



**International Conference on Engineering,  
Natural Sciences, and Technological  
Developments (ICENSTED 2024)**

**PROCEEDINGS BOOK**

**July 19-21, 2024**

**Erdek/Balikesir, Türkiye**

**ISBN: 978-605-9945-44-8**

**Supporters**



International Conference on Engineering,  
Natural Sciences, and Technological  
Developments  
(ICENSTED 2024)

Onsite – Online (Hybrid) Conference  
July 19-21, 2024 | Erdek/Balikesir, Türkiye

**Editor-in-Chief**

Yunus Kaya

**Editors**

Intan Helina Hasan

Nurhafizah Hasim

Selahattin Kosunalp

Umit Yildirim

**ISBN: 978-605-9945-44-8**

**August 2024**

Papers reviewed by at least two reviewers presented at the International Conference on Engineering, Natural Sciences, and Technological Developments (ICENSTED 2024) are included in this proceedings book. Responsibility for all papers presented at ICENSTED 2024 and published in this proceedings book belongs to the respective authors of the papers.

All rights reserved. This publication is free of charge and cannot be sold for money. No part of this publication may be reproduced, stored, retrieved or transmitted, or distributed in any other binding or cover form, without the written permission of the publisher. It can be used by citing the source.

**Bayburt University Publications (Issue: 45)**

**ISBN: 978-605-9945-44-8**

**Publication Date: 21.08.2024**

**Dear Participants,**

We would like to thank all of you for your participation and interest in the International Conference on Engineering, Natural Sciences, and Technological Developments (ICENSTED 2024), which was held as Onsite/Online (Hybrid) in Erdek/Balikesir, Türkiye on July 19-21, 2024.

ICENSTED 2024 was organized for the first time this year with the support of Bayburt University (Türkiye), Gaziantep Islam Science and Technology University (Türkiye), and Citiedge University (Nigeria).

The purpose of the ICENSTED 2024 conference is to provide an international forum for researchers, academics, people in industry and students to discuss the latest research results and present and discuss their ideas, theories, technologies, systems, tools, applications, work in progress. In this direction, the participants will experience all theoretical and practical issues and technological advances emerging in engineering, natural sciences, and other technological fields.

Onsite and online presentations were made by invited speakers and other participants within the scope of ICENSTED 2024. ICENSTED 2024, where 444 oral presentations prepared by 1053 participants from 31 different countries, took place and opened a direction to new cooperation opportunities.

Therefore, we would like to thank Prof. Dr. Mutlu Turkmen (Rector of Bayburt University, Türkiye), Prof. Dr. Sehmus Demir (Rector of Gaziantep Islam Science and Technology University, Türkiye), the invited speakers and all other participants, the members of the scientific committee, the session chairs and all those who contributed to make this conference a great success.

Hope to see you at the next ICENSTED conference.

Best Regards,

On behalf of the ICENSTED 2024 Organizing Committee  
Organizing Committee Chairman  
Assoc. Prof. Dr. Yunus Kaya

## COMMITTEES

### Organizing Committee

#### *Conference Chairman*

Assoc. Prof. Dr. Yunus Kaya, Bayburt University, Türkiye

#### *Members*

Prof. Dr. Paul Daniel Mitchell, University of York, United Kingdom

Prof. Dr. Ugur Cem Hasar, Gaziantep University, Türkiye

Assoc. Prof. Dr. Abdulkarim Ayopo Oloyede, University of Ilorin, Nigeria

Assoc. Prof. Dr. Faieza Abdul Aziz, Universiti Putra Malaysia, Malaysia

Assoc. Prof. Dr. Kubilay Demir, AISOFT Software Corporation, Türkiye

Assoc. Prof. Dr. Marian Janek, University of Žilina, Slovakia

Assoc. Prof. Dr. Selahattin Kosunalp, Bandirma Onyedi Eylul University, Türkiye

Assoc. Prof. Dr. Umit Yildirim, Bayburt University, Türkiye

Asst. Prof. Dr. Hamdullah Ozturk, Gaziantep Islam Science and Technology University, Türkiye

Dr. Hafize Hasar, Gaziantep Directorate of Provincial Agriculture and Forestry, Türkiye

Dr. Intan Helina Hasan, Universiti Putra Malaysia, Malaysia

Dr. Salahedin Rehan, University of Zawiya, Libya

Chief Irukwu Onwuka, Citiedge University, Nigeria

#### *Secretary*

Asst. Prof. Dr. Hilal Kubra Saglam, Ataturk University, Türkiye

Asst. Prof. Dr. Meltem Kizilca Coruh, Ataturk University, Türkiye

### Scientific Committee

Prof. Dr. Ahmet Cansız, İstanbul Technical University, Türkiye

Prof. Dr. Ali Emre Pusane, Boğaziçi University, Türkiye

Prof. Dr. Alyani Ismail, Universiti Putra Malaysia, Malaysia

Prof. Dr. Grigor Yordanov Mihaylov, University of Telecommunications and Post, Bulgaria

Prof. Dr. Jorge Montanari, National University of Hurlingham, Argentina

Prof. Dr. Mehmet Ertugrul, Karadeniz Technical University, Türkiye

Prof. Dr. Mohd Nizar Hamidon, Universiti Putra Malaysia, Malaysia

Prof. Dr. Paul Daniel Mitchell, University of York, United Kingdom

Prof. Dr. Rodrigo Martins, NOVA University Lisbon, Portugal

Prof. Dr. Saravanan Muthupandian, Saveetha Institute of Medical and Technical Sciences (SIMATS),

#### *India*

Prof. Dr. Teodor Iliev, University of Ruse “Angel Kanchev”, Bulgaria

Prof. Dr. Ugur Cem Hasar, Gaziantep University, Türkiye

Assoc. Prof. Dr. Abdulkadir Atalan, Canakkale Onsekiz Mart University, Türkiye

Assoc. Prof. Dr. Abdulkarim Ayopo Oloyede, University of Ilorin, Nigeria

Asst. Prof. Dr. Adem Korkmaz, Bandirma Onyedi Eylul University, Türkiye

Assoc. Prof. Dr. Ezgi Topcu, Ataturk University, Türkiye

Assoc. Prof. Dr. Faieza Abdul Aziz, Universiti Putra Malaysia, Malaysia

Assoc. Prof. Dr. Gokhan Ozturk, Ataturk University, Türkiye

Assoc. Prof. Dr. Halim Kovaci, Ataturk University, Türkiye

Assoc. Prof. Dr. Hulya Ozturk Dogan, Ataturk University, Türkiye

- Assoc. Prof. Dr. Kader Dagci Kiransan, Ataturk University, Türkiye  
Assoc. Prof. Dr. Kubilay Demir, AISOFT Software Corporation, Türkiye  
Assoc. Prof. Dr. Marian Janek, University of Žilina, Slovakia  
Assoc. Prof. Dr. Melike Sevim, Ataturk University, Türkiye  
Assoc. Prof. Dr. Mourad Hebali, University of Mustapha Stambouli Mascara, Algeria  
Assoc. Prof. Dr. Mustafa Tolga Yurtcan, Ataturk University, Türkiye  
Assoc. Prof. Dr. Nuray Demir, Ataturk University, Türkiye  
Assoc. Prof. Dr. Özgür Culfa, University of California San Diego, United States of America  
Assoc. Prof. Dr. Selahattin Kosunalp, Bandirma Onyedi Eylul University, Türkiye  
Assoc. Prof. Dr. Sevda Saritas, Ataturk University, Türkiye  
Assoc. Prof. Dr. Sinan Kul, Bayburt University, Türkiye  
Assoc. Prof. Dr. Tarık Talan, Gaziantep Islam Science and Technology University, Türkiye  
Assoc. Prof. Dr. Umit Yildirim, Bayburt University, Türkiye  
Assoc. Prof. Dr. Yunus Kaya, Bayburt University, Türkiye  
Assoc. Prof. Dr. Zehra Can, Bayburt University, Türkiye  
Asst. Prof. Dr. Erdal Igman, Bayburt University, Türkiye  
Asst. Prof. Dr. Erman Kadir Oztekin, Bayburt University, Türkiye  
Asst. Prof. Dr. Fatih Yilmaz, Bayburt University, Türkiye  
Asst. Prof. Dr. Hamdullah Ozturk, Gaziantep Islam Science and Technology University, Türkiye  
Asst. Prof. Dr. Hilal Kubra Saglam, Ataturk University, Türkiye  
Asst. Prof. Dr. İbrahim Cengiz, Bayburt University, Türkiye  
Asst. Prof. Dr. Latif Akcay, Bayburt University, Türkiye  
Asst. Prof. Dr. Meltem Kizilca Coruh, Ataturk University, Türkiye  
Asst. Prof. Dr. Merve Senol Kotan, Ataturk University, Türkiye  
Asst. Prof. Dr. Mustafa Alptekin Engin, Bayburt University, Türkiye  
Asst. Prof. Dr. Mustafa Ozdemir, Bayburt University, Türkiye  
Asst. Prof. Dr. Nur Ertek Tosun, Ataturk University, Türkiye  
Asst. Prof. Dr. Ramazan Simsek, Bayburt University, Türkiye  
Asst. Prof. Dr. Sebahat Oztekin, Bayburt University, Türkiye  
Asst. Prof. Dr. Yahya Yasin Yilmaz, Bayburt University, Türkiye  
Asst. Prof. Dr. Zeynep Karcioğlu Karakas, Ataturk University, Türkiye  
Dr. Ahmad Ali, University of Mumbai, India  
Dr. Ahmad Ilyas Rushdan, Universiti Teknologi Malaysia, Malaysia  
Dr. Dimitar Totev, Technical University of Sofia, Bulgaria  
Dr. Emine Keles Ozgenc, Trakya University, Türkiye  
Dr. Hafize Hasar, Gaziantep Directorate of Provincial Agriculture and Forestry, Türkiye  
Dr. Intan Helina Hasan, Universiti Putra Malaysia, Malaysia  
Dr. Lawal Mohammed Bello, Bayero University Kano, Nigeria  
Dr. Mojtaba Farhangmehr, Tesla Tajhiz Nano Company, Iran  
Dr. Omowunmi Mary Longe, University of Johannesburg, South Africa  
Dr. Salahedin Rehan, University of Zawiyah, Libya  
Dr. Zainab Yunusa, University of Hafr Al Batin, Kingdom of Saudi Arabia  
Dr. Zeynep Orhan, Ataturk University, Türkiye

## TOPICS

Aircraft-Aeronautical-Aerospace Engineering  
Atmospheric Sciences and Meteorological Engineering  
Automotive Engineering  
Bioengineering  
Biomedical Engineering  
Chemical Engineering  
Civil Engineering  
Computer Sciences and Engineering  
Earth Sciences and Engineering  
Electrical-Electronics and Communication Engineering  
Energy Systems Engineering  
Environmental Sciences and Engineering  
Food Sciences and Engineering  
Industrial Engineering  
Logistics Engineering  
Map Engineering  
Marine and Ship Engineering  
Materials and Metallurgy Engineering  
Mechanical Engineering  
Mechatronics Engineering  
Mining Engineering  
Nuclear Engineering  
Petroleum Engineering  
Software Engineering  
Textile Sciences and Engineering  
Biology  
Chemical  
Mathematics  
Molecular Biology and Genetics  
Physics  
Statistics  
Agriculture, Forestry, and Aquaculture  
Architecture  
City and Regional Planning  
Industrial Design  
Interior Architecture  
Landscape Architecture  
Research-Development  
Technological Production and Developments  
Other Engineering, Natural, and Technological Sciences

## INVITED SPEAKERS

### **Prof. Dr. Rodrigo Martins**

Nova University Lisbon (Caparica, Portugal)

Rodrigo Martins, Portuguese nationality, born in Nova Lisboa, Angola. He got: in 1974 the Honours degree in Electronics Engineering by U. Luanda. In 1977 he got the MSc degree in Semiconductor Materials, by U. of Dundee, Scotland, supervised by W. Spear, the 1977 Euro physicist award; in 1982, the Ph.D. in Energy conversion and Semiconductors, by New University of Lisbon (UNL); in 1988 the Aggregation in Semiconductor Materials and Microelectronics, by UNL. Full Professor at FCT-NOVA since 2002 in Materials Engineering, speciality Materials for Energy, Microelectronics and Nanotechnologies. Professor Honoris Causa by University of Galati, Romania, 2012. Published more than 1000 scientific papers, cited more than 38500, with an h factor of 97 (<https://scholar.google.com/citations?user=5FLD1tUAAAAJ&hl=en>).



He is the running director of i3N; CENIMAT|i3N (<https://www.cenimat.fct.unl.pt/>) and CEMOP/UNINOVA, (<https://cemop.uninova.pt/pt-pt>), President of European Academy of Sciences - EurASc; President of the administration board of the Portuguese cluster in Advanced Materials (NANOMAT); member of the: administration board of the Portuguese cluster on Batteries (BatPower); committee of King Jaume I award for Basic Research ( <https://fprj.es/en/awards/>); coordination board of the Sino-Portugal joint centre in Advanced Materials. Chair of the European Committee Affairs of European Materials Research Society (E-MRS). member of the Portuguese Engineering Academy and of Academia Europaea.

Former: President of International Union of Materials Research Society; Member of the Scientific Council of the European Research Council; president of E-MRS.

In Europe, close to EC, one of the elaborators of the Paper Electronics, Responsible Electronics and Advanced Materials for Industrial Leadership programmes. Mentor of Advanced Materials Academy launched by the EC in 2024 and of the Materials Manifesto 2030.

In China: QiuShi Chair Visiting Professor at Zhejiang University; Honorary Professor of Hefei Institutes of Physical Sciences of the Chinese Academy of Sciences (CAS); Honorary Professor of the Technical University of Wuhan. Coordinator of the Sino-Europe Display Materials Joint Laboratory, launched in Hefei 4<sup>th</sup> July 2024.

He is Editor in Chief of the Journal Materials Discover, from Nature-Springer. Member of the: international advisory board of Advanced Electronics Materials and of the Journal of Physics D; Editor board of the Responsive Materials Journal.

Fields of expertise: advanced functional materials; nanotechnologies, microelectronics, transparent electronics (pioneer) and paper electronics (inventor), with more than 950 papers published, holding an h factor of 96, with more than 35000 citations. Author in 5 books and 31 book chapters and editor in 8 books. He gave so far 157 plenary talks; 260 invited talks; 109 oral presentations and 95 posters, in conferences and workshops.

Patents, awards, and honours: 58 conceived patents (12 are trademark register) and have 7 pending patents related to oxide semiconductors, paper electronics, energy devices, processing technologies; electrochromic devices, memory devices; CMOS technology full oxide based; photodetectors, ink



processing; smart bio detection platforms; x-ray and photodetectors.

Decorated with the gold medal of merit and distinction by the Almada Municipality for his R&D achievements, in 2016; in 2021 he got the Career and Recognition Award given by the Portuguese Society of Materials and Research Nova-Altice Scientific Merit Award, in his first edition. In 2023 selected as PIFI Distinguished Scientist of CAS, the highest honour for overseas talents. Besides that, he got more than 18 international and national prizes and distinctions for his work.

Involvement in Research Projects: 204 projects (96 are national), coordinated 61, responsible in 71, co-responsible in 5 and active member in 62, involving total budget of 78,592,773.18 €.

**Prof. Dr. Saravanan Muthupandian**

Saveetha Institute of Medical and Technical Sciences (SIMATS)  
(Chennai, India)



Dr. Saravanan Muthupandian has over 21 years of teaching and research experience, and he is ranked in the top 2% of scientists worldwide by Stanford University in 2021, 2022 and 2023. Presently working as a Professor, AMR and Nanotherapeutics Lab, Department of Pharmacology, Saveetha University, SIMATS, Chennai, India Since January 2021. He has Graduated in Microbiology, from Madurai Kamaraj University and Doctorate with Specialization in Medical Microbiology and Nanomedicine from Sathyabama University, India. Thereafter, He worked as a Post-Doctoral Researcher, Institute of drug Research, Hebrew University of Jerusalem Israel (2011-2012) focusing his research on Nano-biomaterials & their Biomedical Applications. Prior to his postdoc, he worked as an Assistant Professor (SG), SRM University, and Department of Biotechnology for six Years, from 2005 -2011. and After his post-doctoral research, he worked as Associate Professor, under the United nation development Program, Department of Medical Microbiology and Immunology, School of Medicine, Mekelle University, Ethiopia till January 2021. His Research Specialization: Antimicrobial Resistance (AMR) and Development of Novel biomaterials for emerging and re-emerging Infection in particular Antimicrobial Resistance (AMR) & Cancer for public health importance.

He has published more than 250 research papers including high impact Journal The Lancet and Nature and Nature Medicine with more than 36000 citations and h-index of 72 and i10 index of 169. He has published Nine books and 35 book chapters. He has participated in more than 100 National and International conferences and Reviewers of more than 100 international peer-reviewed journals. Guest editor/ Editors for various reputed PubMed and Scopus indexed journals, in particular, He has an Associate editor in Frontiers in Pharmacology, Frontiers in Oncology and MDPI Functional Biomaterials and Medicinea. He was received many national and international funded projects. In particular he has secured recently two funded projects Sanctioned totalling 1Crore from the ICMR, Government of India in 2023.

He has received many fellowships and Awards notably, IET-Nanobiotechnology premium Awards two-times continuously in the years 2019 and 2020, International Fellowship “Advanced Course on Diagnostics” Sponsored by LSH&TM & Fondation Mérieux, in France 2013, International Fellowship “Pertussis: biology, epidemiology and prevention” meeting Sponsored by Fondation Mérieux & WHO in France 2014, International Union of Microbiological Societies (IUMS) travel grant in 2015 to

Canada, International Fellowship “Advanced Course on Antibiotics” (AdCAB) Sponsored by Institute of Pasteur and Fondation Mérieux France, 2016.

**Prof. Dr. Mohd Nizar Hamidon**

Universiti Putra Malaysia (Selangor, Malaysia)

Mohd Nizar Hamidon is a Professor at Electrical and Electronic Engineering Department and Director of Institute of Nanoscience and Nanotechnology at Universiti Putra Malaysia (UPM). He received the B.Sc in Physics and M.Sc in Microelectronics from Univesiti Malaya (Malaysia) and Universiti Kebangsaan (Malaysia) in 1995 and 2001 respectively. Finally, his Ph.D degrees in Electronic and Electrical Engineering from the University of Southampton (U.K.) in 2005. He joined UPM after BSc at Matriculation Center for 5 years before become UPM engineering faculty member in 2000 until now, where he in charge of research program at the department and faculty. Due to his outstanding research activities, UPM have appointed him as the Director of the institute starting from July 2017 for 7 years.



His research is primarily concerned with the study of electronic and microelectronic devices including the materials (such as oxide and carbon based) and the systems. He has contributed significantly to the development of sensor system such as gas and pressure sensor, and wireless applications. His research has been primarily funded by the international body, government and university internal funding. He has published over 200 technical papers and few book chapters related to his research area. He also had graduated in total of 11 PhD and 15 M.Sc students under his supervision. At the same time, he had registered one Start-up Company known as Serdang Paste Tech Sdn. Bhd.

Mohd Nizar had a good international networking especially with the researchers from Turkey, Japan, Indonesia and Thailand in which they were working together in several different research projects. His also involved in consultancy work for Malaysia government.

He has given many lectures, seminars and invited talks at universities, research institutions and international conferences, and has served as a reviewer for several international conferences and journal. He has been the organizing chair and technical member for several IEEE conferences and The Past Chapter Chair for IEEE Electron Device Malaysia Chapter.

**Prof. Dr. Jorge Montanari**

National University of Hurlingham (Villa Tesei, Argentina)

Jorge Montanari is an Argentine biotechnologist who earned his doctorate in nanotechnology. He directs the Laboratory of Nanosystems with Biotechnological Applications at the National University of Hurlingham in Argentina and is a researcher affiliated with his country’s national science council. He completed his education with postdoctoral stages at UNAM Bilkent in Türkiye, the Czech Academy of Sciences, and Pompeu Fabra University in Barcelona. His research focuses on nanotechnology strategies for developing treatments for skin diseases.



**Dr. Lawal Mohammed Bello**

Bayero University Kano (Kano, Nigeria)

Lawal Muhammad Bello is a Senior Lecturer and researcher in a Telecommunications Research Group, Department of Electrical Engineering, Bayero University, Kano, and a Telecommunications consultant. He received his PhD from University of York, United Kingdom (UK) in January, 2016 (with the subject of his thesis being Intelligent RACH Access strategies for M2M Traffic over Cellular Networks) and MSc in Modern Digital & Radio Frequency Wireless Communications from University of Leeds, UK in 2009. He is an author of several Telecommunications engineering publications and his current research interests include;



- MAC layer design for uplink signaling channel of beyond next generation Cellular Networks.
- Supporting Machine-to-Machine Communications and Internet of Things (IoT) in the existing and future Cellular Networks.
- RACH access strategies of beyond 5G wireless network.
- Resource Management of Cellular Networks among others.

As a University lecturer, Bello has taught different courses, supervised various academic researches, and served as internal and external examiner for undergraduate and postgraduate related to telecommunications.

**Dr. Dimitar Totev**

Technical University of Sofia (Sofia, Bulgaria)

Dr. Dimitar Totev is an engineer, CEO and founder of VPU – an engineering company delivering a full cycle of engineering services in automation and digitalization of industrial processes. He is a lecturer in the Technical University of Sofia in the department of Automation of discrete production engineering.



**Dr. Zainab Yunusa**

University of Hafr Al Batin (Hafr Al Batin, Kingdom of Saudi Arabia)

Zainab Yunusa has completed her PhD from Universiti Putra Malaysia, Malaysia. She has been working in the Department of Electrical Engineering, Bayero University Kano as a Senior Lecturer. She is currently an Assistant Professor in the Department of Electrical Engineering University of Hafr Al Batin Saudi Arabia. She has published more than 25 papers in reputed journals and has been serving as an editorial board member of repute.



**Dr. Ahmad Ali**

University of Mumbai (Mumbai, India)

Dr. Ahmad Ali is currently working as Assistant Professor in the Department of Life Sciences, University of Mumbai, Mumbai, India. Earlier he worked in the National Institute of Pharmaceutical Education and Research (NIPER). He studied at Jamia Hamdard and University of Mumbai obtaining his M. Sc. and Ph. D. degree in Biochemistry and Life Sciences respectively. He has over 17 years of teaching and research experience. Presently he is heading the Molecular Biochemistry Laboratory in the Department where he is supervising MSc and PhD students. His areas of research are Protein and DNA Biochemistry with special contributions on Glycation of biomolecules, DNA damage, antiglycating and anti-aggregating properties of natural products. He has also made significant contributions in the area of artificial sweeteners and their role in the process of glycation. Cyanobacterial systems are another thrust area in his lab where researchers are exploring various applications of these organisms in the field of bioremediation, cosmetics and health benefits. He has received several extramural grants from Government and private funding agencies. He has collaborators from National and International laboratories. He is also a recipient of EMBO Travel Grant to attend European Molecular Biology Organization (EMBO) Research Course and CSIR Travel grant to attend International conference. He is serving as the Reviewer and member of Editorial board of various international journals like Chemosphere, Frontiers in Plant Sciences and Microbiology, Glycobiology, International Journal of Biological Macromolecules, Annals of Phytomedicine and other journals of Elsevier and Springer. He has contributed more than 75 research articles in peer-reviewed national and international journals. He is also author of one book and more than 30 book chapters from Springer, Taylor & Francis and Elsevier publishing houses. He has presented his work in many international and national conferences as Invited Speakers and Resource persons. He has also worked as Member of the organizing committee for many of these conferences.



**ICENSTED 2024 PROGRAM**

**Friday, July 19, 2024**

***Conference Opening***

***Conference Hall (Kiraz Beach Hotel, Erdek)***

09:15 – 09:45	Registration and Tea/Coffee Service	
09:45 – 10:00	Opening Ceremony	Assoc. Prof. Dr. Selahattin Kosunalp – On Behalf of the Organizing Committee
10:00 – 12:30	Opening Session	<p>Materials for Eco-Design Strategies for an Innovative Industry Invited Speaker – Prof. Dr. Rodrigo Martins</p> <p>Emerging Nanotechnologies for Targeting Antimicrobial Resistance: A Special Focus on Chronic Wound Healing Invited Speaker – Prof. Dr. Saravanan Muthupandian</p> <p>Carbon Based Electrode for Gas Sensor Invited Speaker – Prof. Dr. Mohd Nizar Hamidon</p> <p>Vismodegib and Skin: The Challenge of Changing the Administration of an Anticancer Drug with Nanotechnology Invited Speaker – Prof. Dr. Jorge Montanari</p> <p>Evolutionary Trends in RACH Access Techniques Towards a 5G Cellular Invited Speaker – Dr. Lawal Mohammed Bello</p> <p>Integration of Existing Control Systems to the Requirements and Principles of Industry 4.0 Invited Speaker – Dr. Dimitar Totev</p> <p>Deployment of Carbon Based Nanomaterials for Gas Sensing Applications Invited Speaker – Dr. Zainab Yunusa</p> <p>Health Implications of Glycation products in Diabetes and Its Secondary Complications Invited Speaker – Dr. Ahmad Ali</p>
12:30 – 13:30	Lunch (Kiraz Beach Hotel Restaurant)	

***Onsite Sessions***

***Conference Hall (Kiraz Beach Hotel, Erdek)***

Onsite Session – 1 (in English) Head of Session: Assoc. Prof. Dr. Melike Sevim	
13:30 – 14:30	<p>Investigation of the Morphological Structures of PVDF-HFP Flat Sheet Membranes Prepared with Different Concentrations of DMAC/DMF Solvents and Their Performance in DCMD System <i>Ayşe Diskaya*</i>, Ahmet Bora Yavuz, Osman Nuri Ata</p>

	<p>Efficiencies of FePd Nanoparticles in Basic Red 46 Removal <i>Fatma Guclu, <u>Melike Sevim</u>*</i></p>
	<p>Study of the Photoreduction of Co<sup>2+</sup> Ions Under Solar and Visible Light Irradiation <i><u>Samira Tebani</u>*</i>, <i>Lila Kerrai</i>, <i>Samir Ladjali</i></p>
	<p>The Use of Glass and Other Alternative Materials in the Cement Industry <i>Damir Mulamehmedovic, <u>Zehrudin Osmanovic</u>*</i>, <i>Ervin Karic</i>, <i>Belmina Hadžalic</i>, <i>Elma Bajric</i></p>
	<p>Kinetics and Thermodynamics of Thermal Decomposition of Medlar Seed by TG/DTG <i>Zelal Koyuncu, <u>Meltem Kizilca Coruh</u>*</i></p>
	<p>Investigation of Kinetic and Thermodynamic Properties in Response to Thermal Degradation of Ligno-Cellulosic Mixture Prepared from Grape, Pomegranate, and Rosehip Seeds <i><u>Meltem Kizilca Coruh</u>*</i></p>
14:30 – 14:40	Tea/Coffee Break
<p>Onsite Session – 2 (in English) Head of Session: Assoc. Prof. Dr. Selahattin Kosunalp</p>	
14:40 – 15:30	<p>Application and Analysis of Experimental and Numerical Studies to the Film Cooling Turbine Blade <i><u>Amar Berkache</u>*</i>, <i>Rabah Dizene</i></p>
	<p>Recent Trends on Low Pressure Carburizing Furnaces and Process <i><u>Alper Kelesoglu</u>*</i>, <i>Semih Demirci</i>, <i>Beste Ozdeslik</i></p>
	<p>Evaluation of Spectral Efficiency (SE) and Energy Efficiency (EE) of 5G Green Networks Using Soft Computing <i><u>Mahmood Subhi Hussein Sahar</u>*</i>, <i>Koksal Erenturk</i></p>
	<p>Market Shelf Products Detection and Recognition Using YOLO, Faster R-CNN, and SSD Mobilenet <i><u>Alaa Mohamed Jamel Abdulqader Mawlawi</u>*</i></p>
	<p>Energy Efficiency Evaluation of 5G Radio Access Networks Using Fuzzy Logic and ANFIS <i><u>Mohammed Imad Adil Salihi</u>*</i></p>
15:30 – 15:40	Tea/Coffee Break
<p>Onsite Session – 3 (in English) Head of Session: Assoc. Prof. Dr. Selahattin Kosunalp</p>	
15:40 – 16:40	<p>Developing a Software System to Randomly Generate Problem Sets in a Data Analytics Course <i><u>Ahmet Ozkul</u>*</i></p>

	Hysteresis Voltage and Current Control for Fuel Cell Fed Power Circuits <i><u>Unal Yilmaz</u>*</i>
	Factors Influencing the Adoption of Electric Vehicles in the U.S. <i><u>Serkan Varol</u>*</i> , <i>Taylor Ransom</i>
	Experimental Study of Failures of Air Conditioners System Tram in Desert Areas by Applying Preventive Maintenance (Using FEMA and Reliability Lows) <i><u>Khaled Lemnaouer</u>*</i> , <i>Messaoud Louafi</i> , <i>Zoubir Aoulmi</i> , <i>Rabie Karek</i> , <i>Mounia Taleb</i>
	Design of a Low-Profile Metasurface-Based Linear Polarization Converter and RCS Reduction Using This Converter Design <i><u>Yunus Kaya</u>*</i>
	Evaluation of Short-Term Traffic Flow Prediction Approaches in Transportation <i><u>Selahattin Kosunalp</u>*</i> , <i>Yunus Kaya</i>
16:40 – 16:50	Tea/Coffee Break
Onsite Session – 4 (in Turkish) Head of Session: Assoc. Prof. Dr. Ezgi Topcu	
16:50 – 17:30	MnCo <sub>2</sub> O <sub>4</sub> Modified Flexible Graphene Paper for Electrochemical Sensing of Paracetamol <i>Murad Shafiyev</i> , <i><u>Ezgi Topcu</u>*</i> , <i>Elif Ercarikci</i> , <i>Kader Dagci Kiransan</i>
	Investigation of the Cleanability of High Ash Asphaltite Sample Using the Oil Agglomeration Method <i><u>Oyku Bilgin</u>*</i>
	Hydrogen Evolution Reaction on MoO <sub>3</sub> Decorated-CuBi <sub>2</sub> O <sub>4</sub> /Reduced Graphene Oxide Nanocomposite <i>Zeynep Orhan</i> , <i><u>Hulya Ozturk Dogan</u>*</i>
	Flow and Heat Characteristics over Ellipse in the in-Duct Flow <i><u>Neslihan Aydin</u>*</i>
17:30 – 17:40	Tea/Coffee Break
Onsite Session – 5 (in Turkish) Head of Session: Asst. Prof. Dr. Hilal Kubra Saglam	
17:40 – 18:30	Risk Factor Estimation with Ordered Logit and Ordered Probit Models <i><u>Burcu Durmus</u>*</i> , <i>Oznur Isci Guneri</i> , <i>Aynur Incekirik</i>
	Effect of $\alpha$ -Fe <sub>2</sub> O <sub>3</sub> on Gas Detection Performance of MgO Thin Films <i><u>Hilal Kubra Saglam</u></i> , <i>Sevda Saritas*</i>
	Analysis of Quality Risks on the Assembly Line in an Armature Manufacturing Company Using FMEA Method <i><u>Fatma Merve Bayir Kanbur</u>*</i> , <i>Hasan Selim</i>

	A Study on the Effects of Electromagnetic Fields <i>Yunus Kaya*</i> , <i>Selahattin Kosunalp</i>
	Anticancer Activity of Acetaminophen-Platinum (II) Complex Against ER-Positive Breast Cancer <i>Mustafa Tugfan Bilkan*</i> , <i>Meric Arda Esmekaya</i> , <i>Nurhan Ozdemir</i>

**Online Sessions**

**Virtual Hall 1**

Online Session – 1 (in Turkish) Head of Session: Asst. Prof. Dr. Mustafa Ozdemir	
13:30 – 14:50	Impregnation of Wood Material with Magnesium Chloride (MgCl <sub>2</sub> ) and Determination of Leaching Properties <i>Melek Yilmaz Yasbek*</i> , <i>Mehmet Yeniocak</i>
	Determination of Reservoir Water Level by Classical and Artificial Intelligence Methods <i>Sema Karahan*</i> , <i>Zeyneb Kilic</i>
	Historical Environments Affected by the Earthquake in Kahramanmaraş City Center and Restoration Suggestions <i>Hatice Dokme</i> , <i>Sinan Kordon*</i>
	The Sociological Benefits of Green Infrastructure Systems: Inclusive and Healthy Cities for Communities <i>Esra Tan</i> , <i>Sinan Kordon*</i>
	Traditional Uses of Medicinal Plants Naturally Distributed in Yerkesik Basin (Mentese-Mugla) <i>Kenan Akbas*</i>
	Vegetative Anatomy of Two Endemic <i>Muscari</i> L. Species in Türkiye <i>Dudu Ozlem Mavi Idman*</i> , <i>Huseyin Guldal</i> , <i>Ali Gercek</i> , <i>Huseyin Eroglu</i>
	Kombucha-Derived Bacterial Cellulose Production with Herbal Tea and Different Coffee Combinations <i>Nazli Neval Sahin</i> , <i>Nermin Hande Avcioglu*</i>
	Evaluation of Gene Expression Levels of Antimicrobial Peptides (MsDef1 And MsSN1) from <i>M. Sativa</i> Sazova Cultivar During 21-Day Period <i>Busra Albayrak Turgut*</i>
14:50 – 15:00	Break
Online Session – 2 (in Turkish) Head of Session: Asst. Prof. Dr. Mustafa Ozdemir	
15:00 – 16:20	Investigation of the Effect of Chemical Additives on Performance in the Deep Mixing Method with Model Experiments <i>Yunus Emre Colak*</i> , <i>Sukru Ozcoban</i> , <i>Mustafa Mert</i>



	Investigation of the Structure-Pile-Soil Interaction Behaviour in Earthquake Condition of a Reinforced Concrete Building with Pile Foundation <i>Evrin Er*</i> , <i>Sami Oguzhan Akbas</i>
	Determination of Risk Factors within the Scope of Water Supply Management in Water Transmission Systems <i>Yusuf Kilinc*</i> , <i>Cansu Bozkurt</i> , <i>Mahmut Firat</i>
	Defining the Impact Levels of Risk Factors in Water Transmission Systems <i>Yusuf Kilinc*</i> , <i>Cansu Bozkurt</i> , <i>Mahmut Firat</i>
	Determination of Regional Earthquake Risk Distribution of Buildings in the Central Gencosman Neighborhood of Bayburt Province <i>Omer Can</i> , <i>Ertekin Oztekin</i> , <i>Omer Bayrak*</i>
	Use of Bayburt White Stone Waste and Paper Mill Waste Lignin as a Plasticizer/Air-Entraining Concrete Additive in the Production of Carrier and Non-Carrier Lightweight Concrete <i>Omer Bayrak*</i> , <i>Emin Erdem</i>
	An Innovative Method of Getting Impactive Ideas <i>Leyla Erkol*</i> , <i>Murat Arslanoglu</i> , <i>Sevilay Sagtan</i> , <i>Fatih Cagirankaya</i> , <i>Ali Yazgan</i>
	Preservation Issues and Recommendations for Traditional Housings in Urban Centers: The cases from Corum, Turkey <i>Furkan Karahan</i> , <i>Emine Saka Akin*</i>
16:20 – 16:30	Break
Online Session – 3 (in Turkish) Head of Session: Asst. Prof. Dr. Ramazan Simsek	
16:30 – 17:50	Crashworthiness Design and Damage Analysis with Multiple Internal Structure Pattern <i>Hakan Burcin Erdogan*</i>
	Analysis of Diesel/Bio-Oil Blends Produced by Co-Pyrolysis of Spruce with Glycerol <i>Ahmet Rasim Girisen*</i> , <i>Hakan Ozcan</i>
	Investigation of Oxidative Stability Behavior of Kaolin Nanoparticles Doped Bio-Based Palm Lubricants <i>Batuhan Ozakin*</i> , <i>Kursat Gultekin</i> , <i>Nalan Turkoz Karakullukcu</i>
	Production of 3D Woven Textile Composites and Investigation of Their Impact Performance <i>Serkan Erdem*</i> , <i>Mete Onur Kaman</i>
	Evaluation of the Tribological Performance of AA 6061 Coated with Polyurethane/Ti6Al4V Composite <i>Yusuf Burak Bozkurt*</i>

	<p>Numerical Simulation Study of Curvature Radius on the Flexibility and Stress Distribution in Hyperelastic Materials <i>Galip Yilmaz*</i></p>
	<p>Creation of a Digital Twin for Remote Fault Detection of a CNC Machine <i>Cemal Pamukcu*, Numan Dogruay, Abdulsamed Tabak</i></p>
	<p>Design and Analysis of Lightweight 3D-Printed Lattice Structures Using Fused Deposition Modelling <i>Turker Turkoglu*</i></p>
17:50 – 18:00	Break
<p>Online Session – 4 (in Turkish) Head of Session: Asst. Prof. Dr. Ramazan Simsek</p>	
18:00 – 19:20	<p>Numerical Investigation of Heat Transfer Performances in Spiral Dimpled Pipe Profiles <i>Anil Aykut*, Veysel Ozceyhan</i></p>
	<p>Natural Fibers: A Sustainable Alternative for Composite Reinforcements <i>Mehmet Cagri Tuzemen*</i></p>
	<p>Structural Analysis of Hopper Support Frame of Vacuum Road Sweeping Vehicle on Truck Mounted <i>Onur Can Kirit*, Vedat Fetullahoglu</i></p>
	<p>Use of Hardox 500 Tuf in Tippers <i>Resul Akcali*, Akin Zengin, Mustafa Yilmaz</i></p>
	<p>Structural Analysis of Safety Leg on the Vacuum Road Sweeper Mounted on Truck <i>Omer Coskun*, Vedat Fetullahoglu</i></p>
	<p>An Approximate Q-Learning Approach to the Dynamic Pricing and Inventory Control Problem of Perishable Products <i>Tugce Yavuz*, Onur Kaya</i></p>
	<p>Optimizing Workforce and Sub-Lot Scheduling in Seru Production Systems <i>Beren Gursoy Yilmaz*, Emre Cevikcan, Omer Faruk Yilmaz</i></p>
	<p>Development of Beneficiation Flow Diagram of Malatya-Kuluncak Rare Earth Oxide (NTO) Ore <i>Gafure Ersever Angur*</i></p>
19:20 – 19:30	Break
<p>Online Session – 5 (in Turkish) Head of Session: Asst. Prof. Dr. Ramazan Simsek</p>	
19:30 – 20:50	<p><math>A_\alpha</math> – Statistical Limit Superior and Limit Inferior via Ideals <i>Mustafa Gulfirat*</i></p>

	Certain Aspects of Weak Statistical Convergence via Ideals <i><u>Mustafa Gulfirat</u>*</i>
	Investigation of the Conductivity Mechanism of ZnO/C <sub>10</sub> H <sub>10</sub> N <sub>2</sub> pn Heterojunction Produced by Spin Coating Method <i><u>Ramazan Demir</u>*</i>
	A Review of Using of Geopolymers -As an Immobilization Matrix- on Radioactive Waste Management <i><u>Furkan Cinar</u>*</i> , <i>Sema Akyil Erenturk</i>
	Recovery of Critical Metals from Spent Li-Ion Batteries by Deep Eutectic Solvents (DESs) as Green Approach <i><u>Ceren Erust</u>*</i>
	Different Machine Learning Models with Mushroom Comparison <i><u>Idil Sila Gonenc</u>*</i> , <i>Muhammet Cakmak</i>
	Factors Affecting Deterioration of Wall Paintings <i><u>Ozge Karadeniz</u>*</i> , <i>Evin Caner</i>
	Correlation Analysis with the Help of Vector <i><u>Ramazan Simsek</u>*</i>

**Virtual Hall 2**

<p>Online Session – 6 (in English) Head of Session: Asst. Prof. Dr. Sebahat Oztekin</p>	
13:30 – 14:50	Grape Puree-Added and Freeze-Dried Yoghurt Drops: Enumeration of Lactic Acid Bacteria and Determination of Some Physical Properties <i><u>Sebahat Oztekin</u>*</i>
	Contamination by Pesticides of Water and Health Using Artificial Neural Networks <i><u>Benzydane Chahrazed</u>*</i> , <i>Bouharati Khawla</i> , <i>Fenni Mouhamed</i>
	Nutrient-Rich Biofertilizers: The Role of Spirulina Sp and Microalgae in Soil Health Enhancement <i><u>Charef Nassira</u>*</i> , <i>Tamer Fatma Zohra</i> , <i>Saada Zakia</i> , <i>Belaid Boutheina</i> , <i>Bougueroua Karima</i> , <i>Elleuch Jihen</i> , <i>Nasri Hichem</i>
	Growth Control of Cyanobacteria and Cyanotoxins by Biological Methods <i><u>Tamer Fatma Zohra</u>*</i> , <i>Charef Nassira</i> , <i>Nasri Hichem</i>
	Spirulina Sp - Cultivation, Production, and Applications <i><u>Saada Zakia</u>*</i> , <i>Charef Nassira</i> , <i>Tamer Fatma Zohra</i> , <i>Belaid Bouthaina</i> , <i>Elleuch Jihen</i> , <i>Nasri Hichem</i>
	Conditions for Culture and Valorization of Microcystis Cyanobacteria <i><u>Saada Zakia</u>*</i> , <i>Charef Nassira</i> , <i>Tamer Fatma Zohra</i> , <i>Belaid Bouthaina</i> , <i>Elleuch</i>

	<p><i>Jihen, Nasri Hichem</i></p> <p>In Vitro Antioxidant and Anti-Hemolytic Effect of Algerian <i>Centaurea Calcitrapa</i> L. Extracts <i>Krache Imane*</i>, <i>Trabsa Hayat</i>, <i>Boussoualim Naouel</i>, <i>Arrar Lekhmici</i>, <i>Baghiani Abderrahman</i></p> <p>Canopy Dynamics in the Bissa Forest: Chlef, West Algeria <i>Fatima Belhacini*</i>, <i>Djamel Anteur</i>, <i>Faycal Tsourly</i>, <i>Djahida Hedidi</i></p>
14:50 – 15:00	Break
<p>Online Session – 7 (in English) Head of Session: Asst. Prof. Dr. Sebahat Oztekin</p>	
15:00 – 16:20	<p>Biocontrol of Gray Mould in Strawberries with Pectin-Based Coatings Incorporated with Yarrow (<i>Achillea Millefolium</i> L.) Extract <i>Sebahat Oztekin*</i></p>
	<p>Lyophilized Strawberry Slices with Various Thicknesses and Investigation of Their Drying Characteristics <i>Erman Kadir Oztekin</i>, <i>Sebahat Oztekin*</i></p>
	<p>Antibiotic Resistance Pattern of <i>Pseudomonas Sp</i> in Tilapia Fish <i>Oreochromis Sp</i>, and Aquarium Water <i>Romeissa Derdachi*</i>, <i>Sabrina Boucetta</i></p>
	<p>Sample Preparation for Soil Analysis of an Endangered Species in the Sidi Bel Abbes Region (North West Algeria) <i>Mounir Chihab*</i>, <i>Ali Khalifa</i></p>
	<p>Comparative Study of the Effect of Two Irrigation Methods (Drip and Submersion) on the Behavior of Two Varieties of Olive Trees (<i>Olea Europaea</i> L) in the Semi-Arid Zone of Bordj-Bou-Argeridj <i>Faycal Bahlouli*</i>, <i>Hamza Belguerri</i>, <i>Nacira Chourghal</i>, <i>Amel Salamani</i>, <i>Mouhamed Benaini</i>, <i>Khelifa Maamri</i>, <i>Fairouz Mihoubi</i>, <i>Aicha Cherroura</i>, <i>Younes Atek</i>, <i>Fares Aissat</i></p>
	<p>Estimating Aphid Parasitoid Diversity in Guelma's Citrus Orchards, Eastern Algeria <i>Omar Khaladi*</i>, <i>Amira Bouderbala</i></p>
	<p>Egg Quality Characteristics of Local Laying Hens in Oasis Family Farms of Adrar (Algeria) <i>Abderrahmen Boubekeur*</i>, <i>Mohammed Bouallala</i>, <i>Redhwen Bari</i>, <i>Mohammed Souddi</i></p>
	<p>Impact of <i>Thymus Vulgaris</i> and <i>Lavandula Angustifolia</i> Essential Oils on the Carcass Characteristics of Broiler Chickens <i>Benameur Qada*</i>, <i>Laah Jude Attat</i>, <i>Sidi Faruk</i>, <i>Kassous Tahar</i>, <i>Arabi Abed</i></p>
16:20 – 16:30	Break

Online Session – 8 (in English) Head of Session: Asst. Prof. Dr. Mustafa Alptekin Engin	
16:30 – 17:50	Effect of an Essential Oils Mixture on the Growth Performance of Broiler Chickens <i><u>Laah Jude Attat</u>, Benameur Qada*</i> , Sidi Faruk, Kassous Tahar, Arabi Abed
	Comparative Study of the Biogas Yield of Three Olive Mill Wastewater in the Thermophilic Phase <i>Bani Kheiredine*</i> , <i><u>Amrouci Zahra</u></i> , Belmili Zineb, Ghetahem Dalal
	Enhancing the Quality of PET Images Reconstructed by Filtered Back Projection and Ordered Subsets Expectation Maximization <i><u>Benvelles Asma*</u></i> , Korti Amel
	Artificial Intelligence in Camel Racing: Health Maintenance and Prevention <i>Amira Djeddou Benabid*</i> , Hind Houssou, Khaled Djeddi, Dounia Ouachtati
	Antimicrobial Profile of Asian Honey Bee Using Culture Dependent Method <i>Iram Liaqat*</i>
	Medical Image Analysis Using Neural Networks <i><u>Berrimi Fella*</u></i>
	Exploring the Potential of the Genus Achillea on Antiproliferative and Apoptotic Effects of Human Cancer Cell Lines <i><u>Renda Chahna*</u></i>
	Study and Prevention of Occupational Risks (Case of the Elmalabiod Cement Plant) <i><u>Taleb Mounia*</u></i>
17:50 – 18:00	Break
Online Session – 9 (in English) Head of Session: Asst. Prof. Dr. Mustafa Alptekin Engin	
18:00 – 19:20	Effectiveness of Aeration Followed by Statistical Optimization of AOP'S (Ultraviolet/Ultrasonic Active Persulfate/Hydrogen Peroxide) Process Parameters for the Treatment of Young Landfill Leachate <i><u>Hamza Bellouk*</u></i> , Ilham Zouitane, Imane El Mrabet, Naima El Ghachtouli, Hicham Zaitan
	Sono-Pyrolysis of Methane for Enhanced Hydrogen Production <i><u>Aissa Dehane*</u></i> , Slimane Merouani, Atef Chibani
	Photodegradation of Metobromuron by a Photo-Fenton Like Process Using Fe(III)-Picolinic Acid Complex as Catalyst in Aqueous Medium <i><u>Sellam Badreddine*</u></i> , Seraghni Nassira, Bouaziz Chaima, Sehili Tahar
	Photocatalytic Efficiency of Pure and Cu-Doped ZnO Thin Films <i><u>Khemissi Lahouel*</u></i> , Abdecharif Boumaza, Meriem Gasmî

	<p>Exploring the Structural, Optical, and Surface Characteristics of NiO Thin Film for Environmental Applications <i>Meriem Gasmî*, Khemissi Lahouel, Saida Hoggas, Sabiha Hakkar</i></p> <p>Voltametric and Molecular Docking Investigations of Ferrocenylmethylaniline and Its N-Acetylated Derivative Interacting with DNA <i>Asma Yahiaoui*, Benyza Nabil, Amel Messai, Touhami Lanez, Elhafnaoui Lanez</i></p> <p>Response Surface Methodology Study of Corrosion Behavior in Presence of a Pharmaceutical Drug <i>Naceur Benhadria*, Tarik Attar, Abbes Benchadli, Esmâ Choukchou-Braham</i></p> <p>Synthesis, Crystal Structure, Thermal Behavior, and Magnetic Study of 1D Cobalt (II) Coordination Polymer with Dinitrogen Tetrahydride as Bridging Ligand <i>Safaa Hidaoui*, Najlaa Hamdi, Michal Dusek, Nicola Morley, Mohammed Lachkar, Brahim El Bali</i></p>
19:20 – 19:30	Break
<p>Online Session – 10 (in English) Head of Session: Asst. Prof. Dr. Mustafa Alptekin Engin</p>	
19:30 – 20:50	<p>Vibrational Spectroscopic Analysis of 2,6-Bis(4-Fluorophenyl)-3,3-Dimethylpiperidin-4-One (BFDP), DFT, and Molecular Docking Study <i>Kheira Hammou*, Mohamed Cherif Terkhi, Nourdine Boukabcha</i></p> <p>Elastic Anisotropies and Electronic Properties of Tetragonal Spinel CuBi<sub>2</sub>O<sub>4</sub>: A DFT Calculation <i>Rania Charif*, Rachid Makhloufi</i></p> <p>Investigation of the Effect of Membrane Type on Ammonia Formation from Ammonium Chloride and Sodium Chloride in Two-Compartment Bipolar Membrane Electrodialysis <i>Fatemeh Abbasi*, Duygu Adiguzel, Osman Nuri Ata</i></p> <p>Synthesis of Quinoxaline Containing Thiazole Moiety Derivative, Biological Activities, Docking Studies, and ADMET Analysis <i>Anissa Boumati*, Imane Idris, Omar Berradj</i></p> <p>Investigation into Mathematical Modeling of Light Naphtha Isomerization Using Bi-Functional Catalysts <i>Boudjema Amir Lehtihet*, Tayeb Fakhreddine Boukezoula, Lahcène Bencheikh</i></p> <p>Effects of Operating Parameters on the Crystallization Yield of Copper Sulfate: An Experimental Study <i>Amira Boufrioua*, Sarra Guilane, Leila Benmansour</i></p> <p>Exploring CA/CuO in Adsorption and Photocatalysis for Toxic Wastewater Treatment: Preparation, Mechanisms <i>Oumnia Rayane Benkouachi*, Abdallah Bougeuttoucha, Kamilia Madi</i></p>

	Determination and Study of Pollution in Chemical Variables in Industrial Waste Water for the Concrete Factories <i>Mohamed Nadjib Rebizi*</i>
--	--

**Saturday, July 20, 2024**

***Online Sessions***

***Virtual Hall 1***

Online Session – 11 (in English) Head of Session: Asst. Prof. Dr. Erman Kadir Oztekin	
09:00 – 10:20	A Magnetic Field's Impact on a Spiral Porous Fin Exposed to Radiation and Convection <i>Nadia Daradi*</i> , <i>Bouaziz Mohamed Nadjib</i>
	Investigation of the Applicability of Ni-P-Cu Coatings to the Expanded Graphite/PCM Composite Blocks Surfaces by Electrolysis <i>Onur Guler</i> , <i>Mustafa Yusuf Yazici*</i>
	Modeling the Phenomenon of Degradation of a TK31 Centrifugal Compressor by Aleatory Processes <i>Souhila Bouleghlem*</i> , <i>Naima Tamaloussi</i> , <i>Lamia Benzaid</i>
	Challenges of Latent Heat Energy Storage for Energy Efficiency Enhancement <i>Mohamed Teggat*</i>
	Effect of Resin Coating on Mechanical Properties of 3D Printed Parts <i>Abdurrahim Temiz*</i> , <i>Fatih Huzeyfe Ozturk</i>
	Numerical Study of Magneto-Double-Diffusive Natural Convection of a Nanofluid Flowing in a Concentric Annular Space <i>Nesrine Rachedi*</i> , <i>Messaoud Guellal</i>
	Preventive Maintenance of an Industrial Reciprocating Compressor by Oil Analysis <i>Lamia Benzaid*</i> , <i>Naima Tamaloussi</i> , <i>Toufik Sebah</i>
	Flow Analysis for a Light Commercial Vehicle with a Vertical Axis Turbine Added for Power Generation <i>Erman Kadir Oztekin*</i>
10:20 – 10:30	Break
Online Session – 12 (in English) Head of Session: Asst. Prof. Dr. Erman Kadir Oztekin	
10:30 – 11:50	Energy Consumption and Moisture Extraction Optimization in a Heat Pump Tumble Dryer <i>Berkay Yilmaz*</i> , <i>Mehmet Alper Sav</i> , <i>Yusuf Balsever</i>
	Numerical Investigations on the Effect of Isothermal Multi-Jets in Air Curtains

	with LES Approach <i>Sahnoun Rachid*</i> , <i>Drai Ismail</i> , <i>Merouane Habib</i>
	Numerical Study of Flow Around Counter Rotating Cylinder <i>Drai Ismail*</i> , <i>Sahnoun Rachid</i> , <i>Merouane Habib</i> , <i>Yahiaoui Tayeb</i>
	The Effect of Bluff Body Geometry on the Combustion of CH <sub>4</sub> /Air <i>Merouane Habib*</i> , <i>Drai Ismail</i> , <i>Sahnoun Rachid</i>
	Design and Implementation of an Intelligent Irrigation System <i>Toufik Sebbagh*</i> , <i>Islam Boukhadra</i>
	The Production of Bamboo Based Natural Composite Materials and Comparison of Their Material Properties with Particleboard MDF Boards <i>Ali Gumustekin*</i> , <i>Sedat Ozden</i> , <i>Fehmi Nair</i>
	Elastic Repair Analysis for the Interaction Between Two Semi-Elliptical Cracks in a Damaged Aeronautical Structure <i>Belhamiani Mohamed*</i> , <i>Bouzitouna Wahiba Nesrine</i> , <i>Oudad Wahid</i> , <i>Djebbar Noureddine</i>
	Investigation of the Effects of a Heated Vest on Blood Pressure and Body Temperature of Male Individuals <i>Emre Demirci</i> , <i>Erman Kadir Oztekin*</i>
11:50 – 12:00	Break
<p>Online Session – 13 (in English) Head of Session: Asst. Prof. Dr. Erman Kadir Oztekin</p>	
12:00 – 13:20	Microstructure Analysis of Ni-Mn-Ga Epitaxial Thin Films on MgO (100) <i>Gizem Durak Yuzuak*</i>
	Effect of Using Phosphate Sludge in Geopolymerization: A Review <i>Nour El Houda Benghalem*</i> , <i>Nadia Tebbal</i> , <i>Zine El Abidine Rahmouni</i> , <i>Mekki Maza</i>
	Enhancing Mechanical Properties of Titanium Alloys Through Microstructural Control and Alloying Additions <i>Mohamed Boudiaf*</i>
	Synthesis of Iron Copper Binary Nanoparticles Based Phosphate and Application in Multi-Components Reaction <i>Berrichi Amina*</i> , <i>Bachir Redouane</i>
	Innovative Hybrid Systems for Improving Organic Solar Cells: Encapsulation of Organic Molecules in Carbon and Boron Phosphide Nanotubes <i>Soufiane Elhadfi*</i> , <i>Jamal Chenouf</i> , <i>Brahim Fakrach</i> , <i>Hassane Chadli</i>
	Unlocking the Potential of Waste Steel Fibers for Improving High-Performance Concrete <i>Rekia Zouini*</i> , <i>Makani Abdelkadir</i> , <i>Tafraoui Ahmed</i>



	<p>Numerical Performance Simulation of a MoSe<sub>2</sub>-Based Solar Cell Using SCAPS-1D Simulator <i>M'hamed Semlal, Mohamed Khuili*, Nejma Fazouan, El Houssine Atmani</i></p> <p>The Impact of the Alkali-Bleaching Treatment on the Isolation of Natural Cellulosic Fibers from Juncus Effesus L Plant <i>Mona Benali*, Abdallah Oumekki, Jamil Toyir</i></p>
13:20 – 13:30	Break
<p>Online Session – 14 (in English) Head of Session: Asst. Prof. Dr. Ramazan Simsek</p>	
13:30 – 14:50	<p>Noble Metal Nanomaterials in Biosensors <i>Adil Bouhadiche*, Soulef Benghorieb</i></p>
	<p>Bound States of 2D Dirac Oscillator in the Deformed Space <i>Lakhdar Sek*, Mokhtar Falek, Mustafa Mounni</i></p>
	<p>The Applied Physics for Electronic Systems: Detecting of Pollutant Gas Based Pure SnO<sub>2</sub> Semiconductors <i>Youssef Doubi*, Bouchaib Hartiti, Maryam Siadat, Hicham Labrim, Mounia Tahri, Phillipe Thevenin</i></p>
	<p>Optimization for High-Efficient and More Stable RbGeI<sub>3</sub> Perovskite Solar Cells <i>Abdelkader Bouhenna*, Kada Boualem, Nabil Beloufa, Soufi Hadjer, Aboubakr Seddik Kebaili</i></p>
	<p>Approximation Solutions of Time dependent Schrodinger Equation for Deng-Fan Potential Using the Nikiforov-Uvarov-Functional Analysis <i>Medjber Salim*</i></p>
	<p>Conceptual Study of Surface Plasmon Resonance Sensor for Glucose Level Monitoring <i>Mohamed Esseddik Ouardi*, Kada Abdelhafid Meradi, Fatima Tayeboun</i></p>
	<p>Comparative Study of Performance of Different Perovskite Solar Cells Based on Organic and Inorganic Thin Films <i>Riane Houaria*, Bidi Sara, Boussaada Salah Eddine, Mouchaal Younes</i></p>
	<p>Evanescent Wave Coupling Surface Plasmon Resonance (SPR) Sensors <i>Fariza Hanim Suhailin*</i></p>
14:50 – 15:00	Break
<p>Online Session – 15 (in English) Head of Session: Asst. Prof. Dr. Ramazan Simsek</p>	
15:00 – 16:20	<p>Exploring the Optoelectronic Properties of NaAuF<sub>4</sub>: Insights and Applications <i>Ishak Mebarkia*</i></p>
	<p>Exploring the Optical and Thermoelectric Properties of Eco-Friendly Perovskite Alloys for Solar Cell Applications</p>

	<p><i><u>Lakhdar Benahmedi</u></i><sup>*</sup>, <i>Anissa Besbes, Redouane Djelti</i></p> <p>Probing the Electronic, Optical, and Transport Properties of Halide Double Perovskites Cs<sub>2</sub>AgSb(Cl,Br)<sub>6</sub> for Thermoelectric Applications <i><u>Hamza Kerrai</u></i><sup>*</sup>, <i>Ahmed Zaim, Mohamed Kerouad</i></p> <p>Computational Insights into the Superior Efficiency of K<sub>2</sub>(Se,Te)Br<sub>6</sub> Double Halide Perovskite Solar Cells <i><u>Hamza Kerrai</u></i><sup>*</sup>, <i>Ahmed Zaim, Mohamed Kerouad</i></p> <p>An Introduction to Carbon Nanotubes and Their Production Processes <i><u>Maryam Abdolahpour Salari</u></i><sup>*</sup>, <i>Gunay Merhan Muglu, Volkan Senay, Sevda Saritas</i></p> <p>Analyzing the Physical Properties of a Ternary Half-Heusler RhTiP for Industrial Applications <i><u>Aya Righi</u></i><sup>*</sup>, <i>Fatima Bendahma, Abess Labdelli, Khedidja Mechehoud, Mohamed Mana</i></p> <p>QCD Phase Diagram with a Crossover and a First Order Phase Transition <i><u>Mohamed Amine Lakehal</u></i><sup>*</sup>, <i>A. Ait El Djoudi</i></p> <p>Electronic and Nonlinear Optical Properties of (E)-N'-(3-Methoxybenzylidene)-2-(Quinolin-8-Yloxy) Acetohydrazide: A Comprehensive Computational Study <i><u>Mohammed Hadj Mortada Belhachemi</u></i><sup>*</sup>, <i>Zohra Douaa Benyahlou, Amine Ould Rabah, Kheira Hammou</i></p>
16:20 – 16:30	Break
<p>Online Session – 16 (in English) Head of Session: Dr. Mohd Hafizuddin Ab Ghani</p>	
16:30 – 17:50	<p>Theoretical Investigation of MoSSe Janus as Promising Anode Material for Libs Using First-Principles Calculations <i><u>Malak Bounbaa</u></i><sup>*</sup>, <i>Mohamed Khuili, Nejma Fazouan, El Houssine Atmani, Isam Allaoui</i></p> <p>Investigating the Behaviour of Some Response Functions Characterising the Thermal QCD Deconfinement Phase Transition in a Finite Volume for Several Hadronic and QGP Systems <i><u>Rokaya Djida</u></i><sup>*</sup>, <i>Amal Ait El Djoudi</i></p> <p>Cauchy Wavelet Application to Detect Multi-Scale Structures of the Turbulent Flow <i><u>Kenza Zaibak</u></i><sup>*</sup>, <i>Nora Nait Bouda, Fawzia Mekideche-Chafa</i></p> <p>Arbitrary Amplitude Solitary Waves in a Degenerate Plasma System <i><u>Muhammad Asaduzzaman</u></i><sup>*</sup></p> <p>Elimination of Indigenous Dairy Biofilms from Milk Reception Lines by Implementing an Appropriate Cleaning-in-Place CIP Protocol <i><u>Dahou Abdelkader El Amine</u></i><sup>*</sup>, <i>Tahlaiti Hafida, Medjahed Mostefa, Seddar Yagoub</i></p>

	<p><i>Fatima, Doubbi Bounouaa Lahcen, Benabdelmoumene Djilali, Doukani Koula</i></p> <p>Evaluation of the Suitability of Bovine Milk from the Experimental Farm for Industrial Processing <i>Doubbi Bounouaa Lahcen, <u>Dahou Abdelkader El Amine</u><sup>*</sup>, Seddar Yagob Fatma, Tahlaïti Hafida, Bounaama Khalil, Homrani Abdelkader</i></p> <p>Food Packaging Reinforced Active Agent MOF-Based and Their Synthesis Methods <i>Mohd Hafizuddin Ab Ghani</i><sup>*</sup>, Ismayadi Ismail, Rosnah Nawang, Intan Helina Hasan, Juraina Md Yusof, Che Azurahaman Che Abdullah, Siti Hajar Othman, Josephine Liew Ying Chyi, Umer Rashid, Nishata Royan Rajendran Royan, Ruey Shan Chen, Chawalit Ngamcharussrivichai</p> <p>Processing and Conservation of Mussels from the Ain Temouchent Region (West Algerian) <i>Fatima Belhacini</i><sup>*</sup>, Arifa Chegrouche, Dinedane Hadjer Amel</p>
17:50 – 18:00	Break
<p>Online Session – 17 (in English) Head of Session: Asst. Prof. Dr. Galip Yilmaz</p>	
18:00 – 19:20	<p>Design and Project Management for Unmanned Aerial Vehicles <i>Ahmed Khaled Salaheldin Ali</i><sup>*</sup>, Onur Tuncer</p> <p>Enhancing Urban Resilience: Evaluating Earthquake Park Design in Kahramanmaras, Turkey <i>Sinan Kordon</i><sup>*</sup>, Aliye Kaya, Dilan Tokgoz, Meryem Yilmaz, Ozge Akilli</p> <p>Analysis of the Flow Through a Contoured Nozzle Using CFD <i>Sabrina Benlembarek</i><sup>*</sup>, Kamel Talbi</p> <p>Balancing Techniques Comparison on an Inbalanced Payment Company Dataset <i>Mehmet Sukru Aygun</i><sup>*</sup>, Mehmet Fatih Akay</p> <p>Optimization of Incremental Conductance Using Fuzzy Logic Control for MPPT of a Photovoltaic Stand-Alone System <i>Beddi Abdelraouf</i><sup>*</sup>, Hicham Serhoud, Nacer Hebbir, Zoubir Aoulmi, Moussa Attia</p> <p>Enhancing Impact Resistance of Engineering Solutions Through Multiscale Structural Optimization <i>Ilhan Taber</i><sup>*</sup>, Ramazan Karakuzu</p> <p>Comparative Study of Empirical Expressions for Modulus of Soil Reaction and Pipe Displacement in Soil-Pipe System <i>Chahrazad Bacha</i><sup>*</sup>, Meriem Zoutat, Mohamed Mekki</p> <p>Nature-Based Solutions for Flood and Water Management in Urban Areas: Global Practices <i>Emine Keles Ozgenc</i><sup>*</sup></p>

19:20 – 19:30	Break
Online Session – 18 (in English) Head of Session: Assoc. Prof. Dr. Selahattin Kosunalp	
19:30 – 20:50	Differential Geometry and Natural Metrics <i><u>Chaoui Saadia</u></i> <sup>*</sup>
	New Conjugate Gradient Method Using SWP Line search for Nonlinear Unconstrained Optimization <i><u>Souli Choubeila</u></i> <sup>*</sup> , <i><u>Ziadi Raouf</u></i>
	A Stochastic BFGS Algorithm for Bound-Constrained Global Optimization <i><u>Raouf Ziadi</u></i> <sup>*</sup> , <i><u>Bencherif Madani Abdellatif</u></i>
	Characterizations of Weighted Triebel-Lizorkin Spaces Associated with Hermite Operators <i><u>Chichoune Romaiissa</u></i> <sup>*</sup> , <i><u>Saibi Khedoudj</u></i> , <i><u>Mokhtari Zouhir</u></i>
	On a Sojourn Time Formula and Applications in Engineering and Simulation <i><u>Abdelatif Bencherif Madani</u></i> <sup>*</sup>
	Magnetized Fe <sub>3</sub> O <sub>4</sub> /CoFe <sub>2</sub> O <sub>4</sub> Hybrid Ferrofluid with Magnetic Field-Dependent Viscosity over a Slip-Stretching Sheet <i><u>Nur Ilyana Kamis</u></i> <sup>*</sup> , <i><u>Noraihan Afiqah Rawi</u></i> , <i><u>Lim Yeou Jiann</u></i> , <i><u>Sharidan Shafie</u></i>
	An Efficient Numerical Approach for Fractional Integro-Differential Equations of Fredholm Type <i><u>Nouria Arar</u></i> <sup>*</sup> , <i><u>Zineb Laouar</u></i>
	Solutions of Linear Dynamic Systems with the Help of Eigenvalue - Eigenvector <i><u>Ramazan Simsek</u></i> <sup>*</sup>

**Virtual Hall 2**

Online Session – 19 (in English) Head of Session: Asst. Prof. Dr. Mustafa Alptekin Engin	
09:00 – 10:20	Boosting Communication Efficiency: WDM-Distributed Compensation Fiber Integration in Optical Systems <i><u>Hadj Abdelkader Benghenia</u></i> <sup>*</sup> , <i><u>Hadj Ali Bakir</u></i>
	Maximizing Solar Installation Power Using Fuzzy Control <i><u>Amel Ourici</u></i> <sup>*</sup> , <i><u>Abderaouf Bahi</u></i>
	Improving the Electrical Properties of the Smart Temperature Sensor Using CMOS (Si and SiC) Technology <i><u>Mourad Hebali</u></i> <sup>*</sup> , <i><u>Benaoumeur Ibari</u></i> , <i><u>Menouer Bennaoum</u></i> , <i><u>Hocine Abdelhak Azzeddine</u></i> , <i><u>Abdelkader Maachou</u></i> , <i><u>Mohammed El-Amine Beyour</u></i>
	An Overview of Medium Access Control Protocols for Terrestrial Wireless Sensor Networks

	<u>Selahattin Kosunalp</u> *
	Silicon-Integrated GaAs Single-Junction Solar Cell: Design and Performance Improvement <u>Mohammed El-Amine Beyour</u> *, <u>Mourad Hebali</u> , <u>Benaoumeur Ibari</u> , <u>Menouer Bennaoum</u> , <u>Hocine Abdelhak Azzeddine</u> , <u>Abdelkader Maachou</u>
	Microstrip Patch Antenna with Triple-Band Using Metamaterial <u>Hadda Ouguissi</u> , <u>Nail Alaoui</u> *
	Dipole Antenna Based on Metamaterials for RFID <u>Hadda Ouguissi</u> , <u>Nail Alaoui</u> *
	Machine Learning Based Diamond Cut Quality Classification <u>Mustafa Alptekin Engin</u> *, <u>Latif Akcay</u>
10:20 – 10:30	Break
Online Session – 20 (in English) Head of Session: Asst. Prof. Dr. Mustafa Alptekin Engin	
	Study of New Model of SBD Structure Proposed to Elaborate Mixer Design <u>Reguieg Khadidja</u> *, <u>Souar Zeggai</u> , <u>Hebali Mourad</u>
	Investigation of the Electrical Behavior of DG-MOSFET Transistors in Silicon Carbide Using Series and Parallel Equivalent Electronic Circuits <u>Mourad Hebali</u> *, <u>Benaoumeur Ibari</u> , <u>Hocine Abdelhak Azzeddine</u> , <u>Bennaoum Menouer</u> , <u>Ibrahim Farouk Bouguenna</u> , <u>Mohammed El-Amine Beyour</u>
	Towards Service Discovery and Selection Approaches in IoT Applications <u>Selahattin Kosunalp</u> *, <u>Yunus Kaya</u>
	Design of a New Multiband Pentagon Patch Antenna Array <u>Khouloud Mohammed Belhadj</u> *, <u>Souheyla Ferouani</u> , <u>Djalal Ziani Kerarti</u>
10:30 – 11:50	Energy Distribution Analysis Using DWT for the Airgap Eccentricity in Induction Machine <u>Moutaz Bellah Bentradi</u> *, <u>Adel Ghoggal</u> , <u>Tahar Bahi</u>
	Advanced Control Strategy for Grid-Connected Voltage Source Inverters with LCL Filters Dedicated to Renewable Energy Grid Integration Systems <u>Houssam Eddine Mansouri</u> *, <u>Billel Talbi</u> , <u>Idris Messaoudene</u> , <u>Moussa Abderrahim Mehiris</u>
	Efficient QRS Complex Extraction from ECG Signals Using DWT <u>Hadda Ouguissi</u> , <u>Nail Alaoui</u> *
	Microstrip Antenna Design for 5G Communication <u>Hadda Ouguissi</u> , <u>Nail Alaoui</u> *
11:50 – 12:00	Break
Online Session – 21 (in English)	

Head of Session: Asst. Prof. Dr. Mustafa Alptekin Engin	
12:00 – 13:20	Removal of Pollutant by Bacteria Isolated from Oilfield via Biosurfactant Production <i>Nesrine Lenchi*</i> , <i>Wissam Ahmedi</i> , <i>Salima Kebbouche-Gana</i>
	Investigating the Modulatory Effects of Phenolic-Rich Extract on Pancreatic $\beta$ -Cell Gene Expression in Oxidative Stress Conditions <i>Anfel Benmanseur*</i> , <i>Fatma Zahra Hab</i> , <i>Rania Derguine</i> , <i>Rechda Amel Tachour</i> , <i>Mustapha Tacherfiout</i> , <i>Bachra Khettal</i> , <i>Abdelmalek Rezgui</i> , <i>Widad Sobhi</i>
	An Investigation into the Impact of Tannic Acid and Gallic Acid on the Surface Characteristics of 3D-Printed Polylactic Acid in Relation to Adhesion of <i>Pseudomonas Aeruginosa</i> and <i>Staphylococcus Aureus</i> <i>Badr Errabiti*</i> , <i>Amal El Aabedy</i> , <i>Sara Er-Rahmani</i> , <i>Soumya El Abed</i> , <i>Saad Ibensouda Koraichi</i>
	Exploring the Inhibitory Effect of Alpha-Hederin, the Active Saponin of <i>Nigella Sativa</i> , Against the Main Protease M <sup>pro</sup> of SARS-CoV-2 <i>Selma Houchi*</i> , <i>Seoussen Kada</i> , <i>Hanane Khither</i>
	Thymol's Protective Effects on CCl <sub>4</sub> -Induced Oxidative Stress in Female Rats: Assessing Hepatic and Plasmatic Markers <i>Hanane Khither*</i> , <i>Soraya Madoui</i> , <i>Selma Houchi</i> , <i>Asma Mosbah</i>
	Antioxidant Activity, Total Phenolic, and Total Flavonoid Contents of Crude Extract of <i>Inula Viscosa</i> 's Leaves <i>Nadjat Azzi*</i> , <i>Younes Douffa</i> , <i>Nour El Houda Belabas</i> , <i>Haifaa Laroui</i> , <i>Thoraya Guemmaz</i> , <i>Fatima Zerargui</i> , <i>Karima Saffidine</i> , <i>Abderrahmane Baghiani</i>
	Experimental Study on the Healing Effect of the Crude Extract of the Aerial Part of <i>Cytisus Triflorus</i> on Skin Wounds <i>Soraya Madoui*</i> , <i>Hanane Khither</i> , <i>Karima Madoui</i> , <i>Noureddine Charef</i>
	Exploring Phenolic Composition and Scavenging Effects Against Reactive Oxygen Species of Nettle Crude Extract <i>Hamza Kemchache*</i> , <i>Khalil Kaouane</i> , <i>Ayoub Bekka</i> , <i>Mondher Fradjia</i> , <i>Sabrina Manel Kaddour</i> , <i>Rayene Bouaita</i> , <i>Noureddine Charef</i> , <i>Soraya Madoui</i> , <i>Hanane Khither</i>
13:20 – 13:30	Break
Online Session – 22 (in English) Head of Session: Assoc. Prof. Dr. Selahattin Kosunalp	
13:30 – 14:50	Antioxidative Characteristics of Aqueous and Ethanol Extracts of <i>Anethum Graveolens</i> L. Seeds <i>Nour El Houda Belabas*</i> , <i>Nadjat Azzi</i> , <i>Younes Douffa</i> , <i>Haifaa Laroui</i> , <i>Thoraya Guemmaz</i> , <i>Fatima Zerargui</i> , <i>Karima Saffidine</i> , <i>Abderrahmane Baghiani</i>
	Evaluation of In Vitro Antioxidant Activity of Natural Compounds in Atriplex

	Halimus Leaf Extract Using Hydrogen Peroxide and Hydroxyl Radical Assays <i>Khalil Kaouane*</i> , <i>Hamza Kemchache</i> , <i>Ayoub Bekka</i> , <i>Mondher Fradjia</i> , <i>Rayene Bouaita</i> , <i>Sabrina Manel Kaddour</i> , <i>Noureddine Charef</i> , <i>Hanane Khither</i> , <i>Soraya Madoui</i>
	In Vitro Assessment of Biological Activity in Elaeagnaceae Leaves <i>Rayene Bouaita*</i> , <i>Randa Djemil</i> , <i>Samira Bouhalit</i> , <i>Saber Boutella</i> , <i>Khalil Kaouane</i> , <i>Hamza Kemchache</i>
	Evaluation of the Bio-Remedial Effect of Bacillus Atrophaeus to Treat Soil Polluted by Heavy Metals <i>Mondher Fradjia*</i> , <i>Rima Belattar</i> , <i>Abdelhakim Sellal</i> , <i>Wissam Nour Elhouda Ahmedi</i> , <i>Hamza Kemchache</i> , <i>Khalil Kaouane</i> , <i>Nora Laouicha</i> , <i>Amor Benchikh</i>
	Phytotherapy Study of Medicinal Plants Used in the Northern Region of the Wilaya of Setif (Ain El Kebira) <i>Nouioua Wafa*</i> , <i>Madoui Soraya</i>
	ABTS Radical Scavenging Activity and Ferrous Chelating Ability of Ethyl Acetate Extract of Pistacia Atlantica Seeds <i>Younes Douffa*</i> , <i>Nadjet Azzi</i> , <i>Nour El Houda Belabas</i> , <i>Haifaa Laroui</i> , <i>Thoraya Guemmaz</i> , <i>Karima Saffidine</i> , <i>Fatima Zerargui</i> , <i>Abderahmane Baghiani</i>
	Phytochemical Analysis and Biological Activities of Essential Oil and Lavandula Stoechas Harvested in Algeria <i>Amina Benazzouz-Touami*</i> , <i>Driffa Bouchene</i> , <i>Nabila Iaouadaren</i>
	Tolerance Mechanism Study to Polluted Ecosystems of Bioremediants <i>Laouicha Nora*</i> , <i>Sellal Abdelhakim</i> , <i>Bencheikh Amor</i> , <i>Belattar Rima</i> , <i>Fradjia Mondher</i> , <i>Ahmedi Wissam Nourelhouda</i>
14:50 – 15:00	Break
Online Session – 23 (in English) Head of Session: Assoc. Prof. Dr. Selahattin Kosunalp	
15:00 – 16:20	Evaluation of Antibacterial Activity of <i>Thymus Vulgaris</i> Extracts <i>Mohamed Khiari*</i> , <i>Zine Kechrid</i>
	Evaluation of Antibiotic Resistance Pattern and Biofilm Production in Vaginal Isolates in Women <i>Anfal Kara*</i> , <i>Feryal Belfihadj</i> , <i>Naouel Boussoualim</i> , <i>Meriem Elkolli</i>
	Evaluation of Antioxidant and Antibacterial Activities of <i>Ruta Montana</i> Crude Extract from the Mila Region <i>Zineb Bouamrane*</i> , <i>Saber Boutellaa</i> , <i>Hakima Belattar</i> , <i>Mouna Menakh</i> , <i>Nedjla Derbal</i>
	Evaluation of Antibiotic Resistance in Enterobacteria Isolated from Hospital Cockroaches <i>Ben Djaballah Wafa*</i> , <i>Bouguenoun Widad</i> , <i>Trabsa Hayat</i> , <i>Kebkoub Narimane</i> ,

	<p><i>Serraye Fatima</i></p> <p>G-Protein Coupled Estrogen Receptor Expression in Estrogen Receptor Alpha (ER<math>\alpha</math>) Negative Breast Cancer Tissues of Algerian Patients <i>Yasmine Mostaphaoui*</i>, <i>Rafik Menad</i>, <i>Elara N'tima Moudilou</i>, <i>Chahla Bencharif</i></p> <p>Exploring the Insecticidal Potency and Growth Inhibition Effect of <i>Pistacia Lentiscus</i> and <i>Lauris Nobilis</i> Oils and Extracts on <i>Culex Pipiens</i> (Diptera: Culicidae) Larvae <i>Menakh Mouna*</i>, <i>Saber Boutellaa</i>, <i>Zineb Bouamrane</i></p> <p>Unlocking the Power of Nigella: Exploring the Antioxidant Abilities of This Ancient Medicinal Plant <i>Dalia Nafir</i>, <i>Noureddine Belattar*</i></p> <p>The Biological Activity of the Ethanolic Extract from Bee Pollen <i>Oumamar Loubna*</i>, <i>Soltani El Khamza</i>, <i>Khalil Kaouane</i>, <i>Ayoub Bekka</i>, <i>Hamza Kemchache</i></p>
16:20 – 16:30	Break
<p>Online Session – 24 (in English) Head of Session: Assoc. Prof. Dr. Selahattin Kosunalp</p>	
16:30 – 17:50	<p>Tumor Microenvironment in Hepatocellular Carcinoma: A Comprehensive Review <i>Yusra Zarlashat*</i>, <i>Hassan Mushtaq</i></p> <p>Ecological Classification of Soil-Plant Cover Areas Contaminated by Drilling and Mineralized Waters in the Siyazan Region (Azerbaijan) <i>Sanubar Aslanova*</i></p> <p>The Use of Pectin Extracted from Lemon Bark as an Encapsulation Matrix <i>Djerri Rofia*</i>, <i>Himed Louiza</i>, <i>Barkat Malika</i></p> <p>Utilizing <i>Aspergillus Oryzae</i> for Expression of SARS-CoV-2 Spike Protein Domains: Insights into COVID-19 Research <i>Elif Karaman*</i>, <i>Serdar Uysal</i></p> <p>Indirect Effects of Microplastics on Climate Change and Community-Based Solutions to Atmospheric Microplastic Pollution <i>Enes Ozgenc*</i>, <i>Gunay Yildiz Tore</i></p> <p>In Silico Analysis of Phytochemicals from Selected Medicinal Plant Species to Inhibit Alpha-Glucosidase as a Receptor Protein to Treat Type-2 Diabetes Mellitus <i>Ghulam Mustafa*</i>, <i>Shoukat Hussain</i>, <i>Anas Bilal</i>, <i>Rawaba Arif</i></p> <p>Biotin-Functionalized Nanoparticle Systems for Targeted Lung Cancer Therapy <i>Fatma Sayan Poyraz*</i>, <i>Banu Mansuroglu</i></p> <p>Epidemiological, Immunohistochemical, and Molecular Study of Breast Cancer in</p>



	<p>Young Algerian Patients from “Bejaia” <i>Sara Ouari*</i>, <i>Hania Ouahmed-Boudaoud</i>, <i>Chahla Bencharif</i>, <i>Chahira Mazouzi</i></p>
17:50 – 18:00	Break
<p>Online Session – 25 (in English) Head of Session: Asst. Prof. Dr. Sebahat Oztekin</p>	
18:00 – 19:20	<p>Microencapsulation: A Way to Preserve Bioactive Compounds from Food Waste for Novel Food Formulations – A Review <i>Tusneem Kausar*</i>, <i>Ashiq Hussain</i>, <i>Sobia Noreen</i></p>
	<p>Estimation of Total Phenolic Compounds in Three Date Fruits Cultivars from Biskra (Algeria) <i>Amel Barkat*</i>, <i>Hayat Trabsa</i>, <i>Chaima Mezghiche</i>, <i>Yasmine Mabrouka Mizab</i>, <i>Abderahmane Baghiani</i>, <i>Abdelnacer Agli</i></p>
	<p>Estimation of Total Flavonoids Compounds in Three Date Fruits Cultivars from Biskra (Algeria) <i>Amel Barkat*</i>, <i>Hayat Trabsa</i>, <i>Chaima Mezghiche</i>, <i>Yasmine Mabrouka Mizab</i>, <i>Abderahmane Baghiani</i>, <i>Abdelnacer Agli</i></p>
	<p>Antibacterial Activity of Garlic (<i>Allium Sativum</i>) Against <i>Staphylococcus</i> Strains Isolated from Nile Tilapia (<i>Oreochromis Niloticus</i>) <i>Romeissa Derdachi*</i>, <i>Sabrine Boucetta</i></p>
	<p>Health and Nutritional Complications in Newborns of Diabetic Mothers <i>Salima Taleb*</i>, <i>Bouthaina Brakni</i>, <i>Fairouz Dilmi</i></p>
	<p>Assessment of Antimicrobial Activity of Lactic Acid Bacteria Isolated From Artisanal Dairy Products Against <i>Escherichia Coli</i> ATCC 25922 and <i>Staphylococcus Aureus</i> ATCC 29213 <i>Roumaissaa Belkacem*</i>, <i>Qada Benameur</i></p>
	<p>Utilizing Lentil Flour in the Gluten-Free Cake Formulations <i>Sebahat Oztekin*</i></p>
	<p>Potent Inhibitory and Stimulatory Effects of Various Metal Ions on Polyphenol Oxidase Activity Extracted from Algerian Desert Truffles <i>Abdelhafid Bouremana*</i>, <i>Fatima El-Houaria Zitouni-Haouar</i></p>
19:20 – 19:30	Break
<p>Online Session – 26 (in English) Head of Session: Dr. Nurhafizah Hasim</p>	
19:30 – 20:50	<p>Experimental Measurement on a Shaking Table of the Dynamic Characteristics of Structures <i>Abdellatif Bentifour</i>, <i>Abderaouf Daci</i>, <i>Nassima Benmansour</i>, <i>Rachid Derbal*</i></p>
	<p>Evaluation of the Dynamic Characteristics of a 3DOF Reduced Scale Model Using RISAM Shaking Table</p>

	<i><u>Abderaouf Daci</u>, Abdellatif Bentifour, Nassima Benmansour, Rachid Derbal*</i>
	Evaluation of the Carbonation of Concrete with the Addition of Pozzolana and Marble Powder Under the Effect of Temperature <i><u>Ahlem Houaria Mohammed Belhadj*</u>, Rachid Derbal</i>
	Characterization and Application of Sewage Sludge in Cement Products <i><u>Mahmoud Bouslah*</u>, Mekki Maza, Zine El Abidine Rahmouni, Nadia Tebbal</i>
	The Impact of Surface Roughness on Energy Dissipation and Dimensions of Non-Rectangular Stilling Basins: An Experimental Investigation for Sustainable Environmental Practices <i><u>Seyfedine Benabid*</u>, Sonia Cherhabil, Sid Ali Dajfri, Taqiyeddine Assas</i>
	Development of Geopolymer Binders Based on Industrial Waste with Different Treatment Methods: A Review <i><u>Hanane Zadri*</u>, Nadia Tebbal, Zine El Abidine Rahmouni, Mekki Maza</i>
	Valorization of Mining Waste into Construction Materials: Literature Review <i><u>Medjida Touahria*</u>, Nadia Tebbal, Zine El Abidine Rahmouni, Mekki Maza</i>
	The Effect of Limestone on Virgin Cork Concrete Mechanical Properties and Durability <i><u>Samah Hariz*</u>, Fouad Ghomari, Brahim Touil</i>

**Virtual Hall 3**

<p>Online Session – 27 (in Turkish) Head of Session: Asst. Prof. Dr. Ramazan Simsek</p>	
09:00 – 10:20	Investigation of the Microstructure and Hardness Properties of Fe Based High Entropy Alloys Produced by Powder Metallurgy Method <i><u>Murat Bodur</u>, M. Emre Turan, Yavuz Sun*</i>
	Investigation of Delamination Factor in Bi-Directional Drilling of Glass Fiber Reinforced Plastic Materials <i>Erhan Karatas, Oguz Kocar*, <u>Nurettin Baran Zulfikar</u>, Nergizhan Anac, Furkan Parmaksiz</i>
	Using Shape Memory Alloys for Energy Harvesting Systems <i><u>Gokhan Kilic*</u>, Omar Abboosh</i>
	Analysis of Performance Values of Stabilizer Link Parts Produced by Additive Manufacturing Method in Automotive Suspension Systems <i><u>Sevilay Sagtan*</u>, Burak Ates</i>
	Gradient Graphene Sponge for Solar Steam Generation Applications <i><u>Kader Dagci Kiransan*</u>, Ezgi Topcu, Elif Erçarikci</i>
	Investigation of the Effect of Current Density on Ammonia Formation from Ammonium Chloride and Sodium Chloride in Two-Compartment Bipolar Membrane Electrodialysis

	<i>Duygu Adiguzel*</i> , <i>Fatemeh Abbasi</i> , <i>Osman Nuri Ata</i>
	Evaluating the Pb (II) Removal Efficiency of <i>Prunus Laurocerasus</i> : Isotherms, Kinetic and Thermodynamic Studies <i>Zehra Seba Keskin*</i> , <i>Zeynep Mine Senol</i>
	Upgraded Bio-Oil with Co-Pyrolysis of Spruce Sawdust with Glycerol <i>Ahmet Rasim Girisen*</i> , <i>Hakan Ozcan</i>
10:20 – 10:30	Break
Online Session – 28 (in Turkish) Head of Session: Asst. Prof. Dr. Hamdullah Ozturk	
10:30 – 11:50	Comparative Classification Performance Evaluation of Machine Learning and Deep Learning Techniques for BreakHis, Wisconsin, and DDSM Breast Cancer Datasets <i>Oben Adak*</i> , <i>Cigdem Inan Aci</i> , <i>Dogu Ilmak</i>
	A Review on Data Visualization: Usage Fields, Importance, and Examples <i>Durmus Ozkan Sahin*</i>
	Recognition of Human Activities Using Accelerometer and Gyroscope Sensors in Mobile Devices <i>Merve Buluslu*</i> , <i>Adem Korkmaz</i>
	A New Metaheuristic Algorithm for Optimization Problem: Artificial Circulation System Algorithm <i>Nermin Ozcan*</i> , <i>Semih Utku</i>
	Development of an Artificial Intelligence Supported Identity Verification System (KYC) <i>Ceren Goksu*</i> , <i>Kerim Guler</i> , <i>Duygu Keles</i> , <i>Halil Sahin</i>
	Breast Cancer Prediction Using Machine Learning Algorithms <i>Gokberk Kozak*</i> , <i>Erol Ozcekic</i>
	A Drum Wheel Bearing Design in Tumble Dryer <i>Abdullah Berk Ince*</i> , <i>Cevdet Caner Akgun</i>
	Examining the Trend of MOOC Related Studies with Data Mining: Voyant Analyst <i>Bunyami Kayali*</i> , <i>Mehmet Yavuz</i>
11:50 – 12:00	Break
Online Session – 29 (in Turkish) Head of Session: Asst. Prof. Dr. Ramazan Simsek	
12:00 – 13:20	A Research on Staling in Wafers <i>Sibel Koca Cetinkaya</i> , <i>Amine Beyza Ozata*</i> , <i>Ozge Akgul</i> , <i>Begum Ceren Memecan</i>
	Grapevine Leaf Powder as a Functional Food Additive: Physicochemical and Bioactive Properties

	<p><u><i>Mehmet Ali Salik*</i></u></p> <p>A Popular Probiotic Dairy Product-Kefir: Overview on Functional Mechanism of Action and Plant-Based Fermented Beverages</p> <p><u><i>Mehmet Ali Salik*</i></u></p> <p>Cytocompatibility of PVA/Chitosan Electrospun Scaffold Loaded with Antioxidant Amino Acid on Fibroblast and Neuroblastoma Cells</p> <p><u><i>Betul Mutlu*</i></u>, <u><i>Cem Bulent Ustundag</i></u>, <u><i>Rabia Cakir</i></u></p> <p>Characterization and Study of the <i>In Vitro</i> Effects of Polysaccharide-Based Nanofibers Obtained Using the Method of Coaxial Electrospinning to Improve Tympanic Membrane Perforations</p> <p><u><i>Busra Akgul*</i></u>, <u><i>Cansu Gulcan</i></u>, <u><i>Selay Tornaci</i></u>, <u><i>Merve Erginer</i></u>, <u><i>Ebru Toksoy Oner</i></u>, <u><i>Emrah Sefik Abamor</i></u>, <u><i>Serap Acar</i></u>, <u><i>Adil M. Allahverdiyev</i></u></p> <p>Statistical Investigation of Surface Modification Polymerization Methods in Global and Turkish Scale</p> <p><u><i>Nursel Karaoglan*</i></u></p> <p>Determination of Thiamethoxam with Molecular Imprinted Affinity Monolithic Column</p> <p><u><i>Ilgim Gokturk*</i></u></p> <p>Determination of Metalaxyl Using SPR Sensors</p> <p><u><i>Kivilcim Caktu Guler*</i></u></p>
13:20 – 13:30	Break
<p>Online Session – 30 (in Turkish)</p> <p>Head of Session: Asst. Prof. Dr. Hamdullah Ozturk</p>	
13:30 – 14:50	<p>Parameter Extraction of Proton Exchange Membrane Fuel Cell Using Metaheuristic Optimization Techniques: Evaluation and Comparison</p> <p><u><i>Huseyin Bakir*</i></u></p> <p>Classification of Coconut Tree Diseases Using GoogleNet for Agriculture Management</p> <p><u><i>Ebru Ergun*</i></u></p> <p>A Digital Predictive Peak Current Mode Control for Power Factor Correction</p> <p><u><i>Ahmet Talha Dudak*</i></u>, <u><i>Ahmet Faruk Bakan</i></u></p> <p>A Low-Cost Cloud-Based Wearable Accelerometer Data Recording System</p> <p><u><i>Ayse Zehra Caglar</i></u>, <u><i>Cagri Gul</i></u>, <u><i>Sabri Altunkaya*</i></u></p> <p>Nanobioelectronics Used in Targeted Drug Delivery Systems</p> <p><u><i>Gencay Sevim*</i></u>, <u><i>Gulay Buyukkoroglu</i></u></p> <p>A Satellite-Based Augmentation System for Turkey to Enhance Navigation Capabilities</p> <p><u><i>Ibrahim Oz*</i></u></p>

	Optimized Performance Compact Wide-Band Microstrip Filter-Antenna for 4G Applications <i>Husain Ali*</i> , <i>Ugur Cem Hasar</i>
	Simplified Reference-Plane-Invariant Method for Permittivity Extraction of Low-Loss Dielectrics via One-Port Waveguide Measurements <i>Ugur Cem Hasar*</i> , <i>Husain Ali</i>

**Sunday, July 21, 2024**

***Online Sessions***

***Virtual Hall 1***

Online Session – 31 (in English) Head of Session: Asst. Prof. Dr. Mustafa Alptekin Engin	
09:00 – 10:20	A Theoretical Comparative Study of the 1,3-Dipolar Cycloaddition Reaction of Some Alkenes with Nitrene <i>Boulanouar Messaoudi*</i>
	A Kinetic Mechanism Study of the Reaction of Triplet Oxygen O( <sup>3</sup> P) with the But-3-Enal Aldehyde <i>Boulanouar Messaoudi*</i>
	Effect of Si <sup>4+</sup> and Ga <sup>3+</sup> Co-Doping on Structure and Ionic Conductivity of BiSiGaVOx System <i>Abdelmajid Agnaou*</i> , <i>Wafaa Mhaira</i> , <i>Rachida Essalim</i> , <i>Fabrice Mauvy</i> , <i>Maati Alga</i> , <i>Mohamed Zamama</i> , <i>Abdelaziz Ammar</i>
	Thermodynamic Properties at Infinite Dilution of Hydrocarbons in Ionic Liquids <i>Fadhila Rabhi*</i> , <i>Hocine Sifaoui</i> , <i>Fabrice Mutelet</i>
	Modification of Polycaprolactone Through Grafting with an Aromatic Acid: Synthesis and Characterization <i>Nacera Leila Belkhir*</i> , <i>Mohammed Amin Bezzekhami</i> , <i>Kaouter Bentedlaouti</i> , <i>Mahmoud Belalia</i> , <i>Amine Harrane</i>
	Synthesis of New Azomethines Based on Vitamin B6 <i>Samira Ismayilova*</i> , <i>Alakbar Huseynzada</i> , <i>Ulviyya Hasanova</i> , <i>Aygun Israyilova</i>
	Synthesis of New Heterocyclic Nitrogen Derivatives Derived from Pyridopyrazine <i>Mohamed El Yaqoubi*</i> , <i>Yusra Seqqat</i> , <i>Mouad Lahyaoui</i> , <i>Houda Lamssane</i> , <i>Fouad Chahdi Ouazzani</i> , <i>Youssef Kandri Rodi</i>
	Synthesis and Characterization of Layered Double Hydroxides with Different Cations (Mg, Cu, Al) and EDTA Intercalated <i>Fadhila Bouhella*</i> , <i>Boukoussa Bouhadjar</i> , <i>Abdelkader Elaziouti</i> , <i>Hadjer Addou</i> , <i>Nadjia Belmehdi</i>
10:20 – 10:30	Break

Online Session – 32 (in English) Head of Session: Asst. Prof. Dr. Mustafa Alptekin Engin	
10:30 – 11:50	A Chemotherapeutic Supplement, Green Synthesized Silver Nanoparticles Using <i>Papaver Rhoeas</i> for Human Pancreatic Cancer Treatment <i>Cigdem Dikbas*</i> , <i>Muberra Andac</i>
	Theoretical Study, Intermolecular Charge Transfer, MEP, and Nonlinear Optics Application for an Organic Molecule <i>Zohra Douaa Benyahlou*</i> , <i>Mohammed Hadj Mortada Belhachemi</i> , <i>Salem Yahiaoui</i> , <i>Kheira Hammou</i> , <i>Abdelkader Chouaih</i>
	A simple and Efficient One-Pot Synthesis of Hantzsch 1,4-Dihydropyridines Using Heteropolyacid Catalyst Under Mild Condition <i>Fella Gaad*</i> , <i>Sabrina Halit</i> , <i>Malika Makhloufi</i> , <i>Tassadit Mazari</i> , <i>Marchal Catherine Roch</i>
	Nickel Catalyst for Isoxazol Synthesis <i>Benali Belgharri*</i> , <i>Amina Berrichi</i> , <i>Sarah Abbou</i> , <i>Zahra Hamiani</i> , <i>Redouane Bachir</i>
	Phosphotungstic Heteropolyacid Based New Hybrid Materials for Biomass Recovery <i>Feriel Toumi*</i> , <i>Yasmina Idrissou</i> , <i>Tassadit Mazari</i> , <i>Rabia Cherifa</i> , <i>Anne Ponchel</i> , <i>Kania Nicolas</i>
	Semisynthesis of New Isoxazolines from (E)- $\alpha$ -Atlantone: Experimental and Theoretical Investigations <i>Houria Raji</i> , <i>Rida Nejari</i> , <i>Ahmed Chekroun</i> , <i>Abdellah Zeroual*</i> , <i>Noureddine Mazoir</i> , <i>Ahmed Benharref</i>
	Study of Properties of Tin Oxide Thin Films Elaborated by USP Method <i>Sabrina Roguai*</i> , <i>Abdelkader Djelloul</i>
	Synthesis of CuO Nps for Photocatalytic Applications <i>Sabrina Roguai*</i> , <i>Abdelkader Djelloul</i>
11:50 – 12:00	Break
Online Session – 33 (in English) Head of Session: Asst. Prof. Dr. Mustafa Alptekin Engin	
12:00 – 13:20	Photothermal Activity and <i>In Vitro</i> Evaluation of Gold Nanorods for Potential Therapeutic Application in Cutaneous Leishmaniasis Treatment <i>Magali R. Di Meglio*</i> , <i>Cristian Lillo</i> , <i>Jorge Montanari</i>
	Valuation of Essential Oils from Aleppo Pine ( <i>Pinus Halepensis</i> Mill.) Harvested in Two Regions of Algeria <i>Nacira Amara*</i> , <i>Mohamed Kouider Amar</i> , <i>Sabrina Amara</i> , <i>Nadjet Harazi</i>
	Natural Antifungal Agents as Alternatives for <i>Alternaria Alternata</i> Control

	<p><i>Teodora Kukrić*</i>, <i>Renata Iličić</i>, <i>Boris Popović</i></p> <p>Some Derivatives of 3,4-Di-Hydropyrimidin-2(1H)-Thiones Derivatives: Synthesis, Biological Assessment, ADMET, and Drug-Likeness Analysis <i>Noura Kichou*</i>, <i>Nabila Guechtouli</i>, <i>Manel Taferguennit</i></p> <p>Hybrid Electrode Based on Ionic Liquid and Pt and Pd Nano-Clusters: For the Hydrogen Evolution Reaction (HER) Catalysis <i>Hocine Moussouni</i>, <i>Mourad Mechouei*</i>, <i>Jalal Ghilane</i></p> <p>Evaluation of the Antidiabetic Activity of Extracts and Essential Oil of Myrtus Communis Harvested in Algeria <i>Melissa Bessaci*</i>, <i>Amina Benazzouz-Touami</i></p> <p>The Environmentally Friendly Synthesis of Amide Based on Triethylenetetramine <i>Fargana Alizadeh*</i>, <i>Alakbar Huseynzada</i>, <i>Aygun Israyilova</i>, <i>Ulviyya Yolchuyeva</i>, <i>Ulviyya Hasanova</i>, <i>Eldar Gasimov</i>, <i>Goncha Eyvazova</i>, <i>Fuad Rzayev</i>, <i>Orkhan Isayev</i>, <i>Aida Ahmadova</i>, <i>Elshan Aliyev</i></p> <p>Synthesis and Biological Evaluation of Amide Derivative as Novel Antibacterial Agent <i>Fargana Alizadeh*</i>, <i>Alakbar Huseynzada</i>, <i>Aygun Israyilova</i>, <i>Ulviyya Yolchuyeva</i>, <i>Ulviyya Hasanova</i>, <i>Eldar Gasimov</i>, <i>Goncha Eyvazova</i>, <i>Fuad Rzayev</i>, <i>Orkhan Isayev</i>, <i>Aida Ahmadova</i>, <i>Elshan Aliyev</i></p>
13:20 – 13:30	Break
<p>Online Session – 34 (in English) Head of Session: Dr. Intan Helina Hasan</p>	
13:30 – 14:50	<p>Examining How CeO<sub>2</sub> Addition Affects the Microstructure and Wear of Cu-Al-Mn-Fe Shape Memory Alloy <i>Fatih Dogan*</i></p> <p>Catalytic Oxidation of Lignocellulosic Biomass to Biofuels Using Reusable Mixed Oxide as a Catalyst in a Green Solvent <i>Mona Benali*</i>, <i>Abdallah Oumekki</i>, <i>Jamil Toyir</i></p> <p>Thermal Behavior Kinetics of Macromolecular Nickel (II) complex using Thermogravimetric Analysis (TG/DTG) <i>Djoughra Aggoun*</i>, <i>Yasmina Ouennoughi</i></p> <p>Synthesis, Spectral Approach and Electrochemical Properties of Nickel (II) and Copper (II) Organometallic Schiff Base Complexes <i>Yasmina Ouennoughi</i>, <i>Djoughra Aggoun*</i></p> <p>Bibliometric Analysis of Research Trends in Additive Manufacturing in Metallurgical Engineering: A Scopus Database Study by Turkish Scholars <i>Oussama Zaidi*</i></p> <p>Analysis of Electrical Field Norm Distribution at the Cathode/Arc Interface in TIG Welding</p>

	<p><i>Merazi Sayah* , Leila Belgacem</i></p> <p>DFT Insights for Structural, Electronic, and Optical Characteristics of Cs<sub>2</sub>XBr<sub>6</sub> (X = Pb, Sn) Double Perovskites for Low-Cost Solar Cell Applications</p> <p><i>Rekia Larbi* , Omar Sahnoun, Mohamed Sahnoun</i></p> <p>Milling Effect on Structural, Microstructural, and Magnetic Properties of FeCo Based Alloy</p> <p><i>Chaffia Djebbari*</i></p>
14:50 – 15:00	Break
<p>Online Session – 35 (in English)</p> <p>Head of Session: Assoc. Prof. Dr. Selahattin Kosunalp</p>	
15:00 – 16:20	<p>Mapping of Tectonic Fractures in the Zat Region (Western High Atlas, Morocco): Using Remote Sensing and Structural Geology</p> <p><i>Abdelfattah Aboulfaraj* , Abdelhalim Tabit, Ahmed Algouti, Abdellah Algouti, Said Moujane, Saloua Agli</i></p>
	<p>Achieving Full Control of Industrial Robot: Kinematic and Dynamic Modeling with FOPID Controller Tuned using GWO Approach</p> <p><i>Benaoumeur Ibari* , Mourad Hebali, Baghdadi Rezali, Omar Medjad, Menaouer Bennaoum, Hocine Abdelhak Azzedine, Abdelkader Maachou</i></p>
	<p>Analysis of Technical Indicators in Cryptocurrency Market</p> <p><i>Asli Boru Ipek*</i></p>
	<p>IIoT as an Enabler for Data Analytics to Optimize Industrial Processes</p> <p><i>Federico Walas Mateo* , Andrés Redchuk</i></p>
	<p>Q-Learning Enhanced Swarm-Based Algorithms for the 0-1 Knapsack Problem</p> <p><i>Fehmi Burcin Ozsoydan*</i></p>
	<p>Optimizing Risk Management Strategies in the Oil and Gas Industry: Dynamic Assessment and Modeling of Accident Consequences</p> <p><i>Imane Aila* , Samia Chettouh, Djamel Haddad</i></p>
	<p>An Overview of Artificial Intelligence Techniques in Supply Chain Management: AI-Driven Strategies for Risk Management</p> <p><i>Lara J. M. Naser* , Seval Ene Yalcin</i></p>
	<p>An Efficient Design of a Multi-Echelon and Multi-Product Supply Chain Network with Price-Sensitive Demands</p> <p><i>Pinar Yunusoglu* , Derya Eren Akyol, Fehmi Burcin Ozsoydan</i></p>
16:20 – 16:30	Break
<p>Online Session – 36 (in English)</p> <p>Head of Session: Dr. Intan Helina Hasan</p>	
16:30 – 17:50	<p>Production of Graphene by Electrochemical Method and Energy Applications</p> <p><i>Gulbahar Bilgic Tuzemen*</i></p>



	<p>Advanced Hierarchical Control of Islanded AC Microgrids Using Modulated Model Predictive Control <i>Moussa Abderrahim Mehiris*</i>, <i>Billel Talbi</i>, <i>Idris Messaoudene</i>, <i>Houssam Eddin Mansouri</i></p>
	<p>Applications and Future of Unmanned Aerial Vehicles in the Field of Occupational Health and Safety <i>Mustafa Ozdemir*</i></p>
	<p>Model Predictive Control of a PUC7-Based Power Factor Correction (PFC) Rectifier <i>Abdeslem Sahli*</i>, <i>Billel Talbi</i>, <i>Abbes Kihal</i>, <i>Abdelbaset Laib</i>, <i>Abdelbasset Krama</i></p>
	<p>Internal Parameters Identification of a Lithium-Ion Battery <i>Abderrahmane El Djallil Rabhi*</i>, <i>Kamel Djamel Eddine Kerrouche</i></p>
	<p>Influence of the Temperature on the Performance of Conventional Organic Solar Cells <i>Samia Moulebhar*</i>, <i>Chahrazed Bendenia</i>, <i>Hanaa Merad-Dib</i>, <i>Souhila Bendenia</i>, <i>Sarra Merabet</i>, <i>Sid Ahmed Khantar</i></p>
	<p>Optimization of Sabbath Mode Algorithms Used in Refrigerators <i>Mazlum Koray Dirican*</i>, <i>Bulent Ozcan</i></p>
	<p>A Numerical Study on the Aerodynamic Performance of the S1223 Airfoil in Low Reynolds Number Conditions <i>Onur Usta*</i></p>
17:50 – 18:00	Break
<p>Online Session – 37 (in English) Head of Session: Assoc. Prof. Dr. Selahattin Kosunalp</p>	
18:00 – 19:20	<p>Simulation Study of Methylammonium Lead Iodide (CH<sub>3</sub>NH<sub>3</sub>PbI<sub>3</sub>)-Based Perovskite Solar Cell via Silvaco TCAD <i>Sid Ahmed Khantar*</i>, <i>Chahrazed Bendeni</i>, <i>Souhila Bendenia</i>, <i>Hanaa Merad-Dib</i>, <i>Samia Moulebhar</i>, <i>Sarra Merabet</i></p>
	<p>Optimization of Distributed Generations Placement and Sizing in Radial Distribution System Through ABC Algorithm <i>Badreddine Bendriss*</i>, <i>Samir Sayah</i>, <i>Abdellatif Hamouda</i></p>
	<p>Analysis of CdTe Solar Cell Performance Using SCAPS-1D Simulation as a Function of Various Buffer Layers <i>Merabet Sarra*</i>, <i>Bendenia Chahrazed</i>, <i>Bendenia Souhila</i>, <i>Merad Hanae</i>, <i>Moulebhar Samia</i>, <i>Khantar Sid Ahmed</i></p>
	<p>Advancements and Challenges of Photovoltaic Technology in Algeria's Desert <i>Chekal Affari Belhadi*</i>, <i>Kahoul Nabil</i>, <i>Younes Mohammed</i>, <i>Daoudi Lina</i>, <i>Cheghib Hocine</i>, <i>Kherici Zoubida</i></p>

	<p>Contribution to the Study of the Structural, Electronic, Optical, and Thermoelectric Properties of Heusler Alloys: A Material with Great Promise for the Future of Clean Energy <i><u>Khedidja Mechehoud</u>*</i>, <i>Mohamed Mana</i>, <i>Aya Righi</i>, <i>Mouffok Redouane Ghezzar</i>, <i>Fatima Bendahma</i>, <i>Bilel Achir</i></p>
	<p>Energy Management of Photovoltaic/Battery Power Source for Stand-Alone Application <i><u>Lina Daoudi</u>*</i>, <i>Amel Ourici</i>, <i>Siham Ghoudelbourg</i>, <i>Chekal Affari Belhadj</i></p>
	<p>Enhancing Pressure Regulation in PEMFC: PID Conventional and PID Optimized by PSO in Response to Variable Load Demand <i><u>Sabah Kabache</u>*</i>, <i>Djelloul Reguieg</i>, <i>Essaid Bousbiat</i>, <i>Djamel Kendil</i></p>
	<p>Enhanced Grid-Connected Photovoltaic System Using Five-Level Packed U Cell Topology and Advanced Control Approaches <i><u>Abderraouf Touafek</u>*</i>, <i>Fateh Krim</i>, <i>Hamza Afghoul</i>, <i>Billel Talbi</i></p>
19:20 – 19:30	Break
<p>Online Session – 38 (in English) Head of Session: Assoc. Prof. Dr. Selahattin Kosunalp</p>	
19:30 – 20:50	<p>Detection and Classification of Power Quality Disturbances Using Variational Mode Decomposition and Convolutional Neural Networks <i><u>Yahia Bousseloub</u>*</i></p>
	<p>Improving Solar Cell Efficiency: Exploring High-Performance Tandem Solar Cells Integrating Lead-Free Perovskite on Silicon (PVK/Si) via Design and Numerical Analysis <i><u>Hadjer Soufi</u>*</i>, <i>Abdelkader Bouhenna</i>, <i>Khadidja Rahmoun</i>, <i>Mohamed El Amine Slimani</i>, <i>Wisseem Benaissa</i></p>
	<p>Optimal Sizing of a Renewable Energy System for Sustainable Power and Hydrogen Generation Under the Northeastern Algerian Climate <i><u>Toufik Sebbagh</u>*</i></p>
	<p>Active and Reactive Power Control of a Grid-Connected Photovoltaic/Fuel Cell Hybrid System <i><u>Hocine Abdelhak Azzeddine</u>*</i>, <i>Mourad Hebali</i>, <i>Djamel-Eddine Chaouch</i>, <i>Benaoumeur Ibari</i>, <i>Menaouer Benaoum</i></p>
	<p>Artificial Neural Network MPPT and Perturb and Observ MPPT Comparison <i><u>Hocine Abdelhak Azzeddine</u>*</i>, <i>Mourad Hebali</i>, <i>Djamel-Eddine Chaouch</i>, <i>Benaoumeur Ibari</i>, <i>Menaouer Benaoum</i></p>
	<p>Optimization of Forced Circulation Solar Water Heating Systems for Enhanced Residential Energy Efficiency in Algeria <i><u>Ahmed Remlaoui</u>*</i>, <i>Driss Nehari</i></p>
	Investigation of the Effects of Silver Alloying and Transparent Conductive Oxide

	Layer Thickness on the Chalcopyrite Thin Film Solar Cells <i>Semih Agca*</i>
	The Characteristics of an Organic Solar Cell at the Base of Polymeric Material <i>Chahrazed Bendenia*</i> , <i>Souhila Bendenia</i> , <i>Hanaa Merad-Dib</i> , <i>Samia Moulebhar</i> , <i>Sid Ahmed Khantar</i> , <i>Sarra Merabet</i>

**Virtual Hall 2**

Online Session – 39 (in English) Head of Session: Asst. Prof. Dr. Latif Akcay	
09:00 – 10:20	Microstrip Dipole Antenna Design for RFID Application <i>Hadda Ouguissi</i> , <i>Nail Alaoui*</i>
	Chua Circuit and Its Behavior <i>Hadda Ouguissi</i> , <i>Nail Alaoui*</i>
	Harmonic Forecasting for Future Offshore Wind Farm System in the Ayvalik Region of the North Aegean Sea by Using Deep Learning <i>Alp Karadeniz*</i>
	Evaluation of Speech Encryption Algorithm Based on Chaotic Systems <i>Salah Mokhnache*</i> , <i>Tewfik Bekkouche</i> , <i>Nacira Diffellah</i>
	A Design of AI-Based-Smart Glasses, Which Offer Navigation in Addition to Correcting Vision <i>Syed Arif Kamal*</i>
	Impact of Image Size on Classification of Synthetically Generated Window and Door Images <i>Safak Altay Acar*</i>
	Few-Shot and Zero-Shot Video Classification from Large Visual Models Perspective <i>Erol Citak*</i> , <i>Mine Elif Karsligil</i>
	Machine Learning Techniques for Software Fault Prediction: A Distinctive Systematic Literature Review <i>Aleena Rafique*</i> , <i>Sania Bhatti</i>
10:20 – 10:30	Break
Online Session – 40 (in English) Head of Session: Asst. Prof. Dr. Latif Akcay	
10:30 – 11:50	Principal Component Analysis for Database Scan Using Hierarchical KNN Model for Telecom Customer Segmentation <i>Oluwasegun William Ijibadejo*</i> , <i>Saja Murtadha Hashim</i>
	Classification of Plant Leaves Using Vision Transformer Model <i>Kadriye Karadeniz*</i> , <i>Kursat Mustafa Karaoglan</i>

	<p>Artificial Intelligence and Statistics Based Call Count and Average Talk Time Prediction for Call Centers <i>Hasan Huseyin Yurdagul*</i>, Adem Seller, Idris Senocak, Hatice Ozdemir, Ceren Ulus, Mehmet Fatih Akay</p>
	<p>Understanding Large Language Models in Cybersecurity Domain <i>Bugra Kurt*</i>, Aysu Irem Adem, Mahmut Furkan Bakal, Hussain Alburki, Arda Sezen</p>
	<p>Enhancing FOPID Controller Performance in a 3-DOF Planar Manipulator <i>Benaoumeur Ibari*</i>, Mourad Hebali, Baghdadi Rezali, Omar Medjad, Menaouer Bennaoum, Hocine Abdelhak Azzedine, Abdelkader Maachou</p>
	<p>Can NLP Combined with AI Prevent Language Extinction: A Case Study of Turkish <i>Anil Kus*</i>, Cigdem Inan Aci</p>
	<p>CASTEP Investigation of Structural, Electronic, and Optical Properties of CoSb<sub>2</sub>O<sub>6</sub> <i>Rania Charif*</i>, Rachid Makhloufi</p>
	<p>Density Functional Theory (DFT) Investigation on the Structure and Electronic Properties of ZnSb<sub>2</sub>O<sub>6</sub> <i>Rania Charif*</i>, Rachid Makhloufi</p>
11:50 – 12:00	Break
<p>Online Session – 41 (in English) Head of Session: Asst. Prof. Dr. Latif Akcay</p>	
12:00 – 13:20	<p>Effects of Instagram Weddings on Financially Strains, Local Traditions, Stress, Unrealistic Expectations, Privacy Issues, and Digital Disconnect Among Youth of Pakistan <i>Ghulam Safdar*</i>, Mahnoor Bibi</p>
	<p>A Multifaceted Approach to Fault Diagnosis: Comparing Traditional and Deep Learning Methods <i>Ceren Asilkefeli*</i>, Fehmi Burcin Ozsoydan</p>
	<p>Convolutional Neural Network Application for Control Chart Pattern Recognition <i>Ceren Asilkefeli*</i>, Fehmi Burcin Ozsoydan</p>
	<p>Theoretical Investigations of Structural, Mechanical, and Elastic Properties of Novel Quaternary Heusler Alloys for Spin Polarized and Waste Heat Recycling Systems <i>Saadiya Benatmane*</i></p>
	<p>Design of Image Processing Accelerators for TTA Processors <i>Latif Akcay*</i>, Tugce Demirkol</p>
	<p>Enhancing the Performance of Twofish Cipher via Instruction Set Extension</p>

	<p><i><u>Latif Akcay</u></i><sup>*</sup>, <i>Mustafa Alptekin Engin</i></p> <p>Studying the Gender Gap in Advanced Digital Skills: Coding, Data Science, and Cybersecurity</p> <p><i><u>Anxhela Ferhataj</u></i><sup>*</sup>, <i>Fatmir Memaj</i></p> <p>resEARcher: A Sentence-Transformers Guided Tool for Visually Impaired Researchers</p> <p><i>Eylul Hickiran</i>, <i><u>Emrah Inan</u></i><sup>*</sup></p>
13:20 – 13:30	Break
<p>Online Session – 42 (in English)</p> <p>Head of Session: Assoc. Prof. Dr. Selahattin Kosunalp</p>	
13:30 – 14:50	<p>Effect of the Smagorinski Coefficient in LES Turbulence Model at Lateral Diversions</p> <p><i><u>Firat Gumgum</u></i><sup>*</sup></p>
	<p>Numerical Simulation of Investigating the Group Impact on Settlement in the Soft Soil Reinforced by Rigid Inclusions Under Seismic Loads</p> <p><i><u>Oussama Benmerabet</u></i><sup>*</sup>, <i>Salah Messioud</i></p>
	<p>Effect of Calcination Time and Temperature on the Pozzolanic Reactivity of Dam Sediment Slurry</p> <p><i><u>Hanaa Kawther Terrah</u></i><sup>*</sup>, <i>Zine El Abidine Kameche</i>, <i>Hocine Siad</i>, <i>Mohamed Lachemi</i>, <i>Youcef Houmadi</i></p>
	<p>Seismic Evaluation of an Existing Reinforced Concrete Building Based on FEMA P-2018 Methodology</p> <p><i><u>Atakan Emin Aksoy</u></i><sup>*</sup>, <i>Sadik Can Girgin</i>, <i>Ozgur Bozdog</i></p>
	<p>Experimental Study on the Mechanical Behaviour of Fiber Reinforced Sandy Soil</p> <p><i><u>Wiam Khebizi</u></i><sup>*</sup></p>
	<p>Enhancing Self-Compacting Concrete with Recycled Fine Aggregates and Polyethylene Terephthalate Fibers</p> <p><i><u>Meriem Bayah</u></i><sup>*</sup>, <i>Farid Debieb</i></p>
	<p>Synergistic Effect of Ground Granulated Blast-Furnace Slag and Metakaolin on the Performance of Recycled Self-Compacting Concrete</p> <p><i><u>Boubakeur Asmaa</u></i><sup>*</sup>, <i>Menadi Belkacem</i></p>
	<p>Impact of Particle Diameter and Flow Velocity on Particle Transport Behaviour in Saturated Soil</p> <p><i><u>Bouragaa Kheira</u></i><sup>*</sup>, <i>Bennacer Lyacine</i>, <i>Ahfir Nasre-Dine</i></p>
14:50 – 15:00	Break
<p>Online Session – 43 (in English)</p> <p>Head of Session: Dr. Nurhafizah Hasim</p>	
15:00 – 16:20	Effect of the Use of Plastic Waste as Sand on Concrete Properties

	<p><i>Wassila Boughamsa</i><sup>*</sup>, <i>Assia Abdelouahed</i>, <i>Houria Hebhoub</i>, <i>Wassila Mouats</i></p> <p>Study of the Durability of Sand Concrete Based with Wood Ash (0.1%, 0.2%, and 0.3%)</p> <p><i>Abdelouahed Assia</i><sup>*</sup>, <i>Mouats Wassila</i>, <i>Houria Hebhoub</i>, <i>Wassila Boughamsa</i>, <i>Toufik Sebbagh</i></p> <p>Comparative Study on the Valorization of Recycled Plastic Waste in the Formulation of Mortars</p> <p><i>Houria Hebhoub</i><sup>*</sup>, <i>Said Berdoudi</i>, <i>Wassila Boughamsa</i>, <i>Assia Abdelouahed</i>, <i>Wassila Mouats</i>, <i>Mohammed Ichem Benhalilou</i></p> <p>Fresh and Hardened Properties and Durability of Self-Compacting Repair Mortar Made with Ceramic Powder as Cement Substitute</p> <p><i>Messaouda Belouadah</i><sup>*</sup>, <i>Zine El Abidine Rahmouni</i>, <i>NadiaTebbal</i></p> <p>Enhancing Mechanical Strength of Concrete Through Polypropylene Fiber Incorporation</p> <p><i>Shiraz Baloch</i><sup>*</sup>, <i>Farah Naz</i>, <i>Umer Shahzad</i>, <i>Muhammad Abrar Faiz</i></p> <p>Identifying the Main Predictors for Job Satisfaction of Construction Workers: Hierarchical Regression Approach</p> <p><i>Gokhan Kazar</i><sup>*</sup></p> <p>A Comparative Study of Recycled Tire Chips, Jute Fiber, Polyester Fiber, Plastic Fiber Waste for Stabilizing Sand as Retaining Wall Backfill</p> <p><i>Lina Zaidi</i><sup>*</sup>, <i>Fatima Zohra Benamara</i>, <i>Aya Zelti</i>, <i>Issam Mesbahi</i>, <i>Atmane Zeghdi</i></p> <p>Thermal Deformation Model for Concrete Incorporating Silica Fume</p> <p><i>Farid Bouziadi</i><sup>*</sup>, <i>Touhami Tahenni</i>, <i>Abdelkader Haddi</i>, <i>Bensaid Boulekbache</i>, <i>Mostefa Hamrat</i></p>
16:20 – 16:30	Break
<p>Online Session – 44 (in English)</p> <p>Head of Session: Assoc. Prof. Dr. Selahattin Kosunalp</p>	
16:30 – 17:50	<p>Static Analysis of Sigmoid Functionally Graded Plates (S-FGM) by Using Higher Order Shear Deformation Plate Theory</p> <p><i>Habib Hebali</i><sup>*</sup></p> <p>Buckling response of Functionally Graded Plates Using a Novel Four Variable Refined Plate Theory</p> <p><i>Habib Hebali</i><sup>*</sup></p> <p>Using PET Plastic Flakes and Waste Tire Chips as Wall Backfill</p> <p><i>Fatima Zohra Benamara</i><sup>*</sup>, <i>Chiraz Kechkar</i>, <i>Marwa Feligha</i>, <i>Ghania Nigri</i>, <i>Lina Zaidi</i>, <i>Aya Zelti</i></p> <p>Study of the Behavior of A Clay Embankment Reinforced with Recycled Waste</p> <p><i>Aya Zelti</i><sup>*</sup>, <i>Fatima Zohra Benamara</i>, <i>Marwa Feligha</i>, <i>Lina Zaidi</i></p>

	<p>Improvement in Structural Analysis: Creation of a Rectangular Finite Element for Analyzing Membrane Structures <i>Randa Bourenane*</i>, <i>Sifeddine Abderrahmani</i>, <i>Abdulrahman Mutahar Al-Nadhari</i></p>
	<p>Acid and Sulfate Resistance of Concrete Containing Recycled Aggregate: A Comprehensive Experimental Study <i>H. Alperen Bulut*</i></p>
	<p>Effect of Granite Waste on Concrete Performance <i>Ramdane Rihab*</i>, <i>Kherraf Leila</i></p>
	<p>Numerical Study of the Seismic Bearing Capacity of Offshore Skirted Foundations on Sand Using Finite Element Limit Analysis <i>Alaoua Bouaicha*</i>, <i>Abdeldjalil Chamekh</i>, <i>Nour El Islam Boumekik</i>, <i>Abdelhak Mabrouki</i></p>
17:50 – 18:00	Break
<p>Online Session – 45 (in English) Head of Session: Dr. Nurhafizah Hasim</p>	
18:00 – 19:20	<p>Numerical Analysis of the Seismic Bearing Capacity of Strip Footings Near a Frictional Soil Slope <i>Abdeldjalil Chamekh*</i>, <i>Alaoua Bouaicha</i>, <i>Abderraouf Messai</i></p>
	<p>3D Failure Envelopes of Strip Footings on Sand over Non-Homogeneous Clay Using Limit Analysis Method <i>Alaoua Bouaicha*</i></p>
	<p>Prediction of the Maximum Shear Strength of Fiber-Reinforced Soils Using Artificial Intelligence <i>Leyla Bouaricha*</i>, <i>Yasmine Mohamed Bouteben</i>, <i>Azeddine Chehat</i>, <i>Ahmed Djafar Henni</i></p>
	<p>Implementation of Five-Noded Mapped Infinite Element to OpenSees <i>Sefa Uzun*</i>, <i>Yusuf Ayyaz</i></p>
	<p>Thermal Properties and Microstructure Investigation of Sustainable Self-Compacting Concrete-Based Coal Bottom Ash Aggregate <i>Ibtissam Boulahya*</i>, <i>Abdelkadir Makani</i>, <i>Ahmed Taфраoui</i></p>
	<p>Effect of Thermal Gradient on the Initial Stiffness of End-Plate Beam-Column Connections Exposed to Fire <i>Yasmina Douah*</i>, <i>Anis Abidelah</i>, <i>Hichem Rakib Sebbagh</i>, <i>Djamel Eddin Kerdal</i>, <i>Abdelhamid Bouchair</i></p>
	<p>Numerical Analysis of the Static and Cyclic Behavior of a T-Stub Steel Connection <i>Mohammed Mokhtar Fekir*</i>, <i>Hichem Rakib Sebbagh</i>, <i>Anis Abidelah</i>, <i>Abdelhamid Bouchair</i>, <i>Djamel Eddine Kerdal</i></p>

	Numerical Study to Optimize the Best Locations for Building a New Tunnel Next to the Old One by Two Behaviors the Mohr-Coulomb and Drucker-Prager <i>Taleb Hosni Abderrahmane*</i> , <i>Guemidi Ismahene</i>
19:20 – 19:30	Break
Online Session – 46 (in English) Head of Session: Dr. Nurhafizah Hasim	
19:30 – 20:50	Parameter Estimation for a Mechanistic Model of Cell Population Damage from High-Dose Irradiation Using Nelder-Mead Simplex and Particle Swarm Optimization <i>Nabil Haazim Mohd Amirrudin*</i> , <i>Fuaada Mohd Siam</i>
	A Collocation Approach for Solving Space Fractional Partial Differential Equations Using Generalized Lucas Polynomials <i>Zineb Laouar*</i> , <i>Nouria Arar</i>
	Study of the Influence of Grinding on the Characteristics of Natural Phosphate Mining in Kef Esnoun (Algeria) <i>Hadda Rezzag*</i> , <i>Amina Grairia</i> , <i>Saida Bouyegh</i> , <i>Samira Tlili</i> , <i>Lynda Bahloul</i>
	Modeling of the Working Flow Propagation in the Well Ejection System Flow Part <i>Denys Panevnyk*</i>
	Design of Ring Yarn Structures: Physical-Mechanical Properties of Different Yarns for Improved Sustainability and Performance <i>Ivana Salopek Čubrić*</i>
	Assessment of Material Sensory Properties: Focus on bipolar attributes of Stiffness-Softness and Roughness-Smoothness <i>Ivana Salopek Čubrić</i> , <i>Goran Čubrić*</i>
	Artificial Hydrophobic Surfaces Based on MgO Thin Film: Elaboration and Characterization <i>Zehira Belamri*</i>
	Exergy Analysis of Combined Cooling, Heating, and Power Systems Integrated with Carbon Capture and Storage for an LNG Carrier <i>Engin Guler</i> , <i>Selma Ergin*</i>

**Virtual Hall 3**

Online Session – 47 Head of Session: Assoc. Prof. Dr. Selahattin Kosunalp	
09:00 – 10:20	Potential Use of Materials Based on Alginate Beads for Treating Contaminated Water <i>Dhirar Ben Salem*</i> , <i>Amel Riah</i>
	Carbon Nanostructured as an Efficient Adsorbent for High Concentrations of



	<p>Crystal Violet Removal <i>Amel Riah*</i>, <i>Salim Bousba</i></p>
	<p>Lead (Pb) Pollution: A Food Safety Issue <i>Mahmood Ur Rahman*</i></p>
	<p>Exploring the Adsorption Capacities of Olive Mill Solid Waste Biochar for Polyphenols: Experimental Optimization and DFT/B3LYP Analysis <i>Imad Rabichi*</i>, <i>Kawtar Ezzahi</i>, <i>Abdelrani Yaacoubi</i>, <i>Abdelaziz Bacaoui</i>, <i>Mohamed Hafidi</i>, <i>Loubna Elfels</i></p>
	<p>Removal of Total Phenols from Olive-Mill Wastewater Using an Agricultural By-Product, Olive Stone <i>Kawtar Ezzahi*</i>, <i>Imad Rabichi</i>, <i>Abdelghani Yaacoubi</i>, <i>Abdelaziz Bacaoui</i>, <i>Rachid Idouhli</i>, <i>Nabil Rochdi</i>, <i>Mohamed Hafidi</i>, <i>Loubna El Fels</i></p>
	<p>Extraction of Phosphocalcic Biomaterial from the Animals Bones Bio-Waste <i>Saida Bouyegh*</i>, <i>Sabrina Ladjama</i>, <i>Hadda Rezzag</i>, <i>Sihem Benayache</i>, <i>Samira Tlili</i></p>
	<p>Synthesis and Characterisation of Hybrid Membranes for Removal of Rhodamine B <i>Amina Aoues*</i>, <i>Ouarda Merdoud</i>, <i>Mohamed Oualid Boulakradeche</i>, <i>Djamal Abdessemed</i>, <i>Omar Arous</i></p>
	<p>Numerical Assessment of Seismic Behavior in Earth Dams: A Case Study of Fontaine Gazelles Dam, Biskra, Algeria <i>Alaoua Bouaicha*</i></p>
10:20 – 10:30	Break
<p>Online Session – 48 (in English) Head of Session: Assoc. Prof. Dr. Selahattin Kosunalp</p>	
10:30 – 11:50	<p>Isocratic High-Performance Liquid Chromatographic Separation and Determination of Elution Order of Some Quinolone's Enantiomers via Cellulose-Amylose as Chiral Selector <i>Mohamed Nadjib Rebizi*</i></p>
	<p>Evaluation of the Photophysical and Photodynamic Properties of Carbon Quantum Dots Obtained from Plant Extracts <i>Martín Lemos Vilches*</i>, <i>Cristian Lillo</i>, <i>Jorge Montanari</i></p>
	<p>X-Ray Scans Super-Resolution with a Novel Hierarchical Multi-Scale Attention Network <i>Rania Saoudi*</i>, <i>Djameleddine Boudechiche</i>, <i>Zoubeida Messali</i></p>
	<p>Traditional Phytotherapeutic Practices in the South-Eastern Anti-Atlas Mountains: An Ethnobotanical Survey of Medicinal Flora in Iznaguen, Morocco <i>Younesse El-Ouazzani*</i>, <i>Fouad Msanda</i>, <i>Khalil Cherifi</i></p>
	<p>Preparation and Evaluation of Dermatological Gel Based on Aromatic and Medicinal Plant Extracts</p>

	<p><i><u>Fouzia Benoudjit</u></i><sup>*</sup>, <i>Imene Hamoudi, Asmaa Aboulouz</i></p> <p>Electrochemical Exfoliation and Characterization of Graphene for Symmetric Supercapacitors: A Comprehensive Study</p> <p><i><u>Abdelmalik Zemieche</u></i><sup>*</sup>, <i>Loubna Chetibi, Djamel Hamana, Slimane Achour</i></p> <p>Contribution to the Study of Microstructural Properties of Quasicrystals in AlCuFe Alloys</p> <p><i><u>Wafa Boumechta</u></i><sup>*</sup>, <i>Moussa Zahzouh</i></p> <p>Resonance Study of FGM Shells Reinforced with Carbon Nanotubes</p> <p><i><u>Zakia Hammou</u></i><sup>*</sup>, <i>Zakia Guezzen, Zouaoui Sereir, Yamna Hammou</i></p>
11:50 – 12:00	Break
<p>Online Session – 49 (in English)</p> <p>Head of Session: Assoc. Prof. Dr. Selahattin Kosunalp</p>	
12:00 – 13:20	<p>Research Trends in the Use of ChatGPT in Education: A Bibliometric Analysis</p> <p><i><u>Mehmet Donmez</u></i><sup>*</sup></p> <p>Decentralized Collaborative Multi-Agent Reinforcement Learning for Air Attack Scenarios</p> <p><i><u>Berire Gunduz</u></i><sup>*</sup>, <i>Mehmet Dikmen</i></p> <p>Phenotypic and Technological Characterization of Lactic Acid Bacteria Isolated from Algerian Artisanal Dairy Products</p> <p><i><u>Roumaissaa Belkacem</u></i><sup>*</sup>, <i>Qada Benameur</i></p> <p>Contribution of Lorentz Force in Cathode/Arc Coupling During TIG Welding</p> <p><i><u>Merazi Sayah</u></i><sup>*</sup>, <i>Leila Belgacem</i></p> <p>Structural, Morphological, and Optical Properties of Zinc Oxide Prepared by Sol-Gel Method</p> <p><i><u>Khemissi Lahouel</u></i><sup>*</sup>, <i>Meriem Gasmi, Saida Hoggas, Sabiha Hakkar</i></p> <p>Effect of Extract Concentration on Green Synthesis of Silver Nanoparticles</p> <p><i><u>Roufaida Aissa Brahim</u></i><sup>*</sup>, <i>Hadjer Mabrouki, Djamel-Eddine Akretche</i></p> <p>The Methode of Adobe in Building</p> <p><i><u>Hammache Soumia</u></i><sup>*</sup></p> <p>CBD-Loaded Lipid-Based Nanoparticles for Topical Application Against Skin Cancer</p> <p><i><u>Ana Paula Sanguinetti</u></i><sup>*</sup>, <i>Mirian Scavone, Magali Di Meglio, Pablo Raies, Paulo Maffia, Jorge Montanari, Maria Natalia Calienni</i></p>
13:20 – 13:30	Break
<p>Online Session – 50 (in English)</p> <p>Head of Session: Dr. Nurhafizah Hasim</p>	
13:30 – 14:50	<p>Spatial Analysis of Soil Heavy Metals Based on Geostatistical Approach in the North of Iraq</p>

	<p><u>Mohammed Oday Al Hamdani</u><sup>*</sup>, <u>Ali Volkan Bilgili</u>, <u>Sureyya Betul Rufaioglu</u></p> <p>A New Approach for the Degradation By-Products Pesticide Detection in Trace Level</p> <p><u>Chemseddine Zekkaoui</u><sup>*</sup>, <u>Tarek Berrama</u>, <u>Salima Dadou</u>, <u>Assia Beriber</u>, <u>Nassime Doufene</u>, <u>Kadmi Yassine</u></p> <p>Application of Doehlert Design Experimental Methodology for the Optimal Emerging Pollutant Degradation with Fenton Process</p> <p><u>Chemseddine Zekkaoui</u><sup>*</sup>, <u>Tarek Berrama</u>, <u>Salima Dadou</u>, <u>Assia Beriber</u>, <u>Nassime Doufene</u>, <u>Kadmi Yassine</u></p> <p>Optimization by the Surface Response Methodology of a Fenton Like Process by CrVI of an Anthraquinonic Dye Type Green Acid 25</p> <p><u>Benidris Elbatoul</u><sup>*</sup>, <u>Slamani Samira</u>, <u>Hachemi Chaimaa</u>, <u>Abdelmalek Fatiha</u>, <u>Ghezzar Mouffek Redouane</u></p> <p>Pellets from Olive Mill Waste: Densification and Characterization for Sustainable Waste Management Solutions</p> <p><u>Zaina Izghri</u><sup>*</sup>, <u>Fatima Ezzahra Yaacoubi</u>, <u>Chaima Sekkouri</u>, <u>Imad Rabichi</u>, <u>Abdelaziz Ounas</u>, <u>Karima Ennaciri</u>, <u>Abdelaziz Bacaoui</u>, <u>Abdelrani Yaacoubi</u></p> <p>Microplastic Pollution in Surface Waters of Ergene River: Sources and Spread</p> <p><u>Enes Ozgenc</u><sup>*</sup>, <u>Gunay Yildiz Tore</u>, <u>Erdi Bulus</u>, <u>Yesim Muge Sahin</u></p> <p>Diatomite Formation Associated with Sogucak Pyroclastics (Sandikli, Türkiye)</p> <p><u>Bala Ekinici Sans</u><sup>*</sup>, <u>Zeynep Doner</u></p> <p>Effects of Titanium Dioxide on the Ultrasonic and Structural Properties of Zinc–Strontium–Lithium Phosphate Glass</p> <p><u>Nurhafizah Hasim</u><sup>*</sup>, <u>Nur Hidayah Ahmad</u>, <u>Nur Asilah Zulkifeli</u>, <u>Anis Nazihah Mat Daud</u></p>
14:50 – 15:00	Break
<p>Online Session – 51 (in English)</p> <p>Head of Session: Assoc. Prof. Dr. Yunus Kaya</p>	
15:00 – 16:40	<p>Strategic Coordination of P2P Energy Trading in Smart Microgrids</p> <p><u>Kubra Nur Sahin</u><sup>*</sup>, <u>Muhammed Sutcu</u></p> <p>Advancing Turkish-to-English Translation: A Transformer-Based Neural Model Approach</p> <p><u>Nurzhan Amantay</u><sup>*</sup>, <u>Yasin Ortakci</u></p> <p>Contribution to the Application of Condition Maintenance for Followed and Diagnostic Breakdowns of a Rotating Machine</p> <p><u>Naima Tamaloussi</u><sup>*</sup>, <u>Lamia Benzaid</u>, <u>Zina Azzez</u>, <u>Azzedine Bouzaouit</u></p> <p>Recycling of Urban Waste in the Manufacture of Concretes</p> <p><u>Ben Khadda Ben Ammar</u><sup>*</sup></p>

	An Artificial Neural Network-Based Microwave Technique for Bianisotropic Materials Electromagnetic Property Extraction <i>Mehmet Akif Ozkaya*</i> , <i>Ugur Cem Hasar</i>
	Improved Propagation Constant Determination Using Two-Line Measurements <i>Ugur Cem Hasar*</i> , <i>Husain Ali</i>
	Increasing the Reflection Parameter in Microstrip Patch Antennas by Trying Different Shapes <i>Hamdullah Ozturk*</i>
	A Study on General Safety Precautions Against Electrical Accidents in Daily Life <i>Yunus Kaya*</i> , <i>Selahattin Kosunalp</i>
	VO2 Based Adaptive Wideband THz Metamaterial Absorber <i>Merve Kurt*</i> , <i>Gokhan Ozturk</i>
	The Impact of Telework on Gender Equality and Occupational Health <i>Mustafa Ozdemir*</i>

\* : Corresponding Author

\_ : Presenter

### Summary of Sessions

<b>Friday, July 19, 2024</b>		
<i>Conference Hall</i>	<i>Virtual Hall 1</i>	<i>Virtual Hall 2</i>
Opening Session	Online Session – 1	Online Session – 6
Onsite Session – 1	Online Session – 2	Online Session – 7
Onsite Session – 2	Online Session – 3	Online Session – 8
Onsite Session – 3	Online Session – 4	Online Session – 9
Onsite Session – 4	Online Session – 5	Online Session – 10
Onsite Session – 5		
<b>Saturday, July 20, 2024</b>		
<i>Virtual Hall 1</i>	<i>Virtual Hall 2</i>	<i>Virtual Hall 3</i>
Online Session – 11	Online Session – 19	Online Session – 27
Online Session – 12	Online Session – 20	Online Session – 28
Online Session – 13	Online Session – 21	Online Session – 29
Online Session – 14	Online Session – 22	Online Session – 30
Online Session – 15	Online Session – 23	
Online Session – 16	Online Session – 24	
Online Session – 17	Online Session – 25	
Online Session – 18	Online Session – 26	
<b>Sunday, July 21, 2024</b>		

<i>Virtual Hall 1</i>	<i>Virtual Hall 2</i>	<i>Virtual Hall 3</i>
Online Session – 31	Online Session – 39	Online Session – 47
Online Session – 32	Online Session – 40	Online Session – 48
Online Session – 33	Online Session – 41	Online Session – 49
Online Session – 34	Online Session – 42	Online Session – 50
Online Session – 35	Online Session – 43	Online Session – 51
Online Session – 36	Online Session – 44	
Online Session – 37	Online Session – 45	
Online Session – 38	Online Session – 46	

## CONTENTS

### Invited Speakers

Materials for Eco-Design Strategies for an Innovative Industry <i>Rodrigo Martins, Suman Nandy, Pedro Barquinha, Luís Pereira1, Tomás Pinheiro, Henrique Almeida, Rui Igreja, Emanuel Carlos, Elvira Fortunato</i>	1
Emerging Nanotechnologies for Targeting Antimicrobial Resistance: A Special Focus on Chronic Wound Healing <i>Saravanan Muthupandian</i>	2
Carbon Based Electrode for Gas Sensor <i>Mohd Nizar Hamidon, Azlinda Abu Bakar, Mohd Hanif Yaacob, Wan Nursheila Wan Jusoh, Suriati Paiman, Haslina Jaafar, Intan Helina Hassan</i>	3
Vismodegib and Skin: The Challenge of Changing the Administration of an Anticancer Drug with Nanotechnology <i>Jorge Montanari, M. Natalia Calienni</i>	4
Evolutionary Trends in RACH Access Techniques Towards a 5G Cellular <i>Lawal Mohammed Bello</i>	5
Integration of Existing Control Systems to the Requirements and Principles of Industry 4.0 <i>Dimitar Totev</i>	6
Deployment of Carbon Based Nanomaterials for Gas Sensing Applications <i>Zainab Yunusa, Mohd Nizar Hamidon</i>	7
Health Implications of Glycation products in Diabetes and Its Secondary Complications <i>Ahmad Ali</i>	8

### Oral Presentations

Investigation of the Morphological Structures of PVDF-HFP Flat Sheet Membranes Prepared with Different Concentrations of DMAC/DMF Solvents and Their Performance in DCMD System <i>Ayse Diskaya, Ahmet Bora Yavuz, Osman Nuri Ata</i>	9
Efficiencies of FePd Nanoparticles in Basic Red 46 Removal <i>Fatma Guclu, Melike Sevim</i>	16
Study of the Photoreduction of Co <sup>2+</sup> Ions Under Solar and Visible Light Irradiation <i>Samira Tebani, Lila Kerrai, Samir Ladjali</i>	17
The Use of Glass and Other Alternative Materials in the Cement Industry <i>Damir Mulamehmedovic, Zehrudin Osmanović, Ervin Karic, Belmina Hadžalic, Elma Bajric</i>	18
Kinetics and Thermodynamics of Thermal Decomposition of Medlar Seed by TG/DTG <i>Zelal Koyuncu, Meltem Kizilca Coruh</i>	26
Investigation of Kinetic and Thermodynamic Properties in Response to Thermal Degradation of Ligno-Cellulosic Mixture Prepared from Grape, Pomegranate, and Rosehip Seeds	27

*Meltem Kizilca Coruh*

Application and Analysis of Experimental and Numerical Studies to the Film Cooling Turbine Blade	33
<i>Amar Berkache*, Rabah Dizene</i>	
Recent Trends on Low Pressure Carburizing Furnaces and Process	48
<i>Alper Kelesoglu, Semih Demirci, Beste Ozdeslik</i>	
Evaluation of Spectral Efficiency (SE) and Energy Efficiency (EE) of 5G Green Networks Using Soft Computing	49
<i>Mahmood Subhi Hussein Sahar, Koksal Erenturk</i>	
Market Shelf Products Detection and Recognition Using YOLO, Faster R-CNN, and SSD Mobilenet	53
<i>Alaa Mohamed Jamel Abdulqader Mawlawi</i>	
Energy Efficiency Evaluation of 5G Radio Access Networks Using Fuzzy Logic and ANFIS	57
<i>Mohammed Imad Adil Salihi</i>	
Developing a Software System to Randomly Generate Problem Sets in a Data Analytics Course	61
<i>Ahmet Ozkul</i>	
Hysteresis Voltage and Current Control for Fuel Cell Fed Power Circuits	62
<i>Unal Yilmaz</i>	
Factors Influencing the Adoption of Electric Vehicles in the U.S.	69
<i>Serkan Varol, Taylor Ransom</i>	
Experimental Study of Failures of Air Conditioners System Tram in Desert Areas by Applying Preventive Maintenance (Using FEMA and Reliability Lows)	70
<i>Khaled Lemnaouer, Messaoud Louafi, Zoubir Aoulmi, Rabie Karek, Mounia Taleb</i>	
Design of a Low-Profile Metasurface-Based Linear Polarization Converter and RCS Reduction Using This Converter Design	71
<i>Yunus Kaya</i>	
Evaluation of Short-Term Traffic Flow Prediction Approaches in Transportation	76
<i>Selahattin Kosunalp, Yunus Kaya</i>	
MnCo <sub>2</sub> O <sub>4</sub> Modified Flexible Graphene Paper for Electrochemical Sensing of Paracetamol	82
<i>Murad Shafiyev, Ezgi Topcu, Elif Ercaikci, Kader Dagci Kiransan</i>	
Investigation of the Cleanability of High Ash Asphaltite Sample Using the Oil Agglomeration Method	83
<i>Oyku Bilgin</i>	
Hydrogen Evolution Reaction on MoO <sub>3</sub> Decorated-CuBi <sub>2</sub> O <sub>4</sub> /Reduced Graphene Oxide Nanocomposite	88
<i>Zeynep Orhan, Hulya Ozturk Dogan</i>	
Flow and Heat Characteristics over Ellipse in the in-Duct Flow	91
<i>Neslihan Aydin</i>	

Risk Factor Estimation with Ordered Logit and Ordered Probit Models <i>Burcu Durmus, Oznur Isci Guneri, Aynur Incekirik</i>	97
Effect of $\alpha$ -Fe <sub>2</sub> O <sub>3</sub> on Gas Detection Performance of MgO Thin Films <i>Hilal Kubra Saglam, Sevda Saritas</i>	98
Analysis of Quality Risks on the Assembly Line in an Armature Manufacturing Company Using FMEA Method <i>Fatma Merve Bayir Kanbur, Hasan Selim</i>	99
A Study on the Effects of Electromagnetic Fields <i>Yunus Kaya, Selahattin Kosunalp</i>	100
Anticancer Activity of Acetaminophen-Platinum (II) Complex Against ER-Positive Breast Cancer <i>Mustafa Tugfan Bilkan, Meric Arda Esmekaya, Nurhan Ozdemir</i>	106
Impregnation of Wood Material with Magnesium Chloride (MgCl <sub>2</sub> ) and Determination of Leaching Properties <i>Melek Yilmaz Yasbek, Mehmet Yeniocak</i>	107
Determination of Reservoir Water Level by Classical and Artificial Intelligence Methods <i>Sema Karahan, Zeyneb Kilic</i>	115
Historical Environments Affected by the Earthquake in Kahramanmaraş City Center and Restoration Suggestions <i>Hatice Dokme, Sinan Kordon</i>	116
The Sociological Benefits of Green Infrastructure Systems: Inclusive and Healthy Cities for Communities <i>Esra Tan, Sinan Kordon</i>	117
Traditional Uses of Medicinal Plants Naturally Distributed in Yerkesik Basin (Mentesi-Mugla) <i>Kenan Akbas</i>	123
Vegetative Anatomy of Two Endemic <i>Muscari</i> L. Species in Türkiye <i>Dudu Ozlem Mavi Idman, Huseyin Guldal, Ali Gercek, Huseyin Eroglu</i>	129
Kombucha-Derived Bacterial Cellulose Production with Herbal Tea and Different Coffee Combinations <i>Nazli Neval Sahin, Nermin Hande Avcioğlu</i>	130
Evaluation of Gene Expression Levels of Antimicrobial Peptides (MsDef1 And MsSN1) from M. Sativa Sazova Cultivar During 21-Day Period <i>Busra Albayrak Turgut</i>	131
Investigation of the Effect of Chemical Additives on Performance in the Deep Mixing Method with Model Experiments <i>Yunus Emre Colak, Sukru Ozcobañ, Mustafa Mert</i>	135
Investigation of the Structure-Pile-Soil Interaction Behaviour in Earthquake Condition of a Reinforced Concrete Building with Pile Foundation	140



*Evrin Er, Sami Oguzhan Akbas*

Determination of Risk Factors within the Scope of Water Supply Management in Water Transmission Systems 141

*Yusuf Kilinc, Cansu Bozkurt, Mahmut Firat*

Defining the Impact Levels of Risk Factors in Water Transmission Systems 147

*Yusuf Kilinc, Cansu Bozkurt, Mahmut Firat*

Determination of Regional Earthquake Risk Distribution of Buildings in the Central Gencosman Neighborhood of Bayburt Province 152

*Omer Can, Ertekin Oztekin, Omer Bayrak*

Use of Bayburt White Stone Waste and Paper Mill Waste Lignin as a Plasticizer/Air-Entraining Concrete Additive in the Production of Carrier and Non-Carrier Lightweight Concrete 161

*Omer Bayrak, Emin Erdem*

An Innovative Method of Getting Impactive Ideas 168

*Leyla Erkol, Murat Arslanoglu, Sevilay Sagtan, Fatih Cagirankaya, Ali Yazgan*

Preservation Issues and Recommendations for Traditional Housings in Urban Centers: The cases from Corum, Turkey 174

*Furkan Karahan, Emine Saka Akin*

Crashworthiness Design and Damage Analysis with Multiple Internal Structure Pattern 186

*Hakan Burcin Erdogus*

Analysis of Diesel/Bio-Oil Blends Produced by Co-Pyrolysis of Spruce with Glycerol 187

*Ahmet Rasim Girisen, Hakan Ozcan*

Investigation of Oxidative Stability Behavior of Kaolin Nanoparticles Doped Bio-Based Palm Lubricants 195

*Batuhan Ozakin, Kursat Gultekin, Nalan Turkoz Karakullukcu*

Production of 3D Woven Textile Composites and Investigation of Their Impact Performance 201

*Serkan Erdem, Mete Onur Kaman*

Evaluation of the Tribological Performance of AA 6061 Coated with Polyurethane/Ti6Al4V Composite 207

*Yusuf Burak Bozkurt*

Numerical Simulation Study of Curvature Radius on the Flexibility and Stress Distribution in Hyperelastic Materials 208

*Galip Yilmaz*

Creation of a Digital Twin for Remote Fault Detection of a CNC Machine 216

*Cemal Pamukcu, Numan Dogruay, Abdulsamed Tabak*

Design and Analysis of Lightweight 3D-Printed Lattice Structures Using Fused Deposition Modelling 222

*Turker Turkoglu*

Numerical Investigation of Heat Transfer Performances in Spiral Dimpled Pipe Profiles 223

*Anil Aykut, Veysel Ozceyhan*

Natural Fibers: A Sustainable Alternative for Composite Reinforcements 224

*Mehmet Cagri Tuzemen*

Structural Analysis of Hopper Support Frame of Vacuum Road Sweeping Vehicle on Truck Mounted 225

*Onur Can Kirit, Vedat Fetullahoglu*

Use of Hardox 500 Tuf in Tippers 231

*Resul Akcali, Akin Zengin, Mustafa Yilmaz*

Structural Analysis of Safety Leg on the Vacuum Road Sweeper Mounted on Truck 239

*Omer Coskun, Vedat Fetullahoglu*

An Approximate Q-Learning Approach to the Dynamic Pricing and Inventory Control Problem of Perishable Products 244

*Tugce Yavuz, Onur Kaya*

Optimizing Workforce and Sub-Lot Scheduling in Seru Production Systems 245

*Beren Gursoy Yilmaz, Emre Cevikcan, Omer Faruk Yilmaz*

Development of Beneficiation Flow Diagram of Malatya-Kuluncak Rare Earth Oxide (NTO) Ore 254

*Gafure Ersever Angur*

$A_\alpha$  – Statistical Limit Superior and Limit Inferior via Ideals 255

*Mustafa Gulfirat*

Certain Aspects of Weak Statistical Convergence via Ideals 256

*Mustafa Gulfirat*

Investigation of the Conductivity Mechanismus of ZnO/C<sub>10</sub>H<sub>10</sub>N<sub>2</sub> pn Heterojunction Produced by Spin Coating Method 257

*Ramazan Demir*

A Review of Using of Geopolymers -As an Immobilization Matrix- on Radioactive Waste Management 258

*Furkan Cinar, Sema Akyil Erenturk*

Recovery of Critical Metals from Spent Li-Ion Batteries by Deep Eutectic Solvents (DESs) as Green Approach 266

*Ceren Erust*

Different Machine Learning Models with Mushroom Comparision 267

*Idil Sila Gonenc, Muhammet Cakmak*

Factors Affecting Deterioration of Wall Paintings 268

*Ozge Karadeniz, Evin Caner*

Correlation Analysis with the Help of Vector 269

*Ramazan Simsek*

Grape Puree-Added and Freeze-Dried Yoghurt Drops: Enumeration of Lactic Acid Bacteria 270

and Determination of Some Physical Properties

*Sebahat Oztekin*

Contamination by Pesticides of Water and Health Using Artificial Neural Networks 274

*Benzidane Chahrazed, Bouharati Khawla, Fenni Mouhamed*

Nutrient-Rich Biofertilizers: The Role of Spirulina Sp and Microalgae in Soil Health Enhancement 275

*Charef Nassira, Tamer Fatma Zohra, Saada Zakia, Belaid Boutheina, Bougueroua Karima, Elleuch Jihen, Nasri Hichem*

Growth Control of Cyanobacteria and Cyanotoxins by Biological Methods 276

*Tamer Fatma Zohra, Charef Nassira, Nasri Hichem*

Spirulina Sp - Cultivation, Production, and Applications 277

*Saada Zakia, Charef Nassira, Tamer Fatma Zohra, Belaid Bouthaina, Elleuch Jihen, Nasri Hichem*

Conditions for Culture and Valorization of Microcystis Cyanobacteria 278

*Saada Zakia, Charef Nassira, Tamer Fatma Zohra, Belaid Bouthaina, Elleuch Jihen, Nasri Hichem*

In Vitro Antioxidant and Anti-Hemolytic Effect of Algerian *Centaurea Calcitrapa* L. Extracts 279

*Krache Imane, Trabsa Hayat, Boussoualim Naouel, Arrar Lekhmici, Baghiani Abderrahman*

Canopy Dynamics in the Bissa Forest: Chlef, West Algeria 280

*Fatima Belhacini, Djamel Anteur, Faycal Tsourly, Djahida Hedidi*

Biocontrol of Gray Mould in Strawberries with Pectin-Based Coatings Incorporated with Yarrow (*Achillea Millefolium* L.) Extract 281

*Sebahat Oztekin*

Lyophilized Strawberry Slices with Various Thicknesses and Investigation of Their Drying Characteristics 285

*Erman Kadir Oztekin, Sebahat Oztekin*

Antibiotic Resistance Pattern of Pseudomonas Sp in Tilapia Fish *Oreochromis* Sp, and Aquarium Water 290

*Romeissa Derdachi, Sabrina Boucetta*

Sample Preparation for Soil Analysis of an Endangered Species in the Sidi Bel Abbes Region (North West Algeria) 291

*Mounir Chihab\*, Ali Khalifa*

Comparative Study of the Effect of Two Irrigation Methods (Drip and Submersion) on the Behavior of Two Varieties of Olive Trees (*Olea Europaea* L) in the Semi-Arid Zone of Bordj-Bou-Argeridj 292

*Faycal Bahlouli\*, Hamza Belguerri, Nacira Chourghal, Amel Salamani, Mouhamed Benaini, Khelifa Maamri, Fairouz Mihoubi, Aicha Cherroua, Younes Atek, Fares Aissat*

Estimating Aphid Parasitoid Diversity in Guelma's Citrus Orchards, Eastern Algeria 300

*Omar Khaladi, Amira Bouderbala*

Egg Quality Characteristics of Local Laying Hens in Oasis Family Farms of Adrar (Algeria) 301  
*Abderrahmen Boubekour, Mohammed Bouallala, Redhwen Bari, Mohammed Souddi*

Impact of *Thymus Vulgaris* and *Lavandula Angustifolia* Essential Oils on the Carcass 302  
Characteristics of Broiler Chickens  
*Benameur Qada, Laah Jude Attat, Sidi Faruk, Kassous Tahar, Arabi Abed*

Effect of an Essential Oils Mixture on the Growth Performance of Broiler Chickens 303  
*Laah Jude Attat, Benameur Qada, Sidi Faruk, Kassous Tahar, Arabi Abed*

Comparative Study of the Biogas Yield of Three Olive Mill Wastewater in the Thermophilic 304  
Phase  
*Bani Kheiredine, Amrouci Zahra, Belmili Zineb, Ghetahem Dalal*

Enhancing the Quality of PET Images Reconstructed by Filtered Back Projection and Ordered 305  
Subsets Expectation Maximization  
*Benyelles Asma, Korti Amel*

Artificial Intelligence in Camel Racing: Health Maintenance and Prevention 306  
*Amira Djeddou Benabid, Hind Houssou, Khaled Djeddi, Dounia Ouachtati*

Antimicrobial Profile of Asian Honey Bee Using Culture Dependent Method 307  
*Iram Liaqat*

Medical Image Analysis Using Neural Networks 308  
*Berrimi Fella*

Exploring the Potential of the Genus *Achillea* on Antiproliferative and Apoptotic Effects of 309  
Human Cancer Cell Lines  
*Renda Chahna*

Study and Prevention of Occupational Risks (Case of the Elmalabiod Cement Plant) 310  
*Taleb Mounia*

Effectiveness of Aeration Followed by Statistical Optimization of AOP'S 311  
(Ultraviolet/Ultrasonic Active Persulfate/Hydrogen Peroxide) Process Parameters for the  
Treatment of Young Landfill Leachate  
*Hamza Bellouk, Ilham Zouitane, Imane El Mrabet, Naima El Ghachtouli, Hicham Zaitan*

Sono-Pyrolysis of Methane for Enhanced Hydrogen Production 312  
*Aissa Dehane, Slimane Merouani, Atef Chibani*

Photodegradation of Metobromuron by a Photo-Fenton Like Process Using Fe(III)-Picolinic 313  
Acid Complex as Catalyst in Aqueous Medium  
*Sellam Badreddine, Seraghni Nassira, Bouaziz Chaima, Sehili Tahar*

Photocatalytic Efficiency of Pure and Cu-Doped ZnO Thin Films 314  
*Khemissi Lahouel\*, Abdecharif Boumaza, Meriem Gasmi*

Exploring the Structural, Optical, and Surface Characteristics of NiO Thin Film for 315  
Environmental Applications

*Meriem Gasmı, Khemıssi Lahouel, Saida Hoggas, Sabıha Hakkar*

Voltametric and Molecular Docking Investigations of Ferrocenylmethylaniline and Its N-Acetylated Derivative Interacting with DNA 316

*Asma Yahiaoui, Benyza Nabil, Amel Messai, Touhami Lanez, Elhafnaoui Lanez*

Response Surface Methodology Study of Corrosion Behavior in Presence of a Pharmaceutical Drug 317

*Naceur Benhadria, Tarik Attar, Abbes Benchadli, Esmā Choukchou-Braham*

Synthesis, Crystal Structure, Thermal Behavior, and Magnetic Study of 1D Cobalt (II) Coordination Polymer with Dinitrogen Tetrahydride as Bridging Ligand 318

*Safaa Hidaoui, Najlaa Hamdi, Michal Dusek, Nicola Morley, Mohammed Lachkar, Brahim El Bali*

Vibrational Spectroscopic Analysis of 2,6-Bis(4-Fluorophenyl)-3,3-Dimethylpiperidin-4-One (BFDP), DFT, and Molecular Docking Study 319

*Kheira Hammou, Mohamed Cherif Terkhi, Nourdine Boukabcha*

Elastic Anisotropies and Electronic Properties of Tetragonal Spinel  $\text{CuBi}_2\text{O}_4$ : A DFT Calculation 320

*Rania Charif, Rachid Makhloufi*

Investigation of the Effect of Membrane Type on Ammonia Formation from Ammonium Chloride and Sodium Chloride in Two-Compartment Bipolar Membrane Electrodialysis 321

*Fatemeh Abbasi, Duygu Adiguzel, Osman Nuri Ata*

Synthesis of Quinoxaline Containing Thiazole Moiety Derivative, Biological Activities, Docking Studies, and ADMET Analysis 326

*Anissa Boumati, Imane Idris, Omar Berradj*

Investigation into Mathematical Modeling of Light Naphtha Isomerization Using Bi-Functional Catalysts 327

*Boudjema Amir Lehtihet, Tayeb Fakhreddine Boukezoula, Lahcène Bencheikh*

Effects of Operating Parameters on the Crystallization Yield of Copper Sulfate: An Experimental Study 328

*Amira Boufrioua, Sarra Guilane, Leila Benmansour*

Exploring CA/CuO in Adsorption and Photocatalysis for Toxic Wastewater Treatment: Preparation, Mechanisms 329

*Oumnia Rayane Benkouachi, Abdallah Bougeuttoucha, Kamilia Madi*

Determination and Study of Pollution in Chemical Variables in Industrial Waste Water for the Concrete Factories 330

*Mohamed Nadjib Rebizi*

A Magnetic Field's Impact on a Spiral Porous Fin Exposed to Radiation and Convection 331

*Nadia Daradj, Bouaziz Mohamed Nadjib*

Investigation of the Applicability of Ni-P-Cu Coatings to the Expanded Graphite/PCM Composite Blocks Surfaces by Electrolysis 332

*Onur Guler, Mustafa Yusuf Yazici*

Modeling the Phenomenon of Degradation of a TK31 Centrifugal Compressor by Aleatory Processes 333

*Souhila Bouleghlem, Naima Tamaloussi, Lamia Benzaid*

Challenges of Latent Heat Energy Storage for Energy Efficiency Enhancement 334

*Mohamed Tegggar*

Effect of Resin Coating on Mechanical Properties of 3D Printed Parts 335

*Abdurrahim Temiz, Fatih Huzeefe Ozturk*

Numerical Study of Magneto-Double-Diffusive Natural Convection of a Nanofluid Flowing in a Concentric Annular Space 340

*Nesrine Rachedi, Messaoud Guellal*

Preventive Maintenance of an Industrial Reciprocating Compressor by Oil Analysis 341

*Lamia Benzaid, Naima Tamaloussi, Toufik Sebah*

Flow Analysis for a Light Commercial Vehicle with a Vertical Axis Turbine Added for Power Generation 342

*Erman Kadir Oztekin*

Energy Consumption and Moisture Extraction Optimization in a Heat Pump Tumble Dryer 347

*Berkay Yilmaz, Mehmet Alper Sav, Yusuf Balsever*

Numerical Investigations on the Effect of Isothermal Multi-Jets in Air Curtains with LES Approach 348

*Sahnoun Rachid, Draï Ismail, Merouane Habib*

Numerical Study of Flow Around Counter Rotating Cylinder 349

*Draï Ismail, Sahnoun Rachid, Merouane Habib, Yahiaoui Tayeb*

The Effect of Bluff Body Geometry on the Combustion of CH<sub>4</sub>/Air 350

*Merouane Habib, Draï Ismail, Sahnoun Rachid*

Design and Implementation of an Intelligent Irrigation System 351

*Toufik Sebbagh, Islam Boukhadra*

The Production of Bamboo Based Natural Composite Materials and Comparison of Their Material Properties with Particleboard MDF Boards 352

*Ali Gumustekin, Sedat Ozden, Fehmi Nair*

Elastic Repair Analysis for the Interaction Between Two Semi-Elliptical Cracks in a Damaged Aeronautical Structure 358

*Belhamiani Mohamed, Bouzitouna Wahiba Nesrine, Oudad Wahid, Djebbar Nouredine*

Investigation of the Effects of a Heated Vest on Blood Pressure and Body Temperature of Male Individuals 359

*Emre Demirci, Erman Kadir Oztekin*

Microstructure Analysis of Ni-Mn-Ga Epitaxial Thin Films on MgO (100) 365

*Gizem Durak Yuzuak*

Effect of Using Phosphate Sludge in Geopolymerization: A Review <i>Nour El Houda Benghalem, Nadia Tebbal, Zine El Abidine Rahmouni, Mekki Maza</i>	366
Enhancing Mechanical Properties of Titanium Alloys Through Microstructural Control and Alloying Additions <i>Mohamed Boudiaf</i>	367
Synthesis of Iron Copper Binary Nanoparticles Based Phosphate and Application in Multi-Components Reaction <i>Berrichi Amina, Bachir Redouane</i>	368
Innovative Hybrid Systems for Improving Organic Solar Cells: Encapsulation of Organic Molecules in Carbon and Boron Phosphide Nanotubes <i>Soufiane Elhadfi, Jamal Chenouf, Brahim Fakrach, Hassane Chadli</i>	369
Unlocking the Potential of Waste Steel Fibers for Improving High-Performance Concrete <i>Rekia Zouini, Makani Abdelkadir, Tafraoui Ahmed</i>	370
Numerical Performance Simulation of a MoSe <sub>2</sub> -Based Solar Cell Using SCAPS-1D Simulator <i>M'hamed Semlal, Mohamed Khuili, Nejma Fazouan, El Houssine Atmani</i>	377
The Impact of the Alkali-Bleaching Treatment on the Isolation of Natural Cellulosic Fibers from <i>Juncus Effesus</i> L Plant <i>Mona Benali, Abdallah Oumekki, Jamil Toyir</i>	378
Noble Metal Nanomaterials in Biosensors <i>Adil Bouhadiche, Soulef Benghorieb</i>	379
Bound States of 2D Dirac Oscillator in the Deformed Space <i>Lakhdar Sek, Mokhtar Falek, Mustafa Moumni</i>	380
The Applied Physics for Electronic Systems: Detecting of Pollutant Gas Based Pure SnO <sub>2</sub> Semiconductors <i>Youssef Doubi, Bouchaib Hartiti, Maryam Siadat, Hicham Labrim, Mounia Tahri, Phillipe Thevenin</i>	381
Optimization for High-Efficient and More Stable RbGeI <sub>3</sub> Perovskite Solar Cells <i>Abdelkader Bouhenna, Kada Boualem, Nabil Beloufa, Soufi Hadjer, Aboubakr Seddik Kebaili</i>	382
Approximation Solutions of Time dependent Schrodinger Equation for Deng-Fan Potential Using the Nikiforov-Uvarov-Functional Analysis <i>Medjber Salim</i>	383
Conceptual Study of Surface Plasmon Resonance Sensor for Glucose Level Monitoring <i>Mohamed Esseddik Ouardi, Kada Abdelhafid Meradi, Fatima Tayeboun</i>	384
Comparative Study of Performance of Different Perovskite Solar Cells Based on Organic and Inorganic Thin Films <i>Riane Houaria, Bidi Sara, Boussaada Salah Eddine, Mouchaal Younes</i>	389
Evanescent Wave Coupling Surface Plasmon Resonance (SPR) Sensors <i>Fariza Hanim Suhailin</i>	390

Exploring the Optoelectronic Properties of NaAuF <sub>4</sub> : Insights and Applications <i>Ishak Mebarkia</i>	391
Exploring the Optical and Thermoelectric Properties of Eco-Friendly Perovskite Alloys for Solar Cell Applications <i>Lakhdar Benahmedi, Anissa Besbes, Redouane Djelti</i>	395
Probing the Electronic, Optical, and Transport Properties of Halide Double Perovskites Cs <sub>2</sub> AgSb(Cl,Br) <sub>6</sub> for Thermoelectric Applications <i>Hamza Kerrai, Ahmed Zaim, Mohamed Kerouad</i>	396
Computational Insights into the Superior Efficiency of K <sub>2</sub> (Se,Te)Br <sub>6</sub> Double Halide Perovskite Solar Cells <i>Hamza Kerrai, Ahmed Zaim, Mohamed Kerouad</i>	397
An Introduction to Carbon Nanotubes and Their Production Processes <i>Maryam Abdolahpour Salari, Gunay Merhan Muglu, Volkan Senay, Sevda Saritas</i>	398
Analyzing the Physical Properties of a Ternary Half-Heusler RhTiP for Industrial Applications <i>Aya Righi, Fatima Bendahma, Abess Labdelli, Khedidja Mechehoud, Mohamed Mana</i>	399
QCD Phase Diagram with a Crossover and a First Order Phase Transition <i>Mohamed Amine Lakehal, A. Ait El Djoudi</i>	400
Electronic and Nonlinear Optical Properties of (E)-N'-(3-Methoxybenzylidene)-2-(Quinolin-8-Yloxy) Acetohydrazide: A Comprehensive Computational Study <i>Mohammed Hadj Mortada Belhachemi, Zohra Douaa Benyahlou, Amine Ould Rabah, Kheira Hammou</i>	401
Theoretical Investigation of MoSSe Janus as Promising Anode Material for LIBs Using First-Principles Calculations <i>Malak Bounbaa, Mohamed Khuli, Nejma Fazouan, El Houssine Atmani, Isam Allaoui</i>	402
Investigating the Behaviour of Some Response Functions Characterising the Thermal QCD Deconfinement Phase Transition in a Finite Volume for Several Hadronic and QGP Systems <i>Rokaya Djida, Amal Ait El Djoudi</i>	403
Cauchy Wavelet Application to Detect Multi-Scale Structures of the Turbulent Flow <i>Kenza Zaibak, Nora Nait Bouda, Fawzia Mekideche-Chafa</i>	404
Arbitrary Amplitude Solitary Waves in a Degenerate Plasma System <i>Muhammad Asaduzzaman</i>	405
Elimination of Indigenous Dairy Biofilms from Milk Reception Lines by Implementing an Appropriate Cleaning-in-Place CIP Protocol <i>Dahou Abdelkader El Amine, Tahlaoui Hafida, Medjahed Mostefa, Seddar Yagoub Fatima, Doubbi Bounouaa Lahcen, Benabdelmoumene Djilali, Doukani Koula</i>	406
Evaluation of the Suitability of Bovine Milk from the Experimental Farm for Industrial Processing <i>Doubbi Bounouaa Lahcen, Dahou Abdelkader El Amine, Seddar Yagoub Fatma, Tahlaoui Hafida,</i>	407



*Bounaama Khalil, Homrani Abdelkader*

Food Packaging Reinforced Active Agent MOF-Based and Their Synthesis Methods	408
<i>Mohd Hafizuddin Ab Ghani, Ismayadi Ismail, Rosnah Nawang, Intan Helina Hasan, Juraina Md Yusof, Che Azurahaman Che Abdullah, Siti Hajar Othman, Josephine Liew Ying Chyi, Umer Rashid, Nishata Royan Rajendran Royan, Ruey Shan Chen, Chawalit Ngamcharussrivichai</i>	
Processing and Conservation of Mussels from the Ain Temouchent Region (West Algerian)	409
<i>Fatima Belhacini, Arifa Chegrouche, Dinedane Hadjer Amel</i>	
Design and Project Management for Unmanned Aerial Vehicles	410
<i>Ahmed Khaled Salaheldin Ali, Onur Tuncer</i>	
Enhancing Urban Resilience: Evaluating Earthquake Park Design in Kahramanmaras, Turkey	411
<i>Sinan Kordon, Aliye Kaya, Dilan Tokgoz, Meryem Yilmaz, Ozge Akilli</i>	
Analysis of the Flow Through a Contoured Nozzle Using CFD	412
<i>Sabrina Benlembarek, Kamel Talbi</i>	
Balancing Techniques Comparison on an Imbalanced Payment Company Dataset	413
<i>Mehmet Sukru Aygun, Mehmet Fatih Akay</i>	
Optimization of Incremental Conductance Using Fuzzy Logic Control for MPPT of a Photovoltaic Stand-Alone System	417
<i>Beddi Abdelraouf, Hicham Serhoud, Nacer Hebbir, Zoubir Aoulmi, Moussa Attia</i>	
Enhancing Impact Resistance of Engineering Solutions Through Multiscale Structural Optimization	418
<i>Ilhan Taber, Ramazan Karakuzu</i>	
Comparative Study of Empirical Expressions for Modulus of Soil Reaction and Pipe Displacement in Soil-Pipe System	433
<i>Chahrazad Bacha, Meriem Zoutat, Mohamed Mekki</i>	
Nature-Based Solutions for Flood and Water Management in Urban Areas: Global Practices	434
<i>Emine Keles Ozgenc</i>	
Differential Geometry and Natural Metrics	442
<i>Chaoui Saadia</i>	
New Conjugate Gradient Method Using SWP Line search for Nonlinear Unconstrained Optimization	443
<i>Souli Choubeila, Ziadi Raouf</i>	
A Stochastic BFGS Algorithm for Bound-Constrained Global Optimization	444
<i>Raouf Ziadi, Bencherif Madani Abdellatif</i>	
Characterizations of Weighted Triebel-Lizorkin Spaces Associated with Hermite Operators	445
<i>Chichoune Romaisa, Saibi Khedoudj, Mokhtari Zouhir</i>	
On a Sojourn Time Formula and Applications in Engineering and Simulation	446
<i>Abdelatif Bencherif Madani</i>	

Magnetized Fe <sub>3</sub> O <sub>4</sub> /CoFe <sub>2</sub> O <sub>4</sub> Hybrid Ferrofluid with Magnetic Field-Dependent Viscosity over a Slip-Stretching Sheet	447
<i>Nur Ilyana Kamis, Noraihan Afiqah Rawi, Lim Yeou Jiann, Sharidan Shafie</i>	
An Efficient Numerical Approach for Fractional Integro-Differential Equations of Fredholm Type	448
<i>Nouria Arar, Zineb Laouar</i>	
Solutions of Linear Dynamic Systems with the Help of Eigenvalue - Eigenvector	455
<i>Ramazan Simsek</i>	
Boosting Communication Efficiency: WDM-Distributed Compensation Fiber Integration in Optical Systems	456
<i>Hadj Abdelkader Benghenia, Hadj Ali Bakir</i>	
Maximizing Solar Installation Power Using Fuzzy Control	463
<i>Amel Ourici, Abderaouf Bahi</i>	
Improving the Electrical Properties of the Smart Temperature Sensor Using CMOS (Si and SiC) Technology	471
<i>Mourad Hebali, Benaoumeur Ibari, Menouer Bennaoum, Hocine Abdelhak Azzeddine, Abdelkader Maachou, Mohammed El-Amine Beyour</i>	
An Overview of Medium Access Control Protocols for Terrestrial Wireless Sensor Networks	472
<i>Selahattin Kosunalp</i>	
Silicon-Integrated GaAs Single-Junction Solar Cell: Design and Performance Improvement	476
<i>Mohammed El-Amine Beyour, Mourad Hebali, Benaoumeur Ibari, Menouer Bennaoum, Hocine Abdelhak Azzeddine, Abdelkader Maachou</i>	
Microstrip Patch Antenna with Triple-Band Using Metamaterial	477
<i>Hadda Ouguissi, Nail Alaoui</i>	
Dipole Antenna Based on Metamaterials for RFID	478
<i>Hadda Ouguissi, Nail Alaoui</i>	
Machine Learning Based Diamond Cut Quality Classification	479
<i>Mustafa Alptekin Engin, Latif Akcay</i>	
Study of New Model of SBD Structure Proposed to Elaborate Mixer Design	483
<i>Reguieg Khadidja, Souar Zeggai, Hebali Mourad</i>	
Investigation of the Electrical Behavior of DG-MOSFET Transistors in Silicon Carbide Using Series and Parallel Equivalent Electronic Circuits	484
<i>Mourad Hebali, Benaoumeur Ibari, Hocine Abdelhak Azzeddine, Bennaoum Menouer, Ibrahim Farouk Bouguenna, Mohammed El-Amine Beyour</i>	
Towards Service Discovery and Selection Approaches in IoT Applications	485
<i>Selahattin Kosunalp, Yunus Kaya</i>	
Design of a New Multiband Pentagon Patch Antenna Array	489
<i>Khouloud Mohammed Belhadj, Souheyla Ferouani, Djalal Ziani Kerarti</i>	

Energy Distribution Analysis Using DWT for the Airgap Eccentricity in Induction Machine <i>Moutaz Bellah Bentradi, Adel Ghoggal, Tahar Bahi</i>	490
Advanced Control Strategy for Grid-Connected Voltage Source Inverters with LCL Filters Dedicated to Renewable Energy Grid Integration Systems <i>Houssam Eddine Mansouri, Billel Talbi, Idris Messaoudene, Moussa Abderrahim Mehiris</i>	495
Efficient QRS Complex Extraction from ECG Signals Using DWT <i>Hadda Ouguissi, Nail Alaoui</i>	500
Microstrip Antenna Design for 5G Communication <i>Hadda Ouguissi, Nail Alaoui</i>	501
Removal of Pollutant by Bacteria Isolated from Oilfield via Biosurfactant Production <i>Nesrine Lenchi, Wissam Ahmedi, Salima Kebbouche-Gana</i>	502
Investigating the Modulatory Effects of Phenolic-Rich Extract on Pancreatic $\beta$ -Cell Gene Expression in Oxidative Stress Conditions <i>Anfel Benmanseur, Fatma Zahra Hab, Rania Derguine, Rechda Amel Tachour, Mustapha Tacherfiout, Bachra Khettal, Abdelmalek Rezgui, Widad Sobhi</i>	503
An Investigation into the Impact of Tannic Acid and Gallic Acid on the Surface Characteristics of 3D-Printed Polylactic Acid in Relation to Adhesion of <i>Pseudomonas Aeruginosa</i> and <i>Staphylococcus Aureus</i> <i>Badr Errabiti, Amal El Aabedy, Sara Er-Rahmani, Soumya El Abed, Saad Ibnsouda Koraichi</i>	504
Exploring the Inhibitory Effect of Alpha-Hederin, the Active Saponin of <i>Nigella Sativa</i> , Against the Main Protease M <sup>pro</sup> of SARS-CoV-2 <i>Selma Houchi, Seoussen Kada, Hanane Khither</i>	505
Thymol's Protective Effects on CCl <sub>4</sub> -Induced Oxidative Stress in Female Rats: Assessing Hepatic and Plasmatic Markers <i>Hanane Khither, Soraya Madoui, Selma Houchi, Asma Mosbah</i>	506
Antioxidant Activity, Total Phenolic, and Total Flavonoid Contents of Crude Extract of <i>Inula Viscosa</i> 's Leaves <i>Nadjat Azzi, Younes Douffa, Nour El Houda Belabas, Haifaa Laroui, Thoraya Guemmaz, Fatima Zerargui, Karima Saffidine, Abderrahmane Baghiani</i>	507
Experimental Study on the Healing Effect of the Crude Extract of the Aerial Part of <i>Cytisus Triflorus</i> on Skin Wounds <i>Soraya Madoui, Hanane Khither, Karima Madoui, Nouredine Charef</i>	508
Exploring Phenolic Composition and Scavenging Effects Against Reactive Oxygen Species of Nettle Crude Extract <i>Hamza Kemchache, Khalil Kaouane, Ayoub Bekka, Mondher Fradjia, Sabrina Manel Kaddour, Rayene Bouaita, Nouredine Charef, Soraya Madoui, Hanane Khither</i>	509
Antioxidative Characteristics of Aqueous and Ethanol Extracts of <i>Anethum Graveolens</i> L. Seeds <i>Nour El Houda Belabas, Nadjat Azzi, Younes Douffa, Haifaa Laroui, Thoraya Guemmaz,</i>	510

*Fatima Zerargui, Karima Saffidine, Abderrahmane Baghiani*

Evaluation of In Vitro Antioxidant Activity of Natural Compounds in Atriplex Halimus Leaf Extract Using Hydrogen Peroxide and Hydroxyl Radical Assays 511

*Khalil Kaouane, Hamza Kemchache, Ayoub Bekka, Mondher Fradjia, Rayene Bouaita, Sabrina Manel Kaddour, Noureddine Charef, Hanane Khither, Soraya Madoui*

In Vitro Assessment of Biological Activity in Elaeagnaceae Leafs 512

*Rayene Bouaita, Randa Djemil, Samira Bouhalit, Saber Boutella, Khalil Kaouane, Hamza Kemchache*

Evaluation of the Bio-Remedial Effect of Bacillus Atrophaeus to Treat Soil Polluted by Heavy Metals 513

*Mondher Fradjia, Rima Belattar, Abdelhakim Sellal, Wissam Nour Elhouda Ahmedi, Hamza Kemchache, Khalil Kaouane, Nora Laouicha, Amor Benchikh*

Phytotherapy Study of Medicinal Plants Used in the Northern Region of the Wilaya of Setif (Ain El Kebira) 514

*Nouioua Wafa, Madoui Soraya*

ABTS Radical Scavenging Activity and Ferrous Chelating Ability of Ethyl Acetate Extract of Pistacia Atlantica Seeds 515

*Younes Douffa, Nadjat Azzi, Nour El Houda Belabas, Haifaa Laroui, Thoraya Guemmaz, Karima Saffidine, Fatima Zerargui, Abderahmane Baghiani*

Phytochemical Analysis and Biological Activities of Essential Oil and Lavandula Stoechas Harvested in Algeria 516

*Amina Benazzouz-Touami, Driffa Bouchene, Nabila Iaouadaren*

Tolerance Mechanism Study to Polluted Ecosystems of Bioremediants 517

*Laouicha Nora, Sellal Abdelhakim, Bencheikh Amor, Belattar Rima, Fradjia Mondher, Ahmedi Wissam Nourelhouda*

Evaluation of Antibacterial Activity of *Thymus Vulgaris* Extracts 518

*Mohamed Khiari, Zine Kechrid*

Evaluation of Antibiotic Resistance Pattern and Biofilm Production in Vaginal Isolates in Women 519

*Anfal Kara, Feryal Belfihadj, Naouel Boussoualim, Meriem Elkolli*

Evaluation of Antioxidant and Antibacterial Activities of *Ruta Montana* Crude Extract from the Mila Region 520

*Zineb Bouamrane, Saber Boutellaa, Hakima Belattar, Mouna Menakh, Nedjla Derbal*

Evaluation of Antibiotic Resistance in Enterobacteria Isolated from Hospital Cockroaches 521

*Ben Djaballah Wafa, Bouguenoun Widad, Trabsa Hayat, Kebkoub Narimane, Serraye Fatima*

G-Protein Coupled Estrogen Receptor Expression in Estrogen Receptor Alpha (ER $\alpha$ ) Negative Breast Cancer Tissues of Algerian Patients 522

*Yasmine Mostaphaoui, Rafik Menad, Elara N'tima Moudilou, Chahla Bencharif*

Exploring the Insecticidal Potency and Growth Inhibition Effect of *Pistacia Lentiscus* and 523

<i>Lauris Nobilis</i> Oils and Extracts on <i>Culex Pipiens</i> (Diptera: Culicidae) Larvae <i>Menakh Mouna, Saber Boutellaa, Zineb Bouamrane</i>	
Unlocking the Power of Nigella: Exploring the Antioxidant Abilities of This Ancient Medicinal Plant <i>Dalia Nafir, Noureddine Belattar</i>	530
The Biological Activity of the Ethanolic Extract from Bee Pollen <i>Oumamar Loubna, Soltani El Khamsa, Khalil Kaouane, Ayoub Bekka, Hamza Kemchache</i>	531
Tumor Microenvironment in Hepatocellular Carcinoma: A Comprehensive Review <i>Yusra Zarlashat, Hassan Mushtaq</i>	532
Ecological Classification of Soil-Plant Cover Areas Contaminated by Drilling and Mineralized Waters in the Siyazan Region (Azerbaijan) <i>Sanubar Aslanova</i>	533
The Use of Pectin Extracted from Lemon Bark as an Encapsulation Matrix <i>Djerri Rofia, Himed Louiza, Barkat Malika</i>	534
Utilizing <i>Aspergillus Oryzae</i> for Expression of SARS-CoV-2 Spike Protein Domains: Insights into COVID-19 Research <i>Elif Karaman, Serdar Uysal</i>	535
Indirect Effects of Microplastics on Climate Change and Community-Based Solutions to Atmospheric Microplastic Pollution <i>Enes Ozgenc, Gunay Yildiz Tore</i>	536
In Silico Analysis of Phytochemicals from Selected Medicinal Plant Species to Inhibit Alpha-Glucosidase as a Receptor Protein to Treat Type-2 Diabetes Mellitus <i>Ghulam Mustafa, Shoukat Hussain, Anas Bilal, Rawaba Arif</i>	542
Biotin-Functionalized Nanoparticle Systems for Targeted Lung Cancer Therapy <i>Fatma Sayan Poyraz, Banu Mansuroglu</i>	543
Epidemiological, Immunohistochemical, and Molecular Study of Breast Cancer in Young Algerian Patients from “Bejaia” <i>Sara Ouari, Hania Ouahmed-Boudaoud, Chahla Bencharif, Chahira Mazouzi</i>	544
Microencapsulation: A Way to Preserve Bioactive Compounds from Food Waste for Novel Food Formulations – A Review <i>Tusneem Kausar, Ashiq Hussain, Sobia Noreen</i>	551
Estimation of Total Phenolic Compounds in Three Date Fruits Cultivars from Biskra (Algeria) <i>Amel Barkat, Hayat Trabsa, Chaima Mezghiche, Yasmine Mabrouka Mizab, Abderahmane Baghiani, Abdelnacer Agli</i>	552
Estimation of Total Flavonoids Compounds in Three Date Fruits Cultivars from Biskra (Algeria) <i>Amel Barkat, Hayat Trabsa, Chaima Mezghiche, Yasmine Mabrouka Mizab, Abderahmane Baghiani, Abdelnacer Agli</i>	553

Antibacterial Activity of Garlic ( <i>Allium Sativum</i> ) Against <i>Staphylococcus</i> Strains Isolated from Nile Tilapia ( <i>Oreochromis Niloticus</i> ) <i>Romeissa Derdachi, Sabrina Boucetta</i>	554
Health and Nutritional Complications in Newborns of Diabetic Mothers <i>Salima Taleb, Bouthaina Brakni, Fairouz Dilmi</i>	555
Assessment of Antimicrobial Activity of Lactic Acid Bacteria Isolated From Artisanal Dairy Products Against <i>Escherichia Coli</i> ATCC 25922 and <i>Staphylococcus Aureus</i> ATCC 29213 <i>Roumaissaa Belkacem, Qada Benameur</i>	556
Utilizing Lentil Flour in the Gluten-Free Cake Formulations <i>Sebahat Oztekin</i>	557
Potent Inhibitory and Stimulatory Effects of Various Metal Ions on Polyphenol Oxidase Activity Extracted from Algerian Desert Truffles <i>Abdelhafid Bouremana, Fatima El-Houaria Zitouni-Haouar</i>	558
Experimental Measurement on a Shaking Table of the Dynamic Characteristics of Structures <i>Abdellatif Bentifour, Abderaouf Daci, Nassima Benmansour, Rachid Derbal</i>	559
Evaluation of the Dynamic Characteristics of a 3DOF Reduced Scale Model Using RISAM Shaking Table <i>Abderaouf Daci, Abdellatif Bentifour, Nassima Benmansour, Rachid Derbal</i>	560
Evaluation of the Carbonation of Concrete with the Addition of Pozzolana and Marble Powder Under the Effect of Temperature <i>Ahlem Houaria Mohammed Belhadj, Rachid Derbal</i>	561
Characterization and Application of Sewage Sludge in Cement Products <i>Mahmoud Bouslah, Mekki Maza, Zine El Abidine Rahmouni, Nadia Tebbal</i>	562
The Impact of Surface Roughness on Energy Dissipation and Dimensions of Non-Rectangular Stilling Basins: An Experimental Investigation for Sustainable Environmental Practices <i>Seyfedine Benabid, Sonia Cherhabil, Sid Ali Dajfri, Taqiyeddine Assas</i>	563
Development of Geopolymer Binders Based on Industrial Waste with Different Treatment Methods: A Review <i>Hanane Zadri, Nadia Tebbal, Zine El Abidine Rahmouni, Mekki Maza</i>	564
Valorization of Mining Waste into Construction Materials: Literature Review <i>Medjida Touahria, Nadia Tebbal, Zine El Abidine Rahmouni, Mekki Maza</i>	565
The Effect of Limestone on Virgin Cork Concrete Mechanical Properties and Durability <i>Samah Hariz, Fouad Ghomari, Brahim Touil</i>	566
Investigation of the Microstructure and Hardness Properties of Fe Based High Entropy Alloys Produced by Powder Metallurgy Method <i>Murat Bodur, M. Emre Turan, Yavuz Sun</i>	567
Investigation of Delamination Factor in Bi-Directional Drilling of Glass Fiber Reinforced Plastic Materials	573

---

<i>Erhan Karatas, Oguz Kocar, Nurettin Baran Zulfikar, Nergizhan Anac, Furkan Parmaksiz</i>	
Using Shape Memory Alloys for Energy Harvesting Systems <i>Gokhan Kilic, Omar Abboosh</i>	583
Analysis of Performance Values of Stabilizer Link Parts Produced by Additive Manufacturing Method in Automotive Suspension Systems <i>Sevilay Sagtan, Burak Ates</i>	584
Gradient Graphene Sponge for Solar Steam Generation Applications <i>Kader Dagci Kiransan, Ezgi Topcu, Elif Ercarikci</i>	592
Investigation of the Effect of Current Density on Ammonia Formation from Ammonium Chloride and Sodium Chloride in Two-Compartment Bipolar Membrane Electrodialysis <i>Duygu Adiguzel, Fatemeh Abbasi, Osman Nuri Ata</i>	593
Evaluating the Pb (II) Removal Efficiency of <i>Prunus Laurocerasus</i> : Isotherms, Kinetic and Thermodynamic Studies <i>Zehra Seba Keskin*, Zeynep Mine Senol</i>	600
Upgraded Bio-Oil with Co-Pyrolysis of Spruce Sawdust with Glycerol <i>Ahmet Rasim Girisen, Hakan Ozcan</i>	601
Comparative Classification Performance Evaluation of Machine Learning and Deep Learning Techniques for BreakHis, Wisconsin, and DDSM Breast Cancer Datasets <i>Oben Adak, Cigdem Inan Aci, Dogu Ilmak</i>	608
A Review on Data Visualization: Usage Fields, Importance, and Examples <i>Durmus Ozkan Sahin</i>	614
Recognition of Human Activities Using Accelerometer and Gyroscope Sensors in Mobile Devices <i>Merve Buluslu, Adem Korkmaz</i>	615
A New Metaheuristic Algorithm for Optimization Problem: Artificial Circulation System Algorithm <i>Nermin Ozcan, Semih Utku</i>	622
Development of an Artificial Intelligence Supported Identity Verification System (KYC) <i>Ceren Goksu, Kerim Guler, Duygu Keles, Halil Sahin</i>	623
Breast Cancer Prediction Using Machine Learning Algorithms <i>Gokberk Kozak, Erol Ozcekic</i>	624
A Drum Wheel Bearing Design in Tumble Dryer <i>Abdullah Berk Ince, Cevdet Caner Akgun</i>	631
Examining the Trend of MOOC Related Studies with Data Mining: Voyant Analyst <i>Bunyami Kayali, Mehmet Yavuz</i>	632
A Research on Staling in Wafers <i>Sibel Koca Cetinkaya, Amine Beyza Ozata, Ozge Akgul, Begum Ceren Memecan</i>	638
Grapevine Leaf Powder as a Functional Food Additive: Physicochemical and Bioactive	639

## Properties

*Mehmet Ali Salik*

A Popular Probiotic Dairy Product-Kefir: Overview on Functional Mechanism of Action and Plant-Based Fermented Beverages 645

*Mehmet Ali Salik*

Cytocompatibility of PVA/Chitosan Electrospun Scaffold Loaded with Antioxidant Amino Acid on Fibroblast and Neuroblastoma Cells 651

*Betul Mutlu, Cem Bulent Ustundag, Rabia Cakir*

Characterization and Study of the *In Vitro* Effects of Polysaccharide-Based Nanofibers Obtained Using the Method of Coaxial Electrospinning to Improve Tympanic Membrane Perforations 652

*Busra Akgul, Cansu Gulcan, Selay Tornaci, Merve Erginer, Ebru Toksoy Oner, Emrah Sefik Abamor, Serap Acar, Adil M. Allahverdiyev*

Statistical Investigation of Surface Modification Polymerization Methods in Global and Turkish Scale 654

*Nursel Karaoglan*

Determination of Thiamethoxam with Molecular Imprinted Affinity Monolithic Column 665

*Ilgim Gokturk*

Determination of Metalaxyl Using SPR Sensors 666

*Kivilcim Caktu Guler*

Parameter Extraction of Proton Exchange Membrane Fuel Cell Using Metaheuristic Optimization Techniques: Evaluation and Comparison 667

*Huseyin Bakir*

Classification of Coconut Tree Diseases Using GoogleNet for Agriculture Management 668

*Ebru Ergun*

A Digital Predictive Peak Current Mode Control for Power Factor Correction 673

*Ahmet Talha Dudak, Ahmet Faruk Bakan*

A Low-Cost Cloud-Based Wearable Accelerometer Data Recording System 682

*Ayse Zehra Caglar, Cagri Gul, Sabri Altunkaya*

Nanobioelectronics Used in Targeted Drug Delivery Systems 689

*Gencay Sevim\*, Gulay Buyukkoroglu*

A Satellite-Based Augmentation System for Turkey to Enhance Navigation Capabilities 690

*Ibrahim Oz*

Optimized Performance Compact Wide-Band Microstrip Filter-Antenna for 4G Applications 702

*Husain Ali, Ugur Cem Hasar*

Simplified Reference-Plane-Invariant Method for Permittivity Extraction of Low-Loss Dielectrics via One-Port Waveguide Measurements 707

*Ugur Cem Hasar, Husain Ali*



A Theoretical Comparative Study of the 1,3-Dipolar Cycloaddition Reaction of Some Alkenes with Nitroene <i>Boulanouar Messaoudi</i>	713
A Kinetic Mechanism Study of the Reaction of Triplet Oxygen O(3P) with the But-3-Enal Aldehyde <i>Boulanouar Messaoudi</i>	714
Effect of Si <sup>4+</sup> and Ga <sup>3+</sup> Co-Doping on Structure and Ionic Conductivity of BiSiGaVO <sub>x</sub> System <i>Abdelmajid Agnaou*, Wafaa Mhaira, Rachida Essalim, Fabrice Mauvy, Maati Alga, Mohamed Zamama, Abdelaziz Ammar</i>	715
Thermodynamic Properties at Infinite Dilution of Hydrocarbons in Ionic Liquids <i>Fadhila Rabhi, Hocine Sifaoui, Fabrice Mutelet</i>	716
Modification of Polycaprolactone Through Grafting with an Aromatic Acid: Synthesis and Characterization <i>Nacera Leila Belkhir, Mohammed Amin Bezzekhami, Kaouter Bentedlaouti, Mahmoud Belalia, Amine Harrane</i>	717
Synthesis of New Azomethines Based on Vitamin B6 <i>Samira Ismayilova, Alakbar Huseynzada, Ulviyya Hasanova, Aygun Israyilova</i>	718
Synthesis of New Heterocyclic Nitrogen Derivatives Derived from Pyridopyrazine <i>Mohamed El Yaqoubi, Yousra Seqqat, Mouad Lahyaoui, Houda Lamssane, Fouad Chahdi Ouazzani, Youssef Kandri Rodi</i>	719
Synthesis and Characterization of Layered Double Hydroxides with Different Cations (Mg, Cu, Al) and EDTA Intrcalated <i>Fadhila Bouhella, Boukoussa Bouhadjar, Abdelkader Elaziouti, Hadjer Addou, Nadjia Belmehdi</i>	720
A Chemotherapeutic Supplement, Green Synthesized Silver Nanoparticles Using <i>Papaver Rhoas</i> for Human Pancreatic Cancer Treatment <i>Cigdem Dikbas, Muberra Andac</i>	721
Theoretical Study, Intermolecular Charge Transfer, MEP, and Nonlinear Optics Application for an Organic Molecule <i>Zohra Douaa Benyahlou, Mohammed Hadj Mortada Belhachemi, Salem Yahiaoui, Kheira Hammou, Abdelkader Chouaih</i>	722
A simple and Efficient One-Pot Synthesis of Hantzsch 1,4-Dihydropyridines Using Heteropolyacid Catalyst Under Mild Condition <i>Fella Gaad, Sabrina Halit, Malika Makhloufi, Tassadit Mazari, Marchal Catherine Roch</i>	723
Nickel Catalyst for Isoxazol Synthesis <i>Benali Belgharri, Amina Berrichi, Sarah Abbou, Zahra Hamiani, Redouane Bachir</i>	724
Phosphotungstic Heteropolyacid Based New Hybrid Materials for Biomass Recovery <i>Feriel Toumi, Yasmina Idrissou, Tassadit Mazari, Rabia Cherifa, Anne Ponchel, Kania Nicolas</i>	725
Semisynthesis of New Isoxazolines from (E)- $\alpha$ -Atlantone: Experimental and Theoretical	726

## Investigations

- Houria Raji, Rida Nejjari, Ahmed Chekroun, Abdellah Zeroual, Nouredine Mazoir, Ahmed Benharref*
- Study of Properties of Tin Oxide Thin Films Elaborated by USP Method 727  
*Sabrina Roguai, Abdelkader Djelloul*
- Synthesis of CuO Nps for Photocatalytic Applications 728  
*Sabrina Roguai, Abdelkader Djelloul*
- Photothermal Activity and *In Vitro* Evaluation of Gold Nanorods for Potential Therapeutic Application in Cutaneous Leishmaniasis Treatment 729  
*Magali R. Di Meglio, Cristian Lillo, Jorge Montanari*
- Valuation of Essential Oils from Aleppo Pine (*Pinus Halepensis* Mill.) Harvested in Two Regions of Algeria 730  
*Nacira Amara, Mohamed Kouider Amar, Sabrina Amara, Nadjat Harazi*
- Natural Antifungal Agents as Alternatives for *Alternaria Alternata* Control 731  
*Teodora Kukrić, Renata Iličić, Boris Popović*
- Some Derivatives of 3,4-Di-Hydropyrimidin-2(1H)-Thiones Derivatives: Synthesis, Biological Assessment, ADMET, and Drug-Likeness Analysis 732  
*Noura Kichou, Nabila Guechtouli, Manel Taferguennit*
- Hybrid Electrode Based on Ionic Liquid and Pt and Pd Nano-Clusters: For the Hydrogen Evolution Reaction (HER) Catalysis 737  
*Hocine Moussouni, Mourad Mechouet, Jalal Ghilane*
- Evaluation of the Antidiabetic Activity of Extracts and Essential Oil of *Myrtus Communis* Harvested in Algeria 738  
*Melissa Bessaci, Amina Benazzouz-Touami*
- The Environmentally Friendly Synthesis of Amide Based on Triethylenetetramine 739  
*Fargana Alizadeh, Alakbar Huseynzada, Aygun Israyilova, Ulviyya Yolchuyeva, Ulviyya Hasanova, Eldar Gasimov, Goncha Eyvazova, Fuad Rzayev, Orkhan Isayev, Aida Ahmadova, Elshan Aliyev*
- Synthesis and Biological Evaluation of Amide Derivative as Novel Antibacterial Agent 740  
*Fargana Alizadeh, Alakbar Huseynzada, Aygun Israyilova, Ulviyya Yolchuyeva, Ulviyya Hasanova, Eldar Gasimov, Goncha Eyvazova, Fuad Rzayev, Orkhan Isayev, Aida Ahmadova, Elshan Aliyev*
- Examining How CeO<sub>2</sub> Addition Affects the Microstructure and Wear of Cu-Al-Mn-Fe Shape Memory Alloy 741  
*Fatih Dogan*
- Catalytic Oxidation of Lignocellulosic Biomass to Biofuels Using Reusable Mixed Oxide as a Catalyst in a Green Solvent 742  
*Mona Benali, Abdallah Oumekki, Jamil Toyir*
- Thermal Behavior Kinetics of Macromolecular Nickel (II) complex using Thermogravimetric 743

Analysis (TG/DTG)

*Djoughra Aggoun, Yasmina Ouennoughi*

Synthesis, Spectral Approach and Electrochemical Properties of Nickel (II) and Copper (II) Organometallic Schiff Base Complexes 744

*Yasmina Ouennoughi, Djoughra Aggoun*

Bibliometric Analysis of Research Trends in Additive Manufacturing in Metallurgical Engineering: A Scopus Database Study by Turkish Scholars 745

*Oussama Zaidi*

Analysis of Electrical Field Norm Distribution at the Cathode/Arc Interface in TIG Welding 746

*Merazi Sayah, Leila Belgacem*

DFT Insights for Structural, Electronic, and Optical Characteristics of  $\text{Cs}_2\text{XBr}_6$  (X = Pb, Sn) Double Perovskites for Low-Cost Solar Cell Applications 747

*Rekia Larbi, Omar Sahnoun, Mohamed Sahnoun*

Milling Effect on Structural, Microstructural, and Magnetic Properties of FeCo Based Alloy 748

*Chaffia Djebbari*

Mapping of Tectonic Fractures in the Zat Region (Western High Atlas, Morocco): Using Remote Sensing and Structural Geology 749

*Abdelfattah Aboulfaraj, Abdelhalim Tabit, Ahmed Algouti, Abdellah Algouti, Said Moujane, Saloua Agli*

Achieving Full Control of Industrial Robot: Kinematic and Dynamic Modeling with FOPID Controller Tuned using GWO Approach 750

*Benaoumeur Ibari, Mourad Hebali, Baghdadadi Rezali, Omar Medjad, Menaouer Bennaoum, Hocine Abdelhak Azzedine, Abdelkader Maachou*

Analysis of Technical Indicators in Cryptocurrency Market 751

*Asli Boru Ipek*

IIoT as an Enabler for Data Analytics to Optimize Industrial Processes 752

*Federico Walas Mateo, Andrés Redchuk*

Q-Learning Enhanced Swarm-Based Algorithms for the 0-1 Knapsack Problem 757

*Fehmi Burcin Ozsoydan*

Optimizing Risk Management Strategies in the Oil and Gas Industry: Dynamic Assessment and Modeling of Accident Consequences 763

*Imane Aila, Samia Chettouh, Djamel Haddad*

An Overview of Artificial Intelligence Techniques in Supply Chain Management: AI-Driven Strategies for Risk Management 764

*Lara J. M. Naser, Seval Ene Yalcin*

An Efficient Design of a Multi-Echelon and Multi-Product Supply Chain Network with Price-Sensitive Demands 765

*Pinar Yunusoglu, Derya Eren Akyol, Fehmi Burcin Ozsoydan*

Production of Graphene by Electrochemical Method and Energy Applications <i>Gulbahar Bilgic Tuzemen</i>	771
Advanced Hierarchical Control of Islanded AC Microgrids Using Modulated Model Predictive Control <i>Moussa Abderrahim Mehiris, Billel Talbi, Idris Messaoudene, Houssam Eddin Mansouri</i>	777
Applications and Future of Unmanned Aerial Vehicles in the Field of Occupational Health and Safety <i>Mustafa Ozdemir</i>	778
Model Predictive Control of a PUC7-Based Power Factor Correction (PFC) Rectifier <i>Abdeslem Sahli, Billel Talbi, Abbas Kihal, Abdelbaset Laib, Abdelbasset Krama</i>	783
Internal Parameters Identification of a Lithium-Ion Battery <i>Abderrahmane El Djallil Rabhi, Kamel Djamel Eddine Kerrouche</i>	791
Influence of the Temperature on the Performance of Conventional Organic Solar Cells <i>Samia Moulebhar, Chahrazed Bendenia, Hanaa Merad-Dib, Souhila Bendenia, Sarra Merabet, Sid Ahmed Khantar</i>	792
Optimization of Sabbath Mode Algorithms Used in Refrigerators <i>Mazlum Koray Dirican, Bulent Ozcan</i>	793
A Numerical Study on the Aerodynamic Performance of the S1223 Airfoil in Low Reynolds Number Conditions <i>Onur Usta</i>	798
Simulation Study of Methylammonium Lead Iodide (CH <sub>3</sub> NH <sub>3</sub> PbI <sub>3</sub> )-Based Perovskite Solar Cell via Silvaco TCAD <i>Sid Ahmed Khantar, Chahrazed Bendeni, Souhila Bendenia, Hanaa Merad-Dib, Samia Moulebhar, Sarra Merabet</i>	805
Optimization of Distributed Generations Placement and Sizing in Radial Distribution System Through ABC Algorithm <i>Badreddine Bendriss, Samir Sayah, Abdellatif Hamouda</i>	806
Analysis of CdTe Solar Cell Performance Using SCAPS-1D Simulation as a Function of Various Buffer Layers <i>Merabet Sarra, Bendenia Chahrazed, Bendenia Souhila, Merad Hanae, Moulebhar Samia, Khantar Sid Ahmed</i>	807
Advancements and Challenges of Photovoltaic Technology in Algeria's Desert <i>Chekal Affari Belhadj, Kahoul Nabil, Younes Mohammed, Daoudi Lina, Cheghib Hocine, Kherici Zoubida</i>	808
Contribution to the Study of the Structural, Electronic, Optical, and Thermoelectric Properties of Heusler Alloys: A Material with Great Promise for the Future of Clean Energy <i>Khedidja Mechehoud, Mohamed Mana, Aya Righi, Mouffok Redouane Ghezzar, Fatima Bendahma, Bilel Achir</i>	809
Energy Management of Photovoltaic/Battery Power Source for Stand-Alone Application	810

*Lina Daoudi, Amel Ourici, Sihem Ghoulbourg, Chekal Affari Belhadj*

Enhancing Pressure Regulation in PEMFC: PID Conventional and PID Optimized by PSO in Response to Variable Load Demand 811

*Sabah Kabache, Djelloul Reguieg, Essaid Bousbiat, Djamel Kendil*

Enhanced Grid-Connected Photovoltaic System Using Five-Level Packed U Cell Topology and Advanced Control Approaches 822

*Abderraouf Touafek, Fateh Krim, Hamza Afghoul, Billel Talbi*

Detection and Classification of Power Quality Disturbances Using Variational Mode Decomposition and Convolutional Neural Networks 823

*Yahia Bousseloub*

Improving Solar Cell Efficiency: Exploring High-Performance Tandem Solar Cells Integrating Lead-Free Perovskite on Silicon (PVK/Si) via Design and Numerical Analysis 824

*Hadjer Soufi, Abdelkader Bouhenna, Khadidja Rahmoun, Mohamed El Amine Slimani, Wissem Benaissa*

Optimal Sizing of a Renewable Energy System for Sustainable Power and Hydrogen Generation Under the Northeastern Algerian Climate 825

*Toufik Sebbagh*

Active and Reactive Power Control of a Grid-Connected Photovoltaic/Fuel Cell Hybrid System 826

*Hocine Abdelhak Azzeddine, Mourad Hebali, Djamel-Eddine Chaouch, Benaoumeur Ibari, Menaouer Benaoum*

Artificial Neural Network MPPT and Perturb and Observ MPPT Comparison 827

*Hocine Abdelhak Azzeddine, Mourad Hebali, Djamel-Eddine Chaouch, Benaoumeur Ibari, Menaouer Benaoum*

Optimization of Forced Circulation Solar Water Heating Systems for Enhanced Residential Energy Efficiency in Algeria 828

*Ahmed Remlaoui, Driss Nehari*

Investigation of the Effects of Silver Alloying and Transparent Conductive Oxide Layer Thickness on the Chalcopyrite Thin Film Solar Cells 829

*Semih Agca*

The Characteristics of an Organic Solar Cell at the Base of Polymeric Material 834

*Chahrazed Bendenia, Souhila Bendenia, Hanaa Merad-Dib, Samia Moulebhar, Sid Ahmed Khantar, Sarra Merabet*

Microstrip Dipole Antenna Design for RFID Application 835

*Hadda Ouguissi, Nail Alaoui*

Chua Circuit and Its Behavior 836

*Hadda Ouguissi, Nail Alaoui*

Harmonic Forecasting for Future Offshore Wind Farm System in the Ayvalik Region of the North Aegean Sea by Using Deep Learning 837

*Alp Karadeniz*

Evaluation of Speech Encryption Algorithm Based on Chaotic Systems 838

*Salah Mokhnache, Tewfik Bekkouche, Nacira Diffellah*A Design of AI-Based-Smart Glasses, Which Offer Navigation in Addition to Correcting  
Vision 839*Syed Arif Kamal*

Impact of Image Size on Classification of Synthetically Generated Window and Door Images 844

*Safak Altay Acar*

Few-Shot and Zero-Shot Video Classification from Large Visual Models Perspective 848

*Erol Citak, Mine Elif Karsligil*Machine Learning Techniques for Software Fault Prediction: A Distinctive Systematic  
Literature Review 855*Aleena Rafique, Sania Bhatti*Principal Component Analysis for Database Scan Using Hierarchical KNN Model for Telecom  
Customer Segmentation 861*Oluwasegun William Ijibadejo, Saja Murtadha Hashim*

Classification of Plant Leaves Using Vision Transformer Model 871

*Kadriye Karadeniz, Kursat Mustafa Karaoglan*Artificial Intelligence and Statistics Based Call Count and Average Talk Time Prediction for  
Call Centers 880*Hasan Huseyin Yurdagul, Adem Seller, Idris Senocak, Hatice Ozdemir, Ceren Ulus, Mehmet  
Fatih Akay*

Understanding Large Language Models in Cybersecurity Domain 891

*Bugra Kurt, Aysu Irem Adem, Mahmut Furkan Bakal, Hussain Alburki, Arda Sezen*

Enhancing FOPID Controller Performance in a 3-DOF Planar Manipulator 899

*Benaoumeur Ibari, Mourad Hebali, Baghdadi Rezali, Omar Medjad, Menaouer Bennaoum,  
Hocine Abdelhak Azzedine, Abdelkader Maachou*

Can NLP Combined with AI Prevent Language Extinction: A Case Study of Turkish 900

*Anil Kus, Cigdem Inan Aci*CASTEP Investigation of Structural, Electronic, and Optical Properties of  $\text{CoSb}_2\text{O}_6$  907*Rania Charif, Rachid Makhoulfi*Density Functional Theory (DFT) Investigation on the Structure and Electronic Properties of  
 $\text{ZnSb}_2\text{O}_6$  908*Rania Charif, Rachid Makhoulfi*Effects of Instagram Weddings on Financially Strains, Local Traditions, Stress, Unrealistic  
Expectations, Privacy Issues, and Digital Disconnect Among Youth of Pakistan 909*Ghulam Safdar, Mahnoor Bibi*

A Multifaceted Approach to Fault Diagnosis: Comparing Traditional and Deep Learning 910

## Methods

*Ceren Asilkefeli, Fehmi Burcin Ozsoydan*

Convolutional Neural Network Application for Control Chart Pattern Recognition 915

*Ceren Asilkefeli, Fehmi Burcin Ozsoydan*Theoretical Investigations of Structural, Mechanical, and Elastic Properties of Novel  
Quaternary Heusler Alloys for Spin Polarized and Waste Heat Recycling Systems 919*Saadiya Benatmane*

Design of Image Processing Accelerators for TTA Processors 920

*Latif Akcay, Tugce Demirkol*

Enhancing the Performance of Twofish Cipher via Instruction Set Extension 927

*Latif Akcay, Mustafa Alptekin Engin*

Studying the Gender Gap in Advanced Digital Skills: Coding, Data Science, and Cybersecurity 932

*Anxhela Ferhataj, Fatmir Memaj*

resEARcher: A Sentence-Transformers Guided Tool for Visually Impaired Researchers 938

*Eylul Hickiran, Emrah Inan*

Effect of the Smagorinski Coefficient in LES Turbulence Model at Lateral Diversions 944

*Firat Gumgum*Numerical Simulation of Investigating the Group Impact on Settlement in the Soft Soil  
Reinforced by Rigid Inclusions Under Seismic Loads 945*Oussama Benmerabet, Salah Messioud*Effect of Calcination Time and Temperature on the Pozzolanic Reactivity of Dam Sediment  
Slurry 946*Hanaa Kawther Terrah, Zine El Abidine Kameche, Hocine Siad, Mohamed Lachemi, Youcef  
Houmadi*Seismic Evaluation of an Existing Reinforced Concrete Building Based on FEMA P-2018  
Methodology 947*Atakan Emin Aksoy, Sadik Can Girgin, Ozgur Bozdog*

Experimental Study on the Mechanical Behaviour of Fiber Reinforced Sandy Soil 955

*Wiam Khebizi*Enhancing Self-Compacting Concrete with Recycled Fine Aggregates and Polyethylene  
Terephthalate Fibers 956*Meriem Bayah, Farid Debieb*Synergistic Effect of Ground Granulated Blast-Furnace Slag and Metakaolin on the  
Performance of Recycled Self-Compacting Concrete 957*Boubakeur Asmaa, Menadi Belkacem*Impact of Particle Diameter and Flow Velocity on Particle Transport Behaviour in Saturated  
Soil 958*Bouragaa Kheira, Bennacer Lyacine, Ahfir Nasre-Dine*

Effect of the Use of Plastic Waste as Sand on Concrete Properties <i>Wassila Boughamsa, Assia Abdelouahed, Houria Hebhouh, Wassila Mouats</i>	963
Study of the Durability of Sand Concrete Based with Wood Ash (0.1%, 0.2%, and 0.3%) <i>Abdelouahed Assia, Mouats Wassila, Houria Hebhouh, Wassila Boughamsa, Toufik Sebbagh</i>	964
Comparative Study on the Valorization of Recycled Plastic Waste in the Formulation of Mortars <i>Houria Hebhouh, Said Berdoudi, Wassila Boughamsa, Assia Abdelouahed, Wassila Mouats, Mohammed Ichem Benhalilou</i>	965
Fresh and Hardened Properties and Durability of Self-Compacting Repair Mortar Made with Ceramic Powder as Cement Substitute <i>Messaouda Belouadah, Zine El Abidine Rahmouni, Nadia Tebbal</i>	966
Enhancing Mechanical Strength of Concrete Through Polypropylene Fiber Incorporation <i>Shiraz Baloch, Farah Naz, Umer Shahzad, Muhammad Abrar Faiz</i>	967
Identifying the Main Predictors for Job Satisfaction of Construction Workers: Hierarchical Regression Approach <i>Gokhan Kazar</i>	976
A Comparative Study of Recycled Tire Chips, Jute Fiber, Polyester Fiber, Plastic Fiber Waste for Stabilizing Sand as Retaining Wall Backfill <i>Lina Zaidi, Fatima Zohra Benamara, Aya Zelti, Issam Mesbahi, Atmane Zeghdi</i>	982
Thermal Deformation Model for Concrete Incorporating Silica Fume <i>Farid Bouziadi, Touhami Tahenni, Abdelkader Haddi, Bensaid Boulekbache, Mostefa Hamrat</i>	983
Static Analysis of Sigmoid Functionally Graded Plates (S-FGM) by Using Higher Order Shear Deformation Plate Theory <i>Habib Hebali</i>	984
Buckling response of Functionally Graded Plates Using a Novel Four Variable Refined Plate Theory <i>Habib Hebali</i>	985
Using PET Plastic Flakes and Waste Tire Chips as Wall Backfill <i>Fatima Zohra Benamara, Chiraz Kechkar, Marwa Feligha, Ghania Nigri, Lina Zaidi, Aya Zelti</i>	986
Study of the Behavior of A Clay Embankment Reinforced with Recycled Waste <i>Aya Zelti, Fatima Zohra Benamara, Marwa Feligha, Lina Zaidi</i>	987
Improvement in Structural Analysis: Creation of a Rectangular Finite Element for Analyzing Membrane Structures <i>Randa Bourenane, Sifeddine Abderrahmani, Abdulrahman Mutahar Al-Nadhari</i>	988
Acid and Sulfate Resistance of Concrete Containing Recycled Aggregate: A Comprehensive Experimental Study <i>H. Alperen Bulut</i>	989



Effect of Granite Waste on Concrete Performance <i>Ramdane Rihab, Kherraf Leila</i>	996
Numerical Study of the Seismic Bearing Capacity of Offshore Skirted Foundations on Sand Using Finite Element Limit Analysis <i>Alaoua Bouaicha, Abdeldjalil Chamekh, Nour El Islam Boumekik, Abdelhak Mabrouki</i>	997
Numerical Analysis of the Seismic Bearing Capacity of Strip Footings Near a Frictional Soil Slope <i>Abdeldjalil Chamekh, Alaoua Bouaicha, Abderraouf Messai</i>	998
3D Failure Envelopes of Strip Footings on Sand over Non-Homogeneous Clay Using Limit Analysis Method <i>Alaoua Bouaicha</i>	999
Prediction of the Maximum Shear Strength of Fiber-Reinforced Soils Using Artificial Intelligence <i>Leyla Bouaricha, Yasmine Mohamed Bouteben, Azeddine Chehat, Ahmed Djafar Henni</i>	1000
Implementation of Five-Noded Mapped Infinite Element to OpenSees <i>Sefa Uzun, Yusuf Ayvaz</i>	1001
Thermal Properties and Microstructure Investigation of Sustainable Self-Compacting Concrete-Based Coal Bottom Ash Aggregate <i>Ibtissam Boulahya, Abdelkadir Makani, Ahmed Tafraoui</i>	1008
Effect of Thermal Gradient on the Initial Stiffness of End-Plate Beam-Column Connections Exposed to Fire <i>Yasmina Douah, Anis Abidelah, Hichem Rakib Sebbagh, Djemel Eddin Kerdal, Abdelhamid Bouchair</i>	1009
Numerical Analysis of the Static and Cyclic Behavior of a T-Stub Steel Connection <i>Mohammed Mokhtar Fekir, Hichem Rakib Sebbagh, Anis Abidelah, Abdelhamid Bouchair, Djamel Eddine Kerdal</i>	1010
Numerical Study to Optimize the Best Locations for Building a New Tunnel Next to the Old One by Tow Behaviors the Mohr-Coulomb and Drucker-Prager <i>Taleb Hosni Abderrahmane, Guemidi Ismahene</i>	1011
Parameter Estimation for a Mechanistic Model of Cell Population Damage from High-Dose Irradiation Using Nelder-Mead Simplex and Particle Swarm Optimization <i>Nabil Haazim Mohd Amirrudin, Fuaada Mohd Siam</i>	1012
A Collocation Approach for Solving Space Fractional Partial Differential Equations Using Generalized Lucas Polynomials <i>Zineb Laouar, Nouria Arar</i>	1013
Study of the Influence of Grinding on the Characteristics of Natural Phosphate Mining in Kef Esnoun (Algeria) <i>Hadda Rezzag, Amina Grairia, Saida Bouyegh, Samira Tlili, Lynda Bahloul</i>	1019
Modeling of the Working Flow Propagation in the Well Ejection System Flow Part	1024

*Denys Panevnyk*

Design of Ring Yarn Structures: Physical-Mechanical Properties of Different Yarns for Improved Sustainability and Performance 1025

*Ivana Salopek Čubrić*

Assessment of Material Sensory Properties: Focus on bipolar attributes of Stiffness-Softness and Roughness-Smoothness 1030

*Ivana Salopek Čubrić, Goran Čubrić*

Artificial Hydrophobic Surfaces Based on MgO Thin Film: Elaboration and Characterization 1036

*Zehira Belamri*

Exergy Analysis of Combined Cooling, Heating, and Power Systems Integrated with Carbon Capture and Storage for an LNG Carrier 1037

*Engin Guler, Selma Ergin*

Potential Use of Materials Based on Alginate Beads for Treating Contaminated Water 1048

*Dhirar Ben Salem, Amel Riah*

Carbon Nanostructured as an Efficient Adsorbent for High Concentrations of Crystal Violet Removal 1049

*Amel Riah, Salim Bousba*

Lead (Pb) Pollution: A Food Safety Issue 1050

*Mahmood Ur Rahman*

Exploring the Adsorption Capacities of Olive Mill Solid Waste Biochar for Polyphenols: Experimental Optimization and DFT/B3LYP Analysis 1051

*Imad Rabichi, Kawtar Ezzahi, Abdelrani Yaacoubi, Abdelaziz Bacaoui, Mohamed Hafidi, Loubna Elfels*

Removal of Total Phenols from Olive-Mill Wastewater Using an Agricultural By-Product, Olive Stone 1052

*Kawtar Ezzahi, Imad Rabichi, Abdelghani Yaacoubi, Abdelaziz Bacaoui, Rachid Idouhli, Nabil Rochdi, Mohamed Hafidi, Loubna El Fels*

Extraction of Phosphocalcic Biomaterial from the Animals Bones Bio-Waste 1053

*Saida Bouyegh, Sabrina Ladjama, Hadda Rezzag, Sihem Benayache, Samira Tlili*

Synthesis and Characterisation of Hybrid Membranes for Removal of Rhodamine B 1059

*Amina Aoues, Ouarda Merdoud, Mohamed Oualid Boulakradeche, Djamel Abdessemed, Omar Arous*

Numerical Assessment of Seismic Behavior in Earth Dams: A Case Study of Fontaine Gazelles Dam, Biskra, Algeria 1060

*Alaoua Bouaicha*

Isocratic High-Performance Liquid Chromatographic Separation and Determination of Elution Order of Some Quinolone's Enantiomers via Cellulose-Amylose as Chiral Selector 1061

*Mohamed Nadjib Rebizi*

Evaluation of the Photophysical and Photodynamic Properties of Carbon Quantum Dots Obtained from Plant Extracts	1062
<i>Martín Lemos Vilches, Cristian Lillo, Jorge Montanari</i>	
X-Ray Scans Super-Resolution with a Novel Hierarchical Multi-Scale Attention Network	1063
<i>Rania Saoudi, Djameleddine Boudechiche, Zoubeida Messali</i>	
Traditional Phytotherapeutic Practices in the South-Eastern Anti-Atlas Mountains: An Ethnobotanical Survey of Medicinal Flora in Iznaguen, Morocco	1069
<i>Younesse El-Ouazzani, Fouad Msanda, Khalil Cherifi</i>	
Preparation and Evaluation of Dermatological Gel Based on Aromatic and Medicinal Plant Extracts	1070
<i>Fouzia Benoudjit, Imene Hamoudi, Asmaa Aboulouz</i>	
Electrochemical Exfoliation and Characterization of Graphene for Symmetric Supercapacitors: A Comprehensive Study	1071
<i>Abdelmalik Zemieche, Loubna Chetibi, Djamel Hamana, Slimane Achour</i>	
Contribution to the Study of Microstructural Properties of Quasicrystals in AlCuFe Alloys	1072
<i>Wafa Boumechta, Moussa Zahzouh</i>	
Resonance Study of FGM Shells Reinforced with Carbon Nanotubes	1073
<i>Zakia Hammou, Zakia Guezzen, Zouaoui Sereir, Yamna Hammou</i>	
Research Trends in the Use of ChatGPT in Education: A Bibliometric Analysis	1074
<i>Mehmet Donmez</i>	
Decentralized Collaborative Multi-Agent Reinforcement Learning for Air Attack Scenarios	1078
<i>Berire Gunduz, Mehmet Dikmen</i>	
Phenotypic and Technological Characterization of Lactic Acid Bacteria Isolated from Algerian Artisanal Dairy Products	1088
<i>Roumaissaa Belkacem, Qada Benameur</i>	
Contribution of Lorentz Force in Cathode/Arc Coupling During TIG Welding	1089
<i>Merazi Sayah, Leila Belgacem</i>	
Structural, Morphological, and Optical Properties of Zinc Oxide Prepared by Sol-Gel Method	1090
<i>Khemissi Lahouel, Meriem Gasmi, Saida Hoggas, Sabiha Hakkar</i>	
Effect of Extract Concentration on Green Synthesis of Silver Nanoparticles	1091
<i>Roufaida Aissa Brahim, Hadjer Mabrouki, Djamel-Eddine Akretche</i>	
The Methode of Adobe in Building	1092
<i>Hammache Soumia</i>	
CBD-Loaded Lipid-Based Nanoparticles for Topical Application Against Skin Cancer	1093
<i>Ana Paula Sanguinetti, Mirian Scavone, Magali Di Meglio, Pablo Raies, Paulo Maffia, Jorge Montanari, Maria Natalia Calienni</i>	
Spatial Analysis of Soil Heavy Metals Based on Geostatistical Approach in the North of Iraq	1094
<i>Mohammed Oday Al Hamdani, Ali Volkan Bilgili, Sureyya Betul Rufaioglu</i>	

A New Approach for the Degradation By-Products Pesticide Detection in Trace Level <i>Chemseddine Zekkaoui, Tarek Berrama, Salima Dadou, Assia Beriber, Nassime Doufene, Kadmi Yassine</i>	1103
Application of Doehlert Design Experimental Methodology for the Optimal Emerging Pollutant Degradation with Fenton Process <i>Chemseddine Zekkaoui, Tarek Berrama, Salima Dadou, Assia Beriber, Nassime Doufene, Kadmi Yassine</i>	1104
Optimization by the Surface Response Methodology of a Fenton Like Process by CrVI of an Anthraquinonic Dye Type Green Acid 25 <i>Benidris Elbatoul, Slamani Samira, Hachemi Chaimaa, Abdelmalek Fatiha, Ghezzar Mouffek Redouane</i>	1105
Pellets from Olive Mill Waste: Densification and Characterization for Sustainable Waste Management Solutions <i>Zaina Izghri, Fatima Ezzahra Yaacoubi, Chaima Sekkouri, Imad Rabichi, Abdelaziz Ounas, Karima Ennaciri, Abdelaziz Bacaoui, Abdelrani Yaacoubi</i>	1110
Microplastic Pollution in Surface Waters of Ergene River: Sources and Spread <i>Enes Ozgenc, Gunay Yildiz Tore, Erdi Bulus, Yesim Muge Sahin</i>	1111
Diatomite Formation Associated with Sogucak Pyroclastics (Sandikli, Türkiye) <i>Bala Ekinçi Sans, Zeynep Doner</i>	1116
Effects of Titanium Dioxide on the Ultrasonic and Structural Properties of Zinc–Strontium–Lithium Phosphate Glass <i>Nurhafızah Hasim, Nur Hidayah Ahmad, Nur Asilah Zulkifeli, Anis Nazihah Mat Daud</i>	1117
Strategic Coordination of P2P Energy Trading in Smart Microgrids <i>Kubra Nur Sahin, Muhammed Sutcu</i>	1118
Advancing Turkish-to-English Translation: A Transformer-Based Neural Model Approach <i>Nurzhah Amantay, Yasin Ortakci</i>	1119
Contribution to the Application of Condition Maintenance for Followed and Diagnostic Breakdowns of a Rotating Machine <i>Naima Tamaloussi, Lamia Benzaid, Zina Azzez, Azzedine Bouzaouit</i>	1127
Recycling of Urban Waste in the Manufacture of Concretes <i>Ben Khadda Ben Ammar</i>	1128
An Artificial Neural Network-Based Microwave Technique for Bianisotropic Materials Electromagnetic Property Extraction <i>Mehmet Akif Ozkaya, Ugur Cem Hasar</i>	1129
Improved Propagation Constant Determination Using Two-Line Measurements <i>Ugur Cem Hasar, Husain Ali</i>	1135
Increasing the Reflection Parameter in Microstrip Patch Antennas by Trying Different Shapes <i>Hamdullah Ozturk</i>	1141

A Study on General Safety Precautions Against Electrical Accidents in Daily Life <i>Yunus Kaya, Selahattin Kosunalp</i>	1146
VO2 Based Adaptive Wideband THz Metamaterial Absorber <i>Merve Kurt, Gokhan Ozturk</i>	1149
The Impact of Telework on Gender Equality and Occupational Health <i>Mustafa Ozdemir</i>	1157



---

## Materials for Eco-Design Strategies for an Innovative Industry

Rodrigo Martins<sup>\*1</sup>, Suman Nandy<sup>1</sup>, Pedro Barquinha<sup>1</sup>, Luís Pereira<sup>1</sup>, Tomás Pinheiro<sup>1</sup>,  
Henrique Almeida<sup>1</sup>, Rui Igreja<sup>1</sup>, Emanuel Carlos<sup>1</sup>, Elvira Fortunato<sup>1</sup>

<sup>1</sup>Materials Science Department, CENIMAT|I3N and CEMOP/UNINOVA, Faculty of Sciences and Technology, NOVA University Lisbon,  
2829-516 Caparica, Portugal

---

### Abstract

With the growing smartness in electronic manufacturing worldwide, printed electronics technologies draw tremendous attention because of their ability to overcome the limitation of traditional high-cost manufacturing approach which is mostly based on rigid silicon substrate. In these issues, printing technology can be used to fabricate devices on various kind of flexible substrate such as paper, textile, bendable polymers even on human skin. On the other side, printed electronics has a great potential to offer biodegradable and recyclable solutions, by choosing low-cost substrate for printing devices, that may be recycled and/or naturally degraded in nature. This is a way forward to minimize the electronic waste (e-waste) caused by the everincreasing number of disposable electronic devices. Relevantly, “printing electronics on paper” technology is rapidly developing in both research and electronic industry fields during the last decade [1]. Generally, printing processes involve a sequence of tasks, starting with the selection of functional materials along with the envisioned functionality, moving to the formulation of inks, and then the selection of a suitable substrate. Printing technique depending on the ink’s properties and intended features for the printed film. There are several printing technologies, that are being used in research and industrial sectors from lab-scale to large-scale application, such as screen printing, flexographic (or flexo-) printing, gravure printing, gravure-offset printing, and roll-to-roll (R2R) printing. A long list of functional materials, from conductive polymers, ionic liquids, and carbon nanostructures to metallic nanoparticles, and metal oxide nanostructures with conductive, semiconducting, or dielectric properties, can be used to formulate these inks [2-4]. The development of stable, cost-effective, non-toxic, and eco-friendly printable inks with desired printability is crucial to deposit and pattern these materials onto a substrate to enable the production of a new class of devices for electronics and energy purposes that are extremely lightweight, affordable, readily customizable, thin, flexible, and recyclable.

**Keywords:** *Flexible electronics, Responsible electronics, Sustainable electronics*

---

### References

- [1] S. Nandy, S. Goswami, A. Marques, D. Gaspar, P. Grey, I. Cunha, D. Nunes, A. Pimentel, R. Igreja, P. Barquinha, L. Pereira, E. Fortunato, and R. Martins, “Cellulose: A contribution for the zero e-waste challenge,” *Adv. Mater. Technol.*, vol. 6, no. 7, art. no. 2000994, 2021.
- [2] G. Hu, J. Kang, L. W. T. Ng, X. Zhu, R. C. T. Howe, C. G. Jones, M. C. Hersam, and T. Hasan, “Functional inks and printing of two-dimensional materials,” *Chem. Soc. Rev.*, vol. 47, no. 9, pp. 3265–3300, 2018.
- [3] W. Wu, “Inorganic nanomaterials for printed electronics: A review”, *Nanoscale*, vol. 9, no. 22, pp. 7342–7372, 2017.
- [4] L. W. T. Ng, G. Hu, R. C. T. Howe, X. Zhu, Z. Yang, C. G. Jones, and T. Hasan, *Printing of Graphene and Related 2D Materials*, Springer Cham, 2019.



## Emerging Nanotechnologies for Targeting Antimicrobial Resistance: A Special Focus on Chronic Wound Healing

Saravanan Muthupandian<sup>\*1</sup>

<sup>1</sup>AMR and Nanomedicine Lab., Department of Pharmacology, Saveetha Dental College, Saveetha Institute of Medical and Technical Sciences (SIMATS), Chennai 600077, India

---

### Abstract

Nanobiotechnology is a branch of biotechnology that focuses on the use of nanoscale materials and processes to create innovative biomaterials for disease detection, treatment, and prevention. Nano-biotechnology breakthroughs have been achieved in recent years in an effort to reduce and combat bacterial resistance, multidrug resistance (MDR), and bacterial biofilm in order to minimise this major problem. Nanotechnology-based approaches have significantly contributed to the field of nanomedicine, and they have proven to be the most effective alternative antimicrobial materials. Microbe infections are resistant to antibiotic treatment and can result in serious and potentially fatal invasive infections. Bacteria that are resistant to several antibiotics have a substantial negative impact on public health because they reduce the efficacy of therapeutic products that are already in use. Meanwhile, in the present scenario, nanomedicine plays an essential role in the development of alternative and more successful treatment techniques for microbial infections, particularly chronic wound healing.

**Keywords:** *Nanomaterials, Antimicrobial resistance, Nanomedicine, Wound healing*

---



## Carbon-Based Electrode for Flexible Gas Sensor

**Mohd Nizar Hamidon<sup>\*1,2</sup>, Azlinda Abu Bakar<sup>1,3</sup>, Mohd Hanif Yaacob<sup>4</sup>, Wan Nursheila Wan Jusoh<sup>3</sup>, Suriati Paiman<sup>1</sup>, Haslina Jaafar<sup>2</sup>, Intan Helina Hassan<sup>1</sup>**

<sup>1</sup>Functional Nanotechnology Device Laboratory, Institute of Nanoscience and Nanotechnology, Universiti Putra Malaysia, 43400 UPM Serdang, Selangor, Malaysia

<sup>2</sup>Department of Electrical and Electronic, Faculty of Engineering, Universiti Putra Malaysia, 43400 UPM Serdang, Selangor, Malaysia

<sup>3</sup>Malaysians Institute of Aviation Technology, Universiti Kuala Lumpur, 43000 Dengkil, Selangor, Malaysia

<sup>4</sup>Department of Computer and Communication Systems, Faculty of Engineering, Universiti Putra Malaysia, 43400 UPM Serdang, Selangor, Malaysia

---

### Abstract

The sensors are used to gather a wealth of information from the process that can improve operational efficiency of the industry and quality of life which involving a mass of data that need to be analysis especially with the merging of the Internet of Things. Leading edge research in gas sensors has been propelled by the advancements made in fabrication, signal processing and material technology in the last decade and these the scientific world is now on the verge of delivering gas sensors with radically new capabilities for the human societies. This talk will be focusing on carbon-based interdigitated electrode (IDE) which will also influences the response, sensitivity and resistivity of a gas sensor. The interdigitated electrode will be fabricated using thick film fabrication technology on Kypton (a flexible substrate) for more wider applications especially in wearable electronics. The characterization of carbon-based interdigitated electrode and sensing films was done using field emission scanning electron microscopy (FESEM) and Energy Dispersive X-Ray (EDX). The performance of gas sensors was measured by exposed the sensing layer which was made from TiO<sub>2</sub>/MWCNT to are different concentrations of hydrogen between 100 to 1000 ppm at various operating temperature from 100 to 250 °C with a bending condition from 0° to 45°. Analysis from the measurement results showed that the sensor with the operating temperature of 150 °C produced the best sensitivity of gradient  $15.1 \times 10^{-4}$  and they were reliable up to 15° bending angle with 1000 cycle flexibility test.

**Keywords:** Flexible substrate, Carbon-based electrode, Thick film, Hydrogen gas

---





## **Vismodegib and Skin: The Challenge of Changing the Administration of an Anticancer Drug with Nanotechnology**

**Jorge Montanari<sup>\*1,2,3</sup>, M. Natalia Calienni<sup>1,2,3,4</sup>**

<sup>1</sup>Laboratory of Nanosystems for Biotechnology Application (LANSAB), National University of Hurlingham, Villa Tesei, Argentina

<sup>2</sup>National Scientific and Technical Research Council, Argentina

<sup>3</sup>Scientific Research Commission of the Province of Buenos Aires, La Plata, Argentina

<sup>4</sup>Dept. Pharmaceutical and Pharmacological Sciences, University of Padova, Padova, Italy

---

### **Abstract**

Vismodegib, a Hedgehog signalling pathway inhibitor drug indicated for treating basal cell carcinoma, is administered orally, often causing numerous side effects that can lead patients to discontinue treatment. Over the past five years, our group has demonstrated the potential to change its administration route, drastically reducing its dosage and altering its biodistribution. By loading or complexing the drug into various nanoscale particulate systems, we have shown the capability to deliver the drug deep into the skin through user-friendly topical applications, achieving higher drug concentrations near tumors using up to 2500 times less of the drug. In this presentation we will review the incorporation of vismodegib into ultra-deformable liposomes, ethosomes, polymeric micelles, dendrimers, cubosomes, and other novel systems, comparing them with other attempts to achieve topical delivery, and will discuss its repositioning by leveraging the pathway's activation in other tumor types.

**Keywords:** *Vismodegib, Nanotechnology, Skin, Cancer*

---



## Evolutionary Trends in RACH Access Techniques Towards a 5G Cellular Network

Lawal Mohammed Bello<sup>\*1</sup>

<sup>1</sup>*Department of Electrical Engineering, Bayero University Kano, Kano, Nigeria*

---

### Abstract

In an effort to improve rate of information transfer as well as communication from one place to another, cellular networks have seen rapid evolutionary trends. This led to the realization of various generations, from first generation (1G) to the current fifth generation (5G). On the other hand, Random Access Channel (RACH) has been considered to be an essential uplink channel that plays a significant role in establishing an initial connection between a device and a cellular network. The connection is established using Random Access (RA) procedure where collision must to be managed since the access is random (i.e., none of the devices is aware of each other's transmission or known by the cellular network). RACH access is also experiencing similar evolutions seen by the cellular networks, which realize various techniques in order to manage collisions amongst devices during RA procedure. The evolution is as a result of differences in applications and requirements of the cellular network generations. This presentation is a review of different RACH access techniques, highlighting the differences in each of the cellular generations.

**Keywords:** 5G, RACH, Technique

---



## **Integration of Existing Control Systems to the Requirements and Principles of Industry 4.0**

**Dimitar Totev<sup>\*1</sup>**

*<sup>1</sup>Technical University of Sofia, Sofia, Bulgaria*

---

### **Abstract**

Nowadays more than 70% of the industrial processes are automated. The existing control systems are of many different types in terms of complexity, functionality and level of automation. Most of them are in the middle of their lifecycle. At the same time with the fast development of the new technologies new requirements appear, most of them defined by the concept "Industry 4.0". All these bring the question – how we can integrate the existing control system to the new requirements? What are the main goals and directions and what are the problems?

**Keywords:** *Industry 4.0, Automation, Control*

---



## Deployment of Carbon Based Nanomaterials for Gas Sensing Applications

Zainab Yunusa<sup>\*1</sup>, Mohd Nizar Hamidon<sup>2</sup>

<sup>1</sup>Department of Electrical Engineering, University, Hafr Al Batin, Hafr Al Batin, Kingdom of Saudi Arabia

<sup>2</sup>Department of Electrical and Electronic Engineering, Universiti Putra Malaysia, Selangor, Malaysia

---

### Abstract

The miniaturization of electronic devices and advances in nanomaterial research and production has made the application of functional nanomaterials at the forefront of scientific and industrial attention. Recent advances in carbon nanomaterials such as carbon nanotubes, graphene, graphene nanoribbons (GNRs) and other green carbon nanomaterials from organic sources such as rice husk and carbon charcoal have shown excellent results when deployed in electronics, bioelectronics, optoelectronics and photonic applications. In this paper, different carbon nanomaterials will be employed as a sensing material for gas sensors. The advantage of using organic carbon nanomaterials for electronic application is that it is more cost effective and reduces pollution due to the dumping of waste which results to an eco-friendly environment. The results obtained when deployed as a gas sensing material has shown enhanced selectivity, good response and recovery times and stability at room temperature.

**Keywords:** Gas sensor, Rice husk, Carbon nanomaterial, GNRs

---



## Health Implications of Glycation products in Diabetes and Its Secondary Complications

Ahmad Ali\*<sup>1</sup>

<sup>1</sup>Department of Life Sciences, University of Mumbai, Mumbai, India

---

### Abstract

Biomolecular interactions are important for the cellular physiology and homeostasis. Sometimes these interactions are altered and lead to unhealthy conditions. Glycation, a reaction between sugars and proteins, is one such condition that leads to pathophysiological conditions like Diabetes, cataract, neurodegenerative disorders etc. The effect of glycation is realised during sustained hyperglycaemia as a result of accumulation of glycation products. These products alter the structure and function of biomolecules especially proteins and nucleic acids. In this study we have analysed the generation of glycation products in an in vitro system wherein glucose was incubated with BSA for four weeks at 37 °C. The glycation products were found to accumulate manifold in the glycation system (Glu+BSA) as compared to control (without glucose). There was significant alteration in the structure of glycated BSA as revealed by spectroscopic and electrophoretic techniques. The generation of glycation products and structural alteration of protein was suppressed in the presence of a natural product, thymoquinone. These results indicate that glycation causes structural and functional alteration of proteins and natural products can be used for the reversal or suppression of toxic effects of glycation products.

**Keywords:** Albumin, Glycation, Sugars, Thymoquinone

---



## Investigation of the Morphological Structures of PVDF-HFP Flat Sheet Membranes Prepared with Different Concentrations of DMAC/DMF Solvents and Their Performance in the DCMD System

Ayşe Diskaya<sup>\*1</sup>, Ahmet Bora Yavuz<sup>2</sup>, Osman Nuri Ata<sup>3</sup>

<sup>1</sup>Department of Chemical Engineering, Bolu Abant İzzet Baysal University, Bolu, Türkiye

<sup>2</sup>Department of Chemistry, Agri Ibrahim Cecen University, Agri, Türkiye

<sup>3</sup>Department of Chemical Engineering, Ataturk University, Erzurum, Türkiye

### Abstract

In recent years, membrane distillation (MD) processes have been widely researched to meet the increasing need for fresh water and to offer a permanent solution to the emerging water scarcity problem. MD processes are frequently preferred in academic and industrial studies because they have many advantages such as being able to operate at lower pressures than conventional separation processes, not needing to be heated to the boiling point, taking up less space, being more resistant to contamination, being used with waste/renewable energy sources, and being open to development. It is not known how the preparation of poly (vinylidene fluoride-co-hexafluoropropylene) (PVDF-HFP) membranes using different concentrations of dimethylacetamide (DMAC)/dimethylformamide (DMF) solvent mixtures affects their performance in membrane distillation systems. Therefore, this study aimed to investigate the effect of DMAC/DMF solvent mixtures at different concentrations on the morphological structures of PVDF-HFP flat sheet membranes and their performance in the (DCMD) system. In the study, 4 membranes were prepared using the immersion precipitation method using 12% PVDF-HFP copolymer, 3% polyethylene glycol (PEG), and different DMAC and DMF solvent mixtures concentrations. Performance experiments for flux and salinity removal of the prepared PVDF-HFP flat sheet membranes were performed using the (DCMD) system. Membranes were characterized using liquid inlet pressure, contact angle, porosity, thickness measurements, and SEM images. The study conducted experiments at 5 different temperature differences by changing the feeding side temperature (40-50-60-70-80 °C) and keeping the cold side constant at 20 °C. Firstly; distilled water was used as a hot feed solution and then 0.1 M NaCl. The study, it was observed how the concentration changes of DMAC and DMF solvents in the produced membranes affected the flux and salinity removals in the DCMD system depending on the temperature; It was observed that the increase in DMF concentration and decrease in DMAC concentration caused a reduction in flux and salinity removals.

**Keywords:** PVDF-HFP membrane, Direct contact membrane distillation, Non-solvent induced phase separation

## 1 INTRODUCTION

In recent years, the increasing demand for freshwater along with population growth and the unconscious consumption of resources has become a major problem of our age, causing freshwater crises. To provide permanent solutions to the emerging water scarcity problem and increase meet need for freshwater, have been widely used membrane distillation (MD) processes. MD processes are frequently preferred in academic and industrial studies because they have many advantages such as being capable operate at lower pressures than conventional separation processes, not needing to be heated to the boiling point, taking up less space, being more resistant to contamination, being used with waste/renewable energy sources and being open to development. Membrane distillation (MD) is one of the non-isothermal separation processes in which only volatile vapor molecules are transported through porous hydrophobic membranes [1]. MD process must transported through the dry pores of the membranes only vapour, and the feed liquid solution must not wet the membrane pores [2]. The hydrophobic structure of the membrane does not allow liquid to enter the pores of the membrane due to surface tension forces [3]. The MD driving force is supplied by the vapour pressure difference resulting from a temperature difference between two surfaces' membrane sides [4]. The main requirements for polymers used in the fabrication of MD membranes are high hydrophobicity, high liquid entry pressure, chemical inertness, optimum pore size and low thermal conductivity, optimum thickness, high thermal stability, less susceptible to fouling and long-term permeance stability [5]. Three basic techniques are used in the preparation of hydrophobic porous membranes: stretching and heating, thermally induced phase separation (TIPS), and non-solvent induced phase separation (NIPS) [6].

Different polymers such as polytetrafluoroethylene (PTFE), polypropylene (PP), polysulfone, and poly (vinylidene fluoride) (PVDF) have been used to prepare MD membranes. Recently, PVDF- HFP polymer, is one of the most attractive polymers used in membranes prepared as PVDF copolymer. PVDF- HFP is often preferred because of its outstanding properties in terms of mechanical and thermal stability and because it enhances the hydrophobic character of the membranes compared to (PVDF) due to the presence of the Hexafluoropropylene (HFP) group [7]. In this study, flat sheet membranes have been prepared by the NIPS technique under a temperature of 50°C using different DMF concentrations and 12% PVDF-HFP, 3% PEG. The effects of the DMF concentration on the morphological properties of the flat sheet membranes have been studied in terms of scanning electron microscopy (SEM), LEP, contact angle, and void volume fraction. The PVDF-HFP flat sheet membranes prepared with different DMF concentrations were tested in DCMD.

## 2 MATERIAL AND METHOD

The chemicals used in the membrane solutions prepared and experimental system in this study, their properties, and the given which the chemicals were obtained are given in Tab. 1. All chemicals were used at the given purities.

**Table 1.** Composition of the membrane solutions

Chemical Name	Brand	Place of Use
Poly(vinylidene fluoride-co-hexafluoropropylene) (PVDF-HFP, Mw = 455, > 99.5%)	Sigma-Aldrich	Polymer
<u>Polyethylene Glycol</u> (PEG, Mw = 600, >99.5%)	Sigma-Aldrich	Pore former
N, N Dimethylacetamide (DMAC, >99%)	Sigma-Aldrich	Solvent
N, N Dimetilformamid (DMF, >99%)	Sigma-Aldrich	Solvent
Isopropyl Alcohol (IPA, 99%)	Sigma Aldrich	Wetting liquid
Sodium Chloride (NaCl, 99.9%)	Sigma-Aldrich	Feed solution

### 2.1 Preparation of Membranes

The concentration values of the polymer solutions of the membranes to be used in the experiments are presented in Tab. 2. Each membrane solution was prepared by undergoing the same pre-treatments before the casting process. The membrane solutions were stirred for about 24 hours in a magnetic stirrer containing water and the temperature was fixed at 50 °C. The aim here is to ensure that the temperature is the same at every point of the solution and to obtain a completely homogenous solution. Then, the completely homogenized solution was kept in an ultrasonic bath for a certain period to remove the gas bubbles in the solution. Then, it was rested in an oven with a temperature set to 50 °C for about 24 hours. The rested solution was finally allowed to cool to room temperature and made ready for the casting process. The prepared completely homogeneous ready-to-cast solution was poured onto the surface of a glass support material and the casting process was carried out on the glass support surface at a speed of 30 mm/sec with the help of an automatic film application device using a 200 µm thick doctor blade. The solution spread on the glass support surface was immediately taken and immersed in a coagulation bath containing distilled water. In the coagulation bath; as a result of mass transfers between the solution on the glass support surface and distilled water in the coagulation bath, the solution separates from the glass surface and turns into a solid phase and the formation of the membrane structure takes place. To completely remove the solvent chemicals from the surfaces of the obtained membranes, they were placed in a second coagulation bath at room temperature and kept for about 24 hours. Afterward, the membranes were placed between paper towels and left to dry for 24 hours under room conditions to prevent the formation of dust, etc. contamination on the membranes. Finally, characterization tests of each dried membrane were carried out.

**Table 2.** Dope solution composition of the prepared membranes

Membrane Code	Polymer	Solvents		Pore Former
	PVDF-HFP (wt%)	DMF (wt%)	DMAC (wt%)	PEG (wt%)
M1	12		85	3
M2	12	21.5	63.75	3
M3	12	42.5	42.5	3
M4	12	63.75	21.5	3

## 2.2 Characterization of Membranes

The membranes, used in membrane distillation, have been characterized by the following membrane performance parameters: performance of membranes, thickness of the membrane, porosity of the membrane, liquid-entry-pressure of water, contact angle, and SEM.

### 2.2.1 Performance of Membrane

The flux and salinity removal of the prepared membranes were measured using the Lewis cell. First distilled water was used as the feed solution in the system, then 0.1 M saline solution was used to determine the flux and salinity removals per unit time. The effect of feed temperature on DCMD current and salinity removal is given in Tab. 3. Flux and salinity removals were calculated using Eq. (1) and (2) given below.

$$\text{Flux (J)} \left( \text{kg} \cdot \text{m}^{-2} \cdot \text{h}^{-1} \right) = \frac{W_{\text{tp}}}{A \cdot t} \quad (1)$$

$$\text{Salt Rejection (\%)} \gamma = \left( 1 - \frac{C_p}{C_f} \right) \cdot 100 \quad (2)$$

Where  $W_{\text{tp}}$  is the total weight of material collected on the permeate side,  $A$  is the membrane area,  $t$  is the experimental time,  $C_p$  is the permeate concentration and  $C_f$  is the feed concentration.

**Table 3.** Effect of feed temperature on DCMD flux and salinity rejection

Tr (°C)	40			50			60			70			80		
	Distile water flux $\left( \frac{\text{kg}}{\text{m}^2 \cdot \text{h}} \right)$	0.1 M NaCl flux $\left( \frac{\text{kg}}{\text{m}^2 \cdot \text{h}} \right)$	Rejection (%) $\gamma$	Distile water flux $\left( \frac{\text{kg}}{\text{m}^2 \cdot \text{h}} \right)$	0.1 M NaCl flux $\left( \frac{\text{kg}}{\text{m}^2 \cdot \text{h}} \right)$	Rejection (%) $\gamma$	Distile water flux $\left( \frac{\text{kg}}{\text{m}^2 \cdot \text{h}} \right)$	0.1 M NaCl flux $\left( \frac{\text{kg}}{\text{m}^2 \cdot \text{h}} \right)$	Rejection (%) $\gamma$	Distile water flux $\left( \frac{\text{kg}}{\text{m}^2 \cdot \text{h}} \right)$	0.1 M NaCl flux $\left( \frac{\text{kg}}{\text{m}^2 \cdot \text{h}} \right)$	Rejection (%) $\gamma$	Distile water flux $\left( \frac{\text{kg}}{\text{m}^2 \cdot \text{h}} \right)$	0.1 M NaCl flux $\left( \frac{\text{kg}}{\text{m}^2 \cdot \text{h}} \right)$	Rejection (%) $\gamma$
M1	2.17	1.33	99.81	3.29	2.74	99.74	5.22	4.04	99.6	7.42	6.04	99.37	10.97	8.61	99.98
M2	1.69	0.99	99.71	2.27	1.66	98.85	3.41	2.74	98.76	5.32	3.92	98.34	7.73	6.16	96.97
M3	1.35	0.55	99.85	1.92	1.52	99.74	3.01	2.05	99.64	4.73	3.17	99.54	6.98	5.15	99.33
M4	0.93	0.45	99.97	1.88	1.26	99.94	2.5	1.96	99.89	3.63	2.59	99.81	4.41	3.77	99.75

The flux and salinity removal of each membrane were investigated by varying the feed temperature between 40, 50, 60, 70, 80 °C and keeping the filtrate side temperature constant at 20 °C. By keeping the filtrate side temperature at 20 °C and varying the feed temperature between 40-80 °C, it was aimed to transfer the vapour phase from the hydrophobic pores of the membrane to the filtrate side by creating a vapour pressure difference between the hot and cold side. The transported vapour phase accumulates on the cold filtrate side and the accumulated filtrate was taken from the top of the system the fluxes of the membranes were calculated by recording the amount of filtrate transported per unit area per unit time from the total filtrate weight. In the system, mass transfer takes place from the hot side to the cold side through the membrane pores. Therefore, a decrease in liquid level occurs on the feed side. To prevent both the pressure difference that will occur with the decrease in the liquid level here and to prevent the increase in the concentration of the feed liquid, the liquid transferred from the hot side was fed back into the system with the feed provider.

### 2.2.2 Liquid Entry Pressure of Water

The liquid entry pressure (LEP) of membranes is one of the important parameters in evaluating the performance of membranes and should have as large values as possible. LEP value varies depending on the hydrophobicity and pore size of the membrane. The setup given in Fig. 1 was used to determine the liquid entry pressure (LEP) values of the membranes. Distilled water was used as the feed liquid in the setup. After the membrane is placed in the system, the valve is opened and pressure is sent to the system. Wait for 5 minutes at each pressure value and continue the process by gradually increasing the pressure value by 0.1 bar every 5 minutes until the liquid drop comes from the bottom of the membrane. The first liquid drop is recorded as the liquid inlet pressure value of the membrane. Measurements were repeated at least 3 times for each membrane and the average LEP value was calculated. The values obtained are given in the Tab. 4.



### 2.2.3 Membrane Porosity

The porosity of the membrane is defined as the volume of the pores divided by the total volume of the membrane; the symbol for the porosity is  $\varepsilon$  [8]. To determine the porosity values of the membrane, calculations were performed using two liquids, distilled water, and isopropyl alcohol, which have surface tension with the help of a pycnometer. While water does not penetrate the pores of the PVDF-HFP membrane with a hydrophobic structure, isopropyl alcohol penetrates the membrane pores. Thus, the density of the membrane can be calculated using a pycnometer and a precision balance. Calculations for porosity measurements of the Smolder–Franken equation have been used [9].

$$\text{Porosity}[\% \varepsilon] = \left( 1 - \frac{\rho_m}{\rho_{\text{pol}}} \right) \times 100 \quad (3)$$

where  $\rho_m$  and  $\rho_{\text{pol}}$  are the densities of the membrane and the polymer material, respectively. First, the density of the membrane can be calculated according to the following formula:

$$\rho_m = \frac{\rho_{\text{water}} w_3}{w_1 + w_3 - w_2} \quad (4)$$

in which  $w_1$  = weight of the pycnometer with water;  $w_2$  = weight of the pycnometer with water and membrane;  $w_3$  = dry weight of the membrane. In the same way, the density of the polymer material is calculated using the following formula:

$$\rho_{\text{pol}} = \frac{\rho_{\text{IPA}} w_{t3}}{w_{t1} + w_{t3} - w_{t2}} \quad (5)$$

in which  $w_{t1}$  = weight of the pycnometer with IPA,  $w_{t2}$  = weight of the pycnometer with IPA and membrane;  $w_{t3}$  = dry weight of the membrane.

### 2.2.4 Contact Angle

The contact angle is expressed as the angle between a liquid droplet and a solid surface in contact or as a value of the wettability of a solid surface by a liquid [10]. The contact angle value provides information about the hydrophobicity of the membrane. The hydrophobicity of the membrane is the membrane's affinity for water and can be evaluated by measuring the membrane's contact angle [11]. The values obtained are given in the Tab. 4.

### 2.2.5 Membrane thickness

The thickness of membranes is an important parameter for the evaluation of perforation pressure and mechanical strength of membranes. The mechanical strength of the membrane increases with increasing thickness, but this leads to a decrease in flux as it increases the resistance to molecular transport. The flux and thickness of membranes are inversely proportional. Membrane thicknesses were determined by SEM analysis and side sectioning. The values obtained are given in the Tab. 4.

### 2.2.6 SEM

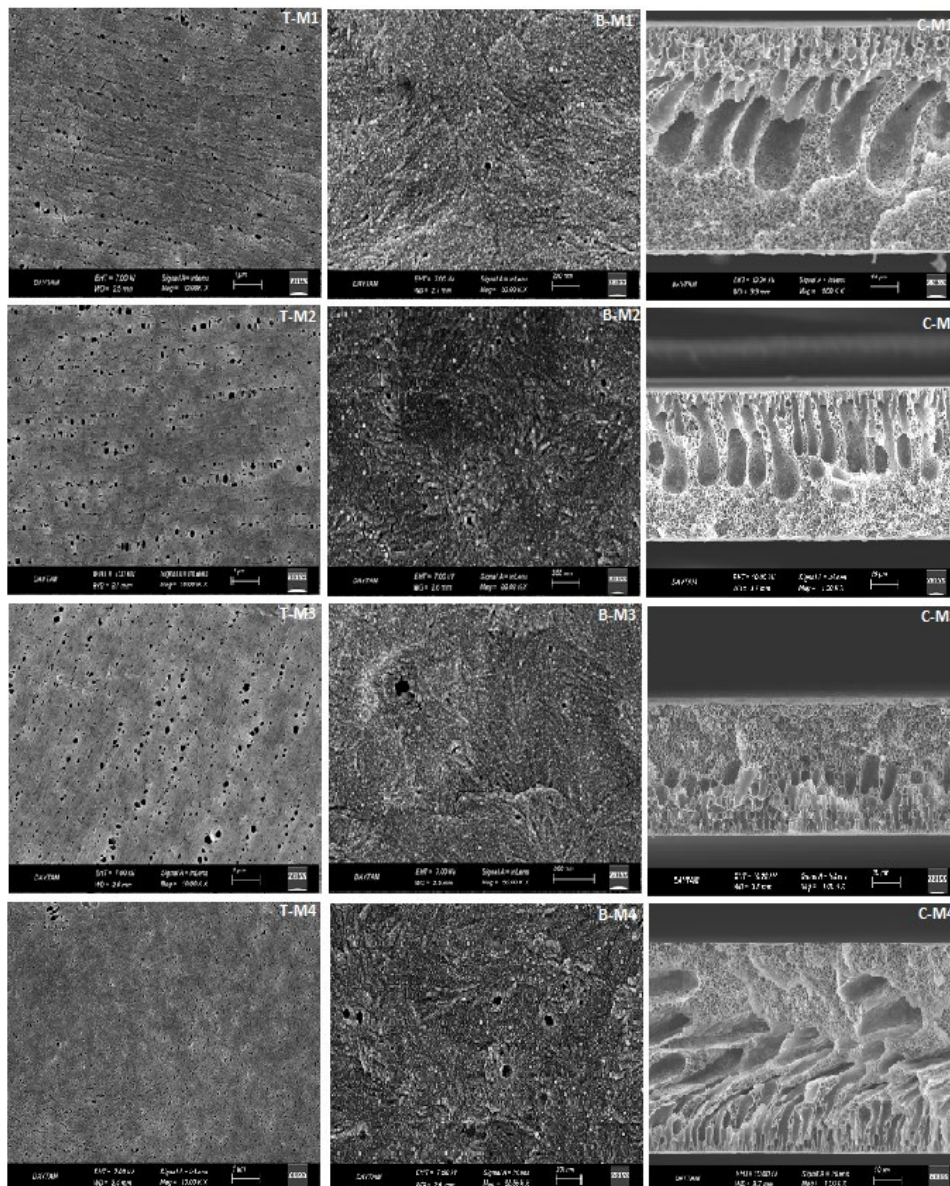
SEM images of the bottom surface, top surface, and side sections of the membranes were taken to evaluate the effects of DMF, and DMAC solvent concentrations on the morphological structure of the produced PVDF-HFP microporous flat sheet membranes. For SEM analyses, services were obtained from DAYTAM. Here, images of the bottom, top, and side surfaces of the membranes were taken using the (SEM, Zeiss-Sigma 300) model device. With the help of the information obtained from the SEM images about the thickness, porosity, pore size, and distribution of the membranes, comments and evaluations were made about the morphological structures of the membranes.

### 3 RESULTS

#### 3.1 Characterization Results

##### 3.1.1 SEM analysis

The morphology for the top, bottom surface, and cross-section of M1, M2, M3, and M4 membranes were studied and reported in Fig. 1. When looking at the SEM images, it can be seen that the bottom surface of all the prepared membranes is dense and can be observed by comparing the bottom surface and cross-sections of the membranes.



**Figure 1.** SEM pictures of the obtained PVDF-HFP flat sheet membranes. (T) Top surface, (B) Bottom surface, and (C) Cross-section

When looking at the top and bottom surfaces of the M1 membrane prepared without DMF solvent, it presents an asymmetric structure a more porous and finger-like macrovoid on the top with a dense layer on the bottom surface (T-M1 and B-M1, respectively) and a porous layer on the top surface and a sponge-like layer on the bottom surface (C-M1). The formation of the sponge-like morphology is greatly affected by the selected solvent and the amount of non-solvent (water) required for the membrane[12]. Generally, high affinity for the solvent/non-solvent pair tends to result in the formation of a sponge-like structure due to instantaneous mixing, while low affinity leads to delayed mixing with a denser structure[7]. Although the presence of macro voids is predicted to improve

membrane performances (flow), they significantly increase membrane wettability as the fluid path is open from the membrane surface to the permeable side without much tortuosity[13]. The formation of microvoids depends on the polymer-solvent-insolvent interaction. Recent studies clearly show that the formation of macrovoids is due to the competition between polymer solidification rate and solvent-insolvent exchange rate[13].

### 3.1.2 Porosity and Thickness

Membrane porosity, thickness, liquid entry pressure, and contact angle were measured and the results are shown in Tab. 3. Porosity is one of the parameters that influences the performance flux and the efficiency of MD. The fabricated flat sheet membranes observed a liquid entry pressure (LEP) range of 2.9–4.8 bar and porosity values ranging from 36.39% to 78.51% with a contact angle variance from 88.32° to 94.64°.

**Table 4.** Membrane contact angle, LEP, porosity and thickness, and pore size for the prepared membranes

Membrane Code	Contact Angle ( $\theta^\circ$ )	Lep (bar)	$\varepsilon$ (%)	$\delta$ ( $\mu\text{m}$ )
				Ortalama
M1	92.19	2.9	58.012	65.99
M2	88.32	4.2	78.51	42.54
M3	90.09	4.6	75.95	38.19
M4	94.64	4.8	36.39	61.41

Looking at the SEM analysis the M1 membrane prepared at 85 wt% of DMAC solvent showed that I have the 58.012 porosity and 65.99 thickness. Membrane M2 exhibited the highest porosity 78.51% and thickness 42.54  $\mu\text{m}$ . DMAC and DMF solvents used at different concentrations in the casting solution affected the formation of the membrane structure depending on the exchange rate between solvent and non-solvent in the coagulation bath. With the decrease in DMAC solvent concentration, spongy structures were formed as a result of mixing between solvent and non-solvent, and thickness and porosity values decreased. Membrane porosity and thickness have been also influenced by the DMAC and DMF solvent concentration in the casting dope solution and by the preparation procedure. By increasing the concentration of DMF from 25 to 75 wt% (M2, M3, and M4 membranes respectively) the porosity decreased from 78.51 % to 36.39 % and the thickness changed from 42.54  $\mu\text{m}$  to 61.41  $\mu\text{m}$ , respectively. According to the contact angles of PVDF-HFP flat sheet membranes prepared by NIPS as given in Tab. 3, the highest team angle was  $\sim 94.64^\circ$  for the M4 membrane. The contact angle values of the membranes increased from  $88.32^\circ$  to  $94.64^\circ$  with increasing DMF concentration.

### 3.1.3 Performance Effects on DTMD

The effect of all prepared PVDF-HFP membranes on DTMD was investigated by varying the feed temperature (between 40 and 80  $^\circ\text{C}$ ), first using distilled water as feed. Then, using 0.1 M NaCl aqueous solution as feed solution, the permeate temperature was kept constant at 20  $^\circ\text{C}$ . Flux measurements and calculated salt removal results using distilled water and 0.1 M NaCl are given in Tab. 3. According to the data obtained in Tab. 1, it was observed how the concentration changes of DMAC and DMF solvents in the produced membranes affected the flux and salinity removals in the DCMD system depending on the temperature. It was observed that the increase in DMF concentration and decrease in DMAC concentration caused a decrease in flux. Increasing feed concentration reduces vapor pressure and increases temperature polarization. For this reason, there is a decrease in the permeate flux. Salt removal rates have been determined to be approximately 99%. The decrease in flux is observed for 0.1 M NaCl containing non-volatile components compared to the distilled water flux. This is attributed to the decrease in water vapor pressure with the addition of solutes due to the decrease in water activity in the feed solution. In addition, the temperature polarization effect and the concentration polarization effect also contribute [14].

### 3.1.4 Contact Angle and Liquid Entry Pressure

For MD processes, the contact angle must be greater than  $90^\circ$ , since LEP largely depends on the hydrophobicity of the membrane [15]. For membranes to have high liquid entry pressures, they must have small room inlet sizes and high hydrophobicity. Among the prepared membranes, M4 has the highest LEP content. With the increase in DMF concentration, liquid entry pressure values increased from 2.9 bar to 4.8 bar. Similarly, when looking at the contact angle values, increased from  $88.32^\circ$  to  $94.64^\circ$  with the increase in DMF concentration.

## 4 CONCLUSION

Flat sheet PVDF-HFP membranes were prepared by non-solvent induced phase separation technique (NIPS) for membrane distillation applications. DMF and DMAC were used as solvents during the phase inversion procedure, which enabled the production of flat sheet membranes suitable for MD applications. Membrane morphology was studied by acting on the composition in the casting dope solution of the DMF and DMAC mixed solvent concentration. Membranes prepared from different concentrations of DMAC and DMF exhibited similar sponge-like structures and finger-like various surface porosities across the membrane. Reducing the DMAC concentration from 85% to 21.5% changed the membrane thickness from 42 to 61 and led to reductions in permeability and salt rejection as a result of reduced porosity. With the increase in DMF concentration, the macrovoid finger-like structure was replaced by a spongy structure. In addition, in DCMD, the fluxes have decreased due to the reduction in the size of the pores and the prominence of the spongy structure.

## References

- [1] M. Khayet, "Membranes and theoretical modeling of membrane distillation: A review," *Adv. Colloid Interface Sci.*, vol. 164, no. 1–2, pp. 56–88, 2011.
- [2] M. El-Bourawi, Z. Ding, R. Ma, and M. Khayet, "A framework for better understanding membrane distillation separation process," *J. Membr. Sci.*, vol. 285, no. 1–2, pp. 4–29, 2006.
- [3] M. S. El-Bourawi, Z. Ding, R. Ma, and M. Khayet, "A framework for better understanding membrane distillation separation process," *J. Membr. Sci.*, vol. 285, no. 1, pp. 4–29, 2006/11/15/ 2006.
- [4] M. García-Payo, M. Essalhi, and M. Khayet, "Effects of PVDF-HFP concentration on membrane distillation performance and structural morphology of hollow fiber membranes," *J. Membr. Sci.*, vol. 347, no. 1-2, pp. 209–219, 2010.
- [5] B. S. Lalia, E. Guillen-Burrieza, H. A. Arafat, and R. Hashaikeh, "Fabrication and characterization of polyvinylidene fluoride-co-hexafluoropropylene (PVDF-HFP) electrospun membranes for direct contact membrane distillation," *J. Membr. Sci.*, vol. 428, pp. 104–115, 2013.
- [6] C. Feng, R. Wang, B. Shi, G. Li, and Y. Wu, "Factors affecting pore structure and performance of poly (vinylidene fluoride-co-hexafluoro propylene) asymmetric porous membrane," *J. Membr. Sci.*, vol. 277, no. 1-2, pp. 55–64, 2006.
- [7] S. Saïdi *et al.*, "Preparation and characterization of hydrophobic P (VDF-HFP) flat sheet membranes using TamiSolve® NxG solvent for the treatment of saline water by direct contact membrane distillation and membrane crystallization," *Sep. Purif. Technol.*, vol. 275, art. no. 119144, 2021.
- [8] A. Alkudhiri and N. Hilal, "Membrane distillation—Principles, applications, configurations, design, and implementation," in *Emerging Technologies for Sustainable Desalination Handbook*, Elsevier, 2018, pp. 55–106.
- [9] C. Smolders and A. J. D. Franken, "Terminology for membrane distillation," *Desalin.*, vol. 72, no. 3, pp. 249–262, 1989.
- [10] R. Hebbbar, A. Isloor, and A. Ismail, "Contact angle measurements," in *Membrane Characterization*, Elsevier, 2017, pp. 219–255.
- [11] M. S. Bingöl, O. N. Ata, N. J. R. Alemdar, and F. Polymers, "Development of a new route for cation exchange membrane fabrication by using GO reinforced styrenated oil," *React. Funct. Polym.*, vol. 178, art. no. 105336, 2022.
- [12] T. Marino, F. Russo, A. Criscuoli, and A. J. J. o. M. S. Figoli, "TamiSolve® NxG as novel solvent for polymeric membrane preparation," *J. Membr. Sci.*, vol. 542, pp. 418–429, 2017.
- [13] Y. J. Song *et al.*, "Controlling the morphology of polyvinylidene-co-hexafluoropropylene (PVDF-co-HFP) membranes via phase inversion method," *Membrane Journal*, vol. 28, no. 3, pp. 187–195, 2018.
- [14] Y. Guan, J. Li, F. Cheng, J. Zhao, and X. J. D. Wang, "Influence of salt concentration on DCMD performance for treatment of highly concentrated NaCl, KCl, MgCl<sub>2</sub> and MgSO<sub>4</sub> solutions," *Desalin.*, vol. 355, pp. 110–117, 2015.
- [15] S. Fadhil *et al.*, "Novel PVDF-HFP flat sheet membranes prepared by triethyl phosphate (TEP) solvent for direct contact membrane distillation," *Chem. Eng. Process. Process Intensif.*, vol. 102, pp. 16–26, 2016.



---

## Efficiencies of FePd Nanoparticles in Basic Red 46 Removal

Fatma Guclu<sup>1</sup>, Melike Sevim<sup>\*1</sup>

<sup>1</sup>Chemistry Department, Science Faculty, Ataturk University, 25240, Erzurum, Türkiye

---

### Abstract

Environmental pollution is a huge problem today. Especially dyestuffs, organic substances and pharmaceutical wastes mixed into wastewater threaten human and environmental health. For these reasons we developed a new catalyst that can provide BasicRed46 pollution removal from wastewater. This study consists of two stages. In the first step, iron-palladium nanoparticles were synthesized under nitrogen atmosphere in a four-neck reactor in the presence of reducing agent, surfactant and co-surfactant under mild conditions. Iron acetylacetonate and palladium acetylacetonate salts were dissolved in 3 ml of oleylamine. Borane-tert-butyl-amine was subjected to the reaction and maintained at 120°C for 1 hour. Colloidal FePd nanoparticles with a uniform structure of 3-3.5 nm were obtained. Colloidal FePd nanoparticles were supported by self-deposition method into mesoporous graphitic carbon nitride structure in liquid phase. It was observed that FePd/mpg catalyst had the highest Basic Red 46 removal. Finally, repeatability tests of the adsorbent were performed. At this stage, the characterization of the adsorbent was done by TEM, XRD, XPS and ICP-MS techniques. It was seen that adsorbent did 91 % Basic Red 46 removal. Thus, a new active catalyst was introduced to the literature.

**Keywords:** *Iron-palladium, Basic Red46, Catalyst, Removal*

---



## Study of the Photoreduction of $\text{Co}^{2+}$ Ions Under Solar and Visible Light Irradiation

Samira Tebani<sup>\*1</sup>, Lila Kerrai<sup>1</sup>, Samir Ladjali<sup>2</sup>

<sup>1</sup>Environmental and Process Engineering, University of Science and Technology Houari Boumediene, Algeria

<sup>2</sup>Process Engineering Department, Faculty of Science and Technology, University of Mustapha Stambouli Mascara, Algeria

---

### Abstract

Water pollution constitutes a serious problem for living beings. Therefore, the depollution of water contaminated by heavy metals is essential for environmental protection. Currently, photocatalysis offers a promising alternative to partially address this pollution issue. A comparative study of the photoreduction of  $\text{Co}^{2+}$  ions under solar and artificial irradiation was conducted using heterogeneous photocatalysis with a  $\text{CuFeO}_2/\text{SnO}_2$  heterogeneous system. The objective was to determine the effect of the mass ratio of the heterogeneous system, pH, and the initial concentration of the  $\text{Co}^{2+}$  solution. The results show that photocatalytic degradation is optimal at a pH of approximately 6, with a mass ratio of  $\text{CuFe}_2\text{O}_4/\text{SnO}_2$  of 50/50 mg per 100 ml of solution to be treated, and an initial cobalt concentration of 50 mg/L. The photoreduction rate of  $\text{Co}^{2+}$  ions under solar irradiation reaches 62.26%, which is significantly higher than the 47.72% rate obtained under visible light irradiation.

**Keywords:** Water pollution, Artificial irradiation, Solar irradiation, Heterogeneous system, Photocatalysis

---



---

## The Use of Glass and Other Alternative Materials in the Cement Industry

Damir Mulamehmedovic<sup>1</sup>, Zehrudin Osmanovic<sup>\*2</sup>, Ervin Karic<sup>2</sup>, Belmina Hadžalic<sup>2</sup>,  
Elma Bajric<sup>2</sup>

<sup>1</sup>Lukavac Cement, Lukavac, Bosnia and Herzegovina

<sup>2</sup>Department for Chemical Engineering, University of Tuzla, Faculty of Technology, Tuzla, Bosnia and Herzegovina

---

### Abstract

Cement production is based on the use of natural raw materials such as: limestone, marl, clay, sand, iron ore, gypsum, slate and bauxite. However, due to their chemical compatibility, alternative materials such as various types of industrial waste, side products or unwanted products of certain processes can be economically and technically acceptable as raw materials for cement production. Increasing requirements to reduce CO<sub>2</sub> emissions into the atmosphere further contribute to the increasing use of alternative raw materials in the production of cement. The use of alternative raw materials for the production of cement is one of the most important methods for reducing CO<sub>2</sub> emissions into the atmosphere from the cement industry. The reason is that the use of alternative raw materials has a preventive effect on the very creation of CO<sub>2</sub>, reducing the exploitation of natural resources. In this way, a raw material mixture is provided which is often more economically acceptable than a raw material mixture based on natural raw materials. Alternative raw materials can often generate additional costs in the industry because it is necessary to carry out ecological disposal. The focus of this paper is the use of industrial waste and other unwanted products in industries as raw materials for the production of cement clinker. It is important to emphasize that chemical compatibility is the first and basic condition for the use of certain alternative materials in the cement industry. With the help of a mathematical model, the economic and ecological effects of the use of different alternative raw materials are shown. The mathematical model provides data on the optimal raw material mixture that meets the required clinker quality parameters, minimizing the costs of the raw material mixture and CO<sub>2</sub> emissions into the atmosphere.

**Keywords:** *Cement, Glass, Alternative materials, Mathematical model*

---

## 1 INTRODUCTION

So far, many professional and scientific works have been written and published in the field of the use of alternative raw materials in the cement industry. Rohrbach, R. (1969) presented in his work the use of oil shale in the amount of 8% directly in the pre-calciner. Shale ash was integrated into the clinker composition, and the quality of the clinker was such that it was not necessary to add gypsum when grinding the clinker into cement [1]. Miller, F.M. (1980) presented the use of fly ash in a cement plant located in Ålborg, Denmark. 10 % of fly ash from the total raw material mixture was dosed directly into the firing zone. The clinker was of good quality with a good phase distribution in the firing process. Later, during 1988, certain changes were made in the fly ash dosing system as well as the construction of a pre-calciner, after which the amount of fly ash in the clinker was raised to 24%. By 1999, 2.3 million tons of fly ash were consumed in this plant, of which 50% of the ash was used as an alternative raw material (Borgholm, 1999), [2]. Valkova I.S. with a colleague (1980) used different types of slag (crystallized and vitreous) in the raw material mixture for the production of clinker. These slags contained significant amounts of barium and manganese oxides. The slag improved the reactivity of the raw material mixture, and the admixtures of barium and manganese contributed to the modification of the alite crystal, which resulted in a clinker with higher strength [3].

Ahluwalia, S. et al. (1981), presented in their paper the advantages of using low-quality limestone as a raw material for clinker production. Limestone with a high magnesium and silicon content and a lower calcium content was subjected to a separation process to concentrate the calcium content in the limestone, which would later be used in the production of cement. Other methods considered were differential grinding and sieving, electrostatic separation, photometric sorting and bacterial washing. These limestones were considered to be more suitable for wet and semi-wet clinker production, although it could also be used in other types of clinker production processes, [4]. Mori, T. (1982), presented a paper dealing with the use of SiO<sub>2</sub>-rich fly ash in a Japanese cement plant. The fly ash control and treatment plant at the Takehara thermal power plant has been installed and managed in such a

way that the resulting fly ash is of suitable quality for clinker production. Fly ash replaced the use of clay in the amount of 20 % to 40 %, depending on which of the two types of ash was used for the production of clinker [5].

Bhatty, J.I. et al. (1985) presented in their paper the possibility of using mineral tailings produced in the process of copper and nickel production. Tailings rich in SiO<sub>2</sub> in combination with other raw materials contributed to the production of clinker which had better strength parameters in cement than commercial cement type 1 [6]. Laxmi, S.A. et al. (1985), considered the use of red mud that is produced as a waste in the production of aluminum. Sludge containing 9.6% SiO<sub>2</sub>, 18.6 % Al<sub>2</sub>O<sub>3</sub>, 15.4 % CaO and 26.65% Fe<sub>2</sub>O<sub>3</sub>, added in an amount of 2.5 %, completely replaced the iron ore used until then. The properties of clinker have not changed significantly. The early strengths in cement were slightly higher, while the strengths remained the same after 28 days, [7]. NCB Report (1987), as a report on the subject, presented the use of carbide sludge as a substitute for limestone in the amount of 30% in the raw material mixture. The addition of this material resulted in raw flour that had good baking properties, and the produced clinker had very good characteristics. Alite and belite crystals were very well formed, and the specific energy consumption for the firing process was significantly lower [8].

Purohit, M. et al. (1987), due to the lack of quality limestone, also presented a paper where they presented the use of a raw material mixture with limestone enriched by the calcium filtration method. Using this kind of raw material in a rotary kiln with a two-stage cyclone heat exchanger, clinker production was successfully carried out in a capacity of 1780 tons/day, with the production of clinker of normal strength, setting time and other physical characteristics. The produced clinker had the following composition: 41% C<sub>3</sub>S, 48% C<sub>2</sub>S, 5% C<sub>4</sub>AF, and 6 % C<sub>3</sub>A, [9]. Puertas, F.M. et al. (1988), demonstrated the use of crystallized slag in the production of clinker. With a high content of CaO, SiO<sub>2</sub> and Al<sub>2</sub>O<sub>3</sub>, the slag replaced significant amounts of limestone, sand and clay in the raw material mixture. An example of the mineralogical composition of clinker from this test is: 63.33 % C<sub>3</sub>S, 14.66 % C<sub>2</sub>S, 7.22 % C<sub>4</sub>AF, and 11.65 % C<sub>3</sub>A, [10]. Harada, M. (1991), presented a study of the use of fly ash as an alternative raw material for clay in the clinker production process.

No significant problems were observed in the production process, and traces of non-combustible residue in the ash did not significantly affect negative changes in the production process, [11]. Ghosh, S.P. et al. (1992), presented work based on the use of ash from rice flakes, created as waste in the process of burning the flakes in boilers for energy production. Ash from rice flakes partially replaced stone with a high SiO<sub>2</sub> content (sandstone) in the raw material mixture. Considering that the ash of rice flakes also contained non-combustible carbon residue, the consumption of coal in the process was partly reduced. Rice husk ash improved the reactivity of the raw material mixture and improved the quality of the clinker [12]. Mullick, A.K. et al. (1992), presented a study of the use of fly ash in a cement plant in India. The chemical composition of the ash was approximately the same as that of the clay used until then, so the clay was almost completely substituted with fly ash [13].

Kelly, R.J. (1994), presented in his paper the findings that the control of the degree of saturation, silicate modulus and aluminate modulus using fly ash in the raw material mixture is superior to the raw material mixture where shale is used as raw material. The test on the basis of which the conclusions were drawn consisted of replacing 3.5% of shale with fly ash. Clinker with ash contained the same amounts of C<sub>3</sub>S and C<sub>2</sub>S, but also an increased content of C<sub>3</sub>A. The increased content of C<sub>3</sub>A contributed to a better control of early strengths and setting time in cement, [14]. Everett, D. (1995), presented in his paper the possibility of using fly ash as a raw material substitute for oil shale. In one of the largest cement plants in North America, the shale used as raw material contained up to 5% sulfur, resulting in the plant generating large amounts of filter dust (CKD) as a by-product that could not be returned to the process. Replacing 50% of the shale with fly ash contributed to a 50 % reduction in the resulting filter dust.

The produced cement was low-alkaline and the emission of SO<sub>2</sub> into the atmosphere was significantly reduced, [15]. Singh, N.B. et al. (1995), published a paper where the use of waste material from landfills of coal-fired thermal power plants was presented. The waste material contained a mixture of fly ash and slag. The use of 4 % of the aforementioned mixture in the raw material mixture did not jeopardize the production process, while the non-combustible residue contributed to better energy efficiency. The satisfactory quality of the clinker and the easier grinding of the clinker have confirmed the possibility of using this material in the production of clinker and cement, [16]. In his paper, Du Toit (1996) presented the results of an industrial trial in a cement plant from South Africa, where limestone with 46.21 % CaO was replaced with limestone that has a CaO content of about 40.8 %. The composition of the raw material mixture was 80 % limestone (46.21 % CaO), 10 % limestone (40.8 % CaO), 9 % slag from boiler plants and 1 % magnetite.

The produced clinker had similar characteristics as clinker in normal production, [17]. Young, R.D. (1996), in his patent protected the knowledge about the use of unground blast furnace slag as a raw material component.



Replacing the usual raw materials with 30 % slag resulted in the production of clinker with an acceptable chemical and mineralogical composition, [18]. Freiman, L.S. with collaborators (1997), in his work presented research related to the use of oil shales that have a high calcium content. The research was done in a cement plant in Russia, and the composition of the oil shale was from 34.5 % to 38.9 % CaO and from 28.1 % to 38. % SiO<sub>2</sub>. The shale contained from 6 % to 8 % of organic fuel, and therefore it was dosed to the pre-calciner in the amount of 8 % of the raw material mixture. The residual fuel component in the shale contributed to energy savings, and the clinker had a satisfactory chemical and mineralogical composition, [19].

Singh, N.B. et al. (1997), presented the use of rice husk ash in vertical shaft kilns for clinker production. The addition of ash contributed to a better burnability of the raw material mixture, the production capacity was increased by 10 %, and the non-combustible residue contributed to energy savings. The produced clinker was of adequate quality, [20]. Bhatt, J.I. et al. (1998), demonstrated the use of fly ash containing 20 % non-combustible residue. The ash content in the raw material mixture with limestone and shale in the amount of 6 % was limited due to the chemical composition of the ash. During the demonstration, the production process ran smoothly and without major changes from the usual state. As a result, production was achieved with energy savings of 4 % and an increase in clinker production capacity of 10 %. The produced clinker was of satisfactory quality, but with a lower content of sulphate and alkali. The quality of the cement produced from the test clinker was comparable to the quality of commercial cement, [21]. Ajiwe, V.I.E. et al. (2000), used 24.5 % rice husk ash in the white cement production process. In combination with other raw materials, the produced cement did not deviate from the quality of commercial cement in terms of chemical and physical properties [22].

Bhatt, J.I. with colleagues (2000) presented a scientific paper using slag from thermal power plants as a potential raw material in the production of cement. These are materials with a similar composition to fly ash, but the particles are much larger. Usually, slag is added as raw material directly to the raw material mill together with other raw materials in the amount of 3 % to 5 % (depending on the chemical composition of the slag). The produced clinker did not show significant deviations in quality, [23]. Bhatt, J.I. (2002), in his study investigated the possibility of using foundry sand as a source of SiO<sub>2</sub> in the raw material mixture. Foundry sand completely replaced ordinary sand, and the produced clinker had a higher hardness due to larger quartz crystals. Grindability of this clinker was more difficult, but the strengths after 28 days were significantly higher, [24]. Xiaoquan, G. with associates (2023), based on the aspiration for CO<sub>2</sub> neutral cement production by 2060, considered the possibility of reducing CO<sub>2</sub> emissions through the use of alternative raw materials, as well as raw materials that had the potential to replace clinker in cement production. In this paper, three scenarios in the use of alternative raw materials were considered: 13 %, 17 % and 20 %. All testing was done in Guangdong, China [25].

However, based on the European Commission's plan to reduce greenhouse gas emissions by 55 % by 2030, it is clear that many industries, including the cement industry, must make certain changes in the production process. The transition of production processes to more environmentally friendly ones is gradual but necessary, and it is necessary to process all potentials that can contribute to the transition itself. The production of clinker requires a large amount of thermal energy, which is on average about 3500 kJ/kg of clinker, [26].

## 2 MATERIAL AND METHOD

The production of clinker, and later cement, with natural or alternative raw materials is identical, and the same restrictions apply to the production process, regardless of whether the raw materials are natural or industrial sources. Alternative raw materials in the cement industry are mainly industrial wastes from other industrial plants, and they are acceptable for the cement industry for three basic reasons:

- Alternative raw material often has a lower cost than natural,
- By using industrial waste as an alternative raw material, industrial waste landfills are reduced and
- The use of alternative raw materials preserves reserves of natural raw materials for future generations.

Materials that were created as products of thermal processes in other industries and contain increased amounts of calcium, silicon, aluminium and iron oxides are very good raw materials for use in the raw material mixture for the production of clinker. A critical point in the use of alternative raw materials created from waste is the compatibility of the chemical composition in order to partially or completely replace one of the natural raw materials [27].

The basic criteria for choosing certain alternative raw materials are:

- Chemical and physical compatibility,

- Availability of alternative raw materials at an economically justified distance from the cement plant,
- The price of the alternative raw material and the economic justification of its use,
- The alternative raw material must be ecologically justified,
- The use must not limit the quality and quantity of the process or product and
- Available amounts of alternative raw materials must meet the needs of continuous production.

Alternative raw materials, which are available only occasionally in limited quantities, can be used in the cement industry, but since it is a continuous production process, it is necessary to consider the risks that can be caused by discontinuous changes in the process. Taking into account all the limitations in the selection of raw materials, it is clear that there are many limitations. Some restrictions are exclusive, while others are acceptable subject to certain conditions. The selection of raw materials according to their physical characteristics is a process that is specific to each industrial plant, while chemical compatibility is exclusive and theoretically the same for most cement plants in the world. Environmental compatibility represents legal restrictions that may be different depending on the type of legal restrictions at the location where the facility is located. When a potential raw material is identified, the first step is to establish communication with the owner of the potential raw material, determine the steps of the visual inspection, agree on the exclusion of samples for analysis purposes, and prepare the financial conditions necessary for the economic evaluation of the justification of use.

A visual inspection of the potential raw material is important so that the potential user can quickly determine whether the physical properties of the raw material are compatible with the process equipment. Alternative raw materials can very often be in the physical form of sludge, fine powder, thick viscous mass, etc., which requires the installation of special equipment for dosing and processing. Of course, the investment in the installation of new equipment can be justified if it is established as a fact after an economic evaluation. After sampling and analysis of the potential raw material, it is necessary to model the raw material mixture and evaluate the chemical compatibility. Together with the check of chemical compatibility, the check of the compliance of the raw material with the requirements for ecological compliance is also carried out. In picture no. 1 shows the flow diagram of the selection of potential raw materials for the production of clinker.

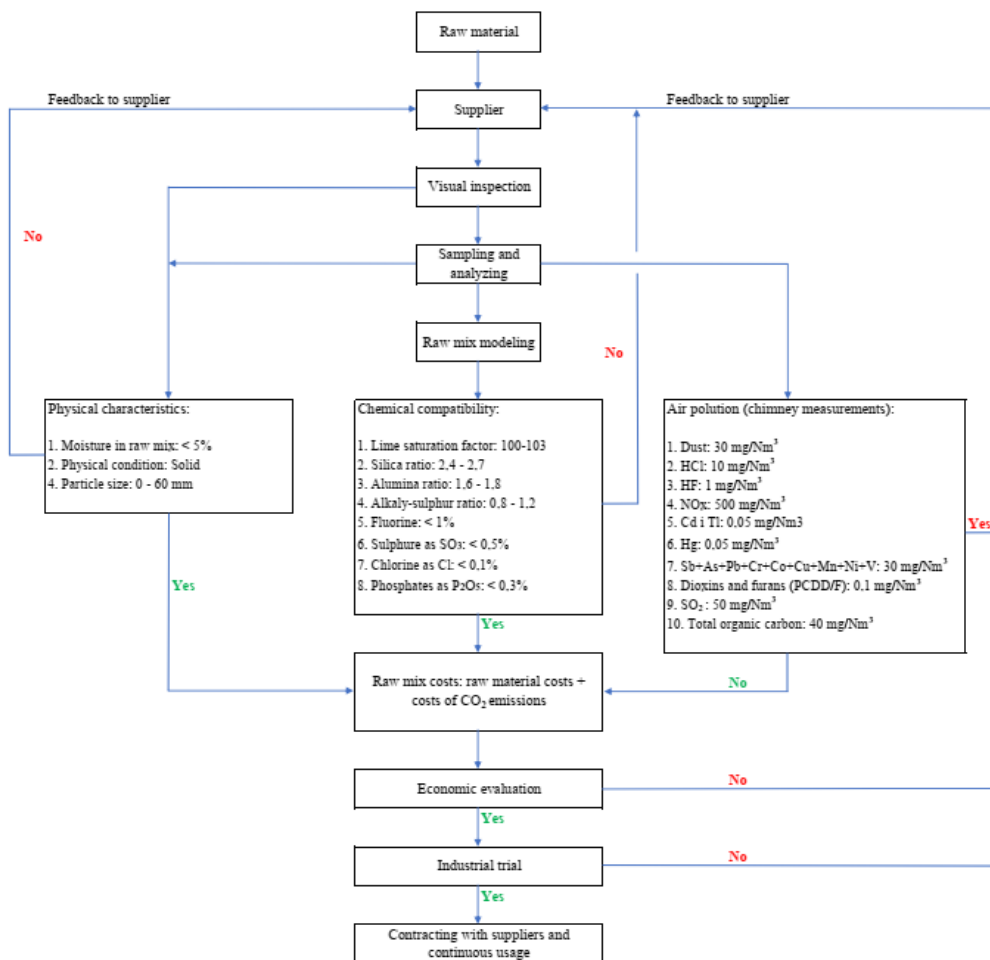


Figure 1. Algorithmic steps of selecting an alternative component in the formation of the raw material mixture

In addition to the basic raw materials for the production of cement, limestone, marl and sand, alternative raw materials such as ash from the thermal power plant, slag from the boilers of the thermal power plant, slag from blast furnaces, waste aerated concrete and waste glass were analysed.

**Table 1.** Chemical composition of alternative ash raw material

Chemical Composition	CaO	SiO <sub>2</sub>	Al <sub>2</sub> O <sub>3</sub>	Fe <sub>2</sub> O <sub>3</sub>	Loss on Ignition	Moisture	Unit
Ash	9.20	54.04	18.80	9.68	1.86	1.00	%

Slag is a waste product of coal combustion in a thermal power plant. The slag from the boilers is rapidly cooled with water, thereby retaining its solid structure. It is granular in shape, black in colour, and resembles slag/slag from blast furnaces.

**Table 2.** Chemical composition of alternative raw material, slag from blast furnaces

Chemical Composition	CaO	SiO <sub>2</sub>	Al <sub>2</sub> O <sub>3</sub>	Fe <sub>2</sub> O <sub>3</sub>	Loss on Ignition	Moisture	Unit
Slag	25.11	41.7	19.83	9.13	0.50	10.00	%

Slag (ground granulated blastfurnance slag - GGBFS) is a side product in iron production. Slag is a water-cooled granular material with a large amount of glassy phase. For many years, blast furnace slag has been recognized in the cement and construction industry as a good material that can be used as an addition to clinker in the cement grinding process. It is characterized by high pozzolanic properties and is ideal for the production of cement with a low heat of hydration.

**Table 3.** Ground granulated blastfurnance slag – GGBFS

Chemical Composition	CaO	SiO <sub>2</sub>	Al <sub>2</sub> O <sub>3</sub>	Fe <sub>2</sub> O <sub>3</sub>	Loss on Ignition	Moisture	Unit
Blastfurnance slag	37.01	39.76	9.57	0.82	0.60	10.00	%

Aerated concrete is a product that belongs to the group of lightweight fine-grained concrete. Other names for aerated concrete are: cellular, foam or aerated concrete. Lightweight concrete has a lower weight per unit volume than conventional concrete. Their volumetric weight is usually less than 1900 kg/m<sup>3</sup>. Aluminium powder in the form of fine colloidal dust is most often used to create gas. In the case of most mineral raw materials of industrial and natural origin, loss by annealing is the thermal decomposition of some carbonate, usually CaCO<sub>3</sub>. During the thermal treatment of aerated concrete, CO<sub>2</sub> will not be emitted, that is, this CO<sub>2</sub> has already been released during the production of CaO, which is used as a raw material in the production of this building material.

**Table 4.** The chemical composition of the alternative raw material “gas-concrete”

Chemical Composition	CaO	SiO <sub>2</sub>	Al <sub>2</sub> O <sub>3</sub>	Fe <sub>2</sub> O <sub>3</sub>	Loss on Ignition	Moisture	Unit
Gas-concrete	27.94	42.62	4.43	2.25	39.00	13.11	%

Given that the cement industry is still a large consumer of fossil and alternative fuels, the appearance of sulphur contained in the fuel usually causes problems in the process. These problems manifest themselves in the form of stickers in rotary kilns. Sulphur control is carried out by an adequate ratio of alkali in the raw materials in relation to the sulphur content. The alkali/sulphate ratio in the raw material mixture should be less than 1. If there is not enough potassium or sodium in the raw materials to bind to the sulphur from the fuel, it is necessary to find a raw material or an additive through which alkali can be introduced into the system. Glass is a good source of sodium and silicon, essential constituents in clinker.

**Table 5.** Chemical composition of alternative raw material, waste glass

Chemical Composition	CaO	SiO <sub>2</sub>	Al <sub>2</sub> O <sub>3</sub>	Fe <sub>2</sub> O <sub>3</sub>	Na <sub>2</sub> O	Moisture	Unit
Waste glass	13.36	66.12	1.97	0.55	15.24	0.40	%

### 3 RESULTS

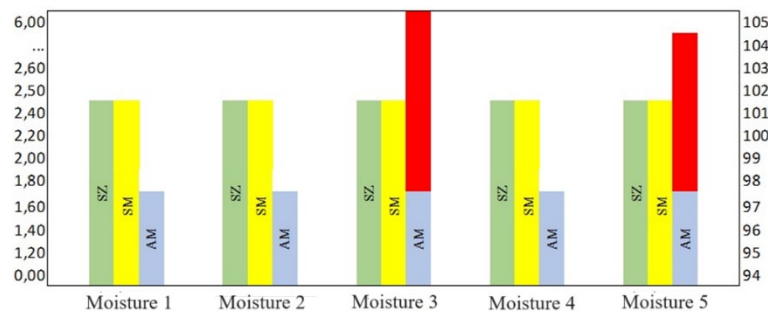
Five mixtures for the production of clinker were analysed:

- i. Raw material mixture: limestone, marl and sand
- ii. Raw material mixture: limestone, slag produced in the thermal power plant and waste glass

- iii. Raw material mixture: limestone, thermal power plant ash and gas concrete
- iv. Raw material mixture: limestone, ash created by burning coal and slag from blast furnaces for iron production
- v. Raw material mixture: limestone, thermal power plant ash and slag from blast furnaces for iron production

### 3.1 Selection According to the Compatibility of the Chemical Composition of the Mixture

As the requirement for the degree of saturation, silicate modulus and aluminite modulus is limiting, the first selection of the potential raw material mixture refers to the exclusion of the raw material mixture that cannot meet the theoretical limitations due to its composition.

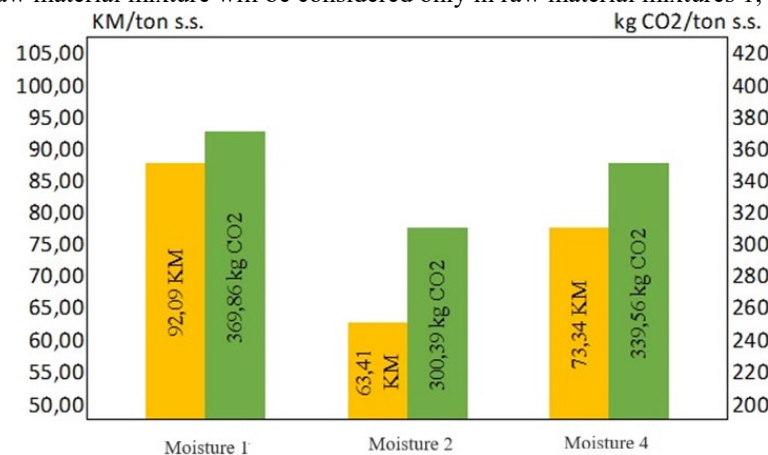


**Figure 1.** Compatibility of a particular raw material mixture in relation to degree of saturation and modulus

Potential raw material mixtures No. 3 and No. 5 can be excluded from consideration at this time due to the high values of the aluminite modulus.

### 3.2 Selection by the Price of the Raw Material Mixture

Raw material mixtures No. 3 and No. 5 do not meet the parameters of the aluminite module, so the selection based on the price of the raw material mixture will be considered only in raw material mixtures 1, 2 and 4.



**Figure 2.** Raw material mixture costs and CO<sub>2</sub> emissions per ton of raw material mixture used

Raw material mixture number 2 represents the optimal choice among all other alternative mixtures that were taken into consideration. The use of limestone as a natural raw material and alternative raw materials ash 2. and aerated concrete, represents a significant reduction in the use of natural resources with better financial results of the company and more environmentally responsible production.

Based on the processed methodology, in addition to choosing the optimal raw material mixture, it is also possible to define a ranking among the raw material mixtures. This can give certain cement companies a significant strategic advantage in the event of changes in the market or facilitate long-term business planning.

## 4 CONCLUSION

During the research, three prerequisites for the quality selection and evaluation of the optimal raw material mixture in the cement plant were observed:

- The choice of raw materials for the production of clinker is possible only if there is a functional primary selection methodology,
- It is necessary to develop a compatibility model of each raw material in the mixture in relation to ecological, production and economic criteria and
- The development of software tools significantly shortens the time of finding the optimal solution, that is, choosing the optimal raw material mixture.

The primary selection methodology ensured the elimination of potential raw materials that could threaten the production process, product quality or have a negative impact on the environment. The primary selection of raw materials is characteristic for each plant individually, but the model presented in this paper enables a systematic approach in the selection process itself, regardless of the specifics of individual plants.

The development of the raw material compatibility model in the raw material mixture is based on theoretically known parameters that guarantee the stability of the production process, product quality, ecological compliance and economic profit. On the basis of the developed model, an optimal raw material mixture was reached, the use of which can be expected to produce clinker of the required quality and quantity, with a reduction in the average cost of the raw material mixture and lower CO<sub>2</sub> emissions.

The mixture of limestone, slag from the thermal power plant and waste glass proved to be the best, where alternative raw materials in the raw material mixture partially replaced natural raw materials with 31.92%. In this case, the price of raw materials per produced ton is lower by 31.09 %, the emission of CO<sub>2</sub> into the atmosphere is lower by 26.80 %. The amount of 31.92 % of the used alternative raw material represents a reduction of the emission of industrial waste into the environment by the same amount and the reduction of CO<sub>2</sub> emission provides more space for planning and better financial results, considering that CO<sub>2</sub> is an object of international trade.

The model presented in this work is flexible to the types of raw materials that can be an alternative in the production of cement.

## References

- [1] R. Rohrbach, "Production of oil shale cement and recovery of electrical energy from oil shale using the rohrbach-lurgi process," pp. 293–296, 1969.
- [2] M. F. MacGregor, "Flames, fuels & vaporization of volatile compounds," in *Research on the Manufacture and Use of Cements: Proceedings of the Engineering Foundation Conference*, New England College, Henniker, New Hampshire, 1985..
- [3] I. S. Valkova and R. G. Dogandzhieva, "Producing Portland cement clinker using blast furnace barrick-manganese slag," in *Proceedings of the 7th International Congress on the Chemistry of Cement*, Paris, France, 1980, vol. 1.
- [4] S. C. Ahluwalia, S. Laxmi, and S. K. Chopra, "High magnesia and marginal grade limestone prospects, problems and technology of utilization," *All India Seminar on Cement Manufacture*, vol. 1, 1981.
- [5] T. Mori, "Features of coal storage and coal ash treatment systems for large scale coal-fired power generation at EPDC's takehara thermal power station, no. 3 extension unit," in *Sixth International Conference on Coal Research, National Coal Board*, London, 1982, vol. 6.
- [6] J. I. Bhatti, J. Marijnissen, and K. J. Reid, "Portland cement production using mineral wastes," *Cement and Concrete Research*, vol. 15, no. 3, pp. 501–510. 1985.
- [7] S. Laxmi and A. K. Parashar, "Potentials of utilisation of wastes from fertilizer and aluminum industries for building materials: an overview," in *National Seminar on Role of Building Materials Industries in Conversion of Waste into Wealth*, 1985, pp. 101–111.
- [8] Q. Wang, S. K., Sun, Z. M., Wang, and X. J. Lyu, "Physical properties, hydration mechanism, and leaching evaluation of the Portland cement prepared from carbide residue," *Journal of Cleaner Production*, vol. 366, art. no. 132777, 2022
- [9] M. A. Purohit, S. M. Rasal, and R. D. Shaha, "Kiln feed filtration for semi dry conversion," in *First NCR International Seminar on Cement and Building Materials*, New Delhi, India, vol. 2. pp. 59–74.
- [10] F. Puertas et al., "Reactivity and burnability of raw mixes made with crystallized blastfurnace slags. I," *Zkg International*, vol. 41, no. 8, pp. 398–402, 1988.
- [11] M. Harada, "Recovery and utilization of coal ash," *Shigen to Sozai, Japan*, vol. 107, pp. 85–91, 1991.
- [12] S. P. Ghosh, K. Mohan, and R. K. Gandhi, "Effects of using rice husk and its ash as fuel and raw material component, respectively, in cement manufacture," in *Int. Congr. Chem. Cem.*, 1992, pp. 224.

- [13] A. K., Mullick, and S. C. Ahluwalia, "Utilization of wastes in Indian cement industry," in *Proceedings of 1st International Symposium on Cement Industry Solutions to Waste Management*, Alberta, Canada, Oct. 1992, pp. 489–512.
- [14] R. J. Kelly, "Coal ash-a useful raw material for Portland cement manufacture," in *2. International Symposium on Ash - A Valuable Resource*, 1994, vol. 2, pp. 373–380.
- [15] D. Everett, "Raw materials are the key to CKD reduction," *Rock Products*, vol. 98, no. 7, pp. 16–21, 1995.
- [16] N. B., Singh, K. N. Bhattacharjee, and A. K. Shukla, "Pond ash-A potential reactive raw material in the black meal process of cement manufacture by vertical shaft kiln (VSK) technology," *Cement and Concrete Research*, vol. 25, no. 3, pp. 459–464, 1995.
- [17] D. T. Pieter, "The use of tswana-only limestone for clinker: Production at the blue circle cement Lichtenburg plant in South Africa," in *Proceedings of 18th International Conference on Cement Microscopy*, Houston, Texas, USA, 1996, vol. 18.
- [18] R. D. Young, "Method and apparatus for using blast-furnace slag in cement clinker production," U.S. Patent No. 5,494,515. 27, Feb. 1996.
- [19] L. S. Freiman and M. W. Kougija, "Residues from oil shale processing used as cement raw material," *ZKG International*, vol. 50, no. 1, pp. 44–49, 1997.
- [20] N. B. Singh, K. N. Bhattacharjee, and A. K. Shukla "Rational utilization of rice husk ash in mini cement plants," *ZKG International*, vol. 50, no. 10, pp. 594–600, 1997.
- [21] J. I. Bhattya et al. "Use of high carbon fly ash as a component of raw mix for cement manufacture," *Report WO*, 5661-01, 1998.
- [22] V. I. E. Ajiwe, C. A. Okeke, F. C. Akigwe, "A preliminary study of manufacture of cement from rice husk ash," *Bioresource Technology*, vol. 73, no. 1, pp. 37–39, 2000,
- [23] J. I., Bhattya, J. Gajda, and F. M. Miller, "Use of high-carbon Illinois fly ash in cement manufacturing," Final Report No. 99-1/2.1 A, 2000.
- [24] J. I. Bhattya, "Role of trace element on cement manufacture and use a laboratory study," *Portland Cement Association*, Skokie, 2002.
- [25] G. Xiaoquan et al. "A scenario simulation of material substitution in the cement industry under the carbon neutral strategy: A case study of Guangdong," *Sustainability*, vol. 15, no. 7, art. no. 5736, 2023.
- [26] [Online]. Available: <https://cembureau.eu/library/reports/2050-carbon-neutrality-roadmap/>
- [27] Z. Osmanovic, N. Haračić, and J. Zelić, "Properties of blastfurnace cements (CEM III/A, B, C) based on Portland cement clinker, blastfurnace slag and cement kiln dusts," *Cement and Concrete Composites*, vol. 91, pp. 189–197. 2018.



---

## Kinetics and Thermodynamics of Thermal Decomposition of Medlar Seed by TG/DTG

Zelal Koyuncu<sup>1</sup>, Meltem Kizilca Coruh<sup>1\*</sup>

*<sup>1</sup>Department of Chemical Engineering, Atatürk University, Erzurum, Türkiye*

---

### Abstract

Türkiye is an agricultural country. In response to 184.593.134 tons of field, garden and vegetable plant production annually, 62.206.754 tons of vegetable waste is generated. In response to this waste rate, 6.009.049 energy units are obtained annually. Therefore, the use of biomass resources in energy production has gained importance in Türkiye. The aim of this study is to examine the kinetics of the degradation process of the energy values of medlar seeds belonging to the Rosaceae subfamily of Rosaceae as an energy source, using the TG/DTG analyzer. In order to examine the kinetics of the thermal decomposition of the medlar seeds, kinetic and thermodynamic parameters will be calculated with temperature and time-dependent weight loss data during decomposition using the data obtained as a result of thermogravimetric analysis at four different heating rates. The widely used Flynn-Wall-Ozawa (FWO), Kissinger-Akahira-Sunose (KAS), Starink, Tang and Coats-Redfern methods will be used to find kinetic parameters such as activation energy, reaction order and pre-exponential factor from the data obtained as a result of thermogravimetric analysis. This study will examine the thermal profile of medlar seeds and contribute to their energy potential and their use as fuel.

**Keywords:** *Medlar core, Thermal decomposition, Kinetic, Thermodynamic, TG/DTG*

---



## Investigation of Kinetic and Thermodynamic Properties of Thermal Degradation of Ligno-Cellulosic Blend Prepared from Grape, Pomegranate, and Rosehip Seeds

Meltem Kizilca Coruh<sup>\*1</sup>

<sup>1</sup>Department of Chemical Engineering, Atatürk University, Erzurum, Türkiye

### Abstract

In our country, grapes, pomegranates, rose hips, almonds, peaches, walnuts, hazelnuts, apricots, sour cherries, pistachios, olives, peanuts, and tea have an important share among the products widely produced in agriculture, and almost all of them are among the top ten in world production. The processing of these crops in agricultural and industrial settings results in the release of residues such as kernels, hulls, slag, and stems. These residues represent two-thirds of renewable energy sources as biomass energy. Therefore, to obtain energy from biomass, it has become important to utilize biomass in energy production by applying methods such as chemical, biological, and thermochemical processes. The aim of this study is to investigate the kinetics of the degradation process of the energy values of the lignocellulosic mixture prepared from grape, pomegranate, and rosehip seeds as an energy source using a TG/DTG analyzer. To study the degradation kinetics of the mixture, the data obtained from thermogravimetric analysis at four different heating rates are used to calculate the kinetic and thermodynamic parameters with temperature and time-dependent weight loss data during degradation. The Flynn-Wall-Ozawa (FWO) and Kissinger-Akahira-Sunose (KAS) methods, which are widely used to find kinetic parameters such as activation energy, reaction order, and pre-exponential factor from thermogravimetric analysis data, will be used.

**Keywords:** Grape, Pomegranate, Rosehip, FWO, KAS, Degradation, Biomass, Energy

## 1 INTRODUCTION

The overall energy demand is increasing due to a growing world population coupled with rising living standards. Worldwide, in response to this demand for energy, the reserves of existing traditional fossil fuel sources, such as oil and coal, are rapidly depleting. In addition, extracting these resources is challenging due to global environmental problems and price fluctuations. Therefore, the transition to unconventional or non-fossil energy sources, such as renewable energy sources, looks very promising and will play an important role in the energy mix of the future. Solar energy, wind energy, geothermal energy, hydroelectric energy, biomass energy, and wave energy are among the renewable energy sources. The largest potential renewable energy source for the future is biomass energy, as it is widely available after coal and oil, easy to store and transport, and the application of this technology is becoming increasingly widespread and accepted. All-natural substances of plant or animal origin, the main components of which are carbohydrate compounds, are defined as Biomass Energy Sources. The energy produced from these sources is defined as Biomass Energy. Biomass sources include agricultural crops, wood and wood waste, urban waste, waste from food processes, animal waste, aquatic plants, and algae. Most biomass energy is produced from wood and wood waste, municipal solid waste, and agricultural waste, respectively. Agricultural wastes consisting of stalks (sunflower, corn, cotton, tomato, rapeseed, etc.), husk-sheath (coffee, soybean, rice, peanut, hazelnut, walnut, etc.), stalk-straw (wheat, barley, rye, oat, etc.) and fruit pits are the most important potential source for fuel production as they are rich in sugar, oil starch, and cellulose. Thus, both agricultural areas are utilized, and plants are used as fuel. The methods used in obtaining energy from biomass can be categorized under two main headings: biochemical and thermochemical. Biochemical methods include biomethanization and fermentation methods; biogas and bioethanol are formed as products. Thermochemical methods include combustion, pyrolysis, liquefaction, and gasification. The most widely used of these methods is pyrolysis. Pyrolysis is the process of thermal degradation of biomass in an oxygen-free environment. As a result, carbon-rich solid products, oily liquid products, and hydrocarbon-rich gas are widely used processes. To design appropriate systems for these processes, it is necessary to know the pyrolysis kinetics of biomass [1–4].

In recent years, interest in the thermal degradation of biomass has been increasing. The design of suitable systems for pyrolysis processes of plant biomass sources is closely related to pyrolysis kinetics. Therefore, it is important to know how parameters such as heating rate, temperature, and chemical composition modify biomass degradation [5–7]. Previously, research has been conducted to investigate the thermal suitability of different biomasses for



bioenergy production, including agricultural waste, woody biomass, and fruit peels [8–18]. However, each biomass has its own unique properties and composition, thus showing the different nature of thermal decomposition. Therefore, this study aimed to calculate kinetic parameters based on thermogravimetric analysis data obtained under pyrolysis conditions of grape, pomegranate, and rosehip seeds used as agricultural waste. For this purpose, activation energy was calculated using the FWO and KAS methods. Thus, since it is possible to develop, design, and optimize the pyrolysis processes of grape, pomegranate, and rosehip seeds, the study will enable the evaluation of existing biomass samples with pyrolysis process and will enable the design of the production of renewable, environmentally friendly fuel materials in the industrial sector.

## 2 MATERIAL AND METHOD

Grape, pomegranate, and rose hip were used as raw materials from a local Ankara market. The biomasses were pre-dried in air and sun for 2 weeks. The dried kernels were subjected to crushing and grinding in the mill to a grain size of less than 250  $\mu\text{m}$ , then dried in an oven at 100  $^{\circ}\text{C}$  for 12 hours and analyzed.

### 2.1 Characterization

Elemental analysis of grape, pomegranate, and rosehip seeds was performed in the THERMO (SCIENTIFIC) brand analyzer model FLASH 2000. C, N, H, and S amounts were measured simultaneously.

Partial analysis of biomass was performed in a muffle furnace. For volatile matter determination, 1 g of the grain mixture was placed in a crucible and a muffle furnace at 950  $^{\circ}\text{C}$  for 10 min. The crucibles were cooled and weighed, and the volatile content was calculated. For ash analysis, 1 g of the seed mixture was placed in a crucible and kept in a muffle furnace at 900  $^{\circ}\text{C}$  for 1 hour. The crucibles were cooled and weighed, and the ash content was calculated. For moisture determination, 1 g of the seed mixture was placed in a crucible and kept in an oven at 105 $^{\circ}\text{C}$  for 24 hours. Then, crucibles were cooled and weighed, and the moisture content was calculated.

Thermogravimetric analyses were performed on a NETZSCH STA 449 C Jupiter TGA-DTA instrument. Approximately 10 mg of the sample was placed in a platinum sample cup and placed in the instrument. Analyses were performed at heating rates of 10, 20, and 30 K/min and a flow rate of 50 mL/min in an inert nitrogen gas atmosphere in the temperature range of 273-1173 K. Sample mass loss was recorded as a function of temperature and time.

### 2.2 Kinetic

In general, the rate of solid decomposition under non-isothermal conditions is expressed by the following equation:

$$\frac{d\alpha}{dt} = k(T) \cdot f(\alpha) \quad (1)$$

Where  $t$  is time,  $T$  is the absolute temperature,  $f(\alpha)$  is the temperature-independent transformation function, and  $\alpha$  is the fractional transformation of biomass.  $k$  is the rate constant, and its temperature dependence is given by the Arrhenius equation.

$$\alpha = \frac{W_0 - W_t}{W_0 - W_s} \quad (2)$$

$$k = A \cdot \exp(-E_a / RT) \quad (3)$$

Substituting the rate constant expression of Equation 3 into Equation 1 gives Equation 4 as the general expression for the rate of solid decomposition.

$$\frac{d\alpha}{dT} = \frac{A}{\beta} \exp\left(-\frac{E_a}{RT}\right) \cdot f(\alpha) \quad (4)$$

Based on Equation 4, many methods have been developed to determine the kinetic parameters. The most widely used of these methods are FWO and KAS. The equations of the KAS and FWO methods are given below:

$$\ln(\beta) = \ln\left(\frac{AE_a}{g(\alpha)R}\right) - 5,331 - 1,052\left(\frac{E_a}{RT}\right) \quad (5)$$

$$\ln\left(\frac{\beta}{T_{max}^2}\right) = \ln\left(\frac{AR}{E_a}\right) - \frac{E_a}{RT_{max}} + \ln\frac{df(\alpha)}{d(\alpha)} \quad (6)$$

### 3 RESULTS

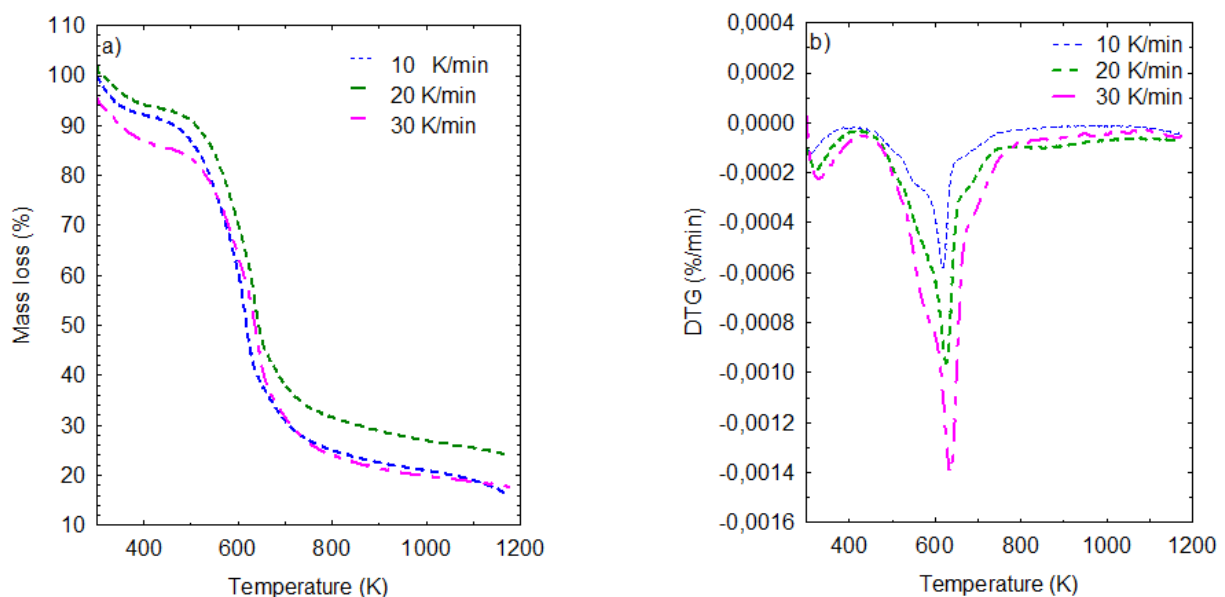
The partial, elemental, and calorific results of the raw material blends are shown in Table 1. When Table 1 is examined, it contains 49.88% carbon, 7.55% moisture and 1.52% ash. Due to the relatively high carbon and low ash content, it can be said that the mixture is a very suitable material for fuel production. The main combustible elements of the fuels, C and H, were determined to be 49.88% and 8.59%, respectively. Both the C (47.73%) and H (6.09%) values of typical biomass and the O content of the mixture (40.41%) are very close to the O value of typical biomass (39.43%). The N and S contents were 1.07% and 0.05%, respectively. Therefore, fuels derived from blended biomass are advantageous for pollutant gases such as SO<sub>x</sub> and NO<sub>x</sub> released during combustion.

**Table 1.** Partial and elemental analysis of biomass products

Partial analysis (%)	Biomass mixture
Volatile matter	75.44
Moisture	7.55
Ash	1.52
*Fixed carbon	15.49
Elemental analysis (%)	
C	49.88
H	8.59
N	1.07
S	0.05
O	40.41
Thermal value (KJ/kg)	22.41

\*Calculated from the difference.

Figure 1 shows the TG-DTG curve of the raw material mixture used in the experiments. It was found that significant mass loss occurred in the structure due to temperature increase. It is known from the literature that hemicellulose, cellulose, and lignin, which are the three main components of biomass, thermally degrade at temperature ranges of 210-325, 310-400, and 160-900 K, respectively [1, 12, 16]. This is due to the separation of the volatile components formed by the thermal degradation of the molecules. As seen in Figure 1, there is a significant, albeit small, separation of volatile components in the 400-700 K range. Above 700 K, there is no significant mass loss and almost complete thermal decomposition and separation of volatile components from the structure.



**Figure 1.** a) TG, b) DTG graph

### 3.1 Kinetic calculations

The FWO and KAS methods were used for kinetic calculations based on data obtained from thermogravimetric analysis of the biomass mixture under non-isothermal conditions. Plots of  $\ln(\beta)$  versus  $1000/T$  for conversion values using the FWO method in equation 5 are shown in Figure 2. For the KAS method, the plots of  $\ln(\beta/T^2)$  versus  $1000/T$  for the conversion values using Equation 6 are shown in Figure 2. It can be seen that the lines obtained with the KAS and FWO methods are quite parallel to each other, and the values of the activation energies calculated with the conversion fraction are close to each other. The activation energies ( $E_a$ ) calculated by the FWO and KAS methods are given in Table 2. The differences in the  $E_a$  values obtained by the FWO and KAS methods are due to the different approaches to temperature integration. This has been observed in studies with a variety of biomass materials, such as pistachio shells [19], walnut shells [10], cherry stalks [16], hazelnut shells [20], corn stalks [21], and palm kernels [22].

According to Table 2, the average activation energy for the mixture was found to be  $104.66 \text{ kJ mol}^{-1}$  according to the FWO method and  $101.48 \text{ kJ mol}^{-1}$  according to the KAS method. When these activation energy values are compared with the values found in the literature for other biomass products [23, 24], it is seen that they are in close agreement.

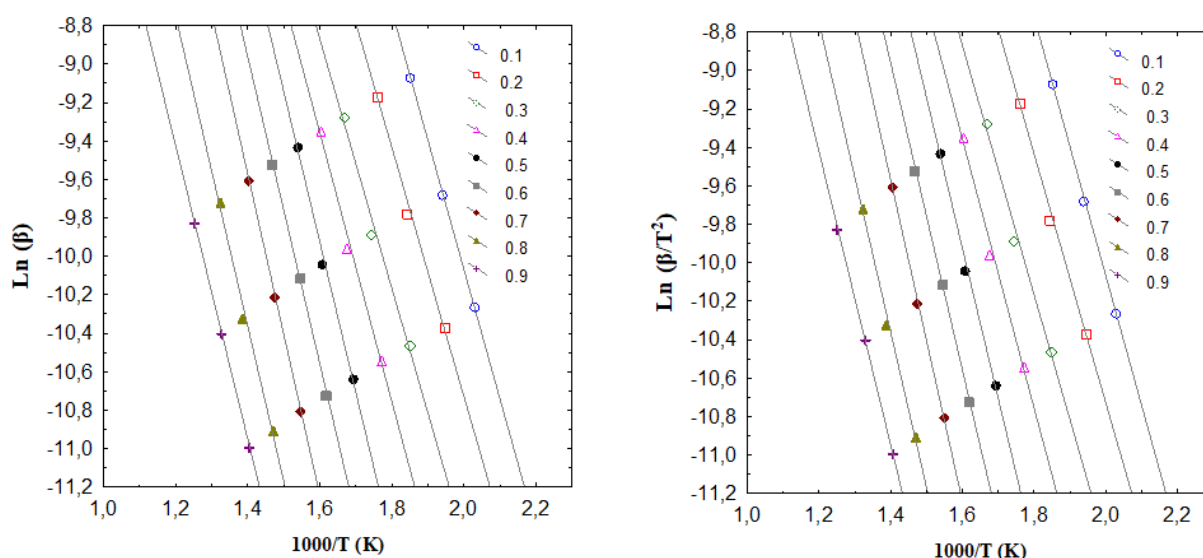


Figure 2. FWO and CAS graph

Table 2. Kinetic parameters

	FWO		KAS	
$\alpha$	EA	A	EA	KAS A
0.1	105.2648	2.23E+07	102.5737	2.82E+09
0.2	104.7655	2.00E+07	100.0029	1.89E+08
0.3	101.5251	9.98E+06	99.1865	1.82E+07
0.4	102.2677	1.17E+07	100.5849	4.72E+07
0.5	102.4746	1.22E+07	101.7091	5.20E+08
0.6	104.8076	2.02E+07	103.8313	6.62E+08
0.7	106.9807	1.02E+08	102.2605	3.54E+07
0.8	103.2927	4.46E+07	100.2691	2.00E+08
0.9	105.2648	2.23E+07	102.9398	3.55E+08
AV.	104.6622		101.4842	

## 4 CONCLUSION

In this study, the pyrolysis of a mixture prepared from grape, pomegranate, and rosehip seeds was studied by non-isothermal thermogravimetric analysis at temperatures of 273-1173 K and heating rates of 10, 20, and 30 K/min. The kinetic parameters of the active pyrolysis steps were calculated using the widely used FWO and KAS methods. The activation energy values obtained are in agreement with the range of values reported in the literature for hemicellulose, cellulose, and lignin, which are the main organic components of the mixture prepared from grape, pomegranate, and rosehip seeds. The low moisture and ash content and the high volatile matter content make the

biomass mixture a potential candidate for the production of biochemicals. The kinetic data obtained from the TGA analysis will be useful for modeling, designing, and developing thermochemical systems for hazelnut shells.

## References

- [1] K. Acikalin, "Thermogravimetric analysis of walnut shell as pyrolysis feedstock," *J. Therm. Anal. Calorim.*, vol. 105, pp. 145–150, 2011.
- [2] K. Acikalin, "Pyrolytic characteristics and kinetics of pistachio shell by thermogravimetric analysis," *J. Therm. Anal. Calorim.*, vol. 109, pp. 227–235, 2012.
- [3] K. Acikalin, "Thermogravimetric analysis of walnut shell as pyrolysis feedstock," *J. Therm. Anal. Calorim.*, vol. 105, no. 1, pp. 145–150, 2012.
- [4] A. Ahmed, E. A. Afolabi, M. U. Garba, U. Musa, M. Alhassan, and K. Ishaq, "Effect of particle size on thermal decomposition and devolatilization kinetics of melon seed shell," *Chem. Eng Commun.*, vol. 206, no. 9, pp. 1228–1240, 2019.
- [5] N. Alias, M. A. A. Zaini, and M. J. Kamaruddin, "Roles of impregnation ratio of K<sub>2</sub>CO<sub>3</sub> and NaOH in chemical activation of palm kernel shell," *J. Appl. Sci. Process Eng.*, vol. 4, no. 2, pp. 195–204, 2017.
- [6] H. Balat and E. Kirtay, "Hydrogen from biomass—present scenario and future prospects," *Int. J. Hydrogen Energy*, vol. 35, pp. 7416–7426, 2010.
- [7] S. Ceylan and Y. Topcu, "Pyrolysis kinetics of hazelnut husk using thermogravimetric analysis," *Bioresource Technology*, vol. 156, pp. 182–188, 2014.
- [8] J. C. G. da Silva, J. L. F. Alves, W. V. A. Galdino, R. F. P. M. Moreira, H. J. José, R. F. de Sena, and S. L. F. Andersen, "Combustion of pistachio shell: physicochemical characterization and evaluation of kinetic parameters," *Environ. Sci. Pollut. Res. Int.*, vol. 25, no. 22, pp. 21420–21429, 2018.
- [9] R. Font, A. Marcilla, J. Devesa, and E. Verdú, "Gas production by almond shell pyrolysis at high temperature," *J. Anal. Appl. Pyrolysis.*, vol. 28, no. 1, pp. 13–27, 1994.
- [10] G. Gozke and K. Acikalin, "Pyrolysis characteristics and kinetics of sour cherry stalk and flesh via thermogravimetric analysis using isoconversional methods," *J. Therm. Anal. Calorim.*, vol. 146, pp. 893–910, 2020.
- [11] S. Gupta, G. K. Gupta, and M. K. Mondal, "Thermal degradation characteristics, kinetics, thermodynamic, and reaction mechanism analysis of pistachio shell pyrolysis for its bioenergy potential," *Biomass Convers. Biorefin.*, vol. 12, no. 11, pp. 4847–4861, 2022.
- [12] X. Hu and M. Gholizaed, "Biomass pyrolysis: A review of the process development and challenges from initial researches up to the commercialisation stage," *J. Energy Chem.*, vol. 39, pp. 109–143, 2019.
- [13] R. Kaur, P. Gera, M. K. Jha, and T. Bhaskar, "Pyrolysis kinetics and thermodynamic parameters of castor (*Ricinus communis*) residue using thermogravimetric analysis," *Bioresour. Technol.*, vol. 250, pp. 422–428, 2018.
- [14] G. Ozsin and A. E. Putun, "Kinetics and evolved gas analysis for pyrolysis of food processing wastes using TGA/MS/FT-IR," *Waste Manag.*, vol. 64, pp. 315–326, 2017.
- [15] N. L. Panwar, R. Kothari, and V. V. Tyagi, "Thermochemical conversion of biomass—ecofriendly energy routes," *Renew. Sustain. Energy Rev.*, vol. 16, pp. 1801–1816, 2012.
- [16] M. Radojević, B. Janković, V. Jovanović, D. Stojiljković, and N. Manić, "Comparative pyrolysis kinetics of various biomasses based on model-free and DAEM approaches improved with numerical optimization procedure," *Plos One*, vol. 13, no. 10, pp. 1–25, 2018.
- [17] T. Raj, M. Kapoor, R. Gaur, J. Christopher, B. Lamba, D. K. Tuli, and R. Kumar, "Physical and chemical characterization of various Indian agriculture residues for biofuels production," *Energy Fuel*, vol. 29, pp. 3111–3118, 2015.
- [18] T. Rasool, V. C. Srivastava, and M. N. S. Khan, "Kinetic and thermodynamic analysis of thermal decomposition of Deodar sawdust and rice husk as potential for pyrolysis," *Biomass Convers. Biorefin.*, vol. 8, pp. 647–657, 2018.
- [19] J. C. G. D. Silva, J. L. F. Alves, W. V. D. A. Galdino, R. D. F. P. M. Moreira, H. J. José, R. F. D. Sena, and S. L. F. Andersen, "Combustion of pistachio shell: physicochemical characterization and evaluation of kinetic parameters," *Environ. Sci. Pollut. Res.*, vol. 25, pp. 21420–21429, 2018.
- [20] K. Slopiecka, P. Bartocci, and F. Fantozzi, "Thermogravimetric analysis and kinetic study of poplar wood pyrolysis," *Appl. Energy*, vol. 97, pp. 491–497, 2012.
- [21] S. S. Tuly, M. Parveen, M. R. Islam, M. S. Rahman, and H. Haniu, "Pyrolysis kinetics study of three biomass solid wastes for thermochemical conversion into liquid fuels," *AIP Conference Proceedings*, vol. 1851, no. 1, pp. art. no. 020083, 2017.
- [22] G. Wang, Y. Dai, H. Yang, Q. Xiong, K. Wang, J. Zhou, Y. Li, and S. Wang, "A review of recent advances in biomass pyrolysis," *Energy Fuels*, vol. 34, pp. 15557–15578, 2020.

- [23] M. Zhai, L. Guo, Y. Zhang, P. Dong, G. Qi, and Y. Huang, "Kinetic parameters of biomass pyrolysis by TGA" *BioResources*, vol. 11, no. 4, pp. 8548–8557, 2016.
- [24] X. Zhang, M. Xu, and L. Sun , "Study on biomass pyrolysis kinetics," *J. Eng. Gas Turbines Power*, vol. 128, no. 3, pp. 493–496, 2004.



---

## Application and Analysis of Experimental and Numerical Studies to the Film Cooling Turbine Blade

Amar Berkache<sup>\*1</sup>, Rabah Dizene<sup>2</sup>

<sup>1</sup>Department of Mechanical Engineering, Faculty of Technology, University Mohamed Boudiaf of M'Sila, Algeria

<sup>2</sup>Advanced Mechanics Laboratory, Mechanical Engineering School, University of Science and Technology Houari Boumediene, Algeria

---

### Abstract

Experimental and numerical investigations on transverse jet flow ( $R < 1$ ) are conducted using discrete jets on a surface exposed to a wall boundary layer, resembling discrete-hole cooling systems for turbine blades. Coolant flow characteristics at hole exits of film-cooled blades are derived from prior analyses with discretized hole pipes and coolant plenum. The ENSMA tunnel facility employs a flat plate with staggered rows of holes for experimentation. A three-dimensional FLUENT code computes mainstream/jet velocity fields' characteristics on the flat plate. Simulation results are presented for both flat and cambered plates, focusing on the accuracy of averaged results and film-cooling flow physics to assess Reynolds averaged equations' predictive accuracy with turbulence models. Calculations involve solving governing equations with turbulence modeling, considering three-dimensional external flow, free-stream turbulence, and stream curvature effects. Comparisons between experimental and numerical results for two turbulence models reveal discrepancies near the wall, which are identified and discussed.

**Keywords:** Turbine blade, Turbulence modeling, Compressible cross flow, Injection holes, Blowing rate, Film cooling, Efficiency

---

## 1 INTRODUCTION

Turbine blade heat transfer prediction is crucial for efficient blade cooling schemes, but turbulence modeling is often the main cause of disagreement with experimental data. This is due to complex flow phenomena in turbine passage and the interaction of injection with aerodynamic curved surface flow around blades. Factors such as stagnation flow heat transfer, steep pressure gradients, free stream turbulence, high Mach number, blowing rate ratio, and three-dimensional effects are presented. Understanding coolant film behavior and its interaction with mainstream flow is essential. Interest in this field has grown, but many studies have focused on simple geometries.

## 2 PROBLEM DEFINITION

With increases in turbine inlet temperature, gas turbine designers are looking to improve cooling effectiveness without raising the amount of coolant usage. Typically, film cooling is used to protect the blade outer surface by injecting cooler air through holes or slots on the blade surface. Film cooling is commonly employed to provide effective blade protection and is realized by injecting coolant jets into the crossflow of hot gases from film cooling holes or slots, on the blade surface. The injected coolant is bent over by the cross flow and forms a film over the blade surface (see Fig. 1) and protects the surface from the hot crossflow gases

The complex flow field produced by the interaction of the jet and the crossflow has been extensively studied and reported in the literature. Experimental studies of [1] have revealed that the near field of the jet is highly complex, three-dimensional, and characterized by large-scale coherent structures in the form of jet shear layer vortices which dominate the initial portion of the jet, the horseshoe vortex wrapping around the base of the jet, the counter-rotating vortex pair which results from the impulse of the cross-flow on the jet and dominate the turbulence structure in formed mixing layer. So, strong distortions in the jet section result from the counter-rotating vortex effects, and the wake vortices formed in the jet wake. The overview of the complex flow field produced by the interaction of the jet and crossflow is shown in Fig. 2.

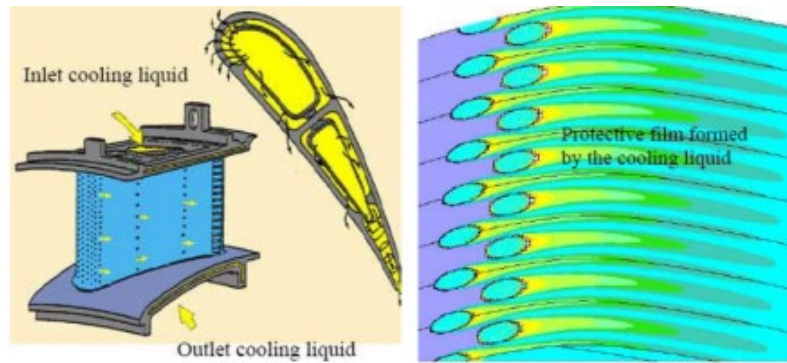


Figure 1. General view - problem definition

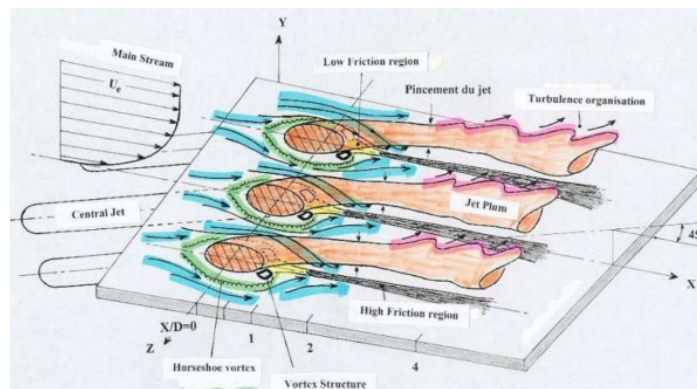


Figure 2. Flow diagram of a row of jets based on experimental results [2]

### 3 PREVIOUS RESEARCH OF FILM COOLING

#### 3.1 RANS Studies

The majority of the reported film cooling simulation studies are based on the time-averaged (RANS) equations. A few representative studies and papers performed several computational studies using turbulence modeling with a commercially available flow solver (Fluent) are presented. [3] carried out an investigation using a high Reynolds RST model employing wall functions to avoid solving the Reynolds stresses all the way to the wall.

The effects of the inclination of the holes on the film cooling heat transfer coefficient have been studied by [4]. An additional study conducted by [5], defers the effect of the angle on the adiabatic efficiency. [6] examined the orientation of the inclination of the hole and its influence on film cooling. They claimed that the injection ports laterally inclined produce cooling holes better than facing forward.

Not only the shape but also the inclination of the holes can alter the performance of film cooling. [7] measured the adiabatic efficiency through liquid crystal thermography. They studied the influence of the injection ratio and orientation downstream of the inclination angle on efficiency. Three angles (30°, 60°, and 90°) were tested. The angle of 30° gave the best cooling characteristics. [8] in their paper presented detailed measurements of the film-cooling effectiveness for three single, scaled-up film-cooling hole geometries. The hole geometries investigated include a cylindrical hole and two holes with a diffuser-shaped exit portion. As compared to the cylindrical hole, both expanded holes show significantly improved thermal protection of the surface downstream of the ejection location, particularly at high M-blowing ratios. The predictions of several Reynolds-Averaged Navier-Stokes solutions for a baseline film cooling geometry are analyzed and compared with experimental data.

#### 3.2 LES Studies

There have been several studies that have utilized LES for film cooling. [9] performed a Large Eddy Simulation (LES) of a high blowing ratio ( $M = 1.7$ ) film cooling flow with a density ratio of unity. Mean results are compared with experimental data to show the degree of fidelity achieved in the simulation. The experimental flow field and heat transfer measurements are available for the flat plate at many axial locations for fixed inlet Mach number, Reynolds number, inlet turbulence intensity as well as the inlet boundary layer thickness. By far the most popular

turbulence models utilized today for flow and heat transfer calculations are the high and low Reynolds number two-equation eddy viscosity models. The  $k\text{-}\epsilon/k\text{-}\omega$  are the most used models. These models often offer a good balance between complexity and accuracy. The ability to predict transition to turbulence which is often present on turbine blades and the ability to integrate into the walls are other reasons for their wide use.

In this paper, both numerical turbulent simulations and experimental measurements have been performed. This study focuses on the efficient computation of film-cooling flows. The main objective is to establish how reliably film cooling flows can be predicted, using commercial software.

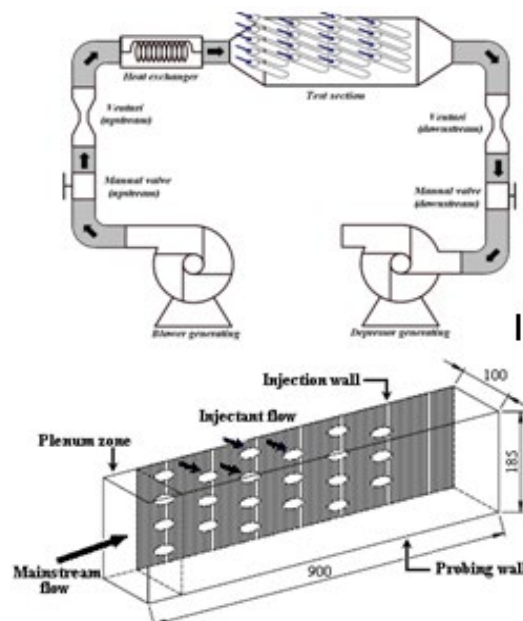
Two numerical calculations are conducted in this work. The first one is compared with the experiment measurements that is carried out on several staggered rows of jet-in-a-crossflow problems. The second one is only numerical calculation. Simulation results are presented for both flat plate and cambered plate represented by three cambered NACA profiles. A two-equation turbulence model (the realizable  $k\text{-}\epsilon$  model) and a two-layer zonal near-wall treatment method (the enhanced wall treatment in FLUENT) have been used to show if it is necessary that the Reynolds averaged equations RANS with turbulence models need anisotropy and realizability corrections to provide correct predictions for the cooling effectiveness, or two-equation turbulence model provide the needed quantitative accuracy and the rich flow physics representing such flows.

All simulations employed the  $k\text{-}\epsilon$  turbulence model with non-equilibrium wall functions. While the standard  $k\text{-}\epsilon$  model is a high-Reynolds-number model, its theory does not provide an analytically derived differential formula for effective viscosity that accounts for. For this reason, we combine the  $k\text{-}\epsilon$  and  $k\text{-}\omega$  models in a way that would allow them to be used in the low-Reynolds-number effects regions. In other words, the method uses the  $k\text{-}\epsilon$  model near the wall, but switches through a function  $F1$  to the  $k\text{-}\omega$  equations away from the wall, these equations having been transformed to a  $k\text{-}\omega$  format.

Note that effective use of this feature does depend on an appropriate treatment of the near-wall region.

#### 4 MODEL AND EXPERIMENTAL DETAILS

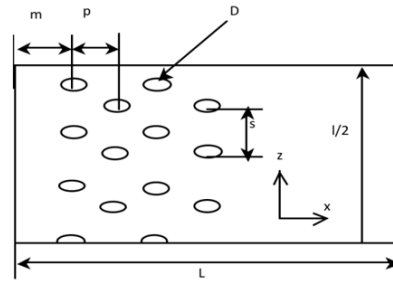
Although experimental tests of a primary air flow pass by a secondary flow on a flat wall perforated was performed. The basic aim of these proposed geometries is to allow more uniform spreading of the jet along the surface resulting in uniform higher cooling. The experimental measurements have been conducted on the ISAE-ENSMA tunnel facility using a flat plate with several staggered rows of holes, at the P' institute in Poitiers (France). Fig. 3 shows the ISAE-ENSMA tunnel facility and the positions of several staggered rows of 81 cylindrical cooling holes inclined at  $30^\circ$  from the wall with a 6mm diameter of each one with elliptical edge ends whose value of the major diameter is equal to 12 mm.



**Figure 3.** General description of the tunnel facility and the flat plate

Fig. 4 shows the geometrical distribution of the holes.

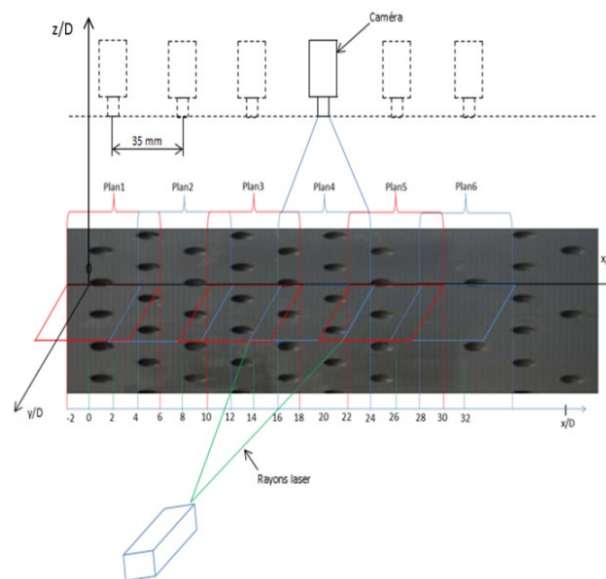




**Figure 4.** Upper view of the flat plate

The temperatures of the two flows are 22 °C for the cooling air and 40 °C for the hot air. The purpose of this study is to show us how is formed the cooling film generated by the cold airflow used in cooling turbine blades. Both mean and fluctuation velocity field measurements are realized using P.I.V. system. A double-pulsed Nd-Yag LASER (Quantel Big Sky) is used to set up the light sheet of the P.I.V. setup. The exit energy is nearly 20 mJ for each LASER pulse. The wavelength is 532 nm. The laser beams are focused onto a sheet by one cylindrical ( $f=0.02$  m) and one spherical ( $f=0.5$  m) lens. The time delay between two pulses, which depends on the velocity and the size of the observation fields, varies from 20 to 50 ms. The video images are recorded with a Hi-Sense Dantec camera. The frame grabber, using a pixel clock, digitizes the analogue video signal to an accuracy of 8 bits. In the frame grabber, each field is digitized in 1280\*1024 pixels with grey levels. The acquisition frequency is 4 Hz. Interrogation of the recorded images is performed by two-dimensional digital cross correlation analysis using “Flow Manager”. The final window has a size of 16 by 16 pixels (0.592 by 0.592 mm) and there is a 50 % overlap. The flows are seeded with smoke generator. A previous study of the drop size distribution has shown that the mean diameter is equal to 5  $\mu$ m. For each velocity field, 300 P.I.V. images have been recorded. We used these 300 velocity fields to calculate the different parameters such as mean velocity and velocity variance fields. The computation of the convergence of the first two moments of the velocity shows that 300 velocity fields are sufficient. Our experience of the PIV was made on a testing flat plate crossed by four open rows of coolant jets ( $Re=0, 6$ ) inclined by 30 degrees relative to the horizontal direction, which is the transverse flow direction. The two main flows and injection are located in the same plane (x,y). To do our experiments we divided our plate into 6 shooting plans. The camera can move in the plane (x, z) along the z-axis with a displacement of 35 mm between each plane.

Fig. 5 illustrates the six measure planes on the test facility. The experiment results obtained will be used to validate the numerical results obtained by RANS simulation conducted in the same conditions and using k- $\epsilon$  and Shear Stress Transport (SST) turbulence models in order to choose which one of the two models will give the best agreement with the experiments. So, the chosen model will be used to investigate and estimate the curvature effect on the coolant jets/crossflow interaction. The main flow is the movement in the x direction with a linear velocity equal to 2 m/s, against the direction of flow of the injection air is in a direction inclined at an angle of 30° relative to the x-axis in the plane (x, z).



**Figure 5.** Measurement plans available with PIV

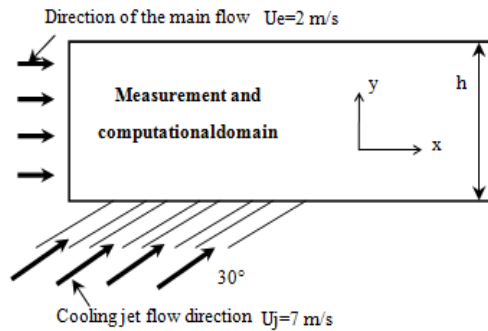


Figure 6. Calculation domain and experimental setup

## 5 3-D AND 2-D COMPUTATIONAL DOMAIN AND BOUNDARY CONDITIONS

### 5.1 3-D Computational Details for the Incompressible Flow: Comparison with the Experiments

In this part, we aim to compare the incompressible 3-D study flow numerical results with the experiments, under the influence of the two-turbulence model. Fig. 7 shows the numerical 3-D flow domain (one symmetrical half) which is the same at the ISAE-ENSMA test facility. Four staggered rows of cylindrical cooling holes ( $D = 6 \text{ mm}$ ;  $s/D = 4$ ) were located on the flat plate. The hole spacing ratio in the transverse direction  $s/D$  is 4 and in the axial direction  $p/D$  is 4.

The commercial finite-volume code FLUENT was used in this investigation and the boundary conditions taken for the compute are shown in Fig. 6. The second-order upwind scheme has been used for the discretization.

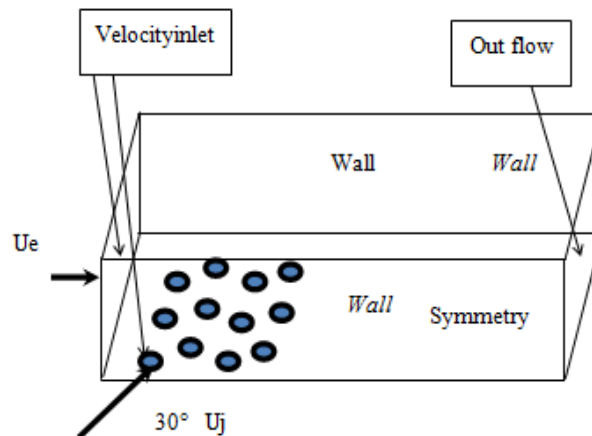


Figure 7. Experimental and numerical studies: 3-D domain and boundary conditions

The dimensions of the experimental study (real) and numerical are given in Tab. 1.

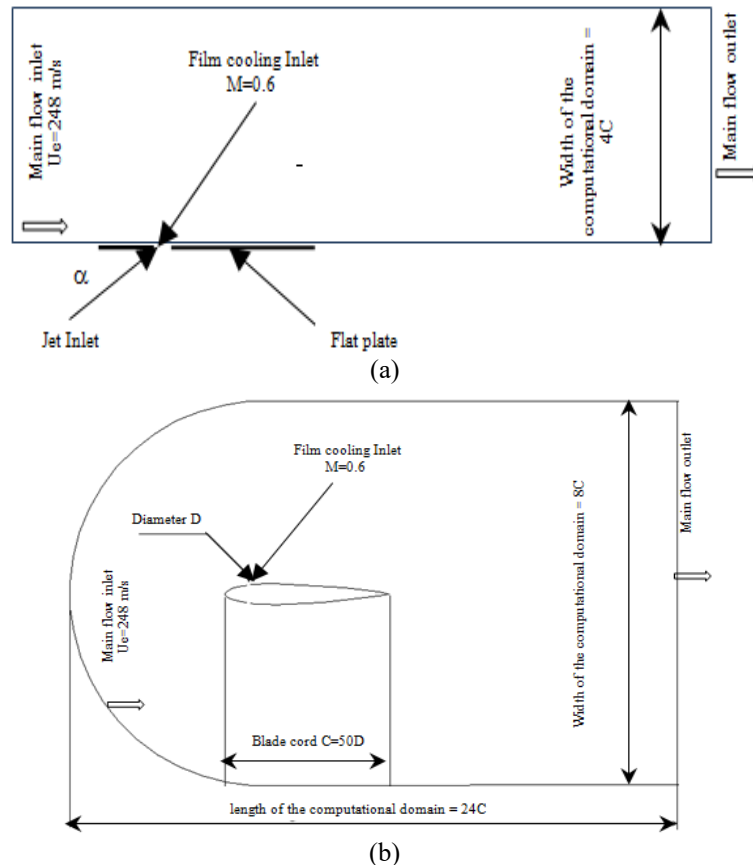
**Table 1.** Grid spacing computation for a given  $Y^+$

	Incompressible Flow	Compressible Flow
$U_e \text{ (m/s)}$	2.0	248.0
$L \text{ (m)}$	0.90	0.25
$Re_C$	1.2 10 <sup>5</sup>	4.13. 10 <sup>6</sup>
$Y^+$	10.0	10.0
$Y_w \text{ (m)}$	0.00151	16. 10 <sup>-6</sup>

### 5.2 2-D Computational Domain for Numerical Compressible Study

To be in such conditions of cooling of gas turbine blades, we considered a single row of holes (film cooling). Simulation calculations are conducted for both flat and cambered plates represented by the three cambered NACA profiles (NACA 0012, 6512, and 8520) with the key emphasis here on the accuracy of the curvature effects on the film-cooling flow physics and the turbulence models.

The single row of jets in interaction with the compressible crossflow is investigated. The jet-to-cross-stream blowing ratio  $M$  is 0.6 and the Mach number is taken to correspond to incompressible flow. Components of mean velocities are compared with experimental results data at upstream and downstream locations in the  $x$ - $y$  plane injection (the symmetrical center plane). The velocity is dimensionless with the cross-stream velocity. The modeled transport equations were solved using a two-dimensional CFD FLUENT code. A non-uniform staggered grid and 33060 mesh cells including the jet injection region are set up in the computational domain shown in Fig. 8(a). The topology of the CH-type grid used in this study is described by the rectangular west external boundary, which is corresponding to the inlet and outlet regions, the east boundary is corresponding to the NACA surface and the south and north internal grid lines forming the connection region to close the C-topology. The inlet region (part of the west boundary) and the exit region (also part of the west boundary) were placed respectively far upstream and downstream of the leading and trailing edge of the profile.



**Figure 8.** (a) Two-dimensional computational flat plate domain and (b) two-dimensional computational Naca0012 profoil domain

### 5.3 Boundary conditions

The elliptical partial differential equations nature requires boundary conditions at all boundaries. It was therefore considered especially in the present work, three types of boundary conditions, as shown in the figure below (see Fig. 8). These three types are:

- The entrance of the jet
- The flow away from the blade
- The rigid walls of the blade

$\alpha$  is the jet penetration angle =  $30^\circ$

$D$  is the slot width = 0.005 m

$C$  is the blade cord = 0.25 m

The same domain was used to simulate the three NACA 0012, 6512, and 8520 fluid flow profiles. Whereas in the case of the flat plate, only the upper face is used. The boundary conditions considered are those of a compressible turbulent flow. These conditions are defined as follows:

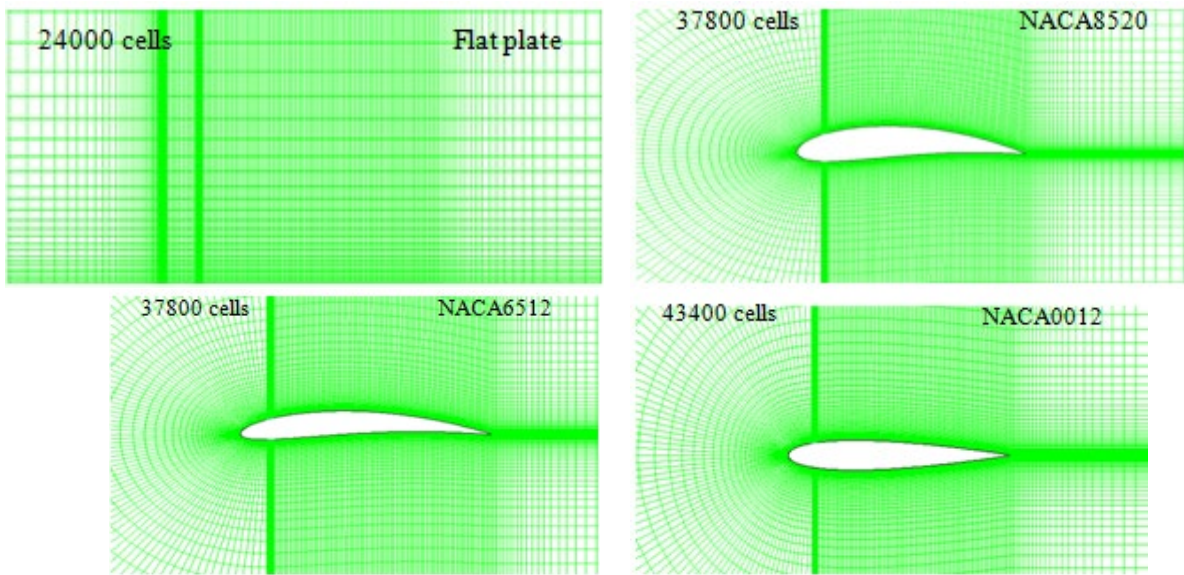
- The flow of the main entrance and the far walls: Pressure far field
- Entry of the jet: Mass flow inlet
- Wall of the blade and the flat plate: Wall

One major step in simulating fluid flows with a turbulence model is the choice of appropriate inlet values of the solved primary variables  $u$ ,  $v$ ,  $k$ ,  $\epsilon$  or  $\omega$  for the flow entering the computational domain. The boundary conditions are derived from the experimental measurements. On the jet exit surface, the axial and the vertical velocity components are defined, while the lateral velocity is neglected. In the upstream boundary, the axial velocity profile, profiles are also specified. The axial velocity component is given in the external flow, while the kinetic turbulent energy and the dissipation rate are calculated. The upstream and downstream conditions have zero gradients for all the state variables.

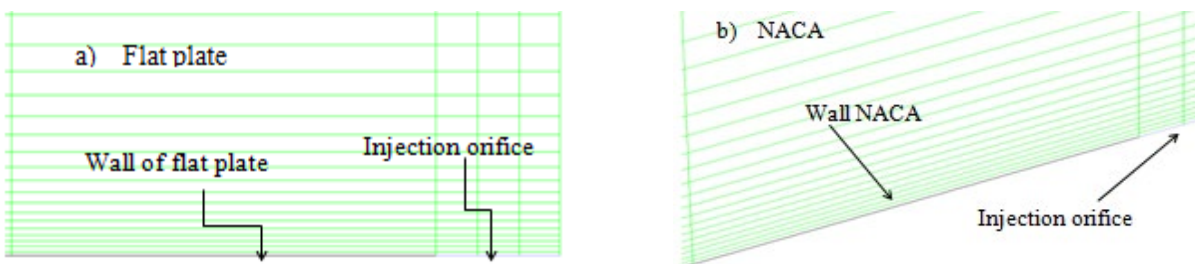
**5.4 Meshing process for two calculations.**

To choose a suitable mesh for the flat plate and for the NACA profiles in the case of the two conducted calculations, we realized two different meshes: the first one used for the half flat plate which consists of 24000 meshes and the second one consists of tighter at the level of the wall with a 10 times thinner step. The formulas used for estimating  $y^+$  are given by the Schlichting skin-friction relationship. For a turbulent boundary layer on a smooth flat plate, the correlation is valid for  $Re < 109$ . The density and viscosity given by default in the form are for air at sea level and room temperature (20°C). Applied to the incompressible and compressible studied flow, it is so able to estimate  $y^+$  for the corresponding grids. Results are presented in the following table 1. To include points in the sub-viscous layer (wall treatment), both numerical calculations meshing have two different nodal grids in an amount of 600000 cells in the half field corresponding to the three-dimensional incompressible flow. This represents over 70% of the total number of meshes in the half domain considered near the wall. Table 1 shows the grid characteristics in this region.

It was noted that the results obtained from these two meshes are almost identical. Therefore, to minimize computational time, a less refined mesh was performed close to the wall as well as the case of the flat plate for the different NACA profiles. The different meshes are shown in the following figures:



**Figure 9.** Views of the computational domain used



**Figure 10.** Zoom of the mesh close of injection orifice: a) flat plate and b) NACA profile

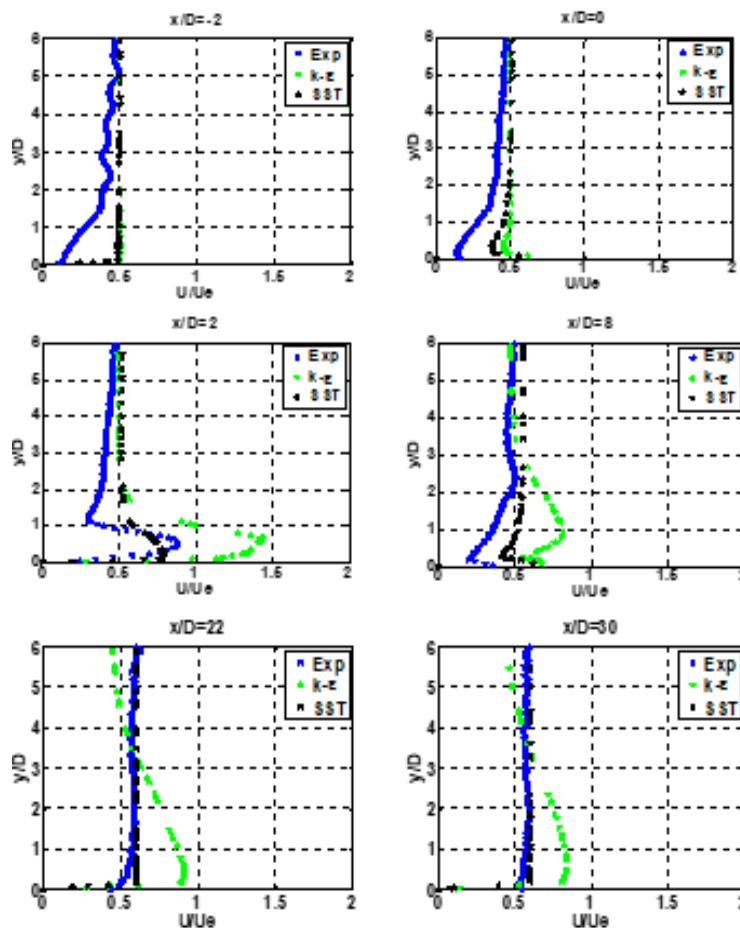
## 6 RESULTS AND DISCUSSIONS

In this section, we will present representative results from experiments and RANS studies, focusing on determining each method's predictive capabilities. The discussion of the results consists of a comparison of numerical and experimental data to show the quality of the computational method. Then the exit jets area and the spreading are analyzed, and the mixing process is investigated. The RANS simulation method of the present study is validated by comparing the time-averaged flow field with the particle-image velocimetry (PIV) measurements of the present work. To obtain the mean and the time-averaged quantities the flow field has been sampled over 6 combined streams-wise and spanwise planes. Here, one of the combined planes corresponds to one measure. So, six measures have been conducted for the crossflow fluid that needs to pass over the complete measurement domain that contains the six rows of jets.

### 6.1 Three-Dimensional Incompressible Flow Calculation

#### 6.1.1 Comparison Between the Experiment and the Calculation Results on Flat Plate

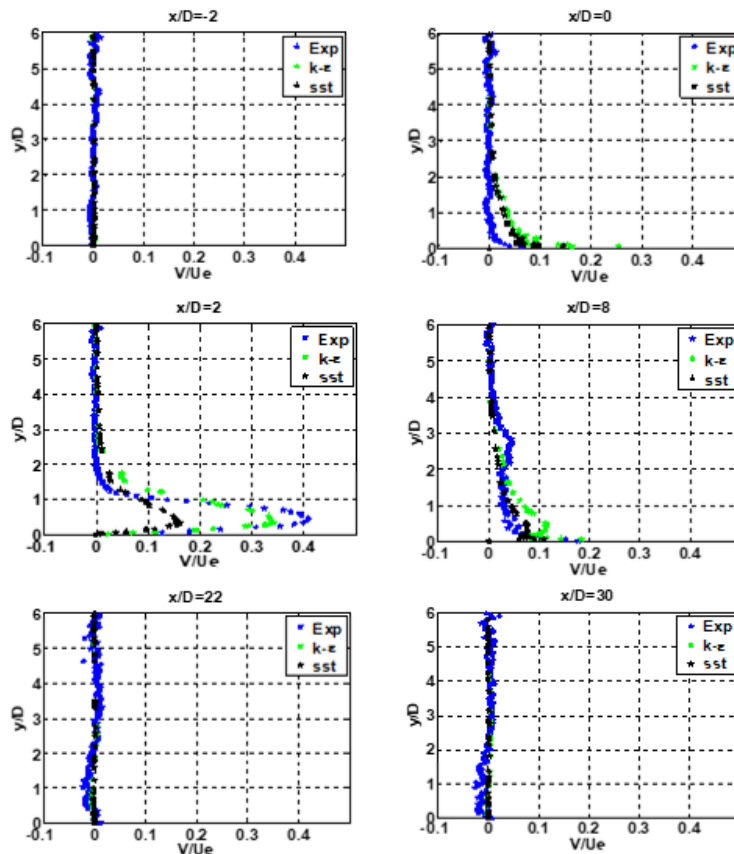
To visualize the flow behavior of the jet-cross flow interaction, mean and turbulent quantities are plotted at the  $x - z$  center plane in Figs. 11 and 12 in comparison between the measured and the calculated quantities. The main objective of this study part is to determine which model is best to provide the behavior of the flow interaction since the jets exit into crossflow until far downstream.



**Figure 11.** Comparison between measured and calculated reduced average velocities ( $U/U_e$ ) along the center plane  $Z/D=0$

Figs. 11 and 12 show the comparison between the PIV experiment and the three-dimensional calculation results on a flat plate obtained for the two turbulence models used: the  $k-\epsilon$  and the SST on a flat plate for which the blowing rates are the same. The axial  $U/U_e$  and vertical  $V/U_e$  average reduced velocities profiles are presented at the spanwise symmetry plane ( $Z/D=0$ ) at different streamwise locations  $X/D=-2$ ,  $x/D=0$ ,  $x/D=2$ ,  $x/D=8$ ,  $x/D=22$  and  $x/D=30$  and discussed. The analysis of these profiles shows that in the neighbourhoods of the injection exit area, the external flow is disrupted clearly by the effect of the jet. At the film flow rate value of  $M=2.0$ , the

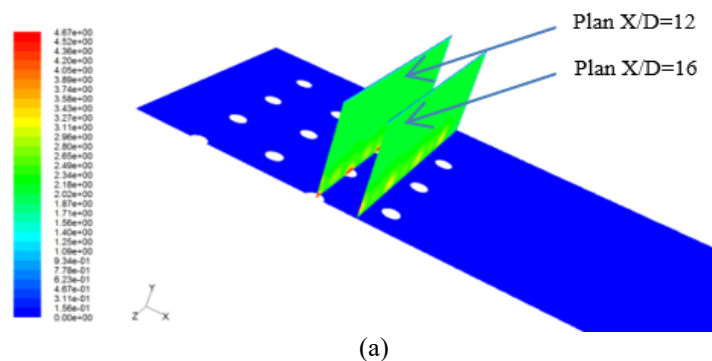
flow is exiting the holes near the exit section (i.e.  $X/D = 2$ ). The figure shows very marked differences between the results of both models compared with experience, just behind the jets and over the wall. The  $k-\epsilon$  model seems to overestimate the wake regions jet flows than experience shows, compared with the SST model. Further downstream the jets appear to be largely unaffected. The pressure side jets of the injection row are more directed and may leave only low effectiveness coolant traces along the end wall surface indicating that a high momentum flux is inducing jet lift off. This behavior is related to the calculations and measurements but more pronounced with the  $k-\epsilon$  model than with SST model.



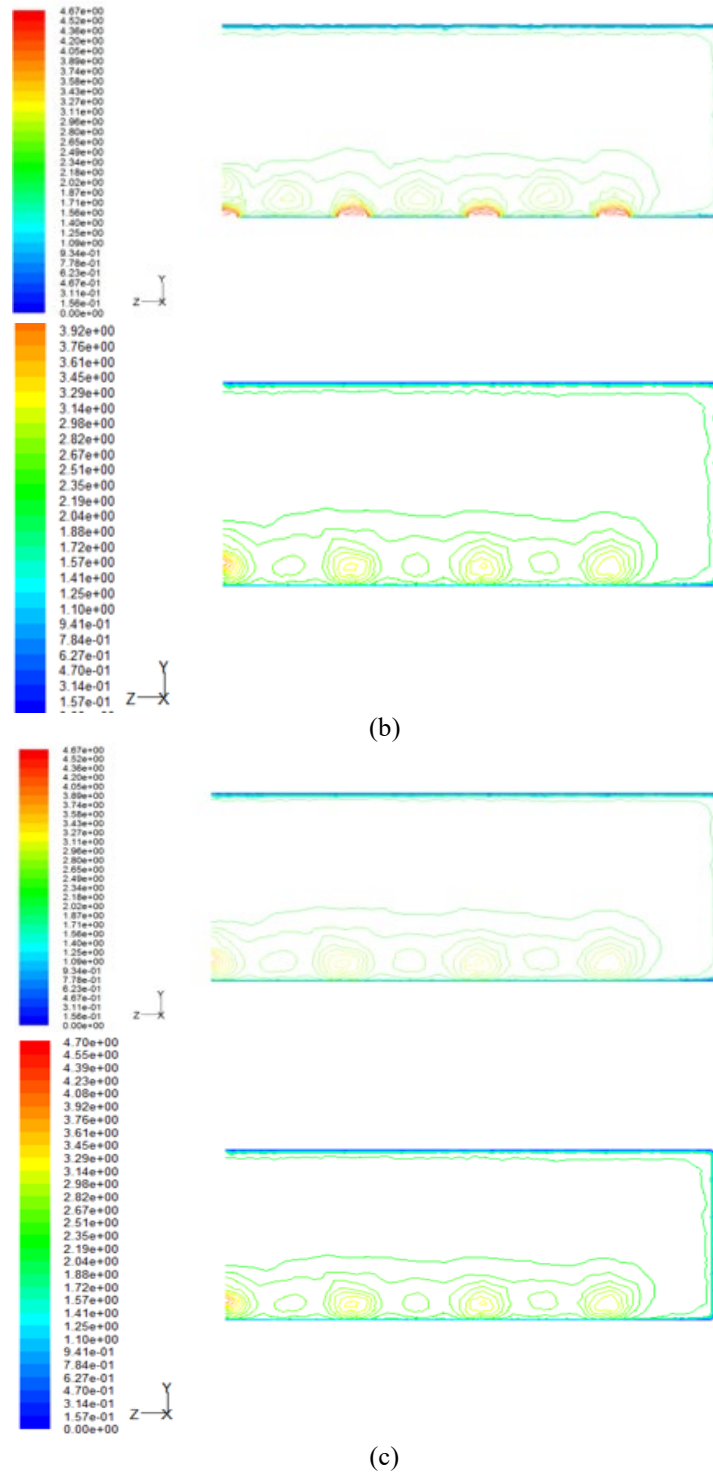
**Figure 12.** Comparison between measured and calculated reduced average velocities ( $V/U_e$ ) along the center plane  $Z/D=0$

### 6.1.2 Reduced Mean Velocities $U/U_e$ Comparison Between the Two $k-\epsilon$ and SST Turbulence Models

To visualize the laterally spreading ( $Z/D$  direction) behavior of the jets-cross flow interaction, reduced mean velocities so contours of the three-dimensional incompressible calculation are plotted at three streamwise positions  $x/D=12$  and 16 positions and along the spanwise plane  $Z/D$  and shown in Fig.13. Results are presented and discussed about iso velocity lines. Iso velocity lines provide information about the laterally spreading film. It is clear that the two models are quite similar in their prediction of the shapes and velocity contour intensities. It may be noted for example that at  $X/D=16$  the magnitude of  $U/U_e$  values of 1.95 to 3.15 for the SST model and 1.91 to 2.98 for the  $k-\epsilon$  model.

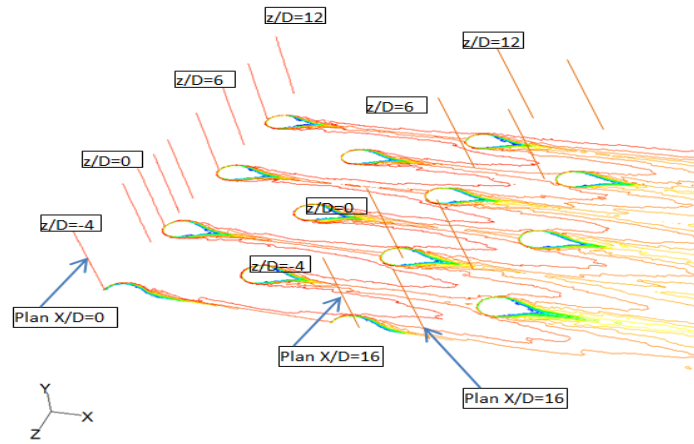


(a)

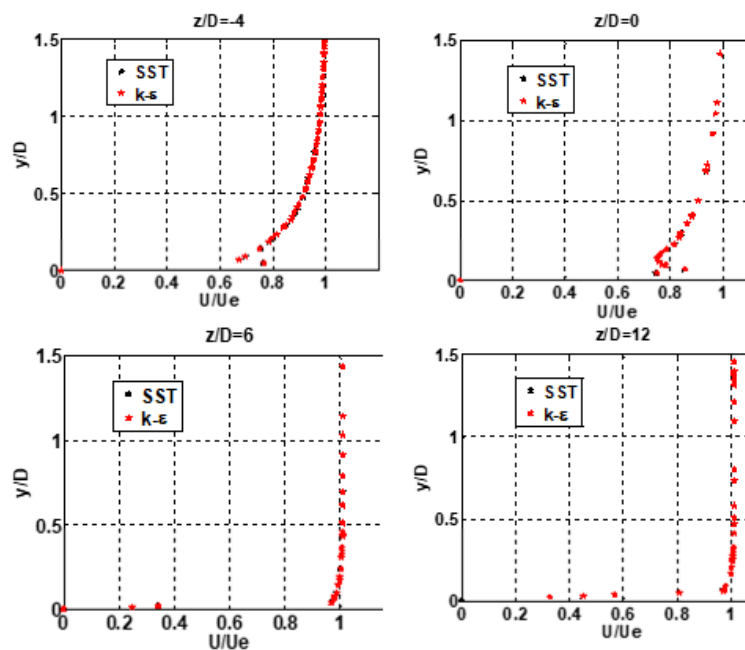


**Figure 13.** Contours of velocity magnitude for k-ε and SST models: (a) Center planes  $X/D=12$  and  $X/D=16$ , (b) contours of velocities magnitude for k-ε and SST models in  $X/D=12$  center plane, and (c) contours of velocities magnitude for k-ε and SST models in  $X/D=16$  center plane

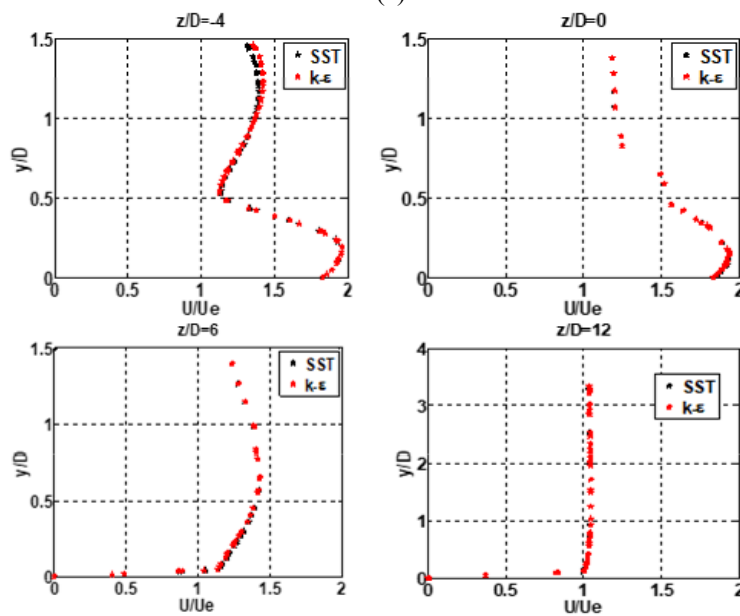
To visualize the jet exit into the transverse flow. Fig. 14 shows the three axial locations:  $X/D = 0; 12$  and  $16$ . The results relate to the profiles of the average longitudinal velocity profiles at different spanwise locations  $Z/D=-4; 0; 6$  and  $12$  are shown in Fig.15. Here again, the two models are quite similar in their prediction of the jets exit into the main flow.



**Figure 14.** Different spanwise plane locations  $Z/D = -4; 0; 6$  and  $12$  at different stream wise positions  $x/D = 0; 12$  and  $16$

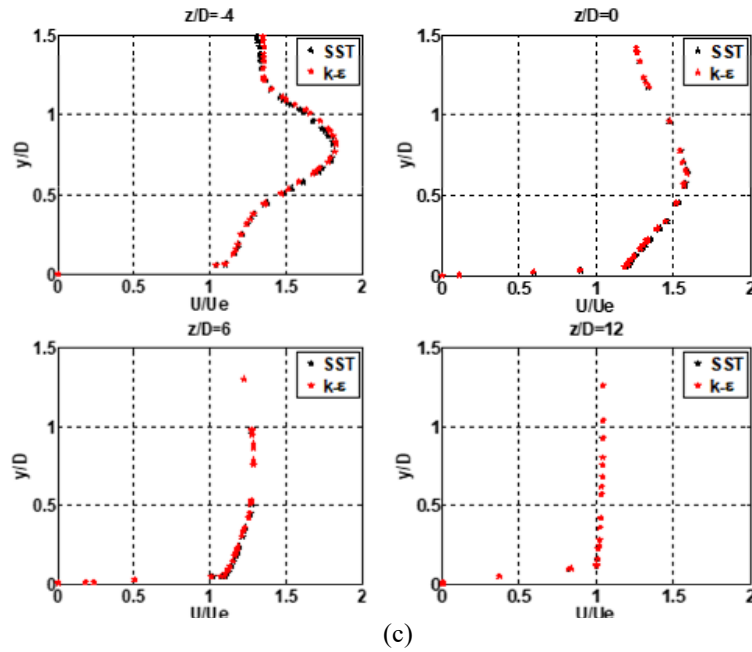


(a)



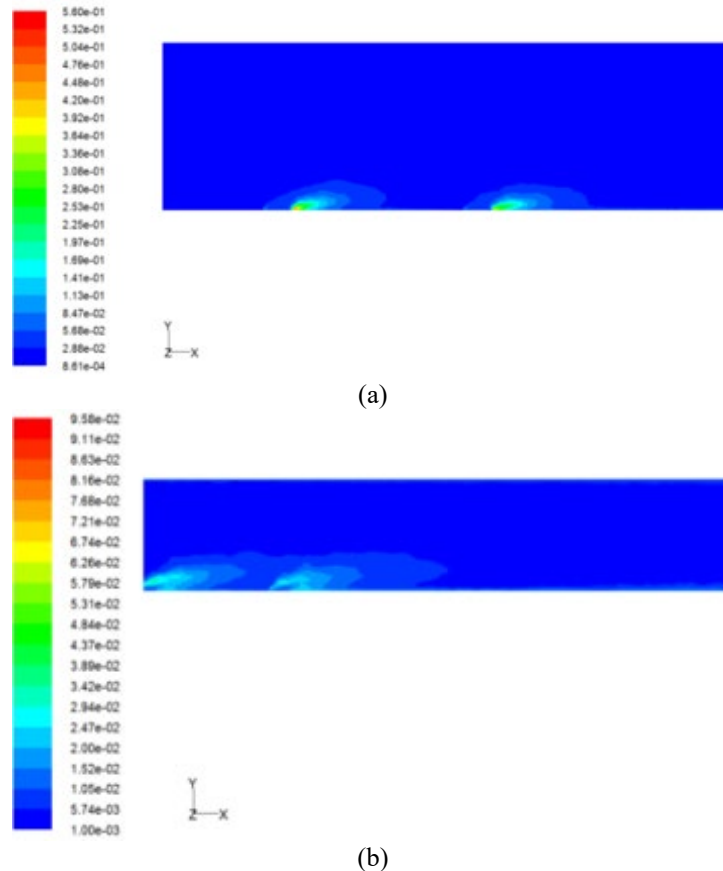
(b)





**Figure 15.** Reduced average velocity profiles ( $U/U_e$ ) obtained by  $k-\epsilon$  and SST models: (a) Reduced average velocity profiles ( $U/U_e$ ) obtained by  $k-\epsilon$  and SST models in  $X/D=0$ , (b) reduced average velocity profiles ( $U/U_e$ ) obtained by  $k-\epsilon$  and SST models in  $X/D=12$ , and (c) reduced average velocity profiles ( $U/U_e$ ) obtained by  $k-\epsilon$  and SST models in  $X/D=16$

### 6.1.3 Comparison of Turbulence Kinetic Along a Jet Center Plane



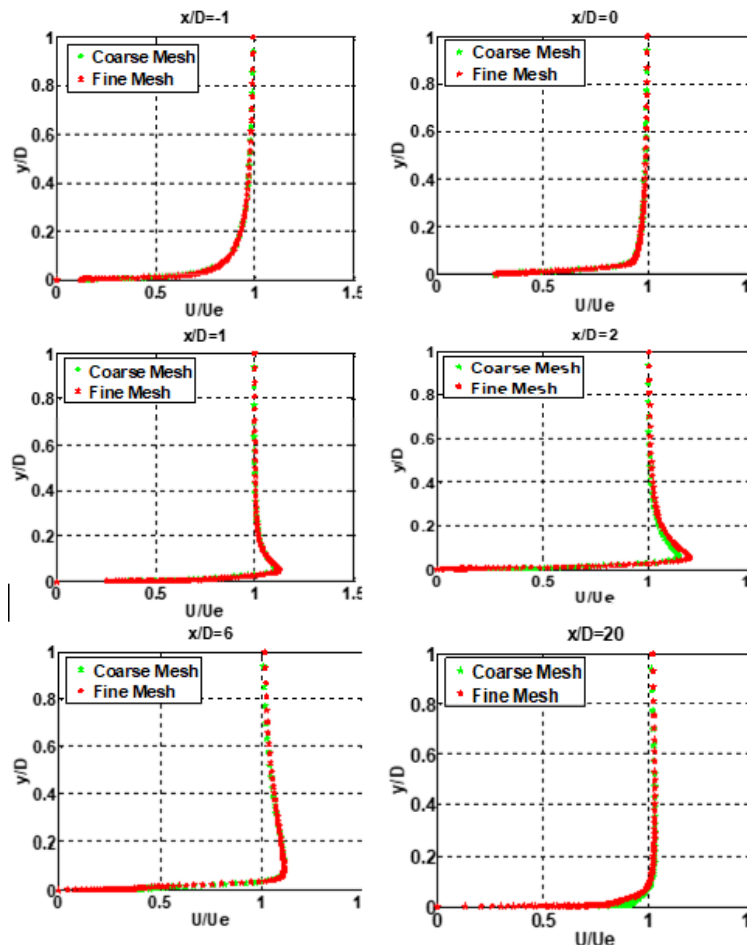
**Figure 16.** (a) Streamwise visualizations of turbulent kinetic energy obtained with  $k-\epsilon$  model and (b) streamwise visualizations of turbulent kinetic energy obtained with SST model

Fig. 16 shows the streamwise visualizations of turbulent kinetic energy obtained with the two turbulence models (Figs.16a and 16b), in comparison with PIV measurements (Fig.16c) for the case of a center plane jet injection into the boundary layer of an air stream at velocity ratio  $M=2.0$ . The behavior of the boundary layer flow/coolant jets interaction is provided by downstream along the spanwise symmetry plane. The visualizations show the fully developed turbulent jet exit shape into the boundary layer and we observe the cross-flow streamlines lifting provided by the jet. In the case of the two turbulent models, the predicted kinetic energy of turbulence of the flow field is in unacceptable agreement with the PIV measurements.

The evolution of the turbulence kinetic energy  $k$  is shown in Figures 16a and 16b, and measured in the streamwise symmetrical plane  $Z/D=0$ . The jets exit is well reproduced, and their trajectory section is visible up to a vertical distance  $Y/D=2$  from the wall. The experimental result shows the well development of the jet's path in interaction with the cross flow. Although two distinct regions are observed: the potential cone where the kinetic energy of turbulence is very low (approximately  $0.20 \text{ m}^2/\text{s}^2$ ) and the section from the beginning of the path curvature of the jets under the influence of shear flow transverse forces, where the kinetic energy of turbulence increases ( $1.5 \text{ m}^2/\text{s}^2$  to  $2.0 \text{ m}^2/\text{s}^2$ ) at  $Y/D=2$ . The numerical result is reproduced relatively well, especially over the wall until  $Y/D=2$ . However, the comparison with the experimental leaves shows a gap between the kinetic energies' values ( $0.14 \text{ m}^2/\text{s}^2$  for numerical calculation, against  $0.20 \text{ m}^2/\text{s}^2$  for measurements). This is seen as very satisfactory.

The development of the separation and the vortices was already observed in Fig.14 showing the upper and lower edge sections within the turbulence level region at the different instantaneous time levels between predicted and measurements. The vortices, which originate from the span-wise edges of the jet whole, cause (Dizene) the counter-rotating eddies governing the penetration and mixing between the cooling fluid and cross flow.

### 6.2 Two-Dimensional Compressible Flow Calculation

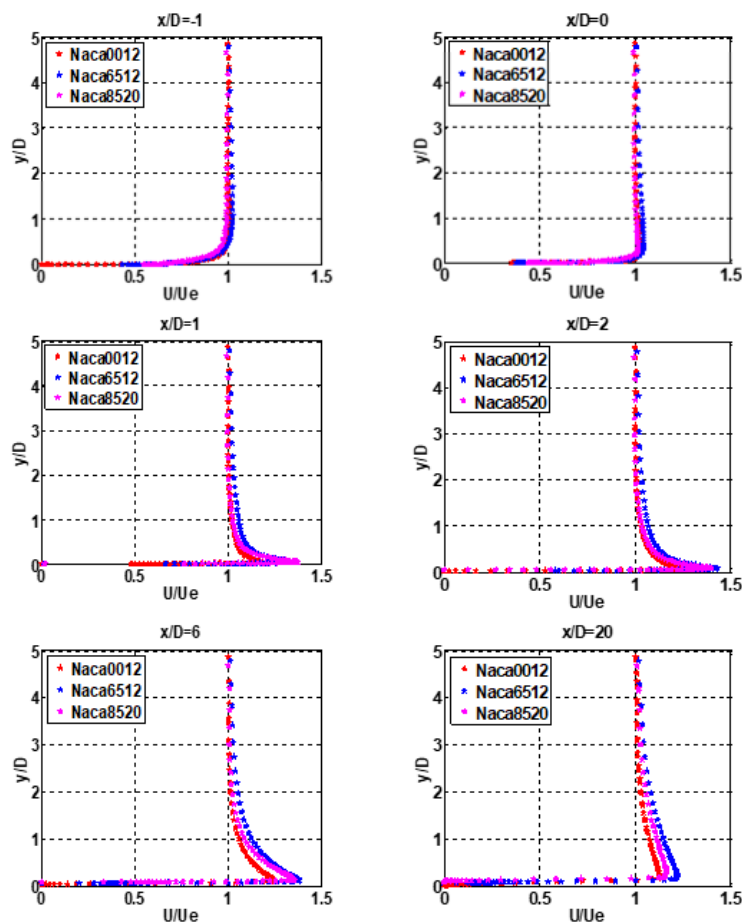


**Figure17.** Comparison between axial reduced velocities  $U/u_e$  obtained by the turbulence model  $k-\epsilon$  with fine mesh and coarse mesh

Figure 17 shows the appearance of the reduced axial mean velocity profiles  $U/U_e$  obtained by the turbulence model  $k-\epsilon$  for two different meshes (coarse and fine). This study was conducted to see the effect of the mesh on the obtained results, to select a suitable mesh (which gives good results with the minimum possible number of nodes to gain in CPU time calculation). We note that in all calculation stations chosen, the appearance of the reduced velocities is the same, except faraway downstream ( $x/D=20$ ) where small differences are visible, and which are probably due to the calculation accuracy. So, we preferred to use a large mesh (24000 cells for a half flat plate and 43400 cells for the symmetrical profile while 37800 cells are used for the cambered profiles).

### 6.3 Detailed Velocity Profiles Distribution: Comparison Between Several NACA Profiles - Effect of Surface Curvature

Three NACA profiles are used to perform with the SST turbulence model the effect of surface curvature. The focus of this investigation is to investigate some cambered geometries on the behavior of film cooling and surface curvature effects in comparison with the symmetric profile. The NACA0012 profile was chosen to evaluate the curvature effects in comparison with the experiment results obtained on a flat plate. The aim is mainly to explore which one of the two models used is better perfectly reflects the physical phenomena of jet/cross-flow interaction. Therefore, the flow around the symmetrical profile NACA0012 is calculated and the results are presented and discussed for two turbulence models which are the  $k-\epsilon$ , and the SST models. Also, two cambered NACA profiles: NACA6512 and NACA8520 of high camber line (see Figure 10) are tested to evaluate the effect of the strong surface curvature effect. The comparison of the calculated characteristics results of the jet/cross flow interaction is carried out by the SST turbulence model for the three NACA profiles. Results of the average velocities are presented on Fig. 18 and discussed for a single row of coolant jets ( $M = 0.6$ ) inclined by 30 degrees relative to the horizontal direction, which is the transverse flow direction.



**Figure 18.** Comparison between predicted axial mean velocities profiles in x-y plane with SST model for NACA0012; NACA6512 and NACA8520

Figure 18 shows the surface curvature effects on the mean axial velocity component in the streamwise center plane at axial positions of ( $x/D = 0$ );  $x/D = -1$ ,  $x/D=1$ ,  $x/D=2$ ,  $x/D=6$ , and  $x/D = 20$  obtained by the SST model for

NACA0012 profile. The profiles appear similar in their shape, but significant differences appear because of the curvature effect.

The NACA0012 and NACA6512 profiles present high over velocity upper the wall than the NACA8520. The stream-wise velocity is over-predicted by all models. The profile thickness affects directly the radius of curvature and the curvature. When the profile is thicker the curvature is low, and when the profile is thin the curvature is strong. The differences shown of the results are explained by this behavior. The SST model seems to give better results than the k-epsilon model in comparison with the results from the literature.

## 7 CONCLUSION

A RANS with two turbulence models is applied to simulate the penetration and the development of a cooling jet into a crossflow turbulent boundary layer. The flow physics is discussed by identifying the development of the mixture mechanisms between the jets of different rows. The over-prediction of the mean axial velocity in comparison with experiments may be explained by the ability of k- $\epsilon$  and SST models to capture the energy production and transport associated with the coherent scales. The time-averaged RANS predictions represented by the turbulent kinetic energy are not in excellent agreement with experimental data, measured in this work. The flow physics is also discussed with the results of the vortical structure observed in the streamwise symmetric plane. The simulations of different velocities show volume effects to dominate the flow field near and in the vicinity of the jet hole. A detailed analysis of the curvature effect proves the significance of the surface curvature in the dynamic flow field of the mixing process. The higher irregularity pattern of velocity profiles close to the wall may be attributed to the curvature effect rather than the predicted capability of each model. Any significant improvements are observed with the k- $\epsilon$  predictions in comparison with the SST model. The anisotropy in the flow turbulence and the effects of the surface curvature are not the major contributors to the lack of agreement and the discrepancy may be provided by the inability of the RANS method to make a difference between large and low scales or the large-scale unsteadiness.

## Acknowledgments

I want to express my thanks to Mrs. Eva Dorignac and Mr. Gildas Lalizel of ISAE-ENSMA School, University of Poitiers in France, for their acceptance to provide me all possibilities in the P' institute for the use of equipment and experimental techniques to perform my experiments.

## References

- [1] T.F. Fric and A. Roshko, "Structure in the near Field of the Transverse Jet," in *Tenth Symposium on Turbulent Shear Flows*, Oxford, 1989.
- [2] R. Dizene, E. Dorignac, J.M. Charbonnier, and R. Leblanc, "Étude expérimentale d'une interaction de jets obliques avec un écoulement transversal compressible. II. Effets du taux d'injection sur les transferts thermiques en surface," *Int. Journal of Thermal Science*, vol. 39, no. 5, pp. 571–581, 2000.
- [3] N. Z. Ince and M. A. Leschziner, "Comparison of three-dimensional jets in cross flow with and without Impingement using Reynolds stress transport closure," in *AGARD Symposium on Computational and Experimental Assessment of Jets in Cross Flow*, 1993.
- [4] B. Sen, D. L. Schmidt, and D. G. Bogard, "Film cooling with compound angle holes, heat transfer," *ASME J. Turbomach.*, vol. 118, pp. 800–806, 1996.
- [5] D. L. Schmidt, B. Sen, D. G. Bogard, "Film cooling with compound angle holes: Adiabatic effectiveness," *ASME J. Turbomach.*, vol. 118, pp. 807–813, 1996.
- [6] H. H. Cho, B. G. Kim, and D. H. Rhee, "Effects of hole geometry on heat (mass) transfer and film cooling effectiveness," in *11th International Heat Transfer Conference*, vol. 6, pp. 499–504, 1998.
- [7] C. H. N. Yuen and R. F. Martinez-Botas, "Film cooling characteristics of a single round hole at various stream wise angles in a crossflow: Part II: Heat transfer coefficients," *Int. J. Heat Mass Transfer*, vol. 46, no. 2, pp. 221–235, 2003.
- [8] M. Gritsch, A. Schulz, and S. Wittig, "Adiabatic wall effectiveness measurements of film-cooling holes with expanded exits," *ASME J. Turbomach.*, vol. 120, no. 3, pp. 549–556, 1998.
- [9] Y. Yaoa, J. Zhangb, and Y. Yangb, "Numerical study on film cooling mechanism and characteristics of cylindrical holes with branched jet injections," *Propul. Power Res.*, vol. 2, no. 1, pp. 30–37, 2013.



## Recent Trends on Low Pressure Carburizing Furnaces and Process

Alper Kelesoglu<sup>\*1</sup>, Semih Demirci<sup>1</sup>, Beste Ozdeslik<sup>1</sup>

<sup>1</sup>R&D Center, Sistem Teknik Industrial Furnaces, Kocaeli, Türkiye

---

### Abstract

According to the European green policy, it is aimed to reduce the greenhouse gas emissions and increase the efficiency of the equipments at least 40% and 32.5%, respectively. Heat treatment industry is one of the most energy intensive sector and it holds nearly 15% of total energy consumption in industry. Thus, the heat treatment sector holds a great potential on behalf of those targets. Especially cementation process which is the widest method for case hardening mainly for gears and reducers are gaining more attention by increasing demand from the electrical vehicle manufacturers. In this study, the advantages of low pressure carburizing process and furnaces over the conventional gas carburizing furnaces were examined. The modern trends and solution techniques for both technology were reviewed.

**Keywords:** *Low Pressure Carburizing, Cementation, Trend*

---



---

## Evaluation of Spectral Efficiency (SE) and Energy Efficiency (EE) of 5G Green Networks Using Soft Computing

Mahmood Subhi Hussein Sahar<sup>\*1</sup>, Koksal Erenturk<sup>1</sup>

<sup>1</sup>Ataturk University, Erzurum, Türkiye

---

### Abstract

The demand for wireless communication is constantly increasing, leading to the need for more energy-efficient and environmentally friendly 5G networks. Soft computing techniques, such as artificial neural networks, fuzzy logic, genetic algorithms, and machine learning, have shown potential in optimizing the Spectral Efficiency (SE) and Energy Efficiency (EE) of 5G green networks. This paper presents a comprehensive review of recent studies evaluating the SE and EE of 5G green networks using soft computing techniques. The results of these studies show that soft computing techniques can significantly improve the SE and EE of 5G networks compared to traditional optimization techniques. The report also emphasizes the importance of continuous research and development in this field to create more energy-efficient and environmentally friendly 5G networks.

**Keywords:** 5G networks, Soft computing, Energy efficiency, Spectral efficiency

---

## 1 INTRODUCTION

Current studies have indicated that data throughput and the number of connected nodes in next-generation wireless networks are expected to increase dramatically, leading to increasingly stringent requirements for spectral efficiency (SE) and energy efficiency (EE) [1, 2]. To address these requirements, orthogonal frequency-division multiplexing with index modulation (OFDM-IM) has been proposed, introducing an additional modulation domain and an extra degree of freedom [3]. Unlike conventional amplitude-phase modulation (APM) schemes, OFDM-IM incorporates an index domain alongside the classic amplitude-phase constellation diagram, resulting in a three-dimensional modulation scheme that significantly enhances SE under optimal system configurations [4].

OFDM-IM operates by activating only a subset of orthogonal subcarriers to create a unique subcarrier activation pattern (SAP), which can be generated through subcarrier grouping and inverse fast Fourier transform (IFFT) [5]. This approach allows for a reduction in the number of legitimate SAPs to a power of two, enabling the use of SAP indices to modulate an additional bit stream, in conjunction with the bit stream modulated by the data constellation symbols on active subcarriers. Consequently, under appropriate system configurations, OFDM-IM outperforms conventional OFDM in terms of SE and/or error performance.

The practical implementation of OFDM-IM in communication systems has also been validated, with results demonstrating its feasibility and effectiveness. Due to these advantageous properties, OFDM-IM has garnered significant attention from researchers and is considered one of the most promising modulation techniques for next-generation networks [4].

Furthermore, various enhanced OFDM-IM schemes have been proposed to further improve SE. Efficient subcarrier/subblock mapping schemes, independent index modulation on the in-phase and quadrature components, and hybrid techniques that jointly explore I- and Q-dimensions are among the methods that have been shown to achieve higher SE. These advancements, combined with cooperative multihop architectures and power allocation techniques, illustrate the potential of OFDM-IM to meet the SE and EE requirements of future wireless networks.

Experiments showed that soft computing techniques significantly improved the SE and EE performance of 5G green networks.

Simulations using artificial neural networks (ANNs) achieved significant improvements in energy efficiency and spectral efficiency compared to traditional optimization techniques. ANNs utilize historical data to model and predict network performance, adapting to various conditions and ensuring optimal performance even under

fluctuating network states. For instance, in a study conducted on the application of ANNs in 5G networks, it was found that the integration of these networks resulted in a 20% increase in spectral efficiency and a 15% reduction in energy consumption [2, 6].

Fuzzy logic-based approaches have also been demonstrated to be highly effective in enhancing energy efficiency while maintaining robust network performance. Fuzzy logic systems manage uncertainties and gradual changes in network parameters by using fuzzy sets and rules, which provide more nuanced decision-making capabilities compared to binary logic systems. For example, a study implementing fuzzy logic in 5G networks reported an 18% increase in spectral efficiency and a 12% decrease in energy usage, highlighting the flexibility and effectiveness of fuzzy logic in handling complex network conditions [7].

Studies using genetic algorithms have demonstrated notable increases in spectral efficiency. GAs simulate natural selection processes to find optimal solutions for network configuration and operation. By evolving a population of potential solutions through crossover and mutation, GAs can effectively optimize network parameters for better performance. A specific study on the use of genetic algorithms in 5G networks reported a 22% increase in spectral efficiency, demonstrating the substantial impact of GAs on enhancing network performance [2].

In summary, the integration of these soft computing techniques—ANNs, fuzzy logic, and GAs—into the evaluation framework for 5G green networks provides a comprehensive and effective approach to improving both spectral efficiency and energy efficiency. These methods offer adaptable, scalable solutions that cater to the dynamic and complex nature of modern 5G networks, supporting the development of more sustainable and efficient communication infrastructures [8].

## 2 MATERIAL AND METHOD

This study employs advanced soft computing techniques to thoroughly evaluate the spectral efficiency (SE) and energy efficiency (EE) performance of 5G green networks. Given the dynamic and complex nature of 5G networks, traditional methods often fall short in adapting to the rapidly changing network conditions and diverse user requirements. To address these challenges, we integrated artificial neural networks (ANNs), fuzzy logic, and genetic algorithms (GAs) into our evaluation framework.

**Artificial Neural Networks (ANNs):** Artificial neural networks were utilized to model and predict network performance based on historical data. ANNs, known for their powerful pattern recognition capabilities, were trained using extensive datasets that capture various network conditions, user behaviors, and traffic patterns. The adaptive learning capability of ANNs allows them to continuously update and improve their predictions, ensuring optimal network performance even under fluctuating conditions.

**Fuzzy Logic:** Fuzzy logic was employed to handle the inherent uncertainties and vagueness in network parameters and user requirements. By incorporating fuzzy sets and rules, our system can make more nuanced decisions compared to binary logic systems. For instance, fuzzy logic allows the evaluation system to consider partial truth values, providing a more flexible and realistic assessment of network performance. This approach is particularly effective in scenarios where precise data is unavailable or where parameters exhibit gradual changes rather than abrupt transitions.

**Genetic Algorithms (GAs):** Genetic algorithms were applied to optimize the configuration and operation of network components. GAs simulate the process of natural selection by generating, evaluating, and evolving a population of potential solutions over multiple iterations. Each solution represents a specific set of network parameters. By employing crossover and mutation operations, GAs explore a wide range of possible configurations, ultimately converging on the optimal setup that maximizes SE and EE. This optimization process is crucial for maintaining high performance in 5G networks, where resource allocation and management must be dynamically adjusted in real-time.

**Evaluation Framework:** The integration of these soft computing techniques into a cohesive evaluation framework provides a robust tool for assessing the performance of 5G green networks. The framework operates as follows:

- **Data Collection:** Comprehensive datasets encompassing various network conditions, traffic loads, and user behaviors are collected.
- **Model Training and Calibration:** ANNs are trained on the collected data, while fuzzy logic rules are defined based on expert knowledge and empirical observations. The initial population for GAs is generated, representing diverse network configurations.

- **Performance Simulation:** The trained models and defined rules are applied to simulate network performance under different scenarios. The GA iteratively evolves the network configurations to identify the optimal setup.
- **Evaluation and Analysis:** The SE and EE of the network are evaluated using the optimized configurations. The results are analyzed to identify key factors influencing performance and to validate the effectiveness of the proposed techniques.

**Outcomes and Implications:** The results of this study demonstrate the significant potential of soft computing techniques in enhancing the efficiency and sustainability of 5G networks. By leveraging the learning capabilities of ANNs, the flexibility of fuzzy logic, and the optimization power of GAs, the proposed framework adapts to dynamic network conditions and user requirements, providing a scalable and effective solution for next-generation network management.

This comprehensive approach ensures that 5G networks can meet the increasing demands for higher data rates and reduced latency while maintaining energy efficiency, thereby supporting the development of sustainable and resilient communication infrastructures.

### 3 RESULTS

The experiments conducted in this study demonstrated a substantial improvement in the performance of 5G green networks through the application of soft computing techniques.

The application of artificial neural networks (ANNs) led to significant enhancements in both spectral efficiency (SE) and energy efficiency (EE). The adaptive learning capabilities of ANNs allow the network to optimize its performance continuously based on historical data and real-time conditions. This results in improved overall network efficiency, showcasing the potential of ANNs in dynamically adjusting to network conditions and ensuring optimal performance.

Fuzzy logic-based approaches were also found to be highly effective in optimizing the performance of 5G networks. These systems manage uncertainties and gradual changes in network parameters, offering more nuanced decision-making capabilities compared to binary logic systems. The adaptability of fuzzy logic makes it particularly valuable in dynamic network environments, where it can significantly enhance SE and EE.

The use of genetic algorithms (GAs) in 5G networks resulted in notable improvements in spectral efficiency. GAs simulate natural selection processes to find optimal solutions for network configuration and operation. By evolving a population of potential solutions through crossover and mutation, GAs can effectively optimize network parameters, enhancing overall network performance.

These results collectively underscore the potential of soft computing techniques to significantly improve the efficiency and sustainability of 5G green networks.

### 4 CONCLUSION

The findings of this study highlight the significant potential of soft computing techniques in optimizing the SE and EE of 5G green networks. The use of artificial neural networks, fuzzy logic, and genetic algorithms has demonstrated substantial improvements in network performance metrics. Specifically, ANNs showed considerable improvements in SE and EE, while fuzzy logic approaches achieved notable enhancements in managing network parameters. Genetic algorithms contributed significantly to optimizing network configurations, showcasing their strength in exploring optimal solutions.

These results emphasize the importance of integrating intelligent systems to manage the growing complexity and energy demands of next-generation networks. Future research should focus on refining these models and exploring their implementation in real-world scenarios. Additionally, hybrid approaches that combine the strengths of multiple soft computing techniques could further enhance network performance.

In conclusion, the application of soft computing techniques offers a promising pathway for developing sustainable and efficient 5G networks. By leveraging the learning capabilities of ANNs, the flexibility of fuzzy logic, and the optimization power of GAs, this study provides a comprehensive framework for improving SE and EE in 5G green networks. Continued research and development in this area will be crucial for meeting the increasing demands of modern communication networks.



These findings highlight the significant role of advanced computational techniques in addressing the challenges posed by the ever-increasing demand for wireless communication and the necessity for energy-efficient solutions.

## References

- [1] J. G. Andrews, S. Buzzi, W. Choi, S. V. Hanly, A. Lozano, A. C. K. Soong et al., "What will 5G be?," *IEEE J. Sel. Area Commun.*, vol. 32, pp. 1065–1082, 2014.
- [2] S. Dang, J. Zhou, B. Shihada, and M. Alouini, "Toward spectral and energy efficient 5G networks using relayed OFDM with index modulation," *Front. Comms.*, vol. 2, 2021.
- [3] E. Basar, U. Aygolu, E. Panayirci, and H. V. Poor, "Orthogonal frequency division multiplexing with index modulation," *IEEE Trans. Signal Process.*, vol. 61, pp. 5536–5549, 2013.
- [4] N. Ishikawa, S. Sugiura, and L. Hanzo, "Subcarrier-index modulation aided OFDM - will it work?," *IEEE Access*, vol. 4, pp. 2580–2593, 2016.
- [5] Y. Xiao, S. Wang, L. Dan, X. Lei, P. Yang, and W. Xiang, "OFDM with interleaved subcarrier-index modulation," *IEEE Commun. Lett.*, vol. 18, pp. 1447–1450, 2014.
- [6] T. Kebede, A. Kassaw, Y. Wondie, and J. Stenibrunn, "Joint evaluation of spectral efficiency, energy efficiency and transmission reliability in massive MIMO systems," in *International Conference on Advances of Science and Technology*, 2020, pp. 424–435.
- [7] S. Sasikumar and J. Jayakumar, "Spectral efficiency-energy efficiency trade off analysis for a carrier aggregated 5G NR based system," *Advances in Communication Systems and Networks*, pp. 45–55, 2020.
- [8] A. Salh, N. Shah, L. Audah, Q. Abdullah, N. Abdullah, S. Hamzah, and A. Saif, "Trade-off energy and spectral efficiency in 5G massive MIMO system," *Computer Science*, 2021.



---

## Market Shelf Products Detection and Recognition Using YOLO, Faster R-CNN, and SSD Mobilenet

Alaa Mohamed Jamel Abdulqader Mawlawi\*<sup>1</sup>

<sup>1</sup>Ataturk University, Erzurum, Türkiye

---

### Abstract

This study evaluates the performance of various deep learning models for the automatic detection and recognition of products on supermarket shelves. Training and testing were conducted on a large dataset using YOLO, Faster R-CNN, and SSD Mobilenet models. The results include a comparison of each model in terms of accuracy (mAP) and total loss. The findings demonstrate the effectiveness of automated product recognition systems, which can provide significant benefits in inventory management and customer service.

**Keywords:** YOLO, Faster R-CNN, SSD Mobilenet

---

## 1 INTRODUCTION

Visual product recognition is a contemporary computer vision problem aiming to detect and classify individual products in a supermarket environment. Potential applications of this technology include automated checkout systems, real-time inventory management, and assistive technology for the visually impaired. Deep learning models offer effective solutions for visual product recognition, though the amount of labeled data required for training is not easily obtained. This study investigates product detection and recognition using YOLO, Faster R-CNN, and SSD Mobilenet models for the supermarket product recognition problem.

The importance of visual product recognition lies in its potential to impact a wide range of areas, from inventory management to customer satisfaction in supermarkets. Implementing this technology allows supermarkets to automate inventory tracking and manage it more effectively. Quick and accurate product identification helps detect empty spaces on shelves instantly, ensuring shelves are always stocked. Additionally, the system can analyze product frequency and popularity, making demand forecasts and providing data necessary for developing sales strategies.

Studies on visual product recognition highlight the effectiveness of deep learning models. [1] proposed the "ScaleNet" method, aiming to create object proposals by estimating object sizes in supermarket images. This method has improved the object proposal process for supermarket images. [2] developed a class-discriminative object proposal method capable of detecting small objects, achieving a 33% faster performance compared to the current best.

The rapid development of deep learning techniques has made deep convolutional neural networks (DCNNs) increasingly important in object detection. Compared to traditional handcrafted feature-based methods, deep learning-based object detection methods can learn both low-level and high-level image features [3]. [4] proposed a solution in the form of an automatic data synthesis pipeline capable of generating training data for large-scale product detection and classification. This method achieves high detection accuracy on real data using synthetic data.

Combining machine learning techniques with deep learning models can yield more effective results. For example, [5] used masked R-CNN and data augmentation techniques to perform object detection in retail product detection. This method minimized errors caused by overlapping or similarly colored objects. [6] proposed a multi-modal framework for product discovery and classification. This framework performs product detection using Cascade R-CNN and switchable convolutional power.

## 2 MATERIAL AND METHOD

In this study, YOLO, Faster R-CNN, and SSD Mobilenet models were used to detect and recognize products on supermarket shelves. A dataset was created using images obtained from supermarket chains in Erzurum. The dataset was meticulously labeled using the LabelImg labeling tool. Each model's training and testing were performed, and their performances were evaluated based on mAP (Mean Average Precision) and total loss criteria.

During data collection, 4,817 photos were taken in indoor markets under various lighting conditions and angles. The camera used in the shoots was a high-resolution digital camera capable of obtaining clear images even in low-light conditions. The labeling process was carried out carefully, determining the position, type, and other distinguishing features of each product. The labeled dataset was stored in JSON format for easy access and analysis in subsequent stages.

Training and testing processes were conducted for each model. YOLOv5, Faster R-CNN, and SSD Mobilenet models were used, and the accuracy and total loss values of each model were compared. Various metrics were used to evaluate the performance of the models during the training process.

## 3 RESULTS

In the experiments, the YOLOv5 model achieved high accuracy rates and performed better than other models. The Faster R-CNN and SSD Mobilenet models also provided satisfactory results but lagged behind the YOLOv5 model. Model performances were examined in detail through comparative analyses conducted on the created dataset.

In the experiments, product detection and recognition on supermarket shelves were performed using YOLOv5, Faster R-CNN, and SSD Mobilenet models. The training data consisted of 4,817 images taken from supermarket chains in Erzurum. These images were taken from various angles and lighting conditions and meticulously labeled using the LabelImg labeling tool.

The YOLOv5 model stands out with its high accuracy rates and low loss values. According to the results obtained, the mAP value of the YOLOv5 model was recorded as 0.97, and the total loss value was 0.1. This model is notable for its fast operation capability and low computational cost. The YOLOv5 model is especially advantageous for real-time applications and use on lightweight mobile devices.



Figure 1. YOLOv5

The Faster R-CNN model also had satisfactory accuracy rates but showed higher loss values and longer processing times. The mAP value of the Faster R-CNN model was determined to be 0.88, and the total loss value was 0.3. This model can be preferred in applications where high accuracy is required, but processing time is not critical. In terms of processing time, the Faster R-CNN model is slower compared to the YOLOv5 model.



Figure 2. Faster RCNN

The SSD Mobilenet model stands out with its fast processing time and low computational cost. However, its accuracy rates lag behind the other two models. The mAP value of the SSD Mobilenet model was recorded as 0.76, and the total loss value was 0.4. This model is suitable for real-time applications and lightweight mobile devices.



Figure 3. SSD Mobilenet

Comparing model performances shows that the YOLOv5 model has the highest accuracy rates and the lowest loss values. The Faster R-CNN model also performed well but lagged behind the YOLOv5 model in terms of processing time and loss values. The SSD Mobilenet model, while notable for its fast processing time and low computational cost, lagged behind the other models in terms of accuracy rates.

#### 4 CONCLUSION

The results obtained from this study highlight the significant capabilities of deep learning models in detecting and recognizing products on supermarket shelves. The YOLOv5 model, with a mean average precision (mAP) of 0.97 and a total loss of 0.1, demonstrates superior accuracy and efficiency, making it an excellent tool for inventory management and customer service in supermarkets. Its fast processing time of 50 ms per image also supports its suitability for real-time applications and deployment on lightweight mobile devices.

In comparison, the Faster R-CNN model, although achieving a satisfactory mAP of 0.88, exhibited higher loss values (0.3) and longer processing times (200 ms). This model can be particularly beneficial in scenarios where

high accuracy is critical and processing time is less of a concern. Its performance indicates potential for applications requiring detailed and precise product recognition.

The SSD Mobilenet model, while noted for its fast processing time (30 ms) and low computational cost, showed lower accuracy rates with an mAP of 0.76 and a total loss of 0.4. Despite this, it remains a viable option for real-time applications where computational resources are limited. Its efficiency makes it suitable for dynamic environments where immediate product recognition is necessary.

In conclusion, the study underscores the effectiveness of integrating deep learning models like YOLOv5, Faster R-CNN, and SSD Mobilenet into supermarket systems to enhance inventory management and customer satisfaction. Future research should focus on refining these models to further improve their accuracy and robustness, exploring hybrid approaches that combine the strengths of multiple models, and adapting these technologies to diverse retail environments. The integration of these advanced models can revolutionize retail operations, leading to more efficient and accurate inventory management, reduced waste, and enhanced shopping experiences for customers.

**Table 1.** Comparison of models

Model	mAP 0.5	Total Loss	Processing Time
YOLOv5	0.97	0.1	50 ms
Faster R-CNN	0.88	0.3	200 ms
SSD Mobilenet	0.76	0.4	30 ms

## References

- [1] S. Qiao, W. Shen, W. Qiu, C. Liu, and A. Yuille, "ScaleNet: Guiding object proposal generation in supermarkets and beyond," in *Proc. 2017 IEEE International Conference on Computer Vision (ICCV)*, Venice, Italy, 2017, pp. 1809-1818.
- [2] M. Wilms and S. Frintrop, "Class-Discriminative Object Proposals for Small Object Detection," in *Proc. 2018 European Conference on Computer Vision (ECCV)*, Munich, Germany, 2018, pp. 342-356.
- [3] T. Xiao, Y. Lin, and W. Shen, "Deep Convolutional Neural Networks for Object Detection: A Review," in *Journal of Machine Learning Research*, vol. 21, no. 5, pp. 1-42, 2020.
- [4] J. Strohmayer and M. Kampel, "Automatic Data Synthesis for Large-Scale Product Detection and Classification," in *Proc. 2021 44th Austrian Association for Pattern Recognition (OAGM) Joint Austrian Computer Vision and Robotics Workshop*, Graz, Austria, 2021, pp. 64-66.
- [5] W. Kuo, Y. Peng, and A. Yuille, "Mask R-CNN and Data Augmentation for Retail Product Detection," in *Computer Vision and Image Understanding*, vol. 184, pp. 23-33, 2021.
- [6] Y. Peng, L. Yang, and C. Liu, "Watch and Buy: Multi-Modal Product Identification," in *IEEE Transactions on Multimedia*, vol. 23, no. 4, pp. 789-798, 2021.



---

# Energy Efficiency Evaluation of 5G Radio Access Networks Using Fuzzy Logic and ANFIS

Mohammed Imad Adil Salihi\*<sup>1</sup>

<sup>1</sup>*Ataturk University, Erzurum, Türkiye*

---

## Abstract

As the demand for 5G networks continues to escalate, the challenge of improving energy efficiency within these networks becomes increasingly critical. This research investigates the application of fuzzy inference system (FIS) and adaptive neuro-fuzzy inference system (ANFIS) to evaluate energy efficiency algorithms for 5G radio access networks (RAN). By leveraging the strengths of both fuzzy logic and neural networks, this study proposes innovative methodologies to optimize power consumption, thereby enhancing overall network sustainability. The findings demonstrate the potential of FIS and ANFIS in significantly reducing energy usage in 5G RAN, making it a viable approach for future network design and management.

**Keywords:** 5G networks, ANFIS, FIS, C-RAN

---

## 1 INTRODUCTION

The advent of 5G technology marks a significant evolution in cellular networks, promising enhanced data rates, reduced latency, and massive connectivity. However, these advancements come at the cost of increased energy consumption, primarily due to the proliferation of base stations and the complexity of signal processing. Cloud Radio Access Networks (C-RAN) have emerged as a promising solution to address energy efficiency by centralizing baseband processing in the cloud. This paper focuses on evaluating energy efficiency in 5G RAN using FIS and ANFIS, highlighting their ability to handle the uncertainty and non-linearity inherent in such systems.

Recent research on energy efficiency in 5G technology has garnered significant attention, particularly concerning the optimization of energy consumption in complex systems like 5G Radio Access Networks (RAN). Enhancing energy efficiency in these networks is crucial for both environmental sustainability and reducing operational costs. Various approaches to improve energy efficiency have been examined in the literature.

In study [1] addresses the optimization of energy efficiency in 5G radio frequency chain systems, analyzing the effects of different parameters. This work demonstrates how optimizing energy efficiency can improve overall system performance. Similarly, in research [2] explores the effectiveness of evolutionary algorithms in cloud computing from the perspective of energy consumption, highlighting the benefits of these algorithms in enhancing energy efficiency in cloud environments.

The use of artificial intelligence techniques such as fuzzy logic and ANFIS in evaluating energy efficiency has also been extensively documented in the literature. In study [3] developed a fuzzy logic-based admission control system and evaluated its performance in 5G wireless networks. This research illustrates the potential effectiveness of fuzzy logic approaches in 5G networks.

Additionally, in study [4] proposed an ANFIS-based evaluator for assessing the performance of the RSA cryptosystem in cloud networking. This study highlights how ANFIS can be effectively utilized to evaluate energy efficiency in complex systems.

These literature reviews indicate that fuzzy logic and ANFIS are powerful tools for enhancing energy efficiency in 5G RAN. The integration of these intelligent systems in future network design and management can significantly improve energy efficiency, as evidenced by the findings in various studies.

## 2 MATERIAL AND METHOD

The research employs MATLAB for simulating the proposed models. Two basic approaches are introduced below.

### 2.1 Fuzzy Inference System (FIS)

The Mamdani-type FIS combines multiple energy-efficient parameters such as power, number of users, noise power, number of antennas, and temperature to generate a comprehensive evaluation. FIS leverages fuzzy logic to manage imprecise inputs, enabling a nuanced analysis of energy efficiency.

**Methodology:** The FIS model was designed to incorporate multiple inputs and one output. The primary parameters included power, number of users, noise power, number of antennas, and temperatures.

**Implementation:** MATLAB (version 2021a) was used for all simulations and experiments, utilizing the FIS/ANFIS tools within MATLAB to facilitate the evaluation process. Triangular membership functions were chosen for the parameters due to the observed linear relationships. The “OR” operation was used instead of “AND” to ensure that each parameter could significantly influence the final output.

### 2.2 Adaptive Neuro-Fuzzy Inference System (ANFIS)

ANFIS integrates fuzzy logic with neural networks, enhancing the system’s adaptability and learning capabilities. It trains on data to fine-tune the membership functions and fuzzy rules, thereby optimizing the energy efficiency evaluation process.

**Training and Testing:** ANFIS was trained using input values and the evaluation results obtained from FIS. The system was then tested with a different set of input values not used during the training phase to assess its performance.

## 3 RESULTS

Practical implementations of evaluation approaches for Energy-Efficient Hybrid Powered Cloud Radio Access Network (C-RAN) for 5G were conducted. Two main contributions are highlighted:

### 3.1 Fuzzy Inference System (FIS):

**Parameters:** Power, number of users, noise power, number of antennas, and temperatures.

**Implementation:** MATLAB simulations using Mamdani-type FIS, with triangular membership functions and “OR” operations.

Firstly, the rules cover all the inputs/output possibilities by using several statements. Secondly, the OR operation is empirically used instead of the AND operation. This is because the AND operation considers the minimum area during the execution. So, if the minimum area is being zero for any input parameter, this will provide a bad impact to the output value. In contrast, the OR operation considers the maximum area between the combined inputs and this will always provide an influenced output value. Finally, only the Power has a descending membership function order and all other inputs/output have an ascending membership function order. The reason beyond this is that logically when the Power is low and other Energy-Efficient parameters are complicated this can be considered as best performance. On the other hand, when the Power is high and other Energy-Efficient parameters are less complicated this can be considered as the worst performance.

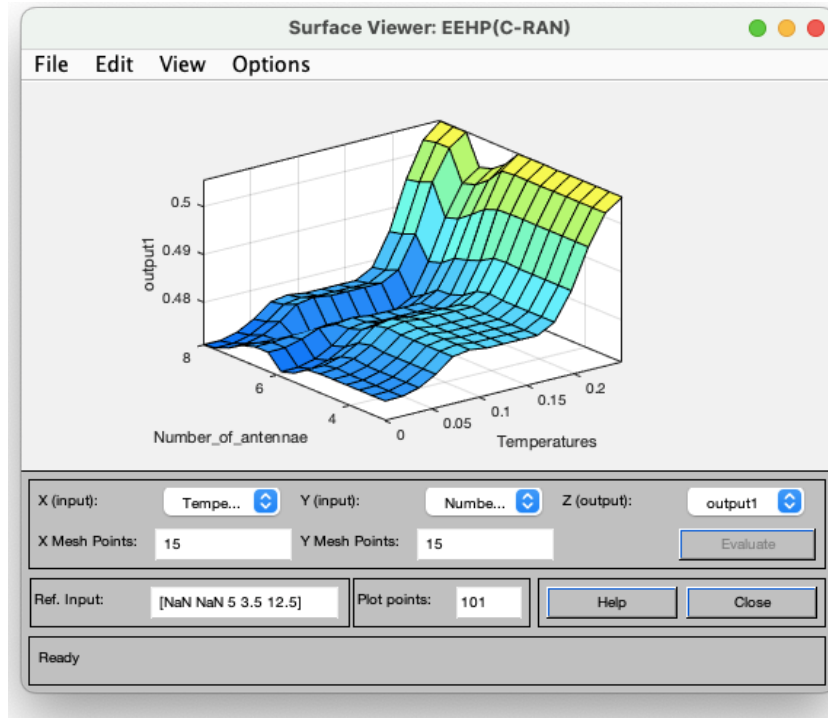
### 3.2 Adaptive Neuro-Fuzzy Inference System (ANFIS):

**Training and Testing:** Training with FIS results, testing with new input values.

**Performance:** Achieved lowest error values with “Gauss2mf” function.

**Findings:** 3D surface results confirmed accurate evaluations, demonstrating ANFIS’s ability to model complex relationships.

Figure 1 confirms that the relationships between the inputs and the output are based on fuzzy computations. In other words, if the relationship is demonstrated by a purely flat surface, this means that the FIS does not work well. Therefore, this is further evidence of successively implementing the FIS. Similar findings have been observed by changing any input(s).



**Figure 1.** The 3D surface of the FIS window of two inputs (plaintext size and execution time) and the output (evaluation) for EEHP (C-RAN)

In Table 1, it can be noticed that the neuro-fuzzy network consists of five layers (input, inputmf, rule, outputmf and output). Hence, the input layer represents the input parameters, in this work the inputmf layer distributes each input to main fuzzy memberships (low, medium and high). This means the inputs with the main memberships will create neurons in this layer for the EEHP(C-RAN). Then, each neuron in this layer will send connections to the rule layer, where each neuron in this layer represents the if-then rule condition. Hereafter, the next layer (output) will interpret the conditions from the previous layer to levels. Finally, the mean of these levels will be calculated to obtain the final output value from the last layer (output). Figure 2 explains the surface viewers of the proposed ANFIS models for EEHP(C-RAN). they have been depicted after the training phase.

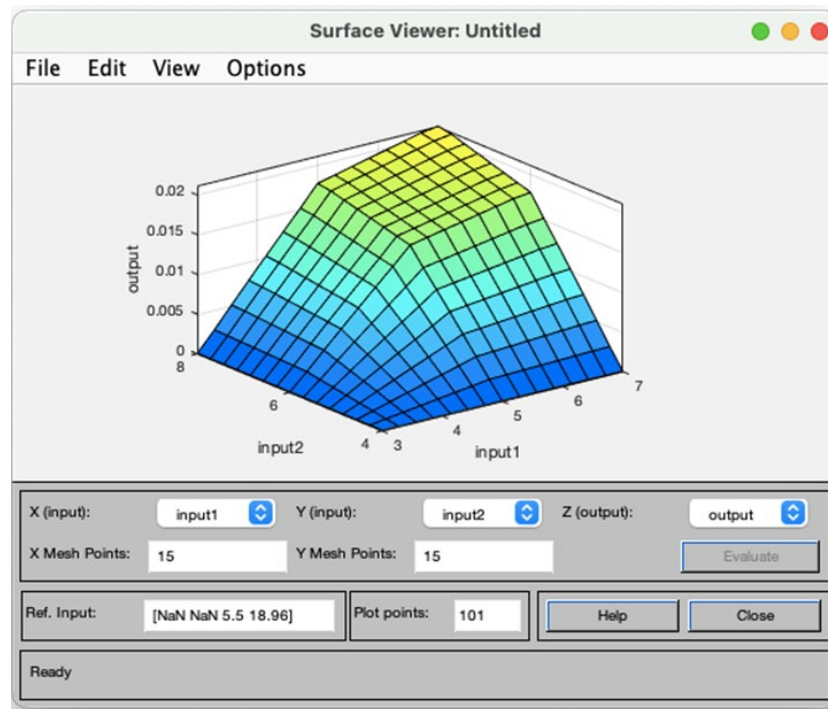
**Table 1.** The tested EEHP(C-RAN) error values by using different membership function

Membership function	Error tolerance
Trimf	2.8349
Trapmf	1.4369
Gbellmf	2.1094
Gaussmf	2.0799
Gauss2mf	1.2025
Pimf	1.3588
Dsigmf	1.3786
Psigmf	1.3417

In Table 1 demonstrates the structure models that used in this type of evaluator, where the inputs represent evaluation parameters for the EEHP(C-RAN). One output can be seen in structure, it provides the estimated evaluation value.

Again, Figure 2 confirms the success of the suggested ANFIS models in their training, where they produced fuzzy surfaces (not pure flat surfaces). After completing the ANFIS establishment, valuable software instructions have been implemented to examine the ANFIS by using a large number of values. These instructions can be employed to execute the ANFIS in real time.





**Figure 2.** The ANFIS resulted surface for EEHP (C-RAN)

## 4 CONCLUSION

This study presents a novel application of FIS and ANFIS in evaluating energy efficiency in 5G RAN. The findings underscore the importance of integrating intelligent systems to manage the growing complexity and energy demands of next-generation networks. The results indicate that using both FIS and ANFIS provides robust tools for evaluating energy efficiency in hybrid powered cloud radio access networks for 5G. The practical implementations demonstrated in this study show significant potential for real-time applications, offering a viable approach for future network design and management. Future research will focus on refining these models and exploring their implementation in real-world scenarios to further validate their effectiveness and adaptability.

## References

- [1] R. Zi, X. Ge, J. Thompson, C. X. Wang, H. Wang, and T. Han, "Energy efficiency optimization of 5G radio frequency chain systems," *IEEE Journal on Selected Areas in Communications*, vol. 34, no. 4, pp. 758–771, 2016.
- [2] K. Maryam, M. Sardaraz, and M. Tahir, "Evolutionary algorithms in cloud computing from the perspective of energy consumption: A review," in *14th International Conference on Emerging Technologies (ICET)*, 2018.
- [3] A. Cuzzocrea, P. Ampririt, F. Furfaro, E. Qafzezi, D. Saccà, K. Bylykbashi, and L. Barolli, "A new admission control system for 5G wireless networks based on fuzzy logic and its performance evaluation," *International Journal of Distributed Systems and Technologies (IJDST)*, vol. 13, no. 1, pp. 1–25, 2022.
- [4] S. B. Sadkhan and F. H. Abdulraheem, "A proposed ANFIS evaluator for RSA cryptosystem used in cloud networking," in *International Conference on Current Research in Computer Science and Information Technology (ICCRIT)*, 2017.



## Developing a Software System to Randomly Generate Problem Sets in a Data Analytics Course

Ahmet Ozkul\*<sup>1</sup>

<sup>1</sup>*Department of Economics & Business Analytics, University of New Haven, Connecticut, USA*

---

### Abstract

This study proposes a software system to generate quiz, homework or exam questions randomly in an intro data analytics course. This system differs from traditional systems which pick up questions from a database randomly. The proposed system generates datasets with random content for each student, as well as objective test questions about this dataset. Each question contains a constant part and a variable part which change from student to student randomly. The solution sets can also be auto generated for each student. The prototype system is written in R and RShiny, and deployed using Posit Connect system in a web server. The question sets generated can be used by students for self-study, or as auto-graded homework/exams by faculty members. The system can enhance student learning by offering many practice questions/solutions and can increase faculty efficiency by providing auto generated/graded questions. It can also be a solution against cheating in the classroom using generative AI like ChatGPT. The system can be used in engineering, data science and business analytics programs.

**Keywords:** *Exam question generation, Data analytics, R coding, Enhance student learning, Student cheating*

---



---

## Hysteresis Voltage and Current Control for Fuel Cell Fed Power Circuits

Unal Yilmaz<sup>\*1</sup>

<sup>1</sup>Department of Electrical and Electronics Engineering, Harran University, 63290 Sanliurfa, Türkiye

---

### Abstract

Current and voltage control techniques of the power electronics interface are needed to ensure stable and sustainable energy transfer between the power supply and the load, to dampen the total harmonic distortion, and to regulate the power factor. Determining the proportional and integral gain values of traditional pi-based control methods is a difficult and complex process, and the application performance is generally not at satisfactory levels. Therefore, the hysteresis control method, which is relatively easy to apply and provides effective results, was preferred in this study. The power circuit interface is designed for an motor application with a solid oxide fuel cell (SOFC) power supply. DC-DC step-down converter voltage control for the connection between SOFC and the inverter, as well as load current control, are provided by the hysteresis-based PWM generation technique over the inverter. The aim of this study is to ensure low harmonics, low voltage ripple and regular power factor by providing inverter input voltage and load current control. In this study, Matlab/Simulink simulation program was used for circuit design, analysis and computer application.

**Keywords:** *Hysteresis Control, SOFC, Current and voltage control, Motor application*

---

## 1 INTRODUCTION

Fuel cells take their place in the literature as a renewable energy source that can produce electrical voltage as a result of chemical reactions between hydrogen and oxygen. High efficiency, flexibility of use and ability to perform in a wide temperature band make fuel cells competitive among renewable energy sources [1]. Due to their ability to perform efficiently at high temperatures and use different hydrocarbon fuels, SOFC fuel cells are preferred as an energy production source in heat-power generators and residences [2]. For industrial loads fed by renewable energy sources, there is a need to design power electronic converters between the power supply and the load. Among these power circuits, the dc-dc converter is used to regulate the level of voltage produced by the fuel cell and to keep the input voltage of the dc-ac inverter at the reference value. To perform these operations, voltage control methods are needed. Moreover, dc-ac inverters are used to convert dc energy into ac energy for electrical load, to regulate load current and voltage, to suppress harmonic distortion and to regulate the power factor. In addition, in order to perform harmonic suppression between the dc-ac inverter and the load, L, LC, LCL... etc. available in the literature. filters are used. After the physical connection between the electrical load and the power source is established, both the voltage control method to keep the voltage at the reference value in the dc-dc converter and the current control methods to provide reliable and appropriate current from the dc-ac inverter to the electrical load will be needed [3, 4]. In this context, the Hysteresis control method attracts attention due to its ease of application and ability to follow variable reference values [5–7]. Therefore, in this study, hysteresis control method was applied for both voltage and current control. The circuit structure and control schemes designed for the proposed study are presented in Figure 1.

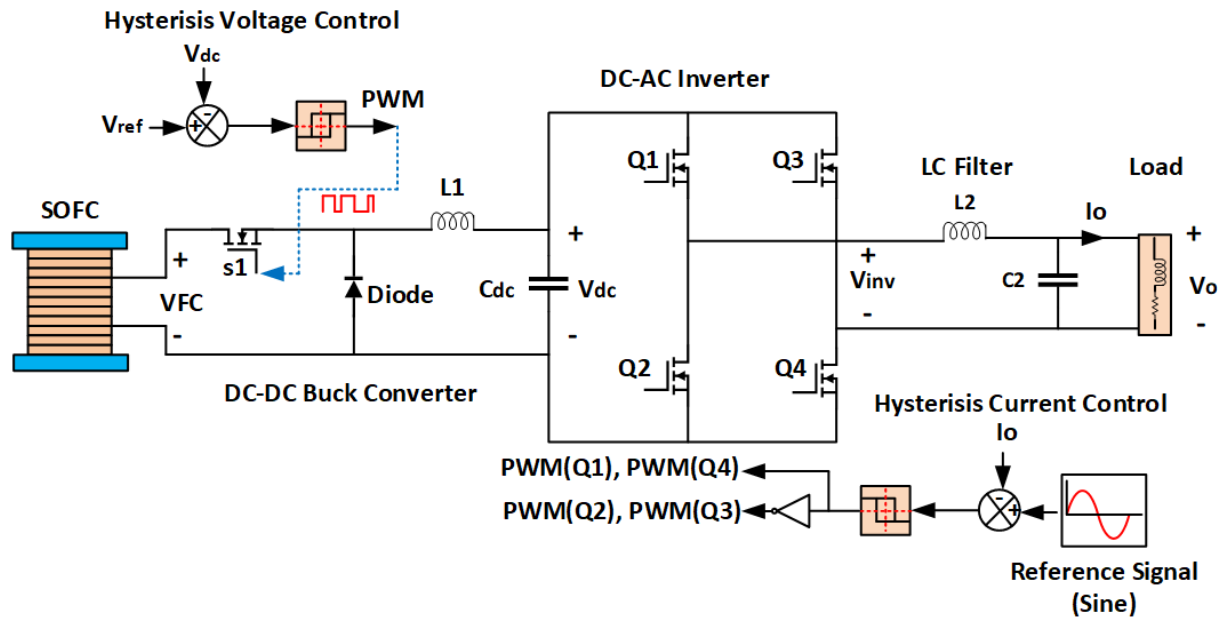


Figure 1. Proposed system model

In this study, as seen in Figure 1, SOFC was used as the power source and a dc-dc buck converter was designed for the power circuit extending to the inverter connection. In order to provide energy flow to the electrical load, a dc-ac full bridge single phase inverter and LC filter design for harmonic suppression have been carried out.

## 2 MATERIAL AND METHOD

For the first step of the study, the Hysteresis voltage controlled DC-DC Buck Converter design was realized as shown in figure 1 to keep the voltage produced by the fuel cell at the reference value. SOFC fuel cell, current-voltage and current-power characteristic curves are presented in Figure 2.

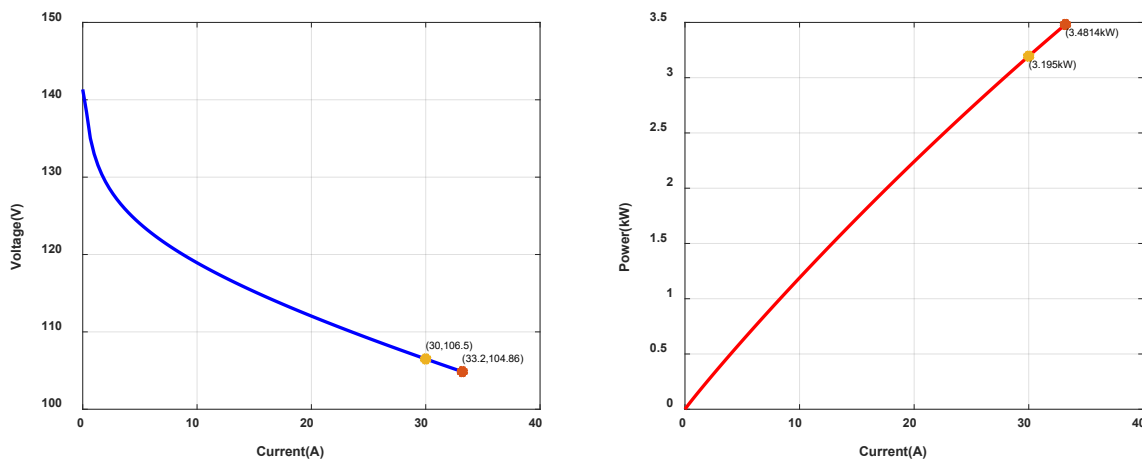


Figure 2. SOFC current-voltage and current-power characteristic curves

The electrical properties and welding parameters of SOFC fuel cell are presented in Table 1.

Table 1. Electrical properties of SOFC

Voltage	Power	Temperature	Pressure Fuel	Pressure Air	Efficiency	Number of Series Stack
282.68	6 kW	600 °C	1.35 Bar	1 Bar	52%	2

The ratio between the input and output voltages of the dc-dc buck converter is shown in the following equation.

$$V_{dc} = D \cdot V_{FC} \tag{1}$$

Where, the  $V_{FC}$  SOFC fuel cell voltage,  $V_{dc}$  output voltage,  $D$  refers to the duty cycle [8].

Hysteresis voltage control creates switching impacts for voltage regulation based on the error signal and hysteresis bandwidth consisting of the difference between the reference voltage and the measured value. The deviation of the actual signal from the reference voltage is called an error signal. Thus, the error signal created is given as an input signal to the controller's hysteresis band. The switching occurs when the error signal deviates beyond the reference hysteresis band limit. If the error signal is above the reference band, the switch on-state error signal reaches lower levels and the switch generates a signal for the off-state [9, 10]. The basic structure of hysteresis control is presented in Figure 3.

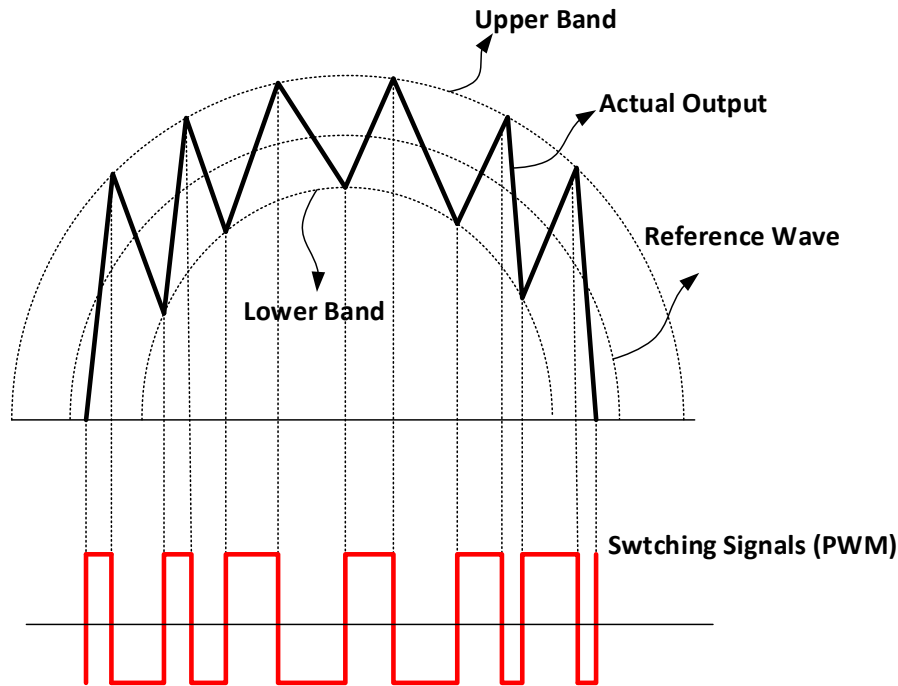


Figure 3. Hysteresis control basic structure

In the second part of the study, Hysteresis current controlled full bridge DC-AC inverter design was performed. In addition, as presented in figure 1, LC filter circuit design has been made for harmonic suppression. The following equation is used to find the effective value of the full bridge single phase DC-AC inverter. Here,  $V_s$  inverter input voltage  $V_o$  inverter output voltage and  $T$  is period [8].

$$V_o = \left( \frac{2}{T} \int_0^{T/2} V_s^2 dt \right)^{1/2} = V_s \quad (2)$$

Full bridge single phase inverter is performing according to the on and off states of 4 semiconductor switch (shown in figure 1). In this context, the output voltage value varies according to the transmission conditions of the switches. The output voltage depending on status of the switches are presented in Table 2.

Table 2. Output voltage and status of the switches

Q1	Q2	Q3	Q4	Status	$V_o$
on	off	off	on	1	$V_s$
off	on	on	off	2	$-V_s$
on	off	on	off	3	0
off	on	off	on	4	0

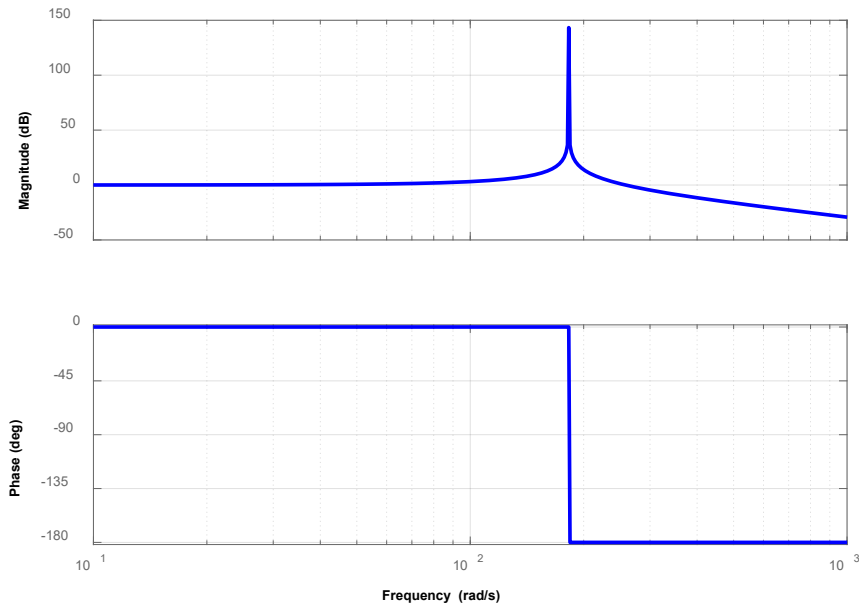
As with Hysteresis voltage control based on error signal and hysteresis bandwidth, Hysteresis current control (HCC) creates switching signals for current regulation. The error signal of the difference between the reference current (sine) and the current measured is given as a signal to the Hysteresis band of the HCC. The switching process occurs when the reference signal of the reference signal goes beyond the limit of the hysteresis band limit. When the error signal exceeds the lower band or exceeds the upper limit, a on/off signal is created for semiconductor switches. This constantly produces signals to switches, thus producing AC output current. As the last stage of

modeling LC filter design has been implemented to dampen total harmonic distortion at the output of the full bridge single phase inverter. The transfer function of the LC filter is given in the equation below [11].

$$G(s) = \frac{V_{inv}}{V_o} = \frac{1}{s^2LC+1} \quad (3)$$

Here  $V_{inv}$  represents the inverter output voltage,  $V_o$  represents the load voltage,  $L$  represents the filter inductor,  $C$  represents the filter capacitor (shown in Figure 1).

The bode diagram of the LC filter according to the transfer function is presented in Figure 4.



**Figure 4.** Bode diagram of LC filter

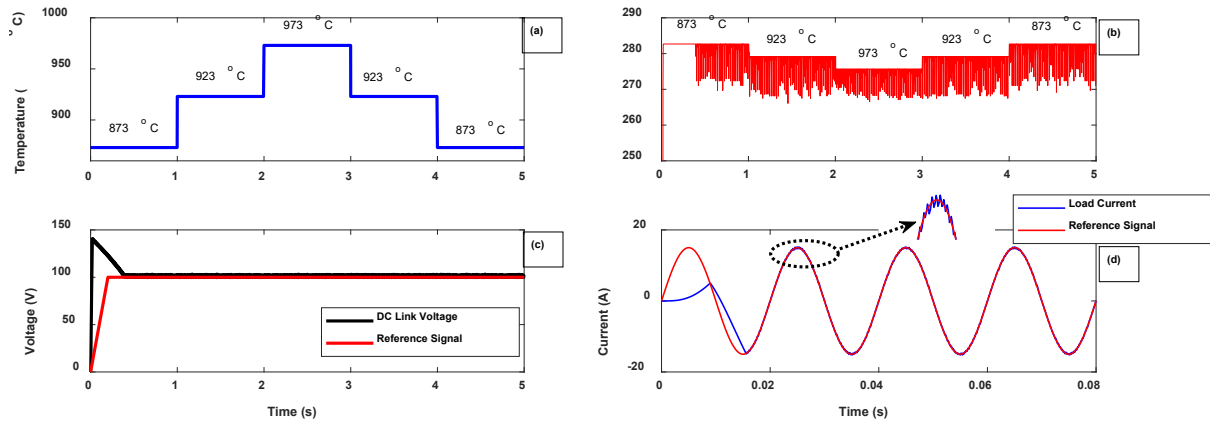
Circuit parameters based on the modeling and design of the proposed system are presented in Table 3.

**Table 3.** System parameters

Parameter	Definition	Value
Lbuck	Buck Converter Inductor	1mH
Cbuck	Buck Converter Capacitor	10mF
L filter	Filter Inductor	3mH
C filter	Filter Capacitor	1mF
Cout	Output Capacitor	1mF
Rload	Load Resistor	10Ω
Lload	Load Inductor	5mH
VFC	Fuel Cell Voltage	280 Vdc
Vdc	DC Link Voltage	100 Vdc
Vout	Output Voltage	50 Vac

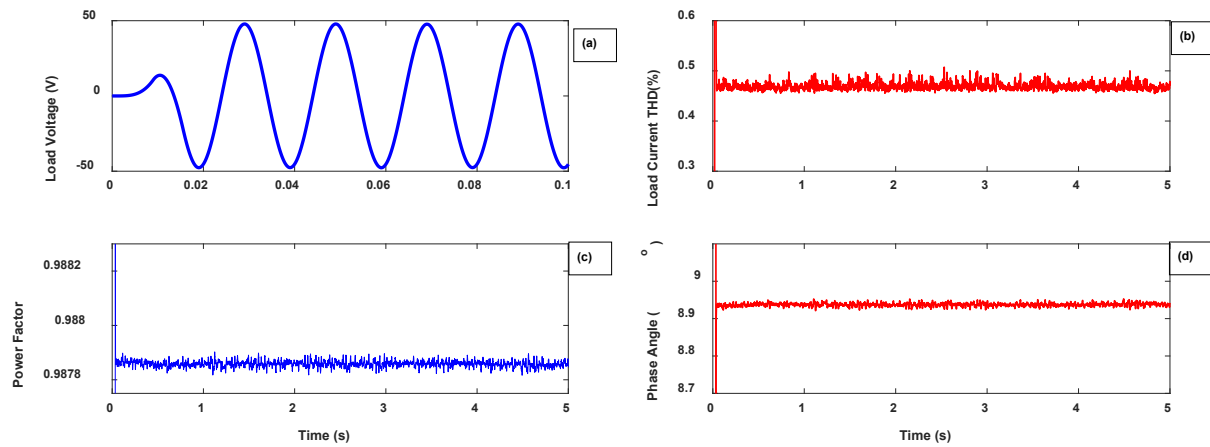
### 3 RESULTS

In this part of the study, simulation results and different situation analyzes were carried out. Under variable temperature, the voltage produced by the SOFC fuel cell will change depending on the temperature. In this case, the dc link voltage is kept at a constant 100 volts thanks to hysteresis voltage control. Thanks to hysteresis current control, the load current is kept at the reference value of 15 A. Fuel cell voltage, variable temperature curves, dc link voltage and output current and reference values are presented in Figure 5.



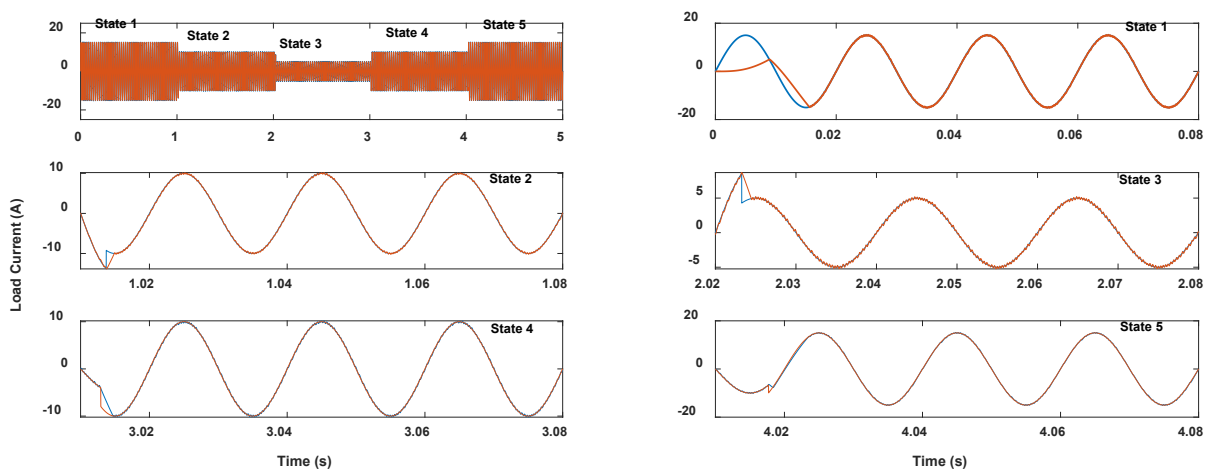
**Figure 5.** (a) Variable temperature, (b) fuel cell voltage, (c) DC link voltage, and (d) load current

The load voltage, total harmonic distortion, power factor and phase angle are presented in Figure 6.



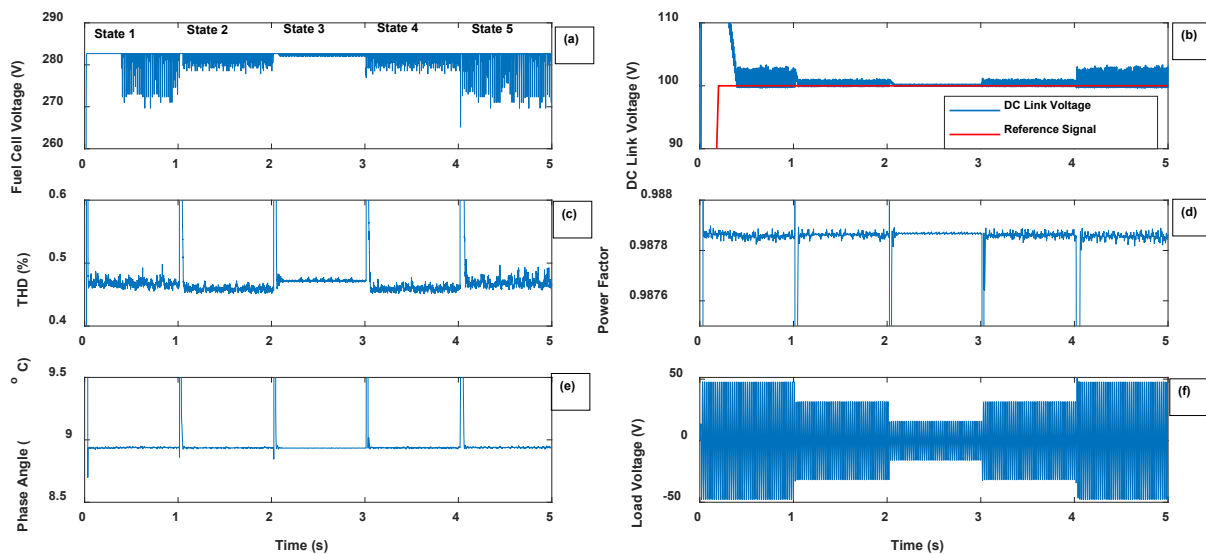
**Figure 6.** (a) Load voltage, (b) load current THD%, (c) power factor, and (d) phase angle

Depending on variable current reference values, sudden changes in the fuel cell voltage and dc link voltage may occur. In this context, thanks to hysteresis voltage control, the fuel dc line voltage is kept at the reference value of 100 V. At the same time, reference current monitoring was carried out using hysteresis current control at different current reference values, and impressive results were achieved. Hysteresis current control performance and load current depending on different current reference values (15 A, 10A, 5A) are presented in Figure 7.



**Figure 7.** Load Current with variable reference values

Depending on the variable reference current values, the dc link voltage is kept constant at the reference value thanks to the hysteresis voltage control. In this context, fuel cell voltage, dc link voltage, THD%, power factor, phase angle and load voltage are presented in Figure 8.



**Figure 8.** (a) SOFC voltage, (b) DC link voltage, (c) THD%, (d) power factor, (e) phase angle, and (f) load voltage

## 4 CONCLUSION

In this study, the power circuit interface for engine supply as a SOFC fuel cell power source was modeled and its computer application was implemented. RL load was modeled for the motor, and a dc-dc buck converter was designed for the power interface in the first stage and a dc-ac single phase full bridge inverter was designed in the second stage (Figure 1). Additionally, an LC filter was applied due to its harmonic suppression feature. Hysteresis voltage control was applied to the dc-dc buck converter to ensure that the voltage produced from the fuel cell remained constant at the reference value while being transferred to the dc-link, and the results are presented in Figures 5(c) and 8(b). Hysteresis current control is used to provide load current control. The performance of the designed control method was tested at different reference values and satisfactory results were obtained (Figure 7). It is obvious that the proposed study can be a strong alternative for stand-alone or on-grid connections of different renewable energy systems (PV system, Wind Turbine, etc.). In the study, system modeling, analysis and simulation were carried out in the Matlab/Simulink program.

## References

- [1] F. Ramadhani, M. A. Hussain, H. Mokhlis, and S. Hajimolana, "Optimization strategies for Solid Oxide Fuel Cell (SOFC) application: A literature survey," *Renewable and Sustainable Energy Reviews*, vol. 76, pp. 460–484, 2017, doi: 10.1016/j.rser.2017.03.052.
- [2] A. Choudhury, H. Chandra, and A. Arora, "Application of solid oxide fuel cell technology for power generation - A review," *Renewable and Sustainable Energy Reviews*, vol. 20, pp. 430–442, 2013, doi: 10.1016/j.rser.2012.11.031.
- [3] U. Yilmaz and O. Turksoy, "Artificial intelligence based active and reactive power control method for single-phase grid connected hydrogen fuel cell systems," *International Journal of Hydrogen Energy*, vol. 48, no. 21, pp. 7866–7883, Mar. 2023, doi: 10.1016/j.ijhydene.2022.11.211.
- [4] B. Goncu and U. Yilmaz, "Different DC-link control methods with multilevel inverter for low harmonic and efficient power transfer in grid-tied hydrogen fuel cell systems," *DUMF Muhendislik Dergisi*, Jun. 2023, doi: 10.24012/dumf.1293293
- [5] H. Khalkhali, A. Oshnoei, and A. Anvari-Moghaddam, "Proportional hysteresis band control for DC voltage stability of Three-phase single-stage PV systems," *Electronics*, vol. 11, no. 3, Feb. 2022, doi: 10.3390/electronics11030452.
- [6] S. Pulendran and J. E. Tate, "Hysteresis control of voltage source converters for synchronous machine emulation," in *15th International Power Electronics and Motion Control Conference (EPE/PEMC)*, Novi Sad, 2012, pp. LS3b.2-1-LS3b.2-8, doi: 10.1109/EPEPEMC.2012.6397432.



- [7] G. Chacko, L. Syamala, N. James, B. M. Jos, and M. Kallarackal, "Switching frequency limited hysteresis based voltage mode control of single-phase voltage source inverters," *Energies*, vol. 16, no. 2, Jan. 2023, doi: 10.3390/en16020783.
- [8] D.W. Hart, *Power Electronics*, New York: McGraw-Hill Book Company, 2011.
- [9] M. Inci, "Performance analysis of T-type inverter based on improved hysteresis current controller," *Balkan Journal of Electrical and Computer Engineering*, vol. 7, no. 2, pp. 149–155, Apr. 2019, doi: 10.17694/bajece.510412.
- [10] M. Chinnari, T. Mounika, K. Swetha, A. Bharathi, and A. H. Chander, "Implementation of hysteresis voltage control for different inverter topologies," in *2020 IEEE India Council International Subsections Conference*, Visakhapatnam, 2020, pp. 272–277, doi: 10.1109/INDISCON50162.2020.00062.
- [11] M. Hojabri and M. Hojabri, "Design, application and comparison of passive filters for three-phase grid-connected renewable energy systems," *ARPJ Journal of Engineering and Applied Sciences*, vol. 10, no. 22, Dec. 2015.



## Factors Influencing the Adoption of Electric Vehicles in the U.S.

Serkan Varol<sup>\*1</sup>, Taylor Ransom<sup>1</sup>

<sup>1</sup>Engineering Management and Technology, University of Tennessee at Chattanooga, Chattanooga, TN, USA

---

### Abstract

The current state of the problem with electric vehicle (EV) adoption rates is that despite the numerous incentives and efforts by governments and automakers to promote their usage, their adoption rate is still relatively low compared to traditional gasoline-powered vehicles. Barriers to EV adoption include the cost of EVs, perceived driving range, and charging time. In this research, the contribution to the field of EV adoption rates has been studied by using K-Means clustering for a wide range of variables that can influence EV adoption rates in different US states. To conduct our analysis, data on EV adoption rates was collected from multiple sources, including government reports, industry publications, and census surveys. Data was also collected on factors that could influence the current EV adoption numbers, such as various fuel and electricity pricing, charging infrastructure availability, government incentives, average income per capita, population statistics, electric power generation types, and capacities per state. This study approach found the main elements connected with either greater or lower EV adoption rates by classifying the states into clusters and assessing several variables. The findings show that increasing the availability of charging infrastructure, more specifically level 2 and DC fast charging stations, and generating more electric power could help to increase the adoption rates of EVs. Overall, this approach provides a more comprehensive understanding of the factors that influence EV adoption rates and can help policymakers and industry stakeholders make informed decisions to promote the widespread adoption of electric vehicles.

**Keywords:** *Electric vehicles, K-Means clustering, EV adoption rates, Charging infrastructure*

---



## **Experimental Study of Failures of Air Conditioners System Tram in Desert Areas by Applying Preventive Maintenance (Using FEMA and Reliability Lows)**

**Khaled Lemnaouer<sup>\*1</sup>, Messaoud Louafi<sup>1</sup>, Zoubir Aoulmi<sup>2</sup>, Rabie Karek<sup>3</sup>, Mounia Taleb<sup>1</sup>**

<sup>1</sup>*Electromechanics, Environnement Laboratory, Larbi Tbessi University, Tebessa, Algeria*

<sup>2</sup>*Mining Sciences Laboratory, Larbi Tbessi University, Tebessa, Algeria*

<sup>3</sup>*Mechanical Engineering - Mechanics and Energy Systems Laboratory, Kasdi Merbah University, Ouargla, Algeria*

---

### **Abstract**

Preventive maintenance is considered the health record of industrial machines and transport vehicles in the world of industry because of its contribution to always protecting these machines and vehicles. Therefore, a tight preventive maintenance plan must always be developed to ensure reliability stability. This article aims to solve the problem of complete failure of the air conditioning (AC) system in trams in the desert region of Algeria, in the context of high temperatures, which resulted in the loss of many passengers and a significant drop in company income. Reliability laws will be applied to the way being obstructed as a result of an error applied in the welding process, which led to the ACHAPS shutdown of the air conditioning system, since the average reliability percentage was 59.01% before fixing the problem and became 81.73% after fixing the problem.

**Keywords:** *Tramway, Air condition system, Drier filter, Preventive maintenance, Reliability, Failures*

---



## Design of a Low-Profile Metasurface-Based Linear Polarization Converter and RCS Reduction Using This Converter Design

Yunus Kaya<sup>\*1</sup>

<sup>1</sup>Department of Electronics and Automation, Bayburt University, Bayburt, 69010 Türkiye

### Abstract

In this study, a low profile metasurface-based linear polarization (LP) converter operating in reflective-mode for microwave X-band (8.2–12.4 GHz) applications is suggested. The suggested design, created with metal termination, an easily accessible and inexpensive FR4 substrate, and a simply designed metasurface, offers polarization conversion ratio (PCR) of over 90% in the frequency range of 9.24–12.21 GHz and over 99% in the frequency range of 9.73–11.48 GHz in the microwave X-band. Moreover, the suggested LP converter design is rearranged with appropriate geometry and the radar cross section (RCS) reduction is provided to be over 10 dBsm in the microwave X-band in the range of 8.84–10.96 GHz compared to the perfect electric conductor (PEC) plate of the same size with the created metasurface structure. The design and simulation applications of LP and RCS reduction were carried out in the frequency range of 6–14 GHz using CST Microwave Studio, a commercial 3D electromagnetic simulator.

**Keywords:** Metasurface, Linear polarization, X-band, RCS reduction

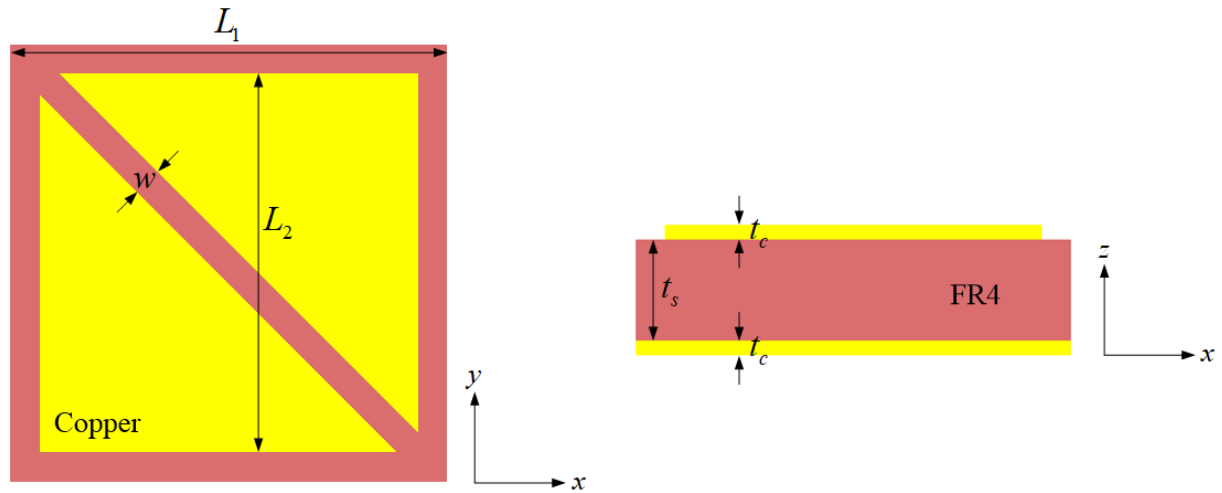
## 1 INTRODUCTION

Controlling the polarization of an electromagnetic wave is an important phenomenon in various application areas such as antenna [1], radar cross section [2], and remote sensing [3]. Therefore, polarization plays a vital role in the performance of microwave devices. Conventional polarization converters constructed with various methods such as optical grating and Faraday effect show limited performance due to reasons such as their large volume, narrow band, manufacturing difficulties and power loss [4, 5]. Therefore, conventional polarization converters are not suitable for practical applications. To eliminate these disadvantages, metasurface-based polarization converters have been suggested instead of conventional polarization converters in recent years. In the microwave [6], terahertz [7], and infrared [8] frequency regions, the unit cell of metasurface-based polarization converters can be designed in the reflective- or transmittive-modes as single [6] or multilayer [9] and are also used in radar cross section (RCS) reduction applications by rearranging the unit cell with the appropriate geometry [10].

In this study, a metasurface-based reflective-mode linear polarization (LP) converter is suggested for microwave X-band (8.2–12.4 GHz) applications. In the suggested converter design, FR4 dielectric material with a thickness of 1.6 mm, which is widely used in the market and is cheap to supply, was used as the substrate material. While the suggested unit cell design shows LP conversion feature over a wide frequency range in the microwave X-band, it is also shown that this design can be used in RCS reduction applications by rearranging it with appropriate geometry.

## 2 CONVERTER DESIGN AND THEORY

The front and side surface views of the suggested metasurface-based LP converter design are shown in Fig. 1, respectively. In the suggested design, a FR4 dielectric material (with a dielectric constant of 4.3 and a loss tangent of 0.025) with a thickness of 1.6 mm ( $t_s$ ), which is widely used in the market, and cheap to supply, is used as the substrate material. The square-shaped substrate has a side of 6 mm ( $L_1$ ). The bottom layer of the substrate is terminated with copper with a conductivity of  $5.8 \times 10^7$  S/m and a thickness of 35  $\mu\text{m}$  ( $t_c$ ). The metasurface on the top layer is created with the same copper material by rotating a 0.4 mm ( $w$ ) wide strip 45° counterclockwise and removing it from a square structure with a side of 5.2 mm ( $L_2$ ).



**Figure 1.** Front and side surface views-dimensioning of the suggested metasurface-based LP converter design, respectively

An electromagnetic wave ( $E^i$ ) traveling in the  $z$ -direction to the metasurface and having an electric field component in the  $y$ -direction ( $y$ -polarized) can reflect ( $E^r$ ) in the same direction (co-polarization, i.e.  $y$ -polarized) or in the opposite direction (cross-polarization, i.e.  $x$ -polarized). Similarly, the opposite is true for the  $x$ -polarized incident wave. Accordingly, for a  $y$ -polarized incident wave, the co- and cross-polarized reflection coefficients are  $R_{yy} = E^{ry} / E^{iy}$ , respectively. Here,  $E^{iy}$  represents the component of the incident wave in the  $y$ -axis, while  $E^{ry}$  and  $E^{rx}$  represent the components of the reflected wave in the  $y$ - and  $x$ -axes, respectively.

Polarization conversion ratio (PCR) is used to evaluate the LP performance of the suggested converter. For a  $y$ -polarized incident wave, the PCR is calculated as follows [2, 6, 7, 10]:

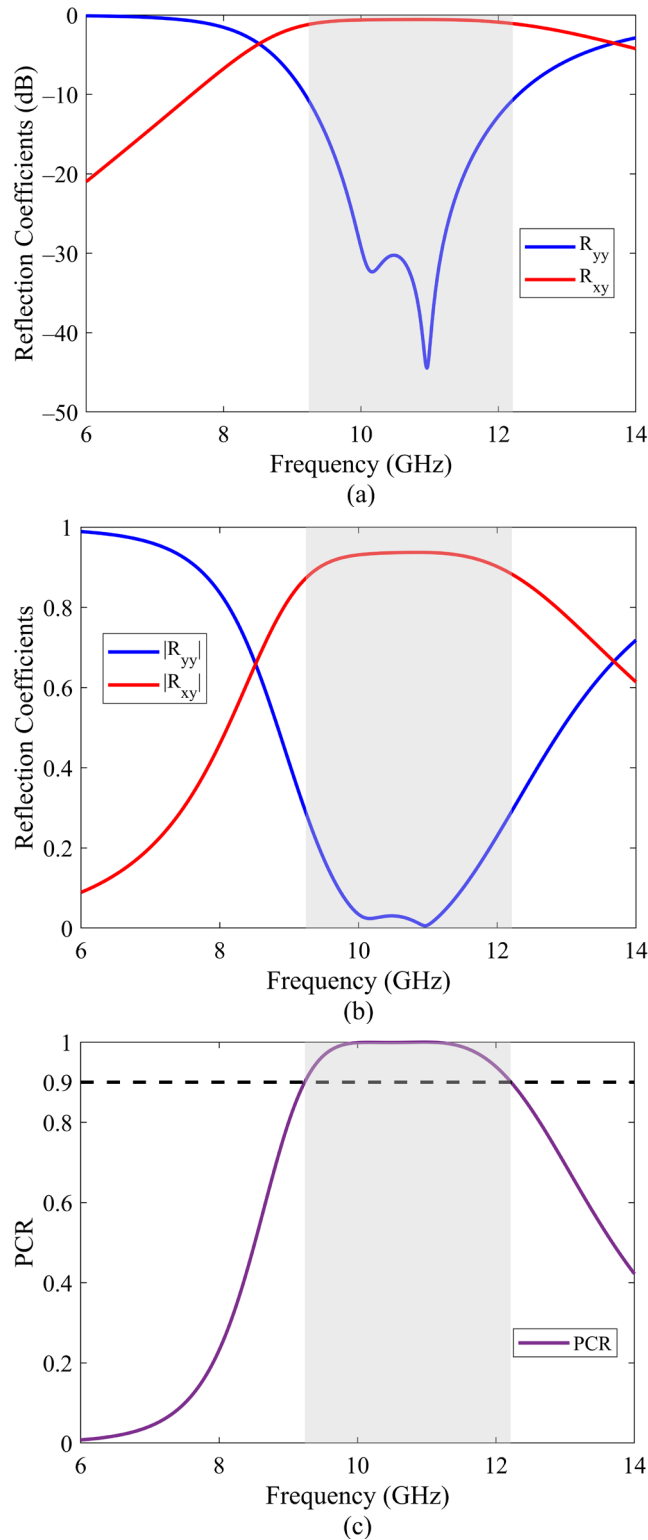
$$\text{PCR} = \frac{|R_{xy}|^2}{|R_{xy}|^2 + |R_{yy}|^2}. \quad (1)$$

Here  $|\star|$  indicates the magnitude of the complex quantity “ $\star$ ”. According to Eq. (1), the closer the  $|R_{xy}|$  value is to 1 and the closer the  $|R_{yy}|$  value is to 0, the closer the PCR value will be to 1. That is, a  $y$ -polarized incident wave will be reflected as  $x$ -polarized.

### 3 SIMULATION RESULTS

The suggested design was modeled and simulated with the 3D electromagnetic simulation program CST Microwave Studio. In the simulations, the boundary conditions were selected as unit cell in the  $x$ - and  $y$ -directions and open in the  $z$ -direction. Tetrahedral mesh type was used as the mesh type. Using these adjustments, simulations were performed in the frequency range of 6–14 GHz under normal incidence ( $0^\circ$ ) and the obtained reflection coefficients in dB and amplitude are given in Fig. 2(a) and Fig. 2(b), respectively. Then, PCR values were obtained from these reflection coefficients according to Eq. (1) and these values are shown against frequency in the same frequency range in Fig. 2(c).

When Fig. 2(a) is examined, it is seen that  $R_{yy}$  is below  $-10.5$  dB and  $R_{xy}$  is above  $-1.25$  dB at the frequency range of 9.24–12.21 GHz in the microwave X-band. When Fig. 2(b) is analysed, it is seen that in the same frequency range, the reflection coefficient amplitudes  $|R_{yy}|$  and  $|R_{xy}|$  approach 0 and 1, respectively. In addition, when Fig. 2(a) and Fig. 2(b) are examined together,  $|R_{yy}|$  is almost 0 and  $|R_{xy}|$  is almost 1 at the resonance frequencies of 10.16 GHz and 10.96 GHz. The PCR performance of the suggested metasurface-based polarization converter design is presented in Fig. 2(c). Accordingly, when Fig. 2(c) is examined, PCR is over 90% in the frequency range of 9.24–12.21 GHz, while it is over 99% in the frequency range of 9.73–11.48 GHz. Additionally, the suggested design offers approximately 100% PCR at the 10.16 GHz and 10.96 GHz resonance frequencies.

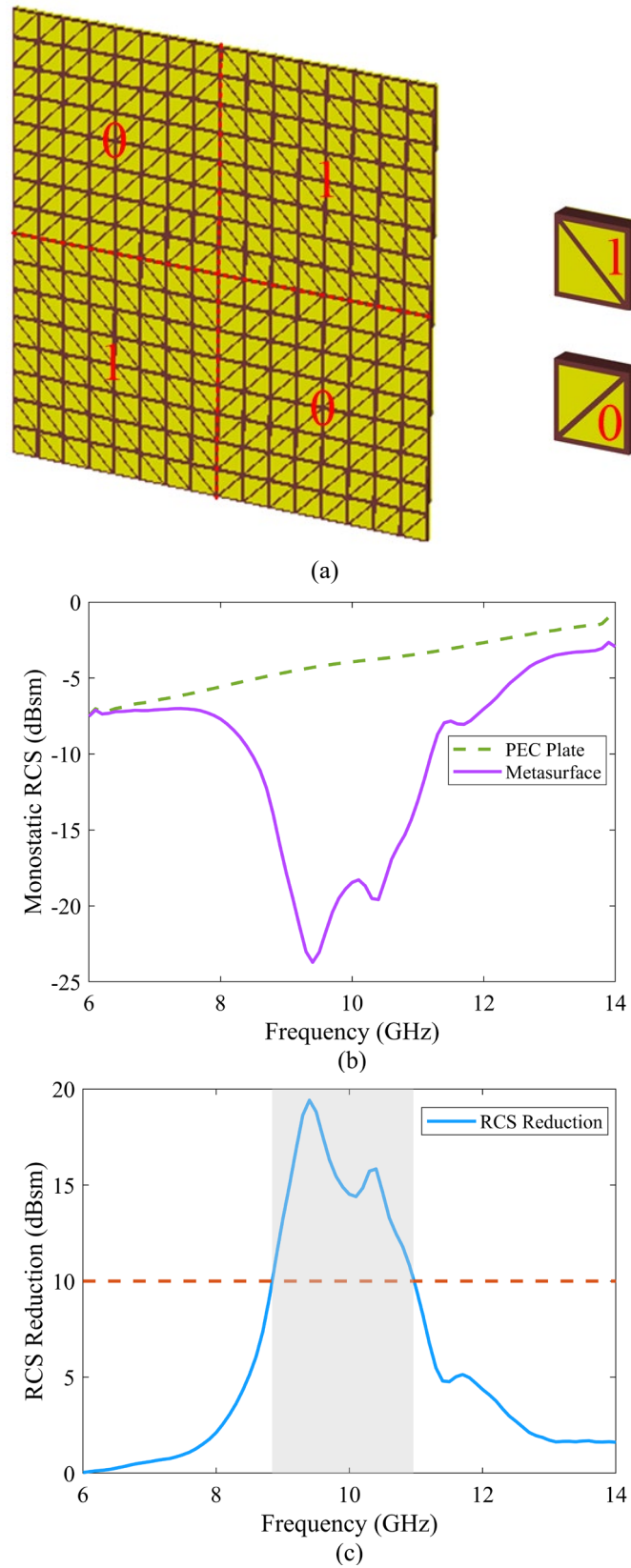


**Figure 2.** Reflection coefficients in (a) dB and (b) amplitude and (c) PCR value of the suggested polarization converter design

#### 4 RCS REDUCTION USING SUGGESTED CONVERTER DESIGN

In recent years, multi-functional designs can be carried out by appropriately modifying the architecture of metamaterials. In particular, the unit cell of LP converters is used in RCS reduction applications by rearranging it with appropriate geometry [10, 11]. For this purpose, a new metasurface structure of  $16 \times 16$  size was created by coding 01/10 (0 means the suggested polarization converter design rotated  $90^\circ$  clockwise and 1 means the suggested polarization converter design) as shown in Fig. 3(a) for RCS reduction by using the suggested converter

design. In Fig. 3(b), the metasurface structure created for RCS reduction and the monostatic RCS values of the perfect electric conductor (PEC) plate of the same dimensions are given. Fig. 3(c) shows the RCS reduction of the metasurface structure created for RCS reduction compared to the PEC plate.



**Figure 3.** (a)  $16 \times 16$  sized metasurface structure created for RCS reduction using the suggested LP converter design, (b) Monostatic RCS values of the created metasurface structure and the PEC plate of the same dimensions, and (c) RCS reduction of the created metasurface structure compared to the PEC plate

Firstly, when the simulated monostatic RCS values of the PEC plate of the same size as the metasurface created for RCS reduction in the frequency range of 6–14 GHz are examined in Fig. 3(b), it is seen that the RCS value of the suggested metasurface is lower than the PEC at every frequency. Secondly, it is noted from Figure 3(c) that the RCS reduction of the metasurface created for RCS reduction is over 10 dBsm in the range of 8.84–10.96 GHz compared to the PEC plate of the same size.

## 5 CONCLUSION

In this study, a metasurface-based LP converter is presented that offers over 90% PCR in the frequency range of 9.24–12.21 GHz and over 99% PCR in the frequency range of 9.73–11.48 GHz in the microwave X-band. The suggested design is constructed with FR4 dielectric material with a thickness of 1.6 mm, which is widely used in the market as substrate material, cheap to supply and has a low profile. In addition, a  $16 \times 16$  metasurface structure was created for RCS reduction by using the suggested LP converter design, and the RCS reduction of this metasurface compared to the PEC plate of the same size was achieved to be over 10 dBsm in the range of 8.84–10.96 GHz.

## References

- [1] M. Li, Z. H. Zhang, and M. C. Tang, "A compact, low-profile, wideband, electrically controlled, tri-polarization-reconfigurable antenna with quadruple gap-coupled patches," *IEEE Trans. Antennas Propag.*, vol. 68, no. 8, pp. 6395–6400, Aug. 2020.
- [2] Y. T. Jia, Y. Liu, Y. J. Guo, K. Li, and S. X. Gong, "Broadband polarization rotation reflective surfaces and their applications to RCS reduction," *IEEE Trans. Antennas Propag.*, vol. 64, no. 1, pp. 179–188, Jan. 2016.
- [3] C. Z. Han, Y. H. Bi, S. Duan, and G. P. Lu, "Rain rate retrieval test from 25-GHz, 28-GHz, and 38-GHz millimeter-wave link measurement in Beijing," *IEEE J. Sel. Top. Appl. Earth Obs. Remote Sens.*, vol. 12, no. 8, pp. 2846–2858, Aug. 2019.
- [4] M. Mutlu and E. Ozbay, "A transparent 90° polarization rotator by combining chirality and electromagnetic wave tunneling," *Appl. Phys. Lett.*, vol. 100, no. 5, art. no. 051909, Jan. 2012.
- [5] C. Chen, Y. P. Sheng, and W. Jun, "Computed a multiple band metamaterial absorber and its application based on the figure of merit value," *Opt. Commun.*, vol. 406, pp. 145–150, Jan. 2018.
- [6] Y. Kaya, "Cheaper, wide-band, ultra-thin, and multi-purpose single-layer metasurface polarization converter design for C-, X-, and Ku-band applications," *Symmetry*, vol. 15, no. 2, art. no. 442, Feb. 2023.
- [7] B. Yin and Y. Ma, "Broadband terahertz polarization converter with anomalous reflection based on phase gradient metasurface," *Opt. Commun.*, vol. 493, art. no. 126996, Aug. 2021.
- [8] Z. C. Liu, Z. C. Li, Z. Liu, H. Cheng, W. W. Liu, C. C. Tang, C. Z. Gu, J. J. Li, H. T. Chen, S. Q. Chen, and J. G. Tian, "Single-layer plasmonic metasurface half-wave plates with wavelength-independent polarization conversion angle," *ACS Photonics*, vol. 4, no. 8, pp. 2061–2069, Aug. 2017.
- [9] P. Wang, Y. Zhang, Y. Wang, H. C. Zhou, and Z. M. Yan, "Multifunctional polarization converter based on multilayer reconfigurable metasurface," *Defence Technol.*, vol. 28, pp. 136–145, Oct. 2023.
- [10] M. A. Shukoor, S. Dey, S. K. Koul, A. K. Poddar, and U. L. Rohde, "Broadband linear-cross and circular-circular polarizers with minimal bandwidth reduction at higher oblique angles for RCS applications," *Int. J. RF Microwave Comput. Aided Eng.*, vol. 31, no. 7, art. no. e22693, Jul. 2021.
- [11] G. Ozturk, U. C. Hasar, M. Ertugrul, F. Tutar, M. F. Corapsiz, M. Kurt, K. Donmez, I. Ismail, and M. S. S. Alfaqawi, "An efficient cost effective wide-angle metasurface-based linear and circular polarization converter for X-, Ku- and K-band applications," *Opt. Laser Technol.*, vol. 163, art. no. 109404, Aug. 2023.





---

## Evaluation of Short-Term Traffic Flow Prediction Approaches in Transportation

Selahattin Kosunalp<sup>\*1</sup>, Yunus Kaya<sup>2</sup>

<sup>1</sup>Department of Computer Technologies, Gonen Vocational School, Bandirma Onyedi Eylul University, Bandirma/Balikesir, 10200 Türkiye

<sup>2</sup>Department of Electronics and Automation, Bayburt University, Bayburt, 69010 Türkiye

---

### Abstract

The implications of recent developments in technology have paved a way for designing high-quality applications in transportation engineering. One problem in dense urban area is the high volume of vehicles travelling on main roads. This requires efficient utilization of road capabilities to allow more secure and comfortable travel. Researchers have focused on the development of short-term traffic flow prediction algorithms. This study aims to review the recent proposed prediction approaches to give an insight for potential researchers. The operating principles of the proposed approaches are covered along with their strong and weak points. Finally, a potential future work direction is presented.

**Keywords:** *Transportation engineering, Short-term, Flow, Prediction*

---

## 1 INTRODUCTION

Intelligent Transportation Systems (ITS) represent a transformative approach to modernizing and optimizing transportation networks through the integration of advanced information and communication Technologies [1]. These systems are designed to enhance the safety, efficiency, and sustainability of transportation by providing real-time data, facilitating communication between various components of the transportation infrastructure, and improving decision-making processes for both operators and users. ITS concept has its roots in the 1960s and 1970s, with the advent of early traffic management systems and computer-based traffic signal control. In the 1990s, the U.S. Department of Transportation launched a significant initiative to promote the development and deployment of ITS, recognizing its potential to address growing transportation challenges.

ITS encompasses a broad range of applications, including traffic management, public transportation management, emergency response coordination, and vehicle-to-vehicle (V2V) and vehicle-to-infrastructure (V2I) communication systems [2]. These applications are designed to work together to create a more integrated and efficient transportation network. For instance, traffic management systems can use real-time data to optimize traffic signal timings, reduce congestion, and improve traffic flow. Public transit systems can benefit from ITS by providing real-time information to passengers, improving schedule adherence, and increasing overall system reliability. The implementation of ITS has been driven by several factors, including the need to reduce traffic congestion, lower greenhouse gas emissions, and enhance road safety. With the growing availability of data and advancements in machine learning and artificial intelligence, ITS is becoming increasingly sophisticated, enabling predictive analytics and autonomous vehicle technologies to be integrated into transportation systems.

The rapid urbanization and the increasing demand for efficient transportation have led to the exploration of innovative solutions to address traffic congestion, reduce environmental impacts, and enhance the overall user experience [3]. ITSs emerge as a pivotal solution, leveraging the power of technology to revolutionize how transportation networks are managed and utilized. By incorporating a range of technologies, such as sensors, cameras, GPS, and data analytics, ITS enables the collection and analysis of vast amounts of data that can be used to monitor traffic conditions, manage public transit systems, and ensure road safety. In summary, Intelligent Transportation Systems represent a critical advancement in the management and operation of transportation networks. By harnessing the power of technology, ITS can significantly improve the efficiency, safety, and sustainability of transportation, making it an essential component of future urban planning and infrastructure development.

Short-term traffic flow prediction is a critical component of modern traffic management systems, aimed at forecasting traffic conditions over a short period, typically ranging from a few minutes to a couple of hours [4]. Accurate short-term traffic flow prediction is essential for optimizing traffic signal timings, managing congestion,

enhancing the efficiency of transportation networks, and providing real-time information to travelers. By predicting traffic patterns in the near future, transportation authorities can make informed decisions to alleviate congestion, reduce travel time, and improve overall road safety.

The need for effective traffic flow prediction has grown in response to the increasing urbanization and the corresponding rise in traffic volumes on road networks. Traditional traffic management strategies often relied on historical data and static models, which could not adequately account for the dynamic nature of traffic conditions. This limitation led to the development of short-term traffic flow prediction models that use real-time data to anticipate changes in traffic patterns. Early approaches to short-term traffic flow prediction were based on statistical methods, such as time series analysis, linear regression, and autoregressive integrated moving average (ARIMA) models. These methods aimed to identify patterns in traffic flow data and extrapolate them to predict future traffic conditions. While these techniques provided a foundation for traffic prediction, they often struggled to capture the complexity and non-linearity inherent in traffic dynamics.

With advancements in computational power and the increasing availability of high-quality traffic data, more sophisticated methods have been developed. Machine learning and deep learning algorithms, such as artificial neural networks (ANNs), support vector machines (SVMs), and recurrent neural networks (RNNs), have emerged as powerful tools for short-term traffic flow Prediction [5]. These models can learn complex patterns from large datasets, making them well-suited to handle the variability and unpredictability of traffic flow. Short-term traffic flow prediction models are now being integrated into Intelligent Transportation Systems (ITS), enabling real-time decision-making and dynamic traffic management. These models are also essential for the development of autonomous vehicles, as they provide the predictive capabilities necessary for safe and efficient navigation in complex traffic environments. To sum up, short-term traffic flow prediction is a vital aspect of modern traffic management, driven by the need for real-time, accurate, and actionable insights into traffic conditions. The evolution from simple statistical models to advanced machine learning techniques reflects the growing complexity of traffic systems and the demand for more precise and adaptable prediction tools. This paper seeks to summarize recent advancements in short-term traffic flow prediction, emphasizing the progress achieved in this field.

## **2 FUNDAMENTALS OF SHORT-TERM TRAFFIC FLOW PREDICTION APPROACHES**

Short-term traffic flow prediction is an essential aspect of traffic management, aimed at forecasting traffic conditions over a brief time horizon, typically ranging from a few minutes to a couple of hours. The fundamental principle behind these approaches involves dividing time into discrete slots and predicting traffic flow for each slot based on various data sources and predictive models. The time slot-based approach enables the modeling of dynamic traffic patterns by capturing the temporal variations in traffic flow, which are influenced by factors such as time of day, weather conditions, and traffic incidents. As a result, short-term traffic flow prediction approaches that divide time into slots are fundamental to modern traffic management systems. By leveraging a combination of data collection, preprocessing, and advanced predictive modeling techniques, these approaches provide real-time insights into traffic conditions, enabling more effective traffic management and improved road safety. As technology continues to advance, the accuracy and reliability of these predictions are expected to improve, making them an indispensable tool for transportation planners and operators.

### **2.1 Time Slot Division**

The division of time into slots is a crucial step in short-term traffic flow prediction. These time slots, often ranging from a few seconds to several minutes, serve as the fundamental units for analysis. The selection of an appropriate time slot length depends on the specific application and the required prediction accuracy. Shorter time slots provide more granular predictions but require more data and computational resources, while longer time slots may smooth out short-term fluctuations, leading to less precise predictions. For instance, in urban traffic management systems, time slots of 5 to 15 minutes are commonly used to capture the variability in traffic flow during peak hours and to respond to sudden changes such as accidents or road closures. The choice of time slot length directly impacts the performance of prediction models, as it determines the resolution of the forecast and the ability to capture rapid changes in traffic conditions.

### **2.2 Data Collection and Preprocessing**

Accurate short-term traffic flow prediction relies heavily on the quality and quantity of data collected. Various data sources are utilized, including loop detectors, cameras, GPS devices, mobile phones, and connected vehicles. These sources provide real-time information on traffic volume, vehicle speed, occupancy rates, and other relevant

parameters. The collected data is then preprocessed to remove noise, fill in missing values, and normalize the data for further analysis. Preprocessing steps often include outlier detection, data smoothing, and feature extraction. These steps are essential to ensure that the data accurately reflects the current traffic conditions and is suitable for input into prediction models. Additionally, historical traffic data is often combined with real-time data to improve the accuracy of predictions by capturing long-term patterns and trends.

### 2.3 Predictive Modeling Approaches

Once the data is preprocessed and time is divided into slots, various predictive modeling approaches are employed to forecast traffic flow for each time slot. Traditional statistical methods, such as autoregressive integrated moving average (ARIMA) models, have been widely used in early traffic flow prediction systems. These models predict future traffic flow by identifying patterns in historical data and extrapolating them into the future. However, the non-linear and complex nature of traffic flow has led to the adoption of more sophisticated machine learning and deep learning techniques. Machine learning models, such as support vector machines (SVMs), decision trees, and k-nearest neighbors (k-NN), can capture non-linear relationships between input variables and traffic flow. These models are trained on historical data and can make real-time predictions based on the input features.

Deep learning models, particularly recurrent neural networks (RNNs) and long short-term memory (LSTM) networks, have shown great promise in short-term traffic flow prediction. These models are capable of learning from sequential data and capturing temporal dependencies between time slots. LSTM networks, for example, are well-suited for traffic flow prediction because they can retain information over longer time periods, making them effective at predicting traffic patterns in highly dynamic environments.

### 2.4 Model Evaluation and Adaptation

After developing a prediction model, its performance is evaluated using various metrics such as mean absolute error (MAE), root mean square error (RMSE), and mean absolute percentage error (MAPE). These metrics help in assessing the accuracy and reliability of the predictions. Model evaluation is often conducted using cross-validation techniques to ensure that the model generalizes well to unseen data. To maintain accuracy, predictive models are regularly updated and adapted to reflect changes in traffic patterns. This is particularly important in urban environments where traffic conditions can change rapidly due to construction, road closures, or changes in public transportation schedules. Adaptive models that can learn from new data in real-time are crucial for maintaining the relevance and accuracy of short-term traffic flow predictions.

## 3 OVERVIEW OF RECENT PREDICTION APPROACHES

A novel approach is presented for improving short-term traffic flow predictions, critical for effective traffic management [6]. The authors introduce the CMPGM model, which integrates partial differential equations with a control matrix to better capture the spatiotemporal dynamics of traffic data. The CMPGM model is designed to handle the inherent uncertainties and small sample sizes commonly encountered in traffic data. By introducing a control matrix into the partial grey model, the authors enhance the model's ability to capture the underlying dynamics of traffic flow, leading to more accurate and stable predictions. The model's effectiveness is validated through extensive experiments, where it is compared with several existing models, including traditional statistical methods, machine learning approaches, and deep learning techniques. The results demonstrate that the CMPGM model outperforms these alternatives, particularly in terms of mean squared error (MSE), mean absolute percentage error (MAPE), and root mean square percentage error (RMSPE).

An innovative model aimed at improving the precision of short-term traffic flow predictions, a critical component for effective traffic management in ITS [7]. The proposed model, named the Spatio-Temporal Residual Graph Convolutional Network (STRGCN), combines two powerful techniques: the Deep Full Residual Graph Convolutional Network (DFRGCN) for capturing spatial correlations in traffic networks, and the Bidirectional Gated Recurrent Unit (Bi-GRU) enhanced with an attention mechanism to accurately model temporal dependencies. This dual approach allows the STRGCN model to better understand and predict the complex and dynamic relationships in traffic data. The model was tested on multiple publicly available traffic datasets, where it consistently outperformed existing prediction models, demonstrating significant improvements in both accuracy and stability. The research underscores the model's ability to handle the intricate spatio-temporal interactions inherent in traffic systems, making it a valuable tool for real-time traffic flow prediction. By effectively addressing the challenges of traditional models, STRGCN has the potential to enhance decision-making processes in ITS, leading to more efficient traffic management and reduced congestion in urban environments.

A sophisticated approach is introduced to address the challenges of predicting long-term traffic flow in complex urban environments [8]. Given the unpredictable nature of urban traffic, influenced by factors like weather, holidays, and nearby traffic conditions, traditional models often struggle to maintain accuracy over extended periods. The proposed hybrid model leverages the strength of Convolutional Neural Networks (CNNs) in extracting meaningful features from traffic data while utilizing Bidirectional Long Short-Term Memory (BiLSTM) networks to capture and learn from temporal dependencies in both forward and backward directions. This dual approach allows the model to effectively handle the intricacies of traffic patterns over time. The authors validate their model using data from four major roadways in Madrid, comparing its performance against eight widely-used baseline models. The results clearly show that the CNN-BiLSTM hybrid model achieves superior accuracy, as evidenced by improved mean absolute error (MAE), root mean square error (RMSE), and classification accuracy. The model not only excels in forecasting traffic flow up to 72 hours in advance but also adapts well to the varying conditions of different urban roads. The study emphasizes the practical implications of these findings, suggesting that the model could be a valuable tool for urban planners and traffic management systems, helping to alleviate congestion and optimize traffic flow through better-informed decision-making.

An advanced methodology is proposed for short-term traffic flow prediction by combining the strengths of the K-Nearest Neighbor (KNN) algorithm and the Bidirectional Long Short-Term Memory (BiLSTM) network [9]. This hybrid approach effectively captures both the spatial and temporal dynamics of traffic data, addressing a critical gap in previous models that largely neglected spatial correlations in traffic flow. The KNN algorithm is utilized to identify and select relevant spatial data points with high correlation, which are then used as input for the BiLSTM model to predict traffic flow. The BiLSTM model, with its ability to process information in both forward and backward directions, further enhances the prediction accuracy by capturing long-term dependencies in the data. The study is validated using real-time traffic data from high-speed roads in the United Kingdom, showcasing the model's superior performance compared to traditional models like Support Vector Regression (SVR), standard LSTM, GRU, and CNN-LSTM. The KNN-BiLSTM model demonstrated significant improvements in mean absolute error (MAE), root mean square error (RMSE), and mean absolute percentage error (MAPE), with performance enhancements of up to 77% in some cases. The results highlight the practical applicability of this model in real-world traffic management systems, where accurate short-term predictions are crucial for optimizing traffic flow, reducing congestion, and improving overall transportation efficiency. The research contributes valuable insights into the development of more robust and accurate traffic prediction models, paving the way for more intelligent and adaptive traffic management solutions.

An approach aims to improve the accuracy and efficiency of short-term traffic flow predictions, particularly in large-scale traffic networks with numerous sensors [10]. The proposed Spatio-Temporal Shared Gated Recurrent Unit (STSGRU) model leverages a shared weight mechanism that allows for simultaneous many-to-many predictions across different sensors, significantly reducing the computational resources and time required for large-scale predictions. By avoiding the need to map traffic networks to images or complex graph structures, the model simplifies the prediction process while maintaining high accuracy. Additionally, the authors incorporate a weekly pattern module based on Fourier transform to capture the inherent periodicity in traffic flow. This module helps to smooth out data fluctuations and provides more stable inputs to the prediction model, enhancing its ability to forecast traffic trends over multiple time steps. The model's effectiveness is validated through extensive experiments on several real-world traffic datasets, including the Caltrans Performance Measurement System (PeMS). The results show that the STSGRU model not only achieves prediction accuracy comparable to that of more complex graph neural networks but also offers greater flexibility and efficiency, making it particularly suitable for deployment in ITS. This research marks a significant advancement in traffic flow prediction, offering a scalable, efficient, and highly accurate solution for managing traffic in large urban areas.

A comprehensive approach is designed to improve the accuracy and reliability of short-term traffic flow predictions, which are critical for effective traffic management and congestion mitigation [11]. The authors propose a hybrid model that combines Variational Mode Decomposition (VMD) and an Improved Dung Beetle Optimization (IDBO) algorithm to enhance the performance of a Long Short-Term Memory (LSTM) network. VMD is employed to decompose the raw traffic data into several intrinsic modal components, effectively isolating the complex and nonlinear aspects of traffic flow from the noise. This decomposition allows for a more precise and focused prediction process. The IDBO algorithm, which integrates chaos mapping, a variable spiral search strategy, and Levy flight, is then used to optimize the LSTM model parameters, further improving the model's ability to handle the intricacies of traffic data. The combination of these methods results in a highly accurate and stable prediction model. The model was tested on real-world traffic data from California's interstate highways, where it demonstrated superior performance compared to other methods, such as traditional LSTM, EMD-LSTM, and VMD-LSTM models. The VMD-IDBO-LSTM model showed significant reductions in mean absolute error

(MAE), mean absolute percentage error (MAPE), and root mean square error (RMSE), indicating its effectiveness in addressing the challenges of nonlinearity and data noise.

A comprehensive methodology is introduced for enhancing the accuracy and efficiency of short-term traffic flow predictions, a key aspect of modern intelligent transportation systems [12]. The authors propose an ensemble model that synergistically combines optimized Variational Mode Decomposition (VMD) with a Long Short-Term Memory (LSTM) network and its bidirectional variant (BiLSTM). The innovative use of an improved Bat Algorithm optimizes the VMD parameters, ensuring that the traffic flow data is decomposed into more stable intrinsic mode functions (IMFs). This preprocessing step significantly improves the predictive capabilities of the LSTM and BiLSTM models by providing cleaner, more stable data inputs. The empirical validation of the model using real-world traffic data from Changsha City showcases its superior performance compared to conventional models. Specifically, the ensemble approach demonstrates marked improvements in prediction accuracy, as measured by metrics such as mean absolute error (MAE) and root mean square error (RMSE). The study also includes a detailed comparative analysis and ablation experiments, underscoring the effectiveness of each component of the ensemble model. The findings suggest that this integrated approach can substantially enhance short-term traffic flow predictions, offering valuable insights for traffic management systems aiming to reduce congestion and improve urban mobility. Additionally, the research highlights the potential of ensemble machine learning methods to address the complexities and non-linearities inherent in traffic data, paving the way for more robust and adaptive predictive models in transportation engineering.

An innovative hybrid approach is suggested that integrates the strengths of the Autoregressive Integrated Moving Average (ARIMA) model and Long Short-Term Memory (LSTM) neural networks to improve the precision of short-term traffic flow predictions [13]. ARIMA is utilized to effectively capture the linear, stochastic patterns inherent in traffic data, while LSTM networks are employed to model the more complex, nonlinear temporal dependencies. By dynamically weighting the predictions from both models, the proposed method ensures that the final output reflects the most accurate aspects of each approach. The research highlights the flexibility and robustness of the combined model, particularly in handling diverse traffic conditions across different highways. The model was rigorously tested on real-world traffic datasets from three major highways (AL215, AL2206, and AL2292), where it consistently outperformed standalone models like ARIMA and LSTM, as well as an equal-weight combination method. The evaluation metrics, including mean absolute error (MAE), mean squared error (MSE), root mean square error (RMSE), and mean absolute percentage error (MAPE), all indicated superior performance by the hybrid model.

## 4 CONCLUSION

In conclusion, this paper provides a comprehensive review and evaluation of recent advancements in short-term traffic flow prediction approaches, which are crucial for optimizing traffic management systems in increasingly congested urban environments. By analyzing a variety of methodologies, including statistical models, machine learning techniques, and hybrid approaches, the study highlights the strengths and limitations of each method in handling the complex and dynamic nature of traffic flow. The findings suggest that while traditional methods like ARIMA have their merits in capturing linear patterns, more sophisticated models such as LSTM and hybrid models offer superior performance by effectively addressing non-linear and temporal dependencies in traffic data. The paper emphasizes the importance of integrating advanced data processing and predictive modeling techniques to enhance the accuracy and reliability of short-term traffic predictions, thereby contributing to more efficient and responsive traffic management systems. Future research should continue to explore the potential of emerging technologies and innovative approaches to further improve the prediction accuracy and applicability in real-world traffic scenarios.

## References

- [1] P. Arthurs, L. Gillam, P. Krause, N. Wang, K. Halder, and A. Mouzakitis, "A taxonomy and survey of edge cloud computing for intelligent transportation systems and connected vehicles," *IEEE Trans. Intell. Transp. Syst.*, vol. 23, no. 7, pp. 6206–6221, Jul. 2021.
- [2] L.S. Iyer, "AI enabled applications towards intelligent transportation," *Transp. Eng.*, vol. 5, art. no. 100083, Sep. 2021
- [3] Z. Lv, R. Lou and A. K. Singh, "AI empowered communication systems for intelligent transportation systems," *IEEE Trans. Intell. Transp. Syst.*, vol. 22, no. 7, pp. 4579–4587, Jul. 2020.
- [4] L. Chen, L. J. Zheng, J. Yang, D. Xia, and W. N. Liu, "Short-term traffic flow prediction: From the perspective of traffic flow decomposition," *Neurocomputing*, vol. 413, pp. 444–456, Nov. 2020.
- [5] K. Lee, M. Eo, E. Jung, Y. Yoon, and W. Rhee, "Short-term traffic prediction with deep neural networks:

- A survey,” *IEEE Access*, vol. 9, pp. 54739–54756, 2021.
- [6] H. Duan and G. Wang, “Partial differential grey model based on control matrix and its application in short-term traffic flow prediction,” *Appl. Math. Modell.*, vol. 116, pp. 763–785, Apr. 2023.
  - [7] Q. Y. Zhang, M. F. Tan, C. W. Li, H. W. Xia, W. F. Chang, and M. L. Li, “Spatio-temporal residual graph convolutional network for short-term traffic flow prediction,” *IEEE Access*, vol. 11, pp. 84187–84199, 2023.
  - [8] M. Méndez, M. G. Merayo, and M. Núñez, “Long-term traffic flow forecasting using a hybrid CNN-BiLSTM model,” *Eng. Appl. Artif. Intell.*, vol. 121, art. no. 106041, May. 2023.
  - [9] W. Zhuang and Y. Cao. “Short-term traffic flow prediction based on a K-nearest neighbor and bidirectional long short-term memory model,” *Appl. Sci.*, vol. 13, no. 4, art. no. 2681, Feb. 2023.
  - [10] X. Y. Sun, F. H. Chen, Y. C. Wang, X. F. Lin, and W. F. Ma, “Short-term traffic flow prediction model based on a shared weight gate recurrent unit neural network,” *Physica A: Statistical Mechanics and its Applications*, vol. 618, art. no. 128650, May. 2023.
  - [11] K. Zhao, D. D. Guo, M. Sun, C. A. Zhao, and H. B. Shuai, “Short-term traffic flow prediction based on VMD and IDBO-LSTM,” *IEEE Access*, vol. 11, pp. 97072–97088, 2023.
  - [12] G. Dai, T. Jinjun and L. Wang, “Short-term traffic flow prediction: An ensemble machine learning approach,” *Alexandria Eng. J.*, 74, pp. 467–480, Jul. 2023.
  - [13] S. Q. Lu, Q. Y. Zhang, G. S. Chen, and D. W. Seng, “A combined method for short-term traffic flow prediction based on recurrent neural network,” *Alexandria Eng. J.*, vol. 60, pp.87–94, Feb. 2021.



## MnCo<sub>2</sub>O<sub>4</sub> Modified Flexible Graphene Paper for Electrochemical Sensing of Paracetamol

Murad Shafiyev<sup>1</sup>, Ezgi Topcu<sup>\*1</sup>, Elif Erçarikci<sup>1</sup>, Kader Dagci Kiransan<sup>1</sup>

<sup>1</sup>Department of Chemistry, Faculty of Science, Ataturk University, Erzurum, Türkiye

### Abstract

The increasing demand for modern, flexible, and portable electronic devices has made the production of flexible materials a frequently researched topic in recent years [1]. However, the search for a low-cost, ideally functionalized, and lightweight material for such devices is still ongoing. Paper-like conductive materials emerge as an alternative due to their use in applications such as Li-ion batteries, supercapacitors, fuel cells, catalysis, and sensors [2].

In this study, a free-standing flexible electrode was developed for the electrochemical determination of paracetamol (PC). This graphene-based paper electrode was prepared using graphene and MnCo<sub>2</sub>O<sub>4</sub> dispersion with a mold-casting method followed by chemical reduction (Figure 1). The morphology and structure of our flexible paper electrode (MnCo<sub>2</sub>O<sub>4</sub>/GP) were characterized by scanning electron microscopy, energy-dispersive, X-ray diffraction, X-ray photoelectron, and Raman spectroscopies. The as-prepared flexible MnCo<sub>2</sub>O<sub>4</sub>/GP showed outstanding sensing performance for PC, as compared to GP, due to the excellent electrochemical properties of MnCo<sub>2</sub>O<sub>4</sub>. The proposed sensor exhibited a wide linear range of 4.64–1000 μM for electrochemical determination of PC with a low detection limit of 1.39 μM. Furthermore, MnCo<sub>2</sub>O<sub>4</sub>/GP was successfully applied for PC syrup and tablets with good accuracy results. For the first time, the present study demonstrated the fabrication and utilization of MnCo<sub>2</sub>O<sub>4</sub>-modified graphene paper to develop a flexible and sensitive electrode for monitoring PC.

**Keywords:** Paracetamol, MnCo<sub>2</sub>O<sub>4</sub>, Flexible graphene-based paper, Electrochemical sensor

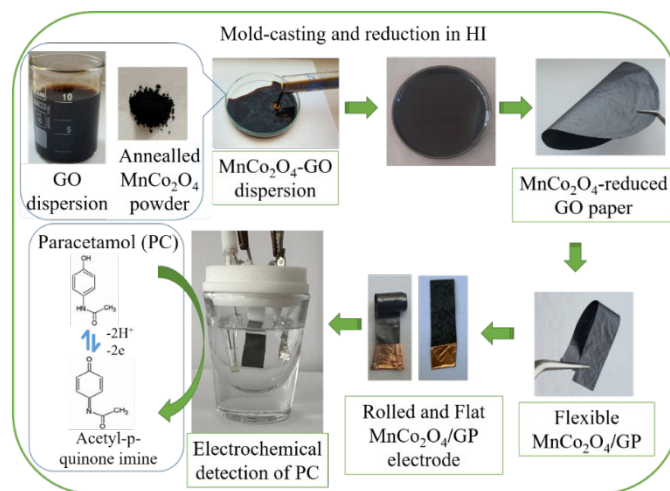


Figure 1. Schematic illustration of the preparation of electrochemical MnCo<sub>2</sub>O<sub>4</sub>/GP sensor

### Acknowledgments

This study was supported by TÜBİTAK under project no: 122Z684

### References

- [1] C. Zhou *et al.*, “Laser-induced MnO/Mn<sub>3</sub>O<sub>4</sub>/N-doped-graphene hybrid as binder-free anodes for lithium ion batteries,” *Chem. Eng. J.*, vol. 385, p. 123720, 2020, doi: 10.1016/j.cej.2019.123720.
- [2] E. Topcu and K. Dagci Kiransan, “Flexible gold nanoparticles/rGO and thin film/rGO papers: Novel electrocatalysts for hydrogen evolution reaction,” *J. Chem. Technol. Biotechnol.*, vol. 94, no. 12, pp. 3895–3904, 2019, doi: 10.1002/jctb.6187.

\*ezgitopcu@atauni.edu.tr



## Investigation of the Cleanability of High Ash Asphaltite Sample Using the Oil Agglomeration Method

Oyku Bilgin<sup>\*1</sup>

<sup>1</sup>Mining Engineering, Sirnak University, Sirnak, Türkiye

### Abstract

Asphaltite reserves are located in and around Şırnak province in the Southeastern Anatolia Region of Turkey. Although they have similar properties to coal, they show structural differences in formation. Asphaltites are a petroleum-based energy source. Chemical analysis values generally vary between approximately 2700-5700 kcal/kg, ash rates range between 35-55% and total sulfur rates vary between 3-8%. High ash and sulfur rates also cause environmental pollution. Asphaltites with high ash content; Coal can be cleaned by applying preparation and enrichment methods and turned into a higher quality, higher calorie energy raw material. For this reason, the energy source with significant high reserves needs to be cleaned and evaluated with enrichment methods, taking into account environmental conditions. On the other hand, an increase in the amount of very fine-sized asphaltite is observed during the application of asphaltite production methods. Most of these fine-sized asphaltites are thrown away without being used and cannot be evaluated economically and cause environmental pollution. All methods used in cleaning coal can also be applied on asphaltites. One of these methods is the oil agglomeration method. In this study, the oil agglomeration enrichment method was applied with different oil types on the asphaltite sample taken from the Avgamasya mining area operating within the borders of Sirnak province, reducing the ash% and obtaining better quality asphaltite.

**Keywords:** Asphaltite, Oil agglomeration, Cleaning, Enrichment

## 1 INTRODUCTION

Asphaltite is a hydrocarbon rock of petroleum origin. Asphalt materials are formed by settling in cracks and voids underground due to factors such as pressure, temperature, and time. Asphaltites have almost the same properties as coal in appearance and chemically, and both are used as energy raw materials. The formation of asphaltites is petroleum-based, while the formation of coals is organic (plant residues, etc.) [1]. While the amount of oxygen in asphaltic materials (especially asphaltic pyrobitumen) is around 3%, this rate varies between 3% and 44% in different types of coal.

Şırnak province, one of the most border provinces of the Southeastern Anatolia Region of Turkey [2], is the source of asphaltites, an important energy raw material. Asphaltite deposits in the Şırnak region are located in phylons. These are; Silopi-Harbul, Silopi-Silip, Silopi-Üçkardeşler, Avgamasya, Milli, Segürük, Nivekara, Karatepe, Seridahli, İspindoruk, Rutkekurat and Uludere-Ortasu phylons. According to the asphaltite license data of TKİ in 2018; there is a total reserve of approximately 67,500,000 tons in Şırnak-Merkez and Silopi. The total reserve is reported as 82,000,000 tons according to the 1978 data of MTA [3–7]. Chemical analyzes of asphaltites generally show approximately, moisture content 0.33-5.40%; ash content 35-52%; sulfur ratio is 3.48-8.23%; and its calorific value is between 2850-5550kcal. Considering the high calorific value of asphaltite, it is suitable for use as an energy raw material in thermal power plants for electricity production and in industrial areas. The ash/sulfur emission rate can be reduced by having circulating fluidized beds and using limestone in thermal power plants. Asphaltite is used as an energy raw material in the 3x135MW thermal power plant located in Şırnak-Silopi [8–10]. High ash and sulfur ratios also cause environmental pollution. Asphaltites with high ash ratios can be cleaned by applying coal preparation and enrichment methods and can be turned into higher quality, higher calorie energy raw materials. For this reason, the energy source in significant high reserves should be cleaned and evaluated with enrichment methods by taking environmental conditions into consideration. On the other hand, an increase in the amount of very fine-grained asphaltite is observed during the application of asphaltite production methods. Asphaltite sample is given in Figure 1.





Figure 1. Asphaltite sample

Most of these fine-sized asphaltites are thrown away without being used and cannot be evaluated economically, and they cause environmental pollution. All methods used in cleaning coals can also be applied on asphaltites. One of these methods is the oil agglomeration method. In this study, the oil agglomeration enrichment method was applied with different oil types on the asphaltite sample taken from the Avgamasya mine site operating within the borders of Şırnak province, and the % ash ratios were reduced and higher quality asphaltite was obtained.

Oil agglomeration (spherical agglomeration), as in flotation, is a method of enrichment that can make selective separation by taking advantage of the differences in the surface properties of coal and the accompanying mineral substances. Coal is naturally more hydrophobic than the accompanying inorganic substances. When oil is added to the suspension of powdered coal in water and mixed, the hydrophobic coal particles are coated with a thin layer of oil [11–13]. As a result of mixing, the oil-coated coal particles collide and form agglomerates by adhering to each other with the binding effect of the oil on their surfaces. Hydrophilic mineral substances, on the other hand, remain in suspension in a dispersed state. Agglomerates resistant to dispersion are removed from the suspension by a mechanical method (sieving) [14–18]. Hydrophobic coal particles are wetted with oil, but hydrophilic clay particles and other residues are not. The coal particles are then collected into particles large enough to be separated, separated from the residues by a sieve.

## 2 MATERIAL AND METHOD

The asphaltite sample used in the experiments applied in this study was taken from Şırnak-Avgamasya asphaltite field. The experimental flow diagram is shown in the Figure 2. Experimental conditions with fuel oil/sunflower oil/ kerosene are shown in Table 1 and Figure 3 shows the agglomeration product.

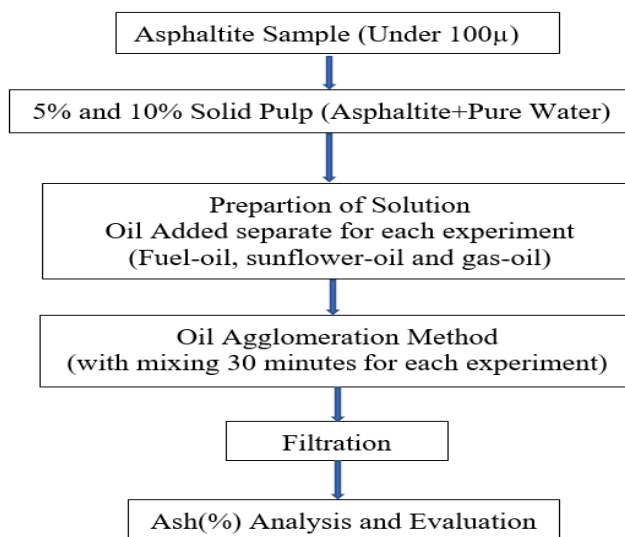
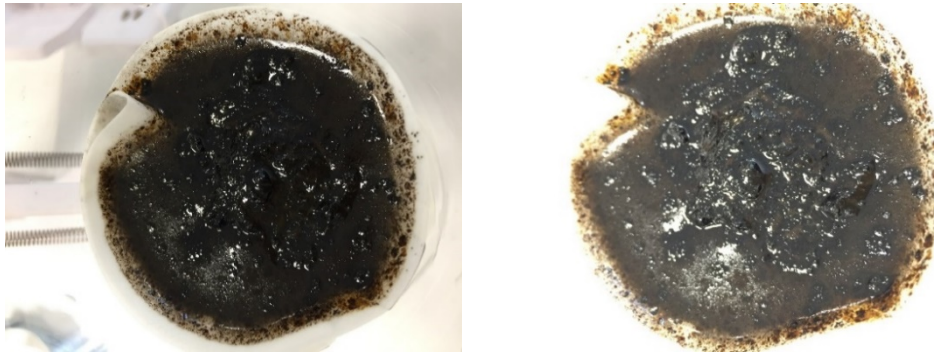


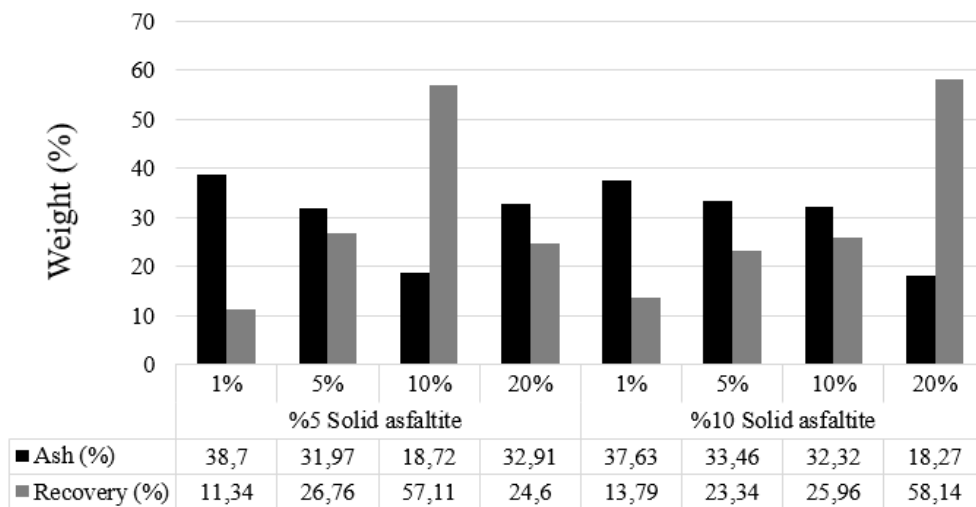
Figure 2. Experiment flow diagram [1]

**Table 1.** Experimental conditions with fuel oil/ sunflower oil

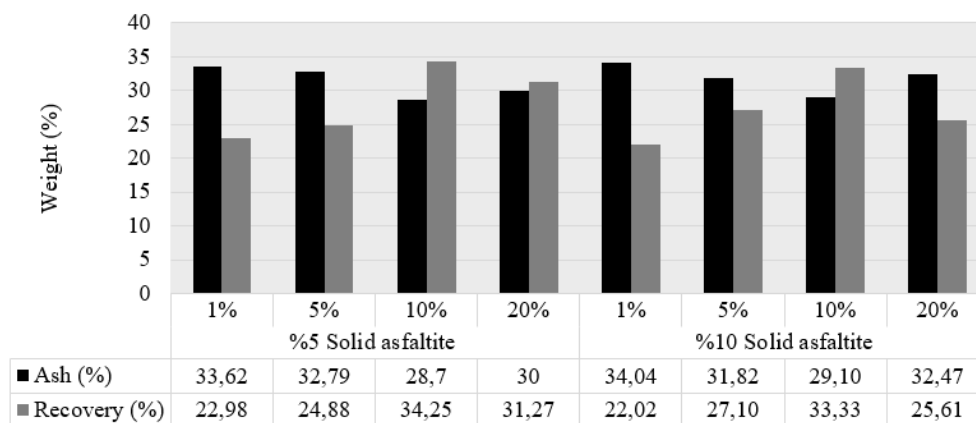
Experimental conditions with fuel oil/sunflower oil	Asfaltite sample
Sample quantity	5%-10% solid pulp (asphaltite+pure water)
Oil type and quantity	1%-5%-10%-20% fuel oil/sunflower oil
Mixing speed	1000 rpm
Mixing time	30 minutes
Washing product	Acetone
Product	Agglomerate
Drying oven	105 °C
Oven	Ash analysis%



**Figure 3.** Agglomeration product



**Figure 4.** Agglomeration product comparison of fuel oil and solids ratios



**Figure 5.** Agglomeration product comparison of sunflower oil and solids ratios

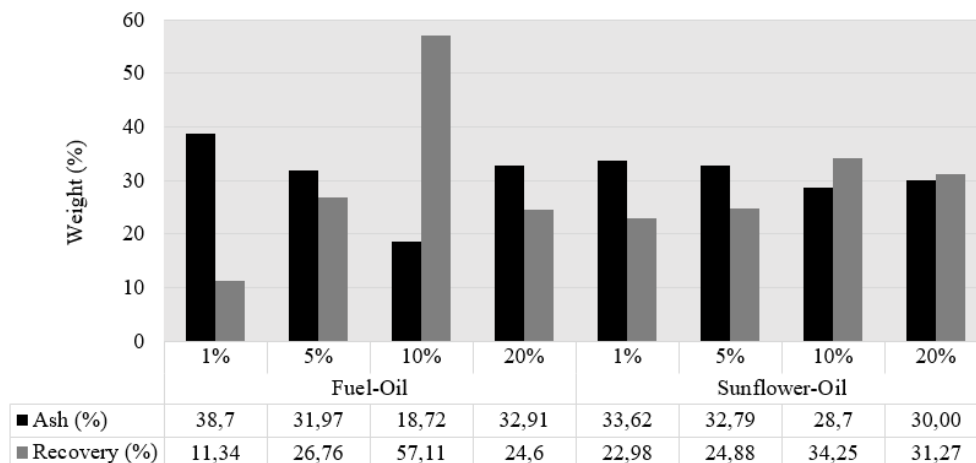


Figure 6. Comparison of oil agglomeration with fuel oil and sunflower oil with 5% solids ratio

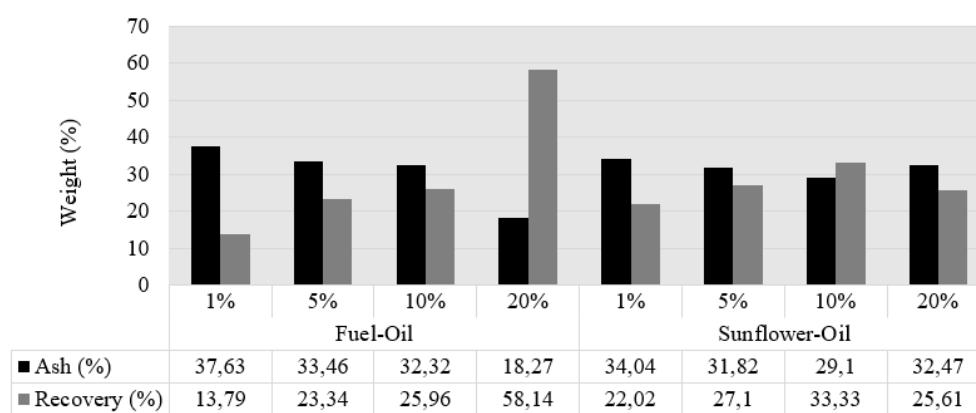


Figure 7. Comparison of oil agglomeration with fuel oil and sunflower oil with 10% solids ratio

### 3 RESULTS

Figure 4 shows agglomeration product comparison of fuel oil and solids ratios. Figure 5 shows the agglomeration product comparison of sunflower oil and solids ratios graph. Figure 6 shows the comparison of oil agglomeration with fuel oil and sunflower oil with 5% solids ratio values. Figure 7, comparison of oil agglomeration with fuel oil and sunflower oil with 10% solids ratio is shown.

### 4 CONCLUSION

The ash ratio of sample asphaltite was calculated as 43.65%. The results of sample asphaltite oil agglomeration test. analysis of the results; in the fuel-oil trial, the best 5% solid enrichment was obtained when 10% fuel-oil was added, while the lowest 18.72% ash ratio was obtained with a yield of 57.11%. The best enrichment was obtained with a solid ratio of 10%. The lowest ash ratio was 18.27% and the yield was 58.14%. In the experiment with sunflower oil; the best enrichment was obtained at 5%; in the agglomeration trial with 10% sunflower oil, the lowest 28.70% ash yield was calculated as 34.25% [1]. In the agglomeration trial carried out with the addition of 10% sunflower oil to the best enrichment ratio of 10%, the lowest ash content of 29.10% was calculated with a yield of 33.33%. As a result; the ash of sample asphaltite sample was reduced from 43.65% to 18.72%.

### References

- [1] O. Bilgin, "Cleaning of fine asphaltite by oil agglomeration", *Energy sources, part a: Recovery, utilization, and environmental effects*, 2020, doi:10.1080/15567036.2020.1810175.
- [2] E. Nakoman, "Güneydoğu anadolu asfaltik hadde zuhurları," *Bilimsel Madencilik Dergisi*, vol. 16, no. 6, pp. 41–51, 1977.
- [3] O. Kural and S. Piskin, "Asfaltitlerin değerlendirilmesi ve Konya İlgin komurlerinde katkı maddesi olarak kullanılması," in *Türkiye 6. Kömür Kongresi*, 1988, pp. 261–264.

- [4] Maden Tetkik Arama Genel Müdürlüğü Raporu, “Asfaltit rezervlerimiz ve değerlendirme imkanları,” Ankara, s. 10. 1982.
- [5] Maden Tetkik Arama Genel Mudurlugu, “Asfaltitler ve Türkiye’deki asfaltit yatakları,” Ankara, 1990.
- [6] I. Senguler, “Küresel enerji politikaları ve Türkiye gercegi asfaltit ve bitumlu seylin Türkiye’deki potansiyeli ve enerji degeri” in *TMMOB, Türkiye VI. Enerji Sempozyumu-MTA*, 2007, pp. 186–195.
- [7] I. Alp, “Asfaltit,” *Bilimsel Madencilik Dergisi*, vol. 16, no. 3, pp. 5–9, 1997.
- [8] O. Bilgin, “Sırnak asphaltites and mining”, in *Istanbul International Modern Scientific Research Congress–III*, Istanbul, 2022.
- [9] DPT Sekizinci Bes Yillik Kalkinma Planı, “Madencilik özel ihtisas komisyonu raporu,” pp. 9–58,2001
- [10] Silopi Elektrik. (2024, Mar. 17), *Enerji ve madencilik* [Online]. Available: <https://www.cinergroup.com.tr/enerji-madencilik/silopi-elektrik-uretim>.
- [11] J. Spoelstra, “The modelling of oil agglomeration of coal fines,” *Journal of Computational and Applied Mathematics*, vol. 28, pp. 359–366, 1989.
- [12] A. Gurses, K. Doymus, and S. Bayrakceken, “Selective oil agglomeration of brown coal: A systematic investigation of the design and process variables in the conditioning step,” *Fuel*, vol. 75, pp. 1175–1180, doi: 10.1016/0016-2361(96)00077-4.
- [13] A. Gurses, K. Doymus, and S. Bayrakceken, “Evaluation of response of brown coal to selective oil agglomeration by zeta potential measurements of the agglomerates,” *Fuel*, vol. 76, pp. 1439–1444, 1997.
- [14] A. Gurses, S. Bayrakçeken, K. Doymus, and M. S. Gülaboglu, “Secimli yag aglomerasyonu ile komurun artırılması,” in *IX. Kimya ve Kimya Mühendisliği Sempozyumu*, Trabzon, 1993, pp. 320.
- [15] C. E. Capes, “Principles and applications of size enlargement in liquid systems,” in *Fine Particles Processing*, New York: P. Aime, 1980, vol. 2, pp. 1442–1462.
- [16] E. K. Aksay, V. Arslan, and H. Polat, “Toz komurlerin zenginlestirilmesinde yag aglomerasyonu yontemi ve yenilikler,” *Istanbul Yerbilimleri Dergisi*, vol. 23, no. 2, pp. 97–108, 2010.
- [17] O. Bajor and O. Trass, “Modified oil agglomeration process for coal beneficiation. I. Mineral matter Liberation by Fine Grinding With The Szego Mill,” *The Canadian Journal of Chemical Engineering*. Vol. 66, pp. 282–285, Apr. 1988.
- [18] O. Yasar and T. Uslu, “Effect of particle size in recovering of coal fines from washery tailings by oil agglomeration,” *Journal of the Polish Mineral Engineering Society*, vol. 19, no. 1, pp. 115–118. June. 2018, doi: 10.29227/IM-2018-01-19.



## Hydrogen Evolution Reaction on MoO<sub>3</sub> Decorated-CuBi<sub>2</sub>O<sub>4</sub>/Reduced Graphene Oxide Nanocomposite

Zeynep Orhan<sup>1</sup>, Hulya Ozturk Dogan<sup>\*2</sup>

<sup>1</sup>East Anatolia High Technology Application and Research Center, Ataturk University, Erzurum, Türkiye

<sup>2</sup>Department of Chemistry and Chemical Processing Technologies, Vocational School of Technical Sciences, Ataturk University, Erzurum, Türkiye

### Abstract

In recent years, hydrogen production using the hydrogen evolution reaction (HER) has been studied quite frequently among clean energy sources. HER reaction is highly preferred because it offers high energy density and has zero pollutant emissions. Production of hydrogen via the electrochemically HER reaction is both economical and can be easily implemented under ambient conditions. Limited quantities and high costs of metal-based electrocatalysts (such as Pt) limit the use of these catalysts for HER. Therefore, it is crucial to develop relatively low-cost and durable electrocatalysts. In this study, CuBi<sub>2</sub>O<sub>4</sub> and reduced graphene oxide (rGO) nanocomposites were synthesized on the nickel foam electrode surface using the one-pot electrochemical co-deposition method. The surfaces of the obtained nanocomposites were decorated with MoO<sub>3</sub> nanoparticles by electrochemical deposition at a constant potential. The high electrocatalytic properties of the synthesized modified electrodes for the HER reaction were investigated using linear scanning voltammetry.

**Keywords:** MoO<sub>3</sub>, CuBi<sub>2</sub>O<sub>4</sub>, Reduced graphene oxide, Hydrogen evolution reaction, Electrocatalyst

## 1 INTRODUCTION

Air pollution due to the emission of carbon products by the combustion of fossil fuels proves a major environmental threat. Although, hydropower, solar, and wind are some of the alternative renewable energy resources yet they possess low energy conversion efficiency. We need strategies to store and transport energy resources such as chemical fuels. One of the promising candidates in this regard is hydrogen, due to its highest value of gravimetric energy density of 142 MJ/kg among all the chemical fuels [1]. Hydrogen as a fuel does not emit carboncontaining pollutants like CO<sub>2</sub>, CO, etc., like other fossil fuels; therefore it is an environment-friendly fuel [2].

Hydrogen evolution reaction (HER) is the simplest electrocatalytic reaction. With development of renewable energy sources electrolytic production of hydrogen becomes an alternative way of hydrogen production for internal combustion engines and fuel cells. In particular, the hydrogen evolution reaction (HER) occurred on cathode in electrolytic bath provides pure H<sub>2</sub> gas. But, this reaction generally depends on the considerable electrocatalysts due to the high overpotential needed in the process [3]. The utilization of electrocatalysts could accelerate the reaction kinetics and lower energy barrier of water dissociation, thereby decreasing the overpotential. HER proceeds through the Volmer, Heyrovsky and Tafel reaction mechanism. HER involves hydrogen adsorption at the electrode surface and as the adsorption energy depends on the nature of electrode materials used so does the kinetics of HER [4]. Noble metal-based materials (such as Pt/C and RuO<sub>2</sub>) are the most effective HER electrocatalysts. However, their practical applications are mainly hindered by the scarcity, instability, and high costs [5]. So the development of new and efficient electrocatalyst design strategies to improve the electrocatalytic activity and stability of existing materials is an urgent problem to be solved. Carbon-based materials have received widespread attention due to their unique advantages for designated catalysis, such as tunable molecular structures, exotic electronic properties as well as strong tolerance to acid/alkaline environments.

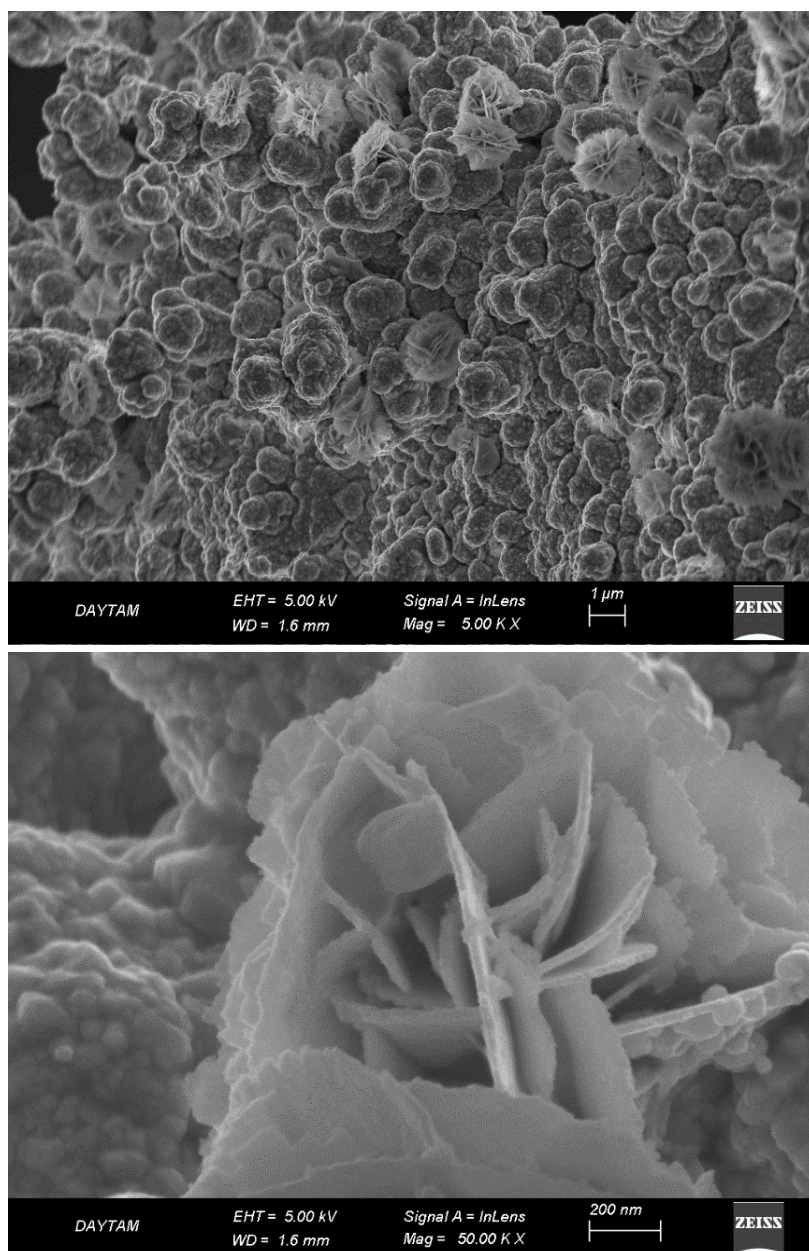
## 2 MATERIAL AND METHOD

Firstly, CuBi<sub>2</sub>O<sub>4</sub>/rGO nanostructures were prepared on the Ni foam electrode surface. CuBi<sub>2</sub>O<sub>4</sub>/rGO was produced in a three-electrode cell system using electrochemical techniques under a constant potential of -400 mV for 15 minutes. The electrode was thermally annealed at 450 °C for 2 hours to form the oxide.

To decorate the CuBi<sub>2</sub>O<sub>4</sub>/rGO surface with MoO<sub>3</sub>, 50 mM KCl solution containing 10 mM MoO<sub>3</sub> was chosen as the electrolyte. By cycling voltammograms from 0V to -1V, MoO<sub>3</sub> was allowed to come to the surface electrochemically for 10 cycles. The prepared MoO<sub>3</sub>@CuBi<sub>2</sub>O<sub>4</sub>/rGO electrodes were characterized by techniques such as XRD, XPS, SEM, and EDS. Linear sweep voltammograms of as-fabricated MoO<sub>3</sub>@CuBi<sub>2</sub>O<sub>4</sub>/rGO electrodes in 0.1 M KOH electrolyte were recorded for the HER application.

### 3 RESULTS

Morphological characterization of MoO<sub>3</sub>@CuBi<sub>2</sub>O<sub>4</sub>/rGO modified Ni foam electrodes were analyzed by SEM (Fig. 1). These SEM images showed that the Ni foam surface was completely covered with nanostructures. Additionally, at high magnifications, MoO<sub>3</sub> growth occurred in the form of nanoflowers.



**Figure 1.** SEM images of MoO<sub>3</sub>@CuBi<sub>2</sub>O<sub>4</sub>/rGO electrode

The HER is an electrochemical process where a redox reaction takes place. Hence, depending upon the pH values of the electrolytes, the mechanism in which the reaction progresses, changes [6]. In Fig. 2, the HER activities of various electrodes in an alkaline medium were compared. The highest current density and relatively low overpotential value in the KOH electrolyte were obtained at the MoO<sub>3</sub> decorated CuBi<sub>2</sub>O<sub>4</sub>/rGO electrode.

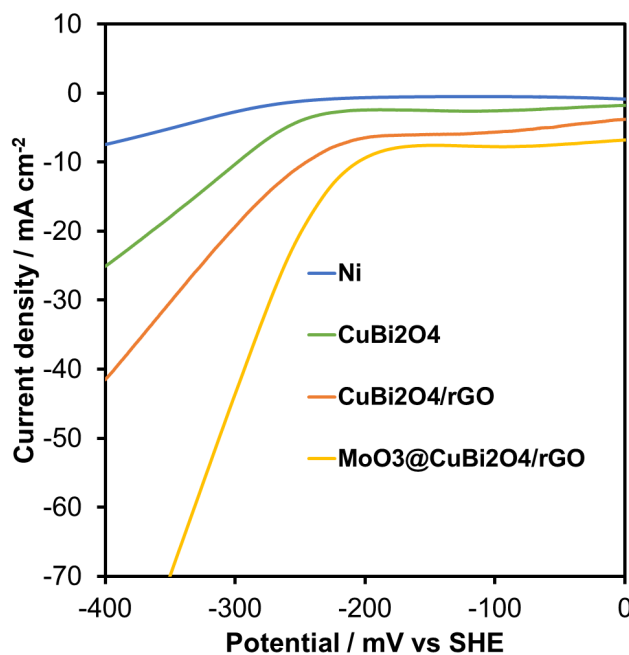


Figure 2. Linear sweep voltammograms of Ni foam, CuBi<sub>2</sub>O<sub>4</sub>, CuBi<sub>2</sub>O<sub>4</sub>/rGO, MoO<sub>3</sub>@CuBi<sub>2</sub>O<sub>4</sub>/rGO electrodes

## 4 CONCLUSION

In this study, MoO<sub>3</sub> decorated CuBi<sub>2</sub>O<sub>4</sub>/rGO electrodes were prepared for use in the hydrogen evolution reaction. The electrochemical technique was chosen as the production method. The characterizations supported the formation of MoO<sub>3</sub> nanostructures on CuBi<sub>2</sub>O<sub>4</sub>/rGO surfaces. MoO<sub>3</sub>@CuBi<sub>2</sub>O<sub>4</sub>/rGO electrode to be a superior HER electrocatalyst, showing a small overpotential of 206 mV at 10 mA cm<sup>-2</sup> in KOH solution.

## References

- [1] G. Zhao, P. Li, K. Rui, Y. Chen, S. X. Dou and W. Sun. "CoSe<sub>2</sub>/MoSe<sub>2</sub> heterostructures with enriched water adsorption/dissociation sites towards enhanced alkaline hydrogen evolution reaction," *Chem. Eur. J.* vol. 24, no 43, pp. 11158–11165, May 2018.
- [2] M. M. Mohideen, B. Subramanian, J. Sun, J. Ge, H. Guo, A. V. Radhamani, et al., "Techno-economic analysis of different shades of renewable and non-renewable energy-based hydrogen for fuel cell electric vehicles," *Renew. Sustain. Energy Rev.*, vol. 174, art. no. 113153, Mar. 2023.
- [3] P. Yu, F. Wang, T. A. Shifa, X. Zhan, X. Lou, F. Xia, and J. He. "Earth abundant materials beyond transition metal dichalcogenides: A focus on electrocatalyzing hydrogen evolution reaction," *Nano Energy*, vol. 58, pp. 244–276, April 2019.
- [4] A. Lasia, "Mechanism and kinetics of the hydrogen evolution reaction," *Int. J. Hydrogen Energy*, vol. 44, no 36, pp. 19484–19518, July 2019.
- [5] Y. Chen, "Interfacial engineering of carbon-based materials for efficient electrocatalysis: Recent advances and future," *Energy Chem.*, vol. 4, no 3, art. no. 100074, May 2022.
- [6] S. Baiju, U. Masuda, S. Datta, K. Tarefder, J. Chaturved, S. Ramakrishna, and L. N. Tripathi Photo-electrochemical green-hydrogen generation: Fundamentals and recent developments, *Int. J. Hydrogen Energy*, vol. 51, pp. 779–808, Jan. 2024.



## Flow and Heat Characteristics over Ellipse in the in-Duct Flow

Neslihan Aydin\*<sup>1</sup>

<sup>1</sup>*Department of Machinery and Metal Technologies, Bursa Uludag University, Bursa, Türkiye*

### Abstract

The study of flow and heat characteristics over an ellipse in an in-duct flow involves analyzing the behavior of fluid and heat transfer around an elliptical object placed within a duct. This analysis is important for various engineering applications, including heat exchangers, aerodynamic design, and fluid machinery. In this study, the flow and heat transfer characteristics in a 100 m long channel were examined over the ellipse placed inside the channel. In the in-channel flow, the focus is on cooling the ellipse by giving air and water flow over the ellipse. The analyzes were analyzed using ANSYS 2022 Fluent. The inlet temperature of air and water was taken as 300 K and the temperature above the aluminum ellipse was taken as 373 K. The inlet velocities of air and water were taken as 5 m/s, 10 m/s and 15 m/s for flow analyses, respectively. SST-k.omega, a turbulence model suitable for heat transfer and flow characteristics, was selected in the analyses. As a result, temperature distribution, velocity distribution, contours and streamlines on the ellipse were obtained for Reynolds numbers and Nusselt numbers at different speeds for the cooling process with the effect of air and water coming on the ellipse.

**Keywords:** *Flow characteristics in-duct flow, Heat characteristics in duct flow, ANSYS 2022 Fluent.*

## 1 INTRODUCTION

Studying flow and heat characteristics over an ellipse in an in-duct flow involves considering both fluid dynamics and heat transfer principles. Fluid Dynamics; analyze how the fluid flows around and over the ellipse. This includes understanding boundary layer development, separation points, and vortex shedding. Velocity profiles; determine how the velocity varies over the surface of the ellipse and in the surrounding flow field. This could involve experimental measurements or computational fluid dynamics (CFD) simulations. Pressure distribution; investigate how pressure varies over the surface of the ellipse and its surroundings. This can provide insights into lift and drag forces acting on the ellipse. Heat transfer characteristics; convection: evaluate how heat is transferred from the surface of the ellipse to the surrounding fluid through convection. This depends on factors such as velocity gradients, fluid properties, and surface temperature. Temperature distribution; examine how temperature varies over the surface of the ellipse and in the surrounding fluid. This includes understanding thermal boundary layers and how they interact with the flow field. Nusselt Number; calculate the Nusselt number to quantify the heat transfer coefficient and compare it with theoretical predictions or empirical correlations. Boundary Conditions; Specify boundary conditions for the flow and heat transfer problem. This includes inlet velocity, temperature, and pressure conditions, as well as any wall boundary conditions for the surface of the ellipse. Modeling approach; decide on the modeling approach, whether it's analytical, numerical (such as finite element analysis or CFD), or experimental (using wind tunnel tests or other methods). Choose appropriate simplifications or assumptions based on the specific problem and desired level of detail. Validation and analysis; validate your model or experimental setup against known solutions or experimental data, if available. Analyze the results to draw conclusions about the flow and heat transfer characteristics over the ellipse. This may involve sensitivity analyses, parametric studies, or comparisons with other geometries or flow conditions. Overall, studying flow and heat characteristics over an ellipse in an in-duct flow requires a multidisciplinary approach integrating fluid dynamics, heat transfer, and possibly other fields like numerical methods or experimental techniques. Modekurti in 2017, In his master's thesis, he performed CFD analysis for non-Newtonian fluids through elliptically bent ducts [1]. Kabus and Oshio in 2005, They investigated experimentally and theoretically the thermal performance of a pipe array heat collector [2]. Ekiciler et al. 2018, they used computational fluid dynamics for nanofluidized SiO<sub>2</sub> in back-stepped slotted in-channel flow. By solving the conservation equations, heat and flow characteristics were tested for different Reynolds numbers [3]. Riaz et al. 2023 also investigated electro-osmotic and thermal effects in a ciliary biased flow model of a viscous fluid connected to an exterior battery passing through an elliptical channel [4]. In their study in 2018, Ragueb and Mansouri obtained the solution of a laminar forced flow of nanofluid in a flow flowing through an elliptical channel [5]. Ibrahim and Alturaihi 2023 also numerically investigated the properties of thermal flow over pipe banks. They investigated the effect of two-phase flow in water air with many different

\*neslihanaydin@uludag.edu.tr



types of vortex generators [6]. In their 2013 study, Tang, Yang and Chen investigated incompressible-Newtonian, fully developed, steady-state laminar flow in different types of channels: equilateral triangular, rectangular, elliptical and super elliptical channels [7]. Zheng et al. 2019 also numerically analyzed the improvement of cooling performance of channel cooling in v-shaped slots for different concepts of slots [8]. In their 2019 study of Du et al., the realizable k-epsilon turbulence model was used to study the flow and heat characteristics in the channel. Numerical analyses were performed by changing the transverse and longitudinal geometries of the flow in a rotating rectangular channel, changing the Reynolds number to 7000 and the rotation number between 0 and [9]. In their study in 2018, Singh and Singh performed three-dimensional flow analyses of the thermal and hydraulic performance of a non-uniform square wave profile solar air heater with ANSYS FLUENT 15.0 [10]. In this study, the characteristics of heat and flow through an elliptical duct in in-channel flow are investigated.

## 2 MATERIAL AND METHOD

In the problem solution, ANSYS FLUENT 2022 version was used. For the problem solution, an elliptical cylinder with a diameter of 1 m is placed in the heat exchanger channel and air and water are given to cool it at different fluid velocities.

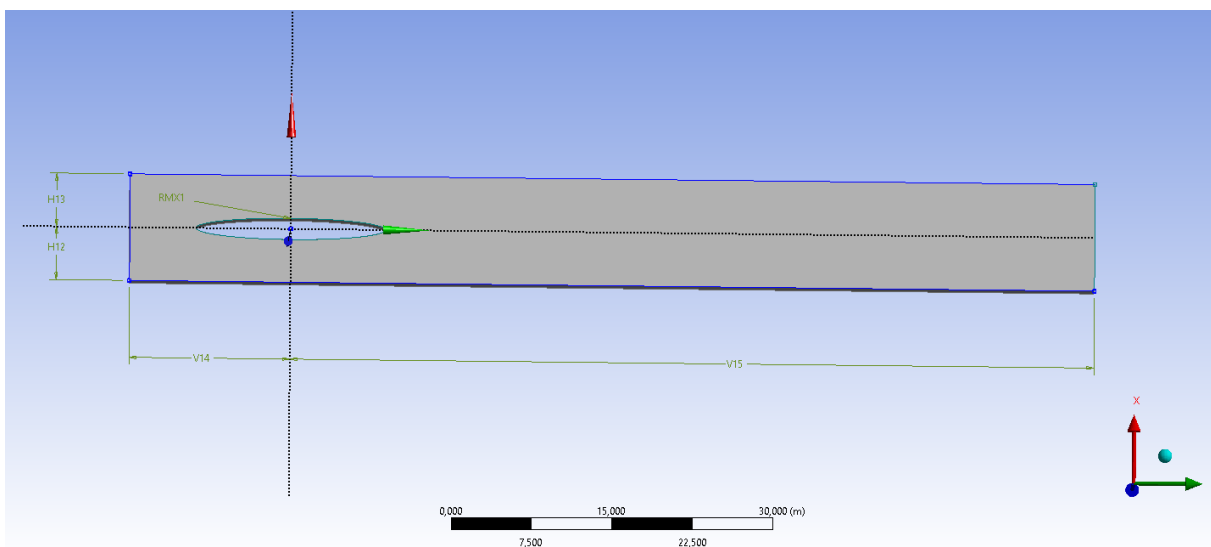


Figure 1. Problem geometry in ANSYS-FLUENT 2022

The channel was given 5 m up and 5 m down by selecting the ellipse origin on both sides symmetrically from the centre. A fully hydrothermal and hydrodynamically developed flow was selected by choosing 15 m on the -y side and 75 m on the +y side from the channel ellipse origin. The length of the ellipse was chosen to be symmetrical on both sides, 1 m.

Dimensions: 5	
<input type="checkbox"/> H12	5 m
<input type="checkbox"/> H13	5 m
<input type="checkbox"/> RMX1	1 m
<input type="checkbox"/> V14	15 m
<input type="checkbox"/> V15	75 m

Figure 2. Details of geometry ellipse in duct flow

The governing equations of incompressible fluid flow can be written as follows:

$$\nabla \cdot \vec{V} = 0 \tag{1}$$

$$\rho(\vec{V} \cdot \nabla \vec{V}) = -\nabla \vec{P} + \nabla \vec{\tau} \tag{2}$$

Where  $\vec{V}$ ,  $\rho$ ,  $\vec{P}$ , and  $\vec{\tau}$  are the velocity vector, density, static pressure and stress tensor, respectively.

Energy equation:

$$u \frac{\partial T}{\partial x} + v \frac{\partial T}{\partial y} + w \frac{\partial T}{\partial z} = \frac{1}{RePr} \left(1 + \frac{\alpha_t}{\alpha}\right) \nabla^2 T \tag{3}$$

Where  $u, v$  and  $w$  are velocities of fluid in  $x, y$  and  $z$  directions.  $\alpha$  and  $\nu$  are thermal expansion coefficient and kinematic viscosity. SST  $k-\omega$  model is used for the solution of turbulent flow. At the inlet, uniform velocity profile has been imposed. No-slip boundary condition has been implemented (i.e.  $u = v = w = 0$ ) over the channel wall.

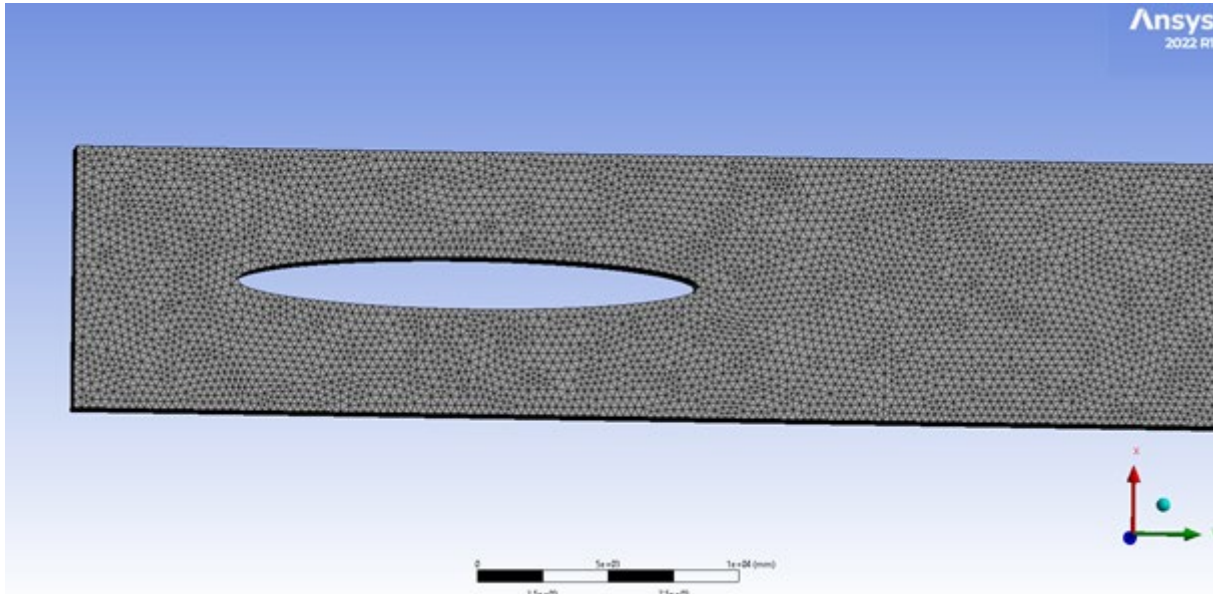


Figure 3. Meshing form for in-channel ellipse

The following Fig. 3 shows the frequent mesh image and Fig. 4 shows the number of meshes 646904, respectively.

Statistics	
Nodes	207815
Elements	646904

Figure 4. The number of meshes for in-channel ellipse

### 3 RESULTS

#### 3.1 Velocity Profiles

Firstly, the cooling of the ellipse in the channel at low speed and the velocity distribution were numerically tested. Afterwards, the speed was gradually increased and the velocity and temperature distributions were taken from ANSYS 2022. When the velocity distribution is examined, for 5-10 and 15 m/s, as the speed continues to increase, turbulence kinetic energy increases, the velocity distribution wake region for the flow following the ellipse has lengthened and its distribution in the channel has spread towards the back of the ellipse. Especially at high velocities, the flow over the blade is symmetrical over the ellipse for  $Re: 8.423 \times 10^5$  and the velocity reaches up to 19.4 m/s in Fig.5, Fig 6, and Fig.7.

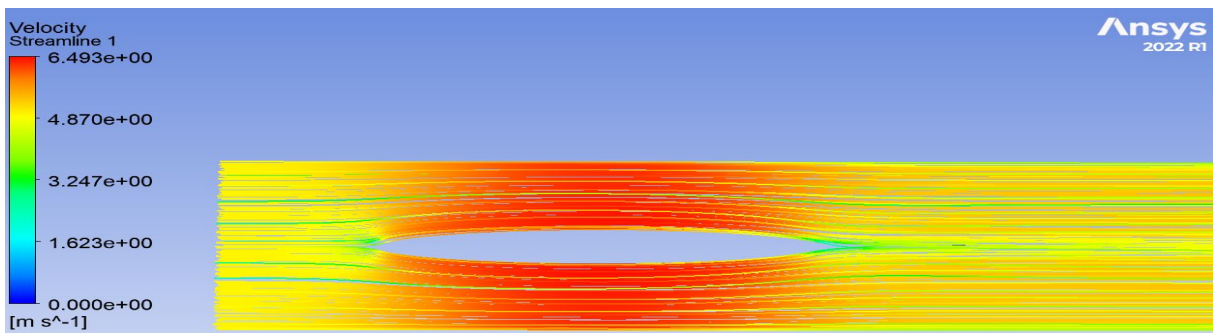


Figure 5. Velocity profile for  $Re: 2.80 \times 10^5$

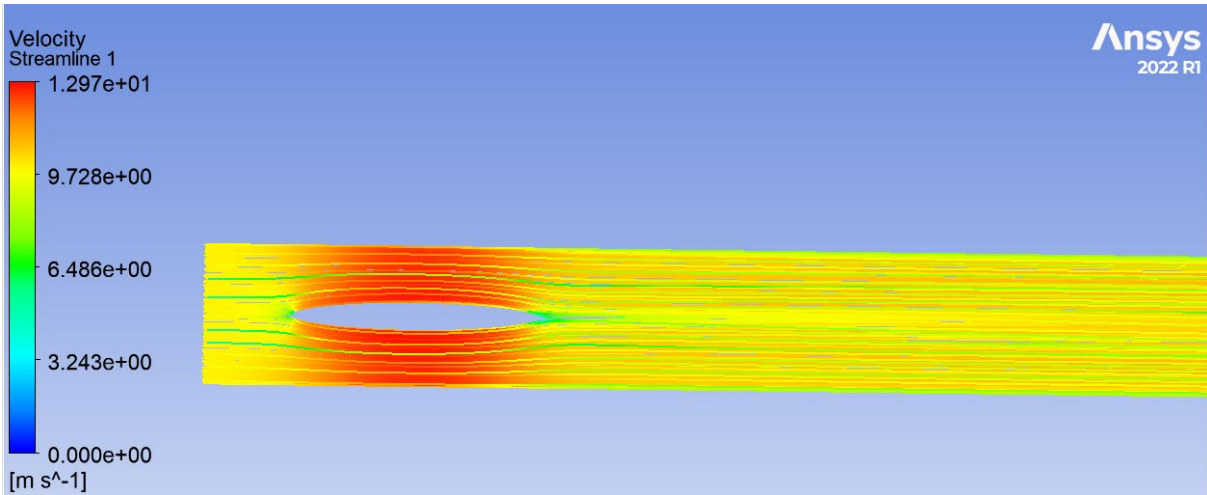


Figure 6. Velocity profile for  $Re: 5.617 \times 10^5$

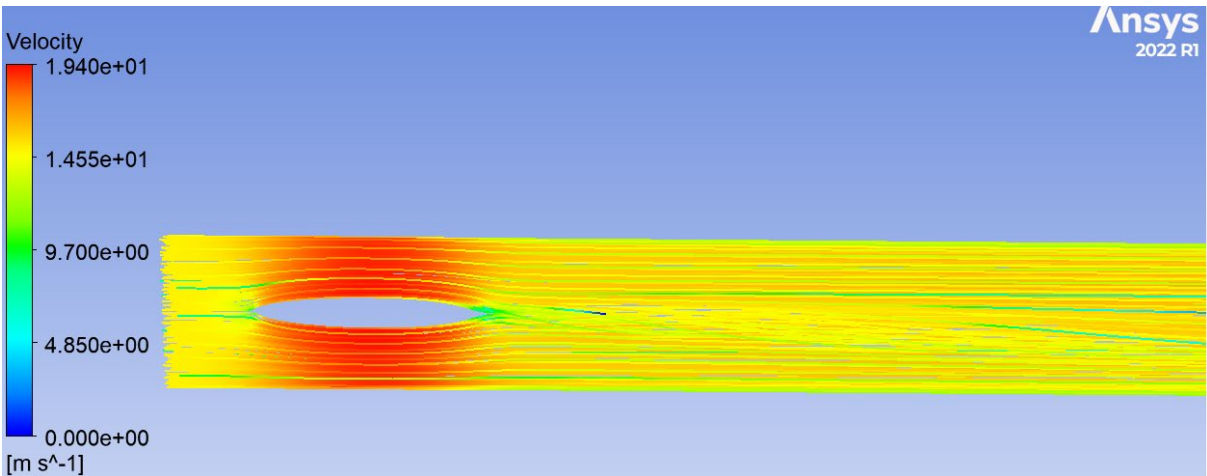


Figure 7. Velocity profile for  $Re: 8.423 \times 10^5$

### 3.2 Temperature Distributions

When the temperature distribution is analysed on the ellipse, it is observed that the temperature increases especially towards the exit of the channel and this increases with increasing speed, which extends the wake region as in the side velocity profiles. Especially at high speeds, it can be seen that the effect of the higher temperatures continues behind the duct with the effect of the ellipse, but full cooling is still achieved.

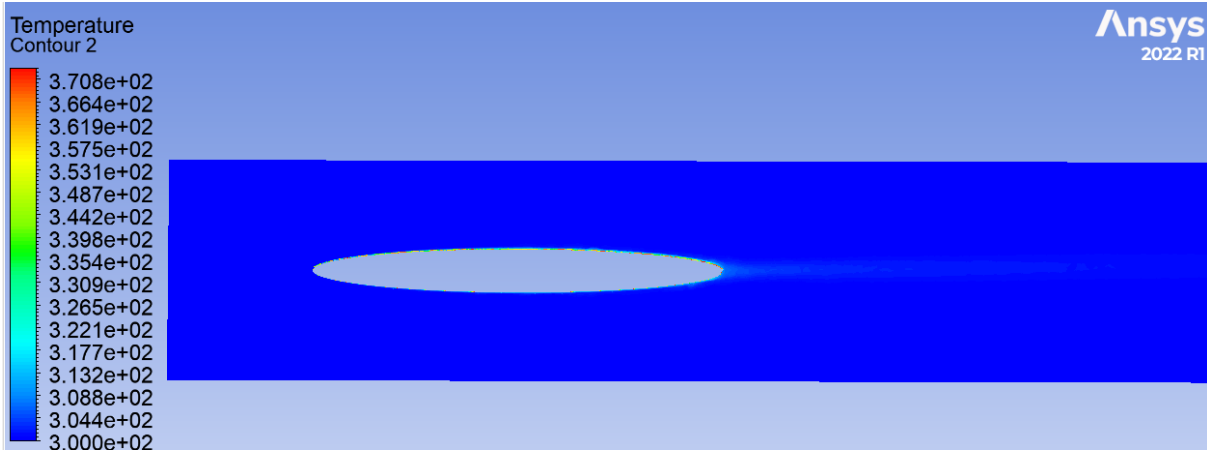


Figure 8. Temperature distribution for  $Re: 2.80 \times 10^5$

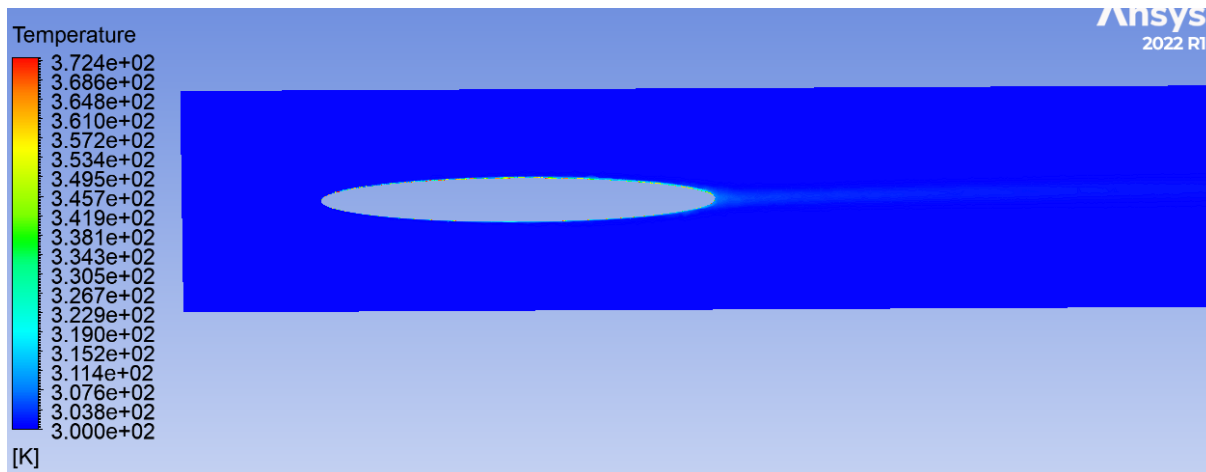


Figure 9. Temperature distribution for  $Re:5.617 \cdot 10^5$

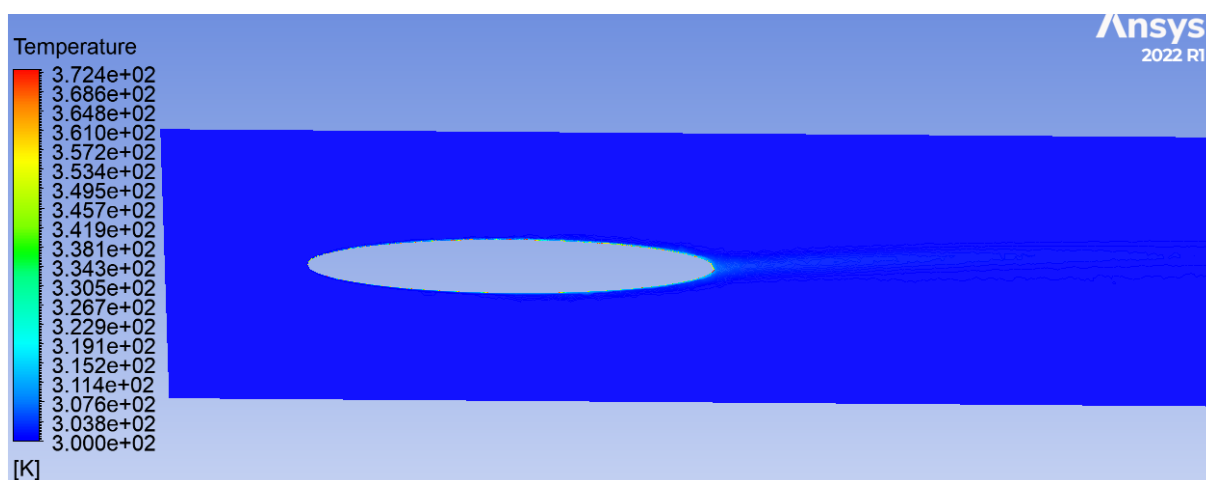


Figure 10. Temperature distribution for  $Re:8.423 \cdot 10^5$

#### 4 CONCLUSION

This study investigates the flow behind the ellipse and the thermal properties of the flow inside the channel. Especially at high velocities for  $Re:8.423 \cdot 10^5$ , the wake region increased and continued in length until the channel exit.

#### References

- [1] A. ModekurtiI, "Numerical investigation of fluid flow and heat transfer for non-newtonian fluids flowing through twisted ducts with elliptical cross-sections" M.S. thesis, Department of Mechanical and Materials Engineering of the College of Engineering and Applied Science, GITAM University, Visakhapatnam, 2013.
- [2] C. J. Kobus and T. Oshio, "An experimental and theoretical investigation into the thermal performance characteristics of a staggered vertical pin fin array heat sink with assisting mixed convection in external and in-duct flow configurations" *Experimental Heat Transfer*, vol. 19, no. 2, pp. 129–148C, 2016.
- [3] R. Ekiciler, E. Aydeniz, and K. Arslan, "The effect of volume fraction of  $SiO_2$  nanoparticle on flow and heat transfer characteristics in a duct with corrugated backward-facing step," *Thermal Science*, 2018,
- [4] A. Riaz,, K. Saleem, and M. Raza, "Cilia-driven flow in a symmetric elliptical duct with electric double layer and thermal effects: Exact solutions," *Arab. J. Sci. Eng.*, vol. 48, pp. 8189–8206, 2023.
- [5] H. Ragueb and K. Mansouri, "An analytical study of the periodic laminar forced convection of non-Newtonian nanofluid flow inside an elliptical duct," *International Journal of Heat and Mass Transfer*, vol. 127, part B, pp. 469–483, 2018.
- [6] A. Q. Ibrahim and R. S. Alturaihi, "Numerical investigation for single-phase and two-phase flow in duct banks with multi types of vortex generators," *International Journal of Technology*, vol. 14, no. 3, pp. 484–500, 2023.

- [7] H.-W. Tang, Y. T. Yang, and C.-K. Chen, "Application of double side approach method to the solution of fully developed laminar flow in duct problems," *Journal of Mechanics*, vol. 29, no. 3, pp. 471–479, Sep. 2013,
- [8] D. Zheng, X. Wang, and Q. Yuan, "Numerical investigation on the flow and heat transfer characteristics in a rectangular channel with V-shaped slit ribs," *Infrared Physics & Technology*, vol. 10, pp. 56–671, 2019.
- [9] W. Du, L. Luo, S. Wang, J. Liu, and B.A. Sunden, "Enhanced heat transfer in a labyrinth channels with ribs of different shape," *International Journal of Numerical Methods for Heat & Fluid Flow*, vol. 30, no. 2, pp. 724–741, 2020.
- [10] I. Singh and S. Singh, "CFD analysis of solar air heater duct having square wave profiled transverse ribs as roughness elements," *Solar Energy*, vol. 162, pp. 442–453, 2018.



## Risk Factor Estimation with Ordered Logit and Ordered Probit Models

Burcu Durmus<sup>\*1</sup>, Oznur Isci Guneri<sup>1</sup>, Aynur Incekirik<sup>2</sup>

<sup>1</sup>Department of Statistics, Faculty of Science, Mugla Sıtkı Kocman University, Mugla, Türkiye

<sup>2</sup>Department of Econometrics, Faculty of Economics and Administrative Sciences, Manisa Celal Bayar University, Manisa, Türkiye

---

### Abstract

The dependent variable examined in most of the studies in the field of health is categorical and ordinal. Ordered logit and probit models are used when the categories of the dependent variable are more than two (at least 3) and in a naturally ordered structure. These models are also known as generalized linear models. For logit models, as in multiple regression analysis, there is no normality and continuity assumption prerequisite. A dataset consisting of data obtained from a survey conducted with patients was used in this study. For this data set, ordered logit and probit models were compared and the parallel slope assumption was investigated. While the validity of the models was tested with likelihood ratio test statistics, tests such as AIC and BIC for Goodness of Fit and deviation statistics were used.

**Keywords:** *Generalized linear models, Ordered logit, Ordered probit, Parallel slope assumption*

---



## Effect of $\alpha$ -Fe<sub>2</sub>O<sub>3</sub> on Gas Detection Performance of MgO Thin Films

Hilal Kubra Saglam<sup>1</sup>, Sevda Saritas<sup>\*2</sup>

<sup>1</sup>Department of Electrical and Electronics Engineering, Faculty of Engineering, Ataturk University, Erzurum, Türkiye

<sup>2</sup>Department of Electrical and Energy, Ispir Hamza Polat Vocational School, Ataturk University, Erzurum, Türkiye

---

### Abstract

Various metal oxide nanostructures such as Fe<sub>3</sub>O<sub>4</sub>, MgO, ZnO and TiO<sub>2</sub> have been synthesized for wide applications. MgO is an inexpensive non-toxic material with unique electrical, chemical, optical and mechanical properties. Reasons for common use include: high surface reactivity, wide bandwidth, chemical stability, thermal stability. Moreover, due to its wide band gap, the dominant light absorption of MgO is in the UV range. MgO has been used as a chemical sensor due to the large mobility of electrons.

The effect of  $\alpha$ -Fe<sub>2</sub>O<sub>3</sub> film grown on MgO film was investigated. XRD studies showed that both films had similar morphological structures with approximately the same planes. Despite this, no sensor response could be obtained from MgO film, while  $\alpha$ -Fe<sub>2</sub>O<sub>3</sub> film showed sensor properties.

**Keywords:** Gas sensor, Thin film, MgO, Spray pyrolysis, Sputter

---



---

## Analysis of Quality Risks on the Assembly Line in an Armature Manufacturing Company Using FMEA Method

Fatma Merve Bayir Kanbur<sup>\*1,2</sup>, Hasan Selim<sup>3</sup>

<sup>1</sup>The Graduate School of Natural and Applied Sciences, Dokuz Eylul University, Izmir, Türkiye

<sup>2</sup>R&D Center, E.C.A. Valfsel Inc., Manisa, Türkiye

<sup>3</sup>Dokuz Eylul University, Department of Industrial Engineering, Izmir, Türkiye

---

### Abstract

In the globalizing world, the rapid advancement of technology and the onset of the information age have not only made things easier in many areas of life, but also changed the understanding of production. The place of machines in production is increasing day by day. This makes things faster and easier. Production on the assembly line is carried out on a large scale and serially. In this way, time and labour loss are tried to be minimized. Therefore, assembly lines play an important role in the efficiency of production systems.

The impact of assembly line risks on customer satisfaction is very significant. In this context; Risks in quality, delivery, communication, warranty and support services, and security must be addressed and managed effectively. In order to minimize the impact of assembly line risks on customer satisfaction, it is essential to strengthen quality control processes, provide training to employees, implement effective communication strategies and establish rapid problem resolution methods.

In this study it is aimed to increase customer satisfaction by reducing quality risks that may occur during the assembly of products in a manufacturing firm operating in armature sector. Failure Modes and Effects Analysis (FMEA), which is a step-by-step approach for identifying all possible failures in a design, a manufacturing or assembly process, or a product or service, is employed in analysing the assembly processes. Actions to be taken to reduce or eliminate quality risks on the assembly lines are determined and forwarded to the company management.

**Keywords:** *Assembly line, Risk analysis, Quality risks, FMEA, Customer satisfaction*

---





## A Study on the Effects of Electromagnetic Fields

Yunus Kaya<sup>\*1</sup>, Selahattin Kosunalp<sup>2</sup>

<sup>1</sup>Department of Electronics and Automation, Bayburt University, Bayburt, 69010 Türkiye

<sup>2</sup>Department of Computer Technologies, Gonen Vocational School, Bandirma Onyedi Eylul University, Bandirma/Balikesir, 10200 Türkiye

### Abstract

During the transmission and use of electrical energy, electromagnetic (EM) fields are created that can affect the environment and people. With the development of technology and the rapid increase in population, it is known that all living things are under the influence of EM fields due to the increasing use of electrical energy in every area of life. In this study, in order to provide guidance for protection from the effects of EM fields; firstly, basic expressions on EM fields are defined, EM spectrum and radiation are mentioned and the effects of EM fields on humans are mentioned. Afterwards, some suggestions were made to protect from EM radiation and fields.

**Keywords:** EM field, Radiation, Effect, Suggestion

## 1 INTRODUCTION

The use and need for electrical energy is increasing due to industrialization and technological development. Electromagnetic (EM) fields are one of the common environmental influences that we are increasingly concerned about as technology advances. People, animals, and plants, in short the entire environment, are exposed to EM fields at various levels today, and our exposure to them continues to increase with the advancement of technology. EM radiation has existed since the dawn of the universe, and light is its most familiar form [1, 2].

EM field refers to the force field containing EM energy, which has electric and magnetic field components, arising from the motion of electric charges. The EM fields we are probably most familiar with are those that occur in nature. The magnetic field that we can detect at the Earth's surface is thought to be produced by electric currents generated deep within the Earth's semi-liquid ferromagnetic core [1].

We are constantly exposed to EM waves in the environments where we live. This can sometimes occur when passing under a high voltage line or sometimes by radiation from base stations near our home. However, even the mobile phones we carry around all the time or the energy-saving light bulbs in our rooms in daily life emit EM radiation. In short, wherever we go in the universe, EM waves will not leave us alone [3, 4].

With the advancement of technology, a rapid increase has been observed in the number of electrically powered devices around us. All the electrical devices we use to make life easier, the low, medium, and high voltage lines that make them work, transformers, microwave ovens, and everything from the sun that illuminates our world are sources of EM fields. Therefore, all of these sources contribute to the EM radiation that surrounds us. The issues of what extent this environmental pollution is and what effects it has on people have been the source of many scientific studies. Numerous scientific studies have been conducted to measure all EM field pollution from low to high frequencies [3, 5].

This paper is a general study on the effects of EM fields and the rest of the paper is organized as follows. Firstly, in Section 2, basic expressions on the EM field are defined, EM spectrum and radiation are mentioned, and the effects of EM fields on humans are mentioned. Finally, in Section 3, some recommendations are made for protection from EM radiation and fields.

## 2 EM FIELD AND ITS EFFECTS

In this section, brief and concise basic information about electric, magnetic, and EM fields, EM spectrum, and radiation is given, and then the effects of EM fields on humans are mentioned.

### 2.1 EM Field

Electric field refers to the attractive or repulsive force effect created by one electric charge on another electric charge. Every electric charge produces an electric field. What creates the electric field is the presence of electric charges. Therefore, a lamp connected to the mains creates an electric field even if no current is passing through it and it is not lit. As the supply voltage of a device increases, the resulting electric field also increases. The unit of electric field intensity is expressed as volts per meter (V/m) [6].

The magnetic field occurs when electric charges change places, that is, when there is an electric current circulation. When the lamp is on, in addition to the electric field, there is also a magnetic field caused by the current passing from the supply cable to the lamp. Tesla (T) or Gauss (G) is used as the unit of measurement for the magnetic field. The higher the current, the higher the resulting magnetic field [6].

Both electric and magnetic field intensities decrease rapidly with distance from the source. While even a small insulating obstacle (building, tree, etc.) blocks the electric field in an electric field, this is not the case in magnetic fields [7].

EM fields occur when electric and magnetic fields come together. Here, the electric wave and the magnetic wave travel together at the speed of light ( $3 \times 10^8$  m/s). The distinctive features of EM fields are their frequencies and wavelengths. Frequency is the number of oscillations of the wave in one second and its unit is Hertz (Hz). Wave length is the distance traveled by the wave during one oscillation [6, 7].

### 2.2 EM Spectrum and Radiation

Electric and magnetic fields are part of the EM radiation spectrum, which extends from static electric and magnetic fields to radio-frequency and infrared radiation and X-rays. EM spectrum; EM waves describe frequencies and wavelengths. At one end of the EM spectrum, which shows all EM waves together, there are gamma rays with high energy and wavelengths in the nanometer range, while at the other end there are low energy and very low frequency rays with wavelengths in the kilometers range (as shown in Figure 1) [1, 8].

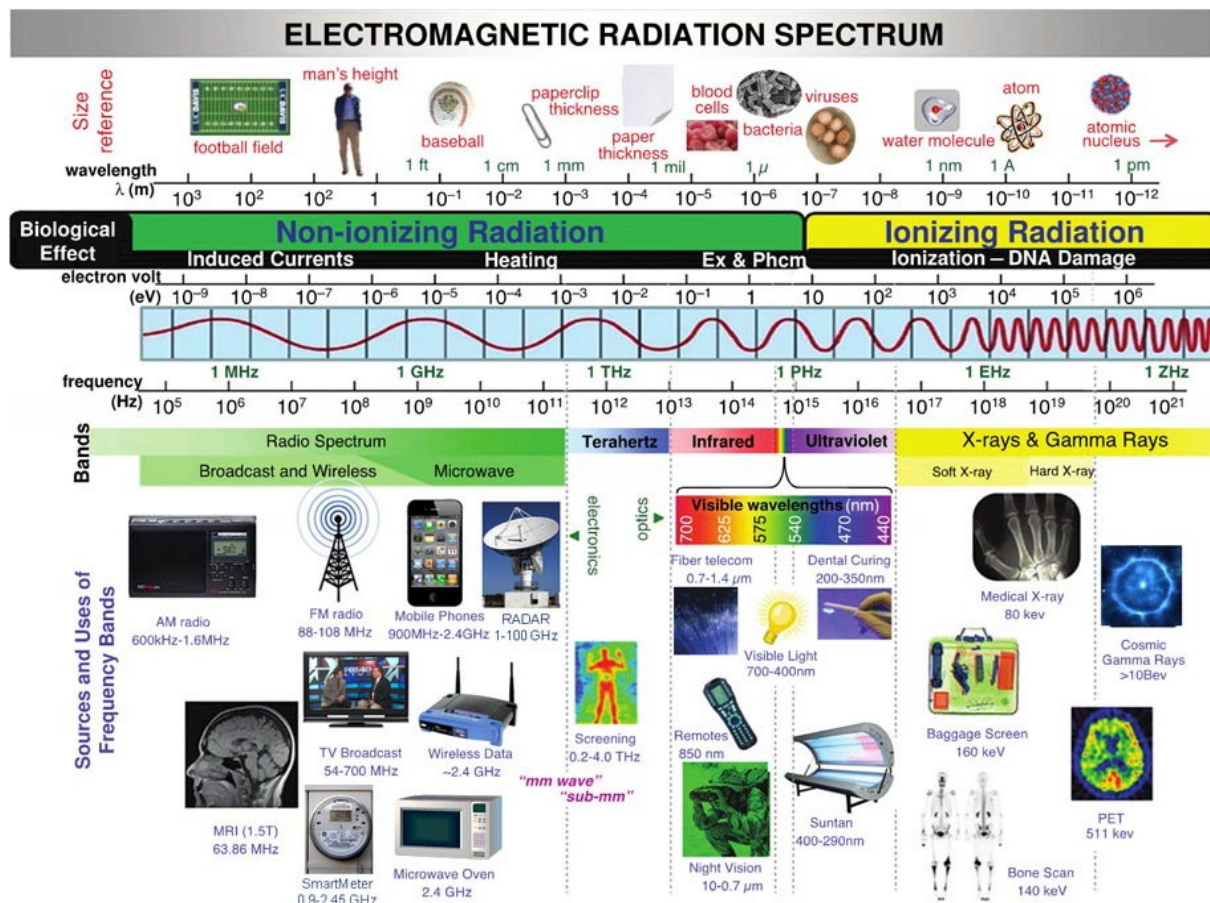


Figure 1. EM spectrum [8]

EM radiation is the emission or transmission of energy traveling in the form of waves or particles that penetrate objects and the human body [3]. EM radiation can be divided into two groups, ionizing and non-ionizing radiation, depending on its interaction with matter [9, 10]. In the spectrum, the region between 0 Hz (direct current (DC)) and 300 GHz is called the non-ionizing radiation region and above 300 GHz is called the ionizing radiation region [2].

Radiation means particle emission (particle emission), it is used for rays that can penetrate into matter. They are divided into two groups according to whether they penetrate into matter and ionize atoms (remove electrons) or not. The type of radiation that ionizes the atoms in the medium directly or indirectly by transferring its energy to the medium as it passes through the substance is called ionizing radiation. Ionizing nuclear radiation (such as neutrons, protons, alpha, beta particles, X and gamma rays) at very high frequencies (above 300 GHz); EM photons have enough energy to break chemical bonds [2, 11]. When these rays with very high energies hit the molecules, they ionize them and disrupt their molecular structure, that is, their vital functions [9, 10, 12]. For this reason, these rays are defined as “ionizing EM radiation”. High-energy ionizing EM waves can cause molecular changes that can damage biological tissue including DNA and genetic material. For this effect to occur, the tissue must interact with high-energy photons such as X and gamma rays. It is known that ionizing radiation affects the DNA of cells, causing mutation and cancer [9].

Not having ionizing properties; radiation originating from fixed telecommunication devices such as base stations, radio and television transmitters and very low frequency (50 Hz) electric and magnetic fields originating from electrical networks, transformer substations, and electrical household appliances are included in the EM radiation group, which is referred to as non-ionizing radiation. At lower frequencies, the energy of the photon is too small to affect chemical bonds [2, 11].

As examples of systems operating in the frequency range of 10 kHz – 300 GHz in the EM spectrum; radio, television, and wireless systems, radar systems, satellite communication systems, microwave ovens, systems operating at RF frequency in medicine and industry, and GSM communication systems are provided. Specific absorption rate (SAR) is defined as the measure of the interaction of EM radiation created by the systems in question with living tissue. SAR is related to the power absorbed in the tissues and converted into heat [6].

“Basic limits” and “derived limits” are defined to determine the limits that may be harmful to human health. Based on the definition in the standards that “absorption of EM energy that will increase body temperature by one degree in the average human body is harmful”, the value of 4 W/kg was accepted as the limit value. According to this assumption, the highest power value that tissues can absorb per kilogram is 4 W/kg. Based on a safety margin of 10 times for workplaces and 50 times for all places where people are present, the basic limits have been set at 0.4 W/kg SAR for workplaces and 0.08 W/kg SAR for general public places. These values are the SAR value given for the whole body for an exposure time of 6 minutes [2]. Specifically, the EM Field Project conducted by the World Health Organization recommends a maximum SAR value of 0.1 W/kg for mobile phone SAR values [6].

### **2.3 Effects of EM Fields on Humans**

Most people, at home and at work, are exposed to a mixture of weak electric and magnetic fields from the use of household appliances and industrial equipment, as well as from the conduction of electricity, telecommunications, and broadcasting. Even in the absence of any external electric field, very small electric currents exist in the human body due to chemical reactions that are part of normal body functions [1].

The way in which EM fields affect health depends on the frequency, intensity, and duration of exposure. The frequency of the applied field is also important in the context of the consequences of the effect. Because different frequencies interact with the body in different ways, the effects of low-frequency fields are not the same as those produced by higher frequencies. Low frequency fields cause stimulation of nerves and muscles, while high frequency fields cause heating of tissues. Occupational exposure limit values are determined in such a way that no adverse health effects will occur as long as these values are adhered to. In other words, for any adverse effect to occur, the exposure limit value must be exceeded at this frequency [1].

It has not yet been definitively proven that the EM field is a cancer-causing factor. Therefore, long-term, epidemic, and experimental studies on humans are necessary to definitively address this issue. Today, interpretations are made only based on the results obtained from studies conducted on animals. As a result of experiments conducted on animals, the effects of EM fields that increase the risk of cancer have been observed. The occurrence of these effects depends on the frequency of the EM field, its intensity, body size, electrical properties of the body, the

distance of the EM field and most importantly the duration of the effect. Accordingly, those who work on high voltage lines or high voltage facilities, radio, and television transmitters are most affected [2, 13, 14].

As a result of exposure to non-ionizing EM fields, two types of effects may occur in living things. These are thermal and non-thermal effects [2].

Thermal effects are stated as the EM energy absorbed by the body converting into heat and increasing body temperature. This temperature increase continues until the heat is balanced by being removed through blood circulation. The temperature increase that very low frequency can cause is actually very small and can most likely be eliminated by the body's normal mechanisms [2].

Disorders and diseases claimed to be due to non-thermal effects include changes in brain activity, sleep disorders, attention disorders, increased headaches, and dizziness. The non-thermal effects of the EM field can cause great disturbances in the human organism. For example, the molecules and atoms of the body may lose the electrical balance they have established among themselves, may be affected by biochemical activities, and most importantly, the electrical structure of the cell and therefore the functioning of the tissues may be disrupted. Related disorders may occur in the cardiovascular system, immune system, and nervous system. It is one of the effects that have been raised about the fact that the constant weakening of the body's immune system will have "an effect that increases cancer or initiates or triggers cancer". There are studies linking the increased risk of blood cancer in children and the change in blood table to EM fields. The number of studies investigating the biological effects of electric fields, which now constitute a risk factor for human health, has begun to increase rapidly [2, 15].

Very low fields are suspected to have the following effects in laboratory studies on animal cells and tissue [2, 15].

- It affects intercellular activity,
- It affects the hormone secretion,
- It affects the body's defense system,
- It causes premature cataracts in the eyes of young people,
- It causes rashes on the facial skin,
- It affects abnormal developments in embryos,
- It disrupts the immune system, and
- It causes an increase in the rates of hallucinations, headaches and depression.

It is possible to summarize the results of some of the epidemiological and experimental studies carried out as follows [2].

In the report of the US Office of Technology Assessment on the effects of electric and magnetic fields produced by transmission lines on public health; it is stated that the interaction of electric and magnetic fields with the cell occurs in the cell membrane and that even a small change in the signal that EM fields can create in the body's electrical system is sufficient for biochemical changes that are critical to the functioning of the cell. In addition, EM fields affect the cells that carry out the normal growth process and disrupt their properties [15].

In the study [16], the link between adult cancers and power lines was examined and it was stated that power lines cause brain cancer but do not cause leukemia. In the study [17], it was found that the risk of brain cancer among those working on power lines was 7 times higher. In the study [18], an increase in leukemia was found in adults living within 100 meters of high voltage power lines. In the study [19], no association was found between exposure to electric fields and cancer in children living within 50 meters of power lines. In the study [20], an increased risk of miscarriage was found between high voltage power lines. In the study [21], it was determined that there was an increase in the rate of leukemia in those living within the 0–600 m range of very low frequency lines. In the study [22], a link between alzheimer's and power supplies was reported. In the study [23], it was reported that alzheimer's disease was observed in men who were exposed to EM fields for a long time due to their occupation, while this was not the case for women.

EM radiation can also have positive effects at different frequencies, with varying durations of effect and depending on the type of tissue exposed. Many scientists have researched these positive effects. Although it is known that EM radiation has cancer-causing effects, it can also be used in cancer treatments to destroy cancer cells or reduce their spreading effect [3].

It has been discovered through experimental results that EM waves in the 30–70 GHz frequency band provide positive results in the treatment of diseases such as ear-nose-larynx cancers, coronary artery diseases, hypertension, pulmonary tuberculosis, and ulcers in their cellular applications [3, 24].

Devices that produce EM waves show positive effects when operated with short-term repetitions and low-intensity powers. For example, in the study [25], time-varying current was created in tissues with EM waves. In tissues whose osteogenesis is increased, the thermal biological healing process is shortened. Thanks to low-frequency EM fields, the healing time can be brought forward by the radiation generated in the bones [3, 26, 27].



**Figure 2.** Low frequency EM field commercial device and clinical application [28]

### 3 CONCLUSION AND SUGGESTIONS

It would be a correct approach to consider that the effects of EM radiation and field-generating devices may pose very serious health risks for public health, that it may take many years for these negativities to be revealed, and therefore, by taking precautions, possible harms that may occur in the future can be prevented. For this reason, some suggestions for protection from EM radiation and fields are presented below [3, 29]:

- Electrical devices should be operated as far away as possible because EM effects decrease rapidly with distance.
- You should either turn off or unplug electrical devices that you are not using. As long as the devices remain in the “Stand by” position, they will create EM pollution. Düşük radyasyonlu bilgisayar ekranı kullanmaya özen gösterilmeli ya da ekran filtresi kullanılmalıdır.
- In order to have a restful sleep, there should be no television, radio etc. in the bedroom.
- You should not be in environments close to high voltage lines.
- Electric massage beds or electric blankets should not be used for long periods of time while in operation.
- Alarm clocks, telephones, and night lamps should be placed at least 2 m away from where we sleep.
- The computer should be used at least an arm's length away.
- Electronic devices plugged into the socket should be avoided.
- If possible, you should not use economy lamps (halogen and fluorescent), and if you do, you should keep them away from you.
- You should not keep your mobile phones above your heart, at waist or chest level, when they are on.
- You should keep an open mobile phone at a safe distance from you (preferably 1 m) and use a headset when making calls. Mobile phones with a SAR value lower than 1 W/kg should be preferred.
- Since the magnetic field of the hair dryer is very high, it should be used intermittently and for short periods of time rather than continuously.
- You should stay at least 1 m away from the microwave oven when it is operating.
- You should stay at least 50 cm away from photocopy machines (they have a high magnetic field).
- Electric shavers should not be used or should be used with a charger.
- You should stay at least 2 m away from the television screens (front and back).
- You should not be near devices such as washing machines and dishwashers while they are operating.

### References

- [1] T.C. Aile, Calisma ve Sosyal Hizmetler Bakanligi İş Sagligi ve Guvenligi Genel Mudurlugu (ISGGM), “Elektromanyetik alanlara iliskin genel bilgiler,” [Online], Jun. 10 2024. Available: [https://www.csgeb.gov.tr/media/61322/elektromanyetik-alanlara-iliskin-genel-bilgiler\\_seri-1.pdf](https://www.csgeb.gov.tr/media/61322/elektromanyetik-alanlara-iliskin-genel-bilgiler_seri-1.pdf)

- [2] G. G. Guclu, "50 Hz elektromanyetik alanlar ve biyolojik etkileri," M.S. thesis, Enerji Bilim ve Teknoloji, Istanbul Technical University, Istanbul, 2011.
- [3] O. Bayram, "Elektromanyetik isinim ve insan sagligina etkileri," M.S. thesis, Electrical and Electronics Engineering, Balikesir University, Balikesir, 2017.
- [4] O. Cerezci, Z. Kartal, K. Pala, and A. Turkkan, *Elektromanyetik Alan ve Sağlık Etkileri*, 1st ed. Bursa: F. Ozsan Matbaacilik, 2012.
- [5] M. Cansiz, A. R. Celik, and M. B. Kurt, "Measurements of electric and magnetic field intensities at 50 Hz mains frequency and comparison of measurement results to ICNIRP's reference levels for general public exposure," *Pamukkale University Journal of Engineering Sciences*, vol. 20, no. 8, pp. 294–299, Aug. 2014.
- [6] TMMOB EMO, "Elektromanyetik alanlarin etkileri," [Online], Jun. 11 2024. Available: [https://www.emo.org.tr/ekler/99bb08f940d7461\\_ek.pdf](https://www.emo.org.tr/ekler/99bb08f940d7461_ek.pdf)
- [7] D. Daymaz and M. Parlak, "Elektromanyetik alan ve etkileri," [Online], Jun. 10 2024. Available: <https://halksagligi.hacettepe.edu.tr/diger/toplumayonelik/emaveetkileri.pdf>
- [8] Stop OC Smart Meters. (2024, Jun. 11). *What is electromagnetic radiation (EMR)?* [Online]. Available: <https://stopocsmartmeters.com/what-is-electromagnetic-radiation-emr.html>
- [9] Z. D. Yakinci, "Elektromanyetik alanin insan sagligi uzerindeki etkileri," *Inonu Universitesi Saglik Hizmetleri Meslek Yuksek Okulu Dergisi*, vol. 4, no. 2, pp. 44–54, Dec. 2016.
- [10] R. Chang, *Physical Chemistry for the Biosciences*, USA: University Science Books, 2005.
- [11] L. Sevgi, "Cevremizdeki elektrik ve manyetik alanlar," *Endustriyel Otomasyon Dergisi*, 2005.
- [12] D. McQuarrie and J. Simon, *Physical Chemistry: A Molecular Approach*, Sausalito CA: University Science Books, 1997.
- [13] A. Canseven and N. Atalay Seyhan, "Elektromanyetik kirlenme ve biyolojik boyutlari" *EMO Dergisi*, vol. 39, pp. 87–91, 1995.
- [14] H. M. Ozaktas. "Gunluk hayatta karsilasilan elektromagnetik alanlar ve insan sagligi," in *Bilisim Toplumuna Giderken Elektromagnetik Kirlilik Etkileri Sempozyumu*, Ankara, 1999, pp. 7–12.
- [15] S. Seker and O. Cerezci, *Cevremizdeki Radyasyon ve Korunma Yontemleri*, Istanbul: Bogazici Universitesi Yayinlari, 1997.
- [16] N. Wertheimer and E. Leeper, "Electrical wiring configurations and childhood cancer" *Am. J. Epidemiol.*, vol. 109, no. 3, pp. 273–284, Mar. 1979.
- [17] S. Seker and O. Cerezci. "Elektromanyetik enerjinin kullaniminda risk analizi," in *Elektrik Mühendisligi 5. Ulusal Kongresi*, Trabzon, 1993, pp. 386–391.
- [18] C. Y. Li, G. Thériault, and R. S. Lin, "Residential exposure to 60-Hertz magnetic fields and adult cancers in Taiwan," *Epidemiology*, vol. 8, no. 1, pp. 25–30, Jan. 1997.
- [19] UK Childhood Cancer Study Investigators, "Childhood cancer and residential proximity to power lines," *Br. J. Cancer*, vol. 83, no. 11, pp. 1573–1580, Nov. 2000.
- [20] G. M. Lee, R. R. Neutra, L. Hristova, M. Yost, and R. A. Hiatt, "A nested case-control study of residential and personal magnetic field measures and miscarriages," *Epidemiology*, vol. 13, no. 1, pp. 21–31, Jan. 2002.
- [21] G. Draper, T. Vincent, M. E. Kroll, and J. Swanson, "Childhood cancer in relation to distance from high voltage power lines in England and Wales: a case-control study," *Br. Med. J.*, vol. 330, no. 7503, pp. 1290–1292A, Jun. 2005.
- [22] H. Harmanci, M. Emre, H. Gurvit, B. Bilgic, H. Hanagasi, E. Gurol, H. Sahin, and S. Tinaz, "Risk factors for alzheimer disease: A population-based case-control study in Istanbul, Turkey," *Alzheimer Dis. Assoc. Disord.*, vol. 17, no. 3, pp. 139–145, Jul.-Sep. 2003.
- [23] C. X. Qiu, L. Fratiglioni, A. Karp, B. Winblad, and T. Bellander, "Occupational exposure to electromagnetic fields and risk of alzheimer's disease," *Epidemiology*, vol. 15, no. 6, pp. 687–694, Nov. 2004.
- [24] O. Coskun, S. Comlekci, M. Naziroglu, and S. Ozkorucuklu, "Augmentation of bone repair by inductively coupled electromagnetic fields," *Suleyman Demirel Universitesi Fen Bilimleri Enstitusu Dergisi*, vol. 13, no. 2, pp. 186–192, Feb. 2014.
- [25] C. A. Bassett, R. J. Pawluk, and A. A. Pilla, "Effect of magnetic fields on nerve conduction parameters in rats," *Science*, vol. 184, no. 4136, pp. 575–577, May. 1974.
- [26] K. Paksoy, "Elektromanyetik kirlilik, etkileri, korunma ve yararlanma yontemleri," M.S. thesis, Physics, Erciyes University, Kayseri, 2001.
- [27] A. Keysan, "Balikesir ili sehir merkezi ve Balikesir Universitesi Cagis Yerleskesi'nin elektromanyetik alan haritasi," M.S. thesis, Electrical and Electronics Engineering, Balikesir University, Balikesir, 2015.
- [28] A. Aslan, "The effects of low and high frequency electromagnetic fields on fracture healing," *Kafkas J. Med. Sci.*, vol. 2, no. 1, pp. 34–42, 2012.
- [29] TED Ankara Koleji. (2024, Jun. 11). *Elektromanyetik radyasyonlar ve insan sagligina olumsuz etkileri?* [Online]. Available: <https://www.tedankara.k12.tr/index.php/elektromanyetik-radyasyonlar-ve-insan-sagligina-olumsuz-etkileri>



---

## Anticancer Activity of Acetaminophen-Platinum(II) Complex Against ER-positive Breast Cancer

Mustafa Tugfan Bilkan<sup>\*1</sup>, Meric Arda Esmekaya<sup>2</sup>, Nurhan Ozdemir<sup>3</sup>

<sup>1</sup>Department of Biophysics, Faculty of Medicine, Tokat Gaziosmanpasa University, Tokat, Türkiye

<sup>2</sup>Department of Biophysics, Faculty of Medicine, Gazi University, Ankara, Türkiye

<sup>3</sup>Department of Medical Services and Techniques, Vocational School of Health Services, Ankara Medipol University, Ankara, Türkiye

---

### Abstract

Estrogen receptor-positive (ER+) breast cancer is the most common breast cancer subtype. The present study examined the possible anti-cancer activity of a new platinum complex of acetaminophen ( $[\text{C}_8\text{H}_9\text{NO}_2]_2\text{PtCl}_2$ , APAP-Pt) on ER+ breast cancer cells (MCF-7). The platinum-based complex has been synthesized and characterized using experimental and theoretical spectroscopic methods. MCF-7 cells were treated with APAP-Pt compound at 5, 25, 50, and 75  $\mu\text{g}/\text{ml}$  concentrations. The cytotoxic effects of the complex were investigated on MCF-7 cells. The spectroscopic findings and elemental analyses indicated that two acetaminophen molecules were covalently bonded with platinum (II) chloride. The viability of APAP-Pt treated cells was reduced compared to untreated control cells. APAP-Pt treatment induced apoptotic cell death via the mitochondrial way in a dose-dependent manner. These results revealed that APAP-Pt has an important anti-cancer activity against ER+ breast cancer cells.

**Keywords:** Acetaminophen, Platinum complexes, ER-positive breast cancer, Cancer treatment, Spectrophotometry

---



## Impregnation of Wood Material with Magnesium Chloride ( $MgCl_2$ ) and Determination of Leaching Properties

Melek Yılmaz Yasbek<sup>\*1</sup>, Mehmet Yeniocak<sup>1</sup>

<sup>1</sup> Woodworking Industrial Engineering, Faculty of Technology, Mugla Sıtkı Kocman University, Mugla, Türkiye

### Abstract

The purpose of this study; it is the determination of the leaching properties of wood material by impregnating with magnesium chloride ( $MgCl_2$ ). In this context; magnesium chloride dissolved in water at the rates of 5%, 10% and 15% was applied to Scots pine (*Pinus sylvestris* L.) and oriental beech (*Fagus orientalis* L.) wood material samples measuring 19x19x19 mm by spraying and dipping methods. Samples applied with magnesium chloride were subjected to leaching tests at pH (3, 7 and 11), temperature (10, 22 and 40 °C) parameters to determine the permanence of the impregnation material. As a result of the tests, it was observed that the dipping method generally provided better adhesion in wood samples with a pH of 11. It has been observed that it provides better adhesion to wood samples. According to the results obtained, it is thought that magnesium chloride, which is harmless to human health, can be an environmentally friendly and alternative material for the protection of wood materials.

**Keywords:** Magnesium chloride ( $MgCl_2$ ), Impregnation, Leaching

## 1 INTRODUCTION

Considering all the advantages of wood material, it is aimed to eliminate its disadvantages or minimize its negative aspects. Wood material is degraded by biological organisms and environmental factors according to environmental conditions. Wood coatings, varnish and impregnating chemicals are used to avoid this negative effect. However these chemicals respect to environmental health is reported in recent years [1]. Therefore, this subject; society, especially in this product customers, the administrative unit, has become a topic of industry professionals and researchers carefully followed [2]. Drying, impregnation and surface treatments are applied to protect the wood material against these negative effects [3]. However, this method has not always been healthy and preferable. Research and the development of technology support new methods that prioritize human health. This issue has become a matter of great interest to the public, especially the government, industry professionals and researchers who are the customers of this product. Inorganic minerals/compounds play an important role in flame retardancy and smoke suppression [4]. Harmful substances contained in preservatives used in wood materials compounds have carcinogenic and cytotoxic effects on the environment and human health as a result, it causes damage to the respiratory tract and the formation of tumors in the liver known [5]. Among these substances; magnesium chloride ( $MgCl_2$ ) can be obtained from salt water or sea water. It's most important feature is that it is preferred in the production of fire extinguishing chemicals and fireproof materials. The fact that it is preferred in the production of skin care materials, pharmaceuticals and cosmetics sector proves that it is harmless to human health.

If this substance is applied to the wood material at the right rate and with the right method, the negative properties observed in the wood material will be minimized. In this study; magnesium chloride applied to wood samples reduced the disadvantages of wood material and the application did not harm the health of living organisms.

## 2 MATERIAL AND METHOD

### 2.1 Material

Scots pine (*Pinus sylvestris* L.) and oriental beech (*Fagus orientalis* L.) wood materials, which are widely preferred in the wood sector, were used in the study. *Pinus sylvestris* L., a species of the genus *Pinus sylvestris* reaches 20-40 m. up to 0.6-1.0 m in height and more than 0.6-1.0 m in diameter, with cylindrical stems, pointed tops and slender It is a branched, thickly branched evergreen tree [6].



In the heartwood there may be trachs filled with impurities and there may also be veils. Trachs inter passages are horizontal rows or sometimes stair-like. Longitudinal parenchyma very are numerous. There is a scattered trachy structure. It is easy to impregnate with this feature [7]. Magnesium chloride (MgCl<sub>2</sub>) was preferred as impregnation agent. Scot pine is a wood species with many health, economic and ecological benefits. Besides being an important resource for the wood industry, the trunk of the tree is smooth and cylindrical, usually brown-gray in color. It also stabilizes the soil, prevents erosion and helps absorb carbon dioxide from the atmosphere.

Oriental beech is a tree that sheds its leaves in winter. It is easy to care for and can grow in many areas in the north where woodlands dominate. One of their most distinctive features is their light gray color and their uniform trunk structure throughout their life. They prefer cool, calcareous and deep soils. Their wood is hard and heavy but easy to process. Their areas of use are quite wide.

Magnesium chloride (MgCl<sub>2</sub>) is an inorganic and irregular compound soluble in water. Magnesium chloride was first used as an antiseptic in the health field during World War I by a French surgeon named Pierre Delbet. The fact that it is still used in the field of health today has proved to us that it is a harmless substance in terms of health. Magnesium chloride is preferred as a coating in fire extinguisher formulas and in fireproofing agents.

## 2.2 Method

### 2.2.1 Preparation of Wood Material

The wood test specimens to be used in the washing tests were prepared from the wood pieces of scots pine (*Pinus sylvestris* L.) and oriental beech (*Fagus orientalis* L.) according to TS 2470, with smooth fibers, without arcs, knots, cracks, color and density differences, with annual rings perpendicular to the surfaces and from the sapwood parts. The timbers supplied were brought to their net dimensions after measured cutting, and were made ready for use after scraping and sanding. Test specimens with dimensions of 19x19x19 mm and water repellency tests were prepared. These test specimens were kept at a temperature of 20±2 °C and a relative humidity of 65 ± 5% until they reached a moisture content of approximately 12%. The wood materials in the test samples were grouped and coded systematically.

### 2.2.2 Preparation of Impregnating Agent Magnesium Chloride (MgCl<sub>2</sub>)

The magnesium chloride was purchased from the market. Magnesium chloride (MgCl<sub>2</sub>) substance to be used in the experiments to be carried out was dissolved with water at the rates of 5%, 10%, 15%. The magnesium chloride substance to be applied to the wood materials to be impregnated by dipping and spraying method is completely dissolved with water. Magnesium chloride was purchased from a chemical company trading in this business.

### 2.2.3 Application of Magnesium Chloride Solution to Wood Samples

Two different methods, dipping and spraying, were used to apply water-solubilized magnesium chloride to the experimental samples. Application parameters are given in Table 1.

**Table 1.** Application conditions of Magnesium Chloride to wood test samples

Impregnation Material	Application Method	Temperature (°C)	Period (min.)
Magnesium Chloride (MgCl <sub>2</sub> )	Dipping	20–22	60
	Spraying	20–22	60

The solutions obtained after the preparation of the magnesium chloride solution were applied to the wood samples for 60 minutes at a temperature of 20-22 °C in the ultrasonic bath device in the immersion method with the classical (immersion) method. The magnesium chloride solution to be applied to the wood material samples by spraying method was applied to the wood samples for 60 minutes at a temperature of 20-22 °C. The test pieces were dried in an oven to constant weight before and after dipping and spraying.

### 2.2.4 Leaching Test

A UV spectrophotometer (Libra/Biochrom brand) was used to measure the maximum wave length of magnesium chloride solutions, which was used as the absorbance reference point. Two wood samples from each group were placed in an Erlenmeyer flask along with 250 milliliters of distilled water. For 120 minutes, Erlenmeyer flasks (JSR/JSSP-30 T brand) were submerged in a shaking water bath. In order to obtain the required amount of solution,

Erlenmeyer’s water was pulled out every 5, 15, 30, 45, 60, 75, 90, and 120 minutes. The solution was then absorbed into the water and measured using a reference UV spectrophotometer. Leach water was maintained at various pH levels (3, 7, 11), temperatures (10, 22, and 40 °C), and leaching rates were compared.

### 3 RESULTS

The maximum wavelength of the magnesium chloride solution was found using a UV spectrophotometer (Table 2). The adsorption of each solution was determined using these parameters as a point of reference.

**Table 2.** Maximum wavelength of MgCl<sub>2</sub>

Magnesium chloride (MgCl <sub>2</sub> ) substance (%)	Max. wavelength (nm)
5	210
10	231
15	300

#### 3.1.1 Leaching Data at pH: 3

When we look at the values given in Table 3, we can see that the maximum leaching value is 0.363 abs for the experimental samples with a temperature of 10 °C and a pH value of 3 in scots pine wood at a rate of 5%. The leaching is seen in beech wood impregnated by spraying method at 15%. This value is 0,006 abs.

In Table 4, according to the leaching data with 3 pH at 22 °C temperature, the leaching value of the scots pine wood sprayed is 0.175 abs. We see the least leaching in beech wood impregnated by spraying method with a value of 15%.

When the values in Table 5 are examined, the tree with the highest washing at 40 °C temperature and 3 pH scots beech wood with 5% impregnation applied by spraying method. This value is 0,852 abs. In oriental beech wood impregnated with dipping method at 15%, the least leaching is 0,022 abs. By looking at the value, we can say that the least leaching is in this group.

As a result, leaching rates increase as the temperature increases. However, the increase in impregnation rates is directly proportional to the fact that it provides more protection than the leaching data.

**Table 3.** Leaching data temperature and a pH: 3 (abs)

Wood Type	Rating	Method	5	15	30	60	75	90	120
			min.	min.	min.	min.	min.	min.	min.
Scot Pine ( <i>Pinus Sylvestris</i> L.)	% 5	Spraying	0.120	0.170	0.174	0.231	0.277	0.296	0.363
		Dipping	0.098	0.096	0.128	0.170	0.204	0.222	0.256
	% 10	Spraying	0.000	0.005	0.013	0.037	0.045	0.071	0.103
		Dipping	0.010	0.007	0.015	0.042	0.044	0.058	0.079
	% 15	Spraying	0.061	0.038	0.046	0.032	0.034	0.030	0.016
		Dipping	0.078	0.077	0.077	0.069	0.072	0.070	0.062
Oriental Beech ( <i>Fagus Orientalis</i> L.)	% 5	Spraying	0.20	0.312	0.367	0.460	0.527	0.573	0.660
		Dipping	0.035	0.034	0.062	0.091	0.127	0.129	0.155
	% 10	Spraying	0.011	0.009	0.025	0.045	0.065	0.068	0.079
		Dipping	0.003	0.008	0.020	0.043	0.053	0.065	0.089
	% 15	Spraying	0.042	0.047	0.049	0.027	0.024	0.021	0.006
		Dipping	0.069	0.064	0.064	0.053	0.052	0.048	0.034

**Table 4.** Leaching data temperature of 22 °C and a pH: 3 (abs)

Wood Type	Rating	Method	5 min.	15 min.	30 min.	60 min.	75 min.	90 min.	120 min.
Scot Pine ( <i>Pinus Sylvestris</i> L.)	% 5	Spraying	0.055	0.065	0.071	0.092	0.121	0.150	0.175
		Dipping	0.028	0.034	0.047	0.073	0.091	0.120	0.147
	% 10	Spraying	0.008	0.012	0.020	0.034	0.059	0.075	0.095
		Dipping	0.017	0.020	0.027	0.038	0.045	0.065	0.085
	% 15	Spraying	0.052	0.053	0.059	0.064	0.078	0.101	0.111
		Dipping	0.057	0.066	0.072	0.085	0.089	0.111	0.126
Oriental Beech ( <i>Fagus Orientalis</i> L.)	% 5	Spraying	0.064	0.086	0.119	0.168	0.202	0.210	0.207
		Dipping	0.021	0.027	0.038	0.062	0.078	0.101	0.112
	% 10	Spraying	0.013	0.019	0.027	0.040	0.067	0.082	0.101
		Dipping	0.032	0.034	0.047	0.065	0.075	0.105	0.117
	% 15	Spraying	0.035	0.037	0.042	0.043	0.050	0.065	0.074
		Dipping	0.066	0.072	0.076	0.081	0.084	0.097	0.108

**Table 5.** Leaching data temperature of 40 °C and a pH: 3 (abs)

Wood Type	Rating	Method	5 min.	15 min.	30 min.	60 min.	75 min.	90 min.	120 min.
Scot Pine ( <i>Pinus Sylvestris</i> L.)	% 5	Spraying	0.210	0.301	0.422	0.575	0.650	0.761	0.817
		DIPPING	0.133	0.157	0.238	0.340	0.391	0.477	0.510
	% 10	SPRAYING	0.008	0.067	0.126	0.185	0.210	0.254	0.283
		DIPPING	0.041	0.121	0.162	0.248	0.276	0.330	0.351
	% 15	SPRAYING	0.047	0.030	0.032	0.025	0.035	0.057	0.062
		DIPPING	0.001	0.066	0.105	0.162	0.179	0.224	0.230
Oriental Beech ( <i>Fagus Orientalis</i> L.)	% 5	Spraying	0.250	0.353	0.468	0.624	0.688	0.815	0.852
		DIPPING	0.195	0.229	0.327	0.492	0.590	0.640	0.674
	% 10	SPRAYING	0.033	0.086	0.133	0.185	0.221	0.270	0.294
		DIPPING	0.011	0.042	0.091	0.144	0.174	0.216	0.240
	% 15	SPRAYING	0.025	0.003	0.007	0.080	0.077	0.086	0.096
		DIPPING	0.053	0.043	0.025	0.010	0.003	0.014	0.022

### 3.1.2 Leaching Data at pH: 7

When we look at the values given in Table 6, we can see that the maximum leaching value is 0.329 abs for the experimental samples with a temperature of 10 °C and a pH value of 7 in scots pine wood at a rate of 5%. The leaching is seen in beech wood impregnated by spraying method at 15%. This value is 0.030 abs.

In Table 7, according to the leaching data with 7 pH at 22 °C temperature, the leaching value of the scots pine wood sprayed is 0.015 abs. We see the least leaching in beech wood impregnated by spraying method with a value of 15%.

When the values in Table 8 are examined, the tree with the highest washing at 40 °C temperature and 7 pH scots beech wood with 5% impregnation applied by spraying method. This value is 1.279 abs. In oriental beech wood impregnated with dipping method at 15%, the least leaching is 0.046 abs. By looking at the value, we can say that the least leaching is in this group.

As a result, leaching rates increase as the temperature increases. However, the increase in impregnation rates is directly proportional to the fact that it provides more protection than the leaching data.

**Table 6.** Leaching data temperature of 10 °C and a pH: 7 (abs)

Wood Type	Rating	Method	5 min.	15 min.	30 min.	60 min.	75 min.	90 min.	120 min.
Scot Pine ( <i>Pinus Sylvestris</i> L.)	% 5	Spraying	0.050	0.063	0.108	0.181	0.226	0.270	0.329
		Dipping	0.013	0.036	0.061	0.105	0.140	0.164	0.194
	% 10	Spraying	0.016	0.010	0.041	0.065	0.086	0.103	0.135
		Dipping	0.033	0.042	0.048	0.043	0.062	0.080	0.112
	% 15	Spraying	0.075	0.080	0.065	0.062	0.059	0.050	0.041
		Dipping	0.071	0.075	0.064	0.054	0.047	0.050	0.032
Oriental Beech ( <i>Fagus Orientalis</i> L.)	% 5	Spraying	0.085	0.111	0.150	0.230	0.275	0.325	0.370
		Dipping	0.001	0.025	0.067	0.088	0.112	0.136	0.169
	% 10	Spraying	0.004	0.009	0.028	0.061	0.077	0.093	0.117
		Dipping	0.015	0.013	0.022	0.032	0.046	0.059	0.081
	% 15	Spraying	0.058	0.055	0.037	0.024	0.020	0.025	0.030
		Dipping	0.074	0.073	0.050	0.054	0.045	0.043	0.032

**Table 7.** Leaching data temperature of 22 °C and a pH: 7 (abs)

Wood Type	Rating	Method	5 min.	15 min.	30 min.	60 min.	75 min.	90 min.	120 min.
Scot Pine ( <i>Pinus Sylvestris</i> L.)	% 5	Spraying	0.070	0.085	0.110	0.230	0.255	0.302	0.343
		Dipping	0.068	0.090	0.130	0.248	0.279	0.335	0.374
	% 10	Spraying	0.007	0.015	0.030	0.041	0.067	0.104	0.105
		Dipping	0.004	0.013	0.032	0.057	0.081	0.101	0.119
	% 15	Spraying	0.008	0.009	0.020	0.018	0.007	0.003	0.015
		Dipping	0.010	0.030	0.036	0.071	0.087	0.112	0.124
Oriental Beech ( <i>Fagus Orientalis</i> L.)	% 5	Spraying	0.098	0.110	0.130	0.223	0.251	0.297	0.330
		Dipping	0.065	0.076	0.095	0.162	0.202	0.219	0.249
	% 10	Spraying	0.002	0.013	0.035	0.041	0.063	0.075	0.089
		Dipping	0.017	0.041	0.076	0.100	0.126	0.154	0.172
	% 15	Spraying	0.002	0.019	0.031	0.043	0.024	0.030	0.045
		Dipping	0.009	0.018	0.036	0.045	0.031	0.040	0.048

**Table 8.** Leaching data temperature of 40 °C and a pH: 7 (abs)

Wood Type	Rating	Method	5 min.	15 min.	30 min.	60 min.	75 min.	90 min.	120 min.
Scot Pine ( <i>Pinus Sylvestris</i> L.)	% 5	Spraying	0.343	0.462	0.871	1.005	1.061	1.218	1.279
		Dipping	0.193	0.304	0.609	0.717	0.727	0.879	0.941
	% 10	Spraying	0.110	0.205	0.300	0.356	0.378	0.447	0.479
		Dipping	0.095	0.210	0.314	0.394	0.412	0.483	0.509
	% 15	Spraying	0.010	0.015	0.049	0.072	0.085	0.109	0.123
		Dipping	0.029	0.059	0.079	0.099	0.114	0.158	0.160
Oriental Beech ( <i>Fagus Orientalis</i> L.)	% 5	Spraying	0.472	0.604	1.015	1.098	1.115	1.270	1.340
		Dipping	0.216	0.296	0.599	0.726	0.750	0.857	0.912
	% 10	Spraying	0.150	0.198	0.259	0.305	0.349	0.378	0.405
		Dipping	0.033	0.153	0.221	0.260	0.273	0.311	0.333
	% 15	Spraying	0.050	0.090	0.108	0.098	0.105	0.127	0.138
		DIPPING	0.018	0.020	0.025	0.027	0.028	0.037	0.046

### 3.1.3 Leaching Data at pH: 11

When we look at the values given in Table 9, we can see that the maximum leaching value is 0.685 abs for the experimental samples with a temperature of 10 °C and a pH value of 11 in scots pine wood at a rate of 5%. The leaching is seen oriental beech wood impregnated by spraying method at 15%. This value is 0.004 abs.

In Table 10, according to the leaching data with 11 pH at 22 °C temperature, the leaching value of the scots pine wood sprayed is 0.104 abs. We see the least leaching in oriental beech wood impregnated by dipping method with a value of 15%.

When the values in Table 11 are examined, the tree with the highest washing at 40 °C temperature and 11 pH scots beech wood with 5% impregnation applied by dipping method. This value is 2.800 abs. In oriental beech wood impregnated with dipping method at 15%, the least leaching is 0.295 abs. By looking at the value, we can say that the least leaching is in this group.

As a result, leaching rates increase as the temperature increases. However, the increase in impregnation rates is directly proportional to the fact that it provides more protection than the leaching data.

**Table 9.** Leaching data temperature of 10 °C and a pH: 11 (abs)

Wood Type	Rating	Method	5 min.	15 min.	30 min.	60 min.	75 min.	90 min.	120 min.
Scot Pine ( <i>Pinus Sylvestris</i> L.)	% 5	Spraying	0.443	0.504	0.579	0.619	0.656	0.666	0.685
		Dipping	0.185	0.215	0.270	0.315	0.316	0.313	0.328
	% 10	Spraying	0.048	0.068	0.087	0.108	0.129	0.141	0.145
		Dipping	0.086	0.132	0.160	0.200	0.232	0.246	0.262
	% 15	Spraying	0.050	0.038	0.035	0.023	0.016	0.020	0.023
		Dipping	0.010	0.048	0.071	0.100	0.106	0.110	0.106
Oriental Beech ( <i>Fagus Orientalis</i> L.)	% 5	Spraying	0.306	0.316	0.337	0.358	0.395	0.433	0.447
		Dipping	0.140	0.173	0.188	0.222	0.245	0.253	0.278
	% 10	Spraying	0.003	0.026	0.034	0.058	0.067	0.082	0.091
		Dipping	0.026	0.051	0.058	0.100	0.103	0.110	0.119
	% 15	Spraying	0.042	0.032	0.028	0.009	0.011	0.004	0.004
		Dipping	0.048	0.042	0.038	0.025	0.023	0.021	0.025

**Table 10.** Leaching data temperature of 22 °C and a pH: 11 (abs)

Wood Type	Rating	Method	5 min.	15 min.	30 min.	60 min.	75 min.	90 min.	120 min.
Scot Pine ( <i>Pinus Sylvestris</i> L.)	% 5	Spraying	0.205	0.208	0.210	0.215	0.216	0.217	0.219
		Dipping	0.206	0.217	0.209	0.213	0.214	0.214	0.217
	% 10	Spraying	0.140	0.144	0.155	0.165	0.170	0.176	0.190
		Dipping	0.173	0.182	0.196	0.208	0.219	0.220	0.229
	% 15	Spraying	0.112	0.105	0.107	0.112	0.115	0.117	0.123
		Dipping	0.119	0.125	0.130	0.141	0.144	0.147	0.152
Oriental Beech ( <i>Fagus Orientalis</i> L.)	% 5	Spraying	0.206	0.209	0.210	0.216	0.216	0.217	0.219
		Dipping	0.201	0.202	0.205	0.211	0.207	0.210	0.209
	% 10	Spraying	0.126	0.124	0.132	0.138	0.139	0.141	0.150
		Dipping	0.143	0.131	0.141	0.141	0.152	0.154	0.160
	% 15	Spraying	0.107	0.108	0.107	0.113	0.112	0.113	0.116
		Dipping	0.093	0.096	0.096	0.101	0.104	0.103	0.104

**Table 11.** Leaching data temperature of 40 °C and a pH: 11 (abs)

Wood Type	Rating	Method	5 min.	15 min.	30 min.	60 min.	75 min.	90 min.	120 min.
Scot Pine ( <i>Pinus Sylvestris</i> L.)	% 5	Spraying	2.225	2.301	2.345	2.417	2.519	2.522	2.573
		Dipping	2.450	2.618	2.625	2.610	2.722	2.896	2.800
	% 10	Spraying	0.321	0.359	0.381	0.418	0.499	0.496	0.547
		Dipping	0.829	0.999	1.165	1.356	1.589	1.670	1.868
	% 15	Spraying	0.096	0.134	0.176	0.252	0.273	0.287	0.338
		Dipping	0.744	0.898	1.072	1.138	1.369	1.440	1.622
Oriental Beech ( <i>Fagus Orientalis</i> L.)	% 5	Spraying	2.269	2.296	2.303	2.356	2.478	2.535	2.545
		Dipping	2.144	2.121	2.190	2.250	2.331	2.411	2.455
	% 10	Spraying	0.403	0.440	0.503	0.579	0.675	0.716	0.822
		Dipping	0.265	0.259	0.339	0.398	0.472	0.505	0.586
	% 15	Spraying	0.120	0.134	0.145	0.203	0.289	0.344	0.394
		Dipping	0.097	0.136	0.145	0.194	0.220	0.241	0.295

## 4 CONCLUSION

Depending on the amount of leaching and time, it was observed that the eastern beech wood impregnated with 15% spraying method showed less change in the leaching test in the table at 10 °C temperature and 3 pH value.

It was determined that the most leakage was observed in eastern beech wood impregnated with 5% spraying method. In the table at 10 °C temperature and 7 pH value, it was observed that the eastern beech wood impregnated with 15% spray method showed less change in the leaching test. It was determined that the highest leaching was observed in eastern beech wood impregnated with 5% spray method. In the table at 10 °C temperature and 11 pH value, it was observed that the eastern beech wood impregnated with 15% spray method showed less change in the leaching test. The highest leakage was observed in yellow pine wood treated with 5% spray method.

In the table at 22 °C temperature and 3 pH value, it was observed that the eastern beech wood impregnated with 15% spray method showed less change in the leaching test. It was determined that the most leakage was observed in the eastern beech wood impregnated with 5% spray method. Depending on the amount of leaching and time, it was observed that yellow pine wood impregnated with 15% spray method showed less change in the table at 22 °C temperature and 7 pH value.

As a result, it was observed that oriental beech wood impregnated with 15% immersion method at 22 °C temperature and 7 pH value showed less change in leaching tests depending on the amount and duration of leaching. In all experimental samples, wood materials impregnated with 5% spraying method were the least protected.

According to the results obtained from the study, wood materials impregnated with 15% dipping method provide the most protection.

## References

- [1] A. Kurtoglu, *Protection of Wood Materials and Environmental Health Effects of chemical wood preservatives*, 1rd ed., National Productivity Center Publications, 1988.
- [2] T. Salthammer, M. Bednarek, F. Fuhrmann, R. Funaki and S. I. Tanabe, "Formation of organic indoor air pollutants by UV-curing chemistry," *Journal of Photochemistry and Photobiology A*, vol. 152, no.5, pp. 1–9, 2002.
- [3] T. L. Higley and King, *Biological Degradation of Wood*, 3rd ed., American Chemical Society, January 1990.
- [4] S. Aslan, *Wood Pest Protection and Impregnation Techniques*, 1rd ed., Ankara, KOSGEB Publications, 1998.
- [5] K. Sinha, P.D. Saha, and S. Datta, "Extraction of natural dye from petals of forest flame (butea monosperma) flower: Process optimization using response surface methodology (RSM)," *Dyes and*

- Pigments*, vol. 94, pp. 212–216, 2012.
- [6] A.Y. Bozkurt ve Y. Goker, *Physical and Mechanical Wood Technology*, 2rd ed., Istanbul, Istanbul University Faculty of Forestry Publications, 1996.
- [7] Y. Bozkurt, Y. Goker, and N. Erdin, “Impregnation technique,” *Forest Faculty Journal*, vol. 54, no. 2, pp. 98–100, 2004.



## Determination of Reservoir Water Level by Classical and Artificial Intelligence Methods

Sema Karahan<sup>\*1</sup>, Zeyneb Kilic<sup>2</sup>

<sup>1</sup>Civil Engineering Department, Institute of Science and Technology, Adiyaman University, Adiyaman, Türkiye

<sup>2</sup>Civil Engineering Department, Engineering Faculty, Adiyaman University, Adiyaman, Türkiye

---

### Abstract

In water structures such as dams, accurate estimation of the water level and water volume in the dam reservoir is very important in terms of the use of water resources, the safety of the dam, planning of dam-related works and operation of the dam. The importance of water level in dams is increasing day by day due to reasons such as increasing climate changes due to global warming, environmental pollution, globalization, industrialization, unconscious use of water, population growth and urbanization.

This review aims to indicate the advantages of revealing the reservoir volume and water level with classical regression and artificial intelligence methods and to emphasize the importance of the subject. Such research, which is important for regions such as Adiyaman where climate conditions are hot, evaporation is high, agricultural irrigation is intensive and dams are numerous, aim to provide special information for water management practices and sustainable use of water. Reservoir level estimates are very informative in determining periodic water supply strategies, hydroelectric energy calculations and flood management studies. Therefore, determining the dam reservoir water level with classical and artificial intelligence methods enables obtaining very useful information in water resources management studies such as the use, conservation, water quality modelling, management and studies of water in dam reservoirs.

Our work aims to promote sustainability and issue awareness of industrial, agricultural and municipal water systems. It is important to investigate strategies to protect water resources, which is a source of concern in many regions such as Adiyaman, in order to address the critical problem of water scarcity. The data obtained as a result of the study will support similar studies and raise awareness for studies on the subject.

**Keywords:** Adiyaman, Dam, Climate, Water, Artificial intelligence methods

---





## Historical Environments Affected by the Earthquake in Kahramanmaras City Center and Restoration Suggestions

Hatice Dokme<sup>1</sup>, Sinan Kordon<sup>\*1</sup>

<sup>1</sup>Department of Landscape Architecture, Kahramanmaras Sutcu Imam University, Kahramanmaras, Türkiye

---

### Abstract

Historical environments consist of building types that carry traces of the past from the day they were created until today. These structures are important in terms of preserving them as heritage and leaving them as inheritance for the future. Today, the protected historical areas have sometimes been deformed due to human influence and sometimes due to physical deterioration. In Turkey, although there are numerous historical buildings, many of them have turned into ruins due to the lack of conservation awareness. The biggest cause of deterioration in historical buildings is natural disaster. The most destructive and damaging of these natural disasters is the earthquake. One of these devastating earthquakes occurred in Kahramanmaras City on February 6, 2023. In the Kahramanmaras earthquake, which is called the "disaster of the century", most part of the city was affected, thousands of buildings were damaged or even destroyed. The impact of the earthquake also caused serious damage to historical environments and cultural heritage areas. This study investigates the effects of Kahramanmaras-centered earthquakes on the historical and cultural heritage structures in Kahramanmaras city center and the status of these historical structures after the earthquake. During the research, the damage of the historical buildings in the city center was determined, and the deteriorations on the buildings were added to the study through photographs. Finally, suggestions were made for the restoration process and for possible future damages.

**Keywords:** *Historical environment, Cultural landscape, Historical building, Earthquake, Cultural heritage*

---



---

## The Sociological Benefits of Green Infrastructure Systems: Inclusive and Healthy Cities for Communities

Esra Tan<sup>1</sup>, Sinan Kordon<sup>\*1</sup>

<sup>1</sup>Department of Landscape Architecture, Kahramanmaraş Sutcu Imam University, Kahramanmaraş, Türkiye

---

### Abstract

Rapid and intensive urbanization has led to environmental pollution, traffic congestion, and the reduction of green spaces in cities. These challenges trigger various economic, ecological, and sociological problems, causing cities to lose their sustainability. To mitigate these negative impacts, the implementation of green infrastructure systems, such as green roofs, green walls, rain gardens, and urban forests, is gaining importance in urban areas. Recent studies from various disciplines have highlighted the benefits of green infrastructure systems. However, comprehensive research on their sociological benefits remains limited. This study aims to thoroughly examine the sociological benefits of green infrastructure systems and their positive impacts on urban communities. Using a systematic literature review method, this study analyzed 5 theses, 10 review articles, and 33 research articles. As preliminary data, a classification table of sociological benefits was created, categorizing them under 9 main headings and 35 subcategories. The findings indicate that disciplines such as forest engineering, urban and regional planning, and landscape architecture predominantly examine the benefits related to social bonds, health, and education. Future research directions are discussed, emphasizing the prioritization of specific benefits of green infrastructure systems. This study provides crucial insights into which disciplines focus on the sociological benefits of green infrastructure and suggests topics for future research. This study also makes valuable recommendations for landscape architects, architects, urban planners, and other professionals in developing sustainable cities.

**Keywords:** Sustainable cities, Green infrastructure, Ecosystem services, Disaster resilience infrastructure literature review

---

## 1 INTRODUCTION

Rapid urbanization has led to a surge in industrial facilities, vehicles, and intense human activities, which have significantly worsened environmental pollution. The negative impacts manifest in various forms, such as air, water, and soil pollution, posing serious threats to both human health and natural ecosystems. With the increase in population, traffic and buildings have become a major problem in cities. This problem causes time loss and stress and increases air pollution and other environmental challenges [1].

One of the major environmental challenges is the reduction of green spaces and parks because of the development pressures. The loss of urban green spaces disrupts people's connection with nature, threatens biodiversity, worsens the impacts of climate change, and negatively influences the quality of resident's life [2, 3]. As a result, fast and uncontrolled urbanization created poorly planned, densely constructed, and energy-inefficient buildings, which has increased ecological, economic, and social problems and resulted in unsustainable living conditions [4].

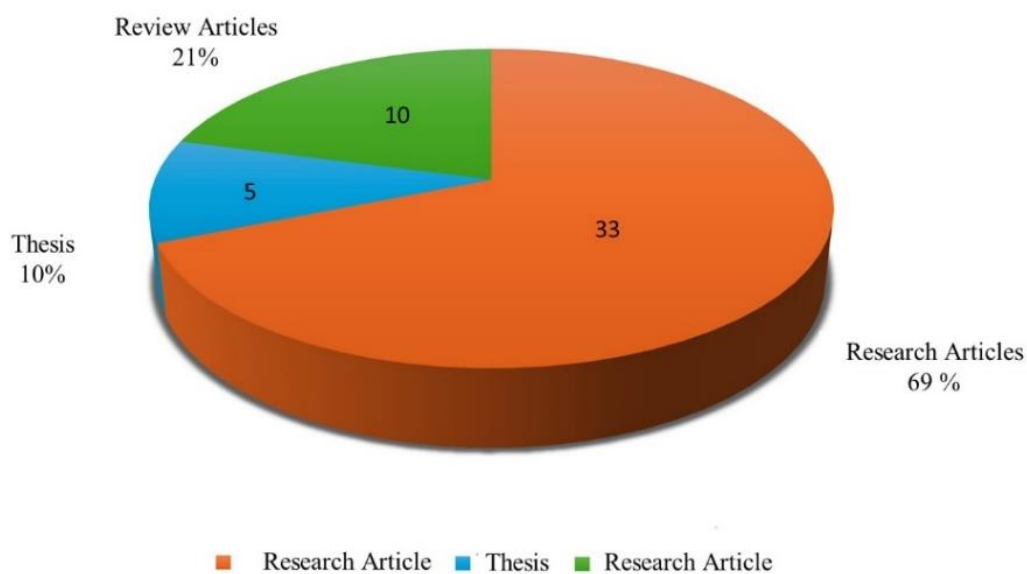
To mitigate the influences of these issues, green infrastructure systems have become popular in cities. These systems offer solutions for the negative consequences of rapid urbanization and provide ecological, economic, and social benefits. Additionally, they combine natural and engineered components to enhance environmental sustainability, improve air and water quality, and provide socio-economic advantages [1, 2]. Examples of green infrastructure include green roofs, green walls, urban forests, permeable pavements, biological water treatment systems, and green corridors [5].

Green infrastructure systems offer numerous economic, ecological, and sociological benefits in urban areas. These systems not only protect the natural environment but also provide various advantages to society. Economically, green infrastructure helps reduce costs by saving energy, increasing property values, and lowering disaster risk [6]. Ecologically, it enhances air quality and supports biodiversity [7]. From a sociological perspective, green spaces strengthen social connections, improve citizens' physical and mental health, and boost the overall quality of urban life [8].

While the literature often emphasizes the ecological and economic benefits of green infrastructure, fewer studies comprehensively examine its sociological advantages. This study aims to address this gap by evaluating the benefits of green infrastructure from a sociological perspective. Additionally, it highlights which benefits are more prominently discussed in the literature, identifies less explored areas, and suggests potential research topics for future studies.

## 2 MATERIAL AND METHOD

In this study, a systematic literature review was conducted from academic databases using numerous keywords related to green infrastructure systems and their benefits. A total of 138 references were reviewed. Abstracts, introductions, and conclusions of these articles were examined, and 90 studies that were not directly related to the topic were excluded from the detailed review. For this study, 48 references were selected. Among the selected 48 studies, 21% were review papers (10), 10% were thesis (5), and 69% were research articles (33). The distribution of the reference type is listed in Figure 1.



**Figure 1.** Distribution of reference type

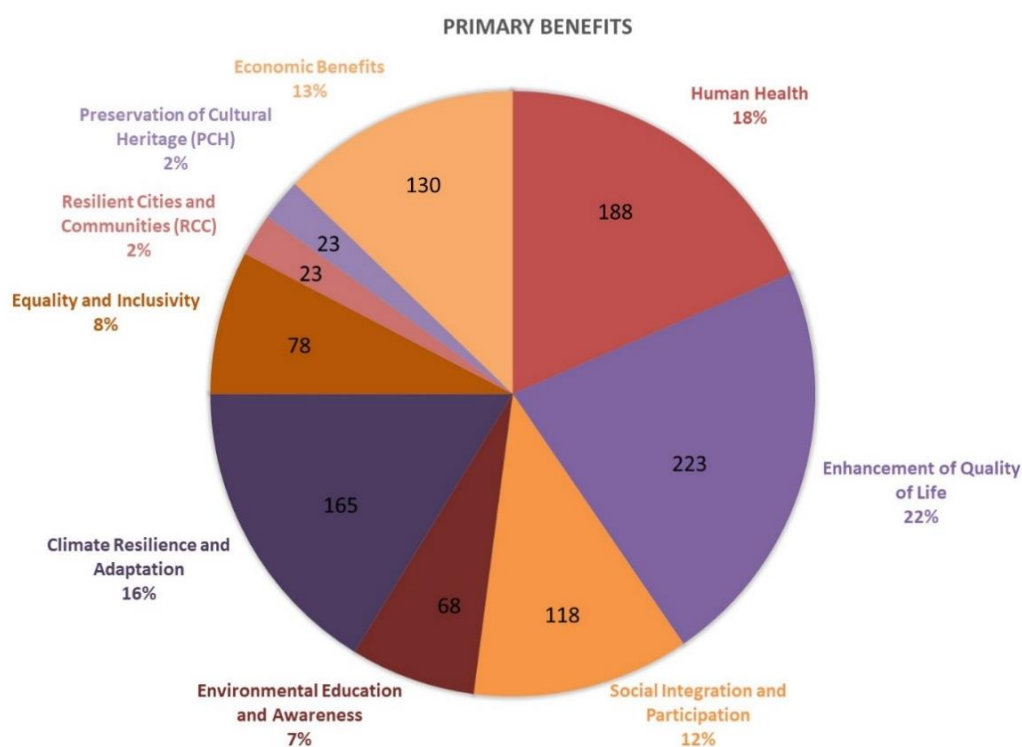
The selected 48 articles were thoroughly analyzed, focusing on the sociological benefits discussed in each. These benefits were then coded into an Excel spreadsheet. This review process allowed for a detailed classification of the sociological benefits of green infrastructure systems and provided insights into which benefits are frequently highlighted in the literature. The Excel spreadsheet was turned into a data analysis table based on the selected references. This table includes the bibliography of each study, the type of study, and the coded sociological benefits mentioned in the references (e.g., PA: Physical Activity, SR: Stress Reduction) (Table 1). Table 1 shows a snapshot from the analysis table. Stars in the table indicate which benefits are discussed in each source. To quantitatively assess the findings, each star was assigned 1 point, and the total points were used to identify the benefits highly mentioned in the literature. Findings were categorized into two main groups, primary benefits and secondary benefits.

**Table 1.** Example of reference analysis table

References	Human Health					Improving Quality of Life					
	PA	SR	SI	IAQ	PS	AV	RLA	TB	SP	SCR	RHN
[1]	*	*	*	*						*	*
[2]	*	*	*	*	*	*	*	*	*	*	*
[3]					*	*	*				
[4]		*	*	*	*	*	*	*			*
[5]	*	*	*	*	*	*	*	*	*	*	*
[6]	*			*		*	*		*	*	
[7]	*	*	*			*	*	*	*	*	
[8]	*	*	*	*		*	*	*	*	*	*
[9]		*	*			*	*	*	*		*
[10]		*	*	*	*	*	*	*			*
[11]		*	*	*	*	*	*	*	*		*
[12]	*	*	*	*	*	*	*	*	*		*
[13]				*			*				*
[14]	*	*	*	*		*	*	*	*		*
[15]	*	*	*	*		*	*	*	*	*	*
[16]	*	*	*	*	*	*	*	*	*	*	*
[17]				*		*					*
[18]	*	*	*	*	*	*	*	*	*	*	*

### 3 RESULTS

Based on the findings nine main categories of primary benefits were identified. These are, Improving Quality of Life, Human Health, Climate Resilience and Adaptation, Economic Benefits, Social Integration and Participation, Equity and Inclusivity, Environmental Education and Awareness, Resilient Cities and Communities, and Preservation of Cultural Heritage (Figure 2).



**Figure 2.** List and scores of primary benefits

Among these benefits, the highest score is attributed to the enhancement of quality of life, with a score of 223. Human health ranks second with 188 points, and climate resilience and adaptation are third with 165 points. The benefits with the lowest scores are the preservation of cultural heritage and resilient cities and communities, both scoring 23 points. Environmental education and awareness rank second lowest with 68 points, while equity and inclusivity are third lowest with 78 points. The nine main categories are subdivided into 33 subcategories. Among these, Recreation and Leisure Activities, Stress Reduction, and Social Interaction received the highest three scores 45, 44, and 43, respectively (Figure 3). In contrast, Commercial Return and Public Awareness received the lowest two scores 12 and 15, respectively. Volunteering opportunities, Intergenerational Interaction and Communication, and Reduction in violence and crime rates received the third lowest scores, 20. This score ranking does not imply that one benefit is more important than another; it merely reflects the frequency with which these topics are discussed in the literature.

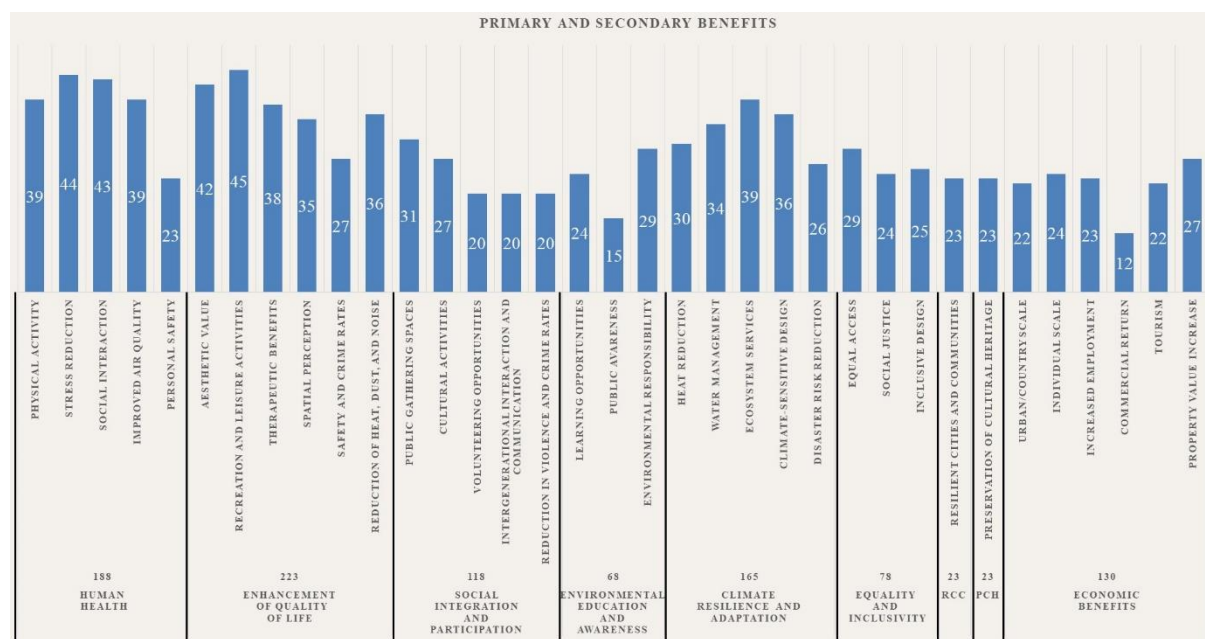


Figure 3. List and scores of primary and secondary benefits

The evaluation of the primary and secondary benefits chart demonstrates that green infrastructure systems offer valuable benefits not only from environmental and economic perspectives but also from sociological viewpoints.

#### 4 CONCLUSION

This study aimed to identify the sociological benefits of green infrastructure systems and explore the frequency with which these topics are discussed in the literature. The results suggest that green infrastructure systems play an important role in enhancing the social well-being of individuals in numerous ways. In addition, the high scores of Recreation and Leisure Activities, Stress Reduction, and Social Interaction show the importance of urban green infrastructure systems for individuals' psychosocial and social needs. On the other hand, the low scores for Commercial Return and Citizen Awareness imply that more research is needed to identify the effects of green infrastructure systems on these benefits. Similarly, the low score of Intergenerational Interaction and Communication highlights the necessity of further research on the interaction between green infrastructure and intergenerational bonds.

In addition, results show that green infrastructure systems play a critical role in developing sustainable environments by enhancing ecosystem services, preserving biodiversity, and mitigating the negative effects of climate change. These systems also support economic sustainability by providing long-term cost savings, energy efficiency, and new job opportunities. From the social aspect, these systems also have great potential for cities. They offer social cohesion and increased participation, enhance the quality of life, and positively influence individuals' physical and mental health.

This comprehensive assessment highlights the multifaceted benefits of green infrastructure systems, serving as a guide for policymakers, urban planners, designers, and community leaders. In light of these findings, it is crucial

to understand the sociological benefits in the formulation of urban policies and development strategies. At the same time, steps should be taken to enhance academic research on all the benefits green infrastructure systems provide. This balanced approach will contribute to creating environmentally, economically, and socially more sustainable and inclusive urban development.

To effectively realize and support the benefits identified in this study, various implementations should be undertaken in our cities. Examples include community gardens, urban parks, green roof systems, green walls, green corridors, and open recreational areas, all of which support green infrastructure in urban settings. Future studies should focus on less-discussed benefits of these systems such as preservation of cultural heritage and resiliency of cities and communities, as found in this study. Given the potential of these implementations in enhancing post-disaster resilience, they should be considered as part of the development of a comprehensive disaster resilience infrastructure system in cities.

In addition, research investigating the perceived benefits and usage of green infrastructure systems by different socio-economic groups is crucial for ensuring equitable access to these benefits. Such research can contribute to more inclusive green infrastructure projects. Also, to raise public awareness, the number of educational programs regarding the benefits of green infrastructure systems should be increased.

Lastly, the collaboration and coordination among various professional groups, including but not limited to landscape architects, architects, urban planners, educators, local authorities, and policymakers should be enhanced to ensure the success, accessibility, and sustainability of green infrastructure projects and supporting policies. The findings and recommendations of this study surely provide valuable academic and practical contributions to the relevant professionals and disciplines.

## Acknowledgments

This study was conducted as a part of Esra Tan's graduate studies under the supervision of Assist. Prof. Dr. Sinan Kordon.

## References

- [1] A. Koc, S. Yılmaz, and E. Mutlu, "Effect of large green areas on air quality in center of Erzurum," *Iğdir University Journal of the Institute of Science and Technology*, vol. 6, no. 4, pp. 109-112, 2016.
- [2] Y. Aksoy and A. Akpınar, "A research about public green area use and green area demand in Istanbul Fatih district," *Istanbul Commerce University Journal of Science*, vol. 10, no. 20, pp. 81-96, 2011.
- [3] U. Ünal and D. E. Akyüz, "Importance of swales in the context of green infrastructure applications and its evaluation by sustainable urban understanding," *İklim Değişikliği ve Çevre*, vol. 3, no. 2, pp. 55-63, 2018.
- [4] O. K. Aksoy and E. S. Arslan, "The role of green infrastructure and ecosystem services reducing potential effects of climate change in cities," *İnsan ve İnsan*, vol. 9, no. 33, pp. 53-62, 2022.
- [5] A. Tuna, "Examination of green infrastructure concept in UK through practice examples," *European Journal of Science and Technology*, no. 21, pp. 416-423, 2021.
- [6] N. Güneroğlu, "The effect of restoration process on riparian landscapes," *Artvin Coruh University Journal of Forestry Faculty*, vol. 18, no. 1, pp. 10-20, 2017.
- [7] C. Bogenc, B. Bekci, and M. Uçok, "Visual quality assessment in socialization spaces in urban parks; Rize coastal park example," in *Proceedings of European Conference on Science, Art & Culture (ECSAC-2018)*, Antalya, 2018, pp. 381-386.
- [8] N. Gürer and A. Uğurlar, "User satisfaction in urban parks: Ankara Kugulu Park case," *Megaron*, vol. 12, no. 3, 2017.
- [9] S. Sahin, R. Taban, G. Ok, and A. Bakkaloglu, "The evaluation of the landscape performance of urban open and green areas within the scope of certain spatial indicators: The case of southeast Ankara city," *İdealkent*, vol. 15, no. 40, pp. 376-405, 2023.
- [10] U. Akkemik, D. Tolunay, C. Erdonmez, E. Atmis, and O. Kurdoglu, "Evaluation of green walls and suggestions in terms of green space problems of Istanbul," *Journal of Bartın Faculty of Forestry*, vol. 23, no. 1, pp. 337-345, 2021.
- [11] B. B. Aras, "Green roof practices in the context of urban sustainability," *MANAS Journal of Social Studies*, vol. 8, no. 1, pp. 469-504, 2019.
- [12] A. Akpınar, "Assessing effects of the quality of urban green spaces on people's health and physical activity," *Artvin Coruh University Journal of Forestry Faculty*, vol. 20, no. 1, pp. 36-46, 2019.
- [13] Y. Aksoy and N. Ergun, "A research on urbanization and green area problem, Istanbul City's Bakirkoy district as a sample," *Journal of TUBAV Bilim*, vol. 2, no. 4, pp. 426-438, 2009.

- [14] S. A. Bıcak and N. C. Erkan, "Method for determining the effects of green space and physical activity on human happiness," *The Journal of Social Sciences Institute*, no. 48, pp. 345-362, 2020.
- [15] M. Bekar and D. U. G. Sekban, "Evaluation of Trabzon coastal route for user satisfaction," *Journal of the International Scientific Researches*, vol. 3, no. 2, pp. 563-576, 2016.
- [16] D. E. Basalma, U. Aysel, and P. S. Kormecli, "An evaluation of quality indicators in urban parks: A case study of Ankara's 100th Year Unity Park," *International Journal of Landscape Architecture Research* vol. 1, no. 1, pp. 08-13, 2017.
- [17] D. Bertiz, I. Eksi, M. Tokmak, D. Ozbey, M. Ak, and A. Gunes, "Comparison of international and national green building certification systems in terms of green infrastructure," *Peyzaj*, vol. 1, no. 2, pp. 31-39, 2019.
- [18] D. M. Cosgun, "The importance of green infrastructure in improvement of quality of life in cities: The case of Bartın," M.S. thesis, Landscape Architecture, Bartın University, Bartın, 2022.



## Traditional Uses of Medicinal Plants Naturally Distributed in Yerkesik Basin (Mentese-Mugla)

Kenan Akbas\*<sup>1</sup>

<sup>1</sup>Department of Herbal and Animal Production, Koycegiz Vocational School, Mugla Sitki Kocman University, Mugla, Türkiye

### Abstract

As a result of face-to-face surveys conducted with local people in the Yerkesik basin, 38 plant samples belonging to 24 families used for medicinal purposes were identified. Among all the plants evaluated, *Salvia fruticosa* Mill. and *Origanum onites* L. are the most preferred plants by the local people. The most common preparation of plants among the local people is infusion and decoction. Other uses include; external application, syrup, tincture, soaking in olive oil, poultice. Parts of plants used in treatment; leaves, flowers, seeds, fruits, resin, cones, latex, balsam, roots and tubers.

**Keywords:** Ethnobotany, Flora, Natural plants, Traditional medicine

## 1 INTRODUCTION

Plants have been used in the treatment of many diseases throughout human history, thanks to the specific or broadly effective compounds they contain. For this reason, approximately 3.5-4 billion of the world's population benefits from medicinal plants. A large part of people, especially those living in rural areas, benefit from local plants in the treatment and prevention of diseases [1].

Considering the latest studies on the flora of our country, there are approximately 12,000 plant taxa in species and subspecies categories. Approximately 1000 of these plant taxa are used for therapeutic purposes [2]. Due to this rich plant diversity of Mugla, many studies have been carried out to identify medicinal and aromatic plants [3–12].

Yerkesik basin, determined as the research area, is located in Mentese district of Mugla province and covers 15 neighborhoods. These neighborhoods; They are Akkaya, Gulagzi, Dogankoy, Yenice, Yerkesik, Kuyucak, Derinkuyu, Yenibagyaka, Algi, Denizova, Sarnic, Bagyaka, Meke, Zeytin, and Dagpinari.

No research conducted around the Yerkesik basin was found as a result of the literature review. With these ethnobotanical studies, it is attempted to preserve this traditional knowledge and transfer it unchanged from generation to generation.

## 2 MATERIAL AND METHOD

Face-to-face interviews were conducted with people of different ages, cultures and educational backgrounds in order to determine the plant species with medicinal and aromatic values that grow naturally in the Yerkesik basin and how these plant species are used by the local people. Due to the continuation of the pandemic during the study, the decisions of the Provincial Hygiene Board regarding the application of the survey were strictly adhered to. The survey was conducted in open areas and the survey duration did not exceed 10 minutes.

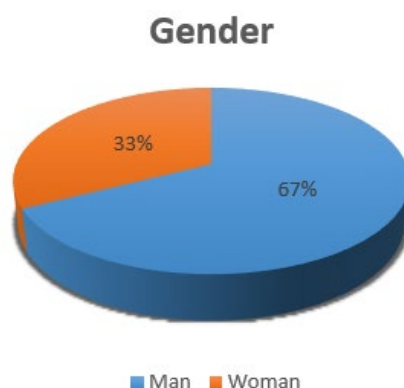
During these interviews, questions were asked to the source people in line with the prepared survey. In addition to the questions asked in the content of the surveys, data such as the purpose and use of the plants used, the local name of the plant, the location where the plant sample was obtained, characteristics of the person surveyed such as age, gender, educational status and occupation information were also determined.

Plants whose use was determined as a result of the surveys; It was identified after it was collected from its natural habitat, pressed, and herbarium samples were prepared, based on the information received from the surveyed people, markets, herbalists, or local people.



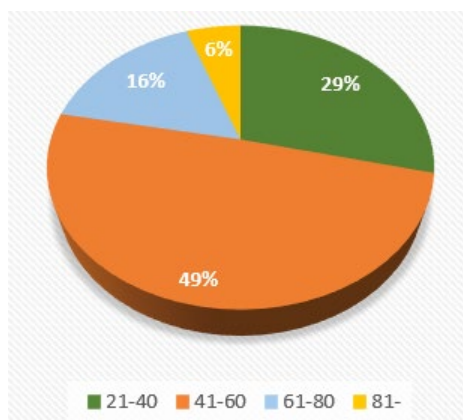
### 3 RESULTS

A survey was conducted with 123 people in the neighbourhoods included in the research area. In the survey study, 83 of the interviews were conducted with men and 40 with women. The proportion of men is higher because the work is mostly done in public areas such as coffeehouses and squares (Figure 1).



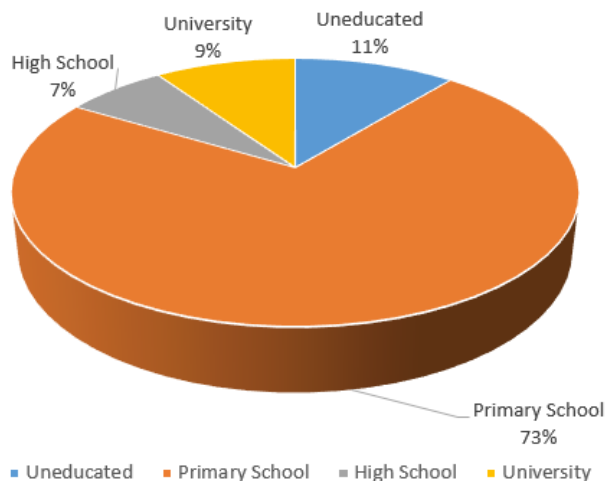
**Figure 1.** Gender distribution of survey participants

Of the people interviewed, 14 people are between the ages of 21-40, 42 people are between the ages of 41-60, 60 people are between the ages of 61-80 and 7 people are between the ages of 81 and over. The rate of individuals over the age of 40 is 71% (Figure 2).



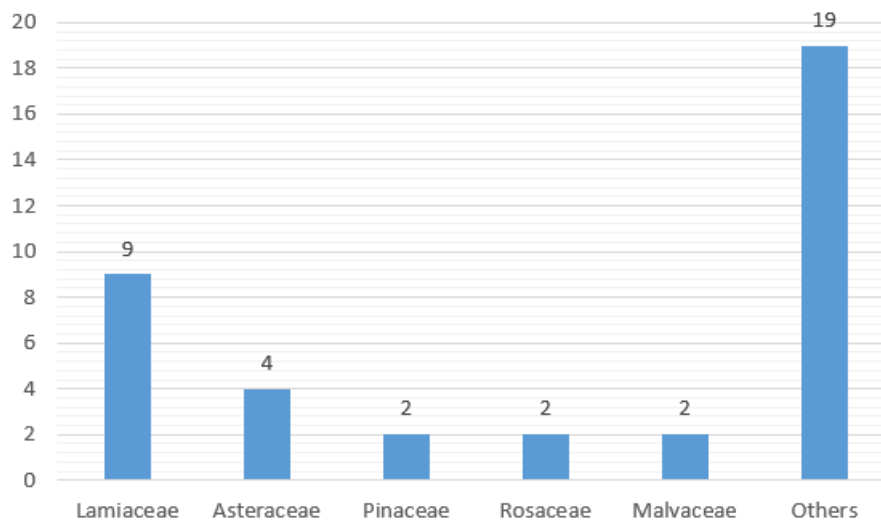
**Figure 2.** Age distribution of survey participants

Among the people interviewed, 4 people (3%) did not receive any education, 97 people (79%) were primary school graduates, 11 people (9%) were high school graduates and 11 (9%) people were educated at university level (Figure 3).



**Figure 3.** Educational status of survey participants

As a result of interviews with local people, 38 plant taxa were identified (Appendix-1). Among the plants used, the plant families with the most taxa are Lamiaceae; (9 taxa), Asteraceae (4 taxa), Cupressaceae (2 taxa), Malvaceae (2 taxa) and Rosaceae (2 taxa) (Figure 4).



**Figure 4.** Plant families with the most taxa used for medicinal purposes in the research area

Consistent with our study, in other studies conducted in Mugla, the plant family with the most used taxa by the local people is Lamiaceae [4–12]. This is a natural result of the Lamiaceae family being the second largest family with the most taxa in our country and containing many species with medicinal value.

In our study area, *Origanum onites* L. and *Salvia fruticosa* Mill. It is generally used for colds and stomach aches. Consistent with our study, in other studies conducted in Mugla, the plant taxon most used by the local people is *Origanum onites* [4–7, 9–12]. Similar uses have been reported in other regions of Türkiye [3, 5, 13, 14].

Another of the most used plants in the field of research is *Sideritis libanotica* subsp. *linearis* (Benth.) Bornm. (Mountain stream). It is used by local people for stomach aches and colds. They have been used for similar purposes in the literature [15].

While the traditional uses of plants in the research area are significantly similar to other studies, *Tulipa orphanidea* Boiss. ex Heldr. and *Crocus muglaensis* Rukšāns taxa were revealed for the first time. In addition, while the medical use of *Onopordum caricum* Hub.-Mor. is included in the literature, information about the purpose for which it is used could not be found in the source [16].

## 4 CONCLUSION

Traditional medicinal uses of 38 plant taxa belonging to 24 families in the research area were revealed as a result of surveys conducted with local people.

Among all plants evaluated; *Salvia fruticosa* and *Origanum onites* are seen as the most preferred plants by the local people. People use these plants as infusions in village coffeehouses and homes. *Lavandula stoechas* subsp. *stoechas*, *Hypericum perforatum* subsp. *veronense*, *Thymbra spicata* subsp. *spicata* and *Sideritis libanotica* subsp. *linearis* are also among the commonly used plants.

The most common preparation of plants among the local people is infusion and decoction. Other uses include; external application, syrup, tincture, soaking in olive oil, poultice. Parts of plants used in treatment; leaves, flowers, seeds, fruits, resin, cones, latex, balsam, roots and tubers.

Local people mostly use plants in the treatment of respiratory diseases, gastrointestinal diseases and pain. As a result of our interviews with local people, we see that plants are still widely used for medicinal purposes in their daily lives. However, we believe that there is a gradual decline in this traditional knowledge.

There is already a lavender garden in Yeniköy called “Fragrance Valley”. The garden, which is visited by many local and foreign tourists every year, constitutes a good example of tourism for the local people. In this sense, the

vacant lands in the region; thyme, St. John's wort, sage, lavender, etc., which have medicinal value and are compatible with the ecological structure of the region. Supporting by "Local Governments" the use of plants to grow species such as and the extraction of essential oils and aromatic juices by processing the grown products will also provide an economic return to the local people.

As a result, this study will guide floristic, phytosociological and ethnobotanical research to be carried out in nearby areas. We also believe that it will make a contribution to those who will cultivate medicinal plants in the region.

## Acknowledgments

This study was supported by the BAP project numbered 21/118/07/1/4, titled "Determination of the Floristic Structure of the Yerkesik Basin and Its Evaluation in Terms of Naturally Distributed Medicinal and Aromatic Plants". We would like to thank Mugla Sitki Kocman University Scientific Research Projects Coordination Unit for their assistance.

## References

- [1] S. A. Sargin, "Plants used against obesity in Turkish folk medicine: A review," *Journal of Ethnopharmacology*, vol. 270, art. no. 113841, 2021.
- [2] S. Yildirimli, "Ethnobotany and Turkish ethnobotany," *Kekibec*, vol. 17, pp. 175–193, 2004.
- [3] F. Ertug, "Wild edible plants of the Bodrum area (Mugla, Turkey)," *Turkish Journal of Botany*, vol. 28, no. 1–2, pp. 161–174, 2004.
- [4] D. Kazan, "Ethnobotany of Ortaca (Mugla)," M.S. thesis, Department of Biology, Mugla Sitki Kocman University, Mugla, 2007.
- [5] G. Uysal, "Ethnobotany of Köyceğiz (Mugla)," M.S. thesis, Department of Biology, Mugla Sitki Kocman University, Mugla, 2008.
- [6] B. Gurdal and S. Kultur, "An ethnobotanical study of medicinal plants in Marmaris (Mugla, Turkey)," *Journal of Ethnopharmacology*, vol. 146, no. 1, pp. 113–126, 2013.
- [7] M. Sagiroglu, S. Dalgiccedil, and S. Toksoy, "Medicinal plants used in Dalaman (Mugla), Turkey," *Journal of Medicinal Plants Research*, vol. 7, no. 28, pp. 2053–2066, 2013.
- [8] Y. Sicak, O. F. Colak, V. Ilhan, E. Sevindik, and N. Alkan, "Some medicinal and aromatic plants used commonly among the public in Koycegiz region," *Anadolu Doga Bilimleri Dergisi*, vol. 4, no. 2, pp. 70–77, 2013.
- [9] H. Akan, A. Oz, and H. Pekmez, "Some of the plants species used among the local people in Ortaca (Mugla)," *Turkish Journal of Agriculture - Food Science and Technology*, vol. 6, no. 9, pp. 1168-1174, 2018.
- [10] S. Kincal, O. Ceylan, and G. Görk, "Ethnobotanical features of Ula (Mugla/Turkey) district," *Biological Diversity and Conservation*, vol. 14, no. 1, pp. 69–81, 2021.
- [11] E. Guneri, T. Turkoglu, M. Yildiztekin, "Investigation of sustainability of traditionally used medicinal plants in Koycegiz-Dalyan special environmental protection area," *Journal of the Institute of Science and Technology*, vol. 13, no. 1, pp. 130–142, 2023.
- [12] K. Akbas, M. Citakolu, and S. Davran, "Natural plants of the Sandras Mountain (Köycegiz-Mugla) traditionally employed for therapeutic purposes," *Turkish Journal of Forestry*, vol. 25, no. 1, pp. 32–40, 2024.
- [13] G. Honda, E. Yesilada, M. Tabata, E. Sezik, T. Fujita, Y. Takeda, Y. Takaishi, and T. Tanaka, "Traditional medicine in Turkey VI. Folk medicine in west Anatolia: Afyon, Kutahya, Denizli, Mugla, Aydin provinces," *Journal of Ethnopharmacology*, vol. 53, no. 2, pp. 75–87, 1996.
- [14] E. Tuzlaci, *Plants and Life in Bodrum*, Istanbul: Fine Arts Press, 2005.
- [15] H. Fakir, M. Korkmaz, and B. Guller, "Medicinal plant diversity of western Mediterranean region in Turkey," *Journal of Applied Biological Sciences*, vol. 3, no. 2, pp. 30–40, 2009.
- [16] A. O. Sari, B. Oguz, A. Bilgic, N. Tort, A. Guvensen, and S. G. Senol, "Asteraceae species used as indigenous remedies at the western Anatolia," *Anadolu J. of AARI*, vol. 18, no. 1, pp. 1–15, 2008.

**Appendix-1: Medicinal uses of plants in the research area**

Family	Scientific Name	Part used	Purpose of usage	Preparation
Altingiaceae	<i>Liquidambar orientalis</i> Mill.	Balm, Oil	Ulcer	With honey
Anacardiaceae	<i>Pistacia terebinthus</i> subsp. <i>terebinthus</i> L.	Fruit	Gastrointestinal disorders	Decoction
Apiaceae	<i>Coriandrum sativum</i> L.	Flowers and leaves	Stomach disorders	Infusion
Araceae	<i>Dracunculus vulgaris</i> Schott	Bulbs	Hemorrhoids, Painkiller	Mush
Asteraceae	<i>Helichrysum orientale</i> (L.) Gaertn.	Flowers and leaves	Kidney stone, Prostate, Bowel	Infusion, Decoction
	<i>Anthemis chia</i> L.	Flowers	Sedative, kidney stone reducer	Infusion
	<i>Taraxacum aleppicum</i> Dahlst.	Roots	Asthma, Cancer	Decoction
	<i>Onopordum caricum</i> Hub.-Mor., Endemic	Roots Flowers and leaves	Stomach disorders, Constipation	Externally, Decoction
Cucurbitaceae	<i>Ecballium elaterium</i> (L.) A.Rich.	Fruit	Ringworm	Sliced and spread
Cupressaceae	<i>Cupressus sempervirens</i> L.	Cone	Bronchitis	Decoction
	<i>Juniperus oxycedrus</i> subsp. <i>oxycedrus</i> var. <i>oxycedrus</i> L.	Seeds	Bronchitis	Decoction
Euphorbiaceae	<i>Euphorbia rigida</i> M.Bieb.	Latex	Wart	Direct
Ericaceae	<i>Arbutus unedo</i> L.	Fruit	Stomache ache	Decoction, consumed raw
Fagaceae	<i>Quercus coccifera</i> L.	Leaves	Burns	Decoction
Hypericaceae	<i>Hypericum perforatum</i> subsp. <i>veronense</i> (Schrank) H.Linb.	Flowers and leaves	Ulcers, burns and wounds	Soaked in olive oil
Iridaceae	<i>Crocus muglaensis</i> Rukšāns, Endemic	Bulbs	Stomache ache	Consumed raw
Lamiaceae	<i>Sideritis libanotica</i> subsp. <i>linearis</i> (Benth.) Bornm.	Flowers and leaves	Cold, Abdominal pain	Infusion
	<i>Salvia fruticosa</i> Mill.	Flowers and leaves	Cold, Abdominal pain	Infusion
	<i>Origanum onites</i> L.	Flowers and leaves	Cold, Abdominal pain, Indigestion	Infusion
	<i>Rosmarinus officinalis</i> L.	Flowers and leaves	Abdominal pain	Infusion
	<i>Teucrium polium</i> subsp. <i>polium</i> L.	Flowers and leaves	Abdominal pain	İnfüzyon
	<i>Thymbra spicata</i> subsp. <i>spicata</i> L.	Flowers and leaves	Abdominal pain	Infusion
	<i>Mentha</i> L.	Leaves	Flu/Cold, Leg aches	Infusion, Oil,
	<i>Lavandula stoechas</i> subsp. <i>stoechas</i> L.	Flowers <sup>a</sup> , Leaves <sup>b</sup>	Cardiovascular opener <sup>a</sup> , cold <sup>a</sup> , Kidney stone <sup>b</sup>	Infusion
	<i>Vitex agnus-castus</i> L.	Seeds	Menstrual pain	Infusion
Lauraceae	<i>Laurus nobilis</i> L.	Leaves	Cold, Cough	Infusion
Liliaceae	<i>Tulipa orphanidea</i> Boiss. ex Heldr.	Flowers and leaves	Pain	Mush
Malvaceae	<i>Alcea biennis</i> Winterl	Flowers <sup>a</sup> ,	Cough <sup>a</sup> ,	Infusion <sup>a</sup> ,

		Seeds <sup>b</sup> , Leaves <sup>c</sup>	Abdominal pain <sup>b</sup> , Pain <sup>c</sup>	Infusion <sup>b</sup> , Mush <sup>c</sup>
	<i>Malva sylvestris</i> L.	Leaves	Abdominal pain, Cough	Infusion
Moraceae	<i>Ficus carica</i> subsp. <i>carica</i> L.	Leaves <sup>a</sup> , Latex <sup>b</sup>	Against Snake and Scorpion bites <sup>a</sup> , liver disease <sup>b</sup>	Mush <sup>a</sup> , Mixed into water <sup>b</sup>
Myrtaceae	<i>Myrtus communis</i> subsp. <i>communis</i> L.	Leaves <sup>a,c</sup> , Fruit <sup>b</sup>	Headache <sup>a</sup> Eye health <sup>b</sup> , Vascular occlusion <sup>c</sup>	Infusion <sup>a</sup> , consumed raw <sup>b</sup> , Tincture <sup>c</sup>
Oleaceae	<i>Olea europaea</i> subsp. <i>europaea</i> L.	Leaves	Diabetes	Infusion
Platanaceae	<i>Platanus orientalis</i> L.	Leaves	Cough, Rheumatism	Infusion and mush
Pinaceae	<i>Pinus brutia</i> var. <i>brutia</i> Ten.	Resin <sup>a</sup> , Cones <sup>b</sup>	wound treatment <sup>a</sup> , Lung disorders <sup>b</sup> , Reduces bronchitis and intestinal worms <sup>b</sup>	Externally <sup>a</sup> , Syrup <sup>b</sup>
Polygonaceae	<i>Rumex crispus</i> L.	Seeds	Diarrhea, Lung clearing, Shortness of breath	Infusion
Rosaceae	<i>Rosa canina</i> L.	Fruit	Cold, Abdominal pain and indigestion	Decoction
	<i>Crataegus monogyna</i> var. <i>monogyna</i> Jacq.	Fruit	Heart diseases	Consumed raw
Urticaceae	<i>Urtica membranacea</i> Poiret ex Savi	Seeds <sup>a</sup> , Leaves <sup>b</sup>	Cancer <sup>a</sup> , Diabetes <sup>b</sup>	Decoction <sup>a</sup> , Infusion <sup>b</sup>



---

## Vegetative Anatomy of Two Endemic *Muscari* L. Species in Türkiye

Dudu Ozlem Mavi Idman<sup>\*1</sup>, Huseyin Guldal<sup>1</sup>, Ali Gercek<sup>1</sup>, Huseyin Eroglu<sup>2</sup>

<sup>1</sup>Department of Collection, National Botanical Garden of Türkiye, Ankara, Türkiye

<sup>2</sup>Department of Biology, Van Yuzuncu Yil University, Van, Türkiye

---

### Abstract

Türkiye, that has many plant species that grow naturally and are traded, also has a very rich flora in terms of bulbous, tuberous and rhizome plant species called geophytes. Geophytes, which can be easily grown and used as landscape, balcony, indoor and outdoor ornamental plants and cut flowers, are in the angiosperm group of seed plants. A Project (TAGEM/BBAD/Ü/20/A7/P9/1947), supported by General Directorate of Agricultural Research and Policies (TAGEM), was carried out to protect and exhibit important geophytes by establishing a geophyte collection within the newly established National Botanical Garden of Türkiye. Two endemic *Muscari* L. species collected within the scope of this project constitute the subject of this study.

In this study, the root, scape and leaf anatomy of endemic *Muscari serpentanicum* Yildirim, Altıoğlu & Pirhan and *Muscari atillae* Yildirim, whose anatomies have not been studied before, were detailed within the scope of creating microscopic slide collections in another project (TAGEM/BBAD/B/20/A1/P9/1949) supported by TAGEM. Both qualitative and quantitative characters were evaluated. Characteristics such as hairiness in the roots, leaf widths, epidermis dimensions, stoma sizes and density of leaves, and root and scape diameters were examined in detailed.

**Keywords:** *Muscari serpentanicum*, *Muscari atillae*, Endemic, Anatomy

---



---

## **Kombucha-Derived Bacterial Cellulose Production with Herbal Tea and Different Coffee Combinations**

**Nazlı Neval Sahin, Nermin Hande Avcioglu<sup>\*1</sup>**

<sup>1</sup>*Biotechnology Section, Biology Department, Faculty of Science, Hacettepe University, Ankara, Türkiye*

---

### **Abstract**

Plant cellulose serves as a prevalent raw material for the production of films derived from natural polymers or composite materials. However, the purification of plant cellulose requires high energy requirement and the use of chemicals, and the waste products formed after purification are known to negatively affect aquatic and terrestrial ecosystems. Therefore, bacterial cellulose (BC) is emerging as a unique biopolymer that is beginning to replace plant-derived cellulose and it is especially characterized by its nanostructured porosity, purity (absence of lignin, pectin, and hemicellulose), mechanical strength, non-allergenic properties, transparency, and ability to form dynamic fibers. Considered one of the traditional foods known as 'nata de coco' among the Filipino people, BC is very popular in Asian countries due to its distinctive soft texture and high fiber content. Kombucha tea is one of the most popular traditional fermented beverages consumed for its potential health benefits. The symbiotic bacterial and yeast community (SCOBY) in the Kombucha allows the tea to acidify and produce carbon dioxide gas during fermentation, allowing a fermented beverage to be obtained. It is also stated that consumption of this tea, which contains some beneficial probiotic bacteria and yeasts, supports digestive health for people. In addition to being a beneficial beverage, kombucha enables the formation of BC due to its symbiotic association. Therefore, it is possible to increase BC yield by isolating the microorganisms in this symbiosis and use them in different combinations of herbal teas and coffee containing fermentation media. Thus, it is possible to obtain BC with a wide industrial usage area, low cost and unique properties.

**Keywords:** *Bacterial cellulose, Kombucha tea, Mate, Coffee*

---



## Evaluation of Gene Expression Levels of Antimicrobial Peptides (MsDef1 And MsSN1) from *M. Sativa* Sazova Cultivar During 21-Day Period

Busra Albayrak Turgut<sup>\*1</sup>

<sup>1</sup>*Molecular Biology and Genetics, Erzurum Technical University, Erzurum, Türkiye*

### Abstract

Antimicrobial peptides in plant is comprised the first line of defense against pathogen microorganisms and pests. They are expressed constitutively or induced by a stimulus and also, they can be tissue-specific. The continuous expression of them is important to plants during an infection. In this study, it was aimed the detection of MsDef1 and MsSN1 gene expressions in different parts of *M. sativa* Sazova cultivar during 21-day growth period. In order to determine their gene expressions, qPCR method was used after plant parts (cotyledon, leaf, root and shoot) were collected. It was determined that *MsDef1* and *MsSN1* genes were expressed in the different plant parts of *M. sativa* Sazova cultivar. *MsDef1* gene expression was detected on 7<sup>th</sup> day in cotyledon with the highest value. Its expression in cotyledon was dramatically decreased on 14<sup>th</sup> and 21<sup>st</sup> day. A slight increase of this gene expression was determined during the 21-day period. In shoot on 7<sup>th</sup> day, the gene expression was detected and it was decreased over time. On the other side, the highest value of MsSN1 gene expression was on 3<sup>rd</sup> day in cotyledon. After 3<sup>rd</sup> day, cotyledons had the same MsSN1 gene expression level. In leaves and roots, the gene expression increased during the 21-day period. On the contrary, in shoots, it was decreased on 14<sup>th</sup> and 21<sup>st</sup> day. Within this study, it was showed that MsDef1 and MsSN1 genes are expressed during the first 21-day growth of *M. sativa* seedlings without a stimulus, which is important for *M. sativa* to protect against pathogen microorganism.

**Keywords:** Gene expression, *M. sativa*, Sazova cultivar, Antimicrobial peptide

## 1 INTRODUCTION

Antimicrobial peptides (AMPs) are peptides with small molecular weight produced in all living beings against microorganisms, virus, pest and insects [1]. Many AMPs were identified from various plant species. AMPs have also been identified from *Medicago* species, which belong to the *Fabaceae* (legume) family and are excluded from the human diet, but are most used as a forage plant due to its high nutritional value. In particular, defensins MtDef2, MtDef4.2, MtDef5 and MtDefMd1 have been characterized from *Medicago truncatula*, which is a model organism and whose genomes are highly similar to alfalfa [2–5]. MtDef4.2 showed an inhibitory effect against different *Fusarium* species at an IC50 value of 0.5-1.8  $\mu$ M [3].

It is also known that approximately 3% of the *Arabidopsis thaliana*, rice, and *alfalfa* (*Medicago sativa*) genomes encode AMP [6, 7]. This ratio shows that *M. sativa* contains many AMPs, but only three AMPs have been identified from *M. sativa* until today. These AMPs are MsDef1, MsSN1 (*M. sativa* snakin-1) and MsDef2.1 [8–10]. MsDef1 defensin is the first AMP characterized from *M. sativa* seeds and there are various studies on this defensin [8]. MsDef1 is an antifungal peptide inhibiting *Fusarium graminearum* and *Verticillium dahlia*. MsSN1 inhibits bacterial growth and fungal spore germination such as *Agrobacterium tumefaciens* and *Phoma medicaginis* [10].

Like animals, AMPs are expressed constitutively or induced by a specific impact in plants. The constitutive expression of AMPs is important to create a defense barrier against pathogens or pests. Previous studies showed that transgenic plants expressing AMP constitutively develop self-resistance against pathogens [10–16]. However, there are a few studies on AMP expression in plants during the growth. This is important for plant defense system because it reveals which AMPs participates in the first line of plant defense. In this study, it was aimed the evaluation of MsDef1 and MsSN1 gene expression levels in *M. sativa* plants (Sazova cultivar) during the 21-day period.



## 2 MATERIAL AND METHOD

### 2.1 Plant Tissue Culture

In vitro culture was prepared according to MS medium (Murashige and Skoog 1962). Sazova seeds sterilized by using 3% sodium hypochlorite solution were planted in MS medium and then, incubated at 25 °C with a 16-hour light and 8-hour dark cycle. Leaves, cotyledons, roots and shoot parts were collected 3, 7, 14 and 21 days after seed planting.

### 2.2 RNA Isolation

RNA was isolated from the samples collected 3, 7, 14 and 21 days after using RNA-solv reagent (Omega Bio-Tek Nocross, Georgia, USA). Isolation steps were carried out according to the protocol of the product.

### 2.3 cDNA Synthesis

cDNA synthesis was performed using 1,000 ng (1 µg) of the isolated RNA samples. It was performed using the cDNA synthesis mix (Nucleogene, Istanbul, Türkiye) using the given method supplied with the mix. According to the kit protocol, mixture including RNA was kept at 25 °C for 30 minutes and at 85 °C for 5 minutes respectively.

### 2.4 qPCR

To determine *M. sativa* MsDef1 and MsSN1 gene expression, qPCR was used. Primers were obtained using the Primer 3 online program and these primers were synthesized by Oligomer (Ankara, Türkiye). qPCR reaction was prepared using synthesized cDNA, primers and 5X Hot FIREPol Evagreen qPCR mix (Solis BioDyne, Tartu, Estonia). qPCR conditions were set to 40 cycles of 15 s at 95 °C, 20 s at 61 °C, and 30 s at 72 °C after waiting at 95 °C for 12 min. MtAct2 (*M. sativa* actin 2) gene was used as the housekeeping gene. qPCR results were evaluated with the 2- $\Delta\Delta$ Ct method.

### 2.5 Statistical Analysis

All data were analyzed with One-way ANOVA - Duncan test using SPSS 22.0 software package. program and the effects of peptide treatments were evaluated statistically. All tests were performed in triplicate. The determination of significant differences was achieved using Duncan's Multiple Comparison Test at a significance level of  $p \leq 0.05$ .

## 3 RESULTS

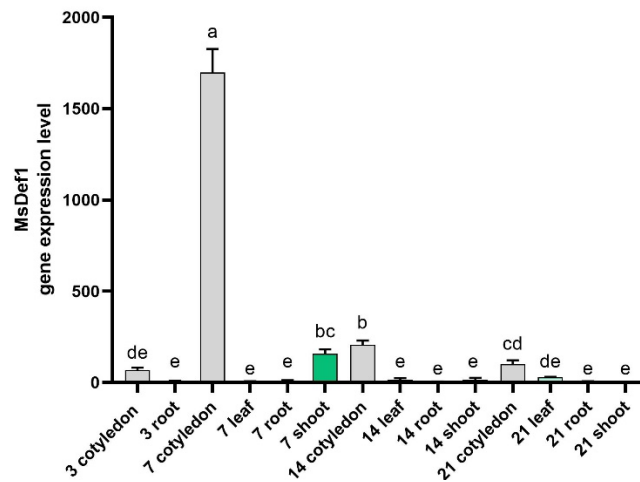
The gene expression level of MsDef1 and MsSN1 in *M. sativa* Sazova cultivar during plant growth over a 21-day period was analysed. *M. sativa* plant growth after the 3rd, 7th, 14th and 21st day was observed as shown in the Figure 1. In 3<sup>rd</sup> day, there were cotyledon and primer root. After 7<sup>th</sup> day, roots, cotyledons, leaf and shoot were observed and continue to grow during 21-day.



Figure 1. *M. sativa* plant growth stages during the 21-day period

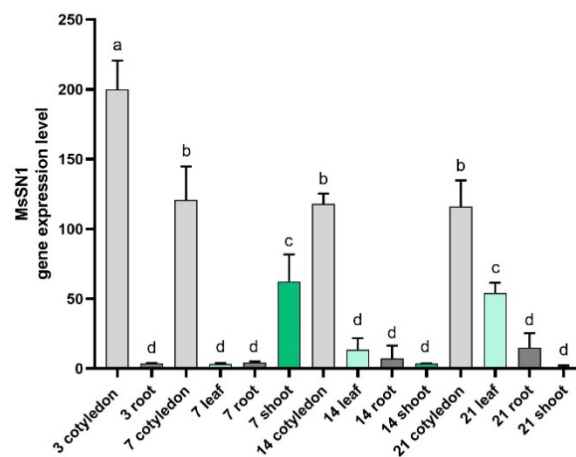
MsDef1 is an antimicrobial peptide in the defensin group containing 45 amino acids and a molecular weight of 5,483 kDa [8]. It was found in the seed of *M. sativa* but it is expressed in roots in response to fungal infection, and its expression can be increased with the application of salicylic acid [17]. According to the relative expression

analysis in the different plant parts, the highest gene expression of *MsDef1* peaked on 7<sup>th</sup> day in cotyledon and decreased dramatically on the 14<sup>th</sup> and 21<sup>st</sup> days (Figure 2). *MsDef1* expression was detected in shoot on 7<sup>th</sup> day and, then it decreased in time. On the contrary, it was observed a slight increasing in leaves over time. During the plant growth, no significant *MsDef1* expression was detected in roots.



**Figure 2.** *MsDef1* gene expression in different plant parts of *M. sativa* Sazova cultivar. Distributions are shown according to Duncan test ( $p < 0.05$ )

*MsSN1* was first identified from the roots of *M. sativa* seedlings [10]. *MsSN1* containing 91 amino acids and having a molecular mass of 9.9 kDa is an antimicrobial peptide belonging to the snakin family. Different parts of the plant were used for the gene expression analysis of *MsSN1* without any stimuli. The highest *MsSN1* expression was detected in cotyledon on 3<sup>rd</sup> day. A decrease in *MsSN1* gene expression was detected on 7<sup>th</sup> day, and there was no significant change on 14<sup>th</sup> and 21<sup>st</sup> days in cotyledon. Its expression in leaves and roots increased during the 21-day period, and it may increase as plant development continues. On the other hand, in the shoots, the highest *MsSN1* expression was detected on 7<sup>th</sup> day and a dramatic decrease was seen on 14<sup>th</sup> day. After 21- period, probably *MsSN1* expression won't exist in the shoots. Similar to our study, Herbel et al. (2017) [18] reported that the gene expression of Snakin-2, is an AMP, varies in different organs of *Solanum lycopersicum* (tomato), such as root, stem, leaf and seed.



**Figure 3.** *MsSN1* gene expression in different plant parts of *M. sativa* Sazova cultivar. Distributions are shown according to Duncan test ( $p < 0.05$ )

#### 4 CONCLUSION

This present study was aimed to determine whether *MsDef1* and *MsSN1* as AMPs identified from *M. sativa* are expressed in this plant during the first 21-day growth period. It was determined that these AMPs were expressed in cotyledon, leaf, roots, and shoots with different levels. The results indicated that these AMPs were expressed for the first 21-day growth period to protect *M. sativa* plant against various pathogens and pests. In the next, to

understand plant and pathogen relationships, new studies on the expression of AMPs during plant growth are needed.

## References

- [1] A. Di Somma, A. Moretta, C. Canè, A. Cirillo, and A. Duilio, “Antimicrobial and antibiofilm peptides,” *Biomolecules*, vol. 10, no. 4, art. no. 652, Apr. 2020.
- [2] R. G. Spelbrink, N. Dilmac, A. Allen, T. J. Smith, D. M. Shah, and G. H. Hockerman, “Differential antifungal and calcium channel-blocking activity among structurally related plant defensins,” *Plant Physiology*, vol. 135, no. 4, pp. 2055–2067, Agu. 2004.
- [3] J. Kaur, M. Thokala, R.S. Alexandre, P. Zhao and H. Peyret, “Subcellular targeting of an evolutionarily conserved plant defensin MtDef4.2 determines the outcome of plant–pathogen interaction in transgenic *A. rabidopsis*,” *Molecular Plant Pathology*, vol. 13, no. 9, pp. 1032–1046, Dec. 2012.
- [4] K. T. Islam, S. L. S. Velivelli, R. H. Berg, B. Oakley, and D. M. Shah, “A novel bi-domain plant defensin MtDef5 with potent broad-spectrum antifungal activity binds to multiple phospholipids and forms oligomers,” *Sci. Rep.*, vol. 7, no. 1, art. no. 16157, Nov. 2017.
- [5] M. Uhe, C. Hogeckamp, R. M. Hartmann, N. Hohnjec, and H. Kuster, “The mycorrhiza-dependent defensin MtDefMd1 of *Medicago truncatula* acts during the late restructuring stages of arbuscule-containing cells,” *Plos One*, vol. 13, no. 1, art. no. e0191841, Jan. 2018.
- [6] P. Mergaert, K. Nikovics, Z. Kelemen, N. Maunoury, D. Vaubert, A. Kondorosi, and E. Kondorosi, “A novel family in *Medicago truncatula* consisting of more than 300 nodule-specific genes coding for small, secreted polypeptides with conserved cysteine motifs,” *Plant Physiology*, vol. 132, no. 1, pp. 161–173, May 2003.
- [7] K. A. T. Silverstein, W. A. Moskal, H. C. Wu, B. A. Underwood, M. A. Graham, C. D. Town, and K. A. VandenBosch, “Small cysteine-rich peptides resembling antimicrobialpeptides have been under-predicted in plants,” *The Plant Journal*, vol. 51, pp. 262–280, Mar. 2007.
- [8] A.-G. Gao, S. M. Hakimi, C. A. Mittanck, Y. Wu, and B. M. Woerner, “Fungal pathogen protection in potato by expression of a plant defensin peptide,” *Nat. Biotechnol.*, vol. 18, no. 12, pp. 1307–1310, Dec. 2000.
- [9] J. N. Hanks A. K. Snyder, M. A. Graham, R. K. Shah, L. A. Blaylock, M. J. Harrison, and D. M. Shah, “Defensin gene family in *Medicago truncatula*: structure, expression and induction by signal molecules,” *Plant Mol. Biol.*, vol. 58, no. 3, pp. 385–399, Jun. 2005.
- [10] A. N. García N. D. Ayub, A. R. Fox, M. C. Gómez, and M. J. Diéguez, “Alfalfa snakin-1 prevents fungal colonization and probably coevolved with rhizobia,” *BMC Plant Biol.*, vol. 14, no. 1, art. no. 248, Dec. 2014.
- [11] K. Kazan, A. Rusu, J. P. Marcus, K. C. Goulter, and J. M. Manners, “Enhanced quantitative resistance to *Leptosphaeria maculans* conferred by expression of a novel antimicrobial peptide in canola (*Brassica napus* L.),” *Mol. Breed.*, vol. 10, pp. 63–70, Febr. 2002.
- [12] D. Deb, A. Shrestha, L. Sethi, N. C. Das, V. Rai, A. B. Das, I. B. Maiti, and N. Dey, “Transgenic tobacco expressing *Medicago sativa* Defensin (Msdef1) confers resistance to various phyto-pathogens,” *Nucleus*, vol. 63, no. 2, pp. 179–190, Agus. 2020.
- [13] L. A. Ivanova and R. A. Komakhin, “Efficiency of the alpha-hairpinin SmAMP-X gene promoter from *Stellaria media* plant depends on selection of transgenic approach,” *Transgenic Res.*, vol. 33, no. 1-2, pp. 1–19, Nis. 2024.
- [14] M. Fallah Ziarani, M. Tohidfar, and M. H. Mirjalili, “Evaluation of antibacterial properties of nisin peptide expressed in carrots,” *Sci. Rep.*, vol. 13, no. 1, art. no. 22123, Dec. 2023.
- [15] E. A. Istomina, T. V. Korostyleva, A. S. Kovtun, M. P. Slezina, ve T. I. Odintsova, “Transcriptome-wide identification and expression analysis of genes encoding defense-related peptides of *Filipendula ulmaria* in response to *Bipolaris sorokiniana* infection,” *JoF*, vol. 10, no. 4, art. no. 258, Mar. 2024.
- [16] V. Nahirňak, N. I. Almasia, V. V. Lia, H. E. Hopp, and C. Vazquez Rovere, “Unveiling the defensive role of Snakin-3, a member of the subfamily III of Snakin/GASA peptides in potatoes,” *Plant Cell Rep.*, vol. 43, no. 2, art. no. 47, Feb. 2024.
- [17] B. Albayrak Turgut ve İ. Bezirganoğlu, “Foliar application of CaO nanoparticles and salicylic acid on *Medicago sativa* seedlings enhances tolerance against *Fusarium oxysporum*,” *Physiological and Molecular Plant Pathology*, vol. 122, art. no. 101926, Nov. 2022.
- [18] V. Herbel, J. Sieber-Frank, and M. Wink, “The antimicrobial peptide snakin-2 is upregulated in the defense response of tomatoes (*Solanum lycopersicum*) as part of the jasmonate-dependent signaling pathway,” *Journal of Plant Physiology*, vol. 208, pp. 1–6, Jan. 2017.



## Investigation of the Effect of Chemical Additives on Performance in the Deep Mixing Method with Model Experiments

Yunus Emre Colak<sup>\*1</sup>, Mehmet Sukru Ozcoban<sup>1</sup>, Mustafa Mert<sup>2</sup>

<sup>1</sup>Civil Engineering, Yıldız Technical University, Istanbul, Türkiye

<sup>2</sup>Civil Engineering, Fatih Sultan Mehmet Vakıf University, Istanbul, Türkiye

### Abstract

This study aims to improve clayey soils by deep mixing method and investigate the effect of magnesium oxide (MgO) on this process. Clay soils are a difficult soil type that negatively affects the durability and stability of structures. Therefore, in our study, the effect of MgO in the deep mixing method for the improvement of clayey soils was examined.

The experiments were carried out in a laboratory environment, and clay soils were improved by using the small-scale model deep mixing method. This method is a technique to improve the mechanical properties of the soil.

It aims to investigate the use of magnesium oxide (MgO), which is low-cost and environmentally friendly, as an alternative to cement and chemical remediation techniques. Cement and magnesium oxide were used together within the scope of the project. The percentage of cement and MgO was determined as the percentage by weight of dry clay, the amount of cement was chosen as 20%, and the amount of MgO was chosen as 0%, 5% and 10%. The water/binder ratio was determined as 1 and the soil was prepared with optimum water content.

The samples prepared in the experiments were subjected to the unconfined pressure test and the results were examined. The results obtained show that the strength increases with increasing MgO content. These results show that it is possible to improve clayey soils by deep mixing with magnesium oxide, which is an environmentally friendly and economical alternative.

This study has the potential to provide an effective solution that can be used in the construction industry and offers an alternative approach to cement-based remediation techniques. Additionally, it offers a new perspective in the field of geotechnical engineering, emphasizing the importance of the use of environmentally friendly materials

**Keywords:** Deep mixing method,, Clayey soil, MgO, Unconfined compression test

## 1 INTRODUCTION

Construction and infrastructure development on a global scale requires the constant search for innovations and improvements in the field of geotechnical engineering. Especially the negative effects of clayey soils on the durability and stability of structures are a frequently encountered problem in engineering applications. Improving the mechanical properties of this soil type and increasing structural safety is of great engineering importance.

In this context, the deep mixing method and the potential effects of chemical additives on the improvement of clayey soils are of great importance. The deep mixing method is an effective method to improve the mechanical properties of the soil. This method has been used successfully in many applications such as strengthening the foundations of buildings and increasing the bearing capacity of the ground.

Magnesium oxide (MgO) offers various benefits in ground improvement as highlighted in research articles. MgO is effective in increasing soil strength by absorbing significant amounts of carbon dioxide (CO<sub>2</sub>). It contributes to reducing CO<sub>2</sub> levels in the atmosphere [1]. It plays an important role in the construction industry, having been used in the mortar material of some ancient buildings due to its high binding properties when appropriate curing conditions are provided [2]. Additionally, studies in the literature show that when 6% nano magnesium oxide is mixed with clay soils, the engineering properties of clay increase significantly [3].

Compared with traditional activators such as lime or Portland cement, MgO exhibited superior performance in terms of strength and permeability, thus ensuring high stabilization efficiency in improving soft soils [4]. Within the scope of soil improvement, the formation of magnesium-aluminium-silicate hydrate (M-A-S-H) gels using

MgO has been examined in various studies. There are findings that by filling the voids of the soil with M-A-S-H gel, the bond between particles is strengthened and the durability of the soil increases [5, 6].

In general, MgO addition plays an important role in the formation and properties of M-A-S-H gel in cementitious systems and affects its mechanical, physical and microstructural properties [6–8]. Research has proven that magnesium oxide can significantly increase the physical and mechanical properties of the soil when mixed with the soil under appropriate curing conditions and correctly.

As a result, the use of environmentally friendly and economical materials such as magnesium oxide can offer an effective solution for improving clay soils. However, more research is needed to determine the effectiveness and appropriate dosages of these materials. The aim of this study is to improve clayey soils by deep mixing method and examine the effect of MgO in this process. In particular, the potential of using magnesium oxide (MgO), which is low-cost and environmentally friendly, as an alternative to cement-based chemical remediation techniques, has been investigated. According to research, it is of great importance as it has the potential to provide an effective solution that can be used in the construction industry and offers an alternative approach to cement-based improvement techniques.

## 2 MATERIAL AND METHOD

In this study, CEM-I 42.5 R type cement, 98% purity magnesium oxide (MgO), Esbka-7 Clay containing reactive silicon dioxide ( $\text{SiO}_2$ ), iron oxide ( $\text{Fe}_2\text{O}_3$ ) and aluminum oxide ( $\text{Al}_2\text{O}_3$ ) were used. The general and situational properties of the soils were determined by various index tests, and these properties are presented in Tables 1 and 2. According to the specific gravity and hydrometer analysis of Esbka-7 Clay, it has 2.62  $\text{gr}/\text{cm}^3$  and 53% clay and 47% silt material ratios.

**Table 1.** Chemical composition of Esbka-7 Clay

Chemical Composition	Esbka-7
$\text{SiO}_2$ (%)	54.00 ± 1.00
$\text{Al}_2\text{O}_3$ (%)	31.00 ± 1.00
$\text{Fe}_2\text{O}_3$ (%)	1.40 ± 0.20
TiO <sub>2</sub> (%)	1.00 ± 0.10
CaO (%)	0.20 ± 0.10
MgO (%)	0.40 ± 0.10
$\text{Na}_2\text{O}$ (%)	0.20 ± 0.10
$\text{K}_2\text{O}$ (%)	0.80 ± 0.20
A.Z. (LoI) (%)	11.00 ± 1.00
Soluble Salt (%)	0.40 ± 0.10
Soluble $\text{SO}_4$ (%)	0.20 ± 0.10

**Table 2.** General features of Esbka-7 Clay

Ground Characteristics	Results
Maximum Dry Density ( $\text{g}/\text{cm}^3$ )	1.40
Specific Gravity (Gs)	2.62
Plasticity Index	20
Optimum Water Content (%)	21
USCS Soil Classification	CL

In this study, the effect of magnesium oxide on the deep mixing method was examined. MgO was added at rates of 0%, 5% and 10% of the dry clay weight, and the unconfined compressive strength of the soil improved in this way was evaluated by keeping it for various curing periods. He carried out crushing experiments after 10, 15, 21 and 28 days.

The tank used in the experimental setup is cylindrical in shape, 40 cm in diameter and 30 cm in height. The tank was prepared by preserving the standard Proctor energy ( $600 \text{ kW}/\text{m}^3$ ) in 6 layers and compacting it at optimum water content with a vibratory compactor. The prepared tank was placed on the machine. The injection material was selected at 20% cement and 0%, 5% and 10% MgO as weight percentage of dry clay. These different ratios were chosen to determine the effect of magnesium oxide (MgO) on the mechanical properties of the soil. The water/binder ratio was chosen as 1.

The specified amount of materials is added to the chamber of the mixing machine. Wait until it becomes a homogeneous mixture. Afterwards, 1 bar pressure determined with the help of the compressor comes to the mixing machine. The drill bit pierces the ground and is lowered to the lowest part. Then, the drill bit rotates in the opposite direction, ensuring mixing of the ejection material.

The material prepared with the small-scale DSM system created homogeneous columns in clay. The mixing process was carried out with the tip rotating at 60 revolutions per minute and 1 bar pressure. A system that moves 30 cm vertically in 20 seconds was used. The experimental setup is shown in Figure 1.



**Figure 1.** Small scale deep mixing system

Unconfined pressure tests were carried out on samples left at certain curing times. The results obtained were analyzed to evaluate the effect of different MgO ratios on the strength of the soil. In this way, it is aimed to determine the optimum additive amounts and combinations.

### 3 RESULTS

The samples prepared in our study were subjected to uniaxial unconfined pressure testing after 10, 15, 21 and 28 days of curing periods. Samples and results are shown in Figures 2 and 3.



**Figure 2.** Prepared samples



Figure 3. Example of tests

The obtained unconfined compressive strength results are presented in Figure 4. These data show the effects of different magnesium oxide ratios on the strength of clay soils.

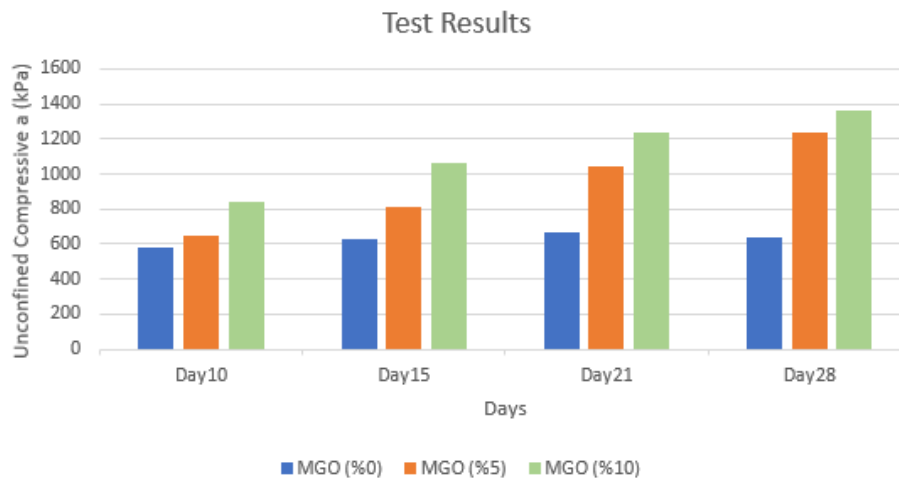


Figure 4. Unconfined compressive strength of samples subjected to 10, 15, 21 and 28-day cure

According to the results obtained, it was observed that magnesium oxide (MgO) had a positive effect on the mechanical properties of clay compacted at optimum water content. Unconfined compressive strength of the samples after 28 days; While it was 635.13 kPa at 0% MgO content, this value increased by 194% to 1237.07 kPa at 5% MgO content and increased by 214% to 1360.73 kPa at 10% MgO content. The unconfined compressive strength increased for each MgO content, and the effect of the curing time was most clearly seen in the 28-day sample containing 10% MgO. According to the results of the free pressure test, it was seen that there was no big difference between 5 and 10 percent MgO content. According to the Force - Elongation graphs, it was seen that the columns became ductile and did not break suddenly.

Increasing the curing time provided the necessary time for the hydration reactions between MgO and water to occur, and the resulting hydration products filled the gaps and increased the strength of the soil. These results show that MgO additive plays an effective role in improving clayey soils and increasing the curing time further increases the strength.

With the increase of the curing time, it has been determined that compounds such as Magnesium-Silica-Hydrate (MSH) and Magnesium Aluminium Hydrate (MAH), which are formed as a result of the interaction of  $Mg(OH)_2$  with  $SiO_2$  and  $Al_2O_3$  during the 28-day period, make positive contributions to the axial strength of the clay. During the long curing period, these products formed in the porous structure of  $Mg(OH)_2$ , creating more durable internal structures. These durable structures contributed to the clay soil becoming more resistant to external influences. As a result, extending the curing time improves the mechanical properties of the clay, allowing a more stable and durable soil to be obtained in terms of engineering.

## 4 CONCLUSION

This study investigated the improvement of clay soils by deep mixing method and the effect of using magnesium oxide (MgO) on this process. MgO, which is presented as an economical and environmentally friendly alternative to traditional cement-based stabilization methods, has been found to significantly increase the strength and stability of clay soils as a result of laboratory experiments.

The deep mixing method is an effective technique used for soil improvement and was combined with MgO in this study. The innovative use of MgO by deep mixing method, especially when used in combination with cement, offers an effective solution to geotechnical engineering problems and has the potential to reduce environmental impacts and reduce costs compared to traditional methods. This research highlights the importance of exploring alternative materials compatible with sustainable construction practices.

The effect of curing time and MgO ratio on the strength of the soil was also evident. The increased strength observed in the 28-day cured samples demonstrated the improvement achieved when allowing the hydration of MgO and the formation of beneficial compounds such as Magnesium-Silica-Hydrate (MSH) and Magnesium-Aluminate-Hydrate (MAH). Thus, extending the curing time and increasing the amount of MgO caused the sample to become brittle by reducing the water content of the soil, thus contributing to a tighter and denser formation between the soil particles.

In conclusion, this study not only reveals the potential of MgO as a soil stabilizer by deep mixing method, but also paves the way for future research. The successful integration of MgO in ground improvement projects can help solve current and future geotechnical engineering challenges, contributing to the construction of more sustainable and resilient infrastructures. These findings constitute an important step towards adopting new and innovative approaches in the construction industry.

## Acknowledgments

This study has been supported by the Yıldız Technical University Scientific Research Projects Coordination Unit (BAP) under the project number 6007. I would like to thank my advisors who helped me in my study. I would like to thank Tümke Makina for helping in machine manufacturing.

## References

- [1] M. M. Awad, et al., "Ground improvement and its role in carbon dioxide reduction: A review," *Environmental Science and Pollution Research*, vol. 28, pp. 8968–8988, 2021.
- [2] M. Bravo, et al., "Performance of Mortars with commercially-available reactive magnesium oxide as alternative binder," *Materials*, no. 14, no. 4, art. no. 938, 2021.
- [3] A. Sadiq, M. Y. Fattah, and M. F. Aswad, "Enhancement of the acid resistance of silty clay using nano-magnesium oxide," *Materials*, no. 16, no. 14, art. no. 5035, 2023.
- [4] Y. Yi, M. Liska, and A. Al-Tabbaa, "Initial investigation into the use of GGBS-MgO in soil stabilization," in *Grouting and Deep Mixing 2012*, 2012, pp. 444–453.
- [5] E. Bernard, "Research progress on magnesium silicate hydrate phases and future opportunities," *RILEM Technical Letters*, vol. 7, pp. 47–57, 2022.
- [6] T. Zhang, H. Fu, and J. Han, "Deformation mechanisms of magnesium silicate hydrate cement with a shrinkage-reducing admixture under different curing conditions," *Minerals*, vol. 13, no. 4, art. no. 563, 2023.
- [7] C. Dewitte, et al., "Chemical and microstructural properties of designed cohesive MSH pastes," *Materials*, vol. 15, no. 2, art. no. 547, 2022.
- [8] M. R. Marsiske, et al., "Uncovering the Early Stages of Magnesium Silicate Hydrate Formation: A Nonclassical Multistep Pathway," *ACS Applied Engineering Materials*, vol. 1, no. 1, pp. 696–707, 2023.





---

## Investigation of the Structure-Pile-Soil Interaction Behaviour in Earthquake Condition of a Reinforced Concrete Building with Pile Foundation

Evrin Er<sup>\*1</sup>, Sami Oguzhan Akbas<sup>1</sup>

<sup>1</sup>Civil Engineering, Gazi University, Ankara, Türkiye

---

### Abstract

In pile foundation systems, which are frequently used in our country for structures built on soils with bearing capacity or settlement problems, it has become mandatory to make solutions with building-soil interaction on ZD, ZE and ZF class soils, according to the Turkish Building Earthquake Regulation (TBDY 2018). In TBDY 2018, it was stated that the structure-pile-soil interaction, especially piles, significantly affects the earthquake behavior of buildings built with piles on relatively soft soils. Piles are subjected to significant plastic deformations due to the effect of earthquake waves generated by the earthquake ground motion defined in the bedrock and propagating within the ground. On the other hand, piles can significantly change the effective foundation movement of the building foundation in terms of both amplitude and frequency content. For these reasons, it is necessary to consider the structure-pile-soil interaction in buildings that sit on weak ground and have pile foundations. The regulation offers 3 methods regarding soil-structure interaction analysis methods and design applications for pile foundations, depending on Local Soil Class, Building Height Class (BYS) and Earthquake Design Class (DTS). The most comprehensive of these is Method I and it is mandatory to apply it in buildings with DTS = 1, 1a, 2, and building height class BYS = 1. In this method, the ground environment must be modelled in three dimensions using the finite element method. In Method II and Method III, there is no need to model the soil ground. In all three methods, kinematic interaction must be made to calculate the effect of earthquake waves propagating in the ground environment on the piles. This study aims to solve the structure-pile-soil interaction of a reinforced concrete building with a piled raft foundation on a ground with bearing capacity problem according to Method I, Method II and Method III, and compare the results between these three methods. Midas GTS-NX program will be used in the analyzes to be carried out according to Method I. In Method II and Method III, the soil model will be modeled in the DeepSoil program, and the pile and superstructure will be modeled in the Sap2000 program.

**Keywords:** TBDY 2018, Structure-pile-soil interaction, Kinematic interaction analysis, Finite elements, Nonlinear analysis

---



## Determination of Risk Factors within the Scope of Water Supply Management in Water Transmission Systems

Yusuf Kilinc<sup>\*1</sup>, Cansu Bozkurt<sup>2</sup>, Mahmut Firat<sup>1</sup>

<sup>1</sup>Civil Engineering Department, Inonu University, Malatya, Türkiye

<sup>2</sup>Technical Vocational School, Ardahan University, Ardahan, Türkiye

### Abstract

High water losses in water supply and distribution systems constitute a serious problem in many countries and in our country. Water losses cause significant economic losses and high amounts of water waste. The insufficient of existing water resources requires more economical and regular use of water. In water distribution systems, reducing water losses that cause water, energy and financial inefficiency, delivering sufficient and clean water to the public and its sustainable management are quite important. However, the methods applied in water loss management and network sustainability are time consuming and costly. Therefore, the most appropriate method should be chosen by taking into account the current capacity of the administration (personnel, technical, equipment and financial). It is great importance to determine and evaluate the possible risks to the network in order to reduce the negative factors that threaten the network. This study aims to define risk components in water supply in water transmission systems. In this context, possible risks that may cause disruption of water transmission were determined. While determining the risk components, basic data measurement, information management systems, water balance management were taken into consideration. The study plans to determine the risk level based on the effects of the factors in question on the network and their probabilities of occurrence.

**Keywords:** *Non-revenue water, Water losses, Risk factors, Risk level*

## 1 INTRODUCTION

As a result of the rapid increase in population, the inability of existing water resources to meet the demand requires more economical and regular use of water. In addition, the decrease in precipitation and the rapid depletion of existing water resources due to global warming threaten many regions as well as our country. It is estimated that our country will be a water-poor country in the coming years. On the other hand, an average of 45% of the water supplied to the network in municipalities in our country is lost due to various reasons [1]. Instead, effective and efficient management of existing water resources can prevent waste of resources. Water losses are basically examined under two main headings; Administrative Losses and Physical Losses. Administrative losses refer to the total amount of illegal use and meter and reading errors. Physical losses refer to the losses that occur in the stages (transmission and distribution lines, tanks and subscriber lines) that water passes from its source to the subscriber [2]. They stated that water supply systems generally consist of water sources, transmission pipes, treatment facilities and distribution networks from the source to the tap. They divided the hazards affecting the amount or quality of water into three groups: natural, human-induced and operational. To assess the reliability of water supply systems, they used risk assessment tools to identify threats, their probability, consequences and the status of each element of these systems against hazards [3].

Due to the increasing and urgent need for efficient management of insufficient water resources, it has become imperative for administrations to work on developing and implementing water management strategies and tools that will help in integrated and automated management of these networks. Such asset management strategies will help the administration to assess the condition of the water distribution network, evaluate historical event data and failure risk, visualize high-risk areas, propose “repair or maintenance” strategies and prioritize work [4]. Drinking water safety management is evolving towards an integrated risk assessment and risk management approach that covers all processes in the water supply system from the water collection system to the consumers [5].

The data obtained should aim to provide authorities from the water sector, water authorities and professional associations with all the information necessary to understand the origin, structure and impact of water losses, to develop and implement a customized counter-strategy and to choose the most efficient methods. There are many different causes and factors that affect the amount and type of water lost in a water distribution network. Without

sufficient knowledge of the nature of water losses, it is impossible to find the right and most efficient solutions to reduce them. Therefore, it is necessary to have a good understanding of water losses in order to reduce water loss. In this way, basic questions can be answered:

- where is water lost in the system,
- how is water lost,
- why is it lost,
- how much is lost.

## 2 MATERIAL AND METHOD

### 2.1 Determining Risk Categories and Sub-Categories

Urban water distribution networks are considered as one of the basic infrastructure facilities and equipment in urban areas. Pipes are one of the main and fundamental components of a water distribution network failure due to various factors during operation. Therefore, developing models for pipe failure rate prediction can be one of the most important tools for managers and stakeholders to optimally operate the water distribution network. In the last decade, various studies have been conducted to predict the failure rate of water distribution pipes using statistical and flexible models, each with its strengths and weaknesses [6].

Earthquakes are natural disasters that humans cannot control and cause significant damage to the economy and society. Earthquakes, in particular, affect not only buildings but also lifeline structures such as water distribution. The disruption of these networks is critical because it can directly damage facilities and also cause long-term loss of the overall system of society. Therefore, it is important to estimate the damage with possible earthquake scenarios and to consider the factors affecting lifeline structures [7].

Among the objectives of water companies is to maintain the performance of pipes in the water distribution system; It is provided through activities such as renovation works, maintenance activities, pressure management and other improvement operations. Therefore, it is useful to determine the risks related to pipes when planning such renovation works [8]. As a result of the research conducted by considering all the elements from the source to the subscriber, the risk categories were created as follows;

- Water source
- Purification and transmission line
- Storage tank
- Distribution system
- Institutional structure and management
- Information data

The main headings of the risks, namely the risk categories, are general headings for the drinking water network, and although they are based on all the elements from the source to the subscriber, they are divided into sub-parts under each category that ensure the integrity of the system. As a result of the literature review, the risk categories were determined as follows and the processes were planned to proceed in this direction.

**Table 1.** Risk categories

Risk Categories					
Water Source	Purification And Transmission	Storage	Distribution System	Institutional Structure And Management	Information Data
Source	Treatment	Maintenance	Physical Loss	Personnel	GIS
Pump	Transmission Line	Design	Administrative Loss	Control	System
	Energy			Equipment	SCADA
					Finance

## 2.2 Identifying Risk Factors

While determining the factors that constitute the risk, the determination was made by taking the following points into consideration.

- Situations that prevent the realization of strategic goals and objectives,
- Works and transactions that may cause its activities to fail,
- Weaknesses of the administration in carrying out its activities,
- Activities that may lead to corruption or irregularities,
- Activities that spend more than the anticipated cost,
- Critical decisions and tasks based on discretion,
- Complex activities and processes,
- Activities with criminal sanctions,
- Works within the field of activity that require advanced technical expertise,
- The emergence of new units or tasks,
- Corporate restructuring,
- Activities that may cause loss of labor, loss of life, or occupational disease,
- Activities that may prevent income increase or cause decrease,
- Activities defined in the business process charts created,
- The issues identified in the internal and external audit reports were taken into account.

While determining the risk factors, their applicability in the field, requirements (data, technological infrastructure, methods or processes that need to be applied beforehand), difficulty levels in implementation and economic requirements were taken into account. The aim here is to reveal the current status of the administration at each application level. Thus, information that will constitute a reference in determining the risky sub-components will be produced. In addition to the issues listed above, the entire system was divided into sub-headings within itself, ensuring both a better grouping of risk factors and revealing the risks belonging to each unit.

**Administration Management:** Under this main heading, the perspective of the institution's senior management on water loss management, management and organizational structure, unit and personnel status, technical equipment adequacy level, training and awareness activities, roadmap-planning, audit and budgeting policy are evaluated.

**Basic Data Measurement:** Under this main heading, the measurement frequency and quality of the basic data required within the scope of water loss management in the administration are questioned. For this purpose, evaluations are made for the most basic parameters such as network length, number of service connections, service connection length on private property, number of valves, number of subscribers, meter information, measurement frequency and quality of water produced and supplied to the system.

**Information Management Systems and Databases:** Under this main heading, the existence and application level of systems and databases used in monitoring and managing water management components in the administration are questioned. In this context, basic queries such as SCADA system (water production, storage, isolated zone inlet flow and pressure monitoring), GIS database (network, valve, network maintenance-repair, valve maintenance-repair), subscriber and meter databases, integration of management systems with each other and data sharing are made.

**Water Balance Management:** This main title basically includes inquiries regarding the applicability of water balance and roadmap, determination of administrative and physical loss subcomponents in the field. For this purpose, losses resulting from meter errors, unbilled legal uses, illegal uses, determination of leakages, GGS and indicators calculated for subcomponents are taken into consideration.

**Administrative Loss Management:** This main title basically includes evaluations within the scope of monitoring the reading efficiencies of legal subscribers, monitoring, analyzing administrative loss components, developing strategies for prevention and defining targets.

**Physical Loss Management:** This main title basically includes inquiries and evaluations within the scope of developing strategies for detection of leakages, defining the roadmap, monitoring, analyzing physical loss components, developing strategies for prevention and defining targets.

Water Loss Management Process and Performance Monitoring: This main title basically includes inquiries and evaluations within the scope of performance monitoring system, data updating and monitoring, billing, analysis of the performance of administrative loss and physical loss prevention methods, defining the roadmap and monitoring.

Economic Analysis: Under this main heading, basically, inquiries and evaluations are made within the scope of water production, fault management and network operation costs, administrative and physical losses cost, unbilled usage cost, cost of methods applied to prevent leaks and administrative losses.

The risk factors created as a result of the literature review are divided into various classes, and even if their locations are different, it is revealed by which unit or units they should be carried out [9]. In this context, risk factors;

- design,
- operation,
- maintenance,
- external factor,
- monitoring,
- control,
- economic,
- personnel,
- training,
- technology,
- data

risk factors classes were determined.

**Table 2.** Water source, purification and transmission line risk factors

No.	Risk Category	Risk Subcategory	Risk factors	Risk factor class
1	Water Source	Source	Failure to meet water demand due to insufficient water source	External Factor
2		Source	Failure to meet water demand due to pollution of water source	External Factor
3		Source	Inability to meet water demand due to lack of alternative water source	External Factor
4		Pump	Failure to deliver water due to failure of the pump in the water source	Care
5		Pump	Failure to deliver water due to the malfunction of the promotion pump	Care
6		Pump	Prolongation of repair time for pump malfunction and failure to deliver water due to insufficient maintenance and repair team	Employee
7		Pump	Failure of pumps due to energy problem in the pump station	Care
8		Pump	Failure of pumps due to power surge in pumping station	Care
9		Pump	Failure to meet water demand due to insufficient pump capacity	Design
10		Source	Inability to provide water supply due to damage to the source after natural disasters	External Factor
11th	Purification and Transmission Line	Purification	Failure to meet water demand in case of malfunction in treatment plant pipelines	Care
12		Transmission line	Water supply disruption due to inlet control valve failure	Care

13		Energy	Failure to meet water demand due to energy outage	External Factor
14		Transmission line	Failure to meet water demand due to malfunction in the facility control and monitoring system	Technology
15		Purification	Failure to provide water supply due to washing water capacity	External Factor
16		Purification	Failure to meet water demand due to algal bloom	External Factor
17		Transmission line	Failure to transmit water due to damage to the transmission line after natural disasters (landslides)	External Factor
18		Transmission line	Missing or damaged art structures	Design
19		Purification	Lack or insufficient cathodic protection in the transmission line	Economic
20		Transmission line	Illegal connection in the transmission line	Control
21		Transmission line	Failure to deliver water as a result of external intervention in the transmission line	Control
22		Transmission line	Use of low quality materials in the transmission line	Economic
23		Transmission line	Poor quality workmanship in the transmission line	Employee
24		Energy	Pump malfunctions in the transmission line	Control
25		Energy	Transmission line pump (promotion) station energy problem occurs	Economic
26		Transmission line	Difficulty in water transmission due to low pressure problem in the transmission line	Design

### 3 RESULTS

Managing the drinking water system and predicting any possible risks in the network is very important for a sustainable system. As a result of the study, the entire system from the source to the subscribers was evaluated and risk factors were determined. In order to easily determine and manage risk factors, the network was divided into 6 categories: water source, treatment and transmission line, storage, distribution system, institutional structure and management and information data. The categories created were divided into subcategories and evaluated. Risk factors were created for each of the headings in the subcategory by conducting literature and field studies. While determining the risk factors, the general structure of the institutions was taken into consideration, and within the scope of their activities, cost-generating situations and elements affecting water transmission were taken into consideration in accordance with their strategic goals and objectives. Again, during the determination of the factors, their applicability in the field, requirements (data, technological infrastructure, methods or processes to be applied beforehand), and difficulty levels in application were taken into consideration and the determination was made. Within the scope of determining the factors, 10 parameters in 2 subcategories belonging to the water source and 16 parameters in 3 subcategories belonging to the treatment and transmission line were determined. Although the determined parameters are common for almost all administrations, the number can be increased depending on the special circumstances of the administrations.

### 4 CONCLUSION

The study aimed to determine the risk by considering all the situations that may occur in institutions working within the scope of drinking water. The determined risk factors can be used by the administrations by adding or removing, thus not requiring a new study. With the study, the administrations will be able to foresee possible risks that may occur in their systems and make early interventions. Thanks to the categories and subcategories created, the administrations will be able to make a risk assessment under the desired title, thus both the study will be carried out regarding the main problematic area and the determination of the risk will be faster. The study aimed to facilitate the detection of failures by creating a reference for institutions struggling with high water losses and failure costs. It can reveal the adequacy status of the administrations in these matters by ensuring that they question

their institutional structure and technological infrastructure. If taken as a basis by the administrations, it aims to reduce water loss rates to a great extent.

## References

- [1] S. Toprak, A. Koc, U. Bacanlı, F. Dikbas. M. Firat, and A. Dizdar, “K losses in drinking water distribution systems and prowat project,” in *5th Urban Infrastructure National Symposium*, 2007, pp. 15–30.
- [2] S. Yilmaz, “Investigation of the effect of customer meters on water loss,” M.S. thesis, Inonu University, Malatya, 2017.
- [3] A. Roozbahani, B. Zahraie, and M. Tabesh , “Integrated risk assessment of urban water supply systems from source to tap,” *Stoch Environ. Res. Risk Assess.*, vol. 27, no. 4, pp. 923–944, 2013.
- [4] S. Christodoulou, C. Charalambous, and A. Adamou, “Rehabilitation and maintenance of water distribution network assets,” *Water Sci. Technol.: Water Supply*, vol. 8, no. 2, pp. 231–236, 2008.
- [5] F. Sun, J. Chen, Q. Tong, S. Zeng, “Integrated risk assessment and screening analysis of drinking water safety of a conventional water supply system,” *Water Sci. Technol.*, vol. 56, no. 6, pp. 47–56, 2007, doi: 10.2166/wst.2007.583.
- [6] A. R. Zahiri, S. M. Jafari, O. Bozorg-Haddad, and M. R. Tabari, “New approach for prediction of water distribution network pipes failure based on an intelligent hybrid model (case study: gorgan water distribution network),” *J. Water Soil Conserv.*, vol. 27, no. 5, pp. 149-166, 2021, doi: 10.22069/JWSC.2021.17670.3319.
- [7] S. Yoon, Y. J. Lee, and H. J. Jung, “Acomprehensive framework for seismic risk assessment of urban water transmission networks,” *International Journal of Disaster Risk Reduction*, vol. 31, pp. 983–994, 2018.
- [8] S. Salehi, M. J. Ghazizadeh, M. Tabesh, S. Valadi, and S. P. S. Nia, “A risk component-based model to determine pipes renewal strategies in water distribution networks,” *Struct. Infrastruct. Eng.*, vol. 17, no. 10, pp. 1338–1359, 2020, doi: 10.1080/15732479.2020.1842466.
- [9] C. Orhan et al., “Performance indicators for monitoring fault maintenance and repair processes in drinking water distribution systems,” *European Journal of Science and Technology*, no. 34, pp. 126–134, 2022.



## Defining the Impact Levels of Risk Factors in Water Transmission Systems

Yusuf Kilinc<sup>\*1</sup>, Cansu Bozkurt<sup>2</sup>, Mahmut Firat<sup>1</sup>

<sup>1</sup>Civil Engineering Department, Inonu University, Malatya, Türkiye

<sup>2</sup>Technical Vocational School, Ardahan University, Ardahan, Türkiye

### Abstract

In drinking water distribution systems, the reduction and sustainable management of water losses that cause water, energy and financial inefficiency is quite important. Therefore, the factors causing water losses should be identified. In addition, possible risks in the system should be determined to ensure safe water delivery to customers. Various risks can be observed in water supply, water production and transmission stages. The impact of these risks is generally at different levels. It is important to define the impact levels of risks in order to perform risk assessment in each system. In this study, the impact levels (weights) of risk factors defined within the scope of safe water delivery to customers were determined. The FUCOM (Full Consistency Method) method was used in the study to determine the weight coefficients. The parameters were ranked according to their importance. FUCOM (Full Consistency Method) is a multi-criteria decision-making method in which the criteria weights can be determined based on the decision maker's priorities. The method consists of ranking the criteria according to their importance, comparing the ranked criteria and determining comparative priorities, and finally calculating the final weights of the criteria. Weights were calculated for the risk factors that cause disruption of water supply. Risk factors were prioritized by taking these weights into account. It is thought that the results obtained from the study will serve as a reference for decision makers and technical personnel in water administrations.

**Keywords:** *Non-revenue water, Water losses, Risk factors, Risk level, FUCOM*

## 1 INTRODUCTION

The drinking water supply and distribution system is the whole that includes all the structures and systems created from the source of water to the subscriber. The structures that make up the system are the water source, transmission line, purification structures, tanks, distribution system, service connections and auxiliary structures such as mast, suction cup, maneuver room, zoning systems, and energy units[1, 2]. The main purpose of the drinking water distribution system is to deliver safe and sufficient water to subscribers. The reduction and sustainable management of water losses that cause energy and financial inefficiency during the realization of the said purpose are very important [3, 4].

The transfer of water from the source to the final point, the subscribers, contains various risks. Risks in the water source;

Inadequate water source

- Pollution of water source
- Lack of alternative water source
- Pump failure in water source
- Pump failure
- Inadequate maintenance and repair team
- Energy problem in pump station
- Power fluctuation in pump station
- Insufficient pump capacity
- Damage to source after natural disasters

Risks in treatment transmission line;

- Failure in treatment plant pipelines
- Inlet control valve failure



- Power outage
- Failure caused by facility control and monitoring system
- Washing water capacity
- Algae bloom
- Natural disasters
- Lack of engineering structures
- Lack of cathodic protection in the transmission line
- Illegal connection in the transmission line
- External intervention in the transmission line
- Use of low quality materials in the transmission line
- Low quality workmanship in the transmission line
- Pump failures in the transmission line
- Energy problem in the transmission line pump (lift) station
- Low pressure problem in the transmission line.

The impact of these risks is generally at different levels. In order to make a risk assessment in each system, it is very important to define the impact levels of the risks. As a result of determining the risk levels, the drinking water supply and distribution system parts are scored among themselves, prioritization is made, the current status of the administrations is revealed and the success rate in intervention to the fault increases [5].

FUCOM method is a method used to determine the importance density of the factors and to optimize and develop the ranking of the available alternatives in multi-purpose problems. This method includes mathematical calculations and thus gives more consistent results [6].

## 2 MATERIAL AND METHOD

### 2.1 Determination of Weight Coefficients

The FUCOM (Full Consistency Method) method was used in the study to determine the weight coefficient. With this method, the parameters were ranked according to their importance. In the selection process to be made among various alternatives with more than one criterion, the most important factor affecting the decision is the determination of the importance degree of the criteria in question on the alternatives. Since each criterion has a different level of importance, the order of the selection decision to be made among the alternatives also changes depending on the weight of these criteria. For this reason, the weighting process of the criteria according to their importance degrees on the alternatives has an important place in the application of multi-criteria decision-making methods [7].

Criteria weighting methods are among the processes that should be done before the decision process in multi-criteria decision-making problems. There are many criterion weighting methods used in multi-criteria decision-making problems [8].

The FUCOM method is used to obtain the criteria weights to rank the alternatives. The FUCOM method was developed to improve the process of determining the criteria weights. Similar methods are often used to determine the criteria weights or to rank the alternatives. The ranking is performed based on pairwise comparisons. On the other hand, many other methods are used to determine the criteria weights, where it is necessary to determine the best and worst criteria before making pairwise comparisons. FUCOM has considerable advantages over other methods [9].

FUCOM (Full Consistency Method) is a multi-criteria decision-making method in which the criteria weights can be determined based on the decision maker's priorities. The method consists of the steps of ranking the criteria according to their importance, comparing the ranked criteria and determining the comparative priorities, and finally calculating the final weights of the criteria [10].

Step 1: The order of importance of the criteria is determined from the predefined set of evaluation criteria ( $C = \{C_1, C_2, \dots, C_n\}$ ). This ordering is done according to the degree of importance of the criteria. In other words, a ranking is created from the criterion expected to have the highest weight coefficient to the least significant criterion, and the criteria are ranked according to the expected values of the weight coefficients as shown below, where  $k$  is the order of the criteria.

$$(1) > (2) > \dots > C_j(k) \tag{1}$$

Step 2: The ranked criteria are compared and the comparative priority of the evaluation criteria ( $\varphi_{k/(k+1)}$ ,  $k = 1, 2, 3, \dots, n$ ) is determined. The comparative priority of the criterion ranked in the  $k$ th place shows the advantage of the criterion ranked in the  $(k+1)$ st place. With this process, the following comparative priority vectors are obtained:

$$\Phi = (\varphi_{1/2}, \varphi_{2/3}, \dots, \varphi_{k/(k+1)}) \tag{2}$$

Step 3: In the third step, the final values of the weight coefficients of the evaluation criteria ( $w_1, w_2, \dots, w_n$ ) T (3) are calculated. The ratio of the weight coefficients must be equal to the comparative priority ( $\varphi_{k/(k+1)}$ ) between the observed criteria defined in Step 2; that is, the following condition must be met.

Condition 1. The comparative priority of the ratio of the weight coefficients must be equal

Condition 2. The weight coefficients must provide mathematical transitivity [11].

Within the scope of the method, weight coefficient calculations were made for 6 risk categories of the network, namely water source, treatment and transmission line, storage, distribution system, institutional structure and management and information data, and their subcategories and risk factors. In the study, water source, treatment and transmission line categories; their subcategories and weight coefficient calculations of risk parameters are shown.

The 6 parameters in the risk category were named respectively and weightings were made among them in the first stage.

**Table 1.** Main categories

Main Criteria	
K	Management
S	Water supply
A	Purification Transmission
D	Storage
I	Drinking Water Distribution System
B	Information Data

**Table 2.** Ranking table

Number of Criteria = 6	Criterion 1	Criterion 2	Criterion 3	Criterion 4	Criterion 5	Criterion 6
Criterion Name	K	S	A	D	I	B
Arrangement	2	5	4	3	1	6
Criteria (in order of importance)	I	K	D	A	S	B
Comparative Priorities	one	3	5	6	7	9

First of all, the named criteria are listed from the most important to the least important in terms of their potential to create risks in water supply and distribution systems.

Then, scoring was made using the "Standard Preference Table" given below among the criteria listed in order of importance. While scoring, the most important criterion is always compared with the others.

**Table 3.** Preference table

Standard Preference Table	
Importance Values	Value Definitions
1	Equal
3	A little more important
5	Pretty important
7	Very important
9	Highly important
2,4,6 and 8	Intermediate values

**Table 4.** Main criteria weight results

Weights	I	K	D	A	S	B
	0.512	0.171	0.102	0.085	0.073	0.057

**Table 5.** Weight results

Weight Results of Risk Factors						
Main Criterion	wana	Subcategory	wka	Subcriterion	Walt	Wintegrated
Water supply	0.170593	Source	0.875	Sk1	0.404624	0.0603978
				Sk2	0.202312	0.0301989
				Sk3	0.080925	0.0120796
				Sk4	0.080925	0.0120796
				Sk5	0.057803	0.0086283
				Sk6	0.057803	0.0086283
				Sk7	0.057803	0.0086283
				Sk8	0.057803	0.0086283
		Pump	0.125	Sp1	0.514391	0.0109689
				Sp2	0.171464	0.0036563
				Sp3	0.102878	0.0021938
				Sp4	0.073484	0.001567
				Sp5	0.073484	0.001567
				Sp6	0.064299	0.0013711
Purification Transmission	0.102356	Purification	0.8333333	Aa1	0.583468	0.0497678
				Aa2	0.116694	0.0099536
				Aa3	0.097245	0.0082946
				Aa4	0.072934	0.006221
				Aa5	0.06483	0.0055298
				Aa6	0.06483	0.0055298
		Transmission line	0.1666667	Ai1	0.384263	0.0065553
				Ai2	0.128088	0.0021851
				Ai3	0.096066	0.0016388
				Ai4	0.076853	0.0013111
				Ai5	0.076853	0.0013111
				Ai6	0.064044	0.0010925
				Ai7	0.064044	0.0010925
				Ai8	0.054895	0.0009365
				Ai9	0.054895	0.0009365
				Ai10	0.054895	0.0009365
				AI11	0.054895	0.0009365
				AI12	0.048033	0.0008194

### 3 RESULTS

There are various risks in the drinking water system from the source to the subscriber. It has become mandatory for the administrations fighting against loss and leakage to define the risks in question, categorize them and conduct separate studies for each risk. In the studies conducted for each risk, the risk should be prioritized and intervention should be made in the right place on time. First of all, one of the simple methods of choosing the most dangerous situation is to weight each risk. In this study, the risks in the network that are categorized are listed with the weighting method FUCOM method. In the study, weighting among the 6 main headings, weighting for 2 subheadings and weighting studies for the risks in these 2 subheadings were conducted. With the study, the drinking water distribution system had the highest weight with a value of 0.512 among the main headings. In the comparative calculation, the weighting ratios were determined so that the totals would be 1, and easy-to-understand and clear results were obtained.

### 4 CONCLUSION

The biggest problem of the administrations managing the drinking water system is the difficulty of predicting the fault in the network and the inability to work systematically. In order to correct these situations, a risk map belonging to the system should be created by the administrations and intervention should be provided by

continuous monitoring. While the study provides convenience to the administrations with the risk parameters it offers, it aims to identify the riskier sections with the weighting studies. The system parts are ranked from important to less important by using the weighting coefficient method. In this way, it can be easily determined where the available financing, equipment, labor, and technology will be used first by the administrations. The disruptions in the system can be reduced by saving the resources and time in question. Since any administration using the study will make a weighting coefficient by considering its own conditions, the results will be specific to each administration and will make it easier for the administration to decide.

## References

- [1] M. Babaei, A. Roozbahani, and M. Hashemy Shahdany, "Risk assessment of agricultural water conveyance and delivery systems by fuzzy fault tree analysis method," *Water Resour. Manag.*, vol. 32, no. 12, pp. 4079–4101, 2018.
- [2] T. Dawood, et al., "Water pipe failure prediction and risk models: State of the art review," *Canadian Journal of Civil Engineering*, vol. 47, no. 10, 2019, doi: 10.1139/Cjce-2019-0481.
- [3] R. C. Marques and A. J. Monterio, "Application of performance indicators in water utilities management—A case-study in Portugal," *Water Sci. Technol.*, vol. 44, no. 2–3, pp. 95–102, 2001.
- [4] J. Gao, K. Li, W. Wu, J. Chen, T. Zhang, L. Deng, and P. Xin, "Innovative water supply network pressure management method," *The Establishment and Application of the Intelligent Pressure-Regulating Vehicle Energies*, vol. 15, art. no. 1870, 2022, doi: 10.3390/en15051870.
- [5] S. Abedzadeh, A. Roozbahani, and A. Heidari, "Risk assessment of water resources development plans using fuzzy fault tree analysis," *Water Resour. Manag.*, vol. 34, no. 8, pp. 2549–2569, 2020.
- [6] T. Mercan and A. Can, "Evaluation of the factors affecting personnel selection with fucom method: An application in an airline company," *Suleyman Demirel University Visionary Journal*, vol. 14, no. 40, pp. 1311–1329, 2023.
- [7] G. Demir and H. Birca, "Comparison of BWM and FUCOM methods of criteria weighting methods and an application," *Sivas Cumhuriyet University Journal of Economics and Administrative Sciences*, vol. 21, no. 2, 2020, doi: 10.37880/cumuiibf.616766.
- [8] M. Tabesh, A. Roozbahani, F. Hadigol, and E. Ghaemi, "Risk assessment of water treatment plants using fuzzy fault tree analysis and monte carlo simulation," *Iranian Journal of Science and Technology, Transactions of Civil Engineering*, vol. 46, pp. 643–658, 2022.
- [9] M. C. Ong, Y. T. Leong, Y. K. Wan, and I. M. L. Chew, "Multi-objective optimization of integrated water system by FUCOM-VIKOR approach," *Process Integration and Optimization for Sustainability*, vol. 5, no. 1, 43–62, 2021, doi: 10.1007/s41660-020-00146-3.
- [10] Ž. Stević, N. Mujaković, A. Goli, and S. Moslem, "Selection of logistics distribution channels for final product delivery: FUCOM-MARCOS model," *J. Intell. Manag. Decis.*, vol. 2, no. 4, pp. 172–178, 2023, doi: 10.56578/jimd020402.
- [11] D. Pamučar, Ž. Stević, and S. Sremac, "A new model for determining weight coefficients of criteria in MCDM models: Full consistency method (FUCOM)," *Symmetry*, vol. 10, art. no. 393, 2018.



## Determination of Regional Earthquake Risk Distribution of Buildings in the Central Gencosman Neighborhood of Bayburt Province

Omer Can<sup>1</sup>, Ertekin Oztekin<sup>2</sup>, Omer Bayrak<sup>\*3</sup>

<sup>1</sup>Construction Technology, Canakkale Vocational School of Technical Sciences, Canakkale Onsekiz Mart University, Canakkale, Türkiye

<sup>2</sup>Civil Engineering, Gumushane University, Gumushane, Türkiye

<sup>3</sup>Civil Engineering, Bayburt University, Bayburt, Türkiye

### Abstract

The biggest Earthquakes in the Country history had been experienced by Erzincan province. The Bayburt province is very close to the Erzincan Province and determination of earthquake risk distribution of buildings in this province is mandatory for the estimations of scenarios after earthquakes and for taking necessary precautions before earthquakes. In many residential regions of our country, a lot of studies had been completed and also a lot of studies continues in order to determine regional earthquake risk distribution. In contrast, it has not performed any study about this subject in the Bayburt province until now.

In this study, determination of the earthquake risk distributions of the reinforced concrete and masonry buildings in the Central Gencosman Neighborhood of Bayburt Province was aimed.

For this aim, fist step evaluation method described in the Annex-A of Law No. 6306 in our country was used in order to determine regional earthquake risk distribution.

The parameters such as short column, soft story, cantilever, big cantilever, visual building quality, impact effect, hill-hillside effect, story numbers, building dimensions, building location were determined in this study. All information collected by the visual screening during Street view will be used in the calculation of performance score of the buildings. All scores were used in the determination of the risks and/or risk ranking of buildings.

By this study, the question of which building has more risk and needs precaution works for a possible earthquake was replied. By this way, an idea about whether an urban transformation is required for this region or not was obtained from this study. Hereby, this study will suply very big contribution to preventing of the life and property losses. This study will lead the similar studies for the other regions of the Bayburt province.

**Keywords:** Earthquake, Bayburt, Distribution of building

## 1 INTRODUCTION

Considering what earthquakes leave behind, it is necessary to take all necessary precautions against this natural event very quickly to avoid similar situations. Almost all of the loss of life and material damage in earthquakes are caused by damage to structures built by human beings themselves. When it comes to preparations or precautions against earthquakes, the first thing that comes to mind is to identify the risky buildings, strengthen them if possible, and if strengthening is not possible, evacuate and demolish them as soon as possible. Although the process can be expressed in this way in one sentence, serious, long and laborious studies need to be carried out in order to fully decide whether even a single building is really risky or safe. Considering the building stock in our country and the world, it becomes clear that it is not possible to detect all truly risky buildings at once. This being the case, as in many countries around the world and in our country, some cruder but faster methods have been developed to take urgent measures. All the studies that need to be done and the methods that can be used to identify risky buildings in our country and determine the regional earthquake risk distribution of buildings are given in detail in the annexes of the Law No. 6306 on the Transformation of Areas Under Disaster Risk dated 16.05.2012 (Annex-2, Annex-A). In other words, within the scope of this law, simplified methods are given that take into account building characteristics and earthquake hazard, which can be used to determine the regional distribution of buildings that may be risky in certain areas and to make prioritization decisions. This law also includes; "In order to determine priorities in certain areas and the regional distribution of potentially risky buildings; First Stage Assessment Methods, which take into account building characteristics and earthquake hazard, can be used. If the ranking to be made is desired to be more precise, Second Stage Evaluation Methods can also be used. In the first stage evaluation methods, parameters determined from the outside and partly from the inside of the building and

affecting the earthquake behavior are used". It is said. This method proposed in this law is used for existing reinforced concrete buildings with 1 to 7 floors and existing masonry buildings with 1 to 5 floors

Many studies have been carried out using this and similar methods to determine building risk distribution in many residential areas of our country. Tokgoz and Bayraktar (2015) using the street scanning method to detect risky buildings in Kaynaşlı district of Düzce Province 2112 buildings were examined [1]. Isik (2015) carried out the evaluation of the masonry building stock in Bitlis Province by street scanning method. Bitlis urban building stock. When the earthquake scores of 296 masonry and mixed buildings examined in all neighborhoods in the first stage evaluation for masonry and mixed buildings, which constitute 40%, are examined; 16% of the total 296 buildings examined were first priority; 44% were in the second priority and 40% were in the third priority building group to be examined [2]. In 2015, the same author comparatively used the first stage evaluation methods used in Japan, Canada and Turkey on the existing reinforced concrete Çeltiksuyu Regional training school building of the same province. In each method, it was revealed that the mentioned reinforced concrete building was extremely risky [2]. Aslankara et al. (2005) collected information about 1700 buildings located on 2009 parcels in Denizli province by street scanning method and made risk assessments of these buildings [3]. Bayrak used the first stage evaluation method for Erzincan province in 2011. For this purpose, 400 buildings located in the central districts of Erzincan province were evaluated using the first stage evaluation method [4].

## 2 MATERIAL AND METHOD

The method to be used in this study is the First Stage Evaluation Method, which is one of the simplified methods in Annex-A of Annex-2 of the Law No. 6306 on the Transformation of Areas at Disaster Risk, which takes into account building characteristics and earthquake hazard. According to the law in question, the same method can be applied for Reinforced Concrete and Masonry buildings. However, although the method is the same, the evaluation criteria for reinforced concrete and masonry buildings are made differently. In the annex of Law No. 6306 (Annex-A in Annex-2) [5], the method is explained as follows for reinforced concrete and masonry buildings.

### 2.1 First Stage Evaluation Method for Reinforced Concrete Buildings (Law No. 6306 (Annex-2 - Annex-A))

This method can be used for existing reinforced concrete buildings with 1 to 7 floors. The parameters required to use the method are given below:

**Carrier System Type:** The carrier system of the building will be determined and selected as one of the reinforced concrete frame (RFB) (DBYBHY Table 2.5, Article 1.1) and reinforced concrete frame and curtain (BACP) (DBYBHY Table 2.5, Article 1.4) systems

**Number of Floors:** The number of free floors (nff) will be determined by taking the critical floor into account.

**Current Condition and Apparent Quality:** The apparent quality of the building reflects the importance given to the quality of materials and workmanship and the maintenance of the building. The apparent quality of the building will be classified as good, medium and poor.

**Soft Story/Weak Story:** It will be determined observationally, taking into account the difference in storey height as well as the significant stiffness difference between floors.

**Vertical Irregularity:** It will be taken into account to reflect the effect of vertically discontinuous frames and changing floor areas. Columns or curtains that do not continue along the height of the building create vertical irregularities.

**Heavy Overhangs:** The difference between the floor area resting on the ground and the floor area above the ground will be determined.

**Irregularity/Torsion Effect in the Plan:** It is defined as the plan not being geometrically symmetrical and the vertical structural elements being placed irregularly. Plan irregularities that may cause torsion in the building will be taken into account.

**Short Column Effect:** At this stage, only short columns observed from the outside will be taken into account in the evaluation.

Note: All information under this heading was taken directly, without modification, from ANNEX-2 (Annex A) of Law No. 6306 [5]

**Building Order/Collision Effect:** The locations of adjacent buildings can affect earthquake performance due to collision. Buildings located on the edge are most negatively affected by this situation, and this negativity increases even more if the floor levels of the adjacent building are different. Situations where the impact of a collision occurs will be determined by external observations.

**Hill/Slope Effect:** This effect will be taken into account in buildings built on slopes above a certain slope.

**Earthquake Hazard and Ground Class:** It will be taken in accordance with the earthquake zones and ground classes specified in DBYBHY.

A performance score (PC) will be calculated for each building by evaluating the collected data. The results obtained can be used to determine the risk priorities of the regions. Performance scores of reinforced concrete buildings will be calculated based on parameters that reflect the earthquake hazard of the location where the buildings are located and the existing building characteristics. A base score (BC) will be determined for the building examined using Table 1, depending on the earthquake hazard zone and the number of floors where the building is located. The relationship between the earthquake hazard zones to be used in the method and the soil classes given in the Turkey Earthquake Zones Map and DBYBHY, which came into force with the decision of the Council of Ministers dated 18/04/1996 and numbered 96/8109, is given in Table 2.

The effect of the carrier system type will be taken into account as a positive score. No additional points will be given for buildings with other load-bearing systems, and positive parameter scores will be given for buildings with other load-bearing systems, using Table 1.

**Table 1.** Base and structural system score table

Total floor base score	Structural system score (SSS)					
	Danger zone				Structural system	
	I	II	III	IV	RFB	RFSWB
1 and 2	90	120	160	195	0	100
3	80	100	140	170	0	85
4	70	90	130	160	0	75
5	60	80	110	135	0	65
6 and 7	50	65	90	110	0	55

Determinations as “yes” or “absent” will be made for all negativity parameters other than the apparent quality. The negativity parameter values (O<sub>i</sub>) corresponding to these determinations will be taken as 1 and 0 for “present” and “absent” cases, respectively. If the apparent quality rating is “good”.

The negativity parameter value (O<sub>i</sub>) will be taken as 0, 1 if it is “medium” and 2 if it is “bad”. The negativity coefficients corresponding to each parameter are shown in Table 4.

The performance score (PC) for the building will be calculated by applying Equation 1.

$$PC = BC + \sum_{i=1}^n O_i \times OP_i + SSS \tag{1}$$

In Equation 1, TP represents the base score, O<sub>i</sub> represents each negativity parameter (i=1 to 8), OP<sub>i</sub> represents the negativity parameter score (Table 4), and SSS represents the positive parameter score. Structural system scores (SSS) are given in Table 1.

As a result of applying the method to the buildings in the examined region, the performance score PC will be calculated for each building. Calculated performance scores will be sorted from largest to smallest. Using the distribution of scores calculated in this way, risk priorities can be determined between regions.

**Table 2.** Earthquake zones determined according to DBYBHY

Danger zone	Earthquake zones	
I	1	Z3/Z4
II	1	Z1/Z2
	2	Z3/Z4
III	2	Z1/Z2
	3	Z3/Z4
IV	3	Z1/Z2
	4	All floors

**Table 3.** Negativity parameter values (Oi) BHY floor class

Negation parameter number	Negativity parameter	Case 1		Case 2	
		Parameter determination	Parameter value	Parameter determination	Parameter value
1	Soft floor	None	0	There is	1
2	Heavycantilevered	None	0	There is	1
3	Visible quality	Good	0	Fair (Bad)	1 (2)
4	Short colon	None	0	There is	1
5	Hill/Slope effect	None	0	There is	1
6	Irregularity in plan	None	0	There is	1

**Table 4.** Odds parameter score (OPi) table

Total number of floors	Odds parameter score (OPi) table											
	Soft floor	Visible quality	Heavy Cantilevered	Floor level/Independent building					Vertical irregularity	Irregularity in plan / Torsio	Short colon	Hill/slope effect
				Same Middle	Same Middle	Edge	Differant Middle	Different Edge				
1,2	-10	-10	-10	0	-10	-5	-15	-5	-5	-5	-3	
3	-20	-10	-20	0	-10	-5	-15	-10	-10	-5	-3	
4	-30	-15	-30	0	-10	-5	-15	-15	-10	-5	-3	
5	-30	-25	-30	0	-10	-5	-15	-15	-10	-5	-3	
6,7	-30	-30	-30	0	-10	-5	-15	-15	-10	-5	-3	

## 2.2 First Stage Evaluation Method for Masonry Buildings (Law No. 6306 (Annex-2 - Annex-A))

This method can be used for existing masonry buildings from 1 to 5 stories. The parameters required to use the method are given below:

- i. **Masonry Building Type:** The load-bearing system of the building will be determined and one of the unreinforced masonry, surrounded masonry, reinforced masonry and mixed (masonry wall + reinforced concrete frame) systems will be selected as the building system.
- ii. **Number of Free Floors:** The number of free floors will be determined by taking the critical floor into account.
- iii. **Building Order and Its Relationship with the Adjacent Building:** Whether separate or adjacent buildings and building floor levels are the same or different will be determined. Five different situations will be determined for this parameter: Separate, adjacent and middle-floor level is the same, adjacent and middle-floor level is different, adjacent and edge/corner-floor level is the same, adjacent and edge/corner-floor level is different.
- iv. **Current State and Apparent Quality:** Material type and quality and masonry workmanship will be checked separately, and classification will be made separately as good, medium and poor for both of these determinations. Additionally, it will be determined whether there is any existing damage and a determination will be made as to whether there is damage to the building or not.
- v. **Negativities in the Plan:** Plan geometry, wall void ratio and whether there is a beam/lintel will be determined. Plan geometry will be specified in two ways, Regular or Irregular. On the critical floor of the building (usually the ground floor), the length of the facade wall in both directions perpendicular to each other will be determined. Accordingly, the amount of walls of the building is defined as "Multiple" if the length of the door and window openings on the front or side facades on the ground floor is less than 1/3 of the facade length, and "Medium" if the length of the gaps is between 1/3 and 2/3 of the facade length. If the length of the gaps is more than 2/3 of the facade length, it will be considered "Low".



- vi. Negatives in Vertical: Vertical wall space arrangement, difference in the number of floors according to the facades and whether there are soft floors will be determined. Vertical space arrangement; They will be classified as “Regular”, “Less Regular” and “Irregular”. If the window and door spaces on the floors are completely overlapped, it will be defined as “Regular”, and if they are placed staggered, it will be defined as “Irregular”. Buildings that fall between these two limit states will be classified as “Less Regular”.
- vii. It will be determined if different facades of the building located on sloping land have different number of floors. It will be determined whether there is a wall discontinuity in the vertical direction.
- viii. Disadvantages of Out-of-Plane Behavior: It will be determined whether masonry walls tend to show out-of-plane behavior. Negativities that trigger out-of-plane behavior in masonry buildings and can generally be detected from outside the building can be listed as follows:
  - a. Weak wall-wall and wall-floor connections (crack or damage where the connections are located, absence of beams)
  - b. Not having a slab that exhibits rigid diaphragm behavior (only masonry structures with reinforced concrete slabs will be considered to show this type of behavior).
  - c. The situation where the mortar quality is too low or there is no mortar at all (causing the wall to separate out of plane).
  - d. Outward out-of-plane deformation in masonry walls
  - e. Masonry structures with gable-wall roof type have the potential to be damaged out of plane.
- ix. Roof Type: This parameter will be determined only for masonry buildings with earthen ceiling slabs.
- x. Earthquake Hazard and Ground Class: It will be taken into account as described in A.2.1.4, in accordance with the earthquake zones and ground classes specified in DBYBHY.

### 3 RESULTS

An attempt was made to investigate the earthquake risk distribution of the region by street scanning method from the buildings in the Central GenCosman District of Bayburt province. In the light of the studies carried out, some statistical data about the buildings in the region were also obtained. These data can be seen in Tables 5, 6 and 7.

**Table 5.** Number of reinforced concrete and masonry-mixed buildings in the sub-regions

Region No	Reinforced Concrete Building	Masonry or Mixed Building	Total
1	21	3	24
2	48	6	54
3	37	7	44
4	96	16	112
5	24	33	57
6	50	0	50
7	19	0	19
8	60	0	60
9	35	0	35
10	20	1	21
Total	410	66	476

**Table 6.** Distribution of some important negativity parameters of reinforced concrete buildings by sub-regions (R: Region)

Immortality Parameters		R1	R2	R3	R4	R5	R6	R7	R8	R9	R10	Total
Short Colon	There is	0	0	21	79	1	38	13	2	7	2	163
	None	21	48	16	17	23	12	6	58	28	18	247
Extreme console	There is	11	32	22	14	5	4	13	18	1	4	124
	None	10	16	15	82	19	46	6	42	34	16	286
Soft Floor	There is	0	0	22	78	17	17	16	27	0	3	164
	None	21	48	15	18	33	33	3	33	35	17	246
Collision Effect	There is	5	29	5	53	17	17	16	34	0	0	168
	None	16	19	32	43	33	33	3	26	35	20	242
Visible Build Quality	Good	6	18	9	2	8	6	1	15	24	18	100
	Middle	9	15	16	14	42	19	3	29	7	1	129
	Bad	6	15	12	80	7	25	15	16	4	1	181

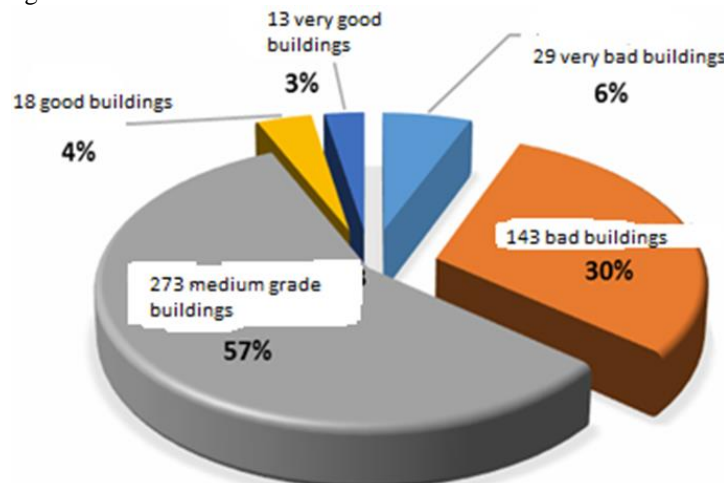
Similar to such negativities in reinforced concrete buildings, some important parameters that may affect the earthquake performance of masonry and mixed buildings in the study area include the total number of floors, wall void ratio, wall void arrangement, collision effect and apparent construction quality.

Of the 66 masonry + masonry buildings in the risk scanned area, 16 have 1 storey, 32 have 2 floors, 14 have 3 floors and finally 4 have 4 or more floors.

**Table 7.** Distribution of some important negative parameters of Masonry + Mixed buildings according to sub-regions (R: Region)

Immortality Parameters	R1	R2	R3	R4	R5	R6	R7	R8	R9	R10	Total	
Total Number of Floors	1	2	3	0	5	0	3	0	2	1	0	16
	2	0	1	0	1	0	8	0	22	0	0	32
	3	0	2	0	0	0	4	0	8	14	0	0
	4 and Above	1	0	0	1	0	1	0	1	4	0	0
Wall Void Ratio	Little	3	2	0	0	0	2	0	11	18	0	0
	Middle	0	4	0	4	0	9	0	11	28	0	0
	A lot	0	0	0	3	0	5	1	11	20	0	0
Wall Space Layout	Organized	2	4	0	4	0	4	0	16	30	0	0
	Less Regular	1	1	0	0	0	5	0	15	22	0	0
	Irregular	0	1	0	3	0	7	1	2	14	0	0
Wall Gap Layout	Yes	3	3	0	2	0	10	0	23	41	0	0
	No	0	3	0	5	0	6	1	10	25	0	0
Visible Build Quality	Good	0	1	0	1	0	0	0	7	9	0	0
	Middle	1	4	0	1	0	8	0	26	40	0	0
	Bad	2	1	0	5	0	8	1	0	17	0	0

In order to determine the risk distributions of buildings in the Gencosman District of Bayburt city center, building performance scores of each reinforced concrete, masonry and/or mixed building were scanned from the street using the method specified in Annex-2 and Annex-A of Law No. 6306 given under the Materials and Methods Section of this study. It was calculated using the data collected by. Buildings for which performance scores are calculated are divided into five different building classes depending on the performance score. Buildings with Performance Score (PC) less than 50 ( $PC \leq 50$ ) are very bad, buildings with  $50 < PC \leq 100$  are bad, buildings with  $100 < PC \leq 150$  are medium, buildings with  $150 < PC \leq 200$  are good,  $200 < PC \leq 250$  The buildings are classified as very good. According to the classification tried to be explained, 29 of the 476 buildings in the region subject to the study were classified as very bad, 143 as bad, 273 as average, 18 as good and 13 as very good. This situation can also be seen from Figure 1.



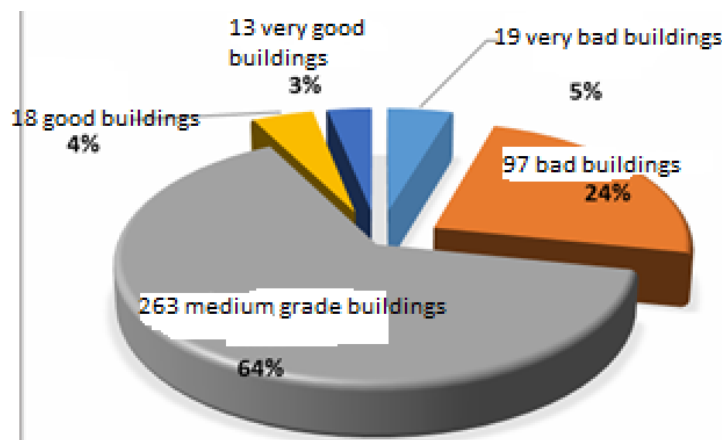
**Figure 1.** Distribution of building classes by performance score

The distribution of the data shown in Figure 1 according to the 10 sub-regions of the entire region is as given in Table 8.

**Table 8.** Distribution of building classes according to performance score based on sub-regions

	1st Region	2 nd Region	3 rd Region	4 th Region	5 th Region	6 th Region	7th Region	8.th Region	9 th Region	10 th Region	Total
$PC \leq 50$ (Very poor)	3	2	7	7	0	0	8	1	0	1	29
$50 < PC \leq 100$ ( Poor )	6	22	21	27	36	6	7	5	0	13	143
$100 < PC \leq 150$ (Medium)	15	29	14	78	21	43	4	33	29	7	273
$150 < PC \leq 200$ (Good)	0	0	1	0	0	1	0	11	5	0	18
$200 < PC \leq 250$ (Very good)	0	1	1	0	0	0	0	10	1	0	13

While this is the case for all buildings, when the situation is evaluated for reinforced concrete buildings, 19 and 97 buildings are classified as very bad and bad respectively, 263 reinforced concrete buildings are classified as medium grade, and 18 and 13 buildings are classified as good and very good reinforced concrete buildings. This situation is shown in Figure 2 for reinforced concrete buildings. Evaluation based on sub-regions for reinforced concrete buildings is given in Table 9.

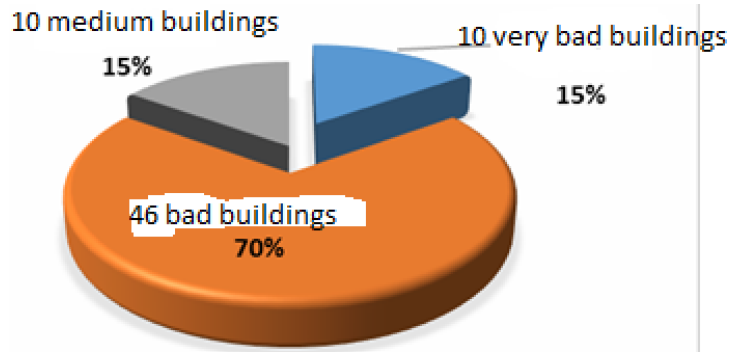


**Figure 2.** Distribution of reinforced concrete building classes according to performance score

**Table 9.** Distribution of Reinforced Concrete building classes according to performance score based on sub-regions

	1st Region	2 nd Region	3 rd Region	4 th Region	5 th Region	6 th Region	7th Region	8.th Region	9 th Region	10 th Region	Total
$PC \leq 50$ (Very poor)	2	0	5	2	0	0	8	1	0	1	19
$50 < PC \leq 100$ ( Poor )	4	19	18	23	3	6	7	5	0	12	97
$100 < PC \leq 150$ (Medium)	15	28	12	71	21	43	4	33	29	7	263
$150 < PC \leq 200$ (good)	0	0	1	0	0	1	0	11	5	0	18
$200 < PC \leq 250$ (Very good)	0	1	1	0	0	0	0	10	1	0	13

Similar to reinforced concrete buildings, if masonry and mixed buildings are classified according to their performance scores, a distribution as shown in Figure 3 is obtained. As can be seen from this figure, no good or very good masonry buildings could be observed in the region. While 15% (10) of the Masonry & Mixed Buildings are in the middle grade, 70% (46) and 15% (10) are in the bad and very bad building class, respectively. The classification made according to the performance scores of masonry and mixed buildings based on sub-regions is given in Table 10.



**Figure 3.** Distribution of Masonry & Mixed building classes according to performance score

**Table 10.** Distribution of Masonry & Mixed building classes according to performance score on sub-regions basis

	1st Region	2 nd Region	3 rd Region	4 th Region	5 th Region	6 th Region	7 th Region	8.th Region	9 th Region	10 th Region	Total
$PC \leq 50$ (Very poor)	1	2	2	5	0	0	0	0	0	0	10
$50 < PC \leq 100$ ( poor )	2	3	3	4	33	0	0	0	0	1	46
$100 < PC \leq 150$ (Medium)	0	1	2	7	0	0	0	0	0	0	10
$150 < PC \leq 200$ (Good)	0	0	0	0	0	0	0	0	0	0	0
$200 < PC \leq 250$ (Very good)	0	0	0	0	0	0	0	0	0	0	0

Following these mathematical classifications, all buildings were rendered in different colors on the map of the region obtained from the map application on the web page of the General Directorate of Land Registry and Cadastre. Figure 4 was obtained by depicting very bad buildings in red, bad buildings in orange, average buildings in yellow, good buildings in light green and very good buildings in dark green.



■ Very bad buildings    
 ■ Bad buildings    
 ■ Medium quality buildings    
 ■ Good buildings    
 ■ Very good buildings

**Figure 4.** Bayburt Province Central Gencosman District Building risk distribution map obtained by street scanning method

## 4 CONCLUSION

As can be seen from the map in Figure 4, it will be immediately understood that the buildings in the upper left and lower right regions of the map are in bad and very bad classes. It can easily be said that the buildings in these two sections, which constitute the building stock in the region, are at risk of earthquake. In order to prevent loss of life and property in the event of a possible earthquake, precautions against earthquakes must be taken urgently in the region. It becomes clear that regional improvement is needed, especially in the upper left part. In other words, it would be quite appropriate to implement urban transformation projects in the regions where the orange and red colored buildings in the upper left part of the map are concentrated, and for the orange and red buildings in the lower right and other parts of the map, the condition of the buildings should be determined with further earthquake analysis, if necessary. It can be said that strengthening is necessary.

It is important to remind here that the method used in this study carried out within the scope of this project is the street scanning method. This method has weaknesses due to visuality and person-dependent evaluations. For this reason, the results obtained from the study are not definitive. Much further study and analysis is required for definitive results. This method showed the relative distribution of earthquake risk distribution in the region.

## Acknowledgments

This study was funded by the Scientific Research Project Coordinatorship of Bayburt University.

## References

- [1] H. Tokgoz and H. Bayraktar, "Application of Street scanning method in detecting risky buildings in Kaynasli district of Duzce province," *Duzce University Journal of Science and Technology*, vol. 3, pp. 107–116, 2015.
- [2] E. Isik, "Investigation of an existing RC building with different rapid assessment methods," *Bitlis Eren Univ J Sci & Technol*, vol. 5, no. 2, pp. 71–74, 2015.
- [3] Y. Aslankara, M. Inel, and S. Toprak, "Estimation of building damages in scenario earthquake at urban scale," in *Earthquake Symposium*, Kocaeli, 2005.
- [4] O. Bayrak, "A field study on determining the earthquake risks of buildings with the first stage assessment method, Erzincan example," M.S. thesis, Karadeniz Technical University, Trabzon, 2011.
- [5] Principles Regarding the Identification of Risky Buildings (Turkish Law) No. 6306 Annex-2, Annex-A.



## Use of Bayburt White Stone Waste and Paper Mill Waste Lignin as a Plasticizer/Air-Entraining Concrete Additive in the Production of Carrier and Non-Carrier Lightweight Concrete

Omer Bayrak<sup>\*1</sup>, Emin Erdem<sup>2</sup>

<sup>1</sup>Civil Engineering, Bayburt University, Bayburt, Türkiye  
<sup>2</sup>Inorganic Chemistry, Pamukkale University, Denizli, Türkiye

### Abstract

Today, cement-based concrete and reinforced concrete elements are mostly used as durable building materials. Concrete with different properties can be produced with chemical and mineral additives added to concrete. In recent years, many studies have been carried out on the evaluation of industrial wastes as mineral and chemical additives used in concrete. In this study, the usability of Bayburt white stone (BWS) waste produced as natural stone in Bayburt as aggregate and paper mill waste lignin (solid lignin) as plasticizer/air entraining in concrete production were investigated. The results obtained were compared with the results obtained from carrier (CLC) and non-carrier lightweight concretes (NCLC) prepared with pumice and perlite aggregates used in the market. The optimum amount of lignin added was determined as 0.6% of the cement weight for a 0.50 water/cement ratio of 5 - 9 cm slump value (S2 class). It was determined that the 28 and 90-day strengths of the BWS used increased significantly (30.4%) despite the decrease in unit volume weight values. Due to the fact that the aggregates used contained water-soluble compounds and the continuation of pozzolanic reactions, the hydration progressed slowly and the strength increase continued effectively until the 90th day. Industrial evaluation of waste BWS and waste lignin, which cause significant environmental problems with such a use, was carried out in the production of CLC and NCLC.

**Keywords:** Waste lignin, Lightweight concrete, Tuff, Bayburt stone, Waste management

## 1 INTRODUCTION

Natural resources are rapidly depleting in parallel with the increasing world population. For this reason, in recent years, many studies have been conducted on recycling and evaluating industrial wastes that cause environmental pollution. Tuffs, which are formed as a result of volcanism in the Bayburt region and provide an important source of income for the local people, are generally used as coating, decoration and insulation materials in buildings after being processed. In addition to being natural and easy to process, Bayburt stone, which is light, produces up to 70% waste during the extraction, cutting and processing processes. A very small portion of the waste generated is generally used as filling material in construction, while the majority is thrown away as waste and causes environmental pollution. Bayburt stone contains high levels of silica and alumina and has pozzolanic properties. Therefore, it has the potential to be used as a pozzolanic additive by grinding in cements or as aggregation by sizing. Being light is another advantage. Tekin et al. in their study in 2020, they produced lightweight concrete blocks with compressive strengths varying between 4-9 MPa using waste zeolitic tuffs at cement dosages of 150 to 250 kg/m<sup>3</sup> and using three different superplasticizers [1]. Another industrial waste is lignin, which is a natural polymer that occurs in paper factories. Millions of tons of lignin are produced each year during paper production and this lignin is either discarded or used as fuel after some processes in the plant. Lignin, a natural polymer, has the potential to be used as a cement chemical additive because it contains groups similar to lignosulphate compounds used as superplasticizers and air-entraining in cements.

Chromium found in cements is mainly found in the form of Cr(III) and Cr(VI), while it is also found in smaller amounts in the form of Cr(IV) and Cr(V) [2]. Cr(VI) compounds are 10 to 100 times more toxic than Cr(III) compounds [3]. For this reason, standards have set limits for the level of sub-chromium compounds. Erdem et al. determined that solid lignin obtained from lignin liquor, when used at a rate of 0.44% of the cement weight, reduces the Cr(VI) level of Portland cement to below 2 ppm values [4]. Reducing toxic chromium amounts can be shown as another important advantage of using lignin in cements.

Baykus et al. 2016 examined the effects of lignin sulfonate-based construction chemicals on the fresh and hardened properties of concrete by making a comparison of chemical additives. For C25/30 and C20/25 target concrete classes, the amount of cement and chemical additives is fixed; Changes were made in the amount of water and aggregate. As a result, they determined that the use of lignin sulfonate-based construction chemicals did not negatively affect the compressive strength development of the concrete due to changes in the properties of fresh concrete such as consistency, temperature and unit weight [5].

In this study, it is aimed to evaluate BWS waste and waste lignin in the production of CLC and NCLC. As a result of this industrial evaluation, a contribution will be made to the solution of environmental problems caused by wastes.

## 2 MATERIAL AND METHOD

### 2.1 Material

#### 2.1.1 Cement

The cement/binder used in the mixtures is CEM I PC 42.5 R type, in accordance with TS- EN 197-1, and was obtained from Askale Cement Factory. Physical and mechanical analysis values are given in Table 1.

**Table 1.** Physical and mechanical analysis results of cement

Compressive Strength MPa			Setting Times hour		Specific Gravity g/cm <sup>3</sup>	Blaine cm <sup>2</sup> /g	Volume Expansion mm
2 <sup>th</sup> day	7 <sup>th</sup> day	28 <sup>th</sup> day	Initial	Final			
26	-	52.6	2.8	3.8	3.12	3370	3

#### 2.1.2 Aggregate

Waste aggregates used in the experiments in the production of load-bearing and non-bearing lightweight concrete were supplied from ŞİMŞEK Stone Enterprises in Bayburt province. Perlite aggregate was supplied from Erzincan PERSAN enterprise and pumice aggregate was supplied from Erzincan ERKALE BIMS enterprise. Chemical analysis of aggregates is given in Table 2. Bayburt stone chemical analyzes were carried out and patented by Bayburt Municipality (TPE / Natural Stones, 442) [6].

**Table 2.** Chemical properties of aggregates (%)

	CaO	SiO <sub>2</sub>	Al <sub>2</sub> O <sub>3</sub>	Fe <sub>2</sub> O <sub>3</sub>	Others
BWS (MTA)	2,95	69,2	25,95	1,1	0,80
Perlite [7]	0,75	74,6	13,2	0,48	10,9
Pumice [8]	11	45	21	7	16

#### 2.1.3 Plasticizer/Air-Entraining Additive (Solid Lignin)

In the study, solid dry lignin obtained by chemical separation from OYKA paper mill waste (lignin liquor) was used as a plasticizer and air entraining additive.

#### 2.1.4 Obtaining Solid Lignin

Solid lignin was separated from the liquor by adding 2% sulfuric acid solution to the lignin liquor supplied from OYKA Paper Factory. Then, the precipitated lignin was filtered and dried at 70 °C and was ground and passed through a 125 micron sieve. Before being added as an additive to the concrete, lime milk and mixing water were added to neutralize the excess acid used during precipitation. Figures 1, 2 and 3 show the stages of obtaining lignin.



**Figure 1.** Lignin liquor obtained from paper mill waste



**Figure 2.** Obtaining pure lignin from liquor by precipitation process



**Figure 3.** Formation of stable air bubble from pure lignin

### 2.1.5 Mixing Water

Bayburt city tap water (pH 7.5-8.5) was used as concrete mixing water.

### 2.2 Method

Sample preparation of the aggregates used in the experiments was carried out according to TS EN 932-1 and TS 707. After the aggregates were brought from the enterprises, they were divided into three classes with dimensions of 0-2, 2-4 and 4-11.2mm, in accordance with the TS EN 1097-6, 2013 standard, and density and water absorption tests were carried out. In addition, specific gravity tests of filler material between 0-0.063 mm were carried out with the pycnometer method in accordance with TS EN 1097-7. The results of the aggregate tests are given collectively in Table 3.

The collapse test was carried out in accordance with TS EN12350-2 and the pressure resistance test was carried out in accordance with TS EN 12390-3.



**Table 3.** Bulk results of BWS aggregate tests

	4 - 11.2 mm	2 - 4 mm	0 - 0.063 mm
Dry density, g/cm <sup>3</sup>	1.71	1.76	1.90
Saturated, surface dry density, g/cm <sup>3</sup>	1.97	2.01	2.10
Apparent grain density, g/cm <sup>3</sup>	2.31	2.35	2.37
Water absorption, %	15.14	14.34	10.37
Loose density, g/cm <sup>3</sup>	1.07	Mehtod TS EN 1097-3	
Compact density, g/cm <sup>3</sup>	1.14	Method TS EN 1097-3	
Filler (0-0.063)			2.55

Table 4 gives the % values of BWS aggregate granulometry created for Dmax 11.2 mm used in CLC production.

**Table 4.** Aggregate granulometry of BWS for CLC

Sieve size, mm	11.2	8	4	2	1	0,5	0.25	0.125	0.063
Passing, %	100	86	63	42	30	20	10	4	2

Table 5 gives the % values of BWS aggregate granulometry created for Dmax 11.2mm used in NCLC production.

**Table 5.** Aggregate granulometry of BWS for NCLC

Sieve size, mm	11.2	8	4	2	1	0.5	0.25	0.125	0.063
Passing, %	100	86	63	42	24	14	8	4	2

Table 6 gives the amounts of materials used in the production of 1 m<sup>3</sup> CLC and NCLC.

**Table 6.** CLC and NCLC mixture amounts, kg/m<sup>3</sup>

	CLC	NCLC
Aggregate, kg/m <sup>3</sup>	1205.54	1611.8
Water, kg/m <sup>3</sup>	225	100
Cement, kg/m <sup>3</sup>	450	200
Water/cement	0,50	0.50
Air, dm <sup>3</sup>	28	30
Lignin, % (as a plasticizer)	0.6	0.6

### 3 RESULTS

#### 3.1 CLC Production with BWS, Perlite, and Pumice Aggregates

As seen in Figure 4 and Table 7, it was determined that the compressive strengths of CLCs produced with BWS showed similar properties to traditional lightweight concretes (perlite and pumice) and they gave higher strengths than pumice and lower strengths than perlite. In addition, the 32.2% increase in the compressive strength of CLC produced with BWS at the end of 90 days shows that the pozzolanic activity continues.

**Table 7.** Comparison of strengths of BWC Pumice and Perlite with CLC

	Bayburt Stone	Pumice	Perlite
7th d., MPa	16.5	17.1	27
28th d., MPa	22.3	14.4	41.7
90th d., MPa	29.5	20.5	46
Density, g/cm <sup>3</sup>	1.888	1.763	1.926

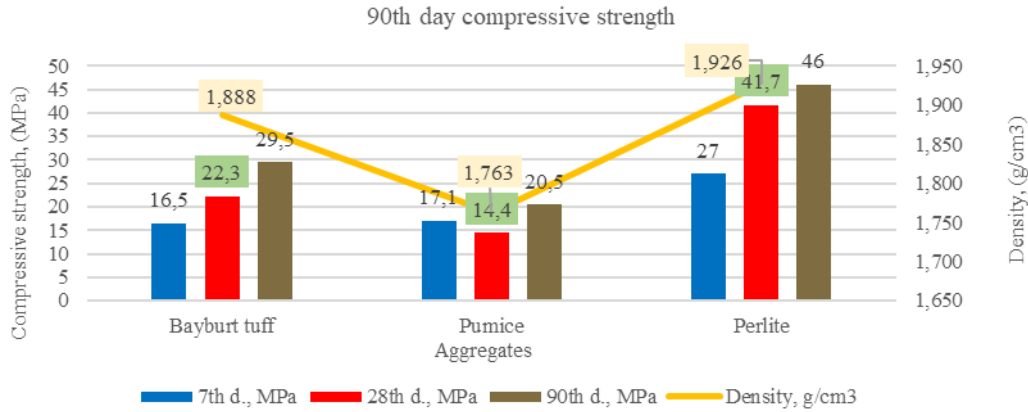


Figure 4. Comparison of compressive strength of aggregates

### 3.2 Determination of Lignin Usage Ratio and Its Effect on CLC

Table 8 gives the results of the experiments conducted to determine the optimum usage ratio of solid lignin. Lignin was added to CLC at the ratios of 0, 0.6 and 0.8% of the cement weight.

Table 8. Effect of lignin on CLC

Adding Amount, %	0 (Ref.)	0,6	0,8
pH	7,3	7,4	7,2
Final setting , (H)	8,6	9,7	10,2
Compact density, g/cm <sup>3</sup>	2,064	1,958	1,989
7 <sup>th</sup> day. Strength, MPa	13,5	14,1	14,5
28 <sup>th</sup> day. Strength, MPa	28,7	25,9	26,6
28 <sup>th</sup> day. Saturated density, g/cm <sup>3</sup>	1.878	1.805	1.840
90 <sup>th</sup> day. Strength, MPa	38.7	32.7	32

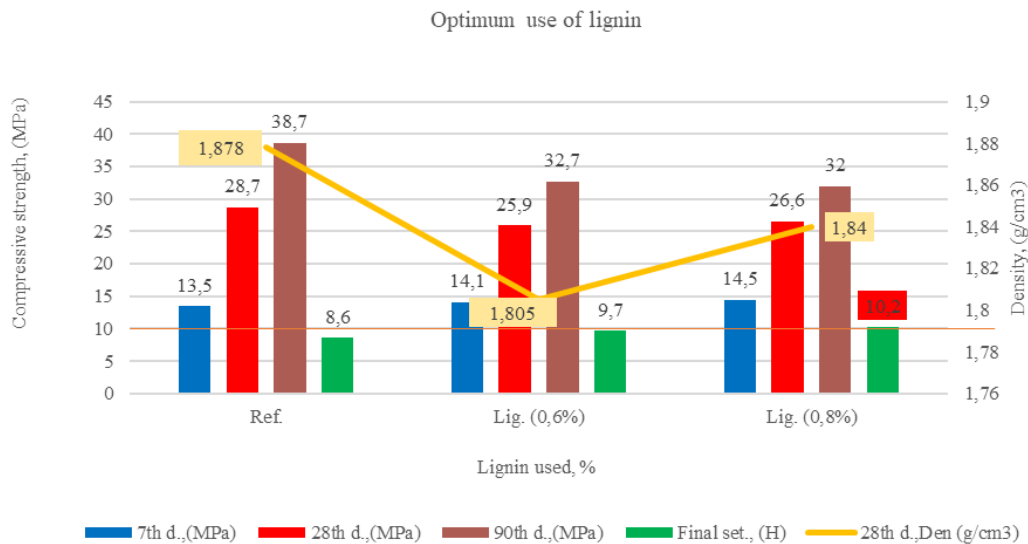


Figure 5. Determination of lignin usage rate and its effect on CLC

As seen in Figure 5., the 28-day compressive strength values of CLCs produced with BWS aggregate decreased by 6 - 7.3%, respectively, when 0.6% and 0.8% lignin was added to the mixture. It is known that every 1 percent increase of air added to concrete reduces the compressive strength of concrete by 2 to 6 percent [9]. Figure 5 also shows that lignin entrains air, causing a decrease in strength. Lignin, which precipitates on the cement particles after dissolving in water, on the one hand delays the formation of hydration products, causing the setting time to extend, and on the other hand, it precipitates at the interface of the aggregate and the paste, causing the adherence

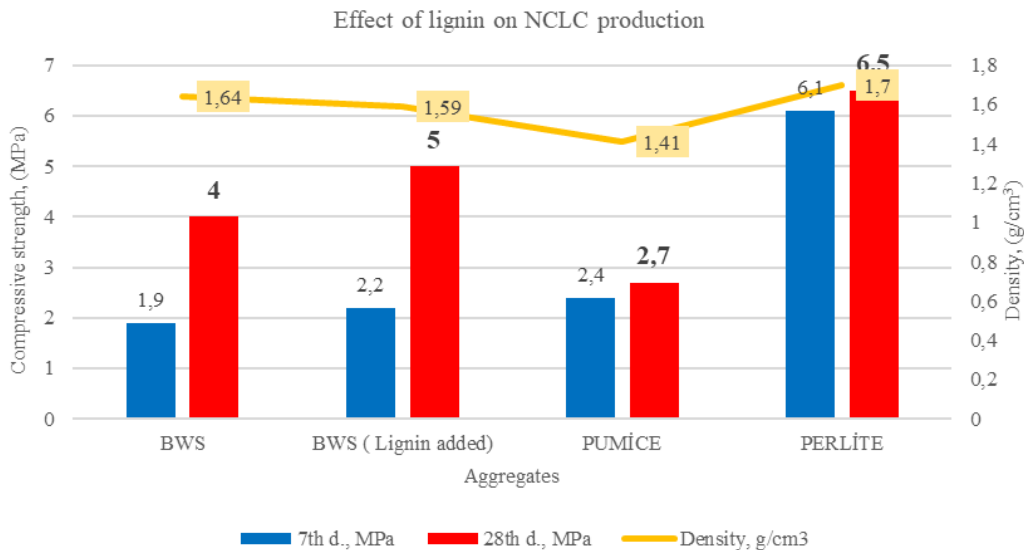
to weaken. Since adding 0.8% lignin to the mixture caused the setting time to exceed 10 hours, the optimum usage rate was determined as 0.6%.

### 3.3 Comparison of NCLCs produced with BWS, Perlite, and Pumice

NCLC production was carried out with BWS, perlite and pumice aggregates. In addition, in order to see the effect of lignin, a comparison was made by adding solid lignin at the rate of 0.6% of the cement weight to the BWS aggregate mixture. The aim here is to produce lightweight blocks (10×10×10 cm in size) with a 28-day compressive strength of at least 5 MPa with a binder dosage of 200 kg/m<sup>3</sup>. Information about the test results is given in Table 9 and Figure 6.

**Table 9.** Effect of lignin on NCLC production

	BWS	BWS (Lignin added)	Pumice	Perlite
7 <sup>th</sup> d., MPa	1.9	2.2	2,4	6.1
28 <sup>th</sup> d., MPa	4	5	2,7	6.5
Density, g/cm <sup>3</sup>	1.640	1.590	1.700	1.410



**Figure 6.** Effect of lignin on NCLC production

As seen in Figure 6, the targeted lowest 5 MPa compressive strength value was reached after 28 days with perlite aggregate mixture and lignin-added BWS mixtures. Here, although the lignin contribution reduces the density value by creating air entrainment, it is seen that the strength increases by 25%, and the lignin compensates for the losses in compressive strength caused by air entrainment by showing a fluidizing effect.

## 4 CONCLUSION

- Aggregates obtained from BWS can be successfully used in the production of carrier and non-carrier lightweight concrete according to the relevant standards (TS 2511),
- In the production of CLC, using lignin at a rate of 0.6% of the cement weight provides 15% water reduction and 10% strength increase,
- In the production of NCLC, using lignin at a rate of 0.6% of the cement weight, the targeted dry density value (1.4 - 1.6 g/cm<sup>3</sup>) and compressive strength (5MPa) values can be achieved and it is suitable for block element production,
- In particular, the compressive strengths of NCLC samples that will be prepared with less water and produced under factory conditions by applying high pressure will be higher,
- The use of lignin as a normal water reducer/plasticizer additive in concrete does not cause any negative effects on concrete and will be useful in protecting concrete from effects such as freezing and thawing,

- It will eliminate the toxic effects caused by reducing Cr (VI) in cements and contribute to the elimination of heavy metal pollution originating from concrete,
- Although the air entrainment feature of lignin causes strength losses in concrete, this It can be used successfully in the production of CLC and NCLC, where the negativity is eliminated with the plasticizing/water reducing effect,
- It can be said that the utilization of both industrial wastes will both get rid of environmental problems and provide economic contribution.

## References

- [1] I. Tekin and H. Sahin 2020, *Cement and Concrete World*, no. 146, Jul.-Aug. 2020.
- [2] A. Mishulovich, "Oxidation states of chromium in Clinker," *Portland Cement Association, Skokie, Illinois, USA*, 1995, p. 6.
- [3] S.A. Katz and H. Salem, "The toxicology of chromium with respect to its chemical speciation: A review," *J. Appl. Toxicol.*, vol. 13, pp. 217–224, 1993.
- [4] E. Erdem, R. Donat, K. Esen, and T. Tunc, "Removal of soluble of Cr(VI) in cement by ferrous sulphate monohydrate, solid lignin and other materials," *J. Ceram. Silik.*, vol. 55, pp. 85–93, 2011.
- [5] C. E. Ekin, S. Ay, N. Baykus, and A. Ay, "Examination of the impact of lignin sulfonate based structure chemicals on fresh and hardened concrete," *Pamukkale University Journal of Engineering Sciences*, vol. 22, no. 6, pp. 478–485, 2016.
- [6] Bayburt Natural Stones, Patent Registration No: 442, Bayburt Municipality.
- [7] E. Aksay et al. "The preparation and enrichment of pumice ore," *Afyon Kocatepe University, Journal of Science and Engineering Sciences*, vol. 16, pp. 384–390, 2016.
- [8] I. Ulusu, "Investigation of the producibility of high strength lightweight concrete using raw perlite aggregate," Ph.D. thesis, Ataturk University Institute of Science and Technology, Erzurum, 2007.
- [9] S. Kosmatka, B. Kerkhoff, and W.C. Panarese, *Design and Control of Concrete Mixtures*, 14th ed. Portland Cement Association, Skokie, 2002.



## An Innovative Method of Getting Impactive Ideas

Leyla Erkol<sup>\*1</sup>, Murat Arslanoglu<sup>1</sup>, Sevilay Sagtan<sup>1</sup>, Fatih Cagirankaya<sup>1</sup>, Ali Yazgan<sup>1</sup>

<sup>1</sup>Teknorot Automotive Products Industry and Trade Inc., Duzce, Türkiye

### Abstract

In order to meet customer demands and expectations, businesses are obliged to meet these expectations through continuous improvement by using quality-oriented, low-cost and sustainable flexible production methods and techniques with minimum waste. In this context, the main goal is to focus on efficiency, effective use of resources and innovation activities. Innovative business behavior is a process that includes the practices of putting forward and implementing ideas that will benefit the organization, explaining problems and solving these problems in the organizational environment. Innovative work behavior; while performing the responsibilities of the employee in a business environment; it is dealing with the idea of renewing and implementing new ideas, products, methods, processes. In this sense, using the labor resource effectively is very important for businesses and managers. For this reason, the leading role in increasing productivity belongs to the employees, that is, the employees. This study focuses on identifying and understanding the barriers to receiving qualified suggestions from employees and how these barriers can be overcome to become sustainable. By applying the Hawthorne effect experiments "interview program" and "serial bagging room observations", a total of 1000 employee experiences in two groups, the suggestions received over a period of 1 year were evaluated. When the results were analyzed, it was seen that the high value-added suggestions received for the 2nd group increased by 32% compared to the 1st group.

**Keywords:** Suggestion system, Method, Added value, Blue collar, Innovation

## 1 INTRODUCTION

Suggestion systems are incentive systems that reward employees for ideas that contribute to organizational effectiveness [1]. While obtaining employee ideas that improve company operations is often defined as the objective of any suggestion system, the actual purpose of these systems is fundamentally different. Most suggestion systems aim to foster company pride and commitment among employees by giving them the sense that their suggestions are acknowledged by the organization and management, allowing them to participate in planning processes as integral members [2].

Employees who contribute to production processes with their creativity play a significant role not only in specific tasks but also in enhancing overall efficiency. Therefore, the voluntary and high-quality suggestions made by employees critically contribute to a company's sustainable competitive advantage. A process of continuous interaction to receive innovative suggestions of high-added value from employees can significantly contribute to a firm's development. Janssen's (2000) definition of creative work behavior describes it as consciously addressing new problems, proposing new methods to resolve them, and actively informing and implementing new ideas to benefit a team or organizational environment [3]. Creative employees are crucial actors in the innovation process. They tend to identify opportunities for new products, discover new applications for existing methods or equipment, and generate new and feasible ideas related to their work [4].

The knowledge and insights that employees possess regarding daily work processes and operations contribute significantly to the company's development. Employees who take ownership of their tasks approach daily work processes more attentively and can identify potential improvements more swiftly. However, they may encounter challenges in receiving high-quality suggestions. At the root of this issue are various barriers that psychologically affect employees and diminish their sense of trust. For example:

- Fear that their suggestions will be perceived by others as funny, too poor, or too simplistic,
- Feeling compelled to adhere strictly to rules imposed by managers,
- Sensation of being overly scrutinized by colleagues,
- Fear of being misunderstood and consequently dismissed from their job,
- Feeling that spending extra time to write a suggestion might not be valued,

- Internal barriers based on their own personality traits.

These barriers constitute the most significant obstacles to receiving quality suggestions in the suggestion process. Establishing a culture of suggestions within the company is crucial for obtaining quality ideas in businesses. This culture provides employees with a safe and comfortable environment to freely express their ideas and makes them feel valued. While collaboration and open communication encourage the sharing of suggestions, feedback from management increases the number of qualified suggestions.

For the system to be sustainable and effective, various factors need to come together harmoniously. One of these factors is strong support from management in idea generation. The manager should serve as a role model in the establishment, implementation, and maintenance of the suggestion system, and should encourage employee participation. Leadership and support increases employees' confidence in the suggestion process, increasing the likelihood of the process being successful. On the other hand, the Hawthorne experiments conducted by Western Electric represent a significant milestone in understanding factors affecting productivity in businesses. These experiments examine the impact of employees' psychological states, personal skills, and recognition in the workplace on productivity. Western Electric, located near Chicago in the town of Hawthorne, conducted a series of six group experiments over eight years involving its facilities and personnel [5]. Table 1 includes the number, name, and objectives of each Hawthorne experiment.

**Table 1.** Hawthorne experiment

Experiment No	Experiment Name	Purpose of The Experiment
1	Illumination Experiments	Enhancing productivity through various lighting configurations in the work areas
2	Relay Assembly Test Room Study	The impact of the number and duration of rest breaks and the length of the workday on productivity
3	II. Relay Assembly Test Room Study	Examining the impact of group wages on production
4	Mica Splitting Test Room Study	Examining the effect on production of keeping the wage variable constant, giving working breaks and shortening the working period
5	Series Connecting Room	Investigating the impact of compassion and mental emotions on production by bringing together employees engaged in different tasks
6	Bank Wiring Observation Room Study	Investigating the impact of compassion and mental emotions on production by bringing together employees engaged in different tasks

Specifically, the "Interview Program Experiment" conducted between 1928 and 1930 within the Hawthorne experiments achieved significant success. This study demonstrated how psychological conditions, personal skills, and factors such as being valued and appreciated by others reflect in productivity [5]. Brainstorming, a method used in businesses for idea generation, plays a critical role in providing quality suggestions. Brainstorming, along with methods like forming teams for group discussions, encourages innovative thinking by bringing together various perspectives. The regular use of these methods contributes to the continuous generation of creative solutions and quality suggestions. The brainstorming method was first used by Osborn (1957), an advertiser, to generate innovative names and slogans for new products. Later, it was applied as a teaching method in psychology and the art of writing. This method has been widely used to enhance group members' creative thinking skills, generate alternative solutions, and reveal their creative potential [6]. Brainstorming is seen as an effective method to maximize the potential of productive employees and increase the innovation of the business. The history of brainstorming dates back to Alex Osborn's discovery of this concept in 1953 [7].

Humans are not born with fixed characteristics; rather, they are shaped and developed under the influence of their environment and various other factors. As Sophocles stated, "There are many wonders in the world, but none is as wonderful as man". "Indeed, it is humanity, which has achieved tremendous inventions and works and led the revolution known today as the "information age", unlike any other being" [8]. Production personnel should be involved not only in daily operations but also in the continuous search for improvement and innovation. Brainstorming allows employees to share their ideas and make suggestions for optimizing work processes. Employees in production can provide solutions to emerging problems based on their accumulated experiences and daily observations in their fields. The innovative ideas that employees generate through brainstorming play a crucial role in increasing the competitive advantage of the business. There are certain techniques for effective brainstorming. These include clarifying the focus of the problem, setting rules, developing others' ideas, having

written materials available, reviewing the performed processes, increasing mental flexibility, and effectively using existing resources [9]. These techniques strengthen the success of the business in areas such as developing new products, reducing costs, and creating more efficient production processes.

The “win-win” principle in the suggestion process is also a method applied in companies for motivation. The concept of win-win does not only encompass material elements; it also includes many individual, social, material, and spiritual concepts such as future expectations, trust, and contribution to society [10]. The impact of recognizing and accepting humans as humans on motivation within the system cannot be underestimated. Valuing and implementing ideas, as well as improving physical working conditions, show that these factors are as critical as money.

## 2 METHOD

The study was carried out by Teknorot Otomotiv Ürünleri San.ve Tic. AŞ company, which produces front suspension parts for passenger cars and light commercial vehicles in the Automotive Supply Industry, in the 1st Organized Industrial Zone in Düzce. To increase the number of quality suggestions, a study was conducted involving 1,089 blue-collar workers. The suggestion system at the company is implemented through a digital portal, allowing employees to directly convey their ideas to managers. This system provides significant ease of access and use for employees, enabling every employee to easily participate. All ideas are securely stored in a reliable environment, and employees can easily access their data. In addition, feedback is quickly provided to employees via this portal through their mobile phones.



**Figure 1.** Factory production area

Teknorot conducts various studies based on the methods of the Hawthorne experiments to use the suggestion system more effectively and increase the number of quality suggestions, taking into account its work structure and human resources portfolio. For this purpose, the focus was on the 5th and 6th experiments in Table 1. The study was conducted from a broader perspective by combining the semi-structured interview system, serial attachment room practices and brainstorming methods.

The Interview Program Experiment aims to evaluate the impact of certain skills and psychological factors on employees by bringing small groups together. Serial Attachment Room Observations investigate the effect of mental-emotional complexity on production by bringing together employees engaged in different tasks. Brainstorming is a group thinking technique that encourages creative thinking freely in a comfortable and unrestricted environment. These techniques were combined to conduct studies aimed at obtaining quality suggestions.



**Figure 2.** Method Used in The Study

Managers have utilized fieldwork in the implementation of specific techniques. Within these studies, groups of 10 to 15 employees, working in different roles such as CNC operator, methods technician, and data entry clerk, have been formed. These groups were brought together with their managers to discuss their work and processes, aiming to develop quality and creative suggestions from different perspectives and to encourage participation in the suggestion system. This approach stands out as an effective strategy to enhance work efficiency and promote innovation in the workplace. The study was designed as an initiative aimed at obtaining quality suggestions. The focus of these efforts includes the following points:

- **Communication and Trust Environment:** An environment of clear communication and trust was created to allow employees to share their ideas voluntarily. By adopting a transparent management approach, employees were allowed to ask questions and express their thoughts freely.
- **Leadership Support:** It is crucial for senior management to take on a leadership role in this process and demonstrate support for the suggestion culture. Managers encourage employees to give quality suggestions by setting an inspiring example for them.
- **Evaluation and Feedback:** Managers increased employees' participation by providing rapid feedback on suggestions from them. Employees were also given clear information directly from authorities about how suggestions were evaluated and implemented.
- **Rewarding:** To encourage quality suggestions, the reward system and its rules were reviewed in consultation with managers.
- **Positive Impact in Feedback:** Managers engaging in sincere conversations with employees, especially those newly hired, created a positive atmosphere in feedback.

The application process with the gathered employee groups includes the working methods used among the groups. In the Hawthorne experiments and the Brainstorming process, various questions were directed to encourage employees to share their ideas. This process was designed to increase employee participation and produce quality suggestions from various perspectives. The questions included:

- Have you had any scrap production in the last month?
- If you have, what do you think caused it?
- Have you encountered any incidents affecting occupational health and safety?
- What are your suggestions for making your work process more efficient?
- What measures can be taken to increase employee motivation?
- How can collaboration among employees be encouraged to develop innovative solutions?
- Do you have any suggestions for increasing production efficiency?
- What improvements can be made to products and services based on customer feedback?
- What strategy should we adopt to keep up with industry developments to maintain a competitive advantage?

Such questions significantly help employees write quality suggestions. Additionally, employees can share their ideas on making improvements in work processes, occupational health and safety, customer satisfaction, and maintaining competitive advantage. The suggestion process plays a significant role as part of Teknorot's approach focused on quality suggestions.

### 3 RESULT

Within the scope of the study, two groups consisting of a total of 1089 people were obtained, as shown in Figure 4. The first group consists of 512 employees in the regions where no work is done, while the second group consists of 577 people in the regions where the work is done.

Group 1: Only 12% of the 1164 suggestions submitted by 512 employees in the regions where work was not carried out were evaluated as qualified suggestions.

**Table 2.** Performance report of non-studied personnel

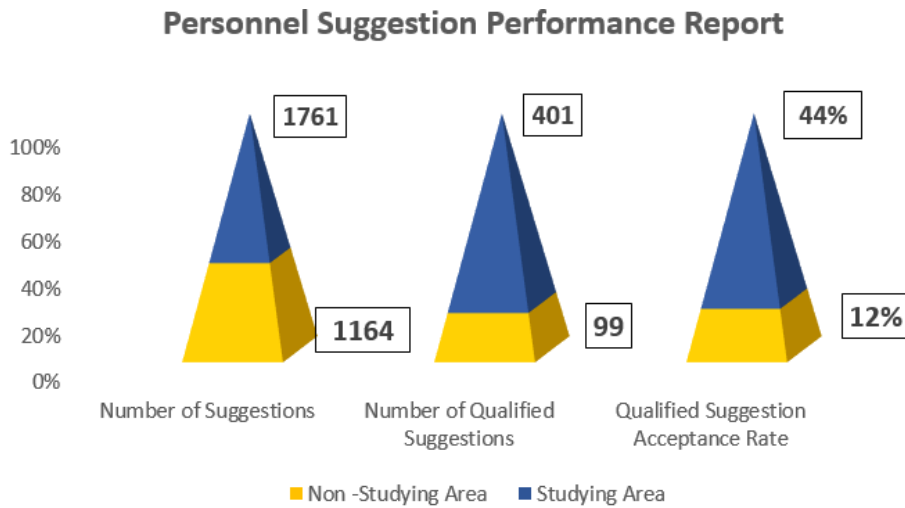
Personnel Suggestion Performance Report			
Number of People	Number of Suggestions	Number of Qualified Suggestions	Qualified Suggestion Acceptance Rate
512	1164	99	12%

Group 2: In the regions where the study was carried out, a one-on-one study was conducted with 577 people and a total of 1761 suggestions were collected. 44% of these suggestions were evaluated as qualified suggestions.



**Table 3.** Performance report of studied personnel

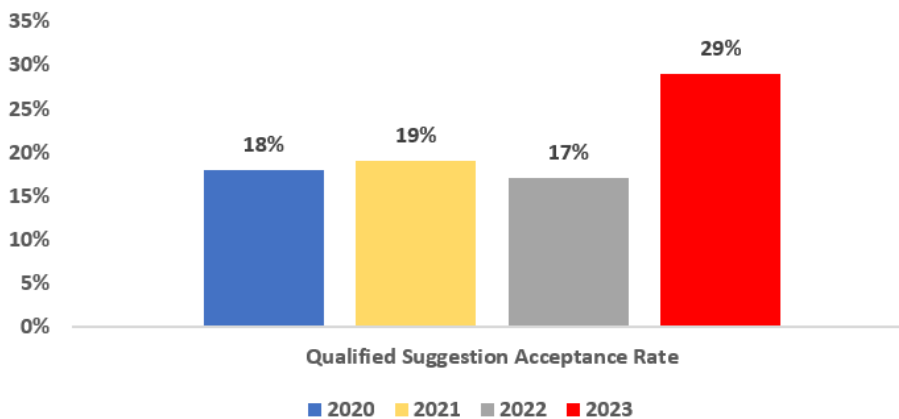
Personnel Suggestion Performance Report			
Number of People	Number of Suggestions	Number of Qualified Suggestions	Qualified Suggestion Acceptance Rate
577	1761	401	44%



**Figure 3.** Personnel suggestion performance report

Based on data covering the period from 2019 to 2023, the evolution of qualified suggestion rates within the company was carefully examined. As shown in Figure 4, while the qualified suggestion rates did not exceed the average level of 18% between 2020 and 2022, considering the results of the study conducted in 2023, it was observed that the qualified suggestion acceptance rates increased to 29%. This notable increase reflects a significant improvement in the company’s quality suggestion culture.

**PERCENTAGE OF ACCEPTED SUGGESTIONS BY YEAR**



**Figure 4.** Quality suggestions accepted rate over the years

## 4 DISCUSSION

As a result, obtaining qualified suggestions from employees is a critical factor for businesses to achieve sustainable competitive advantage. Teknorot has effectively utilized various strategies to utilize its employees' potential and establish a suggestion system filled with valuable solutions. A culture of collaboration and innovation has alleviated employees’ hesitations about sharing their creativity. Supported by management, employees have been able to express their ideas more freely, positively impacting the quality of suggestions.

Particularly, interactions with managers in the field have encouraged employees to share their thoughts without fear of negative reactions. Employees with low self-esteem have been emboldened to make bold suggestions due to the support from managers and the emphasis placed on ideas.

As a result, the risk of valuable suggestions being overlooked has been mitigated, transforming the system into a contemporary, high-quality, and sustainable “suggestion system” rather than a mere “wish and complaint box”. Methods such as the Hawthorne experiments and brainstorming serve as effective tools to encourage employees to share their ideas and generate quality suggestions by leveraging diverse perspectives. The regular use of these methods contributes to businesses’ continuous acquisition of innovative solutions and qualified recommendations.

## References

- [1] W. L. French, *Human Resource Management*, Houghton Mifflin Company, 1994.
- [2] Y. Monden, *Toyota Production System*, USA: Industrial Engineering and Management Press, 1983.
- [3] I. Akkoc, A. Caliskan, and O. Turan, “Gelisim kulturu ve lider desteginin yenilikci davranis ve is performansina etkisi: Is-aile çatismasinin aracilik rolu,” in *9. Ulusal Yonetim ve Organizasyon Kongresi*, Çanakkale, 2011.
- [4] G. Ozcan, “Personel guclendirme ve yenilikci is davranisi arasindaki iliski: Orgutsel yaraticiligin aracilik etkisi,” M.S. thesis, Business, Hatay Mustafa Kemal University, 2020.
- [5] Yonetim ve Organizasyon. (2018, Jan. 02). *Hawthorne deneyleri* [Online]. Available: <https://canergenel.blogspot.com/2018/01/hawthorne-deneyleri-westernelectric.html>
- [6] I. Davies, *The Management of Learning*, London: Mc. Graw Hill, 1971.
- [7] C. C. Aktan, “Organizasyonlarda insan yonetimi: Insan muhendisligi,” *Organizasyon ve Yonetim Bilimleri Dergisi*, vol. 3, no. 2, pp. 387–406, 2011.
- [8] S. Bulba. (2020, Sep. 25). *Fikir uretmek icin kullanabileceginiz design thinking metotlari* [Online]. Available: <https://www.userspots.com/rehber/fikir-gelistirmek-icin-kullanabileceginiz-design-thinking-metotlari>
- [9] E. Turgut and M. Bezenirbas, “The role of social capital and innovative climate on innovative behaviour of employees: A research in health sector,” *Kara Harp Okulu Bilim Dergisi*, vol. 23, no. 2, pp. 101–124, 2013.
- [10] F. Yuan and R. Woodman, “Innovative behaviour in the workplace: The role of performance and image outcome expectation,” *Academy of Management Journal*, vol. 53, no. 2, pp. 323–342, Woodman



## Preservation Issues and Recommendations for Traditional Housings in Urban Centers: The cases from Corum, Turkey

Furkan Karahan<sup>1</sup>, Emine Saka Akin<sup>\*1</sup>

<sup>1</sup>Architecture, Karadeniz Technical University, Trabzon, Türkiye

### Abstract

Traditional housing architecture, shaped by local characteristics, is increasingly confronted with numerous challenges in rapidly expanding urban centers across Turkey, leading to the gradual loss of its unique traits. Due to evolving technologies, changes in production methods, shifts in family structures, and alterations in living conditions, traditional houses have lost their original functionality. Consequently, they are either abandoned or repurposed for inappropriate uses within dense urban centers. The aim of this study is to examine the present usage and conditions of traditional houses located in the urban center of Corum province in Turkey, while identifying preservation challenges and providing recommendations to address them effectively. To achieve this goal, a comprehensive investigation was conducted through both literature review and fieldwork, alongside analysis of data obtained from a 2009 inventory study, focusing on examining the current usage conditions, structural integrity, and functional roles of 50 traditional houses identified in Corum city center. Following in-depth analysis and assessment, it is evident that nearly half of these structures, with seven lost over time, have deteriorated to a state of ruin in the last 15 years. Moreover, many of these buildings lack suitable functionality and face numerous challenges, including traffic congestion, intensified urbanization, commercial interests, and legal ambiguity within the urban center. This underscores the necessity for a holistic preservation approach. Consequently, this study highlights the preservation challenges faced by traditional houses in Corum, whose numbers are steadily decreasing, and offers enhanced recommendations for their conservation and adaptation to future requirements, considering their distinctive functions, spatial adequacy, contextual relevance, and the evolving needs of the city.

**Keywords:** *New function, Spatial suitability, Integrated preservation, Corum*

## 1 INTRODUCTION

The first type of structure built by human beings on earth was for shelter. These structures for the shelter, which were primarily built to protect themselves from the physical environment, have over time turned into residential structures that meet all the psychological and social needs of people. These structures, which were created based on local data and called traditional houses, reflect the culture of the society in which they are located and are shaped in a way that is compatible and respectful of nature. These traditional houses, which have space organization suitable for the extended family structure and production styles of the traditional society, could not meet the needs and expectations of people with the Industrial Revolution. With the industrialization movements, the population in cities increased rapidly, with the help of technology to meet the housing needs of the increasing population, housing production that challenged the nature have become widespread, and production methods, society and family structure has changed. The fact that the spatial organization of traditional houses is not suitable for the modern society and elementary family structure has caused these houses to be either abandoned or used for inappropriate uses, and they are faced with being lost in rapidly growing cities. Especially in urban centers, these traditional houses, which give identity to cities and have an important place in the urban memory, are both non-functional and exposed to urban pressures, making it more difficult to preserve and transfer them to the future.

Changing technology and production styles day by day have changed settlements and their architectures by changing change lifestyles. Considering that this cycle is continuous, it is clear that the conservation efforts of the monumental and traditional structures and textures that form the urban identity and urban memory must be sustainable. In this context, integrated conservation efforts that will ensure the maintenance and reuse of traditional residential buildings that are subject to physical and functional obsolescence are important for the sustainability of these structures. National and international non-governmental organizations and institutions are carrying out many studies to establish boundaries and principles for the protection of these structures and textures that are disappearing day by day in city centers. Among these studies, urban settlements were included in the concept of "historical monument" in the first article of the Venice Charter. In the fifth article of the same charter, it is stated that in the

protection of monuments, a new function can be given for a useful social purpose without changing the plan and decorative elements of the building [1]. Again, the three-year campaign process, which was initiated by the European Council in 1972 with the recommendation to protect the European Architectural Heritage, was completed with the declaration of 1975 as the "European Architectural Heritage" year and the Amsterdam Declaration. This declaration stated that the holistic protection of all urban and rural areas will be possible with integrated practices and policies. In the seventh article of this agreement, which makes recommendations on many issues such as carrying out urban and regional planning actions, taking multi-disciplinary, multi-participatory, legal, administrative and economic measures, better researching conservation, restoration and improvement methods and techniques and expanding their scope, it is stated that urban centers and It was emphasized that interventions in rural settlements should also take into account the social texture, in addition to all technical issues [2]. The multi-dimensional integrated approach regarding the protection of historical cities and urban areas was also put forward by the Valletta Principles, which were adopted at the 17th ICOMOS General Assembly held in Paris in 2011 [3].

In order to facilitate long-term, sustainable conservation in historical cities, it is important to enact the necessary legislation, relevant planning statutes, regulations and laws with public participation [4]. The city of Bruges, Belgium, where conservation practices in historical cities and urban areas are constantly monitored, directed and controlled, continues to reflect the character it has had for centuries. In the sustainability of this character, it was important that the awareness movement initiated by the public in the early 1970s and the framework of the city's planning and policy practices were drawn very well with the master plan made in 1972. Within the framework of these planning and policies, where even the choice of preserving historical buildings or demolishing them and building new buildings is considered a sensitive issue, efforts to protect, develop and organize the cultural heritage of the city are still continuing [5].

Regulation works to be carried out in settlements with a historical context and cultural background will interfere with an established social environment, making the protection of historical cities and urban areas more complicated [6]. Preservation in historical cities and urban areas is an effort to deal with many interrelated and contradictory problems in a balanced way. For example, the new function given to structures that have lost their function to ensure the continuity of historical urban textures on an urban scale is a conservation method. However, in addition to being suitable for the needs of the city, the architectural integrity and spatial characteristics of the building, the new function also has the potential to change the social texture and culture with its new function, because the change in function creates spatial, physical and social changes/transformations. This change/transformation, expressed in recent years with the concept of gentrification, is not only a population change movement caused by the rehabilitation of historical areas, on the contrary, this concept is a dimension of the class restructuring of city centers [7]. Especially the use of historical urban areas for tourism stands out as a very common attitude. This situation, as stated in the Valletta Principles [3], indicates that only tourism and holiday-oriented transformations of historical urban areas will cause them to become places that are not suitable for the daily life of local people, and that gentrification, in this sense, affects societies and carries the risk of making the areas they live in unlivable, and that these areas have a negative impact on their identity. It has been stated that it can go as far as destroying one's character.

Today, especially in historical cities, the lack of sufficient physical space for traffic and parking needs has dramatically changed public spaces in historical urban areas. In addition, it has brought along many problems such as sound, air and visual pollution [8]. It is important to ensure the continuity of financial flows, to monitor the problems of transportation and mass tourism very carefully, and to ensure that coalitions and subsequent political wills respect and maintain the approved urban planning and policy practices in the sustainable preservation of cultural heritage with an understanding that all these problems are taken into consideration [5].

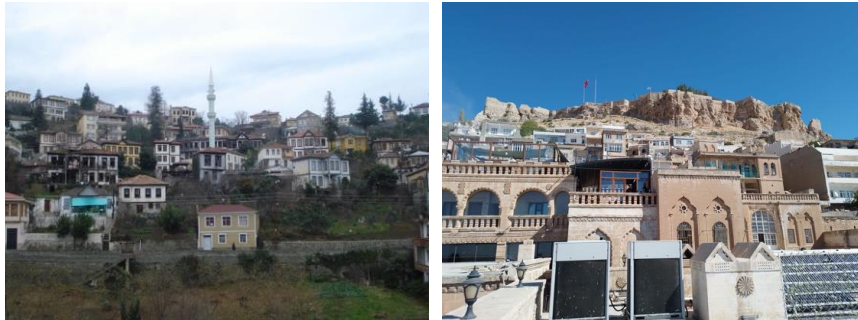
Türkiye, as a country party to the statutes, declarations and resolutions of international institutions and organizations regarding the conservation of historical cities and urban areas, has its own national conservation policies. Despite these conservation policies, there are deficiencies in urban-scale conservation practices in small cities in Anatolia, and the traditional textures of these cities have been severely damaged. The current situation of the traditional houses in the historical city center of Corum, which are discussed within the scope of the study, will be revealed and the conservation efforts in the city and the conservation problems in the historical city center will be revealed.

### **1.1 Anatolian Traditional Architecture**

Traditional houses built with traditional techniques and local materials in Anatolia have architectural and settlement typologies that take into account socio-cultural and natural environmental data. Since respect for nature and human being, rationality, function, frugality, closest selection of materials, interior-exterior harmony, flexibility [9]. and

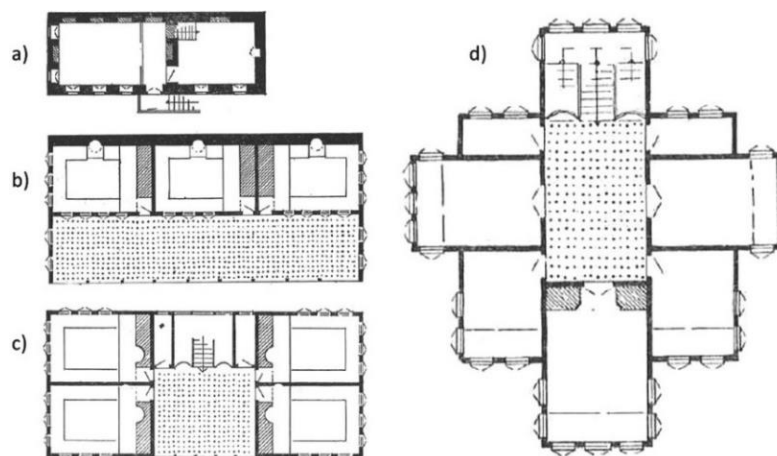
privacy are effective design principles in the formation of these typologies in traditional houses where large families live with a socio-economic structure based on traditional production methods, they reflect the same order.

While the natural environment such as topography, climate, prevailing wind and sunbathing are taken into consideration in the layout of the traditional house, the sun, wind and view of other residential buildings in the surrounding environment are also respected [9]. (Figure 1).



**Figure 1.** Traditional houses that are compatible with the topography and do not block each other's views, sun and wind (E. S. Akin Archive)

Although traditional houses were generally single-story in the early periods, the number of floors increased over time. But, although the number of floors has increased, the main floor, which is the living space, is single and the one at the top. The lower floors are service areas such as kitchens, warehouses and stables and are not included in the traditional housing plan typology [10]. In regions where the climate is harsh, two-story traditional houses also have intermediate floors with low ceiling heights in order to be better heated during the winter months. The location of the sofa determines the plan typologies of Anatolian traditional houses, which consist of the main layout of the living floor, sofa and room spaces [11]. Eldem (1954) created a plan typology of traditional houses with the data he obtained from his study on traditional houses in a wide area of Anatolian geography [10]. As a result of this study, he basically divided the traditional houses, which he described as Turkish Houses, into four plan types: without a sofa, with an inner sofa, with an outer sofa and with a middle sofa, and determined that these also varied within themselves (Figure 2).



**Figure 2.** Plan types defined by Sedat Hakkı Eldem, a) Plan type without sofa, b) Plan type with outer sofa, c) Plan type with inner sofa, d) Plan type with middle sofa [11, 12]

Since ensuring privacy is an important design principle, traditional houses have high garden walls [13], a sofa (stony, living room) between the garden/street and the house [14], ground floors on facades facing the street are closed to the outside, depending on the size of the house, many precautions were taken such as harem and greeting rooms, door knockers being designed with different sounds for men, women and children, secret cabinets, passages, and cages in window openings [12]. If the entrance of a traditional house is on the street, the ground floor on the street front is closed to the outside and the garden at the back of the house is surrounded by walls (Figure 3). Traditional houses in Anatolia contain unique typological elements on the facades, such as the number of floors on the facade, protrusion (bay window, shahnishin, etc.), window proportions, window railings and shutters, entrance or garden doors, floor moldings, color and exterior covering material [15].



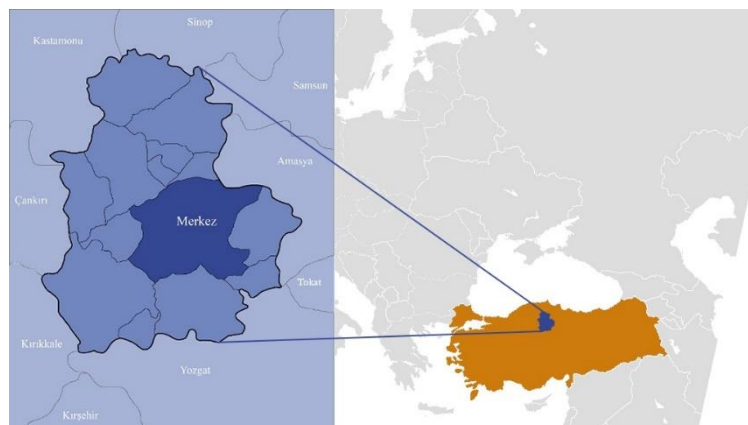
**Figure 3.** Walls separating the street and the garden and ground floors closed to the outside (E. S. Akin Archive)

In traditional residential architecture, construction techniques and materials vary depending on the climatic conditions of the region where they are built and the type of materials available there. Kuban (1982) describes the use of construction techniques and materials according to regions in Anatolia [16];

- Stone house architecture; In the culture produced jointly by Northern Syria and Southeastern Anatolia
- Stone house architecture with wooden beams; Beyond Erzurum, in the culture produced jointly by Northeastern Anatolia, the Caucasus and Dagestan
- Timber-framed house architecture; In the culture produced by the Eastern Black Sea Region
- Cubic stone house architecture with flat roofs; In the culture produced by the Aegean and Mediterranean regions
- Stone housing architecture; In the culture produced by the Niğde and Kayseri (Old Cappadocia) regions of Central Anatolia
- Adobe housing architecture; In the culture that remained in the village and small city environment of Central Anatolia and whose roots date back to the New Stone Age
- Residential architecture made with the hyphae technique (building technique with mostly stone floors, wooden frames and adobe-filled materials); It is divided into seven parts: the coasts of Anatolia, Central Anatolia, and sometimes other regions and the culture produced by the Balkans.

## 2 MATERIAL AND METHOD

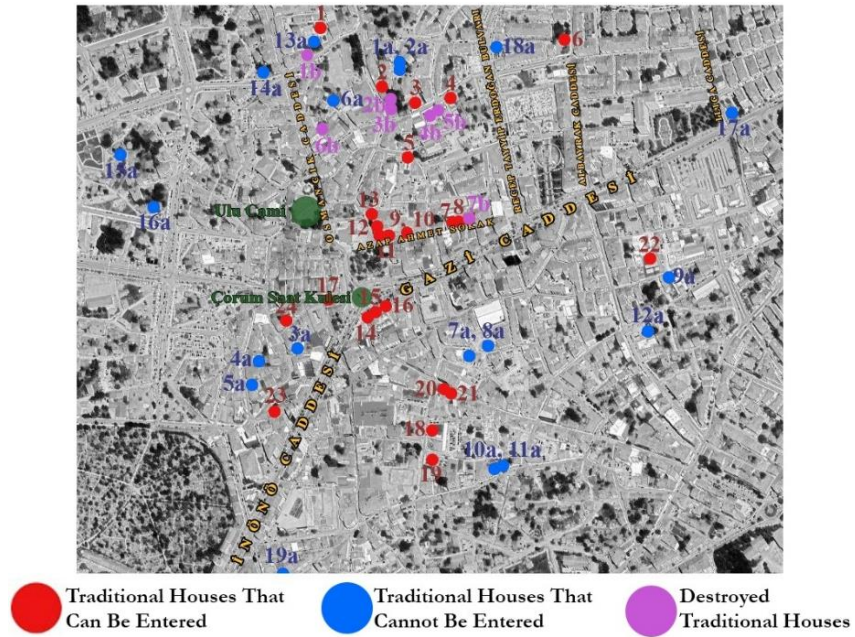
The 50 traditional houses in Corum historical city center, inventoried by the Governorship in 2009, constitute the material of this study. Located in the Central Black Sea Region of Turkey, Corum is a city with a continental climate, 801 meters above sea level (Figure 4).



**Figure 4.** Border map of Corum province and its districts

In this study, it was aimed to determine the structural and usage situations of 50 traditional houses in Corum city center and to reveal the problems and suggestions for their continued sustainability (Figure 5). Literature and field studies have been carried out for this purpose. Information about the city of Corum and its traditional houses was obtained from archives and libraries. Later, through fieldwork, traditional houses were identified, observed, examined and photographed on the site. During these studies, it was observed that seven of the 50 traditional residential buildings in 2009 had not survived to the present day, two of them had completely lost their originality due to inappropriate reconstruction, and many of them were in non-residential use or empty. During these studies,

the role and effectiveness of the public, local and central governments in the conservation projects regarding the historical city center were questioned, the problems in the Corum historical city center were determined, and conservation recommendations were given for the protection of the area.



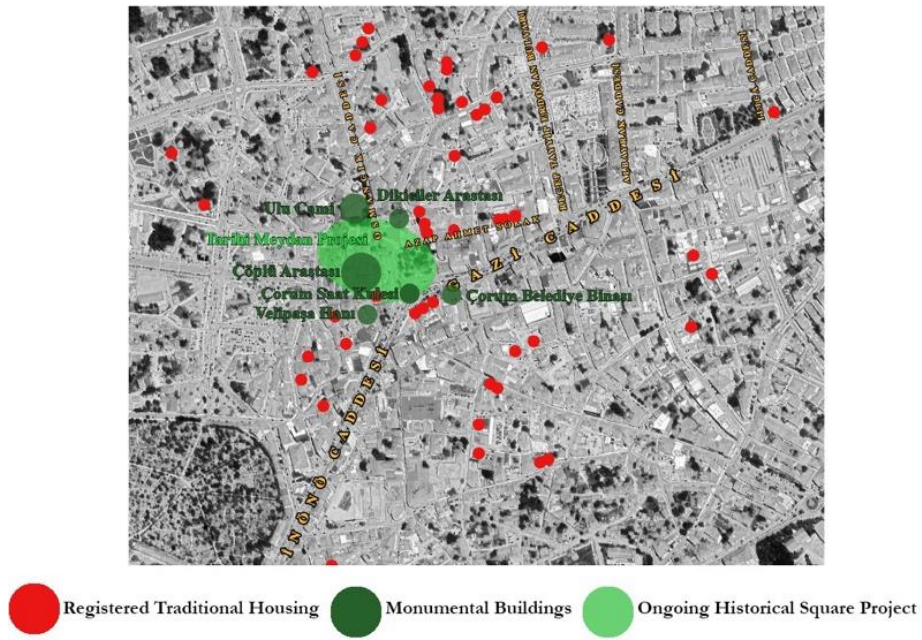
### 3 CORUM HISTORICAL CITY CENTER AND CONSERVATION WORKS

While the monumental buildings in Corum city center are the Clock Tower, Muradi Rabi Ulu Mosque, Veli Pasha Inn, Dikiciler Bazaar, Çöplü Arasta and Corum Municipality Building, there are also 43 registered and unregistered traditional houses. The restoration work on monumental buildings in the city center has been completed, and the Historical City Square restoration and landscaping project continues on an urban scale (Figure 6).



Figure 6. Traditional urban texture with identity as seen in the old photograph of Corum city center [17]

The Historical Square project started to be implemented by Corum Municipality as of 2021 and continues today. This area, which includes the Clock Tower, Muradi Rabi Ulu Mosque, Veli Pasha Inn, Historical Çöplü and Dikiciler Arasta is aimed to pedestrianize the historical city center and create a public space. While facade renovation and street landscaping works are carried out for this purpose, it is aimed to find a solution to the traffic problem. However, during these works, it was observed that examples of traditional texture were also destroyed (Figure 7, 8, and 9).



**Figure 7.** Architectural infrastructure of Corum city (Produced by the author)



**Figure 8.** Working area of Corum Historical Square Project



**Figure 9.** 3D examples of the Historical Square Project, the construction of which has started [18]

The Historical Çöplü Arasta, which is within the scope of the Historical Square project, is popularly known as the shoemakers' arasta and this region has an important value for the history of Corum. It is an iconic region for the local people with its proximity to the Corum Clock Tower, shoe shops in the area and tea houses around it (Map 3). Within the scope of the Historical Square Project, infrastructure and road works were carried out by the municipality on this street, and the shop fronts started to be renewed. Thus, it is planned to integrate with the Historical Square project and use the same language on the facades of the buildings (Figure 10 and 11).





**Figure 10.** Çöplü/Shoemakers Arasta (Hanefi Bayburtlu Archive) in the year of 1954 and today (F. Karahan Archive)



**Figure 11.** Digital visuals prepared for the facades planned to be applied in the same manner in Arasta [18].

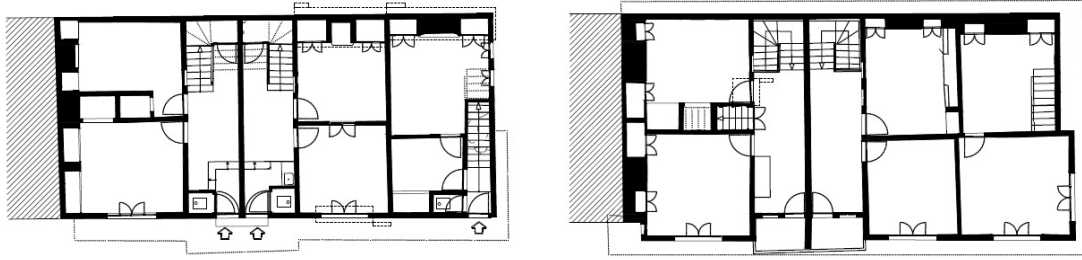
Historical Dikiciler Street/Eskiciler Street, which is also within the scope of the Historical Square project, is 1.5 meters wide and 30 meters long and is known as the narrowest street in the world. In place of the Government Mansion, which was located on this street and became unusable as a result of the fire in 1956, a total of 29 shops, each with an area of 4 m<sup>2</sup>, were built on both opposite sides of the street in 1957 and are called Dikiciler Arasta [18], (Figure 12).



**Figure 12.** Dikiciler Arasta and Eskiciler street before restoration (left) (Habercim19 Archive) and its current state (right) (F. Karahan Archive)

### 3.1 Corum Traditional Houses

The general characteristics of Anatolian Traditional Houses in terms of plan and detail are also seen in Corum Traditional Houses. Corum Traditional Houses also reflect the room and sofa setup and plan types with inner, middle and outer sofas (Figure 13). It is seen that the sofas are generally oriented towards the south [19]. When the settlement characteristics of Corum Traditional Houses are examined, examples with or without gardens are seen depending on their location. Most of the buildings were built adjacent to the street border. In the spatial organization of Corum Traditional Houses, just like the traditional houses in Anatolia, the windows on the ground floors are smaller and fewer in number than the windows on the upper floors, and the windows on the ground floor of the street facades are elevated so that the inside cannot be seen from the road level, giving importance to privacy. In these traditional houses, as in other regions, climate characteristics are an important factor in the selection of building materials and the use of adobe materials is more common (Figure 14).

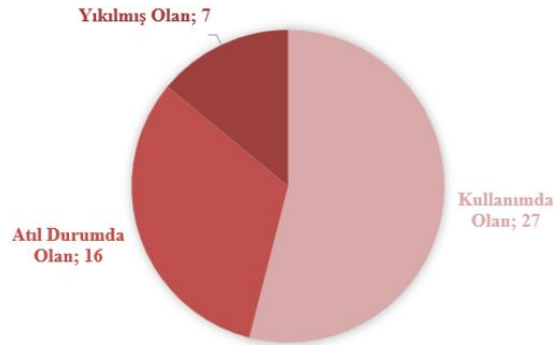


**Figure 13.** Ground (left) and upper (right) floor plans of the traditional house located in Çepni District, Merih Street, No: 20 [18]

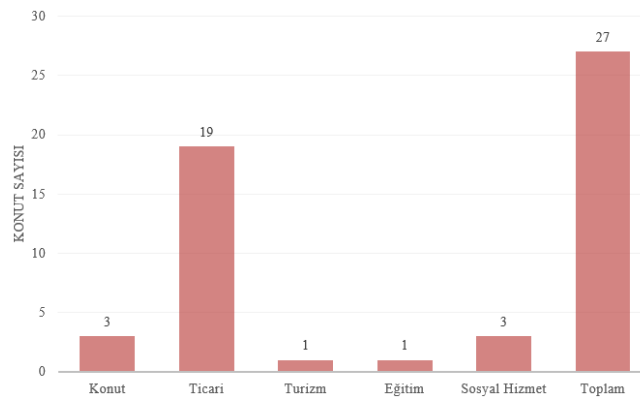


**Figure 14.** Corum Traditional Houses (F. Karahan Archive)

As a result of the field studies, it was seen that seven of the 50 registered traditional houses in the cultural inventory published by the governorship in 2009 were demolished, 16 were abandoned and 27 are being used (Figure 15 and 16). Comprehensive restoration has been made in 12 of the 27 used residences and all of them are used for non-residential commercial, cultural and social purposes. The other 15 used houses are still standing with simple repairs and have some structural problems. It was observed that only three of these standing houses were used in their original function as residences, two houses were empty and unused, and the others were used for other purposes. It was observed that six of the abandoned houses were in very bad condition and were protected with metal protection to prevent harm to the environment (Figure 17, 18 and 19).



**Figure 15.** Status of registered residences in Corum (Produced by the author)



**Figure 16.** Current functions of 27 registered historical houses in use (Produced by the author)



**Figure 17.** Bilaller Mansion (left), which was restored and functioned as the Provincial Directorate of Culture and Tourism, and the house, which was not restored and whose ground floor was used as a wooden shop and the upper floor was used as a warehouse, Üçtutlar Mahallesi No: 2 (F. Karahan Archive)



**Figure 18.** Traditional house used as house number 35 (left) and empty, unused house number 31-33 (right) on Milönü street (F. Karahan Archive)



**Figure 19.** Ruined traditional houses on Kulaksız 1. Street (left) and Alaybay Street (right) (F. Karahan Archive)

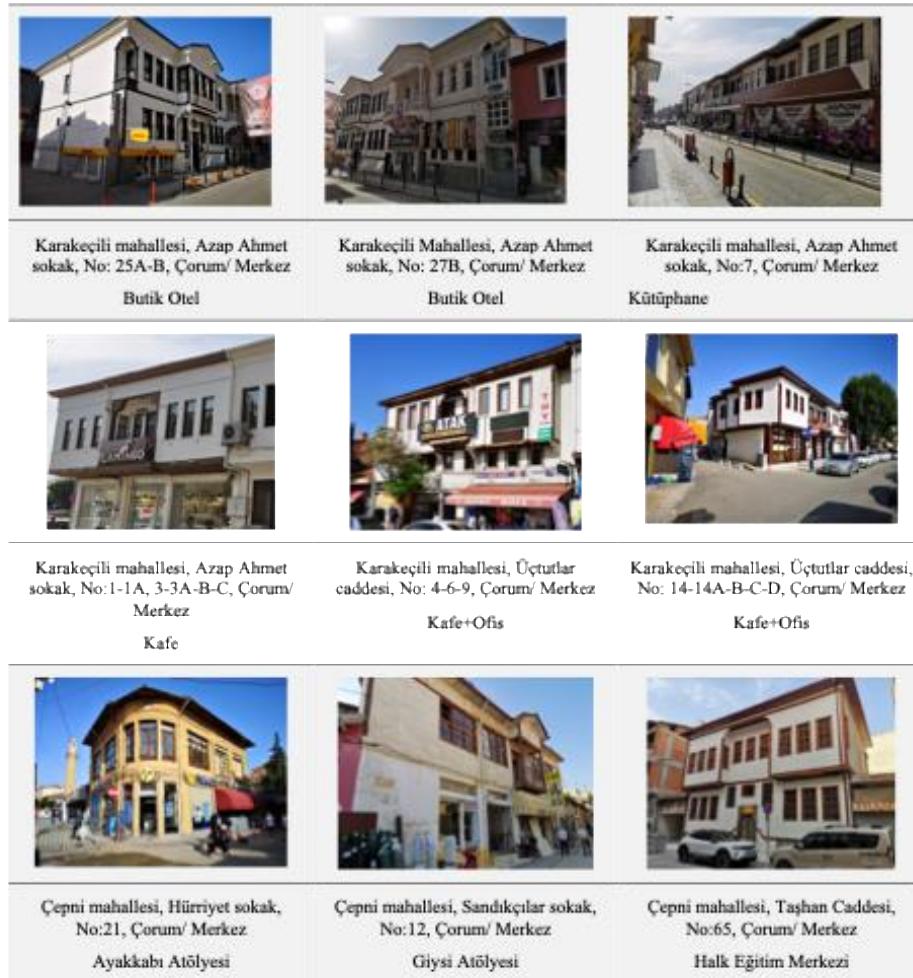
#### 4 DISCUSSION AND EVALUATION

Historical cities that reflect the culture and identity of a society are stratified and survive until today and reflect the evolution of their spatial development [3]. A settlement acquires its identity over many years and is constantly changing. Although it is important to adopt international integrated strategies for the sustainable protection of these changes and the historical and cultural heritage, it is necessary to adapt them according to the unique values, culture and conditions of the country where the heritage is located [20]. Bektaş (1992) states that freezing the past or making that environment uninhabitable for today's people is not conservation in the preservation of historical buildings in urban areas [21]. In the renewal or transformation of cities in a changing world, it is necessary to start with identity awareness and to understand and perceive the transfer of identity from the past to the future as

continuity [22]. Erder (2007) also emphasizes the importance of considering this continuity in the context of continuity [23]. Historical and cultural heritages were shaped according to the needs and expectations of societies in time. In the changing world, people's needs and expectations have also changed and the original functions of these heritages have become unable to meet the needs of the age and many of them have become unusable. For this reason, these historical buildings, which are isolated from society day by day, are abandoned and become neglected and unimportant objects, losing their ability to give identity to their environments and to be a part of the culture in which they are located [24]. Thus, structures isolated from their context become furniture in their environment. For this reason, conservation efforts will be successful by bringing the old and new together in continuity and integrity [25]. The contemporary concept of conservation is comprehensive, from economy to information, from aesthetics to policies, from technology to public awareness, from society's morality to culture [26]. For this reason, efforts to protect dilapidated historical city centers should be considered in this context and solutions should be produced to ensure the integration of historical buildings with urban life. Giving new functions to historical buildings that have lost their functions in recent years is frequently used as one of the conservation methods. However, the new function must provide a balance that is both in line with the spirit and spatial capabilities of the building and also establishes its relationship with other buildings and the city in its area. For this reason, the new function must be made within certain limits, both at the building and city scale [23]. In this way, historical buildings will be kept alive through conservation work carried out within the scope of the limitations and needs of the day, the city and the building, and will be included in the daily lives of the citizens.

In order to sustainably preserve the cultural heritage of Corum as a city with an identity and to transfer it to the future with scientific methods, 50 registered traditional houses located in Corum city center in 2009 were discussed within the scope of this study. The evaluations consisted of categories such as the current usage conditions of the buildings, their usage/structural status, and their usage functions. When traditional houses, especially those located in the heart of cities, are taken as the starting point in urban planning, attraction points can be created at different points for the city by reconstructing the charm of the past in a way adapted to today's conditions. While creating these points, the current needs of the city should be taken into consideration, starting from the city scale and detailing down to the neighborhood, street and single building scale, and environmental conditions should be included in the evaluation. When we look at the traditional houses in the city center of Corum, they have become furniture in the city, left to the fate of people, some of them are used for different functions, some of them have inappropriate uses, and some of them are abandoned to their fate. Although the buildings used for different functions look good from the outside, most of the traditional houses with poor structural conditions are in danger of collapse in the coming years. Because in buildings used for different functions, wall divisions or additions that are not included in any restoration project have been made and are used unconsciously without being structurally controlled. The conservation works carried out with the Corum Historical City Square Project, which is planned to be built in the city center of Corum and whose construction has started partially, continue in a non-integrated manner, and within the scope of this project, four registered traditional houses were demolished for the construction of a car park. In fact, within the scope of the project, new two-storey buildings similar to traditional Corum traditional houses will be built in the historical city center. Similarly, the blocks located in Azap Ahmet Street are now being transformed into commercial areas and workplaces as a single example. Although these methods are not scientific and sustainable, they are also the re-creation of an identity that does not exist in the city through imitation. These traditional houses, which are trying to maintain their existence in the city center by decreasing their numbers day by day and being exposed to many pressures, should be handled with multi-stakeholders with an integrated conservation approach and should not be left to the fate of individuals.

Within the scope of this study, taking into account the Historical Square project and its tourism potential, function suggestions were made for traditional houses located in the commercial area of the historical city center and for which direct interior analyzes were performed (Figure 20).



**Figure 20.** Function suggestions given to traditional houses located in the commercial area of Corum historical city center

## 5 CONCLUSION

In this research, where the current conditions of 50 registered traditional houses in the cultural inventory published by the Corum governorship in 2009 were investigated, the preservation status of the traditional houses in Corum city center was revealed. In a 15-year period from 2009 to the present day, 43 of these houses have survived to the present day. There are 27 traditional residences in use and 16 unused. It has been observed that the majority of unused houses are in ruins with structural problems. Most of these 16 unused traditional houses are expected to be demolished on their own in the near future. 12 of the 27 used houses have been restored and are used for non-residential trade, education, cultural and social functions. Only three of the used and unrestored houses continue to function as residences, and the others are used for commercial, educational, cultural and social activities. However, the usage and structural conditions of these traditional houses, which are in use and not restored, are not suitable for traditional houses. As a result, it has been concluded that among these traditional houses built in accordance with the housing function, only three houses continue to exist with their original function and that the space organization of traditional houses is not suitable for today's family life. For this reason, these structures have either been abandoned or are used unconsciously for different functions. However, depending on the required spatial adequacy of these different functions, dividing walls were either removed or added to the interior spaces of the houses. In addition to the addition of wall removal in this way, functions that put too much load on the building, such as a wedding hall or market, also damage the structural conditions of traditional residential buildings. When we look at the conservation works carried out on an urban scale in Corum city center, it is seen that populist and imitative works are carried out, and an approach is taken where precautions are not taken for buildings that are in danger of collapse. When looked at on a city scale, historical buildings scattered within the regions should be evaluated in harmony with each other and with the life in the region. Thus, historical buildings within the region should be planned in a way that they turn into a historical texture, not as individual structures specialized in the area where they are located. As a result, conservation efforts should be carried out with systematic planning, in harmony with the environment and integrated into today's life. In this process, conscious local people should be

contacted and necessary steps should be taken for the area. It should not be forgotten that this process should not be done unilaterally, but with the common opinions of competent people on this subject.

## Acknowledgments

This study was produced from Furkan Karahan's Master's Thesis titled "Analysis and Evaluation of Traditional House Architecture in Contemporary Cities: Traditional Houses of Corum", which was completed in 2023 at Bozok University Graduate Education Institute, Department of Architecture, under the supervision of Assoc. Prof. Emine Saka Akin.

## References

- [1] Venice Charter, 1964.
- [2] The Declaration of Amsterdam, 1975.
- [3] ICOMOS, *Valetta Convention*, 2011.
- [4] N. M. Cohen, *Urban Conservation*, Cambridge, Massachusetts, MIT Press, 1998.
- [5] B. Beernaert and W. Desimpelaere, "Bruges, Belgium," in *Management Historic Centres*, Robert Pickard, Ed. London and New York, 1st published: Spoon Press, 2000, pp. 8–30.
- [6] J. Warren, "The historic context: Principles and philosophies", in *Context: New Building in Historic Setting*, John Warren, John Worthington, Sue Taylor, Eds. 1st published, Great Britain: Bath Press, 1998.
- [7] Z. M. Enlil, "Yeniden islevlendirme ve soylulastirma: Bir sinifsal proje olarak eski kent merkezlerinin ve tarihi konut dokusunun yeniden ele gecirilmesi," *Domus*, no. 8, pp. 46–49. 2000.
- [8] J. Gehl and L. Gemzge, *New City Spaces*, 3rd ed., Copenhagen: Danish Architectural Press, 2003.
- [9] C. Bektas, "Korumak," *Mimarlik*, no. 1, pp. 72–73, 1991.
- [10] S. H. Eldem, *Türk Evi Plan Tipleri*, Istanbul: ITU Faculty of Architecture Press, 1954.
- [11] O. Küçükerman, *Kendi mekaninin arayışı icinde Türk Evi*, Türkiye Turing ve Otomobilcilik Kurumu, 1996.
- [12] E. S. Akin, A. Kalinbayrak Ercan, S.S Mumcuoglu, and E. Yaprak Basaran, "A refunctioned traditional House: Vasfi Susoy House, Tokat," *Türkiye Bilimler Akademisi Kultur Envanteri*, no. 17, pp. 119–139, 2018.
- [13] H. H. Halac and B. Saglam Doruk, "Regulations for privacy in Turkish Housing," *Akademik Sosyal Arasturmalar*, vol. 6, no. 38, pp. 50–72, 2019.
- [14] H. Yurekli and F. Yurekli, *Türk Evi Gozlemler ve Yorumlar*, Yapı Endüstri Merkezi, 2005.
- [15] E. S. Akin, "Tokat kentinin fiziksel gelismisi, anitsal ve sivil mimari orneklerinin analizi ve degerlendirilmesi," Ph.D. thesis, Dept. Architecture, Karadeniz Teknik Universitesi, Trabzon, TR, 2009.
- [16] D. Kuban, *Türk Ev Gelenegi Uzerine Gozlemler, Türk ve Islam Sanati Uzerine Denemeler*, Arkeoloji ve Sanat Yayinlari, 1982.
- [17] CVİKTM, Corum Valiligi II Kultur ve Turizm Mudurlugu.
- [18] Corum Municipality, 2021.
- [19] M. Akok, "Corum'un eski evleri," *Arkitek*, vol. 09-10, no. 237–238, pp. 171–189, 1951.
- [20] E. Madran, "Tarihi cevrenin tarihi: Osmanlı'dan gunumuze tarihi çevre: Tavirlar-duzenlemeler," *Dosya*, vol. 14, no. 1, pp. 6–15, 2009.
- [21] C. Bektas, *Koruma Onarim*, YEM Yayını, 1992.
- [22] B. Guvenc, *Insan ve Kultur*, 2nd ed., Remzi Kitabevi, 1974.
- [23] C. Erder, *Tarihi Cevre Bilinci*, Orta Dogu Teknik Universitesi Yayinlari, 2007.
- [24] B. Asiliskender, H. Gokmen and N. Yilmaz, "Anit kavrami, kimligin surekliligi degisim: Gevher Nesibe Medresesi deneyimi," *Mimarlık*, no. 322, pp. 55–59, 2005.
- [25] D. Kuban, *Tarihi Cevre Korumanin Mimarlik Boyutu*, YEM Yayini, 2000.
- [26] Z. Gorgulu, "Imar planlama, koruma ve planci iliskileri uzerinde bir degerlendirme," *Yapi*, no. 137, pp. 35–39, 1993.



## **Crashworthiness Design and Damage Analysis with Multiple Internal Structure Pattern**

**Hakan Burcin Erdogan<sup>\*1</sup>**

<sup>1</sup>*Machinery Programme, Department of Machinery and Metal Technologies, Izmir Kavram Vocational School, Izmir, Türkiye*

---

### **Abstract**

In automobile crashworthiness, the effect of geometric properties on absorption is examined in studies. The kinetic energy generated by the first peak force occurring at the time of the collision is damped by the sequential deformation of the crashworthiness. This study prepared internal structure patterns for aluminium alloy crashworthiness designs with three different geometries and equal mass. In the finite element model, the crushing and performance parameters of the crashworthiness were investigated with the help of flat and two different angle inclined plates. For this, reference data were taken into account to observe the damage initiation and progression in the aluminium alloy material model. According to the results of the analysis, it has been observed that the structure in the K1 design, which has a square outer frame and whose internal structure is divided into eight equal sections, provides resistance to crushing by inclined plates. However, it was observed that the crushing damage in the flat plate effect was higher in the ellipsoid (E2) and circle (D1) shaped crashworthiness due to the impact of the collision, and the efficiency decreased due to the bending of the crashworthiness by the inclined plate compression.

**Keywords:** *Crashworthiness design, Energy absorption, Multi-cell structure design*

---



## Analysis of Diesel/Bio-Oil Blends Produced by Co-Pyrolysis of Spruce with Glycerol

Ahmet Rasim Girisen\*<sup>1</sup>, Hakan Ozcan<sup>1</sup>

*Mechanical Engineering Department, Ondokuz Mayıs University, Samsun, Türkiye*

### Abstract

This study examined the fuel properties of bio-oil produced by co-pyrolysis of spruce with glycerol. In addition, the fuel properties of diesel/bio-oil blends with different mixing ratios as 2.5%, 5% and 10% was also investigated. The bio-oil produced via fixed bed reactor. The spruce co-pyrolyzed with glycerol at 20% mixing ratio. Pyrolysis parameters like temperature, heating rate and carrier gas flow rate were adjusted as 550 °C, 10 °C/sec and 100 ml/sec, respectively. The density, kinematic viscosity, flash point, cetane index, water content, calorific value and cold filter plugging point of diesel/bio-oil blends was compared. As a result, water content, kinematic viscosity, calorific value, density and flash point adversely affected by bio-oil additive into the commercial diesel fuel. Although, the mixing ratio is increased up to 10%, there is no significant difference in properties such as the flash point, density and calorific value. In addition, the water content, lower heating value, flash point and viscosity of the diesel/bio-oil blend complied with the standards at %5 mixing ratio. The results showed that the bio-oil production is successful and its blends can be used as a fuel additive safely. Moreover, the cetane index of diesel/bio-oil blends increased. The cetane index directly effects ignition delay of fuel. The start of ignition of diesel/ bio-oil blends with high cetane index will be retarded and it allow controlled combustion.

**Keywords:** Diesel, Bio-oil, Glycerol, Fuel properties, Co-pyrolysis

## 1 INTRODUCTION

The increasing population cause high energy demands. This energy demand is mostly supply by fossil fuels. However, the fossil fuel reserves are limited and existed in specific regions across the globe. Therefore, there is a need for an energy source that can be obtained from each part of the world [1]. Biomass is an attractive energy resource in this scope and can keep the world clean for the upcoming generation. Biomass is an environmentally friend, cheap and abundant source. Biomass can be transform using methods such as coking [2], pyrolysis [3] or gasification [4] to clean energy.

Crude bio-oil obtained through pyrolysis has properties such as high viscosity, acidity, high oxygen content, and chemical instability that make it unsuitable for use as fuel. Therefore, bio-oil properties need to be improved to be used directly. The bio-oil is a complex structure consisting of various oxygen-containing components such as ketones, aldehydes, phenols and sugars. Co-pyrolysis has given an alternative way to improve bio-oil properties. In many studies, co-pyrolysis or catalytic pyrolysis methods have been used to reduce the oxygen content and increase the H/C ratio of bio-oil obtained from pyrolysis. The purpose of co-pyrolysis or catalytic pyrolysis is to remove the oxygen contained in the bio-oil by converting it into CO<sub>2</sub>, CO, etc. gases or to ensure that the carbons in the structure bind excess Hydrogen. The co-pyrolysis characterizations of glycerol have been widely investigated. Bartocci et al. in [5] revealed that the glycerol could increase the hydrogen content in the obtained gases. Delgado et al. in [6] was examined slow co-pyrolysis of corn straw with glycerol and found that the feedstocks interact between with different degrees throughout the process. Wang et. al in [7] was investigated the co-pyrolysis of *Chlorella vulgaris* and glycerol and confirmed a synergistic effect of glycerol on the production of alcohols and esters.

Spruce sawdust (SS) is a renewable carbon source; however, its low hydrogen-to-carbon ratio limits the direct use of bio-oil in combustion systems. Whereas, some liquid wastes such as GLY might be introduced to the pyrolysis system to increase the H/C ratio. The present experimental study focused on the co-pyrolysis of spruce sawdust with GLY to producing diesel fuel carbon range bio-oils. Pyrolysis was conducted in a nitrogen atmosphere using a fluidized bed reactor at various temperatures (400, 450, 500, and 550°C) and mixing ratios (10 wt%, 20 wt%, and 30 wt%). The yields of bio-oils were optimized, and bio-oil ingredients were also examined with the elemental



analysis, GC-MS and FTIR analysis methods. In addition, the bio-oil obtained by co-pyrolysis mixed with diesel fuel with different mixing ratios (2.5%, 5% and 10%). The fuel properties of diesel/bio-oil blends investigated.

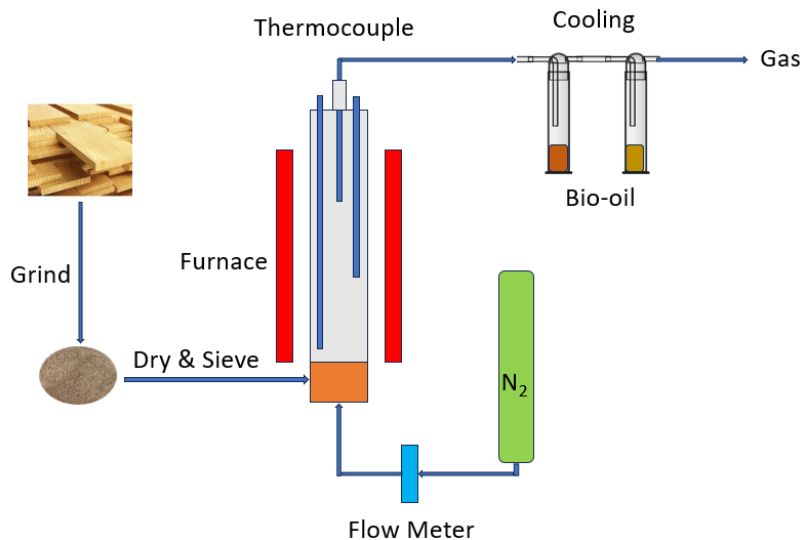
## 2 MATERIAL AND METHOD

### 2.1 Pyrolysis materials

SS was supplied by a local manufacturer and sieved to sizes between 0.75-1.2 mm. SS dried at 110°C for 18 hours to remove moisture. The elemental analysis was conducted, and the results are presented in Table 1. GLY purity of 99.7 % were purchased from Beyanlab Laboratory Products Industry Trade Limited Company. The GLY was mechanically mixed by the SS at the rates of 10 wt%, 20 wt%, and 30 wt%. In this way, it was provided to completely absorb the GLY into the SS.

### 2.2 Bio-oil production

The pyrolysis reactor system was used in experiments as shown in Fig. 1. The inner diameter of the reactor is 50 mm and the height is 400 mm. The reactor is heated by a resistance with a power of 4 kW. Nitrogen as a carrier gas was introduced into the reactor from the bottom at a constant flow rate of 150 mL/min. Bio-oil was collected in a condensation unit at the exit of the reactor. The pyrolysis reactor ensures that the system is in complete balance by taking temperature measurements from 7 different points. A total of 40 grams of raw material was loaded in each process. The reactor's gases were passed through the condenser at 0 °C. Additionally, a second cooler and gas washing chamber were used to increase the condensation of the gases. The liquid products in the glass containers were weighed to determine the total mass. The liquid products were filtered using filter paper and separated from solid particles. The pyrolysis experiments were conducted at temperature of 550 °C, heating rate of 10 °C/sec and carrier gas flow rate of 100 ml/sec. The bio-oil obtained from pyrolysis mixed with diesel fuel with mixing ratio of 2.5% (DB2.5), 5% (DB5), and 10% (DB10). The diesel/bio-oil blends were stirred with magnetic stirrer of 30 min.



**Figure 1.** Experimental setup of co-pyrolysis

### 2.3 Determination of fuel properties

Density, kinematic viscosity, lower heating value (LHV), cold filter plugging point (CFPP), flash point (FP), water content (WC) of the obtained diesel/bio-oil blends were measured in Shell & Turcas Petrol SADAŞ Fuel Analysis Laboratory. The cetane index (CI) of diesel/bio-oil blends were calculated using Equation 1 according to ASTM-D976 standards.

$$CI = 454.74 - 1.641416 \cdot \rho + 0.00077474 \cdot \rho^2 - 0.554 \cdot t_{50} + 97.803 \cdot \log^2(t_{50}) \quad (1)$$

where: CI = Cetane index,  $\rho$  = Density at 15 °C of fuel,  $t_{50}$  = 50% recovery temperature.

The properties of the diesel/bio-oil blends were evaluated according to ASTM D6751 and TS EN 14214 standards, and the properties of diesel fuel were evaluated according to the TS EN 590 standard. The standard values of the investigated fuel properties showed Table 2.

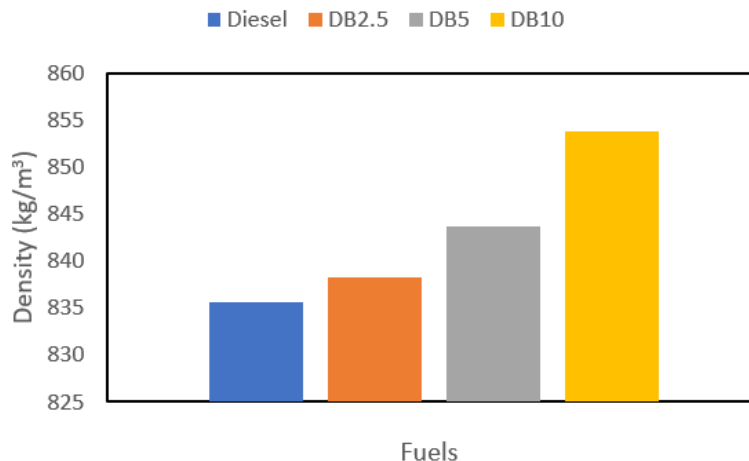
**Table 2.** Standards and limits for fuel properties

Properties	Unit	Limits of ASTM D6751		Limits of EN 14214		TS EN 590	
		Minimum	Maximum	Minimum	Maximum	Minimum	Maximum
Density at 15 °C	kg/m <sup>3</sup>	-	-	860	900	820	845
Kinematic Viscosity at 40 °C	mm <sup>2</sup> /s	1.9	6.0	3.5	5.0	2.0	4.5
CFPP	°C	-	-	-	-	-15 (winter)/+5 (summer)	-
WC	mg/kg	-	500	-	500	-	200
FP	°C	93	-	101	-	55	-
CI	-	47/-	-	51/-	-	51/46	-

### 3 RESULTS

#### 3.1 Density

The density is a significant factor for the flow and cold flow properties of the fuel. On the other hand, density is related to other fuel properties such as cetane index and calorific value. Because, the density value is used in calculating the cetane index. The density values of the diesel/bio-oil blends and diesel fuel are showed in Fig. 2. The density values of all diesel/bio-oil blends are higher than diesel fuel. The density of diesel fuel and DB10 blend is 835.7 and 853.8, respectively. The density of the mixture increased due to the density of bio-oil being higher than diesel fuel. Fuel density for DB10 increased by approximately 35.8% compared to diesel fuel. A fuel blend with a higher density value has a higher energy per unit volume, which increases the power output [8]. Because, high density fuel will lead more fuel to be injected into the cylinders by mass. This situation is theoretically increased the engine power. However, injection of more fuel in to the cylinder might cause a rich mixture in combustion chamber. Homogenous air/fuel mixture will not obtain in this situation and combustion will be affect negatively. Therefore, the suitability of fuel density for the fuel system elements is important.

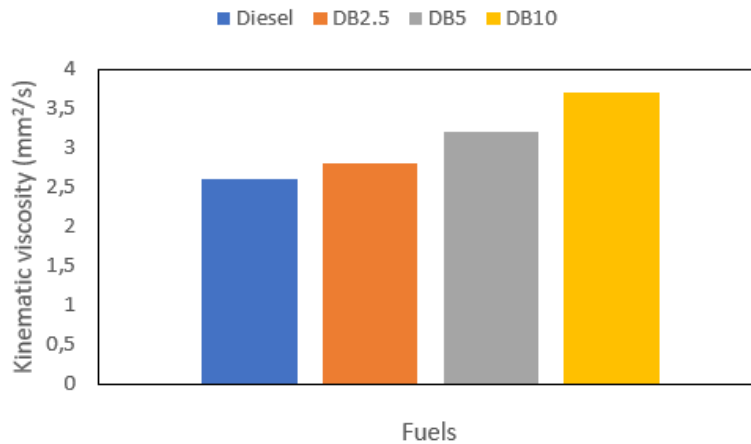


**Figure 2.** Density variation of diesel/bio-oil blends

#### 3.2 Kinematic viscosity

The viscosity is important for fuels because of the flow characteristic. High viscosity has significant negative effects and causes insufficient atomization at the time of injection. The injection duration in diesel engines is between 0.001 and 0.002 s and the diameter of the fuel droplet must be lower than 0.025 mm to maintain the

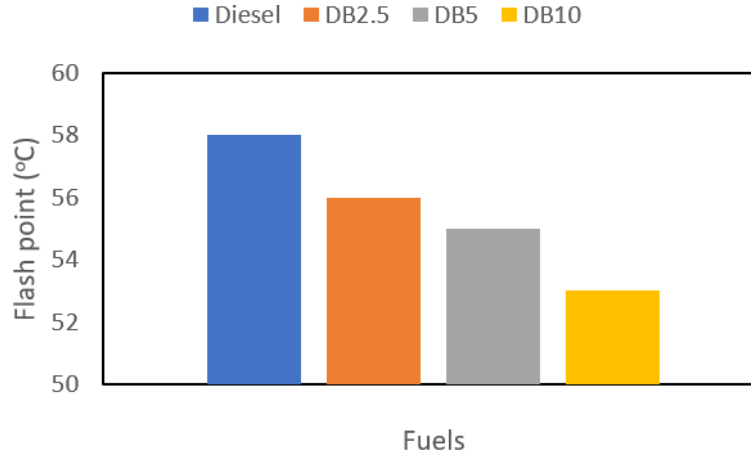
quality of the fuel combustion [8]. Moreover, high viscosity causes more resistance and increase the fuel pressure. This situation adversely affects the operation of the parts of fuel system. Bio-oil and biodiesel have a higher viscosity compared to diesel fuel [9]. Therefore, the viscosity of diesel-bio-oil blends increased slightly as the volume percentage of bio-oil to 10%. The viscosity of diesel and diesel/bio-oil blends are shown in Figure 3. Despite the increase in viscosity, the DB10 mixture remained within standards.



**Figure 3.** Kinematic viscosity variation of diesel/bio-oil blends

### 3.3 Flash point

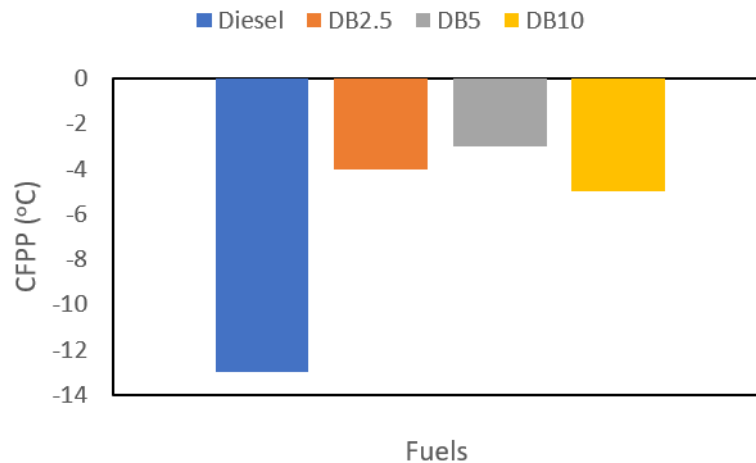
Flash point is an important to safety storage and transport fuels. The flash point for fuels is the minimum temperature at which the fuel can produce a vapor that forms an ignitable mixture with air. The bio-oil contains alcohol-derived compounds and it creates a flammable air/steam mixture at lower temperatures. This situation causes decreasing of the flash point diesel/bio-oil blends. Flash point values of diesel/bio-oil blends are shown in Figure 4.



**Figure 4.** Flash point variation of diesel/bio-oil blends

### 3.4 Cold filter plugging point

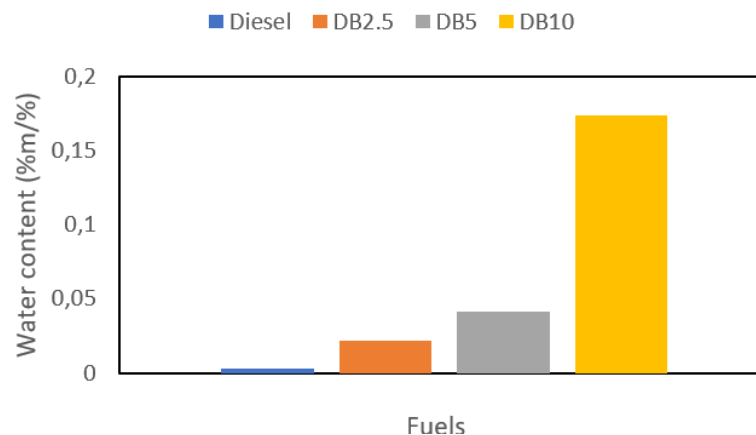
The CFPP of the fuel is important parameter of availability at different geographical conditions. Cold flow properties can be predicted with density and viscosity values. CFPP is the lowest temperature at which a given volume of fuel still passes through a standardized filtration device in a specified time. CFPP gives an information for a fuel will give trouble free flow at low temperature. CFPP values of diesel/bio-oil blends are shown in Figure 5. It can be seen that the CFPP temperatures of diesel/bio-oil blends are higher than those of diesel fuel due to the bio-oil content. The CFPP temperature of DB10 mixture slightly lower than DB2.5 and DB5.



**Figure 5.** Cold filter plugging point variation of diesel/bio-oil blends

### 3.5 Water content

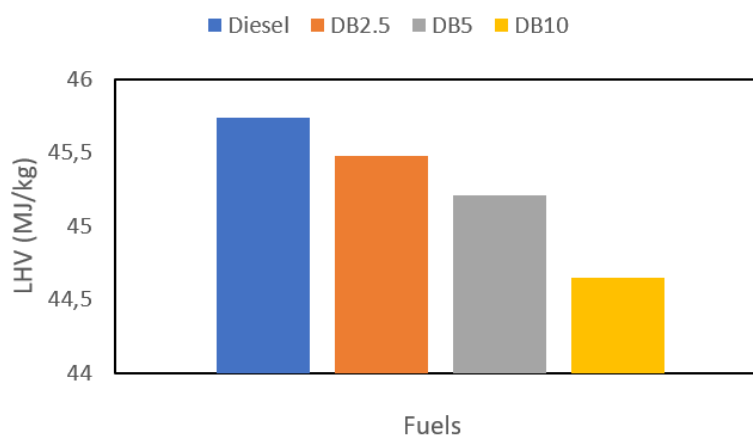
The presence of water content in fuel depends on many reasons. Water content in biodiesel mostly caused from washing process. On the other hand, the water content in the bio-oil obtained from pyrolysis depends on moisture content present in the feedstock and dehydration reactions in pyrolysis. The water content have some adverse impact such as low heating value, ignition delay, and lower combustion rate [10]. A little water content in fuel leads to micro explosion of droplets, a more uniform temperature distribution in combustion chamber and lowers the NO<sub>x</sub> emissions [11, 12]. The amount of water higher than the standards causes a decrease in the quality of the fuel, especially the cold flow properties of the fuel, worsening of the combustion characteristics and corrosion in the fuel system. On the contrary, the water content in fuel higher than the standards decrease quality of the fuel, adversely affect the cold flow properties, deteriorating of the combustion and cause corrosion in the fuel system. The water contents of diesel/bio-oil blends are shown in Figure 6. Water content of DB2.5 and DB5 complies with the standards. But, DB10 mixture have high amount of water.



**Figure 6.** Water content variation of diesel/bio-oil blends

### 3.6 Lower heating value

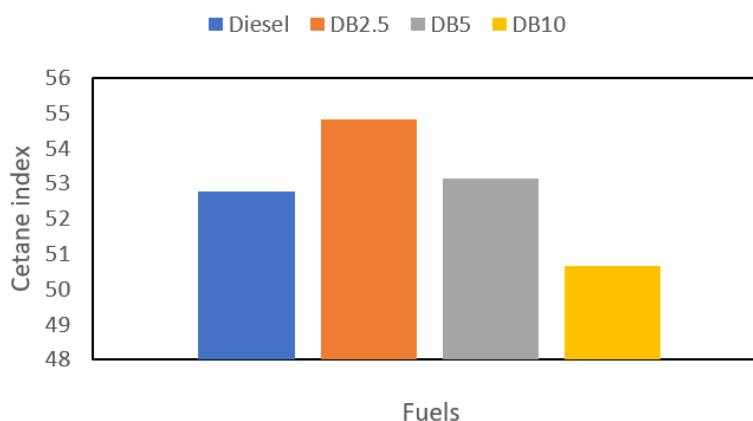
LHV is directly affect the performance of the engine. LHV indicates the amount of energy released of the fuel the end of the combustion. The fuel becomes more efficient as the calorific value increases and improves engine performance during combustion. Bio-oil and biodiesel have lower LHV compared to diesel because of their oxygen content. But, the presence of oxygen in the fuel leads to completely burnt of fuel [13]. Thank to high oxygen content in fuel, CO and HC emissions decrease and NO<sub>x</sub> and CO<sub>2</sub> emissions increase. The calorific value of the bio-oil is always lower than petroleum fuels and it's found within 15-36 MJ/kg in the literature [14–16]. The LHV of bio-oil obtained from co-pyrolysis is approximately 35.14 MJ/kg. All diesel/bio-oil blends in this study have lower LHW than diesel fuel.



**Figure 7.** Lower heat value variation of diesel/bio-oil blends

### 3.7 Cetane index

The cetane index can be describe as the measurement of ignition quality and the self-igniting tendency of the fuel in an engine. The cetane index of fuels is a very crucial property for the combustion characteristics. The longer carbon chains and presence of saturation in molecules effects the cetane index. Therefore, the cetane index of biodiesel is higher than pure diesel [13, 17, 18]. The cetane index directly affects the ignition delay. Fuels with higher cetane index allow controlled combustion because they will have shorter ignition delay. On the contrary, fuels with low cetane index start to burn much later than injection and control of combustion becomes difficult. Cetane indexes of diesel/bio-oil blends are shown in Figure 8. Among all fuels, the highest cetane index belongs to DB2.5 as 54.82. However, the lowest cetane index belong to DB10 as 50.66.



**Figure 8.** Cetane index variation of diesel/bio-oil blends

## 4 CONCLUSION

The fuel properties of the produced diesel/bio-oil blends are examined and the result showed that;

- It is seen that the density values of all diesel/bio-oil blends comply with TS EN14214 standards, and the DB10, which has the highest density value, is 2.16% higher than diesel fuel. On the other hand, DB2.5 and DB 5 only comply with TS EN 590 standarts.
- The viscosity values of the obtained fuels comply with ASTM D6751, TS EN 14214 and TS EN 590 standards. The highest viscosity obtained from DB10. The DB10 is 42.30% higher than diesel fuel.
- The water content of DB10 does not comply with TS EN 590 standarts. However, DB2.5 and DB5 comply with ASTM D6751, TS EN 14214 and TS EN 590 standards.
- There is no significant difference between the lower calorific values of diesel-bio-oil blends. The DB10, which has the lowest lower calorific value, is 2.38% lower than that of diesel fuel.

The main purpose of this study is investigation of the possibilities in using biooils obtained from biomass with diesel fuel. For this reason, the bio-oil obtained from co-pyrolysis of SS dust with GLY and the bio-oil mixed with diesel fuel at different ratios. It can be said that the fuel properties of the diesel/bio-oil blend up to 5% are within the standards and it will be suitable for use as fuel. In order to determine the negative effects of the obtained fuel

blends like density and viscosity detailed studies such as adjusting the injection pressure, changing the injection advance, and evaluate in different compression ratios can be done. In addition, the catalytic co-pyrolysis experiments with different catalyst can be upgrade the bio-oil properties and provide the production of diesel like fuels.

## Acknowledgments

Ahmet Rasim Girisen reports financial support was provided by Council of Higher Education of the Republic of Turkey (YOK 100/2000 Scholarship). Ahmet Rasim Girisen reports financial support was provided by the Scientific and Technological Research Council of Turkey (TUBITAK 2211-A Scholarship). Hakan Ozcan reports financial support was provided by Ondokuz Mayıs University.

## References

- [1] M. A. Sokoto, L. G. Hassan, M. A. Salleh, S. M. Dangoggo, and H. G. Ahmad, "Quality assessment and optimization of biodiesel from lagenaria vulgaris (calabash) seeds oil," *International Journal of Pure and Applied Sciences and Technology*, vol. 15, no. 1, pp. 55–66, Mar. 2013.
- [2] W.-H. Chen, J. Peng, and X. Bi, "A state-of-the-art review of biomass torrefaction, densification and applications," *Renewable and Sustainable Energy Reviews*, vol. 44, pp. 847–866, 2015, doi: 10.1016/j.rser.2014.12.039.
- [3] O. Azeta, A. O. Ayeni, O. Agboola, and F. Elehinafe, "A review on the sustainable energy generation from the pyrolysis of coconut biomass," *Scientific African*, vol. 13, art. no. e00909, Sep. 2021, doi: 10.1016/j.sciaf.2021.e00909.
- [4] H. C. Ong, W.-H. Chen, A. Farooq, Y. Y. Gan, T. Lee, and A. Veeramuthu, "Catalytic thermochemical conversion of biomass for biofuel production: A comprehensive review," *Renewable and Sustainable Energy Reviews*, vol. 113, art. no. 109266, 2019, doi: 10.1016/j.rser.2019.109266.
- [5] P. Bartocci et al., "Pyrolysis of pellets made with biomass and glycerol: Kinetic analysis and evolved gas analysis," *Biomass and Bioenergy*, vol. 97, pp. 11–19, 2017, doi: 10.1016/j.biombioe.2016.12.004.
- [6] R. Delgado, J. G. Rosas, N. Gómez, O. Martínez, M. E. Sanchez, and J. Cara, "Energy valorisation of crude glycerol and corn straw by means of slow co-pyrolysis: Production and characterisation of gas, char and bio-oil," *Fuel*, vol. 112, pp. 31–37, 2013, doi: <https://doi.org/10.1016/j.fuel.2013.05.005>.
- [7] S. Wang, H. Shang, A. E.-F. Abomohra, and Q. Wang, "One-step conversion of microalgae to alcohols and esters through co-pyrolysis with biodiesel-derived glycerol," *Energy Conversion and Management*, vol. 198, art. no. 111792, 2019, doi: 10.1016/j.enconman.2019.111792.
- [8] P. Wu, C. Miao, X. Zhuang, W. Li, X. Tan, and T. Yang, "Physicochemical characterization of levulinate esters with different alkyl chain lengths blended with fuel," *Energy Science & Engineering*, vol. 11, no. 1, pp. 164–177, 2023, doi: <https://doi.org/10.1002/ese3.1320>.
- [9] A. Hoang, "Prediction of the density and viscosity of biodiesel and the influence of biodiesel properties on a diesel engine fuel supply system," *Journal of Marine Engineering & Technology*, vol. 20, pp. 1–13, 10/12 2018, doi: 10.1080/20464177.2018.1532734.
- [10] Q. Lu, W.-Z. Li, and X.-F. Zhu, "Overview of fuel properties of biomass fast pyrolysis oils," *Energy Conversion and Management*, vol. 50, no. 5, pp. 1376–1383, 2009, doi: 10.1016/j.enconman.2009.01.001.
- [11] R. Calabria, F. Chiariello, and P. Massoli, "Combustion fundamentals of pyrolysis oil based fuels," *Experimental Thermal and Fluid Science*, vol. 31, no. 5, pp. 413–420, 2007, doi: 10.1016/j.expthermflusc.2006.04.010.
- [12] A. E. Pütün, A. Özcan, and E. Pütün, "Pyrolysis of hazelnut shells in a fixed-bed tubular reactor: yields and structural analysis of bio-oil," *Journal of Analytical and Applied Pyrolysis*, vol. 52, no. 1, pp. 33–49, 1999, doi: 10.1016/S0165-2370(99)00044-3.
- [13] A. M. Ashraful, et al., "Production and comparison of fuel properties, engine performance, and emission characteristics of biodiesel from various non-edible vegetable oils: A review," *Energy Conversion and Management*, vol. 80, pp. 202–228, 2014, doi: 10.1016/j.enconman.2014.01.037.
- [14] B. Biswal, S. Kumar, and R. K. Singh, "Production of hydrocarbon liquid by thermal pyrolysis of paper cup waste," *Journal of Waste Management*, vol. 2013, 01/01 2013, doi: 10.1155/2013/731858.
- [15] C. Mullen, A. Boateng, N. Goldberg, I. Lima, D. Laird, and K. Hicks, "Bio-oil and bio-char production from corn cobs and stover by fast pyrolysis," *Biomass and Bioenergy*, vol. 34, pp. 67–74, 2010, doi: 10.1016/j.biombioe.2009.09.012.
- [16] M. Bertero, H. Gorostegui, C. Orrabalís, C. Guzmán, E. Calandri, and U. Sedran, "Characterization of the liquid products in the pyrolysis of residual chañar and palm fruit biomasses," *Fuel*, vol. 116, pp. 409–414, 2014, doi: 10.1016/j.fuel.2013.08.027.

- [17] K. Muhammad Usman, F. Anafi, S. Umaru, J. Nuskowski, and D. Kulla, "GC/MS analysis of methyl esters of biodiesel produced from cotton seed oil," *Nigerian Journal of Solar Energy*, vol. 27, 2016.
- [18] K. Muhammad Usman, N. Tijjani, Z. A. U. Magaji, and Y. Bello Habib, "Production of biodiesel from wild grape seed," *NSE Technical Transaction Journal*, 2011.



## Investigation of Oxidative Stability Behavior of Kaolin Nanoparticles Doped Bio-Based Palm Lubricants

Batuhan Ozakin<sup>\*1</sup>, Kursat Gultekin<sup>2</sup>, Nalan Turkoz Karakullukcu<sup>3</sup>

<sup>1</sup>Mechanical Engineering Department, Samsun University, Samsun, Türkiye

<sup>2</sup>Mechanical Engineering Department, Ondokuz Mayıs University, Samsun, Türkiye

<sup>3</sup>Blacksea Advanced Technology Research and Application Center, Ondokuz Mayıs University, Samsun, Türkiye

### Abstract

Oxidation stability is a crucial property of lubricants used in the metalworking industry. Recently, researchers have been turning to bio-based lubricants for sustainability. However, bio-based lubricants show poor oxidation stability, and improving these properties is considered an important issue. In recent years, significant progress has been made in improving the oxidative properties of lubricants by incorporating nanoscale mineral additives. In this context, in the presented study, 0.25% oleic acid-modified kaolin nanoparticles by weight were doped to bio-based palm lubricants, and the lubricants were exposed to oxidation by a hot oil oxidation test (HOOT). The Fourier Transform Infrared Spectroscopy (FT-IR) spectra revealed that the band intensity of palm lubricant with kaolin additive was lower compared to pure palm lubricant. The thermogravimetric analysis (TGA) graphs indicated that palm lubricants with added kaolin could delay the onset of oxidation by about 10.8 °C compared with pure palm lubricants. The synergy between the TGA graphs and FT-IR spectra findings confirms that kaolin nanoparticles improve the oxidative stability of palm lubricants.

**Keywords:** Metalworking industry, Hot oil oxidation test (HOOT), Thermogravimetric analysis (TGA), Surface modification, FT-IR spectroscopy

## 1 INTRODUCTION

Oxidation stability, a key attribute in lubrication technology, signifies the lubricant's ability to withstand oxidation. Lubricants with inadequate oxidation stability tend to have a significantly reduced service life. Moreover, oxidation in lubricants leads to a rise in viscosity and the creation of sludge [1, 2]. Therefore, lubricants are desired to possess high oxidation stability. Current research is focused on improving the oxidation stability of vegetable oils to enhance their sustainability. Therefore, it will be achievable to produce lubricants that serve as alternatives to conventional options, are cost-effective, and importantly, sustainable. Insertion of nanoparticles with antioxidant properties into lubricants is proposed to enhance their oxidative stability for this purpose [3]. While studies on the effectiveness of doping nanoparticles to lubricants for improving oxidation stability are scarce, there has been a recent uptick in interest regarding this issue. The literature respectively showcases studies sequentially demonstrating the improvement of oxidation stability by incorporating nanoparticles into lubricants. Tan et al. stated that nano-sized zeolite in palm oil effectively slows down the oxidation process with a significantly lower degree of polymerization and lower content of acidic oxidation products in the oil [4]. Ali and Xianjun stated that Al<sub>2</sub>O<sub>3</sub>/TiO<sub>2</sub> hybrid nanolubricants improved oxidation by delaying the oxidation onset temperature [5]. Ranjan et al. stated that the lubricants produced with the mechanism they proposed, with optimized concentration, have a lubricating behavior and that the nano additive (TiO<sub>2</sub>/gC<sub>3</sub>N<sub>4</sub>) provides protection from oxidation due to the nitrite and oxides it contains [6]. In their study, Sadiq et al. added graphene and maghemite nanoparticles to coconut oil and found that these nano additives improved oxidation stability by delaying thermal degradation [7]. Kamal et al. reported that incorporating SiO<sub>2</sub> nanoparticles into rice bran oil enhanced its oxidation stability [8]. Kumar et al. showed that the oxidation degradation of ZnO nano-doped engine oil is lower than the base engine oil [9]. In recent years, there has been a growing number of studies in the literature demonstrating that nanoparticles enhance oxidative stability. Brito et al. stated that kaolin has antioxidant properties [10]. There is a lack of research in the literature regarding the use of kaolin nanoparticles to improve the oxidative stability of lubricants.

In this study, oleic acid-modified kaolin nanoparticles were doped to bio-based palm lubricants and subjected to oxidation by a hot oil oxidation test (HOOT). Fourier Transform Infrared Spectroscopy (FT-IR) and thermogravimetric analysis (TGA) have indicated that kaolin nanoparticles enhance the oxidative stability of bio-based palm lubricants.



## 2 MATERIALS AND METHODS

### 2.1 Materials

In this study, palm oil, kaolin particles, oleic acid, and sorbitan monooleate (span80) compounds were commercially obtained and used. The average grain size of kaolin particles was determined as 950 nm. Kaolin particles were milled in an axial ball mill for 8 hours with balls of varying sizes, five times the amount of kaolin, to produce kaolin nanoparticles averaging 350 nm in grain size.

### 2.2 Methods

#### 2.2.1. Surface Modification of Kaolin

Kaolin nanoparticles were subjected to surface modification to have more stable dispersion properties in palm oil. During the surface modification process, 10 g of kaolin particles were dispersed in the homogenizer with acetone. While preserving the molar balance, 10.93 g of oleic acid was added to the solution and thoroughly mixed. The obtained solution was stirred at 1250 rpm using a magnetic stirrer for 5 hours at 35°C, with precautions taken to prevent acetone from evaporating [11]. Then, the solution was washed with acetone and dried at room temperature to obtain modified kaolin particles. Furthermore, research indicates that employing surfactants effectively enhances dispersion stability properties.

#### 2.2.2. Nanolubricant Production

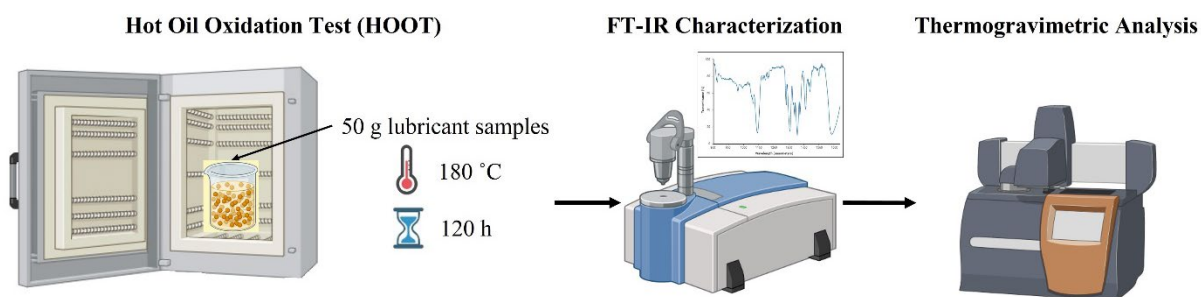
Bio-based palm lubricants with oleic acid-modified kaolin nanoparticles doped have superior dispersion properties. The previous study demonstrated that oleic acid-modified kaolin nanoparticles, combined with span 80 surfactant, effectively ensured superior dispersion stability [12]. Therefore, this method was preferred in nanolubricant production.

First, some palm oil was added to the beaker. Subsequently, kaolin nanoparticles treated with 0.25% oleic acid were added after being accurately weighed using a precision balance. Once more, 0.25% span 80 surfactant was introduced. The resulting mixture was prepared by stirring at 1500 rpm with a magnetic stirrer at 50°C for 90 minutes, followed by an additional hour of mixing using an ultrasonic mixer.

The dispersion stability of the nanolubricant was assessed using the UV-VIS spectroscopy method. These measurements were conducted using the Cary 60 UV-VIS Spectrophotometer (Agilent). Absorbance measurements obtained at 7 and 14 days provided a more conclusive assessment of dispersion stability. The dispersion stability was analysed using relative concentration graphs, where the initial absorbance value of 100 was assumed from UV-VIS spectra measurements.

#### 2.2.3. The Hot Oil Oxidation Test (HOOT) and Characterization Methods

In order to evaluate the oxidative stability of oil samples, a hot oil oxidation test (HOOT) was performed in this study according to the American Society of Oil Chemists (AOCS Cd-12-57). The hot oil oxidation test was conducted with 50 g of sample in a 100 ml glass beaker, kept in an oven at 180°C for 120 hours [13]. The schematic picture of the hot oil oxidation test (HOOT) and characterization methods used in this study is given in Figure 1.



**Figure 1.** The hot oil oxidation test (HOOT) and characterization methods

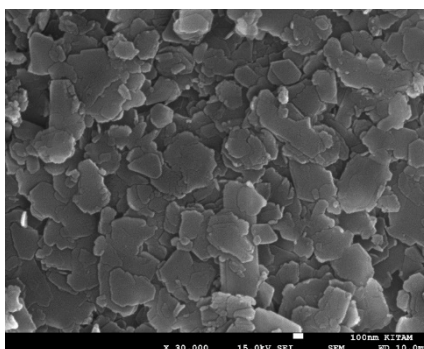
After the oxidation test using the Fourier Transform Infrared Spectroscopy (FT-IR) method, the changes in the peak spectra and structure of the lubricants in the visible region were examined. For this purpose, FT-IR spectra

were obtained using a PerkinElmer Spectrum Two spectrometer with a resolution of  $4\text{ cm}^{-1}$  over the wave number range of  $650\text{--}4000\text{ cm}^{-1}$ .

Thermogravimetric analyses (TGA) were performed using the TA Q-600 SDT brand thermal analyser. Approximately 10 mg of lubricant sample was placed into the device. For evaluating the natural thermal stability of lubricants, analysis was performed under an inert nitrogen atmosphere with a flow rate of 50 ml/min. The temperature was increased programmatically from  $25\text{ }^{\circ}\text{C}$  to  $700\text{ }^{\circ}\text{C}$  at a heating rate of  $10\text{ }^{\circ}\text{C}/\text{min}$  [14]. The onset temperatures of oxidation and mass losses were obtained from the TGA graphs.

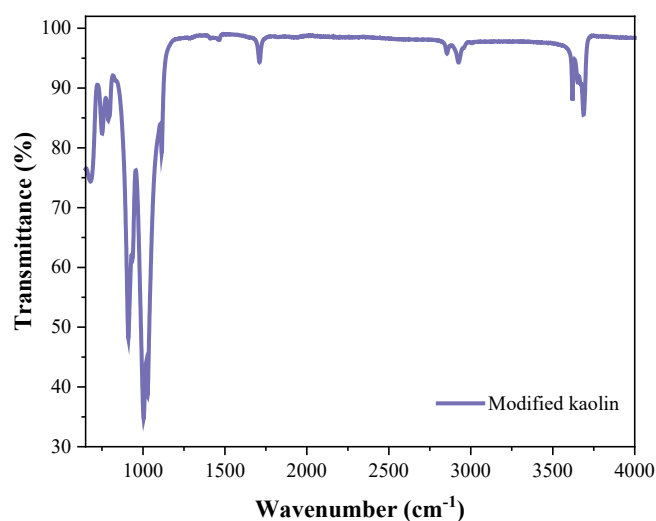
### 3 RESULTS AND DISCUSSION

Figure 2 shows the SEM image of the kaolin particle obtained after 8 hours of grinding in the axial mill. This image clearly shows that the grain distribution spans approximately 10 nm to 500 nm. After 8 hours of milling, the average grain size was determined to be approximately 350 nm.



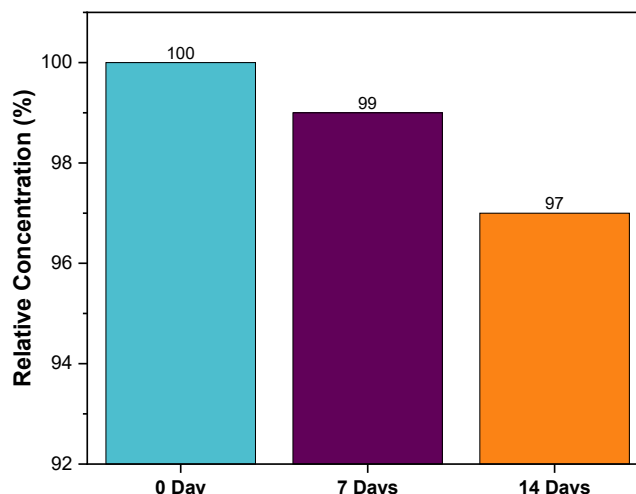
**Figure 2.** SEM images of kaolin nanoparticles [15]

The Fourier Transform Infrared Spectroscopy (FT-IR) spectrum of the kaolin nanoparticle modified with oleic acid is shown in Figure 3. When examining the FT-IR spectrum, the bands appearing at  $3692\text{ cm}^{-1}$ ,  $3668\text{ cm}^{-1}$ ,  $3652\text{ cm}^{-1}$ , and  $3621\text{ cm}^{-1}$  are characteristic of the hydroxyl groups in the kaolin nanoparticles. The bands observed at wave numbers  $1115\text{ cm}^{-1}$ ,  $1030\text{ cm}^{-1}$ , and  $1007\text{ cm}^{-1}$  correspond to the siloxane groups in kaolin. The bands at  $2923\text{ cm}^{-1}$ ,  $2854\text{ cm}^{-1}$ ,  $1710\text{ cm}^{-1}$ ,  $1463\text{ cm}^{-1}$ , and  $1244\text{ cm}^{-1}$  correspond to the oleic acid molecule. This observation points to the modification of kaolin nanoparticles with oleic acid [16].



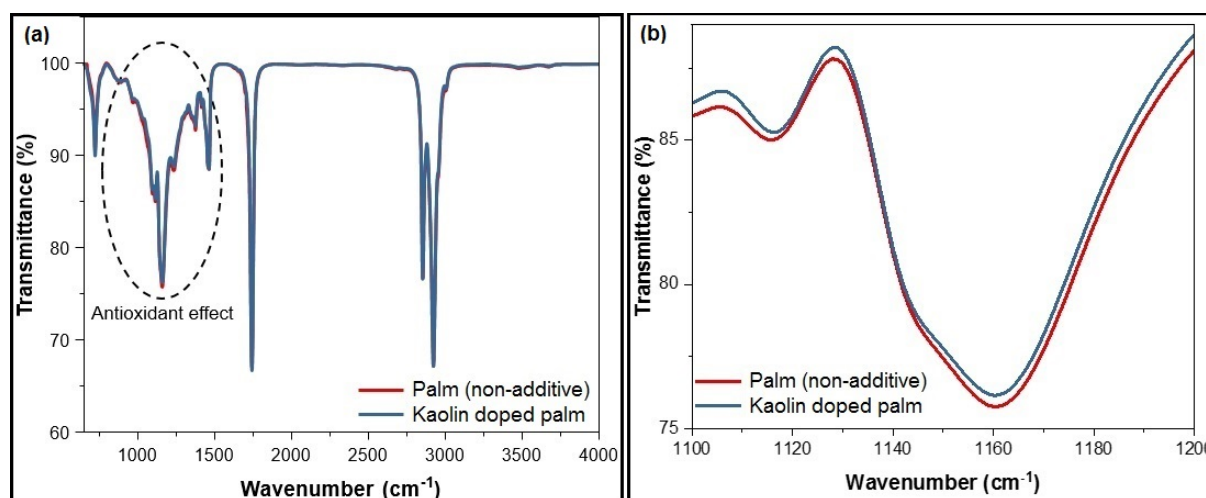
**Figure 3.** FT-IR spectrum of oleic acid-modified kaolin nanoparticle

Relative concentration graphs obtained on different days, representing the dispersion stability of kaolin nanoparticle-doped (0.25% by weight) palm lubricants, are presented in Figure 4. The absorbance value obtained immediately upon completion of the preparation process of the doped palm lubricants is assumed to be 100. The relative concentration values of the lubricants were recorded as 99 and 97 after 7 and 14 days, respectively. Upon evaluating the obtained relative concentration values, it is possible to indicate that the distribution stability was well preserved throughout the 14-day testing period, suggesting the attainment of a stable lubricant.



**Figure 4.** Relative concentration graphs obtained on different days in kaolin nanoparticles doped palm lubricants

The FT-IR spectra obtained after the hot oil oxidation test of kaolin nanoparticle-doped and undoped palm lubricants are shown in Figure 5(a). Furthermore, the bands observed at  $1160\text{ cm}^{-1}$  and  $1117\text{ cm}^{-1}$  correspond to C-O stretching vibrations indicating the presence of alcohols and esters [17]. These bands can be monitored as bands related to oxidation. Changes in transmittance values are noticeable in the spectral region where these bands are located, and Figure 5(b) presents the FT-IR spectra corresponding to the oxidation bands. The band density of kaolin-added palm lubricants at wave numbers  $1117\text{ cm}^{-1}$  and  $1160\text{ cm}^{-1}$ , which represents the bands associated with oxidation, is less than that of pure palm oil. This indicates that the oxidative reaction of kaolin nanoparticles slows down due to increased unsaturation [18, 19].



**Figure 5.** (a) The FT-IR spectroscopy curve of doped and undoped palm lubricants, (b) Section of the FT-IR spectroscopy curve showing bands associated with oxidation

Thermogravimetric analysis (TGA) was used to examine the degradation behavior of palm lubricants with and without kaolin nanoparticles during thermal treatment. Figure 6 displays the thermogravimetric analysis (TGA) curves of doped and undoped palm lubricants. Kaolin nanoparticle-enhanced palm lubricants exhibit a faster rate of weight loss compared to those without additives. When analyzing the TGA plots in Figure 6, it is evident that the oxidation onset temperatures for palm lubricants containing kaolin nanoparticles and those without additives are approximately  $387.3\text{ }^{\circ}\text{C}$  and  $398.1\text{ }^{\circ}\text{C}$ , respectively. These findings reveal that palm lubricants with 0.25% kaolin nanoparticles by weight can delay the oxidation onset temperature by approximately  $10.8\text{ }^{\circ}\text{C}$  compared to palm lubricants without additives. Kaolin nanoparticles play a crucial role in enhancing the oxidative stability of palm lubricants, as indicated by this finding. It can also be stated that it supports the findings obtained in FT-IR spectra. The literature demonstrates that certain nanoparticles are effective in enhancing oxidation stability [5, 7].

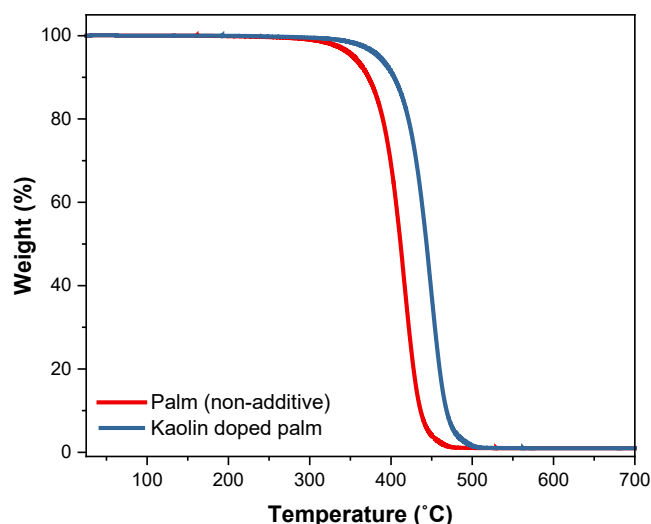


Figure 6. Thermogravimetric analysis (TGA) curves of doped and undoped palm lubricants

## 4 CONCLUSION

Oleic acid-modified kaolin nanoparticles were added to bio-based palm lubricants and subjected to oxidation by hot oil oxidation test. Oxidative stability behaviors were studied using Fourier Transform Infrared Spectroscopy (FT-IR) and thermogravimetric analysis (TGA), yielding the following outcomes.

- The FT-IR spectra indicated that the absorbance intensity of kaolin-incorporated palm oil at wavelengths  $1117\text{ cm}^{-1}$  and  $1160\text{ cm}^{-1}$ , representing oxidation-related bands of the lubricants, was lower compared to pure palm oil.
- Thermogravimetric analysis (TGA) curves showed that palm lubricants with 0.25% kaolin nanoparticles by weight could delay the oxidation onset temperature by approximately  $10.8\text{ }^{\circ}\text{C}$  when compared to palm lubricants without additives.
- The results from TGA curves and FT-IR spectra complement each other, demonstrating that kaolin nanoparticles enhance the oxidative stability of palm lubricants.

Further investigations are underway in future studies focusing on the oxidation stability of palm lubricants fortified with kaolin nanoparticles, exploring factors like particle concentration, size, lubricant preparation methods, and other relevant parameters, thus paving the way for new research avenues in this domain.

## Acknowledgments

This study was supported by Scientific and Technological Research Council of Turkey (TUBITAK) under the Grant Number 222M413. The authors thank to TUBITAK for their supports.

## References

- [1] N. J. Fox and G. W. Stachowiak, "Vegetable oil-based lubricants—a review of oxidation," *Tribology International*, vol. 40, no. 7, pp. 1035–1046, 2007.
- [2] S. Duangkaewmanee and A. Petsom, "Synergistic and antagonistic effects on oxidation stability of antioxidants in a synthetic ester based oil," *Tribology International*, vol. 44, no. 3, pp. 266–271, 2011.
- [3] C. Murru, R. Badía-Laíño, and M. E. Díaz-García, "Oxidative stability of vegetal oil-based lubricants," *ACS Sustainable Chemistry & Engineering*, vol. 9, no. 4, pp. 1459–1476, 2021.
- [4] K. H. Tan, H. Awala, R. R. Mukti, K. L. Wong, T. C. Ling, S. Mintova, and E. P. Ng, "Zeolite nanoparticles as effective antioxidant additive for the preservation of palm oil-based lubricant," *Journal of the Taiwan Institute of Chemical Engineers*, vol. 58, pp. 565–571, 2016.
- [5] M. K. A. Ali, and H. Xianjun, "Improving the heat transfer capability and thermal stability of vehicle engine oils using  $\text{Al}_2\text{O}_3/\text{TiO}_2$  nanomaterials," *Powder Technology*, vol. 363, pp. 48–58, 2020.
- [6] N. Ranjan, R. C. Shende, M. Kamaraj, and S. Ramaprabhu, "Utilization of  $\text{TiO}_2/\text{gC}_3\text{N}_4$  nanoadditive to boost oxidative properties of vegetable oil for tribological application," *Friction*, vol. 9, pp. 273–287, 2021.
- [7] I. O. Sadiq, M. A. Suhaimi, S. Sharif, N. Mohd Yusof, and M. J. Hisam, "Enhanced performance of bio-

- lubricant properties with nano-additives for sustainable lubrication,” *Industrial Lubrication and Tribology*, vol. 74, no. 9, pp. 995–1006, 2022.
- [8] V. V. Kamal, N. Pradeep, R. Santhakumari amma, M. Arif, A. D. Thampi, and S. Edla, “Tribological property and oxidation stability evaluation of rice bran oil with silicon dioxide nanoparticles and spicy aroma-based herbal oils as additives,” *Proceedings of the Institution of Mechanical Engineers, Part J: Journal of Engineering Tribology*, vol. 237, no. 8, pp. 1712–1720, 2023.
- [9] A. Kumar, T. C. S. M. Gupta, and A. Shukla, “Performance and stability evaluation of nanoadditives for engine oil applications,” *Journal of the Brazilian Society of Mechanical Sciences and Engineering*, vol. 45, no. 2, art. no. 92, 2023.
- [10] C. Brito, A. Gonçalves, E. Silva, S. Martins, L. Pinto, L. Rocha, et al., “Kaolin foliar spray improves olive tree performance and yield under sustained deficit irrigation,” *Scientia Horticulturae*, vol. 277, art. no. 109795, 2021.
- [11] X. Rao, C. Sheng, Z. Guo, X. Zhang, H. Yin, C. Xu, and C. Yuan, “Anti-friction and self-repairing abilities of ultrafine serpentine, attapulgite and kaolin in oil for the cylinder liner-piston ring tribo-systems,” *Lubrication Science*, vol. 34, no. 3, pp. 210–223, 2022.
- [12] B. Özakin, and K. Gültekin, “Kaolin partikülleri katkılı bitkisel esaslı palm yağlayıcıların dağılım stabilitesinin geliştirilmesi,” in *3rd International Conference on Engineering, Natural and Social Sciences*, Konya, Türkiye, 2024, pp. 646–651.
- [13] M. Chao, R. Fan, L. Zhang, X. Wang, Q. Shu, J. Gao, et al., “Synthesis and antioxidant properties of a novel arylamine antioxidant,” *Bulletin of the Korean Chemical Society*, vol. 42, no. 11, pp. 1440–1445, 2021.
- [14] G. Uguz, A. Cakmak, C. D. S. Bento and N. Turkoz Karakullukcu, “Experimental investigation of fuel properties and engine operation with natural and synthetic antioxidants added to biodiesel,” *Biofuels*, vol. 14, no. 4, pp. 405–420, 2023.
- [15] B. Ozakin and K. Gultekin, “Kaolin nanopartikülleri katkılı bitkisel esaslı palm yağlayıcıların viskozite davranışlarının incelenmesi,” in *Ases II. International Kayseri Scientific Research Conference*, Kayseri, Türkiye, 2024, pp. 65–74.
- [16] P. G. Sieben, F. Wypych, and R. A. de Freitas, “Oleic acid as a synergistic agent in the formation of kaolinite-mineral oil pickering emulsions,” *Applied Clay Science*, vol. 216, art. no. 106378, 2022.
- [17] A. Rohman and Y. C. Man, “Fourier transform infrared (FTIR) spectroscopy for analysis of extra virgin olive oil adulterated with palm oil,” *Food Research International*, vol. 43, no. 3, pp. 886–892, 2010.
- [18] M. Garcia-Perez, T. T. Adams, J. W. Goodrum, K. C. Das, and D. P. Geller, “DSC studies to evaluate the impact of bio-oil on cold flow properties and oxidation stability of bio-diesel,” *Bioresource Technology*, vol. 101, no. 15, pp. 6219–6224, 2010.
- [19] G. Uguz, “Antioxidant effect of clove oil on biodiesel produced from waste cooking oil,” *Biomass Conversion and Biorefinery*, vol. 13, no. 1, pp. 367–373, 2023.



## Production of 3D Woven Textile Composites and Investigation of Their Impact Performance

Serkan Erdem<sup>\*1</sup>, Mete Onur Kaman<sup>1</sup>

<sup>1</sup>Department of Mechanical Engineering, Firat University, Elazig, Türkiye

### Abstract

In this study, glass fiber reinforced three-dimensional (3D) woven composite plates, whose use is increasing especially in applications where impact damping is required, were produced. The glass fiber fabric obtained by 3D weaving was impregnated with epoxy matrix by hand laying, and then the composite production was completed with vacuum infusion. Charpy impact test was applied to the produced 3D woven glass fiber reinforced composite samples. As a result of the experiment, the impact damping energy of the composite plate was compared with St37 steel material for unit density. According to the results obtained, it was determined that the impact damping performance of the 3D woven glass fiber reinforced composite plate was significantly effective.

**Keywords:** 3D woven, Glass fiber yarn, Charpy test, Impact, Composite

## 1 INTRODUCTION

Due to their high mechanical properties, the usage areas of fiber reinforced composite materials are increasing day by day. In order to meet this need in areas where impact damping is available, an effort has been made to increase impact resistance by producing 3D woven composite materials from fiber-reinforced composite materials, and many studies have been carried out on this subject. When the studies are examined: Jabbar et al. [1] presented an investigation of the mechanical performance of novel 3D woven composite structures. Various 3D woven fabrics with variation in stuffer yarn density were designed, produced and their mechanical properties such as tensile, shear, drop weight impact and compression after impact were investigated. Reinforcements were developed on a modified Dobby loom from flax yarn with four different levels of stuffer yarn densities. Composites were fabricated using these 3D woven fabrics as reinforcement and green epoxy as a matrix. Abbasi et al. [2] presented a new approach for greatly increasing the delamination resistance of fiber reinforced polymer composites via through-the-thickness weaving of high-strength, high-toughness metal z-filaments. Dry carbon fabric preforms were woven in the through-thickness direction with thin and continuous stainless steel or copper filaments, and then infused with epoxy resin to create 3D woven composites. A new in situ experimental method was proposed to realize the non-destructive observation of the failure process of 3D woven carbon-fiber reinforced composites by Li et al. [3]. Synchrotron radiation computer tomography (SRCT), an in-situ load frame and new-style specimens were integrated. With the method, the 3D crack initiation and propagation can be continuously recorded by the SRCT scanner. Through analyzing the experimental results, the out-plane failure mechanism under tension and shear loads was found. Stig et al. [4] developed three analytical models for prediction of the longitudinal Young's modulus of carbon fiber composite materials containing fully interlaced 3D-woven textile reinforcement. Two of the non-linear models utilize rods and springs and were designed to handle an idealized periodic repetitive volume element of the composite material. For validation, an experimental study was performed, and a more detailed model was built using existing textile software (TexGen and WiseTex). All models were employed to explore the effect of 3D yarn crimp on the longitudinal Young's modulus. Tableau et al. [5] focused on the experimental identification of the first damage envelope in a 3D woven composite with polymer matrix, under multi-axial loadings including combined in-plane tension and out-of-plane shear loadings. Proportional tensile-torsion tests on rectangular bars were performed to induce different multiaxial stress states. To enable envelopes identification, onset of the first damage has been evaluated thanks to the correlation of various and complementary investigation measurement techniques, such as Stereo-Digital Image Correlation (Stereo-DIC), Acoustic Emission (AE) and in-situ microscopic observations. In addition, a specific data reduction process has been used to manage accurate quantification of the stress state induced by the multiaxial loadings. Wang et al. [6] studied the mechanical behavior and the complicated failure mechanism of a novel aluminum matrix composites reinforced with 3D orthogonal woven carbon fiber. The quasi-static tensile behavior, local stress response and progressive failure process were investigated via numerical and experimental approach. According to the microstructure at fiber and yarn scale, microscopic and mesoscopic finite element models were established to carry out multiscale simulation.

In this study, 3D composite plate was produced manually using glass fiber yarn. The produced composite plates were subjected to impact testing and their impact performance was compared graphically with St37 steel material.

## 2 MATERIAL AND METHOD

In the study, firstly, 3D woven fabric was obtained by using glass fiber yarn. Afterwards, the composite plate was obtained by impregnating the 3D woven fabric with resin using the vacuum infusion method. First of all, a wooden mold with dimensions of 210x290x20 mm was prepared to obtain 3D weaving, as seen in Figure 1. The inside of the wooden mold is designed to be 20 mm deep for knitting. Afterwards, nails were driven into all edges of the mold at equal intervals of 5 mm (Figure 2).

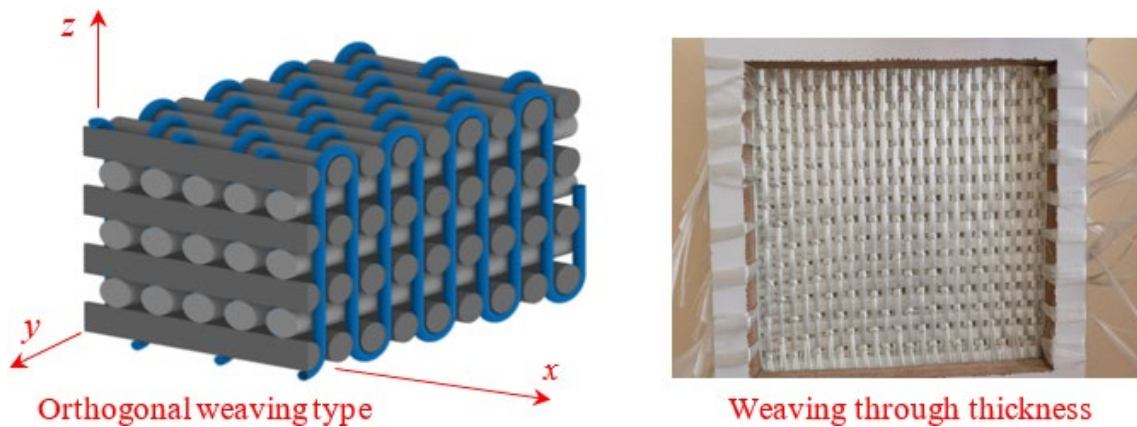


Figure 1. Orthogonal weaving [7]

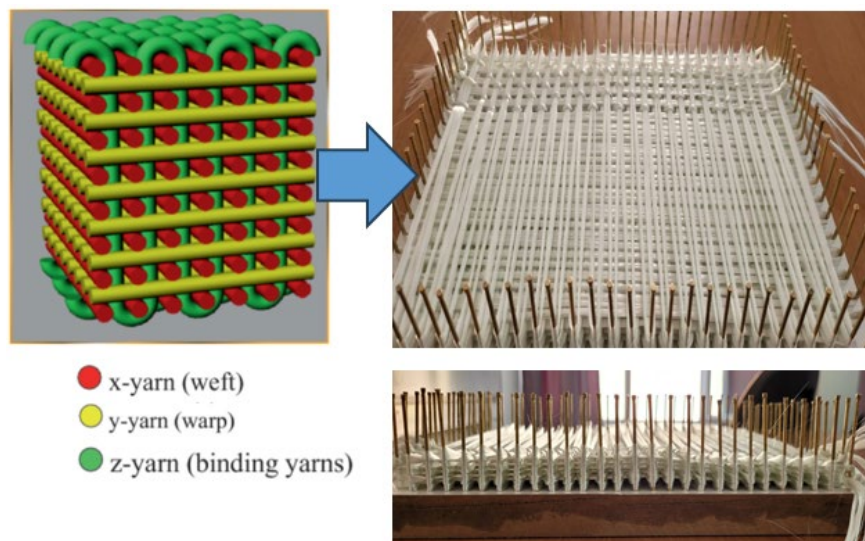


Figure 2. Weaving by placing nails around the mold [8]

After the nails were fixed, the first blind loop was cast from one corner of the mold to prevent the glass fiber yarn from being removed. Afterwards, the knitting was completed in the plane by first following the nails along the long edge. In the second stage, a blind loop was cast from another corner and the knitting in this direction was made in the plane by turning around the nails along the short edge. Thus, the process was repeated 5 times and the knitting in the  $-x$  and  $-y$  directions was completed (Figure 1). Finally, 3D fabric production was carried out by knitting this fabric, which started from a corner, in the  $-z$  direction from one bottom to the other of each loop, with glass fiber attached to the needle. The fabric was pressed with a metal mold to prevent any gaps between the layers in the  $-z$  direction. Orthogonal interlock weaves, are characterized by warp weavers oriented from orthogonal to other in-plane directions and run through the thickness of the preform. The  $-x$  and  $-y$  yarns of the angle-interlock and orthogonal structures are not interlaced [9].

In the production of composite plate, it is aimed to obtain an optimum and homogeneous epoxy distribution at every point of the fabric. The fabric must be impregnated with resin before being removed from the wooden mold.

However, due to the geometry of the mold, the fabric was first wetted by hand and then the excess resin was extracted by vacuum infusion (Figure 3). First of all, a release film was laid on the vacuum infusion bench and fixed to the bench with double-sided tape. Afterwards, the mold containing the resin-impregnated 3D fabric was placed on the release film. After the composite plate was produced, resin was applied so that the consumables could be easily separated, and then peel ply was laid on the 3D fabric (Figure 4).

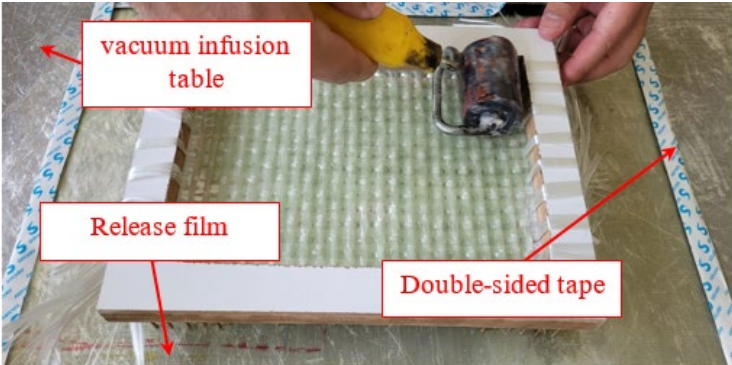


Figure 3. Impregnation of epoxy resin on 3D woven fabric

A mesh has been placed on the peel ply to facilitate the removal of excess resin. After the mesh laying process, the nails on the mold were covered with wooden pieces to prevent them from piercing the vacuum nylon. Additionally, a spiral hose is placed to facilitate the easy flow of excess resin (Figure 5).

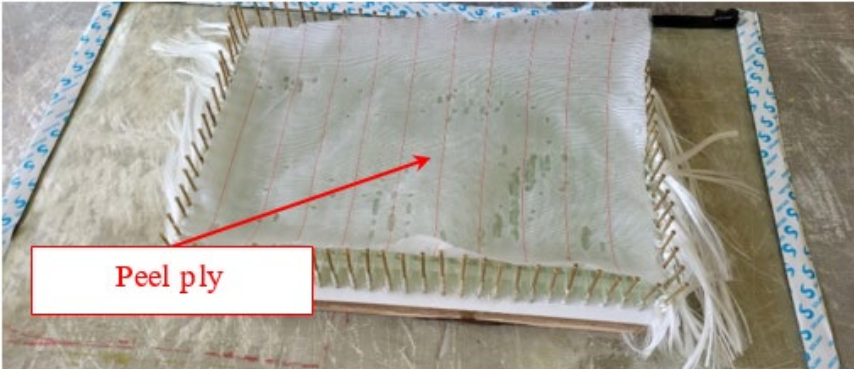


Figure 4. Placement of peel ply on resin impregnated fabric

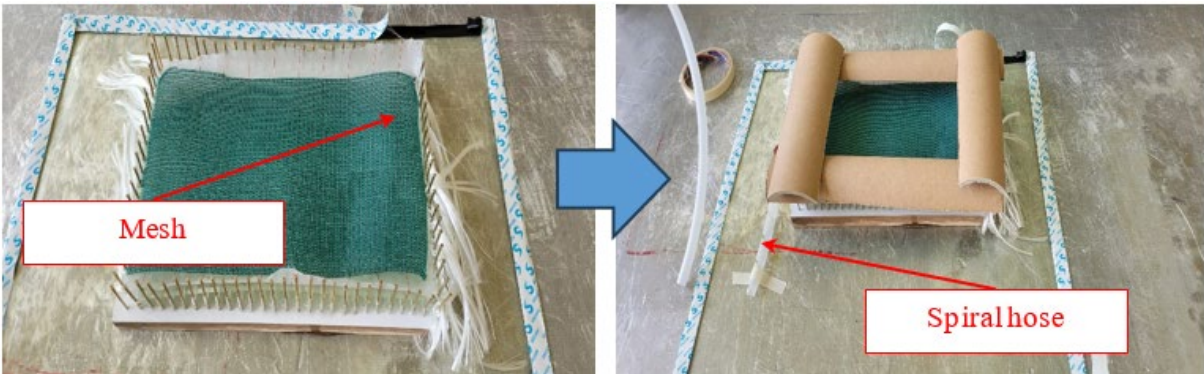


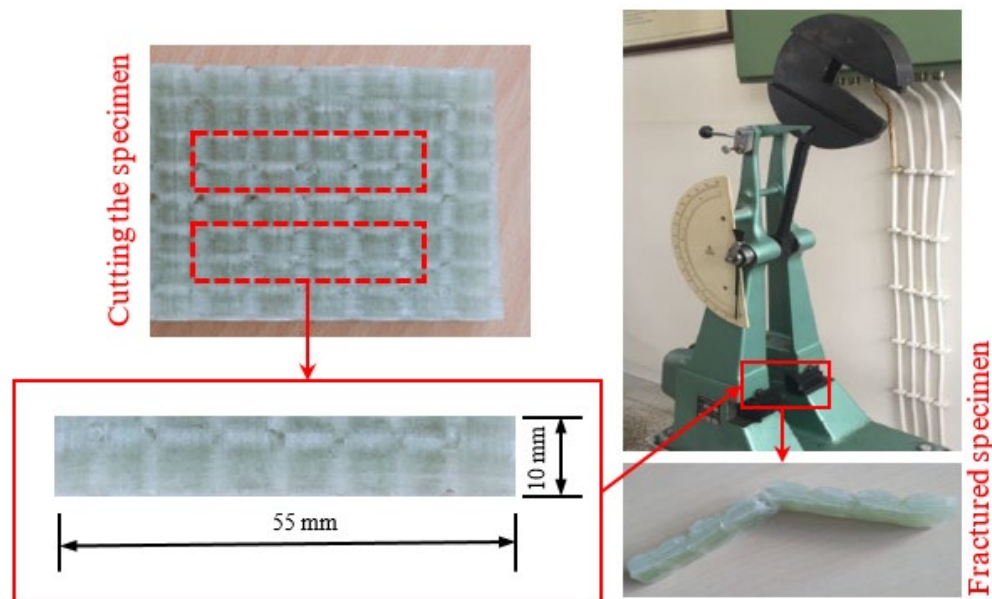
Figure 5. Placing mesh on resin impregnated fabric





**Figure 6.** Removing excess resin from the mold

Finally, vacuum nylon was laid on the double-sided tape. However, the nylon has been shaped according to the form of the cheetah, so that it does not stretch and tear during vacuum. Afterwards, the vacuum infusion bench was heated to 70 °C to increase the fluidity of the resin, thus facilitating the removal of excess resin. Finally, the vacuum was turned on and the excess resin was thrown out (Figure 6). The temperature was increased to 100 °C and kept constant at this value for one hour, then allowed to cool at room temperature. Test samples from the produced 3D composite plate were cut on a wet marble cutting machine (Figure 7). The thickness of each test sample was obtained as 4.5 mm for 5 layers in the plane. The cut test samples were placed in the Veb Werkstoffprüfmaschinen Leipzig brand Charpy impact device and the experiments were carried out. A total of 4 samples were used in the experiments.



**Figure 7.** Test samples prepared for impact test

### 3 RESULTS

The energy absorbed by the 3D woven composite plate as a result of the impact test was obtained as 11.67 J on average. In the experiments, the weight and dimensions of each sample were measured. Accordingly, the density of the produced composite is 2352 kg/m<sup>3</sup>. The resulting absorption amount was divided by the material density. The normalized energy obtained is compared with St37 steel material and presented in Figure 8. Density for steel material is kg/m<sup>3</sup>. In the study conducted by Albayrak and Kaman [10], the absorption energy for steel was calculated as 12.78 J. According to these results; It can be said that the absorbed energy for the composite is approximately similar to St37. However, for both types of materials, it is important to examine the normalized absorption energy, as such a comparison will not be meaningful since the weights and volumes of the test samples are different. While the normalized energy for the 3D woven composite plate was ~0.005 J/(kg/m<sup>3</sup>), this value

was obtained as  $\sim 0.0016 \text{ J}/(\text{kg}/\text{m}^3)$  for steel. This shows that the amount of energy for composite is  $\sim 3$  times that of steel.

In 2D composites, interlayer delamination is a significant damage. Because, it is shown that the interface property is the leading factor affecting out-plane strengths [3]. In the composite, which stands out with its lightness, especially in structures where weight is important, the resistance properties against loads perpendicular to its plane are also increased with the use of 3D woven fabric. This difference emerges thanks to the  $-z$ -direction yarn used throughout the thickness. As seen in Figure 7, one of the factors that prevent the damaged sample from breaking completely is the fibers used throughout the thickness. Abbasi et al. [2] showed that steel  $z$ -filament increases the mode I delamination resistance by over 50 times, with the fracture toughness value being the highest reported value for composite laminates. On the other hand, the increase of warp or weft density could improve the tensile strength and elastic modulus, but the tensile elongation decreases with the increase of weft density [6].

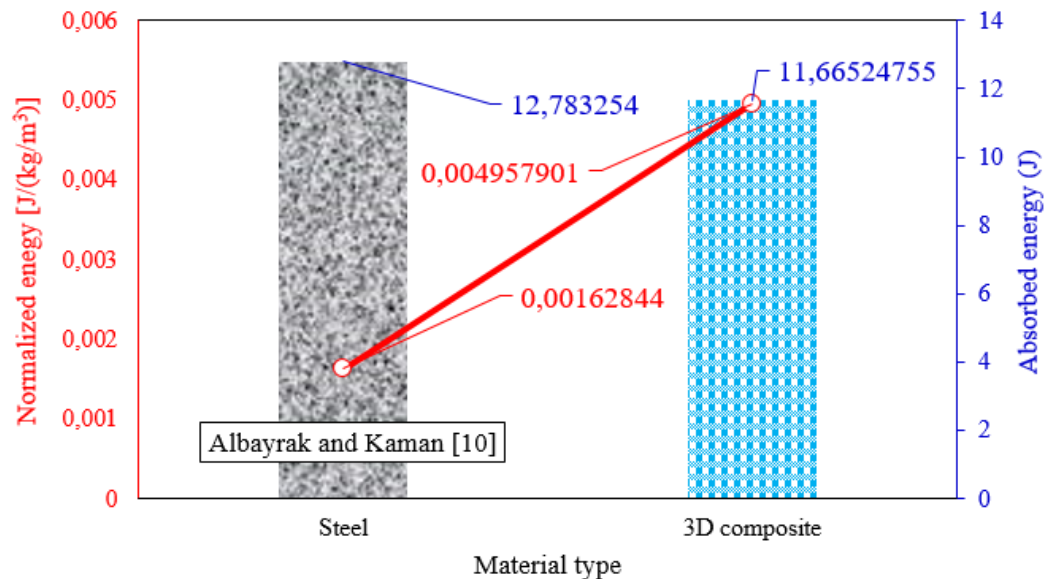


Figure 8. Normalized energy value for 3D woven composite

#### 4 CONCLUSION

Especially since fiber reinforced composites have weight advantages, their usage area is increasing day by day. At this point, 3D woven composites provide a great advantage in absorbing high energy. The yarn added throughout the thickness plays a primary role in absorbing the loads, especially perpendicular to the plane. In this way, delamination damage is prevented and toughness increases. In the presented study, weaving was done by hand. If standard weaving is achieved with the high-tech machines to be used and a more homogeneous structure is provided with vacuum infusion, the impact advantage of 3D woven composites will become more prominent. On the other hand, it should also be noted that the relationship between multiaxial loadings and 3D weaving architecture will affect the results [5].

#### Acknowledgments

Authors thank Mechanical Engineers Emre Coban and Faruk Kaynak, for assistance with weaving of 3D.

#### References

- [1] M. Jabbar, K. Shaker, Y. Nawab, and M. Umair, "Effect of the stuffer yarns on the mechanical performance of novel 3D woven green composites," *Composite Structures*, vol. 269, pp. 1–9, 2021.
- [2] S. Abbasi, R.B. Ladani, C.H. Wang, and A.P. Mouritz, "Improving the delamination resistance of fibre reinforced polymer composites using 3D woven metal Z-Filaments," *Composites Science and Technology*, vol. 198, pp. 1–12, 2020.
- [3] Z. Li, L. Guo, L. Zhang, and Q. Wang, "In situ experimental investigation on the out-plane damage evolution of 3D woven carbon-fiber reinforced composites," *Composites Science and Technology*, vol. 162, pp. 101–109, 2018.
- [4] F. Stig and S. Hallström, "Influence of crimp on 3D-woven fibre reinforced composites," *Composite*

- Structures*, vol. 95, pp. 114–122, 2013.
- [5] N. Tableau, Z. Aboura, K. Khellil, F. Laurin, and J. Schneider, “Multiaxial loading on a 3D woven carbon fiber reinforced plastic composite using tensile-torsion tests: Identification of the first damage envelope and associated damage mechanisms,” *Composite Structures*, vol. 227, pp. 1–12, 2019.
- [6] Z. Wang, W. Zhao, F. Wang, X. Teng, C. Cai, J. Xiao, and Y. Zhang, “Tensile behavior and failure mechanism of 3D woven fabric reinforced aluminum composites,” *International Journal of Mechanical Sciences*, vol. 244, pp.1–17, 2023.
- [7] Tex Tech Industries. (2019, Nov. 18). *New research in 3D woven fabrics reveals the potential for higher performance textiles* [Online]. Available: <https://textechindustries.com/blog/new-research-3d-woven-fabrics-reveals-potential-higher-performance-textiles/>
- [8] A. F. M. Seyam, “3D orthogonal woven fabric formation, structure, and their composites,” *Advanced Weaving Technology*, vol. 1, pp. 361–399, 2022.
- [9] N. S. Karaduman, Y. Karaduman, H. Ozdemir, and G. Ozdemir, “Textile reinforced structural composites for advanced applications,” *Textiles for Advanced Applications*, pp. 87, 2017.
- [10] M. Albayrak and M. O. Kaman, “Experimental and numerical analysis of Charpy impact test”, *DUMF MD*, vol. 10, pp. 945–957, 2019.



---

## Evaluation of the Tribological Performance of AA 6061 Coated with Polyurethane/Ti6Al4V Composite

Yusuf Burak Bozkurt\*<sup>1</sup>

<sup>1</sup>*Department of Mechanical Engineering, Atatürk University, Erzurum, Türkiye*

---

### Abstract

AA 6061 series is a light alloy type that is frequently preferred especially in the aviation/space and automotive industries. Due to its weight advantage, it is preferred in construction and machine elements that do not require high strength. Therefore, they are exposed to loads under different lubrication conditions under static and dynamic loads. Apart from these, the most important mechanism they deal with is wear. The wear damage caused by metallic parts moving relative to each other on the surface significantly reduces the material life under service conditions. Especially in machine elements, the surface hardness of AA 6061 alloys is weak compared to steel grade products. One of the most effective ways to increase the surface hardness of this group of alloys is to apply coating. In this study, the surface of AA 6061 samples was coated by electrowriting. The wear performances of the coated surfaces were examined. Ti6Al4V metal particles were loaded into polyurethane-based resin and then printed on the surface. Thus, harder surfaces were exposed to wear with different sliding balls. The coefficients of friction and wear rates were calculated. Thanks to harder Ti6Al4V particles, wear rates have improved compared to untreated surfaces.

**Keywords:** AA 6061, Electrowriting, Tribology, Ti6Al4V, Polyurethane

---



## Numerical Simulation Study of Curvature Radius on the Flexibility and Stress Distribution in Hyperelastic Materials

Galip Yilmaz<sup>\*1</sup>

<sup>1</sup>Electronic and Automation Department, Bayburt University, Bayburt, Türkiye

### Abstract

This study aims to investigate the enhancement of flexibility in relatively stiff hyperelastic materials by introducing wavy structure models. Finite element method (FEM) simulations were used to analyze the mechanical behavior of these materials under varying curvature radii and stress conditions. The materials were modeled using a Mooney-Rivlin hyperelastic material model, with properties derived from the mechanical tensile test. The simulations were conducted in SolidWorks 2021, focusing on nonlinear, two-dimensional hyperelastic simulations. Four sample types were subjected to analysis: a simple rod (S1) and three wavy samples with radii of 0.5 mm (S2), 1.0 mm (S3), and 1.5 mm (S4). The results indicated that the wavy structures considerably influenced the materials' flexibility and stress distribution. The maximum principal stress values were the highest at the connection points, indicating that these locations may be susceptible to failure for accurate results. The study revealed that strain energy and strain energy density varied with curvature radius. Samples with wavy structures demonstrated lower energy densities than the regular sample. This indicates that wavy geometries can significantly enhance the flexibility of hyperelastic materials, rendering them more appropriate for biomechanical applications such as artificial tissue engineering and prosthetic design. These findings offer new insights into the potential of geometric modifications to enhance the mechanical properties of hyperelastic materials.

**Keywords:** *Finite Element Method (FEM), Hyperelastic Materials, Mooney-Rivlin Model, Wavy Geometries*

## 1 INTRODUCTION

Predicting the mechanical behavior of hyperelastic materials with precision represents a significant challenge for engineers. This challenge arises from the complex structures and vast variety of hyperelastic materials. These materials are utilized in a multitude of fields, spanning from bioengineering, where they are employed in the development of artificial organs and tissue engineering, to the creation of everyday tools and equipment [1–3].

Predicting the mechanical behavior of these materials, particularly in the context of variable load and deformation conditions, represents a highly intricate task. The existence of diverse material types, each endowed with distinctive properties and performance criteria, serves to complicate this process further [4–7]. The utilization of simulation programs is critically important in determining hyperelastic behavior. In particular, the structural softening of relatively stiff materials through the use of wavy or foamed structures offers significant advantages in the context of biomechanical applications. It is of great consequence to accurately model the mechanical properties of these materials for a multitude of engineering and medical applications [8–10]. It is necessary to employ advanced simulation techniques to predict the behavior of hyperelastic materials. These simulations permit the detailed analysis of the responses of materials subjected to complex deformation and loading conditions [11, 12]. In particular, the softening of stiffer materials through wavy or foam-like structures allows for their implementation in biomechanical applications. For example, in the context of artificial tissue engineering or prosthetic design, these materials can offer flexibility and durability that closely resemble those of natural tissues [6, 9, 13, 14].

The objective of this study is to determine how a relatively rigid material can be rendered more flexible through the utilization of wavy structures, employing the Finite Element Method (FEM) for simulation purposes. In this process, the curvature radii of the geometric model were incrementally applied, and the maximum and minimum principal stress values, along with the strain energy storage, were examined under progressively elevated extension ratios. This research aims to develop innovative approaches to enhance the flexibility of relatively stiff materials. In particular, the softening of stiff materials through the use of wavy configurations offers significant advantages in the field of biomechanics, particularly in the areas of artificial tissue engineering and prosthetic design. The data obtained will contribute to developing more flexible and durable materials for engineering and medical fields.

## 2 MATERIAL AND METHOD

### 2.1 Material

Table 1 presents the material properties utilized in the simulation program. A room-temperature vulcanizing silicone film was punched and subjected to a mechanical tensile test at 5 mm/min. The resulting data were employed in the MatEditor2024 program to ascertain the two-degree constants of the Mooney-Rivlin solid hyperelastic material model, which are presented in the accompanying table. Further details regarding the software and the material model can be found in the relevant literature [15–17].

**Table 1.** Material properties, including Poisson’s ratio and two material constants

Property	Value	Unit
Poisson’s Ratio	0.49	-
First Material Constant (A)	33253	N/m <sup>2</sup>
Second Material Constant (B)	-7940	N/m <sup>2</sup>
Mass Density	1.1	g/cm <sup>3</sup>

### 2.2 Simulation Settings

The material data were entered manually into the SolidWorks 2021 material library, and the same material was used for all sample types. Table 2 lists the settings and selections applicable to all samples within the SolidWorks simulation program. A nonlinear, two-dimensional hyperelastic simulation was constructed.

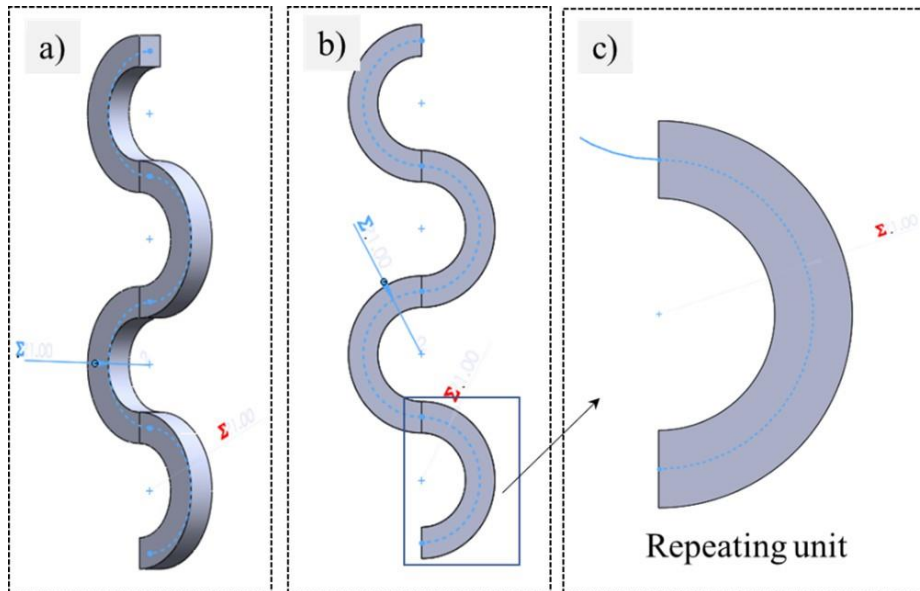
**Table 2.** Common simulation settings for all sample types

Properties	Setting
Analysis type	Nonlinear
Simplification	Static 2D
Mesh type	Planar 2D Mesh
Start time	0 s
End time	1 s
Time increment	Automatic set
Compute free body forces.	NA
Large displacement formulation:	Activated
Update load direction with deflection:	NA
Large strain formulation	NA
Solver choice	Large Problem Direct Sparse
Incompatible bonding options	Simplified option
Control method	Force
Numerical method	Newton’s method
Numerical integration	Newmark-beta

Table 3 tabulates the sample types and properties. The S1 sample was constructed as a simple rod, while the S2, S3, and S4 samples were designed with radii of 0.5 mm, 1.0 mm, and 1.5 mm, respectively. Figure 1 illustrates the methodology employed to determine the wavy structure and the repeating unit. The SolidWorks solid modeling tool created a wavy computer-aided design (CAD) model. Modelling and simulation together were performed in same platform. The models were generated using a linear pattern of interconnected half-circles, and the repeating unit, which is the half-circle, was subsequently drawn separately and utilized in the simulations. In the tensile test of a semicircle, the diameter value was accepted as the initial length and the extension values were calculated with this length as reference. For example, for the curved S2 sample with a radius of 0.5 mm, the initial length was taken as 1.0 mm. Similarly, the initial length of the S3 sample with a radius of 1.0 mm was taken as 2.0 mm, and finally, the initial length value for the 1.5 mm radius of the S4 sample was taken as 3.0 mm. This assumption was thought to be necessary for the reliable test of samples.

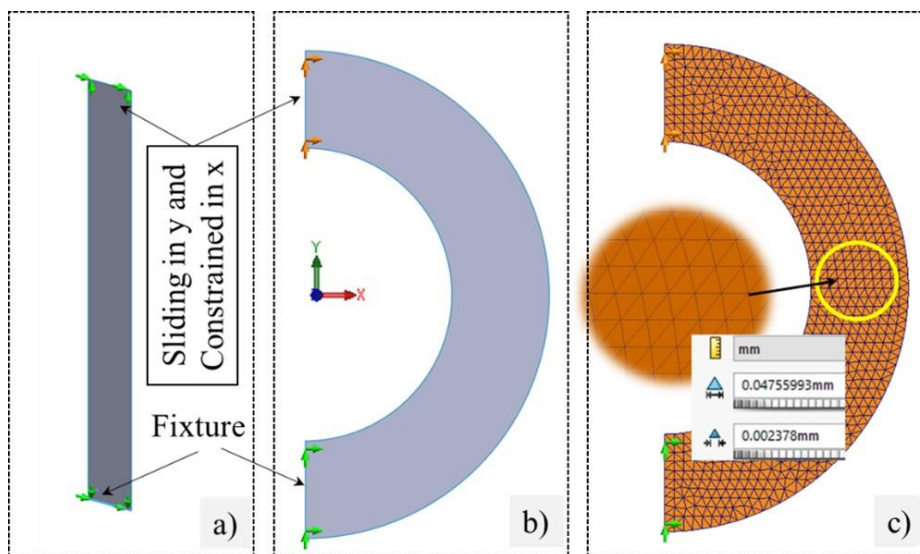
**Table 3.** Sample types, names, and size properties in mm

Name	Radius	Initial length
S1	Inf	5
S2	0.5	1
S3	1.0	2
S4	1.5	3



**Figure 1.** Modeling of the wavy structure in the CAD program and determination of the repeating unit: a) View of the 3D structure, b) View of the 2D cross-section, and c) Image of the repeating unit subjected to simulation

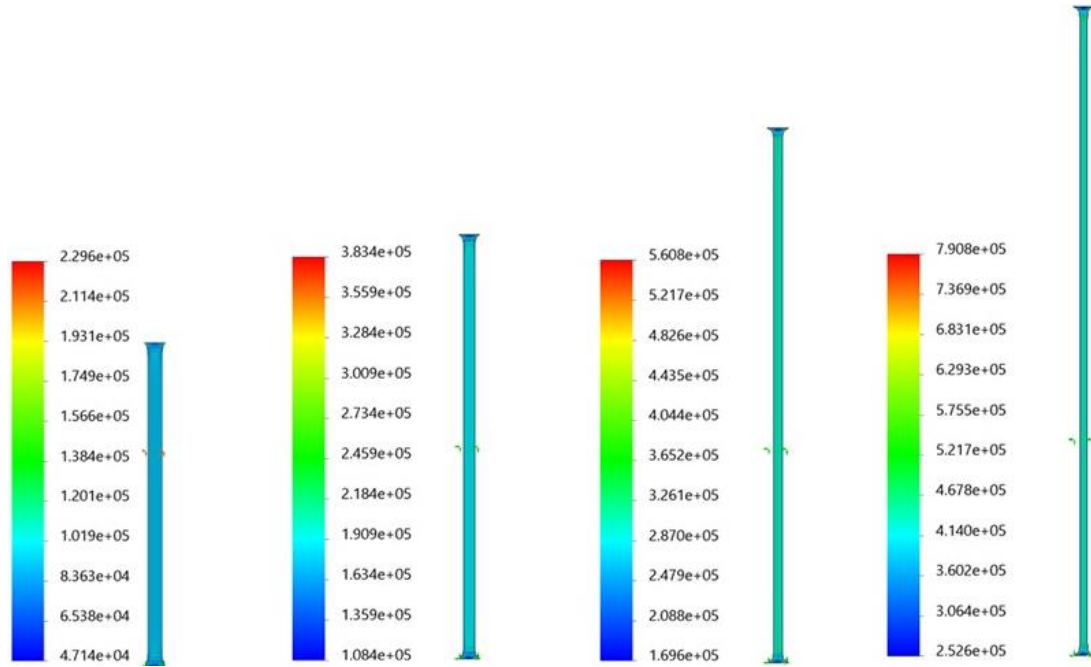
Figure 2 depicts the boundary conditions utilized in the simulation environment. Figure 2a depicts the boundary conditions for the regular S1 sample, whereas Figure 2b illustrates the conditions for the wavy samples. The fixture boundary condition was applied to the lower edges. The upper edges were constrained in the x-direction and permitted a fixed movement in the y-direction, thus achieving the desired extension value. Figure 2c provides an example of the mesh and its dimensions. In that order, the samples were subjected to 0.5, 1.0, 1.5, and 2.0 extension values.



**Figure 2.** Simulation boundary conditions and a mesh example: a) Regular sample, b) Half-circle used for wavy samples (wall thickness 0.5 mm), and c) Image of the generated mesh

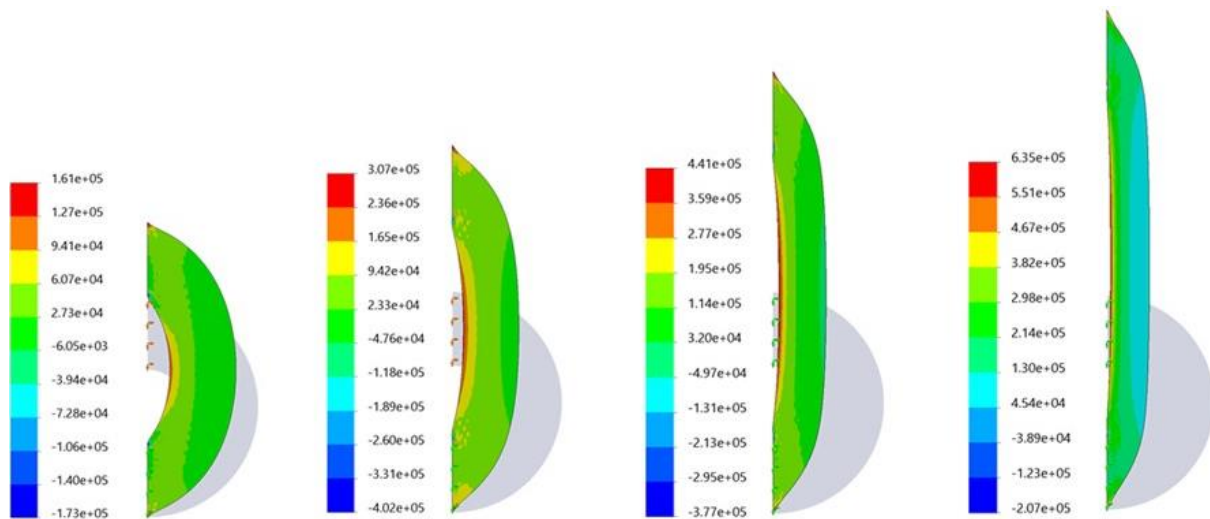
### 3 RESULTS

Figure 3 illustrates the principal stress values from subjecting the regular sample to extension values of 0.5, 1.0, 1.5, and 2.0, from left to right, respectively. As anticipated, the samples exhibited thinning and stretching with increasing extension values. The highest stress values were observed at the points of connection.



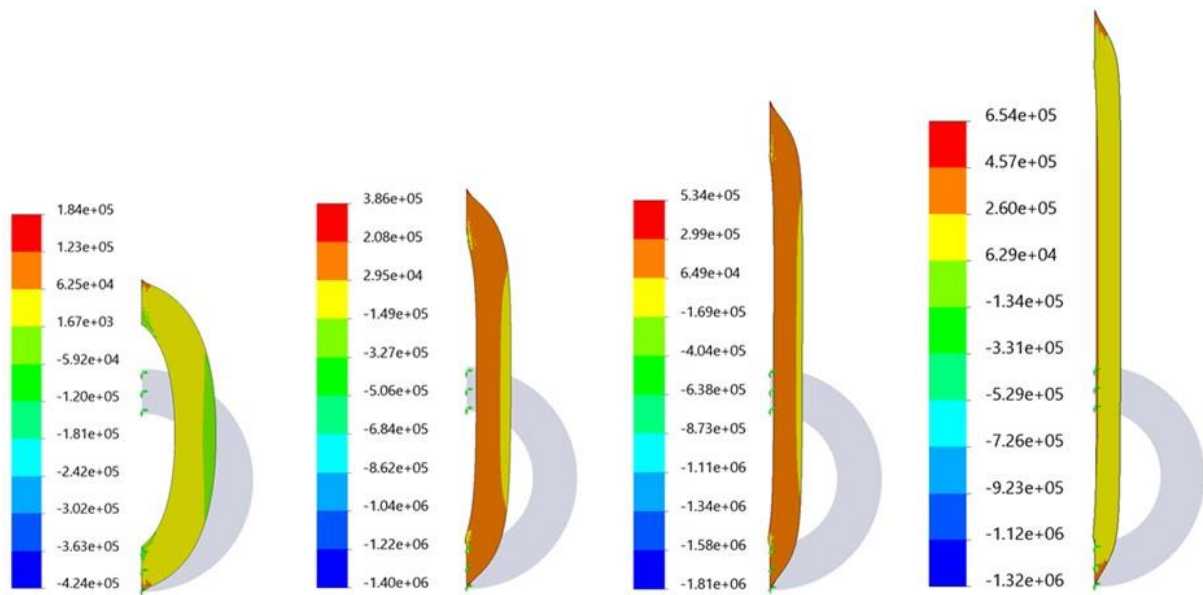
**Figure 3.** Graphs of the principal stress (N/m<sup>2</sup>) of the regular sample (S1) with increasing extension values

Figures 4, 5, and 6 illustrate the principal stress (N/m<sup>2</sup>) graphs for the wavy samples S2, S3, and S4 under increasing extension values. The final extension value of the S4 sample yielded no results, as the process was terminated due to a "Solution failure." This outcome may have been influenced by a number of factors, including the following: This may be indicative of the solution reaching a buckling or limit point. This issue originated from the considerable expansion in radius and elevated extension amount, coupled with the unvarying material thickness, which precluded a reliable outcome. The highest stress values were observed at the connection points in these graphs. The numerical results obtained from the graphs are presented in tabular form.

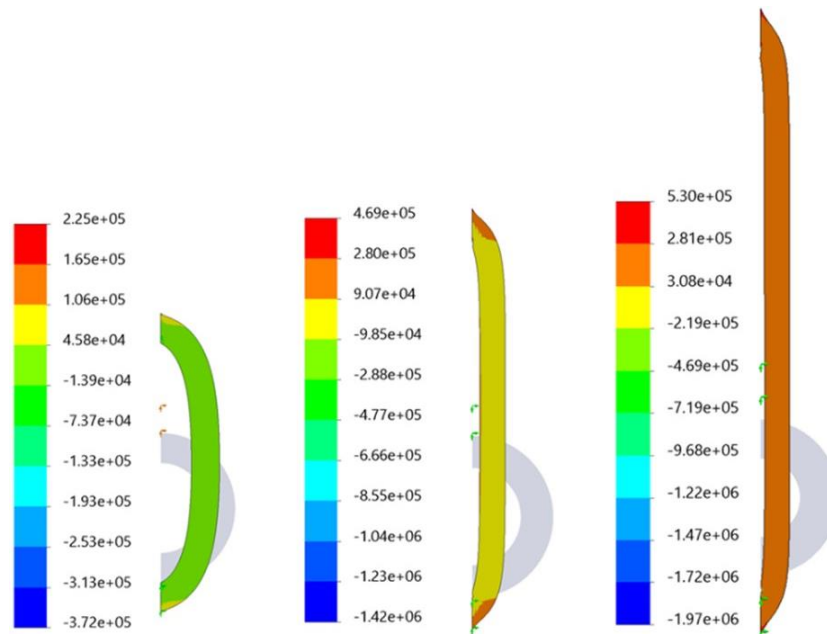


**Figure 4.** Graphs of the principal stress (N/m<sup>2</sup>) of the S2 sample with increasing extension values





**Figure 5.** Graphs of the principal stress (N/m<sup>2</sup>) of the S3 sample with increasing extension values



**Figure 6.** Graphs of the principal stress (N/m<sup>2</sup>) of the S4 sample with increasing extension values

Table 4 presents the maximum values derived from the probe feature graphs. As anticipated, the maximum stress values for all samples demonstrate an increase in correlation with the extension values. Upon examination of the minimum stress values presented in Table 5, it becomes evident that the regular sample did not exhibit any negative stress values, as was anticipated. These values remained positive and exhibited a corresponding increase parallel to the extension values.

In contrast, the wavy samples exhibited negative or compressive stress values. This phenomenon can be attributed to the excess material on the outer edges of the curves becoming compressed as the curves attempt to expand under the influence of deformation. Initially, these values increase for the wavy samples but subsequently decrease with a significant increase in the extension value.

Finally, it should be noted that all curved samples must fully expand their folded structure for an extension value of 1.5. Because the length of the curved structure is the product of the pi number and its radius. This roughly means 1.5 times its initial length value. In the deformation graphs of all curved samples, it can be observed that for an extension value of 1.5, the inner part of the samples is almost completely straightened.

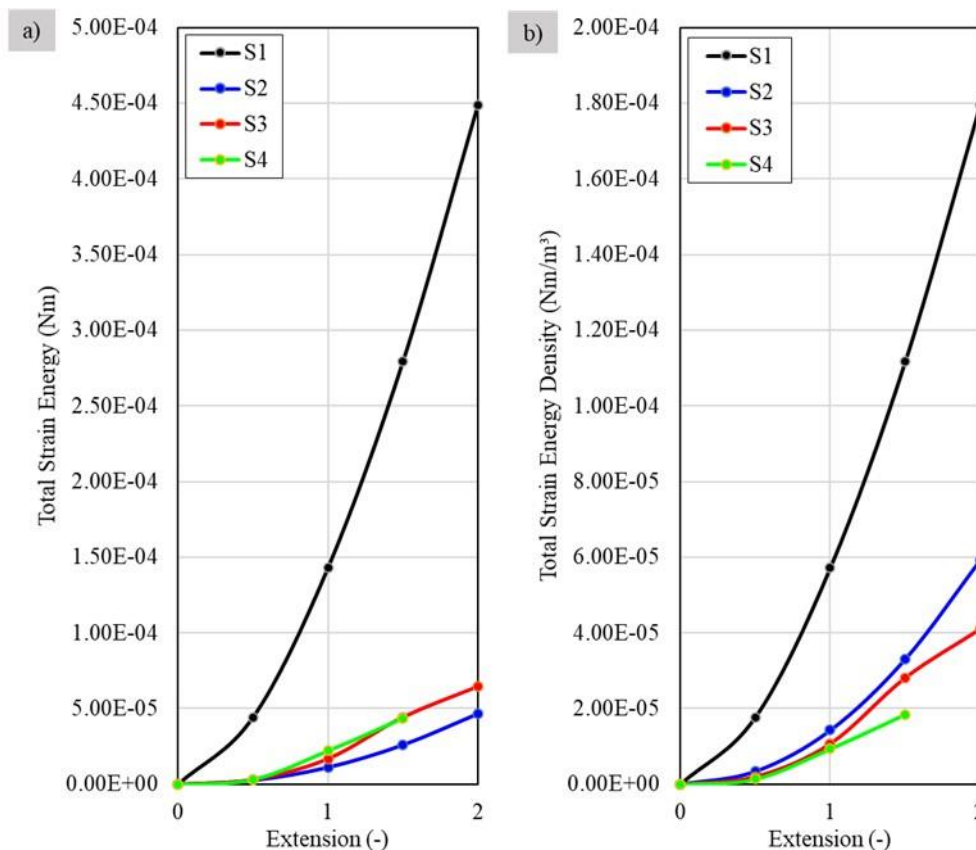
**Table 4.** Maximum normal stress in the first principal direction (Pa)

Extension [-]	S1	S2	S3	S4
0.5	2.30E+05	1.6E+05	1.84E+05	2.25E+05
1.0	3.83E+05	3.1E+05	3.86E+05	4.69E+05
1.5	5.61E+05	4.4E+05	5.34E+05	5.30E+05
2.0	7.91E+05	6.4E+05	6.54E+05	NA

**Table 5.** Minimum normal stress in the first principal direction (Pa)

Extension [-]	S1	S2	S3	S4
0.5	4.71E+04	-1.7E+05	-4.24E+05	-3.72E+05
1.0	1.08E+05	-4.0E+05	-1.40E+06	-1.42E+06
1.5	1.70E+05	-3.8E+05	-1.81E+06	-1.97E+06
2.0	2.53E+05	-2.1E+05	-1.32E+06	NA

To ascertain the flexibility afforded by the wavy structure, the total strain energy values were ascertained and divided by the initial volumes of the samples, thus reporting the total strain energy density values. The graphical representation of these values can be observed in Figure 7 and Table 6.



**Figure 7.** Total strain energy and energy density graphs of the samples: a) Total energy and b) Energy density graphs

Upon examination of Figure 7a, it became evident that a definitive result could not be obtained due to the inconsistency in sample volumes. The graphs that include the volumes in the analysis are presented in Figure 7b for reference. As anticipated, the samples retained their hyperelastic characteristics. It is evident that as the curvature radius increases, the flexibility of the samples also increases. The S4 sample, which exhibited the lowest energy storage, can be attributed to its wider curvature and larger radius. The S3 sample exhibited an energy storage density that fell between that of S2 and S4, which can be attributed to its intermediate curvature radius. The S1 sample exhibited the highest energy storage density, with an order of magnitude difference, demonstrating the greatest resistance to increasing extension.

**Table 6.** Strain energy (U) values in Nm and strain energy density (W) values in N/m<sup>2</sup>

Extension [-]	S1		S2		S3		S4	
	U	W	U	W	U	W	U	W
0.5	4.42E-05	1.77E-05	2.68E-06	3.41E-06	3.18E-06	2.02E-06	3.21E-06	1.36E-06
1.0	1.43E-04	5.72E-05	1.12E-05	1.43E-05	1.68E-05	1.07E-05	2.20E-05	9.33E-06
1.5	2.79E-04	1.12E-04	2.60E-05	3.31E-05	4.42E-05	2.81E-05	4.32E-05	1.83E-05
2.0	4.49E-04	1.80E-04	4.65E-05	5.93E-05	6.44E-05	4.10E-05	NA	NA

## 4 CONCLUSION

This study designed a thin (0.5 mm) hyperelastic material with a wavy form based on a reference flat geometry to investigate the achievable flexibility levels under varying curvature radii in a simulation environment. The following results were obtained:

- The maximum stress values were observed at the points of connection. In practice, these would be expected to form at the opening points of the curves. This indicates that the simulation boundary conditions may be inadequate or inappropriate.
- It was determined that examining total strain energy would be an adequate method for determining the flexibility and hyperelastic behavior of the samples. However, it is essential to normalize these values by volume and to consider the energy density values.
- It was observed that the energy density values exhibited a decline with an increase in the curvature radii of the samples. Furthermore, even at the smallest radius value, a notable reduction was observed compared to the regular sample, illustrating the impact of increasing flexibility requirements on the wavy structure.

In future studies, it would be beneficial to revise the boundary conditions to more accurately represent the actual structure and test different curve designs. Conducting additional experimental studies to corroborate the simulation values would be beneficial.

## References

- [1] A. Ali, M. Hosseini, and B. B. Sahari, "A review and comparison on some rubber elasticity models," *Journal of Scientific and Industrial Research*, vol. 69, no. 7, pp. 495–500, 2010.
- [2] S. K. Melly, L. Liu, Y. Liu, and J. Leng, "A review on material models for isotropic hyperelasticity," *International Journal of Mechanical Systems Dynamics*, vol. 1, no. 1, pp. 71–88, 2021, doi: 10.1002/msd2.12013.
- [3] G. He, B. Xia, Y. Feng, Y. Chen, L. Fan, and D. Zhang, "Modeling the damage-induced softening behavior of brain white matter using a coupled hyperelasticity-damage model," *J Mech Behav Biomed Mater*, vol. 141, art. no. 105753, May 2023, doi: 10.1016/j.jmbbm.2023.105753.
- [4] Y. Yao, J. Chen, J. Liu, and S. Chen, "An alternative constitutive model for elastic particle-reinforced hyperelastic matrix composites with explicitly expressed Eshelby tensor," *Compos Sci Technol*, vol. 221, art. no. 109343, 2022, doi: 10.1016/j.compscitech.2022.109343.
- [5] Z. Guo and L. J. Sluys, "Application of a new constitutive model for the description of rubber-like materials under monotonic loading," *Int J Solids Struct*, vol. 43, no. 9, pp. 2799–2819, 2006, doi: 10.1016/j.ijsolstr.2005.06.026.
- [6] K. K. Dwivedi, P. Lakhani, S. Kumar, and N. Kumar, "A hyperelastic model to capture the mechanical behavior and histological aspects of the soft tissues," *J Mech Behav Biomed Mater*, vol. 126, art. no. 105013, 2022, doi: 10.1016/j.jmbbm.2021.105013.
- [7] S. Talebi and H. Darjani, "A pseudo-strain energy density function for mechanical behavior modeling of visco-hyperelastic materials," *Int J Mech Sci*, vol. 208, art. no. 106652, 2021, doi: 10.1016/j.ijmecsci.2021.106652.
- [8] F. Safshekan, M. Tafazzoli-Shadpour, M. Abdouss, and M. B. Shadmehr, "Mechanical characterization and constitutive modeling of human trachea: Age and gender dependency," *Materials*, vol. 9, no. 6, art. no. 456, 2016, doi: 10.3390/ma9060456.
- [9] T. Liu, Z. Ye, B. Yu, W. Xuan, J. Kang, and J. Chen, "Biomechanical behaviors and visco-hyperelastic mechanical properties of human hernia patches with polypropylene mesh," *Mechanics of Materials*, vol. 176, art. no. 104529, 2023, doi: 10.1016/j.mechmat.2022.104529.
- [10] T. A. Carniel and E. A. Fancello, "A transversely isotropic coupled hyperelastic model for the mechanical behavior of tendons," *J Biomech*, vol. 54, pp. 49–57, 2017, doi: 10.1016/j.jbiomech.2017.01.042.

- [11] N. Gariya, P. Kumar, and B. Prasad, "Stress and bending analysis of a soft pneumatic actuator considering different hyperelastic materials," in *Materials Today: Proceedings*, 2022, doi: 10.1016/j.matpr.2022.05.352.
- [12] A. A. Soufivand, N. Abolfathi, S. A. Hashemi, and S. J. Lee, "Prediction of mechanical behavior of 3D bioprinted tissue-engineered scaffolds using finite element method (FEM) analysis," *Addit Manuf*, vol. 33, art. no. 101181, 2020, doi: 10.1016/j.addma.2020.101181.
- [13] L. Liu and Y. Li, "A visco-hyperelastic softening model for predicting the strain rate effects of 3D-printed soft wavy interfacial layer," *Mechanics of Materials*, vol. 137, 2019, doi: 10.1016/j.mechmat.2019.103128.
- [14] B. Sanborn and B. Song, "Poisson's ratio of a hyperelastic foam under quasi-static and dynamic loading," *Int J Impact Eng*, vol. 123, art. no. 103128, 2019, doi: 10.1016/j.ijimpeng.2018.06.001.
- [15] B. Kim *et al.*, "A comparison among Neo-Hookean model, Mooney-Rivlin model, and Ogden model for chloroprene rubber," *International Journal of Precision Engineering and Manufacturing*, vol. 13, no. 5, pp. 759–764, May 2012, doi: 10.1007/s12541-012-0099-y.
- [16] T. Gopesh and J. Friend, "Facile analytical extraction of the hyperelastic constants for the two-parameter Mooney-Rivlin model from experiments on soft polymers," *Soft Robot*, vol. 8, no. 4, 2021, doi: 10.1089/soro.2019.0123.
- [17] A. A. Smirnov, A. L. Ovsepyan, P. A. Kvindt, F. N. Paleev, E. V. Borisova, and E. V. Yakovlev, "Finite element analysis in the modeling of the heart and aorta structures," *Almanac of Clinical Medicine*, vol. 49, no. 6, pp. 375–384, 2021, doi: 10.18786/2072-0505-2021-49-043.



## Creation of a Digital Twin for Remote Fault Detection of a CNC Machine

Cemal Pamukcu<sup>\*1</sup>, Numan Dogruay<sup>2</sup>, Abdulsamed Tabak<sup>1</sup>

<sup>1</sup>*Mechatronics Engineering Department, Necmettin Erbakan University, Konya, Türkiye*

<sup>2</sup>*Virmode Inc., Konya, Türkiye*

### Abstract

In recent years, the concept of digital twins has gained increasing importance in a wide variety of fields, including industrial manufacturing, healthcare, education, the energy sector, the automotive industry, urban planning, and entertainment. Digital twins serve as exact virtual replicas of physical objects or systems, and their applications span a wide range of areas, including simulation, analysis, training, maintenance, security, and visualization. For calibration errors, energy efficiency, and overheating issues in CNC machines, there is no need for technical service to be physically present at the machine's location. A digital twin of a CNC machine has been created using the popular game engine UNITY and the open-source software development kit OPENXR to diagnose and resolve these issues remotely. This will result in time and cost savings through remote fault diagnosis enabled by the digital twin. In this study, digital twin technology will be used to diagnose and resolve faults such as vibration abnormalities, overheating, calibration errors, and energy efficiency issues remotely.

**Keywords:** *Digital twin, CNC machine, Remote diagnosis, Unity and OpenXr*

## 1 INTRODUCTION

CNC (Computer Numerical Control) machines are computer-controlled, high-precision manufacturing tools. They are used for cutting and shaping materials such as metal, wood, and plastic. These machines are widely preferred in many industries, including automotive, aerospace, and medical fields. CNC machines speed up production processes, reduce costs, and improve quality. Through automation and digital control, the margin of error is reduced and efficiency is increased, making CNC machines indispensable in modern manufacturing [1].

A digital twin is a technology that creates a virtual model of physical objects. This model encompasses the object's lifecycle and is designed to simulate its behavior and monitor operations using real-time data. It was initially used by NASA for spacecraft maintenance and repair. Today, it is widely used in many sectors such as energy, automotive, healthcare, manufacturing, and transportation. Digital twins are employed in a wide range of applications, from optimizing production processes to reducing errors and enabling predictive maintenance. The primary goal of this technology is to ensure perfect alignment between physical assets and their digital counterparts [2].

Augmented Reality (AR) technologies are bringing about a revolutionary transformation in the machinery sector, leading to radical changes in design, manufacturing, and training processes. The usage of these technologies has rapidly evolved from the past to the present and has been widely adopted in industrial applications [3].

OpenXR is an industry standard published in 2017 with the aim of enabling interoperability among various VR and AR devices. The primary objective of this standard is to provide developers and users with more flexibility and options by offering a compatible experience across different platforms. OpenXR facilitates compatibility between different devices, allowing users to have similar experiences across various platforms.

In previous studies, Digital Twin (DT) was proposed as a control system for real-time monitoring of machines. They not only implemented the developed DT to monitor machine conditions in real-time but also applied it to a milling machine. A panel-based task center was created to visualize the machine's status in real-time. The task center comprises three main functions: real-time machine monitoring, overall equipment effectiveness, and order planning [4]. In a recent study, researchers aimed to develop a Digital Twin (DT) model for manufacturing systems. In the second phase of their study, they utilized the developed DT model to predict the completion time of linear motion commands on flexible manufacturing system machines. Multiple machine learning algorithms were employed in the prediction phase, and their performances were compared [5]. In a comprehensive study,

researchers applied a Failure Mode and Effects Analysis (FMEA) method in the machining workshop of a company producing industrial kitchen products. With hundreds of main products and thousands of semi-finished products in its product range, the company's machining workshop monitored the real-time status of 12 machines using Programmable Logic Controller (PLC) cards. Through the PLC cards, they recorded machine operating conditions, capacity utilization times, operating times, waiting times for parts to be clamped only for horizontal lathe machines, idle waiting times, operating times, and downtime durations [6].

In this study, the process of transferring a CNC machine to a virtual environment using Unity and OpenXR was discussed in technical detail, and concrete examples were provided on how these technologies can be utilized in the machine sector. Additionally, the discussion was enriched by making predictions about future trends, taking into account the development of these technologies from the past to the present [7].

## 2 MATERIAL AND METHOD

The equipment and tools used for the study are described in this section.

### 2.1 CNC 1610 Machi

The CNC 1610 is designed as a desktop-sized CNC routing machine. As seen in Figure 1, its compact and portable structure makes it ideal for use in home or small workshop environments. Typically, it has a processing area of 160 mm x 100 mm x 45 mm, which determines the size of the parts that can be processed. The CNC 1610 is equipped with high-precision stepper motors capable of precise processing. These motors control movement in the X, Y, and Z axes, positioning the workpiece to the desired location. Using various cutting tools, the CNC 1610 can process different materials, and is typically ideal for materials such as wood, plastic, and PCBs. The control unit determines the processing path and operates the machine through computer-based control software.

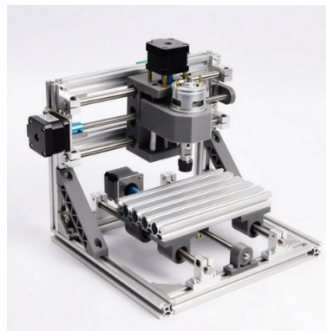


Figure 1. CNC 1610

### 2.2 MKS DLC32 V2.1 Controller Board

The MKS DLC32 V2.1 is a control board used for printers and CNC machines, as shown in Figure 2, offering advanced features. Its 32-bit architecture provides faster processing power and smooth motion control. This control board allows for system expansion and customization by supporting various additional modules and sensors. Extended connectivity options such as USB, SD card, and Ethernet provide flexibility in communication with different devices. Some models have convenient connection points for directly controlling touchscreen displays, allowing users to easily manage the processor. Popular 3D design software applications are equipped with various security features that ensure users can safely operate their systems. These features are crucial for protecting users' data and maintaining system security [8].

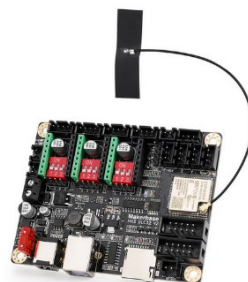


Figure 2. MKS DLC 32 V2.1 controller board

### 2.3 Solidworks

SolidWorks is a computer-aided design (CAD) software developed by Dassault Systèmes. It offers functions such as 3D modeling, simulation, technical drawing, and product data management. SolidWorks facilitates engineering and design processes and is widely used in various industries such as automotive, aerospace, and mechanical engineering. With its user-friendly interface and powerful features, as shown in Figure 3, it enables efficient and creative work.

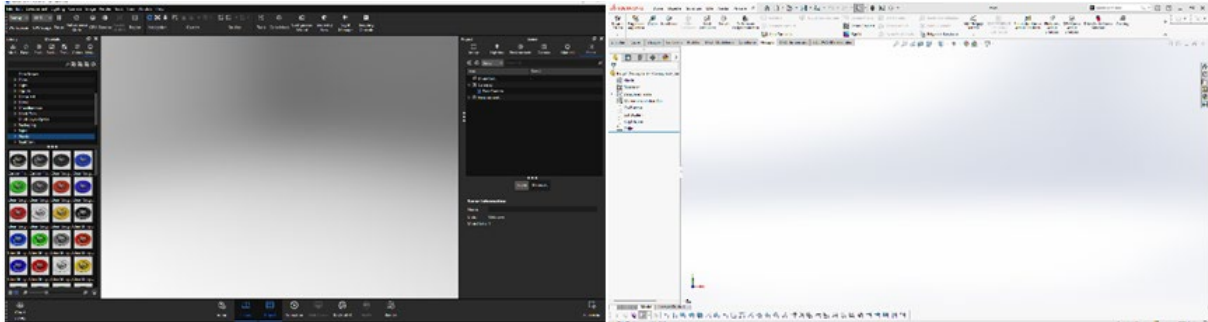


Figure 3. Solidworks and Keyshot login screen

### 2.4 Keyshot

KeyShot is a software used for visualization and rendering. It stands out with its fast-rendering engine, realistic material and lighting options, as well as easy-to-use and integration features. It can integrate with various 3D modeling software and can be used in many fields. KeyShot is particularly preferred in product design and marketing areas.

### 2.5 Unity

Unity is a popular game engine and integrated development environment used for game development and creating interactive 3D applications. It provides developers with ease of use through its user-friendly interface, multi-platform support, and wide range of features. Impressive visual experiences can be created with its graphic features, pre-defined effects, and built-in physics engine. Unity's support for various programming languages, especially C#, enables coding and scripting, offering developers flexibility and customization options. Its extensive asset store and active community support aid in rapid prototyping and finding solutions tailored to specific needs. The applications of Unity are not limited to the gaming industry; it is also used in various fields such as education, architecture, simulation, virtual reality, and augmented reality. Figure 4 illustrates the interface of the Unity program.

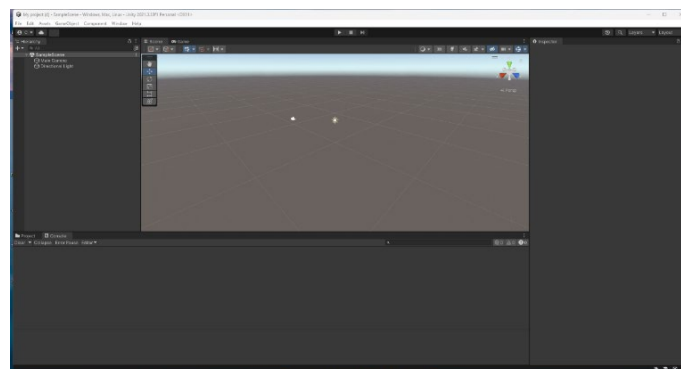


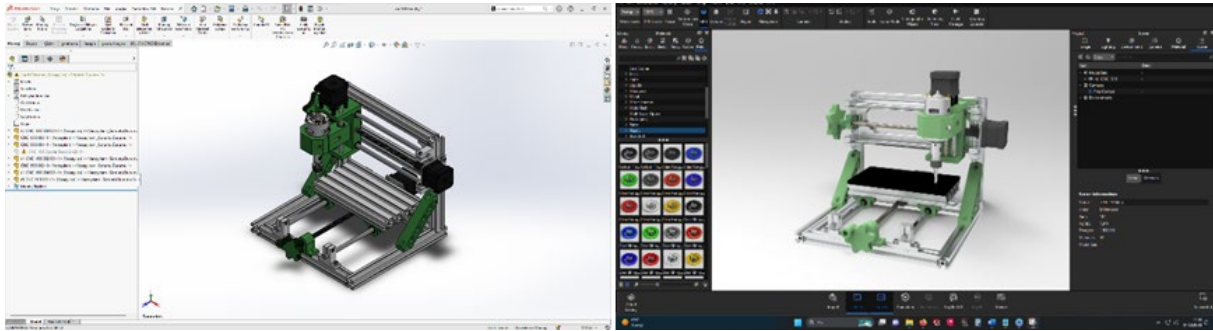
Figure 4. Unity login screen

### 2.6 OpenXr

OpenXR is an industry standard for virtual reality (VR) and augmented reality (AR). It ensures compatibility across different devices and platforms, allowing developers to support multiple devices and platforms using a single API. This standard enables extended reality applications to reach a broader audience and makes the development process more efficient. Managed by the Khronos Group, an open standard, OpenXR has been widely adopted across the industry and is supported by many major VR and AR platforms [9].

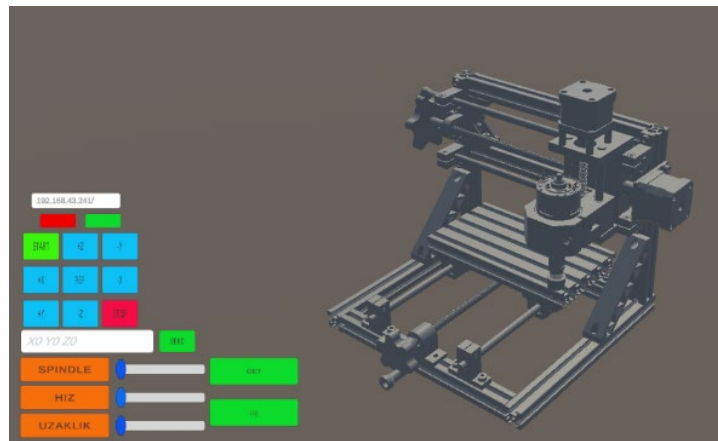
### 3 RESULTS

In this study, the process of transferring the CNC machine to a virtual environment was carried out using the Unity game engine and the OpenXR standard. The first step in transferring machines to a virtual environment was to create a detailed 3D model of the CNC machine in the real world. In this process, professional Computer-Aided Design (CAD) software such as SolidWorks and Blender were used to accurately reflect the design details. During the modelling process, important factors such as the real dimensions of the machine, part details, and functionality were meticulously considered. This approach ensured that the machine in the virtual environment was created as closely as possible to reality and aimed to provide the user with a realistic experience, as shown in the SolidWorks and KeyShot image in Figure 5.



**Figure 5.** Design of CNC machine with Solidworks and Keyshot

Machine models were transferred to the Unity game engine environment to create the virtual environment. Unity is known as a powerful game engine and development environment, facilitating processes such as creating virtual worlds, animation, physics simulation, and interaction. In the study, many of these processes were implemented with code written in C# using Visual Studio. The machine model was placed within Unity using the scene editor and the movements of the machine in the real world were simulated in Unity. The model created in Unity is shown in Figure 6, representing the 3D model of the CNC machine in Unity.



**Figure 6.** 3D application of CNC machine in unity program

Real-time communication and interaction with the machine in the virtual environment were achieved using WebSocket. WebSocket is a communication protocol that provides full duplex communication between the browser and the server. With this protocol, users can control and interact with the machines in the virtual environment in real-time. This is an important step to make the user experience more immersive and realistic. The communication protocol was integrated into the Unity project, allowing users to interact with virtual machines. Communication was done using WebSocket via C#. Figure 7 shows the WebSocket flow diagram.





Figure 7. Websocket flow diagram

The OpenXR standard was used to ensure that virtual reality experiences work seamlessly across different devices. It interacts with Unity's APIs, enabling control over objects, components, and systems within Unity. Through integration with this standard, the Unity project became compatible with various VR and AR devices. In this integration process, using the OpenXR SDK in the Unity project was the starting point. The OpenXR SDK provides Unity with an API that supports the OpenXR standard and enables different VR and AR devices to work together compatibly.

Within the Unity project, necessary configurations were made for an OpenXR compatible Android device. These configurations integrated the device's tracking, input, and control systems into the Unity project. Through the application shown in Figure 8, controlled via the OpenXR API, the machine is operated on an Android device. The developed Unity project was deployed to and tested on the Android device. At this stage, users were able to enter the augmented reality environment, examine the machine in detail, and interact with it. Feedback obtained during testing was taken into account for further development and improvement of the project. Thus, through the combination of machine modelling, Unity game engine usage, OpenXR integration, and testing on Android devices, the process of successfully transferring the machine to the augmented reality environment was completed.

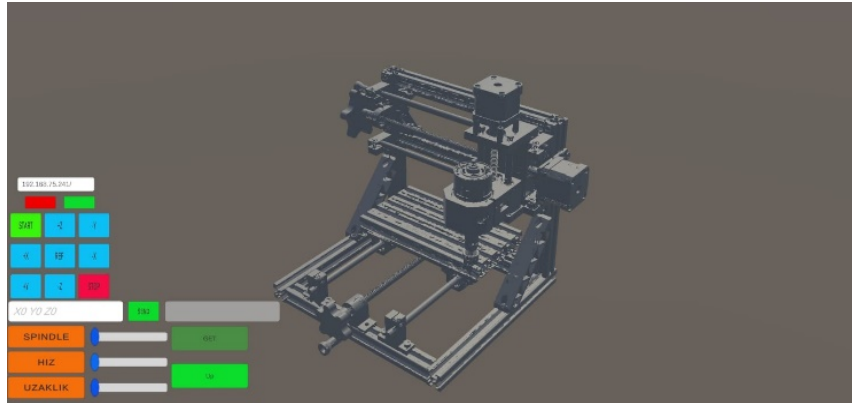


Figure 8. Control panel view on android device

## 4 CONCLUSION

This study has extensively examined the process of transferring CNC machines to a virtual environment and discussed the methods followed to successfully complete this process. The combination of steps presented in the study has enabled the successful transfer of machines to the virtual environment, demonstrating the effectiveness of the methods used in this process. The detailed modelling of real-world machines during the 3D modelling process, the utilization of the Unity game engine, the integration of the OpenXR standard, and the creation of an augmented reality experience compatible with Android have facilitated this achievement. Additionally, it has been observed that the feedback obtained during testing played a significant role in the development and improvement of the project. These feedback loops have provided valuable insights for future work and contributed to further optimizing the process of transferring machines to the virtual environment.

As a result of this study, it has been concluded that digital twin technology can be effectively utilized for the remote diagnosis and resolution of faults such as vibration abnormalities, overheating, calibration errors, and energy efficiency issues. Based on a digital twin model and a data-driven approach, this study presents significant potential for predicting faults in CNC machines and preventing productivity losses through rapid interventions. The sample study conducted on tool life estimation has demonstrated the applicability of the proposed method and

how the technique provides more accurate and timely results than a single approach. This study highlights the potential of digital twin technology for reliable predictive maintenance and rapid intervention in CNC machines.

## Acknowledgments

This study was supported by the Scientific Research Projects Coordination (BAP) Unit of Necmettin Erbakan University (NEU, Project Number: 23GAP19016).

## References

- [1] M. El Jazzer, M. Piskernik, and H. Nassereddine, "Digital twin in construction: An empirical analysis," in *EG-ICE 2020 Workshop on Intelligent Computing in Engineering*, 2020, pp. 501–510, 2020.
- [2] J. Vitorino et al., "Industry 4.0 - Digital twin applied to direct digital manufacturing," *Applied Mechanics and Materials*, vol. 890, pp. 54–60, 2019, doi: 10.4028/www.scientific.net/amm.890.54.
- [3] S. M. Hasan, K. Lee, D. Moon, S. Kwon, S. Jinwoo, and S. Lee, "Augmented reality and digital twin system for interaction with construction machinery," *Journal of Asian Architecture and Building Engineering*, vol. 21, no. 2, pp. 564–574, 2022, doi: 10.1080/13467581.2020.1869557.
- [4] K. J. Wang, T. L. Lee, and Y. Hsu, "Revolution on digital twin technology—a patent research approach," *International Journal of Advanced Manufacturing Technology*, vol. 107, no. 11–12, pp. 4687–4704, 2020, doi: 10.1007/s00170-020-05314-w.
- [5] Y. Li, "Anti-fatigue and collision avoidance systems for intelligent vehicles with ultrasonic and Li-Fi sensors," in *2020 3rd IEEE International Conference on Information Communication and Signal Processing (ICICSP 2020)*, 2020, pp. 203–209, doi: 10.1109/ICICSP50920.2020.9232054.
- [6] H. Haße, B. Li, N. Weißenberg, J. Cirullies, and B. Otto, "Digital twin for real-time data processing in logistics," in *Hamburg International Conference of Logistics (HICL)*, Berlin, 2019, pp. 4–28, [Online]. Available: <https://www.econstor.eu/bitstream/10419/209367/1/hicl-2019-27-004.pdf>
- [7] G. De Cicco, B. Morten, M. Prudenziati, and A. Taroni, "A temperature compensated ultrasonic sensor operating in air for distance and proximity measurements," *IEEE Transactions on Industrial Electronics*, vol. IE-29, no. 4, pp. 336–341, 1982, doi: 10.1109/TIE.1982.356688.
- [8] M. Murshed and M. S. Chowdhury, "An IoT based car accident prevention and detection system with smart brake control," in *International Conference on Applications and Techniques in Information Science (iCATIS2019)*, Dhaka, 2019.
- [9] S. K. Pal, D. Mishra, A. Pal, S. Dutta, D. Chakravarty, and S. Pal, "Digital twin application," in *Digital Twin – Fundamental Concepts to Applications in Advanced Manufacturing*, 2022, Springer, pp. 413–465, doi: 10.1007/978-3-030-81815-9\_7.



---

## Design and Analysis of Lightweight 3D-Printed Lattice Structures Using Fused Deposition Modelling

Turker Turkoglu<sup>\*1</sup>

<sup>1</sup>*Mechanical Engineering Department, Balıkesir University, Balıkesir, Türkiye*

---

### Abstract

This study examines the application of Fused Deposition Modelling (FDM) technology to design and evaluate the mechanical properties of 3D-printed structures, with a specific focus on polylactic acid (PLA) and lattice structures. FDM is recognized for its ability to fabricate complex geometries with varied internal architectures, making it an ideal method for producing lightweight yet mechanically robust components. PLA, a biodegradable thermoplastic, is widely used in FDM due to its ease of processing, biocompatibility, and adequate mechanical properties. The importance of weight reduction in design is emphasized, particularly in industries where minimizing mass without sacrificing strength is critical. Lattice structures, characterized by their repeating geometric patterns, offer a promising solution for weight reduction. Among these, face-centered cubic (FCC), body-centered cubic (BCC), and gyroid structures are prominent due to their distinctive mechanical properties and efficient load distribution.

In this research, cube designs with dimensions of 40x40x40 mm and a lattice thickness of 3 mm were fabricated using different lattice structures. Compression tests were conducted to evaluate the mechanical performance of these designs. The results indicated that the gyroid lattice structure exhibited the highest compressive strength, outperforming the FCC and BCC structures. This superior performance is attributed to the continuous and smooth surface of the gyroid structure, which provides enhanced stress distribution and load-bearing capacity. These findings demonstrate the potential of utilizing lattice structures in 3D-printed designs to achieve significant weight reduction while maintaining or enhancing mechanical performance. The study highlights the importance of selecting appropriate lattice geometries to optimize the structural integrity and functionality of 3D-printed components.

**Keywords:** *Additive manufacturing, Fused deposition modelling, Lattice structures, Mechanical properties*

---



---

## Numerical Investigation of Heat Transfer Performances in Spiral Dimpled Pipe Profiles

Anil Aykut<sup>\*1</sup>, Veysel Ozceyhan<sup>1</sup>

<sup>1</sup>Department of Mechanical Engineering, Erciyes University, Kayseri, Türkiye

---

### Abstract

Heat transfer and hydrodynamic flow characteristics are examined numerically in spiral pipe profiles having dimpled surface. Investigated diameter was left constant is  $D=50$  mm pipe profile diameter, the number of twist ( $n=0.5, 1$  and  $2$  rounds) of the pipes with different Reynolds number ( $Re$ ) flows ( $3000 \leq Re \leq 8000$ ) according to velocity of fluid and the dimpled surfaces were taken as a parameter. A constant heat flux is applied on the outer surface of the pipe profile. Investigated parameters of the circular dimpled are taken as dimple diameter ( $D_d=3, 5,$  and  $8$  mm), and pitch length of dimples ( $PL=20$  mm). The results are evaluated and calculated in terms of the Nusselt number ( $Nu$ ), friction factor ( $f$ ), and performance evaluation criteria (PEC) as functions of the Reynolds number ( $Re$ ). This study conducts an extensive analysis of Computational Fluid Dynamics (CFD) and Conjugate Heat Transfer (CHT) simulations utilizing the capabilities of Ansys Fluent. Tetrahedral mesh structure has been preferred for this study for the better adaptation to the complex geometries and irregular shapes present such as dimpled surfaces. RNG turbulence model was adopted for all cases. RNG transport equation for turbulence distribution with kinetic energy  $k$  and  $\epsilon$ . Within the scope of this study, smooth pipe, spiral pipe and dimpled spiral pipe geometries were examined with CFD simulation studies. According to the results obtained, an increase in heat transfer was observed in the spiral pipe compared to the smooth pipe. It has been observed that when a dimple is applied to the spiral pipe (dimpled spiral pipe), the heat transfer efficiency increases compared to the smooth spiral pipe.

**Keywords:** *CFD, Flow characteristic, Heat transfer enhancement, Numerical method, Twisted dimpled tube*

---



## Natural Fibers: A Sustainable Alternative for Composite Reinforcements

Mehmet Cagri Tuzemen\*<sup>1</sup>

<sup>1</sup>*Department of Metallurgy and Material Engineering, Nevsehir Haci Bektas Veli University, Nevsehir, Türkiye*

---

### Abstract

The interest and use of composite materials are increasing day by day thanks to their high specific strength. Composite materials generally consist of reinforcement elements and matrix elements. The use of various synthetic materials such as glass, carbon and, aramid as reinforcement elements is quite common. However, as the use of composites increases, waste material, recycling and, sustainability issues also gain importance. For this reason, natural reinforcement fibers have come to the fore in recent years. Natural fibers can be plant (cellulose), animal or, mineral based. Jute, hemp, flax, cotton, bamboo, wool, and silk can be given as a few examples of natural reinforcement. While natural fibers have advantages such as low density, biodegradability, and low cost, they also have disadvantages such as moisture absorption and low strength. Various studies are being carried out to eliminate its disadvantages. Manufacturing hybrid composites by using natural fibers and synthetic fibers together to increase strength is one of them. Several surface modifications are made to reduce moisture absorption. To achieve this goal, various chemicals such as alkaline are used. Thus, it is aimed to strengthen the bond between the fiber and the matrix. Natural fiber composites are presently in the early stages of development and their uses are currently limited. However, they have tremendous potential as an environmentally friendly replacement for traditional synthetic fibers.

**Keywords:** *Natural fibers, Polymer composite, Sustainability*

---



## Structural Analysis of Hopper Support Frame of Vacuum Road Sweeping Vehicle on Truck Mounted

Onur Can Kirit<sup>\*1</sup>, Vedat Fetullahoglu<sup>1</sup>

<sup>1</sup>Koluman Automotive Industry Inc, Mersin, Türkiye

### Abstract

The increasing demand for vacuum road sweeping vehicles mounted on trucks brings with it the necessity for the equipment used in these vehicles to provide the best performance and long life. Some of these equipment requires detailed structural analysis as they are of high security importance. This study focuses on the structural analysis of the road sweeper under-hopper support frame, which is a critical component and is subjected to various dynamic loads during operation.

The design and modelling of the road sweeper under-hopper support chassis was carried out using CATIA V5, known for its precision in creating detailed and complex geometries; ANSYS 2023 R2, which offers advanced finite element analysis (FEA) capabilities, was used to evaluate structural integrity and identify areas for improvement. The materials used in the chassis design are of S355 quality. The forces required for chassis analysis were determined by taking into account the situations that the sweeping vehicle would encounter in real world use. In bad condition, half of the hopper chassis was loaded with a maximum of 3.5 tons. In order to simulate the effect of dynamic forces and create a safety factor, analysis was made by applying an extra force of 2 tons.

According to the results of FEA, the maximum stress was measured as 320 MPa when the safety coefficient was 1.57, and no plastic deformation was observed. Critical stress accumulation points and deformation models were revealed in the chassis design. Special modifications have been proposed to strengthen high-stress areas and increase the structural strength and durability of the chassis. The study highlights the importance of using advanced design and analysis tools to develop high-performance, durable chassis for industrial applications.

**Keywords:** Vacuum road sweeper, Structural analysis, Finite element analysis (FEA), Chassis design, Hopper design

## 1 INTRODUCTION

Road sweepers (Refer to Figure 1), which also known as street sweepers, are vehicles or machines that designed to clean streets, roads, and other paved surfaces. They are equipped with brooms, brushes, and vacuum systems to remove debris, dirt, and litter from the roadways. Generally, road sweepers can be divided two categories as truck-mounted or self-propelled, and all models have water systems to help control dust during the sweeping process.



Figure 1. Road sweeper example

There are a lot of aims of road sweepers vehicles: One of them is keeping clean the streets and public spaces by removing trash, leaves, and other debris that accumulate on roadways. Another one is providing safety by removing debris, litter and slippery liquids from roads, so sweepers help reduce the risk of accidents caused by obstructions or slippery surfaces [1].

Regular use of road sweepers helps maintain the visual appeal of urban areas, making them more pleasant for people. Clean streets reduce the spread of diseases, also contribute to overall public health and well-being.

## 2 MATERIAL AND METHOD

This study involves the design and structural analysis of hopper support chassis of a road sweeper as utilizing advanced engineering tools. The chassis was designed and modeled using CATIA V5, chosen for its precision in creating complex geometries. For the structural integrity assessment, ANSYS 2023 R2 was employed, leveraging its advanced finite element analysis (FEA) capabilities to simulate real world conditions. The chassis material was selected S355, known for its high strength and durability. The analysis considered the operational scenarios, where the chassis was subjected to a maximum load of 3.5 tons also with an additional 2 tons applied for to simulate dynamic forces and to ensure a robust safety factor. The FEA results provided critical insights into stress distribution and deformation and also guided the design modifications to enhance the chassis's strength and durability.

### 2.1 Method

Finite Element Analysis (FEA) is a computational method widely used in engineering and physical sciences. This method is employed to simulate the behavior of complex structures, components, or systems. FEA works by breaking down large and complex problems into small and finite elements and by analyzing the behavior of each element individually. And then it predicts the overall behavior of the entire system by combines these elements [1].

Main objectives of FEA:

- i. Structural analysis: To analyze mechanical properties such as stress, strain, deformation, and vibration of a component or structure.
- ii. Thermal analysis: To evaluate heat transfer, temperature distribution, and thermal stresses within a material or structure.
- iii. Fluid dynamics: To model the movement and interactions of fluids.
- iv. Electromagnetic analysis: To simulate the behavior of electric fields, magnetic fields, and electromagnetic waves.

FEA allows to engineers and designers to test the performance, safety, and durability of a product or structure in a virtual environment. This tests reduce the number of physical prototypes, lower the costs, and speed up the product development process.

### 2.2 Material

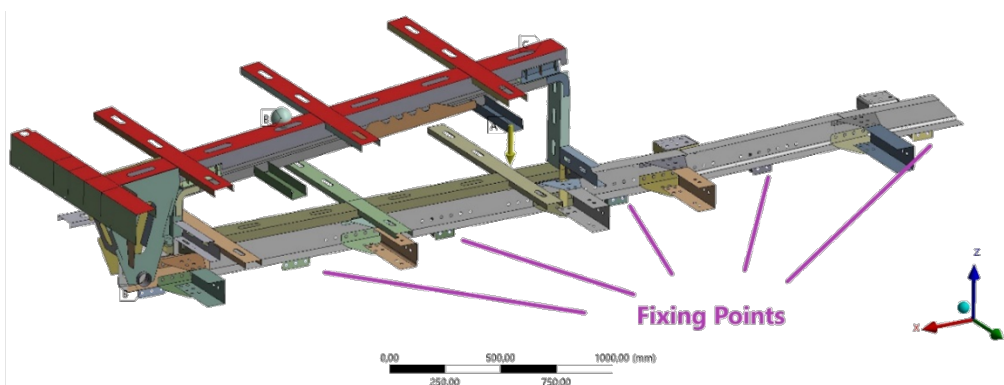


Figure 2. Analysis geometry and fixing points

The analysis was carried out as a semi-model. In the analysis, a 3.5-ton weight was applied to simulate the pressure field where the water tank was located (red surface in Figure 2). In addition, a force of 20 kN was applied from

the pressure surfaces of the water tank (red surface in Figure 2) to simulate dynamic loads. The total force was applied for 1 second and then reduced to zero at the 2<sup>nd</sup> second to observe the steady state. All materials were assigned as S355NL. The fixation was provided by means of auxiliary chassis connection brackets. The analysis geometry and fixing points is shown in Figure 2 [2] .

### 3 RESULTS

In this section, the stress and deformation results which occurred on the support frame based on the static analysis have been discussed and correlated.

According to equivalent stress at 1 second (Transient Condition) in below Figure 3;

- The maximum stress was measured as 375 MPa.
- Stresses above the yield point were generally observed at overlapping areas and in the joining regions.
- Maximum point can be seen circled in Figure 3.

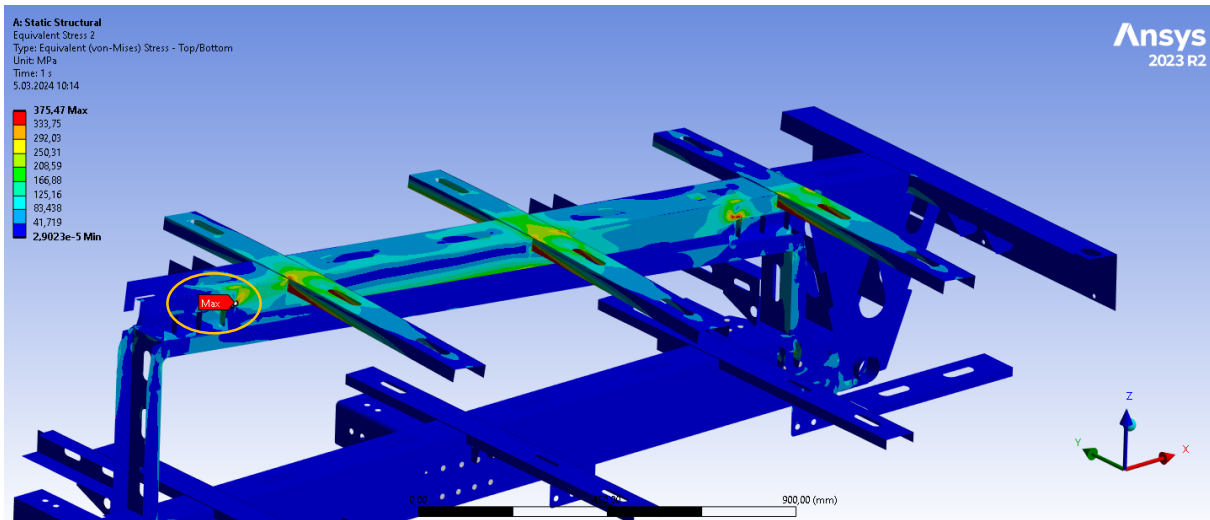


Figure 3. Equivalent stress at 1 second

The regions close to yield limit at 1 second for the equivalent stress can be seen in Figure 4 and Figure 5.

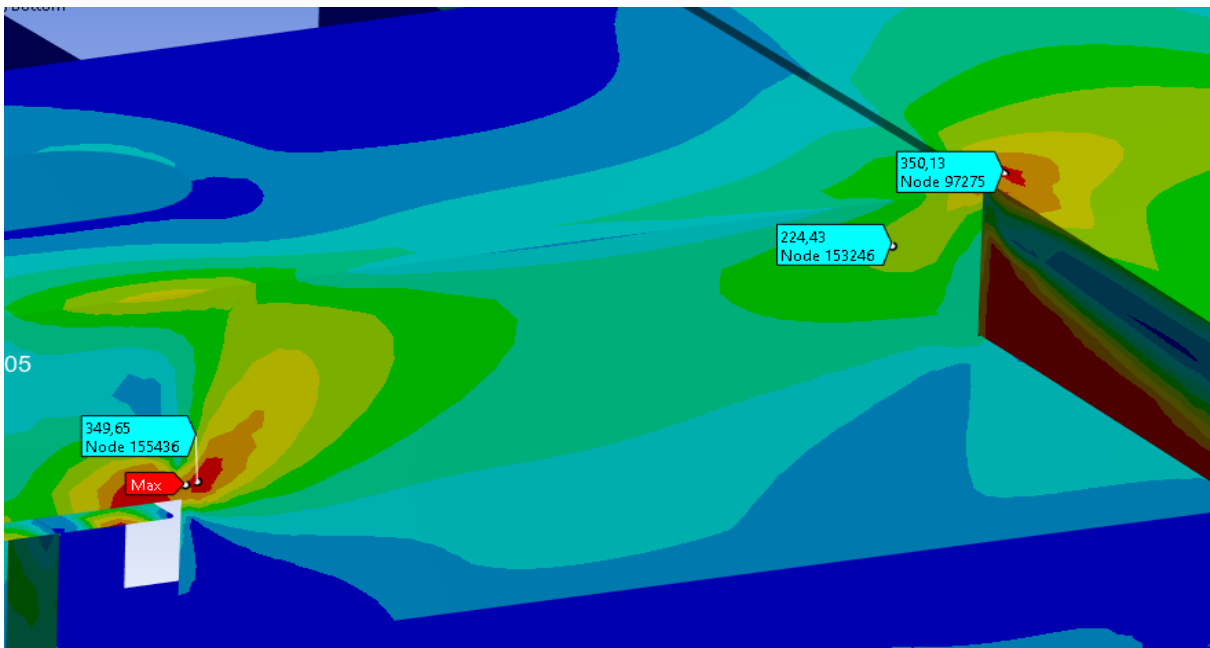
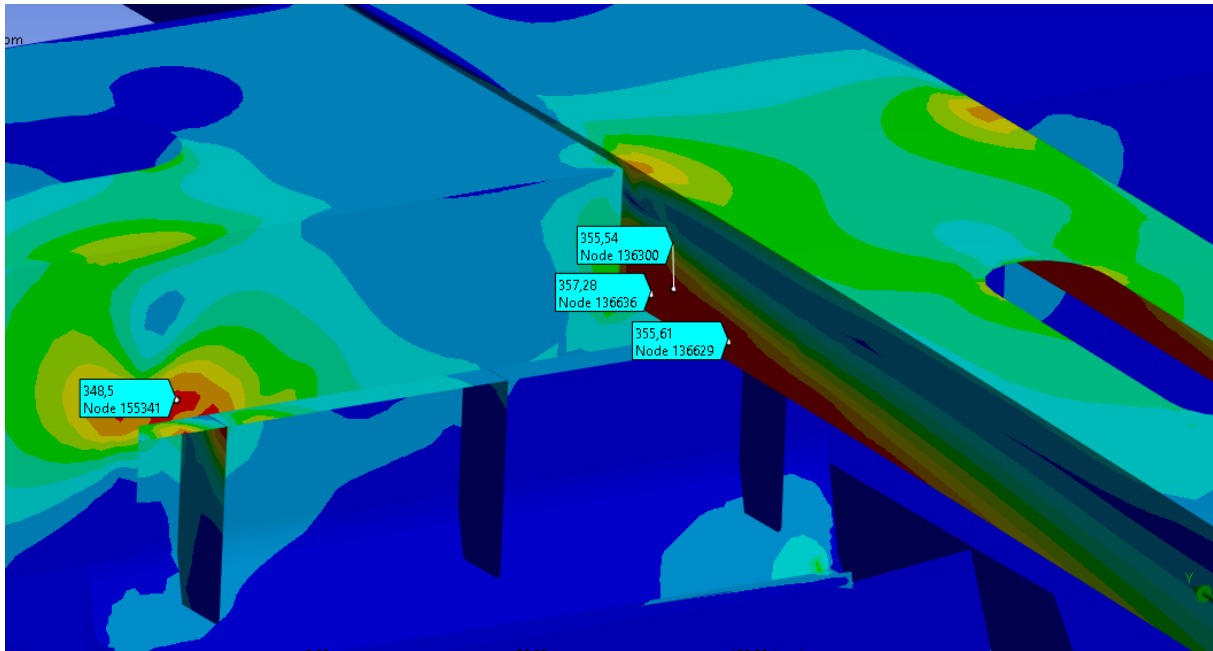


Figure 4. The maximum stress points 1

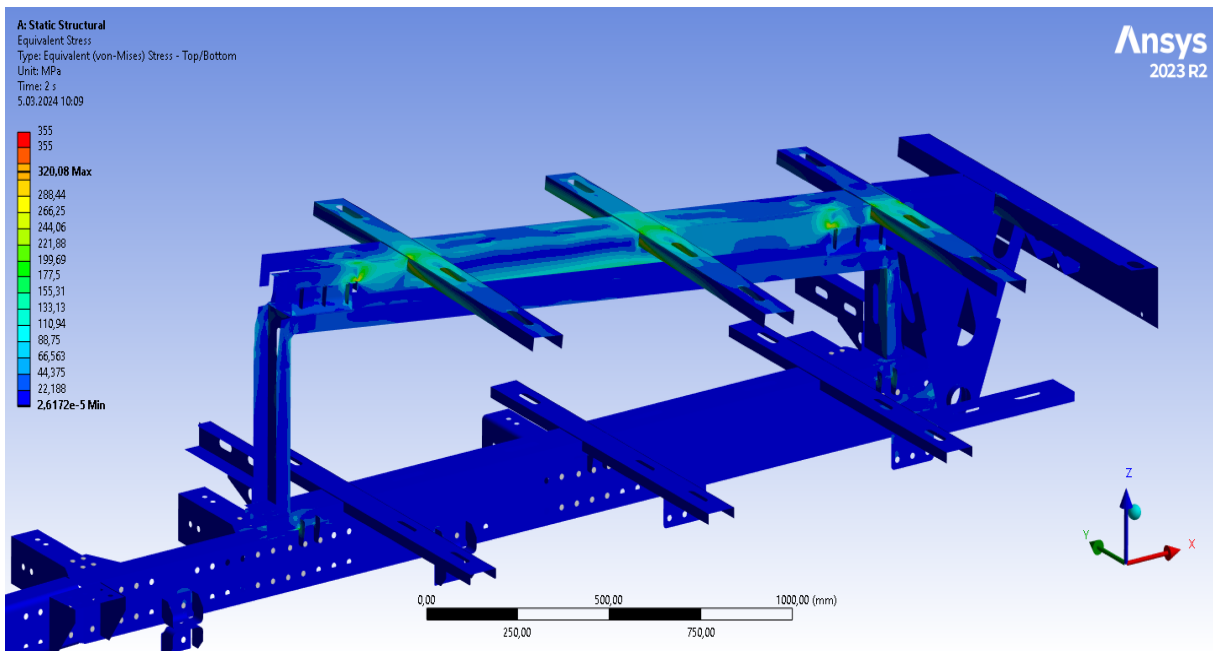




**Figure 5.** The maximum stress points 2

According to equivalent stress at 2 second (Transient Condition) in Figure 6;

- The maximum stress was measured as 320 MPa.
- No behavior was observed above the yield point after the force was released.



**Figure 6.** Equivalent stress at 2 second

According to Stress-Strain ratio, the deformation above 0.02 is interpreted as permanent deformation. Capillary permanent deformation was observed in the five specified regions (Circled in Figure 7).

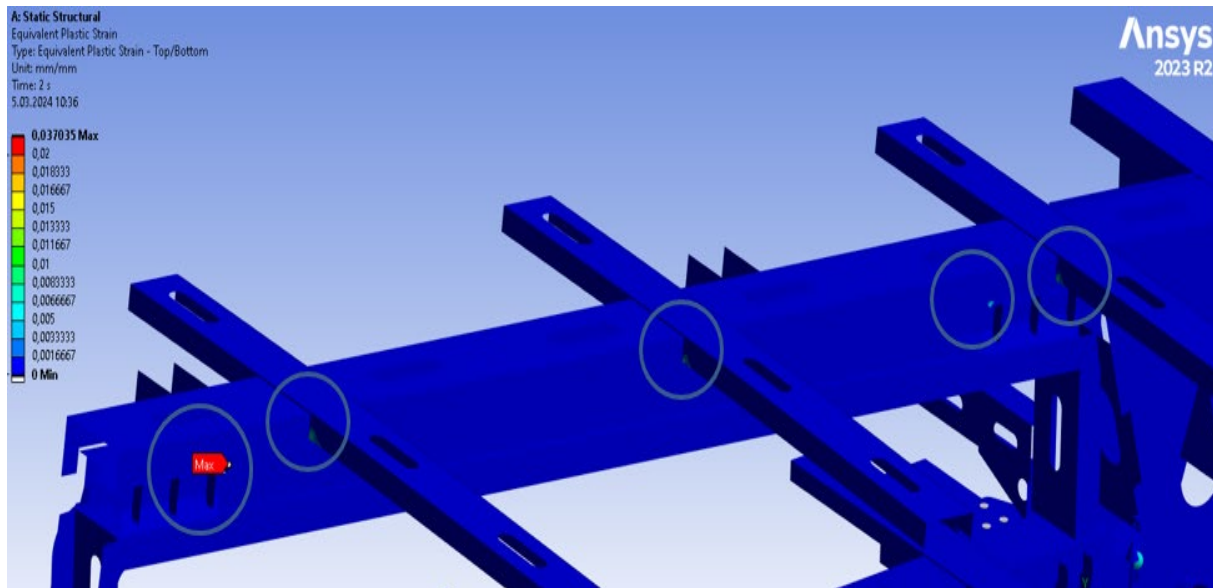


Figure 7. Plastic stress-strain

When total deformation was looking at, the maximum total deformation was observed as 35 mm in the end regions. However, these regions do not undergo permanent deformation because they are not stress-concentrating areas. They result from the ductility of structural steel. The distribution of total deformation can be seen in Figure 8 [3].

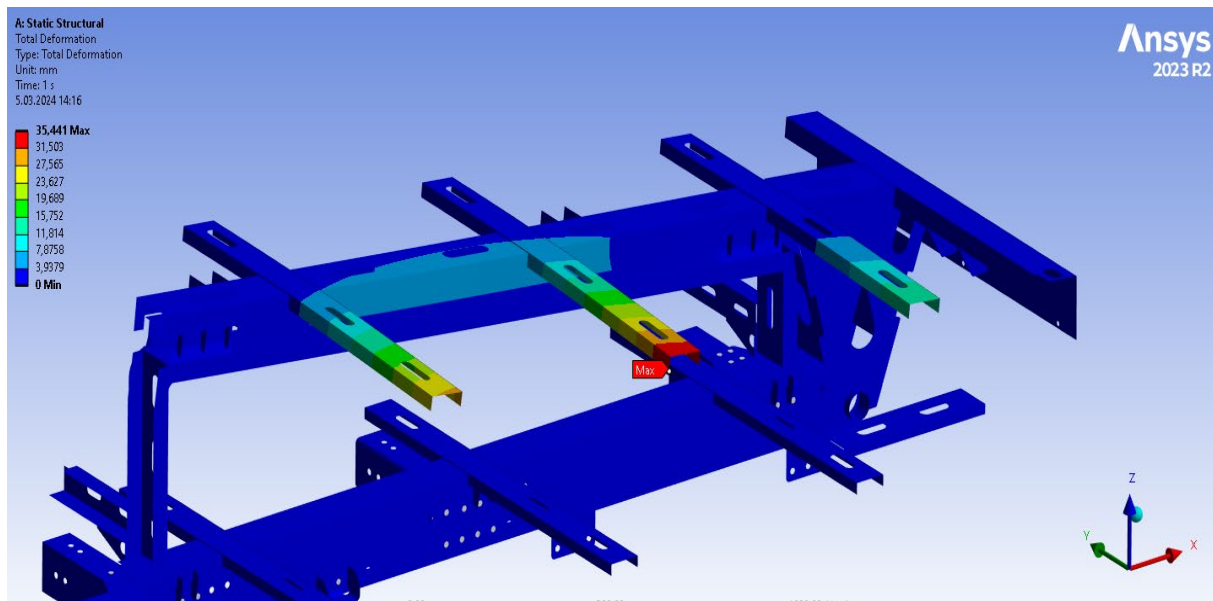


Figure 8. Total deformation

#### 4 CONCLUSION

In the analyses, in addition to the 3,5 ton weight of the tank, a force equivalent to 2 tons was applied from the pressing surfaces of the tank.

In the evaluation: The observed stresses above the yield point are generally at the material's yield limit. However, they have caused a small amount of plastic deformation. This deformation was mainly observed at the joints of the U-profiles, and the amount of plastic deformation is relatively small.

Although these plastic deformations will not be ignored, they may have resulted from singularities caused by the mesh generation during the analysis. It would be appropriate to monitor this with newly produced vehicle.

The study emphasizes the importance of using advanced design and analysis tools to develop high performance and durable chassis for industrial applications.

### **Acknowledgments**

We extend our heartfelt thanks to Koluman Automotive Industry for their generous support and for granting us the opportunity to conduct this study, thanks to our colleague Omer Coskun for analyses support, thanks to our another colleague Hakan Delebe for design ideas, thanks to our another colleague Mesut Yildirim to give support to production process. Their contribution has been invaluable in the pursuit of this research.

### **References**

- [1] O. C. Zienkiewicz, *The Finite Element Method in Engineering Science*, McGrawHill, 1971.
- [2] D. Forni, B. Chiaia, and E. Cadoni, in *Proceedings of the VII European Congress on Computational Methods in Applied Sciences and Engineering, ECCOMAS2016*, Greece, 2016, p. 4920.
- [3] M. Tavakkolizadeh and H. Saadatmanesh, "Strengthening of Steel-Concrete Composite Girders using Carbon Fiber Reinforced Polymers Sheets," *ASCE Journal of Structural Engineering*, vol. 129, no. 1, pp 30–40, 2003.



## Use of Hardox 500 Tuf in Tippers

Resul Akcali<sup>\*1</sup>, Akin Zengin<sup>2</sup>, Mustafa Yilmaz<sup>1</sup>

<sup>1</sup>R&D Engineer, Koluman Automotive Industry Inc., Mersin, Türkiye

<sup>2</sup>R&D Team Leader, Koluman Automotive Industry Inc., Mersin, Türkiye

### Abstract

The superstructures of dump trailers generally used for transporting excavated material on highways have been examined. Improvements related to the abrasion-resistant steel plates, which constitute almost the entire structure, have been adapted to production and daily use.

The results obtained have been analyzed using analysis programs. “The studies were conducted with the consideration of using sand and basalt rock, which are two of the most commonly used materials in the industry”. In the studies conducted using Hardox brand steel plates; Firstly, the Hardox 450 grade, 5mm thick steel plates, which we currently use in 80% of the superstructure during our dump trailer production, were examined separately while transporting sand and basalt rock. Abrasion tests were conducted using analysis programs. Subsequently, the same design and dimensions were used, but instead of Hardox 450 grade 5mm thick steel plates, Hardox 500 Tuf grade 4mm thick steel plates were used. It was planned to use sand and basalt rock during the tests, The reactions against abrasion were analyzed using the same programs. During the tests, various minerals and structures contained within sand and basalt rocks were also examined.

As a result of the analyses; when a 4 mm thick plate is used instead of a 5 mm thick plate, It has been observed that there is approximately a 20% reduction in the weight of the dump trailer's superstructure. During testing intended for sand transport, it was observed that there was a 3% reduction in the service life of dump trailers using Hardox 500 Tuf, 4mm thick plates instead of HARDOX 450, 5mm thick plates. Conversely, during testing intended for basalt rock transport, a 9% increase in service life was observed for dump trailers using Hardox 500 Tuf, 4mm thick plates instead of Hardox 450, 5mm thick plates [1].

**Keywords:** *Tipper, Material quality, Wear resistance, Hardox*

## 1 INTRODUCTION

In the dump trailers we produce in-house: We examined the reactions of 5mm Hardox 450 abrasion-resistant steel sheets and 4mm Hardox 500 Tuf abrasion-resistant steel sheets, used in the side walls and floor of the body, also known as the superstructure, in the transport of two different materials. The first of which is basalt rocks, and the second is sands.

### 1.1 Basalt Rock

The basalt rock we referenced consists of two different mineral groups. The first of these are minerals called Plagioclase. The second is the mineral group called Pyroxene. It contains 43% Plagioclase and 57% Pyroxene in its composition [2].



Figure 1. Basalt rock

### Plagioclase

It is particularly common in igneous rocks. It forms the basis for the classification of igneous rocks.

Chemical composition:  $\text{NaAlSi}_3\text{O}_8 - \text{CaAl}_2\text{Si}_2\text{O}_8$

Crystal System: Triclinic crystal structure (cage-shaped)

Crystal Form: Prismatic or tabular crystal form; massive (natural)

Hardnes: 6–6.5 Rockwell

Specific gravity: 2.6–2.8  $\text{gr}/\text{cm}^3$

Color and transparency: Usually white, sometimes pink, greenish, or brownish; transparent to translucent.

Luster: Glassy.

Distinctive Features: It separates by polysynthetic twinning from potassium feldspars. Depending on changes in chemical composition, there are different types such as albite, oligoclase, andesine, labradorite, bitovnit, and anorthite. These minerals can be distinguished from each other under a microscope [2].



**Figure 2.** Plagioclase

### Piroksen

It is believed to be one of the important components of manton, a complex inosilicate mineral group commonly found in igneous and metamorphic rocks.

Chemical composition: It contains single-chain structures with iron and magnesium. It has approximately  $90^\circ$  distinct cleavage angles. Ojite is the most common mineral in the pyroxene group.

Crystal Form: Tabular cubic crystals

Hardnes: 6 Rockwell

Specific gravity: 3.2–3.6  $\text{gr}/\text{cm}^3$

Color And Transparency: Black [2].



**Figure 3.** Piroksen

### 1.2 Sands

Secondly, the structure of the sand intended to be used in the loading was examined. It consists of a combination of 5 different minerals: 89% quartz, 2% calcite, 3% feldspar, 4% biotite, and 2% hematite [2].



**Figure 4.** Sands

### Quartz

Quartz has the formula  $\text{SiO}_2$  and in its pure form, it contains 46.5% Si and 53.3% O<sub>2</sub>. Its hardness on the Mohs scale is 7 (Rockwell).

Specific Gravity: 2.65 g/cm<sup>3</sup>

Melting Point: 1785 °C

It is one of the most common minerals in the Earth's crust [2].



Figure 5. Quartz

### Kalsit

Chemical Composition:  $\text{CaCO}_3$

Hardness: 3 Specific

Gravity: 2.65 g/cm<sup>3</sup>

Color and Transparency: When pure, it is colorless or white; it can also be observed in gray, yellow, brown, red, green, blue, and black; transparent to semi-transparent [2].



Figure 6. Kalsit

### Felidispat

Table 1. Feldispat properties [2]

Name	Formula	Color and Brightness	Specific Gravity (gr/cm <sup>3</sup> )	Rockwell
Albit	$\text{NaAlSi}_3\text{O}_8$	Colorless, white, white-colored, transparent, translucent, vitreous, pearly	2.6	6–6.5
Anortit	$\text{CaAl}_2\text{Si}_2\text{O}_8$	Colorless, white, off-white, pinkish, red, transparent, translucent, glassy	2.74	6–6.5
Mikroklin	$\text{KAlSi}_3\text{O}_8$	White, off-white, gray, pinkish, transparent, translucent, glassy	2.56	6–6.5
Ortoz	$\text{KAlSi}_3\text{O}_8$	Colorless, white, gray, yellow, reddish, greenish, transparent, translucent, glassy, pearly	2.55	6–6.5



**Figure 7.** Feldspat

### **Biotite**

Chemical Composition:  $K(Mg,Fe)_3(Al,Fe)Si_3O_{10}(OH,F)_2$

Crystal System: Monoclinic

Crystal Form: Platy or short prismatic crystals; flaky and disseminated aggregates

Hardness: 2.5–3 (Rockwell)

Specific Gravity: 2.7–3.4 g/cm<sup>3</sup>

Color and Transparency: Black, dark shades of brown, reddish-brown, green, and rarely white; transparent to nearly opaque

Luster: Submetallic, vitreous [2]



**Figure 8.** Biotite [2]

### **Hematite**

Chemical Composition:  $Fe_2O_3$

Crystal System: Trigonal

Hardness: 5–6

Specific Gravity: 5.26

Color and Transparency: Steel gray-black, opaque

Luster: Metallic [2]



**Figure 9.** Hematite [2]

## 2 MATERIAL AND METHOD

### 2.1 Hardox 450 Wear-Resistant Plate

#### 2.1.1 Mechanical Properties of Hardox 450 Wear-Resistant Plate

##### Mechanical Properties

Hide/Show specific columns [EDIT](#)

PRODUCT	THICKNESS (mm)	HARDNESS <sup>1)</sup> (HBW)	TYPICAL YIELD STRENGTH (MPa), NOT GUARANTEED
Hardox® 450 CR sheet	0.8 - 2.10	425 - 475 <sup>2)</sup>	1250
Hardox® 450 sheet	2.0 - 8.0	425 - 475 <sup>2)</sup>	1250

Figure 10. Mechanical properties [3]

#### 2.1.2 Impact Properties of Hardox 450 Wear-Resistant Plate

##### Impact Properties

Hide/Show specific columns [EDIT](#)

PRODUCT	LONGITUDINAL TEST, TYPICAL IMPACT ENERGY, CHARPY V 10X10 MM TEST SPECIMEN	TRANSVERSE TEST, GUARANTEED IMPACT ENERGY, CHARPY V 10X10 MM TEST SPECIMEN <sup>1)</sup>
Hardox® 450 sheet & plate	50 J / -40 °C	–
Hardox® 450 Tuf	–	27 J / -20 °C <sup>2)</sup>

Figure 11. Impact properties [3]

#### 2.1.3 Chemical Composition of Hardox 450 Wear-Resistant Plate

##### Chemical Composition (heat analysis)

Hide/Show specific columns [EDIT](#)

PRODUCT TYPE	C <sup>1)</sup> (MAX %)	SI <sup>1)</sup> (MAX %)	MN <sup>1)</sup> (MAX %)	P (MAX %)	S (MAX %)	CR <sup>1)</sup> (MAX %)	NI <sup>1)</sup> (MAX %)	MO <sup>1)</sup> (MAX %)	B <sup>1)</sup> (MAX %)
CR sheet	0.19	0.30	1.50	0.020	0.005	0.10	0.10	0.05	0.004
Sheet & plate	0.26	0.70	1.60	0.025	0.010	1.40	1.50	0.60	0.005

Figure 12. Chemical composition [3]

#### 2.1.4 Carbon Equivalent CET of Hardox 450 Wear-Resistant Plate

##### Carbon Equivalent CET(CEV)

Hide/Show specific columns [EDIT](#)

PRODUCT TYPE	CR sheet	Sheet	Plate	Plate	Plate	Plate	Plate	Plate
Thickness (mm)	0.8 - 2.10	2.0 - 8.0	3.2 - 4.9	5.0 - 9.9	10.0 - 19.9	20.0 - 39.9	40.0 - 80.0	80.1 - 160.0
Max CET(CEV)	0.36 (0.49)	0.36 (0.49)	0.37 (0.48)	0.38 (0.49)	0.39 (0.52)	0.41 (0.60)	0.43 (0.74)	0.41 (0.67)
Typ CET(CEV)	0.32 (0.46)	0.33 (0.47)	0.33 (0.46)	0.33 (0.45)	0.36 (0.48)	0.38 (0.56)	0.40 (0.71)	0.39 (0.64)

$$CET = C + \frac{Mn + Mo}{10} + \frac{Cr + Cu}{20} + \frac{Ni}{40} \quad CEV = C + \frac{Mn}{6} + \frac{Cr + Mo + V}{5} + \frac{Cu + Ni}{15}$$

Figure 13. Carbon equivalent [3]

### 2.2 Hardox 500 TUF Wear-Resistant Plate

#### 2.2.1 Mechanical Properties of Hardox 500 TUF Wear-Resistant Plate

##### Mechanical Properties

Hide/Show specific columns [EDIT](#)

PRODUCT	THICKNESS (mm)	HARDNESS <sup>1)</sup> (HBW)	TYPICAL YIELD STRENGTH (MPa), NOT GUARANTEED
Hardox® 500 Tuf sheet	3.0 - 6.5	475 - 505	1370
Hardox® 500 Tuf plate	4.0 - 38.1	475 - 505	1370

Figure 14. Mechanical properties [3]



## 2.2.2 Impact Properties of Hardox 500 TUF Wear-Resistant Plate

### Impact Properties

Hide/Show specific columns [EDIT](#)

PRODUCT	LONGITUDINAL TEST, TYPICAL IMPACT ENERGY, CHARPY V 10X10 MM TEST SPECIMEN <sup>1)</sup>	TRANSVERSE TEST, GUARANTEED IMPACT ENERGY, CHARPY V 10X10 MM TEST SPECIMEN
Hardox® 500 Tuf sheet	50 J / -40 °C	27 J / -40 °C
Hardox® 500 Tuf plate	50 J / -40 °C	27 J / -20 °C

Figure 15. Impact properties [3]

## 2.2.3 Chemical Composition of Hardox 500 TUF Wear-Resistant Plate

### Chemical Composition (heat analysis)

Hide/Show specific columns [EDIT](#)

C <sup>1)</sup> (MAX %)	SI <sup>1)</sup> (MAX %)	MN <sup>1)</sup> (MAX %)	P (MAX %)	S (MAX %)	CR <sup>1)</sup> (MAX %)	NI <sup>1)</sup> (MAX %)	MO <sup>1)</sup> (MAX %)	B <sup>1)</sup> (MAX %)
0.30	0.70	1.60	0.020	0.010	1.50	1.50	0.60	0.005

Figure 16. Chemical composition [3]

## 2.2.4 Carbon Equivalent CET of Hardox 500 TUF Wear-Resistant Plate

### Carbon Equivalent CET(CEV)

Hide/Show specific columns [EDIT](#)

PRODUCT TYPE	Sheet	Plate	Plate	Plate
Thickness (mm)	3.0 - 6.5	4.0 - 16.0	16.1 - 25.4	25.5 - 38.1
Max CET(CEV)	0.38 (0.54)	0.38 (0.54)	0.39 (0.55)	0.44 (0.63)
Typ CET(CEV)	0.35 (0.52)	0.36 (0.52)	0.37 (0.53)	0.40 (0.59)

$$CET = C + \frac{Mn + Mo}{10} + \frac{Cr + Cu}{20} + \frac{Ni}{40} \quad CEV = C + \frac{Mn}{6} + \frac{Cr + Mo + V}{5} + \frac{Cu + Ni}{15}$$

Figure 17. Carbon equivalent [3]

## 3 RESULTS

### 3.1 Basalt Rock Transportation

In the first case, it is anticipated that the dump trailers will transport sand. During the analysis, the properties of the materials and steel, as well as the tests conducted, are specified in the table below [4] .

**Table 1.** Material upgrade from Hardox® 450 to Hardox® 500 Tuf

Estimated Service Life	101.8 Months	9% Increased service life
Corresponding Thickness	4 mm	20% Decreased weight

#### Abrasive

##### Basalt

Plagioclase: Fraction 43%

Pyroxene: Fraction 57%

##### Steel

Current Steel: Hardox® 450 [450 HB]

Thickness: 5 mm

Service Life: 93.3 months

Unloads: 19441

Upgrade Steel: Hardox® 500 Tuf [490 HB]  
 Thickness: 4 mm  
 Service Life: 101.8 months  
 Unloads: 21201

**3.2 Sand Transport**

In the second case, it is anticipated that the dump trailers will transport sand. During the analysis, the properties of the materials and steel, as well as the tests conducted, are specified in the table below.

**Table 2.** Material upgrade from Hardox® 450 to Hardox® 500 Tuf

Estimated Service Life	58.1 Months	3% Decreased service life
Corresponding Thickness	4 mm	20% Decreased weight

**Abrasive**

Sand

Quartz : Fraction 89%  
 Calcite: Fraction 2%  
 Feldspar: Fraction 3%  
 Biotite: Fraction 4%  
 Hematite: Fraction 2%

**Steel**

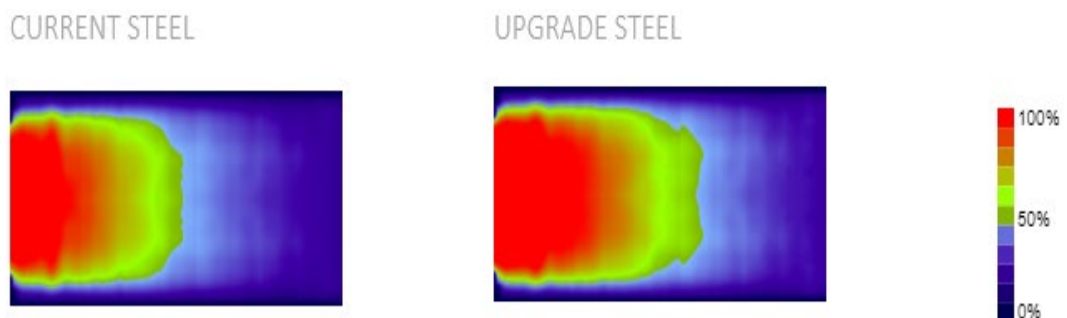
Current Steel: Hardox® 450 [450 HB]  
 Thickness: 5 mm  
 Service Life: 60.1 months  
 Unloads: 12514

Upgrade Steel: Hardox® 500 Tuf [490 HB]  
 Thickness: 4 mm  
 Service Life: 57.1 months

**4 CONCLUSION**

**4.1 Results obtained from basalt rock transportation**

As seen in the table, the reaction to wear is shown for the U-type dump trailer, which is designed for basalt rock transportation, when 4mm Hardox 500 Tuf is used instead of 5mm Hardox 450 in the floor and side wall plates. The characteristics and operating conditions of the dump trailer are specified in Figure 18. The weight of the dump body has been reduced by approximately 20%. This result allows the dump trailer to carry more load with the same dimensions. The service life of the dump trailer has been extended by approximately 9%.



**Figure 18.** Test

## 4.2 Results obtained from sand transportation

As seen in the table, the reaction to wear is shown for the U-type dump trailer, which is designed for sand transportation, when 4mm Hardox 500 Tuf is used instead of 5mm Hardox 450 in the floor and side wall plates. The characteristics and operating conditions of the dump trailer are specified in Figure 19. The weight has been reduced by approximately 20%. This result allows the dump trailer to carry more load with the same dimensions. The service life of the dump trailer has been reduced by approximately 3%.



Figure 19. Test

## Acknowledgments

I would like to thank Akın Zengin and Mustafa Yılmaz for their contributions during the study, and the companies from which I received support: SSAB, the General Directorate of MTA, ERGA BAZALT, Muhendishane, Wikipedia, Ankara University and KUMOCAK.

## References

- [1] Wikipedia. (2005). *Types of morphemes* [Online]. Available: <https://tr.wikipedia.org/wiki/Dilininim>
- [2] MTA Info Bank. [Online]. Available: <https://www.mta.gov.tr/en/#>
- [3] SSAB. *WearCalc* [Online]. Available: <https://www.ssab.com/en>



## Structural Analysis of Safety Leg on the Vacuum Road Sweeper Mounted on Truck

Omer Coskun<sup>\*1</sup>, Vedat Fetullahoglu<sup>1</sup>

<sup>1</sup>Koluman Automotive Industry Inc, Mersin, Türkiye

### Abstract

The increasing demand for vacuum road sweeping vehicles mounted on trucks brings with it the necessity for the equipment used in these vehicles to provide the best performance and long life. One of the components that enable the determination of the performance criteria of these equipment is comprehensive structural analysis. This study focuses on the structural analysis of the road sweeper safety leg, which is a critical component and is subjected to various dynamic loads during operation.

The design and modelling of the safety leg was carried out using CATIA V5, known for its precision in creating detailed and complex geometries; ANSYS 2023 R2, which offers advanced finite element analysis (FEA) capabilities, was used to evaluate structural integrity and identify areas for improvement. When the hopper of the road sweeping vehicle is lifted while the vehicle is in a stationary position, the materials collected in the hopper gather at the back of the hopper due to the slope, causing a load to be placed on the joints in the rotation centre at the bottom rear of the hopper and the safety leg in the middle bottom part of the hopper. In order to perform the strength analysis of the safety leg, a 3500 kg load was applied to half of the hopper chassis with a simplified model, representing the hopper at maximum load and providing a safety coefficient of 1.5.

The analyses were made by considering two different hopper positions: In the 1st case, the position in which the chamber was fully raised and in the last safety position was evaluated, and in the 2nd case, the position in which the chamber was in the first safety position, where it was close to closing, was evaluated. The accumulated load on the safety leg was measured as 83 MPa in the 1<sup>st</sup> case and 94 MPa in the 2<sup>nd</sup> case. As a result of both analyses, no plastic deformation was observed in the safety leg region.

**Keywords:** Vacuum road sweeper, Safety leg, Structural analysis, Finite element analysis (FEA), Dynamic loads

## 1 INTRODUCTION

The demand for efficient and durable truck-mounted vacuum road sweepers has increased, necessitating comprehensive structural analysis to ensure optimal performance and longevity. This study focuses on the structural analysis of the safety leg, a critical component subjected to various dynamic loads during operation. So, two different hopper position were considered, first one is called the fully raised position, second one is called the initial safety position (see Figure 1 and Figure 2 for details).

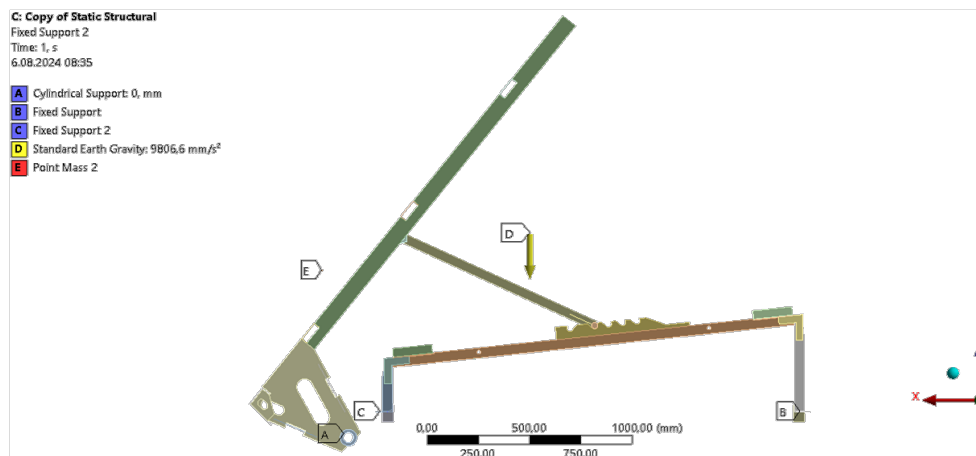


Figure 1. The fully raised position

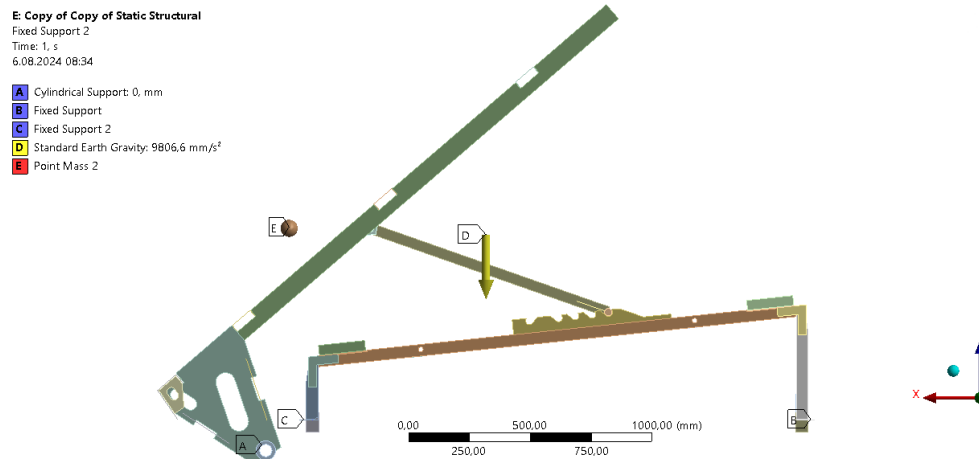


Figure 2. The initial safety position

## 2 MATERIAL AND METHOD

This section details the materials used and the methodology employed in the structural analysis of the safety leg for the vacuum road sweeper.

### 2.1 Materials

The materials used in the design and construction of the safety leg for the vacuum road sweeper include high-strength steels. Specifically, S355 steel was selected for the chassis, and C1040 steel was chosen for the solid components. These materials were chosen due to their high durability and capacity to withstand the dynamic loads experienced during the road sweeper's operation.

### 2.2 Method

The analysis considered a maximum load scenario, where a 3500 kg load was applied to half of the hopper chassis. This load was represented as a point mass applied from the center of gravity of the hopper. Two different hopper positions were analyzed:

- i. The fully raised position.
- ii. The initial safety position, where the hopper is close to closing.

The fixing regions were defined to ensure the accuracy of the simulation. The boundary conditions included constraints that reflect the real-world attachments and supports of the safety leg to the hopper chassis. The finite element model was set up with the defined loading and boundary conditions. Non-linear and symmetrical analysis methods were employed to simulate the realistic behavior of the safety leg under load. The analyses were conducted for both hopper positions to evaluate the stress distribution and potential deformation.

## 3 RESULTS

This section presents the results obtained from the finite element analysis (FEA) of the safety leg for the vacuum road sweeper. The analysis aimed to evaluate the structural integrity and performance of the safety leg under different loading and boundary conditions.

### 3.1 Stress Distribution

The stress distribution results showed that in the fully raised position (Refer to Figure 3), the maximum stress accumulated in the safety leg was 83 MPa (Refer to Figure 4). The stress distribution results showed that in the initial safety position (Refer to Figure 5), where the hopper is close to closing, the maximum stress observed was 94 MPa (Refer to Figure 6). Both two stress values are well within the yield strength limits of the materials used, indicating that the safety leg can handle the applied loads without yielding.

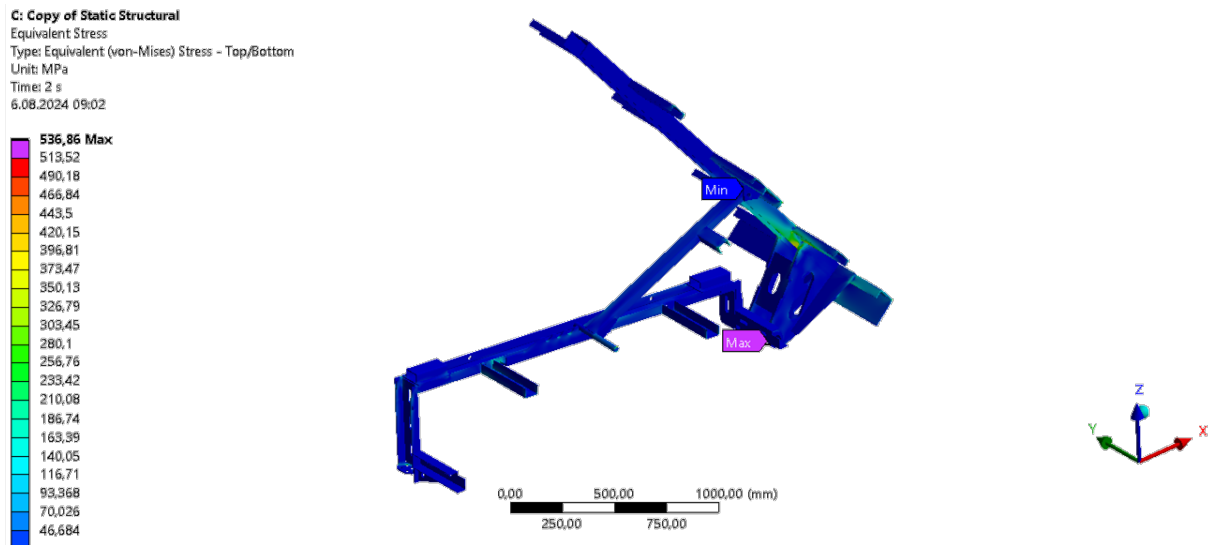


Figure 3. Stress distribution of fully raised position

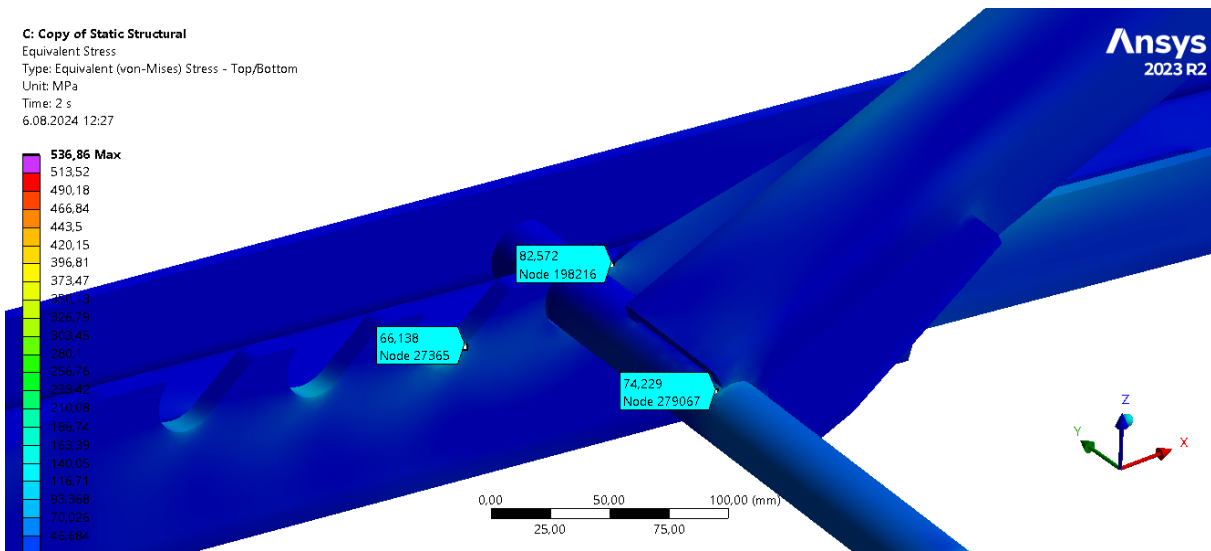


Figure 4. Maximum stress points of fully raised position

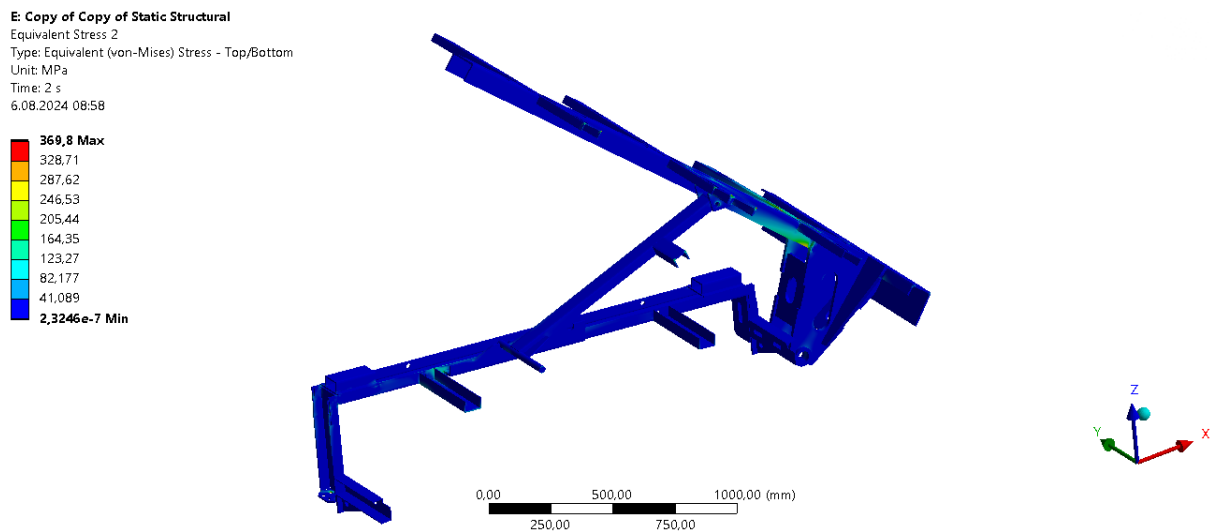


Figure 5. Stress distribution of the initial safety position

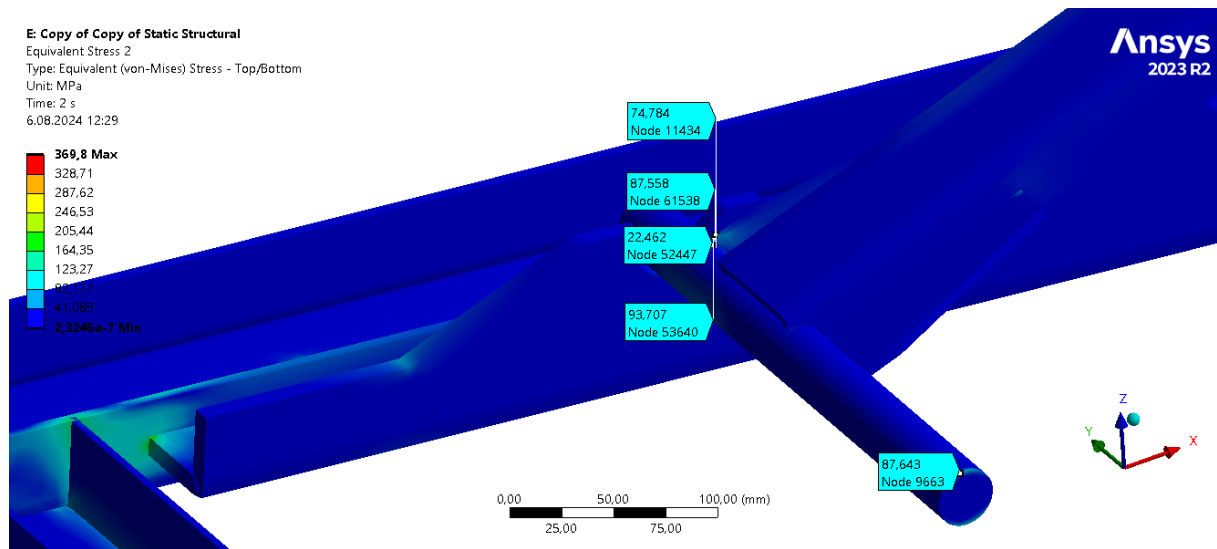


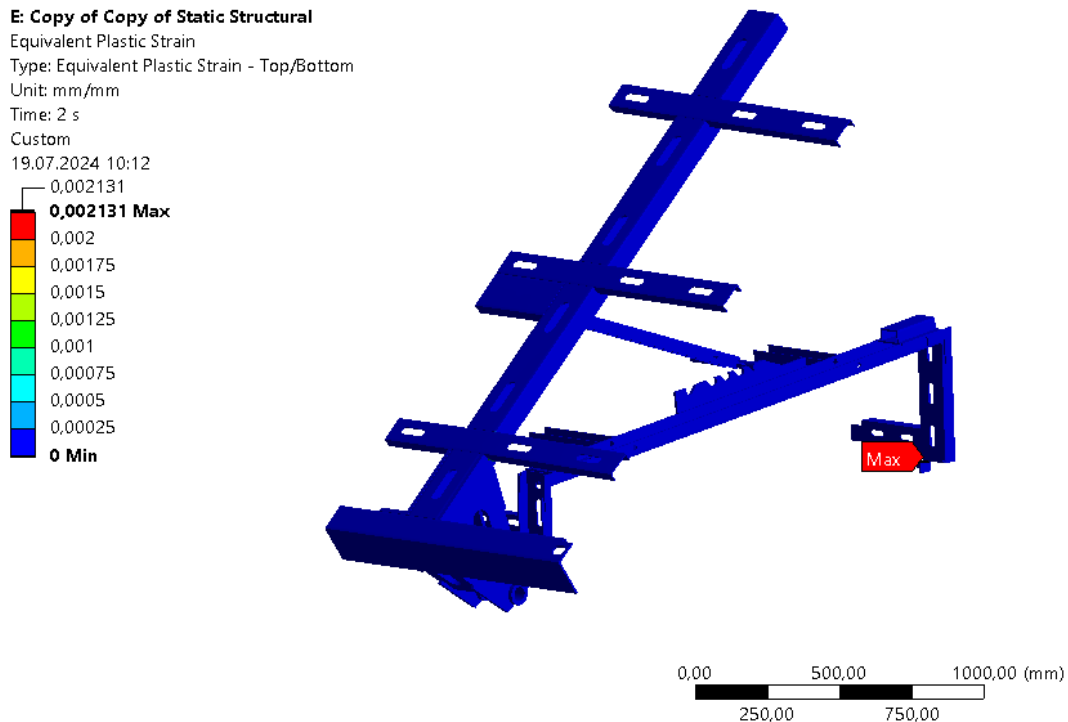
Figure 6. Maximum stress points of the initial safety position

### 3.2 Deformation Analysis

No significant plastic deformation was observed in the safety leg regions which was analyzed (Refer to Figure 7 and Figure 8). The absence of plastic deformation confirms that the design is robust and capable of maintaining its structural integrity under the given load conditions.



Figure 7. The amount of plastic strain in fully raised position



**Figure 8.** The amount of plastic strain in the initial safety position

## 4 CONCLUSION

The structural analysis of the safety leg for the vacuum road sweeper has demonstrated that the design is both robust and reliable. The finite element analysis (FEA) conducted under various loading conditions showed that the safety leg can withstand the dynamic and static loads during operation without experiencing significant stress or deformation.

In conclusion, the safety leg design meets the necessary performance criteria and provides a reliable solution for supporting the hopper under both static and dynamic loads. In the future works, it can be focus on optimizing the design for weight reduction without compromising strength and also investigating the long-term durability under repeated loading cycles.

## Acknowledgments

We extend our heartfelt thanks to Koluman Automotive Industry for their generous support and for granting us the opportunity to conduct this study, thanks to our colleague Onur Can Kirit for analyses support, thanks to our another colleague Tevfik Kaygisiz for design ideas, thanks to our another colleague Erkan Ozcan to give support to production process. Their contribution has been invaluable in the pursuit of this research.

## References

- [1] Ł. Gierz, W. Łykowski, G. Ślaski, and M. Nowakowski, "Design and strength analysis of a new construction of a sweeper with an independent surface copying system dedicated to small loaders and front loaders," *Journal of Physics: Conference Series*, vol. 2714, no. 1, art. no. 012013, 2024, doi: 10.1088/1742-6596/2714/1/012013.
- [2] S. Dheeraj and R. Sabarish, "Analysis of Truck Chassis Frame Using FEM," *Middle-East Journal of Scientific Research*, vol. 20, no. 5, pp. 656–661, 2014, doi: 10.5829/idosi.mejsr.2014.20.05.11375.





## An Approximate Q-Learning Approach to the Dynamic Pricing and Inventory Control Problem of Perishable Products

Tugce Yavuz<sup>\*1</sup>, Onur Kaya<sup>1</sup>

<sup>1</sup>Industrial Engineering, Eskisehir Technical University, Eskisehir, Türkiye

---

### Abstract

In today's developed countries, 40 per cent of fresh food is wasted before it can be consumed. An effective pricing and inventory control policy is important to ensure that these perishable products are consumed before their short shelf life expires. In this study, we focus on solving the dynamic pricing and inventory control problem for perishable goods. In this problem, the problem size increases exponentially as the shelf life of the product increases. This increase in problem size requires an approximate solution method rather than an exact solution method such as Dynamic Programming. In this study, we use the Deep Q-Learning (DQL) algorithm to solve the problem and propose a problem-specific, time-efficient and robust to overestimation DQL approach. Unlike the literature, we consider the simultaneous sale of products of different ages with a shelf life of more than 2 periods. As a result of our comparisons with the dynamic programming algorithm and various heuristic algorithms, we see that the proposed approach achieves better results in a shorter time.

**Keywords:** *Deep Q-learning, Joint dynamic Pricing and inventory decision, Perishable products*

---



---

## Optimizing Workforce and Sub-Lot Scheduling in Seru Production Systems

Beren Gursoy Yilmaz<sup>\*1</sup>, Emre Cevikcan<sup>1</sup>, Omer Faruk Yilmaz<sup>2</sup>

<sup>1</sup>Department of Industrial Engineering, Istanbul Technical University, Istanbul, Türkiye

<sup>2</sup>Department of Industrial Engineering, Karadeniz Technical University, Trabzon, Türkiye

---

### Abstract

Seru Production Systems (SPS) have increasingly replaced traditional assembly lines due to the growing product variety and demand variability in response to customer needs. SPS merges the effectiveness of assembly lines with the adaptability of jobshop manufacturing, offering features such as designability, transportability, waste reduction, simplified operation, and efficient worker transfer capabilities. These attributes make SPS attractive to businesses seeking higher operational efficiency, enhanced flexibility, and rapid responsiveness to market changes. This study focuses on workforce scheduling problems for SPS with a variable sub-lot size division strategy. To address this problem, an optimization model is proposed to minimize makespan. Small-sized problem instances are solved using the GAMS 24.7/CPLEX solver. Sensitivity analysis is conducted to determine which parameters most significantly affect objective function. Computational results demonstrate that the number of serus and sub-lots are the most critical factors influencing makespan in the seru system. The findings highlight the importance of optimizing these parameters to enhance the overall operational performance of SPS. The outcomes suggest that careful consideration of seru and sub-lot configurations can lead to substantial improvements in production efficiency and adaptability, making SPS a viable and competitive alternative to traditional production methodologies.

**Keywords:** Seru production system, Worker scheduling, Variable sub-lot size, Worker transfer

---

## 1 INTRODUCTION

In today's competitive environment, traditional assembly lines are insufficient due to their long cycle times, inability to meet changing demands, unbalanced workloads, and reliance on single-skilled workers [1]. Therefore, small and medium sized enterprises have transitioned their production systems from traditional assembly lines to SPS, which combine flexibility and efficiency. SPS integrates the flexibility of job shop production system with the efficiency of traditional assembly lines, creating a dynamic, human-oriented, and cellular manufacturing system [2]. The reconfigurability and worker empowerment features of SPS offer businesses greater flexibility and responsiveness compared to traditional assembly lines. Moreover, SPS's ability to facilitate worker transfers, known as Shojinka, ensures effective cycle times, allowing businesses to swiftly adapt to changing customer demands [3]. Shojinka refers to the practice of adjusting the number of workers on a production line according to fluctuating demand levels, thereby maintaining optimal efficiency without overstaffing or underutilizing resources [4].

Since SPS needs to meet high variety and low volume demand, determining lot sizes in these production systems is crucial. The lot sizing problem has been a subject of research since the 1960s [5], and over time, lot streaming strategies have become a popular approach in various manufacturing systems to improve operational efficiency [6]. Essentially, there are three main lot streaming strategies: equal, variable, and consistent sub-lots. Considering the autonomous and independent nature of serus, variable and consistent sub-lots are often used interchangeably. Equal sub-lots maintain fixed sub-lot sizes, while variable sub-lots provide flexibility in sub-lot sizes [7]. Implementing lot streaming strategies facilitates production in smaller and variable lot sizes and allows workers to quickly transition between different serus, enhancing adaptability and efficiency within the production system [8]. With SPS's adaptability, companies can ensure performance continuity and gain a competitive advantage in changing conditions.

The development of SPS emerged in response to the economic and competitive pressures experienced by the Japanese electronics industry in the 1990s [9]. Since then, SPS has become increasingly widespread, garnering significant attention and being extensively studied in the literature. Initially, studies focused on problem related to

the design and implementation of SPS. [10] examined the seru design problem, focusing specifically on converting conveyor assembly lines into SPS. [11] devised a multi-objective line-cell conversion model for transforming assembly lines into seru systems to reduce the number of workers without decreasing productivity. [12] formulated a mathematical model to determine the optimal number, capacity, and placement of serus to achieve maximum efficiency and flexibility. Most of these studies emphasized that converting traditional assembly lines to serus reduces lead times and production costs.

Subsequently, researchers' attention turned to assignment and scheduling problems, which are fundamental concerns within SPS. [13] tackled the multi-skilled worker training and assignment problem for SPS, employing a mathematical programming model and designing a two-phase heuristic method to minimize the total system cost. [14] studied the multi-skilled worker assignment problem in SPS, accounting for worker heterogeneity, and proposed a mathematical model with the objective of minimizing workload imbalance. [15] utilized an exact solution method to address seru scheduling problems that involve past-sequence-dependent setup times and learning effects. [16] formulated an integer programming model for the seru scheduling problem, aiming to minimize total weighted completion time. Moreover, the integration of lot streaming problems in SPS has broadened the framework in the literature. [17] employed a genetic algorithm for the order acceptance and scheduling problem in SPS, considering limited processing capability, promised delivery time, and lot streaming concurrently. [18] proposed an optimization model for the seru scheduling and worker assignment problem, considering lot streaming, processing sequence, and setup time. [19] developed a branch-and-bound algorithm to solve lot streaming and learning effects within a seru scheduling problem. [20] investigated seru balancing and assignment problems with a focus on lot streaming, finding that the division of lots significantly enhances system performance. Additionally, [3] addressed the seru and worker scheduling problem, introducing the concept of worker transfer to the literature. This novel concept underscores its significant contributions to enhancing SPS performance. Collectively, numerous studies on scheduling and assignment problems have also contributed various methodologies and managerial insights that enhance the effectiveness and efficiency of SPS. A majority of these studies emphasize that optimizing both worker and product scheduling can significantly reduce lead times, improve resource utilization, and boost operational efficiency within SPS.

Therefore, this study aims to tackle the worker and sub-lot scheduling problem for SPS employing an optimization model designed to minimize makespan. The model includes operational-level decisions such as determining variable sub-lot sizes and scheduling workers, including transferring between serus. The GAMS 24.7/CPLEX solver is utilized to solve small-sized problems efficiently. Furthermore, sensitivity analysis is conducted to assess the impact of various parameters on the objective function, including the number of serus, sub-lots, workers, and lot sizes. Based on the computational results, the study provides several important insights to fully leverage the potential of the proposed model. These insights can guide businesses in optimizing their workforce scheduling and sub-lot division strategy to enhance the efficiency and responsiveness of their production systems.

The study is organized as follows: Section 2 presents the materials and methods, including the problem description and optimization model. Section 3 provides a detailed analysis of the computational results and sensitivity analysis. Lastly, Section 4 presents the conclusions, along with recommendations for future studies.

## 2 MATERIAL AND METHOD

### 2.1 Problem Description

This study deals with the challenge of scheduling workers and lot/sub-lot assignments in SPS. In this framework, each SPS functions as an independent system comprising one or more serus, where workers execute tasks to meet customer demands. Each SPS can produce various product types, with known tasks, sequences, and processing times for each type. The number of serus and workers is predetermined. A seru can be operated by a single worker, who performs all tasks, or by multiple workers, each handling non-overlapping tasks. Each task is allocated to a single station, although a station can handle multiple tasks. Similarly, while a sub-lot is designated to one seru, a seru can process multiple sub-lots from different product types. This study aims to minimize the makespan by scheduling sub-lots and workers, ensuring that a worker does not undertake tasks for two different sub-lots simultaneously. The completion time of a sub-lot in the SPS is affected by the assignments of lot/sub-lot to seru and worker to seru, along with the scheduling decisions, which are made concurrently. Important decisions include determining the utilization of each SPS for sub-lot size, assigning workers to tasks within serus, and making scheduling decisions for production. Addressing facility utilization and worker assignment for SPS involves considering the cycle time within each SPS for each customer demand. Given the ability to adjust the number of workers, it is essential to use Shojinka to effectively adapt the SPS to meet customer demand.

The following assumptions are taken into consideration while formulating the problem.

- All sub-lots are ready for operation in the SPS from time zero.
- Sub-lot preemption is prohibited; once operation starts, it must proceed without interruption.
- A group of workers is ready and available for task assignments from time zero.
- The execution times for tasks associated with each type of product are predefined.

## 2.2 Optimization Model

In the following, the optimization model along with modules are presented. All notations, indices, parameters, and decision variables are summarized in below.

### Indices and Sets

$l$ : Index of lots  $\{l \in L\}$

$l', l''$ : Index of sub-lots  $\{l' \in L'_l, l'' \in L''_l\}$

$p$ : Index of product  $\{p \in P\}$

$t$ : Index of tasks  $\{t \in T\}$

$w$ : Index of worker  $\{w \in W\}$

$s$ : Index of serus  $\{s \in S\}$

### Parameters

$\varphi_{l'p}$ : Indicates if sub-lot  $l'$  belongs to product  $p$ , 1; otherwise, 0

$e_{tp}$ : Indicates if product type  $p$  requires task  $t$  to be performed, 1; otherwise, 0

$m_{tp}$ : The operation time of task  $t$  from product  $p$

$Q_l$ : The quantity of lot  $l$

$I$ : A large constant

$N_{l'}$ : The maximum number of workers permitted in a seru for sub-lot  $l'$

$\Omega$ : The upper bound on the number of sub-lots from a lot ( $|L| \times \Omega = \sum_l |L'_l|$ )

### Decision variables

$C_{max}$ : Makespan

$c_{l'}$ : The completion time of sub-lot  $l'$

$p_{l'}$ : The processing time of sub-lot  $l'$

$\kappa_{l'}$ : The starting time of the operation for sub-lot  $l'$

$B_{wl'}$ : Indicates if the tasks of sub-lot  $l'$  are accomplished by worker  $w$ , 1; otherwise, 0

$\omega_{l'l''}$ : Indicates if the starting time of the operation for sub-lot  $l'$  is smaller than the starting time of the operation for sub-lot  $l''$ , 1; otherwise, 0

$\varpi_{l'l''}$ : Indicates if the completion time of sub-lot  $l'$  is larger than the completion time of sub-lot  $l''$  in period  $h$ , 1; otherwise, 0

$g_{wl'}$ : The cycle time of worker  $w$  for sub-lot  $l'$

$\varepsilon_{l'}$ : The cycle time of sub-lot  $l'$

$A_{l's}$ : The auxiliary variable to calculate the size of sub-lot  $l'$  in seru  $s$

$\delta_{l'}$ : The quantity of sub-lot  $l'$

$x_{l's}$ : Indicates if seru  $s$  is employed for sub-lot  $l'$ , 1; otherwise, 0

$y_{l'l''s}$ : Indicates sub-lot  $l'$  precedes sub-lot  $l''$  in seru  $s$ , 1; otherwise, 0

$z_{ll'}$ : Indicates if sub-lot  $l'$  is included as a sub-lot of lot  $l$ , 1; otherwise, 0

$\phi_{wtl'}$ : Indicates if worker  $w$  performs task  $t$  of sub-lot  $l'$ , 1; otherwise, 0

### Objective functions

$$\text{Min } f = C_{max} \quad (1)$$

The makespan objective is formulated by Equation (1).

### Subject to

$$C_{max} \geq c_{l'} \tag{2}$$

$$c_{l'} = p_{l'} + \kappa_{l'} \quad l' \in L'_l, l \in L \tag{3}$$

$$p_{l'} = \varepsilon_{l'} \times \delta_{l'} \quad l' \in L'_p, l \in L \tag{4}$$

$$\varepsilon_{l'} \geq g_{wl'} \quad w \in W, l' \in L'_p, l \in L \tag{5}$$

$$g_{wl'} = \sum_{p \in P} \sum_{t \in T} m_{tp} \times \varphi_{l'p} \times \phi_{wtl'} \quad w \in W, l' \in L'_l, l \in L \tag{6}$$

$$\sum_{l' \in L'_l} \delta_{l'} = Q_l \quad l \in L \tag{7}$$

$$\mathcal{B}_{wl'} \geq \phi_{wtl'} \quad w \in W, t \in T, l' \in L'_l, l \in L \tag{8}$$

$$\sum_{w \in W} \phi_{wtl'} = z_{ll'} \times \sum_{p \in P} \varphi_{l'p} \times e_{tp} \quad t \in T, l' \in L'_l, l \in L \tag{9}$$

$$\sum_{w \in W} \mathcal{B}_{wl'} \leq N_{l'} \quad l' \in L'_l, l \in L \tag{10}$$

$$\kappa_{l''} - c_{l'} + I \times (3 - y_{l'l''s} - x_{l's} - x_{l''s}) \geq 0 \quad l' \in L'_l, l'' \in L''_l, l' \neq l'', l \in L \tag{11}$$

$$\delta_{l'} / I \leq z_{ll'} \leq \delta_{l'} \quad l' \in L'_l, l \in L \tag{12}$$

$$z_{ll'+1} \leq z_{ll'} \quad l' \in L'_l, l \in L \tag{13}$$

$$y_{l'l''s} + y_{l''l's} \leq 1 \quad l' \in L'_l, l'' \in L''_l, l' \neq l'', l \in L \tag{14}$$

$$y_{l'l''s} + y_{l''l's} \leq x_{l's} + x_{l''s} \quad l' \in L'_l, l'' \in L''_l, l' \neq l'', l \in L \tag{15}$$

$$x_{l's} + x_{l''s} - 1 \leq y_{l'l''s} + y_{l''l's} \quad l' \in L'_l, l'' \in L''_l, l' \neq l'', l \in L \tag{16}$$

$$\sum_{s \in S} x_{l's} = z_{ll'} \quad l' \in L'_l, l \in L \tag{17}$$

$$A_{l's} \leq x_{l's} \times I \quad s \in S, l' \in L'_l, l \in L \tag{18}$$

$$\delta_{l'} = \sum_{s \in S} A_{l's} \quad s \in S, l' \in L'_l, l \in L \tag{19}$$

$$3 - (\omega_{l'l''} + \varpi_{l'l''}) \geq \mathcal{B}_{wl'} + \mathcal{B}_{wl''} \quad l' \in L'_l, l'' \in L''_l, l' \neq l'', l \in L \tag{20}$$

$$I \times \omega_{l'l''} \geq \kappa_{l''} - \kappa_{l'} \quad l' \in L'_l, l'' \in L''_l, l' \neq l'', l \in L \tag{21}$$

$$I \times \varpi_{l'l''} \geq c_{l'} - \kappa_{l''} \quad l' \in L'_l, l'' \in L''_l, l' \neq l'', l \in L \tag{22}$$

$$x_{l's}; \phi_{wtl'}; y_{l'l''s}; z_{ll'}; \varpi_{l'l''}; \omega_{l'l''}; \alpha_{ws}; \mathcal{B}_{wl'} \in \{0,1\} \quad w \in W, t \in T, s \in S, l' \in L'_l, l'' \in L''_l, l \in L, \tag{23}$$

$$\delta_{l'}; c_{l'}; p_{l'}; \kappa_{l'}; \varepsilon_{l'}; A_{l's}; g_{wl'}; C_{max} \geq 0 \quad w \in W, s \in S, l' \in L'_l, l \in L, \tag{24}$$

Equation (2) determines the makespan. Equation (3) compute that the completion time of a sub-lot, with the processing times calculated using Equation (4). Equation (5) stipulates that the cycle time for a sub-lot in a seru must be at least as long as the cycle times of workers performing tasks for the same sub-lot in the same seru. To determine cycle times for all workers assigned to the same seru, Equation (6) is employed. Equation (7) ensures that the total size of sub-lots for a given lot matches the lot size. Equation (8) mandates that if a worker is assigned to perform a task for a sub-lot, the worker must also be assigned to the sub-lot, maintaining consistency in worker assignments. Equation (9) specifies that if a task must be performed for a sub-lot and this sub-lot is part of the relevant lot, a worker must be allocated to perform the task. To limit the number of workers assigned to each sub-lot in a seru, Equation (10) is used. Equation (11) establishes the relationship between the starting and completion times of successive sub-lots within a seru. It ensures that if sub-lot  $l'$  precedes sub-lot  $l''$ , the starting time of sub-lot  $l''$  must be later than the completion time  $l'$ . Equation (12) prevents a sub-lot from being included in the scheduling decision if its size is not greater than zero. According to Equation (13), a sub-lot cannot be included in the schedule unless the previous sub-lot from the same lot is also considered. Equations (14-16) prevent the

simultaneous processing of different sub-lots in the same seru by establishing the processing order of sub-lots. Equation (17) guarantees that each considered sub-lot is assigned to a seru, allowing for two distinct sub-lots from the same lot to be assigned to different serus. Equations (18) and (19) ensure that a sub-lot is assigned to only one seru, and its size is greater than zero. To fully leverage Shojinka, Equations (20-22) are designed to facilitate worker transfer within the SPS. Finally, Equations (23) and (24) specify the binary and sign restrictions for the variables, respectively, ensuring that the model's constraints are met.

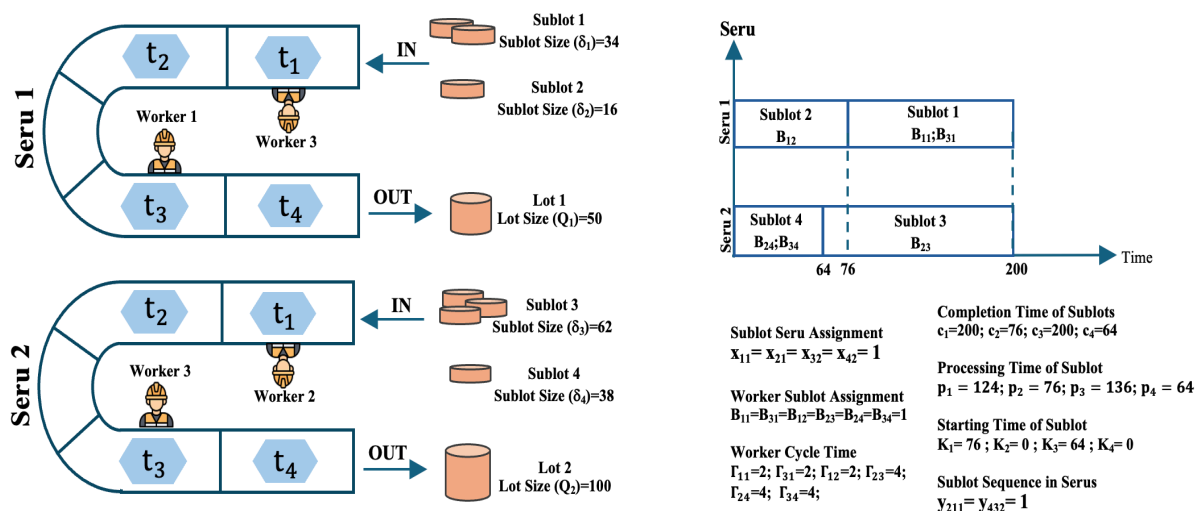
### 3 RESULTS

In this section, a numerical example is provided to validate the proposed model using hypothetical data. The analysis was performed with the GAMS 24.7/CPLEX software on a computer equipped with a 2.50 GHz processor and 16 GB of RAM. The example considered two lots with sizes of 100 and 50 units, divided into a total of 4 sub-lots, and processed by 2 serus and 3 workers over 1 period. The scenario included 4 tasks, each requiring 1 minute of processing time, and involved 1 product type. The evaluation aimed to identify effective sub-lot sizes and optimal worker assignments within the SPS to minimize the makespan. The model focused on determining the most efficient scheduling of sub-lots and the strategic allocation of workers to serus. By doing so, it sought to enhance the overall production efficiency and reduce the maximum completion time. The results from this numerical example are illustrated in Figure 1, which shows the optimized schedule and sub-lot distribution. Additionally, the detailed model statistics are presented in Table 1.

**Table 1.** Model statistics

Objective Function	200
CPU Time (sec.)	6.48
Number of Constraints	24
Number of Continuous Variables	8
Number of Binary Variables	7
Number of Iterations	30193

As illustrated in the figure, the first lot of 50 units is subdivided into two sub-lots of 34 and 16 units, both assigned to the first seru. The second lot, consisting of 100 units, is divided into two sub-lots of 63 and 37 units, assigned to the second seru. By transferring a third worker, each seru has two workers, which facilitates the completion of tasks for each sub-lot. Specifically, the task requirements are 2 tasks for the first sub-lot, 2 tasks for the second sub-lot, 4 tasks for the third sub-lot, and 4 tasks for the fourth sub-lot. In the first seru, processing begins with the second sub-lot, while the second seru starts with the fourth sub-lot. The strategic scheduling of sub-lots and workers, considering the given processing times, leads to an effective workflow within each seru. The overall makespan, calculated based on the allocated resources and scheduled tasks, amounts to 200 minutes. This timeline includes the complete processing of all sub-lots in their respective serus, demonstrating how the coordination of sub-lot assignments and worker distribution can impact the total production time. This example highlights the importance of careful scheduling and resource management in achieving optimal production efficiency.



**Figure 1.** Illustration of results

### 3.1 Sensitivity Analysis

In this section, a sensitivity analysis is conducted to investigate the parameters that affect the proposed model. Specifically, the impact of four key parameters on the objective function is examined. These parameters include the number of serus, the number of workers, the number of sub-lots, and the lot size. By analysing these factors, we aim to understand how variations in these parameters influence the performance and efficiency of the model. This analysis helps identify the critical parameters that significantly affect the model’s outcomes and provides insights for optimizing the system.

The results of the comparative analysis are presented in Table 2. The table illustrates the impact of simultaneous changes in parameters at different levels on the makespan. Specifically, the analysis examines how variations in the number of serus, the number of workers, the number of sub-lots, and the lot size influence the overall performance. Each parameter is tested at multiple levels to observe its effect under different conditions. Additionally, the CPU values of the model are provided in the table, offering insights into the computational efficiency of the model. This comprehensive analysis helps in understanding the sensitivity of the model to various parameter changes and assists in identifying optimal configurations.

**Table 2.** Result of sensitivity analysis

	NS	NW	NST	Makespan	CPU (sec.)
Lot Sizes: 50/100	2	3	4	200	6.48
	4	3	4	270	8.76
	2	4	4	180	10.94
	4	4	4	250	10.30
	2	5	4	170	11.49
	4	5	4	230	12.94
	2	3	6	155	11.84
	4	3	6	190	13.44
	2	4	6	145	12.59
	4	4	6	170	15.98
	2	5	6	170	14.95
	4	5	6	190	14.49
Lot Sizes: 100/200	2	3	4	285	25.04
	4	3	4	295	26.05
	2	4	4	260	28.49
	4	4	4	270	30.48
	2	5	4	255	31.94
	4	5	4	270	34.13
	2	3	6	270	31.35
	4	3	6	210	32.43
	2	4	6	200	35.95
	4	4	6	230	36.21
	2	5	6	250	34.05
	4	5	6	260	37.24

NS: Number of seru, NW: Number of workers, NST: Number of sub-lots

Figure 2 illustrates the impact of each parameter on the objective function. When the number of serus is increased, while holding other parameters constant, the makespan initially decreases. This suggests that a higher number of serus can improve system efficiency up to a certain point. However, beyond a specific threshold, further increases in the number of serus do not yield additional benefits, indicating diminishing returns. Similarly, increasing the number of workers and the number of sub-lots both result in a reduction of the objective function. This demonstrates that having more workers and dividing lots into smaller sub-lots can enhance productivity and reduce overall processing time. Conversely, increasing the lot sizes leads to an increase in the makespan, as it raises the

demand and the number of products to be produced. Larger lot sizes require more time and resources to process, which negatively impacts the system’s efficiency.

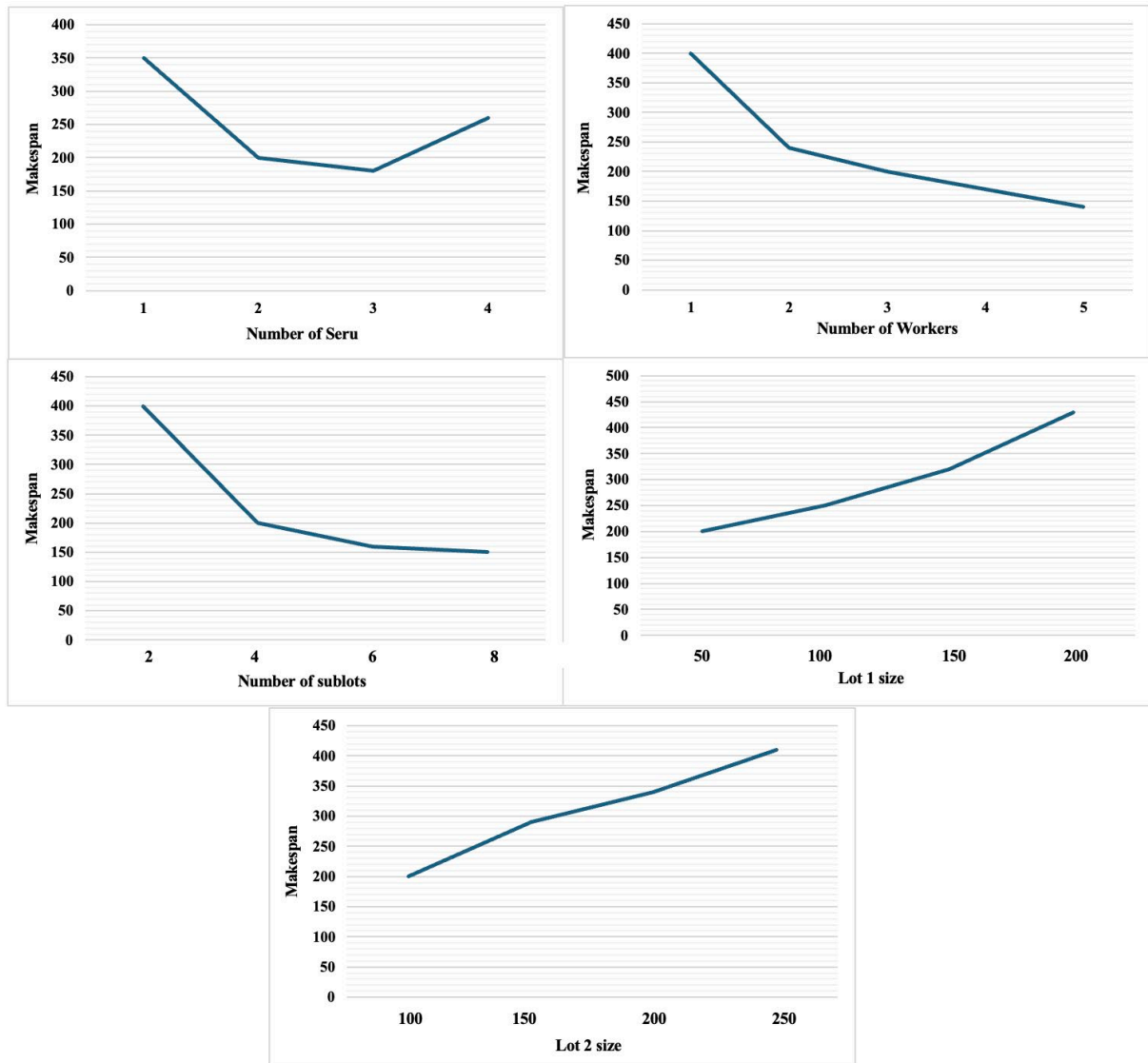


Figure 2. Results of parameter analysis

#### 4 CONCLUSION

This study explores the problem of scheduling workers and sub-lots within SPS, focusing on operational-level decisions such as worker transfers and variable sub-lot sizes. An optimization model is developed to minimize the makespan, providing valuable insights into the impact of different sub-lot sizes and worker transfers on the overall efficiency of the SPS. The findings highlight the crucial role of operational planning in optimizing production schedules and resource utilization. The problem is solved using GAMS 24.7/CPLEX solver, leading to the development of an optimal schedule for workers and sub-lots to achieve the minimum makespan. Following this, a sensitivity analysis examines the parameters influencing the model. The results reveal that the number of serus, the number of sub-lots, and the number of workers are critical parameters affecting the model's performance. These findings underscore the importance of carefully selecting these parameters to optimize system efficiency. Furthermore, the analysis indicates that the interplay between these parameters can significantly influence the system's productivity, suggesting that a balanced approach is necessary for effective operational management. The study also emphasizes the potential for adaptive strategies that respond to dynamic changes in production environments, thereby enhancing flexibility and resilience.

To guide future studies and address the limitations of this research, several recommendations are proposed. Firstly, exploring a multi-objective model of this problem can account for divergent objectives, such as cost minimization



and quality maximization, providing a more comprehensive understanding of trade-offs. Secondly, incorporating uncertainties such as demand and processing time into the problem can enhance its realism and applicability to real-world scenarios. Thirdly, developing metaheuristic algorithms can help manage large-scale problem instances, offering robust solutions in a computationally efficient manner. Lastly, investigating tactical-level decisions for workforce scheduling in SPS can provide deeper insights into operational efficiency and strategic planning, ultimately leading to more effective resource allocation and process improvements. Additionally, integrating advanced data analytics and machine learning techniques could further refine the optimization process by predicting trends and identifying patterns that inform decision-making. Collaborative research efforts that combine theoretical modelling with practical case studies can validate the proposed methods and facilitate the translation of findings into industry practices. Overall, this study lays a foundation for future research aimed at enhancing the efficiency and effectiveness of SPS through informed operational and strategic planning.

### Acknowledgments

This work was supported by the Scientific and Technological Research Council of Türkiye (TUBITAK) BIDEB 2214-A.

### References

- [1] C. Liu, N. Yang, W. Li, J. Lian, S. Evans, and Y. Yin, "Training and assignment of multi-skilled workers for implementing seru production systems," *The International Journal of Advanced Manufacturing Technology*, vol. 69, no. 5–8, pp. 937–959, Jun. 2013
- [2] F. Liu, B. Niu, M. Xing, L. Wu, and Y. Feng, "Optimal cross-trained worker assignment for a hybrid seru production system to minimize makespan and workload imbalance," *Computers & industrial engineering*, vol. 160, pp. 107552–107552, Oct. 2021
- [3] O. F. Yilmaz, "Attaining flexibility in seru production system by means of Shojinka: An optimization model and solution approaches," *Computers & Operations Research*, vol. 119, art. no. 104917, Jul. 2020
- [4] O. F. Yilmaz, "Operational strategies for seru production system: a bi-objective optimisation model and solution methods," *International Journal of Production Research*, vol. 58, no. 11, pp. 3195–3219, Sep. 2019
- [5] S. Reiter, "A system for managing job-shop production," *The Journal of Business*, vol. 39, no. 3, art. no. 371, Jan. 1966,
- [6] B. Gürsoy Yilmaz and O. F. Yilmaz, "Lot streaming in hybrid flowshop scheduling problem by considering equal and consistent sublots under machine capability and limited waiting time constraint," *Computers & Industrial Engineering*, vol. 173, art. no. 108745, Nov. 2022
- [7] Z. Zhang, L. Shao, and Y. Yin, "PSO-based algorithm for solving lot splitting in unbalanced seru production system," *International journal of industrial and systems engineering*, vol. 35, no. 4, pp. 433–433, Jan. 2020.
- [8] B. Gürsoy Yilmaz, Ö.F Yilmaz, and E. Çevikcan, "Lot streaming in workforce scheduling problem for seru production system under Shojinka philosophy," *Computers & industrial engineering*, vol. 185, pp. 109680–109680, Nov. 2023
- [9] Y. Fujita, K. Izui, S. Nishiwaki, Z. Zhang, and Y. Yin, "Production planning method for seru production systems under demand uncertainty," *Computers & Industrial Engineering*, vol. 163, art. no. 107856, Jan. 2022.
- [10] C. Liu, W. Li, J. Lian, and Y. Yin, "Reconfiguration of assembly systems: From conveyor assembly line to serus," *Journal of Manufacturing Systems*, vol. 31, no. 3, pp. 312–325, Jul. 2012
- [11] Y. Yu, J. Tang, W. Sun, Y. Yin, and I. Kaku, "Reducing worker(s) by converting assembly line into a pure cell system," *International Journal of Production Economics*, vol. 145, no. 2, pp. 799–806, Oct. 2013.
- [12] W. Sun, Q. Li, C. Huo, Y. Yu, and K. Ma, "Formulations, features of solution space, and algorithms for line-PureSeruSystem conversion," *Mathematical Problems in Engineering*, vol. 2016, pp. 1–14, Jan. 2016.
- [13] K.-C. Ying and Y.-J. Tsai, "Minimising total cost for training and assigning multiskilled workers in seru production systems," *International Journal of Production Research*, vol. 55, no. 10, pp. 2978–2989, Jan. 2017
- [14] J. Lian, C. Liu, W. Li, and Y. Yin, "A multi-skilled worker assignment problem in seru production systems considering the worker heterogeneity," *Computers & Industrial Engineering*, vol. 118, pp. 366–382, Apr. 2018.
- [15] Y. Jiang, Z. Zhang, X. Gong, and Y. Yin, "An exact solution method for solving seru scheduling problems with past-sequence-dependent setup time and learning effect," *Computers & industrial engineering*, vol. 158, pp. 107354–107354, Aug. 2021.
- [16] Z. Zhang, X. Song, H. Huang, X. Zhou, and Y. Yin, "Logic-based Benders decomposition method for the seru scheduling problem with sequence-dependent setup time and DeJong's learning effect," *European*

- Journal of Operational Research*, vol. 297, no. 3, pp. 866–877, Mar. 2022
- [17] J. Wang, N. Ye, and Y. Peng, “Case studies on design for seru manufacturing,” *Procedia Manufacturing*, vol. 39, pp. 1090–1096, 2019
- [18] L. Shen, Z. Zhang, and Y. Yin, “An improved genetic algorithm for seru scheduling problem with worker assignment considering lot-splitting,” *International Journal of Applied Decision Sciences*, vol. 14, no. 6, pp. 710–710, Jan. 2021.
- [19] Z. Zhang, X. Song, H. Huang, Y. Yin and B. Lev, “Scheduling problem in seru production system considering DeJong’s learning effect and job splitting,” *Annals of Operations Research*, vol. 312, pp. 1119–1141, May. 2022.
- [20] Q. Miao, Z. Bai, X. Liu, and Muhammad Awais, “Modelling and numerical analysis for seru system balancing with lot splitting,” *International Journal of Production Research*, vol. 61, no. 21, pp. 7410–7433, Nov. 2022.



---

## Development of Beneficiation Flow Diagram of Malatya-Kuluncak Rare Earth Oxide (NTO) Ore

Gafure Ersever Angur<sup>\*1</sup>

<sup>1</sup>Rare Earth Elements Application and Research Center, Munzur University, Tunceli, Türkiye

---

### Abstract

The increase in the variety and quantity of metals used in the industry increases the amount and prices of metals needed worldwide due to the developing industry and technological developments. Rare earth elements (REE), thanks to their properties, are used in products that require high technology and have strategic and critical importance. Rare earth elements (REE) are one of the most critical raw materials with ever-increasing demand and supply risk within the scope of transformation to green technologies. China is the largest supplier in the world, accounting for production of more than 95% of the world's rare earth oxides (REO). To reduce the influence of China on the REE market, some countries have started to develop their own national strategies for the production and use of REE-bearing resources. As a result of the exploration activities carried out by the MTA institution, the second largest REE deposit of our country is located in Malatya - Kuluncak. Although there is no production activity, grade and reserve studies are currently carried out by MTA. In light of the information obtained from MTA, Malatya-Kuluncak mineralization field has a reserve of 128,214,000 tons and a NTO grade of 0.18%. Considering this grade percentage, there is a total of 230,785 tons of NTO in the mineralization area. In this study, a flow chart has been proposed for the beneficiation of Malatya-Kuluncak REE ore based on the studies in the literature.

**Keywords:** *Strategic raw material, Rare earth elements, Mineral processing*

---



## $A_\alpha$ – Statistical Limit Superior and Limit Inferior via Ideals

Mustafa Gulfirat<sup>\*1</sup>

<sup>1</sup>Department of Mathematics, Ankara University, Ankara, Türkiye

---

### Abstract

In this study, we deal with notations of  $A$  – statistical limit superior and limit inferior. Firstly, we define a new type of statistical limit points using the concept of  $A$  – statistical convergence with the rate of  $o(a_n)$  via ideals where  $A = (a_{nk})$  is a non-negative regular summability matrix and  $a = (a_n)$  is a positive non-increasing sequence. After that, we present some analogues of properties of  $A$  – statistical limit points of a sequence via ideals.

**Keywords:**  $A_\alpha$  – statistical convergence,  $A_\alpha$  – statistical limit points, Ideals, Ideal convergence, Statistical convergence with a rate via ideals

---



## Certain Aspects of Weak Statistical Convergence via Ideals

Mustafa Gulfirat\*<sup>1</sup>,

<sup>1</sup>*Department of Mathematics, Ankara University, Ankara, Türkiye*

---

### Abstract

The main object of this presentation is to define a new type of weak statistical convergence of a sequence in a normed space  $X$ . In [ICOMAA-2024, May 8-11, 2024], the presenter introduced a new type of the concept of statistical convergence with a rate using the ideals. In this presentation, we apply the concept of ideals to the weak statistical convergence with a rate. In addition, we also investigate some basic properties of the new concept.

**Keywords:** *Weak convergence, Continuous dual space, Ideal, Ideal convergence, Statistical convergence*

---



---

## Investigation of the Conductivity Mechanismus of ZnO/C<sub>10</sub>H<sub>10</sub>N<sub>2</sub> pn Heterojunction Produced by Spin Coating Method

Ramazan Demir\*<sup>1</sup>

<sup>1</sup>Technical Science Vocational School, Canakkale Onsekiz Mart University, Canakkale, Türkiye

---

### Abstract

In this research, a p-n heterojunction diode was fabricated using a p-type 4-amino-2-methylquinoline (C<sub>10</sub>H<sub>10</sub>N<sub>2</sub>) on an n-type zinc oxide (ZnO) film and its conductivity mechanism was studied. First, a thin ZnO film was deposited on an ITO substrate by spin coating. A (C<sub>10</sub>H<sub>10</sub>N<sub>2</sub>) film was then deposited on the ZnO film using the same technique. To investigate the transport mechanism, the log (I)–log (V) graph was plotted. The current-voltage characteristics were analyzed using the I~V<sup>m</sup> relationship, where V represents the voltage and m represents the power index. The m values were calculated for each region. We found m values from the slope of the graph in the first region, within the low voltage range of 0-1.24 volts, was 1.07, while in the second region, voltage 1.24-3.00 volts, it was 9.69 was. From these slope values we concluded that ohmic conduction predominates in the first area, while conduction limited by the trap charge predominates in the second area

**Keywords:** ZnO, 4-amino-2-methylquinoline, C<sub>10</sub>H<sub>10</sub>N<sub>2</sub>, Ohmic, Trap charge limited

---



---

## A Review of Using of Geopolymers -As an Immobilization Matrix- on Radioactive Waste Management

Furkan Cinar<sup>\*1</sup>, Sema Akyil Erenturk<sup>1</sup>

<sup>1</sup>Energy Institute, Istanbul Technical University, Istanbul, Türkiye

---

### Abstract

Population growth and the man-made climate crisis are increasing the importance of sustainable energy and waste management practices. The rising interest in nuclear energy is paralleled by an increasing trend towards the development of innovative materials. In this paper, we address an interesting topic, the use of geopolymers as immobilization matrices in radioactive waste management.

Geopolymers, which are mainly used in the construction industry, stand out as a high potential alternative to traditional materials due to their low leachability, high adsorption capacity, thermal and chemical resistance as well as their cost-effectiveness. Geopolymers are often compared to Portland cement (PC) in terms of durability, leaching resistance and waste loading capacities, and are considered to be a more environmentally friendly solution.

Although there are studies in the literature on the use of geopolymers to immobilize various wastes such as <sup>137</sup>C contaminated soils and used ion exchange resins, there has been a significant increase in the number of publications in recent years. The International Atomic Energy Agency's (IAEA) Coordinated Research Project (CRP) on geopolymers also aims to establish specific testing protocols to demonstrate the durability and suitability of geopolymers.

Geopolymers with high strength and adaptable gel network structure can effectively reduce radionuclide migration or dispersion in undesirable situations as immobilization matrix of radioactive wastes by meeting Waste Acceptance Criteria (WAC). On the other hand, there is still a long way to go in the development of analytical tools and technical processes for the synthesis of geopolymers on an industrial scale, geopolymerization kinetics, gel formation, determination of composition, morphology and microstructure of the structures.

**Keywords:** *Radioactive wastes, Geopolymer, Solidification, Immobilization, Hazardous waste management*

---

## 1 INTRODUCTION

Today with the human population exceeding the threshold of eight billion, it is obvious that it is necessary to reduce the negative impacts of production and consumption processes on the planet's ecosystem. When this situation is taken together with the goal of reducing greenhouse gas emissions to limit global warming as stated in the Paris Agreement, the importance of turning to clean energy emerges. Renewable energy sources, such as solar, wind, hydropower, and nuclear, play a vital role in reducing reliance on fossil fuels and mitigating climate impact.

The focus on nuclear energy is rising day by day due to factors current geopolitical reasons such as the Ukraine-Russia crisis. In addition to the 416 reactors worldwide with a total net electrical capacity of 374.7 GW(e), 59 reactors with a total net electrical capacity of 51.6 GW(e) are under construction [1, 2].

However, the expansion and increased use of nuclear energy brings with it the need for innovative technologies for radioactive waste management. In this context, the development of new materials to isolate radioactive wastes from the biosphere until their radioactivity drops to levels below established safety limits is being widely studied. It is extremely important that new alternative options are put forward in addition to widely accepted methods such as cementation, bituminization, confinement of radioactive wastes in glass and ceramic matrices. Geopolymers, which are mostly used in the construction industry, are one of the promising candidate materials studied for the immobilization and solidification of radioactive wastes with their properties. The reason for this interest is that geopolymers have low leachability, high adsorption capacity, high thermal and chemical resistance as well as being cost-effective [3].

## 2 PROPERTIES OF GEOPOLYMERS

Cement production has a high carbon footprint due to the limestone calcination process and the need for high temperatures to produce clinker. The production of one ton of Portland Cement (PC) results in the emission of about one ton of CO<sub>2</sub> [4]. The global industry of cement, product that mankind produces in the highest volume, is responsible for about 8% of anthropogenic CO<sub>2</sub> emissions [5]. Therefore, much effort is being devoted to developing more sustainable alternatives to PC [4]. Geopolymers are more environmentally friendly option for the construction sector compared to conventional Portland cement. One of their biggest advantages is that they can be produced from by-products such as fly ash from other industries [6].

Geopolymers are semi-crystalline amorphous materials synthesized by inducing and/or catalysing the polymerization reaction between aluminosilicate source materials and alkaline reagents by applying heat [6]. There are three-dimensionally bonded SiO<sub>4</sub> and AlO<sub>4</sub> in its structure [7]. SEM photographs of the geopolymer material are shown in Fig. 1 [8].

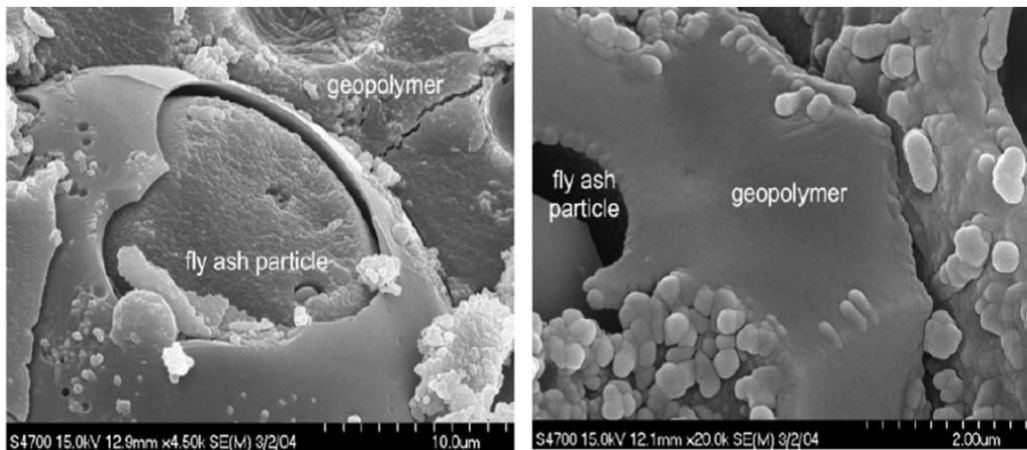


Figure 1. SEM photos of geopolymer material [8]

As seen in Fig. 2, it is possible to produce geopolymers by reacting aluminosilicate materials such as fly ash, metakaolin, calcined clay with alkaline activators containing alkali hydroxides, silicates, aluminates, carbonates and/or sulphates. The synthesis process of geopolymers can take place at room temperature or at temperatures as high as 90°C [9].

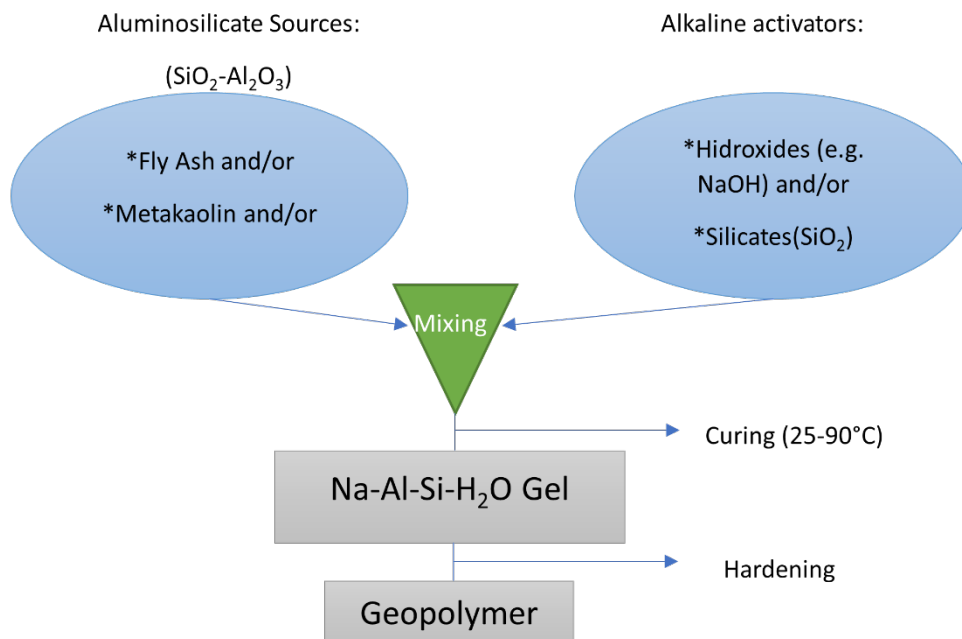
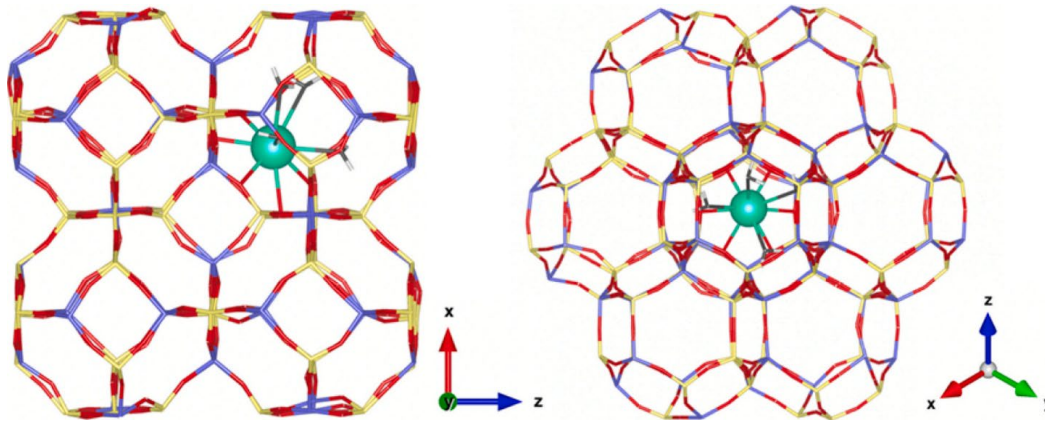


Figure 2. Geopolymer synthesis process [9]



Since the amorphous aluminosilicate compounds in the structure of zeolites are similar in geopolymers, their cation exchange properties are close to each other. Therefore, geopolymers have been successfully used to remove toxic metals from aqueous solutions [6]. Geopolymers behave like zeolites by retaining specific cations [10]. Geopolymers can also retain radioactive elements such as Cesium, Molybdenum and Strontium [11].

Fig. 3 shows the Cs ion trapped in the crystal structure of the geopolymer material.

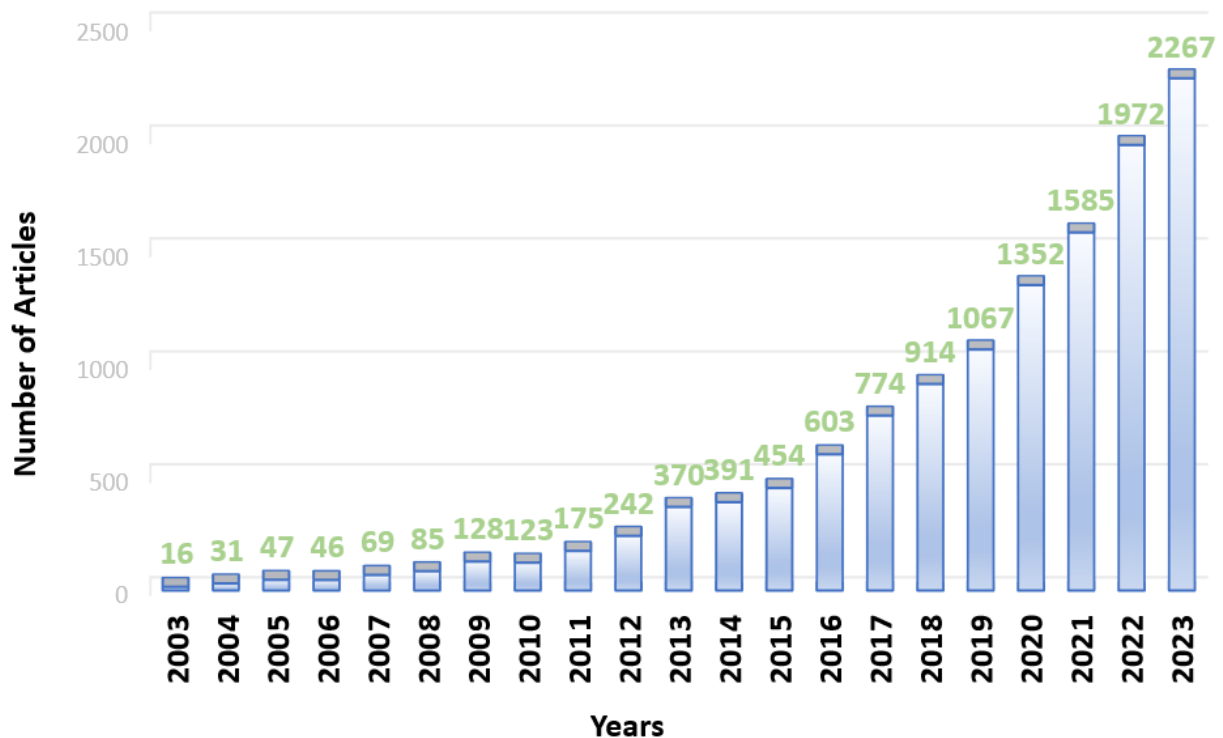


**Figure 3.** The Cs ion in the crystal structure of the geopolymer is represented by a turquoise sphere. The bonds between Si, Al and O atoms in the structure of the geopolymer are represented by yellow, purple and red coloured bars [4]

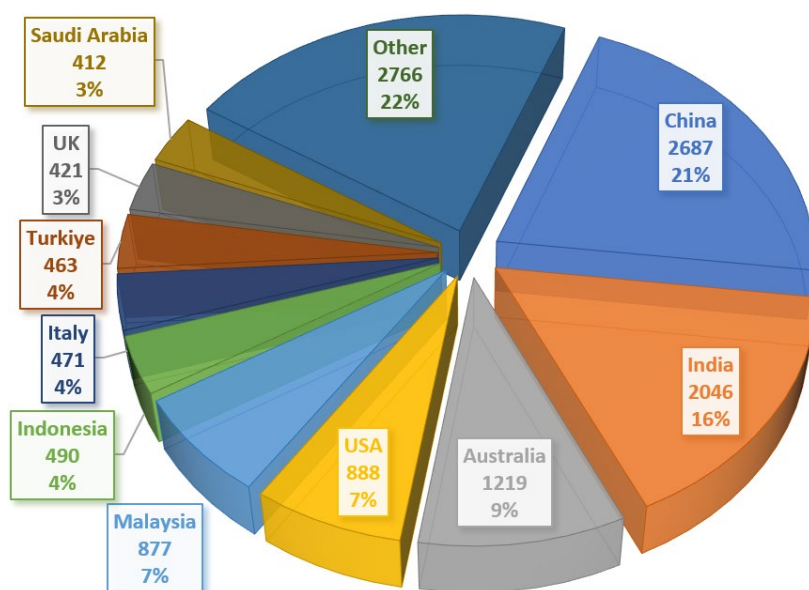
### 3 CURRENT LITERATURE REVIEW

The positive results of research into the properties and advanced applications of geopolymers have led to a growing research interest. As shown in Fig. 4, the increase between 2003 and 2023 has been dramatic.

The top ten countries that have recently shown great interest in research on geopolymers are shown in Fig 5.



**Figure 4.** Articles published on geopolymer materials between 2003-2023 in Scopus (Data extraction date: Jul. 04, 2024)



**Figure 5.** Articles published on geopolimer materials between 2003-2023 in Scopus (Data extraction date: Jul. 04, 2024)

Nearly all of the pores in the structure of geopolymers are meso or micropores, which means higher adsorbability and adsorption capacity for alkali metal ions [12, 13]. Thus, geopolymers appear as a highly usable material for radioactive waste management.

Research on geopolymers reveals that it is possible to use geopolimer waste forms to immobilize various wastes such as  $^{137}\text{Cs}$  contaminated soils, used ion exchange resins [14-20].

#### 4 C COMPARISON WITH TRADITIONAL METHODS

Geopolymer matrices are gaining a place next to the traditionally used glass, concrete, ceramic, bitumen matrices [3]. Multiple factors are considered in the evaluation of waste forms for radioactive waste management.

First of all, mechanical and thermal properties, fire resistance, leaching and biodegradability resistance should be proved to the long-term reliability of the waste form. In addition to, optimizing the waste loading factor without compromising the requirements of the Waste Acceptance Criteria (WAC) is crucial for waste volume reduction [21].

In the literature, geopolymers are most commonly compared with Portland cement. It was reported that the 28-day compressive strength of the geopolymer was measured in the interval of 50-80 MPa, while that of PC varied between 20 and 60 MPa [22]. For leaching resistance, after 42 days of leaching in deionized water at 25 °C, more than 40 times more  $\text{Cs}^+$  and 1000 times more  $\text{Sr}^{2+}$  was leached from PC than geopolymer [23].

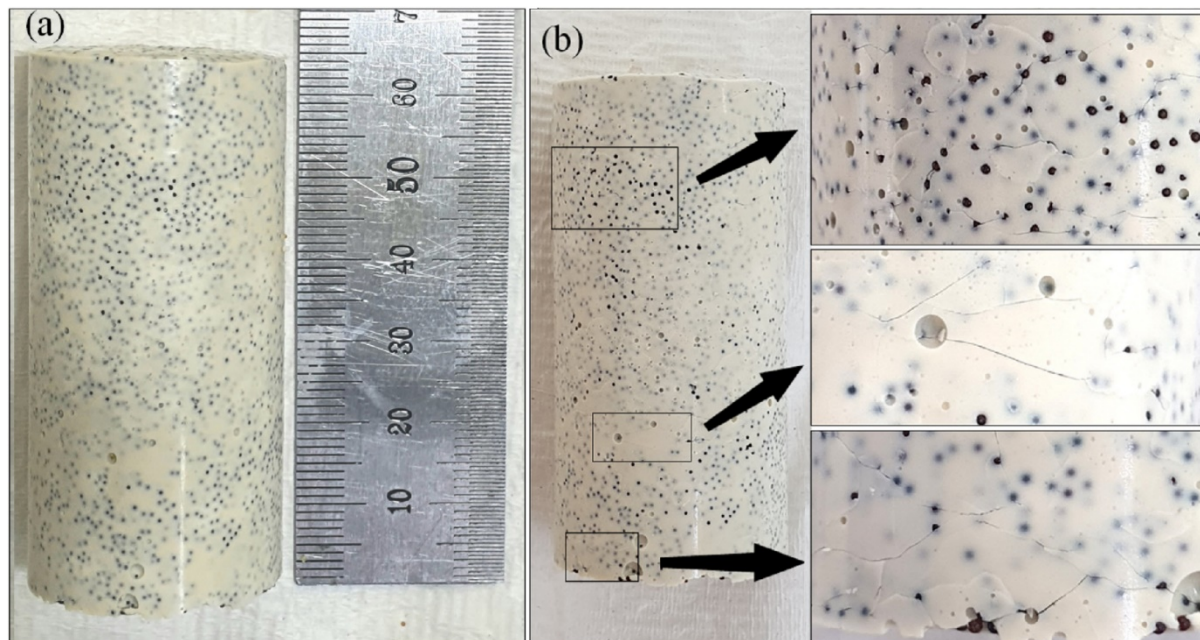
Leaching tests are key indicators of the safety of the waste storage and disposal system, as they show the degree of immobilization of radionuclides in a long-term perspective [24]. The superior structural stability of the geopolymer allows for higher waste loading capacities [25]. The physical changes in the form of geopolymer samples as the waste loading rate increases are shown in Fig. 6.



**Figure 6.** Cubic geopolymer samples containing recycled polyurethane powder (rPU). From left to right, rPU loading factor is 0%, 5% and 10% by weight [21]

According to the Japan Atomic Energy Agency, the amount of  $^{137}\text{Cs}$  leached when using metakaolin-based geopolymers was found to be  $<0.1\%$ , which is about 300 times less than cement [26].

Like others, geopolymer waste forms also suffer structural damage when exposed to water. As the ion exchange resin (IER) in a geopolymer matrix absorbs water and expands, the cracks formed in the material are shown in Fig. 7 [25].



**Figure 7.** Cracks in the geopolymer waste form containing ion exchange resin (IER); (a) before immersion in water (b) after immersion in water for 10 days [25].

Another difference between concrete and geopolymer matrices is the processing temperatures. The inevitable evaporation of highly volatile  $^{137}\text{Cs}$  during processes such as high-temperature melting/sintering, which is necessary for trapping radioactive waste in matrices such as glass, ceramics and SYNROC, will produce secondary airborne contaminants [27, 28].

However, geopolymers can be prepared at room temperature below  $100\text{ }^{\circ}\text{C}$ , thus avoiding  $\text{Cs}^+$  volatilization [29-31].

The stability of the waste matrix depends on the composition of the geopolymer mixture. There is a strong correlation between the amount of calcium in the base material of the geopolymer and the resistance to chemical attack. Geopolymers made from high calcium base material such as fly ash have been shown to be more vulnerable to sulphate attack and carbonation than those with low calcium content [32].

Different durability tests have been developed to demonstrate the safety function of geopolymer waste forms in the long term [33-36].

## 5 IAEA'S COORDINATED RESEARCH PROJECT

The IAEA launched a Coordinated Research Project (CRP) with the code T21029 on 6 September 2023 to demonstrate the performance of geopolymers and promote their use [37]. This project aims to build the scientific and technical knowledge base to support the development of specific test protocols to demonstrate the durability and suitability of geopolymer waste forms [37].

It is obvious that the IAEA, the largest authority in the field of nuclear energy, calling for research on geopolymers is an important sign of the potential of geopolymers.

As stated on the project website; geopolymers show significant promise in stabilizing radioactive waste, but also several tests need to be performed to ensure that the geopolymer waste form complies with the relevant storage and disposal Waste Acceptance Criteria [38].

The purpose of the tests is to determine the long-term durability performance of the waste form under storage and disposal conditions. Due to the lack of established international standards for evaluating the performance of geopolymers waste form, researchers have used various processes, particularly testing protocols established for cementitious matrices. Differences in the application of protocols and test procedures make it difficult to compare test results each other [37].

The IAEA's Coordinated Research Project (CRP) aims to address precisely these challenges. The CRP aims to compare established cementitious protocols with new procedures developed for geopolymer matrix test [37]. The IAEA's efforts to promote the use of geopolymers will help raise awareness among decision-makers on the use of geopolymers for radioactive waste management.

## 6 CONCLUSION

Geopolymers, also known as alkali-activated aluminosilicate binders, have the capability to effectively reduce radionuclide migration or dispersion by helping to immobilize and stabilize radioactive wastes. Geopolymers with low environmental impact have a composition that produces a high strength and adaptable gel network structure, thus complying with radioactive waste disposal requirements. It has a wide range of applications for the construction of future nuclear power plants and waste disposal facilities. It is foreseen that studies on the use of geopolymer matrices for the immobilization of nuclear waste will continue to increase.

Future research proposals for geopolymers include:

- New methods for the synthesis of geopolymers on an industrial scale should be developed.
- To explore the synthesis mechanism of various geopolymers, utilize advanced analytical tools to evaluate the kinetics of geopolymerization, gel formation and determine the composition, morphology and microstructure of the structures.
- Technical processes to characterize and improve the surface and interface properties of geopolymers are required to contribute to pollutant management at industrial scale [39].

## References

- [1] IAEA, "PRIS - Reactor status reports - In operation & suspended operation - By country," [Online], Jul. 09, 2024. Available: <https://pris.iaea.org/PRIS/WorldStatistics/OperationalReactorsByCountry.aspx>
- [2] IAEA, "PRIS - Reactor status reports - Under construction - By country," [Online], 2024. Available: <https://prs.iaea.org/PRIS/WorldStatistics/UnderConstructionReactorsByCountry.aspx>
- [3] R. O. Abdel Rahman, E. Phillip, C. Thye Foo, and N. Khairuddin, "On the Sustainable Utilization of Geopolymers for Safe Management of Radioactive Waste: A Review," *Sustainability*, vol. 15, art. no. 1117, Jan. 2023, doi: 10.3390/su15021117.
- [4] E. Duque-Redondo, K. Yamada, E. Masoero, J. Bañuelos Prieto, and H. Manzano, "Adsorption and migration of Cs and Na ions in geopolymers and zeolites," *Mater Today Commun*, vol. 36, art. no. 106496, 2023, doi: 10.1016/j.mtcomm.2023.106496.
- [5] S. A. Miller, A. Horvath, and P. J. M. Monteiro, "Readily implementable techniques can cut annual CO2 emissions from the production of concrete by over 20%," *Environmental Research Letters*, vol. 11, no. 7, art. no. 074029, 2016, doi: 10.1088/1748-9326/11/7/074029.
- [6] H. Castillo, H. Collado, T. Droguett, M. Vesely, P. Garrido, and S. Palma, "State of the art of geopolymers: A review," vol. 22, no. 1, pp. 108–124, 2022, doi: 10.1515/epoly-2022-0015.
- [7] J. Davidovits, "Geopolymers: Ceramic-like inorganic polymers," *Journal of Ceramic Science and Technology*, vol. 8, pp. 335–350, Jan. 2017, doi: 10.4416/JCST2017-00038.
- [8] F. Škvára, T. Jilek, and L. Kopecky, "Geopolymer Materials Based on Fly Ash," *Ceramics - Silikaty*, vol. 49, pp. 195–204, Jan. 2005.
- [9] J. Davidovits, *Geopolymer Chemistry and Applications*, Institut Géopolymère, 2008.
- [10] M. Y. Khalil and E. Merz, "Immobilization of intermediate-level wastes in geopolymers," *Journal of Nuclear Materials*, vol. 211, no. 2, pp. 141–148, 1994, doi: 10.1016/0022-3115(94)90364-6.
- [11] M. A. Salam, M. Mokhtar, S. M. Albukhari, D. F. Baamer, L. Palmisano, and M. R. Abukhadra, "Insight into the role of the zeolitization process in enhancing the adsorption performance of kaolinite/diatomite geopolymer for effective retention of Sr (II) ions; batch and column studies," *J Environ Manage*, vol. 294, art. no. 112984, 2021, doi: 10.1016/j.jenvman.2021.112984.

- [12] J. Provis, G. Lukey, and J. Van Deventer, "Do Geopolymers Actually Contain Nanocrystalline Zeolites? A Reexamination of Existing Results," *Chemistry of Materials - CHEM MATER*, vol. 17, May 2005, doi: 10.1021/cm050230i.
- [13] E. Ofer- Rozovsky, M. Haddad, G. Bar-Nes, and A. Katz, "The formation of crystalline phases in metakaolin-based geopolymers in the presence of sodium nitrate," *J Mater Sci*, vol. 51, May 2016, doi: 10.1007/s10853-016-9767-0.
- [14] J. Lee, B. Kim, J. Kang, J. Kang, won-S. Kim, and W. Um, "Comparative study between geopolymer and cement waste forms for solidification of corrosive sludge," *Journal of the Nuclear Fuel Cycle and Waste Technology (JNFCWT)*, vol. 18, pp. 465–479, Dec. 2020, doi: 10.7733/jnfcwt.2020.18.4.465.
- [15] J. Ahn, won-S. Kim, and W. Um, "Development of metakaolin-based geopolymer for solidification of sulfate-rich HyBRID sludge waste," *Journal of Nuclear Materials*, vol. 518, Mar. 2019, doi: 10.1016/j.jnucmat.2019.03.008.
- [16] G. Tan *et al.*, "Phosphoric acid-activated metakaolin-based geopolymer: Optimizing P/A molar ratio to solidify Cs+ and Sr2+ in nuclear waste," *Nuclear Engineering and Design*, vol. 424, art. no. 113300, 2024, doi: 10.1016/j.nucengdes.2024.113300.
- [17] X. Ke, S. A. Bernal, T. Sato, and J. L. Provis, "Alkali aluminosilicate geopolymers as binders to encapsulate strontium-selective titanate ion-exchangers," *Dalton Transactions*, vol. 48, no. 32, pp. 12116–12126, 2019, doi: 10.1039/C9DT02108F.
- [18] V. Cuccia, C. B. Freire, and A. C. Q. Ladeira, "Radwaste oil immobilization in geopolymer after non-destructive treatment," *Progress in Nuclear Energy*, vol. 122, art. no. 103246, 2020, doi: 10.1016/j.pnucene.2020.103246.
- [19] W.-H. Lee, T.-W. Cheng, Y.-C. Ding, K.-L. Lin, S.-W. Tsao, and C.-P. Huang, "Geopolymer technology for the solidification of simulated ion exchange resins with radionuclides," *J Environ Manage*, vol. 235, pp. 19–27, 2019, doi: 10.1016/j.jenvman.2019.01.027.
- [20] W. Lin, H. Chen, and C. Huang, "Performance study of ion exchange resins solidification using metakaolin-based geopolymer binder," *Progress in Nuclear Energy*, vol. 129, art. no. 103508, 2020, doi: 10.1016/j.pnucene.2020.103508.
- [21] E. Mossini *et al.*, "Pre-impregnation approach to encapsulate radioactive liquid organic waste in geopolymer," *Journal of Nuclear Materials*, vol. 585, art. no. 154608, 2023, doi: 10.1016/j.jnucmat.2023.154608.
- [22] M. L. Y. Yeoh *et al.*, "Mechanistic impacts of long-term gamma irradiation on physicochemical, structural, and mechanical stabilities of radiation-responsive geopolymer pastes," *J Hazard Mater*, vol. 407, art. no. 124805, 2021, doi: 10.1016/j.jhazmat.2020.124805.
- [23] P. He *et al.*, "Interplay between storage temperature, medium and leaching kinetics of hazardous wastes in Metakaolin-based geopolymer," *J Hazard Mater*, vol. 384, art. no. 121377, 2020, doi: 10.1016/j.jhazmat.2019.121377.
- [24] M. Ojovan, G. Varlakova, Z. Golubeva, and O. Burlaka, "Long-term field and laboratory leaching tests of cemented radioactive wastes," *J Hazard Mater*, vol. 187, pp. 296–302, Mar. 2011, doi: 10.1016/j.jhazmat.2011.01.004.
- [25] Y. Shin, B. Kim, J. Kang, H. Ma, and W. Um, "Estimation of radionuclides leaching characteristics in different sized geopolymer waste forms with simulated spent ion-exchange resin," *Nuclear Engineering and Technology*, vol. 55, no. 10, pp. 3617–3627, 2023, doi: 10.1016/j.net.2023.06.026.
- [26] N. Kozai *et al.*, "Sewage sludge ash contaminated with radiocesium: Solidification with alkaline-reacted metakaolinite (geopolymer) and Portland cement," *J Hazard Mater*, vol. 416, art. no. 125965, 2021, doi: 10.1016/j.jhazmat.2021.125965.
- [27] M. Xu, Y. Wu, and Y. Wei, "Stable solidification of silica-based ammonium molybdophosphate absorbing cesium using allophane: mechanical property and leaching studies," *J Radioanal Nucl Chem*, vol. 316, May 2018, doi: 10.1007/s10967-018-5887-0.
- [28] Z. Jing, Y. Yuan, W. Hao, and J. Miao, "Synthesis of pollucite with Cs-polluted incineration ash mixed with soil for immobilization of radioactive Cs," *Journal of Nuclear Materials*, vol. 510, Jul. 2018, doi: 10.1016/j.jnucmat.2018.07.047.
- [29] S. Bernal, J. Deventer, and J. Provis, *What Happens to 5 Year Old Metakaolin Geopolymers? the Effect of Alkali Cation*, Springer, 2015, doi: 10.1007/978-94-017-9939-3\_39.
- [30] C. Bai and P. Colombo, "Processing, properties and applications of highly porous geopolymers: A review," *Ceram Int*, vol. 44, no. 14, pp. 16103–16118, 2018, doi: 10.1016/j.ceramint.2018.05.219.
- [31] E. Ofer-Rozovsky *et al.*, "Cesium immobilization in nitrate-bearing metakaolin-based geopolymers," *Journal of Nuclear Materials*, vol. 514, pp. 247–254, 2019, doi: 10.1016/j.jnucmat.2018.11.003.
- [32] L. B. de Oliveira, A. R. G. de Azevedo, M. T. Marvila, E. C. Pereira, R. Fediuk, and C. M. F. Vieira, "Durability of geopolymers with industrial waste," *Case Studies in Construction Materials*, vol. 16, art. no. e00839, 2022, doi: 10.1016/j.cscm.2021.e00839.

- [33] R. O. Abdel Rahman and M. Ojovan, "Techniques to test cementitious systems through their life cycles," in *Sustainability of Life Cycle Management for Nuclear Cementation-Based Technologies*, 2021, pp. 407–430, doi: 10.1016/B978-0-12-818328-1.00018-6.
- [34] Z. Jiang, Z. H. Xu, Q. Shuai, P. Li, and Y. H. Xu, "Thermal Stability of Geopolymer - Sr Contaminated Zeolite A Blends," *Key Eng Mater*, vol. 727, pp. 1089–1097, 2017, doi: 10.4028/www.scientific.net/KEM.727.1089.
- [35] I. Bošković *et al.*, "Radiological and physicochemical properties of red mud based geopolymers," *Nuclear Technology and Radiation Protection*, vol. 33, pp. 188–194, Jun. 2018, doi: 10.2298/NTRP1802188B.
- [36] R. O. Abdel Rahman and M. I. Ojovan, "6 - Sustainability of cementitious structures, systems, and components (SSC's): Long-term environmental stressors," in *Sustainability of Life Cycle Management for Nuclear Cementation-Based Technologies*, R. O. Abdel Rahman and M. I. Ojovan, Eds., Woodhead Publishing, 2021, pp. 181–232, doi: 10.1016/B978-0-12-818328-1.00001-0.
- [37] IAEA, "Geopolymers as an immobilization matrix for radioactive waste," [Online], Jul. 10, 2024. Available: [www.iaea.org/projects/crp/t21029](http://www.iaea.org/projects/crp/t21029)
- [38] IAEA, "NEW CRP: Geopolymers as an immobilization matrix for radioactive waste (T21029)," [Online], 2023. Available: [https://www.iaea.org/sites/default/files/styles/original\\_image\\_size/public/crpgeopolymer.png?itok=jP9OVc7Y](https://www.iaea.org/sites/default/files/styles/original_image_size/public/crpgeopolymer.png?itok=jP9OVc7Y)
- [39] M. El Alouani *et al.*, "A comprehensive review of synthesis, characterization, and applications of aluminosilicate materials-based geopolymers," *Environmental Advances*, vol. 16, art. no. 100524, 2024, doi: 10.1016/j.envadv.2024.100524.



---

## Recovery of Critical Metals from Spent Li-Ion Batteries by Deep Eutectic Solvents (DESs) as Green Approach

Ceren Erust<sup>\*1</sup>

<sup>1</sup>Munzur University Rare Earth Elements Application and Research Center, TR62100, Tunceli, Türkiye

---

### Abstract

DESs as the non-toxic, low-cost, and safe approaches are proposed by various investigations for the extraction of metals from spent Li-Ion batteries. Battery cathode material contains critical metals such as Li, Co, Ni, and Mn. In this study, ChCl:Urea and ChCl:Urea:EG as DESs were designed for comparison investigations. The leaching results indicated that temperature has a direct effect on the extraction of critical metals in presence of all DESs. ChCl:Urea:EG has an optimal extraction rate (Li:98%, Co:40%, Ni:41%, and Mn:35%). Kinetics modelling results indicated that the mixed control model by shrinking core model (diffusion and chemical control) was the optimal model fitting with coefficient of determination ( $R^2$ )>0.90 and activation energies between 13-42KJ/mol.

**Keywords:** Critical metals, Deep eutectic solvent, Green chemistry, Recovery, Li-ion batteries

---



## Different Machine Learning Models with Mushroom Comparison

Idil Sila Gonenc<sup>\*1</sup>, Muhammet Cakmak<sup>2</sup>

<sup>1</sup>Mechanical Engineering, Sinop University, Sinop, Türkiye

<sup>2</sup>Computer Engineering, Sinop University, Sinop, Türkiye

---

### Abstract

This study examines the performance of machine learning models for determining whether mushrooms are edible or poisonous using the Mushroom Dataset from the UCI Library. Given the significance of accurately identifying mushrooms—some of which are nutritious or medicinal while others pose serious health risks—this classification problem holds considerable importance. Traditional methods, which often demand expert knowledge and extensive research, are time-consuming. In contrast, machine learning offers a more efficient and effective solution. The dataset underwent rigorous preprocessing, including modal imputation, one-hot encoding, z-score normalization, and feature selection, to ensure data quality and enhance model performance. It consists of 9 columns detailing features such as cap diameter, cap shape, gill attachment, gill color, stem height, stem width, stem color, and season, with the target class indicating edibility (0 for edible, 1 for poisonous). The study employed three machine learning models—Random Forest, Support Vector Classifier (SVC), and Logistic Regression—to determine the most effective approach for mushroom classification. The Random Forest model demonstrated the highest accuracy with a success rate of 99.2%, indicating its robustness in handling this classification task. The SVM model achieving a success rate of 64.4% and the Logistic Regression model showed a lower but notable performance with a 62.5% success rate. These findings underscore the critical role of data preprocessing and model selection in achieving high classification accuracy. The success of machine learning models in this study has significant implications for applications in agriculture and food safety, providing a foundation for developing precise and rapid mushroom classification methods. This research contributes to the ongoing exploration of machine learning's potential in enhancing food safety and supports future studies aimed at improving classification techniques for various biological datasets.

**Keywords:** Mushroom dataset, Binary classification, Machine learning, Random forest, SVC, Logistic regression, Data preprocessing, Model performance

---





---

## Factors Affecting Deterioration of Wall Paintings

**Ozge Karadeniz\*<sup>1</sup>, Evin Caner<sup>1</sup>**

*<sup>1</sup>Department of Conservation and Restoration of Cultural Properties, Institute of Social Sciences, Ankara University, Ankara, Türkiye*

---

### **Abstract**

Wall paintings are a significant part of humanity's cultural heritage and have existed as a widespread art form worldwide since ancient times. One of the earliest examples of wall paintings is the negative and positive handprints made on cave walls during the Upper Paleolithic period, around 30,000 BCE. Over time, these paintings developed technically, and detailed designs were typically applied on plaster layers. The materials and techniques used in wall paintings vary depending on the region and the artist's access to materials. Important types of plaster include clay, lime, gypsum, and pozzolan. These materials were used to harden the plaster layer and ensure the paint adhered to the surface. Additionally, the pigments used in wall paintings are classified as natural mineral, artificial mineral, natural organic, synthetic organic, and metal pigments. These pigments determine the colors and durability of the paintings. Wall paintings deteriorate over time for various reasons, and the factors causing this deterioration cover a wide range. Factors such as humidity, rain, frost, salts, microorganisms, higher plants, insects, animals, birds, and bats, light, temperature, wind, atmospheric pollution, dust, vibration, vandalism, flooding, the use of poor-quality materials, defective construction techniques, and incorrect conservation practices contribute to the deterioration.

The aim of this study is to emphasize the importance of thoroughly examining and understanding the factors that cause deterioration in wall paintings for comprehending the deteriorations and selecting the appropriate conservation and restoration methods. Correctly identifying the factors that cause deterioration is crucial not only for preserving the historical and artistic values of wall paintings and ensuring their longevity but also for applying the correct methods in future conservation and restoration works and contributing to the preservation of cultural heritage.

**Keywords:** *Wall painting, Fresco, Secco, Deterioration, Conservation, Restoration*

---



## Correlation Analysis with the Help of Vector

Ramazan Simsek<sup>\*1</sup>

<sup>1</sup>*Department of Mathematics and Science Education, Faculty of Education, Bayburt University, Bayburt, Türkiye*

---

### Abstract

Correlation is a measure of the change in any two variables together and takes a value between +1 and -1. Correlation analysis is a statistical concept and involves the calculation of the relationship between variables, the direction and severity of this relationship. If the collinearity value is positive, it means that there is a linear relationship between the variables in the same direction, and if it is negative, it means that there is a relationship in the opposite direction. In this study, we will first express the variables whose correlation will be calculated as a centralized vector. Then we will calculate the relationship between the vectors with the help of scalar product and find the correlation coefficient.

**Keywords:** *Vector, Scalar product, Correlation, Correlation coefficient*

---



## Grape Puree-Added and Freeze-Dried Yoghurt Drops: Enumeration of Lactic Acid Bacteria and Determination of Some Physical Properties

Sebahat Oztekin <sup>\*1</sup>

<sup>1</sup>Department of Food Engineering, Bayburt University, Bayburt, Türkiye

### Abstract

This study examined freeze-dried yoghurt drops containing fresh grape purees, focusing on the enumeration of surviving lactic acid bacteria (LAB) and the assessment of various physical properties, including water activity, color ( $L^*$ ,  $a^*$ ,  $b^*$  values), and ash content. Yoghurt was mixed with fresh grape purees in varying ratios (5%, 10%, and 20%) before being freeze-dried to produce yoghurt drops. The survival rates of yogurt bacteria, specifically *Lactobacillus bulgaricus* and *Streptococcus thermophilus*, were determined using MRS (De Man-Rogosa-Sharp) and M17 agar media, respectively. The results showed that both the addition of fresh grapes (5% and 10%) and the freeze-drying process significantly influenced bacterial counts. Notably, the LAB survival rate remained high, indicating the process preserved the viability of these essential yoghurt-making microorganisms. The total lactic acid bacteria survived at least 10.0 log cfu/g dry matter, demonstrating the feasibility of maintaining probiotic benefits in the final product. The addition of grapes also enhanced the total phenolic content and antioxidant activity of the yoghurt drops. Increased grape puree content led to higher water activity, moisture content,  $L^*$  value, and ash content. These findings suggest that yoghurt drops enriched with fresh grapes and processed through freeze-drying can be produced successfully, retaining favorable physical properties and high survival rates of lactic acid bacteria. This innovative product offers a promising way to deliver the health benefits of yoghurt and grapes in a convenient and stable form, appealing to health-conscious consumers and potentially expanding the market for functional foods.

**Keywords:** Yoghurt, Freeze-drying, Functional food, Yoghurt bacteria

## 1 INTRODUCTION

Yoghurt, a popular fermented dairy product, is widely consumed due to its beneficial health properties, primarily attributed to the presence of lactic acid bacteria (LAB). Among these, *Lactobacillus bulgaricus* and *Streptococcus thermophilus* are traditionally used probiotic LAB in the yoghurt production [1]. These symbiotic bacteria play a crucial role in promoting gut health and enhancing the immune system [2]. The incorporation of fruit purees, such as Cornelian, Morello Chery and Rose hip marmalade, grape molasses and date pulp, and grape puree into yoghurt products has gained attention not only for the added nutritional value but also for the potential to enhance flavor and appeal to consumers seeking functional foods. In addition, the grape purees boost the total phenolic content and antioxidant activity of the freeze-dried yoghurt drops, providing additional health benefits. [3].

Freeze-drying a method known for preserving the bioactive compounds and probiotic viability in food products, has emerged as a promising technique for developing innovative yoghurt-based snacks and also as a space food. This innovative technique can help to produce functional and nutritionally-enhanced snack for babies, athletes, or even for astronauts [4]. Freeze drying (lyophilization) involves quickly freezing a product to preserve its nutritional and sensory qualities. The frozen material is then exposed to a vacuum, causing the frozen water to sublime. This process creates a porous structure that allows for quick rehydration and retains flavor compounds. The freeze-dried product can be consumed as is, rehydrated, or used as an ingredient in other formulations. Lyophilization preserves nutritional and sensory qualities, significantly reduces weight, enhances solubility, extends shelf life at moderate temperatures, and allows for customizable rehydration levels [5].

This study investigates freeze-dried yoghurt drops infused with fresh Isabella grape (*Vitis labrusca*) puree at varying concentrations (5%, 10%, and 20%). The research focuses on the enumeration of lactic acid bacteria to evaluate the probiotic potential, alongside the assessment of key physical properties such as water activity, color ( $L^*$ ,  $a^*$ ,  $b^*$  values), and ash content. By understanding these parameters, the study aims to optimize product quality and contribute to the development of innovative, health-oriented dairy products with extended shelf life and enhanced functional benefits.

## 2 MATERIAL AND METHOD

### 2.1 Preparation of Freeze-dried Yoghurt Drops

First of all, yoghurt is traditionally made using a combination of *Lactobacillus bulgaricus* and *Streptococcus thermophilus*. The temperature was set to 43-45 °C during yoghurt-making process. Then, fresh grapes (flesh and skin) were pureed and added to yoghurt (5%, 10%, and 20%) and mixed properly. The yoghurt-grape puree were then subjected to a freeze-drying process to produce the final yoghurt drops. This technique preserved the probiotic bacteria and enhances the shelf-life of the product (Figure 1).

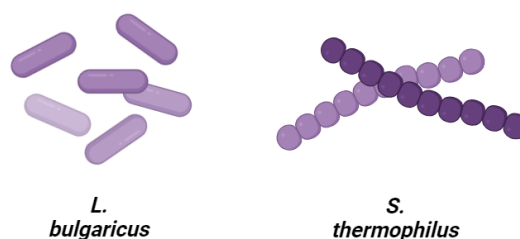


**Figure 1.** Preparation steps of grape puree-added and freeze-dried yoghurt drops

The survival of LAB was evaluated through microbiological analyses;

- *L. bulgaricus*: MRS (De Man-Rogosa-Sharp), double-layered, 37 °C for 72 hours.
- *S. thermophilus*: M17 agar media, under aerobic incubation at 37 °C for 48 hours.

*L. bulgaricus* is essential for the fermentation process in yoghurt, contributing to its distinctive flavor and texture. Its high survival rate in the freeze-dried yoghurt drops is crucial for maintaining the product's health benefits. *S. thermophilus* has a symbiotic relationship with *L. bulgaricus* with to create the perfect balance of acidity and creaminess. Its survival during the freeze-drying process ensures the preservation of the yoghurt's probiotic properties (Figure 2).

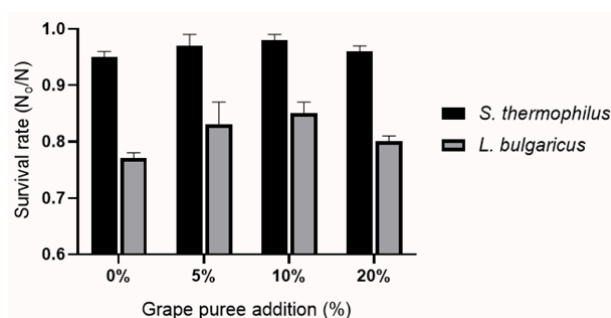


**Figure 2.** Morphological properties of *Lactobacillus bulgaricus* and *Streptococcus thermophilus*

The water activity, moisture content [6], color (Hunterlab  $L^* a^* b^*$ ) [7], ash [8], antioxidants (1,1- diphenyl-2-picrylhydrazyl; DPPH) [9] and total phenolic contents (Folin ciocalteu) [10] of grape puree-added and freeze-dried yoghurt drops were determined in further steps.

## 3 RESULTS

The results showed that freeze-drying preserved high LAB survival rates (at least 10.0 log cfu/g dry matter) in both plain and grape-added yoghurts, ensuring the yoghurt drops retained their probiotic benefits (Figure 3).



**Figure 3.** Survival ratio (N/N<sub>0</sub>) of *Streptococcus thermophilus* and *Lactobacillus bulgaricus* in grape puree-added and freeze-dried yoghurt drops

The results indicated that *S. thermophilus* had better survival rates than *L. bulgaricus* after freeze-drying. This aligns with previous studies showing that *S. thermophilus* is more resistant to freeze-drying, while *L. bulgaricus* is more susceptible due to increased membrane permeability [11].

Color was measured with a Hunterlab Colorflex-EZ colorimeter, recording values as  $L^*$  (lightness),  $a^*$  (redness), and  $b^*$  (yellowness). These values represent luminosity, and chromaticity on the red-green and blue-yellow axes [10]. The addition of grape purees caused a decrease in the  $L^*$  and  $b^*$  values but increase in  $a^*$  value, resulting in a more vibrant and appealing visual appearance (Table 1).

**Table 1.** Color analysis of grape puree-added and freeze-dried yoghurt drops

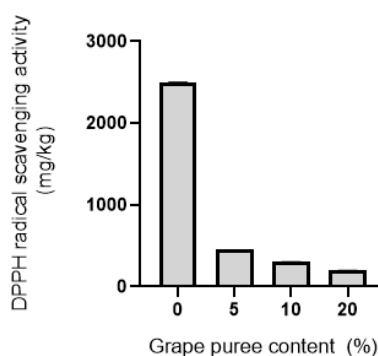
Grape-puree ratio (%)	$L$	$a$	$b$	$\Delta E$
0	90.26 ± 0.11	-1.80 ± 0.05	8.05 ± 0.11	18.46
5	49.40 ± 0.03	8.76 ± 0.15	5.30 ± 0.33	16.01
10	30.01 ± 0.12	10.74 ± 0.03	3.28 ± 0.41	17.06
20	15.31 ± 2.40	24.78 ± 0.17	1.45 ± 0.03	9.40

Grape puree incorporation increased the ash content of the freeze-dried yoghurt drops, indicating a higher mineral content and potential nutritional benefits (Table 2).

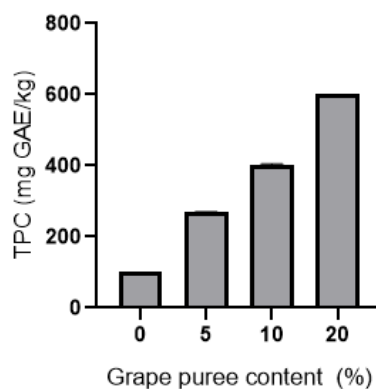
**Table 2.** Proximate analysis of grape puree-added and freeze-dried yoghurt drops

Grape-puree ratio (%)	Moisture content (% wb)	Water activity	Ash content	pH
0	5.16 ± 0.05	0.33 ± 0.01	6.90 ± 0.15	4.10 ± 0.01
5	3.42 ± 0.03	0.33 ± 0.15	7.40 ± 0.33	3.90 ± 0.01
10	2.05 ± 0.12	0.30 ± 0.03	8.50 ± 0.41	3.60 ± 0.01
20	1.50 ± 0.40	0.28 ± 0.17	9.23 ± 0.03	3.56 ± 0.01

The grape-puree added freeze-dried yoghurt samples showed enhanced antioxidant activity (DPPH radical scavenging activity; low DPPH scavenging activity indicates high antioxidant activity as the grape puree concentration increases) together with having high total phenolic content (Figure 4 and 5).



**Figure 4.** DPPH radical scavenging activity of grape-puree added lyophilized yoghurt drops



**Figure 5.** Total phenolic content (mg GAE/kg) of grape-puree added lyophilized yoghurt drops

## 4 CONCLUSION

The study found that adding fresh grapes at 10% to yoghurt and freeze-drying it increased the LAB survival rate (in both plain and grape-added yoghurts) remained high (at least 10.0 log cfu/g dry matter) after the freeze-drying process, ensuring the yogurt drops retained their probiotic benefits. In all cases, the survival rate of *S. thermophilus* was higher than that of *L. bulgaricus*. The addition of grapes (20%) also enhanced phenolic content, antioxidant activity, and significantly influenced physical properties like moisture content, acidity and color. These findings confirm that freeze-dried yoghurt drops enriched with fresh grapes can maintain both probiotic benefits and desirable physical qualities.

## References

- [1] H. Horiuchi and Y. Sasaki, "Effect of oxygen on symbiosis between *Lactobacillus bulgaricus* and *Streptococcus thermophilus*," *J. Dairy Sci.*, vol. 95, no. 6, pp. 2904–2909, 2012.
- [2] R.-A. Munteanu-Ichim, C.-M. Canja, M. Lupu, C.-L. Bădărașu, and F. Matei, "Tradition and Innovation in Yoghurt from a Functional Perspective—A Review," *Fermentation*, vol. 10, no. 7, art. no. 357, 2024.
- [3] Z. Tarakci and E. Kucukoner, "Physical, chemical, microbiological and sensory characteristics of some fruit-flavored yoghurt," *Yuzuncu Yil Universitesi Vet. Fakultesi Derg.*, vol. 14, no. 2, pp. 10–14, 2003.
- [4] E. Venir, M. Del Torre, M. L. Stecchini, E. Maltini, and P. Di Nardo, "Preparation of freeze-dried yoghurt as a space food," *J. Food Eng.*, vol. 80, no. 2, pp. 402–407, 2007.
- [5] G. dos Santos, R. I. Nogueira, and A. Rosenthal, "Powdered yoghurt produced by spray drying and freeze drying: a review," *Brazilian J. Food Technol.*, vol. 21, art. no. e2016127, 2018.
- [6] G. dos Santos, T. P. Nunes, M. Silva, A. Rosenthal, and A. A. C. Pagani, "Development and acceptance of freeze-dried yogurt" powder yogurt," *Int. Food Res. J.*, vol. 25, no. 3, pp. 1159–1165, 2018.
- [7] K. K. Hnin, M. Zhang, S. Devahastin, and B. Wang, "Combined infrared freeze drying and infrared drying of rose-flavored yogurt melts—Effect on product quality," *Food Bioprocess Technol.*, vol. 13, pp. 1356–1367, 2020.
- [8] E. A. Ismail, A. A. Aly, and A. A. Atallah, "Quality and microstructure of freeze-dried yoghurt fortified with additives as protective agents," *Heliyon*, vol. 6, no. 10, 2020.
- [9] J.-M. Sung *et al.*, "Effects of freeze-dried mulberry on antioxidant activities and fermented characteristics of yogurt during refrigerated storage," *Korean J. food Sci. Anim. Resour.*, vol. 35, no. 6, art. no. 807, 2015.
- [10] M. Demirkol and Z. Tarakci, "Effect of grape (*Vitis labrusca* L.) pomace dried by different methods on physicochemical, microbiological and bioactive properties of yoghurt," *LWT*, vol. 97, pp. 770–777, 2018.
- [11] B. Koc, M. S. Yilmazer, P. Balkir, and F. K. Ertekin, "Spray drying of yogurt: Optimization of process conditions for improving viability and other quality attributes," *Dry. Technol.*, vol. 28, no. 4, pp. 495–507, 2010.



## Contamination by Pesticides of Water and Health Using Artificial Neural Networks

**Benzidane Chahrazed<sup>\*1</sup>, Bouharati Khawla<sup>2</sup>, Fenni Mouhamed<sup>1</sup>**

<sup>1</sup>Faculty of Natural Science and Life, UFAS Setif1 University, Algeria

<sup>2</sup>Laboratory of Health and Environment, Faculty of Medicine, UFAS Setif1 University, Algeria

---

### Abstract

Pesticides are considered groundwater contaminants, especially in agricultural areas. The chemical composition of these products is often harmful to human health. The degree of contamination depends on several parameters such as rainfall, the nature of the soil, the microbiological composition of the rhizosphere, the depth of the groundwater, etc. Given this situation, it is very difficult to model such a phenomenon using conventional mathematical techniques in order to determine the impact on the health of the population. In this study, a technique of artificial intelligence including artificial neural networks is proposed. Because neural networks have the ability to support multiple combined variables, their application in this area is adequate.

Based on field data, we have established a predictive model that associates input parameters with their effects on public health as the output variable of the system. This allows upstream action on the quality and quantity of pesticides and chemicals used in agriculture to preserve the public health of the inhabitants of these areas

**Keywords:** *Groundwater, Pesticides, Public health, ANN*

---



## **Nutrient-Rich Biofertilizers: The Role of Spirulina Sp and Microalgae in Soil Health Enhancement**

**Charef Nassira<sup>1</sup>, Tamer Fatma Zohra<sup>1</sup>, Saada Zakia<sup>1</sup>, Belaid Boutheina<sup>1</sup>, Bougueroua Karima<sup>1</sup>, Elleuch Jihen<sup>1</sup>, Nasri Hichem<sup>1</sup>**

*<sup>1</sup>Laboratory of Biodiversity and Pollution of Ecosystems, Department of Biology, University of Chadli Bendjdid El Tarf, Algeria*

---

### **Abstract**

The adoption of sustainable agricultural practices is increasingly imperative in addressing global food security and environmental challenges. Microalgae, characterized by their renewable nature and nutritional richness, offer a unique opportunity to revolutionize conventional farming techniques. This work delves into the fabrication of organic fertilizer from microalgae cultivation, showcasing its potential to foster eco-friendly agricultural systems while enhancing soil health and crop productivity. Among these, *Spirulina* sp, a filamentous cyanobacterium renowned for its nutrient profile, takes center stage in addressing nutritional deficiencies. Harvested from Oubeira Lake and carefully cultivated, *Spirulina* biomass, alongside other microalgae strains, becomes integral to the development of eco-friendly agriculture fertilizers. The overarching objective of this endeavor is clear: to pioneer biofertilizers that minimize reliance on environmentally damaging chemicals, promoting the well-being of ecosystems, animals, and human health. Bloom collected from Oubeira Lake in October 2022, *spirulina* sp were isolated then cultured using Zarrouk's medium in a culture room at  $35 \pm 2$  °C. The culture is then harvested by centrifugation, and the biomass is freeze dried then preserved at -80 °C until further analysis. *Spirulina* biomass in addition to other microalgae strains will be used for the fabrication of the agriculture fertilizer.

**Keywords:** *Spirulina sp., Biofertilizers, Sustainable agriculture, Chemical fertilizer, Environment risque*

---





## Growth Control of Cyanobacteria and Cyanotoxins by Biological Methods

Tamer Fatma Zohra\*<sup>1</sup>, Charef Nassira<sup>1</sup>, Nasri Hichem<sup>1</sup>

<sup>1</sup>Laboratory of Biodiversity and Pollution of Ecosystems, Department of Biology, University of Chadli Bendjdid El Tarf, Algeria

---

### Abstract

The cyanobacteria blooms are a serious threat to water safety. *Microcystis* sp. is a species of cyanobacteria that can form harmful algal blooms in water bodies. Cyanobacterial toxins are discharged into the surrounding environment through the senescence and lysis of blooms. Three cyanobacterial genera that are potentially toxigenic and known for forming blooms are *Microcystis*, *Anabaena*, and *Oscillatoria*. These genera pose hazards due to their ability to produce secondary metabolites and endotoxins. The use of aquatic macrophyte to combat nuisance algae is a promising and environmentally friendly solution. In this work, we evaluated the inhibitory effect of 1% aqueous extracts of *Nymphaea alba* leaves on the growth of *Microcystis* sp. Purified strains of *Microcystis* sp. were exposed for 12 days to 1% aqueous extracts from the leaves of *Nymphaea alba*. Results suggest that the cell density of *Microcystis* sp. cell density decreased compared with the control group, equivalent to 81%, and the concentration of chlorophyll a decreased. This confirms the power of this macrophyte to control the intensive growth of *Microcystis* sp.

**Keywords:** *Cyanobacteria, Microcystis sp, Macrophytes, Nymphaea alba*

---



## **Spirulina Sp - Cultivation, Production, and Applications**

**Saada Zakia<sup>\*1</sup>, Charef Nassira<sup>1</sup>, Tamer Fatma Zohra<sup>1</sup>, Belaid Bouthaina<sup>1</sup>, Elleuch Jihen<sup>1</sup>, Nasri Hichem<sup>1</sup>**

*<sup>1</sup>Ecosystem Biodiversity and Pollution Laboratory, Bio Marine Department, Chadli Ben Jdid El Tarf University, Algeria*

---

### **Abstract**

Microalgae are recognized as a source of numerous active compounds of interest. These include hydrocolloids, phenolic compounds, pigments, vitamins and oligominerals, which are of great interest in the pharmaceutical, par pharmaceutical and cosmetics fields. *Spirulina* sp, a filamentous cyanobacterium, is an excellent source of protein, minerals, vitamin B12, iron and antioxidants such as phycocyanin and gallic acid. Phycocyanin, a protein found in *Spirulina*, which gives it its bluish hue, has numerous benefits for the body. In fact, this protein is said to have positive effects on oxidative stress and inflammation, as well as on red blood cell production. It is also beneficial in preventing certain cancers and diabetes. The research objective is to grow the *spirulina* sp strain from the Taman asset region in nutrient-rich Zarrouk medium, mainly sodium bicarbonate with a basic PH of 10.7. The resulting paste is oven-dried and ground to a powder to extract the phycocyanin, and the extraction yield is compared using 4 extraction methods: distilled water extraction, sonication and freezing, and solvent extraction.

Spectrophotometer readings are taken at absorbances of 615 nm, 620 nm, 652 nm and 280 nm, with Ab 620 indicating phycocyanin concentration and Ab 280 indicating protein concentration. *Spirulina* phycocyanin concentration ranges from 0.8-0.45 mg /ml, with solvent extraction giving higher phycocyanin concentrations than other methods. This study will introduce it into the manufacture of medicines as a valuable antioxidant.

**Keywords:** *Microalgae, Specie , Culture, Phycocyanin, Extraction*

---



## Conditions for Culture and Valorization of Microcystis Cyanobacteria

Saada Zakia<sup>\*1</sup>, Charef Nassira<sup>1</sup>, Tamer Fatma Zohra<sup>1</sup>, Belaid Bouthaina<sup>1</sup>, Elleuch Jihen<sup>1</sup>, Nasri Hichem<sup>1</sup>

<sup>1</sup>*Ecosystem Biodiversity and Pollution Laboratory, Bio Marine Department, Chadli Ben Jdid El Tarf University, Algeria*

---

### Abstract

Cyanobacteria are microscopic organisms that can thrive in nutrient-rich, shallow, stagnant, surface freshwater. They can form abundant, generally blue-green deposits and mosses known as "algal blooms". They have long been assimilated to algae ("blue-green algae"), and there is a very large number of species. Some species of cyanobacteria are capable of producing toxins that are potentially dangerous to health. Microcystis is a genus of freshwater cyanobacteria that includes *Microcystis aeruginosa*, which forms harmful algal blooms that can produce neurotoxins and hepatotoxins, such as microcystin and cyanopeptoline. The aim of the work was to culture *Microcystis* sp cells from the Lac des oiseaux wilaya of ElTaref and to monitor the culture. Single-cell strains of *Microcystis* sp were isolated, purified and cultured in BG11 culture medium at a photoperiod of 16h light and 8h dark at a temperature of 25 °C. The results show that colonies started to grow from 3 days and reached the exponential phase between days 20 and 25 with  $16 \times 10^6$  cells/ml, after 25 days 500 ml of *Microcystis* sp efflorescence material was centrifuged, lyophilization, and stored in a freezer at -20 C for chemical and toxin evaluation of *Microcystis*.

**Keywords:** *Cyanobacteria, Microcystis sp, Culture, Isolation, Growth*

---



---

## **In Vitro Antioxidant and Anti-Hemolytic Effect of Algerian *Centaurea Calcitrapa* L. Extracts**

**Krache Imane<sup>\*1</sup>, Trabsa Hayat<sup>1,2</sup>, Boussoualim Naouel<sup>1</sup>, Arrar Lekhmici<sup>1</sup>, Baghiani Abderrahman<sup>1</sup>**

<sup>1</sup>Laboratory of Applied Biochemistry, Department of Biochemistry Faculty of Natural and Life Sciences, University Ferhat Abbas of Setif 1, Algeria

<sup>2</sup>Department of Nature and Life Sciences, Faculty of Exact Sciences and Nature and Life Sciences, University of Biskra, Algeria

---

### **Abstract**

In the present study, aerial part of *Centaurea calcitrapa* L. were extracted with solvent of varying polarity allowed their separation into three main subfractions, the analysis of methanol crud (CrE), chloroform (ChE) and ethyl acetate (EaE) extracts, showed that the EaE contains the highest amount of flavonoids ( $50,71 \pm 0,65$  mg Eq / Quercetin g dry extract and  $31,96 \pm 0,39$  mg Eq Rutin / g dry extract). Total antioxidant capacity of plasma and red blood cells was measured. The half-life ( $HT_{50}$ ), which corresponds to 50% of cell lysis was calculated, the results showed that both groups treated with plant extract had a protective effect against erythrocytes hemolysis (CrD<sub>2</sub>:  $HT_{50} = 167,3 \pm 3,72$  min). The CrD<sub>2</sub> group showed a strong scavenging activity using DPPH assay ( $51,64 \pm 5,24$  %), higher than that of Vit C group ( $38,92 \pm 1,72$  %). All results confirmed that the extracts have a dose dependent effect on the growth of overall antioxidant defenses. These results support the use of this plant against anti-inflammatory diseases in traditional medicine.

**Keywords:** *Centaurea calcitrapa* L., DPPH, Hemolysis, Flavonoids

---



## Canopy Dynamics in the Bissa Forest: Chlef, West Algeria

Fatima Belhacini<sup>\*1,2</sup>, Djamel Anteur<sup>3</sup>, Faycal Tsourly<sup>1,2</sup>, Djahida Hedidi<sup>4</sup>

<sup>1</sup>University of Ain Temouchent Belhadj Bouchaib, Algeria

<sup>1</sup>Ecology and Management of Natural Ecosystems Laboratory, Tlemcen, Algeria

<sup>2</sup>University of Saida Moulay Tahar, Algeria

<sup>3</sup>University of Chlef Hassiba Benbouali, Algeria

---

### Abstract

The area covered by our contribution is located in the north-east of the wilaya of Chlef (western Algeria); it is an integral part of the Dahra Mountains. The aim of this contribution is to provide an overview of the vegetation cover in the Bissa forest. Floristic surveys were carried out in 100 m<sup>2</sup> plots. The floristic inventory includes more than 147 taxa, divided into 53 families, 36.7% of which are influenced by Mediterranean bioclimatic characteristics. Recent observations show a rapid degradation of these natural forests, which have been invaded by a pyrophilous matorral dominated by *Erica arborea* and *Cistus mospeliensis*. Correspondence factorial analysis (CFA) has enabled us to identify the various factors influencing the development and distribution of species in these groups.

**Keywords:** *Vegetation, Bissa forest, Dynamics, CFA, Chlef-Algeria*

---



## Biocontrol of Gray Mould in Strawberries with Pectin-Based Coatings Incorporated with Yarrow (*Achillea Millefolium L.*) Extract

Sebahat Oztekin <sup>\*1</sup>

<sup>1</sup>Department of Food Engineering, Bayburt University, Bayburt, Türkiye

### Abstract

Gray mould, caused by the fungus *Botrytis cinerea*, presents a significant challenge during the storage of strawberries following postharvest period, leading to considerable economic losses and food loss/waste. To address this issue, this study investigates the effectiveness of pectin-based coatings enhanced with yarrow (*Achillea millefolium L.*) extract as a biocontrol method against *B. cinerea* in strawberries. Pectin, a natural polysaccharide derived from fruits, is a biocompatible and edible material suitable for creating protective coatings on strawberries. Yarrow extract, renowned for its antimicrobial and antioxidant properties due to its high concentrations of phenolic compounds and flavonoids, is integrated into the pectin matrix to boost its bioactive potential. For this reason, 5% of the pectin solution was incorporated with 1% and 2% of yarrow extracts. Further, microbiological, physicochemical, and sensory properties of coated and non-coated strawberry fruits were investigated during 10<sup>th</sup> and 20<sup>th</sup> days at both at 4 °C and 25 °C. Findings showed that strawberries coated with pectin-2% yarrow extracts stored at 4 °C reduced the gray mould incidence up to 90%. Moreover, this coating effectively maintained the antioxidant capacity, phenolic content, hardness and levels of ascorbic acid in strawberries throughout the storage duration. In conclusion, pectin-based coatings incorporated with yarrow extract effectively and sustainably bio-controlled the gray mould in strawberries.

**Keywords:** Biocontrol, Strawberry, Gray mould, Yarrow extract

## 1 INTRODUCTION

Strawberry (*Fragaria ananassa*), a member of the Rosaceae family, is rich in phenolic compounds (anthocyanins, proanthocyanidins, ellagic and other phenolic acids, ellagitannins), minerals, dietary fiber and flavonoids [1]. In 2022, Türkiye produced an average of 728.112 tonnes of strawberries with a yield of 326.918 g/ha. Türkiye was the third-largest grape producer globally, contributing 3.8% of the total, behind China and the United States [2]. Strawberries are popular for their flavor, color, and nutrition but are highly perishable due to their high moisture content, leading to a short shelf life and greater spoilage risk. Strawberries are commonly affected by the necrotrophic fungus *Botrytis cinerea*, which causes gray mold disease during storage and postharvest stages [3]. This pathogen not only affects fruit quality but also leads to substantial economic losses and increased food waste. Traditional methods for managing gray mold often involve synthetic fungicides, which raise environmental and health concerns [4].

Pectin, a complex polysaccharide found in plant cell walls, consists of D-galacturonic acid linked by  $\alpha$ -1,4-glycosidic bonds. It can be extracted from various sources like citrus peels, apples, and banana peels. Pectin's gel-forming ability makes it useful as a stabilizer, emulsifier, and thickening agent. Its branched structure, anionic nature, water solubility, and biodegradability make it ideal for food packaging films, thanks to its non-toxic, edible nature, and cost-effectiveness [5].

Yarrow (*Achillea millefolium L.*) is a medicinal plant known for its antimicrobial and antioxidant properties. The yarrow extract is rich in phenolic compounds and flavonoids [6], which can contribute to the biocontrol and preservation of strawberries against gray mould disease [7]. This study aimed to enhance strawberry preservation using lemon pectin-based coatings with yarrow extract, a cost-effective, biocompatible, and sustainable material. It focused on evaluating the effectiveness of these coatings in controlling gray mold and maintaining strawberry quality.

## 2 MATERIAL AND METHOD

Strawberry fruits were randomly selected from a local organic store, ensuring uniformity in size, color, maturity, and absence of defects. Yarrow was collected from Bayburt province, Türkiye. The aqueous yarrow extracts were prepared [8]. Then, pectin was extracted from lemon peels using traditional extraction method (Figure 1). For this purpose, lemon peels were dried in an oven at 60 °C overnight. Citric acid was added to distilled water to adjust the pH to 2.0 (12 g/100 ml). The citric acid solution was mixed with the dried citrus peels at a 1:25 ratio and extracted at 90 °C for 1.5 hours. The resulting mixture was cooled to 40 °C and then centrifuged at 10,000 rpm for 10 minutes. The filtrate was transferred to an empty beaker, where 96% ethanol was added at a ratio of 4:1 and stored in a refrigerator (+4 °C) for 1 day. The following day, the precipitated pectin was filtered using a cheesecloth and washed at least twice with 96% ethanol. The obtained pectin gel was dried in an oven at 50 °C for 1 day, then ground into a powder [9].

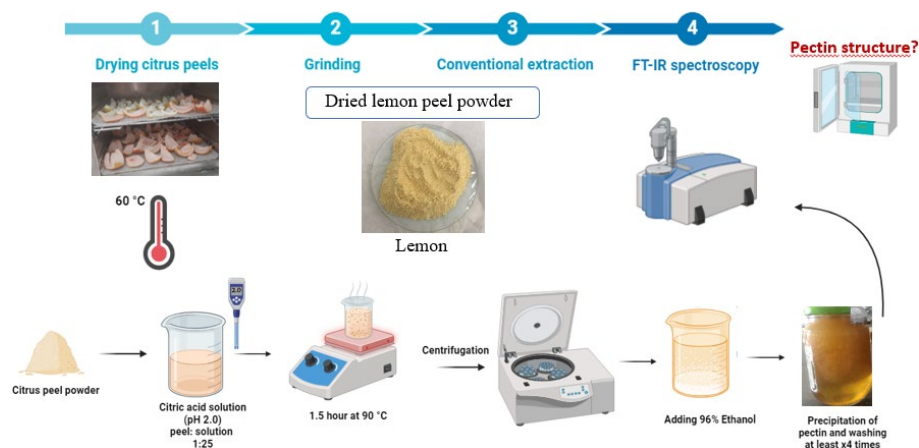


Figure 1. Pectin extraction from lemon peels

The Fourier Transform Infrared (FT-IR) spectroscopic analysis of lemon pectin was performed using a Perkin Elmer Spectrum 65 device. Before starting the measurements, a background scan was taken with air, and the resolution was set to 4  $\text{cm}^{-1}$ . The measurements of the samples were compared with the device's library, and the results were matched with pectin. The FT-IR analysis was conducted in transmission mode at 25°C, covering wavelengths between 4000 and 400  $\text{cm}^{-1}$ , with a resolution of 4  $\text{cm}^{-1}$  [10].

The FT-IR spectra are shown in Figure 2. The range of 3328-3355  $\text{cm}^{-1}$  indicates the presence of -OH groups, suggesting the water solubility of pectin. The carbonyl/carboxyl groups (C=O) between 1600-1734  $\text{cm}^{-1}$  reflect the free and esterified carboxyl groups of pectin. Aromatic C=C ring structures and aliphatic  $\text{CH}_2$  and  $\text{CH}_3$  deformations are identified in the bands between 1300-1440  $\text{cm}^{-1}$ . The region between 1600-1800  $\text{cm}^{-1}$  is specific to pectin and is used for its identification and quality determination. The band at 2932-2940  $\text{cm}^{-1}$  corresponds to the methyl groups of methyl esters in the structure of galacturonic acid [9].

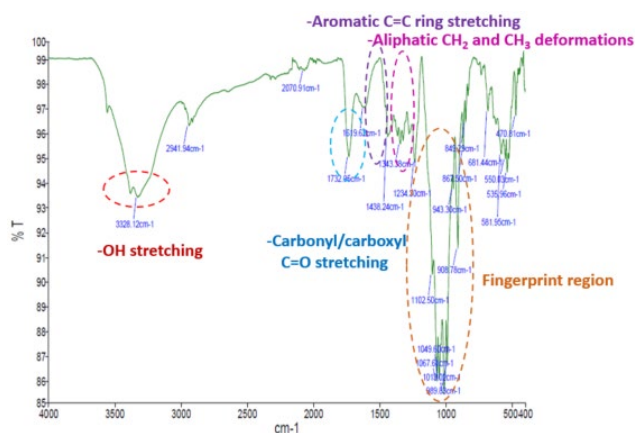
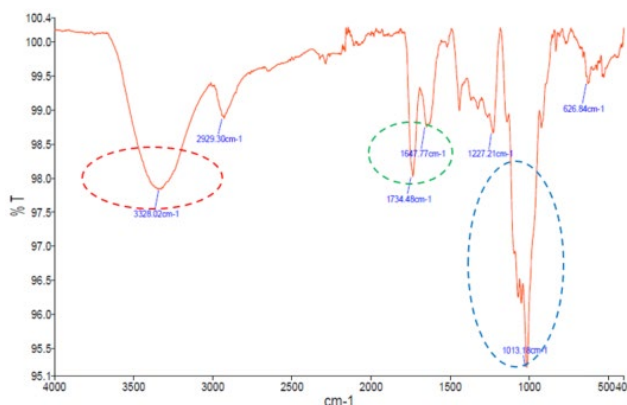


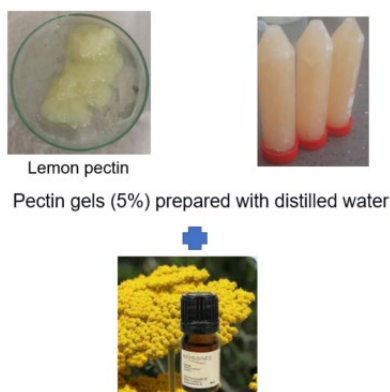
Figure 2. Structure of commercial citrus pectin by FT-IR analysis

The FT-IR result of the commercial citrus pectin was compared with lemon peel pectin, revealing consistency with the typical polysaccharide structure of pectin, which confirms the successful extraction (Figure 3).



**Figure 3.** Confirmation of lemon peel pectin structure by FT-IR analysis

5 % pectin solution (w/v) was prepared with the addition of 1% and 2% yarrow extract (Figure 4). Before the coating treatment, strawberries were washed in cold, sterile, distilled water for 2 minutes, then dried for 30 minutes at room temperature. The control samples were submerged in distilled water for 2 minutes and dried. Test samples were immersed in Pectin (P), Pectin + 1% Yarrow extract (YE), and Pectin + 2% Yarrow extract (YE) solutions for 2 minutes, drained for 1 minute. Then, the coated strawberries were then dried for 1 hour [11].

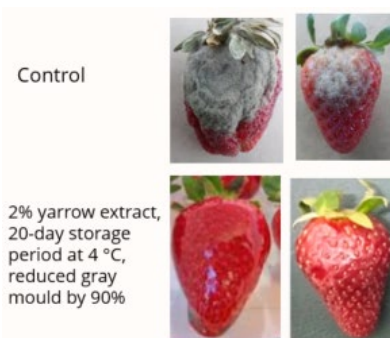


**Figure 4.** Pectin gels (5%) prepared from lemon pectin and yarrow extract (%1 and %2)

The control and treated strawberries were incubated at 4 °C and 25 °C for 10 and 20 days [11]. The antioxidant capacity, phenolic content, hardness and ascorbic acid levels of strawberries were conducted based on the Bhimrao Muley’s method [11].

### 3 RESULTS

The results showed that pectin-based coating containing 2% yarrow extract was the most effective, reducing gray mould incidence by up to 90% during 20 days of storage at 4 °C (Figure 5). The uncoated strawberry shows the typical signs of gray mould infection, with visible fungal growth and deterioration of the fruit. The pectin-based coating infused with yarrow extract demonstrates even greater inhibition of the gray mould fungus, indicating the synergistic biocontrol effects.



**Figure 5.** Control (infected with gray mould) and lemon pectin-yarrow coated strawberries



The pectin-based coating with 2% yarrow extract preserved and even enhanced the antioxidant capacity, phenolic content, and ascorbic acid levels of strawberries (Table 1).

**Table 1.** Antioxidant capacity, phenolic content, and ascorbic acid levels of strawberries

		Storage time (day)		
		0	10	20
DPPH• scavenging activity, IC50* (mg/L)	C	0.08	0.09	0.115
	P	0.078	0.092	0.105
	P+2% YE	0.065	0.082	0.09
Total Phenolic Content (mg GAE/kg)	C	345.78	277	192
	P	386.41	295	201
	P+2% YE	455.32	316	245
Ascorbic Acid Content (mg/100 g)	C	370.2	215	135
	P	332.85	280	142
	P+2% YE	382.12	305	196

## 4 CONCLUSION

This study evaluated pectin-based coatings enhanced with yarrow extract as a biocontrol method. The lemon pectin-based coating with 2% yarrow extract was the most effective, reducing the incidence of gray mould by up to 90% during the 20-day storage period at 4 °C. Additionally, these coatings preserved antioxidant capacity, phenolic content, hardness, and ascorbic acid levels in strawberries. Thus, pectin-based coatings with yarrow extract offer an effective and sustainable solution for controlling gray mold in strawberries.

## References

- [1] M. Pukalskienė *et al.*, “Recovery of bioactive compounds from strawberry (*Fragaria* × *ananassa*) pomace by conventional and pressurized liquid extraction and assessment their bioactivity in human cell cultures”, *Foods*, vol. 10, no. 8, p. 1780, 2021.
- [2] FDA. (2024) *Food and drug administration (FDA)* [Online]. Available: <https://www.fda.gov/>
- [3] S. Petrasch, S. J. Knapp, J. A. L. Van Kan, and B. Blanco-Ulate, “Grey mould of strawberry, a devastating disease caused by the ubiquitous necrotrophic fungal pathogen *Botrytis cinerea*,” *Mol. Plant Pathol.*, vol. 20, no. 6, pp. 877–892, 2019.
- [4] S. Oztekin and F. Karbancioglu-Guler, “Recruiting grape-isolated antagonistic yeasts for the sustainable bio-management of *Botrytis cinerea* on grapes,” *Food Energy Secur.*, vol. 13, no. 1, art. no. e528, Jan. 2024.
- [5] S. Firdaus, F. Ahmad, and S. Zaidi, “Preparation and characterization of biodegradable food packaging films using lemon peel pectin and chitosan incorporated with neem leaf extract and its application on apricot fruit,” *Int. J. Biol. Macromol.*, vol. 263, art. no. 130358, 2024.
- [6] N. Karaaslan Ayhan, M. G. Karaaslan Tunc, S. A. A. Noma, A. Kurucay, and B. Ates, “Characterization of the antioxidant activity, total phenolic content, enzyme inhibition, and anticancer properties of *Achillea millefolium* L.(yarrow),” *Instrum. Sci. Technol.*, vol. 50, no. 6, pp. 654–667, 2022.
- [7] C. El-Kalamouni, P. R. Venskutonis, B. Zebib, O. Merah, C. Raynaud, and T. Talou, “Antioxidant and antimicrobial activities of the essential oil of *Achillea millefolium* L. grown in France,” *Medicines*, vol. 4, no. 2, art. no. 30, 2017.
- [8] S. M. Sousa and L. F. Viccini, “Cytotoxic and genotoxic activity of *Achillea millefolium* L., Asteraceae, aqueous extracts,” *Rev. Bras. Farmacogn.*, vol. 21, pp. 98–104, 2011.
- [9] M. T. Yılmaz, A. Muslu, S. Karasu, F. Bozkurt, and E. Dertli, “Portakal posasından modifiye pektin eldesi ve optimizasyonu, kompozisyonel ve yatsikan faz ozelliklerinin karakterizasyonu,” *Tekirdag Ziraat Fakültesi Derg.*, 2017.
- [10] P. Sharma, K. Osama, V. K. Gaur, A. Farooqui, S. Varjani, and K. Younis, “Sustainable utilization of Citrus limetta peel for obtaining pectin and its application in cookies as a fat replacer,” *J. Food Sci. Technol.*, vol. 60, no. 3, pp. 975–986, 2023.
- [11] A. B. Muley and R. S. Singhal, “Extension of postharvest shelf life of strawberries (*Fragaria ananassa*) using a coating of chitosan-whey protein isolate conjugate,” *Food Chem.*, vol. 329, art. no. 127213, 2020.



## Lyophilized Strawberry Slices with Various Thicknesses and Investigation of Their Drying Characteristics

Erman Kadir Oztekin<sup>1</sup>, Sebahat Oztekin<sup>\*2</sup>

<sup>1</sup>Department of Mechanical Engineering, Bayburt University, Bayburt, Türkiye

<sup>2</sup>Department of Food Engineering, Bayburt University, Bayburt, Türkiye

### Abstract

This study examines the drying characteristics of lyophilized strawberry slices with thicknesses of 3 mm and 5 mm. The strawberries were cut to these specified thicknesses and underwent a freeze-drying process. During the drying period, mass losses of the slices were precisely measured and recorded at regular intervals. Moisture ratios (MR) were also calculated to assess the drying efficiency and behavior of the slices. The gathered data was utilized to develop and evaluate several kinetic drying models using MATLAB software. Mass losses of 100 g strawberry slices were measured every two hours over a 10-hour drying period. Results indicated that the thinner 3 mm slices dried faster due to their lower moisture content compared to the 5 mm slices. Eight different kinetic drying models, including the Page, Henderson-Pabis, Logarithmic, and Two-term exponential models, were tested. The Page model was identified as the most accurate in predicting the drying behavior of the strawberry slices. For the 3 mm and 5 mm slices, the reduced chi-square ( $X^2$ ) values were  $7.184 \times 10^{-5}$  and  $4.235 \times 10^{-4}$ , respectively. The root mean square error (RMSE) values were approximately 0.007348 for the 3 mm slices and 0.004178 for the 5 mm slices. The coefficient of determination ( $R^2$ ) values for both thicknesses were 0.9999, indicating an excellent fit between the experimental data and the selected model. Additionally, the study calculated the effective diffusivity coefficients, which were  $1.95 \times 10^{-10}$  m<sup>2</sup>/s for the 3 mm slices and  $2.75 \times 10^{-10}$  m<sup>2</sup>/s for the 5 mm slices. These results highlight the considerable influence that slice thickness has on the drying rates and overall efficiency of lyophilized strawberry slices. The results provide valuable insights for optimizing freeze-drying processes in food preservation, emphasizing the importance of considering slice thickness to achieve desired drying outcomes.

**Keywords:** Lyophilization, Strawberry, Drying, Thickness, Drying kinetics

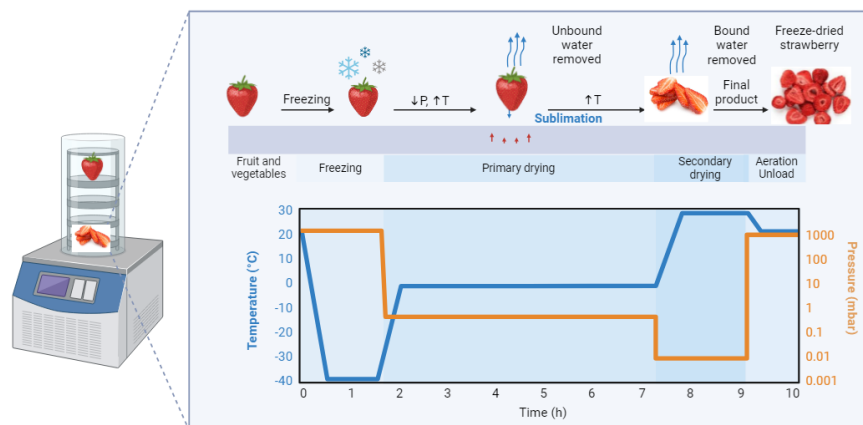
## 1 INTRODUCTION

Strawberry production in Türkiye averaged 728.112 tonnes with a production yield of 326.918 g/ha in 2022. Türkiye ranked third in producing 3.8% of the world's grapes, after China and the United States [1]. Strawberries are widely consumed due to their appealing flavor, color, and high nutritional content. However, their high moisture content makes them highly perishable, resulting in a limited shelf life and increased susceptibility to spoilage [2]. To extend the shelf life of strawberries while preserving their quality, lyophilization, or freeze-drying, has become a preferred preservation technique. This process removes moisture from the fruit by sublimation, directly converting frozen water into vapor under low pressure and temperature conditions. This method is particularly effective in retaining the sensory and nutritional properties of strawberries, such as their vitamins and antioxidants [3].

The efficiency of the lyophilization process can be significantly influenced by the thickness of the strawberry slices. The slice thickness affects both the drying time and the final quality of the product. Thicker slices may result in longer drying times, which can lead to uneven moisture removal and potential degradation of the fruit's structure and nutrients. Conversely, thinner slices may dry more quickly but are at risk of structural damage and loss of delicate flavor compounds [4]. Therefore, understanding the relationship between slice thickness and drying characteristics is crucial for optimizing the lyophilization process [5]. This study aims to investigate the drying behavior of strawberry slices with varying thicknesses (3 mm and 5 mm) during lyophilization. By analyzing the drying kinetics and assessing the physical and chemical properties of the lyophilized slices, this research seeks to identify optimal conditions that ensure high-quality freeze-dried strawberry products with improved shelf life and preserved nutritional value.

## 2 MATERIAL AND METHOD

The yediveren strawberry (*Fragaria virginiana* L.) fruits were purchased from a local organic store by random selection based on their uniform size, color, maturity, and defect-freeness. Then, the strawberry fruit weighs 100 grams and is sliced into 3 mm and 5 mm thick pieces, which are then placed in a test container in 8 pieces and left for freezing at -18 °C [6]. After these preparations, the strawberry samples was subjected to lyophilization using Biobase -40 °C vacuum freeze dryer machine for 10 hours (Figure 1). The study was carried out under 0.01 kPa pressure by the help of vacuum pump.



**Figure 1.** Freeze-drying (Lyophilization) process of strawberries

The weight loss of strawberries were determined in every two hours using a precision balance (with 0.001 g sensitivity). This process is repeated for other date samples at 2, 4, 6, 8, and 10 hours, with mass loss determined at each interval [7].

$$MR = \frac{M_t - M_d}{M_0 - M_d} \quad (1)$$

$$DR = \frac{M_t + dt - M_0}{dt} \quad (2)$$

The change in moisture rate (MR) over time (t), a dimensionless term, is determined using Equations (1) and (2). In these equations, ( $M_0$ ) represents initial moisture content, ( $M_t$ ) is the moisture content at time t, and ( $M_d$ ) is the equilibrium moisture content. These equations provide the MR values, showing the moisture ratio as a function of drying time for the strawberries [8].

$$RMSE = \left[ \frac{1}{N} \sum_{i=1}^N (MR_{pre, i} - MR_{exp, i})^2 \right]^{1/2} \quad (3)$$

$$X^2 = \sum_{i=1}^N (MR_{exp} - MR_{pre})^2 / N - z \quad (4)$$

$$R^2 = 1 - \left[ \frac{\sum (MR_{exp} - MR_{pre})^2}{\sum (MR_{pre})^2} \right] \quad (5)$$

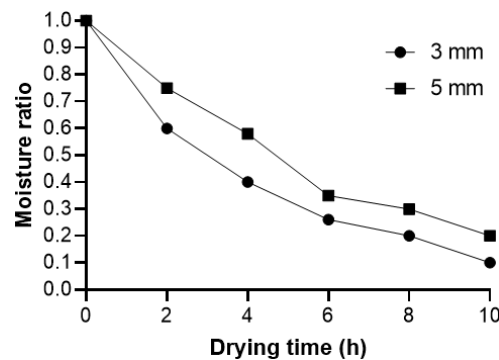
Equations 3, 4, and 5 are used to calculate the root mean square error (RMSE), reduced chi-square ( $X^2$ ), and coefficient of determination ( $R^2$ ) of kinetic models, respectively, to statistically verify the agreement between experimentally obtained moisture ratios and those estimated by the models [9]. Table 1 shows the eight different kinetic drying models used in MATLAB to determine the estimated moisture ratio of strawberries.

**Table 1.** Empirical and semiempirical equations for drying kinetics

Model No	Model Name	Model
1	Newton	$MR = \exp(-kt)$
2	Page	$MR = \exp(-kt^n)$
3	Modified Page I	$MR = \exp[-(kt)^n]$
4	Henderson ve Pabis	$MR = a \cdot \exp(-kt)$
5	Logarithmic	$MR = a \cdot \exp(-kt) + c$
6	Two-term eksponential	$MR = a \exp(-kt) + (1-a) \exp(-kat)$
7	Wang and Singh	$MR = 1 + at + bt^2$
8	Diffusion approach	$MR = a \exp(-kt) + (1-a) \exp(-kbt)$

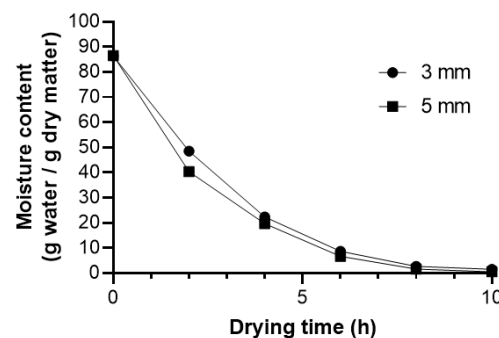
### 3 RESULTS

Figure 2 shows the moisture ratio curves of strawberry slices at different thicknesses of 3 mm and 5 mm, plotted against drying time. The results indicate that as thickness increases, the moisture ratio also rises over time.



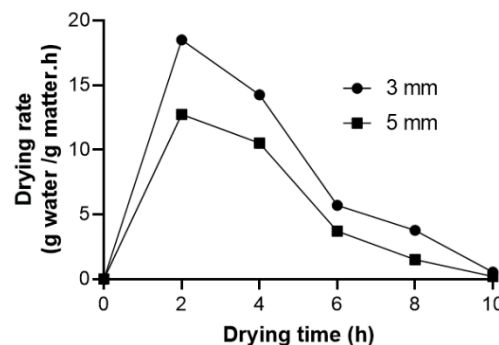
**Figure 2.** The moisture ratio curves of strawberry slices plotted against drying time

Figure 3 shows that the drying rate decreases as moisture content declines. Comparing different thicknesses, the specimen with a 5 mm thickness dries more slowly due to its higher moisture content, while the 3 mm thick specimen dries more quickly as it contains less moisture. The sublimation process causes water vapor to move through the dried regions of the freeze-dried specimen via capillaries.



**Figure 3.** The moisture content of strawberry slices plotted against drying time

Figure 4 presents the moisture content curve of the strawberry, which represents the ratio of water content to dry matter. Initially, the moisture content decreases rapidly during the first 2 hours, followed by a slower decline. As the thickness of the strawberry slices increased, a decrease in the drying rate was observed.



**Figure 4.** The drying rate curves of strawberry slices as a function of drying time

Figure 5 shows the drying rate of freeze-dried strawberry slices having 3 mm and 5 mm thickness. Initially, the drying rate increases due to the high moisture concentration at the surface. However, within the first 2 hours, the drying rate rapidly declines as the plate temperature in the freeze-drying device is around  $-30^{\circ}\text{C}$ .

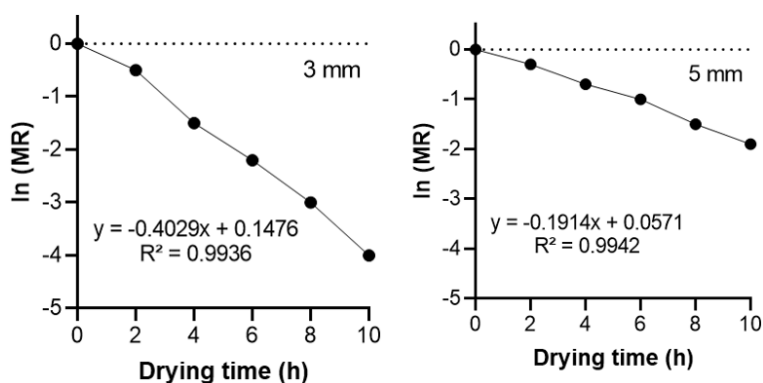


Figure 5. Plot of ln (MR) versus freeze-drying time for strawberry slices

Table 2 presents the  $R^2$ ,  $X^2$ , and RMSE results calculated by eight kinetic drying models. The Page model was identified as the most suitable for both 3 mm and 5 mm thicknesses, with an  $R^2$  value of 0.9999 (closest to 1) and  $X^2$  values of  $7.184 \times 10^{-5}$  and  $4.235 \times 10^{-4}$  (closest to 0) for the respective thicknesses. Additionally, the RMSE values of 0.007348 for 3 mm and 0.004178 for 5 mm, being closest to 0, further support the Page model's suitability for strawberry lyophilization.

Table 2. The results obtained from eight kinetic drying models

Model No	Model Name	Slice Thickness (mm)	Model Parameters	$R^2$	$X^2$	RMSE
1	Newton	3	k: 0.4275	0.9975	$7.52 \times 10^{-4}$	0.03598
		5	k: 0.2478	0.9860	$2.56 \times 10^{-3}$	0.03956
2	Page	3	<b>k: 0.2203</b> <b>n: 1.250</b>	<b>0.9999</b>	<b><math>7.184 \times 10^{-5}</math></b>	<b>0.007348</b>
		5	<b>k: 0.1102</b> <b>n: 1.347</b>	<b>0.9999</b>	<b><math>4.235 \times 10^{-4}</math></b>	<b>0.004178</b>
3	Modified Page I	3	k: 0.3055 n: 1.3002	0.9990	$7.4825 \times 10^{-5}$	0.008654
		5	k: 0.2225 n: 1.2657	0.9994	$8.2236 \times 10^{-4}$	0.007435
4	Henderson and Papis	3	a: 1.035 k: 0.4785	0.9985	$8.21 \times 10^{-4}$	0.02369
		5	a: 1.027 k: 0.2254	0.9988	$5.12 \times 10^{-4}$	0.03865
5	Logarithmic	3	a: 1.254 c: -0.04582 k: 0.2074	0.9952	$8.4789 \times 10^{-4}$	0.075851
		5	a: 1.3669 c: -0.2447 k: 0.1565	0.9921	$2.2357 \times 10^{-3}$	0.06520
6	Two-term exponential	3	a: 1.7458 k: 0.5856	0.9900	$7.905 \times 10^{-5}$	0.098967
		5	a: 1.8521 k: 0.2365	0.9921	$4.6532 \times 10^{-4}$	0.032456
7	Wang ve Sing	3	a: -0.2036 b: 0.01452	0.9875	$2.448 \times 10^{-3}$	0.068542
		5	a: -0.1638 b: 0.00214	0.9758	$1.523 \times 10^{-4}$	0.013546
8	Diffusion Approach	3	a: 4.235 b: 0.9524 k: 0.2885	0.9880	$5.6845 \times 10^{-5}$	0.02654
		5	a: 5.3698 b: 0.9526 k: 0.2589	0.9921	$4.5628 \times 10^{-4}$	0.03258

## 4 CONCLUSION

The results provide valuable insights for optimizing freeze-drying processes in food preservation, emphasizing the importance of considering slice thickness to achieve desired drying outcomes. The proper kinetic drying model was the Page model because the  $R^2$  value was about 0.9999,  $X^2$  values for 3 mm and 5 mm thicknesses were about  $7.184 \times 10^{-5}$  and  $4.235 \times 10^{-4}$ , RMSE values for 3 mm and 5 mm were about 0.007348 and 0.004178, respectively, further confirming the model's accuracy. Taking into account the moisture content and drying rates, it was observed that strawberry slices with a thickness of 5 mm dried more slowly due to their higher moisture content. In contrast, strawberry slices with a thickness of 3 mm dried faster because they contained less moisture.

## References

- [1] FAO, "Food and agricultural organization of the united nations. FAO statistical databases and data sets," *Food Agric. Organ. United Nations*, 2024.
- [2] S. Menéndez-Cañamares, A. Blázquez, I. Albertos, J. Poveda, and A. Díez-Méndez, "Probiotic *Bacillus subtilis* SB8 and edible coatings for sustainable fungal disease management in strawberry," *Biol. Control*, vol. 196, art. no. 105572, 2024.
- [3] O. Kilic, B. Azak, and S. Ersus, "The effect of different drying temperature profiles on the shrinkage and physical quality of the freeze-dried strawberries," *J. Food Process Eng.*, vol. 47, no. 1, art. no. e14523, 2024.
- [4] X. Sun *et al.*, "Effect of pectin addition on the drying characteristics of freeze-dried restructured strawberry blocks," *LWT*, vol. 192, art. no. 115716, 2024.
- [5] J. Hu *et al.*, "Effect of guar gum, gelatin, and pectin on moisture changes in freeze-dried restructured strawberry blocks," *Food Chem.*, vol. 449, art. no. 139244, 2024.
- [6] A. Bahadir, A. Dagdeviren, M. Ozkaymak, and A. R. Guinalah, "Freeze drying process of kiwi slices with various thicknesses and investigation drying characteristic of process," *Politek. Derg.*, vol. 26, no. 1, 415–423, 2023.
- [7] J. P. George and A. K. Datta, "Development and validation of heat and mass transfer models for freeze-drying of vegetable slices," *J. Food Eng.*, vol. 52, no. 1, pp. 89–93, 2002.
- [8] A. Bahadir, A. Dagdeviren, B. M. Yildiz, and M. Ozkaymak, "Determination freeze-drying characteristics of ottoman strawberries," *Gazi Univ. J. Sci.*, vol. 36, no. 3, pp. 1247–1257, 2023.
- [9] A. Vega-Gálvez, M. Miranda, C. Bilbao-Sáinz, E. Uribe, and R. Lemus-Mondaca, "Empirical modeling of drying process for apple (cv. Granny Smith) slices at different air temperatures," *J. Food Process. Preserv.*, vol. 32, no. 6, pp. 972–986, 2008.



---

## Antibiotic Resistance Pattern of *Pseudomonas Sp* in Tilapia Fish *Oreochromis Sp* and Aquarium Water

Romeissa Derdachi<sup>\*1,2,3</sup>, Sabine Boucetta<sup>1</sup>

<sup>1</sup>Department of Nature and Life Sciences, University of August 20, 1955, Skikda, Algeria

<sup>2</sup>Laboratory of Interactions, Biodiversity, Ecosystems and Biotechnology, University of August 20, 1955, Skikda, Algeria

<sup>3</sup>Laboratory of Optimization of Agricultural Production in Subhumid Zones, University of August 20, 1955, Skikda, Algeria

---

### Abstract

Aquaculture is the fastest-growing food production sector in the world, playing a significant role in the economy. A main issue derived from the huge growing and production of the industry is the vulnerability to noteworthy stock losses due to bacterial diseases, which solution requires the intensive use of antimicrobials. Therefore, the intensive use of antibiotics can lead to the spread of antibiotic-resistant bacteria. This study aimed to investigate the presence and antimicrobial susceptibility profile of *Pseudomonas sp* in aquarium water and tilapia fish from a fish farm in Algeria.

Aquarium water was collected in a sterile tube, samples of fish were diluted in sterile saline then the streak plate method was used to isolate the bacteria in cetrimide agar and chocolate agar, and Petri dishes were incubated at 37° for 24h then the colonies were streaked to obtain pure cultures. The identification was done by morphological characteristics and biochemical tests such as motility, citrate utilization test, nitrate reduction test, catalase test, and cytochrome oxidase test. The drug-resistant pattern was determined by the Kirby-Bauer disc diffusion technique on Muller Hinton agar using five antibiotics: tetracycline, gentamicin, ciprofloxacin, ampicillin and erythromycin.

The results showed the absence of *Pseudomonas sp* in fish samples and the presence of one strain in aquarium water which was motile and presented cytochrome oxidase, the Kirby Bauer test showed that the strain was resistant to erythromycin and sensible to the rest of the antibiotics.

In conclusion, this study determined the presence of *Pseudomonas sp* in aquarium water where tilapia fish are harvested, its presence may pose a health risk to human beings and may cause disease to susceptible individuals, especially immune-compromised consumers. Accordingly, proper hygienic measures from farm to fork and hygienic education for fish handlers/traders and consumers are required.

**Keywords:** *Tilapia*, *Oreochromis sp*, *Pseudomonas sp*, Antibiotic resistance

---



## Sample Preparation for Soil Analysis of an Endangered Species in the Sidi Bel Abbes Region (North West Algeria)

Mounir Chihab<sup>\*1,2</sup>, Ali Khalfa<sup>1,3</sup>

<sup>1</sup>Department of Agri-Food, Faculty of Science and Technology, University of Ain Temouchent - Belhadj Bouchaib, Ain Temouchent, Algeria

<sup>2</sup>Laboratory of Applied Hydrology and Environment, Ain Temouchent, Algeria

<sup>3</sup>Laboratory of Applied Hydrology and Environment, Ain Temouchent, Oran, Algeria

---

### Abstract

Mediterranean forests are critical natural habitats supporting diverse ecosystems and biodiversity. Among them, the Tenira forest in the Sidi Bel Abbes region of Algeria stands out for its exceptional plant diversity, categorized by a specific biological spectrum according to Raunkiaer's classification. This unique ecological profile underscores the forest's ecological significance and the intricate relationships between its flora and environmental conditions.

However, the biodiversity of the Tenira forest faces challenges from human activities, particularly the impact of livestock farming. These anthropogenic influences have significantly altered the natural balance and species composition within the forest ecosystem, posing threats to the survival of many plant species, including several endangered and geophytic species.

This research specifically targets a threatened geophytic species within the Tenira forest, aiming to analyze and understand the physicochemical properties of the soils where these species thrive. Through comprehensive soil analysis, it was found that the soils predominantly exhibit a sandy-loam texture, with a slightly alkaline pH level and generally non-saline conditions. Moreover, the presence and distribution of limestone vary significantly across different sampling stations, indicating localized geological influences.

The interpretation of these findings provides valuable insights into the ecological requirements and habitat preferences of the studied geophyte species. Furthermore, it underscores the importance of considering soil characteristics and their spatial variability in conservation strategies aimed at preserving the biodiversity of Mediterranean forests, particularly in regions affected by anthropogenic activities.

**Keywords:** *Mediterranean forest, Soil analysis, Endangered species, Conservation*

---





## Comparative Study of the Effect of Two Irrigation Methods (Drip and Submersion) on the Behavior of Two Varieties of Olive Trees (*Olea Europaea* L) in the Semi-Arid Zone of Bordj-Bou-Arreridj

Faycal Bahlouli<sup>\*1,5</sup>, Hamza Belguerri<sup>1,6</sup>, Nacira Chourghal<sup>1,6</sup>, Amel Salamani<sup>1</sup>,  
Mouhamed Benaini<sup>2</sup>, Khelifa Maamri<sup>1,6</sup>, Fairouz Mihoubi<sup>1</sup>, Aicha Cherroura<sup>1</sup>, Younes  
Atek<sup>3</sup>, Fares Aissat<sup>4</sup>

<sup>1</sup>Departement of Agronomic Sciences, University Mohamed El Bachir El Ibrahim, Bordj-Bou-Arreridj, Algeria

<sup>2</sup>Departement of Agronomic Sciences, University of Djillali Bounaama, Khemis Miliana, Algeria

<sup>3</sup>Departement of Agronomic Sciences, University of Mohamed Khaider, Biskra, Algeria

<sup>4</sup>Departement of Agronomic Sciences, University of Mohamed Boudiaf, M'sila, Algeria

<sup>5</sup>Laboratory of Biodiversity and Biotechnological Techniques for the Valorization of Plant Resources, University of M'sila, Algeria

<sup>6</sup>Laboratory of Characterization and Valorization of Natural Resources, University of Bordj-Bou-Arreridj, Algeria

### Abstract

Olive cultivation in semi-arid zones has shown significant progress in recent years. In this context, this study focuses on the behavior of two olive varieties, Arbequina and Seviollana, grown under two irrigation methods: drip irrigation and submersion. The investigation considers various aspects, including morphological, physiological, and phenological parameters. The experiment is conducted in the municipality of El Annasser, Bordj-Bou-Arreridj province. The primary findings favor drip irrigation over submersion for different parameters such as shoot growth, and chlorophyll content. The Seviollana variety demonstrates favorable results compared to the Arbequina variety for several characteristics, including stomatal density, floral bud count per branch, and cluster count per branch.

**Keywords:** Olive, Variety, Characteristic, Semi-arid, Irrigation, Behavior

## 1 INTRODUCTION

The cultivation of the olive tree (*Olea europaea*, L.) is one of the oldest and most widespread activities in arid and semi-arid areas of the Mediterranean basin, owing to its great adaptation to water deficit conditions [1]. The olive tree, like other fruit trees such as almond and pistachio, plays a significant role in maintaining the balance of the semi-desert ecosystem. In sloped areas, plantations often arranged in terraces contribute to reducing erosion problems and soil loss. Olive groves serve as a refuge and a source of food for certain animal species, thereby contributing to biodiversity conservation [2].

In Algeria, the olive tree holds a privileged position in Algerian agriculture and agricultural production [3]. However, olive oil production in Algeria remains low, influenced by various biotic and abiotic factors. The traditional orchard is extensively established in unfavorable pedological and topographical conditions (slope, poor soil, climate). This makes cultural practices (pruning, soil management, and phytosanitary care) challenging, and the destructive actions of various pests further complicate the situation [2].

The Bordj Bou Arreridj province ranks fourth nationally, with an olive orchard covering an estimated area of 23,919.00 hectares, including 133,200.00 productive olive trees. For the 2022/2023 season, olive oil production is estimated at 10,459.00 hectoliters, with a total olive yield of 5.57 Qx/ha [4].

Irrigation is a technique aimed at compensating for rainfall deficits to benefit agricultural production. It involves artificially providing water to cultivated plants to increase production and improve plant development. Irrigation begins at the end of winter (late March) and continues until autumn (late September). The irrigation doses vary depending on soil type, climate, crop density, cultural methods, and the means employed. Irrigation techniques range from the simplest practices (submersion irrigation) to more advanced methods (drip irrigation).

The objective of this study is to examine the effect of two types of irrigation, drip irrigation and submersion irrigation, on the behavior of two olive varieties, Arbequina and Sevillana, based on various phenological, morphological, and physiological parameters.

## 2 MATERIAL AND METHOD

The experimentation was conducted on a private farm located in the municipality of El Anasser, along National Road No. 5, 5 km from the city center of Bordj Bou Arréridj, at coordinates 36.04249°N and 4.50290°E.

The plant material consisted of two olive varieties: Arbequina and Sevillana. Sixteen trees were tested for each variety, employing two types of irrigation-drip irrigation and submersion in basins. Eight trees were used for each irrigation type. Various characteristics were studied based on the olive tree characterization established by [5], including phenotypic, morphological, physiological, and phenological traits.

### 2.1 Irrigation

In our experimentation, two types of irrigation were applied for each of the two tested varieties. To meet the tree's water needs adequately, irrigation doses were calculated using the ET<sub>c</sub> calculation method [6]:

$$ET_c = ET_o \times K_c \times K_r \quad (1)$$

Where:

- ET<sub>o</sub>: Reference crop evapotranspiration.
- K<sub>c</sub>: Cultural coefficient specific to the olive tree, dependent on age, species, variety, phenological stage, and management method.
- K<sub>r</sub>: Soil cover coefficient by the total canopy, determined using the lysimetric method.

Weekly irrigation was carried out for both types submersion and drip irrigation on the various tested trees, with the water quantity adjusted based on changes in the ET<sub>c</sub> value.

### 2.2 Morphological Characteristics

Measured morphological characteristics included leaf area, overall tree appearance, length of year shoots, number of floral buds per branch, number of clusters per branch, number of floral buds per linear meter (floral intensity), and fertilization rate.

### 2.3 Physiological Characteristics

Measured physiological characteristics included chlorophyll content.

### 2.4 Phenological Characteristics

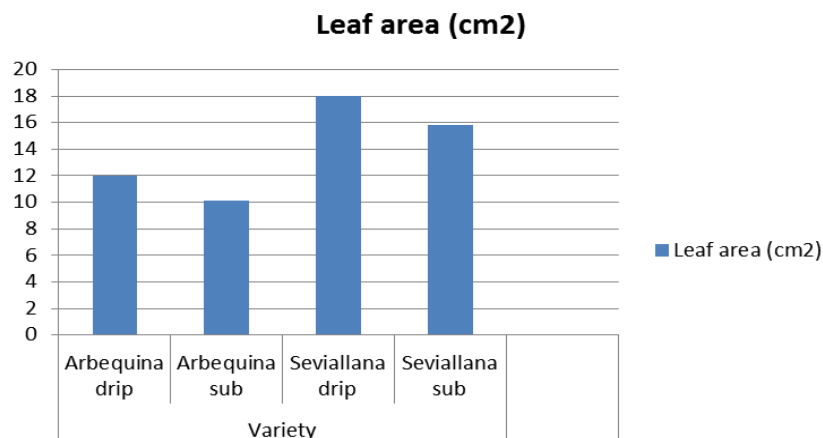
Various phenological stages were monitored, including bud break, flowering, and fertilization.

## 3. RESULTS

### 3.1 Morphological Characteristics

#### 3.1.1 Leaf Area

The Sevillana variety recorded the highest average value at 16.79 cm<sup>2</sup>, compared to the Arbequina variety with an average value of 11.2 cm<sup>2</sup>. A clear comparison between irrigation methods highlights the dominance of drip irrigation by over 5.59 cm<sup>2</sup> compared to submersion irrigation (Figure 01).



**Figure 1.** Leaf area of the two varieties under two irrigation methods

Variance analysis revealed non-significant differences between irrigation methods and for the variety x irrigation interaction. However, there is a highly significant difference between varieties, leading to the emergence of two groups: the first group comprises the Sevillana variety with 16.6 cm<sup>2</sup>, and the second group includes the Arbequina variety with 11.3 cm<sup>2</sup> (Table 1).



**Table 1.** Analysis of variance for the leaf area parameter

Case	Degree of Freedom	Leaf Area		
		Average Square	Average Square	Probability
Variety	1	0.1	228.445	THS 0.000232
Irrigation	1	351.1	8.715	NS 0.416655
Variety x Irrigation	1	741.1	11.40	NS 0.353783

### 3.1.2 Overall Tree Appearance

The results of observations regarding the overall appearance of the trees for the two studied varieties are presented in Table 2 with accompanying illustrations.

**Table 2.** Presentation of the observed overall appearance of the two studied varieties

Variety	Overall Appearance	Photo
Arbequina	Vigor: Moderate. Canopy: Spread, typical of the natural habit of the species Foliage Density: Loose, with openings allowing light in	
Sevillana	Vigor: Moderate Canopy: Upright, branches show strong apical dominance Foliage Density: Loose, with openings allowing light in	

Observation of these traits indicates that both studied varieties exhibit moderate vigor. The Arbequina variety has a spread canopy, characteristic of the species' natural habit, while the Sevillana variety has an upright canopy with branches showing strong apical dominance. Foliage density is moderate for both varieties.

### 3.1.3 Length of Year Shoots

Figure 2 indicates a slight difference in the length of shoots between the two irrigation methods, with a slight advantage for drip irrigation. This suggests the favorability of using drip irrigation, especially if this irrigation method is applied over several years.

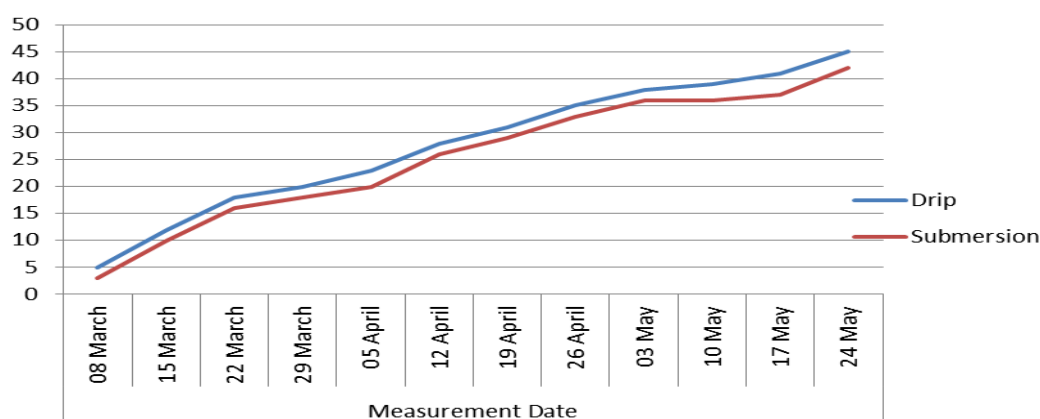


Figure 2. Length of shoots under the two irrigation methods

### 3.1.4 Number of Floral Buds Per Branch

The results show that the number of floral buds per branch varies between varieties, with the highest value recorded by the Sevillana variety at 2137 buds per branch, compared to 1296.5 buds per branch for the Arbequina variety (Table 3).

Table 3. Number of floral buds per branch and number of clusters per branch for the two studied varieties under the two irrigation methods

	Irrigation Method	Number of Floral Buds Per Branch	Average	Number of Clusters Per Branch	Average
Arbequina	Submersion	885	1296,5	73	100
	Drip Irrigation	1708		127	
Sevillana	Submersion	3232	2137	203	150
	Drip Irrigation	1042		97	

Statistically, there are non-significant differences between varieties and irrigation types. However, the interaction variety x irrigation is highly significant, revealing the existence of three groups: Sevillana under submersion with 404 buds/branch, the second group comprises Arbequina under submersion with 213.5 buds/branch, and the third group includes Sevillana under drip irrigation with 130.25 buds/branch and Arbequina under submersion with 110.6 buds/branch (Table 4).

Table 4. Analysis of variance for the parameter number of floral buds per branch

Case	Degree of Freedom	Number of Floral Buds per Branch	
		Average Square	Probability
Variety	1	88305	NS 0.125372
Irrigation	1	58397	NS 0.209407
Variety x Irrigation	1	283693	THS 0.008480

### 3.1.5 Number of Clusters Per Branch

The highest average number of clusters per branch is recorded for the Sevillana variety with 150 clusters/branch, in contrast to the Arbequina variety which has a lower number with 100 clusters/branch.

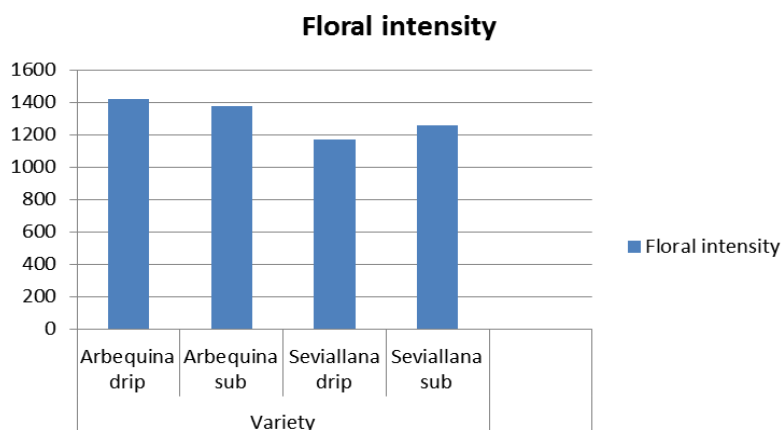
**Table 5.** Analysis of variance for the parameter number of clusters per branch

Case	Degree of Freedom	Number of Clusters per Branch	
		Average Square	Probability
Variety	1	312500	NS 0.099404
Irrigation	1	84500	NS 0.383045
Variety x Irrigation	1	800000	S 0.010909

The variation is significant for the interaction variety x irrigation, with the emergence of three heterogeneous groups: Sevillana under submersion with 25.4 clusters/branch, the second group consists of Arbequina under drip irrigation with 15.9 clusters/branch and Sevillana under drip irrigation with 12.1 clusters/branch, and the third group is formed by Arbequina under submersion with 9.1 clusters/branch (Table 5).

### 3.1.6 Number of Floral Buds Per Linear Meter (Floral Intensity)

The results show that the number of floral buds per branch per linear meter varies according to the variety and irrigation type. The highest average is recorded for Arbequina under submersion and Sevillana under submersion with 1435.46 and 1368.62 floral buds per linear meter, respectively. The lowest average is recorded for drip irrigation for both varieties, with 1138.26 and 1294.38 floral buds per linear meter (Figure 3).



**Figure 3.** Floral intensity of the two varieties under the two irrigation methods

From a statistical perspective, there are no significant differences between varieties, irrigation types, or the interaction of variety x irrigation for the floral intensity parameter.

### 3.1.7 Fertilization Rate

The same measurements taken for flowering were retained to evaluate the fertilization rate.

**Table 6.** Average fertilization rate

Variety	Arbequina		Sevillana	
	Submersion	Drip Irrigation	Submersion	Drip Irrigation
Average (%)	1.62%	1.13%	2.65%	0%

The highest fertilization rate is recorded for the Sevillana variety under submersion irrigation with 2.65%, and 0% for drip irrigation. The Arbequina variety shows average values around 1.62% for submersion irrigation and 1.13% for drip irrigation (Table 6). The low fertilization rate observed for both varieties is attributed to water shortage and, consequently, water stress that may impact fruit formation through pistillar abortion [7].

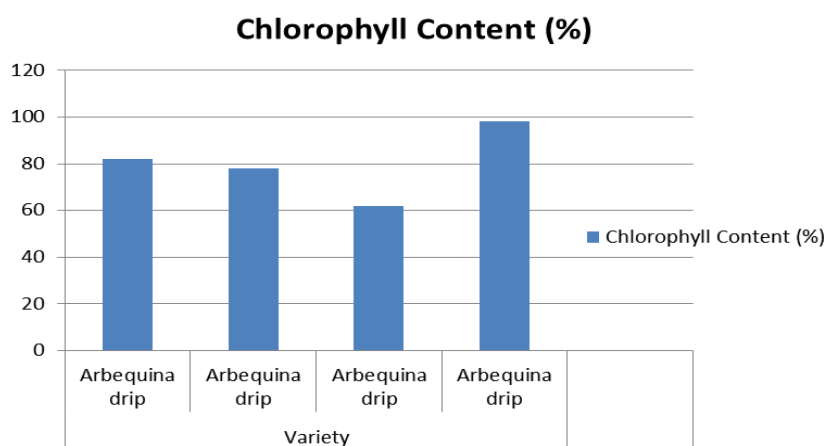
**Table 7.** Analysis of variance for the fertilization rate parameter

Case	Degree of Freedom	Fertilization rate	
		Average Square	Probability
Variety	1	0.02475	NS 0.832445
Irrigation	1	19.76633	THS 0.000002
Variety x Irrigation	1	9.34200	THS 0.000282

There are non-significant differences between varieties. However, differences are highly significant for the irrigation factor and the interaction variety x irrigation. For the irrigation factor, two groups emerge: submersion with a higher fertilization rate than drip irrigation, with 2.14% and 0.57%, respectively. For the interaction, three groups are recorded: the first includes the Sevillana variety under submersion with 2.6%, the second includes Arbequina under submersion with 1.6% and Arbequina under drip irrigation with 1.13%, and the third group represents Sevillana under drip irrigation with 0% (Table 7).

### 3.2 Physiological Leaf Characteristics

Analysis of the results for the chlorophyll content parameter showed that the highest value was recorded for the Sevillana variety irrigated by submersion with 98.54%. In contrast, the lowest value was observed for the Sevillana variety irrigated with drip irrigation at 62%. Meanwhile, the chlorophyll content values recorded for the Arbequina variety were moderate (Figure 4).



**Figure 4.** Chlorophyll content of the two varieties under the two irrigation methods

The increase in total chlorophyll content is a consequence of the reduction in the size of leaf cells due to water stress, resulting in a higher concentration [8]. On the other hand, the decrease in chlorophyll content is a consequence of the reduction in stomatal opening, aimed at limiting water loss through evapotranspiration and increasing resistance to the entry of atmospheric CO<sub>2</sub> necessary for photosynthesis [9]. The quantity of leaf chlorophyll can be influenced by various factors such as leaf age, leaf position, and environmental factors like light, temperature, and water availability [10].

There is a significant variation in chlorophyll content for the Variety x Irrigation interaction, forming three heterogeneous groups: the first group with Sevillana under Submersion at 92.7%, the second with Arbequina under Drip Irrigation at 80.6%, and Arbequina under Submersion at 73.01%. The third group includes Sevillana under Drip Irrigation at 71.4% (Table 8).

**Table 8.** Analysis of variance for the parameter chlorophyll content

Case	Degree of Freedom	Chlorophyll Content	
		Average Square	Probability
Variety	1	218.4	NS 0.453204
Irrigation	1	374.0	NS 0.328047
Variety x Irrigation	1	1673.3	HS 0.044341

### 3.3 Phenological Characteristics

Phenology studies the biological cycles of plants and their connection with climatic conditions. The study of phenology involves recording the different stages of growth and development of plants, for both varieties under the two irrigation types (Table 9).

**Table 9.** Dates of phenological phases for the two studied varieties under both irrigation types

Variety		Budburst Date	Cluster Formation Date	Flowering Date	Fertilization Date
Arbequina	Drip Irrigation	Mar. 17, 2023	Apr. 25, 2023	May 16, 2023	Jun. 13, 2023
	Submersion	Mar. 15, 2023	Apr. 25, 2023	May 14, 2023	Jun. 12, 2023
Syviana	Drip Irrigation	Mar. 15, 2023	Apr. 20, 2023	May 13, 2023	-----
	Submersion	Mar. 16, 2023	Apr. 24, 2023	May 16, 2023	Jun. 12, 2023

#### 3.3.1 Bud Break

The reproductive cycle of the olive tree begins with rising temperatures, typically in late February or early March. The bud break stage is a varietal criterion influenced by the climate of the tree's region.

The onset of bud break is nearly the same for both varieties and both irrigation types, around Mar. 15, 2023 for Arbequina with submersion and Syviana with drip, followed by Syviana with submersion around Mar. 16, 2023, and finally Arbequina with submersion on Mar. 17, 2023 (Table 9). The irrigation type seems to have a negligible effect on bud break.

#### 3.3.2 Cluster Formation

Inflorescences consist of long clusters with 4 to 6 secondary ramifications. The number of flowers varies based on the cluster's position on the branch [12].

Cluster appearance begins on Apr. 20, 2023 for Syviana trees irrigated with drip. After a few days, clusters on Syviana irrigated with submersion appear around Apr. 24, 2023. For the Arbequina variety, clusters appear for both irrigation types around Apr. 25, 2023 (Table 9).

#### 3.3.3 Flowering

Floral buds transform into flower parts to produce flowers; this stage begins around May 13, 2023 for Syviana trees under drip irrigation, followed by May 14, 2023 for Arbequina under submersion. After two days, this stage is reached for Arbequina under drip and Syviana under submersion, both flowering around May 16, 2023 (Table 9).

#### 3.3.4 Fertilization

The same shoots used to measure flowering were retained to assess the fertilization rate. The fertilization rate calculation is performed on Jun. 15, 2023 (Table 9).

The appearance of young fruits begins on Jun. 11, 2023 for both varieties under submersion irrigation. After one day, it begins for Arbequina under drip irrigation around Jun. 13, 2023. However, no fruit was recorded for Syviana under drip irrigation due to the presence of a disease.

## 4. CONCLUSION

Olive cultivation plays a crucial role in our country's social and economic life, representing 15% of the national agricultural product and contributing significantly as a source of currency.

The goal of our study was to compare the effect of irrigation types, specifically drip and submersion, on the phenological, morphological, and physiological development of two olive tree varieties: Arbequina and Syviana. The results obtained are as follows:

- The largest leaf area is observed in Syviana under drip irrigation with 18.02 cm<sup>2</sup>.
- The overall appearance of the trees indicates that both varieties exhibit moderate vigor, with a spreading canopy for Arbequina and an upright posture for Syviana, with loose leaf density.
- Chlorophyll levels are highest in Syviana under submersion with 98.54%.
- The number of stomata/mm<sup>2</sup> is highest in leaves of trees subjected to drip irrigation.
- The number of floral buds per branch and the number of clusters per branch favor Syviana with 2175 floral buds per branch and 150 clusters per branch, respectively.
- Floral intensity (number of floral buds/linear meter) is higher for submersion irrigation compared to drip irrigation.
- Fertilization rate is highest for Syviana under submersion with 2.56%, while Syviana under drip shows 0%.

Phenological stages of olive trees in the study area reveal slight differences between the two tested varieties, with bud break in mid-March, cluster formation in late April, flowering in mid-May, and fertilization in mid-June.

Variance analysis shows non-significant differences between varieties for most measured traits, except for leaf area. However, the Variety x Irrigation interaction is highly significant for many traits, such as stomata/mm<sup>2</sup>, floral buds per branch, and fertilization rate.

In conclusion, drip irrigation yields better results for many measured traits, including shoot growth, stomata/mm<sup>2</sup>, and chlorophyll levels. Irrigation significantly influences the productive and qualitative performance of olive trees by promoting vegetative growth. Therefore, drip irrigation appears to be suitable and economical for olive cultivation.

Syviana exhibits interesting characteristics from a morphological and physiological perspective, including chlorophyll levels, stomata/mm<sup>2</sup>, floral buds per branch, and clusters per branch.

## References

- [1] J. E. Fernandez, "Understanding olive adaptation to abiotic stresses as a tool to increase crop performance," *Environmental and Experimental Botany*, vol. 103, pp. 158–179, 2014.
- [2] N. Zouiten and I. El Hadrami. "The olive psylla: State of knowledge and perspectives for control," *Cahiers Agricultures*, vol. 10, no. 4, pp. 225–233, 2001.
- [3] O. Hobaya, "Contribution to the study of pests of the olive tree (*Olea europaea* L.) in Tlemcen", thesis, University of Tlemcen, 2012.
- [4] Directorate of Agricultural Services of Bordj Bou Arreridj, 2023.
- [5] Methodology for Primary Characterisation of Olive Varieties, Project RESGEN-CT (67/97), EU/IOC, International Olive Council (IOC), 1997.
- [6] G. Allen, S. Pereira, D. Raes, and M. Smith, "Crop evapotranspiration, guidelines for computing crop water requirements," FAO Irrigation and Drainage, 1998.
- [7] L. Rallo, G. C. Martin, and S. Lavee, "Relationship between abnormal embryo sac development and fruitfulness in olive," *Journal of the American Society for Horticultural Science*, vol. 106, no. 6, pp. 813–817, 1981.
- [8] N. Siakhène, "Effect of water stress on some areas of annual alfalfa," thesis, Engineering Memory, El Harrach, 1984.
- [9] R. Bousba, N. Ykhlef, and A. Djekoun. "Water use efficiency and flat photosynthetic response to water deficit of durum wheat (*Triticum durum* Desf)," *World Journal of Agricultural Sciences*, vol. 5, no. 5, pp. 609–616, 2009.
- [10] K. Hikosaka, K. Ishikawa, A. Borjigidai, O. Muller, and Y. Onoda, "Temperature acclimation of photosynthesis: mechanisms involved in the changes in temperature dependence of photosynthetic rate," *Journal of Experimental Botany*, vol. 57, no. 2, pp. 291–302, 2006.
- [11] L. Trabelsi, "Adaptation of nutritional strategies of the olive tree (*Olea europaea* L.) to different water regimes in an arid environment," Ph.D. thesis, National Engineering School of Sfax, Tunisia, 2020.
- [12] A. Ouksili, "Contribution to the study of the floral biology of the olive tree (*Olea europaea* L.). from the formation of flowers to the period of effective pollination," Ph.D. thesis, E.N.S.A.M. Montpellier, 1983.





## Estimating Aphid Parasitoid Diversity in Guelma's Citrus Orchards, Eastern Algeria

Omar Khaladi<sup>\*1</sup>, Amira Bouderbala<sup>2</sup>

<sup>1</sup>Department of Ecology and Environmental Engineering, University 8 May 1945 Guelma, BP 401, Guelma, 24000, Algérie

<sup>2</sup>Laboratory of Agriculture and Ecosystem Functioning, Department of Agronomy Sciences, Faculty of Natural and Life Sciences, Chadli Bendjedid University - El Tarf, Algeria

---

### Abstract

The importance of understanding beneficial insects in agroecosystems has increased due to the excessive use of chemicals that disrupt their presence and sometimes lead to their unintentional extermination. This study aims to conduct an initial inventory of aphid parasitoids belonging to the subfamily Aphidiinae during the spring sap flow period from 2016 to 2019 in orange orchards located in the Guelma region (Eastern Algeria) and to estimate their richness using four non-parametric estimators. Ten species were captured: *Aphidius matricariae* (Haliday, 1834), *Aphidius* sp., *A. ervi* (Haliday, 1834), *Binodoxys angelicae* (Haliday, 1833), *B. acalephae* (Marshall, 1896), *Diaeretiella rapae* (McIntosh, 1855), *Ephedrus plagiator* (Nees, 1811), *Praon volucre* (Haliday, 1833), *Lipolexis gracilis* (Foerster, 1862), and *Lysiphlebus testaceipes* (Cresson, 1880). The most dominant species were *L. testaceipes*, *B. angelicae*, and *A. matricariae*. The non-parametric estimators indicated an average of  $11.39 \pm 0.54$  species, suggesting that the potential richness could extend to 12 species with a sampling accuracy of 87.74%.

**Keywords:** *Aphidiinae*, *Guelma province*, *Eastern Algeria*, *Citrus*, *Parasitoids*

---



---

## Egg Quality Characteristics of Local Laying Hens in Oasis Family Farms of Adrar (Algeria)

Abderrahmen Boubekour<sup>\*1,2</sup>, Mohammed Bouallala<sup>2</sup>, Redhwen Bari<sup>2</sup>, Mohammed Souddi<sup>2</sup>

<sup>1</sup>Higher School of Saharan Agriculture, Adrar, Algeria

<sup>2</sup>Saharan Natural Resources Laboratory, Faculty of Natural and Life Sciences, University of Ahmed Draia, Adrar, Algeria

---

### Abstract

This study aimed to evaluate the morphological characteristics, in terms of composition, of local hens eggs exploited in Adrar. A total of 60 eggs from six family breeding farms were analyzed. The studied egg quality parameters included weights (egg, yolk, albumen, shell) and dimensions (length, large diameter). The shape index, the yolk/albumin ratio and the proportion of albumin, yolk and shell were calculated.

The eggs from local chickens collected had an average weight of  $44.42 \pm 0.71$  g. Weighing of different parts of the egg showed that the weight of albumin, yolk and shell were  $24.72 \pm 0.65$  g,  $14.96 \pm 0.22$  g and  $4.87 \pm 0.07$  g respectively. The average egg dimensions were  $52.06 \pm 0.24$  mm for length and  $36.93 \pm 0.25$  mm for large diameter with an average shape index of  $0.71 \pm 0.005$ . The yolk/albumin ratio was  $0.63 \pm 0.02$  and the proportions of albumin, yolk and shell were respectively  $55.24 \pm 0.73\%$ ,  $34.19 \pm 0.64\%$  and  $11.04 \pm 0.16\%$ . The shades of shell coloring (redhead = 45.0%; white = 31.7%; brown = 23.3%) were listed for all the eggs, which reflects the diversity of hens exploited. The values recorded for yolk pH tend towards acidity (6.70) and the values recorded for albumin pH tend towards alkalinity (9.29). All combinations of correlation between egg weight and other variables are significant ( $p < 0.01$ ) except the combination with yolk weight which is not significant ( $P > 0.05$ ). The yolk weight is not as correlated with the other parameters studied (length, diameter, albumin weight, shell weight and shape index).

These results make it possible to classify the eggs produced by these farms in commercial category "D". Thus, the high proportion of yolk (34.19%) can be considered favorable from the point of view of the nutritional value of egg.

**Keywords:** Algeria, Family breeding, Oasis, Local chicken, Food security

---



---

## Impact of *Thymus Vulgaris* and *Lavandula Angustifolia* Essential Oils on the Carcass Characteristics of Broiler Chickens

Benameur Qada<sup>\*1</sup>, Laah Jude Attat<sup>1</sup>, Sidi Faruk<sup>1</sup>, Kassous Tahar<sup>2</sup>, Arabi Abed<sup>3</sup>

<sup>1</sup>Department of Agronomy, Faculty of Natural and Life Sciences, Abdelhamid Ibn Badis Mostaganem University, 27000 Mostaganem, Algeria

<sup>2</sup>Algeria Animal Care, Algeria

<sup>3</sup>Department of Biology, Faculty of Natural and Life Sciences, Abdelhamid Ibn Badis Mostaganem University, 27000 Mostaganem, Algeria

---

### Abstract

This study aimed to evaluate the impact of *Thymus vulgaris* and *Lavandula angustifolia* essential oils (TEO and LEO) on carcass traits of broiler chickens. A total of 160 day-old broiler chicks (Cobb 500) of both sexes were used in the form of a completely randomized design with 5 treatment batches. Broiler chickens in batches 1, 2 and 3 received drinking water supplemented with TEO 250 $\mu$ L/L, LEO 250 $\mu$ L /L, and TEO 125 $\mu$ L /L + LEO 125 $\mu$ L /L, respectively. Those in batch 4 (negative control) were received drinking water with no EO addition. Broiler chickens in batch 5 (positive control) were treated with several antimicrobial and antiparasitic agents. To investigate the characteristics of the carcass, three birds were randomly selected for each replicate, and their weights were recorded before and after slaughtering. The weight of the whole carcass and its different parts, the internal organs and abdominal fat were also measured. The percentage of each component was measured by dividing the weight of each section by the pre-slaughter live weight before slaughtering. The results of this study showed that the T+LEO group had the highest carcass percentage (74.6) while the control group had the lowest (69.7) ( $P < 0.05$ ). The TEO group had the highest thigh percentage (18.9%)( $P < 0.05$ ). The negative control group had the highest liver weight percentage (3.07%), while the TEO and T+L EO groups had lower liver weight percentages (2.4 and 2.48% respectively)( $P < 0.05$ ). In conclusion, TEO and LEO alone or combined can improve growth performance and carcass characteristics in broiler chickens, providing a viable alternative to antibiotics in poultry farming.

**Keywords:** *Thyme, Lavender, Essential oil, Antibiotics, Carcass characteristics, Broiler chicken*

---



---

## Effect of an Essential Oils Mixture on the Growth Performance of Broiler Chickens

Laah Jude Attat<sup>1</sup>, Benameur Qada<sup>\*1</sup>, Sidi Faruk<sup>1</sup>, Kassous Tahar<sup>2</sup>, Arabi Abed<sup>3</sup>

<sup>1</sup>Department of Agronomy, Faculty of Natural and Life Sciences, Abdelhamid Ibn Badis Mostaganem University, 27000 Mostaganem, Algeria

<sup>2</sup>Algeria Animal Care, Algeria

<sup>3</sup>Department of Biology, Faculty of Natural and Life Sciences, Abdelhamid Ibn Badis Mostaganem University, 27000 Mostaganem, Algeria

---

### Abstract

The primary goal of this research was to evaluate the effect of an essential oils (EOs) mixture (*Thymus vulgaris* and *Lavandula angustifolia* essential oils: TEO and LEO) on the growth performance of broiler chickens. A total of 160 day-old Cobb 500 broiler chickens of both sexes were randomly subjected to five different treatment batches having four replicates per treatment with eight birds in each replicate. The experimental treatments 1, 2 and 3 received, respectively, drinking water supplemented with TEO 250 $\mu$ L/L, LEO 250 $\mu$ L /L, and TEO 125 $\mu$ L /L + LEO 125 $\mu$ L /L, without antibiotics and antiparasitics. Birds in batch 4 (negative control) were received drinking water without additives and those in batch 5 (positive control) were treated with several antimicrobial and antiparasitic agents. Throughout the 42-day trial, growth metrics, feed intake, and feed conversion ratio (FCR) were recorded every week to determine the growth performance. The results of this study showed that TEO, T+LEO and LEO supplementation increased body weight by 10.37%, 5.42% and 4.33% at 42 day of age, respectively ( $P < 0.05$ ). The feed intake was reduced in the group received an EOs mixture by 2.27% when compared to the control group ( $P < 0.05$ ) and it was increased by 12.16% in the positive control group ( $P < 0.05$ ). Also, the feed conversion ratio (FCR) decreased and the average daily gain (ADG) increased in chickens that had EOs added to drinking water when compared to the negative control group ( $P < 0.05$ ). In conclusion, TEO and LEO alone or in combination may be suggested as an alternative for antibiotic growth promoter in stimulating the productivity of commercial broilers.

**Keywords:** *Thyme, Lavender, Essential oil mixture, Growth performance, Broiler chicken*

---



## Comparative Study of the Biogas Yield of Three Olive Mill Wastewater in the Thermophilic Phase

Bani Kheiredine<sup>\*1</sup>, Amrouci Zahra<sup>1</sup>, Belmili Zineb<sup>2</sup>, Ghetahem Dalal<sup>2</sup>

<sup>1</sup>Laboratory for Research on Medicine and Sustainable Development (REMEED), University Constantine 3, Algeria

<sup>2</sup>University Constantine 3, Algeria

---

### Abstract

The research work in this thesis concerns the study of the biodegradability of three Olive mill wastewater from three regions of Algeria (Mila, Jijel, Bejaia), in anaerobic mode. The tests were carried out in a series of 150ml and 250ml reactors in the thermophilic phase (55°C). The characteristics before incubation showed that the three Olive mill wastewater had good solubility. The solubility of Jijel Olive mill wastewater had the best DCOs/DCOt ratio, equal to 88.88%.

The study of biodegradability by the process of anaerobic digestion in the thermophilic phase revealed that Jijel Olive mill wastewater gave the best specific biogas and methane production of the order of 192.25ml/gTVS in the thermophilic phase.

**Keywords:** Olive mill wastewater, Solubility, Biodegradability, Methane

---



## Enhancing the Quality of PET Images Reconstructed by Filtered Back Projection and Ordered Subsets Expectation Maximization

Benyelles Asma<sup>\*1</sup>, Korti Amel<sup>1</sup>

<sup>1</sup>Department of Biomedical Engineering, University of Aboubakr Belkaid, Tlemcen, Algeria

---

### Abstract

Positron emission tomography (PET) is a medical imaging technique that uses scintigraphy to examine the physiological function of the human body. It involves the use of a high-performance gamma camera to detect gamma rays emitted by radioactive elements injected into the patient's body. These rays pass through the gamma camera's components and are converted into a scintigraphy image, which shows the distribution of the radioactive elements in the target organ. However, the scintigraphy image reconstruction process can encounter challenges due to the selection of image reconstruction techniques or the various components of the gamma camera. These factors can result in a decline in the quality of the image. This paper utilizes the analytical reconstruction method known as filtered back projection (FBP) and the iterative method called ordered subset expectation maximization (OSEM). We then devise a system that enhances the quality of the reconstructed image to eliminate artifacts that occur during the acquisition process. The evaluation of these data will be conducted using two performance evaluation parameters: the signal-to-noise ratio (PSNR) and the mean square error (MSE). Based on the acquired results, it is evident that our system yields an optimal outcome using both methods. However, the iterative method requires more computational time compared to the analytical method.

**Keywords:** *Gamma camera, Reconstruction methods, Artifacts, PET, Improvement, Image quality, Image processing*

---



## Artificial Intelligence in Camel Racing: Health Maintenance and Prevention

Amira Djeddou Benabid<sup>\*1,2</sup>, Hind Houssou<sup>1,2</sup>, Khaled Djeddi<sup>1,2</sup>, Dounia Ouachtati<sup>1,2</sup>

<sup>1</sup>Institut of Agronomic and Veterinary Sciences, Souk Ahras University, Algeria  
<sup>2</sup>Laboratory of Sciences and Techniques of the Living, Souk Ahras University, Algeria

---

### Abstract

Traditional camel racing is a popular sport in many countries and it is infused with cultural significance. The integration of artificial intelligence (AI) has brought promising innovations that continue to revolutionize this traditional sport, AI can provide real-time data analysis that can lead to precision training, optimized nutrition, and the prevention of injuries as well as illnesses. Here are some ways in which AI is implemented in camel racing: Performance Forecasting and AI-Assisted Training; capable of providing personalized feedback that helps optimize training programs for each camel, Nutrition Optimization; using biometric tracking sensors, monitoring devices, smart scales, and nutritional management software, specific nutrition plans are recommended for each camel based on its age, weight, energy requirements, and physical condition. Advanced Medical Management by combining a Camel Behavior Monitoring System; using sensors that identify various physiological indicators such as heart rate, respiratory rate, body temperature, blood pressure, and oxygen saturation to detect signs of fatigue or stress, with Advanced Veterinary Technologies such as Magnetic Resonance Imaging (MRI) and CT scanners, the aim is to swiftly diagnose injuries and illnesses and provide appropriate treatment. Not forgetting Dr. Doumir's innovation: The "Camel Racing Diagnostic Boots," a device that diagnoses lameness in racing camels using specialized sensors. These applications of AI contribute to modernizing camel racing, bringing significant benefits in terms of performance, animal well-being, and the overall competition experience.

**Keywords:** *AI, Camel racing, Diagnostic, Prevention, Veterinary technologie*

---



---

## Antimicrobial Profile of Asian Honey Bee Using Culture Dependent Method

Iram Liaqat<sup>\*1</sup>

<sup>1</sup>Microbiology Laboratory, Department of Zoology, Government College University, Lahore, Pakistan

---

### Abstract

The bacteria residing in the gut of honey bees (HB) has demonstrated a significant role in protecting bees against various pathogens, production of honey and wax. However, no information exists about the antibacterial potential of bacterial isolates from gut of Asian HB, *Apis cerana Indica* F. (Hymenoptera: Apidae), against human pathogens. This study aims to investigate the antibacterial and multienzyme potential of aerobic bacteria from *A. cerana* gut using culture dependent approach. A total of 12 HB gut bacteria were characterized morphologically and biochemically. These strains were further screened for their antimicrobial activity against pathogenic human microorganisms. Preliminary characterization of cell-free supernatant (CFS) of two promising isolates was performed by measuring lactic acid concentrations, enzymatic digestion of antimicrobial compounds, stability over a range of temperature, pH and amplification of *spaS* (subtilin) and *spoA* (subtilosin) genes. In primary screening, among 12 HB isolates, eight strains showed statistically significant highest zones of inhibition ( $p \leq 0.05$ ) against *E. coli*, *K. pneumoniae* and *P. aeruginosa*. 16S rRNA sequencing revealed that these isolates belong to *Bacillus* genus, identified as *B. tequilensis*, *B. pumilus*, *B. xiamenensis*, *B. subtilis*, *B. amyloliquefaciens*, *B. safensis*, *B. licheniformis*, *B. altitudinis* (Accession numbers: MT186230-MT186237). Secondary screening revealed that among eight isolates, *B. subtilis* and *B. amyloliquefaciens* showed statistically significantly strong inhibition ( $p \leq 0.05$ ) against all tested pathogens. Antibiotic susceptibility testing revealed that both isolates were resistant to antibiotics and possesses proteolytic, lipolytic and cellulolytic activities. The nature of the compound causing inhibitory activity was found to be proteinaceous and showed stability over a wide range of temperature as well as pH. PCR study confirmed the presence of bacteriocins by successful amplification of important antimicrobial peptide biosynthesis genes *spaS* and *spoA*.

**Keywords:** Honey bees, Gut microbes, Antimicrobial activity, *B. amyloliquefaciens*, *B. subtilis*, *A. cerana*

---





## Medical Image Analysis Using Neural Networks

**Berrimi Fella<sup>\*1</sup>**

*<sup>1</sup>Department of Computer Science, University of Ferhat Abbas, Setif, Algeria*

---

### **Abstract**

Medical image analysis through neural networks is reshaping healthcare by revolutionizing the interpretation of medical images. These neural networks, inspired by the human brain's structure, process complex medical data such as X-rays, MRIs, CT scans, and ultrasounds. Through supervised learning, where models learn from labeled examples, neural networks adjust their parameters to minimize errors between predicted and actual outputs. This involves preprocessing data, splitting it into training, validation, and test sets, training the model, and evaluating its performance.

Convolutional Neural Networks (CNNs), a specialized architecture within neural networks, excel in analyzing spatial data like images. They extract hierarchical features from medical images, enabling tasks like classification, segmentation, and detecting abnormalities. Applications of medical image analysis using neural networks are vast, including tumor detection, organ segmentation, and clinical outcome prediction. These techniques support healthcare professionals in diagnosis and treatment planning, automating tasks and improving efficiency.

However, challenges remain, such as the need for large labeled datasets, algorithmic bias, and ensuring model interpretability and transparency. Overcoming these challenges is essential for the safe and effective integration of neural network-based medical image analysis into clinical practice.

In summary, medical image analysis through neural networks promises enhanced diagnostic capabilities, streamlined workflows, and improved patient outcomes. With continued research and collaboration, this transformative technology will advance medical imaging and revolutionize healthcare delivery.

**Keywords:** *Medical image analysis, Neural networks, Supervised learning, Clinical decision-making*

---



## Exploring the Potential of the Genus *Achillea* on Antiproliferative and Apoptotic Effects of Human Cancer Cell Lines

Renda Chahna\*<sup>1</sup>

<sup>1</sup>Laboratory of Plant Biology and Environment, Department of Biology, Faculty of Sciences, Badji Mokhtar University, Annaba, 23000, Algeria

---

### Abstract

Plants have been used for medical purposes since the beginning of human history and are the basis of modern medicine. Most chemotherapeutic drugs for cancer treatment are molecules identified and isolated from plants or their synthetic derivatives. Our hypothesis was that whole plant extracts selected according to ethnobotanical sources of historical use might contain multiple molecules with antitumor activities that could be very effective in killing human cancer cells. This study examined the effects of one plant extract (ethanol extraction) on human tumor cells. The extracts were from *Achillea cretica* (*Asteraceae*). Our plant extract exhibited dose- and time-dependent killing capabilities in various human derived tumor cell lines and primary cultures established from patients' biopsies.

The killing activity was specific toward tumor cells, as the plant extract had no effect on primary cultures of healthy human cells. Cell death caused by the whole plant extracts is via apoptosis. Plant extract (*Achillea cretica*) showed particularly strong anticancer capabilities since it inhibited actual tumor progression. Our results suggest that the aerial parts of our plant extract is promising anticancer reagent

**Keywords:** Anticancer, *Achillea cretica*, Ethnobotanical, Cancer cell line

---



## **Study and Prevention of Occupational Risks (Case of the Elmalabiod Cement Plant)**

**Taleb Mounia<sup>\*1</sup>**

*<sup>1</sup>Department of Mines and Geotechnology, Echahid Cheikh Larbi Tebessi University, Tebessa, Algeria*

---

### **Abstract**

The main purpose of safety is to eliminate unacceptable risks that could be responsible for physical injuries, harm to human health, or even death, degrade the environment and causes high-cost production. It is also methodologies to follow, technical means to deploy. For this, different methods can be used to determine the safety integrity level of a SIL safety instrumented function. This study is carried out at the Elmalabiod Tébessa cement plant. Having the objective of controlling professional risk in order to evaluate the SIL level in this company. Thus, providing an improvement in the operation and performance of its installations, as well as their security. In this study, we used the what-if method to identify all the scenarios and dissect their sequences, and we finalized our work by proposing a new risk management method, this is the HAZOP method.

**Keywords:** *Occupational risk, Prevention, What if method, HAZOP, Risk management*

---



---

## Effectiveness of Aeration Followed by Statistical Optimization of AOP'S (Ultraviolet/Ultrasonic Active Persulfate/Hydrogen Peroxide) Process Parameters for the Treatment of Young Landfill Leachate

Hamza Bellouk<sup>\*1</sup>, Ilham Zouitane<sup>2</sup>, Imane El Mrabet<sup>3</sup>, Naima El Ghachtouli<sup>2</sup>, Hicham Zaitan<sup>\*1</sup>

<sup>1</sup>Laboratory of Process's, Materiel's and Environment, Faculty of Sciences and Techniques Sidi Mohamed Ben Abdellah University Fez, Morocco

<sup>2</sup>Laboratory Microbial Biotechnology and Bioactive Molecules, Faculty of Sciences and Techniques Sidi Mohamed Ben Abdellah University Fez, Morocco

<sup>3</sup>Team of Applied Chemistry, Geo-Mining, and Modeling (CAG2M), Polydisciplinary Faculty of Ouarzazate, Ibnou Zohr University, 45000, Ouarzazate, Morocco

---

### Abstract

In this study, young leachate from the Fez City landfill underwent biological pretreatment through aeration and treatment via a novel advanced oxidation process (AOP) employing a blend of two inorganic oxidation systems (potassium persulfate (K<sub>2</sub>S<sub>2</sub>O<sub>8</sub>) and hydrogen peroxide (H<sub>2</sub>O<sub>2</sub>)) simultaneously applied with UV-A irradiation and ultrasonic (US) treatment. Initial aeration treatment yielded removal efficiencies of 53% for COD, 55% for Abs<sub>254</sub>, and 78% for CN. The effectiveness of the AOP was statistically evaluated, and optimal operational conditions were determined using Box-Behnken Design (BBD) to examine the impact of three operating variables (pH, S<sub>2</sub>O<sub>8</sub><sup>2-</sup>, and H<sub>2</sub>O<sub>2</sub>) on three target responses: COD, Abs<sub>254</sub>, and color removal. Statistical and graphical analyses revealed that the sequential process involving aeration as pretreatment followed by the application of the H<sub>2</sub>O<sub>2</sub>-PS-US-UV-A system achieved maximum efficiencies of 77% for COD, 99% for color removal, and 91% for Abs<sub>254</sub>, respectively, under optimal conditions of [H<sub>2</sub>O<sub>2</sub>] of 500 mg/L, [S<sub>2</sub>O<sub>8</sub><sup>2-</sup>] of 1671 mg/L, and a pH of 3. Microbiological analyses demonstrated complete removal of total coliforms, fecal coliforms, and total mesophilic flora through sequential AOPs and aeration treatment. This underscores the potential of the combined processes as a promising technique for eliminating high concentrations of pathogenic microorganisms in young leachates.

**Keywords:** Leachate, AOP, Aeration, Box-behnken design

---



## Sono-Pyrolysis of Methane for Enhanced Hydrogen Production

Aissa Dehane<sup>\*1</sup>, Slimane Merouani<sup>1</sup>, Atef Chibani<sup>2</sup>

<sup>1</sup>Laboratory of Environmental Process Engineering, Department of Chemical Engineering, Faculty of Process Engineering, University Constantine 3 Salah Boubnider, P.O. Box 72, Constantine 25000, Algeria

<sup>2</sup>Research Center in Industrial Technologies CRTI, P.O. Box 64, Cheraga, Algiers 16014, Algeria

---

### Abstract

The use of sonolysis on specific substrates in water has demonstrated its effectiveness in improving the sonochemical production of hydrogen. This study explores the sonolysis of methane within a single acoustic bubble (microreactor) across frequencies ranging from 140 to 515 kHz. Regardless of the amount of methane present within the bubble, the hydrogen yield notably increased as the wave frequency decreased, ranging from 515 to 140 kHz. At driving frequencies of 140, 213, 355, and 515 kHz, the hydrogen production reached its maximum levels with methane concentrations of 20%, 15%, 10%, and 10%, respectively. At 213 kHz, with 10% methane present, the hydrogen yield increases by 111 times compared to when the gas atmosphere is saturated only with argon. The highest methane conversions (close to 100% for 2%, 5%, and 7% CH<sub>4</sub>) were achieved at 140 and 213 kHz. When considering the formation of hydrogen and the decay of methane, the utilization of 140 kHz was determined to be the most effective option. An interesting observation was made that at 140 and 213 kHz, with methane mole fractions of 30% or lower and 10% or lower, respectively, there could be simultaneous maximal formation of H<sub>2</sub> and a significant production of OH radicals.

**Keywords:** Ultrasound, Sonolysis, Sono-hydrogen, Methane, Hydroxyl radicals

---



---

## Photodegradation of Metobromuron by a Photo-Fenton Like Process Using Fe(III)-Picolinic Acid Complex as Catalyst in Aqueous Medium

Sellam Badreddine<sup>\*1</sup>, Seraghni Nassira<sup>1</sup>, Bouaziz Chaima<sup>1</sup>, Sehili Tahar<sup>1</sup>

<sup>1</sup>Department of Chemistry, Laboratory of Environmental Sciences and Technologies, University Constantine 1, Constantine, Algeria

---

### Abstract

Phenylurea herbicides represent one of the largest categories of organic compounds with significant environmental risks, given their widespread agricultural usage. Among these herbicides, metobromuron is considered one of the most effective compounds against a wide range of troublesome weeds. Due to its extensive use, it is present in surface water and groundwater, posing threats to both human health and the environment. Therefore, there is a pressing need to eliminate these compounds.

The adoption of Advanced Oxidation Processes (AOPs) stands as a potent approach for eliminating recalcitrant compounds from aqueous streams and attaining substantial levels of mineralization. Amongst AOPs are photo-Fenton-like processes, which involve the addition of iron(III)-ligand complex in the presence of light.

This study investigated the effect of ultraviolet (UVA) enhancement and the Fe(III)-picolinic Complex on the degradation of metobromuron (MTB) in photo-Fenton-like system. We examined different variables, including the concentration of metobromuron, Fe(III)-picolinic acid, pH value, and reaction time, the effect of the irradiation source was studied using two sources (365nm monochromatic lamp and simulated sun light).

The results revealed that the efficiency of photocatalytic degradation was limited when photolysis was conducted in the absence of the Fe(III)-picolinic acid complex. However, the presence of both Fe(III)-picolinic acid and UVA radiation significantly enhanced the photodegradation process. Consequently, after 240 minutes of reaction, approximately 60.6% of MTB was removed. This modality of treatment can be a good alternative for decontamination and detoxification of wastewater polluted with Phenylurea herbicides compounds.

**Keywords:** *Metobromuron, Photo-fenton-like process, Fe(III)-picolinic, Photodegradation*

---



## Photocatalytic Efficiency of Pure and Cu-Doped ZnO Thin Films

**Khemissi Lahouel<sup>1\*</sup>, Abdecharif Boumaza<sup>1</sup>, Meriem Gasmi<sup>1</sup>**

<sup>1</sup>Laboratory of Structures, Proprieties and Inter Atomic Interactions, Faculty of Science and Technology, University of Abbes Laghrour, Khenchela 40000 Algeria

---

### Abstract

The synthesis of ZnO thin films doped with copper (Cu) was prepared and tested for their photocatalytic efficiency in the removal of methylene blue dye (MB). In this work, pure and copper-doped zinc oxide thin films are synthesized as a starting material by the sol-gel method and dip-coating technique and then deposited on a glass substrate to form thin layers. These films were annealed at 500 °C. The structural and optical properties of the prepared ZnO thin film were measured by X-ray diffraction (XRD) and ultraviolet spectroscopy (UV-visible) respectively, thin films are polycrystalline with a ZnO hexagonal wurtzite crystal structure and a P63mc space group (JCPDS card no. 00-036-1451), according to the structural investigation, and no other phases were found, UV-Visible transmittance All of these film spectra showed good transparency in the visible range. The SEM analysis of Cu-doped ZnO showed a nanorod smooth surface with an average diameter of about 23 nm, In addition, there is a narrow distance between each nanorod, which gives difficult access to this pore, and the EDX verified the elemental composition and uniformity of these films.

**Keywords:** Photocatalytic, Sol-gel, Thin film, X-ray diffraction, EDX, FESEM

---



---

## Exploring the Structural, Optical, and Surface Characteristics of NiO Thin Film for Environmental Applications

Meriem Gasmi<sup>\*1</sup>, Khemissi Lahouel<sup>1</sup>, Saida Hoggas<sup>1</sup>, Sabiha Hakkar<sup>1</sup>

<sup>1</sup>Laboratory of Structures, Proprieties and Inter Atomic Interactions, Faculty of Science and Technology, University of Abbes Laghrour, Khenchela, 40000 Algeria

---

### Abstract

Environmental contamination is one of the most widely discussed issues in the world today. In this study, Photocatalytic elimination of the toxic chemicals in water effluents is of interest as a green approach and surface area of the catalyst material is critical for high performance. The photocatalytic activities under UV illumination of the sample was investigated against the pollutant methylene blue dye (MB) by the photodegradation process. NiO thin film was synthesized by Sol-Gel dip coating technique (SG) is prepared on glass substrate. The structure and optical properties of thin film coating were determined by X-ray diffraction (XRD), UV-Vis spectroscopy, and scanning electron microscopy (SEM) techniques. XRD results reveals that the NiO film present a cubic structure highly oriented along (200) direction. UV- visible transmittance spectra of the prepared film revealed a good transparency in the visible region. Thin film was observed in the form of nanostructure with small size 14 nm in the SEM image. The photocatalytic properties of the NiO exhibit a good photocatalytic activity under UV light irradiation, the degradation rate of methylene blue equal to 80% for 4h of irradiation.

**Keywords:** NiO thin film, Sol-ge, Methylene blue, Photocatalytic degradation

---





---

## Voltametric and Molecular Docking Investigations of Ferrocenylmethylaniline and Its N-Acetylated Derivative Interacting with DNA

Asma Yahiaoui<sup>\*1,2</sup>, Benyza Nabil<sup>2</sup>, Amel Messai<sup>3</sup>, Touhami Lanez<sup>1</sup>, Elhafnaoui Lanez<sup>1</sup>

<sup>1</sup>VTRS Laboratory, Chemistry Department, University of El Oued, B.P.789, 39000, El Oued, Algeria

<sup>2</sup>Laboratory of Sensors, Instrumentations and Process, University of Khenchela, B.P. 1252, 40000 Khenchela, Algeria

<sup>3</sup>ISMA Laboratory, Faculty of Sciences and Technology, University of Khenchela, B.P. 1252, 40000 Khenchela, Algeria

---

### Abstract

Research on the potentially anticancer properties of ferrocene derivatives began in the late 1970s, following a groundbreaking discovery by Brynes and his colleagues. They found that ferrocene derivatives containing amine or amide functionalities exhibited antitumor effects against lymphoid leukemia. Since then, many other ferrocene derivatives have been synthesized and evaluated for their anticancer abilities. The pharmacological properties of ferrocene derivatives, especially ferrocenylanilines, have sparked considerable interest. These compounds, whether directly linked to the ferrocene fragment or separated by a methylene group, have shown promise as potential candidates for anticancer and antioxidant drugs.

The synthesis and full characterization of N-ferrocenylmethyl-aniline (FA) and its N-acetyl derivative (NFA) were carried out employing a range of physicochemical techniques, including <sup>1</sup>H and <sup>13</sup>C NMR spectroscopy. In order to study interactions between FA and NFA with chicken blood DNA, detailed analysis was performed. The techniques employed in this study were cyclic voltammetry (CV) and molecular docking (MD). The results imply a strong binding affinity of FA and NFA with the minor groove of the double helix DNA predominantly via electrostatic interactions. This inference is supported by evidence such as a negative change in the formal potential observed in CV and the effect of ionic strength. The MD analysis results closely align with those derived from CV measurements, evident through similar binding constants and free energy values. Furthermore, the binding site size was evaluated from voltammetric data.

**Keywords:** *Ferrocene derivative, DNA minor groove binding, Binding site size, Binding free energy, Docking simulations*

---



---

## Response Surface Methodology Study of Corrosion Behavior in Presence of a Pharmaceutical Drug

Naceur Benhadria<sup>\*1</sup>, Tarik Attar<sup>1</sup>, Abbes Benchadli<sup>2</sup>, Esma Choukchou-Braham<sup>2</sup>

<sup>1</sup>Department of Preparatory Class, Higher School in Applied Sciences, Tlemcen, Algeria

<sup>2</sup>Department of Chemistry, University of Abou Bekr Belkaid, Algeria

---

### Abstract

By integrating response surface methodology (RSM) into the corrosion analysis and conducting gravimetric tests, a quadratic model equation was constructed to elucidate the intricate relationships between the specified parameters and the resulting inhibition efficiency. This comprehensive investigation provided valuable insights into the interactions and effects of these variables on the corrosion inhibition process. The practical implementation of these models facilitated the identification of optimal conditions for maximizing the inhibition efficiency of a pharmaceutical compound. According to the RSM findings, the predicted inhibition efficiencies closely matched the actual experimental results, thus confirming the accuracy and reliability of the models. The optimization results vividly demonstrated a remarkable inhibition efficiency of around 98% under optimal conditions: 0.87% v/v of the pharmaceutical compound, at a temperature of 29.5°C, for duration of 6 hours and 0.5M sulfuric acid solution. Additionally, the RSM analysis revealed that the values of R<sup>2</sup> and R<sup>2</sup><sub>adj</sub> were nearly unity, indicating a strong fit of the data to the model with a confidence level of 95%. Overall, the study underscores the potential of the organic pharmaceutical compound as a potent corrosion inhibitor, providing valuable insights into its adsorption mechanism and performance under various experimental conditions.

**Keywords:** Corrosion, Inhibition, Pharmaceutical drug, RSM, Carbon steel

---



---

## Synthesis, Crystal Structure, Thermal Behavior, and Magnetic Study of 1D Cobalt (II) Coordination Polymer with Dinitrogen Tetrahydride as Bridging Ligand

Safaa Hidaoui<sup>\*1</sup>, Najlaa Hamdi<sup>1</sup>, Michal Dusek<sup>2</sup>, Nicola Morley<sup>3</sup>, Mohammed Lachkar<sup>1</sup>,  
Brahim El Bali<sup>4</sup>

<sup>1</sup>Engineering Laboratory of Organometallic and Molecular Materials, Faculty of Sciences, University Sidi Mohamed Ben Abdellah, Fez, Morocco

<sup>2</sup>Institute of Physics of the Czech Academy of Sciences, Na Slovance 2, 182 21 Praha 8, Czech Republic

<sup>3</sup>Royal Society Leverhulme Trust Senior Research Fellow 2018-2019 Department of Materials Science and Engineering, University of Sheffield, Sheffield S1 3JD, United Kingdom

<sup>4</sup>Independent Scientist, Marrakech, Morocco

---

### Abstract

A new 1D coordination polymer  $[(N_2H_5)_2Co(HPO_4)_2]$  was prepared using slow evaporation technique at room temperature. The X-ray diffraction analysis revealed that the compound crystallizes in the monoclinic system (S.G :  $P2_1/c$ ) with the cell parameters ( $\text{\AA}$ ,  $^\circ$ ) :  $a=5.3665(3)$ ,  $b= 11.1271(6)$ ,  $c= 7.7017(4)$ ,  $\beta= 104.843(4)$ ,  $V= 444.55(4) \text{\AA}^3$  and  $Z= 2$ . The crystal structure, consisting of a linear chain, is made of rings of  $[CoN_2O_4]$  octahedra and  $[PO_3(OH)]$  tetrahedra sharing vertices via oxygen atoms coordinated to cobalt centers. The rings are linked to chains running along  $[100]$  and form thereby polymeric chains that are connected by hydrogen bonds in a three-dimensional arrangement. The thermal behavior consists mainly of the loss of dinitrogen tetrahydride moieties leading thus to the formation of anhydrous cobalt phosphate. The ac magnetic susceptibility shows a peak indicating antiferromagnetic order with a Neel temperature of 5.5 K. Fitting the Curie-Weiss equation to the ac magnetic susceptibility above 50 K gives the average Curie-Weiss Constant to be -11.8 K.

**Keywords:** Cobalt, Crystal structure, Magnetism

---



---

## Vibrational Spectroscopic Analysis of 2,6-Bis(4-Fluorophenyl)-3,3-Dimethylpiperidin-4-One (BFDP), DFT, and Molecular Docking Study

Kheira Hammou<sup>\*,1,2</sup>, Mohamed Cherif Terkhi<sup>1</sup>, Nouridine Boukabcha<sup>2,3</sup>

<sup>1</sup>Laboratory of Environmental Science and Technology and Valorisation(STIVA), Materials Process Engineering, University of Abdelhamid Ibn Badis, Mostaganem, Algeria

<sup>2</sup>Laboratory of Technology and Solid Proprieties(LTPS), Materials Process Engineering, Universit of Abdelhamid Ibn Badis, Mostaganem, Algeria

<sup>3</sup>Laboratory of Technology and Solid Proprieties(LTPS), Chemistry Department, Faculty of Exact Sciences and Informatic, University of Hassiba Benbouali, Chlef, Algeria

---

### Abstract

The current study aimed to evaluate the potential of a compound called 2,6-bis(4-fluorophenyl)-3,3-dimethylpiperidin-4-one (BFDP) as a treatment for Parkinson's disease, lung cancer, and human infectious agents. To achieve this, BFDP was synthesized and analyzed using various spectroscopic methods, including NMR and FT-IR spectral studies. Vibration spectroscopy was used to identify the individual functional groups present in the material, which is a common practice in organic chemistry. Computational calculations for the molecule were performed using density functional theory (DFT) at the B3LYP/6-311G++ (d,p) level of theory. X-ray diffraction (XRD) was used to analyze the crystalline structure of BFDP. The assessment of intermolecular interactions can be done using 3D Hirshfeld surfaces (3D-HS) and 2D fingerprint plots. Additionally, quantum calculations and the DFT technique, along with topological ELF and LOL, can be used for NCI-RDG. The calculation of Hirshfeld surfaces has proven to be a useful tool for crystallographers and crystal engineers as it provides further insight into weak intermolecular forces. The molecular orbitals and their characteristics, especially in terms of energy, were used to predict the most likely type of several reactions for the molecule. Chemical reactivity and molecular structure have a significant correlation with global chemical reactivity descriptor (GCRD) parameters. To investigate the pharmacokinetic characteristics of BFDP, a molecular docking study and an in silico ADMET study were conducted.

**Keywords:** BFDP, DFT, X-ray, GCRD, Molecular docking

---



---

## Elastic Anisotropies and Electronic Properties of Tetragonal Spinel $\text{CuBi}_2\text{O}_4$ : A DFT Calculation

Rania Charif<sup>\*1</sup>, Rachid Makhloufi<sup>1</sup>

<sup>1</sup>Laboratory of Applied Chemistry (LCA), Department of Matter Sciences, Faculty of Exact Sciences and SNV, University of Biskra, P.O. Box 145, 07000, Biskra, Algeria

---

### Abstract

The aim of this work is a study of the structural, and elastic properties of the spinel  $\text{CuBi}_2\text{O}_4$ . The quantum DFT approximation used for this work was applied on the Copper Bismuth Oxide with a space group  $P4/ncc$  (130) and crystallized in tetragonal structure, with unit-cell parameters:  $a = 8.4996$ ,  $c = 5.8172$  Å. Without needing to make physical measurements, the structural characteristic of a material can be investigated by optimizing the first-principles computation. By utilizing the CASTEP code based on the pseudo-potential plane-wave within Material Studio software. This compound, known as Copper Bismuth Oxide, falls under the category of spinel oxides. It's a type of mixed metal oxide where copper ( $\text{Cu}^{2+}$ ) and bismuth ( $\text{Bi}^{3+}$ ) ions are combined with oxygen ( $\text{O}^{2-}$ ) ions.

Spinel-structured  $\text{CuBi}_2\text{O}_4$  mixed oxide, with a narrow band-gap of 1.5 eV, is a compound with intriguing properties. These distinct characteristics have motivated investigations into its potential applications. Notable among these applications are its magnetic, dielectric, and optical traits. Moreover, it shows promise in the field of photocatalytic pollutant degradation.

In this study,  $\text{CuBi}_2\text{O}_4$ 's geometrical optimization was done using a semi-local generalized gradient approximation (GGA) with the Perdew-Burke-Ernzerhof (PBE) for exchange - correlation functional. After optimization, both records of bandgap and DOS of  $\text{CuBi}_2\text{O}_4$  to understand its electronic properties. The  $\text{CuBi}_2\text{O}_4$ 's electronic properties were determined by examining the electronic band structure and density of states, which are determinants of  $\text{CoSb}_2\text{O}_6$  as a narrow gap semiconductor with a direct band gap. Additionally, we determined the elastic constants, bulk, shear and Young's moduli, Pugh ratio, Poisson's ratio, and universal anisotropy. All studied compositions of this compound show structural stability.

**Keywords:** *Density functional theory, CASTEP, Band structure, Density of states, Elastic properties,  $\text{CuBi}_2\text{O}_4$*

---



## Investigation of the Effect of Membrane Type on Ammonia Formation from Ammonium Chloride and Sodium Chloride in Two-Compartment Bipolar Membrane Electrodialysis

Fatemeh Abbasi<sup>\*1</sup>, Duygu Adiguzel<sup>1</sup>, Osman Nuri Ata<sup>1</sup>

<sup>1</sup>Chemical Engineering, Ataturk University, Erzurum, Türkiye

### Abstract

In this paper, the feasibility of using a two-compartment bipolar membrane electro dialysis (BMED) process to replace the distillation unit where ammonia is recovered in synthetic soda production was investigated. The effect of two different membrane types on ammonia formation in the bipolar membrane electro dialysis system was analysed. One of the most important environmental problems of the Solvay process, which is one of the synthetic soda production processes, is the liquid and solid wastes generated by the distillation unit. Disposal of distillation waste directly into the environment without any treatment can cause serious ecological problems in the long term. For this paper, the BMED process was used to replace the unit of distillation in the Solvay process to recover ammonia and produce HCl without generating waste. Bipolar membranes (BPM) and anion exchange membranes (AEM) were utilized in this study in which the BMED cell was designed as a two-compartment, three-repeat design. The experiments were carried out by keeping the current/voltage values (14V/4.8A) constant in the system using direct current (DC). Two different commercial membrane types, FumaTech and PCCell, were used as parameters in the study. The initial feed concentrations were kept constant and the conversion of salt solution to ammonia and HCl acid was monitored. The results showed that HCl and NH<sub>4</sub>OH concentrations were higher in PCCell membranes. The results showed that acid and base production from ammonium chloride can be realized simultaneously with both membranes and distillation waste can be disposed of.

**Keywords:** Solvay process, Soda, Bipolar membrane electro dialysis

## 1 INTRODUCTION

The Solvay process is widely used to make synthetic soda ash (Na<sub>2</sub>CO<sub>3</sub>) [1]. Applications Soda ash is extensively utilized in various industries such as glass, detergent, paper, automotive, construction, and water treatment [2]. This process generates waste from the distillation unit (DW), including NaCl, NH<sub>4</sub>Cl, and CaCl<sub>2</sub>. It is imperative to desalinate this wastewater for environmental and economic reasons [3, 4]. Methods like crystallization, evaporation, and others are used. However, these methods are associated with drawbacks like secondary salt pollution and high operational costs [5, 6].

The bipolar membrane electro dialysis (BMED) process was developed as the distillation step in the Solvay process [3, 7]. The method generates HCl, NaOH, NH<sub>3</sub>, and purified water using a BMED system with a modeled distillation column feed (DCF) composed of NaCl and NH<sub>4</sub>Cl, without any added chemicals [1, 8]. After completing the BMED, NaOH and HCl can be considered commercial goods, while NH<sub>3</sub>·H<sub>2</sub>O is recycled to the column of the absorption to meet the ammonia demand of the Solvay process [9]. The BMED process integrates the salt splitting mechanism found in traditional electro dialysis (ED) with the water decomposition function of bipolar membrane (BM) processes under an electrical field [10].

The feasibility of generating NH<sub>3</sub>·H<sub>2</sub>O and Hydrochloric acid and desalinating NH<sub>4</sub>Cl wastewater by BMED was proven by Li et al. [11]. In another study, Öner et al. concluded that temperature changes did not have a beneficial impact on base and acid production with the BMED system from NaCl- NH<sub>4</sub>Cl feed [7]. Öner et al. also examined how working parameters influenced performance criteria and identified optimal conditions using multi-criteria decision-making methods. Their study found that the major parameter that affects all performance criteria is the primary salt concentration [12]. Valorization of brine to produce Sodium Hydroxide (NaOH) and Hydrochloric Acid (HCl), through variations in the number of triplets, the type of membrane, and various current intensities, has been widely reviewed by Street. The experiments highlighted that increasing both the number of triplets and the

current density led to higher concentrations of acid and base. Furthermore, PCCell membranes exhibited greater efficiency compared to FumaTech membranes [13].

This research was conducted with the aim of the applicability of PCCell and FumaTech membranes in the conversion of waste NaCl and NH<sub>4</sub>Cl in a two-chamber BMED process, where concentrated NaOH and HCl are obtained. For the whole BMED process, which uses anion exchange membranes (AEM) together with the bipolar membrane (BM), the current density value and the number of cells were 75 A/m<sup>2</sup> and 3, respectively. In the present work, the setup of the BMED experimental system was successfully done, along with the generation of acids and bases. The experiments demonstrated that PCCell membranes were more efficient than FumaTech membranes.

## 2 MATERIAL AND METHOD

### 2.1 Membranes and Reagent

The chemicals used in this work were provided by Merck Co. Feed solution, acid solution, and electrolyte solution respectively consisted of (1.2 M NaCl and 3.17 M NH<sub>4</sub>Cl), 0.1M HCl, and 1.5M NaOH, with each fed into the system from their related tanks in the amount of 1L.

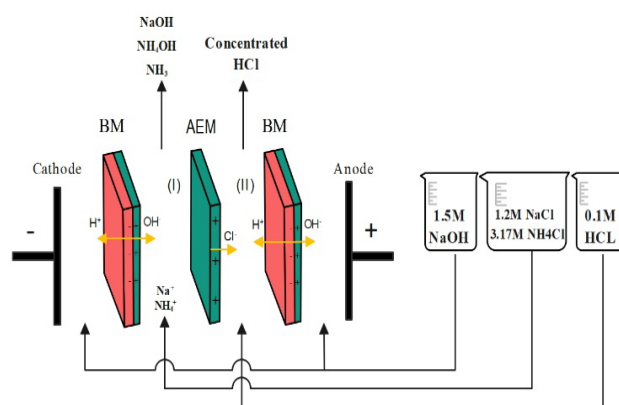
Additionally, Table 1 gives the commercial membranes' main properties used in this work.

**Table 1.** Characteristics of, bipolar membranes and anion exchange membranes used in the tests

Stack	Membrane identification	Thickness (μm)	Area resistance (Ω cm <sup>2</sup> )	Water splitting efficiency (%)	Water splitting voltage (V)	IEC (meq g <sup>-1</sup> )
BM(PCCell)	PC BP	200-350	-	>95	0.8-1.0	
BM(FumaTech)	FBM	110-160	-	>98	< 1.2	
AEM (PCCell)	PC Acid 60	100-110	~ 2	~ 17	-	1.14
AEM(FumaTech)	FAB-PK-130	110-150	< 8.5	-	-	1.0-1.1

### 2.2 Experimental Apparatus and Procedure

The electro dialysis system produced by PCCell GmbH, Heusweiler, Germany was used for the BMED process. Figure 1 illustrates the schematic of the BMED process. The experiments were conducted using a two-compartment electro dialysis process with BP-A configuration and three cells. The membrane stack used in this work is composed of three anion-exchange membranes, two mixed metal oxide electrodes coated with titanium, four bipolar membranes (PCCell and FumaTech), and spacers (ED 640004). The variable was the type of membrane, with PCCell and FumaTech membranes used. The applied current and voltage were 5 A/16 V, respectively.



**Figure 1.** Schematic of the BMED system

To ensure the removal of any noticeable air bubbles within the membrane stack, the solution in each tank was circulated before electric currents were applied. Then the electrodes were connected to a DC power source.

A bipolar membrane contains an anion exchange and a Cation exchange layer, arranged parallel between two electrodes. Water penetrating the BM dissociates into  $\text{OH}^-$  and  $\text{H}^+$  ions in the catalyst layer between the cation and anion exchange membranes using an electric field created by the applied voltage difference. On the other hand, the binary salt solution enters the feed compartment and is split into cation and anion ions under the electric field. The AEM allows only the chlorides formed in the feed compartment to enter the acid compartment and repels the cation ions. This selective transfer is performed by the fixed-charged groups present in the membrane. Then,  $\text{Cl}^-$  joins with  $\text{H}^+$  produced by the BM to form Hydrochloric acid in the acid compartment. Additionally, the remaining cation ions in the feed compartment combine with  $\text{OH}^-$  to produce  $\text{NH}_4\text{OH}$  as well as  $\text{NaOH}$ , respectively.

### 2.3 Data Analysis

Samples were taken from the solutions every half hour for concentration analysis, and the feed solution conductivity was also monitored. The concentrations of base, acid, and  $\text{Cl}^-$  ions were determined through titration with standard solutions of  $\text{NaOH}$ ,  $\text{HCl}$ , and  $\text{AgNO}_3$  in the presence of a potassium chromate ( $\text{K}_2\text{CrO}_4$ ) indicator.

The acid-base concentrations and conversions were calculated by using Equation 1 and 2 [14].

$$C_i = \frac{n_{i,t}}{V_{i,t}} \quad (1)$$

$C_i$ ; final acid-base concentration (mole/l),  $n_{i,t}$ ; final acid-base amount (mole),  $V_{i,t}$ ; final acid-base tank volume (l).

$$\% \text{ Conversion} = \frac{C_{i,t} - C_{i,0}}{C_{total}} \quad (2)$$

$C_{i,t}$ ; final acid-base concentration (M),  $C_{i,0}$ ; initial acid-base concentration (M),  $C_{total}$ ; total acid-base concentration for the total salt conversion (M).

## 3 RESULTS

The BMED stack performance can be influenced by the type of utilized BM. So, it is important to choose suitable bipolar membranes to compare the BMED efficiency [15].

In this instance, the models of bipolar membranes (PCCell / FumaTech) were tested to treat  $\text{NH}_4\text{Cl} + \text{NaCl}$  by Electro dialysis by ion-exchange membranes ion exchange membranes with selective monovalent properties.

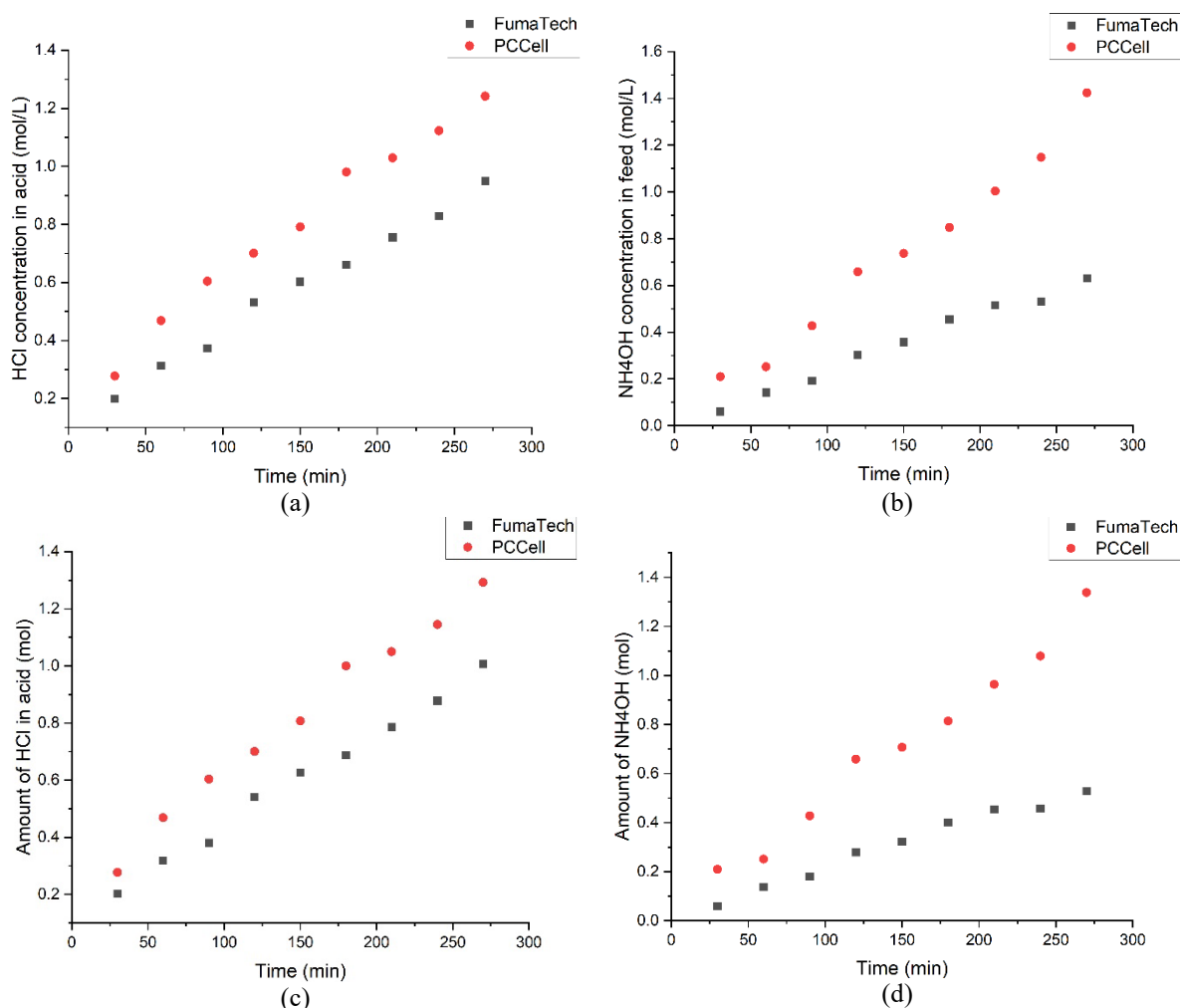
### 3.1 Base and Acid Concentrations

The consequence of different membranes on concentrations and amounts of acid and base are indicated in Fig 2 at constant current densities ( $75 \text{ A/m}^2$ ). The experiment duration was 270 min. As expected, the  $\text{HCl}$  and  $\text{NH}_4\text{OH}$  concentrations and amounts increased over time. This occurs as the anions and cations in the feed compartment interact with the  $\text{H}^+$  and  $\text{OH}^-$  produced by the BM, forming the corresponding acid or base when subjected to an electrical field.

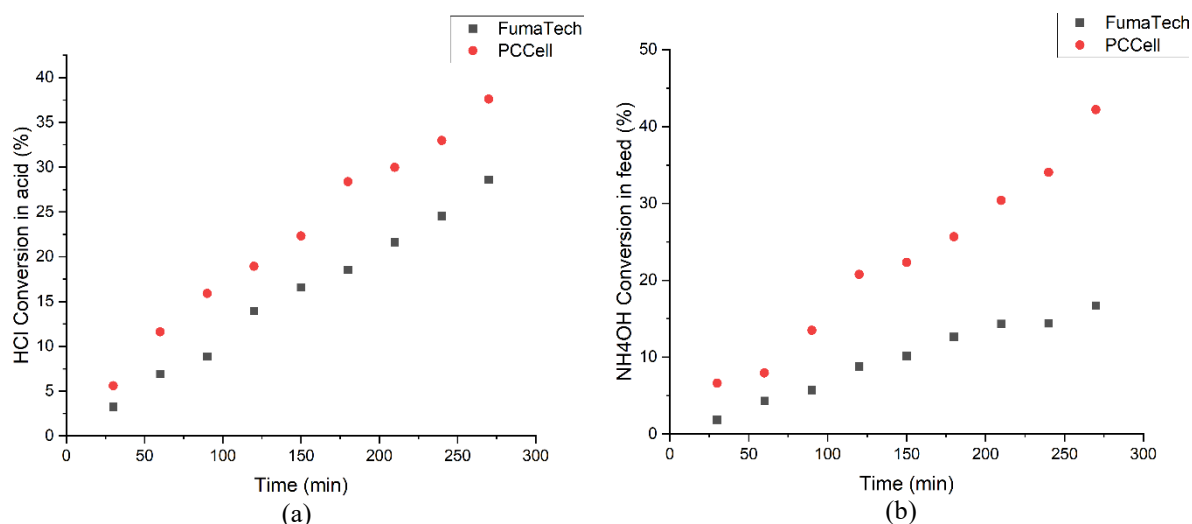
The important point was the non-constant rate of concentration increase. Indeed, in the first hour of the experiments, it was shown that the rate of concentration increases for  $\text{HCl}$  and  $\text{NaOH}$  decreased in the FumaTech membrane, whereas in the PCCell membrane, it decreased for  $\text{H}^+$  but increased for  $\text{OH}^-$ . In the last hour of the experiment, the concentration increase rate fell for  $\text{NaOH}$  (in both membranes) and  $\text{HCl}$  (in FumaTech), whereas it increased for  $\text{HCl}$  (in the PCCell).

Further, the experimental results demonstrate the supremacy of the PCCell compared to the FumaTech, considering either produced base and acid concentration at constant current densities. In the case of  $\text{HCl}$  concentration, the PCCell AEM has a higher ion exchange capacity (IEC) than the FumaTech AEM (Table 1) which is why it allows more ions to pass through. The higher the amount of  $\text{Cl}^-$  transferred from the feeding chamber to the acid, the higher the amount of  $\text{NH}_4^+$  released. Since these cations cannot move through the membrane, they combine with  $\text{OH}^-$ , which is made from the dissociation of water by the BM, in the feed compartment. As a result,  $\text{NaCl}$  and  $\text{NH}_4\text{OH}$  compounds are formed in the feed compartment. The ammonia requirement of the Solvay process is met by the  $\text{NH}_4\text{OH}$  compound. The water decomposition efficiency in the FumaTech bipolar membrane is higher than the PCCell, but there is no significant difference between them. However, the PCCell has a higher base concentration than the FumaTech, due to its higher selectivity.





**Figure 2.**  $H^+$ (a)/ $OH^-$ (b) concentrations and moles of  $H^+$ (d)/ $OH^-$ (c) produced by PCCell and FumaTech membranes stacks as a function of time



**Figure 3.** Acid (a) and base (b) conversion by PCCell and FumaTech membranes stacks as a function of time

### 3.2 Acid and Base Conversion

Base and acid converted from salt for two types of membrane are shown in Figure 3. By Figure 3, the highest acid conversion (38%) was gained in the presence of PCCell. The figure also indicates that the greatest acid conversion is so close for PCCell and FumaTech membranes. Similar to acid conversion, PCCell gives the highest base

conversion (~42%). The low conversion rates in the BMED process can be linked to unwanted mass transfer phenomena. These include back diffusion, co-ion migration, and hydrated ion migration, all of which arise from concentration disparities between the compartments. Such undesirable transports result in decreased concentrations in the targeted compartments, ultimately causing low conversion rates [7]. Generally, the PCCell gains more base as well as acid conversion in the shortest processing time as a result of the high mole amount and concentration value.

## 4 CONCLUSION

This research offers important findings on the efficiency of BMED systems in generating acidic and alkaline solutions from NaCl and NH<sub>4</sub>Cl feed by using FumaTech and PCCell membranes. Additionally, the study explores the potential of BMED to replace the Solvay Process Distillation Unit to eliminate the waste problem. Results show that PCCell is considered the optimum membrane according to the concentration of the final product.

## References

- [1] L. Dursun, O. N. Ata, and A. Kanca, "Bipolar membrane electro dialysis for binary salt water treatment: valorization of type and concentration of electrolytes," *Industrial & Engineering Chemistry Research*, vol. 60, no. 5, pp. 2003–2010, 2021.
- [2] M. R. Oner and O. N. Ata, "The effect of temperature on acid and base production from nh<sub>4</sub>cl-nacl salt solution by bipolar membrane electro dialysis," in *ISASE2018*, Erzurum, 2018, pp. 254.
- [3] M. R. Oner, O. N. Ata, A. B. Yavuz, and H. E. Saygin, "Investigation of the effect of impurity concentration in the simulated industrial saline water on the scaling phenomenon on ion exchange membranes," *Journal of Environmental Chemical Engineering*, vol. 11, no. 5, art. no. 111119, 2023.
- [4] Y. Luo, Y. Liu, J. Shen, and B. Van der Bruggen, "Application of bipolar membrane electro dialysis in environmental protection and resource recovery: A review," *Membranes*, vol. 12, no. 9, art. no. 829, 2022.
- [5] R. M. Harrison, W. Sturges, A.-M. Kitto, and Y. Li, "Kinetics of evaporation of ammonium chloride and ammonium nitrate aerosols," *Atmospheric Environment. Part A. General Topics*, vol. 24, no. 7, pp. 1883–1888, 1990.
- [6] P. Sessiecq, F. Gruy, and M. Cournil, "Study of ammonium chloride crystallization in a mixed vessel," *Journal of crystal growth*, vol. 208, no. 1–4, pp. 555–568, 2000.
- [7] M. R. Oner, A. Kanca, O. N. Ata, S. Yapici, and N. A. Yaylali, "Bipolar membrane electro dialysis for mixed salt water treatment: Evaluation of parameters on process performance," *Journal of Environmental Chemical Engineering*, vol. 9, no. 4, art. no. 105750, 2021.
- [8] Y. Liu, Y. Sun, and Z. Peng, "Evaluation of bipolar membrane electro dialysis for desalination of simulated salicylic acid wastewater," *Desalination*, vol. 537, art. no. 115866, 2022.
- [9] T. Kasikowski, R. Buczkowski, and M. Cichosz, "Utilisation of synthetic soda-ash industry by-products," *International Journal of Production Economics*, vol. 112, no. 2, pp. 971–984, 2008.
- [10] K. Ghyselbrecht, M. Huygebaert, B. Van der Bruggen, R. Ballet, B. Meesschaert, and L. Pinoy, "Desalination of an industrial saline water with conventional and bipolar membrane electro dialysis," *Desalination*, vol. 318, pp. 9–18, 2013.
- [11] Y. Lv, H. Yan, B. Yang, C. Wu, X. Zhang, and X. Wang, "Bipolar membrane electro dialysis for the recycling of ammonium chloride wastewater: Membrane selection and process optimization," *Chemical Engineering Research and Design*, vol. 138, pp. 105–115, 2018.
- [12] M. Oner, O. Ata, and S. Yapici, "Bipolar membrane electro dialysis for mixed salt water treatment: determination of optimum conditions by topsis-based taguchi method," *International Journal of Environmental Science and Technology*, vol. 20, no. 1, pp. 587–604, 2023.
- [13] A. Ruiz Street, "Producción de ácido y base mediante electrodiálisis con membranas bipolares a partir de salmuera," 2024.
- [14] A. Kanca, H. Senol, D. Adiguzel, C. Medin, and O. N. Ata, "Boric acid recovery in dilute during the desalination process in BMED system," *Desalination*, vol. 538, art. no. 115920, 2022.
- [15] A. Filingeri *et al.*, "Acid/base production via bipolar membrane electro dialysis: brine feed streams to reduce fresh water consumption," *Industrial & Engineering Chemistry Research*, vol. 63, no. 7, pp. 3198–3210, 2024.



---

## Synthesis of Quinoxaline Containing Thiazole Moiety Derivative, Biological Activities, Docking Studies, and ADMET Analysis

Anissa Boumati<sup>\*1</sup>, Imane Idris<sup>1</sup>, Omar Berradj<sup>1</sup>

<sup>1</sup>Laboratory of Physics and Chemistry of Materials, Department of Chemistry, University of Mouloud Mammeri, Tizi-Ouzou, Algeria

---

### Abstract

The quinoxaline ring, with its rigid aromatic heterocyclic structure, gives many derivatives remarkable biological properties for pharmaceutical applications. These compounds have demonstrated a wide range of antibacterial, antifungal, antiviral, anticancer and anti-inflammatory activities by targeting various enzymes, receptors or nucleic acids. Some have been shown to be excellent inhibitors of key enzymes such as kinases, proteases or topoisomerases, representing promising avenues for the treatment of serious pathologies. Quinoxalines also have favourable pharmacokinetic properties, with good bioavailability, metabolism and elimination. This versatility makes the quinoxaline motif a preferred core in medicinal chemistry for the discovery and optimisation of innovative new therapeutic agents.

Moreover, the recent trend of hybrid compounds aims to develop one substance by combining several pharmacophore segments with various biological activities. We are attempting to develop an idea of and synthesize a molecule that combines the quinoxaline and thiazole rings. The objective is to use the intrinsic biological properties of these two heterocycles with the objective of eventually creating a therapeutic agent. The recently synthesized molecule's structure has been determined by FT-IR, <sup>1</sup>H-NMR, <sup>13</sup>C-NMR, and mass spectrometry analyses. The antibacterial and antioxidant properties were also evaluated.

In addition, an *in silico* prediction study of the compound's physicochemical, pharmacokinetic and toxicological properties was carried. The results showed that the compound has good pharmacokinetic characteristics. Also, a molecular docking study was carried out by Autodock Vina and DiscoveryStudio2021 to investigate the possible binding interaction of the synthesized compound to act as inhibitors of  $\alpha$ -glucosidase. This approach to hybrid heterocycle synthesis paves the way for the development of new agents with innovative pharmacological activities.

**Keywords:** Quinoxaline, Thiazole, Doking Molecular, ADMET

---



---

## Investigation into Mathematical Modeling of Light Naphtha Isomerization Using Bi-Functional Catalysts

Boudjema Amir Lehtihet<sup>\*1</sup>, Tayeb Fakhreddine Boukezoula<sup>1,2</sup>, Lahcène Bencheikh<sup>1</sup>

<sup>1</sup>Chemical Process Engineering Laboratory, Department of Process Engineering, Faculty of Technology, Ferhat Abbas University Setif 1, Setif, Algeria

<sup>2</sup>Department of Chemistry, Faculty of Science, Ferhat Abbas University Setif 1, Setif, Algeria

---

### Abstract

Naphtha isomerization holds significant importance within the petroleum industry, presenting a necessity for a streamlined and cost-efficient technology in the production of clean fuel with a high-octane rating. The isomerization process holds an important role in refineries, facilitating the production of clean fuels through a simple and cost-effective technology that keeps investment expenses low. This is why catalytic isomerization carries socio-economic and ecological benefits within the industrial site. Its primary objective is to transform linear normal paraffins into branched isoparaffins, reducing aromatic content, and constraining lead levels. Furthermore, this process is employed to attain high-octane products and enhance utilization efficiency.

In this study, our objective was to identify a sustainable kinetic model that aligns with industrial data. Additionally, comprehending the various operational modes of the process, the diverse reactor types, catalysts employed, and the conversion chemistry of light naphtha proved crucial. Moreover, understanding the different chemical reactions occurring within isomerization reactors was essential to our research.

Indeed, our goal in this work or is to investigate the cut-isomerization process ( $C_5/C_6$ ) within an industrial plant. Our focus is on selecting an appropriate kinetic model, essential for constructing the necessary mathematical model tailored to this industry. Simultaneously, we aim to optimize operational conditions to enhance gasoline and hydrogen production while reducing coke deposits and lead content.

The current study into  $C_5/C_6$  isomerization on Pt/ $Al_2O_3$ -Chlorinated catalysts was carried out under industrial conditions. Consequently, the focus of extreme significance lies on the yield and composition of the products obtained in this process.

The data collected from the isomerization unit aligns well with the established kinetic model. Hence, the remaining steps of our work involve transforming this kinetic model into a mathematical representation using reaction rates corresponding to the reactions within the reactors and other relevant parameters. Our aim is to complete this process with minimal error, ensuring a precise mathematical model that reflects the kinetics of the system accurately.

**Keywords:** *Catalytic Isomerization, Paraffins, Light naphtha, Environmental impact, Mathematical modelling, Bi-functional catalyst*

---



## Effects of Operating Parameters on the Crystallization Yield of Copper Sulfate: An Experimental Study

Amira Boufrioua<sup>\*1</sup>, Sarra Guilane<sup>2</sup>, Leila Benmansour<sup>2</sup>

<sup>1</sup>Laboratory of Organic Synthesis, Modelling and Optimization of Chemical Process (LOMOP), University of Badji Mokhtar, Annaba, Algeria

<sup>2</sup>Laboratory of Environmental Engineering, University of Badji Mokhtar, Annaba, Algeria

---

### Abstract

Cooling crystallization is a versatile and efficient technique essential for the production of high-quality crystalline materials. This experimental study investigates the influence of key operating parameters : saturation temperature, stirring speed, and cooling temperature on the crystallization yield of copper sulfate. By systematically varying these parameters, we aim to optimize the crystallization process and enhance yield efficiency. The study reveals that higher saturation temperatures facilitate greater solubility of copper sulfate, leading to improved nucleation rates upon cooling. Optimal crystallization of 65.65% is achieved at a saturation temperature of 70 °C, a stirring speed of 400 rpm, and a cooling temperature of 10 °C. These results shed light on the intricate interplay between operating parameters and their impact on crystallization outcomes. The findings provide valuable insights into the optimal conditions for maximizing copper sulfate crystallization yield, offering potential improvements for industrial applications. Furthermore, the study underscores the importance of fine-tuning process parameters to achieve desired product characteristics and yield efficiency in crystallization processes.

**Keywords:** *Copper sulfate, Crystallization, Optimization, Cooling crystallization*

---



## Exploring CA/CuO in Adsorption and Photocatalysis for Toxic Wastewater Treatment: Preparation, Mechanisms

Oumnia Rayane Benkouachi<sup>\*1</sup>, Abdallah Bougeuttoucha<sup>1</sup>, Kamilia Madi<sup>1</sup>

<sup>1</sup>Process Engineering, Farhat Abbas 1, Setif, Algeria

---

### Abstract

The escalating levels of industrial and urban wastewater necessitate the development of effective treatment methods to remove toxic contaminants. Activated carbon (CA) and copper oxide (CuO) have shown promise in the fields of adsorption and photocatalysis, respectively. This study explores the preparation, mechanisms, and efficacy of CA/CuO composites for toxic wastewater treatment. CA is prepared from natural precursors through carbonization and activation, while CuO is synthesized via precipitation or sol-gel methods. The CA/CuO composites are then formed through impregnation or in situ synthesis techniques. The adsorption mechanism primarily involves physical and chemical interactions, as well as pore filling, while the photocatalytic mechanism includes photon absorption, electron-hole pair generation, and subsequent redox reactions. The synergistic effect of combining CA and CuO results in enhanced removal efficiencies for both heavy metals and organic pollutants. This comprehensive approach leverages the high surface area and adsorption capacity of CA with the photocatalytic properties of CuO, offering a viable solution for the treatment of toxic wastewater. Future research should focus on optimizing composite synthesis and understanding the detailed interaction mechanisms to facilitate real-world applications.

**Keywords:** Adsorption, Photocatalyse, Copper oxide, Activated carbon

---



## Determination and Study of Pollution in Chemical Variables in Industrial Waste Water for the Concrete Factories

Mohamed Nadjib Rebizi\*<sup>1</sup>

<sup>1</sup>*Organic Chemistry and Natural Substances Laboratory, Faculty of Exact Sciences and Computer Science, University of Djelfa, PO Box 3117, Djelfa 17000, Algeria*

---

### Abstract

The aim of this work is to examine the impact of industrial effluents generated by concrete factories on the environment. In this work we collect, analyze, and interpret data on discharges over a period of one year and evaluated the extent of environmental pollution, especially with heavy metals, by determining the concentrations of heavy metal elements in the liquid waste of the concrete production of the National Construction Company 'Cosidar' in Djelfa, where we monitored the following parameters: temperature, pH, chemical oxygen demands (COD), and one of the most notable results obtained was pH=12.9, as the pH value exceeded national and international standards according to the World Health Organization. This is due to the large number of chemical additives in concrete production as well as the concentration of the following heavy metals: (Plomb, Cadmium, Chrome, Cobalt, Cuivre, Nickel, Zinc) exceed the reference values, which led to water pollution. This is due to the components of mineral origin and the materials used in preparing concrete.

**Keywords:** *Liquid waste, Concrete factories, Heavy metals, Environment, Industrial effluents*

---



---

## A Magnetic Field's Impact on a Spiral Porous Fin Exposed to Radiation and Convection

Daradji Nadia<sup>\*1</sup>, Bouaziz Mohamed Nadjib<sup>2</sup>

<sup>1</sup>*Biomaterials and Transport Phenomena Laboratory, University Medea, 26000, Algeria*

---

### Abstract

Extended surfaces that are well known as fins are commonly used to enhance heat transfer in many industries. Fins are widely used to increase the rate of heat transfer from a primary wall surface; and that's why applications for finned surfaces are widely seen in air-conditioning, refrigeration, cryogenics, and electronic devices as well as in heat exchangers and power generators working with high temperature. Besides the traditional applications, we can find fins in nuclear technology. On the other hand, heat transfer takes place in porous materials of various types. A primary aim is common to maximize either the thermal resistance or the rate of thermal equilibration between the material and a fluid passing through it - i.e. to facilitate heat exchange, and less material is consumed in the case of a solid fin is replaced by a porous fin, knowing that to reduce the size and price of fins are the first fins industry goals.

The current study describes how a magnetic field affects a convective-radiative spiral porous fin's temperature attribute. The main advantages of a spiral heat exchanger are its high overall heat transfer coefficient, compact size for a given heat exchange area, relatively low- pressure drop and ease of cleaning. Spiral heat exchanger flow may be countercurrent flow, concurrent flow or cross flow.

The magnetic heat flow has a linear relationship with the magnetic field, the speed of the fluid particles and temperature. The interaction between the porous medium and the fluid is simulated by Darcy's formulation. The effects of Hartman number, Rayleigh number, porosity, fin parameter, and the radiative parameter are experimentally investigated. The mathematical representation resulting from an analysis is a highly non-linear 2nd order differential equation. Complemented by the boundary conditions, the nonlinear system was solved numerically using MATLAB software.

**Keywords:** *Spiral porous fin, Magnetic field, Convection, Radiation*

---





---

## Investigation of the Applicability of Ni-P-Cu Coatings to the Expanded Graphite/PCM Composite Blocks Surfaces by Electrolysis

Onur Guler<sup>1</sup>, Mustafa Yusuf Yazici<sup>\*2</sup>

<sup>1</sup>Metallurgical and Materials Engineering, Karadeniz Technical University, Trabzon, Türkiye

<sup>2</sup>Mechanical Engineering, Samsun University, Samsun, Türkiye

---

### Abstract

Energy storage systems play a crucial role in various applications today, such as electric vehicles, portable devices, and renewable energy systems. The demand for high-performance batteries is increasingly essential for the successful operation of these applications. However, the heat-related issues arising during the use of these batteries can lead to performance degradation and a shortened lifespan. Expanded graphite (EG) and phase change material (PCM) composites offer significant advantages in the passive thermal management of batteries. Ni-P-Cu coatings on these composites can bring innovations such as improved thermal conductivity, enhanced mechanical strength, corrosion resistance, durability, and customizable application parameters. These innovations contribute to addressing challenges associated with passive thermal management in batteries, promoting more efficient and reliable energy storage systems. In this study, we conducted Ni-P-Cu coating processes using the parameters encompassed configurations with a 4 cm anode-cathode gap employing a current density of 2 A/dm<sup>2</sup>. The successful application of electrolytic Ni-P-Cu coating on composites was followed by a thorough analysis of the resulting coating layer using SEM and EDS techniques. Examination revealed a distinctive cauliflower-like and spherical particle morphology in the Ni-P-Cu coating layer, with Cu content around 40 wt%. Furthermore, the microstructure of the Ni-P coating layer exhibited an absence of foreign elements, highlighting the exclusive presence of Ni, P, and Cu elements.

**Keywords:** *Electrolytic Ni-P-Cu coating, Phase change material, Expanded graphite, Material*

---



## Modeling the Phenomenon of Degradation of a TK31 Centrifugal Compressor by Aleatory Processes

Souhila Bouleghlem<sup>\*1</sup>, Naima Tamaloussi<sup>1</sup>, Lamia Benzaid<sup>1</sup>

<sup>1</sup>Department of Mechanical Engineering, Faculty of Technology, University of Skikda, Algeria

---

### Abstract

In this work, the Wiener process is used to model the degradation phenomenon of a sliding bearing at the level of a compressor. The goal is to evaluate the service life, and therefore the evolution over time of the compressor. Change in operating state the physical quantity presented in this study is the bearing temperature.

The measurements forming the sample of the temperatures recorded on a sliding bearing are tested by using a statistical software, the overall idea of which is to compare the distribution of the temperatures collected (measurements taken), with respect to the theoretical distribution function. First, a modeling of the temperature values by such a stochastic process, followed by a simulation of the evolution of the physical quantity studied have been proposed,

Performing a statistical test on the sample of temperatures measured at the sliding bearing in question shows that they follow a normal law. The monitoring of the evolution over time of the degradation of the bearing, therefore allows us to model such a phenomenon by the Wiener process. The corresponding Wiener model gives a good estimate of the probability of stoppages linked to the degradation of the bearing. Indeed, the evolution of the cumulative temperatures according to the proposed model as well as those calculated analytically has the same pace.

Adjusting the sample to the monitored parameters allowed us to successfully simulate the temperature change. The simulation result is important for the prediction of failures that may occur on the studied element. The proposed Wiener model is very powerful because it accurately describes the evolution of temperatures on the sliding bearing studied. So, we came to a better interpretation of the degradation process.

**Keywords:** *Degradation, Aleatory process, Wiener process, Modeling, Simulation*

---



## Challenges of Latent Heat Energy Storage for Energy Efficiency Enhancement

Mohamed Teggat<sup>\*1</sup>

<sup>1</sup>LMe Laboratory, Department of Mechanical Engineering, Laghouat University, Laghouat, Algeria

---

### Abstract

Enhancing energy efficiency is essential for energy savings and reduction of emissions. Energy storage is one of the solutions to enhance energy efficiency through bridging the gap between energy availability and need. Latent heat energy storage is considered as the most promising type of thermal energy storage but is still under development and applied research. In this analysis, it is aimed to discuss the prospects of latent heat energy storage for improvement of energy efficiency as well as their challenges. Research conducted in this field is examined with focus on applications in solar energy and buildings. Cooling and heating applications are discussed as well. The impact of latent heat energy storage is highlighted including energy savings and carbon footprint. Limitations and ways to further improve latent heat energy storage are highlighted for sustainability of thermal engineering applications based on both conventional and renewable energy.

**Keywords:** *Energy storage, Latent heat, Energy efficiency, Carbon footprint*

---



## Effect of Resin Coating on Mechanical Properties of 3D Printed Parts

Abdurrahim Temiz<sup>\*1</sup>, Fatih Huzeyfe Ozturk<sup>1</sup>

<sup>1</sup>Department of Industrial Design Engineering, Karabuk University, Karabuk, Türkiye

### Abstract

Fused filament fabrication (FFF) is a well-known and widely used additive manufacturing (3D printing) process that uses a thermoplastic wire-shaped filament to build a workpiece layer-by-layer. This method offers advantages such as cost-effectiveness, design flexibility, and rapid prototyping capabilities. These benefits stem from the ability to create complex geometries with various materials, enabling quick iteration and customization. However, there is still a requirement to improve the load-bearing capacity and surface characteristics of these components. The objective of this study was to enhance the load carrying capacity of FFF printed PLA parts by applying a surface coating of Anycubic standard SLA resin. The coating technique involved the utilization of a homemade dip coating apparatus. The tensile sample printed on the printer was immersed in the resin in a container and maintained in the resin for 10 seconds with the assistance of this device. These samples were then removed from the resin and the coating process was completed by curing for 10 minutes in the Anycubic Wash&Cure device. Mixed-level design experiment and Taguchi L8 orthogonal array optimization was used to understand and optimize the effects of process parameters, reducing the number of experiments. Tensile test results were used to compare the coated and uncoated specimens. The experimental design has 3 different levels: layer thickness (0.1 mm, 0.2 mm, 0.3 mm, and 0.4 mm), infill pattern (lines and grid), and coating status (coated, uncoated). According to the Taguchi result, the optimum combination is 0.4 mm layer thickness, lines infill pattern and coated sample. The ANOVA results indicate that the coating condition has a statistically significant effect ( $p \leq 0.05$ ), however the filling pattern and layer thickness do not show statistically significant effects. Furthermore, the model's accuracy rate, determined by the R2 value, is 95.30%.

**Keywords:** Additive manufacturing, Surface coating, Taguchi optimization

## 1 INTRODUCTION

Additive manufacturing, commonly known as 3D printing, involves the layer-by-layer production of components [1]. Fused Filament Fabrication (FFF) is a prevalent 3D printing technique that allows for the creation of intricate shapes with ease [2]. FFF utilizes different infill patterns to produce objects, offering versatility in design [3]. This method is cost-effective and efficient, enabling the fabrication of complex items [4]. FFF is particularly popular for its ability to create components with complicated geometries and suitable mechanical properties [5]. It is widely used in various fields, including medicine and materials science [6]. FFF has been instrumental in the development of shape memory polymers and solid polymer electrolytes [1, 2]. The technique's versatility extends to the production of metal structures and composite materials [7]. FFF's applications range from prototyping to industrial-scale manufacturing [8]. The method's adaptability allows for the printing of a wide array of materials, including polymers and ceramics [9]. FFF's automated fabrication process and improving resolution make it a promising alternative for rapid prototyping [10]. Overall, FFF is a versatile and cost-efficient 3D printing method with widespread applications in various industries [6, 8].

The mechanical properties of FFF printed components, particularly those made from PLA, are significantly influenced by layer thickness and printing patterns. Studies have shown that varying the layer thickness can impact the mechanical properties of PLA and ABS 3D printed specimens, with thinner layers resulting in improved internal cavities, surface quality, layer bonding, and overall mechanical properties [11]. Additionally, the infill pattern and raster orientation have been identified as factors that significantly affect the mechanical properties of FFF samples, highlighting the importance of printing patterns in determining mechanical characteristics [12]. Furthermore, the impact of layer thickness on the mechanical properties of PLA and ABS specimens has been investigated, emphasizing the need to consider this parameter in optimizing the mechanical performance of FFF printed parts [13].

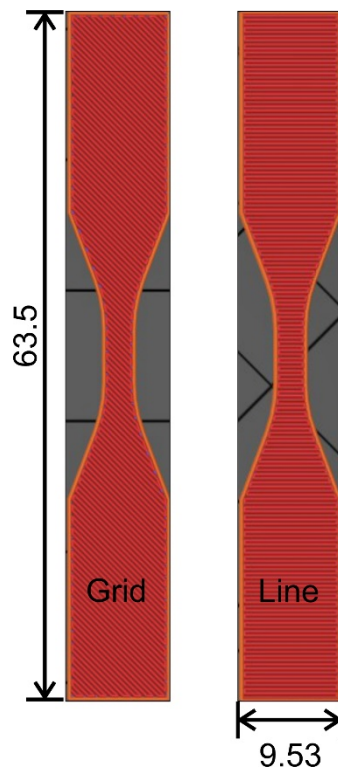
To enhance the impact strength of FFF printed PLA components, resin coating has been explored as a viable solution. Studies have shown that resin coating can significantly improve the impact resistance of FFF processed parts. Taborda et al., (2021) demonstrated that resin coating increases the impact resistance of parts processed by FFF by almost 100% compared to uncoated parts [14]. Additionally, Musgrove et al. (2023) found that resin coatings, specifically parylene-C coating, protect 3D printed devices from erosion, cytotoxicity, and enhance material integrity, making them suitable for various applications [15]. By coating PLA filaments with resin, it is possible to improve the mechanical properties and overall performance of FFF printed objects, making them more durable and resilient [14].

The Taguchi method optimizes manufacturing processes by determining the best combination of input parameters. This statistical tool evaluates multiple responses at once, improving factors like material removal rate, surface roughness, and tool wear. Widely used in various fields, the Taguchi method systematically varies and analyzes parameters to identify optimal conditions, enhancing product quality and efficiency.

The aim of this study was to increase the load-bearing capability of FFF printed PLA components by applying a surface coating of Anycubic standard SLA resin. The coating process employed the use of a custom-made dip coating device. The study aimed to examine the impact of coating, in conjunction with various printing parameters, on the characteristics of samples. Specifically, the investigation focused on comparing the effects of coated and uncoated samples with varying layer thicknesses and printing patterns. The study employed a mixed-level design experiment and utilized Taguchi L8 orthogonal array optimization to comprehensively analyze and enhance the impact of process factors, while minimizing the required number of experiments. ANOVA was used to determine the differences between the groups by analyzing the variance of the data.

## 2 MATERIAL AND METHOD

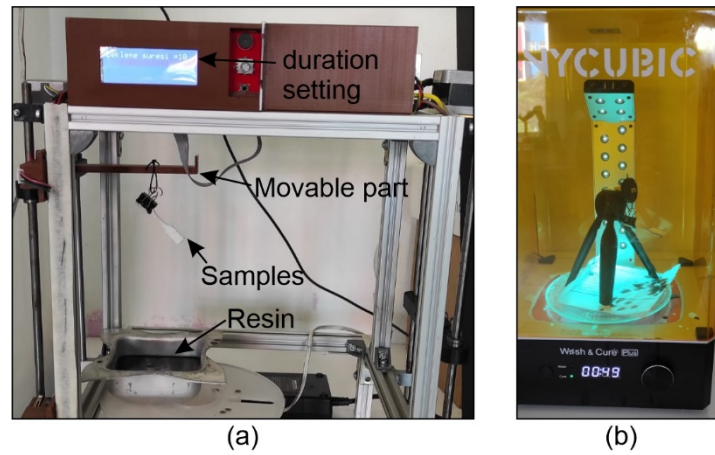
PLA filament with a diameter of 1.75 mm from Esun company was used for printing the samples. For the printed parts, Zaxe X1 3D printer with 0.4 mm nozzle was used with the parameters recommended for PLA materials; print speed 60 mm/s, print temperature 210 °C and bed temperature 60 °C. In the study, the effects of printing pattern (lines and grid) and layer thickness (0.2, 0.3 and 0.4 mm) values were examined to determine the effect of coating on mechanical properties. Figure 1 shows the ASTM D638 Type 5 geometry and printing patterns used.



**Figure 1.** Schematic representation of tensile test specimen

After the printing of the samples was finished, the PLA parts were cleaned and any dust or dirt was removed from the surface to ensure the coating was smooth. Anycubic standard SLA resin was used to coating the PLA samples.

The samples were placed in the dip coating device (Figure 2(a)) and dipped in the resin for 10 s. The samples were then removed from the resin, excess resin was dripped off and placed in the Anycubic Wash&Cure device (Figure 2(b)) for curing. The specimens were exposed to the curing process for 10 min to allow the resin to harden and increase its strength.



**Figure 2.** Devices (a) dip coating and (b) Anycubic Wash&Cure

Optimization was performed with Taguchi L8 array to determine the effect of the coating process on the printed samples with the determined parameters. The variables were determined as printing pattern, layer thickness and coating process. This array is given in Table 1. L and G denote lines and grid, U and C denote un-coated and coated, respectively.

**Table 1.** Taguchi L8 array

Factor	Levels	Values
Layer thickness (mm)	4	0.1; 0.2; 0.3; 0.4
Infill pattern	2	L; G
Coating	2	U; C

All the samples were subjected to a tensile test with Shimadzu tensile test machine at room temperature at a speed of 5 mm/min for 3 repetitions to determine their mechanical properties. Maximum stress values were recorded to determine the effect of variables.

### 3 RESULTS

This section provides and assesses the mechanical reaction obtained from tensile tests conducted on materials C and U. Tensile tests were employed to determine the ultimate tensile strength (UTS). The measurements were averaged over the repeated specimens, and the results, including the mean values and standard deviations, are presented in Table 2. The tensile strengths reach a maximum value of 70.47 MPa for a layer thickness of 0.4 mm, with a L pattern type and C sample. They decrease to 43.76 MPa for a layer thickness of 0.3 mm, with a G pattern type and U sample.

**Table 2.** DOE with L8 Taguchi orthogonal array and results of the tensile tests

Layer thickness (mm)	Infill pattern	Coating	UTS (MPa)
0.1	L	U	48.06±0.2
0.1	G	C	56.65±1.1
0.2	L	U	50.82±0.6
0.2	G	C	60.49±1.3
0.3	L	C	59.26±0.9
0.3	G	U	43.76±0.3
0.4	L	C	70.47±1.5
0.4	G	U	44.52±0.2

Table 3 displays the analysis of variance (ANOVA) findings for ultimate tensile strength (UTS). The F-value quantifies the impact of factors on the response variable. Upon examination of the ANOVA table, it is evident that the F-Value (32.30) is the most influential factor for the coating condition. The F-Value for layer thickness (1.14) has the least impact. The P-value in the ANOVA table determines the statistical significance of the result. Results are deemed statistically significant if the P-Value is below 0.05. Upon examination of the table, it is evident that the only factor that exhibits statistical significance is the coating condition, as indicated by the P-value of 0.03. In addition, the R<sup>2</sup> value of the model is 95.30%, indicating a high level of accuracy. Nevertheless, the R<sup>2</sup> value for Prediction is significantly low at 24.88%.

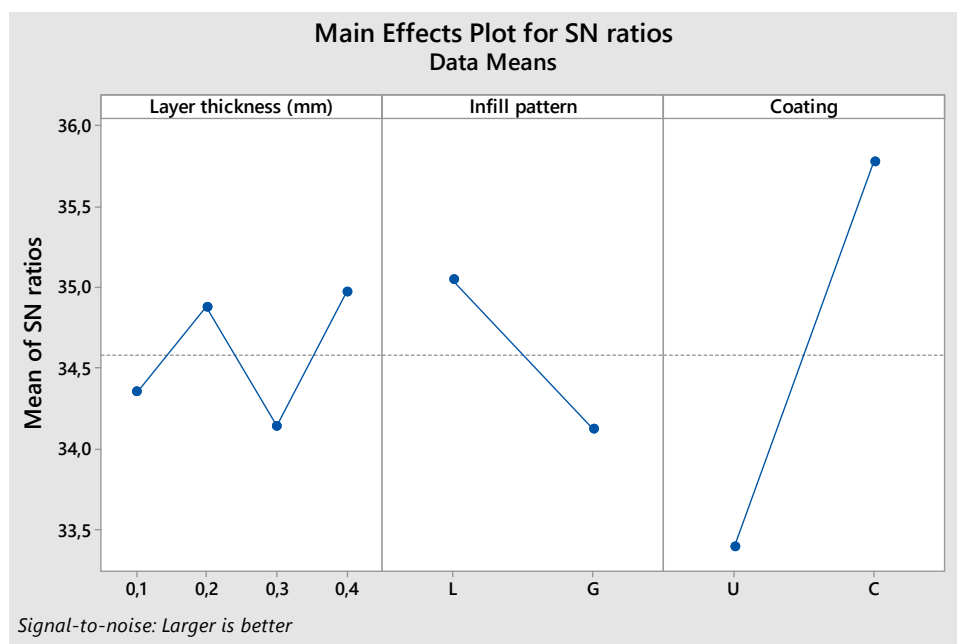
**Table 3.** Analysis of variance

Source	DF	Adj	F-Value	P-Value
Layer Thickness (mm)	3	47.21	1.14	0.499
Infill Pattern	1	67.22	4.87	0.158
Coating	1	445.66	32.30	0.030
Error	2	27.59		
Total	7	587.68		
Model Summary				
R <sup>2</sup>	R <sup>2</sup> (adj)	R <sup>2</sup> (pred)		
95.30	83.57	24.88		

The equation for the regression model is displayed below.

$$\begin{aligned}
 UTS (MPa) = & 54.25 - 1.90 \text{ Layer thickness}_{0.1} + 1.40 \text{ Layer thickness}_{0.2} \\
 & - 2.74 \text{ Layer thickness}_{0.3} + 3.24 \text{ Layer thickness}_{0.4} + 2.90 \text{ Infill pattern}_{L} \\
 & - 2.90 \text{ Infill pattern}_{G} - 7.46 \text{ Coating}_{U} + 7.46 \text{ Coating}_{C}
 \end{aligned}
 \tag{1}$$

Figure 3 illustrates the outcomes of modifying parameters that impact the UTS using the Taguchi design methodology. The optimal signal-to-noise ratio (S/N) yields the most precise values for the operational parameters in the S/N ratio data. The optimum combination of components for UTS, which is A4-B1-C2, is clearly seen in Figure 3. The optimal UTS value was achieved using a layer thickness of 0.4 mm, a printing pattern of L, and a coated sample. The results obtained through the Taguchi design methodology, in conjunction with the application of coatings and optimization of printing parameters, play a vital role in achieving the optimal UTS values. By carefully selecting and optimizing these parameters, it is possible to enhance the mechanical properties of materials, leading to improved performance and durability. Studies on the effect of printing patterns, infill density, and layer thickness on mechanical properties highlight the importance of these parameters in determining the UTS of printed parts. The optimization of 3D printing parameters, including layer thickness and printing pattern, has been shown to enhance surface quality and wear resistance, contributing to improved mechanical performance.



**Figure 3.** S/N values of factor levels for UTS

## 4 CONCLUSION

This study conducted a comparison of the mechanical properties of test samples produced from a FFF 3D printer and a commercially accessible PLA filament. The comparison was based on the coating condition and printing parameters. Based on the Taguchi analysis, the optimal configuration consists of a layer thickness of 0.4 mm, lines infill pattern, and a coated sample. The ANOVA results demonstrate that the coating condition has a statistically significant impact ( $p \leq 0.05$ ), but the filling pattern and layer thickness do not exhibit statistically significant effects. Moreover, the model's accuracy, as measured by the  $R^2$  score, is at 95.30%.

## References

- [1] S. Valvez, P. N. B. Reis, L. Susmel, and F. Berto, "Fused filament fabrication-4D-printed shape memory polymers: A review", *Polymers*, vol. 13, no. 5, art. no. 701, 2021, doi: 10.3390/polym13050701.
- [2] F. Bourseau, "3D printing of solid polymer electrolytes by fused filament fabrication: Challenges towards in-space manufacturing", *Journal of Physics Energy*, vol. 6, art. no. 012001, 2023, doi: 10.1088/2515-7655/ad02be.
- [3] A. Bulavskaya, "X-ray study of the density distribution of FFF-printed samples with different fill patterns", *Journal of Instrumentation*, vol. 19, art. no. C06013, 2024, doi: 10.1088/1748-0221/19/06/c06013.
- [4] S. Demir, "The investigation of printing parameters effect on tensile characteristics for triply periodic minimal surface designs by Taguchi", *Polymer Engineering & Science*, vol. 64, no. 3, pp. 1209–1221, 2023, doi: 10.1002/pen.26608.
- [5] J. Khaliq, "Effects of infill line multiplier and patterns on mechanical properties of lightweight and resilient hollow section products manufactured using fused filament fabrication", *Polymers*, vol. 15, no. 12, art. no. 2585, 2023, doi: 10.3390/polym15122585.
- [6] M. A. Caminero, A. M. Romero, J. M. Chacón, P. J. Núñez, E. G. Plaza, and G. P. Rodríguez, "Additive manufacturing of 316L stainless-steel structures using fused filament fabrication technology: Mechanical and geometric properties", *Rapid Prototyping Journal*, vol. 27, no. 3, pp. 583–591, 2021, doi: 10.1108/rpj-06-2020-0120.
- [7] C. Tosto, J. Tirillò, F. Sarasini, ve G. Cicala, "Hybrid Metal/Polymer Filaments for Fused Filament Fabrication (FFF) to Print Metal Parts", *Applied Sciences*, vol. 11, no. 4, art. no. 1444, 2021, doi: 10.3390/app11041444.
- [8] N. Vidakis *et al.*, "High-performance medical-grade resin radically reinforced with cellulose nanofibers for 3D printing", *Journal of the Mechanical Behavior of Biomedical Materials*, vol. 134, art. no. 105408, Oct. 2022, doi: 10.1016/j.jmbbm.2022.105408.
- [9] G. Tselikos, S. Rasul, P. Groen, C. Li, ve J. Khaliq, "In situ printing and functionalization of hybrid polymer-ceramic composites using a commercial 3D printer and dielectrophoresis—A novel conceptual design", *Polymers*, vol. 13, no. 22, art. no. 3979, 2021, doi: 10.3390/polym13223979.
- [10] M. Zeraatkar, M. D. de Tullio, A. Pricci, F. Pignatelli, ve G. Percoco, "Exploiting limitations of fused deposition modeling to enhance mixing in 3D printed microfluidic devices", *Rapid Prototyping Journal*, vol. 27, no. 10, pp. 1850–1859, Jan. 2021, doi: 10.1108/RPJ-03-2021-0051.
- [11] H. Bakhtiari, M. Nikzad, and M. Tolouei-Rad, "Influence of three-dimensional printing parameters on compressive properties and surface smoothness of polylactic acid specimens," *Polymers*, vol. 15, no. 18, art. no. 3827, 2023, doi: 10.3390/polym15183827.
- [12] J. Bonada, M. M. Pastor, and I. Buj-Corral, "Influence of infill pattern on the elastic mechanical properties of fused filament fabrication (FFF) parts through experimental tests and numerical analyses", *Materials*, vol. 14, no. 18, art. no. 5459, Jan. 2021, doi: 10.3390/ma14185459.
- [13] Y. Chen, K. Shergill, and S. Bull, "Size effects in 3D printed materials", in Research Square, doi: 10.21203/rs.3.rs-2321970/v1.
- [14] L. L. López Taborda *et al.*, "Experimental study of resin coating to improve the impact strength of fused filament fabrication process pieces", *Rapid Prototyping Journal*, vol. 27, no. 3, pp. 475–486, 2021, doi: 10.1108/rpj-08-2018-0194.
- [15] H. B. Musgrove, S. R. Cook, and R. R. Pompano, "Parylene-c coating protects resin 3D printed devices from materials erosion and cytotoxicity", *Analytical Chemistry*, 2023, doi: 10.26434/chemrxiv-2023-42969.





## Numerical Study of Magneto-Double-Diffusive Natural Convection of a Nanofluid Flowing in a Concentric Annular Space

Nesrine Rachedi<sup>\*1</sup>, Messaoud Guellal<sup>1</sup>

<sup>1</sup>Laboratory of Chemical Process Engineering, Faculty of Technology, Ferhat Abbas Setif-1 University, Algeria

---

### Abstract

The investigation of natural convection in nanofluid-filled concentric annular spaces has become a focal point due to its relevance across various engineering applications. This research delves into the numerical analysis of magneto-double-diffusive natural convection within such setups. The nanofluid, comprising nanoparticles dispersed within a base fluid, experiences thermal and solutal buoyancy forces in addition to a transverse magnetic field. Utilizing finite volume methods, the governing equations encompassing mass, momentum, energy, and species conservation are solved numerically. Through this study, the impact of crucial parameters like nanoparticle volume fraction, Rayleigh number, Hartmann number, and Lewis number on flow dynamics and heat transfer properties is examined. Findings reveal intricate fluid flow patterns and notable enhancements in heat transfer rates owing to nanoparticle presence and magnetic field influence. Furthermore, the study explores the influence of various parameters on Nusselt number distribution. By shedding light on the behavior of magneto-double-diffusive natural convection in nanofluid-filled concentric annular spaces, this research offers valuable insights for optimizing thermal management systems and designing advanced heat exchangers.

**Keywords:** *Magneto-double-diffusive, Nanofluid, Natural convection, Hartmann number*

---



## **Preventive Maintenance of an Industrial Reciprocating Compressor by Oil Analysis**

**Lamia Benzaid<sup>\*1</sup>, Naima Tamaloussi<sup>1</sup>, Toufik Sebah<sup>1</sup>**

*<sup>1</sup>Mechanical Engineering Department, University of Skikda, Algeria*

---

### **Abstract**

Oil analysis as a preventive maintenance instrument began to be applied in specific sectors of industry as early as the 1950s. Thanks to these measures we can detect anomalies and prevent breakdowns, plan maintenance, and optimize oil change intervals. In this work we will be particularly interested in the analysis of samples of lubricating oil in service used for the lubrication of a reciprocating compressor in order to determine the physicochemical characteristics of the oil on one side and to determine its degradation and its contamination on the other side.

**Keywords:** *Preventive maintenance, Compressor, Oil analysis, Lubricating oil*

---



## Flow Analysis for a Light Commercial Vehicle with a Vertical Axis Turbine Added for Power Generation

Erman Kadir Oztekin<sup>\*1</sup>

<sup>1</sup>Department of Mechanical Engineering, Bayburt University, Bayburt, Türkiye

### Abstract

The energy required to meet the heating or cooling loads required in transportation can be provided by different techniques. In the simplest way, this energy can be met indirectly from the mechanical energy produced by the transport vehicle or directly from the battery. Nowadays, obtaining energy by using inexhaustible and sustainable energy sources is gaining importance. By using vertical axis turbines, energy can be obtained by using the fluid masses passing through the both sides of the transport vehicle. However, it is necessary to know the disruptive effects of these vertical axis turbine volumes on the flow. In particular, the effects of back pressure and friction, which will cause the vehicle to consume more fuel, need to be investigated. In this study, it will be examined to what extent the flow on the vehicle is affected by adding vertical turbine volumes of different diameters to a light commercial vehicle model. To do this, the cross-sectional area of the vehicle in the direction of progress, pressure and friction forces and the change in friction coefficients will be examined.

**Keywords:** Vertical turbine, Energy, External flow, Drag, Force

## 1 INTRODUCTION

It is important to conduct aerodynamic tests of innovative designs whose fuel consumption depends on the final degree of vehicle aerodynamics. The air flow coming to the vehicle circulates around and through the body of the vehicle, affecting the performance of the vehicle [1]. Streamlines coming to the vehicle generally follow the vehicle body smoothly, but they separate at the rearest edge of the vehicle and create large wakes which can be easily observed. At 100 km/h, aerodynamic drag in a medium-sized European car makes up around 80% of the total road resistance. Aerodynamic drag acting on vehicles can be considered as the sum of pressure drag and viscous drag. While pressure drag depends on the shape and size of the vehicle, viscous drag results from the friction of the outside of the vehicle with the flow around the body. The drag force and other forces and moments acting on the vehicle change in proportion to the square of the vehicle's speed.

The expression for the complete drag force can be given as:

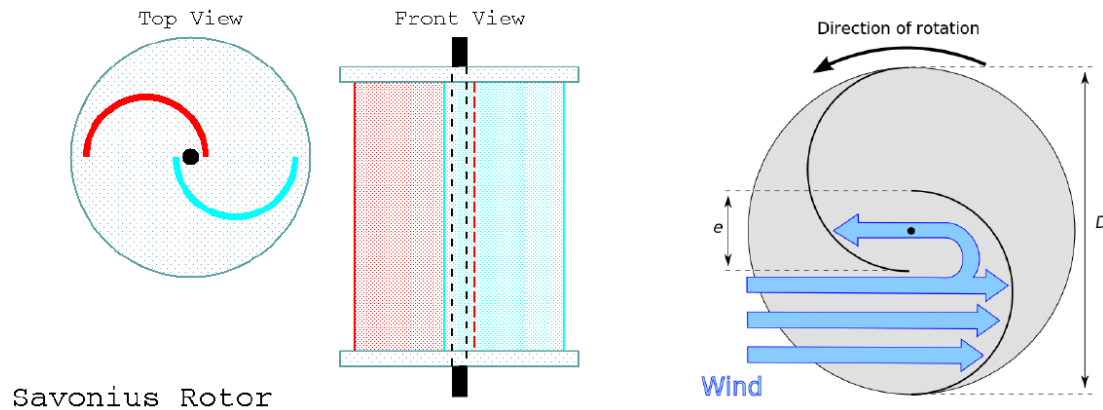
$$F_D = C_D A \frac{\rho}{2} V^2 \quad (1)$$

where  $F_D$  is the drag acting on the vehicle,  $C_D$  is the drag coefficient,  $A$  is the frontal area of the vehicle,  $\rho$  is the density of the fluid and  $V$  is the speed of the object relative to the fluid. The car's design must be such that any additional forces and moments are kept to a minimum so as not to significantly impair directional stability.

Vehicles such as trucks, trailers, transporter minivans and panel vans travel long distances under certain loads and consume large amounts of fuel. Vehicles in this style of light commercial vehicle class can perform both urban and intercity transportation. While the vehicle is driving, there is a need for heating and cooling for the people inside the vehicle. Additionally, extra cooling loads arise when the items being transported are food, fresh meat, fish or biological materials. Extra cooling units integrated into the vehicle meet the power needs from the vehicle itself and increase fuel consumption. Vertical axis turbines can be used to meet cooling loads because their rotation axes can be conveniently integrated into the vehicle body and because they are a very popular renewable energy source.

Vertical axis turbines can be used at low wind speeds and operate more quietly [2]. Vertical axis turbines rotate around an axis perpendicular to the incoming flow and are divided into two main groups: Savonius type and

Darrieus type. In Savonius type wind turbines, two semi-cylindrical buckets facing each other are placed at a certain distance [3]. Although the power production in such turbines is good, the effectiveness may be low. The Darrieus type rotors can capture more wind energy per unit of swept area since their design is dependent on the lift force. The Darrieus airfoils go through the air in a circular motion in the air. A Savonius type turbine will be considered for this study because it can be integrated into vehicles and has lower vibration to avoid disrupting driving orientation.



**Figure 1.** Savonius type wind turbine geometry and flow motion [4]

Savonius type turbines can be produced by changing various parameters. Small scale vertical axis turbine with different blade shapes was produced and its performance was tested by Shah [4]. The rotor diameter and height of the rotor shape were 0.9 m and 1.3 m, respectively. Loganathan et. al. produced and tested two sets of rotors, one with a diameter of 300 mm and a height of 160 mm, and the other with a diameter of 600 mm and a height of 320 mm, with different numbers of blades. They concluded that doubling the size increased power output by about 80% [5]. Zein an Omar designed mini Savonius wind turbine with three helical blades to integrate bikes [6]. The height of the rotor was 100 mm and the diameter of the rotor is less than 110 mm. The calculated the RPM and efficiencies at different wind speeds. Savonius type turbines can be produced by integrating Darrieus airfoils to both utilize lift and grad effects. Higher efficiencies can be observed by this way [7]. Montelpare et. al. experimentally tested modified Savonius wind rotor to meet energy requirement for street lighting systems [8]. They used rotors with different axially connected modular element angles. The rotor diameter is given as 384 mm and the rotor height is designed to be approximately 1 meter. Outside the rotor, there are two pieces of flow guides called deflector and conveyor. While the conveyor allows the flow to go further to the blades, the deflector prevents the reverse flow to the returning blade.

As a result, in order to meet the cooling loads of light commercial vehicles, vertical axis turbines that can be integrated into additional vehicles can be used and produced with different characteristics. In this study, the effects of symmetrical vertical axis turbine volumes of different diameters with a certain height on the flow, especially on the drag acting on the vehicle, will be examined.

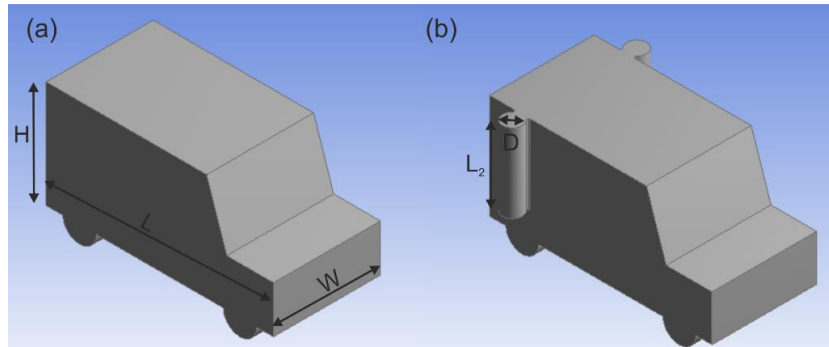
## 2 MATERIAL AND METHOD

Three-dimensional CFD analysis was performed using the ANSYS Fluent program in this inquiry. Since they serve as the foundation for computational fluid dynamics (CFD) and allow us to simulate intricate turbulent flows, the Reynolds-Averaged Navier-Stokes Equations (RANS) have played a significant role in this breakthrough. Applications of the RANS model include marine solutions, aerospace and aeronautical engineering, industrial and automotive solutions, and more. The standard  $k-\epsilon$  turbulence model consists a set of equations which can be applied to a large number of turbulent applications.

Geometry with characteristic lengths of the vehicle can be seen from Figure 2. The vertical axes turbine (VAT) is placed at the rear of the car closer to the area where fluid separation occurs. The characteristic values of the vehicle are considered as follows:  $H=1.6$  m,  $L=3.4$  m,  $W=1.6$  m,  $L_2=1.2$  m, and 0.1, 0.3, 0.5 m values are also considered as  $D$  value.

The air assumed to approach a vehicle with the velocity of 100 km/h (27.7 m/s). No-slip wall conditions for the surfaces were defined. Selected boundary conditions have been consistently implemented for both analysis models. Element size was optimized to get a good result of pressure drag and high inflation numbering (more than 15) was

preferred for more accurate viscous drag results [9]. Tetrahedron and wedge elements were used in the mesh and then the mesh was converted to polyhedral for fasted convergence and to improve the overall mesh quality. Total number of 932,972 elements and number of 220,426 nodes were used for basic vehicle model which is a good level of having accurate results for stationary domain [9]. Whereas total number of 4,127,830 elements and number of 1,575,911 nodes were used for vehicle integrated with vertical axes turbine with the diameter of 0.3 m.



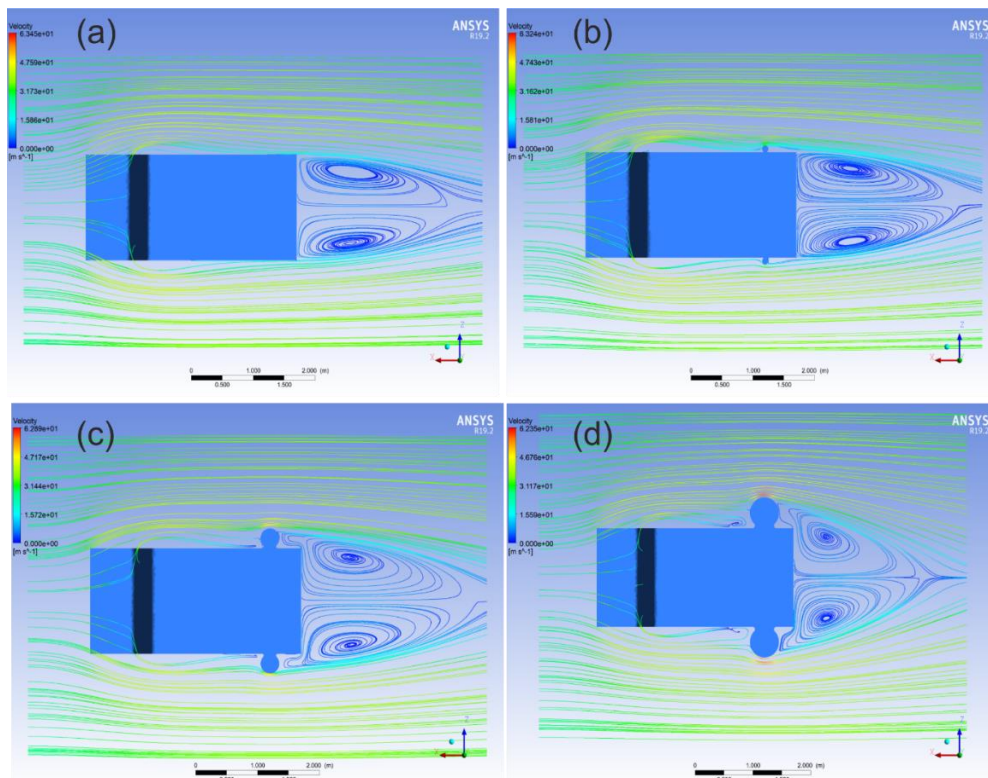
**Figure 2.** Geometry and characteristic parameters

### 3 RESULTS

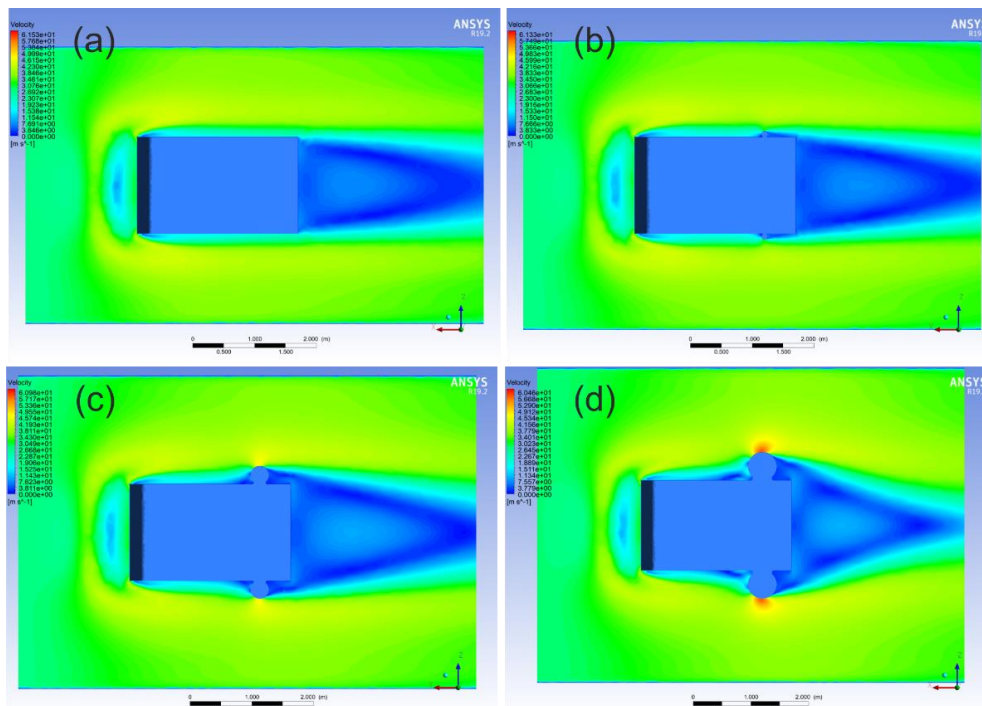
Table 1 shows the projected area, total drag and drag coefficient values for each case.

**Table 1.** Results for each case

Diameter of the VAT (m)	Projected Area (m <sup>2</sup> )	Percent Change (%)	Pressure Drag (N)	Viscous Drag (N)	Total Drag (N)	Percent Change (%)	Coefficient (C <sub>D</sub> )
Basic	2.701673		2298.491000	8.574954	2307.065900		1.806864
0.1	2.991450	10.72584363	2355.062700	6.595275	2361.658000	2.3662999	1.679851
0.3	3.462213	28.15070722	2650.085700	6.909817	2656.995500	15.167733	1.623844
0.5	4.034901	49.34826305	3107.197300	9.200369	3116.397600	35.080562	1.634365



**Figure 3.** Streamlines of (a) basic geometry, (b) VAT D=0.1 geometry, (c) VAT D=0.3 geometry, and (d) VAT D=0.5 geometry



**Figure 4.** Velocity contours of (a) basic geometry, (b) VAT D=0.1 geometry, (c) VAT D=0.3 geometry, and (d) VAT D=0.5 geometry

## 4 CONCLUSION

There is a chance of integrating vertical axes turbines to vehicles for producing energy. The following inferences can be made with the results obtained here.

- Pressure drag always increases while the projected area increases when the diameter of the VAT change. However viscous drag decreases first and increases again with increasing projected area. So there is a limited area that VAT can be integrated to the vehicle without a lot of loss.
- Different types of wall structures, such as wavy structures, can be created and energy can be produced from them.
- As vertical turbine technologies develop and their efficiency increases, such applications will become more prominent as more energy is produced in smaller volumes.
- Such integration applications can be considered not only for light commercial vehicles but also for different transportation vehicles such as trains.
- For vehicles different types of casing structures can be used to prevent blades from damage and also to guide more air into the blades.

## References

- [1] *Aerodynamics of Road Vehicles from Fluid Mechanics to Vehicle Engineering*, W.-H. Hucho, Ed.: Butterworth-Heinemann, 1987.
- [2] R. Kumar, K. Raahemifar, and A. S. Fung, "A critical review of vertical axis wind turbines for urban applications," *Renewable and Sustainable Energy Reviews*, vol. 89, pp. 281-291, 2018.
- [3] C. Kang, H. Liu, and X. Yang, "Review of fluid dynamics aspects of Savonius-rotor-based vertical-axis wind rotor," *Renewable and Sustainable Energy Reviews*, vol. 33, pp. 499-508, 2014.
- [4] S. Shah, "Small scale vertical axis wind turbine," M.S. thesis, Toronto Metropolitan University, Toronto, Ontario, 2015.
- [5] B. Loganathan et al., "Effect of sizing of a Savonius type vertical axis micro wind turbine," *Energy Procedia*, vol. 110, pp. 555-560, 2017.
- [6] Zein, H. and H. Omar, "Designing and manufacturing of miniature savonius wind turbine," in *International Engineering Conference and Exhibition IECE*, Riyadh, 2017.
- [7] S. Bhuyan and A. Biswas, "Comparative investigation of Savonius and hybrid H-Savonius wind rotor - an energy and exergy analysis," *EAI Endorsed Transactions on Energy Web*, vol. 8, art. no. 166362, 2018.

- [8] S. Montelpare et al., "Experimental study on a modified Savonius wind rotor for street lighting systems. Analysis of external appendages and elements," *Energy*, vol. 144, p. 146-158, 2018
- [9] K. A. H. Al-Gburi et al., "Enhancing savonius vertical axis wind turbine performance: A comprehensive approach with numerical analysis and experimental investigations," *Energies*, vol. 16, no. 10, art. no. 4204, 2023.



## Energy Consumption and Moisture Extraction Optimization in a Heat Pump Tumble Dryer

Berkay Yilmaz<sup>\*1</sup>, Mehmet Alper Sav<sup>1</sup>, Yusuf Balsever<sup>1</sup>

<sup>1</sup>*Vestel White Goods Tumble Dryer R&D Center, Manisa, Türkiye*

---

### Abstract

There are many variables that affect energy consumption and moisture extraction efficiency in heat pump tumble dryers. In this study, the amount of refrigerant, fan speed and drum speed that affect energy consumption and moisture extraction efficiency were investigated. A statistical software program was used to optimize energy consumption, moisture extraction rate (MER) and specific moisture extraction rate (SMER) with these variables. The results obtained showed that these three variables have different effects on the outputs. As a result of the study, the parameter values that will keep the energy consumption at the lowest value and the SMER value at the highest value were determined and verified by experiments.

**Keywords:** *Heat pump tumble dryer, Energy efficiency, Moisture extraction, Optimization*

---





## Numerical Investigations on the Effect of Isothermal Multi-Jets in Air Curtains with LES Approach

Sahnoun Rachid<sup>\*1</sup>, Draï Ismail<sup>1</sup>, Merouane Habib<sup>1</sup>

<sup>1</sup>Mechanical Department, University Mustapha Stambouli, Mascara, Algeria

---

### Abstract

This work focuses on the analysis of the turbulent intensity of the flow field resulting from planar jets applied in air curtains systems, which are used in various industry sectors. The air curtains allow realizing cellular containment. Hence, the main objective is to improve the quality of confinement's separation by air curtains. In order to achieve this target, the jet flow must be as laminar as possible. Numerical LES investigations are carried out in this study. A jet impingement against a flat and a smooth surface without recirculation has been used for this assessment. The WALE (Wall Adapting Local Eddy) structure models the subgrid-scale tensor. First, the configuration of air curtain with a single jet and then with a twin-jet are investigated. Result comparisons to available experimental measurements have been performed and good agreements have been noticed. The study is then extended for the first time to air curtain configurations with more than two planar jets. The configuration of the triple jet indicates a lower turbulence level than the single jet and the twin-jet ones. This improves the confinement's separation quality. However, increasing the number of jets highlights a limit because the turbulence decrease will be not significant beyond a certain number of jets taking into account the operating conditions. In this study, an effective process shows that, the four jets configuration is considered as the better compromise under the considered operating conditions.

**Keywords:** *Multi-jets, LES approach, Plan curtain, Planar jet, Turbulence*

---



## Numerical Study of Flow Around Counter Rotating Cylinder

**Drai Ismail\*<sup>1</sup>, Sahnoun Rachid<sup>1</sup>, Merouane Habib<sup>1</sup>, Yahiaoui Tayeb<sup>2</sup>**

<sup>1</sup>*Mechanical Department, University Mustapha Stambouli, Mascara, Algeria*

<sup>2</sup>*Mechanical Department, University of Science and Technology, Oran, Algeria*

---

### Abstract

Recent advancements in automotive aerodynamics and new product design emphasize the significance of aerodynamic phenomena. This study focuses on analyzing the pressure coefficient distributions of aerodynamic forces applied to a rotating cylinder and a container to gain a better understanding of the underlying physical phenomena described by theory.

Initially, the flow around the container is examined for various angles of incidence, enabling the analysis of the velocity field in the wake and the pressure field on its surface. Subsequently, the flow around a rotating cylinder is investigated.

This research relies on numerical simulation using the finite volume method to solve the three-dimensional compressible Navier-Stokes equations. These equations are statistically averaged and closed using a turbulence model. The turbulence model employed in this study is the k-epsilon model.

The numerical results demonstrate a reduction in aerodynamic forces when the cylinders are in rotation. This observation highlights the effectiveness of this technique in mitigating the adverse aerodynamic effects on the container and cylinder, which can have significant implications for the design of new aerodynamic products.

**Keywords:** *Aerodynamics, Product design, Pressure coefficients, Container, Rotating cylinder, Flow, Numerical simulation, Finite volume method, Navier-Stokes equations, k-epsilon turbulence model*

---



## The Effect of Bluff Body Geometry on the Combustion of CH<sub>4</sub>/Air

Merouane Habib<sup>\*1</sup>, Draï Ismail<sup>1</sup>, Sahnoun Rachi<sup>1</sup>

<sup>1</sup>Department of Mechanical Engineering, University of Mascara, Algeria

---

### Abstract

In this work we present a numerical study on the combustion of methane-air in a combustion chamber of different diameters of the bluff body. This study allows us to see the effect of bluff body on the behaviour of the flame in a turbulent flow. This study is carried out using a CFD code calculation based on the finite volume method for the discretization of the differential equations which control the phenomenon. Two models were chosen for the prediction of combustion and turbulence, namely the k-epsilon model for the prediction of turbulence and the EDM (Eddy Dissipation Model) model for combustion. The numerical results obtained are discussed and analyzed.

**Keywords:** *Non-premixed combustion, Bluff body, CFD, k-epsilon model, EDM model*

---



## Design and Implementation of an Intelligent Irrigation System

Toufik Sebbagh<sup>\*1</sup>, Islam Boukhadra<sup>1</sup>

<sup>1</sup>*LGMM Laboratory, University of Skikda, Skikda, Algeria*

---

### Abstract

Agriculture has been a cornerstone of human civilization since ancient times, embodying tradition and sustenance. The success of crop cultivation hinges on favorable environmental conditions and precise moisture levels. In this context, the implementation of advanced technologies becomes imperative for maximizing agricultural productivity while conserving vital resources like water.

The focal point of this research lies in the deployment of an intelligent irrigation control system, facilitated by a microcontroller, to vigilantly monitor agricultural fields. This system operates with a keen eye on efficiency, utilizing sensors strategically positioned within the fields to detect crucial parameters such as soil moisture, humidity, and precipitation. The data collected from these sensors is then relayed to a centralized hub accessible via the Internet, ensuring real-time monitoring and analysis.

Moreover, a user-friendly application interface enables farmers to remotely toggle the operation of the water pump between ON and OFF states, granting them unprecedented control over irrigation processes. In automatic mode, the system autonomously gauges soil moisture levels and triggers irrigation when levels dip below a predetermined threshold, thereby optimizing water usage.

By integrating these technological advancements into agricultural practices, farmers can not only boost crop yields but also mitigate water wastage, fostering sustainable farming methods. This holistic approach underscores the pivotal role of technology in addressing contemporary agricultural challenges and advancing towards a more efficient and environmentally conscious future.

**Keywords:** *Irrigation, Microcontroller, Control, Arduino, Soil humidity*

---



## The Production of Bamboo Based Natural Composite Materials and Comparison of Their Material Properties with Particleboard MDF Boards

Ali Gumustekin<sup>\*1</sup>, Sedat Ozden<sup>\*1</sup>, Fehmi Nair<sup>\*1</sup>

<sup>1</sup>Mechanical Engineering, Erciyes University, Kayseri, Türkiye

### Abstract

Bamboo is a fast-growing plant also cultivated in Türkiye. Bamboo-based composite materials offer advantages such as high strength, lightness, effective thermal conductivity, environmental sustainability, and a low carbon footprint. Particleboard and MDF, commonly used in the furniture industry, require wood chips from slow-growing trees. This study shows that bamboo-based sandwich composites have significant potential as an alternative due to their notable mechanical properties.

In this study, eight types of bamboo-based natural composite materials were produced using two different molds with stacking methods. While the size and lining parameters of bamboo sticks were kept constant, the type of adhesive and the state of the bamboo (whether hollow or filled) were varied. After being removed from the mold, the material was cut into 12 mm thick strips using a bandsaw. Plywood sheets of 3 mm thickness were glued to the top and bottom of these strips. The resulting sandwich composites were tested for compression strength, indentation strength, and thermal conductivity in laboratory conditions.

MDF boards and particleboards have densities of 700 kg/m<sup>3</sup> and 610 kg/m<sup>3</sup>, respectively. Bamboo-based composite made with D4 wood adhesive and hollow sticks has a density of 430 kg/m<sup>3</sup> approximately. The thermal conductivity of MDF and particleboard are 0.097 W/mK and 0.099 W/mK, respectively. The best thermal conductivity value of 0.090 W/mK was achieved in composites made with D3 wood adhesive, with hollow bamboo sticks. The highest compression and indentation strengths were achieved in composites using D4 wood adhesive, with an average compression strength of 23.34 N/mm<sup>2</sup>. The best results in the indentation test with a 20 mm diameter steel ball were also achieved with D4 adhesive. As a result, it was shown that the new bamboo-based material possesses improved properties compared to traditional board materials in terms of thermal conductivity and density.

**Keywords:** Bamboo, Sandwich composites, Compression test, Thermal conductivity coefficient

## 1 INTRODUCTION

In recent years, there has been a growing interest in sustainable and eco-friendly materials within the construction and furniture industries. This shift is driven by the need to reduce the environmental and cost impact of traditional materials, such as particleboard and medium-density fibreboard (MDF), which often involve high energy consumption, the use of synthetic resins that release harmful emissions and high weight problems. Bamboo, a fast-growing and renewable resource, has emerged as a promising alternative due to its exceptional mechanical properties and minimal environmental footprint.

Bamboo's inherent strength, flexibility, and rapid growth cycle make it an ideal candidate for developing natural composite materials. Bamboo-based composites are created by combining bamboo fibres with resins or adhesives, resulting in materials that offer excellent mechanical properties while being environmentally sustainable. These composites can be used in various applications, including construction, furniture, and interior design.

In this study, 8 different bamboo-based sandwich composite materials are produced. These composites are evaluated in laboratory conditions. These results are compared with each other and also MDF and particleboard.

## 2 MATERIAL AND METHOD

### 2.1 Materials

## Bamboo

Bamboo is a fast-growing, renewable resource with excellent mechanical properties. It has been used for centuries in construction, furniture, and various other applications. Bamboo's high strength-to-weight ratio, rapid growth rate, and sustainability make it an attractive material for modern engineering applications [1].

## Marine Adhesive-D4

Marine adhesive D4 is a high-performance adhesive used in the construction of marine vessels and other applications requiring strong, waterproof bonding. It is resistant to water, heat, and chemicals, making it suitable for harsh environments [2].

## MDF Wood Adhesive-D3

MDF wood adhesive D3 is a type of adhesive used for bonding MDF and other wood-based materials. It is known for its strong bond, ease of application, and water resistance [3].

## Polyurethane Foam

Polyurethane foam is a versatile material used in various applications, including insulation, cushioning, and composite cores. It is available in different densities and can be rigid or flexible [4].

## Wood Chips

Wood chips are small pieces of wood produced by chipping larger wood pieces. They are used as a raw material in the production of particleboard, MDF, and other wood-based products [5].

## MDF

MDF is an engineered wood product made from wood fibres bonded with resin under heat and pressure. MDF is known for its smooth surface, uniform density, and ease of machining. It is commonly used in furniture, cabinetry, and interior panelling [6].

## Particleboard

Particleboard is an engineered wood product made from wood particles (such as chips, sawdust, and shavings) bonded with resin and compressed into sheets. It is a cost-effective alternative to solid wood and plywood, commonly used in furniture, flooring, and wall panelling [7].

## 2.2 Methods

In this study, eight types of bamboo-based natural composite materials were produced using two different molds with stacking methods. Work flow is seeing on below chart. While the size and lining parameters of bamboo sticks were kept constant, the type of adhesive and the state of the bamboo (whether hollow or filled) were varied. After being removed from the mold, the material was cut into 12 mm thick strips using a bandsaw. HDF sheets of 3 mm thickness were glued to the top and bottom of these strips (below figure). The resulting sandwich composites were tested for compression strength, indentation strength, and thermal conductivity in laboratory.



**Figure 1.** Bamboo based composite side sectional view

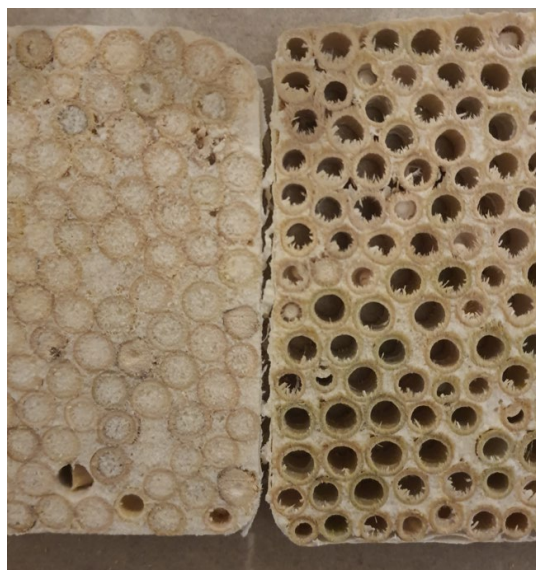


Figure 2. Filled (left) and hollow (right) bamboo core

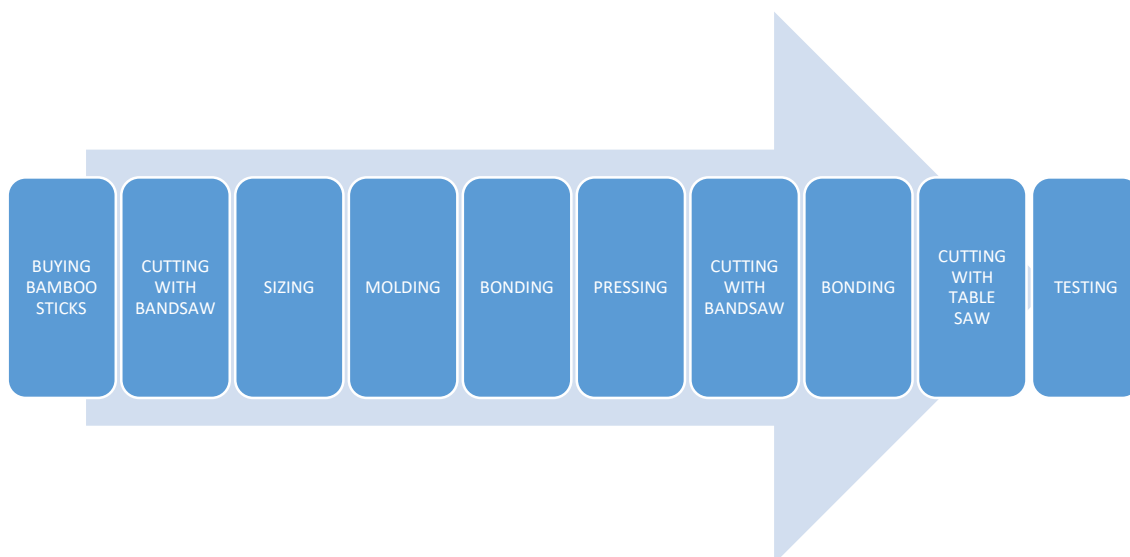


Figure 3. Bamboo composite manufacture process and work flow

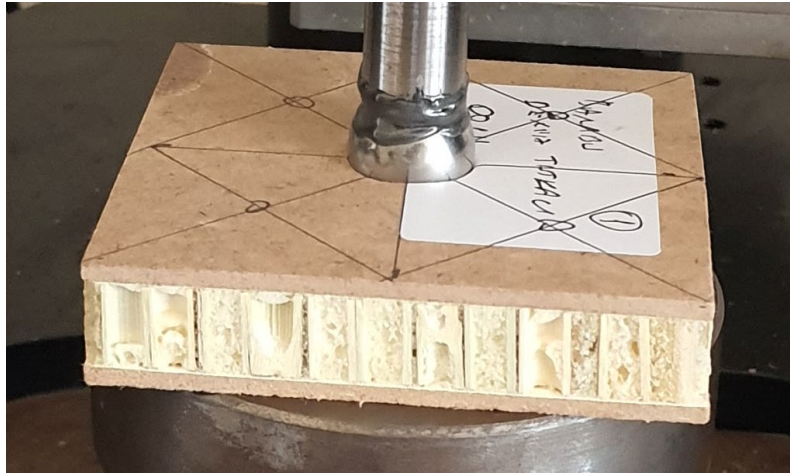
Table 1. Material list

Item Number	Material Explanation	Short Explanation
1	Bamboo + D4 + Filled	1- D4+F
2	Bamboo + D4 + Hollow	2- D4+H
3	Bamboo + Polyurethane + Filled	3- PU+F
4	Bamboo + Polyurethane + Hollow	4- PU+H
5	Bamboo + MDF D3 Adhesive + Filled	5- D3+F
6	Bamboo + MDF D3 Adhesive + Hollow	6- D3+H
7	Bamboo + %95 D3 MDF Adhesive + %5 Saw Dust + Filled	7- D3+S+F
8	Bamboo + %95 D3 MDF Adhesive + %5 Saw Dust + Hollow	8- D3+S+H
9	Particle Board	9-PB
10	MDF-Medium Density Fibreboard	10-MDF

Specific weight calculations were made by using a Precisa LS 220A SCS scale and a caliper with an accuracy of 0,05 mm and range of 0-150 mm.

Compression tests were conducted using a Shimadzu, AG-X 50kN testing machine with samples of 40 mm x 40 mm. The compression speed was 2 mm/min. After the force reached the top peak value, it dropped smoothly on the chart.

Indentation test was conducted using a Shimadzu, AG-X 50kN testing machine with samples of 90 mm x 90 mm. The test involved pressing a 20 mm diameter steel sphere into the composite material at a speed of 2 mm/min, and it was stopped after a 9 mm vertical displacement through the samples.



**Figure 4.** Indentation Test

Thermal conductivity tests were conducted using a Thermtest HFM-100 machine. A minimum sample size of 150 mm x 150 mm was required for the test. Therefore, composite materials were enlarged by using a 20 mm thick EPS board, expanding from 90 mm x 90 mm to 150 mm x 150 mm in size.

### 3 RESULTS

The lightest average specific weight, 428 kg/m<sup>3</sup>, was obtained with the D4 + H composite, making it nearly 39% lighter than MDF.

**Table 2.** Material list

Item Number	Material Explanation	Short Explanation	Avarage Specific Weight (kg/m <sup>3</sup> )
1	Bamboo + D4 + Filled	1- D4+F	503
2	Bamboo + D4 + Hollow	2- D4+H	428
3	Bamboo + Polyurethane + Filled	3- PU+F	464
4	Bamboo + Polyurethane + Hollow	4- PU+H	463
5	Bamboo + MDF D3 Adhesive + Filled	5- D3+F	687
6	Bamboo + MDF D3 Adhesive + Hollow	6- D3+H	476
7	Bamboo + %95 D3 MDF Adhesive + %5 Saw Dust + Filled	7- D3+S+F	645
8	Bamboo + %95 D3 MDF Adhesive + %5 Saw Dust + Hollow	8- D3+S+H	586
9	Particle Board	9-PB	610
10	MDF-Medium Density Fibreboard	10-MDF	700

The D4 + F composite had the highest compression strength. The compressive strength of D4 + F was 86%, 56%, and 28% greater than the compressive strengths of PU + F, D3 + F, and D3 + S + F, respectively. Hollow composites made with D3 adhesive and foamed polyurethane showed better results compared to filled ones.

**Table 3.** Compression test results and top peak values (N)

Comperession Test (N)	Filled	Hollow
D4	<b>37,342</b>	34,674
PU	20,082	<b>28,543</b>
D3	23,942	<b>32,449</b>
D3 + S	29,112	<b>33,700</b>

Similarly, the D4 + F composite had the highest indentation strength. The indentation strength of D4 + F was 98%, 134%, and 79% greater than the indentation strengths of PU + F, D3 + F, and D3 + S + F, respectively. Hollow



composites made with D3 adhesive and foamed polyurethane performed better in indentation tests compared to filled ones.

**Table 4.** Indentation test results and top peak values (N)

Indentation Test (N)	Filled	Hollow
D4	<b>4,975</b>	3,690
PU	2,518	<b>3,523</b>
D3	2,128	<b>3,066</b>
D3 + S	2,774	<b>3,884</b>

Thermal conductivity test results are shown in the chart below. Hollow bamboo composites consistently revealed lower thermal conductivity results compared to filled ones. The lowest thermal conductivity value, 0.0900 W/mK, was achieved with the D3 + H composite. The highest value, 0.1214 W/mK, was obtained with the D3 + S + F composite.

**Table 5.** Thermal conductivity test results (W/mK)

Thermal Conductivity W/mK	Filled	Hollow
D4	0.1005	<b>0.0933</b>
PU	0.1031	<b>0.0978</b>
D3	0.1182	<b>0.0900</b>
D3 + S	0.1214	<b>0.1194</b>

## 4 CONCLUSION

In this study, we produced eight different bamboo-based natural composite materials, varying the adhesive types and bamboo states (hollow or filled). Our results demonstrate that hollow composites are both lightweight and strong, with significant advantages in compression, indentation, and thermal conductivity.

The lightest composite, D4+H, had a specific weight of 428 kg/m<sup>3</sup>, making it 39% lighter than MDF. The D4 + F composite showed the highest compression strength, 86%, 56%, and 28% greater than PU + F, D3 + F, and D3 + S + F, respectively. Indentation tests also highlighted D4 + F's superior performance, with indentation strengths 98%, 134%, and 79% greater than PU + F, D3 + F, and D3 + S + F. Thermal conductivity results indicated that hollow composites have better insulation, with the D3 + H composite achieving the lowest value of 0.0900 W/mK.

These findings confirm that hollow bamboo-based composites are sufficient, offering a promising alternative to conventional materials like MDF and particleboard.

## Acknowledgments

I would like to express my sincere gratitude to the laboratory staff for their invaluable assistance during the experimental phase of this study. My heartfelt thanks go to Erciyes University for providing the necessary resources and support. Finally, I am deeply appreciative of the guidance and feedback from my supervisors, whose insights were instrumental in the successful completion of this project.

## References

- [1] G. Marsh, "Composites consolidate in commercial aviation," *Journal of Reinforced Plastics*, vol. 60, no. 5, pp. 302–305, 2016.
- [2] K. Naresh, K. Shankar, and R. Velmurugan, "Reliability analysis of tensile strengths using Weibull distribution in glass/epoxy and carbon/epoxy composites," *Composites Part B: Engineering*, vol. 133, pp. 129–144, 2018.
- [3] A. Muhammad, M. R. Rahman, and R. Bainsi, "Applications of sustainable polymer composites in automobile and aerospace industry," in *Advances in Sustainable Polymer Composites*, S. Bhansali and A. Vasudev, Eds. Cambridge: Woodhead, 2021, pp. 185–207.

- [4] J. N. Hall, J. Wayne Jones, and A. K. Sachdev, "Particle size, volume fraction and matrix strength effects on fatigue behavior and particle fracture in 2124 aluminum-SiCp composites," *Materials Science and Engineering A*, vol. 183, no. 1–2, pp. 69–80, 1994.
- [5] R. F. J. McCarthy, G. H. Haines, and R. A. Newley, "Polymer composite applications to aerospace equipment," *Composites Manufacturing*, vol. 5, no. 2, pp. 83–93, 1994.
- [6] W. Harizi, R. Azzouz, A. Martins, K. Hamdi, Z. Aboura, and K. Khellil, "Electrical resistance variation during tensile and self-heating tests conducted on thermoplastic polymer-matrix composites," *Composite Structures*, vol. 224, art. no. 111001, 2019.
- [7] K. Naresh, K. Shankar, and R. Velmurugan, "Reliability analysis of tensile strengths using Weibull distribution in glass/epoxy and carbon/epoxy composites," *Composites Part B: Engineering*, vol. 133, pp. 129–144, 2018.



## Elastic Repair Analysis for the Interaction Between Two Semi-Elliptical Cracks in a Damaged Aeronautical Structure

Belhamiani Mohamed<sup>\*1</sup>, Bouzitouna Wahiba Nesrine<sup>1</sup>, Oudad Wahid<sup>1</sup>, Djebbar Nouredine<sup>1</sup>

<sup>1</sup>Mechanical Engineering Department, University of Ain Temouchent, Ain Temouchent, Algeria

---

### Abstract

Cracks within structures typically interact with one another under the influence of external loads. The extent of this interaction is significantly influenced by the distribution of applied stresses. The objective of our research is to conduct a numerical analysis using the finite element method to investigate the fracture behavior of an aeronautical structure containing two semi-elliptical cracks. We focus on understanding the interaction between these cracks, utilizing the stress intensity factor as a critical parameter. This study is rooted in the principles of linear elasticity and fracture mechanics, encompassing a range of three-dimensional geometric configurations.

**Keywords:** Crack interaction, Patch, FIC KI, Von mises, Repair

---



## Investigation of the Effects of a Heated Vest on Blood Pressure and Body Temperature of Male Individuals

Emre Demirci<sup>1</sup>, Erman Kadir Oztekin<sup>\*2</sup>

<sup>1</sup>Department of First and Emergency Aid, Bayburt University, Bayburt, Türkiye

<sup>2</sup>Department of Mechanical Engineering, Bayburt University, Bayburt, Türkiye

### Abstract

Nowadays, the number of heated wearable products equipped with resistive heating elements in the fashion market is increasing. The human body interacts with the temperature of the environment and reacts to these changes. These heated clothes are in close contact with the human body and can also affect blood pressure and body temperature. A person's blood pressure and skin temperature may change with respect to changes at the ambient conditions. People may even experience heart-related health problems in extremely cold and extremely hot weather. In this study, the effects of a heated vest on human health were examined by considering systolic blood pressure, diastolic blood pressure and body temperature data. All three datasets are collected over 30 minutes while the male participants are wearing heated vest when the heating feature is active. The changes in these data are examined by using Friedman test. Detailed statistics are applied by using Wilcoxon Signed Ranks Test in order to see the difference within each group.

**Keywords:** Heated vest, Blood pressure, Temperature, Friedman, Statistics

## 1 INTRODUCTION

With developing technology, smarter products can be designed by improving the functions of wearable products. These products tend to come into direct contact with human body. For example thermal blankets have been developed for space travel [1]. The goal of the definition of thermal comfort is to keep people's skin and internal organs from being exposed to extreme heat or cold for extended periods of time while maintaining a pleasant temperature [2]. According to the definition of thermal comfort, the heat losses from the person's skin to the environment per unit time and the temperature difference between the skin and the body centre should be in balance. The thermal comfort of people in cold environments can be improved both indoors and outdoors with clothing such as coats and vests produced with standard style fabrics. In addition, one of the innovations resulting from integration with technology is coats and vests equipped with self-heating pads. In these heated vests, pads with carbon fiber heating wire are connected to a power unit to provide active heating within the vest or coat [3]. Other wires with different resistance characteristics can also be used as a heating element for heated vests [3, 4]. As a result, thanks to such elements, thermal comfort can be provided even in very cold environments or in jobs where activity is low, such as guarding. Heated pads are generally integrated into the back and chest areas of these wearable products [5]. In this context, thermal comfort can be discussed as the state in which the body exerts minimum physiological effort in the given environment for a healthy individual. Because the body's skin temperature may vary and the body tries to thermally adapt to the environment by using some internal effort [6]. As the body adapts to the environment, vessels may expand (vasodilation) or contract (vasoconstriction). The increase in ambient temperature also causes an increase in body temperature. It is known that temperature increase has an effect on the body's vital values [7]. While blood pressure increases in cold weather due to the structure of the body, blood pressure decreases in warmer weather. Since the vessels narrow in cold weather, blood pressure increases and blood circulation is ensured by the body [8]. Clothing affects heat transfer between the body and the environment. These are important parameters in terms of thermal comfort. Since these clothes are in direct contact with the body, their health effects need to be examined. Moreover, seasonal temperature drops are known to trigger heart diseases [8]. Therefore, it is necessary to know the effects of these products, which come into direct contact with the body, on human health. It should be investigated what additional effects the use of such heated clothing may cause, especially in situations that require effort, such as mountaineering or military operations. In this study, the effects of a commercial heated vest equipped with carbon fiber heating wire heating pads on male individuals' systolic blood pressure, diastolic blood pressure and body (skin) temperature when worn for half an hour will be examined.

## 2 MATERIAL AND METHOD

In the experiments, male participants wore a Monthermo brand large size micro polyester fabric heated vest (model MH34001). The heated vest is temperature controlled and has three operating temperatures: 25, 35 and 45°C. Experiments were conducted while the vest was operated at 45 °C, which is the highest operating temperature. For the study, two probe thermometers were placed on heating pads on the front (chest) and back (back) parts of the jacket. In this way, the effectiveness of the heating pads was checked and it was observed whether they reached the desired temperature. Moreover, the humidity and temperature of the environment were observed during the experiments using a smart room thermometer to ensure that these values do not change too much during the experiments. Before each experiment, the battery was fully charged and the heating was turned on and its temperature was observed to stabilize. Then, as soon as the participant wore the vest, his body temperature, systolic and diastolic blood pressure were measured five times consecutively. Polygreen (model KI 8280) brand thermometer was used to measure body temperature (forehead measurement), Omron (model M2) brand digital blood pressure meter was used to measure blood pressure. The participant's data at the first time (0th minute), the second time (15th minute) and the last time (30th minute) were recorded. After the volunteer took off the jacket at the end of the experiment, the jacket was cooled and the battery was charged again to reach full charge.

## 3 RESULTS

The results of the study will be presented in this section.

### 3.1 Normality Analysis

In this section, it will be examined whether the data shows a normal distribution. For this purpose, skewness and kurtosis values will be presented. In Table 1 the results of skewness test of all datasets are presented. In Table 2 the results of kurtosis test of all datasets are presented.

**Table 1.** Skewness test results of all datasets

Skewness Tests			
Data Name	Statistics	Standard Deviation	Ratio
Systolic blood pressure (minute 0)	-0.212948	0.687043	-0.309948
Systolic blood pressure (minute 15)	-0.124371	0.687043	-0.181023
Systolic blood pressure (minute 30)	0.869028	0.687043	1.264881
Diastolic blood pressure (minute 0)	-0.446260	0.687043	-0.64953
Diastolic blood pressure (minute 15)	-0.640679	0.687043	-0.932516
Diastolic blood pressure (minute 30)	0.364956	0.687043	0.531198
Body temperature (minute 0)	-0.491969	0.687043	-0.716067
Body temperature (minute 15)	0.186934	0.687043	0.272084
Body temperature (minute 30)	0.562291	0.687043	0.818421

**Table 2.** Kurtosis test results of all datasets

Kurtosis Tests			
Data Name	Statistics	Standard Deviation	Ratio
Systolic blood pressure (minute 0)	-1.692466	1.334249	-1.268478
Systolic blood pressure (minute 15)	0.421715	1.334249	0.316069
Systolic blood pressure (minute 30)	-0.103982	1.334249	-0.07793
Diastolic blood pressure (minute 0)	1.690329	1.334249	1.266876
Diastolic blood pressure (minute 15)	-0.120538	1.334249	-0.090341
Diastolic blood pressure (minute 30)	-1.399100	1.334249	-1.048604
Body temperature (minute 0)	0.614178	1.334249	0.460317
Body temperature (minute 15)	-0.762008	1.334249	-0.571113
Body temperature (minute 30)	0.759937	1.334249	0.569561

According to values given in the Table 1 and Table 2 the violation of normality can be argued. Then, histogram of each data and normal Q-Q plots are also investigated. The distribution of the data around the normal curve and histogram graphs clearly showed non-normal distribution. That is, no bell curve profile in the form of a histogram was found. These graphs will not be presented in the here. It has been proven that the data does not show a normal distribution. Repeated (relational) measurements are used in the fields of health and social sciences. However data should show normal distribution [9]. As can be seen from the results, the data were obtained from equal scales,

but did not show a normal distribution. Therefore, the Friedman test was applied to examine whether there was a significant difference in the statistical distribution of the data taken from the participants between the determined periods [10]. Wilcoxon Signed Ranks Test was then applied to examine the time groups with significant differences and to determine which time groups had differences.

### 3.2 Non-Parametric Tests

**Table 3.** Detailed Friedman test results of systolic blood pressure data

Friedman Test Results				
	N	25th	Percentiles	
			50th (Median)	75th
Systolic blood pressure (minute 0)	10	110.2	118.5	121.6
Systolic blood pressure (minute 15)	10	111.3	115.5	116.7
Systolic blood pressure (minute 30)	10	104.5	108.5	115.4
Ranks				
Systolic blood pressure (minute 0)	2.60			
Systolic blood pressure (minute 15)	2.10			
Systolic blood pressure (minute 15)	1.30			
Test Statistics				
N	10			
Chi-Square	8.60			
df	2			
Asymp. Sig.	0.014			

**Table 4.** Wilcoxon signed ranks test results of systolic blood pressure data

Wilcoxon Signed Ranks Test Results			
		N	Asymp. Sig. (2-tailed)
Systolic blood pressure (minute 15) - Systolic blood pressure (minute 0)	Negative Ranks	7	0.830
	Positive Ranks	3	
	Ties	0	
	Total	10	
Systolic blood pressure (minute 30) - Systolic blood pressure (minute 15)	Negative Ranks	8	0.320
	Positive Ranks	2	
	Ties	0	
	Total	10	
Systolic blood pressure (minute 30) - Systolic blood pressure (minute 0)	Negative Ranks	9	0.009
	Positive Ranks	1	
	Ties	0	
	Total	10	

**Table 5.** Detailed Friedman test results of diastolic blood pressure data

Friedman Test Results				
	N	25th	Percentiles	
			50th (Median)	75th
Diastolic blood pressure (minute 0)	10	68.95	71.20	73.40
Diastolic blood pressure (minute 15)	10	66.50	70.60	73.50
Diastolic blood pressure (minute 30)	10	60.00	63.30	72.30
Ranks				
Diastolic blood pressure (minute 0)	2.55			
Diastolic blood pressure (minute 15)	2.15			
Diastolic blood pressure (minute 15)	1.30			
Test Statistics				
N	10			
Chi-Square	8.36			
df	2			
Asymp. Sig.	0.015			

**Table 6.** Wilcoxon signed ranks test results of diastolic blood pressure data

Wilcoxon Signed Ranks Test Results			
		N	Asymp. Sig. (2-tailed)
Diastolic blood pressure (minute 15) - Diastolic blood pressure (minute 0)	Negative Ranks	6	0.214
	Positive Ranks	3	
	Ties	1	
	Total	10	
Diastolic blood pressure (minute 30) - Diastolic blood pressure (minute 15)	Negative Ranks	8	0.022
	Positive Ranks	2	
	Ties	0	
	Total	10	
Diastolic blood pressure (minute 30) - Diastolic blood pressure (minute 0)	Negative Ranks	9	0.009
	Positive Ranks	1	
	Ties	0	
	Total	10	

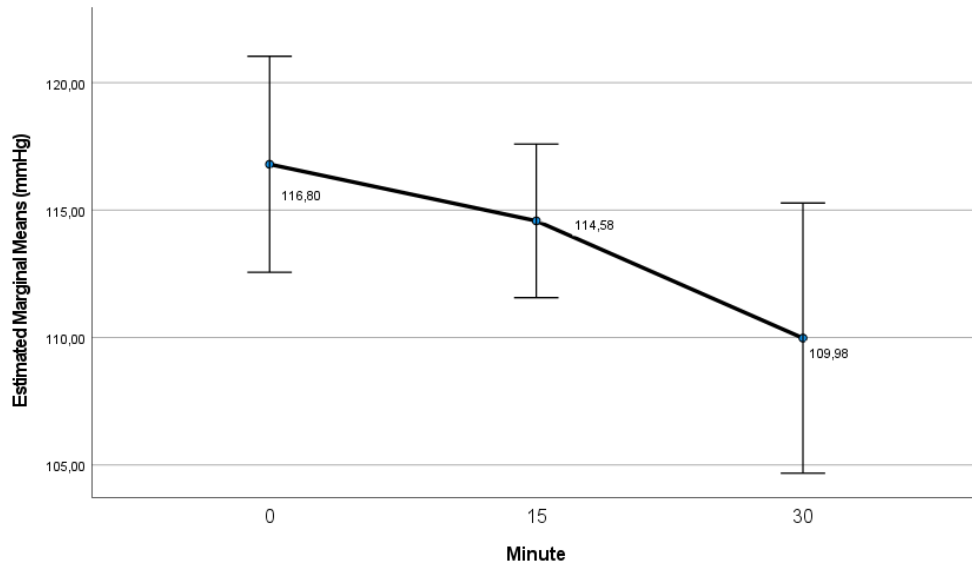
**Table 7.** Detailed Friedman test results of body temperature data

Friedman Test Results				
	N	25th	Percentiles	
			50th (Median)	75th
Body temperature (minute 0)	10	36.50	36.64	36.93
Body temperature (minute 15)	10	36.51	36.73	36.92
Body temperature (minute 30)	10	36.69	36.84	36.94
	Ranks			
Body temperature (minute 0)	1.45			
Body temperature (minute 15)	1.95			
Body temperature (minute 15)	2.60			
	Test Statistics			
N	10			
Chi-Square	7.00			
df	2			
Asymp. Sig.	0.03			

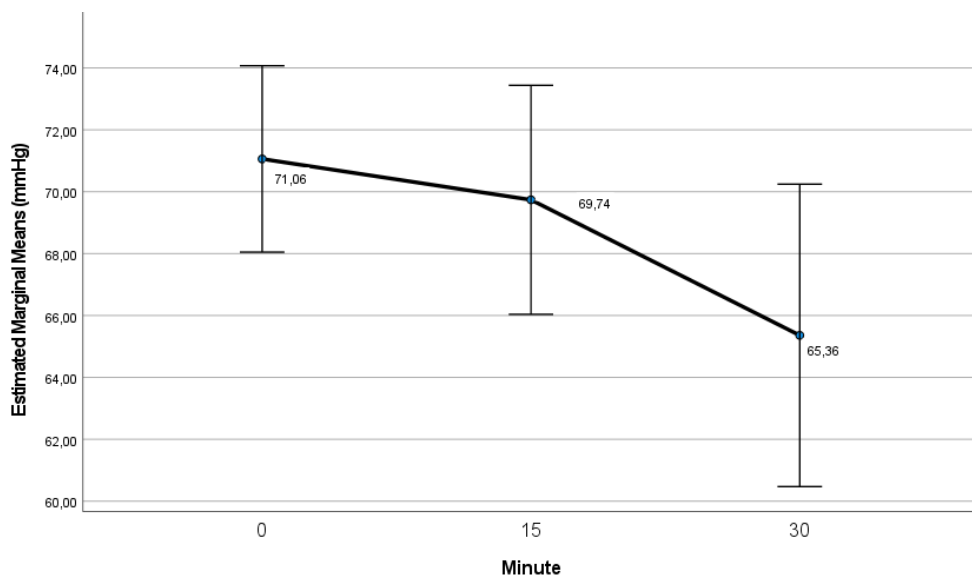
**Table 8.** Wilcoxon signed ranks test results of body temperature data

Wilcoxon Signed Ranks Test Results			
		N	Asymp. Sig. (2-tailed)
Body temperature (minute 15) - Body temperature (minute 0)	Negative Ranks	4	0.307
	Positive Ranks	6	
	Ties	0	
	Total	10	
Body temperature (minute 30) - Body temperature (minute 15)	Negative Ranks	3	0.075
	Positive Ranks	6	
	Ties	1	
	Total	10	
Body temperature (minute 30) - Body temperature (minute 0)	Negative Ranks	0	0.008
	Positive Ranks	9	
	Ties	1	
	Total	10	

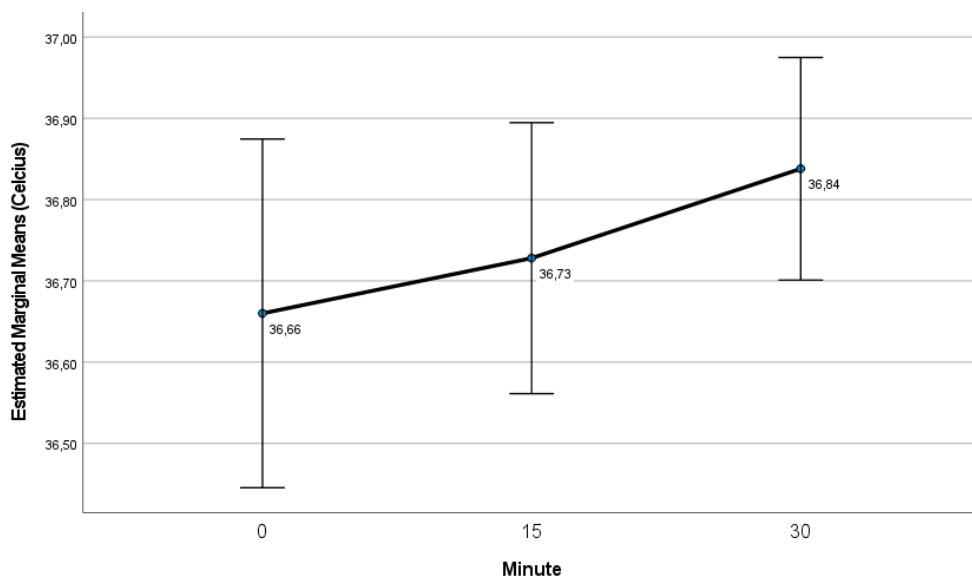
Friedman test results are given in Table 3, Table 5, and Table 7. According to the asymptotic 2-sided significance results, there appears to be statistical significance (value<0.05) within time groups for blood pressure and body temperature measurements. The significance of each time groups can be seen from Table 4, Table 6, and Table 8.



**Figure 1.** Estimated marginal means of systolic blood pressure



**Figure 2.** Estimated marginal means of diastolic blood pressure



**Figure 3.** Estimated marginal means of body temperature



Figure 1, Figure 2, and Figure 3 shows estimated marginal means of systolic blood pressure, diastolic blood pressure, and body temperature, respectively. The decrease in blood pressure and the increase in body temperature can be seen as expected. Estimated marginal means are given at the data points, and error bars with 95 percent confidence intervals are shown around them.

## 4 CONCLUSION

Friedman test results, asymptotic 2-sided significance lower than 5 percent, indicate statistical significance for systolic blood pressure, diastolic blood pressure, and body temperature measurements. In other words, it can be said with at least 95 percent statistical confidence that changes among the measurements depend on the wearing of the vest. The ranks given at the Wilcoxon Signed Ranks Test shows decrease in blood pressure measurements and increase in body temperature measurement. It can also be validated by investigating Figure 1, Figure 2, and Figure 3 where marginal means show decrease in in blood pressure measurements and increase in body temperature measurement. The result is expected. So, it can be concluded that the decrease in blood pressure and increase in body temperature are due to heated vest which is statistically validated. But the changes in blood pressure and body temperature is low in real. Additionally, Wilcoxon Signed Ranks Test results showed that the effects of wearing heated vest started at minute 15. This shows that the selected time interval is sufficient to investigate the changes. The research showed that wearing a heated vest does have an effect on the selected values of male individuals but not significant.

## Acknowledgments

This study was funded by the Scientific and Technological Research Council of Turkey (TUBITAK) in the scope of 2209-A – Research Project Support Programme for Undergraduate Students. Ethical permission for the study was presented to the TUBITAK in the final report.

## References

- [1] E. L. Christiansen and D.M. Lear, “Toughened Thermal Blanket for Micrometeoroid and Orbital Debris Protection,” *Procedia Engineering*, vol. 103, pp. 73–80, 2015.
- [2] F. Wang et al., “A review of technology of personal heating garments,” *Int J Occup Saf Ergon*, vol. 16, no. 3, pp. 387–404, 2010.
- [3] S. Fang et al., “A review of flexible electric heating element and electric heating garments,” *Journal of Industrial Textiles*, vol. 51, no. 1S, pp. 101S–136S, 2022.
- [4] S. Krzemińska et al., “Evaluation of Heating Inserts in Active Protective Clothing for Mountain Rescuers—Preliminary Tests,” *Applied Sciences*, vol. 13, no. 8, art. no. 4879, 2023.
- [5] Q. Zhang et al., “Advancements and challenges in thermoregulating textiles: Smart clothing for enhanced personal thermal management,” *Chemical Engineering Journal*, vol. 488, art. no. 151040, 2024.
- [6] O. Kaynakli and M. Kilic, “Vazodilatasyonun insan fizyolojisine etkisi ve terleme ile karsilastirilmesi,” *Uludag Universitesi Muhendislik Dergisi*, vol. 9, no. 1, pp. 183–194, 2004.
- [7] G. W. Kirschen et al., “Relationship between body temperature and heart rate in adults and children: A local and national study” *The American Journal of Emergency Medicine*, vol. 38, no. 5, pp. 929–933, 2020.
- [8] S. Park et al., “The influence of the ambient temperature on blood pressure and how it will affect the epidemiology of hypertension in Asia,” *J Clin Hypertens (Greenwich)*, vol. 22, no. 3, pp. 438–444, 2020.
- [9] M. J. Blanca et al., “Non-normal data in repeated measures ANOVA: Impact on type I error and power,” *Psicothema*, vol. 35, no. 1, pp. 21–29, 2023.
- [10] L. Hendrickx, L. Gijs, and P. Enzlin, “Who’s distressed by sexual difficulties? Exploring associations between personal, perceived partner, and relational distress and sexual difficulties in heterosexual men and women,” *J Sex Res*, vol. 56, no. 3, pp. 300–313, 2019.



---

## Microstructure Analysis of Ni-Mn-Ga Epitaxial Thin Films on MgO (100)

Gizem Durak Yuzuak<sup>\*1</sup>

<sup>1</sup>Rare Earth Elements Application and Research Center, Munzur University, Tunceli, 62100, Türkiye

---

### Abstract

NiMnGa alloys are highly sought after for applications, in actuators, sensors and magnetic refrigeration. It is crucial to grow these alloys as films on substrates to integrate their functionalities into devices effectively. This study explores the features of NiMnGa films grown epitaxially on MgO via magnetron sputtering from the single NiMnGa target with different film thicknesses. The aim is to examine the impact of film thickness, on its crystal structure, surface appearance and the occurrence of flaws. The X-ray diffraction analysis revealed a relationship, between the NiMnGa films and the MgO. Matched the expected phases indicating a level of crystallographic alignment and successful formation of epitaxial layers. Scanning electron microscope images showed a surface morphology with defined grain boundaries. The grain size and distribution were found to be influenced by substrate temperature and sputtering power. Atomic force microscopy measurements indicated a relatively low surface roughness. The topography images showed uniform surface features, corroborating the electron microscopy results and indicating good surface quality essential for device applications. The study demonstrated that film thickness significantly influences the microstructural properties of NiMnGa thin films. Thicker films exhibited improved crystallinity, larger grain sizes, and reduced defect densities compared to thinner films. The increased presence of twin boundaries in thicker films is advantageous for their magnetic shape memory properties.

The integration of NiMnGa thin films with varying thicknesses on MgO substrates presents significant potential for developing high-performance devices in various technological fields.

**Keywords:** Ni-Mn-Ga, Thin film, Martensite structure

---

### Acknowledgment

This work was supported by the Scientific and Technological Research Council of Turkey (TUBITAK) with project number 223M517.

### References

- [1] A. Backen, et. al, "Epitaxial Ni–Mn–Ga films for magnetic shape memory alloy microactuators," *Advanced Engineering Materials*, vol. 14, no. 8, pp. 696-709, 2012, doi: 10.1002/adem.201200069.
- [2] P. J. Webster, et. al, "Magnetic order and phase transformation in Ni<sub>2</sub>MnGa," *Philos. Mag. B*, vol. 49, no. 3, pp. 295-310, 1984, doi: 10.1080/13642817408246515.



---

## Effect of Using Phosphate Sludge in Geopolymerization: A Review

Nour El Houda Benghalem<sup>\*1</sup>, Nadia Tebbal<sup>2</sup>, Zine El Abidine Rahmouni<sup>1</sup>, Mekki Maza<sup>1</sup>

<sup>1</sup>Geomaterials Development Laboratory, Civil Engineering Department, Faculty of Technology, M'sila University, M'sila 28000, Algeria

<sup>2</sup>Geomaterials Development Laboratory, Institute of Technical Urban Management, M'sila University, M'sila 28000, Algeria

---

### Abstract

The phosphate industry faces serious environmental problems due to the waste generated after extracting the ores. The use of these wastes in the manufacture of environmental binders currently seems interesting for the building materials industry.

Several studies have used phosphate sludge in the manufacture of geopolymers, phosphate sludge is a by-product of the phosphate mining industry. It is formed during the purification of phosphate extracted from mineral deposits, mainly contains phosphate and other minerals rich in calcium carbonate and silica. Geopolymerization is the chemical process that brings together all the reactions transforming solid rich in silica (Si) and alumina (Al), such as fly ash, blast furnace slag or clay, an alkaline activator, such as sodium hydroxide (NaOH) or potassium hydroxide (KOH), to form an alkaline solution, under different experimental conditions, into aluminosilicate gel. This chemical reaction, called polymerization, enables the elements present in the raw materials to bind together to form a solid three-dimensional network, similar to that of Portland cement. This network gives geopolymeric materials high mechanical strength

According to the literature, phosphate sludge has been used with and without heat treatment, at various temperatures; it has been found that the calcination temperature plays an important role in the development of the workability and compressive strength of the system. Some studies have mixed uncalcined phosphate slurry with metakaolin, which is a pozzolanic material produced by the calcination of kaolinite typically between 600 and 900 degrees Celsius in a controlled environment, these studies have confirmed promising results for use as durable surfacing materials, which could substantially promote cleaner production in the construction sector and phosphate mines.

In this work, we will explain some of the works that evaluate the use of phosphate residues in creating environmentally friendly materials

**Keywords:** *Geopolymer, Alkali-activation, Phosphate sludge, Temperature*

---



## Enhancing Mechanical Properties of Titanium Alloys Through Microstructural Control and Alloying Additions

Mohamed Boudiaf<sup>\*1</sup>

<sup>1</sup>University 20 August 1955, Skikda, Algeria

---

### Abstract

Titanium alloys are extensively utilized in various engineering applications owing to their exceptional combination of high strength-to-weight ratio, corrosion resistance, and biocompatibility. In this study, we investigate the effects of microstructural control and alloying additions on the mechanical properties of titanium alloys. Through a comprehensive experimental approach, we systematically vary the processing parameters, including heat treatment conditions and alloy compositions, to tailor the microstructure and optimize the mechanical performance of the alloys. Microstructural characterization techniques such as optical microscopy, scanning electron microscopy, and X-ray diffraction are employed to analyze the phase constituents, grain size distribution, and texture evolution. Mechanical testing, including tensile, hardness, and fatigue tests, is conducted to evaluate the mechanical behavior of the alloys under different conditions. The results reveal significant improvements in the strength, ductility, and fatigue resistance of the titanium alloys by optimizing the microstructure and introducing appropriate alloying elements. This research provides valuable insights into the design and development of advanced titanium alloys with enhanced mechanical properties for demanding engineering applications.

**Keywords:** *Microstructural control, Titanium, Alloys, Mechanical properties*

---



## Synthesis of Iron Copper Binary Nanoparticles Based Phosphate and Application in Multi-Components Reaction

Berrichi Amina<sup>\*1,2</sup>, Bachir Redouane<sup>1</sup>

<sup>1</sup>Laboratory of Catalysis and Synthesis in Organic Chemistry, Faculty of Science and technology, University of Tlemcen BP 119,13000, Tlemcen, Algeria

<sup>2</sup>University of Ain Temouchent, BP 284, 46000, Ain Temouchent, Algeria

---

### Abstract

Phosphate material have a wide range of applications such as fluorescent materials where fluorescent lanthanide orthophosphate were used and it shown a fluorescent properties during their internalization into human umbilical vein endothelial cell. In addition, it has been considered as ceramic materials with high magnetic and electrochemical properties.

Since the calcium phosphate nanoparticles utilization in biological, therapeutic and bio-medicinal fields such as treatment of cancers, caries inhibition, researchers decrease their researches by using other metals and modification of phosphate materials. For example cobalt phosphate nanoparticles, modified this one by Nickel, and Zirconium phosphate nanoparticles which are used as electro-catalyst for water treatment, dyes removal and treatment of cancers. Several methods were used to synthesize phosphate material, such as precipitation, co-precipitation, impregnation, deposition and others, and hydrothermal rout. This later can be lead to different shape and structure.

In this study, we prepared iron copper nanoparticles based phosphate (FeCuP) using hydrothermal rout, during preparation several conditions were used modifying the urea amount. So, different structures were achieved. The material was characterized by SEM, EDX, UV-Vis and XRD. The material was used as catalyst for synthesis of propargylamines. The nanoparticles catalyst was reused with high activity and stability.

**Keywords:** *FeCuP, Nanoparticles, Phosphate material, Minerals*

---



## **Innovative Hybrid Systems for Improving Organic Solar Cells: Encapsulation of Organic Molecules in Carbon and Boron Phosphide Nanotubes**

**Soufiane Elhadfi<sup>\*1</sup>, Jamal Chenouf<sup>1</sup>, Brahim Fakrach<sup>1</sup>, Hassane Chadli<sup>1</sup>**

<sup>1</sup>Laboratory for the Study of Advanced Materials and Applications (LEM2A) Moulay Ismail University, FSM-ESTM Meknes, Morocco

---

### **Abstract**

This study is aimed at investigating new hybrid systems constructed from organic molecules encapsulated in carbon and boron phosphide nanotubes for integration into the photoactive layer of organic solar cells. The encapsulation of these organic molecules in these nanomaterial is intended to enhance the efficiency of converting light into electricity and to shield the compounds from undesirable interactions. The unique properties of carbon nanotubes, such as their high electrical conductivity and large specific surface area, are leveraged in this approach, while boron phosphide contributes its benefits as a semiconductor for optoelectronics. The findings of this study present promising prospects for the development of more efficient and long-lasting organic solar cells through this innovative blend of materials.

**Keywords:** *Organic solar cells, SWCNT, SWBP, DFT study*

---



---

## Unlocking the Potential of Waste Steel Fibers for Improving High-Performance Concrete

Rekia Zouini<sup>\*1</sup>, Makani Abdelkadir<sup>1</sup>, Tafraoui Ahmed<sup>1</sup>

*Department of Civil Engineering&Hydraulic, Tahri Mohamed University, Bechar (08000), Algeria*

---

### Abstract

High-performance concrete is concrete with 50 MPa compressive strength over 28 days, but it is fragile under tension. To create sustainable and functionally enhanced green high-performance concrete, all of this material's qualities, including the high-recycled materials used in its composition, must be studied. For instance, concrete performance may be increased by incorporating fibers that help increase ductility as well as flexural and tensile strengths in addition to preventing cracks. Moreover, Durability pertains to concrete's capacity to endure degradation resulting from its surrounding conditions. It's essential to emphasize that concrete's durability encompasses not just its mechanical strength but also its internal resilience against harsh environmental factors. This research paper investigates the mechanical and microstructure behaviour of high-performance concrete with waste steel fibers. The concrete samples were immersed in 5% HCL acid and MGSO<sub>4</sub> solutions for a duration of 90 days. The study examines factors such as the microstructure change of concrete in aggressive environments. The results demonstrate that high-performance concrete, when reinforced with waste steel fibers, displays notable improvements in compressive strength and satisfactory resilience in flexural strength with the addition of fibers. However, there is a noticeable alteration in the concrete's microstructure after exposure to aggressive environments.

**Keywords:** *Aggressive environment, Durability, Mechanical behavior, Recycled fibers*

---

## 1 INTRODUCTION

Due to its strength and durability, high-performance concrete is a widely used construction material. However, traditional concrete manufacturing requires a significant amount of new materials, leading to excessive exploitation of natural resources and an increase in construction waste. The use of recycled fibers from car tires and construction waste has been presented as a promising solution to address this situation.

The addition of reinforcing fibers has a significant impact on the mechanical, physical properties, and behavior of concrete. Fibers can make concrete a versatile and high-performing construction material by increasing its strength, durability, and resistance to cracks. The addition of reinforcing fibers can make concrete stronger and safer by increasing its resistance to bending and tension. By restraining nascent cracks and preventing their propagation through the concrete matrix, fibers also help control crack propagation. This improves the durability of concrete by reducing the risk of cracks.

The incorporation of fibers generally has little impact on the ascending portion of the stress-strain diagram, as well as on the increase in the strength and modulus of elasticity of concrete, with typical fiber contents ranging up to about 2.5% by volume. However, the addition of fibers can improve the performance of cementitious materials in the hardened state [1, 2].

The incorporation of metallic fibers into concrete significantly reinforces its flexural strength, leading to an improvement of 200% or more. Flexural strength is influenced by various factors such as the shape, orientation, and adhesion of fibers to the concrete matrix. These fibers alter the degradation process under static load by delaying the onset of initial cracks. Additionally, they act as stitches on the cracks, thus increasing the maximum load sustained before rupture. An increase in fiber length results in higher values of forces associated with ultimate load, due to improved anchorage, length, and shape of fibers, as well as more favorable orientations of longer fibers [3, 4].

The durability of concrete can be affected by various factors, whether they come from the external environment such as freeze-thaw cycles, moisture, abrasion, or chemical attacks, or from internal factors such as reactions

between constituent materials, volume variations, or corrosion. As a result, different types of concrete require durability levels adapted to their environment and the required properties [5].

## 2 EXPERIMENTAL PROCEDURE

### 2.1 Materials

The experimental procedure involved the utilization of various materials sourced from the Bechar region, each possessing specific characteristics as detailed below:

**Cement:** For the experiment, a top-tier Portland cement type I, boasting a strength rating of 42.5 MPa, was meticulously chosen. This sulfate-resistant cement is crafted through precise milling of clinker with low calcium aluminate and gypsum content. The chemical characteristics of the cement, which significantly influence the concrete's overall performance, are detailed in Table 1.

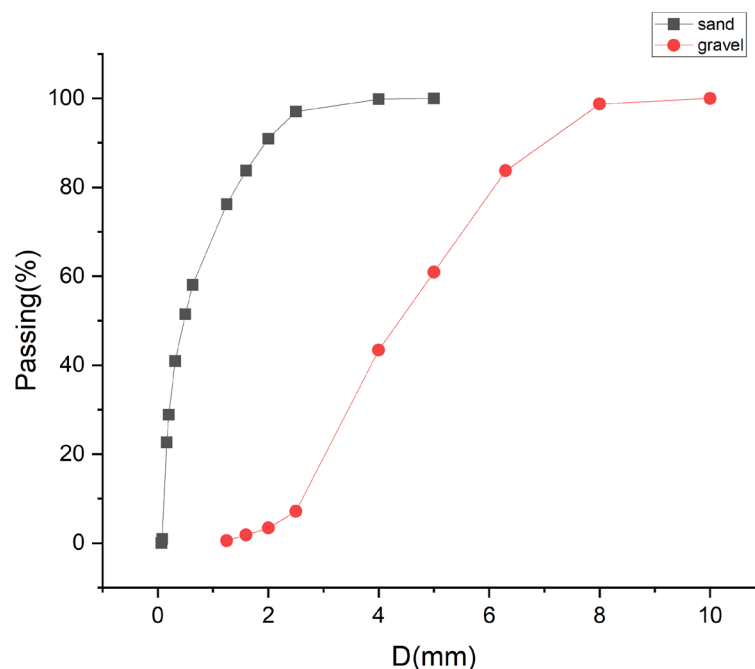
**Table 1.** The percentages of chemical compounds for the cement used (%)

Al <sub>2</sub> O <sub>3</sub>	SO <sub>3</sub>	SiO <sub>2</sub>	CaO	MgO	Fe <sub>2</sub> O <sub>3</sub>	K <sub>2</sub> O	LOI
6.40	1.8–3	20.05	61.23	1.2–3	3.45	0.01–0.05	0.5–3

**Water:** The water utilized in the concrete mixture underwent rigorous scrutiny to ensure its purity and appropriateness for the experiment. It was imperative for the water to be devoid of any solid, mineral, or organic contaminants. Additionally, chemically, the water had to possess a low concentration of dissolved salts, thereby precluding the use of seawater, which could potentially introduce impurities and compromise the structural integrity of the concrete.

**Superplasticizer:** To optimize the workability of the concrete, a high-performance SikaViscoCrete superplasticizer was utilized. This superplasticizer, characterized by its 29% dry extract and a density of 1.085, played a pivotal role in improving the fluidity and flow characteristics of the concrete mixture. This, in turn, facilitated enhanced cohesion and ease of handling during the experiment.

**Aggregates:** The experiment employed locally sourced aggregates obtained from the Bechar region. These aggregates comprised crushed sand-class limestone, possessing a fine particle size of 0.3 cm, as well as gravel crushed to a size of 3/8 inch. The Particle Size Analysis of Aggregates, as illustrated in Figure 1 [EN 933-1], provided a comprehensive insight into the distribution and composition of the aggregates. Additionally, the physical properties of the aggregates, crucial in determining the mechanical strength and durability of the concrete, underwent thorough examination and are detailed in Table 2.



**Figure 1.** The coarse and fine aggregate gradients



**Table 2.** The physical properties of aggregate used

Aggregate Type	Apparent density (kg/m <sup>3</sup> )	Absolute density (kg/m <sup>3</sup> )	Fineness Modulus
Gravel	2.60	1.25	-
Sand	2.54	1.53	2.78

Fibers: To bolster the structural integrity of the concrete, recycled fibers sourced from building waste were methodically integrated into the experiment. These fibers, measuring 2 and 3 cm in length with a diameter of 1 mm, served to reinforce the concrete and enhance its resistance to cracking. Stringent monitoring and control of their properties were maintained in accordance with the EN 14889-1 code within the university laboratory, guaranteeing uniformity and dependability in the experimental outcomes.

### 3 METHODS

Mix proportions: The concrete mixture was meticulously crafted with a water/cement ratio of 0.37, striking a fine equilibrium between workability and strength. Following the guidelines outlined in the EN 196-1 standard, specimens measuring 4\*4\*16 cm were precisely cast. Preparation involved the formulation of both plain concrete and concrete infused with waste fibers, each in diverse volume proportions meticulously detailed in Table 3.

**Table 3.** The concrete composition

Composition	RC	WB1L2	WB1L3	WB2L2	WB2L3
Cement (kg/m <sup>3</sup> )	400	400	400	400	400
Sand (kg/m <sup>3</sup> )	665	665	665	665	665
Gravel (kg/m <sup>3</sup> )	1111	1093	1093	1075	1075
Water (kg/m <sup>3</sup> )	148	148	148	148	148
Superplasticizer (%)	1.75	1.75	1.75	1.75	1.75
Fiber Volume (%)	-	1	1	2	2
Fiber length (mm)	-	20	30	20	30
W/C ratio			0.37		

Curing and preparation: Curing, Testing, and Durability Evaluation: Post-casting, specimens underwent a curing regimen to facilitate gradual strength development. Curing periods of 7, 28, and 90 days were allotted to represent distinct concrete ages. At each interval's conclusion, physical and mechanical properties, encompassing compressive strength, flexural strength, density, and porosity, were meticulously assessed. To gauge concrete durability under specific conditions, specimens endured extended exposure to diverse environments. Over a 90-day period, immersion in water, HCl (hydrochloric acid), and MgSO<sub>4</sub> (magnesium sulfate) solutions ensued. Subsequent SEM, and XRD analyses delved into the microstructural evolution of the specimens post-exposure.

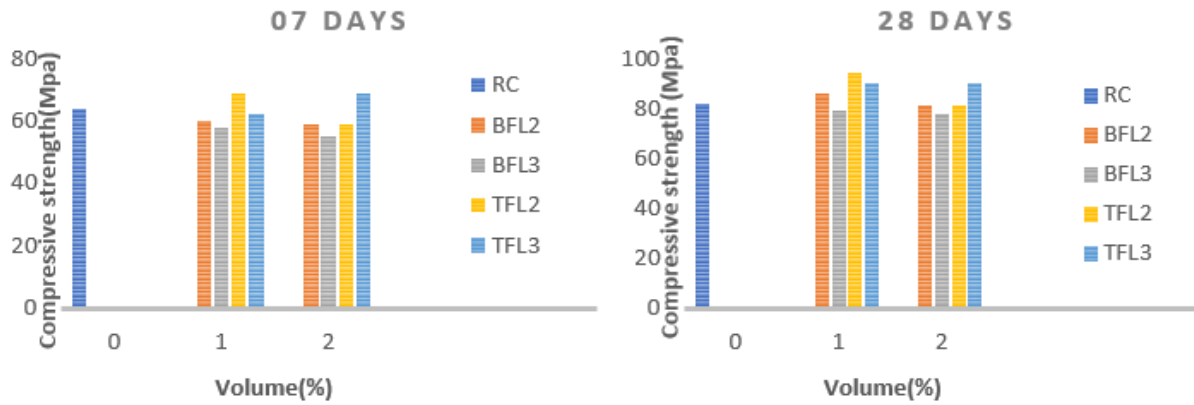
### 4 RESULTS AND ANALYSES

In this section, the importance and effects of the study should be clearly stated. In the conclusion part, the results should not be repeated.

Compressive strength: Using fibers in high-performance concrete improved the mechanical properties of concrete; specifically, fibers in concrete enhanced the compressive strength. This difference was based on the type of fiber used and geometric characteristics – the fiber volume fraction considerably boosted the compressive strength [6]. The mechanical performance of these composites was greatly improved when the aspect ratio of the fibers was increased, a finding supported both experimentally and theoretically [7].

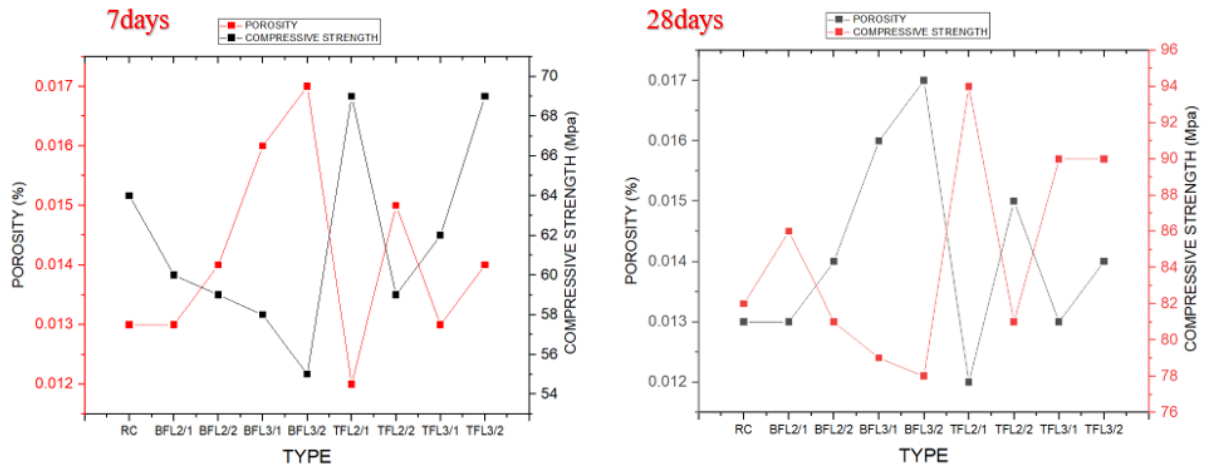
Figure 2 presents the results of compressive strength tests of cubes specimens. A remarkable increase in the compressive strength was observed. Adding industrial steel fiber and recycled steel fiber can improve the mechanical properties of high-performance concrete and reduce its explosive spalling [8].

The compressive strength of concrete on the 28th day was 20% greater than concrete on the 7th day. With the high strength recorded in the car tire fibers, no more change was observed with waste building fibers concrete.



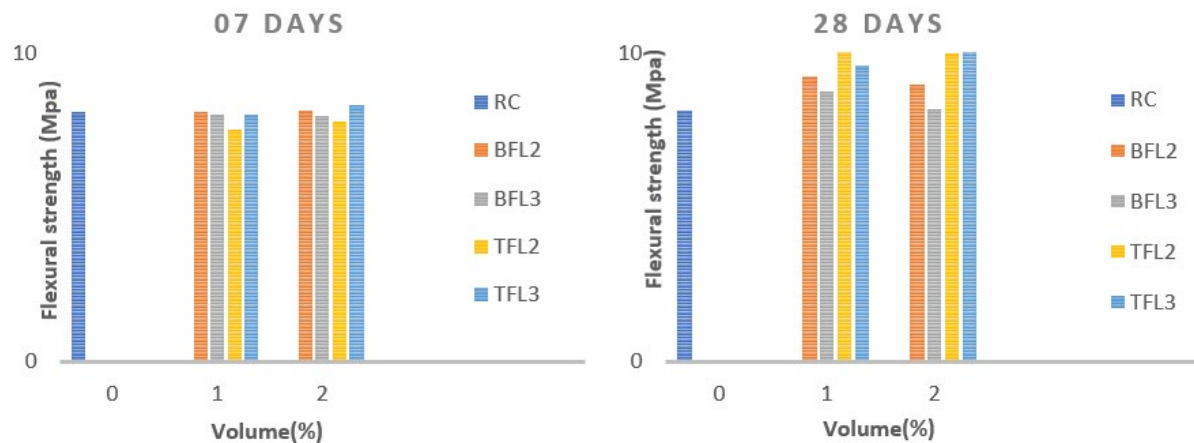
**Figure 2:** Average compressive strength results for concrete mixtures incorporating different type of fibers (RC: Reference concrete, B: Concrete with waste building fibers, and T: Concrete with waste tiers fibers)

Figure 3 represents the effect of porosity on compressive strength. For each mix, the compressive strength was inversely related to porosity; the compressive strength increased as porosity decreased. This finding stems from the permeability of concrete – water absorption is a more appropriate parameter to evaluate the quality of concrete materials [9]. The lowest strength was reported in the sample of concrete containing waste tire fibers 2 cm in length comprising 1% of the total volume.

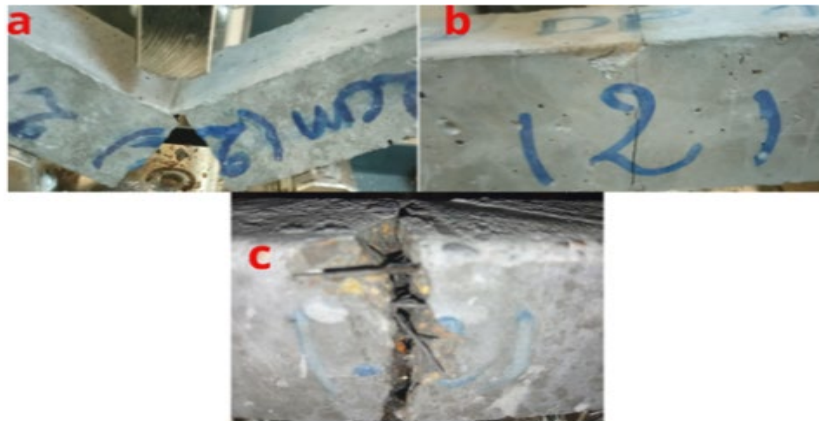


**Figure 3:** The effect of porosity on the compressive strength of high-performance reinforced concrete

Flexural strength: As indicated in Figure 4, the flexural strength increased gradually as fiber volume was increased to 2 and 3%. The highest flexural strength was recorded in concrete with 2% fiber by volume with fibers 2 cm in length. This increase occurred because, after matrix cracking, the fibers carried the concrete’s load until the interfacial bond between the fibers and the matrix failed [10]. The fibers held together the cracks in concrete after a flexible charge (Figure 5b,c), and without reinforcement, big cracks could be observed, as seen in Figure 5a.



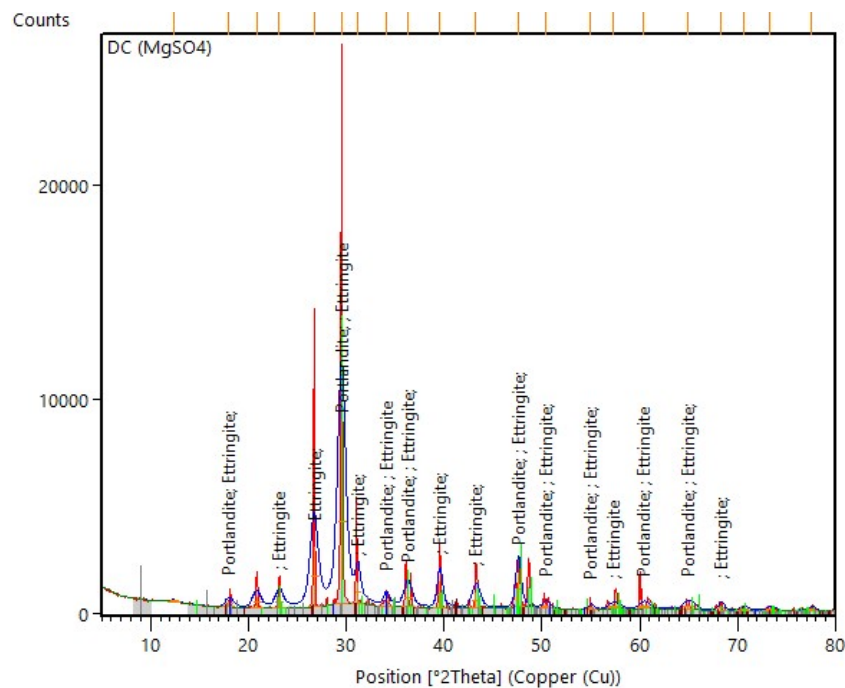
**Figure 4.** Flexural strength of high-performance concrete at 7 and 28 days



**Figure 5.** Cracks in high-performance concrete after flexural strength tests

SEM and DRX Analysis: As shown in Figure 6 through XRD analysis and SEM (scanning electron microscopy), the reaction between concrete and  $MgSO_4$  and  $HCl$  can alter the composition of the concrete. The XRD analysis results reveal a significant decrease in the intensity of peaks corresponding to the main crystalline phase of concrete, which is calcium silicate hydrate (C-S-H). This decrease is consistent with the dissolution of the C-S-H phase due to acid attack and sulfates, as observed in Figure 7. The analysis also revealed the presence of new peaks corresponding to calcium sulfate ( $CaSO_4$ ) and calcium carbonate ( $CaCO_3$ ), which are the products of the reaction between the  $MgSO_4$  environment and the concrete. The mechanism of acid attack involves the reaction between hydrochloric acid and calcium hydroxide present in the cement paste, as represented by the equation:  $2HCl + Ca(OH)_2 \rightarrow CaCl_2 + 2H_2O$ .

This reaction results in the creation of soluble calcium chloride, contributing to the observed weight loss. The composition of the altered concrete, particularly the formation of calcium chloride, was examined using X-ray diffraction (XRD) and energy-dispersive X-ray spectroscopy (EDX) techniques. It is noteworthy that the presence of fibers inhibits the formation of voids that allow acid penetration into the concrete, thus mitigating corrosion and subsequent degradation.



**Figure 6.** XRD Analysis of high performance fibers reinforced concrete after immersing in  $MgSO_4$  solution



- The compressive strength when using fibers was maximal when using steel fiber recycled from car tires at a volume of 1%.
- Adding fibers to high-performance concrete improved flexural strength of concrete because the fibers held together small cracks in the concrete.
- The mechanical characteristics of high performance concrete with short fibers were more impacted than those of concrete with long fibers.
- The presence of compounds such as calcium chloride and the reaction with substances like MgSO<sub>4</sub> can significantly impact the durability and strength of concrete. These reactions alter the microstructure of concrete, affecting its bonding properties and overall resilience. Understanding these mechanisms is crucial for mitigating degradation in concrete structures, especially in environments prone to aggressive chemical exposure.

## Acknowledgments

You can include your acknowledgments information here. If it is not applicable just delete this section.

The authors wish to thank the Directorate General for Scientific Research and Technological Development (D.G.R.S.D.T., Algeria) for financially supporting this work. Thanks to the professors and student members of the Laboratory of Eco-Materials: Innovations & Applications (EMIA ex. LFGM).

## References

- [1] M. S. Ekkehard Fehling, T. L. Joost Walraven, and S. Fröhlich, "Ultra-high performance concrete UHPC," in *Ultra-High Performance Concrete UHPC*, 2014.
- [2] N. Roussel, *Understanding the Rheology of Concrete*, 2011.
- [3] K. Abdou, "Influence des fibres d'acier sur les variations dimensionnelles et pondérales des matrices cimentaires," *Sciences & Technologie B, Sciences de l'ingénieur*, no. 26, pp. 43–48, 2007.
- [4] A. Syed and J. Punkki, "Development of Ultra High Performance Fiber Reinforced Concrete," 2014.
- [5] A. Surahyo, "Concrete construction practical problems and solutions," *Springer*, vol. 39, no. 993, 2019.
- [6] P. Riedel and T. Leutbecher, "Effect of fiber orientation on compressive strength of ultra-high-performance fiber-reinforced concrete," *Materials Journal*, no. 118, no. 2, pp. 199–210, 2021, doi: 10.14359/51730417.
- [7] B. Mobasher, *Mechanics of Fiber and Textile Reinforced Cement Composites*, 2011.
- [8] J. Yang, G.-F. Peng, G.-S. Shui, and G. Zhang, "Mechanical properties and anti-spalling behavior of ultra-high performance concrete with recycled and industrial steel fibers," *Materials*, vol. 12, no. 5, art. no. 783, 2019, doi: 10.3390/ma12050783.
- [9] S. Zhang, P. He, and L. Niu, "Mechanical properties and permeability of fiber-reinforced concrete with recycled aggregate made from waste clay brick," *Journal of Cleaner Production*, vol. 268, art. no. 121690, 2020, doi: 10.1016/j.jclepro.2020.121690.
- [10] V. Afroughsabet, L. Biolzi, and T. Ozbakkaloglu, "High-performance fiber-reinforced concrete: A review," *Journal of Materials Science*, vol. 51, no. 14, pp. 6517–6551, 2016, doi: 10.1007/s10853-016-9917-4.
- [11] Z. Li, X. Zhou, H. Ma, and D. Hou, *Advanced Concrete Technology*, 2022.



## Numerical Performance Simulation of a MoSe<sub>2</sub>-Based Solar Cell Using SCAPS-1D Simulator

M'hamed Semlal<sup>1</sup>, Mohamed Khuili<sup>\*1,2</sup>, Nejma Fazouan<sup>1</sup>, El Houssine Atmani<sup>1</sup>

<sup>1</sup>Laboratory of Nanostructures and Advanced Materials, Mechanics and Thermo fluids, Faculty of Sciences and Technologies, Hassan II University of Casablanca, Mohammedia, Morocco

<sup>2</sup>CRMEF of Beni Mellal-Khénifra, Morocco

---

### Abstract

Due to their low manufacturing cost and simple structure, the 2D Transition metal dichalcogenides material Molybdenum diselenide (MoSe<sub>2</sub>) have attracted tremendous attentions as an absorbent layer of new solar cells. Simulation studies using SCAPS-1D have already been carried out on this type of perovskite to determine the optimized parameters of this solar cell. In our study, we used TiO<sub>2</sub> and In<sub>2</sub>Te<sub>3</sub> as electron and hole-collecting layers respectively. The effects on solar cell performance of temperature, active layer thickness and the density of defects inside and at the interface of this layer are calculated. Our findings indicate that increases in these factors lead to a degradation in device performance. The results, based on power conversion efficiency ( $\eta$ ), open-circuit voltage ( $V_{oc}$ ), fill factor (FF), and short-circuit current ( $J_{sc}$ ) curves, show that with optimized parameters, an efficiency greater than 20% and comparable to that of MoS<sub>2</sub>-based solar cells can be achieved. This research provides theoretical guidance for designing new high-performance solar cells for future studies and manufacturing.

**Keywords:** Photovoltaics, SCAPS-1D, Solar cells, MoSe<sub>2</sub>

---



## The Impact of the Alkali-Bleaching Treatment on the Isolation of Natural Cellulosic Fibers from *Juncus Effesus L* Plant

Mona Benali\*<sup>1</sup>, Abdallah Oumekki<sup>1</sup>, Jamil Toyir<sup>2</sup>

<sup>1</sup>Laboratory of Processes, Materials and Environment (LPME), Faculty of Science and Technology of Fes, Sidi Mohamed Ben Abdellah University, BP. 2202, Morocco

<sup>2</sup>Laboratory of Processes, Materials and Environment (LPME), Sidi Mohamed Ben Abdellah University, FP-Taza, B.P 1223, Morocco

---

### Abstract

Considering their recyclability, availability, and low cost, using lignocellulosic fibers as an alternative cellulosic feedstock is an intriguing option in contemporary applications like biopolymers and biomaterials that have lately attracted attention. The goal of the current research is to develop an efficient technique for isolating natural cellulosic fiber from the Soft Rush (SR) plant. The process is based on a series of alkalization and bleaching procedures, followed by an evaluation of the material's morphology. SR is a widely grown perennial herbaceous plant that is most suited to damp environments and is prized for its sedative and anti-tumor properties, but most significantly, its high cellulose content. In light of this, the primary goal of our work is to create the ideal environment for accessing the (SR) cellulose-rich microfibre from the cementing matrix, which primarily consists of lignin and hemicellulose. therefore, sodium hydroxide 8% was employed in an alkalization procedure, which was followed by a bleaching procedure using different agents. Scanner electron microscopy (SEM), Fourier transform infrared (FTIR), and X-ray diffraction (XRD) were used to establish the relationship between the type of treatment and the fiber's surface structure as well as the network density. To confirm the type of fiber that was recovered from the (SR) stem, the chemical composition was also examined. Based on the output data, the bleaching treatment with sodium hypochlorite yields a positive result due to effective delignification and enhanced fiber density.

**Keywords:** Lignocellulosic fibers, Cellulose, Soft rush, Isolation, Characterization

---



## Noble Metal Nanomaterials in Biosensors

Adil Bouhadiche<sup>\*1</sup>, Soulef Benghorieb<sup>1</sup>

<sup>1</sup>Research Unit in Optics and Photonics (UROP), Center for Development of Advanced Technologies (CDTA), Setif, 19000, Algeria

---

### Abstract

Noble metal nanoparticles (NPs) have played a crucial role in the development of biosensors, such as: Nanobiosensors for point of care disease diagnosis, nanoprobes for in vivo sensing/imaging, cell tracking and monitoring disease pathogenesis or therapy monitoring ... thanks to their simplicity, physiochemical malleability and high surface areas. NPs exhibit peculiar properties linked to their sizes (localized surface plasmon resonance LSPR) which differ considerably from those of their bulk counterpart. Noble metal NPs, particularly gold and silver, are among the most studied nanomaterials for molecular diagnostics, imaging, drug delivery, and therapeutics. LSPR have been explored for the development of new biosensors. This work will focus on studying the unique plasmonic properties of noble metal NPs, using the discrete dipole approximation (DDA) method. LSPR spectroscopy depends on size, shape, composition, core-shell ... of NPs. Silver displays sharper LSPR bands, desirable for plasmonic application in sensors.

**Keywords:** Noble metal nanomaterials, Optical biosensors, DDA, LSPR, Sensitivity

---





## Bound States of 2D Dirac Oscillator in the Deformed Space

Lakhdar Sek<sup>\*1,2</sup>, Mokhtar Falek<sup>2</sup>, Mustafa Mounni<sup>2</sup>

<sup>1</sup>New Technology and Local Development Laboratory, University of ElOued, ElOued, Algeria

<sup>2</sup>Laboratory of Photonic Physics and Nano-Materials (LPPNM), Department of Matter Sciences, University of Biskra, Algeria

---

### Abstract

We analytically examine the equation for a two-dimensional deformed fermionic oscillator that applies to charged particles, including  $1/2$  spin particle, in the presence of a uniform magnetic field. The equation accounts for a minimal uncertainty in momentum due to the anti-de Sitter model. We use the Nikiforov-Uvarov (NU) method to solve this system. Our analysis yields exact energy eigenvalues and corresponding wave functions. We observe that the deformed spectrum remains discrete even for high principal quantum numbers.

**Keywords:** Dirac oscillator, Deformed space, Energy eigenvalues, Nikiforov uvarov method

---



---

## The Applied Physics for Electronic Systems: Detecting of Pollutant Gas Based Pure SnO<sub>2</sub> Semiconductors

**Youssef Doubi<sup>\*1,2</sup>, Bouchaib Hartiti<sup>1</sup>, Maryam Siadat<sup>2</sup>, Hicham Labrim<sup>3</sup>, Mounia  
Tahri<sup>4</sup>, Phillippe Thevenin<sup>5</sup>**

<sup>1</sup>LVOBEEN Laboratory, MEEM & DD Group, Hassan II University of Casablanca, FSTM BP 146, 20650 Mohammedia, Morocco

<sup>2</sup>LCOMS Laboratory, University of Lorraine, 57070 Metz, France

<sup>3</sup>Advanced Systems Engineering Laboratory, National School of Applied Sciences, Ibn Tofail University, 14000 Kenitra, Morocco

<sup>4</sup>SECNDCM-L2MC, ENSAM-Meknes, Moulay Ismail University, Meknes, Morocco

<sup>5</sup>LMOPS Laboratory, University of Lorraine, 57070 Metz, France

---

### Abstract

In this study, we have synthesized tin dioxide thin layers using the spray pyrolysis technique. We explore the impact of substrate temperature on various properties of tin dioxide. Characterization of the thin layers is carried out using X-ray diffraction (XRD), Raman spectrometry (RS), and UV-visible spectrophotometry. XRD analysis reveals the formation of SnO<sub>2</sub> thin layers with a preferential orientation along <110>. RS confirms the presence of characteristic vibration modes associated with the rutile phase of SnO<sub>2</sub>, indicating the formation of a single-phase material. UV-visible spectrophotometry allows for the investigation of optical properties including absorbance, transmittance, and optical band-gap. Additionally, we assess the electrical properties under different gas environments using a low-cost electronic system developed in our laboratory, highlighting the potential of tin dioxide as a candidate material for gas sensor devices.

**Keywords:** SnO<sub>2</sub>, Thin layers, Rutile, Transmittance, Optical band gap

---



## Optimization for High-Efficient and More Stable RbGeI<sub>3</sub> Perovskite Solar Cells

Abdelkader Bouhenna<sup>\*1</sup>, Kada Boualem<sup>1</sup>, Nabil Beloufa<sup>2,3</sup>, Soufi Hadjer<sup>4</sup>, Aboubakr Seddik Kebaili<sup>5</sup>

<sup>1</sup>Science of Materials and Applications Laboratory (LSMA), Physics Department, University of an Témouchent, Algeria

<sup>2</sup>Hydrometeorological Institut for Formation and Research IHFR, Oran, Algeria

<sup>3</sup>Laboratory of Micro and Nanophysics (LaMiN) National Polytechnic School Oran, ENPO-MA, BP 1523, El M'Naouer, 31000, Oran, Algeria

<sup>4</sup>Materials and Renewable Energy Research Unit, university of Tlemcen, Abou Bekr Belkaid, BP 119, Tlemcen 13000, Algeria

<sup>5</sup>The Materials, Processes and Environment Research Unit (URMPE) of the UMBB, Algeria

---

### Abstract

For accurate modelling of the electrical output characteristics of photovoltaic solar cells, the basic semiconductor equations are the hole and electron continuity equations and the Poisson equation. It is available free of charge to the photovoltaic research community and can be freely downloaded. It runs on a Windows operating system environment. With this software you can analyse the characteristic curve I - V, spectral response (QE) of a device, power conversion efficiency (PCE), form factor (FF), short-circuit current  $I_{cc}$ , open-circuit voltage  $V_{co}$ , energy bands of the materials used in the solar cell and concentration of the different materials used by solving the basic semiconductor equations. The study of the different structures will consist of studying the FTO/WS<sub>2</sub>/RbGeI<sub>3</sub>/MoO<sub>3</sub> cell. The steps to be followed for the two parts will be as follows: i. Study of the influence of the thickness of the ETL layer, ii. Study of the influence of the thickness of the absorbing layer, iii. Study of the influence of temperature, and iv. Study of the NA doping density of the absorbing layer.

**Keywords:** FTO/WS<sub>2</sub>/RbGeI<sub>3</sub>/MoO<sub>3</sub>, PCE, ETL, Solar cell

---



---

## Approximation Solutions of Time dependent Schrodinger Equation for Deng-Fan Potential Using the Nikiforov-Uvarov-Functional Analysis

Medjber Salim<sup>\*1</sup>

<sup>1</sup>Department of Physics, University of M'sila, M'sila, Algeria

---

### Abstract

The time dependent Schrödinger equation for the Deng–Fan potential is studied. This potential is not studied in the literatures. This non stationary potential is not studying in the literature. The Deng and Fan potential is a simple potential model for diatomic molecules called the Deng–Fan (DF) oscillator potential. The DF potential was called a general Morse potential whose analytical expressions for energy levels and wave functions have been derived and related to the Manning–Rosen potential (also called Eckart potential by some authors) is anharmonic potential. To obtain the energies spectrum and the wave functions we use a new method for solving a second order differential equation of the hypergeometric type called Nikiforov–Uvarov-Functional Analysis (NUFA) method and the method of variables separation. The (NUFA) method is composed of the concepts of the Nikiforov-Uvarov (NU) method, the parametric Nikiforov-Uvarov method and the functional analysis method. This method is a simple and elegant method for solving a second order differential equation of the hypergeometric type. This method is easy and simple just as the parametric NU method. Unlike the NU method which involved looking for the square of the polynomials and other conditions which makes it complicated, the NUFA can easily be used to obtain the energy and the wave function once the wave equations have been properly transformed and the singularities identified. So its simplicity eliminates the rigorous mathematical manipulations, as encountered in other techniques. The eigensolutions obtained using NUFA method are in agreement with the ones obtained in literatures for the stationary potential models considered. This method can be used to solve few body problems in nuclear physics, particle physics, as well as molecular and chemical physics.

**Keywords:** *Nikiforov–Uvarov-functional analysis method, Time dependent Schrödinger equation, Deng-Fan potential, Wave function, Method of variables separation*

---



## Conceptual Study of Surface Plasmon Resonance Sensor for Glucose Level Monitoring

Mohamed Esseddik Ouardi<sup>\*1</sup>, Kada Abdelhafid Meradi<sup>1</sup>, Fatima Tayeboun<sup>2</sup>

<sup>1</sup>Institute of Science and Technology, University of Ain Temouchent, Ain Temouchent, Algeria

<sup>2</sup>Faculty of Technology, University Djillali Liabes, Sidi-Bel-Abbes, Algeria

### Abstract

Diabetes mellitus is a metabolic disorder disease where blood carries a high sugar level [1]. The purpose of this research is to design and analyze the performances of a surface plasmon resonance sensor for diabetes supervising. For this research to be done, a SPR sensor configuration was designed and theoretically studied, the SPR sensor is based on the Kretschmann configuration [2], for a wavelength of the incident light at 633 nm. The results of the simulation showed that the proposed sensor indicated a sensitivity of 238 deg.RIU-1, a figure of merit of 62.4 RIU-1.

**Keywords:** Surface plasmon resonance, Sensor, Diabetes, Transfer matrix method, Biosensing

## 1 INTRODUCTION

Diabetes is a metabolic disorders disease. It is a condition where a high amount of sugar level is carried by human blood for a prolonged period of time [1]. Diabetes can cause many terrible diseases such as cardiovascular disease, chronic kidney disease, strokes, end even death sometimes [3, 4]. Diabetes can be identified by the glucose concentration in blood. Table 1 represents the categories of diabetes detection.

**Table 1.** Diabetes detection categories [1]

Glucose Condetration in Blood (mM)	Diabetes Category
< 8	Healthy
7.8 – 11.11	Pre-diabetes
> 11.11	Diabetes

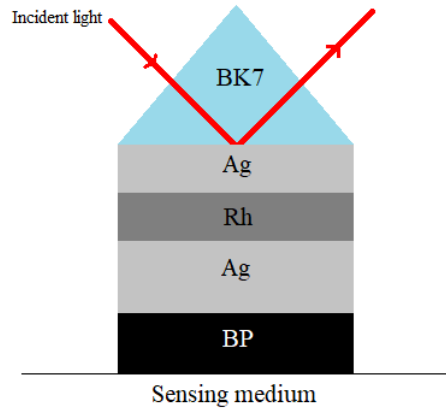
We can deduct that 8 mM of glucose concentration in the blood means that 1 L of human blood contains 0.008 mol of glucose. We can easily get the percentage of glucose in the blood by dividing the glucose mass (in grams) with 1000 mL and multiplying by 100 [5]. In order to sense such a low-level concentration of biomolecules, a sensor with high sensitivity is required. Surface plasmon resonance is one of the widely used label-free optical methods in the design and enhancement of various sensors, they have many applications such as in biological, medical, biochemical application. SPR sensors can be used for monitoring different sorts of substances such as DNA, blood components, viruses, etc. it is a time-saving sensing method [6].

SPR utilizes the shift in the resonance due to the minute change in the refractive index of the sensing medium [7, 8]. The variation in the glucose density causes the refractive index of the solution itself. This change in the RI of the glucose solution will cause a shift in the SPR curve.

The performance of a SPR sensor vary based on its sensitivity, FWHM, figure of merit, detection accuracy, these characteristics are the key values to better performance sensors [9]. In this paper, a novel SPR sensor is proposed based on the Kretschmann configuration [2], the structure consists of a BK7 prism, Silver and Rhodium along with BP.

## 2 MATERIAL AND METHOD

The most used coupling method in SPR-based sensors is the prism coupling technique, this latter has two possible configurations: Kretschmann configuration and Otto configuration [10], they are based on the principle of attenuated total reflectance. The proposed sensor is based on the Kretschmann configuration as shown in Figure 1.



**Figure 1.** Structure of the proposed SPR sensor

The proposed sensor is set up on the Kretschmann configuration, using a layer of 0.5 nm of Rhodium, placed between two layers of Silver with their respective thicknesses 0.5 nm and 45 nm, and six layers of Black Phosphorus, coated on a BK7 prism. The wavelength of the p-polarized incident light is considered as 633nm. The parameters of the configuration are detailed in table 2.

**Table 2.** Configuration parameters of the proposed structure

Layer	Material	Thickness (Nm)
Prism	BK7	/
1	Ag	0.5
2	Rh	0.5
3	Ag	45
4	BP	6*0.53

In this paper, we study the responsiveness of the SPR sensor to the changes in the glucose amount in blood, the refractive index of the analyte is highly sensitive to the smallest changes in glucose concentration. The refractive index of different glucose amount in blood are issued based on the statistics of diabetic human as seen in Table 3 [11]. The glucose concentration of 0.13% (7 mM) is the reference point of a healthy human, values between 0.22% and 0.31% (12 mM and 17 mM respectively) refer to human with diabetes. In order to inspect the stability of the sensor and find out the limit of detection, we incorporate the variation for higher values of the concentration (0.40% and higher).

**Table 3.** Refractive index for different glucose concentrations

Glucose Concentration		Refractive Index (RIU)
%	nM	
0	0	1.3391
0.13	7	1.3481
0.22	12	1.3572
0.31	17	1.3671
0.4	22	1.3765
1	55.5	1.3853
2	111	1.3940
3	166.6	1.4014

In order to test out the performance of the proposed SPR sensor, we use the famous transfer matrix method TMM under MATLAB programming environment, which provides relevant results.

The relation between the first and the last layers is given in (1):

$$\begin{bmatrix} U_1 \\ V_1 \end{bmatrix} = M \begin{bmatrix} U_{N-1} \\ V_{N-1} \end{bmatrix} \tag{1}$$

$U_1$  and  $V_1$  are respectively the tangential elements of the electric and magnetic fields for the first layer, and so on for the  $N^{th}$  layer.  $M$  represents the characteristics matrix, defined as:

$$M_{ij} = (\prod_{k=2}^{N-1} M_k)_{ij} = \begin{pmatrix} M_{11} & M_{12} \\ M_{21} & M_{22} \end{pmatrix} \tag{2}$$

Where,

$$M_k = \begin{pmatrix} \cos \beta_k & -(i \sin \beta_k)/q_k \\ -iq_k \sin \beta_k & \cos \beta_k \end{pmatrix} \tag{3}$$

and

$$q_k = \left(\frac{\mu_k}{\epsilon_k}\right)^{\frac{1}{2}} \cos \theta_k = \frac{(\epsilon_k - n_1^2 \sin^2 \theta_1)^{\frac{1}{2}}}{\epsilon_k} \tag{4}$$

$$\beta_k = \frac{2\pi}{\lambda} n_k \cos \theta_k (z_k - z_{k-1}) = \frac{2\pi d_k}{\lambda} (\epsilon_k - n_1^2 \sin^2 \theta_1)^{\frac{1}{2}} \tag{5}$$

The reflection coefficient becomes then [12]:

$$r_p = \frac{(M_{11} + M_{12}q_N)q_1 - (M_{21} + M_{22}q_N)}{(M_{11} + M_{12}q_N)q_1 + (M_{21} + M_{22}q_N)} \tag{6}$$

Thus, the reflection intensity is given by (7):

$$R_p = |r_p|^2 \tag{7}$$

The most important step in order to verify the performance of the SPR sensor is to calculate its sensitivity (S), its detection accuracy (DA) and figure of merit (FOM) [12]. A good candidate is a SPR sensor that performs well in term of high sensitivity and detection accuracy, the sensitivity can be simply calculated using the ratio of the resonance angle shift to the variation of the refractive index of the analyte:

$$S = \frac{\delta \theta_{SPR}}{\delta n} \tag{8}$$

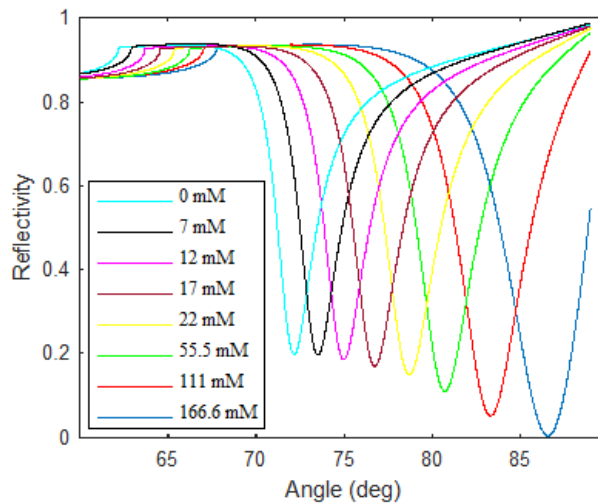
The detection accuracy is the inverse of the full width at half maximum of the curve:

$$DA = \frac{1}{FWHM} \tag{9}$$

As for the figure of merit, we can deduct it from the previous relations [13]:

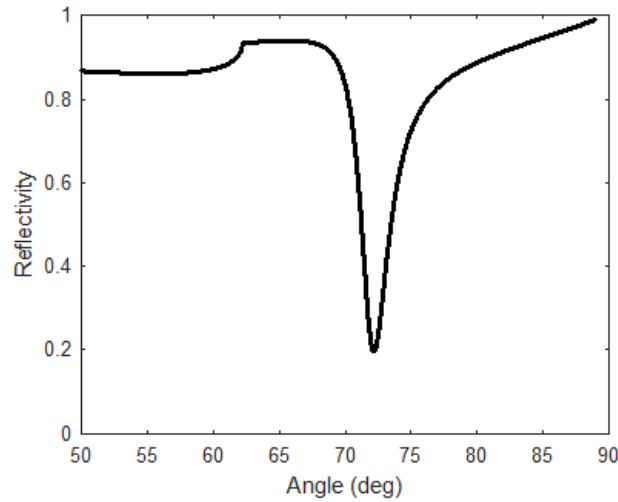
$$FOM = \frac{S}{FWHM} = S \times DA \tag{10}$$

### 3 RESULTS



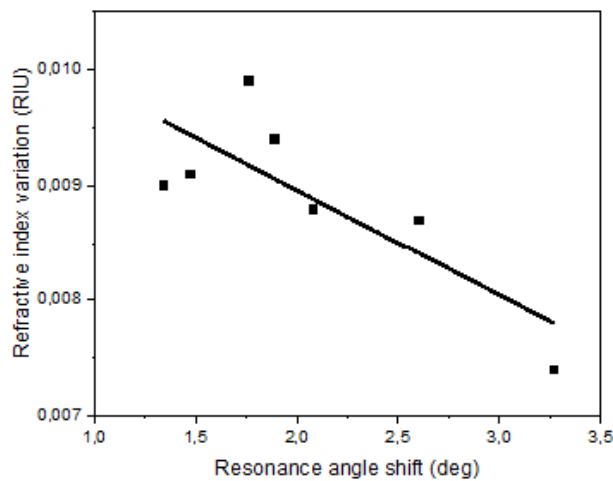
**Figure 2.** The response of the proposed sensor for diabetes monitoring

In this study, for an incident light of 670nm wavelength with an incident angle varying from 60° to 89°. We notice a dramatic shift of the resonance angle (dip) for different values of the refractive index of the analyte. We take the glucose concentration 0 mM as a baseline in order to observe the ability of the proposed SPR sensor.



**Figure 3.** SPR curve for 0mM glucose concentration in blood.

This curve shows a resonance angle at 72.18°, and a minimum value of reflectivity equal to 0.197 a.u., the full width at half maximum 1.60. The ability of the proposed SPR sensor for glucose observing has been determined by the ability to manifest shifting in resonance angle for small variations of glucose concentration in Figure 4.



**Figure 4.** Resonance shift response to glucose refractive index variation.

The SPR sensor indicates a maximum sensitivity of 238 Deg.RIU-1 and a detection accuracy of 0.26 for a FWHM of 3.8134. the figure of merit is thus equal to 62.4, These performance parameters make the proposed sensor reliable in order to sense low levels of glucose amount variations in human blood.

**Table 4.** Comparison between the proposed sensor and other studies

Reference	Configuration	Sensitivity (Deg/RIU)
[14]	Kretschmann conventional structure	116.69
[15]	SF10/Au/Si/MoS <sub>2</sub>	131.70
[16]	BK7/Au/WSe <sub>2</sub>	179.32
This work	BK7/Ag/Rh/Ag/BP	238

Moreover, the minimum detection limit was 0-7 mM which makes the proposed SPR sensor able to detect normal human glucose amounts (<8 mM after meals and <6 mM during fasting).



## 4 CONCLUSION

In this paper, a surface plasmon resonance sensor was proposed and simulated for glucose levels sensing and monitoring, the sensor showed a resonance shift for the variation of glucose amount in human blood for healthy human to diabetic human. Moreover, the sensitivity of the SPR sensor was 238 deg.RIU-1. This sensor may be used for observing diabetes and glucose levels in blood.

## References

- [1] American Diabetes Association, "Classification and diagnosis of diabetes," *Diabetes Care*, vol. 38, pp. S8–S16, 2015.
- [2] E. Kretschmann and H. Raether, "Radiative decay of non-radiative surface plasmons by light," *Z. Naturforsch.*, vol. 23, pp. 2135–2136, 1968.
- [3] J. Tuomilehto, J. Lindström, J. G. Eriksson et al., "Prevention of type 2 diabetes mellitus by changes in lifestyle among subjects with impaired glucose tolerance," *N. Engl. J. Med.*, vol. 344, no. 18, pp. 1343–1350, 2001.
- [4] R. Varma, N. M. Bressler, Q. V. Doan et al., "Prevalence of and risk factors for diabetic macular edema in the United States," *JAMA Ophthalmol.*, vol. 132, no. 11, pp. 1334–1340, 2014.
- [5] P. Anastas and N. Eghbali, "Green chemistry: principles and practice," *Chem. Soc. Rev.*, vol. 39, no. 1, pp. 301–312, 2010.
- [6] J. Homola, "Present and future of surface plasmon resonance biosensors," *Anal. Bioanal. Chem.*, vol. 377, no. 3, pp. 528–539, 2003.
- [7] W. Bogaerts, P. De Heyn, T. Van Vaerenbergh et al., "Silicon microring resonators," *Laser Photonics Rev.*, vol. 6, no. 1, pp.47–73, 2012.
- [8] S. Fouad, N. Sabri, Z. A. Z. Jamal, and P. Poopalan, 'Surface plasmon resonance sensor sensitivity enhancement using gold-dielectric material', *Int. J. Nanoelectron. Mater.*, vol. 10, pp.149–158, 2017.
- [9] A. Verma, A. Prakash, and R. Tripathi, "Sensitivity enhancement of surface plasmon resonance biosensor using graphene and air gap," *Opt. Commun.*, vol. 357, pp. 106–112, Dec. 2015.
- [10] V. G. Achanta, "Surface waves at metal-dielectric interfaces: Material science perspective," *Rev. Phys.*, vol. 5, art. no. 100041, Nov. 2020.
- [11] A. Belay and G. Assefa, "Concentration, wavelength and temperature dependent refractive index of sugar solutions and methods of determination contents of sugar in soft drink beverages using laser lights," *J. Lasers, Opt. Photonics*, vol. 5, no. 2, pp.1–5, 2018
- [12] M. S. Rahman, M. S. Anower, M. R. Hasan, M. B. Hossain, and M. I. Haque, "Design and numerical analysis of highly sensitive Au-MoS<sub>2</sub>-graphene based hybrid surface plasmon resonance biosensor," *Opt. Commun.*, vol. 396, pp. 36–43, Aug. 2017.
- [13] M. S. Anower, M. M. Rahman, and M. S. Rahman, "Hybrid heterostructures for SPR biosensor," in *Biosensor-Current and Novel Strategies for Biosensing*, London, U.K.: IntechOpen, 2020.
- [14] H. Nugroho, L. Hasanah, C. Wulandari et al., "Silicon on insulator-based microring resonator and Au nanofilm Kretschmann-based surface plasmon resonance glucose sensors for lab-on-a-chip applications," *International Journal of Nanotechnology*, vol. 17, pp. 29–41, 2020, doi: 10.1504/IJNT.2020.109348.
- [15] Q. Ouyang, S. Zeng, L. Jiang et al., "Sensitivity enhancement of transition metal dichalcogenides/silicon nanostructure-based surface plasmon resonance biosensor," *Sci Rep*, vol. 6, art. no. 28190, 2016, doi: 10.1038/srep28190.
- [16] D. Nurrohman and N. Chiu, "Surface plasmon resonance biosensor performance analysis on 2d material based on graphene and transition metal dichalcogenides," *ECS Journal of Solid State Science and Technology*, vol. 9, art. no. 115023, 2020, doi: 10.1149/2162-8777/abb419.



## Comparative Study of Performance of Different Perovskite Solar Cells Based on Organic and Inorganic Thin Films

Riane Houaria<sup>\*1</sup>, Bidi Sara<sup>1</sup>, Boussaada Salah Eddine<sup>1</sup>, Mouchaal Younes<sup>1</sup>

<sup>1</sup>Physics Department, Sciences Exactes Faculty, Mascara University, Mascara, Algeria

---

### Abstract

Solar cells have recently received a lot of attention. In order to reduce production costs and convert sunlight more efficiently using advanced technologies. In this context, perovskite solar cells emerged as a new form of solar cell. In this work, we studied the photovoltaic performance of inorganic solar cells based on perovskite hybrid materials  $\text{CH}_3\text{NH}_3\text{PbI}_3$ ,  $\text{CH}_3\text{NH}_3\text{GeI}_3$  and  $\text{CH}_3\text{NH}_3\text{SnI}_3$ , using the SCAPS unidimensional simulation tool. The main objective is to improve the performance of solar cells by determining the optimal parameters for their operation. In this context, the influence of several physical parameters which help to improve their yields, including the effect of the thickness of the perovskite and HTM and ETM layers, the effect of temperature, the effect of the density of defects and the constraining of the perovskite layer on the characteristics of the solar cell. In addition, we obtained encouraging results for JSC (25.2082mA/cms), VOC(1.5238V), FF (90.48%) and energy conversion efficiency of 34.75%, at T =300K.

**Keywords:** Solar cells, Perovskite, SCAPS, JSC, VOC

---



## Evanescent Wave Coupling Surface Plasmon Resonance (SPR) Sensors

Fariza Hanim Suhailin<sup>\*1,2</sup>

<sup>1</sup>Physics Department, Faculty of Science, Universiti Teknologi Malaysia (UTM), 81310 Skudai, Johor Bahru, Malaysia

<sup>2</sup>Laser Center, Ibnu Sina Institute for Scientific & Industrial Research (ISI-SIR), Universiti Teknologi Malaysia (UTM), 81310 Skudai, Johor Bahru, Malaysia

---

### Abstract

The efficient waveguiding of electromagnetic wave in the core of optical fiber has opens up to many advanced opportunities in fundamental research and applications. Structural modification via post-processing methods will disrupt the continuous translational symmetry of the optical fiber structure, hence affecting their waveguiding properties. Tapering or side-polishing the optical fiber to specific ratio or at certain values of polishing length and depth, respectively, will expand the fundamental mode field (spot size) until the field spread into the surrounding air near the fiber interface. This mode is known as evanescent wave. In this work, we will first review the numerical mode analysis on the evanescent wave propagation as we tapered and side-polished the silica-based optical fibers. Then, we will highlight some of our experimental findings of which the evanescent wave is used to couple and excite the plasmonic modes in the metal-coated post-processed optical fibers. These configurations were utilized as a spectroscopic technique based on surface plasmon resonance (SPR) for detection of various physical parameters and biomolecules such as heavy metal ions and deoxyribonucleic acid (DNA).

**Keywords:** *Optical fiber, Evanescent wave, Surface plasmon resonance, Heavy metal ions detection, DNA detection*

---



## Exploring the Optoelectronic Properties of NaAuF<sub>4</sub>: Insights and Applications

Ishak Mebarkia\*<sup>1</sup>

<sup>1</sup>Quantum Electronics Laboratory, Department of Radiation Physics, Faculty of Physics, University of Science and Technology Houari Boumediene, B.P. 32, El Alia, Bab Ezzouar, 16111, Algiers, Algeria

### Abstract

This study investigates the structural and optoelectronic properties of NaAuF<sub>4</sub> material to assess its potential applications, utilizing ab-initio calculations within the framework of density functional theory. Employing the pseudopotential plane wave method, we analysed the structural parameters of NaAuF<sub>4</sub> ternary compound, yielding results that closely align with experimental values documented in the literature. In terms of electronic structure, NaAuF<sub>4</sub> exhibits characteristics of a semiconductor with a direct band gap, holding considerable promise for various optoelectronic applications. Furthermore, our investigation delves into the optical properties of NaAuF<sub>4</sub>, encompassing the real and imaginary components of the dielectric function, refractive index, and absorption coefficient. Notably, our findings reveal significant optical absorption in the UV range for NaAuF<sub>4</sub>, indicating its potential suitability for the development of UV photodetectors. Importantly, this study represents the first comprehensive theoretical analysis of NaAuF<sub>4</sub>, laying the groundwork for future experimental inquiries driven by our insights.

**Keywords:** Optoelectronic properties, Semiconductor material, NaAuF<sub>4</sub> ternary compound, Ab-initio calculations

## 1 INTRODUCTION

Alkali metal tetrafluoroaurates represent a compelling subset within the fluoride single crystal family, boasting attributes conducive to optoelectronic applications. Notably, their expansive ultraviolet absorption range, wide band gaps, and lower refractive indices render them promising candidates [1]. These compounds, characterized by the formula XAuF<sub>4</sub>, feature an alkali metal element (X = Li, Na, K, Rb, and Cs) as a cation, coexisting with the [AuF<sub>4</sub>] anion.

Efforts to elucidate the crystal structure of these ternary compounds have been extensive, employing techniques such as powder diffraction and single-crystal X-ray diffraction analysis. Consensus among researchers indicates that LiAuF<sub>4</sub> adopts a monoclinic crystal structure with the space group P2/c (No. 13) [2,3]. Conversely, the series comprising NaAuF<sub>4</sub>, KAuF<sub>4</sub>, and RbAuF<sub>4</sub> crystallizes in a tetragonal configuration, characterized by the space group type I4/mcm (No. 140) [2–5]. Additionally, the CsAuF<sub>4</sub> ternary compound exhibits orthorhombic symmetry, denoted by Immm (No. 71) [6].

Prior investigations have explored the fundamental physical properties of select alkali metal tetrafluoridobromates and tetrafluoroaurates through theoretical analyses [7,8]. This study, however, focuses specifically on the NaAuF<sub>4</sub> ternary compound, which crystallizes in a tetragonal structure. Employing ab-initio calculations within the framework of density functional theory (DFT) and utilizing the pseudopotential plane wave method (PP-PW), our research delves into the compound's structural, electronic, and optical properties.

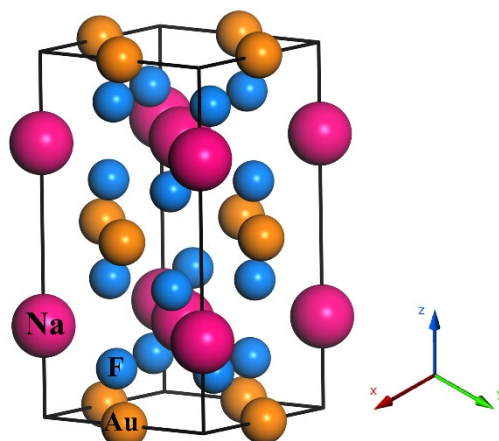
## 2 MATERIAL AND METHOD

Ab-initio calculations were conducted to analyse the optoelectronic properties within the density functional theory (DFT) framework, employing the pseudopotential plane wave (PP-PW) method as implemented in the Cambridge Serial Total Energy Package (CASTEP) code [9]. The generalized gradient approximation for solids (GGA PBEsol) served as the chosen exchange correlation function [10]. Specific elements were assigned diverse valence electron configurations in pseudoatomic computations: Na (3s<sup>1</sup>), Au (6s<sup>1</sup>), and F (2s<sup>2</sup> 2p<sup>5</sup>). A cut-off energy of 60 Ry was set for the plane wave basis set, while a mesh of 4×4×2 special k-points within the first Brillouin zone was utilized.

### 3 RESULTS

#### 3.1 Crystalline Structure

The NaAuF<sub>4</sub> material adopts a tetragonal structure under ambient conditions, characterized by the space group I4/mcm (No. 140). Illustrated in Figure 1, the cell comprises four formula units ( $Z = 4$ ), with the Na atom situated at the Wyckoff site 4a (0, 0, 1/4) and the Au atom at the Wyckoff site 4d (0, 1/2, 0). Conversely, the Wyckoff site of the F atom 16l ( $x_F$ ,  $y_F$ , and  $z_F$ ) remain unfixed by the cell.



**Figure 1.** The unit cell of NaAuF<sub>4</sub> ternary compound

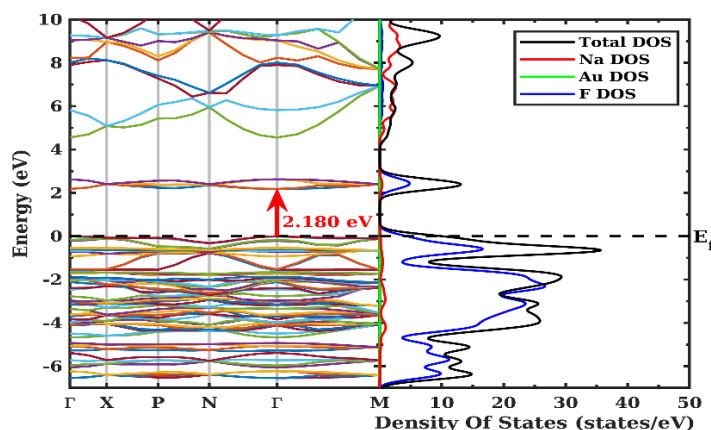
Table 1 provides both the calculated and experimental equilibrium structural parameters, encompassing lattice constants ( $a$  and  $c$ ) and the internal coordinates of the fluorine atom ( $x_F$ ,  $y_F$ , and  $z_F$ ). A notable concurrence is observed between our calculated values and the experimental data, affirming the robustness of our computations.

**Table 1.** The equilibrium lattice constants ( $a$  and  $c$  in Å) and the internal coordinates of fluorine atom ( $x_F$ ,  $y_F$ , and  $z_F$ )

	$a$	$c$	$x_F$	$y_F$	$z_F$
calc.	5.67	10.45	0.172	0.672	0.130
Expt. [2]	5.64	10.49	0.177	0.677	0.135

#### 3.2 Optoelectronic Properties

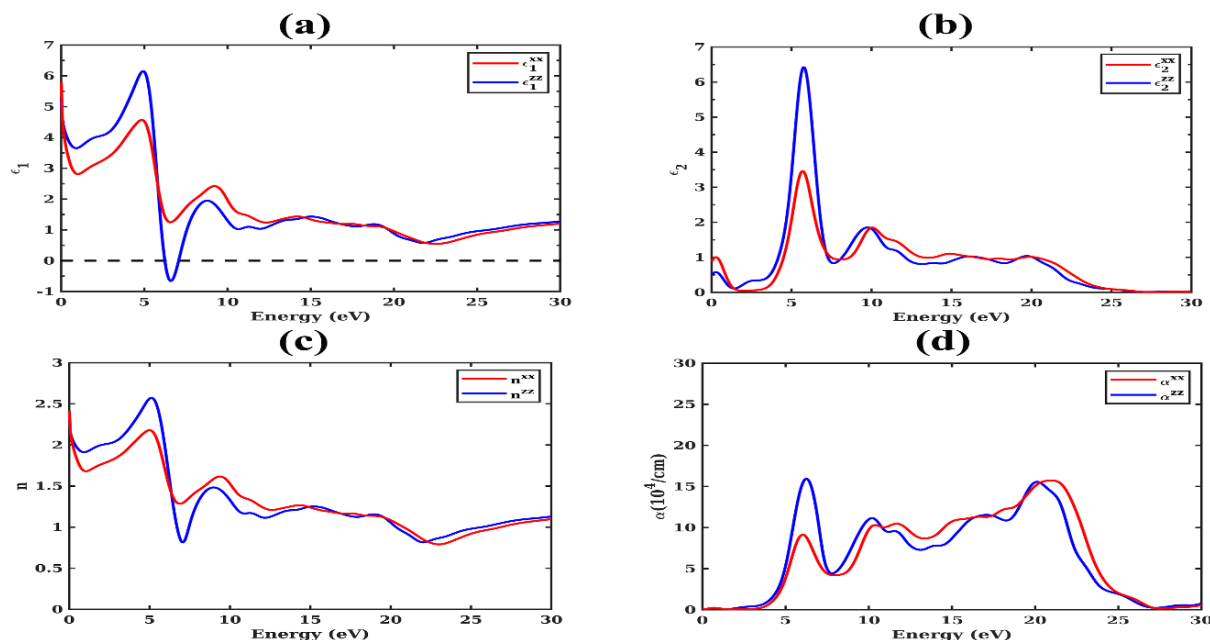
The electronic band structure is illustrated in Figure 2, encompassing the total density of states and the partial density of states for each constituent element: Na, Au, and F.



**Figure 2.** The band structure and the density of states of NaAuF<sub>4</sub>

The computed energy gap measures 2.180 eV, indicating NaAuF<sub>4</sub>'s semiconductor nature characterized by a broad band gap. Notably, it features a direct band gap, attributed to the alignment of its valence band maximum and conduction band minimum at the  $\Gamma$  point.

Figure 3 depicts the optical spectra of the dielectric function  $\epsilon_1(\omega)$  and  $\epsilon_2(\omega)$ , the refractive index  $n(\omega)$ , and the absorption coefficient  $\alpha(\omega)$  along both the x and z directions. Notably, the polarized components exhibit discernible discrepancies for energies below 25 eV, suggesting optical anisotropy within this range for the NaAuF<sub>4</sub> material. Analysis reveals a dielectric response to a static electric field (Drude behavior), evident in the zero-frequency limits for  $\epsilon_1^{xx}(0)$  and  $\epsilon_1^{zz}(0)$ . The energetic peaks observed in  $\epsilon_2^{xx}(\omega)$  and  $\epsilon_2^{zz}(\omega)$  spectra originate from optical transitions between the highest occupied valence and lowest unoccupied conduction bands.



**Figure 2.** The different optical spectra for NaAuF<sub>4</sub> ternary compound (a) The real part, (b) The imaginary part of the dielectric function, (c) The refractive index, and (d) The absorption coefficient

Notably, we observed broad optical absorption in the UV range for NaAuF<sub>4</sub>, hinting at its potential utility in the development of UV photodetectors. Remarkably, our investigation marks the first comprehensive theoretical study of NaAuF<sub>4</sub>, paving the way for future experimental explorations inspired by our findings.

## 4 CONCLUSION

This study provides an in-depth theoretical analysis of the structural, electronic, and optical properties of the NaAuF<sub>4</sub> ternary compound using ab-initio calculations within the density functional theory framework. The findings demonstrate the compound's potential in optoelectronic applications, particularly in UV photodetectors, due to its wide band gap and notable UV absorption characteristics. By establishing a robust agreement between calculated and experimental structural parameters, this work lays a solid foundation for further experimental investigations. The observed optical anisotropy and semiconductor nature of NaAuF<sub>4</sub> underline its relevance in advanced material science and technology, offering significant insights for future research and practical applications in the field of optoelectronics.

## References

- [1] A. J. Stevenson, H. Serier-Brault, P. Gredin, and M. Mortier, "Fluoride materials for optical applications: Single crystals, ceramics, glasses, and glass-ceramics," *J. Fluor. Chem.*, vol. 132, no. 12, pp. 1165–1173, Dec. 2011.
- [2] R. Hoppe and R. Homann, "Neue Untersuchungen an Fluorkomplexen mit dreiwertigem Silber und Gold," *Zeitschrift für Anorg. und Allg. Chemie*, vol. 379, no. 2, pp. 193–198, Dec. 1970.
- [3] U. Engelmann and B. G. Müller, "Darstellung und Struktur der Tetrafluoroaurate(III) MI[AuF<sub>4</sub>] mit MI = Li, Rb," *Zeitschrift für Anorg. und Allg. Chemie*, vol. 598, no. 1, pp. 103–110, Jun. 1991.
- [4] R. Hoppe and W. Klemm, "Über Fluorokomplexe des Palladiums und des Goldes," *ZAAC - J. Inorg. Gen. Chem.*, vol. 268, no. 4–6, pp. 364–371, 1952.
- [5] A. J. Edwards and G. R. Jones, "Fluoride crystal structures. Part VIII. Neutron diffraction studies of potassium tetrafluorobromate(III) and potassium tetrafluoroaurate(III)," *J. Chem. Soc. A Inorganic, Phys. Theor. Chem.*, no. 0, pp. 1936–1938, Jan. 1969.

- [6] R. Schmidt and B. G. Müller, "Einkristalluntersuchungen an Cs[AuF<sub>4</sub>], Cs[Au<sub>2</sub>F<sub>7</sub>] und U<sub>2</sub>F<sub>7</sub>[AuF<sub>4</sub>]," *Zeitschrift für Anorg. und Allg. Chemie*, vol. 630, no. 13–14, pp. 2393–2397, 2004.
- [7] I. Mebarkia, A. Manallah, and R. Belghit, "The first foreseen of structural, mechanical, electronic and optical properties of novel alkali metal tetrafluoridobromate ABrF<sub>4</sub> (A=Na, K and Rb)," *Phys. B Condens. Matter*, vol. 624, no. September 2021, p. 413450, 2022.
- [8] I. Mebarkia, "First-principles study of structural , elastic , and optoelectronic properties of alkali metal tetrafluoroaurate materials MAuF<sub>4</sub> ( M = Na , K , and Rb )," *Indian J. Phys.*, vol. 4, 2024.
- [9] S. J. Clark *et al.*, "First principles methods using CASTEP," *Zeitschrift für Krist.*, vol. 220, no. 5–6, pp. 567–570, 2005.
- [10] J. P. Perdew *et al.*, "Restoring the density-gradient expansion for exchange in solids and surfaces," *Phys. Rev. Lett.*, vol. 100, no. 13, pp. 1–4, 2008.



## Exploring the Optical and Thermoelectric Properties of Eco-Friendly Perovskite Alloys for Solar Cell Applications

Lakhdar Benahmedi<sup>\*1</sup>, Anissa Besbes<sup>1</sup>, Redouane Djelti<sup>1</sup>

<sup>1</sup>Laboratory of Technology and Properties of Solids, Abdelhamid Ibn Badis University, Mostaganem, Algeria

---

### Abstract

In this comprehensive study, we delve into the intricate world of density functional theory (DFT), utilizing the full-potential linearized augmented plane wave (FP-LAPW) method in tandem with the generalized gradient approximation (GGA). Our focus is to meticulously examine the structural, electronic, optical, and thermoelectric properties of an innovative perovskite-type alloy. Upon thorough analysis, we discovered that the alloy exhibits a cubic crystalline structure, characterized by a lattice parameter meticulously measured at 4.80 Å. A deep dive into its electronic properties unveiled its semiconducting nature, distinguished by a direct band gap which is pivotal for its functionality. To quantify the thermoelectric properties, we employed the semi-classical Boltzmann transport theory, as encapsulated in the BoltzTraP computational code. The results were remarkable, indicating that the material boasts an exceptionally high electrical conductivity coupled with a remarkably low thermal conductivity. Such a unique combination of properties culminates in a substantial ZT coefficient, which remains impressively stable across a broad temperature spectrum. The implications of these findings are profound, suggesting that this material holds great promise as a high-performance thermoelectric candidate. Its ability to efficiently convert thermal energy into electrical power, or vice versa, positions it as a potential game-changer in the realm of energy conversion technologies. With sustainability and energy efficiency at the forefront of global priorities, the exploration of such materials could pave the way for groundbreaking advancements in thermoelectric applications.

**Keywords:** Perovskite, BoltzTraP, Wien2K, Dft, Thermoelectric applications

---





---

## Probing the Electronic, Optical, and Transport Properties of Halide Double Perovskites $\text{Cs}_2\text{AgSb}(\text{Cl},\text{Br})_6$ for Thermoelectric Applications

Hamza Kerrai<sup>\*1</sup>, Ahmed Zaim<sup>1</sup>, Mohamed Kerouad<sup>1</sup>

<sup>1</sup>Faculty of Sciences, Moulay Ismail University, B.P. 11201, Zitoune, Meknes, Morocco

---

### Abstract

Double halide perovskites containing halides have garnered considerable attention as efficient semiconductors suitable for thermoelectric and optoelectronic applications due to their outstanding environmental stability, efficiency, and non-toxic nature. In our investigation, we thoroughly examined the structural, electronic, optical, and thermoelectric properties of halide double perovskites  $\text{Cs}_2\text{AgSb}(\text{Cl},\text{Br})_6$  using density functional theory. Applying Born stability and tolerance factor criteria, we confirmed the structural stability of  $\text{Cs}_2\text{AgSb}(\text{Cl},\text{Br})_6$ . Additionally, we conducted a comprehensive assessment of their electronic, optoelectronic, and thermoelectric properties. The band structure analysis revealed that  $\text{Cs}_2\text{AgSbBr}_6$  and  $\text{Cs}_2\text{AgSbCl}_6$  possess semiconducting indirect band gaps of 1.64 eV and 2.44 eV, respectively. Furthermore, an investigation of the optical properties based on the complex dielectric function demonstrated that both compounds exhibit low reflectivity, not exceeding 15%, and very high absorption coefficients in the order of  $10^5 \text{ cm}^{-1}$  in the visible and UV regions. Moreover, the thermoelectric properties were investigated using the BoltzTraP simulation package. The findings unveiled a strong Seebeck coefficient and noteworthy electrical conductivity. These results highlight the adaptability of these materials, indicating their potential for diverse applications, including thermoelectric and optoelectronic devices.

**Keywords:** Double halide perovskites, Optoelectronic, Thermoelectric, DFT, Band gaps

---



---

## Computational Insights into the Superior Efficiency of $K_2(\text{Se,Te})\text{Br}_6$ Double Halide Perovskite Solar Cells

Hamza Kerrai<sup>\*1</sup>, Ahmed Zaim<sup>1</sup>, Mohamed Kerouad<sup>1</sup>

<sup>1</sup>Faculty of Sciences, Moulay Ismail University, B.P. 11201, Zitoune, Meknes, Morocco

---

### Abstract

In this study, the structural stability, electronic, optical, and thermoelectric properties of  $K_2(\text{Se,Te})\text{Br}_6$  halide double perovskites were investigated using first-principles calculations. By applying Born stability and tolerance factor criteria, the structural stability of the compounds was confirmed. Band structure analysis revealed that  $K_2\text{SeBr}_6$  and  $K_2\text{TeBr}_6$  exhibit semiconducting indirect band gaps of 2 eV and 2.42 eV, respectively. Additionally, a study of the optical properties utilizing the dielectric constants indicated that both substances display minimal reflectivity, remaining below 18%, alongside remarkably high absorption coefficients reaching around  $10^5$  cm in the visible spectra. Furthermore, the thermoelectric properties were explored through the BoltzTraP simulation package, revealing a Seebeck coefficient and noteworthy electrical conductivity. These outcomes underscore the versatility of these materials, suggesting their potential suitability for various applications such as solar cells and thermoelectric devices.

**Keywords:** Double halide perovskites, Optoelectronic, Thermoelectric, DFT, Band gaps

---



---

## An Introduction to Carbon Nanotubes and Their Production Processes

Maryam Abdolahpour Salari<sup>\*1</sup>, Gunay Merhan Muglu<sup>2</sup>, Volkan Senay<sup>3</sup>, Sevda Saritas<sup>1</sup>

<sup>1</sup>Department of Physics, Ataturk University, Erzurum, Türkiye

<sup>2</sup>Department of Opticianry, Ataturk University, Erzurum, Türkiye

<sup>3</sup>Department of Opticianry, Bayburt University, Bayburt, Türkiye

---

### Abstract

Carbon nanotubes (CNTs) stand as a pinnacle in nanotechnological advancements, boasting unparalleled properties and characteristics. Multiple production methodologies exist, encompassing laser ablation, electric arc discharge, chemical vapor deposition (CVD), CVD with plasma enhancement, pulsed laser deposition, low-frequency ultrasound waves, bulk polymer heating, and bulk sputtering. The mechanical and thermal excellence of CNTs is intricately linked to their structural nuances. Particularly noteworthy are functionalized magnetic CNTs, pivotal in the realm of biomedicine for applications like magnetic force microscopy. The incorporation of CNTs into kaolinite demonstrates a notable enhancement in both its liquid and plastic limits. In medicine, CNTs exhibit a diverse array of applications, ranging from gene transfer to cancer treatment, drug delivery, and tissue regeneration. Their inherent antioxidant properties further extend their utility to cosmetics and dermatological products. The paramount feature of nanotubes lies in their electrical conductivity, dictated by atomic arrangements. Consequently, they emerge as prime candidates for structural applications, with their properties augmentable through composite formations with metals. The integration of metals into CNT cores can be facilitated through various means, including solid-state reactions, electric arc discharge, and electrochemical techniques. Notably, the capacity for hydrogen gas absorption in CNTs spans a wide range, from 0.4% to 67% by mass. This versatility and adaptability underscore the significance of CNTs across an array of industries, from cutting-edge biomedicine to innovative material science applications, promising a future rich with transformative technological advancements.

**Keywords:** Carbon nanotubes, Synthesis, Composite, Graphite, Electrical conductivity

---



## Analyzing the Physical Properties of a Ternary Half-Heusler RhTiP for Industrial Applications

Aya Righi<sup>\*1</sup>, Fatima Bendahma<sup>1</sup>, Abess Labdelli<sup>2</sup>, Khedidja Mechehoud<sup>1</sup>, Mohamed Mana<sup>2</sup>

<sup>1</sup>Laboratory of Technology and Solid Properties, Abdelhamid Ibn Badis University, Mostaganem, Algeria

<sup>2</sup>Biotechnology Laboratory Applied to Agriculture and Environmental Preservation, Abdelhamid Ibn Badis University, Mostaganem, Algeria

---

### Abstract

Structural, electronics, elastic, as well as thermoelectric characteristics of the half Heusler RhTiP considered by using the linearly augmented plane wave method based on the functional theory of the density implemented in the Wien2k Code. The investigation confirms the alloy's structural stability and identifies a semiconducting behavior with an indirect band gap. The elastic constants are calculated and the conditions of the criterion of mechanical stability have been theoretically confirmed. The electron transport properties were studied by examining electrical conductivity, thermal conductivity, Seebeck coefficient, and figure of merit. The results indicate a significant figure of merit (ZT) value, positioning RhTiP as a potential candidate for thermoelectric devices, thereby advancing the development of environmentally sustainable energy technologies.

**Keywords:** Half heusler, FP-LAPW, Wien2k code, Thermoelectric devices, Figure of merit

---



## QCD Phase Diagram with a Crossover and a First Order Phase Transition

Mohamed Amine Lakehal<sup>\*1,2</sup>, A. Ait El Djoudi<sup>2</sup>

<sup>1</sup>Physics Department, University M'hamed Bouguera Boumerdes, 35000, Algeria

<sup>2</sup>Laboratory of Particle Physics and Statistical Physics – Kouba, B P. 92, 16050, Vieux Kouba, Algiers, Algeria

---

### Abstract

We analyze the phase diagram of QCD by using the equations of state of the hadronic and quark gluon plasma (QGP) phases in the presence of massive and massless particles, for which an MIT bag model is adopted. A switching function is used to perform the transition between the two phases in separate regions of the phase diagram. We examine the influence of some parameters as the finite mass by calculating some thermodynamic quantities well describing the system around the transition, and we study their variations with varying temperature at zero baryochemical potential. We compare our results with Lattice QCD data.

**Keywords:** QCD phase diagram, Equation of state, Finite mass effects, Lattice QCD

---



---

## Electronic and Nonlinear Optical Properties of (E)-N'-(3-Methoxybenzylidene)-2-(Quinolin-8-Yloxy) Acetohydrazide: A Comprehensive Computational Study

Mohammed Hadj Mortada Belhachemi<sup>\*1</sup>, Zohra Douaa Benyahlou<sup>1</sup>, Amine Ould Rabah<sup>1</sup>, Kheira Hammou<sup>1</sup>

<sup>1</sup>Laboratory of Technology and Solid Properties, Abdelhamid Ibn Badis University of Mostaganem, 27000 Mostaganem, Algeria

---

### Abstract

In this study, we investigate the electronic properties and nonlinear optical (NLO) behavior of the organic compound (E)-N'-(3-methoxybenzylidene)-2-(quinolin-8-yloxy) acetohydrazide (MBQA). Utilizing density functional theory (DFT) with the B3LYP functional and the 6-311G(d,p) basis set, we computed the electronic properties, including the electric dipole moment ( $\mu$ ), polarizability ( $\alpha$ ), and hyperpolarizability ( $\beta$ ) along with second-order hyperpolarizabilities ( $\gamma$ ).

Our examination of MBQA's NLO properties encompassed a comprehensive frontier molecular orbitals (FMO) analysis, which included evaluating the HOMO-LUMO energies, determining the energy band gap and assessing global chemical reactivity descriptors. This analysis provided insights into the compound's electronic transitions and chemical stability.

Additionally, we performed a molecular electrostatic potential (MEP) simulation to identify optimal sites for electrophilic and nucleophilic attacks, providing a map of reactive regions within the molecule.

We further conducted Hirshfeld surface (HS) analysis to investigate intermolecular interactions, providing insight into the nature of these interactions within MBQA. To supplement this, a reduced density gradient (RDG) analysis was carried out to explore various types of intermolecular interactions, including repulsive, attractive and Van der Waals forces, while distinguishing between strong and weak interactions.

Our comprehensive approach combining DFT, HS and RDG analyses provides a detailed understanding of the electronic properties and intermolecular interactions of MBQA, contributing valuable insights into its potential applications in nonlinear optics and chemical reactivity.

**Keywords:** Interaction, Optic, Band gap, MEP, DFT

---



---

## Theoretical Investigation of MoSSe Janus as Promising Anode Material for Libs Using First-Principles Calculations

**Malak Bounbaa<sup>\*1</sup>, Mohamed Khuli<sup>1,2,3</sup>, Nejma Fazouan<sup>1</sup>, El Houssine Atmani<sup>1</sup>, Isam Allaoui<sup>4</sup>**

<sup>1</sup>Laboratory of Nanostructures and Advanced Materials, Mechanics and Thermofluids, Faculty of Sciences and Technologies, Hassan II University of Casablanca. Mohammedia, Morocco

<sup>2</sup>CRMEF of Beni Mellal-Khénifra, Morocco

<sup>3</sup>Superior School of Technology, Sultan Moulay Slimane University of Beni Mellal. Khenifra, Morocco

<sup>4</sup>Laboratory of Condensed Matter and Interdisciplinary Sciences(LaMCSi), B.P. 1014, Faculty of Science-Mohammed V University, Rabat, Morocco

---

### Abstract

In recent decades, energy storage technology has attracted much attention in order to meet the considerable energy demands of modern society. Because of their affordable price, high specific capacity, and convenient operating voltage, lithium-ion batteries (LIBs) are a significant component of energy storage systems. Recently, the first requirement for lithium-ion batteries (LIBs) has been the development of new electrode materials to meet the increasing demands for energy density and, in particular, anode materials, which are widely studied. Inspired by molybdenum dichalcogenides MoX<sub>2</sub> (X = S, Se, and Te) and their favorable properties, we have investigated the adsorption and diffusion of Li-ion on Janus MoSSe for Li-ion battery anodes. As a two-dimensional (2D) polarized layered material, Janus MoSSe has an intrinsic dipole, which gives rise to interesting electronic properties. Using first-principles calculations density functional theory calculations integrated with the Quantum ESPRESSO package, we study the adsorption and diffusion of a single Li atom on the Janus MoSSe structure. Lithium adsorption and mobility differ on the upper and lower sides of the Janus. From our results, the band structure of a lithiated MoSSe monolayer suggests that this material is a direct gap semiconductor with a gap energy of 1.04 eV for the S face versus 1.22 eV for the Se face. The calculated density of states (DOS) indicates that it has good electrical conductivity. The optimized adsorption energies were found to be -4.62 eV for the S face and -4.21 eV for the Se face, which are large enough to ensure stability and safety during operation. In addition, MoSSe has low lithium-ion diffusion barriers of 0.21 eV and 0.11 eV for the S and Se faces, respectively, ensuring rapid lithium-ion migration. With a high storage capacity of 452,601 mAh/g and considering all these advantages, we conclude that Janus MoSSe can be considered an excellent candidate for anodes in LIBs.

**Keywords:** DFT, Janus MoSSe, Lithium-ion batteries

---



## Investigating the Behaviour of Some Response Functions Characterising the Thermal QCD Deconfinement Phase Transition in a Finite Volume for Several Hadronic and QGP Systems

Rokaya Djida<sup>\*1</sup>, Amal Ait El Djoudi<sup>1</sup>

<sup>1</sup>Laboratoire de physique des Particules et Physique Statistique (LPPPS), Ecole Normale Supérieure-Kouba, BP 92, Vieux-Kouba, 16050, Algiers, Algeria

---

### Abstract

In the present work, we investigate the characteristics of the thermal QCD deconfinement phase transition, from a confined nuclear matter to a deconfined Quark Gluon Plasma (QGP) phase in a finite volume at non zero chemical potential. This is a continuation of our previous works where we were considering the Hadronic Gas (HG) phase consisting of pions, and we aim to probe the differences between the previous case of a pionic hadronic phase and the present one where the hadronic gas is a nuclear matter containing nucleons (protons and neutrons). Furthermore, we consider that the QGP consists of massless  $u$  and  $d$  quarks in a first step, then of massless  $u$  and  $d$  quarks and massive  $s$  quarks. For this purpose, we calculate the partition functions of both phases, then that of the total HG-QGP system, within the model of coexisting phases. Based on those partition functions, we calculate the mean values of some thermodynamics quantities, called response functions, then we illustrate their behaviour with varying temperature and volume. The main results is that the value of the transition temperature is lowered when considering the nucleons in the hadronic phase instead of pions, as well as in the case of a QGP phase containing additional  $s$  quarks.

**Keywords:** *Confinement, QCD phase transition, Nuclear matter, Response functions*

---





## Cauchy Wavelet Application to Detect Multi-Scale Structures of the Turbulent Flow

**Kenza Zaibak<sup>\*1</sup>, Nora Nait Bouda<sup>2</sup>, Fawzia Mekideche-Chafa<sup>3</sup>**

<sup>1</sup>Laboratory of Particle Physics and Statistical Physics, Ecole Normale Supérieure, BP 92 Vieux Kouba, 16050 Algiers, Algeria

<sup>2</sup>Laboratory of Theoretical and Applied Fluid Mechanics, Faculty of Physics, University of Sciences and Technology Houari Boumediene, Algiers, Algeria

<sup>3</sup>Theoretical Physics Laboratory, Faculty of Physics, University of Sciences and Technology Houari Boumediene, Algiers, Algeria

---

### Abstract

Continuous wavelet transforms (CWT) is mathematical tool for decomposing time series of signal due to its unique ability of revealing temporal information of energetic event together with its spectral information. For this reason, the CWT seems a very good tool for a detailed study into the dynamics of spatial structures, particularly the structures that arising in turbulent flows. In this paper, we perform a multi-scale decomposition by wavelet transform to velocity field of turbulent wall jet, considering two different instants of its evolution. We will use here the Cauchy wavelet. This method shows that, the energetic zones are the most irregular characteristic in the velocity field corresponding to passage of eddies.

**Keywords:** Cauchy wavelet, Continuous wavelet transforms, Velocity field, Turbulent wall jet, Energetic zones

---



## Arbitrary Amplitude Solitary Waves in a Degenerate Plasma System

Muhammad Asaduzzaman<sup>\*1</sup>

<sup>1</sup>*Department of Physics, Khulna University of Engineering & Technology, Khulna, Bangladesh*

---

### Abstract

The fundamental characteristics of arbitrary amplitude solitary potential (associated with the self-gravitational field), which are found to exist in an unmagnetized degenerate quantum plasma system containing inertial heavy nuclei and non-inertial degenerate electron species, have been investigated by employing the pseudo-potential approach, which is valid for nonlinear waves with arbitrary amplitudes. It is found from the nonlinear analysis that the considered degenerate plasma model can support solitary waves only with negative potential. The magnitude of the amplitude of the solitary self-gravitational waves first increases and then decreases with the increase of propagation speed. The width of the solitary waves changes linearly with the propagation speed. The implications of our results to some astrophysical plasma systems are briefly mentioned.

**Keywords:** *Pseudo-potential, Solitary waves, Self-gravitational perturbation, Degenerate pressure, Relativity*

---



---

## Elimination of Indigenous Dairy Biofilms from Milk Reception Lines by Implementing an Appropriate Cleaning-in-Place CIP Protocol

**Dahou Abdelkader El Amine<sup>\*1</sup>, Tahlalti Hafida<sup>1</sup>, Medjahed Mostefa<sup>1</sup>, Seddar Yagoub  
Fatima<sup>1</sup>, Doubbi Bounouaa Lahcen<sup>1</sup>, Benabdelmoumene Djilali<sup>1,2</sup>, Doukani Koula<sup>3</sup>**

<sup>1</sup>Laboratory of Sciences and Techniques of Animal Production, Faculty of Nature and Life Sciences, Abdelhamid Ibn Badis University, Mostaganem, Algeria

<sup>2</sup>Applied animal physiology laboratory, Faculty of Nature and Life Sciences, Abdelhamid Ibn Badis University, Mostaganem, Algeria

<sup>3</sup>Faculty of Nature and Life Sciences, Ibn khaldoun University Tiaret, Algeria

---

### Abstract

Microbial contamination of surfaces remains a topical issue in many sectors of the agri-food industry, particularly in the dairy sector. The presence of constituent microbial flora in cow's milk is a cause for concern, as biofilms are known to be the source of serious economic and health problems. In this study, we were able to isolate strains of *Staphylococcus aureus* and *Bacillus cereus* from rinsing water recovered from a CIP cleaning-in-place of a dairy's fresh milk reception line. Our contribution was to characterize bacterial biofilm patterns on a dairy receiving line (i.e. spoilage and pathogenic flora), carry out cleaning kinetics and model them in order to optimize CIP with available equipment. Our scientific contribution was to discriminate between the respective actions of each stage or activity involved in cleaning, i.e. soaking by hydration in treated water combined with chemical attack, rinsing by mechanical action alone, cleaning by combining mechanical action with chemical action. This approach has enabled us to put forward solutions for combating the contaminants characterized as initiators of dangerous dairy biofilms, and to explain the response to be modeled by the action of physical, biological and/or chemical phenomena. Bacterial inactivation is more or less easily eliminated by an adapted mechanical action, linked to chemistry via concentration, combining the passage of two solutions, one alkaline and the other acidic, to a biocidal disinfection.

**Keywords:** *Bacterial biofilm, Receiving line, CIP, Chemical action, Mechanical action*

---



## Evaluation of the Suitability of Bovine Milk from the Experimental Farm for Industrial Processing

**Doubbi Bounoua Lahcen<sup>1</sup>, Dahou Abdelkader El Amine<sup>\*1</sup>, Seddar Yagob Fatma<sup>1</sup>,  
Tahlaiti Hafida<sup>1</sup>, Bounaama Khalil<sup>1</sup>, Homrani Abdelkader<sup>1</sup>**

<sup>1</sup>Laboratory of Sciences and Techniques of Animal Production, Faculty of Nature and Life Sciences, Abdelhamid Ibn Badis University,  
Mostaganem, Algeria

---

### Abstract

This study concerns the monitoring of the hygienical quality and physico-chemical characteristics of fresh milk produced by the experimental farm, affiliated to the university of Mostaganem, Algeria, from lactating dairy cows of the Prim-Holstein breed. The aim of this study is to evaluate, over a period of six months, the cheese-making ability of milk from the experimental farm compared with reconstituted milk powder of standardized cheese-making quality, and to try to explain the results of tests carried out in relation to milk composition such as protein content, coagulation ability and total dry extract yield of the cheese-making coagulates obtained. The average physico-chemical results obtained for cow's milk samples generally fail to meet IDF standards (in terms of protein content, dry matter and freezing point), compared with samples of reconstituted milk of standardized cheese quality. From a hygienic point, the tested milks are of very satisfactory quality according to IDF standards, with a class A and lacto-fermentation suitable for cheese processing. Repetition of the tests on samples of fresh milk produced by the experimental farm, compared with reconstituted cheese-quality milk, enabled us to detect wetting and a low protein content in the samples of fresh cow's milk, requiring improvement either through breeding and production practices or through a protein amendment providing the balance necessary for good milk processing and obtaining the expected cheese extract yield.

**Keywords:** *Cow's milk, Physico-chemical properties, Cheesemaking aptitude, Lacto-fermentation, Dry extract yield*

---



## Food Packaging Reinforced Active Agent MOF-Based and Their Synthesis Methods

**Mohd Hafizuddin Ab Ghani<sup>\*1</sup>, Ismayadi Ismail<sup>1</sup>, Rosnah Nawang<sup>1</sup>, Intan Helina Hasan<sup>1</sup>,  
Juraina Md Yusof<sup>1</sup>, Che Azurahaman Che Abdullah<sup>1</sup>, Siti Hajar Othman<sup>1</sup>, Josephine  
Ying Chyi Liew<sup>1</sup>, Umer Rashid<sup>1</sup>, Nishata Royan Rajendran Royan<sup>2</sup>, Ruey Shan Chen<sup>3</sup>,  
Chawalit Ngamcharussrivichai<sup>4</sup>**

<sup>1</sup>Universiti Putra Malaysia, Institute of Nanoscience and Nanotechnology, Serdang, Malaysia

<sup>2</sup>UOW Malaysia KDU University College, School of Engineering, Shah Alam, Malaysia

<sup>3</sup>Universiti Kebangsaan Malaysia, Faculty of Science and Technology, Bangi, Malaysia

<sup>4</sup>Chulalongkorn University, Faculty of Science, Bangkok, Thailand

---

### Abstract

Metal-organic frameworks (MOFs) are finding increasing applications in food packaging, with selection criteria based on intended application and processing methods. Traditional methods of food packaging are struggle with issues like microbial growth, unwanted gas molecules such as oxygen and ethylene that accelerate spoilage. MOFs, however, offer a potential solution to these issues. Their antimicrobial properties can solve food spoilage, while some MOFs can act as scavengers, actively removing unwanted molecules. Additionally, MOFs are generally biocompatible and non-reactive with food, making them a safe and effective solution for food packaging. The integration of MOFs into active packaging has the potential to create a safer, more efficient, and sustainable food supply chain. In this short review, some of the fabrication techniques for MOFs active food packaging are discussed. Among the techniques are microwave synthesis, electrochemical synthesis and diffusion synthesis method.

**Keywords:** Food packaging, Active agent, Metal-organic frameworks, Electrochemical, Polymerization

---



## Processing and Conservation of Mussels from the Ain Temouchent Region (West Algerian)

Fatima Belhacini<sup>\*1,2</sup>, Arifa Chegrouche<sup>1,2</sup>, Dinedane Hadjer Amel<sup>1,2</sup>

<sup>1</sup>Department of Agri-Food, Faculty ST, University Ain Temouchent, Algeria

<sup>2</sup>Research Laboratory Ecology and Management of Natural Ecosystems, Tlemcen, Algeria

---

### Abstract

In Algeria, mussels are of relatively high economic and commercial interest, especially the *Mytilus galloprovincialis* mussel. This study is a first attempt, aimed at the conservation, processing and evaluation of shellfish species of commercial interest in particular, where it is based on the physicochemical and microbiological analysis of preserved mussels. Mussels, like other seafood, are quality products of great commercial importance, but fragile. At certain times of the year, the quantities of molluscs and crustaceans caught exceed the immediate food requirements of the local population, but in other circumstances, it is important to conserve the food for later consumption, particularly after cyclones, when food resources are scarce.

This study is a first attempt, aimed at the conservation and evaluation of shellfish species of commercial interest. Indeed, the conservation of mussels and the exploitation of shellfish is one of the main solutions for sustainable development because of its close relationship with economic growth and the protection of natural resources.

This work aims to describe the various methods that can be used to extend the shelf life of seafood products and preserve them in good condition so that they retain all their qualities and can be consumed at a later date, with particular reference to the use of organic raw materials and new agro-industrial technologies.

**Keywords:** Shellfish, *Mytilus galloprovincialis*, Preservation, Processing, Ain Temouchent Algeria

---



## Design and Project Management for Unmanned Aerial Vehicles

Ahmed Khaled Salaheldin Ali<sup>\*1</sup>, Onur Tuncer<sup>2</sup>

<sup>1</sup>Aeronautics and Astronautics Engineering Department, Istanbul Technical University, Istanbul, Türkiye

<sup>2</sup>Aeronautical Engineering Department, Istanbul Technical University, Istanbul, Türkiye

---

### Abstract

Unmanned Aerial Vehicles (UAVs) have become increasingly important in both civilian and military applications due to their versatility and advanced capabilities. This study explores the comprehensive framework of UAV project management, emphasizing the application of the Theory of Inventive Problem Solving (TRIZ) to address and resolve design challenges. Initially, the study examines various classifications of UAVs based on size, range, weight, engine type, and configuration, highlighting the distinctions between manned and unmanned aerial systems. The project management section outlines critical milestones, from project initiation to acceptance and production readiness reviews, and addresses specific challenges related to resources, technology, human factors, and institutional constraints. A detailed project management plan is developed, incorporating methods such as Critical Path, Gantt Charts, and Earned Value Management to ensure effective coordination and requirement management. Moreover, the study presents a comprehensive risk management strategy, identifying internal and external risks associated with UAV operations and proposing mitigation techniques. The discussion includes a case study on UAV accidents, which provides practical insights. In addition, applying TRIZ methodologies, such as contradiction analysis and inventive principles, offers innovative solutions to design problems. One of the aims of this research is to equip project managers with a thorough understanding of the entire UAV development process, enabling them to manage their projects more effectively. By integrating TRIZ into the project management process, this research presents a systematic approach to enhancing UAV development and operational efficiency, ultimately contributing to the advancement of UAV technology and its applications.

**Keywords:** UAV, Project management, Design phases, Project manager, TRIZ

---



## Enhancing Urban Resilience: Evaluating Earthquake Park Design in Kahramanmaras, Turkey

Sinan Kordon<sup>\*1</sup>, Aliye Kaya<sup>1</sup>, Dilan Tokgoz<sup>1</sup>, Meryem Yilmaz<sup>1</sup>, Ozge Akilli<sup>1</sup>

<sup>1</sup>Department of Landscape Architecture, Kahramanmaras Sutcu Imam University, Kahramanmaras, Türkiye

---

### Abstract

Turkey is located in a significant earthquake zone, and, as in the past, there is a high probability of encountering such destructive disasters in the future. Therefore, the presence and adequacy of emergency gathering and shelter areas within urban limits are crucial. Earthquake parks have emerged as urban open spaces whose global importance is increasing to meet this need. These parks are vital for mitigating the negative effects of earthquakes, providing first aid, gathering people in safe areas, and enhancing societal solidarity during crises.

However, for these parks to fulfill their functions effectively, they must be designed according to specific criteria. Recent earthquakes centered around Kahramanmaras have once again underscored the importance of these areas. Therefore, this study aims to achieve two goals. First, it aims to identify design criteria for earthquake parks. Second, it evaluates four different urban parks in Kahramanmaras city center from the perspective of earthquake park design criteria and their suitability as disaster gathering areas. Based on the findings, the strengths and weaknesses of each park for use in a post-disaster scenario have been identified. Important recommendations have been proposed for future green space planning to provide healthier and safer gathering areas for the public during potential disasters. The insights gained from this study in Kahramanmaras could inform crisis management planning following potential disasters and serve as a model for other cities

**Keywords:** *Earthquake parks, Urban resilience, Disaster preparedness, Crisis management, Landscape architecture*

---





## Analysis of the Flow Through a Contoured Nozzle Using CFD

Sabrina Benlembarek\*<sup>1</sup>, Kamel Talbi<sup>1</sup>

<sup>1</sup>Department of Mechanical Engineering, University of Mentouri 1, Constantine, Algeria

---

### Abstract

The performance of the propulsion system is the most important factor in producing efficient flying vehicles. The nozzle is an important component of any high-performance engine or rocket motor. Convergent Divergent Nozzles are commonly employed in rockets; the primary aim of a nozzle is to accelerate the flow to greater exit velocity. To attain acceptable performance characteristics with minimal energy losses, a nozzle must meet all design requirements under all operating situations. The computational work is done on a 2D axi-symmetric density-based coupled solver with a viscous kw-SST turbulence model. To solve complicated partial differential equations, we employ the finite volume method, which consists of linearizing the system of equations and making it easier to solve, nozzle, and analyze the flows (ANSYS FLUENT). The current study aims to investigate supersonic flow in a contour nozzle, and visualization of the shock event found parallels between the formation of the Mach disk and its reflection patterns. The contour nozzle resulted in a higher exit velocity.

**Keywords:** *Convergent-divergent nozzle, Contour nozzle, CFD, Supersonic flow*

---



---

## Balancing Techniques Comparison on an Imbalanced Payment Company Dataset

Mehmet Sukru Aygun<sup>\*1</sup>, Mehmet Fatih Akay<sup>1</sup>

<sup>1</sup>Computer Engineering, Cukurova University, Adana, Türkiye

---

### Abstract

Data imbalance refers to unequal distribution of data samples to different classes in the data set. The research community has been faced imbalanced data in many fields such as medical diagnosis, fraud detection, information retrieval systems. While most of the samples belong to majority (negative) class, the others belong to minority (positive) class in binary datasets. Imbalance ratio (IR) states the proportion of positive class samples to negative class samples. Imbalanced data complicates the learning of minority class samples in classification problems, hence results in a large classification error. Classifier needs balanced data to reduce its classification error and to maximize its overall accuracy. Such as Random Oversampling, Synthetic Minority Oversampling Technique (SMOTE), Adaptive Synthetic Sampling (ADASYN) are oversampling methods that are used to equal minority and majority class samples with increasing minority class samples count. On the other side, undersampling equals the count of both class samples by removing majority class ones. In this study, an imbalanced churn dataset (IR=1:3) provided by a payment company is balanced and classified with different techniques, then compared the results. SMOTE, ADASYN, Random Oversampling and Random Undersampling techniques are used to balance the data, Extreme Gradient Boosting (XGBoost), Support Vector Machines, Logistic regression, C4.5 Decision Tree, Random Forests are used for the classification and F-score is used for evaluation.

**Keywords:** *Imbalanced data, Undersampling, Oversampling, Classification*

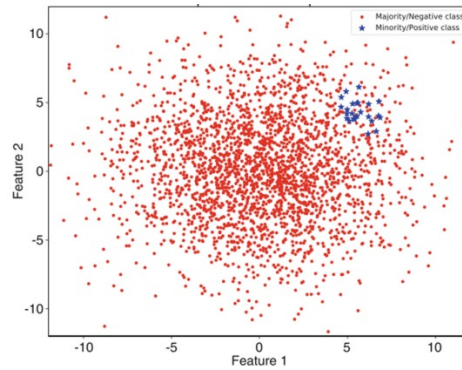
---

## 1 INTRODUCTION

Data imbalance is the term used to describe the unequal distribution of classes within a dataset in the field of data science and machine learning. This phenomenon arises when one or more classes are considerably underrepresented in comparison to others, resulting in difficulties in the training and evaluation of models. The performance of predictive models can be negatively impacted by data imbalance, as algorithms may become biased toward the majority class, thereby compromising the model's accuracy and generalizability on the minority class. In applications where the minority class represents critical or sensitive outcomes, such as fraud detection, medical diagnosis, and uncommon event prediction, it is essential to address data imbalance. This is a prerequisite for the development and implementation of specialized techniques and methodologies to improve the robustness and fairness of machine learning models and to mitigate the effects of imbalance.

Classification problems are based on predicting samples belonging to different classes correctly. To identify positive samples correctly in imbalanced data classification is much more important in general. Typically, traditional classifier learning algorithms tend to favor the majority class by assigning higher weights to rules that accurately predict examples from that class. This bias is influenced by the accuracy metric or cost function used. Alternatively, if there are specific rules that can predict samples from the minority class, they may be disregarded and considered as noise, as more generic principles are given preference.

The imbalance rate (IR), also known as the imbalance ratio or imbalance degree, is a quantitative measure used to assess the level of imbalance in a dataset, specifically in the context of classification difficulties. The term is frequently employed in the fields of machine learning and statistics to characterize the distribution of classes within a dataset. An imbalanced dataset is characterized by a substantial variation in the number of instances across various classifications. The imbalance rate is determined by dividing the number of instances in the majority class by the number of instances in the minority class (Figure 1).



**Figure 1.** Imbalanced data (IR= 1:100)

This study conducts a comparison of various data balancing strategies utilizing identical classification algorithms on a customer churn dataset from a payment provider, where the imbalance ratio (IR) was 1:3.

## 2 MATERIAL AND METHOD

Customer churn prediction models are often solely evaluated on their predictive performance, or their ability to discriminate between churners and non-churners. Over the last 20 years more advanced techniques have been proposed and evaluated [1]. Most churn prediction literature concentrates on comparing various algorithms to decrease a classification error. They concentrate on improving the accuracy of prediction by applying a new preprocessing method and comparing various algorithms. Few studies have tried to conduct churn prediction in emerging businesses rather than standardized businesses such as telecommunication and finance [2].

In churn prediction, class imbalance naturally occurs because churners are usually less frequent than non-churners. Imbalanced data may cause classification techniques to experience difficulties in learning which customers are about to churn, resulting in poor classification power [3].

To deal with absolute and relative rarity of the minority class, the data-level approaches are used to balance data [4]. These are categorized under three different headings:

- i. Oversampling methods: They create a superset of the original dataset by replicating some instances or creating new instances from existing ones.
- ii. Undersampling methods: They discard samples from the majority class and oversampling duplicates or constructs samples from the minority class to create a more balanced dataset.
- iii. Hybrids methods: They combine both sampling approaches.

Oversampling, that tries to duplicate or develop additional positive examples in order to gain relevance. The most popular oversampling methods are Random Over-Sampling, Synthetic Minority Over-sampling Technique (SMOTE), ADASYN (Adaptive Synthetic Sampling) and Borderline-SMOTE.

Undersampling, that consists of decreasing the data by deleting examples belonging to the majority class with the objective of equalizing the number of examples of each class. Random Subsampling and Cluster Centers are some of the methods used.

In this study, SMOTE, ADASYN, Random Oversampling and Random Undersampling techniques are used to balance the data. Five Machine Learning Algorithms are used for churn prediction. They are Logistic regression, C4.5 Decision Tree, Support Vector Machines, Random Forests and eXtreme Gradient Boosting (XGBoost). While first four ones frequently used as benchmark classifiers, XGBoost is rarely used for churn prediction.

Confusion matrix is a summary of prediction results on a classification problem (Table 1).

**Table 1.** Confusion matrix

		Actual	
		+	-
Predicted	+	True positive (TP)	False positive (FP)
	-	False negative (FN)	True negative (TN)

In confusion matrix, there are 4 parts (TP, FP, FN, TN) which hold the information about prediction results. For churning classification, majority class (non-churners) samples are evaluated as positive samples, minority class (churners) samples are evaluated as negative samples. The meanings of them are described as:

- True Positives (TP) are predicted as positive samples, they are positive in actual.
- False Negatives (FN) are predicted as negative samples, they are negative in actual.
- False Positives (FP) are predicted as positive samples, they are negative in actual.
- True Negatives (TN) are predicted as negative samples, they are positive in actual.

The sensitivity or true positive rate measures the proportion of positive examples which are predicted to be positive ( $TP/(TP + FN)$ ). (i.e.. the percentage of churners that is correctly classified), whereas the specificity or the true negative rate measures the proportion of negative examples which are predicted to be negative ( $TN/(TN + FP)$ ) (i.e. the percentage of non-churners that are correctly classified) [5].

F-score is a measure of a test's accuracy. It is calculated from the precision and sensitivity of the test, where the precision is the number of true positive results divided by the number of all positive results ( $TP/(TP + FP)$ ). The F1 score is the harmonic mean of the precision and sensitivity. It is formulated as  $F\text{-score} = 2 * (\text{precision} * \text{sensitivity}) / (\text{precision} + \text{sensitivity})$

Dataset is provided by an payment company. The dataset includes the customer's information between 10/05/2017 and 16/03/2021. It has 7842 records with 18 features. The churner customer count is 1962 and % 25 of all customers while the non-churner customer count is 5580.

### 3 RESULTS

4 resampling (+Imbalanced Data) and 5 classification techniques are implemented on the same preprocessed data with 5x2 Cross Validation. All results are shown below (Table 2-6).

**Table 2.** Unbalanced data results

	Mean Accuracy	Mean Precision	Mean Recall	Mean F-Score
XGBoost	0.776138	0.788809	0.788809	0.767935
SVM	0.671162	0.711655	0.711655	0.629843
Logistic Regression	0.663999	0.694742	0.694742	0.628946
C4.5 Decision Tree	0.725504	0.728270	0.728270	0.719760
Random Forests	0.791136	0.818330	0.818330	0.779188

**Table 3.** SMOTE results

	Mean Accuracy	Mean Precision	Mean Recall	Mean F-Score
XGBoost	0.790105	0.821931	0.821931	0.859612
SVM	0.739482	0.742277	0.742277	0.841813
Logistic Regression	0.741395	0.752348	0.752348	0.839758
C4.5 Decision Tree	0.732851	0.811776	0.811776	0.813008
Random Forests	0.768046	0.807778	0.807778	0.844755

**Table 4.** ADASYN results

	Mean Accuracy	Mean Precision	Mean Recall	Mean F-Score
XGBoost	0.839084	0.867075	0.867075	0.832683
SVM	0.693993	0.726986	0.726986	0.669938
Logistic Regression	0.678080	0.710447	0.710447	0.651257
C4.5 Decision Tree	0.847578	0.905546	0.905546	0.835777
Random Forests	0.872162	0.920686	0.920686	0.864220

**Table 5.** Random oversampling results

	Mean Accuracy	Mean Precision	Mean Recall	Mean F-Score
XGBoost	0.767228	0.779476	0.779476	0.763175
SVM	0.667894	0.709045	0.709045	0.634452
Logistic Regression	0.660176	0.687770	0.687770	0.635914
C4.5 Decision Tree	0.722362	0.729221	0.729221	0.719830
Random Forests	0.780241	0.806436	0.806436	0.771651

**Table 6.** Random undersampling results

	Mean Accuracy	Mean Precision	Mean Recall	Mean F-Score
XGBoost	0.732770	0.732666	0.732666	0.732684
SVM	0.679411	0.710231	0.710231	0.655009
Logistic Regression	0.675630	0.706895	0.706895	0.648827
C4.5 Decision Tree	0.668079	0.669269	0.669269	0.666108
Random Forests	0.718096	0.722070	0.722070	0.715210

ADASYN and Random Forest combination gives the best performance with 0.864220 of F-Score. 0.733256 of F-Score is obtained as the average of 5 techniques with unbalanced data.

## 4 CONCLUSION

Balancing imbalanced data is essential in machine learning because it directly impacts the model's ability to learn and make accurate predictions. In datasets where one class significantly outnumbers another, models tend to become biased towards the majority class, often neglecting the minority class. This bias can result in high overall accuracy but poor performance in identifying and predicting instances of the minority class. Such outcomes are especially problematic in critical applications like healthcare, fraud detection, and risk assessment, where the minority class often represents rare but significant cases. Balancing the data ensures that the model pays appropriate attention to all classes, leading to more reliable and actionable predictions.

Additionally, balanced datasets contribute to fairer and more equitable models. In contexts where decision-making impacts real lives, such as credit scoring, hiring, and criminal justice, biased models can reinforce existing inequalities and result in unfair outcomes. By ensuring that all classes are adequately represented during training, we promote fairness and reduce the risk of systemic biases. Furthermore, balanced data enables the use of more informative evaluation metrics, like precision, recall, and F1-score, which offer a better understanding of model performance across all classes. This holistic approach to evaluation helps in developing robust models that generalize well to diverse real-world scenarios.

## References

- [1] A. De Caigny, K. Coussement, and K. W. De Bock, "A new hybrid classification algorithm for customer churn prediction based on logistic regression and decision trees," *European Journal of Operational Research*, vol. 269, pp. 760–772, 2018.
- [2] S. Kima and H. Leeb, "Customer churn prediction in influencer commerce: An application of decision trees," *Procedia Computer Science*, vol. 199, pp. 1332–1339, 2022.
- [3] W. Verbeke, K. Dejaeger, D. Martens, J. Hur, and B. Baesens, "New insights into churn prediction in the telecommunication sector: A profit driven data mining approach," *European Journal of Operational Research*, vol. 218, pp. 211–229, 2012.
- [4] A. Fernández, S. García, M. Galar, R. C. Prati, B. Krawczyk, and F. Herrera, *Learning from Imbalanced Data Sets*, Springer International Publishing, 2018.
- [5] N. Gordini and V. Veglio, "Customers churn prediction and marketing retention strategies. an application of support vector machines based on the AUC parameter-selection technique in B2B E-commerce industry," *Industrial Marketing Management*, vol. 62, pp. 100–107, 2017.



## Optimization of Incremental Conductance Using Fuzzy Logic Control for MPPT of a Photovoltaic Stand-Alone System

Beddi Abdelraouf<sup>\*1</sup>, Hicham Serhoud<sup>2</sup>, Nacer Hebbir<sup>1</sup>, Zoubir Aoulmi<sup>1</sup>, Moussa Attia<sup>1</sup>

<sup>1</sup>Larbi Tebessi University, Algeria

<sup>2</sup>University of El Oued, Algeria

---

### Abstract

The objective of this paper is to enhance the maximum power point tracking (MPPT) capability of a standalone PV system by proposing the optimization of Incremental Conductance (INC) by using the Fuzzy Logic Control. The PV standalone system comprises an MPPT controller, photovoltaic modules, a constant load, and a DC/DC boost converter. The key objectives of the study include enhancing convergence speed, reducing steady-state oscillations, and improving tracking effectiveness while considering cost-effectiveness. It is well known that the conventional INC technique struggles to adapt to rapid increases in solar irradiance, which pushed us to combine it with FLC. To validate the proposed system, the optimization of incremental conductance (INC-FLC) is compared to the traditional incremental conductance by using the Sim-Power System in MATLAB. The results confirm that the INC-FLC optimization exhibits satisfactory performance with reduced oscillations and improved efficiency compared to other techniques.

**Keywords:** Control, Optimization, MPPT, Photovoltaic system

---



## Enhancing Impact Resistance of Engineering Solutions Through Multiscale Structural Optimization

Ilhan Taber<sup>\*1</sup>, Ramazan Karakuzu<sup>2</sup>

<sup>1</sup>The Graduate School of Natural and Applied Sciences, Dokuz Eylul University, Izmir, Türkiye

<sup>2</sup>Department of Mechanical Engineering, Dokuz Eylul University, Izmir, Türkiye

### Abstract

This study investigates the impact resistance of bottom-freezer refrigerators during transportation, focusing on drop impact testing and damage analysis. Utilizing industry standards (ASTM D5276, ASTM D880) and LS-DYNA simulations, the research examines how packaging solutions and design modifications can enhance refrigerator durability. The finite element model incorporates various material models, such as MAT\_PIECEWISE\_LINEAR\_PLASTICITY (MAT24) for DC04 steel and MAT\_ELASTIC for other steel parts, MAT\_SOIL\_AND\_FOAM for foam components, and MAT\_RIGID for indenters and fixtures, to simulate realistic impact scenarios. AUTOMATIC\_SINGLE\_SURFACE is used for initial contact definitions and enhances the model with TIED\_NODES\_TO\_SURFACE and TIED\_SURFACE\_TO\_SURFACE to manage interactions. The gravity affecting the product unit is defined using the *LOAD\_BODY\_Y* keyword. Mass elements represent the compressor weight, and beam load models are used for packaging straps. Computational efficiency is achieved using Massively Parallel Processing (MPP), the MPP\_IO\_BINOUTONLY keyword, and precise output management techniques. Recommendations for design and material enhancements are based on testing results, contributing to improved product reliability.

**Keywords:** Drop impact testing, White goods, Refrigerators, Finite element analysis, LS-DYNA

## 1 INTRODUCTION

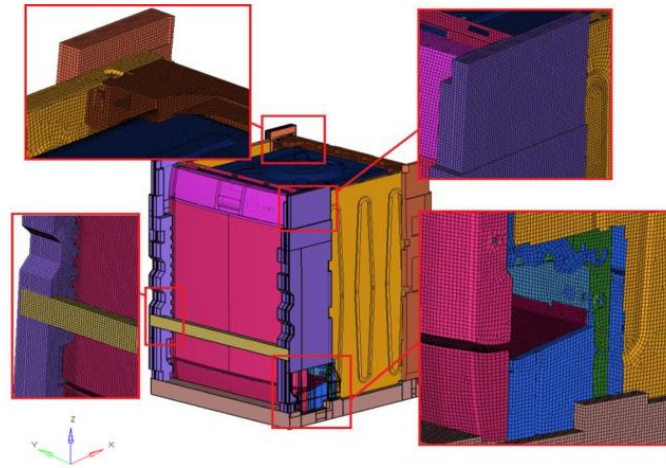
Ensuring the safe transportation of refrigeration systems necessitates robust packaging capable of withstanding various impacts. This study evaluates and enhances the impact resistance of bottom-freezer refrigerators through drop impact testing and design improvements, adhering to industry standards like ASTM D5276 [1] and ASTM D880 [2]. The research involves rigorous damage analysis and subsequent design modifications, with the effectiveness of these improvements assessed through further testing. The objective is to enhance refrigerator durability and safety, contributing to higher product reliability and customer satisfaction.



**Figure 1.** Product stowing and transfer view in factory storage

### 1.1 Historical Developments on Refrigerator Drop Impact Studies

Packaging for refrigeration systems must absorb and dissipate impact energy effectively. Standards such as ASTM D4168 [3] guide the design of packaging solutions. Research highlights the use of computational tools like LS-DYNA to simulate impact scenarios and evaluate packaging performance [4, 5]. Impact testing methods have evolved to assess material and structural resilience. Foundational methods [6, 7] and advancements in Finite Element Analysis (FEA) [8, 9] have improved the assessment of complex impact scenarios. FEA is crucial for optimizing packaging designs by simulating various loading conditions. Studies [10, 11] demonstrate FEA’s role in enhancing design accuracy and reducing material waste.

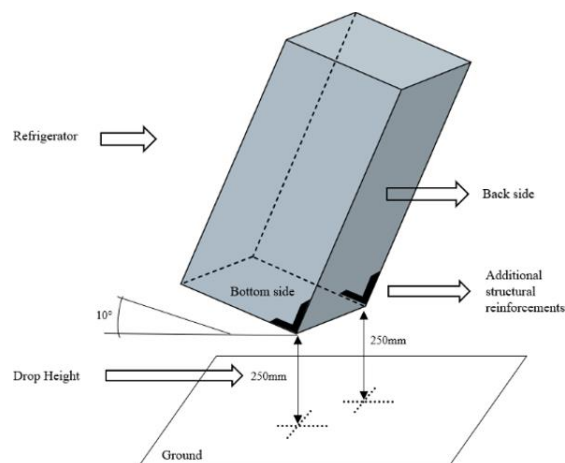


**Figure 2.** FEA model mesh optimization [11]

LS-DYNA is effective in simulating drop impacts due to its computational efficiency. Research [12, 13] showcases its capability to assess and improve packaging materials under impact conditions. Current research often lacks comprehensive studies correlating FEA simulations with real-world tests. This study addresses these gaps by integrating simulation with experimental validation, focusing on detailed model parameterization to improve predictive accuracy.

## 2 OVERVIEW OF METHODOLOGICAL APPROACH

The study uses drop impact tests to simulate handling stresses, following standardized procedures. LS-DYNA, an advanced FEA software, is employed to simulate impacts and predict outcomes before physical testing. The methodology includes precise equipment checks, controlled test conditions, and post-test inspections to ensure accuracy. Integrating experimental validation with computational analysis is crucial. The framework involves comparing simulation results with empirical data, examining pre- and post-test conditions, and calibrating material models against experimental benchmarks. Drop testing includes various impact scenarios (flat, edge, corner) to evaluate packaging strength. Focus is on optimizing drop impact resistance for refrigerator door mechanisms and considering compressor weight and positioning.



**Figure 3.** Drop scenario of the product



The study optimizes drop impact resistance, particularly for edge impacts, by improving EPS foam configurations and reinforcing structural components. The impact of the compressor weight is also considered.

Tests involve dropping the refrigerator from 250 mm onto a rigid surface, with specific parameters including weight, dimensions, packaging type, and environmental conditions. Post-test measurements assess the impact on structural integrity, focusing on door mechanisms and alignment. Variations in functionality and dimensional changes are analyzed.

To measure dimensional changes in critical components such as door hinges, hinge stiffeners, fasteners, and attachment holes, measuring tools such as calipers and rulers are used to ensure accuracy. For certain distances measurements are taken. It can be evaluated whether the measured differences deviate from the original specifications.

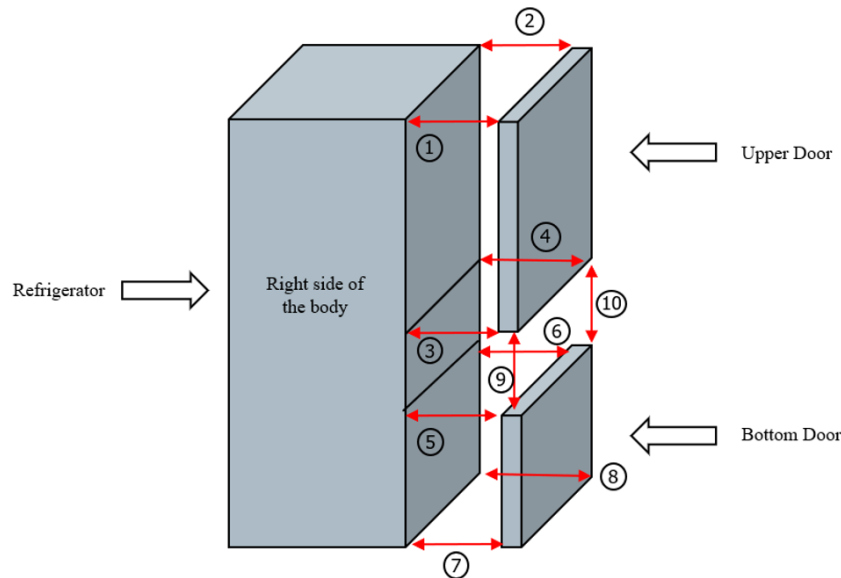


Figure 4. 3D view of measurement points after drop test performed

## 2.1 Materials Used in Refrigerator

The study evaluates the performance of materials like galvanized and stainless steel against drop impacts, crucial for maintaining structural integrity.

Table 1. Materials' mechanic properties

Materials	Elastic Modulus (MPa)	Poisson's Ratio	Density (kg/m <sup>3</sup> )	Refrigerator Components
DC04 EN 10130 (Cold-Rolled Steel)	180000	0.283	7851	Hinge, Reinforcement, Chassis
POM (Polyoxymethylene)	3500	0.499	1410	Hinge connection structures, Panel reinforcement structure
DC01 EN 10130 (Cold-Rolled Steel)	210000	0.300	8000	Sheet metal (0.5mm)
HIPS (High Impact Polystyrene)	1900	0.350	1040	Interior plastic surface structure
ABS (Acrylonitrile Butadiene Styrene)	2890	0.230	12.5	Door caps
PP (Polypropylene)	1400	0.400	1400	Plastic bushing structures
PU (Polyurethane)	2	0.430	27	Insulation walls
EPDM (Ethylene Propylene Diene Monomer)	4826	0.480	860	Door gasket
EPS (Expanded Polystyrene)	22	0.000	20	EPS Absorption foams
PET (Polyethylene Terephthalate)	2.30	0.400	140	Straps
Carton (Corrugated Fiberboard)	2194	0.340	800	Carton box

## 2.2 Finite Element Method Approach

FEA offers efficiency and precision in solving engineering problems. The method involves dividing structures into smaller elements, enabling solutions for complex geometries and loading scenarios. A detailed finite element model of the refrigerator is created, including critical components. Simulations are conducted using LS-DYNA, with defined material models and boundary conditions. Numerical approaches such as direct integration are used for solving dynamic systems. The equations of motion are applied to simulate the refrigerator's response to impact.

Material properties for the refrigerator components are specified, including elastic modulus, Poisson's ratio, and density for various materials like DC04 steel, POM, HIPS, and EPS. A detailed finite element model of the refrigerator, including components such as the door, hinges, and reinforcements, was developed using HyperMesh2019 and LS-Prepost. Cross-validation was performed with LS-DYNA R13. The model incorporates drop height, orientation, and initial conditions to simulate impact scenarios accurately.

Numerical methods like direct integration and modal superposition offer efficient solutions to equilibrium equations in nonlinear, dynamic systems. Direct integration method was employed due to their compatibility with the nonlinear characteristics of the drop test scenario. The equations of motion are defined as:

$$Mu''(t) + Cu'(t) + Ku(t) = F(t) \quad (1)$$

where:

- $M$  is the mass matrix,
- $C$  is the damping matrix,
- $K$  is the stiffness matrix,
- $u''(t)$  is the acceleration vector,
- $u'(t)$  is the velocity vector,
- $u(t)$  is the displacement vector, and
- $F(t)$  is the external force vector.

The central difference method solves differential equations with constant coefficients by calculating velocity and acceleration at each time step. The method is described by:

$$u'_n = \frac{1}{2\Delta t}(u_{n+1} - u_{n-1}) \quad (2)$$

$$u''_n = \frac{1}{(\Delta t)^2}(u_{n+1} - 2u_n + u_{n-1}) \quad (3)$$

The equation of motion for a dynamic system in the finite element analysis context can be written as:

$$(m + \frac{1}{2}\Delta t c)u_{n+1} + 1 = \Delta t^2 p_n - (\Delta t^2 k - 2m)u_n - (m - \frac{\Delta t}{2} c)u_{n-1} \quad (4)$$

where:

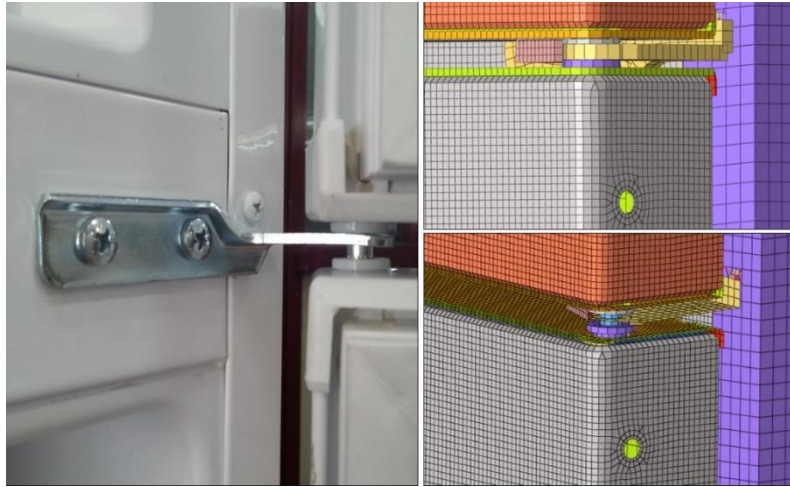
- $m$  is the mass,
- $c$  is the damping coefficient,
- $k$  is the stiffness,
- $u$  is the displacement,
- $u'$  is the velocity,
- $u''$  is the acceleration,
- $p$  is the external force, and
- $\Delta t$  is the time step size.

This explicit integration method was selected for its effectiveness in capturing dynamic responses during the drop test.

The LS-DYNA simulation model was developed through a systematic process: creating geometry, meshing, defining material models, and verifying boundary conditions. The model must reflect the drop test setup, including

drop height and orientation. Accurate material properties and contact interfaces were essential for simulating impact events.

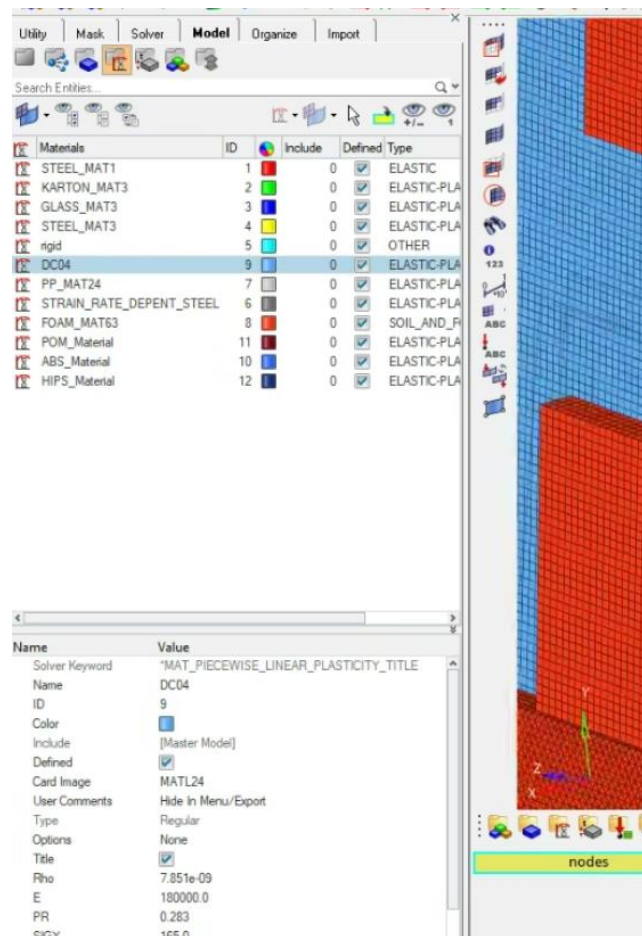
Mesh generation and optimization are crucial for accurate finite element analysis. Mesh refinement, adaptive remeshing, and sensitivity analysis were employed to balance accuracy with computational efficiency.



**Figure 5.** Middle hinge midplane view (shell element)

Simplifications in the model facilitate computation while maintaining accuracy. Mesh quality and element types are adjusted to address numerical issues and ensure efficient simulations.

### 2.3 Material Models and Finite Element Modelling



**Figure 6.** Material LS-DYNA keywords

When we tested dropping the refrigerator using LS-DYNA we used material models to represent its parts. The finite element model was created in HyperMesh 2019 with mesh elements tailored to each component of the refrigerator. We modeled DC04 steel using MAT\_PIECEWISE\_LINEAR\_PLASTICITY (MAT24) to capture its elastic plastic behavior. The steels properties included a density of  $7.85 \times 10^{-9} \text{ kg/mm}^3$  a modulus of 180 GPa a Poisson’s ratio of 0.283 a yield stress of 165 MPa and a tangent modulus of 0.0. We used MAT\_ELASTIC for steel parts MAT\_SOIL\_AND\_FOAM for foam components and MAT\_RIGID, for indenters and fixtures to represent materials in the simulation. Although we considered models like Johnson Cook [14] for strain rate and temperature effects, the selected models proved accurate, for our research purposes.

The selection of material models that correspond with the central difference time integration method employed in the simulation guarantees a portrayal of material reactions during impact. This method allowed for in-depth observations into how refrigerator components behave under drop test scenarios underscoring the significance of employing material models in simulations.

### 2.4 Models and Finite Element Modelling

Defining contact and interactions in LS-DYNA is crucial for accurate simulations. We used AUTOMATIC\_SINGLE\_SURFACE for initial contact definitions and enhanced the model with TIED\_NODES\_TO\_SURFACE and TIED\_SURFACE\_TO\_SURFACE to manage interactions between components. To address boundary conditions, we implemented 120 constraints, including 119 NODAL\_RIGID\_BODY limitations and one INTERPOLATION term. These constraints ensured reliable momentum and energy transfer and maintained the model’s accuracy in predicting real-world impact behavior.

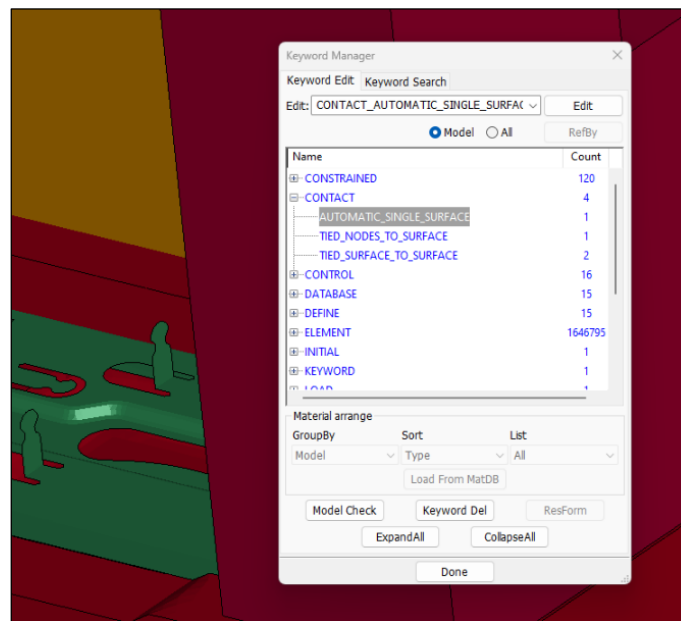


Figure 7. AUTOMATIC\_SINGLE\_SURFACE for initial contact definitions

### 2.5 Simulation Setup and Execution

In the LS-DYNA simulation, it is crucial to specify the starting speed and gravitational pull. The gravity affecting the refrigerator unit is defined using the *LOAD\_BODY\_Y* keyword with the following parameters: Load Curve ID (LCID) for the gravitational force is 11, and the Scale Factor (SF) is applied. The gravitational acceleration is set to  $-9810.000 \text{ mm/s}^2$  (as LS-DYNA requires acceleration in  $\text{mm/s}^2$ ). During the refrigerator drop test, the unit is released from a height of 0.25 meters. LS-DYNA software computes the impact velocity using the equation:

$$V_o = \sqrt{2gh} \tag{5}$$

$$V_o = \sqrt{2 \times 9.8066 \text{ m/s}^2 \times 0.25 \text{ m}} \tag{6}$$

$$V_o = 2.2147 \text{ m/s} \tag{7}$$

Therefore, the impact velocity of the refrigerator unit when dropped from a height of 0.25 meters is approximately 2.2147 m/s.

This arrangement guarantees that the simulation faithfully imitates the circumstances of a refrigerator drop test delivering information on how the refrigerator unit reacts when it hits the ground. The weight of the compressor is simulated using mass components to represent its mass and inertial consequences. Placed at the rear of the refrigerator the 9.2 kg load is distributed to show its influence during the drop test.

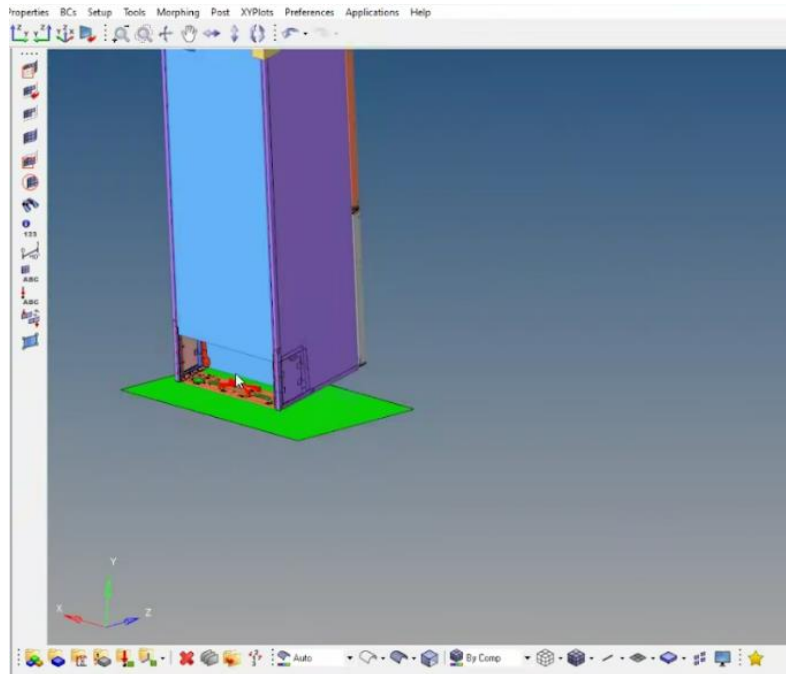


Figure 8. Final FEA model drop simulation condition

Massively Parallel Processing (MPP) and the explicit method enhance simulation efficiency. LS-Prepost R13 and the “MPP\_IO\_BINOUTONLY” keyword streamline file management and speed up computations. The combination of MPP and precise output management optimizes simulation performance and data handling.

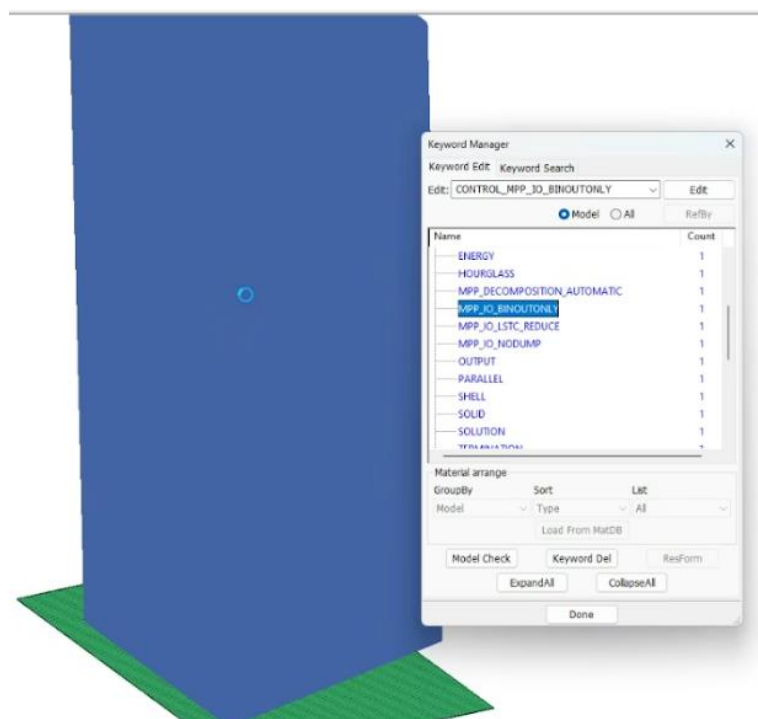


Figure 9. MPP\_IO\_BINOUTONLY keyword streamline file management

### 3 RESULTS

#### 3.1 FEA Analysis Results

Von Mises stress analysis reveals critical stress points: the compressor area has the highest stress at 354.74 MPa, while the chassis ranges from 283.80 to 319.27 MPa, and hinge locations show stress between 248.32 and 283.80 MPa. Although these stress levels are acceptable, they suggest potential issues with door functionality under impact. Plastic deformation is noted primarily in the compressor and hinge areas, with strains indicating a need for design improvements. Stress concentrations at the hinges, despite being high, do not significantly affect structural integrity.

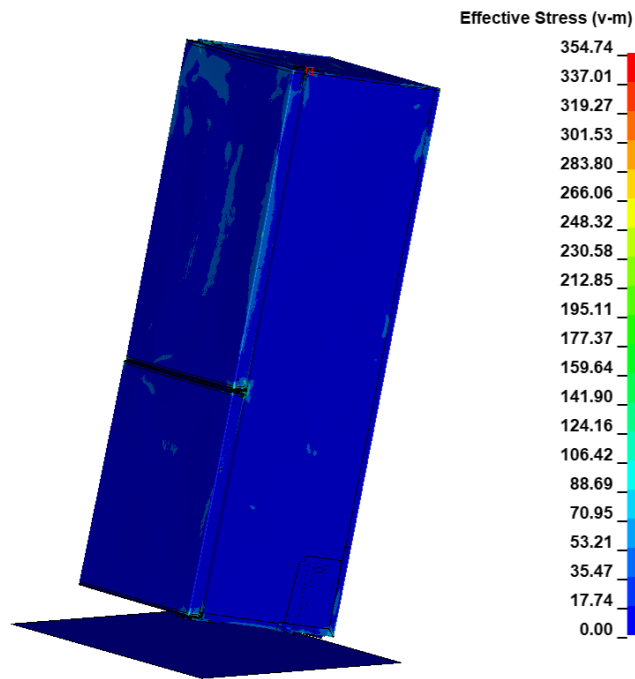


Figure 10. Baseline design Von Mises stress results

In the compressor part plastic deformations vary from 0.12, to 0.20 suggesting a requirement for enhancing the design to increase longevity. The hinges also show deformations ranging between 0.12 and 0.27 which could affect the functionality and efficiency of the door. These results underscore the importance of enhancing the design in these regions.

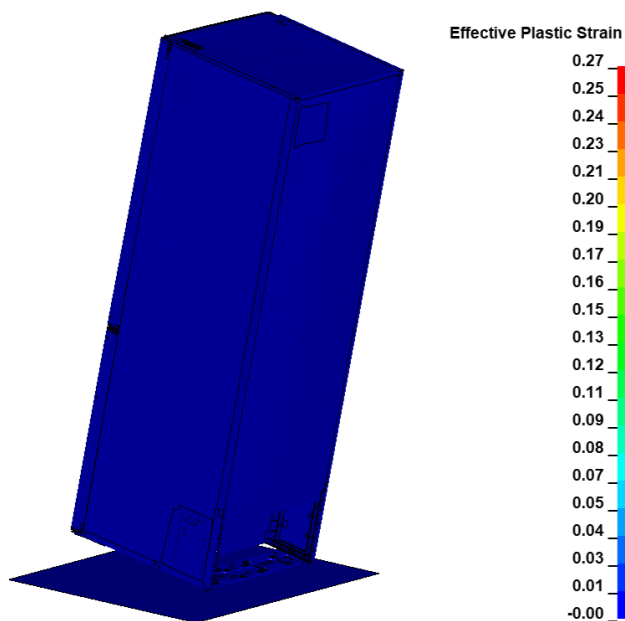


Figure 11. Post-improvement plastic strain results

The examination of EPS indicates strain around the edges caused by the weight of the compressor underscoring the necessity for enhancements, in design to bolster durability in these regions.

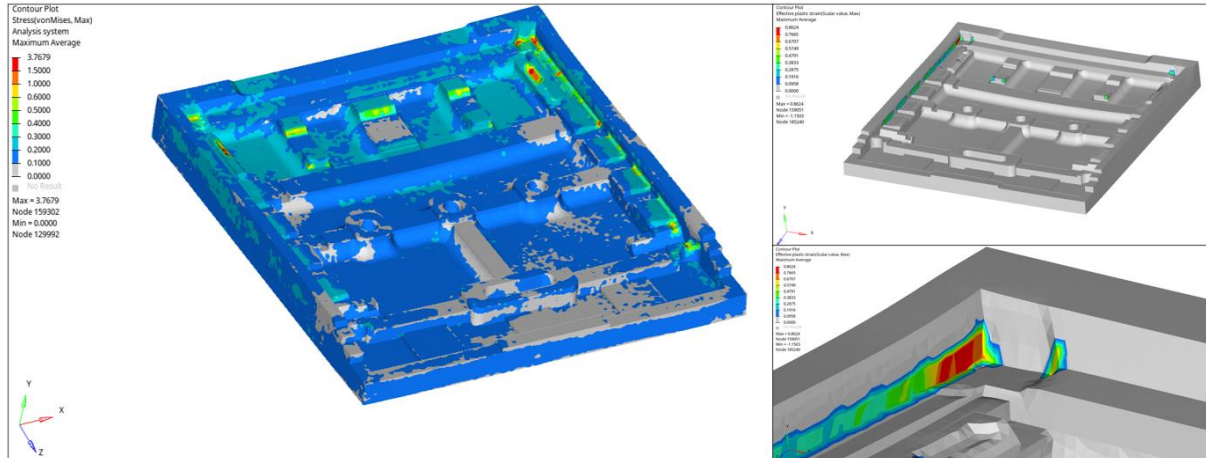


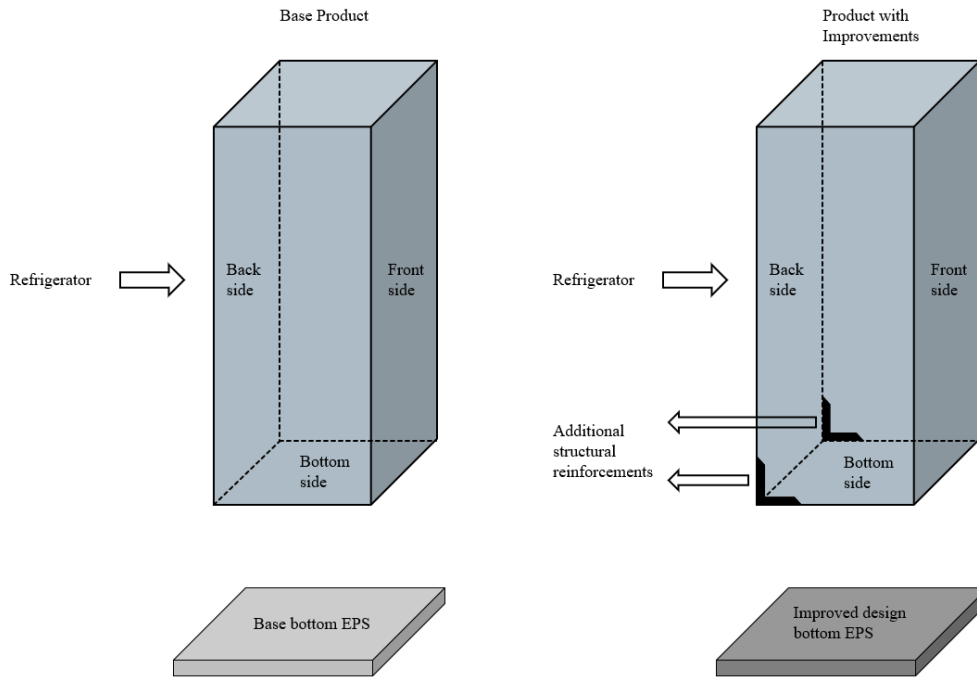
Figure 12. Bottom Styrofoam stress examination view

The initial FEA simulations reveal discrepancies, in the default 12 mm distance suggesting alignment problems arising from negative distances.

Table 2. Base design post-drop test door position measurements (mm)

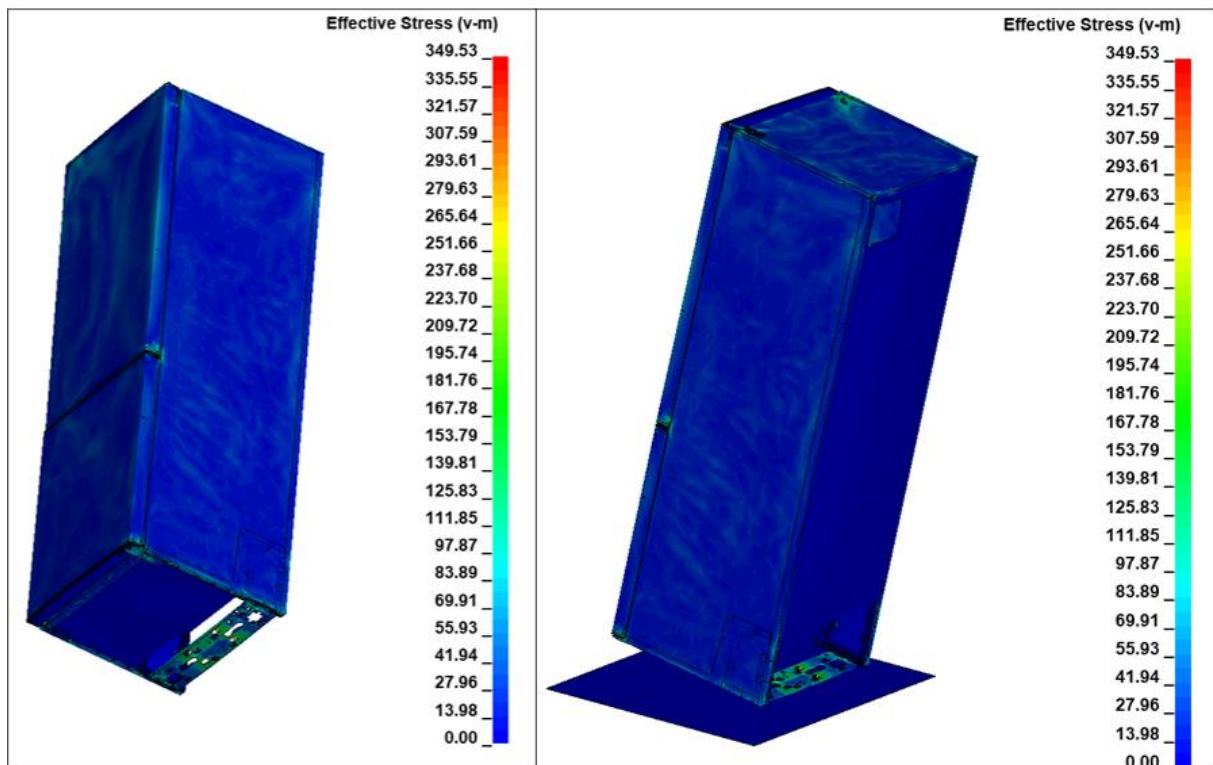
Measurement Points	Baseline Design Theoretical/3D Door Distances	Baseline Door Distances	Distances					
		Before Drop Test	After	After	After	After	After	After
			Drop Test 1	Drop Test 2	Drop Test 3	Drop Test 4	Drop Test 5	Drop Test 6
1	12 mm	12.22	8.87	9.65	9,14	8.95	9.71	9.75
2	12 mm	11.95	11.56	11.64	11.47	11.55	11.57	11.62
3	12 mm	12.15	5.56	6.24	6.45	5.97	7.12	5.63
4	12 mm	11.98	11.55	11.43	11.66	11.62	11.57	11.45
5	12 mm	12.17	7.56	8.05	7.91	7.45	8.34	7.97
6	12 mm	11.92	11.23	11.35	11.36	11.39	11.45	11.39
7	12 mm	12,06	9.34	8.94	9.23	8.85	8.77	9.14
8	12 mm	11.96	11.31	11.46	11.58	11.42	11.33	11.35
9	12 mm	11.9	5.76	5.85	6.12	6.05	5.99	6.08
10	12 mm	11.87	11.64	11.56	11.51	11.48	11.65	11.57

Improvements in design focused on enhancing the compressor section and EPS component to improve energy absorption and impact resistance. The effectiveness of these modifications was validated through FEA simulations.



**Figure 13.** Design improvements

Post-improvement FEA results show reduced stress, with the highest Von Mises stress at 349.53 MPa. Plastic strains of up to 0.26 indicate areas needing further attention. Overall, the improvements reduced stress concentrations and enhanced impact resistance.



**Figure 14.** Post-improvement Von Mises stress results

FEA results show permanent deformation in the refrigerator, with peak plastic strains reaching 0.26 near the compressor and hinges. Strains in the compressor range from 0.12 to 0.20, suggesting a need for material strengthening. Hinges exhibit strains from 0.12 to 0.27, which could affect door functionality. These findings highlight the need for targeted design improvements in these critical areas.



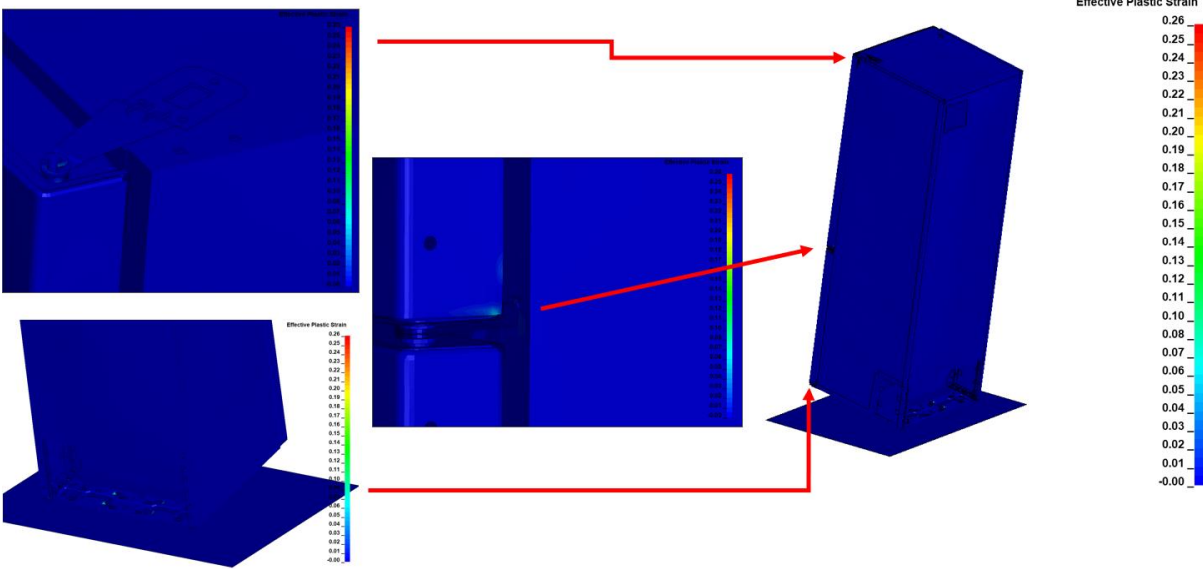


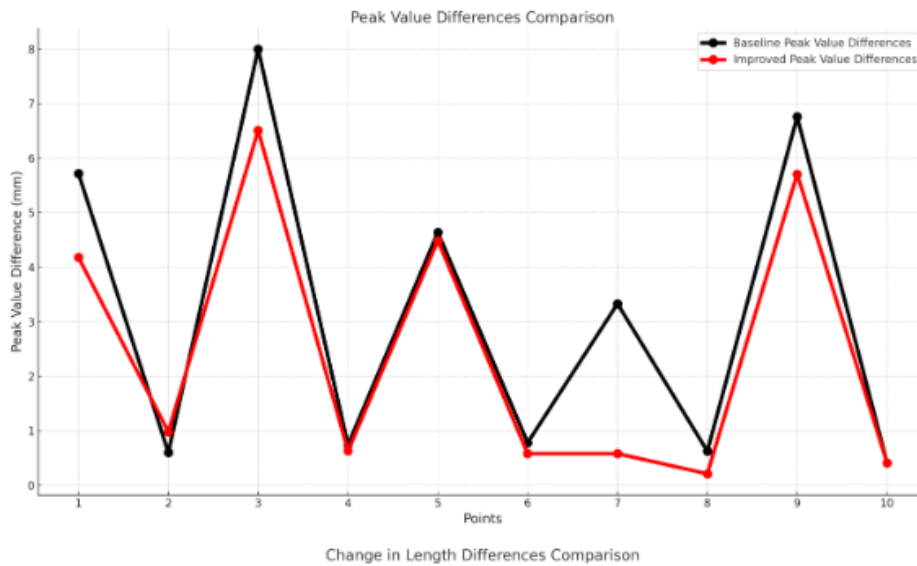
Figure 15. Post-improvement plastic strain results

Table 3. Post-improvements drop test door position measurements (mm)

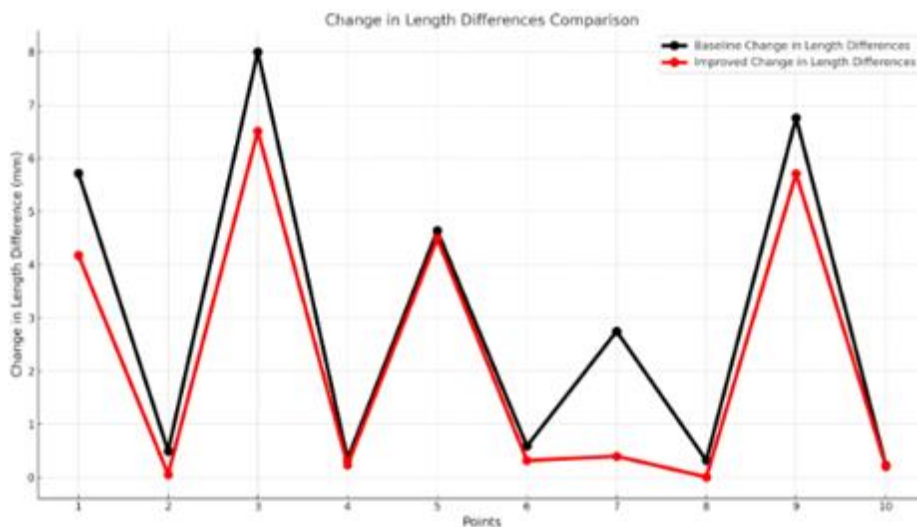
Measurement Points	Baseline Design Theoretical/3D Door Distances	Baseline Door Distances	Distances					
		Before Drop Test	After	After	After	After	After	After
			Drop Test 1	Drop Test 2	Drop Test 3	Drop Test 4	Drop Test 5	Drop Test 6
1	12 mm	12.17	9.15	9.66	9.51	9.86	9.78	9.8
2	12 mm	11.96	11.91	11.93	11.92	11.92	11.94	11.92
3	12 mm	12.08	6.54	6.61	7.13	7.45	7.86	6.23
4	12 mm	11.96	11.7	11.63	11.72	11.69	11.75	11.53
5	12 mm	12.11	8.87	8.13	8.27	7.96	8.12	7.81
6	12 mm	11.94	11.35	11.46	11.21	11.53	11.42	11.79
7	12 mm	12.04	9.9	10.23	9.56	9.67	9.45	9.21
8	12 mm	11.94	11.86	11.9	11.83	11.92	11.89	11.87
9	12 mm	11.86	7.61	8.86	7.71	7.12	6.24	6.73
10	12 mm	11.79	11.78	11.95	11.84	11.82	11.79	11.85

**Table 4.** FEA analysis door distance peak value and change in length measurements

	Baseline Design FEA Measurements (mm)		Post-Improvements Design FEA Measurements (mm)	
	Peak Value	Change in Length	Peak Value	Change in Length
1	-5.72	-5.72	-4.18	-4.18
2	-0.601	-0.5	0.98	-0.06
3	-8	-8	-6.51	-6.51
4	-0.741	-0.35	0.628	0.24
5	-4.64	-4.64	-4.49	-4.49
6	-0.78	-0.59	-0.58	-0.32
7	-3.33	-2.75	-3.17	-2.65
8	-0.624	-0.32	0.21	0.01
9	-6.76	-6.76	-5.71	-5.71
10	-0.411	-0.23	-0.411	-0.21



**Figure 16.** Peak value comparison between baseline FEA results and improved FEA results



**Figure 17.** Change in length comparison between baseline FEA results and improved FEA results

The updated design shows reduced peak deformation:

- Measurement Point 3: Improved from 8 mm to 6.51 mm.
- Measurement Point 5: Enhanced from 4.64 mm to 4.49 mm.
- Measurement Point 9: Reduced from 6.76 mm to 5.71 mm.

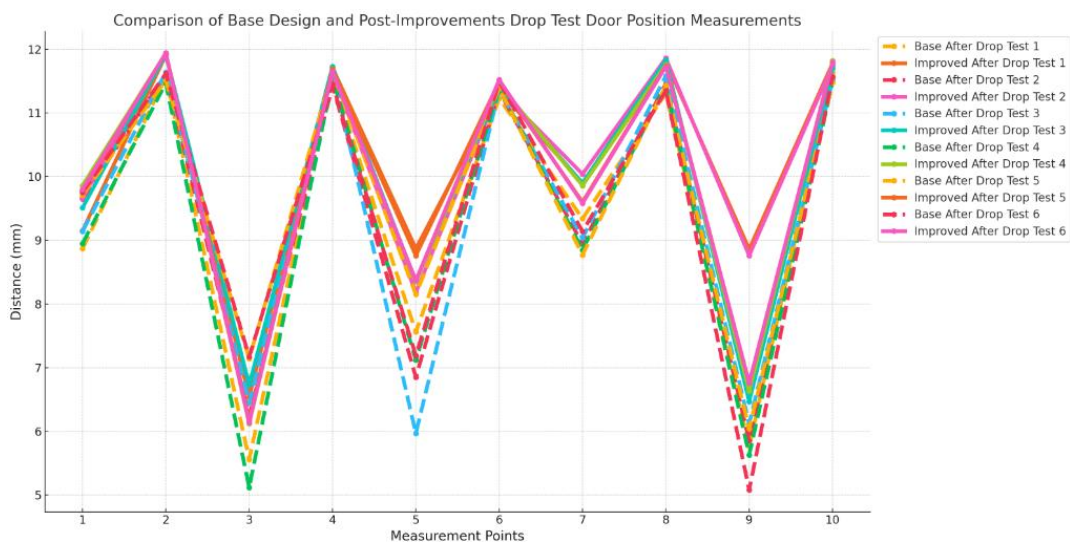
The updated design exhibits minimal length changes, with Measurement Point 2 improving from 0.5 mm to 0.06 mm, reflecting better stability.

### 3.2 Drop Test Results

The original design had differences, from the 12 mm standard at points 3 and 9 suggesting potential structural issues. The enhanced design showcased stability with measurements, to the 12 mm standard:

- Measurement Point 3 had measurements, between 6.12 mm and 6.73 mm.
- Measurement Point 9 ranged from 6.47 mm to 8.86 mm.

The revised layout minimized. Enhanced steadiness when contrasted with the original, displaying effectiveness and resilience, against impact.



**Figure 18.** Baseline design and post-Improved design drop test door distance measurement result comparison in chart



**Figure 19.** Baseline design and post-Improved design drop test door distance measurement average results comparison in chart

## 4 CONCLUSION

The research shows that making changes to the design greatly improves the refrigerator assembly's ability to withstand impact and remain stable. Through FEA simulations and drop tests it has been proven that the new design performs better, showing variations from the distance and lower levels of stress during peak moments. These upgrades guarantee a structure and increased stability when facing impacts bringing the product more in line with design expectations.

FEA and physical tests reveal that the improved design performs better under impact conditions compared to the base design. Initial measurements showed significant deviations, with points 3 and 9 dropping to 5.56 mm and 5.76 mm, respectively. The improved design reduced these deviations to 6.12 mm and 6.47 mm. Stress analysis confirms reduced peak stress values and improved stability, despite some stress concentrations at the hinges, which remain structurally robust.

Future research should focus on:

- EPS Enhancement: Reducing EPS size while maintaining protection.
- Design Refinement: Continual improvements to minimize errors.
- Strain Measurement: Using strain gauges in multiple orientations for detailed data.
- FEA Mesh Refinement: Expanding mesh elements for accuracy.
- Material Testing: Exploring different plastics for better impact resistance.
- Broader Application: Applying methods to various refrigerator models.
- Alternative Criteria: Investigating other failure criteria for plastics.
- Dynamic Observation: Capturing drop tests on camera for comparison with FEA results.

These measures will improve the longevity, robustness, and overall dependability of the product.

## References

- [1] American Society for Testing and Materials, "Standard Test Method for Impact Testing for Shipping Containers and Systems," ASTM D5276, 2019.
- [2] American Society for Testing and Materials, "Standard Test Method for Impact Testing for Shipping Containers and Systems," ASTM D880, 2002.
- [3] American Society for Testing and Materials, "Standard Test Method for Impact Testing for Shipping Containers and Systems," ASTM D4168, 2021.
- [4] D. Neumayer, M. Chatiri, and M. Höermann, "Drop test simulation of a cooker including foam packaging and pre-stressed plastic foil wrapping," in *Simulation Technology, 9th International LS-DYNA Users Conference*, 2006.
- [5] K. Gui and X. Wang, "Design and analysis of cushioning packaging for home appliances," *Procedia Engineering*, vol. 174, pp. 904–909, 2017.
- [6] Y. Liu, F. J. H. G. Kessels, W. D. van Driel, and J. A. S. van Driel, "Comparing drop impact test method using strain gauge measurements," *Microelectronics Reliability*, vol. 49, no. 9, pp. 1299–1303, 2009.
- [7] C. Y. Zhou, T. X. Yu, and S.-W. R. Lee, "Drop/impact tests and analysis of typical portable electronic devices," *International Journal of Mechanical Sciences*, vol. 50, no. 5, pp. 905–917, 2008.
- [8] Y. Y. Wang, C. Lu, J. Li, X. M. Tan, and Y. C. Tse, "Simulation of drop/impact reliability for electronic devices," *Finite Elements in Analysis and Design*, vol. 41, no. 6, pp. 667–680, 2005.
- [9] S. Abrate, *Impact on Composite Structures*. Cambridge University Press, 1998.
- [10] T. Fadji, C. J. Coetzee, T. M. Berry, A. Ambaw, and U. L. Opara, "The efficacy of finite element analysis (FEA) as a design tool for food packaging: A review," *Biosystems Engineering*, vol. 174, no. 1, pp. 20–40, 2018.
- [11] O. Mulkoglu, M. A. Guler, E. Acar, and H. Demirbag, "Drop test simulation and surrogate-based optimization of a dishwasher mechanical structure and its packaging module," *Structural and Multidisciplinary Optimization*, vol. 55, no. 4, pp. 1507–1522, 2017.
- [12] M. Willford, R. Sturt, Y. Huang, I. Almufti, and X. Duan, "Recent advances in non-linear soil-structure interaction analysis using LS-DYNA," in *Workshop on Soil Structure Interaction Knowledge and Effect on the Seismic Assessment of NPPs Structures and Components*, Ottawa, Canada, 2010.
- [13] N. Lengas, S. Johann, D. Kadoke, K. Müller, E. Schlick-Hasper, M. Neitsch, and M. W. Zehn, "Damage assessment of complete, filled fiberboard boxes in regulative vertical impact tests by dropping," *Materials Today Proceedings*, vol. 93, no. 9, 2023.

- [14] G. R. Johnson and W. H. Cook, "A constitutive model and data for metals subjected to large strains, high strain rates and high temperatures," in *7th Int. Symp. on Ballistics*, The Hague, Netherlands, pp. 541–547, 1983.



## Comparative Study of Empirical Expressions for Modulus of Soil Reaction and Pipe Displacement in Soil-Pipe System

Chahrazad Bacha<sup>\*1</sup>, Meriem Zoutat<sup>1</sup>, Mohamed Mekki<sup>1</sup>

<sup>1</sup>Department of Civil Engineering, University of Science and Technology of Oran - Mohamed Boudiaf, Algeria

---

### Abstract

One of the important structures designed for fluid transport is the pipe, a hollow cylinder with a circular cross-section used to convey fluids. Typically, these pipes are arranged in buried networks known as soil-pipe interaction systems. The resilience of these systems under various loads is crucial. In 1867, Winkler introduced a significant coefficient for describing soil-pipe interaction systems: the modulus of soil reaction. This modulus is essential for analysing the structural interaction between soil and pipe, representing how buried pipes respond to loads and providing valuable insights into the soil-pipe interaction system. Over time, researchers have conducted numerous analyses on this modulus of soil reaction, resulting in various empirical expressions documented in the literature. This work aims to present and compare the expressions proposed by Vesic, Meyerhof and Baieke, Kloppel and Glock, Biot, and Selvadurai.

The main goal is to rank these expressions in defining the modulus of soil reaction and, subsequently, to determine their rank in defining the displacement along buried pipes. The comparison based on these empirical equations rank reveals an inverse order in defining pipe displacement compared to defining the modulus of soil reaction.

**Keywords:** *Soil-pipe system, Empirical expressions, Modulus of soil reaction, Pipe displacement*

---



## Nature-Based Solutions for Flood and Water Management in Urban Areas: Global Practices

Emine Keles Ozgenc\*<sup>1</sup>

<sup>1</sup>Department of Landscape Architecture, Trakya University, Edirne, Türkiye

### Abstract

Rapid urbanization and climate change are global issues creating significant social and environmental challenges in urban areas worldwide. Nature-based solutions (NbS), developed to solve these problems and transform cities into sustainable and resilient living spaces, have gained considerable attention in recent years. Using natural ecosystems and processes, NbS strategies aim to provide ecological, economic, and social benefits. These solutions promote ecosystem services, increase resilience to climate change, and improve water management and flood control by integrating natural elements such as green spaces and water bodies. Specifically, in urban flood and water management, NbS reduce flood risks, improve water quality, and support biodiversity by naturally regulating the water cycle. This study examines the potential of NbS against challenges in urban areas. The study also highlights the advantages of successfully implementing NbS and projects worldwide in urban areas.

**Keywords:** *Urbanization, Natural ecosystems, Nature-based solutions, Water management*

## 1 INTRODUCTION

Today, cities face numerous societal challenges due to rapid population growth, climate change, and land use changes. In particular, cities are vulnerable to land use changes driven by the rapidly growing population and the anticipated effects of climate change [1]. Climate change is causing increasingly frequent and severe extreme weather conditions in urban areas. Over half of the world's population currently lives in urban areas, and this proportion is expected to exceed 70% by 2050 [2]. This situation indicates that cities will need to address many issues in the coming decades [3]. In rapidly urbanising areas, a significant proportion of urban development is likely to take place in dense, poor quality and unplanned settlements. These areas are often located in high-risk zones, such as flood plains or steep slopes, exacerbating the effects of climate change. Infrastructure problems, such as inadequate drainage systems and impervious surfaces, exacerbate hazards such as flooding and the urban heat island effect [4]. Therefore, maintaining environmental sustainability and addressing societal challenges in urban areas is becoming increasingly important. The Sustainable Development Goal 11 (SDG11), which aims to "Make cities and human settlements inclusive, safe, resilient, and sustainable", has made urban resilience a critical issue globally [1]. The impact of urbanization, land use, and climate change processes is expected to further increase urban resilience issues over time. Climate change is anticipated to increase the frequency and severity of certain natural hazards, while urbanization is likely to place people and assets in cities at greater risk [4].

Global climate change and rapid land use changes have made water resource management an urgent priority for contemporary cities. According to European Union (EU) reports, the pressure on water resources is increasing, necessitating adopting sustainable approaches in urban water management [5]. Urban drainage systems and water management processes change significantly as cities grow and expand. These changes make water management a critical perspective for adapting to climate change. Flooding in urban areas poses serious risks to communities and negatively impacts cities as one of the most severe climate change-related disasters worldwide [1]. Considering the effects of climate change, it is projected that by 2050, the frequency of current 100-year flood events will at least double globally [6]. Floods disrupt physical infrastructure and affect hydrological processes and associated biotic communities, impacting the flood mitigation functions of natural ecosystems [7]. In this context, green-blue spaces and ecological measures in urban areas have increasingly been adopted as sustainable and effective solutions in water management. Nature-based Solutions (NbS) aim to utilize the natural services of local ecosystems to reduce flood hazards, enhance biodiversity, and improve future climate resilience [6]. Protecting and restoring ecosystems and green-blue spaces in addressing urban challenges is becoming increasingly important. NbS are defined as nature-inspired solutions that provide economic and environmental benefits while addressing various societal challenges [8]. Integrating NbS into urban planning and governance is crucial for creating resilient, healthy, and sustainable cities [1]. NbS are adopted as multifunctional approaches that provide

numerous ecosystem services by restoring degraded ecosystems and reestablishing necessary functions to maintain, sustain, and enhance urban system resilience [3].

In cities, NbS provide effective measures to address various environmental challenges, including mitigating and adapting to climate change, reducing surface runoff, increasing infiltration through permeable surfaces, reducing disaster risk, improving water quality, creating and restoring aquatic biodiversity, supporting ecological coastal management, fostering economic and social development, enhancing human health, and ensuring food and water security [9-11]. This multifunctional and solution-oriented approach significantly contributes to enhancing urban sustainability and resilience. NbS harness nature's power and complexity to transform environmental, social, and economic challenges into innovation opportunities [12]. International policy frameworks, such as the Sustainable Development Goals, the Flood Directive, the Biodiversity Strategy, the Climate Change Adaptation Strategy, and the Green Deal, promote implementing NbS in urban areas [13]. These policies aim to enhance environmental sustainability in cities and offer opportunities for societal well-being and economic development. NbS provide many valuable ecosystem services, such as reducing disaster risks, regulating microclimates, improving human health and promoting socially inclusive green growth. In addition, NbS create synergies by reducing flood and drought risks while improving water quality and availability [5].

This study highlights the role and importance of NbS in achieving sustainability in urban water management. It examines the adverse effects of climate change on cities and the potential of NbS to mitigate these effects, evaluating the steps needed to create sustainable and resilient cities. Additionally, the study discusses practical solutions by reviewing examples and strategies for implementing NbS. In this context, the study aims to develop innovative and effective strategies for achieving sustainable city development, addressing environmental, social, and economic dimensions.

## 2 DEFINITION OF NBS

The concept of NbS was introduced by the World Bank in 2008 to describe approaches that use ecosystem processes rather than technical engineering to address societal challenges. Later, it was adopted by the International Union for Conservation of Nature (IUCN) during its 2013-2016 program, serving as an umbrella term for various ecosystem-based approaches addressing societal challenges [14]. Within this framework, approaches such as Ecosystem-Based Adaptation (EbA), Ecological Disaster Risk Reduction (eco-DRR), Green Infrastructure (GI), Blue-Green Infrastructure (BGI), Water Sensitive Urban Design (WSUD), Sustainable Urban Drainage Systems (SuDS), and Natural Climate Solutions (NCS) are also considered under NbS. Despite their differences, these approaches share a common characteristic of being nature-based compared to gray infrastructure [8].

NbS are based on the understanding that natural and managed ecosystems produce various services dependent on human well-being [8]. NbS are often defined as actions inspired by nature, supported by nature, or modeled after nature [15, 16]. In scientific literature, international reports, and various studies, definitions of NbS have been provided across a broad spectrum (Table 1). These definitions offer a wide framework for conserving, managing, and restoring natural and modified ecosystems while referring to solutions inspired by or supported by nature [14]. The IUCN [17] definition emphasizes the importance of nature conservation and restoration, while the European Commission [18] provides a broader perspective focused on overall sustainability. OECD [8] combines these definitions, describing NbS as "measures that protect, sustainably manage, or restore nature to maintain or enhance ecosystem services to address various social, environmental, and economic challenges." Recently, there has been an emphasis on whether natural processes are actively managed to achieve water-related goals, such as flood and drought reduction, regardless of whether an ecosystem is natural [9]. Both definitions argue that NbS address societal challenges by utilizing ecosystem processes and providing various benefits for nature and people.

**Table 1.** Definitions of NbS

References	Definitions
[17]	"Actions that effectively and adaptively address social challenges while providing benefits for human well-being and biodiversity through the conservation, sustainable management, and restoration of natural and modified ecosystems. They typically offer a wide range of ecosystem conservation and restoration interventions."
[18]	"Actions inspired by, supported by, or copied from nature, aimed at helping communities address various environmental, social, and economic challenges in sustainable ways."
[8]	"Measures that protect, sustainably manage, or restore nature to maintain or enhance ecosystem services to address various social, environmental, and economic challenges."
[19]	"NbS inspired by and supported by nature, using or mimicking natural processes, target secondary benefits such as better water management and adaptation to, mitigation of, and



	resilience to climate change. These solutions optimize ecosystem services natural processes offer and provide social, environmental, and economic benefits.”
[14]	“Actions that aim to address social challenges effectively and coherently while supporting both human well-being and biodiversity, through the conservation, sustainable management, and restoration of natural and modified ecosystems.”
[20]	“Nature-based interventions proposed to address sustainability issues such as resource scarcity, flood and heat risks, and ecosystem degradation caused by urbanization and climate change.”
[1]	“Using biodiversity and ecosystem conservation, enhancement, and restoration as a tool to address multiple concerns simultaneously.”
[21]	“A process aimed at helping communities address various environmental, social, and economic challenges sustainably. In the context of urban and landscape planning, NbS include (i) actions that address well-defined social challenges, (ii) using ecosystem processes of spatial, blue, and green infrastructure networks, and (iii) actions embedded within feasible governance or business models.”
[22]	“A broader definition encompassing the use of nature and how biological diversity can be sustainably protected and used in challenges such as climate change, food security, water resources, or disaster risk management.”
[23]	“A transition to the use of ecosystem services by reducing inputs of non-renewable natural capital and increasing investments in renewable natural processes.”
[16]	“Aims to use various natural features and processes resource-efficient and sustainably. These solutions redefine the role of nature in urban, rural, and natural environments by being adapted to local systems at various spatial scales, providing numerous benefits, and supporting sustainable development and resilience.”

NbS stand out as effective adaptation measures in cities against the impacts of climate change. For example, urban parks can reduce the urban heat island effect, absorb stormwater, provide recreational value, improve air quality, and enhance economic attractiveness [24]. NbS contribute to addressing problems caused by climate change by offering flexibility in adapting to changing conditions. In summary, NbS provide integrated, multifunctional solutions to existing urban and rural issues by promoting the use of nature and natural processes [18, 25].

NbS focus on issues such as reviewing implications for implementation in urban areas, developing solutions in the context of vulnerability to natural disasters, and evaluating the relationships between ecosystem-based adaptation and ecosystem services. Particularly in recent years, a framework has been proposed to enhance climate resilience in urban areas [21]. NbS represent three key innovations: (i) a strong normative focus on developing actionable solutions, (ii) a systematized and concrete perspective, and (iii) the co-creation, development, and implementation of actions through an interdisciplinary approach to mitigate challenges and leverage shared benefits. Therefore, NbS are considered actions that use ecosystem processes to address challenges and are integrated into applicable governance or business models. NbS can address urban challenges, including improving human health and well-being, food security, climate change adaptation and mitigation, sustainable urban development, disaster risk management, and the conservation and enhancement of biodiversity [26]. NbS use green and blue infrastructure and ecosystem processes to ensure the protection or enhancement of ecosystem services. This approach can contribute to alleviating societal challenges while also providing economic, human security, social/cultural, and ecological co-benefits [21].

NbS are based on four fundamental principles: First, the concept that “nature can take many forms” is central. For example, practices like permeable pavements or urban forests are examples of this principle. Second, NbS are characterized by “multifunctionality and solution-orientation”, which involves addressing environmental, social, and economic challenges together. The third principle emphasizes the “necessity of holistic and integrated governance and planning approaches,” highlighting the need to integrate multiple values and disciplines. The fourth principle is the “importance of adapting to place-based conditions”. NbS interact with their surroundings in various ways and address urban challenges through sensitivity to socio-spatial contexts.

### 3 WATER MANAGEMENT AND NBS IN URBAN AREAS

Increasing human pressure and rapid urbanization make cities more vulnerable to natural and climate-related hazards [27]. The extensive coverage of land surfaces and intense urbanization are leading to changes in hydrological regimes, increasing flood risks. These changes are among the most significant driving forces behind alterations in the water cycle [28]. Cities are at high risk from extreme weather events such as floods and urban storms. Therefore, water management has become an increasingly important issue in urban areas. Sustainable urban water management is an approach to urban planning and design that aims to minimize the impacts of

urbanization by supporting natural hydrological processes [29]. NbS can potentially enhance urban resilience and sustainability through locally adapted, resource-efficient, and systematic interventions [30]. By integrating natural elements with engineering approaches, the capacity of NbS to provide ecosystem services offers significant contributions to supporting a sustainable and resilient urban water cycle [31]. In particular, NbS target urban challenges such as climate change, urban heat island effects, water inundation, and impaired health and well-being [30].

NbS encompass a range of urban ecosystem-based approaches, including “urban ecosystem services”, “sponge cities”, “green-blue infrastructure”, “ecological engineering”, and “natural capital” [26]. The ecosystem services provided by NbS play a crucial role in addressing urban challenges. Well-designed NbS can also offer social and economic co-benefits, such as enhancing habitat quality, reducing artificial infrastructure costs, and promoting social engagement and equal access to opportunities. NbS can simultaneously contribute to achieving multiple Sustainable Development Goals, including human well-being and environmental protection.

NbS provide significant opportunities to address various issues related to anthropogenic impacts on the water cycle. These include low water quality, water availability conservation, stormwater management, water treatment, water reclamation, wetland habitat management, soil water management, waste recycling, and enhancing ecological quality [18, 32]. Implementing NbS throughout a city enables the restoration of natural water balance, reduction of peak flows and volumes, and promotion of infiltration, retention, and evaporation. Groundwater replenishment plays a critical role in the drinking water supply in many cities. Creating urban green spaces can facilitate infiltration processes and contribute to groundwater recharge. NbS practices such as afforestation, green space promotion, and green facades can effectively increase evaporation and mitigate the urban heat island effect [31].

A key step towards more sustainable urban water management is to assess and strengthen urban resilience to the water cycle [33]. In this context, NbS have emerged as sustainable solutions for increasing urban resilience. NbS are fundamental to stormwater management when addressing climate change challenges, including conserving or rehabilitating natural ecosystems and enhancing or creating natural processes in modified or artificial ecosystems [31]. Examples of NbS for stormwater management include infiltration basins, green roofs, artificial wetlands, and vegetated swales. Implementing NbS and establishing synergies across different sectors offer various nature-based opportunities for climate change adaptation and mitigation [18]. The European Commission underscores the need for holistic and integrated nature-based strategies to address and adapt to climate change. These strategies should incorporate grey, green, and blue infrastructure, ensuring their applicability across various sectors and challenges. NbS can create synergies that mitigate risks like drought and flooding, aligning with European regulatory objectives. In this context, NbS can significantly enhance urban resilience, particularly in managing stormwater. The regulatory role of NbS on urban surface runoff [34] and their benefits in controlling water pollution [35] have been analyzed. The current global situation encourages experts to build an evidence base to understand NbS contribution to urban resilience.

By 2050, 68% of the global population is projected to live in cities. This situation can lead to flood hazards in areas with inadequate drainage due to heavy rainfall, causing infrastructure systems to overflow and exposing city residents to health risks. The increase in urban population and changes in precipitation patterns due to climate change expose people to greater urban flood risks. Rapid urbanization transforms high-risk floodplains and riverbank areas into residential zones, making cities more vulnerable to flood risks. NbS can help mitigate flood risk by increasing stormwater absorption. NbS are often used with grey infrastructure components, integrated into comprehensive urban development plans, and offer effective solutions. Incorporating NbS into flood management strategies can improve the engineering infrastructure and reduce the stress on the system. These solutions are particularly useful in mitigating the effects of short-term flooding. NbS to reduce the risk of river flooding typically require large-scale efforts and must be carefully planned to meet the needs of affected communities [36]. As seen in Table 2, NbS can be considered an important planning tool in urban areas.

**Table 2.** NbS options in urban areas and their benefits

NbS options	NbS benefits
Urban parks, forests, and street trees	Cooling air temperature
Green buildings	Regulating water flow
Green roofs	Improving water quality
Rewilding abandoned areas	Enhancing noise quality and comfort
Water management (biological swales, retention ponds, rainwater harvesting)	Supporting biodiversity Carbon sequestration

Sustainable urban drainage systems (permeable pavements, etc.)	Rehabilitating degraded areas
Rejuvenated soils	Providing recreational and aesthetic value
Community gardens	Increasing land and property value
Pollinator biodiversity	Improving health and quality of life

In cities, some NbS practices that contribute to reducing flood risk include [36]:

- **Green roofs:** Green roofs on building surfaces, which encourage rainwater infiltration, can potentially reduce rainwater runoff. These roofs can retain between 50% and 100% of rainwater. Many countries promote green roof installations locally. In Canada, new buildings with a gross area larger than 2000 m<sup>2</sup> are required to have green roofs, while Denmark has mandated green roofs for all flat-roofed buildings since 2010. Additionally, cities like New York, San Francisco, and Washington have enacted laws to promote and require green roof usage.
- **Permeable pavements:** Permeable concrete, asphalt, or interlocking pavements that allow rainwater infiltration at the point of contact with the surface effectively reduce rainwater runoff.
- **Bioretention areas:** Bioretention areas, such as rain gardens and bioswales, are vegetated ditches designed to help manage rainwater. These areas can control peak flows and filter pollutants, with the capacity to remove up to 90% of heavy metals from rainwater.
- **Open spaces such as parks and greenways:** Open spaces like parks and greenways can be strategically built or preserved to capture runoff from upstream and surrounding areas. A study in Beijing showed that the city’s green spaces stored 154 million m<sup>3</sup> of rainwater, equivalent to the city’s annual water demand.
- **Constructed wetlands:** Constructed wetlands can capture and retain rainwater, allowing for increased water infiltration. A one-acre wetland can store 3.8 to 5.7 million liters of floodwater and reduce the load on existing rainwater and wastewater systems.
- **Floodplains and bypasses:** Floodplains and bypasses can capture and gradually release excess water and sediment during flood events. Bypasses are constructed diversions designed to manage floodwater volume, whereas floodplains are natural areas that absorb water.
- **Inland wetlands:** Inland wetlands can mitigate flood risk by storing water during periods of heavy rainfall and releasing it during dry spells.
- **Stream beds and banks:** Preserving or restoring natural features like meandering river paths and vegetated banks can help to decelerate river flow.
- **Upland forests:** Upland forests with deep soils have the capacity to slow down and retain surface runoff, resulting in reduced peak flows. Managing forests is an effective strategy for controlling and slowing down moderate short-term floods before the soil becomes saturated.

In addition to helping with urban flood control, NbS provide additional benefits within urban communities. These include reducing the urban heat island effect, lowering air pollution, and offering cool refuges for city residents and wildlife. In particular, green roofs and walls offer opportunities to reduce thermal stress and improve city air quality.

**Table 3.** Using NbS to manage urban flooding and water in different cities

Challenge	City	NbS	Description
Urban flooding	Sri Lanka/Beddagana Wetland Park	Urban green spaces, reservoirs, wetlands	Initiated by the Government of Sri Lanka, this project uses a mix of green and gray infrastructure to reduce flood risk, improve drainage, and provide recreational opportunities in the Colombo metropolitan area. NbS, such as wetland conservation and restoration and the integration of flood parks, are applied alongside traditional approaches like coastal protection walls. These solutions help to slow down the infiltration of rainwater, thus reducing the volume of water that needs to pass through overloaded built systems.
Water quality	United States/Portland, Oregon	Keep stormwater, green streets, permeable pavements, bioswales	Portland, Oregon, uses a combined sewer system that carries stormwater and wastewater through a single pipe. The increased runoff volume from impervious surfaces directly affects water quality and public health. Solutions have been developed to keep rainwater from combined sewer systems and control stormwater using green streets

				and NbS. This includes installing permeable pavements and bioswales, which have resulted in an 80-94% reduction in peak flow in targeted areas.
Urban flooding	China		Sponge cities	Rapid urban population growth, inadequate infrastructure, and the degradation of watercourses have led to severe water issues in China. With 62% of cities exposed to floods, the “sponge cities” NbS solution has been implemented to capture, store, filter, and treat rainwater for reuse. The Chinese government supports this approach with green roofs, permeable pavements, and wetland restorations.
Urban flooding	Sweden/Augustenborg, Malmö		Natural drainage measures	In Sweden, approximately 22 million Euros have been invested in strengthening drainage systems in Augustenborg and Malmö using natural measures. This investment has resulted in a 50% reduction in runoff and a significant increase in biodiversity.
Urban flooding	Portland, Oregon		Rainwater management	An investment of 8 million USD in green streets and tree planting in Portland, Oregon, has saved 250 million USD in rainwater infrastructure costs.
Urban flooding	Canada/Toronto		Green roofs	Local authorities in Toronto, Canada, have encouraged green roofs. In 2009, a regulation mandating green roofs on new buildings with a gross floor area larger than 2,000 m <sup>2</sup> was introduced.
Urban flooding	London/Elizabeth Park	Queen Olympic	Green roofs	London’s Olympic Park has been designed using ecocriticism principles for previously abandoned areas. Green roofs with photovoltaic panels have been implemented to enhance habitat diversity. Compared to other green roofs in London, the park has shown a high diversity of invertebrates. The park covers 560 acres, includes 6.5 km of waterways and 15 acres of woodland, and features over 6,000 new trees.
Urban flooding, Climate change	West Manchester	Gorton Park,	Sponge park, permeable surfaces, rainwater management	NbS have been used in the "sponge park" design process to mitigate and adapt to the potential effects of climate change. Permeable surfaces that filter rainwater for plant nourishment and effective rainwater management have been implemented. The provision of natural vegetation has also supported biodiversity.
Urban flooding	Vuores Tampere/Finland	Central Park,	Bioswales, retention ponds, wetlands, willow treatment, alluvial meadows biofiltration system	The park has developed effective flood mitigation measures through aesthetically pleasing blue-green spaces, green corridors, and alluvial meadows for recreation. Additionally, solutions have been developed to improve rainwater management and enhance water quality specific to the area.

Implementing NbS in various countries has facilitated the integration of natural system processes into human environments, thereby enhancing ecosystem services in urban areas. For example, a well-managed forest can provide multiple ecosystem services, including regulatory, supportive, and cultural benefits. In addition to positive effects such as increased resilience to climate change and enhanced biodiversity, NbS develop a process that underpins sustainability in urban and rural areas. In particular, it offers opportunities to improve and sustain human livability for current and future urban generations [37].

## 4 CONCLUSION

Integrating NbS into urban environments has proven to be a pivotal approach in enhancing ecosystem services and fostering sustainable development. By incorporating natural processes into urban planning, cities can mitigate the effects of climate change, improve biodiversity, and offer many ecosystem services such as regulatory, supportive,

and cultural benefits. Implementing NbS, such as green roofs, permeable pavements, bioretention areas, and constructed wetlands, has demonstrated significant potential in addressing urban challenges, including flood risk reduction, water management, and improving air quality. In addition to environmental benefits, NbS contribute to social and economic advantages, such as enhanced recreational and aesthetic values and improved public health and well-being. The successful examples from various cities worldwide underscore the effectiveness of NbS in creating resilient and livable urban spaces. As cities continue to grow and face the impacts of rapid urbanization and climate change, adopting NbS offers a sustainable pathway to harmonize urban development with natural processes, ensuring the well-being of current and future generations. In conclusion, NbS address immediate urban challenges and pave the way for a holistic and integrated approach to urban resilience and sustainability. By leveraging the benefits of natural ecosystems, cities can create environments resilient to climate impacts and vibrant, healthy, and inclusive for all residents. The widespread adoption and implementation of NbS are crucial to achieving sustainable urban development and fostering a harmonious relationship between human activities and natural systems.

## References

- [1] N. Kabisch *et al.*, “Nature-based solutions to climate change mitigation and adaptation in urban areas: perspectives on indicators, knowledge gaps, barriers, and opportunities for action,” *Ecology and society*, vol. 21, no. 2, 2016.
- [2] B. Wijesiri, A. Liu, and A. Goonetilleke, “Impact of global warming on urban stormwater quality: From the perspective of an alternative water resource,” *Journal of Cleaner Production*, vol. 262, art. no. 121330, 2020, doi: 10.1016/j.jclepro.2020.121330.
- [3] S. Bona, A. Silva-Afonso, R. Gomes, R. Matos, and F. Rodrigues, “Nature-based solutions in urban areas: a European analysis,” *Applied Sciences*, vol. 13, no. 1, art. no. 168, 2022, doi: 10.3390/app13010168.
- [4] World Bank, “A catalogue of nature-based solutions for urban resilience,” World Bank, 2021.
- [5] S. Bona, F. Rodrigues, R. Gomes, and A. Silva-Afonso, “Nature-based solutions for water resilience in thriving European urban areas,” *Urban Water Journal*, pp. 1–14, 2024, doi: 10.1080/1573062X.2024.2359661.
- [6] K. Zhou *et al.*, “Urban flood risk management needs nature-based solutions: a coupled social-ecological system perspective,” *NPJ Urban Sustainability*, vol. 4, no. 1, art. no. 25, 2024, doi: 10.1038/s42949-024-00162-z.
- [7] M. Hemmati, K. Kornhuber, and A. Kruczkiewicz, “Enhanced urban adaptation efforts needed to counter rising extreme rainfall risks,” *NPJ Urban Sustainability*, vol. 2, no. 1, art. no. 16, 2022.
- [8] OECD, “Nature-Based Solutions for Adapting to Water-Related Climate Risks-Policy Perspectives,” ed: Organization for Economic Cooperation and Development Paris, France, 2020.
- [9] M. Lalonde, F. Drenkhan, P. Rau, J. R. Baiker, and W. Buytaert, “Scientific evidence of the hydrological impacts of nature-based solutions at the catchment scale,” *Wiley Interdisciplinary Reviews: Water*, art. no. e1744, 2024.
- [10] A. M. Vega Sánchez and L. M. Mejía, “Soluciones basadas en la naturaleza para la mitigación y la adaptación al cambio climático en ciudades de América Latina,” 2023.
- [11] Y. Recalde, L. A. Popartan, and I. Rodriguez-Roda, “Nature-based solutions for water management: Analysis of the Andean context,” *Blue-Green Systems*, vol. 6, no. 1, pp. 153–168, 2024.
- [12] S. Moosavi, G. R. Browne, and J. Bush, “Perceptions of nature-based solutions for Urban Water challenges: Insights from Australian researchers and practitioners,” *Urban Forestry & Urban Greening*, vol. 57, art. no. 126937, 2021, doi: 10.1016/j.ufug.2020.126937.
- [13] Z. Kalantari, C. S. S. Ferreira, H. Pan, and P. Pereira, “Nature-based solutions to global environmental challenges,” vol. 880, ed: Elsevier, 2023, art. no. 163227.
- [14] E. Cohen-Shacham, G. Walters, C. Janzen, and S. Maginnis, “Nature-based solutions to address global societal challenges,” *IUCN: Gland, Switzerland*, vol. 97, pp. 2016–2036, 2016, doi: 10.2305/IUCN.CH.2016.13.en.
- [15] E. Cohen-Shacham *et al.*, “Core principles for successfully implementing and upscaling Nature-based Solutions,” *Environmental Science & Policy*, vol. 98, pp. 20–29, 2019, doi: 10.1016/j.envsci.2019.04.014.
- [16] D. Kolokotsa, A. A. Lilli, M. A. Lilli, and N. P. Nikolaidis, “On the impact of nature-based solutions on citizens’ health & well being,” *Energy and buildings*, vol. 229, art. no. 110527, 2020, doi: 10.1016/j.enbuild.2020.110527.
- [17] IUCN, “Global standard for nature-based solutions. A user-friendly framework for the verification, design and scaling up of NbS,” Gland, Switzerland, 2020.
- [18] European Commission, “Towards an EU research and innovation policy agenda for nature-based solutions & re-naturing cities: Final report of the horizon 2020 expert group on nature-based solutions and re-naturing cities,” 2015.

- [19] WWAP, “UN world water development report, nature-based solutions for water,” 2018.
- [20] H. Dorst, A. Van der Jagt, R. Raven, and H. Runhaar, “Urban greening through nature-based solutions—Key characteristics of an emerging concept,” *Sustainable Cities and Society*, vol. 49, art. no. 101620, 2019.
- [21] C. Albert *et al.*, “Addressing societal challenges through nature-based solutions: How can landscape planning and governance research contribute?,” *Landscape and urban planning*, vol. 182, pp. 12–21, 2019, doi: 10.1016/j.landurbplan.2018.10.003.
- [22] E. Balian, H. Eggermont, and X. Le Roux, “Outputs of the strategic foresight workshop “nature-based solutions in a BiodivERsA context”,” in *Brussels: BiodivERsA Workshop Report*, 2014: BiodivERsA Brussels, Belgium.
- [23] J. Maes and S. Jacobs, “Nature-based solutions for Europe's sustainable development,” *Conservation letters*, vol. 10, no. 1, pp. 121–124, 2017.
- [24] K. Brown and A. Mijic, “Integrating green and blue spaces into our cities: Making it happen,” *Grantham Institute, London*, 2019.
- [25] A. Dumitru and L. Wendling, “Evaluating the impact of nature-based solutions: A handbook for practitioners,” 2021.
- [26] N. Kabisch, N. Frantzeskaki, and R. Hansen, “Principles for urban nature-based solutions,” *Ambio*, vol. 51, no. 6, pp. 1388–1401, 2022, doi: 10.1007/s13280-021-01685-w.
- [27] J. Marsalek, *Urban water cycle processes and interactions: urban water series-UNESCO-IHP*. CRC press, 2014.
- [28] C. S. Ferreira, A. C. Duarte, M. Kasanin-Grubin, M. Kapovic-Solomun, and Z. Kalantari, “Hydrological challenges in urban areas,” in *Advances in Chemical Pollution, Environmental Management and Protection*, vol. 8, no. 1: Elsevier, 2022, pp. 47–67.
- [29] M. Disse, T. Johnson, J. Leandro, and T. Hartmann, “Exploring the relation between flood risk management and flood resilience,” *Water Security*, vol. 9, p. 100059, 2020.
- [30] J. B. Almenar *et al.*, “Nexus between nature-based solutions, ecosystem services and urban challenges,” *Land use policy*, vol. 100, art. no. 104898, 2021, doi: 10.1016/j.landusepol.2020.104898
- [31] H. V. Oral *et al.*, “Management of urban waters with nature-based solutions in circular cities—Exemplified through seven urban circularity challenges,” *Water*, vol. 13, no. 23, art. no. 3334, 2021.
- [32] N. Frantzeskaki *et al.*, “Nature-based solutions for urban climate change adaptation: linking science, policy, and practice communities for evidence-based decision-making,” *BioScience*, vol. 69, no. 6, pp. 455–466, 2019.
- [33] K. Diao, C. Sweetapple, R. Farmani, G. Fu, S. Ward, and D. Butler, “Global resilience analysis of water distribution systems,” *Water Research*, vol. 106, pp. 383–393, 2016.
- [34] T. Zölch, J. Maderspacher, C. Wamsler, and S. Pauleit, “Using green infrastructure for urban climate-proofing: An evaluation of heat mitigation measures at the micro-scale,” *Urban Forestry & Urban Greening*, vol. 20, pp. 305–316, 2016.
- [35] C. Liqueste, A. Udias, G. Conte, B. Grizzetti, and F. Masi, “Integrated valuation of a nature-based solution for water pollution control. Highlighting hidden benefits,” *Ecosystem Services*, vol. 22, pp. 392–401, 2016.
- [36] S. Ozment, G. Ellison, and B. Jongman, “Nature-based solutions for disaster risk management: Booklet,” 2018.
- [37] EC, “Evaluating the impact of nature-based solutions: a handbook for practitioners,” ed: Publications Office of the European Union Luxembourg, Luxembourg, 2021.



## Differential Geometry & Natural Metrics

Chaoui Saadia<sup>\*1</sup>

<sup>1</sup>*Department of Mathematic, University of Relizane, Relizane, Algeria*

---

### Abstract

The bundle tangent to a manifold plays a key role in differential geometry. It becomes a space Riemannian more interesting when equipped with the Sasaki metric (the base manifold being assumed Riemannian). However, although it is "naturally" defined from the base metric, Sasaki's metric presents an extreme rigidity" with respect to the basic metric; this has been made natural the introduction of other Riemannian metrics on the tangent bundle (the Cheeger-Gromoll metric in is an example).

In this work, we introduce the geometry of tangent bundles in particular "the natural metrics on the tangent bundle". Our work aims the study of the more general class of natural metrics on the tangent bundle. This made it possible, among other things, to highlight the properties of heredity of these metrics, an extreme rigidity of the elements of a subclass of these metrics and to obtain structures interesting geometries on the tangent bundle endowed with a natural metric of a certain type.

**Keywords:** *Differential geomrtry, natural metrics, Tangent bundle, Levi-civita connexion, Riemannian curvature tensor*

---



## **New Conjugate Gradient Method Using SWP Line search for Nonlinear Unconstrained Optimization**

**Souli Choubeila<sup>\*1</sup>, Ziadi Raouf<sup>1</sup>**

<sup>1</sup>*Department of Mathematics, University Ferhat Abbas setif1, Setif, Algeria*

---

### **Abstract**

This paper introduces a novel hybrid conjugate gradient method for addressing nonlinear unconstrained optimization problems. Notably the proposed algorithm guarantees a sufficient descent condition without necessitating any line search, while also demonstrating global convergence under both usual and strong wolfe line search assumptions. The effectiveness of the algorithm is validated through numerical experiments on a set of 100 test function. The comparison with seven existing methods shows that the proposed method is promising and effective.

**Keywords:** *Unconstrained optimizations, Hybrid conjugate gradient, Global convergence, Image restoration*

---





## A Stochastic BFGS Algorithm for Bound-Constrained Global Optimization

Raouf Ziadi\*<sup>1</sup>, Bencherif Madani Abdellatif<sup>1</sup>

<sup>1</sup>Laboratory of Fundamental and Numerical Mathematics (LMFN), Department of Mathematics, University Ferhat Abbas Setif 1, Setif, Algeria

---

### Abstract

This work presents a stochastic modification of a limited memory BFGS method to solve bound-constrained global minimization problems with a differentiable cost function with no further smoothness. The approach is a stochastic descent method where the deterministic sequence, generated by a limited memory BFGS method, is replaced by a sequence of random variables. To enhance the performance of the proposed algorithm and make sure the perturbations lie within the feasible domain, we have developed a novel perturbation technique based on truncating a multivariate double exponential distribution to deal with bound-constrained problems; the theoretical study and the simulation of the developed truncated distribution are also presented.

Theoretical results ensure that the proposed method converges almost surely to the global minimum. The performance of the algorithm is demonstrated through numerical experiments on some typical test functions as well as on some further engineering problems. The numerical comparisons with stochastic and meta-heuristic methods indicate that the suggested algorithm is promising.

**Keywords:** *Global optimization, Limited memory BFGS method, Stochastic perturbation, Truncated multivariate double exponential distribution*

---



## Characterizations of Weighted Triebel-Lizorkin Spaces Associated with Hermite Operators

Chichoune Romai<sup>1</sup>, Saibi Khedoudj<sup>2</sup>, Mokhtari Zouhir<sup>1</sup>

<sup>1</sup>Department of Mathematics, University of Batna2, Batna, Algeria

<sup>2</sup>Department of Mathematics, University of Zhejiang Normal, China

---

### Abstract

Let  $H = -\Delta + |x|^2$  be the Hermite operator on the Euclidean space  $\mathbb{R}^n$ . The purpose of this article is to explore the weighted Triebel-Lizorkin spaces associated with the Hermite operator. Moreover, we establish the molecular decomposition of our spaces.

**Keywords:** *Weighted Triebel-Lizorkin, Hermite operator, Molecular decomposition, Dyadic cube*

---



## On a Sojourn Time Formula and Applications in Engineering and Simulation

Abdelatif Bencherif Madani<sup>\*1</sup>

<sup>1</sup>*Ferhat Abbas University Setif 1, Algeria*

---

### Abstract

We present a Markovian model technique for calculating sojourn times. Let  $X$  be a real standard Markov process, e.g. an SDE with Lipschitz coefficients. For a regular point  $x_0$  in the state space  $E$ , let  $L(t, x_0)$  be the local time (at  $x_0$ ), i.e. loosely speaking the time spent in  $x_0$  up to  $t$ . The right-continuous inverse local time  $L^{-1}$ , i.e.  $L^{-1}(\tau) = \inf\{t: L(t, x_0) > \tau\}$ , is a subordinator, i.e. an increasing Lévy process. Let  $n, k$  be integers,  $\tau > 0$  and  $N(n, \tau)$  be the number of dyadic intervals  $I_{n,k}$  of length  $2^{-n}$ ,  $k \geq 0$ , that intersect the range  $S([0, \tau])$ , i.e. this is box counting for the range. We study normalizing factors  $H(n)$  s.t. the box counting functional  $N(n, \tau)/H(n)$  converges to  $c \tau$  as  $n \rightarrow \infty$  a.s. where  $c$  is some constant. In the author's joint paper 3 below a condition (which is fairly general but rather difficult to check in practice) was given under which that strong law holds. Our aim is to give a mainstream self-contained and unified treatment of the (essentially) regularly varying Lévy measure densities and this turns out to be quicker dealt with than checking the conditions A1, A2 and B in that paper. We shall proceed directly using basic results of Karamata's regular variation theory and related results. A corollary of this result concerns sojourn times  $S(t, B)$  in Borel subsets  $B$  of the state space. Direct applications include e.g. efficient Monte Carlo simulations in engineering.

**Keywords:** *Sojourn time, Application*

---



---

## Magnetized $\text{Fe}_3\text{O}_4/\text{CoFe}_2\text{O}_4$ Hybrid Ferrofluid with Magnetic Field-Dependent Viscosity over a Slip-Stretching Sheet

Nur Ilyana Kamis<sup>1</sup>, Noraihan Afiqah Rawi<sup>\*1</sup>, Lim Yeou Jiann<sup>1</sup>, Sharidan Shafie<sup>1</sup>

<sup>1</sup>Department of Mathematical Sciences, Faculty of Science, University Teknologi Malaysia, 81310 Johor Bahru, Johor, Malaysia

---

### Abstract

The purpose of the present study is to investigate the behavior of  $\text{Fe}_3\text{O}_4/\text{CoFe}_2\text{O}_4$ , mixed with ethylene glycol and water, which is called a hybrid ferrofluid, on a slip-stretching sheet. Hybrid ferrofluids have unique thermal and magnetic properties that make them valuable in biomedical applications. This fluid can be precisely guided to targeted regions with the assistance of external magnetic fields, enhancing drug delivery especially in cancer treatment. The problem is modeled with partial differential equations, which are reduced to ordinary differential equations by employing appropriate similarity variables. The numerical results are attained through the MATLAB solver *bvp4c*. The velocity of the hybrid ferrofluid decreases with the increase in slip velocity and magnetohydrodynamic (MHD) effects. However, the slip velocity enhances the thermal boundary layer of the fluid. A similar trend in temperature is also observed with the MHD parameters. It is found that the magnetic field-dependent viscosity (MFDV) parameter enhances both the velocity and temperature fields. These findings indicate that slip velocity, MHD, and MFDV may facilitate the transport of drug-containing ferrite nanoparticles.

**Keywords:** Hybrid ferrofluid, MFDV, Slip velocity, MHD, *bvp4c*

---



---

# An Efficient Numerical Approach for Fractional Integro-Differential Equations of Fredholm Type

Nouria Arar<sup>\*1</sup>, Zineb Laouar<sup>2,3</sup>

<sup>1</sup>Department of Mathematics, University Constantine 1, Mentouri Brothers, Constantine, Algeria

<sup>2</sup>Laboratory of Applied Mathematics and Didactics, Higher Normal School, Constantine, Algeria

<sup>3</sup>Abdelhafid Boussouf University Center, Mila, Algeria

---

## Abstract

In this study, we develop a collocation method to solve fractional integro-differential equations of Fredholm type using generalized Lucas polynomials. The fractional derivative is handled in the Caputo sense. We employ the operational matrix for the fractional derivative of the generalized Lucas polynomials in conjunction with the collocation method to transform the problem into a system of algebraic equations. Finally, several numerical examples are presented to validate and support the theoretical findings.

**Keywords:** Fractional integro-differential equations, Caputo derivative, Collocation method, Numerical simulation

---

## 1 INTRODUCTION

The resolution of fractional differential and integro-differential equations is a significant research area due to their applications in science and engineering [1, 2]. Fredholm-type fractional equations present unique challenges due to their complexity and the inclusion of fractional derivatives and integrals.

Various numerical methods have been developed to solve complex fractional integro-differential equations. Techniques like the operational Tau approximation [3], least squares with Chebyshev polynomials [4, 5], Haar wavelets, the Chebyshev wavelet method, and approach for linear and multivariable order equations [6–8]. Generalized Lucas polynomials [9] and the spectral collocation method with shifted Legendre polynomials [10], while another study focuses on Volterra-Fredholm equations using third-kind Chebyshev polynomials [11].

In this study, we develop a numerical approach for solving fractional Fredholm-type integro-differential equations using generalized Lucas polynomials (GLPs). By leveraging the operational matrix for the fractional derivative in conjunction with the collocation method, we transform the problem as a set of algebraic equations.

The article is organized as follows: Section 2 covers preliminaries on fractional calculus and the properties of generalized Lucas polynomials. Section 3 details the development of the suggested approach. Section 4 presents examples from the literature to demonstrate the method's effectiveness, comparing our results with existing ones. Finally, the paper concludes with a general conclusion.

## 2 PRELIMINARIES

This section explains the basics of fractional calculus and explores key properties of the GLPs.

### 2.1 Fractional Caputo derivative and properties

In this section, we outline the definition and properties of fractional derivative theory utilized within this work. For a comprehensive understanding, readers are encouraged to refer to [2].

**Definition 2.1** Let  $\nu > 0$ ,  $r \in \mathbb{N}$  the smallest integer greater than  $\nu$  and a function  $u \in L_1[0,1]$ . The Caputo derivative of fractional order  $\nu$  is defined by

$${}^c D^\nu u(x) = \begin{cases} \frac{1}{\Gamma(r-\nu)} \int_0^x (x-s)^{r-\nu-1} u^{(r)}(s) ds, & x > 0, \quad r-1 < \nu < r, \\ \frac{d^r u(x)}{dx^r}, & \nu = r. \end{cases}$$

The properties are as follows

- ${}^c D^\nu C = 0$ ;  $C$  is a constant.
- Let  $[v]$  represent the integer part of  $v$ , and let  $\mathbb{N}_0 = 0, 1, 2, \dots$ . Then, we obtain

$${}^c D^\nu x^\gamma = \begin{cases} 0, & \gamma \in \mathbb{N}_0, \gamma < [\alpha], \\ \frac{\Gamma(\gamma+1)}{\Gamma(\gamma+1-\nu)} x^{\gamma-\nu}, & \gamma \in \mathbb{N}_0, \gamma \geq [v]. \end{cases}$$

- Caputo fractional differentiation is a linear operation
- ${}^c D^\nu (\lambda u + \theta v)(x) = \lambda {}^c D^\nu u(x) + \theta {}^c D^\nu v(x), \quad \forall \lambda, \theta \in \mathbb{R}$ .

### 2.2 Essential Properties and Relations of GLPs

GLPs, denoted as  $\mathcal{L}_j^{\alpha,\beta}(x)$  for nonzero constants  $\alpha$  and  $\beta$ , extend classical Lucas polynomials and are defined over  $[0, 1]$ . They are valuable in mathematical physics, and for solving differential and difference equations, offering versatile applications and enhancing mathematical analysis. GLPs are generated by the relation:

$$\begin{cases} \mathcal{L}_j^{\alpha,\beta}(x) = \alpha x \mathcal{L}_{j-1}^{\alpha,\beta}(x) + \beta \mathcal{L}_{j-2}^{\alpha,\beta}(x), & j \geq 2, \\ \mathcal{L}_0^{\alpha,\beta}(x) = 2, \quad \text{and} \quad \mathcal{L}_1^{\alpha,\beta}(x) = \alpha x \end{cases} \quad (1)$$

The first GLPs are given by:

$$\mathcal{L}_0^{\alpha,\beta}(x) = 2, \quad \mathcal{L}_1^{\alpha,\beta}(x) = \alpha x, \quad \mathcal{L}_2^{\alpha,\beta}(x) = \alpha^2 x^2 + 2\beta, \quad \mathcal{L}_3^{\alpha,\beta}(x) = \alpha^3 x^3 + 3\alpha\beta x.$$

Lucas polynomials can be derived from the GLPs  $\mathcal{L}_j^{\alpha,\beta}(x)$  by setting  $\alpha = \beta = 1$ . Furthermore, several other polynomials can be derived as particular instances of  $\mathcal{L}_j^{\alpha,\beta}(x)$ . Specifically:

- The Pell-Lucas polynomials arise when  $\alpha = 2$  and  $\beta = 1$ ,
- The Fermat-Lucas polynomials emerge for  $\alpha = 3$  and  $\beta = -2$ ,
- The first-kind Chebyshev polynomials manifest when  $\alpha = 1$  and  $\beta = -0.5$ .
- The first kind Dickson polynomials for  $\alpha = 1$  and  $\beta = -v$ .

Let  $u(x)$  be a square-integrable function on  $(0, 1)$  in the Lebesgue sense, and suppose it can be represented as a sum of linearly independent GLPs, given by:

$$u(x) = \sum_{r=0}^{\infty} \mu_r \mathcal{L}_r^{\alpha,\beta}(x).$$

Suppose that  $u(x)$  can be expressed as

$$u(x) \approx u_N(x) = \sum_{r=0}^N \mu_r \mathcal{L}_r^{\alpha,\beta}(x) = U^T \mathcal{L}(x), \quad (2)$$

where

$$U^T = (\mu_0, \mu_1, \dots, \mu_N), \quad \text{and} \quad \mathcal{L}(x) = (\mathcal{L}_0^{\alpha,\beta}(x), \mathcal{L}_1^{\alpha,\beta}(x), \dots, \mathcal{L}_N^{\alpha,\beta}(x))^T. \quad (3)$$

For the successive derivatives of the GLP vector  $\mathcal{L}(x)$ , we consider the following relation for all  $v > 0$ :

$${}^c D^\nu \mathcal{L}(x) = x^{-\nu} \mathbf{D}^\nu \mathcal{L}(x) \quad (4)$$

where  $\mathbf{D}^\nu = (d^\nu)$  and  $d_{ij}^\nu$  are explicitly defined as

$$d_{ij}^\nu = \begin{cases} \omega_\nu(i, j), & \text{for } i \geq [\nu], \quad i \geq j \\ 0, & \text{otherwise.} \end{cases}$$

Here,  $[\nu]$  represents the smallest integer greater than or equal to  $\nu$ , and

$$\omega_\nu(i, j) = \sum_{k=[\nu]}^i \frac{i \rho_j \zeta_{i+k} \zeta_{j+k} (-1)^{\frac{k-j}{2}} \beta^{\frac{i-j}{2}} \Gamma(k+1) \Gamma(\frac{i+k}{2})}{\Gamma(\frac{i-k}{2}+1) \Gamma(\frac{k-j}{2}+1) \Gamma(\frac{j+k}{2}+1) \Gamma(1+k-\nu)} \quad (5)$$

where  $\rho_j$  and  $\zeta_\ell$  are defined respectively by:

$$\rho_j = \begin{cases} 0.5, & \text{if } j = 0 \\ 1, & \text{if } j \geq 1 \end{cases} \quad \text{and} \quad \zeta_\ell = \begin{cases} 1, & \text{if } \ell \text{ is even} \\ 0, & \text{if } \ell \text{ is odd} \end{cases} \quad (6)$$

### 3 OVERVIEW OF THE PROPOSED METHODOLOGY AND NUMERICAL FRAMEWORK

Consider the following linear fractional integro-differential equation in  $L^2(0,1)$ .

$${}^c D^{\nu_q} u(x) + \sum_{i=1}^{q-1} \lambda_i(x) {}^c D^{\nu_i} u(x) + \mu(x) u(x) = f(x) + \int_0^1 W(x, \tau) u(\tau) d\tau, \quad x \in [0,1] \quad (7)$$

where  $\nu_i < \nu_{i+1}$  and  $i < \nu_i \leq i + 1$ ,  $i = 1, 2, \dots, q - 1$ , with the initial conditions:

$$u^{(i)}(0) = c_i, \quad i = 0, 1, \dots, q - 1 \quad (8)$$

where  $\lambda_i(x)$ ,  $\mu(x)$ ,  $f(x)$  are known continuous functions, and  $W$  is the integral kernel. The primary idea is to assume that  $u(x)$  can be approximated by formula (2). By replacing  $u(x)$  in the equation (7) by its approximation  $u_N(x)$ , leads to

$$U^T (x^{-\nu_q} \mathbf{D}^{\nu_q} \mathcal{L}(x) + \sum_{i=1}^{q-1} \lambda_i(x) x^{-\nu_i} \mathbf{D}^{\nu_i} \mathcal{L}(x) + \mu(x) \mathcal{L}(x) - \int_0^1 W(x, \tau) \mathcal{L}^{\alpha, \beta}(\tau) d\tau) \approx f(x) \quad (9)$$

with the initial conditions

$$U^T \mathbf{D}^i \mathcal{L}(0) = c_i, \quad i = 0, 1, \dots, q - 1. \quad (10)$$

So the residual  $R(x, U)$  of equation (9) is given by:

$$R(x, U) = U^T (x^{-\nu_q} \mathbf{D}^{\nu_q} \mathcal{L}(x) + \sum_{i=1}^{q-1} \lambda_i(x) x^{-\nu_i} \mathbf{D}^{\nu_i} \mathcal{L}(x) + \mu(x) \mathcal{L}(x) - \int_0^1 W(x, \tau) \mathcal{L}^{\alpha, \beta}(\tau) d\tau) - f(x)$$

To find the coefficients of the vector  $U$ , we propose a spectral approach based on the collocation method. The collocation points for this method are chosen, according to the following formula:

$$x_p = \frac{p}{N + 1}, \quad p = 1, 2, \dots, N - q + 1$$

By replacing  $x$  with  $x_p$  in the residual  $R(x, U)$ , enforcing it to vanish at interior points  $x_p$ , and considering the initial conditions (10), we obtain the system :

$$\begin{cases} R(x_p, U) = 0, & p = 1, 2, \dots, N - q + 1 \\ U^T \mathbf{D}^i \mathcal{L}(0) = c_i, & i = 0, 1, \dots, q - 1 \end{cases} \quad (11)$$

The solution of this system can be determined using the Gauss elimination method.

### 4 NUMERICAL ILLUSTRATIONS

In this section, we provide some examples to demonstrate the effectiveness of our method. We aim to compare the approximate solutions obtained with those from the existing literature and the exact solution  $u(\kappa)$ . To facilitate this comparison, we define the absolute error as

$$\mathcal{E}(\kappa) = |u(\kappa) - u_N(\kappa)|,$$

and the maximum absolute error as

$$\mathcal{E}_{max} = \max|u(\kappa) - u_N(\kappa)| \quad \kappa \in [0,1].$$

**Example 4.1** [12] Let's consider the following fractional Fredholm integro-differential equation

$${}^c D^\nu u(\kappa) = \frac{86}{1155} + \frac{75\sqrt{\pi}\kappa^2}{16} - \frac{1575\sqrt{\pi}\kappa^4}{64} + \frac{3003\sqrt{\pi}\kappa^6}{128} + \int_0^1 u(\tau)d\tau, \tag{12}$$

with the initial condition  $u(0) = 0$ . The exact solution for  $\nu = 0.5$  is given by

$$u(\kappa) = 16\kappa^{\frac{13}{2}} - 20\kappa^{\frac{9}{2}} + 5\kappa^{\frac{5}{2}}.$$

Table 1 demonstrates that with  $\alpha = \beta = 1$  and  $N = 10$ , the approximate solution values closely align with the exact solution as  $\kappa$  varies across  $[0,1]$ , especially at  $\nu = 0.5$ , confirming convergence. Table 2 shows that error values decrease as  $N$  increases for various values of  $(\alpha, \beta)$ . The smallest absolute error occurs when  $\alpha = \beta = 1$ , indicating that Lucas polynomials outperform other polynomials. Figure 1 further illustrates this convergence, showing that the approximate solution approaches the exact solution as  $\nu$  nears 0.5 from both higher and lower values.

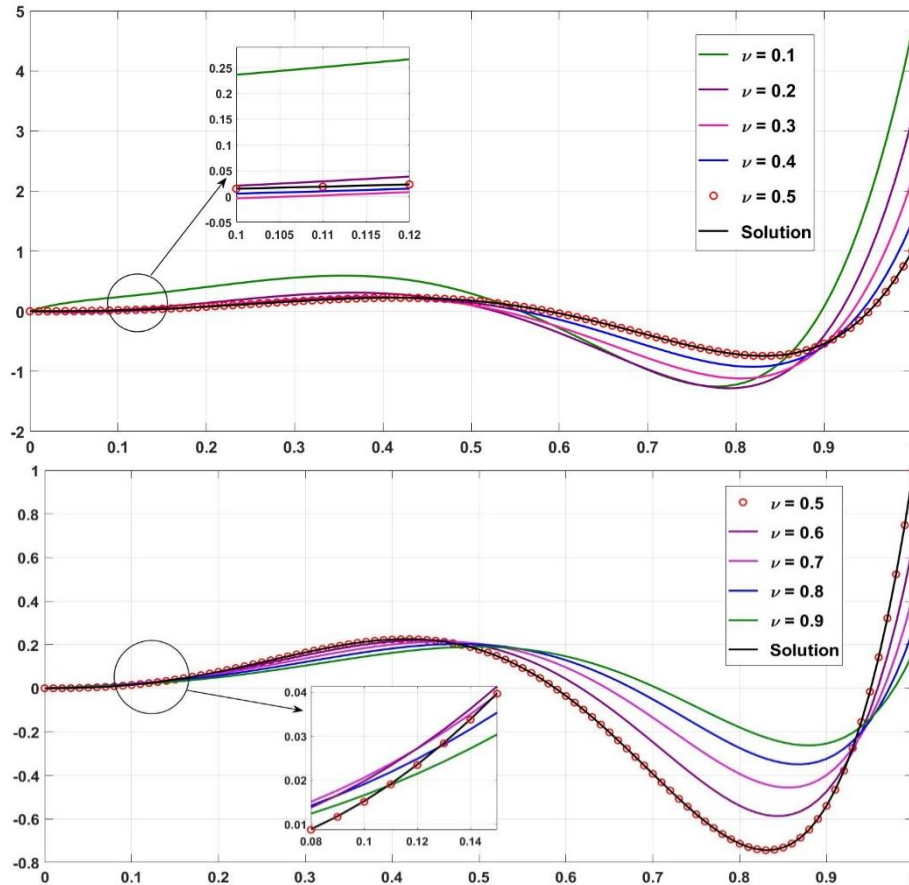
**Table 1.** Approximate values of the solution for  $\alpha=\beta=1$  and  $N = 10$  at different points of  $\kappa$  and for various values of  $\nu$  (Example 4.1)

$\kappa$	$\nu = 0,3$	$\nu = 0,7$	$\nu = 0,9$	$\nu = 0.5$	Exact
.1	-0.0036	0.0205	0.0165	0.0151	0.0152
.2	0.0841	0.0661	0.0498	0.0755	0.0756
.3	0.1967	0.1366	0.1038	0.1640	0.1641
.4	0.2382	0.2003	0.1623	0.2235	0.2236
.5	0.1037	0.2039	0.1901	0.1766	0.1768
.6	-0.2610	0.0955	0.1462	-0.0354	-0.0352
.7	-0.7786	-0.1348	0.0091	-0.3931	-0.3929
.8	-1.1177	-0.3934	-0.1798	-0.7137	-0.7135
.9	-0.5599	-0.3990	-0.2539	-0.5399	-0.5397

**Table 2.**  $\mathcal{E}_{max}$  for different values of  $N$  (Example 4.1)

$N$	8	12	16	20	24
$(\alpha, \beta)=(1,1)$	8.3698e-04	1.8194e-04	5.1147e-05	2.5051e-05	1.3330e-05
$(\alpha, \beta)=(2,1)$	8.3698e-04	1.8194e-04	6.2236e-05	2.6713e-05	4.7405e-05
$(\alpha, \beta)=(3,-2)$	8.3698e-04	1.8194e-04	6.2295e-05	2.7716e-04	5.8256e-05
$(\alpha, \beta)=(1,-0.5)$	8.3698e-04	1.8194e-04	6.4684e-05	2.6879e-05	8.5491e-05





**Figure 1.** Exact and numerical solutions when  $\alpha = \beta = 1, N = 10$  and for  $\nu \leq 0.5$  (up),  $\nu \geq 0.5$  (down) (Example 4.1)

**Example 4.2** [8] Let's consider the following fractional Fredholm integro-differential equation

$${}^c D^\nu u(\kappa) = -\frac{3\kappa^{\frac{1}{6}}\Gamma(\frac{5}{6})(-91 + 216\kappa^2)}{91\pi} + (5 - 2e)\kappa + \int_0^1 \kappa e^\tau u(\tau) d\tau, \tag{13}$$

with the initial condition  $u(0) = 0$ . The exact solution for  $\nu = \frac{5}{6}$  is  $u(\kappa) = \kappa - \kappa^3$ .

Table 3 displays the absolute error produced by the proposed algorithm for solving equation (14) with parameters  $\alpha = \beta = 1$  and  $N = 3,4$ . The results clearly demonstrate that our method outperforms those reported in [8], highlighting the effectiveness of our approach.

**Table 3.**  $\mathcal{E}(\kappa)$  at different points of  $\kappa$  and for  $\alpha = \beta = 1$  (Example 4.2)

$\kappa$	$N = 3$ [8]	$N = 3$ Present	$N = 4$ [8]	$N = 4$ Present
.1	4.510281038e-17	0	1.105886216e-16	0
.2	8.326672685e-17	0	1.301042607e-16	0
.3	1.110223025e-16	0	1.110223025e-16	0
.4	1.110223025e-16	0	6.938893904e-17	0
.5	5.551115123e-17	0	0.0	0
.6	5.551115123e-17	0	2.775557562e-17	0
.7	5.551115123e-17	0	8.326672685e-17	0
.8	1.665334537e-16	0	8.326672685e-17	0
.9	1.387778781e-16	0	2.775557562e-17	0

**Example 4.3** [13] Consider the following fractional Fredholm integro-differential equation:

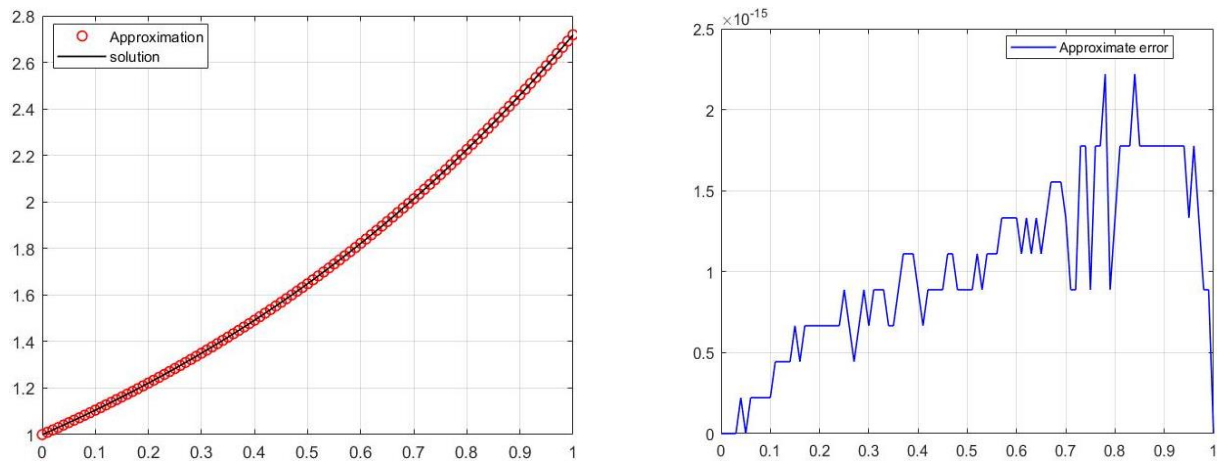
$${}^c D^{\frac{3}{2}} u(x) - D^{\frac{1}{2}} u(x) = e^x - e^{x+1} + \int_0^1 e^x u(\tau) d\tau, \tag{14}$$

with the boundary conditions  $u(0) = 1, u(1) = e$ . The exact solution is  $u(x) = e^x$ .

Table 4 demonstrates that error values decrease significantly as  $N$  increases incrementally for various values of  $(\alpha, \beta)$ . Similar to the previous example, we observe that the  $\mathcal{E}_{max}$  is smallest when  $\alpha = \beta = 1$  compared to other cases, reinforcing that Lucas polynomials outperform the other polynomials considered in this example. Figure 2 shows the exact solution and its estimated approach on the left side, while the approximation error is depicted on the right side, for  $N = 12$  and  $\alpha = \beta = 1$ . The numerical solution closely matches the exact solution, demonstrating high accuracy and effectively capturing the exact solution's behavior.

**Table 4.**  $\mathcal{E}_{max}$  for different values of  $N$  (Example 4.3)

$N$	4	6	8	10	12
$(\alpha, \beta)=(1,1)$	6.0013e-04	3.0797e-06	8.0383e-09	1.2745e-11	2.2204e-15
$(\alpha, \beta)=(2,1)$	6.0013e-04	3.0797e-06	8.0383e-09	1.2747e-11	8.4377e-15
$(\alpha, \beta)=(3,-2)$	6.0013e-04	3.0797e-06	8.0383e-09	1.2747e-11	1.4211e-14
$(\alpha, \beta)=(1,-0.5)$	6.0013e-04	3.0797e-06	8.0383e-09	1.2746e-11	1.2434e-14



**Figure 2.** Plot of the exact solution and its approximation on the left and approximate error on the right for  $\alpha=\beta=1$  and  $N = 12$ . (Example 4.3)

## 5 CONCLUSION

In the presented study, we have developed a numerical method using GLPs and the operational matrix for fractional derivatives, coupled with the collocation method, to solve fractional Fredholm-type integro-differential equations. The results from several examples demonstrate that our method is highly effective, achieving accurate approximations that closely match existing solutions. This confirms the robustness and reliability of the proposed approach. Our method not only simplifies the solution process but also provides a powerful tool for tackling complex fractional integro-differential equations.

## References

- [1] I. Podlubny, *Fractional Differential Equations: An Introduction to Fractional Derivatives, Fractional Differential Equations, to Methods of Their Solution and Some of Their Applications*, Elsevier, 1998.
- [2] A. A. Kilbas, H. M. Srivastava, and J. J. Trujillo, *Theory and Applications of Fractional Differential Equations*, Amsterdam, The Netherlands, 2006.
- [3] S. K. Vanani, S. Karimi, and A. Aminataei, "Operational Tau approximation for a general class of fractional integro-differential equations," *Computational & Applied Mathematics*, vol. 30, pp. 655–674, 2011.

- [4] A. M. S. Mahdy, E. M. H. Mohamed, and G. M. A. Marai, "Numerical solution of fractional integro-differential equations by least squares method and shifted Chebyshev polynomials of the third kind method," *Theoretical Mathematics & Applications*, vol. 6, no. 4, pp. 87–101, 2016.
- [5] A. Benzahi, N. Arar, N. Abada et al, "Numerical investigation of fredholm Fractional integro-differential equations by least squares method and compact combination of shifted chebyshev Polynomials," *Journal of Nonlinear Mathematical Physics*, vol. 30, pp. 1392–1408, 2023.
- [6] A. Rohul, S. Kamal, A. Muhammad et al, "An efficient algorithm for numerical solution of fractional integro-differential equations via Haar wavelet," *Journal of Computational and Applied Mathematics*, vol. 381, art. no. 113028, 2021.
- [7] F. Zhou, and X. Xu, "Numerical solution of fractional Volterra-Fredholm integro-differential equations with mixed boundary conditions via Chebyshev wavelet method," *International Journal of Computer Mathematics*, vol. 96, no. 2, pp. 436–456, 2019.
- [8] F. Ghomanjani, "A new approach for solving linear fractional integro-differential equations and multi variable order fractional differential equations," *Proyecciones*, vol. 39, no. 1, pp. 199–218, 2020.
- [9] W. M. Abd-Elhameed, and Y. H. Youssri, "Generalized Lucas polynomial sequence approach for fractional differential equations," *Nonlinear Dynamics*, vol. 89, no. 2, pp. 1341–1355, 2017.
- [10] Z. Laouar, N. Arar, and A. Ben Makhlof, "Spectral collocation method for handling integral and integrodifferential equations of n-th order via certain combinations of shifted Legendre polynomials," *Mathematical Problems in Engineering*, vol. 2022, no. 1, art. no. 9043428, 2022.
- [11] Z. Laouar, N. Arar and A. Ben Makhlof, "Theoretical and numerical study for Volterra-Fredholm fractional integro-differential equations based on Chebyshev polynomials of the third kind," *Complexity*, vol. 2023, no. 1, art. no. 6401067, 2023.
- [12] A. Setia, Y. Liu, and A. S. Vatsala, "Solution of linear fractional Fredholm integro-differential equation by using second kind Chebyshev wavelet," in *11th International Conference on Information Technology: New Generations IEEE*, 2014.
- [13] M. Gulsu, Y. Ozturk, and A. Anapali, "Numerical approach for solving fractional fredholm integro-differential equation," *International journal of Computer Mathematics*, vol. 90, no. 7, pp. 1413–1434, 2013.



## **Solutions of Linear Dynamic Systems with the Help of Eigenvalue - Eigenvector**

**Ramazan Simsek<sup>\*1</sup>**

*<sup>1</sup>Department of Mathematics and Science Education, Faculty of Education, Bayburt University, Bayburt, Türkiye*

---

### **Abstract**

A dynamic equation is an equation in which there is a change over time with respect to a variable. The solution of the ensemble of such equations depends on functions whose change at any instant is equal to the values at that instant. The solutions of these equations, which have many applications in engineering, have been handled by different methods. In this paper, we will first define a first order linear dynamical system. Then we will find the solution of this type of system with the help of eigenvalues and eigenvectors using exponential functions  $e^t$  whose derivative is equal to itself.

**Keywords:** *Eigenvalue, Eigenvector, Derivative, Dynamic system of equations*

---



---

## Boosting Communication Efficiency: WDM-Distributed Compensation Fiber Integration in Optical Systems

Hadj Abdelkader Benghenia<sup>\*1</sup>, Hadj Ali Bakir<sup>2</sup>

<sup>1</sup>Faculty of science and technology, Ain Temouchent University Belhadj Bouchaib, Algeria

<sup>2</sup>University of Chlef, Algeria

---

### Abstract

This research explores the optimization of transmission efficiency in optical fiber communication systems by integrating wavelength-division multiplexing (WDM) with dispersion compensation fiber (DCF). Dispersion within optical fibers often results in signal degradation, imposing limitations on transmission distance and data rate. By incorporating DCF into the system, the detrimental effects of dispersion can be effectively mitigated. Additionally, the implementation of WDM facilitates the simultaneous transmission of multiple signals at varying wavelengths, thereby augmenting overall transmission capacity. Through comprehensive simulations and analysis, our study showcases a substantial enhancement in transmission performance achieved through the synergistic combination of WDM and DCF. Our findings reveal notable improvements in signal quality, extended transmission distances, and heightened data rates, underscoring the potential of this integrated approach as a compelling solution for high-speed and long-distance optical communication systems.

**Keywords:** *Optical fiber communication, WDM, DCF, Transmission efficiency, Signal degradation, Data rate, Transmission distance*

---

## 1 INTRODUCTION

Optical fiber communication systems have revolutionized modern telecommunications by enabling high-speed and long-distance data transmission. However, one of the key challenges in these systems is the dispersion effect, which can degrade signal quality and limit transmission distances. Dispersion arises due to the varying velocities of different wavelengths of light traveling through the optical fiber, leading to pulse spreading and inter-symbol interference.

To address this challenge, dispersion compensation fiber (DCF) has emerged as a critical component in optical communication systems. DCF is designed to introduce a precisely controlled amount of dispersion that compensates for the dispersion accumulated during transmission, thereby enhancing signal quality and extending transmission distances [1].

Moreover, the integration of wavelength-division multiplexing (WDM) with DCF has garnered significant attention in recent years. WDM technology enables the simultaneous transmission of multiple signals over a single optical fiber by utilizing different wavelengths for each signal. By combining WDM with DCF, the benefits of both technologies can be leveraged synergistically to further enhance transmission efficiency and capacity [2]. While leveraging wavelength-division multiplexing (WDM) alone for dispersion management in optical fiber communication systems offers certain advantages, it also presents limitations that can affect system performance and scalability.

One limitation arises from the inherent dispersion properties of optical fibers, which can lead to dispersion-induced distortions in WDM systems. Without dispersion compensation techniques like dispersion compensation fiber (DCF), these distortions can limit the achievable transmission distances and data rates, particularly in long-haul transmission scenarios [3].

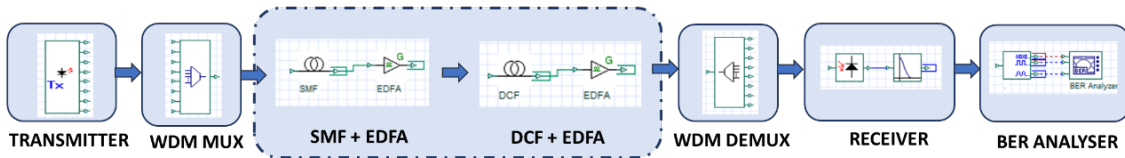
Furthermore, WDM-based dispersion management may face challenges in effectively mitigating dispersion over a wide range of wavelengths. Optical fibers exhibit wavelength-dependent dispersion characteristics, meaning that different wavelengths may experience varying levels of dispersion. Without tailored dispersion compensation mechanisms for each wavelength channel, WDM systems may struggle to maintain signal quality and system performance across the entire spectral range [4].

Additionally, the scalability of WDM-based dispersion management solutions may be limited by the availability of suitable optical components and signal processing techniques. As the number of wavelength channels increases in WDM systems, the complexity of dispersion management also grows, requiring more sophisticated dispersion compensation methods and higher-performance optical components. This can result in increased system costs and complexity, potentially limiting the scalability of WDM-based dispersion management approaches [4].

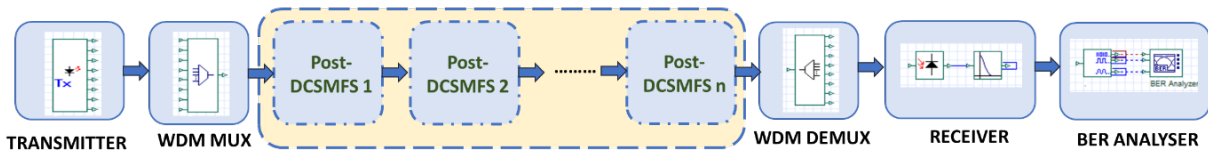
This study aims to explore the synergistic benefits of integrating WDM with DCF in optical fiber communication systems. Through comprehensive simulations and analysis, we investigate the impact of this integrated approach on transmission performance, including signal quality, transmission distance, and data rate.

Figure 1 illustrates both the post-compensation and distributed post-compensation schemes. When dealing with multiple single-mode fibers (SMFs), it may be necessary to employ multiple dispersion compensating fibers (DCFs), resulting in the utilization of a distributed layout for the chromatic dispersion compensation module (CDCM). This distributed layout, depicted in Figure 1, accommodates the need for multiple DCFs when working with multiple SMFs. The structure of this paper unfolds as follows. In Section 2, we delve into a more comprehensive discussion of the theoretical model adopted in this study. Section 3 provides clarity on the layout settings and outlines the simulation parameters. The presentation of simulation results, along with supportive diagrams and an in-depth analysis of the most effective technique, is presented in Section 4. Finally, Section 5 encapsulates the key conclusions drawn from this study.

(a)



(b)



**Figure 1.** Illustrates dispersion compensation schemes using DCF. (a) Post compensation and (b) distributed post-compensation

## 2 DISPERSION COMPENSATION TECHNOLOGY USING DCFS

To enhance overall system performance and minimize the impact of dispersion on transmission quality, numerous dispersion compensation technologies have been suggested [5]. Within the literature, certain techniques stand out as promising solutions for dispersion compensation and management. These include dispersion compensating fibers (DCF), chirped fiber Bragg gratings (FBG), and high-order mode (HOM) fiber [6]. The concept of utilizing dispersion compensation fibers for managing dispersion was initially proposed as early as 1980. However, it wasn't until the invention of optical amplifiers that dispersion compensation fibers (DCF) began to garner widespread attention and research focus.

Due to their maturity, stability, resistance to temperature fluctuations, and wide bandwidth capabilities, dispersion compensation fibers (DCF) have emerged as one of the most effective methods for managing dispersion and have undergone extensive research. Single-mode fibers (SMFs) inherently exhibit positive second-order and third-order dispersion values. In contrast, DCFs possess negative dispersion values. By introducing a DCF into the optical path, the average dispersion approaches zero [7]. In modeling the transmission of signals over longer fiber links, factors such as Four-Wave Mixing (FWM) and Cross-Phase Modulation (XPM) are often disregarded, focusing instead on Self-Phase Modulation (SPM) and dispersion effects. The signal transmission behavior can be accurately simulated by solving the nonlinear Schrödinger equation.

$$\frac{\partial A_j(z,t)}{\partial z} + \frac{1}{2} i\beta_2(\lambda_j) \frac{\partial^2 A_j(z,t)}{\partial t^2} - i\gamma |A_j(z,t)|^2 A_j(z,t) + \frac{\alpha}{2} A_j(z,t) = 0 \quad (1)$$

$A_j(z, t)$  is complex amplitude of  $j$  channel optical pulse,  $\beta_2(\lambda_j)$  is the dispersion parameter of  $j$  channel,  $r$  is the nonlinear coefficient,  $\alpha$  is the loss coefficient. After  $N$ -section dispersion compensation of DCF, the channel residual dispersion can be expressed as

$$\Delta D(\lambda_j) = NL_{SMF} \left[ (1 - \mu_p)D_{SMF}(\lambda_p) + (j - p)\Delta\lambda \left( \frac{dD_{SMF}(\lambda_p)}{d\lambda} - \frac{\mu_p D_{SMF}(\lambda_p)}{D_{SMF}(\lambda_p)} \frac{dD_{DCF}(\lambda_p)}{d\lambda} \right) \right] \quad (2)$$

In the formula,  $\mu_p$  is the dispersion compensation rate of  $p$ -channel

$$\mu_p = \frac{D_{DCF}(\lambda_p)L_{DCF}}{D_{SMF}(\lambda_p)L_{SMF}} \quad (3)$$

$L_{SMF}$  and  $L_{DCF}$  are the conventional single-mode fiber length and dispersion compensation fiber length within the amplifier spacing.  $\Delta\lambda$  is the channel wavelength spacing.

$D_{DCF}(\lambda_p)$  and  $D_{SMF}(\lambda_p)$  are the dispersion coefficient of conventional single-mode fiber and dispersion compensation fiber at the  $\lambda_p$  wavelength.

### 3 SIMULATION SETUP

An 8-channel Wavelength Division Multiplexing (WDM) optical network was designed to operate at data rates of 20, 40, and 80 Gbps using the Optisystem 7.0 simulator software. The fundamental block diagram of the simulation setup is depicted in Fig.1. Within the transmitter section, a data source generates a pseudo-random bit sequence at data rates of 20, 40, and 80 Gbps. The electrical pulse generator, operating in either Non-Return-to-Zero (NRZ) or Return-to-Zero (RZ) modulation formats as per the required modulation scheme, transforms the binary data into electrical pulses. These electrical pulses then modulate the laser signal via the Mach-Zehnder modulator. In the simulation setup, eight laser sources are employed to generate optical signals with varying wavelengths. The channel spacing utilized between these wavelengths is set at 50 GHz.

The multiplexer integrates the input channels and sends them through an optical fiber channel, composed of both Single-Mode Fiber (SMF) and Dispersion Compensating Fiber (DCF). Upon reaching the receiver, a 1:8 demultiplexer divides the composite signal into four distinct channels. Subsequently, the output of the demultiplexer undergoes detection by a PIN photodetector, followed by filtration through a low-pass electrical Bessel filter. Finally, the signal is analyzed for Bit Error Rate (BER) using a BER Analyzer.

The positioning of Single-Mode Fiber (SMF) and Dispersion Compensating Fiber (DCF) within the optical link is crucial and is chosen based on the compensation scheme employed. In distributed post-compensation schemes, the number of spans is assumed to be 2 or more. In optical communication systems, a “span” refers to a segment of optical fiber between two amplification points or dispersion compensation points. Each span represents a length of fiber over which the optical signal propagates before it may experience signal degradation due to factors like attenuation or dispersion. EDFAs are used between the links in order to amplify the signals.

Dispersion-Compensated Single-Mode Fiber Systems (DCSMFS) are advanced optical communication systems engineered to address the challenge of dispersion, particularly chromatic dispersion, encountered in single-mode fiber (SMF) transmission. In SMFs, different wavelengths of light propagate at varying speeds, leading to signal distortion and degradation over long distances.

To mitigate dispersion effects, DCSMFS employ dispersion compensation techniques, prominently utilizing Dispersion-Compensating Fiber (DCF). DCF is a specialized type of fiber engineered with opposite dispersion characteristics to SMF. By strategically integrating DCF segments into the optical link at appropriate intervals, dispersion compensation is applied to counteract the dispersion-induced signal distortion, thereby maintaining signal integrity and quality.

To evaluate the performance of the Wavelength Division Multiplexing (WDM) system across different transmission distances, specific lengths of Single-Mode Fiber (SMF) and Dispersion Compensating Fiber (DCF) have been selected, as detailed in Table 1. Furthermore, the simulation incorporates various parameters for both SMF and DCF, as outlined in Table 2. These parameters are essential for accurately modeling the optical transmission characteristics and dispersion compensation capabilities within the system. By varying the lengths of SMF and DCF and adjusting their respective parameters, the simulation enables a comprehensive analysis of the WDM system's performance under different transmission conditions.

**Table 1.** Different cases of transmission distance

Length of SMF (km)	Length of DCF (km)
100	20
200	40
300	60
400	80
500	100
600	120
700	140
800	160
900	180
1000	200

**Table 2.** Simulation parameters

Parameter	SMF	DCF
Dispersion(ps/nm/km)	16	-80
Attenuation(dB/km)	0.2	0.6
Dispersion slope (ps/nm <sup>2</sup> .km)	0.075	0.2
Effective area (μm <sup>2</sup> )	80	30

## 4 RESULTS AND DISCUSSION

In this section, we present the results obtained from our experiments and engage in a comprehensive discussion of their implications. We analyze the performance of Dispersion-Compensated Single-Mode Fiber Systems (DCSMFS) across various configurations of Single-Mode Fiber (SMF) and Dispersion-Compensating Fiber (DCF), as well as the impact of different transmission distances. Through an in-depth examination of the data, we explore the effectiveness of dispersion compensation techniques, assess signal quality, transmission efficiency, and discuss the implications for practical applications in optical communication systems. Additionally, we identify key insights and potential areas for further research in the field.

The Q-factor plots presented in Figure 2 underscore the importance of dispersion compensation strategies in maintaining signal quality over varying transmission distances. Employing a split between SMF and DCF allows for more effective dispersion compensation, resulting in improved Q-factor values and enhanced system performance. Further analysis and optimization of dispersion compensation techniques are warranted to maximize the Q-factor and ensure reliable communication in Dispersion-Compensated Single-Mode Fiber Systems (DCSMFS).

The Figure 3 and Table 3 provides a comparison of the maximum Q-factor values obtained for two dispersion compensation schemes: Without Split, and Split SMF=50km & DSF=10km, and Split SMF=100km & DSF=20km. The results are categorized based on the transmission distances (in kilometers) and data rates (20Gbps, 40Gbps, and 80Gbps).

In our initial experiment, we opted not to employ a split between Single-Mode Fiber (SMF) and Dispersion-Compensating Fiber (DCF). This decision entailed utilizing a continuous length of either SMF or DCF, without alternating between them. By adopting continuous lengths of either SMF or DCF, our aim was to explore the performance of the optical communication system under varying dispersion compensation scenarios. This setup allowed us to assess the impact of dispersion compensation at different intervals along the transmission distance.

The absence of a split between SMF and DCF in our experiments had significant implications for dispersion compensation efficiency. Without alternating between SMF and DCF segments, dispersion compensation may have been less effective over longer transmission distances. This continuous length of either SMF or DCF may not have adequately mitigated dispersion effects, resulting in signal degradation and reduced transmission distance.

At higher data rates, such as 20 Gbps, 40 Gbps and 80 Gbps, signal degradation becomes more pronounced over longer distances due to dispersion, attenuation, and nonlinear effects. Without robust dispersion compensation mechanisms, maintaining signal quality becomes increasingly challenging. The observed limitation in transmission distance can be attributed to the heightened sensitivity of higher data rates to signal degradation, exacerbated by the absence of effective dispersion compensation strategies.



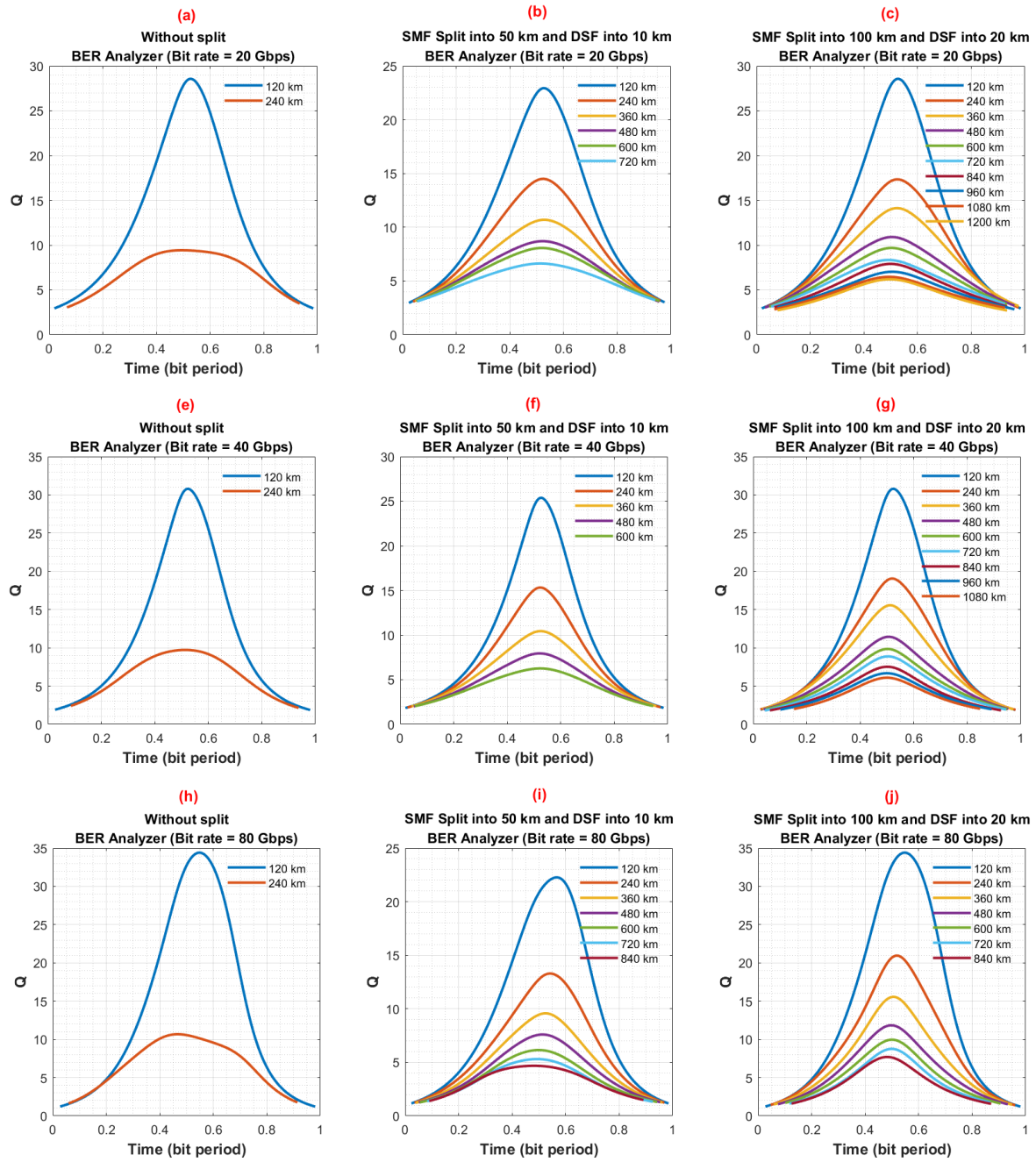


Figure 2. Comparison of Q-factor performance across different dispersion compensation scenarios

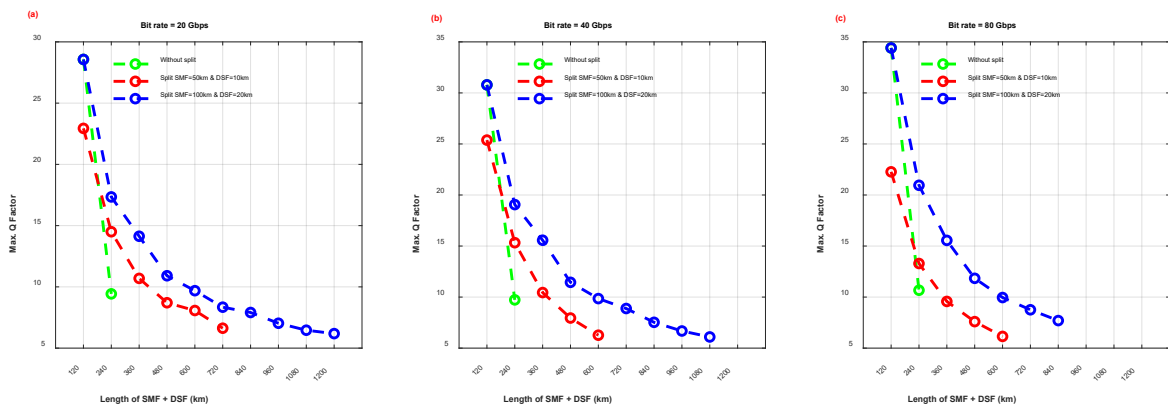


Figure 3. Maximum Q-factor values for dispersion compensation schemes at various transmission distances and data rates

**Table 3.** Summary of maximum Q-factor values for dispersion compensation schemes at various transmission distances and data rates

SMF+ DSF (km)	Max. Q Factor								
	Without Split			Split SMF=50km & DSF=10km			Split SMF=100km & DSF=20km		
	20 Gbps	40 Gbps	80 Gbps	20 Gbps	40 Gbps	80 Gbps	20 Gbps	40 Gbps	80 Gbps
120	28.5673	30.7897	34.4100	22.9388	25.3800	22.2698	28.5673	30.7897	34.4100
240	9.4297	9.7257	10.6714	14.5007	15.3263	13.2892	17.3431	19.0602	20.9512
360	***	***	***	10.6932	10.4430	9.5735	14.1325	15.5698	15.5538
480	***	***	***	8.7035	7.9479	7.5953	10.9077	11.4446	11.8374
600	***	***	***	8.0702	6.2650	6.1458	9.6887	9.8522	9.9554
720	***	***	***	6.6254	***	***	8.3433	8.8803	8.7554
840	***	***	***	***	***	***	7.9080	7.5270	7.6981
960	***	***	***	***	***	***	7.0302	6.6780	***
1080	***	***	***	***	***	***	6.4621	6.0942	***
1200	***	***	***	***	***	***	6.1840	***	***

Max. Q Factor (\*\*\*) < 6)

The study's findings illuminate significant disparities in the performance of Dispersion-Compensated Single-Mode Fiber Systems (DCSMFS) across various dispersion compensation scenarios. Notably, both the Split SMF=50km & DSF=10km and Split SMF=100km & DSF=20km configurations showcased superior efficacy compared to the Without Split scenario. Particularly, the Split SMF=100km & DSF=20km scenario emerged as the most effective. Here's an elucidation of these results:

In the Split SMF=50km & DSF=10km scenario, alternating segments of 50 km Single-Mode Fiber (SMF) and 10 km Dispersion-Compensating Fiber (DSF) were employed. This approach demonstrated enhanced dispersion compensation, especially evident at longer transmission distances. However, its performance was eclipsed by the Split SMF=100km & DSF=20km configuration.

The Split SMF=100km & DSF=20km setup, featuring longer segments of both SMF (100 km) and DSF (20 km), exhibited superior dispersion compensation performance. Across all transmission distances and data rates, this scenario yielded higher Q-factor values, indicative of enhanced signal quality and dispersion compensation efficiency.

Comparatively, the results underscored the efficacy of extending the lengths of both SMF and DSF segments in bolstering dispersion compensation performance. The Split SMF=100km & DSF=20km configuration, with its longer segments, minimized signal degradation and improved transmission reliability, particularly over extended distances.

These findings underscore the critical importance of optimizing dispersion compensation strategies in DCSMFS to ensure robust signal transmission. The superior performance of the Split SMF=100km & DSF=20km scenario underscores the need for further research and optimization efforts to refine dispersion compensation techniques for enhanced system performance in practical optical communication applications.

## 4 CONCLUSION

In conclusion, our study underscores the significance of dispersion compensation strategies in optimizing the performance of Single-Mode Fiber Systems. Through comparative analysis, configurations employing a split between SMF and DSF demonstrated superior dispersion compensation efficiency, with the Split SMF=100km & DSF=20km scenario emerging as the most effective. These findings emphasize the importance of refining dispersion compensation techniques to ensure robust signal transmission in optical communication networks.

## References

- [1] M. R. Salehi and G. P. Agrawal, *Optical WDM Networks: Principles and Practice*, Springer Science & Business Media, 2009.
- [2] G. Keiser, *Optical Fiber Communications*, 4th ed.: McGraw-Hill Education, 2011.
- [3] G. P. Agrawal, *Fiber-Optic Communication Systems*, 4th ed.: Wiley, 2010.
- [4] R. Ramaswami and K. N. Sivarajan, *Optical Networks: A Practical Perspective*, 3rd ed.: Morgan Kaufmann, 2010.
- [5] J. Yu and B. Yang, "Dispersion-allocated soliton technology with long amplifier spacing and long distance," *IEEE Photonics Technology Letters*, vol. 9, no. 7, pp. 952–954, 1997.

- [6] M. Yadav, A. K. Jaiswal, N. Agrawal, and N. Nitin, "Design performance of high-speed optical fiber WDM system with optimally placed DCF for dispersion compensation," *International Journal of Computer Applications*, vol. 122, no. 20, Jul. 2015.
- [7] T. Bobruk, "Chromatic dispersion compensation in existing fiber optic telecommunication lines with the growing bit rates needs of DWDM system," *Informatyka, Automatyka, Pomiar w Gospodarce i Ochronie Środowiska*, vol. 11, no. 4, 2021.



---

## Maximizing Solar Installation Power Using Fuzzy Control

Amel Ourici<sup>\*1</sup>, Abderaouf Bahi<sup>2</sup>

<sup>1</sup>Department of Electrical Engineering, Badji Mokhtar Annaba University, Algeria

<sup>2</sup>Department of Computer Science, University of Chadli Bendjedid El Taref, Algeria

---

### Abstract

The growing demand for renewable energy sources has led to increased interest in solar power systems. To enhance the efficiency and power output of solar installations, researchers have explored the implementation of advanced control techniques. One such approach is fuzzy control, which leverages fuzzy logic to optimize the performance of solar systems. This paper focuses on how fuzzy control method are applied to maximize the power generation of solar installations, taking advantage of their adaptability and ability to handle uncertainties inherent in solar energy generation, and under variable weather conditions. The study aims to provide valuable insights into improving the overall efficiency and viability of solar energy as a sustainable power source.

**Keywords:** Solar power, Fuzzy control, Renewable energy, Inference rules, Energy optimization

---

## 1 INTRODUCTION

With the increasing global emphasis on sustainable and clean energy sources, solar power has emerged as a promising solution to meet the ever-growing demand for electricity. The utilization of solar photovoltaic (PV) installations has become widespread, as they harness sunlight to produce renewable electricity without harmful emissions. However, the efficiency of solar power systems [1, 2] heavily depends on the fluctuating nature of solar irradiance and temperature, posing challenges to maintain stable and optimal energy production. To address these challenges, researchers and engineers have turned their attention to advanced control techniques to enhance the performance of solar installations. Among these control strategies, fuzzy control [3, 4] has gained significant attention due to its ability to deal with uncertainties and nonlinearities prevalent in solar energy generation. Fuzzy logic, developed by Lotfi A. Zadeh in the 1960s, provides a means of handling imprecise or ambiguous data, making it particularly suited for applications in dynamic and complex systems like solar power plants. The primary objective of this research is to investigate how fuzzy control can be effectively applied to maximize the power output of solar installations. By integrating fuzzy logic into the control system, the solar plant can adapt to varying environmental conditions, achieving an optimal balance between energy generation and consumption. This study aims to contribute to the growing body of research in renewable energy optimization, focusing specifically on the unique challenges faced in solar power systems. In this paper, we will explore the principles of fuzzy control and its relevance to solar energy applications. We will delve into the characteristics of solar installations, including their nonlinearity, variability, and uncertainty, which makes traditional control methods less efficient in capturing the full potential of solar energy. By considering these intricacies, we will outline the key advantages of using fuzzy control in enhancing the performance of solar power plants. Furthermore, this research will discuss the implementation of fuzzy logic-based controllers in a simulated solar power system. The simulation will include representative data of solar irradiance and ambient temperature to mimic real-world scenarios. By comparing the performance of fuzzy control with traditional control techniques, we aim to demonstrate the superiority of fuzzy logic in maximizing solar installation power output under varying environmental conditions. In conclusion, this study strives to shed light on the significance of fuzzy control in the context of solar energy optimization. The integration of fuzzy logic-based controllers holds the potential to revolutionize the solar power industry by enabling solar installations to operate at their highest efficiency levels regardless of external factors. By contributing valuable insights into this domain, we hope to encourage further research and development of advanced control methods that will accelerate the global transition to sustainable and renewable energy sources.

## 2 RESEARCH METHOD

Solar energy is a promising energy worldwide, Figure 1 shows the existence of this energy in several countries around the world. In this paper, we used a fuzzy controller to have the maximum power of a photovoltaic installation.

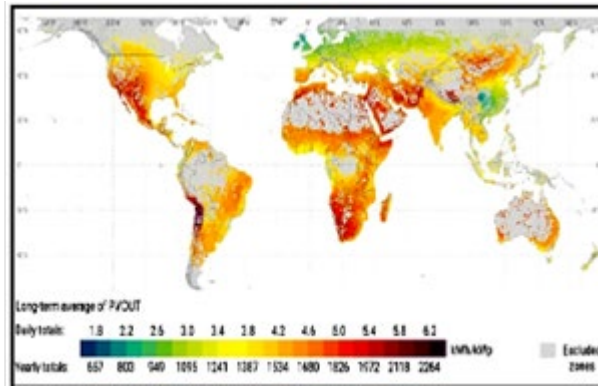


Figure 1. World average solar irradiation map from the World Bank (2021)

### 2.1 Solar Installation Studied

As a first approach, our project involved a 100 kW PV array utilizing SunPower SPR-305-WHT modules, each containing 96 cells. The array was designed with 5 modules connected in series per string and a total of 66 parallel strings. We integrated a boost chopper and implemented perturb and observe maximum power point tracking control. Figure 2 illustrates the setup of the PV array along with the boost chopper.

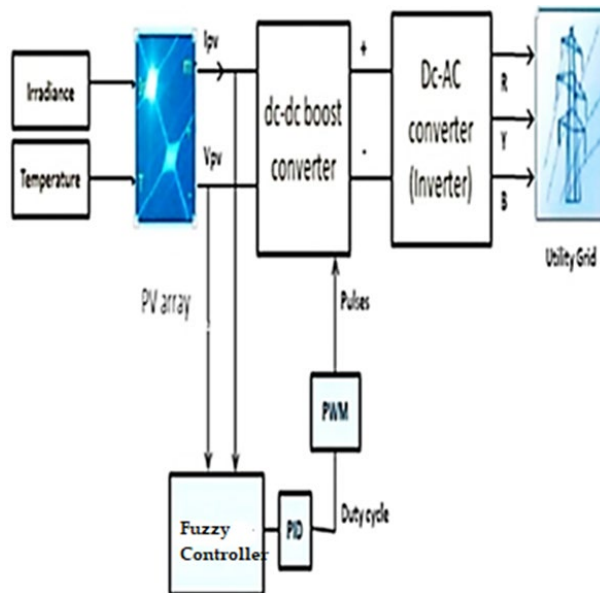


Figure 2. Scheme of photovoltaic generator studied

Observing properties at the terminals of the PV array requires the inclusion of additional parameters in the basic equations, as the array comprises several interconnected PV cells.

$$I = I_{PV} - I_0 \left[ \exp \left( \frac{V + R_s I}{V_t \alpha} \right) - 1 \right] - \frac{V + R_s I}{R_p} \tag{1}$$

Where  $I_{PV}$  and  $I_0$  are the PV current and saturation currents, respectively, of the array and  $V_t = N_s k T / q$  is the thermal voltage of the array with  $N_s$  cells connected in series.  $R_s$  is the equivalent series resistance of the array and  $R_p$  is the equivalent parallel resistance. Due to variations in ambient temperature and solar radiation, the maximum output of a solar system will fluctuate. Solar systems require real-time peak power point trackers as the available maximum power continuously changes with atmospheric conditions. The literature proposes three distinct categories for maximum power point tracking (MPPT) schemes: Direct method, intelligent method, and indirect method [5–9]. The direct method, referred to as the truth-seeking approach for MPPT, involves continuously disturbing the operating point of the PV generator to find the maximum power point. Within this category, schemes like perturbations and observations (P&O), hill climbing (HC), and incremental conductance (INC) have found widespread application in PV systems. In the P&O method, the PV array's working voltage is perturbed to attain

the MPPT. Similarly, the hill-climbing method perturbs the duty cycle of the DC/DC interface converter, following a method similar to P&O [10–13]

**2.2 Fuzzy Control Adopted**

Fuzzy logic is also called “linguistic logic” because its values of truth are words of the common vocabulary: “Rather true, rather false, far, far enough, close enough, strong, weak...”. Fuzzy logic is used to study the representation of uncertain knowledge, to approximate reasoning and to model vague notions of natural language. Fuzzy logic works by identifying and applying rules that combine expert inputs with desired outputs. There are generally four determining stages of fuzzy logic: the fuzzification interface, the knowledge base, the inference block and the defuzzification interface [14–17].

In the following we will detail the steps of designing a fuzzy controller in order to pursue the maximum power point. Like us have previously introduced the fuzzy controller has three blocks, so three stages which consists in the fuzzification of input variables by the use of belonging functions, then the inference or variables fuzzified are compared with predefined sets to determine the appropriate answer, and finally defuzzification to convert fuzzified subsets into values.

**2.2.1 Fuzzification**

The purpose of fuzzification is to define the belonging functions for the different variables, which makes it possible to blur the input variables. A preliminary step is to define a maximum allowable variation range for input variables. The purpose of fuzzification is to transform input variables into linguistic or fuzzy variables [18, 19]. In our case, we have two input variables which are the error  $E(k)$  and the error variation  $\Delta E(k)$  at the moment sampling  $k$  defined as follows:

$$E(k) = \frac{P(k) - P(k-1)}{V(k) - V(k-1)} \tag{2}$$

$$\Delta E(k) = E(k) - E(k-1) \tag{3}$$

Where  $P(k)$  is the power of the photovoltaic generator and  $V(k)$  the voltage of the photovoltaic generator therefore:  $E(k)$  is zero at the maximum power point of the photovoltaic generator, these input variables are expressed in terms of language variables such as LN (large negative), SN (small negative), EZ (zero equal), SP (small positive), LP (large positive).

The control rule must be designed so that the input variable ( $E$ ) is always zero.

**Table 1.** Rules of inference

$\Delta E$	LN	SN	EZ
$E$			
LN	EZ	EZ	LP
SN	EZ	EZ	SP
EZ	SP	EZ	EZ
SP	SN	SN	SN
LP	LN	LN	LN

In the inferences we will use fuzzy operators such as AND, OR, the operator AND is used within a rule, while the operator OR binds the different rules, and in our study we will rely on the max-min inference method. For this method of inference the operator AND is performed by the minimum training, the operator OR is performed by the maximum training, and THEN (the implication) is performed by the minimum training

**2.2.2 Defuzzification**

Finally, we must carry out the reverse operation of the fuzzification, here we must calculate a numerical value understandable by the external environment from a fuzzy definition is the purpose of the defuzzification. Defuzzification can be achieved using the center of gravity method.

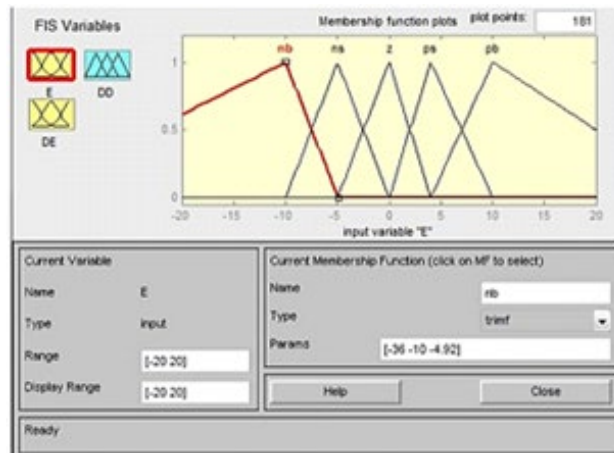


Figure 3. Calculation of the error in the proposed fuzzy logic controller

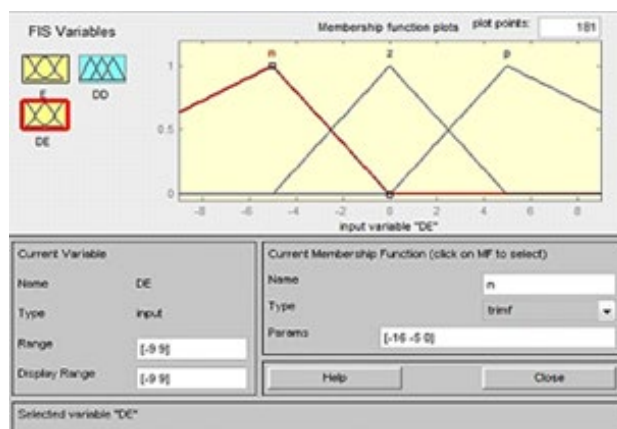


Figure 4. Calculation of the error variations in the proposed fuzzy logic controller

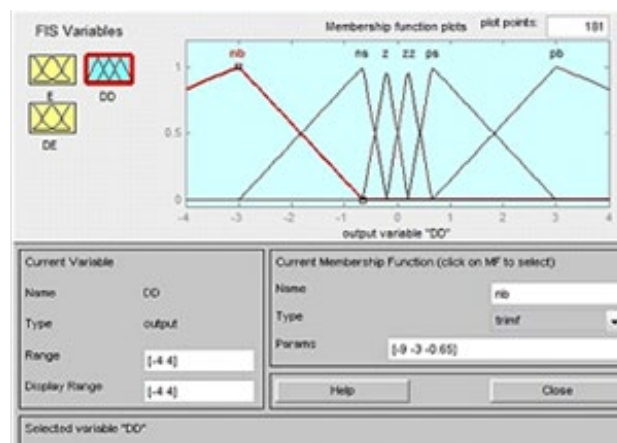
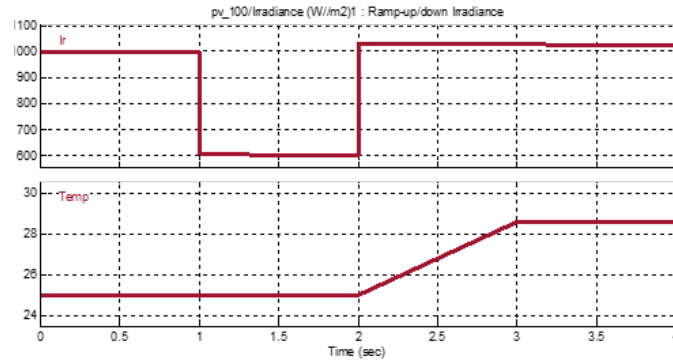


Figure 5. Calculation on the duty cycle in the proposed fuzzy logic controller

### 3 RESULTS AND DISCUSSION

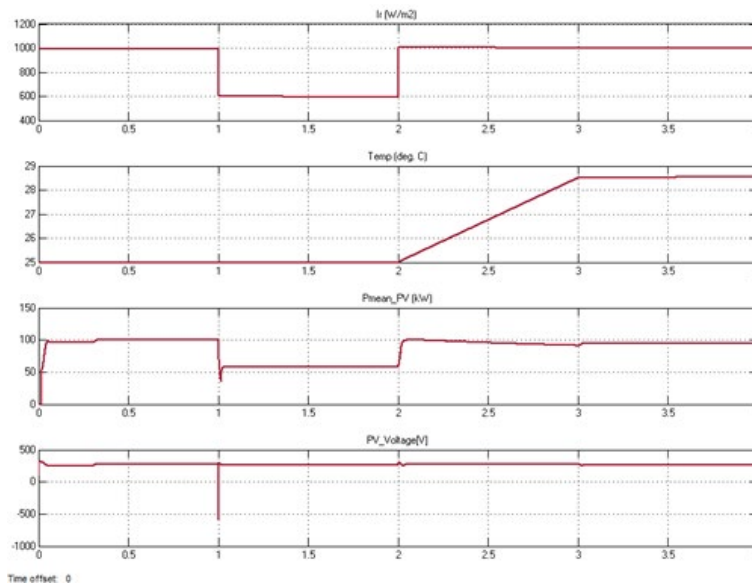
We tested the fuzzy control on our photovoltaic system under various climatic conditions, namely irradiation and ambient temperature.

Figure 6 illustrate Required variations in irradiation and temperature, where we see that the two quantities vary at the same time.



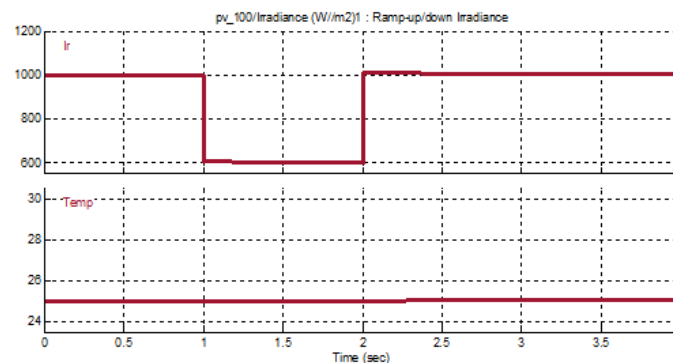
**Figure 6.** Required variations in irradiation and temperature (case 1)

Figure 7 shows the variations of the output power and the voltage of our PV installation, according with irradiation and temperature variations, we can see easily that the maximum power of 100 kW was reached, and the voltage was kept constant



**Figure 7.** Irradiation and temperature imposed, output power and voltage of the PV array (case 1)

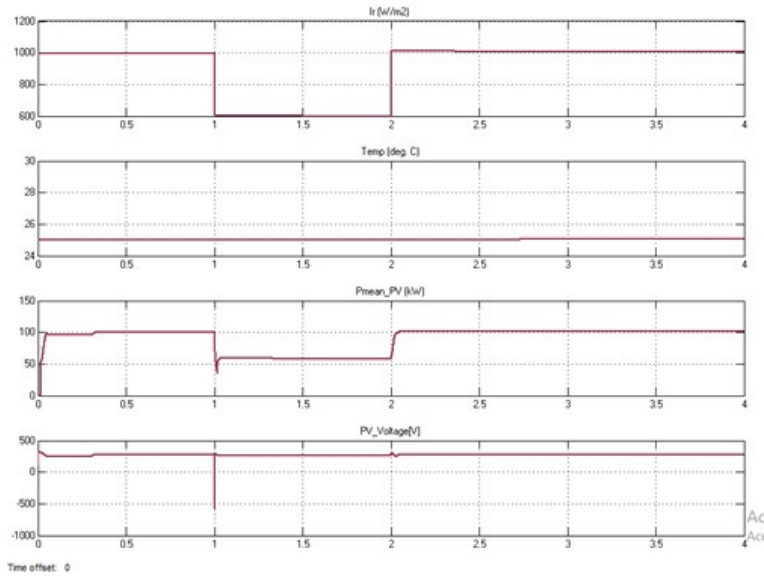
Figure 8 shows that temperature was maintained at 25 °C, with a variable irradiation



**Figure 8.** Variations in irradiation for a constant temperature (case 2)

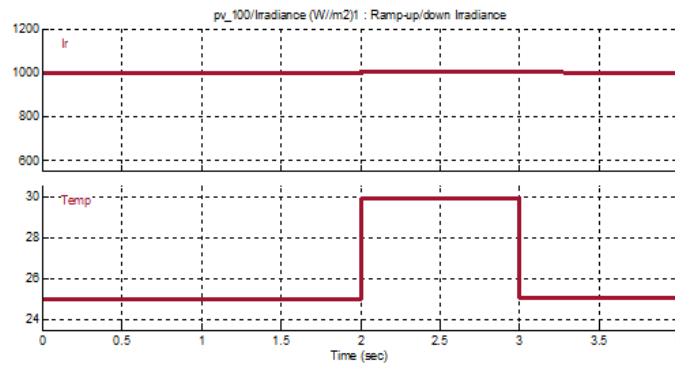
Figure 9 illustrate also the output power and the voltage of our system, under variations of figure 5 we can see that the voltage is sensitive to the variations of the irradiation, when the latter is changed, the voltage has a rather large peak. On the other hand, the power easily reaches its maximum despite the variations of these two climatic conditions.



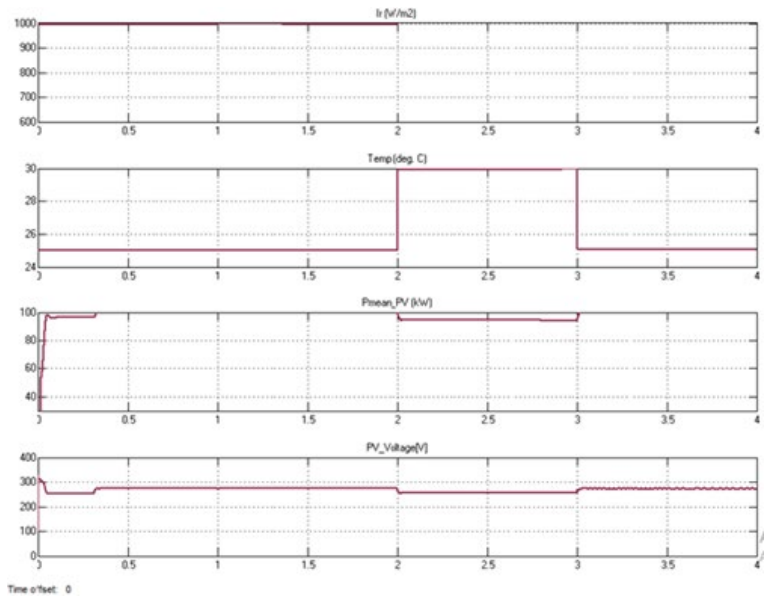


**Figure 9.** Irradiation and temperature, output power and voltage of the PV array case (2)

Figure 10 shows that the irradiance was maintained constant 1000 W/m<sup>2</sup>, with variable temperature. Figure 11 demonstrate that with temperature variations of Figure 6, the output power don't ric hits maximum value , especially when temperature riches 30 °C , but the voltage does not peak in this case.



**Figure 10.** Variation in temperature for a constant irradiation case (3)



**Figure 11.** Irradiation and temperature imposed, output power and voltage of the PV array

## 4 CONCLUSION

In this paper, we have studied and simulated the fuzzy control method applied to solar power systems. The results have demonstrated the effectiveness of fuzzy control in achieving precise maximum power point tracking. Moreover, we observed that this method exhibits remarkable robustness and insensitivity to transient regimes, making it a reliable and efficient approach for enhancing solar power generation under varying environmental conditions.

By integrating fuzzy logic into the control system, we successfully optimized the power output of the solar installation, ensuring maximum energy harvesting from the available solar irradiance and ambient temperature. The adaptability of fuzzy control allowed the system to continuously adjust and respond to changing weather conditions, thereby ensuring consistent and efficient power generation.

This study contributes valuable insights into the application of fuzzy control for solar energy optimization, paving the way for further advancements in renewable energy technologies. With its ability to handle uncertainties and nonlinearities inherent in solar energy generation, fuzzy control presents a promising avenue for maximizing the potential of solar installations and promoting sustainable energy solutions for a greener future.

## References

- [1] L. Zhang, S. S. Yu, T. Fernando, H. H. C. Lu, and K. P. Wong, "An online maximum power point capturing technique for high-efficiency power generation of solar photovoltaic systems," *J. Mod. Power Syst. Clean Energy*, vol. 7, no. 2, pp. 357–368, Mar. 2019, doi: 10.1007/s40565-018-0440-2.
- [2] A. F. Murtaza, M. Chiaberge, F. Spertino, U. T. Shami, D. Boero, and M. De Giuseppe, "MPPT technique based on improved evaluation of photovoltaic parameters for uniformly irradiated photovoltaic array," *Electr. Power Syst. Res.*, vol. 145, pp. 248–263, 2017, doi: 10.1016/j.epsr.2016.12.030.
- [3] O. Guenounou, B. Dahhou, and F. Chabour, "Adaptive fuzzy controller based MPPT for photovoltaic systems," *Energy Convers. Manag.*, vol. 78, pp. 843–850, 2014, doi: 10.1016/j.enconman.2013.07.093.
- [4] W. S. E. Abdellatif, M. S. Mohamed, S. Barakat, and A. Brisha, "A fuzzy logic controller based MPPT technique for photovoltaic generation system," *International Journal on Electrical Engineering and Informatics*, vol. 13, pp. 394–417, 2021, doi: 10.15676/ijeei.2020.13.2.9.
- [5] N. Karami, N. Moubayed, and R. Outbib, "General review and classification of different MPPT techniques," *Renew. Sustain. Energy Rev.*, vol. 68, pp. 1–18, 2017, doi: 10.1016/j.rser.2016.09.132.
- [6] M. Abou El Ela and J. A. Roger, "Optimization of the function of a photovoltaic array using a feedback control system," *Solar Cells*, vol. 13, pp. 107–119, 1984, doi: 10.1016/0379-6787(84)90002-4.
- [7] B. Bendib, H. Belmili, and F. Krim, "A survey of the most used MPPT methods: Conventional and advanced algorithms applied for photovoltaic systems," *Renewable and Sustainable Energy Reviews*, vol. 45, pp. 637–648, 2015, doi: 10.1016/j.rser.2015.02.009.
- [8] S. Motahhir, A. El Hammoumi, and A. El Ghzizal, "Photovoltaic system with quantitative comparative between an improved MPPT and existing INC and P&O methods under fast varying of solar irradiation," *Energy Reports*, vol. 4, pp. 341–350, 2018, doi: 10.1016/j.egy.2018.04.003.
- [9] R. Khan, L. Khan, S. Ullah, I. Sami, and J. S. Ro, "Backstepping based super-twisting sliding mode MPPT control with differential flatness oriented observer design for photovoltaic system," *Electronics*, vol. 9, art. no. 1543, 2020, doi: 10.3390/electronics9091543.
- [10] A. Anurag, S. Bal, S. Sourav, and M. Nanda, "A review of maximum power-point tracking techniques for photovoltaic systems," *International Journal of Sustainable Energy*, vol. 35, pp. 478–501, 2016, doi: 10.1080/14786451.2014.918979.
- [11] P. Joshi, and S. Arora, "Maximum power point tracking methodologies for solar PV systems—A review," *Renewable and Sustainable Energy Reviews*, vol. 70, pp. 1154–1177, 2017, doi: 10.1016/j.rser.2016.12.019.
- [12] A. Trivedi, A. Gupta, R.K. Pachauri, and Y. K. Chauhan, "Comparison of perturb & observe and ripple correlation control MPPT algorithms for PV array," in *2016 IEEE 1st International Conference on Power Electronics, Intelligent Control and Energy Systems (ICPEICES)*, Delhi, 2016, doi: 10.1109/ICPEICES.2016.7853459.
- [13] Y. Zhu, M. K. Kim, and H. Wen, "Simulation and analysis of perturbation and observation-based self-adaptable step size maximum power point tracking strategy with low power loss for photovoltaics," *Energies*, vol. 12, art. no. 92, 2019, doi: 10.3390/en12010092.
- [14] L. Farah, H. Amir, K. Abdelfateh, I. Cosimo, A. Jamil, and M. Mufti, "A highly-efficient fuzzy-based controller with High reduction inputs and membership functions for a grid-connected photovoltaic system," *IEEE Access*, vol. 8, pp. 163225–163237, 2020, doi: 10.1109/ACCESS.2020.3016981.

- [15] T. Sutikno, A. C. Subrata, and A. Elkhateb, "Evaluation of fuzzy membership function effects for maximum power Point tracking technique of photovoltaic system," *IEEE Access*, vol. 9, pp. 109157–109165, 2021, doi: 10.1109/ACCESS.2021.3102050.
- [16] N. Ali, K. Mahmoud, M. Lehtonen, and M. M. F. Darwish, "An efficient fuzzy-logic based variable-step incremental conductance MPPT method for grid-connected PV systems," *IEEE Access*, vol. 9, pp. 26420–26430, 2021, doi: 10.1109/ACCESS.2021.3058052.
- [17] N. U. R. Joy, M. Rana, and F. Rahman, "Extraction of maximum power of grid connected PV systems using advanced FLC," *International Journal of Renewable Energy Research-IJRER*, vol. 11, no. 4, 2021.
- [18] M. Dehghani, M. Taghipour, G. B. Gharehpetian, and M. Abedi, "Optimized fuzzy controller for MPPT of grid-connected PV systems in rapidly changing atmospheric conditions," *J. Mod. Power Syst. Clean Energy*, vol. 9, no. 2, pp. 376–383, 2021, doi: 10.35833/MPCE.2019.000086.
- [19] K. H. Kapumpa and D. Chouhan, "A fuzzy logic based MPPT for 1MW standalone solar power plant," in *2017 Recent Dev. Control. Autom. Power Eng. RDCAPE 2017*, Noida, 2017, vol. 3, pp. 153–159, doi: 10.1109/RDCAPE.2017.8358258.



## Improving the Electrical Properties of the Smart Temperature Sensor Using CMOS (Si and SiC) Technology

**Mourad Hebali<sup>\*1</sup>, Benaoumeur Ibari<sup>1</sup>, Menouer Bennaoum<sup>1</sup>, Hocine Abdelhak Azzeddine<sup>1</sup>, Abdelkader Maachou<sup>1</sup>, Mohammed El-Amine Beyour<sup>1</sup>**

*<sup>1</sup>Department of Electrotechnical, University Mustapha Stambouli Mascara, 29000 Mascara, Algeria*

---

### Abstract

CMOS technology has various electronic applications, including the design of temperature sensor circuits. In this paper, the electrical properties of smart temperature sensor in 130 nm technology were improved using OrCAD PSpice software. The proposed CMOS circuit was developed to provide the first smart temperature sensor based on two different semiconductor technologies (Si and 4H-SiC) integrated on the same chip. These technologies are activated separately according to the temperature range (Low and High). The study of this smart sensor have shown that they operate under a low voltage less than 0.8 V and ultra-low power of order nW. In addition, it is characterized by high sensitivity and good linearity across a temperature range from – 120 °C to 500 °C. It is expected that the use of Si and 4H-SiC technologies for both temperature ranges (low and high) respectively will increase the life of this sensor.

**Keywords:** *Si, 4H-SiC, CMOS, Smart sensor, 130 nm technology*

---



---

# An Overview of Medium Access Control Protocols for Terrestrial Wireless Sensor Networks

Selahattin Kosunalp<sup>\*1</sup>

<sup>1</sup>Department of Computer Technologies, Gonen Vocational School, Bandirma Onyedi Eylul University, Bandirma/Balikesir, 10200 Türkiye

---

## Abstract

Wireless sensor networks (WSNs) have become a popular research area due to their interesting advantages such as cost-effective and large coverage. A typical WSN enables a specific number of tiny and resource-limited devices, so-called sensor nodes, to work together for achieving a common mission. The interoperability of these devices is therefore critical to provide the desired goal. Medium access control (MAC) protocols hold a significant role to ensure an efficient working operation among the nodes. A large body of MAC protocols have been proposed to maintain a good quality of service in terms of channel utilization and energy-efficiency since invention of WSNs. It is well-known that researchers produced several survey studies to cover the main MAC protocols, but there have been few attempts to examine the most-recent MAC protocols. Therefore, this study aims to re-visit the recent MAC approaches proposed in the last 3 years and outline their main mechanisms.

**Keywords:** *Networking, Wireless sensor networks, Medium access control*

---

## 1 INTRODUCTION

Wireless networking and communications have been one of most popular research areas as all real-life applications can benefit from a networking solution [1]. Recent technological developments in terms of wireless communication have paved a way for further utilization of wireless networking. Wireless sensor network (WSN) is perhaps the starting point in wireless networking domain and received a lot of attention over time. The first studies in WSN domain have been carried out for terrestrial purposes. This was later expanded to aerial and underwater platforms [2]. The practical applications of WSNs have been difficult to find a real-life trace. The application scope of WSNs is now high, thanks to recent developments in internet of things (IoT) and unmanned aerial vehicles (UAVs).

In recent years, WSNs have been combined with other areas that permits more efficient and intelligent solutions. For example, a traditional WSN scenario was designed to observe the animal activities in harsh environments with the aid of reinforcement learning strategy [3]. Due to remote deployment, UAVs are employed to collect the data from the nodes. In other work, WSNs, UAVs and IoT are integrated into a framework for agricultural goals [4]. It has its basics on the integration of WSNs with UAV for real-time data collection. UAVs act as a bridge from sensor nodes to a central point for providing an efficient IoT-enabled precision agriculture technique. On the other hand, WSNs are currently utilized in underwater networking as the environment faces rapidly changing conditions [5]. This work modified a terrestrial WSN approach to adapt it to varying conditions of underwater channels.

In all WSN-based applications, a critical effort is placed on the interoperability of sensor nodes for a better network operation. This can be achieved to permit the nodes to consume the energy source in an efficient manner. This is because energy is limited and redundant usage of energy will eventually result in short lifetime of an entire network. The most energy-consuming operation is wireless communication unit, so that MAC protocols take the responsibility of controlling the wireless transmission strategy of the nodes. A well-designed MAC protocol should be able to provide an acceptable performance in terms of channel utilization and delay, in addition to energy-efficient operation. Many MAC protocols have been designed and provided good performance outputs. This paper takes the opportunity of covering most-recent MAC protocols, in order to summarize the progress within MAC domain. We first start with a basic background information on WSN in the next section. Later, the operating principles of the MAC protocols included will be described in details. The paper will be concluded in the last section.

## 2 OVERVIEW OF WIRELESS SENSOR NETWORKS

### 2.1 Architecture of Sensor Node

A sensor node has different hardware units to complete its task. It has a sensor to sense data, a wireless communication unit to transmit the sensed data, a processor to process all activities and energy unit to supply the required power. To handle the limited-energy issue in WSNs, energy-harvesting phenomena is exploited to harvest energy from environment. For instance, a small solar panel has the potential to harvest solar energy for a perpetual operation of sensor nodes. This is demonstrated by fig. 1 below. Harvesting ambient energy has different problems to mitigate due to time-varying harvestable energy. There is maximum energy to harvest when sun is up, but there is no energy after sunset. Therefore, the harvested energy should be carefully consumed, and some energy should be saved when no energy is available to extract.

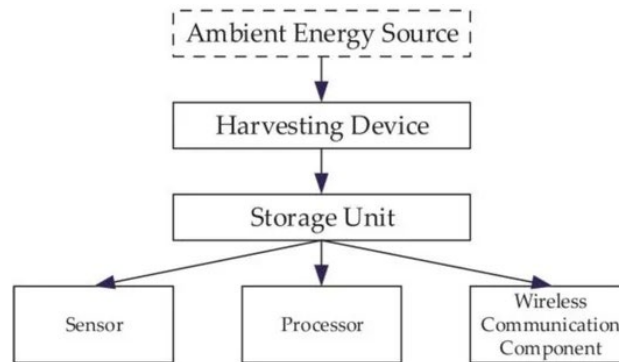


Figure 1. Main parts of a sensor node

### 2.2 Main Body of Wireless Sensor Networks

Traditionally, WSNs includes a group of sensor nodes that team up with each other to accomplish a common duty. An environmental information is the main target to be sensed and reported to a remote central point as depicted in fig. 2 below. The examples of environmental information are temperature, humidity, movement and pressure. Each sensor node shares and contends for the medium with equal chance. This is subject to concurrent transmissions from different nodes, leading to packet collisions. This essentially results in destruction of all collided packets and each collided packet will be retransmitted. This process consumes extra energy and also reduces the channel utilization. Therefore, an efficient MAC protocol should avoid packet collisions. Previous MAC protocols suffer from high-complexity nature and high overhead. This is because the performance evaluations are mostly conducted using simulation-based tool that present perfect conditions and no limitations. Various unrealistic assumptions are employed to achieve better performance. However, the real sensor nodes are limited in size, memory and energy capacity. This makes the implementation of high-complexity MAC protocols difficult in practice. Thus, there is a significant need to develop simpler protocols meeting the capacity of sensor nodes.

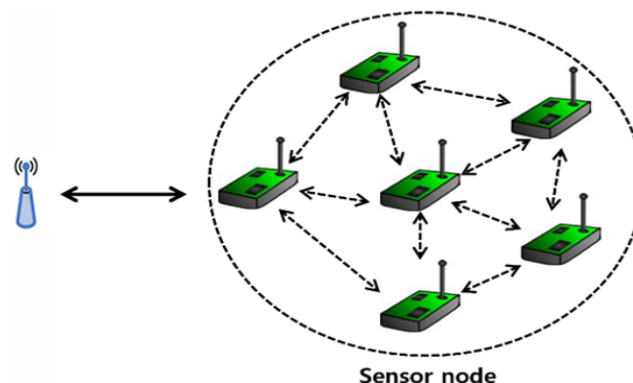


Figure 2. A typical WSN environment

## 3 MAC PROTOCOLS

The IRIS protocol is a novel cross-layer protocol designed for long-range WSNs with an ultra-low duty cycle of less than 1%, enabling energy-efficient monitoring of extensive infrastructures such as rivers, coastlines, and

pipelines [6]. It integrates network discovery, medium access control, and routing, ensuring operation with minimal energy consumption and adhering to spectrum regulations. The protocol is robust against unreliable wireless connections and node failures, using periodic ping packets for route discovery and data forwarding. Simulations and long-term network tests have validated its performance, demonstrating efficient route formation and stable operation over extensive deployment.

Another work proposes a framework for designing wireless network protocols using distributed reinforcement learning (RL) to enhance medium access control (MAC) in IoT and sensor networks [7]. It models MAC behavior as a Multi-agent Markov Decision Process (MAMDP) and uses temporal difference RL methods, allowing network nodes to independently learn optimal transmission strategies to maximize throughput. Unlike traditional protocols like ALOHA, which perform poorly under high load and heterogeneous conditions, the proposed RL-based approach adapts dynamically to traffic variations and topological changes, achieving near-benchmark performance with improved fairness and efficiency. The framework is scalable and effective in diverse network conditions, ensuring equitable bandwidth distribution and adaptability to dynamic traffic environments.

A recent study presents an enhanced TDMA-based medium access control (MAC) protocol designed specifically for wireless sensor networks (WSNs) integrated with Internet of Things (IoT) capabilities [8]. The proposed scheme, named IoT-TDMA, aims to improve channel throughput and reduce latency in WSNs by leveraging IoT features. Practical implementations on real-world single-hop and multi-hop network topologies demonstrated significant performance improvements over existing MAC protocols, particularly in terms of reduced end-to-end delay and higher throughput. The study also highlights the energy efficiency of IoT-TDMA, though it notes that energy consumption increases with higher traffic loads due to frequent packet transmissions via the Internet. Overall, IoT-TDMA shows promise for future applications in IoT-enabled WSNs, with further research suggested on fully developing MAC protocols based on this approach and conducting large-scale experiments.

ALOHA is the first medium access control (MAC) protocol, known for its simplicity but limited by low channel throughput due to packet collisions. The paper aims to improve the ALOHA protocol's performance by increasing channel utilization and reducing collisions, particularly in IoT applications using reinforcement learning [9]. Instead of fixed-length packets, the proposed method uses dynamically selected packet lengths to reduce collisions and improve throughput. The enhanced ALOHA protocol is adapted for IoT scenarios, where smart devices communicate with minimal human intervention. An IoT-ALOHA version is proposed, leveraging IoT capabilities to make smarter transmission decisions. A stateless Q-learning algorithm is used to optimize the transmission policy, aiming to maximize throughput. Q-learning helps determine the best times to transmit packets based on previous transmission outcomes. The proposed enhancements result in a significant throughput increase from about 18% with traditional ALOHA to approximately 58%. The paper validates the enhancements through practical implementations and analytical models, demonstrating notable performance improvements.

Another attempt explores the development of an energy-efficient MAC protocol designed to extend the lifetime and reduce latency in WSNs [10]. The proposed LELLMAC protocol aims to improve energy efficiency, reduce latency, and increase throughput in WSNs. It utilizes a hybrid algorithm combining multiple strategies to optimize the protocol's performance. Logical Link Decision (LLD) is used for sending data and adaptive reception methods for receiving data. The protocol's performance is evaluated through extensive simulations and analytical models. LELLMAC significantly reduces energy consumption, latency, and improves throughput compared to existing techniques. The LELLMAC protocol outperforms existing MAC protocols in terms of energy efficiency, latency, and throughput.

A fresh paper focuses on developing an improved Media Access Control (MAC) protocol tailored for wireless sensor networks (WSNs) used in mission-critical applications [11]. The core of the paper introduces the Mission-Critical MAC (MC-MAC) protocol. This protocol employs an adaptive learning-centered approach to optimize channel access and route selection based on the current network scenario. It ensures that critical data packets are transmitted with higher priority to meet time-bound requirements. Machine learning techniques are utilized to dynamically adjust to changing network conditions and optimize the transmission paths for critical data packets. The proposed idea aims to provide a reliable and timely transfer of data by considering factors like network traffic, node energy levels, and link quality. The design and implementation section details the system model and the functioning of the MC-MAC protocol. It explains how the protocol adapts to network changes and allocates channels for data transmission. The MC-MAC protocol is designed to support varying network scenarios, ensuring efficient and reliable communication for mission-critical applications. The paper provides a thorough evaluation of the MC-MAC protocol through simulations. The results demonstrate that the proposed protocol outperforms existing protocols in terms of throughput, end-to-end delay, and energy efficiency. The MC-MAC protocol shows

significant improvements in handling emergency data packets, ensuring they are delivered within the required time bounds.

## 4 CONCLUSION

Wireless sensor networks (WSNs) have long been an attractive study area for at least 20 years. Medium access control (MAC) protocol design for terrestrial WSNs received a lot of research activities and currently its popularity is still increasing. With the development of internet of things (IoT), artificial intelligence (AI) and reinforcement learning (RL), more powerful and intelligent MAC protocols are designed for diverse environments, from aerial to underwater. Therefore, this paper places its emphasis on reviewing the recent MAC protocols proposed for terrestrial WSNs. Several MAC schemes are introduced along with their operating principles.

## References

- [1] W. Saad, M. Bennis, M. Mozaffari, and X. Lin, X. *Wireless Communications and Networking for Unmanned Aerial Vehicles*, Cambridge University Press, 2020.
- [2] Q. Wang, H. N. Dai, Q. Wang, M. K. Shukla, W. Zhang, and C.G. Soares, "On connectivity of UAV-assisted data acquisition for underwater internet of things," *IEEE Internet of Things Journal*, vol. 7, no. 6, pp. 5371–5385, 2020.
- [3] S. Ergunsah, V. Tumen, S. Kosunalp, and K. Demir, "Energy-efficient animal tracking with multi-unmanned aerial vehicle path planning using reinforcement learning and wireless sensor networks," *Concurrency and Computation: Practice and Experience*, vol. 35, no. 4, art. no. e7527, 2023.
- [4] P.K. Singh and A. Sharma, "An intelligent WSN-UAV-based IoT framework for precision agriculture application," *Computers and Electrical Engineering*, vol. 100, art. no. 107912, 2022.
- [5] S. H. Park, P. D. Mitchell, and D. Grace, "Reinforcement learning based MAC protocol (UW-ALOHA-QM) for mobile underwater acoustic sensor networks," *IEEE Access*, vol. 9, pp. 5906-5919, 2020.
- [6] Y. Chu, P. D. Mitchell, D. Grace, J. Roberts, D. White, and T. Mickus, "IRIS: A low duty cycle cross-layer protocol for long-range wireless sensor networks with low power budget," *Computer Networks*, vol. 225, art. no. 109666, 2023.
- [7] H. Dutta and S. Biswas, "Distributed reinforcement learning for scalable wireless medium access in IoTs and sensor networks," *Computer Networks*, vol. 202, art. no. 108662, 2022.
- [8] S. Kosunalp and Y. Kaya, "IoT-TDMA: A performance evaluation of TDMA scheme for wireless sensor networks with Internet of Things," *Concurrency and Computation: Practice and Experience*, vol. 34, no. 21, art. no. e7063, 2022.
- [9] S. Acik, S. Kosunalp, M.B. Tabakcioglu, and T. Iliev, "Improving the performance of ALOHA with internet of things using reinforcement learning," *Electronics*, vol. 12, no. 17, art. no. 3550, 2023.
- [10] T. Hai, J. Zhou, T. V. Padmavathy, A. Q. Md, D. N. A. Jawawi, and M. Aksoy, "Design and validation of lifetime extension low latency MAC protocol (LELLMAC) for wireless sensor networks using a hybrid algorithm," *Sustainability*, vol. 14, no. 23, art. no. 15547, 2022.
- [11] A.R. Raut and S.P. Khandait, "An intelligent MAC protocol for mission critical applications in wireless sensor networks," *Concurrency and Computation: Practice and Experience*, vol. 35, no. 23, art. no. e7813, 2023.





---

## Silicon-Integrated GaAs Single-Junction Solar Cell: Design and Performance Improvement

**Mohammed El-Amine Beyour<sup>\*1</sup>, Mourad Hebali<sup>2</sup>, Benaoumeur Ibari<sup>2</sup>, Menouer Bennaoum<sup>2</sup>, Hocine Abdelhak Azzeddine<sup>1,2</sup>, Abdelkader Maachou<sup>1</sup>**

<sup>1</sup>LSTE Laboratory, University of Mascara, Mascara 29000, Algeria

<sup>2</sup>Department of Electrotechnical, University Mustapha Stambouli Mascara, 29000 Mascara, Algeria

---

### Abstract

Recently, the integration of silicon technology with III-V semiconductor materials has become critical for the development of future solar devices, particularly solar cells. In this paper, the electrical performance of a Si/GaAs/Si single-junction solar cell was enhanced by varying the position of the GaAs layer using SILVACO 2D-Atlas simulation software. Under standard illumination conditions (AM1.5G) and at room temperature, various static characteristics including current-voltage (I-V) and power-voltage (P-V) were analyzed. These static properties were used to extract various electrical parameters such as short-circuit current ( $I_{sc}$ ), open-circuit voltage ( $V_{oc}$ ), maximum power ( $P_{max}$ ), and fill factor (FF). The electrical characteristics of the cell improved as the GaAs layer approached its cathode electrode, resulting in enhanced performance of the Si/GaAs/Si solar cell with changes in the GaAs layer position. Among all the GaAs layer positions tested, the ITO/p-Si/Si/GaAs/n-GaAs/ITO solar cell demonstrated the highest performance and optimal electrical parameters.

**Keywords:** *Silicon technology, GaAs, Single-junction solar cell, Static characteristics, Electrical parameters*

---



## Microstrip Patch Antenna with Triple-Band Using Metamaterial

Hadda Ouguissi<sup>1</sup>, Nail Alaoui<sup>\*2</sup>

<sup>1</sup>Materials, Energetic Systems, Renewable Energies, and Energy Management Laboratory (LMSEERGE), Faculty of Technology, Ammar Thelidji University of Laghouat, Laghouat, Algeria

<sup>2</sup>Research Laboratory for Modeling, Simulation and Optimization of Real Complex Systems, University of Djelfa, 17000 Djelfa, Algeria

---

### Abstract

This paper introduces the concept of a multiband microstrip patch antenna that use a Complementary Split Ring Resonator (CSRR). By incorporating a complementary split ring resonator (CSRR) onto the ground plane of the standard rectangular patch antenna, several frequency bands can be achieved, resulting in the reduction of the antenna's size. This paper analysed and compared the outcomes of the microstrip antenna with two, four, and six CSRR inclusions. The multiband antenna design became practical due to the quasi-static resonance features of the complementary split square resonators.

**Keywords:** CST Studio, Metamaterial, Complementary split ring resonator, Microstrip antenna, Triple-band

---



## Dipole Antenna Based on Metamaterials for RFID

Hadda Ouguissi<sup>1</sup>, Nail Alaoui<sup>2\*</sup>

<sup>1</sup>*Materials, Energetic Systems, Renewable Energies, and Energy Management Laboratory (LMSEERGE), Faculty of Technology, Ammar Thelidji University of Laghouat, Laghouat, Algeria*

<sup>2</sup>*Research Laboratory for Modeling, Simulation and Optimization of Real Complex Systems, University of Djelfa, 17000 Djelfa, Algeria*

---

### Abstract

The paper presents an innovative approach to antenna design miniaturization through the utilization of metamaterials. In order to enhance frequency characteristics while simultaneously reducing antenna size, we propose an innovative approach. The foundation of this approach lies in the interconnection of a resonant element with two divided circles. This investigation focuses on the parameters of the proposed antenna, which include the resonant frequency, return loss, bandwidth, radiation pattern, gain, directivity, electromagnetic field, and current supplied. All simulation results are produced by CST software.

**Keywords:** *CST Studio, Metamaterial, Complementary split ring resonator, Microstrip antenna, Triple-band*

---



## Machine Learning Based Diamond Cut Quality Classification

Mustafa Alptekin Engin<sup>\*1</sup>, Latif Akcay<sup>1</sup>

<sup>1</sup>Department of Electrical and Electronics Engineering, Bayburt University, Bayburt, Türkiye

### Abstract

Diamond, the hardest known mineral, must undergo processing in order to be utilized in jewelry. The cut of the diamond is the least agreed of the relevant parameters as it has an effect on the appearance of the light behaviour in the diamond. The classification of these diamond parameters, which have a non-linear relationship between them, is a complex process. In this study, machine-learning classification of diamond cut quality was performed using 9 parameters on 53940 diamonds. Price, carat, colour, clarity, length, width, depth, total depth percentage and table parameters were used to determine the cut quality defined as fair, good, very good, premium, ideal. The current study utilises a number of classification method, including ensemble bagged tree, linear discriminant, support vector machine, k nearest neighbour and naïve bayes, as well as neural network algorithms. The data set was divided into two distinct subsets, designated as the training and test phases, respectively. The training subset constituted 90% of the data set, while the test subset constituted 10%. In the training phase, a 25% hold-out validation method was employed. Among the machine learning-based methods, an 80.5% classification accuracy value was calculated by hyperparameters optimisation of the trilayered neural network classifier.

**Keywords:** *Diamond cut classification, Machine learning, Classification, Trilayered neural network*

## 1 INTRODUCTION

The economic and cultural significance of diamonds in the global context has a far-reaching impact that transcends geographical boundaries. Furthermore, this material is employed in a multitude of fields, including engineering, art, and science, due to its scarcity, flexibility, and aesthetic appeal. The use of diamonds, together with other precious materials, such as gold and silver, in the creation of jewellery has become a global symbol of wealth, loyalty, and prestige. Diamond extraction and distribution represents a multifaceted sector that transcends geographical boundaries, economic cycles and ethical values. As a result, the pathway of diamond extraction and distribution can be considered a complex expression of the global political network. [1]. The 2024 Diamond Global Market Report indicates that the market size of diamonds, which has been developing strongly in recent years, is increasing from \$2.43 billion in 2023 to \$2.59 billion in 2024, with a compound annual growth rate (CAGR) of 6.7% [2]. The same report predicts that growth in 2028 will reach \$3.29 billion. The forecast period will see the emergence of new trends, including the customisation of jewellery, an increase in disposable income, shifts in consumer behaviour and the integration of artificial intelligence in the grading of diamonds. It is notable that numerous studies employing machine learning methodologies have been conducted in the field of diamond grading. In one of the studies on overcoming human error in diamond price prediction, a random forest regression method through machine learning demonstrated a 98% success rate [3]. In another study on the use of extreme learning machines for the prediction of the diamond price range, an 83.75% classification accuracy was calculated [4]. In another study on the prediction of diamond prices using WEKA data mining software, different machine learning classifiers were compared, with the random forest classifier emerging as the most successful method [5]. In a study on the evaluation of the prediction performance of supervised machine learning algorithms for the diamond pricing model, it was found that Random Forest Regression was the most successful method [6]. However, it should be noted that all the studies mentioned above are on the estimation of diamond pricing. In addition to the natural properties of the diamond mineral, it is mentioned in the literature that the cut made during the processing stage is also very important [7]. Therefore, in this study, the effects of other properties of diamond on the cut quality classification process were investigated. In this study, the Kaggle Diamond Record Repository was employed to train machine learning classifiers [8]. Among the machine learning classification algorithms utilised, the trilayered neural network classifier was identified as the most efficacious method, exhibiting a classification accuracy of 80.5% via hyperparameters optimisation. The following framework outlines the structure of this study: In Part 2, the database and classification methods are presented. In Part 3, the findings on machine learning-based classification models are discussed. Finally, in Part 4, the overall analysis of the results is presented.

## 2 MATERIAL AND METHOD

The methodology employed in the study is illustrated in Figure 1.

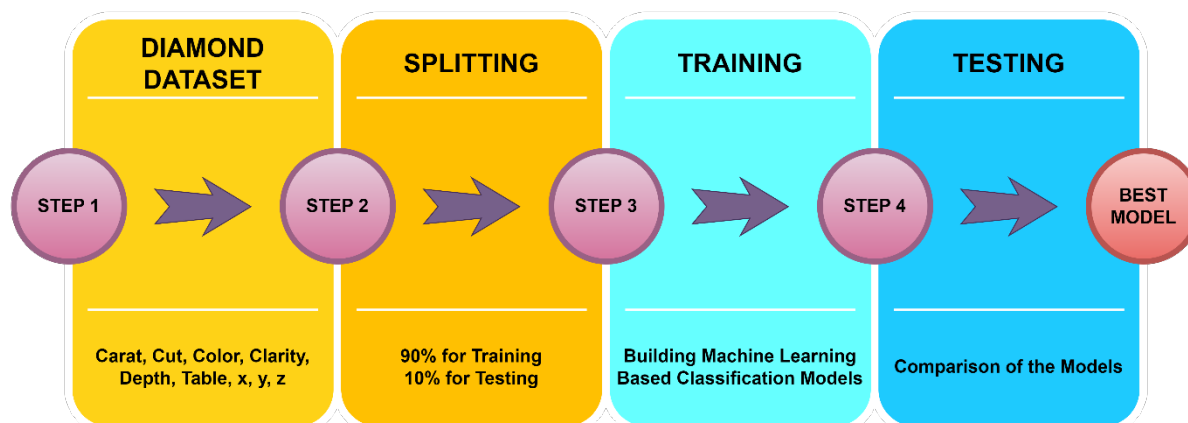


Figure 1. Process steps of the study

### 2.1 Dataset

In this study, the Diamond Record Repository in the Kaggle community, which provides a forum for researchers to discuss and share different machine learning techniques, was employed [8]. The database contains 53940 diamond features. Additionally, the descriptive features of the database are presented in Table 1.

Table 1. Diamonds dataset

Feature	Description	Value Range
Cut	Quality of the cut	Fair, Good, Very Good, Premium, Ideal
Carat	Weight of the diamond	0.20-5.01
Color	Diamond colour	J, I, H, G, F, E, D
Clarity	A measurement of how clear the diamond is	I1, SI2, SI1, VS2, VS1, VVS2, VVS1, IF
Table	Width of top of diamond relative to widest point	43-95
x	Length in mm	0-10.74
y	Width in mm	0-58.90
z	Depth in mm	0-31.8
Depth	Total depth percentage= $z/mean(x,y)$	43-79
Price	Price in US dollars	326-18823

### 2.2 Data Splitting

The initial step in the construction of the classification model to be employed with machine learning is to divide the database into two distinct subsets, with a specific ratio allocated to each, for use in the subsequent training and test phases. In this study, the ratio of 90/10 was chosen for the training and testing phases, respectively. In order to ensure a blind and fair classification, the data included in this ratio were randomly selected.

### 2.3 Classification

Once the training data had been selected, the classification model was developed utilizing a number of different algorithms, including support vector machines (SVM), k-nearest neighbor (KNN), ensemble bagged tree (EBT), trilayered neural network (TNN), naïve bayes (NB), and linear discriminant (LDA). These algorithms are frequently preferred in classification studies.

In the support vector machines method, the quadratic kernel function was selected. In the case of the K-nearest neighbour (KNN) algorithm, the coarse method, which utilises a value of 100 as the number of nearest neighbours, was employed in conjunction with the Euclidean distance metric. In the EBT algorithm, the maximum number of

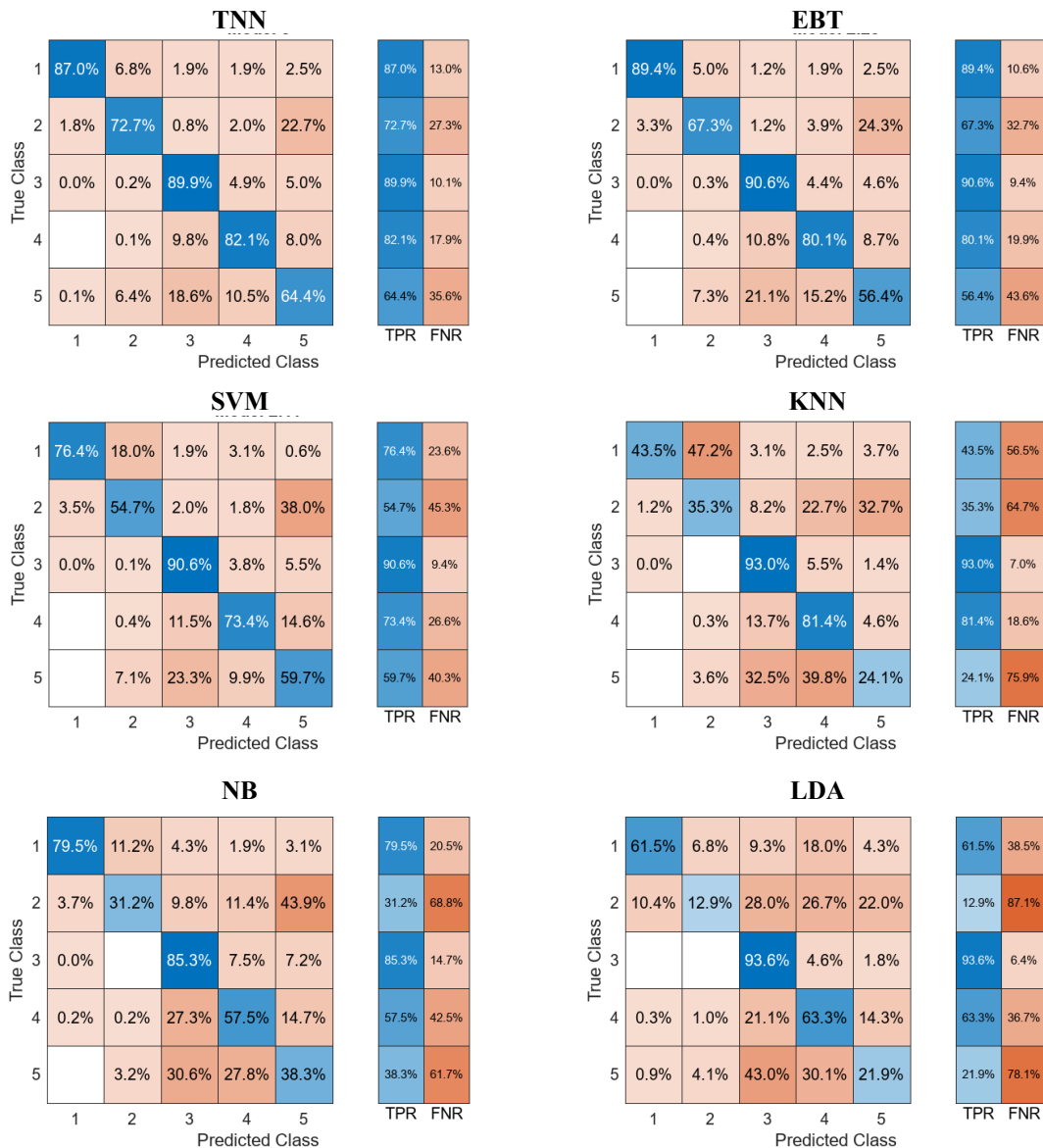
splits is 48545, and the number of learners is 30. In the TNN method, the layers were utilised with ReLU activation, with a regularisation strength value of 3.7321e-05, and layers of size 70, 295 and 57, respectively. In the NB method, a Gaussian kernel was utilised, whereas in the LDA method, the full covariance structure was employed.

### 3 RESULTS

Table 2 presents a comparative analysis of the machine learning-based classification models employed in this study in terms of classification accuracy. Figure 2 presents the test confusion matrices, with the true positive rates (TPR) and false negative rates (FNR) expressed as a percentage for each model.

**Table 2.** Comparison of the classification models

Method	Accuracy
TNN	80.5
EBT	78.1
SVM	75.6
KNN	67.9
NB	62.6
LDA	61.5



**Figure 2.** Test confusion matrices of classification models

## 4 CONCLUSION

In this study, we evaluated the performance of various classifiers in predicting the cut quality of 53,940 diamonds, categorized into five grades: Fair, Good, Very Good, Premium, and Ideal. The classifiers assessed included the Trilayered Neural Network (TNN), Ensemble Bagged Trees (EBT), Support Vector Machines (SVM), K-Nearest Neighbors (KNN), Naive Bayes (NB), and Linear Discriminant Analysis (LDA). The confusion matrices for each model provided detailed insights into their classification capabilities, and we also compared the True Positive Rates (TPR) and False Positive Rates (FPR) for each classifier. The results demonstrated that the TNN classifier outperformed the others, achieving the highest overall accuracy. Specifically, TNN exhibited the highest TPR across most cut quality grades, indicating its superior ability to correctly identify the true quality of diamonds. Furthermore, TNN maintained relatively low FPRs, minimizing the rate of misclassifications. The EBT classifier also showed strong performance, closely trailing TNN. EBT's ensemble approach, which combines multiple decision trees, resulted in high TPRs, particularly for the middle grades (Good, Very Good, Premium). The SVM classifier demonstrated solid accuracy and balanced TPRs and FPRs across all grades. Its strength in finding optimal hyperplanes for class separation made it a reliable choice, particularly effective in distinguishing between well-defined classes like Premium and Ideal. The KNN classifier displayed moderate performance, with decent TPRs for the lower and middle grades (Fair, Good, Very Good), but it struggled with the higher grades (Premium, Ideal), leading to higher FPRs. The LDA classifier yielded moderate results, with reasonable TPRs for the middle grades but higher FPRs overall. LDA's assumption of normally distributed classes likely limited its effectiveness in handling the complex variability of diamond attributes. The NB classifier showed the least satisfactory performance, with lower TPRs and higher FPRs across all grades. The strong independence assumption of NB is less suitable for this dataset, where attributes are likely correlated, leading to poorer classification performance. In summary, the Trilayered Neural Network classifier emerges as the most effective tool for the classification of diamond cut quality, followed closely by Ensemble Bagged Trees and Support Vector Machines. These classifiers demonstrated high TPRs and manageable FPRs, making them reliable for practical applications in diamond quality assessment. Ultimately, both the gemological industry and consumers will benefit from future work that builds on the current findings to develop more accurate and reliable diamond cut quality classification models by adding additional features such as advanced gemological parameters or high-resolution imaging data to provide more comprehensive input to the models.

## References

- [1] Research and Markets Ltd., "Global diamond market overview, 2024-29," [Online], Jun. 08, 2024. Available: <https://www.researchandmarkets.com/reports/5953034/global-diamond-market-overview-29>
- [2] The Business Research Company, "Diamond market trends, growth drivers, share forecast to 2033," [Online], Jun. 08, 2024. Available: <https://www.thebusinessresearchcompany.com/report/diamond-global-market-report>
- [3] T. Ramaswamy, S. Sanjana, T. Meghana, "Machine learning algorithms for diamond price prediction," *European Chemical Bu.*, vol. 12, no. 8, pp. 2529–2534, 2023.
- [4] J. Ramírez, D. Zabala-Blanco, R. Ahumada-García, J. P. Rivelli Malc, A. D. Firoozabadi, and M. Flores-Calero, "Extreme learning machines for predict the diamond price range," in *2023 IEEE CHILEAN Conference on Electrical, Electronics Engineering, Information and Communication Technologies (CHILECON)*, 2023.
- [5] M. S. Amzad Basha, M. Martha Sucharitha, A. U. Devi, M. Ashok, and P. M. Oveis, "Exploring machine learning models to predict the Diamond price: A data mining utility using weka," in *2023 9th International Conference on Advanced Computing and Communication Systems (ICACCS)*, 2023.
- [6] S. N. Kigo, E. O. Omondi, and B. O. Omolo, "Assessing predictive performance of supervised machine learning algorithms for a diamond pricing model," *Sci. Rep.*, vol. 13, no. 1, art. no. 17315, 2023.
- [7] T. M. Moses *et al.*, "A foundation for grading the overall cut quality of round brilliant cut diamonds," *Gems Gemol.*, vol. 40, no. 3, pp. 202–228, 2004.
- [8] S. Agrawal, "Diamonds," [Online], Jun. 08, 2024. Available: <https://www.kaggle.com/datasets/shivam2503/diamonds>



---

## Study of New Model of SBD Structure Proposed to Elaborate Mixer Design

Reguieg Khadidja<sup>\*1</sup>, Souar Zeggai<sup>2</sup>, Hebali Mourad<sup>1</sup>

<sup>1</sup>Electronic Department, University of Mascara, Algeria

<sup>2</sup>Electronic Department, University of Saida, Algeria

---

### Abstract

This paper reports on the use of a Schottky Barrier Diode (SBD) as a non-linear element to improve mixer performance. In the field of electronics, a mixer is a device that combines two or more electrical signals into a composite output signal.

Mixers are essential components in many systems, including radio receivers, transmitters, radar systems, and satellite communications. They are used to perform frequency conversion, shifting signals from one frequency range to another. The performance of mixers is characterized by parameters like conversion gain, conversion loss, and noise figure. Researches in this domain insure that parameter's mixer significantly influenced by the choice of material combination used to form the metal/semiconductor (M/Sc) junction of non linear element. Our model employs gold (Au) as metal and indium phosphide (InP) from the III-V semiconductor compound to create the junction of SBD. The designed diode is a circular planar type with an average radius of 0.5  $\mu\text{m}$  and a junction capacitance of 8 fF. The doping density of the sample is  $5 \times 10^{17} \text{ cm}^{-3}$ . This model ensures an ideality factor ( $\eta$ ) of 1.31 and a saturation current ( $I_s$ ) of 4.17  $\mu\text{A}$ , and it can achieve a sensitivity ( $S_i$ ) of 27.96 A/W. These parameters are critical for characterizing the SBD and and subsequently guaranteeing valuable metrics for mixer performance. The article concludes with the summary and perspective developments of mixers.

**Keywords:** Mixer, SBD, Sensitivity, Ideality factor

---





---

## Investigation of the Electrical Behavior of DG-MOSFET Transistors in Silicon Carbide Using Series and Parallel Equivalent Electronic Circuits

**Mourad Hebali<sup>\*1</sup>, Benaoumeur Ibari<sup>1</sup>, Hocine Abdelhak Azzeddine<sup>1</sup>, Bennaoum Menouer<sup>1</sup>, Ibrahim Farouk Bouguenna<sup>1</sup>, Mohammed El-Amine Beyour<sup>1</sup>**

*<sup>1</sup>Department of Electrotechnical, University Mustapha Stambouli Mascara, 29000 Mascara, Algeria*

---

### Abstract

In this paper, the electrical behavior of Double Gate (DG) MOSFET transistors in SiC with 130 nm technology was investigated using two equivalent electronic circuits (Series and Parallel) based on the Single Gate (SG) MOSFET transistor. The  $I_D$ - $V_{DS}$ ,  $I_D$ - $V_{GS}$ , and  $g_m$ - $V$  characteristics, as well as subthreshold operation of these DG-MOSFET transistors, were studied and compared with the SG-MOSFET transistor using OrCAD PSpice with the BSIM3v3 model. The obtained results showed that the different transistors are characterized by an ultra-low  $I_{OFF}$  leakage current of the order of 1 pA, a very high  $I_{ON}/I_{OFF}$  ratio of the order of  $10^7$  and  $10^6$ , and a high Subthreshold Slope (SS) of the order of 86 mV/dec and 85 mV/dec for the transistors in 4H-SiC and 6H-SiC, respectively. They also operate under a low voltage less than 1.2V and low power for both models like the SG-MOSFET transistor, especially the series DG-MOSFET transistor, which is characterized by ultra-low power consumption. Additionally, these transistors also exhibited higher transconductance efficiency, especially the parallel DG-MOSFET transistor.

**Keywords:** 4H-SiC, 6H-SiC, 130nm technology, DG-MOSFET transistor, BSIM3 model

---



## Towards Service Discovery and Selection Approaches in IoT Applications

Selahattin Kosunalp<sup>\*1</sup>, Yunus Kaya<sup>2</sup>

<sup>1</sup>Department of Computer Technologies, Gonen Vocational School, Bandirma Onyedi Eylul University, Bandirma/Balikesir, 10200 Türkiye

<sup>2</sup>Department of Electronics and Automation, Bayburt University, Bayburt, 69010 Türkiye

### Abstract

The Internet of Things (IoT) is a transformative paradigm where everyday physical objects are interconnected through the internet, equipped with sensors, software, and network connectivity. These smart devices can collect, exchange, and act upon data autonomously, enabling real-time monitoring, control, and optimization of processes across various environments such as homes, cities, industries, and beyond. IoT enhances operational efficiency, promotes innovative services, and improves the quality of life by seamlessly integrating the physical and digital worlds. Service discovery is a critical component in IoT applications for several reasons. IoT environments are inherently dynamic, with devices constantly joining, leaving, or moving within the network. Efficient service discovery helps optimize resource usage by ensuring that IoT devices can find the most appropriate services quickly and with minimal energy consumption. The scope of this paper is to cover most recent IoT service discovery approaches.

**Keywords:** *Internet of things, Service discovery, Service selection, Objects*

## 1 INTRODUCTION

The Internet of Things (IoT) refers to the network of interconnected physical devices embedded with sensors, software, and other technologies, enabling them to collect and exchange data over the internet [1]. Key components of IoT include sensors and actuators, connectivity, data processing, and user interfaces. Sensors gather data from the environment, while actuators perform actions based on the data received. Connectivity involves the various communication protocols and networks that facilitate data transmission between devices. Data processing encompasses the analysis and interpretation of collected data, often leveraging cloud computing resources. User interfaces, such as mobile apps or dashboards, allow users to interact with and manage IoT devices. The architecture of IoT typically consists of four layers: the perception layer (sensors and actuators), the network layer (connectivity), the processing layer (data processing and storage), and the application layer (user interfaces and applications) [2]. This layered approach ensures efficient data flow, management, and utilization, ultimately enabling a wide range of applications from smart homes and cities to industrial automation and healthcare.

Service discovery and selection in IoT (Internet of Things) applications refer to the mechanisms and processes by which IoT devices identify, locate, and choose services available within a network [3]. These services could include data acquisition, data processing, storage, communication, and other functionalities that IoT devices might need to perform their tasks. IoT environments are highly dynamic, with devices frequently joining or leaving the network, changing locations, or altering their operational status. Service discovery allows devices to continuously identify available services and adapt to these changes. IoT ecosystems often consist of heterogeneous devices from different manufacturers, each with varying capabilities and communication protocols. Effective service discovery and selection mechanisms ensure that these devices can work together seamlessly. IoT devices are often resource-constrained, with limited processing power, memory, and energy. By efficiently discovering and selecting the most appropriate services, these devices can optimize their resource usage and extend their operational lifespan. As the number of IoT devices in a network grows, manual configuration and management of services become impractical. Automated service discovery and selection enable the system to scale efficiently without significant manual intervention. Different IoT applications have varying QoS requirements, such as latency, bandwidth, reliability, and security. Service selection allows IoT devices to choose services that meet their specific QoS needs, ensuring the overall system performance and user satisfaction. In the event of service failures or disruptions, effective discovery and selection mechanisms allow IoT devices to quickly find alternative services, enhancing the system's fault tolerance and resilience.

IoT service discovery relying on a central point refers to a centralized architecture where a central server or service registry manages and facilitates the discovery of IoT services. In this model, IoT devices and services register their capabilities, endpoints, and metadata with the central point. When an IoT device or application needs to discover a service, it queries the central registry to obtain the necessary information. Centralized control makes it easier to manage, update, and monitor IoT services and devices. Centralized databases can provide fast and efficient lookup for services, reducing the time and complexity involved in service discovery. A central point can enforce security policies and authentication, ensuring that only authorized devices and services can interact. The central registry represents a single point of failure. If it goes down, the entire service discovery mechanism can be disrupted. Depending on the network architecture and distance, querying a central server may introduce latency, which can be critical in time-sensitive applications. While centralized IoT service discovery offers several benefits, it is essential to balance these with the potential challenges, especially regarding reliability, scalability, and security. Some IoT architectures also explore decentralized or distributed approaches to mitigate these challenges.

IoT service discovery without relying on a central point refers to decentralized or distributed approaches where devices autonomously discover and interact with each other without the need for a centralized server [4]. This model leverages peer-to-peer (P2P) communication, distributed hash tables (DHTs), and other decentralized protocols to facilitate service discovery. Eliminating a single point of failure enhances system reliability and availability. If one node fails, the system can continue to operate. Decentralized systems can scale more easily as each device can contribute to the service discovery process, reducing the load on any single point. Localized discovery can reduce latency, as devices can find and connect to nearby services directly. Decentralized architectures can provide better privacy, as there is no central repository of data that can be targeted by attackers. Implementing decentralized discovery protocols can be more complex than centralized approaches, requiring sophisticated algorithms for efficient operation. IoT devices often have limited computational and communication resources, which can constrain the implementation of decentralized discovery mechanisms. Decentralized IoT service discovery offers a robust alternative to centralized systems, particularly in environments requiring high resilience, scalability, and privacy. However, it necessitates careful design to address the inherent challenges and ensure efficient and secure operation. This paper aims to summarize recent advancements in IoT service discovery and selection approaches, highlighting the progress made in this domain.

## 2 IOT SERVICE DISCOVERY AND SELECTION APPROACHES

A novel approach to improving IoT service recommendations through a hybrid system that integrates collaborative filtering with ontology is presented in [5]. The authors address the challenge of information overload caused by the proliferation of smart devices and IoT services. Traditional IoT recommender systems often rely on data from users' own devices, which can lead to inefficiencies due to missing data. The proposed hybrid technique leverages Social IoT (SIoT) to utilize data generated by IoT devices owned by users' friends and friends of friends. This approach incorporates social relationships among objects into the recommendation process, enhancing personalization and accuracy. Ontology is used to model the SIoT, capturing the relationships between objects and users, while collaborative filtering predicts ratings and generates recommendations. In summary, this paper contributes to the field by introducing a hybrid recommender system that effectively combines social network principles with IoT data, resulting in more accurate and personalized IoT service recommendations. The integration of ontology and collaborative filtering in the SIoT context presents a significant advancement in addressing the complexities and challenges of IoT service recommendation systems.

A recent study presents a method for optimizing the composition of IoT services based on Quality of Service (QoS) constraints [6]. The authors address the complexity of selecting appropriate IoT services from a vast number of candidates that offer similar functionalities but differ in QoS properties. This selection process is an NP-hard problem due to the high number of candidate services and the need to meet both functional and non-functional user requirements. To tackle this challenge, the authors propose a hybrid approach combining Genetic Algorithms (GA) and Neural Networks (NN) for global QoS optimization in large-scale environments. The method involves decomposing QoS attributes into multiple levels and using a neural network to classify IoT services into different QoS categories. Initially, GA is applied to theoretical QoS levels to obtain an ideal theoretical composition. The neural network then evaluates and filters out inappropriate concrete services, retaining only those that match the QoS categories of the ideal theoretical composition. Finally, GA is applied again to these filtered services to achieve a near-optimal concrete composition. The proposed approach is demonstrated to outperform existing methods in terms of composition time, hypervolume indicator, and compositional optimality, while maintaining similar performance to other advanced techniques like TS-QCA. The effectiveness of the approach is validated through simulations, showing its ability to improve both the search space and execution time for IoT service compositions under global QoS constraints. This work contributes significantly to the field by providing a scalable

and efficient method for QoS-aware IoT service composition, leveraging the strengths of genetic algorithms and neural networks.

Another work addresses the challenge of efficiently combining IoT services to balance energy consumption and Quality of Service (QoS) [7]. The increasing deployment of smart devices in IoT has necessitated the development of methods to integrate services provided by these devices into comprehensive composite services that meet user demands and optimize energy usage. It proposes a novel approach called FSCA-EQ (Fast Service Composition Algorithm - Energy and QoS aware), which utilizes hierarchical optimization. This approach involves two main steps: first, using the Compromise Ratio Method (CRM) to pre-select services that meet the user's QoS requirements, and second, applying the concept of relative dominance to choose the optimal service based on its energy profile, QoS attributes, and user preferences. The CRM is used to identify services that provide a good balance of cost, execution time, and reliability, while the relative dominance concept ensures the selected services also minimize energy consumption. The proposed FSCA-EQ algorithm is validated through simulations, showing superior performance compared to other methods in terms of selection time, energy consumption, and overall optimality. The results demonstrate that FSCA-EQ can quickly and effectively balance QoS levels and energy consumption, making it particularly suitable for large-scale IoT environments. However, the authors note that the algorithm does not account for dynamic changes in user preferences and the scale of composite services, which presents areas for future research.

A similar study addresses the complex challenge of composing IoT services in a manner that optimizes both energy consumption and Quality of Service (QoS) [8]. Given the energy constraints and dynamic nature of IoT environments, traditional service composition methods often fall short in simultaneously meeting energy and QoS requirements, leading to suboptimal performance and reduced service lifetime. The authors propose a novel group teaching-based energy efficient and QoS-aware services composition approach (GT-EQCA) that mitigates these issues. The GT-EQCA method employs a hierarchical process where only relevant services are considered during composition, thereby reducing computation time and enhancing composition lifetime and utility. The approach leverages the group teaching optimization method, which does not require specific parameter tuning, making it more adaptable and efficient. This method preselects services based on their energy profiles and QoS attributes using lexicographic optimization and relative Pareto dominance principles. The preselected services are then refined through the group teaching optimization process to achieve a composite service that meets global QoS constraints with minimal energy consumption. The authors validate the GT-EQCA approach through large-scale simulations using a real dataset, demonstrating its superiority over four baseline algorithms in terms of composition time, energy consumption, and QoS utility. The results highlight the approach's potential to significantly enhance the efficiency and effectiveness of IoT service composition, offering a promising solution for managing the growing complexity of IoT environments.

An advanced hybrid multi-objective metaheuristic algorithm designed to address the complexities of selecting IoT services in multi-cloud environments is presented in [9]. The integration of IoT with cloud computing has led to the formation of extensive networks of interconnected devices and services, creating the need for effective service selection mechanisms that can optimize Quality of Service (QoS). The service selection problem is classified as NP-hard, necessitating the use of metaheuristic algorithms for efficient resolution. The proposed pRTMNSGA-III algorithm combines the strengths of two existing algorithms, RNSGA-III and TMNSGA-III, and introduces a parallel evaluation approach to enhance computational efficiency. It leverages a more effective fuzzy membership function to select the best solutions based on the requester's preferred QoS. The evaluation of pRTMNSGA-III on multiple datasets demonstrates its superiority over state-of-the-art algorithms, including RNSGA-III, TMNSGA-III, NSGA-III, pNSGA-II, NSGA-II, and NSPSO. Experimental results show that pRTMNSGA-III outperforms these algorithms by up to 37% in terms of the number of non-dominated solutions generated.

An efficient method for selecting IoT services that optimize both energy consumption and Quality of Service (QoS) is described in [10]. The proposed system aims to efficiently aggregate and rank IoT services using a combination of Hidden Markov Model (HMM), K-Nearest Neighbors (KNN), and Extreme Gradient Boosting (XGBoost). The system begins by identifying and categorizing services using a fuzzy rule-based KNN classifier, which considers factors like energy availability and response time. XGBoost is then employed to dynamically select the best services from the categorized list, ensuring minimal energy consumption and high reliability. HMM is used to predict future QoS values based on historical data, further refining service selection to maintain optimal performance. Experimental results in an Openstack environment demonstrate the proposed system's effectiveness, showing significant improvements in response time and energy efficiency compared to traditional methods. This approach is particularly beneficial for applications requiring real-time data processing and high reliability, such as in medical IoT systems.

A novel mechanism to address the challenges of discovering and selecting appropriate IoT services that meet Quality of Service (QoS) requirements in dynamic environments is proposed in [11]. The proposed solution, PAMSer, utilizes a peer-to-peer (P2P) resource discovery approach and an optimization algorithm called OptSel to enhance the reliability and efficiency of IoT service selection. PAMSer employs a k-random walk algorithm to gather near-real-time QoS information from user nodes, thereby reducing message overhead and avoiding the scalability issues associated with centralized approaches. OptSel optimizes service selection by assigning a dominance value to each service based on its QoS attributes and energy levels, ensuring the selection of the most suitable services while avoiding those with potentially critical weaknesses. Extensive simulations demonstrate that PAMSer significantly outperforms existing methods in terms of message overhead, latency, scalability, reliability, and QoS accuracy, making it a promising approach for managing the complex and dynamic nature of IoT environments.

### 3 CONCLUSION

In conclusion, this paper presents a comprehensive overview of various service discovery and selection mechanisms in IoT applications, emphasizing the critical role of Quality of Service (QoS) and energy efficiency. The proposed solutions, such as PAMSer and OptSel, leverage advanced algorithms like k-random walk, fuzzy membership functions, and group teaching optimization to enhance service reliability, scalability, and efficiency. Through extensive simulations and evaluations, these methods have demonstrated significant improvements over traditional approaches, offering promising advancements in managing the dynamic and complex nature of IoT environments. The insights and methodologies discussed provide a solid foundation for future research and development in optimizing IoT service discovery and selection processes.

### References

- [1] M. A. Jamshed, K. Ali, Q. H. Abbasi, M. A. Imran, and M. Ur-Rehman, "Challenges, applications, and future of wireless sensors in internet of things: A review," *IEEE Sensors Journal*, vol. 22, no. 6, 5482–5494, 2022.
- [2] S. Acik, S. Kosunalp, and M. B. Tabakcioglu, "Evaluating the lifetimes of energy-harvesting wireless sensor networks with ALOHA," *Engineering Proceedings*, vol. 41, no. 1, art. no. 10, 2023.
- [3] M. Achir, A. Abdelli, L. Mokdad, and J. Benothman, "Service discovery and selection in IoT: A survey and a taxonomy," *Journal of Network and Computer Applications*, vol. 200, art. no. 103331, 2022.
- [4] S. Kosunalp and K. Demir, "SARL: A reinforcement learning based QoS-aware IoT service discovery model," *Journal of Electrical Engineering*, vol. 71, no. 6, pp. 368–378, 2020.
- [5] H. Bouazza, B. Said, and F. Z. Laallam, "A hybrid IoT services recommender system using social IoT," *Journal of King Saud University-Computer and Information Sciences*, vol. 34, no. 8, pp. 5633–5645, 2022.
- [6] R. Boucetti, O. Hioual, and S. M. Hemam, "An approach based on genetic algorithms and neural networks for QoS-aware IoT services composition," *Journal of King Saud University-Computer and Information Sciences*, vol. 34, no. 8, pp. 5619–5632, 2022.
- [7] Z. Y. Chai, M. M. Du, and G. Z. Song, "A fast energy-centered and QoS-aware service composition approach for internet of things," *Applied Soft Computing*, vol. 100, art. no. 106914, 2021.
- [8] S. Hameche, M. E. Khanouche, A. Chibani, and A. Tari, "A group teaching optimization-based approach for energy and QoS-aware internet of things services composition," *Journal of Network and Systems Management*, vol. 32, no. 1, art. no. 4, 2024.
- [9] A. Zebouchi and Y. Aklouf, "pRTMNSGA-III: A novel multi-objective algorithm for QoS-aware multi-cloud IoT service selection," *Annals of Telecommunications*, pp. 1–22, 2024.
- [10] L. SaiRamesh, and S. Sabena and K. Selvakumar, "Energy efficient service selection from IoT based on QoS using HMM with KNN and XGBOOST," *Wireless Personal Communications*, vol. 124, no. 4, pp. 3591–3602, 2022.
- [11] K. Demir, "A QoS-aware service discovery and selection mechanism for IoT environments," *Sādhanā*, vol. 46, no. 4, art. no. 242, 2021.



## Design of a New Multiband Pentagon Patch Antenna Array

**Khouloud Mohammed Belhadj<sup>\*1</sup>, Souheyla Ferouani<sup>2</sup>, Djalal Ziani Kerarti<sup>3</sup>**

<sup>1</sup>Smart Structure Laboratory SSL of Temouchent, Department of Electronic and Telecommunications, University of Ain Temouchent, Belhadj Bouchaib, Ain Temouchent, Algeria

<sup>2</sup>LTT laboratory of Tlemcen, Department of Electronic and Telecommunications, University of Ain Temouchent, Belhadj Bouchaib, Ain Temouchent, Algeria

<sup>3</sup>LARATIC laboratory at National Institute of Telecommunications and ICT of Oran, Department of Post Graduated and Specialties, Oran, Algeria

---

### Abstract

Antenna design and simulation is a fast-growing field among researchers. Antennas play an essential role in telecommunications. Today, the microstrip patch antenna is extremely useful in the fields of advanced electronic devices, while microstrip array antennas are also mainly used in telecommunication systems. They are used to obtain a necessary pattern that cannot be achieved with a single element. This work proposes the design of a pentagonal microstrip patch antenna array with 1 patch (1×1) operating at 3.5GHz, and 2 patches (1×2) offering the 4 resonant frequencies: 2.33 GHz, 2.95GHz, 3.51GHz and 5.045 GHz using CST simulation software. The substrate used is FR4 with a permittivity of  $\epsilon_r = 4.35$  and a thickness of  $h=1.5\text{mm}$ . The proposed antenna is validated in practice for operation in 5G, 4G/LTE in some regions, Wifi, and S-band.

**Keywords:** *Microstrip array antenna, CST, 5G, Wifi, S-band*

---



## Energy Distribution Analysis Using DWT for the Airgap Eccentricity in Induction Machine

Moutaz Bellah Bentrad<sup>\*1</sup>, Adel Ghoggal<sup>1</sup>, Tahar Bahi<sup>2</sup>

<sup>1</sup>Electrical Engineering Department (LGEB), Mohamed Khider University, Biskra, Algeria

<sup>2</sup>Electrical Engineering Department (LASA), Badji Mokhtar University, Annaba, Algeria

### Abstract

This paper presents an energy distribution analysis of airgap eccentricity in induction machines using discrete wavelet transform (DWT). Airgap eccentricity, a common fault in induction machines, is categorized into static, dynamic, and mixed types. This study aims to investigate the energy characteristics of these fault types under various operational conditions and different degrees of defect severity. By applying DWT to the current signals of induction machines, we decompose the signals into various frequency components and analyse the energy distribution at each decomposition level. The analysis reveals distinct energy patterns associated with each type of airgap eccentricity and varying defect levels. These findings provide valuable insights for early fault detection and condition monitoring of induction machines, enhancing their reliability and operational efficiency. The proposed approach demonstrates the effectiveness of DWT in isolating and identifying specific fault characteristics, offering a robust tool for predictive maintenance and fault diagnosis in industrial applications.

**Keywords:** Induction machine, Diagnosis, DWT, Eccentricity, Energy distribution

## 1 INTRODUCTION

Induction motors have long been favoured in industrial applications because of their simplicity. However, extended operation or adverse operating conditions can lead to malfunctions, typically caused by mechanical or electrical issues [1]. Examples of mechanical failures include seat and coil misalignment, bearing failure, and dynamic and static eccentricity. The primary types of electrical faults are insulation faults, rotor faults, and magnetic circuit faults. Induction motors commonly experience issues related to bearings, stators, rotors, and eccentricity disturbances [2, 3]. Lateral damage to ball bearings can lead to shaft tilt and rotor eccentricity. This increase in eccentricity results in unbalanced magnetic attraction, excessive vibration, and a rise in rotor temperature [4].

This paper presents an energy distribution analysis of airgap eccentricity in induction machines using discrete wavelet transform (DWT), as a first step of the conducted work, raw data of stator current signal will be decomposed to segments with various frequency bands to many levels to extract the best approximation level that contains vital information connected to health condition of the machine, and these results will be accompanied with an energy distribution analysis for the classification task.

### 1.1 Wavelet Transform

The wavelet transform, similar to the Fourier transform, is a powerful signal processing tool. Unlike the Fourier transform, which uses different frequencies, the wavelet transform decomposes the signal into scaled and shifted versions of a mother wavelet. This method's primary advantage is its flexibility in representing transient signals. The wavelet transform is particularly valuable for analysing signals with variable speed or load, resembling Fourier analysis in this regard. Unlike the sinusoidal functions in Fourier analysis, wavelets typically exhibit rapid decay of the oscillation function.

$$\Psi_{a,b}(t) = \Psi\left(\frac{t-b}{a}\right) \quad (1)$$

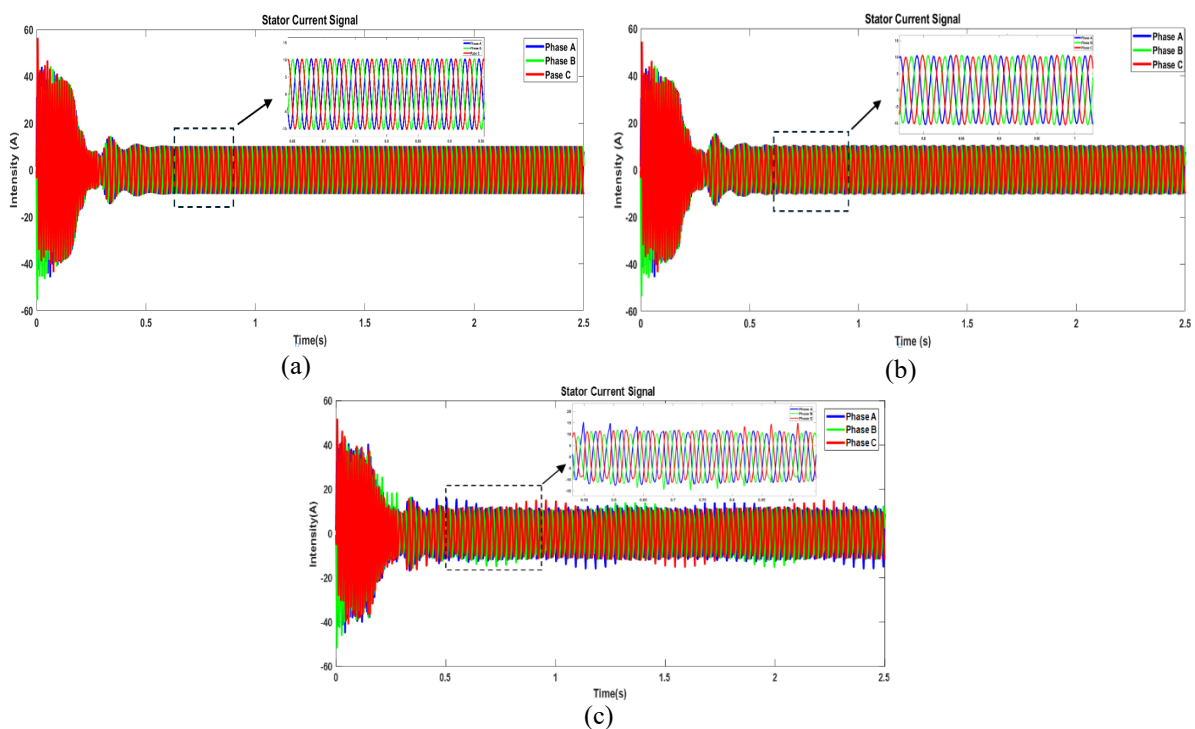
Where,  $a$  is the scaling parameter and  $b$  is the shifting parameter [5, 6]

## 2 AIRGAP ECCENTRICITY FAULT DETECTION BY WAVELET TRANSFORM

Air gap irregularity profiles chosen in this research are 10% deemed tolerable percentage, since even newly manufactured machines contain a certain level of irregularity, 20% which is a worrisome level that should be treated with caution, 30% which is an alarming percentage that requires an immediate intervention in order to avoid catastrophic drawbacks.

**Table 1.** Machine parameters

Parameter	Identification
Machine type	3-phase squirrel cage with inclined bar
Number of bars	40
Frequency	50 Hz
Rated Voltage	415 V
Winding number	28
Air gap radius	82 mm
Air gap thickness	0.8 mm



**Figure 1.** Stator current signal with air gap irregularity: (a) 10%, (b) 20%, and (c) 30%

### 2.1 Wavelet Decomposition Analysis

The sampling frequency has been set 5 KHz. The original stator current signal  $s$  has been decomposed upto 12th level of decomposition for healthy as well as for airgap irregularity condition.

The decomposition was carried out up to the 12th level to extract low-frequency information hidden within the time-domain waveform. While the 11th-level low-frequency approximation signal shows minimal changes in the stator current signal, the 12th-level low-frequency approximation signal contains highly significant information. It is strongly advised to use high decomposition levels because, at lower levels, the mother wavelet is more localized in time and oscillates more rapidly within a short period [7].



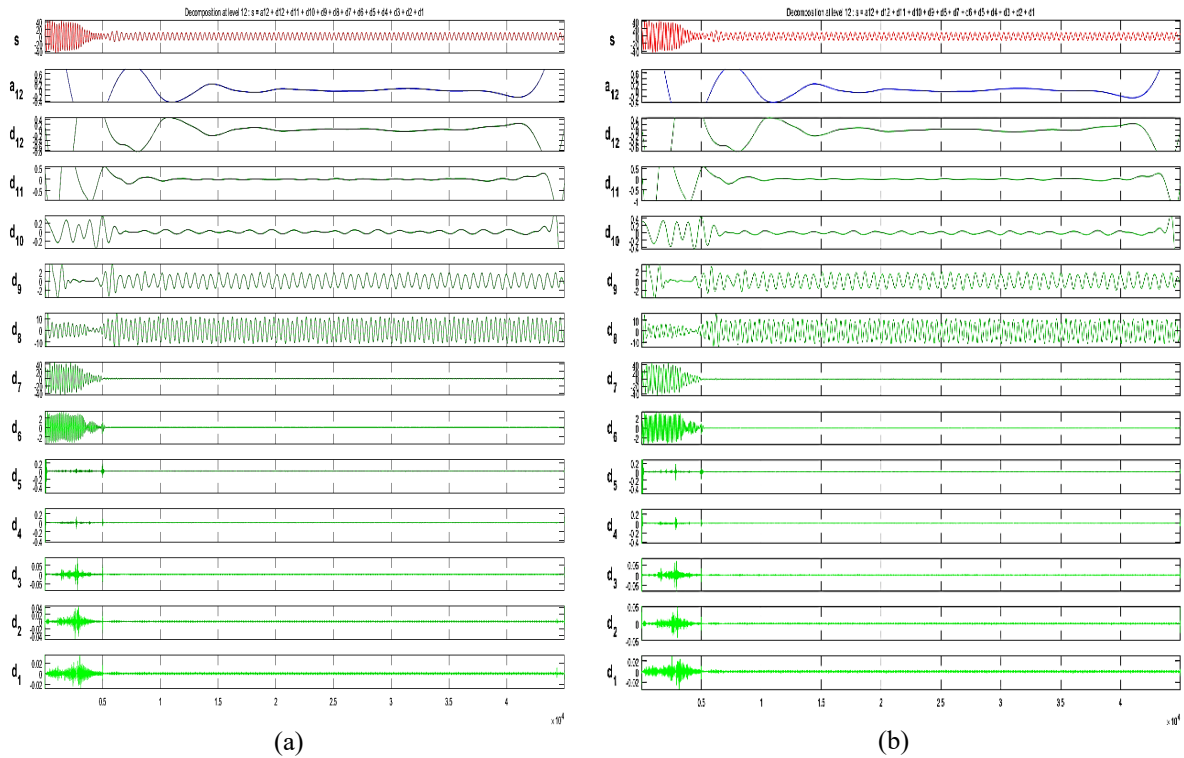


Figure 2. DWT decomposition of the raw stator current signal: (a) Healthy and (b) faulty airgap

## 2.2 Proposed Method

After the decomposition of the raw signal of the stator current, two types of decomposition are generated: high frequency (detailed decomposition) and low frequency (approximation decomposition), each level contains a certain frequency band for the decomposed signal, after decomposition each level will be compared between healthy and faulty air gap, the following results shown in figure 2 showcase the levels of the detailed frequency decomposition in which we can notice differences in frequency of each level, which indicate a promising results that can be used for the comparison and later on the classification of each current signal based on its frequency.

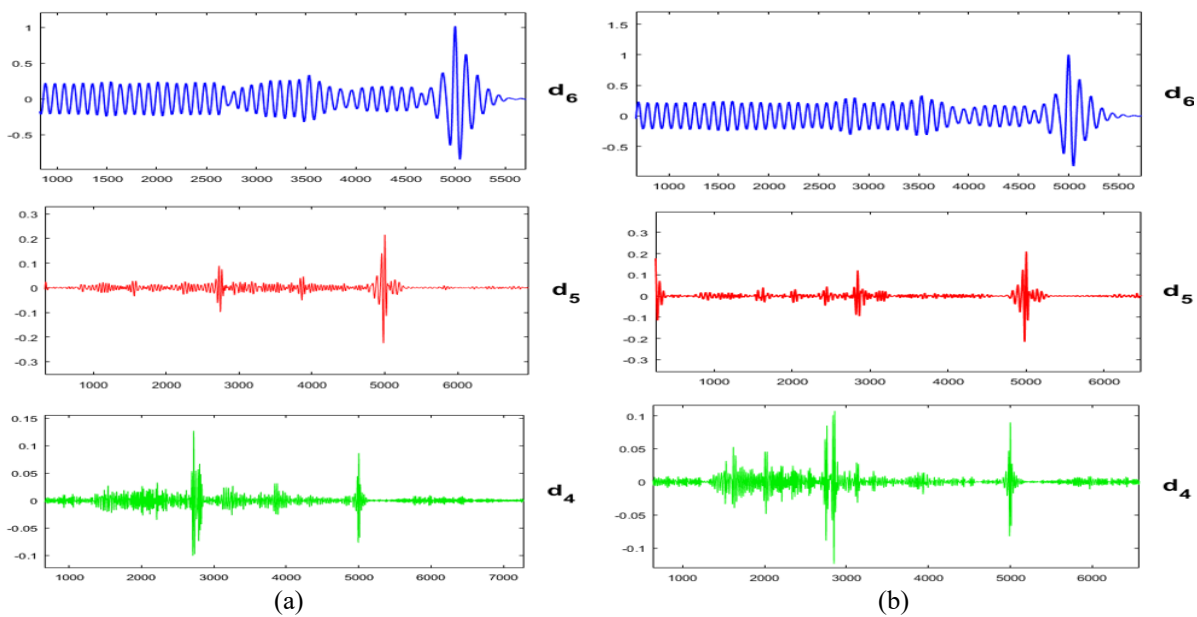


Figure 3. DWT analysis of the high frequency levels for current signal: (a) Healthy and (b) faulty airgap

### 3 RESULTS AND DISCUSSION

After conducting decomposition for the current signal in the previous section, many levels of the decomposition are acquired which can be used for the energy analysis in order to be used later on for the feature extraction task, we notice the existence of three specific levels that hold frequencies that deliver a vital information about the dissipated energy at each level relative to each type of air gap eccentricity which are; Level 6, 7, and 8.

An energy analysis is performed at each level to determine the most suitable decomposition level that can be used for feature extraction

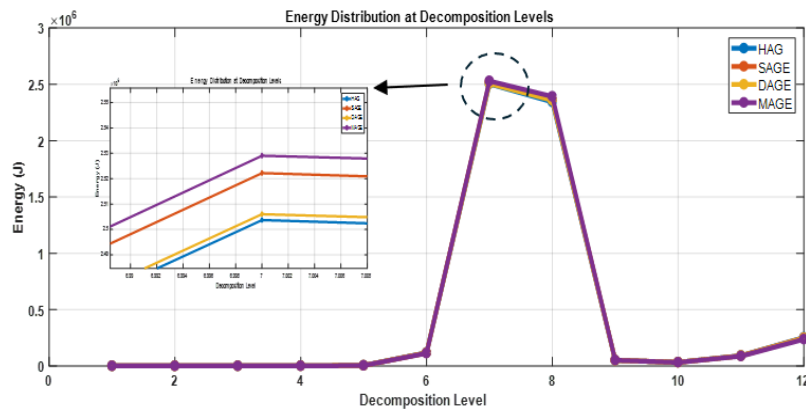
**Table 2.** Energy distribution analysis of decomposition levels

Machine Condition	Decomposition Level	Dissipated energy (J)
Healthy	D6	$1.173 \times 10^5$
	D7	$2.504 \times 10^6$
	D8	$2.344 \times 10^6$
Static air gap	D6	$1.164 \times 10^5$
	D7	$2.522 \times 10^6$
	D8	$2.363 \times 10^6$
Dynamic air gap	D6	$1.155 \times 10^5$
	D7	$2.206 \times 10^6$
	D8	$2.359 \times 10^6$
Mixed air gap	D6	$1.126 \times 10^5$
	D7	$2.529 \times 10^6$
	D8	$2.392 \times 10^6$

It is clear that the chosen decomposition levels exhibit approximate results of dissipated energy levels with a slight advantage in the 7<sup>th</sup> level that delivered better and more precise results relative to each type of the defect, which indicates that it is suitable for feature extraction of the air gap irregularity with regards to its types and operational conditions.

Figure 4 illustrates the performance of the results achieved:

HAG: healthy air gap, SAGE: static air gap, DAGE: dynamic air gap, MAGE: mixed air gap.



**Figure 4.** Energy Distribution analysis of the 12 decomposition levels

### 4 CONCLUSION

We can conclude that with the help of discrete wavelet decomposition, energy distribution can be used as strong feature for the detection of air gap irregularity in the induction machine with its various types, operational conditions, that indicates its reliability for early fault detection which could later on preserve the condition of the induction machine against undesirable and unpredictable breakdowns.

### References

[1] A. J. Bazarro, E. C. Quispe, and R. C. Mendoza, “Causes and failures classification of industrial electric

- motor,” in *2016 IEEE ANDESCON*, 2016, pp. 1–4.
- [2] A. Glowacz, “Fault diagnosis of single-phase induction motor based on acoustic signals,” *Mech. Syst. Signal Process.*, vol. 117, pp. 65–80, 2019.
- [3] D.-J. Choi, J.-H. Han, S.-U. Park, and S.-K. Hong, “Diagnosis of electric motor using acoustic noise based on CNN,” in *2019 22nd International Conference on Electrical Machines and Systems (ICEMS)*, 2019, pp. 1–4.
- [4] E. Artigao, A. Honrubia-Escribano, and E. Gómez-Lázaro, “In-service wind turbine DFIG diagnosis using current signature analysis,” *IEEE Trans. Ind. Electron.*, vol. 67, no. 3, pp. 2262–2271, 2019.
- [5] G. Inuso, F. La Foresta, N. Mammone, and F. C. Morabito, “Brain activity investigation by EEG processing: Wavelet analysis, kurtosis and Renyi’s entropy for artifact detection,” in *2007 International Conference on Information Acquisition*, Seogwipo, Korea, 2007, pp. 195–200.
- [6] E. Ghaderpour, S. D. Pagiatakis, and Q. K. Hassan, “A survey on change detection and time series analysis with applications,” *Appl. Sci.*, vol. 11, art. no. 6141, 2021.
- [7] K. M. Siddiqui and V. K. Giri, “Broken rotor bar fault detection in induction motors using wavelet transform,” in *2012 International Conference on Computing, Electronics and Electrical Technologies (ICCEET)*, Nagercoil, India, 2012, pp.1–6.



## Advanced Control Strategy for Grid-Connected Voltage Source Inverters with LCL Filters Dedicated to Renewable Energy Grid Integration Systems

Houssam Eddine Mansouri<sup>\*1</sup>, Billel Talbi<sup>1</sup>, Idris Messaoudene<sup>1</sup>, Moussa Abderrahim Mehiris<sup>1</sup>

<sup>1</sup>ETA Laboratory, Department of Electronic, University Mohamed El Bachir El Ibrahimi, Bordj Bou Arreridj, Algeria

### Abstract

This study investigates the design and implementation of a control strategy for a three-phase grid-connected VSI (voltage source inverter) employing an *LCL* filter. The proposed controller leverages integral sliding mode control (ISMC) for its inherent robustness to system uncertainties and external disturbances. Additionally, space vector modulation (SVM) is incorporated to achieve minimal total harmonic distortion (THD) in the output voltage waveform while maintaining satisfactory dynamic response characteristics. The effectiveness and robustness of the proposed controller are validated through simulations conducted in the MATLAB®/Simulink® environment.

**Keywords:** *Grid-connected inverter, Voltage source inverter, Integral sliding mode control (ISMC)*

## 1 INTRODUCTION

In recent years, there has been a notable emphasis on addressing environmental concerns by augmenting energy production in an eco-friendly manner [1–2]. Typically, energy derived from renewable sources such as wind, solar, and fuel cells undergoes a processing phase before being integrated into the grid to comply with established standards [3–4]. The Voltage Source Inverter (VSI) plays a prominent role in this process, as it handles the direct current voltage generated from the renewable source and feeds it into the grid via a filter. The primary goal of a grid-connected VSI is to generate a sinusoidal current with a specified frequency and transmit it to the grid through a filter. Generally, an *L*, *LC* or *LCL* type filter is employed to facilitate the injection of the current produced by the VSI into the grid. The injection of grid currents must be performed with low total harmonic distortion (THD %). In this context, sliding mode control (SMC) theory is widely introduced in power electronic converters control [5–8]. The implementation of SMC not only delivers a high control performance but also allows for straightforward experimental setup [5–10]. However, it is plagued by an undesired phenomenon known as chattering with persisting steady-state error. This prompted the advancement of SMC theory to augment control performance, mitigating its drawbacks by introducing an integral term to the sliding surface, resulting in what is known as an integral sliding mode controller (ISMC). This paper applies ISMC theory to craft efficient and straightforward controller for a three-phase grid-connected inverter using *LCL* filter. Additionally, the control law design has been adjusted, incorporating an approximation of the signum function as the switching mechanism. This modification yields a substantial reduction in the chattering phenomenon and guarantees the injection of generated DC power into the grid with high-quality grid current. To validate the control performance of the proposed ISMC-based scheme, numerical simulations are conducted using MATLAB®/ Simulink® simulation environment.

## 2 MATERIAL AND METHOD

### 2.1 Grid Connected Voltage Source Inverter

The topology of the three-phase *LCL* grid-connected inverter with the suggested controller is shown in Figure 1, where the wind turbine and photovoltaic systems are replaced by a DC voltage source. The grid connected inverter converts DC voltage to AC voltage by controlling the on-off state of the IGBT, which will introduce harmonics in the modulation process. The AC voltage is finally delivered to the power grid after passing it through a filter. In Figure 1, *C* is the filter capacitor, *L*<sub>1</sub> and *L*<sub>2</sub> are the inverter-side and grid-side filter inductance respectively with their series equivalent resistances *r*<sub>1</sub> and *r*<sub>2</sub>.

The inverter model after Clark transformation can be written in the state equation form to indicate the specific relationships of the quantities of the inverter system:

$$\begin{bmatrix} \frac{di_{i,\alpha\beta}}{dt} \\ \frac{di_{g,\alpha\beta}}{dt} \\ \frac{dv_{c,\alpha\beta}}{dt} \end{bmatrix} = \begin{bmatrix} \frac{u_{i,\alpha\beta} - v_{c,\alpha\beta} - r_1 i_{i,\alpha\beta}}{L_1} \\ \frac{v_{c,\alpha\beta} - v_{g,\alpha\beta} - r_2 i_{g,\alpha\beta}}{L_2} \\ \frac{i_{i,\alpha\beta} - i_{g,\alpha\beta}}{C} \end{bmatrix} \quad (1)$$

where  $(v_{i,\alpha\beta})$  is the control input, inverter output current is  $(i_{i,\alpha\beta})$  grid current  $(i_{g,\alpha\beta})$  capacitor voltage  $(v_{c,\alpha\beta})$  and  $(v_{g,\alpha\beta})$  are grid voltage in  $\alpha\beta$  reference frame. To inject current waveform in-phase with grid voltages the reference for grid current  $(i_{g,\alpha\beta}^*)$  is obtained by utilizing the utility grid voltage phase angle extracted through the phase locked loop (PLL). Based on the system dynamics, inverter side reference current,  $(i_{i,\alpha\beta}^*)$  can be written as follows:

$$i_{i,\alpha\beta}^* = (1 - CL_2\omega^2)i_{g,\alpha\beta}^* \quad (2)$$

and  $\omega$  is obtained by utilizing the utility grid voltage phase angle extracted through the phase locked loop (PLL).

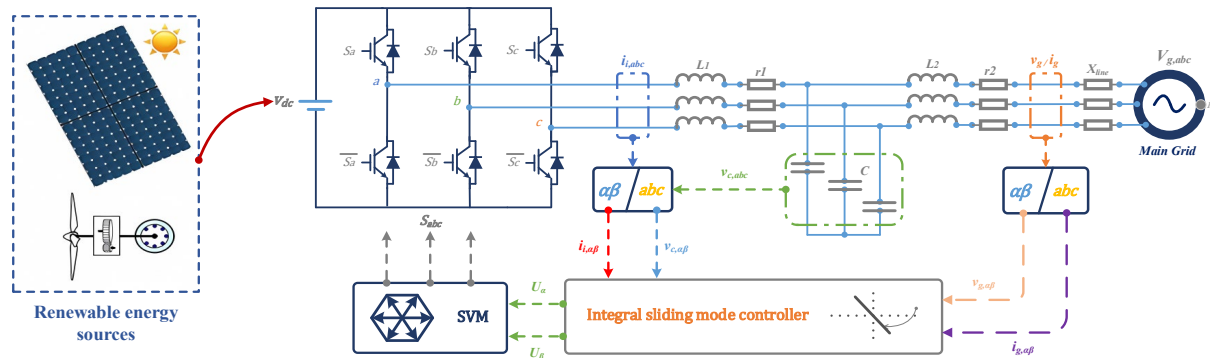


Figure 1. Three-phase grid-connected inverter with the suggested ISMC controller

## 2.2 Integral sliding mode Controller design

In order to design the controller, error terms are introduced as the difference between desired and the actual values, while the integral action is applied on (5) to improve the reference tracking performance:

$$x_1 = i_{i,\alpha\beta}^* - i_{i,\alpha\beta} \quad (3)$$

$$x_2 = i_{g,\alpha\beta}^* - i_{g,\alpha\beta} \quad (4)$$

$$x_3 = \int (i_{i,\alpha\beta}^* - i_{i,\alpha\beta}) \quad (5)$$

The pivotal element in the SMC, which governs the behavior of the controlled variables, is the sliding surface. The proposed sliding surfaces and its time derivative are defined as follows:

$$S_{\alpha\beta} = k_1 x_{1,\alpha\beta} + k_2 x_{2,\alpha\beta} + k_3 \int x_{1,\alpha\beta} dt \quad (6)$$

$$\dot{S}_{\alpha\beta} = k_1 \dot{x}_{1,\beta\alpha} + k_2 \dot{x}_{2,\beta\alpha} + k_3 x_{1,\beta\alpha} \quad (7)$$

where  $k_1$  and  $k_2$  are the sliding coefficients responsible for the rate of convergence of the trajectory. Now, to carry out the stability analysis of the proposed controller, let us consider the following Lyapunov function:  $V = \frac{1}{2} S^2$  and  $\dot{V} = S \cdot \dot{S}$ ,

$$\dot{V} = S \cdot \left[ -\frac{k_1}{L_1} (u_i - v_c - r_1 i_i) + k_1 i_1^* + k_2 x_1 + k_3 \dot{x}_2 \right] \quad (8)$$

According to sliding mode theory, the control law can be divided into two parts: the equivalent control and the switch control and after simplifying (7) for the control law ( $u_i$ ) we get:

$$u_i = v_c + r_1 i_1 + L_1 \dot{i}_1^* + \frac{k_2}{k_1} L_1 x_1 + \frac{k_2}{k_1} L_1 \dot{x}_2 + \frac{L_1}{k_1} \frac{\lambda \cdot S}{|S| + \delta} \quad (9)$$

Now, putting (9) into (8) and to guarantee the convergence of  $V$ , it should be verified that the derivative of  $V$  is negative as follows:

$$\dot{V} = \frac{L_1}{k_1} \frac{\lambda \cdot S^2}{|S| + \delta} < 0 \quad (10)$$

Additionally,  $\lambda$  must be chosen negative in order to satisfy the reaching condition of the controller.

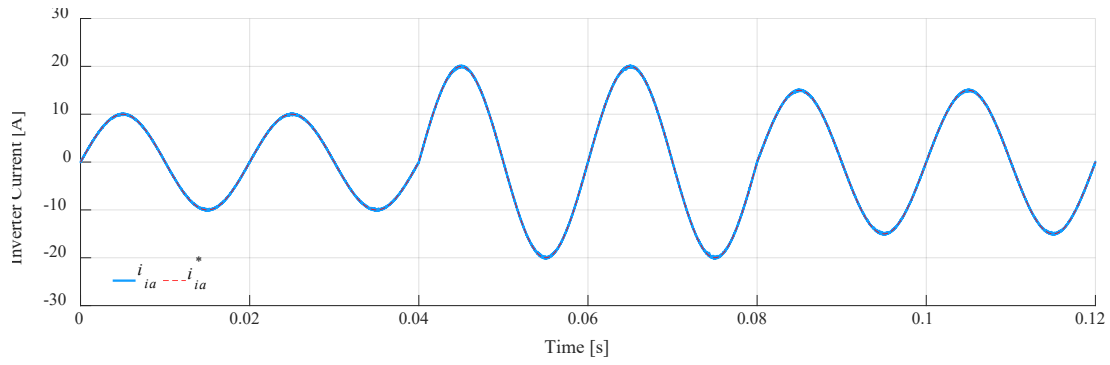
### 3 RESULTS

Numerical simulations using MATLAB®/Simulink® environment are carried out to confirm the performance of the suggested controller. System parameters are listed in Table 1.

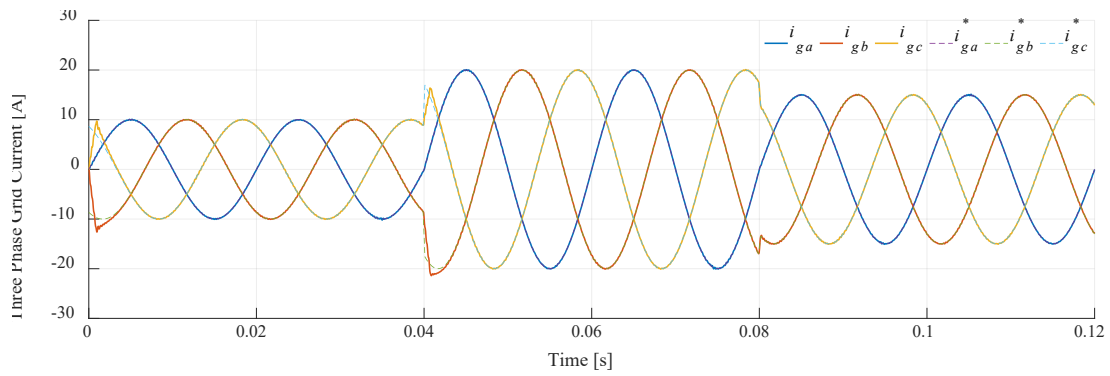
**Table 1.** System parameters

Parameter	Value
DC link voltage $V_{dc}$	450 V
Filter inductance $L_1 / L_2$	2.5 mH
Filter resistance $r_1 / r_2$	0.2 $\Omega$
Filter Capacitance $C$	5 $\mu$ F
Grid frequency $f_g$	50 Hz
Grid voltage peak $V_{g,max}$	$110\sqrt{2}$ V
SVM switching frequency $f_{SVM}$	10 kHz

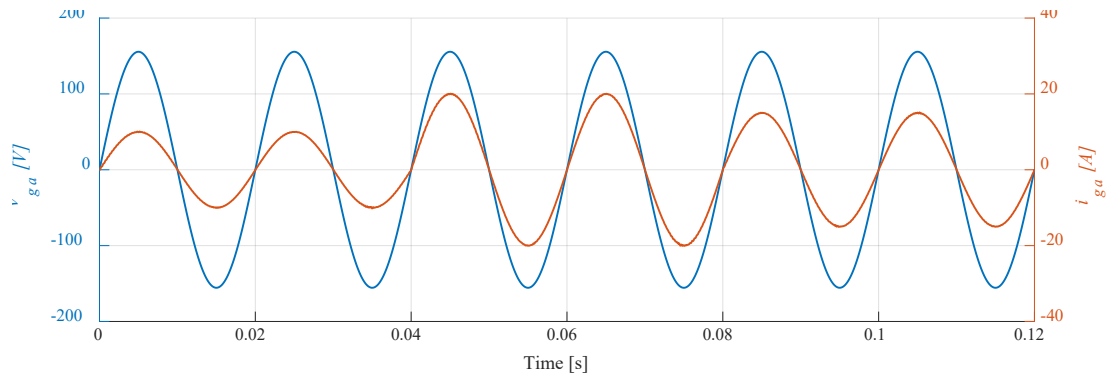
The simulation result with different inverter current reference in natural frame ( $i_{ia}^*$ ) is shown in Figure 2. It can be seen that the ISMC controller tracks perfectly the reference of inverter current during the transient and steady-state condition with minimal ripple leading to a more efficient operation. It should be noted that the values of the sliding controller are chosen to be ( $k_1 = k_2 = 10^3, k_3 = 1$ ). Figure 3 presents the simulated response of the injected grid currents in the natural frame ( $i_{ga}, i_{gb}, i_{gc}$ ) with their references ( $i_{ga}^*, i_{gb}^*, i_{gc}^*$ ). It is found that the injected grid currents exhibit fast response with minimum fluctuations, the grid currents and their amplitudes (10A, 20A, 15A) almost instantaneously follow the changes in references currents, without any steady-state error. The simulated responses of the grid voltage and current for phase- $a$  ( $v_{ga}, i_{ga}$ ) are plotted in Figure 4. It can be noted that the grid current is in phase with the grid voltage, thereby confirming the operation at unity power factor. The phase- $a$  grid current ( $i_{ga}$ ) and its FFT are showed in Figure 5, where the THD is found 0.53% (below 5%). Figure 6 displays the obtained simulation results when the filter inductance and capacitance ( $L1, L2, C$ ) are varied within the specified range. It can be noticed that these variations have minimal impact on the grid current THD. These results are very promising and demonstrate that the suggested ISMC controller exhibits low sensitivity to changes in these parameters.



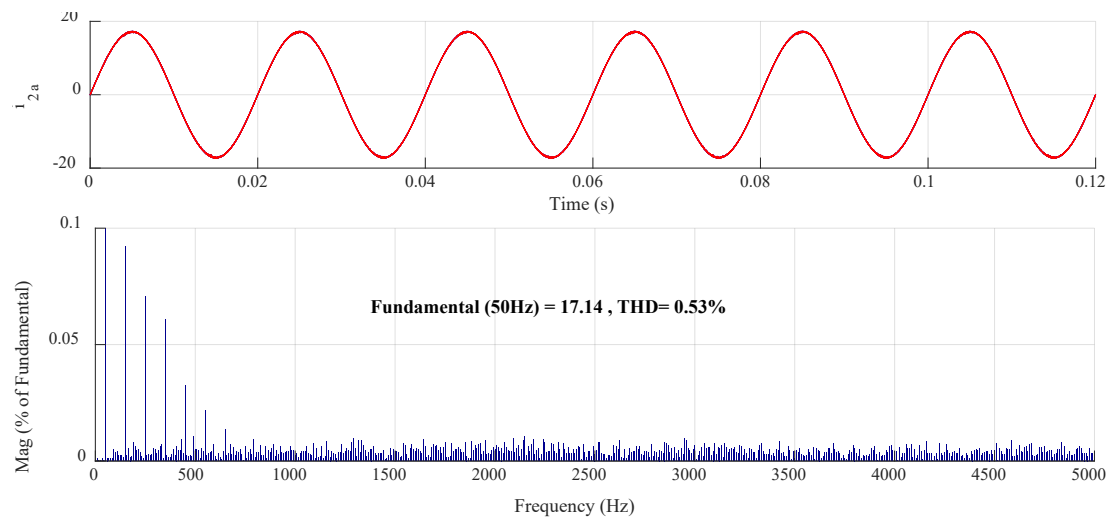
**Figure 2.** Simulation results for phase a inverter current with its reference



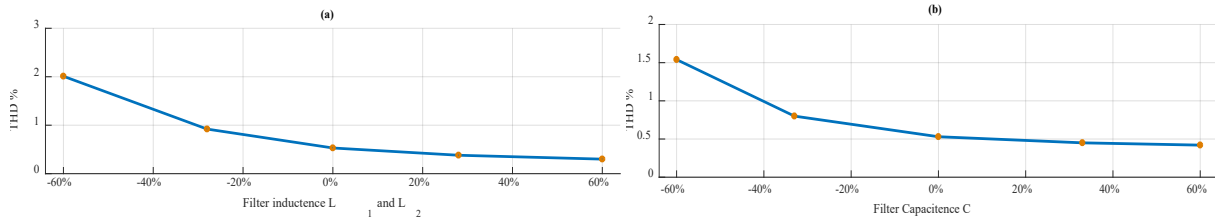
**Figure 3.** Simulation results for the injected grid currents with their references in the natural frame



**Figure 4.** Simulation results for the phase-a grid voltage and injected current



**Figure 5.** Simulation results for phase-a grid current and its FFT



**Figure 6.** Simulation results with grid filter parameters variations. (a) Inductance variation and (b) capacitance variation

## 4 CONCLUSION

This paper devised an integral sliding mode control strategy for three phase grid-connected inverter, aiming to suppress the harmonics and simplify the controller design. Mathematical model of the inverter system is established and detailed controller design is presented. The designed controller in a rotating reference frame guarantees the asymptotic stability of the desired system and injects sinusoidal current into the grid. MATLAB®/Simulink® platforms are used to carry out a simulation of the entire system. Furthermore, simulation results show that this control method has strong robustness and decent dynamics and steady state characteristics, significantly reducing the high-frequency harmonics as well as achieving unity power factor operation.

## References

- [1] F. Blaabjerg, R. Teodorescu, M. Liserre, and A. V. Timbus, "Overview of control and grid synchronization for distributed power generation systems," *IEEE Trans. Ind. Electron.*, vol. 53, no. 5, pp. 1398–1409, Oct. 2006.
- [2] I. Sefa, and N. Altin, "Grid interactive photovoltaic inverters-A review," *Journal of the Faculty of Engineering and Architecture of Gazi University*, vol. 24, no. 3, pp. 409–424, 2009.
- [3] IEC 61000-3-2 International Standard, International Electrotechnical Commission, 1998.
- [4] IEEE 519 Recommended Practices and Requirements for Harmonic Control in Electrical Power Systems, IEEE Standard, 1993.
- [5] V. I. Utkin, "Sliding mode control design principles and applications to electric drives," *IEEE Trans. Ind. Electron.*, vol. 40, pp. 23–36, 1993.
- [6] C. Edwards and S. Spurgeon, *Sliding Mode Control: Theory and Applications*, Boca Raton, FL, USA, CRC Press, 1998.
- [7] S. C. Tan, Y. M. Lai, and C. K. Tse, *Sliding Mode Control of Switching Power Converters: Techniques and Implementation*, Boca Raton, FL, USA, CRC Press, 2011.
- [8] F. Sebaaly, H. Vahedi, H. Y. Kanaan, N. Moubayed, and K. Al-Haddad, "Sliding mode fixed frequency current controller design for grid-connected NPC inverter," *IEEE J. Emerg. Select. Top. Power Electron.*, 4, pp. 1397–1405, 2016.
- [9] E. Van Dijk, J. N. Spruijt, D. M. O'sullivan, and J. B. Klaassens, "PWM-switch modeling of DC-DC converters," *IEEE Trans. Power Electron.*, vol. 10, pp. 659–665, 1995.
- [10] E. Bianconi, J. Calvente, R. Giral, E. Mamarelis, G. Petrone, C. A. Ramos-Paja, G. Spagnuolo, and M. Vitelli, "A fast current-based MPPT technique employing sliding mode control," *IEEE Trans. Ind. Electron.*, vol. 60, pp. 1168–1178, 2013.





## Efficient QRS Complex Extraction from ECG Signals Using DWT

Hadda Ouguissi<sup>1</sup>, Nail Alaoui<sup>\*2</sup>

<sup>1</sup>Materials, Energetic Systems, Renewable Energies, and Energy Management Laboratory (LMSEERGE), Faculty of Technology, Ammar Thelidji University of Laghouat, Laghouat, Algeria

<sup>2</sup>Research Laboratory for Modeling, Simulation and Optimization of Real Complex Systems, University of Djelfa, 17000 Djelfa, Algeria

---

### Abstract

The method described in this work employs the Discrete Wavelet Transform to eliminate noise from authentic ECG data and identify the QRS complex. Wavelets offer versatility through a range of wavelet functions, each possessing distinct attributes, while also furnishing both temporal and spectral details. The dataset utilized as an example was obtained from the MIT-BIH Noise Stress Test Database.

**Keywords:** ECG, QRS complex, Discrete wavelet transform, Threshold

---



## Microstrip Antenna Design for 5G Communication

Hadda Ouguissi<sup>1</sup>, Nail Alaoui<sup>\*2</sup>

<sup>1</sup>Materials, Energetic Systems, Renewable Energies, and Energy Management Laboratory (LMSEERGE), Faculty of Technology, Ammar Thelidji University of Laghouat, Laghouat, Algeria

<sup>2</sup>Research Laboratory for Modeling, Simulation and Optimization of Real Complex Systems, University of Djelfa, 17000 Djelfa, Algeria

---

### Abstract

A millimeter wave microstrip patch antenna and its array are proposed for 5G applications. The 5G Microstrip patch is constructed on a Rogers RT Duroid 5880 substrate with a standard thickness of 1.575 mm, a relative dielectric constant ( $\epsilon_r$ ) of 2.2, and a tan of 0.0013. The antenna has a resonance frequency of 27.95 GHz, a return loss of -25.84 dB, and a bandwidth of 1.863 GHz. The proposed antenna is designed as a 1x2 array with tapered line feeding. The antenna array resonates at 28 GHz frequency. With the array of antennas, there is a noticeable improvement in gain. Because of its small size, the antenna and its array can be used for 5G mobile communication.

**Keywords:** Millimeter wave, Array antenna, Mobile communication, 5G applications

---



---

## Removal of Pollutant by Bacteria Isolated from Oilfield via Biosurfactant Production

Nesrine Lenchi<sup>\*1,2</sup>, Wissam Ahmedi<sup>3</sup>, Salima Kebbouche-Gana<sup>2</sup>

<sup>1</sup>Department of Natural Sciences and Life, University of Algiers, Benyoucef Benkhedda, Algeria

<sup>2</sup>Laboratory of Bioinformatics, Applied Microbiology and Biomolecules, Faculty of Sciences, M'hamed Bougara University of Boumerdes, Algeria

<sup>3</sup>Laboratory of Phytotherapy Applied to Chronic Diseases, Faculty of Nature and Life Sciences, University Ferhat Abbas of Setif 1, Algeria

---

### Abstract

Heavy metals rank as highly hazardous pollutant with significant implications for public health. There are several health problems linked to heavy metal toxicity, which has been shown to be a serious threat. Despite having no biological function, these metals nevertheless have toxic effects that are detrimental to the health of humans and their ability to operate normally. They may occasionally function as a fictitious component of the body or even obstruct metabolic processes. Certain metals, like aluminum, can be eliminated through elimination processes, but other metals accumulate and show persistent symptoms in the body and food chain. Consequently, the demand for its elimination has increased. It is advisable to employ cost-effective, eco-friendly green technology for the remediation of this contaminant. This study aims to evaluate the bioremediation potential of microbial strain isolated from an Algerian oilfield in removing heavy metals.

In this presented study, bacteria named NL4 isolated from produced waters, which is able to grow in heavy metal medium and produce biotechnologically interesting metabolite like biosurfactants, were used to investigate its bioremediation abilities. This bacteria is able to produce biosurfactant after 10 days of incubation, the strain can reduce more than 80% of heavy metals. Meanwhile, this bacteria showed a good biosurfactant production with an Emulsification index of 65%. This strain was also able to lower the surface tension. These encouraging findings suggest that these bacteria might be applied in more intricate heavy metal-polluted settings, making them excellent choices for use in further bioremediation projects.

**Keywords:** Oilfield, Bacteria, Heavy metal, Biosurfactant

---



---

## Investigating the Modulatory Effects of Phenolic-Rich Extract on Pancreatic $\beta$ -Cell Gene Expression in Oxidative Stress Conditions

Anfel Benmansour\*<sup>1</sup>, Fatma Zahra Hab<sup>1</sup>, Rania Derguine<sup>2</sup>, Rechda Amel Tachour<sup>1</sup>,  
Mustapha Tacherfiout<sup>1</sup>, Bachra Khettal<sup>1</sup>, Abdelmalek Rezgui<sup>3</sup>, Widad Sobhi<sup>3</sup>

<sup>1</sup>Department of Microbiology, Faculty of Natural Sciences, University of Abderrahmane Mira, 06000, Bejaia, Algeria

<sup>2</sup>Department of Biochemistry, Faculty of Natural Sciences, University of Ferhat Abbas Setif 1, 19000, Setif, Algeria

<sup>3</sup>Biotechnology Research Center, 25000, Constantine, Algeria

---

### Abstract

Oxidative stress is a significant factor in the development of metabolic disorders, such as diabetes mellitus. Pancreatic  $\beta$ -cells, which are responsible for insulin secretion, are particularly vulnerable to oxidative damage due to their high metabolic activity and low antioxidant capacity. Phenolic compounds, which are known for their potent antioxidant properties, have demonstrated promising effects in reducing oxidative stress-related damage. This study investigates the potential modulatory effects of a phenolic-rich extract on the gene expression profile of pancreatic  $\beta$ -cells under oxidative stress conditions. Using in vitro models, pancreatic  $\beta$ -cells were exposed to oxidative stress inducers, such as streptozotocin, in the presence or absence of a phenolic-rich extract. Quantitative real-time PCR was used to analyse gene expression and evaluate changes in key genes involved in oxidative stress response, antioxidant defence, and insulin secretion pathways. The results showed significant alterations in the expression levels of genes associated with oxidative stress defence mechanisms following treatment with the phenolic-rich extract. This suggests a potential protective role against oxidative damage in pancreatic  $\beta$ -cells. Additionally, an analysis of genes related to insulin secretion suggests a potential improvement in  $\beta$ -cell function after treatment. In general, our study emphasises the promising modulatory effects of phenolic-rich extracts on pancreatic  $\beta$ -cell gene expression in oxidative stress conditions, providing valuable insights into potential therapeutic strategies for diabetes management.

**Keywords:** Phenolic-rich extract, Oxidative stress, Pancreatic  $\beta$ -cells, Gene expression modulatory effects

---



---

## **An Investigation into the Impact of Tannic Acid and Gallic Acid on the Surface Characteristics of 3D-Printed Polylactic Acid in Relation to Adhesion of *Pseudomonas Aeruginosa* and *Staphylococcus Aureus***

**Badr Errabiti\*<sup>1</sup>, Amal El Aabedy<sup>1</sup>, Sara Er-Rahmani<sup>1</sup>, Soumya El Abed<sup>1</sup>, Saad Ibsouda Koraichi<sup>1</sup>**

*<sup>1</sup>Laboratory of Microbial Biotechnology and Bioactive Molecules, Faculty of Science and Technology, Sidi Mohamed Ben Abdellah University, Fez, Morocco*

---

### **Abstract**

In this work, the impact of tannic acid (TA) and gallic acid (GA) on the physicochemical features of PLA surface was examined. TA and GA exhibited a considerable antibacterial impact on both *P. aeruginosa* (P) and *S. aureus* (S) strains. Contact angle measurements were used to assess hydrophobicity, surface tension components, electron donor and electron acceptor characteristics of untreated and treated PLA. The untreated PLA surface was qualitatively hydrophilic and quantitatively hydrophobic, and the electron donor property was more relevant than the electron acceptor one. Potentially, the PLA surface improved qualitatively and quantitatively after all treatments by shifting to a hydrophilic character and largely electron-donating except for the MICGA/S treatment. Using the Derjaguin-Landau-Verwey-Overbeek approach, the total free energy of adhesion determined the adherence of *P. aeruginosa* and *S. aureus* to the treated and untreated PLA. In fact, except for PLA treatment with MICGA/S, the total free energies of *S. aureus* and *P. aeruginosa* adherence to PLA increased following all treatments, demonstrating that adhesion is negative. Besides, According to SEM image analysis, the proportion of adhesion dropped throughout treatments, suggesting that PLA- MICGA/P therapy had the highest anti-adherence effectiveness.

**Keywords:** *Contact angle, Bacterial adhesion, Tannic acid, Gallic acid, PLA, Anti-adhesion*

---



---

## Exploring the Inhibitory Effect of Alpha-Hederin, the Active Saponin of *Nigella Sativa*, Against the Main Protease M<sup>pro</sup> of SARS-CoV-2

Selma Houchi<sup>\*1</sup>, Seoussen Kada<sup>1</sup>, Hanane Khither<sup>1</sup>

<sup>1</sup>Laboratory of Applied Biochemistry, Department of Biochemistry, Faculty of Life and Nature Sciences, University of Ferhat Abbas Setif-1, Algeria

---

### Abstract

As a consequence of the recent appearance of severe acute respiratory syndrome coronavirus 2 (SARS-CoV-2), a worldwide pandemic of coronavirus disease 2019 (COVID-19) has occurred. One of the main targets for therapeutic research is the SARS-CoV-2 main protease (M<sup>pro</sup>), which is essential for viral replication. This study aimed to identify the inhibitory effect of Alpha-Hederin, the active saponin of *Nigella sativa*, against M<sup>pro</sup>. The molecular docking study showed that Alpha-Hederin produced a stable complex at the active site with an impressive binding energy of -8.54 kcal/mol. It has two hydrogen donor-bonds with His 41, Cys 145, and one hydrogen acceptor-bonds with Gln 189. Its scoring energy and its interaction with the amino acid residues of the catalytic dyad of the M<sup>pro</sup> active site, His 41 and Cys 145 with Hydrogen bonds, demonstrated its inhibitory impact. Molecular weight, hydrogen bond acceptors and donors are the three areas where Alpha-Hederin fails to pass Lipinski's filter in terms of its physicochemical and drug-likeness characteristics. Because of its physicochemical features, it was shown to have limited intestinal absorption. These findings suggest that Alpha-Hederin could be a good candidate for structural modification and more research to find more effective anti-SARS-CoV-2 treatment medicines.

**Keywords:** Alpha-hederin, M<sup>pro</sup>, SARS-CoV-2, Inhibition

---



---

## Thymol's Protective Effects on CCl<sub>4</sub>-Induced Oxidative Stress in Female Rats: Assessing Hepatic and Plasmatic Markers

Hanane Khither<sup>\*1</sup>, Soraya Madoui<sup>1</sup>, Selma Houchi<sup>1</sup>, Asma Mosbah<sup>2</sup>

<sup>1</sup>Laboratory of Applied Biochemistry, Faculty of Natural and Life Sciences, University of Ferhat Abbas Setif 1, Setif 19000, Algeria

<sup>2</sup>Laboratory of Applied Biochemistry, Faculty of Natural and Life Sciences, University Constantine 1, Constantine 25000, Algeria

---

### Abstract

Carbon tetrachloride (CCl<sub>4</sub>) is a toxic chemical that induces oxidative stress in the body. When the liver metabolizes CCl<sub>4</sub>, it generates reactive free radicals, mainly trichloromethyl free radicals ( $\bullet\text{CCl}_3$ ), which can damage cell membranes, proteins, and DNA through lipid peroxidation and oxidative stress. Thymol, a bioactive molecule found in thyme, has gained recognition for its antioxidant properties and therapeutic potential. This study aims to evaluate the effects of thymol on oxidative stress markers induced by CCl<sub>4</sub> in Albino Wistar female rats. The intoxicated rats were treated with thymol for seven days at doses of 100 and 200 mg/kg/day. The assessment of oxidative stress induced by CCl<sub>4</sub> was conducted by evaluating the activity of antioxidant enzymes such as superoxide dismutase (SOD) and catalase, as well as the levels of malondialdehyde (MDA). The results indicate a significant increase in hepatic levels of oxidative stress markers by 18.56 times for MDA, 2.05 times for CAT, and 2.22 times for SOD. At the plasma level, MDA levels increased by 2.86 times, while SOD and CAT showed slight decreases (2.06 for CAT and 2.66 for SOD). Curative treatment of rats with thymol at doses of 100 and 200 mg/kg/day for seven days led to a significant decrease in MDA plasma and hepatic concentrations by 87.57% and 85.19%, respectively. Furthermore, compared to the CCl<sub>4</sub>-intoxicated group, the curative treatment significantly increased plasma catalase and SOD activity by 52.77% and 99.2%, respectively, and significantly decreased hepatic levels by 107.92% and 109.86%. Finally, thymol has a very important healing effect and a strong antioxidant effect in living things that protects against CCl<sub>4</sub>-induced liver damage. A dose of 200 mg/kg/day is thought to be a good example of a therapeutic effect.

**Keywords:** Carbon tetrachloride,, Oxidative stress, Protective effect, Thymol

---



---

## Antioxidant Activity, Total Phenolic, and Total Flavonoid Contents of Crude Extract of *Inula Viscosa*'s Leaves

Nadjat Azzi<sup>\*1</sup>, Younes Douffa<sup>1</sup>, Nour El Houda Belabas<sup>1</sup>, Haifaa Laroui<sup>1</sup>, Thoraya Guemmaz<sup>1</sup>, Fatima Zerargui<sup>1</sup>, Karima Saffidine<sup>1</sup>, Abderrahmane Baghiani<sup>1</sup>

<sup>1</sup>Laboratory of Applied Biochemistry, Department of Biochemistry, Faculty of Nature and Life Sciences, Farhat Abbas University of Setif 1, Setif 19000, Algeria

---

### Abstract

Medicinal plant has been used for a long time for its many therapeutic properties such as prevention of cardiovascular diseases, inflammation disorders, or reducing the risk of cancer. The aim of this study was to evaluate the antioxidant activity of the crude extract (CrE) of *Inula viscosa*'s leaves. Extraction was carried out by maceration in methanol. The quantification of total phenolic and flavonoids were estimated through the use of Folin-Ciocalteu and aluminum trichloride reagents, respectively. The potential of natural antioxidant presents in CrE to inhibit free radicals and chelating of metals was evaluated using the stable radical 2, 2- diphenyl -1- picrylhydrazyl (DPPH•) stable radical and reducing power methods. Total polyphenols and flavonoid amounts were  $309.42 \pm 0.15 \mu\text{g GAE/mg E}$  and  $11.78 \pm 0.12 \mu\text{g QE/mg E}$ , respectively. Crude extract performed a potent activity in scavenging DPPH• ( $\text{IC}_{50} = 15.2 \pm 0.75 \mu\text{g/ml}$ ) and in reducing power ( $\text{EC}_{50} = 21.05 \pm 0.36 \mu\text{g/ml}$ ). The presence of polyphenols and flavonoids could to some extent justify the observed antioxidant effect in the current study, thus opening new prospects for research and innovative phytopharmaceuticals developments.

**Keywords:** *Inula viscosa*, Polyphenols, Flavonoids, Antioxidant activity, DPPH, Reducing power

---





## Experimental Study on the Healing Effect of the Crude Extract of the Aerial Part of *Cytisus Triflorus* on Skin Wounds

Soraya Madoui <sup>1\*</sup>, Hanane Khither<sup>1</sup>, Karima Madoui<sup>2</sup>, Nouredine Charef<sup>1</sup>

<sup>1</sup>Laboratory of Applied Biochemistry, University Ferhat Abbas Setif, 19000, Algeria

<sup>2</sup>Laboratory of Applied Optics, Institute of Optics Mechanics, University Ferhat Abbas Setif, Algeria

---

### Abstract

The purpose of this test is to investigate the healing effect of the crude extract of the aerial part of *Cytisus triflorus* on experimental wounds. The extracts were prepared in vaseline at a concentration of 5%. The animals were anesthetized by intraperitoneal injection of 1ml of 2% urethane. Circular wounds of 300 mm<sup>2</sup> were created on the dorsal level. The wounds were dressed daily once a day. Measurements of the wounds were taken every three days until complete healing. The appearance, color, and odor of the wounds were noted throughout the treatment period. The healing process occurred in several phases: a gradual disappearance of inflammation, a contraction phase (the wounds became hard and covered with slightly blackish crusts). The treatment resulted in complete healing of the wounds. The use of *Cytisus triflorus* in ointment preparation promoted absence of infection. The wounds were odorless throughout the treatment

**Keywords:** *Cytisus triflorus* L., Inflammation, Resolution and healing effect

---



---

## Exploring Phenolic Composition and Scavenging Effects Against Reactive Oxygen Species of Nettle Crude Extract

**Hamza Kemchache<sup>\*1</sup>, Khalil Kaouane<sup>1</sup>, Ayoub Bekka<sup>1</sup>, Mondher Fradjia<sup>1</sup>, Sabrina Manel Kaddour<sup>1</sup>, Rayene Bouaita<sup>2</sup>, Nouredine Charef<sup>1</sup>, Soraya Madoui<sup>1</sup>, Hanane Khither<sup>1</sup>**

<sup>1</sup>Departement of Biochemistry, University of Farhat Abbas Setif-1, Setif, Algeria

<sup>2</sup>Departement of Molecular and Cellular Biology, University of Khenchela, Khenchela, Algeria

---

### Abstract

Reactive oxygen species (ROS) and free radicals are highly reactive and unstable molecules known to cause damage to biological systems, including DNA, proteins, and lipids, contributing to various health conditions such as cardiovascular and neurodegenerative diseases. Fortunately, certain secondary metabolites called antioxidants can neutralize these harmful species. In this study, we investigated the phenolic composition and antioxidant activity of a methanolic crude extract obtained from the aerial parts of nettle. The total polyphenol content was quantified using the Folin-Ciocalteu reagent, yielding a content of  $31.875 \pm 2.17$  mg EAG/g of extract. Additionally, the extract exhibited concentration-dependent inhibition of hydrogen peroxide, with  $IC_{50}$  values of  $0.292 \pm 0.002$  mg/mL, and scavenging activity against hydroxyl radicals, with an  $IC_{50}$  of  $1.791 \pm 0.068$  mg/ml. These findings suggest that nettle may represent a promising natural source of antioxidants.

**Keywords:** *Antioxidant, Hydrogen peroxide, Hydroxyl radical, Nettle, Polyphenols*

---



---

## Antioxidative Characteristics of Aqueous and Ethanol Extracts of *Anethum Graveolens* L. Seeds

Nour El Houda Belabas<sup>\*1</sup>, Nadjat Azzi<sup>1</sup>, Younes Douffa<sup>1</sup>, Haifaa Laroui<sup>1</sup>, Thoraya Guemmaz<sup>1</sup>, Fatima Zerargui<sup>1</sup>, Karima Saffidine<sup>1</sup>, Abderrahmane Baghiani<sup>1</sup>

<sup>1</sup>Laboratory of Applied Biochemistry, Department of Biochemistry, Faculty of Nature and Life Sciences, Farhat Abbas University of Setif 1, Setif 19000, Algeria

---

### Abstract

Researchers have confirmed that foods rich in natural antioxidants play a significant role in the prevention and treatment of many disorders, particularly cancers, and cardiovascular disease. The study aimed to evaluate the antioxidant potential of seed extracts from *Anethum graveolens* L., which is widely accepted by consumers and have various applications in food flavoring, and also in natural medical treatments in the pharmaceutical industries. This plant is rich in valuable compounds that show a remarkable antioxidant power and are associated with many health benefits. Ethanol and Aqueous extracts are obtained by maceration and decoction and they were comparatively evaluated for their *in vitro* antioxidant properties. The extracts were characterized by total phenol content (TPC), total flavonoid content (TFC) analysis and antioxidant activities with different assays, such as 1,1-diphenyl 1-2-picryl-hydrazyl (DPPH) and iron binding ability of chelators. Our results showed that the aqueous extract of the studied plant exhibited a high content of phytochemicals and promising antioxidant properties. The highest polyphenols and favonoids content was detected for aqueous extract ( $50.62 \pm 0.91 \mu\text{g GAE/mg DW}$ ) ( $8.56 \pm 0.57 \mu\text{gQE/g DW}$ ) respectively. however, this study demonstrated that these plant extracts of seeds are excellent sources of natural antioxidants. Significant additional differences that were found in the phytochemical composition could be exploited in future research for pharmaceutical purposes.

**Keywords:** *Anethum graveolens* L., Aqueous extract, Ethanol extract, Antioxidant activity, Seeds

---



---

## Evaluation of In Vitro Antioxidant Activity of Natural Compounds in *Atriplex Halimus* Leaf Extract Using Hydrogen Peroxide and Hydroxyl Radical Assays

**Khalil Kaouane<sup>\*1</sup>, Hamza Kemchache<sup>1</sup>, Ayoub Bekka<sup>1</sup>, Mondher Fradjia<sup>1</sup>, Rayene Bouaita<sup>2</sup>, Sabrina Manel Kaddour<sup>1</sup>, Nouredine Charef<sup>1</sup>, Hanane Khither<sup>1</sup>, Soraya Madoui<sup>1</sup>**

<sup>1</sup>Department of Biochemistry, University of Setif 1, Algeria

<sup>2</sup>Department of Molecular and Cellular Biology, University of Khenchela, Algeria

---

### Abstract

Oxidative stress-related diseases, such as cancer, diabetes, neurodegenerative disorders, and cardiovascular diseases, often result from the accumulation of free radicals in the body. Numerous studies worldwide aim to identify natural antioxidants from plant sources, as plants are fundamental to traditional medicinal treatments. *Atriplex halimus* (Family: *Chenopodiaceae*) is one such plant, traditionally used by herbalists in Arabic countries to treat conditions such as rheumatism, diabetes, and heart ailments. The present study aims to evaluate the antioxidant activity of the methanolic leaf extract of *Atriplex halimus*. The extract was analyzed for its total phenolic content (TPC) and total flavonoid content (TFC) using spectrophotometric methods. The antioxidant activity was assessed through various *in vitro* assays, including the hydrogen peroxide scavenging assay and hydroxyl radical scavenging assay. The TPC and TFC of the methanolic extract were found to be  $27.93 \pm 0.28$  mg GAE/g and  $9.44 \pm 0.07$  mg QAE/g, respectively. The leaf extract demonstrated significant antioxidant activity, with 72.71% inhibition for hydrogen peroxide scavenging compared to ascorbic acid 81.63%. For the hydroxyl radical assay, the extract showed 59.82% inhibition compared to BHT 85.91%. These findings suggest that the leaf extract could be a potent natural antioxidant, potentially useful for applications in health and nutrition.

**Keywords:** *Atriplex halimus*, Total phenolic, Total flavonoid, Hydrogen peroxide, Hydroxyl radical

---



---

## In Vitro Assessment of Biological Activity in Elaeagnaceae Leafs

Rayene Bouaita<sup>\*1</sup>, Randa Djemil<sup>1</sup>, Samira Bouhalit<sup>1</sup>, Saber Boutella<sup>2</sup>, Khalil Kaouane<sup>3</sup>,  
Hamza Kemchache<sup>3</sup>

<sup>1</sup>Molecular and Cellular Biology, University of Abbes Laghrour Khenchela, Khenchela, Algeria

<sup>2</sup>Biochemistry, University of Abdelhafid Boussouf, Mila, Algeria

<sup>3</sup>Biochemistry, University Ferhat Abbas, Setif1, Algeria

---

### Abstract

Natural substances from biomass plant have taken advantage of multiple interests in the biotechnology industries both in food, cosmetic and pharmaceutical. Between these compounds are found much of secondary metabolites which are mainly illustrated in therapeutics. Traditional medicines has used for long time plant materials for healing without knowing what had caused their actions, then studies of secondary metabolites are the subject of numerous studies based on in vitro cultures of plant tissues. These include phenolic compounds, polyphenols, flavonoids, anthocyanins, tannins ... which are the subject of our study, compounds widely used in therapeutics as vasculoprotective, anti-inflammatory, enzyme inhibitors, antioxidant and anti free radical. Our work has brought the excerpts from an algerian plant belong to the family of Elaeagnaceae, traditionally used to treat many diseases. The methodology developed for the analysis of these extracts has been applied for the determination of leaves of this plant. This study presents an attempt to evaluate the antioxidant activity of two dry organic extracts: Hydromethanolic (HMEA) and Hydroéthanolic (HEEA) extracts . The qunatitative estimation of total polyphenols (by the Folin-Ciocalteu method) and total flavonoids (by the method of aluminium trichloride) showed that the extracts are richer in these compounds. Assessment in vitro antioxidant activity using 2,2-diphenyl-bpicrylhydrazyl (DPPH), which showed a significant antioxidant activity as following : for HMEA 92% inhibition and 91% inhibition HEEA . using a assay showed that the Hydromethanolic extract exhibited good antioxidant activity with 92% inhibition rate by the DPPH method. However, this activity is less inferior to ascorbic acid (positive control).

**Keywords:** Polyphenols, DPPH, Antioxidant, Elaeagnaceae

---



## Evaluation of the Bio-Remedial Effect of *Bacillus Atrophaeus* to Treat Soil Polluted by Heavy Metals

Mondher Fradjia<sup>\*1</sup>, Rima Belattar<sup>2</sup>, Abdelhakim Sellal<sup>2</sup>, Wissam Nour Elhouda  
Ahmedi<sup>1</sup>, Hamza Kemchache<sup>1</sup>, Khalil Kaouane<sup>1</sup>, Nora Laouicha<sup>3</sup>, Amor Benchikh<sup>3</sup>

<sup>1</sup>Departement of Biochemistry, University of Ferhat Abbas Setif-1, Setif, Algeria

<sup>2</sup>Health and Environment Research Laboratory, Elbachir El Ibrahimi University BBA, University of Farhat Abbas Setif-1, Setif, Algeria

<sup>3</sup>Applied Microbiology Laboratory, Ferhat Abbas University, Setif 1, Algeria

---

### Abstract

Heavy metals are among the main inorganic pollutants in the soil. They are continually added to the soil by various activities such as metallurgical activities. Soil contamination by heavy metals is one of the major factors limiting plant productivity and, therefore, agricultural production. The objective of this study is to analyze the bio-remedial effect of strains of *Bacillus atrophaeus* sp (B16) and their protective effect of a plant species, the bean (*Vicia faba* L) in the case of a soil contaminated with copper (Cu). This work carried out in vivo consists of evaluating variations in morphological and biochemical parameters such as stem height, number of branches, leaf surface and total chlorophyll content. The results obtained show an increase in stem height of 35.33cm for plants grown in soils treated with B16 in comparison with those treated with EDTA (standard chelator) of 34.33cm and the negative control (untreated) 27cm. The calculation of the leaf area also shows an increase with plants grown in the presence of bio-remediant of 17 cm<sup>2</sup> for B16 and EDTA compared to that obtained with C- of 8.11 cm<sup>2</sup>. The results also show an overproduction recorded for the total chlorophyll content of 50.63 CCI for B16 in comparison with the standard and the negative control of 44.93 CCI and 29.96 CCI respectively.

**Keywords:** Heavy metals, Pollution, Bioremediation, Rehabilitation, *Bacillus*

---



## **Phytotherapy Study of Medicinal Plants Used in the Northern Region of the Wilaya of Setif (Ain El Kebira)**

**Nouioua Wafa<sup>\*1</sup>, Madoui Soraya<sup>2</sup>**

<sup>1</sup>Laboratory of Medicinal Plants Applied to Chronic Diseases, Faculty on Natural and Life Sciences, Ferhat Abbas University Setif-1, El Bez, Setif 19000, Algeria

<sup>2</sup>Laboratory of Applied Biochemistry, Faculty of Nature and Life Sciences, Ferhat Abbas University Setif-1, Setif 19000, Algeria

---

### **Abstract**

This research adds to our understanding of the therapeutic plants that are employed in conventional phytotherapy. The 250 persons that were questioned were included in the questionnaire that we used to do this. Many people have questions about us, especially in relation to the use of medicinal plants. This poll suggests that 63.33% of respondents take conventional medications. This finding demonstrates the value of medicinal herbs in the field of modern medicine. The collected data allowed for the identification of sixty-three medicinal plants, grouped into thirty-two families (the most common being Lamiaceae), three of which are dominant: Apiaceae, Lamiaceae, and Asteraceae. The leaves and the entire plant are the portions that are used the most. Most popular techniques are infusion and decoction.

**Keywords:** *Medicinal plants, Traditional phytotherapy, Questionnaires, Modern therapeutics, Ain el kebira*

---



---

## ABTS Radical Scavenging Activity and Ferrous Chelating Ability of Ethyl Acetate Extract of Pistacia Atlantica Seeds

Younes Douffa<sup>\*1</sup>, Nadjat Azzi<sup>1</sup>, Nour El Houda Belabas<sup>1</sup>, Haifaa Laroui<sup>1</sup>, Thoraya Guemmaz<sup>1</sup>, Karima Saffidine<sup>1</sup>, Fatima Zerargui<sup>1</sup>, Abderahmane Baghiani<sup>1</sup>

<sup>1</sup>Laboratory of Applied Biochemistry, Department of Biochemistry, Faculty of Nature and Life Sciences, Ferhat Abbas University of Setif 1, Setif 19000, Algeria

---

### Abstract

Reactive oxygen species (ROS) are a class of extremely reactive molecules that are frequently produced as byproducts of biological reactions. They are associated in the onset of degenerative diseases. Phenolic compounds of medicinal plants have the ability to shield the body from free radical damage. The main objective of this study was to evaluate the total content of phenol (TPC) and flavonoids (TFC) of ethyl acetate extract (EAES) prepared from the seeds of Pistacia atlantica, as well as their antioxidant activity using 2, 2'-azino-bis 3-ethylbenzothiazoline-6-sulfonic acid (ABTS) scavenging and ferrous chelating assays. EAES contain a high amount of TPC and TFC corresponding to  $266.34 \pm 15.50$  mg GAE/g and  $62.7 \pm 0.4$   $\mu$ g QE/g, respectively. This extract showed a strong activity in scavenging ABTS radical and chelating ferrous ion with corresponding IC<sub>50</sub> of  $3.21 \pm 0.07$  and  $380.76 \pm 22.09$   $\mu$ g/ml, respectively. The present study has demonstrated that EAES have a potent antioxidant effect that has contributed to the therapeutic benefits.

**Keywords:** ABTS, Antioxidant activity, Ferrous chelating, Flavonoids, Polyphenols

---





---

## Phytochemical Analysis and Biological Activities of Essential Oil and Lavandula Stoechas Harvested in Algeria

Amina Benazzouz-Touami<sup>\*1</sup>, Driffa Bouchene<sup>1</sup>, Nabila Iaouadaren<sup>1</sup>

<sup>1</sup>Laboratory of Physics and Chemistry of Materials (LPCM), Department of Chemistry, Faculty of Sciences, Mouloud Mammeri University,  
Tizi Ouzou 15000, Algeria

---

### Abstract

This study aims to thoroughly analyze the essential oil of *Lavandula stoechas* (commonly known as French lavender or butterfly lavender) harvested in the Tizi-Ouzou region of Algeria. The extraction of the oil was performed using hydrodistillation, a method that involves distilling the plant material with water to capture volatile compounds. The extraction yield obtained from this process was 1.23%. To characterize the extracted essential oil, physicochemical analyses were conducted to determine its properties and chemical composition. The analysis by gaseous chromatography (GC) and by gaseous chromatography coupled by a mass spectrometer (GC / MS) allowed us to determine the chemical composition of studied essential oil. The phytochemical screening of the aerial parts (dried leaves) of *Lavandula stoechas* revealed the presence of several chemical compounds with interesting biological activities. The aqueous extract of *L. stoechas* is rich in tannins, saponins, sterols, and triterpenes. However, it does not contain alkaloids and flavonoids. Additionally, infrared (IR) spectroscopic analysis was carried out. The study also focused on evaluating the antimicrobial effect of the essential oil against various bacterial strains. Among these, the most significant inhibition was observed against *Escherichia coli* (*E. coli*). This antimicrobial effect highlights the potential of *Lavandula stoechas* essential oil as a natural agent in combating certain bacterial infections. The study of the antioxidant power was realized by the method of reduction of the radical DPPH · showed the existence of an antioxidant activity of our essences.

**Keywords:** *Lavandula stoechas*, Antimicrobial effect, Antioxydant activity, Chromatography in gas phase coupled by mass spectrometry (GC / MS), Essential oil

---



---

## Tolerance Mechanism Study to Polluted Ecosystems of Bioremediants

Laouicha Nora<sup>\*1</sup>, Sellal Abdelhakim<sup>2</sup>, Bencheikh Amor<sup>1</sup>, Belattar Rima<sup>2</sup>, Fradjia Mondher<sup>3</sup>, Ahmedi Wissam Nourelhouda<sup>3</sup>

<sup>1</sup>Biochemistry, Applied Microbiology Laboratory Ferhat Abbas University1, Setif, Algeria

<sup>2</sup>Biochemistry, Health and Environment Laboratory, Elbachir El-Ibrahimi University, Bordj Bou Arreridj, Algeria

<sup>3</sup>Biochemistry, Laboratory of Phytotherapy Applied to Chronic Diseases University, Setif1, Algeria

---

### Abstract

The consequences of industrial activities, particularly metallurgical ones, persist today. The objective of this study is to evaluate the remedial effect of the soil through the use of bio-remediants, in particular a plant species which is the sunflower (*Helianthus annuus*), and two bacterial strains namely: *Pseudomonas laurentiana* M11 and *Bacillus atrophaeus* B16, via the evaluation of their heavy metal chelating capacity, in vitro, using a colorimetric test based on the reduction in the absorbance of the murexide-Zn/Cu complex. Strains B16 and M11 demonstrated an exceptional Zn chelation potential with a maximum of 92% for B16 and 90% for M11 at a volume of only 25µl and a Cu chelation potential with a rate of 83% for B16 and 68. % for M11 at 25µl, in comparison with EDTA which gave rates of 88% for the chelation of Zn and 35% for Cu with the same volume. A microplate test was performed with a double serial dilution method to estimate Cu tolerance. The copper concentrations used in this resistance test were between 6.4 mg/ml and 0.2 mg/ml. Strains M11, B14, and B16 showed normal growth up to a minimum inhibitory concentration (MIC) of 0.4 mg/mL.

**Keywords:** Heavy metal, EDTA, Chelation, bioremediation, Bacillus, Pseudomonas

---



## Evaluation of Antibacterial Activity of *Thymus Vulgaris* Extracts

Mohamed Khiari\*<sup>1</sup>, Zine Kechrid<sup>2</sup>

<sup>1</sup>Department of Biology, University of Souk Ahras, Souk ahras, Algeria

<sup>2</sup>Department of Biochemistry, University of Annaba, Annaba, Algeria

---

### Abstract

The use of medicinal plants today is the form of the most widespread medicine worldwide. Utilizing aromatic plants as interesting source of phytochemicals constitute one of the largest scientific concerns. Thymus is a medicinal and aromatic plant belonging to the Lamiaceae family, it is used and recognized for its therapeutic virtues in traditional medicine. The present study aims to evaluate the antioxidant activity of aqueous, methanolique and essential oil extracts of *Thymus vulgaris* L. collected from Ouled Driss region, Souk Ahras. Furthermore, the antibacterial activity was valuated using three bacterial strains: *Staphylococcus aureus*, *Escherichia coli* and *Klibesiella pneumoniae*. Commercial antibiotics were used as references. The phytochemical analysis indicated that leaf of *T. vulgaris* comprising anthocyanins, leucoanthocyanins, flavonoids, tanins and terpenoids. The obtained results showed also that essential oil of *T. vulgaris* in its pure state has the greatest antibacterial effect against the three strains, superior or equal to the all antibiotics used. On the other hand, the aqueous extract has weak activity only against the *S. aureus* strain. Dilution of extracts in DMSO reduced their antibacterial power. The present research demonstrated the antibacterial activities of *T. vulgaris* extracts against three strains of bacteria. It was suggested that essential oil of the present plant could be use as an antibacterial agent.

**Keywords:** *Thymus vulgaris*, Essential oil, Antibacterial activity, *Staphylococcus*, *Escherichia coli*

---



---

## Evaluation of Antibiotic Resistance Pattern and Biofilm Production in Vaginal Isolates in Women

Anfal Kara<sup>1\*</sup>, Feryal Belfihadj<sup>2</sup>, Naouel Boussoualim<sup>1</sup>, Meriem Elkolli<sup>2</sup>

<sup>1</sup>Laboratory of Applied Biochemistry, University of Setif, Algeria

<sup>2</sup>Laboratory of Applied Microbiology, University of Setif, Algeria

---

### Abstract

The vagina serves as a suitable ecosystem that harbours diverse communities of microorganisms. Among these, *Lactobacillus*, recognized as vaginal flora. Bacterial vaginosis, an infection arising from the disruption of the normal balance of vaginal bacteria, poses a threat to the vaginal environment. Vaginal infections pose a substantial health concern for females due to challenges such as high recurrence rates, drug resistance, occurrence of virulence genes, and the emergence of persistent strains. Our study aims to elucidate the etiology of vaginal infections, assess antibiotic resistance, and profile biofilm activity. Twenty strains were isolated from hospitalized and non-hospitalized women aged between 24 -50 years. Biochemical and microbiological standard tests were employed for sample identification, Kirby Bauer Disk method was used for testing antimicrobial sensitivity. Screening of ESBL strains were confirmed by disk diffusion method, and biofilm were assed through a microplate assay. Results indicated that 62.5% of the isolates were *Staphylococcus aureus*, while *Enterobacter aerogenes*, *Escherichia coli*, and *Klebsiella* each constituted 12.5%. A significant proportion (62.5%) of the strains exhibited multi-drug resistance, with 75% displaying high acquired resistance, particularly against  $\beta$ -lactams, cephalosporins, macrolides, and aminoglycosides, such as Cephalexin, Cefoxitin, Cefixime, Ceftazidime, Cefotaxime, Oxacillin, Gentamycin, Kanamycin, and Erythromycin. Notably, 62% exhibited notable resistance to imipenem, nalidixic acid, and ciprofloxacin. Furthermore, 37.5% of bacteria demonstrated an Extended Spectrum Beta-Lactamase (ESBL) character. All strains exhibited biofilm activity, with 37% demonstrating moderate production and 63% exhibiting weak production. In conclusion, our study sheds light on vaginal infections, revealing a predominant presence of multi-drug resistant strains, heightened resistance to key antibiotics, and widespread biofilm activity.

**Keywords:** Vaginal infections, Antibiotic resistance, Biofilm activity, Multi-drug resistance, Bacterial vaginosis, Extended Spectrum  $\beta$ -Lactamase (ESBL)

---



---

## Evaluation of Antioxidant and Antibacterial Activities of *Ruta montana* Crude Extract from the Mila Region

Zineb Bouamrane<sup>\*1</sup>, Saber Boutellaa<sup>1</sup>, Hakima Belattar<sup>1</sup>, Mouna Menakh<sup>2</sup>, Nedjla Derbal<sup>1</sup>

<sup>1</sup>Laboratory of Natural Sciences and Materials (LSNM), Institute of Sciences and Technology, University Center Abdehafid Boussouf, Mila, Algeria

<sup>2</sup>Department of Nature and Life Sciences, University Center Abdehafid Boussouf, Mila, Algeria

---

### Abstract

This study aims to evaluate the antioxidant and antibacterial activities of the crude extract of *Ruta montana*, a medicinal plant widely spread in the Mila region. Bioactive compounds such as polyphenols and flavonoids are specifically studied for their potential beneficial properties. The crude extract of *R. montana* was obtained by macerating the plant, harvested at the fruiting stage, in 80% ethanol. The polyphenol and flavonoid contents were quantified using the Folin-Ciocalteu and aluminum trichloride methods, respectively. Additionally, the antioxidant activity was evaluated using the DPPH free radical scavenging method by comparing the IC<sub>50</sub> of the crude extract with that of ascorbic acid. The antibacterial activity was tested against several bacterial strains, including *Klebsiella pneumoniae*, *Pseudomonas aeruginosa*, *Escherichia coli*, *Staphylococcus aureus*, and *Bacillus subtilis*, using the disk diffusion method. Analyses revealed a polyphenol content of 50.8 µg GAE/mg of extract and a flavonoid content of 16.6 µg QE/mg of extract. The crude extract of *R. montana* exhibited moderate antioxidant activity with an IC<sub>50</sub> of 68.45 µg/ml, compared to ascorbic acid with an IC<sub>50</sub> of 3.56 µg/ml. Regarding antibacterial activity, the extract showed no inhibitory effect against the tested strains.

Although the crude extract of *R. montana* presents notable antioxidant activity, it is inferior to that of ascorbic acid. However, no antibacterial activity was observed against the tested bacterial strains. These results highlight the need for further research to isolate and identify the specific active compounds of *R. montana* and to assess their therapeutic potential.

**Keywords:** *Ruta montana*, Crude extract, Polyphenols, Flavonoids, Antioxidant activity (DPPH), Antibacterial activity

---



---

## Evaluation of Antibiotic Resistance in Enterobacteria Isolated from Hospital Cockroaches

**Ben Djaballah Wafa<sup>\*1,2</sup>, Bouguenoun Widad<sup>1</sup>, Trabsa Hayat<sup>1,3</sup>, Kebkoub Narimane<sup>1</sup>,  
Serraye Fatima<sup>1</sup>**

<sup>1</sup>Faculty of Exact Sciences and Natural and Life Sciences, University of Biskra, Biskra 07000, Algeria

<sup>2</sup>Laboratory for the Promotion of Innovation in Agriculture in Arid Regions (PIARA), Department of Agronomic Sciences, University of Biskra, Biskra, Algeria

<sup>3</sup>Laboratory of Applied Biochemistry, Faculty of Natural and Life Sciences, Ferhat Abbas Setif 1 University, Setif 19000, Algeria

---

### Abstract

Cockroaches are undesirable pests, often living in close proximity to humans, and their presence in hospitals poses a major public health problem as they can contribute to the spread of pathogenic bacteria, thereby increasing the risk of nosocomial infections. Among these bacteria are Enterobacteriaceae. The aim of this study is to isolate Enterobacteriaceae from the external surface and the interior of cockroaches and to determine their level of antibiotic resistance. Forty cockroaches were collected from two hospitals in the Biskra province over ten days. The isolation and purification of bacteria were carried out on selective media: Hektoen, MacConkey, and Chromagar, and identification were done according to standard microbiological methods. Antibiotic resistance profiles of the isolates were determined by antibiogram according to EUCAST 2022. In total, 35 Gram-negative bacteria were isolated from the 40 cockroaches, of which 15 strains (43%) were Enterobacteriaceae. 46% of the strains were identified as *Klebsiella* sp. and *Serratia* sp., followed by *Enterobacter* sp. (40%), and *E. coli* and *Proteus* sp. at 7%. According to the antibiogram, the isolates from the external surface of cockroaches showed the highest resistance rate (91.6%) for the antibiotics Amoxicillin, Ceftazidime, and Gentamicin, while for the isolates from the interior of the cockroaches, the highest resistance rate was 33.33% against Ceftazidime. A resistance rate of 8.33% against Ertapenem was revealed, which is noteworthy. All isolates remained sensitive to Imipenem. In conclusion, cockroaches can be mechanical and biological vectors of multi-resistant Enterobacteriaceae in hospitals, posing a threat to public health. This underlines the necessity of finding solutions to control these pests.

**Keywords:** *Cockroaches, Nosocomial infections, Multi-resistant, Enterobacteriaceae, Antibiotic*

---



## G-Protein Coupled Estrogen Receptor Expression in Estrogen Receptor Alpha (ER $\alpha$ ) Negative Breast Cancer Tissues of Algerian Patients

Yasmine Mostaphaoui\*<sup>1</sup>, Rafik Menad<sup>1,2</sup>, Elara N'tima Moudilou<sup>3</sup>, Chahla Bencharif<sup>4</sup>

<sup>1</sup>Laboratory of Valorization and Bioengineering of Natural Resources Department of Natural and Life Sciences, Faculty of Sciences, University of Algiers, Algiers, Algeria

<sup>2</sup>Laboratory of Research on Arid Areas, Small Vertebrates Reproduction Faculty of Biological Sciences, Houari Boumediene University of Sciences and Technology, Algiers, Algeria

<sup>3</sup>Sciences and Humanities, Lyon Catholic University, Lyon, France

<sup>4</sup>Anatomy and Pathology Laboratory, CHU Khelil Amrane, Bejaia, Algeria

### Abstract

G Protein-Coupled Estrogen Receptor 1 (GPER1) has emerged as a pivotal player in the molecular pathogenesis of breast cancer. Its expression influences critical processes such as cell proliferation, migration and metastasis [1, 2]. Approximately 60% of breast tumors express GPER [3], suggesting its potential as a therapeutic target. Breast cancer remains a significant health challenge in Algeria, where it is the most prevalent cancer among women with 14 601 new cases in 2022 and a leading cause of cancer related deaths with 4 893 cases according to GLOBOCAN [4], so further research is needed to understand GPER1's specific impact on breast cancer in the Algerian population.

This study aims to analyze this receptor's expression in primary invasive breast cancer tissues, particularly those that are negative for estrogen receptor alpha (ER $\alpha$ ), in an Algerian population. Formalin-fixed, paraffin-embedded tissue samples from patients diagnosed with primary invasive breast cancer of no special type were collected from Khelil Amrane hospital in Bejaia. These patients had received no radiotherapy or neoadjuvant chemotherapy prior to their surgery. GPER1 expression was analysed by immunohistochemistry using a detection kit from Vector Laboratories. Results showed two different GPER1 localisations, cytoplasmic and nuclear with a predominant nuclear localisation in these samples which correlates with a more aggressive phenotype. However, the study's scope was limited by the patient sample size, suggesting that an increased number of participants could enhance the validity of the findings.

In conclusion, understanding GPER1's expression pattern and elucidate its role in tumor progression could be transformative for breast cancer treatment in Algeria. Further research with larger sample sizes is essential to substantiate these preliminary findings and develop effective targeted therapies especially for invasive breast cancers that are ER  $\alpha$  negative such as triple negative breast cancer, having no molecular target and patients are only receiving chemotherapy as treatment.

**Keywords:** GPER1, Immunohistochemistry, Invasive breast cancer, ER negative breast cancer

### References

- [1] A. Vivacqua, "GPER1 and microRNA: Two players in breast cancer progression," *Int. J. Mol. Sci.*, vol. 22, no. 1, pp. 1–16, 2021, doi: 10.3390/ijms22010098.
- [2] E. J. Filardo *et al.*, "Distribution of GPR30, a seven membrane-spanning estrogen receptor, in primary breast cancer and its association with clinicopathologic determinants of tumor progression," *Clin. Cancer Res.*, vol. 12, no. 21, pp. 6359–6366, 2006, doi: 10.1158/1078-0432.CCR-06-0860.
- [3] L. H. Hsu, N. M. Chu, Y. F. Lin, and S. H. Kao, "G-protein coupled estrogen receptor in breast cancer," *Int. J. Mol. Sci.*, vol. 20, no. 2, 2019, doi: 10.3390/ijms20020306.
- [4] J. Ferlay, M. Ervik, F. Lam, M. Laversanne, M. Colombet, L. Mery, M. Piñeros, A. Znaor, I. Soerjomataram, and F. Bray, (2024). Global Cancer Observatory: Cancer Today. Lyon, France: International Agency for Research on Cancer. Available: <https://gco.iarc.who.int/today>, Accessed: June 19, 2024.



## Exploring the Insecticidal Potency and Growth Inhibition Effect of *Pistacia lentiscus* and *Laurus Nobilis* Oils and Extracts on *Culex pipiens* (Diptera: Culicidae) Larvae

Menakh Mouna<sup>\*1</sup>, Saber Boutellaa<sup>2</sup>, Zineb Bouamrane<sup>2</sup>

<sup>1</sup>Department of Biological and Agricultural Sciences, Institute of Natural and Life Sciences, Abdelhafid Boussouf University Center Mila 43000, Algeria

<sup>2</sup>Laboratory of Natural Sciences and Materials Laboratory, Abdelhafid Boussouf University Center Mila 43000, Algeria

### Abstract

This study assessed the larvicidal and emergence inhibitory effects of Mastic Tree (*Pistacia lentiscus* L.), and Bay Laurel (*Laurus nobilis* L.) essential oils and extracts on *Culex pipiens* L. mosquito larvae, a significant public health threat as a vector for various diseases. Our analysis encompassed individual and combined evaluations of these natural products. Gas chromatography–mass spectrometry (GC-MS) analysis revealed distinctive chemical compositions in *P. lentiscus* and *L. nobilis* essential oils, featuring noteworthy compounds such as spathulenol,  $\beta$ -caryophyllene, linalool, and 1,8-cineole. HPLC analysis showed richness in phenolic compounds in both extracts, including benzoic acid, quercetin, and catechin hydrate. Biological tests were performed according to a standard methodology inspired by the WHO protocol. Individual larvicidal assessments demonstrated *L. nobilis* essential oil as the most potent, with an LC<sub>50</sub> of 31.94 ppm and an LT<sub>50</sub> of 6.14 h. Followed by *P. lentiscus* essential oil (LC<sub>50</sub> of 46.59 ppm, LT<sub>50</sub> of 33.77 h), *L. nobilis* ethanolic extract (LC<sub>50</sub> of 73.17 ppm, LT<sub>50</sub> of 11.55 h) and *P. lentiscus* ethanolic extract (LC<sub>50</sub> of 135.60 ppm, LT<sub>50</sub> of 47.69 h). Remarkably, synergistic combinations of *P. lentiscus* and *L. nobilis* extracts, especially essential oils exhibited heightened larvicidal effects, surpassing individual extract efficacy. Noteworthy is the synergistic activity observed by blending *P. lentiscus* and *L. nobilis* essential oils in volume ratios of 1:4, 2:3, and 2:2. Additionally, *P. lentiscus* and *L. nobilis* essential oils displayed inhibitory effects on larvae emergence, with synergistic activity observed in specific combinations. Our findings underscore the potential of these natural extracts, both individually and synergistically, as effective eco-friendly larvicidal agents against *C. pipiens*.

**Keywords:** *Pistachia lentiscus*, *Laurus nobilis*, *Culex pipiens*, Larvicidal effect, Emergence inhibition

## 1 INTRODUCTION

*Culex pipiens*, the common house mosquito, represents a major public health threat by spreading diseases like West Nile virus and causing allergic reactions such as angioedema and urticarial [1]. Effective mosquito population control is critical for global health, but traditional chemical insecticides pose environmental concerns and lead to resistance. As a result, there is increasing interest in exploring alternative, eco-friendly, and sustainable methods to manage mosquito vectors [2]. Natural products from plants have gained attention as potential alternatives to synthetic insecticides due to their biodegradability, low toxicity to non-target organisms, and effectiveness against mosquito larvae [3]. Essential oils and botanical extracts have shown promise in this regard. *Pistacia lentiscus* (mastic) and *Laurus nobilis* (bay laurel), native to the Mediterranean region, have been recognized for their therapeutic properties and potential natural insecticidal compounds [4, 5].

This study aims to evaluate the larvicidal activity and emergence inhibitory effects of *P. lentiscus* and *L. nobilis* extracts against the third instar *C. pipiens* larvae. By assessing the effectiveness of these natural products both individually and in combination, the research seeks to contribute valuable insights to the development of novel and sustainable mosquito control strategies, expanding the arsenal of eco-friendly solutions in the fight against mosquito-borne diseases.



## 2 MATERIAL AND METHOD

### 2.1 Preparation of extracts

Using a modified cleverger-type apparatus, 100 g of dried leaves were hydrodistilled for three hours to extract the essential oils. The collector solvent in this case was diethyl ether. Following solvent evaporation, the oil was kept at 4 °C in sealed vials shielded from light. *P. lentiscus* and *L. nobilis* ethanolic extracts were prepared using a Soxhlet apparatus. Approximately 50 g of samples were extracted in 250 mL of 80 % ethanol for 4 hours then, the solutions were filtered, concentrated under vacuum pressure at 45 °C and were kept at 4 °C prior analysis [6]

### 2.2 Gas Chromatography–Mass Spectrometry (GC-MS)

Essential oils were analyzed using an Agilent 6890 GC-MS system with a 5973 mass spectrometry detector and an HP-5 MS capillary column. The temperature program increased from 60 to 250°C over 8 minutes at 2°C/min, with helium as the carrier gas at 0.6 mL/min and a split ratio of 100:1. Scans covered a mass range of 50–550 m/z every second. Component identification involved comparing fragmentation patterns to WILEY and NIST05 reference libraries and determining Kovats retention indices using n-alkanes (C8–C40) [7].

### 2.3 HPLC-DAD Screening of Phenolics

Shimadzu reverse phase high performance liquid chromatography (Shimadzu Cooperation, Japan) system that consists of a Shimadzu model LC-20AT solvent delivery unit and a Shimadzu model SPD-M20A diode array detector and is monitored by LC-solution software was used to analyze ethyle acetate and butanolic extracts as well as 27 standard phenolics. The results were presented as micrograms per gram of dry weight, and their characterization was based on a comparison of the retention times [8].

### 2.4 Larvicidal Bioassay Test

Mosquito larvae used in this study were from a *Cx. pipiens* biotype *molestus* laboratory colony, kept at 26–27°C, 50–60% relative humidity, and a 16:8 h photoperiod (L). Adults were housed in 33 cm mesh-covered cages and fed a 10% sucrose solution. Due to autogeny, females did not require blood for egg development. Essential oils and ethanolic extracts were prepared in water with Tween 80 as an emulsifier, tested at concentrations ranging from 25 to 200 ppm and 50 to 400 ppm, respectively, against early third instar *C. pipiens* larvae in 250 mL cups with distilled water. Mortality was monitored at regular intervals over 72 hours with five replications per concentration, using a control group of distilled water and Tween 80 [9].

### 2.5 Emergence Inhibition Effect

To assess adult emergence inhibition (IE50 and IE90), cups containing larvae were covered with netting to prevent adult escape. Mortality and survival were monitored every few days until all adults emerged. The experiment maintained a temperature range of 25–28 °C and a 12L:12D photoperiod. Results were expressed as IE%, indicating the percentage of larvae failing to develop into viable adults, including those that did not fully separate from pupal cases [6].

### 2.6 Preparation of Mixtures

We utilized the ten-point approach to explore the potential enhancement of specific extracts' effects by combining them in different ratios. According to this idea, the half-lethal concentrations of substances A and B are influenced by the potency of a and b. As a result, we evaluated the mixes with the co-toxic factor approach. In particular, the concentration gradient order of the following five ratios was taken into consideration: 1:4, 2:3, 2:2, 3:1, and 4:1 [10].

## 3 RESULTS

### 3.1 GC-MS Analysis

The essential oils from *P. lentiscus* and *L. nobilis* exhibited distinct chemical compositions, as detailed in Table 1 and Table 2, respectively, through GC-MS analysis. In the *P. lentiscus* essential oil, the prominent compounds identified were spathulenol (16.73%),  $\beta$ -caryophyllene (11.60%), germacrene-D (8.03%), and carvacrol (7.12%).

In addition, the *L. nobilis* essential oil showcased linalool (25.68%), 1,8-cineole (23.29%), methyleugenol (15.48%), camphene (15.01%) and eugenol (5.02%) as major compounds in this oil.

**Table 1.** Chemical composition of the essential oil from *P. lentiscus* (RT: Retention time, RI: Retention index)

No	Compound	RT	RI	%
1	$\alpha$ -pinene	4.74	939	2.40
2	Camphene	5.18	942	0.24
3	$\beta$ -Pinene	6.87	954	2.01
4	$\alpha$ -Thujene	7.41	957	0.57
5	$\alpha$ -Terpinene	8.06	1062	0.01
6	<i>p</i> -Cymene	8.52	1065	3.23
7	$\beta$ -Phelladrene	8.76	1066	4.82
8	$\gamma$ -Terpinene	10.56	1179	3.46
9	$\alpha$ -Terpinolene	13.28	1197	2.38
10	4-Terpineol	18.13	1229	2.10
11	$\alpha$ -Terpineol	19.09	1236	0.63
12	Pulegone	22.31	1258	4.00
13	Phellandral	24.56	1273	2.64
14	Bornyl acetate	25.52	1442	2.44
15	Carvacrol	26.98	1447	7.12
16	2-Bornene	29.73	1457	1.32
17	Copaene	31.03	1512	0.27
18	$\beta$ -Caryophyllene	33.69	1525	11.60
19	$\alpha$ -Caryophyllene	35.68	1535	1.85
20	Aromadendrene	36.11	1537	1.37
21	$\gamma$ -Cadinene	37.12	1542	5.29
22	Germacrene-D	37.47	1543	8.03
23	$\alpha$ -Muurolene	38.78	1550	1.30
24	$\alpha$ -Amorphene	39.47	1553	0.89
25	$\alpha$ -Farnesene	39.72	1554	0.33
26	$\delta$ -Cadinene	40.18	1557	3.81
28	Spathulenol	43.14	1571	16.73
29	$\beta$ -Cadinene	45.90	1585	1.18
31	$\alpha$ -Cadinol	47.39	1592	6.73
Total identified			98.75%	

**Table 2.** Chemical composition of the essential oil of leaves of *L. nobilis*

No	Compound	RT	RI	%
1	$\alpha$ -pinene	4.873	936	0.68
2	Camphene	5.325	939	15.01
3	Sabinene	6.314	946	2.84
4	$\beta$ -Pinene	7.08	952	0.19
5	1,8-Cineole	9.549	1022	23.29
6	$\gamma$ -Terpinene	10.869	1031	0.24
7	4-Terpineol	11.355	1084	2.21
8	$\alpha$ -Terpinolene	12.658	1093	0.1

9	Linalool	14.795	1107	25.68
10	trans-Pinocarveol	16.041	1115	0.37
11	Borneol	17.825	1177	0.28
12	Nerol	18.088	1179	0.49
13	Phellandral	22.397	1258	0.44
14	Carvacrol	24.397	1272	0.25
15	Elemol	25.003	1276	0.23
16	Linalyl acetate	25.952	1282	0.74
17	l-Bornyl acetate	27.347	1291	0.51
18	Eugenol	31.09	1317	5.02
19	$\beta$ -Elemene	32.708	1327	0.31
20	Methyleugenol	34.52	1340	15.48
21	germacrene A	39.218	1479	0.33
22	$\alpha$ -Amorphene	39.966	1485	0.16
23	$\delta$ -Cadinene	40.544	1539	0.47
24	Spathulenol	43.601	1562	2.96
25	Alloaromadendrene	46.351	1583	0.48
26	$\beta$ -Eudesmol	47.414	1590	0.99
Total identified			99.74%	

### 3.2 HPLC Analysis

The HPLC analysis results of *P. lentiscus* and *L. nobilis*, ethanolic extracts, presented in Figure 1 showcased the presence of distinct compounds. *P. lentiscus* extract revealed 5 compounds, while the *L. nobilis* extract contained 6 compounds. In the *P. lentiscus* extract, the identified compounds were benzoic acid (17.35%), catechin hydrate (9.45%), galic acid (2.58%), ascorbic acid (2.11%), and quercetine (0.75%). Additionally, the *L. nobilis* extract revealed quercetine (7.89%), Benzoic acid (3.39%), myrecitine (2.94%), 3-hydroxyflavone (1.75%), coumaric acid (1.43%), and catechin hydrate (1.09%) as its identified compounds.

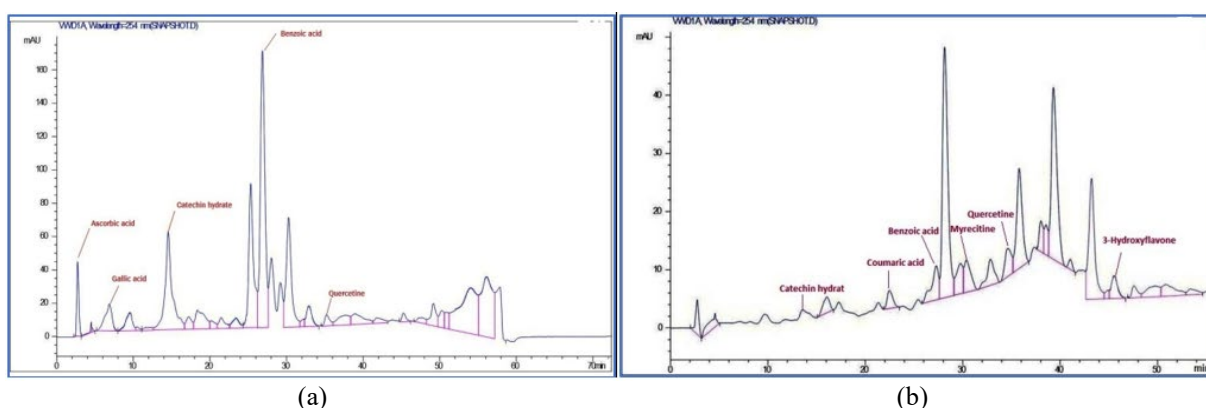


Figure 1. (a) HPLC Chromatogram of *P. lentiscus* and *L. nobilis* and (b) ethanolic extracts

### 3.3 Larvicidal Potency

The individual larvicidal effects of *P. lentiscus*, and *L. nobilis*, extracts against *C. pipiens* larvae were detailed in Table 3. The findings highlighted *L. nobilis* essential oil as the most potent extract, exhibiting an  $LC_{50}$  of 31.94 ppm and an  $LT_{50}$  of 6.14 h. Following this, *P. lentiscus* essential oil showed moderate effectiveness with an  $LC_{50}$  of 46.59 ppm and an  $LT_{50}$  of 33.77 hours. Subsequently, *L. nobilis* ethanolic extract displayed an  $LC_{50}$  of 73.17 ppm with an  $LT_{50}$  of 11.55 hours, while *P. lentiscus* ethanolic extract showed comparatively lower effectiveness, with an  $LC_{50}$  of 135.60 ppm and an  $LT_{50}$  of 47.69 hours.

The outcomes of the synergistic larvicidal effect of *P. lentiscus* and *L. nobilis* extracts against *C. pipiens* larvae were depicted in Table 4. Our findings indicated that combining these extracts in various ratios enhanced their effectiveness against mosquito larvae.

**Table 3.** Individual Larvicidal effect of *P. lentiscus* and *L. nobilis* extracts against *C. pipiens* larvae (LC<sub>50</sub>- LC<sub>90</sub> Lethal concentration and LT<sub>50</sub>- LT<sub>90</sub> Lethal time kills 50% and 90% of the exposed larvae at LC<sub>50</sub> respectively, UCL Upper confidence limit, LCL Lower confidence limit, X<sup>2</sup> Chi-square E.O essential oil, E.E ethanolic extract)

Extracts	LC <sub>50</sub> (LCL-UCL)	X <sup>2</sup>	LT <sub>50</sub> (LCL-UCL)	X <sup>2</sup>
<i>P. lentiscus</i> E.O	46.59 (34.66-59.77)	1.48	33.77 (23.57-52.75)	5.36
<i>P. lentiscus</i> E.E	135.60 (104.09-176.31)	0.41	47.69 (33.77-87.35)	2.42
<i>L. nobilis</i> E.O	31.94 (22,72-40.08)	1.26	6.14 (4.96-9.56)	0.03
<i>L. nobilis</i> E.E	73.17 (49.29-95.46)	0.71	11.55 (8.96-13.37)	5.09

**Table 4.** Synergistic Larvicidal effect of *P. lentiscus* and *L. nobilis* extracts against *C. pipiens* larvae (CTC Co-toxicity Index, CTC =100 indicated an additive effect, CTC > 100 indicated a synergistic effect, and CTC < 100 indicated an antagonistic effect)

Mixtures	LC <sub>50</sub> (ppm) (LCL-UCL)	X <sup>2</sup>	CTC	LT <sub>50</sub> (h) (LCL-UCL)	X <sup>2</sup>	CTC
<i>P. lentiscus</i> E.O/ <i>L. nobilis</i> E.O						
1 :4	30.06 (19.06-44.06)	0.45	106.25 <sup>S</sup>	7.06 (5.94-21.66)	5.25	86.96 <sup>an</sup>
2 :3	31.34 (19.34-49.34)	1.53	101.91 <sup>S</sup>	8.34 (7.66-22.24)	3.63	73.62 <sup>an</sup>
2 :2	30.65 (22.65-48.65)	2.55	104.20 <sup>S</sup>	10.65 (7.35-24.85)	2.87	57.65 <sup>an</sup>
3 :2	33.56 (21.56-47.56)	0.54	95.17 <sup>an</sup>	7.56 (6.44-14.02)	1.54	81.21 <sup>an</sup>
4 :1	36.03 (28.03-50.03)	3.06	88.64 <sup>an</sup>	11.03 (8.44-24.72)	3.86	55.66 <sup>an</sup>
<i>P. lentiscus</i> E.E/ <i>L. nobilis</i> E.E						
1 :4	74.64 (62.64-88.64)	2.86	98.03 <sup>an</sup>	14.64 (11.14-28.68)	0.74	78.89 <sup>an</sup>
2 :3	73.11 (63.11-89.11)	3.42	100.08 <sup>ad</sup>	11.10 (9.89-25.11)	1.95	104.05 <sup>S</sup>
2 :2	73.64 (61.64-87.64)	0.87	99.36 <sup>an</sup>	13.64 (11.56-27.23)	1.63	84.67 <sup>an</sup>
3 :2	76.66 (66.76-91.57)	1.75	95.44 <sup>an</sup>	12.66 (10.63-36.45)	3.81	91.23 <sup>an</sup>
4 :1	80.34 (67.34-93.34)	1.05	91.07 <sup>an</sup>	10.34 (8.66-24.34)	2.86	111.70 <sup>S</sup>

### 3.4 Emergence Inhibition Efficacy

As depicted in Table 5, *L. nobilis* E.O and *P. lentiscus* E.O displayed intriguing inhibitory effects on the emergence of *C. pipiens* larvae, with LC<sub>50</sub> values of 27.64 ppm and 42.33 ppm, respectively. However, ethanolic extracts exhibited a moderate impact, showcasing LC<sub>50</sub> values of 121.50 ppm, 70.23 ppm, and 83.44 ppm, respectively. Regarding their synergistic effects, the combination of *P. lentiscus* and *L. nobilis* essential oils demonstrated synergistic activity when mixed in volume ratios of 1:4 and 2:2.

**Table 5.** Emergence inhibition efficacy of *P. lentiscus* and *L. nobilis* extracts against *C. pipiens* larvae (CTC Co-toxicity Index, CTC =100 indicated an additive effect, CTC > 100 indicated a synergistic effect, and CTC < 100 indicated an antagonistic effect)

Extracts	LC <sub>50</sub>	LCL-UCL	X <sup>2</sup>	CTC
<i>P. lentiscus</i> E.O	42.33	32.23-51.65	2.45	-
<i>P. lentiscus</i> E.E	121.50	100.15-153.22	1.31	-
<i>L. nobilis</i> E.O	27.64	20.55-38.21	1.76	-
<i>L. nobilis</i> E.E	70.23	42.67-91.66	1.61	-
<i>P. lentiscus</i> E.O / <i>L. nobilis</i> E.O (1:4)	26.89	17.23-40.66	2.75	102.79 <sup>S</sup>
<i>P. lentiscus</i> E.O / <i>L. nobilis</i> E.O (2:3)	29.59	18.37-45.77	1.43	93.41 <sup>an</sup>
<i>P. lentiscus</i> E.O / <i>L. nobilis</i> E.O (2:2)	21.88	15.73-39.25	1.05	126.33 <sup>S</sup>
<i>P. lentiscus</i> E.O / <i>L. nobilis</i> E.O (3:2)	30.44	18.51-37.33	0.77	90.80 <sup>an</sup>
<i>P. lentiscus</i> E.O / <i>L. nobilis</i> E.O (4:1)	32.66	23.65-46.88	0.89	84.63 <sup>an</sup>
<i>P. lentiscus</i> E.E / <i>L. nobilis</i> E.E (1:4)	70.34	58.24-80.44	2.42	99.84 <sup>an</sup>
<i>P. lentiscus</i> E.E / <i>L. nobilis</i> E.E (2:3)	69.22	60.51-81.33	3.83	98.95 <sup>an</sup>
<i>P. lentiscus</i> E.E / <i>L. nobilis</i> E.E (2:2)	70.45	59.34-80.23	1.56	99.69 <sup>an</sup>
<i>P. lentiscus</i> E.E / <i>L. nobilis</i> E.E (3:2)	72.05	61.43-85.53	1.36	97.47 <sup>an</sup>
<i>P. lentiscus</i> E.E / <i>L. nobilis</i> E.E (4:1)	75.33	61.11-90.05	2.62	93.23 <sup>an</sup>

#### 4 CONCLUSION

This study highlights the larvicidal and emergence inhibitory effects of essential oils from *P. lentiscus* and *L. nobilis* against *C. pipiens* larvae. Synergistic effects among these extracts suggest potential for enhanced efficacy in mosquito control. Further research into mechanisms of action and field applications is recommended to validate their eco-friendly potential and ensure environmental safety.

#### Acknowledgments

The authors are grateful to the Ministry of higher education and scientific research of Algeria

#### References

- [1] N. Abutaha, "Larvicidal potential and phytochemical analysis of *Garcinia mangostana* Extracts on controlling of *Culex pipiens* larvae," *Pakistan Journal of Zoology*, vol.56, no.2, pp.679–686, Jul.2022.
- [2] L. Aissaoui, A. Bouaziz, H. Boudjelida, and A. Nazli, "Phytochemical Screening and Biological Effects of *Laurus nobilis* (Lauraceae) Essential Oil Against Mosquito Larvae, *Culex Pipiens* (Linnaeus, 1758) (Diptera: Culicidae) species," *Applied Ecological Environment Research*, vol. 21, no.1, pp. 287–300, Dec. 2023.
- [3] M. Menakh, S. Boutellaa, D. Mahdi, A. Zellagui, and M. Ozturk, "Hepatoprotective effects of *Hertia cheirifolia* butanolic extract and selenium against CCl<sub>4</sub>-induced toxicity in rats," *Journal of Reports in Pharmaceutical Science*, vol.10, no.2, pp. 216–224, Mar.2021.
- [4] M. M. Baz, M. M. Hegazy, H. F. Khater, and Y. A. El-Sayed, "Comparative evaluation of five oil-resin plant extracts against the mosquito larvae, *Culex pipiens* say (Diptera: Culicidae)," *Pakistan Veterinary Journal*, vol.41, no.3, pp.191–196, Sep. 2021.
- [5] J. M. Ben Jemâa, N. Tersim, K.T. Toudert, and M. L. Khouja, "Insecticidal activities of essential oils from leaves of *Laurus nobilis* L. from Tunisia, Algeria and Morocco, and comparative chemical composition," *Journal of Stored Product Research*, vol.48, pp. 97–104, Dec. 2012.
- [6] M. Menakh, S. Boutellaa, K. Benabied, et al, "A comparative Analysis of Algerian natural extracts as Solo and Synergistically against *Culex pipiens* (Diptera: Culicidae) Larvae," *International Journal of Tropical Insect Science*, vol.45, no.1, May. 2024.
- [7] M. Menakh, D. Mahdi, S. Boutellaa, A. Zellagui, M. Lahouel, and C. Bensouici "In vitro antioxidant activity and protective effect of *Hertia cheirifolia* L. n-butanol extract against liver and heart mitochondrial oxidative stress in rat," *Acta Scientifica Naturalis*, vol. 7, no.1, pp. 33–45, Mar. 2020.
- [8] G. Tel-Çayan, M. Ozturk, M. E. Duru et al, "Phytochemical investigation, antioxidant and anticholinesterase activities of *Ganoderma adspersum*," *Industrial Crops Product*, vol.76, pp.749–754. Jan. 2015.
- [9] WHO. (2005). *Guidelines for laboratory and field testing of mosquito larvicides* [Online]. Available: [http://whqlibdoc.who.int/hq/2005/WHO\\_CDS\\_WHOPES\\_GCDPP\\_2005.13.pdf?ua=1](http://whqlibdoc.who.int/hq/2005/WHO_CDS_WHOPES_GCDPP_2005.13.pdf?ua=1)

- [10] J. Y. Liang, J. Xu, Y. Y. Yang, Y. Z. Shao, F. Zhou, and J. L. Wang, "Toxicity and synergistic effect of *Elsholtzia ciliata* essential oil and its main components against the adult and larval stages of *Tribolium castaneum*," *Foods*, vol. 9, no.3, pp. 345–349, Feb. 2020.



## Unlocking the Power of Nigella: Exploring the Antioxidant Abilities of This Ancient Medicinal Plant

Dalia Nafir<sup>\*1</sup>, Nouredine Belattar<sup>1</sup>

<sup>1</sup>Applied Biochemistry Laboratory, Department of Biochemistry, Ferhat Abbas University Setif-1, Algeria

---

### Abstract

*Nigella sativa*, also known as black seed, is a medicinal plant that has been used for centuries for its many health benefits. A study was conducted to assess the effects of nigella in protecting against risks caused by free radicals. Initially, a hydroalcoholic maceration of 36 hours was carried out using ethanol as a solvent to extract all polyphenols. Tests demonstrated that the high concentration of phenolic compounds at 30.85 ( $\mu\text{g GAE/g}$  of extract) and flavonoids at 13.46 ( $\mu\text{g quercetin/g}$  of extract) in nigella led to significant antioxidant activity with an IC<sub>50</sub> of DPPH equal to 0.19 mg/ml compared to BHA, and an A<sub>0.5</sub> absorbance of phynanthroline equal to 114.7  $\mu\text{g/ml}$  compared to the BHA standard, or an A<sub>0.5</sub> equal to 4.11  $\mu\text{g/ml}$ , highlighting its antioxidant properties and its ability to reduce iron. However, despite its many potential benefits, it is important to note that further studies are needed to better understand the mechanisms of action of nigella and confirm its beneficial effects on health.

**Keywords:** *Nigella sativa*, Maceration, Polyphenols, Antioxidants

---



## The Biological Activity of the Ethanolic Extract from Bee Pollen

Oumamar Loubna<sup>\*1</sup>, Soltani El Khamsa<sup>1</sup>, Khalil Kaouane<sup>1</sup>, Ayoub Bekka<sup>1</sup>, Hamza Kemchache<sup>1</sup>

<sup>1</sup>*Applied Biochemistry Laboratory, Ferhat Abbas University Setif 1, Algeria*

---

### Abstract

“Humanity would only have four years left if the bees vanished”. This quotation, purportedly from Albert Einstein, emphasizes how crucial bees are to the equilibrium of the flora. Pollen is one of the hive's outputs. This product is highly beneficial due to its antibacterial and antioxidant qualities, among others. The ethanolic extract's (PE) chemical analysis is the main topic of this investigation. To ascertain its biological activity, the pollen sample that was taken from the Wilaya of Batna, Algeria, underwent preparation and assessment procedures. The yield extraction is 25.7%. The total polyphenol and flavonoid content was determined using the Folin-Ciocalteu reagent and aluminum chlorides, respectively. It is estimated to be 700.155±0.100 mg EAG/g of pollen and 138.5714±0.0180 mg EQ/g. The radical scavenging potential of the extracts was determined by the DPPH method, the results of which show that these extracts have good activity. We measured the antioxidant activity using the DPPH method. The results obtained were very significant, the IC<sub>50</sub> of the ethanolic extract (IC<sub>50</sub> = 0.0155 mg/ml) while the positive control BHT is (IC<sub>50</sub> 0.0937mg/ml). The conclusions of this study led us to conclude that bee pollen is one of the essential products of the hive in terms of nutritional and therapeutic value.

**Keywords:** *Pollen, Polyphenols, Flavonoids, DPPH, Ethanolic extract*

---





---

## Tumor Microenvironment in Hepatocellular Carcinoma: A Comprehensive Review

Yusra Zarlashat<sup>\*1</sup>, Hassan Mushtaq<sup>2,3</sup>

<sup>1</sup>Department of Biochemistry, Government College University Faisalabad, Faisalabad, Pakistan

<sup>2</sup>Health Biotechnology Division, National Institute for Biotechnology and Genetic Engineering-C (NIBGE), Faisalabad, Pakistan

<sup>3</sup>Pakistan Institute of Engineering and Applied Sciences (PIEAS), Islamabad, Pakistan

---

### Abstract

Hepatocellular carcinoma (HCC), the most common form of primary liver cancer, arises predominantly from hepatocytes and is strongly associated with chronic liver inflammation and fibrosis. Viral etiologies such as hepatitis B virus (HBV) and hepatitis C virus (HCV) infections, alongside non-viral factors like alcoholic liver disease and metabolic dysfunction, contribute significantly to its pathogenesis. Non-viral causes such as alcohol-induced steatohepatitis and non-alcoholic steatohepatitis (NASH) exhibit distinct immune landscapes involving platelets, inflammatory cells, and altered metabolic pathways, emphasizing the diverse mechanisms contributing to HCC development. The review explores the role of immune cells in the tumor microenvironment (TME) of HCC, focusing on their interactions and effect on tumor progression and immune evasion mechanisms. Immune cells in HCC, such as regulatory T cells (Tregs), myeloid-derived suppressor cells (MDSCs), and tumor-associated macrophages (TAMs), create an immunosuppressive microenvironment that aids tumor progression. The presence and activity of these cells, along with dysfunctional CD8<sup>+</sup> T cells and regulatory cytokines, influence prognosis and offer potential therapeutic targets. Signaling pathways like WNT- $\beta$ -catenin, transforming growth factor-beta (TGF- $\beta$ ), and MYC, along with mutations in genes such as catenin beta 1 (CTNNB1), Tumor Protein 53 (TP53), and AT-Rich Interactive Domain 1A (ARID1A), contribute to immune evasion and tumor progression in HCC by modulating the immune microenvironment and immune checkpoint protein expression. Conventional systemic therapies for HCC, including combination immunotherapies with checkpoint inhibitors and other agents, show promise in improving patient outcomes, though challenges remain due to the immunosuppressive TME and tumor heterogeneity.

**Keywords:** Hepatocellular carcinoma, Immune landscape, Immune cells, Tumor microenvironment, Immune checkpoint inhibitors, Curative strategies

---



## **Ecological Classification of Soil-Plant Cover Areas Contaminated by Drilling and Mineralized Waters in the Siyazan Region (Azerbaijan)**

**Sanubar Aslanova<sup>\*1</sup>**

<sup>1</sup>*Faculty of Chemistry and Biology, Azerbaijan State Pedagogical University, Baku, Azerbaijan*

---

### **Abstract**

As a result of phytoecological studies conducted in the Siyazan region, measures have been proposed for the recultivation (biological stage) of soils contaminated with oil, oil products, and mineralized waters. In this regard, it is also necessary to purify the microbiological conditions of soils covered with oil products, as well as fuel oil, at oil and gas extraction sites in Azerbaijan to improve their fertility. The effectiveness of biological recultivation also depends on the soil's moisture retention properties, the presence of toxic substances, hydrocarbons, bitumen substances in the granulometric composition of oil-contaminated soils, and a number of ecological indicators. In biological recultivation (after the technical reclamation stage), positive results have been obtained in the planting of trees and shrubs that adapt to the ecological indicators of oil-contaminated soils.

In the biological recultivation of soils contaminated with oil and mineralized waters in the Siyazan region, the use of the following trees and shrubs is recommended: *Salix australis*, *Robinia pseudocacia*, *Platanus orientalis*, *Elaeagnus angustifolia*, *Olea europaea*.

Thus, it is recommended to carry out agrotechnical measures for three years to ensure the normal development of newly planted trees and shrubs and the efficiency of afforestation in the oil field surroundings of the Siyazan region. In the restoration of soil fertility, the results obtained from studying the tree and shrub species used, as well as the soil nutrients (humus, etc.), should be adhered to in the implementation of agrotechnical and biological reclamation measures.

**Keywords:** *Recultivation, Humus, Fuel oil, Bitumen, Landscape*

---



## The Use of Pectin Extracted from Lemon Bark as an Encapsulation Matrix

Djerri Rofia<sup>\*1</sup>, Himed Louiza<sup>1</sup>, Barkat Malika<sup>1</sup>

<sup>1</sup>The Biotechnology and Food Quality Research Laboratory (Biaqual), University of the Brothers Mentouri-Constantine 1, Algeria

---

### Abstract

As the capsules have many functions, various kinds of capsules have been prepared and applied to the various fields such as cosmetics, food materials, medicine, adhesives, information recording materials, textiles, and agricultural materials. The main purposes of encapsulation are to protect the core material from environment, to release the core material according to occasion demands and to handle the gaseous and the liquid core materials as the fine solid particles.

The encapsulation of essential oils was carried out by the pectin- casein complex ; essential oils and pectin are extracted from lemon peels. The extraction of essential oils was carried out by hydro distillation and pectin by conventional process using citric acid under conditions of PH ranges from 1.2 up to 4.2 and temperatures ranges from 40°C up to 90°C with a constant time of 60 minutes. The yield of essential oil obtained by hydro distillation is 3.275%, the pectin yield was 29.57% when the ph is 1.2 and the temperature 90°C in the duration of 60 minutes.

In this study, a preparation was performed in three ratios (essential oil: polymer) which are: HEE (1; 1), HEE (1, 2) and HEE (2; 1) to determine the ratio that ensures the best encapsulation. Thus, the ratio of the polymer complex used (pectin; casein) is (2; 8) and (4;8) The capsules loaded with lemon essential oil obtained have a white color, spherical of relatively homogeneous sizes with diameters ranging from 4.5 to 5 mm. These become solid while retaining the same characteristics. After drying, they become stronger with a reduced size of 4mm.

Finally the results of encapsulation efficacy showed that the efficiency of the HEE (1:2) ratio is 86.73%, while the ration (1:1) is 81, 79 % this indicates the proper process of encapsulation of the essential oil in the casein-pectin biopolymer.

**Keywords:** *Lemon peels, Essential oils, Pectin, Casein, Encapsulation*

---



---

## Utilizing *Aspergillus Oryzae* for Expression of SARS-CoV-2 Spike Protein Domains: Insights into COVID-19 Research

Elif Karaman<sup>\*1</sup>, Serdar Uysal<sup>1</sup>

<sup>1</sup>*Beykoz Institute of Life Sciences and Biotechnology, Bezmialem Vakıf University, Istanbul, Türkiye*

---

### Abstract

The COVID-19 pandemic has underscored the urgent need for effective diagnostics due to the highly contagious nature of SARS-CoV-2, which infects host cells by binding to the ACE2 receptor in the respiratory system. The spike (S) protein of the virus, essential for viral entry, comprises two subunits (S1 and S2) with an N-terminal domain (NTD) and a receptor-binding domain (RBD). Various expression systems have been employed to produce these viral proteins to evaluate their utility as antigens in COVID-19 detection assays. *Aspergillus oryzae*, recognized as Generally Recognized as Safe (GRAS), is widely used in fermentation and enzyme production owing to its high secretion capability, cost-effective media, and environmental resilience. This study demonstrates the successful expression of the NTD and RBD in *Aspergillus oryzae* for the first time, producing them as glucoamylase-fusion proteins. These fusion proteins were purified through metal affinity chromatography and verified by size-exclusion chromatography. Their ability to bind human anti-IgG antibodies was assessed using an ELISA, revealing significant, concentration-dependent interactions. This confirms their functionality in antigen-antibody interactions and establishes *A. oryzae* as a viable platform for producing viral proteins, facilitating scalable and cost-effective production for advanced research, vaccine development, and immunoassay design.

**Keywords:** *Receptor binding domain, N-terminal domain, SARS-CoV-2, Aspergillus oryzae*

---



## Indirect Effects of Microplastics on Climate Change and Community-Based Solutions to Atmospheric Microplastic Pollution

Enes Ozgenc<sup>\*1</sup>, Gunay Yildiz Tore<sup>2</sup>

<sup>1</sup>Vocational School of Health Services, Environmental Health Program, Trakya University, Edirne, Türkiye

<sup>2</sup>Department of Environmental Engineering, Tekirdag Namik Kemal University, Tekirdag, Türkiye

### Abstract

Microplastics (MPs) have become an increasing concern in environmental sciences, with significant impacts on ecosystems and human health. This study examines the indirect effects of MPs on climate change and community-based solutions to atmospheric MP pollution. MPs in the atmosphere significantly influence radiative forcing by altering the reflection and absorption of sunlight, leading to changes in climate systems. Through atmospheric transport mechanisms, MPs are distributed across vast geographical areas, impacting biodiversity and food chains in marine and terrestrial ecosystems, thereby causing disruptions in the carbon cycle. Community-based solutions are of strategic importance in mitigating MP pollution. These solutions include public awareness and education campaigns, collaboration between local governments and non-governmental organizations, improvements in waste management systems, and promotion of individual responsibilities. The study emphasizes the indirect effects of MPs on climate change and the effectiveness of community-based approaches in addressing this issue. The study also provides a scientific perspective on the indirect effects of MPs on climate change and community-based solutions to atmospheric MP pollution.

**Keywords:** Atmospheric pollution, Biodiversity, Climate change, Community-based solutions, Microplastic

## 1 INTRODUCTION

MPs, defined as plastic particles less than 5 mm in size, have become pervasive in the environment, including the atmosphere [1]. Recent studies have shown that MPs can be transported through the air and deposited in various ecosystems, leading to a growing concern about their potential effects on climate change [2]. These tiny particles can absorb and release heat, altering the albedo effect and potentially influencing global temperature patterns [3]. Additionally, the degradation of MPs can release greenhouse gases, such as methane (CH<sub>4</sub>) and ethylene, further exacerbating global warming. The full extent of these indirect effects on the climate system remains largely unexplored, making it a pressing issue for scientific investigation and environmental policy [4].

Efforts to address MP pollution have primarily focused on reducing plastic waste and improving waste management systems. Initiatives such as banning single-use plastics, promoting recycling, and encouraging sustainable consumption have gained traction worldwide [5]. Regarding atmospheric MPs, there is a growing emphasis on monitoring and research to understand their sources, distribution, and impacts [1]. Air quality monitoring networks increasingly incorporate MP analysis to assess their presence in urban and rural environments [6, 7]. While these measures are crucial, they are often limited by a lack of comprehensive data and public awareness, which hampers effective policy-making and community engagement.

A more holistic and community-driven approach is essential to mitigate the indirect effects of MPs on climate change. Community-based solutions can play a pivotal role in addressing atmospheric MP pollution [8]. This includes public education campaigns to raise awareness about the sources and consequences of MP pollution, as well as grassroots initiatives to reduce plastic use and promote sustainable alternatives [9]. Local governments can collaborate with community organizations to implement stricter regulations on plastic emissions and encourage innovative solutions, such as developing biodegradable materials [10, 11]. Additionally, fostering citizen science projects can empower individuals to participate in data collection and monitoring, thereby enhancing the understanding of MP distribution and its environmental impacts [12].

The primary objective of this study is to elucidate the indirect effects of MPs on climate change and propose actionable community-based solutions to mitigate atmospheric MP pollution. Specifically, the research aims to (1) quantify the contribution of atmospheric MPs to global warming through their physical and chemical interactions

in the atmosphere, (2) identify key sources and pathways of MP dispersion in different environments, (3) develop a framework for community engagement and education on MP pollution, and (4) recommend policy measures and practical actions to reduce MP emissions at the local and national levels. By achieving these goals, the study seeks to comprehensively understand the problem and offer viable solutions involving scientific and community efforts.

## 2 THE CONTRIBUTION OF MPS TO GLOBAL WARMING

Significant amounts of greenhouse gases (GHGs), carbon dioxide (CO<sub>2</sub>), CH<sub>4</sub>, etc., are emitted during plastics' production, use, and waste management. The production of plastics requires petrochemical processes, and using fossil fuels in these processes results in CO<sub>2</sub> emissions. During waste management, especially open burning or irregular disposal of plastics, GHGs such as CH<sub>4</sub> can be released into the atmosphere [13]. GHGs can also be released as plastics break down into MPs during environmental degradation processes (UV radiation, oxidation, etc.) [14]. These processes continue throughout the environmental lifetime of plastics and can have a lasting impact on climate change. In the atmosphere, MPs can act as cloud condensation nuclei (CCN) or ice nuclei (INP), especially in marine aerosols or with dust of terrestrial origin [15]. These nuclei allow water vapor to condense into cloud droplets or sublimate to form ice crystals. The surface properties, chemical composition, and size of MPs can influence these processes. For example, hydrophobic surfaces on MPs can hinder the condensation of water vapor, while MPs with hydrophilic surfaces can promote the formation of cloud droplets. These processes can affect the optical properties of clouds, their lifetime, and their capacity to produce precipitation, thus directly affecting regional and global climate [15]. MPs can reflect or absorb sunlight when suspended in the atmosphere. The reflectivity (albedo) and absorption properties of these particles can affect the solar radiation reaching the Earth's surface [16]. Energy absorbed by MPs can cause localized heating of the atmosphere, while reflected energy can increase atmospheric cooling [1]. However, the net effect of these processes depends on the size, chemical composition, and concentration of MPs. Thus, MPs in the atmosphere can cause radiative imbalances, leading to complex interactions in the climate system [17].

MPs can remain suspended in the water column, preventing sunlight from reaching the depths. This can negatively impact the growth and photosynthetic efficiency of phytoplankton, especially photosynthetic organisms [18]. Phytoplankton, as the primary producers of the oceans, play a vital role in the carbon cycle and the food chain of marine ecosystems. The presence of MPs can negatively affect the biological productivity and carbon cycling of the oceans by restricting the light uptake of these organisms [19]. Oceans play a critical role in the carbon cycle and serve as carbon sinks. As MPs circulate in marine ecosystems, they can interfere with biological processes [20]. For example, when MPs are consumed by aquatic organisms, their contribution to the carbon cycle can be reduced [21]. Furthermore, the microbial biofilm that forms on the surface of MPs can affect the biological fixation of carbon. These processes can increase CO<sub>2</sub> levels in the atmosphere by reducing the ocean's capacity to sequester carbon [22]. By adhering to the surfaces of phytoplankton or suspended in the aquatic environment, they can block access to the light these organisms need for photosynthesis [23]. Furthermore, toxic chemicals or pathogens present on the surfaces of MPs can be toxic to phytoplankton, leading to reduced phytoplankton populations and lower photosynthetic efficiency [24]. Phytoplankton decline can impact the food chain in marine ecosystems and reduce the ocean's capacity to sequester carbon [21].

Blue carbon ecosystems (seagrass meadows, mangroves, salt marshes) are known for their carbon storage capacity [25]. MPs can accumulate in these ecosystems and damage carbon fixation processes. For example, MPs accumulating in mangrove roots can inhibit sediment stability and oxygen access to the root zone [26]. In seagrass meadows and salt marshes, MPs can accumulate in plant roots, negatively affecting photosynthetic efficiency and plant growth [27]. Damage to these ecosystems can lead to increased levels of carbon in the atmosphere and accelerate climate change. It can also have significant impacts on soil ecosystems [28]. MPs accumulated in soil can affect the activities of soil organisms, altering organic matter transformation and greenhouse gas emissions [29]. For example, ingestion of MPs by earthworms can cause mechanical damage to their digestive systems, and accumulation of MPs in their intestines can reduce digestive efficiency and the contribution of these organisms to the carbon cycle in soil [30]. Furthermore, the accumulation of MPs in soil can alter water and air permeability, leading to anaerobic conditions and the release of GHGs such as CH<sub>4</sub> [31].

Increased extreme weather events (storms, flooding, heat waves) due to climate change can increase the movement and spread of MPs in the environment. For example, flood waters can carry MPs accumulated on land into rivers and seas. Storms, conversely, can carry MPs through the atmosphere, causing them to spread over large areas. These events can cause MPs to accumulate in previously unaffected areas and expand their impact on ecosystems [32]. They can also facilitate the transport of MPs to deeper soil layers or the seabed. MP pollution and climate change can have mutually reinforcing effects on environmental and biological systems. For example, increased temperatures due to climate change can increase the MP degradation rate, releasing more MPs. Furthermore, the

presence of MPs can reduce the resilience of marine species to stress and make them more vulnerable to the impacts of climate change [33]. This weakens the resilience of ecosystems and exacerbates the impacts of both MP pollution and climate change crises. Thus, the dispersion and accumulation of atmospheric MPs not only threaten air quality and human health but also disrupt the climate balance, complicating global warming and cooling processes, which can negatively impact environmental sustainability and the resilience of ecosystems.

### 3 SOURCES OF ATMOSPHERIC MP DISTRIBUTION

The distribution of atmospheric MPs originates from a variety of sources. These MPs can be emitted into the atmosphere due to natural and anthropogenic processes [1]. One of the most common sources is tire particles from the wear of vehicle tires. In areas with high traffic density, the concentration of such MPs in the atmosphere increases. Synthetic fibers generated during the production and use of textiles are also an important source. These fibers can be mixed with water while washing clothes and may not be completely filtered in water treatment plants and pass into the atmosphere [32]. Plastic dust emitted from industrial plants can enter the atmosphere in large quantities, especially in plastic production and recycling plants. In addition, practices such as waste management and open garbage burning also contribute to the spread of atmospheric MPs. Natural processes can cause these MPs to spread over large areas through mechanisms such as wind and air currents [34]. In conclusion, the source of atmospheric MPs is a combination of human activities and natural processes, and each of these sources increases the potential risks to environmental pollution and human health (Table 1).

**Table 1.** Atmospheric MPs: Sources and processes

Source	Specific Examples	Formation Mechanism	Dispersal Pathway	Potential environmental and health effects
Tire Wear	Car, truck, bicycle tires	Friction and abrasion of tire surface	Wind and air currents from roadsides	Air quality degradation, soil and water contamination, respiratory issues
Synthetic Textile Products	Polyester, nylon, acrylic clothing	Washing, drying, and abrasion of textiles	Ventilation systems, wind	Long-distance transport, atmospheric pollution, food chain impact
Industrial Emissions	Plastic production facilities, petrochemical factories	Gases and particles from production processes	Chimney gases, air currents	Air pollution, adverse effects on vegetation and human health
Road Traffic	Vehicle exhaust, road surface wear	Exhaust emissions, particle release from road surfaces	Air currents, vehicle traffic	Respiratory diseases, general air quality deterioration
Sea Spray	Wave actions, surface foam	Transport of seawater droplets by wind	Wind, aerosol formation	Accumulation in marine and terrestrial ecosystems
Urban Stormwater Drainage	Urban surface water, sewage	MP collection by rainwater and evaporation	Evaporation, rainwater flow	Wide area dispersal of MPs
Dust Storms	Desert dust, volcanic eruptions	Uplifting of dust particles by wind	Wind, atmospheric movements	Long-range transport, air pollution, impact on human and animal health

As shown in Table 1, atmospheric MP dispersion from various sources poses significant environmental and health risks and hazards. Factors such as tire wear, synthetic textiles, industrial emissions, road traffic, sea spray, urban stormwater drainage, and dust storms, which are sources of MPs, cause the formation of particles that can spread over large areas and remain in the atmosphere for long periods of time. These particles can reduce air quality and lead to respiratory diseases, asthma, and other health problems. In addition, the environmental dispersion of MPs can cause soil and water pollution, damage vegetation, and accumulate in marine ecosystems. Considering the potential impacts of MPs on the food chain, this pollution seriously threatens ecosystems and human health. In this context, understanding the source and spread pathways of MP pollution is critical for developing effective measures.

## 4 FUTURE PERSPECTIVES

Addressing atmospheric MP pollution requires active public participation and education. In this regard, public awareness campaigns should be organized at local and national levels, and educational programs on MP pollution should be integrated into school and university curricula. Public education programs and seminars should be held to raise general awareness, and voluntary activities and cleanup campaigns should encourage individual participation. Local governments should support these efforts and provide regular information on MP pollution. Policy measures and practical actions are also necessary to reduce MP emissions. Strict regulations on the production, use, and disposal of plastic products should be implemented, and the use of single-use plastics should be restricted or replaced by environmentally friendly products. Strengthening waste management systems is crucial to increase recycling rates and utilize specialized filtration technologies in water treatment plants. Plastic production facilities should be strictly monitored, and investment in research and development activities for new technologies to reduce MP emissions should be promoted. Additionally, civil society organizations and the private sector should collaborate to organize incentive programs for the public, encouraging individuals to adopt environmentally friendly practices. This framework aims to minimize the effects of MP pollution and reduce its environmental impact.

## 5 CONCLUSION

This study explores the indirect effects of MPs on climate change and community-based solutions to combat atmospheric MP pollution. It has been demonstrated that MPs play a role in atmospheric processes, particularly through their ability to reflect and absorb light, potentially influencing the climate system. This interference can affect local and global climate conditions by altering albedo and creating radiative imbalances. Additionally, transporting MPs through the atmosphere to various ecosystems can disrupt biodiversity and ecosystem balance due to their toxic effects. Community-based solutions are of critical importance in mitigating the negative impacts of MPs on the climate. Firstly, raising public awareness and providing education are seen as initial steps in preventing MP pollution. In this context, educational programs in schools and community centers, media campaigns, and disseminating informative materials are recommended. Secondly, improving waste management systems is necessary. Strengthening recycling processes, separating plastic waste at the source, and promoting using recyclable materials are essential in reducing MP pollution. Moreover, encouraging individuals and communities to develop sustainable consumption habits is crucial. These habits include reducing the use of single-use plastic products, opting for reusable items, and avoiding plastic packaging. Additionally, governments and the private sector must actively engage in addressing this issue. Specifically, enacting laws and regulations to reduce MP pollution, adopting more sustainable production processes in industries, and developing innovative technologies are necessary. In conclusion, understanding the effects of MPs on climate change and minimizing these effects require further research and developing effective action plans. In this regard, community-based solutions and global cooperation are vital in combating atmospheric MP pollution and ensuring the sustainability of our planet. It is essential for everyone to take responsibility and work together to increase environmental awareness.

## References

- [1] Y. Zhang, S. Kang, S. Allen, D. Allen, T. Gao, and M. Sillanpää, "Atmospheric microplastics: A review on current status and perspectives," *Earth-Science Reviews*, vol. 203, art. no. 103118, 2020.
- [2] S. Sharma, V. Sharma, and S. Chatterjee, "Contribution of plastic and microplastic to global climate change and their conjoining impacts on the environment-A review," *Science of The Total Environment*, vol. 875, art. no. 162627, 2023.
- [3] Y. Zhang *et al.*, "Current status and future perspectives of microplastic pollution in typical cryospheric regions," *Earth-Science Reviews*, vol. 226, art. no. 103924, 2022.
- [4] M. Kida, S. Ziembowicz, and P. Koszelnik, "CH<sub>4</sub> and CO<sub>2</sub> Emissions from the decomposition of microplastics in the bottom sediment—preliminary studies," *Environments*, vol. 9, no. 7, art. no. 91, 2022.
- [5] A. Hira, H. Pacini, K. Attafuah-Wadee, D. Vivas-Eugui, M. Saltzberg, and T. N. Yeoh, "Plastic waste mitigation strategies: A review of lessons from developing countries," *Journal of Developing Societies*, vol. 38, no. 3, pp. 336–359, 2022.
- [6] L. Shao *et al.*, "Airborne microplastics: A review of current perspectives and environmental implications," *Journal of Cleaner Production*, vol. 347, art. no. 131048, 2022.
- [7] R. Akhbarizadeh, S. Dobaradaran, M. A. Torkmahalleh, R. Saeedi, R. Aibaghi, and F. F. Ghasemi, "Suspended fine particulate matter (PM<sub>2.5</sub>), microplastics (MPs), and polycyclic aromatic hydrocarbons (PAHs) in air: their possible relationships and health implications," *Environmental Research*, vol. 192, art. no. 110339, 2021.



- [8] J. Vince and B. D. Hardesty, "Governance solutions to the tragedy of the commons that marine plastics have become," *Frontiers in Marine Science*, vol. 5, art. no. 214, 2018.
- [9] L. Henderson and C. Green, "Making sense of microplastics? Public understandings of plastic pollution," *Marine Pollution Bulletin*, vol. 152, art. no. 110908, 2020.
- [10] J. P. Da Costa, C. Mouneyrac, M. Costa, A. C. Duarte, and T. Rocha-Santos, "The role of legislation, regulatory initiatives and guidelines on the control of plastic pollution," *Frontiers in Environmental Science*, vol. 8, art. no. 104, 2020.
- [11] E. Özgenç, "Evaluation of the Spreading Dynamics and interactions of lead-carrier microplastics affected by biofilm: A mini-review," *Water, Air, & Soil Pollution*, vol. 235, no. 5, pp. 1–18, 2024.
- [12] S. E. Nelms *et al.*, "The role of citizen science in addressing plastic pollution: Challenges and opportunities," *Environmental Science & Policy*, vol. 128, pp. 14–23, 2022.
- [13] S. Muenmee, W. Chiemchaisri, and C. Chiemchaisri, "Enhancement of biodegradation of plastic wastes via methane oxidation in semi-aerobic landfill," *International Biodeterioration & Biodegradation*, vol. 113, pp. 244–255, 2016.
- [14] P. R. Sutkar, R. D. Gadewar, and V. P. Dhulap, "Recent trends in degradation of microplastics in the environment: A state-of-the-art review," *Journal of Hazardous Materials Advances*, art. no. 100343, 2023.
- [15] M. Aeschlimann, G. Li, Z. A. Kanji, and D. M. Mitrano, "Potential impacts of atmospheric microplastics and nanoplastics on cloud formation processes," *Nature Geoscience*, vol. 15, no. 12, pp. 967–975, 2022.
- [16] S. Sunil, G. Bhagwat, S. G. T. Vincent, and T. Palanisami, "Microplastics and climate change; the global impacts of a tiny driver," *Science of The Total Environment*, art. no. 174160, 2024.
- [17] M. S. Parvez, H. Ullah, O. Faruk, E. Simon, and H. Czédli, "Role of microplastics in global warming and climate Change: A review," *Water, Air, & Soil Pollution*, vol. 235, no. 3, art. no. 201, 2024.
- [18] S. Du *et al.*, "Environmental fate and impacts of microplastics in aquatic ecosystems: A review," *RSC Advances*, vol. 11, no. 26, pp. 15762–15784, 2021.
- [19] S. Casabianca *et al.*, "Ecological implications beyond the ecotoxicity of plastic debris on marine phytoplankton assemblage structure and functioning," *Environmental Pollution*, vol. 290, art. no. 118101, 2021.
- [20] T. S. Galloway, M. Cole, and C. Lewis, "Interactions of microplastic debris throughout the marine ecosystem," *Nature Ecology & Evolution*, vol. 1, no. 5, art. no. 0116, 2017.
- [21] M. Shen *et al.*, "Can microplastics pose a threat to ocean carbon sequestration?," *Marine Pollution Bulletin*, vol. 150, art. no. 110712, 2020.
- [22] X. Wang, Y. Xing, M. Lv, T. Zhang, H. Ya, and B. Jiang, "Recent advances on the effects of microplastics on elements cycling in the environment," *Science of the Total Environment*, vol. 849, art. no. 157884, 2022.
- [23] Y. Mao *et al.*, "Phytoplankton response to polystyrene microplastics: perspective from an entire growth period," *Chemosphere*, vol. 208, pp. 59–68, 2018.
- [24] V. Nava and B. Leoni, "A critical review of interactions between microplastics, microalgae and aquatic ecosystem function," *Water Research*, vol. 188, art. no. 116476, 2021.
- [25] A. M. Ricart, P. H. York, C. V. Bryant, M. A. Rasheed, D. Ierodiaconou, and P. I. Macreadie, "High variability of Blue Carbon storage in seagrass meadows at the estuary scale," *Scientific Reports*, vol. 10, no. 1, art. no. 5865, 2020.
- [26] X. Liu, H. Liu, L. Chen, and X. Wang, "Ecological interception effect of mangroves on microplastics," *Journal of Hazardous Materials*, vol. 423, art. no. 127231, 2022.
- [27] S. A. Bandh *et al.*, "Importance of blue carbon in mitigating climate change and plastic/microplastic pollution and promoting circular economy," *Sustainability*, vol. 15, no. 3, art. no. 2682, 2023.
- [28] E. Ozgenç, "Advanced analytical techniques for assessing and detecting microplastic pollution in water and wastewater systems," *Environmental Quality Management*, vol. 34, no. 1, art. no. e22217, 2024.
- [29] J. Zhou *et al.*, "Microplastics as an emerging threat to plant and soil health in agroecosystems," *Science of the Total Environment*, vol. 787, art. no. 147444, 2021.
- [30] B. Gao, Y. Li, N. Zheng, C. Liu, H. Ren, and H. Yao, "Interactive effects of microplastics, biochar, and earthworms on CO<sub>2</sub> and N<sub>2</sub>O emissions and microbial functional genes in vegetable-growing soil," *Environmental Research*, vol. 213, art. no. 113728, 2022.
- [31] F. Wang, Q. Wang, C. A. Adams, Y. Sun, and S. Zhang, "Effects of microplastics on soil properties: current knowledge and future perspectives," *Journal of Hazardous Materials*, vol. 424, art. no. 127531, 2022.
- [32] E. Özgenç, E. Keleş, and G. Yıldız Töre, "Assessment of biomarker-based ecotoxic effects in combating microplastic pollution - A review," *Global NEST Journal*, vol. 26, no. 1, pp. 1–24, 2024.
- [33] H. V. Ford *et al.*, "The fundamental links between climate change and marine plastic pollution," *Science of the Total Environment*, vol. 806, art. no. 150392, 2022.

- [34] C. E. Enyoh, A. W. Verla, E. N. Verla, F. C. Ibe, and C. E. Amaobi, "Airborne microplastics: A review study on method for analysis, occurrence, movement and risks," *Environmental Monitoring and Assessment*, vol. 191, pp. 1–17, 2019.



---

## **In Silico Analysis of Phytochemicals from Selected Medicinal Plant Species to Inhibit Alpha-Glucosidase as a Receptor Protein to Treat Type-2 Diabetes Mellitus**

**Ghulam Mustafa<sup>\*1</sup>, Shoukat Hussain<sup>1</sup>, Anas Bilal<sup>1</sup>, Rawaba Arif<sup>2</sup>**

<sup>1</sup>Department of Biochemistry, Government College University Faisalabad, Faisalabad, Pakistan

<sup>2</sup>Department of Biochemistry, University of Jhang, Jhang, Pakistan

---

### **Abstract**

Diabetes mellitus (DM) is a rapidly growing metabolic condition identified by continual high blood sugar levels. The primary consequence of DM is elevated blood sugar levels, which occurs as a result of inadequate insulin production or the malfunction of pancreatic beta cells responsible for insulin production. Chronic hyperglycemia associated with diabetes can lead to chronic harm, impaired function, and eventual organ failure of multiple systems, encompassing the eyes, kidneys, nerves, heart, and blood vessels. To address this, one approach is to inhibit the activity of enzymes such as  $\alpha$ -glucosidase which is involved in carbohydrate digestion. In the current study, the in vitro assessment of *Hordeum vulgare* (IC<sub>50</sub> 216.2  $\pm$  5  $\mu$ g/mL) showcased a potent inhibitory effect on  $\alpha$ -glucosidase, surpassing the standard used i.e., acarbose (IC<sub>50</sub> 246.55  $\pm$  10  $\mu$ g/mL). Moreover, the inhibition of  $\alpha$ -glucosidase was also explored using phytochemicals derived from *H. vulgare* through molecular docking study. Among these compounds, medicagol, euphol, stigmaterol, beta-sitosterol, and fucosterol exhibited strong binding interactions through amino acids Lys903, Glu281, Ala842, Gly828, Leu826, Ala704, and Ile780 with the receptor protein and also fulfilled the criterion of being a potential drug candidate when analyzed for absorption, distribution, metabolism, and excretion profiling. It was also found to be non-Ames toxic and non-carcinogen. Therefore, the compound medicagol has been revealed as a potential or lead compound to be used against diabetes mellitus type 2.

**Keywords:** *Phytochemicals, Molecular docking, Binding interactions, ADMET, Medicagol*

---



## Biotin-Functionalized Nanoparticle Systems for Targeted Lung Cancer Therapy

Fatma Sayan Poyraz\*<sup>1</sup>, Banu Mansuroglu<sup>1</sup>

<sup>1</sup>Department of Molecular Biology and Genetics, Yildiz Technical University, Faculty of Art&Science, Istanbul, Türkiye

### Abstract

Polymeric nanoparticles, developed as an alternative to traditional treatments such as radiotherapy and chemotherapy, which are frequently used in cancer treatment and have very high side effects, increase hydrophobic molecules' solubility, biodistribution and bioavailability [1]. Gentisic Acid (GA), a powerful phenolic compound in terms of antioxidant and free radical scavenging activities, is a molecule known for its pro-apoptotic and antiproliferative effects in various cancerous tissues [2]. 5-Fluorouracil, which shows its activity by interfering with DNA synthesis and mRNA translation, is a rationally designed anticancer agent [3]. Biotin, which is known as a vitamin, is used as a targeting molecule. Cancer cells often overexpress biotin-specific receptors on the cell surface. Therefore, specific interactions between biotin and its receptors can be used to advantage for targeted drug delivery [4].

In this study, the combination of 5-fluorouracil and Gentisic Acid (FUGA) molecules were encapsulated in PLGA (FUGANPs) by double emulsion solvent evaporation method. Then, characterized nanoparticles were coated with biotin (BNPs) and A549 non-small lung cancer cells were targeted. The cytotoxic effect of FUGA, FUGANPs and BNPs on the A549 cell line was determined using the MTT method. Using the determined IC<sub>50</sub> values, cell migration, colony-formation capacity and apoptotic effects were examined on A549 cells. BNPs, FUGANPs and FUGA treatments, respectively, showed a high effect on A549 cells when they were compared with control cells, and it was observed that biotin-targeted nanoparticles were more effective in the treatment. It is thought that this targeted formulation of combined molecules may create a useful model in combined drug treatments and targeting studies.

**Keywords:** 5-Fluorouracil, Gentisic acid, Biotin, Polymeric nanoparticles, Lung cancer

### Acknowledgments

This paper was supported by the Scientific and Technological Research Council of Türkiye (TÜBİTAK) with the 2214-A International Research Fellowship Programme for PhD Students.

### References

- [1] M. A. Beach, U. Nayanathara, Y. Gao, C. Zhang, Y. Xiong, Y. Wang, and G. K. Such, "Polymeric Nanoparticles for Drug Delivery," *Chemical Reviews*, vol. 124, no. 9, pp. 5505–5616, 2024.
- [2] F. Abedi, B. M. Razavi, and H. Hosseinzadeh, "A review on gentisic acid as a plant derived phenolic acid and metabolite of aspirin: Comprehensive pharmacology, toxicology, and some pharmaceutical aspects," *Phytotherapy Research*, vol. 34, no. 4, pp. 729–741, 2020.
- [3] S. Christensen, B. Van der Roest, N. Besselink, R. Janssen, S. Boymans, J. W. Martens et al., "5-Fluorouracil treatment induces characteristic T> G mutations in human cancer," *Nature Communications*, vol. 10, no. 1, art. no. 4571, 2019.
- [4] S. Y. Kim, S. H. Cho, Y. M. Lee, and L. Y. Chu, "Biotin-conjugated block copolymeric nanoparticles as tumor-targeted drug delivery systems," *Macromolecular Research*, vol. 15, pp. 646–655, 2007.



## Epidemiological, Immunohistochemical, and Molecular Study of Breast Cancer in Young Algerian Patients from “Bejaia”

Sara Ouari<sup>\*1</sup>, Hania Ouahmed-Boudaoud<sup>2</sup>, Chahla Bencharif<sup>3</sup>, Chahira Mazouzi<sup>4</sup>

<sup>1</sup>Laboratory of Applied Biochemistry, Faculty of Natural and Life Sciences, Ferhat Abbas University Setif 1, Setif, Algeria

<sup>2</sup>Plant Biotechnology and Ethnobotany Laboratory, Faculty of Natural and Life Sciences, University Abderrehmane Mira, Bejaia, Algeria

<sup>3</sup>Anatomy and Pathology Laboratory, CHU Khelil Amrane, Bejaia, Algeria

<sup>4</sup>Oncology Department, CHU Khelil Amrane, Bejaia, Algeria

### Abstract

Breast cancer is the most frequently diagnosed cancer and the leading cause of cancer death among women in Algeria. Its incidence continues to increase, especially in young women, hence, the aim of our study is to analyze the important risk factors and identify the molecular biomarkers characterizing breast cancer in young women from Bejaia. Our study included women with confirmed breast cancer during the period 2019-2021; medical information on each patient were analyzed using SPSS software version 26, biomarkers characterizing each tumor (Estrogen (ER) and Progesterone (PR) receptors, HER2 oncoprotein, Ki67 antigen, p53 tumor suppressor protein) were identified by immunohistochemical staining, and pedigree of patients with family history of cancer have been established. Of 190 patients: the median age was 42 years; 56.2% had a family history of cancer, qualifying it as the main risk factor; pedigree analysis showed both maternal and paternal heredity, other cancer types were found to be integrally associated with breast cancer in many families, which is maybe due to presence of hereditary mutated gene. IBC-NST formerly known as “invasive ductal carcinoma” is the main histological type found in this study with 78.2% cases, the most frequent histological grade was the average SBR grade (grade II) found at 71.7%; Analysis of molecular biomarkers expression indicated that 73.2% overexpress ER and PR, the Luminal B Her2<sup>-</sup> and Luminal A types were therefore the predominant molecular subtypes, and the first-line treatment was hormonal therapy using “Tamoxifen” a selective estrogen receptor modulator (SERM); p53 protein was found overexpressed in 70% of Triple negative molecular subtype cases, associated with aggressive breast cancer. The lack of awareness and molecular studies is the cause of delays in diagnosing patients. Early detection combined with appropriate treatment will reduce the incidence and diagnosis at an advanced stage and increase survival from breast cancer.

**Keywords:** Breast cancer, Risk factors, Cancer heredity, Molecular subtypes, Immunohistochemical staining

## 1 INTRODUCTION

Breast cancer is the most common cancer and the main cause of morbidity in women worldwide, it is the 5th cause of cancer-related deaths with an estimated number of 2.3 million new cases worldwide according to the GLOBOCAN 2020 data, whose standardized incidence rates are higher for women in industrialized countries than in Asian and African countries [1], Nowadays, breast cancer is increasingly observed in young women, due to several risk factors that are likely to increase the possibility of developing breast cancer at a young age [2].

Breast cancer is a major public health problem in Algeria. In 2020, 12536 new cases were diagnosed, 3.255 deaths or 1.91% of total deaths. Indeed, the incidence increased from 14.5 new cases per 105 inhabitants in 1993 to 70.2 per 105 in 2012 to 143.3 per 105 habitants in 2017 [2]. Among the primary goals of cancer registries in collecting data on new cases and deaths is the reduction of cancer-related morbidity and mortality through the facilitation of cancer research and the education of scientists, clinicians, and the public.

Indeed, the histological classification of carcinomas is realized by histopathological and molecular studies, characteristic molecular markers of breast cancer are detected by immunohistochemical technique, these are crucial steps in the diagnosis, the determination of the prognosis and the therapeutic decision [3], Moreover, early genetic tests in families with a history of cancer will allow a diagnosis of predisposition and thus the proposal of preventive treatments [4]. Different modern medicines (targeted therapy, hormonal therapy, radiation therapy, surgery and chemotherapy) are prescribed to treat breast cancer. Surgery of both breasts is a preventative measure in some increased probability of developing cancer in females [5].

Up to now, no reliable or accurate epidemiological data on BC diagnosed in Bejaia by oncologists/senologists are available in Algeria.

The aims of this work were to study the clinical, histopathological, and molecular aspects of breast cancer by investigating the prevalence, identifying the risk factors, and evaluating tissue expression of molecular markers: Hormonal receptors (Estrogens and Progesterones), HER-2, Ki67, and P53 in young breast cancer patients diagnosed at the University Hospital Center of Bejaia on a sample of 190 patients whose age varies from 26 to 55 years; For a Perspective of revolutionizing the diagnose and prognosis of patients, provide a personalized treatment strategy, and better care to patients with breast cancer due to the unpleasant side effects of the treatments.

## **2 MATERIAL AND METHODS**

### **2.1 General Information**

This study included 190 patients, young women with breast carcinoma, whose age varies from 26 to 55 years, whose operating parts have been received at the anatomy histopathology service and have followed their treatment and consultation at the medical oncology service of the Center of Sidi Ali Lebher, Annex of the University Hospital Center of Bejaia during the last years 2019, 2020 and 2021.

The criteria of selection were: mainly patients who do not exceed 55 years old and patients who were subjected to breast surgery which was either radical or conservative surgery, all of them had undergone full clinical examination and routine laboratory investigations.

### **2.2 Histopathological Examination**

Histological sections of the tumors and breast tissues were sent to the Anatomopathology service for histopathological examination and diagnosis reviewed by the experienced pathologist (C.B). Breast tissues were preserved in formalin and embedded in paraffin wax. Thin sections were made and collected on slides then stained with routine hematoxylin-eosin staining after that they were diagnosed according to the criteria of the World Health Organization (WHO) and graded according to the modified Scarff-bloom and Richardson (SBR) method. The patient's tumor type, size, grade, nodal status, presence of Paget's disease, estrogen receptor (ER) progesterone receptor (PR), human epidermal growth factor 2 (Her2), and the proliferation marker KI-67 status were reported in the histopathological reports.

### **2.3 Tissue Expression of ER, PR, Ki-67 & HER2 in Invasive Breast Carcinoma**

The analysis of ER, PR, HER2 and Ki-67 was done by immunohistochemical staining using the following antibodies: ER (clone EP1, Monoclonal Rabbit Anti-Human, Agilent Dako Autostainer, Carpinteria, CA 93013, USA), PR (clone PgR 636 Monoclonal Mouse Anti-Human, Agilent Dako Autostainer, Carpinteria, CA 93013, USA), HER2 (c-erbB-2 Oncoprotein, Polyclonal Rabbit Anti-Human, Agilent Dako, Glostrup, Denmark), and Ki-67 (clone MIB-1 Monoclonal Mouse Anti-Human, Agilent Dako Autostainer, Glostrup, Denmark). The positive cell staining was evaluated in a quantitative and visual way using light microscopes. The results were expressed as a percentage and intensity of marking defined by the Allred score and ASCO 2013 recommendations respectively and Tumors were classified into different molecular subtypes according to WHO recommendation 2019. Immunohistochemical staining of p53 marker using the following antibodies (Clone DO-7, Monoclonal Mouse Anti-Human, Agilent Dako Autostainer, Carpinteria, CA 93013, USA) was done on 10 samples from patients whose molecular subtype is “Triple Negative (TN)” to assess whether P53 mutations would contribute to aggressive TN type breast cancer.

### **2.4 Statistical Analysis**

The patient information was collected by consulting their archived medical records and from an epidemiological questionnaire applied referring to the risk factors for breast cancer. Data was collected and summarised using descriptive analysis performed with SPSS version 26.

## **3 RESULTS**

### **3.1 Risk Factors Related to Breast Cancer**

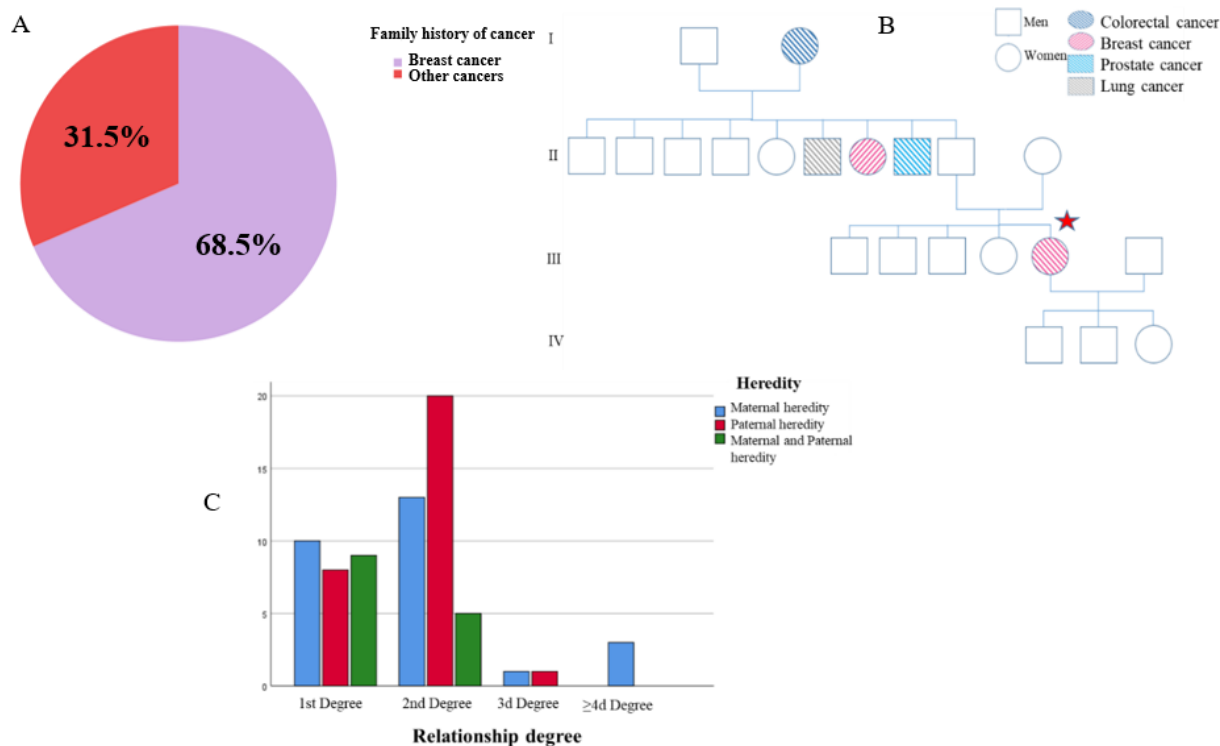
### 3.1.1 Incidence and Mortality

There is no exact data on incidence and mortality related to BC in Bejaia or Algeria. Through our study there was no big difference in the incidence, 41.6% and 40.5% in 2019 and 2020 respectively in patients of ages between 26-55 years. GLOBOCAN gives an average estimation of the most recent rates applied to the 2020 population in Algeria, BC incidence is estimated to 12536 new cases in 2020 in females of all ages, ranked first in the incidence of all other types of cancer, followed by 4 116 cases of death [2].

### 3.1.2 Hereditary

Positive Family History of Cancer: Of 129 patients, 56.2% had a family history, of which 38.6% had a history of BC and 17.6% had a history of other types of cancer (Fig. 1 A). According to various studies, genetic predisposition represents the main risk factor, and our results agree with the data of a study which states that hereditary BC represents about 30% of total cases [11]; Furthermore, an analysis a pedigree of a family (Fig. 1.B) which seems to present hereditary characteristics of cancer in which appears our 50-year-old patient (III-5) suffering from a grade II Invasive BC of No Special Type (IBC-NST), with a second-degree relationship including 2 uncles (II- 6 and II-8) and a paternal aunt (II-7) who died from lung, prostate, and breast cancer respectively, and paternal grandmother from colorectal cancer. According to several studies [12, 13], Colorectal cancer could be integrally associated with BC in a family and this has been proven at the molecular level by the presence of a linkage to the 1100delC mutation in the CHEK2 gene, a cell cycle checkpoint kinase variant that is present in 18% of hereditary breast cancers, and in addition to the major “BRCA1/2” genes that have a function in the repair of double strand DNA breaks in the origin of the high risk of BC, therefore a panel of 13 genes recognized for the clinical utility was established in 2018; Thus pedigree illustrates the importance of the involvement of BC susceptibility genes in a family at high and intermediate risk and demonstrates the place of oncogenetic for the study of cases of predisposition in order to consider surveillance. with a view to early detection of possible cancer, preventive surgery, or hormone prevention in women carrying a gene mutation such as BRCA [4].

Degree of Relationship: The number of cases with a second-degree relationship of BC was the highest with 56.2% followed by first degree with 37%, with no significant difference between maternal and paternal heredity (Fig. 1. C). Studies have shown that the risk is 13.3% if only one of 1st degree relative is affected, while it increases to 21.1% if two 1st degree relatives are affected or several 2nd degree relatives [14].



**Figure 1.** Risk factors related to breast cancer: A. Family history of cancer, B. Pedigree of a family history of cancer, and C. Degree of relationship

### 3.2 Clinical Aspect

#### 3.2.1 Tumor Location

Of 148 patients, there was a slight difference in the location of the tumor which is more in the left breast 48.6%, with 4 bilateral involvements, and dominance in the supero-external quadrant (QSE) with 45.8% for the right breast (Fig. 2. A); The average size of the tumor was found to be 2.24 cm and most patients presented a tumor size between [1–3 cm]. The results obtained match those of the literature where several studies stipulate that BC is a little more often on the left side and rarely bilateral, as well as a dominance of the QSE site [15, 16], this topography is explained by the majority presence of glandular tissue in this supero-external part of the breast.

#### 3.2.2 Clinical Stage

The average clinical stage was stage II, in which 66 patients belong representing 44.9%, and we found 16 patients who reached stage IV (metastasis) with secondary bone, hepatic and pulmonary localizations (Fig. 2. B). The results recorded are consistent with those of other studies where stage II is the most frequent at 49.2% not very advanced stage [17, 18], contrary to the results obtained by another study where Stage IV (Metastatic) was predominant due to ignorance, lack of medium and fear of diagnosis [19]. Algeria is one of the countries where the diagnosis is made at not very advanced stages, for this better awareness would allow early diagnosis for better care.

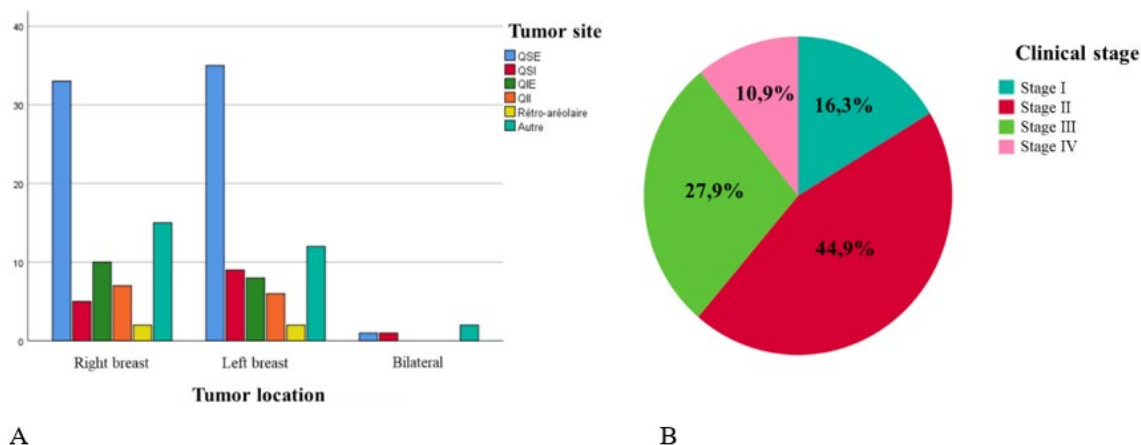


Figure 2. Clinical aspect: A. Tumor location and B. Clinical stage

### 3.3 Anatomopathological and Immunohistochemical Analysis

#### 3.3.1 Histopathological Types

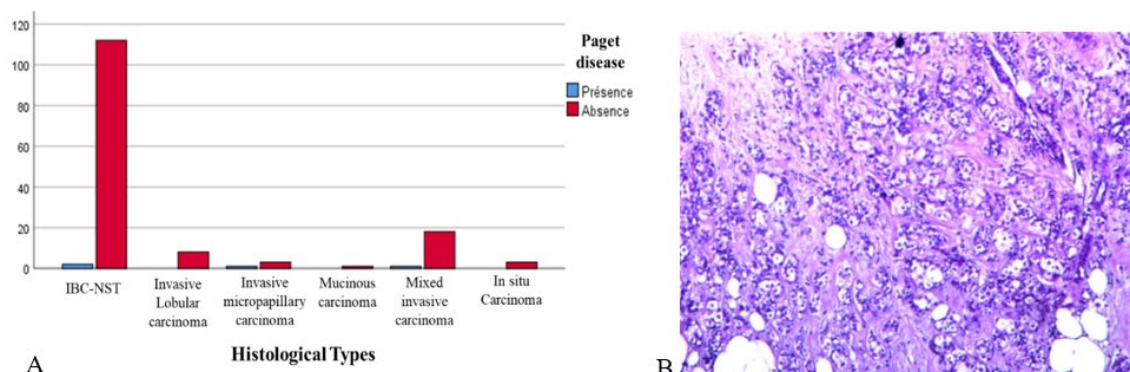


Figure 3. Anatomopathological and immunohistochemical analysis: A. Histogram representing the distribution of the different histological types and the association with Paget’s disease and B. Histological appearance of an IBC-NST type

IBC-NST formerly known as “invasive ductal carcinoma” is the main histological type found in this study with 78.2% cases, followed by Mixed (Ductal & Lobular) Invasive Carcinoma in 11.2% and Invasive Lobular

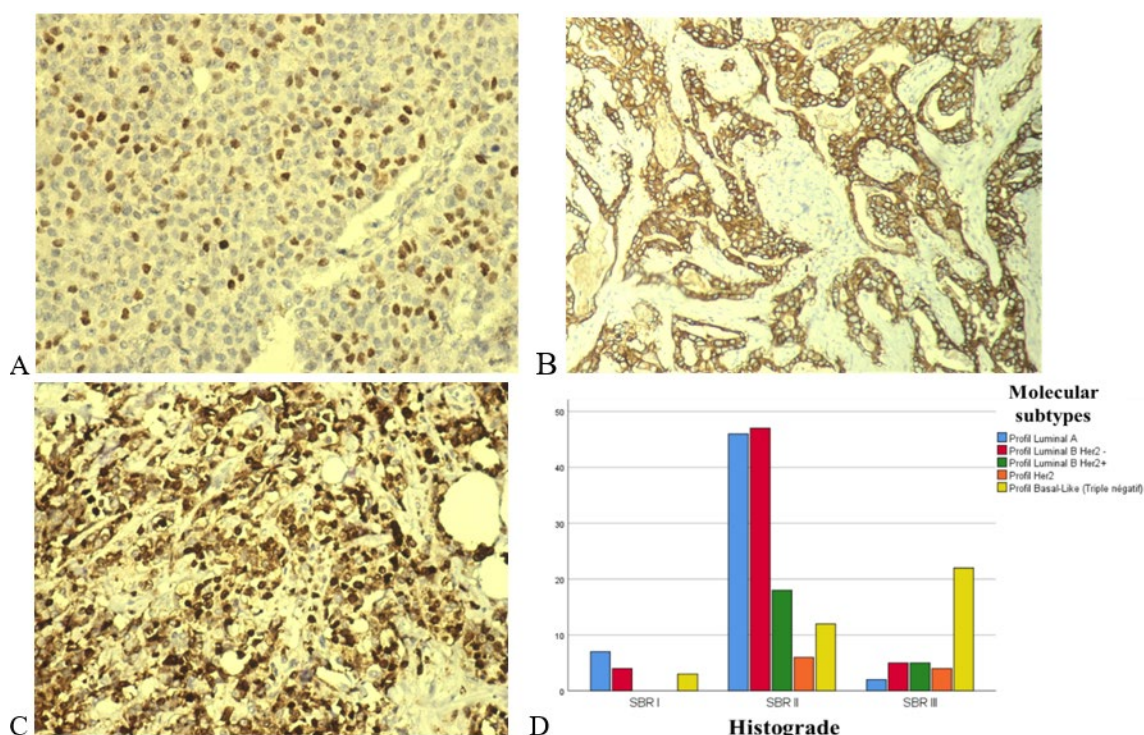


Carcinoma in 5.3%, Paget disease was found associated with 4 cases with a percentage of 2.7%; the most frequent histological grade is the average grade (grade II) found at 71.7%, Grades III and I (SBR III & I) represented respectively 20,9% and 7,5% (Fig. 3. A). The results are consistent with the latest WHO data (2019) as well as a Moroccan study [16] which stipulates that the most common histological type was IBC-NST with a percentage of 73.2% and associated Paget's disease is present in 1–3% of the cases [20]. The Moroccan study was also consistent with the histological grade results, the histoprognostic grade of SBR studied in 621 patients presented a predominance of grade II with a percentage of 60%, followed by grade III at 20% [16], these results are consistent with the results obtained.

### 3.3.2 Molecular Subtypes

Positive ER & PR immunostaining (Fig. 4. A) was found in 73.3% of the cases, the tumor is hormone-dependent (positive hormone receptors) being a good prognosis; HER2 immunostaining (Fig. 4. B) was found positive in 6% of the cases, these tumors are characterized by an overexpression of the protein coded by this gene and defines the positive HER2 status; The Ki67 antigen immunostaining (Fig. 4. C) evaluate the cell proliferation, percentages greater than 20% indicate that the proliferation is high and shows a bad prognosis. According to the results obtained by the Immunohistochemical staining, the Luminal B Her2<sup>-</sup> type and Luminal A are the predominant with respective percentages of 30.6% and 30.1%, followed by the Basal-like type (Triple negative) with 20.8 %. Moreover, by analyzing the relationship between molecular subtypes and SBR grade, we found that the Luminal A and B types are of low and medium grade (I or II) while the Basal-like type is rather a high grade (grade III) (Fig. 4. D).

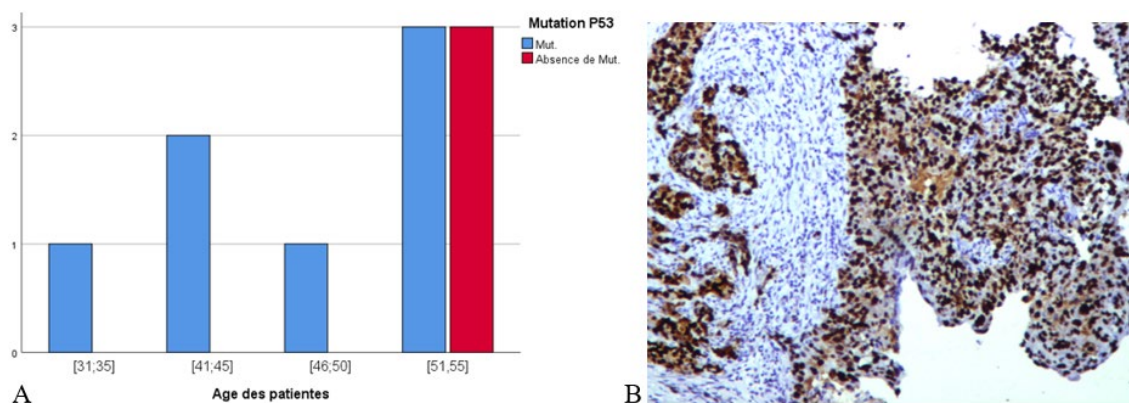
According to studies Luminal A type cancers represent approximately 58.5% [21], this is in contrast with our results and would allow us to confirm that this type (Luminal A) which is characterized by the presence of hormone receptors and absence of HER2 is of lower grade and better prognosis as well as for the Luminal B Her2<sup>-</sup> type. Moreover, the Triple negative type (Basal-like) is found to be 16%, usually grade III, and often high proliferation index. Thus, we can confirm that the low-grade Luminal A and Luminal B molecular types are at low risk and easily treated by hormone therapy with the possibility of adjuvant or neo-adjuvant chemotherapy, while the Her2 and Basal-like types are at high risk in the short term. The Her2 type is treated by targeted therapy (Trastuzumab) with the possibility of adjuvant or neo-adjuvant chemotherapy as well, whereas the Basal-like type characterized by hormone receptor negativity and high Ki-67 levels is treated exclusively by chemotherapy, associated or not with surgery.



**Figure 4.** Molecular subtypes: A. Results of hormone receptor “ER & PR” immunostaining, B. Results of Her2 immunostaining, C. Results of Ki67 immunostaining (G×20), and D. relation between molecular subtypes and histograde)

### 3.3.3 Immunohistochemical p53 Test on Samples from 10 Patients

According to the results of the Immunohistochemical p53 staining on samples from 10 patients with “Triple negative” molecular subtype, 7 of them presented a mutation which is expressed by intense and diffuse nuclear staining and the other 3 were negative for the p53 mutation (Fig 5. A). Somatic mutations in the P53 gene are reported in 19-57% of human BCs [3], several studies showed that the molecular subtype Basal-like Carcinomas on the genomic level has a particularly high mutation rate of the P53 gene [22, 23], this is in perfect agreement with the results obtained where the search for Mutated P53 in 10 patients with triple negative molecular type was confirmed at 70%, this could confirm that this P53 mutation is present and therefore is associated with aggressive BC.



**Figure 5.** A. Histogram representing the number of p53 mutations in “Triple negative” patients according to age and B. Histological result of p53 immunostaining in an IBC-NST (G×10)

## 4 CONCLUSIONS

The present study is the first estimating cancer incidence in Bejaia province. Our findings support that age, oestrogen, overweight, and family history increased the risk of BC. According to the result of our study, BC disease is less common to those in developing countries, with a predominance of invasive ductal carcinoma. However, most of the women studied developed the disease in advanced age. That knowledge of BC trends and its common morphologies in the country can help to reduce its incidence rate in the population, and determine adequate treatment. BC rates are potentially avoidable by prevention programs. Thereby, these findings could be of great value to establish adequate evidence-based awareness and BC preventive measures in Algerian women.

## References

- [1] Y.-S. Sun, Z. Zhao, Z.-N. Yang, F. Xu, H.-J. Lu, Z.-Y. Zhu, W. Shi, J. Jiang, P.-P. Yao, and H.-P. Zhu, “Risk factors and preventions of breast cancer,” *International journal of biological sciences*, vol. 13, no 11, art. no. 1387. 2017.
- [2] International Agency for Research on Cancer, World Health Organization, “The global cancer observatory,” [Online], Mar. 2021. Available: <https://gco.iarc.fr/today/data/factsheets/populations/12-algeria-fact-sheets.pdf>.
- [3] Y. Feng, M. Spezia, S. Huang, C. Yuan, Z. Zeng, L. Zhang, and G. Ren, “Breast cancer development and progression: Risk factors, cancer stem cells, signaling pathways, genomics, and molecular pathogenesis,” *Genes & diseases*, vol. 5, no 2, pp. 77–106. 2018.
- [4] O. Cohen-Haguenaer, “Inherited predisposition to breast cancer (2): Risks and surveillance,” *Medecine Sciences: M/S*, vol. 35, no 4, pp. 332–345. 2019.
- [5] T. A. Moo, R. Sanford, C. Dang, and M. Morrow, “Overview of breast cancer therapy,” *PET Clinics*, vol. 13, no 3, pp. 339–354. 2018.
- [6] H. Najjar And A. Easson, “Age at diagnosis of breast cancer in Arab nations,” *International Journal of Surgery*, vol. 8, no 6, pp. 448–452. 2010.
- [7] M. D. Kristin Rojas and M. D. Ashley Stuckey, “Breast cancer epidemiology and risk factors,” *Clinical Obstetrics and Gynecology*, vol. 59, no 4, pp. 651–672. 2016.
- [8] Collaborative Group on Hormonal Factors in Breast Cancer, “Breast cancer and breastfeeding: Collaborative reanalysis of individual data from 47 epidemiological studies in 30 countries, including 50 302 women with breast cancer and 96 973 women without the disease,” *The Lancet*, vol. 360, no. 9328, pp. 187–195. 2002.

- [9] K. A. Ban and C. V. Godellas, “Epidemiology of breast cancer,” *Surgical oncology clinics*, vol. 23, no. 3, pp. 409–422. 2014.
- [10] T. M. Brasky, Y. Li, D. J. Jaworowicz, N. Potischman, C. B. Ambrosone, A. D. Hutson, and J. L. Freudenheim, “Pregnancy-related characteristics and breast cancer risk,” *Cancer Causes & Control*, vol. 24, pp. 1675–1685. 2013.
- [11] A. Ozsoy, N. Barca, B. A. Dolek, H. Aktas, E. Elverici, L. Araz, and O. Ozkaraoglu, “The relationship between breast cancer and risk factors: A single-center study,” *European Journal of Breast Health*, vol. 13, no. 3, art. no. 145, 2017.
- [12] H. Meijers-Heijboer, M. Wasielewski, A. Wagner, A. Hollestelle, F. Elstrodt, R. Van Den Bos, and M. Schutte, “The CHEK2 1100delC mutation identifies families with a hereditary breast and colorectal cancer phenotype,” *The American Journal of Human Genetics*, vol. 72, no. 5, pp. 1308–1314, 2003.
- [13] J. Moretta, P. Berthet, V. Bonadona, O. Caron, O. Cohen-Haguenaer, C. Colas, and C. D’unicancer, “Recommandations françaises du groupe génétique et cancer pour l’analyse en panel de gènes dans les prédispositions héréditaires au cancer du sein ou de l’ovaire,” *Bulletin Du Cancer*, vol. 105, no. 10, pp. 907–917. 2018.
- [14] Z. Momenimovahed and H. Salehiniya, “Epidemiological characteristics of and risk factors for breast cancer in the World,” *Breast Cancer: Targets and Therapy*, pp. 151–164. 2019.
- [15] G. Sahraoui, F. Khanchel, and E. Chelbi, “Anatomopathological profile of breast cancer in cape bon, Tunisia,” *The Pan African Medical Journal*, vol. 26, pp. 11–11. 2017.
- [16] M. El Fouhi, A. Benider, K. Z. A. Gaëtan, and A. Mesfioui, “Profil épidémiologique et anatomopathologique du cancer de sein au CHU Ibn Rochd,” *Casablanca. Pan African Medical Journal*, vol. 37, no. 1, 2020.
- [17] N. Bouzid, R. Lahmar, S. Tebra, and N. Bouaouina, “Cancer du sein chez la femme jeune de moins de 35 ans en Tunisie : Étude rétrospective à propos de 124 cas,” *Gynécologie Obstétrique & Fertilité*, vol. 41, no. 6, pp. 356–360, 2013.
- [18] D. M. Kasib, M. A. Al-Naqqash, and A. S. Alshewered, “Breast cancer among Iraqi female in their fifth decade: A retrospective study,” *TMR Cancer*, 2019.
- [19] E. Ndounga, A. T. Bambara, A. F. B. Liboko, C. Itoua, D. Moukassa, and J. B. N. Mbon, “Cancer du sein chez la femme de 35 ans et moins au CHU de Brazzaville,” *PAMJ-Clinical Medicine*, vol. 2, no. 94, 2020.
- [20] M. Akram, M. Iqbal, M. Daniyal, and A. U. Khan, “Awareness and current knowledge of breast cancer,” *Biological Research*, vol. 50, pp. 1–23. 2017.
- [21] F. K. Al-Thoubaity, “Molecular classification of breast cancer: A retrospective cohort study,” *Annals of Medicine and Surgery*, vol. 49, pp. 44–48. 2020.
- [22] L. Silwal-Pandit, H. K. M. Vollan, S. F. Chin, O. M. Rueda, S. Mckinney, T. Osako, and A. Langerød, “TP53 mutation spectrum in breast cancer is subtype specific and has distinct prognostic relevance,” *Clinical Cancer Research*, vol. 20, no. 13, pp. 3569–3580. 2014.
- [23] Z. Yi, F. Ma, G. Rong, Y. Guan, C. Li, and B. Xu, “Clinical spectrum and prognostic value of TP53 mutations in circulating tumor DNA from breast cancer patients in China,” *Cancer Communications*, vol. 40, no. 6, pp. 260–269, 2020.



## **Microencapsulation: A Way to Preserve Bioactive Compounds from Food Waste for Novel Food Formulations – A Review**

**Tusneem Kausar<sup>\*1</sup>, Ashiq Hussain<sup>2</sup>, Sobia Noreen<sup>3</sup>**

<sup>1</sup>*Institute of Food Science and Nutrition, University of Sargodha, Sargodha 40100, Pakistan*

<sup>2</sup>*Punjab Food Authority, Lahore, Punjab 54000, Pakistan*

<sup>3</sup>*Institute of Chemistry, University of Sargodha, Sargodha 40100, Pakistan*

---

### **Abstract**

Food by-products have been of great interest of researchers since most of them are rich in bioactive compounds and have potential to be applied into food and pharmaceutical products. Using food waste is important to the world since it involves sustainability (use of residues), economy (development of value-added product), science, technology and health (development of functional products). However, these compounds are unstable when in contact to environmental and industrial process conditions due to their sensitivity to high temperature, light, oxygen losing their functional activity and even produce negative sensory effects on products. Microencapsulation is technology of packaging these compounds in powder form in a continuous film as coating with longer shelf life and better organoleptic properties. Spray drying, extrusion, conservation, emulsification, supercritical fluid technology, ionic gelation, nanoscale manufacture, and fluid bed coating are some of the encapsulating processes utilized in the food industry. The bioactive compounds after microencapsulation can be used as a novel ingredient in various formulations. Several studies have successfully created innovative encapsulation systems that improve food product quality and shelf life.

**Keywords:** *Food waste, Bioactive compounds, Microencapsulation, Food enrichment*

---



---

## Estimation of Total Phenolic Compounds in Three Date Fruits Cultivars from Biskra (Algeria)

Amel Barkat<sup>\*1,2</sup>, Hayat Trabsa<sup>2,3</sup>, Chaima Mezghiche<sup>2</sup>, Yasmine Mabrouka Mizab<sup>2</sup>,  
Abderahmane Baghiani<sup>3</sup>, Abdelnacer Agli<sup>4,5</sup>

<sup>1</sup>Promoting Innovation in Agriculture in Arid Regions (PIAAR), Department of Natural Sciences and Life, Faculty of Exact Sciences Nature and Life Sciences, University of Mohamed Khider, Biskra, Algeria

<sup>2</sup>Department of Natural Sciences and Life, Faculty of Exact Sciences Natural and Life sciences, University of Mohamed Khider, Biskra, Algeria

<sup>3</sup>Laboratory of Applied Biochemistry, Faculty of Nature and Life Sciences, University Ferhat Abbas, Setif, Algeria

<sup>4</sup>Laboratory of Nutrition and Food Technologies, Constantine, Algeria

<sup>5</sup>Institute of Nutrition, Food and Agro-Food Technologies, Constantine, Algeria

---

### Abstract

Date fruits are a national heritage; they are a source of bioactive compounds that are known by their therapeutic effects. Phenolic compounds are one of these bioactive molecules, that have numerous health benefits, including anti-inflammatory and antioxidants properties. This study aimed to estimate and compare the quantity of total phenolic compounds in three cultivars of Algerian date fruits (Ghars, Mech Degla and Deglet Nour) obtained from west of Biskra (Algeria) using hot infusion.

To achieve the objectives, the samples of dates were collected at mature repining stage and prepared. They were homogenized to obtain a uniform sample using 1/10 ratio in hot distilled water and less them to cold down in room temperature. The colorimetric method of Folin-Ciocalteu was used and Gallic acid was used as standard. The total phenolic content was expressed as micrograms of Gallic acid equivalent per gram of fresh weight. To explain results, SPSS v25 was used. Primary results for the yield of extraction, no significant effect of cultivars according to Kruskal-Wallis test ( $0,368 > 0,05$ ), with 65,05% for Ghars, 51,97% for Deglet Nour and 42,07% for Mech Degla. For total phenolic quantification, a significant effect of cultivars on it using One-Way ANOVA test ( $0 < 0,05$ ) where Deglet Nour gave the highest quantity ( $239,927 \pm 72,681 \mu\text{g GAE/mg}$  of extract) followed by both Mech Degla and Ghars ( $95,97 \pm 4,955$  and  $94,14 \pm 8,396 \mu\text{g GAE/mg}$  of extract, respectively). In conclusion, this finding highlights the importance of cultivars in the change of total phenolic content.

**Keywords:** *Deglet nour, Mech degla, Ghars, Hot infusion, Total phenolic content*

---



---

## Estimation of Total Flavonoids Compounds in Three Date Fruits Cultivars from Biskra (Algeria)

Amel Barkat<sup>\*1,2</sup>, Hayat Trabsa<sup>2,3</sup>, Chaima Mezghiche<sup>2</sup>, Yasmine Mabrouka Mizab<sup>2</sup>,  
Abderahmane Baghiani<sup>3</sup>, Abdelnacer Agli<sup>4,5</sup>

<sup>1</sup>Promoting Innovation in Agriculture in Arid Regions (PIAAR), Department of Natural Sciences and Life, Faculty of Exact Sciences Nature and Life Sciences, University of Mohamed Khider, Biskra, Algeria

<sup>2</sup>Department of Natural Sciences and Life, Faculty of Exact Sciences Natural and Life sciences, University of Mohamed Khider, Biskra, Algeria

<sup>3</sup>Laboratory of Applied Biochemistry, Faculty of Nature and Life Sciences, University Ferhat Abbas, Setif, Algeria

<sup>4</sup>Laboratory of Nutrition and Food Technologies, Constantine, Algeria

<sup>5</sup>Institute of Nutrition, Food and Agro-Food Technologies, Constantine, Algeria

---

### Abstract

Date fruits are a popular fruit in arid and semi-arid, and are known for their nutritional value and health benefits. Dates are a good source of various bioactive compounds, including flavonoids. Despite the recognized health benefits of flavonoids, their quantification may influence by the cultivars. This study investigated the quantity of total flavonoids in three date fruits cultivars (Deglet Nour, Mech Degla and Ghars) from west of Biskra (Algeria) using hot infusion. Date fruits were collected at full maturity, and homogenized with hot distilled water. The aluminum chloride assay was used to determine the total flavonoids content. The results showed that the cultivars had no effect on the yield of extraction using Kruskal-Wallis test ( $0,368 > 0,05$ ), with 65,05% for Ghars, 51,97% for Deglet Nour and 42,07% for Mech Degla. For total flavonoids quantification, a significant effect of cultivars on it using One-Way ANOVA test ( $0 < 0,05$ ), where Deglet Nour gave the highest quantity ( $0,1147 \pm 0,004 \mu\text{g QE/mg extract}$ ) followed by Mech Degla ( $0,067 \pm 0,002 \mu\text{g QE/mg extract}$ ) and Ghars ( $0,0497 \pm 0,002 \mu\text{g QE/mg extract}$ ). These finding highlights the importance of cultivars in the change of total flavonoid content in date fruits.

**Keywords:** *Deglet nour, Mech degla, Ghars, Hot infusion, Total flavonoid content*

---



---

## Antibacterial Activity of Garlic (*Allium Sativum*) Against *Staphylococcus* Strains Isolated from Nile Tilapia (*Oreochromis Niloticus*)

Romeissa Derdachi<sup>\*1,2,3</sup>, Sabine Boucetta<sup>1</sup>

<sup>1</sup> Department of Nature and Life Sciences, University of August 20, 1955, Skikda, Algeria

<sup>2</sup>Laboratory of Interactions, Biodiversity, Ecosystems and Biotechnology, University of August 20, 1955, Skikda, Algeria

<sup>3</sup>Laboratory of Optimization of Agricultural Production in Subhumid Zones, University of August 20, 1955, Skikda, Algeria

---

### Abstract

Garlic (*Allium sativum*) has been known for its potent medicinal activities since ancient times. It is one of the most used medicinal plants globally, therefore, the current study aimed to investigate the antibacterial activity of garlic. Samples of fish were diluted in sterile saline. The streak plate method was used to isolate *Staphylococcus* strains on mannitol salt agar, then the identification was done by morphological characteristics and biochemical tests. The diffusion method on Mueller Hinton agar was used to test the antibacterial activity of the aqueous extract of garlic. A volume of the inoculum was spread on the surface of the MH agar, then, a sterile borer was used to form holes which were filled with 100 µl of the aqueous extract. The petri dishes were incubated for 24H at 37 °C. The results show inhibition zones around some holes filled with the aqueous extract. 60% of the strains were sensitive to garlic extract while 40% were resistant. Therefore, this extract has an antibacterial activity against *staphylococcus* strains. In conclusion, garlic is considered a medicinal plant and numerous studies report its antibacterial efficacy against some bacterial species and this was confirmed by the current study.

**Keywords:** *Garlic, Allium sativum, Antibacterial activity, Oreochromis niloticus, Staphylococcus sp*

---



---

## Health and Nutritional Complications in Newborns of Diabetic Mothers

Salima Taleb<sup>\*1,2,3</sup>, Bouthaina Brakni<sup>1</sup>, Fairouz Dilmi<sup>1</sup>

<sup>1</sup>Faculty of Exact Sciences and Natural and Life Sciences, Department of Applied Biology Echahid Cheikh Larbi Tebessi University Tebessa 12000 Algeria

<sup>2</sup>Water and Environment Laboratory, Echahid Cheikh Larbi Tebessi University Tebessa 12000 Algeria

<sup>3</sup>Laboratory of Nutrition and Food Technology (LNTA) University of Constantine 1, Algeria

---

### Abstract

The aim of this work is to study the impact of diabetes during pregnancy on the health and nutritional status of the newborn. Case control study conducted from February 1 to April 15, 2021 at the Khaldi Abdelaziz maternity ward in Tebessa East of Algeria. Newborns of mothers with diabetes were included. Each newborn of a diabetic mother was matched to a newborn of a mother without pathologies chosen at random on the same day of recruitment. We took into consideration all types of diabetes: gestational diabetes and pre-gestational diabetes (type 1 diabetes + type 2 diabetes). The types of diabetes are distributed: 46 cases of gestational diabetes (76.67%) and 14 cases of pre-gestational diabetes (3.33%). The average age of diabetic parturients was  $31.72 \pm 5.41$  years. Multiparas constituted 39.10% in this group and delivery by cesarean section was (66.67%) vs (22.00%) ( $p < 0.0001$ ). Pre-pregnancy BMI and current BMI were significantly correlated with newborn birth weight. Hydramniosis was significantly more common in diabetic mothers (31.67%). Macrosomia was significantly higher in newborns of diabetic mothers (42.86% in mothers with pre-gestational diabetes vs. 30.43% in mothers with gestational diabetes vs. 14% in non-diabetic mothers,  $P = 0.009$ ). Prematurity, malformation, stillbirth and hypoglycemia are significantly more common in diabetic mothers. The impact of diabetes on the health and nutritional status of the newborn is well demonstrated in this study. The existence of diabetes is the factor most associated with neonatal complications. Thus, improving fetal prognosis will require the involvement of a multidisciplinary team before conception, during pregnancy, at delivery and postpartum.

**Keywords:** Diabetes, Pregnancy, New born, Complications

---





---

## Assessment of Antimicrobial Activity of Lactic Acid Bacteria Isolated From Artisanal Dairy Products Against *Escherichia Coli* ATCC 25922 and *Staphylococcus Aureus* ATCC 29213

Roumaissaa Belkacem<sup>\*1</sup>, Qada Benameur<sup>2</sup>

<sup>1</sup>Alimentary Sciences Department, Faculty of Sciences of Nature and Life, University of Abdelhamid Ibn Badis Mostaganem, 27000 Mostaganem, Algeria

<sup>2</sup>Agronomy Department, Faculty of Sciences of Nature and Life, University of Abdelhamid Ibn Badis Mostaganem, 27000 Mostaganem, Algeria

---

### Abstract

Several genera of bacteria and yeast have been reported as probiotics. Researches have been showed that Lactic acid bacteria (LAB) reported antimicrobial activity because they produce several antimicrobial compounds such as bacteriocins. The aim of this study was to isolate probiotics and to evaluate *in vitro* their antagonistic effect against *Escherichia coli* ATCC 25922 and *Staphylococcus aureus* ATCC 29213. The antimicrobial activity of stains was evaluated against *Escherichia coli* ATCC and *Staphylococcus* ATCC using agar disc diffusion assay. The result showed that all isolates exhibited inhibitory effect against pathogenic bacteria except S56, the highest effect was observed by S71 against *Staphylococcus* ATCC with diameter Zone (16±1mm) followed by S2, S21, S38, S29 and S26 with diameter zones ranged from (14±1 mm to 14,33±1.15mm), then the highest inhibitory effect against *Escherichia coli* ATCC was observed by S26 and S71 with diameter zones (12,66±1.15mm) and (12,33±0.57 mm) respectively. The lowest effect was observed by S62 against *Escherichia coli* ATCC and *Staphylococcus* ATCC with diameter zones (7±0.70mm) and (11.33±1.5mm) respectively. It can be conducted that strains S71, S26, S2, S21, S38, S29 had significant inhibitory effect against *Escherichia coli* ATCC and *Staphylococcus* ATCC. Further studies are necessary to evaluate their benefit human and animal health.

**Keywords:** Lactic acid bacteria, Antagonistic effect, Bacteriocins, *Escherichia coli* ATCC 25922, *Staphylococcus aureus* ATCC 29213

---



---

## Utilizing Lentil Flour in the Gluten-Free Cake Formulations

Sebahat Oztekin<sup>\*1</sup>

<sup>1</sup>Department of Food Engineering, Bayburt University, Bayburt, Türkiye

---

### Abstract

Individuals diagnosed with celiac disease must adhere strictly to a gluten-free diet to effectively manage their healthy condition. This dietary regimen necessitates avoiding all foods and products that contain wheat, barley, and rye, along with any items that could potentially be cross-contaminated with gluten. In this study, gluten-free cake formulations were developed by incorporating lentil flour at levels of 10%, 20%, and 30%, while control cakes used whole purpose flour. Proximate composition analysis showed a significant increase in protein content in muffins with lentil flour, which was 1.6 times higher than in gluten-free control samples. However, the addition of lentil flour altered batter properties, resulting in decreased pH and specific volume, while density increased, indicating reduced air incorporation and final cake volume. Various physical properties, including cooking loss, cake yield, browning index, color, volume, and texture, were analyzed. The inclusion of lentil flour led to increased browning indices in both crumb and crust. In conclusion, integrating up to 30% lentil flour into gluten-free cakes provides a realistic option for gluten-intolerant consumers. Despite modifications in certain physical and textural features, sensory quality remained good. This study provides useful insights into the production of gluten-free bakery items enhanced with lentil flour, with the goal of increasing nutritional content while matching customer preferences.

**Keywords:** *Gluten-free, Lentil flour, Cake, Functional food, Celiac disease*

---



---

## Potent Inhibitory and Stimulatory Effects of Various Metal Ions on Polyphenol Oxidase Activity Extracted from Algerian Desert Truffles

Abdelhafid Bouremana<sup>\*1</sup>, Fatima El-Houaria Zitouni-Haouar<sup>1</sup>

<sup>1</sup>Laboratory of Biology of Microorganisms and Biotechnology, Department of Biotechnology, Faculty of Natural and Life Sciences, Oran 1 Ahmed Ben Bella University, Oran 31000, Algeria

---

### Abstract

Enzymatic browning, catalysed by polyphenol oxidase (PPO), significantly impacts the shelf-life and quality of mushrooms, fruits, and vegetables in the food industry. PPO catalyses the oxidation of phenolic compounds to quinones, which polymerize with proteins or amino acids to form brown pigments. Preventing this enzymatic browning is crucial for improving food quality and safety, and numerous natural and synthetic PPO inhibitors have been identified.

In this study, polyphenol oxidase enzyme was extracted and partially purified from the peridium of Algerian desert truffles using the temperature phase partitioning method, resulting in a 62.8% recovery of activity and a purification ratio of 1.3 compared to the crude extract. The number of interfering proteins was halved, and the specific enzyme activity increased to 2.11 U/mg after purification. Furthermore, our work investigated the effects of various metal ions on PPO activity. The present findings revealed that KCl, BaCl<sub>2</sub>, NH<sub>4</sub>Cl, and CaCl<sub>2</sub> inhibited PPO activity to different extents, while MgCl<sub>2</sub> and CuSO<sub>4</sub> increased specific activity. These results highlight the diverse effects of metal ions on PPO, acting as either inhibitors or activators.

Understanding the inhibition and activation of PPO by metal ions is essential in fields such as food technology, biochemistry, and pharmacology. This research provides valuable insights into enzyme regulation and the development of enzyme inhibitors as potential therapeutic agents and effective food preservatives.

**Keywords:** Polyphenol oxidase, Desert truffles, Metals ions, Inhibitors, Food industry

---



## Experimental Measurement on a Shaking Table of the Dynamic Characteristics of Structures

Abdellatif Bentifour<sup>1</sup>, Abderaouf Daci<sup>1</sup>, Nassima Benmansour<sup>1</sup>, Rachid Derbal<sup>\*1,2</sup>

<sup>1</sup>Risk Assessment & Management Laboratory (RISAM), University of Tlemcen, Po Box 230, Tlemcen, Algeria

<sup>2</sup>Department of Civil Engineering and Public Works, University of Ain Temouchent, Po. Box 284, Ain Temouchent, Algeria

---

### Abstract

In earthquake engineering, shaking tables are widely used to predict the dynamic behavior of structures subjected to seismic excitations. Through reduced-scale models, the dynamic characteristics of the structures are identified. The main objective of this work is to carry out experimental measurements on a steel specimen using the shaking table of RISAM laboratory. The specimen is subjected to harmonic dynamic excitations on which an accelerometer is fixed to measure its dynamic response. Through these measurements, the dynamic characteristics of this specimen, such as natural frequency and damping, are determined. Then, a numerical model is developed using a finite element code. The comparison of the numerical and experimental results showed that they are similar. Subsequently, the specimen is subjected to free vibration tests. The damping was calculated using the logarithmic decrement method based on the temporal variations of the accelerations measured during this test. At the end of this work, it can be concluded that the dynamic characteristics, resulting from experimental measurements, are essential for the analysis of the dynamic response of structures.

**Keywords:** *Shaking table, Dynamic characteristics, Natural frequency, Damping, Dynamic response*

---



---

## Evaluation of the Dynamic Characteristics of a 3DOF Reduced Scale Model Using RISAM Shaking Table

Abderaouf Daci<sup>1</sup>, Abdellatif Bentifour<sup>1</sup>, Nassima Benmansour<sup>1</sup>, Rachid Derbal<sup>\*1,2</sup>

<sup>1</sup>Risk Assessment & Management Laboratory (RISAM), University of Tlemcen, Po Box 230, Tlemcen, Algeria

<sup>2</sup>Department of Civil Engineering and Public Works, University of Ain Temouchent, Po. Box 284, Ain Temouchent, Algeria

---

### Abstract

The dynamic behaviour of structures subjected to seismic excitations is often predicted by numerical models. The reliability of these results must be subject to experimental validations. To this end, experimental tests using shaking tables leads to a more realistic prediction of the dynamic behavior of civil engineering structures. The main objective of this work is the detection of vibration signatures of structures under seismic ground motion. For this purpose, a 3 DOF reduced scale model is adopted. Experimental tests are carried out using the RISAM (Risk Assessment and Management) shaking table. The vibration signature of this 3 DOF reduced scale model is mainly characterized by the predominant frequencies and damping. These dynamic characteristics are vital for understanding the dynamic behavior of structures. The predominant frequencies of this reduced model are evaluated using a frequency sweep under a low-intensity white noise signal. The specific damping to this model is determined. Then, dynamic analyses are carried out using a 3D finite elements model of this 3 DOF reduced scale model. The results obtained through these experimental tests show that the approach followed to determine the dynamic characteristics of this 3 DOF reduced scale model proves to be very effective. In addition, a perfect similarity is noted between these numerical and experimental results.

**Keywords:** *RISAM shaking table, Experimental tests, Dynamic characteristics, 3 DOF reduced scale model, 3D finite elements model*

---



---

## Evaluation of the Carbonation of Concrete with the Addition of Pozzolana and Marble Powder Under the Effect of Temperature

Ahlem Houaria Mohammed Belhadj<sup>\*1,2</sup>, Rachid Derbal<sup>2</sup>

<sup>1</sup>Smart Structures Laboratory (SSL), University of Ain Temouchent, Po. Box 284, Ain Temouchent, Algeria

<sup>2</sup>Department of Civil Engineering and Public Works, University of Ain Temouchent, Po. Box 284, Ain Temouchent, Algeria

---

### Abstract

Today, the durability of cementitious material structures is one of the important factors in the field of civil engineering. It is influenced not only by mechanical loads but also by the environment. These influences become more important when it is necessary to guarantee a service life of the material for a long time. One solution to reduce the environmental impact of concrete is to substitute a portion of the cement with mineral additions, such as marble powder and natural pozzolana. However, this substitution must not reduce the material's performance towards carbonation, one of the main phenomena of aging of reinforced concrete structures. Carbonation is a chemical reaction between the cement matrix and the carbon dioxide present in the air. This reaction, in addition to forming calcium carbonate, decreases the pH of the interstitial solution thus making the reinforcements vulnerable to corrosion. Under extreme conditions such as fire, concrete may lose these characteristics. The main purpose of this study is to experimentally characterize the effect of carbonation on concrete with the addition of marble powder and natural pozzolana exposed to high temperatures. Two types of concrete were studied ordinary concrete and concrete with the addition of pozzolana. Cylindrical specimens of  $11 \times 22 \text{ cm}^2$  are used. To evaluate the durability of these two concretes measurements of mass loss and porosity were carried out. The carbonation is calculated after spraying phenolphthalein on specimens of concrete exposed to the open air for + 365 days. The compressive strength measures the mechanical behavior of concretes.

**Keywords:** Pozzolana, Marble powder, Carbonation, High temperature, Concrete

---



## Characterization and Application of Sewage Sludge in Cement Products

Mahmoud Bouslah<sup>\*1</sup>, Mekki Maza<sup>1</sup>, Zine El Abidine Rahmouni<sup>1</sup>, Nadia Tebbal<sup>1</sup>

<sup>1</sup>Civil Engineering Department, Geomaterials Development Laboratory, University of M'sila, Algeria

---

### Abstract

Sewage sludge ash (SSA) has emerged as a promising supplementary cementitious material (SCM) to enhance the performance and durability of cementitious materials. This paper presents a comprehensive review of the characterization and consumption of SSA role in cement structure gives. Chemical composition analysis reveals the presence of silica, alumina, and other oxides important for pozzolanic reactivity. Mineralogical analysis identifies crystalline and amorphous phases, elucidating the potential of SSA. Physical properties such as surface specificity and particle size distribution influence the performance and mechanical properties of cementitious materials. Evaluation of pozzolanic activity by different methods determines the amount of SSA contribution to strength development. The study of hydration kinetics clarifies the early life and long-term performance of cementitious systems containing SSA. Technical testing shows increased compressive, tensile and flexural strength of SSA-modified concrete. Developmental performance studies confirm resistance to chloride penetration, sulfate attack, alkali silica reaction (ASR), and carbonation, ensuring durability of SSA-based cement products. This study provides valuable insights into Effective application of SSA characteristics and applications to sustainable building practices Simple.

**Keywords:** Sewage sludge ash (SSA), Cement-based materials, Mechanical properties, Durability performance, Alkali-silica reaction (ASR)

---



---

## The Impact of Surface Roughness on Energy Dissipation and Dimensions of Non-Rectangular Stilling Basins: An Experimental Investigation for Sustainable Environmental Practices

Seyfeddine Benabid<sup>\*1</sup>, Sonia Cherhabil<sup>2</sup>, Sid Ali Dajfri<sup>2</sup>, Taqiyeddine Assas<sup>2</sup>

<sup>1</sup>Research Laboratory in Subterranean and Surface Hydraulic, LARHYSS, University of Biskra 7000, Algeria

<sup>2</sup>University of Biskra 7000, Algeria

---

### Abstract

The dynamics of downstream flow energy dissipation in hydraulic structures is an interesting topic for hydraulic engineers, and has received special attention in recent years because hydraulic systems such as dams are often subject to heavy flooding. During floods, when a reservoir is full, the water is returned to the river via a spillway. The riverbed is then confronted with a torrential flow of high kinetic energy. This results in harmful traction forces due to its erosive impact, negatively affecting the surfaces of the valleys and potentially causing damage to agricultural lands. The phenomenon of hydraulic jumps is effective in dissipating energy, and studying the characteristics of these jumps is a key factor in the economic and engineering design of charming stilling basins that play a vital role in protecting natural channels and rivers bed. This work presents the results of an experimental study of hydraulic jump flow in a non-rectangular channel over a rough pebble bed, representing a typical natural bed conditions. In this practical work, three rough beds with a roughness height  $k_{(e)}$ , 14.47, 24.47, 30.76 mm were tested in an inclined cross-section of bed to examine the effect of geometric conditions on the hydraulic jump characteristic. The basic flow properties were investigated with a wide range of inflow Froude number ( $3.31 < Fr_1 < 16.05$ ) and flow rate ( $24 \text{ v} < Q < 45 \text{ l/s}$ ). The results showed that increasing the bed roughness and cross-slope of the bed channel leads to a reduction in the characteristics of hydraulics jump compared with a smooth bed such as the relative roller length ( $L_r/d_1$ ) which reduced by 25%; on the other hand, it increases the relative energy loss  $E_{L/E_1}$  by 9.67 %. Based on the experimental data, empirical equations have been proposed to express the characteristics of the hydraulic jump as a function of Froude number and height of the roughness elements.

**Keywords:** Hydraulic jump, Stilling basin, Energy dissipation, Roughness elements, Asymmetric trapezoidal channel

---





---

## Development of Geopolymer Binders Based on Industrial Waste with Different Treatment Methods: A Review

Hanane Zadri<sup>\*1</sup>, Nadia Tebbal<sup>1,2</sup>, Zine El Abidine Rahmouni<sup>1</sup>, Mekki Maza<sup>1</sup>

<sup>1</sup>Geomaterials Development Laboratory, Civil Engineering Department, Faculty of Technology, M'sila University, M'sila 28000, Algeria

<sup>2</sup>Institute of Technical Urban Management, Geomaterials Development Laboratory, M'sila University, M'sila 28000, Algeria

---

### Abstract

In recent years, scientific research into new construction materials has focused on the development of geopolymer cement based on industrial waste or by-products such as blast furnace slag, fly ash, rice husk ash, metakaolin, alkaline activators (NaOH /KOH and Na<sub>2</sub>SiO<sub>3</sub>). The aim of manufacturing geopolymer cement is to protect the environment from CO<sub>2</sub> emissions, reduce the use of natural raw materials (clay and limestone) and create a new ecological and sustainable material. The synthesis of geopolymers depends on a number of parameters, including the type of raw materials used (chemical composition), the activator content and molarity, and the curing conditions. In this paper, we reviewed the importance of this topic and discussed a group of research such as: a recent study investigated the effect of variations in curing temperature and atmospheric exposure and humidity on the mechanical and microstructural properties of fly ash and steel slag mortars. Their results show that thermal curing at 50 °C and exposure to atmospheric air offer the best strength results for alkali-activated mortars. Nagajothi and Elavenil studied the effect of using ground granulated slag and fly ash to produce geopolymer cement, and their results indicated that a compressive strength of 42 MPa was observed within 40 hours of curing under ambient conditions. Rangan studied the durability and mechanical characterisation of geopolymer concrete with different variables such as alkaline activator concentration, curing method and temperature. Gopalakrishma and Pasla studied the effect of using different Fly-Ash-GGBS-MK materials as a binder in the manufacture of GPC mortars, their results indicated that the compressive strength of the materials varies with the percentage of these materials used in the composition. Finally, the use of alkali-activated binders with different mode can reduce carbon dioxide emissions by up to 80% compared with portland cement, making it a promising option for reducing environmental impact.

**Keywords:** *Geopolymer, Cementitious materials, Alkali-activator, Industrial waste*

---



## Valorization of Mining Waste into Construction Materials: Literature Review

Medjida Touahria\*<sup>1</sup>, Nadia Tebbal<sup>2</sup>, Zine El Abidine Rahmouni<sup>1</sup>, Mekki Maza<sup>1</sup>

<sup>1</sup>Geomaterials Development Laboratory, Civil Engineering Department, Faculty of Technology, M'sila University, M'sila 28000, Algeria

<sup>2</sup>Institute of Technical Urban Management, Geomaterials Development Laboratory, M'sila University, M'sila 28000, Algeria

---

### Abstract

The mining industry in Algeria and various countries around the world generates millions of tons of mining waste annually from the extraction stage until manufacturing. Mine waste contains sulphides such as pyrite, galena, and chalcopyrite. These sulfur minerals, under the influence of oxygen and in the presence of water, cause the phenomenon of acid mine drainage. As mining activity is constantly increasing due to its economic importance, controlling the discharge of these wastes has become an urgent matter because they constitute a real burden on the environment. In recent years, many studies have focused on finding ways to revalue these wastes and even benefit from them.

This paper aims to collect some important studies on the revaluation of barite waste. Many researches have found that barium ions can disintegrate ettringite by forming BaSO<sub>4</sub> precipitate. Additionally, barite additions have improved the physical and mechanical properties of the prepared samples, as shown in research by Ting Zhang and al. and A.M. Zayed and al. confirmed that a higher barite content (50%) induced an increase in the compressive strength and simple bending of the sample by approximately 91% and 111% respectively. They also improved the microstructural properties of the chryso-concrete tiles in terms of porosity of the matrix cementitious.

This paper contains the rest of the results, in addition to other important studies.

**Keywords:** Mining waste, Barite, Ettringite, Mechanical strengths, Review

---



---

## The Effect of Limestone on Virgin Cork Concrete Mechanical Properties and Durability

Samah Hariz<sup>\*1</sup>, Fouad Ghomari<sup>1</sup>, Brahim Touil<sup>2</sup>

<sup>1</sup>Department of Civil Engineering, University of Tlemcen, Tlemcen, Algeria

<sup>2</sup>Department of Civil Engineering, University of Saida, Saida, Algeria

---

### Abstract

Globally, the construction industry's increasing use of concrete is heightening energy consumption, exacerbating climate change, and amplifying issues like heatwaves and droughts. Additionally, the corrosion of steel bars due to chloride ion infiltration poses a significant threat to the durability of reinforced concrete structures.

Building on previous research involving the substitution of traditional aggregates with virgin cork at a 25% ratio, significant progress has been made, particularly in thermal insulation. Our study aimed to assess the durability and mechanical properties of this innovative material by incorporating 10% limestone, maintaining a water-to-cementitious materials ratio of 0.45. This resulted in six concrete variants: ordinary concrete, dry or wet cork concrete, limestone and virgin cork (dry & wet) concrete.

Although the inclusion of virgin cork reduced mechanical strength compared to standard concrete, the addition of limestone improved mechanical properties. Notably, both limestone and virgin cork exhibit promising mechanical attributes as construction materials, aligning with RILEM's lightweight concrete classification.

Experiments on porosity and capillary absorption confirmed these findings, showing reduced values with limestone usage. Regarding the diffusion coefficient, a slight decrease occurred with limestone addition, while dry or wet cork increased it. However, combining limestone with dry or wet virgin cork decreased the diffusion coefficient, with the lowest value observed in wet cork combined with limestone.

Our research suggests that dry cork concrete with limestone yields optimal results in mechanical properties, porosity, and capillary absorption. Conversely, wet concrete with limestone excels in mitigating chloride propagation, prolonging concrete lifespan. Further exploration is necessary to fully understand the properties of wet virgin cork concrete.

**Keywords:** *Bio-based concrete, Virgin cork, Limestone, Strength, Diffusion coefficient*

---



## Investigation of the Microstructure and Hardness Properties of Fe Based High Entropy Alloys Produced by Powder Metallurgy Method

Murat Bodur<sup>1</sup>, M. Emre Turan<sup>1</sup>, Yavuz Sun<sup>\*1</sup>

<sup>1</sup>Metallurgical and Materials Engineering Department, Karabuk University, Karabuk, Türkiye

### Abstract

Developing technology has revealed humanity's need for new types of materials. Although existing traditional materials can meet the needs, they may be insufficient in some areas of use. New material designs and studies have increased in the automotive, space and aviation sectors due to features such as low weight and high wear resistance. In this study, two designed high entropy alloys were produced by the powder metallurgy method. Pure element powders were used for the alloys to be produced for the powder metallurgy method. Elemental powders of appropriate grain sizes were pressed under appropriate conditions after being subjected to mechanical alloying. Alloys were obtained by sintering the pressed alloys in atmosphere-controlled furnaces, and they were cooled in Si sand to prevent oxidation. Microstructure characterization and hardness tests were applied to the obtained alloys. As a result of the tests, it was determined that high entropy alloys with Cr addition had higher hardness values than those with Mo addition.

**Keywords:** Powder metallurgy, High entropy alloys, Hardness, Microstructure

## 1 INTRODUCTION

Alloys have evolved from simple to complex compositions based on humankind's ability to develop materials. The improved functions and performances of alloys have enabled civilizations to progress. Over the last century, significant evolution and progress has led to the invention of special alloys such as stainless steels, high-speed steels and superalloys. Although alloys composed of more than one element have higher mixing entropy than pure metals, the improved properties are mostly due to the mixing enthalpy allowing the addition of appropriate alloying elements to increase strength and improve physical and/or chemical properties. Since the turn of the century, more complex compositions with higher mixing entropy have emerged. Such complex compositions do not guarantee a complex structure and microstructure or the accompanying brittleness. Conversely, significantly higher mixing entropy obtained from complex compositions can simplify the structure and microstructure and endow alloys with attractive properties. Jien-Wei Yeh and Brian Cantor independently announced the feasibility of high-entropy alloys and equiatomic multicomponent alloys in their reports published in 2004. This breakthrough in alloying concepts has accelerated research on these new materials worldwide in the last decade [1-4].

Each alloy has its own unique properties. The main factor that determines the mechanical and microstructural properties of high entropy alloys is the phase formed by the alloy. High entropy alloys show better and different mechanical and microstructural properties than conventional alloys. The ideal mixing ratios of the elements used in the high entropy alloys that are the subject of the paper were calculated using a program. In the calculation, the atomic size of the elements, mixing enthalpies, mixing entropies, etc. are taken into account. Alloys were created by investigating and taking into account the parameters.

The preparation processes, production, mechanical and metallographic processing processes of the high- entropy alloys created, and the mechanical and metallographic test results of the high- entropy alloys produced are expressed in this paper.

## 2 EXPERIMENTAL STUDIES

### 2.1 Sample Design and Preparation

Two Fe-based, high entropy alloys were determined to be used in the paper. In designing the alloys, factors such as mixing entropy, mixing enthalpy and Gibbs free energy were taken into consideration, and element selection

and ratios were calculated accordingly. Metal powders were obtained from Nanokar Company. The powder properties supplied by Nanokar Company are given in Table 1.

**Table 1.** Powder properties used in tests

Elements	Purity (%)	Grain Size ( $\mu\text{m}$ )
Fe	99.90	44
Mn	99.90	44
Al	98.85	44
Cr	99.50	44
Ni	99.50	44
Mo	99.95	44

Element percentages of the elements used in the experiments are given in Table 2, and chemical contents by weight of the elements used in the experiments are given in Table 3. Chemical analysis rates by weight were determined and calculated for a total of 30 gr.

**Table 2.** % Ratios of elements used in tests

Test Order	Alloy Type	Alloys	Fe%	Mn%	Al%	Cr%	Ni%	Mo%
1	HEA-1	$\text{Fe}_{50}(\text{MnAlMoNi})_{12.5}$	48.57	11.94	5.87	-	12.76	20.86
2	HEA-2	$\text{Fe}_{50}(\text{MnAlCrNi})_{12.5}$	53.70	13.21	6.49	12.50	14,11	-

**Table 3.** Chemical content by weight of the elements used in the tests

Test Order	Alloy Type	Alloys	Fe%	Mn%	Al%	Cr%	Ni%	Mo%
1	HEA-1	$\text{Fe}_{50}(\text{MnAlMoNi})_{12.5}$	14.57	3.58	1.76	-	3.83	6.26
2	HEA-2	$\text{Fe}_{50}(\text{MnAlCrNi})_{12.5}$	16,11	3.96	1.95	3.75	4.23	-

## 2.2 Production of Alloys

In the mechanical alloying process, each of the high entropy alloys was run at 300 rpm. In the mechanical alloying process, the powders were mixed in 12 cycles, with 30 minutes of work and 10 minutes of break, to obtain a homogeneous structure.

In order to obtain the mechanical and microstructural properties of two high entropy powder alloys produced by obtaining a homogeneous mixture through mechanical alloying process, cold pressing was applied with a 100-ton cold press.

The samples formed after the cold pressing process were sintered at 1000°C. The pressed samples were placed in the oven, the oven worked with a temperature increase of 10 °C per minute and reached 1000 °C in 100 minutes. The samples were kept at 1000°C for approximately 1 hour. The sintered samples were embedded in silica sand in a ceramic crucible and allowed to cool at room temperature. After the sinter process, the samples were allowed to cool in silica sand to prevent oxidation.

## 2.3 Microstructure Characterization

Ø30mm bakelite mold was used in the bakelite process. The device operated under 150 bar at 180 °C with 5 minutes of compression and the bakelite process was carried out. Bakelite high entropy alloys were then surface polished with a surface polishing device. Surface preparation processes were carried out by polishing the surface of 2 high entropy alloys taken from Bakelite before mechanical tests.

XRD device was used to determine the composition and phases in the alloy samples. Continuous scanning was performed using a copper tube in the range of 10-90°. For all measurements, the device was operated under 30 kV and 20 mA parameters.

The most important point in the production of high entropy alloys is microstructure control. Scanning Electron Microscope (SEM) was used to examine the surface morphological properties of high-entropy alloys produced by mechanical alloying method. Elemental distribution analysis (mapping) and point analysis images of the samples were also examined on the same device.

## 2.4 Hardness Analysis of Alloys

After the sample preparations were completed, hardness measurements were made as a result of 15 seconds of load application under 2 high entropy HV1 loads.

## 3 EXPERIMENTAL FINDINGS AND DISCUSSION

### 3.1 Microstructure Results

XRD results of the produced HEA-1, HEA-2 alloys are shown in Figure 1. A second phase was not observed in the produced alloys. The peaks of the alloying elements we added are seen in the XRD results.

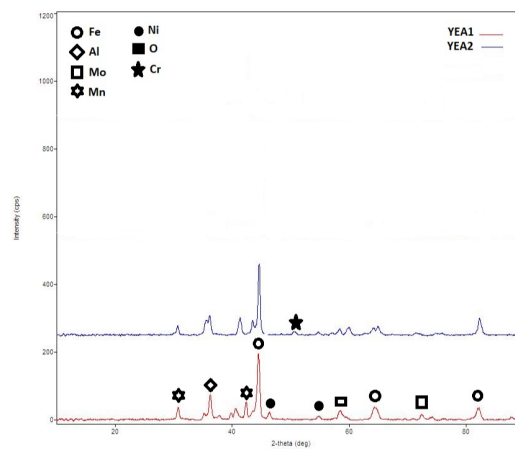


Figure 1. XRD image of HEA-1, HEA-2 alloys

It can be seen in the microstructure images in Figure 2 that the grains in the structure of the HEA-2 alloy, which is a Cr and Ni- containing alloy with high entropy, have grown compared to the HEA-1 alloy.

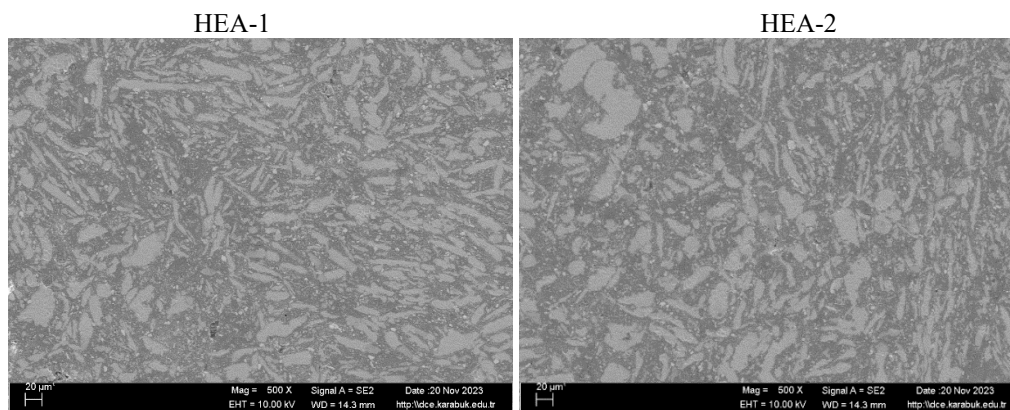
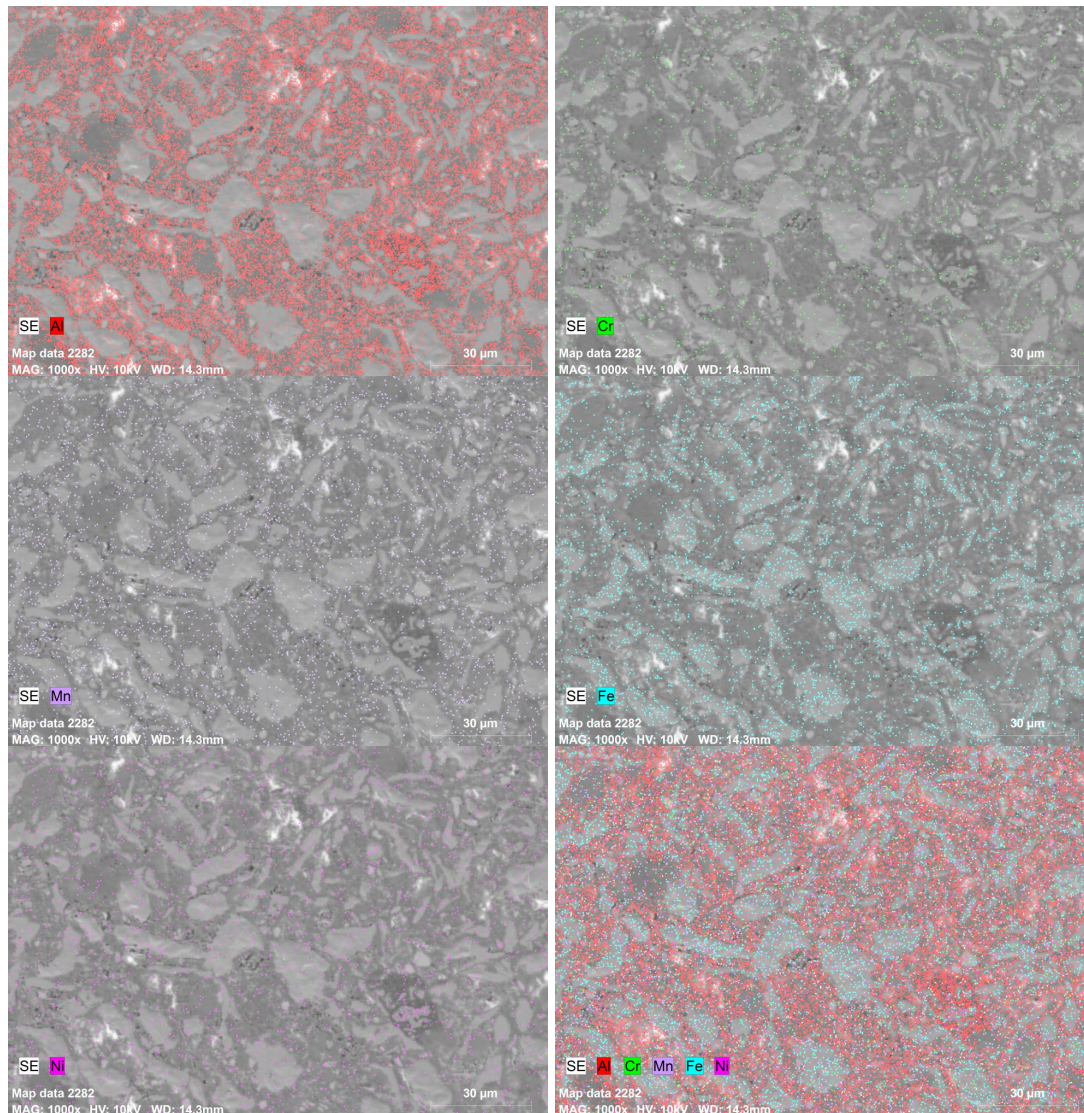


Figure 2. Microstructure image of HEA-1, HEA-2 alloys

As an example, the elemental distribution map of HEA-2 alloy, which is one of the high entropy alloys, was examined. Figure 3 shows the distribution of Al, Cr, Mn, Fe and Ni elements in the HEA-2 alloy. When the elemental distribution map is examined, it is seen that all the alloying elements in Fe are distributed homogeneously and the Al element is more abundant in the structure.



**Figure 3.** HEA-2 elemental distribution map of its alloy

There are several important factors that determine the microstructure and critical properties of HEAs. Among these factors, four main effects are considered to be the main factors: high entropy, lattice distortion, slow diffusion rate and mixing [2].

It is considered that this high entropy facilitates the solubility of the phases within themselves. Therefore, this effect prevents the formation of many undesirable phases. Moreover, the diffusion rate of atoms is low, so the formation of various phases in such alloys is kinetically restricted. As a result, not only the high configurational entropy but also the low diffusion rate in HEAs significantly affects the number of phases to be formed [6]. Some HEAs may contain intermetallic phases due to the strong bonding between metallic elements. Intermetallic phases are also defined as relatively ordered solid solutions. In the solid-state thermodynamic approach, as the temperature increases, the vacancy concentration and the solubility of solutes in the solvent atoms also increase.

Since each solid solution phase in HEAs is part of the multicomponent matrix, each atom is surrounded by different types of atoms and is therefore subject to lattice strain and stress due to the atomic size difference. Apart from the difference in atomic size, the different binding energy and crystal structure between the added elements causes even higher lattice distortion, considering the presence of unsymmetrical neighboring atoms around an atom, i.e. unsymmetrical bonds and electronic structure, and the variation of this unsymmetry from region to region is expected [5]. Therefore, most lattice sites and overall lattice distortion are expected to be more severe than in conventional alloys in which most matrix atoms (or solvent atoms) have the same type of atoms as their neighbors.

Since HEAs can have a single phase or more phases that vary with composition, all phases contribute to the properties of the alloys in terms of their size, shape, and distribution. In fact, the properties of these alloys are very

similar to composite materials consisting of two or more constituent materials with significantly different physical or chemical properties. In other words, each phase can be considered a member of the composite structure. Composite properties arise from both the properties of the elements themselves due to the mixing rule, the interaction of the elements with each other, and the lattice distortion effect. The interaction of elements and the lattice distortion effect are more important contributions compared to the mixing rule. The effects of this feature on different HEAs have been stated in many studies in the literature [6–8].

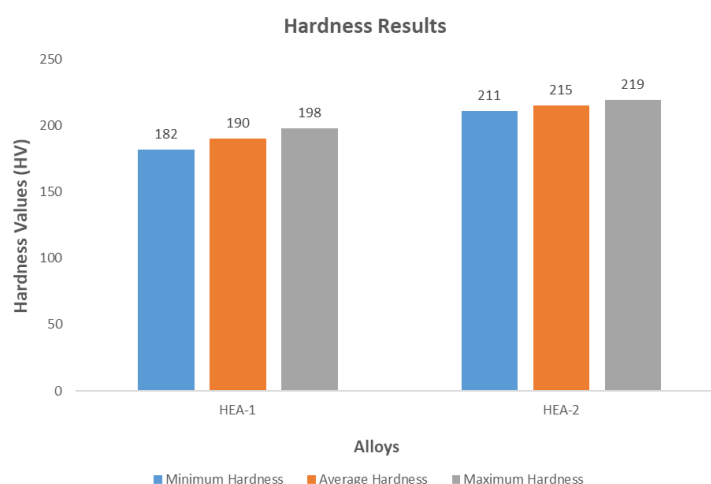
The formation of new phases requires the co-diffusion of many different types of atoms in HEAs. As discussed in the above section, HEAs can contain solid solutions of random or ordered types. The matrices of HEAs can be considered as completely soluble.

### 3.2 Hardness Test Results

Hardness tests of the produced HEA-1 and HEA-2 alloys were carried out under HV1 load with a load application of 15 seconds. The minimum, maximum and average hardness values of the samples are shown in Table 4 and the hardness graph comparison is shown in Figure 4.

**Table 4.** Hardness test results of alloys

Test Order	Alloy Type	Alloy Created	Minimum Hardness	Average Hardness	Maximum Hardness
1	HEA-1	$\text{Fe}_{50}(\text{MnAlMoNi})_{12.5}$	182	190	198
2	HEA-2	$\text{Fe}_{50}(\text{MnAlCrNi})_{12.5}$	211	215	219



**Figure 4.** Hardness test comparison chart for alloys

Due to high mixing entropy, the produced alloys can ideally form stable single-phase solid solutions in which atoms of different sizes are homogeneously distributed. However, enthalpic interactions inevitably alter the local chemical order (LCO) in HEAs, leading to short-range order (SRO) and/or incipient concentration waves. Despite the uncertainty of LCO, a mixture of atoms of different sizes induces severe lattice distortion, which frequently exhibits short-range resistance to dislocation slip, in order to maximize the solid solution strengthening effect in HEAs [5, 6, 9]. These lattice distortions also have a serious effect on the hardness and strength values of the alloy. The high amount of alloying elements added to the system in HEA causes us to expect that the amount of elements dissolved in the lattice structure of the main phase will be higher, which will lead to more lattice degradation.

In literature studies, it has been stated that adding even small amounts of elements such as Mn, Al, Cr, Ni to the alloy structure has an effect on increasing the amount of hardness in the alloy structure. It is known that the lattice distortion effect in HEA alloys causes an increase in hardness values [10, 11].

## 4 GENERAL RESULTS

In this study, high entropy alloys  $\text{Fe}_{50}(\text{MnAlMoNi})_{12.5}$  (HEA-1),  $\text{Fe}_{50}(\text{MnAlCrNi})_{12.5}$  (HEA-2) alloys were produced by powder metallurgy method and mechanical and metallographic examinations were carried out.



Microstructure characterization and hardness tests were carried out on the produced alloys. The findings obtained as a result of the tests applied to the produced alloys are given below.

- The microstructure examination, it was seen that the grains in the alloys showed a homogeneous distribution. No interphase or compound was detected in the microstructures of the alloys. There are several important factors that determine the microstructure and critical properties of HEAs. Among these factors, it can be said that four basic effects are the main factors: high entropy, lattice distortion, slow diffusion rate and mixing.
- The hardness values of high entropy alloys with Cr addition were higher than the hardness values of high entropy alloys with Mo addition. It has been observed that the lattice distortion effect of high- entropy alloys causes an increase in hardness values, and alloying elements such as Ni and Cr add hardness-increasing properties to the structure.

Developing technology has created the need for new types of materials. Although existing traditional materials can meet the needs, they may be insufficient in some cases. High entropy alloys are advantageous because they have high hardness and high wear resistance. High entropy alloys are an open field for research due to low weight and high wear resistance requirements in the automotive, space and aviation sectors.

## Acknowledgments

I would like to thank Karabük University BAP commission and Karabük University Rectorate for their support with the project numbered KBÜBAP-23-YL-022 in the completion of this study.

## References

- [1] F. Tian, Y. Wang, D. L. Irving, and L. Vitos, "Overview of high-entropy alloys", in *Applications of Coherent Potential Approximation to HEAs*, 2016, pp. 299–332.
- [2] P. Shewmon and C. Gill, "Metallurgy Retrieved 2020".
- [3] B. S. Murty, J. W. Yeh, S. Ranganathan, and P. P. Bhattacharjee, *High-Entropy Alloys*, 1st ed. San Diego: Elsevier, 2014.
- [4] C. C. Tasan, Y. Deng, K. G. Pradeep, M. J. Yao, H. Springer, and D. Raabe, "Composition dependence of phase stability, deformation mechanisms, and mechanical features of the CoCrFeMnNi high-entropy alloy system," in *JOM*, 2014, vol. 66, pp.1993–2001.
- [5] K. Y. Tsai, M. H. Tsai, and J. W. Yeh, "Sluggish diffusion in Co-Cr-Fe-Mn-Ni high-entropy alloys," *Acta Materialia*, vol. 61, no. 13, pp. 4887–4897, 2013.
- [6] Q. J. Li, H. Sheng, and E. Ma, "Strengthening in multi- principal element alloys with local-chemical-order roughened dislocation pathways," *Nature Communications*, vol. 10, art. no. 3563, 2019.
- [7] J. W. Yeh, Y. L. Chen, S. J. Lin, and S.K. Chen, "High- entropy alloys - a new era of exploitation", *Materials Science Forum*, vol. 560, pp. 1–9, 2007.
- [8] D. R. Gaskell and D. E. Laughlin, *Introduction to the Thermodynamics of Materials*, 4th ed. London: CRC Press, 2003.
- [9] C. J. Tong, M. R. Chen, J. W. Yeh, S. J. Lin, S. K. Chen, T. T. Shun, and S. Y. Chang, "Mechanical performance of the Al<sub>x</sub>CoCrCuFeNi high-entropy alloy system with multiprincipal elements," *Metallurgical and Materials Transactions A*, vol. 36, pp. 1263–1271, 2005.
- [10] F. Otto, Y. Yang, H. Bei, and E. P. George, "Relative effects of enthalpy oath entropy on the phase stability of equiatomic high-entropy alloys," *Acta Materialia*, pp. 2628–2638, 2013.
- [11] Z. Y. Rao, X. Wang, J. Zhu, X. H. Chen, L. Wang, J. J. Si, Y. D. Wu, and X. D. Hui, "Affordable FeCrNiMnCu high entropy alloys with excellent comprehensive tensile properties," *Intermetallics*, pp. 23–33, 2016.



## Investigation of Delamination Factor in Bi-Directional Drilling of Glass Fiber Reinforced Plastic Materials

Erhan Karatas<sup>1,2</sup>, Oguz Kocar<sup>\*2</sup>, Nurettin Baran Zulfikar<sup>2</sup>, Nergizhan Anac<sup>2</sup>, Furkan Parmaksiz<sup>2</sup>

<sup>1</sup>Mining Machinery Factory, Türkiye Hard Coal Enterprises, Zonguldak, Türkiye

<sup>2</sup>Department of Mechanical Engineering, Faculty of Engineering, Zonguldak Bulent Ecevit University, Zonguldak, Türkiye

### Abstract

Glass fiber reinforced plastics (GRP) are manufactured in layers by adding glass fiber reinforcements to the polymer resin forming the matrix structure. Glass fiber reinforced plastic materials (GRP) are widely used in automotive, construction and many other sectors due to their corrosion resistance, high strength/low weight ratio, thermal resistance and low cost. Machining operations such as drilling and milling can be applied to GRP. As GRP consists of more than one layer, defects called delamination, which disrupt the structural integrity of the hole, occur especially at the entrance and exit of the hole during drilling. This situation both negatively affects product life and causes problems during product assembly. In the literature, there are several studies on the optimization of drilling parameters and drill characteristics (drill point angle, drill material) to reduce the delamination rate. In the studies examined, GRPs were fixed to the vice from two sides, and one-way drilling was applied. In this study, GRP was clamped in a vise from one side and the effects of bi-directional drilling on the delamination rate were investigated. Five different feed rates (200, 400, 600, 800, 800, and 1000 mm/min) and two different tool rotational speeds (1500 and 3000 rpm) were used for drilling. Reference samples (thickness: 5 mm) were drilled from one way. The other samples were bi-directional drilled 1.5, 2.5 and 3.5 mm from the front side and then 3.5, 2.5 and 1.5 mm from the back side by turning the part. The delamination rates of all samples have been calculated. The samples having the lowest and highest delamination ratios were visually inspected. In one-way drilling, the lowest delamination rate of  $1.20 \pm 0.10$  was obtained at 1500 rpm tool rotational speed and 400 mm/min feed rate. For bi-directional drilling, the lowest delamination rate of  $1.16 \pm 0.02$  was obtained at a tool rotational speed of 3000 rpm, a feed rate of 400 mm/min and a drilling distance of 3.5 mm front and 1.5 mm back surface. The results showed that delamination rates were more stable in one-way drilling and increased with feed rate in bi-directional drilling.

**Keywords:** Delamination, Bi-directional drilling, Glass fiber reinforced plastic, Hole drilling process

## 1 INTRODUCTION

The concept of composites has been rapidly adopted since its introduction in literature, leading to increased demand for various composite materials suitable for diverse applications. Composites offer significant advantages, particularly in terms of strength and lightness. Carbon fiber and glass fiber reinforced plastic composite materials are frequently preferred in industrial engineering solutions. Glass fibre reinforced polymer composites are much more widely used because they are cost effective. Glass fiber reinforced plastic (GRP) consists of glass fiber and resin reinforced with a plastic matrix, providing properties such as hardness, fatigue resistance, and chemical resistance [1]. GRP composites can be processed by machining methods. Among these manufacturing methods, drilling is the most used and can be applied as an end process [2, 3]. However, delamination defects often occur when drilling holes in composite parts. Delamination can be defined as the deformation that occurs at the hole entrance and exit during the drilling process. This may reduce operating performance and cause damage to the system [4]. Due to the delamination defect, part continuity is disrupted, and hole size tolerance is disrupted, causing problems during assembly. Products may be discarded. Numerous studies have been conducted and continue to be conducted on reducing delamination in drilling holes in composites. In the literature, various approaches have been proposed to reduce delamination during drilling in composites, including the use of backing plates during drilling, drilling at different feed rates, development of specially designed cutting tools, minimal coolant or cryogenic applications, the use of stepped drills for gradual hole drilling, ultrasonic drilling, and high-speed drilling [5, 6].

It has been revealed that feed rate, cutting speed and tool rotational speed have significant effects on delamination in drilling operations [7]. Studies have emphasized that the effect of tool feed rate on delamination is particularly noteworthy [7–9]. Increasing the feed rate increases the thrust force, causing the tool to apply more force on the

fiber as it passes through the material. This increased thrust force causes the fibers to break, causing delamination at the hole exit [7]. The second most influential process parameter on delamination is cutting speed. Increasing cutting speed allows the fibers to be cut more easily, which reduces layer separation. Proper cutting of fibers helps minimize delamination [9].

Studies have emphasized that drill geometry is another parameter that has an impact on delamination. Drill geometry is defined by features such as the number of cutting edges, diameter, tip angle, tool material and type. Alvares et al. showed that the cutting tip angle has a great effect on delamination. As the cutting tip angle decreased, the contact area of the fiber, which is the reinforcement material, with the drill decreased. Therefore, a decrease in the thrust force of the cutting tool was observed. The decrease in thrust force reduced delamination [10]. In their study, Devi and Palanikumar observed that increasing the diameter of the cutting tool leads to increased contact with fibers within the material and increased thrust force, thereby increasing delamination [11]. Recent research has highlighted that the type of drill bit selected for drilling operations is one of the significant factors affecting delamination [12]. Various types of drill bits such as wood drill bits, step drill bits, twist drills, and specially designed drill bits are available. Upon examining these drill bit types, it becomes evident that using drill bits with geometries and materials that reduce thrust force is key to minimize delamination [12, 13]. Specifically, it has been found that specially designed drill bits and step drill bits, which reduce thrust force, significantly reduce delamination [12]. Furthermore, literature emphasizes that coatings on cutting tools (drill bits) also have a notable effect on delamination. Navneet et al. have stated that coatings reduce drill bit wear and thereby decrease the risk of delamination. However, the high cost of these coatings limits their widespread use in industrial applications [14].

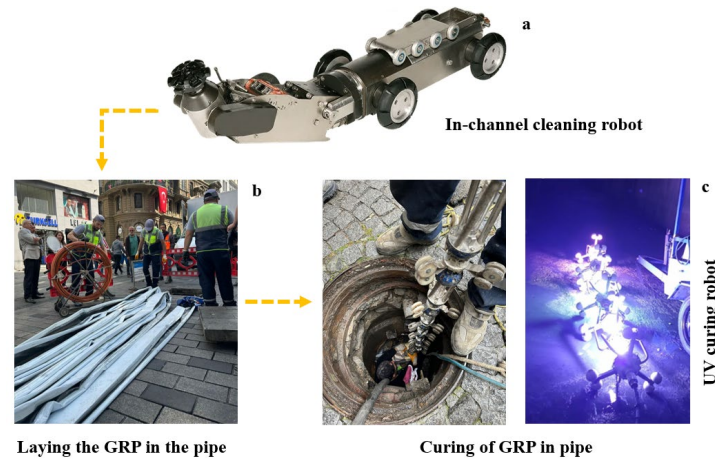
Composite materials' joining factors and contents significantly influence delamination. The mechanical properties, orientation, and distribution of the matrix and reinforcement materials, which are components of composite materials, directly affect the formation and resistance of delamination. Additionally, the chemical structures and curing processes of materials like resins used as matrix materials are factors that impact delamination. Many additives such as organic, metallic and nano-sized particles are added to increase the durability of composite materials. These additives are among the factors that affect delamination during the drilling process. Sundaram et al. investigated the drilling characteristics of glass fibre reinforced composite materials with coconut shell and extract addition. As a result, they observed that the additive materials they used reduced delamination [15]. Anand and Patara stated that during the drilling process, stress occurred in the areas where the fibers were dense. This stress caused separation between the layers. Increasing the volumetric ratio of fibers causes the pushing force and the resulting temperature to increase. They concluded that this situation affects delamination [16]. Geng et al. have found that the orientation angles of fibers are crucial in composite drilling processes. In the study, it was observed that while a more effective cutting process was achieved in the areas where the tool came into contact with the resin during drilling, it was difficult to cut the fibers when it encountered fibers. Consequently, forcing fibres at the hole exit leads to exit delamination, while at the entrance, the rotational motion of the tool causes fibres to peel, resulting in surface layer separation. Additionally, Pawar et al. observed that the increase in the orientation angle of the fibers causes the cutting forces to increase and, as a result, to increase delamination [17]. The mentioned studies were carried out in the conventional hole drilling process. In conventional hole drilling operations, problems with delamination formation due to separation of layers, especially at the hole exits, continue. In this study, the mechanical properties of glass fiber reinforced plastic composite materials produced by hand lay-up technique and the delaminations occurring during two different hole drilling (conventional and bi-directional) were examined. It was aimed to determine the effect of conventional and bidirectional hole drilling on the delamination rate. Five different tool feed rates (200, 400, 600, 800 and 1000 mm/min) and two different tool rotational speeds (1500 and 3000 rpm) were used as drilling process parameters. After the drilling process, images of the holes were taken with a digital microscope and delamination rates were calculated. Hole exit damages in bidirectional and conventional hole drilling processes were examined, and the effects of process parameters on the delamination rate were discussed comparatively.

## 2 MATERIAL METHOD

### 2.1 Glass Fiber Reinforced Composite Material

Glass fiber reinforced plastics materials were supplied from Kanaltek Construction Inc. GRP material is imported from France by Kanaltek Construction Inc. and used in the inner coating of corrugated pipes and high-density polyethylene (HDPE) pipes in wastewater lines using the trenchless method. Wastewater channel lining is preferred to protect the inner and outer surfaces of pipes used for transporting and storing wastewater. The material used in the coating of the inner surface of the pipe helps to extend the life of the duct system by preventing corrosion, abrasion and clogging.

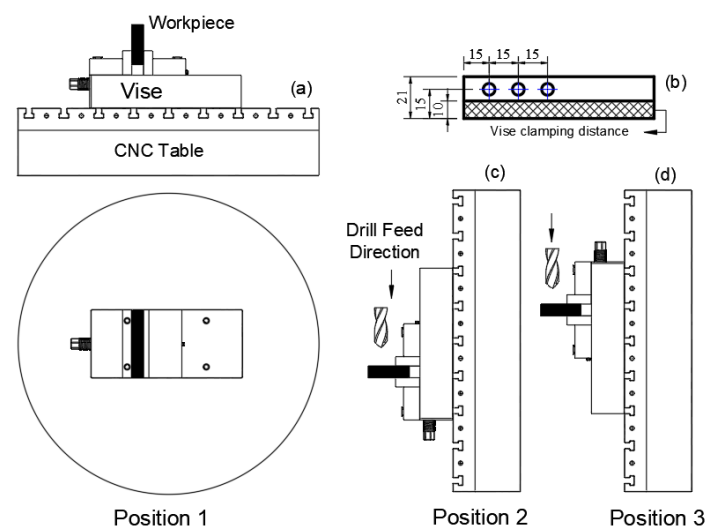
Figure 1 shows the coating process of the pipes inside the channel. Before the GRP material is laid into the channel, the inside of the pipes is cleaned with an in-channel cleaning robot (Figure 1a). After the inside of the channel is cleaned, GRP is placed into the channel (Figure 1b). Then, air is blown into the GRP and it is inflated. Finally, the UV curing robot moves inside the pipe to perform UV light curing (Figure 1c). The GRP obtained from Kanaltek Construction Inc. was supplied in a flat and cured state. Then, it was cut to the specified dimensions and prepared for the drilling process.



**Figure 1.** GRP coating process inside the channel

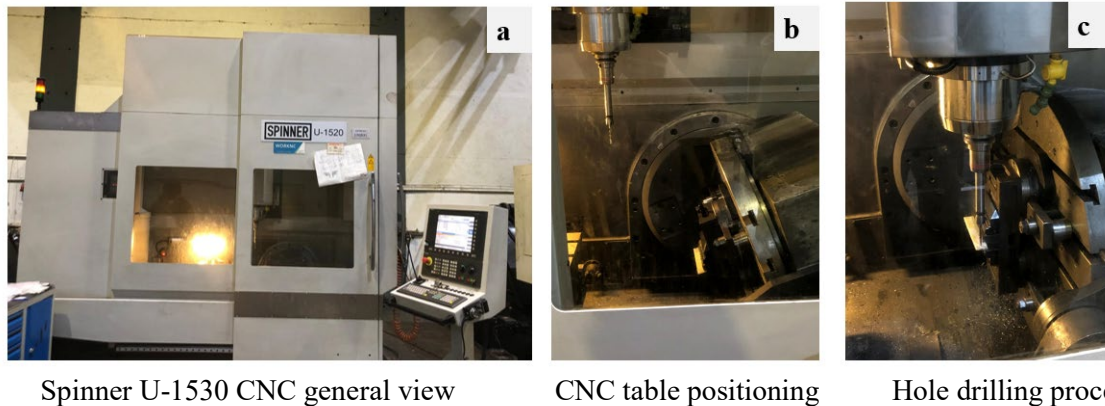
## 2.2 Drilling Process

In the conventional drilling process, the material is first rigidly fixed to the table. Then, the drill enters from the upper surface of the piece and exits through the bottom surface, drilling the piece. In bi-directional drilling process, the drill enters from the upper surface of the piece, then the piece is turned over, and the drilling is repeated from the bottom surface to complete the process. In this study, the drilling operations were carried out at the Turkey Hard Coal Enterprises Central Workshop using a Spinner brand U-1530, 5-axis CNC vertical machining center. The U-1530 5-axis CNC vertical machining center has dual tables (movable table  $\text{\O}630\text{mm}$ , fixed table  $1530 \times 530\text{ mm}$ ), a maximum tool rotational speed of 12,000 rpm, 32 stations, and spindle with 18 kW power and 105 Nm torque. In Figure 2, a schematic representation of the drilling process is given. Figure 2a shows the position of the workpiece relative to the table and the vise. The parts were cut according to the width of the vise jaw. Thus, a more stable attachment of the parts was ensured. Each experiment was performed in three replicates. A distance of 15 mm was left between the holes and 15 mm to the edge of the part. The parts were attached to the vise with a 10 mm hold (Figure 2b). After the part is attached to the vise, the table of the CNC vertical machining center changes position. In Figure 2c, the front surface holes are drilled in both conventional drilling processes and bidirectional drilling processes. Finally, the CNC vertical machining center changes position to perform the drilling on the back surface of the part for the bi-directional drilling process.



**Figure 2.** Schematic representation of bi-directional drilling

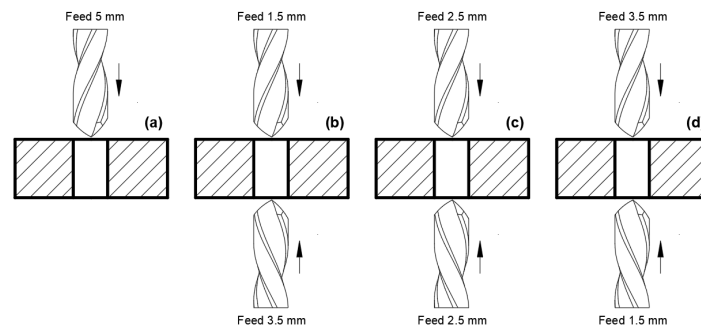
The 3D modeling of the part was prepared using SolidWorks, and the G-codes required for the drilling process were prepared using the commercial software SolidCam. Figure 3 shows the CNC vertical machining center used for the drilling process, the positioning before drilling and the view during drilling.



**Figure 3.** a) CNC vertical machining center used in the drilling process b) positioning of the CNC table and c) hole drilling process

**2.3 Experimental Design**

Figure 4 shows the drilling strategy used in conventional and bidirectional drilling. The GRP material was drilled through in single pass using conventional drilling (Figure 4a). In bi-directional drilling, holes of 1.5, 2.5, and 3.5 mm were drilled from the front surface, and holes of 3.5, 2.5, and 1.5 mm were drilled from the back surface (Figure 4 b-d).



**Figure 4.** Schematic representation of conventional drilling and bi-directional drilling

Table 1 gives the process parameters used in the drilling process. Five different tool feed rates (200, 400, 600, 800 and 1000 mm/min) and two different tool rotational speeds (1500 and 3000 rpm) were used as process parameters.

**Table 1.** Process parameters used in drilling operations

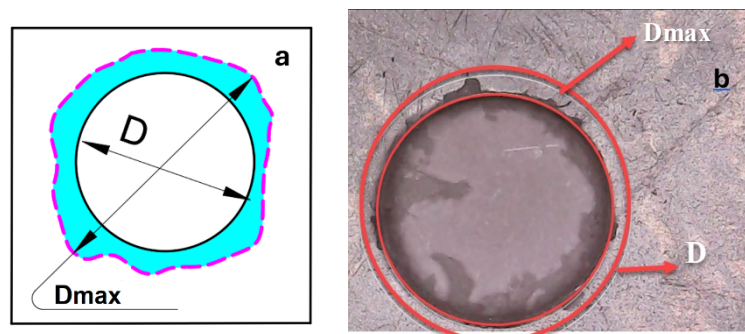
Experimental Number	Feed Rate (mm/min)	Rotational Speeds (rpm)
1	200	1500
2	400	
3	600	
4	800	
5	1000	
6	200	3000
7	400	
8	600	
9	800	
10	1000	

## 2.4 Calculation of Delamination

The schematic (Figure 5a) and post-drilling (Figure 5b) images of the drilled drill diameter and the damaged diameter of the GRP material are provided. Delamination is a type of damage caused by the low strength between the layers in composite materials. The delamination factor ( $D_f$ ) is a parameter used to evaluate surface damage at the entrance/exit of holes during the drilling of composite materials [18, 19]. The delamination rate is calculated using the ratio of the maximum observed diameter in the damage ( $D_{max}$ ) to the drill diameter ( $D$ ) during drilling, as given by the formula (1) below [3].

$$D_f = D_{max}/D \quad (1)$$

In order to calculate the delamination rate from the drilling process, images of all the hole exits were taken using a stereo microscope (10x magnification). To calculate the delamination rate, the images taken were processed in AutoCAD 2024 program by drawing circles appropriate to the damage caused. Figure 5 shows the drill diameter ( $D$ ) and the maximum diameter in the delamination zone ( $D_{max}$ ).



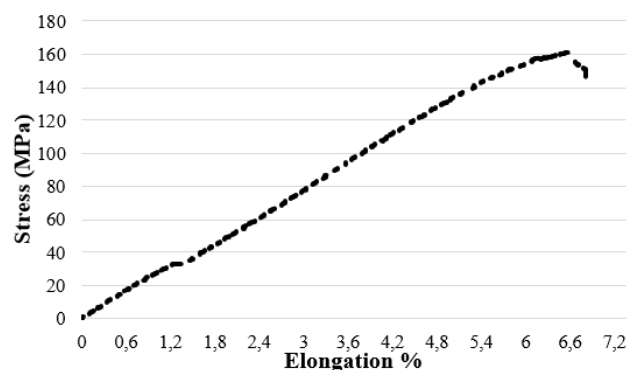
**Figure 5.** Demonstration of delamination factor a) schematic representation of delamination factor, b) view after drilling

## 3 FINDINGS AND DISCUSSION

In the study, hole exit damage in bi-directional and conventional hole drilling of glass fiber reinforced composite material was examined and compared. In the drilling process, tool rotational speeds were determined as 1500 and 3000 rpm, and tool feed rates were determined as 200, 400, 600, 800 and 1000 mm/min. The data obtained were compared and glass fiber reinforced composites were evaluated according to the hole drilling method.

### 3.1 Mechanical Properties of Glass Fiber Reinforced Composite

In composite material production, mechanical properties (type of resin, length and type of glass fiber, production technique, etc.) are influenced by many parameters. Tensile tests were conducted to determine the mechanical properties of glass fiber-reinforced composite materials. The stress-strain curve of the results closest to the average value obtained from the tensile test is shown in Figure 6. According to the tensile test results, the tensile strength was calculated as  $168.4 \pm 6.4$  MPa and the percent elongation as  $6.8 \pm 0.5$ . The hardness of the GFP material was determined to be  $234 \pm 2.1$  HV. Hardness measurements were conducted using an Insize HDT-LP200 Leeb portable device, and the tensile tests were performed with a 50-ton capacity Besmark tensile testing machine.



**Figure 6.** Stress-strain diagram of GRP material

### 3.2 Delamination Ratios

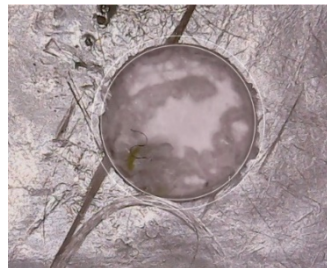
#### 3.2.1 Delamination Rate in Conventional Drilling Process

Table 2 presents the averages of delamination ratios for conventional glass fiber-reinforced composites at different feed rates and a tool rotational speeds. Figure 7 shows images of the samples with the lowest and highest delamination rates. After drilling, the lowest delamination rate was determined to be  $1.20 \pm 0.10$  in experiment number 2, and the highest delamination rate was determined to be  $1.42 \pm 0.08$  in experiment number 7. At a tool rotational speed of 1500 rpm, the delamination rate increased as the feed rate increased. At a tool rotational speed of 3000 rpm, it was determined that the delamination rate varied independently of the feed rate.

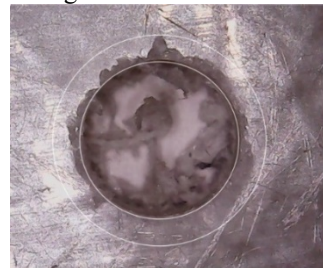
**Table 2.** Delamination rates in conventional (one-sided) drilling

Experimental Number	Rotational Speed (rpm)	Feed Rate (mm/min)	Traditional drilling
1	1500	200	$1.26 \pm 0.14$
2	1500	400	$1.20 \pm 0.10$
3	1500	600	$1.25 \pm 0.07$
4	1500	800	$1.35 \pm 0.14$
5	1500	1000	$1.33 \pm 0.26$
6	3000	200	$1.29 \pm 0.10$
7	3000	400	$1.42 \pm 0.08$
8	3000	600	$1.27 \pm 0.03$
9	3000	800	$1.35 \pm 0.02$
10	3000	1000	$1.35 \pm 0.07$

Traditional Drilling



Experimental Number 2:  
 $1.20 \pm 0.10$  (1500 rpm, 400 mm/min)



Experimental Number 7:  
 $1.42 \pm 0.08$  (3000 rpm, 400 mm/min)

**Figure 7.** The appearance of the holes in the samples with the lowest and highest delamination rates in the traditional drilling process

#### 3.2.2 Delamination Rate in Bi-directional Drilling Process

Table 3 provides the averages of delamination rate for glass fiber-reinforced composites in bi-directional drilling at different feed rates and tool rotational speeds. Figures 8, 9, and 10 show images of samples with the lowest and highest delamination rates in bi-directional drilling (1.5/3.5 mm, 2.5/2.5 mm, and 3.5/1.5 mm, respectively). For bi-directional drilling with 1.5 mm from the front surface and 3.5 mm from the back surface, the lowest delamination rate was determined to be  $1.22 \pm 0.3$  in experiment number 1, and the highest delamination rate was determined to be  $1.60 \pm 0.49$  in experiment number 8. The delamination rate increased up to a feed rate of 600 mm/min at both tool rotational speeds, but improvements were observed at feed rates of 800 and 1000 mm/min. Similar results were obtained at tool rotational speeds of 1500 and 3000 rpm with feed rates of 200 and 400 mm/min. In conventional drilling, while the delamination rate decreases with increasing cutting speed, the delamination rate increases with increasing feed rate [20]. The reason for this is that the layered structure at the hole exits is pushed rather than cut by the cutting tool. In bi-directional drilling, the layered structure is not forced at the hole exits, which reduces the effect of the tool feed rate.

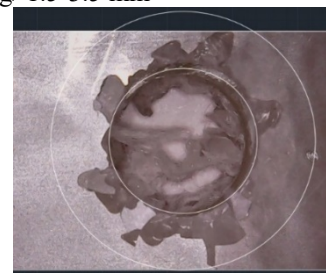
**Table 3.** Delamination ratios in bi-directional drilling process

Experimental Number	Rotational Speed (rpm)	Feed Rate (mm/min)	Bi-directional Drilling		
			1.5 mm / 3.5 mm	2.5 mm/ 2.5 mm	3.5 mm/1.5 mm
1	1500	200	1.22±0.3	1.25±0.14	1.22±0.10
2	1500	400	1.25±0.12	1.56±0.18	1.72±0.09
3	1500	600	1.56±0.23	1.75±0.32	1.75±0.21
4	1500	800	1.34±0.02	1.43±0.27	1.86±0.18
5	1500	1000	1.28±0.12	1.96±0.10	1.82±0.26
6	3000	200	1.25±0.13	1.18±0.16	1.34±0.27
7	3000	400	1.30±0.13	1.54±0.13	1.16±0.02
8	3000	600	1.60±0.49	1.53±0.15	1.60±0.37
9	3000	800	1.39±0.29	1.74±0.36	1.53±0.18
10	3000	1000	1.47±0.41	1.61±0.35	1.50±0.17

Bi-directional Drilling/ 1.5-3.5 mm



Experimental Number 1: 1.22±0.3  
(1500 rpm, 200 mm/min)

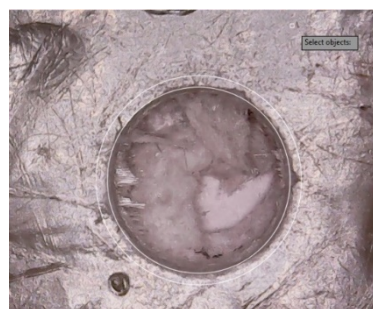


Experimental Number 8: 1.60±0.49  
(3000 rpm, 600 mm/min)

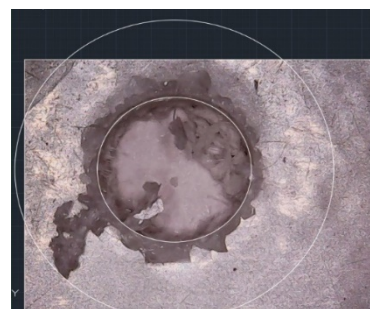
**Figure 8.** The appearance of holes in samples with the lowest and highest delamination rate for bi-directional drilling

For bi-directional drilling with 2.5 mm from the front surface and 3.5 mm from the back surface, the lowest delamination rate was determined to be 1.18±0.16 in experiment number 6, and the highest delamination rate was determined to be 1.96±0.10 in experiment number 5. The delamination rate increased with the increase in tool feed rate at both tool rotational speeds. A decrease in delamination rate occurred as the tool rotational speed increased from 1500 rpm to 3000 rpm.

Bi-directional Drilling/ 2.5-2.5 mm



Experimental Number 6: 1.18±0.16  
(3000 rpm, 200 mm/min)



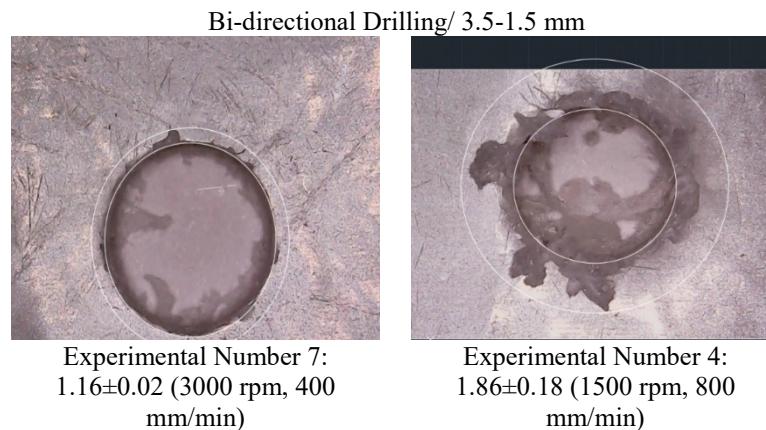
Experimental Number 5:  
1.96±0.10  
(1500 rpm, 1000 mm/min)

**Figure 9.** The appearance of the holes in the samples with the lowest and highest delamination rates in the bi-directional drilling process

For bi-directional drilling with 3.5 mm from the front surface and 1.5 mm from the back surface, the lowest delamination rate was determined to be 1.16±0.02 in experiment number 7, and the highest delamination rate was



determined to be  $1.86 \pm 0.18$  in experiment number 4. The delamination rate increased with the increase in tool feed rate at both tool rotational speeds. An decrease in delamination rate occurred with the increase in tool rotational speed (3000 rpm).



**Figure 10.** The appearance of the holes in the samples with the lowest and highest delamination rates in the bi-directional drilling process

### 3.3 Comparison of Delamination Rates Determined According to Drilling Method

The largest and smallest delamination rates observed at hole exits during the drilling of GRP materials using different drilling methods are presented in Figure 11. The lowest delamination rate (1.16) was determined in the bi-directional drilling with 3.5 mm from the front surface and 1.5 mm from the back surface. The highest delamination rate (1.96) was observed in bi-directional drilling with 2.5 mm from both the front and back surfaces. When examining the difference between the highest and lowest delamination rates, it was found that in samples drilled using the conventional method (1.42-1.20), the difference was calculated as 0.22. In bi-directional drilling, the differences were 0.38 (1.60-1.22), 0.78 (1.96-1.18), and 0.70 (1.86-1.16). This indicates that delamination values were narrower in range with the conventional drilling method. Composite materials drilled with 2.5 mm from both the front and back surfaces in bi-directional drilling were found to be the group most affected by drilling process parameters. In composite materials, there are many parameters that affect the quality of the hole. In the study, information about the manufacturing of the composite materials and the specific resin used is not shared by the manufacturer. Additionally, it is possible that while the upper surfaces hardened well during the curing process performed by the user, the desired level of hardening may not have been achieved in the lower surfaces. According to its application area, this situation can be considered acceptable. This is because the composite material is laid inside the pipe, inflated with air and cured with a curing robot. The cured GRP material will have its upper surface in contact with the fluid. For this reason, the manufacturer considers it sufficient for the material to cure the upper surfaces and reach a certain depth of hardness. However, it is understood that when a connection is attempted by drilling a hole, it may cause the material to deteriorate earlier than expected due to delamination damage.

Figure 11a shows that delamination decreases as the drilling depth from the bottom surface decreases. This indicates that the curing was completed before the subsurface reached full hardness. Figure 12 shows the delamination rates of GRP materials drilled with different drilling techniques according to the feed rate and tool rotational speed. It appears that process parameters have less impact on delamination in conventional drilling. It can be said that the reason for this is that in conventional drilling, heat accumulates during the drilling process and causes regional heating. In bi-directional drilling (1.5/3.5 mm), there was a rapid increase in the delamination rate at a feed rate of 600 mm/min at both tool rotational speeds. This increase in delamination rate decreased again at feed rates of 800 and 1000 mm/min. It was determined that the delamination rate increased with the increase in tool feed speed when 2.5 mm was drilled from the front and back surfaces. In bi-directional drilling (3.5/1.5 mm), the lowest delamination rate was obtained at 1500 rpm tool rotational speed and 200 mm/min feed rate, while the delamination rate increased with the increase of tool feed rate. When the tool rotational speed was 3000 rpm, a low delamination rate was obtained at a feed rate of 200 mm/min and 400 mm/min.

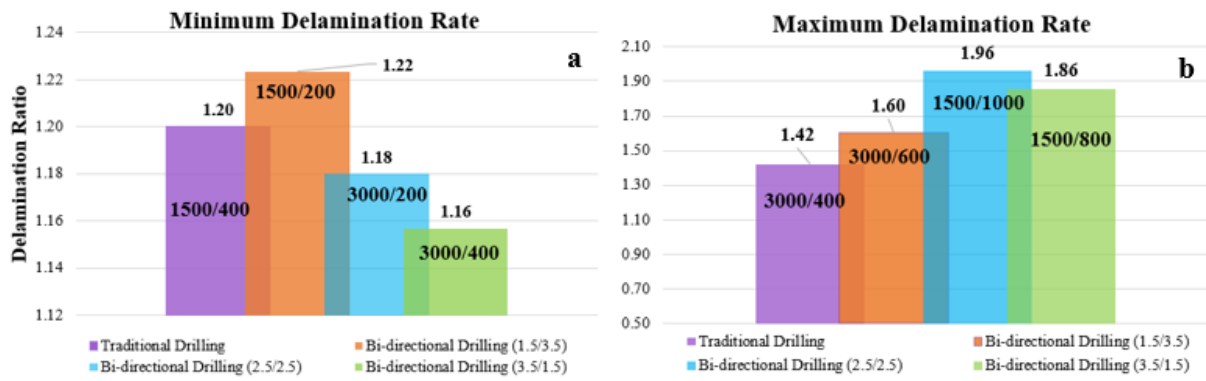


Figure 11. Minimum (a) and maximum (b) delamination rates of GRP with different drilling processes

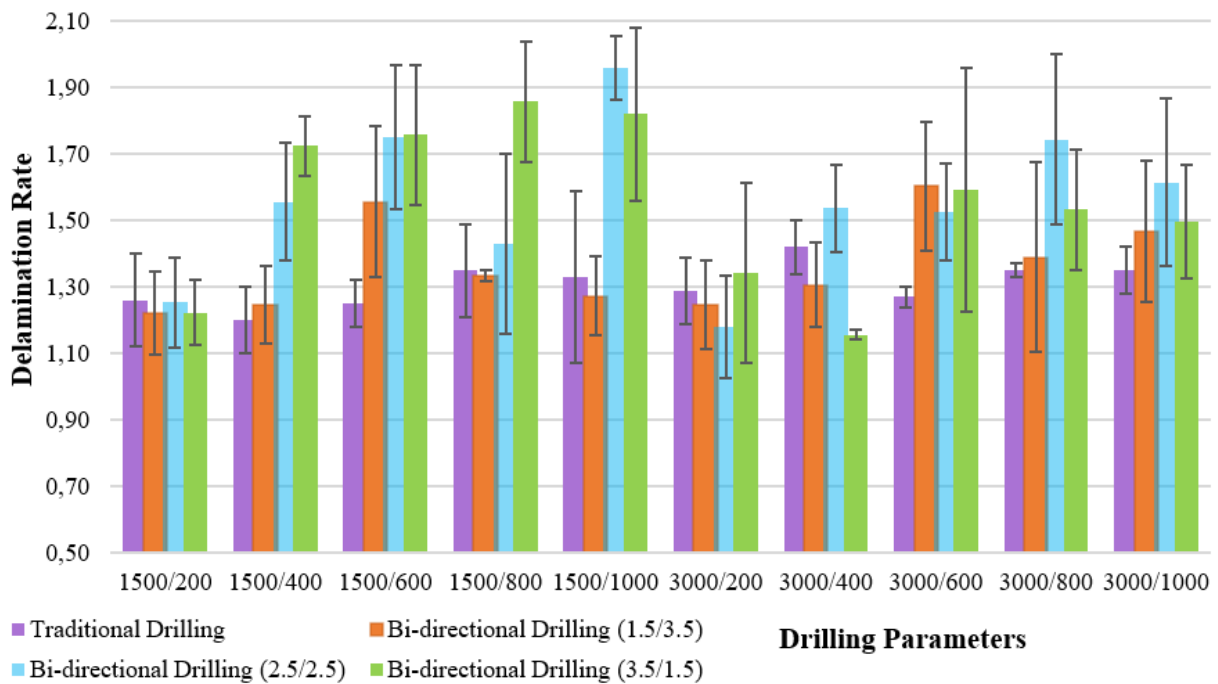


Figure 12. Delamination rates according to drilling method

## 4 RESULTS

GRP composites are widely used in industry due to their mechanical and thermal properties. Since composite materials consist of layers, errors occur during drilling operations that may disrupt their structural integrity. In the study, the drilling process of GRP composites was examined using bidirectional drilling as an alternative to conventional drilling. Five different feed rates (200, 400, 600, 800 and 1000 mm/min) and two different tool rotational speeds (1500 and 3000 rpm) were used in the drilling process. The results obtained are summarized below:

As a result of the tensile test, the tensile strength of the GRP material used was determined as  $168.4 \pm 6.4$  MPa and the hardness was determined as  $234 \pm 2.1$  HV.

In conventional drilling, the lowest delamination rate was determined to be 1.20 at 1500 rpm tool rotational speed and 400 mm/min feed rate. In bi-directional drilling, the lowest delamination rate was obtained as 1.16 at 3000 rpm tool rotational speed and 400 mm/min feed rate in drilling 3.5 mm from the front surface and 1.5 mm from the back surface.

The highest delamination rate in traditional drilling was determined to be 1.42 at a tool rotational speed of 3000 rpm and a feed rate of 400 mm/min. In bi-directional drilling (2.5/2.5 mm), it was determined to be 1.96 at a tool rotational speed of 1500 rpm and a feed rate of 1000 mm/min. There has been less variation in the delamination rate in samples drilled using the conventional drilling method. This is thought to be due to the heat generated

during drilling, which accumulates rather than dissipates throughout the drilling process, causing localized softening of the material.

## References

- [1] H. Ozer, "Surekli cam elyaf takvyeli termoplastik kompozit malzemelerin gelistirilmesi ve mekanik ozelliklerinin deneysel olarak belirlenmesi," M.S. thesis, Department Of Automotive Engineering, Bursa Uludag University, Bursa, 2015.
- [2] S. Bayraktar and Y. Turgut, "Elyaf takviyeli polimer kompozit malzemelerin delinmesi üzerine bir arastirma," in *3. Ulusal Talasli Imalat Sempozyumu*, pp. 4–5, 2012.
- [3] T. Bilge, A. R. Motorcu, and A. Ivanov, "Kompakt laminat kompozit malzemenin tungsten karbur takimlarla delinmesinde delaminasyon faktorunun degerlendirilmesi," *Pamukkale Universitesi Muhendislik Bilimleri Dergisi*, vol. 23, no. 4, pp. 427–436, 2017.
- [4] H. Ho-Cheng and C. Dharan, "Delamination during drilling in composite laminates," *J. Manuf. Sci. Eng.*, vol. 112, no. 3, pp. 236–239, 1990.
- [5] J. Babu, T. Sunny, N. A. Paul, K. P. Mohan, J. Philip, and J. P. Davim, "Assessment of delamination in composite materials: A review," *Proceedings of the Institution of Mechanical Engineers, Part B: Journal of Engineering Manufacture*, vol. 230, no. 11, pp. 1990–2003, 2016.
- [6] S. Sridharan, *Delamination Behaviour of Composites*, Elsevier, 2008.
- [7] J. Fernández-Pérez, J. Díaz-Álvarez, M. Miguélez, and J. Cantero, "Combined analysis of wear mechanisms and delamination in CFRP drilling," *Composite Structures*, vol. 255, art. no. 112774, 2021.
- [8] M. Baraheni, A. Tabatabaeian, S. Amini, and A. R. Ghasemi, "Parametric analysis of delamination in GFRP composite profiles by performing rotary ultrasonic drilling approach: Experimental and statistical study," *Composites Part B: Engineering*, vol. 172, pp. 612–620, 2019.
- [9] N. A. Shahkhosravi, J. Yousefi, M. A. Najfabadi, G. Minak, H. Hosseini-Toudeshky, and F. Sheibanian, "Static strength and damage evaluation of high speed drilled composite material using acoustic emission and finite element techniques," *Engineering Fracture Mechanics*, vol. 210, pp. 470–485, 2019.
- [10] A. Díaz-Álvarez, J. Díaz-Álvarez, N. Feito, and C. Santiuste, "Drilling of biocomposite materials: Modelling and experimental validation," *Simulation Modelling Practice and Theory*, vol. 106, art. no. 102203, 2021.
- [11] G. R. Devi and K. Palanikumar, "Analysis on drilling of woven glass fibre reinforced aluminium sandwich laminates," *Journal of Materials Research and Technology*, vol. 8, no. 1, pp. 1024–1035, 2019.
- [12] L. Gemi, S. Morkavuk, U. Koklu, and D. S. Gemi, "An experimental study on the effects of various drill types on drilling performance of GFRP composite pipes and damage formation," *Composites Part B: Engineering*, vol. 172, pp. 186v194, 2019.
- [13] F. Su, L. Zheng, F. Sun, Z. Wang, Z. Deng, and X. Qiu, "Novel drill bit based on the step-control scheme for reducing the CFRP delamination," *Journal of Materials Processing Technology*, vol. 262, pp. 157–167, 2018.
- [14] N. Khanna, K. Desai, and A. Sheth, "Industry supported experimental studies on drilling of thick multi-directional GFRP composite material," *Procedia CIRP*, vol. 77, pp. 320–323, 2018.
- [15] R. K. Sundaram, N. Sivashanmugam, D. Shameer, R. Deepak, and G. Saikrishnan, "Experimental investigation of mechanical properties and drilling characteristics on polymer matrix composite materials," *Materials Today: Proceedings*, vol. 43, pp. 1057–1063, 2021.
- [16] R. S. Anand and K. Patra, "Mechanistic cutting force modelling for micro-drilling of CFRP composite laminates," *CIRP Journal of Manufacturing Science and Technology*, vol. 16, pp. 55–63, 2017.
- [17] O. A. Pawar, Y. S. Gaikhe, A. Tewari, R. Sundaram, and S. S. Joshi, "Analysis of hole quality in drilling GLARE fiber metal laminates," *Composite Structures*, vol. 123, pp. 350–365, 2015.
- [18] F. Özkaya, F. Özen, E. İlhan, and S. Aslanlar, "Cam küre takviyeli polipropilen kompozit malzemelerin delaminasyon faktörünün deneysel olarak incelenmesi," *Afyon Kocatepe Universitesi Fen ve Muhendislik Bilimleri Dergisi*, vol. 19, no. 3, pp. 843–849, 2019.
- [19] N. Koboevic, M. Jurjevic, and Z. Koboevic, "Influence of cutting parameters on thrust force, drilling torque and delamination during drilling of carbon fibre reinforced composites," *Tehnicki Vjesnik*, vol. 19, no. 2, pp. 391–398, 2012.
- [20] E. Kirhasanoglu and Y. Turgut, "Karbon elyaf takviyeli kompozitlerin istifli delinmesinde delik cikis hasarinin deneysel arastirilmesi," *Gazi Muhendislik Bilimleri Dergisi*, vol. 7, no. 2, pp. 152–159, 2021.



## Using Shape Memory Alloys for Energy Harvesting Systems

Gokhan Kilic<sup>\*1</sup>, Omar Abboosh<sup>2</sup>

<sup>1</sup>Department of Basic Science, Naval Petty-Officer Vocational School, National Defence University, Yalova, Türkiye  
<sup>2</sup>Department of Environmental Health, College of Environmental Science and Technologies, University of Mosul, Mosul, Iraq

---

### Abstract

Shape memory alloys (SHA) have an important place in present and future energy conversion applications due to their reversible solid phase transformation capabilities. The main applications of these alloys are biomedical, aerospace, automobile, energy, electronics, construction and seismic. The main unique properties of shape memory alloys are the ability to recover the deformation without any external intervention even after high deformation (superelasticity) and the ability to recover the material after high deformation rates by heating (shape memory effect). The main reason for the shape recovery in both of the above properties is the solid phase transformations that take place within the material. Thanks to these properties, shape memory alloys are smart materials that are also used for energy harvesting. Vibration energy or thermal energy can be converted into electrical energy using shape memory alloys. At the same time, it allows the energy generated as waste energy to be used as electrical energy. In particular, studies on energy harvesting are carried out by integrating shape memory alloys with piezoelectric technology. In addition, magnetic shape memory alloys can be used to harvest energy without being integrated with other systems. The review also provides some preliminary information on energy harvesting systems with shape memory alloys and their operating principles. Finally, some directions for future work in this field are identified.

**Keywords:** *Energy harvesting, Shape memory alloys, Shape memory effect, Superelasticity*

---



## Analysis of Performance Values of Stabilizer Link Parts Produced by Additive Manufacturing Method in Automotive Suspension Systems

Sevilay Sagtan<sup>\*1</sup>, Burak Ates<sup>1</sup>

<sup>1</sup>R&D Center, Teknorot Automotive Products Industry and Trade Inc., Duzce, Türkiye

### Abstract

The automotive industry increasingly utilizes additive manufacturing (AM) for technological innovations and productivity gains, addressing issues like low-volume production, high mold costs, long lead times, and inventory requirements. This study examines the application of AM to the stabilizer link, a component of the automotive suspension and steering system, focusing on performance effects. Traditionally made with aluminium casting alloys, stabilizer links were produced using Selective Laser Melting (SLM) from AlSi10Mg powder, chosen for its high strength, low weight, and good machinability. Production parameters such as machine type, laser power, layer thickness, and scanning speed were meticulously determined. Post-production heat treatment was applied to enhance durability and optimize structural properties, reducing residual stresses. Performance analysis included surface roughness, axial clearance, torque measurement, tensile, compression, and life tests. Results showed that SLM-produced stabilizer links are superior in mechanical strength and lighter than conventionally cast parts. Positive outcomes in functional tests like surface roughness and ease of assembly indicate that AM will be crucial for the automotive industry, providing high quality, rapid production, and design flexibility.

**Keywords:** Automotive suspension systems, Additive manufacturing, Stabilizer link, Selective laser melting

## 1 INTRODUCTION

Additive manufacturing has emerged as an important innovation in the automotive industry in recent years. The advantages offered by the technology, such as low-volume production, reduced tooling costs and shorter lead times, are revolutionizing the production of automotive components [1]. For low-volume parts, additive manufacturing offers faster and economical advantages over conventional production methods [2]. Offering advantages in automotive applications to improve fuel efficiency and reduce emissions, additive manufacturing methods are a way to produce lightweight components without sacrificing high strength and durability [3]. The method can also produce products that clearly meet customer demand, eliminate warehousing needs and minimize lead time, especially for critical parts [4]. The application areas of the additive manufacturing method in the automotive sector are shown below.

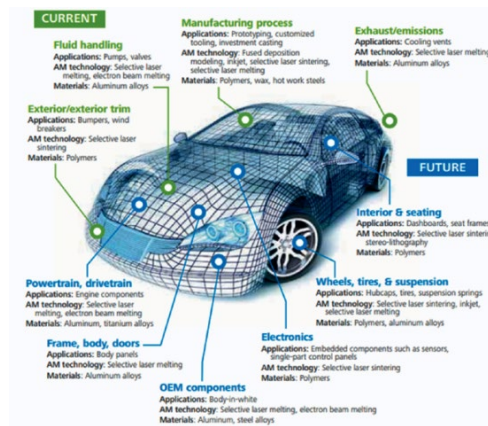


Figure 1. Additive manufacturing applications in automotive industry [5]

Industrial companies of many countries have introduced various additive manufacturing devices and methods. Different parameters are taken into account when classifying additive manufacturing methods. Accordingly, manufacturing processes are categorized into layers according to the chemical and physical events that occur

during production. These are classified as chemical processes, thermophysical processes, liquid jet processes, solid jet processes and ultrasonic processes [6]. Today, additive manufacturing methods are classified as liquid, filament, powder and solid sheet according to the starting material used [7]. Selective laser melting (SLM), one of the additive manufacturing techniques, is used in the production of components with complex internal structures. In this method, high-density parts are formed by melting the powders on the powder bed in a specific scanning direction using an energy source according to CAD data. The SLM method produces parts with fine microstructure due to its fast-cooling rate. Thanks to the advanced microstructure of the parts produced with SLM, they show superior mechanical properties. In addition, parts produced by SLM method exhibit higher density and superior performance compared to conventional production methods [8].

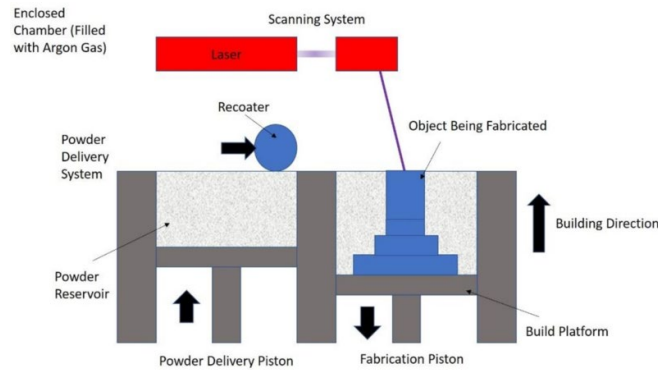


Figure 2. Selective laser melting (SLM) process [9]

Aluminum alloys are used in the aerospace, automotive, marine and medical sectors, as well as in a variety of applications that require special designs. SLM production technology is widely used in the production of Al-Si alloys as well as steel (such as Maraging steel, 316L), titanium, cobalt, copper and nickel alloys [10]. AlSi10Mg, one of the Al-Si alloys, stands out with its high mechanical properties and corrosion resistance and can be produced with a very good surface quality by additive manufacturing method. [11]. AlSi10Mg alloy is an aluminium alloy noted for its high mechanical properties and corrosion resistance. AlSi10Mg alloy also offers engineering properties such as low dimensional shrinkage, weldability, low weight ratio and machinability. When produced by additive manufacturing, a very smooth surface is obtained, and production is achieved without causing structural defects. AlSi10Mg alloys have weldability thanks to their high resistance to hot cracking. The laser beam used in the SLM process has a high power and scanning speed and creates a large temperature gradient during rapid solidification. This can lead to the formation of solidification defects such as pores, inclusions and cracks in the alloy structure. As a result, the alloys may exhibit poor ductility, fatigue and wear life at room temperature. [12]. In the studies carried out in the production with SLM method, the parameters are categorized under four main headings: laser, scanning, powder and temperature.

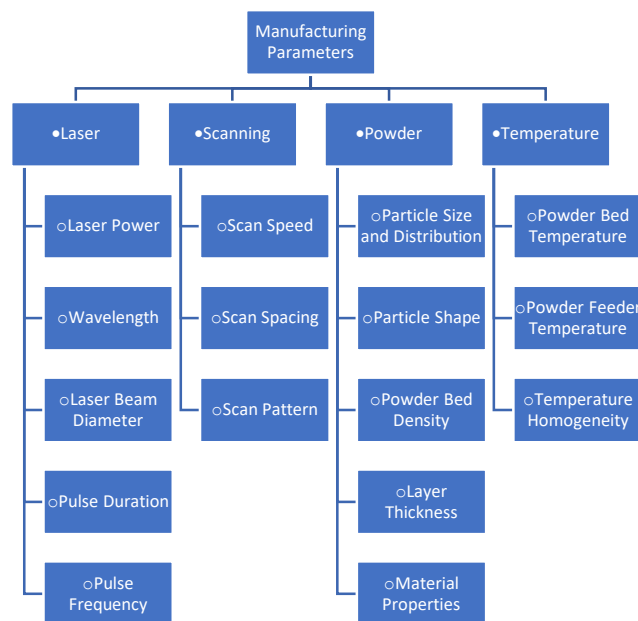
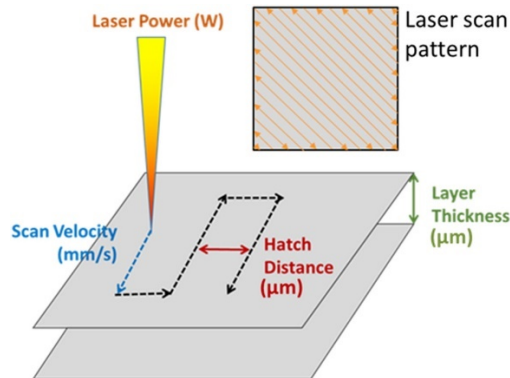


Figure 3. Classification of manufacturing parameters in SLM method

In the production of metal parts by SLM, the input parameters significantly affect the quality of the final product. Input parameters include laser power, scanning speed, scanning interval, layer thickness, scanning pattern, build direction and powder characteristics. Output parameters are defined as relative density, mechanical properties, surface roughness, geometrical accuracy and metallurgical structure [13].



**Figure 4.** Manufacturing parameters commonly used in laser powder bed fusion processes [8]

Surface quality greatly affects the service life of manufactured parts. Rough surfaces are known to adversely affect the fatigue performance of metallic materials. For this reason, high surface quality is preferred for parts that will operate under dynamic loads. While the SLM method offers significant advantages such as design flexibility and part quality, it still has some shortcomings in terms of surface quality. The surface roughness seen on parts produced by additive manufacturing is partly related to the adhesion of molten powder particles to the surface and the additive manufacturing process [14].

This study focuses on the effects of production parameters on product quality in the use of AlSi10Mg alloy in additive manufacturing and its applicability to the stabilizer link part, one of the automotive suspension components produced with cast aluminium alloy in the current production method. Surface roughness, tensile-compression and life tests were carried out to compare the performance of prototype additive manufacturing parts and stabilizer link parts produced with conventional casting alloys.

## 2 MATERIAL AND METHOD

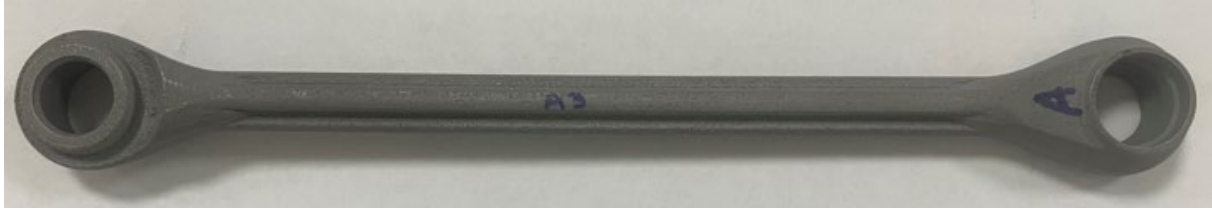
Automotive the stabilizer link part, which is one of the suspension components, is basically a ball joint (ball stud), plastic bearing, housing parts. Operation within Teknorot in order to compare functional requirements within the scope of a stabilizer link part with a high mold cost and low lot quantity has been selected. The body of the selected stabilizer link part has EN AC 43200 material and is produced by aluminum injection method. Same body Selective Laser Production from AlSi10Mg material by smelting (SLM) method in the table below parameters.

**Table 1.** Additive manufacturing production parameters of AlSi10Mg samples

Machine Manufacturer	Model	Preheating	Production Rate	Laser Power	Layer Thickness	Scan Rate	Heat Treatment After Production
SLM Solutions	280 2.0	150 °C	24.5 cm <sup>3</sup> /h	350-370 Watt	30 µm	300-500 mm/s	2 hours at 300 °C normalization



**Figure 5.** EN AC 43200 stabilizer link body manufactured with aluminum injection



**Figure 6.** Stabilizer link body manufactured with AlSi10Mg SLM method

Products produced by SLM method have high strength properties thanks to their advanced microstructure. Tensile tests were performed on tensile bar samples produced by aluminum injection and tensile bar samples produced by SLM and the results are as shown in the table below.

**Table 2.** Yield and tensile test Results

Mechanical Properties	Tensile Specimen Produced by Aluminum Injection	Tensile Specimen Produced by SLM Method
Yield Strength (MPa)	180	252
Tensile Strength (MPa)	240	380

In the stabilizer link part, which is exposed to variable loads on more than one axis during operation in vehicles, surface roughness values have an important place in performance values for the life of the part. Surface roughness values are expected to be optimum in order to prevent cracks, notch effect and breakage of the part over time or with instantaneous loads. Measurements were taken from the parts of the produced parts shown in the figure.



**Figure 7.** Measurement region of surface roughness values

The surface roughness results obtained from the prototypes produced are as shown in the table below.

**Table 3.** Surface roughness values of manufactured bodies

Product No	Aluminum Injection Manufactured Body	Body Manufactured with SLM Method
	Rz (µm)	Rz (µm)
1	10.279	12.841
2	14.699	14.710
3	12.460	10.544
4	7.907	13.428
5	10.751	12.330
6	9.263	15.080

Within the scope of the study, the bodies produced with aluminum injection and SLM were assembled with the same assembly parameters.



**Figure 8.** Stabilizer link part produced by aluminum injection





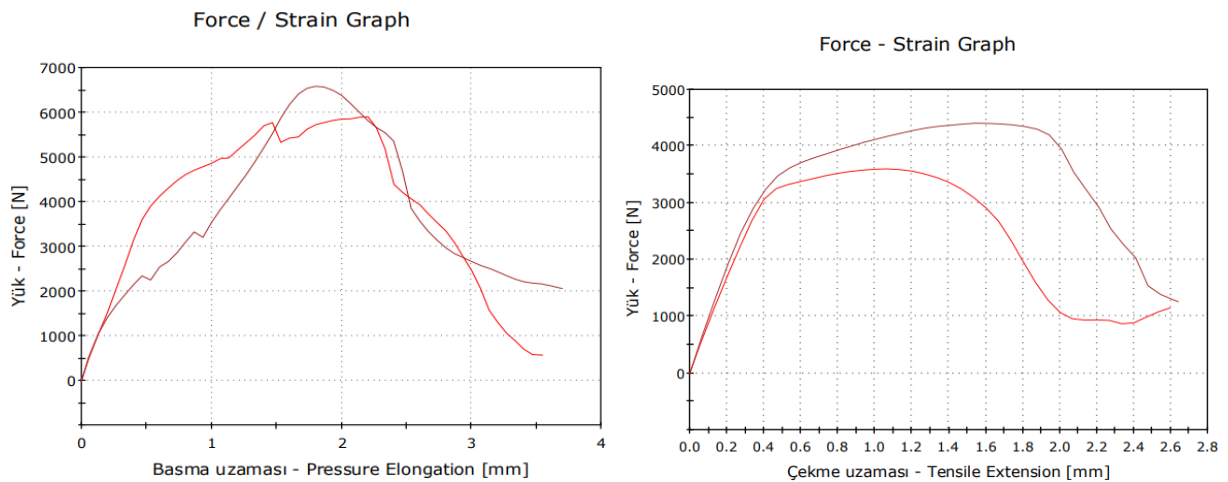
**Figure 9.** Stabilizer link part produced with SLM

During vehicle driving, the ball joint in the stabilizer link part is expected to operate by tilting in the desired axis and angle. During operation, frictional stresses occur in oscillation and rotation movements. These stresses are called torque and low torque values are desired during oscillation and rotation. In addition, in order to ensure driving comfort and long part life, it is desired to have a low clearance value in the ball joint axis in the ball joint, plastic bearing and body assembly. The functional test results applied to the prototype samples are as follows.

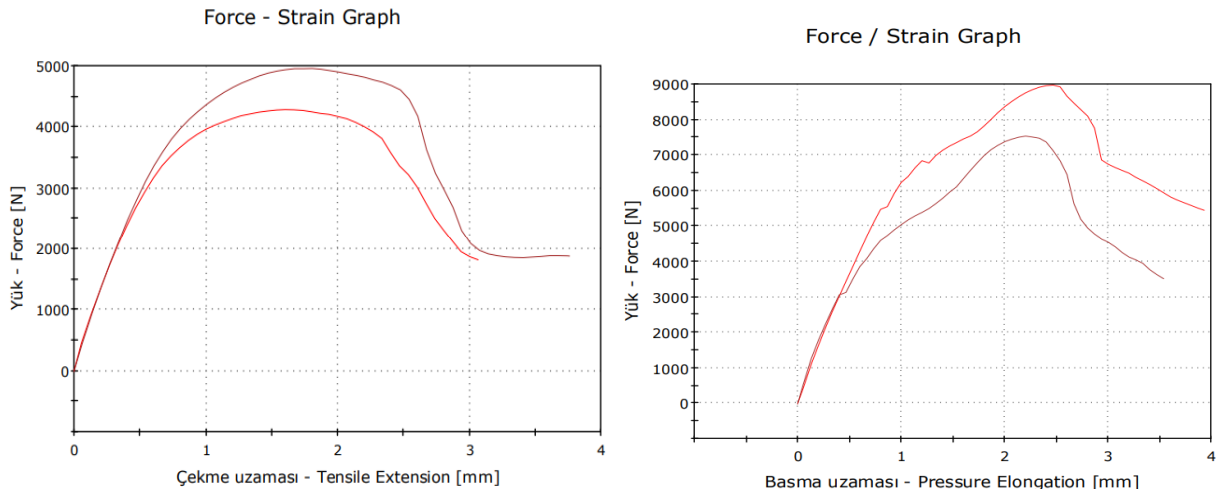
**Table 4.** Functional test results

Functional Tests	Stabilizer Link Part Produced by Aluminum Injection			Stabilizer Link Part Produced with SLM		
	Sample 1	Sample 2	Sample 3	Sample 1	Sample 2	Sample 3
Oscillation Torque (Nm)	1.1	1.2	1.3	0.9	1	0.8
Oscillation Breakdown Torque (Nm)	3.9	3.4	4	3	2.5	2,6
Rotational Torque (Nm)	1.6	1.4	1.6	1	0.8	1.2
Rotational Breakdown Torque (Nm)	2.4	2	2.8	1.6	1.2	2
Axial Gap (mm)	0.127	0.128	0.112	0.143	0.154	0.146

During driving, the stabilizer link part is subjected to loads on the ball joint axis. In order to ensure driving safety, ball stud pull-out and ball stud push-out tests are performed for the ball joint. Although the results are directly applied to the ball joint, the data reveals the mechanical strength of the body material. The graphs of the ball joint pull-out and push-out results are shown in the picture below.



**Figure 10.** Tensile and compression test results of stabilizer link parts produced by aluminum injection

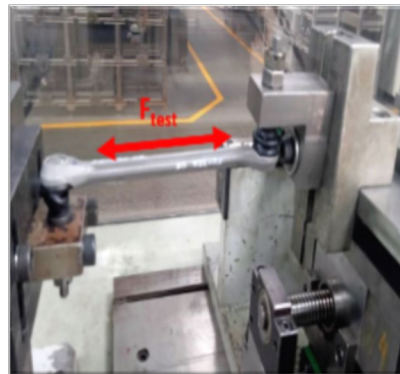


**Figure 11.** Tensile and compression test results of stabilizer link parts manufactured with SLM

**Table 5.** Ball joint compression and tensile tests

Functional Tests	Stabilizer Link Part Produced by Aluminum Injection		Stabilizer Link Part Produced with SLM	
	Sample 1	Sample 2	Sample 1	Sample 2
Ball Joint Compression (N)	5901.68	6578.42	8966.71	7530.76
Ball Joint Tension (N)	3592.09	4393.23	4286.38	4953.7

During driving, the stabilizer link part is not only subjected to static loads, but also to dynamic loads. This results in fatigue of the part. After fatigue, fractures may occur in the body of the stabilizer link part or in the ball joint. A life test is performed to see the fatigue strength of the part. There should be no breakage as a result of the test. At the same time, low rotational torque and low axial clearance values are required in order not to adversely affect driving comfort. Single axis stabilizer link life test parameters were tested with 2,000,000 cycles, 2000 N load and 5 Hz Frequency in accordance with the connection type in the picture below.



**Figure 12.** Single axis stabilizer link life test connection shape

**Table 6.** Lifetime test results

Functional Tests	Stabilizer Link Part Produced by Aluminum Injection		Stabilizer Link Part Produced with SLM	
	Before Test	After Test	Before Test	After Test
Rotational Torque (Nm)	1.8	1.2	2	0.8
Rotational Breakdown Torque (Nm)	4	2.4	3	1.2
Axial Gap (mm)	0.096	0.1	0.148	0.219

### 3 RESULTS

According to the results of the study, significant differences were observed between the stabilizer link part produced by the SLM (Selective Laser Melting) method and the stabilizer link part produced by the traditional aluminium injection method.

- **Surface Roughness:** The bodies produced by both methods have low surface roughness and there is no need for machining to improve the surface quality.
- **Assembly and Weight:** The bodies produced by the SLM method did not encounter any problems during assembly. In addition, the weight of the bodies produced by this method is lower than the bodies produced by aluminium injection.
- **Functional Tests: Ball Joint Compression and Tensile Tests:** The ball joint compression and tensile strengths of stabilizer link parts produced by SLM method are higher than those produced by aluminium injection molding.
- **Life Test:** In the single axis stabilizer link life test, the values of the stabilizer links produced by SLM and the part produced by aluminium injection molding method are close. The results of both parts are acceptable in terms of stabilizer link manufacturability.

Although low surface roughness is achieved in both methods, the SLM method does not require additional machining operations, which speeds up the production process and reduces costs. The lighter weight of the parts produced with SLM can reduce the overall weight of vehicles and improve fuel efficiency. Moreover, the lack of problems during assembly demonstrates the practicality of this method. In addition, reducing material wastage and increasing energy efficiency during the manufacturing process makes SLM an environmentally friendly option by reducing the carbon footprint. Functional tests have shown that parts produced with SLM have higher mechanical strength and perform better in life tests. The SLM method offers fast and flexible production without the need for high mold costs and long production runs. This is a great advantage especially in low-volume production. In addition, the lighter and more durable parts produced with the SLM method indicate that additive manufacturing may be used more widely in the automotive industry in the future. In addition, the SLM method draws attention with its superiority in the production of complex geometries and detailed internal structures. This method enables the realization of designs that are not possible with traditional manufacturing techniques, offering innovative and efficient solutions in the sector. In the coming period, with the developments in SLM technology, it will be possible to produce much more complex and optimized parts in the automotive industry, which will create a significant transformation in the industry.

### 4 CONCLUSION

The stabilizer link part produced with Selective Laser Melting (SLM), which is an additive manufacturing method, meets the functional requirements of the stabilizer link part produced with aluminium, such as torque, axial clearance, ball joint protrusion and compression, life test, surface roughness. With the additive manufacturing method, products in the desired geometry can be produced quickly without waiting for high mold costs and mold production deadlines.

Since the weight of the products produced with the additive manufacturing method is less than the products produced according to traditional production methods, it contributes to reducing the carbon footprint and achieving green consensus. Since the additive manufacturing method produces lightweight and high-strength products, it will play an important role in the future of the automotive industry and will replace many traditional production methods, especially casting.

### Acknowledgments

This work was supported and funded by Teknorot Otomotiv Ürünleri Sanayi ve Ticaret A.Ş. We would like to thank Eskişehir Design and Innovation Center (ETIM) for their valuable contribution for prototype production.

### References

- [1] Gibson, D. Rosen, and B. Stucker, *Additive Manufacturing Technologies - 3D Printing, Rapid Prototyping, and Direct Digital Manufacturing*, Springer, 2015.

- [2] H. Bikas, P. Stavropoulos, and G. Chryssolouris, "Additive manufacturing methods and modelling approaches: a critical review," *The International Journal of Advanced Manufacturing Technology*, vol. 83, pp. 389–405, 2016.
- [3] T. D. Ngo, A. Kashani, G. Imbalzano, K. T. Nguyen, and D. Hui, "Additive manufacturing (3D printing): A review of materials, methods, applications and challenges," *Composites Part B: Engineering*, vol. 143, pp. 172–196, 2018.
- [4] T. T. Wohlers and T. Caffrey, "3D printing and additive manufacturing state of the industry annual worldwide progress report," Wohlers Associates, Fort Collins, Col., 2014.
- [5] G. Ozer, "Eklemeli imalat teknolojileri uzerine derleme," *Nigde Omer Halisdemir Universitesi Muhendislik Bilimleri Dergisi*, vol. 9, no. 1, pp. 606–621, 2020.
- [6] N. Guo and M. C. Leu, "Additive manufacturing: technology, applications and research needs," *Frontiers of Mechanical Engineering*, vol. 8, pp. 215–243, 2013.
- [7] J.-P. Kruth, M. Leu, and T. Nakagawa, "Progress in Additive Manufacturing and Rapid Prototyping," *CIRP Annals*, vol. 47, no. 2, pp. 525–540, 1998.
- [8] Y. Siyambas and Y. Turgut, "Defects, mechanical properties and surface roughness of AlSi10Mg alloy," *Gazi University, Journal of Science*, vol. 10, no. 2, pp. 368–390, 2022.
- [9] L. Jiao, Z. Y. Chua, S. K. Moon, and J. Song, "Femtosecond laser produced hydrophobic hierarchical structures on additive manufacturing parts," *Nanomaterials*, vol. 8, no. 8, art. no. 601, Aug. 2018.
- [10] J. H. Martin, B. D. Yahata, J. M. Hundley, J. A. Mayer, T. A. Schaedler, and T. M. Pollock, "3D printing of high-strength aluminium alloys," *Nature*, vol. 549, pp. 365–369, 2017.
- [11] H. Kahramanzade, Y. Sert, and T. Kucukomeroglu, "Surtunme karistirma isleminin eklemeli imalat yontemi ile uretilen AlSi10Mg alasiminin tribolojik ozelliklerine etkisi," *Avrupa Bilim ve Teknoloji Dergisi*, vol. 28, pp. 1159–1166, 2021.
- [12] M. Tang and P. C. Pistorius, "Oxides, porosity and fatigue performance of AlSi10Mg parts produced by selective laser melting," *International Journal of Fatigue*, vol. 94, no. 2, pp. 192–201, 2017.
- [13] B. Duman and C. Kayacan, "Dogrudan metal lazer sinterleme/ergitme yontemi ile imal edilecek parcanin mekanik ozelliklerinin tahmini," *Teknik Bilim Dergisi*, vol. 7, no. 1, pp. 12–28, 2017.
- [14] W. J. Sames, F. A. List, S. Pannala, R. R. Dehoff, and S. S. Babu, "The metallurgy and processing science of metal additive manufacturing," *International Materials Reviews*, vol. 61, no. 5, pp. 315–360, 2015.
- [15] W. E. Frazier, "Metal Additive Manufacturing: A Review," *Journal of Materials Engineering and Performance*, vol. 23, pp. 1917–1928, 2014.
- [16] S. Sun, M. Brandt, and M. Easton, "Powder bed fusion processes: An overview," in *Laser additive manufacturing: materials, design, technologies, and applications*, M. Brandt, Ed.: Woodhead Publishing, 2017, Chapter 2, pp. 55–77.



## Gradient Graphene Sponge for Solar Steam Generation Applications

Kader Dagci Kiransan<sup>\*1</sup>, Ezgi Topcu<sup>1</sup>, Elif Ercarikci<sup>1</sup>

<sup>1</sup>Department of Chemistry, Science Faculty, Ataturk University, Erzurum, Türkiye

### Abstract

The expectation from the materials used in solar steam generators is that it provides clean water with high efficiency and low cost from direct natural sunlight [1]. The focus for this purpose is to develop materials with both cost-effective and easy scalabilities that can efficiently absorb sunlight and convert it into thermal energy [11]. Recently, metallic nanoparticles such as gold [2] and alumina [3] have been frequently investigated for clean water production in SSG, but their possible practical applications are limited due to their high cost, complex manufacturing processes, and potential safety issues [4]. At this point, 3D graphene sponges with high sunlight absorption and thermal insulation appear as an effective candidate for the photothermal conversion mechanism [5]. Herein, we successfully prepared a 3D graphene sponge material (GSM) possessing hydrophobic character and then brought it into a hydrophilic-hydrophobic gradient structure by a simple acid impregnation method. In this gradient graphene sponge material (GGSM), while the gradient structure provides a fast and effective water transport performance, a high rate of sunlight absorption and photothermal transformation. Compared with GSM, GGSM showed a higher water vapor conversion and steam evaporation efficiency owing to the gradient structure.

**Keywords:** Solar steam generators, Graphene sponge, Gradient material

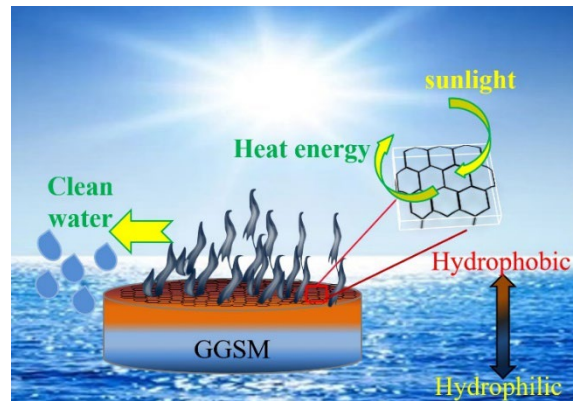


Figure 1. Representative illustration of the use of GGSM in a SSG

### Acknowledgments

This study was supported by TÜBİTAK under project no: 121M347.

### References

- [1] M. Elimelech and W. A. Phillip, "The future of seawater desalination: Energy, technology, and the environment," *Science*, vol. 333 pp. 712–717, 2011,
- [2] L. Zhang, B. Tang, J. Wu, R. Li, and P. Wang, "Hydrophobic light-to-heat conversion membranes with self-healing ability for interfacial solar heating," *Adv. Mater.*, vol. 27, pp. 4889–4894, 2015.
- [3] L. Zhou, Y. Tan, J. Wang, W. Xu, Y. Yuan, W. Cai, S. Zhu, and J. Zhu, "3D self-assembly of aluminium nanoparticles for plasmon-enhanced solar desalination," *Nat. Photonics*, vol. 10, pp. 393–398, 2016.
- [4] K. Bae, G. Kang, S. K. Cho, W. Park, K. Kim, and W. J. Padilla, "Flexible thin-film black gold membranes with ultrabroadband plasmonic nanofocusing for efficient solar vapour generation," *Nat. Commun.*, vol. 6, art. no. 10103, 2015.
- [5] X. Li, W. Xu, M. Tang, L. Zhou, and J. Zhu, "Graphene oxide-based efficient and scalable solar desalination under one sun with a confined 2D water path," *Proc. Natl. Acad. Sci.*, vol. 113, no. 49, pp. 13953–13958, 2016.



## Investigation of the Effect of Current Density on Ammonia Formation from Ammonium Chloride and Sodium Chloride in Two-Compartment Bipolar Membrane Electrodialysis

Duygu Adiguzel<sup>\*1</sup>, Fatemeh Abbasi<sup>1</sup>, Osman Nuri Ata<sup>1</sup>

<sup>1</sup>Chemical Engineering, Ataturk University, Erzurum, Türkiye

### Abstract

In this study, it was aimed to convert synthetically prepared feed solution containing NaCl and NH<sub>4</sub>Cl into ammonia in the bipolar membrane (BMED) process. The Solvay process, which is one of the soda production processes, has an increasing waste problem that cannot be solved and has started to cause great damage to the environment. The feasibility of using two-compartment bipolar membrane electro dialysis (BMED) process instead of distillation unit where ammonia is recovered and abundant liquid and solid wastes are generated in synthetic soda production was investigated. The effect of current/voltage on ammonia formation in the bipolar membrane electro dialysis system was investigated. BMED processes are systems that work on the principle of migration of ions to the relevant compartments under the influence of an electric field. In these systems, which enable the separation of water into its ions, simultaneous acid and base production takes place while the purification process is carried out. Using these features of the BMED system, simultaneous acid and base production was realized from ammonium chloride and sodium chloride solutions. In this study, the BMED cell was designed according to the BPM//ADM//BPM configuration and as a two-compartment six-repeat cell. The initial feed concentrations were kept constant and NH<sub>4</sub>OH (base) and HCl (acid) were produced at current densities of 50 A/m<sup>2</sup>, 75 A/m<sup>2</sup>, 100 A/m<sup>2</sup>. The results obtained showed that varying current densities affected the acid and base concentrations achieved. It was found that acid and base concentrations increased with increasing current density. At current densities of 50 A/m<sup>2</sup> and 100 A/m<sup>2</sup>, the NH<sub>4</sub>OH conversion rate increased by about 22%, while the acid conversion increased by more than 30% at the same current densities. The results showed that the BMED process can be used instead of the distillation unit in the SOLVAY process and waste problems can be solved to a great extent.

**Keywords:** Solvay process, Soda, Bipolar membrane electro dialysis

## 1 INTRODUCTION

In the industry, sodium carbonate is known as sodium carbonate. Soda ash, which has numerous applications, is extensively utilized in various industries such as glass, detergent, paper, automotive, construction, and water treatment. While its usage areas are so widespread, its production is also quite high in the world. According to the information gathered in 2023, China topped the list with 29 million tons of soda ash, followed by Turkey and the United States.

Soda ash is made by the 'Solvay Process'. It is one of the world's most widely used methods for making synthetic soda. So much so that the Solvay process carries out 46% of soda ash production by synthetic methods. The Solvay process's numerous advantages have led to its widespread use. The Solvay process has many advantages. These include easy access to raw materials. Also, low energy costs and recycling most of the ammonia used.[1, 2]. But, the world is developing and changing. So, these Solvay process advantages have started to become less important. Especially with global warming, which is widespread. The solid, liquid, and gaseous wastes released in the Solvay process have started to be seen as a threat. The Solvay process, also called the ammonia-soda process, makes liquid waste. It happens during the ammonia recovery phase. Distillation waste (DW) is the largest waste among all the wastes. The Solvay process produces 10 m<sup>3</sup> of distillation waste for every 1 tonne of soda obtained [3]. This distillation waste generally contains NH<sub>4</sub>Cl, NaCl and a large proportion of CaCl<sub>2</sub>. It has been reported that for 1 million tonnes of soda produced each year, the amount of CaCl<sub>2</sub> in the waste is more than 1 million tonnes and the NaCl content is more than 400,000 tonnes [4]. This waste, which has a dense content, is discharged directly into open water sources or waste collection ponds without any treatment [5]. This situation not only causes environmental pollution but also damages the ecosystem in open water sources and harms the living organisms in the water. However, this waste, which causes pollution in water resources, may also cause water scarcity in the

future [6]. Many methods have been studied by different researchers to minimize the negative conditions caused by this waste. However, the easy availability of  $\text{CaCl}_2$  and low market demand have put the studies on the back burner [7].

$\text{Ca(OH)}_2$  for ammonia recovery is obtained by calcination of  $\text{CaCO}_3$ . Along with  $\text{Ca(OH)}_2$ ,  $\text{CO}_2$  gas is also obtained at this stage for carbonation process. However, it is known that not all of the  $\text{CO}_2$  gas produced is used and approximately 0.2 - 0.4 tonnes of  $\text{CO}_2$  is released to the atmosphere for every 1 tonne of soda production [8]. This is quite a lot, considering that  $\text{CO}_2$  is the most potent greenhouse gas in terms of global warming. In addition, 950 - 1100 °C heat is required to carry out the calcination process [9]. Significant energy is required to reach the necessary heat during this stage. It is recognized that the highest energy consumption in the Solvay process occurs here, with 33% of the total energy consumed in the process being used at this stage [4].

The wastes generated in the Solvay process, the damage of these wastes to the ecosystem, high amounts of energy consumption, and insufficient studies have led to new researches in this field. The most striking among these studies are the studies carried out with bipolar membrane electro dialysis (BMED) processes, which are frequently used in recent years and are an electrochemical method. BMED processes are processes that allow simultaneous acid and base production as well as purification processes. Öner, et al. [10], in their study, it was stated that the BMED system was considered an alternative to the distillation unit and could be integrated into the Solvay process. In another study Dursun, et al. [11], BMED system was considered an alternative to the distillation unit and could be integrated into the Solvay process. Lv, et al. [12] ve Li, et al. [13] in their study, it was stated that the BMED system was aimed to achieve simultaneous HCl and  $\text{NH}_4\text{OH}$  production in the BMED process using  $\text{NH}_4\text{Cl}$ -containing solutions. The goal also included the purification of the  $\text{NH}_4\text{Cl}$ -containing solution. During the studies, high desalination rates and reaching the targeted acid-base concentrations were observed. Additionally, the BMED process demonstrated low energy consumption, which is noteworthy. BMED system was considered an alternative to the distillation unit and could be integrated into the Solvay process.

In this study, it was aimed to produce  $\text{NH}_4\text{OH}$  and HCl from  $\text{NH}_4\text{Cl}$  and NaCl containing solution by using BMED process instead of distillation unit in Solvay process. Recovery of ammonia and avoidance of distillation waste was investigated with the BMED cell designed as two compartments.

## 2 MATERIAL AND METHOD

### 2.1 Reagent and Membranes

$\text{NH}_4\text{Cl}$  - NaCl for the feed tank, HCl for the acid tank and NaOH for the electrolyte tank of the solutions prepared for use in the BMED system were supplied by Merck.

The electro dialysis system manufactured by PCCell GmbH, Heusweiler, Germany was used for the BMED process. PCCell BED 1-4 model BMED system was used in the system where hardware and software programmes are available together. Anion exchange membrane (PC Acid 60) and bipolar membranes and spacers (ED 640004) were supplied from PCCell for use in the BMED cell. The BMED cell, which consists of an anode and cathode end, was provided with an electric field with the help of a DC power supply. In addition to the anode and cathode, experiments were performed in a two-compartment cell with 6 repeats.

### 2.2 Definition of Experimental Set up and BMED Experiments

In addition to the BMED cell consisting of the feed and acid compartments, there is an electrolyte compartment that provides electrical conductivity. The solution tanks of each compartment in the system were filled with 1 liter of simulated solutions. NaCl -  $\text{NH}_4\text{Cl}$  solution was prepared for the feed tank, HCl solution for the acid tank, and NaOH solution for the electrolyte tank. The experiments were carried out by transporting the solution ions in the tanks to the relevant compartments under the applied electric field. The ion transfer in the BMED cell for this study is shown in Figure 1.

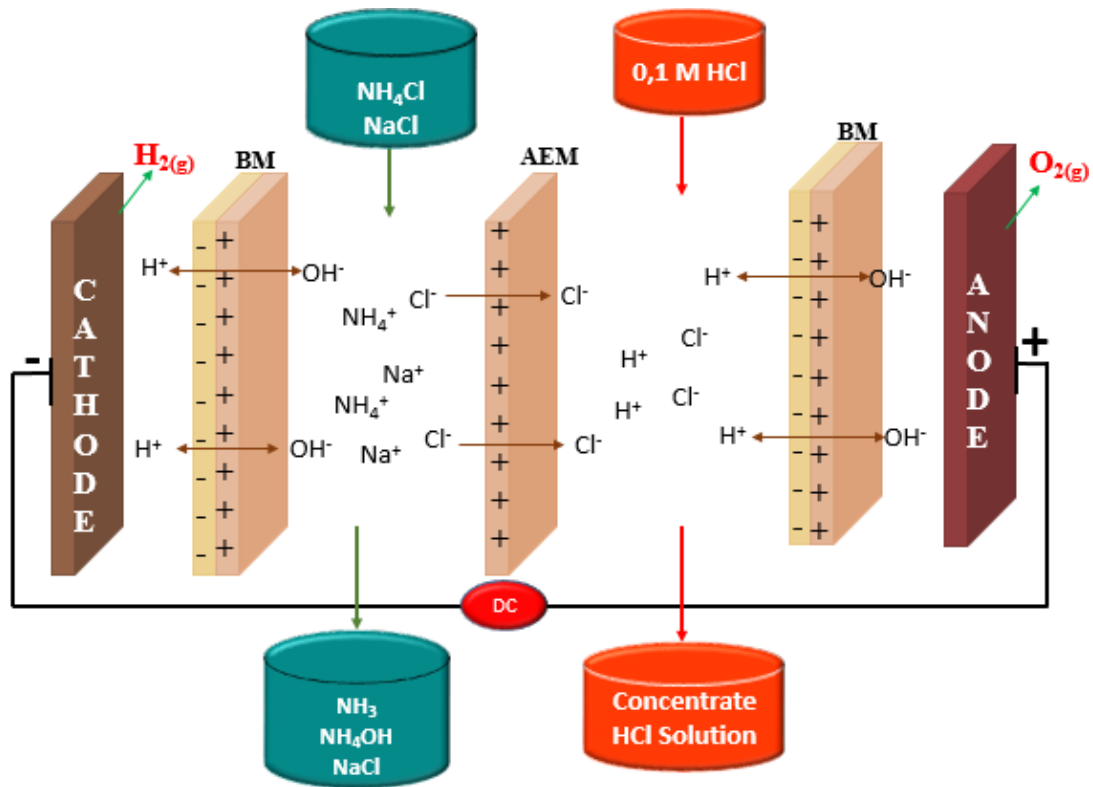


Figure 1. BMED system

The experimental parameters of this study, in which acid-base concentrations and conversions were determined as performance criteria, are given in Table 1.

Table 1. Experimental parameters and their levels

	3.2 A (50 A/m <sup>2</sup> )	4.8 A (75 A/m <sup>2</sup> )	6.4 A (100 A/m <sup>2</sup> )
Initial Feed Concentration	170 g NH <sub>4</sub> Cl + 70 g NaCl	170 g NH <sub>4</sub> Cl + 70 g NaCl	170 g NH <sub>4</sub> Cl + 70 g NaCl
Initial Acid Concentration	0.1 M HCl	0.1 M HCl	0.1 M HCl
Initial Electrolyte Concentration	1.5 M NaOH	1.5 M NaOH	1.5 M NaOH
Flow Rate	10 l/h	10 l/h	10 l/h
Temperature	25 °C	25 °C	25 °C

### 2.3 Data Analysis

During the experiments, acid and base determinations were carried out every 30 minutes by wet methods. For acid concentration determination, 1 ml of solution taken from the acid tank was diluted with distilled water and titrated with 0.1 M HCl solution. For base concentration, 1 ml of solution taken from the base tank was diluted with distilled water and titrated with 0.1 M NaOH solution. The acid-base concentrations and conversions were calculated by using Equation 1 and Equation 2 [14].

$$C_i = \frac{n_{i,t}}{V_{i,t}} \quad (1)$$

$C_i$ ; final acid or base concentration (mole/l),  $n_{i,t}$ ; final acid or base amount (mole),  $V_{i,t}$ ; final acid or base tank volume (l)

$$\% \text{ Conversion} = \frac{C_{i,t} - C_{i,0}}{C_{total}} \quad (2)$$

$C_{i,t}$ ; final acid or base concentration (M),  $C_{i,0}$ ; initial acid or base concentration (M),  $C_{total}$ ; total acid or base concentration for the total salt conversion (M)



### 3 RESULTS

It has been stated that in BMED process, acid and base production can be realised simultaneously through bipolar membranes (BM). Bipolar membranes are double layer membranes consisting of anion exchange and cation exchange surfaces. In addition, these membranes allow the dissociation of water into  $H^+$  and  $OH^-$  ions under an electric field [11]. In addition, ions are transported to the relevant compartment by anion exchange membranes (AEM) in the BMED cell and acid formation occurs

In this study, acid-base formation from feed solution containing  $NH_4Cl$  and  $NaCl$  with the help of BMED process was investigated by considering different current densities. In the experiments, acid-base concentrations and conversions were determined.

#### 3.1 Acid Concentration and Conversion

In this study with a two-compartment BMED cell, HCl production as acid is observed. The variation of acid amounts (moles) versus time in experiments performed at different current values (3.2 A // 4.8 A // 6.4 A) is given in Figure 2.

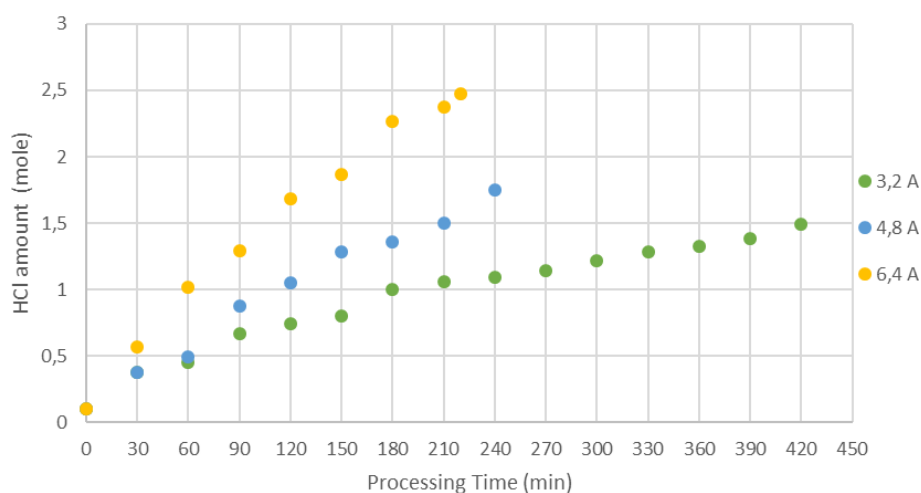


Figure 2. The amount of acid produced with processing time

Based on Figure 2, the concentration of acid increased over time. The study refers to two compartments: the feed and acid compartments, separated by an AEM. In the solution, the  $Cl^-$  anion from  $NH_4Cl$  and  $NaCl$  in the feed tank passes through the AEM and moves towards the acid tank. There, it combines with  $H^+$  ions from BM to form HCl. It can be noted that  $Cl^-$  ions are continuously transported to the acid compartment due to the electric field effect, leading to an increase in the amount of HCl. The experiment conducted at 6.4 A resulted in the highest amount of HCl. This can be attributed to faster ion transitions at higher current densities. [15]. In addition to HCl amounts, HCl concentrations are given in Figure 3.

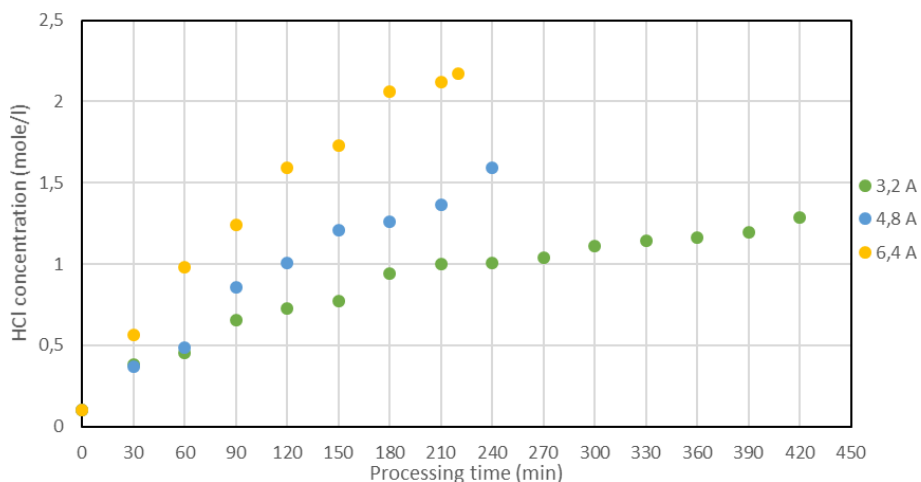


Figure 3. The amount of acid concentration produced with processing time

In Figure 3, the concentration values (mole/l) are lower than the mole amounts. This is because of the hydrated ion transitions resulting from the difference in concentration between the compartments, as well as the ions transported during the BMED process. [10]. The volume of the acid tank increases as hydrated ions are transported into the acid compartment. The concentrations of ions transported decrease as the volume increases. This process occurs independently of the electric field effect. As seen in Figure 3, the experiment conducted with 6.4 A shows the highest concentration value. Lastly, Figure 4 salt-based acid conversion graph is given.

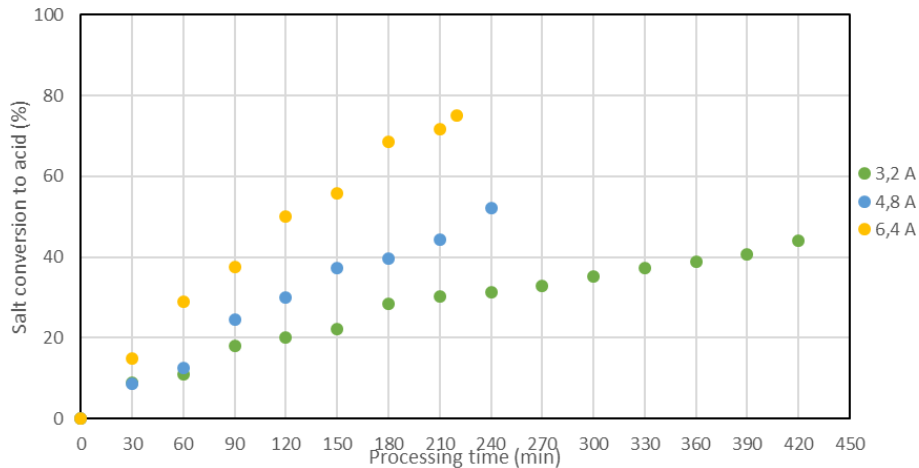


Figure 4. Salt conversion to acid

The amount of HCl formed (in moles) is expected to be theoretically the same as the amount of  $\text{NH}_4\text{Cl}$  (in moles). In the experiments, the initial amount of  $\text{NH}_4\text{Cl}$  was determined to be 3.17 mol, and the conversion rates were calculated accordingly. Analysis of Figure 4 shows that the conversion rates range from 40% to 80% in all experiments. The low conversion rates may be attributed to unwanted transports occurring in the BMED process. Undesirable transports refer to mass transfer phenomena, such as back diffusion, co-ion migration, and hydrated ion migration, which occur due to concentration differences between the compartments during the process. [10]. Undesirable transportation can lead to low concentrations in the relevant compartments, resulting in low conversion rates. Analysis of Figure 4 reveals that the highest conversion is achieved at 6.4 A as a result of the high mole amount and concentration value.

### 3.2 $\text{NH}_4\text{OH}$ Concentration and Conversion

The chloride ions ( $\text{Cl}^-$ ) in  $\text{NH}_4\text{Cl}$  in the feed compartment are moved to the acid compartment, releasing  $\text{NH}_4^+$  ions in the process. Because these ions are cations, they are unable to pass through the AEM and BMs. Instead, they react with  $\text{OH}^-$  ions from BM and form the compound  $\text{NH}_4\text{OH}$ . As a result,  $\text{NaCl}$  and  $\text{NH}_4\text{OH}$  compounds are present in the feed compartment. By obtaining  $\text{NH}_4\text{OH}$ , the Solvay process can fulfill its ammonia requirement. In Figure 5 shows the change in the amount of  $\text{NH}_4\text{OH}$  (measured in moles) over time during the experiments.

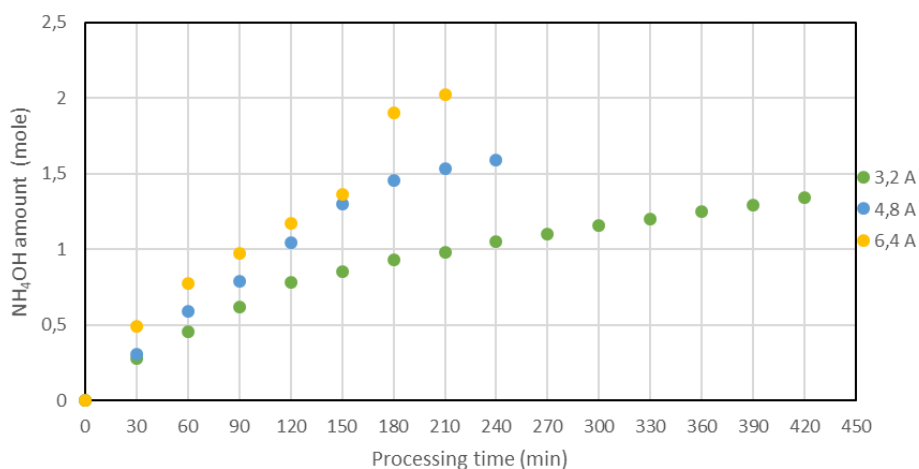
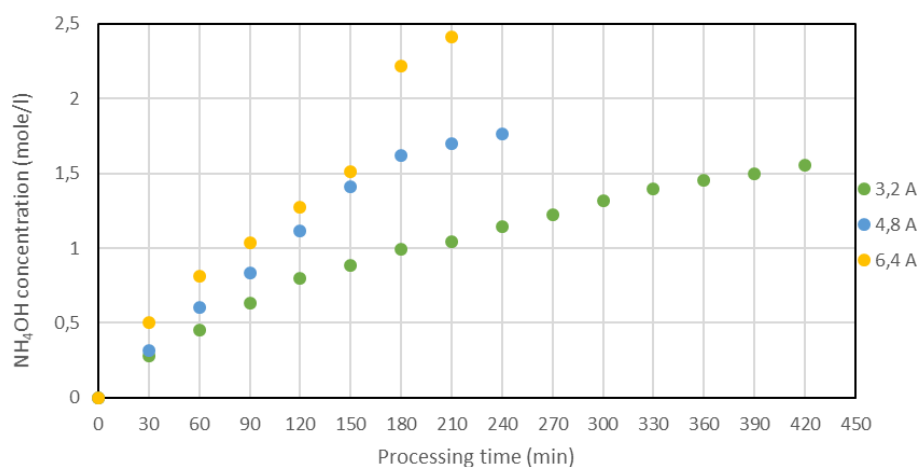


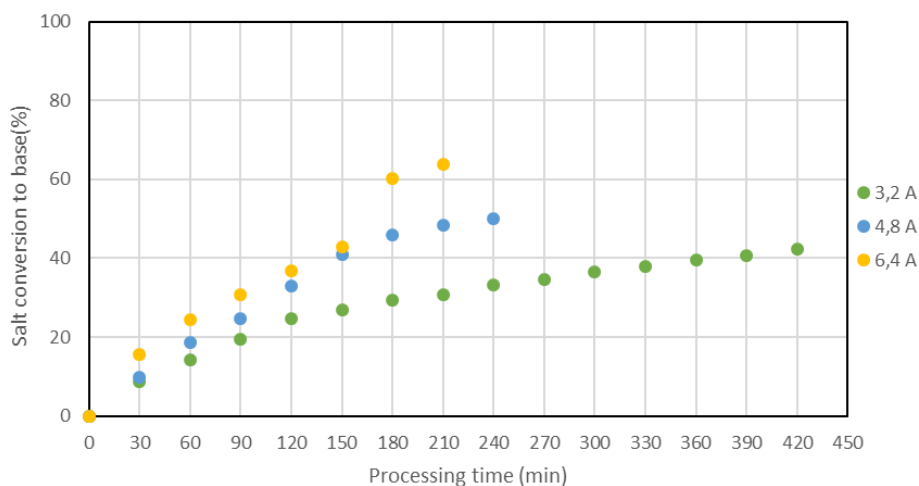
Figure 5. The amount of base produced with processing time

In the experiments conducted at different current values, the amounts of  $\text{NH}_4\text{OH}$  formed showed a similar trend to acid formation. This is evident in Figure 5. The highest  $\text{NH}_4\text{OH}$  conversion occurred in the experiment carried out with 6.4 A. This is attributed to a similar reason as acid formation. As current density increases, ion transport may change in direct proportion and result in higher conversions. The changes in  $\text{NH}_4\text{OH}$  concentration are illustrated in Figure 6.



**Figure 6.** The amount of base concentration produced with processing time

Figure 6 demonstrates that the concentration of  $\text{NH}_4\text{OH}$  increases in comparison to the acid concentration. It was noted that the acid concentration was lower than the amount of acid. However, this is the opposite for the  $\text{NH}_4\text{OH}$  concentration. This can be explained by the transfer of hydrated ions to the acid concentration, which causes a decrease in volume in the feed compartment. As a result, the decrease in volume in the feed compartment leads to an increase in concentration. Consequently, a more concentrated feed solution is obtained at the end of the experiment. The  $\text{NH}_4\text{Cl}$ -based  $\text{NH}_4\text{OH}$  conversion, which is determined as a performance criterion, is presented in Figure 7.



**Figure 7.** Salt conversion to base

In the  $\text{NH}_4\text{OH}$  conversion experiment, we took into consideration  $\text{NH}_4\text{Cl}$  based conversion, similar to acid conversion. We calculated the theoretically expected amount of  $\text{NH}_4\text{OH}$  to match the initial amount of  $\text{NH}_4\text{Cl}$  in moles, and then calculated the conversion rates accordingly. The results show that the conversion rates range between 40% and 80%, following a similar trend to the acid conversion rates. Upon careful analysis of the graphs, we observed that the acid conversion rates are slightly higher, possibly due to the more proportional change in volume and mole changes in the acid compartment.

## 4 CONCLUSION

In this study, an alternative to the distillation unit of the solvay process was investigated to eliminate the waste problem. The study defined parameters and levels, and set performance criteria accordingly. It was found that

higher current values led to higher conversions. However, transport issues such as back diffusion, common ion transitions, and water transport with hydrated ions are limiting factors for concentration and conversion. The data suggests that the BMED process could replace the distillation unit and be integrated into the Solvay process.

## References

- [1] G. Steinhäuser, "Cleaner production in the Solvay Process: general strategies and recent developments," *Journal of Cleaner Production*, vol. 16, no. 7, pp. 833–841, 2008.
- [2] T. Kasikowski, R. Buczkowski, B. Dejewski, K. Peszyńska-Białczyk, E. Lemanowska, and B. Igliński, "Utilization of distiller waste from ammonia-soda processing," *Journal of cleaner production*, vol. 12, no. 7, pp. 759–769, 2004.
- [3] X. Zhang, E. Asselin, and Z. Li, "CaCO<sub>3</sub> precipitation kinetics in the system CaCl<sub>2</sub>–CO<sub>2</sub>–Mg(OH)<sub>2</sub>–H<sub>2</sub>O for comprehensive utilization of soda production wastes," *ACS Sustainable Chemistry & Engineering*, vol. 9, no. 1, pp. 398–410, 2020.
- [4] M. Trypuć and K. Białowicz, "CaCO<sub>3</sub> production using liquid waste from Solvay method," *Journal of Cleaner Production*, vol. 19, no. 6-7, pp. 751–756, 2011.
- [5] P. de Carvalho Pinto, M. de Oliveira Carvalho, F. Linhares, T. Da Silva, and G. de Lima, "A cleaner production of sodium hydrogen carbonate: partial replacement of lime by steel slag milk in the ammonia recovery step of the Solvay process," *Clean Technologies and Environmental Policy*, vol. 17, pp. 2311–2321, 2015.
- [6] Y. M. Shen and T. G. Wang, "NaCl brine preparation from distiller waste and Na<sub>2</sub>SO<sub>4</sub>," *Advanced Materials Research*, vol. 233, pp. 897–902, 2011.
- [7] T. Kasikowski, R. Buczkowski, M. Cichosz, and E. Lemanowska, "Combined distiller waste utilisation and combustion gases desulphurisation method: The case study of soda-ash industry," *Resources, conservation and recycling*, vol. 51, no. 3, pp. 665–690, 2007.
- [8] D. V. Quang, A. Dindi, and M. R. Abu Zahra, "The utilization of CO<sub>2</sub>, alkaline solid waste, and desalination reject brine in soda ash production," *CO<sub>2</sub> Separation, Purification and Conversion to Chemicals and Fuels*, pp. 153–184, 2019.
- [9] U. Sanigok, *Anorganik Endüstriyel Kimya*, Güray Mat. Tic. Limited Şti., 1987.
- [10] M. R. Oner, A. Kanca, O. N. Ata, S. Yapici, and N. A. Yaylali, "Bipolar membrane electro dialysis for mixed salt water treatment: Evaluation of parameters on process performance," *Journal of Environmental Chemical Engineering*, vol. 9, no. 4, art. no. 105750, 2021.
- [11] L. Dursun, O. N. Ata, and A. Kanca, "Bipolar membrane electro dialysis for binary salt water treatment: valorization of type and concentration of electrolytes," *Industrial & Engineering Chemistry Research*, vol. 60, no. 5, pp. 2003–2010, 2021.
- [12] Y. Lv, H. Yan, B. Yang, C. Wu, X. Zhang, and X. Wang, "Bipolar membrane electro dialysis for the recycling of ammonium chloride wastewater: Membrane selection and process optimization," *Chemical Engineering Research and Design*, vol. 138, pp. 105–115, 2018.
- [13] Y. Li, S. Shi, H. Cao, X. Wu, Z. Zhao, and L. Wang, "Bipolar membrane electro dialysis for generation of hydrochloric acid and ammonia from simulated ammonium chloride wastewater," *Water research*, vol. 89, pp. 201–209, 2016.
- [14] A. Kanca, H. Senol, D. Adiguzel, C. Medin, and O. N. Ata, "Boric acid recovery in dilute during the desalination process in BMED system," *Desalination*, vol. 538, art. no. 115920, 2022.
- [15] J. Shen, J. Huang, L. Liu, W. Ye, J. Lin, and B. Van der Bruggen, "The use of BMED for glyphosate recovery from glyphosate neutralization liquor in view of zero discharge," *Journal of Hazardous Materials*, vol. 260, pp. 660–667, 2013.



---

## Evaluating the Pb (II) Removal Efficiency of *Prunus Laurocerasus*: Isotherms, Kinetic and Thermodynamic Studies

Zehra Seba Keskin<sup>\*1</sup>, Zeynep Mine Senol<sup>2</sup>

<sup>1</sup>Department of Pharmacy, Health Services Vocational School, Sivas Cumhuriyet University, 58140 Sivas, Türkiye

<sup>2</sup>Department of Nutrition and Diet, Faculty of Health Sciences, Sivas Cumhuriyet University, 58140, Sivas, Türkiye

---

### Abstract

In the contemporary era, the unregulated discharge of wastewater contaminated with heavy metals, the result of anthropogenic activities and rapid industrialisation, represents a global threat. Among these heavy metals, lead presents a significant risk to the environment and human health due to its stability in the environment and inability to be biologically degraded.

The objective of this study is to ascertain the biosorbent properties of *Prunus laurocerasus* L. (PL) fruit seeds, a by product of agriculture, for the effective removal of Pb<sup>2+</sup> ions from an aqueous solution. A batch biosorption system was employed to investigate the influence of various parameters on the biosorption process, including initial solution pH, temperature, contact time, and initial Pb<sup>2+</sup> concentration.

The morphological characteristics of the PL biosorbent were characterised using SEM-EDX, FT-IR, and PZC analyses before and after biosorption. Isotherm studies indicated that the Langmuir isotherm model ( $R^2=0.987$ ) was the most suitable model for the biosorption process. The biosorption kinetic mechanism was found to follow the pseudo-second-order kinetics ( $R^2=0.765$ ) and the intraparticle diffusion model ( $R^2=0.994$ ).

The maximum biosorption capacity of the PL biosorbent for Pb<sup>2+</sup> ions was determined to be 58 mg g<sup>-1</sup>. Thermodynamic studies indicated that the biosorption mechanism is endothermic, spontaneous, and entropy-increasing. These results indicate that the PL biosorbent has the potential to be a promising, eco-friendly, cost-effective, and sustainable biosorbent for the removal of Pb<sup>2+</sup> ions.

**Keywords:** Biosorption, Biowaste, Lead

---



## Upgraded Biooil with Co-Pyrolysis of Spruce Sawdust with Glycerol

Ahmet Rasim Girisen<sup>\*1</sup>, Hakan Ozcan<sup>1</sup>

<sup>1</sup>Department of Mechanical Engineering, Ondokuz Mayıs University, Samsun, Türkiye

### Abstract

This study examined the co-pyrolysis of spruce sawdust to upgraded bio-oils. For this purpose, a fixed bed reactor was used for experiments. The yields and components of obtained bio-oils at different mixing ratios with glycerol (10, 20, and 30 wt%) and pyrolysis temperatures (400, 450, 500, 550 and 600 °C) were investigated. The results showed that the bio-oil yield improved with an additive of glycerol at all mixing ratio. The highest oil yield (46.4 wt%) was obtained at 20 wt% mixing ratio of glycerol and a pyrolysis temperature of 550 °C. The GC-MS results also showed that the bio-oils ingredients a significant ratio of ketones, phenols and alcoholic compounds. The unoxxygenated hydrocarbons in the bio-oil obtained from the pyrolysis of spruce sawdust was found to be 4.81% (GC-MS peak area). The number of unoxxygenated hydrocarbons increased significantly with co-pyrolysis. The unoxxygenated hydrocarbons in the bio-oils produced by co-pyrolysis were found to be 22.24%. The results of co-pyrolysis also revealed that the average carbon number of the compounds in the bio-oils changed with using glycerol.

**Keywords:** Co-pyrolysis, Biomass, Glycerol, Bio-oil, Hydrocarbons

## 1 INTRODUCTION

The increasing consumption of fossil fuels and the increase in prices have increased the interest in sustainable energy sources and concerns about the necessity of these resources [1]. The environmental footprints left on our world by harmful substances resulting from fossil fuels have inevitably brought about an interest in green and sustainable energy sources [2]. Therefore, it is imperative to find an alternative, cheap and environmentally friendly energy source to meet the amount of energy needed in the future [3]. Considering these situations, the evaluation of biomass using methods such as coking, pyrolysis or gasification plays an essential role in meeting the current energy need in a cleaner and environmentally friendly way.

The main product, bio-oil formed as a result of pyrolysis, has yield values that can reach up to 70% by weight, depending on various factors (reactor operating conditions, holding time, biomass properties, etc.) [4]. In the transportation sector, most fossil fuels are considered gasoline, diesel, aviation and jet fuel. Crude bio-oil obtained through pyrolysis has properties such as high viscosity, acidity and chemical instability that make it unsuitable for use as fuel. For this reason, bio-oil properties need to be improved to be used directly. One obstacle to using bio-oils as a renewable alternative to fossil fuels is that they have a significantly high oxygen content of approximately 50% by weight. Bio-oil is a complex structure consisting of various oxygen-containing components such as ketones, aldehydes, phenols and sugars. The possibilities of using methods used in oil refining processes to obtain high-value-added petroleum products from bio-oil are also being investigated. However, it has disadvantages in fluidized bed pyrolysis and hydrothermal processes. When large quantities of bio-oil are directly processed using fluidized bed pyrolysis, a high amount of coke is formed, decreasing liquid yield. Studies on hydrothermal processes with bio-oil can provide higher degrees of deoxygenation than studies conducted with fluidized beds. In addition, hydrogen creating high partial pressure has led to an increase in process costs [5].

In many studies, co-pyrolysis or catalytic pyrolysis methods have been used to reduce the oxygen content and increase the H/C ratio of bio-oil obtained from pyrolysis. The purpose of co-pyrolysis or catalytic pyrolysis is to remove the oxygen contained in the bio-oil by converting it into CO<sub>2</sub>, CO, etc. gases or to ensure that the carbons in the structure bind excess Hydrogen. Rotliwala and Parikh in [6] studied the co-pyrolysis of high-density polyethylene (HDPE) with defatted *Jatropha* cake (JK) in a batch reactor. The co-pyrolysis process was carried out in nitrogen flow at atmospheric pressure and a temperature of 450 °C. The bio-oil yield obtained from co-pyrolysis was determined as 63%. Bio-oils obtained from co-pyrolysis were analyzed using GC-MS and ASTM D86 standards. The co-pyrolysis of HDPE with JK significantly increased the proportion of components with a gasoline-like carbon range (C<sub>6</sub>-C<sub>12</sub>) by up to 45% compared to when HDPE was pyrolyzed alone. Solak et al. in

[7] obtained the highest bio-oil yield of 79.5% from the co-pyrolysis of cellulose and polyethylene at 500 °C. Brebu et al. in [8] investigated the pyrolysis of lignin with polymers such as PE, PP, PS and PC. The researchers stated that the liquid yield obtained only reached 53.2-62.7% by weight. In addition, they reported that they co-pyrolyzed pine cones with synthetic polymers and found that it gave a liquid yield of 63.9-69.7% by weight. When biodiesel is produced by transesterification of grease, glycerin is released as a significant by-product.

The boiling point of glycerol is 290 °C and when higher temperatures are reached in pyrolysis, components such as CO, H<sub>2</sub>, CO<sub>2</sub>, CH<sub>4</sub> etc. are formed. In this case, Glycerol becomes a usable material in co-pyrolysis for hydrogen enrichment and deoxygenation. Carmines et al. in [9] analyzed by adding different amounts of glycerol (5%, 10% and 15%) to tobacco and collecting the products and particulate matter in the pyrolysis gas produced during the thermal transformation of the mixture. The results showed that glycerol diluted the smoke and increased the humidity. They also found that the acrolein content in the smoke increased in the mixture, where 10% and 15% glycerol were added to the tobacco. Nicotine, acetaldehyde, aromatic amine, propanol, phenols, N-nitrosamines and other compounds have also been shown to be reduced. Skoulou et al. in [10], in their study to prepare hydrogen-enriched fuel from the co-pyrolysis of olive stone and glycerol mixture, found that the hydrogen content in the gas obtained from pyrolysis increased by 11.6% in the mixture created with 25% glycerol.

Spruce sawdust is a renewable carbon source. But its low hydrogen-to-carbon ratio limited using bio-oil from pyrolysis as directly diesel fuel. Whereas, some liquid wastes that are high in hydrogen might be introduced to the pyrolysis system to increase the H/C ratio. The present research on co-pyrolysis of spruce saw dust and hydrogen-donor liquid waste has focused on the preparation of diesel fuel carbon range bio-oils. Glycerol was utilized in this study to investigate the co-pyrolysis of spruce saw dust. In this way, this study will provide guidance on the changes in bio-oil composition during co-pyrolysis and the production of upgraded bio-oil. In this scope, pyrolysis was carried out in a nitrogen atmosphere in a fixed bed reactor at different temperatures (400, 450, 500, 550 and 600 °C) and mixing ratios (10 wt%, 20 wt%, and 30 wt%). The yields and bio-oil contents of liquid products obtained from pyrolysis were investigated. While investigating bio-oil contents, chromatography-mass spectrometry, elemental analysis and FTIR analysis methods were used.

## 2 MATERIAL AND METHOD

### 2.1 Materials

The spruce saw dusts sizes sieved to be 0.75-1.2 mm. The drying process was carried out by keeping it in an oven at 75 °C for 12 hours. Vario Cube Elemental Analyzer was used for elemental analyses. Muffle furnace and convection furnace were used to perform proximate analysis of spruce saw dust samples. The samples were air dried at 105 °C in accordance with the ASTM E871-92 standard and waited in the oven until they reached a constant weight. The samples placed in the lidded porcelain container were heated in a muffle furnace at 850 °C for 70 minutes. After the process, the remaining samples were cooled and their weights were measured. For ash determination according to the ASTM D1102-84 standard, the samples were heated in lidless porcelain containers at 950 °C for 2 hours. The amount of fixed carbon was calculated by subtracting the sum of the resulting ash, moisture and volatile substances from the initial mass. Glycerol was mechanically mixed with spruce saw dusts at the rates of 10 wt%, 20 wt% and 30 wt%.

### 2.2 Thermogravimetric Analysis (TGA)

TA Instruments SDTQ600 device was used in thermogravimetric analysis to determine the thermal behavior of spruce saw dust and temperature-dependent mass losses. The sample mass for experiment was 2 mg. Initial temperature of experiments was set at the room temperature. In analyzes performed up to 800 °C, the heating rate was set as 10 °C/min. Nitrogen gas flow was set at 50 ml/min as entrainer gas and provide inert atmosphere in the analyzes. Furthermore, TGA analysis were performed twice to minimize the experimental error.

### 2.3 Characterization of Bio-Oil

FTIR analyzes were performed to determine the molecular bond structures in the bio-oil obtained from the pyrolysis of spruce saw dusts. Bruker Tensor 27 IR analyzer, which measures in the range of 400-4000 cm<sup>-1</sup>, was used in the analyzes. GC-MS analysis was performed using the Shimadzu GCMS-QP2020 plus device to determine the compounds contained in the bio-oil. The bio-oils to be analyzed were diluted with Methanol at the HPLC level at a ratio of 1/100 by volume. 2 µl of sample was used for each injection. Restek Rxi-5ms (30m x 0.25 mm, 0.25 µm film thickness) column was used in GC-MS analyses. Helium was used as a carrier gas in the sample analysis

and the injector temperature was determined as 250 °C, the program was adjusted to start from 50 °C, reach 280 °C at a speed of 10 °C/min, and wait for 1 minute at 280 °C.

## 2.4 Experimental Setup

The experimental system established to obtain bio-oil from spruce saw dusts by pyrolysis is shown in Figure 1. The raw material was fed into the fixed bed pyrolysis reactor from the top. The reactor, which had an inner diameter of 50 mm and a length of 400 mm, was heated only with electrical heaters. Nitrogen (N) gas was used to entertain gas and provide inert environment during the experiments. Nitrogen gas was connected to the reactor from the bottom and flow was provided at a constant flow rate of 50 ml/min (the flow rate was standardized at 0 °C and 1 atm conditions). Temperatures were measured with a total of 7 thermocouples inside and outside the reactor. Pyrolysis was performed with a total of 40 g of sample in each experimental set. The reactor's gases were passed through the condenser at 0 °C. A second cooler and, finally, a gas washing chamber were used to increase the condensation of the gases. Since the amount of usable, helpful liquid was prioritized when calculating the total liquid yield, the liquid products in the glass containers were weighed to determine the total mass. The obtained products were filtered using filter paper and separated from solid particles.

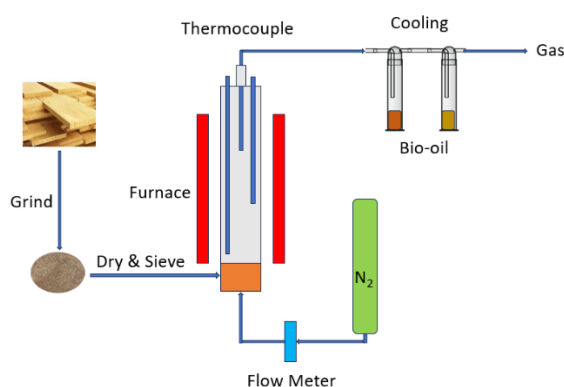


Figure 1. Experimental setup

## 3 RESULTS

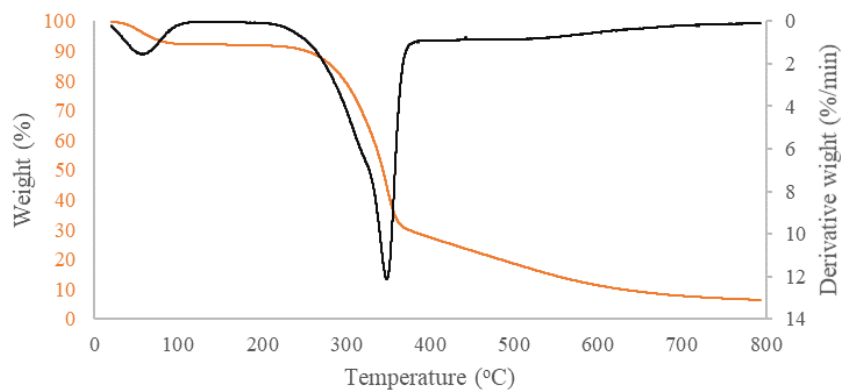
The proximate and ultimate analysis can have a significant impact on the pyrolysis process because of the complex structure of woody biomasses. In thermal analyzes and experimental studies of spruce saw dust, care was taken to ensure that the samples were homogeneous in order to avoid errors due to particle size. The proximate and ultimate analysis results of spruce saw dusts are given in Table 1. As a result of the analysis, the fixed carbon, volatile matter and ash contents of the spruce saw dust samples were found to be 19.96 wt%, 75.54 wt% and 5.49 wt%, respectively. In addition, the moisture content of spruce saw dusts was determined as 9.99 wt%. Excessive humidity may cause negative effects such as high heat requirement for evaporation [11]. It is seen that the carbon, hydrogen, nitrogen and oxygen contents of spruce saw dusts are 45.29 wt%, 6.58 wt%, 0.02 wt% and 48.11 wt%, respectively. It can be seen that spruce saw dust alone cannot provide the desired H/C ratio to obtain diesel fuel-like bio-oil. In addition, the high oxygen content indicates that the bio-oil to be obtained will be rich in oxygen and might be contain acid, alcohol and ketone-like structures. For this reason, bio-oil should be enriched with hydrogen and oxygen removed. It is known that the quality of bio-oil increases, its calorific value increases and its oxygen content decreases thanks to co-pyrolysis [12]. Compared to the process of enriching bio-oils with hydrogen at high pressure, co-pyrolysis is a safer and easier way to produce quality bio-oil [13].

Table 1. Proximate and ultimate analysis of spruce saw dust

	Compound	%wt
Ultimate analysis	C	50.44
	H	6.07
	N	0.3
	O	43.19
Proximate analysis	Fixed Carbon	19.96
	Moisture	9.99
	Volatiles	75.54
	Ash	5.49

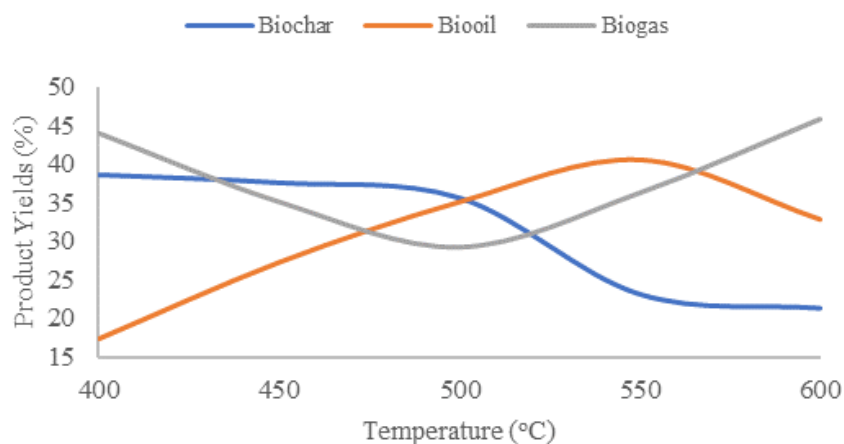


The curves obtained as a result of thermogravimetric analysis applied to spruce saw dust are presented in Figure 2. The mass loss started with the increase in temperature and gave the first peak at approximately 63 °C. As a result of the evaporation of moisture at temperatures up to 207 °C, the spruce saw dust lost approximately 9% mass. Subsequently, with the increase in temperature, the decomposition of hemicellulose began rapidly. It reached its maximum mass loss rate at 345 °C, where hemicellulose and cellulose decompose. At 390 °C, where the curve started to become linear, the total mass loss was observed to be 70%. When the temperature reached 500 °C, the passive pyrolysis zone was entered. This region can also be said to be the region where lignin is slowly degraded.



**Figure 2.** TGA and DTG curves of spruce saw dust

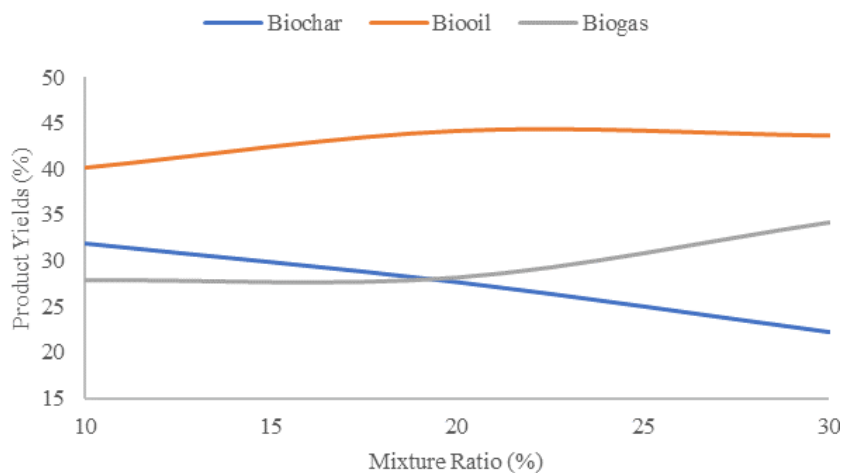
In the pyrolysis of spruce saw dust carried out at different temperatures, the highest liquid product yield was obtained at 550 °C. While the rise in temperature increased the liquid and gas product yield, it caused the biochar yield to decrease. Heating rates were kept constant for all temperatures. In addition, feed rates and entrainer gas flow rates were kept constant. It was not expected to see a difference at the desired level in terms of product conversion when increasing the temperature above 600 °C. For this reason, this temperature was not exceeded. The product yields obtained from the pyrolysis of spruce saw dust at different temperatures are given in Figure 3. In pyrolysis at 400 °C, the product yields of biochar, bio-oil and biogas were determined as 38.69 wt%, 17.32 wt% and 43.99 wt%, respectively. The biochar, bio-oil and biogas yields in pyrolysis at 600 °C were obtained as 21.28 wt%, 32.89 wt% and 45.83 wt%, respectively. The highest bio-oil yield obtained from pyrolysis at 550 °C as 40.66 wt%. The co-pyrolysis and catalytic co-pyrolysis experiments were conducted at 550 °C temperature because the highest bio-oil yield of pyrolysis obtained at this temperature.



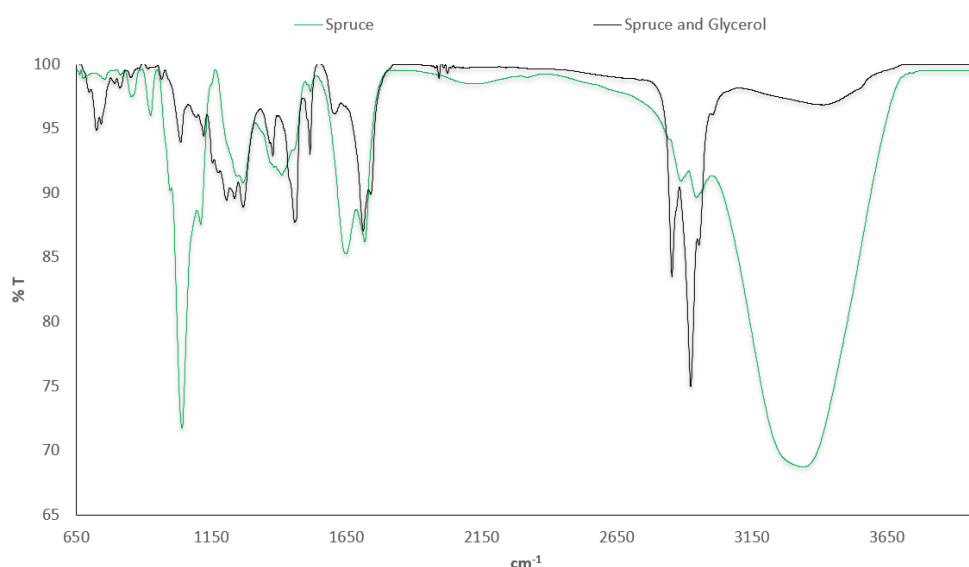
**Figure 3.** Product yields in pyrolysis of spruce saw dusts at different temperature

Co-pyrolysis is a well-known method to improve the quality of bio-oil obtained from pyrolysis [9, 10]. In co-pyrolysis, it is important to choose materials that are compatible with each other and will create a synergistic effect. The co-pyrolysis with glycerol was evaluated to obtain high quality bio-oil from spruce saw dust. It is known in many studies that glycerol has positive effects on bio-oil. Three different mixture ratios were used in the co-pyrolysis of spruce saw dust with glycerol. The yields of the products obtained from the co-pyrolysis of spruce saw dust with glycerol at different rates are given in Figure 4. When the liquid product amounts obtained from each of the mixture ratios were evaluated, it was seen that 20% mixture amount gave the highest liquid yield. The liquid product yields obtained for 10 wt%, 20 wt% and 30 wt% mixing ratios at 550 °C as 40.17 wt%, 44.11 wt%

and 43.59 wt%, respectively. Biochar yield decreased with increasing mixing ratio. It was observed that with the increase in the mixing ratio, more liquid and gaseous products were formed. The results showed that the glycerol had a positive effect on the formation of liquid and gaseous products in the pyrolysis reactions. However, increasing the rate of glycerol, the second component of co-pyrolysis, can enhance the conversion to gas product. In addition, it might be evaporate before the pyrolysis and condense in the condensation zone.



**Figure 4.** Product yields in co-pyrolysis of spruce sawdusts with glycerol at different mixing ratios



**Figure 6.** FTIR curves of bio-oil obtained from pyrolysis of spruce and co-pyrolysis with glycerol

The curves obtained from the FTIR analysis performed to determine the functional groups of the components in bio-oils are given in Figure 6. Since a diesel like bio-oil is targeted, oxygen-containing compounds should not be in the liquid product. However, when the curves for all cases were examined, the peaks between the wavenumbers of 3200-3700  $\text{cm}^{-1}$ , which showed O-H stretching vibrations, showed that there were oxygen-bonded compounds in all of the bio-oils. It appears that there is a lot of oxygenated components in the bio-oil obtained with pyrolysis of spruce sawdusts. The co-pyrolysis results with catalysts showed that oxygen-containing components decreased. It can be said that O-H bonded carboxylic acid and alcohol structures exist in bio-oils. C-H stretching vibrations in the band gap of 2695-3333  $\text{cm}^{-1}$  and C-H bending vibrations in the band gap of 1350-1475  $\text{cm}^{-1}$  showed the presence of alkane and aldehyde structures in the bio-oil. Similar peaks at a wavelength of 1700  $\text{cm}^{-1}$  in all structures indicated C-O bonds, indicating the presence of ketones, carboxylic acids and aldehydes in the bio-oils. In addition, C-O stretching vibrations between 950-1300  $\text{cm}^{-1}$  showed that alcohol and ester structures may be among the compounds [14].

GC-MS analysis was performed to get certain results about the contents of the bio-oils obtained from the experiments. The data obtained from the GC-MS are given in Table 2 for the best results. The commentary about FTIR analysis results were confirmed by GC-MS results. The bio-oil obtained from pyrolysis of spruce sawdusts contained mostly oxygenated hydrocarbons. The broad O-H peak seen in the FTIR analysis supported this

situation. The GC-MS results revealed that furan, aldehyde, alcohol and phenol compounds were in the majority. The amount of oxygen-free hydrocarbons was determined as 4.81 % (peak area). Benzene, alcohol and aliphatic hydrocarbons were mostly seen in bio-oil obtained from co-pyrolysis. The oxygen-free hydrocarbons increased with glycerol at 22.24%. Although the increase is significant, it is not sufficient for use as a diesel fuel.

## 4 CONCLUSION

In this research, Spruce were pyrolyzed with glycerol to investigate the interactions between spruce and glycerol in a fixed bed reactor. The main conclusions are:

- i. The highest biooil rate was observed as 44.11 wt% at 550 °C, 50 ml/min entrained gas flow and 30 °C/min heating rate from co-pyrolysis with glycerol at 20% mixing ratio. In addition, biocoke and biogas yields obtained as 27.68 wt% and 28.21 wt%, respectively.
- ii. The lowest bio-coke rate was obtained as 21.28 wt% in the pyrolysis of spruce at 600 °C. Also, the highest biogas rate obtained as 45.83 wt% in the pyrolysis of spruce at 600 °C.
- iii. The number of oxygenated compounds was dense in structure of biooils according to FT-IR analysis. However, in co-pyrolysis with glycerol, total oxygen amount decreases significantly, and hydrocarbon structures increase.
- iv. The biooil obtained from the co-pyrolysis of glycerol dissolved with diesel fuel by mechanical mixing at room temperature. It maintained homogeneous form without precipitation or phase separation for a week up to 10 wt%.
- v. The biooil contents according to GC-MS results were in the 99.28% gasoline-carbon range from pyrolysis of spruce sawdust. On the other hand, the biooil obtained from co-pyrolysis with glycerol was in the 85.32% diesel fuel carbon range.
- vi. The chemical formula of biooils from co-pyrolysis with glycerol and pyrolysis of spruce sawdust were procured as  $C_{13.7}H_{23.3}O_{1.4}$  and  $C_{6.95}H_{9.15}O_{2.05}$ , according to GC-MS and elemental analysis results, respectively.

Although the biooil obtained from the experiments is unsuitable for direct use as diesel fuel, it can be used in less sensitive systems (liquid fuel boilers, etc.) by mixing with diesel fuel or as low-quality fuel. Based on findings, future researches will be focus on the co-pyrolysis can be repeated with different wastes like hydrogen-rich plastics. Furthermore, the co-pyrolysis can be repeated with zeolite catalysts like HZSM-5 and natural catalysts like dolomite to reduce the oxygen content in the biooil. Additionally, the structure contained valuable chemicals. It is also possible to produce valuable chemicals by using various extraction methods of these components.

## Acknowledgments

Ahmet Rasim GIRISEN reports financial support was provided by Council of Higher Education of the Republic of Turkey (YOK 100/2000 Scholarship). Ahmet Rasim Girisen reports financial support was provided by the Scientific and Technological Research Council of Turkey (TUBITAK 2211-A Scholarship). Hakan OZCAN reports financial support was provided by Ondokuz Mayıs University.

## References

- [1] P. R. Bhoi, A. S. Ouedraogo, V. Soloiu, and R. Quirino, "Recent advances on catalysts for improving hydrocarbon compounds in bio-oil of biomass catalytic pyrolysis," *Renewable and Sustainable Energy Reviews*, vol. 121, art. no. 109676, 2020, doi: 10.1016/j.rser.2019.109676.
- [2] A. K. Koyande, K. W. Chew, K. Rambabu, Y. Tao, D.-T. Chu, and P.-L. Show, "Microalgae: A potential alternative to health supplementation for humans," *Food Science and Human Wellness*, vol. 8, no. 1, pp. 16–24, 2019, doi: 10.1016/j.fshw.2019.03.001.
- [3] C. H. Tan, P.-L. Show, J.-S. Chang, T. Ling, and J. Lan, "Novel approaches of producing bioenergies from microalgae: A recent review," *Biotechnology Advances*, vol. 33, 2015, doi: 10.1016/j.biotechadv.2015.02.013.
- [4] W.-H. Chen, J. Peng, and X. Bi, "A state-of-the-art review of biomass torrefaction, densification and applications," *Renewable and Sustainable Energy Reviews*, vol. 44, pp. 847–866, 2015, doi: 10.1016/j.rser.2014.12.039.
- [5] O. Azeta, A. O. Ayeni, O. Agboola, and F. Elehinafe, "A review on the sustainable energy generation from the pyrolysis of coconut biomass," vol. 13, art. no. e00909, 2021, doi: 10.1016/j.sciaf.2021.e00909.
- [6] Y. Rotliwala and P. Parikh, "Study on thermal co-pyrolysis of jatropha deoiled cake and polyolefins," *Waste Management & Research: The Journal of the International Solid Wastes and Public Cleansing Association, ISWA*, vol. 29, pp. 1251–1261, 2011, doi: 10.1177/0734242X11406948.

- [7] A. Solak and P. Rutkowski, "Bio-oil production by fast pyrolysis of cellulose/polyethylene mixtures in the presence of metal chloride," *Journal of Material Cycles and Waste Management*, vol. 16, pp. 491–499, 2013, doi: 10.1007/s10163-013-0204-z.
- [8] M. Brebu and I. Spiridon, "Co-pyrolysis of LignoBoost lignin with synthetic polymers," *Polymer Degradation and Stability*, vol. 97, pp. 2104–2109, 2012, doi: 10.1016/j.polyimdegradstab.2012.08.024.
- [9] E. Carmines and C. L. Gaworski, "Toxicological evaluation of glycerin as a cigarette ingredient," *Food and chemical toxicology: An international journal published for the British Industrial Biological Research Association*, vol. 43, pp. 1521–1539, 2005, doi: 10.1016/j.fct.2005.04.010.
- [10] V. Skoulou, P. Manara, and A. Zabaniotou, "H<sub>2</sub> enriched fuels from co-pyrolysis of crude glycerol with biomass," *Journal of Analytical and Applied Pyrolysis*, vol. 97, pp. 198–204, 2012, doi: 10.1016/j.jaap.2012.05.011.
- [11] H. C. Ong, W.-H. Chen, A. Farooq, Y. Y. Gan, T. Lee, and A. Veeramuthu, "Catalytic thermochemical conversion of biomass for biofuel production: A comprehensive review," *Renewable and Sustainable Energy Reviews*, vol. 113, art. no. 109266, 2019, doi: 10.1016/j.rser.2019.109266.
- [12] F. Abnisa and W. M. A. Wan Daud, "A review on co-pyrolysis of biomass: An optional technique to obtain a high-grade pyrolysis oil," *Energy Conversion and Management*, vol. 87, pp. 71–85, 2014, doi: 10.1016/j.enconman.2014.07.007.
- [13] A. V. Bridgwater, "Review of fast pyrolysis of biomass and product upgrading," *Biomass and Bioenergy*, vol. 38, pp. 68–94, 2012, doi: 10.1016/j.biombioe.2011.01.048.
- [14] O. Onay and O. Kockar, "Fixed-bed pyrolysis of rapeseed (*Brassica napus* L.)," *Biomass & Bioenergy - Biomass Bioenergy*, vol. 26, pp. 289–299, 2004, doi: 10.1016/S0961-9534(03)00123-5.



## Comparative Classification Performance Evaluation of Machine Learning and Deep Learning Techniques for BreakHis, Wisconsin, and DDSM Breast Cancer Datasets

Oben Adak<sup>\*1</sup>, Cigdem Inan Aci<sup>1</sup>, Dogu Ilmak<sup>2</sup>

<sup>1</sup>Department of Computer Engineering, Mersin University, Mersin, Türkiye

<sup>2</sup>Department of Geomatics Engineering, Mersin University, Mersin, Türkiye

### Abstract

Breast cancer is the most common cancer among women worldwide and is likely to be fatal if diagnosed late. Clinical decision support systems (CDSS) play an important role in helping physicians make decisions about diseases such as breast cancer, where early diagnosis is critical. CDSS aims to successfully classify new data by training them with machine learning and deep learning algorithms. In the literature, mammography, histopathological images, or tabular data have been trained with many machine learning and deep learning algorithms to detect benign or malignant tumors in breast cancer diagnosis. The aim of this study is to measure the success of Wisconsin, BreakHis, and DDSM datasets, which are commonly used in the literature, in breast cancer detection by training and classifying them with machine learning and deep learning algorithms that are different from the literature and the same. In this paper, the machine learning algorithms used were Naive Bayes (NB), Support Vector Machines (SVM), k-Nearest Neighbor (k-NN), and Random Forest (RF). Convolutional Neural Networks (CNN), one of the deep learning algorithms, that gives highly successful results, especially in image classification, was used. A CNN architecture was designed and applied to the Wisconsin dataset. The CNN architectures VGG-16, VGG-19, DenseNet-121, and MobileNet-V2 were used for the BreakHis and DDSM datasets, and the AlexNet architecture was also used for the DDSM dataset. The specified classification methods were developed and trained using Scikit-Learn and TensorFlow libraries, and the performance of the methods was analyzed, and then the results of the performance criteria were recorded. The results of the analyses were compared and the method that gave the most successful accuracy in each dataset was determined. The most successful method on the Wisconsin dataset was SVM with 100% accuracy. The most successful method on the 40x, 100x, 200x, and 400x magnified images of the BreakHis dataset was DenseNet-121 with accuracies of 97.52%, 95.58%, 96.92%, and 96.19%, respectively. The most successful method on the DDSM dataset was SVM with 100% accuracy.

**Keywords:** Breast cancer, Clinical decision support system, Machine learning, Deep learning, Convolutional neural networks

## 1 INTRODUCTION

Breast cancer is the second most common cancer diagnosed in women, surpassed only by non-melanoma skin cancer. It is the leading cause of cancer death in women worldwide [1]. In particular, breast cancer (BC) is one of the most common cancers in women. Mortality from BC is very high compared to other cancers [2]. Detection and diagnosis of BC can be achieved by imaging techniques such as diagnostic mammography (X-ray), magnetic resonance imaging (MRI), ultrasound (sonography), and thermography [3]. Machine learning plays an important role in a wide range of critical applications such as data mining, natural language processing, image recognition, expert systems, and prediction [4]. Clinical decision support systems (CDSS) are an important part of clinical information systems designed to support clinician decision-making during the care process [5]. Based on structured data, AI can support more comprehensive and personalized decision suggestions for clinicians through techniques such as machine learning [6].

In this paper, three different datasets were utilized: The Wisconsin Breast Cancer Dataset, the Breast Cancer Histopathology (BreakHis) Dataset, and the Digital Database for Screening Mammography (DDSM) Dataset. These datasets were trained using various classification methods commonly employed in breast cancer detection, including k-NN, NB, SVM, RF techniques, and CNN. Their success was then evaluated.

## 1.1 Literature Review

Technological developments are also enabling the development of CDSS, so that medical imaging and data analysis can greatly assist physicians in making decisions in many diseases where early diagnosis can save lives, such as breast cancer. Several studies have been and are being conducted in the literature in the area of breast cancer screening.

Salama et al [7] obtained 98.87% accuracy, 98.88% area under the curve (AUC), 98.98% sensitivity, 98.79% precision, and 97.99% F1 score by applying data augmentation with a modified U-Net model and InceptionV3 using the DDSM dataset in 2017. The study result of Ganesh et al. [8] achieved 97.8% accuracy using DenseNet on the DDSM dataset in 2023. Adeniyi et al [9] divided the images into 5 different classes, which are benign, ductal carcinoma, lobular carcinoma, mucinous carcinoma, and papillary carcinoma. They obtained 95.33% accuracy with DenseNet on the 100x magnification images, 94.34% accuracy with DenseNet on the 400x magnification images, 96.56% accuracy with ResNet on the 100x magnification images, 96.3% accuracy with DenseNet on the 400x magnification images using the discriminative fine-tuning. Obaid et al [10] obtained the best accuracy rate result which is 98.1% as quadratic kernel-based SVM using Wisconsin Breast Cancer (Diagnostic) dataset.

## 2 MATERIAL AND METHOD

### 2.1 The Datasets

This study includes three different datasets. The Wisconsin Breast Cancer Dataset contains tabular data used to diagnose breast cancer, the BreakHis dataset contains histopathology images used to perform depth analysis with histopathology images, and the DDSM Dataset contains mammography images used for breast cancer screening. The Wisconsin breast cancer dataset consists of tabular data, comprising 569 cases and 30 characteristics. Some important features include ID number, diagnosis (M = Malignant, B = Benign), and 10 real-valued features computed for each nucleus. BreakHis dataset consists of histopathological images. It contains 7909 microscopic images of breast tumor tissue collected from 82 different patients. These microscopic images are collected using different magnification factors (40X, 100X, 200X, and 400X). There are 2,480 benign and 5,429 malignant features. The DDSM dataset contains mammography images. It consists of 13128 mammography images divided into two classes (benign and malignant). The number of benign samples is 5970 and the number of malignant samples is 7158.

### 2.2 Methods

In this study, each dataset was examined in detail, and the input characteristics of the data were determined. The output was to classify benign or malignant tumors. Machine learning and deep learning algorithms were used to compare the performance metrics between machine learning and deep learning algorithms. The machine learning algorithms used were:

- Naive Bayes: It is based on computing simple statistics from a given training dataset as the learning step following a straightforward (but naive) application of the Bayesian formula for conditional probability in order to obtain a classification [11].
- SVM: Support Vector Machine (SVM) is a classification and regression prediction tool that uses machine learning theory to maximize predictive accuracy while automatically avoiding over-fit to the data [12].
- k-NN: k-NN algorithm is a simple learning algorithm inside the machine. The overall idea is relatively simple: calculate the distance between a point A and all other points, remove the k points with the nearest point, and then count the k points which belong to the classification. The largest proportion, then point A belongs to the classification [13].
- RF: RF classifier is an ensemble method that trains several decision trees in parallel with bootstrapping followed by aggregation, jointly referred as bagging [14].

The deep learning algorithms used were:

- DenseNet-121: In a DenseNet architecture, layers are connected with dense blocks, meaning that each layer utilizes inputs from all previous layers in order to create a feature map that will send data to all of the following layers [15].
- MobileNet-V2: MobileNetV2 is an improvement of its earlier version and came with multiple modifications and optimizations. It saw the introduction of Inverted Residuals with Linear Bottleneck that included skip

connections but used depth wise separable convolutions, unlike the standard convolution layer which operates on the entire volume using the filters, it separates the input images and applies each of the channels with its own set

- of filters after which they are stacked back [16].
- VGG-16: The VGG16 network comprised of convolutional layers 13 in number and fully connected layers three in number [17].
- VGG-19: VGG-19 model is very much similar to VGG-16 model but with 3 additional conv layers [18].
- AlexNet: It uses 3 different types of layer: Convolution layer, Pooling layer and FullyConnected (FC) layers and full architecture of AlexNet is created after making a stack of these layers. The convolution layer is the core building block of this network and each consists of some learnable filters. Every filter is small spatially along width and height [19].

First, the Wisconsin dataset was examined. This dataset was divided into two parts: 10% test data and 90% training data. The dataset was checked for missing values. Then, feature selection was performed using the Pearson correlation method. With this method, input variables that did not have a strong relationship with the output variable were identified and removed from the dataset. Data scaling was performed, and the data were rescaled to a certain range. Then, the grid search method was used to determine the most appropriate parameters of the k-NN, NB, SVM, and RF classification methods. For each method, the hyperparameters that gave the best results were selected, and the dataset was trained using these parameters. The results were evaluated according to the established performance criteria, and a confusion matrix was generated for each model. Additionally, AUC values of the models were compared using receiver operating characteristic (ROC) curves. Subsequently, the Wisconsin dataset was trained with a CNN architecture, and the obtained test results were compared with the results of other classifiers to determine the classifier that yielded the best results.

Secondly, the BreakHis dataset was examined. Each magnified image value was divided into training and test groups as specified in the CSV file. Due to the unbalanced distribution between the two classes in the training folders, the cancer-free data was upsampled to match the cancerous data. The image dimensions were resized to 128x128 pixels. Initially, these histopathological images were trained using VGG-16, VGG-19, DenseNet-121, and MobileNet-V2 architectures, and the results were compared to determine the most successful architecture among them. Subsequently, the images were converted into vectors and trained with different classification methods such as k-NN, NB, SVM, and RF. The grid search method was employed to determine the most appropriate parameters. Finally, the results of all performance measures were compared, and the most successful classification method was determined.

Finally, the DDSM dataset is divided into training and test sets, with 20% allocated for testing. The images are sized at 227x227 pixels. Initially, AlexNet was trained alongside VGG-16, VGG-19, DenseNet-121, and MobileNet-V2 CNN architectures. Subsequently, the images were converted into vectors and trained using (flattening) k-NN, NB, SVM, and RF classification methods. Before the training phase, the grid search method was applied to determine the most appropriate parameters. Finally, the test results of the classification methods were compared, and the method that yielded the best results was determined.

In order to find the most successful machine learning hyperparameters grid search method was applied to all machine learning algorithms. Grid search provides finding these most successful hyperparameters automatically. In this study the grid search method has taken averaged F1-score by applying cross validation.

### 2.3 Performance Metrics

During the process of evaluating a model's performance, a complexity matrix is used that includes four different variables: True Positive (TP), True Negative (TN), False Positive (FP), and False Negative (FN). The accuracy of a prediction model is determined using the formula shown in Equation 1. Precision measures the ability of the classifier to correctly predict relevant data, while Recall measures the proportion of relevant data identified by the classifier. The F1 score is a metric used to evaluate the performance of the model, calculated by taking the harmonic mean of Precision and Recall. The equations (Eq. 2, Eq. 3, and Eq. 4) show the calculation of the Recall, Precision, and F1-Score metrics.

$$\text{Accuracy}(\%) = \frac{(\text{TP} + \text{TN})}{(\text{TP} + \text{TN} + \text{FP} + \text{FN})} \quad (1)$$

$$\text{Recall}(\%) = \frac{TP}{(TP + TN)} \tag{2}$$

$$\text{Precision}(P) = \frac{TP}{(TP + FP)} \tag{3}$$

$$\text{F1-Score} = 2 \times \frac{(\text{Precision} \times \text{Recall})}{(\text{Precision} + \text{Recall})} \tag{4}$$

## 2.4 Results and Discussions

The Wisconsin dataset achieved the highest accuracy rate in the Support Vector Machine classifier with a value of 100%. In addition, a CNN architecture consisting of 119457 parameters and 2 convolutional layers was used. In the CNN architecture, 8 was chosen as the epoch size, and 32 was chosen as the size of the training and test groups. The learning rate was set to 0.001. The optimization algorithm is Adam and the activation function is sigmoid. The performance results of the CNN architecture are shown in Table 1.

**Table 1.** The performance results of CNN on the Wisconsin dataset

Architecture	Accuracy	Precision	F1-Score
CNN	0.9825	0.9565	0.9778

40x, 100x, 200x, and 400x magnified images of the BreakHis dataset achieved the highest accuracy rate in the DenseNet-121 architecture with values of 0.9752, 0.9558, 0.9692, and 0.9619, respectively. In CNN architectures, the epoch value is set to 50, and the size of the training and test groups is set to 32. The learning rate is 0.001 and the images are 128x128 in size. Adam was chosen as the optimization algorithm and Sigmoid as the activation function. The results of the CNN architectures are shown in Table 2. Among the classification methods, the RF classifier showed the most successful results. The grid search results of the RF algorithm are shown in Table 5.

**Table 2.** The performance results of different CNN architectures on the BreakHis dataset

Architecture	Magnification Rate	Accuracy	Precision	F1-Score
VGG-16	x40	0.9204	0.9669	0.9400
VGG-19		0.8887	0.9372	0.9166
DenseNet-121		<b>0.9752</b>	<b>0.9830</b>	<b>0.9817</b>
MobileNetV2		0.9366	0.9519	0.9539
VGG-16	x100	0.9384	0.9680	0.9543
VGG-19		0.8774	0.8994	0.9114
DenseNet-121		<b>0.9558</b>	<b>0.9734</b>	<b>0.9674</b>
MobileNetV2		0.9183	0.9453	0.9398
VGG-16	x200	0.9349	0.9552	0.9528
VGG-19		0.9111	0.9288	0.9361
DenseNet-121		<b>0.9692</b>	<b>0.9733</b>	<b>0.9778</b>
MobileNetV2		0.9367	0.9569	0.9540
VGG-16	x400	0.9358	0.9619	0.9523
VGG-19		0.8976	0.9408	0.9233
DenseNet-121		<b>0.9619</b>	<b>0.9737</b>	<b>0.9719</b>
MobileNetV2		0.9294	0.9597	0.9474

The DDSM dataset showed the highest accuracy rate in the SVM classifier with a value of 100%. Among the CNN architectures, the DDSM dataset showed the most successful results with 99.9% accuracy in DenseNet-121 and MobileNet-V2. In the CNN architectures, the epoch value is set to 8, the training group size is 32, and the test group size is 8. The learning rate is 0.001, and the images are 227x227 in size. Adam was chosen as the optimization algorithm and Sigmoid as the activation function. The results of the performance metrics are shown in Table 3.



**Table 3.** The performance results of different CNN architectures on the DDSM datasets

Architecture	Accuracy	Precision	F1-Score
VGG-16	0.9981	0.9979	0.9982
VGG-19	0.9977	0.9965	0.9979
<b>DenseNet-121</b>	<b>0.9992</b>	<b>1.0000</b>	<b>0.9992</b>
<b>MobileNetV2</b>	<b>0.9992</b>	<b>1.0000</b>	<b>0.9992</b>
AlexNet	0.9901	0.9895	0.9909

**Table 4.** Wisconsin grid search results

Classifiers	Parameters	Accuracy
Naive Bayes	priors: None, var_smoothing: 1e-09	0.9434
k-NN	n_neighbors: 10, p: 1, weights: 'distance'	0.9688
SVM	C: 10.0, gamma: 'scale', kernel: 'rbf'	<b>0.9765</b>
RF	criterion: 'entropy', max_features: 'sqrt', n_estimators: 500	0.9629

**Table 5.** BreakHis best classifier results

Classifiers	RF	
Magnification Rate	Parameters	Accuracy
40x	criterion: 'entropy', n_estimators: 500	<b>0.8773</b>
100x	criterion: 'entropy', n_estimators: 500	<b>0.8660</b>
200x	criterion: 'entropy', n_estimators: 500	<b>0.8615</b>
400x	criterion: 'entropy', n_estimators: 500	<b>0.8711</b>

**Table 6.** DDSM grid search results

Classifiers	Parameters	Accuracy
Naive Bayes	priors: None, var_smoothing: 1e-09	0.8330
k- Nearest Neighbor	n_neighbors: 10, weights: 'distance'	0.9995
SVM	C: 10.0, kernel: 'rbf'	<b>0.9998</b>
RF	criterion: 'entropy', n_estimators: 500	0.9988

### 3 CONCLUSION

Breast cancer is a disease for which early diagnosis is of great importance. Machine learning algorithms and deep learning methods in the literature are used in CDSS so that early diagnosis and treatment of the disease can be carried out easier and faster. This study proves the importance of artificial intelligence in the field of early diagnosis of breast cancer and CDSS. Machine learning and deep learning algorithms are continuously improved, and they can provide more effective and better decision systems. The results achieved a better accuracy rate than the literature.

## Acknowledgments

This study has been supported by TÜBİTAK with project number 1919B012307755 within the scope of 2209-A University Students Research Projects Support Program.

## References

- [1] K. P. Traves and S. E. H. Cokenakes, "Breast cancer treatment," *American Family Physician*, vol. 104, no. 2, Aug. 2021.
- [2] F. A. Spanhol, L. S. Oliveira, C. Petitjean, and L. Heutte, "A Dataset for breast cancer histopathological image classification," *IEEE Transactions on Biomedical Engineering*, vol. 63, no. 7, pp. 1455–1462, Jul. 2016.
- [3] J. E. Joy, E. E. Penhoet and D. B. Petitti, *Saving Women's Lives: Strategies for Improving Breast Cancer Detection and Diagnosis*, USA: Natl. Acad. Press, 2005.
- [4] Niharika G. Maity and Dr. Sreerupa Das, "Machine learning for improved diagnosis and prognosis in healthcare," in *2017 IEEE Aerospace Conf.*, 2017.
- [5] A. Wright, D. F. Sittig, J. S. Ash, S. Sharma, J. E. Pang, and B. Middleton, "Clinical decision support capabilities of commercially-available clinical information systems," *Journal of the American Medical Informatics Association*, vol. 16, no. 5, pp. 637–644, Sept. 2009.
- [6] M. Ji, G. Z. Genchev, H. Huang, T. Xu, H. Lu, and G. Yu, "Evaluation framework for successful artificial intelligence-enabled clinical decision support systems: Mixed methods study," *Journal of medical Internet research*, vol. 23, no. 6, art. no. e25929, Jun. 2021.
- [7] W. M. Salama and M. H. Aly, "Deep learning in mammography images segmentation and classification: Automated CNN approach," *Alexandria Engineering Journal*, vol. 60, pp. 4701–4709, Mar. 2021.
- [8] K. Ganesh and B. P. Rao, "Classification of breast cancer from mammogram images using DenseNET," *Journal of Biomedical Engineering*, vol. 40, no.2, pp. 192–199, 2023.
- [9] A. A. Adeniyi and S. A. Adeshina, "Automatic classification of breast cancer histopathological images based on a discriminatively fine-tuned deep learning model," in *2021 1st International Conference on Multidisciplinary Engineering and Applied Science (ICMEAS)*, Abuja, Nigeria, 2021, pp. 1–5.
- [10] I. O. Obaid, M. A. Mohammed, M. K. A. Ghani, S. Mostafa, and F. T. Al-Dhief, "Evaluating the performance of machine learning techniques in the classification of wisconsin breast cancer," *International Journal of Engineering and Technology*, vol.7 no. 4.36, pp. 160–166, 2018.
- [11] S. Badillo, B. Banfai, F. Birzele, I.I Davydov, L. Hutchinson, T. Kam-Thong, J. Siebourg-Polster, B. Steiert, and J. D. Zhang. "An introduction to machine learning," *Clin. Pharmacol. Ther.*, vol.107, no.4, pp. 871–885, 2020.
- [12] V. R. Jakkula. "Tutorial on support vector machine (SVM)," 2011.
- [13] J. Sun, W. Du, and N. Shi. "A survey of kNN algorithm," *Information Engineering and Applied Computing*, 2018.
- [14] S. Misra and H. Li, "Noninvasive fracture characterization based on the classification of sonic wave travel times," in *Machine Learning for Subsurface Characterization*, S. Misra, H. Li and J. He, Gulf Professional Publishing, 2020, pp. 243–287.
- [15] S. A. Albelwi, "Deep Architecture based on DenseNet-121 model for weather image recognition" *International Journal of Advanced Computer Science and Applications (IJACSA)*, vol. 13, no. 10, pp. 559–565, 2022.
- [16] B. J. Bipin Nair, B. Arjun, S. Abhishek, N. M. Abhinav, and V. Madhavan, "Classification of Indian Medicinal Flowers using MobileNetV2," in *2024 11th International Conference on Computing for Sustainable Global Development (INDIACom)*, New Delhi, India, 2024, pp. 1512–1518.
- [17] G. Sriram, T .R. G. Babu, R. Praveena, and J. V. Anand "Classification of leukemia and leukemoid using VGG-16 convolutional neural network architecture," *Mol. Cellular Biomechanics*, vol. 19, no. 1, pp. 29–40, 2022.
- [18] J. Gupta, S. Pathak, and G. Kumar, "Deep learning (CNN) and transfer learning: A review", *Journal of Physics: Conference Series*, vol. 2273, Feb. 2022.
- [19] S. M. S. Islam, S. Rahman, M. M. Rahman, E. K. Dey, and M. Shoyaib, "Application of deep learning to computer vision: A comprehensive study," in *2016 5th International Conference on Informatics, Electronics and Vision (ICIEV)*, Dhaka, Bangladesh, pp. 592–597, 2016.



## A Review on Data Visualization: Usage Fields, Importance, and Examples

Durmus Ozkan Sahin<sup>\*1</sup>

<sup>1</sup>Department of Computer Engineering, Ondokuz Mayıs University, Samsun, Türkiye

---

### Abstract

Data visualization is the process of transforming information into visual elements with graphs or tables in order to display it in a meaningful and effective way. This study includes the importance of data visualization, its usage areas and example uses in different programming languages. Nowadays, it has become very important to deal with the rapidly increasing amount of data, to analyse and extract information. Data visualization has become very important precisely because of this need. Data visualization is used effectively in many fields, from business to science, from education to health. Large amounts of data are made meaningful with data visualization in business analytics, marketing strategies, financial analysis, scientific research and many other fields. In the study, examples of studies on data visualization are presented. For example, it is supported by sample articles where data visualization is used effectively in many fields, from road traffic analysis to maritime traffic, from big data analysis to COVID-19 vaccine data. Additionally, this study presents examples of data visualization through Matplotlib and Seaborn libraries in the Python programming language and ggplot libraries in the R programming language. These libraries help understand data more effectively by creating various graphs and tables. How to visualize data effectively is explained with examples from each library.

**Keywords:** *Data visualization, Data visualization Libraries, Python programming language, R programming language, Matplotlib, Seaborn, ggplot*

---



## Recognition of Human Activities Using Accelerometer and Gyroscope Sensors in Mobile Devices

Merve Buluslu<sup>\*1</sup>, Adem Korkmaz<sup>2</sup>

<sup>1</sup>Graduate School of Natural and Applied Sciences, Bandirma Onyedü Eylül University, Balıkesir, Türkiye

<sup>2</sup>The Department of Computer Technology, Bandirma Onyedü Eylül University, Balıkesir, Türkiye

### Abstract

In recent years, advancements in sensor technologies in mobile devices have enabled the development of new methodologies for classifying physical activities. This study utilizes data obtained from the gyroscope and three-axis accelerometer sensors in smartphones to explore the potential to detect standing (class 0) and walking (class 1) movements. Initially, a skewed dataset containing 106 standing and 6293 walking instances was analyzed using Random Forest (RF), k-Nearest Neighbors (k-NN), Naive Bayes (NB), and Decision Tree (DT) algorithms. The first classification results showed that the DT algorithm exhibited the highest performance with 97% accuracy. In the second phase of the study, the dataset underwent normalization and was balanced through oversampling with the SMOTE algorithm. Subsequent analyses on the balanced dataset indicated that the RF model achieved superior performance with 98% accuracy. These results demonstrate the capability of the Random Forest algorithm to classify movements with high accuracy in balanced datasets following normalization and SMOTE processes. In conclusion, these findings highlight the significant contributions that mobile sensor technologies can make to the development of real-time and accurate activity recognition systems, offering new opportunities in daily life and health monitoring applications.

**Keywords:** Mobile sensors, Activity recognition, Machine learning algorithms, Data balancing, Real-time monitoring

## 1 INTRODUCTION

Recognition of human activities using accelerometer and gyroscope sensors in mobile devices has emerged as a rapidly evolving field due to the widespread adoption of smartphones equipped with these sensors. Accelerometers and gyroscopes are fundamental components in modern smartphones, enabling the detection of a wide range of movements and orientations. This technology plays a crucial role in various applications including healthcare services, personal fitness, and smart device interactions, providing valuable insights into human behavior and activity patterns [1, 2]. Accelerometers measure the acceleration of a device in three-dimensional space, capturing data about movements such as tilting, shaking, or linear motion, while gyroscopes measure the orientation and rotational motion of the device. Together, these sensors offer a comprehensive understanding of the device's motion and position, making them particularly useful for Human Activity Recognition (HAR) applications [3, 4].

The use of accelerometer sensors has also become significant in areas such as vehicular crash detection. Dong et al. [5] have worked on piezoresistive accelerometers developed for crash detection in the automotive industry, and Fazeen et al. [6] have developed a system using accelerometers in modern smartphones to detect traffic accidents in real-time. These systems utilize advanced algorithms to detect sudden changes in speed during accidents and integrate additional data processing techniques to reduce false alarm rates. Integrated sensors in smartphones offer the advantages of low cost and continuous data flow, providing valuable applications in health monitoring and safety [7]. Specifically, data from these sensors are processed using advanced algorithms and machine learning techniques to ensure accuracy and efficiency in real-time applications. Mantyjärvi et al. [8] have developed methods for identifying human movements using multiple accelerometer sensors, employing principal component analysis and independent component analysis for feature extraction, and classifying these features with multilayer perceptron neural networks. Khan et al. [9] have successfully applied Linear Discriminant Analysis (LDA) techniques to classify basic activities such as running and walking using accelerometer data.

In this study, we utilized data from smartphone sensors as examined by AlSahly et al. [10] for indoor localization and tracking without requiring additional hardware or specific infrastructure. Classification algorithms and techniques were aligned to accurately determine users' walking and standing activities. Details concerning the

dataset used in this study, feature extraction from this dataset, and the classification algorithm are discussed in Section 2; experimental results and evaluations are presented in Sections 3 and 4.

## 2 MATERIAL AND METHOD

In this study, IMU sensors integrated into smartphones, such as Accelerometers and Gyroscopes, were utilized to classify human activities into standing (class 0) and walking (class 1). The data derived from these sensors had been previously recorded and used in academic studies. During the data collection process, data was gathered at a sampling frequency of 10 Hz for five seconds in fixed positions, and additional data was collected while participants were moving, based on their stepping behaviors and speeds on different paths [10].

The analysis of the data was conducted on the Google COLAB platform to evaluate classification algorithms. The dataset comprised six attributes related to the accelerometer and gyroscope data for x, y, and z axes, along with activity attributes indicating whether the subjects were standing or walking. In the initial classification process, Random Forest (RF), k-Nearest Neighbors (k-NN), Naive Bayes (NB), and Decision Tree (DT) algorithms were applied, and their performance was evaluated on an imbalanced dataset.

The Random Forest (RF) algorithm is an ensemble model formed by multiple decision trees, where each tree independently learns from a randomly selected subset of data. This model is known for its high accuracy in classification and regression tasks [11]. The k-Nearest Neighbors (k-NN) algorithm determines the class of a sample based on the majority class among its k-nearest neighbors. It is a simple and effective classification method, particularly suitable for small datasets [12]. The Naive Bayes (NB) algorithm provides probabilistic classification based on Bayes' Theorem. It assumes independence of each feature's contribution to the class and delivers quick results in large datasets [13]. The Decision Tree (DT) algorithm classifies data through decision points or nodes, where each node tests an attribute and divides the dataset into smaller subsets. This method generates models that are easy to understand and interpret [14].

For each of these models, metrics such as precision, recall, F1 score, and support were provided:

- Precision: Indicates how many of the model's positive predictions were correct.
- Recall: Shows how many of the actual positive samples were correctly predicted.
- F1 Score: The harmonic mean of precision and recall, it is a balanced performance metric.
- Support: Indicates the number of samples in each class.
- Standing (0): 106 samples
- Walking (1): 6293 samples

To improve the models' performance, data balancing techniques such as SMOTE and normalization were employed.

- Normalization: This technique enhances data quality by feeding the system algorithms, aiming to reduce variation among the data and standardizing it to a specific range, typically between 0 and 1 or -1 and 1 [15].
- SMOTE: Developed as a solution to the imbalanced class problem by Chawla et al. (2002), this over-sampling technique is suggested to counter the overfitting problem that arises from duplicating observation units [16].

The four different machine learning models applied (RF - Random Forest, k-NN - k-Nearest Neighbors, NB - Naive Bayes, and DT - Decision Tree) were represented with confusion matrices (before and after data balancing). Each confusion matrix summarizes how the models performed for the two classes (1: Walking, 0: Standing).

- True Positive (TP): Identifies positive samples correctly predicted as positive.
- True Negative (TN): Identifies negative samples correctly predicted as negative.
- False Positive (FP): Identifies negative samples incorrectly predicted as positive.
- False Negative (FN): Identifies positive samples incorrectly predicted as negative.

## 3 RESULTS

The results should be clear and concise.

**Table 1.** Classification report of RF, k-NN, NB, and DT

	RF				k-NN			
	Precision	Recall	f1-Score	Support	Precision	Recall	f1-Score	Support
0	0.78	0.17	0.28	106	0.55	0.16	0.25	106
1	0.99	1.00	0.99	6293	0.99	0.99	0.99	6293
Accuracy			0.99	6399			0.98	6399
Macro avg	0.99	0.99	0.99	6399	0.99	0.98	0.98	6399
Weighted avg	0.98	0.99	0.98	6399	0.98	0.98	0.98	6399
	NB				DT			
0	0.00	0.00	0.00	106	0.27	0.33	0.30	106
1	0.98	1.00	0.99	6293	0.99	0.98	0.97	6293
Accuracy			0.98	6399			0.97	6399
Macro avg	0.49	0.50	0.49	6399	0.97	0.97	0.97	6399
Weighted avg	0.97	0.98	0.97	6399	0.98	0.97	0.98	6399

Table 1 presents the classification report for the Random Forest (RF), k-Nearest Neighbors (k-NN), Naive Bayes (NB), and Decision Tree (DT) algorithms. The report includes metrics such as precision, recall, f1-score, and support for each class across the different models.

For the standing class (class 0), the RF model achieved a precision of 0.78, recall of 0.17, and an f1-score of 0.28, supported by 106 instances. The k-NN model, on the other hand, showed lower precision at 0.55, with a recall of 0.16 and an f1-score of 0.25 for the same class. Both models struggled to accurately predict the minority class, as indicated by their low recall values.

In contrast, the walking class (class 1) displayed high predictive performance across all models. The RF model reached near-perfect scores with a precision of 0.99, a recall of 1.00, and an f1-score of 0.99, supported by 6293 instances. Similarly, k-NN maintained high scores with a precision and recall of 0.99 and an f1-score of 0.99. This suggests that all models performed well with the majority class but showed varying degrees of difficulty with the minority class.

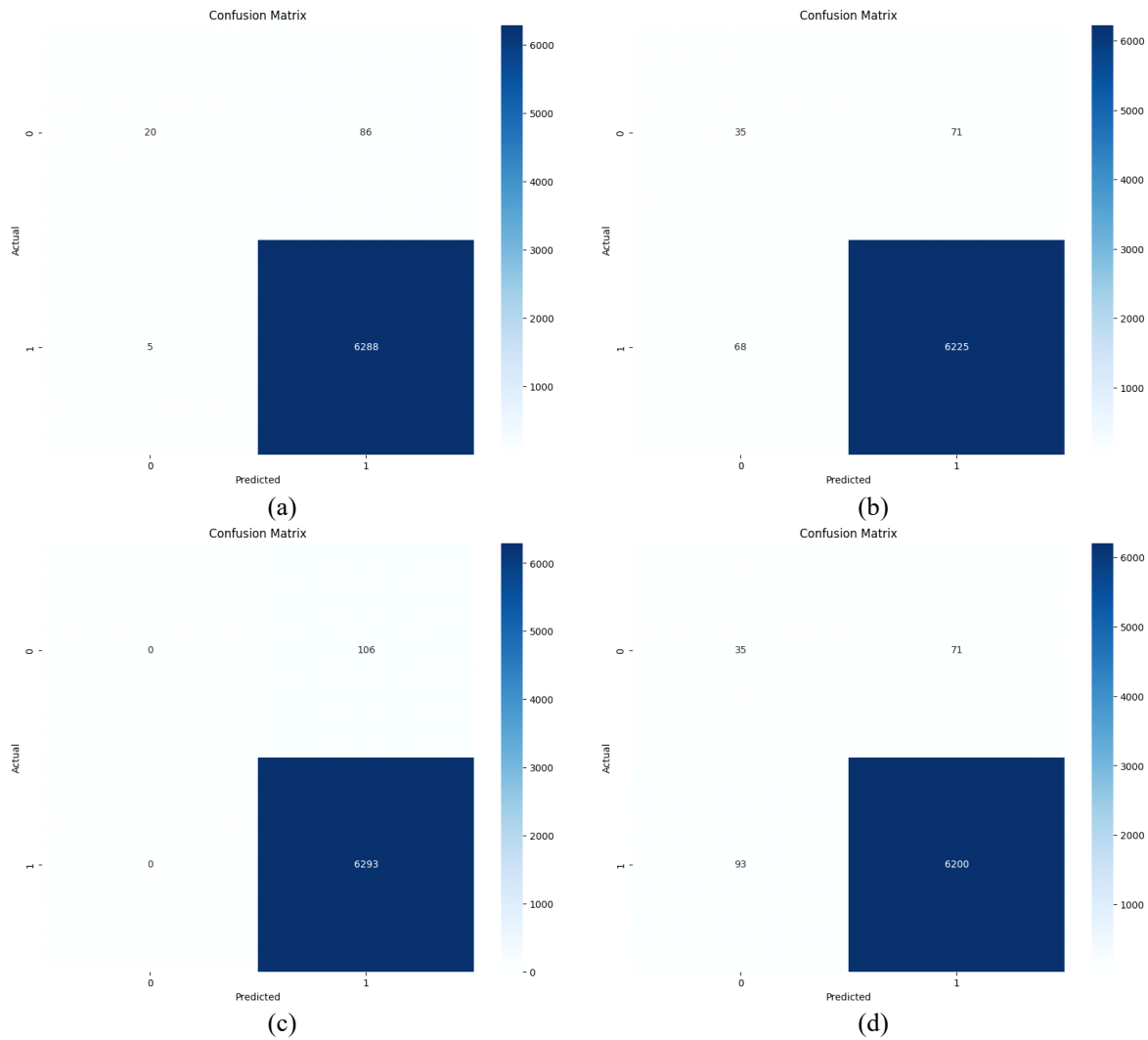
Overall accuracy for RF was recorded at 0.99 for the combined dataset of 6399 instances, slightly higher than the 0.98 achieved by k-NN. This demonstrates the effectiveness of RF in handling this particular dataset.

The Naive Bayes model showed a complete inability to classify the standing class, with all scores at 0.00, highlighting significant limitations with this method in the context of imbalanced data. The Decision Tree model, while not as weak as NB, still showed modest results with a precision of 0.27, recall of 0.33, and an f1-score of 0.30 for class 0.

Macro and weighted averages for the models indicate general trends in performance, with RF and k-NN showing high overall metrics, suggesting robustness across classes, especially in the weighted results which take class imbalance into account.

This detailed classification performance underscores the challenges of imbalanced datasets in machine learning and highlights the effectiveness of certain algorithms over others in managing such disparities. The superior performance of the RF and k-NN models, particularly in terms of accuracy and weighted averages, reflects their potential utility in real-world applications where large imbalances may exist.

Figure 1 displays the confusion matrices for four different machine learning models: Random Forest (RF), k-Nearest Neighbors (k-NN), Naive Bayes (NB), and Decision Tree (DT). Each matrix summarizes how the models performed for two classes (1: Walking, 0: Standing). Upon analyzing the matrices individually, it is observed that the RF model exhibits the best performance in correctly predicting class 1 (Walking). However, it commits more errors in class 0 (Standing), particularly with a high number of false positives (FP). The k-NN model performs well in predicting class 1 but incurs more errors in class 0, especially with a high count of false negatives (FN). The NB model completely misclassifies class 0, with no true negatives (TN) present, yet it is quite successful in predicting class 1. The DT model shows good performance in predicting class 1, but like the others, it is more error-prone in class 0, with a moderate number of false negatives (FN).



**Figure 1.** Confusion matrix results of RF (a), k-NN (b), NB (c), and decision tree (d)

**Table 2.** Classification report of RF, k-NN, NB and DT (Normalization + Smote)

	RF				k-NN			
	Precision	Recall	f1-Score	Support	Precision	Recall	f1-Score	Support
0	0.97	1.00	0.98	6381	0.93	1.00	0.97	6381
1	1.00	0.97	0.98	6187	1.00	0.93	0.96	6187
Accuracy			0.98	12568			0.96	12568
Macro avg	0.98	0.98	0.98	12568	0.97	0.96	0.96	12568
Weighted avg	0.98	0.98	0.98	12568	0.97	0.96	0.96	12568
	NB				DT			
	Precision	Recall	f1-Score	Support	Precision	Recall	f1-Score	Support
0	0.85	0.88	0.87	6381	0.96	0.97	0.97	6381
1	0.88	0.84	0.86	6187	0.97	0.96	0.96	6187
Accuracy			0.87	12568			0.96	12568
Macro avg	0.87	0.87	0.87	12568	0.96	0.96	0.96	12568
Weighted avg	0.87	0.87	0.87	12568	0.96	0.96	0.96	12568

The table presents a detailed classification report following the application of Normalization and SMOTE techniques, analyzing the performance of four machine learning models: Random Forest (RF), k-Nearest Neighbors (k-NN), Naive Bayes (NB), and Decision Tree (DT).

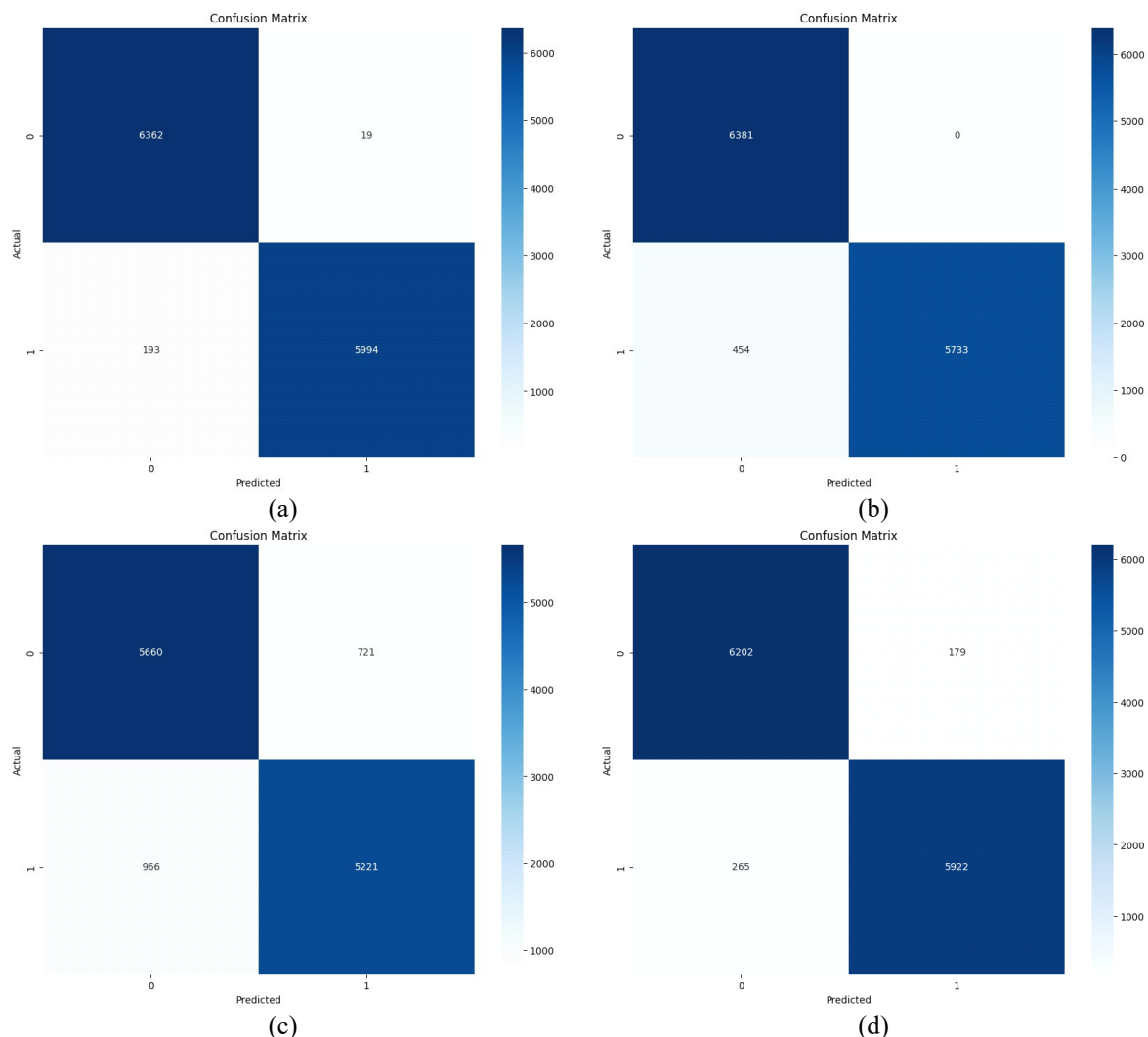
For class 0 (Standing), the RF model achieved impressive metrics with a precision of 0.97, recall of 1.00, and an F1-score of 0.98, supported by 6381 samples. The k-NN model also showed strong results with a precision of 0.93, recall of 1.00, and an F1-score of 0.97. This indicates that both models were highly effective in correctly identifying the standing class, particularly after data balancing techniques were applied.

In class 1 (Walking), the RF model maintained a perfect precision of 1.00 and a recall of 0.97, yielding an F1-score of 0.98. The k-NN model, while still achieving perfect precision, saw a decrease in recall to 0.93, resulting in an F1-score of 0.96. This slight drop suggests a marginal trade-off between precision and recall in the k-NN model for class 1.

The Naive Bayes model showed weaker performance compared to RF and k-NN, with precision and recall around 0.85 and 0.88 respectively for class 0, and slightly lower for class 1. The Decision Tree model closely paralleled the performance of RF, with precision and recall exceeding 0.96 for both classes, indicating robustness in handling balanced datasets.

Overall accuracy of the models ranged from 0.87 for NB to 0.98 for RF, reflecting the effectiveness of the preprocessing steps in enhancing model outcomes. The macro and weighted averages across all models further underline the consistency in model performance, with RF and DT showing particularly high scores, demonstrating their efficacy in a balanced classification context.

This classification report highlights the substantial improvement in model accuracy and balance following the implementation of Normalization and SMOTE, with RF and DT models showing exceptional ability to generalize across both classes.



**Figure 2.** Confusion matrix outcomes for random forest (a), k-nearest neighbors (b), naive bayes (c), and decision tree (d) following normalization and SMOTE techniques

According to the results depicted in Figure 2, the RF model exhibits robust performance with notably low numbers of false positives and false negatives. In contrast, the k-NN model has generated more false negatives compared to RF, indicating difficulties in accurately predicting positive classes. The NB model is particularly characterized by a higher number of false positives compared to other models, suggesting a tendency to over-predict positive



classes. The Decision Tree model also performs well overall but has a higher count of false negatives compared to RF.

Upon evaluating the overall situation, the RF model consistently shows the lowest numbers of false positives and negatives, making it the most reliable model in scenarios where the accuracy of both positive and negative predictions is critical. Conversely, k-NN appears to be at a disadvantage due to its high rate of false negatives. The NB model stands out for its high false positives, indicating a propensity for over-prediction. Although the DT model exhibits higher false negatives than RF, its overall performance remains commendable.

These evaluations assist in determining which models may be more suitable under specific circumstances. For instance, the RF model may be preferred in situations where false negatives are critical, while a choice between DT and RF could be made based on overall accuracy.

## 4 CONCLUSION

In this study, an initial analysis was conducted on an imbalanced dataset using four machine learning algorithms: Random Forest (RF), k-Nearest Neighbors (k-NN), Naive Bayes (NB), and Decision Tree (DT). The initial classification results indicated that the DT algorithm exhibited the highest effectiveness with an accuracy of 97%. In the second phase of the research, the dataset underwent a normalization process and was balanced through oversampling using the SMOTE algorithm. Subsequent analyses on this balanced dataset demonstrated that the RF model performed exceptionally well, achieving an accuracy of 98%. These results highlight the capability of the Random Forest algorithm to classify movements accurately in balanced datasets following normalization and SMOTE processes.

Ultimately, these findings underscore the significant contributions that mobile sensor technologies can make to the development of real-time and accurate activity recognition systems. The application of these technologies presents new opportunities in everyday life and health monitoring applications, indicating their potential to enhance quality of life and healthcare service delivery.

## References

- [1] R. Abdel-Salam, R. Mostafa, and M. Hadhood, "Human activity recognition using wearable sensors: Review, challenges, evaluation benchmark," in *International Workshop on Deep Learning for Human Activity Recognition*, Singapore, 2021, pp. 1–15.
- [2] Saha, U., Saha, S., Kabir, M. T., Fattah, S. A., & Saquib, M. (2024). Decoding human activities: Analyzing wearable accelerometer and gyroscope data for activity recognition. *IEEE Sensors Letters*.
- [3] How do smartphone sensors work? A short guide. (2022). [Online]. Available: <https://kommandotech.com/guides/how-do-smartphone-sensors-work/>
- [4] Sensorlere genel bakis. (2024). [Online]. Available: [https://developer.android.com/develop/sensors-and-location/sensors/sensors\\_overview?hl=tr](https://developer.android.com/develop/sensors-and-location/sensors/sensors_overview?hl=tr)
- [5] P. Dong, X. Li, Y. Wang, S. Feng, and S. Li, "An axial-beam piezoresistive accelerometer for highperformance crash detection of automotive industry," in *5th IEEE Conference on Sensors*, 2006.
- [6] M. Fazeen, B. Gozick, R. Dantu, M. Bhukhiya, and M. C. González, "Safe driving using mobile phones," *IEEE Transactions on Intelligent Transportation Systems*, vol. 13, no. 3, pp. 1462–1468, 2012.
- [7] O. D. Lara and M. A. Labrador, "A survey on human activity recognition using wearable sensors," *IEEE Communications Surveys & Tutorials*, vol. 15, no. 3, pp. 1192–1209, 2012.
- [8] J. Mantyjarvi, J. Himberg, and T. Seppanen, "Recognizing human motion with multiple acceleration sensors," in *2001 IEEE International Conference on Systems, Man and Cybernetics. E-Systems and E-Man for Cybernetics in Cyberspace*, 2001, vol. 2, pp. 747–752.
- A. M. Khan, Y. K. Lee, and S. Y. Lee, "Accelerometer's position free human activity recognition using a hierarchical recognition model," in *The 12th IEEE International Conference on E-Health Networking, Applications and Services*, 2010, pp. 296–301.
- [9] M. AlSahly et al., "Handheld device-based indoor localization with zero infrastructure (HDIZI)," *Sensors*, vol. 22, no. 17, art. no. 6513, 2022, doi: 10.3390/s22176513.
- [10] L. Breiman, "Random forests," *Machine Learning*, vol. 45, pp. 5–32, 2001.
- [11] T. Cover and P. Hart, "Nearest neighbor pattern classification," *IEEE Transactions on Information Theory*, vol. 13, no. 1, pp. 21–27, 1967.
- [12] G. H. Johna and P. Langley, "Estimating continuous distributions in Bayesian classifiers," *arXiv Preprint*, 2013.
- [13] J. R. Quinlan, "Induction of decision trees," *Machine Learning*, vol. 1, pp. 81–106, 1986.

- [14] P. J. M. Ali, R. H. Faraj, E. Koya, P. J. M. Ali, and R. H. Faraj, "Data normalization and standardization: A technical report," *Mach Learn Tech Rep*, vol. 1, no. 1, art. no. 16, 2014..
- [15] K. Ay, and E. Yolacan, "Yeniden ornekleme metotlarının kredi kartı sahtecilik tespiti için topluluk öğrenmesine kapsamlı analizi," *Afyon Kocatepe Üniversitesi Fen ve Mühendislik Bilimleri Dergisi*, vol. 34, no. 2, pp. 123–135, 2022.
- [16] N. V. Chawla, K. W. Bowyer, L. O. Hall, and W. P. Kegelmeyer, "SMOTE: Synthetic minority over-sampling technique," *Journal of Artificial Intelligence Research*, vol. 16, pp. 321–357, 2002, doi: 10.1613/jair.953.



---

## A New Metaheuristic Algorithm for Optimization Problem: Artificial Circulation System Algorithm

Nermin Ozcan<sup>\*1,2</sup>, Semih Utku<sup>3</sup>

<sup>1</sup>Department of Biomedical Technologies, Dokuz Eylul University, Izmir, Türkiye

<sup>2</sup>Department of Biomedical Engineering, Iskenderun Technical University, Hatay, Türkiye

<sup>3</sup>Department of Computer Engineering, Dokuz Eylul University, Izmir, Türkiye

---

### Abstract

Optimization processes play a crucial role in tackling complex problems in engineering, natural sciences, and technological domains. The constraints of industrial research and the intricate nature of design problems impose limitations on current methods, thereby hindering the attainment of optimal solutions. This situation has served as a stimulus for enhancing current methodologies or suggesting novel methodologies with distinct mathematical frameworks. This paper introduces a novel meta-heuristic optimization algorithm known as the Artificial Circulation System Algorithm (ACSA). ACSA mimics the physiological processes involved in the regulatory mechanism of the human circulatory system. The optimization process incorporates neural and hormonal regulators, which are existing systems in the inspiration, into the algorithm's infrastructure. The efficacy of ACSA is evaluated on six widely recognized benchmark functions, and the performance of the algorithm on 2, 10, and 50-dimensional problems is examined through convergence curves. Moreover, the global minima are assessed through statistical analysis and then compared with seven widely-used optimization algorithms. These rigorous studies definitively validate the strength and effectiveness of the proposed algorithm. Furthermore, the algorithm's performance on multidimensional functions showcases its capacity to tackle real-world obstacles. Thus, it is anticipated that the proposed novel algorithm will facilitate its utilization in practical scenarios and serve as a fresh and effective approach.

**Keywords:** *Bio-inspired, Evolutionary, Heuristic, Metaheuristic, Optimization*

---



## Development of an Artificial Intelligence Supported Identity Verification System (KYC)

Ceren Goksu<sup>\*1</sup>, Kerim Guler<sup>1</sup>, Duygu Keles<sup>1</sup>, Halil Sahin<sup>1</sup>

<sup>1</sup>Money pay Payment and Electronic Money Services Inc., Istanbul, Türkiye

---

### Abstract

The rapid advancement of technology is driving significant changes in information security. Particularly, identity verification processes have evolved from traditional methods to biometric database-based authentication systems. Techniques like fingerprint scanning, facial recognition, and retina scanning offer robust security in verifying user identities. However, these systems also pose challenges such as personal data security risks and counterfeit threats.

This study aims to bolster security in identity verification processes through the development of an identity access device integrated with NFC technology using the KEC module. The device aims to swiftly and reliably authenticate documents such as ID cards, thereby minimizing security vulnerabilities. Various technologies have been employed within the project scope to detect counterfeit identity documents using biometric database-based authentication methods. Advanced techniques including machine learning algorithms such as deep learning and artificial neural networks have been utilized to identify attempts at document counterfeiting. Tests and analyses conducted demonstrate that the developed device significantly enhances security and accuracy rates.

The proposed device offers enhanced reliability and user-friendliness compared to existing identity verification systems, with a focus on raising security standards. Additionally, its ease of integration and user-friendly interface enhance its applicability in industrial and commercial settings. In conclusion, this study has demonstrated the effectiveness and usability of a device developed to enhance the security of biometric database-based identity verification systems.

**Keywords:** *Biometric identification system, Security solutions, Authentication technologies*

---



## Breast Cancer Prediction Using Machine Learning Algorithms

Gokberk Kozak<sup>\*1</sup>, Erol Ozcekic<sup>1</sup>

<sup>1</sup>Department of Computer Technology, Balikesir Vocational School, Balikesir University Balikesir, Türkiye

### Abstract

Breast cancer remains a critical global health challenge, necessitating advancements in early detection and predictive methodologies. This study addresses this challenge by evaluating the effectiveness of five distinct machine learning algorithms—Support Vector Machines (SVM), Logistic Regression, Decision Trees, K-Nearest Neighbors (KNN), and Random Forest—in predicting breast cancer outcomes. Utilizing a comprehensive dataset from Kaggle, our analysis leverages Python libraries such as scikit-learn and Matplotlib for model development and evaluation. The models were assessed based on accuracy, with K-Nearest Neighbors achieving the highest accuracy rate of 99.12%, followed by SVM and Random Forest with 96.49% and 95.61%, respectively. The findings underscore the potential of these algorithms to enhance predictive accuracy and inform timely interventions in breast cancer diagnosis, contributing to improved patient outcomes and more effective healthcare strategies.

**Keywords:** Breast cancer Prediction, Machine learning

## 1 INTRODUCTION

Breast cancer is a pressing global health issue that affects millions of individuals each year, with early detection playing a crucial role in improving patient outcomes. As the prevalence of breast cancer continues to rise, there is a compelling need for innovative approaches to enhance prediction and diagnosis [1]. This study explores the application of five distinct machine learning algorithms to develop a robust predictive model for breast cancer detection. Our approach involves using a dataset sourced from UCI machine learning repository, a well-regarded platform for data science competitions and resources [2]. The dataset forms the basis of our analysis, which is performed using Python libraries including scikit-learn for algorithm implementation and Matplotlib for data visualization. The selected algorithms—Support Vector Machines (SVM), Logistic Regression, Decision Trees, K-Nearest Neighbors (KNN), and Random Forest—were chosen for their diverse methodologies and strengths in handling predictive tasks. Each algorithm offers unique advantages: SVM excels in finding optimal decision boundaries, Logistic Regression provides transparency in feature-impact analysis, Decision Trees visualize complex decision rules, KNN identifies patterns based on proximity, and Random Forest enhances accuracy through ensemble learning. By rigorously evaluating these models, we aim to identify the most effective approach for predicting breast cancer, thereby contributing to the global effort to improve early detection and intervention strategies. This study highlights the potential of advanced machine learning techniques in transforming breast cancer diagnosis and underscores the importance of continued innovation in healthcare analytics.

## 2 MATERIAL AND METHOD

### 2.1 Collection of Samples

The dataset used in this study was sourced from digitized fine needle aspiration (FNA) images of breast masses. FNA involves using a thin needle to extract cells from a breast mass, which are then captured in digital form for analysis. Features such as cell shape, size, and texture are extracted from these images to characterize the samples. This dataset, acquired from a reputable machine learning repository, provides a comprehensive and standardized basis for developing and evaluating predictive models in breast cancer detection [3].

**Table 1.** Distribution of patients types

Diagnosis	Number of Cases
Benign	357
Malignant	212

## 2.2 Data Preprocessing

To ensure that the machine learning models operate effectively, the dataset underwent normalization and standardization. These preprocessing steps are crucial for handling features with different scales and distributions.

- Normalization adjusts feature values to a common scale, typically  $[0, 1]$ . This is achieved by subtracting the minimum value of the feature and dividing by the range of the feature values. Normalization is particularly useful when the model relies on distance metrics or gradient-based optimization, as it helps prevent features with larger scales from dominating the learning process.
- Standardization involves rescaling features to have a mean of zero and a standard deviation of one. This is done by subtracting the mean of the feature and dividing by its standard deviation. Standardization is essential for algorithms that assume features are normally distributed or when they involve computations that are sensitive to the scale of data, such as Support Vector Machines (SVM) and Logistic Regression.

By applying normalization and standardization, we ensure that all features contribute equally to the model's performance and that the learning algorithms can converge more efficiently.

Feature selection and engineering are pivotal in enhancing model performance and interpretability.

- Feature Selection involves identifying and retaining the most relevant features for the predictive model while discarding irrelevant or redundant ones. This process helps in reducing the dimensionality of the data, improving model accuracy, and decreasing training time. Methods such as recursive feature elimination, feature importance from tree-based models, and statistical tests were employed to select the most influential features. Feature selection not only optimizes model performance but also enhances interpretability by focusing on the most critical attributes.
- Feature Engineering entails creating new features or modifying existing ones to better capture the underlying patterns in the data. This could involve generating interaction terms, polynomial features, or aggregating multiple features to create composite indicators. For this dataset, feature engineering included deriving new metrics based on existing cell characteristics to better capture the nuances of breast mass properties. Effective feature engineering helps in revealing hidden patterns and improving model predictive power.

Together, normalization/standardization and feature selection/engineering play a critical role in preparing the data for machine learning models, ensuring that they are trained on a well-structured and relevant set of features for optimal performance.

## 2.3 Description of Machine Learning Models

In this study, we utilized a variety of machine learning algorithms to predict breast cancer outcomes. Each model brings distinct strengths to the table, contributing to a comprehensive predictive framework. Here is a detailed description of each model used

### 2.3.1 Support Vector Machines (SVM)

Support Vector Machines (SVM) are a powerful classification technique that works by finding the optimal hyperplane that separates different classes in the feature space. SVM aims to maximize the margin between data points of different classes, thus creating the most robust boundary for classification. This model is particularly effective in high-dimensional spaces and is versatile in handling linear and non-linear classification tasks through the use of different kernel functions, such as linear, polynomial, and radial basis function (RBF) kernels [4]. SVM is known for its effectiveness in cases where the number of dimensions exceeds the number of samples, making it suitable for complex breast cancer data.

### 2.3.2 Logistic Regression

Logistic Regression is a fundamental classification algorithm used to model the probability of a binary outcome. It estimates the probability that a given input belongs to a particular class using a logistic function (sigmoid function) to produce an output between 0 and 1. Logistic Regression provides interpretability by offering coefficients that indicate the relationship between each feature and the outcome. This model is straightforward and effective, particularly when the relationship between features and the target variable is approximately linear. It is often used as a baseline model for binary classification tasks like predicting breast cancer.

### 2.3.3 Decision Tree

Decision Trees are intuitive models that create a flowchart-like structure where each internal node represents a decision based on a feature, each branch represents the outcome of that decision, and each leaf node represents a class label. The tree is built by recursively splitting the dataset into subsets based on feature values that best separate the classes. Decision Trees are valuable for their interpretability, as they visually represent decision rules and are easy to understand. However, they can be prone to overfitting, particularly with complex datasets. Techniques like pruning and setting a maximum depth can help mitigate this issue.

### 2.3.4 K-Nearest Neighbors (KNN)

K-Nearest Neighbors (KNN) is a non-parametric algorithm used for classification and regression tasks. It classifies a data point based on the majority class among its 'k' nearest neighbors in the feature space. The distance between points is usually measured using metrics such as Euclidean distance. KNN is simple and effective, especially when the decision boundary is not linear. It does not require a training phase as it makes predictions based on the entire training dataset, which can be computationally expensive for large datasets. KNN is sensitive to the choice of 'k' and the distance metric, making hyperparameter tuning crucial for optimal performance.

### 2.3.5 Random Forest

Random Forest is an ensemble learning method that combines multiple Decision Trees to improve classification accuracy and robustness. It constructs a multitude of decision trees during training and outputs the mode of the classes (for classification) or the mean prediction (for regression) of the individual trees. Random Forest mitigates overfitting by averaging the results of various trees, which reduces variance and increases generalization. This model is highly effective for handling large datasets with complex interactions among features. It also provides feature importance scores, which can be valuable for understanding the contribution of different features to the model's predictions.

Each of these models offers unique advantages and contributes to a comprehensive analysis of breast cancer predictions. By leveraging their individual strengths, we aim to develop a robust and accurate predictive framework.

## 2.4 Model Training

In our study, model training and validation were crucial steps in developing and assessing the performance of the predictive algorithms. This process involves several key stages to ensure that the models are well-trained, reliable, and capable of generalizing to new, unseen data.

### 2.4.1 Training Process

The training process involves feeding the machine learning models with the dataset to learn from the data and adjust their parameters accordingly. The dataset was split into training and testing sets to facilitate this process:

- Training Set: A portion of the dataset, typically 70-80%, was used to train the models. During training, the models learn the relationships between the features and the target variable (e.g., benign or malignant). The training phase includes:
  - Algorithm Selection: Choosing the appropriate algorithm based on the problem and dataset characteristics.
  - Parameter Tuning: Adjusting hyperparameters (such as the number of neighbors in KNN or the depth of trees in a Decision Tree) to optimize model performance. Techniques such as grid search or random search were used to find the best combination of parameters.
  - Fitting the Model: Using the training data to fit the model, which involves adjusting the model parameters to minimize the prediction error.

### 2.4.2 Validation Method

To evaluate the performance of the models and ensure they generalize well to new data, several validation methods were employed:

- Cross-Validation: The dataset was divided into multiple subsets (folds), and the model was trained and validated on different combinations of these subsets. A common approach is k-fold cross-validation, where the

data is split into  $k$  equal parts. The model is trained  $k$  times, each time using  $k-1$  folds for training and the remaining fold for validation [5]. The performance metrics are averaged across all  $k$  iterations to provide a more robust estimate of model performance.

- **Validation Set:** Alternatively, a separate validation set (typically 20-30% of the data) was used to assess the model's performance after training [6]. This set was not seen by the model during training, providing an independent measure of its ability to generalize.
- **Performance Metrics:** The models were evaluated using various metrics to assess their predictive accuracy and reliability:
  - **Accuracy:** The proportion of correctly classified instances out of the total number of instances.
  - **Precision and Recall:** Precision measures the proportion of true positives among the predicted positives, while recall measures the proportion of true positives among the actual positives.
  - **F1 Score:** The harmonic mean of precision and recall, providing a single metric that balances both aspects.
  - **Confusion Matrix:** A table showing the true positives, false positives, true negatives, and false negatives, which helps in understanding the model's performance in more detail.

### 2.4.3 Model Evaluation and Selection

After training and validating the models, a comparative analysis was conducted to select the best-performing model. This involved:

- **Comparing Metrics:** Evaluating the performance metrics of each model to determine which provided the highest accuracy, precision, recall, and F1 score.
- **Assessing Overfitting and Underfitting:** Ensuring that the model does not overfit (perform exceptionally well on training data but poorly on new data) or underfit (perform poorly on both training and test data) [7].

By systematically training and validating the models, we aimed to ensure that they are robust, accurate, and capable of providing reliable predictions for breast cancer diagnosis. This comprehensive approach to model evaluation and selection contributes to the overall effectiveness of our predictive framework.

## 3 RESULTS

In this section, we present the performance of the various machine learning models used in predicting breast cancer outcomes. The evaluation was conducted using confusion matrices and classification reports for each model, which provide insights into their accuracy, precision, recall, and overall effectiveness.

### 3.1 Model Performance Overview

The models were assessed on their ability to correctly classify cases as benign or malignant. Key performance metrics, including accuracy, precision, recall, and F1 score, were computed for each model [8]. The confusion matrices for each model illustrate the number of true positives, true negatives, false positives, and false negatives, while the classification reports summarize these metrics in detail.

### 3.2 Confusion Matrices

The confusion matrices visually represent the performance of each model in distinguishing between benign and malignant cases. They provide a clear view of how many cases were correctly classified and where the models made errors. Each matrix is followed by a detailed breakdown of true positive, true negative, false positive, and false negative counts [9].



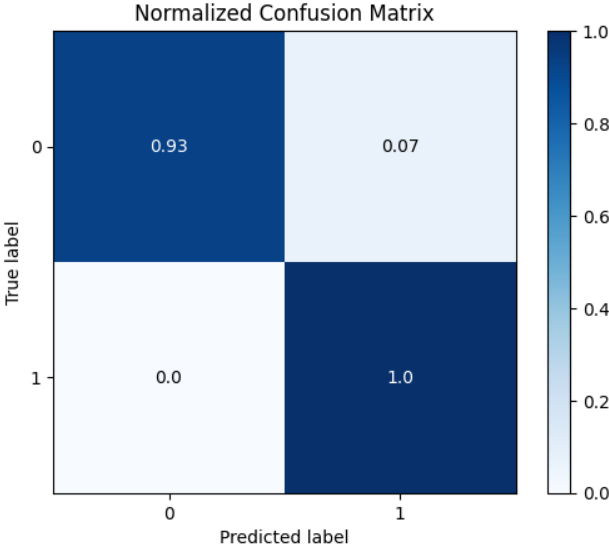


Figure 1. Random forest confusion matrix

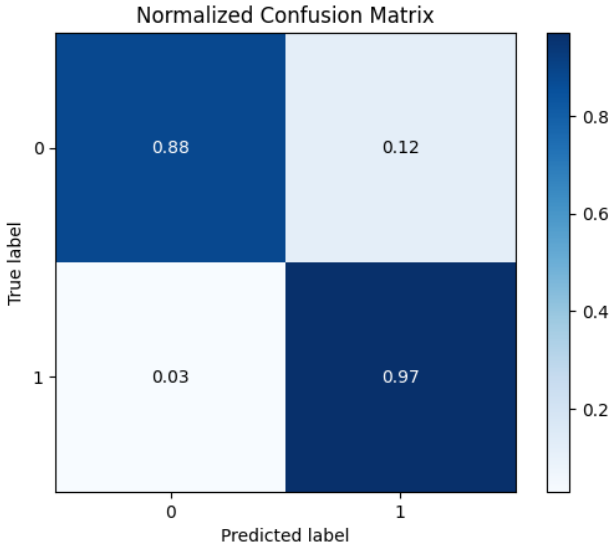


Figure 2. Decision tree confusion matrix

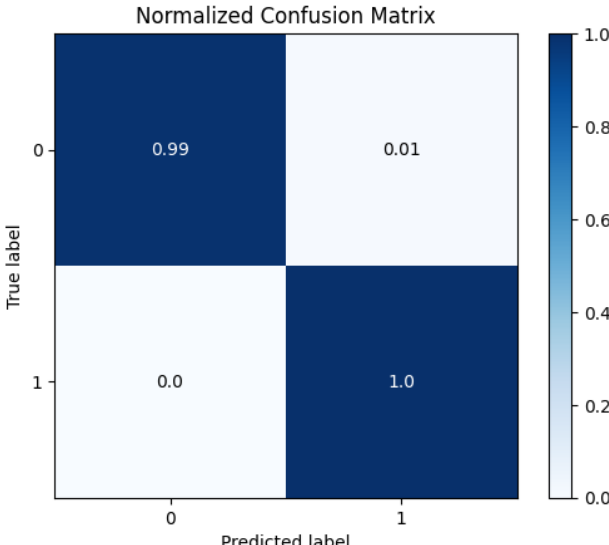
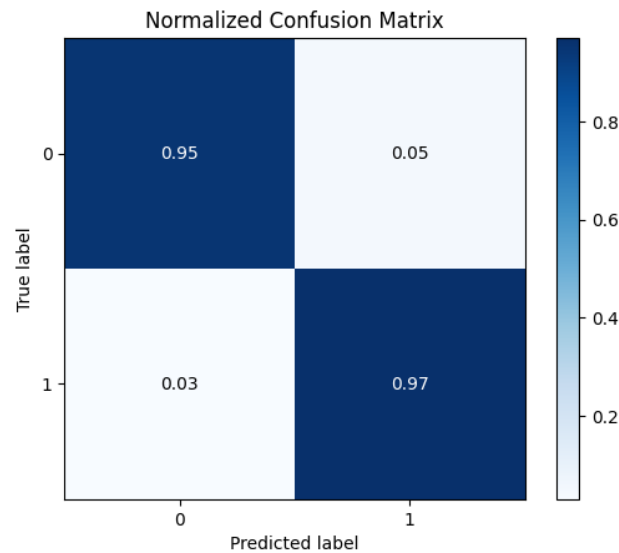
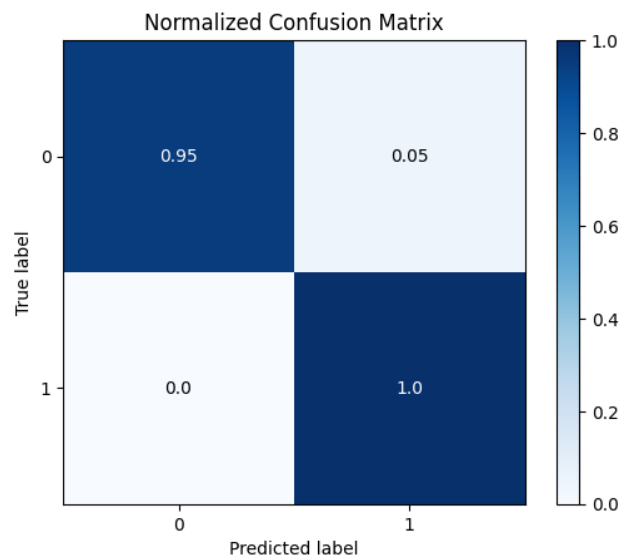


Figure 3. K-nearest neighbors confusion matrix



**Figure 4.** Logistic regression confusion matrix



**Figure 5.** Support vector machine confusion matrix

### 3.3 Classification Reports

The classification reports offer a comprehensive evaluation of each model's performance metrics:

- Accuracy: The proportion of correctly classified cases.
- Precision: The ratio of true positive predictions to the total predicted positives.
- Recall: The ratio of true positive predictions to the total actual positives.
- F1 Score: The harmonic mean of precision and recall, providing a single metric for model performance.

These metrics help in understanding how well each model performs and in comparing their relative strengths and weaknesses [10]. The results from these evaluations are crucial for selecting the most effective model for breast cancer prediction.

Further details, including the specific confusion matrices and classification reports for each model, are provided in the subsequent sections. These visualizations and reports will guide the interpretation of the models' performance and their potential for practical application in breast cancer diagnosis.

**Table 2.** Class: 0 classification report

	Model Name	Precision	Recall	F1-Score
1	Support Vector Machine	1.00	0.95	0.97
2	Logistic Regression	0.99	0.95	0.97
3	Decision Tree Classifier	1.00	0.95	0.97
4	KNN (k-Nearest Neighbors)	1.00	0.95	0.97
5	Random Forest Classifier	1.00	0.93	0.97

**Table 3.** Class: 1 classification report

	Model Name	Precision	Recall	F1-Score
1	Support Vector Machine	0.91	1.00	0.95
2	Logistic Regression	0.90	0.97	0.94
3	Decision Tree Classifier	0.91	1.00	0.95
4	KNN (k-Nearest Neighbors)	0.91	1.00	0.95
5	Random Forest Classifier	0.89	1.00	0.94

## 4 CONCLUSION

This study evaluated several machine learning models for predicting breast cancer outcomes, utilizing a dataset derived from digitized fine needle aspiration (FNA) images. The models assessed include Support Vector Machines (SVM), Logistic Regression, Decision Tree, K-Nearest Neighbors (KNN), and Random Forest. Our findings indicate that each model offers unique strengths in terms of predictive accuracy and interpretability. K-Nearest Neighbors achieved the highest accuracy, highlighting its effectiveness in identifying patterns within the dataset. Support Vector Machines and Random Forest also demonstrated strong performance, with high accuracy rates and robustness across different scenarios. Logistic Regression, while slightly less accurate, provided valuable insights into feature relationships, and Decision Trees offered intuitive decision-making processes. The evaluation through confusion matrices and classification reports revealed nuanced details about each model's performance. Metrics such as precision, recall, and F1 score were instrumental in understanding the models' strengths and areas for improvement. In summary, the comprehensive analysis underscores the potential of machine learning models in enhancing early detection and prediction of breast cancer. The choice of model may depend on specific needs such as interpretability or computational efficiency. Future work could explore combining models or integrating additional data sources to further refine predictive accuracy and clinical applicability. This study contributes to the ongoing efforts in improving breast cancer diagnosis and highlights the importance of utilizing diverse algorithms to address this critical health challenge effectively.

## References

- [1] G. Bertoli, C. Cava, and I. Castiglioni, "MicroRNAs: New biomarkers for diagnosis, prognosis, therapy prediction and therapeutic tools for breast cancer," *Theranostics*, vol. 5, no. 10, art. no. 1122, 2015.
- [2] D. Dua and C. Graff, "UCI Machine Learning Repository," Irvine, CA: University of California, School of Information and Computer Science, 2019. Available: <http://archive.ics.uci.edu/ml>
- [3] L. Jelen, T. Fevens, and A. Krzyzak, "Classification of breast cancer malignancy using cytological images of fine needle aspiration biopsies," *International Journal of Applied Mathematics and Computer Science*, vol. 18, no. 1, art. no. 75, 2008.
- [4] S. Amarappa and S. V. Sathyanarayana, "Data classification using support vector machine (SVM), a simplified approach," *Int. J. Electron. Comput. Sci. Eng.*, vol. 3, pp. 435–445, 2014.
- [5] D. Krstajic et al. "Cross-validation pitfalls when selecting and assessing regression and classification models," *Journal of cheminformatics*, vol. 6, pp. 1–15, 2014.
- [6] S. Raschka, "Model evaluation, model selection, and algorithm selection in machine learning," *arXiv Preprint, arXiv:1811.12808*, 2018.
- [7] O. A. Montesinos López, A. Montesinos López, and J. Crossa, "Overfitting, model tuning, and evaluation of prediction performance," in *Multivariate Statistical Machine Learning Methods for Genomic Prediction*, Cham: Springer International Publishing, 2022. pp. 109–139.
- [8] R. Yacouby and D. Axman, "Probabilistic extension of precision, recall, and f1 score for more thorough evaluation of classification models," in *Proceedings of the First Workshop on Evaluation and Comparison of NLP Systems*, 2020. pp. 79–91.
- [9] J. Liangi "Confusion matrix: Machine learning," *POGIL Activity Clearinghouse*, vol. 3, no. 4, 2022.
- [10] J. P. Craig, K. K. Nichols, E. K. Akpek, B. Caffery, H. S. Dua, C. K. Joo et al., "TFOS DEWS II definition and classification report," *The Ocular Surface*, vol. 15, no. 3, pp. 276–283, 2017.



---

## A Drum Wheel Bearing Design in Tumble Dryer

Abdullah Berk Ince<sup>\*1,2</sup>, Cevdet Caner Akgun<sup>\*1,2</sup>

<sup>1</sup>R&D Department, Vestel White Goods/Tumble Dryer Factory, Manisa, Türkiye

<sup>2</sup>Dokuz Eylul University, Manisa, Türkiye

---

### Abstract

This study focuses on bearing design of a motor-driven drum, used in tumble dryer, which is supported at two points to enable axial rotation. The bearing support is provided through the rear panel and front shield sides, by utilizing reduction screws and bushings for bearing assembly rigidity.

The main purpose of this study is to eliminate the bushing in the existing structure and replace its function with plastic reinforcement figures added to the front shield. In order to validate the new design, fatigue analyses and lifecycle tests were performed.

In the new design, bushings were omitted, ensuring that displacement and fatigue resistance values under dynamic loads on the screw region remained within limits during operation. The reinforced plastic support featured circumferential plastic additions around the screw socket, increasing wall thickness based on load distribution.

ANSYS were used during the analysis of the design. Fatigue analysis for both existing and new designs showed no damage, considering infinite life as  $10^6$  according to Y normal stress.

Comparisons revealed that the new design had reduced displacement compared to the existing design. Due to the brittle material behavior of the front shield, the Coulomb Criterion was applied using maximum and minimum principal stresses in the screw socket region. Von Mises stresses were considered for the screw, and capillary ribs were added to the inside of the socket hole to ensure assembly rigidity and create a pre stress. Analyses confirmed 60% reduction in stresses on the screw in the new design (without bushing element), verifying its suitability. The design was adapted to the plastic injection mold, and six-month lifetime tests were conducted.

The study resulted in an annual cost saving of 70,000€ by eliminating the bushings in product. In addition, amount of bushing-related scrap and assembly labor have reduced. Procurement process has simplified.

**Keywords:** Displacement analysis, ANSYS static structural analysis, Fatigue analysis, Wheel support, reinforced design

---



## Examining the Trend of MOOC Related Studies with Data Mining: Voyant Analyst

Bunyami Kayali<sup>\*1</sup>, Mehmet Yavuz<sup>2</sup>

<sup>1</sup>Vocational School of Technical Sciences, Bayburt University, Bayburt, Türkiye  
<sup>2</sup>Distance Education Application and Research Center, Bingöl University, Bingöl, Türkiye

### Abstract

This study aims to determine the profile and trend of the studies on MOOC with the Voyant text mining tool. In this direction, the text mining method was used in the study. Web of Science (WoS) database was searched with the related words MOOC, "massive open online course", "MOOCs", and "massive open online courses", and 2822 studies with open access constituted the sample of the study. The data were analysed using Voyant Tool, an online and open-source text mining tool. The abstracts of the studies were brought together and uploaded to the online web page <https://voyant-tools.org/>, and various analyses were performed. The most recurring words in the abstracts are "MOOC", "students", "education", "open", "online", "learning", "massive", and "course". These words were followed by "study", "learners", "research", "massive" and "data". "Online", "students", "MOOCs", and "MOOC" were the most used words with "learning". The words "epidemic", "devices", "frequency", "improve", and "curriculum" have a high correlation with learning. While the use of the word "learning" in the studies showed a continuously increasing trend, the use of "MOOC" showed a decreasing and then increasing trend. In some studies, it was observed that it was used in similar numbers with learning. Other words such as "online", "source", "open", and "education" showed similar trends. As a result of the study, it is recommended for researchers to scan the literature by using these words in their studies on the field in question, to determine the keywords related to their studies among these words, and to use the related words expressed here together while determining the titles of the studies.

**Keywords:** MOOC, Data mining, Voyant tool

## 1 INTRODUCTION

The philosophy of openness in education is based on the idea that knowledge produced collectively by people is a shared value of humanity. An important starting point of the openness movement was the 'Open Course Resources' project launched by the Massachusetts Institute of Technology (MIT) in 2001. The university announced to the world that it would freely share all its knowledge. In 2012, UNESCO published the "Paris Declaration on Open Educational Resources" [1]. In the declaration, open educational resources are characterised as freely accessible and usable without restrictions [2].

The positive and expansionist attitude of this movement towards ensuring equality of opportunity in education and the developments in information and communication technologies (ICT) has brought along a series of practices with an openness philosophy in the field of education [3]. Thanks to ICT tools, providing time and space flexibility within the scope of educational activities, increasing presentation capacity and interaction between stakeholders have paved the way for some of the applications mentioned above in the e-learning field [4]. Massive Open Online Courses (MOOCs) are the most current and widespread applications in e-learning [5].

The idea of a MOOC first emerged when Siemens and Downes decided to design a course format that could overlap with the theory of connectivism. In this context, Siemens and Downes' "Connectivism and Connective Knowledge" course, which they gave at their own university in 2008, was recorded as the first application of the online history course [6]. While the course was taken for credit by only 25 people, it was free of charge and without credit by 2300 people worldwide [7]. After the implementation, MOOC was defined as the accessibility of any online course, its openness to many people, and the free provision of educational resources and materials [8]. The openness-oriented movement is also an evolved form that emerged mainly with networked learning [9].

MOOCs' first and foremost goal is to provide free and open educational opportunities to as many people as possible [10]. MOOCs are flexible and easy-to-access applications that provide equal opportunity for participants

with the flexibility of time and place. Participants' ages, income levels, locations or education levels are ignored [11]. Anyone with an internet connection can access the shared content, communicate with other participants, and participate in the MOOC at length. Short educational videos, multiple-choice exams, and peer-supported online discussions in the form of questions and answers form the general structure of the course. MOOCs can create a sense of community, allow you to connect over the internet and develop lifelong learning skills [8]. It can create a personal learning network, especially for Generation Z, who are prone to learning through visuals and online thanks to the rapid flow of data.

Following the spread of the philosophy of openness in education through open course materials, MOOCs have steadily increased in popularity [12]. A few years after its emergence, it has aroused great interest worldwide [13]. The advantages of higher education, such as the opportunity to work with experts, international participant interaction, sharing of various instructional materials, low cost, more accessibility and providing individualised support [14], have attracted the attention of universities and further increased the popularity of the MOOCs. This is so much so that the effort of universities to go beyond the physical campus walls and reach a more significant number of students has been put into practice with MOOCs. Universities such as Harvard, MIT, YALE, Duke, Stanford, UC Berkeley and UCLA offer courses and certificates in thousands of different subjects on websites such as Coursera, edX, and Udemy [15]. As of 2019, nearly 120 million students have been reached through approximately 2500 courses organised on these platforms [16].

As a result, the fact that MOOCs are structured by elite higher education institutions with institutional identity all over the world and that people prefer them so intensively has led researchers to focus more on this field [17]. In this direction, considering the abundance of studies on MOOCs in the literature, it is thought that such a study to be conducted on the studies on MOOCs is essential in determining the trend in this field. In this direction, considering the abundance of studies on MOOCs in the literature, it is thought that such a study is essential in determining the trend in this field. In addition, it is thought that the data obtained from this study will significantly contribute to further research, development of publication policies, and guidance of researchers in the field. In this context, 2822 open access articles on MOOCs in the Web of Science database were analysed with the help of data mining according to different variables (most used word, related words). The current study aims to reveal the profile and trend of studies on MOOCs. For this purpose, answers to the following research questions will be sought throughout the study.

- i. What are the most recurring words in study abstracts?
- ii. Which words are related to each other?

## **2 MATERIAL AND METHOD**

In this section, the methodology, sampling, and data analysis of the study are presented. Detailed explanations associated with the literature are given under each heading.

### **2.1 Research Method/Design**

The text mining method was used in the research. Text mining is the process of analysing text to extract valuable information from text for specific purposes [18]. It is also a method that helps the analytical process and interpretation of the research [19].

### **2.2 Sample**

On July 12, 2024, the Web of Science (WoS) database was searched with the keywords “MOOC”, “massive open online course”, “MOOCs”, and “massive open online courses”. 8876 studies were reached, and 2822 with open access constituted the study's sample. These studies were downloaded in Excel format. The abstracts were gathered and uploaded to the online web page “<https://voyant-tools.org/>”.

### **2.3 Data Analysis**

In the study, the data were analysed using the content analysis method. The analysis was conducted using the Voyant tool. Voyant is an open-source, online-based tool for text analysis. This tool uses computational algorithms to generate visuals by making various inferences from texts of different sizes, genres and languages within seconds [20]. In addition to the humanities [21], it has been used in different fields such as literature [22], engineering [23] and medicine [24].

One of the main features of Voyant Tools is to extract repeated words throughout a document and display them in various graphs so that the user can thoroughly learn a body’s central ideas or themes. The terms extracted from Voyant Tools can be used as keywords or converted into topics [25]. Voyant, one of the text mining tools used in the research, performs 24 different analyses such as frequency, distribution, and word cloud of terms.

While conducting the analysis, first, irrelevant words (such as a, so, then, where, which, next, nine, if, and him) in the related studies should be removed. For this, the Stopwords feature in the Voyant tool was used. Here, English, the language of the relevant studies, was selected and 485 irrelevant words in the database were removed. Thus, a more valid and reliable analysis was conducted.

### 3 RESULTS

The study aims to reveal the profile of the studies on MOOCs. In this context, the abstracts of 2822 studies were subjected to Cirrus analysis. The word cloud resulting from the analysis is shown in Figure 1.



Figure 1. Word cloud of the most frequently used words from Cirrus analysis

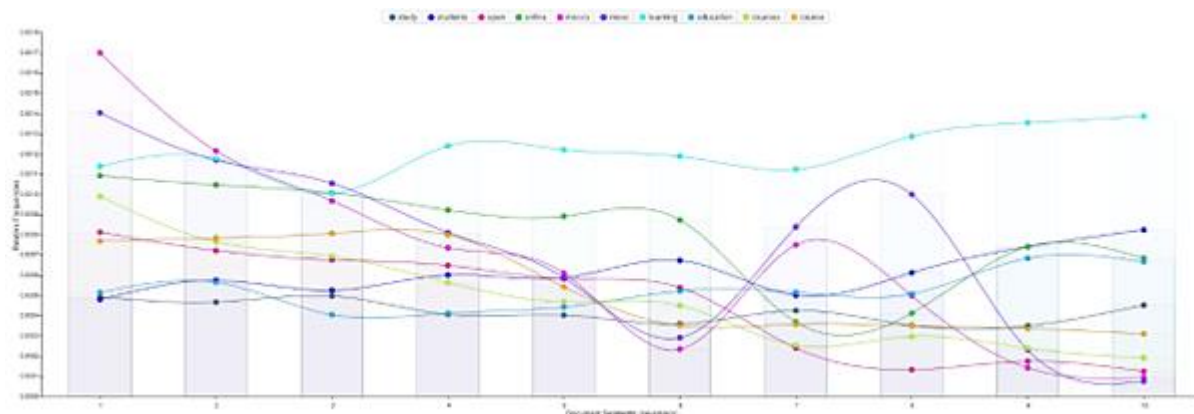
When Figure 1 is examined, it is seen that the 50 most repeated words in the study abstracts are given in the word cloud. As seen in the figure, words such as “MOOC”, “students”, “education”, “open”, “online”, “learning”, “massive”, and “course” stand out as the most repeated words. These words were followed by “study”, “learners”, “research”, “massive” and “data”. The repetition rates of these words because of the analysis are given in Figure 2.

Document Terms				
#	Term	Count	Relative	Trend
1	learning	6416	12.118	
1	online	4254	8.035	
1	mooc	3949	7.459	
1	moocs	3677	6.945	
1	students	3238	6.116	
1	course	2861	5.404	
1	education	2770	5.232	
1	courses	2598	4.907	
1	open	2461	4.648	
1	study	2224	4.201	

Figure 2. Most frequently used words and number of repetitions

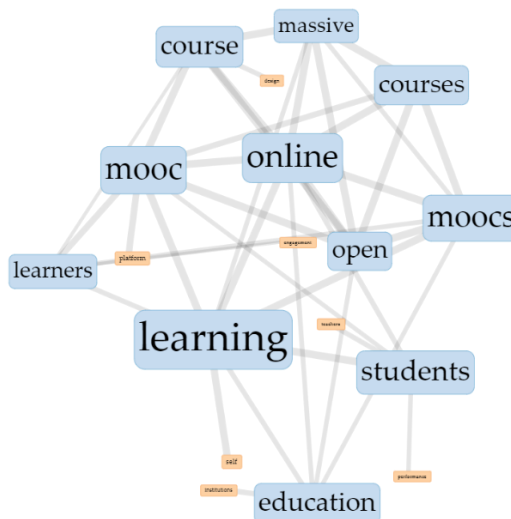
Figure 2 shows the numbers and relative values of the most repeated words as a result of the analysis. Accordingly, it is seen that the most recurring word is “learning” (C=6414, R=12.118). The words “online”, “students”,

“MOOCs”, and “MOOC” were the most frequently used words with "learning". The words “online” (C=4254, R=8.035) and “MOOC” (C=3949, R=7.459) mainly were used with “learning”. The words “epidemic”, “devices”, “frequency”, “improve” and “curriculum” have high correlations with learning. The Trends tool examined the most frequently used words more closely. The Trends tool is used to create a line graph showing the distribution of a word in a text or document. The results of the analysis performed with the Trends tool are presented in Figure 3.



**Figure 3.** Trends tool analysis result

When Figure 3 is analysed, the trends of the ten most repeated words are compared with each other. Among the related words, “learning” showed an increasing trend. On the other hand, “MOOC” showed a decreasing and then an increasing trend. In some studies, it was observed that it was used in similar numbers with learning. The other words “online”, “source”, “open”, and “education” showed similar trends. According to the figure, different words stand out in different studies. Collocates Graph analysis was performed to find out the relationship between the related words and which expressions repeat together the most. This analysis represents words and terms nearby as a power-oriented network graph. The result of the analysis is given in Figure 4.



**Figure 4.** Collocates Graph analysis result

When Figure 4 is analysed, the database's most used main terms are shown with blue boxes, while orange boxes represent the words most associated with the term in question. In addition to the relationship between the main terms, the analysis also revealed that there are sub-relationships such as "education institutions", "performance", "learning-self", "teachers-students", "learners-engagements", "MOOC-platform", and "course design".

Scatterplot analysis was conducted to show how the words that emerged from the analysis were clustered in a text. Along with this analysis, similarity, correspondence analysis, principal component analysis and t-stochastic Neighbor Embedding (t-SNE) analysis were performed. The t-SNE analysis results obtained within the scope of the study are given in Figure 5.



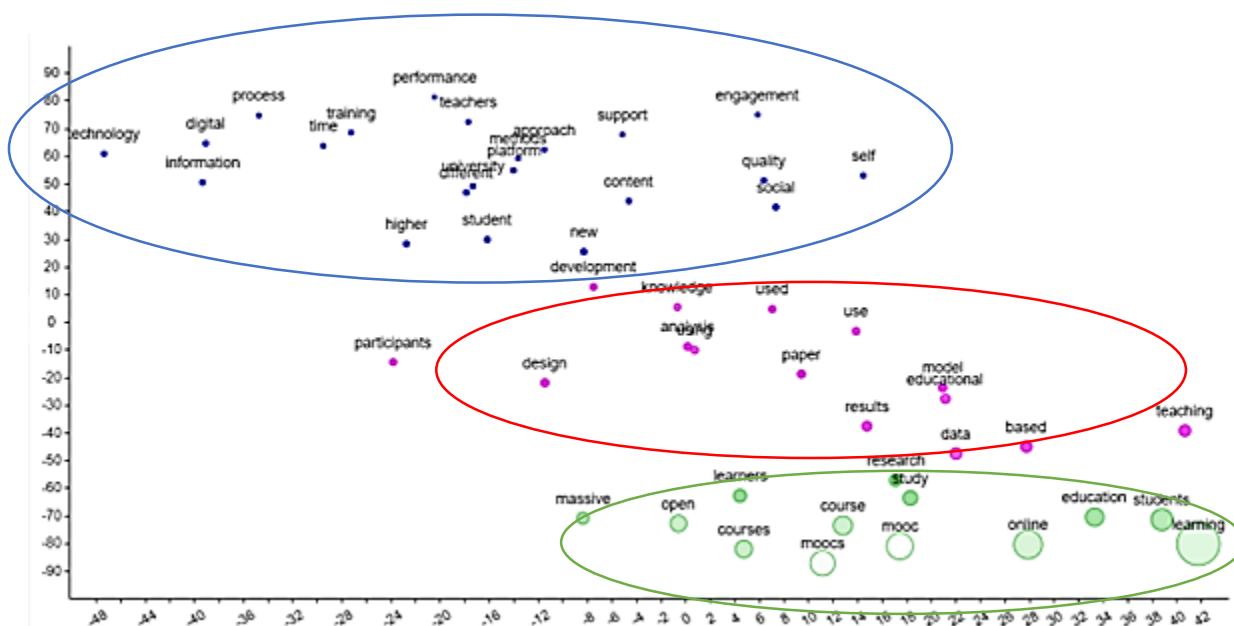


Figure 5. t-SNE analysis result

When Figure 5 is examined, the first 50 words were combined in the cluster shown with three different colours. These words, which are listed according to relative frequency, better visualise the pattern between words with a strong relationship. These words were grouped into green, red and blue clusters. The words with the highest relationship and bond were grouped in the green cluster, while the red and blue clusters were grouped with words with weaker bonds. This can be explained by the fact that green circles are more significant than red and blue circles.

## 4 CONCLUSION

In this study, 2822 study abstracts were analysed using the data mining method in order to determine the profile and trend of the studies conducted in the literature. In this context, the data were analysed using the online text mining tool called Voyant, and the results obtained from the analysis are presented in this section. In line with the results, suggestions for researchers are also included in the section.

The most recurring words in the study abstracts were “MOOC”, “students”, “education”, “open”, “online”, “learning”, “massive”, and “course”. These words were followed by “study”, “learners”, “research”, “massive” and “data”. “Online”, “students”, “MOOCs”, and “MOOC” were the most used words with “learning”. The words “epidemic”, “devices”, “frequency”, “improve”, and “curriculum” have a high correlation with learning. While the use of the word “learning” in the studies showed a continuously increasing trend, the use of “MOOC” showed a decreasing and then increasing trend. In some studies, it was observed that it was used in similar numbers with learning. The other words “online”, “source”, “open”, and “education” showed similar trends.

Based on these results, it is recommended for researchers to scan the literature by using these words in their studies on the field in question, to determine the keywords related to their studies among these words and to use the related words expressed here together while determining the titles of the studies. In addition, researchers who will conduct similar studies can conduct more comprehensive studies in which variables such as country, author, year of publication and type of publication are analysed in addition to these variables.

## References

- [1] A. Bozkurt, “Acik egitsel kaynaklardan acik egitsel uygulamalara: Turk yuksekogretimi baglaminda ekolojik bakis acisiyla bir degerlendirme,” *Acikogretim Uygulamaları ve Arastirmaları Dergisi*, vol. 5, no. 3, pp. 127–150, 2019.
- [2] R. McGreal, T. Anderson, and D. Conrad, “Open educational resources in Canada,” *International Review of Research in Open and Distributed Learning*, vol. 16, no. 5, pp. 161–175, 2015.
- [3] JISC, “Overcoming barriers and finding enablers,” Bristol: JISC, 2015. [Online]. Available: <https://www.jisc.ac.uk/guides/open-educational-resources/overcoming-barriers-and-finding-enablers>

- [4] K. Kikkas, M. Laanpere, and H. Põldoja, "Open courses: The next big thing in elearning," in *Proceedings of the 10th European Conference on e-Learning*, A. Rospigliosi, Ed., Reading: Academic Publishing Limited, 2011, pp. 370–376.
- [5] K. F. Hew and W. S. Cheung, "Students' and instructors' use of massive open online courses (MOOCs): Motivations and challenges," *Educational Research Review*, vol. 12, pp. 45–58, 2014.
- [6] J. Mackness, S. Mak, and R. Williams, "The ideals and reality of participating in a MOOC," in *Proceedings of the 7th International Conference on Networked Learning 2010*, L. Dirckinck-Holmfeld et al., Eds., University of Lancaster: Lancaster, 2010, pp. 266–275.
- [7] D. Kassabian, "Massive Open Online Courses (MOOCs) at elite, early-adopter universities: Goals, progress, and value proposition," Ph.D. dissertation, University of Pennsylvania, Pennsylvania, USA, 2014.
- [8] S. Zutshi, S. O'Hare, and A. Rodafinos, "Experiences in MOOCs: The perspective of students," *American Journal of Distance Education*, vol. 27, no. 4, pp. 218–227, 2013.
- [9] O. Zawacki-Richter and S. Naidu, "Mapping research trends from 35 years of publications in distance education," *Distance Education*, vol. 37, no. 3, pp. 245–269, 2016.
- [10] L. Yuan and S. Powell, "MOOCs and open education: Implications for higher education," *Cetis White Paper*, pp. 1–21, 2013.
- [11] S. Peter and M. Deimann, "On the role of openness in education: A historical reconstruction," *Open Praxis*, vol. 5, no. 1, pp. 7–14, 2013.
- [12] C. M. Stracke, "How can e-learning and MOOCs reveal and exploit the hidden treasures of open research and open education?" in *From Education to Employment and Meaningful Work with ICTs: Proceedings of EDEN Annual Conference*, A. M. Teixeira, A. Szűcs, and I. Mázár, Eds., Zagreb: European Distance and E-Learning Network, 2014, p. 11.
- [13] O. A. Bozkurt, "Kitlesel acik cevrimiçi dersler (Massive Open Online Courses - MOOCs) ve sayisal bilgi çağında yasamboyu ogrenme firsati," *Acikogretim Uygulamalari ve Arastirmalari Dergisi*, vol. 1, no. 1, 2015.
- [14] S. I. de Freitas, J. Morgan, and D. Gibson, "Will MOOCs transform learning and teaching in higher education? Engagement and course retention in online learning provision," *British Journal of Educational Technology*, vol. 46, no. 3, pp. 455–471, 2015.
- [15] C. Blake and E. Scanlon, "Online teaching: Applying distance learning principles to MOOCs," in *Handbook of Research on Emerging Priorities and Trends in Distance Education: Communication, Pedagogy, and Technology*, IGI Global, 2014, pp. 186–200.
- [16] D. Shah, "By the Numbers: MOOCs in 2018 Class Central," 2019. [Online]. Available: <https://www.classcentral.com/report/mooc-stats-2018/>
- [17] R. Baker, B. Evans, E. Greenberg, and T. Dee, "Understanding persistence in MOOCs (Massive Open Online Courses): Descriptive & experimental evidence," in *Proceedings of the European MOOC Stakeholder Summit 2014 (EMOOCs 2014)*, U. Cress and C. D. Kloos, Eds., Lausanne, Switzerland, Feb. 10-12, 2014, pp. 5–10. [Online]. Available: <http://www.emoocs2014.eu/sites/default/files/Proceedings-Moocs-Summit-2014.pdf>
- [18] A. Visa, "Technology of text mining," in *International Workshop on Machine Learning and Data Mining in Pattern Recognition*, Berlin, Heidelberg: Springer Berlin Heidelberg, Jul. 2001, pp. 1–11.
- [19] A. Miller, "Text mining digital humanities projects: Assessing content analysis capabilities of voyant tools," *Journal of Web Librarianship*, vol. 12, no. 3, pp. 169–197, 2018.
- [20] E. Alhudithi, "Review of Voyant Tools: See through your text," *Language Learning & Technology*, vol. 25, no. 3, pp. 43–50, 2021.
- [21] M. E. Welsh, "Review of Voyant tools," *Collaborative Librarianship*, vol. 6, no. 2, pp. 96–98, 2014.
- [22] K. Ramsby, "Text-mining short fiction by Zora Neale Hurston and Richard Wright using voyant tools," *CLA Journal*, vol. 59, no. 3, pp. 251–258, 2016.
- [23] H. Hendrigan, "Digital humanities and STEM librarianship, or why I stopped rolling my eyes at word clouds," 2018.
- [24] I. D. Maramba et al., "Web-based textual analysis of free-text patient experience comments from a survey in primary care," *JMIR Medical Informatics*, vol. 3, no. 2, art. no. e3783, 2015.
- [25] K. Gregory, L. Geiger, and P. Salisbury, "Voyant tools and descriptive metadata: A case study in how automation can compliment expertise knowledge," *Journal of Library Metadata*, vol. 22, no. 1–2, pp. 1–16, 2022.



## A Research on Staling in Wafers

Sibel Koca Cetinkaya<sup>1</sup>, Amine Beyza Ozata<sup>\*1</sup>, Ozge Akgul<sup>1</sup>, Begum Ceren Memecan<sup>1</sup>

<sup>1</sup>Sagra Group Food Inc., Ordu, Türkiye

---

### Abstract

Although it varies depending on the wafer type; it is a crunchy and low-moisture snack that contains many ingredients, such as sheet, cream and chocolate products. The ingredients of wafer sheets can generally be listed as wheat flour, starch, water, raising agents, sugar, oil, lecithin, milk powder, whey powder, enzyme and salt. The quality of wafer sheets is mainly affected by parameters such as flour properties, amount of water, mixture type, cooking time and temperature. Staling includes physical and chemical events such as moisture redistribution, drying, starch retrogradation, increase in hardness, loss of aroma and flavor. In order to delay staling and extend the shelf life, applications such as the use of enzymes such as alpha amylase, hemicellulase, lipase, emulsifiers, hydrocolloids or their combinations, and rearrangement of production processes are carried out. Since amylases are effective in starch retrogradation, they help to obtain products that are resistant to staling; proteases provide stability in such products by reducing gluten elasticity; lipases provide softness and volumetric improvement; hemicellulases have a positive effect on dough viscosity and leaf hardness, especially in wafers prepared with strong flours. Lecithin, another wafer sheet component, has been reported to extend shelf life in some studies. Based on all this information, dough recipes in different formulations were prepared by making changes in enzyme and emulsifier inputs in order to delay staling, and the final product was evaluated. Wafers made with different sheet formulations were subjected to aging tests and evaluated sensory, chemical and textural. When looking at the texture analysis results, where differences between samples are seen, it can be seen that the study is promising and has areas open to development.

**Keywords:** *Wafer sheet, Staling, Enzyme*

---



## Grapevine Leaf Powder as a Functional Food Additive: Physicochemical and Bioactive Properties

Mehmet Ali Salik<sup>\*1</sup>

<sup>1</sup>Department of Food Processing, Bingol University, Bingol, Türkiye

### Abstract

The grapevine (*Vitis vinifera* L.) is one of the most cultivated important perennial crops in the world, especially in the Mediterranean area. The grapevine is composed of grape fruit (including parts such as seeds, pulp and skin) and leaves. Grapevine leaves, which are usually thrown out by grape producers, have been consumed fresh or pickled in Turkish culinary culture for years. In addition, it has a range of uses in pharmaceuticals, cosmetics, teas, and other food supplements in some countries, especially in Europe. Studies have shown that grapevine leaves have beneficial effects on human health due to their anti-cancerogenic, anti-inflammatory, anti-diabetic, antimicrobial, analgesic, antipyretic, antioxidant, and immunomodulatory properties. In this study, some physicochemical and bioactive properties of grapevine leaf powder (GLP) obtained from the famous grape cultivar "Karaerik" (*Vitis vinifera* spp., Cimin) grown in Turkey were investigated. According to the results, in GLP sample was determined as dry matter 92.48%, ash 7.33%, protein 2.70%, pH 3.39, titration acidity 5.60%, water activity ( $a_w$ ) 0.46,  $L^*$  value 39.84,  $a^*$  value -2.34,  $b^*$  value 15.06,  $H^\circ$  value 98.82 and  $C^*$  value 15.24. Total phenolic content (TPC), total flavonoid content (TFC), total antioxidant capacity (DPPH•, CUPRAC and FRAP), chlorophyll *a* and chlorophyll *b* contents of the GLP determined as 54.90 mg GAE/g, 1619.53 mg QE/g, 94.76 mg TE/g, 167.30 mg TE/g, 17.40 mg TE/g, 510.89 µg/g and 87.47 µg/g, respectively. The results suggest that GLP is a potential source of nutraceutical compounds with valuable antioxidant properties that can be used as functional additive in the food industry.

**Keywords:** Grapevine leaf, Functional food additive, Antioxidant, Chlorophyll, Bioactive compounds

## 1 INTRODUCTION

Grapevine (*Vitis vinifera* L.) is one of the most widely cultivated fruit crops of economic importance worldwide [1, 2]. Grapes are consumed as table grapes or processed into products such as wine, raisins, juices, and other derived products [3, 4]. Turkey is the location of the world with a suitable climate for cultivating grapevines and is the origin of the vine genes [5]. In addition to their market worth, grapes, and their byproducts contain nutritional and bioactive compounds [6, 7]. Grapes are composed of parts such as leaves, seeds, skins, and pulp, which contain many chemical components such as polyphenols, anthocyanins, minerals, sugars, enzymes, organic acids, and amino acids [1, 8, 9].

Grapevine leaves are an abundant byproduct of vineyards. While they are considered a delicacy in many countries in the Mediterranean Basin, in some regions they are considered a waste, and strategies to valorize them are nonexistent [6]. Grapevine leaves have been consumed in fresh and canned forms for years. Stuffed grape leaves (dolma), which are made with fresh or pickled grape leaves, are a famous dish (stuffed with minced meat, rice, or vegetables) cooked by Turkish, Balkan, and Middle Eastern nations for centuries [2, 5]. In addition, grapevine leaves have a range of uses in pharmaceuticals, cosmetics, teas, and other food supplements in some countries, especially in Europe [3, 8]. Hefnawy et al. [10] demonstrated that grape leaf powder can be used as a natural antioxidant in biscuit baking. Grapevine leaves are rich in bioactive compounds with nutraceutical potential. Studies have shown the presence of various organic acids, phenolic acids, flavonols, tannins, procyanidins, anthocyanins, lipids, enzymes, vitamins, carotenoids, terpenes and sugars in grapevine leaves [4, 7]. Furthermore, studies have reported that grapevine leaves have beneficial effects on human health due to their anti-cancerogenic, anti-inflammatory, anti-diabetic, antimicrobial, analgesic, antipyretic, antioxidant, and immunomodulatory properties [1, 6, 7, 9, 11].

In the light of these findings, the present study aimed to draw attention to the potential of grapevine leaves to be used as functional additives in the food industry. For this purpose, grapevine leaf powder (GLP) obtained from the

famous “Karaerik” (*Vitis vinifera* spp., Cimin) grape variety grown in Turkey was analyzed in terms of some parameters and its bioactivity and nutritional composition were revealed.

## 2 MATERIAL AND METHOD

### 2.1 Material

In the study, fresh leaf samples obtained from the famous grape cultivar “Karaerik” (*Vitis vinifera* spp., Cimin) were randomly collected in June as material from a vineyard (Figure 1) in the Bayırbağ village (GPS location 39°41'48"N 39°43'11"E) of Erzincan (Turkey).



Figure 1. A vineyard in the Bayırbağ village of Erzincan

### 2.2 Preparation of the Grapevine Leaf Powder (GLP)

Fresh grapevine leaves (Figure 2a) were washed after de-stemming and dried in the shade until completely dehydrated (4-5 days). Then, the dried grapevine leaves were ground to a fine powder using a laboratory blender (Blender 8011ES, HGB2 WTS3 Model, USA) and the particle size was standardized by passing through a 500-micron mesh sieve. The GLP was maintained at +4 °C until analyses (Figure 2b).

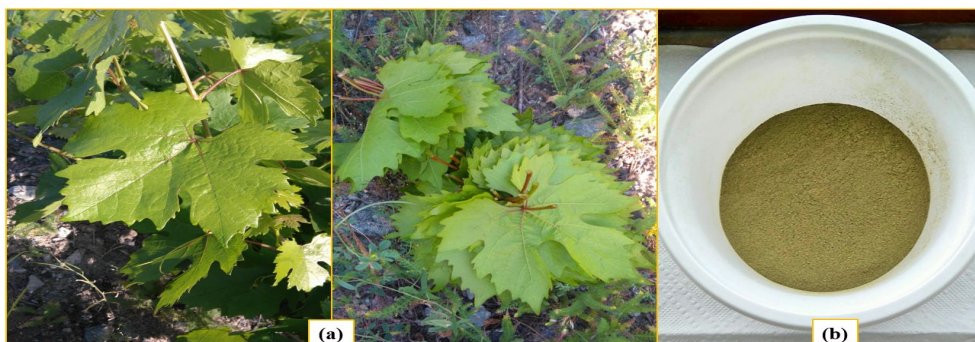


Figure 2. Fresh grapevine leaves (a) and GLP (b) samples

### 2.3 Physical and Chemical Analysis

The dry matter, ash, protein (N% x 6.25), pH, titration acidity, and water activity analyses of the GLP were carried out using the methods reported by Cemeroglu [12]. The color properties of GLP were obtained by measuring  $L^*$  (brightness, 0: black, 100: white),  $a^*$  (+: redness, -: greenness),  $b^*$  (+: yellowness, -: blueness),  $H^\circ$  (hue angle; 0°: red, 90°: yellow, 180°: green, 270°: blue, 360°: red) and  $C^*$  (colour saturation) values using a Chroma Meter (Minolta CR-200, Minolta Chromometer, Japan) [2].

### 2.4 Bioactivity analysis

#### 2.4.1 Extraction Process for GLP

Two independent extractions for GLP were carried out as described by Pintać et al. [11] with some modifications. To prepare the extracts, 1 g of sample was transferred into Falcon tubes, added with 20 mL of methanol (75%,

v/v), and extracted in an orbital shaker (IKA Heidolph Unimax 1010, Almany) for 2h at room temperature, followed by centrifugation at 5000 rpm (WUC-D03H, Germany) for 15 min. The supernatants were filtered through Whatman No. 1 filters, and the methanolic extracts were stored at  $-20^{\circ}\text{C}$  in the dark until analyses.

#### 2.4.2 Determination of the Total Phenolic Content (TPC)

The TPC of GLP was performed by the Folin-Ciocalteu spectrophotometric method as specified by Singleton and Rossi [13]. The results are reported as mg gallic acid equivalent (GAE)/100 g sample.

#### 2.4.3 Determination of the Total Flavonoid Content (TFC)

The TFC of GLP was performed by the aluminum chloride spectrophotometric method as specified by Dewanto et al. [14]. The results are reported as mg quercetin equivalent (QE)/g sample.

#### 2.4.4 Determination of the Total Antioxidant Activity

The 2,2-diphenyl-1-picrylhydrazyl (DPPH•) radical scavenging capacity of the GLP was performed by measuring the absorbance at 517 nm as reported by Al Juhaimi et al. [3]. The cupric ion-reducing antioxidant capacity (CUPRAC) of the GLP was performed at 450 nm using the method of Apak et al. [15]. The ferric-reducing antioxidant power (FRAP) of the GLP was performed at 593 nm using the method of Benzie and Strain [16]. The results are reported as mg trolox equivalent (TE)/g sample.

#### 2.4.5 Determination of the Chlorophyll (Chl) Pigment Content

Chl *a* and chl *b* pigment contents of GLP were performed using the spectrophotometric method reported by Barros et al. [17]. The absorbance was measured at 645 nm and 663 nm using a UV-Vis spectrophotometer (Shimadzu, UV-VIS 1800, Japan). The results are reported as  $\mu\text{g}$  per g sample.

### 3 RESULTS

#### 3.1 Physicochemical Properties

The results of the analysis of the physicochemical properties of the GLP are given in Table 1. The dry matter amount of the GLP was determined as 92.48%, ash amount as 7.33%, protein amount as 2.70%, pH value as 3.39, titration acidity as 5.60%, and water activity value as 0.46 (Table 1). Banjanin et al. [8] determined the dry matter contents in the range of 91.80-92.61% and protein contents in the range of 9.38-20.30% for 11 grapevine leaves collected from Bosnia and Herzegovina. Gülcü et al. [2] reported the dry matter content of 10 varieties of fresh grapevine leaves collected in Tekirdağ (Turkey) between 19.11 and 38.08%.  $L^*$ ,  $a^*$ ,  $b^*$ ,  $H^{\circ}$ , and  $C^*$  values of the GLP were determined as 39.84, -2.34, 15.06, 98.82, and 15.24, respectively. The  $H^{\circ}$  value of the GLP indicates a color between  $90^{\circ}$  (yellow) and  $180^{\circ}$  (green). Similarly, Gülcü et al. [2] reported that the  $L^*$  value varied between 30.80-42.39, the  $a^*$  value between -5.20(-9.52), and the  $b^*$  value between 9.96-26.07 in fresh grapevine leaves.

**Table 1.** Physicochemical properties of the grapevine leaf powder (GLP)

Properties	GLP
Dry matter (%)	92.48±0.09
Ash (%)	7.33±0.09
Protein (%)	2.70±0.02
pH	3.39±0.00
Titration acidity (%)	5.60±0.03
Water activity	0.46±0.01
$L^*$	39.84±0.71
$a^*$	-2.34±0.07
$b^*$	15.06±0.23
$H^{\circ}$	98.82±0.27
$C^*$	15.24±0.23

#### 3.2 Bioactive Properties

The results of the analysis of the bioactive properties of the GLP are given in Table 2. The TPC of the GLP was determined as 54.90 mg GAE/g, TFC as 1619.53 mg QE/g, DPPH• radical scavenging capacity as 94.76 mg TE/g,

CUPRAC as 167.30 mg TE/g, and FRAP as 17.40 mg TE/g (Table 2). There are many studies on the antioxidant activity, phenolic profile, and bioactive properties of grapevine leaves. Some of these are summarized in Table 3. The results showed that grapevine leaves have high TPC, TFC, and antioxidant activity (DPPH•, FRAP, ABTS, etc.) and are a rich natural source of phenolic compounds (especially caffeic acid, ellagic acid, ferulic acid, catechin, rutin, etc.) and phytochemicals (tocopherols, tannins, carotenoids, etc.) (Table 3). The contents of chl *a*, chl *b*, and total chl in the GLP sample were determined as 510.89 µg/g, 87.47 µg/g, and 598.36 µg/g, respectively. Similarly, Maia et al. [18] determined the chl *a* content in the range of 230.69-374.26 µg/g fw and chl *b* content in the range of 198.53-281.04 µg/g fw for 7 different grapevine leaf varieties (Trincadeira, Cabernet Sauvignon, Pinot noir, Tintabarroca, 'Castelão', Bastardo and C19) collected from France and Portugal.

**Table 2.** Bioactive properties of the grapevine leaf powder (GLP)

Properties	GLP
TPC (mg GAE/g)	54.90±6.80
TFC (mg QE/g)	1619.53±104.37
DPPH (mg TE/g)	94.76±0.58
CUPRAC (mg TE/g)	167.30±5.83
FRAP (mg TE/g)	17.40±0.34
Chl <i>a</i> (µg/g)	510.89±96.49
Chl <i>b</i> (µg/g)	87.47±36.07
Total chl (µg/g)	598.36±132.12

**Table 3.** Bioactive properties of grapevine leaf (GL) samples compiled from literature

Source of the GL	Bioactive Properties	R
Sfax/Tunisia (1 variety)	<b>TPC:</b> 790.59 mg GAE/g dw, <b>TFC:</b> 137.34 mg QE/g, <b>Total flavonols:</b> 58.0 mg RE/g dw, <b>Condensed tannin:</b> 42.86 CE/g dw, <b>DPPH:</b> 11.18 EC <sub>50</sub> (µg/mL).	[1]
Tekirdağ/Türkiye (10 variety)	<b>TPC:</b> 19.49-78.66 mg GAE/g dw, <b>TFC:</b> 8.09-27.68 mg CE/g dw, <b>Total tannin:</b> 19.31-96.89 mg TAE/g dw, <b>ABTS:</b> 334.27-715.85 µmol TE/g dw, <b>12 phenolic compounds:</b> Caftaric acid, kaempferol-3-glucoside, rutin trihydrate, (+)-catechin, and ferulic acid are the main compounds.	[2]
Tekirdağ/Türkiye (5 variety)	<b>TPC:</b> 11.63-15.48 mg GAE/g, <b>TFC:</b> 306.60-575.25 mg CE/g, <b>DPPH:</b> 17.43-45.24 EC <sub>50</sub> (µg/mL), <b>Total carotenoid:</b> 47.04-74.39 µg/g, <b>16 phenolic compounds:</b> (+)-catechin, 1,2-dihydroxybenzene, 3,4-dihydroxybenzoic acid and trans-ferulic acid are the main compounds.	[3]
Manisa/Türkiye (5 variety)	<b>TPC:</b> 9.72-14.22 mg GAE/g, <b>TFC:</b> 5.08-7.22 mg CE/g, <b>(+)-catechin:</b> 91.20-131.73 mg/kg, <b>Epicatechin:</b> 20.07-55.50 mg/kg, <b>Vanilic acid:</b> 60.0-78.92 mg/kg, <b>Galic acid:</b> 6.02-6.67 mg/kg, <b>Caffeic acid:</b> 45.10-70.14 mg/kg.	[5]
Italy (1 variety)	<b>TPC:</b> 15.39-18.63 mg GAE/g fw, <b>DPPH:</b> 21.85-22.19 mg TE/g fw, <b>Total carotenoids:</b> 0.47-1.01 mg/g fw, <b>Total phytosterols:</b> 0.10-0.19 mg/g fw, <b>Total tocopherols:</b> 0.41-1.87 mg/g fw, <b>13 phenolic compounds:</b> Hyperoside, kaempferol-3-glucoside, shikimic acid, and catechin are the main compounds.	[7]
Trebinje/Bosnia and Herzegovina (11 variety)	<b>TPC:</b> 12.98-17.48 mg GAE/g, <b>TFC:</b> 52.18-117.96 mg QE/g, <b>Total carotenoid:</b> 13.92-60.46 µg/g, <b>DPPH:</b> 20.60-20.79 mmol TE/kg, <b>14 phenolic compounds:</b> 3,4-dihydroxybenzoic acid, (+)-catechin, 1,2-dihydroxybenzene, rutin-trihydrate, quercetin, apigenin-7-glucoside, and caffeic acid are the main compounds.	[8]
Artvin/Türkiye (17 variety)	<b>TPC:</b> 172.66-483.33 µg GAE/mg dw, <b>DPPH:</b> 17.43-45.24 EC <sub>50</sub> (µg/mL), <b>ABTS:</b> 10.01-35.88 EC <sub>50</sub> (µg/mL).	[9]
Serbia (8 variety)	<b>DPPH:</b> 11.40-62.6 EC <sub>50</sub> (µg/mL), <b>FRAP:</b> 25.70-50.70 mg AAE/g dry extract, <b>28 phenolic compounds:</b> Quercetin 3-o-glucoside, hyperoside, kaempferol 3-ogluoside, rutin, ellagic and chlorogenic acids are the most abundant compounds.	[11]
Serbia (22 variety)	<b>TPC:</b> 27.5-76.0 mg GAE/g dw, <b>DPPH:</b> 0.43-0.87 mmol TE/kg, <b>22 phenolic compounds:</b> Ellagic acid and rutin are the most abundant compounds.	[19]

**Abbreviations; R:** References; **GAE:** Gallic acid equivalent, **QE:** Quercetin equivalent, **TE:** Trolox equivalent, **RE:** Rutin equivalent, **CE:** Catechin equivalent, **TAE:** Tannic acid equivalent, **AAE:** Ascorbic acid equivalent, **dw:** dry weight, **fw:** fresh weight.

## 4 CONCLUSION

The analytical findings show that grapevine leaf powder (GLP) obtained from the famous “Karaerik” grape variety (*Vitis vinifera* spp., Cimin) proved to be a rich source of natural bioactive compounds such as flavonoids,

phenolics, and chlorophyll pigments. GLP is also remarkable for its ash (7.73%) and protein (2.70%) content. The GLP, which has strong antioxidant properties, can be used as a functional ingredient/additive for processing into nutraceutical and health foods in the food industry.

## References

- [1] A. Aouey, A. M. Samet, H. Fetoui, M. S. J. Simmonds, and M. Bouaziz, "Anti-oxidant, anti-inflammatory, analgesic and antipyretic activities of grapevine leaf extract (*Vitis vinifera*) in mice and identification of its active constituents by LC–MS/MS analyses," *Biomedicine & Pharmacotherapy*, vol. 84, pp. 1088–1098, Dec. 2016.
- [2] M. Gulcu, K. Ghafoor, F. Al-Juhaimi, M. M. Ozcan, N. Uslu, E. E. Babiker, I. A. M. Ahmed, and I. U. Azmi, "Effect of grape (*Vitis vinifera* L.) varieties and harvest periods on bioactive compounds, antioxidant activity, phenolic composition, mineral contents, and fatty acid compositions of *Vitis* leave and oils," *Journal of Food Processing and Preservation*, vol. 44, no. 11, pp. 1–7, Nov. 2020.
- [3] F. Al Juhaimi, N. Uslu, M. M. Ozcan, M. Gulcu, I. A. M. Ahmed, H. A. S. Alqah, M. A. Osman, and M. A. Gassem, "Effect of fermentation on antioxidant activity and phenolic compounds of the leaves of five grape varieties," *Journal of Food Processing and Preservation*, vol. 43, no. 7, pp. 1–7, Jul. 2019.
- [4] D. Barreales, R. Malheiro, J. A. Pereira, J. Verdial, A. Bento, P. A. Casquero, and A. C. Ribeiro, "Effects of irrigation and collection period on grapevine leaf (*Vitis vinifera* L. var. Touriga Nacional): Evaluation of the phytochemical composition and antioxidant properties," *Scientia Horticulturae*, vol. 245, pp. 74–81, Feb. 2019.
- [5] A. Guler and A. Candemir, "Total phenolic and flavonoid contents, phenolic compositions and color properties of fresh grape leaves," *Turkish Journal of Agricultural and Natural Sciences*, vol. 1, no.1, pp. 778–782, Mar. 2014.
- [6] A. Lima, A. Bento, I. Baraldi, and R. Malheiro, "Selection of grapevine leaf varieties for culinary process based on phytochemical composition and antioxidant properties," *Food Chemistry*, vol. 212, pp. 291–295, Dec. 2016.
- [7] F. K. Nzekoue, M. L. K. Nguefang, L. Alessandroni, A. M. Mustafa, S. Vittori, and G. Caprioli, "Grapevine leaves (*Vitis vinifera*): Chemical characterization of bioactive compounds and antioxidant activity during leave development," *Food Bioscience*, vol. 50, art. no. 102120, pp. 1-8, Dec. 2022.
- [8] T. Banjani, N. Uslu, Z.R. Vasic, and M. M. Ozcan, "Effect of grape varieties on bioactive properties, phenolic composition, and mineral contents of different grape-vine leaves," *Journal of Food Processing and Preservation*, vol. 45, no. 2, pp. 1–7, Feb. 2021.
- [9] H. Yildiz, O. Cakir, K. Cakiroglu, and N. Karatas, "A comparative study on the bioactivity and mineral content of different grapevine (*Vitis vinifera* L.) leaves cultivated in Türkiye," *Applied Fruit Science*, vol. 66, pp. 657–666, Apr. 2024.
- [10] H. Hefnaw, G. A. El-Shourbag, and M. F. Ramadan, "Phenolic extracts of carrot, grape leaf and turmeric powder: antioxidant potential and application in biscuits," *Journal of Food Measurement and Characterization*, vol. 10, no. 3, pp. 576–583, Sep. 2016.
- [11] D. Pintača, D. Četojević-Simin, S. Berežni, D. Orčić, N. Mimica-Dukić, and M. Lesjak, "Investigation of the chemical composition and biological activity of edible grapevine (*Vitis vinifera* L.) leaf varieties," *Food Chemistry*, vol. 286, pp. 686–695, Jul. 2019.
- [12] B. Cemeroglu, *General Methods in Food Analysis*, in *Food Analysis*, B. Cemeroglu, Ed. Ankara: Food Technology Association Publications, 2010, pp. 87–93.
- [13] V. L. Singleton and J. A. Rossi, "Colorimetry of total phenolics with phosphomolybdic-phosphotungstic acid reagents," *American journal of Enology and Viticulture*, vol. 16, no. 3, pp. 144–158, 1965.
- [14] V. Dewanto, X. Wu, K.K. Adom, and R.H. Liu, "Thermal processing enhances the nutritional value of tomatoes by increasing total antioxidant activity," *Journal of Agricultural and Food Chemistry*, vol. 50, pp. 3010–3014, Apr. 2002.
- [15] R. Apak, K. Guclu, M. Uzyurek, S. E. Karademir, and E. Ercag, "The cupric ion reducing antioxidant capacity and polyphenolic content of some herbal teas," *International Journal of Food Sciences and Nutrition*, vol. 57, no. 5-6, pp. 292–304, Jul. 2009.
- [16] I. F. F. Benzie and J. J. Strain, "The ferric reducing ability of plasma (FRAP) as a measure of "antioxidant power" the FRAP assay," *Analytical Biochemistry*, vol. 239, no. 1, pp. 70–76, Jul. 1996.
- [17] L. Barros, L. Cabrita, M.V. Boas, A.M. Carvalho, and I.C.F.R. Ferreira, "Chemical, biochemical and electrochemical assays to evaluate phytochemicals and antioxidant activity of wild plants," *Food Chemistry*, vol. 127, no. 4, pp. 1600–1608, Aug. 2011.
- [18] M. Maia, A. R. Cavaco, G. Laureano, J. Cunha, J. Eiras-Dias, A. R. Matos, B. Duarte, and A. Figueiredo, "More than just wine: The nutritional benefits of grapevine leaves," *Foods*, vol. 10, no. 10, art. no. 2251, Sep. 2021.



- [19] M. M. Pantelić, D. Č. D. Zagorac, I. Ž. Ćirić, M. V. Pergal, D. J. Relić, S. R. Todić, and M. M. Natić, “Phenolic profiles, antioxidant activity and minerals in leaves of different grapevine varieties grown in Serbia,” *Journal of Food Composition and Analysis*, vol. 62, pp. 76–83, Sep. 2017.



## A Popular Probiotic Dairy Product-Kefir: Overview on Functional Mechanism of Action and Plant-Based Fermented Beverages

Mehmet Ali Salik<sup>\*1</sup>

<sup>1</sup>Department of Food Processing, Bingol University, Bingol, Türkiye

### Abstract

Fermentation is one of the oldest, economic, and natural methods used to improve the nutritional and sensory quality of foods and increase their shelf life. Kefir is a fermented popular probiotic milk beverage different in consistency and taste from other dairy products such as “yogurt” and “ayran”. Kefir is a refreshing traditional dairy drink originating from the Caucasus and produced by fermentation of animal milk such as cow, sheep, and goat by “kefir grains” containing lactic acid bacteria, acetic acid bacteria, and yeast. Kefir contains food components and fermentation metabolites such as vitamins, minerals, fatty acids, organic acids (lactic, acetic, gluconic, etc.), amino acids, bioactive peptides, polysaccharides (kefiran), ethanol, and carbon dioxide (CO<sub>2</sub>). These compounds have been related to health-promoting benefits such as anti-inflammatory, anti-carcinogenic, anti-allergenic, antimicrobial, and anti-diabetic effects, lowering serum cholesterol levels, improved digestion (lactose tolerance) and gut health, a reduction in hypertension, and regulation of reactive oxygen species. Today, plant-based fermented beverages (PBFs) are gaining attention from the scientific community, food industry, and consumers as milk alternatives (especially for people with lactose intolerance, milk allergy, a prevalence of hypercholesterolemia, and vegans). In addition, PBFs are of particular interest to consumers due to their functional properties and the presence of beneficial microorganisms. Plant-based beverages are a liquid mixture of plant materials homogenized with water. Recent research has shown the use of various plant matrices such as legumes (soy, peanut, pea, lupin, cowpea, etc.) cereals (oat, rice, corn, spelt, etc.), nuts (almond, coconut, hazelnut, pistachio, peanut, walnut, cashew, etc.), pseudocereals (quinoa, teff, amaranth, etc.), and seeds (sesame, flaxseed, hemp, sunflower, black cumin, apricot, etc.) in the production of plant-based beverages. This study provides an overview of plant-based beverages fermented with kefir culture and the functional mechanism of action of kefir, a popular dairy product.

**Keywords:** Fermentation, Kefir, Functional foods, Plant-based beverages, Health benefits

## 1 INTRODUCTION

Fermentation is one of the oldest, economic, and natural methods used to improve the nutritional and sensory quality of foods and increase their shelf life [1, 2]. Consumption of fermented foods is a rising trend worldwide due to their health-promoting effects [3]. In this respect, fermented dairy products are important sources of bioactive components (serum proteins,  $\alpha$ -lactalbumin,  $\beta$ -lactoglobulin, serum albumin, immunoglobulins, glycomacropptides, lactoferrin, lactoperoxidase, docosahexaenoic acid, eicosapentaenoic acid, conjugated linoleic acid, phospholipids, sterols, vitamins, melatonin, etc.) that strengthen the immune system and play a role in the regulation of many functional activities in the human body [4, 5]. Kefir is a refreshing traditional dairy drink originating from the Caucasus and produced by fermentation (at room temperature under anaerobic conditions of 24-36 h) of animal milk such as cow (mainly), sheep, and goat by "kefir grains" containing (combined in an extracellular polysaccharide matrix) lactic acid bacteria, acetic acid bacteria and yeast [3, 6-9]. In addition, kefir is also commercially produced industrially with starter kefir culture [8, 10].

Increasing consumer demand for healthy foods and changing dietary habits have stimulated efforts to develop new foods [6, 11]. Nowadays, it is possible to see a large number of new functional foods on the market, with dairy products and beverages representing an important segment [6]. While probiotics, which play an important role in the functional food market, are typically found in fermented dairy products, non-dairy probiotic foods have also become popular [11]. Today, plant-based fermented beverages (PBFs) are gaining attention from the scientific community, food industry, and consumers as milk alternatives [2]. PBFs have attracted the attention of consumers as an alternative to dairy products, especially for people with lactose intolerance, milk allergy and hypercholesterolemia prevalence [2, 6]. While this phenomenon was initially driven by an increase in vegan and animal product intolerant consumers, today the search for alternative, sustainable and eco-efficient food has

become a collective interest [2, 6, 12]. Plant-based beverages refer to products obtained exclusively from plant sources. According to the latest data, the annual growth rate of the plant-based beverage market is estimated to be 6.7% by 2026 [12]. This study, the nutritional importance of kefir, a popular dairy product, its functional mechanism of action, and general information about kefir-like plant-based beverages fermented using kefir culture were given.

## 2 THE IMPORTANCE OF KEFIR IN NUTRITION

The chemical composition and nutritional values of kefir are shown in Table 1. Kefir contains adequate amounts of food components (protein, fat, carbohydrates, vitamins, and minerals) that are important in nutrition [10]. The pH value of kefir, a fermented milk product, varies between 4.0 and 4.6. Kefir may be manufactured from whole, semi-skimmed, and skimmed milk [8]. Kefir contains food components and fermentation metabolites such as vitamins, minerals, fatty acids, organic acids (lactic, acetic, gluconic, etc.), amino acids, bioactive peptides, polysaccharides (kefiran), ethanol, CO<sub>2</sub>, acetaldehyde, acetoin, and diacetyl [8, 13]. Kefir is rich in various amino acids (serine, valine, lysine, alanine, phenylalanine, threonine, methionine, tryptophan, and isoleucine) compared to unfermented milk [8]. Kefir produced from whole milk is also a good source of vitamin K<sub>2</sub>, which is essential for calcium metabolism [3].

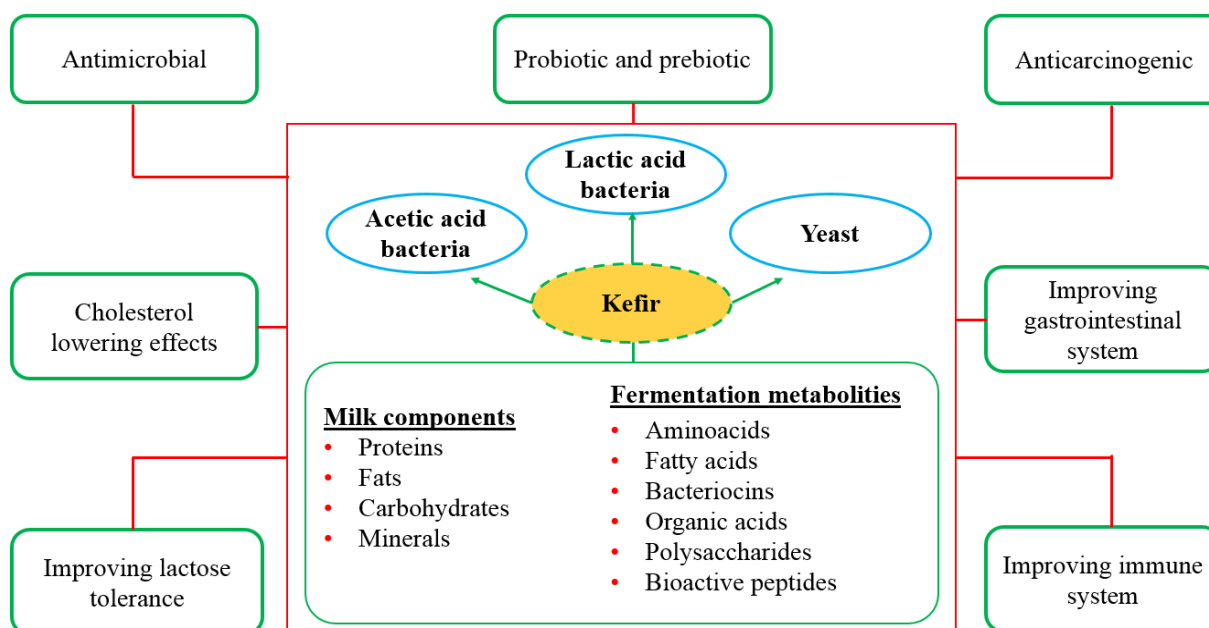
**Table 1.** Chemical composition and nutritional values of kefir [10]

Component	100 g	Component	100 g	Component	100 g
Energy (kcal)	65	Methionine + Cysteine (g)	0.12	Vitamin E (mg)	0.11
Fat (g)	3.5	Lysine (g)	0.27	Calcium (g)	0.12
Protein (g)	3.3	Valin (g)	0.22	Phosphor (g)	0.10
Lactose (g)	4.0	Vitamin A (mg)	0.06	Magnesium (g)	0.12
Ethyl alcohol (g)	0.9	Vitamin B <sub>1</sub> (mg)	0.04	Potassium (g)	0.15
Lactic acid (g)	1.0	Vitamin B <sub>2</sub> (mg)	0.17	Sodium (g)	0.05
Cholesterol (mg)	13.0	Vitamin B <sub>3</sub> (mg)	0.09	Chloride (g)	0.10
Tryptophan (g)	0.05	Vitamin B <sub>6</sub> (mg)	0.05	Iron (mg)	0.05
Phenylalanine + Tyrosine (g)	0.35	Vitamin B <sub>12</sub> (mg)	0.50	Copper (µg)	12.0
Leucine (g)	0.34	Carotene (mg)	0.02	Molybdenum (µg)	5.50
Isoleucine (g)	0.21	Vitamin C (mg)	1.00	Manganese (µg)	5.00
Threonine (g)	0.17	Vitamin D (mg)	0.08	Zinc (mg)	0.36

The composition and microbial flora of kefir are influenced by the type and composition of milk, the composition and number of kefir grains or culture, culture medium, fermentation temperature, fermentation time, and storage conditions [3, 9, 11]. Lactic acid and acetic acid bacteria and yeasts, which are symbiotic in the natural microflora of kefir grains, play a key role in the formation of the taste and aroma of kefir produced by traditional methods. Lactic acid and ethyl alcohol formed as a result of the activity of these microorganisms in milk are effective on the taste of kefir [11]. In industrial kefir production, standard kefir culture is used and production is carried out under more controlled conditions, resulting in products with more standardized properties compared to kefir produced by traditional methods [8, 10]. Kefirs are classified into 3 groups in terms of the fermentation metabolites they contain; weak kefir (poor in acid, alcohol and CO<sub>2</sub>), medium kefir and strong kefir (rich in acid, alcohol and CO<sub>2</sub>) [14, 15].

## 3 FUNCTIONAL MECHANISM OF ACTION OF KEFIR

Kefir is one of the functional foods and its beneficial effects on health have been scientifically proven [3, 16]. The probiotic shelf life of kefir beverages is affected by the stability of the microbial population. Numerous species have been isolated from kefir, including lactobacilli (*Lactobacillus acidophilus*, *Levilactobacillus brevis*, *Lactobacillus kefir*, *Lactocaseibacillus casei*, *Lentilactobacillus parakefiri*, etc.), lactococci (*Lactococcus lactis* ssp. *lactis*, *Lactococcus lactis* ssp. *cremoris*, *Streptococcus thermophiles*, *Leuconostoc mesenteroides*, *Leuconostoc cremoris*, etc.), acetic acid bacteria (*Acetobacter aceti*, *Acetobacter fabarum*, *Acetobacter genera*, etc.) and yeast (*Saccharomyces cerevisiae*, *Kluyveromyces marxianus*, *Kluyveromyces lactis*, etc.) [3]. It is recommended that the total lactic acid bacteria count should be >10<sup>7</sup> CFU/mL and the yeast count should be >10<sup>4</sup> CFU/mL during the shelf life of kefir [6]. Many scientific reports highlighted the health benefits of kefir due to its antimicrobial, antiviral, anticancer, gastrointestinal tract effects, intestinal microbiota modulation, cholesterol-lowering activity, anti-diabetic effects, tolerance to lactose, anti-allergenic activity, reduced kidney hypertrophy, and anti-mutagenic effect [3, 6, 7, 11]. Some functional properties of kefir are given in the schematic diagram in Figure 1 [8, 16].



**Figure 1.** Functional properties of kefir

In the fermentation of milk by kefir microorganisms, primary components and secondary metabolites such as organic acids, antimicrobial peptides, polysaccharides, CO<sub>2</sub>, hydrogen peroxide (H<sub>2</sub>O<sub>2</sub>), and bacteriocins are synthesized. Many of these bioactive metabolites have been demonstrated to inactivate the growth of food spoilage and pathogenic microorganisms [8]. Lactic acid and acetic acid reduce the pH of the food and have an inhibitory effect on pathogenic microorganisms such as *Escherichia coli* and *Salmonella* spp. On the other hand, H<sub>2</sub>O<sub>2</sub> provides an antimicrobial effect by creating an antagonistic effect directly on pathogens [17]. According to the World Health Organization (WHO), probiotics are defined as live microorganisms that, when taken in adequate amounts, benefit host health [18]. As a result of clinical studies, it has been determined that probiotics have positive effects on strengthening the immune system and gastrointestinal diseases [3, 16, 17]. In this respect, kefir supports the positive effects of probiotics on human health as it contains probiotics with different properties. Given these benefits, it is concluded that kefir should be consumed regularly as a part of the daily diet.

#### 4 PLANT-BASED KEFIR-LIKE BEVERAGES

Recent developments in fermented foods have led to renewed interest in the use of functional ingredients in their production [7]. Plant-based beverages are a liquid mixture of plant materials homogenized with water. Physicochemically, plant-based beverages can also be described as colloidal suspensions of dispersed plant material or oil-in-water emulsions. Since milk is an oil-in-water emulsion, plant-based beverages imitate milk in some characteristics such as consistency, stability, mouth-feel and taste [2]. It is seen in the literature that these beverages are also called “milk”, such as plant-based milk or non-dairy milk [7, 11]. However, European Union regulations declare that in many countries the term “milk” may only be used for the marketing and advertising of products obtained from animal milk. Therefore, worldwide it should be agreed to refer to plant-based liquid products as “beverages” or “drinks” instead of milk, as in Mexico [2].

The interest and acceptance of plant-based beverages by consumers is steadily increasing and the sector is showing a strong growth trend [19]. Novel kefir-like products may represent important foods providing beneficial microorganisms for vegetarians with limited access to fermented products [6]. The beverages fermented by kefir microorganisms have a pleasant taste and aroma due to the organic acids, ethanol, CO<sub>2</sub>, and volatile compounds produced during fermentation. Moreover, plant-based beverages fermented using kefir culture positively affect consumer health as they contain probiotic microorganisms that support the intestinal microflora [12]. In the search for alternative products for milk intolerant individuals, the scientific community has investigated various plant matrices such as legumes (soy, peanut, pea, lupin, cowpea, etc.), cereals (oat, rice, corn, spelt, etc.), nuts (almond, coconut, hazelnut, pistachio, peanut, walnut, cashew, etc.), pseudocereals (quinoa, teff, amaranth, etc.), and seeds (sesame, flaxseed, hemp, sunflower, black cumin, apricot, etc.) for their functional properties due to the nutritional and health compounds they contain [3]. The information on some of the studies conducted for this purpose and the important findings obtained are compiled in Table 2.

**Table 2.** Plant-based beverages fermented with kefir culture for lactose-intolerant and vegan populations

Plant-Based Substrates Used	Concentration / Fermentation / Cultures Used	Important findings or impacts	R
Hemp seed (HS)-based kefir beverages	1:9 ratio (seed:water)/for 24 h at 28 °C/Kefir grains	Kefir fermentation increased the amount of organic acids (tartaric, malic, lactic, acetic, succinic, butyric, etc.), free fatty acids, and free amino acids in HS-based beverages. Fermentation also increased the particle size, viscosity, and phase-separation resistance of the final product.	[1]
Sweet blue lupin (SBL)-based kefir beverages	5%, 10% and 15% (seed:water)/for 24 h at 25°C/Commercial kefir grains	All the samples showed good viability for LAB (>10 <sup>7</sup> CFU/mL) and yeasts (>10 <sup>6</sup> CFU/mL) during 21 days of storage (6 °C). Kefir fermentation increased the amount of free amino acids and antioxidant activity in SBL-based kefir beverages.	[6]
Nut (almond, peanut, hazelnut, walnut, and cashew)-based kefir beverages	1:5 ratio (seed:water)/at 25 °C until pH 4.6/Commercial kefir starter culture	In all samples, high probiotic viability (>10 <sup>7</sup> CFU/mL) was preserved in all microorganisms except yeasts at the end of the storage period. Almond-based kefir beverage is the best example in terms of microbiological and rheological features.	[11]
Licuri-based kefir beverages	1:3 ratio (seed:water)/for 48 h at 25 °C/Water kefir grains ( <i>Lactobacillus hilgardii</i> and <i>Brettanomyces bruxellensis</i> are the dominant species)	All the samples showed good stability in terms of acidity, pH, and viability for LAB (≥10 <sup>8</sup> CFU/mL) and yeasts (10 <sup>4</sup> -10 <sup>5</sup> CFU/mL) during 28 days of storage (4 °C).	[12]
Soybean-based kefir beverages	1:10 ratio (seed:water)/for 36-48 h at 28°C/Kefir grains	Kefir fermentation increased the amount of glutamic acid and sensory quality in soybean-based kefir beverages. <i>Lactobacillus kefir</i> and <i>Kazachstania unispora</i> were the dominant species in soybean-based kefir drink.	[13]
Black cumin oil cake-based kefir beverages	20% and 30% (seed:water)/for 24 h at 25 °C/Commercial kefir grains	All the samples showed good viability for LAB (>10 <sup>7</sup> CFU/mL) and yeasts (>10 <sup>5</sup> CFU/mL) during 21 days of storage (6 °C). The results obtained in rheological and textural measurements are comparable to the well-known structure of conventional milk kefir.	[19]
Flaxseed oil cake-based kefir beverages	5%, 10% and 15% (seed:water)/for 24 h at 25°C/Commercial kefir grains	All the samples showed good viability for LAB (>10 <sup>7</sup> CFU/mL) and yeasts (>10 <sup>6</sup> CFU/mL) during 21 days of storage (6 °C). As a result of fermentation, antioxidant activity in beverages increased.	[20]
Quinoa-based fermented beverages	7.5% (seed:water)/37°C until pH < 4.0/ <i>Lactiplantibacillus plantarum</i> , <i>Lactobacillus kefir</i> , acid mother cultures and kefir grains	Fermented quinoa beverage obtained with <i>Lactiplantibacillus plantarum</i> strain demonstrated better growth and high antioxidant activity at fermentation.	[21]
Apricot seed extract (ASE)-based fermented milk	Apricot kernel extract mixed with cow's milk in various ratios (0:100, 25:75, 50:50, 75:25, 100:0)/for 12-18 h at 24 °C/Commercial kefir culture	Angiotensin-converting enzyme-inhibitory (ACE), antioxidant activities, and content of amino acids including Gln, Gly and Arg increased with the increasing levels of ASE used in the kefir production. Yeast, lactobacilli and lactococci counts also increased with the addition of ASE.	[22]
Various plant (chickpeas, rice, and raw almonds)-based kefir beverages	20% (seed:water)/for 8 h at 25 °C/Water kefir grains	Almond and chickpea kefir were rich in potassium mineral. Ethyl acetate, acetic acid, propionic acid, hexanoic acid and benzenemethanol are the main volatile compounds in almond and chickpea kefir.	[23]

R: References, CFU: Colony-forming unit

## 5 CONCLUSION AND FUTURE PERSPECTIVE

Kefir, also known as the “elixir of youth”, kefir is an important fermented beverage that has been consumed for thousands of years. Kefir naturally contains probiotic microorganisms, which provide additional health benefits. No food in nature can substitute and/or replace milk. Milk is a food secreted by mammals that is vital for health and nutrition because it contains unique types and amounts of components (casein and serum proteins, fat, lactose, calcium, phosphorus, etc.). In recent years, with the change in people's dietary habits, the popularity of veganism, lactose intolerance, milk allergy, and hypercholesterolemia prevalence, there has been a growing interest in alternative plant-based foods in the diet of individuals. In this respect, PBFs have succeeded in attracting attention. As a result of the literature research, it has been observed that the fermentation process, especially in the production of PBFs, increases the bioactivity of the products, improves sensory quality, and increases the expected functional effects of the products. Research has shown that kefir has important effects on human nutrition and health and that kefir should be consumed regularly in the daily diet. It was also concluded that PBFs can be consumed as a good source of nutrients and probiotics in the diet of vegan and dairy-intolerant individuals. In the future, it is foreseen that kefir and/or kefir-like PBFs formulations with a rich bioactive compound profile and high nutritional value, enriched with different flavors and/or aromatic fruits, preserve their sensory quality and the number of probiotic microorganisms during shelf life will be developed that appeal not only to vegans but also to all consumer groups. Furthermore, we must promote the acceptance of the term “plant milk” as a “plant-based beverage” or “plant-based extract”, which has become established in the literature. In this direction, it would be useful to establish practical legislation in all countries and to use a standardized correct term in the scientific community.

## References

- [1] X. Li, Y. He, Y. Xie, L. Zhang, J. Li, and H. Liu, “Effects of fermentation with Kefir grains on nutrient composition, flavor volatiles, and product physical stability of a hemp seed (*Cannabis sativa* L.) beverage,” *LWT-Food Science and Technology*, vol. 183, art. no. 114934, Jun. 2023.
- [2] B. Hidalgo-Fuentes, E. de Jesús-José, A. de J. Cabrera-Hidalgo O. Sandoval-Castilla, T. Espinosa-Solares, R. M. González-Reza, M. L. Zambrano-Zaragoza, A. M. Liceaga, and J. E. Aguilar-Toalá, “Plant-based fermented beverages: Nutritional composition, sensory properties, and health benefits,” *Foods*, vol. 13, no. 6, art. no. 844, Mar. 2024.
- [3] D. Dahiya and P.S. Nigam, “Therapeutic and dietary support for gastrointestinal tract using kefir as a nutraceutical beverage: Dairy-milk-based or plant-sourced kefir probiotic products for vegan and lactose-intolerant populations,” *Fermentation*, vol. 9, no. 4, art. no. 388, Apr. 2023.
- [4] A. Arslaner and M. A. Salik, “Sutun fonksiyonel nitelikli biyoaktif bileşenleri (Functional bioactive components of milk),” *Erzincan Üniversitesi Fen Bilimleri Enstitüsü Dergisi*, vol. 12, no. 1, pp. 124–135. March 2019.
- [5] M. A. Salik and S. Cakmakci “Sut ve konjuge yağ asidinin sağlık ve beslenme üzerindeki önemi,” *3. Uluslararası Baku Bilimsel Araştırmalar Kongresi*, Baku, Azerbaycan, 2021, pp. 736-741.
- [6] L. Łopusiewicz, E. Drożdżowska, P. Trocer, P. Kwiatkowski, A. Bartkowiak, A. Gefrom, and M. Sienkiewicz, “The effect of fermentation with kefir grains on the physicochemical and antioxidant properties of beverages from blue lupin (*Lupinus angustifolius* L.) seeds,” *Molecules*, vol. 25, no. 24, art. no. 5791, pp. 2–14, Dec. 2020.
- [7] D. S. Atik, B. Gurbuz, E. Boluk, and I. Palabiyik, “Development of vegan kefir fortified with *Spirulina platensis*,” *Food Bioscience*, vol. 42, art. no. 101050, Aug. 2021.
- [8] V. Ganatsios, P. Nigam, S. Plessas, and A. Terpou, “Kefir as a functional beverage gaining momentum towards its health promoting attributes,” *Beverages*, vol. 7, no. 3, art. no. 48, Jul. 2021.
- [9] Z. B. Guzel-Seydim, C. Gokirmakli, and A. K. Greene, “A comparison of milk kefir and water kefir: Physical, chemical, microbiological and functional properties,” *Trends in Food Science & Technology*, vol. 113, pp. 42–53, Jul. 2021.
- [10] S. Otles and O. Cagindi, “Kefir: A probiotic dairy composition, nutritional and therapeutic aspects,” *Pakistan Journal of Nutrition*, vol. 2, no. 2, pp. 54–59, Feb. 2023.
- [11] E. M. Comak Gocer, and E. Koptagel, “Production and evaluation of microbiological & rheological characteristics of kefir beverages made from nuts,” *Food Bioscience*, vol. 52, art. no. 102367, Apr. 2023.
- [12] J. de Carvalho Alves, C. O. de Souza, L. de Matos Santos, S. N. A. Viana, D. de Jesus Assis, P. P. L. G. Tavares, E. d. R. Requião, J. M. R. B. D. S. Ferro, and M. N. Roselino, “Licuri kernel (*Syagrus coronata* (Martius) Beccari): A promising matrix for the development of fermented plant-based kefir beverages,” *Foods*, vol. 13, no. 3, art. no. 2056, Jun. 2024.
- [13] J. Luo, S. Liu, H. Lu, Q. Chen, and Y. Shi, “Microbial community variations and bioconversion improvements during soybean-based fermentation by kefir grains,” *Foods*, vol. 12, no. 8, art. no. 1588. Ap. 2023.

- [14] C. Kocak and A. Gursel, "Kefir," *Gida*, vol. 6, no. 4, pp. 11–14, 1981.
- [15] M. Ciftci and N. Oncul, "Sut urunlerinde starter kultur kullanimi," *Gaziosmanpasa Bilimsel Arastirma Dergisi*, vol. 10, no. 3, pp. 62–76, Dec. 2021.
- [16] Z. B. Guzel Seydim, T. Kok Tas, A. K. Greene, and A. C. Seydim, "Functional properties of kefir," *Critical Reviews in Food Science and Nutrition*, vol. 51, no. 3, pp. 261–268, Mar. 2011.
- [17] P. Karatepe and H. Yalcin, "Kefirli saglik," *Igdir Universitesi Fen Bilimleri Enstitusu Dergisi*, vol. 4, no. 2, pp. 23–30, Jun. 2014.
- [18] FAO/WHO, "Guidelines for the Evaluation of Probiotics in Food. Food and Agriculture Organization of the United Nations and World Health Organization Expert Consultation Report", pp. 111, 2002.
- [19] Ł. Łopusiewicz, N. Smietana, D. Paradowska, and E. Drożdowska, "Black cumin (*Nigella sativa* L.) seed press cake as a novel material for the development of new non-dairy beverage fermented with kefir grains," *Microorganisms*, vol. 10, no. 2, art. no. 300, Jan. 2022.
- [20] L. Łopusiewicz, E. Drożdowska, P. Siedlecka, P. Mezynska, A. Bartkowiak, M. Sienkiewicz, H. Zielinska-Blizniewska, and P. Kwiatkowski, "Development, characterization, and bioactivity of non-dairy kefir-like fermented beverage based on flaxseed oil cake," *Foods*, vol. 8, no. 11, art. no. 544, Nov. 2019.
- [21] A. Pugliese, M. Ulzurrun, F. C. Leskow, G. De Antoni, and E. Kakisu, "Microbiological and chemical characterization of fermented quinoa beverages obtained with kefir microorganisms," *Journal of Food and Nutrition Research*, vol. 62, no. 4, pp. 363–373, Nov. 2023.
- [22] K. Uruc, A. Tekin, D. Sahingil, and A. A. Hayaloglu, "An alternative plant-based fermented milk with kefir culture using apricot (*Prunus armeniaca* L.) seed extract: Changes in texture, volatiles and bioactivity during storage," *Innovative Food Science and Emerging Technologies*, vol. 82, art. no. 103189, Dec. 2022.
- [23] M. Ustaoglu-Gencgonul, C. Gokirmakli, B. Ucgul, Y. Karagul-Yuceer, and Z. B. Guzel-Seydim, "Chemical, microbial, and volatile compounds of water kefir beverages made from chickpea, almond, and rice extracts," *European Food Research and Technology*, vol. 250, pp. 2233–2244, Apr. 2024.



---

## Cytocompatibility of PVA/Chitosan Electrospun Scaffold Loaded with Antioxidant Amino Acid on Fibroblast and Neuroblastoma Cells

**Betul Mutlu<sup>\*1</sup>, Cem Bulent Ustundag<sup>1</sup>, Rabia Cakir<sup>1</sup>**

<sup>1</sup>*Bioengineering Department, Yildiz Technical University, Istanbul, Türkiye*

---

### Abstract

2-aminoethanesulfonic acid, taurine, is an amino acid with antioxidant properties not involved in protein production found in large amounts as a free amino acid in many cell types and tissues. In this study, taurine amino acid-loaded PVA/Chitosan electrospun mats were successfully produced by electrospinning and characterized from various aspects. Microstructural analysis of the electrospun mats showed that the increase in the amount of amino acids caused significant changes in fiber diameter. In the chemical analysis examined with FT-IR, the inclusion of the amino acid in the nanofiber structure was confirmed by observing taurine-specific peaks on the electrospun mats. To evaluate the usability of free taurine and the produced electrospun mats as tissue scaffolds, their cytotoxic activities were investigated on the mouse fibroblast cell line and human neuroblastoma cell line using the XTT cell viability test. The results show that taurine does not produce cytotoxic effects on fibroblast and neuroblastoma cells up to 1000 µg/ml. Indirect cytotoxic activity results of taurine-loaded nanofibrous mats confirm that they are cytocompatible for fibroblast and neuroblastoma cells. Findings show that taurine-loaded PVA/Chitosan electrospun mats can be an antioxidant and cytocompatible tissue scaffold for nerve and skin tissue engineering applications.

**Keywords:** *Taurine, Cytotoxicity, Electrospun scaffolds, Nanofiber*

---





## Characterization and Study of the *In Vitro* Effects of Polysaccharide-Based Nanofibers Obtained Using the Method of Coaxial Electrospinning to Improve Tympanic Membrane Perforations

Busra Akgul<sup>\*1</sup>, Cansu Gulcan<sup>1</sup>, Selay Tornaci<sup>2</sup>, Merve Erginer<sup>3</sup>, Ebru Toksoy Oner<sup>2</sup>,  
Emrah Sefik Abamor<sup>1</sup>, Serap Acar<sup>1</sup>, Adil M. Allahverdiyev<sup>4</sup>

<sup>1</sup>Bioengineering, Yildiz Technical University, Istanbul, Türkiye

<sup>2</sup>Bioengineering, Marmara University, Istanbul, Türkiye

<sup>3</sup>Institute of Nanotechnology and Biotechnology, Istanbul University-Cerrahpasa, Istanbul, Türkiye

<sup>4</sup>The V. Akhundov Scientific Research Medical Preventive Institute, Baku, Azerbaijan

### Abstract

The tympanic membrane (TM) is a transparent, thin curtain that separates the middle ear and the outer ear. It is responsible for protecting the inner part of the ear from external factors and transmitting sound [1]. Perforations occur in the tympanic membrane due to infection, traumatic and iatrogenic reasons [2]. Today, tissue engineering approaches have begun to be used as an alternative to traditional surgical methods to close perforations [3]. Natural polysaccharides are more preferred in tissue engineering applications compared to synthetic materials due to their anti-inflammatory, antioxidant, immune response regulator, cell migration guiding, wound healing promoting, cell proliferation inducing effects and low cytotoxicity [4].

In this study, nanofibers were developed to close chronic perforations that do not heal spontaneously and to ensure the improve of the perforated area in a short time. These nanofibers based on PCL and PCL-polysaccharide based were obtained by coaxial electrospinning method. Characterization and *in vitro* cell culture studies of the obtained nanofibers were carried out. It was determined that PCL-polysaccharide based nanofibers are more hydrophilic, more biodegradable, and have higher swelling capacity than PCL nanofibers. Also, the diameters of PCL and PCL-polysaccharide based nanofibers were obtained as 247 nm and 149 nm, respectively. Warton gel stem cells and L929 fibroblast cells were used in cell culture studies. In these studies, when the biocompatibility, cell adhesion and wound closure properties of nanofibers were compared, it was determined that PCL-polysaccharide based nanofibers had better cell interactions than PCL nanofibers.

Considering these results, it is concluded that PCL-Polysaccharide based nanofibers may be effective in the regeneration of TM perforations. Accordingly, in future studies, its *in vivo* activities will be examined and its potential as an alternative patch to autografts will be investigated.

**Keywords:** Tympanic membrane perforation, Polysaccharide, Coaxial electrospinning, Nanofiber

### Acknowledgments

This study was supported by Yildiz Technical University Scientific Research Projects Coordination Unit (BAP) under project number TSA-2023-5371 (YTU, ADEP, 5371). Busra Akgul was supported by the Turkish Scientific and Technological Research Council (TUBITAK) scholarship (Grant No: 2211A) and Council of Higher Education (YOK), 100/2000 Scholarship Programme of Doctorate, in the fields of Biomaterials and Tissue Engineering during this study.

### References

- [1] N. H. Cho, M. E. Ravicz, and S. Puria, "Human middle-ear muscle pulls change tympanic-membrane shape and low-frequency middle-ear transmission magnitudes and delays," *Hearing Research*, vol. 430, art. no. 108721, 2023.
- [2] V. Pontillo, G. Cavallaro, F. Barbara, M. Mastrodonato, A. Murri, and N. Quaranta, "Recurrent tympanic perforation after myringoplasty: A narrative literature review and personal experience," *Acta Otorhinolaryngologica Italica*, vol. 43, pp. S41–S41, 2023.

- [3] M. A. Villar-Fernandez and J. A. Lopez-Escamez, "Outlook for tissue engineering of the tympanic membrane," *Audiology Research*, vol. 5, no. 1, art. no. 117, 2015.
- [4] H. Xu, Y. Che, R. Zhou, L. Wang, J. Huang, W. Kong et al., "Research progress of natural polysaccharide-based and natural protein-based hydrogels for bacteria-infected wound healing," *Chemical Engineering Journal*, art. no. 153803, 2024.



## Statistical Investigation of Surface Modification Polymerization Methods in Global and Turkish Scale

Nursel Karaoglan<sup>\*1</sup>

<sup>1</sup>Department of Electrical and Energy, TOBB Vocational School of Technical Sciences, Karabuk University, Karabuk, Türkiye

### Abstract

This study aims to statistically examine the global and local research trends of advanced polymerization techniques such as Controlled Radical Polymerization (CRP), Atom Transfer Radical Polymerization (ATRP), Reversible Addition-Fragmentation Chain Transfer (RAFT), Nitroxide Mediated Polymerization (NMP), and Photoinitiated Polymerization (PIMP). These methods are critical for the controlled synthesis of complex molecular structures in polymer science and hold significant application potential, especially in surface modification, materials science, biotechnology, and nanotechnology. Within the scope of this study, the numerical distributions of articles published using these methods, categorized by year and country, were analyzed using the Web of Science (WoS) database. These analyses reveal the international research trends related to these polymerization techniques. Additionally, a focused examination of publications on these polymerization methods in Turkey was conducted, and visual mappings of associated keywords and research topics were created using co-occurrence analysis. This study comprehensively evaluates the development of research in polymerization methods and Turkey's contributions in this field, offering significant findings that could guide future research endeavors.

**Keywords:** *Polymerization methods, Surface modification, Global trends, Turkish scale, Scientific analysis*

## 1 INTRODUCTION

The synthesis of polymer brushes on the surface is one of the most common and effective methods of surface modification of the substrate. This structure, called a polymer brush, consists of polymer chains that are chemically tightly bonded to the substrate through covalent bonds and have a brush-like appearance [1, 3]. Depending on how the polymer chains are bonded and the type of substrate, the polymer chains can form hierarchical structures. These structures are formed by bonding to another polymer chain (one-dimensional, 1D) on a planar surface (two-dimensional, 2D) or a spherical or cylindrical solid (three-dimensional, 3D) [4]. The nanoscale layering of polymers chemically attached to the surface can significantly modify the surface's physicochemical properties. Such modifications are carried out using surface-initiated polymerization techniques, which have emerged as a powerful tool in producing polymer brushes. The number of publications on polymer brushes is increasing yearly, and research topics span a wide range of fields, such as physics, materials science, food science, biomedical, and medical science. This demonstrates the versatile application potential of polymer brushes and the growing academic and industrial interest [5, 7].

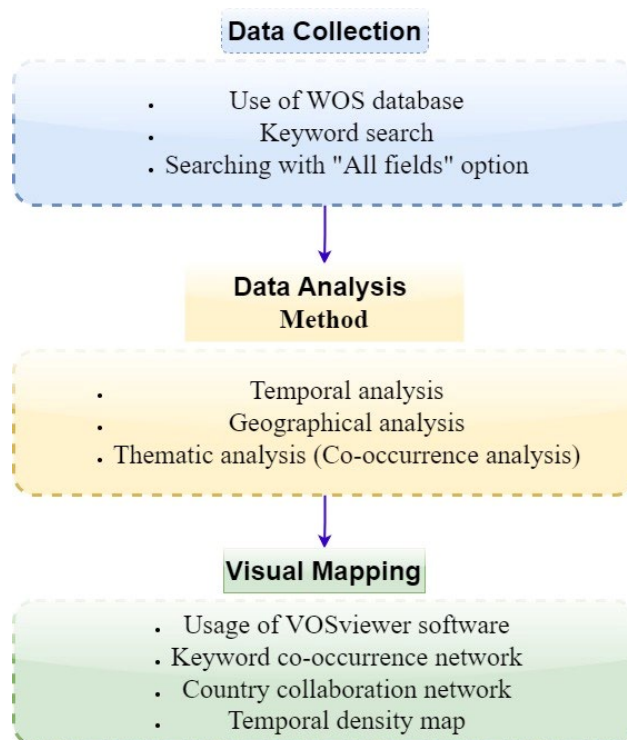
The traditional radical polymerization method can be used to synthesize polymers. However, the uncontrollability of molecular weight in this method and undesired chain terminations lead to deviations from desired chain lengths and broad molecular weight distribution, which limits the synthesis of polymer surfaces with specific architectures [8] [9]. Molecular weight, dispersion, and molecular architecture (composition, topology, and functionality) are the most critical factors affecting the properties and applications of polymers. The increasing demand for functional polymeric materials with specific properties has accelerated the development of innovative and effective modification methods. In this context, macromolecular engineering enables the design of polymers for specific applications through precise synthesis and comprehensive characterization [10]. Controlled Radical Polymerization (CRP) techniques with specific methods have been developed to improve these properties. CRP is a technique that encompasses other polymerization methods and has made significant progress in both academic and industrial fields. Starting in 1982 with the pioneering work of Otsu and co-workers in the controlled radical photopolymerization of MMA using benzyl dithiocarbamate as an iniferter [11], this field has attracted a great deal of attention with more than 30,000 publications and more than 4,000 patents in the last 40 years. Moreover, the CRP technique has revolutionized the field of macromolecular synthesis by combining the ease of use of free radical polymerization and the high standard of control provided by living ionic polymerization in a single polymerization process [12, 14].

CRP offers various applications by precisely controlling polymers' molecular weight, dispersion, and architecture. The various sub-methods of CRP use different techniques and reagents to achieve this goal. Commonly applied methods include Atom Transfer Radical Polymerization (ATRP) [15, 16], Reversible Addition-Fragmentation Chain Transfer (RAFT) [17], Nitroxide Mediated Polymerization (NMP) [18] and Photoinitiated Polymerization (PIMP) [19]. These methods offer many adjustable experimental variables with parameters such as the type of reagents used, reaction time, concentration, and temperature [20]. However, polymer brushes' efficient and controlled preparation still poses a significant challenge. Furthermore, a better understanding of the structure (composition, architecture, and length) of the attached polymer chains and their effect on the matrix is required to optimize the performance of polymer brushes.

In this study, co-occurrence analysis and statistical comparisons were performed with the data obtained from the Web of Science (WoS) database to understand the global and local research trends of advanced polymerization techniques such as CRP, ATRP, RAFT, NMP, and PIMP and to identify research gaps. Turkey-based and global studies were examined, and a trend analysis was performed for the studies in this field in the literature. These analyses reveal the importance of polymerization methods in scientific and industrial application areas, especially in critical areas such as materials science, biotechnology, nanotechnology, and surface modification. In polymer science, investigating these methods, which offer great potential for the controlled synthesis of complex molecular structures, contributes to identifying strategic directions and directing future research efforts locally and globally. In addition, the annual numerical distribution of polymerization methods on a global and Turkish scale was examined, and visual maps of relevant keywords and research topics were created using VOSviewer [21, 22] software. In this context, the aim and significance of the study is to significantly contribute to the advancement of the research field by comprehensively evaluating the existing literature and filling the knowledge gaps in this field.

## 2 METHODOLOGY

This study adopted a comprehensive bibliometric analysis method to examine the global and local research trends of advanced polymerization techniques. These systematic approaches are designed to ensure the reliability and reproducibility of the study. In this context, the methodology section is presented under three sub-headings: Data Collection, Data Analysis Method, and Visual Mapping Techniques. In the Data Collection phase, the process of obtaining the research data and the criteria used are explained in detail. Data Analysis Methods reveals the processing process of the collected data and the analysis methods applied. Finally, the Visual Mapping Techniques section describes how the analysis results were visualized, and the software platform used. Figure 1 presents the flowchart detailing the methodology systematically applied in the study.



**Figure 1.** Flowchart showing the research methodology and steps employed

## 2.1 Data Collection

In the data collection phase of this study, the WoS database was used to examine global and local research trends related to CRP and its related advanced polymerization methods, ATRP, RAFT, NMP, and PIMP techniques. The data collection strategy was designed separately for each technique and to cover all techniques. The WoS database was searched using the keywords “Controlled Radical Polymerization,” “Atom Transfer Radical Polymerization” or “ATRP,” “Reversible Addition-Fragmentation Chain Transfer” or “RAFT,” “Nitroxide-Mediated Polymerization” or “NMP,” “Photoinitiated Polymerization” or “PIMP.” These keywords were queried by selecting “all fields” on the WoS platform, including the title, abstract, and WoS keywords. In addition, a comprehensive query created by combining all these keywords was also used, aiming at a holistic analysis of the related techniques. The raw data were carefully analyzed to eliminate duplicate records and irrelevant publications. Standard data cleaning procedures were applied to ensure consistency and reliability of the data, and publications suitable for analysis were selected. In this process, the bibliometric information of the publications (publication year, author information, institutions, countries, keywords, etc.) was systematically extracted.

## 2.2 Data Analysis Method

The raw data was systematically reviewed to eliminate duplicate records and irrelevant publications. Relevant publications for the analysis were identified, and their bibliometric information was extracted. Data analysis encompassed several steps: temporal analysis, which examined the distribution of publications over the years for each polymerization technique; geographical analysis, which assessed the distribution of publications by country; and thematic analysis, which included the co-occurrence analysis of keywords used in the publications. The number of publications from Turkey was compared to global publication counts to evaluate Turkey’s position and contribution in the field. At this stage, publications related to CRP, ATRP, RAFT, NMP, and PIMP techniques were individually examined for their distribution over the years. This analysis revealed the temporal development and potential trends in the research area.

Subsequently, the distribution of publications by country was examined, identifying international contributions and geographical concentrations. This analysis highlighted which countries are leading in this field and potential collaboration opportunities. The number of publications from Turkey was again compared to global publication counts to assess Turkey’s position and contribution. Additionally, a co-occurrence analysis of keywords used in the publications was performed. This analysis elucidated the thematic structure and trends within the research area, identifying popular research topics and potential new research areas. The five advanced polymerization methods were collectively analyzed to evaluate trends from different perspectives. These analyses aim to comprehensively present the overall status of the CRP, ATRP, RAFT, NMP, and PIMP techniques, Turkey’s position in the field, and potential future research directions.

## 2.3 Visual Mapping Techniques

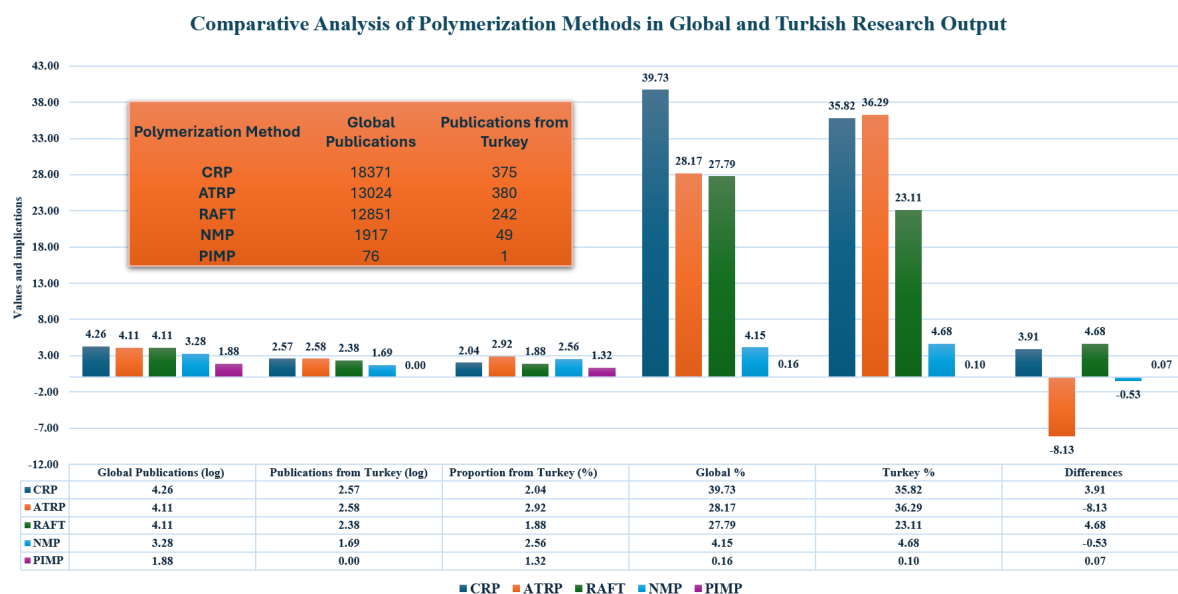
VOSviewer software was used to visualize and make the results of bibliometric analyses more understandable. This software is designed to process large bibliometric datasets and visualize complex network structures. Keywords such as co-occurrence network, country collaboration network, and temporal density map were created with VOSviewer [23]. The keyword co-occurrence network shows the key concepts in the research field and the relationships between these concepts; this map helps to identify research clusters and sub-disciplines in the field. The country collaboration network reveals international research collaborations and geographical collaboration patterns, while the temporal density map shows the distribution of research activities over time. This methodological approach allows for a comprehensive and systematic analysis of research dynamics in CRP and related advanced polymerization techniques. Visual mapping techniques created with VOSviewer contribute to more effective analysis and presentation of research dynamics in the field of CRP, ATRP, RAFT, NMP, and PIMP techniques by making complex bibliometric data more understandable and interpretable [2].

## 3 RESULTS

This section is dedicated to the presentation of the analyses performed and the findings obtained. The analyses conducted and the results acquired elucidate the significant themes within the research domain and the interrelationships among these themes. Data sourced from the WoS was imported into the VOSviewer software, facilitating the execution of keyword co-occurrence analyses. These analyses are crucial for visualizing thematic clusters and relationships within the research field. The visualization tools provided by VOSviewer render the frequency of keyword usage and their interconnections more comprehensible. The study also incorporates critical metrics such as the Co-occurrence Value, which denotes the number of distinct documents in which a particular

keyword appears alongside other keywords, and the Link, representing the relationship or connection between two items. For instance, if the co-occurrence value of the keyword ‘‘CRP’’ is indicated as 5, this signifies that this keyword appears in 5 different articles or documents in conjunction with other keywords. The link value denotes the connections a keyword has with five distinct other keywords.

Figure 2 is intended to present a comparative display of research outputs on polymerization methods at both the global and Turkish scales. The graph visualizes the publication numbers on a logarithmic scale, thereby elucidating the prevalence of various polymerization techniques within the field of polymer science and highlighting Turkey’s contributions to this domain.



\*The above statistical information was obtained from the WOS database as of 8 July 2024.

**Figure 2.** General perspective: Comparison of research outcomes

CRP holds the highest number of publications globally (18,371), accounting for 39.73% of the total publications. This indicates that CRP is a widely used and researched method in polymer synthesis. In Turkey, studies on CRP (375 publications, 35.82%) also hold a significant place, albeit with a relatively lower percentage compared to the global figures (difference: 3.91%). ATRP ranks second globally (13,024 publications, 28.17%), and stands out as the most studied method in Turkey (380 publications, 36.29%). This suggests that Turkish researchers have a higher interest in ATRP compared to global trends (difference: -8.13%). While RAFT holds a significant place in the global literature (27.79%), it is relatively less studied in Turkey (23.11%). This difference (4.68%) indicates potential research opportunities in the field of RAFT polymerization in Turkey. Both NMP and PIMP methods are less studied on both global and Turkish scales. Particularly, the fact that there is only one publication from Turkey in the field of PIMP suggests substantial potential for future research in this area. These data indicate that the research conducted in Turkey on polymerization techniques, when compared to global prevalence and trends, reveals certain gaps and opportunities in specific areas.

The graph in Figure 3, illustrating the global distribution of studies on polymerization techniques over the years, provides a comprehensive analysis of research trends in the field of polymer science. The dataset, spanning from 2001 to 2024, highlights the research intensity of CRP, ATRP, RAFT, PIMP, and NMP techniques. The consistently dominant position of CRP demonstrates its extensive application in polymer synthesis. Additionally, the flexibility of the CRP model and its compatibility with various monomers render this technique more advantageous compared to other polymerization methods. The ability of CRP to encompass the principles of other controlled/living polymerization techniques, such as ATRP and RAFT, contributes to its widespread acceptance in the research domain. The steady rise of the RAFT technique reflects the increasing interest in controlled/living radical polymerization. The decline in ATRP and NMP techniques can be attributed to the maturation of these methods or the development of alternative approaches. The low but steady number of studies on the PIMP technique indicates that this area remains a niche research topic. The general decline observed in 2023-2024 can be explained by the incomplete data collection process or the impact of global factors; this suggests that additional analysis may be required to predict future research trends.

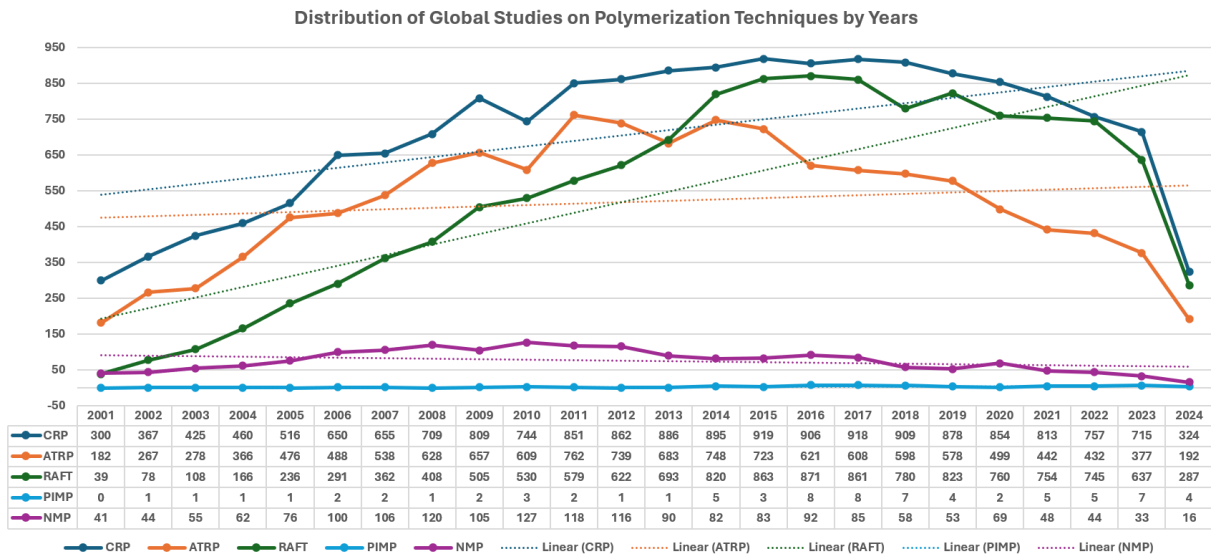


Figure 3. Distribution of global studies on polymerisation techniques by years

Figures 4-7 present graphs showing the number of publications by country for CRP, ATRP, RAFT, NMP, and PIMP techniques, respectively. These graphs visually represent the research productivity and international research share of each polymerization technique in different countries. The distribution of publication numbers by country for each technique allows for the analysis of the global popularity of these methods and the research intensity across countries.



Figure 4. The CRP graph of number of publications by country



Figure 5. The ATRP graph of number of publications by country



Figure 6. The RAFT graph of number of publications by country

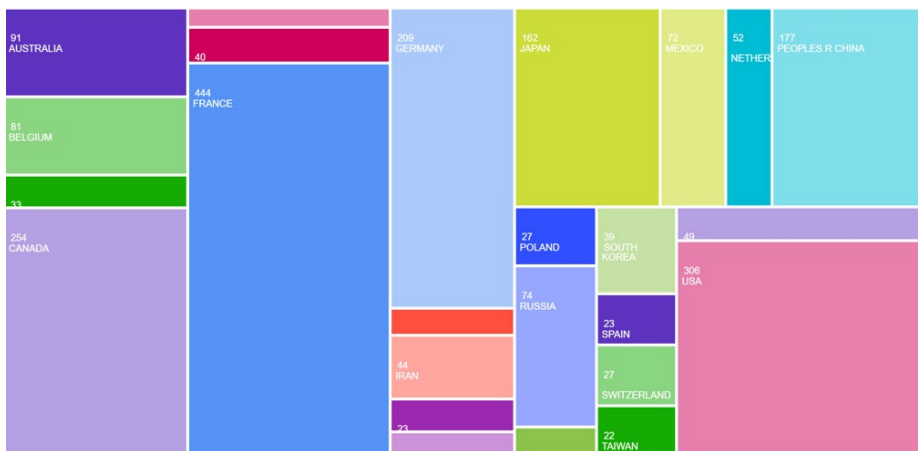


Figure 7. The NMP graph of number of publications by country

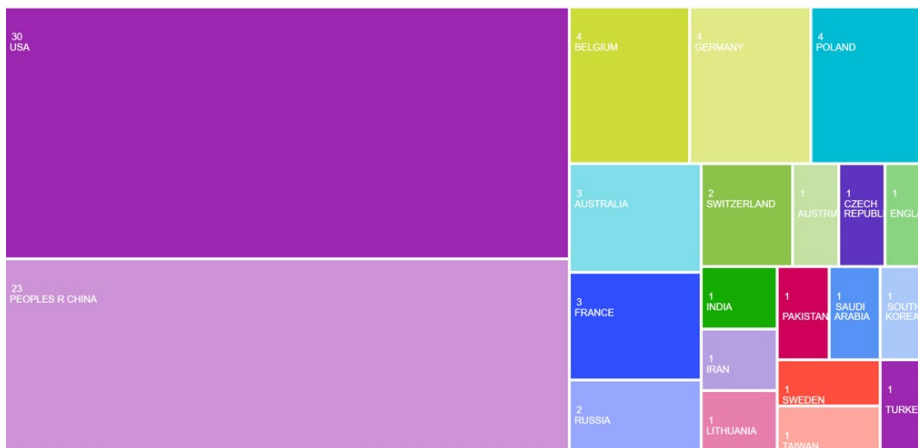


Figure 8. The PIMP graph of number of publications by country

The country-based publication ranking presented in Figure 9 reveals a multifaceted panorama of global academic productivity. Various bibliometric indicators, such as CRP, ATRP, RAFT, NMP, and PIMP shown in the table, have been employed to quantitatively evaluate the scientific output of different countries. Turkey’s average ranking of 13.8 reflects its position in the international academic arena. This dataset indicates that while Turkey demonstrates strong performance in certain areas (e.g., 9th place in ATRP), there is potential for development in others (e.g., 21st place in PIMP). This comprehensive analysis highlights the relative strengths and weaknesses of the research ecosystems in various countries, providing valuable insights for researchers and academic institutions.



Countries/Regions	CRP	Countries/Regions	ATRP	Countries/Regions	RAFT	Countries/Regions	NMP	Countries/Regions	PIMP
PEOPLES R CHINA	4485	PEOPLES R CHINA	4823	PEOPLES R CHINA	4021	FRANCE	444	USA	30
USA	3700	USA	2669	USA	2101	USA	306	PEOPLES R CHINA	23
JAPAN	1814	JAPAN	898	AUSTRALIA	1564	CANADA	254	BELGIUM	4
FRANCE	1374	GERMANY	702	GERMANY	1070	GERMANY	209	GERMANY	4
GERMANY	1365	FRANCE	519	ENGLAND	995	PEOPLES R CHINA	177	POLAND	4
AUSTRALIA	976	SOUTH KOREA	474	FRANCE	928	JAPAN	162	AUSTRALIA	3
ENGLAND	817	CANADA	440	JAPAN	834	AUSTRALIA	91	FRANCE	3
CANADA	742	ENGLAND	436	INDIA	437	BELGIUM	81	RUSSIA	2
INDIA	590	<b>TURKEY</b>	<b>380</b>	CANADA	358	RUSSIA	74	SWITZERLAND	2
SOUTH KOREA	584	INDIA	377	SOUTH KOREA	324	MEXICO	72	AUSTRIA	1
BELGIUM	419	POLAND	300	BELGIUM	286	NETHERLANDS	52	CZECH REPUBLIC	1
RUSSIA	415	IRAN	279	NETHERLANDS	266	<b>TURKEY</b>	<b>49</b>	ENGLAND	1
NETHERLANDS	379	SINGAPORE	269	<b>TURKEY</b>	<b>242</b>	IRAN	44	INDIA	1
<b>TURKEY</b>	<b>375</b>	BELGIUM	253	IRAN	229	ENGLAND	40	IRAN	1
ITALY	328	NETHERLANDS	243	RUSSIA	181	SOUTH KOREA	39	LITHUANIA	1
IRAN	320	AUSTRALIA	231	ITALY	148	BRAZIL	33	PAKISTAN	1
POLAND	314	TAIWAN	231	MEXICO	148	POLAND	27	SAUDI ARABIA	1
SPAIN	279	ITALY	213	SPAIN	145	SWITZERLAND	27	SOUTH KOREA	1
SWITZERLAND	271	SWITZERLAND	195	SWITZERLAND	134	IRELAND	23	SWEDEN	1
TAIWAN	240	SPAIN	156	TAIWAN	120	SPAIN	23	TAIWAN	1
BRAZIL	216	RUSSIA	132	SINGAPORE	113	CZECH REPUBLIC	22	<b>TURKEY</b>	<b>1</b>
PAKISTAN	197	SWEDEN	97	POLAND	106	TAIWAN	22		
SINGAPORE	179	SAUDI ARABIA	96	BRAZIL	89	INDIA	19		
MEXICO	174	PORTUGAL	86	SOUTH AFRICA	88	ITALY	16		
SAUDI ARABIA	146	CZECH REPUBLIC	83	GREECE	81	SAUDI ARABIA	13		
<b>Turkey's average ranking: 13.8</b>									
*Only the first 25 countries are listed.									

Figure 9. Country-based publication ranking

Figure 10 provides a detailed presentation of country-specific publication distributions through combined keyword searches applied in the WoS database. The primary aim of this analysis is to comprehensively evaluate the potential and research activity of polymerization techniques among countries from a global perspective. Combined keywords have been utilized to more accurately reflect the main trends in literature and the contributions of different countries in this field. In this context, as shown in Figure 10, Turkey’s publication performance in polymerization is ranked 11th. This ranking highlights Turkey’s significant position in terms of research and publication productivity related to polymerization techniques on an international level. When assessed in terms of local and global research trends, this finding underscores the importance of Turkey’s scientific contributions and research potential in polymerization techniques.



Figure 10. Country-based publication distribution using combined keyword searches in WOS database

Figure 11 illustrates the co-occurrence and connection map of keywords used in Turkey, reflecting their intensities over the years. The map visualizes the relationships between keywords and the temporal changes through color coding. It is observed that central terms such as “atom transfer radical polymerization (ATRP)” possess strong connections with many other terms, emphasizing the significance of this topic in the field and the intensity of research. The color scale represents the period from 2005 to 2020, with the intensity of colors indicating the frequency of keyword usage in specific years. Blue tones represent earlier years, while green and yellow represent more recent years. This map analyzes how research trends around specific keywords have evolved and which topics have garnered more interest.

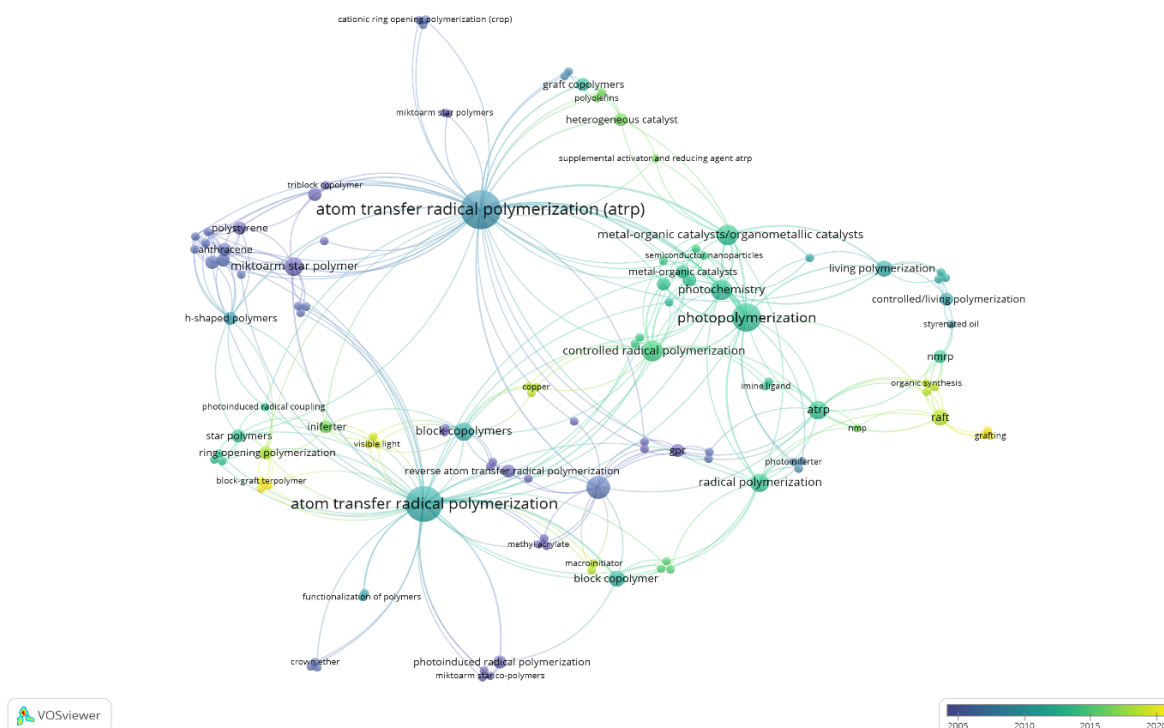


Figure 11. Co-occurrence and link map of keywords in Turkey (Year-based density)

Figure 12 presents an overview of the co-occurrence and connection map of keywords in Turkey. The map visualizes the relationships between specific keywords and their connections within the research domain through color coding. This map facilitates the analysis of research trends and the interrelationships between specific topics. For instance, the term “atom transfer radical polymerization (ATRP)” is positioned at the center of the map, showing solid connections with many other keywords; this underscores the significance of the topic in the literature. Different colors on the map represent specific keyword groups and the relationships between these groups. Blue, green, red, orange, and other colors highlight the clustering of relevant topics and emphasize their importance in research. For example, blue may represent terms related to photopolymerization, while red could signify terms associated with radical polymerization. Overall, this map provides valuable insights into how keywords in various subfields of polymer research in Turkey are used together and which topics play a more central role. These insights have the potential to help researchers identify which areas have been more extensively studied and which areas require more collaboration.

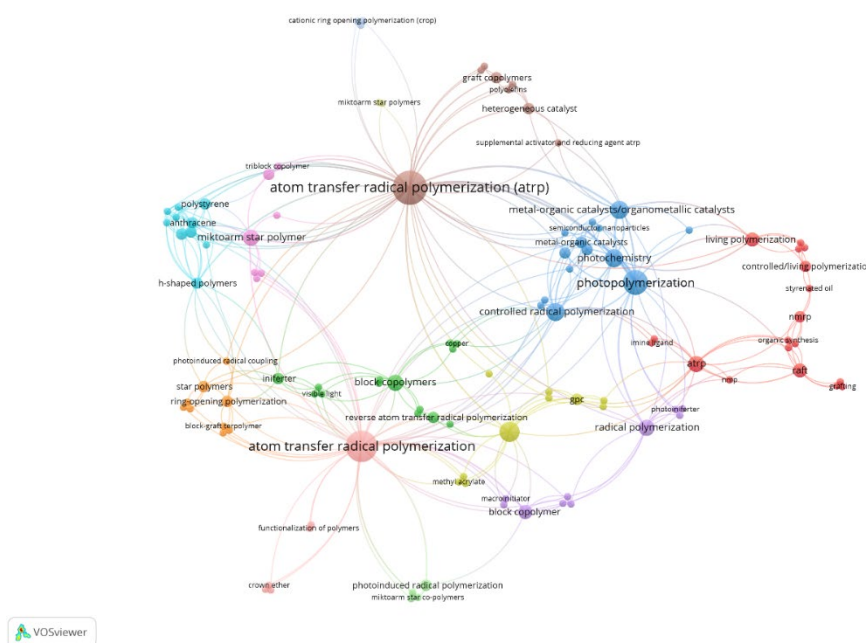


Figure 12. Co-occurrence and link map of keywords in Turkey (Overview)

Figure 13 illustrates the results of the co-occurrence analysis conducted using the VOSviewer software. The analysis examines the frequency of keyword usage in articles and the strength of the connections between these keywords. The table presents the keywords' ranking, frequency of occurrence, and total link strength. Among the top-ranked keywords are terms such as "atom transfer radical polymerization (ATRP)" and "photopolymerization". The term "atom transfer radical polymerization (ATRP)" is used 16 times and has a total link strength of 62, securing the highest rank. The term "photopolymerization" is used nine times and has a total link strength of 41. These keywords indicate intense research activity in polymerization and photochemical processes, highlighting their central role in literature. The table also reveals the prevalence of studies on various polymerization techniques and types of polymers. For instance, terms such as "controlled radical polymerization," "living polymerization", and "block copolymers" represent significant topics within their respective research areas.

Order	Keyword	Occurrences	Total link strength
1	atom transfer radical polymerization (atrp)	16	62
2	atom transfer radical polymerization	14	56
3	photopolymerization	9	41
4	methyl methacrylate	6	20
5	controlled radical polymerization	5	22
6	metal-organic catalysts/organometallic catalysts	5	21
7	photochemistry	5	22
8	atrp	4	16
9	block copolymers	4	14
10	miktoarm star polymer	4	14
11	radical polymerization	4	17
12	block copolymer	3	11
13	living polymerization	3	12
14	raft	3	12
15	anthracene	2	14
16	controlled/living polymerization	2	6
17	diels-alder reaction	2	14
18	gpc	2	8
19	graft copolymers	2	7
20	h-shaped polymers	2	14
21	heterogeneous catalyst	2	8
22	iniferter	2	10
23	maleimide	2	14
24	metal-organic catalysts	2	12
25	nmrp	2	7
26	organometallic catalysts	2	12
27	photoinduced radical polymerization	2	6
28	polystyrene	2	12
29	reverse atom transfer radical polymerization	2	5
30	ring-opening polymerization	2	9
31	stable free-radical polymerization (sfrp)	2	5
32	star polymers	2	9
33	visible light polymerization	2	11
34	atom-transfer radical polymerization (atrp)	1	4
35	azobenzene	1	4
36	block-graft terpolymer	1	4
37	cationic polymerization	1	2
38	cationic ring opening polymerization (crop)	1	3
39	chain scission	1	3
40	chlorinated polypropylene	1	4

**Figure 13.** The numerical values of co-occurrence and link maps of keywords in the Turkey scale

#### 4 DISCUSSION AND FUTURE WORK

This study aims to statistically examine global and local research trends in advanced polymerization techniques such as CRP, ATRP, RAFT, NMP, and PIMP. These methods are critical for the controlled synthesis of complex molecular structures in polymer science and have significant potential for application in surface modification, materials science, biotechnology, and nanotechnology. The research used a large dataset from the WoS database. The data collected through WoS was used to comprehensively analyze key bibliometric indicators such as keywords and publication counts. These data were processed systematically to gain an in-depth understanding and assessment of global and local research trends related to polymerization techniques.

The findings of this study provide a comprehensive assessment of global and local research trends related to CRP techniques. The results indicate that the ATRP method has the highest publication count, followed by RAFT, NMP, and PIMP in succession. Interest in these techniques has significantly increased since the late 1990s, with a marked rise in annual publication numbers for ATRP and RAFT particularly noted from the mid-2010s. NMP has a higher publication count than PIMP and exhibits a more stable growth trend. By country, the United States, China, and France are leading research on these polymerization techniques. Turkey is actively engaged in research in this field, ranking between 11 and 13.8 globally. Research trends in Turkey reveal that ATRP is the most studied method, followed by RAFT. Although research on NMP and PIMP is less prevalent, studies in these areas also exist. The co-occurrence analysis reveals that these polymerization techniques are closely related to various application areas. The potential of CRP techniques in nanotechnology, biomedical applications, and materials science is emphasized. Turkey's contributions to advanced polymerization techniques, particularly in ATRP and RAFT, underscore significant research efforts. The findings suggest that controlled radical polymerization techniques are gaining increasing global interest and hold substantial potential across various scientific and industrial domains. Turkish research could further advance this dynamic and evolving field. In this context, the findings outline the current state of advanced polymerization techniques and Turkey's contributions and provide important directions for future research. Firstly, it is recommended that more profound studies be conducted on the potential of CRP, ATRP, and RAFT techniques, particularly in areas such as nanotechnology, biomedical applications, and materials science. Research into the performance and innovative application methods of these techniques could expand the boundaries of polymer science. Furthermore, a more detailed examination of Turkey's contributions could facilitate the development of strategies aligned with international research trends. Encouraging collaborations and joint projects among research centers and universities in Turkey could lead to more

comprehensive studies on CRP and RAFT techniques, strengthening Turkey's role in the global polymer science community.

Future research should focus on further exploring the application potential of PIMP and NMP techniques. Increasing research in these areas could enhance their roles and effectiveness in industrial applications. Specifically, the potential applications of PIMP in nanomaterials and biomedical devices could broaden research opportunities in this field. Lastly, co-occurrence analysis and other data visualization methods are crucial in identifying new trends and research topics. Applying these methods to larger datasets could provide valuable insights into the development process of polymerization techniques and predict future research directions. These recommendations may contribute to advancing knowledge in polymer science and uncovering new research opportunities.

## References

- [1] R. Yang, X. Wang, S. Yan, A. Dong, S. Luan, and J. Yin, "Advances in design and biomedical application of hierarchical polymer brushes," *Progress in Polymer Science*, vol. 118, art. no. 101409, 2021, doi: 10.1016/j.progpolymsci.2021.101409.
- [2] M. Krishnamoorthy, S. Hakobyan, M. Ramstedt, and J. E. Gautrot, "Surface-initiated polymer brushes in the biomedical field: Applications in membrane science, biosensing, cell culture, regenerative medicine and antibacterial coatings," *Chemical Reviews*, vol. 114, no. 21, pp. 10976–11026, 2014, doi: 10.1021/cr500252u.
- [3] Y. Zou, J. N. Kizhakkedathu, and D. E. Brooks, "Surface modification of polyvinyl chloride sheets via growth of hydrophilic polymer brushes," *Macromolecules*, vol. 42, no. 9, pp. 3258–3268, 2009.
- [4] C. Feng and X. Huang, "Polymer Brushes: Efficient Synthesis and Applications," *Accounts of Chemical Research*, vol. 51, no. 9, pp. 2314–2323, 2018, doi: 10.1021/acs.accounts.8b00307.
- [5] R. Wang, Q. Wei, W. Sheng, B. Yu, F. Zhou, and B. Li, "Driving Polymer Brushes from Synthesis to Functioning," *Angewandte Chemie*, vol. 135, no. 27, 2023, doi: 10.1002/ange.202219312.
- [6] D. Li, L. Xu, J. Wang, and J. E. Gautrot, "Responsive polymer brush design and emerging applications for nanotheranostics," *Advanced Healthcare Materials*, vol. 10, no. 5, art. no. 2000953, 2021.
- [7] S. Nastyshyn *et al.*, "Temperature-responsive polymer brush coatings for advanced biomedical applications," *Polymers*, vol. 14, no. 19, art. no. 4245, 2022.
- [8] M. Szwarc, "'Living' polymers," *Nature*, vol. 178, no. 4543, pp. 1168–1169, 1956.
- [9] R. B. Grubbs and R. H. Grubbs, "50th Anniversary Perspective: Living Polymerization—Emphasizing the Molecule in Macromolecules," *Macromolecules*, vol. 50, no. 18, pp. 6979–6997, 2017.
- [10] S. Dworakowska, F. Lorandi, A. Gorczyński, and K. Matyjaszewski, "Toward Green Atom Transfer Radical Polymerization: Current Status and Future Challenges," *Advanced Science*, vol. 9, no. 19, 2022, doi: 10.1002/advs.202106076.
- [11] T. Otsu and M. Yoshida, "Role of initiator-transfer agent-terminator (iniferter) in radical polymerizations: Polymer design by organic disulfides as iniferters," *Die Makromolekulare Chemie, Rapid Communications*, vol. 3, no. 2, pp. 127–132, 1982.
- [12] Y.-N. Zhou, J.-J. Li, T.-T. Wang, Y.-Y. Wu, and Z.-H. Luo, "Precision polymer synthesis by controlled radical polymerization: Fusing the progress from polymer chemistry and reaction engineering," *Progress in Polymer Science*, vol. 130, art. no. 101555, 2022.
- [13] J. Nicolas, Y. Guillauneuf, C. Lefay, D. Bertin, D. Gigmes, and B. Charleux, "Nitroxide-mediated polymerization," *Progress in Polymer Science*, vol. 38, no. 1, pp. 63–235, 2013, doi: 10.1016/j.progpolymsci.2012.06.002.
- [14] V. Mittal, *POLYMER*.
- [15] K. Matyjaszewski and J. Xia, "Atom transfer radical polymerization," *Chemical reviews*, vol. 101, no. 9, pp. 2921–2990, 2001.
- [16] V. Coessens, T. Pintauer, and K. Matyjaszewski, "Functional polymers by atom transfer radical polymerization," *Progress in polymer science*, vol. 26, no. 3, pp. 337–377, 2001.
- [17] E. V Chernikova and E. V Sivtsov, "Reversible addition-fragmentation chain-transfer polymerization: Fundamentals and use in practice," *Polymer Science, Series B*, vol. 59, pp. 117–146, 2017.
- [18] J. Nicolas, Y. Guillauneuf, C. Lefay, D. Bertin, D. Gigmes, and B. Charleux, "Nitroxide-mediated polymerization," *Progress in Polymer Science*, vol. 38, no. 1, pp. 63–235, 2013.
- [19] Y. Yagci, S. Jockusch, and N. J. Turro, "Photoinitiated polymerization: advances, challenges, and opportunities," *Macromolecules*, vol. 43, no. 15, pp. 6245–6260, 2010.
- [20] N. P. Truong, G. R. Jones, K. G. E. Bradford, D. Konkolewicz, and A. Anastasaki, "A comparison of RAFT and ATRP methods for controlled radical polymerization," *Nature Reviews Chemistry*, vol. 5, no. 12, pp. 859–869, 2021, doi: 10.1038/s41570-021-00328-8.

- [21] N. J. Van Eck and L. Waltman, "Text mining and visualization using VOSviewer," *arXiv preprint arXiv:1109.2058*, 2011.
- [22] N. J. van Eck and L. Waltman, "Software survey: VOSviewer, a computer program for bibliometric mapping," *Scientometrics*, vol. 84, no. 2, pp. 523–538, 2010, doi: 10.1007/s11192-009-0146-3.
- [23] N. Ranjan, "Chitosan with PVC polymer for biomedical applications: A bibliometric analysis," *Materials Today: Proceedings*, vol. 81, no. 2, pp. 894–898, 2021, doi: 10.1016/j.matpr.2021.04.274.



## Determination of Thiamethoxam with Molecular Imprinted Affinity Monolithic Column

Ilgim Gokturk\*<sup>1</sup>

<sup>1</sup>Department of Chemistry, Hacettepe University, Ankara, Türkiye

### Abstract

Agricultural pesticide use boosts crop yields, but when applied carelessly and incorrectly, it can also negatively impact human and environmental health. Thiamethoxam (TMX), with its chlorothiazole structure, is a second-generation neonicotinoid insecticide [1, 2]. It has been shown that TMX can negatively affect the fertility of non-target organisms and can be hepatotoxic, especially for hepatocellular carcinoma, which poses a significant threat to the ecosystem and humans [3]. Due to their superior flow characteristics, ease of fabrication, and exceptional performance over traditional beads in separating biomolecules, monolith materials are now regarded as a fresh generation of stationary phases [4]. In this study, amino acid-based molecularly imprinted affinity monolithic columns for TMX determination were characterized by SEM and FTIR. The effect of different parameters such as initial TMX concentration (0.01-1.0 mg/mL), flow rate (0.25-1.5 mL/min), temperature (4-45 °C), and ionic strength (0.01-0.1 M NaCl) on the adsorption capacity of molecularly imprinted monolithic column was examined. The analyses were carried out with an HPLC (Dionex, Ultimate 3000, UV detector) system. The maximum adsorption capacity of the monolithic column was found to be 11.2 mg/g polymer.

**Keywords:** Column, Monolith, Molecular imprinting, Pesticide

### References

- [1] F. J. Tian, C. K. Qiao, C. X. Wang, T. Pang, L. L. Guo, J. Li, R. L. Pang, and H. Z. Xie, "The fate of thiamethoxam and its main metabolite clothianidin in peaches and the wine-making process," *Food Chemistry*, vol. 382, art. no. 132291, 2022.
- [2] N. Ajermoun, A. Loudiki, A. Farahi, S. Lahrach, S. Saqrane, M. Bakasse, and M. A. El Mhammedi, "Review—Sensor evaluation for thiamethoxam detection in different matrices," *Journal of the Electrochemical Society*, vol. 168, art. no. 116508, 2021.
- [3] F. Wang, Y. Wang, Y. Li, S. Zhang, P. Shi, H. Li-Byarlay, and S. Luo, "Pesticide residues in beebread and honey in Apis cerana cerana and their hazards to honey bees and human," *Ecotoxicology and Environmental Safety*, vol. 238, art. no. 113574, 2022.
- [4] L. Uzun, R. Say, and A. Denizli, "Porous poly (hydroxyethyl methacrylate) based monolith as a new adsorbent for affinity chromatography," *Reactive and Functional Polymers*, vol. 64, pp. 93–102, 2005.



---

## Determination of Metalaxyl Using SPR Sensors

Kivilcim Caktu Guler\*<sup>1</sup>

<sup>1</sup>*Department of Chemistry, Hacettepe University, Ankara, Türkiye*

---

### Abstract

In recent years, SPR sensors have seen increased applications due to their rapid results, low cost, and applicability to different analytes. Pesticides that protect plants from pests should be applied at the right time and in the right amount for the plants. If these parameters are not followed, the pesticides will first contaminate the plants and soil, and then take over the food chain, threatening all living beings. To prevent excessive and unnecessary application and to monitor their presence in food, we developed sensors with Metalaxyl recognition regions. Metalaxyl-imprinted Poly (2-hydroxyethyl methacrylate-N-methacryloyl-L-phenylalanine methyl ester (PHEMAPA)) nanoparticles were immobilized on the surface of an SPR chip. For the characterization of Metalaxyl-imprinted sensors, FTIR, zeta, and SEM analyses were performed. AFM, SEM, and FTIR-ATR analyses were conducted for the characterization of the sensor surface. Solutions were prepared in the concentration range of 0.01-10 mg/L for Metalaxyl, and kinetic analyses were conducted using the SPR system. Meptyldinocap was chosen to perform the selectivity analyses of the sensor. It was observed that the sensor was 5.8 times more selective compared to Meptyldinocap. All analyses were conducted with the same sensor, which was also found to have high reusability.

**Keywords:** *SPR sensors, Pesticide, Metalaxyl*

---



---

## Parameter Extraction of Proton Exchange Membrane Fuel Cell using Metaheuristic Optimization Techniques: Evaluation and Comparison

Huseyin Bakir<sup>\*1</sup>

<sup>1</sup>*Department of Electronics and Automation, Vocational School, Dogus University, Istanbul, Türkiye*

---

### Abstract

Proton Exchange Membrane Fuel Cells (PEMFCs) are a type of fuel cell that efficiently convert chemical energy from hydrogen into electricity. This technology is attractive for clean energy applications due to its zero emissions and high efficiency. To create a reliable PEMFC model, it is necessary to accurately extract the values of key parameters that affect its behaviour. However, the complex and nonlinear nature of PEMFC poses a significant challenge in estimating these parameters. To overcome this, powerful optimization tools are required. With this in mind, the present study focuses on testing novel metaheuristic optimization algorithms in PEMFC parameter extraction. In this direction, Nonlinear Marine Predator Algorithm (NMPA), Exponential Distribution Optimizer (EDO), Beluga Whale Optimization (BWO), Golden Jackal Optimization (GJO), Horse Herd Optimization Algorithm (HOA), Seagull Optimization Algorithm (SOA) and Kepler Optimization Algorithm (KOA) are implemented to identify the parameters of the commercial 500 W NedStack PS6 PEMFC model. The algorithms were run 30 times with the settings given in their original articles for the objectivity and reproducibility of the results. The stopping criterion for the metaheuristic search process is 500 iterations. The metaheuristic algorithms are trained on the experimental V-I dataset of the NedStack PS6 PEMFC and tested for minimizing the sum of squared error (SSE) objective function, which measures the difference between the experimental and estimated voltage. The minimum result of the SSE is calculated to be 2.0656 for NMPA, 2.1049 for EDO, 2.0871 for BWO, 2.14 for GJO, 2.1331 for HOA, 2.1187 for SOA and 2.0659 for the KOA algorithm. Based on the results of the mean and standard deviation metrics, it was observed that the NMPA algorithm had the highest statistical robustness among all the algorithms with the SSE results of 2.0656 mean and 4.5118E-04 standard deviation. In summary, this study strongly reports that the NMPA algorithm is an effective and reliable method in the parameter extraction problem of the PEMFC model.

**Keywords:** Proton Exchange Membrane fuel cell, Parameter extraction, Metaheuristic algorithms, Clean energy

---





## Classification of Coconut Tree Diseases Using GoogleNet for Agriculture Management

Ebru Ergun<sup>\*1</sup>

<sup>1</sup>Department of Electrical and Electronics Engineering, Faculty of Engineering and Architecture, Recep Tayyip Erdogan University, Rize, Türkiye

### Abstract

Coconut tree diseases are a critical issue for the agricultural and plant pathology research communities, as they can severely impact the coconut industry and food security. Traditional methods for diagnosing these diseases often rely on manual observation and labour-intensive identification processes. However, recent advancements in deep learning techniques have significantly improved the automatic classification of coconut tree diseases, offering a more efficient and accurate approach. In this study, a dataset recorded in India, comprising 5,798 images of various coconut tree diseases such as Bud Root Dropping, Bud Rot, Gray Leaf Spot, Leaf Rot, and Stem Bleeding, was utilized. We focused on the application of a deep learning-based method for the classification of these multiple coconut tree disease classes. Specifically, we were employed to effectively a GoogleNet-based model distinguishes between the disease types. The experimental results underscored the efficacy of GoogleNet in identifying coconut tree diseases, achieving a classification accuracy of 98.24% with the deep learning architecture. These findings demonstrate the potential of deep learning models in enhancing disease diagnosis and management in the agricultural sector.

**Keywords:** Agricultural research, Deep learning techniques, Classification, Coconut, GoogleNet

## 1 INTRODUCTION

Coconut tree diseases pose a substantial challenge to experts in agriculture and plant pathology, as these diseases have the potential to cause widespread disruption within the coconut industry and pose a serious threat to food security [1]. The traditional approaches to diagnosing these diseases are primarily reliant on manual inspections, which require significant time and effort. These methods often involve labour-intensive processes that not only demand substantial human resources but are also susceptible to human error, leading to inconsistencies and potential misdiagnoses.

In recent years, however, the field has witnessed remarkable advancements in deep learning technology, which have introduced innovative and highly effective alternatives to traditional diagnostic methods. Deep learning, a subset of artificial intelligence, involves the use of neural networks with multiple layers that can learn and make decisions from vast amounts of data [2]. These advancements have led to the development of sophisticated models capable of analysing and classifying diseases with a level of accuracy and efficiency previously unattainable.

By leveraging deep learning techniques, researchers have been able to create models that can automatically identify and classify various coconut tree diseases from images. These models significantly reduce the need for manual labour and the associated errors, providing a more reliable and consistent method for disease diagnosis. The ability of deep learning models to process large datasets and identify patterns that might be missed by the human eye makes them an invaluable tool in the fight against agricultural diseases [3].

The impact of these technological advancements extends beyond merely improving the speed and accuracy of disease diagnosis. By integrating deep learning models into agricultural practices, there is the potential to enhance overall crop management and health monitoring systems. This integration can lead to early detection of diseases, timely intervention, and ultimately, better management of resources to ensure the sustainability and productivity of coconut plantations. The advancements in deep learning not only address the immediate challenges posed by coconut tree diseases but also pave the way for a more resilient and efficient agricultural sector.

In the literature, Toradmalle et al. focused on detecting diseases in coconut trees using image processing technologies, computer vision, and deep learning models. They reviewed various methodologies and applied them

to a dataset of leaf images classified into five distinct diseases. By employing CNN, DenseNet121, InceptionResNetV2, and ANN algorithms, they achieved a disease detection accuracy of approximately 99% [4]. In another study, Singh et al. developed an end-to-end framework for detecting stem bleeding disease, leaf blight disease, and pest infections in coconut trees using image processing and deep learning technologies. They utilized a set of hand-collected images and applied various segmentation algorithms to identify abnormal boundaries. Their custom-built 2D convolutional neural network (CNN) achieved a validation accuracy of 96.94%, while fine-tuned pre-trained models, such as InceptionResNetV2 and MobileNet, attained accuracies of 81.48% and 82.10%, respectively [5]. Additionally, Nesarajan et al. aimed to improve coconut production in Sri Lanka by developing a system for detecting pest attacks and nutrient deficiencies in coconut leaves. They employed advanced machine learning and image processing techniques to monitor leaves following pesticide and fertilizer applications. An Android mobile application was created to facilitate the automatic recognition of pests and diseases. Their method, which included pre-processing steps such as converting RGB to greyscale and resizing, achieved notable classification accuracies of 93.54% with SVM and 93.72% with CNN. This project is designed to enhance coconut production and provide significant benefits to farmers through more efficient disease detection methods [6].

In this research, we utilized a comprehensive dataset [7] from India, consisting of 5,798 images depicting various coconut tree diseases, including Bud Root Dropping, Bud Rot, Gray Leaf Spot, Leaf Rot, and Stem Bleeding. Our goal was to implement a deep learning-based approach to accurately classify these disease types. We employed a GoogleNet-based model for this purpose, leveraging its sophisticated architecture to distinguish between the different diseases effectively.

The results of our experiments demonstrated the impressive capabilities of GoogleNet in identifying coconut tree diseases, achieving a high classification accuracy of 98.24%. These findings highlight the potential of deep learning models to significantly improve disease diagnosis and management in agriculture, offering a robust solution to ensure the health and productivity of coconut trees.

## 2 MATERIAL AND METHOD

### 2.1 Dataset Description

In this study, we utilized the Coconut Tree Disease Dataset recorded by Thite et al. in India [7]. This dataset consists of high-resolution images, each measuring 768 pixels wide by 1024 pixels high, with a resolution of 72 dots per inch. This high quality ensures that the images provide clear and detailed visual information about the diseases affecting coconut trees.

The dataset includes images categorised into five disease classes: “Bud Root Dropping”, “Bud Rot”, “Grey Leaf Spot”, “Leaf Rot” and “Stem Bleeding”. This diverse representation provides a balanced view of the various diseases affecting coconut trees, as detailed in Figure 1, which shows sample images for each disease category.

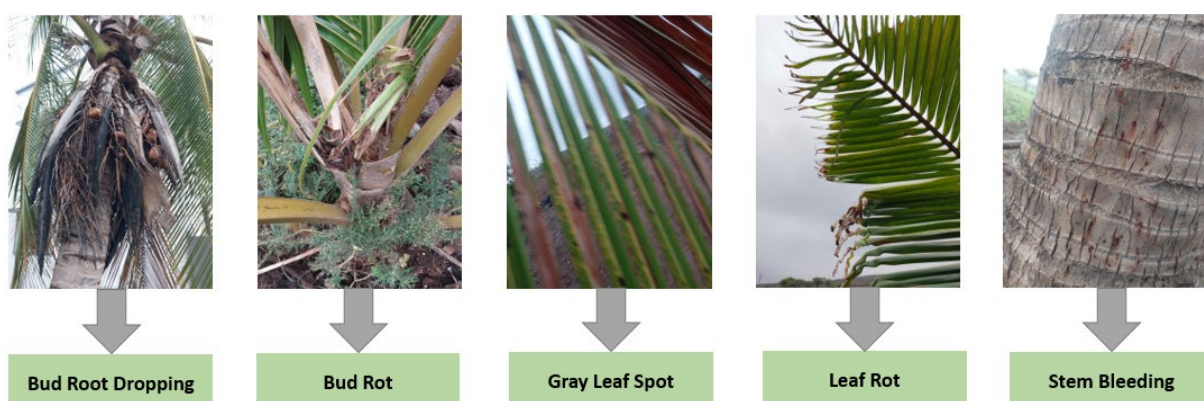
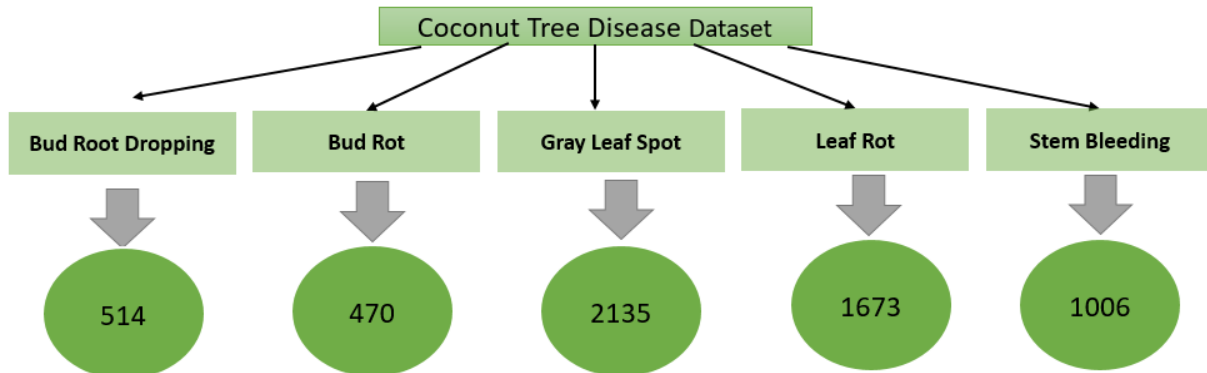


Figure 1. Images of coconut disease dataset [7]

Understanding these diseases is crucial as they can have a significant impact on the health and productivity of coconut plantations. For example, Bud Root Dropping can inhibit early growth, Bud Rot can rapidly destroy groves, Grey Leaf Spot can cause extensive defoliation, Leaf Rot affects photosynthesis and Stem Bleeding gradually weakens the tree structure. Effective management of these diseases is critical to maintaining the viability of coconut plantations.

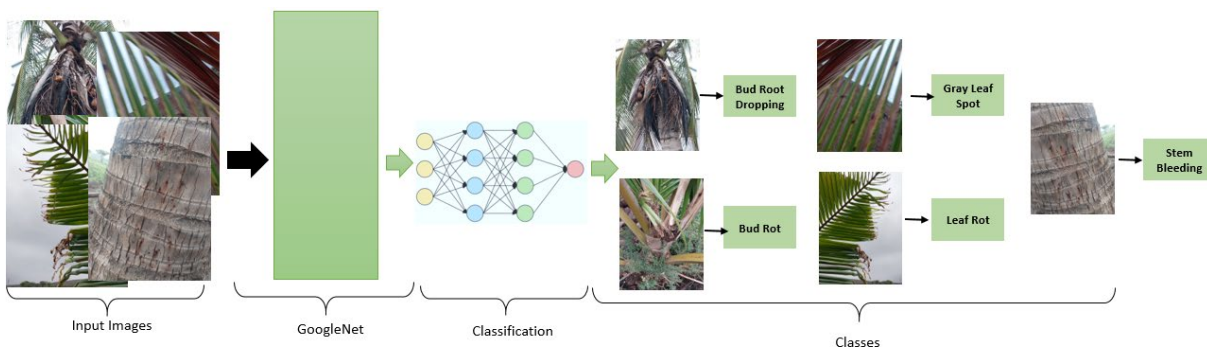
The dataset, captured using the rear cameras of Samsung F23 5G mobile phones, was collected in Kendur, Maharashtra (18°47'06.4"N 74°01'19.5"E). The use of mobile cameras provides flexibility and ensures that the images reflect real conditions in the coconut plantations. The high resolution of the dataset and the practical method of data collection enhance its quality and authenticity. Each image is carefully labelled and organised into separate folders for easy access and identification, as shown in Figure 2, which shows the directory structure of the coconut tree disease dataset. This resource is invaluable to researchers and practitioners focused on developing advanced disease detection and classification models.



**Figure 2.** The dataset for coconut tree disease is organized into directories [7]

## 2.2 Proposed Methods

A convolutional neural network (CNN) is a type of artificial neural network used to process structured grid data such as photographs. Unlike standard neural networks, CNNs use convolutional layers to learn spatial feature hierarchies from input data in an autonomous and adaptive manner. This method uses filters on the input image to recognise patterns such as edges, textures and shapes [8]. CNNs often consist of several types of layers, such as convolutional layers, pooling layers, and fully connected layers, which work together to progressively extract and refine information. This design allows CNNs to be more successful at tasks such as image categorisation and object recognition by collecting and recognising complex patterns in the visual input. In this study, the CNN architecture employed is based on GoogleNet, with models trained on images of five different coconut tree disease classes. Figure 3 illustrates the general architecture of CNNs as applied in the proposed method.



**Figure 3.** Proposed method

GoogleNet is a deep convolutional neural network architecture developed by Google [9]. It is remarkable for its novel usage of inception modules, which enable the network to effectively collect characteristics across many sizes. An inception module comprises of many concurrent convolutional and pooling procedures with varying filter sizes. The results of these processes are concatenated and sent to succeeding levels. This approach enables GoogleNet to manage computational complexity while maintaining excellent speed [10]. Furthermore, GoogleNet uses dimensionality reduction techniques in these inception modules to improve the network's efficiency. As a consequence, GoogleNet performs admirably in picture classification tasks while being computationally cheap when compared to other deep learning architectures.

In this study, we employed classification accuracy to evaluate the performance of the proposed method. Classification accuracy is a key metric that measures the proportion of correctly classified instances out of the total number of instances [11], [12]. To ensure the robustness and generalizability of our results, we utilized 5-fold cross-validation. In this approach, the dataset is divided into five equal-sized folds. The model is trained on four

of these folds and tested on the remaining fold. This process is repeated five times, with each fold serving as the test set once. The final classification accuracy is obtained by averaging the accuracy scores from each fold.

### 3 RESULTS

In this study, we used a transfer learning approach to classify coconut tree diseases using a comprehensive image dataset. The images, standardised to a resolution of 224×224 pixels, were processed to balance computational efficiency with high quality feature extraction. Using GoogleNet with 144 frozen layers, we optimised the model's hyperparameters, setting the maximum number of epochs to 10, mini batch size to 16, and initial learn rate to 0.00001. Given the class imbalance in the dataset, classification accuracy was chosen as the evaluation metric.

The dataset consisted of a total of 5,798 images divided into five disease categories: “Bud Root Dropping” with 514 images, “Bud Rot” with 470 images, “Grey Leaf Spot” with 2,135 images, “Leaf Rot” with 1,673 images and “Stem Bleeding” with 1,006 images. The images were randomly divided into training and test sets, with 4,639 images used for training and 1,159 images reserved for testing to ensure robust model evaluation. In addition, the distribution of training and test images for each class, as well as details for a single fold, are shown in Table 1.

The 5-fold cross-validation yielded an impressive average classification accuracy of 98.24%. This high accuracy highlights the effectiveness of GoogleNet in managing and classifying the diverse range of coconut tree diseases within this dataset, demonstrating the strong performance and reliability of the model in this application.

**Table 1.** Distribution of training and test images for each class

Classes	Number of test images	Number of train images
Bud Root Dropping	102	412
Bud Rot	94	376
Gray Leaf Spot	427	1708
Leaf Rot	335	1338
Stem Bleeding	201	805

It is also important to highlight that in their study, Thite et al. [7] achieved a classification accuracy of 94% using ResNet. Our proposed method, employing a GoogleNet-based model, surpasses this performance by a margin of 4.24%, achieving an accuracy of 98.24%. This significant improvement underscores the robustness and effectiveness of our approach in accurately classifying coconut tree diseases.

### 4 CONCLUSION

In conclusion, addressing coconut tree diseases is of paramount importance for both agricultural practices and plant pathology research, given their substantial impact on the coconut industry and global food security. Traditional diagnostic methods, which rely heavily on manual observation and labour-intensive processes, have been largely supplemented by recent advancements in deep learning technologies. This study utilized a dataset of 5,798 images from India, covering various coconut tree diseases including Bud Root Dropping, Bud Rot, Gray Leaf Spot, Leaf Rot, and Stem Bleeding, to explore the effectiveness of deep learning techniques for disease classification. By employing a GoogleNet-based model, we achieved a remarkable classification accuracy of 98.24%. These results highlight the effectiveness of deep learning models in improving the accuracy and efficiency of disease diagnosis and management. The findings suggest that such advanced models hold significant potential for transforming disease detection practices in the agricultural sector, ultimately leading to better management and mitigation strategies for coconut tree diseases.

### References

- [1] C. D. Wijethunga, K. C. Ishanka, S. D. N. Parindya, T. J. N. Priyadarshani, B. Harshanath, and S. Rajapaksha, “Coconut plant disease identified and management for agriculture crops using machine learning,” *International Journal of Engineering and Management Research*, vol. 13, no. 5, pp. 79–88, 2023.
- [2] M. Maray, A. A. Albraikan, S. S. Alotaibi, R. Alabdan, M. Al Duhayyim, and W. K. Al-Azzawi, “Artificial intelligence-enabled coconut tree disease detection and classification model for smart agriculture,” *Computers and Electrical Engineering*, vol. 104, no. 10, pp. 83–99, 2022.
- [3] V. Kavithamani and S. UmaMaheswari, “Investigation of Deep learning for whitefly identification in coconut tree leaves,” *Intelligent Systems with Applications*, vol. 20, no. 20, pp. 2v9, 2023.

- [4] D. Toradmalle, N. Bhanushali, M. Dama, and M. Dhote, "Deep learning framework for early detection of diseases in coconut tree from leaf images," in *2023 6th International Conference on Advances in Science and Technology*, ICAST, 2023, pp. 137–142.
- [5] P. Singh, A. Verma, and J. S. R. Alex, "Disease and pest infection detection in coconut tree through deep learning techniques," *Computers and electronics in agriculture*, vol. 182, no. 10, pp. 59–86, 2021.
- [6] D. Nesarajan, L. Kunalan, M. Logeswaran, S. Kasthuriarachchi, & D. Lungalage, "Coconut disease prediction system using image processing and deep learning techniques," in *2020 IEEE 4th International Conference on Image Processing, Applications and Systems*, IPAS, 2020, pp. 212–217.
- [7] S. Thite, Y. Suryawanshi, K. Patil, and P. Chumchu, "Coconut (*Cocos nucifera*) tree disease dataset: A dataset for disease detection and classification for machine learning applications," *Data in Brief*, vol. 10, no. 9, pp. 59–69, 2023.
- [8] S. Lawrence, C. L. Giles, A. C. Tsoi, and A. D Back, "Face recognition: A convolutional neural-network approach," *IEEE Transactions on Neural Networks*, vol. 8, no. 1, pp. 98–113, 1997.
- [9] N. Yang, Z. Zhang, J. Yang, Z. Hong, & J. Shi, "A convolutional neural network of GoogLeNet applied in mineral prospectivity prediction based on multi-source geoinformation," *Natural Resources Research*, vol. 30, no. 6, pp. 3905–3923, 2021.
- [10] I. N. Yulita, M. F. R. Rambe, A. Sholahuddin, and A. S. Prabuwno, "A convolutional neural network algorithm for pest detection using GoogleNet," *AgriEngineering*, vol. 5, no. 4, pp. 2366–2380, 2023.
- [11] E. Ergun, O. Aydemir, and O. E. Korkmaz, "Investigating the informative brain region in multiclass electroencephalography and near infrared spectroscopy based BCI system using band power based features," *Computer Methods in Biomechanics and Biomedical Engineering*, pp. 1–16, 2024.
- [12] E. Ergun, "Deep learning based multiclass classification for citrus anomaly detection in agriculture," *Signal, Image and Video Processing*, pp.1–10, 2024.



---

## A Digital Predictive Peak Current Mode Control for Power Factor Correction

Ahmet Talha Dudak<sup>\*1</sup>, Ahmet Faruk Bakan<sup>2</sup>

<sup>1</sup>Department of Power and Control System Design Engineering, ASELSAN, Ankara, Türkiye

<sup>2</sup>Electrical Engineering, Yildiz Technical University, Istanbul, Türkiye

---

### Abstract

In this paper, a digital predictive peak current control (PPCC) method for power factor correction (PFC) circuits is proposed. With the proposed current control method, the peak current reference value to be used in current control is predicted and pulse width modulation (PWM) is generated. The peak current control is based analog and has a fast dynamic response. It is suitable for the high frequency applications. In addition, the PPCC is implemented by using the internal comparator and digital to analog converter (DAC) of a digital signal processor (DSP) without external components. The proposed current control method is performed for a interleaved totem pole PFC (ITPFC) circuit. The operation of the method is investigated for different load, input voltage and varying circuit parameters.

**Keywords:** Predictive peak current control (PPCC), Power factor correction (PFC), Digital control

---

## 1 INTRODUCTION

AC-DC converters are widely used in industry. These power converters consist of a diode bridge, input capacitor and switched DC-DC converter. In such converters with input capacitance and semiconductor, the total harmonic distortion (THD) of the input current is high and the power factor (PF) is low. PFC circuits are used in order to provide low THD and high PF. There are many different control methods in PFC circuits. These are peak current control, average current control, hysteresis current control etc. These methods can be performed with analog integrated circuits (IC). With the developing processor technology, these control methods can also be performed digitally. Thus, more complex control algorithms can be performed by processors.

Most digitally controlled PFC circuits are based on average current mode control [1–6]. However, due to the time delay in digital control, the current control bandwidth is limited to one tenth of the sampling frequency. As a result, the input current distortion increases in conventional control methods. In order to improve the performance, methods that derive the duty ratio with feed-forward have been developed. However, due to the differences in discontinuous current mode (DCM) and continuous current mode (CCM) operation, input current distortion is inevitable in DCM. In addition, the high ripple in the inductance current in average current mode operation makes it difficult to obtain the current average accurately. In order to prevent this, the value of the inductance is increased, which leads to the use of larger inductance. However, this case is not valid in peak current control. The high ripple in the inductance current does not affect the operation of the control. Thus, operation with lower inductance values can be realised and the cost is reduced.

The predictive current control method used in PFC circuits [2–7] eliminates the input current distortion caused by the low control bandwidth. However, input current distortion is still existed in DCM operation. In addition, parametric variations in the circuit cause a negative effect on the control performance. For a good reference tracking, non-ideal conditions should also be taken into account. In conclusion, there are three main challenges in the predictive current control method. Firstly, the dependence on the accuracy of the model leads to errors in the tracked current, secondly, the increased complexity due to modelling all known non-ideal states and the resulting difficulty of digital implementation, and thirdly, the measurement or estimation of non-ideal states and parametric variations of the converter is challenging.

This paper is organized as follows. In section II, the average input current estimation with ideal circuit parameters, the non-ideal situations and disruptive effects are analyzed for the ITPFC. Section III discusses the simulation results of the ITPFC for the different load and input voltages. Section IV concludes the paper.

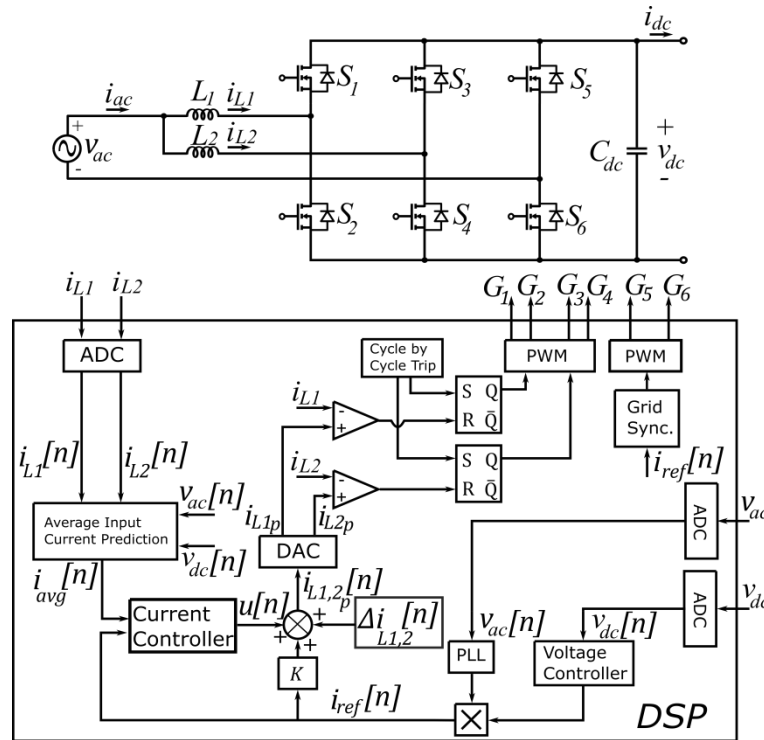


Figure 1. The proposed control method for the ITPFC

## 2 DIGITAL PPCC IN INTERLEAVED TOTEM POLE PFC

The proposed control method is shown in Figure 1.  $v_{ac}$ ,  $i_{ac}$ ,  $i_{L1}$  and  $i_{L2}$  represent grid voltage, grid current,  $L_1$  inductance current and  $L_2$  inductance current respectively.  $S_1$ ,  $S_2$ ,  $S_3$  and  $S_4$  are switches operating at switching frequency.  $S_5$  and  $S_6$  are switches operating at grid frequency.  $G_1$ ,  $G_2$ ,  $G_3$ ,  $G_4$ ,  $G_5$  and  $G_6$  are the gate signals of the  $S_1$ ,  $S_2$ ,  $S_3$ ,  $S_4$ ,  $S_5$  and  $S_6$  switches respectively.  $C_{dc}$  is the output capacitor,  $v_{dc}$  output voltage and  $i_{dc}$  is the output current.  $K$  represents the phase number in the ITPFC.  $u[n]$  is the output of the current controller. In the range where the  $v_{ac}$  is positive, when  $S_2$  and  $S_4$  turn on, the inductance currents are exposed to the  $v_{ac}$  and increase linearly. When  $S_1$  and  $S_3$  turn on, the energized inductances transfer their energy to  $C_{dc}$ . When the  $v_{ac}$  is positive, the slow switch  $S_6$  is active. In the range where the  $v_{ac}$  is negative, when  $S_1$  and  $S_3$  turn on, the inductance currents are exposed to the  $v_{ac}$  and increase linearly in the negative direction. When  $S_2$  and  $S_4$  turn on, the energized inductances transfer their energy to  $C_{dc}$ . When the  $v_{ac}$  is negative, the slow switch  $S_5$  is active.

The main features of the proposed digital PCMC method are presented as follows.

- i. The output voltage controller is the same as that of the conventional APMC
- ii. The grid synchronization of the input current is performed with digital phase locked loop (PLL) algorithm.
- iii. The average current following the reference current is derived by estimation. Using the current data sensed at the beginning of the PWM, the average current data in the relevant switching period is estimated.
- iv. The proposed method is used to minimize the error between the estimated average current and the reference current and to ensure reference tracking despite non-ideal situations and variations.
- v. The predicted peak current value is loaded into the digital to analog converter (DAC) and cycle-by-cycle current control is performed using fast comparators in the DSP.

### 2.1 Average Input Current Prediction

PFC converters can operate in different operating modes such as CCM, boundary conduction mode (BCM) and DCM. In CCM operation, where the inductance current is not zero during a switching period, the MOSFET switching loss is high due to hard switching, while the inductance core losses are low compared to other operating modes due to low inductance current ripple. In DCM operation, switching losses are reduced due to zero voltage conduction (ZVS) when the MOSFET is turned on, while core losses are increased due to high inductance current ripple. Figure 2 shows the inductance current waveforms for operation modes.

In digital current control methods, when the current is sampled in the middle of the PWM, the sampled value is equal to the average current value for CCM operation, while in DCM operation, the current value sampled in the middle of the PWM is not equal to the average value. In conventional digital applications, in order to accurately sample the average inductance current in DCM operation, it is necessary to sample multiple regions in one switching period.

$$i_L[n] = \frac{i_L[n]_{peak}}{2} \quad (1)$$

$$i_L[n]_{avg} = \frac{i_L[n]_{peak}}{2} \left( \frac{(d[n] + d'[n])T_s}{T_s} \right) \quad (2)$$

In (1),  $i_L[n]$  represents the value of the sampled inductor current. The average inductor current is derived in (2). If the equation (1) is substituted in (2), the equation (3) is obtained.

$$i_L[n]_{avg} = i_L[n](d[n] + d'[n]) \quad (3)$$

In the analysis of the average current prediction, the equations will not be given separately for each of the  $i_{L1}$  and  $i_{L2}$  currents for the ITPFC. Only the equations for one inductor current will be expressed. When the grid voltage is positive, the duty ratios is given in (4) and (5) for the CCM and DCM operation.

$$i_L[n]_{avg} = i_L[n](d[n] + d'[n]) \quad (4)$$

$$d[n]_{dcm} = \sqrt{\frac{(2L_{1,2}i_{refL_{1,2}}[n](v_{ac}[n] - v_{dc}))}{((v_{ac}[n] - v_{dc})v_{ac}[n]T_s - v_{ac}^2[n]T_s)}} \quad (5)$$

In (5),  $L_{1,2}$  represents the common value for each inductor.  $i_{refL_{1,2}}$  represents the current reference for each inductance current. The average current value is given in (6) and (7) for the CCM and DCM operation.

$$i_{avg}[n]_{ccm} = i_L[n-1] + \frac{v_{ac}[n-1]}{2L_{1,2}}d[n-1]_{ccm}T_s + \frac{(v_{ac}[n-1] - v_{dc})(1 - d[n-1]_{ccm})T_s}{L_{1,2}} + \frac{v_{ac}[n]}{2L_{1,2}}d[n]_{ccm}T_s \quad (6)$$

$$i_{avg}[n]_{dcm} = \frac{v_{ac}[n]}{2L_{1,2}}d[n]_{dcm}T_s \quad (7)$$

When the grid voltage is negative, the duty ratio and average current equations is like following.

$$d[n]_{ccm} = 1 + \frac{v_{ac}[n]}{v_{dc}} \quad (8)$$

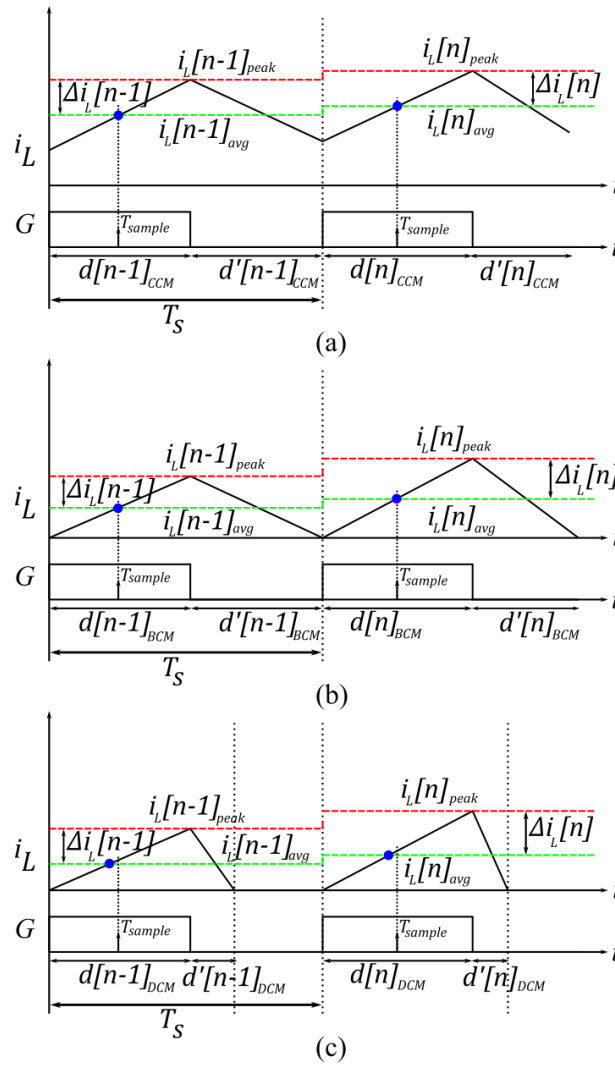
$$d[n]_{dcm} = \sqrt{\frac{(2L_{1,2}i_{refL_{1,2}}[n](v_{ac}[n] + v_{dc}))}{((v_{ac}[n] + v_{dc})v_{ac}[n]T_s - v_{ac}^2[n]T_s)}} \quad (9)$$

$$i_{avg}[n]_{ccm} = i_L[n-1] + \frac{v_{ac}[n-1]}{2L_{1,2}}d[n-1]_{ccm}T_s + \frac{(v_{ac}[n-1] + v_{dc})(1 - d[n-1]_{ccm})T_s}{L_{1,2}} + \frac{v_{ac}[n]}{2L_{1,2}}d[n]_{ccm}T_s \quad (10)$$

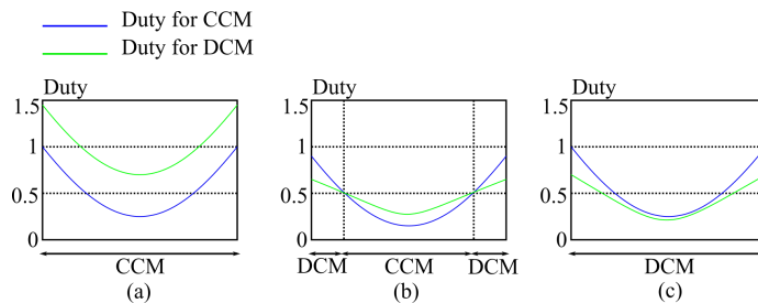
$$i_{avg}[n]_{dcm} = \frac{v_{ac}[n]}{2L_{1,2}}d[n]_{dcm}T_s \quad (11)$$

In the average current prediction, the calculated duty rates can be used to determine the CCM or DCM operating conditions. If the duty rate calculated for DCM is less than the duty rate calculated for CCM, the operation will be DCM, if the duty rate calculated for CCM is less than the duty rate calculated for DCM, the operation will be CCM. Figure 3 shows an illustration of the determination of the duty rate for CCM and DCM operation.





**Figure 2.** The inductor current waveforms for the operation modes: (a) CCM, (b) BCM, and (c) DCM.



**Figure 3.** Determination of CCM and DCM operation zone according to the estimated occupancy rate: (a) Heavy load, (b) intermediate load, and (c) low load

After predicting the average current values for  $L_1$  and  $L_2$ , the current value  $i_{ac}[n]$  to be drawn from the input is predicted by summing them. This value is compared with  $i_{ref}[n]$  and the error signal input for the current controller is obtained. The current controller is converged to zero the error. The output signal of the current controller is summed with the reference peak current value. The reference peak current value is derived in (12). The predicted peak current value is derived in (13).

$$\Delta i_{L_{1,2}}[n] = \frac{v_{ac}[n]}{L_{1,2}} d[n] T_s \tag{12}$$

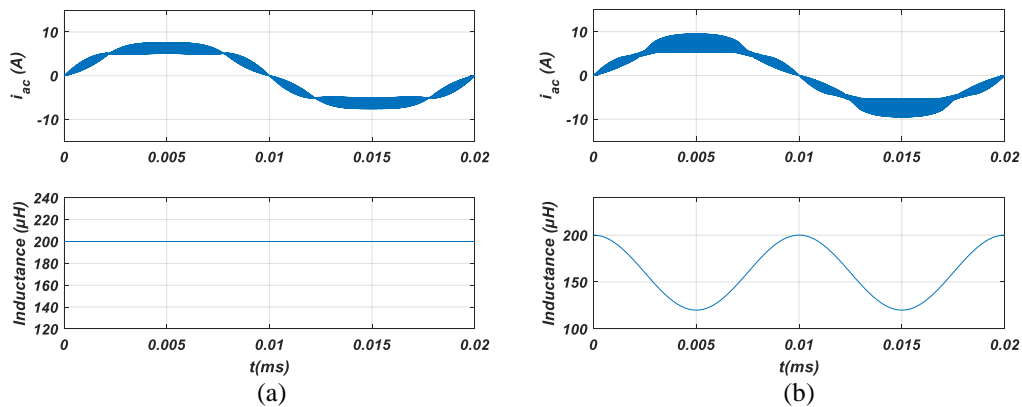
$$i_{L_{1,2}p}[n] = u[n] + \frac{i_{ref}[n]}{K} + \Delta i_{L_{1,2}}[n] \tag{13}$$

## 2.2 Analysis of Non-Ideal Situations and Disruptive Effects

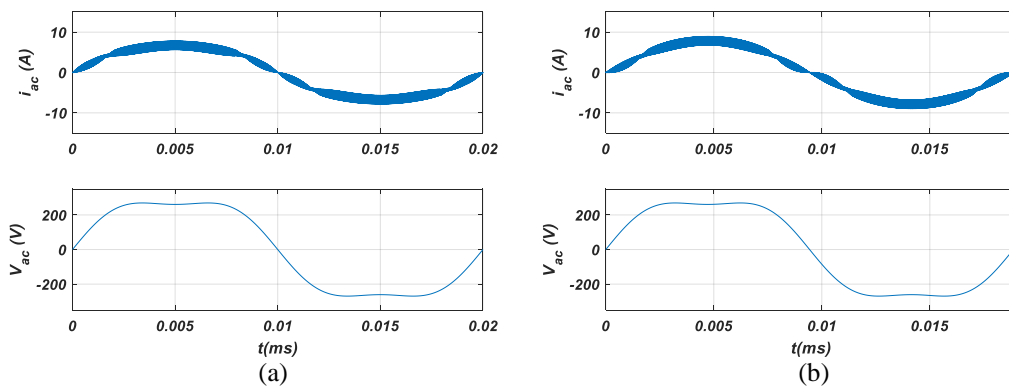
### 2.2.1 Effect of the Inductance Variation

Saturated inductance is often preferred in inductance design in PFC circuits. The magnetic permeability of them changes at high currents. In other words, the inductance value tends to decrease at high currents. As a result of this situation, the changing inductance value causes differences in the circuit model and this situation should be considered in the control. If this is not considered in classical PCC methods, successful current reference tracking becomes difficult and the input current THD value increases. Therefore, additional prediction processes are performed to accurately estimate the inductance value. This prediction process must also be completed within one switching period.

For the proposed control method, the waveform of the current drawn from the input according to the inductance change is shown in Figure 4. It is seen that the waveforms change from DCM to CCM for the saturated inductance model. It is seen that the current ripple increases at the transition to CCM. With the proposed method, the peak current value changes in a way to compensate the change in the system. Thus, the current drawn from the grid corresponds to the average input current in all cases.



**Figure 4.** Input current waveforms depending on inductance value with the proposed control method (a) for ideal inductance, (b) for saturated inductance



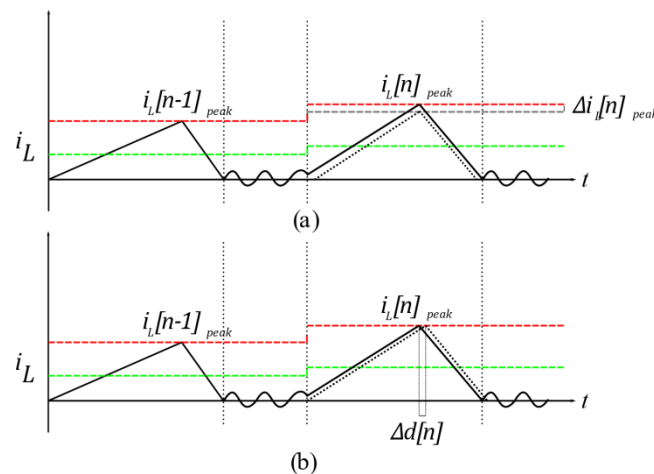
**Figure 5.** Waveform of the current drawn from the input for the proposed method (a) in case of harmonic in the grid voltage (b) in case the frequency of the grid containing harmonics also changes

### 2.2.2 Effect of Grid Voltage Harmonics and Frequency Variation

In case the grid voltage is harmonic, the control method should be able to perform reference tracking successfully. Grid harmonics can be easily compensated by the proposed control method. In addition, when there is a change in the operating frequency of the grid, the control should be able to adapt to it. Against this situation, PLL algorithms that can accurately follow the grid are preferred. Thus, a current reference can be obtained in the same phase with the read input voltage. Figure 5 shows the current waveform drawn from the grid for the proposed method when the 3rd harmonic is added to the grid and the grid frequency changes to 53Hz. It can be seen that the current reference can be accurately tracked with the proposed method.

### 2.2.3 Parasitic Effects

In DCM mode operation, after the inductance current drops to zero, a resonance occurs between the inductance and the parasitic capacitance of the semiconductors. During this resonance, the inductance current oscillates around the zero axis. At the end of this oscillation, if the current value does not equal zero, the inductance current increases linearly with an initial value when the inductance is energized with the next switching signal. This initial value can be positive or negative. Due to this situation, incorrect results are obtained in the average current estimation. Precautions should be taken against this situation in order to perform the control successfully. Figure 6 shows the waveforms for average current control and peak current control for this case. As can be seen from the waveforms, since the current has the first value in the average current mode control, a shift in the peak current value occurs. In peak current mode control, the duty cycle is changed by accurately adjusting the peak value. In classical or predictive peak current mode control, this situation must be compensated for by making a prediction calculation. In the proposed method, the peak current value is set automatically without the need for additional operations. This provides an advantage for ease of control. In conventional methods, it may be necessary to use a snubber as a solution. This means additional loss.



**Figure 6.** Parasitic effect in the inductor current for DCM operation: (a) Average current control, (b) peak current control

### 2.2.4 Difficulty of Current Prediction in DCM Mode

DCM mode of operation occurs when the grid voltage is low or the output power is low. Closed loop systems with linear controllers designed for CCM mode do not perform as well in DCM mode and it becomes difficult to track the reference current. Additional measures need to be taken for this. According to the waveform in Figure 2.c., in order to estimate the average value of the current in DCM mode, complex calculations are required as shown in equations (5) and (9). In particular, calculations that add additional load to the processor, such as square root, pose a problem for time-critical applications. This is an obstacle to operation at high frequencies.

### 2.2.5 Zero Crossing Distortion

In conventional average current mode controllers, distortions occur in the input current waveform at zero crossing regions of the grid. This is due to the fact that the controller does not follow the current reference quickly and accurately. This causes the THD value to increase. In the totem pole PFC circuit, spikes occur in the inductance current during positive to negative or negative to positive transitions due to phase transitions. If no precautions are taken against this at zero crossing regions, the THD value deteriorates significantly. In order to take precautions against this, soft start is performed at zero crossing regions and this effect is minimized by increasing gradually the duty rate. However, the proposed method can compensate the zero crossing distortions very quickly without any additional operation.

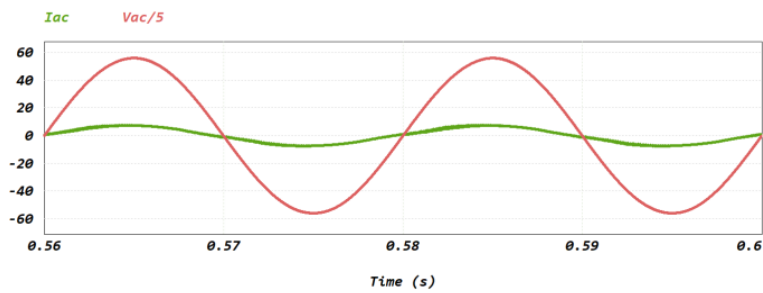
## 3 SIMULATION RESULTS

The proposed method for the interleaved totem pole PFC circuit is tested for a 1kW prototype. The circuit parameters are given in Table 1. Figure 7 shows the input current and voltage waveforms. Here, the input current THD is below 5% and the PF is 0.99. Figure 8 shows the output voltage waveform. It is seen that the voltage ripple is approximately 5%. Figure 9 shows the inductance currents in each phase of ITPPFC. Figure 10 shows that the

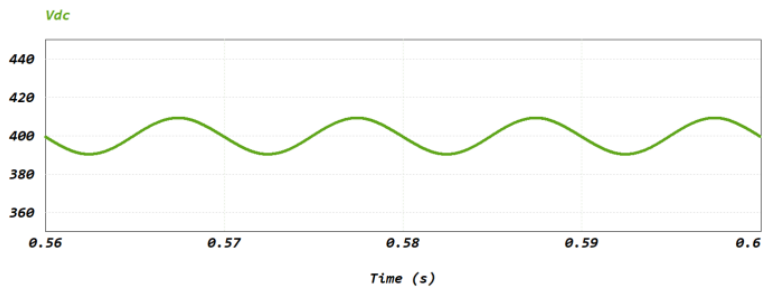
average value of the input current follows the reference current very smoothly. Figure 11 shows the ability of the input current to follow the current reference against the instantaneous variation of the current reference. Here, stable operation is successfully achieved with the proposed control method. Figure 12 shows the variation of the input current and output voltage against the instantaneous load change. It is seen that the control is realized in a stable manner.

**Table 1.** Circuit parameters

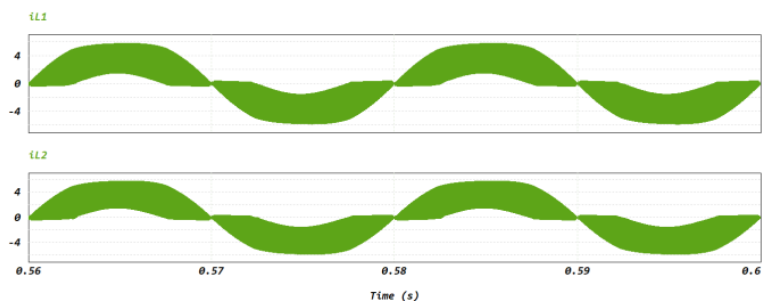
Symbol	Quantity	Value
$v_{ac}$	Input Voltage	195-265 $V_{ac}$
$v_{dc}$	Output Voltage	400 $V_{dc}$ (5%)
$i_{ac}$	Input Current	5 $A_{rms}$
$L_1, L_2$	Inductance	200 $\mu H$
$P_o$	Output Power	1 kW
$f_L$	Grid Frequency	47-53 Hz
$f_p$	Switching Frequency	100 kHz
$C_{dc}$	Output Capacitance	440 $\mu F$



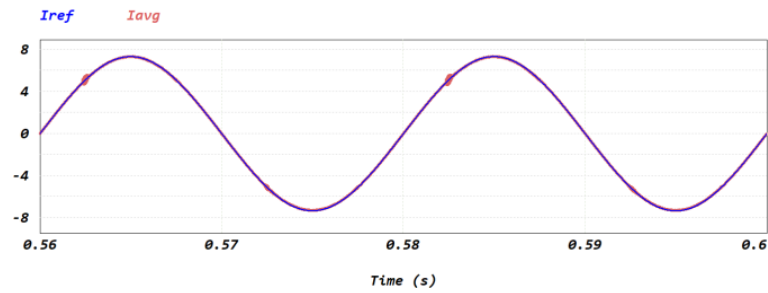
**Figure 7.** The Input current and voltage waveforms



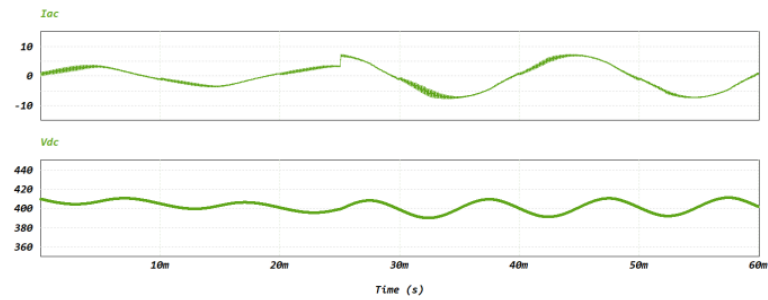
**Figure 8.** Output voltage waveform



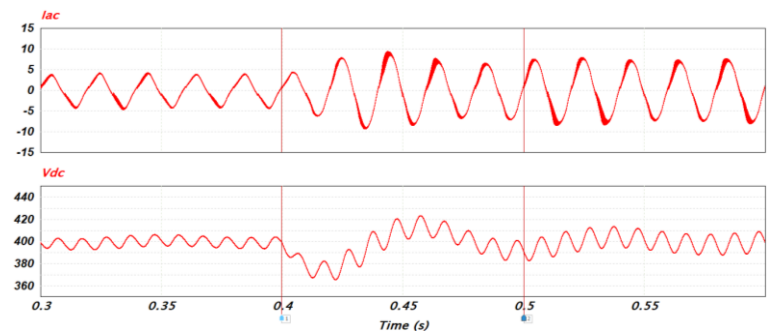
**Figure 9.** Inductance currents for ITPFC



**Figure 10.** Reference tracking performance of the average input current



**Figure 11.** Response of the controller to the step change of the current reference



**Figure 12.** Dynamic response of the proposed controller against load variation

## 4 CONCLUSION

In this paper, a digital PPCC method for ITPFC circuit is proposed. The proposed PPCC has a good dynamic response. In addition, PPCC is considered suitable for applications with high switching frequencies since it is performed as analog the current control. The proposed method provides a good current reference tracking in spite of the non-ideal situations and variations. The non-ideal situations and variations such as variable inductance value, non-sinusoidal grid voltage, difficulties in predicting average current in DCM operation, parasitic effects and zero crossing distortions are investigated in this paper. The proposed method successfully compensates the peak value of the controlled current. The proposed current control method is implemented for a 1kW ITPFC circuit under different load conditions and input voltage.

## References

- [1] K. Gusseme, D. Sype, A. Bossche, and J. Melkebeek, "Digitally controlled boost power-factor-correction converters operating in both continuous and discontinuous Conduction Mode," *IEEE Trans. on Ind. Electron.*, vol. 52, no.1, pp. 88–97, Feb. 2005.
- [2] W. Zhang, G. Feng, Y. Liu, and B. Wu, "A digital power factor correction (PFC) control strategy optimized for DSP," *IEEE Trans. on Power Electron.*, vol. 19, no.6, pp. 1474–1485, Nov. 2004.
- [3] W. Zhang, Y. Lui, and B. Wu, "A new duty cycle control strategy for power factor correction and FPGA implementation," *IEEE Trans. on Power. Electron.*, vol. 21, no.6, pp. 1745–1753, Nov. 2006.
- [4] Y. Cho and J. Lai, "Digital plug-in repetitive controller for single-phase bridgeless PFC converters," *IEEE Trans. on Power. Electron.*, vol. 28, no.1, pp. 165–175, Jan. 2013.

- [5] H. Youn, J. Park, K. Park, J. Baek, and G. Moon, "A digital predictive peak current control for power factor correction with low-input current distortion," *IEEE Trans. on Power. Electron.*, vol. 31, no.1, pp. 900-912, Jan. 2016.
- [6] J. Park, D. Kim, and K. Lee, "Predictive control algorithm including conduction-mode detection for PFC converter," *IEEE Trans. on Ind. Electron.*, vol. 31, no.1, pp. 900-912, Jan. 2016.
- [7] H. Youn, J. Park, K. Park, J. Baek, and G. Moon, "A digital predictive peak current control for power factor correction with low-input current distortion," *IEEE Trans. on Power. Electron.*, vol. 31, no.1, pp. 900-912, Jan. 2016.



---

## A Low-Cost Cloud-Based Wearable Accelerometer Data Recording System

Ayşe Zehra Caglar<sup>1</sup>, Çağrı Güllü<sup>1</sup>, Sabri Altunkaya<sup>\*1</sup>

<sup>1</sup>Electrical and Electronics Engineering, Necmettin Erbakan University, Konya, Türkiye

---

### Abstract

This study proposes a cheap, affordable, and easy-to-use acceleration recording system for various biomedical applications. The system will utilize a wearable device equipped with an accelerometer sensor and a microcontroller. A mobile application will control the device via Wi-Fi, enabling data recording and transfer to a cloud storage platform, thereby making all data readily accessible. This study consists of two parts: hardware and software. The hardware consists of an accelerometer sensor, Li-ion battery, battery charging circuit, a button, two LEDs, and a microcontroller that control all of the hardware. The microcontroller software reads the sensor data, communicates with the mobile phone interface via Wi-Fi, and transfers the data. Mobile phone software will be used to control the hardware and embed data in the cloud. As a result, a low-cost, cloud-based accelerometer data recording system was realized. Thanks to this system, people's acceleration signals can be recorded cheaply and easily evaluated remotely.

**Keywords:** Accelerometer sensor, Cloud-based data storage, Wearable device design

---

## 1 INTRODUCTION

Wearable technologies are used in a wide variety of fields, such as health, fitness, sports, military, and entertainment. Wearable devices help collect important information about physical activity, health metrics, and environmental interactions by leveraging advances in sensor technology, data analytics, and wireless communications [1–4]. In the field of health, disease prevention, personalized treatment approaches, home care, and remote measurement issues come to the fore. As wearable technologies develop, it is anticipated that in addition to a general overview, such as the patient going to the hospital for healthcare services and performing the necessary tests and measurements, necessary measurements will be taken and evaluated during the patient's daily life activities when necessary [5–7]. Wearable technologies are therefore becoming the focus of research and development in various scientific disciplines. In this context, wearable technologies that can constantly monitor personal physiological and activity data are important tools. These devices enable researchers and clinicians to obtain deeper assessments of health status and disease progression by allowing real-time data collection under daily living conditions, if desired [2, 8, 9].

The use of wearable technologies in the field of healthcare is quite wide. These include activity tracking [10, 11], heart rate [12] and blood pressure monitoring [13], sleep quality assessment [14], and fall detection [15, 16]. These are just a few of the areas. The sensors and devices used vary depending on the areas of use. Accelerometers, gyroscopes, magnetometers, heart rate sensors, electrocardiograph (ECG) sensors, and blood pressure sensors are among the most commonly used sensors. Among these, the accelerometer measures the amount and direction of acceleration. Accelerometers are generally very small and wearable devices. It contains a tiny mass and electronic circuits that detect the movement of the mass. By detecting this movement, information is obtained about the magnitude and direction of the acceleration [17]. Accelerometers are used in many healthcare applications.

Rowlands et al. evaluated the accuracy of postural classification using the Sedentary Sphere on data obtained from two commonly used wrist-worn triaxial accelerometers. For this purpose, 34 adults were measured by wearing a GENEActiv and an ActiGraph GT3X+ accelerometer on their non-dominant wrist while performing four lying, seven sitting, and five upright activities [10]. Maher et al. conducted a study to describe the current clinical use of wearable activity monitors in South Australia, identify barriers and facilitators of their implementation, and explore potential opportunities for wider clinical adoption. At the 12 centers in the study, five used primarily Fitbits® (various models), four used research-grade accelerometers (e.g., GENEActiv, ActivPAL, and StepWatch accelerometers), one used Whoop Bands®, and the other used smartphone-based step counters [18]. Al Abiad et al. aimed to develop a fall risk assessment method using wearable sensors independent of sensor placement. The researchers analyzed acceleration data from older adults recorded with a DynaPort motion recorder to identify gait

parameters associated with falls. They used a step detection method that works with sensors placed anywhere on the body to calculate parameters related to gait variability, complexity, intensity, and quantity [19].

The areas where accelerometers are commonly used are detecting conditions such as neurological diseases and musculoskeletal problems by examining people's walking patterns in gait analysis, encouraging healthy lifestyle habits, and helping prevent diseases by measuring the amount of daily movement in physical activity tracking, and detecting falls by analyzing falls or early detection of falls can be given [20, 21].

The integration of wireless data reading and cloud applications into biomedical applications has contributed to the development of modern healthcare. Wireless data reading does not require connection to a device; thus, it prevents cable confusion and facilitates continuous data recording. Cloud applications further enhance the wireless data logging ecosystem by providing robust platforms for data storage, processing, and analysis. This wireless continuous data stream has paved the way for early diagnosis, timely intervention, and personalized treatment plans. It promotes collaborative care and accelerates medical research by facilitating seamless sharing of data among healthcare providers, researchers, and patients. The combination of wireless data transmission and cloud computing provides scalability, accessibility, and security, ultimately improving patient outcomes and transforming the landscape of biomedical applications [22–24].

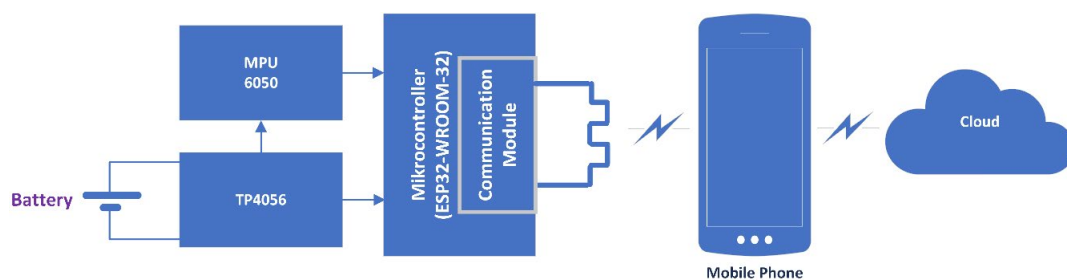
Although the use of acceleration signals in different areas is increasing, there are a limited number of acceleration recorders used. Although existing devices have sufficient features (sampling frequency, acceleration range, resolution and connection options), their prices vary between \$150 and \$900. In addition, these acceleration recorders do not have an international distribution network. Because sales networks remain regional, it is very difficult to purchase and use them. For these reasons, it cannot be effectively used in studies such as gait analysis, physical activity monitoring, fall detection and prevention, and posture assessment, where acceleration signals are used in developing and third-world countries. Therefore, in this study, a low-cost, remote-access accelerometer was designed for gait analysis.

## 2 MATERIAL AND METHODS

The study consists of two parts. The first step is to design and software a data collection hardware that will communicate with the sensor, perform data collection operations, and transfer the collected data to a mobile phone with a built-in Wi-Fi unit. The second task is to write a mobile phone interface program that will communicate with the data collection hardware via Wi-Fi, direct the recording processes, and upload the obtained data to the cloud environment. A block diagram of the proposed system is presented in Figure 1. The block diagram in Figure 4 visually represents the system's architecture, including the interconnections between the microcontroller, sensor, Wi-Fi module, battery management unit, and mobile phone application.

### 2.1 Hardware Design and Software Development

The system utilizes a microcontroller (ESP32-WROOM-32E) to handle data acquisition from the sensor, perform on-board processing, and manage wireless communication. The ESP32-WROOM-32E is a powerful MCU module with integrated Wi-Fi communication developed for various applications, such as low-power sensor networks. An MPU6050 six-axis acceleration sensor module was chosen for its cheap and easy-to-use ability to measure acceleration data. In addition, the MPU 6050 has a programmable option for measurement range and low power consumption. The system employs Wi-Fi communication for data transmission to mobile phones. Wi-fi communication was carried out using a 2.4-GHz Wi-fi module and on-board PCB antenna hardware integrated into the ESP32-WROOM microcontroller. A TP4056 linear Li-ion battery charger was integrated to manage the charging process of the system battery.



**Figure 1.** Block diagram of the proposed accelerometer recorder



C programming language was used to develop the software for the microcontroller hardware. The program was developed using Arduino IDE and the Visual Studio Editor. A flow diagram of the software is shown in Figure 2. The flow diagram in Figure 1 consists of the main program and interrupt subroutine. The main program consists of the steps of introducing the libraries required for the operation of the system, making Wi-Fi settings, making and installing server settings, making acceleration sensor settings, and starting the measurement process with the settings made. Once the system measurement is initiated, the MPU6050 acceleration sensor generates a hardware interrupt each time it finishes the measurement. When this hardware interrupt connected to the microcontroller is active, the microcontroller goes out of sleep mode and executes the interrupt subroutine. In the interrupt subprogram, serial communication with the acceleration sensor is initiated, and the values measured by the MPU6050 are read. These read values are then transferred to the server, and the microcontroller enters sleep mode again.

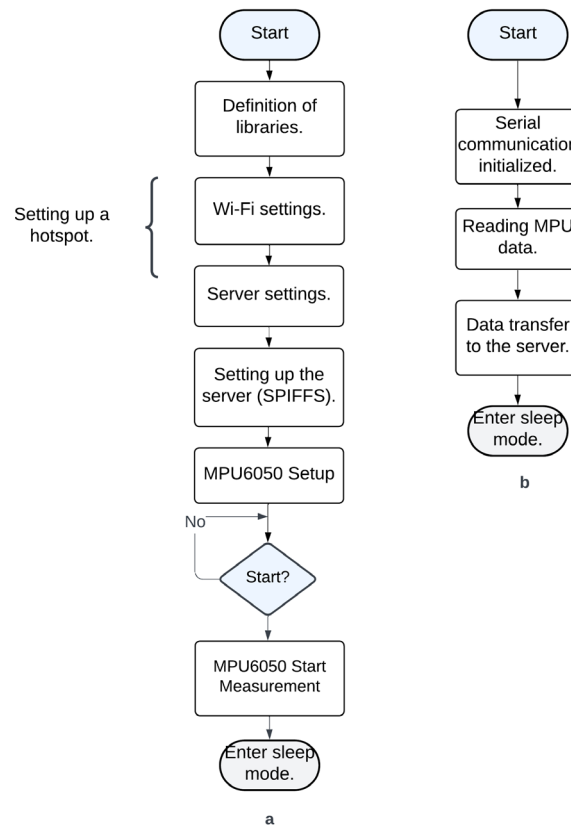


Figure 2. Flow diagram of the microcontroller program a. Main program b. Interrupt subroutine

## 2.2 HTML Server Program

In this study, a web application was designed to initiate data acquisition, visualize, and record the recorded data in real time. A web application created using the HTML, JavaScript, and CSS libraries receives data sent by the microcontroller in JSON format. This application provides real-time data reading using web socket and server-sent events (SSE) technologies. The flow diagram of the application is shown in Figure 3. Real-time accelerometer data are presented visually and numerically using dynamic graphics. Buttons were also added to the interface for user interaction to perform various operations, such as pausing/resuming the data flow, resetting data, and saving data. The data to be recorded were provided as output in Excel format for analysis or reporting. The user interface images of the mobile phone and computer are shown in Figures 4, 5, and 6.

After the registration process is completed, when an Internet connection is available, the data are uploaded to the Cloud. Users can access and review data records in the application. Data synchronization and storage are provided by the Cloud. The Google Firebase cloud platform was selected for data storage and synchronization. Data uploads were managed via the Firebase REST API and provided cloud database synchronization. This protocol combined multiple data entries into a single request, thereby allowing bulk uploads. The Firebase system was preferred due to its features, such as security rules, data encryption, and support for various authentication methods. In addition, the fact that the application is extensible and allows the integration of many Firebase services is another reason for the preference.

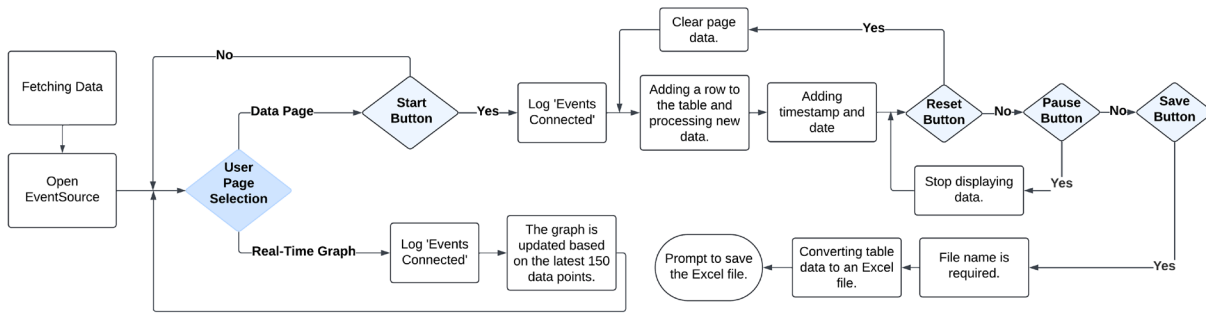


Figure 3. Flow diagram of the HTML server program

Data Page					
X	Y	Z	Time	Date	
1.21	0.36	-0.65	15.25.20.370	24.07.2024	
1.21	0.36	-0.65	15.25.20.370	24.07.2024	
1.21	0.36	-0.65	15.25.20.370	24.07.2024	
1.21	0.36	-0.65	15.25.20.370	24.07.2024	
1.21	0.36	-0.65	15.25.20.370	24.07.2024	
1.21	0.36	-0.66	15.25.20.370	24.07.2024	
1.20	0.36	-0.66	15.25.20.369	24.07.2024	
1.20	0.36	-0.66	15.25.20.369	24.07.2024	
1.20	0.36	-0.66	15.25.20.287	24.07.2024	
1.20	0.36	-0.66	15.25.20.286	24.07.2024	
1.20	0.36	-0.66	15.25.20.286	24.07.2024	
1.20	0.36	-0.66	15.25.20.286	24.07.2024	
1.20	0.36	-0.66	15.25.20.286	24.07.2024	
1.20	0.36	-0.66	15.25.20.286	24.07.2024	
1.20	0.36	-0.66	15.25.20.286	24.07.2024	
1.20	0.36	-0.66	15.25.20.286	24.07.2024	
1.20	0.36	-0.67	15.25.20.286	24.07.2024	
1.20	0.36	-0.67	15.25.20.285	24.07.2024	
1.20	0.36	-0.67	15.25.20.285	24.07.2024	
1.20	0.36	-0.67	15.25.20.200	24.07.2024	

Figure 4. Access to computer data page view

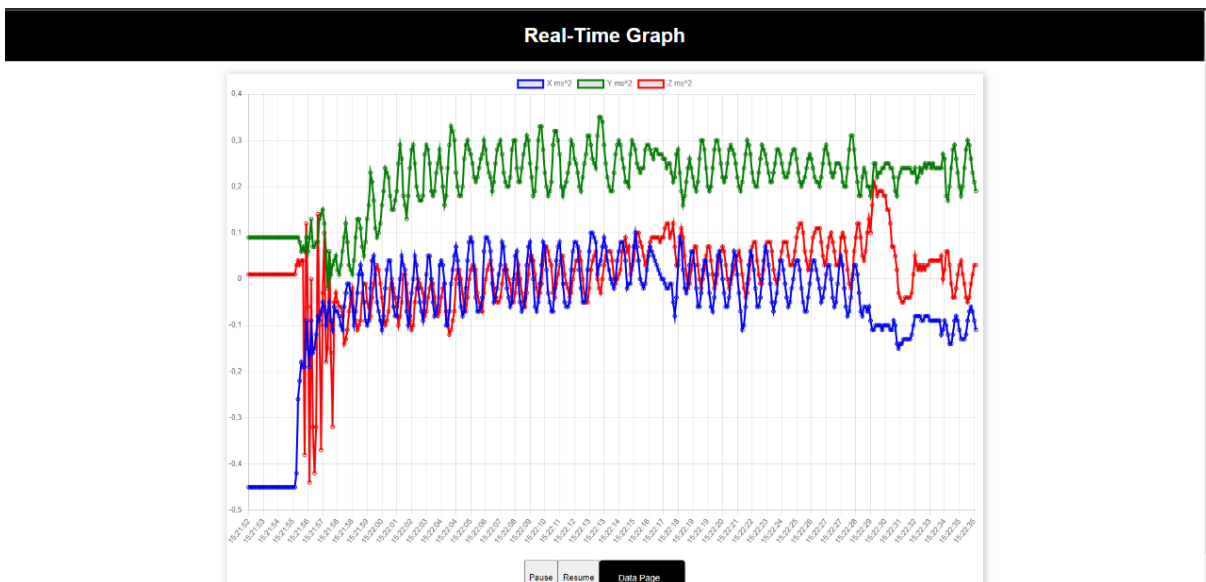


Figure 5. Access from a computer-graphic page view

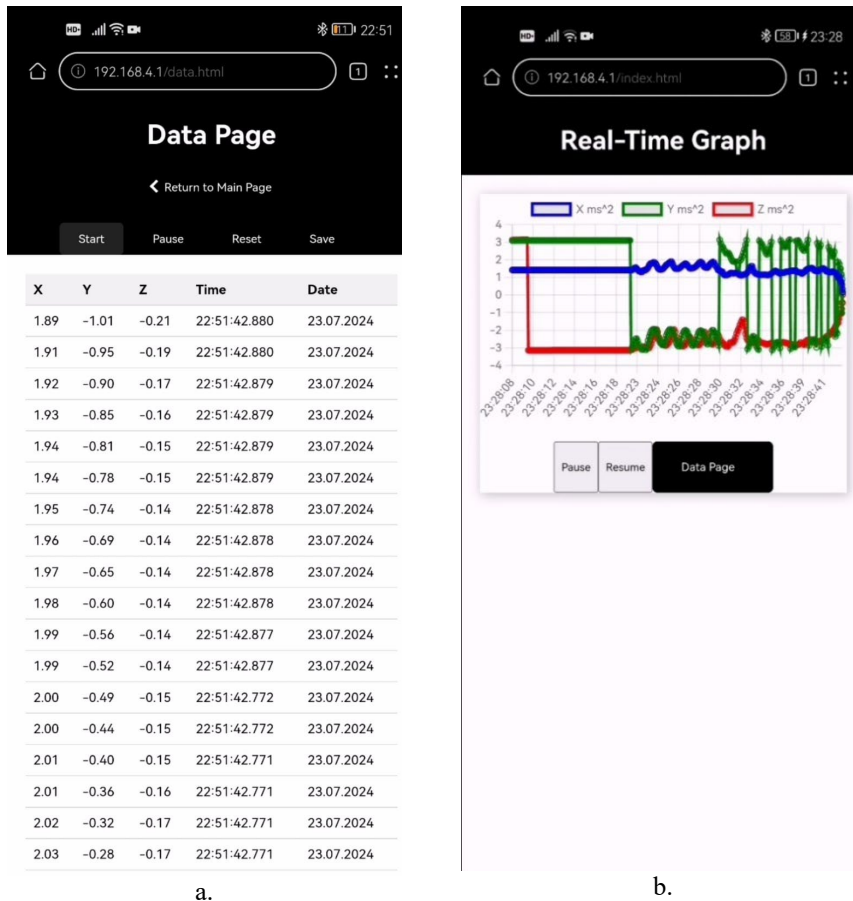


Figure 6. Access from mobile phone a. Data page b. Graph page view

### 3 RESULTS

This section presents the findings related to the development and testing of a low-cost, remote-access accelerometer designed for gait analysis.

#### 3.1 Hardware Design

The designed recording system has a measurement range of +/- 16g and a measurement resolution of 16 bits. It allows data recording at sampling rates up to 100 Hz. Cloud communication can be carried out effectively via Wi-Fi. The designed recording system is 65 mm long and 75 mm wide. The power consumption of the device during sleep was 30 microamps, and the power consumption during measurement and data transmission was 115 mA. Data can be recorded for 110 minutes using an 800-mAh battery. Figure 7 shows the top view of the proposed system.

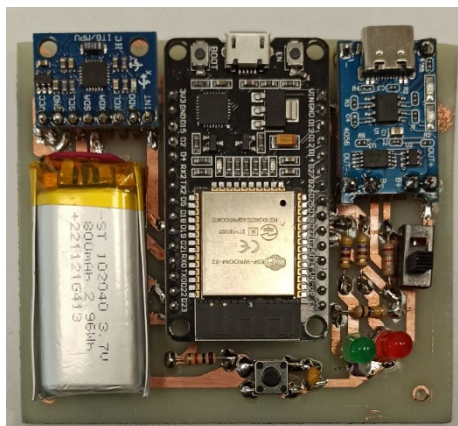


Figure 7. Top view of the proposed system

### 3.2 Cost Analysis

The three most important parameters of the system are the microcontroller module, acceleration sensor module, battery management module, and li-ion battery, and the cost of these modules is \$11, \$3, \$2, and \$10, respectively. In addition, the total cost of materials, such as the key, LED resistor, and printed circuit used in the circuit is \$24. Printing If we add these cost items, the total cost of the acceleration recording system is \$50. Table 1 presents the basic features of the commercially available acceleration recorders that we designed in this study. The selling price of the cheapest commercial product in Table 1 is \$150. The cost of the proposed system was \$50. It is understood that a low-cost acceleration recording system, which is the main purpose of our study, has been achieved.

**Table 1.** Caption of table

	Sensor Range	Sensor Resolution	Sample Frequency	Connectivity	Price
DynoPort	±16 g	2048 LSB/g	100 Hz	Wi-Fi/ Bluetooth	480\$
RunScribe	N	N/A	500 Hz	Bluetooth	600\$
GeneActiv	±16 g	N/A	100 Hz	Wi-Fi/ Bluetooth	260\$
The Opal	±16 g	14 bits	128 Hz	Wi-Fi	N/A
Shimmer3 IMU	±16 g	N/A	N/A	N/A	465\$
Movella Dot	±16 g	16 bits	120 Hz	Bluetooth	150\$
HAM-x16	±16 g	16 bits	400 Hz	SD card	170\$
Our Study	±16 g	16 bits	100 Hz	Wi-Fi	50\$

## 4 CONCLUSION

This study successfully developed a low-cost, wirelessly based remote acceleration data recording system. By integrating an accelerometer, microcontroller, and Wi-Fi-based remote access protocol, a wearable device was designed to measure and record acceleration data wirelessly. This system will pave the way for many research studies by enabling researchers and health professionals to record acceleration data wirelessly in many areas where acceleration measurements are required, such as gait analysis, activity tracking, and athlete performance measurements. The main starting point of this study is the development of an affordable system, and its domestic nature will facilitate the access of researchers to this device.

## Acknowledgments

This work was supported by TÜBİTAK 2209-A Research Project Support Program for Undergraduate Students and the Necmettin Erbakan University Scientific Research Projects Coordination Unit under project number 23GAP19008.

## References

- [1] M. Bongartz, R. Kiss, P. Ullrich, T. Eckert, J. Bauer, and K. Hauer, "Development of a home-based training program for post-ward geriatric rehabilitation patients with cognitive impairment: study protocol of a randomized-controlled trail," *BMC Geriatr*, vol. 17, no. 1, art. no. 214, Sep. 2017.
- [2] R. Buendia *et al.*, "Wearable sensors to monitor physical activity in heart failure clinical trials: State-of-the-art review," *Journal of Cardiac Failure*, vol. 30, no. 5, pp. 703–716, 2024.
- [3] C. Hinchliffe *et al.*, "Evaluation of walking activity and gait to identify physical and mental fatigue in neurodegenerative and immune disorders: Preliminary insights from the IDEA-FAST feasibility study," *J Neuroeng Rehabil*, vol. 21, no. 1, art. no. 94, Jun. 2024.
- [4] M. Yontem, B. Erbil, and B. S. Erdogdu, "Evaluation of renal and thyroid function tests in chronic renal failure patients," *Necmettin Erbakan Üniversitesi Fen ve Mühendislik Bilimleri Dergisi*, vol. 2, no. 2, pp. 52–57, Dec. 2020.
- [5] B. Khan, Z. Riaz, R. u. S. Ahmad, and B. L. Khoo, "Advancements in wearable sensors for cardiovascular disease detection for health monitoring," *Materials Science and Engineering: R: Reports*, vol. 159, 2024.

- [6] J. J. M. Kraaijkamp, M. Stijntjes, J. H. De Groot, N. H. Chavannes, W. P. Achterberg, and E. F. van Dam van Isselt, "Movement patterns in older adults recovering from hip fracture," *Journal of Aging and Physical Activity*, vol. 32, no. 3, pp. 312–320, Jun. 2024.
- [7] N. G. Sengoz and F. Zeybek, "Sharp silhouettes for obtaining 3D body measurements from 2D images," *Necmettin Erbakan Üniversitesi Fen ve Mühendislik Bilimleri Dergisi*, vol. 4, no. 2, pp. 8–25, Dec. 2022.
- [8] J. A. Wullems, S. M. P. Verschueren, H. Degens, C. I. Morse, and G. L. Onambebe-Pearson, "Concurrent validity of four activity monitors in older adults," *Sensors (Basel)*, vol. 24, no. 3, Jan. 2024.
- [9] A. T. Sozer, "Subject-specific sinusoid approach for a brain–computer interface based on single-channel steady-state visual evoked potential," *Necmettin Erbakan Üniversitesi Fen ve Mühendislik Bilimleri Dergisi*, vol. 3, no. 1, pp. 1–12, Jun. 2021.
- [10] A. V. Rowlands, T. Yates, T. S. Olds, M. Davies, K. Khunti, and C. L. Edwardson, "Wrist-worn accelerometer-brand independent posture classification," *Med Sci Sports Exerc*, vol. 48, no. 4, pp. 748–54, Apr. 2016.
- [11] N. A. Edwards, M. K. Talarico, A. Chaudhari, C. J. Mansfield, and J. Onate, "Use of accelerometers and inertial measurement units to quantify movement of tactical athletes: A systematic review," *Appl Ergon*, vol. 109, art. no. 103991, May 2023.
- [12] N. Alugubelli, H. Abuissa, and A. Roka, "Wearable devices for remote monitoring of heart rate and heart rate variability-what we know and what is coming," *Sensors (Basel)*, vol. 22, no. 22, Nov. 2022.
- [13] H. Y. Pan, C. K. Lee, T. Y. Liu, G. W. Lee, C. W. Chen, and T. D. Wang, "The role of wearable home blood pressure monitoring in detecting out-of-office control status," *Hypertens Res*, vol. 47, no. 4, pp. 1033–1041, Apr. 2024.
- [14] N. T. Tran, H. N. Tran, and A. T. Mai, "A wearable device for at-home obstructive sleep apnea assessment: State-of-the-art and research challenges," *Front Neurol*, vol. 14, art. no. 1123227, 2023.
- [15] F. Wu, H. Zhao, Y. Zhao, and H. Zhong, "Development of a wearable-sensor-based fall detection system," *Int J Telemed Appl*, vol. 2015, art. no. 576364, 2015.
- [16] S. Altunkaya, "Frequency domain features of acceleration signals to evaluate fall risk of elderly," *Avrupa Bilim ve Teknoloji Dergisi*, pp. 150–155, 15 Aug. 2020.
- [17] G. Grouios, E. Ziagkas, A. Loukovitis, K. Chatzinikolaou, and E. Koidou, "Accelerometers in our pocket: Does smartphone accelerometer technology provide accurate data?," *Sensors (Basel)*, vol. 23, no. 1, Dec. 2022.
- [18] C. Maher, K. Szeto, and J. Arnold, "The use of accelerometer-based wearable activity monitors in clinical settings: current practice, barriers, enablers, and future opportunities," *BMC Health Serv Res*, vol. 21, no. 1, art. no. 1064, Oct. 2021.
- [19] N. Al Abiad, K. S. van Schooten, V. Renaudin, K. Delbaere, and T. Robert, "Association of prospective falls in older people with ubiquitous step-based fall risk parameters calculated from ambulatory inertial signals: Secondary data analysis," *JMIR Aging*, vol. 6, art. no. e49587, Nov. 2023.
- [20] Y. Celik *et al.*, "Sensor Integration for Gait Analysis," in *Encyclopedia of Sensors and Biosensors*, R. Narayan, Ed. Oxford: Elsevier, 2023, pp. 263–283.
- [21] C. C. Yang and Y. L. Hsu, "A review of accelerometry-based wearable motion detectors for physical activity monitoring," *Sensors*, vol. 10, no. 8, pp. 7772–88, 2010.
- [22] R. K. Dwivedi, S. Singh, and R. Kumar, "Integration of Wireless Sensor Networks with Cloud: A Review," in *2019 9th International Conference on Cloud Computing, Data Science & Engineering (Confluence)*, 2019, pp. 114–119.
- [23] J. Hassan *et al.*, "The rise of cloud computing: data protection, privacy, and open research challenges-a systematic literature review (SLR)," *Comput Intell Neurosci*, vol. 2022, art. no. 8303504, 2022.
- [24] C. R. Panigrahi, J. L. Sarkar, B. Pati, R. Buyya, P. Mohapatra, and A. Majumder, "Mobile cloud computing and wireless sensor networks: A review, integration architecture, and future directions," *IET Networks*, vol. 10, no. 4, pp. 141–161, 2021.



---

## Nanobioelectronics Used in Targeted Drug Delivery Systems

Gencay Sevim<sup>\*1,2</sup>, Gulay Buyukkoroglu<sup>3</sup>

<sup>1</sup>Department of Medical Services and Techniques, Antalya Bilim University, Antalya, Türkiye

<sup>2</sup>Department of Advanced Technologies, Eskisehir Technical University, Eskisehir, Türkiye

<sup>3</sup>Department of Pharmaceutical Biotechnology, Anadolu University, Eskisehir, Türkiye

---

### Abstract

Targeted drug delivery systems enable the effective treatment of many diseases instead of conventional treatments having undesirable effects and harms. Therefore, interest in targeting mechanisms has increased, and different methods have been developed. The purpose of such different studies is to design a biocompatible, biodegradable, and non-toxic targeted drug delivery system that can direct the therapeutic agent to the target region, maintain the therapeutic effect in the target region for the desired time, and prevent drug metabolism and early drug release. These systems have three fundamental components: therapeutic agent, targeting fragment, and drug protective fragment. Among these, the targeting fragment has different working mechanisms. It can be physical, chemical, ligand-based structures, and so on. In the literature, many studies are carried out on such targeting parts. In this context, one prefers nanobioelectronics to use as a targeting fragment due to being suitable for internal and external intervention. The most preferred ones are gold, magnetic, multiferroic, up-conversion nanoparticles, carbon-based structures, quantum dots, triboelectric nanostructures, and different nanoparticle conjugates. They have a high potential to be used as a targeting agent because they can both target drug systems effectively and provide the desired therapeutic duration. Additionally, they offer traceability because they can generate physical signals.

In this study, conducting a comprehensive literature review, one focuses on using nanobioelectronics in drug targeting systems and presents information from different studies. Nanobioelectronics, which have the potential to be used in many areas thanks to their unique physical properties, are particularly remarkable in the field of health. In this context, their interactions with biological systems and their integration into drug systems are discussed in this study.

**Keywords:** Nanobiotechnology, Bioelectronic, Nanobioelectronics, Targeted drug delivery, Targeting mechanisms

---



## A Satellite-Based Augmentation System for Turkey to Enhance Navigation Capabilities

Ibrahim Oz\*<sup>1</sup>

<sup>1</sup>Ankara Yıldırım Beyazıt University TTO, Ankara, Türkiye

### Abstract

Turkey's location at the crossroads of Europe and Asia creates unique challenges and opportunities for regional positioning and time distribution systems. This article explores Turkey's specific needs for positioning accuracy and potential solutions through satellite-based augmentation systems (SBAS).

SBAS supports many Global Navigation Satellite Services (GNSS) applications using techniques like wide-area differential GNSS (DGNSS) and precise point positioning (PPP). These services primarily provide high-accuracy positioning solutions, with availability and integrity being secondary considerations.

Next-generation GNSS satellites that transmit augmentation signals in the L1, L5, and L6 frequency bands. These signals can support a range of augmentation services, such as SBAS, wide-area DGNSS, and PPP, to meet the needs of various industries. Additionally, there are plans to implement next-generation dual-frequency multi-constellation SBAS. Multi-constellation GNSS increases robustness against potential issues with core satellite constellations and extends service coverage. Next-generation SBAS and GNSS are expected to improve GNSS performance's accuracy, integrity, availability, and continuity.

Raw Accuracy gives an initial estimate of positioning accuracy based solely on GNSS measurements, which can be significantly affected by various error sources. Corrected accuracy, achieved through augmentation systems like DGPS or SBAS, offers a more reliable and precise positioning solution by reducing the impact of these errors. To practically investigate wide-area augmentation techniques, we implemented a prototype SBAS system. This system achieved positioning accuracy of 0.3 to 0.6 meters horizontally and 0.4 to 0.8 meters vertically over Turkey during normal ionospheric conditions. However, severe ionospheric activities can degrade positioning performances. The successful implementation and testing of SBAS in Turkey paved the way for enhanced navigation services, improving safety, efficiency, and reliability in various applications. This development aligns with global trends in GNSS augmentation, positioning Turkey at the forefront of advanced navigation technologies.

**Keywords:** GNSS, SBAS, Wide-area augmentation techniques, Satellite-based augmentation systems, Navigation systems

## 1 INTRODUCTION

Positioning and time distribution systems are critical in various sectors, including transportation, telecommunications, agriculture, and defense. In Turkey, the demand for reliable and accurate positioning information is growing rapidly, driven by urbanization, infrastructure development, and the increasing use of location-based services. Additionally, precise timing synchronization is essential for telecommunications, financial services, and power distribution sectors. However, Turkey's unique geographical characteristics, including mountainous terrain, coastal regions, and urban centers, challenge existing positioning and timing systems. Therefore, there is a need to develop specialized solutions tailored to Turkey's specific requirements.

Dense urban environments with tall buildings and complex street layouts characterize Turkey's major cities, including Istanbul, Ankara, and Izmir. These conditions can lead to multipath interference and signal blockage, reducing the accuracy of positioning systems. Therefore, solutions must be developed to mitigate the effects of urban clutter and improve positioning accuracy in urban areas. Turkey has a long coastline bordering the Aegean, Mediterranean, and Black Seas. Coastal regions present challenges for maritime navigation and coastal surveillance, requiring specialized positioning systems to provide accurate location information for vessels and maritime assets. The mountainous terrain in Turkey poses challenges for traditional positioning systems, particularly in remote and rugged areas. Solutions must be developed to ensure reliable positioning information is

available across all regions, including mountainous terrain. Precise timing synchronization is essential for telecommunications, financial services, and power distribution sectors. However, achieving accurate timing synchronization across Turkey's vast territory requires robust timing distribution systems capable of compensating for propagation delays and network latency.

Augmenting existing Global Navigation Satellite Services (GNSS) systems such as Global Positioning System (GPS), GLONASS, and Galileo with regional augmentation systems can improve positioning accuracy and reliability in urban and challenging environments. Differential GNSS (DGNSS) and Satellite-Based Augmentation Systems (SBAS) can provide real-time corrections to GNSS signals, improving accuracy to within a few meters. Establishing regional timing distribution networks using precision timing equipment such as atomic clocks and network time servers can ensure accurate timing synchronization across Turkey. These networks can leverage both satellite-based and terrestrial timing sources to provide redundancy and resilience against disruptions [1, 2].

GPS is known for its wide availability and continuous modernization to improve signal quality and reliability. BeiDou offers various civilian signals with functionalities tailored to various applications. Galileo emphasizes high accuracy and integrity, making it a robust choice for civilian applications in Europe. Quasy Zenith Satellite System (QZSS) is designed to enhance GPS performance in Japan, particularly in urban areas with challenging signal environments. Indian Regional Navigation Satellite System (IRNSS) focuses on providing enhanced coverage and Accuracy within India, addressing regional navigation needs.

Table 1 provides a comparative overview of the key characteristics of various GNSS and their associated augmentation systems.

**Table 1.** Location of monitoring stations

GNSS System	Frequency Bands (MHz)	Signal Type	Civilian accuracy (m)	Key Features
GPS	L1 (1575.42) L2 (1227.6) L5 (1176.45)	C/A, P(Y), M	5-15	- Widely available - Multiple civilian signals - Modernization ongoing
BeiDou	B1 (1561.035) B2 (1207.14) B3 (1268.52)	B1(I), B1-C, B2a, B2b, B3a	5-10	- Multiple civilian signals with varied functionalities
Galileo	E1 (1575.42) E5 (1191.795) E6 (1278.750)	E1 OS, E5a(OS), E5b(CS)	4-8	- European system - Focus on high accuracy and integrity
QZSS	L1 (1575.42) L2 (1227.6) L5 (1176.45)	C/A, L1C, LEX	3-5	- Regional system for Japan - Offers augmentations for improved accuracy
IRNSS	L5 (1176.45) S (5115.2)	NavIC	5-10	- Regional system for India - Focus on improved coverage over India

GPS operates on three primary frequency bands: L1 (1575.42 MHz), L2 (1227.6 MHz), and L5 (1176.45 MHz). These frequencies support various signal types to enhance accuracy and availability. BeiDou uses B1 (1561.035 MHz), B2 (1207.14 MHz), and B3 (1268.52 MHz) frequency bands. Each band provides different signal types tailored to specific applications. Galileo operates on E1 (1575.42 MHz), E5 (1191.795 MHz), and E6 (1278.750 MHz) frequency bands, which are designed to support a range of services with high accuracy and integrity. QZSS utilizes the same frequency bands as GPS (L1, L2, L5) and includes the LEX signal for enhanced performance in the Asia-Oceania region. IRNSS uses L5 (1176.45 MHz) and S (5115.2 MHz) frequency bands to provide navigation services primarily within India [1].

GPS provides Coarse/Acquisition (C/A) code on L1, precise (P(Y)) code on L1 and L2, and military (M) code on L1 and L2 frequencies. BeiDou offers multiple signal types, including B1(I), B1-C, B2a, B2b, and B3a, each serving different applications and user needs. Galileo signals include E1 Open Service (OS), E5a OS, and E5b Commercial Service (CS), designed for high precision and civilian use. QZSS includes C/A, L1C, and LEX signals to provide accurate positioning information and augmentations. IRNSS uses signal to provide reliable navigation services focusing on the Indian region [3–8].

GPS typically provides an accuracy of 5-15 meters for civilian users. BeiDou offers accuracy between 5-10 meters. Galileo aims for higher precision with accuracy ranging from 4-8 meters. QZSS provides a high accuracy of 3-5 meters, benefiting from regional augmentations. IRNSS achieves accuracy between 5-10 meters, focusing on regional needs.



## 1.1 GNSS Range Measurement and Accuracy

In multi-GNSS positioning, pseudo-range measurement can be used to obtain single-point positioning information as it estimates the distance between the satellite and the receiver. The pseudo-range represents the apparent range between the satellite and the receiver, incorporating various sources of error and delays. The pseudo-range equation can be given by [2,11,.17].

$$\rho_i = \|\mathbf{R}_{\text{sat}} - \mathbf{R}_{\text{GS}}\| + c\tau_{\text{delay}} + \Delta d_{\text{trop}} + \Delta d_{\text{ion}} + \epsilon \quad (1)$$

where:

- $\rho_i$ : The pseudo-range between the station/user and the satellite,
- $R_{\text{sat}}$ : The satellite position vector,
- $R_{\text{GS}}$ : The ground station or user position vector,
- $c$ : The speed of light,
- $\tau_{\text{delay}}$ : The combined ground station and transponder time delay,
- $\Delta d_{\text{trop}}$ : the tropospheric delay,
- $\Delta d_{\text{ion}}$ : The ionospheric delay, and
- $\epsilon$ : Represents other errors, such as multipath effects and clock biases.

The range from a ground station to a satellite can be represented by the following equation:

For the GPS satellite's C/A signal code, pseudo range in the L1 frequency, the equation can be expressed as:

$$\rho_c = \rho + c[\Delta t_{\text{GPS}}(t) - \Delta t_U(t)] \quad (2)$$

where:

- $\rho_c$ : The C/A code pseudo-range in L1,
- $c$ : The speed of light,
- $\Delta t_{\text{GPS}}$ : The clock offset of the GPS satellite,
- $\Delta t_U$ : The clock offset of the receiver,
- $T$ : The instant observation time, and
- $\rho$ : The 3D distance between the ground station or user receiver and the GPS satellite.

By using the pseudo-range measurements from multiple satellites, the receiver can solve for its position coordinates (latitude, longitude, altitude) and clock bias, enhancing the accuracy of the positioning information. This process involves solving a system of nonlinear equations to determine the user's location and the receiver clock offset. GNSS augmentation systems, such as SBAS and GBAS, provide additional corrections to mitigate errors from ionospheric and tropospheric delays, satellite clock biases, and orbital inaccuracies, further improving the reliability and precision of the positioning solution [9–14].

### 1.1.1 Multilateration Technique

Multilateration is a fundamental technique in satellite-based navigation systems used to determine the precise location of a receiver by measuring the distances to at least four satellites. This method relies on the principle that the position of a point in three-dimensional space can be uniquely determined if its distances to four known points (the satellites) are known. Each satellite broadcasts signals that contain information about its position and the time the signal was transmitted. The receiver calculates the distance to each satellite by measuring the time it takes for the signal to travel from the satellite to the receiver, known as the pseudo-range.

With three satellites, the receiver can solve for its position in three-dimensional space, but this assumes perfect synchronization between the satellite and receiver clocks. However, because there is typically a clock bias in the receiver, a fourth satellite is necessary to account for this timing error. The additional satellite provides the necessary data to solve the four unknowns: the receiver's three-dimensional coordinates (latitude, longitude, and altitude) and the clock bias. This system of equations is solved simultaneously to pinpoint the receiver's exact location. Using more than four satellites can enhance accuracy and provide redundancy, ensuring reliable position determination even if one or more satellites are temporarily unavailable.

The equations form a system that can be solved using numerical methods or least squares estimation, providing the receiver's precise location. This method is robust and essential for the accurate functioning of modern GNSS systems, including GPS, Galileo, BeiDou, and GLONASS.

### 1.1.2 Dilution of Precision (DOP)

Dilution of Precision (DOP) is a key concept in Global Navigation Satellite System (GNSS) positioning that quantifies the effect of satellite geometry on the precision of position estimates. DOP values indicate how the satellite configuration affects the accuracy of the GNSS receiver's calculated position. Lower DOP values correspond to better geometric configurations and more accurate position estimates [4, 8]. To derive DOP values, we start from the linearized form of the pseudo-range equations, represented in matrix form as:

$$\mathbf{P} = \mathbf{H}\mathbf{x} \quad (3)$$

where:

$\mathbf{P}$  is the vector of pseudo-range measurements.

$\mathbf{H}$  is the geometry matrix, containing the partial derivatives of the pseudo-range equations with respect to the receiver's coordinates and clock bias.

$\mathbf{x}$  is the vector of unknowns (receiver coordinates and clock bias).

The covariance matrix of the position estimate,  $\mathbf{Q}$ , is given by:

$$\mathbf{Q} = (\mathbf{H}^T\mathbf{H})^{-1} \quad (4)$$

The diagonal elements of  $\mathbf{Q}$  provide the variances of the position errors in different directions. The DOP values are derived from the trace of  $\mathbf{Q}$ :

GDOP is a composite value encompassing several specific dilution of precision (DOP) components: PDOP (Position Dilution of Precision), which Reflects the contribution of satellite geometry to three-dimensional position errors. HDOP (Horizontal Dilution of Precision), reflects the impact on horizontal position accuracy (latitude and longitude). VDOP (Vertical Dilution of Precision), reflects the impact on vertical position accuracy (altitude). TDOP (Time Dilution of Precision), reflects the impact on the receiver clock error.

$$\text{GDOP} = \sqrt{\text{trace}(\mathbf{Q})} \quad (5)$$

Each DOP component (HDOP, VDOP, PDOP, and TDOP) can be extracted from the elements of the covariance matrix. Specifically:

$$\text{HDOP} = \sqrt{Q_{xx} + Q_{yy}}$$

$$\text{VDOP} = \sqrt{Q_{zz}}$$

$$\text{TDOP} = \sqrt{Q_{tt}}$$

$$\text{PDOP} = \sqrt{Q_{xx} + Q_{yy} + Q_{zz}}$$

$$\text{GDOP} = \sqrt{Q_{xx} + Q_{yy} + Q_{zz} + Q_{tt}}$$

where,  $Q_{xx}$ ,  $Q_{yy}$ ,  $Q_{zz}$ , and  $Q_{tt}$ : the diagonal elements of the covariance matrix  $\mathbf{Q}$ .

GDOP is an important metric in GNSS that influences the precision of position estimates. Lower GDOP values indicate better satellite geometry and, consequently, higher positioning accuracy.

### 1.1.3 Raw Horizontal and Vertical Accuracy

Raw horizontal and vertical accuracy refer to the initial positioning accuracy obtained directly from GNSS measurements without any corrections applied. This raw accuracy is influenced by factors such as satellite geometry, atmospheric conditions, multipath effects, and inherent errors in the GNSS signals [5].

The raw horizontal Accuracy (Horizontal Positioning Error, HPE) can be expressed as:

$$\text{HPE}_{\text{raw}} = \text{HDOP} \times \sigma_{\text{URE}} \quad (8)$$

The raw vertical Accuracy (Vertical Positioning Error, VPE) can be expressed as:

$$\text{VPE}_{\text{raw}} = \text{VDOP} \times \sigma_{\text{URE}} \quad (9)$$

where:

HDOP (Horizontal Dilution of Precision) and VDOP (Vertical Dilution of Precision) reflect the geometry of the satellite constellation.

$\sigma_{\text{URE}}$  (User Range Error) represents the standard deviation of the range errors from various sources like satellite clock errors, ephemeris errors, and atmospheric delays.

Raw Accuracy gives an initial estimate of positioning accuracy based solely on GNSS measurements, which can be significantly affected by various error sources. Corrected accuracy, achieved through augmentation systems like DGPS or SBAS, offers a more reliable and precise positioning solution by reducing the impact of these errors. Understanding and improving these accuracies are crucial for applications requiring high precision, such as aviation, surveying, and geolocation services.

#### 1.1.4 Corrected Horizontal and Vertical Accuracy

Corrected horizontal and vertical accuracy refers to the improved positioning accuracy obtained after applying correction techniques such as Differential GPS (DGPS) or Satellite-Based Augmentation Systems (SBAS). These corrections help mitigate errors due to atmospheric delays, satellite clock offsets, and other sources, resulting in more accurate position estimates.

The corrected horizontal accuracy can be expressed as [8]:

$$\text{HPE}_{\text{corrected}} = \text{HDOP} \times \sigma_{\text{corrected\_URE}} \quad (10)$$

The corrected vertical accuracy can be expressed as:

$$\text{VPE}_{\text{corrected}} = \text{VDOP} \times \sigma_{\text{corrected\_URE}} \quad (11)$$

In these equations:

$\sigma_{\text{corrected\_URE}}$  represents the standard deviation of the corrected range errors after applying techniques like DGPS or SBAS.

By minimizing the DOP values and improving the signal quality, the GNSS system can provide precise horizontal and vertical position solutions. Horizontal and vertical accuracy are critical metrics in GNSS-based location determination, reflecting the precision of the computed position in the horizontal (latitude and longitude) and vertical (altitude) planes, respectively. These accuracies are influenced by various factors, including satellite geometry, signal quality, and atmospheric conditions.

## 1.2 Error Sources and Corrections

Global Navigation Satellite Systems (GNSS) are susceptible to various error sources that can affect the accuracy of positioning data. The primary error sources include satellite clock errors, which arise from inaccuracies in the satellite's onboard clock, and ephemeris errors, stemming from inaccuracies in the satellite's reported position. Ionospheric and tropospheric delays also significantly impact GNSS signals; the ionosphere can cause delays due to its charged particles, especially during periods of high solar activity, while the troposphere induces delays due to its water vapor and pressure variations. Multipath effects, where signals reflect off surfaces such as buildings and terrain before reaching the receiver, introduce further errors. Additionally, receiver clock errors due to inaccuracies in the user's device and signal obstruction or interference can degrade the quality of the GNSS signals. These errors collectively impact the precision and reliability of GNSS-based positioning, necessitating correction techniques such as those provided by Satellite-Based Augmentation Systems (SBAS).

Table 2 presents a comparison of typical GNSS error sources without correction and with SBAS correction, showing the significant improvement provided by SBAS in mitigating these errors [14–19].

This table highlights the efficacy of SBAS in reducing various GNSS errors, leading to more accurate and reliable positioning data [4].

**Table 2.** Typical error sources without correction and with SBAS correction

Component	GNSS Error (m)	SBAS (m)
Ephemeris	2.1 m	0.1
Satellite clock	2.1 m	0.1
Ionosphere	4.0 m	0.2
Multipath	1.4 m	1.0
Troposphere	0.7 m	0.2
Receiver noise	0.5 m	0.5
Total (RMS)	<b>5.3 m</b>	<b>1.2</b>

Table 3 presents a comparison of horizontal and vertical errors in GNSS positioning without correction and with SBAS correction, highlighting the improvements in accuracy provided by SBAS.

**Table 3.** Horizontal and vertical errors without correction and with SBAS correction

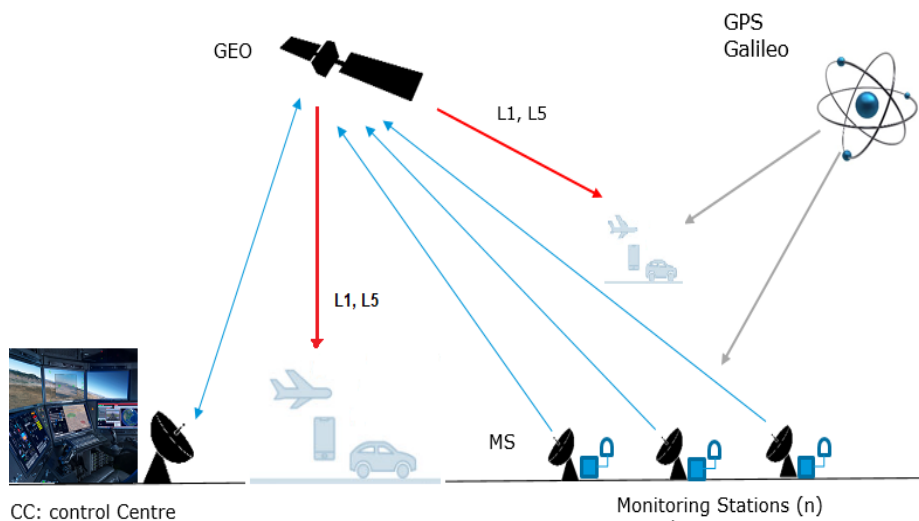
Component	GNSS Error (m)	SBAS (m)
Total Horizontal error (1 sigma, 68%), satellite geometry 1.3	5.2	1.6
Total Horizontal error (2 sigma, 95%), satellite geometry 1.3	10.4	3.2

Table 3 shows that SBAS provides substantial improvements in both horizontal and vertical positioning accuracy. The reduction in errors from GNSS-only to SBAS-corrected measurements, across different confidence intervals, underscores the capability of SBAS to enhance the reliability and precision of GNSS positioning.

### 1.3 General SBAS (Satellite-Based Augmentation Systems) for GNSS

Satellite-Based Augmentation Systems (SBAS) enhance Global Navigation Satellite Systems (GNSS) by improving navigation attributes such as accuracy, reliability, and availability by integrating external information into the calculation process. These systems are designed to transmit additional information about error sources (e.g., clock drift, ephemeris, ionospheric delay) or direct measurements of signal deviations, and they may also incorporate additional vehicle information into the calculations [10].

Figure 1 illustrates the typical operation of a Satellite-Based Augmentation System (SBAS). The process begins with GNSS data collection via a network of monitoring stations distributed across the region. These monitoring stations continuously receive signals from GNSS satellites, which include information such as satellite positions, clock errors, and atmospheric conditions.



**Figure 1.** General SBAS diagram

The collected data are then transmitted to a central control center. At the control center, the data undergo thorough processing to determine the necessary corrections for satellite orbit errors, satellite clock errors, and ionospheric and tropospheric delays. This processed augmentation data is used to generate SBAS correction messages.

Next, these correction messages are uplinked to a geostationary (GEO) satellite via uplink stations. The GEO satellite, positioned in a fixed location relative to the Earth, retransmits the augmentation messages using L-band frequencies [1].

Users equipped with SBAS-capable GNSS receivers receive both the original GNSS signals and the SBAS correction signals from the GEO satellite. The GNSS receivers integrate these signals to determine the user's precise location. The SBAS corrections significantly enhance the accuracy, integrity, and reliability of the positioning information, providing users with improved navigation capabilities.

This system ensures that users, whether in aviation, maritime, agriculture, or personal navigation, benefit from the augmented data, achieving higher precision in their positional information than they would with standard GNSS signals alone.

Implemented or proposed SBAS and Ground-Based Augmentation Systems (GBAS) include several notable examples. The Wide Area Augmentation System (WAAS) is operated by the United States Federal Aviation Administration (FAA), while the European Geostationary Navigation Overlay Service (EGNOS) is managed by the ESSP on behalf of the EU's GSA. Japan's Ministry of Land, Infrastructure and Transport (MLIT) Japan Civil Aviation Bureau (JCAB) operates the Multi-functional Satellite Augmentation System (MSAS). Another Japanese system, the Quasi-Zenith Satellite System (QZSS), began operations in November 2018. India's GPS Aided Geo Augmented Navigation (GAGAN) and Russia's GLONASS System for Differential Correction and Monitoring (SDCM) offer global coverage. Additionally, the Canadian WAAS (CWAAS) is run by NavCanada, and Mexico operates SENEAM WAAS. China's BeiDou Satellite Based Augmentation System (BDSBAS) and the Korean Augmentation Satellite System (KASS) by the Korea Aerospace Research Institute (KARI) are also significant. Finally, the Agency for Aerial Navigation Safety in Africa and Madagascar (ASECNA) provides regional services.

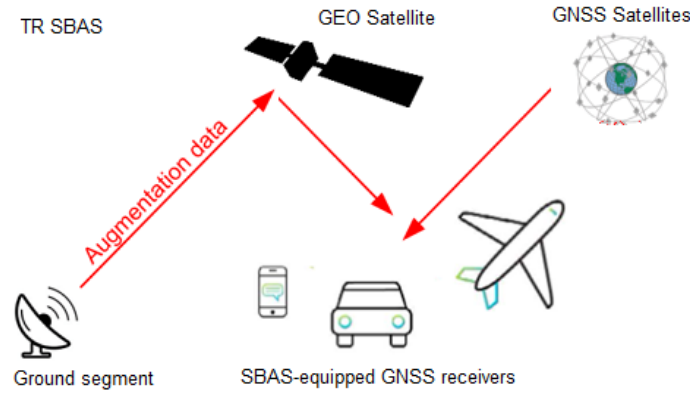
A Satellite-Based Augmentation System (SBAS) is an advanced navigation system that enhances the accuracy, integrity, and availability of Global Navigation Satellite System (GNSS) signals. SBAS improves these signals by using additional satellite signals and ground-based stations to provide users with differential corrections and integrity information. The system comprises three main segments: the ground segment, which includes reference stations that measure GNSS signal errors and send data to master stations for calculating differential corrections and integrity information; the space segment, which uses geostationary satellites to broadcast these corrections to users. Consequently improving coverage and reliability; and the user segment, which consists of SBAS receivers capable of processing these signals and applying corrections to enhance positioning accuracy. SBAS functionality includes providing differential corrections for satellite orbit errors, satellite clock errors, and ionospheric delays, improving positioning accuracy from several meters to within one meter. It also includes integrity monitoring, which continuously assesses the reliability of GNSS signals and issues timely warnings if any signals are unreliable, ensuring high safety levels, particularly in aviation. Additionally, SBAS improves the availability of GNSS signals by using geostationary satellites to ensure continuous service even in challenging environments.

## **2 GROUND AND USER STATIONS FOR TURKEY**

Turkey can design and implement an effective Regional Navigation and Timing Augmentation System (RNTAS) tailored to its specific needs. Figure 2 illustrates the proposed Satellite-Based Augmentation System (SBAS) specifically developed for Turkey. This system operates in a manner similar to the general SBAS architecture depicted in Figure 2, but it is tailored to meet the unique geographical and navigational needs of Turkey.

The Turkish SBAS begins with the establishment of a network of monitoring ground stations strategically distributed across the country. These stations are situated in both urban and rural areas to ensure comprehensive coverage and redundancy. The monitoring stations continuously collect GNSS data, including signals from multiple GNSS satellites, capturing satellite positions, clock errors, and atmospheric data.

The collected data from the monitoring stations are transmitted to two master stations located at strategically chosen sites within Turkey. These master stations process the data to compute the necessary differential corrections, which include satellite orbit errors, clock errors, ionospheric and tropospheric delays, and other relevant parameters. The master stations then generate augmentation messages based on these corrections [11, 13]



**Figure 2.** Proposed SBAS system for Turkey

The augmentation messages are sent to multiple uplink stations, which transmit them to a geostationary (GEO) satellite. For the Turkish SBAS, the system may lease transponders on existing geostationary satellites or utilize dedicated satellites to broadcast the augmentation messages. These satellites are positioned to provide optimal coverage over Turkey and its surrounding regions.

Users equipped with SBAS-capable GNSS receivers in Turkey receive both the standard GNSS signals and the augmentation signals transmitted by the GEO satellite. The receivers integrate these signals to determine highly accurate and reliable position information. The SBAS corrections enhance the positioning accuracy to within 0.5 to 1 meter horizontally and vertically, providing significant improvements over standard GNSS accuracy. The implementation of the Turkish SBAS aims to support a wide range of applications, including aviation, maritime, agriculture, surveying, and personal navigation. The system is designed to ensure high integrity, availability, and reliability, thereby enhancing the safety and efficiency of navigation services across Turkey.

**2.1 System Design**

Considering Turkey's unique geographic location and its need for high-accuracy navigation services, a proposal for a dedicated Satellite-Based Augmentation System (SBAS) for Turkey has been developed, similar to systems like WAAS (USA) and EGNOS (Europe).

The ground segment of the proposed SBAS involves establishing a network of reference stations across Turkey, including key urban centers and rural areas. In the space segment, geostationary satellites would broadcast augmentation messages over the Turkish region and surrounding areas. For the user segment, SBAS-capable GNSS receivers would be developed and distributed for various applications, including aviation, maritime, agriculture, and personal navigation. Key features of the proposed SBAS include achieving positioning accuracy within 0.3 to 1 meter horizontally and vertically under nominal conditions. The system would also incorporate redundancy in both the ground and space segments to maintain continuous service in case of any failures [1, 2].

**2.2 SBAS Test Stations**

Five monitoring ground stations and three user points were selected for system testing. The locations of the monitoring stations are provided in Table 4, while Table 5 provides information about the three user test points.

GNSS data were collected for 24 hours at 10-minute intervals for both the monitoring stations and the user test points. The processed augmentation data were then uplinked to a geostationary (GEO) satellite.

**Table 4.** Location of monitoring stations

	Latitude (°N)	Longitude (°E)	Height (m)
St-1	39.906081	32.740775	876.61
St-2	40.582916	32.548768	1439.82
St-3	39.451735	32.728141	949.32
St-4	39.912122	33.312938	925.88
St-5	39.869260	31.949616	959,78

Both the monitoring stations and the user test points calculated their locations in two different ways: Without Augmentation: This approach relied solely on the raw GNSS data to determine positions. With SBAS Augmentation: This method utilized the Satellite-Based Augmentation System (SBAS) data to correct the GNSS signals, enhancing the accuracy of the calculated positions.

The calculated positions from both methods were compared to evaluate the performance of the augmentation system. The results were analyzed to determine the effectiveness of the SBAS in improving positioning accuracy.

**Table 5.** Location of user stations

	Latitude (°N)	Longitude (°E)	Height (m)
U1	40.022762	32.607893	956.61
U2	39.828181	32.974277	1499.23
U3	39.814742	32.409319	739.21

### 2.2.1 Detailed Procedure

The procedure shows operation principals of Turkey SBAS system [1, 11, 17].

#### i. Data Collection:

- Five monitoring ground stations were strategically placed across different geographical locations to collect GNSS data.
- Similarly, three user points were selected to represent typical end-user locations.
- GNSS data from both monitoring stations and user points were collected continuously for 24 hours with data points recorded every 10 minutes.

#### ii. Data Processing:

- The collected GNSS data from the monitoring stations were processed to generate augmentation corrections. These corrections included compensations for satellite clock errors, ephemeris errors, ionospheric delays, and tropospheric delays.
- The processed augmentation data were then transmitted to a geostationary satellite, which broadcasted these corrections back to the user receivers.

#### iii. Position Calculation:

- Without Augmentation: User points calculated their positions using only the raw GNSS data. This served as a baseline to assess the natural accuracy of the GNSS system without any enhancements.
- With SBAS Augmentation: User points recalculated their positions using the GNSS data corrected by the SBAS. The augmentation data improved the accuracy by correcting various error sources in the GNSS signals.

#### iv. Performance Evaluation:

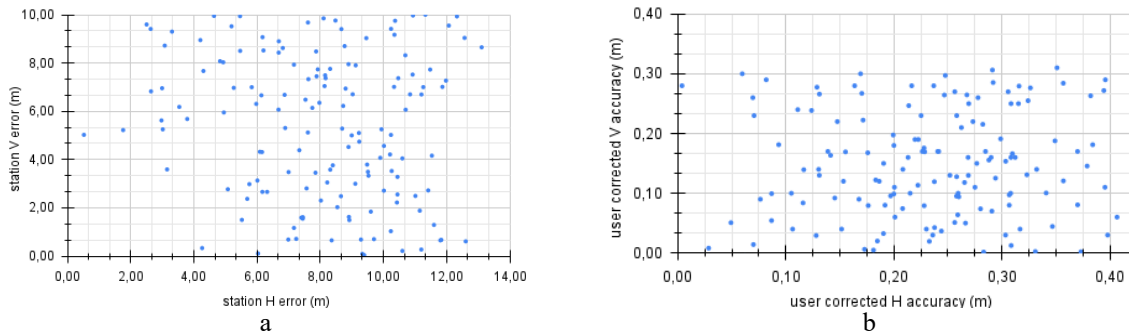
- The positions calculated using both methods were compared against known reference positions to determine the horizontal and vertical positioning errors.
- The improvement in positioning accuracy due to SBAS was quantified by comparing the errors from both methods.
- Statistical analysis was performed to assess the consistency and reliability of the SBAS-enhanced positions over the 24-hour period.

## 3 RESULTS

A comprehensive system testing procedure was designed to implement and evaluate the proposed Satellite-Based Augmentation System (SBAS) for Turkey. This involved strategically selecting five monitoring ground stations and three user test points. The objective was to assess the performance of the SBAS in enhancing GNSS positioning accuracy.

Figure 3.a is a scatter plot displaying the raw horizontal and vertical errors measured at a monitoring station. The horizontal axis represents the horizontal error (H error) in meters, while the vertical axis represents the vertical error (V error) in meters. Each point on the plot corresponds to an individual measurement. The horizontal error ranges from approximately 0 to 13 meters. The distribution of the horizontal errors shows a spread across the entire range, with no clear clustering around a specific value. The vertical error ranges from approximately 0 to 10 meters. Similar to the horizontal errors, the vertical errors are spread across the range, indicating measurement variability. The wide range of errors suggests that the GNSS system's performance can vary significantly, likely due to factors

such as multipath effects, atmospheric conditions, satellite geometry, and signal obstructions. High error values emphasize the necessity of an augmentation system, such as SBAS, to enhance the accuracy and reliability of the GNSS positioning.



**Figure 3.** a. Raw horizontal and vertical accuracy of station-5 b. Corrected horizontal and vertical accuracy of user-3

Figure 3.b shows a scatter plot displaying the corrected horizontal and vertical accuracies for user stations after applying Satellite-Based Augmentation System (SBAS) corrections. The horizontal axis represents the corrected horizontal accuracy (H accuracy) in meters, while the vertical axis represents the corrected vertical accuracy (V accuracy) in meters. Each point on the plot corresponds to an individual measurement. The horizontal accuracy ranges from approximately 0 to 0.4 meters. Most points are clustered below 0.3 meters, indicating improved horizontal positioning accuracy due to SBAS corrections. The vertical accuracy ranges from approximately 0 to 0.4 meters. Similar to the horizontal accuracy, most points are clustered below 0.3 meters, showing improved vertical positioning accuracy. This uniform distribution suggests that the SBAS corrections improve both horizontal and vertical accuracies independently.

The clustering of points around lower accuracy values (0.1 to 0.3 meters) demonstrates the effectiveness of SBAS in significantly enhancing the positioning accuracy for user stations. Compared to the raw error data, the corrected accuracies show reduced variability, highlighting the consistency and reliability of the SBAS corrections. The lack of a strong correlation between horizontal and vertical accuracies suggests that SBAS effectively addresses both dimensions of positioning errors independently.

**Table 6.** Users RMSE (m)

	X	Y	Z
U-1	0.18	0.18	0.17
U-2	0.26	0.28	0.25
U-3	0.22	0.23	0.22

Table 6 presents the Root Mean Square Error (RMSE) in Earth-Centered Earth-Fixed (ECEF) coordinates for three user stations, labeled U-1, U-2, and U-3. RMSE is a commonly used metric in positioning accuracy assessment, as it quantifies the average squared difference between the estimated and true positions. Lower RMSE values indicate higher accuracy in the position estimation.

For user station U-1, the RMSE values in the X, Y, and Z coordinates are all below 0.20 meters, indicating high accuracy in the positioning data. The nearly identical RMSE values for X and Y suggest symmetric errors in the horizontal plane. At the same time, the slightly lower Z-coordinate RMSE indicates slightly better accuracy in the vertical direction. User station U-2 shows higher RMSE values than U-1, with the highest errors in the Y-coordinate. This suggests a slightly reduced positioning accuracy for U-2, particularly in the horizontal plane. Despite this, the vertical accuracy remains relatively consistent, with the Z-coordinate RMSE being only marginally lower than the X and Y coordinates. The RMSE values for user station U-3 are slightly higher than those for U-1 but lower than those for U-2, indicating moderate positioning accuracy. The relatively uniform RMSE values across all three coordinates suggest balanced errors in both the horizontal and vertical directions.

The RMSE values in the table provide a quantitative measure of the accuracy of the positioning data for the three user stations. User Station U-1 demonstrates the highest accuracy among the three, with all coordinates showing RMSE values below 0.20 meters. User Station U-2 has the highest RMSE values, particularly in the Y-coordinate,



indicating more significant errors in the horizontal positioning. User Station U-3 exhibits moderate accuracy, with balanced RMSE values around 0.22 to 0.23 meters.

By comparing this corrected accuracy data with the raw error data, one can clearly see the substantial improvement in positioning accuracy provided by the SBAS, validating its effectiveness for enhancing navigation capabilities in Turkey.

## 4 CONCLUSION

The deployment and evaluation of a Satellite-Based Augmentation System (SBAS) for Turkey, aimed at enhancing the country's navigation capabilities, have yielded promising results. This study's comprehensive analysis underscores the significant improvements in positioning accuracy afforded by SBAS corrections, compared to unaugmented GNSS data.

The observed improvements in positioning accuracy are consistent with the expected benefits of SBAS technology, which integrates corrections for satellite clock errors, orbital inaccuracies, ionospheric delays, and tropospheric delays. This comprehensive correction capability is particularly valuable in Turkey's varied geographic landscape, which includes urban areas, mountainous regions, and coastal zones, each presenting unique challenges for accurate GNSS positioning.

Furthermore, the performance of SBAS in Turkey aligns well with similar implementations globally, such as WAAS in the United States and EGNOS in Europe. These systems have been instrumental in providing enhanced navigation services for critical applications, including aviation and maritime operations. The successful application of SBAS in Turkey demonstrates its potential to deliver comparable benefits, ensuring high-precision navigation across the country.

While the initial results are encouraging, further research and continuous monitoring are essential to ensure sustained performance and reliability of the SBAS in Turkey. Moreover, expanding the network of ground monitoring stations could further enhance the SBAS coverage and accuracy, particularly in remote or underserved areas.

## References

- [1] S. Choy, J. Kuckartz, A. G. Dempster, C. Rizos, and M. Higgins "GNSS satellite-based augmentation systems for Australia," *GPS Solutions*, vol. 21, pp. 835–848, 2017.
- [2] T. Sakai, S. Fukushima, N. Arai, and K. Ito, "Implementation of prototype satellite-based augmentation system (SBAS)," in *IGNSS Symposium*, 2006, pp. 6-9.
- [3] I. Oz, "Proximity monitoring of collocated satellites based on real time measurement", *Journal of the Faculty of Engineering & Architecture of Gazi University*, vol. 39, no. 2, pp. 825–834, 2023.
- [4] U. Tugcular, A. C. Basibuyuk, M. F. Engin, T. C. Sisman, C. Tola, and H. E. Soken, "Türkiye bölgesel seyrüsefer uydusu sisteminin bir artırım sistemi olarak tasarımı ve eniyilemesi," in *UHUK-2020-166*, Ankara, Turkey, 2020, pp. 1–16.
- [5] S. Buyuk, O. U. Oregul, A. C. Basibuyuk, U. Tugcular, T. C. Sisman, and C. Tola, "Preliminary orbit design for Turkish regional navigation satellite system," in *2019 9th International Conference on Recent Advances in Space Technologies (RAST)*, 2019, pp. 279–284.
- [6] A. F. Yagli, M. Gokten, S. Gulgonul, I. Oz, and O. Dalbay, "Regional positioning system using Turksat satellites," in *2013 6th International Conference on Recent Advances in Space Technologies (RAST)*, 2013, pp. 237–240.
- [7] I. Oz, "Coverages stabilization of an inclined orbit communication satellite with two axis biases", *Journal of the Faculty of Engineering & Architecture of Gazi University*, vol. 38, no. 1, pp. 219–230, 2022, doi: 10.17341/gazimmdf.960480.
- [8] F. A. Kaya and M. Saritas, "A computer simulation of dilution of precision in the global positioning system using Matlab," in *Proceedings of the 4th International Conference on Electrical and Electronic Engineering, Bursa, Turkey*, 2005, Vol. 711, pp. 64–69.
- [9] S. Buyuk, O. U. Oregul, A. C. Basibuyuk, U. Tugcular, T. C. Sisman, and C. Tola, "Preliminary orbit design for Turkish regional navigation satellite system," in *2019 9th International Conference on Recent Advances in Space Technologies (RAST)*, 2019, pp. 279–284.
- [10] I. Oz, "Electrical orbit raising: Influence of thrusters in geostationary satellite deployment," in *ASES-2024-Kongreases*, 2024, pp:163–174.
- [11] E. Demircioglu, S. Gulgonul, A. F. Yagli, and H. Ertok, "Ground and on-board systems for GNSS activities

- over Ku-band communication satellites,” in *Ankara International Aerospace Conference*, 2015, pp. 10–12.
- [12] L. S. Lawal and C. R. Chatwin, “Essential parameters of space-borne oscillators that ensures performance of satellite-based augmentation system,” in *3rd IEEE International Conference on Adaptive Science and Technology (ICAST 2011)*, 2011, pp. 42–50.
- [13] I. Oz, “Minimizing satellite residence time in the GEO region through elevated eccentricity method,” *TUJE*, vol. 8, no. 3, pp. 416–426, 2024, doi: 10.31127/tuje.1395250.
- [14] E. Rubinov, C. Marshall, L. Ng, and A. R. Tengku, “Positioning performance of SBAS and PPP technology from the Australia and New Zealand SBAS test-bed,” in *Proceedings of the 15th South East Asian Survey Congress (SEASC2019)*, Darwin, Australia, 2019, pp. 15–18.
- [15] D. Gautam, C. Watson, A. Lucieer, and Z. Malenovský, “Error budget for geolocation of spectroradiometer point observations from an unmanned aircraft system,” *Sensors*, vol. 18, no. 10, pp. 3465–3474, 2018.
- [16] C. Ozarpa and I. Oz “Conjoint analysis of GPS based orbit determination among traditional methods,” *SAUCIS*, vol. 6, no. 3, pp. 189–197, 2023.
- [17] B. Konakoglu and A. Akar, “Elazig ve cevresindeki illerde meydana gelen tektonik hareketlerin TUSAGA-aktif istasyonlarinin konumlarına etkisinin statik deformasyon modeller kullanılarak incelenmesi” *Geomatik*, vol. 6, no. 2, pp. 165–178, 2020.
- [18] S. Yuan, Y. Teng, and H. Li, “Comparison of position dilution of precision (PDOP) at system and user level in multi-GNSS positioning,” in *2020 IEEE 3rd International Conference on Electronics and Communication Engineering (ICECE)*, 2020, pp. 47–50.
- [19] I. Oz, “GEO satellite orbit determination using spaceborn onboard receiver,” *Journal of Polytechnic*, vol. 27, no. 1, pp. 101–108, 2024.
- [20] O. Yildirim, “A comparative analysis of the virtual reference stations (VRS),” *Scientific Research and Essays*, vol. 6, no. 27, pp. 5726–5733, 2011.



# Optimized Performance Compact Wide-Band Microstrip Filter-Antenna for 4G Applications

Husain Ali<sup>\*1</sup>, Ugur Cem Hasar<sup>1</sup>

<sup>1</sup>Electrical and Electronics Engineering, Gaziantep University, Gaziantep, Türkiye

## Abstract

This article presents a performance-optimized compact filter-antenna based on a four-pole broadband planar structure. The design features a 4-cavity planar fourth-order bandpass filter connected to a patch antenna via a microstrip transmission line. Each of the four resonators comprises an E-shaped arm terminating in an open-loop squared ring. We demonstrate several enhancements to the antenna's performance, including re-dimensioning the L-shaped defected ground structure, and redesigning the patch antenna slots. Through re-simulation of the structure with varying sizes, we achieved superior results compared to the original design. The optimized antenna system is smaller and lighter, offering the significant advantage of easier integration into 4G devices.

**Keywords:** Band-pass, Compact, Filter-antenna, Microstrip, 4G

## 1 INTRODUCTION

Consumer mobile usage currently dominates 4G wireless resource consumption, driving an increasing demand for compact wireless transceivers [1–4]. Given their significant impact on wireless communication system performance, planar antennas and filters are regarded as crucial components in microwave systems [4–8]. The microstrip filter-antenna allows designers to characterize both filtering and radiation patterns simultaneously. This structure offers several advantages, including compact size and ease of manufacture, as it can be printed on a PCB, contributing to its widespread adoption as one of the most prevalent RF structures in recent years.

In this paper, we propose an improved version of a wide-band antenna operating in the 2.4 GHz ISM band, with a bandwidth of 1.22 GHz and a fractional bandwidth of 50%, as described in [9]. Significant improvements in filter-antenna performance were achieved by optimizing the dimensions of the L-shaped defected ground structure and redesigning the antenna slot to incorporate two U-shaped slots instead of the traditional slot used in the original design. Multiple dimensions of these U-shaped slots were re-simulated using CST software, resulting in a notable enhancement in performance.

## 2 THE FILTER ANTENNA DESIGN

The filter-antenna structure utilized in this study comprises a microstrip transmission line connected to a rectangular monopole patch antenna. The band-pass filter (BPF) is designed with four E-shaped arms, each terminating in an open-loop squared ring, and is directly integrated with the microstrip transmission line. The BPF's input port is connected to the microstrip line, while its output port interfaces directly with the monopole patch antenna, ensuring seamless signal transmission. Additionally, the structure features a partial ground plane with an etched L-shaped slot, which contributes to improved performance and compactness. This innovative design enhances the integration of filtering and radiating functions, making it highly suitable for advanced compact wireless transceivers.

The characteristic impedance of the microstrip line calculated using equation [10]:

$$Z_c = \frac{120\pi}{\sqrt{\epsilon_{eff} \left[ \frac{w}{h} + 1.393 + 0.667 \ln \left( \frac{w}{h} + 1.444 \right) \right]}} \quad (1)$$

The dimensions of the patch antenna can be calculated using the analytical expressions given in [8] by

$$L = \frac{c}{2f\sqrt{\epsilon_{eff}}} - 2\Delta L \quad (2)$$

$$\Delta L = 0.412h \frac{(\epsilon_{eff} + 0.3) \left(\frac{W}{h} + 0.262\right)}{(\epsilon_{eff} - 0.258) \left(\frac{W}{h} + 0.813\right)} \quad (3)$$

$$\Delta L = 0.412h \frac{(\epsilon_{eff} + 0.3) \left(\frac{W}{h} + 0.262\right)}{(\epsilon_{eff} - 0.258) \left(\frac{W}{h} + 0.813\right)} \quad (4)$$

Whereas the initial width is given by the following expression [11]

$$w = \frac{\lambda_0}{2} \left(\frac{\epsilon_r}{2}\right)^{-\frac{1}{2}} \quad (5)$$

The proposed optimized filter-antenna structure in comparison with the original structure is shown in Figure 1. The optimized structure has two U-shaped slots inside the monopole patch antenna.

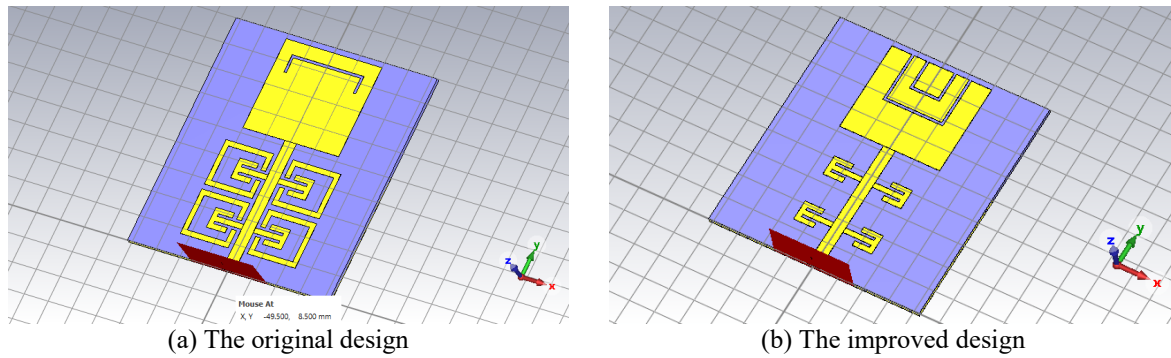


Figure 1. Comparison between two antennas structures

### 3 SIMULATION AND MEASUREMENT RESULTS

To compare the performance of two different structures in terms of reflection coefficient as a function of the frequencies, the exact same simulations conducted in the original paper have been re-introduced for both structures. Figure 2 shows comparison of reflection coefficient (S11) as a function of the frequencies for three different materials (RT5880, RO3003, and FR4) at fixed thickness  $h=0.81$  mm for both original and improved designs. The new optimized structure showed better performance in terms of reflection coefficient, where it reached  $-41$  dB in comparison with  $-24$  dB when using RT5880 material at  $h=0.81$  mm.

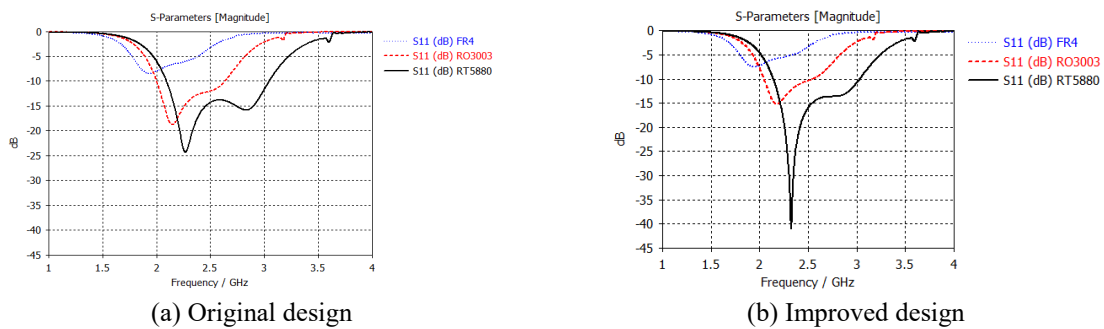


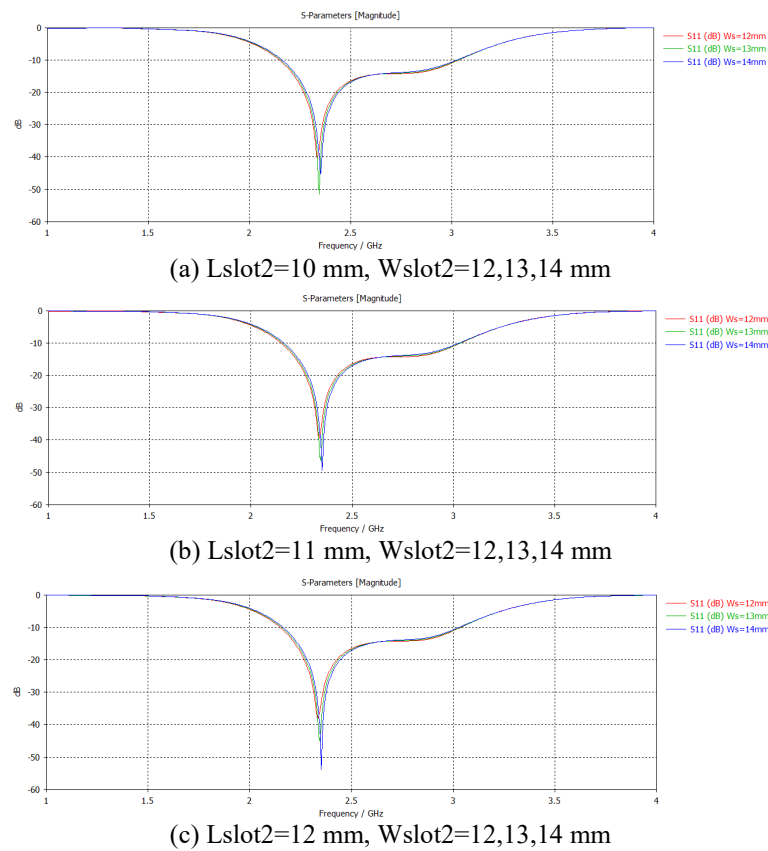
Figure 2. Simulated reflection coefficients (S11) for materials (RT5880, RO3003, and FR4) at fixed thickness  $h=0.81$  mm

FR4 is one of the most widely used substrate materials in the manufacture of printed circuits, consisting of fiberglass fabric embedded in epoxy resin. Typically, FR4 is suitable for designs operating at frequencies below 1 GHz, where its performance is generally acceptable. However, as the operating frequency increases beyond this range, the effects of passive elements become more pronounced and must be carefully considered during the design process. At frequencies above 3 GHz, it becomes essential to account for factors such as surface roughness, the skin effect, the proximity effect, and the dielectric substrate properties [12]. Designing within this higher frequency range necessitates materials with superior properties compared to FR4. Table 1 lists three materials selected to evaluate filter-antenna performance including the FR-4. The differences in the reflection coefficient (S11) resulting from the simulation of these materials are depicted in Figure 2. These simulations highlight the importance of material selection in achieving optimal performance for high-frequency applications.

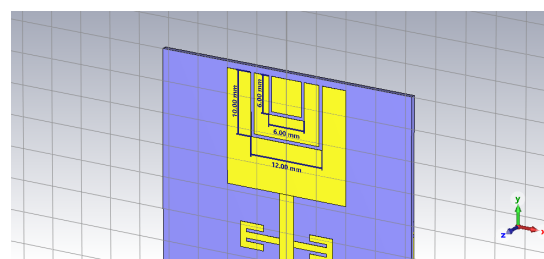
**Table 1.** The used materials and their properties

Material	Material Properties	
	Dielectric Constant ( $\epsilon_r$ )	Loss Tangent ( $\tan\delta$ )
RT5880	2.2	0.0009
RO3003	3	0.0013
FR4	4.3	0.018

As explained previously, one of the most important improvements in antenna performance was achieved by modifying the slot shape in the patch antenna body to become a double U-shaped slot. To reach the best reflection coefficient (S11) through simulation, a parameter sweep of the dimensions of the outer U-shaped slot was tested only, where three different values were selected for each the length and width of the slot without changing slot spacing, the Figure 3 shows the results of this simulation. The tested values are (Lslot2=10, 11, 12 mm, and Wslot2=12, 13, 14 mm). This simulation showed that the best configuration in terms of reflection coefficient (S11) was Lslot2=10 mm, Wslot2=13 mm, where S11 reached -55 dB.



**Figure 3.** Simulated reflection coefficient (S11) using RT5880 substrate at fixed thickness  $h=0.81$  mm with parameter sweep of outer slot dimensions



**Figure 4.** New U-shaped slots structure and dimensions

Defected ground structure (DGS) implemented on ground plane of the filter-antenna affects design's parameters such as effective capacitance and effective inductance [13]. The equivalent LC components cause a slow-wave impact which lead at the end to a smaller design [4]. Figure 5 shows the structure of DGS used in both designs. The results of parameter sweep of the DGS dimensions shown in Figure 6; where three different values were selected

for each t DGS length ( $L_{dg}$ ) and width ( $W_{dg}$ ). The tested values are ( $L_{dg}=4, 5.4, 6.8$  mm, and  $W_{dg}=5, 7.5, 10$  mm). This simulation resulted a slight improvement in reflection coefficient ( $S_{11}$ ), while a result that may be very useful noticed at the dimensions  $L_{dg} = 5.4$  mm and  $W_{dg}=5$  mm where  $S_{11}$  reached  $-55$  dB.

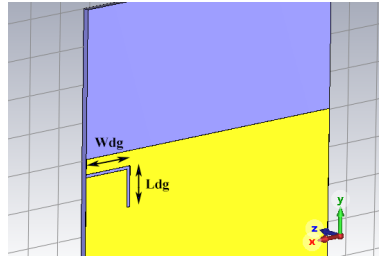
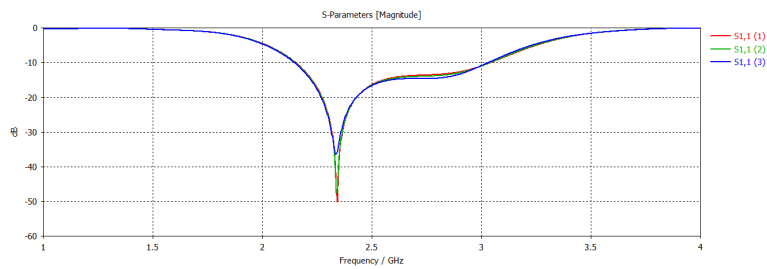
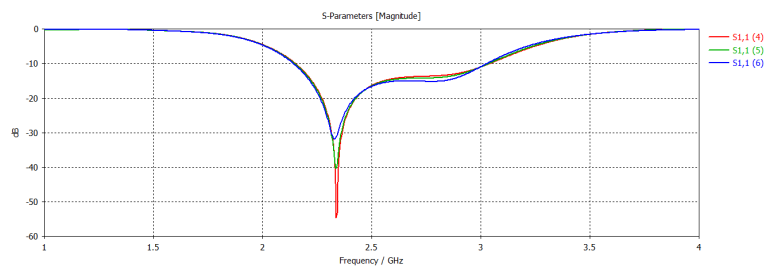


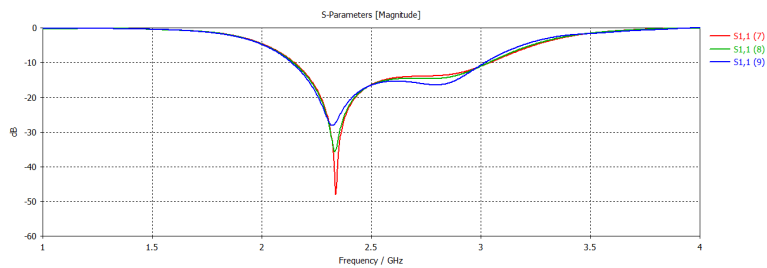
Figure 5. L-shaped slot DGS for both designs



(a)  $L_{dg}=4$  mm,  $W_{dg}=5, 7.5, 10$  mm



(b)  $L_{dg}=5.4$  mm,  $W_{dg}=5, 7.5, 10$  mm



(c)  $L_{dg}=6.8$  mm,  $W_{dg}=5, 7.5, 10$  mm

Figure 6. Simulated reflection coefficient ( $S_{11}$ ) using RT5880 substrate at fixed thickness  $h=0.81$  mm with parameter sweep of DGS dimensions

Other performance analysis of the modified design was implemented; Figure 7 shows a comparison of the filter-antenna efficiency for the same improved design with parameter sweep of both outer slot dimensions and DGS dimensions, and it was found that there is no significant change in the efficiency. Also, Figure 8 shows VSWR for the same sweep, which also did not have a noticeable difference compared to the original antenna.

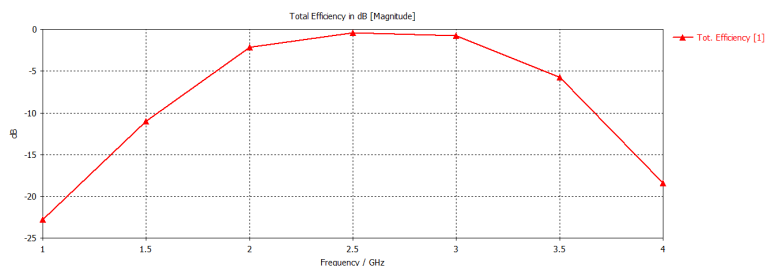


Figure 7. Simulated total efficiency using RT5880 substrate at fixed thickness  $h=0.81$  mm

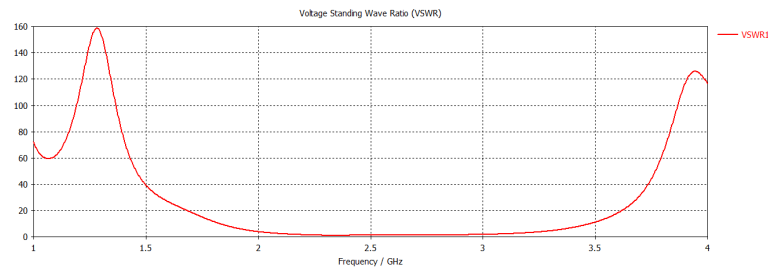


Figure 8. Simulated VSWR using RT5880 substrate at fixed thickness  $h=0.81$  mm

## 4 CONCLUSION

Modifications to the filter-antenna design structure are presented to improve its performance. The shape of the slot in the monopole patch antenna structure was modified to be dual U-shaped slots. In addition, the dimensions of one of the new slots were tested using the parameter sweep method in the simulation, and better results were reached - 55 dB compared to -25 dB in the original design. The same methodology was used to select the dimensions of the DGS, which resulted dual beam at the same reflection coefficient level. There was no noticeable change in antenna efficiency, nor in VSWR.

## References

- [1] O. Parchin, N. Al-Yasir, and R. Abd-Alhameed, *Microwave/RF Components for 5G Front-End Systems*, Telangana, India: Avid Science, 2019.
- [2] H. Liu, "High-temperature superconducting bandpass filter using asymmetric stepped-impedance resonators with wide-stopband performance," *IEEE Transactions on Applied Superconductivity*, vol. 25, no. 5, pp. 1–6, Oct. 2015.
- [3] A. Hussaini, "Green flexible RF for 5G," in *Fundamentals of 5G Mobile Networks*, J. Rodriguez, Ed. Hoboken, NJ, USA: John Wiley and Sons, 2015.
- [4] P. K. Malik, S. Padmanaban, and J. Nielsen, *Microstrip Antenna Design for Wireless Applications*, CRC Press, 2021.
- [5] S. K. Koul and K. G. S., *Antenna Architectures for Future Wireless Devices*, Springer, 2022.
- [6] Z. Hou, C. Liu, B. Zhang, R. Song, Z. Wu, J. Zhang, and D. He, "Dual-/tri-wideband bandpass filter with high selectivity and adjustable passband for 5G mid-band mobile communications," *Electronics*, vol. 9, art. no. 205, 2020.
- [7] Y. I. A. Al-Yasir, N. Ojaroudi Parchin, A. M. Abdulkhaleq, M. S. Bakr, and R. A. Abd-Alhameed, "A survey of differential-fed microstrip bandpass filters: Recent techniques and challenges," *Sensors*, vol. 20, art. no. 2356, 2020.
- [8] Y. I. A. Al-Yasir, N. O. Parchin, A. Abdulkhaleq, R. Abd-Alhameed, and J. Noras, "Recent Progress in the design of 4G/5G reconfigurable filters," *Electronics*, vol. 8, art. no. 114, 2019.
- [9] Y. I. A. Al-Yasir, M. K. Alkhafaji, H. A. Alhamadani, N. Ojaroudi Parchin, I. Elfergani, A. L. Saleh, J. Rodriguez, and R. A. Abd-Alhameed, "A new and compact wide-band microstrip filter-antenna design for 2.4 GHz ISM band and 4G applications," *Electronics*, vol. 9, art. no. 1084, 2020.
- [10] K.-L. Wong, Y.-C. Chen, and W.-Y. Li, "Four LTE low-band smart-phone antennas and their MIMO performance with user's hand presence," *Microw. Opt. Technol. Lett.*, vol. 58, no. 9, pp. 2046–2052, Sep. 2016.
- [11] J. Choi, W. Hwang, C. You, B. Jung, and W. Hong, "Four-element reconfigurable coupled loop MIMO antenna featuring LTE full-band operation for metallic-rimmed smartphone," *IEEE Trans. Antennas Propag.*, vol. 67, no. 1, pp. 99–107, Jan. 2019.
- [12] D. Leys, "Best materials for 3–6 GHz design," *Print. Circuit Des. Manuf.*, pp. 34–39, 2004.
- [13] G. Breed, "An introduction to defected ground structures in microstrip circuits," *High Frequency Electronics*, vol. 7, pp. 50–54, 2008.



## Simplified Reference-Plane-Invariant Method for Permittivity Extraction of Low-Loss Dielectrics via One-Port Waveguide Measurements

Ugur Cem Hasar<sup>\*1</sup>, Husain Ali<sup>1</sup>

<sup>1</sup>Electrical and Electronics Engineering, Gaziantep University, Gaziantep, Türkiye

### Abstract

This paper presents a microwave method for extracting the relative complex permittivity ( $\epsilon_r$ ) of low-loss dielectric samples. This method is distinguished by its simplicity, non-iterative approach, and reference-plane-invariant (RPI) characteristics. It is specifically designed for one-port waveguide measurements using a short-circuit termination. By leveraging reflection-only measurements with a short-circuit termination, this technique effectively eliminates Fabry-Pérot resonances. The proposed method was validated through permittivity measurements of polyvinyl chloride (PVC) and polypropylene (PP) within the X-band frequency range (8.2-12.4 GHz). Various scenarios were examined, including inaccuracies in sample location and thickness. Additionally, a repeatability analysis was conducted to compare the performance of this method with other existing techniques in the literature.

**Keywords:** Material characterization, Non-iterative, One-port measurement, Permittivity, Short-termination

## 1 INTRODUCTION

Electromagnetic properties are intrinsic to materials, serving as a critical means for characterizing non-electromagnetic properties through established correlations. Such correlations are pivotal in a variety of research areas, including cure-state and constituent analysis [1], disbond and corrosion detection [2], adulteration checking and quantification [3, 4], and moisture analysis [5, 6]. Consequently, accurate electromagnetic measurements are a vital and dynamic field of research, particularly for these application areas. Numerous techniques have been proposed in the literature, tailored to different criteria such as sample nature (e.g., soil, liquid, powder, and granular), frequency band, accuracy, and simplicity. These techniques are broadly categorized into resonant and non-resonant methods based on their working principles [7]. This paper focuses on non-resonant methods, given their capability to provide broadband information about electromagnetic properties, making them particularly suitable for comprehensive material characterization.

Among the various non-resonant methods documented in the literature, such as free space, planar, coaxial, waveguide, and open-ended techniques [8–22], our research focuses on waveguide non-resonant methods. These methods are favored due to their high accuracy (owing to wave guiding capability), greater repeatability (non-sex flanges), broader applicability (suitable for low-loss to high-loss solid, liquid, granular, and powder materials), and relative simplicity (requiring less mathematical analysis). Waveguide non-resonant methods utilize reflection and/or transmission responses of a material under test when subjected to an applied electromagnetic field [11–28]. For low-loss or medium-loss materials, both reflection and transmission responses can be used to investigate electromagnetic properties. However, this study specifically concentrates on reflection-only responses [23–28], as they can be implemented using one-port measurements with relatively inexpensive vector network analyzers (VNAs).

Reflection-only non-resonant methods can be categorized in several ways, including their requirements for reference-plane information, whether they are iterative or non-iterative, the type of termination needed, and the implementation requirements. These categorization criteria help in understanding the distinct characteristics and suitability of each method for various applications.

Reflection-only non-resonant methods can be categorized into two primary groups: a) reference-plane-dependent methods (RPD) [23–25] and b) reference-plane-invariant methods (RPI) [26–28]. Specially designed sample holders with consistent sample lengths can mitigate the need for reference-plane information. However, this approach demands the fabrication of multiple sample holders, which is impractical for implementation. Moreover, fabricated samples often do not fit into their holders with substantial lengths. In such cases, accurate retrieval of



electromagnetic properties necessitates precise information about the reference-plane position of the sample. RPI methods can be applied for precise retrieval of these properties [26–28].

Additionally, reflection-only non-resonant methods can be divided into two other groups: a) iterative methods requiring numerical analysis [23, 24, 26, 28] and b) non-iterative methods that do not require numerical analysis [25]. The advantage of non-iterative methods is that they do not require prior information about the sample’s electromagnetic properties, thus avoiding the influence of any incorrect initial guesses. However, all non-iterative reflection-only methods in the studies [25] are RPD methods.

Furthermore, these methods can be categorized based on the required termination: a) methods requiring only short termination [23, 24] and b) methods necessitating match and short terminations or an electronic calibration unit [25–28]. The latter methods require a well-defined match termination, which is challenging to implement across the entire frequency band, or an expensive electronic calibration unit.

Finally, reflection-only non-resonant methods can be classified by their implementation requirements. The methods in studies [23–26] are relatively simpler to apply, requiring easier analysis, whereas methods in studies [27, 28] involve complex expressions or two-tier calibration. Table 1 presents a brief comparison of reflection-only non-resonant methods in the literature for extracting the electromagnetic properties of materials, considering factors such as sample type, number of samples, dispersive nature of the sample, loss character, RPI property, the approach followed, the termination applied, and the implementation requirements.

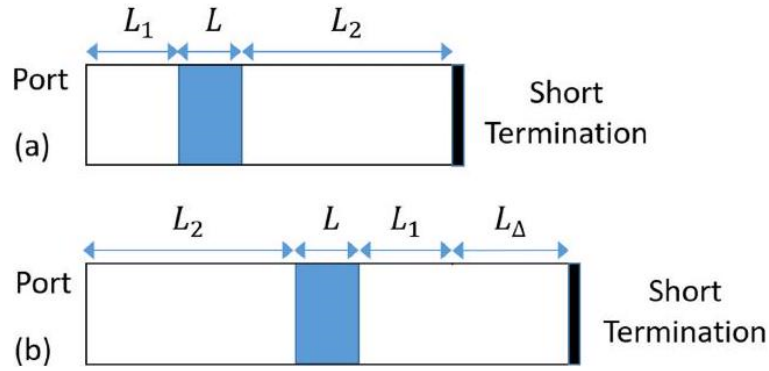
In this study, we focus on non-iterative, relatively simpler-to-apply, reflection-only non-resonant methods that do not require reference-plane information (RPI) and utilize an easier type of termination (short termination). Upon examining the existing reflection-only non-resonant methods in the literature [23–28] (see Table I), we observe that none of them simultaneously satisfy all these criteria. To address this gap, we propose a novel reflection-only, non-iterative, and simple non-resonant method based on RPI expressions for samples terminated by a short termination.

**Table 1.** Comparison of our work with different retrieval reflection-only (one-port) non-resonant techniques

Method	Metric							
	Sample Type	Number of Samples	Dispersive	Loss Character	RPI	Approach	Termination	Requirement
[23]	Solid	One	Yes	Low/Medium	No	Iterative	Short Only	Simpler
[24]	Solid	Two	Yes	Low/Medium	No	Iterative	Short Only	Simpler
[25]	Solid	One	Yes	Low/Medium	No	Non-iterative	Match/Short	Simpler
[26]	Solid	One	Yes	Low/Medium	Yes	Iterative	Match/Short	Simpler
[27]	Liquid	One	Yes	High	Yes	Iterative	Match/Short	Difficult
[28]	Solid	One	Yes	Low/Medium	Yes	Partially Non-iterative	Match/Short	Difficult
This Work	Solid	One	Yes	Low/Medium	Yes	Non-Iterative	Short Only	Simpler

## 2 THE METHOD

Figs. 1(a) and 1(b) presents schematic views of two waveguide measurement configurations in implementation of our method. A dielectric sample with length  $L$  arbitrarily positioned ( $L_1 \neq L_2$ ) into a waveguide measurement cell with length  $L_{\text{cell}} = L_1 + L + L_2$  and ended by a fixed short termination (direct configuration). Here,  $L_1$  and  $L_2$  are the distances from the front and rear terminals of the guide to the sample surfaces. Besides, the configuration in Fig. 1(b) illustrates the configuration of the inverted measurement cell of same sample ended by a variable short termination with an offset of  $L_{\Delta}$  (reverse configuration). It is assumed that the waveguide measurement cell is operated by its dominant mode  $TE_{10}$  [22, 25, 26, 28].



**Figure 1.** Schematic views of measurement configurations of a sample with length  $L$  asymmetrically ( $L_1 \neq L_2$ ) positioned into a waveguide measurement cell with length  $L_{\text{cell}} = L_1 + L + L_2$ : (a) direct configuration with fixed short termination and (b) reverse configuration with variable short termination with an offset  $L_{\Delta}$

## 2.1 Scattering S-Parameters

Reflection S-parameters of the direct and reverse configurations in Figures 1(a) and 1(b) can be obtained for the time reference in the form  $\exp(+j\omega t)$  as [25, 26, 28]

$$S_{11s}^d = R_1^2 \left[ \frac{\Gamma(1-P^2) + R_2^2(\Gamma^2 - P^2)}{(1-\Gamma^2 P^2) + R_2^2 \Gamma(1-P^2)} \right] \quad (1)$$

$$S_{11s}^r = R_2^2 \left[ \frac{\Gamma(1-P^2) + R_1^2 R_{\Delta}^2 (\Gamma^2 - P^2)}{(1-\Gamma^2 P^2) + R_1^2 R_{\Delta}^2 \Gamma(1-P^2)} \right] \quad (2)$$

$$\Gamma = \frac{\gamma_0 - \gamma}{\gamma_0 + \gamma} \quad P = e^{-\gamma L} \quad \gamma = jk_0 \sqrt{\epsilon_r - (f_c/f)^2} \quad (3)$$

$$\gamma_0 = jk_0 \sqrt{1 - (f_c/f)^2} \quad R_u = e^{-\gamma_0 L_u} \quad u = 1, 2, \text{ or } \Delta. \quad (4)$$

Where the subscripts ‘s’ and ‘m’ denote the short and match terminations while the superscripts ‘d’ and ‘r’ designate the direct and reverse configurations;  $P$  and  $\Gamma$  are, respectively, the propagation factor of the sample and the reflection coefficient at the sample surface;  $\gamma_0$  and  $\gamma$  are the propagation constants of air and sample regions, respectively;  $k_0$  is the free-space wavenumber;  $R_1, R_2$ , and  $R_{\Delta}$  are, respectively, the transformation factors corresponding to  $L_1, L_2$ , and  $L_{\Delta}$ ;  $f_c$  and  $f$  are the cutoff and operating frequencies, respectively; and  $\epsilon_r = \epsilon_r' - j\epsilon_r''$  where  $\epsilon_r' \geq 1$  and  $\epsilon_r'' \geq 0$ .

## 2.2 Elimination of Reference-Plane Dependence

Our purpose in this study is to determine  $\epsilon_r$  from RPI expressions, e.g., without knowing  $L_1$  and  $L_2$ . Magnitudes of  $S_{11s}^d$  and  $S_{11s}^r$  can be written as

$$|S_{11s}^d| = \left| \frac{\Gamma(1-P^2) + R_2^2(\Gamma^2 - P^2)}{(1-\Gamma^2 P^2) + R_2^2 \Gamma(1-P^2)} \right| \quad (5)$$

$$|S_{11s}^r| = \left| \frac{\Gamma(1-P^2) + R_1^2 R_{\Delta}^2 (\Gamma^2 - P^2)}{(1-\Gamma^2 P^2) + R_1^2 R_{\Delta}^2 \Gamma(1-P^2)} \right| \quad (6)$$

It is seen from (5) and (6) that if  $R_2^2 = R_1^2 R_{\Delta}^2$ , then  $|S_{11s}^d| = |S_{11s}^r|$ . This means for  $L_2 > L_1$  that if the offset of the variable short can be properly arranged to  $L_{\Delta} = L_2 - L_1$  (validated by measurements), then it is possible to determine  $L_1$  and  $L_2$  by the following simple expressions

$$L_1 = \frac{1}{2}(L_{\text{cell}} - L_{\Delta} - L), \quad L_2 = L_1 + L_{\Delta} \quad (7)$$

## 2.3 Non-Iterative and Simpler Extraction of Permittivity

Assuming that variable short is at (or reset to) its original position ( $L_{\Delta} = 0$ ), next it is possible to determine  $P^2$  from (1) and (2) for known  $R_1$  and  $R_2$  evaluated after applying the before mentioned procedure as

$$P^2 = \frac{R_2^2 \Gamma^2 + \left(1 - \frac{R_2^2 S_{11s}^d}{R_1^2}\right) \Gamma - \frac{S_{11s}^d}{R_1^2}}{(\Gamma + R_2^2) \left(1 - \frac{S_{11s}^d}{R_1^2} \Gamma\right)} = \frac{R_1^2 \Gamma^2 + \left(1 - \frac{R_2^2 S_{11s}^r}{R_2^2}\right) \Gamma - \frac{S_{11s}^r}{R_2^2}}{(\Gamma + R_1^2) \left(1 - \frac{S_{11s}^r}{R_2^2} \Gamma\right)} \quad (8)$$

Then, from the two expressions of  $P^2$  in (8), one can derive

$$(\Gamma^2 - 1)[\Lambda_1 \Gamma^2 + \Lambda_2 \Gamma + \Lambda_1] = 0 \quad (9)$$

Where

$$\Lambda_1 = S_{11s}^d - S_{11s}^r \quad (10)$$

$$\Lambda_2 = (R_2^2 - R_1^2) \left(1 + \frac{S_{11s}^d S_{11s}^r}{R_1^2 R_2^2}\right) + (1 + R_1^2 R_2^2) \left(\frac{S_{11s}^d}{R_1^2} - \frac{S_{11s}^r}{R_2^2}\right) \quad (11)$$

Because for a passive sample,  $|\Gamma| \neq 1$ , then,  $\Gamma$  can be uniquely determined from (9) as

$$\Gamma = -\frac{\Lambda_2}{2\Lambda_1} \mp \sqrt{\left(\frac{\Lambda_2}{2\Lambda_1}\right)^2 - 1} \quad (12)$$

The correct sign in (12) can be ascertained by enforcing the passivity criterion; that is,  $|\Gamma| \leq 1.0$  where  $|\star|$  denotes the magnitude of ' $\star$ '.

Finally,  $\varepsilon_r$  of a dielectric material can be computed from

$$\varepsilon_r = \left(\frac{1-\Gamma}{1+\Gamma}\right)^2 (1 - (f_c/f)^2) + (f_c/f)^2 \quad (13)$$

Or

$$\varepsilon_r = \left(\frac{j \ln(P^2) \mp 2\pi m_b}{2k_0 L}\right)^2 + (f_c/f)^2 \quad (14)$$

where  $m_b$  denotes the branch index value ( $m_b = 0, 1, 2, \dots$ ). Accurate  $m_b$  value can be evaluated by comparing similar  $\varepsilon_r$  values determined from (13) and (14) for some  $m_b$  values [28].

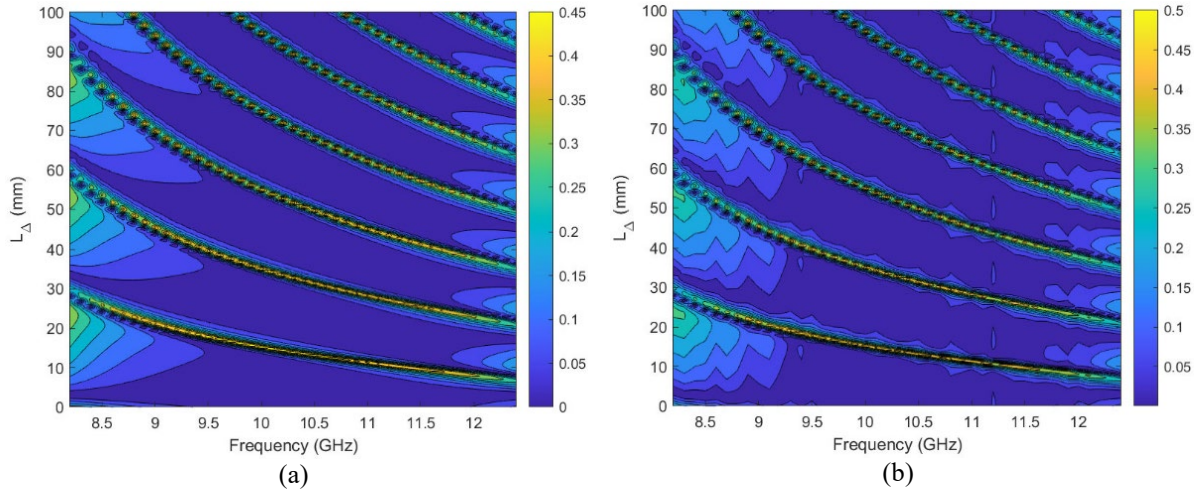
### 3 VALIDATION

We applied a numerical analysis to examine whether  $|F_{\text{obj}}(L_\Delta)|$  results in any null value at different frequencies over the entire band. Here,

$$F_{\text{obj}}(L_\Delta) = |S_{11s}^d| - |S_{11s}^r|(L_\Delta). \quad (15)$$

This analysis will help one to get insight into measurements while finding  $L_\Delta$  value for which  $R_1$  and  $R_2$  can first be calculated and  $\varepsilon_r$  can then be computed non-iteratively and uniquely.

For this goal, we considered a sample with  $\varepsilon_r = 5.2 - j0.3$  and  $L = 10\text{mm}$ , and the length  $L_2 = 8.0\text{mm}$ . Fig. 2(a) illustrates  $|F_{\text{obj}}(L_\Delta)|$  over a plane of  $L_\Delta - f$  over entire frequency band (8.2-12.4 GHz). It is observed from Fig. 2(a) that there is only one  $L_\Delta$  value (10 mm) which results in null value for  $|F_{\text{obj}}(L_\Delta)|$  over entire frequency band. This means that if matching between  $|S_{11s}^d|$  and  $|S_{11s}^r|$  is being examined over entire frequency band in implementation of our method, there will be only one  $L_\Delta$  value. In order to examine the effect of noise on the performance of our proposed method, we applied a Gaussian white noise to S-parameters. For example, Fig. 2(b) illustrates  $|F_{\text{obj}}(L_\Delta)|$  over plane of  $L_\Delta - f$  for the same sample and  $L_2$  value when additive Gaussian noise with 20 dB SNR value is added to  $S_{11s}^d$  only. It is seen from Fig. 2(b) that it is still possible to determine correct  $L_\Delta$  value (10 mm) when noise was added.



**Figure 2.** Dependence of  $|F_{\text{obj}}(L_{\Delta})|$  over plane of  $L_{\Delta} - f$  for a sample with  $\epsilon_r = 5.2 - j0.3$  and  $L = 10\text{mm}$ , and the length  $L_2 = 8.0\text{ mm}$  under two different cases: (a) without any noise and (b) when additive Gaussian noise with 20 dB SNR value is added to  $S_{11s}^d$  only [The guide is an X-band waveguide ( $f_c = 6.557\text{ GHz}$  and  $f = 8.2:12.4\text{ GHz}$ )]

## 4 CONCLUSION

A simpler and non-iterative retrieval method has been developed for determining the relative complex permittivity ( $\epsilon_r$ ) of low-loss dielectric samples using RPI expressions. This method, which relies on reflection-only S-parameter waveguide measurements with short-circuit termination, is unaffected by Fabry-Pérot resonances. The expressions for non-iterative extraction of  $\epsilon_r$  were derived. These expressions were validated by a numerical analysis when an additive Gaussian white noise is present. Although this method is simple, RPI, non-iterative, and free from the effects of Fabry-Pérot resonances, it requires accurate knowledge of the sample thickness for optimal results.

## References

- [1] K. J. Bois, A. D. Benally, P. S. Nowak, and R. Zoughi, "Cure-state monitoring and water-to-cement ratio determination of fresh Portland cement-based materials using near field microwave techniques," *IEEE Trans. Instrum. Meas.*, vol. 47, no. 3, pp. 628–637, Jun. 1998.
- [2] M. T. Ghasr, S. Kharkovsky, R. Zoughi, and R. Austin, "Comparison of near-field millimeter-wave probes for detecting corrosion precursor pitting under paint," *IEEE Trans. Instrum. Meas.*, vol. 54, no. 4, pp. 1497–1504, Aug. 2005.
- [3] W. Guo, X. Zhu, Y. Liu, and H. Zhuang, "Sugar and water contents of honey with dielectric property sensing," *J. Food Eng.*, vol. 97, no. 2, pp. 275–281, Mar. 2010.
- [4] H. Hasar, U. C. Hasar, Y. Kaya, H. Ozturk, M. Izginli, T. Oztas, N. Aslan, M. Ertugrul, J. J. Barroso, and O. M. Ramahi, "Honey-water content analysis by mixing models using a self-calibrating microwave method," *IEEE Trans. Microw. Theory Techn.*, vol. 71, no. 2, pp. 691–697, Feb. 2023.
- [5] A. Lewandowski, A. Szyplowska, A. Wilczek, M. Kafarski, J. Szerement, and W. Skierucha, "One-port vector network analyzer characterization of soil dielectric spectrum," *IEEE Trans. Geosci. Remote Sens.*, vol. 57, no. 6, pp. 3661–3676, Jun. 2019.
- [6] H. Hasar, U. C. Hasar, H. Ozturk, M. Izginli, N. Aslan, T. Oztas, M. Ertugrul, M. Karayilan, and O. M. Ramahi, "Permittivity extraction of soil samples using coaxial-line measurements by a simple calibration," *IEEE Trans. Geosci. Rem. Sens.*, vol. 61, art no. 5300108, 2023.
- [7] L. F. Chen, C. K. Ong, C. P. Neo, V. V. Varadan, and V. K. Varadan, *Microwave Electronics: Measurement and Materials Characterization*, West Sussex, England: Wiley, 2004.
- [8] X. Bao, G. Crupi, I. Ocket, J. Bao, F. Ceysens, M. Kraft, B. Nauwelaers, and D. Schreurs, "Numerical modeling of two microwave sensors for biomedical applications," *Int. J. Numer. Model. El.*, vol. 34, no. 1, Jan./Feb. 2021, Art. No. e2810.
- [9] C. Yang, K. Ma, and J. -G. Ma, "A noniterative and efficient technique to extract complex permittivity of low-loss dielectric materials at terahertz frequencies," *IEEE Antennas Wireless Propag. Lett.*, vol. 18, no. 10, pp. 1971–1975, Oct. 2019.

- [10] Z. Li, A. Haigh, P. Wang, C. Soutis, and A. Gibson, "Dielectric spectroscopy of Baijiu over 2-20GHz using an open-ended coaxial probe," *J. Food Sci.*, vol. 86, no. 6, pp. 2513–2524, Apr. 2021.
- [11] A. M. Nicolson and G. Ross, "Measurement of the intrinsic properties of materials by time-domain techniques," *IEEE Trans. Instrum. Meas.*, vol. 19, no. 4, pp. 377–382, Nov. 1970.
- [12] W. B. Weir, "Automatic measurement of complex dielectric constant and permeability at microwave frequencies," *Proc. IEEE*, vol. 62, no. 1, pp. 33–36, Jan. 1974
- [13] J. Baker-Jarvis, R. G. Geyer, and P. D. Domich, "A nonlinear leastsquares solution with causality constraints applied to transmission line permittivity and permeability determination," *IEEE Trans. Instrum. Meas.*, vol. 41, no. 5, pp. 646–652, Oct. 1992.
- [14] A. -H. Boughriet, C. Legrand, and A. Chapoton, "Noniterative stable transmission/reflection method for low-loss material complex permittivity determination," *IEEE Trans. Microw. Theory Techn.*, vol. 45, no. 1, pp. 52–57, Jan. 1997.
- [15] K. J. Bois, L. F. Handjojo, A. D. Benally, K. Mubarak, and R. Zoughi, "Dielectric plug loaded two-port transmission line measurement technique for dielectric property characterization of granular and liquid materials," *IEEE Trans. Instrum. Meas.*, vol. 48, no. 6, pp. 1141–1148 Dec. 1999.
- [16] T. C. Williams, M. A. Stuchly, and P. Saville, "Modified transmissionreflection method for measuring constitutive parameters of thin flexible high-loss materials," *IEEE Trans. Microw. Theory Techn.*, vol. 51, no. 5, pp. 1560–1566, May 2003.
- [17] U. C. Hasar, "Two novel amplitude-only methods for complex permittivity determination of medium- and low-loss materials," *Meas. Sci. Technol.*, vol. 19, no. 5, Apr. 2008, Art. no. 055706
- [18] K. Chalapat, K. Sarvala, J. Li, and G. S. Paraoanu, "Wideband referenceplane invariant method for measuring electromagnetic parameters of materials," *IEEE Trans. Microw. Theory Techn.*, vol. 57, no. 9, pp. 2257–2267, Sep. 2009.
- [19] U. C. Hasar and C. Westgate, "A broadband and stable method for unique complex permittivity determination of low-loss materials," *IEEE Trans. Microw. Theory Techn.*, vol. 57, no. 2, pp. 471–477, Feb. 2009
- [20] C. Wu, Y. Liu, S. Lu, S. Gruszczynski, and Y. Yashchyshyn, "Convenient waveguide technique for determining permittivity and permeability of materials," *IEEE Trans. Microw. Theory Techn.*, vol. 68, no. 11, pp. 4905–4912, Nov. 2020.
- [21] D. Munalli, M. T. A. Qaseer, and R. Zoughi, "Modified waveguidebased method for microwave characterization of high-loss materials," *IEEE Trans. Instrum. Meas.*, vol. 71, art no. 6002310, 2022.
- [22] A. K. Sharma and S. K. Dubey, "Dielectric characterization for solid with an improved NRW procedure and uncertainty estimation," *IEEE Trans. Instrum. Meas.*, vol. 72, art no. 1009411, 2023.
- [23] S. Roberts and A. V. Hippel, "A new method for measuring dielectric constant and loss in the range of centimeter waves," *J. Appl. Phys.*, vol. 17, no. 7, pp. 610–616, 1946.
- [24] U. C. Hasar, J. J. Barroso, Y. Kaya, M. Ertugrul, M. Bute, and J. M. Catala-Civera, "Two-step numerical procedure for complex permittivity retrieval of dielectric materials from reflection measurements," *Appl. Phys. A*, vol. 116, pp. 1701–1710, 2014.
- [25] C. Yang, H. Huang, and M. Peng, "Non-iterative method for extracting complex permittivity and thickness of materials from reflection-only measurements," *IEEE Trans. Instrum. Meas.*, vol. 71, art. no. 6002908, May 2022.
- [26] C. Yang, "A position-independent reflection-only method for complex permittivity and permeability determination with one sample," *Frequenz*, vol. 74, no. 3–4, pp. 163–167, Mar. 2020.
- [27] U. C. Hasar, C. R. Westgate, and M. Ertugrul, "Noniterative permittivity extraction of lossy liquid materials from reflection asymmetric amplitude-only microwave measurements," *IEEE Microw. Wireless Compon. Lett.*, vol. 19, no. 6, pp. 419–421, Jun. 2009.
- [28] U. C. Hasar, H. Ozturk, and O. M. Ramahi, "Noniterative reference-plane-invariant material parameter retrieval method for low-loss solid samples using one-port waveguide measurements," *IEEE Trans. Microw. Theory Techn.*, vol. 72, no. 2, pp. 1098–1106, Feb. 2024.



## A Theoretical Comparative Study of the 1,3-Dipolar Cycloaddition Reaction of Some Alkenes with Nitron

Boulanouar Messaoudi<sup>\*1,2</sup>

<sup>1</sup>Higher School of Applied Sciences of Tlemcen, ESSA-Tlemcen, BP 165 RP Bel Horizon, Tlemcen 13000, Algeria

<sup>2</sup>Toxicomed laboratory, University of Abou Bekr Belkaid, Tlemcen, 13000, Algeria

---

### Abstract

Heterocyclic reactions chemistry is one of the most important domains nowadays because of its capability to give rise to heterocyclic compounds. This latter are present in natural as well as pharmaceutical products. One of the common used routes to form heterocyclic products is the reaction of [3+2] cycloaddition commonly known as 1,3-dipolar reaction. This type of reactions has been widely studied over decades by both experimental and theoretical chemists in a very large scale. The main interest for theoreticians dealing with these reactions was to explain many observed aspects such as; regioselectivity, stereoselectivity, type of the mechanism, etc. In this contribution, a theoretical investigation of the 1,3-dipolar reaction of a nitron with different alkenes has been done at B3LYP/6-31G\* level of theory. The exploration and the investigation of the experimentally observed regioselectivity has been rationalized using Parr function. Both gas and solution (solvent) phases have been taken into account in order to probe the reaction mechanisms of the studied reactions. The obtained theoretical results based on the energetic profiles show that these reactions follow a one step concerted mechanism. The solvent effect has been studied and analyzed and found to be of importance and impact the geometries and energetics of transition states and products.

**Keywords:** 1,3-dipolar reaction, Parr function, Mechanism, B3LYP

---



---

## A Kinetic Mechanism Study of the Reaction of Triplet Oxygen $O(^3P)$ with the But-3-Enal Aldehyde

Boulanouar Messaoudi<sup>\*1,2</sup>

<sup>1</sup>Higher School of Applied Sciences of Tlemcen, ESSA-Tlemcen, BP 165 RP Bel Horizon, Tlemcen 13000, Algeria

<sup>2</sup>Toxicomed laboratory, University of Abou Bekr Belkaid, Tlemcen, 13000, Algeria

---

### Abstract

In the atmosphere, many reactions occur and take place. These reactions have a crucial impact on our planet and different phenomena dealing with the environment such as air quality. Aldehydes are organic compounds with a significant importance used widely in industry.

They are Volatile Organic Compounds (VOCs) usually released to the atmosphere from a variety of anthropogenic sources. They can also result from the incomplete combustion of hydrocarbons and other organic material such as fuel burning. Moreover, their biogenic source is directly related to photochemical reactions of the flora (plants, trees, etc). Chemical degradation of the aldehyde compounds in the atmosphere leads to a variety of secondary pollutants. Atomic oxygen  $O(^3P)$ , among other active species, plays a very important role in the combustion process of unsaturated hydrocarbons. Unsaturated aldehydes are aldehydes with an unsaturated C-C bond (is this case double bond), so they are characterized with the presence of two functional groups. Nowadays, theoretical approaches and computational modeling are used in order to well investigate and comprehend the reaction channels and understand its mechanisms. In this scientific contribution, the reaction of but-3-enal with the triplet oxygen atom has been studied using different theories such as; Møller-Plesset MP2, G3, and CBS-QB3 to probe the complex and multichannel potential energy surface. Two scenarios of mechanism are possible; the hydrogen abstraction and the O-addition. This latter is the dominant channel.

**Keywords:** *Butenal, MP2, CBS methods, Multichannel mechanism,  $O(^3P)$*

---



---

## Effect of $\text{Si}^{4+}$ and $\text{Ga}^{3+}$ Co-Doping on Structure and Ionic Conductivity of $\text{BiSiGaVO}_x$ system

Abdelmajid Agnaou<sup>\*1</sup>, Wafaa Mhaira<sup>1</sup>, Rachida Essalim<sup>1</sup>, Fabrice Mauvy<sup>2</sup>, Maati Alga<sup>1</sup>,  
Mohamed Zamama<sup>1</sup>, Abdelaziz Ammar<sup>1</sup>

<sup>1</sup>Laboratory of Materials Sciences and Processes Optimization, Faculty of Sciences Semlalia, Cadi Ayyad University, B.P. 2390, Marrakech, Morocco

<sup>2</sup>CNRS, University of Bordeaux, UMR 5026, 87, 33608, Pessac, France

---

### Abstract

In the present work, the Si and Ga co-doped the  $\text{Bi}_4\text{V}_2\text{O}_{11}$  compound, i.e., the  $\text{Bi}_4\text{V}_{2-x}\text{Ga}_{x/2}\text{Si}_{x/2}\text{O}_{11-3x/4}$  system ( $0.1 \leq x \leq 0.9$ ) was studied. The structural study of the  $\text{Bi}_4\text{V}_{2-x}\text{Ga}_{x/2}\text{Si}_{x/2}\text{O}_{11-3x/4}$  solid solution by X-ray diffraction (XRD) revealed that evidence that: stabilization of the  $\alpha$  phase for  $x \leq 0.1$ , stabilization of the  $\beta$  phase for  $0.2 \leq x < 0.4$ , stabilization of the  $\gamma$  phase for  $0.4 \leq x \leq 0.8$ , and the limit of the  $\text{Bi}_4\text{V}_{2-x}\text{Ga}_{x/2}\text{Si}_{x/2}\text{O}_{11-3x/4}$  solid solution is found at  $x \approx 0.9$ . On the one hand, we observed the transition from phase  $\alpha$  to phase  $\beta$  and then to phase  $\gamma$  for increasing substitution rate  $x$ . This was confirmed by the variation of the parameters and volume of the mesh showing the two transitions as a function of  $x$ . Raman and infrared spectroscopic studies confirmed the stabilization of three phases  $\alpha$ ,  $\beta$  and  $\gamma$  of this solid solution. Electrical conductivity is considerably enhanced by substitution with silicon and gallium cations. In all temperature ranges, the compound with  $x = 0.2$  shows the highest conductivity values ( $7.87 \times 10^{-5} \text{ S.cm}^{-1}$ ) at  $300^\circ\text{C}$  and ( $1.1 \times 10^{-1} \text{ S.cm}^{-1}$ ) at  $500^\circ\text{C}$ .

**Keywords:** *BiSiGaVO<sub>x</sub>, XRD, FTIR, Ionic conductivity*

---





## Thermodynamic Properties at Infinite Dilution of Hydrocarbons in Ionic Liquids

Fadhila Rabhi<sup>\*1</sup>, Hocine Sifaoui<sup>1</sup>, Fabrice Mutelet<sup>2</sup>

<sup>1</sup>Laboratory of Physical Chemistry of Materials and Catalysis, University Abderrahmane Mira - Bejaia, Algeria

<sup>2</sup>Reactions and Process Engineering Laboratory, University of Lorraine, 1 Rue Grandville, 54000 Nancy, France

---

### Abstract

Ionic liquids (ILs) gained a lot of attention, from researchers and industries, as alternative liquids for different types of applications, due to their unique intrinsic properties, gotten from the unlimited cation/anion combination. Thermodynamic properties of mixtures containing ionic liquids have been evaluated by the experimental and the theoretical studies to better understand the thermodynamic behavior of ionic liquids and describe molecular interaction between molecules, in order to select the appropriate ionic liquids to a specific application. In this work, the partial molar excess Gibbs free energy, enthalpy and entropy at infinite dilution of various hydrocarbons, including alkanes, alkenes, alkynes, and aromatic hydrocarbons in the investigated ionic liquids were determined from the measured infinite dilution activity coefficient data.

**Keywords:** *Ionic liquids, Hydrocarbons, Thermodynamic properties*

---



## **Modification of Polycaprolactone through grafting with an Aromatic acid: Synthesis and Characterization**

**Nacera Leila Belkhir<sup>\*1</sup>, Mohammed Amin Bezzekhami<sup>1</sup>, Kaouter Bentedlaouti<sup>1</sup>,  
Mahmoud Belalia<sup>1</sup>, Amine Harrane<sup>1</sup>**

*<sup>1</sup>Chemistry Department, University of Abdelhamid Ibn Badis , Mostaganem, Algeria*

---

### **Abstract**

The objective of this study is to develop and synthesize a new biodegradable polymer based on polycaprolactone. The polycaprolactone was chemically modified with an aromatic acid using a naturel clay as an eco-catalyst. The obtained copolymer were characterized by various analytical methods such as FTIR, TGA, and DSC. Subsequently, the antioxydant activity were evaluated in this work.

**Keywords:** *Polycaprolactone, Grafting, Antioxydante properties*

---



---

## Synthesis of New Azomethines Based on Vitamin B6

Samira Ismayilova<sup>\*1,2</sup>, Alakbar Huseynzada<sup>1,2</sup>, Ulviyya Hasanova<sup>1,2</sup>, Aygun Israyilova<sup>1,2,3</sup>

<sup>1</sup>Biomedical Materials Department of ICESCO, Baku State University, Baku, Azerbaijan

<sup>2</sup>GPOGC Scientific Research Institute, Azerbaijan State Oil and Industrial University, Baku, Azerbaijan

<sup>3</sup>ARICH, Baku State University, Baku, Azerbaijan

---

### Abstract

Schiff bases, known as azomethines, are among the most significant synthons in organic chemistry. They appeal to chemists for a variety of biological and synthetic reasons. Multiple investigations have demonstrated that these unique compounds have antibacterial, antiviral, antifungal, anti-HIV, antidiabetic, and anticancer properties.

Natural chemicals containing the pyridine ring include niacins, vitamin B6, nicotinamide adenine dinucleotide, and trigonelline. Furthermore, pyridine derivatives have a wide range of noteworthy biological activity, and many pyridine compounds are employed in clinical practice. Pyridine compounds serve as antioxidants, antivirals, antimicrobials, antidiabetics, antimalarials, antitubercular, psychopharmacological antagonists, antiproliferatives, and anti-inflammatory agents. Pyridine moieties have several biological uses due to their water solubility, chemical stability, capacity to establish hydrogen bonds, and tiny molecular size.

Pyridoxal, a product of vitamin B6, plays a crucial role in vital metabolic activities such as deamination, transamination, and decarboxylation. It also aids in the metabolism of amino acids, sugars, and fats.

Considering everything mentioned, novel azomethines were synthesised based on vitamin B6 and aromatic polyamine. The aldehyde component was pyridoxal hydrochloride and the amine 4-aminobenzylamine. The structures of the novel Schiff bases were verified using <sup>1</sup>H and <sup>13</sup>C NMR, mass spectroscopy, and elemental analysis.

**Keywords:** Schiff bases, Vitamin B6, Aromatic polyamine

---

### Acknowledgments

This work was supported by the Science Development Foundation under the President of the Republic of Azerbaijan – Grant № AEF-GAT-7-2023-2(44)-2917.



## Synthesis of New Heterocyclic Nitrogen Derivatives Derived from Pyridopyrazine

Mohamed El Yaqoubi<sup>\*1</sup>, Yousra Seqqat<sup>1</sup>, Mouad Lahyaoui<sup>1</sup>, Houda Lamssane<sup>1</sup>, Fouad Chahdi Ouazzani<sup>1</sup>, Youssef Kandri Rodi<sup>1</sup>

<sup>1</sup>Laboratory of Applied Organic Chemistry, Faculty of Sciences and Techniques, Sidi Mohamed Ben Abdellah University, Morocco

---

### Abstract

This study presents a novel method for synthesizing heterocyclic systems featuring a pyrido[2,3-*b*]pyrazine core. The initial step involves the reaction of 5-bromo-2,3-diaminopyridine with oxalic acid, yielding 7-bromopyrido[2,3-*b*]pyrazine-2,3(1H,4H)-dione. Subsequent N-alkylation of this compound is performed using halogenated carbon chains under phase transfer catalysis conditions, producing various derivatives. These products were characterized using standard spectroscopic techniques, demonstrating high efficiency in the synthesis process.

**Keywords:** *Heterocyclic, N-alkylation, Condensation, Pyrido[2,3-*b*]pyrazine*

---



---

## Synthesis and Characterization of Layered Double Hydroxides with Different Cations (Mg, Cu, Al) and EDTA Intrcalated

Fadhila Bouhella<sup>\*1</sup>, Boukoussa Bouhadjar<sup>2</sup>, Abdelkader Elaziouti<sup>1</sup>, Hadjer Addou<sup>1</sup>,  
Nadjia Belmehdi<sup>1</sup>

<sup>1</sup>Sciences and Technologies Process Engineering Laboratory, University of Sciences and Technologies of Oran, Algeria

<sup>2</sup>Department of Materials Engineering, University of Sciences and Technologies of Oran, Algeria

---

### Abstract

In this work, M/Al - layered double hydroxides (LDHs) as anionic clays, ( $M^{2+} = Cu^{2+}, Mg^{2+}$  and  $Zn^{2+}$ ) with cationic ratio of 2 - 4, were synthesized by co- precipitation method at constant pH and explored as an potential antimicrobial materials (an antibacterial agent). The as-elaborated materials were characterized by X-ray diffraction (XRD) and Fourier-transform infrared (FTIR) spectroscopy. XRD results showed that additional phase is presented in all samples due to the lattice strains created when more divalent cations ( $M^{2+}$ ) is added and the longer periods of hydrothermal treatment. The as-synthesized samples were calcined at 500°C temperature for formation an oxides and the phase transformations were fully investigated by X-ray diffraction, FTIR spectroscopy. Among these M/Al-LDHs materials,  $Cu_2-Al-500$  and  $Mg_4-Al-CO_3$ ,  $Mg_4-Al-500$  exhibit high antimicrobial activity against both gram-positive (Staphylococcus aureus, [S. aureus] and Enterococcus faecalis, [E. faecalis]), and Gram-negative (Escherichia coli, [E. coli]) bacteria. These results suggest that  $Cu_2/Al-LDHs$ ,  $Mg_4-Al-CO_3$  and  $Mg_4-Al-500$  are the promising host materials for designing efficient antibacterial matrix, contributing to the depollution and improvement of water quality in the environment and to the fight against bacterial resistance to antibiotics. Experiments continue with the Catalytic behavior.

**Keywords:** Layered double hydroxides, Co-precipitation, Synthesis, Environment

---



---

## A Chemotherapeutic Supplement, Green Synthesized Silver Nanoparticles Using *Papaver Rhoeas* for Human Pancreatic Cancer Treatment

Cigdem Dikbas\*<sup>1</sup>, Muberra Andac<sup>1</sup>

<sup>1</sup>Department of Nanoscience and Nanotechnology, Ondokuz Mayıs University, Samsun, Türkiye

---

### Abstract

Due to their physicochemical properties and therapeutic uses, silver nanoparticles (AgNPs) have become the focus of increasing attention in cancer research as a new generation of medical agents. In our study, PR-AgNPs were synthesized by green synthesis method using the extract obtained from the poppy plant (PR), and the cytotoxicity of PR-AgNPs on the MIA PACA (human pancreatic cancer) cell line was investigated. The synthesized PR-AgNPs were characterized utilizing ultraviolet-visible (UV-Vis) spectroscopy, scanning electron microscopy (SEM) and X-ray diffraction (XRD), scanning transmission electron microscopy (STEM), and Fourier transform infrared (FTIR) spectroscopy methods. Surface plasmon resonance (SPR) bands of PR-AgNPs were observed between 450 and 500 nm in the UV-Vis spectrum. PR-AgNPs were spherical in shape and their sizes varied between 5 and 25 nm. The particles' average size was around 10 nm. The formation of face-centered cubic (FCC) structures, determined from the XRD pattern, confirms the presence of metallic silver. According to FTIR results, -OH, -C=C and -CH groups played a role as effective agents in the synthesis and stabilization of NPs. The in vitro cytotoxicity of PR-AgNPs was tested on the MIA PaCa cell line and the inhibitory concentration (IC<sub>50</sub>) was determined as 52.26 µg/ml. PR-AgNPs showed dose-dependent inhibitory effects on MIA PaCa cancer cells (at 24-h exposure). Although silver nanoparticles at low doses do not cause significant cytotoxic effects, it has been determined that the cytotoxicity potential increases as the PR-AgNP concentration increases. This highlights the need for careful optimization and control of dosage in the use of NPs. Consequently, the cytotoxic effects of PR-AgNPs on human cell lines should be comprehensively investigated to ensure their safe and effective use in biomedical applications.

**Keywords:** *Papaver rhoeas*, Silver nanoparticle, MIA PaCa

---



---

## Theoretical Study, Intermolecular Charge Transfer, MEP, and Nonlinear Optics Application for an Organic Molecule

Zohra Douaa Benyahlou<sup>\*1</sup>, Mohammed Hadj Mortada Belhachemi<sup>1</sup>, Salem Yahiaoui<sup>1</sup>,  
Kheira Hammou<sup>1</sup>, Abdelkader Chouaih<sup>1</sup>

<sup>1</sup>Laboratory of Technology and Solid Properties (LTSPS), Abdelhamid Ibn Badis University of Mostaganem, 27000 Mostaganem, Algeria

---

### Abstract

Thiazolidinone derivatives are an important aromatic heterocyclic nucleus. These heterocyclic compounds are extensively used for their biological activities and photovoltaic applications. In this work, we are interested to the 2-thioxo-3N-(2-methoxyphenyl)-5[4'-methyl-3'-N-(2'-methoxyphenyl)thiazol-2'(3'H)-ylidene]thiazolidin-4-one. The knowledge of the crystal structure of these compounds is crucial for understanding the related charge transfer phenomena. On the other hand, the interest in nonlinear optical (NLO) properties of  $\pi$ -conjugated and functionalized organic compounds has greatly increased due to their potential applications in optoelectronics. Theoretical calculations in the ground state have been carried out for the compound studied using the density functional theory DFT/B3LYP with 6-31G++(d,p) basis set, to establish the configuration, stereochemistry and conformations of the molecule. Other physical and chemical parameters such as the frontier orbital energy gap (difference between the HOMO and LUMO), these orbitals determine the way how the molecule interacts with other species and give information about the reactivity/stability of specific regions of the molecule. Furthermore, the molecular electrostatic potential (MEP) surface was mapped. The negative and positive charge density distribution were determined to understand the molecular geometries and the intramolecular charge transfer within the molecule. Calculated frontier molecular orbitals (FMOs) energies and chemical reactivity parameters indicated that the molecule under investigation exhibits high first hyperpolarizability, typical of an NLO material.

**Keywords:** Thiazole, Density function theory (DFT), MEP, FMOs, NLO

---



## A simple and Efficient One-Pot Synthesis of Hantzsch 1,4-Dihydropyridines Using Heteropolyacid Catalyst Under Mild Condition

Fella Gaad<sup>\*1,2</sup>, Sabrina Halit<sup>1</sup>, Malika Makhloufi<sup>1</sup>, Tassadit Mazari<sup>2</sup>, Marchal Catherine Roch<sup>3</sup>

<sup>1</sup>Laboratory of Physics and Chemistry of Materials (LPCM), University of Mouloud Mammeri, Tizi-Ouzou(UMMTO), 15000 Tizi-Ouzou, Algeria

<sup>2</sup>Laboratory Applied Chemistry and Chemical Engineering (LCAGC), University of Mouloud Mammeri Tizi-Ouzou (UMMTO), 15000 Tizi-Ouzou, Algeria

<sup>3</sup>Institute of Lavoisier of Versailles (ILV), University of Saint Quentin en Yvelines, France

---

### Abstract

In recent years, multi-component reactions (MCRs) using nanocatalysts have made remarkable advances. The “one-pot” nature of MCRs means fewer by-products can be formed, reducing costs, time and energy consumption. These advantages, combined with the high efficiency, selectivity and recyclability of nanocatalysts, extend the development potential of catalytic systems for the synthesis of essential organic molecules under environmentally-friendly conditions.

In this study, phosphomolybdic heteropolyacid, H<sub>3</sub>PMo<sub>12</sub>O<sub>40</sub>, noted PMo<sub>12</sub> is selected as an efficient ecofriendly nanomaterial in the synthesis of 1,4-dihydropyridine (DHP) via Hantzsch MCR. The first obtained results were very interesting in terms of both reaction conditions and DHP yield. Product purity was verified using various analytical techniques, including proton and carbon NMR, infrared, Ultraviolet–visible spectroscopy and melting point determination.

**Keywords:** 1,4-dihydropyridine, Green chemistry, Heteropolyacid, Catalyst, Pharmacology

---





---

## Nickel Catalyst for Isoxazol Synthesis

**Benali Belgharri<sup>\*1,2</sup>, Amina Berrichi<sup>1,2</sup>, Sarah Abbou<sup>1,2</sup>, Zahra Hamiani<sup>1,2</sup>, Redouane Bachir<sup>1,3</sup>**

<sup>1</sup>Laboratory of Catalysis and Synthesis in Organic Chemistry, Chemistry Department, University of Tlemcen, B.P.119 Tlemcen 1300, Algeria

<sup>2</sup>University of Ain Temouchent, BP 284, 46000 Ain Témouchent, Algeria

<sup>3</sup>University of Tlemcen, 1300 Tlemcen, Algeria

---

### Abstract

This work focuses on the synthesis and characterization of new materials which is used as a catalyst for the synthesis of heterocyclic molecules. Our research has mainly focused on metal-phosphate materials the invention is to introduce a new transition metal in our starting material iron phosphate III (FePO<sub>4</sub>). These materials undergo heat treatments to increase their structure and activity under organic reactions.

Heterocyclic compound have long been considered fundamental structural elements in the field of therapeutic and pharmaceutical treatments. This is due to their ability to offer a wide range of possibilities to substitute atoms or groups within their ring-shaped structures, highlighting their diversity and adaptability. Isoxazole, in particular, is a preferred structure that has a wide range of biological activities and pharmacological properties. It occupies a significant place in various psychotropic drugs and an important position in the pharmaceutical field.

The new materials obtained were characterized by different physicochemical analysis technique: DRX, IR, SEM, specific surface measurement by BET and UV-Vis. The new catalysts were used in the synthesis of isoxazole from the chalcone taking into account the adequate conditions of the reaction. Catalysts showed good activity in isoxazole synthesis.

**Keywords:** Catalysts, FePO<sub>4</sub>, Heterocycle, Isoxazole, Metal transition

---



---

## Phosphotungstic Heteropolyacid Based New Hybrid Materials for Biomass Recovery

Feriel Toumi<sup>\*1,2</sup>, Yasmina Idrissou<sup>2</sup>, Tassadit Mazari<sup>1,2</sup>, Rabia Cherifa<sup>2</sup>, Anne Ponchel<sup>3</sup>,  
Kania Nicolas<sup>3</sup>

<sup>1</sup>Laboratory of Applied Chemistry and Chemical Engineering (LCAGC), Faculty of Chemistry, University of Mouloud Mammeri Tizi Ouzou (UMMTO), Tizi Ouzou, Algeria

<sup>2</sup>Laboratory of Natural Gas Chemistry (LCGN), Faculty of Chemistry (USTHB), BP 32, 16111, Algiers, Algeria

<sup>3</sup>Jean Perrin Faculty of Sciences, University of Artois, UCCS - UMR CNRS 8181, Lens, France

---

### Abstract

Heteropolyacids (HPAs) are a class of important (nanoparticles) solid acid catalysts widely used in both homogeneous and heterogeneous catalysis as environmentally-friendly alternatives to corrosive mineral acids. However, the need to separate and purify the catalyst products from the reaction product has given rise to new environmental concerns, resulting in a new class of materials known as hybrids. These are just as effective as their counterparts with the option of reutilization.

In this context, hydrogels are considered as promising candidates for the immobilization of catalytic nanoparticles. Consisting of three-dimensional networks of polymer chains and characterized by their high-water retention capacity and hydrated network structure, they offer long-term stabilization for nanoparticles.

In this study, new hybrid organic inorganic materials have been developed based on phosphotungstic acid  $H_3PW_{12}O_{40}$  (HPW) immobilized on different supports: silica ( $SiO_2$ ), Polyacrylamide hydrogel (PAAm),  $\beta$ -Cyclodextrine ( $\beta$ -CD) for biomass valorization application. The as prepared catalytic systems were analyzed by different characterization techniques, spectroscopic and thermal methods, FT-IR analysis, MEB-EDX and ATG. The swelling behavior of materials (HPW/PAAm) and (PAAm/ $\beta$ -CD) was studied in distilled water at 25 °C.

The characterization results confirmed the reliability of the hybrid material synthesis and highlighted the interactions between the support and the HPW, which lead to the formation of new active sites for the catalysis process.

**Keywords:** Heteropolyacid, Polyacrylamide, Hydrogel,  $\beta$ -cyclodextrin, Silica, Biomass, Catalysis

---



---

## Semisynthesis of New Isoxazolines from (E)- $\alpha$ -Atlantone: Experimental and Theoretical Investigations

Houria Raji<sup>1,2</sup>, Rida Nejari<sup>2</sup>, Ahmed Chekroun<sup>1</sup>, Abdellah Zeroual<sup>\*2</sup>, Nouredine Mazoir<sup>2</sup>, Ahmed Benharref<sup>1</sup>

<sup>1</sup>Laboratory of Biomolecular Chemistry, Natural Substances and Reactivity, URAC 16, Faculty of Sciences Semlalia, Cadi Ayyad University, P.O. Box 2390, Marrakech, Morocco

<sup>2</sup>Molecular Modelling and Spectroscopy Research Team, Faculty of Science, Chouaib Doukkali University, P.O. Box 20, 24000 El Jadida, Morocco

---

### Abstract

In the present work, new isoxazolines were semi-synthesized by 1,3-dipolar cycloaddition reactions of nitriloxides on (E)- $\alpha$ -atlantone, a sesquiterpene compound isolated from *Cedrus atlantica* essential oil. The reaction proceeds in a chemo- and periselective manner, leading to two cycloadducts, 3 and 3'. The structures of the obtained cycloadducts were determined using infrared spectroscopy, nuclear magnetic resonance spectroscopy, high-resolution mass spectrometry, and elemental analysis.

In addition, the chemoselectivity of this reaction was investigated through both practical experiments and theoretical approaches based on the Molecular Electron Density Theory (MEDT). Analysis of the Parr functions and electron localization functions (ELF) of the reactants revealed that the reaction exhibits both chemo- and stereoselectivity. These observations were supported by reactivity indices and activation energy calculations. This study thus contributes to deepening our understanding of the epoxidation processes and their selectivity mechanisms.

Furthermore, *in silico* investigations were conducted employing molecular docking, molecular dynamics, ADMET (absorption, distribution, metabolism, excretion, toxicity) tests, as well as drug-likeness evaluation, to complement the experimental findings and enhance our understanding of the potential bioactivity of the compounds at the molecular level.

**Keywords:** *Cedrus atlantica*, MEDT, ADME-TOX, Molecular docking

---



## Study of Properties of Tin Oxide Thin Films Elaborated by USP Method

Sabrina Roguai\*<sup>1</sup>, Abdelkader Djelloul<sup>1</sup>

<sup>1</sup>Department Science of the Matter, Abbes Laghrour University Khenchela, Algeria

---

### Abstract

SnO<sub>2</sub> thin films were deposited by ultrasound pyrolysis spray technique at 450 °C. The films were characterized by X-ray diffraction, Fourier transformed infrared (FTIR), and ultraviolet–visible spectroscopy. The tetragonal rutile-type structure was confirmed by X-ray diffraction with an average crystallite size of 35 nm. In addition, the FTIR study indicated the existence of two distinct characteristic absorptions which correspond to (O-Sn-O) deformations and (O-Sn) stretching modes. For the optical properties, the band gap energy was determined by Wemple DiDomenico model.

**Keywords:** *Thin films, X-ray diffraction, FTIR spectroscopy, Optical properties*

---



## Synthesis of CuO Nps for Photocatalytic Applications

Sabrina Roguai\*<sup>1</sup>, Abdelkader Djelloul<sup>1</sup>

<sup>1</sup>Department Science of the Matter, Abbes Laghrour University Khenchela, Algeria

---

### Abstract

Today, wastewater treatment and the sanitation of potable water supplies are major concerns. Among the most recent advances in water treatment, advanced oxidation processes (AOP) are solutions allowing the mineralization in an aqueous medium of organic molecules that are toxic to the ecosystem. heterogeneous photocatalysis. It is a photo-sensitized reaction based on the adsorption of light radiation by the catalyst, generally a semiconductor using CuO. It has the advantage of not introducing chemical compounds other than CuO into the medium to be treated. In this study, the copper nanoparticles were synthesized by a simple co-precipitation method which was obtained by heating at 80°C for photocatalytic application. The microstructural characterization of the nanopowder obtained was performed using X-ray diffraction (XRD) and SEM microscopy. XRD studies demonstrated that the formation of the CuO monoclinic phase and the average grain size of CuO crystallite was found to be 30 nm. SEM images indicate the morphology as a three-dimensional flower-like structure was successfully prepared for sub-sequent degradation of methylene blue (MB).

**Keywords:** CuO NPs, X-ray diffraction, SEM, Photocatalytic

---



---

## Photothermal Activity and *In Vitro* Evaluation of Gold Nanorods for Potential Therapeutic Application in Cutaneous Leishmaniasis Treatment

Magalí R. Di Meglio<sup>\*1,2,3</sup>, Cristian Lillo<sup>1,2,3</sup>, Jorge Montanari<sup>1,2,3</sup>

<sup>1</sup>Laboratory of Nanosystems for Biotechnology Applications (LANSAB), National University of Hurlingham, Villa Tesei, Argentina

<sup>2</sup>Scientific Research Commission of the Province of Buenos Aires (CIC), La Plata, Argentina

<sup>3</sup>National Council for Scientific and Technical Research (CONICET), Autonomous City of Buenos Aires, Argentina

---

### Abstract

Gold nanorods (AuNRs) absorbing in the near-infrared are well known for their efficacy in photothermal therapy, owing to their unique optical properties related to the surface plasmon resonance phenomenon. This effect allows for the collective oscillation of surface electrons in the nanoparticle in response to incident light at specific wavelengths, leading to a significant increase in local temperature. There are already studies that have demonstrated the efficacy of using AuNRs as potential effectors of photothermal therapy for treating various diseases.

Furthermore, cutaneous leishmaniasis is one of the most significant vector-borne neglected tropical diseases globally. The ulcerative lesions caused by this infection can lead to severe disfigurement and disability if untreated. Conventional treatments are often ineffective, costly, and extensive, with low patient adherence and a high incidence of adverse effects and resistance.

Given this context, we aimed to synthesize, characterize, and study the photothermal activity and cytotoxicity of gold nanorods to develop nanoformulations for topical application as a novel, localized, and enhanced treatment for cutaneous leishmaniasis.

The synthesis of gold nanorods was achieved using the seed-mediated growth method in the presence of the surfactant CTAB. The nanorods were subsequently coated with SiO<sub>2</sub> alone or with PEG and SiO<sub>2</sub>, following a modified Stober method. Characterization of these nanoparticles was performed using UV-visible spectrophotometry, dynamic light scattering (DLS), and transmission electron microscopy (TEM).

Initial assays were conducted to assess the photothermal activity of both bare and coated nanoparticles in water. They were irradiated with an 808 nm laser at power densities of 1 W.cm<sup>-2</sup>, 1.3 W.cm<sup>-2</sup>, and 7.8 W.cm<sup>-2</sup>, with varying concentrations, resulting in significant temperature increases in all cases. Based on these findings, we evaluated the intrinsic cytotoxicity of the nanoparticles and the toxicity induced by laser irradiation at lower power levels in MCF7, SKOV P300 and HaCaT cell lines.

**Keywords:** Gold nanorods, Photothermal therapy, Cutaneous leishmaniasis, Nanotechnology

---



---

## Valuation of Essential Oils from Aleppo Pine (*Pinus Halepensis* Mill.) Harvested in Two Regions of Algeria

Nacira Amara<sup>\*1</sup>, Mohamed Kouider Amar<sup>2</sup>, Sabrina Amara<sup>3</sup>,  
Nadjet Harazi<sup>1</sup>

<sup>1</sup>Biology Department, Saad Dahleb Blida 1 University, Blida, Algeria

<sup>2</sup>Laboratory of Quality Control, Physico-Chemical Department, SAIDAL of Medea, Algeria

<sup>3</sup>Institute of architecture and urban planning, Saad Dahleb Blida 1 University, Blida, Algeria

---

### Abstract

Aromatic plants have considerable assets to offer, thanks to the use of their essential oils (EO) in a variety of applications particularly as antifungal and antibacterial agents. The aim of this study was to determine the chemical composition of *Pinus halepensis* (Mill.) EOs from two national parks, Chrea (Blida) and Theniet El Had (Tissemsilt) Algeria, in order to establish their chromatographic profiles, their chemotypes and assess their antimicrobial activity. The EOs from the fresh leafy branches of *Pinus halepensis* (Mill.) were extracted using the hydrodistillation method. The essential oils obtained were analysed by gas chromatography-mass-spectrometry (GC-MS). The antimicrobial activity of these two essential oils was assessed on eight microbial strains using the aromatogram method. GC-MS analysis of Aleppo pine from the Theniet El Had and Chrea parks revealed the presence three main compounds: Beta Myrcene (24.36%), Alpha Pinene (18.80%), Trans-Caryophyllene (16.56%), Alpha-Pinene (31.89%), Beta-Myrcene (22.91%) and Trans-Caryophyllene (10.40%) respectively. Evaluation of the antimicrobial activity of Chrea EO revealed a sensitivity for the eight strains tested (*Escherichia coli*, *Salmonella typhimurium*, *Pseudomonas aeruginosa*, *Bacillus subtilis*, *Staphylococcus aureus*, *Candida albicans*, *Saccharomyces cerevisiae* and *Aspergillus brasiliensis*). While the EO at Theniet El Had inhibited six microbial strains. The results showed that essential oil of Chrea was potentially toxic against all the microbial strains tested These could contribute to the development of new antimicrobial agents that pose no risk to the environment.

**Keywords:** *Pinus halepensis* mill, Valuation, Essential oils, Regions, GC-MS

---



---

## Natural Antifungal Agents as Alternatives for *Alternaria Alternata* Control

Teodora Kukrić<sup>\*1</sup>, Renata Iličić<sup>2</sup>, Boris Popović<sup>1</sup>

<sup>1</sup>Department of Field and Vegetable Crops, Faculty of Agriculture, University of Novi Sad, Trg Dositeja Obradovića 8, 21000 Novi Sad, Republic of Serbia

<sup>2</sup>Department for Plant and Environmental Protection, Faculty of Agriculture, University of Novi Sad, Trg Dositeja Obradovića 8, 21000 Novi Sad, Republic of Serbia

---

### Abstract

Among phytopathogenic fungi, *Alternaria alternata* is well known for causing diseases in a wide range of plants. *A. alternata* has a broad host range, infecting numerous plant species including vegetables, fruits, ornamental plants, and crops. Symptoms caused by *A. alternata*, such as leaf spots, blights, and rots, can lead to significant crop losses. The fungus is particularly notorious for its ability to produce a variety of secondary metabolites, some of which are toxic to both plants and humans. Due to its cosmopolitan range, there is a need for effective control methods. Integrating cultural practices, chemical treatments, and biological control can help reduce the impact of *A. alternata*, thereby ensuring better yield and quality. Novel fungicides with different modes of action are constantly needed to prevent resistance development, prompting scientific efforts to develop alternative solutions. This study evaluated the efficacy (E%) of hydrophobic deep eutectic solvents (HDES). Eight thymol-based HDES (Thy:Pin, Thy:Lim, Thy:Euc, Thy:Cam, Tim:EG, Tim:1,2PD, Tim:2,3BD and Tim:CapA) were tested in eight concentrations 0.7%, 1.5%, 3.1%, 6.25%, 12.5%, 25%, 50%, 100%. Antifungal activity was assessed *in vitro* and the results were presented as E%. All eight thymol-based HDES showed E% ranging from 18% to 100%. Thy:Pin exhibited the highest, and Thy:EG the lowest cumulative E% across the eight concentrations. The antifungal activity of thymol-based HDES was confirmed in this study, and these results can serve as a basis for further investigations into the biofungicide potential of HDES.

**Keywords:** Biofungicides, HDES, Thymol

---





## Some Derivatives of 3,4-Di-Hydropyrimidin-2(1H)-Thiones Derivatives: Synthesis, Biological Assessment, ADMET, and Drug-Likeness Analysis

Noura Kichou<sup>\*1,3</sup>, Nabila Guechtouli<sup>3</sup>, Manel Taferguennit<sup>2</sup>

<sup>1</sup>Department of Chemistry, Faculty of Sciences, University Mouloud Mammeri of Tizi-Ouzou, Tizi-Ouzou, Algeria

<sup>2</sup>Electrochemistry-Corrosion Laboratory, Metallurgy and Mineral Chemistry, Faculty of Chemistry, University of Science and Technology Houari Boumediene (USTHB), BP 32 El Alia, Bab Ezzouar – 16111 Alger, Algeria

<sup>3</sup>M'Hamed Bougara University of Boumerdes, 35000 Algeria

### Abstract

3,4-di-hydropyrimidin-2(1H)-thiones have attracted considerable interest due to a wide range of biological activities, including antitumor, antioxidant, antibacterial, antifungal, anti-inflammatory and anti-hypertensive properties. Some derivatives of 3,4-di-hydropyrimidin-2(1H)-thiones were synthesized by the Biginelli method, which consists of an easy reaction that is widely used in organic synthesis, which occurs in a single step to obtain multifunctional heterocycles. The structures of the synthesized compounds have been elucidated by IR, <sup>1</sup>H NMR and <sup>13</sup>C NMR.

Synthesized compounds were screened for their antimicrobial activity against the E.coli and staphylococcus aureus and antifungal activity against Aspergillus Niger and penicillium notatum. The ADMET (Absorption, Distribution, Metabolism, Excretion, and Toxicity) and drug-likeness study were carried out to predict the pharmacokinetic parameters and toxicity of the complexes. Good drug binding behaviour and a non-toxic nature were observed for most of the compounds.

**Keywords:** 3,4-di-hydropyrimidin-2(1H)-thiones, Synthesis, Antibacterial activity, ADMET

## 1 INTRODUCTION

3,4-Dihydropyrimidin-2(1H)-thiones, named Biginelli compounds, represent a heterocyclic system of significant pharmacological importance. In the past decades, a wide range of biological effects including anti-inflammatory [antimicrobial, antifungal, calcium channel blockers activities have been described for these compounds. Much of recently published research has been focused on the synthesis of dihydropyrimidines. Dihydropyrimidines which are important compounds due to their therapeutic and pharmacological properties. They can serve as the integral of several calcium channel blockers, antihypertensive agents, and α-1a-antagonists and neuropeptide Y (NPY) antagonists. Dihydropyrimidin-2(1H)-thiones shown to possess potential antioxidant activity [1–4].

## 2 MATERIAL AND METHOD

### 2.1 Synthesis

3,4-Dihydropyrimidin-2(1H)/thione derivatives were synthesized in moderate to high yields via one-pot three component Biginelli reaction of aldehydes, ethyl acetoacetate and urea/thiourea in the presence of ethanol and concentrated hydrochloric acid catalyst, in microwave irradiation. This protocol offers several advantages including good yields of products, short reaction time and easy work-up procedure Figure 1.

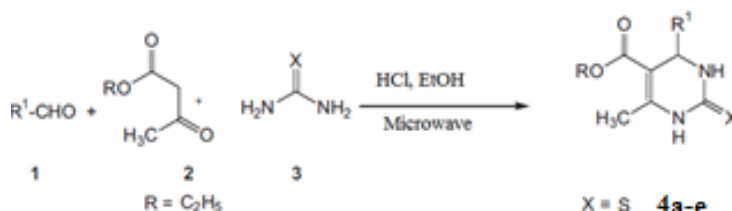
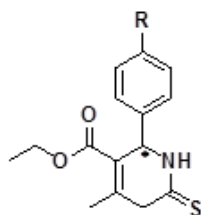


Figure 1. General procedure for the preparation of 3,4-dihydropyrimidinones/thiones



R: H, OH, OCH<sub>3</sub>, Cl, N(CH<sub>3</sub>)<sub>2</sub>

**Figure 2.** Structure of 3,4-dihydropyrimidin-2(1H)-thiones

## 2.2 Anti Microbial Activity

Antimicrobial activity was examined by the agar -diffusion method. The in vitro antimicrobial activity of the synthesized compounds was investigated against *Staphylococcus aureus* (Gram-positive), *Escherichia coli* (Gram-negative), *Aspergillus niger* and *Penicillium notatum* (fungi). Media used were nutrient agar and potato dextrose agar. Non sterile powder of the tested compounds were dissolved in DMSO to yield 250µg/ml and 500µg/ml. Streptomycin and fluconazole were used as reference standards.

All bacterial were incubated overnight at 37 °C and all fungal cultures were incubated at 37° ± 2°C for 48 hrs. After the incubation period, the petri plates were observed for zone of inhibition by using vernier scale. The results evaluated by comparing the zone of inhibition shown by the derivatives with standard drug.

## 2.3 ADMET Prediction

Physicochemical properties and Pharmacokinetics Properties such as Absorption, Distribution, Metabolism, Excretion and Toxicity of the molecular structure of 3,4-dihydropyrimidin-2(1H)-ones were studied via admetSAR [5].

## 3 RESULTS

### 3.1 Characterization

5-Ethoxycarbonyl-6-methyl-4-phenyl-3,4-dihydropyrimidin-2(1H)-thione (**4a**) MP(°C) 208–210; IR (KBr, cm<sup>-1</sup>): 3328 and 3209 (N–H str.), 1702 (C=O str.), 1202 (C= S str.); <sup>1</sup>H NMR (500 MHz, DMSO-d<sub>6</sub>) δ: 1.03 (t, J = 7.4 Hz, 3H, OCH<sub>2</sub>CH<sub>3</sub>), 2.17 (s, 3H, CH<sub>3</sub>), 4.02 (q, J = 7.4 Hz, 2H, OCH<sub>2</sub>CH<sub>3</sub>), 5.11 (s, 1H, CH), 7.21–7.41 (m, 5H, Ar-H), 7.16 (s, 1H, NH-3), 9.57 (s, 1H, NH-1) ppm; <sup>13</sup>C NMR (125 MHz, DMSO-d<sub>6</sub>) δ: 14.4, 18.0, 54.6, 60.1, 99.9, 122.4, 125.9, 129.8, 143.0, 154.6, 165.7, 174.7 ppm [3].

5-Ethoxycarbonyl-6-methyl-4-(4-hydroxyphenyl)-3,4-dihydropyrimidin-2(1H)-thione (**4b**) MP(°C) 172-173 °C, IR (KBr, cm<sup>-1</sup>): 3501(O–H str.) , 3184 and 3016(N–H str.), 1686 and 1580(C=O str.) 1200 (C=S str.), <sup>1</sup>H NMR (400 MHz, DMSO-d<sub>6</sub>): δ 1.11 (t, J = 6.9 Hz, 3H, CH<sub>3</sub>), 2.24 (s, 3H, CH<sub>3</sub>), 3.98 (q, J = 6.7 Hz, 2H, CH<sub>2</sub>), 5.08 (d, J = 2.3 Hz, 1H, CH), 6.69 (d, J = 8.1 Hz, 2H, Ar-H), 7.01 (d, J = 8.1 Hz, 2H, Ar- H), 9.34 (s, 1H, NH), 9.5 (s, 1H, NH), 10.18 (s, 1H, OH) [6].

5-Ethoxycarbonyl-6-methyl-4-(4-methoxyphenyl)-3,4-dihydropyrimidin-2(1H)-thione (**4c**) MP(°C) 155–157; IR (KBr, cm<sup>-1</sup>): 3323 and 3206 (N–H str.), 1697 (C= O str.), 1209 (C=S str.); <sup>1</sup>H NMR (500 MHz, DMSO-d<sub>6</sub>) δ: 1.20 (t, J = 7.4 Hz, 3H, OCH<sub>2</sub>CH<sub>3</sub>), 2.19 (s, 3H, CH<sub>3</sub>), 3.58 (s, 3H, OCH<sub>3</sub>), 3.99 (q, J = 7.4 Hz, 2H, OCH<sub>2</sub>CH<sub>3</sub>), 5.26 (s, 1H, CH), 7.11 (s, 1H, NH-3), 7.01 (d, 2H, J = 8.0 Hz, Ar-H), 7.36 (d, 2H, J = 8.0 Hz, Ar- H), 9.56 (s, 1H, NH-1) ppm; <sup>13</sup>C NMR (125 MHz, DMSO-d<sub>6</sub>) δ: 14.6, 17.2, 54.2, 60.8, 99.5, 122.2, 126.3, 129.6, 143.3, 155.8, 166.0, 175.5 ppm [3].

5-ethoxycarbonyl-6-methyl-4-(4-chlorophenyl)-3,4-dihydropyrimidin-2(1H)-thione (**4d**) IR (KBr, cm<sup>-1</sup>): 3321 and 3212 (N–H str.), 1689 (CO str.), 1206 (CS str.); <sup>1</sup>H NMR (500 MHz, DMSO-d<sub>6</sub>) δ: 2.18 (s, 3 H, CH<sub>3</sub>), 3.55 (s, 3H, OCH<sub>3</sub>), 5.21 (s, 1H, CH), 7.13 (d, 2H, J = 8.2 Hz, Ar-H), 7.33 (d, 2H, J = 8.2 Hz, Ar-H), 7.55 (s, 1H, NH-3), 9.33 (s, 1H, NH-1) ppm; <sup>13</sup>C NMR (125 MHz, DMSO-d<sub>6</sub>) δ: 14.3, 17.7, 54.0, 100.5, 122.1, 126.1, 129.4, 143.0, 155.2, 165.3, 175.2 ppm [6].

5-ethoxycarbonyl-6-methyl-4-(4-N,Ndimethylaminophenyl)-3,4-dihydropyrimidin 2(1H)-thione (**4e**) MP(°C) 208–210 ; (KBr, cm<sup>-1</sup>): 3330 and 3124(N–H str.), 2944 (C–H aliph), 1690 and 1618(C=O str.), 1282 (C=S str.) : <sup>1</sup>H NMR (300 MHz, DMSO-d<sub>6</sub>) δ: 1.16 (t, J=7.9Hz , 3H, OCH<sub>2</sub>CH<sub>3</sub>), 2.40 (s, 3H, CH<sub>3</sub>), 5.47 (s, 1H, CH), 2.71

(s, 6H, N(CH<sub>3</sub>)<sub>2</sub>), 3.35 (q, J=7.9, 2H OCH<sub>2</sub>CH<sub>3</sub>), 8.21 (s, 1H, NH-3), 9.48 (s, 1H, NH-1), 7.30–7.23 (m, 4H, Ar-H) [7].

### 3.2 Antibacterial Activity and Antifungal Activity

These types of bacteria were selected because one of them (*Staphylococcus aureus*) is positive for the Graham stain, while the other (*Escherichia coli*) is negative. 4a is effective against *s.aureus* and *E.coli*. 4b showed the moderate activities (Table 1).

4a and 4b showed significant activity against *A.Niger* and *P.Notatum* when compared to standard (Table 2).

**Table 1.** Antibacterial activity of synthesized compound

Compound	E.Coli (250µg/ml)	E.Coli (500µg/ml)	S.Aureus (250µg/ml)	S.Aureus (500µg/ml)
4a	11	12	15●	18●
4b	10	11	12	13
4c	8	8	8	8
4d	8	8	8	8
Dmso(control)	8	8	8	8
Standard(250µg/ml) Streptomycin	18	18	20	20

● Significant zone of Inhibition

**Table 2.** Antifungal activity of synthesized compounds (Zone of inhibition (mm))

Compound	Aspiggillus Niger (250µg/ml)	Aspiggillus Niger (500µg/ml)	Penicillium Notatum (250µg/ml)	Penicillium Notatum (500µg/ml)
4a	12	13	22*	24*
4b	10	11	12	15
4c	8	8	8	8
4d	8	8	8	8
Dmso (control)	8	8	8	8
Standard (250µg/ml) Fluconazole	21	21	24	24

### 3.3 ADMET Prediction

To confirm a drug and its efficacy as a top candidate against any disease, ADMET is essential. The partition coefficient (cLogP), donor hydrogen bond and drug similarity were calculated using physicochemical methods. Pharmacokinetic studies were also conducted for clinical trials of these derivatives molecules. The results are presented in Table 3.

The topological polar surface area (TPSA) should be less than <140 Å<sup>2</sup> for significant oral bioavailability, our results showed good values of TPSA ranging between 43.3 Å<sup>2</sup> and 75.6 Å<sup>2</sup>. Furthermore, the results describes that all compounds showed high GI adsorption and Caco-2 permeability. Moreover, most of the molecules can be metabolized by the major cytochromes, except molecule (4a), and derivatives containing chlorine radical (molecule 4c) and methoxy radical (molecule 4d). Moreover, all the molecules are non oct-2 -inhibitors, indicating a good excretion.

A drug candidate must first pass a toxicity risk assessment to be considered for drug development. Low toxicity and side effects indicate a high therapeutic index of the drug. For this reason, a toxicity prediction analysis was performed, the results indicate that all the molecules are anticarcinogenic and are non-AMES toxic. However only derivatives that contain methoxy radical (molecule 4d) and amino radical (molecule 4e) are hERG inhibitors which indicates that they act as K<sup>+</sup> channel blockers, known as anti-hypertensives. Interinstegly, the derivatives that contain hydroxy radical (molecule 4b) and methoxy radical (molecule 4c) are presenting an anti-hepatotoxicity. And finally, only the derivative that contains chlorine radical (molecule 4c) presented a non-respiratory toxicity.

Additionally of being anticancer, antihypertensive and anti-hepatotoxic agents as shown from the results above, literature have already revealed that for a majority of the analogues of 3,4-dihydropyrimidine-2(1H)-thiones derivatives, their biological activity is affected by the lipophilicity (logP) and the nature of the substituents; For instance, in *Tale et al* study, it has been found that derivative having chlorine or fluorine as radicals in the para-position on the benzene ring, are having high lipophilicity, and presenting active IL-6 inhibitory effect at concentration of 10  $\mu$ M, and hence they are considered as anti-inflammatory agents. In this study, molecule 4c is the best candidate for being an anti-inflammatory agent, due to its chlorine radical in the para-position, and highest lipophilicity compared to the other molecules (Table 3).

**Table 3.** ADMET prediction results of the five 3,4-dihydropyrimidine-2(1H)-thiones derivatives

Physicochemical properties		(4a)	(4b)	(4c)	(4d)	(4e)
<b>Lipophilicity</b>	Log P	2.44	2.04	2.99	2.57	2.75
<b>Hydrogen bonds</b>	H-bond donors	1	2	0	1	1
	H-bond acceptors	3	3	3	4	3
<b>Molecular weight</b>	MW (g.mol <sup>-1</sup> )	275.37	291.37	292.7	275.3	302.3
<b>Flexibility</b>	Rotatable bonds	4	4	5	5	5
<b>Polarity</b>	TPSA (Å <sup>2</sup> )	55.40	90.65	79.65	64.6	58.64
<b>Solubility</b>	Log S	-2.79	-2.17	-5.17	2.44	-4.43
<b>Saturation</b>	Fraction of C sp <sup>3</sup>	0.33	0.33	0.38	0.33	0.41
Pharmacokinetics properties						
<b>Absorption</b>	GI absorption	High	High	High	High	High
	Caco-2	Yes	No	Yes	Yes	Yes
<b>Distribution</b>	BBB permeability	Yes	No	Yes	Yes	Yes
<b>Metabolism</b>	CYP2D6 inhibitor	No	No	No	No	No
	CYP2C19 inhibitor	Yes	No	Yes	Yes	No
<b>Excretion</b>	Oct-2 inhibitor	No	No	No	No	No
<b>Toxicity</b>	Carcinogenicity (binary)	No	No	No	No	No
	Ames mutagenesis	No	No	No	No	No
	hERG K <sup>+</sup> channel inhibitor	No	No	No	Yes	Yes
	Respiratory toxicity	Yes	Yes	No	Yes	Yes
	Hepatotoxicity	Yes	No	Yes	No	Yes

## 4 CONCLUSION

All the synthesized derivatives of 3,4-dihydropyrimidin-2-thiones were evaluated with Physical, analytical Characterization and Biological methods. All the compounds were subjected to Antimicrobial activity. Compound 4a shows higher zone of inhibition.

The ADMET prediction study showed optimal physicochemical, pharmacological, and bioavailability, with estimating the biological activity of each derivatives of the studied of 3,4-dihydropyrimidine-2(1H)-thiones derivatives, including anticancer, antihypertensive and anti-hepatotoxic, anti-inflammatory, antibacterial and antifungal activities. It was found that amongst all the compounds screened, derivative 4c, besides of its non-respiratory toxicity and anti-hepatotoxicity, showed a promising tendency to be anti-inflammatory active. Derivatives 4 and 5 showed a tendency of being anti-hypertensives, while derivative 4d exhibited also possible antibacterial and antifungal activities, along with derivative 4b that showed also an anti-hepatotoxicity. Globally, the ADMET results showed that the investigated 3,4-dihydropyrimidine-2(1H)-thiones derivatives could be potent biological active compounds.

## References

- [1] V. Lakshmi Harika, K. Konda Ravi Kumar, and S. Afzal Basha, "Synthesis, characterization and biological evaluation of 3,4-dihydropyrimidin- 2(1H)-thione derivatives," *Archives of Applied Science Research*, vol. 6, no. 6, pp. 121–127, 2014.
- [2] C. P. Rathod, N. R. Kadam, S. C. Dhawale, and L. N. Barde, "Synthesis and biological evaluation of 3,4-dihydropyrimidines thiones 2020 derivatives," *International Journal of Health Sciences*, vol 6, no. S4, pp.

- 5929–5936. 2022.
- [3] A, Krishnamoorthy, S. M. Syed, L. Kuppan, N. S. Prasanna, and N. A. Rahim, “Facile synthesis of 3,4-dihydropyrimidin-2(1H)-ones and -thiones and indeno[1,2-d]pyrimidines catalyzed by p-dodecyl benzenesulfonic acid” *Journal of Taibah University for Science*, vol 8, pp. 236–247. 2014.
- [4] N. Kichou, I. Rahou, Z. M. Elamin, Khaled Sekkoum and H. Y. Aboul-Enein” Chiral separation of 3,4-dihydropyrimidin-2(1H)-ones and 3,4-di-hydropyrimidin-2(1H)-thiones enantiomers by HPLC on Chiralcel®OD-H,” *Current Analytical Chemistry*, vol. 16. no.3. pp. 250–255, 2020.
- [5] H. Yang, C. Lou, L. Li, J. Sun, Y. Cai, Z. Wang, W. Li, G. Liu, and Y. Tang, “admetSAR 2.0: Web-service for prediction and optimization of chemical ADMET properties,” *Bioinformatics*, vol. 35, no. 6, pp. 1067–1069. 2019.
- [6] C. A , Ladole, N. G. Salunkhe, R. S. Bhaskar, and A. S. Aswar, “A microwave assisted synthesis of 3,4-dihydro pyrimidin-2(1H)-one/thione derivatives using nano crystalline MgFe<sub>2</sub>O<sub>4</sub> as catalyst,” *European Journal of Chemistry*, vol. 5, no. 1, pp. 122–126, 2014.
- [7] S. S, Mansoor, S. S. Shafi, and S. Z. Ahmed. “The 3,4-dihydropyrimidin-2(1H)-ones (DHPMs) have recently emerged as important target molecules due to their therapeutic and pharmacological properties,” *Arabian Journal of Chemistry*, vol. 9, pp. 846–851. 2016.
- [8] R. H. Tale, A. H. Rodge, G. D . Hatnapure , and A. P. Keche, “The novel 3,4-dihydropyrimidin-2(1H)-one urea derivatives of N-aryl urea: Synthesis, anti-inflammatory, antibacterial and antifungal activity evaluation,” *Bioorganic & Medicinal Chemistry Letters*, vol. 21. no.15, pp. 4648–4651, 2011.



## Hybrid Electrode Based on Ionic Liquid and Pt and Pd Nano-Clusters: For the Hydrogen Evolution Reaction (HER) Catalysis

Hocine Moussouni<sup>1</sup>, Mourad Mechouet\*<sup>1</sup>, Jalal Ghilane<sup>2</sup>

<sup>1</sup>Laboratory of Physics and Chemistry of Materials (LPCM), Department of Chemistry, University of Mouloud Mammeri, Tizi-Ouzou, Algeria

<sup>2</sup>ITODYS Laboratory, University of Paris, 75013 Paris, France

### Abstract

Surface modification with thin organic layers is crucial for designing materials with specific properties to develop practical applications such as supercapacitors, metal-air batteries; fuel cells, corrosion resistance.

In the present work, we focused on the grafting of thin film positively charged based on ionic liquids (LIs) on a glassy carbon electrode (GC), then functionalized with metal nanoparticles (Pt or Pd). The SEM obtained images confirm the modified electrode. Then its catalytic performances towards the hydrogen evolution reaction (HER) were evaluated. Interestingly, the catalytic performances are improved for both prepared electrodes (GC/LI/Pt, GC/LI/Pd), especially the latest one containing palladium and makes it of the best catalysts, regarding the literature. It seems that the ionic layer presence displays an increase catalytic, which is probably due to the synergistic effect existence between the grafted ionic layer and the metallic nanoparticles.

**Keywords:** Ionic liquid, Nanoparticles, Modified electrode, Electrocatalysis, Hydrogen evolution reaction

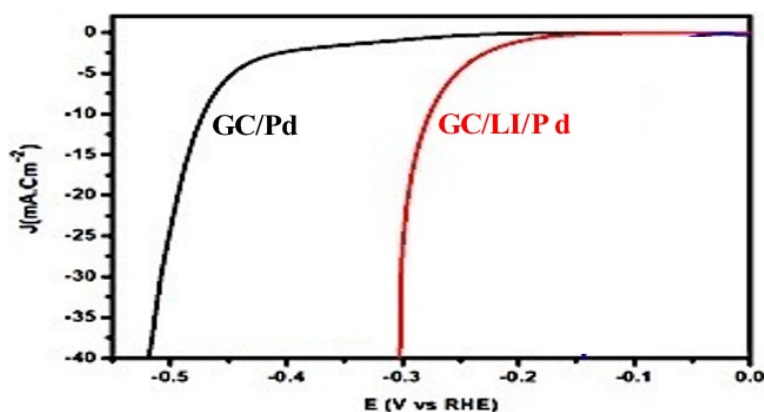


Figure 1. GC/Pd, GC/LI/Pd graph



---

## Evaluation of the Antidiabetic Activity of Extracts and Essential Oil of *Myrtus Communis* Harvested in Algeria

Melissa Bessaci<sup>\*1</sup>, Amina Benazzouz-Touami<sup>1</sup>

<sup>1</sup>Department of Chemistry, Faculty of Sciences, Mouloud Mammeri University, Tizi Ouzou 15000, Algeria

---

### Abstract

This study aims to comprehensively analyze the antidiabetic properties of the essential oil as well as the aqueous and ethanolic extracts of *Myrtus Communis*, collected in the Tizi-Ouzou region of Algeria. The evaluation of antidiabetic activity was conducted in vitro using the glucose absorption capacity determination method by yeast cells. This method involves measuring the glucose transport rate across the yeast cell membrane suspended in glucose solutions of varying concentrations (5, 10, 25 µg/ml) in the presence of extracts and essential oil at different concentrations. The residual glucose amount in the medium after contact time with yeast cells serves as an indicator of glucose absorption by them. It was observed that the extracts exhibit a dose-dependent inhibitory activity, increasing inversely proportionally to the added glucose concentration. The maximum inhibition values reached 78.47%, 78.88%, and 81.09% for the ethanolic extract, while for the aqueous extract, the rates were 77.17%, 77.52%, and 78.03% for concentrations of 100, 200, and 300 µg/ml, respectively. The essential oil demonstrated remarkable inhibitory activity, reaching 79.67%.

**Keywords:** *Myrtus Communis*, Antidiabetic activity, Essential oil, Ethanolic extract, Aqueous extract

---



## The Environmentally Friendly Synthesis of Amide Based on Triethylenetetramine

Fargana Alizadeh<sup>\*1,2</sup>, Alakbar Huseynzada<sup>2,3</sup>, Aygun Israyilova<sup>2,3</sup>, Ulviyya Yolchuyeva<sup>1</sup>,  
Ulviyya Hasanova<sup>2,3</sup>, Eldar Gasimov<sup>4</sup>, Goncha Eyvazova<sup>3</sup>, Fuad Rzayev<sup>4</sup>, Orkhan  
Isayev<sup>4</sup>, Aida Ahmadova<sup>3</sup>, Elshan Aliyev<sup>2</sup>

<sup>1</sup>Institute of Petrochemical Processes, Baku, Azerbaijan

<sup>2</sup>Geotechnological Problems of Oil, Gas and Chemistry, Scientific Research Institute of ASOIU, Baku, Azerbaijan

<sup>3</sup>Baku State University, Baku, Azerbaijan

<sup>4</sup>Azerbaijan Medical University, Baku, Azerbaijan

### Abstract

In many synthetic and natural molecules, bioconjugates, bioactive macrocyclic medicines, multifunctional nanostructures, and well-ordered supramolecular architectures, the amide group is frequently present and plays a significant role in biological and pharmacological products. The formation of amide bonds is therefore an essential step in the synthesis of organic compounds [1, 2].

Only at very high temperatures may an amine and a carboxylic acid directly condense to form an amide; these circumstances are incompatible with the presence of other labile functionalities. Consequently, it is essential to install a good leaving group or activate the acid's acyl carbon. Many synthetic approaches have been established to synthesise amides from different derivatives of carboxylic acid [3]. The acylating agents are typically prepared by converting the carboxy components into the appropriate chlorides, mixed anhydrides, active esters, or isocyanates using mild reagents. In all cases, it is necessary to find the optimal working conditions for the method. It is still vital to have a very effective, reliable, atom-economical, low cost, environmentally friendly and useful technique for the quick and clean realisation of the amide bond [4].

In light of the foregoing, the new chemical was synthesized via benzoyl chloride derivative with triethylenetetramine in a non-catalyzed medium. <sup>1</sup>H and <sup>13</sup>C NMR and mass spectroscopy methods, as well as elemental analysis, were used to study the structures of the generated benzamide. In addition, the antibacterial activity of the synthesized amide was examined against gram-positive and gram-negative bacterial strains such as *Staphylococcus aureus*, *Escherichia coli*, and *Pseudomonas aeruginosa* microorganisms. The twofold microdilution technique was used to determine the examined compound's minimum inhibitory concentration (MIC). The outcomes of the obtained antibiotics were compared to those of the pristine medications (cefotaxime and ceftriaxone). In some concentrations, the chemical showed stronger inhibitory action than the reference drugs against *E. coli*, *P. aeruginosa*, and *S. aureus*.

**Keywords:** *Atom-economical technique, Triethylenetetramine, Acyl chloride, Antimicrobial properties*

### Acknowledgments

This work was supported by the Azerbaijan Science Foundation-Grant No AEF-MCG-2023-1(43)-13/09/3-M-09.

### References

- [1] X. Yu and D. Sun, "Macrocyclic drugs and synthetic methodologies toward macrocycles," *Molecules*, vol. 18, no. 6, pp. 6230–6268, 2013.
- [2] C. J. White and A. K. Yudin, "Contemporary strategies for peptide macrocyclization," *Nature Chemistry*, vol. 3, no. 7, pp. 509–524, 2011.
- [3] V. R. Pattabiraman and J. W. Bode, "Rethinking amide bond synthesis," *Nature*, vol. 80, no. 7378, pp. 471–479, 2011.
- [4] C. A. Montalbetti and V. Falque, "Amide bond formation and peptide coupling," *Tetrahedron*, vol. 61, no. 46, pp. 10827–10852, 2005.





## Synthesis and Biological Evaluation of Amide Derivative as Novel Antibacterial Agent

Fargana Alizadeh<sup>\*1,2</sup>, Alakbar Huseynzada<sup>2,3</sup>, Aygun Israyilova<sup>2,3</sup>, Ulviyya Yolchuyeva<sup>1</sup>,  
Ulviyya Hasanova<sup>2,3</sup>, Eldar Gasimov<sup>4</sup>, Goncha Eyvazova<sup>3</sup>, Fuad Rzayev<sup>4</sup>, Orkhan  
Isayev<sup>4</sup>, Aida Ahmadova<sup>3</sup>, Elshan Aliyev<sup>2</sup>

<sup>1</sup>Institute of Petrochemical Processes, Baku, Azerbaijan

<sup>2</sup>Geotechnological Problems of Oil, Gas and Chemistry, Scientific Research Institute of ASOIU, Baku, Azerbaijan

<sup>3</sup>Baku State University, Baku, Azerbaijan

<sup>4</sup>Azerbaijan Medical University, Baku, Azerbaijan

### Abstract

In addition to being the primary chemical bonds found in proteins, amide linkages are also the building blocks of many of the most functional and extensively used synthetic polymers and drugs [3]. Amides are of great interest in organic chemistry especially due to their high stability and polarity and their conformational diversity.

One of the most significant reactions in organic chemistry—amide bond formation—is often overlooked as a contemporary issue because of the widespread occurrence of amides in modern pharmaceuticals and biologically active substances. But existing methods are reaching their inherent limits, and concerns about their waste and cost are becoming sharper. Due to limitations of existing chemical methods, such as reasons abovementioned, the development of novel approaches is gaining increased interest [1, 2].

All in all, the structural properties of acyl halides and polyamine provide the basis for the synthesis of novel amide N, N'-(piperazine-1,4-diylbis(propane-3,1-diyl))bis(1-naphthamide) from benzoyl chloride derivative and 1,4-Bis(3-aminopropyl)piperazine. According to computational studies, the previously mentioned characteristics have been demonstrated to enhance biological activity. The structure of the synthesised molecule was examined using elemental analysis, mass spectroscopy, and <sup>1</sup>H and <sup>13</sup>C NMR. Using a variety of biological activities, the experiment's next stage was to determine the biological activities of a newly synthesised amide. *Acinetobacter baumannii*, *Klebsiella pneumoniae*, *Pseudomonas aeruginosa*, *Escherichia coli*, *Staphylococcus aureus*, and other gram-positive and gram-negative bacteria were tested to examine the biological activity of the synthesised organic compound. This new amide was shown to have a less inhibitory impact than the reference antibiotics, cefotaxime and ceftriaxone.

**Keywords:** *Naphthamide, Piperazine, Biological activity, Antibacterial agent*

### Acknowledgments

This work was supported by the Azerbaijan Science Foundation-Grant No AEF-MCG-2023-1(43)-13/09/3-M-09.

### References

- [1] S. Kumari, A. V. Carmona, A. K. Tiwari, and P. C. Trippier, "Amide bond bioisosteres: Strategies, synthesis, and successes," *Journal of Medicinal Chemistry*, vol. 63, no. 21, pp. 12290–12358, 2020
- [2] N. J. Oldenhuis, A. M. Whittaker, and V. M. Dong, "Greener methods for amide bond synthesis," in *Green Chemistry in Drug Discovery: From Academia to Industry*, 2022, pp. 35–96,
- [3] V. R. Pattabiraman and J. W. Bode, "Rethinking amide bond synthesis," *Nature*, vol. 480, no. 7378, pp. 471–479, 2011, doi:10.1038/nature10702.



---

## Examining How CeO<sub>2</sub> Addition Affects the Microstructure and Wear of Cu-Al-Mn-Fe Shape Memory Alloy

Fatih Dogan<sup>\*1</sup>

<sup>1</sup>Rare Earth Elements Application and Research Center (MUNTEAM), Munzur University, Tunceli, Türkiye

---

### Abstract

Shape Memory Alloys (SMAs) exhibit superior mechanical properties, notably enhanced wear resistance, in comparison to conventional counterparts with similar surface hardness. Rare earth oxides frequently serve as additives in alloys to enhance their mechanical characteristics. The study presented herein the examination of the impact of varied CeO<sub>2</sub> additions (0.01%, 0.1%, 0.5, and 1.0% CeO<sub>2</sub>) on the attributes of Cu-Al-Mn-Fe SMAs fabricated using powder metallurgy (PM). Various tests were conducted, Optical Microscope (OM), scanning electron microscopy (SEM), energy dispersion spectrometer (EDS), X-ray diffraction (XRD), as well as hardness and wear tests. The experimental results indicate that the addition of the CeO<sub>2</sub> particles affected austenite phase boundaries during martensitic phase transformation may hinder the transition itself, leading to modifications in the wear properties of Cu-Al-Mn-Fe SMA. The change in wear rate predominantly correlates with the formation of precipitates in the inclusion of CeO<sub>2</sub>. The enhancement in wear and hardness properties primarily stems from grain refinement strengthening, and solid solution strengthening following the addition of rare earth oxide (CeO<sub>2</sub>). The wear rate demonstrates with the CeO<sub>2</sub> content elevation from  $1.5 \times 10^{-3}$  mm<sup>3</sup>/m to  $3.4 \times 10^{-3}$  mm<sup>3</sup>/m. The frictional characteristics of Cu-Al-Mn-Fe SMA were improved, with the addition of CeO<sub>2</sub> particle decreased friction coefficient of 0.4 by the addition CeO<sub>2</sub> particle. The incorporation of the quantity of CeO<sub>2</sub> (0.5 % CeO<sub>2</sub>) facilitated the enhancement of grain uniformity in Cu-Al-Mn-Fe SMA, leading to improved wear resistance. The hardness and wear tests showed that incorporating CeO<sub>2</sub> particles into Cu-Al-Mn-Fe SMA enhances the hardness of the samples while exhibiting a reduction in the wear rate with optimum percentages of reinforcements.

**Keywords:** Shape memory alloy, Rare earth, Microstructure, Wear behaviour

---



## Catalytic Oxidation of Lignocellulosic Biomass to Biofuels Using Reusable Mixed Oxide as a Catalyst in a Green Solvent

Mona Benali<sup>\*1</sup>, Abdallah Oumekki<sup>1</sup>, Jamil Toyir<sup>2</sup>

<sup>1</sup>Laboratory of Processes, Materials and Environment (LPME), Faculty of Science and Technology of Fes, Sidi Mohammed Ben Abdellah University, BP. 2202, Morocco

<sup>2</sup>Laboratory of Processes, Materials and Environment (LPME), Sidi Mohammed Ben Abdellah University, FP-Taza, B.P 1223, Morocco

---

### Abstract

Biofuels or liquid fuels derived from natural matter, are one of the most intriguing yet divisive alternatives for petroleum-based fuels. The most common approach to producing biofuels is to transform plant sugars and other carbohydrates into oxygen-deficient chemicals. A growing relevance has been devoted to the direct synthesis of platform molecules from biomass resources, using one-pot or cascade techniques via adequate catalytic system. Tuning and improving the reaction conditions of the above-mentioned bio sourced processes makes this approach as beneficial strategy from an economic and ecological standpoint. In a similar vein the major goal of this contribution was to investigate and enhance the conditions for a selective oxidation of lignocellulosic biomass to yield formic acid (FA), one of the most coveted liquid hydrogen carriers and among the key compounds used in the pharmaceutical, cosmetic, and leather industries. Both oxidizing aqueous hydrogen peroxide and magnesium mixed oxide have been employed at an atmospheric pressure for this purpose. The effect of reaction time, temperature, amount of catalyst and oxidant on the product's yield and selectivity have been investigated. The oxidation of a plant-derived cellulosic fibers at 70 °C provided an impressive result with a high yield and specific activity of 59.8%, 1.14 (g FA/g cellulose/g catalyst) respectively, the latter was confirmed to be relatively close to the one from the oxidation of pure cellulose. Furthermore, the reusability of the catalyst has also been studied which was demonstrated to result in the same yields for 2 consecutive runs.

**Keywords:** Lignocellulosic biomass, Heterogenous catalyst, Catalytic oxidation, Biofuels, Optimization

---



---

## Thermal Behavior Kinetics of Macromolecular Nickel (II) complex using Thermogravimetric Analysis (TG/DTG)

Djoughra Aggoun<sup>\*1</sup>, Yasmina Ouennoughi<sup>1</sup>

<sup>1</sup>Laboratory of Electrochemistry, Molecular Engineering and Redox Catalysis (LEIMCR), Faculty of Technology, University of Ferhat  
Abbas Setif-1, Setif 19000, Algeria

---

### Abstract

Determining of thermal degradation mechanism of synthetic materials remains problematic for researchers. So, the aim of this paper is to study the decomposition kinetics of Divinylbenzene-4-vinylpyridine unmodified copolymer structure with its modified structure with nickel complex were investigated by thermal analysis. These thermogravimetry (TG) and differential thermogravimetry (DTG) analysis were conducted between room temperature 25 and 800 °C using four different heating rates 5, 10, 15 and 20 °C/min. Four methods were used to calculate the values of the activation energies of the thermal decomposition. The obtained values are 198, 183-265 and 209-288 kJ mol<sup>-1</sup> for Kissinger method; 179, 315, and 162 kJ mol<sup>-1</sup>, in the  $\alpha$  conversion ranges (0.25-0.85; 0.55-0.95 and 0.50-0.85) for Ozawa method; 188, 441 and 191 kJ mol<sup>-1</sup>, in the  $\alpha$  conversion ranges (0.30-0.85; 0.55-0.95 and 0.40-0.90) for Friedman method respectively. While for Coats-Redfern method, in the  $\alpha$  conversion range (159-177; 99-150), the resulting activation energies are 86-96 kJ mol<sup>-1</sup>. The activation energy values calculated from Coats-Redfern method are also used to evaluate the thermodynamic parameters like  $\Delta S$ ,  $\Delta H$  and  $\Delta G$  of these compounds.

**Keywords:** Macromolecular nickel complex, Thermal analysis (TG/DTG), Decomposition kinetics, Activation energy, Thermodynamic parameters

---



---

## Synthesis, Spectral Approach and Electrochemical Properties of Nickel (II) and Copper (II) Organometallic Schiff Base Complexes

Yasmina Ouennoughi<sup>1</sup>, Djouhra Aggoun<sup>\*1</sup>

<sup>1</sup>Laboratory of Electrochemistry, Molecular Engineering and Redox Catalysis (LEIMCR), Faculty of Technology, University of Ferhat Abbas Setif-1, Setif 19000, Algeria

---

### Abstract

This paper explores the synthesis, characterization and electrocatalytic behavior of two ferrocenyl-substituted tetradentates complexes of Nickel and copper. The complexes, N,N-Bis[5-(N,N-ferrocenmethylaminophenyl)methylsalicylidyne]-1,2-diaminoethane of M(II) ((Fc-Me-Ani)<sub>2</sub>-LM<sup>II</sup>), were prepared by heating the tetradentate Schiff base ligand ((Fc-Me-Ani)<sub>2</sub>-H<sub>2</sub>L) in the presence of a stoichiometric amount of nickel(II) and copper(II) metal salts, dissolved in a mixture of ethanol and methylene chloride at 50 °C under N<sub>2</sub> atmosphere. The molecular structures of these complexes were deduced from elemental analysis, FT-IR, UV-Vis and mass spectrometry. The electrochemical characterization was investigated by cyclic voltammetry on a glassy carbon electrode and the effect of the solvent (methylenechloride (DCM), dimethylformamide (DMF) and dimethylsulfoxide (DMSO)) was analyzed. The electrochemical characterization of the metal complexes reveals the electron-transfer capability of the two electroactive redox moieties, ie. the ferrocenyl moieties (Fc<sup>+</sup>/Fc) and the metallic centre (Ni<sup>2+</sup>/Ni<sup>+</sup>) or (Cu<sup>2+</sup>/Cu<sup>+</sup>).

**Keywords:** Organometallic compounds, Nickel and copper Schiff base complexes, Spectroscopy, Electrochemistry

---



## **Bibliometric Analysis of Research Trends in Additive Manufacturing in Metallurgical Engineering: A Scopus Database Study by Turkish Scholars**

**Oussama Zaidi<sup>\*1</sup>**

*<sup>1</sup>Mechanical Engineering Department, Construction Engineering Faculty, University of Mouloud Mammeri de Tizi Ouzou, 15000 Tizi-Ouzou, Algeria*

---

### **Abstract**

This paper presents a comprehensive bibliometric analysis of research trends in additive manufacturing within the field of metallurgical engineering, focusing on publications authored by Turkish researchers. Utilizing data extracted from the Scopus database, the study examines scholarly output, citation patterns, collaboration networks, and thematic evolution within the domain of additive manufacturing. Key bibliometric indicators such as publication trends, citation impact, international collaboration, and co-citation networks are analyzed to identify prominent research themes, influential authors, and emerging areas of interest specific to additive manufacturing in metallurgical engineering. The findings provide valuable insights into the trajectory of additive manufacturing research conducted by Turkish scholars, shedding light on the discipline's current status, emerging trends, and future directions within the context of metallurgical engineering. This bibliometric analysis serves as a valuable resource for researchers, practitioners, and policymakers seeking to understand the dynamics of additive manufacturing research in Turkey and globally, and offers a foundation for guiding future research endeavors in this specialized area of metallurgical engineering.

**Keywords:** *Metallurgical engineering, Additive manufacturing, Bibliometric, Scopus*

---



## **Analysis of Electrical Field Norm Distribution at the Cathode/Arc Interface in TIG Welding**

**Merazi Sayah<sup>\*1</sup>, Leila Belgacem<sup>1</sup>**

*<sup>1</sup>Research Center in Industrial Technologies – CRTI, Algiers, Algeria*

---

### **Abstract**

Understanding the distribution of electrical field standards at the cathode/arc interface in tungsten inert gas welding (TIG) is crucial to optimize welding parameters and ensure high quality welds. This study aims to analyze the distribution of the electrical field standard in the vicinity of the cathode and arc during TIG welding processes. Through COMSOL numerical simulations to model cathode/arc coupling, variations in the distribution of electrical field standards are studied under different welding conditions, including arc length variations, current density and electrode geometry. The results highlighted the spatial distribution of the electric field standard, highlighting the regions of high and low field forces at the cathode/arc interface. In addition, the implications of the distribution of electric field standards on weld penetration, heat affected area size and overall weld quality are discussed. The results of this analysis contribute to the optimization of TIG welding processes and the advancement of understanding in the field of arc physics.

**Keywords:** *TIG welding, Electrical field norm, Cathode/arc interface, Distribution analysis, Welding parameters, Computational simulations, Weld quality*

---



---

## DFT Insights for Structural, Electronic, and Optical Characteristics of $\text{Cs}_2\text{XBr}_6$ ( $\text{X} = \text{Pb}, \text{Sn}$ ) Double Perovskites for Low-Cost Solar Cell Applications

Rekia Larbi<sup>\*1</sup>, Omar Sahnoun<sup>1</sup>, Mohamed Sahnoun<sup>1</sup>

<sup>1</sup>Physic Department, Univesity of Mascara, Mascara, Algeria

---

### Abstract

In recent years, the variant forms of perovskites materials have gained significant attention as innovative substances for exploring their potential in photovoltaic applications. In this study, a comprehensive analysis of the structural, electronic, and optical characteristics of a series of mixed-metal double perovskites  $\text{Cs}_2\text{XBr}_6$  ( $\text{X}=\text{Pb},\text{Sn}$ ), has been carried out using first-principles calculations based on density functional theory. We have validated the thermodynamic stability of these compounds through the computation of their formation energy. Furthermore, the computed bandgap is direct in terms of exploring the band structures for all compounds. These calculated bandgap values fall within the visible energy range. Moreover, as the concentration of Sn increases within the  $\text{Cs}_2\text{XBr}_6$  ( $\text{X}=\text{Pb},\text{Sn}$ ) systems, there is a gradual increment in the band gap. Furthermore, a thorough examination of the estimated optical properties against photon energy suggests that they might be employed in solar cell devices with maximal transition and high coefficient absorption in the visible spectrum. The spectroscopic limited maximum efficiency (SLME) metric was used to predict solar cell characteristics of the perovskite absorber layer as a function of thickness. we have demonstrated variations in the behavior of  $J_{sc}$ ,  $V_{OC}$ , and  $\eta$  depending on the concentration of Sn atom.

**Keywords:** Perovskites, Optical properties, Photovoltaic applications, DFT

---





## **Milling Effect on Structural, Microstructural, and Magnetic Properties of FeCo Based Alloy**

**Chaffia Djebbari<sup>\*1</sup>**

<sup>1</sup>*Department of Technology, Faculty of Technology, 20 August 1955 University Skikda, Algeria*

---

### **Abstract**

Mechanical alloying is an economic technique for developing powders of nanostructured materials by the structural disintegration of a coarse-grained structure following severe plastic deformation. Thus, the production of iron cobalt based alloys is done by high energy ball milling in a planetary ball mill P7 under an argon atmosphere. Structural, microstructural and magnetic properties were followed by X-ray diffraction (XRD) and vibrating sample magnetometry (VSM). The result of the X-ray diffractograms refinement revealed the formation of a disordered solid solution Fe(Al,Co) of BCC structure with high density of dislocations. The refinement of the grain size and the increase of the average rate of micro-stresses exhibit significant distortion of the crystal lattices. The powder alloy demonstrated soft magnetic behavior with a saturation magnetization of 186 emu/g and a coercivity of 60 Oe, indicative of multidomain properties based on the Mr/Ms ratio.

**Keywords:** *Mechanical alloying, FeCo based alloys, X-ray diffraction, Magnetic properties*

---



---

## Mapping of Tectonic Fractures in the Zat Region (Western High Atlas, Morocco): Using Remote Sensing and Structural Geology

Abdelfattah Aboulfaraj<sup>\*1</sup>, Abdelhalim Tabit<sup>1</sup>, Ahmed Algouti<sup>1</sup>, Abdellah Algouti<sup>1</sup>, Said  
Moujane<sup>1</sup>, Saloua Agli<sup>1</sup>

<sup>1</sup>2GRNT Laboratory (Geosciences, Geotourism, Natural Hazards and Remote Sensing), Department of Geology, Marrakech, Faculty of  
Sciences Semlalia, Cadi Ayyad University, Morocco

---

### Abstract

This research maps tectonic fractures in the Zat area of the Western High Atlas using optical data (Landsat 8 OLI and ASTER DEM). These images have been treated and enhanced using an appropriate method (filters, ACP) in order to construct a lineament map. It was confirmed in a fully new structural map based on a combination of pre-existing geological data and field information. The described lineaments include four primary directional ranges, N-S, NW-SE, E-W, and NE-SW, with a prevalence of the NE-SW directional family of Atlasic compression. They represent a greater agreement with the faults that are previously acknowledged. Except for the directional range from E-W to NNE-SSW, which contains lineaments connected with Ediacaran dykes. Furthermore, the E-W directional family, which is part of the prior range, might be related with normal faults formed perpendicular to N-S accidents during the opening of the Paleozoic basin. The lineament density grows proportionately from the Phanerozoic cover to the Precambrian substratum due to the development of terrain stiffness and fracturing rate. With the exception of the Precambrian nuclei (Ourika and Afra), were distinguished by a significant decline in density. This shows that these nuclei exercised local lithological control over fracturing during the orogenic compressions that occurred during geological eras. In the context of prospecting and identifying mineralised fractures, as well as the investigation of subsurface flows, this work offers an intriguing structural map. Furthermore, as part of sustainable development, it investigated a major geological hazard that is very sensitive to the ground movements that characterize the area.

**Keywords:** Remote sensing, Lineament, Tectonics, Ediacaran, Hercynian, Atlasic, Precambrian block

---

### References

- [1] Ellero, M. G. Malusà, G. Ottria, H. Ouanaimi, and N. Froitzheim, "Transpressional structuring of the High Atlas belt, Morocco," *Journal of Structural Geology*, vol. 135, art. no. 104021, 2020.
- [2] N. Ennih and J. P. Liégeois, "The boundaries of the West African craton, with special reference to the basement of the Moroccan metacratonic Anti-Atlas belt," *Geological Society*, vol. 297, no. 1, pp. 1–17, 2008.
- [3] N. Ennih and J. P. Liégeois, "The Moroccan Anti-Atlas: The West African craton passive margin with limited Pan-African activity. Implications for the northern limit of the craton," *Precambrian Research*, vol. 112, no. 3–4, pp. 289–302, 2001.
- [4] A. Soulaïmani and H. Ouanaimi, "Anti-Atlas et Haut Atlas, circuit occidental," *Nouveaux Guides Géologiques et Miniers du Maroc*, vol. 3, pp. 9–72, 2011.



## **Achieving Full Control of Industrial Robot: Kinematic and Dynamic Modeling with FOPID Controller Tuned using GWO Approach**

**Benaoumeur Ibari<sup>\*1</sup>, Mourad Hebali<sup>1</sup>, Baghdadi Rezali<sup>1</sup>, Omar Medjad<sup>1</sup>, Menaouer Bennaoum<sup>1</sup>, Hocine Abdelhak Azzedine<sup>1</sup>, Abdelkader Maachou<sup>1</sup>**

<sup>1</sup>*Department of Electrotechnical, University Mustapha Stambouli Mascara, 29000, Mascara, Algeria*

---

### **Abstract**

Industrial robots represent complex systems that merit extensive research and investigation. In this study, we focus on the FANUC M 710iC/70 robot, presenting a comprehensive analysis. In the first, we delve into kinematic modeling, utilizing DH parameter tables for Forward Kinematics and a geometric approach for Inverse Kinematics. Secondly, we address the dynamics of the robot through Euler-Lagrange equations. Finally, we develop an optimal FOPID controller for position control using the Grey Wolf Optimizer (GWO), a metaheuristic optimization algorithm. Simulation results conducted under varying load conditions validate the controller's efficiency, demonstrating improved accuracy and stability in trajectory tracking.

**Keywords:** *6DOF manipulators, Kinematic, Dynamic, Fanuc M 710iC, Trajectory control, FOPID controller, GWO optimizer*

---



---

## Analysis of Technical Indicators in Cryptocurrency Market

Asli Boru Ipek<sup>\*1</sup>

<sup>1</sup>Management Information Systems, Kutahya Dumlupinar University, Kutahya, Türkiye

---

### Abstract

Academic researchers, economists, financial analysts, and investors analyze vast amounts of data using a variety of models to make predictions. Despite the widespread use of technical indicators in the stock market literature, technical indicators in the cryptocurrency market have not been adequately studied. Therefore, the use of technical indicators while developing the hybrid model is one of the important contributions of this study. Multiple methods can be integrated to propose a hybrid methodology. This study will mainly explain the answers to three research questions: (1) how to construct a hybrid method for cryptocurrency price prediction; (2) does the predictive performance vary depending on the types of cryptocurrency; and (3) do technical indicators have an impact on the performance of the proposed hybrid method? In this paper, five cryptocurrencies, including Bitcoin, Ethereum, Cardano, XRP, and Solana, are considered for price prediction. The results of this study show that the hybrid methodology has shown promising results in cryptocurrency price prediction. In the proposed method, the value of the root mean squared error varies between 0.031 and 0.102. Despite the increase in prediction accuracy in financial markets, studies in the literature claim that prediction accuracy can be further increased by searching for new sources of information. The more accurate the prediction, the more risk can be reduced. Also, prediction studies are necessary to ensure the economic progress of a country.

**Keywords:** *Cryptocurrency, Technical indicators, Hybrid methodology*

---



---

## IIoT as an Enabler for Data Analytics to Optimize Industrial Processes

Federico Walas Mateo<sup>\*1</sup>, Andrés Redchuk<sup>2</sup>

<sup>1</sup>*Institute of Engineering and Agronomy, Universidad Nacional Arturo Jauretche (UNAJ), Florencio Varela, Argentine*

<sup>2</sup>*ETSII, Universidad Rey Juan Carlos, Madrid, Spain*

---

### Abstract

This paper develops concepts associated with the generation of data from industrial processes, and its transformation into information so that industrial companies evolve towards the Industry 4.0 model to reach the Industry 5.0 emergent paradigm. Key concepts and an analysis of the state of the art on best practices to integrate data from industrial operations and use it to generate value-added information to optimize industrial processes are presented. Standard topics on Operations Technology (OT) and Information Technology (IT) architecture are discussed, including concepts of Industrial Internet of Things (IIoT), Artificial Intelligence and Machine Learning (AI/ML).

The conceptual framework is developed to analyse AI/ML as a process optimization engine, integration with IIoT and the potential to produce data to feed AI/ML models strictly in the industrial field. At the end of the chapter an analysis of opportunities and weaknesses presented by these solutions for optimizing processes in the industrial field is presented according to the border conditions established for the new production models.

**Keywords:** *Industry 4.0, AI/ML, IIoT platform, ISA 95, Lean Manufacturing*

---

## 1 INTRODUCTION

This paper develops concepts associated with the gathering of data from industrial processes, and its transformation into information to ease process management through descriptive and prescriptive analytics. This is the key for industrial companies to evolve towards the Industry 5.0 (I5.0) paradigm.

The structure of this chapter includes key concepts and an analysis of best practices to integrate data from industrial operations and use it to generate value-added information to improve industrial processes. The chapter continues with the presentation of the case study and the results achieved, to end with the corresponding conclusions.

The market penetration of devices in IIoT architectures, equipped with sensing and communication capabilities, has allowed companies to connect devices in manufacturing plants, developing cyber-physical systems capable of generating and collecting data throughout the industrial space [1].

Standard topics on Operations Technology (OT) and Information Technology (IT) architecture are discussed, including concepts of Industrial Internet of Things (IIoT), Artificial Intelligence and Machine Learning (AI/ML). Technology (OT/IT) convergence, are identified by [2] among the main areas of investment in the short term.

On the other hand, the link between Lean Management (LM) and I5.0 generates interest, with the aim of eliminating waste from business processes to improve their efficiency, as well as their competitiveness, according to [3]. Facilitating the visibility of the operation data impacts the possibility of eliminating tasks that do not add value and identifying opportunities for improvement.

## 2 INDUSTRIAL PROCESS DATA GENERATION, INTEGRATED ARCHITECTURE

To start this topic, let us refer to the article by [4] where the authors highlight the need to consider the systems approach when addressing research on the integration of industrial information. The paper describes the modelling and integration of information flow to contextualize business information with operational data through the architecture proposed by IIoT.

The International Society for Automation (ISA) [5] and the International Electrotechnical Commission (IEC) [6] approach operational information collection and its integration. IEC 62264 multilayer standard based on the ISA-

95 standard defines a framework for an information model exchange which ease the integration of solutions that run in both IT and OT areas. The firms that comply with this standard define interfaces between control and management functions, allowing them to make informed decisions about the data to exchange so that costs and risks are kept low in the event of implementation errors when deploying the solutions.

Figure 1 shows the architecture level proposed by the ANSI/ISA-95 standard. This International Standard has been generated to address problems that arise during the development of automated interfaces in the field of enterprise management systems and control systems. This standard guides the vertical integration of firm information. The ISA 95 standard defines a functional hierarchy model to categorize the functions of industrial companies. This 5-layer model is known as the automation pyramid.

Level 0 is where the production processes are carried out. At that level, the operational frame is measured in milliseconds [7] through sensors (pressure, temperature, flow, etc.), and all field devices (actuators, servo motors, etc.). This tier is where also appearing identification devices, through RFID or Bluetooth technology, among other alternative to trace equipment and goods in the operational process.

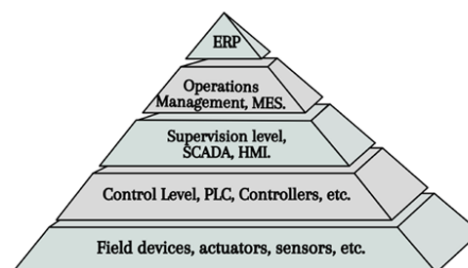
Level 1 represents the first logical layer, where data received from the previous level is processed. The operational processes at this level are based on constant feedback mechanisms. In this instance, control elements such as Programmable Logic Controllers (PLC), and variable speed drives, among others, appear. The time frame is given in seconds.

Level 2 represents the automation layer, where control and automation mechanisms are generated. In this instance appear the Human Machine Interfaces (HMI), Supervision Control, and Data Acquisition systems (SCADA). These systems communicate with lower layers such as PLCs through protocols, and communication standards, such as MODBUS. The time frame at this level is given in minutes.

The next level, 3, is the layer where the contextualization with the product that is manufactured occurs. In this layer, the recipes or Bill of Materials (BOM) are defined and maintained. The system that works in this instance is the Manufacturing Execution System (MES), on this tool it is possible for operators to enter data. The time frame is given in hours to days.

The last level, 4, represents the instance of management, planning, and intelligence of operations and business. The key element is the Enterprise Resource Planning System (ERP).

**INFORMATION INTEGRATION PYRAMID ACCORDING TO ANSI/ISA 95 (ISO/IEC IEC 62264-3)**



**Figure 1.** Information vertical integration model proposed by the ANSI/ISA 95 standard

To conclude this issue, we must note that, although the ISA 95 model and the automation pyramid are still relevant to support smart production technologies and IIoT, it would seem necessary to analyse the extension of this model based on the challenges presented by the new variants. technological. This item is anticipated as one of the future research lines.

### 3 IIOT ARCHITECTURE. IT AND OT INTEGRATION THROUGH IIOT

The OT consists of systems that monitor and control physical processes that manage automated manufacturing processes, and associated applications that are typically safety-critical, in real-time, incorporating additional non-functional properties such as limited latency, reliability, and compliance with safety standards. and industry-specific protection [8, 9]. Until now, IT, such as cloud/edge computing, service-oriented architectures (SOA), and virtualization, have been exploited in industrial applications only in a limited way, that is, only in contexts where very strict requirements were not needed. However, it is becoming increasingly apparent that I5.0 will have a very

significant impact only with full OT/IT convergence driving the deep joint exploitation of the latest computing and communication technologies.

The article [10] develops the conceptual framework for IT and OT infrastructure to facilitate the I5.0 model. The convergence of OT/IT is essential for data integration, and especially for advancing AI solutions in the industrial decision-making process, providing the foundation for a cognitive-capable plant. The article includes a real case that meets the specific needs of IT and OT, achieving a fast and smooth transfer of large volumes of data to the IT layer.

[11] consider that with the rise of trends such as IoT and cloud manufacturing that seek the convergence of IT tools in OT networks, IT and OT analysis are highly sought after in current industries that seek real-time solutions. data analysis. To analyse the data in the IT and OT domain, it is necessary to use models, which not only focus on describing both domains but can also show the relationship between them. This article presents a technique that uses operational data, produced in an organization from IIoT solutions, to model OT, to apply analysis methods.

#### 4. A CASE IN THE FOOD INDUSTRY

To illustrate the scope and strengths of IIoT architecture, an adoption case is developed. The case takes place in an industrial company in the food sector located in the south of the suburbs. The company's production system responds to the continuous process scheme, and at the beginning of the project it had a SCADA architecture for the management of industrial processes, and an ERP platform for business management.

Based on the initiative of the company's Management, a diagnosis of digital maturity was made that made visible the need to advance in a greater integration of data to evolve in the I5.0 model. Within this framework, it was decided to advance in the adoption of an IIoT architecture. For this, a Gateway type device was incorporated to take the data of the plant operation, which is found in the OT network, to the cloud. For the integration of the information of the processes, the OPC UA server that incorporates the existing SCADA platform in the company is used and enables the interoperability of the data so that it can finally be viewed on the IIoT MindSphere platform developed by the German company Siemens [12].

The solution MindSphere is an open, cloud-based IIoT operating system capable of connecting all the plant equipment and systems, extracting industrial process data and converting it into information. This platform has an open action protocol and various functionalities such as remote access to Amazon Web Service cloud services or the PaaS (Platform-as-a-Service) service.

Being an open platform, MindSphere allows connecting with other open platforms such as NodeRed [13], and Grafana [14] among others. NodeRed is a programming tool for connecting hardware devices, APIs, and online services. It provides an editor over a web browser that makes it easy to develop flows using preconfigured nodes. This tool is based on Node.js, and is event driven.

On the other hand, Grafana is an open source platform for data visualization and monitoring. It allows users to create and share dashboards that display real-time data from various sources, including databases, servers, and cloud services. Grafana, according to [14] supports a wide range of data sources, it also includes functions such as alerts, annotations and plugins for data visualization, and integration with other tools. It is commonly used in the fields of system monitoring, IoT, and network monitoring.

Once the integration of the operation information from SCADA was generated, a dashboard system was developed to show different KPIs of the operation, which can be viewed outside the plant environment without affecting the security conditions required by the OT network. Figures 2 and 3 show different ways of viewing the KPIs and equipment status generated with operation data.



**Figure 2.** KPI of the daily operation that is shown in the dashboard generated on the IIoT platform



**Figure 3.** Dashboard that shows the status of a boiler from data gathered by the IIoT architecture

Lastly, it is worth noting that the adoption of the new solution was carried out through a co-creation process facilitated by working with an agile methodology to manage change. In this way, it was possible for process experts to get involved early in the adoption of the solution, and to be able to contribute knowledge of the industrial domain to technology providers.

Finally, the data generated is stored in a cloud database that will ease the evolution of the data architecture, towards a prescriptive analytics model.

#### 4 CONCLUSION

As the first emerging of this work, the fact of achieving a robust IIoT structure from connecting various solutions achieving the convergence of data in the manufacturing environment. One issue that stands out among the results is the possibility of extracting data outside the plant without violating cybersecurity protocols. Achieving the security of the SCADA data is an added value that generates the value proposition of the project. It is worth mentioning that during emergencies that required access to the SCADA from outside the plant, important divergences arose with the company's security standards. The most notorious event occurred during the restrictions imposed by the COVID pandemic.

On the other hand, the empowerment of the people involved in the process was achieved by visualizing the data in a friendlier way through dashboards located in the manufacturing plant. An observation that deserves consideration is the fact that the OT infrastructure had a state-of-the-art SCADA platform that incorporated the functionality of the OPC UA server. Without this functionality, the project would have become more complex and would have consumed more resources.

The IIoT platform generates information that streamlines the process of continuous improvement of the industrial processes carried out by the company. Visualization of the state of production through digital platforms on monitors located in the boiler area and in the process control room. This allows analyzing the state of the assets and the operational processes to address the elimination of waste proposed by the Lean Manufacturing approach, this view integrated with the I5.0 strategy, leads the company to operate within the Lean 5.0 model.

Finally, highlight the importance of open platforms to facilitate the deployment of complex solutions, dynamically and saving development resources. As an example, it can be seen in the paragraph mentioning the OPC UA standard in this section.

#### References

- [1] N. Tapoglou, J. Mehnen, and J. Butans, "Energy efficient machining through evolutionary real-time optimization of cutting conditions on CNC-milling controllers," in *Experiments and Simulations in Advanced Manufacturing*, Berlin/Heidelberg, Germany: Springer, 2021; pp. 1–18, doi: 10.1007/978-3-030-69472-2\_1.



- [2] Gartner. (2024, May 4). When IT and Operational Technology Converge [Online]. Available: <https://www.gartner.com/smarterwithgartner/when-it-and-operational-technology-converge>
- [3] N. Y. G. Lai, K. H. Wong, and D. Halim, "Industry 4.0 enhanced lean manufacturing," in *2019 8th International Conference on Industrial Technology and Management (ICITM)*, pp. 206–211, 2019.
- [4] W. He and L. Xu, "Integration of distributed enterprise applications: A survey," *IEEE Transactions on Industry Informatics*, vol. 10, no. 1, pp. 35–42, Feb. 2014.
- [5] ISA. International Society of Automation. [Online] July 01, 2022. Available: <https://www.isa.org/>
- [6] American National Standards Institute (ANSI), ISA-95.00.01-2010, ISA-95.00.02-2010, ISA-95.00.03-2013, ISA-95.00.04-2012, ISA-95.00.05-2013. North Carolina USA.
- [7] M. Åkerman, *Implementing Shop Floor IT for Industry 4.0*. Department of Industrial and Materials Science, Gothenburg: Chalmers University of Technology, 2018.
- [8] A. Garbugli, A. Bujari, and P. Bellavista, "End-to-end QoS management in self-configuring TSN Networks," in *Proceedings of the IEEE International Conference on Factory Communication Systems (WFCS)*, Linz, Austria, pp. 131–134, 2021.
- [9] A. Arestova, M. Martin, K. S. J. Hielscher, and R. German, "A service-oriented real-time communication scheme for AUTOSAR adaptive using OPC UA and Time-sensitive networking," *Sensors*, vol. 21, art. no. 2337, 2021.
- [10] L. Patera, A. Garbugli, A. Bujari, D. Scotece, and A. Corradi, "A layered middleware for OT/IT convergence to empower Industry 5.0 applications," *Sensors*, vol. 22, art. no. 190, 2022, doi: 10.3390/s22010190.
- [11] P. Lara, M. Sánchez, and J. Villalobos., "Enterprise modelling and operational technologies (OT) application in the oil and gas industry," *Journal of Industrial Information Integration*, 2020.
- [12] Siemens. (2024, Feb. 03). Available: <https://new.siemens.com/es/es/productos/software/mindsphere.html>
- [13] B. N. Musungate and T. Ercan, "A simple Node-RED implementation for digital twins in the area of Manufacturing," *Trends Comput Sci Inf Technol*, vol. 8, no. 2, pp. 50–54, 2023, doi: 10.17352/tcsit.000068.
- [14] E. G. Rani and D. T. Chetana, "Using GitHub and Grafana tools: Data visualization (DATA VIZ) in big data," in *Computer Vision and Robotics*, Singapore: Springer, doi: 10.1007/978-981-19-7892-0\_38.



## Q-Learning Enhanced Swarm-Based Algorithms for the 0-1 Knapsack Problem

Fehmi Burcin Ozsoydan<sup>\*1</sup>

<sup>1</sup>Industrial Engineering Department, Dokuz Eylul University, Izmir, Türkiye

### Abstract

Machine learning-based solution approaches offer quite promising novelties in numerous research areas. In parallel, one can also put forward that swarm population-based metaheuristic algorithms represent promising alternative strategies in solving various optimization problems. Moreover, it is clear from the related literature that, research studies bringing such remarkable approaches together, grab attention of the researchers particularly in the last decade. Accordingly, the present paper introduces a Q-learning method that is capable of promoting or demoting the used population-based algorithms according to their achievements throughout search. As Genetic Algorithm (GA), and Particle Swarm Optimization (PSO), two well-regarded algorithms are adopted by the proposed Q-learning mechanism. Since it has a wide range of application areas in real-life, 0-1 Knapsack Problem is used as the benchmarking environment. 0-1 Knapsack Problem is a constrained binary optimization problem. Therefore, priority based encoding technique, which includes real-valued loci in solution vectors, is used by both algorithms. Thus, the regarding constraint of this problem is implicitly handled without any necessary further modifications. Moreover, it is clear that PSO is intrinsically appropriate for continuous solution encoding technique. In order to adapt GA to such an environment, affine-based crossover is used. It is worth stressing that, canonical modifications of these optimizers without any extensions are adopted. In this regard, performances of GA, PSO and the proposed Q-learning mechanism are compared to each other on the 0-1 Knapsack Problem benchmarking instances taken from the literature. As demonstrated by the experimental study and appropriate statistical tests, attention-grabbing results are achieved.

**Keywords:** Particle swarm optimization, Genetic algorithm, q-learning, 0-1 knapsack problem

## 1 INTRODUCTION

Integration of metaheuristic algorithms with machine learning (ML) techniques grab attention of researchers particular in the last decade. Since, it is apparent that machine learning-based solution approaches offer quite promising opportunities in numerous research fields including optimization research field [1–11].

One can categorize ML techniques into three main categories such as, supervised learning, unsupervised learning and reinforcement learning [6–11]. In the first category, namely, supervised learning, labelled data or target values are used. Unsupervised learning on the other hand makes use of unlabelled data, which is commonly used in segmentation or clustering problems. Finally, in reinforcement learning (RL), agents (virtual entities) choose actions among a group of actions due to a feedback that is gathered out of the environment, which agents interact to. According to the state of the environments, agents attempt to learn the efficient actions via a reward mechanism, which is usually problem or domain specific. Since the present work aims to integrate an RL method to population-based algorithms, these algorithms are presented in the following.

In the related literature, there are lots of population-based (or sometimes interchangeably swarm-based algorithms). Most of these algorithms draw inspiration from some particular mechanisms of living beings that attempt to survive. One can put forward that Genetic Algorithm (GA) [12] is one of the fundamental algorithms in this domain. GA is inspired by evolutionary mechanisms of Darwinian Theory and most of the studies are inspired by the notion of GAs. As another well-known algorithm, Particle Swarm Optimization (PSO) [13], which simulates the behaviours of bird or fish flocks seeking for food, is chosen as another algorithm in the present work.

Accordingly, the present paper introduces a Q-learning (QL) algorithm that is capable of driving population-based algorithms throughout optimization process. As reported above, GA and PSO, which are two well-regarded algorithms are adopted by the proposed QL mechanism. Since it has a wide range of application areas in real-life, 0-1 Knapsack Problem (KP) is used as the benchmarking environment. One should note that 0-1 KP is a constrained binary optimization problem. Therefore, priority based encoding technique that includes real-valued

loci in solution vectors, is used by both algorithms. Thus, the regarding constraint of this problem is implicitly handled without any necessary further modifications. Moreover, In order to adapt GA to such an environment, bled crossover, which is based on affine crossover, is used. It is worth stressing that, canonical modifications of these optimizers without any extensions are adopted. In the experimental study, performances of GA, PSO and QL-driven population-based algorithms are compared to each other on the 0-1 KP benchmarking instances taken from the related literature.

The rest of this paper is organized as follows: mentioned optimization problem along with regarding details and solution methods are presented in Section 2, while computational results and concluding remarks are given in Section 3 and Section 4, respectively.

## 2 PROBLEM AND SOLUTION METHODS

### 2.1 Benchmarking problem

0-1 KP [14] has numerous real-life applications in practice. This is the main motivation in choosing this problem as the benchmarking environment. Some of these applications include project selection, cargo loading, budget management, assignment, cutting stock, etc., [14]. Given a set of items associated to profits and weights, 0-1 KP aims to maximize the total knapsack profit subjected to knapsack capacity constraint. 0-1 KP can be formulated as given in Eqs. 1-3, where  $J = \{1, \dots, n\}$  represents the set of items,  $p_j$  and  $w_j$  are the profit and the weight of the  $j$ th item, respectively. In Eq. 2,  $C$  represents the capacity of the knapsack while  $x_j$  is a binary variable denoting whether the  $j$ th item is included in the knapsack. In this context, Eq. 1, which maximizes the total profit is the objective function and Eq. 2 is the knapsack capacity constraint. Finally, Eq. 3 imposes restrictions on decision variables.

$$\max \sum_{j \in J} p_j x_j \quad (1)$$

$$\text{s.t.} \\ \sum_{j \in J} w_j x_j \leq C \quad (2)$$

$$x_j \in \{0,1\}, \quad j \in J \quad (3)$$

The 0-1 KP formulated above is shown to be an NP-hard problem [14]. Therefore, solution approaches consisting mostly of heuristic approaches are reported. Due to space limitation again, readers are asked to refer to the survey presented by Bhattacharjee and Sarmah [15].

### 2.2 Solution encoding and decoding

There is a notable number of solution representation techniques in the related literature. However, the chosen technique should encompass also the existing constraints of the attacked problem. In this regard, priority-based encoding, where continuous numbers in solution vectors are sorted in ascending or descending order, is adopted in the present work. Solution vectors in this procedure include continuous real-valued numbers. The sorted list of these values indeed gives the precedence of items to be included in the knapsack. Simply, items are assigned to knapsack once at a time according to the sorted list as long as the knapsack capacity constraint is not violated. Thus, a vector can easily be decoded and the capacity constraint is implicitly satisfied. All tested algorithms, GA, PSO and QL adopt this strategy in the present work.

### 2.3 Genetic algorithm

For fair comparisons, the canonical GA [12] is employed. Chromosomes (solution vectors) are randomly generated as random variables  $\in [-1,1]$  in the initial population. Subsequently, some selected chromosomes undergo crossover with respect to a parameter referred to as crossover rate that is denoted by  $xOverRate$ . Afterwards, this population is exposed to mutation operations with respect to another parameter, namely, mutation rate that is denoted by  $mutRate$ . Accordingly, offspring population is obtained. Finally, natural selection is applied subsequent to evaluation of fitness values. Elitism procedure is optionally applied in order not lose the best-found solution in the current population. One should note that blend crossover is used as the crossover operator in GA. Mutation

takes place as generating a new random variable  $\in [-1,1]$  for the corresponding dimension of the corresponding chromosome. A pseudo code for the adopted GA is illustrated by Algorithm 1.

---

**Algorithm 1:** A pseudo code for GA

---

```

1: generate initial population
2: while (termination criterion not met)
3:     select the chromosomes for xover
4:     apply xover and mutation
5:     evaluate fitness
6:     apply natural selection
7:     apply elitism
8: end
9: print gbest

```

---

## 2.4 Particle swarm optimization

PSO [13] is another well-regarded population-based metaheuristic algorithm. Its efficiency is reported and is demonstrated in a great variety of research papers. As already mentioned, PSO is inspired by fish and bird flocks and it simulates the movement of such living beings. More formal definitions regarding PSO is presented in the following.

Solution vectors in PSO are referred to as particles. These solution vectors interact to each other via movement mechanisms formulated by Eqs. 4-5. In these equations,  $w$ ,  $v_{ij}$ ,  $pBest_{ij}$ ,  $x_{ij}$ ,  $gBest_j$ ,  $c_1$  and  $c_2$  represent inertia coefficient, velocity of the  $i$ th vector at the  $j$ th dimension,  $i$ th particle-best vector value at the  $j$ th dimension,  $i$ th vector value at the  $j$ th dimension, best-found solution vector value at the  $j$ th dimension, cognitive and social coefficients, respectively.

$$v_{ij} = wv_{ij} + c_1 \times rand \times (pBest_{ij} - x_{ij}) + c_2 \times rand \times (gBest_j - x_{ij}) \quad (4)$$

$$x_{ij} = x_{ij} + v_{ij} \quad (5)$$

Both initial population and initial values of velocity vectors are defined as random variables  $\in [-1,1]$ . Next, according to the movement functions, population is allowed to evolve. Neither upper nor lower bound limitations for the values are applied in the present work. Therefore, any additional group of constraints does not exist in the proposed algorithm. Finally, a pseudo code for PSO is presented by Algorithm 2.

---

**Algorithm 2:** A pseudo code for PSO

---

```

1: generate initial particles
2: for ( $t = 1; t \leq maxIter; t++$ )
3:     for ( $i = 1; i \leq popSize; i++$ )
4:         for ( $j = 1; j \leq n; j++$ )
5:             evaluate  $v_{ij}$  via Eq. 4
6:             update  $x_{ij}$  via Eq. 5
7:         end
8:         evaluate fitness
9:         update pbest and gbest
10:    end
11: end
12: print gbest

```

---

## 2.5 Q-learning driven algorithms

QL [16] is known to be an off-policy and model-free RL algorithm. QL has some main components such as environment, agent, reward, states and actions. As a virtual entity, an agent interacts to environment in QL. According to a feedback mechanism, agent is either rewarded or penalized. States are positions that switch due to actions taken by agent. Thus, the aim in QL is to choose the most promising actions according to any state that the agent falls into so as to maximize the total cumulative reward.

The mentioned reward mechanism is formulated by Eq. 6. As one can see from this formulation, agent achieves a reward when a solution is improved. If solution gets worse on the other hand, agent is penalized. Otherwise, any reward is not assigned.

$$reward_{t+1} = \begin{cases} +1 & \text{if } f_{new} - f_{X_{best}} > 0 \\ 0 & \text{if } f_{new} - f_{X_{best}} = 0 \\ -1 & \text{if } f_{new} - f_{X_{best}} < 0 \end{cases} \quad (6)$$

In QL, cumulative rewards of the state-action pairs are recorded in a table referred to as Q-table. The values in this table are driven out from Bellman equation as formulated by Eq. 7. The mentioned cumulative rewards of each state-action pairs are denoted by  $(s_t, a_t)$  and in this equation, the parameters  $\alpha_t$  and  $\gamma$  represent learning rate and discount factor, respectively. In the present work,  $\gamma$  is fixed to 0.80,  $\alpha$  is gradually decreased by Eq. 8.

$$Q_{t+1}(s_t, a_t) = Q_t(s_t, a_t) + \alpha_t \left[ reward_{t+1} + \gamma \max_a Q_t(s_{t+1}, a) - Q_t(s_t, a_t) \right] \quad (7)$$

$$\alpha_t = 1 - \left( 0.9 \times \frac{t}{maxIter} \right) \quad (8)$$

In order to avoid premature convergence in QL, the  $\epsilon$ -greedy method [17] is employed. According to this strategy, by  $\epsilon$  % probability, actions are randomly selected. Next, a roulette-wheel selection is applied by  $\chi$  % probability. Finally, by  $1 - \epsilon - \chi$  % probability, the maximum Q-factor method is used.

State-action space of the Q-table in the proposed QL procedure is of size  $2 \times 2$ . In this space, both states and actions are represented by the used algorithms GA and PSO. Therefore, the cumulative rewards of state-action pairs are recorded in a Q-table as given in the following.

$$\begin{bmatrix} GA - GA & GA - PSO \\ PSO - GA & PSO - PSO \end{bmatrix}$$

### 3 RESULTS

#### 3.1 Calibration of parameters

The parameters *maxIter* and *popSize*, which represent the maximum number of iterations and population size in GA and PSO are fixed to 1000 and 50, respectively. The remaining GA related parameters, *xOverRate* and *mutRate* are fixed to 0.95 and 0.001, respectively. Next, the movement coefficients in PSO,  $c_1$  and  $c_2$  are both fixed to 1.80. Finally, the QL related parameters  $\epsilon$  and  $\chi$  are fixed to 0.15 and 0.60 respectively. All these values are obtained via a preliminary work, which points out promising outcomes for all tested algorithms.

#### 3.2 Computational results

All tests are performed over 30 independent replications on a PC with i7-4790K CPU and 32 GB RAM. Obtained results are presented in Table 1, which is comprised of two distinct parts. The first part of Table 1 is associated to the standard 0-1 KP instances [18-19]. Next, the following part represents greater-scaled benchmarking instances. These instances are obtained following the guidelines of Zou et al. [18]. Since the optimum solution is not known for this group of instances, Dantzig upper bound (Eq. 9) is used. In this technique, items are sorted by non-increasing order of profit/weight ratios. These items are included in the knapsack until a specific item  $s$  exceeds the knapsack capacity. Thus, the upper bound for the regarding instance is obtained via Eq. 9. Accordingly, *hit* values in the first part of Table 1, which represent the number of runs that the corresponding algorithm finds the optimum value, do not apply for the second part of the same table.

$$UB = \sum_{r=1}^{s-1} p_r + \left( C - \sum_{r=1}^{s-1} w_r \right) \times \frac{p_s}{w_s} \quad (9)$$

As one can see from the first part of Table 1, all tested algorithms PSO, GA and QL exhibit exactly same performances except for the particular instance *kp8*. In this instance, PSO cannot achieve the optimum values in one of the replications. Nevertheless, this can be considered as an exceptional circumstance and the rest of the

results does not point out any superiority among algorithms. Therefore, one should focus on the second part of Table 1, which illustrates the results for greater-scaled instances.

According to the second part of Table 1, PSO achieves the most promising results in 5 out of 8 instances, while QL exhibits the same performance in 4 out of 8 instances in terms finding the best results. Considering the same performance metric, GA finds the best value in the instance  $kp_{11}$ . According to these results, one can conclude that PSO can be considered as slightly more efficient than QL in terms of finding the best results. This is an expected result, since, QL makes of both GA and PSO according to their rewards, gained throughout optimization process. Moreover, the same findings point out that GA can be considered as a naïve algorithm among the tested algorithms for the same performance metric.

**Table 1.** Computational results

	<i>items</i>	PSO				GA			QL		
		<i>opt.</i>	<i>best</i>	<i>mean</i>	<i>hit</i>	<i>best</i>	<i>mean</i>	<i>hit</i>	<i>best</i>	<i>mean</i>	<i>hit</i>
$kp_1$	10	295	295	295	30	295	295	30	295	295	30
$kp_2$	20	1024	1024	1024	30	1024	1024	30	1024	1024	30
$kp_3$	4	35	35	35	30	35	35	30	35	35	30
$kp_4$	4	23	23	23	30	23	23	30	23	23	30
$kp_5$	15	481.06	481.06	481.06	30	481.06	481.06	30	481.06	481.06	30
$kp_6$	10	52	52	52	30	52	52	30	52	52	30
$kp_7$	7	107	107	107	30	107	107	30	107	107	30
$kp_8$	23	9767	9767	9766.80	29	9767	9767	30	9767	9767	30
$kp_9$	5	130	130	130	30	130	130	30	130	130	30
$kp_{10}$	20	1025	1025	1025	30	1025	1025	30	1025	1025	30
	<i>items</i>	<i>UB.</i>	<i>best</i>	<i>mean</i>	<i>hit</i>	<i>best</i>	<i>mean</i>	<i>hit</i>	<i>best</i>	<i>mean</i>	<i>hit</i>
$kp_{11}$	100	7016.50	<b>7003</b>	7000.46	Na	<b>7003</b>	6996.13	Na	<b>7003</b>	<b>7001.46</b>	Na
$kp_{12}$	200	11639.21	11573	<b>11466.40</b>	Na	11092	10914.96	Na	<b>11590</b>	11430.63	Na
$kp_{13}$	300	14254.57	<b>13858</b>	13452.73	Na	12719	12289.16	Na	13804	<b>13613.70</b>	Na
$kp_{14}$	500	18640.57	17026	16576.53	Na	14984	14619.13	Na	<b>17087</b>	<b>16727.83</b>	Na
$kp_{15}$	800	40607.35	<b>37482</b>	36630.66	Na	34245	33825.16	Na	37414	<b>36898.36</b>	Na
$kp_{16}$	1000	67256.33	65350	<b>64959.60</b>	Na	63525	63234.70	Na	<b>65352</b>	64928	Na
$kp_{17}$	1200	86994.11	<b>86468</b>	<b>86218.70</b>	Na	85591	85459.33	Na	86310	86112.83	Na
$kp_{18}$	1500	103745.10	<b>101399</b>	100850.53	Na	99420	99121.26	Na	101333	<b>100977.43</b>	Na

The obtained mean results in the second part of Table 1 point out a different outcome. As can be seen from this part of Table 1, QL achieves the most promising mean values in 5 out of 8 instances, while PSO exhibits the same performance in 3 out of 8 instances. GA on the other hand, can be considered as a naïve algorithm again in terms of finding the most promising mean values. According to these findings, one can conclude that QL can be considered as slightly more efficient than PSO in terms of finding the most promising mean values. This further points out that robustness of QL can be considered as slightly better than those of the PSO's and GA's.

## 4 CONCLUSION

The present study reports a reinforcement learning (RL) strategy that employs Genetic Algorithm (GA) and Particle Swarm Optimization (PSO) as actions. Accordingly, the proposed strategy either promotes or demotes the regarding action (GA or PSO) based on its achievement throughout optimization process. Q-learning (QL) method is adopted as the RL strategy in the present work. Moreover, in order to avoid premature convergence, the  $\epsilon$ -greedy method is additionally employed by the used QL method. Due to its wide range of applications in practice, 0-1 Knapsack Problem is used as the benchmarking problem. Priority-based encoding technique, which implicitly enables handling knapsack capacity constraint, is used. In order to adapt GA to this problem domain, affine-based crossover is adopted. Canonical modifications of GA and PSO without any further extensions are used.

Carried out comparisons among the tested algorithms GA, PSO and QL point out that PSO achieves the most promising results in 5 out of 8 instances, while QL exhibits the same performance in 4 out of 8 instances in terms finding the best results. On the other hand, QL achieves the most promising mean values in 5 out of 8 instances, while PSO exhibits the same performance in 3 out of 8 instances. As a result one can conclude that while PSO is found to be slightly better than QL in terms of finding the most promising best values, QL seems to be exhibiting a more robust outcome. Finally, GA is found as a naïve algorithm in terms of both best and mean results for the reported testing conditions.

Machine learning research field has striking characteristics and offers essential opportunities and novelties in numerous research fields. One can put forward that optimization field still benefits the improvements in machine

learning. Accordingly, adopting QL method along with different strategies regarding the state evaluation techniques, can be scheduled as a potential future work.

## References

- [1] I. Golcuk, F. B. Ozsoydan, and E. D. Durmaz, "An improved arithmetic optimization algorithm for training feedforward neural networks under dynamic environments," *Knowledge-Based Systems*, vol. 263, art. no. 110274, Mar. 2023.
- [2] F. B. Ozsoydan and I. Golcuk, "A reinforcement learning based computational intelligence approach for binary optimization problems: The case of the set-union knapsack problem," *Engineering Applications of Artificial Intelligence*, vol. 118, art. no.105688, Feb. 2023.
- [3] F. B. Ozsoydan and I. Golcuk, "A hyper-heuristic based reinforcement-learning algorithm to train feedforward neural networks," *Engineering Science and Technology, an International Journal*, vol. 35, art. no. 101261, Nov. 2022.
- [4] I. Golcuk and F. B. Ozsoydan, "Q-learning and hyper-heuristic based algorithm recommendation for changing environments," *Engineering Applications of Artificial Intelligence*, vol. 102, art. no. 104284, Jun. 2021.
- [5] F. B. Ozsoydan, "Artificial search agents with cognitive intelligence for binary optimization problems," *Computers & Industrial Engineering*, vol. 136, pp. 18–30, Oct. 2019.
- [6] M. Al Akasheh, E. F. Malik, O. Hujran, and N. Zaki, "A decade of research on data mining techniques for predicting employee turnover: A systematic literature review," *Expert Systems with Applications*, vol. 238-E, art. no. 121794, Mar. 2024.
- [7] E. Alpaydin, *Introduction to machine learning*, MIT Press, 2020.
- [8] G. James, D. Witten, T. Hastie, and R. Tibshirani, *An Introduction to Statistical Learning*, New York: Springer, 2013.
- [9] M. Alloghani, D. Al-Jumeily, J. Mustafina, A. Hussain, and A. J. Aljaaf, "A systematic review on supervised and unsupervised machine learning algorithms for data science," *Supervised and Unsupervised Learning for Data Science*, pp. 3–21, Sep. 2019.
- [10] J. E. Van Engelen, and H. H. Hoos, "A survey on semi-supervised learning," *Machine Learning*, vol. 109, pp. 373–440, 2020.
- [11] K. Khetarpal, M. Riemer, I. Rish, and D. Precup, "Towards continual reinforcement learning: A review and perspectives," *Journal of Artificial Intelligence Research*, vol. 75, pp. 1401–1476, Dec. 2022.
- [12] J. H. Holland, *Adaptation in Natural and Artificial Systems*, Ann Arbor, MI: The University of Michigan Press, 1975.
- [13] D. Wang, D. Tan, and L. Liu, "Particle swarm optimization algorithm: an overview," *Soft Computing*, vol. 22, no. 2, pp. 387–408, Jan. 2018.
- [14] H. Kellerer, U. Pferschy, and D. Pisinger, "Exact solution of the knapsack problem," *Knapsack Problems*, pp. 117–160, 2004.
- [15] K. K. Bhattacharjee and S. P. Sarmah, "Modified swarm intelligence based techniques for the knapsack problem," *Applied Intelligence*, vol. 46, no. 1, pp. 158–79, Aug. 2017.
- [16] C. J. Watkins and P. Dayan, "Q-learning," *Machine Learning*, vol. 8, pp. 279–292, May 1992.
- [17] H. Mosadegh, S. F. Ghomi, and G. A. Suer, "Stochastic mixed-model assembly line sequencing problem: Mathematical modeling and Q-learning based simulated annealing hyper-heuristics," *European Journal of Operational Research*, vol. 282, no. 2, pp. 530–544, Apr. 2020.
- [18] D. Zou, L. Gao, S. Li, and J. Wu, "Solving 0-1 knapsack problem by a novel global harmony search algorithm," *Applied Soft Computing*, vol. 11, no. 2, pp.1556–1564, Mar. 2011.
- [19] F. B. Ozsoydan, "Effects of dominant wolves in grey wolf optimization algorithm," *Applied Soft Computing*, vol. 83, art. no. 105658, Oct. 2019.



## **Optimizing Risk Management Strategies in the Oil and Gas Industry: Dynamic Assessment and Modeling of Accident Consequences**

**Imane Aila<sup>\*1</sup>, Samia Chettouh<sup>1</sup>, Djamel Haddad<sup>1</sup>**

<sup>1</sup> *Laboratory of Research in Industrial Prevention, Institute of Health & Safety, University of Chadid Mostepha Ben Boulaid-Batna 2, Batna, Algeria*

---

### **Abstract**

Faced with major technological innovations and growing energy demand, the oil and gas industry remains inherently risky. Meticulous risk assessments are essential to protect people, secure equipment, and preserve the environment.

This study offers a substantial contribution to risk management in liquefied petroleum gas facilities, highlighting the importance of a dynamic approach to risk assessment. By focusing on quantitative methods and methods for modeling the effects of potential incidents, this research aims to optimize prevention and protection strategies. The approach adopted not only identifies and quantifies risks, but also simulates the potential consequences of various accident scenarios, facilitating the integration of safety measures into the HSE (health, safety and environment) management system. This proactive approach enriches decision-making processes and improves responsiveness to eventualities, contributing to a safer working environment better prepared for operational challenges.

**Keywords:** *Risk management, Dynamic approach, Effects modeling, Prevention strategies, Safety*

---





---

## **An Overview of Artificial Intelligence Techniques in Supply Chain Management: AI-Driven Strategies for Risk Management**

**Lara J. M. Naser<sup>1</sup>, Seval Ene Yalcin<sup>\*1</sup>**

*Industrial Engineering, Bursa Uludag University, Bursa, Türkiye*

---

### **Abstract**

Supply Chain Risk Management (SCRM) is critical in identifying, assessing, and mitigating risks that could disrupt the supply chain. Artificial Intelligence (AI) has emerged as a powerful tool in SCRM, providing advanced capabilities in predictive analytics and real-time risk monitoring. This study explores the transformative impact of AI in Supply Chain Management (SCM), particularly in risk management and enhancing performance.

AI's positive influence extends across various SCM domains, including demand prediction, distribution, logistics management, sales and marketing strategy, and inventory oversight. AI's predictive abilities result in substantial reductions in inventory costs, optimal supplier selections, and improved forecasting of sales demand, production, logistics, and customer service. Despite the advantages, integrating AI into SCM encounters obstacles like resistance due to job security concerns and the necessity for a high level of expertise to ensure efficient implementation. The research identifies a gap in exploring AI's application in SCM, particularly concerning the human element and training and development of the workforce.

The significance of AI in SCRM is emphasized with AI and machine learning enhancing risk assessment, prediction, and mitigation through sophisticated data analysis, pattern recognition, and process automation. This contributes to boosting supply chain resilience and responsiveness.

This research highlights AI's crucial role in modernizing SCM and its capacity to address modern/contemporary supply chain challenges by introducing innovative risk management solutions.

**Keywords:** *Supply chain Management, Artificial intelligence, Supply chain risk management*

---



## An Efficient Design of a Multi-Echelon and Multi-Product Supply Chain Network with Price-Sensitive Demands

Pinar Yunusoglu<sup>\*1,2</sup>, Derya Eren Akyol<sup>3</sup>, Fehmi Burcin Ozsoydan<sup>3</sup>

<sup>1</sup>Industrial Engineering Department, Izmir Bakircay University, Izmir, Turkiye

<sup>2</sup>Graduate School of Natural and Applied Sciences, Dokuz Eylul University, Izmir, Turkiye

<sup>3</sup>Industrial Engineering Department, Dokuz Eylul University, Izmir, Turkiye

### Abstract

This paper studies the efficient design and planning of a multi-echelon and multi-product supply chain network in which customers have price-sensitive demands. We consider extending a Mixed Integer Linear Programming (MILP) model previously presented in the literature with multiple products and their price-sensitive customer demands. We use a price-response function to determine the price of the products in the Supply Chain Network Design (SCND) Problem. The effectiveness of the proposed solution approach is demonstrated by an illustrative example. It is concluded that integrating the strategic and tactical supply chain network decisions and product pricing decisions gives promising results in the solution to the SCND problem.

**Keywords:** Supply chain network design, Price-sensitive demand, Pricing, Revenue management

## 1 INTRODUCTION

In today's competitive business environment, various revenue management practices have emerged in the design and planning of supply chain networks [1]. Revenue management in Supply Chain Network Design (SCND) handles two categories of decisions: price and quantity decisions. Considering these two decisions in the SCND problem is challenging [1]. Accordingly, this paper handles integrated tactical and strategic planning in the SCND problem, considering the price and quantity decisions with price-sensitive demand of the customers.

In recent years, a substantial amount of work has been done on the facility and demand allocation problems. We refer interested readers to the survey papers presented by [2–5]. Jayaraman [6] handles the capacitated warehouse location and distribution network problem. They propose a MILP model to minimize the cost of servicing the customer demand, outbound transportation costs, and the total fixed costs of opening warehouses. Pirkul and Jayaraman [7] integrate production and distribution planning in the multi-commodity, multi-plant, and capacitated facility location problem. They propose a MILP model and an efficient heuristic based on Lagrangian relaxation for its solution. Tragantalerngsak et al. [8] consider a two-echelon facility location problem. They develop a Lagrangian relaxation-based branch and bound algorithm to determine the number and locations of facilities. Gourdin et al. [9] consider an uncapacitated facility location problem with client matching. They develop a greedy heuristic and a branch-and-cut algorithm and propose valid inequalities and optimality cuts for the problem.

Pricing decisions affect customers' behaviour on whether to purchase a product or service, which ultimately changes revenue per unit of each product. Furthermore, it also affects the structure of the supply chain network, i.e., the number, location, and capacity of the facilities to meet the price-sensitive demand of customers in the SCND problem [1]. The pricing decisions affect the strategic network planning decisions on the capacity side, i.e., determining locations and capacities of supply chain facilities. It also affects the master planning decisions, i.e., purchasing and material requirements planning, production planning, and distribution planning on the demand side. Even though the practicability of pricing decisions in the SCND problem, there are a few studies in the existing literature [10–14] considering facility location problems with price-sensitive demand of customers.

In this paper, we consider the efficient design and planning of a multi-echelon and multi-product supply chain network in which customers have price-sensitive demands. The physical flow of products from production plants to warehouses and from warehouses to customers is considered [15]. The SCND problem considers price-sensitive customer demands and includes production and storage capacity limitations. The objective is to determine the optimal number, location, and capacity of the production plants and warehouses when maximizing the total profit of the SCND problem. This problem has been initially studied by Amiri [15], and they have proposed a MILP

model and an efficient heuristic solution procedure that is Lagrangian relaxation of the problem. The main contribution of the paper is twofold: 1. it extends the SCND problem of Amiri [15] with multiple products and their price-sensitive demands, considering strategic and tactical decisions in a single MILP model; 2. it presents a price-response function initially presented by [1]. We consider discrete price levels so that the integration of the price-response function and a linear programming model is possible.

The remainder of this paper is structured as follows. In Section 2, the extended MILP model is explained in detail. Section 3 presents the illustrative example and its solution and lastly, Section 4 gives conclusions and future research directions.

## 2 MATHEMATICAL MODELING APPROACH

### 2.1 Notation for the Model

The notation required for the mathematical model is as follows.

#### Notation

$N$	Index set of customers
$M$	Index set of potential warehouse sites
$T$	Index set of products
$L$	Index set of price levels
$K$	Index set of potential plant sites
$R$	Index set of capacity levels available to the potential warehouses
$H$	Index set of capacity levels available to the potential plants
$C_{ij}$	Cost of supplying one unit of demand to customer $i$ from warehouse at site $j$
$C_{jk}$	Cost of supplying one unit of demand to warehouse at site $j$ from plant at site $k$
$F_j^r$	Fixed cost per unit of time for opening and operating warehouse with capacity level $r$ at site $j$
$G_k^h$	Fixed cost per unit of time for opening and operating plant with capacity level $h$ at site $k$
$s_j^r$	Capacity with level $r$ for the potential warehouse at site $j$
$e_k^h$	Capacity with level $h$ for the potential plant at site $k$

#### Price-Response Function Parameters

$D_{it}^{max}$	The maximum demand of customer $i$ to product $t$
$a_{it}$	The parameter of the price-response function If $price_{it} < a_{it}$ , potential demand is $D_{it}^{max}$
$b_{it}$	The parameter of price-response function If $price_{it} > b_{it}$ , the potential demand is 0.

#### Decision Variables

$X_{ijt}$	Fraction (regarding $D_{it}$ ) of demand of customer $i$ delivered from warehouse at site $j$
$Y_{jkt}^r$	Fraction (regarding $s_j^r$ ) of shipment from plant at site $k$ to warehouse at site $j$ with capacity level $r$
$U_j^r$	1 if a warehouse with capacity level $r$ is located at site $j$ 0 otherwise
$V_k^h$	1 if a plant with capacity level $h$ is located at site $k$ 0 otherwise
$\Delta_{tl}$	If price level $l$ is selected for product $t$ , equals 1; otherwise, equals 0.

### 2.2 The Price-Response Function

In the extended MILP model, the constraints related to the revenue management and the price-response function are adapted from [1]. We consider the continuous price-response function in Equation 1 where  $Price_{it}$  represents the non-negative continuous variables corresponding to the price of products. This function is a special case of the logit price-response function.

$$D_{it} = \begin{cases} D_{it}^{max}, & Price_{it} \leq a_{it} \\ D_{it}^{max} \left[ \frac{b_{it} - Price_{it}}{b_{it} - a_{it}} \right], & a_{it} < Price_{it} < b_{it} \\ 0, & Price_{it} \geq b_{it} \end{cases} \quad (1)$$

The following price-response function in Equation 2 can be used to estimate the potential demand of price-sensitive customers to the products. However, this function is non-linear. Therefore, we have decided to develop a linear price-response function with discrete price levels.

$$D_{itl} = \max \left\{ \min \left\{ D_{it}^{max}, D_{it}^{max} \left( \frac{b_{it} - PR_{tl}}{b_{it} - a_{it}} \right) \right\}, 0 \right\} \quad (2)$$

The proposed function that calculates the price of the products at price level  $l$  is shown in Equation 3. This function is adopted from [1] to the considered SCND problem.

$$PR_{tl} = \frac{\sum_{i \in I} a_{it} D_{it}^{max}}{\sum_{i \in I} D_{it}^{max}} + \frac{(l-1)}{(|L|-1)} \left( \frac{\sum_{i \in I} b_{it} D_{it}^{max}}{\sum_{i \in I} D_{it}^{max}} - \frac{\sum_{i \in I} a_{it} D_{it}^{max}}{\sum_{i \in I} D_{it}^{max}} \right) \quad \forall t, \forall l \quad (3)$$

### 2.3 Objective Function and Constraints

The proposed mathematical model is given below. We extend the model proposed by Constraints related to revenue management and price-response function are adapted from [1].

$$\begin{aligned} \max \quad & \sum_{i \in N} \sum_{t \in T} \sum_{l \in L} PR_{tl} \cdot D_{itl} \cdot \Delta_{tl} - \sum_{i \in N} \sum_{j \in M} \sum_{t \in T} \sum_{l \in L} C_{ij} \cdot D_{itl} \cdot X_{ijt} - \sum_{j \in M} \sum_{k \in K} \sum_{t \in T} \sum_{r \in R} \bar{C}_{jk} \cdot s_j^r \cdot Y_{jkt}^r - \sum_{j \in M} \sum_{r \in R} F_j^r \cdot U_j^r \\ & - \sum_{k \in K} \sum_{h \in H} G_k^h \cdot V_k^h \end{aligned} \quad (4)$$

$$\sum_{j \in M} \sum_{t \in T} X_{ijt} = 1 \quad \forall i \in N \quad (5)$$

$$\sum_{i \in N} \sum_{t \in T} \sum_{l \in L} D_{itl} \cdot X_{ijt} \leq \sum_{r \in R} s_j^r \cdot U_j^r \quad \forall j \in M \quad (6)$$

$$\sum_{r \in R} U_j^r \leq 1 \quad \forall j \in M \quad (7)$$

$$\sum_{i \in N} \sum_{l \in L} D_{itl} \cdot X_{ijt} \leq \sum_{k \in K} \sum_{r \in R} s_j^r \cdot Y_{jkt}^r \quad \forall j \in M, \forall t \in T \quad (8)$$

$$\sum_{j \in M} \sum_{t \in T} \sum_{r \in R} s_j^r \cdot Y_{jkt}^r \leq \sum_{h \in H} e_k^h \cdot V_k^h \quad \forall k \in K \quad (9)$$

$$\sum_{h \in H} V_k^h \leq 1 \quad \forall k \in K \quad (10)$$

$$\sum_{l \in L} \Delta_{tl} = 1 \quad \forall t \in T \quad (11)$$

$$X_{ijt} \geq 0 \quad \forall i \in N, \forall j \in M, \forall t \in T \quad (12)$$

$$U_j^r \in \{0,1\} \quad \forall j \in M, \forall r \in R \quad (13)$$

$$Y_{jkt}^r \geq 0 \quad \forall j \in M, \forall k \in K, \forall t \in T, \forall r \in R \quad (14)$$

$$V_k^h \in \{0,1\} \quad \forall k \in K, \forall h \in H \quad (15)$$

$$\Delta_{tl} \in \{0,1\} \quad \forall t \in T, \forall l \in L \quad (16)$$

The objective function (4) maximizes the total net contribution, i.e., total profit, where the first term represents the revenues, and the remaining terms includes facility opening and operating and distribution costs. Constraint (5)

guarantees the demand satisfaction of the customers for each product and imposes that each customer may only need one product. Constraint (6) guarantees that total customer demand satisfied by a warehouse cannot exceed the warehouse capacity. Constraint (7) ensures that a warehouse can be assigned at most one capacity level. Constraint (8) guarantees that total customer demand satisfied by a warehouse cannot exceed the total shipments to the warehouse from all plants. Constraint (9) represents the capacity restrictions of the plants in terms of their total shipments to the warehouses. Constraint (10) ensures that a plant can be assigned to at most one capacity level. Constraint (11) ensures that each product can be assigned to only one price level. Constraints (12) - (16) define the domain of the decision variables.

### 3 ILLUSTRATIVE EXAMPLE

An illustrative example is developed to verify the applicability of our solution approach. The illustrative problem data is shown in Tables 1-7. IBM ILOG CPLEX Optimizer 22.1.0 is used to solve the MILP model, and the model is coded in C# on the Microsoft Visual Studio 2022 platform. We run the model using a computer with Intel(R) Core(TM) i7-1165G7 2.80 GHz and 16 GB RAM.

**Table 1.** Parameter  $\overline{C}_{jk}, \forall j \in M, \forall k \in K$

$j/k$	$k1$	$k2$	$k3$
$j1$	3	2	2
$j2$	3	2	3
$j3$	3	2	2
$j4$	3	2	3
$j5$	3	3	2

**Table 2.** Parameter  $C_{ij}, \forall i \in N, \forall j \in M$

$i/j$	$j1$	$j2$	$j3$	$j4$	$j5$
$i1$	2	2	3	2	2
$i2$	2	3	2	2	2
$i3$	2	3	2	3	3
$i4$	2	3	3	2	3
$i5$	2	3	2	2	3
$i6$	2	3	2	2	2

**Table 3.** Parameter  $G_k^h, \forall k \in K, \forall h \in H$

$k/h$	$h1$	$h2$	$h3$	$h4$	$h5$
$k1$	45977	31579	20621	37519	43553
$k2$	38688	19337	39889	46611	27975
$k3$	45977	46978	31622	44877	45541

**Table 4.** Parameter  $F_j^r, \forall j \in M, \forall r \in R$

$j/r$	$r1$	$r2$	$r3$	$r4$	$r5$	$r6$	$r7$
$j1$	16507	19666	17003	20155	15560	16971	20220
$j2$	17437	19528	15753	21068	15308	19133	17190
$j3$	16976	18078	14371	13632	14660	21096	14012
$j4$	19976	19643	15210	18317	14174	19500	14304
$j5$	19402	20429	18333	18729	18099	20557	19131

**Table 5.** Parameter  $D_{it}^{max}, \forall i \in N, \forall t \in T$

$i/t$	$t1$	$t2$	$t3$
$i1$	881	1211	1264
$i2$	1197	808	1165
$i3$	956	822	1044
$i4$	1064	884	1089
$i5$	883	1125	919
$i6$	1101	1166	1029

**Table 6.** Parameter  $a_{it}, \forall i \in N, \forall t \in T$

$i/t$	$t1$	$t2$	$t3$
$i1$	144	146	142
$i2$	148	141	147
$i3$	141	149	145
$i4$	141	149	142
$i5$	142	148	143
$i6$	144	143	146

**Table 7.** Parameter  $b_{it}, \forall i \in N, \forall t \in T$

$i/t$	$t1$	$t2$	$t3$
$i1$	195	196	196
$i2$	195	198	191
$i3$	199	199	199
$i4$	195	200	197
$i5$	194	190	197
$i6$	197	199	191

The computational results are shown in Tables 8-10. We have achieved the optimal solution of illustrative problem instance. The average time elapsed to guarantee the optimal solutions is 2.32 seconds. The total profit is 2445987.57, when total revenue is 2630460.62, warehouse opening and operating costs are 61892, facility opening and operating costs are 38688, the distribution costs of warehouses to customers are 41946.52, and the distribution costs of warehouses to plants are 41946.52.

**Table 8.** Optimal values of warehouse capacity level decisions ( $U_j^r, \forall j \in M, \forall r \in R$ )

$j/r$	$r1$	$r2$	$r3$	$r4$	$r5$	$r6$	$r7$
$j1$	0	0	1	0	0	0	0
$j2$	0	0	0	0	1	0	0
$j3$	0	0	1	0	0	0	0
$j4$	0	0	1	0	0	0	0
$j5$	0	0	0	0	0	1	0

**Table 9.** Optimal values of plant capacity level decisions ( $V_k^h, \forall k \in K, \forall h \in H$ )

$k/h$	$h1$	$h2$	$h3$	$h4$	$h5$
$k1$	0	1	0	0	0
$k2$	1	0	0	0	0
$k3$	0	0	0	0	1

**Table 10.** Optimal values of price decisions ( $\Delta_{tl}, \forall t \in T, \forall l \in L$ )

$t/l$	$l1$	$l2$	$l3$	$l4$	$l5$
$t1$	1	0	0	0	0
$t2$	0	0	1	0	0
$t3$	0	0	0	1	0

## 4 CONCLUSION

This study aims to integrate the multi-echelon and multi-product SCND problem and product pricing decisions in which the customers have price-sensitive demands. We consider a multi-echelon SCND problem of Amiri [15], and we consider extending their MILP model with multiple products and their price-sensitive customer demands. We have used the price-response function initially adopted by [1] to dynamic supply chain network design with capacity planning problem. We have verified the effectiveness of our proposed solution approach with an illustrative example. Future research may consider stochastic components in price-demand relationships of customers. Furthermore, different pricing strategies with cannibalization and arbitrage opportunities can be investigated in detail.

## References

- [1] M. Fattahi, M. Mahootchi, K. Govindan, and S. M. M. Husseini, "Dynamic supply chain network design with capacity planning and multi-period pricing," *Transportation Research Part E: Logistics and Transportation Review*, vol. 81, pp. 169–202, Sep. 2015.
- [2] R. L. Francis, L. F. McGinnis, and J. A. White, "Locational analysis," *European Journal of Operational Research*, vol. 12, no. 3, pp. 220–252, Mar. 1983.
- [3] C. H. Aikens, "Facility location models for distribution planning," *European Journal of Operational Research*, vol. 22, no. 3, pp. 263–279, Dec. 1985.
- [4] M. L. Brandeau and S. S. Chiu, "An overview of representative problems in location research," *Management Science*, vol. 35, no. 6, pp. 645–674, Jun. 1989.
- [5] P. Avella, S. Benati, L. C. Martinez, K. Dalby, D. Di Girolamo, B. Dimitrijevic, G. Ghiani, I. Giannikos, N. Guttmann, and T. H. Hultberg, "Some personal views on the current state and the future of locational analysis," *European Journal of Operational Research*, vol. 104, no. 2, pp. 269–287, Jan. 1998.
- [6] V. Jayaraman, "An efficient heuristic procedure for practical-sized capacitated warehouse design and management," *Decision Sciences*, vol. 29, no. 3, pp. 729–745, Jul. 1998.
- [7] H. Pirkul and V. Jayaraman, "A multi-commodity, multi-plant, capacitated facility location problem: Formulation and efficient heuristic solution," *Computers & Operations Research*, vol. 25, no. 10, pp. 869–878, Oct. 1998.
- [8] S. Tragantalerngsak, J. Holt, and M. Rönnqvist, "An exact method for the two-echelon, single-source, capacitated facility location problem," *European Journal of Operational Research*, vol. 123, no. 3, pp. 473–489, Jun. 2000.
- [9] É. Gourdin, M. Labbé, and G. Laporte, "The uncapacitated facility location problem with client matching," *Operations Research*, vol. 48, no. 5, pp. 671–685, Sep-Oct. 2000.
- [10] A. Ahmadi-Javid and P. Hoseinpour, "Incorporating location, inventory and price decisions into a supply chain distribution network design problem," *Computers & Operations Research*, vol. 56, pp. 110–119, Apr. 2015.
- [11] A. Ahmadi-Javid and R. Ghandali, "An efficient optimization procedure for designing a capacitated distribution network with price-sensitive demand," *Optimization and Engineering*, vol. 15, no. 3, pp. 801–817, Jan. 2014.
- [12] P. Hansen, D. Peeters, and J.-F. Thisse, "Facility location under zone pricing," *Journal of Regional Science*, vol. 37, no. 1, pp. 1–22, Dec. 1997.
- [13] P. Hanjoul, P. Hansen, D. Peeters, and J.-F. Thisse, "Uncapacitated plant location under alternative spatial price policies," *Management Science*, vol. 36, no. 1, pp. 41–57, Jan. 1990.
- [14] J. L. Wagner and L. M. Falkson, "The optimal nodal location of public facilities with price-sensitive demand," *Geographical Analysis*, vol. 7, no. 1, pp. 69–83, Jan. 1975.
- [15] A. Amiri, "Designing a distribution network in a supply chain system: Formulation and efficient solution procedure," *European Journal of Operational Research*, vol. 171, no. 2, pp. 567–576, Jun. 2006.



---

## Production of Graphene by Electrochemical Exfoliation Method and Energy Applications

Gulbahar Bilgic Tuzemen <sup>\*1</sup>

<sup>1</sup>Department of Metallurgy and Material Engineering, Faculty of Engineering-Architecture, Nevsehir Haci Bektas Veli University, Nevsehir 50300, Türkiye

---

### Abstract

Graphene is made up of 2D layers of sp<sup>2</sup> hybridized carbon atoms that resemble honeycombs. Due to its extraordinary mechanical, thermal, and optical abilities, graphene (a single layer of closely spaced carbon atoms organized in a honeycomb-shaped structure) appears to have a promising future. Despite the interesting material's benefits, high manufacturing costs and limited scalability have prevented its widespread use in everyday use. Sensors, batteries, hydrogen storage, and use as an electrode in a solar cell are just a few of the many potentials uses that make graphene a great candidate in the field of energy. Electrochemical exfoliation (EE) of graphite emerges as a valid alternative for large-scale graphene manufacturing, with its environmental friendliness, scalability, and solution processability. Here recent advances in EE in various electrolytes will be summarized. Followed by and the energy applications of exfoliated graphene materials will be highlighted.

**Keywords:** *Electrochemical exfoliation, Graphene, Energy applications*

---

## 1 INTRODUCTION

Graphene consists of 2D sp<sup>2</sup> hybridized layers of carbon atoms that resemble honeycombs. The future of graphene, a single layer of closely spaced carbon atoms arranged in a honeycomb-shaped structure, looks bright due to its outstanding mechanical, electrical, thermal and optical properties [1, 2]. Graphene is an excellent candidate for a variety of possible applications in the energy sector, including sensors, batteries, hydrogen storage, and use as an electrode in a solar cell [3]. Despite all the benefits of this innovative material, high production costs and limited scalability are the main obstacles to its commercialization. [1] Numerous methods, such as bottom-up synthesis from aromatic precursors, epitaxial growth, band isolation, liquid phase exfoliation, gaseous reagents and chemical vapor deposition, do not appear to be easily scalable due to their high price and complex procedures or low efficiency. Recently, wet chemical techniques such as reduction of graphene oxide (GO) and EE of graphite may provide good alternatives for large-scale graphene production. On the other hand, when strong oxidants are applied to graphite, GO is formed, which is highly oxidized and has a disordered structure. Chemical, thermal or electrochemical reduction procedures aimed at converting graphene into reduced graphene oxide (rGO) and restoring graphene's unique properties are unfortunately unstable and always result in some defects in the material. Moreover, with its environmental friendliness, scalability, and solution processability, EE of graphite appears to be a suitable alternative for large-scale graphene synthesis [1–4].

Compared to the Hummers process, EE graphene a graphene-like substance, requires a shorter manufacturing time and significantly less chemical waste. Alternatively, graphite powder can be directly exfoliated in the liquid phase utilizing an external driving force such as shear mixing or ultrasonication [3]. However, with several attempts to speed up the exfoliation process, such as the use of expanded graphite or graphite intercalation compounds, the yields of these methods are still low [4]. Over the past few years, EE of graphite has gained more and more interest as a potentially scalable technique. In general, structural expansion at a graphite electrode (GE) is driven by an electrical current through the use of an electrolyte (such as non-aqueous or an aqueous solution).

Depending on the intercalated ions' charge, the GE represents oxidation or reduction processes by acting as an anode or cathode [4]. Unlike other exfoliation techniques, this procedure works best without a lot of equipment and is usually carried out outside. Compared to other chemical/sonication methods, which frequently use dangerous chemicals or solvents, it is more environmentally friendly [4]. Most notably, EE processes, which depend on graphite precursors, operating voltages, and electrolytes, may produce gram-scale amounts of graphene at the testing proportions with adjustable quality in a matter of minutes to hours. Several graphite precursors, in



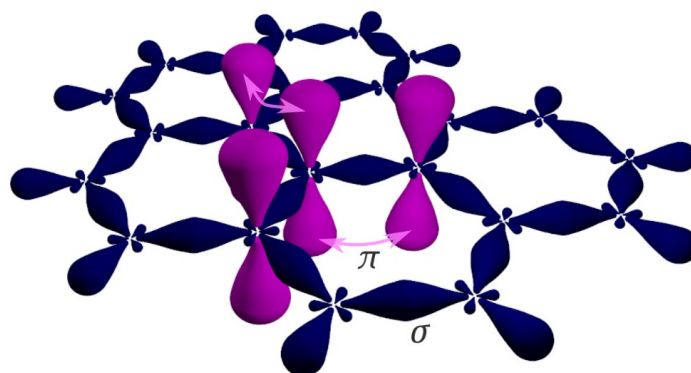
the form of powder, rod, foil or flake, have been studied in EE [4]. These precursors include both synthetic and natural graphite. These processes may be roughly separated into two groups: (1) anodic exfoliation in an aqueous solution of inorganic salts, mineral acids, or a combination of water and ionic liquids; and (2) cathodic exfoliation in organic solvents containing lithium or alkylammonium salts. High-performance drain electrodes for lithium batteries, supercapacitors sodium batteries, fuel cells, electrochemical sensors and counter-electrode materials in dye-sensitized solar cells (DSSC), are just a few of the numerous applications for which EEG materials have been used [5–12].

Table 1 displays graphene's physical characteristics. Graphene is the strongest material yet tested, with an intrinsic tensile strength of 130 GPa and a Young's modulus of over 1 TPa [13]. Graphene monolayers' mechanical resilience is demonstrated by their ability to bend at large angles with little strain. Monolayer graphene retains superior carrier mobility even under severe deformation. Research on graphene's heat transport is expanding, especially because of the material's possible uses in thermal management. Due to the limits of the equipment utilized, the majority of experimental observations have shown significant errors in the thermal conductivity values. Early observations of the thermal conductivity of suspended graphene indicated an extraordinarily high thermal conductivity up to  $5300 \text{ W}\cdot\text{m}^{-1}\cdot\text{K}^{-1}$ . in accordance with expectations for graphene and related carbon nanotubes [14].

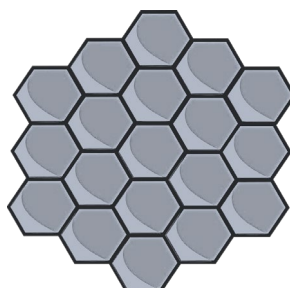
Figure 1 shows the bonds sigma and pi in graphene. While pi bonds are formed by tunneling between the projecting pz orbitals, sigma bonds are produced by the overlap of sp<sup>2</sup> hybrid orbitals. Figure 2 demonstrated image of graphene honeycomb structure.

**Table 1.** Graphene physical properties

Molecular Bond Length	1.42 Å
Spring Constant	1–5 N/m
Theoretical Specific Surface Area	2630 m <sup>2</sup> /g
Thermal Conductivity	5300 W·m <sup>-1</sup> ·K <sup>-1</sup>
Fracture Toughness	4 MPa√m (brittle)
Density (2D)	0.763 mg/m <sup>2</sup>
Young's Modulus	1 TPa
Stiffness	0.5 TPa
Tensile Strength	130 GPa



**Figure 1.** The bonds sigma and pi in graphene. While pi bonds are formed by tunneling between the projecting pz orbitals, sigma bonds are produced by the overlap of sp<sup>2</sup> hybrid orbitals [15]



**Figure 2.** Image of graphene honeycomb structure

## 2 ELECTROCHEMICAL EXFOLIATION METHOD

It has been shown that the choice of electrolytes has a significant impact on the quality of graphene. The optimal electrolyte should act as a dispersion to stabilize the reduced graphene flakes and prevent re-aggregation, as well as effectively induce guest ion intercalation to separate the graphene layers without destroying the graphitic shape. In actuality, anodic exfoliation in aqueous electrolytes promotes the synthesis of thin-layer graphene (1-3 layers), but almost invariably results in EEG oxidation. We recently discovered that the significant oxidation brought on by water electrolysis might be substantially mitigated by adding scavengers to an aqueous electrolyte [4].

Graphite sources have a substantial effect on the oxygen concentration and fault density of exfoliated graphene, in addition to electrolytes. Numerous graphite precursors have been investigated, including graphite foil, expanded graphite, graphite powder, natural graphite flakes and etc. A significant approach to achieving high-quality nanosheets is suggested by the thoughtful selection of starting graphite, which takes into account the requirements of various electrochemical cells. Furthermore, current research shows that the fluctuation of applied voltage on graphite may be a significant factor influencing the quantity and quality of graphene layers, as well as the exfoliation yield [4].

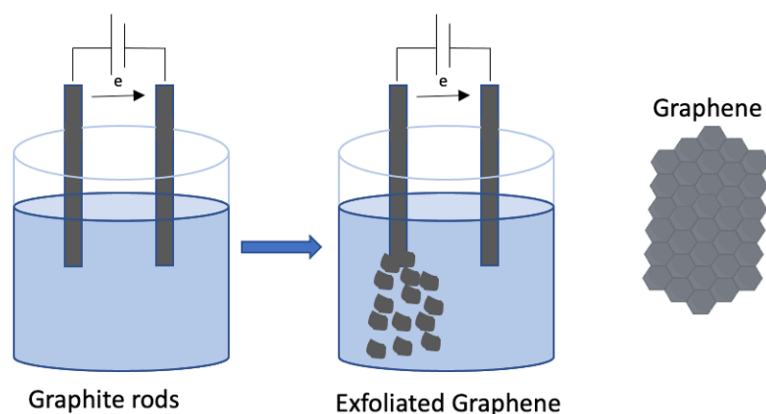
The electrochemical reactions' great intricacy makes the process at the graphite contact difficult. Three steps are basically involved in effective exfoliation: anions/cations intercalating, graphite layers expanding, and exfoliation at the graphite surface. By measuring the structural deformation at the graphite interface, Palermo et al. have shown that effective intercalation and bubble formation inside graphite interlayers are important variables determining speedy and complete exfoliation [16]. The fundamental cause of the broad distribution of graphene layers in practice is that exfoliation can start at any point in graphite and these steps do not occur in the same sequence. The maintenance of graphene quality and exfoliation efficiency appear to be mutually exclusive. Although few-layer graphene is typically the main outcome, cationic intercalation in non-aqueous environments is an additional option that can prevent excessive oxidation.

**Electrolyte:** A suitable electrolyte solution is prepared, typically containing a solvent (such as water or an organic solvent) and salts (e.g., potassium hydroxide, sodium sulfate) to facilitate the electrochemical reactions.

**Electrodes:** GEs are commonly used, where one electrode acts as the anode and the other as the cathode.

**Electrochemical process:** Electrochemical reactions take place at the electrode surfaces when a voltage is applied between the two electrodes submerged in the electrolyte solution. At the anode (positive electrode), graphite or graphite oxide undergoes oxidation reactions, releasing GO or similar species into the solution. At the cathode (negative electrode), reduction reactions take place, where GO or its derivatives are reduced to form rGO or even graphene, depending on the applied potential and conditions. **Formation of Graphene:** The released GO or derivatives in the electrolyte solution can spontaneously reassemble into sheets due to Van der Waals interactions. Further reduction steps, such as post-treatment with chemicals or thermal annealing, may be required to convert GO to rGO or graphene, improving its electrical conductivity and other properties [16–22].

**Collection and Purification:** The graphene or rGO sheets formed in the electrolyte solution can be collected on substrates or filtered out. Purification steps, such as washing with solvents or filtration, may be necessary to remove residual electrolyte salts or by-products [1, 2, 16, 17]. An overview of some current research on the synthesis of materials via EE is shown in Table 2 [23].



**Figure 1.** Schematic representation of EE of graphite rods

**Table 2.** An overview of some recent EE investigations on material synthesis [23]

Electrolytes	Electrodes	Applied voltage (V, DC Anodic)	Additional conditions	Size ( $\mu\text{m}$ )	References
0.1M $\text{K}_2\text{SO}_4$	Graphite foil	+10	Graphite powder	0.2-0.6	[14]
0.5M $\text{H}_2\text{SO}_4$	Graphite foil	+10	Pretreatment in 1M	2.2	[18]
0.05M $\text{NaCl}$	Graphite foil	+10	-	0.6	[19]
0.1M $\text{C}_6\text{H}_5\text{COOH}$	Graphite rod	-1.5	Pulse electrolysis	2-5	[20]
0.1M $(\text{NH}_4)_2\text{SO}_4$	Graphite flake	+10	Packed in dialysis tubing	>30	[121]

### 3 ENERGY APPLICATIONS

DSSC, Fauziah et al. [5] used ultrasonication of EE graphene as a counter electrode (CE). It has been demonstrated that repeated ultrasonication may repair structural flaws in graphene. Reduced rGO by the Hummers technique is 0.714%, whereas EEG with 6 rounds of ultrasonication (EEG\_6) yields the maximum performance as CE in solar cell with an efficiency of 0.890%. Therefore, a more environmentally friendly and high-performing DSSC was produced by using EEG\_6 as the CE.

A ternary deep eutectic melt including acetamide, ammonium nitrate and urea was used for the EE process that Zhang and colleagues devised [6]. This approach is very efficient and scalable. The product mostly comprised of different layer graphene, with a specific surface area ( $878 \text{ m}^2 \text{ g}^{-1}$ ) that was near to the predicted value of three-layer graphene, according to the data, which also revealed that the yield had grown to 76%. Additionally, high areal capacitance of  $120 \text{ mF cm}^{-2}$  as well as high cycling stability were offered by graphene-based all-solid-state flexible supercapacitors. This technique has enabled the large-scale, environmentally benign, and cost-effective manufacture of graphene, and it has great potential for a variety of innovative uses. Ouhib and associates [7] proposed a straightforward method to produce polymer-functionalized graphene sheets. One to five layers of polyacrylonitrile were chemisorbed on graphene sheets as a consequence, with a layer graphene making up the bulk of the layers. As a consequence, we created a straightforward and efficient one-pot EE and functionalization technique. As an anode in Li-ion batteries, this new functionalized graphene exhibits well rate capability without requiring an additional conductive dopant or binder. They were able to include and electropolymerize acrylonitrile between the graphite layer at low cathodic working potentials ( $\sim -2\text{V}$ ). Raman study indicates that the breakdown of graphene sheets is greatly reduced by the low operating voltage. This modified graphene was used to create homogenous coatings on glass that had a good electrical conductivity of  $8.1 \text{ S.cm}^{-1}$ .

In a Pt-free DSSC, Fatya et al. [8] employed a composite of polyaniline (PANI) and graphene as the counter electrode. The team used leftover battery graphite rod to create electrochemically exfoliated graphene (EEG). The EEG had a comparatively low resistance of  $502.72 \Omega/\text{square}$ , according to DC testing. The power conversion efficiency of the PANI/EEG materials is superior to that of the PANI-based counter electrode, according to current density-voltage (J-V) tests.

Chen et al. [9] designed a 3D printed reactor to enable the use of graphite flakes for EE to rapidly obtain arc GO. For high-temperature PEMFC, polybenzimidazole (PBI)/GO composite membranes were created using as-made electrochemically exfoliated graphene oxide (EGO). The produced EGO was utilized in PBI membrane to enhance PEMFC performance at high temperatures. PBI/EGO was found to have the maximum power density and better proton conductivity increased by 29.2%. Additionally, EGO increased mechanical behavior and durability.

EE graphene (EG) is used in a unique way by Zhao et al. [10] to create an anode for long cycle Li-ion batteries. With no binder, the premium EG was sprayed directly onto the copper foil, giving it excellent bridging, conductivity, and volume capacity. With about 100% capacity retention after 6500 cycles, the battery has demonstrated a high capacity of  $356 \text{ mA h g}^{-1}$ .

In aqueous conditions, Edison et al. [11] showed how quickly graphite may be exfoliated anodic electrochemically to form graphene sheets (GS). A constant voltage of +10 V was applied between two identical graphite layers in 0.1 M aqueous ammonium sulfate for the GS synthesis. In a three-electrode system, the maximum specific capacitance of the GS/Ni foam double-layer capacitance is representative of semi-rectangular voltammograms and triangle GCD curves. Furthermore, GS/Ni foam's symmetric two-electrode performance was investigated. This foam demonstrated an excellent power density and energy density.

## 4 CONCLUSION

Exfoliated graphene, a new class of graphene materials obtained by electrochemical methods, has excellent potential for high-performance devices. Considerable attention has been paid to improving the EE process with the goals of producing graphene materials with high yield, excellent product purity, and low manufacturing costs. Generally speaking, graphene production requires graphite exfoliation conditions that minimize graphene damage. As a result, it is preferable to prevent oxidative processes and exfoliate GEs as soon as possible. Advantages include cathodic exfoliation, high-temperature electrolytes, low voltage or pulsed power supply, thin GEs, and robust mechanical forces. Higher quality graphene materials can be obtained from less oxidative electrolytes made of bases, salts, or organic substances because they reduce the oxidative radicals generated during graphite exfoliation. On the other hand, the generation of GO, which will need the proper pretreatment of GEs to intercalate ions, is best achieved in environments with strong oxidative electrolytes, higher applied potentials, high temperatures, and mechanical stresses. To improve structural control over the resulting graphene materials, we must first gain a deeper understanding of the principles behind graphite exfoliation reactions. They interact with graphite materials, much of the information on the precise reaction pathways and reaction kinetics is still lacking. Second, most of the current research uses only modest laboratory setups. Mass transport, heat management, and complex liquid mixing are involved in large-scale material production. Effective equipment design and process optimization depend on research on heat and mass transport processes during EE. Third, different properties of graphene materials are needed for a range of new applications.

## References

- [1] B. Vedhanarayanan, B. Babu, M. M. Shaijumon, and A. Ajayaghosh, "Exfoliation of reduced graphene oxide with self-assembled  $\pi$ -gelators for improved electrochemical performance," *ACS Applied Materials & Interfaces*, vol. 9, no. 23, pp. 19417–19426, Oct. 2016.
- [2] M. J. Allen, V. C. Tung, and R. B. Kaner, "Honeycomb carbon: A review of graphene," *Chemical Reviews*, vol. 110, no. 1, pp. 132–145, Jul. 2009.
- [3] N. Fauziah *et al.*, "Ultrasonication-modified electrochemically exfoliated graphene for counter electrode in dye-sensitized solar cells," *Carbon Trends*, vol. 12, art. no. 100292, Sep. 2023.
- [4] S. Yang, M. R. Lohe, K. Müllen, and X. Feng, "New-generation graphene from electrochemical approaches: Production and applications," *Advanced Materials*, vol. 28, no. 29, pp. 6213–6221, Feb. 2016.
- [5] N. Fauziah *et al.*, "Eco-friendly direct-current pulsed electropolymerization of polyaniline nanofibers on synthetic graphite substrate for counter electrode in dye-sensitized solar cells," *Polymer-Plastics Technology and Materials*, vol. 62, no. 6, pp. 800–815, Dec. 2022.
- [6] Y. Zhang *et al.*, "Electrochemically exfoliated high-yield graphene in ambient temperature molten salts and its application for flexible solid-state supercapacitors," *Carbon*, vol. 127, pp. 392–403, Feb. 2018.
- [7] F. Ouhib *et al.*, "A facile and fast electrochemical route to produce functional few-layer graphene sheets for lithium battery anode application," *J. Mater. Chem. A*, vol. 2, no. 37, pp. 15298–15302, 2014.
- [8] A. I. Fatya, M. Reza, R. R. Sunarya, and V. Suendo, "Synthesis of polyaniline/electrochemically exfoliated graphene composite as counter-electrode in dye-sensitized solar cell," *Polymer-Plastics Technology and Materials*, vol. 59, no. 12, pp. 1370–1378, Mar. 2020.
- [9] J. Chen *et al.*, "One step electrochemical exfoliation of natural graphite flakes into graphene oxide for polybenzimidazole composite membranes giving enhanced performance in high temperature fuel cells," *Journal of Power Sources*, vol. 491, art. no. 229550, Apr. 2021.
- [10] X. Zhao *et al.*, "Electrochemical exfoliation of graphene as an anode material for ultra-long cycle lithium ion batteries," *Journal of Physics and Chemistry of Solids*, vol. 139, art. no. 109301, Apr. 2020.
- [11] T. N. Edison *et al.*, "Electrochemically exfoliated graphene sheets as electrode material for aqueous symmetric supercapacitors," *Surface and Coatings Technology*, vol. 416, art. no. 127150, Jun. 2021.
- [12] J. M. Munuera *et al.*, "Electrochemical exfoliation of graphite in aqueous sodium halide electrolytes toward low oxygen content graphene for energy and environmental applications," *ACS Applied Materials & Interfaces*, vol. 9, no. 28, pp. 24085–24099, Jul. 2017.
- [13] M. Ishigami, J. H. Chen, W. G. Cullen, M. S. Fuhrer, and E. D. Williams, "Atomic structure of graphene on  $\text{SiO}_2$ ," *Nano Letters*, vol. 7, no. 6, pp. 1643–1648, May 2007.
- [14] A. A. Balandin *et al.*, "Superior thermal conductivity of single-layer graphene," *Nano Letters*, vol. 8, no. 3, pp. 902–907, Feb. 2008.
- [15] Wikipedia. *Graphene* [Online]. Available: <https://en.wikipedia.org/wiki/Graphene>
- [16] S. K. Tiwari, S. Sahoo, N. Wang, and A. Huczko, "Graphene research and their outputs: Status and Prospect," *Journal of Science: Advanced Materials and Devices*, vol. 5, no. 1, pp. 10–29, Mar. 2020.

- [17] J. M. Munuera *et al.*, “Electrochemical exfoliation of graphite in aqueous sodium halide electrolytes toward low oxygen content graphene for energy and environmental applications,” *ACS Applied Materials & Interfaces*, vol. 9, no. 28, pp. 24085–24099, Jul. 2017.
- [18] X. Huang *et al.*, “Low defect concentration few-layer graphene using a two-step electrochemical exfoliation,” *Nanotechnology*, vol. 26, no. 10, art. no. 105602, Feb. 2015.
- [19] J. M. Munuera *et al.*, “High quality, low oxygen content and biocompatible graphene nanosheets obtained by anodic exfoliation of different graphite types,” *Carbon*, vol. 94, pp. 729–739, Nov. 2015.
- [20] Ya. I. Kurys, O. O. Ustavyska, V. G. Koshechko, and V. D. Pokhodenko, “Structure and electrochemical properties of multilayer graphene prepared by electrochemical exfoliation of graphite in the presence of benzoate ions,” *RSC Advances*, vol. 6, no. 42, pp. 36050–36057, 2016.
- [21] T. C. Achee *et al.*, “High-yield scalable graphene nanosheet production from compressed graphite using electrochemical exfoliation,” *Scientific Reports*, vol. 8, no. 1, Sep. 2018.
- [22] G. Bilgic, “Reduced graphene synthesis via eco-friendly electrochemical exfoliation method,” *Kastamonu University Journal of Engineering and Sciences*, Jun. 2024.
- [23] F. Liu *et al.*, “Synthesis of graphene materials by electrochemical exfoliation: Recent progress and future potential,” *Carbon Energy*, vol. 1, no. 2, pp. 173–199, Oct. 2019.



# Advanced Hierarchical Control of Islanded AC Microgrids Using Modulated Model Predictive Control

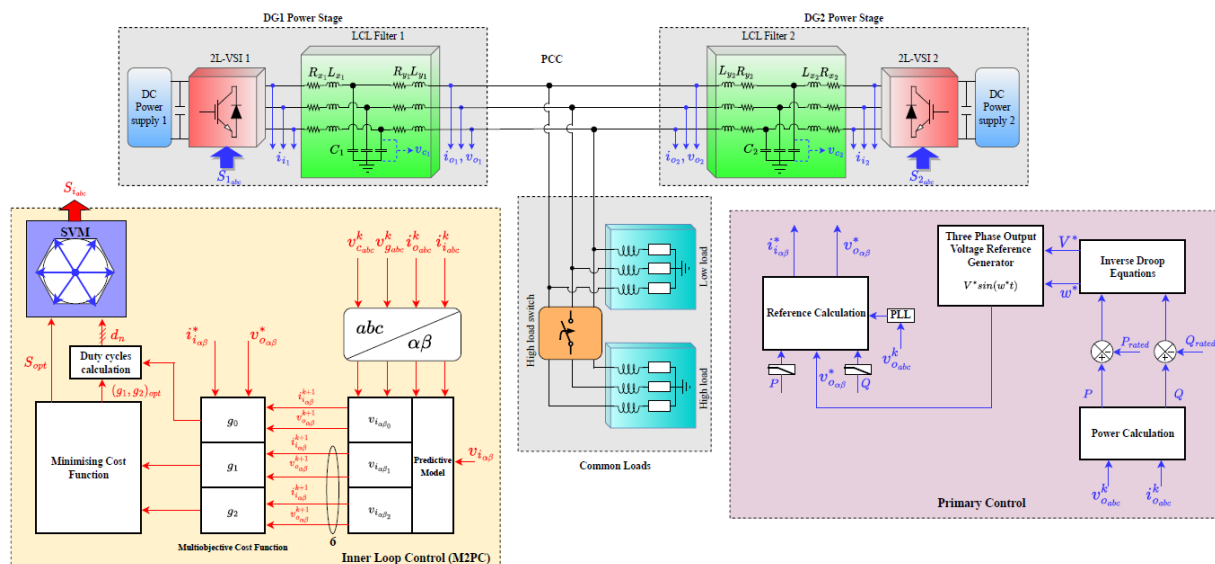
Moussa Abderrahim Mehiris<sup>\*1</sup>, Billel Talbi<sup>1</sup>, Idris Messaoudene<sup>1</sup>, Houssam Eddin Mansouri<sup>1</sup>

<sup>1</sup>ETA Laboratory, Department of Electronics, University Mohamed El Bachir El Ibrahimi of Bordj Bou Arreridj, Bordj Bou Arreridj, Algeria

## Abstract

Microgrids make it possible to integrate renewable energy sources more deeply into the main electrical grid, but doing so requires advanced control systems to manage power flow between the sources and the grid. The goal of this study is to present a novel approach to modulated model predictive control (M<sup>2</sup>PC) that addresses the drawbacks of traditional Finite Control Set Model Predictive Control, specifically the variable switching frequency and resultant ripples. In order to reach the ideal switching state, M<sup>2</sup>PC uses an innovative technique with the evaluation of new cost function based on two subsequent multi-objective cost functions that are computed for successive voltage vectors, following by space vector modulation. An outer loop using inverter droop control generates references, which are tracked by an inner loop using M<sup>2</sup>PC in the hierarchical control scheme. By using this method, harmonic distortion is reduced and switching frequency is stabilized. Our control scheme is used to integrate two distributed generating units into a microgrid configuration consisting of inverters connected by an LCL filter. Voltage magnitude and frequency regulation are focused in islanded mode, whereas power contribution from each distributed generator is the primary priority in grid-connected mode. The proposed M<sup>2</sup>PC successfully tracks changing power generation and dynamic load changes, as demonstrated by simulation results in MATLAB/SIMULINK. It also greatly improves dynamic responsiveness and overall stability under variable load circumstances and disturbances. These results highlight M<sup>2</sup>PC's potential to contribute to the development of decentralized energy systems by significantly increasing the operating efficiency and reliability of islanded AC microgrids.

**Keywords:** M<sup>2</sup>PC, Finite control set model predictive control, Distributed generating, Droop control, Islanded AC microgrids



\* moussaabderrahim.mehiris@univ-bba.dz



---

# Applications and Future of Unmanned Aerial Vehicles in the Field of Occupational Health and Safety

Mustafa Ozdemir<sup>\*1</sup>

<sup>1</sup>Department of Emergency and Disaster Management, Faculty of Applied Sciences, Bayburt University, Bayburt, Türkiye

---

## Abstract

This study examines the applications and future potential of “Unmanned Aerial Vehicle” technology in the field of occupational health and safety. Unmanned aerial vehicles are utilised to enhance safety standards, improve efficiency, and detect hazardous conditions in high-risk sectors such as construction, mining, energy, and agriculture. The study addresses the innovative solutions provided by unmanned aerial vehicles, their benefits, and the challenges encountered while also assessing how future technological advancements can be more effectively integrated into occupational health and safety processes. Conducted through a systematic literature review, this research offers a comprehensive analysis of the current and potential applications of uncrewed aerial vehicles in the occupational health and safety domain.

**Keywords:** *Unmanned aerial vehicles (UAVs), Occupational health and safety (OHS), Industrial UAV Applications*

---

## 1 INTRODUCTION

Due to technological advancements, uncrewed Aerial Vehicles (UAVs) have increasingly been employed across various industrial sectors. Particularly in the field of Occupational Health and Safety (OHS), UAVs have garnered attention for the advantages they offer in risky and hazardous work environments. These devices enhance worker safety, detect dangerous situations in advance, and improve the efficiency of work processes [1]. The applications of UAVs in the OHS field are primarily concentrated in high-risk sectors. UAVs are effectively utilised in critical safety tasks such as inspection, monitoring, and emergency response in the construction, mining, energy, and agriculture industries. For example, UAVs can conduct detailed assessments of structures on construction sites to identify hazards in advance, thus minimising the risks associated with working at heights. In the mining sector, UAVs can rapidly and safely perform crucial tasks such as monitoring ventilation systems and detecting explosive gases in mines [2, 3].

The innovative solutions provided by UAVs not only elevate safety standards but also enhance operational efficiency. Traditional inspection and monitoring methods are often time-consuming and costly, whereas UAVs expedite these processes, providing a cost advantage to businesses. Moreover, using UAVs reduces workers' exposure to hazardous areas, helping prevent occupational accidents and diseases [4].

In the future, as UAV technology continues to evolve, their applications in the OHS field are expected to become even more widespread. Autonomous UAVs, equipped with artificial intelligence and machine learning algorithms, can perform more complex tasks. Consequently, UAVs are anticipated to be more proactive in safety processes, detecting potential hazards in advance and implementing preventive measures. This study examines the applications of UAVs in the OHS field, the challenges encountered, and the possible future uses, drawing upon existing literature [2, 5].

## 2 MATERIAL AND METHOD

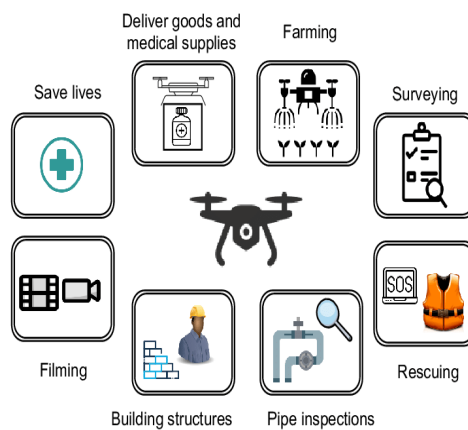
This study is designed as a systematic literature review to examine UAVs' applications and future potential in OHS. Within the scope of the study, academic articles, reports, and other scientific publications concerning the applications and effects of UAVs in the field of OHS were reviewed. Data sources included academic databases such as PubMed, Scopus, Web of Science, and Google Scholar. The keywords “Unmanned Aerial Vehicles”, “Drone”, “Occupational Health and Safety”, “Workplace Safety”, “UAV”, and “OSH” were used in the study. Only studies published in 2010 and beyond examining the applications of UAVs in the field of OHS, published in peer-reviewed journals, conference papers, reports, and theses with full-text access, were included in the study.

Studies examining the military or recreational use of UAVs, studies presented only as abstracts or posters, and regulatory documents other than technical reports and standards were excluded. A literature search was conducted using a search strategy in the identified databases. The obtained publications were examined based on title and abstract, and a preliminary screening was performed according to inclusion and exclusion criteria. The full texts of the studies that passed the initial screening were read for a more detailed evaluation. At this stage, the UAV applications, benefits provided, challenges encountered, and potential future use areas mentioned in the studies were noted. The reviewed studies were evaluated using the thematic analysis method in data analysis. Main themes and sub-themes emerging in the studies were identified, and a comprehensive analysis of the applications and effects of UAVs in the field of OHS was conducted. The findings, benefits, and recommendations mentioned in the studies were also synthesised. This study is limited to specific databases and keywords. Furthermore, only studies with full-text access were evaluated. Therefore, some essential studies may not have been accessible. However, a comprehensive scanning and analysis reviewed a wide range of existing literature.

### 3 RESULTS

#### 3.1 Types of UAVs and Their Applications

UAVs can be classified based on their physical designs and sizes. Different types include fixed-wing, single-rotor, multi-rotor, and hybrid. Multi-rotor UAVs have become ideal for consumer deliveries or aerial photography tasks due to their ability to hover in the air. UAVs can also be classified as military, commercial, and recreational devices [6, 7]. Figure 1 shows some non-military uses of UAVs [8].



**Figure 1.** Some non-military uses of UAVs

UAVs' physical designs and operational capabilities enable their use in various application areas. Fixed-wing UAVs are suitable for long-range reconnaissance missions and monitoring large areas. Single-rotor UAVs are used for specialised tasks because they can perform more complex manoeuvres. At the same time, multi-rotor UAVs are preferred for tasks requiring more excellent stability and precision. Hybrid UAVs combine the advantages of these different designs and can be used for versatile missions [9].

#### 3.1. Regulations on UAVs in European and Turkish Law

Legal regulations on (UAVs) in Europe aim to ensure the sustainable growth of UAV usage by addressing safety, privacy, and liability issues. The European Union Aviation Safety Agency (EASA) has established comprehensive regulations by categorising UAV operations into open, specific, and certified categories based on risk levels. EASA sets safety standards by requiring UAV operators to register and obtain permits for particular flights, ensuring operators undergo appropriate training and certification processes. Regarding privacy and data protection, UAVs must comply with the General Data Protection Regulation (GDPR). UAV operators must also have adequate insurance to cover potential damages [10, 11].

Member states can implement additional regulations at the national level according to their local needs. Flight restrictions may apply, particularly in areas such as around airports and densely populated cities. EASA is also developing regulations for future trends, such as Beyond Visual Line of Sight (BVLOS) flights and the U-Space air traffic management system. Counter-UAV measures to be applied in cases of UAV misuse are also included in the legal framework. These regulations ensure UAV technology's safe, responsible, and efficient use while minimising associated risks [12].



Türkiye UAV usage is regulated by the Directorate General of Civil Aviation (SHGM). SHGM has issued various regulations and guidelines to ensure the safe and orderly use of UAVs. These regulations define UAVs' operational limitations, users' obligations, and safety measures [13].

The fundamental regulation regarding UAV usage in Türkiye is the "Instruction on Unmanned Aerial Vehicles" issued by SHGM. This instruction covers the classification, registration, and certification processes of UAVs, flight permits, and the obligations of operators. UAVs are classified into various categories based on their weight and intended use. Different licenses and registration requirements apply to each category. All UAVs weighing over 500 grams must be registered and certified with SHGM. UAV operators must obtain permission from SHGM to fly in specific areas. Special permits are required in sensitive areas such as city centres, airports, and military zones [14].

The Air Traffic Services (ATS) Regulation contains provisions to prevent UAVs from colliding with other aircraft in the airspace and ensure safe operations. According to this regulation, UAV operators must submit a flight plan in advance for specific flights. UAVs must operate in compliance with designated airspace restrictions and rules.

### 3.2. Applications and Future of UAVs in OHS

UAVs or drones have significant impacts on OHS and healthcare. These impacts emerge positively and negatively when UAVs are integrated into various sectors. While UAVs can potentially reduce physical risks for workers by undertaking hazardous tasks, they can also create new safety concerns and stress factors. The presence of UAVs in workplaces may cause anxiety and long-term stress in some individuals [15].

In healthcare, UAVs have great potential in applications such as emergency response, medication delivery, and elderly care. These devices are seen as solutions to address shortages of healthcare workers and improve service delivery to remote areas. Integrating UAVs' social skills can also enhance human-robot interactions in various environments, including home settings and healthcare scenarios. However, more research is needed on user experience and interaction between humans and UAVs [16, 17].

UAVs can also enhance workplace safety by monitoring hazardous areas, conducting surveillance, and enforcing OHS standards. UAVs can play a significant role in the construction, mining, and disaster response industries. These devices can reduce workers' workloads, although the perceived workload may differ from the actual workload due to 3D space navigation. Industries adopting UAVs to reorganise tasks and gain a competitive advantage often operate on a cost and risk reduction rationale. However, workers will need to adapt to working with UAVs, which can come at a cost, especially concerning privacy issues. Physical and psychological safety concerns are influenced by collision potential concerns [18].

Integrating UAVs in various sectors also brings multiple risks and challenges. These risks include property damage, injuries to operators and the public, privacy violations, and liability issues. These risks require multifaceted management approaches. Health risks posed by UAVs can be direct (physical contact) or indirect (caused by UAV behaviour). Proper maintenance and regular inspections are critical for risk mitigation but can be costly and impact job organisation. Equipping UAVs with obstacle-detection capabilities and developing behaviours that account for human dynamics is essential in reducing stress and accidents [19].

The reliability of UAVs varies significantly between commercial, military, and personal use. Personal UAVs typically have the lowest reliability. The highest-risk components are power sources, navigation systems, and ground control stations. Cybersecurity is a growing concern as UAVs can be used maliciously or become hacking targets. This has led to the development of counter-UAV technologies, which also present new challenges and potential for misuse [20].

Accepting UAVs in workplaces depends on workers' perceptions of their benefits and ease of use. This can be enhanced by making UAVs more social. The concept of autonomous UAV communities that can communicate and self-organize can lead to more efficient task execution and management, potentially reducing the need for human intervention. The idea of UAVs operating as a market-based system using bargaining principles and game theory is also being discussed [21].

Regulatory bodies are developing rules for unmanned aerial systems. Organisations like EASA (European Union Aviation Safety Agency) are working on UAVs' operational safety and integration. Critical areas for future research include privacy, safety, social impacts, human-drone interactions, and regulatory issues. The increasing

number of UAVs brings challenges related to privacy and liability. Slowly evolving legislation may hinder the development of the field through over-regulation and lack of creativity promotion [21].

The potential impacts of UAVs on occupational safety, health, and healthcare highlight opportunities and areas requiring further research and development. Challenges in integrating UAVs include social acceptance, human-drone interaction, and safety concerns. Various studies and reports support the potential benefits of UAVs in disaster management, supply chain improvements, and healthcare delivery [22].

While UAVs offer significant benefits in OHS and healthcare, the risks and challenges of implementing these technologies must also be considered. Successful integration of UAVs requires appropriate interface design, usability testing, regulatory frameworks, and consideration of human factors. Collaboration among all stakeholders and continuous research is critical to fully realising the potential of UAV technology.

## 4 CONCLUSION

The continuous development of UAV technology will further expand these vehicles' applications in the OHS field. Autonomous UAVs and the integration of artificial intelligence (AI) will enable UAVs to perform more complex tasks. For example, autonomous UAVs can help implement proactive safety measures by continuously monitoring hazardous areas and analysing data. AI-supported analyses can process the data collected by UAVs quickly and accurately, allowing for the early detection of potential hazards.

Furthermore, the range of UAV applications is expected to broaden. In the energy sector, UAVs can be used for regular inspections of wind turbines and solar panels. In the agricultural industry, UAVs can monitor the condition of farmlands and assess plant health, thereby increasing productivity. Such applications will allow the benefits of UAVs in terms of safety and efficiency to extend to a broader range of areas.

In conclusion, UAVs are emerging as a significant technological innovation in OHS. Their safety and efficiency advantages contribute to the widespread adoption of these vehicles in industrial applications. However, factors such as the regulation of UAV use, technical limitations, and integration challenges must be considered. In the future, the development of UAV technology and the discovery of new application areas will enable these vehicles to be used more effectively in OHS processes.

## References

- [1] F. Elghaish, S. Matarneh, S. Talebi, M. Kagioglou, M. R. Hosseini, and S. Abrishami, "Toward digitalisation in the construction industry with immersive and drones technologies: a critical literature review," *Smart and Sustainable Built Environment*, vol. 10, no. 3, pp. 345–363, 2021.
- [2] T. R. Wanasinghe, R. G. Gosine, O. De Silva, G. K. Mann, L. A. James, and P. Warriar, "Unmanned aerial systems for the oil and gas industry: Overview, applications, and challenges," *IEEE Access*, vol. 8, pp. 166980–166997, 2020.
- [3] N. Shvahr and T. Komisarenko, "Research of new methods for quality air control after massive explosions in the open mine industry," in *E3S Web of Conferences*, 2020, vol. 166: EDP Sciences, art. no. 02007.
- [4] C. Stocker, R. Bennett, F. Nex, M. Gerke, and J. Zevenbergen, "Review of the current state of UAV regulations," *Remote Sensing*, vol. 9, no. 5, art. no. 459, 2017.
- [5] S. Y. Choi and D. Cha, "Unmanned aerial vehicles using machine learning for autonomous flight; state-of-the-art," *Advanced Robotics*, vol. 33, no. 6, pp. 265–277, 2019.
- [6] C. Barrado, E. Salami, A. Gallardo, L. X. Herranz, and E. Pastor, "Understanding the implications of the future unmanned air traffic growth," in *2021 IEEE/AIAA 40th Digital Avionics Systems Conference (DASC)*, 2021: IEEE, pp. 1–7.
- [7] A.-M. Auvinen, "Understanding the stakeholders as a success factor for effective occupational health care," *Occupational Health*, vol. 29, no. 7, pp. 25–43, 2017.
- [8] T. Alladi, V. Chamola, N. Sahu, and M. Guizani, "Applications of blockchain in unmanned aerial vehicles: A review," *Vehicular Communications*, vol. 23, art. no. 100249, 2020.
- [9] S. A. Wich and L. P. Koh, *Conservation Drones: Mapping and Monitoring Biodiversity*, Oxford University Press, 2018.
- [10] A. Konert and T. Dunin, "A harmonised european drone market?—new EU rules on unmanned aircraft systems," *Adv. Sci. Technol. Eng. Syst. J.*, vol. 5, no. 3, pp. 93–99, 2020.
- [11] F. Nikodem, A. Bierig, and J. S. Dittrich, "The new specific operations risk assessment approach for UAS regulation compared to common civil aviation risk assessment," 2018.

- [12] V. Lappas *et al.*, “EuroDRONE, a European unmanned traffic management testbed for U-space,” *Drones*, vol. 6, no. 2, art. no. 53, 2022.
- [13] G. Dogan Ocak and N. Gurbuz, “Current regulations on civil UAV usage in Turkey,” *GSI Articletter*, vol. 19, art. no. 71, 2018.
- [14] T. Savaş, “Evaluation of flight permissions of unmanned aerial vehicles in Turkey,” *Avrupa Bilim ve Teknoloji Dergisi*, no. 35, pp. 616–624, 2022.
- [15] A. Soeiro, S. Shahedi, and S. Maheronnaghsh, “A framework to implement occupational health and safety innovation,” in *4th Symposium on Occupational Safety and Health Proceedings Book*, 2021.
- [16] S. I. Khan *et al.*, “UAVs path planning architecture for effective medical emergency response in future networks,” *Physical Communication*, vol. 47, art. no. 101337, 2021.
- [17] X. Zhou *et al.*, “Human-robot skills transfer interface for UAV-based precision pesticide in dynamic environments,” *Assembly Automation*, vol. 41, no. 3, pp. 345–357, 2021.
- [18] M. Gheisari and B. Esmaeili, “Applications and requirements of unmanned aerial systems (UASs) for construction safety,” *Safety Science*, vol. 118, pp. 230–240, 2019.
- [19] I. Jeelani and M. Gheisari, “Safety challenges of human-drone interactions on construction jobsites,” *Automation and Robotics in the Architecture, Engineering, and Construction Industry*, pp. 143–164, 2022.
- [20] K. Hartmann and K. Giles, “UAV exploitation: A new domain for cyber power,” in *2016 8th International Conference on Cyber Conflict (CyCon)*, 2016: IEEE, pp. 205–221.
- [21] Q. Peng, H. Wu, and R. Xue, “Review of dynamic task allocation methods for UAV swarms oriented to ground targets,” *Complex System Modeling and Simulation*, vol. 1, no. 3, pp. 163–175, 2021.
- [22] B. Hiebert, E. Nouvet, V. Jeyabalan, and L. Donelle, “The application of drones in healthcare and health-related services in north america: A scoping review,” *Drones*, vol. 4, no. 3, art. no. 30, 2020.



---

## Model Predictive Control of a PUC7-Based Power Factor Correction (PFC) Rectifier

Abdeslem Sahli<sup>\*1</sup>, Billel Talbi<sup>1</sup>, Abbas Kihal<sup>2</sup>, Abdelbaset Laib<sup>2</sup>, Abdelbasset Krama<sup>3</sup>

<sup>1</sup>ETA laboratory, Department of Electronics, University Mohamed El Bachir El Ibrahimy of Bordj Bou Arreridj, El-Anasser 34030, Algeria

<sup>2</sup>Department of Automatic, University of Science and Technology Houari Boumediene, Algiers 16111, Algeria

<sup>3</sup>Hamad Bin Khalifa University, Doha, Qatar

---

### Abstract

In the present investigation, a model predictive control (MPC) methodology is implemented on a packed-u-cell (PUC)-based power factor correction (PFC) rectifier. The particular configuration under examination involves a 7-level PUC converter that facilitates the generation of two levels of DC output voltages. The enhancement of the MPC cost function is executed through the minimization of discrepancies in the DC output voltages across capacitors and the input grid current. Furthermore, the voltages of the targeted capacitors and the peak magnitude of the input current are embedded in the formulated cost function to standardize the discrepancies. Furthermore, a supplementary PI controller is utilized to determine the magnitude of the grid current reference based on the calculated discrepancies in the capacitors' voltages.

The simulations results are provided to showcase the superior dynamic performance and effectiveness of the MPC controller in maintaining the output voltage references amidst variations in load conditions.

**Keywords:** Multi-level Rectifier, Power factor correction (PFC), Model predictive control (MPC)

---

## 1 INTRODUCTION

Several intriguing research studies have recently been published regarding the application of nonlinear techniques to control multilevel converters [1, 2], as an alternative to the traditional predictive control methods. Model Predictive Control (MPC) is commonly utilized in managing plants with intricate dynamics, where the dynamic model of the plant aids in determining the optimal control input at the present time step [3]. This optimal decision is made by solving an optimization problem based on an error cost function, which considers the current measured states, previous states, and predicted states. Forecasted states are estimated from the plant's mathematical model, and control actions are implemented over a finite horizon, with the potential for longer horizons [4].

The type of control input is dictated by the structure of the controlled system. In scenarios involving finite control set issues, MPC demonstrates a variable switching frequency output, with the optimization problem being resolved by assessing an online cost function for all possible control inputs. On the other hand, in continuous input MPC scenarios, a modulator is necessary, resulting in a fixed switching frequency and the possibility of offline optimization problem resolution. Constraints can be integrated into the controller design for both types of MPC problems to enhance system performance. This flexibility is particularly advantageous for model predictive-based controllers, especially when dealing with nonlinear models [5].

The Packed U-cell inverter (PUC) has found applications in various fields such as inverters, grid-connected systems, and industrial applications. The PUC7 rectifier generates two output voltages, one below and one above the grid's rms voltage, reducing the need for filter components on both the ac-side and load side. Unlike nonlinear model predictive control, finite-control-set model predictive control (FCS-MPC) is implemented in packed U-cell converters, where the closed-loop system matrix incorporates the control input, adding complexity to the controller design [6].

In this study, FCS-MPC is applied to a dual output multi-level converter system, where the first dc voltage output is 1/3 the second one, resulting in a 7-level converter input voltage using PUC7 topology. The multilevel voltage waveform helps minimize the filter size required on the grid side. Moreover, the utilization of FCS-MPC controller contributes to reducing the total harmonic distortion of the grid-side input current. The presented controller has exhibited efficient performance in achieving unity power factor from the grid side and effectively managing the

auxiliary capacitor voltages towards their set references. Matlab simulations were conducted to evaluate the controller's performance across various test scenarios.

## 2 MATHEMATICAL MODEL OF THE PUC7 PFC RECTIFIER

The illustration in Figure 1 showcases the evaluated dual output PUC5 rectifier, with power supplied from an AC source (grid) through an L-filter.

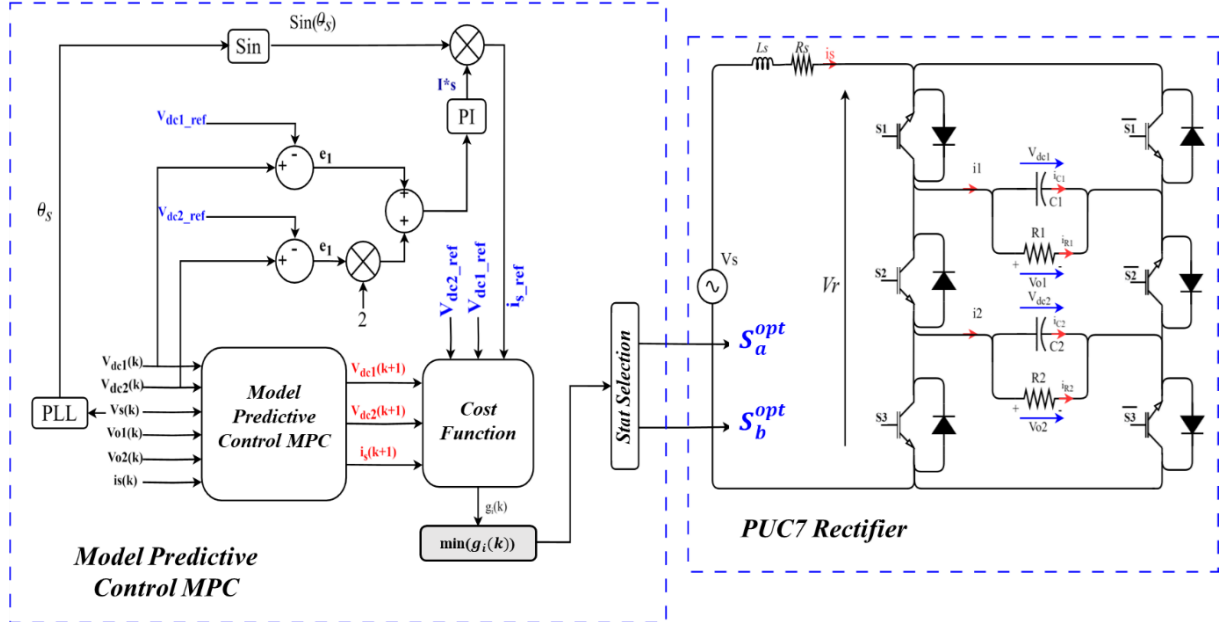


Figure 1. Proposed system synoptic

The filter's inductance and internal resistance are denoted as  $L_s$  and  $r_s$ , respectively. The converter comprises six bidirectional power switches and yields two output DC voltages. The higher DC output voltage ( $v_{o1} = 3E$ ) is three times the lower DC output voltage ( $v_{o2} = E$ ). Following the control sequence outlined in Table 1, both outputs are harnessed to generate a 7-level input voltage to the rectifier, as depicted in Table 1.

Table 1. Control sequence

State	$V_r$	S1	S2	S3
1	$V_{dc1}=3E$	1	0	0
2	$V_{dc1}-V_{dc2}=2E$	1	0	1
3	$V_{dc2}=E$	1	1	0
4	0	0	0	0
5	0	1	1	1
6	$-V_{dc2}=-E$	0	0	1
7	$V_{dc2}-V_{dc1}=-2E$	0	1	0
8	$-V_{dc1}=-3E$	0	1	1

The control input switching function is specified as:

$$\begin{cases} s_1 = s_a - s_b \\ s_2 = s_b - s_c \end{cases} \quad (1)$$

The loads are assumed to be resistive loads (with nominal values of  $R_1$  and  $R_2$ ) connected in parallel with filtering capacitors  $C_1$  and  $C_2$ , correspondingly. The total current drawn from each branch is linked to the source current as:

$$i_1 = s_1 i_s = i_{c1} + i_{R1}, i_2 = s_2 i_s = i_{c2} + i_{R2} \quad (2)$$

thus, yielding the subsequent dynamics for the capacitors:

$$C_1 \frac{dv_{dc1}}{dt} = s_1 i_s - \frac{v_{o1}}{R_1} \quad (3)$$

and

$$C_2 \frac{dv_{dc2}}{dt} = s_2 i_s - \frac{v_{o2}}{R_2} \quad (4)$$

The load voltages are associated with the inverter input voltage in concurrence with the control input signals as outlined in Table I and (1). The PUC rectifier input voltage is characterized as:

$$v_r = s_1 v_{dc1} + s_2 v_{dc2} \quad (5)$$

constituting a 7-level input voltage waveform. Conversely, the source-side current dynamics can be articulated as:

$$\frac{di_s}{dt} = -\frac{r_s}{L_s} i_s + \frac{1}{L_s} (v_s - v_r) \quad (6)$$

### 3 FINITE-CONTROL-SET MODEL PREDICTIVE CONTROLLER

In general, the FCS-MPC method necessitates the discrete-time representation of the controlled system, forecasting of future time step values, and optimization of a real-time cost function. In this particular investigation, the controller must adhere to the ensuing requirements:

- To regulate the dc output voltages  $v_{dc1}$  and  $v_{dc2}$  in proximity to their set reference values  $3E$  and  $E$  (these specific voltage references for capacitors ensure a reliable operation of the PUC7 rectifier),
- To synchronize the input current with the AC source voltage  $v_s$  to achieve a power factor of unity along with minimal total harmonic distortion (THD). The subsequent sections will elaborate on the detailed design process of the controller.

Using first order forward Euler approximation, the discrete equivalent forms of (3) and (4), respectively, are given as:

$$v_{dc1}(k+1) = v_{dc1}(k) + \frac{T_s}{C_1} (s_1(k) i_s(k) - \frac{v_{o1}(k)}{R_1}) \quad (7)$$

and

$$v_{dc2}(k+1) = v_{dc2}(k) + \frac{T_s}{C_2} (s_2(k) i_s(k) - \frac{v_{o2}(k)}{R_2}) \quad (8)$$

Similarly, the discrete form of the grid current dynamic is given as:

$$i_s(k+1) = i_s(k) - \frac{r_s T_s}{L_s} i_s(k) + \frac{T_s}{L_s} (v_s(k) - s_1(k) v_{dc1}(k) - s_2(k) v_{dc2}(k)) \quad (9)$$

The peak reference current  $I_s^*$  is produced through the utilization of the output voltages of the capacitors, using a proportional integral (PI) controller as depicted in Figure 1.

After determining the peak value of the current reference from the source, it is synchronized with the source voltage to achieve a power factor of one for the power derived from the source. By adjusting the phase shift between the

current reference and the source voltage, a specific power factor can be preserved. The selection of the control input pair at time step (k) aims to minimize a normalized cost function, denoted as g,

$$g_i(k+1) = \left( \frac{v_{dc1}(k+1) - v_{dc1-ref}}{v_{dc1-ref}} \right)^2 + \left( \frac{v_{dc2}(k+1) - v_{dc2-ref}}{v_{dc2-ref}} \right)^2 + \lambda \left( \frac{i_s(k+1) - i_{s-ref}^*}{I_s^*} \right)^2 \tag{10}$$

which is calculated for the subsequent sampling time (k+1). A dimensionless gain  $\lambda$  is employed as a weighting factor for the normalized current error, resulting in an overall dimensionless cost function.

Figure 2 depict the FCS-MPC flowchart of the proposed control system.

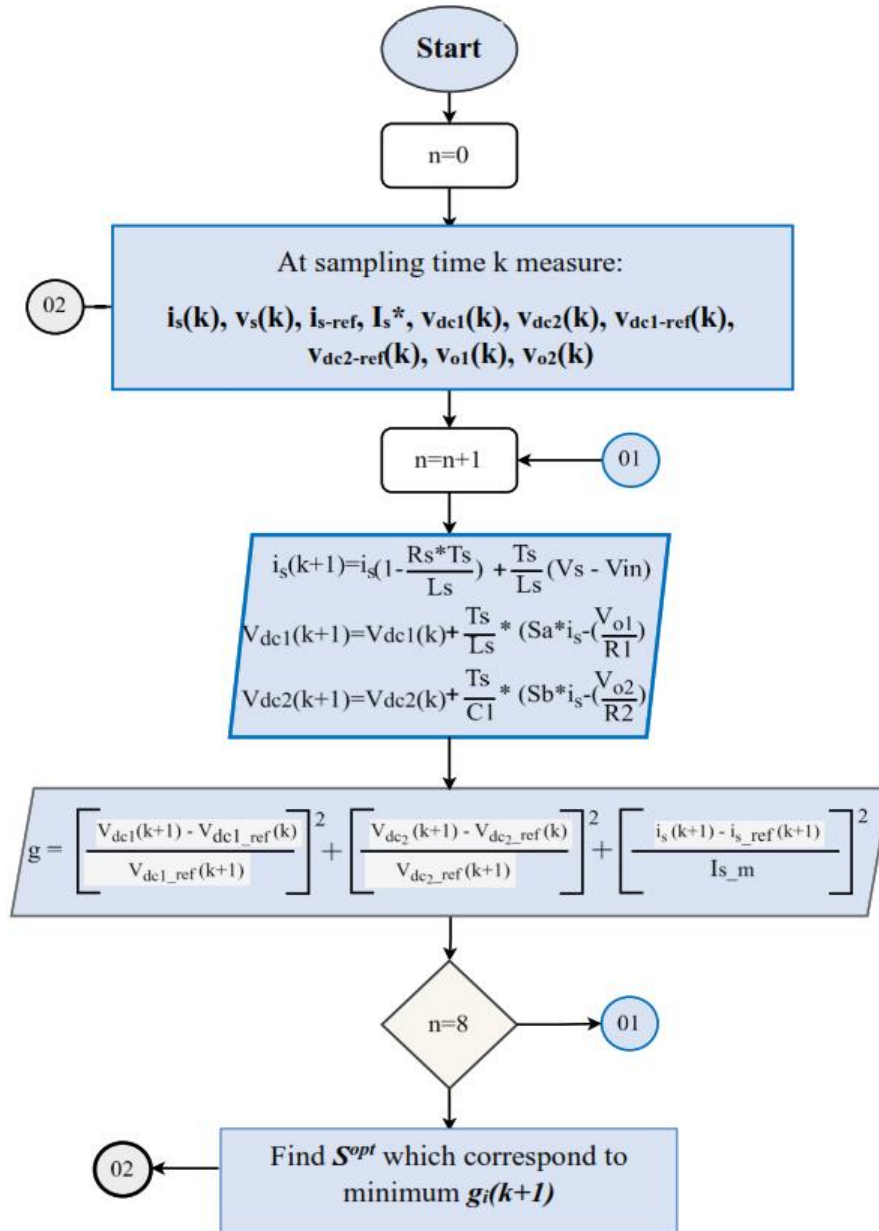


Figure 2. FCS-MPC flowchart

#### 4 SIMULATION RESULTS

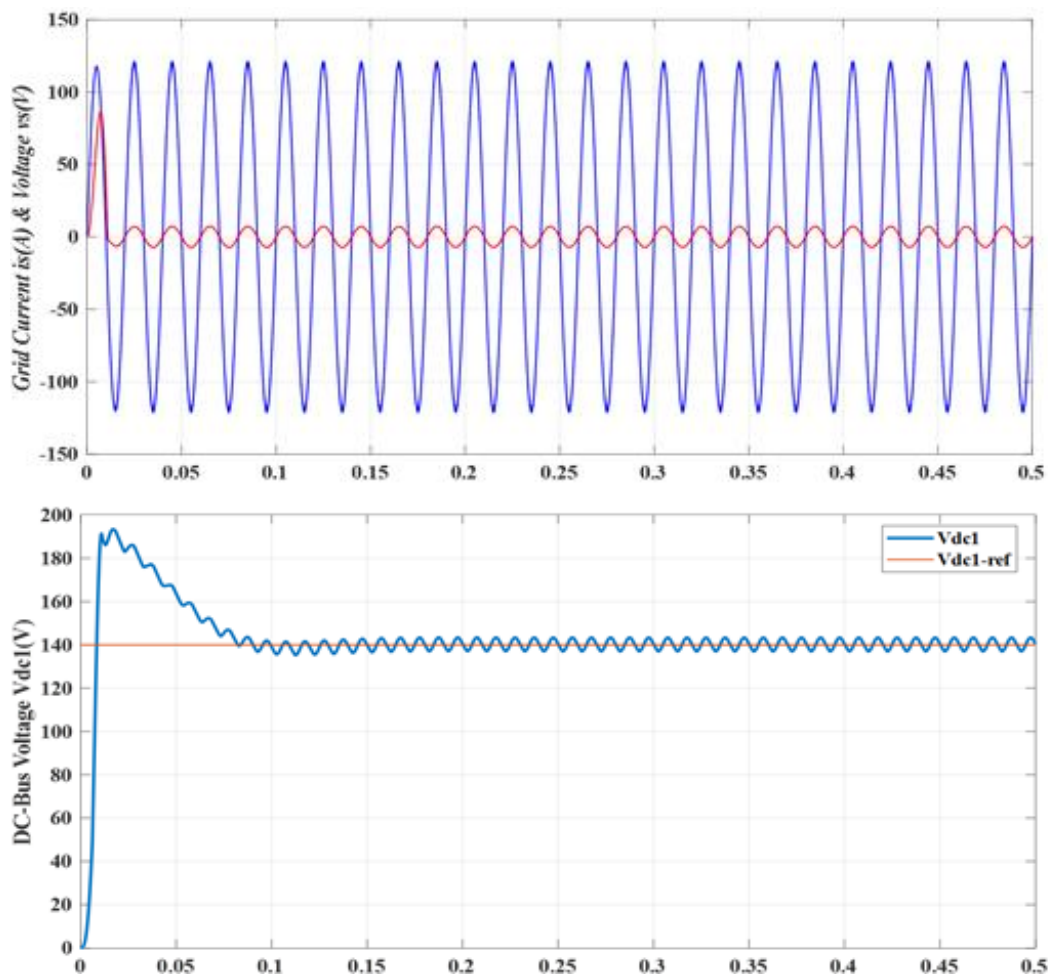
In this section, we offer various simulations to showcase the performance of the controller. The simulations were conducted using Matlab/Simulink with the simulation parameters outlined in Table 2. Various tests were carried out on the multilevel rectifier to assess the effectiveness of the controller.

**Table 2.** Simulation parameters

Parameters	Value
Grid Voltage ( $V_s$ )	120 V
Grid Frequency ( $f_s$ )	50 Hz
Grid Side Inductor ( $L_s$ )	5 mH
DC Capacitors ( $C1$ & $C2$ )	1100 $\mu$ F
Load DC Side Resistor ( $R1$ & $R2$ )	80 $\Omega$
DC Voltage Reference ( $V_{dc1ref}$ & $V_{dc2ref}$ )	140V & 70 V
MPC sampling Time $T_s$	50 $\mu$ s

Firstly, the Steady State Test was conducted with equal load resistances ( $R1 = R2 = 80 \Omega$ ). The simulation test outcome is depicted in Figure 3, demonstrating precise control of both capacitor voltages. The source current is sinusoidal and in phase with the source voltage, indicating unity power factor operation. The total harmonic distortion (THD) of the source current is computed to be 1.70% as depicted in Figure 4.

Moving on to the Load Dynamic Test, the initial load change test involved setting both loads to  $R1 = R2 = 80 \Omega$ , then decreasing the first load resistor to  $30 \Omega$  to simulate an increasing in power consumption by the first load. The simulation result of this test is displayed in Figure 5. This test demonstrate the controller's ability to deliver the necessary power to the loads while maintaining regulated load voltages. Additionally, it is evident that the source current exhibits low harmonic distortion and remains in phase with the source voltage.





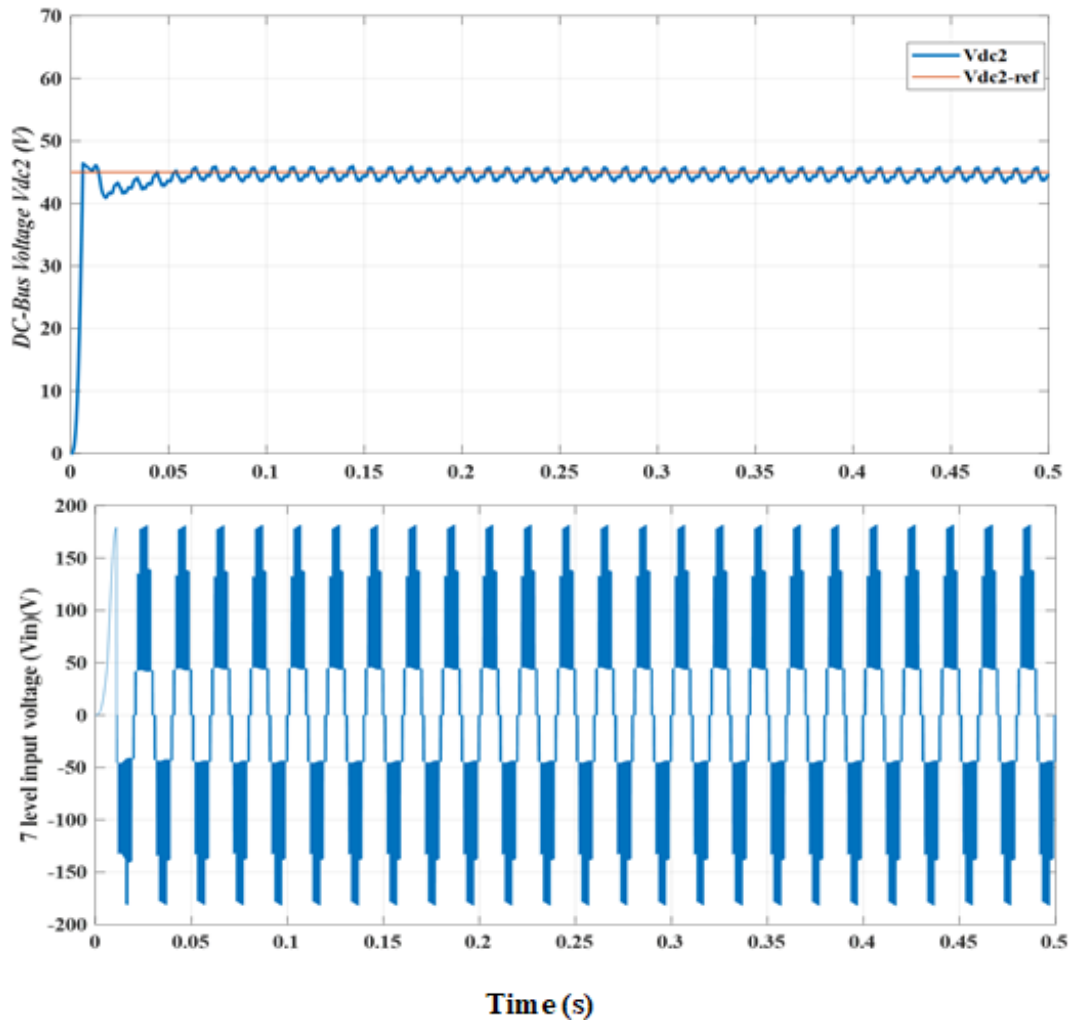


Figure 3. Simulation result of PUC7 rectifier in steady state ( $R_1 = R_2 = 80 \Omega$ )

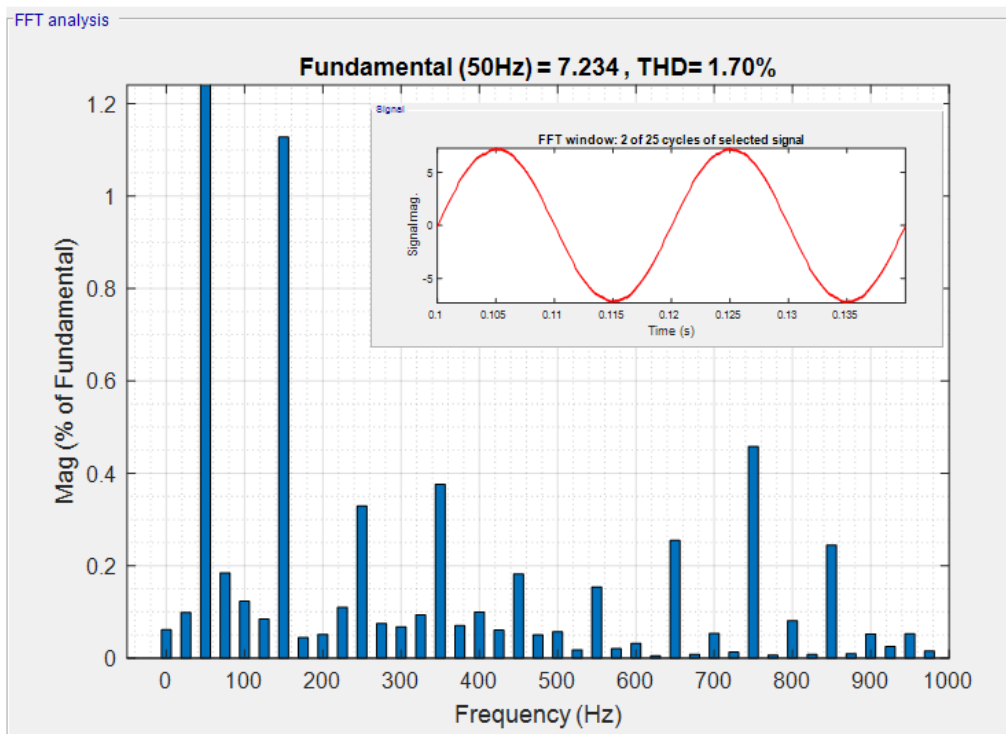


Figure 4. THD analysis of source current in steady state

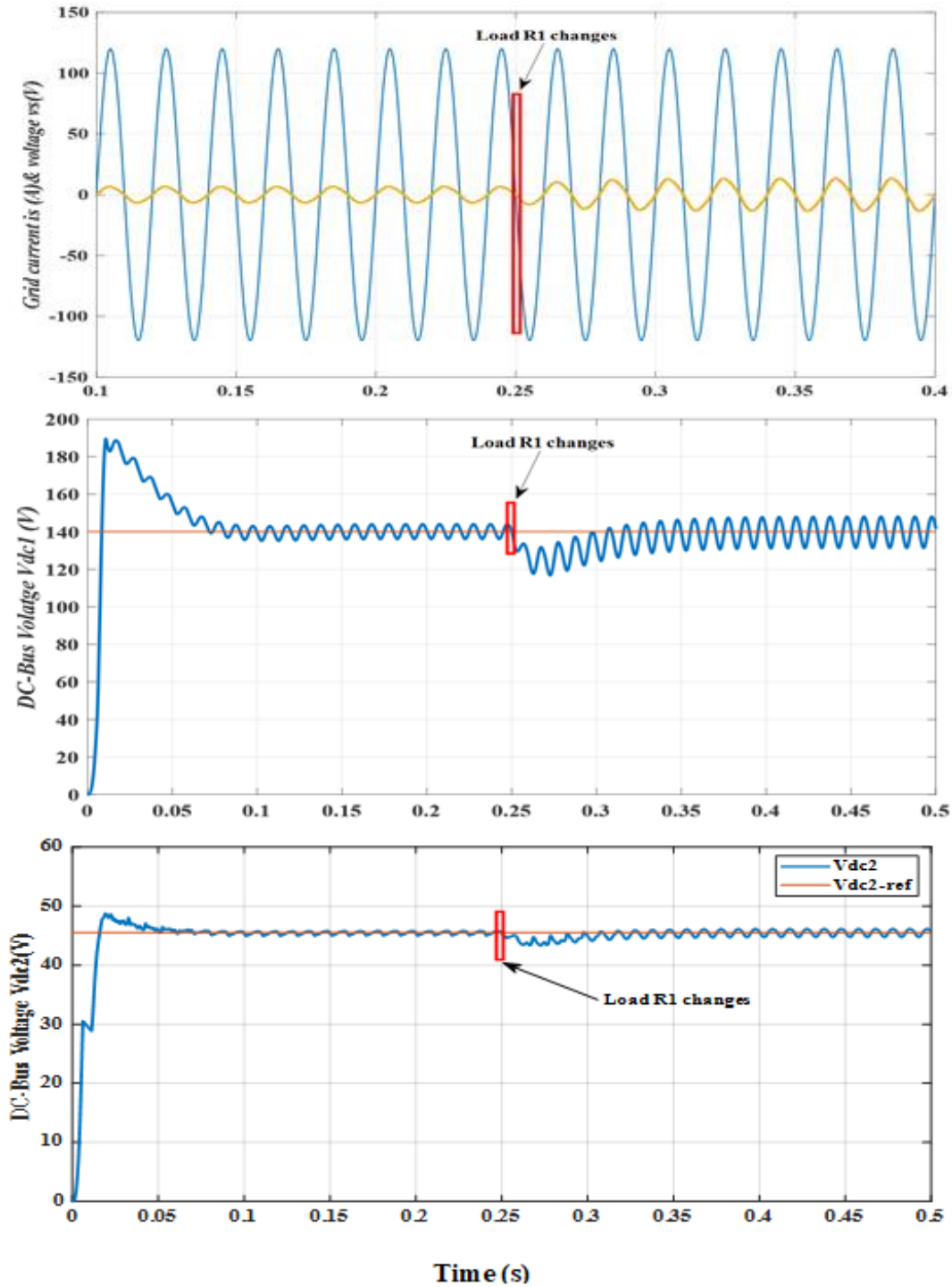


Figure 5. Simulation result of PUC7 rectifier in dynamic state

## 5 CONCLUSION

In this work, a finite control set model predictive controller (FCS-MPC) is suggested for a 7-level PUC (PUC7) PFC rectifier. The proposed method leverages the discrepancies in output voltages (capacitor voltages) and the phase angle of the grid voltage to generate the reference source current. The MPC controller then determines the appropriate control input to reduce a newly formulated cost function that integrates normalized state errors. It is evident from the simulation results provided that the proposed controller shows rapid dynamic performance and effective tracking capabilities. This is achieved by controlling the two output voltages to their target values under unity power factor conditions and with low total harmonic distortion in the input current.

## References

- [1] S. Vazquez, J. I. Leon, J. M. Carrasco, L. G. Franquelo, E. Galvan, J. A. Sanchez, and E. Dominguez, "Controller design for a single-phase two-cell multilevel cascade h-bridge converter," in *2008 IEEE International Symposium on Industrial Electronics*, Jun. 2008, pp. 2342–2347.
- [2] L. M. Kunzler and L. A. C. Lopes, "Power balance technique for cascaded h-bridge multilevel cells in a hybrid power amplifier with wide output voltage range," in *2018 IEEE International Conference on Industrial Technology (ICIT)*, Feb. 2018, pp. 800–805.
- [3] P. Cort'es, M. P. Kazmierkowski, R. Kennel, D. E. Quevedo, and J. R. Rodriguez, "Predictive control in power electronics and drives," *IEEE Trans. Industrial Electronics*, vol. 55, no. 12, pp. 4312–4324, 2008.
- [4] D. Q. Mayne, J. B. Rawlings, C. V. Rao, and P. O. Scokaert, "Constrained model predictive control: Stability and optimality," *Automatica*, vol. 36, no. 6, pp. 789–814, 2000.
- [5] A. Sahli, F. Krim, A. Laib, and B. Talbi, "Energy management and power quality enhancement in grid-tied single-phase PV system using modified PUC converter," *IET Renewable Power Generation*, vol. 13, no. 14, pp. 2512–2521, 2019.
- [6] H. Makhamreh, M. Trabelsi, O. Kukrer, and H. Abu-Rub, "Model predictive control for a PUC5 based dual output active rectifier," in *2019 IEEE 13th International Conference on Compatibility, Power Electronics and Power Engineering (CPE-POWERENG)*, 2019, pp. 1–6.



## Internal Parameters Identification of a Lithium-Ion Battery

Abderrahmane El Djallil Rabhi<sup>\*1</sup>, Kamel Djamel Eddine Kerrouche<sup>1</sup>

<sup>1</sup>Algerian Space Agency, Satellite Development Center, Oran, Algeria

---

### Abstract

Battery management is crucial to increase battery lifetime and save energy. Therefore, it is important to create a robust battery model with accurately identified parameters since it contributes to an optimal battery management system (BMS). In this work, the lithium-ion battery is modeled using an electrical equivalent circuit that consists of electrical components, resistors, and capacitors (RCs), called the Thevenin model, and in order to improve the accuracy, a double RC network is selected. The identification of the lithium-ion battery internal parameters is performed using three main steps. First, a relationship between open circuit voltage (OCV) and state of charge (SOC) is created using the curve fitting method. Then, the internal resistance is identified by the calculation of the instantaneous battery voltage drops. Finally, the identification of RCs components is carried out using the Levenberg-Marquardt optimization method. In addition, all parameters are identified as function of SOC. As a result, a lithium-ion battery model is created with identified variable internal parameters depending on the SOC values.

**Keywords:** *Lithium-ion battery, Battery identification, Battery model, Battery management system*

---



## Influence of the Temperature on the Performance of Conventional Organic Solar Cells

Samia Moulebhar<sup>\*1</sup>, Chahrazed Bendenia<sup>1</sup>, Hanaa Merad-Dib<sup>1</sup>, Souhila Bendenia<sup>1</sup>,  
Sarra Merabet<sup>1</sup>, Sid Ahmed Khantar<sup>1</sup>

<sup>1</sup>Laboratory of Analysis and Modeling of Advanced Materials for Renewable Energies, Abd El Hamid Ibn Badis University, Mostaganem 27000, Algeria

### Abstract

The influence of ambient temperature on the processes of carrier generation, recombination and transport in solar cells is notable. A simulation study was carried out on an organic solar cell, with a temperature variation from 280 to 340 K, as shown in Figure 1.

The results show a significant increase in open circuit voltage ( $V_{oc}$ ) and energy efficiency (PCE), from 0.53 to 0.59 V and from 5.6% to 6.17% respectively. At the same time, the fill factor (FF) fell slightly, from 60.04% to 58.75%. The short-circuit current density ( $J_{sc}$ ) remains unchanged at  $17.72 \text{ mA cm}^{-2}$ . The higher temperature provides increased thermal energy for the production and movement of carriers, particularly excitons, which are neutral. This increase creates a steeper concentration gradient of excitons, which increases the series resistance of the device and therefore the  $V_{oc}$ . However, it also leads to a decrease in the FF values of the device.

**Keywords:** Organic solar cell, Temperature, Performances, SCAPS 1D

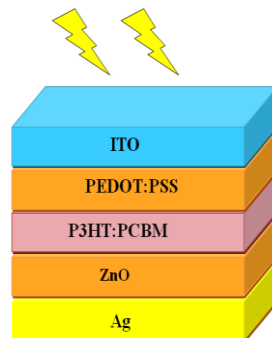


Figure 1. Conventional structure

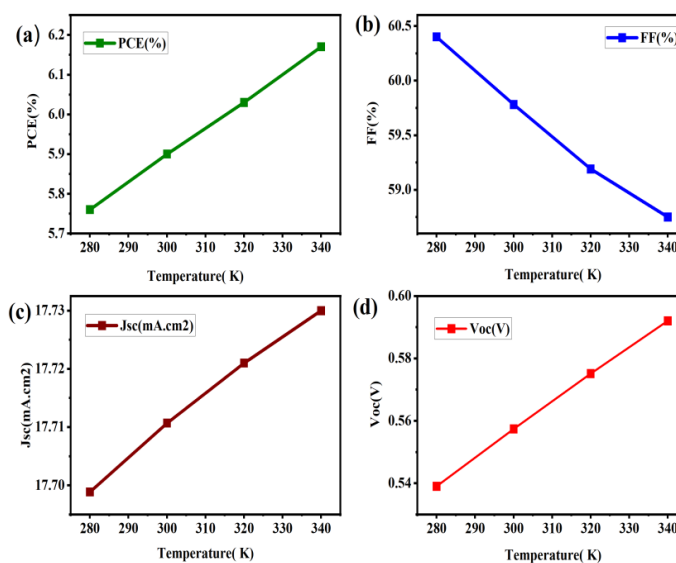


Figure 2. Effect of temperature on: (a) PCE, (b) FF, (c) Jsc, and (d) Voc



## Optimization of Sabbath Mode Algorithms Used in Refrigerators

Mazlum Koray Dirican<sup>\*1</sup>, Bulent Ozcan<sup>2</sup>

<sup>1</sup>Program Manager, Vestel White Goods Co., Manisa, Türkiye

<sup>2</sup>Laboratory Engineer, Vestel White Goods Co., Manisa, Türkiye

### Abstract

According to Jewish belief, the universe was created in six days, and the seventh day, known as the Sabbath, is a sacred day of rest. The Sabbath begins on Friday evening and ends on Saturday, during which business activities are forbidden by the Torah. Jews can continue to use their home appliances in Sabbath mode, which ensures religious use by preventing home appliances from operating with user input during the Sabbath. Sabbath mode on refrigerators generally stipulates that the compressor runs on a timer, the interior lights are turned off, and the fan motors stop operating with the user's interaction. Therefore, the refrigerator operates according to a predetermined scenario rather than environmental conditions. This may result in inadequate cooling or over-cooling, causing foods to spoil or freeze.

In this study, two distinct Sabbath algorithms were investigated to comply with Sabbath day regulations. A set of criteria was used to rate the algorithms. The first algorithm calculates an average operating pattern by examining the refrigerator's operation before the Sabbath, while the second algorithm adjusts the compressor start pattern based on predefined parameters and stops the compressor according to interior sensors. One of the predefined parameters is the calculation of the average heat loss of the refrigerator during the Shabbat in Israel based on season and time. Comparison tests were conducted in the Vestel refrigerator factory's test rooms, using combinations of six different ambient temperatures and three different relative humidity levels. The energy consumption and compartment temperature data were constantly recorded. The test results revealed that the second algorithm consumed 15% less energy and had a  $\pm 2$  degree more steady temperature fluctuation. Future research will focus on creating new adaptive learning sabbath algorithms that regulate compressor stops according to sensor data and are constantly updated according to start-end temperatures and consumed power.

**Keywords:** Sabbath mode, Refrigerator, Energy consumption, Temperature fluctuation

## 1 INTRODUCTION

The sabbatical is a more formalized concept known to the Jewish people in which a Sabbath, which begins from Friday evening to Saturday night, is embraced mainly because the universe creation took six days, and the seventh day is a day of rest. That is why, during this sacred time, there are no various types of work, and even the use of electric gadgets is prohibited. For these religious needs, almost all of the Jewish homes operate their home appliances, including the cool fridges on 'Sabbath mode' to avoid operating in a manner that will contravene the sabbath laws.

Sabbath mode changes how appliances work to stop any manual changes during the Sabbath. For refrigerators, this usually means changing their operations, so they do not react to user inputs. Common changes include setting the compressor on a fixed timer, turning off interior lights, and stopping fan motor activity. These changes make sure the refrigerator works on a set schedule instead of responding to real-time conditions, which can sometimes cause less effective cooling. This might lead to food spoiling due to not enough cooling or freezing due to too much cooling.

This study delves into the effectiveness of two distinct Sabbath algorithms designed to improve refrigerator performance while adhering to Sabbath regulations. The first algorithm sets an average operating pattern based on performance data from the refrigerator collected before the Sabbath. This data-driven method will consequently set a standard operational schedule for the individuals to follow in the Sabbath. The second algorithm presents a more complex method, as the compressor function is now adjusted by employing a mix of variables containing predefined elements and data obtained from the sensors. This algorithm includes parameters such as average heat loss pertaining to the zone where the company carries out its operations, and the seasonal and time variations that

allow the activity of the compressor to maintain the temperature at optimal levels while at the same time taking into consideration the energy usage.

## 2 MATERIAL AND METHOD

### 2.1 Materials

The following resources were used in this study:

- IEC 62552 - Household refrigerating appliances – Characteristics and test methods
- Test room and instrumentation in accordance with Annex A of EN 62552-1
- Domestic Refrigerator [1]
- Refrigerator Kosher Certification Guidelines [2]

### 2.2 Test Method

The domestic refrigerator used in the study is a 530-liter double-door refrigerator-freezer model. Thermocouples are placed in the center of each basket and 5 cm from the surfaces of the. The test environment is maintained at a steady 32°C, simulating typical high-temperature conditions with low fluctuations. Prior to activating the Sabbath mode, the refrigerator-freezer samples are operated for a continuous 24-hour period. This pre-test duration helps establish baseline performance and allows algorithms to gather the environmental data to be used during the mode activation.



**Figure 1.** Photos of thermocouple positions on a sample

The first algorithm examines the refrigerator's typical patterns before the mode is engaged. Before the mode activation, the first algorithm gathers the information about temperature, power, door opening/closing and compressor cycles. For an accurate baseline to be formed, it is important to note that appliance should be run for a certain amount of time before the mode activation, so that shabbat mode can be efficient and reliable.



**Figure 2.** Photos of the first sample that utilizes the first algorithm

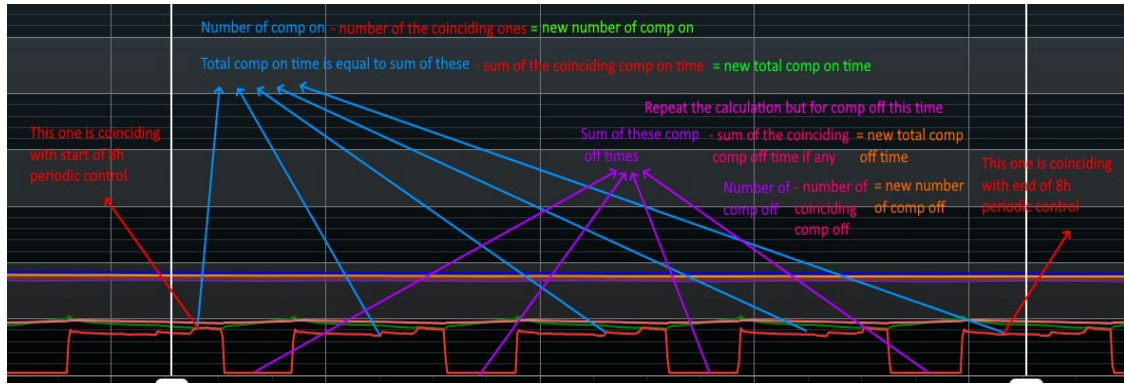


Figure 3. Visualization of the first algorithm work sequence calculation

The second algorithm regulates the running of a refrigerator’s compressor by controlling its start and stop cycle on directives of a set of parameters. One of them is the determination of the average heat loss of the refrigerator and this is done with particular reference to Shabbat. This calculation depends on the location of the building, the season of the year and time of the day. Independent temperature and other conditions sensors inside the refrigerator give the data only if the compressor is in operation, which lets the algorithm set the best mode and time of the compressor functioning according to the initially determined parameters to maintain optimally cool conditions and save energy at the same time. Thus, the approach under discussion guarantees that the refrigerator will work fine and save energy during Shabbat.



Figure 4. Photos of the second sample that utilizes the second algorithm

Table 1. Specification of the second algorithm working logic

Condition	Compressor Starter Timer Value	Compressor Stopper Sensor Value	Compressor Working Speed Value
$T_{amb} < 14\text{ }^{\circ}\text{C}$	Every 80 min	Fridge 5 °C set	According to current season and date
$14\text{ }^{\circ}\text{C} < T_{amb} < 38\text{ }^{\circ}\text{C}$	Every 160 min	Fridge 5 °C set	According to current season and date
$38\text{ }^{\circ}\text{C} < T_{amb}$	Every 240 min	Fridge 5 °C set	According to current season and date

### 3 RESULTS

Results are tabulated for both algorithms. The definition of the variables can be found below:

$T_{amb}$  : Test chamber temperature

$T_m$  : Mean temperature of the fresh/freezer food compartment

$P_{on}$  : Average power consumption of the sample while compressor is working



$P_{off}$  : Average power consumption of the sample while compressor is not working

$WR$  : Working ratio of the compressor of the sample during the test

$P_{ss}$  : Steady-State power consumption of the sample

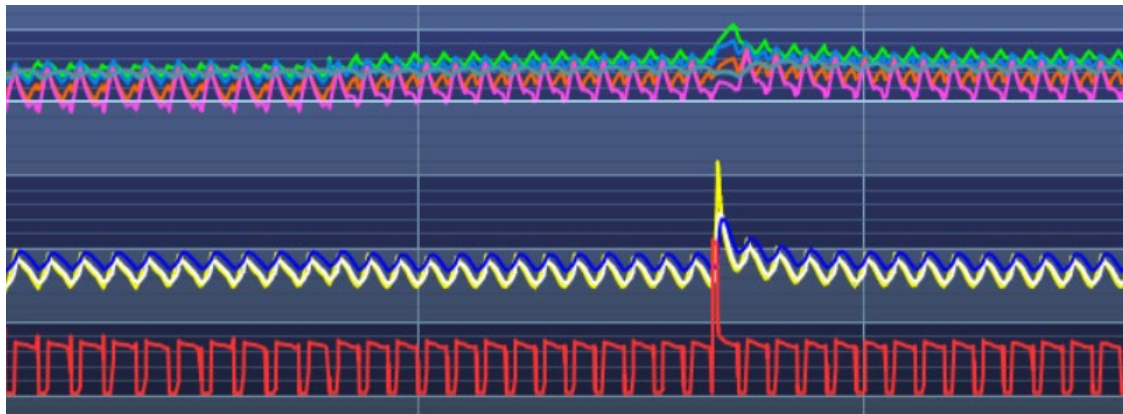
By definition, steady-state power consumption of a sample can be found as follows:

$$P_{ss} = P_{on} \times WR + P_{off} \times (1 - WR) \tag{1}$$

According to test results, there was an increase in both fresh food and freezer compartment in the first sample, 1.4 °C and 0.9 °C respectively. Despite the average power consumption of the sample while compressor is working was stayed the same, there was an increase in the steady-state power consumption of the sample due to change in the working ratio of the compressor of the sample during testing.

**Table 2.** Results of the first algorithm before and during the shabbat mode activated

Variables	Units	Before Shabbat Mode	During Shabbat Mode
Tamb	(°C)	32	32
Tm	(°C)	3.5	4,9
Tfm	(°C)	-20.2	-19.3
Pon	(W)	55.03	55.12
Poff	(W)	1.1	1.1
WR	-	80.5%	86.17%
Pss	(W)	45.4	48.6



**Figure 5.** Test graph of the first algorithm during the testing

Similar to results of the first sample, compartment temperatures of the second sample were increased as well, by 1.2°C and 0.8°C respectively. In the second algorithm, the working ratio of the compressor is lowered significantly, from 80.2% to 67.5%. Huge decrease in the working ratio caused unit to be consume lower power in steady-state condition by 7%.

**Table 3.** Results of the second algorithm before and during shabbat mode activated

Variables	Units	Before Shabbat Mode	During Shabbat Mode
Tamb	(°C)	32	32
Tm	(°C)	3.3	4.5
Tfm	(°C)	-20.1	-19.3
Pon	(W)	55.49	61.63
Poff	(W)	1.2	1.1
WR	-	80.2%	67.5%

P <sub>ss</sub>	(W)	45,7	42,7
-----------------	-----	------	------

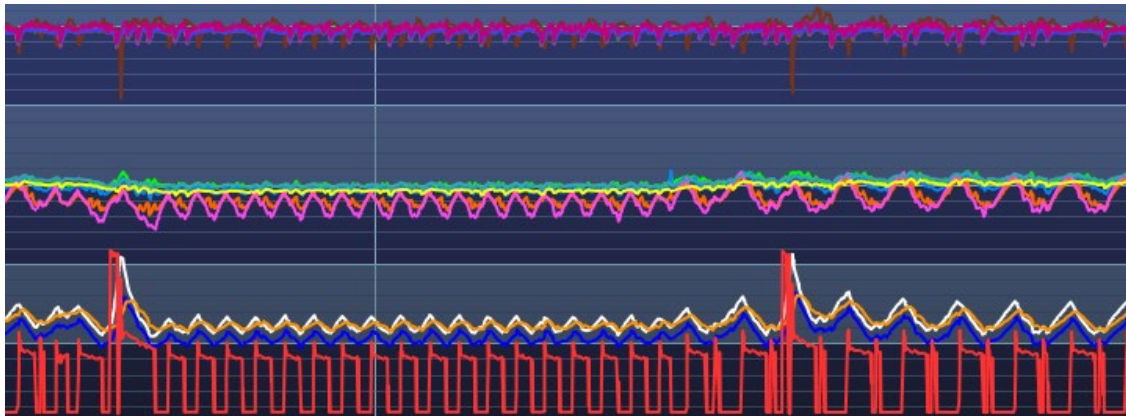


Figure 6. Test graph of the first algorithm during the testing

#### 4 CONCLUSION

The initial algorithm, defined by a fixed patternology, caused the compressor's working ratio to rise. This elevated operational load led to a 13.8% increase in power consumption compared to the second algorithm. Conversely, the second algorithm, which adjusts the compressor dynamically based on sensor data and present parameters, turned out to be more energy-efficient while keeping temperature conditions relatively stable.

In light of these results, the algorithms behind Sabbath mode ought to be enhanced with a view to optimizing energy saving while concurrently enhancing the means of equalizing temperatures. Thus, the comparison of the power consumption clearly manifested the necessity of the optimization of the Sabbath mode.

The research on the subject will advance in the future with the development of self-organizing Sabbath algorithms that will further optimize the energy conservation ratio without compromising the stability of the temperature. These sophisticated algorithms will be developed to run using the actual time sensor feed data and they will be designed to self-adapt in terms of compressor cycles based on the start-end temperatures and power use statistics. This way the present study seeks to refine the efficiency of Sabbath mode appliances so that they are fit for religious use but not at the expense of their performance.

#### References

- [1] Vestel. (2024). *Vestel NFK60112 E GI PRO WIFI 533 Lt No-Frost Buzdolabi* [Online]. Available: <https://www.vestel.com.tr/vestel-nfk60112-e-gi-pro-wifi-533-lt-no-frost-buzdolabi-p-2966>
- [2] R. A. Mushell. (2003). "Keeping Your Cool: All About Refrigerators". *STAR-K* [Online]. Available: Keeping Your Cool: All About Refrigerators | STAR-K Kosher Certification



---

## A Numerical Study on the Aerodynamic Performance of the S1223 Airfoil in Low Reynolds Number Conditions

Onur Usta\*<sup>1</sup>

<sup>1</sup>Department of Naval Architecture and Marine Engineering, Turkish Naval Academy, National Defence University, Istanbul, Türkiye

---

### Abstract

In this study, the performance of an aircraft wing featuring the s1223 airfoil, which is specifically designed for low Reynolds numbers, has been modelled and evaluated through Computational Fluid Dynamics (CFD) analyses. The numerical results from these analyses have been validated against available experimental data from the literature, obtained from wind-tunnel tests at a Reynolds number (Re) of  $2 \times 10^5$ . Following the validation process, the study further investigates the performance characteristics of the s1223 airfoil section under a variety of flow conditions. The focus is particularly on the lift coefficient generated by the wing at different angles of attack and varying velocity combinations. For this purpose, CFD analyses were conducted for the S1223 airfoil at angles of attack (AoA) of 0, 4, and 8 and 12 degrees, within a Reynolds number range of  $1.75 \times 10^5 < Re < 2.5 \times 10^5$ , which are representative of the operational regimes for unmanned aerial vehicles (UAVs). In the CFD simulations, governing equations are modelled by Reynolds-Averaged Navier-Stokes (RANS) method using the standard k-omega turbulence model. This approach enabled a detailed examination of the aerodynamic performance of the S1223 airfoil, particularly in terms of its lift generation capabilities under the specified conditions. The results provide insights into the efficiency and effectiveness of the airfoil design at low Reynolds numbers and high altitude conditions, which is critical for applications for UAVs. The findings from this research contribute to the understanding of airfoil performance in low Reynolds number regimes and offer valuable data for the design and optimization of aircraft wings in similar applications.

**Keywords:** S1223 airfoil, CFD, RANS, Angle of attack, Low Reynolds number, High altitude

---

## 1 INTRODUCTION

The aerospace industry continues to explore innovative solutions to optimize aircraft performance under various operational conditions. In recent years, there has been a growing emphasis on developing airfoils, capable of sustaining efficient flight at low speeds and high altitudes. In the realm of aerodynamic research, understanding the performance characteristics of airfoils at low Reynolds numbers is crucial for a variety of applications ranging from unmanned aerial vehicles (UAVs) to high-altitude pseudo-satellite (HAPS) systems. These platforms demand airfoils that can achieve high lift coefficients while minimizing drag, thereby extending mission durations and operational capabilities.

The airfoil can be considered the “heart” of an aircraft due to its crucial role in producing the necessary lift for flight. Lift generation is essential for maintaining altitude and ensuring stable flight conditions. The design and efficiency of the airfoil significantly impact an aircraft's performance, influencing factors such as fuel efficiency, maneuverability, and overall aerodynamic properties. In essence, the airfoil's ability to generate sufficient lift while minimizing drag is fundamental to the success of any aircraft design. Moreover, the airfoil must exhibit high efficiency, especially in the Low Reynolds number (Re) regime, which is typically encountered by smaller aircraft, unmanned aerial vehicles (UAVs), and during certain flight conditions such as takeoff and landing. Researches by [1] and [2] underscores the importance of optimizing airfoil performance in this regime. Low Re conditions present unique challenges, including increased sensitivity to flow separation and transition effects. Thus, designing airfoils that maintain high lift-to-drag ratios and stable aerodynamic characteristics under these conditions is critical for advancing aerospace technology and improving the performance of various types of aircraft.

The S1223 airfoil profile, developed by Mark Drela and Michael at the University of Illinois in the 1990s, is renowned for its performance at low Reynolds numbers. This makes it ideal for high-lift, low-speed applications such as unmanned aerial vehicles (UAVs), gliders, and solar-powered aircrafts. The S1223 is designed to maximize the lift-to-drag ratio, enhancing efficiency and stability for endurance-focused missions [3, 4].

In the literature, it is observed that the S1223 foil is generally examined in an air environment. However, Oller et al. [5] investigated the lift and drag performance of the S1223 foil geometry in a water environment. This study [5] provides significant insights into the behavior of this geometry in different fluid environments. The authors conducted experiments in a water environment and meticulously analysed the performance characteristics of the S1223 foil based on the obtained data.

This airfoil features a moderately thick and cambered design with a reflexed trailing edge, which helps in delaying flow separation and reducing drag, particularly at high angles of attack. These attributes are beneficial for aircraft requiring sustained flight at low speeds or at high altitudes, where traditional aerodynamic designs might struggle due to the thin air and reduced Reynolds numbers. The S1223 profile's versatility has made it a popular choice not only in the field of solar-powered HAPS (High Altitude Pseudo-Satellite) systems like the Zephyr but also in small-scale UAVs and experimental aircraft aimed at achieving long-duration flights and efficient performance in challenging atmospheric conditions.

The significance of studying the S1223 airfoil lies in its potential to improve the design and operation of lightweight, high-efficiency aircraft used for surveillance, reconnaissance, and environmental monitoring. These applications demand airfoils capable of generating sufficient lift at low speeds while minimizing drag, thereby extending mission durations and enhancing operational flexibility. By leveraging computational fluid dynamics (CFD) simulations, this study seeks to elucidate the complex flow phenomena around the S1223 airfoil and validate its performance metrics against empirical data and theoretical predictions. Moreover, understanding the aerodynamic behavior of the S1223 airfoil in low Reynolds number regimes contributes to broader advancements in aerodynamic theory and computational modelling.

According to Imumbhon et al. [4], the Selig S1223 airfoil profile stands out for its exceptional performance at low Reynolds numbers, high lift capability, and low noise levels at small angles of attack. When combined with the use of high-strength carbon fiber, it becomes an excellent choice for this RA-driven aircraft application.

An altitude of 65000 feet, which is particularly significant for military aircraft, was selected for this study. In aviation, an altitude of 65000 feet (approximately 19812 meters) is important because it is near the edge of the atmosphere, close to the boundary of space. This altitude is beyond the operational ceiling of conventional commercial aircraft and above the altitudes at which some private and military aircraft can fly. This altitude is important for several reasons. One reason is that, at higher altitudes, the air density is lower, which reduces drag and consequently fuel consumption. Aircraft capable of flying at these altitudes can perform more efficiently on long-range missions. The second reason is an aircraft flying at or above 65000 feet can avoid enemy radar and air defense systems. This altitude provides a strategic advantage for surveillance and reconnaissance missions. The third reason is that, most commercial flights operate at lower altitudes, making the airspace above 65000 feet less congested. This reduces the risk of collisions and simplifies air traffic management.

This study includes a fine application of CFD. CFD is a powerful tool for studying fluid dynamics. It can describe the complex flow around geometric boundaries, quickly evaluate preliminary airfoil designs, and make prompt adjustments. This significantly reduces the cost, time, and risks associated with repeated experiments, making CFD an increasingly important method for airfoil design and flow field analysis in recent years [7].

This study aims to provide valuable insights into the aerodynamic performance of the S1223 airfoil in low Reynolds number and high altitude conditions, relevant to various aviation and aerospace sectors. The primary objective is to conduct a detailed numerical investigation of the S1223 airfoil's performance using CFD simulations, validated against experimental wind-tunnel data. Key performance metrics, such as lift and drag, are analysed across a range of AoA and velocities. The study focuses on Reynolds numbers from  $1.75 \times 10^5$  to  $2.5 \times 10^5$ , corresponding to velocities of 20 to 25 m/s, which are typical for UAVs and high-altitude pseudo-satellites (HAPS). Simulations are conducted at angles of attack of  $0^\circ$ ,  $4^\circ$ ,  $8^\circ$ ,  $12^\circ$  to replicate real-world flight conditions and assess the airfoil's performance under different aerodynamic loads.

## 2 S1223 AIRFOIL

### 2.1 Geometrical characteristics

Geometrically, the S1223 airfoil shows specific characteristics that contribute to its efficiency in generating maximum lift force while maintaining a low thickness profile.

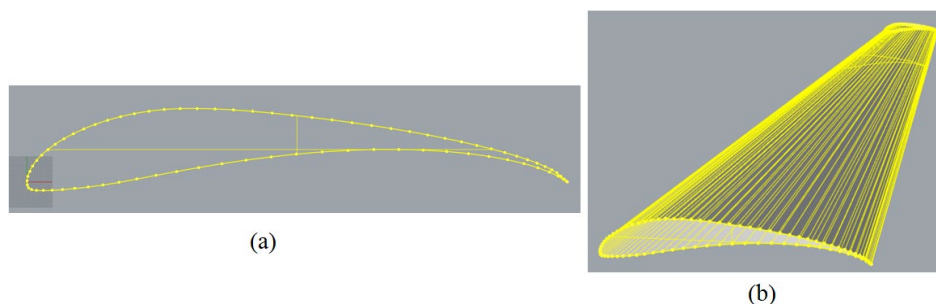
The geometric equation of the S1223 airfoil describes the shape of its upper and lower surfaces, typically defined in terms of a parametric equation. For the S1223 airfoil, the coordinates of the upper and lower surfaces are represented with the equation below:

$$y_u(x) = \frac{t}{0.2} \left( 0.2969\sqrt{x} - 0.1260x - 0.3516x^2 + 0.2843x^3 - 0.1025x^4 \right) \quad (1)$$

$$y_l(x) = -\frac{t}{0.2} \left( 0.2969\sqrt{x} - 0.1260x - 0.3516x^2 + 0.2843x^3 - 0.1025x^4 \right) \quad (2)$$

Where  $t$  represents the maximum thickness of the airfoil as a fraction of the chord length  $c$ , and  $x$  denotes the normalized chordwise position from 0 (leading edge) to 1 (trailing edge).

The S1223 airfoil generated in the 3-D CAD programme in accordance with the above equation is shown in Figure 1.



**Figure 1.** S1223 airfoil geometry (a) 2-D, (b) 3-D

### 3 COMPUTATIONAL MODELING

Pressure distribution on the foil, lift production, drag force, pressure coefficient, lift coefficient, drag coefficient and lift/drag coefficient are used to analyse the performance of aerofoils. Within this respect, these parameters are investigated in this study utilizing the Reynolds-averaged Navier-Stokes (RANS) equations with the standard k-omega turbulence model. This approach allows for a detailed analysis of the flow characteristics around the S1223 airfoil, capturing complex phenomena such as boundary layer development, separation points, and vortex shedding.

#### 3.1 Computational Domain and Mesh

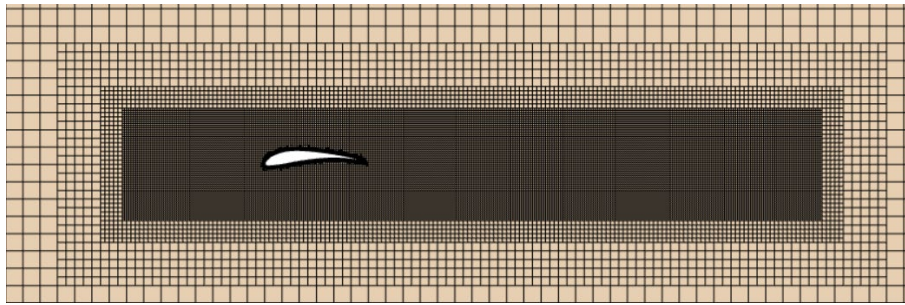
CFD analyses were performed to meet the physical conditions given in Table 1. The computational domain has been designed to be sufficiently large to prevent flow reflections and reverse flow behind the airfoil.

An unstructured polyhedral mesh was generated in the computational domain. The mesh around the airfoil has been generated with high density to accurately model the airflow around the boundary layer. The mesh cells gradually increase in size moving outward from the airfoil, allowing for efficient analysis without excessively straining computational resources.

Computational domain with S1223 airfoil is and mesh around the airfoil are presented in Figure 2 and Figure 3 below.



**Figure 2.** Computational domain with S1223 airfoil



**Figure 3.** Mesh around the airfoil

### 3.2 Numerical parameters

#### *Lift coefficient and drag coefficient*

Lift and drag forces are influenced by various factors including the air's density, the square of the velocity, the air's viscosity and compressibility, the surface area over which the air flows, the shape of the body, and the body's angle relative to the flow. The effects of body shape, inclination, air viscosity, and compressibility are generally very complex. To simplify these complex dependencies, a single variable called the lift coefficient ( $C_L$ ) and the drag coefficient ( $C_D$ ) are used. This approach consolidates all these effects into one equation.

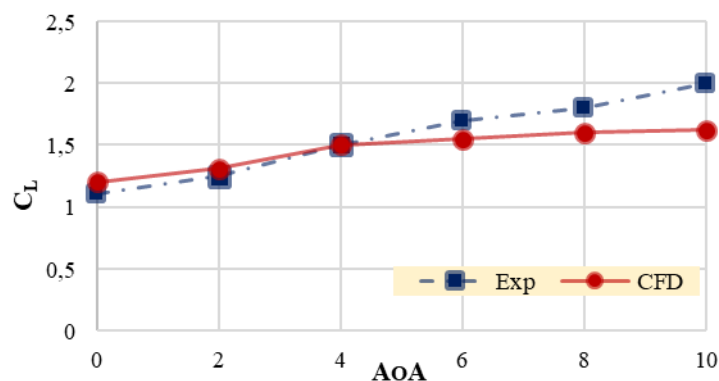
The lift equation expresses that lift ( $L$ ) is equal to the lift coefficient ( $C_L$ ) multiplied by the air density ( $\rho$ ), half the square of the velocity ( $V$ ), and the wing area ( $A$ ).

The drag equation expresses that drag ( $D$ ) is equal to the drag coefficient ( $C_D$ ) multiplied by the air density ( $\rho$ ), half the square of the velocity ( $V$ ), and the wing area ( $A$ ).

## 4 VALIDATION STUDY

Selig and Guglielmo [3] conducted experiments on the S1227 airfoil at  $Re=2 \times 10^5$  conditions in the angle of attack range from 0 degrees to 20 degrees. The experiments were conducted in the open-return subsonic wind tunnel at the University of Illinois [3]. In the validation analyses performed in this study, the experimental results obtained from [3] are used.

Within the scope of this study, lift coefficient values at the range of  $0^\circ$ - $10^\circ$  angles of attack around  $Re=2 \times 10^5$  conditions were obtained and compared with the literature as presented in Figure 4 below.



**Figure 4.** Experimental and numerical results

When the lift coefficient results obtained experimentally (from the literature) and through CFD (in this study) for the AoA conditions mentioned above are carefully examined, it is observed that the results are very close to each other, particularly at 2 and 4 degrees. However, as the AoA increases, the  $C_L$  values from experimental results increase more rapidly, while the rate of increase in  $C_L$  values from the numerical analysis is smaller.

Given that the experimental results closely match the obtained results, validation is considered achieved, allowing the study to proceed to the next step.

## 5 CFD ANALYSIS OF S1223 AIRFOIL FOR VARIOUS AoA AND RE CONDITIONS

After the validation study, CFD analyses were conducted for the S1223 airfoil at angles of attack (AoA) of 0 degrees, 4 degrees, 8 degrees and 12 degrees within a Reynolds number range of  $1.75 \times 10^5 < Re < 2.5 \times 10^5$  which are representative of the operational regimes for unmanned aerial vehicles (UAVs) and High-altitude platform systems (HAPSs).

### 5.1 Flow Conditions

The flow conditions in the study, presented in Table 1 are chosen to be compatible with the operating conditions of a real UAV.

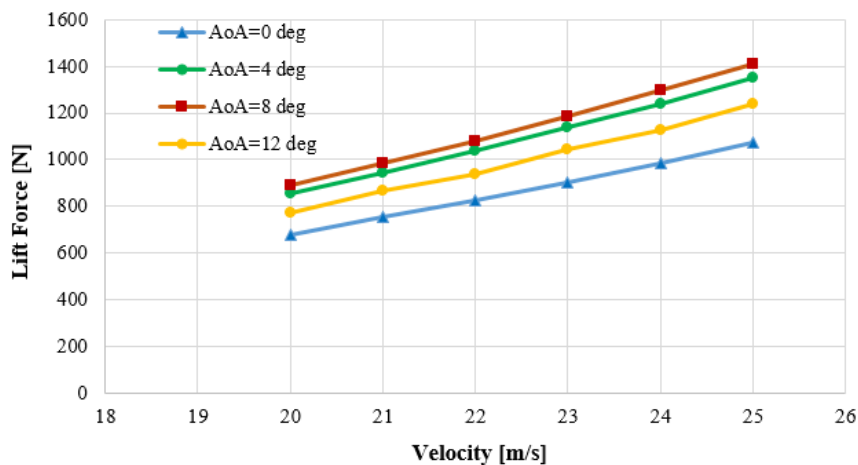
**Table 1.** Flow conditions

AoA [deg]	Air density (kg/m <sup>3</sup> )	Altitude [ft]	Gravity [m/s <sup>2</sup> ]	Temperature [K]	Reynolds number [-]
0, 4, 8, 12	0.092	65000	9.75	216.65	$1.75 \times 10^5$ - $2.5 \times 10^5$

As detailed in the Introduction, 65000 ft is a realistic altitude for a UAV. Density, pressure and temperature values are calculated to reflect realistic conditions for air at this altitude.

### 5.2 Results and Discussions

The results of lift force, drag force and lift/drag obtained by CFD are presented in Figures 5, 6, 7 respectively. The purpose of presenting lift and drag forces instead of dimensionless lift and drag coefficients is to analyze the increase in drag and lift forces in response to increasing speed. When the speed varies in the range of 20 to 25 m/s, as in this study, the dimensionless lift and drag coefficients should theoretically remain constant or exhibit minimal changes due to viscous effects and numerical errors. This behavior has also been observed in the CFD analyses conducted, the lift and drag coefficients remain nearly constant as speed increases.



**Figure 5.** Lift force results obtained by CFD.

Upon examining the graph of lift force variation with speed, it is observed that the lowest lift production, as expected, occurs at a 0 degree AoA. Interestingly, the highest lift production is not at a 12 degree AoA. This indicates that the S1223 airfoil experiences stall before reaching 12 degrees. For the all velocity conditions simulated, the higher lift value is obtained for AoA= 8 degree however, 4 degree AoA is very close to that.

Drag force results obtained by CFD are compared in Figure 6.

Drag is an unwanted force. For this reason, the smaller the drag, the better. In general, the drag force increases with the angle of attack for airfoils. As expected, the smallest drag forces occur at 0 degree and 4 degree AoA.

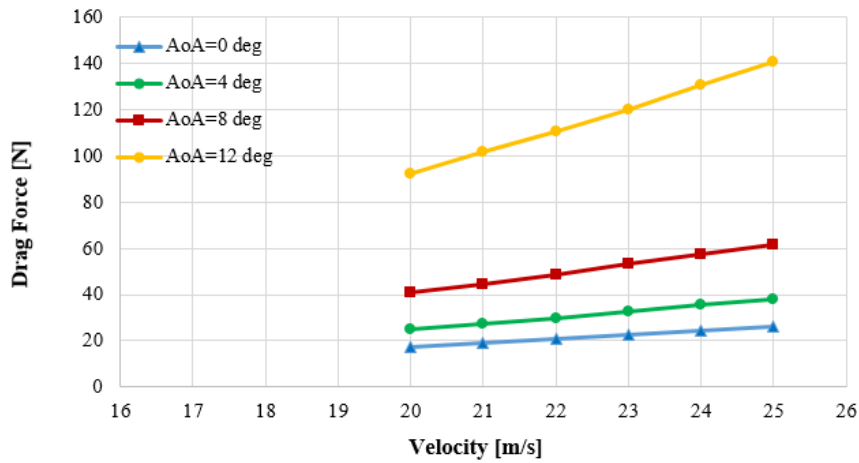


Figure 6. Drag force results obtained by CFD

By dividing the lift force by the drag force, the non-dimensional value that represents performance criteria is determined as presented in Figure 7.

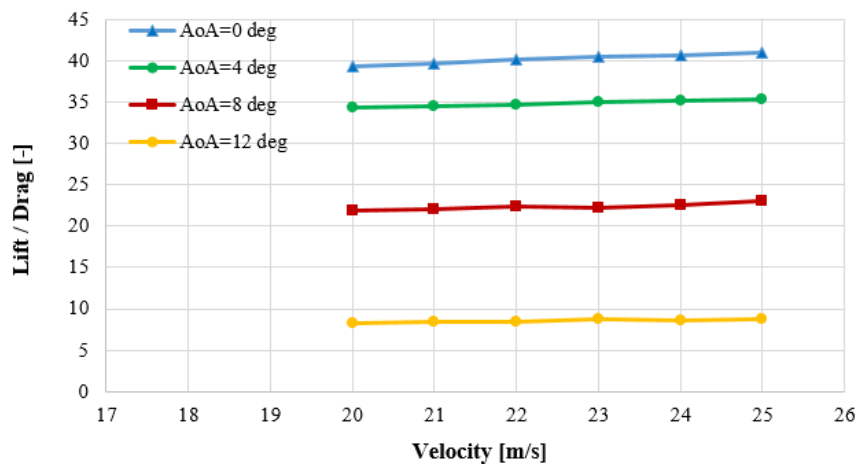


Figure 7. Lift force / Drag force results obtained by CFD

Upon examining the lift-to-drag ratio graphs which are the performance criteria for the airfoil, lift/drag value is almost stable with the variation of velocity, as expected. Moreover, it is clear that 0 degree and 4 degree AoA yield the best performance.

Upon evaluating the lift, drag and lift/drag results together, it is concluded that the optimum angle of attack (AoA) for the S1223 airfoil wing is 4 degrees. Additionally, the numerical study has shown that an aircraft with an S1223 airfoil will experience a significant drop in performance if it cruises at an angle of attack of 12 degrees or higher. At an 8 degree AoA, there is more lift produced compared to 4 degrees; however, considering the drag, the aerodynamic performance at 8 degrees is still worse than at 4 degrees.

## 6 CONCLUSIONS

In this study, the aerodynamic characteristics of the S1223 airfoil, which is commonly used in UAVs, are examined under different Reynolds numbers and angles of attack conditions. The following conclusions were obtained from the study:

- The performance characteristics of an airfoil such as lift production and drag force can be accurately determined CFD analyses.
- The study has shown that the generated model by the RANS method and the k-omega turbulence model, the aerodynamic characteristics of the airfoil under different angles of attack and Reynolds number conditions can accurately predicted.



- The results obtained by CFD indicate that under the operating conditions of a real UAV, the S1223 airfoil exhibits optimal efficiency at angles of attack between 0 and 4 degrees. Beyond 4 degrees, the lift-to-drag ratio declines.
- Under low Reynolds number and 65000 altitude conditions, the most efficient AoA for an aircraft with S1223 wings is between 0 and 4 degrees.

## References

- [1] W. Yuan, M. Khalid, J. Windte, U. Scholz, and R. Radespiel. "An investigation of low-Reynolds-number flows past airfoils," in *23rd AIAA Applied Aerodynamics Conference*, 2005, p. 4607.
- [2] S. G. Kontogiannis, D. E. Mazarakos, and V. Kostopoulos. "ATLAS IV wing aerodynamic design: From conceptual approach to detailed optimization," *Aerospace Science and Technology*, vol. 56, pp. 135–147, 2016.
- [3] M. S. Selig and J. J. Guglielmo, "High-lift low Reynolds number airfoil design," *Journal of aircraft*, vol. 34, no. 1, pp. 72–79, 1997.
- [4] E. Mollica and A. Timmoneri, "CFD analysis of the low Reynolds S1223 airfoil," *International Journal of Engineering, Science and Technology*, vol. 13, no. 4, pp. 46–49, 2022.
- [5] O. Aramayo, S. A. Nallim, L., and S. Oller, "Usability of the Selig S1223 profile airfoil as a high lift hydrofoil for hydrokinetic application," *Journal of Applied Fluid Mechanics*, vol. 9, no. 2, pp. 537–542, 2016.
- [6] J. O. Imumbhon, M. D. Alam, and Y. Cao, "Design and structural analyses of a reciprocating S1223 high-lift wing for an RA-driven VTOL UAV," *Aerospace*, vol. 8, no. 8, art. no. 214, 2021.
- [7] R. Ma and P. Liu, "Numerical simulation of low-reynolds-number and high-lift airfoil S1223," in *Proceedings of the World Congress on Engineering*, London, U.K, 2009.



## Simulation Study of Methylammonium Lead Iodide (CH<sub>3</sub>NH<sub>3</sub>PbI<sub>3</sub>)-Based Perovskite Solar Cell via Silvaco TCAD

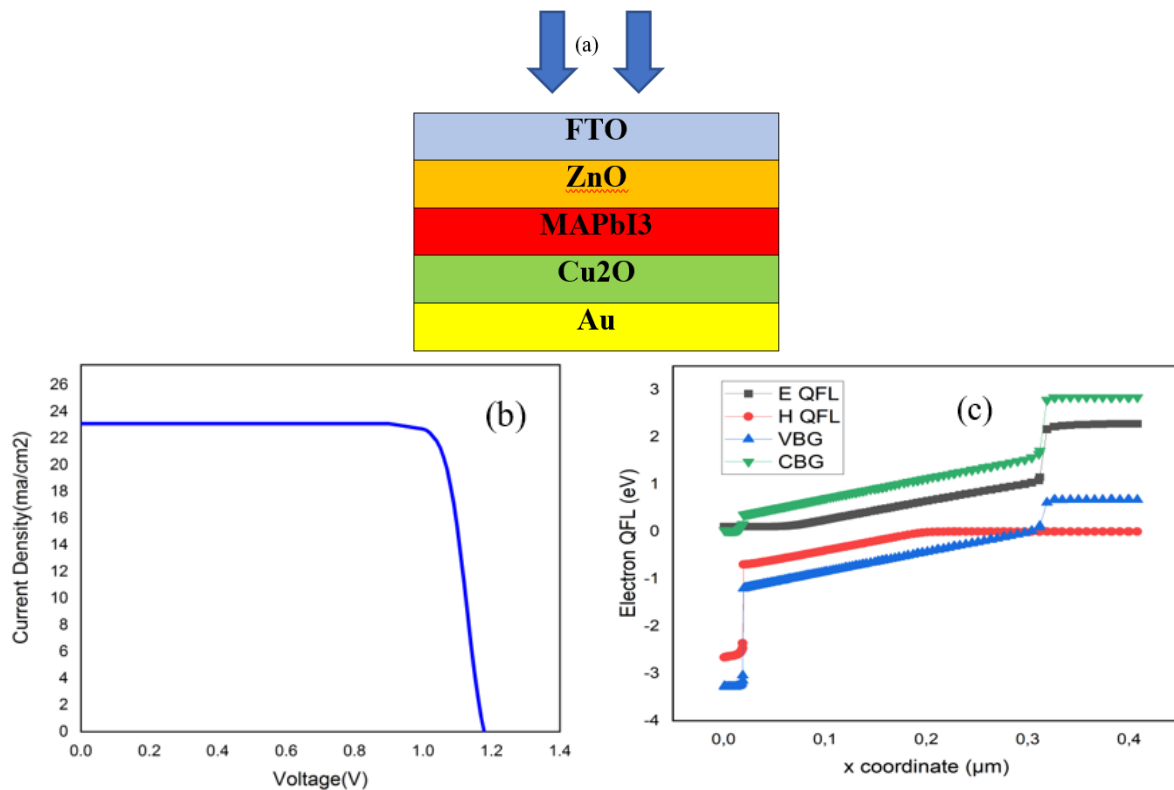
Sid Ahmed Khantar<sup>\*1</sup>, Chahrazed Bendeni<sup>1</sup>, Souhila Bendenia<sup>1</sup>, Hanaa Merad-Dib<sup>1</sup>,  
Samia Moulebhar<sup>1</sup>, Sarra Merabet<sup>1</sup>

<sup>1</sup>Faculty of Sciences and Technology, University Abd El Hamid Ibn Badis, Mostaganem 27000, Algeria

### Abstract

This study presents the demonstration of an organo-metal halide perovskite, n-i-p planar perovskite solar cell (PSC) based on CH<sub>3</sub>NH<sub>3</sub>PbI<sub>3</sub>, utilizing Silvaco TCAD. A material cell design of FTO/ZnO/MAPbI<sub>3</sub>/Cu<sub>2</sub>O/Au was investigated, with a detailed analysis conducted on parameters including thickness, doping concentration of the perovskite layer, electron transport layer (ETL), hole transport layer (HTL), and defect density. Under optimized conditions, the PSC exhibits an energy conversion efficiency of approximately 24.29%, accompanied by a fill factor of 84.85%, an open-circuit voltage of 1.18 V, a short-circuit current density of 24.19 mA/cm<sup>2</sup>, and a quantum efficiency ranging from 80% to 90% under 300 Kelvin temperature. This model underscores the potential of CH<sub>3</sub>NH<sub>3</sub>PbI<sub>3</sub> as a perovskite material, heralding the production of solar cells with high efficiency.

**Keywords:** MAPbI<sub>3</sub>, Cu<sub>2</sub>O, ZnO, Organic-inorganic perovskite solar cell, Silvaco atlas



**Figure 1.** (a) device architecture (b) Simulated J-V characteristic devices (c) energy band diagram of proposed MAPbI<sub>3</sub> based solar cell



---

## Optimization of Distributed Generations Placement and Sizing in Radial Distribution System through ABC Algorithm

Badreddine Bendriss<sup>\*1</sup>, Samir Sayah<sup>1</sup>, Abdellatif Hamouda<sup>2</sup>

<sup>1</sup>Department of Electrical Engineering, Ferhat Abbas University, Algeria

<sup>2</sup>Optics and Fine Mechanics Institute, Ferhat Abbas University, Algeria

---

### Abstract

The surge in electricity consumption across residential, commercial, and industrial sectors has driven the integration of renewable energy-based Distributed Generations (DGs) to meet electrical demands and mitigate greenhouse gas emissions. Effective incorporation of DGs into Radial Distribution Systems (RDS) is critical for improving overall system performance. This paper presents an Artificial Bee Colony (ABC) algorithm designed to identify the optimal size, location, and power factor (PF) of DG units, aiming to minimize total real power losses and enhance the voltage profile, all while adhering to operational constraints. The study evaluates two DG types: one operating at a unity PF and the other at an optimal PF. The study demonstrates that the improved voltage profile and reduced power losses contribute to a more robust and reliable electrical grid. Moreover, the results indicate that DGs functioning at their optimal PF significantly reduce power losses and improve the voltage profile across all buses of the RDS, underscoring the importance of considering the optimal PF in the operation of DGs, as it yields more significant benefits compared to unity PF operation. These insights can guide future renewable energy integration and distribution system optimization developments. The efficacy of the proposed algorithm is demonstrated through simulations conducted on an IEEE 33-bus standard distribution system, with results corroborating findings from existing literature.

**Keywords:** *Artificial bee colony, Distributed generations, Power losses, Voltage profile, Radial distribution systems*

---



---

## Analysis of CdTe Solar Cell Performance Using SCAPS-1D Simulation as a Function of Various Buffer Layers

**Merabet Sarra<sup>\*1</sup>, Bendenia Chahrazed<sup>1</sup>, Bendenia Souhila<sup>1</sup>, Merad Hanae<sup>1</sup>, Moulebhar Samia<sup>1</sup>, Khantar Sid Ahmed<sup>1</sup>**

<sup>1</sup>*Department of Electronics, Abdelhamid Ibn Badis, Mostaganem, Algeria*

---

### Abstract

Cadmium telluride (CdTe)-based cells have emerged as the leading commercialized thin-film photovoltaic technology due to their superior temperature coefficients, higher energy yield, and lower degradation rates compared to silicon (Si) technology. This makes CdTe cells a more efficient and reliable choice for large-scale solar energy production, offering better performance in varying environmental conditions and ensuring more sustainable energy production. In this study, the effect of various buffer layers such as CdS, ZnTe, ZnS, and  $Cd_xZn_{1-x}S$  on CdTe solar cells performance was assessed using SCAPS-1D simulator. The analysis was conducted at a temperature of 300 K under standard AM1.5G illumination. The study focused on altering the buffer layer thickness from 10 nm to 100 nm while keeping other parameters fixed. Modeling results for the Mo/p-CdTe/n-CdS/ZnO solar cell yielded an optimum efficiency of 21.47%, an open-circuit voltage (VOC) of 0.90 V, a short-circuit current density (JSC) of 27.71 mA/cm<sup>2</sup>, and a fill factor (FF) of 86.13%. The CdS layer was replaced by ZnS, ZnTe and  $Cd_xZn_{1-x}S$ , achieving efficiencies of 19.58%, 20.97% and 20.22%, respectively. These findings contribute valuable insights into optimizing CdTe solar cells to improve performance and wider applicability in renewable energy systems. Further experimental validation and optimization efforts are warranted to validate these simulation results and advance the efficient development and eco-friendly CdTe solar cell technologies.

**Keywords:** *Efficiency, Buffer layer, CdTe, Solar cell, SCAPS-1D*

---



---

## Advancements and Challenges of Photovoltaic Technology in Algeria's Desert

**Chekal Affari Belhadj<sup>\*1</sup>, Kahoul Nabil<sup>2</sup>, Younes Mohammed<sup>3</sup>, Daoudi Lina<sup>4</sup>, Cheghib Hocine<sup>2</sup>, Kherici Zoubida<sup>2</sup>**

<sup>1</sup>Laboratory for Modeling of Renewable Energy and Nanoscale Devices, Brother Mentouri University Constantine 1, Constantine, Algeria

<sup>2</sup>Laboratory of Electromechanical Systems, Badji Mokhtar University-Annaba, Annaba, Algeria

<sup>3</sup>Constantine Electrical Engineering Laboratory, Brother Mentouri University, Constantine 1, Constantine, Algeria

<sup>4</sup>Mathematical Modeling and Numerical Simulation, Badji Mokhtar University-Annaba, Annaba, Algeria

---

### Abstract

Algeria is taking significant steps towards for sustainable energy transition and promoting efficient and more sustainable energy future. Algerian Sahara could capture enough solar energy to meet the electricity needs of the entire world. Harsh climatic conditions of Algerian desert create challenges for the performance, reliability, and sustainability of solar photovoltaic installations. This paper explores the primary factors contributing to the degradation of c-Si in desert climates and examines the direct correlation between desert climate and the acceleration of degradation mechanisms. The study was carried out at research unit of renewable energy in Algerian Saharan middle (urerms.cder.dz), Adrar, in the extreme southwest of Algeria. An overview of Algeria's desert climate has been presented, is characterized by high ambient temperatures (exceeds 50 °C in summer) and high solar irradiations (exceeds 1000 W/m<sup>2</sup>). The main contribution of this work is to examine the impact of environmental factors on energy efficiencies. Data base of PV power plant installed in desert has been included. The findings of the analysis demonstrate the significant influence of the desert environment on the power generation performance. The study gives a clearer insight that can help researchers, manufacturers, investors, developers, and governments to develop an adequate PV solar system in similar climates.

**Keywords:** Algeria's desert climate, Power generation monitoring, c-Si, Performance assessment, Lifetime expectancy

---



## **Contribution to the Study of the Structural, Electronic, Optical, and Thermoelectric Properties of Heusler Alloys: A Material with Great Promise for the Future of Clean Energy**

**Khedidja Mechehoud<sup>\*1</sup>, Mohamed Mana<sup>2</sup>, Aya Righi<sup>1</sup>, Mouffok Redouane Ghezzar<sup>3</sup>, Fatima Bendahma<sup>1</sup>, Bilel Achir<sup>1</sup>**

<sup>1</sup>Laboratory of Technology and Solid Properties, Abdelhamid Ibn Badis University, Mostaganem, Algeria

<sup>2</sup>Biotechnology Laboratory Applied to Agriculture and Environmental Preservation, Abdelhamid Ibn Badis University, Mostaganem, Algeria

<sup>3</sup>Environmental and Recovery Sciences and Techniques, Abdelhamid Ibn Badis University, Mostaganem, Algeria

---

### **Abstract**

This study demonstrates the successful application of first-principles calculations for thermal conductivity in promising and environmentally friendly Heusler compounds. We present a systematic analysis of the electronic structure, optoelectronic and thermoelectric properties of two Heusler alloys, Na<sub>2</sub>TlBi and Na<sub>2</sub>TlSb. In this work, density functional theory (DFT) calculations with the modified Becke-Johnson (mBJ) approximation are employed to compute their physical properties. The results reveal that these alloys exhibit structural stability, a direct band gap, and strong ultraviolet light absorption, making them suitable candidates for optoelectronic devices. An investigation of the thermoelectric properties of the two alloys was conducted through calculations. This analysis showed that both alloys possess favorable characteristics, including high electrical conductivity, Seebeck coefficient, and ZT value. The combined optoelectronic and thermoelectric responses suggest these novel Heusler alloys hold significant promise for future applications in optoelectronics and renewable energy.

**Keywords:** *Heusler, Optoelectronic properties, Thermoelectric properties, Renewable energy*

---



## Energy Management of Photovoltaic/Battery Power Source for Stand-Alone Application

Lina Daoudi<sup>\*1</sup>, Amel Ourici<sup>1</sup>, Sihem Ghoulbourg<sup>1</sup>, Chekal Affari Belhadj<sup>2</sup>

<sup>1</sup>Mathematical Modeling and Numerical Simulation laboratory, Badji Mokhtar University, Annaba, Algeria

<sup>2</sup>Laboratory for Modeling of Renewable Energy and Nanoscale Devices, Freres Mentouri Constantine 1 University, Constantine, Algeria

---

### Abstract

This paper presents a control technique for a renewable energy system that combines photovoltaic panels (PV) and battery bank storage device. The PV is utilized as the primary main source and the batteries for storage reasons in case of surplus production or to compensate for temporary deficits of power during peak demand. The strategy proposed herein is a nonlinear technique based on the flatness property. It controls the energy generated and provides for the complete description of the state's trajectories. This method's control law is supplemented with the PI and neural network (PNN) to improve tracking of the reference trajectory signals and stability. The obtained results from simulation show that the proposed flatness-PNN can successfully manage the power flow in the proposed system and provide more stability by reducing the disturbance in the regulated DC bus voltage.

**Keywords:** Energy management, Photovoltaic, Batterie, DC bus, Neural network

---



## Enhancing Pressure Regulation in PEMFC: PID Conventional and PID Optimized by PSO in Response to Variable Load Demand

Sabah Kabache<sup>\*1</sup>, Djelloul Reguieg<sup>2</sup>, Essaid Bousbiat<sup>3</sup>, Djamel Kendil<sup>3</sup>

<sup>1</sup>Coating, Materials and Environment Laboratory, Physics Department, University of Boumerdes, Algeria

<sup>2</sup>Independent Researcher, France

<sup>3</sup>Laboratory of Integrated Sensor-Based Systems, Algeria

### Abstract

In a Proton Exchange Membrane Fuel Cell (PEMFC) setup, maintaining precise pressure levels on both the anode (H<sub>2</sub>) and cathode (O<sub>2</sub>) sides is crucial, particularly during load variations. Failure to control pressure appropriately can result in imbalances that may harm the fuel cell stack's delicate membranes. This study proposes a dual-control approach using a conventional PID regulator and a PSO-regulated PID optimizer to keep membrane pressures stable within acceptable ranges. The effectiveness of these methods was tested on a 5 kW PEMFC stack model subjected to 50 A current jumps, with simulations conducted in Matlab/Simulink. Results indicate that employing conventional regulation with gains optimized by the PSO algorithm effectively mitigated disturbances caused by load changes, maintaining satisfactory performance metrics (response time, overshoot, stability), as evidenced by indices like IAE, ITAE, and ISE.

**Keywords:** PEMFC, O<sub>2</sub> pressure, H<sub>2</sub> pressure, PID, PID tuned by PSO algorithm

## 1 INTRODUCTION

Fuel cells (FC) serve as stationary devices designed to directly convert the electrochemical energy of hydrogen fuel into electricity. This technology is highly regarded in both industrial and research spheres. Among various types, the Proton Exchange Membrane Fuel Cell (PEMFC) holds particular promise for application in both stationary and mobile settings. PEMFC stands out due to its lightweight design, impressive power density, and ability to operate at lower temperatures compared to other fuel cell types [1].

Several studies in the scientific literature have explored different approaches in linear and non-linear control for modeling and controlling fuel cells. Some notable research papers in this field include: Andrés Moran Doran et al. [2] proposes a hybrid scheme using neural networks to model and control fuel cell systems. The study highlights the importance of considering variables beyond reactant supply for fuel cell performance. It demonstrates that a neuro-PID controller alone cannot stabilize voltage without an inverse model control. Kai Ou et al. [3] proposes a feedforward fuzzy-PID controller for regulating the oxygen excess ratio in PEM fuel cell systems. The feedforward fuzzy-PID approach effectively controls the oxygen excess ratio and reduces parasitic power loss. The paper also discusses the combining of PID and fuzzy logic for easy and efficient air flow control implementation. Nicu Bizon et al. [4] proposed a strategy for a fuel saving in proton exchange membrane fuel cell (PEMFC) systems. The strategy involves switching the load-following mode to the fueling regulators, resulting in optimized fuel consumption efficiency and reducing fuel consumption by 14-29% compared to commercial strategies.

In the field of process control, proportional-integral-derivative (PID) controllers remain among the most widely used solutions due to their simplicity and efficiency. However, traditional PID parameter tuning often relies on heuristic or empirical methods, which can lead to sub-optimal performance in complex or variable situations [5]. The optimization of PID parameters has therefore become a major concern for improving the performance of control systems. The Particle Swarm Algorithm (PSO) is emerging as a promising technique for solving this problem. Indeed, PSO is an optimization method based on mechanisms for imitating the collective behavior of a swarm of birds or fish, making it possible to efficiently search the solution space for the best set of parameters [6].

In this study, we introduce a hybrid approach, combining the PID controller with an optimized algorithm (PSO), to develop an adaptive law. This integration enhances the controller's adaptability, enabling it to maintain high performance and effectively handle the complex nonlinear characteristics of the fuel cell (PEMFC), as well as the load disturbances resulting from load demand fluctuations. The performance of the tuned regulator (PID-PSO) is



compared with that of the conventional controller (PID) to enhance gas consumption efficiency and stabilize power output at rated values amidst load variations. The main purpose of this work is to focus on the pressure stability at the terminals of the membranes for oxygen and hydrogen, as their variations affect the system's lifespan and efficiency. The transient performances of the proposed adaptive PID controller are evaluated against those of the classical PID controller (PID-C) using various performance indices.

## 2 SYSTEM COMPONENT

A PEM fuel cell operates by utilizing hydrogen and oxygen (air), both of which require humidification prior to entering the stack. Heat generated during operation must be dissipated through either natural or forced cooling methods to prevent membrane flooding. Consequently, a standard fuel cell system includes various auxiliary components such as hydrogen storage tanks, pressure regulators, humidifiers, air filters, heat exchangers, compressors, water separators, relief valves, pumps, and water tanks, etc. [7].

To streamline the analysis and minimize simulation duration, intricate modeling of these components is sidestepped. Instead, focus is placed on studying reactant flow dynamics and related pressure fluctuations in a simplified manner. The system is treated as spatially lumped and isothermal, with the assumption that the stack temperature remains regulated at 65°C through an independent cooling mechanism.

This paper examines a 5-kW fuel cell stack, comprising 35 cells, each with an active surface area of 232 cm<sup>2</sup>. The stack's output voltage surpasses 19 V (equivalent to 0.53 V per cell), with a maximum current capacity of 300 A. The investigation will focus on the system's performance during H<sub>2</sub>/air operation, utilizing pure hydrogen at the anode and ambient air at the cathode [8].

In this system, a DC-DC power inverter plays a crucial role by converting variable DC output from the fuel cell stack into a consistent load. With an input voltage typically around 19V, it requires precise optimization to maintain a stable output at 120V. This task is managed by a simple yet effective controller, dynamically adjusting the modulation index of the PWM signals that drive the inverter, as shown in Fig 1. This controller ensures the system's stability and reliability by maintaining the desired output voltage levels with precision and efficiency

## 3 DYNAMIC MODELING

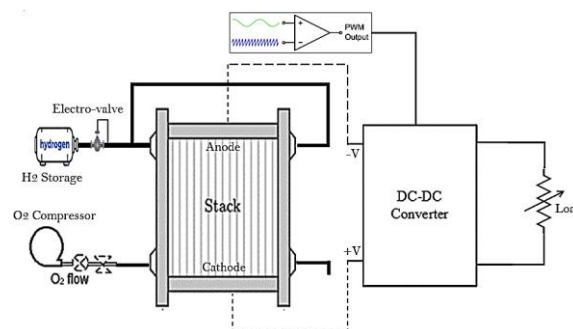
### 3.1 Fuel cell modelling

As depicted in Fig. 1, the fuel cell serves as an electrochemical device responsible for converting the energy stored in hydrogen into electrical power. The operational principle of the fuel cell is elucidated by an electrochemical redox reaction [9]. It facilitates a reaction between hydrogen and oxygen, resulting in the generation of electricity, water, and heat, as outlined by the following overall chemical equation.



The output voltage of the fuel cell can be expressed using the following equation [14].

$$V_{FC} = E_{Nerst} - V_{act} - V_{ohm} - V_{con} \tag{2}$$



**Figure 1.** Load variation fuel cell system

E-Nerst, is the reversible open-circuit voltage, it is described by the Nerst equation as:

$$E_{Nerst} = c_1 - c_2(T_{FC} - c_3) + c_4 \times T_{FC} \left[ \ln(P_{H_2}) + 0.5(P_{O_2}) \right] \quad (3)$$

Where,  $P_{H_2}$  hydrogen pressure (atm),  $P_{O_2}$  oxygen pressure (atm) and T absolute temperature (K).  $V_{act}$  denotes the activation voltage drop, as expressed in the Tafel equation as:

$$V_{act} = \xi_1 + \xi_2 T + \xi_3 T \ln(C_{O_2}) + \xi_4 I_{FC} \quad (4)$$

Here,  $I_{FC}$  denotes the fuel cell current (A), and  $\xi_i$  (where  $i=1-4$ ) represent parametric coefficients corresponding to each cell model.  $C_{O_2}$  denotes the concentration of dissolved oxygen at the interface of the cathode catalyst, which can be determined through the following calculation:

$$C_{O_2} = \frac{P_{O_2}}{5.08 \times 10^6 e^{-\frac{498}{T}}} \quad (5)$$

The total ohmic voltage loss, often denoted as  $V_{ohm}$ , can be formulated as:

$$V_{ohm} = IR_{mem} \quad (6)$$

Where  $R_m$  the membrane resistance is determined by dividing the thickness,  $t_{mem}$ , by the conductivity  $\sigma_{mem}$  as described by the following equation.

$$R_{mem} = t_{mem} / \sigma_{mem} \quad (7)$$

$V_{conc}$  represents the concentration voltage drop, which is defined as:

$$V_{conc} = -B \ln \left( 1 - \frac{J}{J_{max}} \right) \quad (8)$$

Where,  $J_{max}$  is the maximum current density of the cell,  $J$  (A/cm<sup>2</sup>) represents the actual current density of the cell and B is a parametric coefficient, which depends on the cell and its operation state. When  $N_{FC}$  fuel cells are linked in series, the fuel cell stack's output voltage is determined by:

$$V_{stack} = N_{FC} V_{FC} \quad (9)$$

Relevant parameter values are given in Table 1.

**Table 1.** PEMFC Model's parameters

Parameters	Value	Unit
T	353	K
$N_{FC}$	35	
$t_m$	$175 \times 10^{-4}$	cm
F	96485	C kmol <sup>-1</sup>
R	8.31415	J kmol <sup>-1</sup> K <sup>-1</sup>
$K_{O_2}$	$2.11 \times 10^{-5}$	Kmol S <sup>-1</sup> atm
$K_{H_2}$	$4.22 \times 10^{-5}$	Kmol S <sup>-1</sup> atm
$\tau_{O_2}$	3.37	(s)
$\tau_{H_2}$	6.47	(s)
$\xi_1$	-0.944	
$\xi_2$	0.00354	
$\xi_3$	$8 \times 10^{-8}$	
$\xi_4$	$-1.96 \times 10^{-4}$	
C1	1.229	
C2	$8.5 \times 10^{-4}$	
C3	298.15	
C4	$4.3085 \times 10^{-5}$	

### 3.2 Dynamic Gas Flow Model

The hydrogen partial pressure can be determined by considering the input flow rate and the current of the fuel cell, establishing a functional relationship between these variables [9]:

$$P_{H_2} = \left[ \left( 1 / K_{H_2} \right) + \tau_{H_2} s \right] \left( q_{H_2}^{in} - 2K_r I \right) \tag{10}$$

In this context,  $\tau_{H_2}$  represents the input hydrogen flow, while  $K_r$  signifies the hydrogen flow that is consumed. This consumption can be mathematically expressed as follows:

Using identical methods, the oxygen partial pressure is articulated as:

$$P_{O_2} = \left[ \left( 1 / K_{O_2} \right) + \tau_{O_2} s \right] \left( q_{O_2}^{in} - K_r I \right) \tag{11}$$

$$K_r = N_{FC} / 4F \tag{12}$$

where in  $q_{O_2}$  is the input oxygen flow, and  $k_r$  is the hydrogen flow which is consumed, and can be expressed as: Equations (10) and (11) delineate the correlation between the current of the fuel cell and the partial pressures of hydrogen and oxygen, respectively. As the load initiates current flow, both hydrogen and oxygen reactants rise, leading to a corresponding decrease in their partial pressures.

### 3.3 Power Conditioning

The fuel cell functions at a modest output voltage spanning a broad spectrum (18 ~ 36 V). To convert this DC power into high voltage suitable for the load, appropriate power converters are indispensable. This study introduces a boost converter. An H-bridge inverter employing single-phase pulse width modulation (PWM) is employed to convert the DC power into high voltage AC (120 V). Four pairs of insulated gate bipolar transistor (IGBT) diodes are configured as switches within the inverter's two arms [10, 11].

The inverter receives a variable DC input, while the load maintains fixed voltage and frequency values of 120 V and 50 Hz, respectively. To compensate for fluctuations in the stack output, the inverter stage requires control. A straightforward approach involves adjusting the modulation index, denoted as “m”, to alter the PWM gating signals, which govern the switching times of the four IGBTs within the inverter (refer to Fig 1).

A PID controller is specifically designed and calibrated for this objective, while the specifications of the DC/DC converter components are detailed in the accompanying table:

**Table 2.** Converter parameters

Parameters		Valeus
DC/DC components	Inductance	L=6.725e-3 H
	Capacity	C= 1.68e-4 F
	Duty cycle	D=0.24
Regulator gains	Proportional gain	Kp=0.1
	Integral gain	Ki=60

## 4 CONTROL OF THE FUEL CELL SYSTEM

### 4.1 Calculated PID Gains

The conventional PID controller is extensively employed in industrial process control owing to its uncomplicated design and effectiveness in managing both linear and non-linear systems. The controller is given by the mathematical and canonical equation as follows [12, 13]:

$$P(S) = K_p + \frac{K_i}{S} + K_d S \tag{13}$$

The pressure control loop consists of a direct chain and a unitary return chain. The open-loop transfer function (OLTF) is as follows:

$$OLTF = \left( K_p + \frac{K_i}{S} K_d S \right) * \left( \frac{1/K}{\tau_r s + 1} \right) \tag{14}$$

The provided expression represents the closed-loop transfer function (CLTF):

$$CLTF = (OLTF) / (1 + OLTF) \tag{15}$$

$$CLTF = \frac{\left( K_p + \frac{K_i}{S} K_d S \right) * \left( \frac{1/K}{\tau_r s + 1} \right)}{1 + \left[ \left( K_p + \frac{K_i}{S} K_d S \right) * \left( \frac{1/K}{\tau_r s + 1} \right) \right]} \tag{16}$$

$$CLTF = \frac{K}{(\tau_r + K_d) S^2 + (K_p + 1) S + K_i} \tag{17}$$

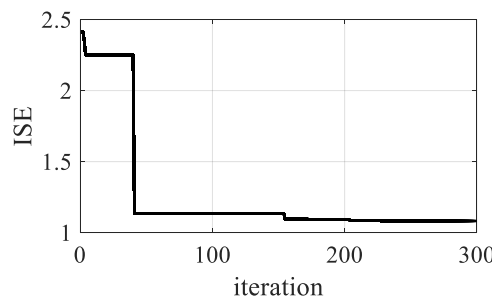
Identifying the transfer function parameters using the canonical form of a second-order system proceeds as follows:

$$\frac{K}{S^2 + 2\xi\omega_n S + \omega_n^2} \tag{18}$$

Here,  $\tau_r + K_d = 1$ ,  $K_p + 1 = 2\xi\omega_n$ , and  $K_i = \omega_n^2$ . The determination of system control gains proceeds as follows:  $K_p = 2\xi\omega_n$ ,  $K_i = \omega_n^2$ , and  $K_d = 1 - \tau_r$ .

#### 4.2 PID Tune by PSO

In this research, we leverage the Particle Swarm Optimization (PSO) algorithm to optimize the gains of the Proportional-Integral-Derivative (PID) controller to enhance the performance of a dynamic system. By integrating the PSO algorithm into PID tuning, our aim is to estimate the best gains to achieve good performance, ensuring stability, faster transient response, and robustness under changing load demand conditions. This novel approach offers significant potential for improving control strategies for complex systems. Through rigorous analysis, we demonstrate the effectiveness and versatility of the PSO-based PID tuning method. Fig. 2 illustrates the convergence of the algorithm, providing visual validation of its effectiveness [14].



**Figure 2.** Convergence integral square error

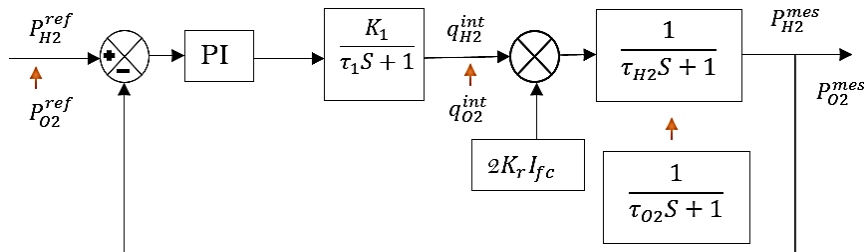
The tuning parameters with the estimated gains after optimization are presented in the table below.

**Table 3.** PSO parameters

Parameters	Description	
Iter=300	Iteration number	
N=300	Initialized population number	
Wmax=0.9	Acceleration max factor	
Wmin=0.4	Acceleration min factor	
Var=3	Number of regulation parameters	
Lb=[0 0 0]	Lower bound of algorithm research	
Ub=[100 100 100]	Highly bound of algorithm research	
Estimated gains	Hydrogen regulator	Kp= 39.8461
		Ki= 7.4197
		Kd= 50
	Oxygen regulator	Kp= 32.7375
		Ki= 3.8694
		Kd= 50

### 4.3 Fuel Flow Control

Theoretical cell voltage is significantly influenced by both hydrogen and oxygen partial pressures. To ensure the stability of these pressures, we suggest employing a proportional integral controller to determine the fuel flow rate of the PEMFC. This controller effectively regulates the fuel flow through an actuator.



**Figure 3.** H2 and O2 flow calculation loop using PI controller

The trial-and-error method and tuned gains by PSO algorithm are used to calculate the controller gains, which presented in the table below for current loop regulation, H2 and O2 pressure loops as follows:

**Table 4.** Regulation parameters

Parameters	Values
Current regulator	Kp=15
	Ki=10
Hydrogen regulator	Kp=1.9
	Ki=1
	Kd=0.15
Oxygen regulator	Kp=2
	Ki=1.5
	Kd=0.2

## 5 SIMULATION RESULT AND DISCUSSION

As part of the modeling study in Matlab Simulink, the aim was to evaluate the performance of the “PEMFC” fuel cell. We examined the effects of varying the load while keeping the pressure constant. This configuration is crucial for understanding the complex interactions between load and pressure, providing valuable insight into system performance. Analyses of the Simulation Results (Hydrogen pressure, oxygen pressure, DC voltage and power consumption are presented as follows:

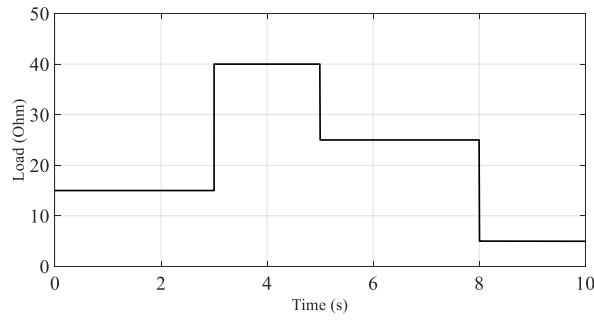


Figure 4. Load profile

5.1 Performance Analysis of H2 and O2 Pressure and DC Voltage

Performance analysis is based on three key parameters in the control chain: H2 pressure, O2 pressure, and DC-voltage, as depicted in Figures 5, 6, and 7, respectively. Optimal control of these factors is crucial for the longevity of the fuel cell and its components, while ensuring good energy efficiency. The performance analyses are presented in the table below.

Table 5. Analysis performance (TDR: Transient damped regime)

Parameters		Performances	
Hydrogen pressure	Manuel regulation	Response time (s)	0.05
		Overshoot (%)	2%
		Stability	0.01
	PSO tuned	Response time (s)	0.03
		Overshoot (%)	TDR
		Stability	0.003
Oxygen pressure	Manuel regulation	Response time (s)	0.3
		Overshoot (%)	0%
		Stability	0.024
	PSO tuned	Response time (s)	0.2
		Overshoot (%)	TDR
		Stability	0.011

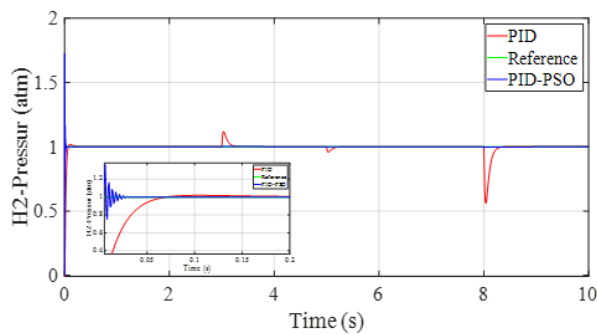


Figure 5. H2 pressure profile

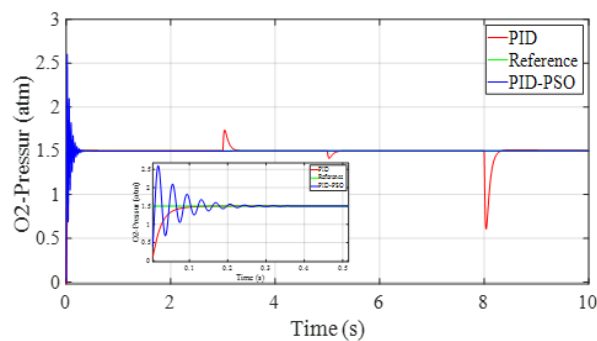
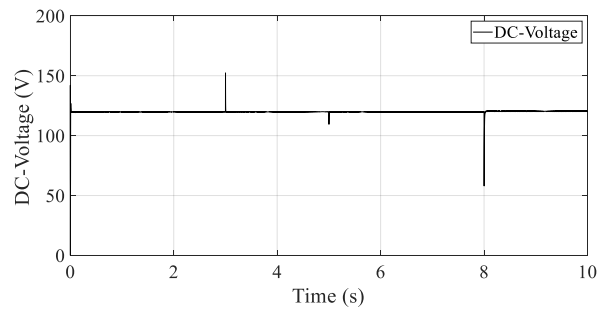


Figure 6. O2 pressure profile



**Figure 7.** DC-voltage profile

The characteristics provided for hydrogen and oxygen conventional (PID) pressure regulation, including a response time of [0.05s-0.3s] for H<sub>2</sub> and O<sub>2</sub> successively, an overshoot of [2%-0%], and stability at [0.01-0.024], collectively indicate a highly efficient and reliable system for fuel cell operation. The rapid response time ensures swift adjustments to changes in demand, minimizing stress on components and potential damage to the fuel cell membrane. The low overshoot signifies precise control, reducing fluctuations around the setpoint and safeguarding against excessive pressure variations. Moreover, the tight stability ensures consistent operating conditions, contributing to prolonged system lifetime and enhanced performance. In summary, these characteristics reflect a pressure regulation system that optimally maintains hydrogen pressure levels, mitigating risks and fostering the longevity and efficiency of the fuel cell system.

The PSO-tuned PID regulation surpasses the conventional PID regulation in key performance metrics. With a faster response time and significantly tighter stability at 0.003, it ensures rapid adjustments and minimal fluctuations around the setpoint, enhancing system responsiveness and stability. Moreover, the PSO-tuned PID's ability to maintain a “Transient Damped Regime” overshoot signifies precise control, minimizing overshoot and reducing the risk of system instability. Overall, these improvements translate to superior pressure regulation, increased efficiency, and enhanced reliability in fuel cell operation compared to the standard PID regulation.

To develop the study and give more accuracy of regulated system, we analyzed the stability of the controller relative to its reference using many indicators: Integral Absolute Error (IAE), Integral Time Absolute Error (ITAE), Integral Square Error (ISE) as presented in the table below:

**Table 6.** Stability analysis of steady state

Parameters		IAE	ITAE	ISE
PID tuned regulator	Hydrogen pressure	0.003	0.005	0.0012
	Oxygen pressure	0.011	0.0013	0.0002
	DC voltage	0.021	0.045	0.006
PID manual regulation	Hydrogen pressure	0.01	0.037	0.0016
	Oxygen pressure	0.024	0.028	0.0037
	DC voltage	0.023	0.05	0.0078

Integral Absolut Error (IAE), Integral Time Absolut Error (AMRE), Integral Square Error (ISE)

The comparison between PID tuned regulation and manual PID regulation across various control scenarios reveals significant differences in stability and performance. In all cases—hydrogen pressure, oxygen pressure, and DC voltage—the PID tuned regulator consistently exhibits lower values for stability indices (IAE, ITAE, and ISE) compared to manual regulation. This indicates superior control performance and reduced oscillations, highlighting the effectiveness of PID tuning, especially when assisted by techniques like PSO. Overall, the results underscore the importance of optimizing control strategies to achieve better stability and performance in diverse control scenarios, ultimately enhancing system efficiency and reliability.

## 5.2 Testing Robustness of H<sub>2</sub> and O<sub>2</sub> Pressure Under Load Variations

The fluctuations in load demand occur at various moments, notably at t=3s, 5s, and 8s, presented in Fig. 8, and Fig. 9, resulting in changes in the required flow rate and thus causing instability in pressure regulation. The assessment of the regulation’s robustness, presented in the Table VII:

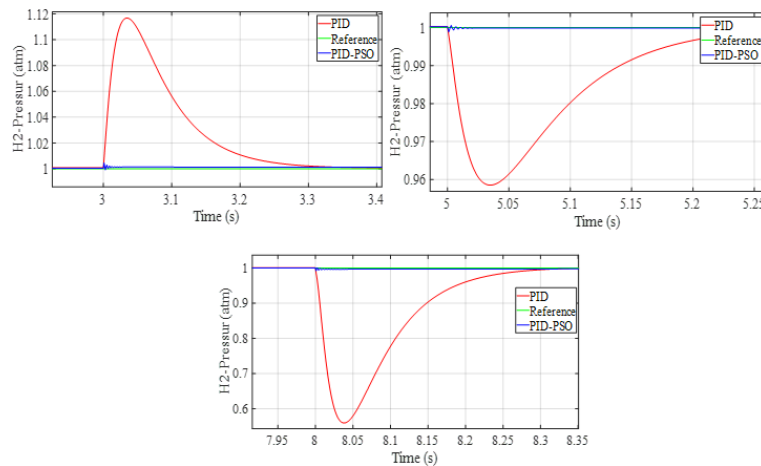


Figure 8. H2-pressure enlargement at t=3, 5s and 8s

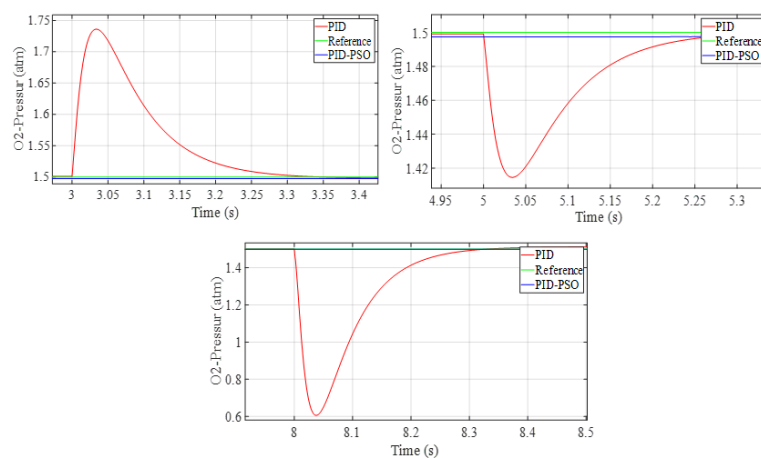


Figure 9. O2-pressure enlargement at t=3, 5s and 8s

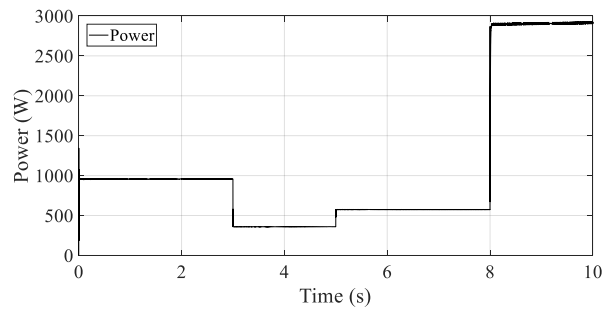
Table 7. Pics under load variations

Parameters		Perturbations			
		Times	Pics (V)	Time (S)	Freq (Hz)
Hydrogen pressure	PID manual tuned	t= 3s	0.11	0.3	3.33
		t= 5s	0.04	0.25	4
		t= 8s	0.35	0.35	2.86
	PID-PSO tuned	All time	0.005	0.02	50
Oxygen pressure	PID manual tuned	t= 3s	0.22	0.35	2.86
		t= 5s	0.08	0.3	3.33
		t= 8s	0.9	0.3	3.33
	PID-PSO tuned	All time	null	null	-

Analysing the variations in load demand for hydrogen and oxygen pressure regulation reveals notable differences between PID manual tuning and PID tuning with PSO optimization. Under PID manual tuning, fluctuations in hydrogen pressure result in peaks with varying magnitudes and response times, potentially subjecting fuel cell membranes to mechanical stress and degradation. Similarly, oxygen pressure regulation under PID manual tuning exhibits fluctuations with peaks of differing intensities and response times. In contrast, PID tuning with PSO optimization consistently maintains minimal peak values and faster response times, suggesting improved stability and precision. This approach reduces mechanical stress on fuel cell membranes and other components, enhancing overall durability and performance. Thus, the comparison underscores the effectiveness of PID tuning with PSO optimization in promoting smoother operation and extending the lifespan of fuel cell systems.

Finally through this Fig 10, we can observe the dynamic changes in power consumption across different time intervals.





**Figure 10.** Power consumption

## 6. CONCLUSION

In this study, we investigate into the dynamic modelling, control, and simulation of PEMFC. Initially, we introduce the dynamic model of PEMFC based on existing literature, incorporating various evolutions of physical parameters. Subsequently, we outline the approach for calculating the flow rates of hydrogen and oxygen. Following this, we present a strategy employing Proportional Integral (PI) controllers for the DC-DC boost converter. The efficacy of our proposed control strategy for the proton exchange membrane fuel cell system across a wide operating range is confirmed through simulations conducted using Matlab/Simulink software. The simulation results of the H<sub>2</sub> and O<sub>2</sub> pressure control loop, based on both conventional PID controllers and tuned PID controllers utilizing the PSO algorithm, have been examined. The findings demonstrate that optimizing the tuning parameters using PSO significantly enhances system performance. This improvement has been evidenced through the analysis of performance indices such as IAE, ITAE, and ISE, particularly in managing load variation peaks. This optimization thereby aids in ensuring constant pressure at the PEMFC membrane terminals.

## References

- [1] G. Bhansali and R. Kumar, "Design analysis and dynamic control of PEM fuel cell for standalone applications," in *2014 IEEE Students' Conf. Electr. Electron. Comput. Sci. SCEECS 2014*, 2014, doi: 10.1109/SCEECS.2014.6804455.
- [2] Y. Li, X. Zhao, S. Tao, Q. Li, and W. Chen, "Experimental study on anode and cathode pressure difference control and effects in a proton exchange membrane fuel cell system," *Energy Technol.*, vol. 3, no. 9, pp. 946–954, 2015, doi: 10.1002/ente.201500077.
- [3] F. Gonzatti, M. Miotto, and F. A. Farret, "Proposal for automation and control of a PEM fuel cell stack," *J. Control. Autom. Electr. Syst.*, vol. 28, no. 4, pp. 493–501, 2017, doi: 10.1007/s40313-017-0322-2.
- [4] R. Geethanjali and R. Sivakumar, "Design of intelligent controller for PEM fuel cell," in *3rd IEEE Int. Conf. Sci. Technol. Eng. Manag. (ICONSTEM 2017)*, 2017, pp. 1050–1053, doi: 10.1109/ICONSTEM.2017.8261316.
- [5] H. Marzougui, A. Kadri, M. Amari, and F. Bacha, "Improvement of energy management algorithm for fuel cell electrical vehicle with fuzzy logic," in *2017 18th Int. Conf. Sci. Tech. Autom. Control Comput. Eng. STA 2017*, 2017, pp. 212–217, doi: 10.1109/STA.2017.8314963.
- [6] Y. Zhu, J. Zou, C. Peng, Y. Xie, and L. Li, "Modelling and fuel flow control of PEMFC considering over-pressure case," in *2017 Chinese Autom. Congr. (CAC 2017)*, 2017, pp. 2222–2225, doi: 10.1109/CAC.2017.8243143.
- [7] Y. Qi, M. Thern, M. Espinoza-Andaluz, and M. Andersson, "Modeling and control strategies of proton exchange membrane fuel cells," *Energy Procedia*, vol. 159, pp. 54–59, 2019, doi: 10.1016/j.egypro.2018.12.017.
- [8] H. P. Regulation, *PEM Fuel Cell Voltage Neural Control Based on*, 2019.
- [9] Y. Rao, Z. Shao, A. H. Ahangarnejad, E. Gholamalizadeh, and B. Sobhani, "Shark smell optimizer applied to identify the optimal parameters of the proton exchange membrane fuel cell model," *Energy Convers. Manag.*, vol. 182, pp. 1–8, 2019, doi: 10.1016/j.enconman.2018.12.057.
- [10] H. C. Nejad, M. Farshad, E. Gholamalizadeh, B. Askarian, and A. Akbarimajd, "A novel intelligent-based method to control the output voltage of proton exchange membrane fuel cell," *Energy Convers. Manag.*, vol. 185, pp. 455–464, 2019, doi: 10.1016/j.enconman.2019.01.086.
- [11] H. Deng, Q. Li, Y. Cui, Y. Zhu, and W. Chen, "Nonlinear controller design based on cascade adaptive sliding mode control for PEM fuel cell air supply systems," *Int. J. Hydrogen Energy*, vol. 44, no. 35, pp. 19357–19369, 2019, doi: 10.1016/j.ijhydene.2018.10.180.

- [12] Y. Cao, Y. Li, G. Zhang, K. Jermsittiparsert, and N. Razmjooy, "Experimental modeling of PEM fuel cells using a new improved seagull optimization algorithm," *Energy Reports*, vol. 5, pp. 1616–1625, 2019, doi: 10.1016/j.egy.2019.11.013.
- [13] M. K. Singla, A. S. Oberoi, and P. Nijhawan, "Trends so far in hydrogen fuel cell technology: State of the art," *Int. J. Adv. Trends Comput. Sci. Eng.*, vol. 8, no. 4, pp. 1146–1155, 2019, doi: 10.30534/ijatcse/2019/23842019.
- [14] H. He, S. Quan, and Y. X. Wang, "Hydrogen circulation system model predictive control for polymer electrolyte membrane fuel cell-based electric vehicle application," *Int. J. Hydrogen Energy*, vol. 45, no. 39, pp. 20382–20390, 2020, doi: 10.1016/j.ijhydene.2019.12.14.



## Enhanced Grid-Connected Photovoltaic System Using Five-Level Packed U Cell Topology and Advanced Control Approaches

Abderraouf Touafek<sup>\*1</sup>, Fateh Krim<sup>1</sup>, Hamza Afghoul<sup>1</sup>, Billel Talbi<sup>2</sup>

<sup>1</sup>Power Electronics and Industrial Control Laboratory (LEPCI), Department of Electronics, University of Sétif-1, 19000 Setif, Algeria

<sup>2</sup>ETA laboratory, Department of Electronics, University Mohamed El Bachir El Ibrahimi of Bordj Bou Arreridj, El-Anasser 34030, Algeria

---

### Abstract

This study introduces a grid-connected photovoltaic (PV) system employing a five-level Packed U Cell (PUC5) topology. It consists of a PV panel with a DC-DC boost converter and a PUC5 multilevel inverter constructing three pairs of switches to generate five voltage levels, thereby reducing component count compared to traditional inverters. The proposed control scheme integrates the perturb and observe (P&O) maximum power point tracking (MPPT) method and predictive current control (PCC). The control scheme aims to maximize power extraction from the PV panel while minimizing the total harmonic distortion (THD) of the current fed into the grid. The simulation results show that the system is capable of effectively and reliably detecting the maximum power points of the PV array, even when there are sudden changes in irradiance. In addition, these results emphasize the capability of the PUC5 topology to decrease the number of components and improve the performance of the system, while also guaranteeing the delivery of high-quality power. This illustrates the system's potential for efficient and consistent grid-connected PV applications.

**Keywords:** Photovoltaic system, PUC5 topology, Predictive current control, Grid-connected, Maximum power point tracking

---



## **Detection and Classification of Power Quality Disturbances Using Variational Mode Decomposition and Convolutional Neural Networks**

**Yahia Bousseloub<sup>\*1</sup>**

*<sup>1</sup>Electromechanical Systems Laboratory, Faculty of Sciences Engineering, Badji Mokhtar Annaba University, Annaba, Algeria*

---

### **Abstract**

Power quality receives more and more attentions because disturbances in power quality may impair equipment security, power availability and system dependability in power system. Detection and classification of the power quality issues is the first stage before adopting efforts to decrease their harmful effects. Common approaches to classify power quality disturbances includes signal processing methods, machine learning methods and deep learning methods. Signal processing methods are good at feature extraction, whereas machine learning methods and deep learning methods are excellent in multi-classification tasks. Via combing their individual benefits, this research provides a combined method based on variational mode decomposition and convolutional neural networks, which takes a small quantity of samples but achieves excellent classification precision. The proposed method is demonstrated to be a qualified and competitive system for the detection and classification of power quality issues.

**Keywords:** *Power quality, Variational mode decomposition, Convolutional neural networks*

---



---

## Improving Solar Cell Efficiency: Exploring High-Performance Tandem Solar Cells Integrating Lead-Free Perovskite on Silicon (PVK/Si) via Design and Numerical Analysis

Hadjer Soufi<sup>\*1</sup>, Abdelkader Bouhenna<sup>2</sup>, Khadidja Rahmoun<sup>1</sup>, Mohamed El Amine Slimani<sup>1</sup>, Wissem Benaissa<sup>1</sup>

<sup>1</sup>Materials and Renewable Energies Research Unit URMER, University of Tlemcen, Abou Bekr Belkaid, BP 119, Tlemcen13000, Algeria

<sup>2</sup>Materials Science and Applications Laboratory (LSMA), University of Ain Temouchent, Belhadj Bouchaib, BP 284, 46000, Algeria

---

### Abstract

This recently, tandem perovskite / silicon solar cells have emerged as a novel advancement in photovoltaic technology, garnering attention for their affordability and potential to surpass traditional cell efficiency limits.

This study conducts device simulations of CsGeI<sub>3</sub>/Si based solar cells employing a glass/FTO/WS<sub>2</sub>/CsGeI<sub>3</sub>/Si/HTL architecture with a metal back contact (Ag). SCAPS-1D software is utilized for simulation, assessing the effectiveness and performance of the solar cell. Various hole transport layers (HTLs) including P3HT, PEDOT: PSS, CFTS, and MoO<sub>3</sub> are investigated. The impact of absorber layer thickness, electron transport layer (ETL) thickness, and HTL thickness are analyzed.

Optimizing the tandem perovskite / silicon solar cell with MoO<sub>3</sub> as the HTL reveals an overall efficiency of 37%, achieved by varying the temperature of solar cells and the thickness of the absorber layer, HTL, and ETL.

**Keywords:** Solar, Cell, Tandem, Perovskite, Scaps-1D

---



## Optimal Sizing of a Renewable Energy System for Sustainable Power and Hydrogen Generation Under the Northeastern Algerian Climate

Toufik Sebbagh\*<sup>1</sup>

<sup>1</sup>*LGMM Laboratory, University of Skikda, Skikda, Algeria*

---

### Abstract

This study represents a thorough examination of the economic and technical viability of a renewable energy system that integrates wind turbines, photovoltaic generators, and storage units to fulfill both electrical and hydrogen energy requirements. Employing advanced simulation tools like the Homer software, the investigation focuses on the Filfila region in Skikda, Northeastern Algeria, meticulously analyzing meteorological parameters such as temperature, irradiation levels, and wind speed profiles.

Through rigorous simulation processes, the proposed system undergoes optimization to identify the most efficient configurations. The envisioned setup includes a combination of wind turbines, solar panels, electrolyzers, batteries, and hydrogen reservoirs, strategically designed to maximize energy output while minimizing costs.

Results from the study unveil an optimal system configuration, featuring a 117 KW PV generator, 55 KWh battery capacity, and a 106 KW wind generator. Furthermore, economic analysis delves into the costs associated with various system components, with PV panels, wind turbines, and electrolyzers identified as the major cost contributors.

Ultimately, this research underscores the economic viability of the selected system setup, offering valuable insights into sustainable energy solutions, particularly for remote and off-grid areas. By showcasing the potential of renewable energy integration, this study contributes to the ongoing discourse on transitioning towards cleaner and more sustainable energy sources.

**Keywords:** *Green hydrogen, Renewable energy, Optimization, Homer, Sustainability*

---



## Active and Reactive Power Control of a Grid-Connected Photovoltaic/Fuel Cell Hybrid System

Hocine Abdelhak Azzeddine<sup>\*1</sup>, Mourad Hebali<sup>2</sup>, Djamel-Eddine Chaouch<sup>1</sup>, Benaoumer Ibari<sup>2</sup>, Menaouer Benaoum<sup>2</sup>

<sup>1</sup>LSTE Laboratory, Mustapha Stambouli University of Mascara, Mascara, Algeria

<sup>2</sup>Mustapha Stambouli University of Mascara, Mascara, Algeria

---

### Abstract

The presented study aims to contribute to the search for innovative ways to improve the multi-modelling environment for the analysis of hybrid systems. The modelling and control of a grid-connected photovoltaic/fuel cell hybrid system is proposed in this article. The photovoltaic module is modelled as well as the Proton Exchange Membrane Fuel Cell (PEMFC). Local neural network-based control of MPPT (Maximum Power Point Tracking) and PEMFC is carried out. The combination of all the component models to constitute a model dedicated to the integrated photovoltaic/fuel cell hybrid system responding to different topologies and external data configurations for the duration of a typical day is carried out in Matlab/Simulink. In addition, an intelligent control of the active and reactive powers injected into the network is proposed.

**Keywords:** Fuel cell, Photovoltaic, Grid, Neural network, Active and reactive power

---



## Artificial Neural Network MPPT and Perturb and Observ MPPT Comparison

Hocine Abdelhak Azzeddine<sup>\*1</sup>, Mourad Hebali<sup>2</sup>, Djamel-Eddine Chaouch<sup>1</sup>, Benaoumeur Ibari<sup>2</sup>, Menaouer Benaoum<sup>2</sup>

<sup>1</sup>LSTE Laboratory, Mustapha Stambouli University of Mascara, Mascara, Algeria

<sup>2</sup>Mustapha Stambouli University of Mascara, Mascara, Algeria

---

### Abstract

This article presents a comparison between a photovoltaic MPPT using the « Perturb and Observ» technique and a MPPT based on an Artificial Radial Basis Function Neural Network (RBFN). A photovoltaic (PV) panel is modeled using the one diode model which model is then used to generate a set of PV panel maximum power points defined by their voltage  $V_{mpp}$  and currents  $I_{mpp}$ , to train a RBFN capable of predicting the maximum power point for any insolation and temperature conditions. Validated, the neural network will be used to control a DC-DC converter to force the panel to permanently provide its maximum power. Compared to a traditional Perturb and Observe MPPT system, the proposed based RBF MPPT shows improved static and dynamic performances. The simulation is performed using MATLAB SIMULINK environment.

**Keywords:** Photovoltaic MPPT, Neural network, Perturb, Observ

---





---

## Optimization of Forced Circulation Solar Water Heating Systems for Enhanced Residential Energy Efficiency in Algeria

Ahmed Remlaoui<sup>\*1</sup>, Driss Nehari<sup>1</sup>

<sup>1</sup>Applied Hydrology and Environment Laboratory, University of Ain Temouchent, 46000 Ain-Temouchent, Algeria

---

### Abstract

This research introduces an advanced numerical simulation for a forced circulation solar water heater (FC-SWHs) tailored to Algeria's climate. It's designed to meet the daily hot water demand of 246 liters for single-family homes. The study employed dynamic TRNSYS modelling to assess the system's efficacy in Ain Temouchent's weather conditions. Validation against established data for collector outlet temperature was performed. Notable results include a highest monthly average outlet temperature of 38 °C in September and a maximum energy gain of 250 W in August. Seasonal fluctuations in auxiliary heating were observed, with a peak energy use of 500 kJ/hr in May to sustain a 60 °C water temperature. Energy inputs at the storage tank's inlet and outputs at the hot water outlet were examined, with inputs reaching 500 W in May. The system maintained average tank temperatures (top, middle, bottom) and post-mixer temperatures suitable for use, between 55 °C and 57 °C. For cooler water needs, the mixer output was kept at 47 °C. The TRNSYS model indicated consistent inlet and outlet tank flow rates, crucial for high-temperature operation starting at 55 °C. At this temperature, the flow rate decreased to 7 kg/hr, while the mixer's outflow increased to 10.5 Kg/hr. The solar fraction (SF) and thermal efficiency were analyzed, showing the lowest SF at 54% in July and the highest over 84% in September, with other months maintaining above 60%. Thermal efficiency varied from 49% to 73% in January, 43% to 62% in April, 48% to 66% in July, and 53% to 69% in October.

**Keywords:** Energy system, Forced circulation solar water heater (FC-SWHs), Energy consumption, Thermal efficiency, TRNSYS modelling

---



## Investigation of the Effects of Silver Alloying and Transparent Conductive Oxide Layer Thickness on the Chalcopyrite Thin Film Solar Cells

Semih Agca<sup>\*1</sup>

<sup>1</sup>Department of Metallurgical and Materials Engineering, Ankara Yildirim Beyazıt University, Ankara, Türkiye

### Abstract

In this study, the effects of silver alloying and transparent conductive oxide layer thickness on the structural properties and solar cell parameters of chalcopyrite thin film solar cells were investigated. The chalcopyrite solar cell was created by physical vapour deposited Cu(In,Ga)Se<sub>2</sub> absorber, chemical bath deposited CdS buffer, sputtered ZnO window and indium tin oxide transparent conductive oxide layers. Back and front contacts were fabricated by sputtered molybdenum and e-beam deposited aluminum and nickel layers, respectively. The absorber layers of the solar cells were deposited with and without silver addition and indium tin oxide transparent conductive oxide layer was deposited with different thicknesses (200 and 300 nm) to understand the effects on the structural properties of the absorber and the solar cell parameters. Results showed that, the silver alloying increased the crystal quality and the average grain size of the absorber leading to an increase in all solar cell parameters. Moreover, increasing the indium tin oxide transparent conductive oxide layer thickness increased open circuit voltage and fill factor. The best power conversion efficiency was obtained in the silver alloyed solar cell having 300 nm indium tin oxide transparent conductive oxide layer.

**Keywords:** Chalcopyrite, Solar cell, Thin film, Silver alloying

## 1 INTRODUCTION

Chalcopyrite semiconductor materials are used in thin film solar cell technologies with the highest efficiencies. Cu(In,Ga)Se<sub>2</sub> (CIGS) is a chalcopyrite structure alloy consisting of CuInSe<sub>2</sub> and CuGaSe<sub>2</sub>. Due to its tunable direct bandgap, low material usage, high absorption coefficient, and short energy pay back times, CIGS is used as an absorber layer in thin film solar cells [1]. The chalcopyrite structure consists of a combination of metals and chalcogens. Since they are in the same group, silver or gold can be used instead of copper, and gallium can be used instead of indium. In chalcogens, sulfur or tellurium is used instead of selenium [2–4]. In recent years, research on the use of silver instead of copper has increased considerably. Erslev et al. have examined samples with different Ag/Cu ratios using capacitance-based characterization methods and found that silver alloying increased the open circuit voltage by reducing defects in the structure [5]. Boyle et al. have investigated the crystallographic structure of samples with Ag/(Ag+Cu) ratio from 0 to 1 in detail using XRD and showed that small amounts of secondary phases were formed in samples with Ag/(Ag+Cu) ratio greater than 0.5 [6]. Edoff et al., after extensive research on samples with different Ag/(Ag+Cu) ratios, have stated that for chalcopyrite solar cells with narrow band gap, the Ag/(Ag+Cu) ratio of 0.2 is very beneficial in terms of the efficiency of the solar cell [7]. Transparent conductive oxide (TCO) layer is responsible from the lateral transportation of photo-generated current in thin film solar cells. Indium tin oxide (ITO) has been the most used TCO to date due to its features such as low resistance and high transparency in the visible wavelength range [8]. In this study, both the effects of silver alloying and the thickness of the ITO TCO layer on the structural properties of the absorber and the solar cell parameters have been investigated.

## 2 MATERIAL AND METHOD

CIGS thin film solar cells were fabricated on 400 nm thick molybdenum coated soda lime glasses. Since there was no diffusion barrier on the substrates, sodium could diffuse from soda lime glass to the absorber layer of the solar cells. The absorber layers of the solar cells were deposited with and without silver addition by three-stage co-evaporation method. Copper, silver, indium, gallium, and selenium were evaporated simultaneously by a multi-source physical vapour deposition chamber. Copper and silver were evaporated in the second stage of the deposition. Indium and gallium were deposited both in first and third stages to get a copper poor stoichiometry while selenium was evaporated during all stages.

The amount of gallium and indium were set according to get a narrow bandgap absorber layer. 2 microns thickness and the desired compositions of the absorbers were set by means of laser light scattering setup. The substrates were heated up to 620 °C and rotated during the deposition to get a homogenous absorber layer. 50 nm thick n-type CdS was deposited by chemical bath deposition on the p-type CIGS absorber layer to create the p-n junction. 100 nm thick ZnO window layer was deposited by RF magnetron sputtering. ITO TCO layer was deposited with different thicknesses (200 and 300 nm) to understand the effect of the TCO thickness on the solar cell parameters. The deposition of the ITO TCO layer was realized by RF magnetron sputtering. Front contacts of the CIGS solar cells were deposited by e-beam evaporation. 30 nm thick nickel depositions were applied before and after the 2 microns thick aluminum front contact wires. The upper nickel coating was deposited to prevent the oxidation of the aluminum layer while the lower one was used to hinder the diffusion of the aluminum to the absorber layer.

The scanning electron microscope (SEM) microstructure photos of the CIGS absorber layers were taken by ZEISS Supra 40VP SEM. The chemical composition of the absorber layers was determined by Bruker EDS which was attached to the SEM. Open circuit voltage ( $V_{oc}$ ) and fill factor (FF) values were obtained by current density-voltage (J-V) measurement technique with a four-point measurement setup. Short circuit current density ( $J_{sc}$ ) values were determined by using external quantum efficiency (EQE) which was equipped with a xenon lamp and a monochromator. J-V and EQE measurements were realized under AM1.5G standard test conditions at room temperature.

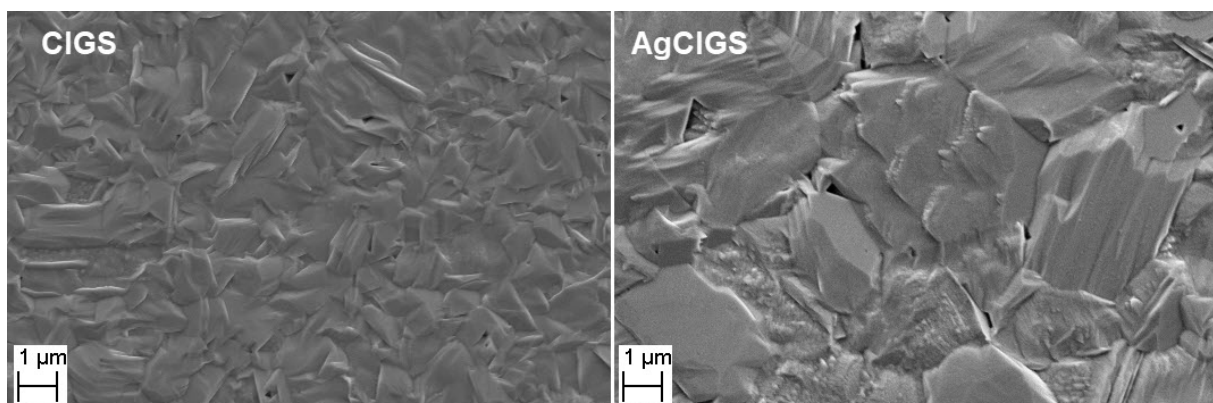
### 3 RESULTS

The chemical compositions of the absorber layers of the CIGS solar cells were analysed by EDS and the results were shown in Table 1.

**Table 1.** The chemical compositions of the absorber layers

Sample	Cu (at. %)	Ag (at. %)	In (at. %)	Ga (at. %)	Se (at. %)
CIGS	22.33	---	16.91	8.20	52.56
AgCIGS	18.01	4.29	16.98	8.38	52.34

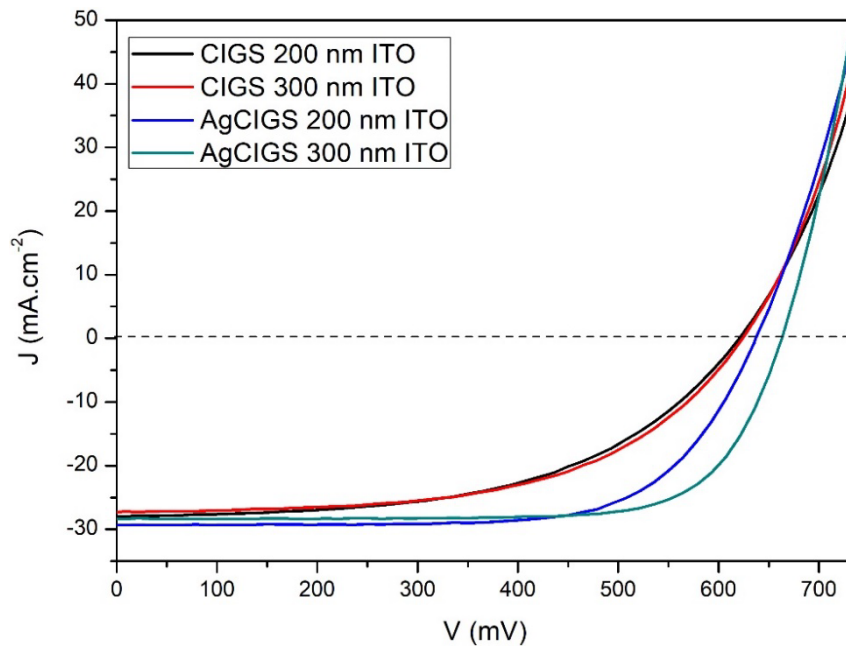
The desired amount of copper in the CIGS sample and the total amount of copper and silver in the AgCIGS sample to get a copper poor stoichiometry were achieved successfully.  $Cu/(Ga+In)$  ratio (CGI) for CIGS sample and  $(Ag+Cu)/(Ga+In)$  ratio (ACGI) for AgCIGS sample were set to about 0.9 which is necessary for high efficiency [9]. On the other hand,  $Ga/(Ga+In)$  ratios (GGI) of the samples were about 0.3 which is also desirable to be able to fabricate highly efficient narrow bandgap chalcopyrite thin film solar cells. The ratio of  $Ag/(Ag+Cu)$  (AAC) was set to 0.2 in AgCIGS sample since it is very beneficial in terms of the efficiency of the solar cell for narrow bandgap chalcopyrite thin film solar cells [7]. The SEM microstructure photos of the CIGS absorber layers were shown in Figure 1.



**Figure 1.** The SEM microstructure photos of the CIGS absorber layers

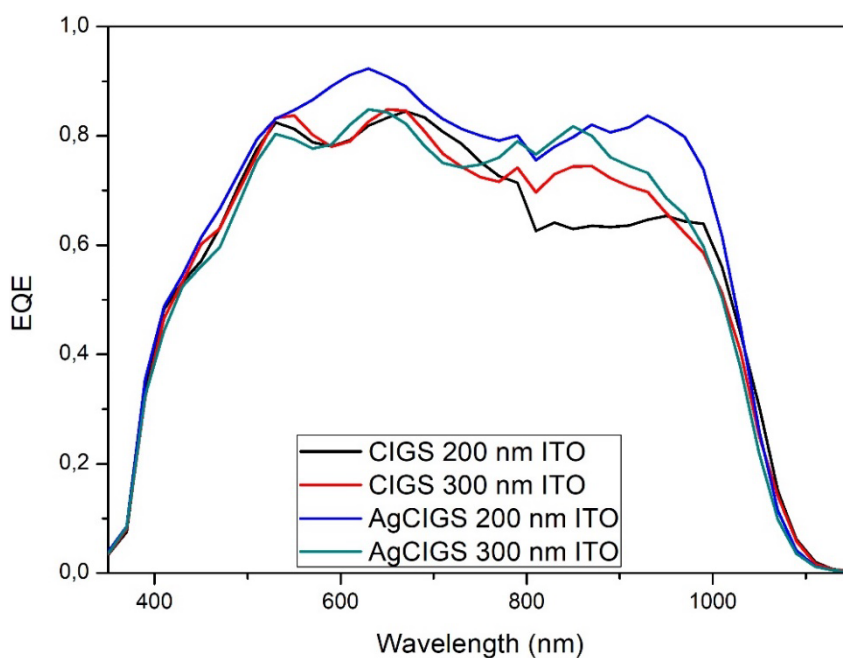
As can be seen in Figure 1, the addition of silver with an AAC ratio of 0.2 has increased the average grain size which is in good agreement with the literature [10]. The increase in average grain size and the resulting improvement in crystal quality were caused by the decrease in the melting temperature of the chalcopyrite structure after the addition of silver and the facilitation of the movements of atoms and grain boundaries [11]. This advantage

of silver alloying provides flexibility in the production temperature of the chalcopyrite solar cell, allowing it to be produced at much lower temperatures and without serious decreases in solar cell efficiency, thus facilitating production on flexible substrates and accelerating the transition to industrial scale [10]. J-V measurement results of the solar cells were shown in Figure 2.



**Figure 2.** J-V measurement results of the solar cells

It can be seen from Figure 2 that, the addition of silver increased both  $V_{oc}$  and FF for all ITO thicknesses. This phenomenon can be explained by the mechanism of decreasing the defects and the grain boundary recombination with the increase in crystal quality and average grain size [5]. On the other hand, the addition of silver also increased the  $J_{sc}$  values of the samples. This was thought to occur because silver alloying widens the bandgap by causing anion displacement and cation electronegativity [12]. Moreover, increasing the thickness of the ITO TCO layer from 200 nm to 300 nm increased  $V_{oc}$  and FF but decreased the  $J_{sc}$ . Normally, there is a compromise as increasing thickness both increases conductivity and decreases transparency [13]. Therefore, the increase in  $V_{oc}$  and FF values can be explained by the increase in conductivity, and the decrease in  $J_{sc}$  value can be explained by the decrease in transparency [14]. EQE measurement results of the solar cells were shown in Figure 3.



**Figure 3.** EQE measurement results of the solar cells

It can be seen from Figure 3 that, the addition of silver increased the current collection at all wavelengths for both samples with ITO TCO layers having 200 nm and 300 nm thicknesses. On the other hand, the increase in ITO thickness caused a greater decrease in current collection in the AgCIGS sample but a slight increase in the CIGS sample. It can be understood by comparing the data from Figure 2 and Figure 3 that, the  $J_{sc}$  values obtained by J-V and EQE measurements were slightly different. Since the  $J_{sc}$  values obtained with EQE are more consistent and realistic than the  $J_{sc}$  values obtained with J-V, the use of  $J_{sc}$  values obtained with EQE was preferred in this study. Solar cell parameters and power conversion efficiency (PCE) values of the solar cells were shown in Table 2.

**Table 2.** The photovoltaic parameters of the solar cells

Sample	Voc (mV)	Jsc (mA.cm <sup>-2</sup> )	FF (%)	PCE (%)
CIGS 200 nm ITO	621	28.13	53.0	9.26
CIGS 300 nm ITO	624	28.51	55.3	9.84
AgCIGS 200 nm ITO	637	31.09	68.8	13.63
AgCIGS 300 nm ITO	663	28.71	74.2	14.12

Increasing ITO thickness and adding silver increased Voc and FF values. On the other hand, increasing the ITO thickness in AgCIGS samples caused a decrease in  $J_{sc}$  by a lower current collection. However, since the effect of the increase in Voc and FF values was more pronounced, the sample with silver addition and 300 nm thick ITO TCO layer was able to reach a higher efficiency value than the others.

## 4 CONCLUSION

Chalcopyrite thin film solar cells having different absorber layers and different ITO TCO layer thicknesses were produced successfully on molybdenum coated soda lime glass substrates by three-stage co-evaporation, chemical bath deposition, RF magnetron sputtering, and e-beam evaporation methods. The addition of silver increased the crystal quality and the average grain size of the absorber. This led to an increase in all solar cell parameters. On the other hand, increasing the ITO thickness also improved the solar cell parameters but decreased the  $J_{sc}$  value of the AgCIGS sample slightly. As a conclusion, although there is always a compromise in solar cell properties, optimized values and the best PCE were obtained in the silver alloyed solar cell having 300 nm ITO TCO layer.

## Acknowledgments

The author would like to thank to PV Group of Prof. Dr. Roland Scheer in the Physics Institute of Martin Luther University Halle-Wittenberg for their support with the laboratory infrastructure.

## References

- [1] S. Siebentritt, "Chalcopyrite compound semiconductors for thin film solar cells," *Current Opinion in Green and Sustainable Chemistry*, vol. 4, pp. 1–7, Apr. 2017.
- [2] S. Agca, "New studies on chalcopyrite thin film solar cells: Silver alloying," *International Journal of Engineering Research and Development*, vol. 16, no. 1, pp. 106–116, Jan. 2024.
- [3] S. Agca and G. Cankaya, "Photovoltaic properties of Cu(In,Ga)(Se,Te)<sub>2</sub> thin film solar cells with different tellurium amounts and a copper-poor stoichiometry," *International Journal of Energy Studies*, vol. 8, no. 4, pp. 849–858, Dec. 2023.
- [4] S. Agca and G. Cankaya, "Effect of gallium content on diode characteristics and solar cell parameters of Cu(In<sub>1-x</sub>Ga<sub>x</sub>)(Se<sub>0.98</sub>Te<sub>0.02</sub>)<sub>2</sub> thin film solar cells produced by three-stage co-evaporation at low temperature," *Gazi University Journal of Science Part C: Design and Technology*, vol. 11, no. 4, pp. 1108–1115, Dec. 2023.
- [5] P. T. Erslev, G. M. Hanket, W. N. Shafarman, and J. D. Cohen, "Characterizing the effects of silver alloying in chalcopyrite CIGS solar cells with junction capacitance methods," *Materials Research Society Symposium Proceedings*, vol. 1165, art. no. 107, 2009.
- [6] J. H. Boyle, B. E. McCandless, G. M. Hanket, and W. N. Shafarman, "Structural characterization of the (AgCu)(InGa)Se<sub>2</sub> thin film alloy system for solar cells," *Thin Solid Films*, vol. 519, no. 21, pp. 7292–7295, Aug. 2011.
- [7] M. Edoff, T. Jarmar, N. S. Nilsson, E. Wallin, D. Högstrom, O. Stolt, O. Lundberg, W. N. Shafarman, and L. Stolt, "High Voc in (Cu,Ag)(In,Ga)Se<sub>2</sub> solar cells," *IEEE Journal of Photovoltaics*, vol. 7, no. 6, pp.

- 1789–1794, Nov. 2017.
- [8] M. Mazur, R. Pastuszek, D. Wojcieszak, D. Kaczmarek, J. Domaradzki, A. Obstarczyk, and A. Lubanska, “Effect of thickness on optoelectronic properties of ITO thin films,” *Circuit World*, vol. 48, no. 2, pp. 140–159, Mar. 2022.
- [9] N. Naghavi, F. Mollica, J. Goffard, J. Posada, A. Duchatelet, M. Jubault, F. Donsanti, A. Cattoni, S. Collin, P. P. Grand, J. J. Greffet, and D. Lincot, “Ultrathin Cu(In,Ga)Se<sub>2</sub> based solar cells,” *Thin Solid Films*, vol. 633, pp. 55–60, Jul. 2017.
- [10] S-C. Yang, J. Sastre, M. Krause, X. Sun, R. Hertwig, M. Ochoa, A. N. Tiwari, and R. Carron, “Silver-promoted high-performance (Ag,Cu)(In,Ga)Se<sub>2</sub> thin-film solar cells grown at very low temperature,” *Solar RRL*, vol. 5, no. 5, art. no. 2100108, May 2021.
- [11] C. Wang, D. Zhuang, M. Zhao, Y. Li, L. Dong, H. Wang, J. Wei, and Q. Gong, “Effect of silver doping on properties of Cu(In,Ga)Se<sub>2</sub> films prepared by CuInGa precursors,” *Journal of Energy Chemistry*, vol. 66, pp. 218–225, Mar. 2022.
- [12] J. H. Boyle, B. E. McCandless, W. N. Shafarman, and R. W. Birkmire, “Structural and optical properties of (Ag,Cu)(In,Ga)Se<sub>2</sub> polycrystalline thin film alloys,” *Journal of Applied Physics*, vol. 115, art. no. 223504, Jun. 2014.
- [13] S-Y. Lien, “Characterization and optimization of ITO thin films for application in heterojunction silicon solar cells,” *Thin Solid Films*, vol. 518, pp. S10–S13, Mar. 2010.
- [14] H. Kim, J. S. Horwitz, G. Kushto, A. Piqué, Z. H. Kafafi, C. M. Gilmore, and D. B. Chrisey, “Effect of film thickness on the properties of indium tin oxide thin films,” *Journal of Applied Physics*, vol. 88, no. 10, pp. 6021–6025, Nov. 2000.



## The Characteristics of an Organic Solar Cell at the Base of Polymeric Material

**Chahrazed Bendenia<sup>\*1</sup>, Souhila Bendenia<sup>1</sup>, Hanaa Merad-Dib<sup>1</sup>, Samia Moulebhar<sup>1</sup>, Sid Ahmed Khantar<sup>1</sup>, Sarra Merabet<sup>1</sup>**

*<sup>1</sup>Laboratory Laboratory for Analysis and Modeling of Advanced Materials for Renewable Energies, University Abd El Hamid Ibn Badis, Mostaganem 27000, Algeria*

---

### **Abstract**

Organic semiconductor materials have attracted a great deal of research interest in the field of bulk heterojunction (BHJ) solar cells in terms of their electrical and optical properties. These materials, which make up the active layer (polymer/fullerene), can be used to improve the performance of the device.

In this context, we are numerically measuring the characteristics of inverted-structure organic solar cells (OSCs) using the SCAPS-1D simulator, which is used to model the physical and electrical behavior of an electronic component based on semiconductor physics, including electrical, optical and thermal properties. This software uses various physical models such as : Monte Carlo, Langevin, Fermi-Dirac, SRH (Shockley Read Hall), recombination, etc...

The results obtained have enabled us to represent the structure and the IV characteristics, namely the short-circuit current (Isc), the open-circuit voltage (Voc), the form factor (FF) and the conversion efficiency (PCE).

**Keywords:** *Semiconductor, Bulk heterojunction, Active layer, Characteristics*

---



## Microstrip Dipole Antenna Design for RFID Application

Hadda Ouguissi<sup>1</sup>, Nail Alaoui<sup>\*2</sup>

<sup>1</sup>*Materials, Energetic Systems, Renewable Energies, and Energy Management Laboratory (LMSEERGE), Faculty of Technology, Ammar Thelidji University of Laghouat, Laghouat, Algeria*

<sup>2</sup>*Research Laboratory for Modeling, Simulation and Optimization of Real Complex Systems, University of Djelfa, 17000 Djelfa, Algeria*

---

### Abstract

This paper explores an innovative way of designing antennas through metamaterial integration and the miniaturization process. In order to boost frequency usability and reduce the antenna size, we propose a new solution. The interaction between the two divided ring resonators with this resonant component is based on this technique. In this experiment the parameters considered include the resonant frequency, the lack of response, and the wavelength, the amount of radiation, and the gain and the power produced by an antenna. CST conducts all simulation effects.

**Keywords:** *CST Studio, Metamaterial, Miniaturization, RFID*

---





## Chua Circuit and Its Behavior

Hadda Ouguissi<sup>1</sup>, Nail Alaoui<sup>\*2</sup>

<sup>1</sup>*Materials, Energetic Systems, Renewable Energies, and Energy Management Laboratory (LMSEERGE), Faculty of Technology, Ammar Thelidji University of Laghouat, Laghouat, Algeria*

<sup>2</sup>*Research Laboratory for Modeling, Simulation and Optimization of Real Complex Systems, University of Djelfa, 17000 Djelfa, Algeria*

---

### Abstract

The Chua circuit is among the simplest non-linear circuits that show most complex dynamical behavior and chaotic structures' depending upon the strength of the forcing parameters. In this work and by studying the stability and the influence of the circuit parameters on the system dynamics, the dynamic characteristics of the proposed chaotic circuit are theoretically analyzed and numerically simulated. The results show that the proposed chaotic circuit has gone through three states: period, bifurcation, and chaos.

**Keywords:** *Chaos theory, Chua's circuit, Parameters of bifurcation, Chaotic behavior*

---



## Harmonic Forecasting for Future Offshore Wind Farm System in the Ayvalik Region of the North Aegean Sea by Using Deep Learning

Alp Karadeniz<sup>\*1</sup>

<sup>1</sup>Electrical and Electronics Engineering, Balikesir University, Balikesir, Türkiye

---

### Abstract

Wind energy plays a crucial role in today's energy sector, offering the potential to reduce reliance on fossil fuels and promote environmental sustainability. Offshore wind farms, in particular, present a promising opportunity for more efficient energy generation, harnessing higher and more consistent wind speeds compared to onshore facilities. However, integrating these offshore structures into electrical systems presents various technical challenges. This research utilizes real-time wind speed data collected from the Ayvalik region between 2005 and 2020 to simulate a 2 MW offshore wind farm connected to a 120 kV grid using Simulink/MATLAB. The primary objective of this study is to develop a forecasting model capable of generating accurate and reliable predictions of harmonics for offshore wind energy systems. To achieve this, a deep learning approach (Long Short-Term Memory (LSTM)) is employed to forecast harmonics generated by a total of 2 MW of renewable generators, specifically double-fed induction generators (DFIGs) operated by wind turbines. These generators produce voltage and current waveforms using real-world data (wind speed) from the Ayvalik region. Harmonics are extracted from these waveforms and used to generate training and testing datasets for the forecasting model. The LSTM model is then applied to predict the harmonics. The results demonstrate that the harmonics predicted by the deep learning method closely match the calculated data.

**Keywords:** *Ayvalik region offshore wind farm, Deep learning, Harmonics, Offshore wind farms, Random forest model*

---



## Evaluation of Speech Encryption Algorithm Based on Chaotic Systems

Salah Mokhnache<sup>\*1</sup>, Tewfik Bekkouche<sup>2</sup>, Nacira Diffellah<sup>2</sup>

<sup>1</sup>*EBT Department University Ferhat Abbas Setif 1, Setif, Algeria*

<sup>2</sup>*Electronics Department, Mohamed El Bachir El Ibrahimi University, Bordj Bou Arréridj, Algeria*

---

### Abstract

This work is done in the context of speech encryption. It highlights the performance of chaotic systems in cryptosystems by consolidating system secret keys that are chaotically generated by maps that are highly sensitive to the slightest changes in initial conditions, such as the standard map and the sine map. Objective and subjective analyses, such as visual examination of the waveform in the time domain, spectrograms, histograms, as well as statistical analyses, were carried out to evaluate the performance of our cryptosystem. The analysis of these performances confirmed that the proposed system shows very acceptable security.

**Keywords:** *Speech encryption, Chaos, Chaotic systems*

---



---

## A Design of AI-Based-Smart Glasses, Which Offer Navigation in Addition to Correcting Vision

Syed Arif Kamal<sup>\*1</sup>

<sup>1</sup>*Meritorious Professor, Project Director, the NGDS Pilot Project, Ex-Acting Vice Chancellor, and Ex-Dean, Faculties of Science & Engineering, University of Karachi, PO Box 8423, Karachi 75270, Sindh, Pakistan*

---

### Abstract

The human eyes are protected in specialized sockets carved out in the human skull. An average human eye in adult has a diameter of approximately 2.5 cm. Because of lack of outdoor activities, increased use of computer, television and smart phones, youngsters are increasingly experiencing defects of vision, most common are myopia or short-sightedness, hypermetropia or long-sightedness/far-sightedness. Prescription eye glasses are needed to correct these defects. At times, children and adults have to wear 3 types of glasses, one for visualizing things far away, another for computer use and the third one for reading, causing a lot of hassle in changing glasses and creating problems in carrying all of them. AI-based-smart glasses are proposed, which have 3 in 1 features, adjusting to far vision, computer vision and reading vision through ultrasound waves (available in cameras). Additionally, antiglare and photosensitive (darkening the glasses in bright sunlight) features are added. In addition, the author proposes to add 4 tiny cameras, 2 between the left- and the right-eye glasses ( $C_1$  one pointing straight and  $C_2$  tilted to provide a view just in front of toes) and 2 at the end of frame,  $C_3$  and  $C_4$ , resting on each tip of ear, all of the cameras equipped with night-vision capability. Bluetooth connectivity is provided to earphones, smart-wrist watch and smart phone.  $C_1$  is equipped with unusual-motion and explosive-trace detection as well as night-vision capability.  $C_2$  is powered with edge-based algorithm to detect any obstacles in front, sounding alarms in all these situations as well as visual warning on the upper-right-hand corner of the right-eye glass and a mirror setup for the left-eye glass.  $C_3$  and  $C_4$  are employed for back vision and sensors  $S_1$  and  $S_2$  for blind-corner vision. Smart-phone features as well as features of cardless-authorization and charge system are incorporated. These glasses are protected through automatic-lock system, based on voice and 3-D-face recognition as well as real-time transmission to a secure location, identity as well as positional coordinates and momenta of possessor to prevent from unauthorized use or snatching.

**Keywords:** *Back and blind-corner vision, Edge-based algorithm, Night vision, Smart-phone features, Unusual-motion and explosive-trace detection*

---

## 1 INTRODUCTION

We, the humans, are blessed with the unique gift from Allah Izz-o-Jal — our eyes. This is a remarkable piece of technology, which provides stereo vision, along with automatic adjustment of focus for near and far objects as well as dark adaptation. The human eyes are protected in specialized sockets carved out in the human skull, an average adult eye possesses a diameter of around 2.5 cm. The white outer region of our eye, which protects the internal parts of our eyes, is called 'sclera'. The transparent portion of our eye that allows the light to enter our eye is termed as 'cornea', which consists of transparent tissue. A circular, thin structure made up of contracting and relaxing muscles in the eye, which controls the light reaching the retina and the size of 'pupil' (part of eye located in iris center), is known as the 'iris'. Pupil allows light to enter the 'retina' (light-sensitive tissue in the inner core of the eye, which sends electrical signals, converted from light, to brain for processing). 'Lens' is a biconvex, transparent structure present in the eye behind the pupil. 'Optic nerve' sends electrical impulses from retina to the brain.

In this paper, the author proposes AI-based-smart glass, which combine automatically-adjusting-prescription glasses for reading, computer use and distance vision with back and blind-corner vision, night vision as well as unusual-motion and explosive-trace detection using smart-phone features.

## 2 MODELS OF IMAGE FORMATION

Mathematical-computer models of image formation include the geometrical model, the image-function model, the radiometrical model, the color model, the spatial-frequency model and the digitizing model. In the context of the geometrical model, the projection of a point in the image plane is located based on equation (1)

$$\frac{1}{u} + \frac{1}{v} = \frac{1}{f} \Rightarrow v = \frac{uf}{u - f} \tag{1}$$

In the above equation, u represents distance of the object from lens center, v distance of the image from lens center and f the focal length (Figure 1).

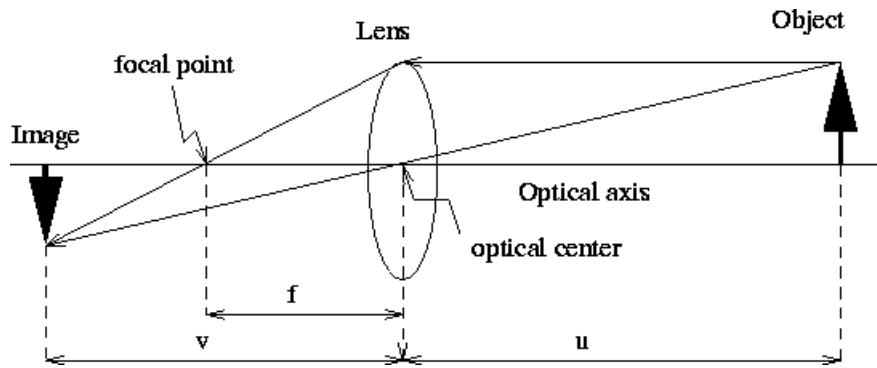


Figure 1. Geometry of image formation

## 3 CARE OF EYES

It is imperative that we protect our eyes through proper diet, exercise and lifestyle adjustment through plans outlined in Tables 7, 11 of [1]. During an outdoor session, children engage in various activities (drawing, singing, painting, jigsaw puzzle) to get the required doses of vitamin D. The children should sit facing away from the sun (physical-education instructor/teacher should face the sun) and their eyes should be protected through UV (ultraviolet)-cutoff glasses or indigenously-made spectacles, made from one layer of completely-exposed photographic film, ASA 100, having high silver content. They should exercise for 5 minutes each after waking up, at the end of every hour and before going to bed — focusing eyes far away and moving eyeballs (up, down, sideways) and applying cold water to eyes every 3-4 hours. It is interesting to notice that in the Muslim faith, wudu/ablution is obligatory for prayers, which are offered 5 times a day. The ritual of ablution has a segment of washing face, which keeps eyes cool. Exercising eyes after every hour should be practiced by adults, too. Adults and children should, also, be wearing UV-cutoff glasses or indigenously-made spectacles, whenever they go outside or travel on city roads, not only, to protect eyes from UV rays, but also, to save eyes from dust and other foreign objects (for persons with normal eyesight, it is recommended to put on zero-power glasses even during night just for this reason). This is most important for adults, who have cataract surgery and have lenses put in their eyes.

There should be a maximum of 2-hour screen time (computer/video games/TV/DVD — computer monitor at eye level) for children. Proper lighting is required for reading/writing/drawing activities. Neck and back should be straight as well as normal to thighs for all the above activities. Smart phones should not be given to children.

If a brown/black spot is seen in eyes or unusual redness is observed (visible clearly using ophthalmoscope — Figure 2), immediate medical attention is needed.



Figure 2. Ophthalmoscope

## 4 DEFECTS OF VISION

Note that a young child does not have 6/6 vision. A 5-year-old child may have 6/12 vision. The letters in children's books/workbooks should be adapted according to age.

Myopia or Near-Sightedness is a defect of vision, in which distant objects appear blurred and objects close to a person are seen clearly. This occurs because the eyeball is either too long or the refractive power of the eye lens is too high. In such situations, the image forms in front of the retina rather than forming on the retinal surface. Correction is achieved by prescribing glasses/contacts made of concave (diverging) lenses, which diverge the rays just enough so that the image forms on retinal surface.

Hypermetropia or Long-Sightedness (sometimes called 'far-sightedness') is a defect of vision, in which nearby objects appear blurred and distant objects are seen clearly. This occurs because the eyeball is either too short or the refractive power of the eye lens is too low. In such situations, the image forms behind the retina rather than forming on the retinal surface. Correction is achieved by prescribing glasses/contacts made of convex (converging) lenses, which converge the rays just enough so that the image forms on retinal surface.

Cataract is clouding of the lens, which obstructs vision and does not allow creation of a sharp and a clear image. A cataract forms when old cells, after their death, stick in a capsule creating clouding over lens with the passage of time, causing blurring of image. Correction is achieved through surgery. An artificial lens is placed in place of the opaque lens, removed via surgery.

Presbyopia or Old-Age Long-Sightedness is a natural defect that occurs with the age. The eye muscles become so weak that no longer a person can see nearby objects clearly. The near point of a person with presbyopia is more than 25 cm. Correction is achieved by wearing bifocal or progressive-addition lenses (PALs), in which the upper portion of the lens consists of concave lens and the lower portion convex lens.

Astigmatism is a defect in which the light rays, which enter the eye, fail to focus light evenly to a single focal point on the retina but instead scatter away. The light rays converge in such a way that some of them focus on the retina and still other focus in front of or behind the retina. This is due to non-uniform curvature of the cornea; resulting in distorted or blurry vision at any distance. Correction of astigmatism is achieved by prescribing spherical-cylindrical lens.

## 5 EYE GLASSES AND POWER OF A LENS

Optical power (also referred to as dioptric power, refractive power, focusing power, or convergence power) is the degree to which a lens converges or diverges light. Mathematically, power of a lens is reciprocal of the focal length. Equation (1), therefore, becomes

$$P = \frac{1}{f} = \frac{1}{u} + \frac{1}{v} \quad (2)$$

SI unit of optical power is diopter (D), which is  $m^{-1}$ . High optical power corresponds to short focal length. If a lens is immersed in a refractive medium, its optical power as well as focal length change. For 2 or more thin lenses close together, the optical power of the combined lenses is the algebraic sum of optical power of individual lenses, which is derived from formula for focus of combined lens, i.e.,

$$\frac{1}{f} = \frac{1}{f_1} + \frac{1}{f_2} \Rightarrow P = P_1 + P_2 \quad (3)$$

The prescription eyeglasses have numbers listed under the heading OS (Oculus Sinister meaning Left Eye) and OD (Oculus Dextrus meaning Right Eye). Occasionally, there would be a number listed under the heading OU, which implies something involving both eyes. These numbers represent diopters. Roughly, farther away from zero is the prescription (compare with 'Away-from-Normality Index' in Growth-and-Obesity Roadmaps 5.0 — Tables 4a, 5a, 8a, 9a in [1]), the worse is the eyesight and the more vision correction (stronger prescription) is needed. A plus sign indicates that the patient has hypermetropia (long-sightedness/far-sightedness) and a minus sign implies that patient is suffering from myopia (near-sightedness). This is because convex lenses have positive optical power, whereas concave lenses have negative optical power. For people, who have astigmatism, there'll be 3 numbers in their

prescription, i. e.,  $S \times C \times Axis$ .  $S$  refers to spherical portion of the prescription,  $C$  to cylindrical portion or astigmatism.  $Axis$  is a number anywhere between  $0^\circ$  and  $180^\circ$ . It documents orientation of the astigmatism.

Generally, people of mature age have to use 3 types of eye glasses — one for reading, the other for computer vision and the third for distance vision. Sometimes glasses for distance vision are embedded with the property that they darken in bright light. However, this poses problems during nighttime driving. The vehicles coming from the opposite direction with bright headlights cause these glasses to darken, making it difficult to drive on highway. The time-lag between darkening and removing the glasses may be critical as serious accident may happen during this short span-of-time. A solution to this problem is proposed in AI-based-smart glasses.

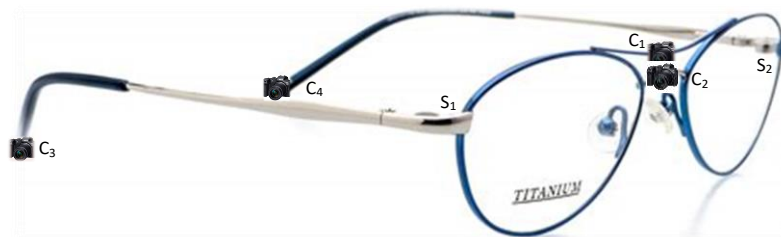
## 6 ARTIFICIAL INTELLIGENCE (AI): BLESSINGS AND CURSES

Artificial intelligence (AI) is considered as the capability of a digital computer or a robot, which is computer-controlled to accomplish tasks usually associated with humans. The term is frequently applied to the task of developing systems embedded with the intellectual processes characteristic of intelligent beings, which include the abilities to reason, to find meaning, to generalize or to learn from previous experience.

Virtual Reality is taking an important role in modern society within very different areas, ranging from industrial applications to entertainment business. It has numerous advantages in the education sector, since it allows 3-D visualization of almost any object or going anywhere in a unique manner. In medical education, in particular, anatomy, its use is especially important because it permits studying any structure of the human body by taking the user inside each one [2]. Earlier this year, an AI-based system for determining risk of acquiring scoliosis in school-going children has been proposed [3].

Concerns have been expressed whether AI would take over humans and their jobs. A very significant misuse of AI is virtual-reality glasses, which if used on roads and public places, make the person oblivious of one's surroundings causing collisions and accidents. These glasses are making both visual and acoustic disconnect with the environment. Previously, use of smart and non-smart phones during driving has been the main source of accidents. Further, access to smart phones to all family members and their constant use has broken the family fabric, deprived them from proper sleep and causing more and more youngsters to wear prescription glasses.

Tyschsen and Foeller studied the effects of immersive virtual-reality-headset viewing on young children by analyzing a sample of 50 children (29 boys; 21 girls), 4-10-year-old. They concluded that younger children tolerate fully immersive 3-D virtual reality game play without noteworthy effects on visuomotor functions [4].



**Figure 3.** A prototype of AI-based-smart glasses

## 7 AI-BASED-SMART GLASSES

In this work, a prototype is given for AI-based-smart glasses, which have 3 in 1 features, adapting for distance vision, computer vision and reading vision through ultrasound waves, which are available in cameras. The author proposes to add 4 tiny cameras:  $C_1$  points straight and is equipped with unusual-motion and explosive-trace detection as well as night-vision capability;  $C_2$  tilted downwards to provide a view just in front of toes, powered with edge-based algorithm to detect any obstacle or ditch in front, sounding alarms in all these situations as well as visual warning on the upper-right-hand corner of right-eye glass and a mirror setup for the left-eye glass;  $C_3$  and  $C_4$  provide back views; sensors,  $S_1$  and  $S_2$  bind-corner view as well as adaptability to adjust focus for reading, computer work and distance vision in addition to intensity-based algorithm for antiglare mechanism and adjusting for bright light during daytime. This is accomplished by programming intensity-based algorithm for darkening of glasses in bright sunlight, so that it is activated, only, during daylight hours. These daylight hours are determined from local sunrise and sunset timings, which are obtained from latitude and longitude of the location of AI-based glasses. The latitude and longitude of the current location is obtained from GPS (Global-Positioning System) [6]. This should take care of the unwanted darkening of the glasses during nighttime driving (Figure 3).

Smart-phone features as well as features of cardless-authorization and charge system [7] are incorporated in these glasses, which are protected through automatic-lock system, based on voice and 3-D-facial recognition [8, 9] as well as real-time transmission to a secure location, identity as well as positional coordinates and momenta of possessor to prevent from unauthorized use or snatching.

## 8 CONCLUSION

AI-enabled smart home products, like Google Assistant, Apple's Siri, and Amazon's Alexa, are taking a more proactive role in smart homes, revolutionizing security systems and home appliances. They recognize the voice commands and accomplish the assigned task. Further, they can automate operations by storing and implementing the user's preferences. In this work, the author has proposed AI-based-smart glasses, which should enhance the user's interaction with the environment by providing an almost 360° vision instead of the normal stereo vision available in human eyes. In future, there is a potential to include features, which should enable persons with severely-impaired vision to be able to see clearly. That should be the true purpose of science — to enhance quality of life for the human beings.

## References

- [1] S. A. Kamal, "Growth-and-Obesity Roadmaps 5.0 for children of still-growing parents — the eleventh-generation solution of childhood obesity-and-malnutrition," *Int. J. Biol. Biotech.*, vol. 20, no. 2, pp. 243–267, Apr. 2023
- [2] S. G. Izard, J. A. J. Méndez, and P. R. Palomera, "Virtual reality educational tool for human anatomy," *J. Med. Syst.*, vol. 41, no. 5, art. no. 76, Mar. 2017
- [3] S. A. Kamal and S. K. Raza, "An AI-based system for determining risk of acquiring scoliosis in school-going children," in *Proceedings of the Fourth International Artificial Intelligence and Data Science Congress (ICADA 2024)*, Izmir, Türkiye, Mar. 2024, pp. 346–362.
- [4] L. Tyschsen and P. Foeller, "Effects of immersive virtual reality headset viewing on young children: visuo-motor function, postural stability and motion sickness," *Am. J. Ophthalmol.*, vol. 209, pp. 151–159, Jan. 2020
- [5] S. A. Kamal, "Combination of moiré contours and edge-based algorithm to study motion in the sagittal plane," *Kar. Univ. J. Sc.*, vol. 24, no. 2, pp. 53–60, Dec. 1996
- [6] C. J. Hegarty, "The global-positioning system (GPS)," in *Springer Handbook of Global Navigation Satellite Systems: Springer Handbooks*, P. J. Teunissen and O. Montenbruck, Eds. Edinburgh: Springer, Cham., 2017, pp. 197–218
- [7] S. A. Kamal, "A cardless-authorization and charge system," in *The Seventh Symposium on Computational Complexities, Innovations and Solutions (CCIS 2012)*, Abbottabad, Pakistan, May. 2012.
- [8] S. A. Kamal, "Pattern recognition using moiré-fringe topography and rasterstereography," in *International Symposium on Biometrics and Security Technologies (IEEE ISBAST 2008)*, Bahria University, Islamabad, Pakistan, Mar. 2008.
- [9] M. Wasim, S. A. Kamal, and A. Shaikh, "A security system employing edge-based rasterstereography," *Int. J. Biol. Biotech.*, vol. 10, no. 4, pp. 243–267, Oct. 2013.





---

## Impact of Image Size on Classification of Synthetically Generated Window and Door Images

Safak Altay Acar<sup>\*1</sup>

<sup>1</sup>Department of Computer Technologies, Yenice Vocational School, Karabuk University, Karabuk, Türkiye

---

### Abstract

This paper presents a classification study of synthetically generated window and door images. Firstly, new synthetic window and door images are generated in two different sizes using the real images. A deep convolutional generative adversarial network is used for the generation process. Then, the generated images are classified as window and door. The classification process is applied separately for images of different sizes using artificial neural network. The results obtained for images of different sizes are presented and the impact of image size is evaluated and discussed.

**Keywords:** Deep convolutional generative adversarial network, Artificial neural network, Window, Door

---

## 1 INTRODUCTION

Synthetic images of building parts are created and used in many studies. Hong et al. [1] propose a cycle-consistent adversarial network (CycleGAN) based study to generate synthetic images of building and bridge parts and they test the dataset they created. Zhu et al. [2] present a study that extracts architectural elements from panoramic images. They implement various applications by performing operations such as image synthesis on the dataset they created. Hu et al. [3] introduce an approach that is semi-supervised adversarial recognition of windows. They use generated window images in their study. Chinese window grill images generation method based on generative adversarial networks is presented by Miao et al. [4]. Kelly et al. [5] introduce a dataset of window images which is created for generating quality synthetic data. Also, there are many studies on the classification and detection of windows, doors, etc. Yang and Förstner [6] propose a study of facade images classification as building, door, window, etc. They use randomized decision forest and local features in their approach. Ramôa et al. [7] present methods for door detection and classification. Their methods classify doors as open, semi-open and closed. A method which detects windows and doors in 3D point clouds is proposed by Jarzabek-Rychard et al. [8]. Sezen et al. [9] present a study which detects door and window by using various deep learning algorithms. Sun et al. [10] introduce a study that researches window opening behavior. Their study contains window detection and window image classification utilizing the VGG16 model. A study which extracts window and door from point cloud data is proposed by Cheng et al. [11]. They present the enhanced Bounding Box algorithm to determine probable openings.

This study aims to find out the impact of image size on classification of synthetically generated window and door images. A deep convolutional generative adversarial network is used to generate synthetic images of different sizes and the generated images are classified using artificial neural network.

## 2 MATERIAL AND METHOD

### 2.1 Dataset

Large Scale Architectural Asset (LSAA) dataset [2] which can be reached from [12] is used in this study. This dataset includes architectural asset images from different cities. Window and door images from the same city are wanted to be used. Images taken in Paris are selected due to the greater number of images. Since there are 11393 door images, the same number of window images are picked. Synthetic images are generated using these real images. Sample window and door images belong to LSAA dataset [2] are shown in Fig. 1.



Figure 1. Sample images belong to LSAA dataset [2] (a) window (b) door

## 2.2 Generation of Synthetic Window and Door Images

Radford et al. proposed Deep Convolutional Generative Adversarial Network (DCGAN) [13]. This network is a variant of Generative Adversarial Network (GAN) [14] and includes convolution layers and transposed convolution layers. In this study, synthetic window and door images are generated using a deep convolutional generative adversarial network that is smaller and contains fewer filters than [13]. Architecture of used deep convolutional generative adversarial network is shown in Fig. 2. There are dense and reshaped layers in the first layers of the architecture of the generator. Also, the generator has four transposed convolution layers which have 256, 128, 64 and 3 filters respectively. After the first three transposed convolution layers, there are batch normalization [15] and ReLU [16] layers. Discriminator has three convolution layers, three batch normalization [15] layers and three Leaky ReLU [17] layers in a regular order. There are 64, 128 and 256 filters in convolution layers respectively. The discriminator ends with flatten, dropout and dense layers. Kernel size is 4x4 in all transposed convolution and convolution layers.

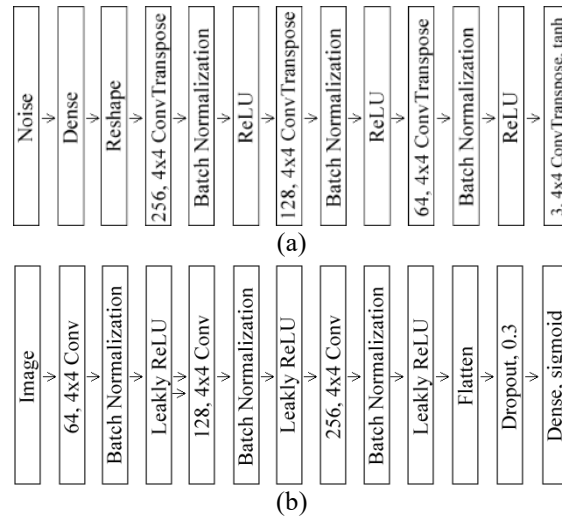


Figure 2. Architecture of used deep convolutional generative adversarial network (a) generator (b) discriminator

Window and door images are synthetically created in two different sizes: 48x64 pixels and 56x72 pixels. Deep convolutional generative adversarial network is trained four times for 500 epochs. 100 sample images are generated at each epoch. Images generated in the last 50 epochs are collected to be used in the classification process. Total number of generated images used in the classification process is given in Table 1. Samples of generated window and door images are shown in Fig. 3.

Table 1. Total number of generated images used in classification process

Architectural Asset	Size (pixels)	Total Number
window	48x64	5000
door	48x64	5000
window	56x72	5000
door	56x72	5000



**Figure 3.** Samples of generated images (a) windows (48x64 pixels) (b) windows (56x72 pixels) (c) doors (48x64 pixels) (d) doors (56x72 pixels)

### 2.3 Classification of Generated Window and Door Images

Artificial neural network (ANN) whose basis model is presented by McCulloch and Pitts [18], imitates the human nervous system and learning process [19]. Synthetically generated window and door images are classified using two different types of artificial neural networks in this study. The input and output neuron numbers of these artificial neural networks are compatible with the image size and number of classes, respectively. There is a difference in the number of neurons in the hidden layers between them. The first one has two hidden layers, each with 10 neurons. The second one has two hidden layers, each with 100 neurons.

## 3 EXPERIMENTAL RESULTS

Software which is required for experimental studies is developed with Python programming language using TensorFlow and Keras libraries. In experiments, synthetically generated window and door images of two different sizes are classified separately using two artificial neural networks. There are 10 neurons in the hidden layers of the first ANN and 100 neurons in the hidden layers of the second ANN. ANNs are trained for 20 epochs and 70% of the images are reserved for training and 30% for testing. The used evaluation metrics are calculated as given in Eq. (1), Eq. (2), Eq. (3) and Eq. (4) [20]. These equations use the terms TP, TN, FP and FN to refer to true positive, true negative, false positive and false negative, respectively.

$$Accuracy = \frac{TP+TN}{TP+FP+FN+TN} \quad (1)$$

$$Precision = \frac{TP}{TP+FP} \quad (2)$$

$$Recall = \frac{TP}{TP+FN} \quad (3)$$

$$F1 - score = 2x \frac{Precision \times Recall}{Precision+Recall} \quad (4)$$

Obtained classification results are given in Table 2 and Table 3. When the results are examined, it is seen that better results are obtained with smaller images. Precision, recall, F1-score and accuracy values belonging to these images are higher. When classification methods are evaluated, the second ANN is more successful. It achieves higher F1-score and accuracy values than the first ANN in 48x64 pixels image size and achieves higher or same precision, recall, F1-score and accuracy values than the first ANN in 56x72 pixels image size.

**Table 2.** Classification results of images generated as 48x64 pixels

Class	First ANN				Second ANN			
	Precision	Recall	F1-score	Accuracy	Precision	Recall	F1-score	Accuracy
door	0.99	0.95	0.97	0.97	0.98	1.00	0.99	0.99
window	0.95	0.99	0.97		1.00	0.98	0.99	

**Table 3.** Classification results of images generated as 56x72 pixels

Class	First ANN				Second ANN			
	Precision	Recall	F1-score	Accuracy	Precision	Recall	F1-score	Accuracy
door	0.93	0.93	0.93	0.93	0.96	0.93	0.95	0.95
window	0.93	0.93	0.93		0.93	0.96	0.95	

## 4 CONCLUSION

Synthetic window and door images are generated using a deep convolutional generative adversarial network and these generated images are classified using two different artificial neural networks. When the impact of image size on classification is evaluated, it is seen that artificial neural networks classify smaller images more accurately. In future studies, the number of classes and image size variety can be increased. Different classification methods can be used. Different types of images and datasets can be studied.

## References

- [1] Y. Hong, S. Park, H. Kim, and H. Kim, "Synthetic data generation using building information models," *Automation in Construction*, vol. 120, art. no. 103871, Oct. 2021.
- [2] P. Zhu, W. R. Para, A. Frühstück, J. Femiani, and P. Wonka, "Large-scale architectural asset extraction from panoramic imagery," *IEEE Transactions on Visualization and Computer Graphics*, vol. 28, no. 2, pp. 1301–1316, Feb. 2022.
- [3] H. Hu, X. Liang, Y. Ding, X. Yuan, Q. Shang, B. Xu, X. Ge, M. Chen, R. Zhong, and Q. Zhu, "Semi-supervised adversarial recognition of refined window structures for inverse procedural facade modelling," *ISPRS Journal of Photogrammetry and Remote Sensing*, vol. 192, pp. 215–231, Oct. 2022.
- [4] C. Miao, J. Wu, J. Chen, S. Xiong, L. Wang, and Q. Wang, "Image generation of traditional Chinese window grilles based on generative adversarial networks," in *International Conference on Culture-Oriented Science and Technology*, Lanzhou, China, 2022, pp. 232–236.
- [5] T. Kelly, J. Femiani, and P. Wonka, "WinSyn: a high resolution testbed for synthetic data," in *IEEE/CVF Conference on Computer Vision and Pattern Recognition*, 2024, pp. 22456–22465.
- [6] M. Y. Yang, and W. Förstner. "Regionwise classification of building facade images," in *ISPRS Conference Photogrammetric Image Analysis*, Munich, Germany, 2011, pp. 209.
- [7] J. G. Ramôa, L. A. Alexandre, and S. Mogo, "Real-time 3D door detection and classification on a low-power device," in *IEEE International Conference on Autonomous Robot Systems and Competitions*, Ponta Delgada, Portugal, 2020, pp. 96–101.
- [8] M. Jarzabek-Rychard, D. Lin, and H-G. Maas, "Supervised detection of façade openings in 3D point clouds with thermal attributes," *Remote Sensing*, vol. 12, no. 3, art. no. 543, Feb. 2020.
- [9] G. Sezen, M. Cakir, M. E. Atik, and Z. Duran, "Deep learning-based door and window detection from building façade," *The International Archives of the Photogrammetry, Remote Sensing and Spatial Information Sciences*, vol. XLIII-B4-2022, XXIV ISPRS Congress, Nice, France, 2022, pp. 315–320.
- [10] C. Sun, X. Guo, T. Zhao, and Y. Han, "Real-time detection method of window opening behavior using deep learning-based image recognition in severe cold regions," *Energy and Buildings*, vol. 268, art. no. 112196, Aug. 2022.
- [11] B. Cheng, S. Chen, L. Fan, Y. Li, Y. Cai, and Z. Liu, "Windows and doors extraction from point cloud data combining semantic features and material characteristics," *Buildings*, vol. 13, no. 2, art. no. 507, Feb. 2023.
- [12] *Large Scale Architectural Asset Dataset* [Online]. Available: <https://github.com/ZPdesu/ljaa-dataset>
- [13] A. Radford, L. Metz, and S. Chintala, "Unsupervised representation learning with deep convolutional generative adversarial networks," arXiv preprint arXiv:1511.06434, 2015.
- [14] I. J. Goodfellow, J. Pouget-Abadie, M. Mirza, B. Xu, D. Warde-Farley, S. Ozair, A. Courville, and Y. Bengio, "Generative adversarial nets," *Advances in Neural Information Processing Systems*, vol. 27, 2014.
- [15] S. Ioffe, and C. Szegedy, "Batch normalization: accelerating deep network training by reducing internal covariate shift," in *International Conference on Machine Learning*, PMLR, 2015, pp. 448–456.
- [16] V. Nair and G. E. Hinton, "Rectified linear units improve restricted boltzmann machines," in *Proceedings of the 27th International Conference on Machine Learning (ICML-10)*, 2010, pp. 807–814.
- [17] A.L. Maas, A.Y. Hannun, and A.Y. Ng, "Rectifier nonlinearities improve neural network acoustic models," in *Proc. ICML*, vol. 30, no. 1, pp. 3, 2013.
- [18] W. S. McCulloch, and W. Pitts, "A logical calculus of the ideas immanent in nervous activity," *Bulletin of Mathematical Biophysics*, 5, pp. 115–133, 1943.
- [19] C. C. Aggarwal, *Neural Networks and Deep Learning: A Textbook*, Springer International Publishing AG, 2018, p. 1.
- [20] A. Tharwat, "Classification assessment methods," *Applied Computing and Informatics*, vol. 17, no. 1, pp.168–192, 2021.



## Few-Shot and Zero-Shot Video Classification from Large Visual Models Perspective

Erol Citak<sup>\*1</sup>, Mine Elif Karsligil<sup>1</sup>

<sup>1</sup>Computer Engineering Department, Yildiz Technical University, Istanbul, Türkiye

### Abstract

In recent years, large visual models have emerged as state-of-the-art solutions for various computer vision challenges, garnering significant attention due to their ability to handle different modalities. These models, trained on extensive datasets, are frequently employed as off-the-shelf solutions for a multitude of problems due to their robustness and versatility. This study investigates the efficacy of two pre-trained large vision models, CLIP and BLIP, specifically in the context of low-shot and zero-shot video classification tasks. By freezing the weights of these models, we conducted a comprehensive comparative analysis of their performance as baseline solutions. Our experimental results indicate that large visual models can achieve substantial performance in few-shot video classification tasks even without additional training, demonstrating their potential for applications where labeled data is scarce. However, in the context of zero-shot video classification, performance varied significantly. These variations were primarily influenced by the frequency and relevance of the keywords used to describe the videos during the models' initial training phase, highlighting the importance of the training data composition in zero-shot learning scenarios. Additionally, we contextualized our findings by comparing them with existing research in the field, providing a broader perspective on the capabilities and limitations of large visual models in video classification. This comparative analysis underscores the potential of these models to serve as powerful tools in computer vision, while also pointing out areas where further refinement and targeted training may be necessary to improve zero-shot classification performance. Overall, our study provides valuable insights into the application of large visual models for few-shot and zero-shot-based video classification, offering a foundation for future research and development in this area.

**Keywords:** Video classification, Few-shot learning, Zero-shot learning, Large visual models, Deep learning

## 1 INTRODUCTION

Large visual models have been providing the most successful SOTA solutions for many problems such as object detection [1], image and optical character recognition [2], and document analysis [3] in recent years. However, the number of trainable weights of these models is considerably higher than some popular deep learning architectures used in the past years [4]. For this reason, these models are implemented as fine-tuning or feature extraction which means completely frozen weights, for use in subtasks. Within the scope of this study, we used these models, which were trained with a lot of multi-modal data during the training phase, in the few-shot and zero-shot video classification problem.

The traditional video classification problem aims to assign videos given as input within the scope of predefined classes to the relevant classes. However, few-shot and zero-shot video classification approaches have become popular in recent years, both because the video content consists of many frames and these frames contain complex information, and because of the high cost of tagging unlabeled videos before learning with a supervised algorithm. The general approach in this few-shot and zero-shot approach, which is an alternative to the traditional video classification problem, can be called learning to learn. The important term in this concept is N-way K-shot, which N refers to number of classes and K refers to number of samples for each class. In this concept, during the training, validation and testing phases, the dataset is first divided into 3 separate parts, that is, they do not contain any common classes. Then, M randomly generated episodes are created from each part. This M number is a hyper-parameter and depends on the system, which is trained and tested. And depending on the N-way K-shot approach in each episode, the system is first trained with N classes and K examples from each class, and then tested with a similar data approach over these M episodes. The final performance value is presented as the average of the performance obtained from M test episodes.

In light of this information, our work aims to solve the video classification problem in a way that requires a low amount of data during the training phase. Within this context, we use the large visual models, CLIP [5] and BLIP [6], as feature extractors from video frames and textual descriptions of videos. CLIP has an image and a text encoder. For the image encoder, it utilizes Resnet50 [7] and Vision Transformer [8]. On the textual information processing side, it uses transformer-based Text Transformer architecture. These two components are trained jointly under the supervision of contrastive learning that tries to maximize the probability of two modalities for the corresponding elements. During the training, it has tried many different learning policies like weight initialization, etc. The total number of parameters of this large visual model is presented for different configurations in Table 1. Besides that, with this number of parameters, the dataset, which is used during training, requires special attention. At this stage, CLIP uses a semi-supervised labeled dataset which means that the study collected nearly ~400 million images and their tags. Then using their tags, the input sentence of the text encoder is constructed in this format; “A photo of <<image\_tag>>”. For example, for a given dog image, the corresponding sentence is “A photo of dog”.

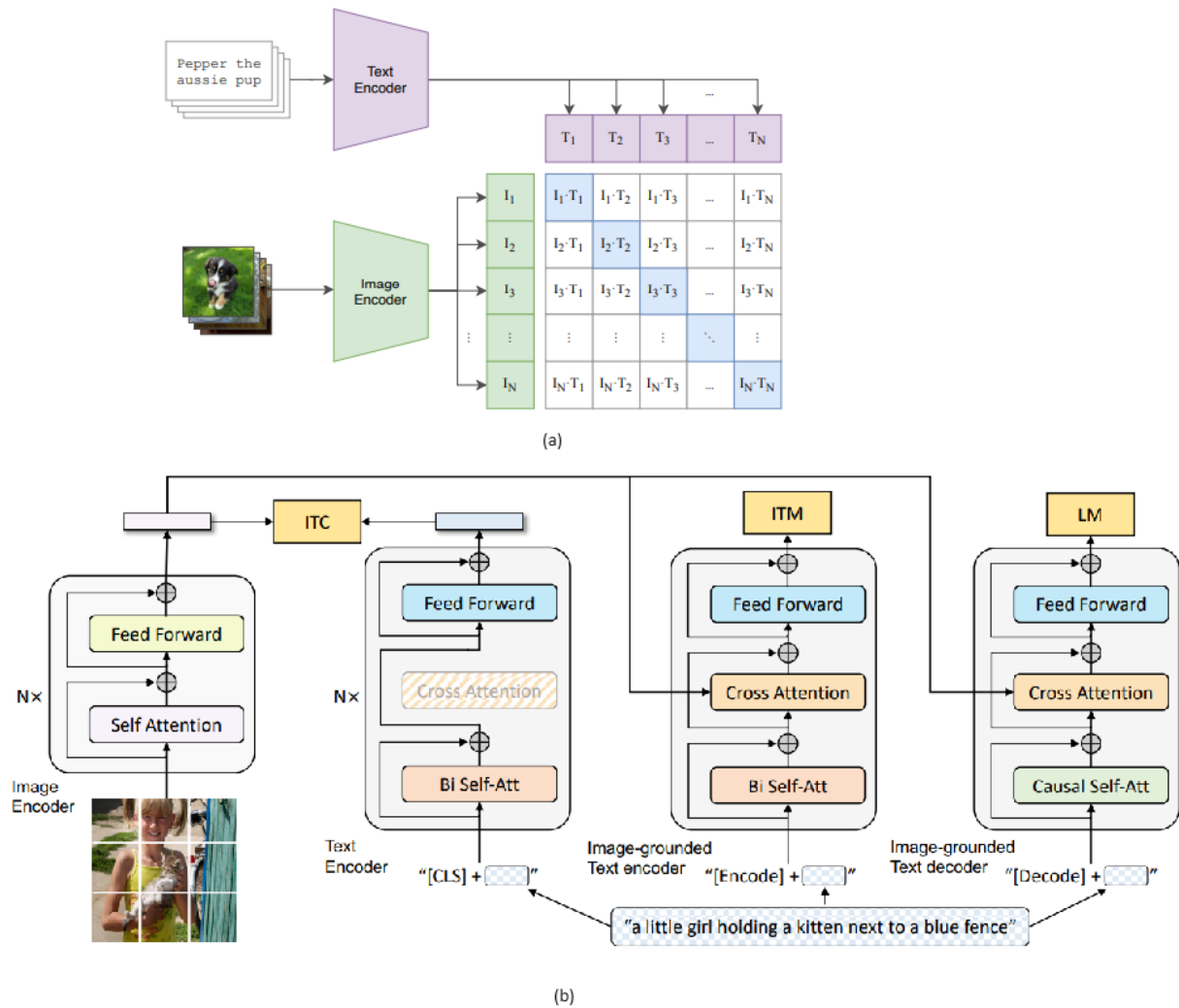
**Table 1.** Number of paramters of CLIP model

<b>Text Encoder</b>	<b>Image Encoder</b>	<b>Text Parameters</b>	<b>Image Parameters</b>	<b>Total Paramters</b>
GPT-2-like (12-layer, 256-dimensional embeddings)	Resnet-50	~63 Million	~102 Million	~165Million
GPT-2-like (12-layer, 256-dimensional embeddings)	Resnet-101	~63 Million	~123 Million	~186 Million
GPT-2-like (12-layer, 256-dimensional embeddings)	Resnet 50x4	~63 Million	~375 Million	~438 Million

Another large visual model, that is experimented with in this study, is BLIP. This model was proposed for various multi-modal tasks like image captioning, visual-question answering, or image-text retrieval. Since BLIP is designed to be an answer for different tasks, it has multiple different objectives. For example, image-text retrieval uses CLIP-based contrastive objective but question answering uses masked language modeling to generate consistent answers for a given image. But in total, their objectives are image-text contrastive (ITC) loss, image-text matching (ITM) loss, and language modeling loss to generate natural sentences. The total number of parameters depends on the system components in text and image encoding and is presented in Table 2. To effectively train these cumbersome models, they utilized several large-scale datasets like COCO [9] and LAION400M [10]. Also, they have proposed an image captioning module to boost the existing datasets, CapFilt, for better performance gain. In the testing they use multiple datasets, COCO and Flickr30k, to get better unbiased results. The overall architectures for both large visual models are presented in Figure 1.

**Table 2.** Number of paramters of BLIP model

<b>Text Encoder</b>	<b>Image Encoder</b>	<b>Text Parameters</b>	<b>Image Parameters</b>	<b>Total Paramters</b>
BERT-base	ViT-Small	~110 Million	~86 Million	~196 Million
BERT-large	ViT-Large	~340 Million	~307 Million	~647 Million



**Figure 1.** Deep neural network-based model architectures of CLIP (a) and BLIP (b) studies

On the dataset hand, we chose to use the HVU-LD [11] dataset, which is derived from the HVU [12] dataset, while performing this comparative analysis within the scope of this study. This dataset was proposed to close the dataset requirement gap between the few and zero-shot learning approaches and video classification. It consists of 64 training, 12 validation, and 24 test classes, each containing 100 video-video depiction pairs. Each sample consists of a video and video description pair. The depictions in this pair show the video it belongs to in 6 different perspectives, which are scene, object, action, event, attribute, and concept. A sample of this dataset is presented in Figure 2.



**Figure 2.** A sample episode from HVU-LD dataset

In summary, the performance of using highly diverse and high-scale data during the training of large visual models in the low-shot and zero-shot video classification problems was measured. At this stage, all weights of these models are completely frozen in order to compare them with each other. And all tests were carried out with the HVU-LD dataset, which is exactly suitable for the nature of the problem. At the same time, the results of the relatively more traditional SS-CADA-VAE study, which was made with a variational autoencoder on the relevant dataset, are also presented, aiming to provide guidance for future studies planned in this field.

## 2 MATERIAL AND METHOD

Our study focuses on two points. The first of these proposes the use of fully frozen large visual models for FSL and ZSL video classification problems. The second is to compare different large visual models both within themselves and with the variational autoencoder, which is relatively more traditional, but this time, unlike large visual models, it has been trained with the relevant dataset. This variational autoencoder-based solution was proposed by the HVU-LD paper and it takes the frames of videos and their keywords as input and then maps these two modalities into a shared common space. With the help of this shared common space, both FSL-based video classification and ZSL-based video classification, which refer to classifying videos using the keywords.

### 2.1 Dataset Preparation

In this study, the HVU-LD dataset with episodic N-way K-shot paradigm is used for all different network types. In detail, since large visual models with completely frozen weights were used in this study, the training and validation set of the relevant dataset was not used. Instead, a comparative analysis was carried out on the test set consisting of 24 classes. In this context, firstly, the normalization process of the input videos was carried out. Since the videos in the test set had different lengths, in order to standardize them, 16 frames were selected from each video uniformly. Since the average length of the videos in the dataset is approximately 7.4 minutes, there is no need for any padding operation. The descriptions corresponding to the videos and analyzing them from 6 different perspectives were subjected to basic natural language processing normalization. These steps were, respectively, conversion to lowercase, removal of stopwords, and stemming. With these steps, both videos and descriptions are ready to be given as input to the relevant models.

After these pre-processing steps, an episodic dataloader process was carried out in accordance with the N-way K-shot principle. In this context, as stated before, it was determined how many episodes would be used in the testing phase. By choosing this M number as 10k, it was aimed to obtain more robust and unbiased results. And during all the tests, tests were carried out for different N and different K values, and these are stated in the results section. However, the important point here is that the classes to be included in these 10K episodes and the videos from which those classes will be selected are completely random, which we think is important for robust and unbiased results.

### 2.2 Large Visual Model Based Networks

As mentioned before, the trained weights of the large visual models in their original state were preserved without any fine-tuning, and features were obtained from the videos and depictions. In this context, the procedure used when testing each model can be given in two steps. The first is to extract the video feature embedding extraction and the second is the video description embedding.

$$k_v = \frac{1}{n} \sum_{(i=1)}^{16} f(x_i) \quad (1)$$

where  $k_v$  is the final video embedding and  $f()$  is the feature extraction method, which is CLIP or BLIP, in this study. For the same mindset, we extracted video description as follows;

$$k_d = \frac{1}{n} \sum_{(i=1)}^j f(x_i) \quad (2)$$

where  $k_d$  is the final video description embedding and  $f()$  is the feature extraction method, which is CLIP or BLIP. But to be more specific, since CLIP and BLIP have visual and textual decoders at the same time, we use the proper encoder modules for each modality.



### 2.3 Testing Procedure

In this subsection, we will mention how the test protocol for N-way K-shot was created after obtaining the features. N-way K-shot approach refers to the few-shot and zero-shot learning policy, which indicates that there are N classes and K shot in an episode. For example, in a 3-way 5-shot episode there will be 3 different classes and 5 different samples for each class are given for learning. But besides that, there are also other samples for each class for testing purposes. In this study we chose the number of test samples for each class as 15. According to this configuration, we will be presenting the classification performance over those samples.

In the light of this testing procedure, first we will be constructing the class embeddings using K samples for each class. Then using these 15 samples for each class, we will be comparing them with the class embeddings. The comparison will be made over the Euclidean distance. The overall testing setting from the class embeddings to comparison is presented as follows.

$$e_c = \frac{\{1\}}{K} \sum_{i=1}^K x_i^c \quad (3)$$

where  $e_c$  is a class embedding of a sample class  $c$ . Then the comparison formula can be given as follows.

$$d(t_j^c, e_c) = \sum_{k=1}^d \frac{1}{d} \sqrt{(t_{jk}^c - e_{ck})^2} \quad (4)$$

Then the class labels are assigned to while taking the distance of each test sample and class embeddings. This assignment operation is finalized with SoftMax function to assign a probability of each distance score. Also, each performance, which will be presented in the next section, is repeated 10k times to improve reliability.

## 3 RESULTS

In this section the results for both few-shot and zero-shot video classification are presented and discussed in detail. Meanwhile the discussion is not just about the large visual models but also about the variational autoencoder based model. Thus, our comparative analysis can be done in depth.

First of the variation autoencoder based model's 1-shot can be given as follows.

**Table 3.** 1-shot and 3, 5, and 10-way few-shot video classification results with different visual feature extraction backbones for the variational autoencoder model [10] (Results are presented in percentage)

N-way	CNN Encoder	ViT Encoder
3	63.91	76.43
5	51.42	65.59
10	37.68	52.38

According to Table 3, it is clearly observed that when the number of classes in an episode increases, the classification performance decreases. The same test for the large visual models is presented in Table 4.

**Table 4.** 1-shot and 3, 5, and 10-way few-shot video classification results with different large visual models (Results are presented in percentage)

N-way	CLIP	BLIP
3	83.75	81.06
5	76.36	72.78
10	64.26	60.34

Table 4 presents the 1-shot and 3, 5, and 10-way few-shot video classification for large visual models. When the comparison is made between CLIP and BLIP, it is observed that CLIP is slightly better than BLIP. But the more critical point is that both of these large visual models have much higher performance than the traditional variational autoencoder.

On the zero-shot video classification setting, Table 5 presents the variational autoencoder based model’s results. Since that model proposes two different visual and textual encoders, we also present the same scores.

**Table 5.** Zero-shot video classification results with different visual and textual architectures for the variational autoencoder model [10] (Results are presented in percentage)

Model Types	CNN	ViT
ELMO [11]	32.46	37.03
BERT [12]	39.72	48.91

Besides the variational autoencoder model, Table 6 presents the same test for the large visual models.

**Table 6.** Zero-shot video classification results with different large visual models (Results are presented in percentage)

Model Types	
CLIP	24.23
BLIP	31.77

Surprisingly, the variational autoencoder model surpasses all large visual models for the zero-shot video classification problem. The one and most important reason in this regard is that since the variational model is trained with the training set of the relevant dataset, it sees some special keywords or word groups before and is trained on that subject. For example, CLIP was not successful compared to the variational autoencoder in this test scenario because it had the “A photo of <<image\_tag>>” structure and BLIP contained information about certain classes and their limited keywords in the COCO dataset. Besides that, it is observed that BLIP is considerably better in zero-shot video classification than CLIP since it has a language model and an image-text retrieval-based losses.

## 4 CONCLUSION

In this study, we have done comprehensive comparisons between large language models and a variational autoencoder model for few-shot and zero-shot video classification problems. The first finding is that the image encoder of large visual models is much more powerful than the traditional models. Due to the high volume of data during training, these models are capable of extracting and solving complex scenes. On the other hand, even if these models have shown promising results, it is shown that they are highly dependent on their training data. This finding appears in the zero-shot video classification setting, which is required to analyse some special keyword or keyword groups.

## References

- [1] J. Bai, S. Bai, S. Yang, S. Wang, S. Tan, P. Wang, and J. Zhou, “Qwen-vl: A frontier large vision-language model with versatile abilities,” *arXiv preprint*, arXiv:2308.12966, 2023.
- [2] H. Liu, C. Li, Y. Li, B. Li, Y. Zhang, S. Shen, and Y. J. Lee, “Llava-next: Improved reasoning, OCR, and world knowledge,” *arXiv preprint*, arXiv:2401.56789, 2024.
- [3] L. Beyer, A. Steiner, A. S. Pinto, A. Kolesnikov, X. Wang, D. Salz, et al., “PaliGemma: A versatile 3B VLM for transfer,” *arXiv preprint*, arXiv:2407.07726, 2024.
- [4] Z. Guo and J. Liu, “Trustworthy large models in vision: A survey,” *arXiv preprint* arXiv:2311.09680, 2023.
- [5] A. Radford, J. W. Kim, C. Hallacy, A. Ramesh, G. Goh, S. Agarwal, et al., “Learning transferable visual models from natural language supervision,” in *Proc. Int. Conf. Mach. Learn.*, 2021, pp. 8748–8763.
- [6] J. Li, D. Li, C. Xiong, and S. Hoi, “Blip: Bootstrapping language-image pre-training for unified vision-language understanding and generation,” in *Proc. Int. Conf. Mach. Learn.*, Jun. 2022, pp. 12888–12900.
- [7] K. He, X. Zhang, S. Ren, and J. Sun, “Deep residual learning for image recognition,” in *Proc. IEEE Conf. Comput. Vis. Pattern Recognit.*, 2016, pp. 770–778.
- [8] A. Dosovitskiy et al., “An image is worth 16x16 words: Transformers for image recognition at scale,” arXiv:2010.11929, 2020.
- [9] T. Y. Lin et al., “Microsoft coco: Common objects in context,” in *Proc. 13th Eur. Conf. Comput. Vis.*, Zurich, Switzerland, Sep. 6-12, 2014, pp. 740–755, Springer, 2014.
- [10] C. Schuhmann et al., “Laion-400m: Open dataset of clip-filtered 400 million image-text pairs,” arXiv:2111.02114, 2021.

- [11] E. Citak and M. E. Karşlıgil, "Multi-modal low-data-based learning for video classification," *Appl. Sci.*, vol. 14, no. 10, art. no. 4272, 2024.
- [12] A. Diba, M. Fayyaz, V. Sharma, M. Paluri, J. Gall, R. Stiefelhagen, and L. Van Gool, "Large scale holistic video understanding," in *Proc. 16th Eur. Conf. Comput. Vis.*, Glasgow, UK, Aug. 23-28, 2020, pp. 593–610, Springer, 2020.
- [13] J. Sarzynska-Wawer, A. Wawer, A. Pawlak, J. Szymanowska, I. Stefaniak, M. Jarkiewicz, and L. Okruszek, "Detecting formal thought disorder by deep contextualized word representations," *Psychiatry Research*, vol. 304, art. no. 114135, 2021.
- [14] J. Devlin, M. W. Chang, K. Lee, and K. Toutanova, "Bert: Pre-training of deep bidirectional transformers for language understanding," *arXiv preprint*, arXiv:1810.04805, 2018.



---

# Machine Learning Techniques for Software Fault Prediction: A Distinctive Systematic Literature Review

Aleena Rafique<sup>\*1</sup>, Sania Bhatti<sup>1</sup>

<sup>1</sup>Department of Software Engineering, Mehran University of Engineering & Technology, Jamshoro, Pakistan

---

## Abstract

Software faults significantly undermine the quality and reliability of software systems, emphasizing the critical need for effective fault prediction and mitigation strategies during the software development lifecycle. This study conducts a comprehensive survey of 291 research papers sourced from Google Scholar and IEEE databases, employing rigorous search criteria to investigate the efficacy of machine learning techniques for software fault prediction. Our analysis focuses on methodologies aimed at anticipating software faults through machine learning approaches, with evaluation metrics including precision, accuracy, and the F1 score. While our findings highlight promising avenues for fault prediction, we acknowledge limitations such as potential bias from search criteria and database selection. To advance future research in this domain, we recommend broadening survey criteria and integrating additional databases to ensure a more comprehensive analysis of available literature.

**Keywords:** *Software fault prediction, Data mining techniques, Feature selection, f-measure, Reliability assurance*

---

## 1 INTRODUCTION

Software engineering involves crafting, testing, and deploying computer applications to address practical issues while adhering to engineering principles and industry standards. It delves into the breadth and depth of literature, revealing insights into the evolving landscape of information and software technology [1]. The complex process of software development encompasses stages like design, implementation, testing, and maintenance. Throughout development, software faults may arise, leading to system crashes and data corruption. Identifying potential faults in software modules before they cause significant problems is crucial. Machine learning techniques show promise in predicting software faults by analyzing past projects and identifying patterns. This aids developers in prioritizing testing efforts, allocating resources efficiently, and improving software quality. A systematic review evaluates the application of machine learning in software fault prediction, providing a comprehensive assessment of techniques within applied soft computing. Insights into the effectiveness and advancements at the intersection of machine learning and software quality assurance are offered [2]. Following a thorough examination of various studies, this paper explores machine-learning techniques for software fault prediction.

Another study [3] investigates the performance of software fault prediction within the context of software engineering, contributing insights into the practical effectiveness and implications of fault prediction techniques. An enhanced approach for cross-project defect prediction is proposed in [4], streamlining training data to improve prediction accuracy across different software projects. The application of machine learning to software fault prediction is explored in [5], contributing to the understanding of how these techniques enhance fault prediction methods. In-depth examinations of various software fault prediction techniques are presented in [6], offering a comprehensive overview and contributing to the assessment of strategies for enhancing software quality.

A focus on unsupervised learning techniques for software defect prediction is outlined in [7], contributing insights into their utilization and efficacy in enhancing defect prediction processes. Another study [8] provides a comprehensive overview of software defect prediction using machine learning, offering valuable insights into the landscape of improving software quality. The proficiency of supervised machine learning algorithms in predicting software refactoring is assessed in [9], contributing insights into the capabilities of various algorithms in predicting refactoring actions. Software fault prediction through data mining, machine learning, and deep learning methods is explored in [10], providing an organized assessment of their effectiveness. Automatic software defect detection using machine learning is investigated in [11], offering insights into the application of machine learning for identifying software defects. The utilization of optimized machine learning techniques for scientific programming in software fault prediction is demonstrated in [12], showcasing advancements in leveraging machine learning for more effective software fault prediction.

A systematic review of software fault prediction research is presented in [13], highlighting the growing use of public datasets and machine learning while advocating for increased adoption of class-level metrics. The impact of model context, choice of independent variables, and modeling techniques is examined in [14], revealing effective models often favor simpler techniques while emphasizing the need for more comprehensive methodology in future research. The effectiveness of simplified metric sets for software defect prediction is investigated in [15], providing practical guidelines for training data selection, classifier choice, and metric subset determination. A comparative effectiveness study of supervised and unsupervised methods in Software Defect Number Prediction (SDNP) is detailed in [8], concluding that the unsupervised method LOC\_D serves as a valuable baseline for future research. Predicting software fault proneness is explored in [5], delving into the performance of three machine learning algorithms on multiple releases and discerning trade-offs between accuracy and other metrics. A Systematic Literature Review (SLR) fills a crucial gap in the understanding of software defect prediction for mobile applications [3], examining 47 relevant studies and revealing prevalent trends, providing insights for future research and practitioners.

The motivation behind this study lies in the increasing importance of software quality assurance and the continuous evolution of machine learning techniques. As the software engineering landscape advances, understanding the effectiveness and advancements at the intersection of machine learning and software quality assurance becomes crucial. This study delves into the nuances of various machine learning methodologies applied to software fault prediction, shedding light on their effectiveness and limitations.

## 2 RESEARCH METHODOLOGY

### 2.1 Conducting the Review

In the quest for research papers, specific studies meeting predefined inclusion and exclusion criteria for software fault prediction emerged as primary references. These criteria involved scrutinizing research paper content to ascertain its relevance to the study's specific focus utilizing software tools for software fault prediction. Papers sharing akin objectives were included, whereas those with broader scopes or misaligned goals were excluded. The visual representation of each step in this process is depicted in Figure 1.

The papers were gleaned from two primary databases, namely Google Scholar and IEEE. Employing the search query ("Software fault Detection", "Machine Learning", "Classification", and NASA PROMISE) yielded a total of 291 papers from both sources. Subsequently, the initially retrieved papers underwent further screening based on selection and exclusion criteria. This entailed evaluating the degree of relevance and alignment of research studies with the scope outlined in this systematic literature review.

**Table 1.** Criteria for paper selection

No	Inclusion Criteria	Exclusion Criteria
1	Accessible and Free	Research papers requiring account creation for access.
2	Limited Scope	Research papers addressing machine learning, classification models, and data mining techniques, focusing solely on software fault/defect prediction.
3	Reputable Sources	Research papers published by well-established institutions, universities, professors, or recognized peers, such as the University of Science and Technology in India.
4	Not Easily Accessible	Research papers published by lesser-known organizations, websites, blogs, and online forums.

#### 2.1.1 Temporal Analysis of Publications

The consistent upward trend in the volume of articles over the past 9 years (Figure 2) emphasizes the enduring relevance of software fault prediction through diverse machine-learning techniques. The y-axis of the figure denotes the count of primary studies conducted within this domain, while the x-axis corresponds to the respective years of research. Notably, the peak in research publications occurred in 2021, with approximately 18 instances in this field. In contrast, the current year, 2023, has witnessed the lowest number of studies to date, with only 2 research instances in this domain.

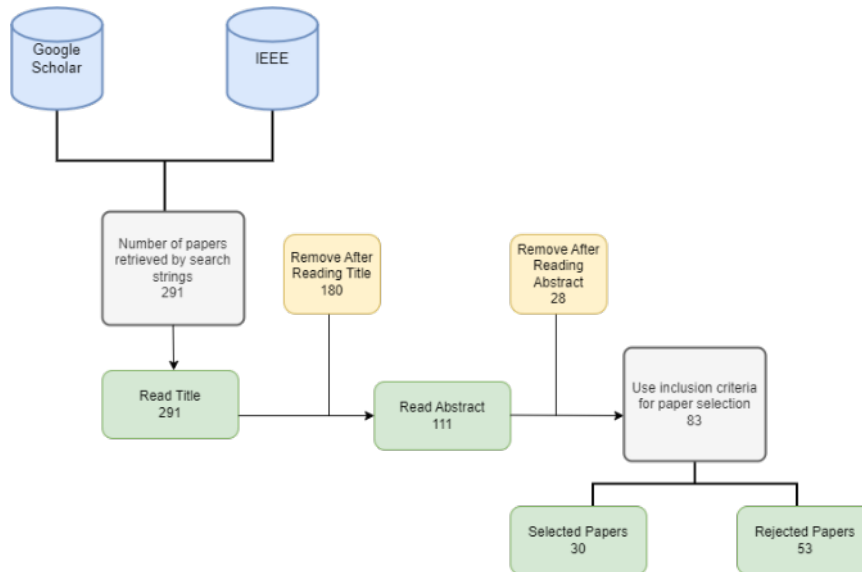


Figure 1. Steps of methodology

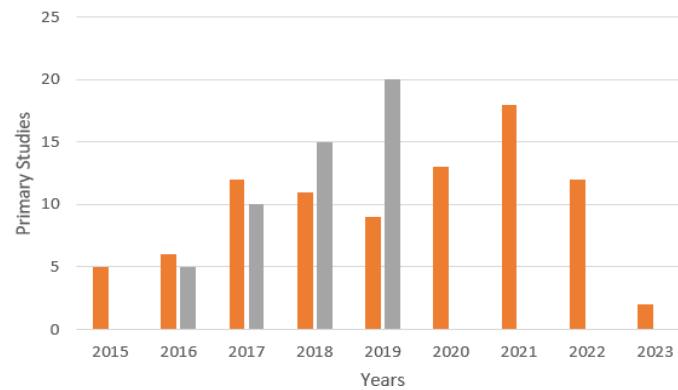


Figure 2. Temporal view of publications

### 2.1.2 Research Questions

The following research questions guide the selection of papers and subsequent analysis in this systematic literature review:

RQ1: What factors influence the effectiveness of software fault prediction models?

Over-fitting, dataset noise, cost parameters, software metrics, and feature selection are among the factors that impact the accuracy of software fault prediction [10]. The utilization of feature selection techniques enhances the prediction of various fault prediction tools.

RQ2: Is predicting faults in Python programs feasible compared to that in C/C++ and Java?

Paper [11] focuses on the experimental evidence that fault-prediction machine learning methods developed for C/C++ and Java programs can be successfully applied to Python programs. The study explores class-level prediction, a finer-grained approach demonstrated through the design and testing of models on ten open-source Python projects.

RQ3: What are the benefits of early fault detection, and which classifiers prove to work better through experimentation?

According to research, early detection of faults in a particular module can reduce the efforts of manpower, allowing concentrated attention on problematic areas in the development phase [12]. Research [16] utilizes MLP, Bayesian Network, and NB classifiers, with the Neural Network Classifier emerging as the most effective in terms of TPR, FPR, and Accuracy.

RQ4: Is it feasible to perform software defect prediction using machine learning techniques?

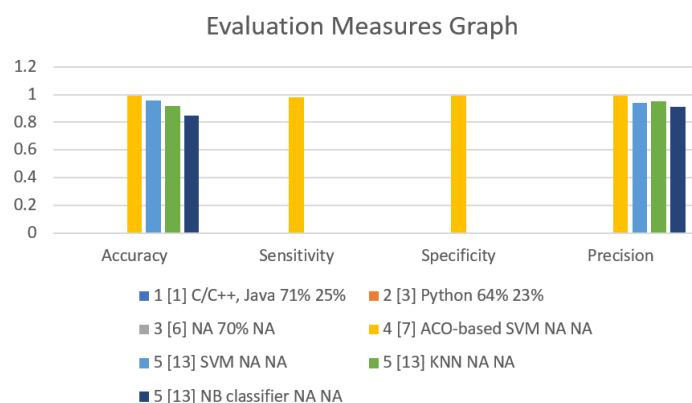
The development of fault-free software is a challenge in the software industry, and machine learning techniques, such as Classification and regression, clustering, are used to build predictive models for software defect learning techniques [16]. Research paper applied Logistic Regression on the PROMISE dataset repository and obtained a 71% accuracy result in the software defect prediction experiment.

RQ5: How does software fault prediction help project managers effectively utilize resources for better quality assurance?

Research paper [14] discusses that activities like software testing, software inspection, formal verification, and software defect/fault prediction help project managers use resources for the best quality assurance. The models, based on machine learning techniques, enable better decision-making for the allocation and usage of available resources in software development tasks.

**Table 2.** Evaluation Measures Comparison

No	Reference	Tested Using Tool/ Language/ Classifier Used	Recall Rate	False Positive	Accuracy	Sensitivity	Specificity	Precision
1	[1]	C/C++, Java	71%	25%	NA	NA	NA	NA
2	[3]	Python	64%	23%	NA	NA	NA	NA
3	[6]	NA	70%	NA	NA	NA	NA	NA
4	[7]	ACO-Based SVM	NA	NA	99%	98%	99%	99%
5	[13]	SVM	NA	NA	96%	NA	NA	94%
		KNN	NA	NA	92%	NA	NA	95%
		NB Classifier	NA	NA	85%	NA	NA	9%



**Figure 3.** Evaluation measures graph

### 3 LIMITATIONS AND CHALLENGES

The analysis [15] may overlook the rapid developments in software engineering post-2002. A subsequent study could be conducted to capture recent trends and emerging themes in the evolving software engineering research landscape. The systematic review's [8] scope might not embrace the latest advancements in machine learning beyond 2015. An updated review could be undertaken to integrate recent developments in machine learning techniques for predicting software faults. The study [5] may not address all potential applications and challenges of machine learning in software fault prediction. A more comprehensive investigation could explore additional contexts and challenges where machine learning contributes to enhancing software quality. The reviewer's [3] findings may not fully encompass newer research and evolving approaches in software fault prediction. An updated survey could include more recent studies and evolving techniques in the software fault prediction domain. The research [13] might not thoroughly address specific constraints or limitations of using optimized machine learning techniques for software fault prediction. Future work could delve into the challenges, biases, or constraints that might arise when applying optimized machine learning to scenarios of software fault prediction. Every study's limitation presents an opportunity for further exploration and improvement, fostering ongoing research and development in the realm of software engineering and quality assurance.

## 4 RESULTS AND DISCUSSION

The outcomes of this investigation enrich our comprehension of software fault prediction models, encompassing their assessment methodologies, adaptability across diverse programming languages, and implications for resource allocation in quality assurance. The results underscore the pivotal role of machine learning techniques in achieving precision and dependability in software fault prediction. Moreover, the standardized evaluation metrics employed in this study offer a consistent framework for gauging the effectiveness of software fault prediction models. The heightened efficiency and mitigated bias evident in machine learning techniques underscore their superiority over preceding approaches, illustrating their practical implementation potential [17].

Overall, the findings from this systematic literature review provide valuable insights into the effectiveness of machine learning techniques for software fault prediction.

## 5 CONCLUSION

In conclusion, this systematic literature review underscores the significance and feasibility of integrating machine learning techniques into software fault prediction. It accentuates the necessity of considering diverse influencing factors in the prediction process, the advantages of early fault detection, the efficacy of various classifiers, the practical application of machine learning in predicting defects in Python programs, and the benefits of software fault prediction in optimizing resource utilization for quality assurance.

It is imperative to acknowledge the inherent limitations in this study, particularly its reliance on specific search criteria and databases, which may have resulted in the omission of relevant papers. To ensure a comprehensive literature analysis, future research should contemplate expanding the search criteria and incorporating additional databases. In brief, the findings from this study enrich the understanding of fault prediction models, their evaluation processes, their applicability across programming languages, and their implications for resource allocation in quality assurance.

## Acknowledgments

There is no conflict of interest among the authors, and each author has contributed equally to the research design, implementation, and execution.

## References

- [1] R. L. Glass, I. Vessey, and V. Ramesh, "Research in software engineering: an analysis of the literature," *Information and Software Technology*, vol. 44, no. 8, pp. 491–506, 2002.
- [2] C. Catal, "Software fault prediction: A literature review and current trends," *Expert Systems with Applications*, vol. 38, no. 4, pp. 4626–4636, Apr. 2011. doi: 10.1016/j.eswa.2010.10.024.
- [3] R. Malhotra, "A systematic review of machine learning techniques for software fault prediction," *Appl. Soft Comput. J.*, vol. 27, pp. 504–518, 2015, doi: 10.1016/j.asoc.2014.11.023.
- [4] S. Dhankhar, "Software fault prediction performance in software engineering," in *International Conference on Computing for Sustainable Global Development, INDIACom 2015*, pp. 228–232, 2015, doi: 10.14569/IJACSA.2023.0140340.
- [5] P. He, Y. He, L. Yu, and B. Li, "An Improved Method for Cross-Project Defect Prediction by Simplifying Training Data," *Math. Probl. Eng.*, vol. 2018, 2018, doi: 10.1155/2018/2650415.
- [6] B. Wójcicki and R. Dąbrowski, "Applying machine learning to software fault prediction," *E-Informatica Softw. Eng. J.*, vol. 12, no. 1, pp. 199–216, 2018, doi: 10.5277/e-Inf180108.
- [7] S. S. Rathore and S. Kumar, "A study on software fault prediction techniques," *Artif. Intell. Rev.*, vol. 51, no. 2, pp. 255–327, Feb. 2019, doi: 10.1007/s10462-017-9563-5.
- [8] N. Li, M. Shepperd, and Y. Guo, "A systematic review of unsupervised learning techniques for software defect prediction," *Information and Software Technology*, vol. 122. Elsevier B.V., Jun. 01, 2020. doi: 10.1016/j.infsof.2020.106287.
- [9] X. Chen, D. Zhang, Y. Zhao, Z. Cui, and C. Ni, "Software defect number prediction: Unsupervised vs supervised methods," *Inf. Softw. Technol.*, vol. 106, pp. 161–181, Feb. 2019, doi: 10.1016/j.infsof.2018.10.003.
- [10] M. Aniche, E. Maziero, R. Durelli, and V. H. S. Durelli, "The Effectiveness of Supervised Machine Learning Algorithms in Predicting Software Refactoring," *IEEE Trans. Softw. Eng.*, vol. 48, no. 4, pp. 1432–1450, Apr. 2022, doi: 10.1109/TSE.2020.3021736.
- [11] I. Batoool and T. A. Khan, "Software fault prediction using data mining, machine learning and deep learning



- techniques: A systematic literature review,” *Comput. Electr. Eng.*, vol. 100, May 2022, doi: 10.1016/j.compeleceng.2022.107886.
- [12] N. Elshamy, A. AbouElenen, and S. Elmougy, “Automatic detection of software defects based on machine learning,” *International Journal of Advanced Computer Science and Applications*, 2023. doi: 10.14569/IJACSA.2023.0140340.
- [13] M. Shafiq, F. H. Alghamedy, N. Jamal, T. Kamal, Y. I. Daradkeh, and M. Shabaz, “Scientific programming using optimized machine learning techniques for software fault prediction to improve software quality,” *IET Softw.*, vol. 17, no. 4, pp. 694–704, 2023, doi: 10.1049/sfw2.12091.
- [14] T. Hall, S. Beecham, D. Bowes, D. Gray, and S. Counsell, “A systematic literature review on fault prediction performance in software engineering,” *IEEE Transactions on Software Engineering*, vol. 38, no. 6, pp. 1276–1304, 2012. doi: 10.1109/TSE.2011.103.
- [15] C. Catal and B. Diri, “A systematic review of software fault prediction studies,” *Expert Systems with Applications*, vol. 36, no. 4, pp. 7346–7354, May 2009. doi: 10.1016/j.eswa.2008.10.027.
- [16] P. He, B. Li, X. Liu, J. Chen, and Y. Ma, “An empirical study on software defect prediction with a simplified metric set,” *Inf. Softw. Technol.*, vol. 59, pp. 170–190, Mar. 2015, doi: 10.1016/j.infsof.2014.11.006.
- [17] X. Chen, D. Zhang, Y. Zhao, Z. Cui, and C. Ni, “Software defect number prediction: Unsupervised vs supervised methods,” *Inf Softw Technol*, vol. 106, pp. 161–181, Feb. 2019, doi: 10.1016/J.INFSOF.2018.10.003.
- [18] Y. A. Alshehri, K. Goseva-Popstojanova, D. G. Dzielski, and T. Devine, “Applying machine learning to predict software fault proneness using change metrics, static code metrics, and a combination of them,” *IEEE SOUTHEASTCON*, Oct. 2018, vol. 2018-April, doi: 10.1109/SECON.2018.8478911.
- [19] M. Jorayeva, A. Akbulut, C. Catal, and A. Mishra, “Machine Learning-Based Software Defect Prediction for Mobile Applications: A Systematic Literature Review,” *Sensors*, vol. 22, no. 7, Apr. 2022. doi: 10.3390/s22072551.



---

## Principal Component Analysis for Database Scan Using Hierarchical KNN Model for Telecom Customer Segmentation

Oluwasegun William Ijibadejo<sup>\*1</sup>, Saja Murtadha Hashim<sup>2</sup>

<sup>1</sup>Department of Computer Engineering, Karabuk University, Karabuk, Turkiye

---

### Abstract

Effective client base segmentation is a difficulty for telecom businesses in order to customise services and marketing tactics. In order to obtain precise telecom consumer segmentation, we provide an approach in this paper that blends Principal Component Analysis (PCA) with a Hierarchical K-nearest neighbours (KNN) model. Using PCA, the telecom customer database's dimensionality is decreased, allowing for the capture of the most pertinent data with the least amount of processing overhead. PCA offers a succinct depiction of the database by locating the primary components that account for the majority of the variance in the data. Principal Component Analysis (PCA) enhances database scans in telecom customer segmentation by reducing high dimensionality, thus improving efficiency. By applying PCA, telecom companies can overcome challenges posed by large datasets with numerous features and noisy data samples, which is crucial for accurate customer segmentation [3]. This reduction in dimensions allows for more efficient database scans, enabling clustering algorithms like K-means to perform better with dimensionally reduced data, ultimately enhancing the accuracy and effectiveness of customer segmentation in the telecom industry.

Next, using the neighbouring data points as a basis for classification, the Hierarchical KNN model is used to group consumers in the smaller feature space. This makes it possible to identify discrete client categories with certain traits and inclinations. We illustrate this approach's efficacy in telecom client segmentation with a case study. The outcomes demonstrate the advantages of consumer profiling, cluster analysis, and dimensionality reduction. These information may be used by telecom businesses to create focused marketing campaigns, allocate resources as efficiently as possible, and improve efforts to acquire and retain customers.

With the help of this approach, telecom businesses may effectively and pragmatically segment their client base, gaining useful insights from sizable customer datasets to help them make strategic decisions in a cutthroat industry.

**Keywords:** *Principal component analysis (PCA), Database scan, Telecom customer segmentation, Customer profiling, Cluster analysis, Machine learning, Marketing strategies*

---

## 1 INTRODUCTION

In the telecommunications industry, client segmentation is essential for comprehending and meeting the wide range of consumer wants. A powerful method for efficiently segmenting telecom consumers and extracting significant insights from enormous databases is to apply Principal Component Analysis (PCA) in conjunction with a Hierarchical K-nearest neighbours (KNN) model.

The most crucial information is preserved when high-dimensional data is converted into a lower-dimensional space using PCA, a dimensionality reduction approach. PCA reduces computing complexity and facilitates effective analysis by allowing for a more succinct representation of the database by finding the principle components that encapsulate the highest variation in the data. The Hierarchical KNN model offers a strong foundation for telecom consumer segmentation when used in conjunction with PCA. Customers are categorised by the KNN algorithm according to how similar they are to nearby data points in the feature space [1–3]. The Hierarchical KNN model allows you to identify different consumer groups with certain traits and preferences by clustering like customers together and exposing underlying patterns and correlations. Understanding consumer behaviour and preferences is essential for businesses to customise services, allocate resources optimally, and raise customer happiness in the fast-paced, fiercely competitive telecom sector. In order to accomplish these objectives, telecom customer segmentation which divides consumers into discrete groups according to their traits and behaviors is essential. When Principal Component Analysis (PCA) and a Hierarchical k-Nearest Neighbours (k-NN) model are used together, it is possible to analyse enormous customer records efficiently and get insightful information. This

integrated technique facilitates effective consumer segmentation by reducing the dimensionality of the data and accurately identifying nearest neighbours. By identifying closest neighbours using the smaller feature space, the hierarchical k-NN model is a useful addition to PCA. By arranging data points into a hierarchical tree structure, this technique improves the efficiency of looking for nearby neighbours. Differentiable customer segments may be identified with the hierarchical k-NN model by taking into account the commonalities among consumers in the reduced feature space.

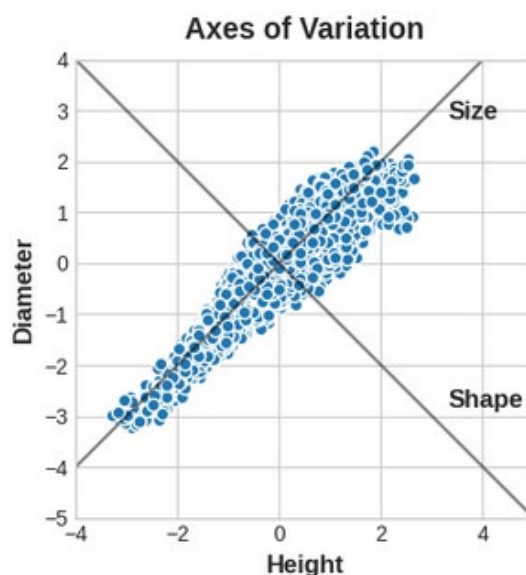
For consumer segmentation, telecom businesses may reap significant benefits from combining PCA with the hierarchical k-NN model. Large client datasets may be mined for insightful information using this method, which helps businesses create more focused marketing campaigns, improve customer happiness, and retain more customers [4].

There are several benefits of using the Hierarchical KNN model in conjunction with PCA for telecom client segmentation. First of all, it makes it possible to thoroughly analyse huge databases, giving telecom companies a better grasp of their clientele. Second, it makes it easier to identify homogenous client groups, which makes it possible to develop specialised service offers and focused marketing campaigns. Finally, it improves decision-making by offering useful information for allocating resources, retaining customers, and pursuing new business. In this work, we investigate the use of a Hierarchical KNN model for telecom customer segmentation in conjunction with Principal Component Analysis for database scans. Through a case study, we illustrate the advantages of dimensionality reduction, cluster analysis, and consumer profiling, and we show how successful this technique is. Telecom firms may satisfy the changing requirements of their consumers in a competitive market by using this technique to fully use their client databases and make well-informed business choices [5].

## 2 PRINCIPAL COMPONENT ANALYSIS OVERVIEW

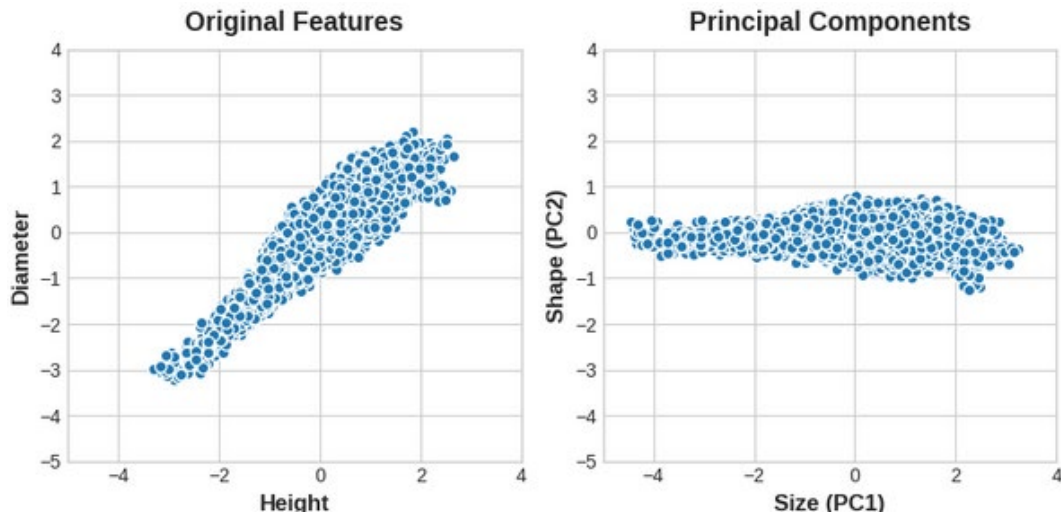
One popular dimensionality reduction method for extracting the most crucial information from high-dimensional datasets is Principal Component Analysis (PCA). A collection of correlated variables is converted mathematically into a new set of uncorrelated variables known as primary components.

Reducing the dimensionality of the data while preserving as much of the original variance as feasible is the primary goal of PCA. As a result, the data may be represented more succinctly, which facilitates analysis, interpretation, and visualisation. In the Abalone dataset are physical measurements taken from several thousand Tasmanian abalone. (An abalone is a sea creature much like a clam or an oyster.) We'll just look at a couple features for now: the "Height" and "Diameter" of their shells. You could imagine that within this data are "axes of variation" that describe the ways the abalone tend to differ from one another. Pictorially, these axes appear as perpendicular lines running along the natural dimensions of the data, one axis for each original feature [6, 7].



**Figure 1.** Perpendicular lines running along the natural dimensions of the data

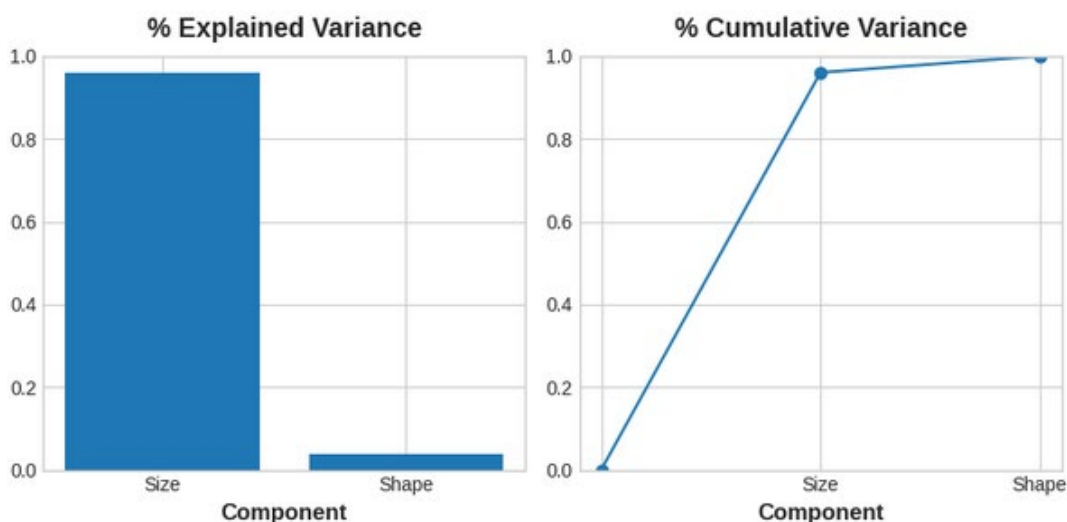
Often, we can give names to these axes of variation. The longer axis we might call the "Size" component: small height and small diameter (lower left) contrasted with large height and large diameter (upper right). The shorter axis we might call the "Shape" component: small height and large diameter (flat shape) contrasted with large height and small diameter (round shape).



**Figure 2.** The principal components become the new features by a rotation of the dataset in the feature space

The following steps are included in the PCA process:

- **Standardisation:** A zero mean and unit variance are usually applied to the input variables. This guarantees that the analysis won't be dominated by variables with disparate scales.
- **Covariance Matrix Calculation:** Using the standardised variables as a basis, the covariance matrix is calculated. Details on the interdependencies and relationships between the variables are provided by the covariance matrix.
- **Computation of Eigenvalue and Eigenvector:** The covariance matrix's eigenvalues and matching eigenvectors are computed. The eigenvectors show the direction or weightings of the original variables in the new transformed space, and the eigenvalues show how much variation is explained by each primary component.
- **Principle Component Selection:** The eigenvalues are used to guide the selection of the principle components. Greater importance is attributed to the components with bigger eigenvalues because they capture more variance in the data.
- **Transformation:** To create the converted dataset, the original data is projected onto the chosen major components. The new uncorrelated variables in this dataset are represented by a linear combination of the original variables for each variable [9].



**Figure 3.** Size accounts for about 96% and the Shape for about 4% of the variance between Height and Diameter

The Size component captures the majority of the variation between Height and Diameter. It's important to remember, however, that the amount of variance in a component doesn't necessarily correspond to how good it is as a predictor: It depends on what you're trying to predict.

**Table 1.** Literature review table

References	Results	Methods Used	Literature Survey	Dataset	Objectives
<b>A Data-Driven Approach to Improve Customer Churn Prediction Based on Telecom Customer Segmentation</b> Tianyuan Zhang	<ul style="list-style-type: none"> <li>Dimension reduction by transforming correlated variables into uncorrelated components</li> <li>Small set of principal components retains most information from original data</li> </ul>	<ul style="list-style-type: none"> <li>Fisher discriminant equations</li> <li>Logistic regression analysis</li> </ul>	<ul style="list-style-type: none"> <li>Technological progress has changed competition and game rules in the telecom industry</li> <li>Telecom companies need to identify high-risk churn customers and focus on customer retention</li> </ul>	<ul style="list-style-type: none"> <li>Data collected from three major Chinese telecom companies</li> <li>Dataset information included demographic and business data</li> </ul>	<ul style="list-style-type: none"> <li>Predict telecom client churn through customer segmentation.</li> <li>Help telecom companies avoid customer churn and increase profits</li> </ul>
<b>Segmentation via principal component analysis for perceptron classification: a case study of kenyan mobile subscribers</b> Khamis Mwero Maneno	<ul style="list-style-type: none"> <li>SF-PCA achieves similar accuracy as non-secure centralized PCA</li> <li>SF-PCA is faster than privacy-preserving alternatives based on secure multiparty computation or homomorphic encryption</li> </ul>	<ul style="list-style-type: none"> <li>K-means, FCM, PCM, Hierarchical neural network</li> <li>Perceptron</li> </ul>	<ul style="list-style-type: none"> <li>Segmentation importance in targeting profitable customer groups</li> <li>Principal Component Analysis for dimension reduction in clustering algorithms</li> </ul>	<ul style="list-style-type: none"> <li>Subscriber data from nine transactions</li> <li>Real case data for segmentation and classification</li> </ul>	<ul style="list-style-type: none"> <li>Segment existing customers</li> <li>Classify new customers using perceptron neural network</li> </ul>
<b>A comparative dimensionality reduction study in telecom customer segmentation using deep learning and PCA</b> Maha Alkhayrat Research on The Anonymous Customer Segmentation Model of Telecom Bin Luo	<ul style="list-style-type: none"> <li>PCA based fuzzy clustering outperforms PCA based K-means</li> <li>FCM algorithm shows better performance compared to K-Means algorithm</li> </ul>	<ul style="list-style-type: none"> <li>Principal Component Analysis (PCA) decomposition</li> <li>Autoencoder Neural Network</li> </ul>	<ul style="list-style-type: none"> <li>The main author performed the literature review for the paper</li> </ul>	<ul style="list-style-type: none"> <li>Real telecom dataset with 220 features</li> <li>Data belonging to 100,000 customers</li> </ul>	<ul style="list-style-type: none"> <li>Evaluate clustering in reduced and latent space</li> <li>Compare clustering results in original and reduced data space</li> </ul>
<b>Improving the efficiency measurement index using principal component analysis (PCA)</b> Ahmed Husham Mohammed	<ul style="list-style-type: none"> <li>Efficient data transmission achieved through PCA technology</li> <li>Original data reconstructed accurately after decoding the data stream</li> </ul>	<ul style="list-style-type: none"> <li>K-means clustering algorithm</li> <li>SVD algorithm</li> </ul>	-	-	<ul style="list-style-type: none"> <li>Classify customers based on value</li> <li>Propose business strategies for different value customer segments</li> </ul>
<b>Understanding customers' behaviour of telecommunication companies increasing the efficiency of clustering techniques</b> Ilias K. Savvas	<ul style="list-style-type: none"> <li>Reduces variables in dataset while retaining original variance</li> <li>Useful in machine learning for efficient data analysis</li> </ul>	<ul style="list-style-type: none"> <li>Principal Component Analysis (PCA)</li> <li>Data Envelopment Analysis (DEA)</li> </ul>	-	-	<ul style="list-style-type: none"> <li>Improve efficiency measurement index</li> <li>Integrate PCA-DEA for better results</li> </ul>

<p><b>Customer Mobile Behavioral Segmentation and Analysis in Telecom Using Machine Learning</b> Eman Hussein Sharaf Addin Analysis of Principal Component Algorithm for Various Datasets Soumyalatha Naveen</p>	<ul style="list-style-type: none"> <li>● PCA is essential for multivariate data analysis and dimension reduction</li> <li>● PCA enhances AI applications like image processing and anomaly detection</li> </ul>	<ul style="list-style-type: none"> <li>● DBSCAN and k-means clustering algorithms</li> <li>● Distributed / multi-core versions of clustering techniques</li> </ul>	<ul style="list-style-type: none"> <li>● Telecommunication Companies' customers' data</li> <li>● No specific mention of other datasets used in the study</li> </ul>	<ul style="list-style-type: none"> <li>● Increase efficiency of clustering techniques for telecommunication customer behavior</li> <li>● Implement distributed/multi-core versions of DBSCAN and k-means algorithms</li> </ul>	
<p><b>Analysis of Principal Component Algorithm for Various Datasets</b></p>	<ul style="list-style-type: none"> <li>● Visualization of customer clusters using graph plotting</li> <li>● Data-driven decision-making based on final clusters</li> </ul>	<ul style="list-style-type: none"> <li>● PCA for dimensionality reduction</li> <li>● K-means algorithm for data clustering</li> </ul>	<ul style="list-style-type: none"> <li>● Customer dataset generated using Faker Python package</li> <li>● Pre-processed dataset with PCA technique for clustering analysis</li> </ul>	<ul style="list-style-type: none"> <li>● Identify customer segments in telecom using machine learning</li> <li>● Develop a web-based dashboard for visualization and analysis</li> </ul>	
<p><b>Principal Component Analysis</b> Soumyatanu Mukherjee</p>	<ul style="list-style-type: none"> <li>● MQSFLA has advantages in convergence rate and accurate value</li> <li>● MQSFLA-k effectively solves telecom customer segmentation for retention</li> </ul>	<ul style="list-style-type: none"> <li>● Principal Component Analysis (PCA)</li> <li>● Statistical method for data reduction</li> </ul>	<ul style="list-style-type: none"> <li>● Breast cancer, Wine, Digits, Iris datasets used for analysis</li> <li>● PCA implemented on various application datasets for monitoring performance</li> </ul>	<ul style="list-style-type: none"> <li>● Evaluate PCA impact on various application datasets</li> <li>● Analyze monitoring performance of PCA on different datasets</li> </ul>	
<p><b>Scalable and Privacy-Preserving Federated Principal Component Analysis</b></p>	<ul style="list-style-type: none"> <li>● Improved telecom customer segmentation accuracy</li> <li>● More scientific and reasonable segmentation results for marketing strategy formulation</li> </ul>	<ul style="list-style-type: none"> <li>● Principal Component Analysis (PCA) algorithm</li> <li>● Statistical method for data reduction</li> </ul>	<ul style="list-style-type: none"> <li>● PCA extracts principal components from correlated features in data matrix</li> <li>● RPCA is an efficient algorithm for PCA using random projection</li> </ul>	<ul style="list-style-type: none"> <li>● Breast cancer, wine, digits, Iris datasets used for analysis</li> <li>● PCA implemented on 2 X 2 process using Python</li> </ul>	<ul style="list-style-type: none"> <li>● Evaluate PCA impact on various application datasets</li> <li>● Analyze PCA performance on different datasets like Wine, Cancer, Digits, Iris</li> </ul>

Publication rate

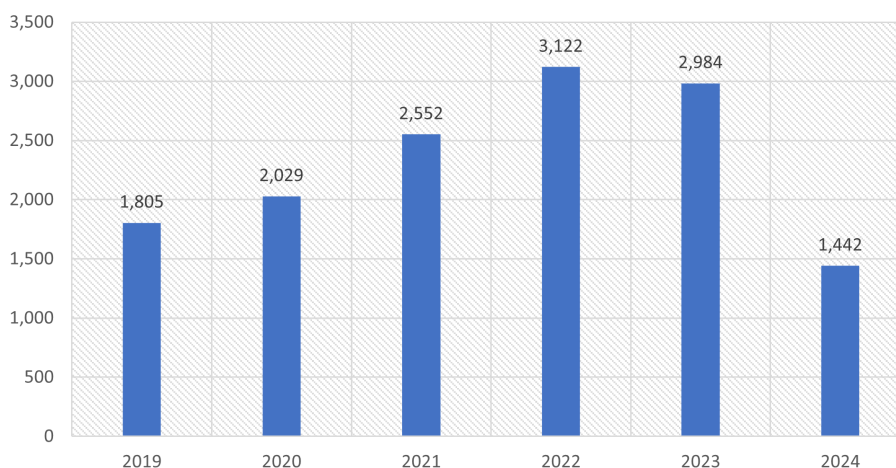


Figure 4. Publication rate in six years

### 3 APPLICATION OF PCA IN TELECOM INDUSTRY

- i. Dimensionality reduction: Call duration, frequency, data consumption, and client demographics are just a few of the many factors that telecom statistics frequently contain. By lowering these dimensions, PCA makes the dataset simpler. When your features are highly redundant (*multicollinear*, specifically), PCA will partition out the redundancy into one or more near-zero variance components, which you can then drop since they will contain little or no information.
- ii. Noise Reduction: By eliminating extraneous information and noise, PCA concentrates on the most important patterns. A collection of sensor readings will often share some common background noise. PCA can sometimes collect the (informative) signal into a smaller number of features while leaving the noise alone, thus boosting the signal-to-noise ratio.
- iii. Visualisation: PCA makes it simpler to visualise and analyse client groups by condensing data into fewer dimensions.
- iv. Anomaly detection: Unusual variation, not apparent from the original features, will often show up in the low-variance components. These components could be highly informative in an anomaly or outlier detection task.
- v. Decorrelation: Some ML algorithms struggle with highly-correlated features. PCA transforms correlated features into uncorrelated components, which could be easier for your algorithm to work with [8, 11].

### 4 HIERARCHICAL K-NEAREST NEIGHBOUR

Machine learning techniques like hierarchical k-NN (k-NN) are frequently applied to regression and classification problems. The k-NN algorithm, a non-parametric technique for estimating a target variable's value based on the values of its k nearest neighbours in the feature space, is extended by this approach. The data is arranged in a hierarchical form, like a tree, in the hierarchical k-NN method to enable effective search and retrieval of closest neighbours. Faster computing and a smaller search space are made possible by this hierarchical structure, particularly with high-dimensional data [10].

Let's consider a dataset with N data points, denoted as  $X = \{x_1, x_2, \dots, x_n\}$ , where each data point  $x_i$  is represented by its feature vector and belongs to a specific class or cluster.

- i. Tree: Construction: The first step in the hierarchical k-NN algorithm is to construct a hierarchical tree structure, such as a binary tree, using the training data X. This tree divides the feature space into regions, making it easier to search for nearest neighbors.
- ii. Nearest Neighbor Search: To classify a new data point x, the algorithm traverses the hierarchical tree to identify the k nearest neighbors. Starting from the root of the tree, the algorithm moves down the tree based on the feature values, narrowing down the search space until the k nearest neighbors are found.

The search process involves comparing the distance between the new data point x and the regions represented by the tree nodes. The distance can be calculated using various metrics such as Euclidean distance, Manhattan distance, or cosine similarity.

- iii. Classification: Once the k nearest neighbors are identified, the algorithm assigns a class label to the new data point x based on the majority vote of the neighbors. In other words, the class label that occurs most frequently among the k nearest neighbors is assigned to the new data point.

Mathematically, the hierarchical k-NN algorithm can be represented as follows:

Given a new data point x, let  $N_k(x)$  represent the set of k nearest neighbors of x, which are determined by traversing the hierarchical tree and considering the distances between x and the tree nodes. [11]

The class label y of the new data point x is determined based on the majority vote of the class labels of the k nearest neighbors:

$$y = \operatorname{argmax}(c) \sum (1/d(x_i, x)) \text{ where } x_i \in N_k(x) \text{ and } c \text{ is the class label.}$$

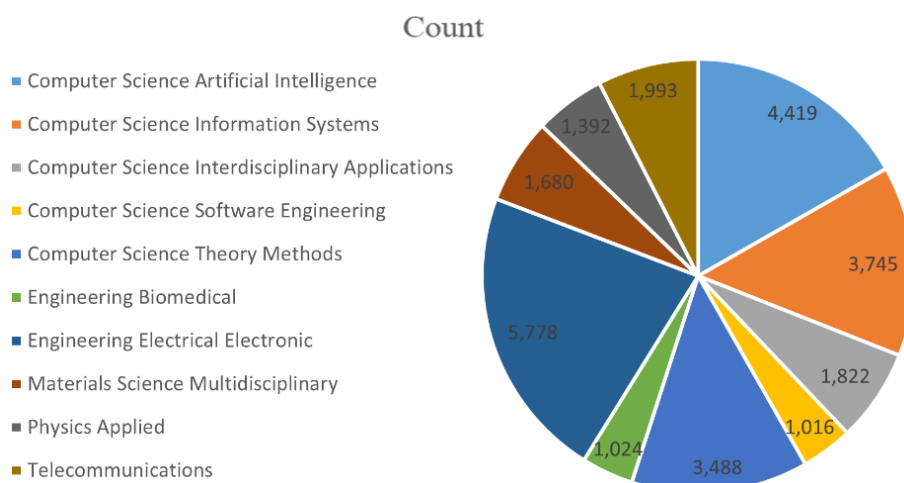
Here,  $d(x_i, x)$  represents the distance metric between the data point  $x_i$  and the new data point x.

The hierarchical k-NN algorithm offers a flexible and efficient approach to classification tasks, enabling accurate predictions based on the similarities between data points in the feature space. By organizing the data in a hierarchical structure and considering the nearest neighbors, this algorithm provides a powerful tool for various applications such as pattern recognition, image classification, and customer segmentation in the telecom industry. The following are the primary steps in the hierarchical k-NN algorithm:

- i. Data Preprocessing: In order to manage missing values, normalise the features, and eliminate any noise or outliers that can compromise the algorithm's accuracy, the input data is usually preprocessed.
- ii. Tree Construction: Using the training data, a hierarchical structure, like a binary tree, is built. The data is arranged in a hierarchical structure according to feature values, which facilitates the process of finding closest neighbours.
- iii. Nearest Neighbour Search: The algorithm searches the hierarchical tree to find the closest neighbours in order to categorise or forecast the target variable for a given test data point. It begins at the base of the tree and descends it in accordance with the feature values, reducing the size of the search area until the k closest neighbours are located.
- iv. Classification or Regression: Based on the majority vote or average of the neighbours, the algorithm, after identifying the k nearest neighbours, assigns a class label (in the case of classification) or estimates the target variable value (in the case of regression).

A few benefits of the hierarchical k-NN method include its enhanced computing efficiency, lower memory use, and resilience to noise and outliers. Large-scale datasets can benefit from its hierarchical data organisation, which speeds up neighbour retrieval and search times.

Applications for the approach may be found in many different fields, such as anomaly detection, recommendation systems, pattern recognition, and picture categorization. It is a well-liked option for many machine learning problems due to its interpretability, simplicity, and capacity to handle both numerical and categorical input. All things considered, the hierarchical k-NN algorithm offers a versatile and effective method for solving regression and classification issues, enabling precise forecasts and judgement calls based on the similarity of data points in the feature space [13].



**Figure 5.** Fields and sectors PCA Hierarchical KNN has been applied

## 5 APPLICATION OF HIERARCHICAL K-NEAREST NEIGHBOUR IN TELECOM INDUSTRY

Telecom applications include:

- i. Customer segmentation: k-NN may divide customers into groups according to how close they are to other customers who exhibit comparable behaviours.
- ii. Predictive modelling uses patterns found in past data to forecast the behaviour and preferences of customers.
- iii. Personalisation: By precisely determining the requirements and preferences of the target audience, personalisation improves marketing initiatives.

Benefits:

1. Flexibility and Simplicity: Suitable for a wide range of datasets and simple to apply.
2. Scalability: It can handle big datasets thanks to its hierarchical nature.



## 6 INTEGRATION OF PCA AND HIERARCHICAL K-NEAREST NEIGHBOUR FOR TELECOM CUSTOMER SEGMENTATION

For telecom customer segmentation, the combination of Principal Component Analysis (PCA) and Hierarchical k-Nearest Neighbours (k-NN) provides a potent method for gaining insightful information from sizable customer databases. Through this integration, the advantages of PCA in terms of dimensionality reduction and information extraction are combined with the potency of the hierarchical k-NN model in terms of distinguishing between different consumer groups [14].

The following procedures are involved in merging PCA and hierarchical k-NN for telecom customer segmentation:

- i. **PCA-Assisted Dimensionality Reduction:** In order to reduce the dimensionality of the telecom customer database, PCA is first used. Finding the primary components that capture the most variance in the data is required for this. By converting the high-dimensional data into a lower-dimensional space, PCA makes analysis easier to understand and makes segmentation more efficient.
- ii. **Construction of a Hierarchical k-NN Model:** Using the modified dataset, a hierarchical k-NN model is built once the dimensionality is decreased. In order to facilitate the efficient search and retrieval of closest neighbours, this model arranges the data in a hierarchical structure, like a tree.
- iii. **Identification of Nearest Neighbours:** In the reduced feature space, each customer's nearest neighbours are found using the hierarchical k-NN model. The model brings comparable consumers together by taking into account the similarities between them based on their feature values.
- iv. **Customer Segmentation:** The telecom customers are then divided into several categories or clusters based on the nearest neighbours that have been found. These clusters enable focused marketing tactics and personalised service offers by representing consumer groupings with certain features and preferences.

There are several benefits of combining PCA and hierarchical k-NN for telecom consumer segmentation. First, by removing unnecessary or less useful variables and emphasising the most important ones, PCA lowers the dataset's dimensionality. This improves computing performance and streamlines the analytical process. Second, by effectively identifying nearest neighbours, the hierarchical k-NN model makes use of the limited feature space, allowing the development of customer segments with comparable qualities. This makes it easier to have a more thorough and in-depth grasp of the clientele [15].

Thirdly, telecom businesses may find hidden patterns and links in their client datasets by combining PCA with hierarchical k-NN. Businesses may better target their marketing campaigns, allocate resources more efficiently, and enhance their efforts to acquire and retain consumers by segmenting their client base according to commonalities.

Thus, hierarchical k-NN combined with PCA offers a strong foundation for telecom client segmentation. This method helps telecom businesses to address the changing demands of their consumers by using nearest neighbour analysis and dimensionality reduction to extract important insights from their customer datasets and make well-informed business choices [16].

## 7 CHALLENGES

Researchers and practitioners may face a number of difficulties while utilising Principal Component Analysis (PCA) for database scans employing a Hierarchical KNN model for telecom consumer segmentation. Among these difficulties are:

- i. **Figuring out the ideal amount of main components** It is important to choose how many principal components to keep. Important information may be lost if there are too few components selected. However, if an excessive number of components are kept, the findings could become harder to understand. A great balance necessitates thoughtful deliberation and examination.
- ii. **Managing multicollinearity:** The linear independence of variables is assumed by PCA. However, variables may show multicollinearity, or strong correlation, in real-world datasets. This may make it difficult to effectively represent the data's underlying structure and have an effect on how well the hierarchical KNN model performs [17].
- iii. **Managing absent data** Databases frequently have missing data, which can have an impact on the precision of PCA and other analyses. To guarantee accurate findings, it could be essential to use imputation techniques or handle missing variables carefully. **Principle component interpretation:** Principal component analysis can be difficult, even if principle component analysis (PCA) reduces dimensionality.
- iv. **Proficiency in the relevant subject and a thorough comprehension of the fundamental variables** are necessary to derive significant understanding from these elements.

- v. Managing computational complexity: Computational efficiency is an issue since large-scale telecom consumer databases may include enormous amounts of data. With these kinds of datasets, PCA may be computationally demanding, particularly when using the hierarchical KNN model. It is crucial to devise ways to strike a compromise between computational complexity and the required degree of accuracy.
- vi. Taking care of class imbalance: Class imbalance is a common occurrence in telecom customer databases, where certain customer categories are noticeably smaller than others. Due to its potential to favour larger classes, this imbalance may have an impact on the hierarchical KNN model's performance. For fair and accurate consumer segmentation, this imbalance must be addressed by altering the KNN algorithm or using suitable sampling strategies.

Careful assessment of the particular context, dataset, and research aims is necessary to address these problems. Researchers and practitioners may use PCA and the hierarchical KNN model to effectively segment telecom customers by recognising these possible roadblocks and putting relevant measures in place to overcome them [5, 18].

## 8 CASE STUDIES AND APPLICATION

- i. Churn Prediction: Telecom businesses may identify customers who are at danger of leaving by first using PCA to reduce the dataset dimensions and then using hierarchical k-NN.
- ii. Usage Pattern Analysis: Principal components associated with customer usage patterns can be found using PCA, and k-NN can then be used to categorise customers into various usage segments.
- iii. Marketing Campaigns: By combining PCA with k-NN, marketing campaigns based on consumer groupings determined by their major components may be targeted more precisely.

## 9 CONCLUSION

In summary, a viable method for telecom customer segmentation is provided by the combination of Principal Component Analysis (PCA) and the Hierarchical k-Nearest Neighbours (k-NN) model. Telecom businesses may efficiently analyse big customer records and gain important insights by using PCA to decrease dimensionality and the hierarchical k-NN model to discover nearest neighbours.

The most crucial information is obtained with the least amount of computational complexity because to PCA's dimensionality reduction capabilities. This makes it possible to express the telecom client database succinctly, which improves the effectiveness of further analysis. Different client groups may be identified using the hierarchical k-NN model based on similarities in the reduced feature space. Telecom firms may create focused marketing campaigns, optimise resource allocation, and enhance customer acquisition and retention by clustering clients based on shared qualities.

For telecom firms, this strategy has several useful advantages, such as the capacity to gather insightful data from sizable client databases and make wise business choices in a cutthroat industry. Telecom firms may better understand their customers' tastes, customise their services, and stay competitive by utilising PCA and the hierarchical k-NN model.

All things considered, the combination of PCA and the hierarchical k-NN model offers a reliable and effective method for segmenting telecom customers. In the fast-paced telecom sector, it enables organisations to get insightful knowledge, raise customer happiness, and spur corporate expansion.

## References

- [1] G. Gao and M. Li, "Telecom customer segmentation based on principal component analysis and K-means clustering," in *4th International Conference on Science and Social Research (ICSSR)*, pp. 1–4, 2018.
- [2] Z. Hao and H. Jiang, "Telecom customer segmentation based on principal component analysis and K-means clustering algorithm," *Journal of Convergence Information Technology*, vol. 11, no. 11, pp. 194–201, 2016.
- [3] X. Li and Q. Zhang, "Telecom customer segmentation based on principal component analysis and K-means clustering," in *5th International Conference on Big Data Analytics*, pp. 101–104, 2021.
- [4] Y. Li and J. Wang, "Telecom customer segmentation based on principal component analysis and K-means clustering," in *12th International Conference on Natural Computation, Fuzzy Systems and Knowledge Discovery (ICNC-FSKD)*, pp. 736–740, 2016.
- [5] Y. Liu and H. Zhu, "Telecom customer segmentation based on PCA and K-means clustering analysis," in *2015 International Conference on Intelligent Transportation, Big Data & Smart City*, pp. 283–285, 2015.
- [6] Z. Liu and L. Li, "Telecom customer segmentation based on principal component analysis and K-means clustering," in *4th International Conference on Artificial Intelligence and Big Data*, pp. 163–167, 2021.

- [7] L. Sun and Y. Hu, "Telecom customer segmentation based on principal component analysis and K-means clustering," in *Sixth International Symposium on Parallel Architectures, Algorithms and Programming*, pp. 282–286, 2014.
- [8] H. Wang and N. Xiong, "Telecom customer segmentation based on principal component analysis and K-means clustering," *Journal of Physics: Conference Series*, vol. 1087, no. 5, art. no. 052136, 2018.
- [9] Q. Wang and Z. Xu, "Telecom customer segmentation based on principal component analysis and K-means clustering," in *3rd International Conference on Information Technology and Computer Application*, pp. 65–69, 2021.
- [10] X. Wang and X. Gao, "Telecom customer segmentation based on principal component analysis and K-means clustering," in *2013 International Conference on Information Science and Applications*, pp. 1–4, 2013.
- [11] Y. Wang and L. Li, "Telecom customer segmentation based on principal component analysis and K-means clustering," in *4th International Conference on Big Data and Internet of Things*, pp. 113–116, 2021.
- [12] W. Yang and L. Zhang, "Telecom customer segmentation based on principal component analysis and K-means clustering," in *3rd International Conference on Systems and Informatics (ICSAI)*, pp. 1196–1200, 2017.
- [13] X. Zhang and H. Zhao, "Telecom customer segmentation based on principal component analysis and K-means clustering," in *IEEE 3rd Information Technology, Networking, Electronic and Automation Control Conference (ITNEC)*, pp. 1951–1954, 2019.
- [14] H. Liu and X. Liu, "Telecom customer segmentation based on principal component analysis and K-means clustering," in *6th International Conference on Computer and Communications Management (ICCCM)*, pp. 106–110, 2020.
- [15] Y. Zhang and J. Wu, "Telecom customer segmentation based on principal component analysis and K-means clustering," in *5th International Conference on Computer Science and Software Engineering*, pp. 452–455, 2021.
- [16] J. Zhao and J. Li, "Application of principal component analysis and hierarchical K-means clustering algorithm in telecom customer segmentation," in *2012 International Conference on Computer Science and Electronics Engineering*, vol. 1, pp. 598–601, 2012.
- [17] C. Zhou and S. Chen, "Telecom customer segmentation based on principal component analysis and K-means clustering," in *4th International Conference on Intelligent Sustainable Systems (ICISS)*, pp. 698–701, 2020.



## Classification of Plant Leaves Using Vision Transformer Model

Kadriye Karadeniz<sup>\*1</sup>, Kursat Mustafa Karaoglan<sup>1</sup>

<sup>1</sup>Computer Engineering, Karabuk University, Karabuk, Türkiye

### Abstract

The Classification of Plant Leaves (CPL) is critically important in biology and ecology. This task is usually performed in current studies using Machine Learning (ML), Deep Learning models, and image processing techniques. The Vision Transformer (ViT) model, which produces high-performance results in image processing, separates images into small patches and processes these patches as a sequence. Thanks to its attention mechanism, it has the potential to exhibit high performance in complex and high-resolution images. This study uses the ViT model to perform the CPL task and evaluate its performance using common ML metrics. Comparisons are made with related studies in the literature. For this purpose, experimental studies were carried out using the ViT model on the Swedish Leaf dataset consisting of 1125 leaf images of 15 different Swedish tree species. The results show that the proposed approach produces high and efficient performance results. In this context, over 95% classification success was achieved in the accuracy metric with the developed ViT-based approach. In addition, applying the proposed approach in the CPL task is among the first approaches in the literature.

**Keywords:** *Plant leaves classification, Vision Transformer, Machine Learning, Plant recognition*

## 1 INTRODUCTION

Plants are one of the fundamental elements of life on earth and play an essential role in the natural environment, ecological balance, industry, and medicine [1]. Today, it is estimated that there are between 220,000 and 420,000 species of flowering plants on Earth [2]. Due to this vast number, a botanist or expert can't identify all plant species. Some plant species can be very similar to each other. Therefore, distinguishing them is time-consuming and costly. Due to these difficulties, computerized systems are needed to identify and classify plants [3]. Identifying plant species is vital in various application areas such as agricultural science, conservation, ecological effects, natural products and drug development where human efforts are involved [4].

Plant species identification has become an actively researched topic by computer vision researchers in recent years due to the difficulty of traditional methods [5]. Various organs of plants, such as leaves, fruits, roots and barks, can be used for identification. Leaves are widely used for plant species identification, especially in tropical regions. Access to the roots of plants is difficult. On the other hand, flowers are available only during the flowering season. Fruits appear at certain times of the year. Leaves can be found in abundance throughout the year compared to other tissues. Plant leaves have a stable shape and structure, so they are suitable for recognition by computer vision methods. Sampling and photographing leaves are economical and practical for creating a dataset [1–3, 7, 8].

Plant leaf classification identifies and classifies plant species according to their features [7]. The first studies on species recognition from plant leaf images were based on classical image processing techniques and manual feature extraction from leaf images. There are frequent studies in the literature on this subject. In the study conducted by Wu et al. [8], 12 leaf features were extracted to classify 32 plant species, and Probabilistic Neural Networks (PNN) were used. 1800 leaves were trained in the study, and according to the experimental results, an accuracy rate of more than 90% was achieved. In the survey conducted by Bakhshipour and Jafari [9], Support Vector Machine (SVM) and Artificial Neural Networks (ANN) were used to detect weeds according to their patterns. In the study, four weed species commonly found in sugar beet fields were examined, and according to the experimental results, ANN achieved an accuracy rate of 93.33%. In another study [10], a method combining three visual features on leaves, namely border shape, texture and color, was proposed using pattern recognition methods. Experiments were conducted on the ImageCLEF 2012 dataset. In the problem of plant recognition based on leaf images, 90.41% accuracy was achieved for 115 species. In a study, SVM and Adaptive Boosting were used. Morphological features such as centre, main axis length, minor axis length, robustness, contour and orientation were extracted from leaf images. Various classifiers, including K-Nearest Neighbor (KNN), Decision Trees (DT) and Multilayer Perceptron, were tested on the Flavia dataset and compared with other classifiers. With the advantage of a 10-fold

cross-validation strategy, a 95.85% accuracy rate was achieved [11]. In another study, which used Artificial Intelligence (AI) techniques such as ANN, Naive Bayes (NB), Random Forest (RF), KNN, and SVM to develop an automatic descriptor for plant leaves, 22 visual features were extracted in 4 groups as size, color, texture and pattern on 637 healthy leaf data taken from 32 different plant species. The SVM model was the most successful descriptor model, with an accuracy rate of 92.91% for the combination, including all groups [12]. In another study, a new five-step algorithm was proposed, which includes image preprocessing, segmentation, feature extraction, dimensionality reduction and classification steps. The proposed algorithm was tested with KNN, DT, NB and SVM on a publicly available dataset called Flavia, consisting of 1600 images. The best-performing KNN method achieved over 90% precision and recall values [13].

The increasing capacity and speed of central and graphics processing units have led to the development of new high-performance methods that can process raw data without manual features. This has been effective in the emergence of Deep Learning (DL) architectures. In further studies using larger datasets, DL models have been applied to perform feature extraction and image classification automatically. In a study using CNN, 94.8% accuracy was achieved on the Flavia dataset [5]. A proposed CNN classifier was tested on the Swedish leaf dataset. The model predicted the category of an unknown plant with minimum error [14]. A study using a dataset containing eight different leaf classes belonging to Bangladeshi plants, VGG16, VGG19, ResNet50, InceptionV3, Inception-Resnetv2 and Xception models, were tested. The architecture with the highest accuracy was determined as VGG16 [15]. In another study, a new CNN-based method called D-Leaf was proposed. Leaf images were pre-processed. Features were extracted using three different CNN models: pre-trained AlexNet, tuned AlexNet and D-Leaf. D-Leaf model achieved a test accuracy of 94.88% compared to AlexNet (93.26%) and tuned AlexNet (95.54%) models [16]. In a study by Lee et al. [7], a new model named Plant-CNN-ViT, which combines the strengths of Vision Transformer (ViT), ResNet50, DenseNet201 and Xception models, was proposed. The experimental results showed superior performance, and the proposed model was tested on four plant leaf datasets (Flavia, Folio, Swedish, MalayaKew).

In addition to plant recognition based on leaf images, studies on disease detection from leaf images have also been frequently included in the literature in recent years. Machine Learning (ML) and DL models were applied to classify tomato diseases such as bacterial spot, early blight and leaf mould on the PlantVillage tomato dataset. Among the ML and DL algorithms, ResNet34 architecture yielded the best results [17]. A study on a CNN model proposed to classify honeysuckle plants into three categories: healthy, diseased, and leaf burn, 457 of 1088 honeysuckle plant leaves were identified as healthy, 509 as diseased and pest infected, and 122 as leaf burn due to excessive dose of fertilizer. The proposed model achieved over 90% classification accuracy [18]. Another study applied the ViT model to the Cassava Leaf Disease dataset to classify Cassava leaf diseases. Experimental results have shown that the ViT model achieves at least 1% higher accuracy than CNN models (EfficientNet and Resnet50d) [19]. In another study, CNN and ViT models were tested for classifying leaf diseases from rice, tea, and maize leaf images. According to the experimental results, the ViT model outperformed CNN on all three datasets [20]. A ViT-based approach was proposed for leaf disease detection and tested on the Plant Pathology 2020 dataset in another study. The experimental results determined that the ViT model significantly outperformed CNN-based models in plant disease detection [21].

This study proposes the ViT model to classify plant species based on leaf images. The dataset used is the Swedish Leaf dataset, which is frequently studied in the literature. The dataset is relatively small. Therefore, the number of images was increased sixfold by using data augmentation techniques to increase the size of the dataset. The proposed model was tested on the Swedish Leaf dataset. This study evaluated the ViT model's performance in classifying plant leaves.

In the introduction of this study, the importance of plant species classification from plant leaf images is emphasized, and related studies in the literature are presented. The second part explains the structure of the ViT model used in the research and its application method. In the third part, the details of the experiments conducted under the headings of experimental environment, used data set, performance metrics, and hyperparameters are given. In the fourth part, the obtained results are presented. In the last part, a general summary of the study is made, the obtained findings are summarized, and suggestions for future research are made.

## 2 METHODOLOGY

ViT [22], introduced by Dosovitskiy et al., is an innovative DL architecture that applies Transformer architecture to image classification problems and has recently attracted significant attention in computer vision. Transformer architecture was first successfully used in Natural Language Processing (NLP) tasks and is known for its ability to effectively model long dependencies thanks to its attention mechanism [23]. ViT emerged as an alternative to

CNN. ViT models have achieved quite competitive performance in image classification [24], image segmentation [25], and object detection [26]. There is a layer in ViT called self-attention [27] layer. This layer enables the global embedding of information in the image. Vision transformers consider input images as image patches, like word sequences in NLP. In other words, like language data, ViT also learns the relationships between patches through self-attention. This mechanism allows the model to capture long-term dependencies between different image regions. Attention between patches enables the model to understand different visual features better. CNNs use pixels as input, but image transformers divide images into some specific visual markers. They first divide the images into pieces and then embed each one. The resulting spatial embedding becomes an input to the transformer encoder. The model also learns how to reconstruct the image during the training phase.

In the training process of the ViT model, 16x16 pixel patches are first created from the images. In the next step, the patches are flattened from 2D vectors to 1D vectors. Then, linear embeddings are made from the patch vectors, and spatial embeddings are included. The result sequence is given to the transformer encoder. The self-attention layer in the transformer encoder captures the dependencies between the patches. It also allows the model to take the global context into account. The encoder has a feed-forward neural network after the self-attention layer. The output of each patch is passed through a feed-forward neural network. This helps to capture the complex nonlinear relationships within the patches. The last layer of the transformer encoder is a classification head.

The structure of the ViT model is shown in Figure 1.

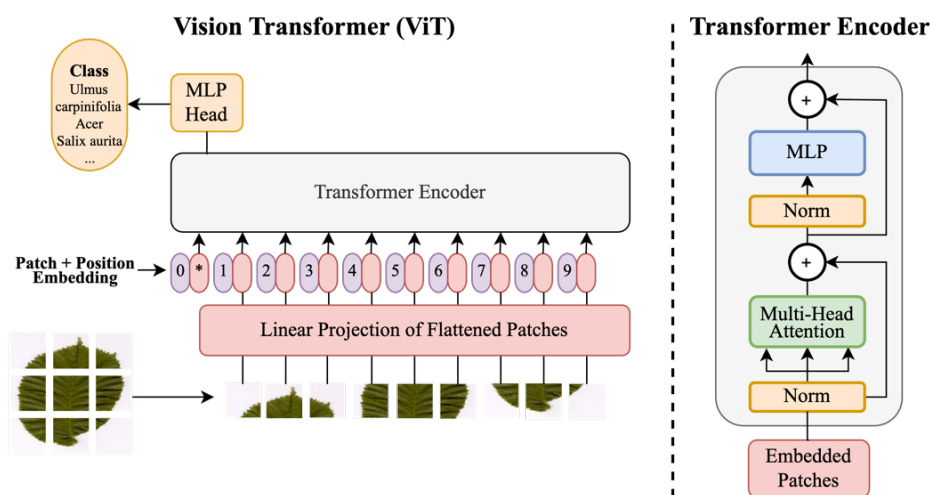


Figure 1. ViT model workflow diagram [22]

ViT achieves superior results compared to CNNs, requiring significantly less computational resources for pretraining. Compared to CNNs, ViT exhibits weaker inductive bias overall, leading to greater reliance on model refinement or data augmentation during training on smaller datasets. ViT performs better when trained on sufficient data, outperforming a similar CNN with fewer computational resources. These transformers have high success rates in NLP models and are now being applied to images for image recognition tasks.

### 3 EXPERIMENTAL STUDY

In this section, experimental studies using the ViT model in the classification of plant leaves are discussed. First, the experimental environment is detailed, and then the analysis results are presented.

#### 3.1 Experimental Environment

The environment in which the experimental studies were conducted was explained. The dataset, performance metrics, and hyperparameters were discussed in this context.

##### 3.1.1 Dataset

The Swedish Leaf dataset, created by Oskar J. O. Söderkvist [28], consists of leaf images of 15 Swedish tree species. There are 1125 leaf images in total in the dataset, which includes 75 images for each species. Each leaf image has a white background and is of different sizes. All images are resized to 224x224 pixels before being fed into the model. Data augmentation techniques such as rotation, shift, shear, zoom, flip, and pixel filling are applied

to the dataset to increase the training data's diversity and prevent over-learning. In addition, each image is duplicated five times, thus increasing the number of images in the dataset by six times. The dataset is divided into two sets: training and testing. The training and test sets are divided equally into each class and contain 360 and 90 samples, respectively. There are 5400 images in the augmented training dataset and 1350 in the augmented test dataset. Figure 2 shows sample images from each class in the Swedish Leaf dataset. Table 1 shows the original image numbers in each class in the data set and after the data augmentation process.

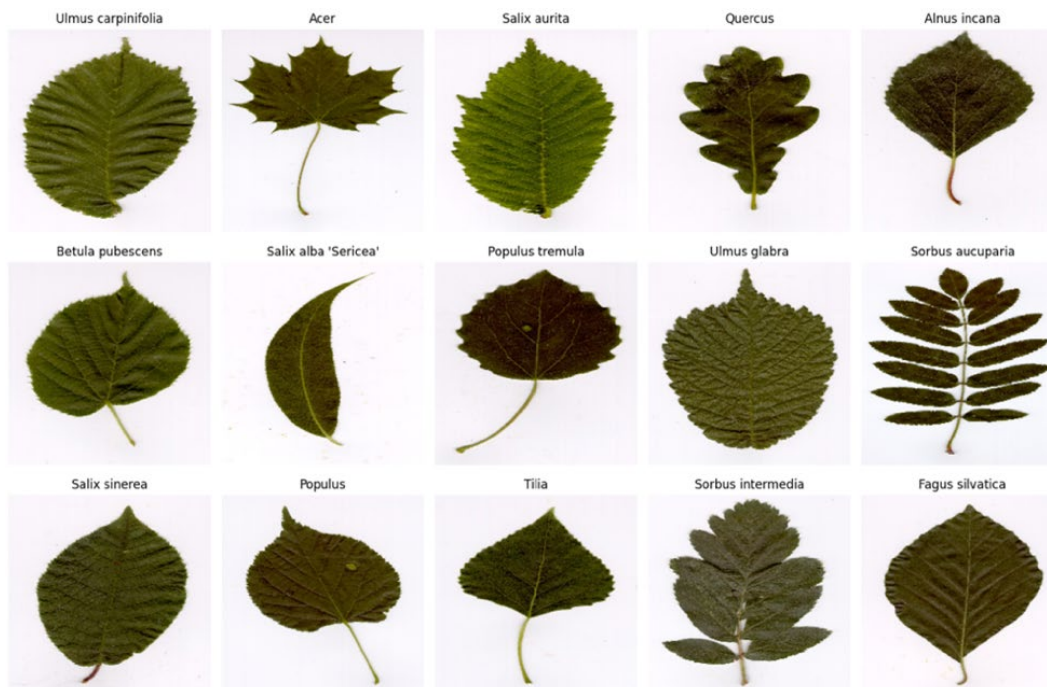


Figure 2. Sample images of the Swedish Leaf dataset

Table 1. Dataset splitting

Class	Number of Examples	Augmented Number of Examples	Augmented Number of Training	Augmented Number of Tests
Ulmus carpinifolia	75	450	360	90
Acer	75	450	360	90
Salix aurita	75	450	360	90
Quercus	75	450	360	90
Alnus incana	75	450	360	90
Betula pubescens	75	450	360	90
Salix alba 'Sericea'	75	450	360	90
Populus tremula	75	450	360	90
Ulmus glabra	75	450	360	90
Sorbus aucuparia	75	450	360	90
Salix sinerea	75	450	360	90
Populus	75	450	360	90
Tilia	75	450	360	90
Sorbus intermedia	75	450	360	90
Fagus sylvatica	75	450	360	90
<b>Total</b>	<b>1125</b>	<b>6750</b>	<b>5400</b>	<b>1350</b>

### 3.1.2 Evaluation Metrics

Evaluation metrics are quantitative measures used to evaluate the effectiveness of a predictive model or the standard of an algorithm's output. In this study, four metrics, namely accuracy, precision, recall, and F1 score, were used to evaluate the performance of the ViT model. These metrics are calculated by the mathematical equations given in equations (1–4).

Here, TP represents the number of positive and positively classified examples, TN represents the number of negative and negatively classified examples, FP represents negative and positively classified examples, and FN represents the number of positive and negatively classified examples.

$$Accuracy = \frac{True\ Positives\ (TP) + True\ Negatives\ (TN)}{Total\ Population\ (TP + TN + FP + FN)} \quad (1)$$

$$Precision = \frac{True\ Positives\ (TP)}{True\ Positives\ (TP) + False\ Positives\ (FP)} \quad (2)$$

$$Recall = \frac{True\ Positives\ (TP)}{True\ Positives\ (TP) + False\ Negatives\ (FN)} \quad (3)$$

$$F1\ Score = 2 \times \frac{Precision \times Recall}{Precision + Recall} \quad (4)$$

### 3.1.3 Hyperparameters

All the hyperparameters selected for successful training of the ViT model are listed in Table 2. This study used an Adam optimizer with a learning rate of 0.001 to optimize the model and minimize the loss. The size of the input images is determined as 224x224 pixels. Patch size is the small pieces into which the photos are divided. The images are divided into fragments of 16x16 pixels. The number of patches indicates how many pieces the images are divided into according to the patch size. Here, when an image of 224x224 pixels is divided into patches with 16x16 pixels, 196 patches with a size of 14x14 pixels are obtained. The batch size indicates the number of data samples presented to the model in each training step, which is 256. The number of passes of the entire training data set over the model is 500 epochs. The number of heads used in the multi-head self-attention mechanism is set to 4. The number of Transformers layers used is 8.

**Table 2.** Hyperparameters of ViT model

Name of the Parameter	Values
Learning Rate	0.001
Weight Decay	0.0001
Batch Size	256
Number of Epochs	500
Image Size	224x224
Patch Size	16x16
Number of Patches	196
Projection Dimension	64
Number of Heads	4
Transformers Layers	8
Transformer Units	128, 64
MLP Heads Units	2048, 1024

## 4 RESULTS

In this section of the paper, the performance of the proposed method is analyzed through a comprehensive discussion of the findings from the evaluation metrics. The architecture is implemented in Python using Keras. ViT is applied to classify fifteen different categories, including *Ulmus carpinifolia*, *Acer*, *Salix aurita*, *Quercus*, *Alnus incana*, *Betula pubescens*, *Salix alba* ‘*Sericea*,’ *Populus tremula*, *Ulmus glabra*, *Sorbus aucuparia*, *Salix sinerea*, *Populus*, *tilia*, *Sorbus intermedia*, *Fagus silvatica*. The proposed model is trained for 500 epochs using a batch size 256. ModelCheckpoint and EarlyStopping methods are also used, and the training is stopped at the stage where the model performs best. During training, Adam optimized with a learning rate of 0.001 is used to optimize the model to minimize the loss.

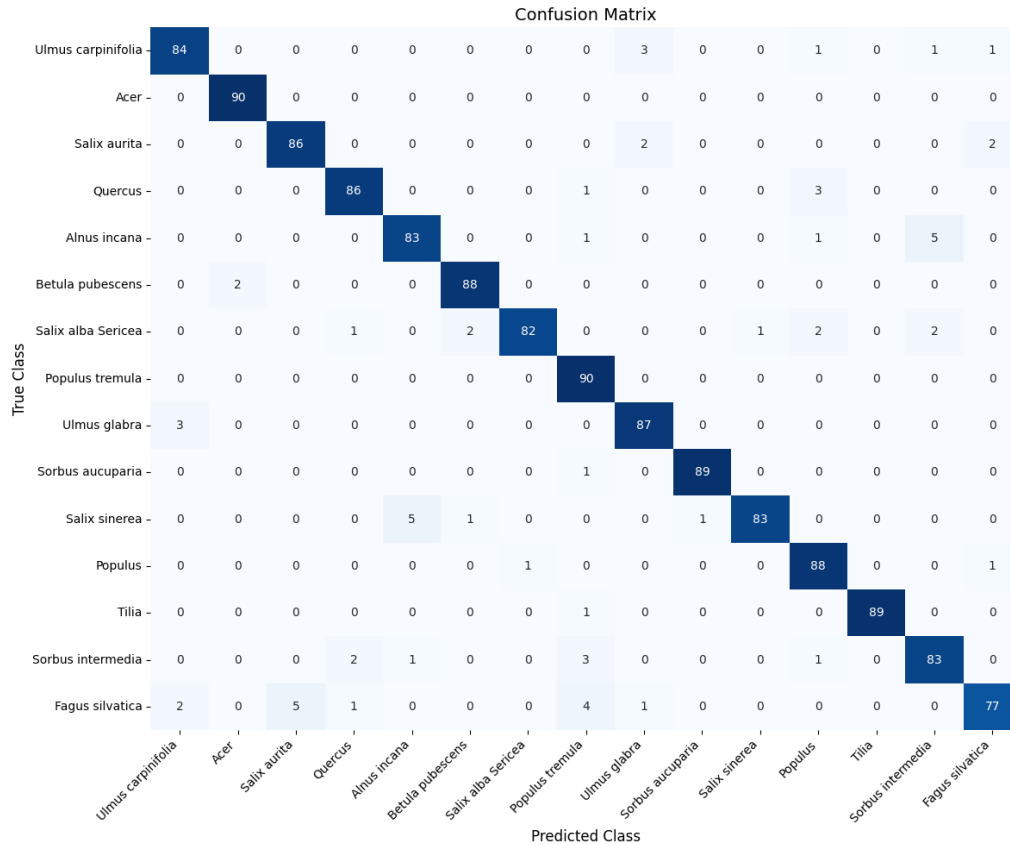
For each fold, training accuracy, training loss, validation accuracy, and validation loss are recorded during the training stage to evaluate the performance of the proposed architecture. The confusion matrix shown in Figure 4 shows that the proposed method successfully categorizes all 15 classes and achieves 95% accuracy, precision, recall, and F1 score values, as shown in Table 3.



**Table 3.** Performance metrics

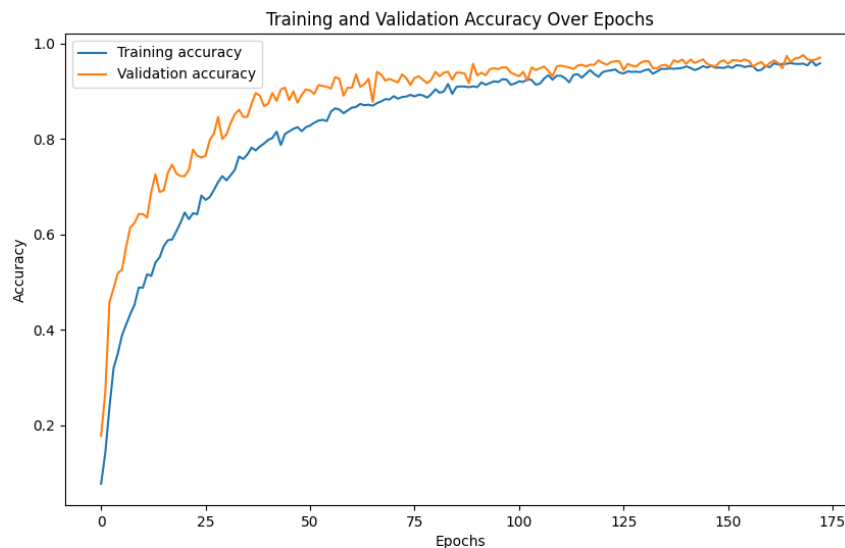
Leaf Classification	Performance Metrics			
	Accuracy	Precision	Recall	F1-Score
ViT	0.952	0.953	0.952	0.952

The complexity matrix, which contains the number of images that the ViT model correctly and incorrectly classified in the test dataset, is presented in Figure 3. The complexity matrix is a matrix that shows how many correct predictions the model made for each class and how many incorrect predictions it made.

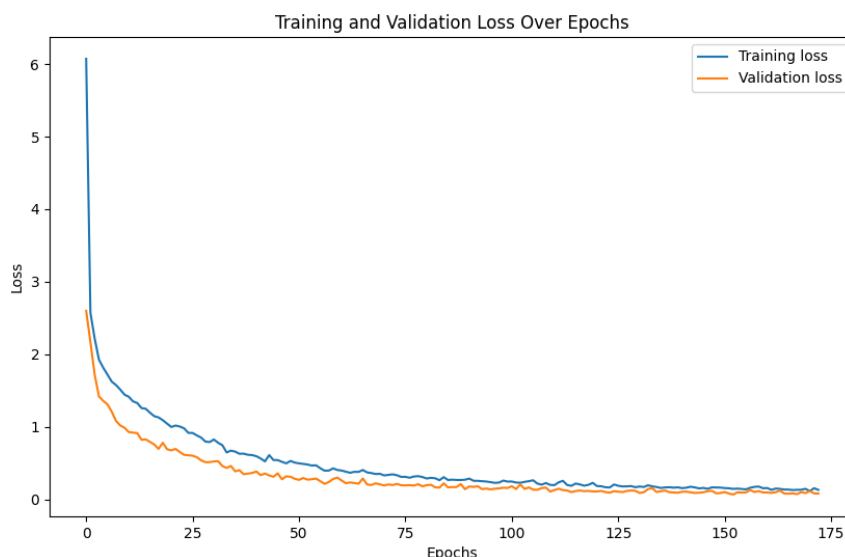


**Figure 3.** Confusion matrix

Figures 4 and 5 show the accuracy and loss graphs of the ViT model.



**Figure 4.** Accuracy graphic obtained as a result of experimental studies



**Figure 5.** Loss graphic obtained as a result of experimental studies

Table 4 shows the classification results obtained on leaf images of 15 different classes using the ViT model to classify plant species. This table shows the success of images belonging to each class with varying metrics as percentages. The table includes precision, recall, F1 score metrics, and the number of test images in each class.

**Table 4.** Classification report

Class	Precision	Recall	F1-Score	Support
Ulmus carpinifolia	0.944	0.933	0.939	90
Acer	0.978	1.0	0.989	90
Salix aurita	0.945	0.956	0.950	90
Quercus	0.956	0.956	0.956	90
Alnus incana	0.933	0.922	0.927	90
Betula pubescens	0.967	0.978	0.972	90
Salix alba 'Sericea'	0.988	0.911	0.948	90
Populus tremula	0.891	1.0	0.942	90
Ulmus glabra	0.935	0.967	0.951	90
Sorbus aucuparia	0.989	0.989	0.989	90
Salix sinerea	0.988	0.922	0.954	90
Populus	0.917	0.978	0.946	90
Tilia	1.0	0.989	0.994	90
Sorbus intermedia	0.912	0.922	0.917	90
Fagus sylvatica	0.951	0.856	0.901	90
<b>Overall</b>				
Accuracy	0.952	0.952	0.952	0.952
Macro Avg	0.953	0.952	0.952	1350
Weighted Avg	0.953	0.952	0.952	1350

In Table 4, the ViT model performed best in the Tilia class with 100% precision, 98.9% recall, and 99.4% F1 score. The ViT model performed worst in the Fagus sylvatica class with 91.5% precision, 85.6% recall, and 90.1% F1 score.

## 5 CONCLUSION

This study proposes an architecture for the Classification of Plant Leaves (CPL), an essential task in biology and ecology, using the ViT model. Known for its high performance in image processing, the ViT model divides images into small patches, unlike CNN, and processes these patches as a sequence. ViT was selected to effectively process complex and high-resolution photos using the attention mechanism that has demonstrated superior success in NLP tasks. This model is used to evaluate the performance of the study with standard machine learning metrics (accuracy, precision, recall, f1 score) and compare the results with the existing literature.

Experimental results show that the ViT model achieves a remarkable classification accuracy exceeding 95% on the Swedish Leaf dataset. This high level of performance highlights the efficiency and effectiveness of ViT-based approaches in CPL tasks. The results also highlight that this approach is one of the first to apply the ViT model in the specific context of plant leaf classification and significantly contribute to the field.

The dataset used in this study is relatively small. Future work can further investigate its application to other larger datasets with varying complexity and resolution to validate the robustness and generalizability of the ViT model. In addition, integrating other advanced machine learning deep learning techniques or hybrid models can improve performance. The number of hyperparameters used in the study can be increased or decreased, enabling the model to perform better. Further work can also investigate the impact of different preprocessing techniques on the accuracy and efficiency of the model, which can provide deeper insights into optimizing CPL tasks using the ViT model.

## References

- [1] H. Wu, L. Fang, Q. Yu, J. Yuan, and C. Yang, "Plant leaf identification based on shape and convolutional features," *Expert Syst Appl*, vol. 219, art. no. 119626, 2023.
- [2] A. Kaya, A. S. Keceli, C. Catal, H. Y. Yalic, H. Temucin, and B. Tekinerdogan, "Analysis of transfer learning for deep neural network based plant classification models," *Comput Electron Agric*, vol. 158, pp. 20–29, 2019.
- [3] J. Wei Tan, S.-W. Chang, S. Abdul-Kareem, H. J. Yap, and K.-T. Yong, "Deep learning for plant species classification using leaf vein morphometric," *IEEE/ACM Trans Comput Biol Bioinform*, vol. 17, no. 1, pp. 82–90, 2018.
- [4] S. H. Lee, C. S. Chan, S. J. Mayo, and P. Remagnino, "How deep learning extracts and learns leaf features for plant classification," *Pattern Recognit*, vol. 71, pp. 1–13, 2017, doi: <https://doi.org/10.1016/j.patcog.2017.05.015>.
- [5] A. E. Minarno, Z. Ibrahim, A. Nur, M. Y. Hasanuddin, N. M. Diah, and Y. Munarko, "Leaf based plant species classification using deep convolutional neural network," in *2022 10th International Conference on Information and Communication Technology (ICOICT)*, 2022, pp. 99–104.
- [6] K. Yang, W. Zhong, and F. Li, "Leaf segmentation and classification with a complicated background using deep learning," *Agronomy*, vol. 10, no. 11, art. no. 1721, 2020.
- [7] C. P. Lee, K. M. Lim, Y. X. Song, and A. Alqahtani, "Plant-CNN-ViT: plant classification with ensemble of convolutional neural networks and vision transformer," *Plants*, vol. 12, no. 14, art. no. 2642, 2023.
- [8] S. G. Wu, F. S. Bao, E. Y. Xu, Y.-X. Wang, Y.-F. Chang, and Q.-L. Xiang, "A leaf recognition algorithm for plant classification using probabilistic neural network," in *2007 IEEE International Symposium on Signal Processing and Information Technology*, 2007, pp. 11–16.
- [9] A. Bakhshipour and A. Jafari, "Evaluation of support vector machine and artificial neural networks in weed detection using shape features," *Comput Electron Agric*, vol. 145, pp. 153–160, 2018.
- [10] A. Oncevay-Marcos, R. Juarez-Chambi, S. Khlebnikov-Núñez, and C. Beltrán-Castañón, "Leaf-based plant identification through morphological characterization in digital images," in *Computer Analysis of Images and Patterns: 16th International Conference, CAIP 2015, Valletta, Malta, 2015, Part II*, pp. 326–335.
- [11] S. Mahajan, A. Raina, X.-Z. Gao, and A. Kant Pandit, "Plant recognition using morphological feature extraction and transfer learning over SVM and AdaBoost," *Symmetry (Basel)*, vol. 13, no. 2, art. no. 356, 2021.
- [12] E. Yigit, K. Sabanci, A. Toktas, and A. Kayabasi, "A study on visual features of leaves in plant identification using artificial intelligence techniques," *Comput Electron Agric*, vol. 156, pp. 369–377, 2019.
- [13] G. Saleem, M. Akhtar, N. Ahmed, and W. S. Qureshi, "Automated analysis of visual leaf shape features for plant classification," *Comput Electron Agric*, vol. 157, pp. 270–280, Feb. 2019, doi: [10.1016/J.COMPAG.2018.12.038](https://doi.org/10.1016/J.COMPAG.2018.12.038).
- [14] D. Bisen, "Deep convolutional neural network based plant species recognition through features of leaf," *Multimed Tools Appl*, vol. 80, no. 4, pp. 6443–6456, 2021.
- [15] S. U. Habiba, M. K. Islam, and S. M. M. Ahsan, "Bangladeshi plant recognition using deep learning based leaf classification," in *2019 International Conference on Computer, Communication, Chemical, Materials and Electronic Engineering (IC4ME2)*, 2019, pp. 1–4.
- [16] J. Wei Tan, S.-W. Chang, S. Abdul-Kareem, H. J. Yap, and K.-T. Yong, "Deep learning for plant species classification using leaf vein morphometric," *IEEE/ACM Trans Comput Biol Bioinform*, vol. 17, no. 1, pp. 82–90, 2018.
- [17] L. Tan, J. Lu, and H. Jiang, "Tomato leaf diseases classification based on leaf images: a comparison between classical machine learning and deep learning methods," *AgriEngineering*, vol. 3, no. 3, pp. 542–558, 2021.

- [18] L. Selvam and P. Kavitha, "Classification of ladies finger plant leaf using deep learning," *J Ambient Intell Humaniz Comput*, pp. 1–9, 2020.
- [19] H.-T. Thai, N.-Y. Tran-Van, and K.-H. Le, "Artificial cognition for early leaf disease detection using vision transformers," in *2021 International Conference on Advanced Technologies for Communications (ATC)*, 2021, pp. 33–38.
- [20] P. Bhuyan and P. K. Singh, "Evaluating Deep CNNs and Vision Transformers for Plant Leaf Disease Classification," in *International Conference on Distributed Computing and Intelligent Technology*, 2024, pp. 293–306.
- [21] H. Keerthan Bhat, A. Mukund, S. Nagaraj, and R. Prakash, "LeafViT: Vision Transformers-Based Leaf Disease Detection," in *International Conference on Innovations in Computational Intelligence and Computer Vision*, 2022, pp. 85–102.
- [22] A. Dosovitskiy *et al.*, "An image is worth 16x16 words: Transformers for image recognition at scale," *arXiv preprint*, arXiv:2010.11929, 2020.
- [23] A. Vaswani *et al.*, "Attention is all you need," in *Advances in Neural Information Processing Systems*, I. Guyon, U. Von Luxburg, S. Bengio, H. Wallach, R. Fergus, S. Vishwanathan, and R. Garnett, Eds., Curran Associates, Inc., 2017. [Online]. Available: [https://proceedings.neurips.cc/paper\\_files/paper/2017/file/3f5e243547dee91fbd053c1c4a845aa-Paper.pdf](https://proceedings.neurips.cc/paper_files/paper/2017/file/3f5e243547dee91fbd053c1c4a845aa-Paper.pdf)
- [24] B. Gheflati and H. Rivaz, "Vision transformers for classification of breast ultrasound images," in *2022 44th Annual International Conference of the IEEE Engineering in Medicine & Biology Society (EMBC)*, 2022, pp. 480–483.
- [25] A. Sagar, "Vitbis: Vision transformer for biomedical image segmentation," in *MICCAI Workshop on Distributed and Collaborative Learning*, 2021, pp. 34–45.
- [26] H. Song *et al.*, "VidT: An efficient and effective fully transformer-based object detector," *arXiv 2021*, *arXiv preprint*, arXiv:2110.03921.
- [27] M. Caron *et al.*, "Emerging properties in self-supervised vision transformers," in *IEEE/CVF International Conference on Computer Vision*, 2021, pp. 9650–9660.



---

## Artificial Intelligence and Statistics Based Call Count and Average Talk Time Prediction for Call Centers

Hasan Huseyin Yurdagul<sup>1</sup>, Adem Seller<sup>1</sup>, Idris Senocak<sup>1</sup>, Hatice Ozdemir<sup>1</sup>, Ceren Ulus<sup>2</sup>,  
Mehmet Fatih Akay<sup>2</sup>

<sup>1</sup>Universal Software, Istanbul, Türkiye

<sup>2</sup>Cukurova University, Department of Computer Engineering, Adana, Türkiye

---

### Abstract

Nowadays, call centers face high demand volumes that are continually increasing due to technological advancements. Accelerating processes and accurately managing workforce planning are crucial to meet customer satisfaction and deliver quality service. Call count and average talk time prediction stands out as a critical tool for workforce planning. In this study, it is aimed to develop call count and average conversation times prediction models using deep learning based Bidirectional Long Short Term Memory (BiLSTM), Gated Recurrent Unit (GRU), Multi-Layer Perceptron (MLP), and statistics-based Moving Average (MA). The data set includes call data between 01.01.2020 and 08.10.2022. The performance of the developed models has been evaluated using Determination Coefficient ( $R^2$ ), Root Mean Squared Error (RMSE), Mean Absolute Error (MAE), and Mean Squared Error (MSE). Results indicate that Bi-LSTM provided the highest prediction performance for call count. Also, MA demonstrated superior performance in average talk time prediction.

**Keywords:** Call center, Count of calls, Average talk time

---

## 1 INTRODUCTION

Today, businesses have begun to attach great importance to customer relations due to increased competition and changing economic balances. Customer satisfaction is a critical factor for the success of businesses. An important way to increase customer satisfaction is to respond to and resolve customer issues quickly. Therefore, businesses need a communication network to quickly respond to customer problems. These communication networks have turned into call centers over time. Call centers are communication centers that answer customers' calls, solve problems and implement action plans. Through call centers, businesses improve customer relations and can resolve problems faster.

With the development of technology, the call center sector has become one of the prominent business areas for the world economy with the added value and employment opportunities it creates. For this reason, call center companies invest in qualified human resources and improving service quality. The services offered in call centers are generally carried out by personnel called customer representatives. Since call centers have large volumes of data traffic and the workload of the staff is high enough, there may be unanswered calls waiting in the queue, which can extend the time it takes to solve the customer's problem, thus creating a negative profile. Carrying the full load of these large-scale operations, scheduling enough agents and ensuring customers can contact agents quickly is a difficult task to manage manually. In this context, call number and average talk time estimation is an important part of efficient call center operation [1].

Call count and average talk time prediction aims to optimize productivity, manage agents' workload, and allocate an appropriate number of agents to be able to deliver the assistance customers need in a timely manner. When the number of future calls and average talk time cannot be predicted; There may be too many or not enough representatives. This situation leads to loss of time and cost. Within the scope of all these, the subject of the study is to develop artificial intelligence and statistics-based number of calls and average conversation time prediction models for call centers.

## 2 LITERATURE REVIEW

In recent times, studies on predicting the number of calls and average conversation duration have been conducted across various sectors to better plan call center operations. For the 112 Emergency Call Center in Isparta, a model using Artificial Neural Networks (ANN) has been developed to predict the number of calls related to health, security, and fire emergencies. The model used a feedforward backpropagation algorithm with momentum and adaptive learning rate to train the network for predicting the likely number of calls in future periods [2]. Machine learning models have been developed for daily call center arrival predictions using data from an online retailer's customer support and complaint queue, consisting of half-hour observations over 174.5 weeks. Results showed that the Random Forest (RF) algorithm provided the best prediction performance [3]. Based on the challenge of predicting the number of expected phone calls within 40 days faced by a company, call volume predictions have been made using statistical and neural network models. The study concluded that statistical models outperformed neural networks [4]. By using data mining and machine learning techniques, past call data have been analyzed, and models have been created to predict future call traffic. The developed models have been tested by addressing a telecom call center traffic congestion that occurred in 2008. The results showed that the proposed method predicted the formation of traffic congestion earlier than existing non-personalized call prediction methods [5]. Different univariate time series methods are evaluated for predicting call center arrivals. Specifically, various methods have been analyzed to predict intra-day arrivals at call centers of a UK retail bank. The methods used include seasonal Autoregressive Integrated Moving Average (ARIMA) modeling, periodic autoregressive modeling, Holt-Winters exponential smoothing, and dynamic harmonic regression. The results indicated that seasonal ARIMA and Holt-Winters methods were effective for short-term forecasts, but simple historical averages showed limited performance over longer delivery times [6]. An arrival counting model based on a Mixed Poisson process approach is presented to predict workload in a call center. When applied to the call center of an Israeli Telecom company, the model accounted for the impact of events like billing on the arrival process by including these events as exogenous variables [7]. A simulation-based machine learning framework has been presented to evaluate the performance of call centers with multiple types of demand [8]. Based on multi-channel data from contact centers, a data-driven modeling approach has been used to predict the likelihood of an individual customer making a call within the next thirty days. The study used datasets from the contact centers of a US insurance company [9]. The use of various univariate time series forecasting methods has been evaluated for predicting daily call arrivals in the presence of outliers. In addition to statistical methods, artificial neural networks were considered [10]. The capabilities of machine learning in modeling and forecasting call load time series, characterized by strong seasonality on a daily and hourly scale, were investigated. Seasonal ANN and Long Short-Term Memory (LSTM) models have been compared with the Seasonal Autoregressive Integrated Moving Average (SARIMA) model, one of the most common statistical methods used by call centers. Model results were performed on three different datasets provided by Teleopti, and SARIMA has been proven to be more accurate in making daily scale predictions across all three datasets [11].

## 3 DATASET GENERATION

In this study, call count data from 01.01.2020 00:00 to 08.10.2022 23:00 was used. The data includes both the number of calls received by the call center and the average talk time values. The attributes of the data used to estimate the count of calls are shown in Table 1, and the attributes of the data used to estimate the average talk time are shown in Table 2.

**Table 1.** Attributes of call count data

Number of Data	Minimum	Maximum	Mean	Standard Deviation
24288	0	494	77.13	73.51

**Table 2.** Attributes of talk time data

Number of Data	Minimum	Maximum	Mean	Standard Deviation
24288	0	3639	584.01	221.59

## 4 METHODOLOGY

In this study, BiLSTM, GRU and MLP algorithms were used for both call count estimation and average talk time estimation. In addition to deep learning-based algorithms, results were also obtained with the statistics-based MA algorithm. Time lag was implemented in the models used to obtain the results. As a result of this method used, the input and output lag numbers have been determined and the training of the algorithms has been completed. The

lag number is determined by specifying how many past time points the algorithm should look at at each step (Input Lag) and how many future time points (Output Lag) it should produce. In order to get better results, firstly, scaling was done between 0-1. In order to better fit the results, sigmoid activation was used in the output layers of the algorithms.

**4.1 Bi-directional Long ShortTerm Memory – BiLSTM**

BiLSTM algorithm is defined as an artificial neural network that aims to capture more comprehensive information by processing time series data both forward and backward. The output at each time step is based on both past and future information [12].

**4.2 Gated Recurrent Unit – GRU**

GRU is one of the Recurrent Neural Network (RNN) structures. It has two main gates: update gate and reset gate. At the update gate, it is decided which information will be kept, discarded, and new information added, while at the reset gate, it is decided how much of the previous information will be forgotten.

**4.3 Multi-Layer Perceptron – MLP**

MLP is one of the most common types of artificial neural networks and is used especially in supervised learning problems such as classification and regression. It consists of an input layer, one or more hidden layers and an output layer.

**4.4 Moving Average – MA**

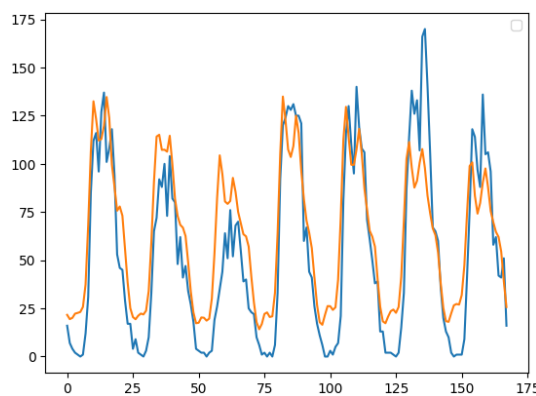
MA is a technique that smoothes data fluctuations by calculating the average of a data series over a specific time period. This method is used to understand the general trends and patterns of the data series. It is generally used in time series analysis and is constantly updated over a certain period.

**5 RESULTS AND DISCUSSION**

**5.1 Results on the Count of Calls**

**Table 3.** Algorithm and parameters

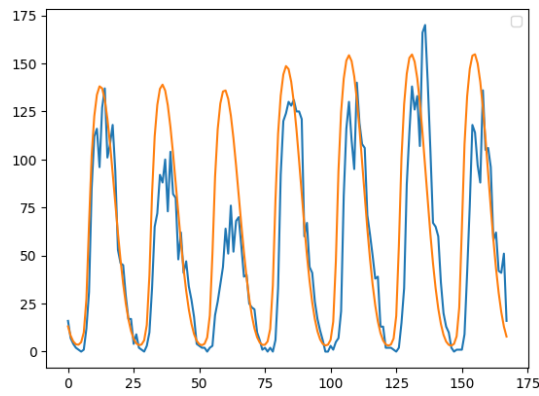
Number of Input Lags	Number of Output Lags	Model	Layer1: Number of Neurons	Epochs	Batch Size
168	1	MLP	128	100	128



**Figure 1.** Comparison of predictive values and actual values

**Table 4.** Algorithm and parameters

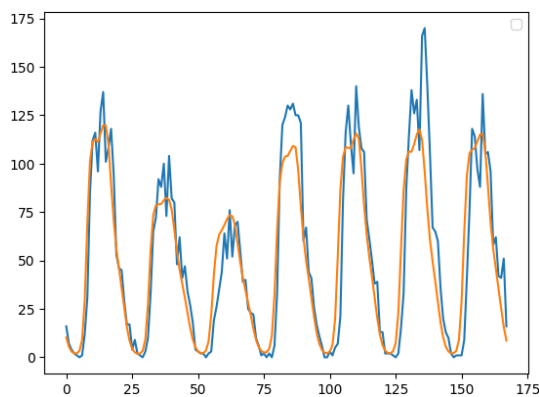
Number of Input Lags	Number of Output Lags	Model	Layer1: Number of Neurons	Epochs	Batch Size
168	1	GRU	32	20	128



**Figure 2.** Comparison of predictive values and actual values

**Table 5.** Algorithm and parameters

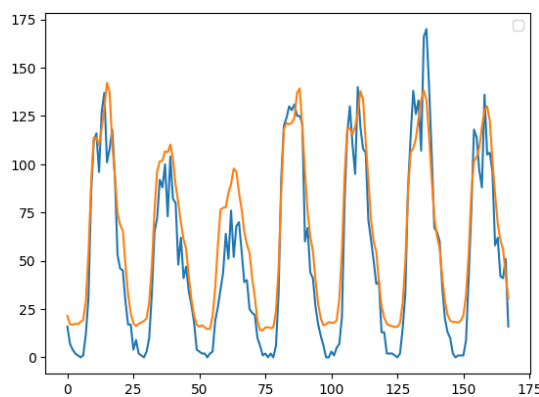
Number of Input Lags	Number of Output Lags	Model	Layer1: Number of Neurons	Epochs	Batch Size
168	1	Bi-LSTM	32	10	128



**Figure 3.** Comparison of predictive values and actual values

**Table 6.** Algorithm and parameters

Number of Input Lags	Number of Output Lags	Model	Layer1: Number of Neurons	Epochs	Batch Size
168	24	MLP	128	100	128

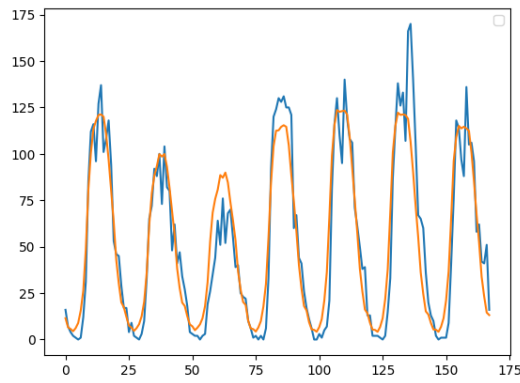


**Figure 4.** Comparison of predictive values and actual values

**Table 7.** Algorithm and parameters

Number of Input Lags	Number of Output Lags	Model	Layer1: Number of Neurons	Epochs	Batch Size
168	1	GRU	32	20	128

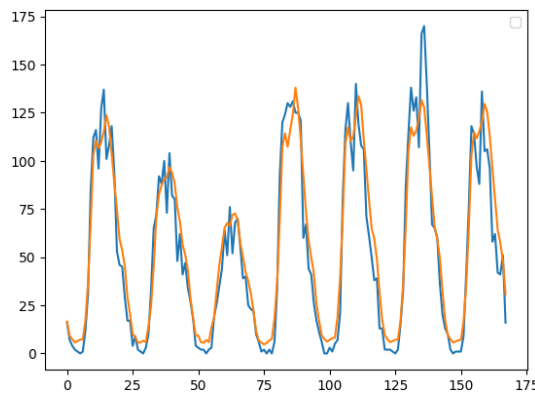




**Figure 5.** Comparison of predictive values and actual values

**Table 8.** Algorithm and parameters

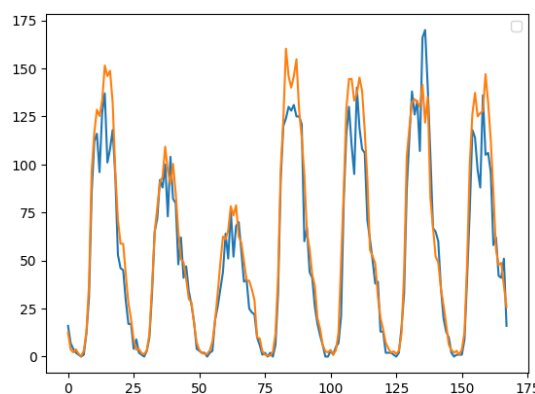
Number of Input Lags	Number of Output Lags	Model	Layer1: Number of Neurons	Epochs	Batch Size
168	1	Bi-LSTM	32	10	128



**Figure 6.** Comparison of predictive values and actual values

**Table 9.** Moving Average and parameters

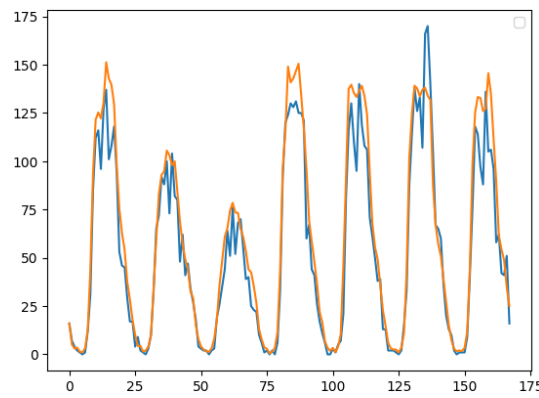
Mooving Window	Period
168	4



**Figure 7.** Comparison of predictive values and actual values

**Table 10.** Moving Average and parameters

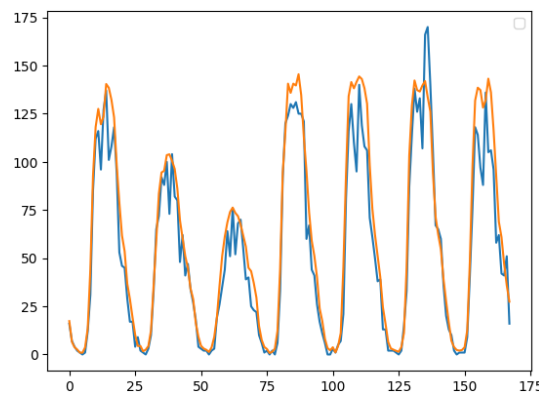
Mooving Window	Period
168	8



**Figure 8.** Comparison of predictive values and actual values

**Table 11.** Moving average and parameters

Mooving Window	Period
168	12



**Figure 9.** Comparison of Predictive Values and Actual Values

**Table 12.** Table of results

	<b>R2</b>	<b>RMSE</b>	<b>MSE</b>	<b>MAE</b>
MLP – 1	0.74	23.76	564.61	19.94
GRU – 1	0.42	35.5	1260.39	24.49
Bi-LSTM – 1	0.82	19.84	393.64	13.83
MLP – 2	0.86	17.46	304.80	15.15
GRU – 2	0.88	16.44	270.19	12.2
Bi-LSTM – 2	0.92	12.90	166.49	10.24
MA – 1	0.91	14.17	200.68	9.6
MA – 2	0.91	13.74	188.91	9.46
MA – 3	0.91	14.16	200.57	9.87

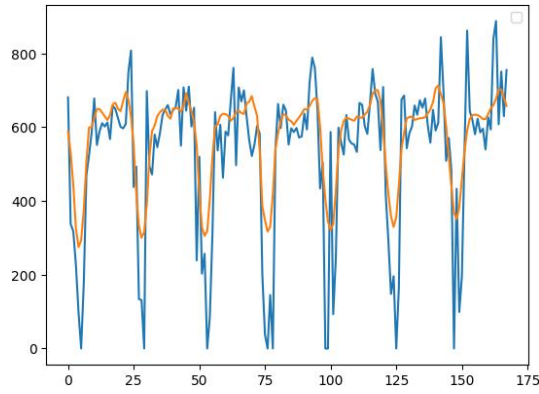
- The Bi-LSTM-2 model shows the best performance. The R2 value of this model is the highest (0.92) and the error metrics (RMSE, MSE, MAE) are the lowest.
- MA models (MA-1, MA-2, MA-3) also show very good performance, they stand out especially with their low MAE values.
- Among MA models, MA-2 performs better than MA-1 and MA-3.
- The GRU-1 model shows very low performance compared to other models.
- Among GRU models, GRU-2 performs better than GRU-1.
- Among MLP models, MLP-2 performs better than MLP-1.

Consequently, further studies on Bi-LSTM-2 and MA models may be beneficial. These models appear to provide the highest accuracy and lowest error rates.

**5.2 Results on the Average Talk Time**

**Table 13.** Algorithm and parameters

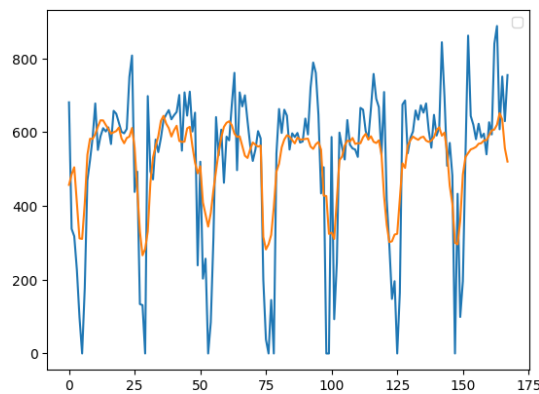
Number of Input Lags	Number of Output Lags	Model	Layer1: Number of Neurons	Layer2: Number of Neurons	Epochs	Batch Size
168	1	MLP	128	64	100	128



**Figure 10.** Comparison of predictive values and actual values

**Table 14.** Algorithm and parameters

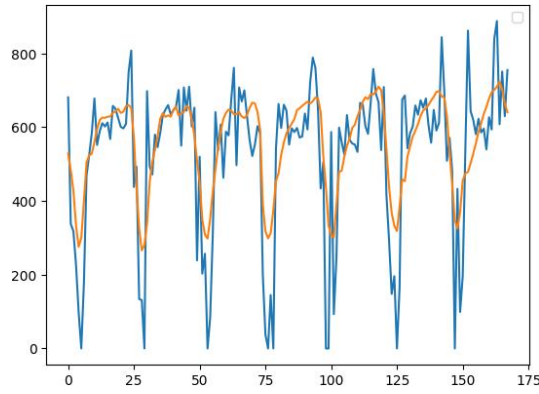
Number of Input Lags	Number of Output Lags	Model	Layer1: Number of Neurons	Layer2: Number of Neurons	Epochs	Batch Size
168	1	GRU	32	16	20	128



**Figure 11.** Comparison of predictive values and actual values

**Table 15.** Algorithm and parameters

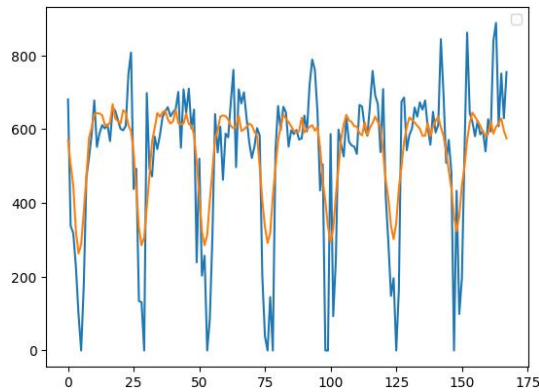
Number of Input Lags	Number of Output Lags	Model	Layer1: Number of Neurons	Layer2: Number of Neurons	Epochs	Batch Size
168	1	Bi-LSTM	32	16	10	128



**Figure 12.** Comparison of predictive values and actual values

**Table 16.** Algorithm and parameters

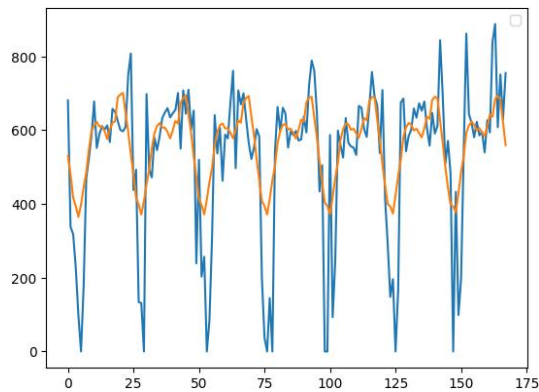
Number of Input Lags	Number of Output Lags	Model	Layer1: Number of Neurons	Layer2: Number of Neurons	Epochs	Batch Size
168	24	MLP	128	64	100	128



**Figure 13.** Comparison of predictive values and actual values

**Table 17.** Algorithm and parameters

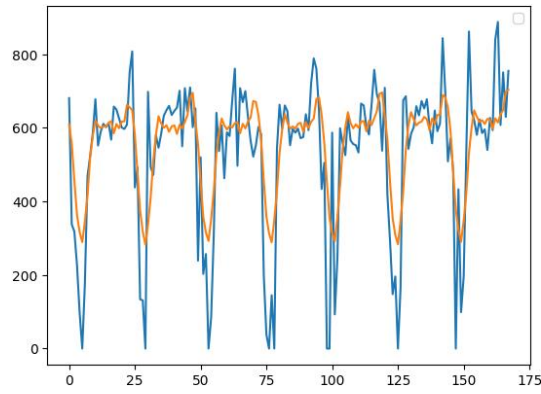
Number of Input Lags	Number of Output Lags	Model	Layer1: Number of Neurons	Epochs	Batch Size
168	1	GRU	64	20	128



**Figure 14.** Comparison of predictive values and actual values

**Table 18.** Algorithm and parameters

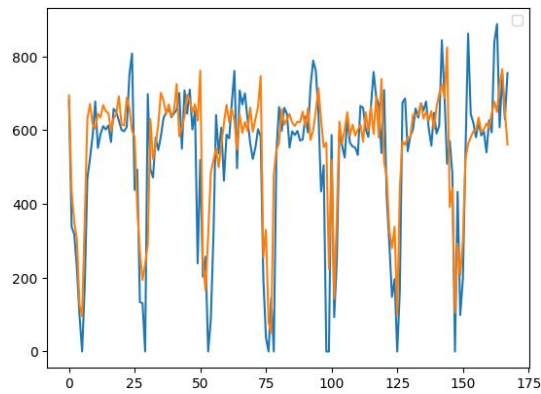
Number of Input Lags	Number of Output Lags	Model	Layer1: Number of Neurons	Epochs	Batch Size
168	1	Bi-LSTM	64	20	128



**Figure 15.** Comparison of predictive values and actual values

**Table 19.** Moving average and parameters

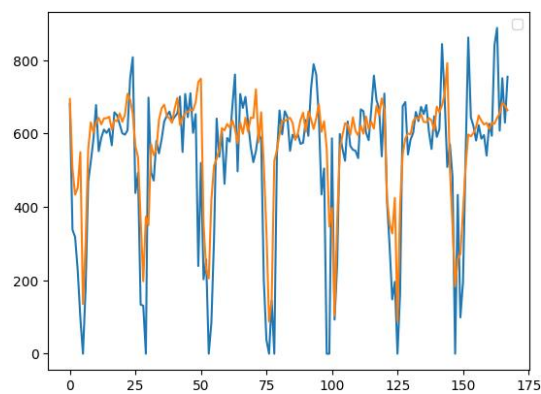
Mooving Window	Period
168	4



**Figure 16.** Comparison of predictive values and actual values

**Table 20.** Moving average and parameters

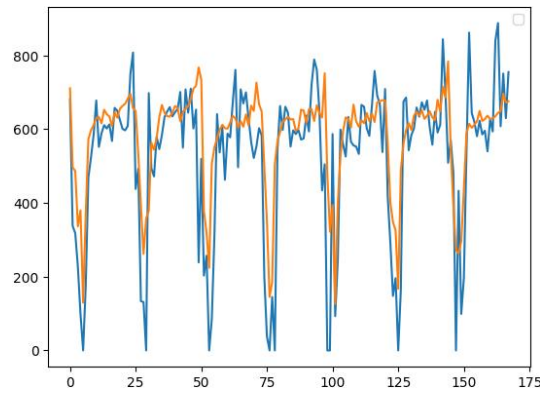
Mooving Window	Period
168	8



**Figure 17.** Comparison of predictive values and actual values

**Table 21.** Moving Average and parameters

Mooving Window	Period
168	12



**Figure 18.** Comparison of predictive values and actual values

**Table 22.** Table of results

	<b>R2</b>	<b>RMSE</b>	<b>MSE</b>	<b>MAE</b>
MLP – 1	0.58	135.47	18351.63	97.65
GRU – 1	0.54	142.71	20365.07	104.61
Bi-LSTM – 1	0.58	136.28	18572.83	100.63
MLP – 2	0.57	137.07	18789.36	98.39
GRU – 2	0.46	153.39	23527.73	108.0
Bi-LSTM – 2	0.58	135.89	18466.85	97.58
MA – 1	0.61	130.27	16970.7	91.12
MA – 2	0.55	140.29	19681.16	96.45
MA – 3	0.54	141.49	20019.79	99.4

- The MA-1 model shows the best performance. The R2 value of this model is the highest (0.61) and the error metrics (RMSE, MSE, MAE) are lower than other models.
- Among MA models, MA-1 performs better than MA-2 and MA-3.
- Bi-LSTM and MLP models generally exhibit similar performance and can be considered good alternatives.
- Among MLP models, MLP-1 performs better than MLP-2.
- The GRU-2 model shows the lowest performance compared to other models.
- Among GRU models, GRU-1 performs better than GRU-2.

Consequently, further studies on the MA-1 model may be beneficial. This model appears to provide the highest accuracy and lowest error rates. Other models also show generally acceptable performance, but the performance of the GRU-2 model needs improvement.

## 6 CONCLUSION

Call count and average talk time prediction aims to optimize productivity, manage agents' workload, and allocate an appropriate number of agents to be able to deliver the assistance customers need in a timely manner. When the number of future calls and average talk time cannot be predicted; There may be too many or not enough representatives. This situation leads to loss of time and cost. For this reason, in this study, artificial intelligence and statistics-based number of calls and average talk time estimation models have been developed for call centers. Prediction models were evaluated with R2, MSE, MAE and RMSE metrics.

According to the results obtained from the developed prediction models, it was seen that the Bi-LSTM-2 and MA models performed better in predicting the number of calls, and the MA-1 model performed better in predicting the average talk time.

## References

- [1] Zendesk. (2024, Jul. 23). *AI call center: A complete guide* [Online]. Available: <https://www.zendesk.com/blog/ai-call-center/>
- [2] E. Aydemir, M. Karaatli, G. Yilmaz, and S. Aksoy, "112 Acil cagri merkezine gelen cagri sayilarini belirleyebilmek icin bir yapay sinir aglari tahminleme modeli gelistirilmesi," *Pamukkale Üniversitesi Mühendislik Bilimleri Dergisi*, vol. 20, no. 5, pp. 145–149, 2014.

- [3] T. Albrecht, T. M. Rausch, and N. D. Derra, "Call me maybe: Methods and practical implementation of artificial intelligence in call center arrivals' forecasting," *Journal of Business Research*, vol. 123, pp. 267–278, 2021.
- [4] D. Leszko, "Time series forecasting for a call center in a Warsaw holding company," Ph.D. thesis, 2020.
- [5] R. A. Mohammed and P. Pang, "Agent personalized call center traffic prediction and call distribution," in *Neural Information Processing: 18th International Conference, ICONIP 2011*, Shanghai, China, 2011, Part II, pp. 1–10.
- [6] J. W. Taylor, "A comparison of univariate time series methods for forecasting intraday arrivals at a call center," *Management Science*, vol. 54, no. 2, pp. 253–265, 2008.
- [7] M. A. Kadioglu and B. Alatas, "Enhancing call center efficiency: Data driven workload prediction and workforce optimization," *The Eurasia Proceedings of Science Technology Engineering and Mathematics*, vol. 24, pp. 96–100, 2023.
- [8] S. Li, Q. Wang, and G. Koole, "Predicting call center performance with machine learning," in *Advances in Service Science: Proceedings of the 2018 INFORMS International Conference on Service Science*, pp. 193v199, 2019
- [9] S. Moazeni and R. Andrade, "A data-driven approach to predict an individual customer's call arrival in multichannel customer support centers," in *2018 IEEE International Congress on Big Data (BigData Congress)*, pp. 66–73, 2018.
- [10] D. Barrow and N. Kourentzes, "The impact of special days in call arrivals forecasting: A neural network approach to modelling special days," *European Journal of Operational Research*, vol. 264, no. 3, pp. 967–977, 2018.
- [11] N. Baldon, "Time series forecast of call volume in call centre using statistical and machine learning methods," 2019.
- [12] M. J. Hamayel and A. Y. Owda, "A novel cryptocurrency price prediction model using GRU, LSTM and bi-LSTM machine learning algorithms," *Ai*, vol. 2, no. 4, pp. 477–496, 2021.



## Understanding Large Language Models in Cybersecurity Domain

Bugra Kurt<sup>\*1</sup>, Aysu Irem Adem<sup>1</sup>, Mahmut Furkan Bakal<sup>2</sup>, Hussain Alburki<sup>1</sup>, Arda Sezen<sup>2</sup>

<sup>1</sup>Software Engineering, Atilim University, Ankara, Türkiye  
<sup>2</sup>Computer Engineering, Atilim University, Ankara, Türkiye

### Abstract

Addressing the use of Artificial Intelligence (AI) and Machine Learning (ML) solutions to handle security concerns is becoming more popular in the field of cybersecurity. Large Language Models (LLMs) have become extremely effective tools in this field, exhibiting remarkable performance on a wide range of prompt-oriented tasks. In this research, we perform a comparative study of four cybersecurity focused LLMs: Lily, Secure BERT, Secure BERT\_Plus, and CySecBERT. Our research attempts to evaluate how well these models perform in answering pre-formulated cybersecurity questions and their paraphrased forms. We determine each model's strengths and weaknesses through in-depth analysis, providing insight into how well it may be used to answer cybersecurity-related issues. Our results contribute to clarifying the complex Q&A aspect of LLM performance.

**Keywords:** Large language model, Artificial intelligence, Cybersecurity, Comparative analysis

## 1 INTRODUCTION

Especially with the enormous developments in technology during recent years, it is possible to say that technological devices are inevitable parts of our both personal and business lives. According to Schmeikal et. al. , technology has affected the individual life styles and the whole nature of the society [1]. Due to this significant role of the technological devices, both the people and the businesses might have the risk of being vulnerable against possible attacks. According to Lachkov et al., cybersecurity attacks are crucial issues for computing systems [2]. In addition, Cody et al. states that cyberattacks directly threaten national security and raise existential concerns [3]. This situation makes cybersecurity important more than ever. As investments are made in applying Artificial Intelligence and Machine Learning (AI/ML) based solutions to gain a strategic advantage in response time, analysis speed, and maneuverability for government and private industry applications, concerns about the inherent vulnerabilities of these technologies are growing [4]. Large language models (LLMs) have recently demonstrated unprecedented performance across a range of tasks based on natural language processing [5]. In this paper, we explore the essential role that LLMs play as platforms for addressing cybersecurity-related queries. In this article, it is evaluated how cybersecurity understanding and practices can be enhanced by comparing the differences between responses provided through direct and paraphrased definitions. For this purpose, both definitions taken from the internet and paraphrased versions of the definitions were asked to Secure BERT\_Plus, Secure BERT, CySec BERT and Lily LLMs and the accuracy percentage of the answers received were compared.

## 2 RELATED WORK

The combination of artificial intelligence (AI) and cybersecurity in recent years has spurred interest in using AI technology to improve penetration testing techniques. Adding AI sparring partners to penetration testers using large-language models (LLMs) like GPT-3.5 is one method. Within security testing assignments, this strategy aims to expedite low-level vulnerability research as well as high-level work planning. Furthermore, the advent of BERT-based language representation, which provides bidirectional context and overcomes the drawbacks of unidirectional models, has completely changed the way that language is understood and analyzed. These developments, demonstrated by research like that of Happe and Cito and Devlin et al., highlight the promise of AI-driven cybersecurity strategies while also posing significant ethical questions [6, 7].

### 2.1 Augmenting Penetration Testing with Large-Language Models (LLMs)

Software security testing, and penetration testing, has historically involved a lot of manual testing and analytical stages and high degrees of knowledge. But recent developments in artificial intelligence (AI) have prompted



researchers to investigate augmenting penetration testers with AI sparring partners by adopting large-language models (LLMs) like GPT-3.5. With security testing assignments, this method seeks to improve both high-level task planning and low-level vulnerability research. A recent study conducted by Happe and Cito explores the potential use of LLMs, specifically GPT-3.5, in penetration testing [6]. The study investigates two distinct use cases: high-level task planning and low-level vulnerability hunting within a vulnerable virtual machine. In the latter scenario, the researchers implemented a closed-feedback loop between LLM-generated low-level actions and a vulnerable virtual machine connected through SSH. This allowed the LLM to analyze the machine state for vulnerabilities and suggest concrete attack vectors, which were automatically executed within the virtual machine. The paper presents encouraging preliminary findings and suggests ways to enhance the use of LLMs for penetration testing assignments. It also brings up significant ethical questions about using AI sparring partners in security testing. By showing how LLMs can help penetration testers find vulnerabilities and increase testing efficiency overall, this study advances the investigation of AI-driven techniques in cybersecurity.

## 2.2 BERT-Based Language Representation

BERT presents a conceptually straightforward but empirically effective method of language representation. BERT produces state-of-the-art results on multiple NLP benchmarks, such as question answering, language inference, and natural language inference, by fine-tuning with just one extra output layer after pretraining on enormous corpus of text data. The BERT model outperforms other methods, like feature-based and fine-tuning approaches, for applying pretrained language representations to downstream tasks. Because BERT is bidirectional, as opposed to conventional unidirectional language models, it can overcome constraints in capturing contextual information, especially for tasks involving sentences and tokens. The “masked language model” (MLM) pretraining objective does this by randomly masking input tokens, and then training the model to predict the original vocabulary id of the masked tokens. BERT performs better on a variety of NLP tasks by removing the unidirectionality limitation and introducing bidirectional context. It is a very effective tool for language understanding and analysis due to its capacity to extract rich contextual information from both left and right contexts [7].

## 3 METHODOLOGY

In this section, the methodology of the study was explained. Primarily, we decided on some commonly used cybersecurity terms and found their definitions on Wikipedia which is used frequently while conducting search on the Internet. These definitions were asked as questions to some LLMs which are specialized in the specific domain of cybersecurity. The question set can be found on Table 1. Additionally, paraphrased versions of these definitions were also asked to same LLMs in order to see the effect of paraphrasing on performance and capability of these LLMs. The LLMs mentioned above are Secure BERT\_Plus, Secure BERT, CySecBERT and Lily.

**Table 1.** Question set

1	The <mask> project is a computer security project that provides information about security vulnerabilities and aids in penetration testing.	Metasploit
2	<mask> modeling is a process by which potential threats, such as structural vulnerabilities or the absence of appropriate safeguards, can be identified and enumerated, and countermeasures prioritized	Threat
3	<mask> is a software utility for automated discovering of SQL injection vulnerabilities in web applications	sqlmap
4	<mask> involves the systematic scanning of systems to gather information about potential vulnerabilities that can be exploited.	Reconnaissance
5	<mask> is the collection and analysis of data gathered from open sources	Open Source Intelligence (OSINT)
6	<mask> is a computer network administration software utility used to test the reachability of a host on an Internet Protocol (IP) network.	Ping
7	Operating System <mask> is the process of identifying the operating system on a targeted host by analyzing the responses to various packets sent to it.	Fingerprinting
8	An <mask> is a device or software application that monitors a network or systems for malicious activity or policy violations	Intrusion Detection System (IDS)

9	An <mask> is a piece of software sequence of commands that takes advantage of a vulnerability to cause unintended or unanticipated behavior to occur on computer software or hardware.	Exploit
10	<mask> is a flaw in a computer system that weakens the overall security of the device/system.	Vulnerability
11	<mask> is the act of proving an assertion, such as the identity of a computer system user.	Authentication
12	A data <mask> is the unauthorized exposure of personal information	Breach
13	A <mask> attack occurs when multiple systems flood the bandwidth or resources of a targeted system, usually one or more web servers	DDoS
14	A <mask> is grouping of multiple private computer networks or local hosts within the same infrastructure	Domain
15	<mask> is the process of encoding information that converts the original representation of the information into a ciphertext.	Encryption
16	<mask> is a network security system that monitors and controls incoming and outgoing network traffic based on predetermined security rules	Firewall
17	<mask> is any software intentionally designed to cause disruption to a computer to gain unauthorized access to system	Malware
18	A <mask> vulnerability is a security hole in a computer system unknown to its owners, developers or anyone capable of mitigating it	Zero-day
19	<mask> engineering is the psychological manipulation of people into performing actions or divulging confidential information	Social
20	A <mask> is a set of changes to a computer program or its supporting data designed to update or repair it	Patch

### 3.1 Secure BERT

Trained on a huge amount of cybersecurity data, SecureBERT is a domain-specific language model based on RoBERTa that has been adjusted and improved to comprehend and express cybersecurity textual data. SecureBERT is used to describe textual data related to cybersecurity. It was trained using a significant amount of in-domain text that was scraped from web sources. The cybersecurity corpus statistics compiled for Secure-BERT training consist of a total of 98,411 words sourced from articles, books, survey papers, blogs/news, Wikipedia articles related to cybersecurity, security reports, and video subtitles.

When compared to other models such as RoBERTa (foundation model), SecBERT, and SciBERT, SecureBERT has shown notably better performance in predicting masked words inside the text. Promising results have also been shown by SecureBERT in maintaining general English language representation [8].

### 3.2 Secure BERT\_Plus

By utilizing the processing capacity of eight A100 GPUs, this model is an enhanced version of the SecureBERT model, trained on a corpus eight times larger than its predecessor. This version, dubbed Secure BERT\_Plus results in an average 9% improvement in Masked Language Model (MLM) task performance. This development is a significant step toward reaching higher levels of competence in language comprehension and representation learning in the field of cybersecurity.

Based on RoBERTa, SecureBERT is a domain-specific language model that has been extensively trained on cybersecurity data and refined to comprehend and accurately represent cybersecurity textual data totaling 253,433 words by using articles, books, survey papers, Blogs/News, cybersecurity documentations, Wikipedia (cybersecurity), security reports, video subtitles and podcasts [9].

### 3.3 CySecBERT

CySecBERT is a general-purpose cybersecurity language model that has been pre-trained and is based on BERT. The methodology involves pre-training the model on a meticulously curated cybersecurity corpus, including scientific literature, Twitter data, web content, and the national vulnerability database. To accomplish this

objective, its is intended to adapt BERT to the cybersecurity domain through the utilization of domain-specific text corpora. The adaptation process is facilitated by a pipeline constructed with Huggingface and Weights&Biases. This ultimately resulted in the development of a pre-trained model based on bert-base-uncased. Training procedures are conducted on the Lichtenberg Cluster, where strategies are implemented to address issues such as catastrophic forgetting. These strategies involve adjustments to the learning rate, training steps, and dataset size, aiming to optimize the model's performance in the cybersecurity context while minimizing the risk of forgetting important learned information [10].

### 3.4 Lily-Cybersecurity-7B-v0.2

Lily works as a cybersecurity assistant. With 22,000 manually generated cybersecurity and hacking-related data pairs, it is a Mistral Fine-tune model. The dataset encompasses a broad range of topics within cybersecurity, covering areas such as threat management, incident response, encryption, network security, compliance, and emerging technologies [11].

## 4 RESULTS & DISCUSSION

The primary objective of this study is to assess the accuracy of responses from four language models specialized in the domain of cybersecurity: SecureBERT, SecureBERT\_Plus, CySecBERT and Lily. Specifically, we analysed the accuracy of four different language models in providing correct answers to predetermined questions and their paraphrased versions. In addition, we compared the performance of these language models on how accurately they answered the questions. This comparison helped us identify the strengths and weaknesses of the models and understand which model performed better in answering domain specific questions.

To achieve this goal, following research questions are prepared:

- RQ1: Which model demonstrates greater accuracy in its responses when providing answers to predetermined questions?
- RQ2: To what extent does the response accuracy differ between responses to predetermined questions and their paraphrased versions?

In this section, the results of the study are presented according to the research questions above. The findings of the study presented in this section provide valuable insights into the performance and capabilities of these language models, offering implications for their practical use and further development in the field of language models and cybersecurity.

### 4.1 RQ1: Which Model Demonstrates Greater Accuracy in Its Responses When Providing Answers to Predetermined Questions?

The performance of the three language models, namely SecureBERT, SecureBERT\_Plus, CySecBERT was evaluated based on their accuracy in answering a set of predetermined questions. SecureBERT correctly answered 12 out of 20 questions, resulting in a 60% accuracy rate. On the other hand, SecureBERT\_Plus demonstrated a slightly lower accuracy, correctly answering 11 out of 20 questions, with a 50% accuracy rate. These results are actually surprising since SecureBERT\_Plus is an advanced version of SecureBERT due to the number of items in datasets that they are trained with. A possible reason for this might be the limitation of our dataset. As it is also indicated in future work part, a deeper dataset with much more number of questions might change this situation. Furthermore, CySecBERT showed the lowest accuracy of all the models, successfully answering only 5 out of 20 questions, or 15% of the total. This indicates a significant need for improvement in its performance compared to the other models. It is also observed that these three language models provide unrelated answers like 'It' or 'This' when the first word of the sentence is the keyword that we are looking for. Therefore, it is recommended to be careful about these kinds of questions while asking them to these language models.

These results demonstrate the varying performance levels of different language models in understanding and responding to given questions in a specific domain. Detailed information about the correctness of the answers of these language models can be found on Table 2. Also the total performance accuracy of models can be found on Table 3.

**Table 2.** Results

SecureBERT	Result	CySecBERT	Result	SecureBERT Plus	Result
OpenVAS (%17)	Wrong	Sans (%34)	Wrong	Metasploit (%17)	Correct
Threat (%96)	Correct	Threat (%97)	Correct	Threat (%95)	Correct
OWASP (%12)	Wrong	Apache (%20)	Wrong	It (%56)	Wrong
It (%86)	Wrong	It (%20)	Wrong	It (%52)	Wrong
OSINT (%99)	Correct	Collection (%17)	Wrong	This (%39)	Wrong
Ping (%84)	Correct	Snort (%29)	Wrong	It (%57)	Wrong
Identification (%74)	Wrong	Identification (%88)	Wrong	Fingerprinting (%68)	Correct
HIDS (%50)	Wrong	Agent (%60)	Wrong	IDS (%61)	Correct
Exploit (%96)	Correct	Exploit (%78)	Correct	Exploit (%97)	Correct
It (%33)	Wrong	There (%32)	Wrong	Vulnerability (%51)	Correct
Authentication (%94)	Correct	Authentication (%13)	Correct	Authentication (%38)	Correct
Breach (%63)	Correct	Breach (%79)	Correct	Breach (%78)	Correct
DDoS (%92)	Correct	Simultaneous (%19)	Wrong	DDoS (%69)	Correct
Federation (%40)	Wrong	LAN (%25)	Wrong	Cluster (%55)	Wrong
Encryption (%96)	Correct	Encoding (%38)	Wrong	Encoding (%35)	Wrong
Firewall (%34)	Correct	Snort (%22)	Wrong	It (%57)	Wrong
Malware (%53)	Correct	Software (%86)	Wrong	Ransomware (%52)	Wrong
Software (%63)	Wrong	Software (%41)	Wrong	Security (%46)	Wrong
Social (%100)	Correct	Social (%95)	Correct	Social (%95)	Correct
Patch (%94)	Correct	Change (%26)	Wrong	Patch (%52)	Correct

**Table 3.** Total accuracy

Language Model	Correct Answer	Wrong Answer	Percentage
SecureBERT	12	8	60
SecureBERT Plus	11	9	55
CySecBERT	5	15	25

Since the other model, Lily, provides a complete sentence as a response to questions, we used Cosine Similarity method to find the similarity between its response and the original definition taken from Wikipedia as already explained in the Methodology part. Cosine Similarity rates can be found in the following table.

**Table 4.** Cosine similarity rates with original definition

Question Asked to Lily	Cosine Similarity of response of Lily with original definition
What is Metasploit?	0.2032
What is Threat Modeling?	0.2277
What is sqlmap?	0.2656
What is Reconnaissance?	0.1611
What is OSINT?	0.1058
What is Ping?	0.0696
What is Operating System Fingerprinting?	0.1825
What is IDS?	0.1656
What is Exploit?	0.1527
What is Vulnerability?	0.2207
What is Authentication?	0.2371
What is Breach?	0.1476
What is DDoS?	0.1292
What is Domain?	0.0778
What is Encryption?	0.0875
What is Firewall?	0.0912
What is Malware?	0.1333
What is Zero-day?	0.1101
What is Social Engineering?	0.1533
What is Patch?	0.1544

Lily provides the answers in its own cheerful way that makes the response somehow unofficial. For instance, it defines a firewall as a “guardian of a computer network” or a malware as a “villain in the cybersecurity world”. Even though these explanations make the usage of Lily fun for cybersecurity enthusiasts, it is observed that this behavior of Lily may decrease the Cosine Similarity rates between its responses and the original definition of commonly used cybersecurity terms. To evaluate this situation, most related and official parts of Lily’s responses to each question were extracted. Then, the Cosine Similarity rates were measured again between these extracted parts and the original definitions. It is found that for 80% of the questions (16 out of 20), there was an increase in the Cosine Similarity rates when the most related parts of Lily’s responses are separated from its funny explanations. Detailed results can be found in the following table.

**Table 5.** Comparison between cosine similarity rates

Cosine Similarity of response of Lily (with her cheerful way) with Wiki definition	Cosine Similarity of response of Lily (modified) with Wiki definition	Change
0.2032	0.2631	5.99%
0.2277	0.2817	5.40%
0.2656	0.3162	5.06%
0.1611	0.3198	15.87%
0.1058	0.2401	13.43%
0.0696	0.1632	9.36%
0.1825	0.3265	14.40%
0.1656	0.2611	9.55%
0.1527	0.2592	10.65%
0.2207	0.3162	9.55%
0.2371	0.6324	39.53%
0.1476	0.1048	-4.28%
0.1292	0.1025	-2.67%
0.0778	0	-7.78%
0.0875	0.1005	1.30%
0.0912	0.1601	6.89%
0.1333	0.2016	6.83%
0.1101	0.0771	-3.30%
0.1533	0.3651	21.18%
0.1544	0.1973	4.29%

#### 4.2 RQ2: To What Extent Does the Response Accuracy Differ Between Responses to Predetermined Questions and Their Paraphrased Versions?

After the above procedures, we applied the paraphrasing process to the questions in the question set we had. Then we asked the new questions to the SecureBERT and SecureBERT\_Plus models we use. While the LILY model gives answers to the questions in the form of explanations, the other three models give five answers with their percentages that can fill a structure called <mask> that we put in the questions. For this reason, the LILY model was not used in this section so that we could compare the paraphrase effect. In addition, the CySecBERT model was not taken into account in this section because it gave incorrect answers to most of the questions. You can find change rates before and after the paraphrasing applied to these two models on following tables.

**Table 6.** Change rates for SecureBERT

	SecureBERT	SecureBERT(Paraphrased)	Change
Q1	Wrong	Wrong	-
Q2	Threat (%96)	Threat (%83)	-13%
Q3	OWASP (%12)	sqlmap (%50)	50%
Q4	Wrong	Wrong	-
Q5	OSINT (%99)	OSINT (%12)	-87%
Q6	Ping (%84)	Ping (%36)	-48%
Q7	Wrong	Fingerprinting (%97)	97%
Q8	Wrong	Wrong	-
Q9	Exploit (%96)	Wrong	-96%
Q10	Wrong	Wrong	-

Q11	Authentication (%94)	Authentication (%87)	-7%
Q12	Breach (%63)	Breach (%83)	20%
Q13	DDoS (%92)	DDoS (%77)	-15%
Q14	Wrong	Wrong	-
Q15	Encryption (%96)	Wrong	-96%
Q16	Firewall (%34)	Wrong	-34%
Q17	Malware (%53)	Wrong	-53%
Q18	Wrong	Wrong	-
Q19	Social (%100)	Social (%100)	0%
Q20	Patch (%94)	Patch (%93)	-1%

**Table 7.** Change rates for SecureBERT\_Plus

	SecureBERT Plus	SecureBERT Plus(Paraphrased)	Change
Q1	Metasploit (%17)	Metasploit (%9)	-8%
Q2	Threat (%95)	Threat (%90)	-5%
Q3	Wrong	sqlmap (%71)	71%
Q4	Wrong	Wrong	-
Q5	Wrong	OSINT (%27)	27%
Q6	Wrong	Wrong	-
Q7	Fingerprinting (%68)	Fingerprinting (%91)	-23%
Q8	IDS (%61)	Wrong	-61%
Q9	Exploit (%97)	Wrong	-97%
Q10	Vulnerability (%51)	Wrong	-51%
Q11	Authentication (%38)	Wrong	-38%
Q12	Breach (%78)	Breach (%84)	6%
Q13	DDoS (%69)	DDoS (%68)	-1%
Q14	Wrong	Wrong	-
Q15	Wrong	Wrong	-
Q16	Wrong	Wrong	-
Q17	Wrong	Wrong	-
Q18	Wrong	Wrong	-
Q19	Social (%95)	Social (%100)	5%
Q20	Patch (%52)	Patch (%81)	29%

According to the data in this table, after paraphrasing, there was a total decrease in accuracy rates of 71% in the SecureBert model and 61% in the SecureBERT\_Plus model. We think that this result is related to the deficiencies in generalization and interpretation ability of these two LLMs caused by insufficient data diversity.

## 5 FUTURE WORK

The most important limitation of this study is about the dataset. Therefore, using a dataset with more number of questions may enhance the reliability of the study especially in terms of the unexpected results. Additionally, there might be more language models to find and use in this study to make it much more general.

## References

- [1] B. Schmeikal, H. Hogeweg-de Haart, and W. Richter, *Impact of Technology on Society: A Documentation of Current Research*, Elsevier, 2013
- [2] P. Lachkov, L. Tawalbeh, and S. Bhatt, "Vulnerability assessment for applications security through penetration simulation and testing," *Journal of Web Engineering*, vol. 21, no. 7, pp. 2187–2208, 2022, doi: 10.13052/jwe1540-9589.2178
- [3] T. Cody, E. Meno, P. Beling, and L. Freeman, "Whole campaign emulation with reinforcement learning for cyber test," *IEEE Instrumentation & Measurement Magazine*, vol. 26, no. 5, pp. 25–30, Aug. 2023, doi: 10.1109/MIM.2023.10208253
- [4] Y. Stefinko, A. Piskozub, and R. Banakh, "Manual and automated penetration testing. Benefits and drawbacks. Modern tendency," in *2016 13th International Conference on Modern Problems of Radio Engineering, Telecommunications and Computer Science (TCSET)*, Lviv, Ukraine, 2016, pp. 488–491, doi: 10.1109/TCSET.2016.7452095.

- [5] K. Tran, M. Standen, J. Kim, D. Bowman, T. Richer, A. Akella, and C.-T. Lin, “Cascaded reinforcement learning agents for large action spaces in autonomous penetration testing,” *Appl. Sci.*, vol. 12, art. no. 11265, 2022, doi: 10.3390/app122111265
- [6] A. Happe and J. Cito, “Understanding Hackers’ work: An empirical study of offensive security practitioners,” in *31st ACM Joint European Software Engineering Conference and Symposium on the Foundations of Software Engineering*, 2023, pp. 1669–1680, doi: 10.1145/3611643.3613900.
- [7] J. Devlin, M. W. Chang, K. Lee, and K. Toutanova, “BERT:Pre-training of deep bidirectional transformers for language understanding,” *arXiv preprint*, arXiv:1810.04805, 2018.
- [8] Ehsanaghaei. GitHub - ehsanaghaei/SecureBERT: SecureBERT is a domain-specific language model to represent cybersecurity textual data. Available: <https://github.com/ehsanaghaei/SecureBERT>
- [9] Ehsanaghaei. GitHub - ehsanaghaei/SecureBERT-plus: An extended version of SecureBERT, trained on top of both base and large version of RoBERTa using 10 GB cybersecurity-related data. Available: <https://github.com/ehsanaghaei/SecureBERT-plus>
- [10] M. Bayer, P. Kühn, R. Shanehsaz, and C. Reuter, “CYSECBERT: A domain-adapted language model for the cybersecurity domain,” *arXiv (Cornell University)*, 2022, doi: 10.48550/arxiv.2212.02974
- [11] segolilylabs/Lily-Cybersecurity-7B-v0.2 · Hugging Face. Available: <https://huggingface.co/segolilylabs/Lily-Cybersecurity-7B-v0.2>



## Enhancing FOPID Controller Performance in a 3-DOF Planar Manipulator

**Benaoumeur Ibari<sup>\*1</sup>, Mourad Hebali<sup>1</sup>, Baghdadi Rezali<sup>1</sup>, Omar Medjad<sup>1</sup>, Menaouer Bennaoum<sup>1</sup>, Hocine Abdelhak Azzedine<sup>1</sup>, Abdelkader Maachou<sup>1</sup>**

<sup>1</sup>*Department of Electrotechnical, University Mustapha Stambouli Mascara, 29000, Mascara, Algeria*

---

### Abstract

This paper introduces a self-tuning approach for FOPID (Fractional Order PID) controller implementation in robot manipulators on the artificial networks. For the proposed approach, the dynamic of 3-DOF planer manipulator model is developed using Euler-Lagrange. The proposed approach takes the advantages to estimate the requirements uncertainty parameters of the FOPID controller. Its solves the problem of the tuning of FOPID controller parameter with regard to disturbances in input torque to improve its control performance. Simulation results using the dynamic of the robot with varying load conditions prove the effectiveness of the proposed approach in the trajectory problems, and artificial algorithm can achieve the robustness and the tracking performance.

**Keywords:** *Robot manipulator, FOPID control, Position tracking, Optimal control*

---





## Can NLP Combined with AI Prevent Language Extinction: A Case Study of Turkish

Anil Kus<sup>\*1</sup>, Cigdem Inan Aci<sup>2</sup>

<sup>1</sup>Computer Technologies, Toros University, Mersin, Türkiye

<sup>2</sup>Computer Engineering, Mersin University, Mersin, Türkiye

### Abstract

Languages are regarded as one of the most crucial elements of a culture. Despite Turkish being a structurally rich language, it has been exposed to a significant influx of foreign words and structures, especially with the advent of the digital age and technological advancements. The frequent use of non-Turkish words within Turkish sentences, especially in social media content and online news, is perceived as a negative trend for the future of the Turkish language. The incorporation of words from different languages disrupts the structure and uniqueness of Turkish, posing a potential threat to the usage of Turkish words in the long term. This study is based on a model designed to identify non-Turkish words in sentences and then reconstruct the sentences using Turkish words to prevent damage to the Turkish language and to preserve it. The deep learning based GPT algorithm, which is one of the Large Language Models that have gained increasing popularity in recent years, was chosen for this study. The results of the study were evaluated using three different similarity algorithms. Similarity scores of up to 96% were obtained for texts written in correct Turkish. It is expected that the results of the study will contribute to Turkish Natural Language Processing studies.

**Keywords:** Turkish language, Text similarity, Large language models, Deep learning

## 1 INTRODUCTION

In the contemporary era of globalization, linguistic variety encounters unparalleled hurdles, with many languages teetering on the verge of disappearing. The swift globalization pace, combined with the supremacy of major languages, has marginalized and put at risk numerous minor languages. Nonetheless, technological progress offers a distinct chance to tackle this predicament and safeguard linguistic diversity for forthcoming generations.

According to the Unesco World Atlas of Languages, there are 8,324 languages (spoken and signed) documented by governments, public institutions and academic communities around the world, out of which approximately 7,000 are still alive. However, the Distribution of these languages is highly disparate. Surprisingly, only 3% of the global population is responsible for speaking 96% of all documented languages, while approximately 97% of the world's population, totaling 7.5 billion individuals, communicate in just around 250 languages. This means that a mere 4% of all documented languages are spoken by the vast majority of people worldwide [1].

Over the course of history, languages have naturally transformed and at times vanished from use. However, the current rate of language loss far exceeds what can be considered "natural". According to some linguists, between 50% and 90% of languages are expected to become highly endangered or extinct by the end of this century. This rapid increase in language endangerment can be caused by cultural, political, and economic marginalization, as well as the dominance of global imperialism [2].

The rise of Artificial Intelligence (AI) signifies a groundbreaking time for the preservation and revival of endangered languages, offering numerous benefits in linguistic documentation, analysis, and education. In the realm of documentation and linguistic analysis, AI technologies play a crucial role in streamlining intricate processes, thereby making notable contributions to safeguarding linguistic legacy. AI-powered automated transcription and translation tools have proven invaluable in accurately transcribing and translating spoken language, thereby facilitating the conservation of oral traditions, grammatical structures, and lexical subtleties characteristic of endangered languages. Additionally, Natural Language Processing (NLP) tools, a branch of AI, provide linguists with powerful analytical capabilities, enabling them to identify linguistic patterns, grammatical structures, and contextual nuances within large datasets. AI-driven morphological analysis enriches linguistic documentation by uncovering the complexities of word structures and their semantic nuances, thereby supporting

the creation of dictionaries and comprehensive linguistic repositories. Furthermore, AI significantly contributes to digital archiving initiatives by facilitating the creation of multimedia archives enhanced with video and audio recordings [3].

The beneficial effects of AI on endangered languages are significant and varied, encompassing linguistic documentation, analysis, and language acquisition. Ongoing technological advancements emphasize the imperative incorporation of AI within collaborative endeavors focused on the conservation and revitalization of endangered languages. This strategic integration safeguards their longevity and cultural vitality, thereby ensuring their preservation for posterity [4]. For instance, AI-based transcription technology has been effectively utilized to document the Cherokee language. Through the automation of transcription, linguists and community members can proficiently translate oral narratives into written format, thereby safeguarding grammatical structures, vocabulary, and cultural subtleties. Consequently, this has streamlined the development of digital repositories and linguistic materials dedicated to the Cherokee language [5]. Another success story is AI-driven language learning apps have been instrumental in the resurgence of the Maori language, is an indigenous language of New Zealand. These apps feature interactive tutorials, gamified components, and tailored learning experiences, fostering heightened engagement and skill development among users. Furthermore, the inclusion of Maori cultural elements in these AI tools ensures authenticity and resonance with the community's language revitalization objectives [3].

In today's digital age, there is an observable trend towards individuals using languages beyond their native tongues. This inclination can be attributed to several factors, including the widespread utilization of diverse linguistic frameworks, the necessity for intercultural communication, and the impacts of global trade and travel. Although Turkish is not categorized as an endangered language, its pristine form is gradually eroding. Despite concerted endeavors by linguists, academicians, and intellectuals to preserve the integrity of the Turkish language, the inexorable penetration of technology, coupled with the burgeoning assimilation of foreign lexicons, particularly prevalent among the younger demographic, precipitates the infiltration of English, German, French, and other linguistic elements into Turkish discourse, thereby eliciting linguistic degeneration. It has become common in visual media and social media to include foreign words in Turkish sentences. This phenomenon may lead to the gradual weakening and eventual extinction of the mother tongue over time. The aim of this study is to preserve the Turkish language using AI-supported NLP methods and to reintroduce the use of Turkish words in texts, videos, and conversations. To achieve this goal, detection of foreign words in Turkish texts (which could be articles or blog posts, as well as subtitles of movies or songs) and automatic replacement of these words with their Turkish equivalents has been implemented.

A study was conducted to develop an application that detects sentences commonly used in social and visual media platforms, internet news websites, and also daily life, which contain foreign words, using Large Language Models (LLMs), followed by automatically reforming these words and generating new sentences in Turkish.

Finally, sentences recreated by LLMs were compared with sentences that should already exist in Turkish grammar rules. This comparison was made using three different similarity algorithms to determine how accurately the system provided results.

## 2 LITERATURE REVIEW

The resurgence of interest in the field of NLP with AI technologies has intensified research in this area. Technologies such as Generative AI and LLMs have the potential to revive languages that are dwindling in usage, particularly those found across the globe. In the literature, there are various studies in multiple languages related to this topic.

Zhang et al. (2022) focus on exploring the potential of NLP in revitalizing endangered languages. Initially, they propose three guiding principles for NLP practitioners to facilitate collaboration with language communities and discuss three ways in which NLP can support language education. They then examine Cherokee, an endangered Native American language, as a case study. After analyzing the language's history, linguistic characteristics, and available resources, they identify meaningful avenues for collaboration between NLP practitioners and community partners. They recommend two strategies for enhancing Cherokee language resources using machine-assisted processing and highlight several NLP tools of interest to the Cherokee community. The study utilizes Machine Translation (MT), Optical Character Recognition (OCR), and Automatic Speech Recognition (ASR) techniques, yielding promising outcomes for Cherokee language revitalization. For instance, employing two ASR models - one for audio-to-phonetic text and another for audio-to-syllabic text-contributes to language documentation, achieving a noteworthy F1-Score of 17.9, indicative of encouraging progress [2].

Prud'hommeaux et al. present findings from a study where linguists and community members, possessing different levels of language proficiency, transcribe audio recordings of an endangered language within specified time constraints, with and without the aid of Automatic Speech Recognition (ASR). Their research reveals notable reductions in both transcription time and error rates when ASR corrections are applied, benefiting language learners across proficiency levels. A total of 12 hours of Seneca recordings were amassed and transcribed. Moreover, various deep neural ASR architectures were explored, encompassing neural models available in Kaldi, DeepSpeech [6], wav2vec [7], and a proprietary fully convolutional architecture (Thai et al., 2020), with and without employing transfer learning and data augmentation techniques. Their most effective system currently achieves word error rates (WER) approaching 25% [8].

Wassie and etc. investigated various approaches to enhance MT for the Ge'ez language, including transfer learning from related languages, optimizing shared vocabulary and token segmentation methods, fine-tuning large pre-trained models, and utilizing LLMs for few-shot translation with fuzzy matches. They devised a multilingual neural machine translation (MNMT) model tailored to the relatedness of languages, yielding an average performance enhancement of approximately 4 BLEU compared to conventional bilingual models. Additionally, they endeavored to fine-tune the NLLB 200 model, among the most sophisticated translation models available, but found its performance lacking with only 4k training samples for Ge'ez. Furthermore, they experimented with employing GPT-3.5, a cutting-edge LLMs, for few-shot translation with fuzzy matches, leveraging embedding similarity-based retrieval to identify contextual examples from a parallel corpus. Their observations revealed that GPT-3.5 achieved an impressive BLEU score of 9.2 without prior knowledge of Ge'ez, albeit still lower than the MNMT baseline of 15.2 [9].

Rijhwani et al. tackled the challenge of extracting text from resources written in critically endangered languages. They curated a benchmark dataset comprising transcriptions from scanned books in three such languages and conducted a comprehensive examination demonstrating the limitations of general-purpose OCR tools in handling the data-scarce nature of endangered languages. To address this issue, they devised an OCR postcorrection technique specifically tailored to facilitate training in this context of limited data availability. This approach led to an average reduction of 34% in recognition error rates across the three languages, showcasing its effectiveness in improving OCR accuracy [10].

### 3 MATERIAL AND METHOD

The increasing trend of using languages other than one's native tongue in the digital age poses a threat to the integrity of the Turkish language. While Turkish is not currently endangered, its authenticity is gradually eroding due to the pervasive influence of foreign languages, particularly among the younger demographic. This phenomenon is exacerbated by the widespread use of digital and visual media platforms, where foreign words are commonly incorporated into Turkish discourse, potentially leading to the gradual weakening and eventual extinction of the mother tongue.

This study suggests addressing the issue by employing proposed methods to conserve and reintegrate Turkish words into texts, videos, and conversations. For this process, the following steps were followed.

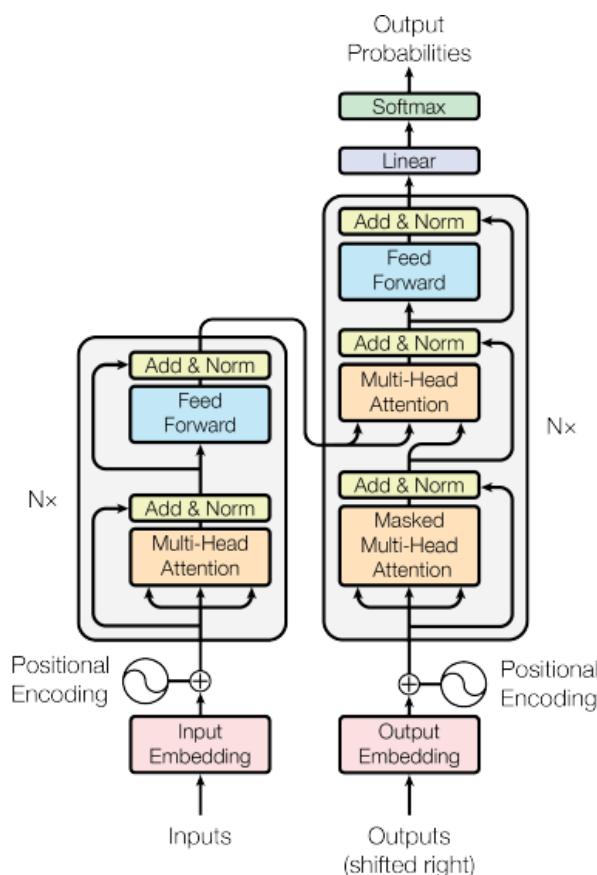
Firstly, due to a lack of an appropriate dataset, we created our own diverse collection of Turkish texts, encompassing academic articles, blog entries, social media posts, online news, and subtitles from various multimedia sources. Then, second step is non-Turkish word detection, advanced NLP algorithms by LLMs is utilized to detect instances of foreign word integration in Turkish discourse. In order to substitute the words, we proposed automated algorithms to replace detected foreign words with their Turkish equivalents. Ensured replacements maintain semantic similarity, contextual relevance, and linguistic integrity. In our model integration, we incorporated Deep Learning (DL) model to iteratively refine the replacement algorithm. Continuously adapting the system to evolving linguistic trends and nuances through ongoing learning.

Finally, the effectiveness of the solution through comparative analysis of texts pre- and post-implementation is evaluated. The most popular similarity algorithms used in order to assess and compare the texts between generated by proposed model and the manually corrected text.

This study seeks to preserve the linguistic purity and vitality of the Turkish language by systematically utilizing AI-driven NLP techniques, aiming to prevent the infiltration of foreign words and ensure its resilience in the digital age.

### 3.1 Large Language Models

Recently, widely used, LLMs are fundamental models utilizing DL in tasks such as NLP and Natural Language Generation. LLMs are pre-trained on vast amounts of data to aid in learning the complexity and connections of language. For this training process, techniques such as fine-tuning, in-context learning, and zero/one/few shot learning are applied. LLMs, essentially Transformer-based neural networks introduced in a paper by Google engineers in 2017, aim to predict the next likely text. The complexity and performance of a model can be evaluated based on the number of parameters it has. These parameters are the factors considered when producing output. Popular LLMs such as BLOOM, NeMO LLM, XLNet, Cohere, and GPT are already available, with their numbers increasing every day. In this study, GPT-3.5 LLMs have been preferred [11].



**Figure 1.** Architecture of transformer model

Figure 1 shows that the Transformer model employs a self-attention mechanism to extract features for each word, determining the significance of all other words in the sentence relative to the word in question. Unlike traditional approaches, it does not rely on recurrent units for feature extraction, opting instead for weighted sums and activations, allowing for highly parallelizable and efficient computations.

The architecture reveals an encoder model on the left and a decoder on the right, each comprising a central block of “an attention and a feed-forward network”, repeated  $N$  times. Before exploring these components, it is essential to thoroughly examine the self-attention mechanism, a core concept of the Transformer model.

### 3.2 Similarity algorithms

Text similarity assessment is a crucial aspect in various NLP tasks like information extraction, machine translation, and text summarization [12]. Similarity algorithms are methods used to measure the likeness or resemblance between texts, documents, or linguistic elements such as words or sentences.

In this study, three different similarity algorithms were employed to compare texts purified of foreign languages by LLMs with texts written according to Turkish language rules. The reason for choosing these algorithms is their frequent usage in the literature concerning text similarity.

**Cosine Similarity:** This algorithm measures the cosine of the angle between two vectors in a multidimensional space. In NLP, documents or sentences are typically represented as vectors, where each dimension corresponds to a word or a feature. Cosine similarity is often used to compare the similarity of documents or sentences based on their word embeddings or vector representations [13].

$$\text{Cosine Similarity } (A, B) = \frac{A \cdot B}{\|A\| \times \|B\|} \quad (1)$$

As shown in Formula (1), it quantifies the similarity of the direction of two vectors irrespective of their magnitude. The result is a value between -1 and 1, where 1 indicates perfect similarity, 0 indicates no similarity, and -1 indicates perfect dissimilarity.

**Jaccard Similarity:** This algorithm calculates the similarity between two sets by comparing their intersection to their union. In NLP, it's frequently used to measure the similarity between two documents or sets of words. For example, when comparing the presence of words in documents or the overlap between sets of words [14].

$$J(A, B) = \frac{|A \cap B|}{|A \cup B|} \quad (2)$$

The Jaccard Similarity coefficient is computed by dividing the count of shared elements between two sets by the total count of distinct elements in those sets. This yields a value ranging from 0 to 1, where 0 signifies absence of shared elements (complete dissimilarity) and 1 signifies that the sets are identical.

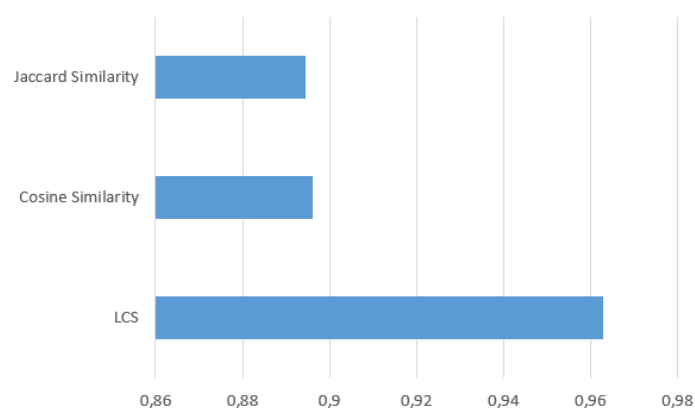
**Longest Common Subsequence (LCS):** LCS identifies the longest shared subsequence between two texts. This subsequence encapsulates the most similar portions of the texts. The algorithm considers the structural similarity between texts, examining not only the order of words but also the specific arrangement of words or characters within the texts [15].

### 3.3 Dataset and Technical Details

An application developed using the Python programming language within the Anaconda platform and coded in the Spyder, Integrated Development Environment (IDE), was created to contribute to the Turkish language. The entire study can be viewed at “<https://github.com/anilkus>”. In the first stage of the study, an original dataset consisting of 100 text files containing sentences with non-Turkish words was created. Subsequently, the corrected versions of these sentences, written in accordance with Turkish grammar rules by the application, were compared. Comparison was conducted by taking the average of the results of three different similarity algorithms. The scores of the similarity algorithms range from 0 to 1, where a score of 1 indicates a higher resemblance as it approaches towards 1.

## 4 RESULTS AND DISCUSSION

In this study, an original dataset comprising sentences used in visual/written media, news websites, or daily life, containing non-Turkish words, was created. The GPT model from the LLMs was utilized to detect and replace foreign words with their Turkish equivalents. The replaced sentences were compared with their counterparts written in accordance with Turkish language rules using similarity algorithms, and success scores were obtained. The average of all scores was calculated, and an evaluation was made accordingly.



**Figure 2.** The success scores of the model according to similarity algorithms

As seen in Figure 2, the similarity ratio of the recreated sentences to the original ones was calculated as 0.9628 in LCS, 0.8962 in Cosine similarity, and 0.8945 in the Jaccard similarity algorithm. As the results indicate, the accuracy rate of the developed system is high. Each similarity metric employs distinct mathematical formulas and computation methods. For instance, LCS focuses on finding the longest common subsequence between two sequences, while Cosine similarity measures the cosine of the angle between two vectors, and Jaccard similarity assesses the intersection over the union of sets. As a result, discrepancies in scores can arise due to these methodological differences. In addition, the characteristics of the language and dataset used can influence the performance of similarity metrics. Certain metrics may handle specific language structures or data distributions more effectively, leading to variations in scores depending on the context.

<b>Cümle</b>	Mülakatlarda hazır olmak çok önemli. Özellikle hardskillslerini göstermek olumlu sonuçlanmasına yardımcı olabilir.
<b>LLM</b>	Mülakatlara hazır olmak çok önemlidir. Özellikle sert becerilerini göstermek olumlu sonuçlanmasına yardımcı olabilir.
<b>Doğrusu</b>	Mülakatlara hazır olmak çok önemlidir. Özellikle teknik becerilerini göstermek olumlu sonuçlanmasına yardımcı olabilir.

**Figure 3.** Example sentence

In Fig 3, an example study is showed where a sentence containing foreign words has been corrected using LLMs. However, due to the direct translation, errors have occurred. It can be said that LLMs are still open to improvement, especially in Turkish translations.

It has been observed that the complex structure of Turkish language leads to semantic errors in many sentences. For instance, in the sentence “Presentable görünmek iş hayatında önemlidir. PR yapmak istiyorsan sosyal medyayı iyi kullanmalısın.” (It is important to appear presentable in business life. If you want to do PR, you should use social media well.), the application translated the word “presentable” as “able to present”, and failed to interpret the term “PR”. Furthermore, the application occasionally detected certain Turkicized words as non-Turkish and felt the need to replace them. These instances have resulted in decreased success scores.

## 5 CONCLUSION

In the current age, the gradual disappearance of languages has emerged as a critical issue. The younger generation, which spends a significant amount of time on digital platforms, often exhibits careless behavior in this regard, frequently using foreign words that harm their native languages. This study presents the development of a system designed to detect non-Turkish words used in the Turkish language and generate revised sentences. The application employs the most common algorithm, GPT-3.5, from LLMs, and the generated texts are evaluated using three different similarity algorithms. The results demonstrate that this approach achieves high success.

One of the limitations of this study is the restricted availability of Turkish datasets. It is also recommended to evaluate the study with different metrics. The limited token count of the algorithm used has also hindered the analysis of longer sentences. Future work aims to develop this system into a real-time correction tool. For instance, during a live conference, the system could immediately correct any incorrect words or sentence structures used by the speaker. It is hoped that this study will contribute to the preservation of the Turkish language.

## References

- [1] B. L. Sañudo, “The role of language technologies and MT in fostering multilingualism by contributing to the revitalization of minor and endangered languages,” *Educación, Investigación e Innovación en Red*, 2023.
- [2] S. Zhang, B. Frey, and M. Bansal, “How can NLP help revitalize endangered languages? A case study and roadmap for the Cherokee language,” in *60th Annual Meeting of the Association for Computational Linguistics*, Dublin, Ireland, 2022, vol. 1, pp. 1529–1541.
- [3] S. Sharofova, “The impact of AI on endangered languages: Can technology save or kill?,” *Texas Journal of Philology, Culture and History*, vol. 25, pp. 52–59, 2023.
- [4] L. Schubert. (2014). *Computational linguistics* [Online]. Available: <https://plato.stanford.edu/archives/spr2020/entries/computational-linguistics/>
- [5] L. Hinton, “Bringing our languages home: Language revitalization for families,” (2013).
- [6] D. Amodei, A. Sundaram, A. Rishita, B. Jingliang, B. Eric, C. Carl, C. Jared et al., “DeepSpeech 2: End-to-end speech recognition in English and Mandarin,” in *33rd International Conference on Machine Learning*, New York, 2016, pp. 173–182.
- [7] S. Schneider, B. Alexei, C. Ronan, and A. Michael, “wav2vec: Unsupervised pre-training for speech

- recognition,” in *The Annual Conference of the International Speech Communication Association*, Graz, 2019, pp. 3465–3469.
- [8] E. Prud’hommeaux, J. Robbie, H. Richard, and M. Karin, “Automatic speech recognition for supporting endangered language documentation,” *Language Documentation & Conservation*, vol. 15, pp. 491–513, 2021.
- [9] A. K. Wassie, “Machine translation for Ge’ez language,” *arXiv preprint*, arXiv:2311.14530, 2023.
- [10] S. Rijhwani, A. Anastasopoulos, and G. Neubig, “OCR post correction for endangered language texts,” *arXiv preprint*, arXiv:2011.05402, 2020.
- [11] A. S. Attila, “OpenAI GPT ve ChatGPT,” *Dikeyksen*, 2023.
- [12] P. Chen, F. Wu, T. Wang, and W. Ding, “A semantic qa-based approach for text summarization evaluation,” in *Thirty-Second AAAI Conference on Artificial Intelligence*, 2018.
- [13] R. Singh and S. Singh, “Text similarity measures in news articles by vector space model using NLP,” *J. Inst. Eng. India Ser. B*, vol. 102, pp. 329–338, 2021, doi: 10.1007/s40031-020-00501-5.
- [14] A. W. Qurashi, V. Holmes, and A. P. Johnson, “Document processing: Methods for semantic text similarity analysis,” in *2020 International Conference on INnovations in Intelligent SysTems and Applications (INISTA)*, Novi Sad, Serbia, 2020, pp. 1–6.
- [15] S. Yavuz, C.-C. Chiu, P. Nguyen, and Y. Wu, “CaLcs: Continuously approximating longest common subsequence for sequence level optimization,” in *Conference on Empirical Methods in Natural Language Processing*, Brussels, Belgium, 2048, pp. 3708–3718.



---

## CASTEP Investigation of Structural, Electronic, and Optical Properties of $\text{CoSb}_2\text{O}_6$

Rania Charif<sup>\*1</sup>, Rachid Makhoulfi<sup>1</sup>

<sup>1</sup>Laboratory of Applied Chemistry (LCA), Department of Matter Sciences, Faculty of Exact Sciences and SNV, University of Biskra, P.O. Box 145, 07000, Biskra, Algeria

---

### Abstract

The aim of this work is a study of the structural, and electronic properties of the trirutile  $\text{CoSb}_2\text{O}_6$ . The quantum DFT approximation used for this work was applied on the cobalt antimonate oxide a trirutile structure with a space group P42/mnm (136) and crystallized in tetragonal structure, with unit-cell parameters:  $a = 0.466$ ,  $c = 0.924$  nm. Without needing to make physical measurements, the structural characteristic of a material can be investigated by optimizing the first-principles computation. By utilizing the CASTEP code based on the pseudo-potential plane-wave within Material Studio software. In this study,  $\text{CoSb}_2\text{O}_6$ 's geometrical optimization was done using a semi-local generalized gradient approximation (GGA) with the Perdew-Burke-Ernzerhof (PBE) for exchange - correlation functional, PBE for solids (PBESOL), Perdew-Wang91 (PW91) and RPBE functionals, as well as the local density approximation (LDA-CAPZ). After optimization, both records of bandgap and DOS of  $\text{CoSb}_2\text{O}_6$  to understand its electronic properties. The  $\text{CoSb}_2\text{O}_6$ 's electronic properties were determined by examining the electronic band structure and density of states, which are determinants of  $\text{CoSb}_2\text{O}_6$  as a narrow gap semiconductor with a direct band gap.

**Keywords:** Density functional theory, CASTEP, Band structure, Density of states,  $\text{CoSb}_2\text{O}_6$

---





---

## Density Functional Theory (DFT) Investigation on the Structure and Electronic Properties of $\text{ZnSb}_2\text{O}_6$

Rania Charif<sup>\*1</sup>, Rachid Makhoulfi<sup>1</sup>

<sup>1</sup>Laboratory of Applied Chemistry (LCA), Department of Matter Sciences, Faculty of Exact Sciences and SNV, University of Biskra, P.O. Box 145, 07000, Biskra, Algeria

---

### Abstract

The aim of this work is a study of the structural, and electronic properties of the trirutile  $\text{ZnSb}_2\text{O}_6$ . The quantum DFT approximation used for this work was applied on the zinc antimonate oxide a trirutile structure with a space group  $P4_2/mnm$  (136) and crystallized in tetragonal structure, with unit-cell parameters:  $a = 0.466$ ,  $c = 0.924$  nm. Without needing to make physical measurements, the structural characteristic of a material can be investigated by optimizing the first-principles computation. By utilizing the CASTEP code based on the pseudo-potential plane-wave within Material Studio software. In this study,  $\text{ZnSb}_2\text{O}_6$ 's geometrical optimization was done using a semi-local generalized gradient approximation (GGA) with the Perdew-Burke-Ernzerhof (PBE) for exchange - correlation functional, PBE for solids (PBESOL), Perdew-Wang91 (PW91) and RPBE functionals, as well as the local density approximation (LDA-CAPZ). After optimization, both records of bandgap and DOS of  $\text{ZnSb}_2\text{O}_6$  to understand its electronic properties. The  $\text{ZnSb}_2\text{O}_6$ 's electronic properties were determined by examining the electronic band structure and density of states, which are determinants of  $\text{ZnSb}_2\text{O}_6$  as a narrow gap semiconductor with a direct band gap.

**Keywords:** Density functional theory, CASTEP, Band structure, Density of states,  $\text{ZnSb}_2\text{O}_6$

---



## **Effects of Instagram Weddings on Financially Strains, Local Traditions, Stress, Unrealistic Expectations, Privacy Issues, and Digital Disconnect Among Youth of Pakistan**

**Ghulam Safdar<sup>\*1</sup>, Mahnoor Bibi<sup>1</sup>**

*<sup>1</sup>Department of Media & Communication Studies, Rawalpindi Women University, Rawalpindi, Pakistan*

---

### **Abstract**

The study examined the ubiquitous impact of social media, especially Instagram, on how people see relationships and weddings. The study investigated the complex impacts of Instagram weddings on the financial strain, local traditions, stress, unrealistic expectations and privacy issues and digital disconnect among youngsters of Pakistan. The study conducted under the light of “*Social Learning Theory*”. The study was quantitative in nature and researchers designed self-designed questionnaire consisted on close-ended questions to collect the data from the (N=217) young male and female using purposive sampling technique residence of Rawalpindi, Pakistan. The study found negative effects like societal comparison, false expectations, and financial pressure are contrasted with positive elements like creativity, inspiration, and a sense of community. The study concluded mixed outcomes. Positively, Instagram marriages are source of joy, creativity, and inspiration. These events give young people a venue to exhibit various ethnic customs and promote a feeling of community. These aesthetically pleasing portrayals may also establish aspirational standards for commitment and relationships. On the other hand, the well-controlled aspect of Instagram weddings leads to societal comparison and inflated expectations. Young people experience pressure to live up to idealized standards for appearance, spending budget, and overall event perfection. This may have an adverse effect on body image and relationship expectations, in addition to causing stress, worry, and financial hardship.

**Keywords:** *Instagram weddings, Youth, Mental health, Financial constraints*

---



## A Multifaceted Approach to Fault Diagnosis: Comparing Traditional and Deep Learning Methods

Ceren Asilkefeli<sup>\*1 2</sup>, Fehmi Burcin Ozsoydan<sup>3</sup>

<sup>1</sup>Business Administration, Social Sciences University of Ankara, Türkiye

<sup>2</sup>Graduate School of Natural and Applied Sciences, Dokuz Eylul University, Izmir, Türkiye

<sup>3</sup>Industrial Engineering, Dokuz Eylul University, Izmir, Türkiye

### Abstract

Mechanical fault diagnosis is crucial for ensuring the stable operation of mechanical equipment by preventing failures and predicting potential issues. This study investigates and compares traditional machine learning algorithms and deep learning methods for bearing fault diagnosis. Specifically, it evaluates the performance of Support Vector Machines (SVMs), Random Forests, and Convolutional Neural Networks (CNNs) using the CRWU roller bearing dataset. SVMs, known for their ability to find complex decision boundaries, and Random Forests, valued for their robustness and versatility, are compared against CNNs, which are adept at capturing hierarchical data representations. The experimental results demonstrate that the Random Forest classifier achieves the highest accuracy at 97%, followed by SVMs and CNNs, both at 94%. These findings underscore the potential of ensemble learning methods like Random Forests in fault diagnosis, while also highlighting the effectiveness of deep learning approaches. The study concludes with discussions on the implications of these results and suggestions for future research directions in the field of mechanical fault diagnosis.

**Keywords:** *Fault diagnosis, Machine learning, Support vector machine (SVM), Random forest, Convolutional Neural network (CNN)*

## 1 INTRODUCTION

Mechanical fault diagnosis can prevent mechanical equipment failures from getting worse and is important for the stable operation of mechanical equipment. To guarantee the machine operates steadily, fault diagnosis for mechanical equipment must monitor, diagnose, and predict the condition of the machinery.

At present, mechanical equipment fault diagnosis methods mainly include the based method of the physical model and signal processing, and data-driven [1]. The deep fault feature representation relationship underlying the data is found through data mining, and the mapping relationship between the data and the fault is established to detect and identify the fault source. These are the data-driven methods for determining the deep fault feature representation relationship behind the data. Data-driven methods have a strong chance of developing because they don't require extensive professional knowledge and just a certain level of intelligence. As an early data-driven method for mechanical fault diagnosis, machine learning has several uses and well-developed algorithm patterns, including logistic regression, support vector machines, decision trees, random forests, naive Bayes, and neural networks.

This paper presents a comprehensive study on fault diagnosis techniques, focusing on the comparison between traditional machine learning algorithms and a deep learning method. Specifically, the effectiveness of Support Vector Machines (SVMs), Random Forests, and Convolutional Neural Networks (CNNs) for bear fault diagnosis is explored. SVMs are powerful classifiers known for their ability to find complex decision boundaries in high-dimensional spaces. Random Forests, as an ensemble learning method, offer robustness and versatility, making them suitable for capturing complex relationships in the data. CNNs, on the other hand, use deep learning architectures to automatically pick up hierarchical data representations; this makes them very useful for jobs that need spatial or picture data.

The remainder of this paper is organized as follows: Section 2 provides a review of existing literature on fault diagnosis techniques, highlighting the advancements in both traditional and deep learning approaches. Section 3 describes the methodology adopted for this study, including dataset preparation, model implementation, and evaluation metrics. Section 4 presents the experimental results and comparative analysis of SVMs, Random

Forests, and CNNs. Section 5 discusses the findings and implications of our study, while Section 6 concludes the paper and suggests avenues for future research.

## 2 LITERATURE REVIEW

In the past, traditional machine learning methods were used for mechanical fault diagnosis. These methods can be summarized as expert system-based, ANN-based, and SVM-based approaches [2]. In the present time, researchers mostly use deep learning-based approaches such as CNN for mechanical fault diagnosis.

SVM works by mapping the input vectors to a high-dimensional feature space by a linear transformation. Next, a hyper plane is established as a decision plane in the feature space, and the edge of the spacer between the positive and negative examples of that plane is maximized [3]. SVM serves as a widely-used machine learning method in health state recognition, especially for fault diagnosis of rolling element bearings, gears, motors, engines, rotor systems, and hydraulic equipment [2]. Due to the lack of feature extraction ability, SVM is generally used in combination with signal processing techniques for feature extraction [4].

A random forest is created by combining different tree predictors so that every tree in the forest is dependent on the values of a random vector that is independently and uniformly sampled [5].

Convolutional neural networks (CNNs) are designed to handle input that is presented as several arrays. For instance, a three-dimensional (2D) array of pixel intensities over three color channels can represent a color image [6]. They are composed by an input layer, convolutional layers, pooling layers, fully connected layers and an output layer. CNN architectures allow them to be separated into two categories: 1D CNN-based diagnosis models and 2-dimensional (2D) CNN-based diagnosis models. In this study 1D CNN-based diagnosis model is used.

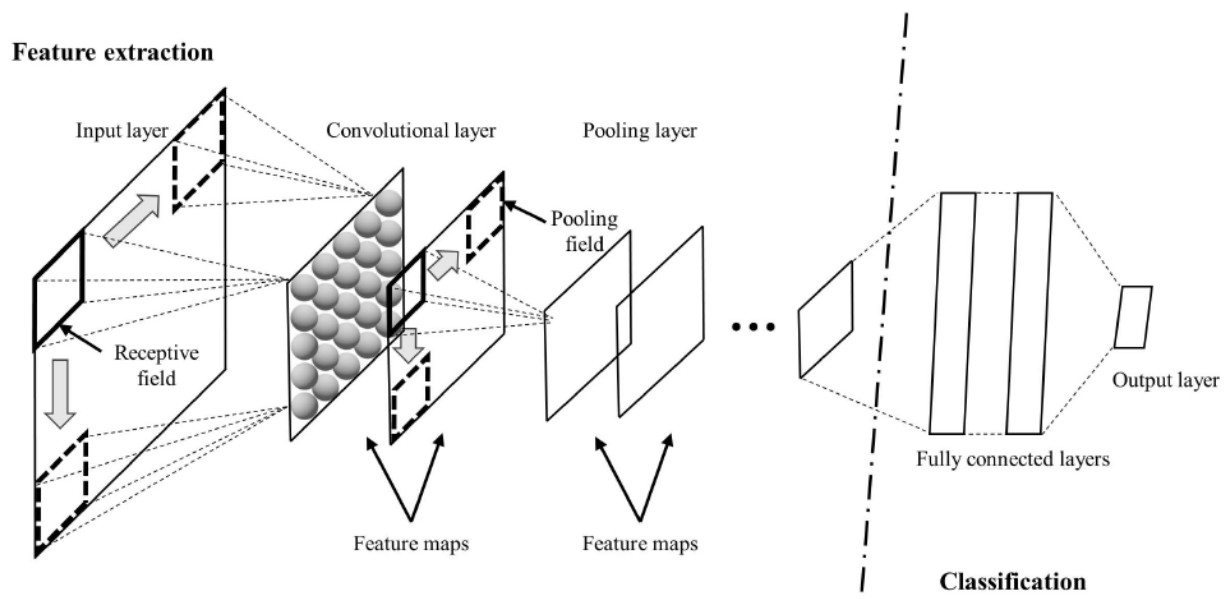


Figure 1. Structure of a CNN [7]

## 3 METHODOLOGY AND EXPERIMENTAL SETUP

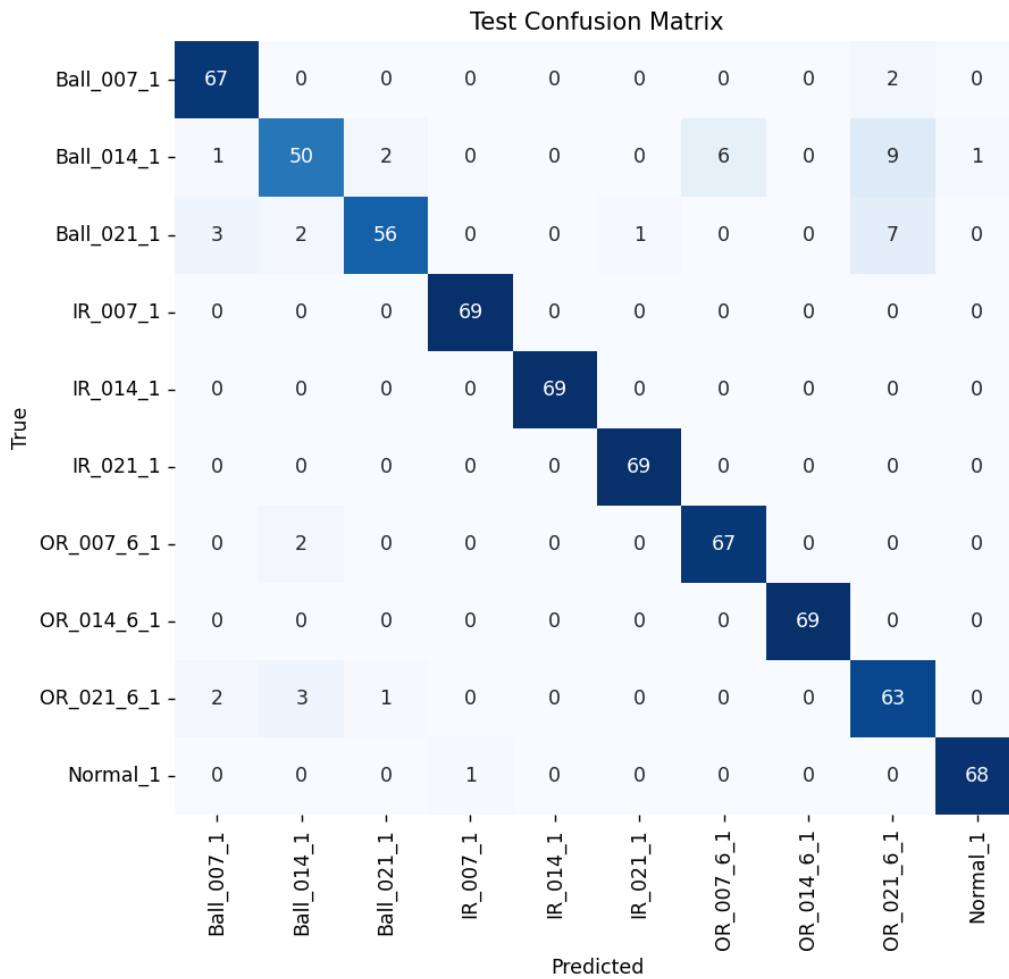
In this study, CRWU roller bearing data set is used for training and testing. To ensure effective and robust of proposed model, each bearing state (including healthy) included 240 samples acquired from accelerometers in the time domain, split into 70% for training and 30% for testing. Thus, 1610 training and 690 test samples are provided in total.

**Table 1.** CRWU roller bearing data

	max	min	mean	sd	rms	skewness	kurtosis	crest	form	fault
0	0.35986	-0.41890	0.017840	0.122746	0.124006	-0.118571	-0.042219	2.901946	6.950855	Ball_007_1
1	0.46772	-0.36111	0.022255	0.132488	0.134312	0.174699	-0.081548	3.482334	6.035202	Ball_007_1
2	0.46855	-0.43809	0.020470	0.149651	0.151008	0.040339	-0.274069	3.102819	7.376926	Ball_007_1
3	0.58475	-0.54303	0.020960	0.157067	0.158422	-0.023266	0.134692	3.691097	7.558387	Ball_007_1
4	0.44685	-0.57891	0.022167	0.138189	0.139922	-0.081534	0.402783	3.193561	6.312085	Ball_007_1
...	...	...	...	...	...	...	...	...	...	...
2295	0.21425	-0.19839	0.010769	0.064100	0.064983	-0.212497	-0.119312	3.297037	6.034174	Normal_1
2296	0.21967	-0.20882	0.013136	0.068654	0.069883	-0.061308	-0.295122	3.143410	5.319958	Normal_1
2297	0.20799	-0.21613	0.012571	0.067128	0.068279	-0.154754	-0.071405	3.046161	5.431299	Normal_1
2298	0.21425	-0.22405	0.012608	0.066813	0.067977	-0.326966	0.023662	3.151821	5.391672	Normal_1
2299	0.19610	-0.24721	0.012209	0.063243	0.064396	-0.351762	0.226294	3.045244	5.274392	Normal_1

### 4 RESULTS

The comparative analysis of Support Vector Machines (SVMs), Random Forests, and Convolutional Neural Networks (CNNs) for roller bearing fault diagnosis reveals that while Random Forests achieve the highest accuracy at 97%, both SVMs and CNNs show significant promise, each achieving an accuracy of 94%. Figure 2,3 and 4 show the confusion matrixes of the results. The robustness of Random Forests in handling complex fault patterns underscores their suitability for fault diagnosis tasks. However, the balanced precision and recall of CNNs highlight the potential of deep learning architectures in this domain. Future research should focus on enhancing deep learning approaches by exploring deeper and more complex CNN architectures, integrating advanced feature extraction techniques, and developing hybrid models that combine the strengths of traditional machine learning and deep learning methods. This could involve the use of transfer learning, attention mechanisms, and unsupervised pre-training to improve the generalization and accuracy of fault diagnosis systems, ultimately leading to more reliable and efficient maintenance of mechanical equipment.



**Figure 2.** Confusion matrix of SVM results

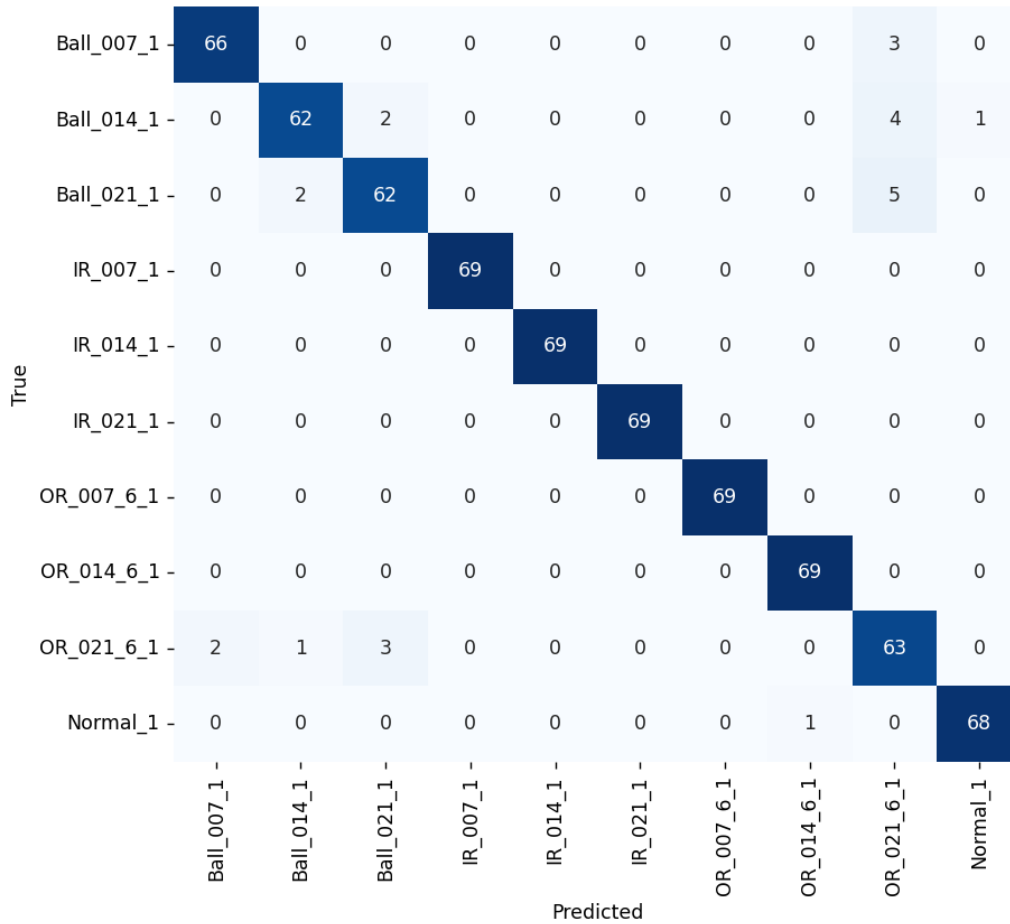


Figure 3. Confusion matrix of random forests results

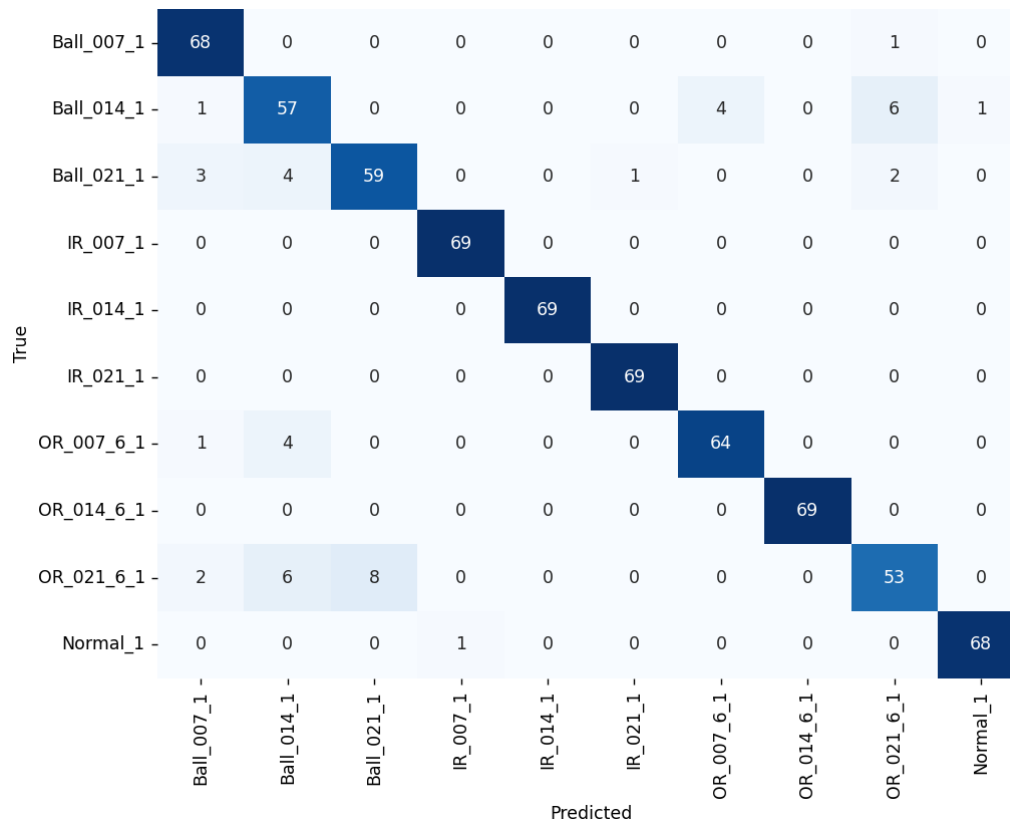


Figure 4 Confusion matrix of CNN results

## 5 CONCLUSION

This study provides a comprehensive comparison of traditional machine learning algorithms and deep learning methods for mechanical fault diagnosis, specifically focusing on the performance of Support Vector Machines (SVMs), Random Forests, and Convolutional Neural Networks (CNNs) using the CRWU roller bearing dataset. The experimental results demonstrate that the Random Forest classifier outperforms both SVMs and CNNs, achieving an accuracy of 97%, compared to 94% for the other two methods.

The superior performance of Random Forests highlights the robustness and versatility of ensemble learning methods in capturing complex relationships within the data. SVMs, while effective in finding complex decision boundaries, and CNNs, with their ability to automatically extract hierarchical features, also show strong potential for fault diagnosis tasks. However, the need for extensive feature extraction in SVMs and the computational intensity of CNNs suggest areas where further optimization and hybrid approaches could be beneficial.

These findings suggest that while traditional machine learning methods remain valuable, deep learning techniques offer promising avenues for advancing fault diagnosis capabilities. Future research should explore hybrid models that combine the strengths of various algorithms, investigate the impact of different feature extraction methods, and consider real-time implementation challenges. By continuing to develop and refine these approaches, we can enhance the reliability and efficiency of mechanical fault diagnosis systems, ultimately contributing to more stable and efficient operation of mechanical equipment.

## References

- [1] J. Hou, X. Lu, Y. Zhong, W. He, D. Zhao, and F. Zhou, "A comprehensive review of mechanical fault diagnosis methods based on convolutional neural network," *Journal of Vibroengineering*, vol. 26, no. 1, pp. 44-65, Nov. 2023.
- [2] Y. Lei, B. Yang, X. Jiang, F. Jia, N. Li, A. K. Nandi, "Applications of machine learning to machine fault diagnosis: A review and roadmap," *Mechanical Systems and Signal Processing*, vol. 138, art. no. 106587, Apr. 2020.
- [3] L. Zhang, B. Zhang, "Relationship between support vector set and kernel functions in SVM," *Journal of Computer Science and technology*, vol. 17, no. 5, pp. 549-555, Sep. 2002.
- [4] R. Liu, B. Yang, E. Zio, and X. Chen, "Artificial intelligence for fault diagnosis of rotating machinery: A review," *Mechanical Systems and Signal Processing*, vol. 108, pp. 33-47, Aug. 2018.
- [5] L. Breiman, "Random Forests," *Machine Learning* vol 45, pp. 5-32, Oct. 2001.
- [6] Y. LeCun, Y. Bengio, and G. Hinton, "Deep learning," *Nature* vol. 521, pp. 436-444, May 2015.
- [7] K. B. Lee, S. Cheon, and C. O. Kim, "A convolutional neural network for fault classification and diagnosis in semiconductor manufacturing processes," *IEEE Transactions on Semiconductor Manufacturing*, vol. 30, no. 2, pp. 135-142, May 2017.



## Convolutional Neural Network Application for Control Chart Pattern Recognition

Ceren Asilkefeli<sup>\*1,2</sup>, Fehmi Burcin Ozsoydan<sup>3</sup>

<sup>1</sup>Business Administration, Social Sciences University of Ankara, Türkiye

<sup>2</sup>Graduate School of Natural and Applied Sciences, Dokuz Eylül University, İzmir, Türkiye

<sup>3</sup>Industrial Engineering, Dokuz Eylül University, İzmir, Türkiye

### Abstract

This study explores the application of 1-Dimensional Convolutional Neural Networks (1D-CNNs) for Control Chart Pattern Recognition (CCPR), building upon the groundwork established by Zan et al. [1]. The proposed model is evaluated on a dataset generated through Monte Carlo simulation, comprising 12,000 instances across six typical control chart patterns. The 1D-CNN structure, closely aligned with the parameters introduced by Zan et al. [1], demonstrates a commendable accuracy of 91% in recognizing control chart patterns. The results affirm the efficacy of the 1D-CNN as a robust and automatic method for extracting intricate features from raw data in the realm of CCPR. Additionally, a detailed analysis, including a confusion matrix, provides insights into the model's performance across different control chart patterns. This study contributes to the evolving field of artificial intelligence in quality control and process monitoring.

**Keywords:** Control chart, Pattern recognition, Convolutional neural network, Statistical process control, Deep learning

## 1 INTRODUCTION

Achieving and sustaining an appropriate and stable level of the intended process quality characteristics is the major goal of process quality control. The process control chart is a conventional tool that is employed in this position. Originally created by Shewhart in 1924, control charts are now one of the most crucial components of statistical process control (SPC) and are frequently used in manufacturing quality control. To identify and rule out assignable causes as soon as feasible, it's also necessary to see if control charts exhibit any particular anomalous patterns. Control charts can be categorized into six fundamental patterns (Figure 1): normal, upward shift, downward shift, upward trend, downward trend and cyclic [1].

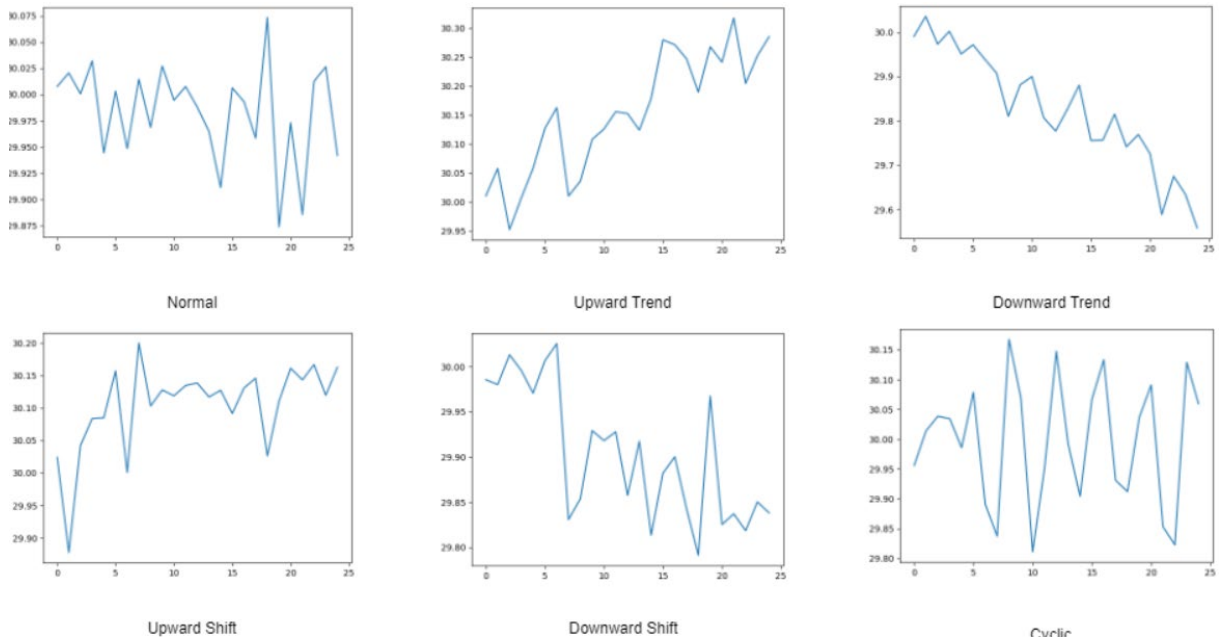


Figure 1. Six basic patterns in control charts



Machine Learning (ML) techniques are widely used in control chart pattern recognition (CCPR) with very good outcomes. Neural networks method is one of the most used ML methods for CCPR.

In this study, 1-Dimensional Convolutional Neural Networks (1D-CNN) method is used for CCPR. The proposed model is experimented on a dataset with 12000 instances which are generated using Monte Carlo simulation.

## 2 LITERATURE REVIEW

There are many neural networks applications for CCPR in the literature. One of the first applications is done for six basic patterns mentioned before [2]. They proposed a neural network model that includes the input layer contains 56 neurons used as input data of 56 consecutive points in a control chart and one hidden layer. They also experimented on mixed abnormal patterns and obtained good results.

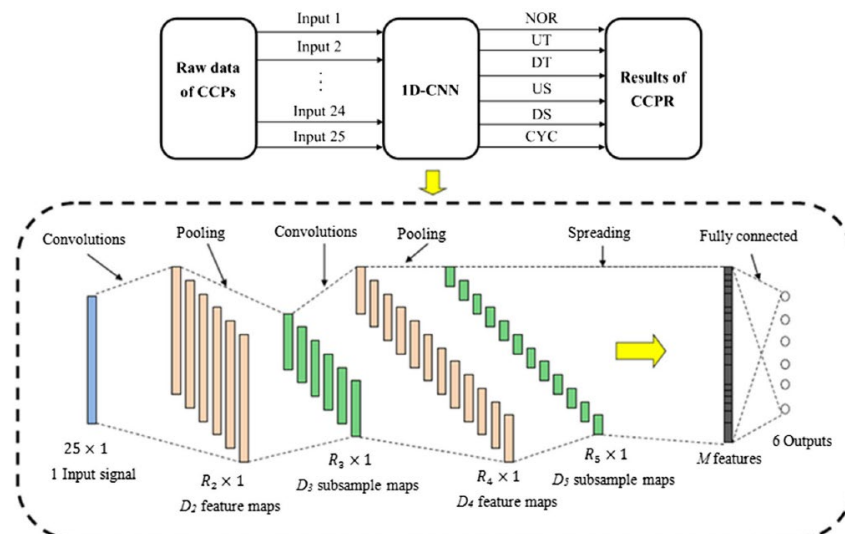
Niaki and Abbasi [3], created a perceptron neural network for monitoring and classifying mean shifts in multi-attribute processes. Three Artificial Neural Network (ANN) for control charts were created by Hosseinifard et al. [4] to track three simple linear profile parameters: the intercept, slope, and residual variance. Two of their control charts were solely for detection, but one was used for both identification and detection. Mohammadzadeh et al. [5], established an SVR (support vector regression) control chart for monitoring a logistic profile by extending Hosseinifard et al.'s [4] study.

Zan et al. [1], proposed a novel 1D-CNN-based CCPR method, eliminating the need for manual feature extraction. The proposed 1D-CNN emerges as a promising solution, offering higher quality feature sets and potential applications in real production environments, promising to advance automation and intelligence in quality management. Future research avenues include exploring online prediction and diagnosis systems based on various deep learning algorithms. To track generalized linear regression profiles, Sabahno and Amiri [6], created various statistical and machine-learning-based control charts with fixed and variable design parameters.

## 3 METHODOLOGY

### 3.1 1D-CNN Structure

In this study, a 1D-CNN to complete the CCPR by Zan et al. [1], is used so as to extract the CCP features through the feature learning. CNNs have an advantage over typical machine learning methods in that they can achieve end-to-end diagnosis or recognition. Stated differently, the neural network receives raw data as input and outputs a pattern type. A CNN's convolution and pooling layers finish feature extraction, feature selection, and feature optimization. The suggested 1D-CNN's structure differs slightly from the typical CNN structure. Since the 1D-CNN structure's feature mapping is a vector rather than a matrix, it is especially sensitive to temporal sequences like CCPs. A fully connection layer, two pooling layers, and two convolution layers make up the proposed CNN structure of the suggested CCPR method, which is depicted in Figure 2. The fully connection layer realizes classification, while the convolution and pooling layers finish feature extraction. Same parameters as Zan et al. [1] are used in this study.



**Figure 2** The structure of the CCPR method (retrieved from [1])

## 4 EXPERIMENTS AND RESULTS

### 4.1 Data Generation

A dataset which contains 12000 samples is generated using Monte Carlo simulation with given parameters (Table 1). The mean  $\mu$  was set to 30, and the standard deviation  $\sigma$  was set to 0.05. The value of the slope  $d$  varied in the range  $[0.1\sigma, 0.3\sigma]$ . The magnitude of the shift  $s$  changed in the range  $[1.5\sigma, 3\sigma]$ , and the amplitude of cyclic patterns  $a$  varied in the range  $[1.5\sigma, 4\sigma]$ . The value of the period of cycle  $\omega$  was respectively set to 4, 5, 6, 7, and 8. The starting position of each unnatural pattern was in the range  $[4, 9]$ . The data length of the CCPs was 25. 8400 samples were used to train, 1800 samples were used for validation and 1800 samples were used for testing.

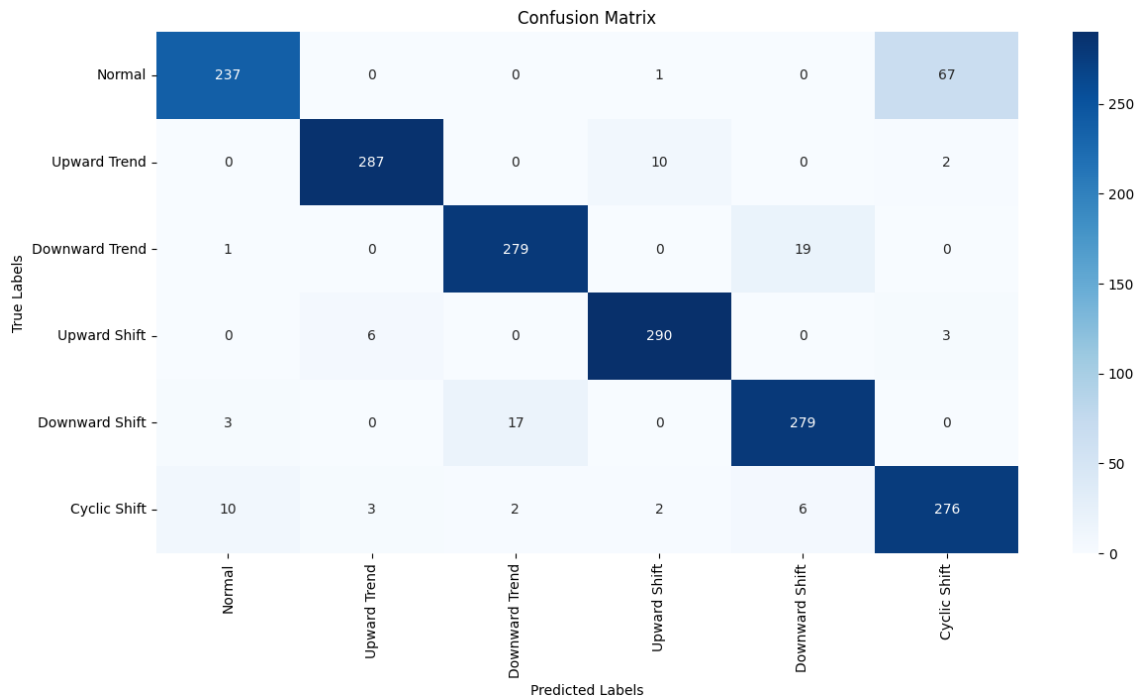
**Table 1** The parameters of six CCPs [1]

Pattern	Mathematical Representation	Parameter Value
Normal	$y(t) = \mu + x(t)$	$\mu=30, \sigma=0.05$
Upward Trend	$y(t) = \mu + x(t) + v \times d \times t$	$d \in [0.1\sigma, 0.3\sigma]$
Downward Trend	$y(t) = \mu + x(t) - v \times d \times t$	$d \in [0.1\sigma, 0.3\sigma]$
Upward Shift	$y(t) = \mu + x(t) + v \times s$	$s \in [1.5\sigma, 3\sigma]$
Downward Shift	$y(t) = \mu + x(t) - v \times s$	$s \in [1.5\sigma, 3\sigma]$
Cyclic	$y(t) = \mu + x(t) + v \times a \times \sin(2\pi/w)$	$a \in [1.5\sigma, 4\sigma], w \in [4, 5, 6, 7, 8]$

### 4.2 Results

The 1D-CNN model, trained and evaluated on the CCPR task, has demonstrated a commendable accuracy with a correct recognition ratio of 91%. This high level of accuracy underscores the efficacy of the 1D-CNN as a suitable method for CCPR, affirming its capability to automatically extract intricate features from raw data.

To gain further insights into the model's performance, a confusion matrix is presented in Fig. 3. The confusion matrix provides a detailed breakdown of the model's predictions across different control chart patterns. Each row represents the true class, while each column corresponds to the predicted class. The diagonal elements of the matrix indicate correct predictions, and off-diagonal elements represent misclassifications.



**Figure 3** Confusion matrix

## 5 CONCLUSION

The application of neural networks in control chart pattern recognition (CCPR) has gained substantial traction over the years, presenting a paradigm shift in the way anomalous patterns are identified and classified. The evolution

of this field has seen various neural network architectures contributing to the accuracy and efficiency of CCPR, providing valuable insights into process monitoring and quality control.

In this study, the field of CNNs for CCPR was explored, building upon the foundation laid by Zan et al. (2020). The proposed 1D-CNN method, with its unique structure tailored for temporal sequences like CCPs, demonstrated promising results. By eliminating the need for manual feature extraction, the 1D-CNN emerged as a robust solution, offering higher quality feature sets for potential applications in real production environments.

The experimental phase involved the application of the proposed 1D-CNN model on a meticulously generated dataset of 12000 instances through Monte Carlo simulation. The dataset encompassed diverse control chart patterns, including normal, upward trend, downward trend, upward shift, downward shift, and cyclic patterns. The model's accuracy, evaluated through a correct recognition ratio of 91%, attests to its capability to autonomously extract intricate features from raw data.

The proposed 1D-CNN method lays the groundwork for future research directions in CCPR. Exploration of online prediction and diagnosis systems based on various deep learning algorithms holds promise for further enhancing automation and intelligence in quality management. The advancements in this field could potentially revolutionize the way industries approach process monitoring and quality control.

## References

- [1] T. Zan, Z. Liu, H. Wang, M. Wang, and X. Gao, "Control chart pattern recognition using the convolutional neural network," *Journal of Intelligent Manufacturing*, vol. 31, pp. 703–716, Apr. 2019.
- [2] R. S. Guh and Y. C. Hsieh, "A neural network based model for abnormal pattern recognition of control charts," *Computers & Industrial Engineering*, vol. 36, no. 1, pp. 97–108, Jan. 1999.
- [3] S. A. Niaki and B. Abbasi, "Detection and classification mean-shifts in multi-attribute processes by artificial neural networks," *International Journal of Production Research*, vol. 46, no. 11, pp. 2945–2963, Apr. 2008.
- [4] S. Z. Hosseinifard, M. Abdollahian, and P. Zeepongsekul, "Application of artificial neural networks in linear profile monitoring," *Expert Systems with Applications*, vol. 38, no. 5, pp. 4920–4928, May 2011.
- [5] M. Mohammadzadeh, A. Yeganeh, and A. Shadman, "Monitoring logistic profiles using variable sample interval approach," *Computers & Industrial Engineering*, vol. 158, art. no. 107438, Aug. 2021.
- [6] H. Sabahno and A. Amiri, "New statistical and machine learning based control charts with variable parameters for monitoring generalized linear model profiles," *Computers & Industrial Engineering*, vol. 184, art. no. 109562, Oc. 2023.



## Theoretical Investigations of Structural, Mechanical, and Elastic Properties of Novel Quaternary Heusler Alloys for Spin Polarized and Waste Heat Recycling Systems

Saadiya Benatmane<sup>\*1,2</sup>

<sup>1</sup>Department of Science and Technology, Faculty of Science and Technology, Abdelhamid Ibn Badis University of Mostaganem, 27000 Mostaganem, Algeria

<sup>2</sup>Laboratory for Modeling and Simulation in Materials Sciences, Djillali Liabes University, 22000 Sidi Bel-Abbes, Algeria

---

### Abstract

In this paper, we employed density functional theory using WIEN2k to study structural, mechanical, electrical, magnetic and thermoelectric properties for quaternary Heusler alloys. The self-consistent field calculation is done with generalized gradient approximation procedure. The structural stability analysis shows that the Heusler alloys are stable in Y-I type structure and having ferromagnetic property. In mechanical stability analysis we identified that all the reported Heusler alloys are ductile in nature. Electronic property calculations of reveals that all are half-metal, having metallic nature in spin up channel and semiconducting nature in spin down channel. The calculated values of spin magnetic moments are consistent with Slater-Pauling rule.

**Keywords:** *Half-metallicity, Quaternary Heusler compounds, Ab initio calculation, Elastic properties*

---



---

## Design of Image Processing Accelerators for TTA Processors

Latif Akcay<sup>\*1</sup>, Tugce Demirkol<sup>2</sup>

<sup>1</sup>Electrical - Electronics Engineering, Bayburt University, Bayburt, Türkiye

<sup>2</sup>Electronics and Automation Department, Bayburt University, Bayburt, Türkiye

---

### Abstract

Digital image processing filters have a vital role in numerous modern applications today. Due to their inherent parallelism and flexibility, transport triggered architecture (TTA) has emerged as a promising application-specific instruction set processor (ASIP) design paradigm for accelerating image processing tasks. In this paper, we present implementation of a few custom accelerators for basic filters on a simple TTA processor. First, we explain the essential concepts of TTA, such as explicit data transfer, parallel computation, customizable instruction sets and register file design approach. It is crucial to grasp these principles in order to comprehend how TTA can be an effective solution for image processing applications. Then, we briefly introduce the open-source TTA processor design environment, OpenASIP, and its tools for processor design, customization, simulation, and implementation. After that, we describe our custom TTA operations developed for commonly used digital image filters. The operations were implemented using Verilog HDL and then integrated into a base processor. Tests were performed on an FPGA to prove the efficiency of the architecture and developed operations in terms of performance and chip area. The results obtained are given in comparative tables for different processor configurations.

**Keywords:** Image Processor, Transport triggered architecture, OpenASIP, ASIP, FPGA

---

## 1 INTRODUCTION

The term 'image processing' can be defined as the extraction of meaningful information from digital pixel data, through the application of various algorithms and techniques [1]. It is a pervasive technology in contemporary computer science, with applications in diverse fields. The applications of image processing are frequently encountered in many different fields, including automotive, entertainment, medical, imaging, security, computer vision, control, and robotics [2]. Image processing techniques allow automating decision-making processes by extracting useful information from the image data.

A variety of digital filter techniques have been developed to facilitate the interpretation of relationships between pixels and their neighbouring elements [3]. Given that the image is typically a data structure comprising a multitude of pixels, the computational load on systems that perform the operations defined in the filters is considerable [4]. Therefore, there is a need for computation systems that can efficiently perform digital filter operations. Achieving this is possible by customizing the processing units according to the target application. Unlike general-purpose processors, application-specific processors contain many custom instructions and data paths tailored to the algorithm or application area they are designed for [5].

Transport-triggered architecture (TTA) is a computational method that facilitates the transfer of processed data between specialized functional units via parallel data buses [6]. This approach makes TTA an ideal framework for developing application-specific instruction set processors (ASIP). Consequently, flexible processor designs can be developed according to the requirements of the target application or an application area. In addition, TTA processors can be developed leveraging a handy and free toolset called OpenASIP, formerly known as TTA-Based Co-Design Environment (TCE) [7].

In this study, custom operations that can be used within TTA processors have been developed for Sobel, Gaussian Blur, Prewitt, Scharr, Median, Laplacian, Sharpening, and Blur filters, which are used extensively in almost every image processing application [3]. A review of the literature reveals no studies that have employed TTA to accelerate these basic filters. The rest of the study are organized as follows: In the second section, the target digital filters for which the operation designs was developed are briefly explained. The general structure of TTA is summarized in the third section. In the fourth section, custom operation designs are explained and the results obtained from the tests are given. Finally, the entire study is concluded in the fifth section.

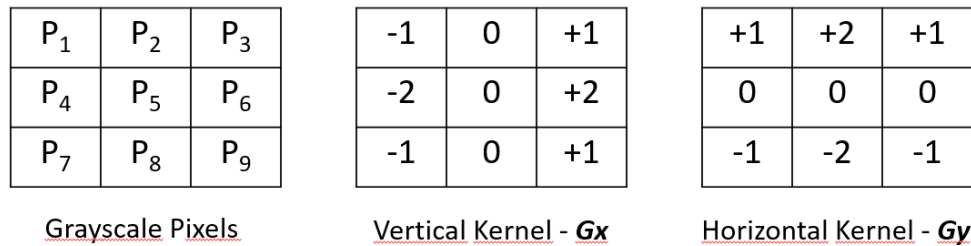
## 2 FUNDAMENTAL IMAGE PROCESSING FILTERS

Fundamental filters play a pivotal role in image processing, facilitating the extraction or enhancement of information through the application of diverse mathematical operations on digital images. These processes encompass a range of techniques, including edge identification, noise reduction, and image enhancement. The fundamental filters represent the basic tools used to perform these operations.

Gradient filters, including Sobel, Prewitt, and Scharr, are employed to identify edges within an image [3]. These filters ascertain the intensity and direction of edges by calculating the derivatives of neighbouring pixels. In practice, these operations entail the application of convolution operations with diverse coefficient matrices to grayscale pixel values. Figure 1 illustrates the methodology for calculating the value of a pixel with a Sobel filter. The detection of edges is frequently a crucial stage in the analysis of images, with applications including object recognition and the operation of automatic driving systems. Another filter used for edge detection is the Laplacian filter. It emphasises rapid intensity changes and is typically employed for the identification of salient structures within an image.

Blur filters are an effective means of reducing noise or softening details in an image [3]. These filters, such as the Gaussian Blur, typically function by averaging pixels or calculating a weighted average. Similarly, the Median filter is a type of filter used to reduce noise in an image. The value of each pixel is replaced by the median value of neighbouring pixels, which effectively reduces noise while preserving edges.

These filters are regarded as the fundamental building blocks of image processing, offering a high degree of versatility for a multitude of applications. Each filter is selected to address a specific issue and is utilised to enhance the precision, clarity, or intelligibility of image analysis.



$$|G_x| = |-P_1 + P_3 - 2P_4 + 2P_6 - P_7 + P_9|$$

$$|G_y| = |P_1 + 2P_2 + P_3 - P_7 - 2P_8 - P_9|$$

$$|G| = |G_x| + |G_y| \text{ (Sobel Value of Related Pixel)}$$

**Figure 1.** Computation of the Sobel filter operation

## 3 PROCESSOR ARCHITECTURE AND DESIGN ENVIRONMENT

In this section, we briefly summarize TTA, the application-specific processor architecture used in this study. In addition, we explain the open-source and free design and development environment OpenASIP which is formerly known as TCE.

### 3.1 Transport-Triggered Architecture

The computational philosophy of Very Long Instruction Word Architecture (VLIW) [8] is to emphasise the benefits of instruction-level parallelisation (ILP) [9]. This approach provides an extremely efficient processor architecture, particularly for applications where the data calculation results are independent of one another, thereby allowing for parallel execution. TTA is, in fact, a methodology for the design of a processor that incorporates a number of enhancements based on the fundamental computing concept of the VLIW architecture. In TTA processors, data is transported between functional units (FUs) via parallel transport lines. The aforementioned FUs are the units in which arithmetic and logical operations are performed. As illustrated in Figure 2, a typical TTA processor comprises multiple parallel data paths and functional units (FUs).

In contrast to general-purpose processors, TTA processors are designed for a specific application or application area. This allows for a high degree of customisation, with almost every part of the architecture, such as FUs, data

paths, and register blocks, being tailored to the requirements of the target application. The flexibility, scalability and customisability of TTA make it an ideal method for application-specific instruction set processor (ASIP) design.

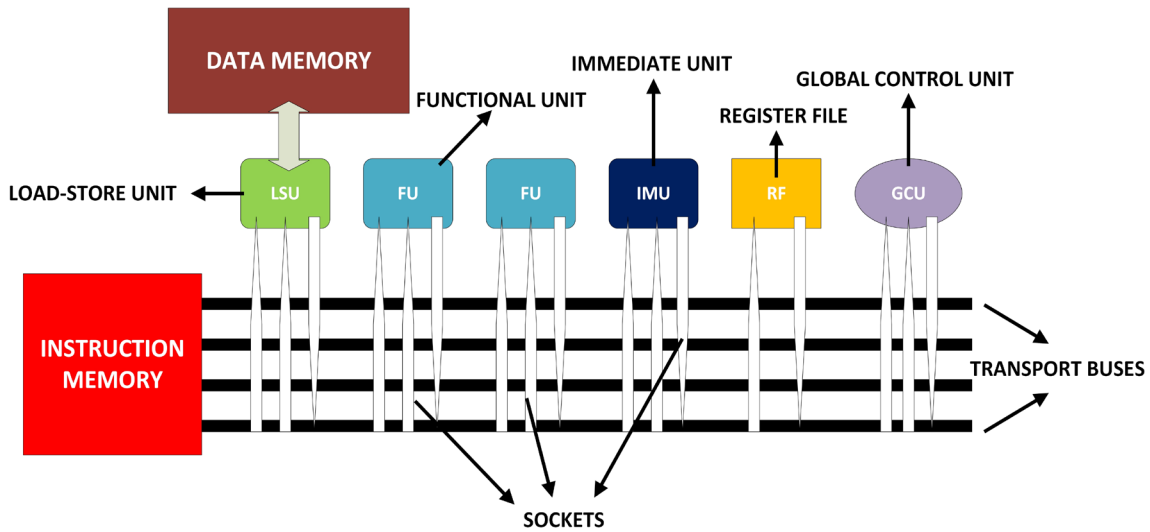


Figure 2. A typical TTA processor and its basic building blocks

### 3.2 OpenASIP

OpenASIP is an open-source and free processor design and development toolkit developed by the University of Tampere [10]. Designers are able to complete the entire development process, up to the point of pre-synthesis, utilising solely the tools provided within OpenASIP, without the necessity for additional tools. OpenASIP boasts a variety of useful interfaces, including the LLVM-based retargetable compiler (tcecc), the processor model development tool (ProDe), a cycle-accurate simulator (Proxim), an operation set editor (OSEd), a hardware data base editor (HDBeditor) and a processor HDL code generator (ProGe) [11]. All of these tools are entirely open source and provided free of charge. Furthermore, supplementary tools such as Design Space Explorer [12], which aims to automatically identify the most effective processor design, enhance OpenASIP's comprehensive and valuable development environment for TTA processors. Figure 3 illustrates a development process with OpenASIP tools led by a designer who has just a high-level application code at the beginning.

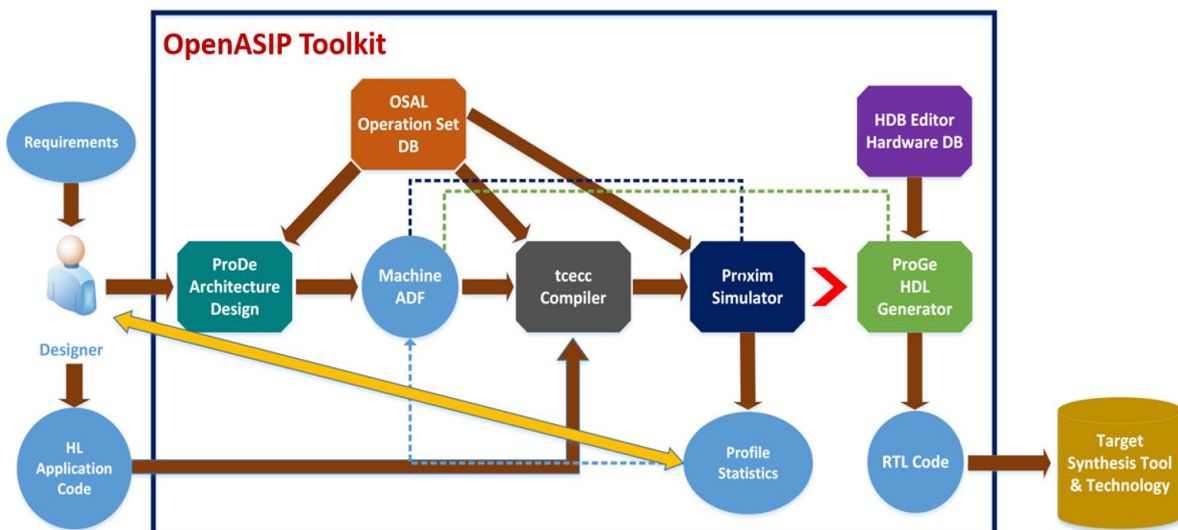


Figure 3. From high-level application to target TTA processor RTL

## 4 PROCESSOR DESIGN AND TESTS

In this section, we explain design and implementation process of our ASIP for the fundamental image processing filters. In addition, we share the comparative test results and resource utilizations for FPGA implementation.

### 4.1 Template Architecture

As is usual practice, the TTA processor development process is initiated with the creation of a preliminary processor model. Subsequently, the model is modified to incorporate customisations, thereby facilitating the gradual development of a more effective processor model. In this study, we employed a TTA processor model, as illustrated in Figure 4, which comprises general-purpose operations. The model, designated GP-1, comprises four transport buses, load and store operations that provide access to data memory, and jump and call operations that control program execution, in addition to general-purpose operations. To examine the impact of the transport bus count on performance, a GP-2 configuration with the same FUs but two buses was developed and used in the test.

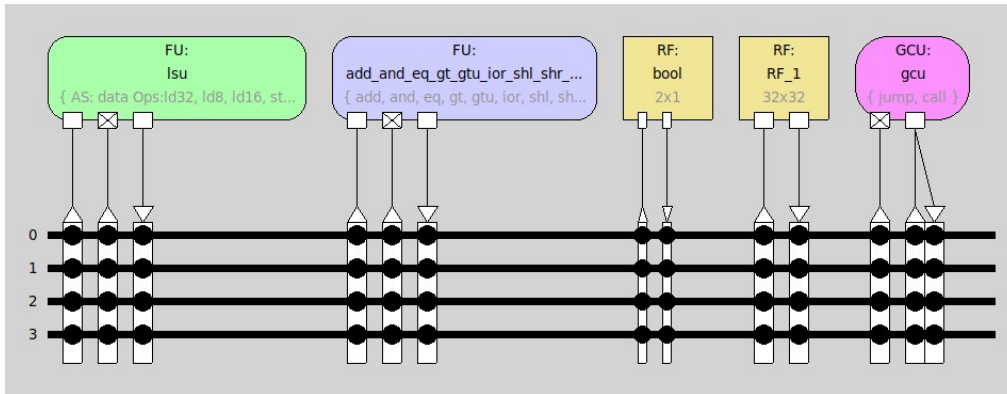


Figure 4. GP-1 core model in ProDe

### 4.2 Design and Integration of Custom Operations

The calculation of the final value of each pixel in image processing filters necessitates a considerable number of mathematical operations, as illustrated in Figure 1. It is practically unfeasible for processors such as GP-1, which are equipped with only general-purpose operations within their FUs, to execute applications utilising such filters in a manner that is both high-performance and efficient. It is therefore necessary for the processor core to be equipped with custom operations that are specifically designed for the fundamental image processing of filters. To this end, custom operations have been developed for each of the eight image filters targeted in this study (Sobel, Scharr, Prewitt, Laplacian, blur, Gaussian blur, median, sharpening).

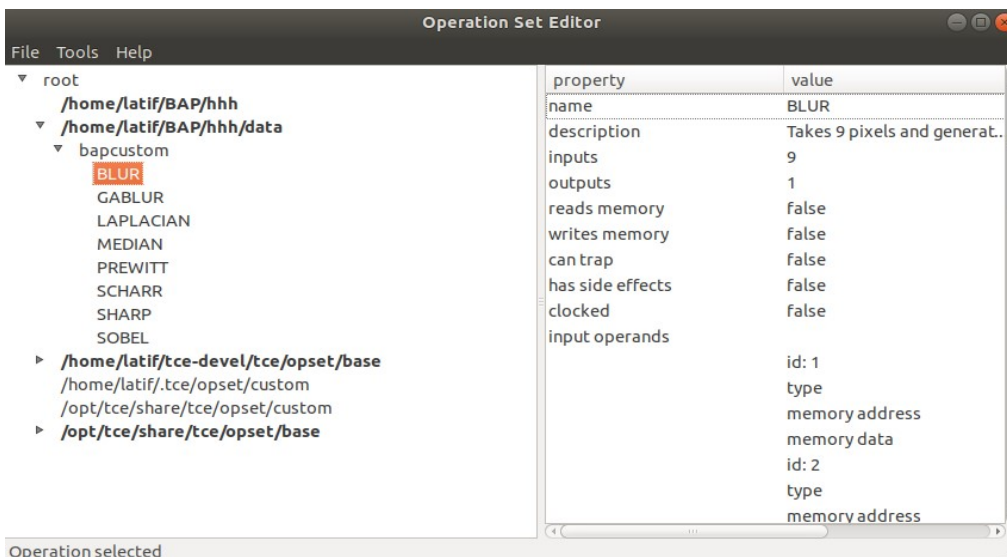


Figure 5. Determining the custom operations properties in OSEd

In the OpenASIP toolkit, the OSEd tool is employed for the purpose of designing and managing application-specific operations. The OSEd tool enables the definition of a range of features, including operation definitions, functions, input-output port numbers, data types, memory relationships and other similar characteristics. In this way, the developed operations can be integrated into any TTA processor. Figure 5 illustrates the definition of the custom operations designed for the filters within the scope of the study in the OSEd tool.



A unifying characteristic of the basic filters is that the values of all neighbouring pixels are needed in the calculation of each pixel. Consequently, each of the operations designed to work on grayscale images contains nine 8-bit wide input ports and one 8-bit wide output port. The functions that the commands are to perform, namely the filter calculations, are developed in a separate OSEd module written in C++. Therefore, all operations are prepared for integration into the processor core and utilisation by the OpenASIP compiler.

Following the compilation of the OSEd modules, the ASIP design, which incorporates image filtering operations, was initiated. The initial step involved the creation of a new function unit (FU), designated as FU\_FILTERS, on the GP-1 model. This unit has nine input ports and one output port, allowing compatibility with custom operations. Subsequently, the operations developed in the OSEd tool were added to the FU\_FILTERS unit using the ProDe tool. The resulting new processor model was named CP-1. Furthermore, a variant of the same configuration, designated CP-2, was developed to examine the impact of the number of transport buses on processor performance. Figure 6 illustrates the block structure of the CP-1 ASIP model.

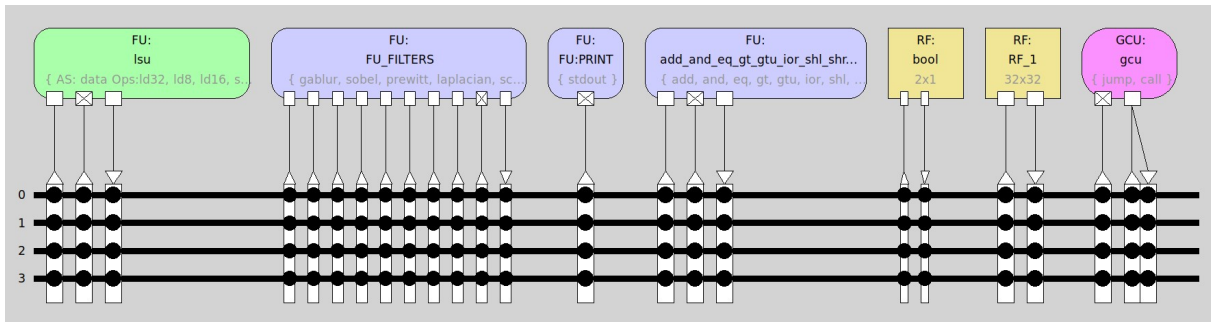


Figure 6. Custom TTA processor (CP-1) model in ProDe

### 4.3 Tests and Results

A continuous test cycle is employed to evaluate the impact of the operations devised during the ASIP design process. The Proxim tool, accessible within the OpenASIP toolkit and equipped with cycle-accurate simulation capabilities, is an invaluable asset for testing and profiling the target application and the core model. Figure 7 illustrates the Proxim analysis, showcasing the number of triggers in the FU\_FILTERS unit as a consequence of our test software's execution on the CP-1 processor model.

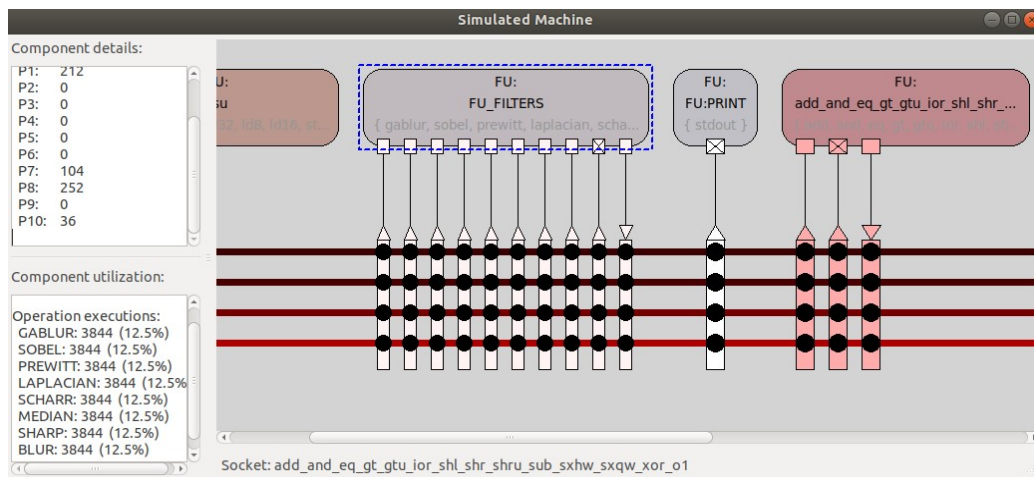


Figure 6. Custom TTA processor (CP-1) model in ProDe

The Proxim tool, which simulates the user application on the processor model, produces accurate performance data in terms of clock cycles. However, in order to ascertain the precise number of clock cycles the processor completes the target application, it is necessary to define the delay information for each custom operations. In this context, the delay in terms of clock cycles for the operations designed for image filtering was determined in the ProDe tool. The HDL implementation of the FU\_FILTERS unit was developed with VHDL in accordance with the delay values given in Table 1.

**Table 1.** The clock-cycle latencies of the custom operations

Operation	Latency
BLUR	3
GABLUR	3
MEDIAN	35
SHARPENING	3
SOBEL	4
SCHARR	3
PREWITT	4
LAPLACIAN	3

In the test phase, a simple application was developed in the C language. The application contains basic filter operations applied sequentially. The grayscale Lenna test images, with dimensions of 64x64, 128x128, and 256x256 pixels, were used for the simulations, which were performed using Proxim analyses. The total number of clock cycles for the GP-1, GP-2, CP-1, and CP-2 configurations are presented in Table 2.

**Table 2.** Performance comparison of the developed TTA processors

Processor	Bus Count	Clock Cycles (64x64)	Clock Cycles (128x128)	Clock Cycles (256x256)
GP-1	4	16,965,778	69,151,243	275,413,123
GP-2	2	22,458,486	91,359,118	363,962,745
CP-1	4	695,228	1,754,443	11,453,204
CP-2	2	852,716	2,546,698	14,218,605

The results demonstrate that the custom operations developed for basic image processing filters significantly enhance performance. Conversely, although the number of transport buses has been observed to have a positive impact on performance, it cannot be concluded that it constitutes a significant factor for our ASIP.

The hardware implementation of the FU\_FILTERS unit was introduced to the OpenASIP toolkit with HDBEditor. Subsequently, the HDL codes of all processors were generated using the ProGe tool. Finally, all processors were synthesised with Xilinx Vivado IDE [13] for an xc7a-100t class FPGA part. Table 3 provides a comparison of the resource utilizations for all TTA processors designed in this study. As anticipated, the implementation of custom operations leads to an increase in the required chip area. Nevertheless, the associated resource increase can be regarded as reasonable in light of the enhanced performance achieved.

**Table 3.** Comparison of FPGA resources for the developed TTA processors

Processor	LUT	FF	DSP
GP-1	1774	865	0
GP-2	1456	768	0
CP-1	3674	2232	10
CP-2	2852	1854	10

## 5 CONCLUSION

The utilisation of image processing applications is pervasive across a multitude of contemporary technological domains. In addition to sophisticated filters, fundamental image processing filters are also employed in these applications for a multitude of purposes. This study examines the potential of ASIP design as an effective solution, particularly in the field of embedded systems, for basic image processing filters. In addition to open-source and free design tools, TTA is regarded as an optimal method for such designs, due to its flexible, customisable, and scalable structure. In the context of this study, custom operations were developed using the OpenASIP toolkit for eight fundamental image filters. Subsequently, a fundamental TTA-based ASIP model was devised by integrating custom operations with general-purpose operations within the same core across distinct FUs. The resulting analysis demonstrated the beneficial impact of custom operations on core performance. Furthermore, the hardware

implementations of all processor models were generated. Finally, the FPGA synthesis results were subjected to comparative analysis. In future studies, it would be beneficial to implement more effective designs that utilise ILP to enhance performance. One potential approach is to develop discrete FUs, which could facilitate the execution of the test code used in this study with enhanced performance.

## Acknowledgments

This work is granted by the Scientific and Technical Research Council of Türkiye (TÜBİTAK) under 2209 programme with the project number 1919B012307030.

## References

- [1] U T. S. Huang, W. F. Schreiber, and O. J. Tretiak, "Image processing," in *Proceedings of the IEEE*, vol. 59, no. 11, pp. 1586-1609, Nov. 1971, doi: 10.1109/PROC.1971.8491.
- [2] T. Acharya and A. K. Ray, *Image Processing: Principles and Applications*, New York: Wiley-Interscience, 2008.
- [3] J. Coady, A. O'Riordan, G. Dooly, T. Newe, and D. Toal, "An overview of popular digital image processing filtering operations," in *2019 13th International Conference on Sensing Technology (ICST)*, 2019.
- [4] Y. Zhou, F. He, and Y. Qiu, "Accelerating image convolution filtering algorithms on integrated CPU-GPU architectures," *J. Electron. Imaging*, vol. 27, no. 03, art. no. 1, 2018.
- [5] A. Nohl, F. Schirrmester, and D. Taussig, "Application specific processor design: Architectures, design methods and tools," in *2010 IEEE/ACM International Conference on Computer-Aided Design (ICCAD)*, 2010.
- [6] L. Akçay and B. Ors Yalcin, "Analysing the potential of transport triggered architecture for lattice-based cryptography algorithms," *Int. J. Embed. Syst.*, vol. 15, no. 5, art. no. 404, 2022.
- [7] L. Akçay and B. Ö. Yalçın, "Lightweight ASIP Design for Lattice-Based Post-quantum Cryptography Algorithms". *Arab J Sci Eng.*, 2024. <https://doi.org/10.1007/s13369-024-08976-w>
- [8] J. A. Fisher, "Very Long Instruction Word architectures and the ELI-512," *Comput. Archit. News*, vol. 11, no. 3, pp. 140-150, 1983.
- [9] A. Aiken, U. Banerjee, A. Kejariwal, and A. Nicolau, "Overview of ILP Architectures," in *Instruction Level Parallelism*, Boston, MA: Springer US, 2016, pp. 9-42.
- [10] K. Hepola, J. Multanen and P. Jääskeläinen, "OpenASIP 2.0: Co-design toolset for RISC-V application-specific instruction-set processors," *2022 IEEE 33rd International Conference on Application-specific Systems, Architectures and Processors (ASAP)*, Gothenburg, Sweden, 2022, pp. 161-165, doi: 10.1109/ASAP54787.2022.00034.
- [11] L. Akçay and B. Ors, "Custom TTA operations for accelerating kyber algorithm," in *2021 13th International Conference on Electrical and Electronics Engineering (ELECO)*, 2021.
- [12] V. A. Zivkovic, R. J. W. T. Tangelder, and H. G. Kerkhoff, "Design and test space exploration of transport-triggered architectures," in *Proceedings Design, Automation and Test in Europe Conference and Exhibition 2000 (Cat. No. PR00537)*, 2002.
- [13] S. Chakraborty, "Vivado Design Tools," *Designing with Xilinx® FPGAs*, pp. 17-21, Oct. 2016, doi: 10.1007/978-3-319-42438-5\_2.
- [14] H. Modi and P. Athanas, "In-system testing of Xilinx 7-Series FPGAs: Part 1-logic," in *MILCOM 2015 - 2015 IEEE Military Communications Conference*, 2015.



---

## Enhancing the Performance of Twofish Cipher via Instruction Set Extension

Latif Akcay\*, Mustafa Alptekin Engin

*Electrical - Electronics Engineering, Bayburt University, Bayburt, Türkiye*

---

### Abstract

Symmetric-key cryptography has a crucial role in providing data protection and securing digital communications in modern systems due to its efficiency in encrypting large data volumes with a single secret key. The Twofish cipher is a well-known block cipher for its speed and security against a wide range of cryptographic attacks. This paper presents simple custom instructions for the Twofish encryption algorithm to improve throughput and reduce computational overhead. The proposed instructions were designed to be compatible with the industry standard RISC-V instruction set architecture. We use a classical five-stage pipelined RV32IM core as a test and integration platform for the custom instructions. Performance evaluations of the test results demonstrate that our instruction set extension provides significant speedup and a reasonable increase in chip area. We explain the hardware and software design and implementation of our approach in detail and give comparative tables that show FPGA resource utilization. In addition, this study also highlights the potential of a more advanced instruction set extension for the Twofish cipher.

**Keywords:** *RISC-V, Cryptography, Custom instruction design, Extending instruction set, FPGA*

---

## 1 INTRODUCTION

In the modern world, where digital security is becoming increasingly important, the use of effective encryption algorithms has become a critical requirement. Symmetric encryption algorithms constitute a fundamental aspect of data protection strategies, offering rapid and secure data encryption and decryption operations [1]. In this context, the Twofish algorithm [2] is a notable example of a robust option in terms of security and performance. Twofish is a versatile block encryption algorithm designed by Bruce Schneier and his team, which encrypts data in 128-bit blocks using variable key size. This algorithm offers a high level security and efficiency and is employed in a range of applications.

However, the efficiency of the algorithms is dependent not only on the security of their design, but also on the capability of the hardware and software environments in which they are implemented. At this point, it is important to consider the role of processor architectures. RISC-V [3], as an open-source instruction set architecture (ISA), offers significant advantages in terms of expandability and customisability. The architectural features of RISC-V offer potential for optimising the performance of encryption algorithms.

This study, as the initial steps of this research process, examined the potential for enhancing the efficiency of the Twofish algorithm through the utilization of the RISC-V instruction set extension technique. The extension possibilities afforded by the RISC-V architecture facilitate improvements in the performance of the encryption and decryption processes associated with the Twofish algorithm. In particular, the objective is to accelerate the computationally intensive operations of Twofish through the utilisation of RISC-V instruction set extensions. This approach seeks to provide notable performance gains in both software and hardware-based implementations by enhancing the speed of the algorithm and optimising its energy efficiency.

The existing literature includes studies on instruction set extensions for comparable encryption techniques, such as the Advanced Encryption Standard (AES) and the Data Encryption Standard (DES) [4-6]. However, to the best of our knowledge, there is no RISC-V-based study that has been proposed for Twofish yet. This study is organized as follows. Section 2 summarizes the Twofish encryption algorithm, the RISC-V architecture, and the soft-core processor used in this study. Section 3 explains the instructions designed and their integration into software and hardware. Section 4 presents the performance analysis and hardware implementation results. Finally, Section 5 concludes the study.

## 2 ALGORITHM AND ARCHITECTURE

This section provides a concise overview of the operational methodology of the Twofish algorithm. Additionally, it highlights the significance of the RISC-V (ISA) and the processor employed as the fundamental platform for this study.

### 2.1 Twofish Block Cipher

Twofish is a secure symmetric encryption algorithm designed by Bruce Schneier and his team for submission to the Advanced Encryption Standard (AES) competition organised by the National Institute of Standards and Technology (NIST) [2]. The expectation of the NIST was that the participants would submit an encryption algorithm that could work with keys of 128, 192, and 256 bits on 128-bit data blocks. Twofish was selected as one of the finalists as an improved version of the previously known Blowfish encryption algorithm [7]. It attracted considerable attention among the candidates for its speed and has strong security guarantees. Currently, there is no known cryptanalysis method that can successfully break Twofish.

The Twofish encryption algorithm is based on a 16-round Feistel network [8]. Each round contains a bijective  $F$  function consisting of 8-by-8-bit S-boxes depending on the key length, a fixed 4-by-4 maximum distance separable (MDS) matrix, a pseudo-Hadamard transform (PHT), and bitwise rotations. Figure 1 illustrates the initial stage of the Twofish encryption algorithm, along with the XOR operations (input whitening) at the beginning. A similar whitening operation is also performed after the 16th round.

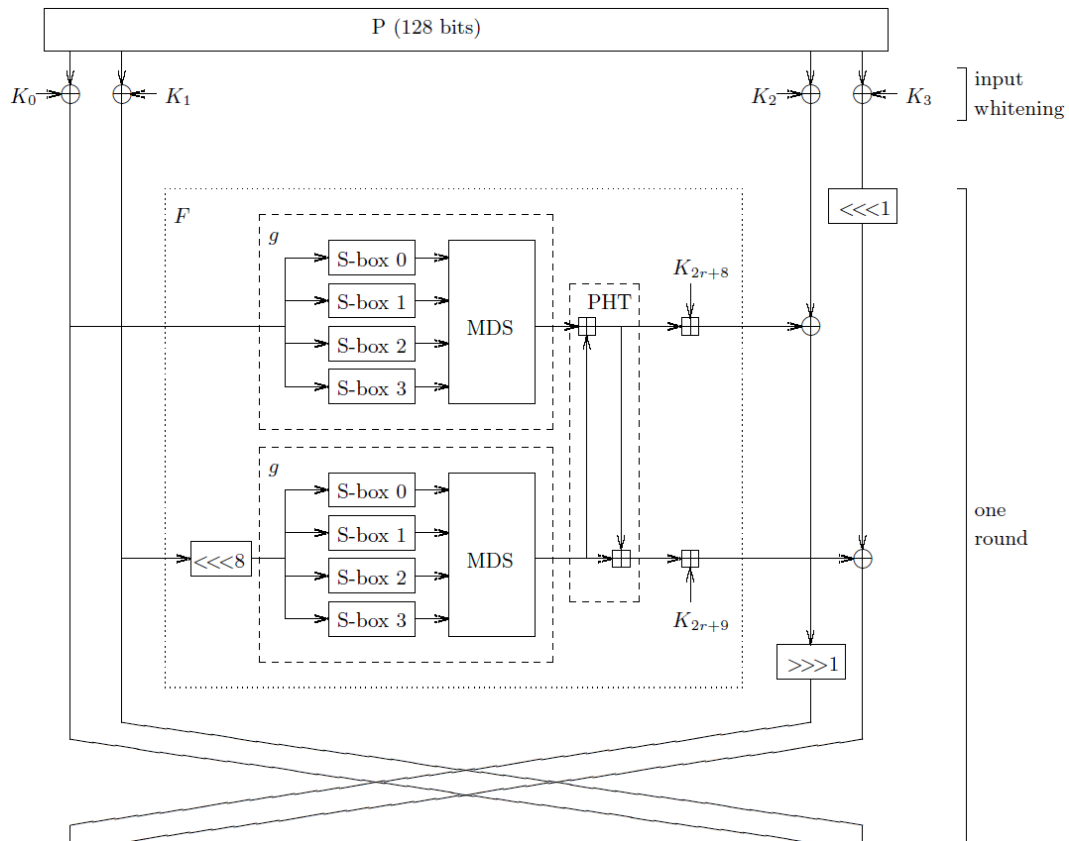


Figure 1. The internal structure of the Twofish encryption algorithm [2]

Based on the security requirements, Twofish can be used with variable key sizes. Besides, the data block size and number of rounds can be arranged according to user needs. The combination of these features makes Twofish an appropriate encryption algorithm for a wide range of applications. However, the Twofish algorithm has some disadvantages compared to the Rijndael algorithm, which won the NIST competition and became the standard AES. Firstly, AES is a less complex encryption method than Twofish. Therefore, software and hardware implementation of Twofish is relatively more difficult. Secondly, Twofish is slightly slower than AES. For all these reasons, although Twofish is not a widely used encryption method like AES, it is still included in some essential software libraries, as in [9].

## 2.2 RISC-V ISA

RISC-V was started to develop as an open-source and free ISA in 2010 at the University of California, Berkeley. The objective of the project was to develop a modular instruction set with royalty-free license rights that could be used in both academia and industry. At that time, the initiative in the ISA field was dominated by private companies. To date, numerous RISC-V standards have been published, and the instruction sets were frozen in 2019. Nevertheless, there are still optional instruction sets that are currently under development.

The RISC-V instruction set defines a set of instructions that are compatible with the classical RISC concept and are available in 32, 64, and 128 bit widths. Additionally, the RISC-V ISA features a carefully selected instruction set that facilitates the design of multiplexers and is suitable for variable size extensions. The popularity of RISC-V ISA has been increasing in many application areas in recent years [10].

## 2.3 Hornet Core

Hornet is a RISC-V-based, single-issue, in-order processor developed at Istanbul Technical University [11]. It implements 32-bit base integer (RV32I) and multiplication instructions (RV32M) defined in the RISC-V ISA manual. Hornet has a 5-stage pipelined classical RISC core architecture. The Hornet project is accessible on the GitHub repository and provided with fully open-source HDL code, useful scripts, example test codes, and detailed documentation. Figure 2 shows a simplified pipeline diagram of the core. Since it is a simple, easy-to-use and FPGA-proven project, we used Hornet as the base processor platform on which we implemented our custom instructions.

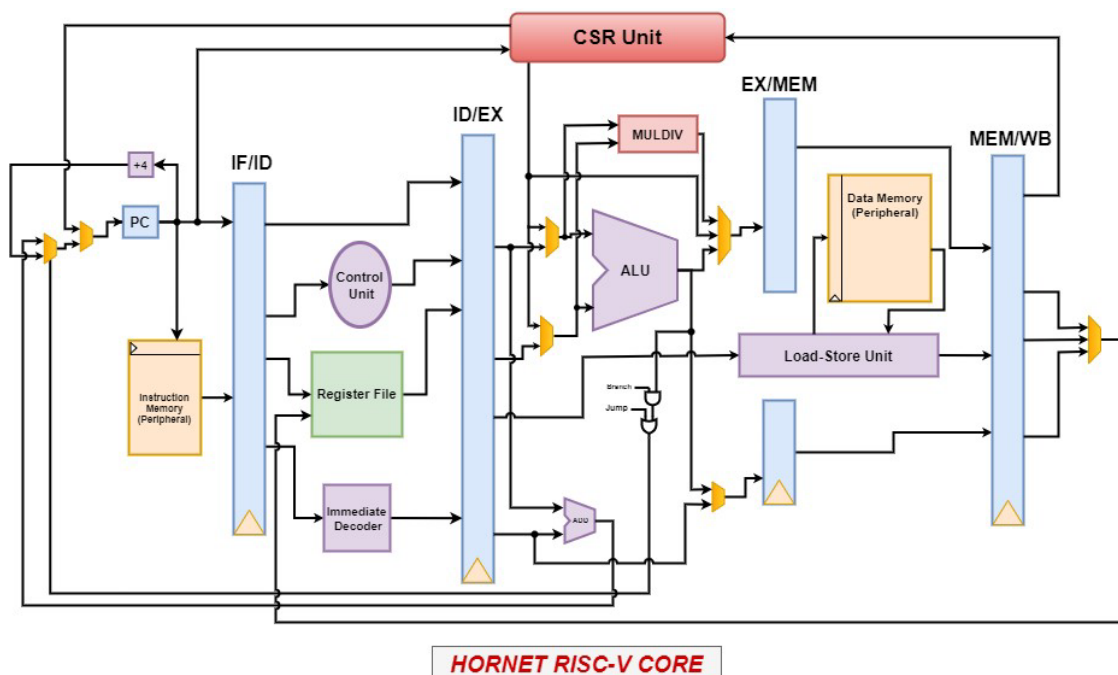


Figure 2. Pipeline architecture of the Hornet RISC-V core [11]

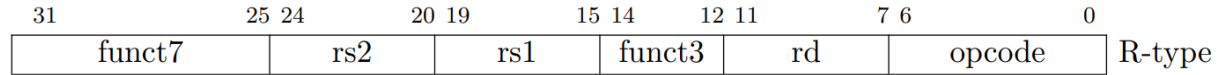
## 3 DESIGN OF CUSTOM INSTRUCTIONS

Excluding the difference in production technologies, there are generally two methods to ensure that an algorithm runs faster and more effectively on a processor [13]. One such method is to design loosely-coupled hardware accelerators that are directly connected to the data buses of the processors. However, this method does not provide an optimal solution, as it significantly increases data traffic and requires a custom design for each processor. The alternative approach is to integrate the most computationally demanding parts of the algorithm into the processor core as tightly-coupled hardware accelerators. Provided that designs are compliant with the relevant instruction set standards, this approach does not result in an increase over data bus traffic. Furthermore, tightly-coupled hardware accelerators can be deployed on other compatible processors.

Figure 1 shows that the Twofish encryption algorithm can be accelerated at a high level if the S-box, MDS and PHT blocks in the F function are implemented in hardware. However, this study is still in its early stages, so these

complex operations have not been designed yet. The algorithm also includes rotation and byte-swap operations. Twofish software implementations often use the following operations:

- $ROL32(x,n) = (((x) \ll (n)) \mid ((x) \gg (8 * \text{sizeof}(\text{word\_t}) - (n))))$
- $ROR32(x,n) = (((x) \gg (n)) \mid ((x) \ll (8 * \text{sizeof}(\text{word\_t}) - (n))))$
- $ROTR4(x, n) = (((x) \gg (n)) \mid (((x) \& (1 \ll ((n)-1))) \ll (4 - (n))))$



**Figure 3.** The R-type base instruction format defined in RISC-V ISA [3]

If these functions are executed in one clock cycle, performance can be increased with a tiny hardware cost in return. Accordingly, these functions were transformed into custom instructions and implemented within the Hornet core. Figure 3 shows the R-type instruction format defined in the official specification of the RISC-V ISA. It can be seen that the ROL32, ROR32 and ROTR4 functions are quite suitable to be designed as R-type instructions. Therefore, we have designed and implemented two custom instructions using Verilog HDL. Then, we have extended the arithmetic logic unit (ALU), control unit, and the decoder implementations of the core to operate the custom instructions which perform the rotation functions.

In order for the compiler to be aware of the instruction set extensions made in the processor hardware, it is necessary to recompile the compiler from the source code and reload it in order to support the newly added instructions. Accordingly, the descriptive codes of the custom instructions have been added to the files named *riscv-opc.c* and *riscv-opc.h* in the RISC-V GNU Toolchain source code. In the Twofish software code, the rotation functions are arranged to work with the newly added instructions in accordance with the RISC-V assembly rules. Finally, the software code, compiler, and hardware chain have been enabled to use custom instructions in a compatible manner.

## 4 FPGA IMPLEMENTATION AND TEST RESULTS

In the test phase, the Twofish software was compiled separately for Hornet configurations with and without the instruction extension. The tests were performed using Xilinx Vivado as a software-hardware co-simulation tool. The total number of clock cycles (CC) obtained from the tests, which indicates the execution time of the Twofish encryption operation, is presented in Table 1 for comparative analysis. Although the observed improvement in performance is relatively modest, it is noteworthy that this was achieved with only a few custom instructions. Furthermore, as outlined in Section 3, this is the initial phase of a longer-term project to extend the instruction set for Twofish cipher.

**Table 1.** Performance gain of the custom instructions

Processor	Maximum Frequency	CC
Hornet	50 MHz	15944
Hornet + custom ins.	50 MHz	14956

A Xilinx xc7a-100t class FPGA was selected for the hardware synthesis. As with the performance analysis, the synthesis operation was conducted separately for Hornet cores with and without custom instructions. The FPGA resource utilization values after synthesis are presented in Table 2. The results demonstrate that the hardware cost of the designed instructions remained at a reasonable level. It is also notable that, despite the newly integrated instructions, the maximum frequency of the processor remains at 50 MHz.

**Table 2.** Hardware resources required for the custom instructions

Processor	LUT	FF	MUX	DSP
Hornet	5548	2562	571	0
Hornet + custom ins.	5872	2623	593	0

## 5 CONCLUSION

The protection of sensitive data is arguably one of the most critical issues of the digital age. When considered in this context, it becomes evident that symmetric encryption algorithms play a crucial role in a multitude of fields.

Twofish is a fast, secure, and easy-to-implement block encryption algorithm used in many applications. In this study, the instruction set extension technique was applied to the Twofish encryption algorithm. We used open-source and free ISA, compiler, and processor platforms to implement our custom instructions. In the tests performed after the hardware and software implementations, it was seen that the performance increased at a reasonable level with a few custom instructions. This was achieved with a minimal hardware cost that proves the efficiency of the extension. This study is the initial phase of a longer project that aims to create a detailed instruction set for the Twofish cipher. In future studies, we intend to focus on the tightly-coupled implementation of blocks such as S-boxes, MDS, and PHT, which are resided in the  $F$  function of the Twofish encryption algorithm and constitute the main computational load.

## References

- [1] N.A. Mohammed, H. Alabdulrazzaq, and N. Q. Mohammad, "Symmetric encryption algorithms: Review and evaluation study," *International Journal of Communication Networks and Information Security*, vol. 12, no. 2, pp. 256–272, 2020.
- [2] B. Schneier et al., "The twofish encryption algorithm: A 128-bit block cipher." NIST AES Proposal, [Online], June 15 1998. Available: [https://karlin.mff.cuni.cz/~kozlik/udk\\_mat/twofish.pdf](https://karlin.mff.cuni.cz/~kozlik/udk_mat/twofish.pdf)
- [3] D. A. Patterson and J. L. Hennessy, *Computer Organization and Design RISC-V Edition: The Hardware Software Interface*, 2nd ed. Oxford, England: Morgan Kaufmann, 2021.
- [4] B. Marshall, G. R. Newell, D. Page, M.-J. O. Saarinen, and C. Wolf, "The design of scalar AES Instruction Set Extensions for RISC-V," *IACR Transactions on Cryptographic Hardware and Embedded Systems*, pp. 109–136, 2020.
- [5] S. O'Melia and A. J. Elbirt, "Enhancing the performance of symmetric-key cryptography via instruction set extensions," *IEEE Trans. Very Large Scale Integr. VLSI Syst.*, vol. 18, no. 11, pp. 1505–1518, 2010.
- [6] L. Pan, G. Tu, S. Liu, Z. Cai, and X. Xiong, "A lightweight AES coprocessor based on RISC-V custom instructions," *Secur. Commun. Netw.*, vol. 2021, pp. 1–13, 2021.
- [7] A. E. Adeniyi, S. Misra, E. Daniel, and A. Bokolo Jr, "Computational complexity of modified Blowfish cryptographic algorithm on video data," *Algorithms*, vol. 15, no. 10, art. no. 373, 2022.
- [8] A. Bogdanov and K. Shibutani, "Generalized Feistel networks revisited," *Des. Codes Cryptogr.*, vol. 66, no. 1–3, pp. 75–97, 2013.
- [9] J. Callas, L. Donnerhacke, H. Finney, D. Shaw, and R. Thayer, "RFC 4880: OpenPGP Message Format," USA, RFC Editor, 2007.
- [10] S. Rout and C. Shekhar, "The rise and popularity of RISC-V," *Techrxiv*, 2024.
- [11] Y.S. Tozlu and Y. Yilmaz, "Design and Implementation of a 32-Bit RISC-V Core", Senior Design Project, Electronics and Communication Engineering Department, İstanbul Technical University, Türkiye, 2021.
- [12] GitHub. (2024). *Hornet RISC-V Core* [Online]. Available: <https://github.com/yavuz650/RISC-V>
- [13] T. Fritzmann, G. Sigl, and J. Sepúlveda, "RISQ-V: Tightly coupled RISC-V accelerators for Post-Quantum Cryptography," *IACR Transactions on Cryptographic Hardware and Embedded Systems*, pp. 239–280, 2020.
- [14] S. Chakraborty, "Vivado Design Tools," *Designing with Xilinx® FPGAs*, pp. 17–21, Oct. 2016, doi: 10.1007/978-3-319-42438-5\_2.
- [15] H. Modi and P. Athanas, "In-system testing of Xilinx 7-Series FPGAs: Part 1-logic," in *MILCOM 2015 - 2015 IEEE Military Communications Conference*, 2015.





---

## Studying the Gender Gap in Advanced Digital Skills: Coding, Data Science, and Cybersecurity

Anxhela Ferhataj<sup>\*1</sup>, Fatmir Memaj<sup>2</sup>

<sup>1</sup> Department of Informatics & Technology, Faculty of Engineering, Informatics and Architecture, European University of Tirana, Tirana, Albania

<sup>2</sup> Department of Statistics and Applied Informatics, Faculty of Economy, University of Tirana, Tirana, Albania

---

### Abstract

Digital skills such as coding, data science and cybersecurity play a crucial role in driving career success and innovation in today's technological landscape. Although there has been a rise in awareness and efforts to promote diversity, gender disparities persist in these critical areas of technology. The work and lives of people are significantly impacted by digital technologies. Advanced skills are a specific set of skills required for a job. They are mainly needed for IT-related jobs such as coding, cybersecurity and data science. Advanced skills are often acquired through formal education. The global digital gender divide is significant.

This study examines the gender gap in advanced digital skills among students, specifically coding, data analytics, and cybersecurity. The research sample consisted of 309 students from the European University of Tirana. The survey instrument is a questionnaire distributed online. The survey assessed a range of digital skills in three key areas: coding, data science and cybersecurity. We also used Likert scale questions to collect student feedback on the importance of digital technologies. Hypotheses are tested with 95% confidence intervals. JASP - 0.18.3 was used for data analysis. The conclusion of the data analysis shows that women, as opposed to men, gave digital skills a greater priority in terms of potential careers in the future. There were notable gender differences in cybersecurity skills as well as the value of digital skills in the labor market, with men probably possessing higher levels of skills.

**Keywords:** *Advanced digital skills, Gender gap, Coding, Data science, Cybersecurity*

---

## 1 INTRODUCTION

Technological advancements have influenced the digital transformation of enterprises, increasing the demand for IT personnel with superior digital capabilities. Several organizations and authors have investigated digital talents and their distribution. Advanced talents are a specific collection of abilities required for a job. They are primarily required for IT-related positions such as coding, cybersecurity, and data science. Advanced skills are frequently obtained through formal education.

The global digital gender difference is enormous. According to the European Commission (2023) [1], digital skills are defined as those required for the safe and critical use of information technology. In accordance with the European Commission (2023) [1], basic digital skills include computer use, whereas advanced digital skills include programming, developing electronic information, online security, and so on. According to Van Dijk (2019) [2], digital gender divides are defined as gender inequalities in ICT access, attitudes towards technology, knowledge and skills, and use and involvement. This study investigates the gender gap in advanced digital skills among students, focusing on coding, data analytics, and cybersecurity.

## 2 LITERATURE REVIEW

Advanced digital skills have become the foundation of Europe's digital future in an age of perpetual technological advancement [1]. Different researchers [3] classify digital divides at three levels. The first level addresses the availability of ICT resources and attitudes about technology. The second level covers gender differences in ICT use, knowledge, and skills. The third level refers to gaps in ICT-related outcomes, such as learning or educational achievement. Cultural, social, and economic inequalities in education are just some of several influencing factors. Different researchers have reported differences between genders in digital knowledge and skills [4–6]. This was identified by several studies [5] that there are gender differences in perceptions of technology that have an

important positive effect on male self-efficacy and attitudes. However, according to some findings, women have a higher level of digital knowledge and abilities [6]. According to other research, male and female students show similar preferences for learning styles [7].

In line with calculates from the European Commission (2023) [1], there will be approximately 10 million ICT specialists in 2023, accounting for 5% of all EU workers. At least 20 million ICT specialists are expected to be employed by 2030, with a gender balance, according to expectations [1]. The increase in demand for employees with advanced digital abilities is impacted by these regulations. The data analysis reveals an important gender gap in the number of employees for the year 2023, with 81% of men and 19% of women employment. Bulgaria (29%), Estonia (27%), and Romania (26%), among other EU nations, have the greatest percentages of women employed in the IT sector. Malta (14%) and the Czech Republic (12%) have the lowest [8]. Though 51% of EU citizens are female, only 1 in 3 STEM graduates and 1 in 5 ICT specialists identify as female [8]. It is evident from the Eurostat data in Figure 1 from 2013 to 2022 that there hasn't been much of a change in the proportion of women employed in ICT.

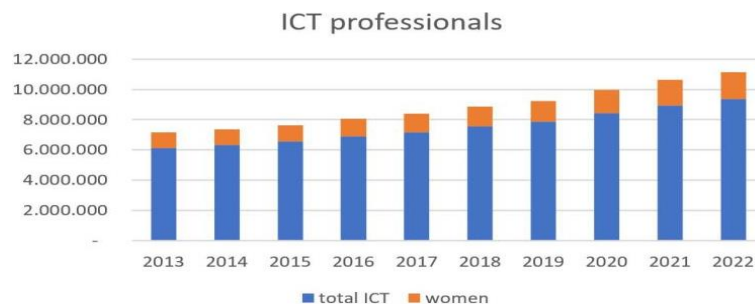


Figure 1. ICT professionals [8]

Since the total percentage of males with at least basic digital abilities was slightly greater than that of women (57% versus 54%), the gender gap varied significantly by age group. Compared to their male colleagues, more young women in the age ranges of 16–24, 25–34, and 35–44 possessed at least basic digital abilities. The situation is reversed among those 45 years of age or older, when the percentages are larger among men and the gender difference grows in the older age groups (refer to figure 2).

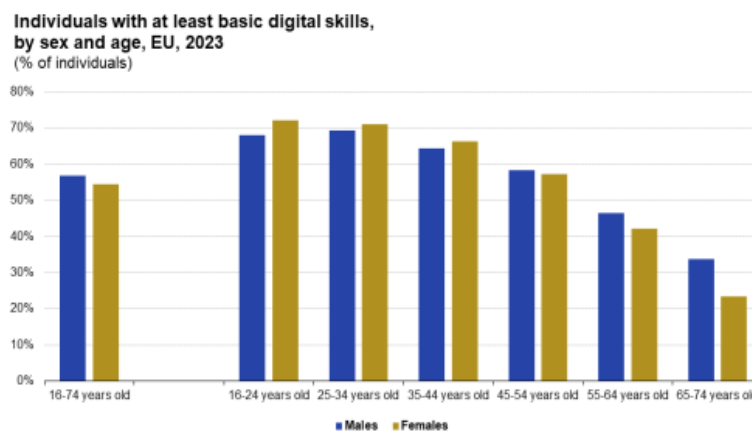


Figure 2. Individuals with at least basic digital skills, by sex and age, EU, 2023 [8]

Cedefop’s composite indicator that measures the performance of EU skills systems is called the European Skills Index (ESI) [9]. The “distance to the ideal” performance of nations is measured by the ESI. All countries’ ratings are calculated and then compared to an ideal performance that varies from 0 to 100. The skills development, skills activation, and skills matching components compose the ESI, and each one evaluates one specific aspect of a skills system. Fifteen different indicators collected from several international datasets form the basis of the ESI.

Information about the conclusion of different educational and training levels (such as adult education and basic education) is given in the “Skills Development” component. Information regarding how well skills systems help the transition to employment and engagement in the labor market is covered under the “Skills Activation” component. Next, the “Skills Matching” component examines how skills are used and whether they are mismatched for a particular job market and nation. The European Skills Index (2024) ranks the performance of each of the three components, with Czechia ranking first out of 31 with a total score of 70.4. It placed first in skills

matching (score: 92.4), 23rd in skills activation (score: 53.9), and 11th in skills development (score: 60.5) at the component level (refer to figures 3).

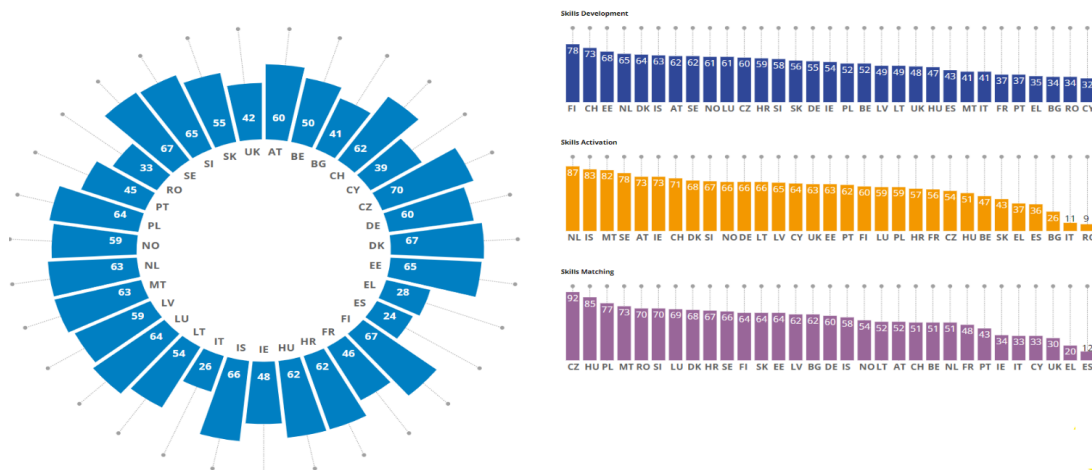


Figure 3. European Skills Index 2024 [9]

The Ready4Cybersecurity Program from Microsoft: Microsoft has acknowledged the large gender gap in cybersecurity and has started steps to improve women’s and girls’ access to cybersecurity capabilities. Approximately 25% of cybersecurity workers worldwide are women. To close this gap and improve diversity in the profession, the program seeks to train and certify 100,000 young women in cybersecurity by 2025. [10]

With reference to Albanian INSTAT data for 2023, 99.1% of businesses employing more than ten people utilize computers with Internet access. This percentage is less than the 2022 figure of 98.7%. In the meantime, compared to 2022, there will be more specialists working in the ICT sector in 2023. In particular, the percentage of ICT workers increased from 26.3% in 2022 to 28.4% in 2023 [11]. This emphasizes the necessity for advanced digital capabilities among ICT specialists. According to Albanian INSTAT data, 68,305 female students—or 58.4% of all students enrolled in higher education will continue their studies across all study cycles at the institution in the academic year 2023–2024. It has been found that women represent most university students [12].

Research Question: How do gender-based differences in exposure to coding, data science, and cybersecurity education influence career choices in these fields?

Research hypotheses are:

- H1: Gender has a significant impact on the development of advanced digital skills, such as coding ( $\alpha = 0.05$ ).
- H2: Gender has a significant impact on the development of advanced digital skills in data science ( $\alpha = 0.05$ ).
- H3: Gender has a significant impact on the development of advanced digital skills in cybersecurity ( $\alpha = 0.05$ ).

### 3 MATERIAL AND METHOD

The questionnaire is used as a research instrument. Three variables are taken as factors in the questionnaire: cybersecurity, data science, and coding. Questions with alternatives are included in the first section, and a 5-point Likert scale survey with responses ranging from “strongly agree” to “strongly disagree” is included in the second. Online distribution of the surveys took place throughout the first semester of the 2023–2024 academic year. There are 199 males and 110 females among the 309 students from the European University of Tirana who are taking part. A total of 350 questionnaires were sent; 309 of them were validly completed, while 41 of them were not completed. 88% of respondents responded. Hypotheses are tested with 95% confidence intervals. JASP - 0. 18. 3 was used for data analysis.

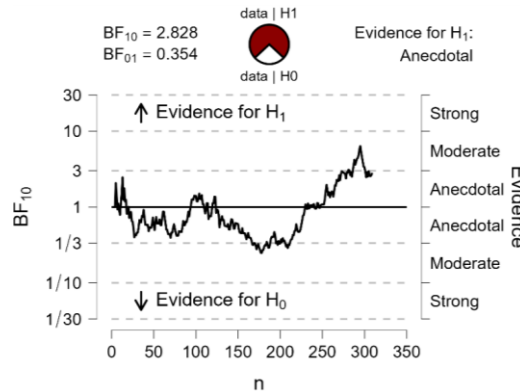
### 4 RESULTS

Data analysis was done applying the Bayesian Independent Samples T-Test, which evaluates the strength of evidence against the null hypothesis (no difference between groups). The Bayes Factor supporting the alternative hypothesis is represented by the  $BF_{10}$  value. The findings show that there are notable differences between men and women in how advanced digital abilities are perceived and performed. Based on the data presented in figure 4, it can be concluded that there are significant differences between both genders regarding the significance of advanced

digital abilities for their future career development. Compared to men, women placed a higher value on digital skills for future employment opportunities. With reference to Table 1, the average for the female gender is 4, while the average for the male gender is 3.693.

**Table 1.** Advanced digital skills and career

	Group	N	Mean	SD	SE	Coefficient of variation	95% Credible Interval	
							Lower	Upper
Advanced digital skills and career	Female	110	4	0.878	0.084	0.219	3.834	4.166
	Male	199	3.693	1.078	0.076	0.292	3.543	3.844



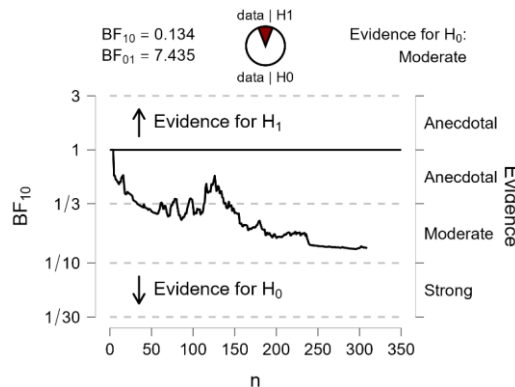
**Figure 4:** Advanced digital skills and career

Table 2 reveals that there are statistically significant differences in cybersecurity among the three skills. There is significant proof supporting the null hypothesis, which states that there is not a difference in coding ability between genders. Because both genders showed similar levels of proficiency, this data shows that initiatives to promote gender equality in coding education may be having a favorable effect. Previous studies have emphasized the value of early exposure and ongoing support in the teaching of coding, especially for female students. These findings are in line with research indicating that inclusive learning settings and focused educational initiatives can help reduce gender gaps in coding. Several initiatives have been implemented in Albania to include girls in ICT.

There is not enough evidence to draw solid conclusions against the null hypothesis, but it does indicate a little gender gap in data science proficiency. There were notable gender differences in cybersecurity skills as well as the value of digital skills in the labor market, with men probably possessing higher levels of skills. Figures 5-7 provide a graphical representation of each of the advanced digital skills.

**Table 2.** Bayesian independent samples T-test

	BF <sub>10</sub>	error %
Advanced Digital Skill: Coding	0.134	0.100
Advanced Digital Skill: Data Science	0.766	0.023
Advanced Digital Skill: Cybersecurity	1.435	0.013



**Figure 5:** Advanced digital skill: Coding

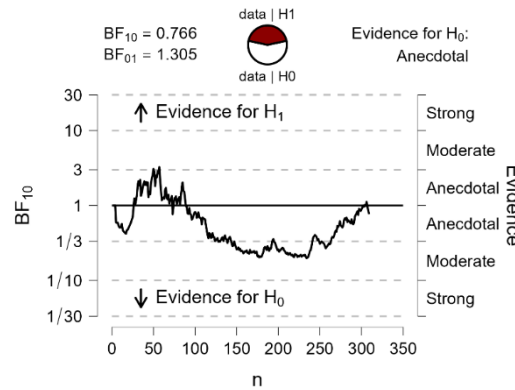


Figure 6: Advanced digital skill: Data science

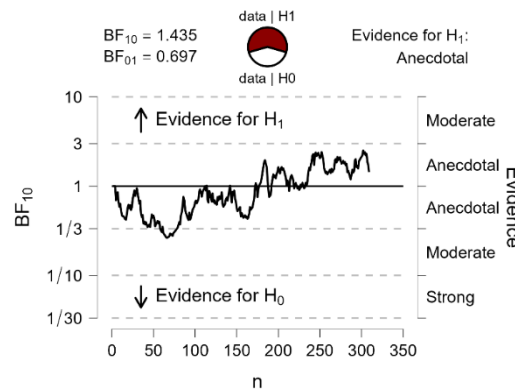


Figure 7: Advanced digital skill: Cybersecurity

Table 3: Advanced digital skills: Coding, data science, and cybersecurity

	Group	N	Mean	SD	SE	Coefficient of variation	95% Credible Interval	
							Lower	Upper
Advanced Digital Skill: Coding	Female	110	2.791	0.69	0.07	0.248	2.66	2.922
	Male	199	2.814	0.83	0.06	0.295	2.698	2.93
Advanced Digital Skill: Data Science	Female	110	2.245	0.78	0.07	0.348	2.098	2.393
	Male	199	2.457	0.99	0.07	0.404	2.318	2.596
Advanced Digital Skill: Cybersecurity	Female	110	2.518	0.8	0.08	0.317	2.367	2.669
	Male	199	2.764	0.98	0.07	0.354	2.627	2.901

## 5 CONCLUSION

The study concluded that women, as opposed to males, gave digital skills a greater priority in terms of potential careers in the future. This conclusion is significant because it implies that women recognize the importance of digital skills for advancing in their careers. The findings are consistent with theoretical viewpoints that highlight the importance of socialization, self-efficacy, and resource accessibility when discussing gender disparities in STEM education.

Considering the growing significance of cybersecurity expertise in the digital economy, this conclusion is alarming. Women have a low representation in cybersecurity sectors, according to earlier research, which is sometimes caused by a lack of opportunity for focused education and enduring gender biases. The findings emphasize the importance of creating programs that encourage and assist female students in the field of cybersecurity, such as awareness campaigns, mentorship programs, and scholarships.

## References

- [1] European Commission, "Shaping Europe's digital future," 10 October 2023. [Online]. Available: <https://digital-strategy.ec.europa.eu/en/policies/digital-skills> [Accessed 3 June 2024].
- [2] J. Van Dijk, *The Digital Divide*, John Wiley & Sons, 2019.

- [3] A. J. A. M. Van Deursen, A. Van der Zeeuw, P. De Boer, G. Jansen, and T. Van Rompay, "Digital inequalities in the internet of things: differences in attitudes, material access, skills, and usage," *Information, Communication & Society*, vol. 24, no. 2, pp. 258–276, 2021.
- [4] D. G. Campos and R. Scherer, "Digital gender gaps in Students' knowledge, attitudes and skills: an integrative data analysis across 32 countries," *Education and Information Technologies*, vol. 29, pp. 655–693, 2024.
- [5] Z. Cai, X. Fan and J. Du, "Gender and attitudes toward technology use: a meta-analysis," *Computers & Education*, vol. 105, pp. 1–13, 2017.
- [6] F. Siddiq and R. Scherer, "Is there a gender gap? A meta-analysis of the gender differences in students, *ICT literacy*," *Educational Research Review*, vol. 27, pp. 205–217, 2019.
- [7] A. Ora, R. Sahatcija, and A. Ferhataj, "Learning styles and the hybrid learning: An empirical study about the impact of learning styles on the perception of the hybrid learning," *Mediterranean Journal of Social Sciences*, vol. 9, no. 1, pp. 137–148, 2018.
- [8] Eurostat, "Digitalisation in Europe," 29 April 2024. [Online]. Available: <https://ec.europa.eu/eurostat/web/interactive-publications/digitalisation-2024> [Accessed 5 June 2024].
- [9] CEDEFOP, "European skills index: 2024 European skills index," 2024. [Online]. Available: <https://www.cedefop.europa.eu/en> [Accessed 12 June 2024].
- [10] Microsoft, "News: Microsoft," 28 April 2023. [Online]. Available: <https://news.microsoft.com/apac/2023/04/28/microsoft-expands-access-to-cybersecurity-skilling-for-women-and-girls-with-ready4cybersecurity-program/> [Accessed 12 June 2024].
- [11] INSTAT, "Use of information and communication technology in enterprises," INSTAT, Tirana, 2023.
- [12] INSTAT, "Education enrollment statistics," INSTAT, Tirana, 2024.



---

## resEARcher: A Sentence-Transformers Guided Tool for Visually Impaired Researchers

Eylul Hickiran<sup>1</sup>, Emrah Inan<sup>\*1</sup>

<sup>1</sup>Department of Computer Engineering, Izmir Institute of Technology, Izmir, Türkiye

---

### Abstract

The scientific literature is growing at an exponential rate, particularly in the fields of Artificial Intelligence (AI) and Machine Learning (ML), where the number of papers published each month doubles every 23 months. Keeping up with the latest trends in this ever-expanding environment is difficult, especially for visually impaired researchers. To alleviate this difficulty, we present a tool called resEARcher, which extracts weekly published papers from arXiv and divides the content of these papers into appropriate sections. Hence, it facilitates listening to specific parts from the extracted sections for visually impaired scientists. Experiments were carried out with the use of abstract texts, considering the target, and with the use of weekly published papers to find similar papers first. For the first case, the highest Pearson's  $r \times 100$  score of 68.84 is achieved by the all-mpnet-base-v2 pre-trained model of the Sentence-Transformers. The second experiment was conducted on computing accuracy of the extracted sections per paper. In this scenario, we used a technique based on regular expressions to extract each section and 0.789, 0.684, 0.526, 0.632, 0.895 scores obtained for the Introduction, Related Work, Method, Evaluation and Conclusion sections respectively.

**Keywords:** Sentence-transformers, PDF extraction, Android, Tool, Impaired users

---

## 1 INTRODUCTION

The scientific literature is growing at an exponential rate, particularly in the fields of Artificial Intelligence (AI) and Machine Learning (ML), where Krenn et al. [1] reveal that the number of papers published each month doubles every 23 months [1]. Keeping up with the latest trends in this ever-expanding environment is difficult, especially for visually impaired researchers [2]. This is particularly critical for individuals who face challenges with traditional reading methods, such as those with visual impairments or busy schedules that limit seated reading time. Existing text-to-speech solutions, particularly for PDFs [3], often neglect the user experience, offering robotic voices or clunky interfaces that hinder usability and engagement.

The motivation behind this work stems from the urgent need to bridge the gap between accessibility of digital content and user experience. By focusing on user-friendly design and advanced text-to-speech technology, the application aims to transform the way users interact with digital text. It addresses specific challenges such as navigating through long documents, understanding complex layouts and finding specific information quickly and efficiently. By providing a tool that converts text into high-quality, audible formats and allows easy navigation between sections, the application enables users to enjoy literature, keep up with academic and professional material, and participate in cultural and civic activities without the barriers imposed by traditional reading methods.

This study presents a mobile application that converts PDFs into audio content, allowing users to effectively consume text-based information through natural-sounding audio. The application analyses PDF content, identifies key sections and narrates them, simplifying navigation and improving accessibility. In addition, the application offers personalised recommendations for new PDFs based on the documents the user adds each week. This feature enhances the user experience by helping them discover relevant content and keep up to date with the latest information in their areas of interest. With its user-friendly interface and optimised performance, the application not only makes information more accessible, but also supports social inclusion by allowing users to efficiently multitask in their daily activities. This project represents a significant step towards removing barriers to information access and contributing to a more equitable research ecosystem.

## 2 MATERIAL AND METHOD

PDF extraction refers to the process of extracting data from a PDF file. This data can include text, images, tables, charts, or other types of content. PDF extraction can be used for a variety of purposes, including document processing, data analysis, digital archiving and more.

### 2.1 Regular Expression-based PDF Extraction Technique

Regular expressions, commonly referred to as “regex [4]”, are a versatile tool for handling text. They provide a flexible way of searching, matching and modifying strings based on defined patterns. In Java, regular expressions are implemented by classes found in the `java.util.regex` package, primarily `Pattern` and `Matcher`. A regular expression is a sequence of characters that defines a search pattern. This pattern is used for various string operations such as searching, validating, splitting and replacing. Although the syntax of regular expressions can be complicated, it is based on basic concepts.

The key challenge is to ensure that the regular expressions accurately capture the relevant data without missing important information or including extraneous data. It can also be difficult to deal with variations in formatting and context within the PDF. Regular expressions must be carefully crafted to account for different patterns and inconsistencies in the document. Table 1 shows the examples of regular expressions for the PDF extraction task:

**Table 1.** Excerpts of regular expressions of the extraction task

Regular Expression	Main objective
<code>[a-zA-Z0-9._-]+</code>	This part specifies the beginning of the email address and includes characters found in email addresses. It accepts uppercase and lowercase letters, numbers, periods (.), underscores ( ) and hyphens (-). The + sign indicates that these characters can be repeated one or more times.
<code>@</code>	This character separates the username from the domain name in the email address.
<code>\\.</code>	This part represents a period (.). The dot can be used in the domain name, but if it needs to be used directly in a regular expression, it should be escaped with a backslash ( ).
<code>[a-z]+</code>	This part specifies the extension of the domain name and only accepts lower case letters. The domain name extension must contain one or more lower case letters.

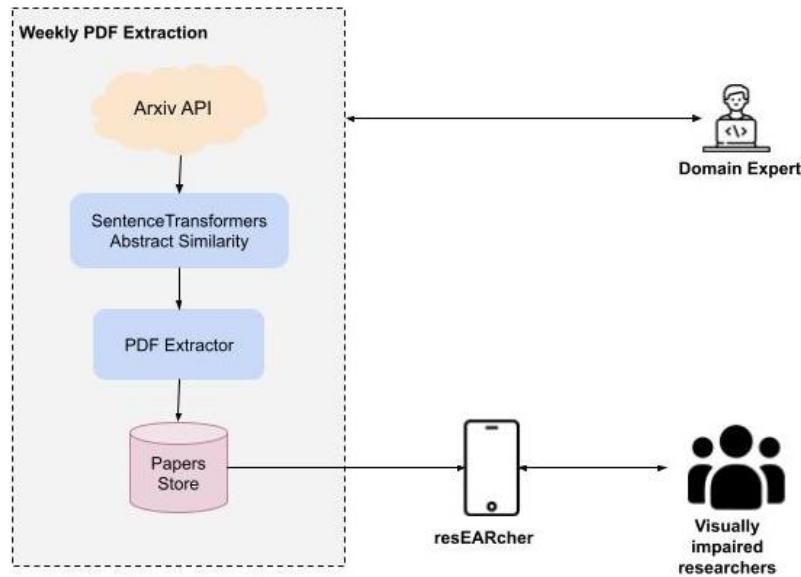
### 2.2 resEARcher Tool

The aim of this application is to facilitate access to and interaction with digital content and to increase accessibility for people who have difficulties with traditional reading methods. With its user-friendly design and advanced text reading technology, the application aims to change the way users interact with digital text. It addresses specific challenges such as navigating through long documents, understanding complex layouts and accessing specific information quickly and efficiently.

The application is developed using Java in Android Studio and manages database operations using SQLite. User information and extracted PDF text are stored in the database. The text-to-speech process is performed using data from the database. User passwords are encrypted using the SHA-256 [5] algorithm before being stored in the database. Users are recommended articles of interest on a weekly basis, facilitated by a batch processing system. A Python application run by the developer updates the database to provide these recommendations.

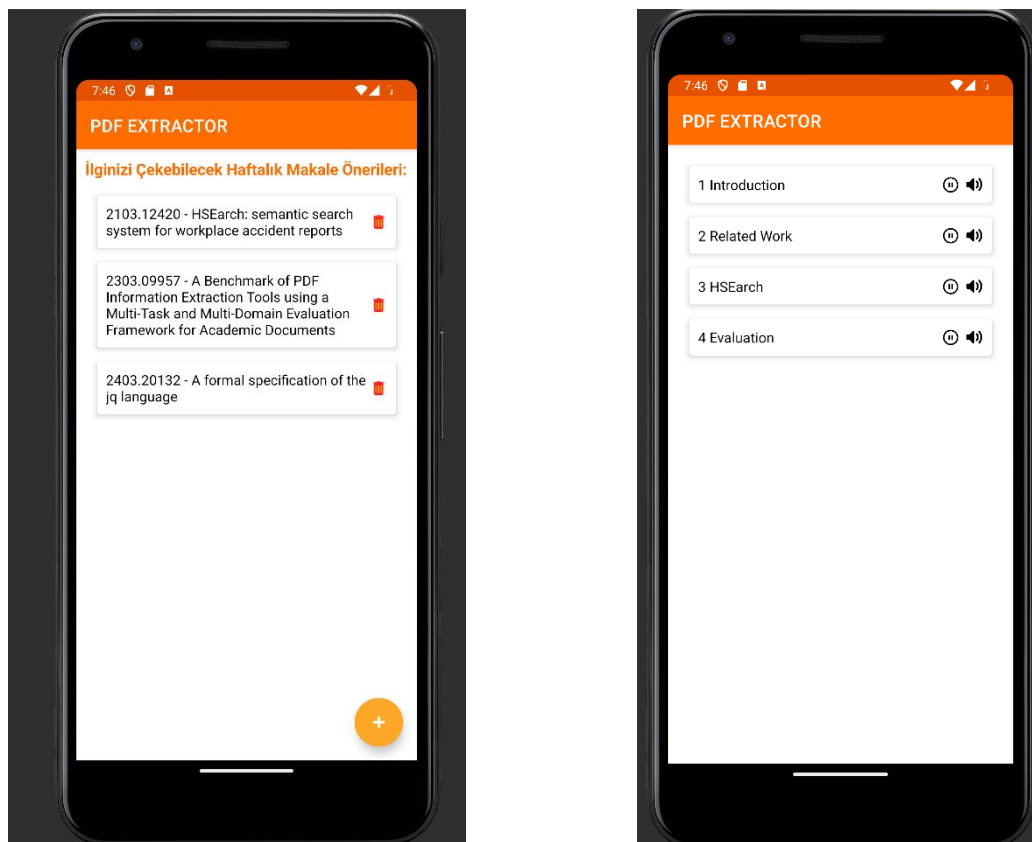
The system integrates restful services tools to facilitate easy access and efficient management of academic papers. It connects directly to Arxiv, a comprehensive repository of academic papers, via the Arxiv API [6]. This ensures that users have access to the latest research as it becomes available, enhancing their academic and professional endeavours. To improve the user experience, the system uses Sentence-BERT [7], an advanced language processing model, to analyse abstracts. Sentence-BERT evaluates the content and extracts thematic similarities between papers. Based on this analysis, the system can recommend academic papers that match the user's interests, updated weekly.





**Figure 1.** General structure of the proposed tool

After retrieving the papers in PDF format using the Arxiv API, the iText library within Android Studio is used to extract content from these documents. A complex regex (regular expression) algorithm is used to accurately identify and capture the titles of the papers. The extracted titles and content are then stored in a database, creating a rich, searchable repository of scholarly material. This repository is conveniently accessible at any time, providing users with invaluable resources for research and learning. Figure 2 denotes the sample graphical user interfaces of the proposed application.



a) List of the extracted PDFs

b) List of headers for a specific extracted PDF file

**Figure 2.** GUIs of the developed software tool

When users open the application, they are presented with a login screen. This screen contains two fields for users to enter their registered email address and password, as well as a login button. Passwords are encrypted using the

SHA-256 algorithm to ensure that information is stored securely in the database. User credentials are checked against the database for authentication. After logging into the application, users will see the PDFs they have previously added (as illustrated in Figure 2.a), and the weekly PDFs recommended by the application. The PDFs are listed on the screen with their IDs and titles. At the bottom of the screen is a “+” button that allows users to add new PDFs. When users click the “+” button, they are taken to the PDF addition screen. Users can delete added or recommended PDFs by clicking the recycle bin icon.

On the Add PDF screen, users are expected to enter the Arxiv ID in the field provided. When the user clicks the 'Add' button, the PDF ID and title are extracted and added to the database. The user is then redirected to the PDF listing screen. When users click on a PDF on the main screen, they are taken to a screen displaying the titles associated with that PDF. These titles are retrieved from the database. When the user clicks on the speaker icon next to a title, the paragraph associated with that title is read aloud. The user can stop the narration at any time by pressing the pause button. When the user clicks on the Speaker button, the relevant field in the database is updated. The text-to-speech process is then performed based on the updated information in the database.

### 3 RESULTS

To compute the similarity between target and weekly published articles, we perform the Pearson’s  $r \times 100$  score to compare the pre-trained models in the sentence transformers [7]. As we have been collecting papers for four weeks, there are a limited number of papers dealing with artificial intelligence and large language models. Hence, we adapted the current study to the Semantic Textual Similarity (STS) task [8].

**Table 1.** Measure of the degree of the correlation strength between target and published paper abstracts

Degree	Score range	Score
The strongest match	[0.80, 1.00]	5
Strong	[0.60, 0.79]	4
Moderate	[0.40, 0.59]	3
Weak	[0.20, 0.39]	2
The weakest match	[0.00, 0.19]	1

Table 1 summarises the degree of correlation between abstract pairs of the target and published papers. It assigns a value of 5 if the similarity score is in the range [0.80, 1.0] as the strongest match for the given abstract pair. Equation 1 denotes the  $r(x, y)$  correlation between the target and the published paper abstract.

$$r(x, y) = \frac{\sum(x - \bar{x})(y - \bar{y})}{\sqrt{\sum(x - \bar{x})^2 \sum(y - \bar{y})^2}} \quad (1)$$

where  $x$  and  $y$  represent the predicted and the actual score of the correlation, respectively. Further,  $\bar{x}$  and  $\bar{y}$  indicate the average scores for the predicted and the actual values. As an initial task, we collected 100 papers over four weeks and Table 2 shows the Pearson’s coefficient scores of the pretrained models. The first model is all-mpnet-base-v2 [9], which was trained on a 1B sentence pair dataset using a contrastive learning objective, where the model predicts a random sample in the dataset for one text from the pair. The second model is all-distilroberta-v1 [10], which uses the pre-trained distilroberta-base model as a distilled version of the RoBERTa model [11]. The last pretrained model is all-MiniLM-L12-v2 [12], and it maps the text onto a dense vector space in 384 dimensions. As denoted in Table 2, the first model all-mpnet-base-v2 [9] performs slightly better than other models considering shows the Pearson’s coefficient scores.

**Table 2.** Pearson’s coefficient scores of the pretrained Sentence-Transformers models

Model	Pearson’s $r \times 100$ score
all-mpnet-base-v2 [9]	68.84
all-distilroberta-v1 [10]	67.77
all-MiniLM-L12-v2 [12]	67.56

After computing the similarities between the target and published paper abstracts, we also calculate accuracy scores for each extracted section of the similar papers. To extract the paper content, we employ the regular expression-based technique in this study and Equation 2 illustrates the accuracy calculation.

$$\text{Accuracy} = \frac{\text{Correctly extracted text for each section}}{\text{Total number of extracted texts per section}} \quad (2)$$

where accuracy is calculated as the ratio of correctly extracted text to the total number of extracted texts for each section.

**Table 3.** Accuracy scores of the extracted texts for each section

Extracted section	Accuracy
Introduction	0.789
Related Work	0.684
Method	0.526
Evaluation	0.632
Conclusion	0.895

As shown in Table 3, the regular expression-based method achieves a competitive accuracy score for all sections, but for the extraction of the conclusion section, it is slightly better than the other sections in terms of accuracy score since this section contains shorter texts with a well-defined format borders.

## 4 CONCLUSION

This study presents resEARcher as an android application that aims to reach visually impaired scientists who have difficulty following trends in the machine learning and artificial intelligence literature. It extracts weekly published papers from arXiv and divides the content of these papers into appropriate sections. This makes it easier for visually impaired researchers to listen to specific parts of the extracted sections. In the results obtained from the data allocated for the test, the first task is to calculate the similarities between the target and the weekly published abstracts of the papers. Experimental results show that the first model all-mpnet-base-v2 [9], trained on a 1B sentence pair dataset using a contrastive learning objective, achieves slightly higher Pearson's coefficient scores than other pre-trained sentence transformer models. Moreover, the regular expression-based method achieves a competitive accuracy score for all sections, but for the extraction of the conclusion section, it is slightly better than the other sections in terms of accuracy score. As a future direction, we will investigate the image processing methodology [13] to extract more accurate section content for the given paper, leveraging a larger benchmark [14]. Furthermore, we will continue to collect weekly articles, considering both single and double column formats based on the selected topics.

## References

- [1] M. Krenn, L. Buffoni, B. Coutinho, S. Eppel, J. G. Foster, A. Gritsevskiy et al., "Forecasting the future of artificial intelligence with machine learning-based link prediction in an exponentially growing knowledge network," *Nature Machine Intelligence*, vol. 5, no. 11, pp. 1326–1335, 2023.
- [2] I. Emara. "Evaluation of qualitative data analysis software by a visually impaired researcher: An autoethnographic study," *International Journal of Qualitative Methods*, vol. 22, pp. 1–11, 2023, doi: 10.1177/160940692312143.
- [3] M. J. U. Chowdhury and A. Hussan. "A review-based study on different Text-to-Speech technologies," *arXiv preprint*, arXiv:2312.11563, 2023.
- [4] T. Venkata. (2024). *Understanding regular expressions in java: A comprehensive guide* [Online]. Available: <https://medium.com/@dattu1993/understanding-regular-expressions-in-java-a-comprehensive-guide-f24e744ad82a>
- [5] C. Geisler, "Future directions for research on the relationship between information technology and writing," *Journal of Business and Technical Communication*, vol. 15, no. 3, pp. 269–308. 2001.
- [6] arXiv API Access. (2024). *arXiv API access* [Online]. Available: <https://info.arxiv.org/help/api/index.html>
- [7] N. Reimers and I. Gurevych. Sentence-bert: Sentence embeddings using siamese bert-networks. In arXiv preprint arXiv:1908.10084. 2019.
- [8] D. Cer, M. Diab, E. Agirre, L. Lopez-Gazpio, and L. Specia, "Semeval-2017 task 1: Semantic textual

- similarity-multilingual and cross-lingual focused evaluation,” *arXiv preprint*, arXiv:1708.00055. 2017.
- [9] all-mpnet-base-v2. (2024). *all-mpnet-base-v2* [Online]. Available: <https://huggingface.co/microsoft/mpnet-base>
- [10] all-distilroberta-v1. (2024). *all-distilroberta-v1* [Online]. Available: <https://huggingface.co/distilbert/distilroberta-base>
- [11] L. Yinhan, M. Ott, N. Goyal, J. Du, M. Joshi, D. Chen, O. Levy, M. Lewis, L. Zettlemoyer, and V. Stoyanov, “RoBERTa: A robustly optimized BERT Pretraining approach,” *arXiv preprint*, arXiv:1907.11692. 2019.
- [12] all-MiniLM-L12-v2. (2024). *all-MiniLM-L12-v2* [Online]. Available: <https://huggingface.co/microsoft/MiniLM-L12-H384-uncased>
- [13] Y. Xu, M. Li, L. Cui, S. Huang, F. Wei, and M. Zhou, “Layoutlm: Pre-training of text and layout for document image understanding,” in *26th ACM SIGKDD International Conference on Knowledge Discovery & Data Mining*, 2020, pp. 1192–1200.
- [14] N. Meuschke, A. Jagdale, T. Spinde, J. Mitrović, and B. Gipp, “A benchmark of pdf information extraction tools using a multi-task and multi-domain evaluation framework for academic documents,” in *International Conference on Information*, Cham, Mar. 2023, pp. 383–405.



---

## Effect of the Smagorinski Coefficient in LES Turbulence Model at Lateral Diversions

Firat Gumgum<sup>\*1</sup>

<sup>1</sup>Civil Engineering Department, Dicle University, Diyarbakir, Türkiye

---

### Abstract

The Smagorinsky coefficient ( $C_s$ ) is a critical parameter in the Large Eddy Simulation (LES) turbulence model, profoundly impacting the accuracy and stability of turbulence predictions. This study is aimed to explore the effects of varying  $C_s$  values on LES performance, specifically focusing on turbulent flows involving lateral diversions. Numerical simulations were conducted using the FLOW-3D software, with  $C_s$  values ranging from 0.02 to 0.2. The mesh size to the diversion channel size ratio was kept constant as 1/50; 1/40; 1/20 on x; y; z directions. The  $C_s$  value choice significantly affected the resolution of vortical structures and the recirculation zone. Lower  $C_s$  values increased the length of the recirculation and captured detailed vortical structures up to 0.05. Beyond this value, lower eddy viscosities resulted in inaccurate flow structures inside the recirculation zone.  $C_s$  values greater than 0.85, including the default value of  $C_s = 0.1$ , also led to inaccurate depiction of the flow field by generating vortices in y direction. These results underscore the importance of carefully calibrating the Smagorinsky coefficient in LES models for flows involving lateral diversions. Achieving a balance that provides realistic turbulent eddy viscosity is crucial for accurately capturing the complex interactions and separation phenomena characteristic of these flows. The Smagorinsky coefficient's effect on eddy viscosity is also influenced by mesh size, which was kept constant in this study, with finer meshes resulting in lower eddy viscosity for a given coefficient, thus requiring careful calibration of  $C_s$ .

**Keywords:** Smagorinsky coefficient, LES, lateral diversions, Flow-3D

---



## Numerical Simulation of Investigating the Group Impact on Settlement in the Soft Soil Reinforced by Rigid Inclusions Under Seismic Loads

Oussama Benmerabet<sup>\*1</sup>, Salah Messioud<sup>1</sup>

<sup>1</sup>LGCE Laboratory, Civil and Hydraulic Engineering Department, Faculty of Sciences and Technology, University of Jijel, Jijel, Algeria

---

### Abstract

The rapid industrialization and urbanization observed in developing countries highlight the continuous rise in land demand for various construction projects. Soil conditions at construction sites may often be unsuitable for supporting structures due to the presence of weak characteristics or unsuitable soil, particularly in areas prone to significant seismic activity. Recent advancements in technology have enabled construction on diverse soil types by enhancing bearing capacity and reducing soil settlement, while also providing cost-effective and environmentally friendly solutions. One of the notable techniques for reinforcing soft soil is the use of rigid inclusions. This study introduces a numerical simulation generated through Code-Aster software about the reinforced soil by rigid inclusions under seismic loading. The investigation primarily examines the influence of the number of inclusions on the soil's behavior, starting with a single inclusion in the initial model and progressively increasing the number in subsequent models to analyze variations in settlement and internal forces. Results indicate that the highest displacement is at the inclusion's top and decreases linearly towards the bottom. The significance of inclusions as an effective reinforcement method is evident from the decrease in displacement with an increase in the number of inclusions in the model. This research aims to evaluate the elastic behavior of the soil and the effect of varying inclusion numbers on horizontal displacement in order to validate the efficacy and reliability of using rigid inclusions as a reinforcement technique for soil subjected to seismic loads.

**Keywords:** Numerical simulation, Reinforced soil, Rigid inclusions, Seismic loading

---



---

## Effect of Calcination Time and Temperature on the Pozzolanic Reactivity of Dam Sediment Slurry

**Hanaa Kawther Terrah<sup>\*1</sup>, Zine El Abidine Kameche<sup>1</sup>, Hocine Siad<sup>2</sup>, Mohamed Lachemi<sup>2</sup>, Youcef Houmadi<sup>3</sup>**

<sup>1</sup>*Civil Engineering and Public Works Department, University Belhadj Bouchaib-UBBAT, Smart Structure Laboratory (SSL), Ain Temouchent, Algeria*

<sup>2</sup>*Civil Engineering Department, Toronto Metropolitan University, Toronto, Canada*

<sup>3</sup>*National School of Administration (ENA), University of Tlemcen, SSL, Algeria*

---

### Abstract

The accumulation of sediments in dams, amplified by natural effects and human activities, disrupts the use of these large water resources. Dredging is crucial to restore the necessary depth, thereby contributing to the preservation of the natural environment and optimizing dam efficiency. Concurrently, within the framework of sustainable sediment management and ecological aspects, the valorization of dam sediment slurry holds great interest in the construction industry due to its potential to become a low-CO<sub>2</sub>-emission pozzolanic material. However, this potential requires thermal treatment through calcination, necessitating optimization of temperature and time for maximal activation with reduced environmental impact. While previous studies have explored various calcination temperatures and durations, there is a clear divergence regarding the optimal values for more effective utilization.

This study employed a method combining microstructure analysis and experimentation to effectively process the dredged sediment powders. Differential thermal analysis (DTA) was conducted initially to observe mass loss in the temperature range up to 1000°C. Based on DTA analysis, two different temperatures were selected, and three calcination durations were examined. X-ray diffraction (XRD) analysis was also performed on raw and calcined clay samples to determine the evolution of kaolinite mineral peaks. Compressive strength testing was conducted to validate the pozzolanic properties of the calcined sediment slurry. Contrary to literature findings, the results indicated that a temperature of 720°C for 1 hour is sufficient to achieve satisfactory pozzolanic activity for dam sediment slurry.

**Keywords:** *Calcination, Pozzolanic reactivity, Dam sediment slurry, DTA, XRD*

---



## Seismic Evaluation of an Existing Reinforced Concrete Building Based on FEMA P-2018 Methodology

Atakan Emin Aksoy<sup>\*1</sup>, Sadik Can Girgin<sup>1</sup>, Ozgur Bozdogan<sup>1</sup>

<sup>1</sup>Civil Engineering Department, Dokuz Eylul University, Izmir, Türkiye

### Abstract

The major earthquakes in Türkiye in recent years have shown the importance of assessing the building stock. However, modeling and assessing these structures realistically is a very time-consuming option. The FEMA P-2018 report, published by the Federal Emergency Management Agency (FEMA), provides a simplified methodology for evaluating older reinforced concrete structures that are likely to collapse, making building stock assessment efforts easier in terms of time. FEMA P-2018 procedures include the following steps: identifying the critical stories and components by estimating effective yield strength based on four collapse mechanisms, calculating drift demands and capacities of critical stories and components, evaluating collapse potential by comparing demand and capacities, determining column and wall ratings and final step is determining collapse potential rating of the structure. This study considers the behavior of an existing reinforced concrete building in Bayraklı, İzmir. The earthquake behavior of the structure was evaluated with FEMA P-2018 guidelines.

**Keywords:** Reinforced concrete frames, Collapse mechanism, Building assessment

## 1 INTRODUCTION

Major earthquakes have demonstrated the vulnerability of reinforced concrete (RC) buildings in regions with high seismic activity in Türkiye. A recent study [1] reported that the earthquakes showed that the primary causes of significant damage to reinforced concrete structures can be summarized as poor material and workmanship quality, poor detailing, lack of code compliance, soft story condition, etc.

Several studies [2, 3] have shown that the existence of older, seismically vulnerable concrete buildings, known as non-ductile reinforced concrete buildings, concerns public safety. Also, in FEMA P-2018 [3] it is stated that the 1971 San Fernando earthquake highlighted the poor performance of concrete frame buildings due to inadequate steel reinforcing in the design codes of that era. Structures need to be evaluated to reduce casualties and lower the cost of disasters. For this purpose, various seismic evaluation methods are used in practical applications in the literature. They can be classified into 3 tiers according to their evaluation detailing. FEMA P-154 [4] report includes the Tier 1 /Rapid Visual Screening (RVS) procedure that has been developed to identify, inventory, and screen potentially seismically hazardous buildings. The RVS procedure employs a method based on conducting a site survey of a building and completing a Data Collection Form based on visual observation of the building's exterior and, if it is accomplishable, its interior. The report [4] suggests that if they are identified as potentially hazardous, an experienced seismic design professional should perform a detailed evaluation of these structures to determine if they are seismically hazardous. A recent study by Erdil et al. (2019) [5] showed that Tier 2 (preliminary) assessment methods seem effective in identifying the seismic vulnerability of buildings, as they allow for an assessment of the seismic performance of an individual building when compared to Tier 1 assessment methods (street survey). In the Tier 3 evaluation approach, a complete analysis of the nonlinear response of the building to is performed, implicitly or explicitly, as defined in ASCE/SEI 41-17 [6].

A simplified approach, Seismic Evaluation of Older Concrete Buildings for Collapse Potential, was proposed by FEMA [3] to evaluate collapse risk by using simplified estimates of drift demands. This methodology aims to make the identification of the subset of buildings that are likely to have a high risk of collapse easier without the requirement for extensive testing or nonlinear analysis. The intention of this methodology is to identify the subsets of these buildings that are of lower relative risk of collapse, termed lower seismic risk buildings, or are of significantly higher relative risk of collapse, termed exceptionally high seismic risk buildings. This methodology focuses on structural deficiencies in vertical structural components. This approach assesses the reinforced concrete frame, bare frame, frame-wall, bearing wall, and infilled frame structures with heights less than 48.77 meters.



## 2 SEISMIC EVALUATION METHOD

### 2.1 Summary of FEMA P-2018 Methodology

The methodology starts with classifying the structure as: frame, frame-wall, bearing wall, or infilled frame-system and determination of the critical story. Then, horizontal spectral acceleration for the recommended seismic hazard level at the site corresponding to the effective fundamental period is to be determined. After that, the global demand-to-capacity ratio and global seismic drift demand of the building, should be calculated. After getting these values, component drift demand and component drift capacity are to be determined. Finally, the building rating should be determined by taking the maximum story rating based on the average of the component ratings. The Building Rating (BR), as defined in FEMA P-2018, is utilized to assess and categorize the relative risk of buildings within an inventory, assigning them to one of three levels of relative risk: exceptionally high seismic risk buildings (if  $BR \geq 0.7$ ), high seismic risk buildings (if  $0.7 > BR > 0.3$ ), and lower seismic risk buildings (if  $0.3 \geq BR$ ). A recommended flowchart for this methodology is shown in Figure 1.

### 2.2 Existing Reinforced Concrete Building

In this study, the seismic risk of an eight-story reinforced concrete building is investigated, which was built in 1992 in Bayraklı/İZMİR. The dimensions of the regular floor plan for the building, as shown in Figure 2, are 20.5 meters by 20.5 meters, and the height of the building is 23.1 meters. The ground-floor height is 3.5 meters, while the others are 2.8 meters. According to the structural drawings, the reinforced concrete structure was made of BS20 concrete and BCI steel type as per TS500/1984 [7]. However, field investigations showed that the compressive strength of concrete was 9 MPa. The building's site class was determined as "D", based on ASCE 7-16 [8]. The building has infilled frames in its regular stories; however, the ground floor has only 5 infilled frames (Figure 3). Thus, the system is classified as an "infilled frame system". For plastic mechanism analysis, loads and component strengths need to be calculated. First, the expected gravity load is calculated using the equation taken from FEMA P-2018 [3]. The equation is presented below (1). With this equation, all expected gravity loads on columns and concrete walls were calculated.

$$P_G = P_D + 0.25P_L \quad (1)$$

Component flexural and shear strengths are calculated based on expected material properties. Concrete and reinforcing steel properties used in component strength calculations shall be expected material properties, as the methodology requires; the expected compressive strength of concrete and expected yield strength of reinforcement are calculated with the following equations (2, 3), and the results are 9.5 MPa and 275 MPa, respectively.

$$f'_{ce} = 1.5f'_c \quad (2)$$

$$f'_{ye} = 1.25f'_y \quad (3)$$

Then, component strengths are calculated, which include columns and walls flexural strength considering P-M interaction, columns and walls shear strength (Eqs. 4, 5), beams flexural and shear strength, columns capacity-limited shear strength, masonry infilled panel strength, and infilled bay strength (Eqs. 6, 7).

$$V_n = k \left( \frac{A_v f'_{ye} d}{s} + \lambda \left( \frac{0.5 \sqrt{f'_{ce}}}{l_{inf} / d} \sqrt{1 + \frac{P_g}{0.5 A_g \sqrt{f'_{ce}}}} \right) 0.8 A_g \right) \quad (4)$$

$$V_n = (\alpha_c \lambda \sqrt{f'_c} + \rho_t f'_y) A_{cv} \quad (5)$$

$$V_m = P_{inf}^{grav} \mu + A_{w,inf} C \quad (6)$$

$$V_{inf,solid} = \max(V_m, P_{inf}^{max} \mu + V_{lc}) \quad (7)$$

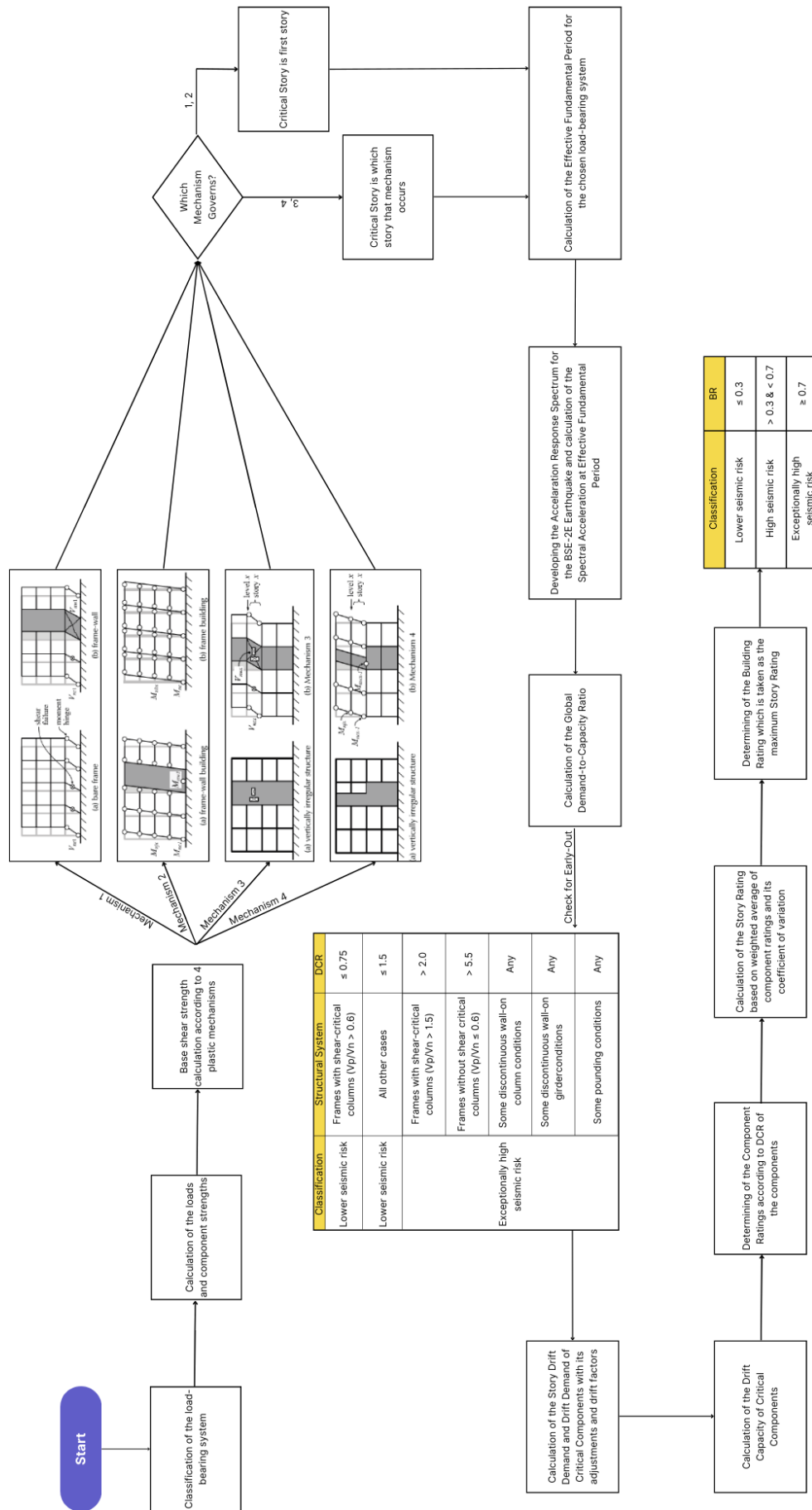


Figure 1. Flowchart for the FEMA P-2018 Methodology

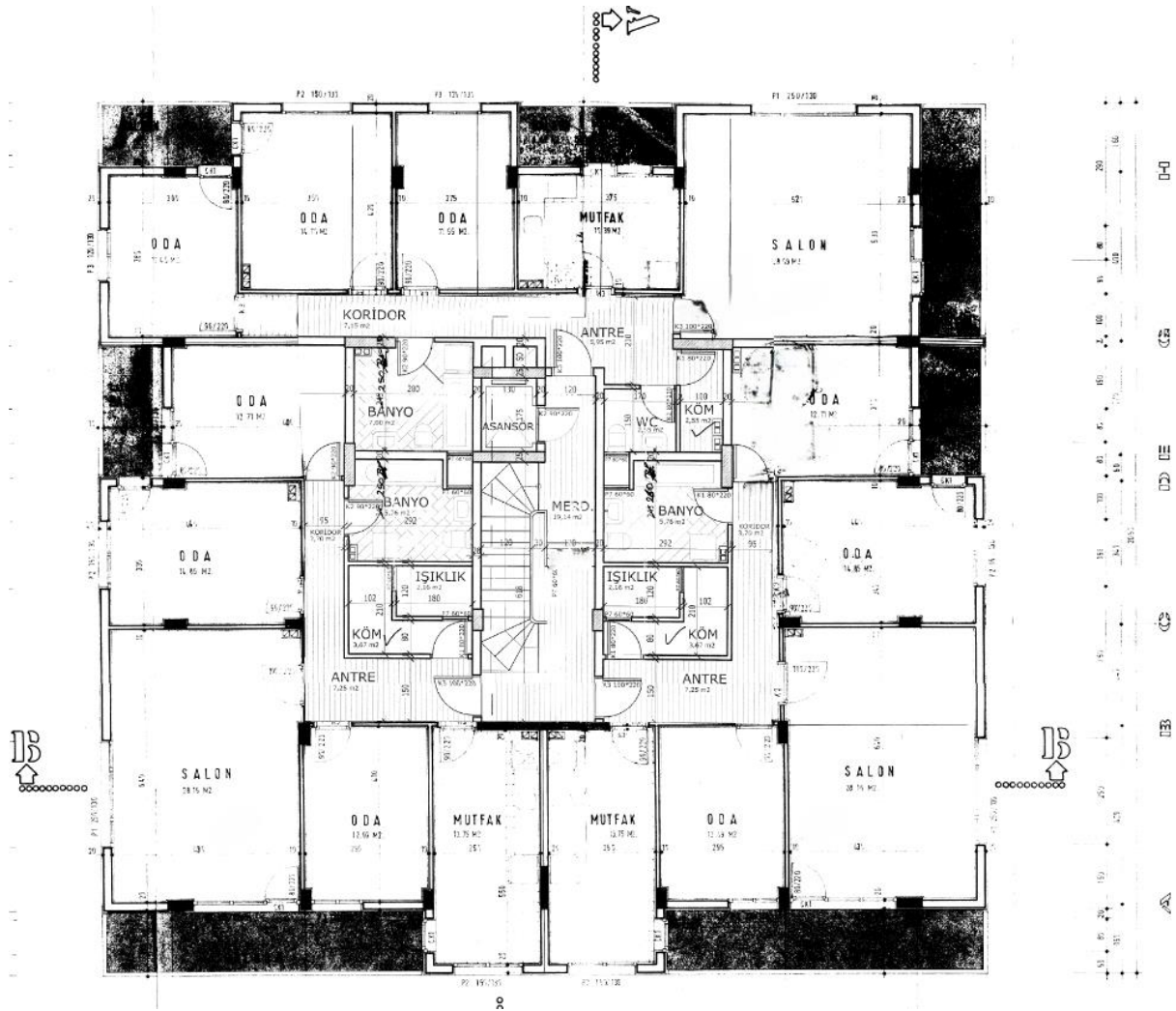


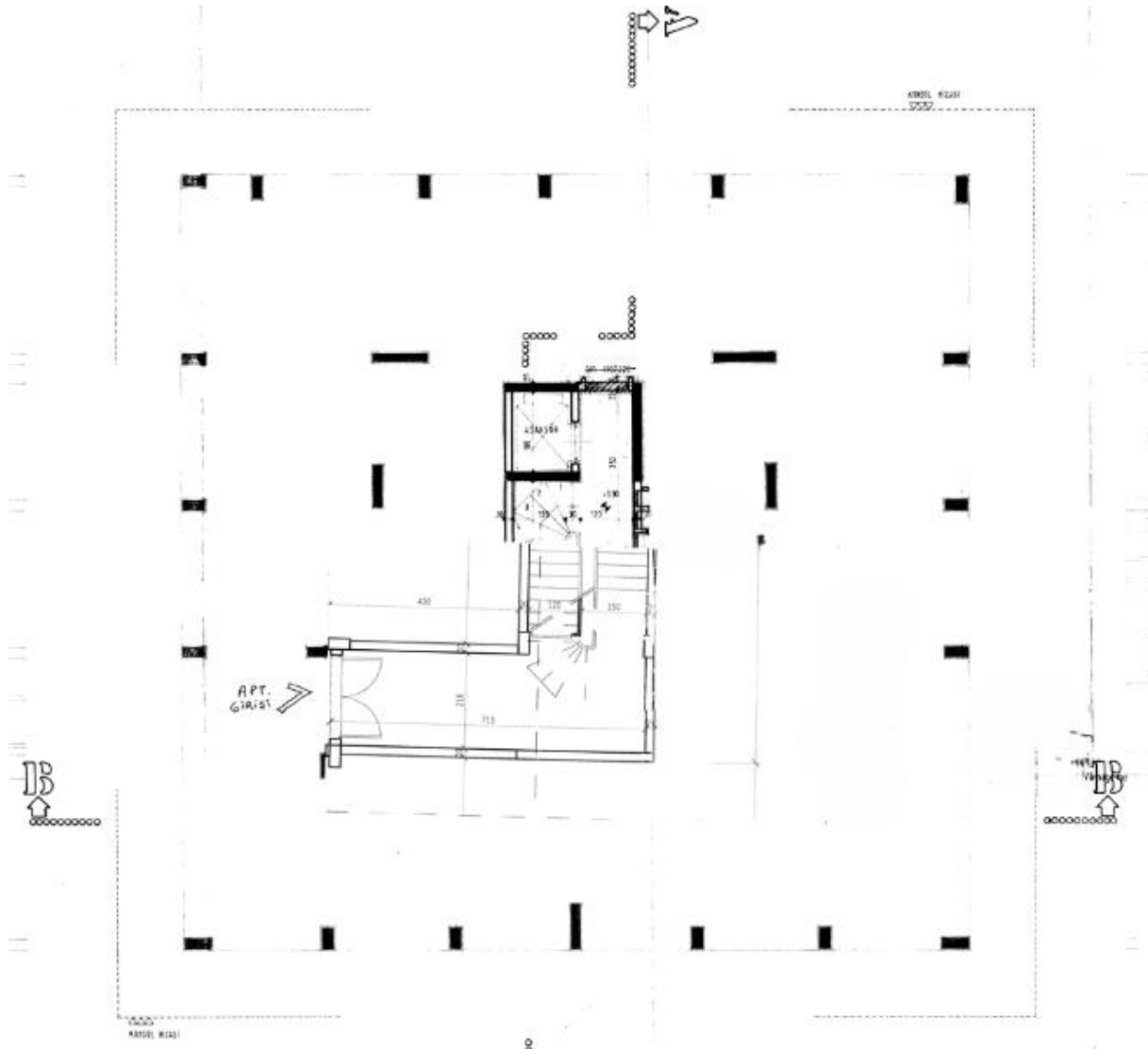
Figure 2. Architectural floor plan (2-8 stories)

### 3 RESULTS

The governing mechanism is determined after obtaining the values below. Plastic mechanism base shear strengths for Mechanism 1 and Mechanism 2 are shown in Table 1. Additionally, the plastic mechanism base shear strength for the infilled frame system is also stated in Table 1. Thus, Mechanism 2 governs in the X direction, and Mechanism 1 governs in the Y direction. Although the base shear strength for Mechanism 2 is lower than Mechanism 1, it is greater than three-quarters (3/4) of the base shear strength for Mechanism 1. Therefore, Mechanism 1 should be taken as the controlling mechanism in the Y direction according to FEMA P-2018 [3]. Also, the plastic mechanism base shear strength for the infilled frame is calculated. When all these shear strengths are compared, plastic mechanism base shear strength for the X direction equals 4151.4 kN, and for the Y direction, it equals 4556.6 kN.

Table 1. Base shear strengths

Cases	X	Y
Mechanism 1	6961.14 kN	5270.98 kN
Mechanism 2	4151.4 kN	4765.52 kN
Infilled Frame	5083.96 kN	4556.6 kN



**Figure 3.** Architectural plan of the ground floor

The effective fundamental period is calculated using the formulas (Eqs. 8- 11) for frame systems, frame-wall systems, and infilled frame systems, which are taken from FEMA P-2018 [3]. The effective fundamental period is 0.482 s and 0.937 s for the X and Y directions, respectively.

$$T_e = 0.07 (h_n)^{0.5} \left( \frac{V_y}{W} \right)^{-0.5} \quad (8)$$

$$T_e = 0.0026 \frac{h_n}{\sqrt{C_w}} \leq T_e \quad (9)$$

$$C_w = \frac{100}{A_{base}} \sum_{i=1}^j \frac{A_{wi}}{1 + 0.83 \left( \frac{h_{wi}}{l_{wi}} \right)^2} \quad (10)$$

$$T_e = \left( 1.6 - 0.6 \frac{V_{p1}}{V_{p1,bare}} \right) T_{e,bare} \quad (11)$$

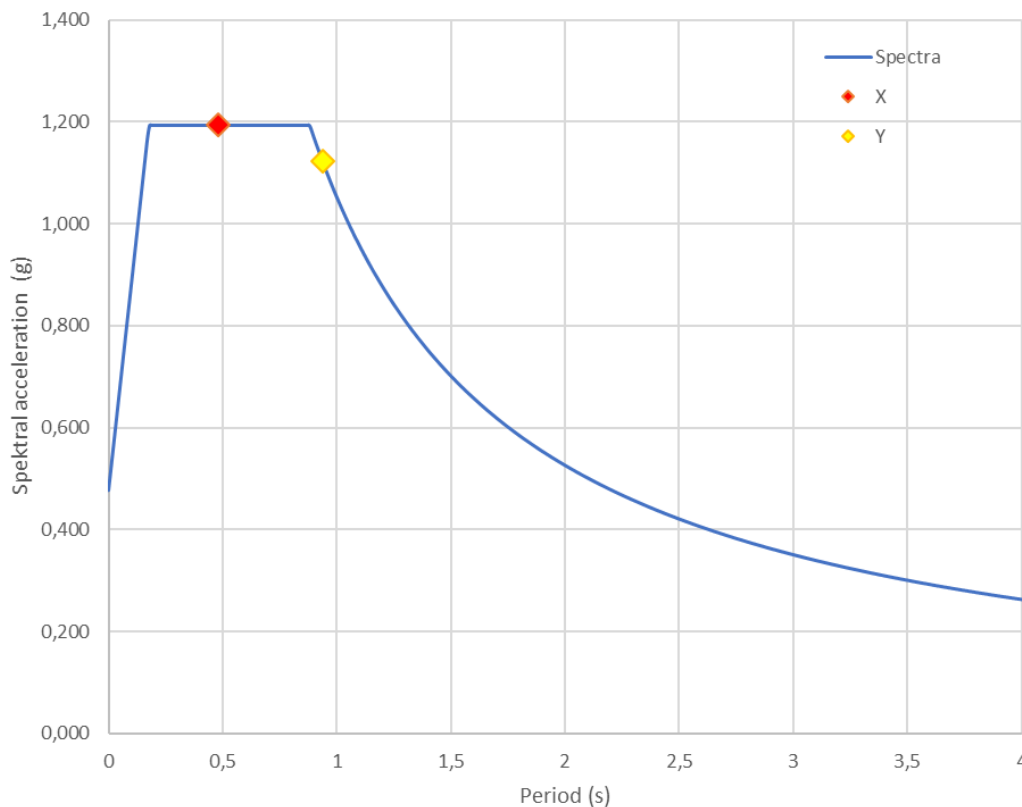
The recommended seismic hazard level for evaluation is the ASCE/SEI 41-17 Basic Safety Earthquake BSE-2E, which corresponds to a 5% probability of exceedance in a 50-year period [3]. In Türkiye there is no such seismic hazard level. There is a 2% probability of exceedance in a 50-year period and a 10% probability of exceedance. A study [9] has shown the relation between two peak ground acceleration levels and two different corresponding periods. That relation was used with modification to get a 5% probability, as shown below (12, 13). Thus, short-period spectral acceleration and spectral acceleration corresponding to a 1-sec period are calculated. Design spectral accelerations are determined by using the appropriate coefficients for the soil classification. With these values, an elastic design spectrum is obtained. Spectral values are given in Table 2, and the spectra are presented in Figure 4. Spectral acceleration values at effective fundamental periods for both orthogonal directions are determined. Spectral accelerations are 1.194 g and 1.124 g, respectively, for the X and Y directions.

$$\frac{S_{a,R1}}{S_{a,R2}} = \left( \frac{T_{R1}}{T_{R2}} \right)^k \tag{12}$$

$$S_{a,N} = \left( \frac{T_N}{T_{R2}} \right)^k \times S_{a,R2} \tag{13}$$

**Table 2.** Spectral values

Return Period	$S_s$	$S_1$	$S_{DS}$	$S_{D1}$
2475	2.120	0.543	1.696	1.148
975	1.472	0.368	1.194	1.053
475	1.111	0.273	1.123	0.801



**Figure 4.** Elastic Response Spectra

The global demand-to-capacity ratio was calculated using spectral accelerations, effective yield strengths, building total seismic weight, and effective mass factor, which equals 1.0 for the 8-story infill wall system. The ratio is 8.4 and 7.2 for the X and Y directions. For early identification, the capacity-limited (plastic) shear strength to nominal shear strength ratio was calculated for all vertical components at the critical story (the first story). The ratio is

lower than 0.6 for both orthogonal directions. Also, the global demand-to-capacity ratio is greater than 5.5 for both orthogonal directions. Therefore, this building could be identified as an “exceptionally high seismic risk building”. If the current structure is to be ranked, seismic demand and the capacity of the components need to be calculated. Global seismic demand needs to be calculated first to calculate component seismic demand. It can be calculated using the global demand-to-capacity ratio, effective fundamental period, spectral acceleration, and soil coefficient. Using these calculations, global seismic drift demand is calculated as 0.137 meters and 0.274 meters for the X and Y directions. Then, story drift demand is calculated with  $\alpha$  coefficient. Coefficient  $\alpha$  modifies story drifts considering the number of stories in a building, the yield mechanism, and whether the story is critical. Story drift demand is 0.109 meters and 0.219 meters, respectively, for the X and Y directions. Lastly, P- $\Delta$  adjustment needs to be calculated. With this adjustment, the adjusted story drift demand is 0.14 meters and 0.367 meters, respectively, for the X and Y directions.

Component drift demand is calculated using the drift factor. Column drift factors are given in Table 3, and the vertical wall drift factor is taken as 1.0. Component drift capacity is calculated using the equation below (14). Using the component drift demand-to-component drift capacity ratio, components can be rated according to Table 4.

**Table 3.** Column drift factors

Ratio of Column Strengths to Beam Strengths	Column Drift Factor
$\leq 0.6$	0.85
1	0.70
$\geq 2.4$	0.30

$$\Delta_c = l_u (\theta_c + 0.01) \tag{14}$$

Using the component ratings and fraction of gravity loads supported by that component, the weighted average story rating can be calculated. Then, adjustment based on the coefficient of variation (standard deviation of all the vertical component ratings at a story divided by the weighted mean vertical component rating at a story) is done. Lastly, story rating is calculated using the adjusted average of column and wall ratings in the story. Story rating is calculated as 0.67 and 0.9 for the X and Y directions, respectively. The building rating, BR, is taken as the maximum story rating. Therefore, BR is 0.9, which corresponds to “exceptionally high seismic risk building”.

**Table 4.** Column and wall rating

Drift Demand to Drift Capacity Ratio	Rating
$\Delta_D / \Delta_C \leq 0.25$	0.0
$0.4 \geq \Delta_D / \Delta_C > 0.25$	0.1
$0.5 \geq \Delta_D / \Delta_C > 0.4$	0.2
$0.7 \geq \Delta_D / \Delta_C > 0.5$	0.3
$0.9 \geq \Delta_D / \Delta_C > 0.7$	0.4
$1.1 \geq \Delta_D / \Delta_C > 0.9$	0.5
$1.4 \geq \Delta_D / \Delta_C > 1.1$	0.6
$1.8 \geq \Delta_D / \Delta_C > 1.4$	0.7
$2.5 \geq \Delta_D / \Delta_C > 1.8$	0.8
$3.0 \geq \Delta_D / \Delta_C > 2.5$	0.9
$\Delta_D / \Delta_C > 3.0$	0.93

## 4 CONCLUSION

In this study, an 8-story reinforced concrete building with infilled frames built in 1990’s is evaluated using the FEMA P-2018 evaluation methodology. Base effective yield strength and critical story of the building based on plastic mechanism analysis and procedures are determined for 3 possible mechanisms. When all these shear strengths are compared, Mechanism 2 is the governing plastic mechanism since base shear strength for the X direction is lower than the strength values in other cases. Also, the global demand-to-capacity ratios (8.4 and 7.2)

are greater than 5.5 for both orthogonal directions. It indicates that the building is classified as an exceptionally high seismic risk building. Besides, the building rating (BR) is calculated as 0.9, which is the highest possible rating for collapse. Therefore, exceptionally high seismic risk buildings should be given the highest priority for more detailed evaluation in an inventory.

## References

- [1] A. Yakut et al., "Performance of structures in Izmir after the Samos Island earthquake," *Bulletin of Earthquake Engineering*, vol. 20, pp. 7793–7818, Sep. 2021.
- [2] A. Liel et al., "Seismic evaluation of older concrete buildings for collapse potential," in *17th World Conference on Earthquake Engineering*, Sendai, Japan, 2020.
- [3] Applied Technology Council (ATC), "Seismic Evaluation of Older Concrete Buildings," FEMA, California, Virginia, FEMA P-2018, 2018.
- [4] "FEMA P-154", ATC-21 – Rapid Vis. Screen. Build. potential Seism. hazards a handbook. Redw. City Appl. Technol. Council. FEMA, vol. 145, pp. 388, January 2015.
- [5] B. Erdil and H. Ceylan, "A detailed comparison of preliminary seismic vulnerability assessment methods for RC buildings," *Iranian Journal of Science and Technology, Transactions of Civil Engineering*, vol. 43, pp. 711–725, Feb. 2019.
- [6] Seismic Evaluation and Retrofit of Existing Buildings, ASCE/SEI 41-17, 2017.
- [7] Design and Construction Rules for Reinforced Concrete Structures, TS-500, 1984.
- [8] Minimum Design Loads and Associated Criteria for Buildings and Other Structures, ASCE/SEI 7-16, 2017.
- [9] M. N. Fardis, "European structural design codes: Seismic actions," in *Encyclopedia of Earthquake Engineering*, M. Beer et al. Berlin Heidelberg: Springer-Verlag, 2015, pp. 1020–1038.



## Experimental Study on the Mechanical Behaviour of Fiber Reinforced Sandy Soil

Wiam Khebizi\*<sup>1</sup>

<sup>1</sup>*Civil Engineering and Architecture Department, Djillali Bounaama University, Khemis Miliana, Algeria*

---

### Abstract

This article explores the possibility of improving the undrained monotonic response of natural loose sand that normally appears susceptible to the phenomenon of static liquefaction. To this end, an experimental study was carried out in the laboratory using a triaxial apparatus on the influence of polypropylene fibers on the undrained behavior of the soil (Chlef sand). The tests were carried out on samples reinforced with fiber percentages (0, 0.3, 0.5 and 0.8%) in the wet state with several initial water content ( $w=0, 2, 3$  and 5%), initial relative density of 30 and at initial confining pressure of 100 kPa.

The results of the tests show that the introduction of fibers reduces the appearance of the post-peak liquefaction and even reduces the potential for the occurrence of the liquefaction. The increase in shear strength is function with increasing fiber percentage and with confining pressure.

We can say that, the potential for initiation of liquefaction decreases on the one hand with the increase in the percentage of fiber and on the other hand, this potential increases with the increase in the water content. We can pass from a perfectly unstable state for a high water content to a very stable state for a low water content and a high rate of reinforcement.

**Keywords:** *Triaxial, Consolidated undrained, Behavior, Shear strength, Fiber*

---





---

## Enhancing Self-Compacting Concrete with Recycled Fine Aggregates and Polyethylene Terephthalate Fibers

Meriem Bayah<sup>\*1</sup>, Farid Debieb<sup>2</sup>

<sup>1</sup>LME Laboratory, Faculty of Technology, University Yahia Fares of Medea, Algeria

<sup>2</sup>Civil Engineering Departement, Faculty of Technology, University Saad Dahleb of Blida 1, Algeria

---

### Abstract

The utilization of recycled aggregates and fibers in concrete has gained significant attention in recent years due to its potential for sustainability and environmental benefits. Recycled aggregates, derived from construction and demolition waste, offer a promising alternative to natural aggregates, reducing the demand for virgin materials and minimizing landfill waste. The incorporation of fibers, such as steel, glass, synthetic, or plastic fibers, enhances the mechanical properties and durability of concrete. This study investigates the effects of recycled fine aggregates (RFA) and different volumetric fractions (Vf) of fibers on the properties of self-compacting concrete (SCC). The recycled fine aggregates (RFA) were sourced from crushed moderate concrete slabs and substituted for natural fine aggregates (NFA) at various mass fractions (25% and 50%). The fibers used include recycled polyethylene terephthalate (PET) fibers. A series of tests were conducted to evaluate the compressive strength, tensile strength, flexural strength, and durability of the concrete mixes. The results indicate that SCC with RFA exhibits comparable compressive strength to conventional SCC, while the inclusion of PET fibers significantly improves the tensile and flexural strengths. Specifically, the concrete mix with 50% RFA and higher volumetric fractions of PET fibers demonstrated the most pronounced enhancement in mechanical properties. Overall, the findings suggest that the combined use of RFA and PET fibers can produce sustainable SCC with enhanced mechanical properties and durability. This approach not only contributes to the conservation of natural resources but also promotes the recycling of construction waste, aligning with the principles of sustainable development and the circular economy. Further research is recommended to optimize the mix designs and explore the long-term performance of fiber-reinforced RFA SCC in various environmental conditions.

**Keywords:** *Self compacting concrete, Recycled aggregates, Flexural strength, Durability, Tensile strength*

---



## **Synergistic Effect of Ground Granulated Blast-Furnace Slag and Metakaolin on the Performance of Recycled Self-Compacting Concrete**

**Boubakeur Asmaa<sup>\*1</sup>, Menadi Belkacem<sup>1</sup>**

<sup>1</sup>*Civil Engineering, University of Blida 1, Blida, Algeria*

---

### **Abstract**

Demolition waste and cement production is responsible for 36% of total waste produced on earth and 8 % of the world's CO<sub>2</sub> emissions, respectively. The use of Supplementary Cementitious Materials (SCMs) and Recycled Concrete Aggregates (RCA) requires greater implementation to produce a sustainable construction industry. In this experimental research, the combined effect of ground granulated blast-furnace slag (GGBFS) and metakaolin (MK) on the performance of recycled self-compacting concrete (RSCC) are investigated. Coarse natural aggregates (CNA) were replaced by coarse recycled concrete aggregates (CRA) at rates 100%, while fine natural aggregates (FNA) were partially substituted at 50% by fine recycled concrete aggregates (FRA). Workability properties such as flowability, viscosity and passing ability, as well as compressive strength and ultrasonic pulse velocity of recycled self-compacting concrete were investigated. The experimental results show that the combined use of GGBFS and MK in RSCC mixes met the EFNARC requirements for filling capacity, passing ability, and resistance to segregation. In the hardened state, compressive strength and ultrasonic pulse velocity decrease with the incorporation of recycled concrete aggregates. However, the combined use of GGBFS and MK in RSCC significantly improve compressive strength and ultrasonic pulse velocity. The optimal replacement percentage for slag and MK is 15%, as RSCC mixes exhibit the best performance at this level of replacement.

**Keywords:** *Ground granulated blast-furnace slag, Metakaolin, Recycled self-compacting concrete, Workability, Compressive strength*

---



## Impact of Particle Diameter and Flow Velocity on Particle Transport Behaviour in Saturated Soil

Bouragaa Kheira<sup>\*1</sup>, Bennacer Lyacine<sup>1</sup>, Ahfir Nasre-Dine<sup>2</sup>

<sup>1</sup>Laboratory of Energy, Environment and Information Systems, University of Adrar, National Road No. 6, 01000, Adrar, Algeria

<sup>2</sup>Normandy University, 76600, Le Havre, France

### Abstract

The transport of silt particles in porous media is a critical area of interest for many fields, such as the internal erosion of earthen hydraulic structures, the facilitated transport of pollutants to groundwater (where particles act as vehicles for contaminants), oil recovery processes involving pore clogging phenomena, and the artificial recharge of groundwater. In the current study, instantaneous injection tracing tests in a laboratory column were conducted to investigate the influence of fine particle size on the transport parameters of a saturated porous medium (sand). Silt particles with two different size distributions, with mean diameters of 13.8  $\mu\text{m}$  and 24.3  $\mu\text{m}$ , were studied. The experimental conditions rigorously controlled physicochemical factors such as pH and ionic strength, alongside varying flow velocities to account for hydrodynamic effects. The size distribution analysis of the recovered particles was carried out using a particle counter. The transport parameters were determined from the breakthrough curves using the analytic solution of one-dimensional advection-dispersion with deposition kinetics. The interpretation of these curves shows that the variation in parameters responds to the flow velocity and the size of the suspended fine particles.

**Keywords:** Silt particles, Size, Hydrodynamic effects, Transport, Deposition

## 1 INTRODUCTION

The migration of fine particles within porous media is a phenomenon intrinsic to fluid flow, garnering substantial research interest across a wide array of application domains. In civil engineering, the detachment of fine particles constituting the material can lead to internal erosion, a primary cause of incidents in hydraulic earth structures. In the environmental field, the transport of solid particles impacts groundwater resources, either directly through particles that are intrinsic pollutants or indirectly by carrying attached pollutants such as bacteria, viruses, pesticides, metals, and radioactive elements, a process known as facilitated transport.

The mechanisms of particle deposition and mobilization in saturated porous media have been extensively studied in recent decades, though most research has focused on dissolved elements and colloids. For example, the work of [1, 2] demonstrated that particles transported in saturated soils could contribute to the rapid transport and/or retardation (clogging) of pollution toward groundwater, posing a significant threat to the environment and human health [3]. Fine suspended particles, typically larger than a micrometer ( $> 1 \mu\text{m}$ ) [4], have attracted significant attention recently due to their size and density [5–8]. Their migration depends on mechanisms related to the physicochemical environment [9, 10], the size and distribution of the saturated soil, the porous medium in which transport occurs, and flow velocity [11]. Many laboratory column studies have been undertaken to control the parameters governing particle transport in saturated porous media. The use of laboratory columns allows for the variation of one parameter at a time while controlling others. An experimental study was conducted to investigate the transport and deposition of particles in a saturated porous medium, focusing on the influence of size and flow velocity on the transport and retention of fine particles in saturated sand. The parameters characterizing the transport and deposition of fine particles were determined using the analytical solution of the convection-dispersion equation with first-order deposition kinetics [10].

## 2 MATERIAL AND METHOD

### 2.1 Materials

The protocol constructed below, illustrated in Figure 1, consists of the pulse injection of fine particles into a Plexiglas column 32 cm long with an internal diameter of 4 cm, containing a porous medium (sand), and subjected

to flow. The column is positioned horizontally and equipped with four piezometers to monitor the hydraulic load evolution during the tracing tests. The sand grains constituting the porous medium exhibit a nearly uniform size distribution, ranging from 1 to 1.25 mm. The porosity of the medium is 0.40, and laboratory measurements indicate a permeability of  $5.5 \times 10^{-3}$  m/s, as determined by Darcy's law. To achieve the objective of this study, two populations of clay particles with a density of 2.65 were selected. The size distribution of the first population is between 8 and 20  $\mu\text{m}$  with a modal diameter of 13.8  $\mu\text{m}$  (denoted Limon 13.8  $\mu\text{m}$ ), and the second population is between 16 and 34  $\mu\text{m}$  with a mode at 24.3  $\mu\text{m}$  (noted Silt 24.3  $\mu\text{m}$ ).

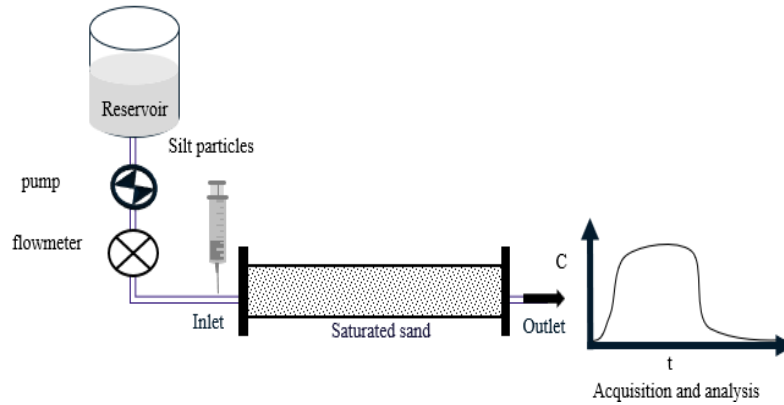


Figure 1. The experimental protocol scheme

In order to control the microparticle size evolution of the particles returned using a particle counter (Coulter Multisizer II), samples were taken at the outlet of the column at peak concentrations. Moreover, to avoid clogging at the entrance to the column, the injected volume  $V_{inj}$  was kept very small compared to the pore volume  $V_p$  of the porous medium [1, 7]. The low concentration of the injected suspension and the instantaneous nature of the injection did not affect the permeability of the medium.

## 2.2 Transport Parameters Identification

The general convection-dispersion equation with first-order deposition kinetics for a one-dimensional steady flow is given as follows [1, 2]:

$$\frac{\partial C}{\partial t} = D_L \frac{\partial^2 C}{\partial x^2} - u \frac{\partial C}{\partial x} - K_{dep} C \quad (1)$$

Where  $C$  is the effluent concentration of particles transported in the mobile liquid phase (g/l),  $D_L$  is the dispersion coefficient ( $\text{cm}^2/\text{s}$ ),  $u$  is the average particle velocity (cm/s),  $K_{dep}$  the kinetic deposition coefficient ( $\text{h}^{-1}$ ), the parameter characterizing the deposition speed during the collision of particles against the grains of the medium and also against other particles.

The initial and boundary conditions regarding the concentrations of suspended particles are stated as follows :

$$\begin{cases} C(t = 0, x) = 0 \\ C(t, x = 0) = m/Q \cdot \delta(t) \\ C(t, x = \infty) = 0 \end{cases} \quad (2)$$

Where  $\delta(t)$  is a time-dependent Dirac-type function [ $\text{T}^{-1}$ ];  $Q$  is the flow rate [ $\text{L}^3 \text{T}^{-1}$ ];  $m$  is the mass of the injected particles [ $\text{M}$ ] which is calculated by:  $m = C_0 \cdot V_{inj}$

$C_0$  is the initial concentration and  $V_{inj}$  is the volume of the injected tracer. The analytical solution of equation (1) with the initial and boundary conditions (2), is given by Wang et al 2000 [5]:

$$C(t) = \frac{m}{Q} \sqrt{\frac{P_c t_c}{4t^3}} \exp(-K_{dep} t) \exp\left(-\frac{P_c}{4t_c} \frac{(t_c - t)^2}{t}\right) \quad (3)$$

For a distance  $L$  fixed between the injection point and the observation point and defining  $P_e = uL/D_L = L/\alpha_L$  as the Péclet number and  $t_c = L/u$  as the transfer time by pure convection

### 3 RESULTS AND DISCUSSION

#### 3.1 Particle Transport Behaviour

The transport parameters are determined by fitting the experimental breakthrough curves by the parabolic regression method [5] based on the analytical solution of equation (1). Figure 2 presents the comparison of the breakthrough curves of the two populations of suspended particles and those simulated by the mathematical model when the flow velocity  $U = 0.42$  cm/s. NVp is the number of pore volumes injected. The relative concentration  $C_R$  of the particles is given as follows:

$$C_R = \frac{CV_p}{M} = \frac{CV_p}{V_{inj}C_0} \tag{4}$$

where  $V_p$  is the pore volume of the porous medium [ $L^3$ ],  $V_{inj}$  is the volume of the injected suspension [ $L^3$ ] and  $C_0$  is the initial concentration of the injected particles [ $M/L^3$ ]. Experimental breakthrough curves are well simulated by the analytical model, regardless of particle size. The peak of the restitution curves decreases with particle size.

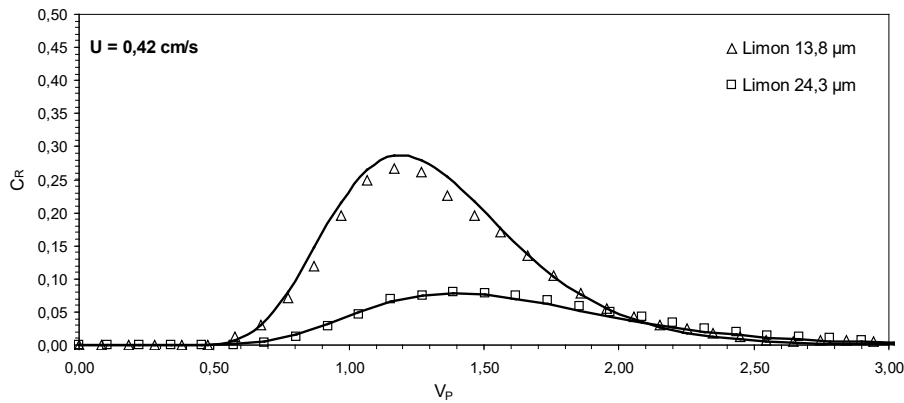


Figure 2. Example of simulation of an experimental curve for the darcy speed  $U = 0.42$  cm/s

Figure 3 shows the hydrodynamic effects and particle size on the recovery rate. Flow velocity is an important hydrodynamic parameter in the transport and deposition of particles in a porous medium. It can be seen that the two populations of particles generally exhibit similar behavior. The recovery rate increases with the flow velocity. For the same flow velocity, the recovery rate is greater when the particle size is small. At low velocity, the hydrodynamic forces exerted by the flow are insufficient to entrain the largest particles, which then remain trapped in the medium. The recovery rate observed for the 24.3 µm silt population is still low. This is linked to the large size of the injected suspensions, which leads to the systematic trapping of the coarsest fractions. For this population consisting of large particles (24.3 µm silt), all the injected particles were retained in the porous medium when the flow velocity was less than 0.15 cm/s.

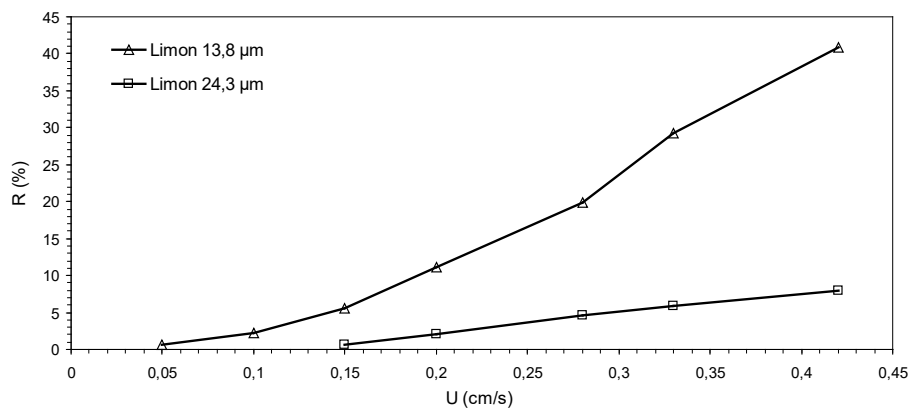


Figure 3. Particle size and flow velocity effects on the recovery rates

### 3.2 Deposition Kinetics Coefficient

The different tracing series carried out with the different populations of particles studied in this study show that the kinetic deposition coefficient ( $K_{dep}$ ) increases with the flow velocity, almost at the same rate as the recovery rate (Figure 4). The evolution of this coefficient with the flow velocity can be represented by a power relation ( $K_{dep} \propto U^\theta$ ). This development has already been observed by other authors. The values of the power coefficient  $\theta$  are respectively 0.26 and 0.27 for the populations (Silt 13.8  $\mu\text{m}$ , Silt 24.3  $\mu\text{m}$ ). As reported by Bennacer et al 2013 [11] the power coefficient  $\theta$  increases with the size distribution of the injected particles.

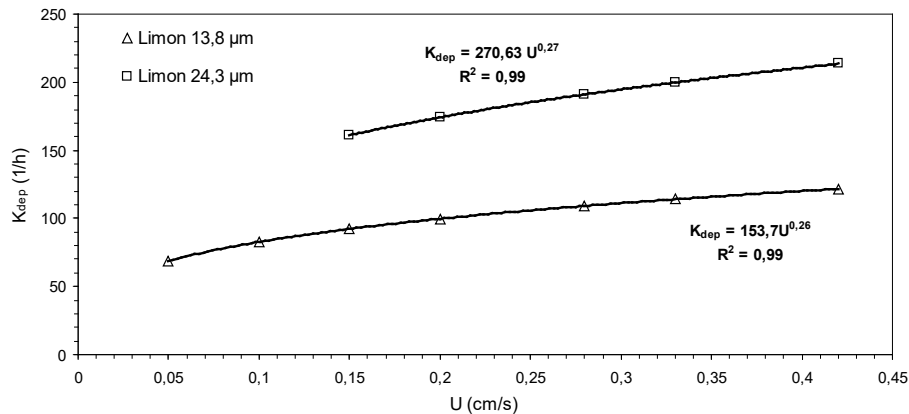


Figure 4. Deposition coefficient as a function of the darcy velocity

## 4 CONCLUSION

This experimental investigation highlighted the significant impact of particle size and flow velocity on various transport parameters in a saturated porous medium. Our findings reveal that an increase in flow rate correlates with a rise in both the recovery rate and the deposition coefficient. Additionally, the size of the injected particles plays a crucial role in determining the recovery rate and the size selection of fine particles at the column outlet. Specifically, large particles are not effectively transported by the flow at low velocities, leading to their deposition within the medium. This study indicates that particle deposition is primarily governed by the effects of sedimentation and mechanical blocking, both of which are heavily influenced by particle size. Overall, our results contribute to a deeper understanding of particle behavior in porous media, providing valuable insights for applications in fields such as environmental engineering, petroleum recovery, and groundwater contamination.

## References

- [1] R. Kretzschmar, K. Barmettler, D. Grolimund, Y. D. Yan, M. Borkovec, and H. Sticher, "Experimental determination of colloid deposition rates and collision efficiencies in natural porous media," *Water Resour. Res.*, vol. 33, pp. 1129–1137, 1997.
- [2] D. Grolimund, M. Elimelech, M. Borkovec, K. Barmettler, R. H. Kretzschmar, and H. Sticher, "Transport of in situ mobilized colloidal particles in packed soil columns," *Environ. Sci. Technol.*, vol. 32, pp. 3562–3569, 1998.
- [3] J. F. McCarthy and J. M. Zachara, "Subsurface transport of contaminants," *Environ. Sci. Technol.*, vol. 23, pp. 496–502, 1989.
- [4] M. Elimelech and C. R. O'Melia, "Effect of particle size on collision efficiency in the deposition of Brownian particles with electrostatic energy barriers," *Langmuir*, vol. 6, pp. 1153–1163, 1990.
- [5] H. Q. Wang, M. Lacroix, N. Massei, and J.-P. Dupont, "Transport of particles in porous media: determination of hydrodynamic parameters and deposition coefficient," *C. R. Acad. Sci. Paris*, vol. 331, pp. 97–104, 2000.
- [6] A. Benamar, H. Q. Wang, N.-D. Ahfir, A. Alem, N. Massei, and J.-P. Dupont, "Effects of flow velocity on the transport and deposition kinetics of suspended particles in saturated porous media," *C. R. Geoscience*, vol. 337, pp. 497–504, 2005.
- [7] N.-D. Ahfir, H. Q. Wang, A. Benamar, A. Alem, N. Massei, and J.-P. Dupont, "Transport and deposition of suspended particles in saturated porous media: hydrodynamic effect," *Hydrogeology Journal*, vol. 15, pp. 659–668, 2007, doi: 10.1007/s10040-006-0131-3.
- [8] A. Alem, A. Elkawafi, N.-D. Ahfir, and H. Q. Wang, "Filtration of kaolinite particles in a saturated porous medium: hydrodynamic effects," *Hydrogeology Journal*, vol. 21, pp. 573–586, 2013.

- [9] Q. Meng et al., “SiO<sub>2</sub> and microparticle transport in a saturated porous medium: effects of particle size and flow rate,” *Appl. Water Sci.*, vol. 14, art. no. 50, 2024, doi: 10.1007/s13201-024-02105-6.
- [10] L. Bennacer, N.-D. Ahfir, A. Bouanani, A. Alem, and H. Q. Wang, “Suspended particles transport and deposition in saturated granular porous medium: particle size effects,” *Transport in Porous Media*, vol. 100, pp. 377–392, 2013.
- [11] L. Bennacer, N.-D. Ahfir, A. Alem, and W. Huaqing, “Influence of particles sizes and flow velocity on the transport of polydisperse fine particles in saturated porous media: Laboratory experiments,” *Water Air Soil Pollut*, vol. 233, no. 7, art. no. 249, Jul. 2022, doi: 10.1007/s11270-022-05732-4.



## Effect of the Use of Plastic Waste as Sand on Concrete Properties

Wassila Boughamsa<sup>\*1</sup>, Assia Abdelouahed<sup>1</sup>, Houria Hebhou<sup>1</sup>, Wassila Mouats<sup>2</sup>

<sup>1</sup>LMGHU Laboratory, Civil Engineering Department, 20 August 1955 University, Skikda, Algeria

<sup>2</sup>Civil Engineering Department, 20 August 1955 University, Skikda, Algeria

---

### Abstract

Recycling and valorization of waste in civil engineering is an important sector, it has two sensitive targets: environment protection and economic improvement. Current study used plastic waste, which has become invasive worldwide and poses environmental hazards due to its bulky and unsightly nature.

The main objective of this work is to test the effect of partial replacement of natural sand by a powder of plastic waste in the composition of concrete, in order to preserve natural resource of sand. To achieve this study, in the composition of a reference concrete formulated using the "Dreux Gorisse" method, dune sand will be substituted by crushed PVC from false ceilings. The chosen substitution rates are: 1%, 2%, 3% and 4%. The behavior of the freshly prepared concretes (workability and density) as well as the hardened state (compressive and flexural strength) and chemical attacks (mass loss in chlorides, mass loss in sulfuric acid) will be evaluated and compared to those of a reference ordinary concrete composed initially of dune sand.

Based on the obtained results, it can be concluded that substituting sand by plastic powder leads to significant decreases in the density of all the studied mixtures, as well as a decrease in the mechanic performance but still acceptable, however, the mixes containing plastic waste were more resistant to sulfuric acid and salt attacks. This possibility represents a promising approach to valorize plastic waste in concrete, aiming to preserve natural resources, reduce concrete production costs, and contribute to environmental protection by limiting waste at its source.

**Keywords:** *Valorisation, Plastic waste, Concrete, Replacement, Durability*

---





## **Study of the Durability of Sand Concrete Based with Wood Ash (0.1%, 0.2%, and 0.3%)**

**Abdelouahed Assia<sup>\*1</sup>, Mouats Wassila<sup>2</sup>, Houria Hebhou<sup>2</sup>, Wassila Boughamsa<sup>2</sup>, Toufik Sebbagh<sup>1</sup>**

<sup>1</sup>University of Skikda, Algeria

<sup>2</sup>20 August 1955 University, Algeria

---

### **Abstract**

In recent years, Algeria has proficient many fires in the forests, leaving a large amount of wood ashes, which made us think about how to exploit these ashes in our field of work by reusing them in the manufacture of concretes. Wood ash is generated as a by-product of combustion in wood fired power plants, paper mills, and wood burning factories.

This work is inserted within the framework of studying the use of ashes in cementitious materials. This study aims to the use of wood ash as additional cementitious materials, use this waste as substitutes for cement to formulate a sand concrete. Wood ash is used in weight ratios of 0.1%, 0.2%, 0.3% and a control sand concrete with 0% ash. All of the properties in the fresh state, the mechanical strength and the weight loss test of each mixture that's treated by sea water or preserved in drinking water were carried out through the experiments carried out.

**Keywords:** *Wood ash, Sand concrete, Durability*

---



## Comparative Study on the Valorization of Recycled Plastic Waste in the Formulation of Mortars

**Houria Hebhou<sup>\*1,2</sup>, Said Berdoudi<sup>1</sup>, Wassila Boughamsa<sup>1</sup>, Assia Abdelouahed<sup>1</sup>, Wassila Mouats<sup>1</sup>, Mohammed Ichem Benhalilou<sup>3</sup>**

<sup>1</sup>LMGHU Laboratory, Department of Civil Engineering, University 20 August 1955-Skikda, Algeria

<sup>2</sup>Mining Department, University Badji Mokhtar, Annaba, Algeria

<sup>3</sup>Batna 2 University, Batna, Algeria

---

### Abstract

The objective of this experimental work is to introduce a plastic waste into the composition of cement mortars, in order to reduce the cost of their manufacture, limit CO<sub>2</sub> emissions, reduce the risk of this waste on human health and preserve the environment. To carry out this comparative study, we created two series of combinations and included plastic waste in the form of sand from the sawing of PVC profiles in the first series and PVC tubes in the second series. This trash will partially replace the sand at the rates of: 2%, 4% and 6%. All mixtures were subjected to the following tests: density, workability, compressive strength and tensile strength.

The results obtained show a reduction in density, workability and mechanical resistance at the age of 28 days but remain acceptable. Mortars based on plastic waste sand obtained by sawing PVC tubes have greater compressive strengths in comparison with mortars based on plastic waste sand obtained by sawing PVC profiles.

**Keywords:** Mortar, Sand, Valorisation, Plastic waste, Characterizations, Performance

---



## **Fresh and Hardened Properties and Durability of Self-Compacting Repair Mortar Made with Ceramic Powder as Cement Substitute**

**Messaouda Belouadah<sup>\*1</sup>, Zine El Abidine Rahmouni<sup>1</sup>, Nadia Tebbal<sup>2</sup>**

<sup>1</sup>*Geomaterials Development Laboratory, Civil Engineering Department, Faculty of Technology, M'sila University, M'sila, Algeria*

<sup>2</sup>*Institute of Technical Urban Management, M'sila University, M'sila (28000), Algeria*

---

### **Abstract**

Self-compacting concretes and mortars are characterized by their great fluidity, since they are carried out without the need for a vibrator, and they are also characterized by the fact that they contain a high percentage of mineral additives which greatly affect their properties in the elastic

The main objective of this work is to study the effect of ceramic powder on the liquid, solid and durability properties of self-compacting mortar. By substituting the quantities of cement with the following percentages: 5%, 10%, 15%, 20%.

The results showed that partial replacement of fine aggregate with sanitary ceramic fillers up to 20% of cement by weight improves mechanical properties and durability of the self-posing mortar. The test results were discussed in the lights of the literature data on influence of ceramic waste on properties of fresh and hardened self-posing mortar.

**Keywords:** *Mortars, Self-compacting, durability, Cement, Ceramic powder*

---



---

## Enhancing Mechanical Strength of Concrete Through Polypropylene Fiber Incorporation

Shiraz Baloch<sup>\*1</sup>, Farah Naz<sup>1</sup>, Umer Shahzad<sup>1</sup>, Muhammad Abrar Faiz<sup>2</sup>

<sup>1</sup>Department of Civil Engineering, Khwaja Fareed University of Engineering & Information Technology, Rahim Yar Khan, Pakistan

<sup>2</sup>Department of Civil & Environmental Engineering, Yonsei University, Seoul, South Korea

---

### Abstract

Concerns about resource depletion and greenhouse gas emissions have prompted a worldwide movement towards sustainable construction practices, which has brought attention to the need for environmentally acceptable alternatives to conventional building materials like concrete. Our research work highlights the need for comprehensive testing to evaluate and optimize the performance of concrete mixed with polypropylene fibres, as we delve into the diversity of these fibres. When compared to other fibre kinds, polypropylene (PP) fibres offer a reasonable amount of control. The purpose of this experiment is to evaluate the durability and mechanical properties of concrete that has been incorporated with polypropylene fibres. The 18 mm long polypropylene fibres utilized as an additional material in this study ranged from 1% to 2% by weight. For the sole purpose of improving workability and increasing durability, silica fume was used in place of some of the cement in fresh concrete at varying percentages. Nevertheless, the main emphasis is on evaluating the effects of fibres individually. As compared to the control samples, samples with 1.5% PP fibre added had 20% higher compressive strength and much higher tensile strength. This study emphasizes the need of employing the right amount of PP fibre strands to make sustainable concrete, which helps to lessen the environmental effect of the building sector without sacrificing structural integrity.

**Keywords:** Sustainable construction, Polypropylene fibers, Durability, Workability, Structural integrity

---

## 1 INTRODUCTION

### 1.1 Background

Concrete, renowned for its durability and longevity, has emerged as one of the foremost building materials globally. Despite its widespread use, concrete is susceptible to cracking due to various factors such as shrinkage, temperature fluctuations, and external loads. These problems can weaken structures over time and lead to costly repairs. Finding ways to improve concrete's durability and performance is essential for ensuring the longevity of infrastructure. However, it's not just about making concrete stronger; factors like sustainability, cost-effectiveness, and ease of construction also play crucial roles in selecting the right solutions. Balancing these considerations is key to addressing the challenges inherent in concrete applications and advancing towards more resilient and sustainable construction practices. Incorporating polypropylene (PP) fibers into concrete mixtures emerges as a promising approach, offering enhancements in both mechanical properties and environmental impact.

### 1.2 Literature Review

Concrete due to its durability and longevity, has become one of the world's most popular building materials. Nonetheless, it can crack for a variety of reasons, including shrinkage, temperature changes, and external loads. The tensile strength of concrete is significantly lower than its compressive strength [1–5]. The weak tensile strength, impact resistance, and susceptibility to moisture are its shortcomings. Anywhere you need it, you can easily shape and thickness it to your specifications [6]. New concrete is in the process of hydrating and losing water through capillary networks, which causes moisture to migrate to the top. Vapors are created and the bulk of concrete starts to shrink as water evaporates. Here, micro-cracks spread over the concrete mass, reducing its strength. Micro-cracks that are now receding spread and grow larger and more noticeable as the process progresses. Concrete with any kind of crack, no matter how small, is unsightly and weakens its quality and durability [7].

The tensile strength and strain capacity of concrete are restricted. It is well-known that concrete's brittleness and tension sensitivity, which leads to low ductility, are major problems with its structural use. There is an increasing

demand for using fibres that can help improve the strength and reduce the carbon footprint in a sustainable way in order to solve these concerns and improve the performance of concrete.

Fibres, according to earlier studies, can greatly improve the mechanical properties of concrete when added to mixtures. For both building and maintenance purposes, ultra-high-performance concrete (UHPC) is being investigated due to its exceptional mechanical qualities. The flexural toughness and tensile strength of UHPC were enhanced by the addition of polypropylene fibres [8]. Lightweight, extremely robust, and corrosion-resistant, polypropylene fibre is a type of polymer. The cracks in PP fibres are prevented from spreading because of this. The optimal rate of PP fibre insertion into concrete increased strength and improved durability, according to scanning electron microscopy (SEM) studies [1].

When dealing with tensile stresses on either side of the exterior surface of a concrete piping that is too thin for the two layers of traditional rebar, a hybrid fibre solution that combines high specific gravity (steel) fibres with low specific gravity (PP) fibres can be an effective solution [9]. The breaking strength is greatly enhanced when PP fibres are added to TRAC [10]. Improving the concrete's resilience to abrasion and freeze-thaw, as well as reducing the volume expansions caused by sulphate attack by alkali silica reaction (ASR), are all outcomes of randomly dispersing polypropylene fibres in the mix [11]. Because the water-to-binder ratio affects the ideal fibre content, it is important to take it into account when talking about how fibres improve the mechanical or microstructural qualities of concrete [12].

Polypropylene fibres have numerous industrial uses due to their versatility [13]. The ductility, fire and impact resistance, and sturdiness of concrete substances can be significantly enhanced by adding fibres, which vary in shape and geometrical properties [14]. In addition to acting as a crack arrestor, the inappropriate packing and dispersion of polypropylene fibres in concrete alters the fresh and cured characteristics, which has a negative impact on concrete [15]. Adding more polypropylene fibre to a mixture in its raw form decreases its workability and makes it more fibrous, making it harder to handle [16]. The workability of concrete is diminished when fibres are added to it. When 0.5% polypropylene fibre was used, the compressive and tensile strengths were enhanced [17]. When added to high-performance self-compacting concrete, polypropylene fibres significantly increase its splitting tensile strength [18].



**Figure 1.** Polypropylene fibers strands

### 1.3 Aim of Research

The core aim of this study is to examine how varying quantities of polypropylene fibers affect both the mechanical attributes and the long-term sustainability of high-strength concrete. In total, four distinct concrete mix formulations were developed, incorporating different proportions of fibers. These mixtures were employed in the production of cylindrical PCC concrete specimens, resulting in the creation of a total of 72 samples. Subsequent testing involved assessing compressive strength and tensile strength at various time intervals.

### 1.4 Contribution to Sustainable Development Goals (SDGs)

The incorporation of polypropylene (PP) fibers in concrete aligns with Sustainable Development Goals (SDGs) 11, 12, and 13. Replacing Portland cement with polypropylene (PP) fibers can reduce carbon emissions associated with traditional Portland cement and promoting sustainable infrastructure development, the research contributes to Goal 11 (Sustainable Cities and Communities). Additionally, the innovation in construction materials and techniques, aimed at minimizing resource consumption and waste generation, supports Goal 12 (Responsible Consumption and Production). Furthermore, the enhanced durability and resilience of PP fiber-reinforced concrete contribute to Goal 13 (Climate Action) by mitigating the environmental impact of construction activities.



**Figure 2.** Sustainable development goals (SDGs) chart

## 2 RESEARCH METHODOLOGY

### 2.1 Materials

The present study used Type 1 (42.5) OPC Cement, which is a multipurpose cement that meets the criteria of ASTM C150 and has several potential uses. At Rahim Yar Khan's Bismillah Building Materials, we picked up two sacks of Maple Leaf cement. In our research work, properties of the cement used are detailed in Table 1 below. In this study, high-quality Maple Leaf cement was used. For mix IDs containing Polypropylene Fibre, the Experimental Setup involved partially substituting cement with different amounts of Silica Fume. Also utilized as fine aggregates were harrow sands that were bought locally. We used Sargodha Crush for the coarse aggregate and harrow sand, which is accessible locally, for the fine aggregate in our experimental setting. We put the coarse and fine aggregates through their paces in the lab, and you can see all the details about their characteristics in Table 2 and Table 3, respectively. Different tests of the materials were performed in lab before concret mix design.

**Table 1.** Chemical & physical properties of cement

Chemical Properties	Percentage (%)	Physical Properties	Results
CaO	64.7	Size	$\leq 75\mu$
SiO <sub>2</sub>	23.6	Fineness of cement	92%
Al <sub>2</sub> O <sub>3</sub>	8.5	Normal consistency	28%
Fe <sub>2</sub> O <sub>3</sub>	1.7	Early setting time	36 min
MgO	2.5	Final setting time	415 min
SO <sub>3</sub>	1.2	Specific Gravity	3.15
K <sub>2</sub> O	2.5	Soundness	1.70%
Na <sub>2</sub> O	0.22	28-dayscomp.str.	42 MPa

**Table 2.** Physical properties of fine aggregate

Physical Property	Description
Source	Local Harrow Sand
Fineness Modulus	2.62
Specific Gravity	2.67
Water Absorption	1.32%
Loose Bulk Density	1.300 g/cm <sup>3</sup>
Compacted Bulk Density	1.475 g/cm <sup>3</sup>

**Table 3.** Properties of coarse aggregate

Physical Property	Description
Source	Sargodha Crush
Max. Size	20mm
Fineness Modulus	6.5
Specific Gravity	2.748 (SSD)
Water Absorption	1%
Impact Value	6.4
Crushing Value	21.26
Los Angeles Abrasion	18.16%
Air Void %	0.50%
Compressive Strength	20.2 MPa
Average Unit Weight	1680 kg/m <sup>3</sup>

We used the MasterRheoBuild superplasticizer in this study at a constant concentration of 0.8% across all samples. Purchased from BASF Karachi was this crucial additive. By increasing workability, decreasing the water-cement ratio, and improving mechanical qualities, superplasticizer help in the production of high-performance concrete. To achieve our performance targets and fine-tune the concrete mix, superplasticizer was an essential component of our project. The development of high-strength concrete often makes use of these chemicals. Our MasterRheoBuild Superplasticizer features are detailed in Table 5. For all PP-incorporated mixes in our study, we used Polypropylene fibres that were 18 mm long. The Clifton, Karachi-based Matrix Duracrete Company was the supplier of these premium fibres. Table 4 provides a comprehensive list of the specs for these microfibers that have already been manufactured. In addition, the reputed SAFE Mix company in North Nazimabad, Karachi is where we sourced our Silica Fume. For this experiment, silica fume is employed in place of some of the OPC cement. The ferrosilicon business produces silica fume, which is a highly effective pozzolanic material that improves the physical properties and durability of concrete. An important factor in concrete's strength and durability is the use of silica fume as a partial cement substitute; this additive boost strength and durability while decreasing water demand and shrinkage during hydration.

**Table 4.** Properties of polypropylene fibers

No	Property	Results
1	Color	Natural
2	Type	Monofilament Fiber
3	Length	18 mm
4	Diameter	18-micron nominal
5	Density	0.95 gm nominal
6	Absorption	Nil
7	Sp. Surface Area	250 m <sup>2</sup> per Kg
8	Ignition Point	365 °C
9	Thermal Conductivity	Low
10	Electrical Conductivity	Low
11	Acid Resistance	High
12	Alkali Resistance	96%

**Table 5.** Properties of superplasticizer

Property	Result
Color of Liquid	Black
Air Entrainment	1.48 at 25 °C
Chloride Content	Nil to BS 5075/BS: EN934
Specific Gravity	1.19

**Table 6.** Chemical and physical properties of silica fume

Chemical Property	Percentage (%)	Physical Property	Results
SiO <sub>2</sub>	87.6	Average Particle size	≤0.2μm
CaO	2.85	Specific Gravity	2.3
Al <sub>2</sub> O <sub>3</sub>	5.7	Color	Grey
Fe <sub>2</sub> O <sub>3</sub>	1.7	Bulk Density (kg/m <sup>3</sup> )	572
MgO	2.5	Solubility	Insoluble
SO <sub>3</sub>	1.9	Surface Area	22 m <sup>2</sup> /g
K <sub>2</sub> O	2.4		
Na <sub>2</sub> O	0.2		

## 2.2 Material Testing

Materials were tested for following tests in the materials testing lab.

**Table 7.** List of performed experiments

Experiments	References
Impact value test of coarse aggregate	ASTM D5874 – 16
Crushing value test of coarse aggregate	BS812-110
Water absorption & specific gravity of coarse aggregate	ASTM C127-15
LAA value test of coarse aggregate	ASTM C-535-16
Fineness modulus of sand	ASTM C136/136M-16
Relative density of sand	ASTM D4254-16
Compressive strength of mortar cubes	ASTM C109/C109M-16
Slump cone test	ASTM C143/143M-15
Compression test of cylinders	ASTM C39
Split tensile test of cylinders	ASTM C496

### 2.3 Concrete Mix Design

In this investigation, we employed Mix M20 (1:1.5:3). A total of eighteen specimens were cast for every mix ID. Out of a total of 72 specimens, 54 had polypropylene fibre added to them, while 18 served as control samples. As seen in figure 3, the mix design specifics are presented. The experimental setting utilized a constant water to cement ratio of 0.56 for all the mixes. Incorporating water and superplasticizer into a mixture of cement, sand, and aggregates was the first step in the process. The next step was to add the fibre strands to the mixer and mix them well so that they were evenly distributed. All of the materials were well mixed by dispersing the fibres. The control samples did not include any silica fume or polypropylene fibres. Slump cone testing is useful for determining if concrete is suitable for use in construction since it assesses the material's flow and consistency. The slump cone test was repeated until a suitable value of w/c was obtained before proceeding for casting cylinders.

**Table 8.** Mix proportions data

Mix ID	Mix Proportion			Cement (kg)	Silica Fume (kg)	Coarse Aggregate (ft <sup>3</sup> )	PP Fibers (kg)	Sand (ft <sup>3</sup> )	Water (ml)	Admixture (ml)
	Cement (%)	CA (%)	PPF (%)							
CS	100%	100	0	39.52	0	2.967	0	1.483	22130	475
PP 1%	C:SF (90:10)	100	1	35.56	3.98	2.967	0.395	1.483	22130	475
PP 1.5%	C:SF (85:15)	100	1.5	33.56	5.96	2.967	0.592	1.483	22130	475
PP 2%	C:SF (80:20)	100	2	31.6	7.92	2.967	0.79	1.483	22130	475

### 2.4 Casting and Curing of Specimens

Each mixture required the casting of eighteen concrete cylinders. A cylinder has a diameter of 6 inches and a length of 12 inches. The specimens were reshaped and then placed in an incubator after 36 hours' time had passed. Careful cure over 7, 14, and 28 days was possible in this controlled laboratory setting.

### 2.5 Compressive Strength Test (ASTM C39/39M)

Using the well-known ASTM C39/C39M standard, we measured the breaking strength of concrete specimens that were cylindrical in shape. Following this specification, the loading rate was between 20 and 50 psi/second, or 0.14 to 0.35 MPa/second. The specimens were subjected to compressive strength evaluations on separate days in our study, following the guidelines set out by ASTM.

### 2.6 Split Tensile Strength Test (ASTM C496/C496M)

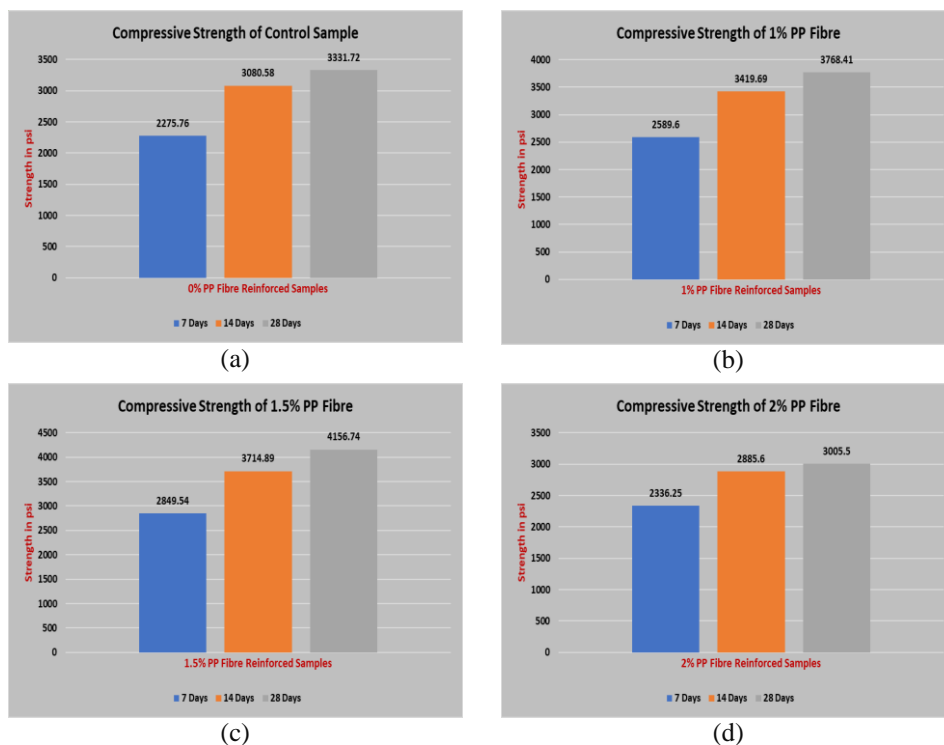
One method for determining the maximum breaking strength of concrete samples is the split tension test, which is also called the indirect tensile force test. The tensile strength of concrete can be measured quantitatively using this method. Our study utilized this test to assess the breaking load of concrete cylinders, which yielded important information on the material's durability and performance.



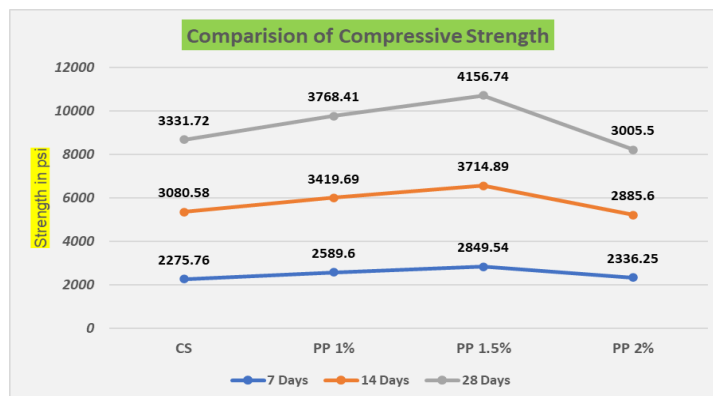
### 3 RESULTS

#### 3.1 Compressive Strength

The compression strength is clearly a defining feature of high-quality concrete, which is also a crucial mechanical element in the field of building construction. The results of the tests for compression performed on specimens of concrete are shown in Figure 3. As shown in Figure 3, the concrete sample underwent compression testing. Compressive strength tests were conducted on specimens at 7, 14, and 28 days as per the protocol. The compressive strength of specimens that had polypropylene fibres added was higher than that of control samples. Results showed the greatest improvement in strength at 1.5% PPF incorporation. About 20% increase in compressive strength for 1.5% PPF incorporated specimens was observed. At 2% decrement in the compressive strength followed but the optimum dosage with improved results were 1.5% PPF mix samples. Generally, the enhancement in the compressive strength observed in fiber incorporated specimens can be attributed to the fibers distinctive capability to impede and slow down the propagation of cracks, while also diminishing stress concentration at crack tips, is noteworthy. Figure 4 presents a comprehensive comparison of compressive strength across different mixtures. When we utilize silica fume as a partial substitute for cement, ranging from 10% to 15%, we can see enhancements not only in compressive & tensile strength but also in overall durability.



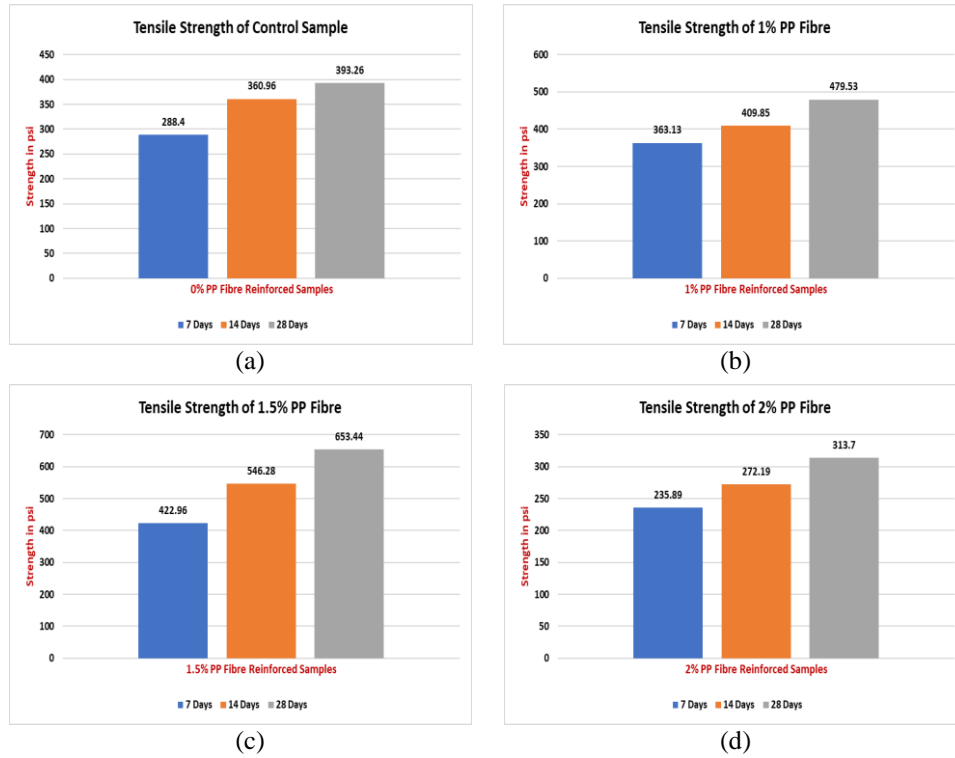
**Figure 3.** (a) Compressive strength of control samples at different days, (b) compressive strength of 1% PPF samples at different days, (c) compressive strength of 1.5% PPF samples at different days, and (d) compressive strength of 2% PPF samples at different days



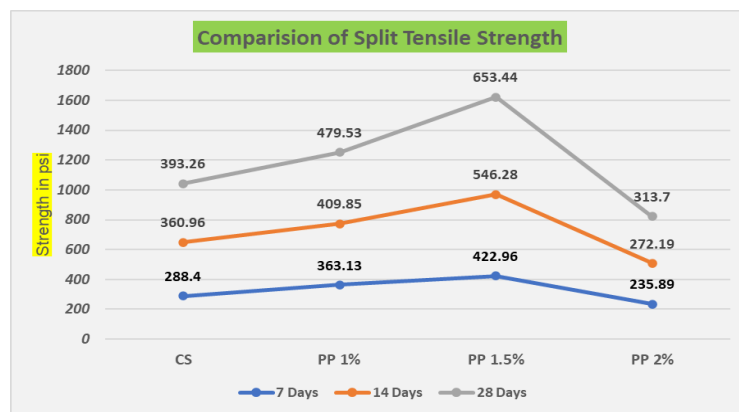
**Figure 4:** Overall comparison of compressive strength of different mix IDs

### 3.2 Split Tensile Strength of Specimens

The tensile strength of concrete stands out as a pivotal attribute, especially considering that structural forces can lead to the development of cracks under tension. Concrete's tensile strength is notably lower than its compressive strength, typically hovering around 10-15% of the compressive strength. In our research, the results of split tensile strength obtained, are displayed in Figures 5 and 6, respectively.



**Figure 5.** (a) Tensile strength of control samples at different days, (b) tensile strength of 1% PPF samples at different days, (c) tensile strength of 1.5% PPF samples at different days, and (d) tensile strength of 2% PPF samples at different days



**Figure 6.** Overall comparison of tensile strength of different mix IDs

## 4 CONCLUSION

Based on the outcomes of this research, several deductions can be drawn. Incorporating 1.5% polypropylene (PP) fibers in concrete mixtures yielded the best balance between fiber distribution and interfacial bonding, enhancing both tensile and compression properties. By blending 1.5% PP fibers with 10-15% silica fume in concrete, synergistic benefits may lead to substantial improvements in mechanical characteristics and durability, including a remarkable 20% boost in compressive strength and enhanced tensile strength observed in samples containing 1.5% polypropylene fibers, though strength decreased at 2% PP fiber content. Polypropylene fiber also showed crack prevention while enhancing the mechanical strength of concrete. Augmenting the polypropylene (PP) fiber

content in concrete results in a decrease in the slump, and when the dosage exceeds 2%, the mixture became overly fibrous, making it challenging to handle and work with effectively. The higher amounts of fiber can affect and decrease the durability and strength of concrete while also influencing the water absorption in concrete. Polypropylene fibers are easily available in the market at affordable rates, given their utilization in concrete as an additive material further makes them cost-effective and sustainable. Enhanced strength, improved durability and cracks mitigation are important benefits of incorporating Polypropylene fibers in concrete for sustainable construction. Optimizing the right combination of fiber content can offer cost-effective solutions in concrete construction, potentially improving performance and durability without significantly raising project costs. Incorporating polypropylene fibers in concrete can also reduce CO<sub>2</sub> emissions, making it an eco-friendly and sustainable option for Civil Engineering projects.

Investigation on the flexural and shear crack patterns in fiber-reinforced concrete, specifically focusing on a comparative study of blended type, micro length, and macro length polypropylene (PP) fibers. Assessing the impact of different curing conditions on the development and propagation of cracks in fiber-reinforced concrete. Evaluating the long-term durability and performance of fiber-reinforced concrete specimens under varying environmental conditions. Exploring the use of advanced imaging techniques (e.g., X-ray CT scanning) to study the internal crack patterns and fiber dispersion within fiber-reinforced concrete.

## Acknowledgments

The authors would like to express their gratitude to the management, academic teaching staff, and non-teaching staff of the Department of Civil Engineering within the Faculty of Chemical, Civil & Environmental Engineering at Khwaja Fareed University of Engineering and Information Technology for their invaluable assistance in completing this study.

## References

- [1] J. Ahmed, D. D. Burduhos-Nergis, M. M. Arbili, S. M. Alogla, A. Majidi, and A. F. Deifalla, "A review on failure modes and cracking behaviors of polypropylene fibers reinforced concrete," *Buildings*, vol. 12, no. 11, art. no. 1951, 2022.
- [2] J. Ahmad, F. Aslam, R. Martinez-Garcia, M. H. E. Ouni, and K. M. Khedher, "Performance of sustainable self-compacting fiber reinforced concrete with substitution of marble waste (MW) and coconut fibers (CFs)," *Scientific Reports*, vol. 11, no. 1, art. no. 23184, 2021.
- [3] S. Acosta-Calderon, P. Gordillo-Silva, N. García-Troncoso, D. V. Bompa, and J. Flores-Rada, "Comparative evaluation of sisal and polypropylene fiber reinforced concrete properties," *Fibers*, vol. 10, no. 4, art. no. 31, 2022.
- [4] A. Saradar, B. Tahmouresi, E. Mohseni, and A. Shadmani, "Restrained shrinkage cracking of fiber-reinforced high-strength concrete," *Fibers*, vol. 6, no. 1, art. no. 12, 2018.
- [5] M. Amran, S. S. Huang, A. M. Onaizi, N. Makul, H. S. Abdelgader, and T. Ozbakkaloglu, "Recent trends in ultra-high-performance concrete (UHPC): Current status, challenges, and future prospects," *Construction Building Materials*, vol. 352, art. no. 129029, 2022.
- [6] K. Thangapandi, R. Anuradha, N. Archana, P. Muthuraman, O. Awoyera Paul, and R. Gobinath, "Experimental study on performance of hardened concrete using nano materials," *KSCE Journal of Civil Engineering*, vol. 24, no. 2, pp. 596–602, 2020.
- [7] H. S. Arel and B. S. Thomas, "The effects of nano- and micro-particle additives on the durability and mechanical properties of mortars exposed to internal and external sulfate attacks," *Results in Physics*, vol. 7, pp. 843–851, 2017.
- [8] D. Shen, C. Liu, Y. Luo, H. Shao, X. Zhou, and S. Bai, "Early-age autogenous shrinkage, tensile creep, and restrained cracking behavior of ultra-high-performance concrete incorporating polypropylene fibers," *Cement and Concrete Composites*, vol. 138, art. no. 104948, 2023.
- [9] A. Faisal, S. Abbas, S. M. S. Kazmi, and M. J. Munir, "Development of concrete mixture for spun-cast full-scale precast concrete pipes incorporating bundled steel and polypropylene fibers," *Materials*, vol. 16, no. 2, art. no. 512, 2023.
- [10] F. Xu, Si. Wang, T. Li, B. Liu, B. Li, and Y. Zhou, "Mechanical properties and pore structure of recycled aggregate concrete made with iron ore tailings and polypropylene fibers," *Journal of Engineering*, vol. 33, art. no. 101572, 2021.
- [11] M. R. Latifi, O. Biricik, and A. Mardani Aghabagalou, "Effect of the addition of polypropylene fiber on concrete properties," *Journal of Adhesion Science and Technology*, vol. 36, no. 4, pp. 345–369, 2022.
- [12] Z. Yuan and Y. Jia, "Mechanical properties and microstructure of glass fiber and polypropylene fiber reinforced concrete: An experimental study," *Construction and Building Materials*, vol. 266, art. no.

- 121048, 2021.
- [13] P. Nuaklong, N. Boonchoo, P. Jongvivatsakul, T. Charinpanitkul, and P. Sukontasukkul, "Hybrid effect of carbon nanotubes and polypropylene fibers on mechanical properties and fire resistance of cement mortar," *Construction and Building Materials*, vol. 275, art. no. 122189, 2021.
- [14] S. Fallah and M. Nematzadeh, "Mechanical properties and durability of high-strength concrete containing macro-polymeric and polypropylene fibers with nano-silica and silica fume," *Construction and Building Materials*, vol. 132, pp. 170–187, 2017.
- [15] A. Lakshmi, P. Pandit, Y. Bhagwat, and G. Nayak, "A review on efficiency of polypropylene fiber-reinforced concrete," in *Sustainability Trends and Challenges in Civil Engineering: Select Proceedings of CTCS 2020*, pp. 799–812, 2022.
- [16] T. A. H. Ahmed and O. M. A. Daoud, "Influence of polypropylene fibres on concrete properties," *IOSR J. Mech. Civ. Eng.*, vol. 13, no. 05, pp. 09–20, 2016.
- [17] H. Hosseinzadeh, A. M. Salehi, M. Mehraein, and G. Asadollahfardi, "The effects of steel, polypropylene, and high-performance macro polypropylene fibers on mechanical properties and durability of high-strength concrete," *Construction and Building Materials*, vol. 386, art. no. 131589, 2023.
- [18] P. Smarzewski, "Fresh and mechanical properties of high-performance self-compacting concrete containing ground granulated blast furnace slag and polypropylene fibres," *Applied Sciences*, vol. 13, no. 3, art. no. 1975, 2023.



## Identifying the Main Predictors for Job Satisfaction of Construction Workers: Hierarchical Regression Approach

Gokhan Kazar<sup>\*1</sup>

<sup>1</sup>Department of Civil Engineering, Istanbul Medeniyet University, Istanbul, Türkiye

### Abstract

Worker productivity is one of the most important issues in construction projects. The productivity of construction workers is highly correlated with their job satisfaction. In this context, mental health status and work-related stressors are primary factors that play a key role in the satisfaction of construction workers. However, to the best of the author's knowledge, there is no detailed study that focuses on assessing the relationship between mental health disorders, work-related stressors and job satisfaction among construction workers. Therefore, the main objective of this study is to identify the most important mental health disorders and job-related factors affecting job satisfaction of construction workers. For this purpose, we conducted a survey among 186 Turkish construction workers and developed hierarchical regression models for mental health disorders and job-related stressors separately. The results of this study show that depression, which is one of the most common health disorders among workers, has a crucial and negative impact on the job satisfaction of construction workers. In addition, managerial factors among job-related stressors are primary predictors of construction workers' job satisfaction. Understanding these parameters allows construction professionals to manage construction workers based on their mental health status and work-related stressors. In particular, personalised mental health support should be provided to workers to understand their problems of low job satisfaction while working. It is generally emphasised that proper management of construction workers will increase worker productivity and prevent poor project performance in construction.

**Keywords:** Hierarchical regression model, Construction management, Worker productivity, Job satisfaction, Mental health

## 1 INTRODUCTION AND BACKGROUND

Labor productivity is a critical factor in determining the overall performance of construction projects. Hussain [1] explored the correlation between construction labor productivity and project performance, highlighting the need to understand this relationship. Mahamid [2] also found a strong relationship between labor productivity and rework in construction projects, indicating that productivity directly affects project quality and efficiency. Chowdhury [3] emphasized that top management support can increase worker motivation, productivity, efficiency, and work quality in construction projects, underscoring the importance of organizational factors and leadership support in improving worker productivity and project performance. Hashiguchi et al. [4] emphasized that addressing motivational factors can lead to sustainable improvements in project productivity. In addition, Enshassi et al. [5] pointed out that external factors such as noise levels can affect the productivity of construction projects, emphasizing the need to consider environmental issues related to worker productivity. In addition, Doloi [6] demonstrated that operational strategies and worker motivation significantly affect project performance, highlighting the critical role of worker motivation in achieving project success.

Worker productivity in the construction industry is significantly influenced by job satisfaction. Research by Hashiguchi et al. [4] shows that high job satisfaction among construction workers is associated with improved professional and technical skills related to construction machinery and specialized equipment, leading to increased productivity. Similarly, Salling et al. [7] identified job satisfaction as a key motivator for improving labor productivity in the construction context. Furthermore, studies such as Xie et al. [8] have shown that supporting the mental health and safety of construction workers can lead to positive well-being and job satisfaction, which ultimately contributes to higher levels of productivity. In addition, research by García [9] suggests that factors such as autonomy, accomplishment, recognition, and personal fulfillment are critical to increasing job satisfaction among workers in creative industries, which can be extrapolated to the construction sector. Furthermore, the study by Stefanovska-Petkovska et al. [10] explores the predictors of job satisfaction among construction workers and pointed out the influence of personal characteristics on job satisfaction. This highlights the importance of

understanding and addressing the factors that contribute to job satisfaction in order to increase productivity in the construction industry.

Job satisfaction, mental health disorders, and work stressors in the construction industry are highly interrelated factors that affect workers' well-being and performance. Several studies provide insight into these relationships. Job satisfaction plays a critical role in mediating the effects of stressors on mental health and work outcomes. Research by Li et al. [11] suggests that job satisfaction acts as a mediator between job stressors and workers' physical and mental health outcomes. Similarly, Chen & Fang [12] found that job satisfaction mediated the relationship between challenge stressors and job performance and between obstruction stressors and job performance. Furthermore, in a study by Ahmad et al. [13] job stress partially mediated the relationship between role conflict and job satisfaction. Mental health disorders have been shown to significantly affect job satisfaction and job tenure. Mohammad et al. [14] showed that several mental health disorders were strongly associated with lower job satisfaction and shorter job tenure. In addition, mental health disorders were found to be related to burnout, with occupational stressors and low job satisfaction playing a role in this relationship, as highlighted by Lu et al. [15]. Work stressors in the construction industry can have a detrimental effect on job satisfaction and mental health. Schaefer & Moos [16] found that relationship and workload stressors were associated with lower job satisfaction and higher work-related distress among long-term care workers. In addition, individual stressors such as poor diet, financial strain, and sleep disturbance were significantly negatively related to job satisfaction among emergency medical services personnel, as reported by Sedlár [17].

In conclusion, the relationship between job satisfaction, mental health disorders, and work stressors in construction is complex and intertwined. Job satisfaction acts as a mediator between stressors and various outcomes, while mental health disorders can impact job satisfaction and overall well-being. Addressing work stressors, promoting job satisfaction, and supporting mental health are essential in fostering a healthy and productive work environment in the construction industry [18]. However, such relationship between job satisfaction, mental health disorders and work stressors are still unclear in the construction industry. Therefore, the main objective of this study is to identify the most important mental health disorders and job-related factors affecting job satisfaction of construction workers. Also, the correlation between each factor was investigated in this study. By understanding these points, it is possible to provide healthier working environment and more satisfied construction workers.

## 2 RESEARCH METHODOLOGY AND RESULTS

To this end, we conducted a survey of 186 Turkish construction workers and developed hierarchical regression models for mental health disorders and work-related stressors separately. A hierarchical regression model, also known as a multilevel or nested model, is a type of regression analysis used when the data have a nested or hierarchical structure. This model takes into account the hierarchical structure of the data, allowing for more accurate estimates of the relationships between variables. Hierarchical models include random effects to account for variability at each level of the hierarchy. This allows the model to account for the fact that observations within the same group (e.g., students in the same classroom) are likely to be more similar to each other than to observations in other groups [19]. By including random effects, hierarchical models can provide more accurate and generalizable estimates of the relationships between variables. Hierarchical regression models, also known as multilevel or mixed effects models, offer several advantages, especially when dealing with complex data structures. By accounting for the hierarchical structure, these models provide more accurate and reliable parameter estimates. They can borrow power from the entire data set to improve estimates for groups with smaller sample sizes. Hierarchical models can partition variance into within-group and between-group components [20]. This helps to understand how much of the variability in the outcome is due to within-group differences versus between-group differences. Hierarchical models can also handle missing data more effectively by using information from other levels in the hierarchy, reducing bias and improving the robustness of results. Hierarchical models allow for the inclusion of predictors at different levels (e.g., individual-level and group-level predictors), providing a more complete understanding of the factors influencing the outcome [21]. Overall, hierarchical regression models provide a powerful framework for analyzing complex data sets with nested structures, leading to more nuanced insights and accurate inferences.

A face-to-face survey method was used for data collection at real construction sites. The survey measured four different parts; i) demographic information, ii) mental health disorder scales for depression, anxiety, and stress, iii) work stressors, and iv) job satisfaction. Each part included measurement items relevant to the administration of the survey. A total of 186 construction workers participated in this study. Among these construction workers, more than half are married (57.5%) and use tobacco (61.6%). While 47.8% of the construction workers live in apartments, the rest live in labor camps. 34.5% of construction workers have more than 15 years of experience in

the construction industry. 58.4% of the construction workers who participated in this study worked on construction projects.

In order to check the reliability of the collected data, we evaluated the Cronbach's alpha values for each factor. The results show that each latent variable is satisfied according to Cronbach's alpha ( $\alpha$ ), since each of them is higher than 0.8 (Table 1) [22]. According to the correlation analysis, depression is significantly correlated with stress and managerial stressors. Also, stress is highly correlated with organizational and working conditions stressors. The results of this study show that depression, which is one of the most common health disorders among workers, has a significant and negative impact on the job satisfaction of construction workers (Table 2). In addition, among job stressors, leadership factors are primary predictors of construction workers' job satisfaction (Table 3).

**Table 1.** Correlation analysis and Cronbach's Alpha ( $\alpha$ ) results

Factors	Depression	Anxiety	Stress	Managerial	Organizational	Project Related	Work Conditions	Cronbach Alpha ( $\alpha$ )
Depression	1	-0.058	<b>0.667</b>	<b>0.582</b>	0.106	0.124	0.091	0.881
Anxiety	-	1	-0.218	0.067	-0.149	-0.211	0.181	0.912
Stress	-	-	1	-0.102	<b>0.513</b>	0.109	<b>-0.644</b>	0.889
Managerial	-	-	-	1	-0.018	0.218	0.106	0.805
Organizational	-	-	-	-	1	<b>0.402</b>	0.245	0.834
Project-Related	-	-	-	-	-	1	0.138	0.824
Work conditions	-	-	-	-	-	-	1	0.901

**Table 2.** Hierarchical regression results for mental health disorders

Model	Independent Variable	B	SE	Beta	Sig.	VIF	R	R <sup>2</sup>	$\Delta$ R <sup>2</sup>	F Change	Sig. Change
1	Constant	1.078	0.027	-	0.000		0.332	0.114	0.114	14.215	<b>0.002</b>
	Depression	-0.058	0.011	-0.328	0.002	1.000					
2	Constant	1.015	0.029	-	0.000		0.402	0.162	0.048	3.518	0.237
	Depression	-0.072	0.031	-0.328	0.002	1.003					
	Anxiety	0.026	0.041	0.176	0.237	1.006					
3	Constant	1.013	0.043	-	0.000		0.406	0.165	0.003	0.041	0.561
	Depression	-0.075	0.021	-0.356	0.007	1.347					
	Anxiety	0.027	0.019	0.217	0.256	1.419					
	Stress	0.000	0.006	0.031	0.561	1.765					

**Table 3.** Hierarchical regression results for work-related stressors

Model	Independent Variable	B	SE	Beta	Sig.	VIF	R	R <sup>2</sup>	$\Delta$ R <sup>2</sup>	F Change	Sig. Change
1	Constant	0.883	0.025	-	0.000		0.008	0.000	0.000	0.011	0.827
	Organizational	0.021	0.035	0.018	0.929	1.000					
2	Constant	0.981	0.025	-	0.000		0.052	0.002	0.002	0.046	0.813
	Organizational	0.020	0.028	0.011	0.945	1.002					
	Work-Conditions	0.065	0.011	-0.052	0.694	1.002					
3	Constant	0.888	0.051	-	0.000		0.532	0.283	0.281	4.678	<b>0.041</b>
	Organizational	0.013	0.023	0.004	0.976	1.763					
	Work-Conditions	0.015	0.018	-0.022	0.745	1.623					
	Managerial	0.069	0.001	0.532	0.967	1.801					
4	Constant	2.446	3.471	-	0.527		0.054	0.005	0.284	0.512	0.712
	Organizational	0.054	0.005	0.036	0.825	1.429					
	Work-Conditions	0.061	0.038	-0.074	0.714	1.512					
	Managerial	0.072	0.004	0.561	0.878	1.224					
	Project-Related	0.031	0.061	-0.051	0.605	1.313					

### 3 DISCUSSION AND CONCLUSION

Depression has a significant impact on job satisfaction in various professions. Numerous studies have consistently shown that depression is correlated with lower levels of job satisfaction [23–25]. Symptoms of depression such as anhedonia, loss of interest, low self-esteem, and feelings of worthlessness are contributing factors to decreased job satisfaction [26]. In addition, elements such as job stress, leadership quality, and job demands are known to mediate the relationship between depression and job satisfaction [14, 16]. Depression and low job satisfaction can interact in both directions. Individuals with depression may experience reduced motivation, energy, and interest in their work, leading to lower job satisfaction. Conversely, low job satisfaction can contribute to feelings of stress, worthlessness, and hopelessness, which can exacerbate or even trigger depression. Poor work environments, such as high job demands, low control, lack of support, and poor working conditions, can contribute to low job satisfaction [27, 28]. These factors can also be stressors that lead to or exacerbate depression. Depression can negatively affect an individual's job performance, leading to conflict, unmet expectations, and negative feedback that further reduces job satisfaction. This negative cycle can perpetuate both depression and dissatisfaction. Depression is often associated with physical symptoms such as fatigue and sleep disturbances, which can make it difficult to perform well at work and enjoy work tasks, leading to lower job satisfaction. In addition, mental health issues such as anxiety and difficulty concentrating can also reduce job satisfaction. Depression can affect interpersonal relationships in the workplace [29, 30]. Depressed individuals may withdraw from colleagues, leading to a lack of social support and feelings of isolation, which can further reduce job satisfaction. Understanding this relationship underscores the importance of addressing both mental health and job satisfaction in the workplace to improve overall employee well-being and productivity. In summary, a body of research highlights the complex interplay between depression and job satisfaction. Depression not only leads to lower job satisfaction, but is also exacerbated by low job satisfaction [31]. Addressing factors that influence job satisfaction and fostering supportive work environments are critical to improving employees' mental well-being and overall job satisfaction.

Managerial factors are found that these parameters can have a significant impact on job satisfaction in the construction industry. Research by Kim & Cho [32] highlights that appropriate managerial intervention can reduce job stress and increase satisfaction for regular employees; however, it can have a negative effect on the satisfaction of irregular employees [32]. This suggests that the type of management approach used can influence how employees perceive their job satisfaction. In addition, the study by Voet & Walle [33] highlights that managerial autonomy plays a crucial role in determining job satisfaction, with higher autonomy being positively correlated with job satisfaction. Furthermore, the study by Bahsri & Zakaria [34] points out that organizational justice is a factor that can affect job satisfaction. This suggests that how fair employees perceive management decisions and actions within the organization can affect their overall satisfaction. Furthermore, research by Pirzadeh [27] indicates that both intrinsic and extrinsic aspects of the job play a role in determining overall job satisfaction, regardless of managerial status. This implies that the nature of the job itself, along with external factors influenced by managerial decisions, can collectively affect job satisfaction levels. In conclusion, managerial factors such as intervention approaches, autonomy, and organizational justice can have a significant impact on job satisfaction in the construction industry [32, 35]. Understanding and addressing these managerial aspects is critical to promoting a positive work environment and increasing job satisfaction among construction workers.

Understanding these parameters allows construction professionals to manage construction workers based on their mental health status and work-related stressors. In particular, personalised mental health support should be provided to workers to understand their problems of low job satisfaction while working. It is generally emphasised that proper management of construction workers will increase worker productivity and prevent poor project performance in construction. Reducing mental health disorders among construction workers requires a multi-faceted approach that addresses both the work environment and individual needs. Here are several strategies that can be implemented:

- Personalized training for construction workers should be provided based on their unique issues and conditions.
- Train supervisors and managers to recognize signs of mental health problems and respond with empathy and support.
- Implement programs that promote physical health, such as fitness programs, nutrition counselling, and regular health screenings.
- Develop and implement workplace policies that specifically address mental health and provide clear guidelines for support and intervention.



## Acknowledgments

The author would like to thank all the construction workers who took part in this study.

## References

- [1] S. Hussain, W. Xuetong, and T. Hussain, "Impact of skilled and unskilled labor on project performance using structural equation modeling approach," *SAGE Open*, 2020, doi: 10.1177/2158244020914590.
- [2] I. Mahamid, "Analysis of schedule deviations in road construction projects and the effects of project physical characteristics," *J. Financ. Manag. Prop. Constr.*, vol. 22, no. 2, pp. 192–210, 2017, doi: 10.1108/JFMPC-07-2016-0031.
- [3] M. M. Islam Chowdhury, K. B. Othman, M. A. Khan, and I. F. Sulaiman, "Role of Effective corporate governance and motivational leadership in increasing productivity and efficiency of human resources," *Glob. J. Manag. Bus. Res.*, 2020, doi: 10.34257/gjmbvol20is10pg29.
- [4] N. Hashiguchi *et al.*, "The effects of psychological factors on perceptions of productivity in construction sites in Japan by worker age," *Int. J. Environ. Res. Public Health*, 2020, doi: 10.3390/ijerph17103517.
- [5] A. Enshassi, E. Al-Swaity, A. R. Abdul Aziz, and R. Choudhry, "Coping behaviors to deal with stress and stressor consequences among construction professionals: A case study at the Gaza Strip, Palestine," *J. Financ. Manag. Prop. Constr.*, 2018, doi: 10.1108/JFMPC-12-2016-0057.
- [6] H. Doloi, "Twinning motivation, productivity and management strategy in construction projects," *EMJ - Eng. Manag. J.*, 2007, doi: 10.1080/10429247.2007.11431738.
- [7] S. T. Salling, C. T. Pérez, and S. Wandahl, "Perception of Project Management Among Construction Workers: A Survey in Denmark," in *Proceedings of the 31st Annual Conference of the International Group for Lean Construction (IGLC31)*, 2023, doi: 10.24928/2023/0124.
- [8] L. Xie, Z. Luo, and B. Xia, "Influence of psychosocial safety climate on construction workers' intent to stay, taking job satisfaction as the intermediary," *Eng. Constr. Archit. Manag.*, 2024, doi: 10.1108/ECAM-12-2021-1082.
- [9] M. del C. López-García, "Theoretical Construction of Job Satisfaction of Workers of Creative Industries in Mexico City," *J. Soc. Sci.*, 2021, doi: 10.3844/jssp.2021.14.18.
- [10] M. Stefanovska-Petkovska, M. Bojazdiev, V. K. Handjiski, and V. Trajkovska, "The 'blue-collar' motivation: Personal and work environment predictors of job satisfaction among construction workers," *Univers. J. Manag.*, 2017, doi: 10.13189/ujm.2017.050306.
- [11] Y. Li, F. Yang, W. Zhang, and Z. Zhang, "The mediating role of job satisfaction in the stressor–strain relationship among Chinese government employees," *Humanit. Soc. Sci. Commun.*, 2023, doi: 10.1057/s41599-023-02386-3.
- [12] S.-C. Fang and H.-L. Chen, "Job stressors and job performance: Modeling of moderating mediation effects of stress mindset," *Pressacademia*, 2019, doi: 10.17261/pressacademia.2019.1020.
- [13] J. Ahmad, S. Zahid, F. F. Wahid, and S. Ali, "Impact of role conflict and role ambiguity on job satisfaction the mediating effect of job stress and moderating effect of islamic work ethics," *Eur. J. Bus. Manag. Res.*, 2021, doi: 10.24018/ejbmr.2021.6.4.895.
- [14] S. Mohammad, M. Miguët, G. Rukh, H. B. Schiöth, and J. Mwinyi, "Job satisfaction and job tenure of people with mental health disorders: a UK Biobank cohort study," *Scand. J. Public Health*, 2023, doi: 10.1177/14034948221119639.
- [15] M. Lu *et al.*, "Do type A personality and neuroticism moderate the relationships of occupational stressors, job satisfaction and burnout among Chinese older nurses? A cross-sectional survey," *BMC Nurs.*, 2022, doi: 10.1186/s12912-022-00865-7.
- [16] J. A. Schaefer and R. H. Moos, "Effects of work stressors and work climate on long-term care staff's job morale and functioning," *Res. Nurs. Heal.*, 1996, doi: 10.1002/(SICI)1098-240X(199602)19:1<63::AID-NUR7>3.0.CO;2-J.
- [17] M. Sedlár, "Job stressors and job satisfaction in emergency medical services crew members in Slovakia," *Pomáhajúce Profesie*, 2021, doi: 10.17846/pp.2021.4.2.22-30.
- [18] P. E. D. Love, D. J. Edwards, and Z. Irani, "Work stress, support, and mental health in construction," *J. Constr. Eng. Manag.*, 2010, doi: 10.1061/(asce)co.1943-7862.0000165.
- [19] P. Bowen, P. Edwards, H. Lingard, and K. Cattell, "Workplace stress, stress effects, and coping mechanisms in the construction industry," *J. Constr. Eng. Manag.*, vol. 140, no. 3, pp. 1–15, 2014, doi: 10.1061/(asce)co.1943-7862.0000807.
- [20] S. A. Radmacher and D. J. Martin, "Identifying significant predictors of student evaluations of faculty through hierarchical regression analysis," *J. Psychol. Interdiscip. Appl.*, vol. 135, no. 3, pp. 259–268, 2001, doi: 10.1080/00223980109603696.
- [21] N. S. Haynes and P. E. D. Love, "Psychological adjustment and coping among construction project

- managers,” *Constr. Manag. Econ.*, vol. 22, no. 2, pp. 129–140, 2004, doi: 10.1080/0144619042000201330.
- [22] D. G. Altman and J. M. Bland, “Statistics notes: Cronbach’s alpha,” *BMJ*, 1996.
- [23] C. Wang, F. A. Mohd-Rahim, Y. Y. Chan, and H. Abdul-Rahman, “Fuzzy Mapping on Psychological Disorders in Construction Management,” *J. Constr. Eng. Manag.*, vol. 143, no. 2, 2017, doi: 10.1061/(asce)co.1943-7862.0001217.
- [24] I. Kamardeen and R. Y. Sunindijo, “Personal characteristics moderate work stress in construction professionals,” *J. Constr. Eng. Manag.*, 2017, doi: 10.1061/(asce)co.1943-7862.0001386.
- [25] R. R. Langdon and S. Sawang, “Construction workers’ well-being: What leads to depression, anxiety, and stress?,” *J. Constr. Eng. Manag.*, vol. 144, no. 2, 2018, doi: 10.1061/(asce)co.1943-7862.0001406.
- [26] B. Netterstrøm *et al.*, “The relation between work-related psychosocial factors and the development of depression,” *Epidemiologic Reviews*. 2008. doi: 10.1093/epirev/mxn004.
- [27] P. Pirzadeh, H. Lingard, and R. P. Zhang, “Job quality and construction workers’ mental health: Life course perspective,” *J. Constr. Eng. Manag.*, vol. 148, no. 12, pp. 1–13, 2022, doi: 10.1061/(asce)co.1943-7862.0002397.
- [28] M. D. Idrees, M. Hafeez, and J. Y. Kim, “Workers’ age and the impact of psychological factors on the perception of safety at construction sites,” *Sustain.*, 2017, doi: 10.3390/su9050745.
- [29] P. Chopra, “Mental health and the workplace: Issues for developing countries,” *International Journal of Mental Health Systems*. 2009. doi: 10.1186/1752-4458-3-4.
- [30] J. Horsfall, M. Cleary, G. E. Hunt, and G. Walter, “Psychosocial treatments for people with co-occurring severe mental illnesses and substance use disorders (dual diagnosis): A review of empirical evidence,” *Harvard Review of Psychiatry*, vol. 17, no. 1. pp. 24–34, 2009. doi: 10.1080/10673220902724599.
- [31] A. P. C. Chan, J. M. Nwaogu, and J. A. Naslund, “Mental ill-health risk factors in the construction industry: Systematic review,” *J. Constr. Eng. Manag.*, vol. 146, no. 3, 2020, doi: 10.1061/(asce)co.1943-7862.0001771.
- [32] K. W. Kim and Y. H. Cho, “The moderating effect of managerial roles on job stress and satisfaction by employees’ employment type,” *Int. J. Environ. Res. Public Health*, 2020, doi: 10.3390/ijerph17218259.
- [33] J. van der Voet and S. Van de Walle, “How cutbacks and job satisfaction are related: The role of top-level public managers’ autonomy,” *Rev. Public Pers. Adm.*, 2018, doi: 10.1177/0734371X15609409.
- [34] N. B. Bahsri and A. B. Zakaria, “Systematic literature review on the job satisfaction of employees in the logistics industry,” *Int. J. Ind. Manag.*, 2023, doi: 10.15282/ijim.17.1.2023.9174.
- [35] M. Leung, Y.-S. Chan, and P. Olomolaiye, “Impact of stress on the performance of construction project managers,” *J. Constr. Eng. Manag.*, vol. 134, no. 8, pp. 644–652, 2008, doi: 10.1061/(asce)0733-9364(2008)134:8(644).



## **A Comparative Study of Recycled Tire Chips, Jute Fiber, Polyester Fiber, Plastic Fiber Waste for Stabilizing Sand as Retaining Wall Backfill**

**Lina Zaidi<sup>\*1</sup>, Fatima Zohra Benamara<sup>1</sup>, Aya Zeltani<sup>1</sup>, Issam Mesbahi<sup>1</sup>, Atmane Zeghdi<sup>1</sup>**

<sup>1</sup>Laboratory of Civil and Hydraulic Engineering (LGCH), Department of Civil Engineering and Hydraulics, University May 8, 1945 Guelma, Guelma, Algeria

---

### **Abstract**

Waste is the product of all companies and industrial enterprises. The reduction and recycling of waste is justified first of all from an environmental and economic point of view. Indeed, this problem can be reduced by finding applications for recycled waste in the field of civil engineering and this as lightweight backfilling materials in geotechnical works and thus contribute to the preservation of natural resources. In this work, we modeled a mechanically stabilized earthen wall (MSE) in finite elements using the PLAXIS 2D software, the backfill of which is composed of a mixture of sand and different recycled waste at different percentages (tire chips, jute fiber, polyester fiber, Plastic fiber). The results obtained from this numerical study were compared and interpreted to confirm the effectiveness of the substitution of recycled waste for sand used as backfill adjacent to retaining structures.

**Keywords:** *Recycled waste, Retaining wall (MSE), Contiguous embankments, 2D PLAXIS, Stability*

---



## Thermal Deformation Model for Concrete Incorporating Silica Fume

Farid Bouziadi\*<sup>1</sup>, Touhami Tahenni<sup>2</sup>, Abdelkader Haddi<sup>3</sup>, Bensaid Boulekbache<sup>1</sup>,  
Mostefa Hamrat<sup>1</sup>

<sup>1</sup>Laboratory of Materials Sciences and Environment, Hassiba Benbouali University of Chlef, Algeria

<sup>2</sup>Laboratory of Acoustic and Civil Engineering, Djilali Bounaama University of Khemis Miliana, Khemis Miliana, Algeria

<sup>3</sup>Civil Engineering and Geo-Environment Laboratory, IMT Lille Douai, Univ. Lille, ULR 4515, Bethune, France

---

### Abstract

This study aims to propose a new approach to predict the thermal deformation behavior of building element at different temperature levels (20 °C, 50 °C, 80 °C), by using nonlinear finite element analysis. The new approach is based on the coupling between Burger's rheological model, two-phase composite material models and maturity concept. Burger's rheological model is employed to predict the thermal deformation. Furthermore, the maturity approach is employed to evaluate the mechanical properties of concrete. However, the thermal properties of concrete used in building element are estimated by two-phase composite material models. The obtained results show that increasing the temperature amplifies the rate and the magnitude of the thermal deformation and stress generated by thermal shrinkage.

**Keywords:** Concrete, Thermal deformation, Two-phase model, Maturity concept, Burger's rheological model

---



## Static Analysis of Sigmoid Functionally Graded Plates (S-FGM) by Using Higher Order Shear Deformation Plate Theory

Habib Hebali\*<sup>1</sup>

<sup>1</sup>Department of Civil Engineering, University of Mustapha Stambouli, Mascara, Algeria

---

### Abstract

This work presents a bending analysis of sigmoid functionally graded plates (S-FGM) by employing a four variable refined plate theory. This model uses only “four variables” and considers trigonometric variation of “transverse shear stress” which is even less than the first shear deformation theory (FSDT). Governing equations are obtained from the principle of minimum total potential energy. A Navier type analytical solution methodology is also presented for simply supported FG plates S-FGM which predicts accurate solution. Numerical results obtained by the present theory are compared with available solutions, from which it can be concluded that the proposed theory is accurate and simple in analyzing the static bending behavior of (S-FGM) plates.

**Keywords:** *Bending , Governing equations, Sigmoid functionally graded plate, Shear deformation theory*

---



## **Buckling response of Functionally Graded Plates Using a Novel Four Variable Refined Plate Theory**

**Habib Hebali<sup>\*1</sup>**

*<sup>1</sup>Department of Civil Engineering, University of Mustapha Stambouli, Mascara, Algeria*

---

### **Abstract**

This work presents a Buckling analysis of functionally graded plates by employing a four variable plate theory. The number of unknown functions involved is reduced to merely four, as against five in other shear deformation theories. The proposed theory does not require a shear correction factor such as the first order shear deformation theory (FSDT). Equations of motion are obtained by utilizing the principle of virtual displacements and solved via Navier's procedure, The convergence and the validations of the proposed theoretical numerical model are performed to demonstrate the efficacy of the model

**Keywords:** *Buckling, Shear correction factor, Governing equations, Navier's procedure*

---



## Using PET Plastic Flakes and Waste Tire Chips as Wall Backfill

Fatima Zohra Benamara<sup>\*1</sup>, Chiraz Kechkar<sup>1</sup>, Marwa Feligha<sup>1</sup>, Ghania Nigri<sup>1</sup>, Lina Zaidi<sup>2</sup>, Aya Zeltni<sup>3</sup>

<sup>1</sup>Civil and Hydraulic Engineering Department, 8 May 1945 Guelma University, Guelma, Algeria

<sup>2</sup>Civil Engineering and Hydraulic Department, 20 August 1955 University, Skikda, Algeria

<sup>3</sup>Laboratory of Civil Engineering and Hydraulic, 8 May 1945 Guelma University, Guelma, Algeria

---

### Abstract

Recycling waste in the civil engineering sector is one way to both protect natural resources and decrease the negative effects of waste on the environment. The purpose of this study is to evaluate the impact of use of recyclable materials as backfill in retaining walls, such as tire chips and plastic. A numerical study has been carried out by using PLAXIS 2D software version 8.6 to model three types of rigid retaining walls, namely: scale wall test, cantilever wall, and gravity wall. In addition, the backfills of those retaining walls are composed of two mixtures. The first is a mixture of sand and tire chips (TC) with different percentages (10%, 30%, 50%, and 70%). The second is a mixture of sand and PET plastic flakes at different percentages (12.5%, 22.5%, and 32.5%). The results obtained from this study confirmed that the use of PET plastic waste and tire chips waste mixed with sand in the backfills of rigid retaining walls contributes effectively to the reduction of horizontal and vertical displacements as well as the earth pressures behind the retaining walls, therefore improving the stability of the retaining walls.

**Keywords:** *Tire chips (TC), PET plastic flakes, Rigid retaining walls, Backfill, PLAXIS 8.6*

---



## Study of the Behavior of A Clay Embankment Reinforced with Recycled Waste

Aya Zeltani<sup>\*1</sup>, Fatima Zohra Benamara<sup>1</sup>, Marwa Feligha<sup>2</sup>, Lina Zaidi<sup>1</sup>

<sup>1</sup>Department of Civil and Hydraulic Engineering, University May 8, 1945, Laboratory of Civil and Hydraulic Engineering (LGCH), Guelma, Algeria

<sup>2</sup>Department of Civil, University August 20, 1955, Skikda, Algeria

---

### Abstract

Poor soils are soils that exhibit unfavourable geotechnical characteristics, such as low bearing capacity or high compressibility. These soils are often used in construction projects, which can lead to several risks. Additives used to treat and stabilize poor soils are often costly and can have a negative impact on the environment. In this regard, recycled waste can improve the geotechnical characteristics of poor soils, thereby increasing the stability of the embankment and reducing the risks of sliding and settling; thus, providing an interesting alternative to traditional additives. Similarly, they are less expensive and have a lower environmental impact considering the current waste management issue. Therefore, it is desirable to consider this solution, especially in the field of geotechnics. In this work, a numerical study using finite element method with Plaxis 2D software was conducted on a reduced model of point-loaded embankment, aiming to evaluate the effect of different types of recycled waste on the stability of an embankment. The embankment consisted of a mixture of clay and various types of recycled waste (fly ash, granulated blast furnace slag, plastic, rubber powder from tires, and eggshell powder), at different percentages. The analysis of the results allowed determining the effects of these on the behaviour of the treated soil and thus gaining a better understanding of the most effective waste. These results will allow considering integration perspectives in future construction projects.

**Keywords:** Clay, Embankment, Recycled waste, Stabilization, Plaxis 2D

---





## Improvement in Structural Analysis: Creation of a Rectangular Finite Element for Analyzing Membrane Structures

**Randa Bourenane\*<sup>1</sup>, Sifeddine Abderrahmani<sup>1</sup>, Abdulrahman Mutahar Al-Nadhari<sup>2</sup>**

<sup>1</sup>Department of Civil Engineering, Laboratory of Applied Civil Engineering (LGCA), University of Echahid Cheikh Larbi Tebessi, Tebessa, Algeria

<sup>2</sup>LARGHYDE Laboratory, Department of Civil Engineering and Hydraulics, Faculty of Sciences and Technology, University of Biskra, BP 145 RP, 07000, Biskra, Algeria

---

### Abstract

This paper introduces a novel rectangular finite element designed for examining membrane element characteristics through a strain-based method, featuring three important external degrees of freedom at every corner node. The analysis revealed that linear membrane strains exhibit superior convergence as compared to other components and the reference solution. Several numerical examples demonstrate that successful convergence can only be achieved with a restricted number of individual components.

**Keywords:** *Membrane element analysis, Finite element method, Strain-based approach, Convergence improvement, Rectangular finite element*

---



## Acid and Sulfate Resistance of Concrete Containing Recycled Aggregate: A Comprehensive Experimental Study

H. Alperen Bulut<sup>\*1</sup>

<sup>1</sup>Department of Civil Engineering, Erzincan Binali Yildirim University, Erzincan, Türkiye

### Abstract

The aim of this study is to comprehensively experimentally investigate the acid and sulfate resistance of concrete produced using recycled aggregates. For this purpose, recycled aggregates at the ratios of 0%, 10%, 25% and 50% by volume were used as fine and coarse aggregates in concrete production instead of natural aggregates. In order to determine the acid and sulfate resistance of concrete, the samples were kept in 5% H<sub>2</sub>SO<sub>4</sub> and Na<sub>2</sub>SO<sub>4</sub> solutions for 7 and 28 days, and then weight loss, compressive strength loss and visual evaluations were made. In addition, comparisons were made by not using recycled aggregate in control concretes. The highest weight losses as a result of acid attack were obtained in concrete produced using 50% recycled aggregate. While the compressive strength loss of the control concrete after 7 days (C/7) acid attack was 4.17%, this loss in the 50% recycled aggregate concrete (RA50/7) increased approximately 8 times and became 35.74%. As the acid exposure duration increased from 7 days to 28 days, compressive strength losses occurred at higher levels in all groups. There was no weight loss in all concretes after sulfate attack, instead there was a slight increase in weight. As the recycled aggregate ratio and the number of days increased, the compressive strength losses experienced by concretes after sulfate attack also increased. The damage conditions obtained as a result of visual evaluation of concrete with 50% recycled aggregate after acid attack and sulfate attack were parallel to other results. As a result of comprehensive experimental studies, it has been determined that the sulfate resistance of concrete produced with recycled aggregates is better than acid.

**Keywords:** Recycled aggregate, Recycled aggregate concrete, Acid attack, Sulfate attack

## 1 INTRODUCTION

The estimated production amount of concrete, which is the most used building material in the world and is produced approximately 4 billion tons annually, is expected to exceed 5 billion tons in 2050 [1]. Aggregates, which make up approximately 80% of the concrete volume, are used in production as an alternative aggregate as a result of the recycling of concrete waste, also called construction and demolition waste [2–5]. Compared to normal concrete aggregate, the high porosity and water absorption properties of recycled aggregates negatively affect concrete performance [6–8]. In addition, recycled aggregates, which have a negative effect on the strength and durability properties of concrete, are thought to be the reasons for this effect, especially the porosity of the old mortar and the weaknesses in the interfacial transition zone [9–11]. For example, it has been reported that the chloride ion permeability values of recycled aggregate concretes are approximately 80% higher than natural aggregate concretes due to the weaknesses arising from the interfacial transition zone [12].

The aim of this study is to comprehensively experimentally investigate the acid and sulfate resistance of concrete produced using recycled aggregates. For this purpose, recycled aggregates at the ratios of 0%, 10%, 25% and 50% by volume were used as fine and coarse aggregates in concrete production instead of natural aggregates. In order to determine the acid and sulfate resistance of concrete, the samples were kept in 5% H<sub>2</sub>SO<sub>4</sub> and Na<sub>2</sub>SO<sub>4</sub> solutions for 7 and 28 days, and then weight loss, compressive strength loss and visual evaluations were made. In addition, comparisons were made by not using recycled aggregate in control concretes. It is thought that the results obtained as a result of examining the effect of aggressive solutions on concrete depending on the recycled aggregate ratios and the number of days will be considered valuable and original in terms of contributing to the literature.

## 2 MATERIAL AND METHOD

CEM I 42.5 R type Portland cement was used in the production of recycled aggregate concretes and control concretes. Technical information about this cement is given in Table 1. The specific gravity of the natural aggregates that make up the control concrete and the recycled aggregates used in various proportions are 2.46 g/cm<sup>3</sup> and 2.31 g/cm<sup>3</sup>, respectively, for fine aggregate and 2.66 g/cm<sup>3</sup> and 2.40 g/cm<sup>3</sup>, respectively, for coarse aggregate. Recycled aggregates at ratios of 0%, 10%, 25% and 50% by volume were used in concrete instead of natural aggregates. No recycled aggregate was included in the control concretes.

**Table 1.** Technical information about cement

<b>CEM I 42.5 R</b>	
<b>Chemical Compositions (%)</b>	
SiO <sub>2</sub>	19.27
Al <sub>2</sub> O <sub>3</sub>	4.29
Fe <sub>2</sub> O <sub>3</sub>	3.26
CaO	63.45
MgO	2.38
SO <sub>3</sub>	2.90
Na <sub>2</sub> O	0.30
K <sub>2</sub> O	0.71
Cl <sup>-</sup>	0.01
Loss on ignition	2.72
Insoluble residue	0.71
<b>Physical Characteristics</b>	
Residue on a 32 micron sieve	7.26
Specific gravity	3.10
Specific surface (cm <sup>2</sup> /g)	3430
Beginning of setting	2hrs-30min
End of setting	3hrs-29min
Volume expansion (mm)	1.0
<b>Compressive strength (MPa)</b>	
2nd day	28.6
28th day	54.1

In the coding, the English abbreviations of the recycled aggregates are indicated with the first letters, the ratios are indicated with the numbers after the letters, without using the (%) sign, and the experimental days are indicated with the numbers after the '/' sign. For example, RA25/28 represents concrete with 25% recycled aggregate and indicates that the test day is day 28. Control concretes are represented by the letter C. The concrete mix design used in concrete production is given in Table 2 without specifying the test days.

**Table 2.** Concrete mix design (kg/m<sup>3</sup>)

Code	Recycled fine aggregate	Recycled coarse aggregate	Natural fine aggregate	Natural coarse aggregate	Cement	Water	Superplasticizer (%)
C	-	-	875.44	769.36	450	202.5	1.1
RA10	81.61	69.37	787.90	692.42	450	202.5	1.17
RA25	204.02	173.43	656.58	577.02	450	202.5	1.24
RA50	408.05	346.86	437.72	384.68	450	202.5	1.42

Acid and sulfate attack tests were performed on cube samples (100x100x100 mm) according to ASTM C 267 [13] and ASTM C 1012 [14] standards. After the samples were kept in 5% H<sub>2</sub>SO<sub>4</sub> and Na<sub>2</sub>SO<sub>4</sub> solutions for 7 and 28 days, weight loss, compressive strength loss and visual evaluations were performed.

### 3 RESULTS

#### 3.1 Weight Loss of Recycled Aggregate Concretes After Acid Attack

The weight losses of concrete produced using different recycled aggregates exposed to acid attack for 7 and 28 days are given in Figure 1. While the 7-day weight loss of control concretes and concretes with 10% and 25% recycled aggregate was almost the same, increasing the recycled aggregate ratio to 50% brought about a weight loss almost 2 times higher. The 28-day acid exposure results were similar among all groups. The highest weight loss results for all days occurred in concrete produced using 50% recycled aggregate.

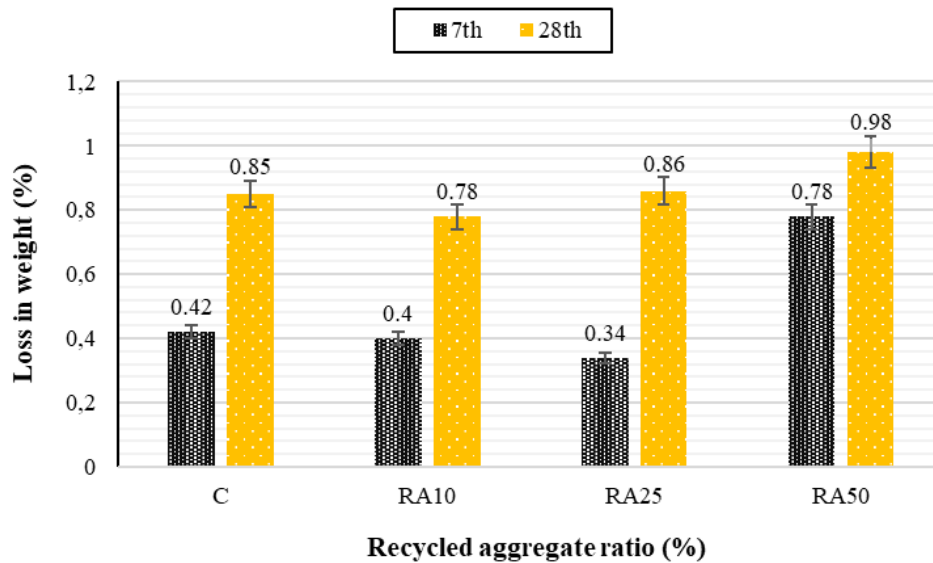


Figure 1. Loss in weight of recycled aggregate concretes after acid attack

#### 3.2 Compressive Strength Loss of Recycled Aggregate Concretes After Acid Attack

7 and 28-day compressive strength losses of concrete groups were calculated according to TS EN 12390-3 [15] standard by taking the percentage of strength results obtained before and after acid and sulfate attack. Strength results are given in Table 3.

Table 3. Compressive strength results of concrete before acid and sulfate attack

Code	7-day compressive strength (MPa)	28-day compressive strength (MPa)
C	34.80	45.25
RA10	32.21	42.8
RA25	27.67	36.17
RA50	25.45	32.39

Based on Table 3, the compressive strength losses of concrete after acid exposure are shown in Figure 2. Accordingly, as the recycled aggregate ratio increased, compressive strength losses increased. For example, while the 7-day (C/7) compressive strength loss of control concrete was 4.17%, this loss in 50% recycled aggregate concrete (RA50/7) increased approximately 8 times and became 35.74%. As the acid exposure duration increased from 7 days to 28 days, compressive strength losses occurred at higher levels in all groups. Just like the weight loss results, the highest ratios of compressive strength losses were seen in concrete with 50% recycled aggregate.

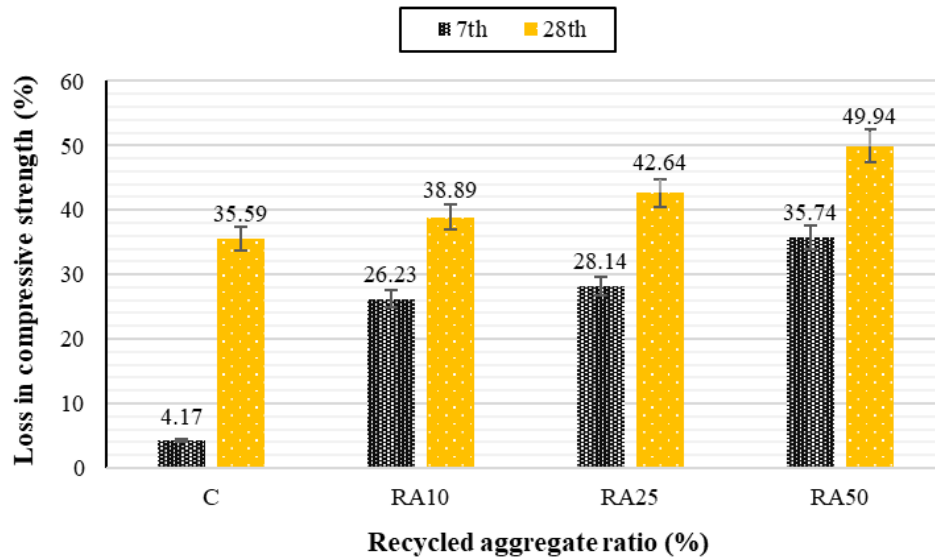


Figure 2. Loss in compressive strength of recycled aggregate concretes after acid attack

### 3.3 Weight Loss of Recycled Aggregate Concretes After Sulfate Attack

The weight loss results of concrete exposed to sulfate attack for 7 and 28 days are given in Figure 3. There was no weight loss after the sulfate attack in all concrete groups, instead there was a slight increase in weight. For example, the weight increase of concrete with 10% recycled aggregate after 7 and 28 days of sulfate attack was 0.97% and 0.85%, respectively. A similar trend was experienced at similar values in all groups.

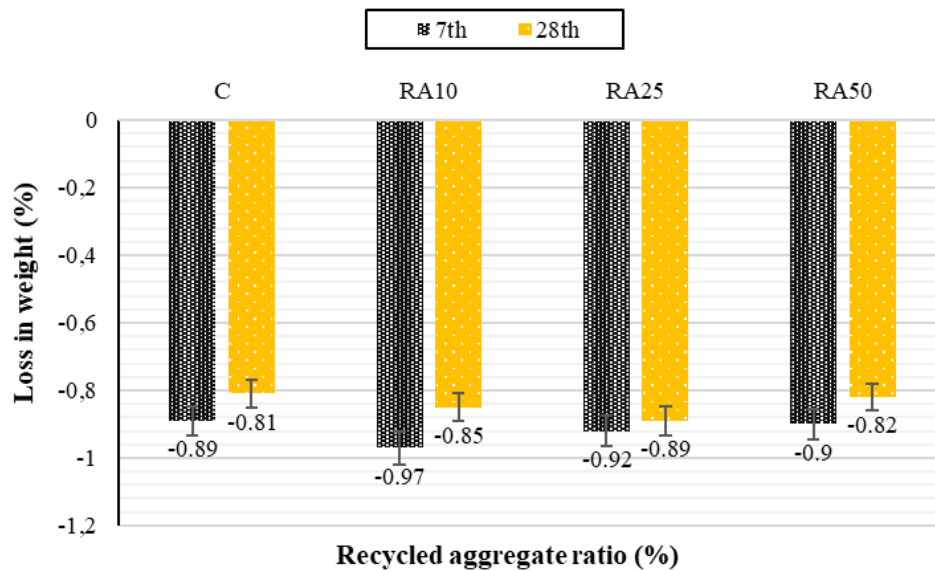
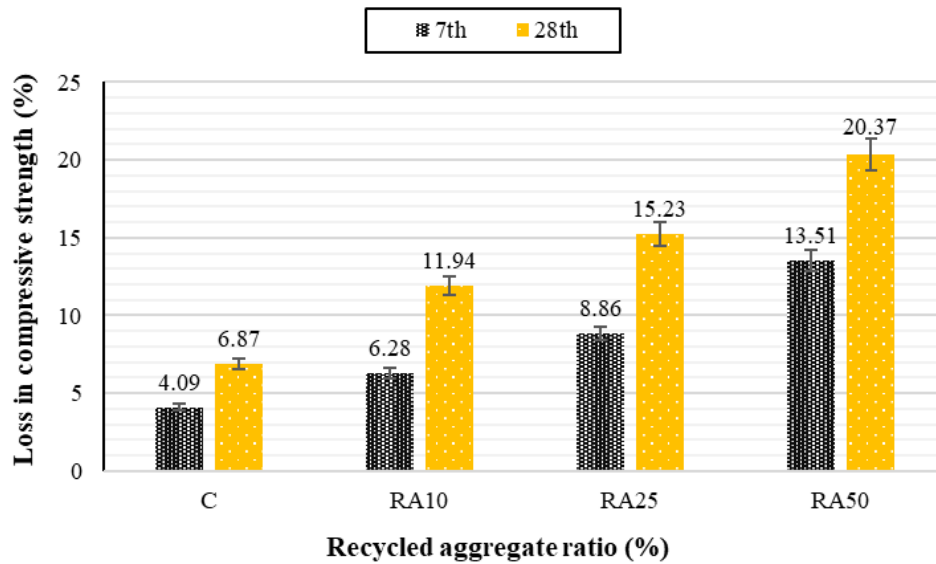


Figure 3. Loss in weight of recycled aggregate concretes after sulfate attack

### 3.4 Compressive Strength of Recycled Aggregate Concretes After Sulfate Attack

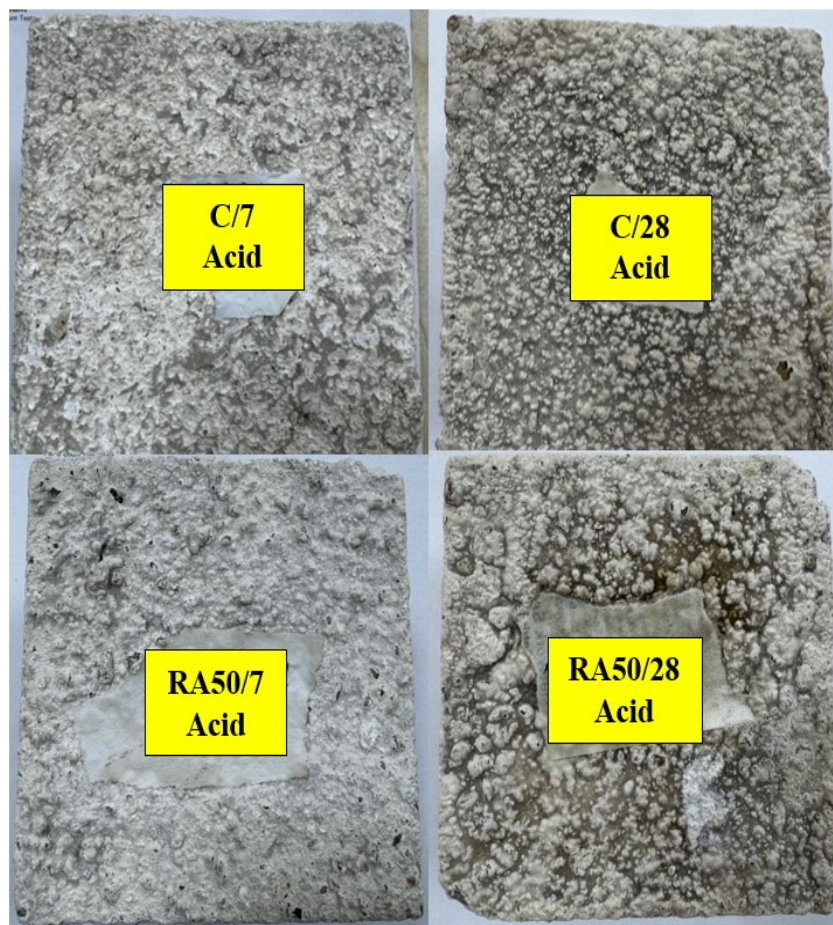
In Figure 4, the compressive strength losses experienced by concrete after sulfate attack are given in line with Table 3. As can be seen clearly in Figure 4, as the recycled aggregate ratio and the number of days increased, the compressive strength losses experienced by the concrete after sulfate attack also increased. For example, while the compressive strength losses of the control concrete after 7 and 28 days of sulfate exposure were 4.09% and 6.87%, respectively, these losses increased in the concrete produced with 25% recycled aggregate, reaching 8.86% and 15.23%, respectively.



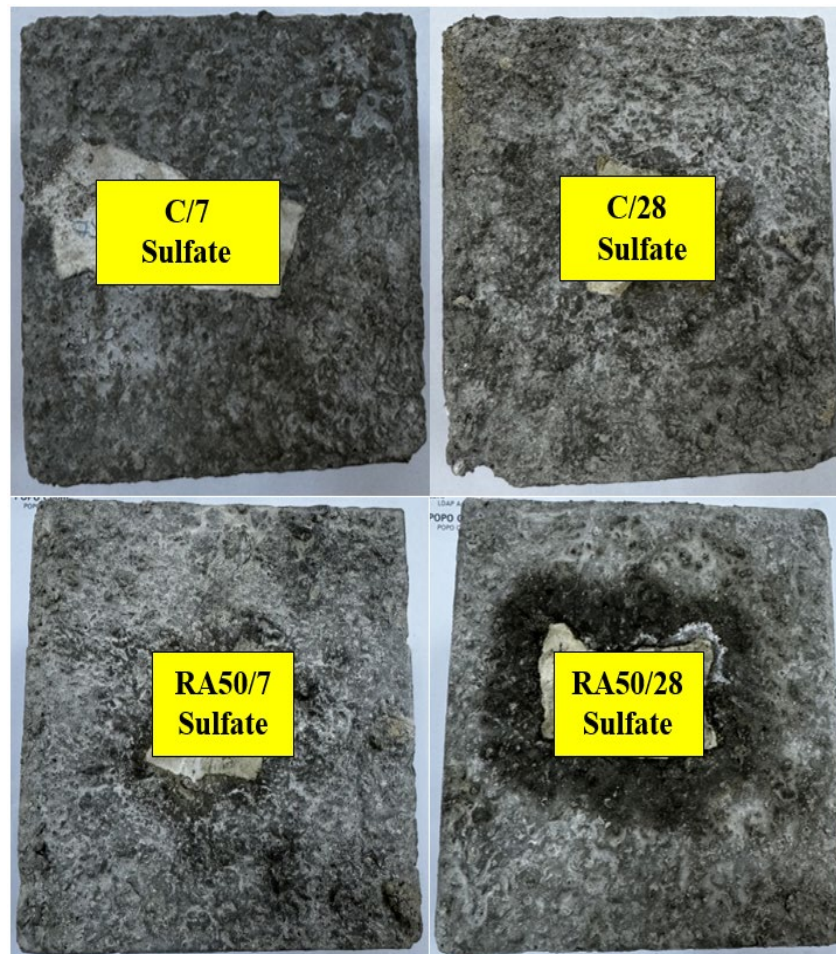
**Figure 4.** Loss in compressive strength of recycled aggregate concretes after sulfate attack

### 3.5 Visual Evaluation Results of Concretes After Acid And Sulfate Attack

Images of control and 50% recycled aggregate concretes exposed to acid and sulfate for 7 and 28 days are given in Figure 5. Accordingly, in Figure 5 (a), as acid exposure increases from 7 to 28 days, damages such as flaking, peeling, disintegration, crumbling, and deterioration of dimensional stability on the surfaces of concrete are clearly seen. In Figure 5 (b), the damages (scour, deterioration, capping, etc.) on the surfaces of concrete with 50% recycled aggregate, especially after 28 days, after sulfate exposure are clearly observed. The visual evaluation results were parallel to the weight and compressive strength losses after acid and sulfate attack.



(a)



(b)

**Figure 5.** Images of concretes exposed to acid and sulfate attack for 7 and 28 days

## 4 CONCLUSION

The results obtained from the study are given below.

- The highest weight losses as a result of acid attack were obtained in concrete produced using 50% recycled aggregate.
- While the compressive strength loss of the control concrete after 7 days (C/7) acid attack was 4.17%, this loss in the 50% recycled aggregate concrete (RA50/7) increased approximately 8 times and became 35.74%. As the acid exposure duration increased from 7 days to 28 days, compressive strength losses occurred at higher levels in all groups.
- There was no weight loss after the sulfate attack in all concrete groups, instead there was a slight increase in weight.
- As the recycled aggregate ratio and the number of days increased, the compressive strength losses experienced by concretes after sulfate attack also increased.
- The damage conditions obtained as a result of visual evaluation of concrete with 50% recycled aggregate after acid and sulfate attack were parallel to other results.
- As a result of comprehensive experimental studies, it has been determined that the sulfate resistance of concrete produced with recycled aggregates is better than acid.

## References

- [1] W. Thae, M. Iwanami, K. Nakayama, and W. Yodsudjai, "Influence of acetic acid treatment on microstructure of interfacial transition zone and performance of recycled aggregate concrete," *Construction and Building Materials*, vol. 417, art. no. 135355, Feb. 2024.
- [2] H. Yuan and L. Shen, "Trend of the research on construction and demolition waste management," *Waste*

- Management*, vol. 31, no. 4, pp. 670–679, Apr. 2011.
- [3] A. Akhtar and A. K. Sarmah, “Construction and demolition waste generation and properties of recycled aggregate concrete: A global perspective,” *Journal of Cleaner Production*, vol. 186, pp. 262–281, Jun. 2018.
  - [4] Y. Zhang, W. Luo, J. Wang, Y. Wang, Y. Xu, and J. Xiao, “A review of life cycle assessment of recycled aggregate concrete,” *Construction and Building Materials*, vol. 209, pp. 115–125, Jun. 2019.
  - [5] L. Lin, J. Xu, J. Yuan, and Y. Yu, “Compressive strength and elastic modulus of RBAC: An analysis of existing data and an artificial intelligence based prediction,” *Case Studies in Construction Materials*, vol. 18, art. no. e02184, Jul. 2023.
  - [6] C.S Poon, Z.H Shui, and L Lam, “Effect of microstructure of ITZ on compressive strength of concrete prepared with recycled aggregates,” *Construction and Building Materials*, vol. 18, no. 6, pp. 461–468, Jul. 2004.
  - [7] J. Xiao, J. Li, and Ch. Zhang, “Mechanical properties of recycled aggregate concrete under uniaxial loading,” *Cement and Concrete Research*, vol. 35, no. 6, pp. 1187–1194, Jun. 2005.
  - [8] M. S. D. Juan and P. A. Gutiérrez, “Study on the influence of attached mortar content on the properties of recycled concrete aggregate,” *Construction and Building Materials*, vol. 23, no. 2, pp. 872–877, Feb. 2009.
  - [9] H. Guo, C. Shi, X. Guan, J. Zhu, Y. Ding, T. Ling, H. Zhang, and Y. Wang, “Durability of recycled aggregate concrete – A review,” *Cement and Concrete Composites*, vol. 89, pp. 251–259, May 2018.
  - [10] S. Pradhan, S. Kumar, and S. V. Barai, “Multi-scale characterisation of recycled aggregate concrete and prediction of its performance,” *Cement and Concrete Composites*, vol. 106, art. no. 103480, Feb. 2020.
  - [11] R. Wang, N. Yu, and Y. Li, “Methods for improving the microstructure of recycled concrete aggregate: A review,” *Construction and Building Materials*, vol. 242, art. no. 118164, May. 2020.
  - [12] S. M. S. Kazmi, M. J. Munir, Y. Wu, I. Patnaikuni, Y. Zhou, and F. Xing, “Effect of recycled aggregate treatment techniques on the durability of concrete: A comparative evaluation,” vol. 264, art. no. 120284, Dec. 2020.
  - [13] ASTM C 267 Standard Test Methods for Chemical Resistance of Mortars, Grouts, and Monolithic Surfacing and Polymer Concretes. ASTM International, West Conshohocken, PA, USA, 2020.
  - [14] ASTM C 1012 Standard Test Method for Length Change of Hydraulic-Cement Mortars Exposed to A Sulfate Solution. ASTM International, West Conshohocken, PA, USA, 2019.
  - [15] TS EN 12390-3, Testing Hardened Concrete Part 3: Compressive Strength of Test Specimens, Turkish Standards Institution, Ankara, Turkey, 2019 (Turkish Codes).





## Effect of Granite Waste on Concrete Performance

Ramdane Rihab<sup>\*1</sup>, Kherraf Leila<sup>2</sup>

<sup>1</sup>Materials and Durability of Constructions Laboratory, Department of Civil Engineering, University of Mentouri, Constantine, Algeria

<sup>2</sup>Materials Geotechnics Habitat and Urban Laboratory, Department of Civil Engineering, University of 20 Aou t 1955, Skikda, Algeria

---

### Abstract

Nowadays, the valorization of industrial waste and the search for new construction materials are major concerns for many countries around the world. The rapid growth of urbanization and industrialization has led to a significant increase in waste production, sparking growing interest in sustainable management and efficient utilization of these wastes.

Our work falls within this same concept and aims to valorize granite waste generated during its use in construction or other fields. Granite is a hard, magmatic stone with many qualities (high load resistance, impermeability, and longevity). It is often used for paving stones, curbs, slabs, etc. The cutting process of these elements produces inert debris (fragments).

The main objective of this investigation is to study the influence of substituting natural gravel with gravel derived from granite waste on the properties of concrete. To achieve this, granite waste in the form of gravel was introduced into the formulation of hydraulic concrete with varying percentages (0%, 20%, and 40%). The influence of this partial substitution on the characteristics of fresh concrete (density, slump) and its hardened state performance (compressive strength, tensile strength) was then studied.

The results obtained show that using up to 40% granite waste gravel as a mass substitution for natural gravel in concrete is a promising way to valorize this waste in hydraulic concrete formulations.

**Keywords:** Valorization, Granite, Waste, Concrete, Characteristics

---



---

## Numerical Study of the Seismic Bearing Capacity of Offshore Skirted Foundations on Sand Using Finite Element Limit Analysis

**Alaoua Bouaicha<sup>\*1,2</sup>, Abdeldjalil Chamekh<sup>3</sup>, Nour El Islam Boumekik<sup>2</sup>, Abdelhak Mabrouki<sup>2</sup>**

<sup>1</sup>Scientific and Technical Research Center on Arid Regions (CRSTRA), Campus of Mohamed Khider University, BP 1682 RP, 07000 Biskra, Algeria

<sup>2</sup>Civil Engineering Research Laboratory (LRGC), Mohamed Khider University, BP 145 RP, 07000 Biskra, Algeria

<sup>3</sup>Civil Engineering Department, Faculty of Technology, Ferhat Abbas Setif 1 University, Setif 19000, Algeria

---

### Abstract

In the realm of offshore infrastructures, skirted foundations emerge as a promising technical solution, effectively optimizing bearing capacity while efficiently controlling settlements. This paper employs the Finite Element Limit Analysis (FELA) to comprehensively study the bearing capacity of a strip skirted foundation situated on sand, all within a seismic context by leveraging the pseudo-static approach. Key parameters are meticulously examined: the depth of the skirt ( $D_s$ ), the intrinsic friction angle of the sand ( $\phi$ ), and the horizontal seismic coefficient ( $k_h$ ). Our conclusions, drawn from rigorous numerical analyses, demonstrate the efficiency and resilience of a strip skirted foundation on sand, highlighting the ramifications of seismic loading. We quantify these observations using the Bearing Capacity Ratio ( $BCR$ ), revealing a notable enhancement in  $BCR$  with the integration of vertical skirts. Moreover, our study indicates that fluctuations in  $k_h$  and  $D_s$  significantly impact the  $BCR$ . To contextualize our results, we juxtapose our results with prior studies available in the scientific corpus.

**Keywords:** Bearing capacity, Limit analysis, Pseudo-static approach, Sand, Skirted footing

---



---

## Numerical Analysis of the Seismic Bearing Capacity of Strip Footings Near a Frictional Soil Slope

Abdeldjalil Chamekh<sup>\*1</sup>, Alaoua Bouaicha<sup>2,3</sup>, Abderraouf Messai<sup>1</sup>

<sup>1</sup>Civil Engineering Department, Faculty of Technology, Ferhat Abbas Setif 1 University, Setif 19000, Algeria

<sup>2</sup>Scientific and Technical Research Center on Arid Regions (CRSTRA), Campus of Mohamed Khider University, BP 1682 RP, 07000 Biskra, Algeria

<sup>3</sup>Civil Engineering Research Laboratory (LRGC), Mohamed Khider University, BP 145 RP, 07000 Biskra, Algeria

---

### Abstract

Strip footings near slopes present unique challenges in civil engineering, especially under seismic loads. This paper evaluates the seismic bearing capacity of strip footings located at the edge of a slope using the pseudo-static approach with the Optum<sup>G2</sup> software, applying the limit analysis method. The parameters analyzed include soil friction angle ( $\phi$ ), horizontal acceleration ( $k_h$ ), slope angle ( $\beta$ ), and normalized distance ( $L/B$ ). The results show that increasing  $k_h$  significantly reduces the seismic bearing capacity factor ( $N_{\gamma E}$ ), particularly pronounced for steep slopes and soils with a high friction angle. Increasing  $L/B$  mitigates this reduction, improving  $N_{\gamma E}$  according to different configurations. The identified failure mechanisms include face, toe, base, and Prandtl-type failures, influenced by  $\beta$ ,  $k_h$ ,  $\phi$ , and  $L/B$ . The comparison of results with theoretical solutions and literature data shows good agreement.

**Keywords:** *Seismic bearing capacity, Strip footings, Slope, Pseudo-static approach, Soil friction angle, Horizontal acceleration, Limit analysis*

---



## 3D Failure Envelopes of Strip Footings on Sand over Non-Homogeneous Clay Using Limit Analysis Method

Alaoua Bouaicha<sup>\*1,2</sup>

<sup>1</sup>Scientific and Technical Research Center on Arid Regions (CRSTRA), Campus of Mohamed Khider University, BP 1682 RP, 07000 Biskra, Algeria

<sup>2</sup>Civil Engineering Research Laboratory (LRGC), Mohamed Khider University, BP 145 RP, 07000 Biskra, Algeria

---

### Abstract

This study employs finite element limit analysis to evaluate the bearing capacity of rough strip footings on sand overlying non-homogeneous clay under combined loading. By utilizing adaptive meshing techniques, the precision of the bearing capacity factors is significantly enhanced. The investigation focuses on several key parameters, including the thickness of the sand layer, the non-homogeneity of the clay's strength, and the nature of the eccentric-inclined loads. The probe loading methods is utilized to construct detailed 3D failure envelopes and identify failure mechanisms under vertical, horizontal, and moment loads.

The results reveal how variations in the sand layer's thickness and the clay's non-homogeneous properties influence the bearing capacity and failure modes. Additionally, the study delineates the complex interaction between vertical, horizontal, and moment loads in shaping the failure envelopes. New insights are provided into the failure mechanisms and 3D failure envelopes, particularly highlighting the significant impact of non-homogeneous clay characteristics. These findings contribute valuable information to the field of geotechnical engineering, offering a more nuanced understanding of foundation behavior under combined loading conditions and improving the design and analysis of strip footings in layered soil systems.

**Keywords:** Failure envelopes, Bearing capacity, Strip footing, Limit analysis, Sand, Clay, Non-homogeneous

---



## Prediction of the Maximum Shear Strength of Fiber-Reinforced Soils Using Artificial Intelligence

Leyla Bouaricha<sup>\*1</sup>, Yasmine Mohamed Bouteben<sup>2</sup>, Azeddine Chehat<sup>1</sup>, Ahmed Djafar Henni<sup>3</sup>

<sup>1</sup>Department of Civil Engineering and Architecture, University of Khemis Miliana 44225, Algeria

<sup>2</sup>University Freres Mentouri - Constantine 1, Constantine, 25017, Algeria

<sup>3</sup>Laboratory of Structures, Geotechnic and Risks (LSGR), University of Hassiba BenBouali Chlef, Algeria

---

### Abstract

Fiber reinforcement is a widely used technique in geotechnical engineering to enhance the mechanical properties of soils. This study focuses on predicting the shear strength properties of fiber-reinforced soils (FRS) using advanced artificial intelligence (AI) models. The objective of the research is to validate the accuracy and reliability of these AI models in predicting the maximum shear strength of FRS, considering the complex interactions between soil and fibers.

The study compiles high-quality data from laboratory tests conducted on FRS between 1983 and 2019. Parameters such as soil type, fiber type, fiber content, and stress conditions are considered. AI techniques, including artificial neural networks (ANN), are used to develop predictive models for the shear strength properties of FRS. The AI models are validated using the compiled database, and their accuracy is compared to traditional theoretical and empirical models. The results demonstrate the effectiveness of AI models in predicting the shear strength properties of FRS, providing engineers with reliable tools for designing geotechnical structures involving FRS.

In conclusion, this study highlights the potential of AI models in predicting the shear strength properties of FRS, offering a promising alternative to traditional models and contributing to advancements in geotechnical engineering.

**Keywords:** *Fiber reinforcement, Shear strength, Artificial intelligence, Prediction*

---



## Implementation of Five-Noded Mapped Infinite Element to OpenSees

Sefa Uzun<sup>\*1</sup>, Yusuf Ayvaz<sup>2</sup>

<sup>1</sup>Civil Engineering Department, Kutahya Dumlupinar University, Kutahya, Türkiye

<sup>2</sup>Civil Engineering Department, Yildiz Technical University, Istanbul, Türkiye

### Abstract

The formulation and implementation of a five-noded mapped infinite element for modelling unbounded domains are presented. In classical quadrilateral elements, the same shape functions are used to discretize both coordinates and displacements. However, in the five-noded mapped infinite element, different shape functions are required for these tasks. The coordinates are discretized using coordinate ascent formulation, while Lagrange polynomials are used for displacements. This element is a quadrilateral with one side extending to infinity and the others remaining finite. Different shape functions are applied for the finite and infinite directions. The stiffness matrix for this element is derived using the standard finite element procedure, with Gauss-Legendre integration employed for its evaluation. The implementation is done in C++ within the OpenSees framework. The proposed infinite element yields accurate results when compared with analytical results from the literature. It proves to be very effective for modelling unbounded domains, demonstrating significant advantages in computation time and memory management compared to using an enlarged domain.

**Keywords:** *Mapped infinite element, Finite element method, Infinite domain, Coordinate ascent formulation*

## 1 INTRODUCTION

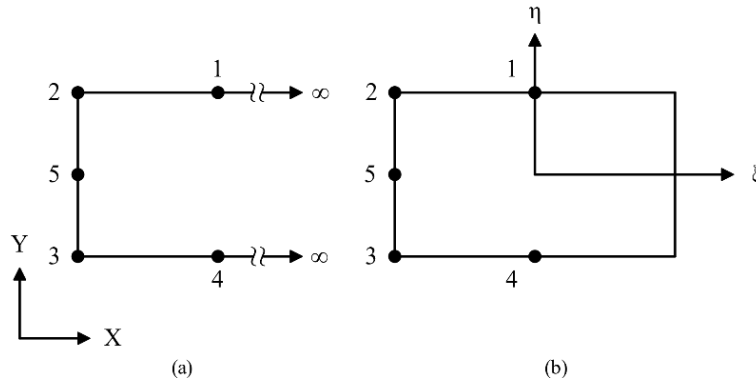
The modelling of an infinite domain often occurs in the simulation of physical applications, the stress field around a circular hole in a solid material being a typical example. However, solving a physical field on an infinite domain is numerically infeasible for volume discretisation methods such as the finite element method. Therefore, different computational methods have been developed to reduce the computational effort by truncating the domain, e.g. the boundary element method. Infinite element is one of these methods.

Beer and Meek [1] introduced a parametric infinite element that permits for modelling of infinite type problems economically. They investigated the holes opened with different shapes in the infinite medium. Kumar [2] developed an advanced infinite element with different forms of decay function. He used the displacement descent and the coordinate ascent formulation in derived the advanced infinite elements. Buchanan and Sallah [3] introduced two different concepts for infinite element. First, they modify the numerical integration scheme. Second, they modify the material matrix. Davies and Bu [4] introduced an efficient infinite element for analysis of half-space problems. They developed a decay function for stress analysis based on the theoretical displacement attenuation away from the source loading. Abd El Fattah et al. [5] developed a new infinite element. The coordinate ascent mapping formulation is used to develop the new infinite element. The reciprocal, exponential, and logarithmic decay functions are considered in the formulation of the infinite element. Houmat [6] introduced a new coordinate ascent hierarchical infinite element. Finite side of the infinite element has an arbitrary number of cubic-order quadrilateral finite element. The highlight points at the proposed infinite element are simplicity of mapping and the holding of standard integration points. Erkal et al. [7] presented an infinite element which is the ease of application and computational efficiency for modelling the unbounded domain. They introduce a comprehensive coordinate and field variable mapping functions for one-dimensional and two-dimensional infinite elements. Liu et al. [8] developed a computer program which analyzes the response of asphalt pavement structures under static loading. Thomas et al. [9] introduced formulation of bi-quadratic infinite element. The element stiffness matrix is computed using two-point Gauss quadrature based on the defined mapping function and standard shape function. Haji et al. [10] presented a comprehensive infinite element formulation. The proposed infinite element reproduced the far-field boundary effect using only one layer of infinite element.

The purpose of this study is to implement the five-noded mapped infinite element to OpenSees [11]. OpenSees is a powerful open-source structural analysis software package. It was written in C++ programming language using object-oriented programming technique.

## 2 5-NODED MAPPED INFINITE ELEMENT

Coordinates and displacements are discretized different functions in the formulation of the five-noded mapped infinite element. Mapping functions is used to discretize coordinates of the five-noded mapped infinite element. Coordinate ascent formulation is used to create the mapping functions of the five-noded mapped infinite element. The generation of the mapping functions of the five-noded mapped infinite element is explained in detail in [9, 12, 13]. Global and local representation of five-noded mapped infinite element are illustrated in Figure 1. As seen from Figure 1, the five-noded mapped infinite element is finite in the local  $\eta$  direction. And the five-noded mapped infinite element extends to infinity in the local  $\xi$  direction. The mapping functions of the five-noded mapped infinite element are given in the (1)-(5).



**Figure 1.** (a) Global and (b) local representation of five-noded infinite element

$$M_1(\xi, \eta) = \left[ \frac{1}{2(1-\xi)} \right] (1+\xi)(1+\eta) \tag{1}$$

$$M_2(\xi, \eta) = \left( \frac{1+\eta}{1-\xi} \right) (\eta - \xi - 1) \tag{2}$$

$$M_3(\xi, \eta) = \left( \frac{1-\eta}{1-\xi} \right) (-\eta - \xi - 1) \tag{3}$$

$$M_4(\xi, \eta) = \left[ \frac{1}{2(1-\xi)} \right] (1+\xi)(1-\eta) \tag{4}$$

$$M_5(\xi, \eta) = \left( \frac{2}{1-\xi} \right) (1-\eta^2) \tag{5}$$

Standard shape functions are used to discretize the displacements of the five-noded mapped infinite element. The shape functions of the five-noded mapped infinite element are derived from the shape functions of the eight-node quadrilateral element. The shape functions of the infinite element are given in (6)-(10).

$$N_1(\xi, \eta) = \frac{1}{2} (1-\xi^2) (1+\eta) \tag{6}$$

$$N_2(\xi, \eta) = \frac{1}{4} (1-\xi)(1+\eta)(-\xi + \eta - 1) \tag{7}$$

$$N_3(\xi, \eta) = \frac{1}{4} (1-\xi)(1-\eta)(-\xi - \eta - 1) \tag{8}$$

$$N_4(\xi, \eta) = \frac{1}{2}(1 - \xi^2)(1 - \eta) \quad (9)$$

$$N_5(\xi, \eta) = \frac{1}{2}(1 - \xi)(1 - \eta^2) \quad (10)$$

The coordinates (x and y) of the infinite element can be written as in (11)-(12) using mapping functions of the infinite element.

$$\begin{aligned} x(\xi, \eta) &= N_1(\xi, \eta)x_1 + N_2(\xi, \eta)x_2 + N_3(\xi, \eta)x_3 + N_4(\xi, \eta)x_4 + N_5(\xi, \eta)x_5 \\ &= \sum_{i=1}^5 N_i(\xi, \eta)x_i \end{aligned} \quad (11)$$

$$\begin{aligned} y(\xi, \eta) &= N_1(\xi, \eta)y_1 + N_2(\xi, \eta)y_2 + N_3(\xi, \eta)y_3 + N_4(\xi, \eta)y_4 + N_5(\xi, \eta)y_5 \\ &= \sum_{i=1}^5 N_i(\xi, \eta)y_i \end{aligned} \quad (12)$$

The horizontal and vertical displacements (u and v) can be written as in (13)-(14) using shape functions of the infinite element.

$$\begin{aligned} u(\xi, \eta) &= N_1(\xi, \eta)u_1 + N_2(\xi, \eta)u_2 + N_3(\xi, \eta)u_3 + N_4(\xi, \eta)u_4 + N_5(\xi, \eta)u_5 \\ &= \sum_{i=1}^5 N_i(\xi, \eta)u_i \end{aligned} \quad (13)$$

$$\begin{aligned} v(\xi, \eta) &= N_1(\xi, \eta)v_1 + N_2(\xi, \eta)v_2 + N_3(\xi, \eta)v_3 + N_4(\xi, \eta)v_4 + N_5(\xi, \eta)v_5 \\ &= \sum_{i=1}^5 N_i(\xi, \eta)v_i \end{aligned} \quad (14)$$

The strain-displacement relation of the infinite element can be written as in (15)-(18).

$$\{\epsilon\} = \begin{bmatrix} \frac{\partial}{\partial x} & 0 \\ 0 & \frac{\partial}{\partial y} \\ \frac{\partial}{\partial y} & \frac{\partial}{\partial x} \end{bmatrix} [N(\xi, \eta)] \begin{Bmatrix} u_1 \\ v_1 \\ \vdots \\ u_5 \\ v_5 \end{Bmatrix} = [B] \begin{Bmatrix} u_1 \\ v_1 \\ \vdots \\ u_5 \\ v_5 \end{Bmatrix} \quad (15)$$

$$[B] = \begin{bmatrix} \frac{\partial N_1}{\partial x} & 0 & \dots & \frac{\partial N_5}{\partial x} & 0 \\ 0 & \frac{\partial N_1}{\partial y} & \dots & 0 & \frac{\partial N_5}{\partial y} \\ \frac{\partial N_1}{\partial y} & \frac{\partial N_1}{\partial x} & \dots & \frac{\partial N_5}{\partial y} & \frac{\partial N_5}{\partial x} \end{bmatrix} \quad (16)$$



$$\begin{Bmatrix} \frac{\partial N_i}{\partial x} \\ \frac{\partial N_i}{\partial y} \end{Bmatrix} = \begin{bmatrix} \frac{\partial \xi}{\partial x} & \frac{\partial \eta}{\partial x} \\ \frac{\partial \xi}{\partial y} & \frac{\partial \eta}{\partial y} \end{bmatrix} = [J]^{-1} \begin{Bmatrix} \frac{\partial N_i}{\partial \xi} \\ \frac{\partial N_i}{\partial \eta} \end{Bmatrix} \tag{17}$$

$$[J] = \begin{bmatrix} \frac{\partial x}{\partial \xi} & \frac{\partial y}{\partial \xi} \\ \frac{\partial x}{\partial \eta} & \frac{\partial y}{\partial \eta} \end{bmatrix} = \begin{bmatrix} \sum_{i=1}^5 \frac{\partial M_i}{\partial \xi} x_i & \sum_{i=1}^5 \frac{\partial M_i}{\partial \xi} y_i \\ \sum_{i=1}^5 \frac{\partial M_i}{\partial \eta} x_i & \sum_{i=1}^5 \frac{\partial M_i}{\partial \eta} y_i \end{bmatrix} = [J(\xi, \eta)] \tag{18}$$

where B is the strain-displacement operator, and J is the Jacobian matrix. The stiffness matrix of the infinite element can be written as in (19).

$$[k] = \sum_{i=1}^3 \sum_{j=1}^3 [B(\zeta_i, \zeta_j)]^T [D] [B(\zeta_i, \zeta_j)] \det [J(\zeta_i, \zeta_j)] W_i W_j \tag{19}$$

where D,  $\zeta$ , and W are material matrix, abscissae of the Gaussian quadrature and weight of the Gaussian quadrature, respectively.

### 3 NUMERICAL MODELS

An infinite plate with a central circular hole subjected to a uniformly distributed outward pressure,  $q_0$  acting on the periphery of the opening, is one of the infinite domain problems of the civil engineering. Representation of an infinite plate with a central circular hole is given in Figure 2. Three different numerical models (Model 1, Model 2, and Model 3) are used to model the infinite plate with a central circular hole. Representation of the numerical models are illustrated in Figure 3. The numerical models are truncated at one point to model the infinite plate with a central circular hole. This point is called as  $R_2$ . The Model 1 is consisting of plane-strain eight-node quadrilateral elements. The nodes along the X direction are constrained in the Y direction. The nodes along the Y direction are constrained in the X direction. However, the nodes along the edge at  $R_2$  are set to free. The Model 2 is consisting of plane-strain eight-node quadrilateral elements. The nodes along the X direction are constrained in the Y direction. The nodes along the Y direction are constrained in the X direction. On the other hand, the nodes along the edge at  $R_2$  are constrained in the X and Y direction. The Model 3 is consisting of eight-node plane-strain quadrilateral elements and five-noded mapped infinite elements. The nodes along the X direction are constrained in the Y direction. The nodes along the Y direction are constrained in the X direction. On the other hand, the edge at  $R_2$  is modelled with five-noded mapped infinite elements. The parameters of the Model 1, Model 2, and Model 3 are given in Table 1. Mesh of the numerical models are illustrated in Figure 4.

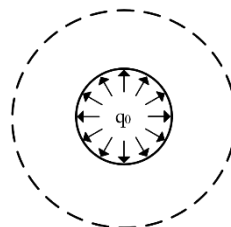


Figure 2. Representation of an infinite plate with a central circular hole

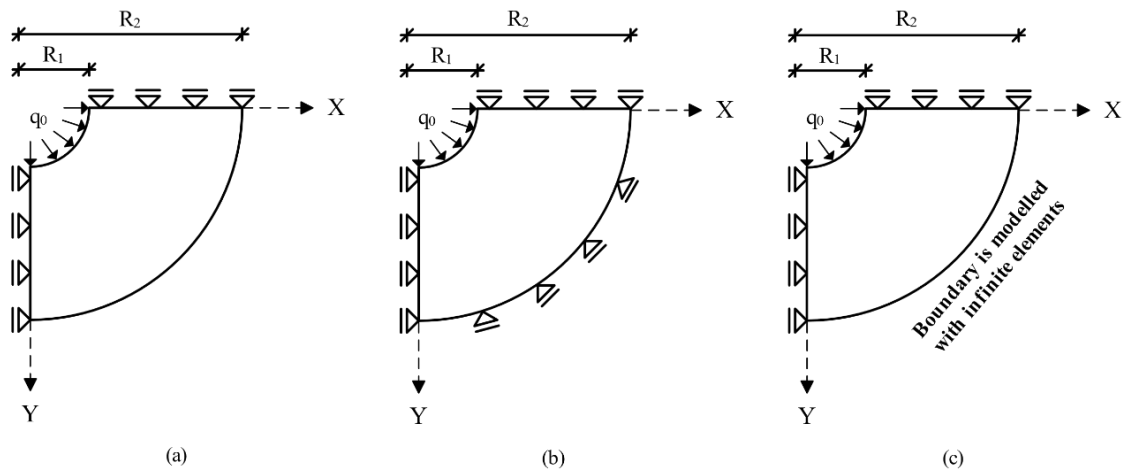


Figure 3. Representation of numerical models; (a) Model 1, (b) Model 2, and (c) Model 3

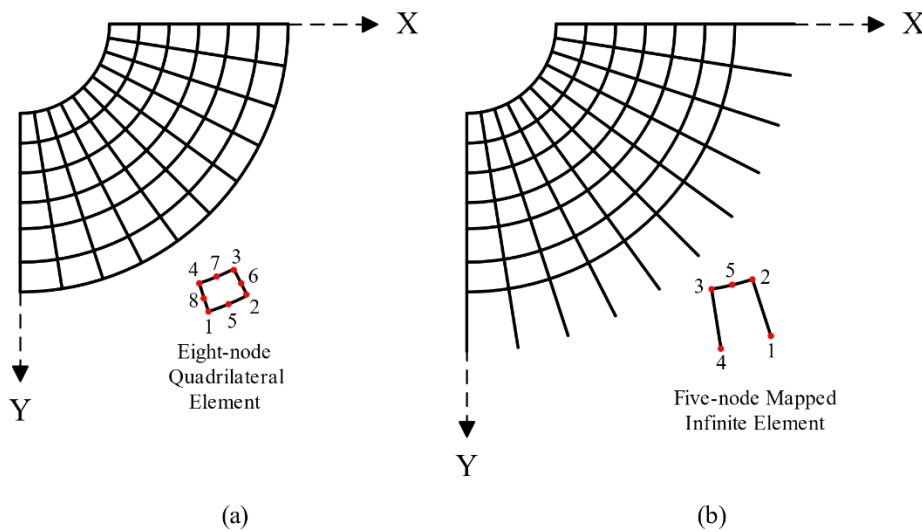


Figure 4. Mesh of the numerical models; (a) Model 1 and Model 2, and (b) Model 3

Table 1. The parameters of the Model 1, Model 2, and Model 3

Parameter	Definition	Value		
		Model 1	Model 2	Model 3
$R_1$	radius of the circular hole		1 m	
$R_2$	radius of the circular plate	varies from 5 m to 50 m		
$q_0$	pressure	1 kN/m <sup>2</sup>		
$E$	modulus of elasticity of the plate	1 kN/m <sup>2</sup>		
$\mu$	Poisson's ratio	0.25		

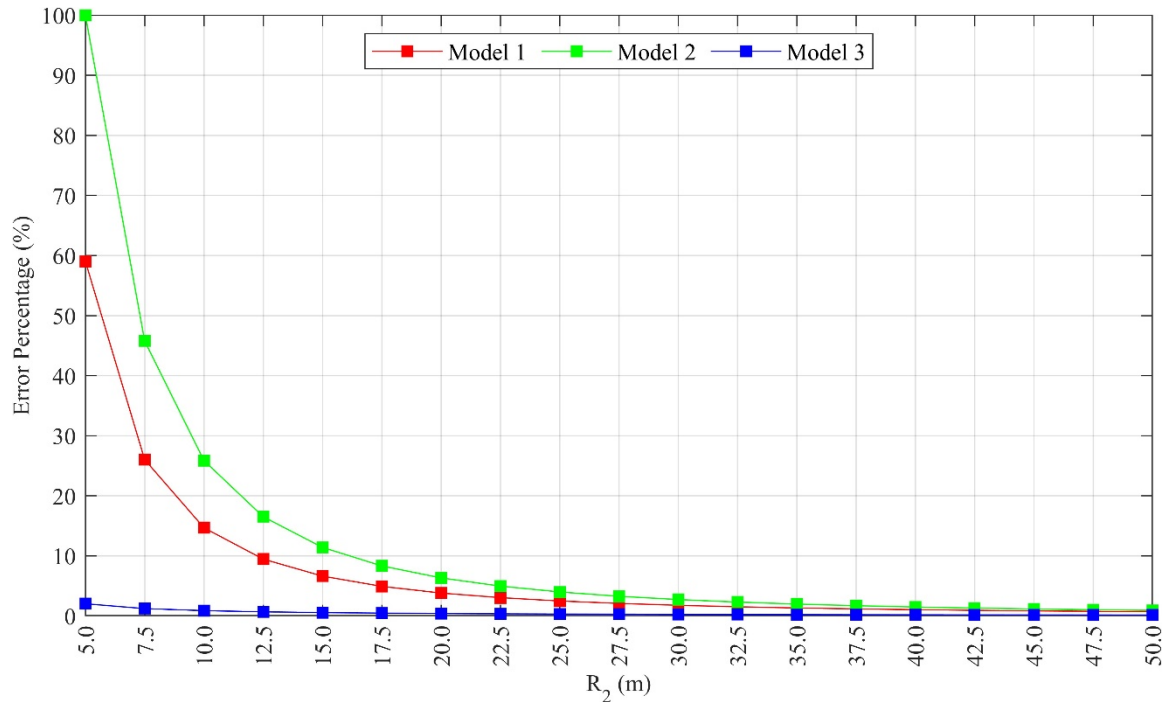
## 4 RESULTS

The analytical solution of an infinite plate with a central circular hole subjected to a uniformly distributed outward pressure,  $q_0$  acting on the periphery of the opening, is given in (20).

$$u_r = \left( \frac{1 + \mu}{E} \right) \left( \frac{q_0 R_1^2}{r} \right) \tag{20}$$

where  $r$  is the radial distance. A number of analyses are performed in OpenSees using the Model 1, Model 2, and Model 3. The error percentages of the radial displacement at  $r=5$  m obtained from the numerical models are

calculated according to the analytical result given in (20). The comparison of the calculated error percentages from the numerical models are illustrated in Figure 5. The numerical value of the calculated error percentages is given in Table 2.



**Figure 5.** Error percentage of the radial displacement of the numerical models at  $r=5$  m according to the analytical result

As seen from Figure 5, the error percentages decrease as the value of  $R_2$  increases for Model 1 and Model 2. On the other hand, the error percentage for the Model 3 is close to zero. The use of small and five-noded mapped infinite element models instead of large, truncated models not only provides a computation time advantage, but also ensures that the results are closer to the analytical results, as shown in Figure 5 and Table 2.

**Table 1.** The error percentage of the radial displacement at  $r=5$  m obtained from the numerical models according to analytical result

R <sub>2</sub>	Model 1	Model 2	Model 3	R <sub>2</sub>	Model 1	Model 2	Model 3
5.00	59.03	100.00	2.03	30.00	1.78	2.73	0.27
7.50	26.02	45.78	1.23	32.50	1.53	2.31	0.25
10.00	14.68	25.87	0.88	35.00	1.33	1.98	0.23
12.50	9.46	16.52	0.69	37.50	1.18	1.71	0.21
15.00	6.63	11.41	0.56	40.00	1.05	1.49	0.20
17.50	4.93	8.33	0.48	42.50	0.94	1.31	0.19
20.00	3.81	6.34	0.41	45.00	0.84	1.16	0.18
22.50	3.05	4.97	0.36	47.50	0.77	1.03	0.17
25.00	2.50	4.00	0.33	50.00	0.70	0.92	0.16
27.50	2.09	3.28	0.29				

## 5 CONCLUSION

Modelling an infinite domain presents a frequent challenge across various engineering disciplines. Truncated models are commonly employed to model infinite domains numerically. However, using the truncated model requires larger model dimensions for satisfactory results. This, in turn, increases computation time and memory usage, which can become insufficient. To address this issue, several solutions have been developed to model infinite domains. The utilization of infinite elements is considered one of the potential solutions. Incorporating infinite elements in the process of modelling infinite domains can effectively reduce both computation time and

memory usage. This study implemented a five-noded mapped infinite element into OpenSees and validated it using analytical results. The analyses results show that the model employing the five-noded mapped infinite element is more efficient than the truncated model.

## References

- [1] G. Beer and J. Meek, "Infinite domain elements," *International Journal for Numerical Methods in Engineering*, vol. 17 no. 1, pp. 43–52, 1981.
- [2] P. Kumar, "Static infinite element formulation," *Journal of Structural Engineering*, vol. 111 no. 11, pp. 2355–2372, 1985.
- [3] G. Buchanan and M. Sallah, "Some simplified methods for infinite elements," *Computational Mechanics*, vol. 6, pp. 167–172, 1990.
- [4] T. Davies and S. Bu, "Infinite boundary elements for the analysis of halfspace problems," *Computers and Geotechnics*, vol. 19, no. 2, pp. 137–151, 1996.
- [5] T. Abd El Fattah, H. Hodhod, and A. Akl, "A novel formulation of infinite elements for static analysis," *Computers and Structures*, vol. 77, pp. 371–379, 2000.
- [6] A. Houmat, "Coupling of finite and hierarchical infinite elements: application to a non-homogeneous cross-anisotropic half-space subjected to a non-uniform circular loading," *International Journal for Numerical and Analytical Methods in Geomechanics*, vol. 37, pp. 1552–1573, 2013.
- [7] A. Erkal, D. Laefer, M. Asce, and S. Tezcan, "Advantages of infinite elements over prespecified boundary conditions in unbounded problems," *Journal of Computing in Civil Engineering*, vol. 29 no. 6, 2015.
- [8] P. Liu, D. Wang, and M. Oeser, "Application of semi-analytical finite element method coupled with infinite element for analysis of asphalt pavement structural response," *Journal of Traffic and Transportation Engineering*, vol. 2, no. 1, pp. 48–58, 2015.
- [9] J. Thomas, P. Jeyakarthykeyan, and K. Ramesh. "Element matrix formulation for bi-quadratic infinite element," in *IOP Conference Series: Materials Science and Engineering*, 2018.
- [10] T. Haji, A. Faramarzi, N. Metje, D. Chapman, and F. Rahimzadeh, "Development of an infinite element boundary to model gravity for subsurface civil engineering applications," *International Journal for Numerical and Analytical Methods in Geomechanics*, vol. 44 no. 3, pp. 418–431, 2020.
- [11] F. McKenna, "OpenSees: A framework for earthquake engineering simulation," *Computing in Science and Engineering*, vol. 13, no. 4, pp. 58–66, 2011.
- [12] W. Moser, C. Duenser, and G. Beer, "Mapped infinite elements for three-dimensional multi-region boundary element analysis," *International Journal for Numerical Methods in Engineering*, vol. 61, no. 3, pp. 317–328, 2004.
- [13] C. Barbier, P. Bettess, and J. Bettess, "Automatic generation of mapping functions for infinite elements using reduce," *Journal of Symbolic Computing*, vol. 14, pp. 523–534, 1992.



---

## Thermal Properties and Microstructure Investigation of Sustainable Self-Compacting Concrete-Based Coal Bottom Ash Aggregate

Ibtissam Boulahya<sup>\*1</sup>, Abdelkadir Makani<sup>1</sup>, Ahmed Tafraoui<sup>1</sup>

<sup>1</sup>Laboratory of Eco-Materials: Innovations & Applications (EMIA), Department of Civil Engineering & Hydraulic, Tahri Mohamed University, Bechar, Algeria

---

### Abstract

Effective solid waste management and recycling are increasingly critical challenges in various industries. Coal bottom ash (CBA) is a residual product derived from coal-fired thermal power plants. Utilizing such waste materials as construction components in civil engineering offers potential environmental benefits and helps mitigate issues associated with coal bottom ash disposal. This study aims to investigate the feasibility of employing CBA, sourced from a defunct Algerian thermal power plant, as coarse and fine aggregates in lightweight self-compacting concrete (LWSCC). The research evaluates the fresh and hardened properties, microstructure (SEM, XRD, TGA), and thermal conductivity of SCC incorporating CBA at full replacement levels relative to natural aggregates. The findings indicate that the workability of mixes using CBA as coarse aggregates improves significantly with complete replacement (100%) of natural coarse aggregates by coarse CBA, while it decreases with full replacement (100%) of natural fine aggregates by Fine CBA. The mixtures satisfy self-compacting concrete standards, although a slight reduction in compressive strength is observed when CBA is used for both coarse and fine aggregates. Additionally, the density mixtures containing CBA aggregate decreases notably. Thermal conductivity values also show a significant decrease, approximately 50% for coarse aggregate replacement and 44.3% for fine aggregate replacement, indicating favorable thermal insulation properties. Moreover, microstructural and TGA analyses suggest that the CSH gel structure is marginally less dense compared to control concrete, and the overall intensity of ettringite remains unchanged with the inclusion of coal bottom ash in the concrete mix. These results underscore the potential of utilizing CBA as aggregates in LWSCC, offering both environmental benefits and improved thermal insulation characteristics.

**Keywords:** *Self-compacting concrete, Coal bottom ash, Thermal conductivity, Microstructure*

---



## Effect of Thermal Gradient on the Initial Stiffness of End-Plate Beam-Column Connections Exposed to Fire

Yasmina Douah<sup>\*1</sup>, Anis Abidelah<sup>1</sup>, Hichem Rakib Sebbagh<sup>1</sup>, Djemel Eddin Kerdal<sup>1</sup>,  
Abdelhamid Bouchair<sup>2</sup>

<sup>1</sup>Civil Engineering Department, LM2SC, USTO-MB, B.P. 1505 El M'Naouer, Oran, Algeria

<sup>2</sup>Pascal Institute, Blaise Pascal University, BP 10448, F-63000 Clermont-Ferrand, France

---

### Abstract

The presence of different elements in the connections (bolts, plates and welds) means that a differential temperature distribution is produced when they are subjected to heating caused by accidental fires. As a result, a non-uniform temperature distribution is observed throughout the depth of the connection, with a significant reduction in the temperatures of the upper flanges of the beams compared with the lower flanges directly exposed to the fire. This phenomenon may influence the behaviour of the connections due to the non-uniform change in the properties of these elements.

In this study, the response of the connections is investigated in terms of initial stiffness in order to examine the effect of the thermal gradient on the actual behaviour of steel column-beam connections. Two approaches were taken into consideration: the first by considering a uniform temperature distribution over the entire depth, and the second by taking into account the temperature distribution observed in previous experimental tests. The study shows that taking into account the thermal gradient provides a more accurate estimation of the stiffness of the connection under the effect of heat, showing a less significant reduction in stiffness compared with a uniform temperature distribution.

**Keywords:** *Thermal gradient, Fire exposure, Beam-column connections, Initial stiffness*

---



## Numerical Analysis of the Static and Cyclic Behavior of a T-Stub Steel Connection

Mohammed Mokhtar Fekir<sup>1\*</sup>, Hichem Rakib Sebbagh<sup>1</sup>, Anis Abidelah<sup>1</sup>, Abdelhamid Bouchair<sup>2</sup>, Djamel Eddine Kerdal<sup>1</sup>

<sup>1</sup>Civil Engineering Department, LM2SC, USTO-MB, B.P. 1505 El M'Naouer, Oran, Algeria

<sup>2</sup>Institute Pascal, University Blaise Pascal, BP 10448, F-63000 Clermont-Ferrand, France

---

### Abstract

The aim of this paper is to study numerically the static and cyclic behavior of a T- stub steel connections. A 3D finite element model is developed with 20-node volume elements, using Cast3m software. The model includes material and geometric non-linearities such as contact, plasticity and large displacements. It is calibrated under monotonic loading using experimental data available in the literature. Based on this validated model, an analysis is carried out to evaluate the influence of the T-stub flange thickness on its global behavior under static and cyclic loading. The cyclic behavior of the T-stub is characterized by the multi-linear response envelope curve. Finally, an analysis of the evolution of the prying forces and bolt forces of the T-stub is also carried out.

**Keywords:** Bolted assembly, T-stub, Monotonic loading, Cyclic loading

---



## Numerical Study to Optimize the Best Locations for Building a New Tunnel Next to the Old One by Tow Behaviors the Mohr-Coulomb and Drucker-Prager

Taleb Hosni Abderrahmane<sup>\*1,2</sup>, Guemidi Ismahene<sup>1</sup>

<sup>1</sup>Department of Civil Engineering, University Chadli Bendjedid, El Tarf, Algeria

<sup>2</sup>FIMAS Laboratory, University of Bechar, Algeria

---

### Abstract

The tunnels are essential infrastructures for enhancing mobility in mountainous regions. They offer several advantages, such as reducing distances, travel time, and improving transportation ease. Engineers often need to construct new tunnels close to existing ones, prioritizing safety. In this study, we used OptumG2 software for a numerical analysis of a new tunnel's position in six different locations: bottom, top, left (at 12 m and 32 m), and right (at 12 m and 32 m) using the finite element method. The analysis was conducted based on two criteria: Mohr-Coulomb and the equivalent Drucker-Prager. We focused on the overall displacement field, the vertical displacement of the model, and the displacement, bending moment, shear, and normal force on the concrete lining. The results showed that constructing a new tunnel at the bottom could significantly impact the stability of the existing tunnel. Additionally, the maximum displacement observed when adding a new tunnel at the bottom aligned with the Drucker-Prager criteria.

**Keywords:** *Tunnels, Locations, Instability, Finite element method, OptumG2*

---





## Parameter Estimation for a Mechanistic Model of Cell Population Damage from High-Dose Irradiation Using Nelder-Mead Simplex and Particle Swarm Optimization

Nabil Haazim Mohd Amirrudin<sup>\*1</sup>, Fuaada Mohd Siam<sup>1</sup>

<sup>1</sup>Department of Mathematical Science, Faculty of Science, Universiti Teknologi Malaysia, 81310, Johor Bahru, Johor, Malaysia

---

### Abstract

Radiotherapy employs high-energy waves to treat cancers and tumors by directly killing cancer cells or creating charged particles that damage the DNA, thereby disrupting cancer cell growth and division. However, high doses of radiation can also harm nearby normal cells, leading to side effects. The primary objective of radiotherapy is to maximize damage to cancer cells while minimizing harm to surrounding normal cells. Various mechanistic models have been developed to study the dynamic behavior of cell populations following high-dose ionizing radiation. Accurate parameter estimation for these models is crucial for understanding the cellular response to radiation. This study aims to estimate the parameter values for a mechanistic model of high-dose irradiation damage using two optimization algorithms: Nelder-Mead Simplex (NMS) and Particle Swarm Optimization (PSO). The performance and efficiency of these algorithms are evaluated based on the minimum value of the sum of squared errors, computational time, and the number of iterations required to compute the objective function. The results indicate that NMS offers higher accuracy and requires less time to minimize the objective function, making it suitable for precise parameter estimation. On the other hand, PSO demonstrates quicker convergence, achieving the objective function faster than NMS, which is advantageous for initial rapid estimations. In conclusion, both algorithms have distinct strengths, with NMS excelling in accuracy and efficiency, while PSO provides faster convergence, thus offering complementary benefits for parameter estimation in mechanistic models of high-dose irradiation damage.

**Keywords:** *Parameter estimation, Radiation effects, DNA damage, Nelder-mead simplex, Particle swarm optimization*

---



## A Collocation Approach for Solving Space Fractional Partial Differential Equations Using Generalized Lucas Polynomials

Zineb Laouar<sup>\*1,2</sup>, Nouria Arar<sup>3</sup>

<sup>1</sup>Laboratory of Applied Mathematics and Didactics, Higher Normal School, Constantine, Algeria

<sup>2</sup>Abdelhafid Boussouf University Center, Mila, Algeria

<sup>3</sup>Department of Mathematics, University Constantine 1, Mentouri Brothers, Constantine, Algeria

### Abstract

This study introduces a computational method to solve the space fractional diffusion equation, where the fractional derivative is treated in the Caputo sense. The numerical simulation combines finite difference schemes for the temporal variable with a collocation technique for the spatial variable. This last utilizes generalized Lucas polynomials as basis functions along with the corresponding collocation nodes. The problem is transformed into an algebraic system by using operational matrices for both fractional and integer derivatives. Numerical examples are provided to demonstrate the efficiency of the proposed approach.

**Keywords:** Fractional diffusion equation, Fractional Caputo derivative, Collocation method, Crank-Nicolson scheme, Numerical simulation

## 1 INTRODUCTION

In this paper, we consider the following space fractional partial differential equation

$$u_t(x, t) = d(x) {}^C\mathcal{D}_x^\beta u(x, t) + f(x, t), \quad 0 \leq x \leq 1, \quad 0 \leq t \leq 1.$$

Where  ${}^C\mathcal{D}_x^\beta u(x, t)$  denotes the fractional derivative of  $u(x, t)$  expressed in the Caputo sense of order  $\beta$  according to the space variable  $x$ .  $d(x)$  is a known coefficient and  $f(x, t)$  is source function. The initial and the boundary conditions are as follows

$$u(x, 0) = \psi(x), \quad u(0, t) = \phi_1(t), \quad u(1, t) = \phi_2(t).$$

This equation models successfully many physical and financial problems, it describes the transport of particles in anomalous diffusion in diverse fields. Many researchers interested in the numerical solution of such problems. For instance, the collocation and tau methods, the finite difference method and spline approach [1–4]. Here, we develop a numerical technique to solve the space fractional partial differential equation basing on generalized Lucas polynomials [5, 6]. By making use of the operational matrix of fractional derivative, the collocation method is performed together with the Crank Nicolson scheme to obtain a final algebraic system to solve. Related works on similar numerical methods, but applied to different types of equations, can be found in [7, 8].

The paper is organized as follows, first we introduce some preliminaries concerning the fractional derivation and generalized Lucas polynomials in Section 2. In Section 3, we detail the steps of the proposed algorithm. Finally, in Section 4, numerical examples are presented and discussed to confirm the efficiency of the method.

## 2 PRELIMINARIES

Hereafter, we introduce the definition of fractional Caputo derivative, including some important properties. Also, generalized Lucas polynomials.

**Definition 2.1** The fractional derivative of a function  $u(x) \in L_1[0,1]$  in the Caputo sense is given by

$${}^c\mathcal{D}^\beta u(x) = \begin{cases} \frac{1}{\Gamma(m-\beta)} \int_0^x (x-z)^{m-\beta-1} u^{(m)}(z) dz, & \beta > 0, x > 0, m-1 \leq \beta \leq m, m \in \mathbb{N}. \\ \frac{d^m u(x)}{dx^m}, & \beta = m. \end{cases}$$

Here are the following properties

- ${}^c\mathcal{D}^\beta C = 0$ ;  $C$  is a constant.
- We denote by  $[\beta]$  the integer part of  $\beta$  and  $\mathbb{N}_0 = \{0, 1, 2, \dots\}$ , then we have

$${}^c\mathcal{D}^\beta x^\gamma = \begin{cases} 0, & \gamma \in \mathbb{N}_0, \gamma < [\beta], \\ \frac{\Gamma(\gamma+1)}{\Gamma(\gamma+1-\beta)} x^{\gamma-\beta}, & \gamma \in \mathbb{N}_0, \gamma \geq [\beta]. \end{cases}$$

- The Caputo fractional differentiation is a linear operation

$${}^c\mathcal{D}^\beta (\lambda u + \theta v)(x) = \lambda {}^c\mathcal{D}^\beta u(x) + \theta {}^c\mathcal{D}^\beta v(x), \quad \forall \lambda, \theta \in \mathbb{R}.$$

### 2.1 About the Generalized Lucas Polynomials

As their name indicate, these polynomials are a generalization of the classical Lucas polynomials. We denote by  $\mathcal{L}_i^{a,b}(x)$  the generalized Lucas polynomial (GLP) of degree  $i$  defined over  $[0,1]$ , where  $a, b$  are nonzero real constants. They are defined using the relation of recurrence [1]

$$\begin{cases} \mathcal{L}_i^{a,b}(x) = ax\mathcal{L}_{i-1}^{a,b}(x) + b\mathcal{L}_{i-2}^{a,b}(x), & i \geq 2, \\ \mathcal{L}_0^{a,b}(x) = 2, \quad \text{and} \quad \mathcal{L}_1^{a,b}(x) = ax. \end{cases} \tag{1}$$

The explicit power formula of  $\mathcal{L}_i^{a,b}(x)$  can be expressed as follows:

$$\mathcal{L}_i^{a,b}(x) = 2i \sum_{k=0}^i \frac{a^k b^{\frac{i-k}{2}} \zeta_{i+k}^{\left(\frac{i+k}{2}\right)} \zeta_{i+k}^{\left(\frac{i-k}{2}\right)}}{i-k} x^k, \quad \forall i \geq 1, \quad \zeta_j = \begin{cases} 1, & \text{if } j \text{ is even,} \\ 0, & \text{if } j \text{ is odd.} \end{cases} \tag{2}$$

The GLP encompass several types of well-known polynomials by varying the values of the constants  $a$  and  $b$ . For instance, the Lucas polynomials for  $a = b = 1$ , the Pell-Lucas polynomials for  $a = 2$  and  $b = 1$ , the Fermat-Lucas polynomials for  $a = 3$  and  $b = -2$  and the first-kind Chebyshev polynomials for  $a = 1$  and  $b = -0.5$ . Now, in order to utilize the GLP in constructing the spectral expansion, we need to formulate some important expressions concerning the approximate solution and its derivative of fractional order. For this, let's consider a square integrable function  $u(x)$  in  $(0,1)$  that can be expressed in terms of the GLP as follows

$$u(x) = \sum_{i=0}^{\infty} c_i \mathcal{L}_i^{a,b}(x).$$

The approximate solution is then considered as the truncation series

$$u(x) \simeq u_N(x) = \sum_{i=0}^N c_i \mathcal{L}_i^{a,b}(x) = U^T(\mathcal{L}(x)), \tag{3}$$

where

$$U^T = (c_0, c_1, \dots, c_N), \quad \text{and} \quad (\mathcal{L}(x)) = (\mathcal{L}_0^{a,b}(x), \mathcal{L}_1^{a,b}(x), \dots, \mathcal{L}_N^{a,b}(x))^T. \tag{4}$$

For the fractional derivative, we denote by  ${}^c\mathcal{D}^\beta \mathcal{L}(x)$  the fractional derivative of GLP of order  $\beta$ , expressed as

$${}^c\mathcal{D}^\beta \mathcal{L}(x) = x^{-\beta} D^\beta \mathcal{L}(x), \quad D^\beta = (d_{ij}^\beta), \quad d_{ij}^\beta = \begin{cases} \omega_\beta(i, j), & \text{for } i \geq [\beta], i \geq j, \\ 0, & \text{otherwise.} \end{cases} \tag{5}$$

Where  $[\beta]$  represents the smallest integer greater than or equal to  $\beta$  and



$$(A_1)_{i,j} = \mathcal{L}_{i-1}^{a,b}(x_{j-1}), \quad \text{for all } i, j = 1, \dots, N + 1.$$

$$(A_2)_i^j = \begin{cases} d(x_{j-1})x_{j-1}^{-\beta}D^\beta \mathcal{L}(x_{i-1}), & \text{for all } i = 2, \dots, N, \\ 0, & \text{for all } i = 1, N + 1. \end{cases}$$

Where  $(A_2)_i^j$  denotes the  $j$ -th row in the matrix  $A_2$  for all  $j = 1, \dots, N + 1$ .

$$(A_3)_{i,j} = \begin{cases} (A_1)_{i,j}, & \text{for all } i = 2, \dots, N \text{ and } j = 1, \dots, N + 1, \\ 0, & \text{for all } i = 1, N + 1 \text{ and } j = 1, \dots, N + 1. \end{cases}$$

#### 4 ILLUSTRATIVE EXAMPLES

In this section, we treat some numerical examples using the present technique. The obtained results of the approximate solution are compared with the values of the exact solution using different types of generalized Lucas polynomials. All the computations were carried out in double precision using Matlab 9.8.0 (R2020a) in AMD Ryzen 5 5600X 6-Core, 3.70 Ghz machine.

**Example 4.1** Let's consider the following fractional heat equation

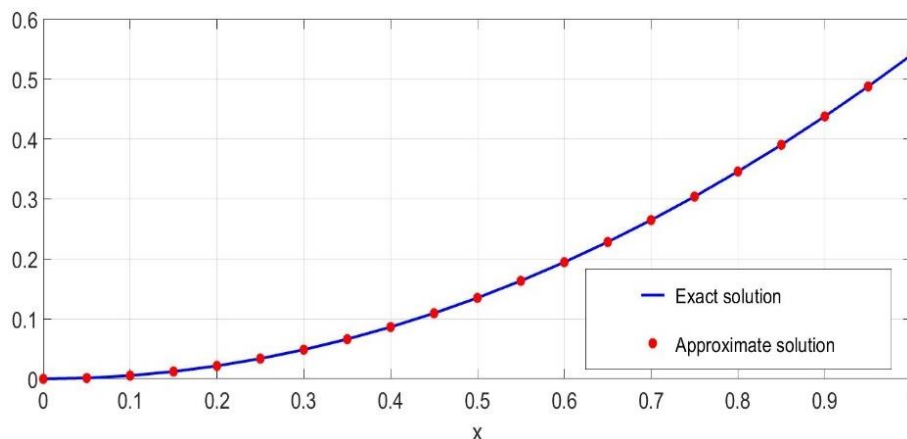
$$u_t(x, t) = v(x)^c D^\beta u(x) + f(x, t), \tag{12}$$

where  $v(x) = \frac{\Gamma(3-\beta)x^\beta}{2}$ ,  $f(x, t) = x^2(\sin(-t) - \cos(-t))$ . The initial condition  $u(x, 0) = x^2$  and the boundary conditions are  $\phi_1(t) = 0, \phi_2(t) = \cos(-t)$ . The exact solution is  $u(x, t) = x^2 \cos(-t)$ .

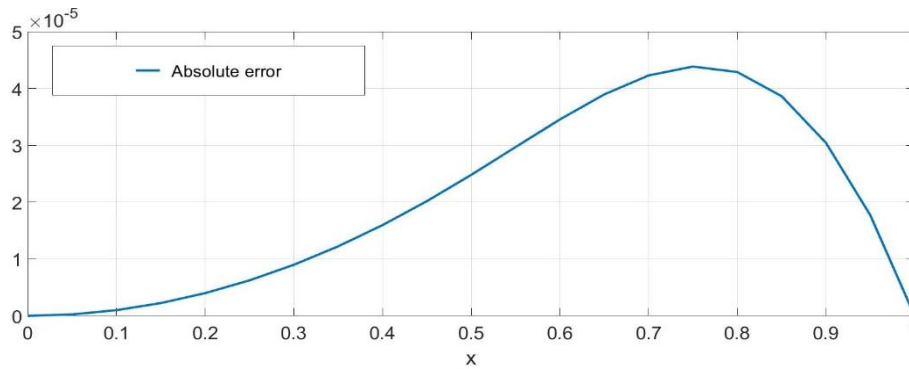
The results presented in Table 1 were obtained for  $N = 12$  with different values of  $\beta$  at various times  $t = 0.1, 0.5, 1$ . Also, in Figure 1, the behavior of the exact and the approximate solutions all over the domain  $[0,1]$  is depicted. The superposition of both curves confirms the efficiency of the proposed technique. Moreover, in Figure 2, the plot of the absolute error curve is presented in the right side, reflecting and affirming the results.

**Table 1.** Approximate values of the solution at different times and for different values of  $\beta$  (Example 4.1)

$t$	$\beta = 1.2$	$\beta = 1.4$	$\beta = 1.6$	$\beta = 1.8$
<b>0.1</b>	$7.2359e - 04$	$6.5654e - 04$	$5.4591e - 04$	$4.7128e - 04$
<b>0.5</b>	$2.2018e - 03$	$1.3784e - 03$	$1.1141e - 03$	$8.8512e - 03$
<b>1</b>	$7.3622e - 02$	$3.8460e - 02$	$6.8638e - 04$	$4.6618e - 04$



**Figure 1.** Behavior of the exact and the approximate solutions in  $[0,1]$  for  $N = 20, \Delta t = 0.001$  (Example 4.1)



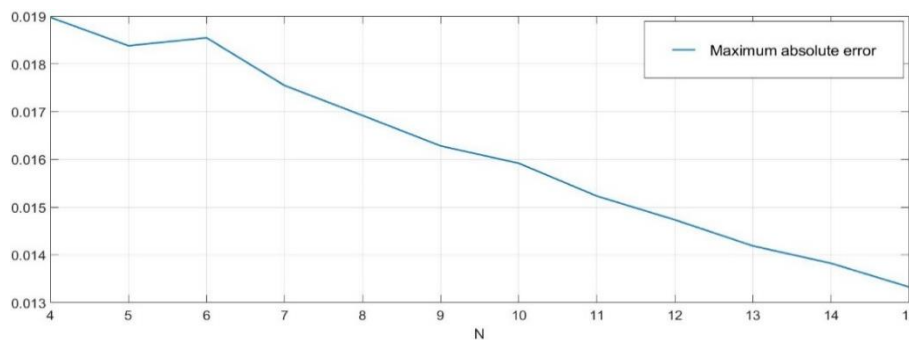
**Figure 2.** Absolute error curve (right) in  $[0,1]$  for  $N = 20$  using  $\Delta t = 0.001$  (Example 4.1)

**Example 4.2** Let's consider the following equation

$$u_t(x, t) = v(x)^c \mathcal{D}^{1.8} u(x) + f(x, t), \tag{13}$$

where  $v(x) = \Gamma(0.2)x^{1.8}$ ,  $f(x, t) = -(2x - 11x^2)\exp(-t)$ . The initial condition  $u(x, 0) = x(1 - x)$  and the boundary conditions are  $\phi_1(t) = \phi_2(t) = 0$ . The exact solution for  $\beta = 1.8$  is  $u(x, t) = (x - x^2)\exp(-t)$ .

In Figure 3, the variations of the maximum absolute error are depicted for various values of  $N$ , showing the decrease in error values while  $N$  increases.



**Figure 3.** Maximum absolute error as a function of  $N$  (Example 4.2)

**Example 4.3** Let's consider the following fractional heat equation

$$u_t(x, t) = v(x)^c \mathcal{D}^{1.8} u(x) + f(x, t), \tag{14}$$

where  $v(x) = \Gamma(1.2)x^{1.8}$ ,  $f(x, t) = 3x^2(2x - 1)\exp(-t)$ . The initial condition  $u(x, 0) = x^2$  and the boundary conditions are  $\phi_1(t) = \phi_2(t) = 0$ . The exact solution is  $u(x, t) = x^2(1 - x)\exp(-t)$ .

In Table 2, the results of the maximum absolute error are calculated for different values of  $N$ . It shows that while using different coefficients  $(a, b)$  of the GLP, which means treating the problem with different families of polynomials, the results remain the same and show the good behavior of the approximate solution compared to the exact one. Also, in Figure 4, the curve of absolute error is depicted using  $N = 20$  and  $(a, b) = (2, 1)$  confirming the obtained results.

**Table 2.** The maximum error for different values of  $N$  using  $\Delta t = 0.01$  (Example 4.3)

$(N, \Delta t)$	$(4, 0.01)$	$(8, 0.001)$	$(12, 0.001)$	$(16, 0.0001)$
$(a, b) = (1, 1)$	$4.6754 - 04$	$4.7197e - 05$	$4.4673e - 05$	$4.3142e - 06$
$(a, b) = (2, 1)$	$4.6754 - 04$	$4.7197e - 05$	$4.4673e - 05$	$4.3756e - 06$
$(a, b) = (3, -2)$	$4.6754 - 04$	$4.7197e - 05$	$4.4673e - 05$	$4.3752e - 06$
$(a, b) = (1, -0.5)$	$4.6754 - 04$	$4.7197e - 05$	$4.4673e - 05$	$4.3847e - 06$

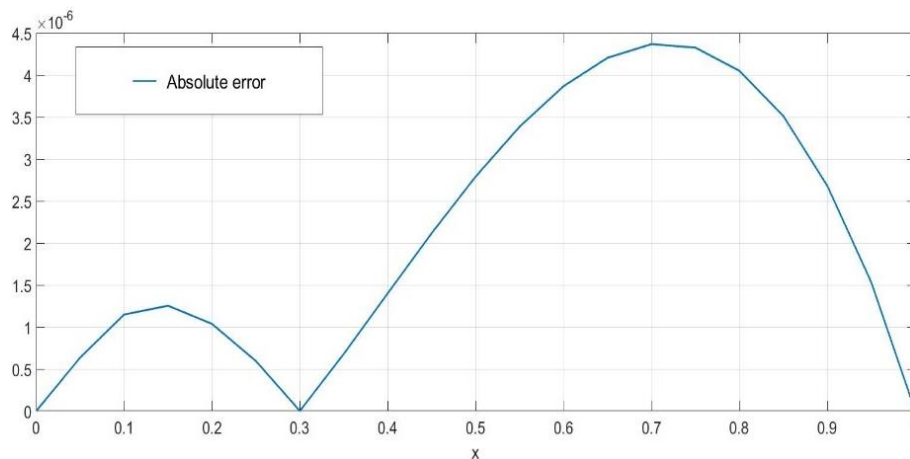


Figure 4. Absolute error curve for  $N = 20$  using  $\Delta t = 0.0001$  (Example 4.3)

## 5 CONCLUSION

In the presented study, we treat the space fractional partial differential equation using a combination of finite differences methods and spectral methods. We start by discretizing the problem according to the temporal variable  $t$  using a Crank Nicolson scheme with an appropriate time step  $\Delta t$ . For the space discretization, the approximate solution is formulated using a spectral expansion based on generalized Lucas polynomials. These polynomials allow us to express the different derivatives of the approximate solution in a matrix form, especially the fractional one, which is of the Caputo sense. After substituting the obtained relations in the temporal scheme together with the boundary conditions, a collocation method is applied to derive the final linear system to solve. The obtained results for the different examples show that with small order values of the selected GLP, we achieve good results, which confirms the applicability for other types of fractional differential equations.

## References

- [1] S. Kheybari, M. T. Darvishi, and M. S. Hashemi, "Numerical simulation for the space-fractional diffusion equations," *Applied Mathematics and Computation*, vol. 348, pp. 57–69, 2019.
- [2] R. Shikrani, M. S. Hashmi, N. Khan, A. Ghaffar, K. S. Nisar, J. Singh, and D. Kumar, "An efficient numerical approach for space fractional partial differential equations," *Alexandria Engineering Journal*, vol. 59, no. 5, pp. 2911–2919, 2020.
- [3] K. Krishnarajulu, R. B. Sevugan, and G. V. Sivaramakrishnan, "A new approach to space fractional differential equations based on fractional order Euler polynomials," *Publications de l'Institut Mathematique*, vol. 104, no. 118, pp. 157–168, 2018.
- [4] M. M. Khader, "On the numerical solutions for the fractional diffusion equation," *Communications in Nonlinear Science and Numerical Simulation*, vol. 16, no. 6, pp. 2535–2542, 2011.
- [5] W. M. Abd-Elhameed, and Y. H. Youssri, "Spectral solutions for fractional differential equations via a novel Lucas operational matrix of fractional derivatives," *Rom. J. Phys.*, vol. 61, no. 5-6, pp. 795–813, 2016.
- [6] Y. H. Youssri, W. M. Abd-Elhameed, A. S. Mohamed, and S. Sayed, "Generalized Lucas polynomial sequence treatment of fractional pantograph differential equation," *International Journal of Applied and Computational Mathematics*, vol. 7, pp. 1–16, 2021.
- [7] Z. Laouar, N. Arar and, A. Ben Makhlof, "Theoretical and numerical study for Volterra-Fredholm fractional integro-differential equations based on Chebyshev polynomials of the third kind," *Complexity*, vol. 2023, no. 1, art. no. 6401067, 2023.
- [8] Z. Laouar, N. Arar, and A. Ben Makhlof, "Spectral collocation method for handling integral and integrodifferential equations of n-th order via certain combinations of shifted legendre polynomials," *Mathematical Problems in Engineering*, vol. 2022, no. 1, art. no. 9043428, 2022.
- [9] W. M. Abd-Elhameed, and Y. H. Youssri, "Generalized Lucas polynomial sequence approach for fractional differential equations," *Nonlinear Dynamics*, vol. 89, pp. 1341–1355, 2017.
- [10] C. Canuto, M. Y. Hussaini, A. Quarteroni, and T. A. Zang, *Spectral Methods: Fundamentals in Single Domains*, Springer Science & Business Media, 2007.



## Study of the Influence of Grinding on the Characteristics of Natural Phosphate Mining in Kef Esnoun (Algeria)

Hadda Rezzag<sup>\*1</sup>, Amina Grairia<sup>1</sup>, Saida Bouyegh<sup>1</sup>, Samira Tlili<sup>1</sup>, Lynda Bahloul<sup>1</sup>

<sup>1</sup>Research Center in Industrial Technologies CRTI, P.O. Box. 64, Cheraga, Algiers, Algeria

### Abstract

Algerian phosphate ores have significant phosphate reserves. In this work, a mechanical treatment by grinding in a high-energy planetary mill was carried out on the phosphate ore extracted from the Kefessnoun deposit with the aim of obtaining a good yield. This could contribute to their valorization as an alternative raw material for the ceramic industry. Several ore characterization techniques have been carried out to determine the characteristics linked to the chemical, particle size and mineralogical composition of the main constituents by X-ray diffraction.

The analyzes carried out on the phosphate in this study are of significant economic interest because of its high P<sub>2</sub>O<sub>5</sub> content of up to 30%. The particle size ranges from 250 to 63 μm. The CaO/P<sub>2</sub>O<sub>5</sub> ratio reaching 1.70 clearly shows that the nature of phosphate ore is very carbonated. The XRD analysis results showed the presence of phosphate elements, carbonate and siliceous minerals such as: Ca<sub>10</sub>(PO<sub>4</sub>)<sub>6</sub>, Ca<sub>10</sub>(PO<sub>4</sub>)<sub>3</sub>(CO<sub>3</sub>)<sub>3</sub>(OH)<sub>2</sub>, Ca<sub>5</sub>(PO<sub>4</sub>)<sub>3</sub>F, CaMg(CO<sub>3</sub>)<sub>2</sub>, CaMg(CO<sub>3</sub>)<sub>2</sub>, CaCO<sub>3</sub> and SiO<sub>2</sub>.

**Keywords:** Phosphate ores, Treatment, Valorization, X-ray diffraction

## 1 INTRODUCTION

Nowadays, the mining sector is significant to the economies of various countries. Algeria's significant phosphate mineral reserves are located in Jebel Onk-Tebessa, in the east of the entire country [1–3]. The phosphate mining company (SOMIPHOS-spa) planned to operate and process phosphate ore from Djebel Onk in order to develop its phosphate production capacities on a national economic scale [4]. Phosphates are extensively utilized in many fields. They are widely used at 80 to 90% in the manufacturing of ceramic products, phosphoric acid, and fertilizers [5–7].

Current research in the field of phosphate mineralurgy aims precisely to find reliable and efficient enrichment processes at the industrial stage, with a view to the rational exploitation of these materials [8]. However, knowledge of the elements of these ores is necessary to guide recovery treatment choices [9–11].

Understanding the chemical and mineralogical characteristics of phosphate ore is the objective of this study in order to develop an adapted and beneficial exploitation strategy in the areas of valorization of this ore.

## 2 MATERIAL AND METHOD

In this research work, we based ourselves on raw phosphate ore from the kef-essnoun - Djebel Onk deposit in the Tebessa city, produced by the national phosphate exploitation company SOMIPHOS. These are the most answered granular phosphates. The grain size varies on average by a few millimeters. The facies are generally mixed in color from beige to brown. These color variations are linked to the content of organic compounds.



Figure 1. Phosphate ore in grains



## 2.1 Grinding Treatment

The dimensions of the phosphate-rich sample used varied between 200 and 80 $\mu$ m. a mechanical preparation by dry grinding was carried out in order to have a sample of very small dimensions (very fine), these powders are suitable for the various required analyzes [12]. Grinding is carried out using a high-energy planetary grinder with a jar rotation speed of 700 rpm for 3 hours.

Particle size analysis makes it possible to determine and observe the different grain diameters that constitute this ore. To do this, the analysis consists of separating and classifying these grains using sieves according to their diameter (250 - 63 $\mu$ m).

## 2.2 Characterization

The structural characterization of the crushed powder was observed using an optical microscope. The identification of the phases was carried out using a Rigaku Ultima IV type diffractometer using the classical  $K\alpha$  radiation of copper ( $\lambda= 1.5406 \text{ \AA}$ ) in the interval of 5-90 of  $2\theta$  with a step of 0 .02°. The X-ray diffraction patterns were compared with the ICSD database.

## 3 RESULTS

### 3.1 Classification of Phosphate Ore

Generally speaking, the quality of phosphate depends on the content of major chemical constituents such as the  $P_2O_5$  content, i.e. phosphoric anhydride, but this content can also be expressed as tricalcium phosphate  $(PO_4)_2Ca_3$  depending on the following relationship [13]:

$$\text{TPL (Tri Basic Phosphate of Lime)} = \%P_2O_5 \times 2.185. \quad (1)$$

In the present case, the phosphate ore quality under investigation in this paper is 66–68% TPL type phosphate.

### 3.2 Chemical Analysis

Generally in nature, the kef-essnoun phosphate ore is not found in its pure state, it is found to form a group of chemical and mineralogical constituents. Phosphate is essentially composed of phosphoric anhydride (30%) mixed with calcium oxide (50 to 53%), silica in small quantities and other impurities such as magnesium oxide, iron and aluminum, sulfides, organic matter and traces of metals [14]. Table 1 shows the analysis results of phosphate ore from a common ore.

**Table 1.** Typical chemical composition of phosphate

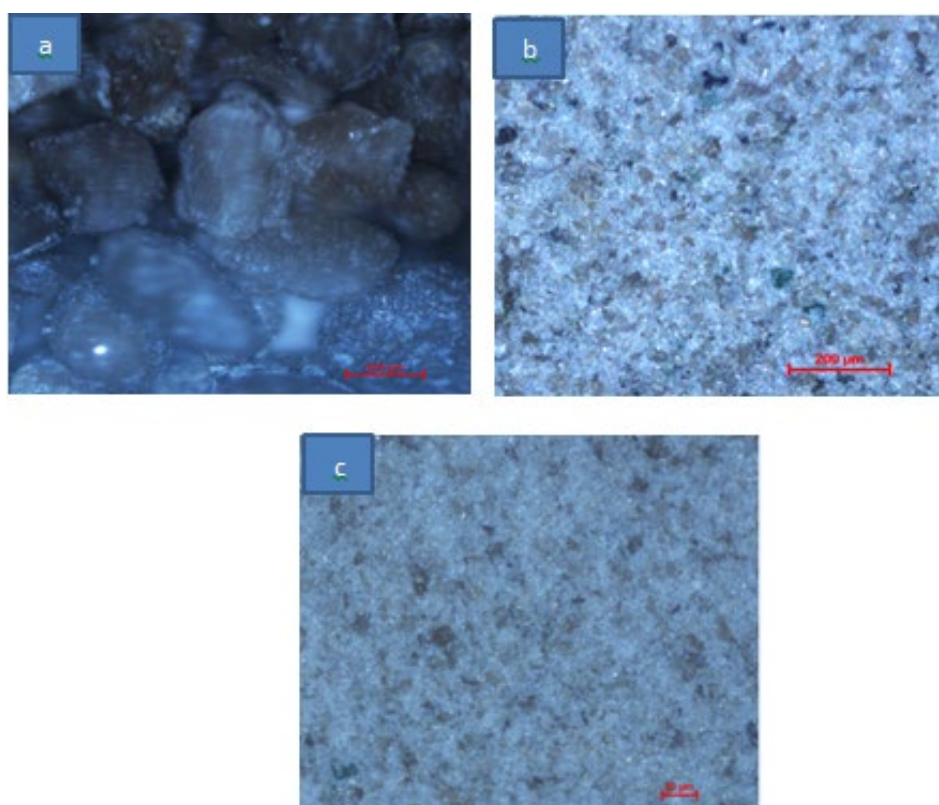
Composants Chimique	Masse (%)
$P_2O_5$	$\geq 30.20$
CaO	50.00-53.00
$CO_2$	5.80-6.30
$SiO_2$	1.20-2.00
$Na_2O$	1.10-1.30
$Al_2O_3$	0.40-0.50
$SO_3$	2.90-3.50
MgO	0.65-0.90
$Fe_2O_3$	0.30-0.40
$K_2O$	0.07-0.10
$H_2O$	0.80-1.50
$CO_2$	2.50-3.00
F	3.00-3.90

According to the chemical composition in major elements ( $P_2O_5$ , CaO) given in Table 1. The CaO/ $P_2O_5$  ratio reaching 1.70 clearly shows that the nature of kefessenoun phosphate ore is very carbonated.

### 3.3 Microscope Observation

The results of the optical microscope observation carried out on the different crushed classes (Figure.2) demonstrated that the natural phosphate of Djebel Onk is mainly composed of phosphate grains of very diverse sizes and shapes linked either by a soft clay matrix, or by a carbonaceous phosphorite matrix. Phosphate grains contain exogangues, such as dolomite, and endogangues.

Clay mineral pellets are mainly composed of quartz and calcite. They generally appear in the form of a stock of crystals, or as endogangue in the structure [15]. Generally speaking, these results confirm the predominance of phosphate elements with gangue elements (dolomite and sometimes quartz).



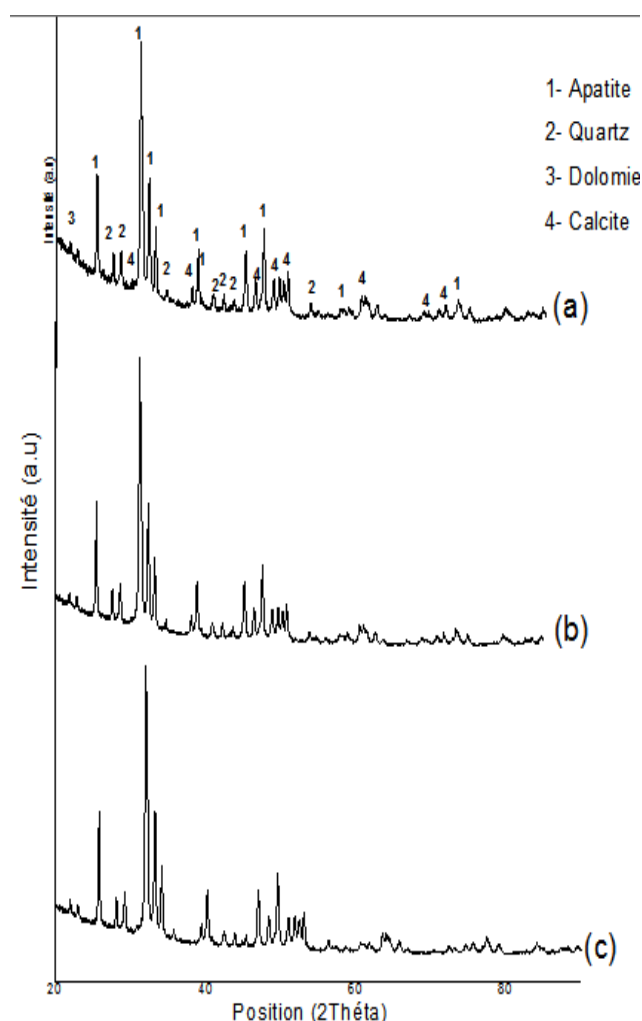
**Figure 2.** Optical microscopy images of phosphate from Jebel Onk. (a) Natural phosphate, (b) Particle size < 90  $\mu\text{m}$ , (c) Particle size < 63  $\mu\text{m}$

### 3.4 Phase Identification by X-Ray Diffraction

The results of X-ray diffractometer (XRD) analysis of raw phosphate ore made it possible to identify the main mineralogical phases. The identification of phases by X-ray diffractometer analysis was done using the JCPDS – ICDD database using HighScore software.

According to the analysis of Figure.1, we notice the presence of the same phases after the treatment by grinding. Therefore the grinding carried out has no influence on the change in the nature of the crystalline phases of these solids.

In this work the ore studied is a phosphate material very rich in carbonate and fluorapatite characterized by the most intense peaks at  $25.81^\circ$ ;  $32.06^\circ$ ;  $33.29^\circ$  and  $34.16^\circ$ , with the presence of other phases such as: calcium carbonate and silica in low intensity, the evolution of the size of the crystallites of each class was highlighted by XRD. We note a decrease in the crystalline size from  $221\text{\AA}$  to  $159\text{\AA}$  of the two classes ( $90\mu\text{m}$  and  $63\mu\text{m}$ ) respectively.



**Figure 3.** XRD diagram of crushed phosphate powder (a) crushed class 90µm, (b) crushed class 63µm, (c) raw class

## 4 CONCLUSION

The chemical and mineralogical analysis of the phosphate minerals studied allowed a qualitative and quantitative verification with the aim of exploiting them as a source of high quality  $P_2O_5$  in the new economic context. The study of phosphate ore from the Djebel-Onk region by grain size analysis allowed us to obtain a fine grain size phosphate ore rich in  $P_2O_5$ , clayey and dolomitic.

X-ray diffraction analysis allowed us to identify the different phases:

- The major phases in phosphate elements such as apatite carbonate, hydroxyapatite carbonate, fluorapatite, fluorapatite carbonate.
- The minor phases of the siliceous and carbonate gangue in small quantities.

A decrease in crystal size from  $221\text{\AA}$  to  $159\text{\AA}$  for the two categories (90 µm and 63 µm), respectively.

## Acknowledgments

We would like to express our sincere thanks to the mining company FERPHOS for its assistance in sampling and providing various data, as well as express our gratitude to the testing, characterization and measurement laboratory of the advanced materials research unit (URMM) – Annaba.

## References

- [1] N. Bezzi, T. Djoudi Merabet, and J. Pivan, “Magnetic properties of the Bled El Hadba phosphate-bearing

- formation (Djebel Onk, Algeria): Consequences of the enrichment of the phosphate ore deposit,” *Journal of African Earth Sciences*, vol. 50, no. 2–4, pp. 255–267, Feb. 2023.
- [2] L. Gadri R. Hadji, F. Zahri, Z. Benghazi, A. Boumezbeur, M. L. Boukelloul, et al., “The quarries edges stability in opencast mines: a case study of the Jebel Onk phosphate mine, NE Algeria,” *Arabian Journal of Geosciences*, vol. 8, pp. 8987–8997, Apr. 2015.
- [3] M. Dassamiour, H. Mezghache, and B. Elouadi, “The use of three physicochemical methods in the study of the organic matter associated with the sedimentary phosphorite in Djebel Onk Basin, Arabian,” *Journal of Geosciences*. vol. 6, pp. 309–319, Sept. 2011.
- [4] L. Bounemia and A. Mellah, “Characterization of crude and calcined phosphates of Kef Essenoun (Djebel Onk, Algeria),” *Journal of Thermal Analysis and Calorimetry*, vol. 146, pp. 2049–2057, Sept. 2021.
- [5] A. E. M. Safhi, A. Amar, Y. El Berdai, M. El Ghorfi, Y. Taha, R. Hakkou, et al., “Characterizations and potential recovery pathways of phosphate mines waste rocks,” *Journal of Cleaner Production*, vol. 374, art. no. 134034, Sept. 2022.
- [6] T.V. Kulakovskaya, V. M. Vagabov, and I. S. Kulaev, “Inorganic polyphosphate in industry, agriculture and medicine: Modern state and outlook,” *Process Biochemistry*, vol. 47, no 1, pp. 1–10, Oct. 2012.
- [7] S. Pal, T. K. Ghosh, R. Ghosh, S. Mondal, and P. Ghosh, “Recent advances in recognition, sensing and extraction of phosphates: 2015 onwards,” *Coordination Chemistry Reviews*, vol. 405, art. no. 213128, Feb. 2020
- [8] J. Drzymala, *Mineral Processing*, 1st ed. Wroclaw University of Technology, 2007.
- [9] A. Z. M. Abouzeid, “Physical and thermal treatment of phosphate ores,” *International Journal of Mineral Processing*, vol. 85, no 4, pp. 59–84, Jan. 2008.
- [10] Z. Abouzeid, A. T. Negm and D. A. Elgillani, “Upgrading of calcareous phosphate ores by flotation: Effect of ore characteristics,” *International Journal of Mineral Processing*, vol. 90, no. 1–4, p. 81–89, 2009.
- [11] M.I. Al-Wakeel, “Effect of mechanical treatment on the mineralogical constituents of Abu-Tartour phosphate ore, Egypt,” *International Journal of Mineral Processing*, vol. 75, no 1–2, pp. 101–112, Jan. 2005.
- [12] E. H. Oelkers and E. Valsami-Jones, “Phosphate mineral reactivity and global sustainability,” *Elements*, vol. 4, no 2, p. 83–87, Apr. 2008.
- [13] M. Amrani., Y. Taha, A. Kchikach, M. Benzaazoua, and R. Hakkou, “Valorization of phosphate mine waste rocks as materials for road construction,” *Minerals*, vol. 9, no 4, art. no. 237, Apr. 2019.
- [14] N. Bezzi, T. Aifa, S. Hamoudi, D. Merabet, “Trace elements of Kef Es Sennoun natural Phosphate (Djebel Onk, Algeria) and how they affect the various Mineralurgic modes of treatment,” *Procedia Engineering*, vol. 42, pp. 1915–1927, Aug. 2012.
- [15] U. Ryszko, P. Rusek and D. Kołodyńska, “Quality of phosphate rocks from various deposits used in wet phosphoric acid and P-fertilizer production,” *Materials*, vol. 16, no 2, art. no. 793, Jan. 2023.



## Modeling of the Working Flow Propagation in the Well Ejection System Flow Part

Denys Panevnyk\*<sup>1</sup>

<sup>1</sup>*Department of Oil and Gas Machines and Equipment, Ivano-Frankivsk National Technical University of Oil and Gas, Ukraine*

---

### Abstract

Based on the use of the mathematical apparatus of the theory of functions of a complex variable, a method is proposed for modeling the propagation of the working flow in the flow path of an ejection well system in the form of a point source placed on the same axis as the mixing chamber of a jet pump. The point source of the working flow is considered as a function of the current reduced to a complex form. The working fluid radially leaves the source symmetrically in all directions. The streamlines of the working flow along the radii are directed from the center of the source. The radial velocity of the outflow decreases with distance from the center in inverse proportion to the first power of the distance to it. Using the equation of the velocity potential and the stream function, a relation is obtained for the complex potential of the plane-radial and spatial working flow. The set of mutually perpendicular streamlines and lines of equal potentials forms a hydrodynamic grid of a plane-radial working flow, which determines the kinematic picture of the working medium motion. The velocity of the liquid remains unchanged along the equipotential lines and changes when moving from one line to another. The flow rate of the liquid is constant along the streamlines and changes when passing to an adjacent line. The spatial hydrodynamic grid is formed by equipotential surfaces and flow surfaces of stream functions and has the form of orthogonally placed coaxial spheres and radial meridional planes. The complex potential obtained in the course of research is a function of the operating flow rate in the flow path of the jet pump and can be used in modeling the process of its symmetrical rotation in the well. This template is designed to guide authors in preparing their papers by direct editing. Although this template was prepared in word format, a similar format can be used in Latex format under the responsibility of authors.

**Keywords:** *Borehole jet pump, Potential flows, Hydrodynamic functions, Complex potential, Stream function*

---



---

## Design of Ring Yarn Structures: Physical-Mechanical Properties of Different Yarns for Improved Sustainability and Performance

Ivana Salopek Čubrić\*<sup>1</sup>

<sup>1</sup>Department of Textile Design and Management, University of Zagreb Faculty of Textile Technology, Zagreb, Croatia

---

### Abstract

The use of polyamide yarns and its significance in the textile industry increases due to its elasticity, flexibility, and ease of maintenance, particularly in sportswear. Besides conventional yarns, the interest is increased towards the use of recycled and functional polyamide yarns. The adoption of recycled yarns offers environmental benefits by reducing resource demand and waste generation, though variations in quality and performance require careful consideration. With a growing emphasis on performance, there's a rising demand for functional yarns offering advanced features like moisture-wicking and antimicrobial properties, despite potential cost implications. This investigation was conducted on a set of polyamide yarns - conventional, recycled, and functional by testing various parameters and physical-mechanical properties. The results of testing provide insights into each yarn type's characteristics, aiding in decision-making for production processes.

**Keywords:** Yarn, Testing, Ring, Functionality, Recycling, Sustainability, Material, Polyamide

---

## 1 INTRODUCTION

Polyamide yarns belong to the group of yarns made of artificial fibres obtained by spinning from the melt of polyamide polymers. Such yarns are very suitable for making products with high elasticity and flexibility, they are easy to maintain and do not wrinkle in use. Furthermore, the advantage of the polyamide yarn use is also seen in the fact that those yarns are not flammable. When used in the fabric, they dry quickly which is why such yarns are widely used for sportswear. The disadvantage of polyamide yarns is charging with static electricity. Polyamide yarns do not retain heat, which may be both advantage and disadvantage, depending on the final product. Recently, a number of studies was published that observed different aspects in the production of polyamide yarns and fibres that are forwarded towards the improvement of properties [1–6]. Regarding the type, polyamide yarns are used either as conventional, recycled or functional yarns with a wide range of possible functionalities. Those yarns are, along with the polyester yarns [7–9], still dominant for the production of sportswear.

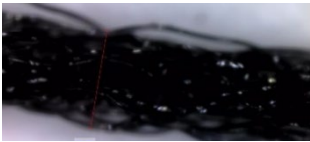
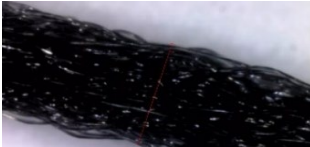

The use of recycled yarns presents numerous advantages. For example, their use reduces the need for new materials, thus decreasing the environmental toll of sourcing and processing raw materials. This leads to lower carbon emissions, decreased energy consumption, and minimized waste generation. However, recycled yarns can vary in quality and performance compared to non-recycled materials. Factors like the origin and treatment of recycled materials may influence yarn characteristics such as strength, elasticity and durability in use. Still, despite potential variations, the use of recycled yarns offers a sustainable approach to manufacturing, aligning with consumer preferences for environmentally friendly products. Nonetheless, careful consideration of quality indices, durability in use, and total costs of production is crucial to effectively integrate recycled materials into production processes.

As the textile industry increasingly prioritizes performance and functionality of a final product, there's a rising demand for functional yarns across diverse sectors, including sports apparel, outdoor wear, medical textiles, and industrial applications. Consumers now seek textiles that not only provide comfort and style but also boast advanced performance features. Functional yarns are engineered to enhance textile performance in various ways, offering improved properties, like moisture/sweat transfer, heat transfer/heat retention, antimicrobial properties, and UV protection. Disadvantage of the use of functional yarns, despite their performance benefits, are seen through increase of the production costs compared to conventional yarns. Therefore, manufacturers must carefully compare the improved properties that those yarns give to the final product and production costs when integrating functional yarns into their products.

## 2 MATERIALS AND METHOD

For the investigation was selected a set consisting of polyamide ring yarns that are conventional, recycled or functional. The description of materials regarding the raw material with accompanying material designation is given in Table 1.

**Table 1.** Materials used for the assessment

Number	Raw Material / Special Function	Material Designation	Microscopic Image
1	100% Polyamide Conventional yarn	YC	
2	100% Polyamide Recycled yarn	YR	
3	100% Polyamide Functional yarn	YF	

The selected yarns were tested for a number of parameters and physical-mechanical properties, like diameter, number of twists, tensile properties, hairiness and abrasion.

**Diameter:** The yarn diameter was determined using a Dino-Lite Pro Hr AM7000/AD7000 series, 5 megapixel microscope, with which yarn specimens were photographed. Before starting the actual measurement, it was necessary to calibrate the microscope, i.e. set it to certain parameters. Each yarn consists of thicker and thinner places, and considering such non-uniformity, an average thickness that extended over the largest part of the yarn was sought. The measurement process was carried out in such a way that each yarn sample was placed on a bright surface, and in different places, with the help of a microscope, yarns were photographed, which was visible on the computer screen. The software DinoCapture 2.0 was used to measure the diameter. A total of 10 measurements was performed for each yarn.

**Number of twists:** On the torziometer device of the brand Twister, Mesdan Lab, the test of the twist of the yarn was carried out for each yarn. A total of 10 measurements was done.

**Tensile properties:** On the device dynamometer Statimat M- produced by Textechno company, the yarns were tested for tensile properties. The total of 50 measurements was performed for each yarn and the testing was conducted in the dry state. The device is fully automated and connected to a computer to which it sends data through a specific program it contains. The device contains two pneumatic clamps, one of which is fixed (upper) and the other is attached to the stretching slide (lower). According to the defined norm, the upper clamp slides towards the lower one, after which the lower one continues to slide and stretch the yarn until the yarn breaks. For the comparison of tensile properties, the focus was placed on yarn tenacity.

**Hairiness:** Yarn hairiness was measured on a yarn hairiness measuring device type G 565 produced by Zweigle. The device works on the photometric principle. For each yarn, 5 measurements were made for four length classes, from the smallest (X1) to the largest (X4). The measuring length was set to 25 m. After reading the number of protruding fibers, the actual number of protruding fibers was calculated. The device functions in such a way that it consists of four channels by means of which the desired length zones are defined, it also has a measuring field consisting of a photoreceptor. At the very entrance of the material to the measuring zone, there is a light that, based on the projection of the shadow of the fibers, counts only those fibers that protrude from the body of the yarn. The received light is converted into an electrical signal by means of a detector.

**Abrasion:** Each sample was tested on an abrasion tester type G550. The abrasion tester works on the principle that a weight is placed on each placed yarn, which after the yarn breaks, falls into its field and marks the number of abrading cycles that were needed until the yarn breaks. Each yarn break causes the sandpaper wrapped around the rod to move left and right. Such a principle shows the maximum durability of a particular yarn.

### 3 RESULTS

The results of yarn testing, including diameter, number of twists, tensile properties, hairiness and abrasion are presented in Figures 1-6.

The results provide insights into the physical and mechanical properties of each type of yarn. As can be seen from Figure 1, the recycled yarn (assigned as YR) has the smallest diameter, indicating it might be spun finer than the other types due to the fact that its raw material has already been in use. In this group of yarns, it was shown that the functional yarn has the highest diameter (Figure 2) which is to be explained by the additional process of yarn functionalization. Regarding the number of twists, it was confirmed that all yarns have approximately the same value.

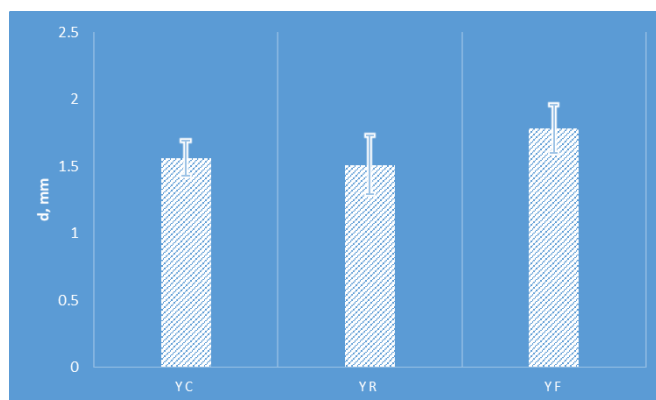


Figure 1. Yarn diameter

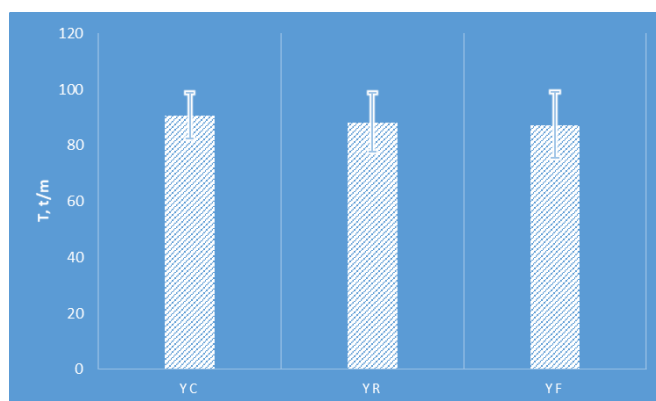


Figure 2. Number of twists

As far as the tenacity is observed, the recycled yarn surprisingly showed the highest values (Figure 3, 4). Such outcome indicates that this yarn is to be more resistant to the forces applied. It is to further investigate how this behaviour influences the fabric hand properties, especially the perception of material softness.

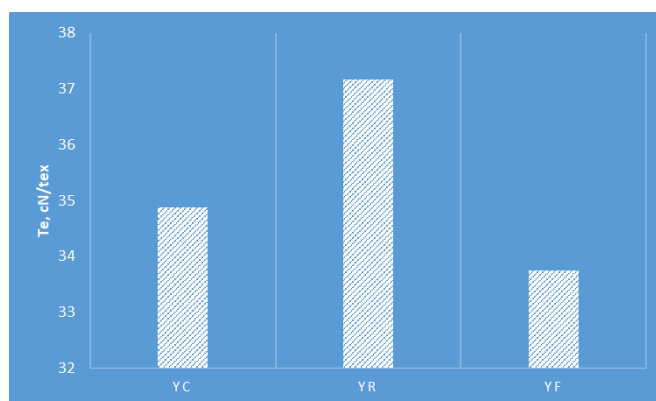


Figure 3. Tenacity



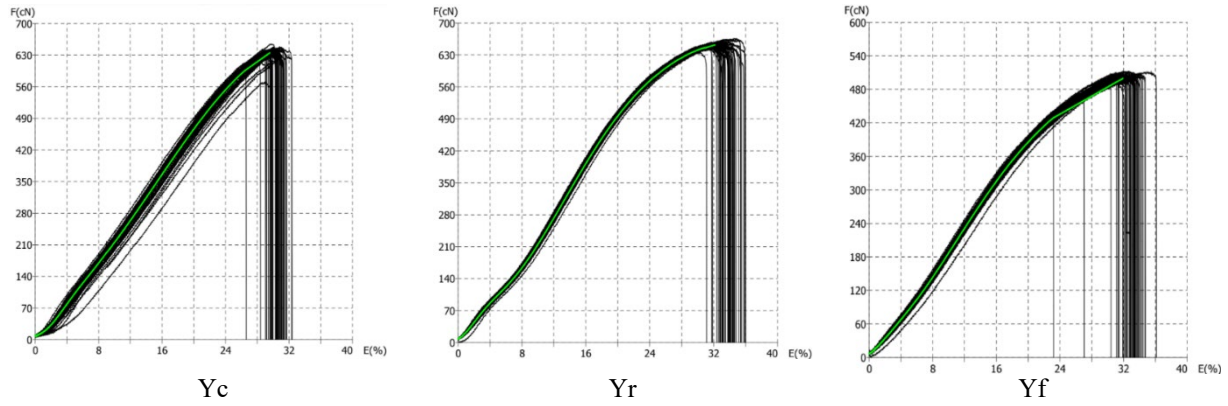


Figure 4. F/E curves

The number of protruding fibers is highest in the recycled yarn, suggesting potential issues with the yarn structure during the further production processes. Still, this number is not so high and is quite unlikely that the users may perceive differences between the yarns regarding this property.

The conventional yarn (assigned as YC) has the highest number of abrading cycles (Figure 6). This outcome points out the fact that it might be much more durable than recycled or functional yarns when used in a garment. In comparison, the number of cycles needed for a recycled and functional yarn to break is 2-3 times lower.

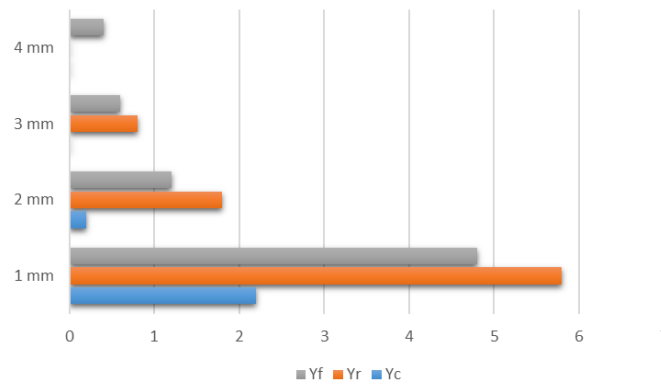


Figure 5. Hairiness – number of protruding fibres

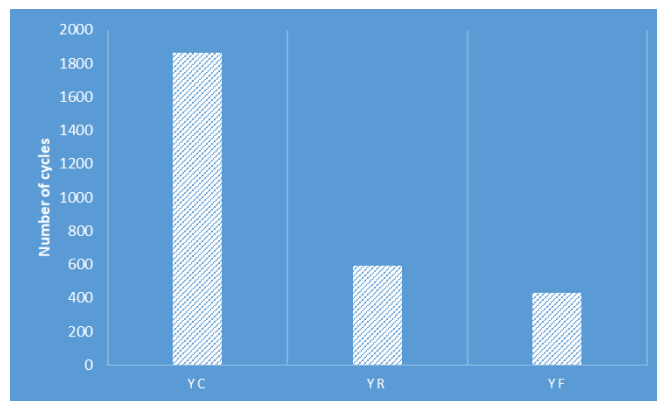


Figure 6. Abrasion – average number of abrading cycles

Determining which yarn is better for the production of materials depends on the specific requirements of the materials being produced and the intended application. Each yarn type has its own set of characteristics that make it suitable for different purposes. The conventional yarn can support a very high number of abrading cycles, indicating good durability of the final product in use. It also has a moderate tenacity, what is durability-related. The standard deviation of diameter and number of twists per meter is relatively low, suggesting consistent quality. Conventional yarns are often cost-effective in comparison to the functional yarns due to standardized production processes. So, very good durability and low production costs are advantages of this yarn type.

Recycled yarns are environmentally friendly as they are made from recycled materials. This can be a significant factor for companies focusing on sustainability. The results have shown that this type of yarn has the smallest diameter among the three yarns, potentially making it suitable for finer fabrics or applications requiring lightweight materials. Great tenacity and average resistance to abrasion compared to the conventional yarn, makes the recycled yarn may still a very good option for many applications.

Functional yarns are engineered to possess specific properties tailored to particular applications. However, the provided results does not indicate a clear advantage in terms of strength or longlasting durability compared to the other yarns, i.e. recycled and conventional. Functional yarns can be customized to meet specific performance requirements, and to have increased properties besides those that were the topics of investigation with this research. Therefore, increase of the special functional property is expected to make them suitable for a specialized application.

## 4 CONCLUSION

The results of the study indicated the differences between three types of polyamide yarns – conventional, recycled and functional. In summary, the choice of yarn depends on the priorities of the production process and the final use of the garment that will be made using those yarns. If durability and consistency are paramount, the conventional yarn may be preferred. For environmentally conscious production or applications requiring finer materials, the recycled yarn could be a better option. If specialized properties or customization are required, the functional yarn may be the most suitable choice. Ultimately, the decision should be based on a comprehensive evaluation of the specific needs and goals of the production process.

## Acknowledgments

This work has been fully supported by Croatian Science Foundation under the project IP-2020-02-5041, Textile Materials for Enhanced Comfort in Sports – TEMPO.

## References

- [1] J. E. Song, H. R. Kim, and S. H. Lee, "Effect of enzymatic hydrolysis on developing support of polyamide woven fabric for enzyme immobilization," *Textile Research Journal*, vol. 89, no. 7, pp. 1345–1360, 2019, doi:10.1177/0040517518767148.
- [2] F. M. Bezerra, D. S. de Carvalho Cotre, A. Plath et al., "β-Cyclodextrin: Disperse yellow 211 complexes improve coloristic intensity of polyamide dyed knits," *Textile Research Journal*, vol. 92, no. 13–14, pp. 2194–2204, 2022, doi:10.1177/00405175211022624.
- [3] B. Rietzler, B. Caven, T. Bechtold, and T. Pham, "Treatment of polyamide 66 fabric for increased ultraviolet protection," *Textile Research Journal*, vol. 90, no. 15–16, pp. 1881–1888, 2020, doi:10.1177/0040517519896752.
- [4] N. Xu, G. Wang, and Y. Tao, "Construction of unsaturated systems on the surface of polyamide fibers," *Textile Research Journal*, vol. 93, no. 23–24, pp. 5336–5344, 2023, doi:10.1177/00405175231193778.
- [5] Y. A. Eltahir, H. A. M. Saeed, C. Yuejun, Y. Xia, and W. Yimin, "Effect of hot drawing on the structure and properties of novel polyamide 5,6 fibers," *Textile Research Journal*, vol. 84, no. 16, pp. 1700–1707, 2014, doi:10.1177/0040517514527378.
- [6] A. H. Hekmati, A. Rashidi, R. Ghazisaeidi, and J.-Y. Drea, "Effect of needle length, electrospinning distance, and solution concentration on morphological properties of polyamide-6 electrospun nanowebs," *Textile Research Journal*, vol. 83, no. 14, pp. 1452–1466, 2013, doi:10.1177/0040517512471746.
- [7] A. Petrov, I. Salopek Čubrić, and G. Čubrić, "Influence of aging on the physical properties of knitted polymeric materials," *Polymers*, vol. 16, no. 4, art. no. 513, 2024, doi: 10.3390/polym16040513.
- [8] I. Katić Križmančić, I. Salopek Čubrić, V. M. Potočić Matković, and G. Čubrić, "Changes in mechanical properties of fabrics made of standard and recycled polyester yarns due to aging," *Polymers*, vol. 15, no. 23, art. no. 4511, 2023, doi: 10.3390/polym15234511.
- [9] I. Salopek Čubrić, G. Čubrić, I. Katić Križmančić, and M. Kovačević, "Evaluation of changes in polymer material properties due to aging in different environments," *Polymers*, vol. 14, no. 9, art. no. 1682, 2022, doi: 10.3390/polym14091682.



---

## Assessment of Material Sensory Properties: Focus on bipolar attributes of Stiffness-Softness and Roughness-Smoothness

Ivana Salopek Čubrić<sup>1</sup>, Goran Čubrić<sup>\*2</sup>

<sup>1</sup>Department of Textile Design and Management, University of Zagreb Faculty of Textile Technology, Zagreb, Croatia

<sup>2</sup>Department of Clothing Technology, University of Zagreb Faculty of Textile Technology, Zagreb, Croatia

---

### Abstract

Extensive research has focused on understanding sensory attributes in relation to human perception, highlighting the critical factors influencing successful sensory evaluations, including assessor profiles, commitment, procedural definition, and overall quality assurance. Market segmentation theory suggests that consumer factors, such as geographic, demographic, psychological, or socio-cultural aspects, significantly impact research outcomes. This study aims to explore how the use of different materials affect fabric attribute perception among evaluators with diverse profiles. Following recommendations from previous studies, particularly concerning material selection and evaluator recruitment, a range of materials used in sportswear and next-to-skin wear was chosen for examination. Bipolar attributes, including stiffness-softness and roughness-smoothness, were carefully selected to address various aspects of tactile perception pertinent to the fabrics assessed by different evaluator groups. The results reveal that fabrics made of 100% man-made yarns were perceived as softer compared to cotton fabrics, irrespective of the addition of elastane. However, the disparities in softness perception were less pronounced among male evaluators, particularly those in the 60-65 age group. Notably, variations in smoothness perception were evident across different evaluator groups with the average ratings from the oldest male group displaying uniformity.

**Keywords:** Sensory analysis, Material, Yarn, Fabric, Stiffness, Softness, Roughness, Smoothness

---

## 1 INTRODUCTION

A number of consumer purchases of textiles and apparel are driven by visual appeal and sensory attraction and in this context, sensory attributes need to be considered as essential sales argument. Researchers point out that fabric hand is a nuclear factor related to comfort of textile and clothing [1]. Therefore, strong efforts have been done towards interpretation of sensory attributes with respect to human senses [2-4]. The success of a sensory evaluation largely depends on a number of influencing factors among which are the profile of assessors, their commitment to evaluation, definition of procedure and assurance of quality of whole procedure. According to the theory of market segmentation [5, 6], the correlation of consumer factors (i.e. geographic, demographic, psychological or socio-cultural) is supposed to have significant impact on research outcomes.

Regarding the material used in the evaluation, scientists have focused at wide range of materials, mainly with significant differences regarding the fabric construction, fibre composition and range of mass per unit area. The total number of fabrics used in investigations is from 4 upwards. In the study of Xue et al., the set of fabrics differed according to the raw material (wool, cotton, polyester, cashmere, rayon and elastane) and fabric weave (satin, tweed, twill, plain, etc.), with fabric mass per unit area in the range 4.30-13.48 mg/cm<sup>2</sup> [4]. The authors concluded that use of simple sensory techniques (in this case free sorting and rating) should be observed as efficient for assessment of relatively large number of fabrics [4]. In another research, the focus was placed towards investigation of non-homogenous set of fabrics (authors define that they are meant to be for common clothing articles) including both knitted and woven fabrics. Additionally, fabrics differed in fiber composition (Tencel®, micro Tencel®, cotton, modal, micro modal, wool, polyester, polyamide), structural parameters, as well as different finishing processes [3]. The results showed good agreement between panel members for attributes of smoothness and softness, but not for warmth. As a limitation of fabric set, authors point out higher differences of fabric parameters (thickness, mass per unit area) and advise other scientists not to use too distinct samples [3]. Park et al. focused at evaluation of coolness of different knitted fabrics (jersey, mesh, tricot, pique, honeycombed pique) produced of Nylon/Spandex, polyester/Nylon, cotton and polyester and with mass per unit area 118-220 g/m<sup>2</sup>. The outcomes of the study showed that differences in assessment are affected by knit type. The study did not confirm consistent influence of fiber composition or yarn fineness [7]. The attempt has been made to evaluate set of 20 fabrics highly differing in mass per unit area (33.80-340.84 g/m<sup>2</sup>), fabric construction (woven - plain,

chiffon, satin, flannel, knitted - rib, single jersey, jacquard and nonwoven) and fiber composition (cotton, linen, polyester, elastane, viscose, Supro, Tencel, wool, nylon, silk). The results are further compared to results of instrumental measurements and significant correlations between results of two used methods are reported [1]. Evaluation of 13 fabrics consisting of cellulosic, wool, polyester and polyamide knitted and woven fabrics with varied mass per unit area (121-158 g/m<sup>2</sup>) showed good agreement between panel members for fabric smoothness and softness [3]. Authors point out that the size of fabric set used in evaluation impacts the precision of outcomes in the way that it decreases with increasing of fabrics within the set [3].

In the Table 1 is given an overview of the profile of evaluators in the studies covering the sensory evaluation of fabric attributes. As can be seen, the total number of evaluators in the studies varies from 7 to 40 and mostly includes both female and male volunteers. In a number of studies, the age range of participating evaluators is quite wide. The other specifics important for the definition of the profile, such as profession, education level or nationality are not taken into consideration in all the studies. Based on the information given, it could be concluded that researchers mostly engage students or employees of the same company.

**Table 1.** The profile of evaluators [8–18]

Total number of evaluators	Age of evaluators	Gender of evaluators (F –female; M - male)	Origin	Education level	Specifics
35	Less than 30- more than 60	F 24 M 11	28 of 35 Germans	Different	5 blind or visually impaired
21	-	-	-	-	Sight disorders
10	23-54	-	Same nationality	-	-
40	23-60	F 24 M 16	-	-	-
30	-	F 20 M 10	-	Students	-
15	-	F 10 M 5	-	-	Employees at the same company
7	-	F 7 M 0	-	Students	-
29	-	-	Japanese	-	-
23	21-45	F 15 M 8	-	-	-
28	23-56	F 14 M 14	From Asia, Africa and Europe	Different	Stayed in Europe for at least 1 month before experiment
23	22-30	F 12 M 11	-	-	-
20	25-41	F 11 M 9	-	Faculty staff, students	Untrained
31	19-38	F 16 M 15	-	University students	-
13	Around 20	-	-	College students	-
8	24-35	-	-	-	-
10	23-54	-	-	-	From the same university

The intention of this study is to determine the effect of knitted material on the perception of fabrics' attributes among evaluators with different profile. In the definition of experiment, the recommendations given by authors of previous studies are taken into account, especially regarding the selection of materials [3] and recruitment of evaluators [3, 4, 19].

## 2 MATERIAL AND METHOD

For the investigation is selected a set of different knitted materials used for the production of next-to-skin wear. The description of materials regarding the raw material with accompanying material designation is given in Table 2.


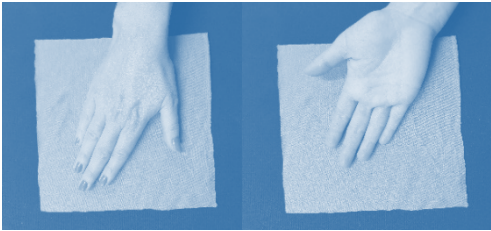
**Table 2** Materials used for the assessment

Number	Raw material	Material designation
1	100% Cotton	CO
2	100% Cotton	CO1r
3	100% Cotton	CO2
4	100% Cotton	CO3
5	92% Cotton + 2% elastane	CO3/EL1
6	98% Cotton + 2% elastane	CO3/EL2
7	100% Viscose	CV
8	100% Polyester	PES
9	100% Lyocell	CLY

In a prior study [20], it was emphasized that assessing sensory qualities requires targeted evaluators. Since the fabrics under evaluation are meant for close-to-skin wear, which appeals to a diverse consumer base, it was crucial to involve evaluators of various genders and ages. To minimize discrepancies influenced by individual factors, a method was devised to precisely define evaluator groups based on age and gender. Recognizing the significance of feedback from diverse evaluator profiles, the recruitment aimed to form six distinct evaluator groups, evenly split between female and male evaluators. These groups were categorized by age: 20-25, 40-45, and 60-65 years old.

The assessment took place in a controlled examination room set at a temperature of 20±2°C and a relative humidity of 65±5%. Evaluators were instructed to refrain from using hand moisturizers on the assessment day to prevent any impact on their perception. Each evaluation was conducted individually, with a facilitator guiding the evaluator through the process. The facilitator provided information on the fabrics' purpose, as well as the bipolar fabric properties and rating scale. Bipolar attributes were selected to cover various aspects of tactile perception relevant to the specific fabrics being assessed. A total of two of key bipolar attributes were examined: stiffness-softness, and roughness-smoothness. The evaluation procedure was outlined briefly, and instructions for handling the fabrics were provided, Table 3.

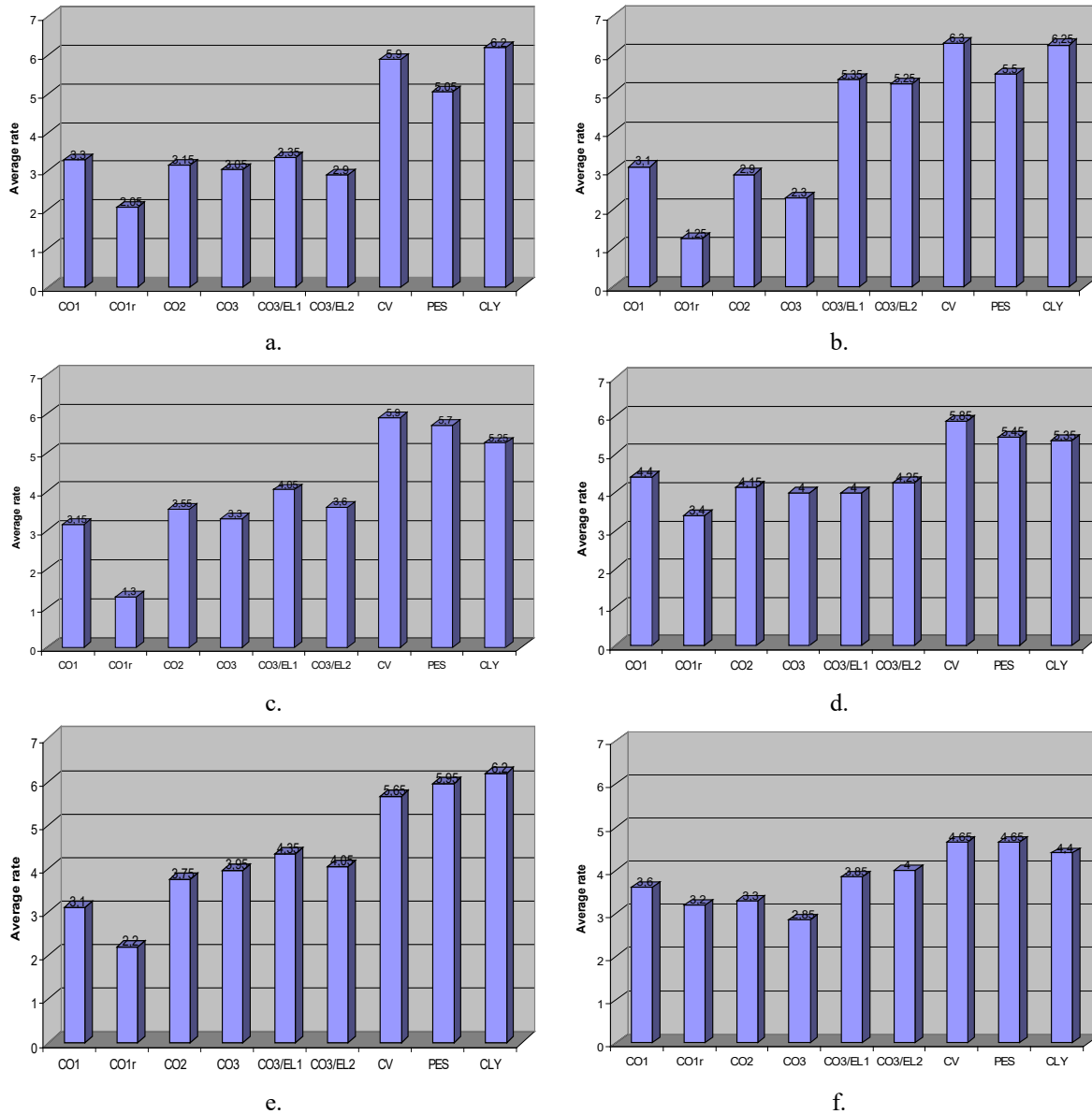
**Table 3.** Bipolar attributes and instructions for manipulation

Bipolar Attributes	Instruction for Manipulation During Evaluation	
Stiffness-Softness	Take the fabric from the flat surface. Rub and squeeze the fabric between thumb and index fingertip; then between thumb and other fingers.	
Roughness-Smoothness	The fabric is placed on the flat surface. Move the palm and fingers over the fabric surface; move the back of the hand in the same way.	

## 3 RESULTS

The results of average rates given by groups of evaluators for two bi-polar attributes are given in the figures 1 and 2.

As can be seen from the Figure 1, all groups of evaluators perceived fabrics produced of 100% man-made yarns (i.e. viscose, polyester and lycell) as softer than fabrics produced of cotton (both with or without addition of elastane). Male evaluators 20-40 years old gave a very high softness rating for cotton material with added elastane (greater than 5). Other groups of evaluators gave this group of samples a lower rating, similar to the rating for materials without elastane. Most groups of evaluators rated the material CO1r (cotton without elastin) as the stiffest. Only the oldest male group rated the material CO3 as the stiffest. Differences between the perceptions of softness are less pronounced for male evaluators, especially those in the age group 60-65. Given the results, it can be concluded that the perception of smoothness differs a lot between different groups of evaluators.

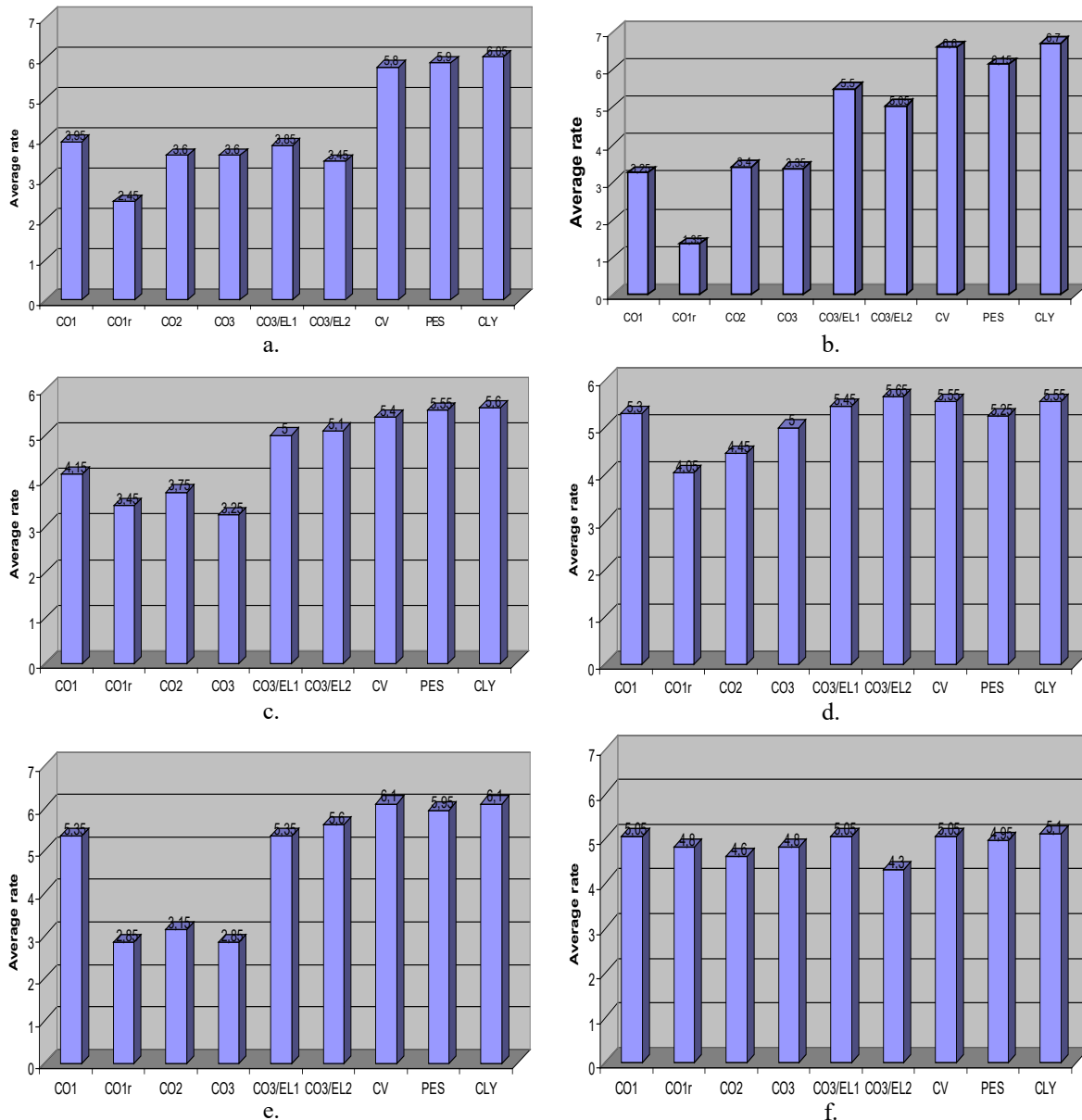


**Figure 1.** Average rating for bipolar attributes stiffness - softness (S-S) given by evaluation group: a. Female 20 years old, b. female 40 years old, c. female 60 years old, d. male 20 years old, e. male 40 years old, and f. male 60 years old

From the Figure 2, it is seen that average rates given by members of the oldest male group are quite uniform. It can be said that this group of evaluators could not detect any differences in the roughness of the material. Male evaluators aged 40-60 years gave quite similar results in the assessment of roughness assessment. Only cotton samples without elastane (CO1r and CO2) were rated as rougher than other materials.

Female evaluators made differences in roughness between the individual material groups of materials (cotton; cotton with elastane; man-made yarns). Female evaluators aged 20-40 years rated the material with elastane similarly to the material without elastane, in contrast to the other two groups of female evaluators. These groups

rated the material with elastane just as well as the materials made from man-made yarns. For these bipolar attributes (roughness-smoothness), it can also be seen that they differ greatly in relation to different groups of evaluators.



**Figure 2.** Average rating for bipolar attributes roughness-smoothness (R-S) given by evaluation group: a. Female 20 years old, b. female 40 years old, c. female 60 years old, d. male 20 years old, e. male 40 years old, and f. male 60 years old

#### 4 CONCLUSION

This study focuses on the evaluation of the sensory perception of knitted fabrics made from different fibres. The materials were evaluated by a panel of assessors comprised of six different groups of evaluators consisting of equal numbers of female and male evaluators. A two important bipolar attributes were analysed: stiffness-softness and roughness-smoothness. All evaluators groups perceived knitted fabrics made from 100% man-made yarns to be softer than knitted fabrics made from cotton with or without elastane. However, the differences in the perception of softness were less noticeable among the male assessors, especially those between 60 and 65 years of age. The average values for the roughness-smoothness attribute given by the members of the oldest male group are uniform, while the female evaluators made differences between the individual material groups in terms of roughness. It can be concluded from this that the influence of the age and gender of the assessors on sensory perception was established for both attributes analysed.

## Acknowledgments

This work has been fully supported by Croatian Science Foundation under the project IP-2020-02-5041, Textile Materials for Enhanced Comfort in Sports – TEMPO.

## References

- [1] X. Liao, Y. Li, J. Hu, X. Wu, and Q. Li, “A Simultaneous measurement method to characterize touch properties of textile materials,” *Fibers and Polymers*, vol. 5, no. 7, pp. 1548–1559, Jul. 2014.
- [2] A.M. Pensé-Lh eritier, C. Guilabert, M.A. Bueno, M. Sahnoun, and M. Renner, “Sensory evaluation of the touch of a great number of fabrics,” *Food Qual Preference*, vol. 17, no. 6, pp. 482–488, Sep. 2006.
- [3] A. B. H. Musa, B. Malengier, S. Vasile, and L. Van Langenhove, “A comprehensive approach for human hand evaluation of split or large set of fabrics,” *Textile Research Journal*, vol. 89, no. 19–20, pp. 4239–4252, Feb. 2019.
- [4] Z. Xue, X. Zeng, L. Koehl, and L. Shen, “Consistency and reliability of untrained consumers’ perceptions of fabric hand of men’s suiting,” *Textile Research Journal*, vol. 86, no. 13, pp. 1425–1442, Aug. 2016.
- [5] L. Schiffman and L. Kanuk, *Consumer Behavior*, 11<sup>th</sup> Edition, Pearson, 2015.
- [6] A. Weinstein, *Handbook of Market Segmentation: Strategic Targeting for Business and Technology Firms*, Haworth Press, 2004.
- [7] J. Park, H-S. Yoo, K. H. Hong, and E. Kim, “Knitted fabric properties influencing coolness to the touch and the relationship between subjective and objective coolness measurements,” *Textile Research Journal*, vol. 88, no. 17, pp. 1931–1942, Sep. 2017.
- [8] S. Wiskott, M.O. Weber, F. Heimlich, and Y. Kyosev, “Effect of pattern elements of weft knitting on haptic preferences regarding winter garments,” *Textile Research Journal*, vol. 88, no. 15, pp. 1689–1709, Aug. 2018.
- [9] D. Grinevi iute, V. Daukantiene, and M. Gutasukas, “Textile hand: Comparison of two evaluation methods,” *Material Science (Medziagotyra)*, vol. 11, no. 1, pp. 57–63, Dec. 2005.
- [10] M.G. Tadesse, R. Harpa, Y. Chen, L. Wang, V. Nierstrasz, and C. Loghin, “Assessing the comfort of functional fabrics for smart clothing using subjective evaluation,” *Journal of Industrial Textiles*, vol. 48, no. 8, pp. 1310–1326, Mar. 2019.
- [11] G. Ozcelik, G. Supuren, T. Gulumser, and I. Tarakcioglu, “A study on subjective and objective evaluation of the handle properties of shirt fabric,” *Fibres and Textiles in Eastern Europe*, vol. 68, no. 3, pp. 56–62, May 2008.
- [12] C. L. Hui, T. W. Lau, S. F. Ng, and K. C. C. Chan, “Neural network prediction of human psychological perceptions of fabric hand,” *Textile Research Journal*, vol. 74, no. 5, pp. 375–383, May 2004.
- [13] A. V. Cardello, C. Winterhalter, and H. G. Schutz, “Predicting the handle and comfort of military clothing fabrics from sensory and instrumental data: development and application of new psychophysical methods,” *Textile Research Journal*, vol. 73, no. 3, pp. 221–237, Mar. 2003.
- [14] R. A. Asad, W. Yu, Q. Siddiqui, M. Vincent, and Q. Wang, “Subjective evaluations of fabric-evoked prickle using the unidimensional rating scale from different body areas,” *Textile Research Journal*, vol. 86, no. 4, pp. 350–364, Mar. 2016.
- [15] H. Kanai, H. Kimura, M. Morishima, U. Shouji, T. Nishimatsu, K. Shibata, and T. Yamamoto, “Microscopic photometry and its parameterization for objective evaluation of aesthetics of woven fabrics,” *Textile Research Journal*, vol. 82, no. 19, pp. 1982–1995, Nov. 2012.
- [16] Z. Xue, X. Zeng, and L. Koehl, “Development of a method based on fuzzy comprehensive evaluation and genetic algorithm to study relations between tactile properties and total preference of textile products,” *Journal of Textile Institute*, vol. 108, no. 7, pp. 1085–1094, 2017.
- [17] Q. Wang, Y. Tao, Z. Zhang, J. Yuan, Z. Ding, Z. Jiang, Z. Jia, and J. Wang, “Representations of fabric hand attributes in the cerebral cortices based on the Automated Anatomical Labeling atlas,” *Textile Research Journal*, vol. 89, no. 18, pp. 3768–3778, Sep. 2019.
- [18] M. G. Tadesse, E. Loghin, M. Pislaru, L. Wang, Y. Chen, V. Nierstrasz, and C. Loghin, “Prediction of the tactile comfort of fabrics from functional finishing parameters using fuzzy logic and artificial neural network models,” *Textile Research Journal*, vol. 89, no. 19-20, pp. 4083–4094, Oct. 2019.
- [19] I. L. Ciesielska-Wr obel, and L. Van Langenhove, “The hand of textiles – definitions, achievements, perspectives – a review,” *Textile Research Journal*, vol. 82, no. 14, pp. 1457–1468, Sep. 2012.
- [20] I. Salopek  ubri , G.  ubri , and P. Perry, “Assessment of knitted fabric smoothness and softness based on paired comparison,” *Fibers and Polymers*, vol. 20, no. 3, pp. 656–667, Apr. 2019.





## Artificial Hydrophobic Surfaces Based on MgO Thin Film: Elaboration and Characterization

Zehira Belamri\*<sup>1</sup>

<sup>1</sup>Phase Transformation Laboratory, Department of Physic, Mentouri Brothers Constantine 1 University, Constantine, 25000 Algeria

---

### Abstract

By simply thermally oxidizing magnesium that had been electrodeposited on aluminium substrates, stable MgO thin films were produced. In this work, we investigated how the molarity of the solution affected the physical characteristics of MgO coatings. The samples were characterized by X-ray diffraction (XRD), Raman spectroscopy, and scanning electron microscopy (FEG-SEM) equipped with energy dispersive X-ray analysis (EDX). The wettability properties of the synthesized films were estimated by measuring the contact angle between the surface of the films and a deposited water drop (WCA). The optimal MgO nanostructure coating crystallizes when magnesium layers are electroplated with 0.2 M of the solution for two hours at 500 °C. The MgO coating's crystal orientation is influenced by the molarity of the solution. Data from the XRD analysis are corroborated by Raman spectroscopy results. Normal vibrational modes that are compatible with the MgO structure were visible in the acquired spectra. The study's findings suggest that the vibration mode of the MgO coating described in this work is affected by changing the solution molarity. This form may be responsible for the MgO<sub>0.2</sub> layer's best hydrophobicity, which is caused by air trapping between the nanowires (fibers) to prevent water from adhering to the film.

**Keywords:** MgO nanowires, Aluminium substrate, Solution molarity, Electroplating, Hydrophobic

---



## Exergy Analysis of Combined Cooling, Heating, and Power Systems Integrated with Carbon Capture and Storage for an LNG Carrier

Engin Guler<sup>1,2</sup>, Selma Ergin<sup>\*1</sup>

<sup>1</sup>Naval Architecture and Marine Engineering Department, Istanbul Technical University, Istanbul, Türkiye

<sup>2</sup>Naval Architecture and Marine Engineering Department, Piri Reis University, Istanbul, Türkiye

### Abstract

The significance of limiting greenhouse gas emissions has grown in the maritime sector and regulations in this regard have become increasingly stricter. This leads to the need for innovative technologies to be used in ships and the development of existing technologies. This study investigates the exergy analysis of cooling, heating, and power systems integration with the carbon capture and storage (CCS) system for a liquefied natural gas (LNG) carrier. Main power, boil-off natural gas (BO-NG) reliquefaction, CO<sub>2</sub> capture, CO<sub>2</sub> liquefaction, and organic Rankine Cycle (ORC) systems are modeled and simulated using Aspen HYSYS. The results show that the total exergy efficiency of the system is 64.5% and the largest source of exergy destruction is the main engine and its components with 59.9% of the total. It was found that the exergy destruction of the ORC and carbon capture system accounted for 28.3% of the total, while CO<sub>2</sub> liquefaction and BO-NG reliquefaction systems accounted for 11.9%. While the total exergy efficiency of CO<sub>2</sub> liquefaction and BO-NG reliquefaction systems is as high as 95.3%, this value is 25.3% for ORC and carbon capture systems. Therefore, it is determined that the efficiencies of ORC and carbon capture systems have the potential to be improved with different thermal designs.

**Keywords:** Solvent-based carbon capture and storage, Organic Rankine cycle, Cooling, heating, and power integration, Exergy analysis

## 1 INTRODUCTION

Reducing CO<sub>2</sub> emissions to mitigate global warming has become crucial over time. The International Maritime Organization has considerably accelerated its work since 2008 and has set rules and regulations in several phases to limit the CO<sub>2</sub> emissions from international maritime activities. As a result of the 72nd Marine Environment Protection Committee meeting held in 2018 agreed that CO<sub>2</sub> emissions emitted from ships will be reduced by 50% by 2050 compared to 2008 [1]. As a result of the meetings held later, it has been decided to take this implementation date even earlier than 2050 in various phases for different ship types and to classify the ships according to the CO<sub>2</sub> rate ships emit [2].

Carbon capture and storage (CCS) systems can effectively reduce CO<sub>2</sub> emissions by up to 95% for land-based plants. As a result, research on the application of CCS systems on ships has gained prominence recently. The first systematic investigation on the application of solvent-based carbon capture for ships was given by Luo and Wang [3]. Ammonia can be used as a solvent in a ship-based CCS system to capture both CO<sub>2</sub> and SO<sub>x</sub> emissions, according to Awoyomi et al. [4]. Feenstra et al. [5] examined the carbon capture feasibility and the cost of the ship CCS system, with the change in the amount of emissions due to the power demand and the use of liquefied natural gas (LNG) or diesel as fuel. Güler and Ergin [6] investigated the viability of CCS systems with various shipboard carbon management techniques and investigated the impact of hydraulic design parameters on CCS systems. In their next study, the authors examined how the use of various solvents affects the cost, equipment size, and emissions of the CCS system [7].

It should be emphasized that employing the CCS system has some drawbacks due to the thermal energy and power requirements, as well as the cost, despite its quite effective outcomes in lowering CO<sub>2</sub> emissions. Therefore, increasing the system's viability has been the main goal of studies that investigate CCS systems. In one of these studies, Lee and Cho [8] show that the liquefaction of CO<sub>2</sub> using cold heat of LNG reduces the electric power demand of cooling for a land facility. Additionally, the waste heat recovery (WHR) system is incorporated into the CCS system rather than drawing electricity in order to meet the thermal requirements of the stripper reboiler in the system. Zhang [9] employed the organic Rankine cycle (ORC) to generate power using exhaust gas heat for the CCS system's power requirements. The authors also investigated the integration of cooling, heating, and power

systems of LNG carriers with the CCS system and conducted 4E analyses for the integration, in their previous study [10]. The authors tried to minimize the costs using genetic algorithm optimization, but the exergy loss mechanisms were not investigated in this study.

The objective of this research is to conduct a comprehensive exergy analysis and to identify systems and equipment that have the potential to reduce exergy destruction according to the results obtained from the analysis for an LNG carrier by combining cooling, heating, and power systems with marine CCS systems. The main power system, carbon capture system, CO<sub>2</sub> liquefaction system, boil-off natural gas (BO-NG) reliquefaction system, and ORC as an auxiliary power system are the five systems that are the focus of this study's modeling and integration. While there have been previous analyses and examinations of the integrations of these systems, this study is the first to conduct a comprehensive exergy analysis and identify exergy efficiency for systems and equipment-based improvements.

## 2 MATERIAL AND METHOD

A Q-Flex type LNG carrier is analyzed for the study and its main dimensions and particulars are shown in Table 1. According to the main dimensions and particulars, the power requirement of the ship is determined and main power system modeling is performed. The carbon capture system is modeled to capture CO<sub>2</sub> in the exhaust gas from the main power system. The captured CO<sub>2</sub> must be temporarily stored on the ship until delivery to the port. Therefore, the CO<sub>2</sub> liquefaction system is modeled. One of the biggest problems encountered in LNG transport is the boiling of natural gas. This situation causes freight and financial loss. Therefore, in order to compensate for the loss, the BO-NG reliquefaction system is modeled. By integrating the BO-NG reliquefaction system with the CO<sub>2</sub> liquefaction system, it is possible to reduce the equipment amount, cost, and energy requirements of the CO<sub>2</sub> liquefaction system. In particular, the reliquefied BO-NG sent to the main engine as fuel has a large cold energy, which is critical for the liquefaction of CO<sub>2</sub>. On the other side, although the temperature is not very high in these modeled systems, there are large waste heat potentials. It is possible to provide auxiliary power from this waste heat, which does not reach very high temperatures, with ORC and reduce the power requirement of the CCS system. For this reason, the ORC system is also modeled as an auxiliary power source. On the other hand, waste heat is very important, especially for CO<sub>2</sub> regeneration and it is possible to reduce the exergy loss with the detailed exergy analyses performed in this study. In this way, it may be possible to capture more CO<sub>2</sub> or to obtain more energy from the ORC system. The integration of the systems is simplified as a schematic and shown in Figure 1.

**Table 1.** Main dimensions and particulars of studied ships

Description	Q-Flex
Scantling ship size (m <sup>3</sup> )	210000
Scantling draught (m)	12.7
Length overall (m)	315
Length between perpendicular (m)	303
Breadth (m)	50
Design draught (m)	12
Maximum ship speed (kn)	20

### 2.1 Modeling of Main Power System

The Series 60 approach estimates the power requirements of the investigated ship based on its size and speed [11]. MAN's LNG-fueled engine is selected in accordance with the estimated power demand, and the features of the selected engine used in modeling at 75% maximum continuous rate (MCR) and calculations are given in Table 2 [12]. The other parameters given by the engine manufacturer and assumptions to be used in modeling the system are available in the literature [10].

As observed in Figure 2, the main power system is represented as turbocharger (TC) compression, air intercooling, cylinder compression, combustion, and power stroke thermal processes, in that order. The air is intercooled twice in this variant. Seawater is used for cooling in the second stage, while process water from the CCS system is utilized as the coolant in the first. Comparing the rich loading CO<sub>2</sub> solubility performances across the literature, the validation investigation of the CCS system modeling reveals a 0.08% discrepancy. It could be argued that there is good agreement between the results [3].

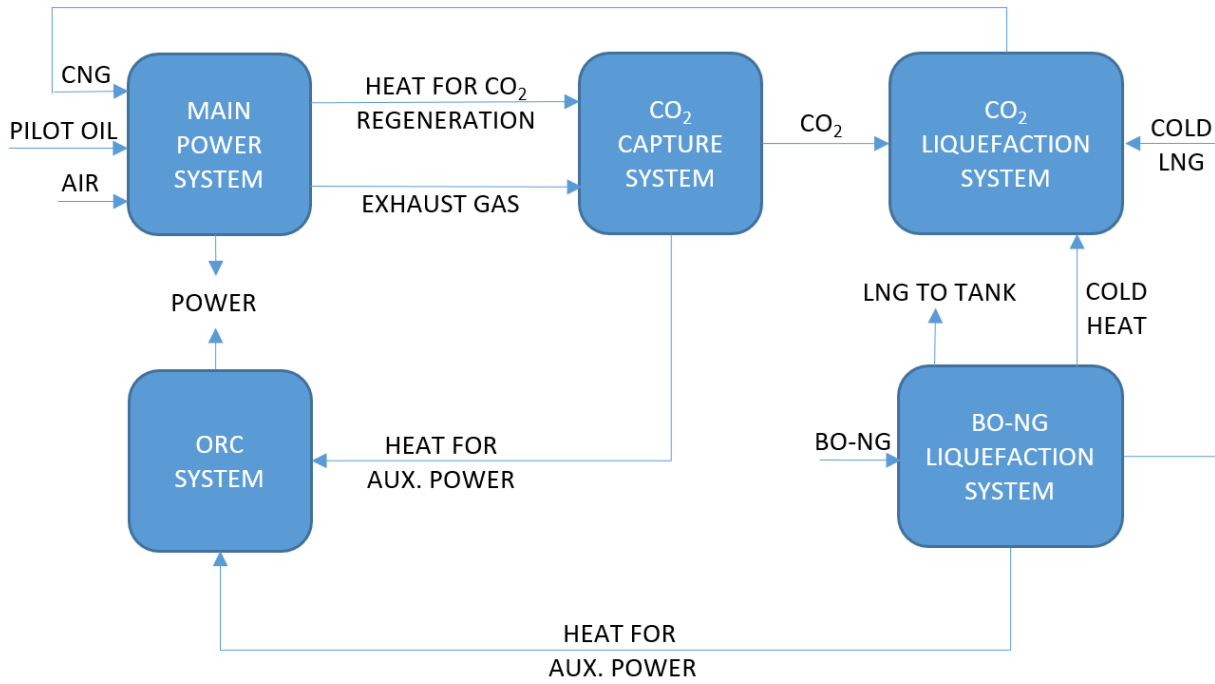


Figure 1. Schematic diagram of systems integration

Table 2. Selected engine and properties for the studied ship

Description	Unit
Estimated maximum main engine power ( )	39300 kW
Selected main engines	7G60ME-C10.5
Total power of main engines at full load ( )	2x19880 kW
Air consumption at 75% MCR	62.4 kg/s
TC compressor outlet pressure at 75% MCR	3.07 bar
Specific pilot oil consumption at 75% MCR	3.06 g/kWh
Specific gas consumption at 75% MCR	135 g/kWh

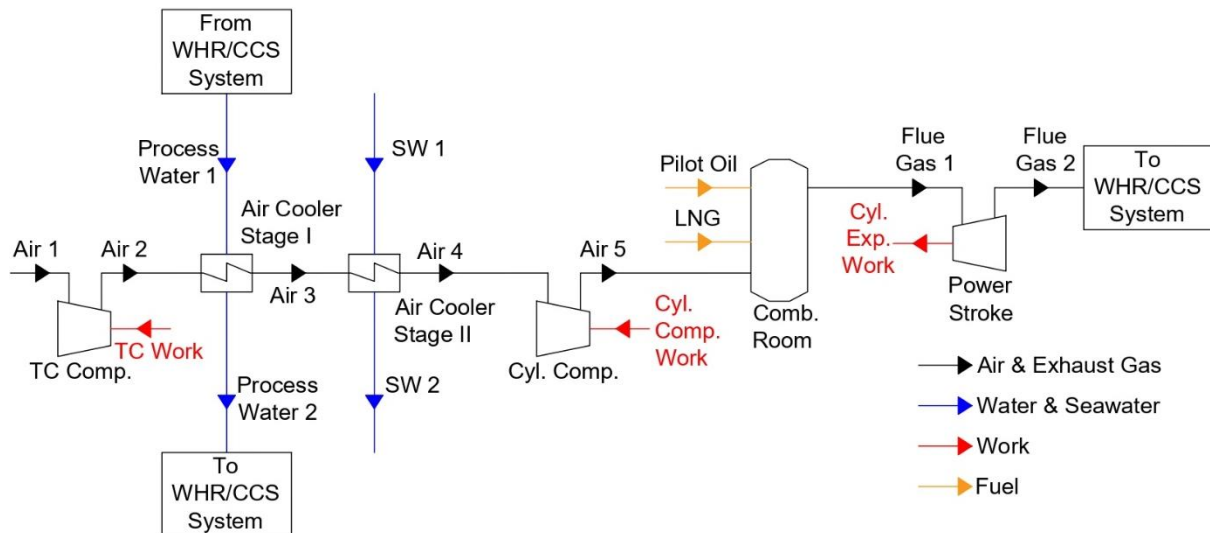


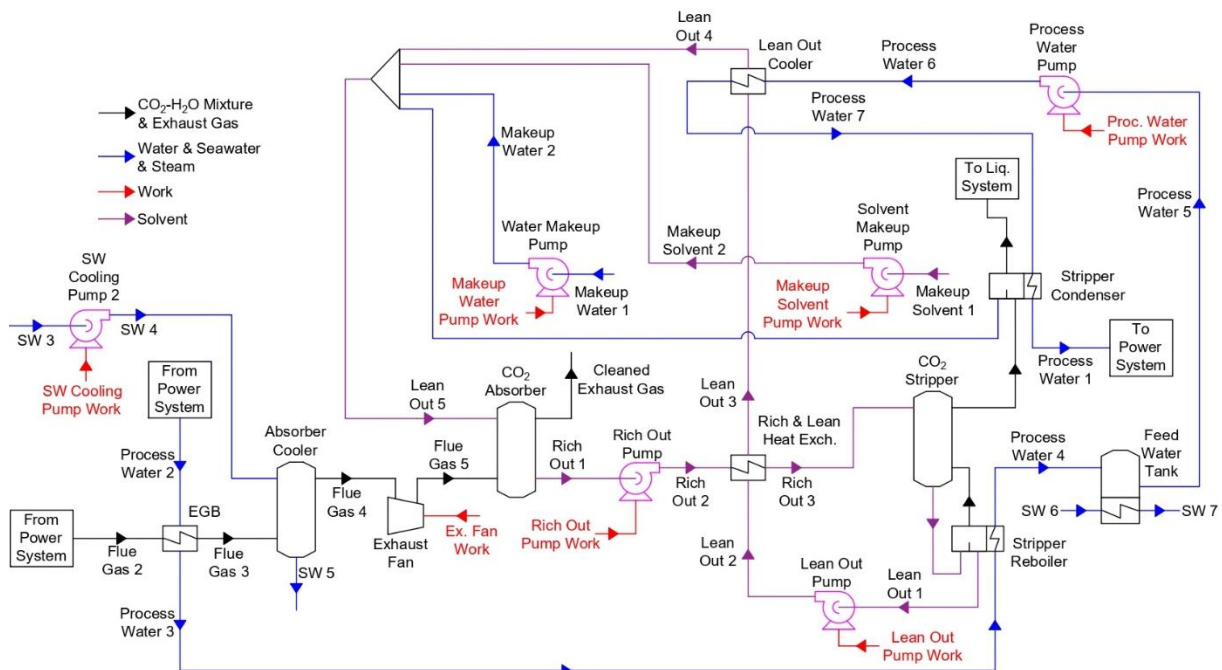
Figure 2. Main power system and its components

2.2 Modeling of the Carbon Capture System

While there are several capture techniques described in the literature, including the use of membranes, adsorption, and the liquefaction of exhaust gas, prior research indicates that solvent-based post-combustion capture is the most

widely used and marketed technique [13, 14]. Being “end-of-pipe” technology is another benefit of this technology. Furthermore, solvent-based scrubbers are a well-known technology because they are frequently used to lower SO<sub>x</sub> emissions for ships. This study uses 30% aqueous piperazine (PZ) as the solvent in a solvent-based CCS system. Compared to traditional amine-based alkanolamines, PZ has a superior reaction rate, reduced volatility, good thermal stability, and does not corrode stainless steel [13, 15].

The carbon capture system is modeled as can be seen in Figure 3. According to Figure 3, Before being pressured to make up for the pressure lost in the absorber, the flue gas going through the exhaust gas boiler (EGB) is first cleaned with seawater in the absorber cooler until its temperature drops to 50 °C. After the CO<sub>2</sub>-lean solvent mixture has chemically absorbed the CO<sub>2</sub>, the CO<sub>2</sub> is finally extracted from the flue gas and cleansed exhaust gas is discharged into the atmosphere. After being preheated by a regenerative heat exchanger (HEX), the CO<sub>2</sub>-rich solvent mixture from the absorber's outlet is pumped to the stripper column. Heat is used in the stripper column to regenerate CO<sub>2</sub>, which then enters the condenser at the top of the column from the solution. This HEX condenses a significant amount of water that evaporates with the CO<sub>2</sub> and recycles it back into the system via a pump. The CO<sub>2</sub> liquefaction system receives the separated CO<sub>2</sub>. Conversely, a pump recycles the CO<sub>2</sub>-lean solvent mixture into the system, the regenerative HEX cools it, and it is then moved to the absorber inlet. By the way, because of column evaporation, pumps pull water and solvent from the makeup reservoirs. The process water, which heats up in the lean-out cooler, stripper condenser, main engine air cooler, and EGB respectively, provides the heat it needs to the stripper reboiler.



**Figure 3.** Model of the CCS system for studied ships

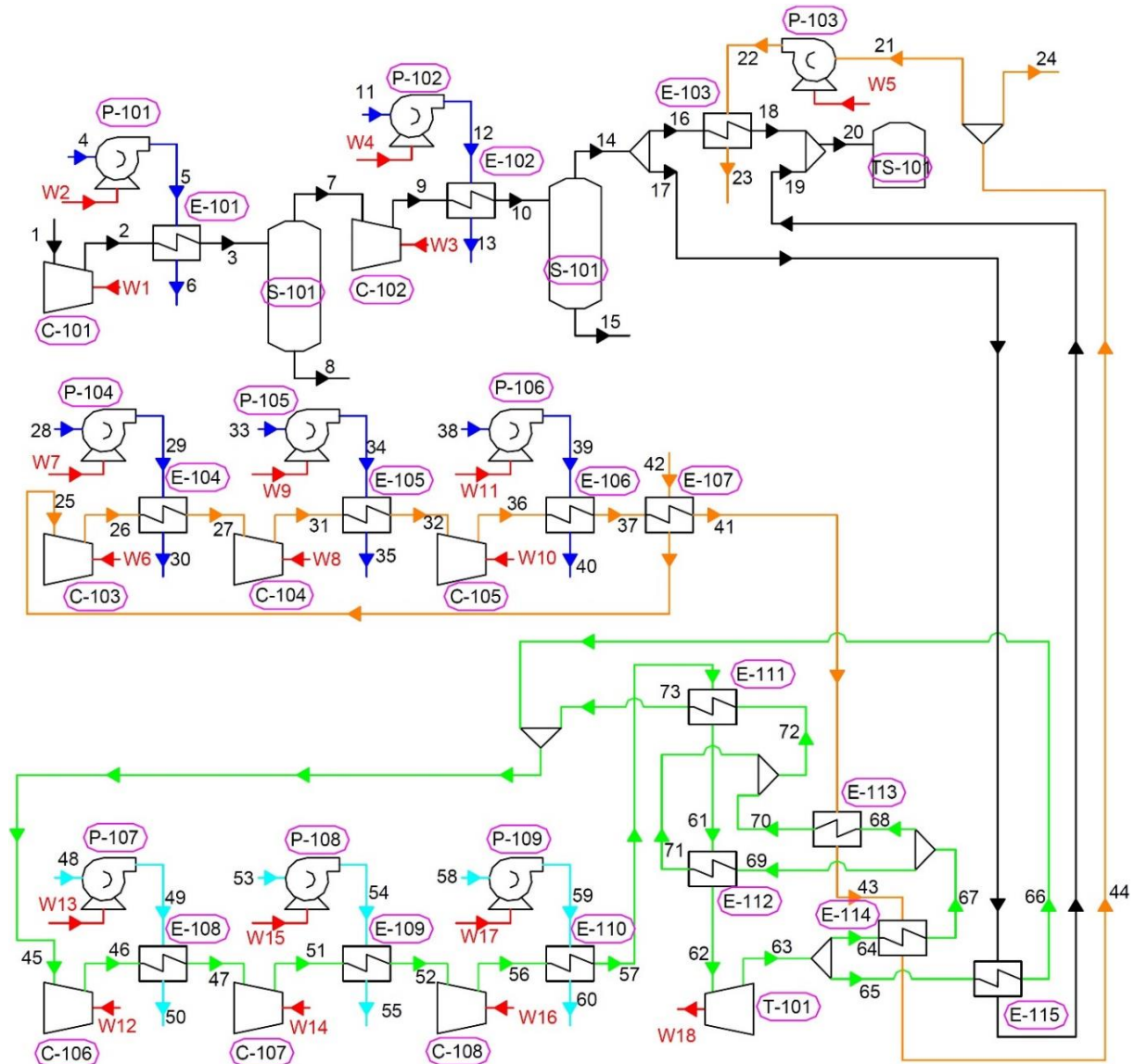
The packing materials and their characteristics used in CO<sub>2</sub> absorber and stripper columns, the chemical reaction and equilibrium equations of these columns, the equilibrium constants used in these reactions, the mathematical model used for the solution, and all other assumptions to the system are available in the literature [10]. Comparing the rich loading CO<sub>2</sub> solubility performances across the literature, the validation investigation of the CCS system modeling reveals a 0.08% discrepancy. It could be argued that there is good agreement between the outcomes [3].

### 2.3 Modeling of the Boil-Off Natural Gas and Carbon Dioxide Liquefaction Systems

Before being moved to a permanent storage facility or used for other purposes, captured CO<sub>2</sub> must be stored on ships. CO<sub>2</sub> can be kept on ships as either a liquid or solid form of carbamate. Liquefaction will be more practical for CO<sub>2</sub> storage in LNG carriers due to the challenges associated with handling solids, the fact that carbamate formation is heavier in the liquefied state than in the liquid state, and the utilization of "end-of-pipe" technology.

As stated earlier, to prevent the loss of cargo due to the BO-NG, a reliquefaction system is modeled. A portion of the reliquefied BO-NG is transported to be utilized as fuel in the main engine. Before it reaches the injector of the engine, LNG is compressed to 300 bar by a pump. Furthermore, cold LNG must be heated until it reaches the

outside temperature. This section of the study recommends using cooled LNG to lower the temperature of CO<sub>2</sub> storage. Furthermore, under some circumstances, cold LNG could not be enough to fully cool the CO<sub>2</sub>. In this instance, the closed N<sub>2</sub> cycle—which is primarily employed for BO-NG reliquefaction—can cool part of the CO<sub>2</sub>. Figure 4 illustrates the integration of the BO-NG reliquefaction and CO<sub>2</sub> liquefaction systems for this purpose.



**Figure 4.** Model of the integration of BO-NG and CO<sub>2</sub> liquefaction systems

As illustrated in Figure 4, a regenerator uses pressurized BO-NG from tanks to cool it. Three-stage compressors pressurize the system. Following the regenerator, a closed N<sub>2</sub> cooling cycle cools and liquefies BO-NG. At last, the liquid BO-NG is separated. Three-stage compressors and intercoolers pressurize N<sub>2</sub> in this closed cooling cycle as well. Regenerative HEXs precool N<sub>2</sub> before it enters the expander following compression. The N<sub>2</sub> is also cooled by the expansion process. After that, expanded N<sub>2</sub> is recycled back into the system via the CO<sub>2</sub> and BO-NG condensers, as well as the regenerative HEXs. Conversely, CO<sub>2</sub> is separated from water and its impurities in two steps after being pressurized by compressors and intercooled. Lastly, a cycle of cold LNG and BO-NG reliquefaction cools and liquefies CO<sub>2</sub> to its storage temperature. The literature contains the integrated model's assumptions and parameters. The BO-NG reliquefaction system and the CO<sub>2</sub> liquefaction system were validated independently of each other. It can be concluded that the results are in good agreement when the amount of cooled CO<sub>2</sub> is compared for the CO<sub>2</sub> liquefaction system and the literature, with a 0.52% difference. [16]. When HEX operating conditions are used, the validation of the BO-NG reliquefaction model reveals a 1.75% variation in the N<sub>2</sub> rate [17]. It could argued that there is good agreement between the outcomes.

### 2.4 Modeling of Organic Rankine Cycle System

Creating energy from waste heat could help lower the CCS system's energy usage. Waste heat can be collected from a variety of sources, most notably cooling cycles. The highest temperature that can be achieved from these waste heat sources isn't considered to be particularly high, though. This is why using ORC rather than the traditional Rankine cycle would be beneficial [18]. Therefore, Figure 5 models and illustrates the ORC system. The BO-NG/CO<sub>2</sub> liquefaction system's organic fluids are collected in a collector. At the stripper column's reboiler output, the upper stream absorbs the heat from the process water. After that, the EGB superheats the collected stream before it reaches the ORC turbine. The turbine's input and exit pressures are 4000 and 740 kPa, respectively, and the organic fluid used is R152a [19]. The organic fluid is cooled to the liquefaction temperature after the turbine outlet. Recycled into the system after that. Figure 4 illustrates that water is utilized in place of R152a for cooling three-staged N<sub>2</sub> compressors. These compressors need a significant quantity of cooling. The turbine inlet temperature would significantly decrease if the waste heat that was extracted from them was utilized for the ORC. Water is used to cool these compressors since doing otherwise would decrease system efficiency and raise the cost of the HEXs. The ORC system model has been verified by the literature, and it has been determined that the power generated by the turbine differs by 1.03% when the study's ideal circumstances are met [19]. It could be argued that there is good agreement between the outcomes.

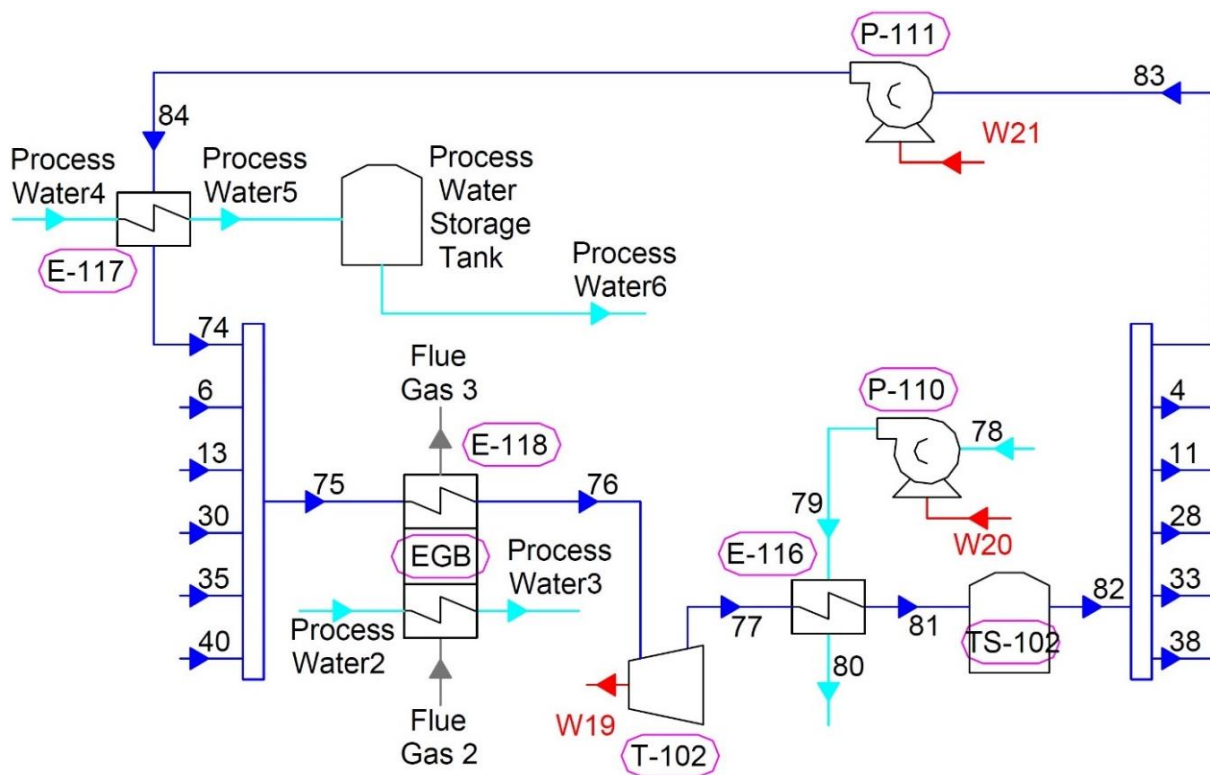
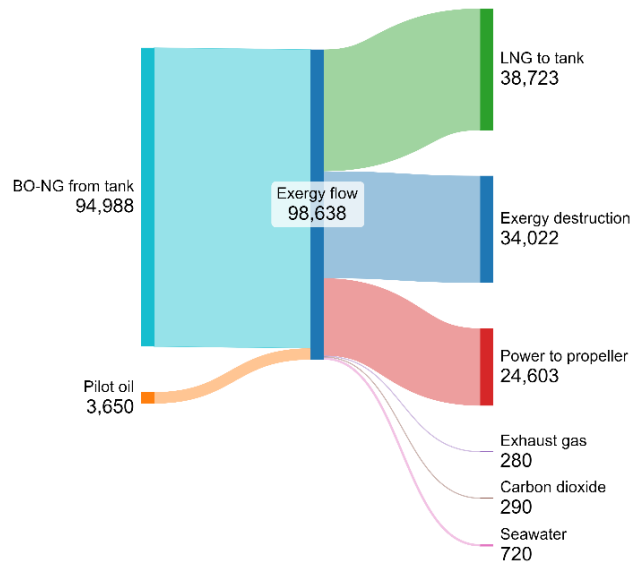


Figure 5. Model of the integrated ORC systems

## 3 RESULTS AND DISCUSSION

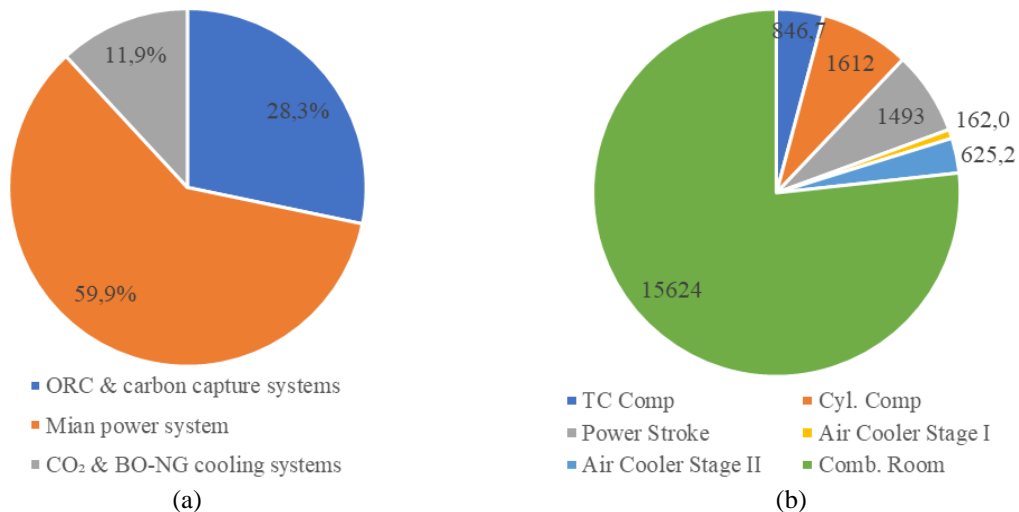
As a result of the analyses, 34.2% of the CO<sub>2</sub> emitted from the exhaust gas is captured. The amount of CO<sub>2</sub> captured here is determined by the amount of heat used for regeneration and it is possible to capture more CO<sub>2</sub> when this heat is increased.

Exergy analyses of the integrated systems of the examined ships are performed and the results are shown with Sankey diagrams in Figure 6. The useful outputs of this integrated system are power transferred to the propeller, reliquefied natural gas, and CO<sub>2</sub> captured and liquefied. According to Figure 6, the total exergy efficiency of the system is 64.5%. The exergy transferred to the environment by exhaust gas and sea water is almost negligible. However, the value of the exergy destroyed is significant and its recovery potential should be analysed.



**Figure 6.** Sankey diagram of the integrated system showing the exergy flow and destruction in kW

To determine the recovery potential of the destroyed exergy, the distribution of exergy destruction depending on the systems is determined and shown in part a) of Figure 7. According to Figure 7, the largest source of exergy destruction with 59.9% is the main engine and its components. The second largest source with 28.3% is the ORC and carbon capture system. CO<sub>2</sub> and BO-NG reliquefaction systems account for only 11.9% of the total exergy destruction. The distribution of the exergy destruction of the components of the main engine is shown in part b of Figure 7. The duty and exergy destruction values of all equipment of the integrated system are shown in Table 3. According to Figure 7, the exergy destruction in the combustion room is 15.62 MW, which is 76.7% of the destruction in the main power system and 45.9% of the destruction in the whole integrated system. Although it is possible to reduce the exergy destruction by reducing the air-fuel ratio of the engine or increasing the cylinder compression ratio, parameters such as operating temperature and pressure limits of the material used, and control of NO<sub>x</sub> emissions limit the reduction of exergy destruction. Other main engine components apart from the combustion chamber are also limited by various parameters and it is very difficult to reduce exergy destruction. Moreover, the exergy efficiencies of other components of the engine are quite high as can be seen in Table 3.



**Figure 7.** (a) Percentage exergy destruction distribution by systems and (b) exergy destruction distribution at the main engine and its components in kW

**Table 3.** Duty, exergy efficiency, and exergy destruction of all equipment

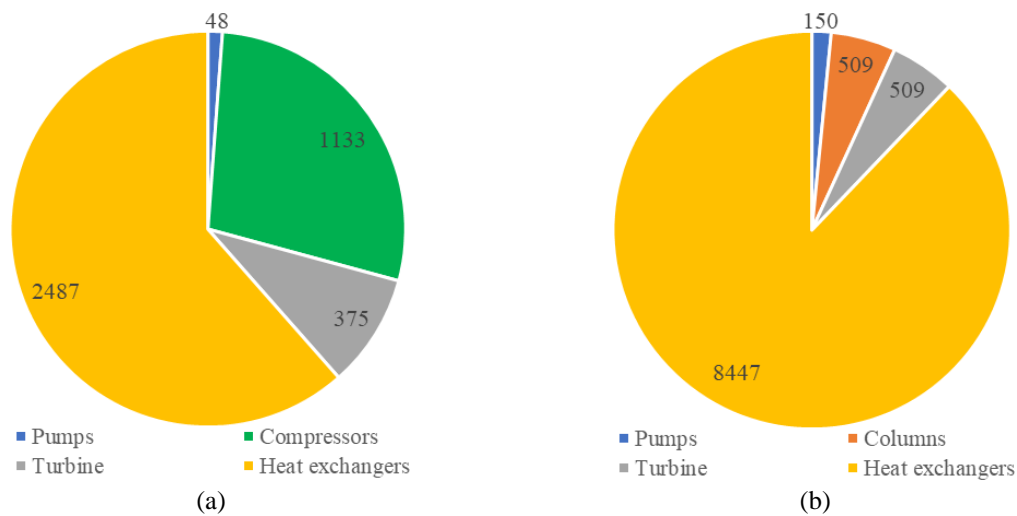
Component	Duty (kW)	$\eta_{ex}$	Ex. Des. (kW)
SW Cooling Pump 2	22.48	0.902	2.194
Rich Out Pump	1.689	0.636	0.615
Lean Out Pump	3.718	0.850	0.557



Makeup Water Pump	0.2239	0.905	0.021
Makeup Solvent Pump	0.0024	0.894	0.000
Process Water Pump	48.73	0.902	4.769
TC Comp	8140	0.896	846.7
Cyl. Comp	14980	0.892	1612
Power Stroke	44800	0.967	1493
Air Cooler Stage I	2844	0.981	162.0
Air Cooler Stage II	4889	0.905	625.2
Comb. Room	57078	0.785	15624
EGB	17414	0.785	3599
Absorber Cooler	8389	0.284	1772
CO <sub>2</sub> Absorber	-	0.863	44.55
Rich & Lean HEX	2746	0.715	140.5
CO <sub>2</sub> Stripper	-	0.832	464.1
Stripper Reboiler	12090	0.805	1124
Lean Out Cooler	889.2	0.764	30.25
Stripper Condenser	9160	0.701	521.6
P101	1.803	0.451	0.990
P102	1.774	0.451	0.974
P103	87.41	0.767	20.33
P104	12.46	0.451	6.844
P105	15.07	0.451	8.278
P106	12.28	0.451	6.745
P107	18.30	0.941	1.077
P108	21.39	0.941	1.259
P109	21.93	0.941	1.291
P110	97.26	0.941	5.724
P111	247.9	0.451	136.2
C101	157.6	0.800	31.52
C102	151.5	0.798	30.66
C103	282.0	0.832	47.45
C104	290.7	0.837	47.40
C105	290.0	0.837	47.26
C106	1897	0.828	325.4
C107	1920	0.842	302.9
C108	1927	0.844	300.8
T101	1119	0.665	375.3
T102	1194	0.574	509.1
E101	157.0	0.961	6.687
E102	154.4	0.983	4.385
E103	407.5	0.860	202.6
E104	240.9	0.966	16.37
E105	294.0	0.975	18.89
E106	239.5	0.980	18.17
E107	615.8	0.857	124.4
E108	1717	0.971	247.1
E109	2007	0.969	305.1

E110	2059	0.972	313.5
E111	4804	0.967	640.9
E112	710.2	0.989	222.7
E113	167.3	0.986	43.88
E114	985.7	0.973	322.4
E115	0.0235	0.696	0.015
E116	3821	0.825	707.0
E117	12775	0.869	553.0

The distribution of the exergy destruction of the components for the ORC and carbon capture systems is shown in part a) of Figure 8, and for the CO<sub>2</sub> and BO-NG reliquefaction system is shown in part b) of Figure 8. According to part a) of Figure 8., about 2.49 MW of exergy is destroyed from the HEXs. Although the potential loss to be recovered seems to be large, according to Table 3, the efficiencies of these HEXs (E101-115) are quite high and it will not be easy to increase these efficiencies further. Here, the exergy destruction due to the compressors is about 1.13 MW. The exergy efficiencies of these compressors are around 80-85% according to Table 3 and by improving the compressor efficiencies, a partial reduction of exergy destruction can be contributed. Especially the exergy loss in pumps is very low and the potential to reduce the exergy destruction from other equipment is low. According to Figure 8 in part b), about 8.45 MW of exergy is destroyed from the HEXs. Moreover, the exergy efficiencies of EGB, absorber cooler, E-116, E-117, stripper reboiler, and condenser as HEXs in these systems are generally low and these HEXs have a great potential to reduce exergy destruction. In addition to these data, when the total exergy efficiencies of the systems are examined, the total exergy efficiency of CO<sub>2</sub> liquefaction and BO-NG reliquefaction systems is calculated as high as 95.3%, while this value is 25.3% in ORC and carbon capture systems. Therefore, it is determined that the efficiencies of ORC and carbon capture systems have the potential to be improved with different thermal designs.



**Figure 8.** (a) Exergy destruction distribution at CO<sub>2</sub> and BO-NG liquefaction system and (b) exergy destruction distribution at ORC, and carbon capture in kW

## 4 CONCLUSIONS

This study presents exergetic analyzes of marine carbon capture and storage (CCS) systems by integrating cooling, heating, and power systems to reduce exergy loss of a liquefied natural gas (LNG) carrier. This study consists of five system modeling and integration: main power system, carbon capture system, CO<sub>2</sub> liquefaction system, BO-NG reliquefaction system, and organic Rankine cycle (ORC) as an auxiliary power system. Although the integrations of these systems have been examined and various analyses have been made before, this study is the first that such a detailed exergy analysis has been made and it has been determined where improvements can be made on the basis of system and equipment.

The conclusions of the study can be listed as follows:

- The total exergy efficiency of the integrated system is 64.5%.

- While the exergy transferred to the environment by exhaust gas and sea water is quite small, the exergy destruction is above 34 MW.
- It is determined that the main power system constituted 59.9%, ORC and carbon capture systems constituted 28.3%, and CO<sub>2</sub> and BO-NG liquefaction systems constituted 11.9% of the total exergy destruction.
- Despite the very high exergy destruction, the potential to reduce exergy destruction from the main power system is evaluated to be low due to the parameters limiting the main engine design.
- Although 2.49 MW of exergy destruction occurs from the heat exchangers (HEX) in the CO<sub>2</sub> and BO-NG reliquefaction system, the potential to reduce exergy loss is low since the exergy efficiency of the HEXs is quite high.
- The exergy loss of HEXs in ORC and carbon capture systems is 8.45 MW and the exergy efficiency of the HEXs is relatively low, so the potential to reduce exergy destruction is high.
- The total exergy efficiency of CO<sub>2</sub> liquefaction and BO-NG reliquefaction systems is calculated as high as 95.3%, while this value is 25.3% in ORC and carbon capture systems. Together with the previous results, improvements in the thermal design of ORC and carbon capture systems will make a great contribution to the integrated system that investigated.

In future studies, the heat needed for the removal of process water and the regeneration of CO<sub>2</sub> should be considered by passing the solution directly through the exhaust gas boiler and the air cooler of the main engine. Thus, by reducing the number of equipment in the system, both complexity and exergy destruction will be reduced, and the captured CO<sub>2</sub> amount can be increased. On the other hand, by using different working fluids for the ORC system, the efficiency of the ORC system and the amount of auxiliary power to be obtained from it can be increased.

## Acknowledgments

The authors express their gratitude to the Istanbul Technical University Scientific Research Projects Coordination Unit (BAP) for providing financial support for the project numbered 44432.

## References

- [1] International Maritime Organization, "Adoption of the initial IMO strategy on reduction of GHG emissions from ships and existing IMO activity related to reducing GHG emissions in the shipping sector," 2018.
- [2] Marine Environment Protection Committee, "Report of the marine environment protection committee on its eightieth session," 2023.
- [3] X. Luo and M. Wang, "Study of solvent-based carbon capture for cargo ships through process modeling and simulation," *Appl. Energy*, vol. 195, pp. 402–413, 2017.
- [4] A. Awoyomi, K. Patchigolla, and E. J. Anthony, "CO<sub>2</sub>/SO<sub>2</sub> emission reduction in CO<sub>2</sub> shipping infrastructure," *Int. J. Greenh. Gas Control*, vol. 88, pp. 57–70, 2019.
- [5] M. Feenstra, J. Monteiro, J. T. van den Akker, M. R. M. Abu-Zahra, E. Gilling, and E. Goetheer, "Ship-based carbon capture onboard of diesel or LNG-fuelled ships," *Int. J. Greenh. Gas Control*, vol. 85, pp. 1–10, 2019.
- [6] E. Guler and S. Ergin, "An investigation on the solvent based carbon capture and storage system by process modeling and comparisons with another carbon control methods for different ships," *Int. J. Greenh. Gas Control*, vol. 110, art. no. 103438, 2021, doi: 10.1016/j.ijggc.2021.103438.
- [7] E. Guler and S. Ergin, "The effects of different solvents on the performance of carbon capture and storage (CCS) systems for different ships," in *The 34th Asian-Pacific Technical Exchange and Advisory Meeting on Marine Structures Conference*, 2021, pp. 320–328.
- [8] J. Lee and J. Cho, "Liquefaction process using LNG cold heat," *Trans. Korean Hydrog. New Energy Soc.*, vol. 31, no. 2, pp. 259–264, 2020.
- [9] L. Zhang, Z. Pan, L. Shang, and L. Dong, "Thermo-economic analysis of organic rankine cycle (ORC) with CO<sub>2</sub> capture system for coal-fired power plant waste heat recovery," *Int. J. Energy a Clean Environ.*, vol. 19, no. 3–4, pp. 303–322, 2018, doi: 10.1615/InterJenerCleanEnv.2018025381.
- [10] E. Guler and S. Ergin, "An investigation of the cooling, heating and power systems integration with carbon capture and storage for LNG carriers," *Ships Offshore Struct.*, pp. 1–15, 2023, doi: 10.1080/17445302.2023.2195245.
- [11] F. H. Todd, "Series 60 methodical experiments with models of single-screw merchant ships," 1963.
- [12] MAN Energy Solutions, "CEAS engine calculations," 2024. Available: <https://www.man-es.com/marine/products/planning-tools-and-downloads/ceas-engine-calculations>
- [13] G. Rochelle, E. Chen, S. Freeman, D. Van Wagener, Q. Xu, and A. Voice, "Aqueous piperazine as the

- new standard for CO<sub>2</sub> capture technology,” *Chem. Eng. J.*, vol. 171, no. 3, pp. 725–733, 2011, doi: 10.1016/j.cej.2011.02.011.
- [14] M. Wang, A. Lawal, P. Stephenson, J. Sidders, and C. Ramshaw, “Post-combustion CO<sub>2</sub> capture with chemical absorption: a state-of-the-art review,” *Chem. Eng. Res. Des.*, vol. 89, no. 9, pp. 1609–1624, 2011.
- [15] F. Vega, M. Cano, S. Camino, L. M. G. Fenandez, E. Portillo, and B. Navarrate, “Solvents for Carbon Dioxide Capture,” in *Carbon dioxide chemistry, capture and oil recovery*, Intechopen, 2018, pp. 142–163. doi: 10.5772/intechopen.71443.
- [16] Y. Seo, H. You, S. Lee, C. Huh, and D. Chang, “Evaluation of CO<sub>2</sub> liquefaction processes for ship-based carbon capture and storage (CCS) in terms of life cycle cost (LCC) considering availability,” *Int. J. Greenh. Gas Control*, vol. 35, pp. 1–12, 2015, doi: 10.1016/j.ijggc.2015.01.006.
- [17] Y. Shin and Y. Pyo, “Design of a boil-off natural gas reliquefaction control system for LNG carriers,” *Appl. Energy*, vol. 86, pp. 37–44, 2009, doi: 10.1016/j.apenergy.2008.03.019.
- [18] I. Dincer and M. E. Demir, *Steam and Organic Rankine Cycles*, vol. 4–5. 2018. doi: 10.1016/B978-0-12-809597-3.00410-7.
- [19] M. Akman and S. Ergin, “Thermo-environmental analysis and performance optimisation of transcritical organic Rankine cycle system for waste heat recovery of a marine diesel engine,” *Ships Offshore Struct.*, vol. 16, no. 10, pp. 1104–1113, 2021, doi: 10.1080/17445302.2020.1816744.



## Potential Use of Materials Based on Alginate Beads for Treating Contaminated Water

Dhirar Ben Salem<sup>\*1</sup>, Amel Riah<sup>2</sup>

<sup>1</sup>Research Laboratory in Subterranean and Surface Hydraulics, University of Biskra, PO Box 145, Biskra, 07000, Algeria

<sup>2</sup>REMEDD Laboratory, Department of Chemical Engineering, University of Constantine 03 Saleh Boubnider, Constantine, Algeria

---

### Abstract

Industrial wastewater often contains high concentrations of heavy metals, posing significant risks to human health and the environment. In this research endeavour, biochar and magnetic biochar were used to prepare two (2) different adsorbent materials using the encapsulation method based on sodium alginate biopolymer. The encapsulation creates magnetic and non-magnetic beads and then were examined in the uptake of copper and cadmium ions from water. Under batch experiments, these engineered beads were thoroughly characterized and evaluated as adsorbents for metal ions, with isotherm studies conducted under pH 5.0 conditions and different initial concentrations.

The findings reveal notable differences in the  $pH_{PZC}$  values of the prepared materials. The prepared beads were considered effective materials for removing copper and cadmium ions. Modelling the adsorption isotherms, the Langmuir model demonstrated a superior fit over the Freundlich model. Furthermore, the adsorption process was influenced by the pH of the solution. One of the key advantages of the developed beads lies in their ability to float on the surface of the solution, facilitating easy collection and separation using an external magnetic field. Moreover, their recyclability renders them highly promising for the efficient removal of heavy metals from industrial wastewater. Thus, presenting a sustainable solution to mitigate environmental contamination.

**Keywords:** Biochar, Alginate bead, Heavy metals, Adsorption, Isotherm

---



---

## Carbon Nanostructured as an Efficient Adsorbent for High Concentrations of Crystal Violet Removal

Amel Riah<sup>\*1</sup>, Salim Bousba<sup>2</sup>

<sup>1</sup>Department of Chemical Engineering, University of Constantine 03 Saleh Boubnider, Constantine, Algeria

<sup>2</sup>Research Laboratory in Subterranean and Surface Hydraulics, University of Biskra, PO Box 145, Biskra 07000, Algeria

---

### Abstract

Nanostructured materials exhibit exceptional properties that make them promising candidates for various applications, particularly in wastewater treatment. This study explores the use of Nano-Structured Carbon material (NAT) as an adsorbent for the efficient removal of crystal violet dye from aqueous solutions. The objective is to assess its performance and potential modifications for future investigations. The NAT samples were thoroughly characterized using various techniques before undergoing adsorption batch experiments. The effect of several key factors such as solution pH, stirring time, and isothermal conditions on crystal violet uptake was investigated.

Results indicate that an increase in solution pH enhances the removal efficiency of crystal violet by the NAT adsorbent. Notably, at lower acidic pH values ( $< 5$ ), Crystal violet dye elimination from water is observed, albeit with reduced efficiency compared to pH values exceeding the point of zero charge ( $pH_{PZC}$ ). The adsorption kinetics data conform well to the pseudo-second-order model. Furthermore, the Langmuir and Freundlich models are identified as the most suitable fits for the isotherm data.

This research underscores the potential of Nano-Structured Carbon material as a highly effective nano-adsorbent for crystal violet adsorption, providing valuable insights for future studies in the field of water treatment by adsorption. These findings highlight the promising application of nano-structured carbon materials in addressing water pollution challenges, emphasizing the importance of continued research and development in this area.

**Keywords:** *Nano-adsorbent, Nano-structured carbon material, Crystal violet, Adsorption, Elimination*

---



## Lead (Pb) Pollution: A Food Safety Issue

Mahmood Ur Rahman\*<sup>1</sup>

<sup>1</sup>Department of Bioinformatics and Biotechnology, GC University – Faisalabad, Allama Iqbal Road, Faisalabad-38000, Pakistan

---

### Abstract

Lead (Pb) is a heavy metal which is added into the environment by various anthropogenic activities, e.g. industries. Lead along with industrial waste is accumulated in the soil causing serious ecological risks, as well as human health hazards through consumption of edible crops grown on such Pb-polluted soils. It is needed to inhibit Pb entry into the human food chain by suitable mechanisms and phytoremediation is one of them. The recent developments in phytoremediation of metals from soil are important milestones. Plants uptake metals from soil and accumulate them, so that the soil is detoxified from the harmful effects of metal pollution. There are more than 400 plants which could be used for phytoremediation. In this way, the toxic heavy metals like Pb could be removed from soil by non-food plants so that they will not enter into the food chain. Several amendments may also be used to detoxify the hyperaccumulator plants so that the toxicity of metal could be minimized. In this way the toxicity of metal will not affect the consumer of that plant. In this lecture, Pb toxicity, phytoremediation, detoxification and various food safety issues will be discussed.

**Keywords:** *Phytoremediation, Heavy metals, Lead, Hyperaccumulator plants, Soil detoxification*

---



## Exploring the Adsorption Capacities of Olive Mill Solid Waste Biochar for Polyphenols: Experimental Optimization and DFT/B3LYP Analysis

Imad Rabichi<sup>\*1,2</sup>, Kawtar Ezzahi<sup>2</sup>, Abdelrani Yaacoubi<sup>1</sup>, Abdelaziz Bacaoui<sup>1</sup>, Mohamed Hafidi<sup>2</sup>, Loubna Elfels<sup>1</sup>

<sup>1</sup>Laboratory of Applied Chemistry and Biomass (LCAB), Faculty of Sciences Semlalia, Cadi Ayyad University, Marrakech, 40000, Morocco

<sup>2</sup>Laboratory of Microbial Biotechnologies Agrosiences and Environment (BioMAgE), Faculty of Sciences Semlalia, Cadi Ayyad University, Marrakech, 40000, Morocco

---

### Abstract

The study focuses on producing biochar from Olive Mill Solid Waste (OMSW) on a semi-industrial scale to serve as an adsorbent for removing phenolic compounds like vanillic acid. Optimization of preparation conditions, including carbonization temperature, residence time, and heating rate, was conducted in the laboratory. The biochar was characterized using various techniques, and its adsorption behavior for vanillic acid was analyzed using different models and kinetics. Experimental data align well with the pseudo-second-order and Langmuir models, indicating a maximum adsorption capacity of 57.47 mg.g<sup>-1</sup>. Density Functional Theory (DFT) was employed to elucidate the adsorption mechanism, revealing that vanillic acid's ability to donate electrons to the biochar surface correlates with its inhibition efficiencies. The computational modeling findings support the experimental results, providing insight into the adsorption process.

**Keywords:** Biochar, Production, Adsorption, Vanillic acid, Kinetics, DFT

---





---

## Removal of Total Phenols from Olive-Mill Wastewater Using an Agricultural By-Product, Olive Stone

**Kawtar Ezzahi<sup>\*1,2</sup>, Imad Rabichi<sup>1,2</sup>, Abdelghani Yaacoubi<sup>2</sup>, Abdelaziz Baçaoui<sup>2</sup>, Rachid Idouhli<sup>2</sup>, Nabil Rochdi<sup>3</sup>, Mohamed Hafidi<sup>1</sup>, Loubna El Fels<sup>1</sup>**

<sup>1</sup>Laboratory of Microbial Biotechnologies Agrosociences and Environment (BioMAGe), Faculty of Sciences Semlalia, Cadi Ayyad University, Marrakech, 40000, Morocco

<sup>2</sup>Laboratory of Applied Chemistry and Biomass (LCAB), Faculty of Sciences Semlalia, Cadi Ayyad University, Marrakech, 40000, Morocco

<sup>3</sup>Laboratory of Innovative Materials, Energy and Sustainable Development (IMED-Lab), Faculty of Sciences Semlalia, Cadi Ayyad University, Marrakech, 40000, Morocco

---

### Abstract

Olive Mill WasteWater (OMWW), a by-product of olive oil production, presents environmental challenges due to its potent pollutants. The heedless release of this effluent into the environment, particularly from smaller olive mills, bears the potential for profound ecological disruption. In response to this pressing environmental concern, an array of treatment modalities has been posited, each seeking to redress the toxicity inherent in OMWW and curtail its adverse environmental impact. This paper presents an innovative solution for addressing environmental challenges in olive oil production by converting Olive Stone (OS) into biochar (BC), which serves as an effective adsorbent for polyphenol recovery or removal from OMWW. The study highlights the pyrolysis process used to convert OS into biochar. Through a comprehensive research approach, we demonstrate the efficacy of successive biochar filtration as a pretreatment method for raw OMWW. Our findings reveal the significant enhancement of total suspended solids (TSS) and mineral matter (MM) removal from raw OMWW, achieving rates of approximately 86% and 75%, respectively. Additionally, a substantial reduction in total phenolic compounds (TP) and chemical oxygen demand (COD) by 52.34% and 40.90%, respectively, is observed. This study underscores the potential of biochar derived from OS as a sustainable tool for OMWW pretreatment, with notable contributions to pollutant removal and environmental impact mitigation. By transforming waste into a valuable resource, this approach exemplifies the transformative power of eco-friendly practices in reshaping industries and fostering a more sustainable future for olive oil production and wastewater management.

**Keywords:** Olive mill wastewater, Biochar, Olive stone, Pyrolysis, Polyphenol

---



## Extraction of Phosphocalcic Biomaterial from the Animals Bones Bio-Waste

Saida Bouyegh<sup>\*1</sup>, Sabrina Ladjama<sup>1</sup>, Hadda Rezzag<sup>1</sup>, Sihem Benayache<sup>1</sup>, Samira Tlili<sup>1</sup>

<sup>1</sup>Research Center in Industrial Technologies CRTI, P.B. 64, Cheraga, Algiers, Algeria

### Abstract

Waste treatment and environmental preservation are today a priority to achieve sustainable development. The objective of this work was to transform Animals bio-waste (bovine bone) into calcium phosphates, which are highly valuable materials. In this study, phosphocalcic biomaterial was produced from bovine bone femur by using decomposition treatment. The thermal transformation process of bovine bone was studied by using a TGA/DSC analyzer. The physical properties of phosphocalcic material were evaluated by different techniques such as scanning electron microscopic (SEM) coupled with energy dispersive spectroscopy (EDS), Fourier-transform infrared spectroscopy (FT-IR) absorbance spectra, and X-ray diffraction (XRD). These methods reveal characteristics about the structural, chemical, morphological, and physicochemical properties of the material that has been produced. This material finds potential applications in several fields such as the bioceramic industry, medical and pharmaceutical fields and environmental pollution control. It could be considered as a low cost and economical material. The bovine bone source is inexpensive, easy to produce, and available in unlimited quantities. This can contribute positively to the economy, the environment and general health. The treatment and recovery of biowaste has generated a lot of interest, particularly from both environmental and economic perspectives.

**Keywords:** Bovine bone, Environmental pollution, Phosphocalcic biomaterial, Bio-waste

## 1 INTRODUCTION

The numerous human activities that are concerned with expanding the economy and population contribute to an increase in food and agricultural resources, which then causes waste from the food industry to become one of the sources of pollution. The accumulation of large quantities of organic waste are considered highly polluting sources. These spills of biological waste cause air pollution, contamination of surface water and groundwater, and are a source of environmental risks. Attempts to valorize these wastes as a source of raw materials for the creation of biomaterials, has become a useful strategy to solve these problems [1]. For the extraction of a more valuable compound, some waste products from natural sources are promising resources. These natural wastes must be transformed using specific procedures and approaches. Bones are composed of 65-70% inorganic and 30-35% organic compounds (collagen (95%) and proteins) [2]. Bones' rigidity and appropriate mechanical characteristics are provided by their mineral components. One of the most important products that may be obtained from natural bone garbage, is calcium phosphate namely hydroxyapatite (HAp) which is the major inorganic component of human bone, with formula  $\text{Ca}_{10}(\text{PO}_4)_6(\text{OH})_2$ . Hydroxyapatite (HAp) can serve as useful raw materials for various applications. Alternative methods have therefore been developed [3–7] to generate HAp from inexpensive and recyclable biological resources. Natural HAp can be derived from natural resources and bio-wastes such as eggshells [8–12], seashells [13, 14] and animal bones [15–19]. There are a few methods of extracting hydroxyapatite from animal bones: thermal decomposition, subcritical process and alkaline hydrolysis [20–24]. The physicochemical characteristics of the hydroxyapatite formed (including the Ca/P molar ratio and surface shape) are influenced by the type of bone raw material and the treatment conditions [25].

In this study bovine bone was chosen as one of the suitable raw materials to produce hydroxyapatite powder and an alternative for the valorization of animal wastes. This is due to the fact that bovine bone, an affordable and accessible material, is morphologically and structurally identical to human bone [26]. Thus, the aim of this research was to provide and characterize HAp from natural bovine bone (BHAp). The method adopted is thermal decomposition. The product's phase content, shape, and types of bonds have been identified by X-ray analysis, scanning electron microscopy (SEM), and Fourier transform infrared spectroscopy (FTIR).

## 2 MATERIAL AND METHOD

### 2.1 Bovine Bone Powder Preparation

Bovine bone, as a raw material, is a potential source of natural HA. This inexpensive and easily accessible material may be a good choice to produce HA powder. Hence, bovine bone was chosen as one of the suitable approaches of producing HA powder as a result. The raw material in this study was bovine femur bones obtained from butcher. The bovine bones were boiled in water for 3 hours to remove adhering impurities, and residual soft material were removed with knife and washed with distilled water several times. The process was followed by drying of the bovine bones in oven at 100°C for 7 hours to denaturalize the protein and to evaporate the absorbed moisture. After that, a mortar and pestle were used to crush up the dried bovine bones into small pieces. The crushed bone was pulverized using a planetary milling process (Fritsch, Pulverisette 7) for 06 hours into a fine enough powder. Finally, the powders were sieved to separate off particle sizes of less than 25  $\mu\text{m}$ .

### 2.2 HAp Powder Calcination

The calcination process provides high biological safety factors by thermally decomposing organic components in bones and removing all disease-related genetic markers [23]. Elevated temperatures during calcination will eradicate every microorganism and prevent the possibility of disease dissemination.

### 2.3 Characterization of Produced HAp

Thermal transformations induced by temperature were evaluated by TGA-DSC analysis (SDT Q600 equipment) between 25 and 1200 °C, at a heating rate of 10 °C/min, in a nitrogen atmosphere. This method allowed us to determine the optimal pathways and temperatures for the complete dissociation of calcium carbonate and the safe deproteinization of bovine bone. The surface morphology and microstructural of the products were perceived by FE-SEM Quanta 250 (FEG, FEI) scanning electron microscopy (SEM) equipped with energy dispersive spectroscopy (EDS). Rigaku Ultima IV equipment PANalytical (X'Pert PRO XRD) was used to assess the phase purity of the powders that were generated. Using  $\text{CuK}\alpha$  ( $\lambda = 1.5406\text{\AA}$ ) radiation, the intensity data were recorded in increments of 0.02 ° over the scanning range of  $2\theta = 10^\circ$  to  $80^\circ$ . The created stages were verified and compared with JCPDS standard files (card no. 09-0432). The functional groups were determined using Fourier transform infrared spectroscopy (FTIR; Model IRAfinity-1S, SHIMADZU). An average of thirty scans were performed on the samples within the wave number range of  $4000\text{ cm}^{-1}$ -  $400\text{ cm}^{-1}$ . The spectrometer has a resolution of  $4\text{ cm}^{-1}$ .

## 3 RESULTS

### 3.1 DSC/TGA

Figure 1 presents the TGA results, confirming the removal of the organic part from bovine bone. Two inflection points were perceived in the TGA curves of the bovine bone at 100 °C and 400 °C, respectively, which indicate the elimination of organic materials and water. The complete elimination of organic components below 600 °C in bovine bone was indicated by the absence of discernible weight loss between 700 °C and 1400 °C.

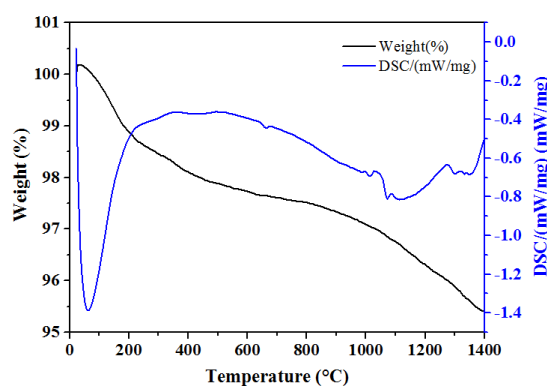


Figure 1. TGA and DSC of raw bovine bone

In this work, thermal decomposition procedures were used to extract HAp from cortical bovine bone. Figure 2 illustrates how the color of bovine bone changes during the calcination process. Due to the elimination of organic

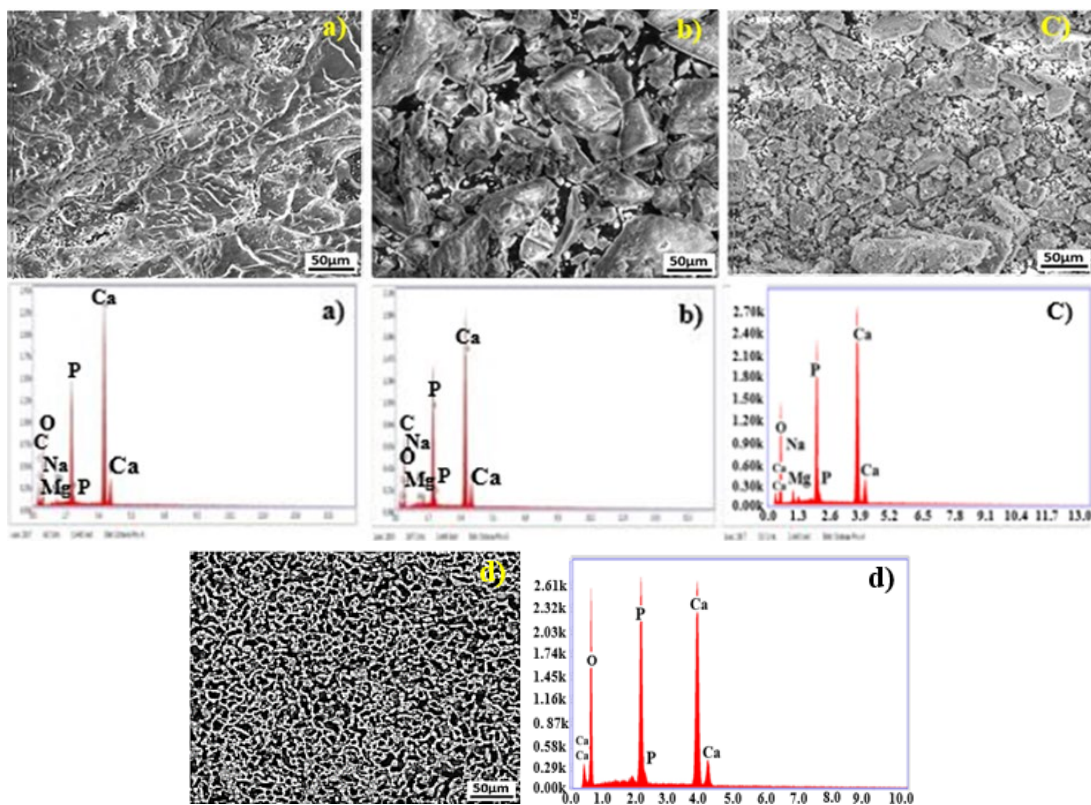
compounds during calcination, the color of the bone changed [27]. As a result, the color of the raw bovine bone changes from yellowish brown to white.



**Figure 2.** Illustration the color of bovine bone changes during the calcination process

### 3.2 Surface morphology

SEM micrographs in Figure 3 (a) to (d) display the morphology and microstructural characteristics of the synthetic (commercial) hydroxyapatite and produced powders bovine bone hydroxyapatite that have been observed at various magnifications. The microstructure of raw bones is highly dense which is due to the presence of organic substances impregnated with the mineral phase associated with bovine bones. In contrast to the raw bovine bone powder, which has a more compacted microsurface, the calcined powder has numerous pores produced by the dissolution of the organic and mineral phase [28]. Similar to what Khoo et al. [16] saw, the morphologies of the raw bone powder as it changed during heat treatment (Figure 3(a) to (c)).



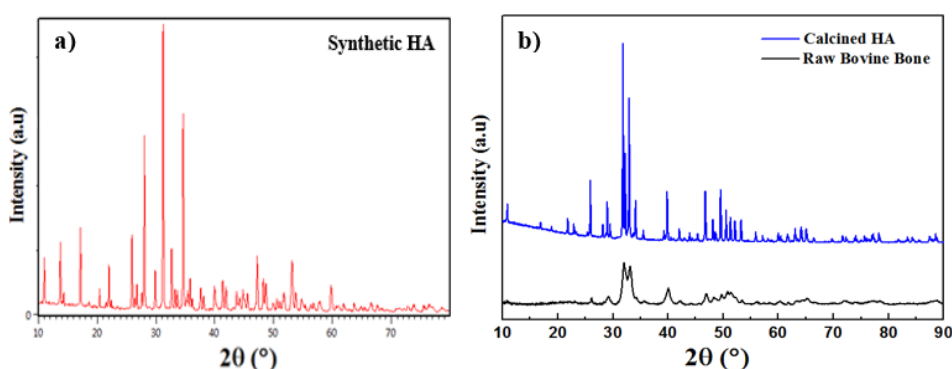
**Figure 3.** SEM image and EDS spectrum of a) raw bovine bone, b) bovine bone powder (BHA) dried at 100 °C, and c) calcined bovine hydroxyapatite (BHA) d) Commercial HA

Using an EDX analyzer, the chemical contents of HAP powder were determined both before and after calcination. Figure 3 presents the results of the EDS investigation into the elemental composition of HAP powders prepared by calcination at 850 °C/ 3h. The EDS spectra of HAP powders are shown in Figures 3(a), 3(b) and 3(c) respectively. The EDS spectrum of raw material and the dried clearly shows the peaks of Ca, P, C and O as expected. The presence of C is quite usual in the case of bovine bone, which has only been dried in the oven at 100°C, whereas in the case of bovine bone, which has been calcined at 900 °C, there is no trace of C. With traces of trace elements like magnesium (Mg) and sodium (Na), the three elements calcium (Ca), phosphorus (P), and oxygen (O) makeup most of the all samples. The elemental makeup of the samples, according to Ramesh et al [29], is strikingly close to the chemical makeup of real bone. This observation was further validated by FT-IR and XRD results. The Ca/P molar ratio (1.68) was qualitatively calculated using EDS data. The predicted value for

pure stoichiometric hydroxyapatite is 1.67, and the Ca/P ratio found in this experiment deviates somewhat from that value [30].

### 3.3 XRD

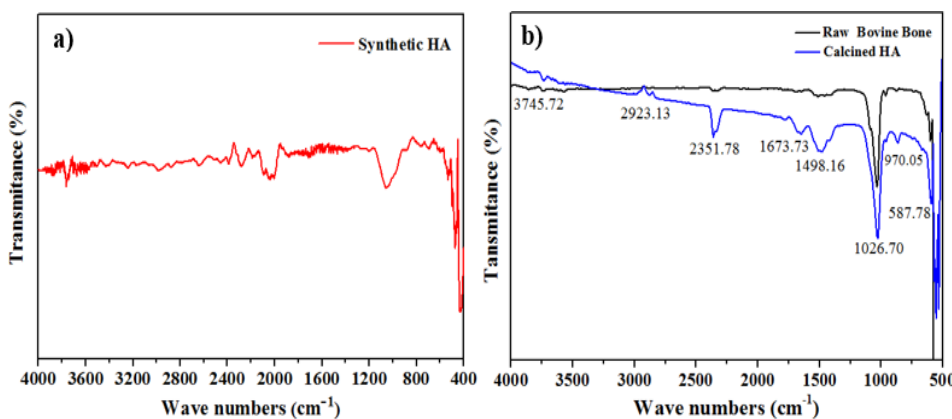
Figure 4 shows the XRD patterns of the HAp extracted from bovine bone and synthetic (commercial) hydroxyapatite. The phase and purity of derived HAp crystals were confirmed with XRD analysis. X-ray diffraction was performed to confirm the presence and crystallinity of hydroxyapatite in the obtained product, as shown in Figure 5. The resultant XRD spectra were compared with standard HAp data from JCPDS 09-0432. All of the crystalline peaks in the XRD spectra, as seen in Figure 4, closely resembled the peaks in the standard HAp, indicating that natural HAp was formed by the thermal process. The calcined bovine bone exhibit three principal peaks, which are the 211, 112, 300, and 202 planes at  $2\theta$  adjacent, 31.9, 33.05, 33.98, and 34.21 in that order of almost equal intensities established the formation of pure hydroxyapatite in crystallite form. The sharp and distinct peaks indicated a high degree of crystallinity. The diffraction peaks' strength clearly increases as the calcination temperature rises, and they also become narrower and sharper. This implies that the amorphous raw bovine bone was changed into crystalline phase with decreasing organic phase and carbonate at a temperature of 850 °C.



**Figure 4.** XRD analysis of a) synthetic HA (SHA) and b) bovine bone HA (BHA) calcined at 850°C

### 3.4 FTIR

Figure 5 reveals the FTIR spectra of uncalcined sample (raw bovine bone) and calcined HAp at 850°C. The FTIR spectra indicate the presence of phosphate ( $\text{PO}_4^{3-}$ ), hydroxyl ( $\text{OH}^-$ ) and carbonate ( $\text{CO}_3^{2-}$ ) groups. Since the cross-linked structure in the raw HAp bovine bone was disrupted during the calcination process, these spectra are clearly apparent in the calcined HAp samples. Numerous bands in the HAp spectrum matched the HAp reference spectrum and agree with the data that has been published on HAp [31]. As shown in Figure 5(b), the bands of raw bovine bone and calcined BHAp are apparently different due to the alterations in their chemical bonds during calcination at 850°C. In contrast, the result is the same as that of the commercial HA powder sample. The FTIR spectrum of calcined bovine bone at 850°C (Figure 5) exhibits good agreement with the spectra of a HA synthetic reference material described by Markovic et al. [32]. It is also revealed that there is no discernible difference between commercial HA and HA that has been taken from bovine. The FT-IR spectra of the HA samples are shown in in Figures 5(a) and 5(b).



**Figure 5.** FTIR results of a) synthetic hydroxyapatite (SHA) and b) bovine bone hydroxyapatite (BHA)

## 4 CONCLUSION

Among the different waste recovery alternatives, the production of hydroxyapatite (HAp) has attracted attention, because animal bones represent a natural source. In this work, natural synthesized hydroxyapatite (HA) powders have been successfully produced using calcination method. Based on the investigation's findings, it could be concluded that bone-derived hydroxyapatite has a lot of potential for usage as a useful and inexpensive material in a variety of applications. Synthesizing HAp from natural sources can contribute significantly towards natural resource management, health care, waste utilization amongst others. The EDS analysis showed the formation of HAp which was spherical in shape and Ca/P ratio of less than 1.68. The thermal decomposition with high temperature was effective for preparation of natural HA from bovine. Since, the process of converting bovine bone into an extremely valuable product (HAp with optimal properties) is an environmentally friendly process. These alternatives are expected to attract increasing attention in the near future.

## References

- [1] D. O. Obada, E. T. Dauda, J. K. Abifarin, D. Dodoo-Arhin, and N. D. Bansod, "Mechanical properties of natural hydroxyapatite using low cold compaction pressure: Effect of sintering temperature," *Materials Chemistry Physics*, vol. 239, no. 2020, art. no. 122099, 2019.
- [2] D. O. Malla et al., "Extraction and characterization of novel natural hydroxyapatite bioceramic by thermal decomposition of waste ostrich bone," *International Journal Biomaterials*, vol. 1690178, pp.1–10, 2020.
- [3] U. Ripamonti, J. Crooks, L. Khoali, and L. Roden, "The induction of bone formation by coral-derived calcium carbonate/hydroxyapatite constructs," *Biomaterials*, vol. 30, pp. 1428–1439, 2009.
- [4] C. Balázs, F. Wéber, Z. Kovér, E. Horváth, and C. Németh, "Preparation of calcium–phosphate bioceramics from natural resources," *Journal of the European Ceramic Society*, vol. 27, pp. 1601–1606, 2007.
- [5] K. S. Vecchio, X. Zhang, J. B. Massie, M. Wang, and C. W. Kim, "Conversion of bulk seashells to biocompatible hydroxyapatite for bone implants," *Acta Biomaterials*, vol. 3, pp. 910–918, 2007.
- [6] Z. Wei, C. Xu, and B. Li, "Application of waste eggshell as low-cost solid catalyst for biodiesel production," *Bioresource Technology*, vol. 100, pp. 2883–2885, 2009.
- [7] M. Sadat-Shojai, M. T. Khorasani, E. Dinpanah-Khoshdargi, and A. Jamshidi, "Synthesis methods for nanosized hydroxyapatite with diverse structures," *Acta Biomaterials*, vol. 9, pp. 7591–7621, 2009.
- [8] N. Elizondo-Villarreal, A. Martinez-de-la-Cruz, R.O. Guerra, J.L. Gomez Ortega, L.M. Torres-Martinez, and V.M. Castano, "Biomaterials from agricultural waste: Eggshell-based hydroxyapatite," *Water Air Soil Pollution*, vol. 223, no. 7, pp. 3643–3646, 2012.
- [9] M. K. Sah and S. N. Rath, "Soluble eggshell membrane: A natural protein to improve the properties of biomaterials used for tissue engineering applications," *Materials Science and Engineering: C*, vol. 67, pp. 807–821, 2016.
- [10] A. R. Ibrahim, W. Wei, D. Zhang, H. Wang, and J. Li, "Conversion of waste eggshells to mesoporous hydroxyapatite nanoparticles with high surface area," *Materials Letters*, vol. 110, pp. 195–197, 2013.
- [11] S. W. Lee, S. G. Kim, C. Balázs, W. S. Chae, and H. O. Lee, "Comparative study of hydroxyapatite from eggshells and synthetic hydroxyapatite for bone regeneration," *Oral Sur. Oral Med. Oral Pathol. Oral Radiol*, vol. 113, no. 3, pp. 348–355, 2012.
- [12] P. Kamalanathan, S. Ramesh, L. T. Bang, A. Niakan, C. Y. Tan, J. Purbolaksono, H. Chandran, and W. D. Teng, "Synthesis and sintering of hydroxyapatite derived from eggshells as a calcium precursor," *Ceramics International*, vol. 40, pp. 16349–16359, 2014.
- [13] J. H. Shariffuddin, M. I. Jones, and D. A. Patterson, "Greener photocatalysts: Hydroxyapatite derived from waste mussel shells for the photocatalytic degradation of a model azo dye wastewater," *Chemical Engineering Research and Design*, vol.91, no. 9, pp. 1693–1704, 2013.
- [14] S. Santhosh and S. Balasivanandha Prabu, "Thermal stability of nano hydroxyapatite synthesized from sea shells through wet chemical synthesis," *Materials Letters*, vol. 97, pp. 121–124, 2013.
- [15] C. Y. Ooi, M. Hamdi, and S. Ramesh, "Properties of hydroxyapatite produced by annealing of bovine bone," *Ceramics International*, vol. 33, pp. 1171–1177, 2007.
- [16] W. Khoo, F. Nor, H. Ardhyanta, and D. Kurniawan, "Preparation of natural hydroxyapatite from bovine femur bones using calcination at various temperatures," *Procedia Manufacturing*, vol. 2, pp. 196–201, 2015.
- [17] A. Niakan, S. Ramesh, P. Ganesan, C. Y. Tan, J. Purbolaksono, H. Chandran, and W.D. Teng, "Sintering behaviour of natural porous hydroxyapatite derived from bovine bone," *Ceramics International*, vol. 41, no. 2, pp. 3024–3029, 2015.
- [18] B. R. Sunil and M. Jagannatham, "Producing hydroxyapatite from fish bones by heat treatment," *Materials Letters*, vol. 185, pp. 411–414, 2016.

- [19] W. Qiao, Q. Liu, Z. Li, H. Zhang, and Z. Chen, "Changes in physicochemical and biological properties of porcine bone derived hydroxyapatite induced by the incorporation of fluoride," *Science Technology Advanced Materials*, vol. 18, no. 1, pp. 110–121, 2010.
- [20] A. Obczak, Z. Kowalski, and Z. Wzorek, "Preparation of hydroxyapatite from animal bones," *Acta of Bioengineering and Biomechanics*, vol. 11, art. no. 4, 2009.
- [21] N. A. M. Barakat, M. S. Khil, A. M. Omran, F. A. Sheikh, and H. Y. Kim, "Extraction of pure natural hydroxyapatite from the bovine bones biowaste by three different methods," *Journal of Materials Processing and Technology*, vol. 209, no. 7, pp. 3408–3415, 2009.
- [22] C. Y.O. OI, M. Hamdi, and S. Ramesh, "Properties of hydroxyapatite produced by annealing of bovine bone," *Ceramics International*, vol. 33, pp. 1171–1177, 2007.
- [23] E. Hosseinzadeh, M. Davarpanah, N. H. Nemati, and S.A. Tavakoli, "Fabrication of a hard tissue replacement using natural hydroxyapatite derived from bovine bones by thermal decomposition method," *Int. Journal of Organ Transplantation in Med*, vol. 5, no. 1, pp. 23–31, 2014.
- [24] J. Venkatesan, B. Lowe, P. Manivasagan, K.H. Kang, E.P. Chalisserry, S. Anil, and S.K. Kim, "Isolation and characterization of nano-hydroxyapatite from salmon fish bone," *Materials*, vol. 8, no. 8, pp. 5426–5439, 2015.
- [25] H. Asgharzadeh Shirazi, M.R. Ayatollahi, and B. Beigzadeh, "Preparation and characterisation of hydroxyapatite derived from natural bovine bone and PMMA/BHA composite for biomedical applications," *Materials Technology*, vol. 31, no. 8, pp. 1–6, 2016.
- [26] A. Loś, Z. Kowalski, K. Krupa-Żuczek, and Z. Wzorek, "Examination of physicochemical properties of bone waste intended for thermal utilization," in *13th Conference on Environment and Mineral Processing*, Ostrava, Czech Republic, 2009.
- [27] E. Kusri and M. Sontang, "Characterization of x-ray diffraction and electron spin resonance: Effects of sintering time and temperature on bovine hydroxyapatite," *Radiation Physics and Chemistry*, vol. 81, pp. 118–125, 2012.
- [28] A. Sobczak, Z. Kowalski, and Z. Wzorek, "Preparation of hydroxyapatite from animal bones," *Acta Bioeng Biomech*, vol. 11, no. 4, pp. 23–28, 2018.
- [29] S. Ramesh, Z. Z. Loo, C. Y. Tan, , W. J. K. Chew, , Y. C. Ching, F. Tarlochan et al., "Characterization of biogenic hydroxyapatite derived from animal bones for biomedical applications," *Ceramics International*, vol. 44, no. 9, pp.10525–10530, 2018.
- [30] K. Ishikawa, S. Matsuya, Y. Miyamoto, and K. Kawate, "Bioceramics," *Bioengineering*, vol. 9, pp. 169–214, 2007.
- [31] A. Boskey and N. Pleshko Camacho, "FT-IR imaging of native and tissue-engineered bone and cartilage," *Biomaterials*, vol. 28, no. 15, pp. 2465–2478, 2007.
- [32] M. Markovic, B. O. Fowler, and M. S. Tung, "Preparation and Comprehensive Characterization of a Calcium Hydroxyapatite Reference Material," *Journal of Research of the National Institute of Standards and Technology*, vol. 109, no. 6, pp. 553–568, 2004.



---

## Synthesis and Characterisation of Hybrid Membranes for Removal of Rhodamine B

Amina Aoues<sup>\*1,2</sup>, Ouarda Merdoud<sup>2,3</sup>, Mohamed Oualid Boulakradeche<sup>2</sup>, Djamel Abdessemed<sup>1</sup>, Omar Arous<sup>2</sup>

<sup>1</sup>Laboratory of Sciences and Industrial Processes Engineering, Department of the Environment Engineering, USTHB, PO Box 32 El Alia, Bab Ezzouar, 16111, Algiers, Algeria

<sup>2</sup>Laboratory of Hydrometallurgy and Inorganic Molecular Chemistry (LHCIM), Faculty of Chemistry, USTHB, PO Box 32 El Alia, Bab Ezzouar, 16111, Algiers, Algeria

<sup>3</sup>Center of Research in Physical and Chemical Analysis (CRAPC), Bousmail, Tipaza, Algeria

---

### Abstract

This work reports the synthesis and characterization of hybrid membranes for removal of Rhodamine B in an aqueous solution. The application of membrane technology to remove pollutant dyes from industrial wastewater has become a priority. Modifying membranes to improve their properties can enhance dye removal efficiency. In this work, flat-sheet membranes were synthesized via the phase inversion technique and immersion precipitation. The composite membranes were fabricated using Algerian clay, a biopolymer and a plasticizer.

The impact of the local clay additive on membrane properties and performance was investigated using some techniques like Scanning Electron Microscopy (SEM), Fourier Transform Infrared spectroscopy (FTIR), contact angle measurements, and Thermogravimetric Analysis (TAG). The prepared composite membranes were evaluated for their ability to retain Rhodamine B.

The newly developed membranes exhibited promising performance, with dye retention exceeding 50%. The inclusion of the Algerian clay modifier influenced membrane morphology, hydrophilicity, and thermal stability, thereby enhancing dye removal efficiency. These findings highlight the potential of clay-based composite membranes for treating industrial wastewater contaminated with organic pollutant dyes. Further optimization of the membrane fabrication process and operating conditions could lead to even higher dye retention capabilities.

**Keywords:** Composite membranes, Biopolymer, Clay, Dye removal

---





## Numerical Assessment of Seismic Behavior in Earth Dams: A Case Study of Fontaine Gazelles Dam, Biskra, Algeria

Alaoua Bouaicha<sup>\*1,2</sup>

<sup>1</sup>Scientific and Technical Research Center on Arid Regions (CRSTRA), Campus of Mohamed Khider University, BP 1682 RP, 07000 Biskra, Algeria

<sup>2</sup>Civil Engineering Research Laboratory (LRGC), Mohamed Khider University, BP 145 RP, 07000 Biskra, Algeria

---

### Abstract

In arid regions vulnerable to seismic activities, ensuring the stability and safety of earth dams becomes even more paramount, especially in the context of climate change that may intensify these challenges. Fontaine Gazelles Dam, located in the arid zone of Biskra, Algeria, exemplifies such vital infrastructure. This research zeroes in on the seismic behavior of the Fontaine Gazelles Dam, utilizing the Finite Element Method (FEM), a sophisticated tool tailored for modeling intricate geotechnical challenges. Using FEM, we explore potential deformations, stress distributions, and the dam's stability under diverse seismic scenarios, with special attention to the exacerbating effects of climate change in such arid regions. Acknowledging the dam's unique geotechnical characteristics, this study emphasizes its resilience and vulnerabilities against both seismic disturbances and climate-induced stresses. The insights gleaned provide a roadmap for potential reinforcements and future design adaptations, especially for dams situated in arid regions facing the dual challenges of seismicity and climate change.

**Keywords:** *Arid regions, Dam stability, Earth dams, Finite element method (FEM), Seismic analysis*

---



---

## Isocratic High-Performance Liquid Chromatographic Separation and Determination of Elution Order of Some Quinolone's Enantiomers via Cellulose-Amylose as Chiral Selector

Mohamed Nadjib Rebizi\*<sup>1</sup>

<sup>1</sup>*Organic Chemistry and Natural Substances Laboratory, Faculty of Exact Sciences and Computer Science, University of Djelfa, PO Box 3117, Djelfa 17000, Algeria*

---

### Abstract

Today in our pharmacies are a lot of developed drugs possess chiral centers, chirality has become increasingly important topic issue in drug research and has attracted increasing consideration in the pharmaceutical industry. The main objective of this work is to applied a simple direct isocratic high-performance liquid-chromatographic methods for chiral separation and determining the enantiomeric purity of some antibacterials drugs using commercialized polysaccharides stationary phases (Chiralcel® OD-H, Chiralcel® OD, Chiralcel® OJ, Chiralpak® AD, Chiralpak® IA and Chiralpak® IB). The result data illustrates the ability of the cellulose and amylose derivatives to yield good resolution. Therefore, this process has advantages over with ease of use. It is more simple and fast procedure for sample pre-treatment, easy preparation of the mobile phase, use of a low flow rate in the chromatographic system, and, consequently, decreased use of organic solvent in the mobile phase. In addition, considering the importance of understanding the chiral recognition mechanisms associated with the chromatographic enantioresolution, computational study by molecular docking were also achieved to determine mechanism of separation and elution order. The modeling studies indicated strong interactions of R-enantiomers with Chiralcel® OD-H chiral selector than S-enantiomers. The supramolecular mechanism of the chiral recognition was established by modeling of chromatographic studies. It was observed that hydrogen bondings and  $\pi$ - $\pi$  interactions are the major forces for chiral separation. The present chiral HPLC method may be used for enantiomeric resolution of quinolones in any matrices.

**Keywords:** *Quinolones, HPLC, Cellulose-amylose CSPs, Docking, Chiral separation*

---



## Evaluation of the Photophysical and Photodynamic Properties of Carbon Quantum Dots Obtained from Plant Extracts

Martín Lemos Vilches<sup>\*1,2,3</sup>, Cristian Lillo<sup>1,2,3</sup>, Jorge Montanari<sup>1,2,3</sup>

<sup>1</sup>Laboratory of Nanosystems for Biotechnology Application (LANSAB), National University of Hurlingham, Av. Vergara 2222 (B1688GEZ), Villa Tesei, Buenos Aires, Argentina

<sup>2</sup>Scientific Research Commission of the Province of Buenos Aires (CIC), Calles 60 y 118 (1900) La Plata, Buenos Aires, Argentina

<sup>3</sup>National Council for Scientific and Technical Research (CONICET), Ciudad Autónoma de Buenos Aires 1425, Argentina

---

### Abstract

Carbon quantum dots (CQDs) constitute a field of growing interest in nanomedicine due to the fluorescent properties and high stability exhibited by these structures. Due to their low toxicity and photodynamic activity through generation of reactive oxygen species (ROS), CQDs can be used as potential biomarkers and phototherapeutic agents for cancer treatment.

The carbon quantum dots synthesized in this study were made from watermelon extracts and dehydrated blueberries. Moreover, stocks of nitrogen-doped carbon quantum dots were prepared by adding urea during the synthesis process. The method used is called solvothermal, which involves subjecting the samples in a steel and Teflon reactor to a solvothermal oxidation process at high pressures and temperatures. Once the suspension is obtained, the material is purified and its concentration is determined through a protocol of filtration, dialysis, and lyophilization.

The optical properties of the carbon quantum dots were characterized using UV-Visible spectroscopy, steady-state and time-resolved fluorescence and FT-IR spectroscopy. The carbon quantum dots obtained from both carbon sources can be excited between 300 and 400 nm and exhibit emission between approximately 350 and 600 nm. The addition of urea during the synthesis process stabilizes the photophysical properties and increases the emission intensity in the different carbon quantum dots. Indirect determinations of molecular oxygen consumption (to detect the formation of singlet oxygen) and using the Colestat enzymatic kit (detection of superoxide anion radical) were performed. Indirect determinations were made through UV-Visible spectroscopy measurements in ABDA assays. The intensity drops in the bands at 342, 359, 378 and 400 nm indirectly indicate ROS production when the suspensions are irradiated. These experiments showed a slight singlet oxygen generation capacity, recorded through the decay of dissolved oxygen concentration.

**Keywords:** *Quantum dots, Photodynamic therapy, Nanobiotechnology, Nanotechnology*

---



---

# X-Ray Scans Super-Resolution with a Novel Hierarchical Multi-Scale Attention Network

Rania Saoudi<sup>\*1</sup>, Djameleddine Boudechiche<sup>1</sup>, Zoubeida Messali<sup>1</sup>

<sup>1</sup>ETA Laboratory, Department of Electronics, University of Mohamed El Bachir El Ibrahimi, Bordj Bou Arreridj, Algeria

---

## Abstract

High-resolution (HR) medical imaging modalities, such as X-ray, plays a pivotal role in modern healthcare. However, acquiring this HR images often comes with limitations that provides Low Resolution (LR) images which can lead to misinterpretations, potentially impacting patient care and outcomes. To address this issue, Super-resolution (SR) techniques specially those based on deep learning, have emerged as a promising solution.

In this work, we propose a novel Hierarchical Multi-Scale Attention Network (HMSAN), a deep learning architecture designed specifically for the X-ray image SR task. The HMSAN employs a hierarchical feature extraction strategy, which is a key innovation of our approach. This architecture utilizes a sequence of Residual Receptive Field Blocks (RRFBs), enabling the network to capture features across multiple scales. A distinctive aspect of our HMSAN is the integration of a channel attention mechanism within the RRFBs. This mechanism enables the model to selectively enhance important features, significantly improving the overall performance of the SR process. The proposed approach outperforms both classical bicubic interpolation and the existing deep learning SR techniques. It demonstrably produces superior visual quality in chest X-ray image SR evidenced by significant improvements in PSNR and SSIM metrics. These findings demonstrate that the hierarchical multi-scale and attention nature of our model can significantly advance the field of medical image SR, which in turn improve patient care and clinical decision making.

**Keywords:** Medical imaging, X-ray, Super resolution, Deep learning, Multi-scale

---

## 1 INTRODUCTION

X-ray imaging is a widely used medical imaging technique that has become an indispensable tool in modern healthcare. Unlike magnetic resonance imaging (MRI), which utilizes a strong magnetic field, X-ray imaging relies on the use of ionizing radiation to produce detailed images of the body internal structures. This non-invasive technique allows healthcare professionals to diagnose various diseases, detect injuries and monitor the progression of conditions affecting the bones, organs, and soft tissues [1]. However, acquiring high-resolution X-ray images often comes with limitations [2]. Technical factors, such as the energy of the X-ray beam, the distance between the patient and the detector, and the sensitivity of the imaging equipment, can impact the quality of the resulting image. Additionally, patient factors, such as body habitus and the presence of metal implants or foreign objects, can further complicate the imaging process and compromise the visual quality of the X-ray. To overcome this weakness, the field of medical imaging has explored the emergence of super-resolution (SR) techniques, particularly those based on deep learning. These advanced methodologies aim to reconstruct a high-resolution (HR) image from a low-resolution (LR) image input, thereby increasing the resolution of MRI scans without the need to additional updates and preserving the original content.

In this context, this paper presents a novel Hierarchical Multi-Scale Attention Network (HMSAN), a cutting-edge deep learning architecture designed for the task of X-ray image SR. Our approach introduces a hierarchical feature extraction strategy that effectively addresses the challenges associated with enhancing the resolution of X-ray images. The HMSAN is characterized by its unique sequence of Residual Receptive Field Blocks (RRFBs) and an integrated channel attention mechanism. The combination of RRFBs and channel attention is a key innovation in our HMSAN architecture. While RRFBs provide the necessary multi-scale feature extraction capabilities, the channel attention module further refines the feature representations by highlighting the most informative channels. Furthermore, the employed model incorporates a skip connection to mitigate the issue of information loss and mitigate overfitting during the training process. Multiple experiments conducted on the X-ray dataset, specifically the Chest dataset, have demonstrated that the hierarchical multi-scale and attention nature of our model exhibits superior performance compared to widely recognized SR models in terms of both visual quality and PSNR and SSIM criterions.

The rest of the content of this paper is organized as follows: In Section 2, we provide the basic mathematical concepts of the conventional SR task. In Section 3, we describe our proposed HMSAN model. The experimental findings are reported in Section 4. In Section 5, we state concluding remarks.

## 2 SUPER RESOLUTION MODEL

In computer vision, Single Image Super Resolution (SISR) task aims to recover a corresponding HR image from its LR counterpart. The LR image is typically the output of a degradation function of the original HR image. Mathematically, the degradation process is defined as:

$$I_{xLR} = d(I_{yHR}, \delta) \quad (1)$$

Where  $I_{xLR}$  denotes the LR image,  $I_{yHR}$  denotes the input HR image or reference image and  $d$  represents the degradation mapping function for converting the HR image to the LR image, and  $\delta$  stands the parameter set of the degradation process (additive noise). The degradation process is unavailable in a real-world environment, and  $I_{xLR}$  is the only the given information input for the inverse degradation function.

The SR process is theoretically aimed to provide the inverse solution  $d^{-1}$  of the original degradation mapping function to reconstruct the HR image from the LR version. So, the SR process can be described mathematically as follows:

$$g(I_{xLR}, \delta) = d^{-1}(I_{xLR}) \approx I_{ySR} \quad (2)$$

The function  $g$  represents the SR function, where  $d$  represents the input degradation parameters of the function  $g$ , and  $I_{ySR}$  denotes the resulting SR value.

Serval studies assume that the degradation of images in reality is influenced by various factors including blurring, additive noise, and attenuation that should be considered in practical applications. Usually, the whole degradation model can be described as follows.

$$I_{xLR} = d(I_{yHR}, \delta) = (I_{yHR} \otimes K) \downarrow s + n \quad (3)$$

Where,  $I_{yHR} \otimes K$  signifies the convolution operation between the ground truth HR image  $I_{yHR}$  and blur kernel  $K$ ,  $\downarrow s$  is typically down-sampling process with scale factor  $s$  and  $n$  refers to the additive noise (generally Gaussian).

Conventional image super-resolution (SR) algorithms, such as those based on interpolation (nearest neighbor, bilinear, and bicubic) [3], estimate pixel values by interpolating information from neighboring pixels. While effective for basic upscaling, these methods often struggle to preserve fine details and introduce artifacts. To overcome these challenges, deep learning-based SR models have emerged. To address these limitations, deep learning-based SR models have emerged. By learning complex mappings between LR and HR image pairs, these models can effectively recover intricate details and outperform traditional interpolation methods [4].

## 3 PROPOSED WORK

In this study, we introduce a novel SR model specifically designed for X-ray images that integrates hierarchical multi-scale and attention mechanisms to significantly enhance feature extraction from Low Resolution (LR) images. The workflow of the proposed HMSAN model is illustrated in Figure1. HMSAN can be categorized into three principal components: Primary: (1) Feature Extraction Module, (2) Deep Feature Attention Modules, and (3) Reconstruction Module. The Primary Feature Extraction Module of our proposed SR algorithm employs  $3 \times 3$  convolutional filters with the Rectified Linear Unit (ReLU) activation function. This initial module is responsible for extracting 64 shallow features from the input sequence of LR images.

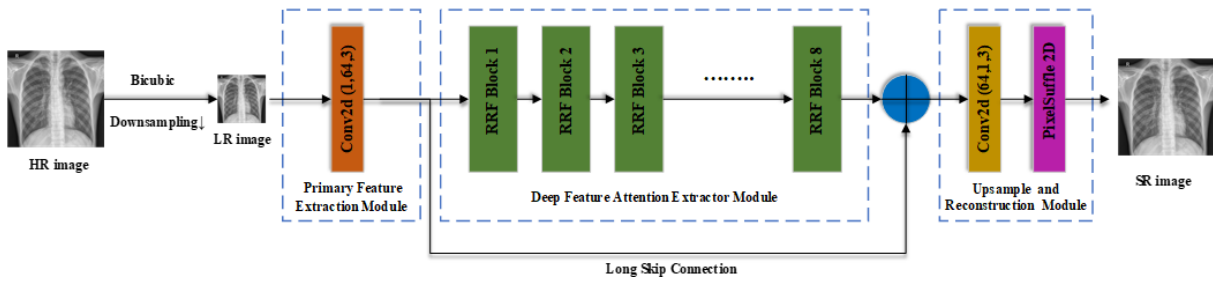


Figure 1. Hierarchical Multi-Scale Attention Network (HMSAN) architecture

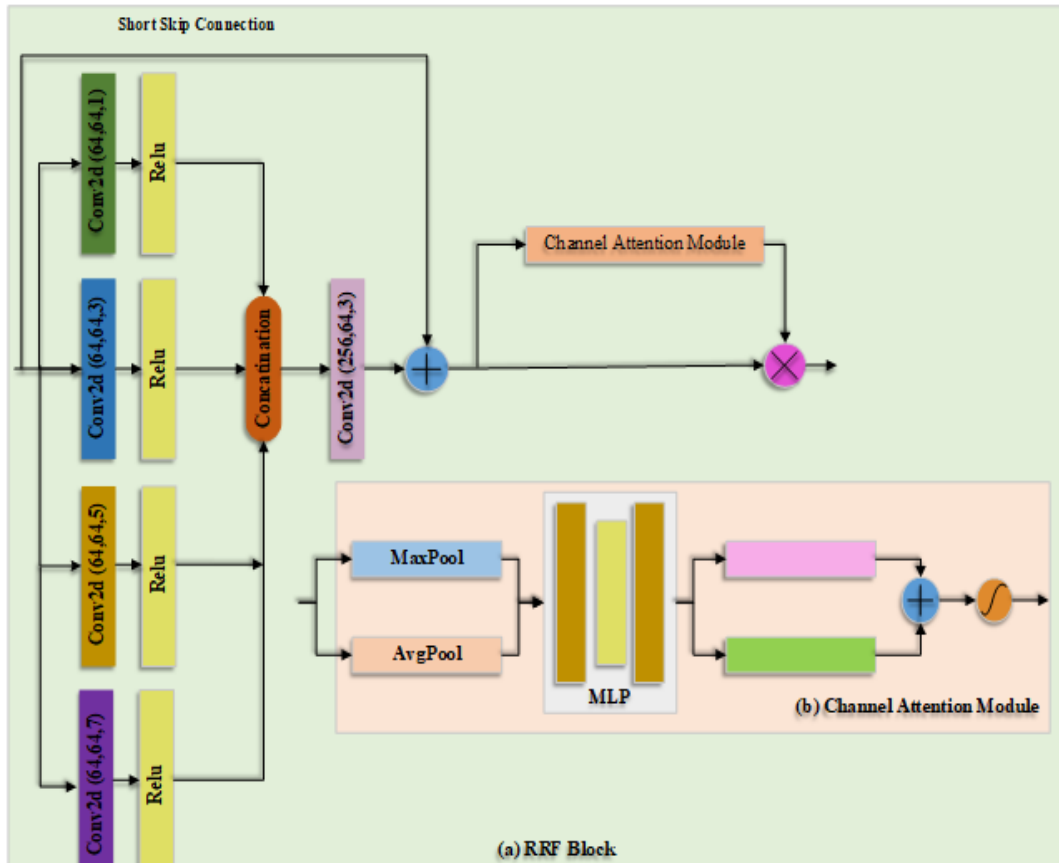


Figure 2. Residual receptive field blocks (RRFBs) structure for the deep features attention modules

Subsequently, the set of 64 shallow features is transmitted to the deep features attention module, wherein more robust features are extracted that comprises of eight consecutive blocks of Residual Receptive Field Blocks (RRFBs). As depicted in Figure2 (panel a) the RRFB consists of four parallel convolutional branches, each convolutional branch uses different kernel sizes (1x1, 3x3, 5x5, and 7x7) to capture features at different scales. The 64 outputs feature from all branches are concatenated and passed through a convolutional layer with filters of 3x3 kernel size to reduce the dimensionality from 256 features to 64 features to apply a skip connection between the original input and the processed output, allowing the network to learn residual mappings, which can mitigate overfitting and enabling the training of deeper networks. To enhance feature representation, we incorporate a Channel Attention Module (as shown in Figure 2, panel b) within each RRFB. This module dynamically recalibrates channel-wise feature responses by adaptively learning attention weights, allowing the model to preserve the most informative features while suppressing less relevant ones. To address potential issues related to network degradation, we implement two types of skip connections: Long Skip Connections (LSCs) and Short Skip Connections (SSCs). The LSCs integrate both the input and output of the residual layer while also incorporating shallow features, thereby enriching the information flow. In contrast, the SSCs focus on merging local depth features, enhancing the model ability to capture fine details critical for accurate image reconstruction.

In the Reconstruction Module, the 64 resultant features from the Deep Feature Attention Modules are fed into a convolutional layer with a 3x3 kernel size, producing an output size of 1 (as we are specifically addressing grayscale images). The feature map is then upsampled by a scale factor of 2 using a PixelShuffle layer, which

rearranges the feature maps to generate a reconstructed SR output. The workflow ensure that the majority of computations in the LR space are completed.

In our proposed model, the process of SR reconstruction is faster and easier than Very Deep Convolutional Networks [5] and Super-Resolution Using a Generative Adversarial Network [6], thanks to the exclusion of batch normalization results in reduced complexity and a 40% decrease in memory space occupation as stated in reference [7].

## 4 EXPERIMENTAL RESULTS

In this section, we first present a comprehensive overview of the implementation specifics. Then, we describe the datasets and the evaluation metrics considered in our study. A quantitative qualitative study is established to highlight the superiority of the proposed model with the recent state-of-the-art SR outcomes.

### 4.1 Implementation Steps

The proposed methodology was implemented with PyTorch software version 1.6, with the training and testing processes conducted on an google colab with T4 GPU. The neural network underwent training for a duration of 30 epochs, with a batch size of 8. The optimization process is achieved by Adam optimizer to minimize the mean-squared error loss between the network output and the HR image, with a learning rate of 0.001. The momentum term  $\beta_1$  and RMSprop term  $\beta_2$  were empirically determined to be 0.9 and 0.999, respectively.

### 4.2 Datasets and Evaluation

The proposed model as well as the considered SR algorithms are applied to a Chest X-ray (CXR) dataset utilized for the purpose of training and evaluating various models of SR techniques specifically designed for X-ray scans as referenced in [8] and [9]. The datasets consisted of two distinct subsets of X-ray scans, specifically normal and pneumonia. Each dataset was divided into three subsets: 70% of the data are used for training, 20% for the testing and 10% for validation The HR or reference images have a size of  $1024 \times 1024$  pixels with 8-bit grayscale values and the LR images were generated from the original HR images using bicubic interpolation.

The performance of the models was assessed using Peak Signal-to-Noise Ratio (PSNR) and Structural Similarity Index (SSIM) metrics, in addition to visual quality evaluation.

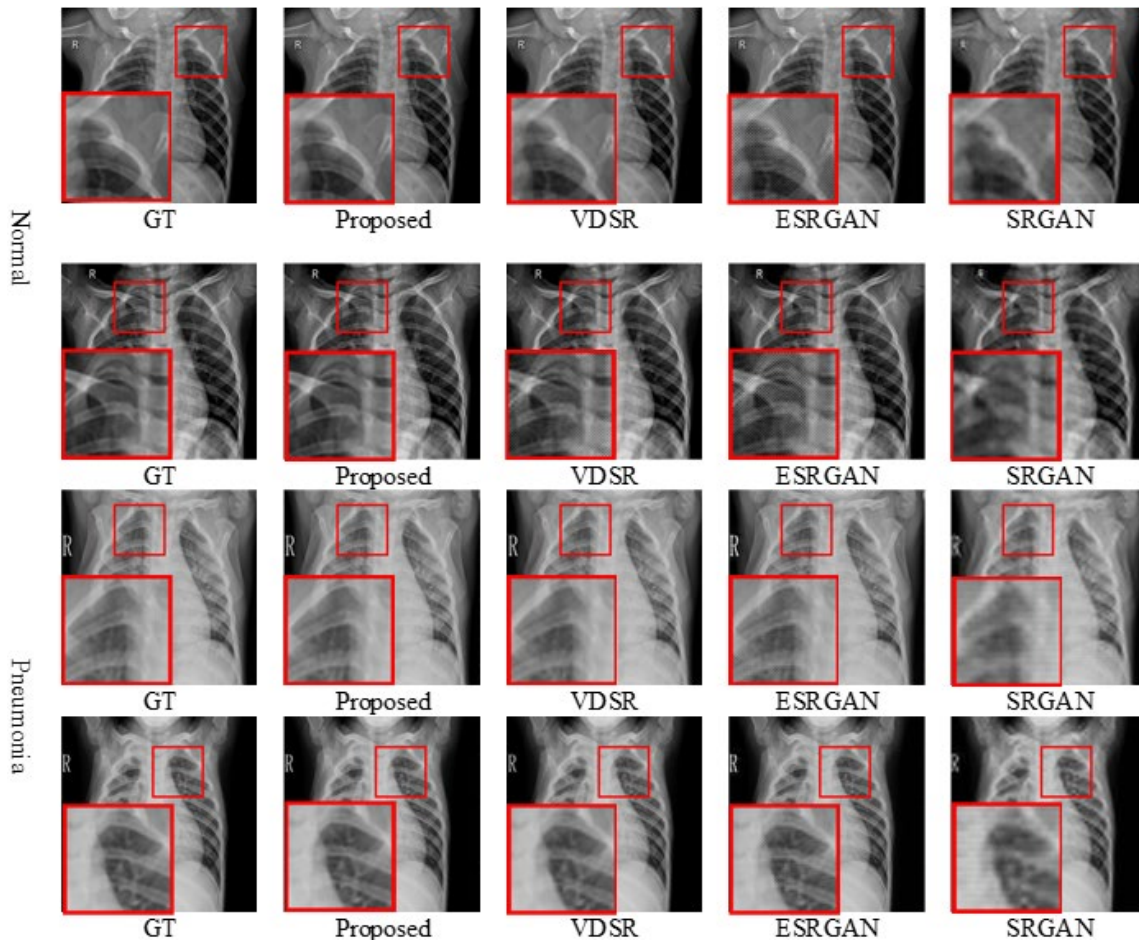
### 4.3 Results

In order to empirically assess the efficiency of the proposed SR model, we conduct a quantitative comparative analysis with the conventional-bicubic interpolation [10] and with three deep learning state-of-the-art SR algorithms including Very Deep Convolutional Networks (VDSR) [5], Super-Resolution Using a Generative Adversarial Network (SRGAN) [6], and Enhanced Super-Resolution Generative Adversarial Networks (ESRGAN) [11]. For the sake of objective comparison, all of the aforementioned models have undergone training using the same dataset and the same number of epochs. Table 1 displays the average values of PSNR and SSIM of normal and pneumonia datasets for bicubic interpolation, VDSR, SRGAN, ESRGAN and the proposed HMSAN networks. The evaluation is conducted using scale factor of 2. The optimal outcomes for both datasets are indicated in bold for clarity and the parameters of each network are also provided in Table 1. The results clearly demonstrate that our proposed model significantly outperforms both classical bicubic interpolation and the state-of-the-art deep learning SR algorithms in terms of PSNR and SSIM for both normal and pneumonia datasets. The evidence strongly supports the effectiveness of our approach in enhancing image quality, making it a valuable contribution to the field of medical image processing.

Figure 3 presents the corresponding resulting SR images of the compared super-resolution (SR) methods mentioned in Table 1. The visualization is conducted on both normal and pneumonia datasets with an upscaling factor of 2. The ground truth HR images, as well as the proposed HMSAN, VDSR, ESRGAN and SRGAN methods, are displayed. The visual superiority of the proposed model over the other methods in both image types is evident from Figure 3. For the sake of clarity, we provide a zoom of the region denoted by the red rectangle discernible in the normal image. SRGAN and ESRGAN results indicate that the reconstruction of this particular area was incomplete. Conversely, VDSR results show some improvement in this regard. However, our model offers accurate representation of the ground truth, with well-defined edges and textures. Consequently, the resulting images from the proposed model exhibit clear reconstruction. Comparable findings can also be seen in pneumonia images.

**Table 1.** PSNR & SSIM average values of the proposed model Vs Bicubic interpolation, VDSR, SRGAN and ESRGAN on both Normal and Pneumonia datasets

SR Methods	Scale	Parameters	Normal		Pneumonia	
			PSNR↑	SSIM↑	PSNR↑	SSIM↑
Bicubic Interpolation	x2	/	34.95	0.9313	33.86	0.9526
VDSR	x2	0.7 M	42.35	0.9985	41.79	0.9982
SRGAN	x2	1.3 M	35.31	0.9348	38.22	0.9923
ESRGAN	x2	13 M	41.16	0.9969	40.25	0.9963
Proposed	x2	2.9 M	42.76	0.9986	41.89	0.9983

**Figure 3.** Visual comparison of different SISR models on (CXR) benchmark datasets with 2× upscaling factor

## 5 CONCLUSION

In this paper, we have presented a novel Hierarchical Multi-Scale Attention Network (HMSAN) tailored for enhancing the quality of X-ray images through super-resolution techniques. By integrating hierarchical multi-scale feature extraction with advanced attention mechanisms, our proposed model effectively captures and emphasizes critical features from low-resolution images, significantly improving the overall image quality. The efficiency of the proposed model was assessed by applying accessible (CXR) datasets. Numerous experiments have been conducted to compare the efficiency of the proposed HMSAN model versus bicubic interpolation, VDSR, ESRGAN and SRGAN. The obtained results demonstrate the superiority of our HMSAN model in terms of PSNR and SSIM metrics.

## References

- [1] G. Hussain and Y. Shiren, “Recognition of COVID-19 disease utilizing X-ray imaging of the chest using CNN,” in 2021 International Conference on Computing, Electronics & Communications Engineering (iCCECE), Southend, 2021.



- [2] A. Khishigdelger, A. Salem, and H. S. Kang, "Enhancing chest X-ray image super-resolution through residual group and channel attention," *Kics*, vol. 49, no. 5, pp. 762–772, May 2024, doi: 10.7840/kics.2024.49.5.762.
- [3] F. Zhu, "A review of deep learning based image super-resolution techniques," *arXiv*, arXiv:2201.10521.
- [4] Y. LeCun, Y. Bengio, and G. Hinton, "Deep learning," *Nature*, vol. 521, no. 7553, pp. 436–444, May 2015, doi: 10.1038/nature14539.
- [5] J. Kim, J. K. Lee, and K. M. Lee, "Accurate image super-resolution using very deep convolutional networks," *arXiv*, arXiv:1511.04587, 2016.
- [6] C. Ledig *et al.*, "Photo-realistic single image super-resolution using a generative adversarial network," *arXiv*, arXiv:1609.04802, 2017.
- [7] B. Lim, S. Son, H. Kim, S. Nah, and K. M. Lee, "Enhanced deep residual networks for single image super-resolution," in *2017 IEEE Conference on Computer Vision and Pattern Recognition Workshops (CVPRW)*, Honolulu, HI, USA, 2017, pp. 1132–1140. doi: 10.1109/CVPRW.2017.151.
- [8] A. Khishigdelger, A. Salem, and H.-S. Kang, "Elevating chest X-ray image super-resolution with residual network enhancement," *Journal of Imaging*, vol. 10, no. 3, art. no. 64, 2024.
- [9] X. Liming, X. Zeng, Z. Huang, W. Li, and H. Zhang, "Low-dose chest X-ray image super-resolution using generative adversarial nets with spectral normalization," *Biomedical Signal Processing and Control*, vol. 55, art. no. 101600, Jan. 2020, doi: 10.1016/j.bspc.2019.101600.
- [10] S. Gao and V. Gruev, "Bilinear and bicubic interpolation methods for division of focal plane polarimeters," *Opt. Express*, vol. 19, no. 27, pp. 26161–26173, Dec. 2011, doi: 10.1364/OE.19.026161.
- [11] X. Wang *et al.*, "ESRGAN: Enhanced super-resolution generative adversarial networks," *arXiv*, arXiv:1809.00219, 2018.



## **Traditional Phytotherapeutic Practices in the South-Eastern Anti-Atlas Mountains: An Ethnobotanical Survey of Medicinal Flora in Iznaguen, Morocco**

**Younesse El-Ouazzani<sup>\*1</sup>, Fouad Msanda<sup>1</sup>, Khalil Cherifi<sup>1</sup>**

<sup>1</sup>*Laboratory of Microbial Biotechnology and Plant Protection, Faculty of Sciences, Ibn Zohr University, Agadir, Morocco*

---

### **Abstract**

Morocco has a rich cultural heritage of traditional medicine, which relies heavily on the use of medicinal plants. These plants have been used for centuries to treat a wide range of ailments, and their efficacy has been passed down through generations. However, this valuable knowledge is often undocumented and at risk of being lost.

An ethnobotanical survey was conducted in the rural commune of Iznaguen, located on the southeast of the Anti-Atlas Mountains, to document medicinal plants used by the local population, gather comprehensive information on their therapeutic applications, and contribute to the preservation of local phytotherapy knowledge. The study area covers 1710 km<sup>2</sup>. The research team conducted field surveys and interviews with 250 respondents in thirty-nine villages. Data were collected through structured and semi-structured interviews with local informants, including herbalists, traditional healers, and the local population who use medicinal plants for health and well-being. The research team conducted field surveys and interviews with 250 respondents across thirty-nine villages. Questionnaires encompassed aspects of plant identification, preparation methods, therapeutic applications, administration methods, and cultural significance. Both quantitative and qualitative methods were employed for data analysis.

The findings of this study provide valuable insights into the traditional medicinal plant knowledge of the local population. The identification of 28 frequently used endemic botanical species highlights the rich biodiversity of the region and the importance of these plants in traditional healthcare practices. Which can be used to support the conservation of medicinal plants, promote sustainable traditional use practices, and develop new phytotherapeutic products.

**Keywords:** *Phytotherapy, Ethnobotany, Medicinal plants, Biodiversity, Rural community*

---



## Preparation and Evaluation of Dermatological Gel Based on Aromatic and Medicinal Plant Extracts

Fouzia Benoudjit<sup>\*1,2</sup>, Imene Hamoudi<sup>3</sup>, Asmaa Aboulouz<sup>3</sup>

<sup>1</sup>Laboratory of Coatings, Materials & Environment, M'hamed Bougara University, Boumerdes, Algeria

<sup>2</sup>Research Unit of Materials, Processes and Environment, M'hamed Bougara University, Boumerdes, Algeria

<sup>3</sup>Department of Chemistry, Faculty of Sciences, M'hamed Bougara University, Boumerdes, Algeria

---

### Abstract

The increasing consumer preference for dermatological formulations highlights the growing awareness of skincare's importance in overall health and wellness. This trend is particularly pronounced in the shift towards formulations based on aromatic and medicinal plant extracts, which are favoured over those containing only chemical ingredients. The advantages of dermatological gels, such as ease of application and enhanced skin absorption, make them an ideal medium for delivering the bioactive compounds present in these plants. Aromatic and medicinal plants are rich in bioactive compounds that offer a variety of skin benefits. The aim of this study was to prepare a dermatological gel using selected local aromatic and medicinal plants extracts, and to evaluate its quality. The characterization of the elaborated gel focused on its organoleptic, physicochemical, and rheological properties. Organoleptic properties such as colour, odour, homogeneity and touch were assessed, while physicochemical parameters including pH, viscosity, and stability were measured. Rheological properties were also analysed to determine the ease of application of the gel and its spreadability on the skin. Results demonstrated that it is possible to obtain a good quality dermatological gel based on local herbal extracts. The formulated gel exhibited desirable organoleptic properties, optimal physicochemical characteristics, and suitable rheological behavior, making it a good product for dermatological applications. This study underscores the potential of integrating aromatic and medicinal plant extracts into dermatological formulations, offering a natural and effective alternative to purely chemical-based products.

**Keywords:** *Dermatological gel, Preparation, Evaluation, Aromatic and medicinal plant extracts*

---



---

## Electrochemical Exfoliation and Characterization of Graphene for Symmetric Supercapacitors: A Comprehensive Study

Abdelmalik Zemieche<sup>\*1</sup>, Loubna Chetibi<sup>1,2</sup>, Djamel Hamana<sup>1,2</sup>, Slimane Achour<sup>1,2</sup>

<sup>1</sup>Laboratory of Advanced Materials Technology, Ecole Nationale Polytechnique de Constantine, Algeria

<sup>2</sup>Phase Transformation Laboratory, University of Constantine 1, Algeria

---

### Abstract

Electrochemical exfoliation presents a simple, cost-effective, environmentally safe, and scalable way for bulk production of high quality graphene and its derivatives from graphite. Graphene derivatives hold immense promise across diverse fields including electronics, sensing technology, energy storage (supercapacitors and batteries), biomedical engineering, and advanced nanocomposites due to their versatile properties.

In this technique, applying a voltage induces ionic species to intercalate within graphite, leading to the formation of gaseous compounds. These compounds cause expansion, resulting in the exfoliation of individual graphene sheets.

This study involved the electrochemical exfoliation of graphene using inorganic electrolyte ((NH<sub>4</sub>)<sub>2</sub>SO<sub>4</sub>) and graphite rods as precursor. Various characterization techniques, including X-ray diffraction (XRD), Raman spectroscopy (RS), Scanning transmission electron microscopy/ energy dispersive spectroscopy (STEM/EDX) analysis, X-ray photoelectron spectroscopy (XPS), and Brunauer-Emmett-Teller (BET) analysis, were employed to assess the physico-chemical properties of the prepared sample. Furthermore, the prepared electrode, deposited on copper foil, underwent testing via cyclic voltammetry (CV) and electrochemical impedance spectroscopy (EIS) to understand the electrochemical behavior of these electrodes.

**Keywords:** *Exfoliated graphene, Characterization techniques, Supercapacitor electrode, Doctor blade*

---



---

## Contribution to the Study of Microstructural Properties of Quasicrystals in AlCuFe Alloys

Wafa Boumechta <sup>\*1</sup>, Moussa Zahzouh <sup>2</sup>

<sup>1</sup>Department of Metallurgy, University Badji Mokhtar, Annaba, Algeria

---

### Abstract

Quasicrystalline alloys are innovative materials that emerged in the last decades. Their unique atomic structure that exhibits nonperiodic long-range order led them to obtain remarkable properties including low electrical and thermal conductivity, unusual optical characteristics, low surface energy, high hardness and coefficient of friction, oxidation resistance and biocompatibility, which makes them highly attractive materials for various applications. The optimization of the quasicrystal's properties is based on different parameters including the cooling rate and the additional elements. This study presents the synthesis and processing methods of quasicrystals based on Al-Cu-Fe. Moreover, the effects of heat treatment parameters and the influence of additional elements on the microstructure evolution of quasicrystalline (QC) AlCuFe alloys are discussed. The results indicate that often some crystals compositions are retained in the sample at room temperature, after solidification, alongside with the quasicrystal. The coexistence of crystalline and quasicrystalline phases, which have different compositional and atomic volumes, significantly influences the material's properties. The experimental observations show that the formation of the QC phase in Al-Cu-Fe compounds is favored by high cooling rates exceeding  $10^4$  °C/s. Additionally, the amount of the QC phase increases with fast solidification. Small addition amounts of Cr ensure the coexistence of the icosahedral and decagonal QCs. Ni additions aid in maintaining the atomic structure of quasicrystals.

**Keywords:** AlCuFe alloy, Quasicrystals, Solidification, Microstructure, Icosahedral phase

---



## Resonance Study of FGM Shells Reinforced with Carbon Nanotubes

Zakia Hammou<sup>1</sup>, Zakia Guezzen<sup>2</sup>, Zouaoui Sereir<sup>2</sup>, Yamna Hammou<sup>3</sup>

<sup>1</sup>Physical Chemistry Department, Chemistry Faculty, University of Science and Technology of Oran, USTO, Oran, Algeria

<sup>2</sup>Composite Structures and Innovative Materials Laboratory, Mechanical Engineering Faculty, University of Science and Technology of Oran, BP 1505 El M'naouer, USTO, Oran, Algeria

<sup>3</sup>Maritime Sciences and Engineering Laboratory, Mechanical Engineering Faculty, University of Science and Technology of Oran, BP 1505 El M'naouer, USTO, Oran, Algeria

---

### Abstract

In the present study, the nonlinear vibration behavior of shallow shell reinforced by carbon nanotubes is investigated. Carbon nanotube-reinforced composite (CNTRC) shells with is used. The reinforcement is considered to be functionally graded (FGM) distribution along the radial direction of the shallow shell. The material properties of functionally graded carbon nanotube reinforced composites (FG-CNTRCs) are assumed to be graded in the thickness direction, and are estimated through a micromechanical model. The nonlinear partial differential equations are obtained based on the Von-Karman geometric nonlinear theory and it is assumed that the shell behaves in a manner consistent with classical shell theory. An approximation based on the Galerkin technique to reduce the problem into an infinite system of nonlinearly with quadratic and cubic nonlinearities. The equations are solved using the method of multiple scales (MMS) for the simply supported boundary conditions. It is found that the distributed carbon nanotubes and curvatures of the shallow shell affect the natural frequencies and the shape modes.

**Keywords:** Galerkin method, Functionally graded carbon nanotube, Fundamental linear frequency, Resonance

---



---

## Research Trends in the Use of ChatGPT in Education: A Bibliometric Analysis

Mehmet Donmez<sup>\*1</sup>

<sup>1</sup>Middle East Technical University, Ankara, Türkiye

---

### Abstract

The integration of ChatGPT into education has seen remarkable growth, driven by its potential to revolutionize teaching and learning. This study uses a bibliometric analysis to investigate the research landscape of ChatGPT in education, reviewing publications up to July 2024 from the Web of Science database. By examining relevant academic works, the study offers insights into current trends and emerging themes. The findings show significant global interest, with major contributions from the United States, China, and the United Kingdom. The analysis highlights key themes such as artificial intelligence, education, and student engagement, with special attention to issues like attitudes and plagiarism. This research showcases the transformative impact of ChatGPT on educational practices, providing a broad view of its diverse applications and implications. The study underscores the importance of ongoing exploration and collaboration among educators, researchers, and policymakers to fully realize ChatGPT's potential, ultimately enhancing learning experiences and outcomes in various educational settings. The comprehensive overview presented in this study serves as a valuable resource for understanding how ChatGPT is being utilized and its potential future directions, aiming to inform and inspire future research and practical applications in the field of education.

**Keywords:** *Data-driven AI, Education, ChatGPT, Bibliometric analysis, Emerging trends*

---

## 1 INTRODUCTION

Data-driven artificial intelligence (AI) is revolutionizing teaching and learning by leveraging large datasets to derive insights and make informed decisions [1]. This transformative technology enhances educational experiences in several ways. Firstly, it supports personalized learning by tailoring educational content to meet individual student needs [2]. This customization helps students learn at their own pace and according to their unique strengths and weaknesses. Secondly, AI streamlines administrative tasks, such as grading and scheduling, making these processes more efficient and less time-consuming for educators. Additionally, AI fosters collaborative environments by supporting group projects and peer learning through intelligent systems that facilitate interaction and cooperation among students. Overall, data-driven AI is a powerful tool transforming education by offering personalized learning, automating tasks, and enhancing collaboration.

A notable example of this transformation is ChatGPT, a cutting-edge language model developed by OpenAI. Utilizing advanced natural language processing (NLP) and machine learning (ML), ChatGPT generates human-like text based on the input it receives, understanding context to provide relevant, coherent responses [3]. For students, ChatGPT offers personalized support by tailoring tutoring to individual needs and learning styles, encouraging active learning and critical thinking, and providing a safe space for questions and exploration [4]. For educators, ChatGPT acts as a teaching assistant, managing routine tasks, providing valuable data insights into student performance, and helping to craft more engaging lesson plans.

While ChatGPT and other AI technologies hold great promise for education, they come with a set of challenges. Privacy is a major concern, especially when it comes to protecting sensitive student information [5]. There's also the issue of making sure these AI tools are accessible to all students, regardless of their socioeconomic status, to avoid deepening existing inequalities. Additionally, AI systems can sometimes reflect and amplify biases, which could perpetuate unfairness and create new forms of discrimination [6]. It's essential to address these issues to ensure that the integration of AI in education is both fair and beneficial for all students.

This paper provides a comprehensive overview of the current landscape of research on ChatGPT in education through a rigorous bibliometric analysis of scholarly publications. By examining publications retrieved from the Web of Science database, the study identifies key themes, research methodologies, and emerging trends in this evolving field. By addressing the transformative potential and associated challenges of data-driven AI in education,

this paper seeks to inform educators, researchers, and policymakers about the opportunities and implications of leveraging AI technologies like ChatGPT to shape the future of education.

## 2 METHODOLOGY

This study employed a bibliometric analysis by focusing on studies conducted up to July 2024 and sourced from the Web of Science database. The chosen keywords for this review included “ChatGPT”, “education”, “learning”, and “teaching”. The objective was to identify and analyze recent academic publications that explore the integration of ChatGPT in educational contexts. By systematically reviewing research within this timeframe, this study aims to concentrate on current trends, emerging themes, and notable findings in utilizing ChatGPT to understand and improve educational practices. This review contributes to the ongoing discourse on integrating ChatGPT in education and seeks to inform future research directions and applications within the field. The inclusion and exclusion criteria for this bibliometric analysis were defined based on the PRISMA guidelines [7]. The specified criteria included articles published in academic journals, written in English, and available in full text, explicitly focusing on educational research that involves ChatGPT, as shown in Table 1.

**Table 1.** Inclusion and exclusion criteria

Inclusion Criteria	Exclusion Criteria
Published in an academic journal	Review or meta-analysis
Written in English	Not written in English
Available in full-text	Not available in full text
Educational research	Not educational research
Using ChatGPT	Focused on other AI tools

Following the PRISMA guidelines, the inquiry and selection process involved the identification, screening, eligibility assessment, and inclusion of articles [8]. In the identification phase, a comprehensive search on the Web of Science yielded a total of 2,118 articles. Subsequently, during the screening stage, titles, abstracts, and keywords were meticulously examined, leading to the exclusion of 662 articles that did not align with the predetermined criteria. Following this, in the eligibility assessment phase, 1,456 articles underwent further examination, resulting in the exclusion of an additional 960 articles. Ultimately, 496 articles met the inclusion and exclusion criteria and were deemed suitable for the review. This systematic process ensures a rigorous and transparent approach to selecting relevant literature, contributing to the robustness and reliability of the forthcoming review on the integration of ChatGPT in education.

During data analysis, a BibTeX file was extracted from the Web of Science database to gather all relevant data. The bibliometric analysis and visualization were then conducted using the biblioshiny web interface, which is integrated with RStudio and the bibliometrix package [9].

## 3 RESULTS

The bibliometric analysis, covering the period from 2022 to 2024, as shown in Figure 1, revealed a rapid growth in research on ChatGPT in education, with an annual growth rate of 1683.26%. A total of 496 documents from 163 sources were analyzed, with each document receiving an average of 7.627 citations. The average document age was 0.361 years, indicating a recent surge in publications. The study identified 1492 Author’s Keywords and 388 Keywords Plus, reflecting a wide range of research themes. A total of 1578 authors contributed, with a notable level of collaboration evident from the 3.44 co-authors per document and 18.55% international co-authorships. The document types included 360 articles and 136 early access articles, highlighting the prominence of journal publications in this field.



**Figure 1.** Summary of the bibliometric analysis

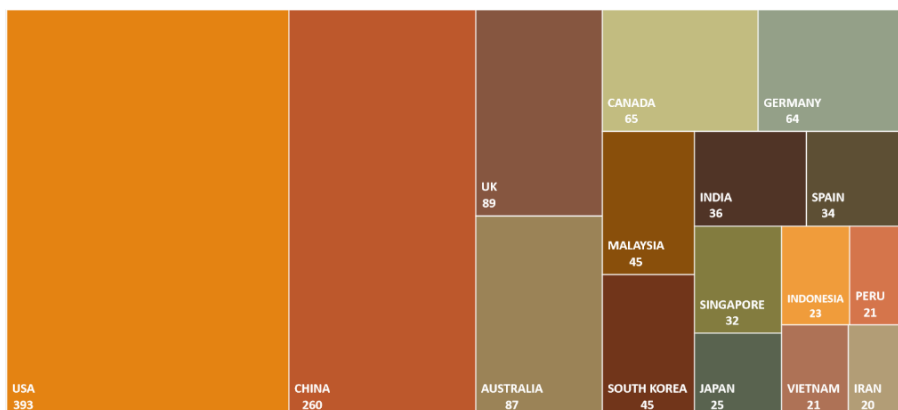


The analysis of host journals reveals that research on ChatGPT in education is widely disseminated across various academic platforms (see Table 2). The leading journal is Education and Information Technologies, with 35 articles, followed by JMIR Medical Education with 32 articles. The Journal of Chemical Education and Education Sciences has 20 and 17 articles respectively. Other notable journals include the International Journal of Technology in Education (16 articles), Interactive Learning Environments (15 articles), and Medical Teacher and TechTrends (13 articles each). Additionally, IEEE Transactions on Learning Technologies and Frontiers in Education have 12 and 11 articles respectively. A significant portion of the research is also published in 153 other journals, contributing a total of 312 articles. This distribution highlights the broad and interdisciplinary interest in the application of ChatGPT across various fields of education.

**Table 2.** Host journals

Journal Name	Number of Publications
Education and Information Technologies	35
JMIR Medical Education	32
Journal of Chemical Education	20
Education Sciences	17
International Journal of Technology in Education	16
Interactive Learning Environments	15
Medical Teacher	13
Techtrends	13
IEEE Transactions on Learning Technologies	12
Frontiers in Education	11
Others (153 Different Journals)	312

The analysis of research on ChatGPT in education reveals a strong global presence, as seen in Figure 2, with the United States leading with 393 publications, followed by China (260) and the United Kingdom (89). Australia (87) and Canada (65) also contribute significantly, along with Germany (64), Malaysia, and South Korea (45 each). Other notable contributors include India (36), Spain (34), and Singapore (32). The data highlights extensive international engagement, with contributions from a diverse range of countries, reflecting the widespread interest and global impact of ChatGPT in educational research.



**Figure 2.** Countries of articles (>20)

The analysis of key terms in research on ChatGPT in education, as seen in Figure 3, reveals that “artificial-intelligence” is the most frequently mentioned term, appearing 38 times, followed by “education” (31) and “students” (24). Other prominent terms include “technology” (21), “acceptance” (15), and “impact” (12). Terms such as “model” and “information-technology” (11 each), and “user acceptance” (10) also feature prominently. The term “chatgpt” appears 8 times, along with related concepts like “knowledge,” “motivation,” “quality,” and “science.” Additional notable terms include “higher-education,” “online,” and “teachers” (7 each), reflecting the educational context. Other frequently mentioned terms include “ai” (6), “attitudes,” “engagement,” and “plagiarism” (6 each), highlighting key areas of focus within the research.

The trend topic analysis of research on ChatGPT in education highlights key focus areas and themes. “Artificial Intelligence” emerges as the dominant topic, with 36% of mentions, underscoring its central role in the discourse. “Education” is the next most frequently discussed topic, accounting for 29% of mentions, reflecting its significant relevance in the research. The topic of “Students” appears in 23% of the publications, indicating a strong focus on

learner-related aspects. “Attitudes” and “Plagiarism” are each discussed in 6% of the mentions, highlighting specific concerns and interests within the research landscape. These trends reveal the primary themes and areas of emphasis in the study of ChatGPT’s impact on education.



Figure 3. Most frequent 50 keywords

## 4 CONCLUSION

This bibliometric analysis provides an in-depth look at the rapidly evolving field of ChatGPT research in education, revealing substantial growth and international interest. The study’s findings highlight an extraordinary annual growth rate of 1683.26%, showing an unprecedented expansion in research activities related to ChatGPT. Notably, the United States, China, and the United Kingdom have emerged as leading contributors to this growing body of knowledge, with significant scholarly engagement also noted from other countries, illustrating the global relevance and widespread adoption of ChatGPT in educational settings. The analysis uncovers dominant themes within the research, including the transformative impact of ChatGPT on educational practices and student engagement.

However, the integration of such advanced AI technologies comes with challenges that must be addressed to harness their benefits entirely. Privacy concerns, ensuring equitable access for all students, and mitigating algorithmic biases are critical issues that need to be carefully managed. Future research should aim to develop effective strategies for these challenges while assessing the long-term effects of ChatGPT in various educational contexts. This study serves as a comprehensive resource for understanding current trends. It provides a foundation for future research, emphasizing the importance of collaborative efforts among educators, researchers, and policymakers to optimize the use of ChatGPT in education.

## References

- [1] Y. Feng, S. Vanam, M. Cherukupally, W. Zheng, M. Qiu, and H. Chen, “Investigating code generation performance of ChatGPT with crowdsourcing social data,” *Proc. - Int. Comput. Softw. Appl. Conf.*, vol. 2023-June, pp. 876–885, 2023.
- [2] S. J. Rao *et al.*, “ChatGPT: A conceptual review of applications and utility in the field of medicine,” *J. Med. Syst.*, vol. 48, no. 1, pp. 1–10, Dec. 2024.
- [3] Y. Xing, “Exploring the use of ChatGPT in learning and instructing statistics and data analytics,” *Teach. Stat.*, vol. 46, no. 2, pp. 95–104, Apr. 2024.
- [4] R. N. Albdarani and A. A. Al-Shargabi, “Investigating the effectiveness of ChatGPT for providing personalized learning experience: A case study,” *Int. J. Adv. Comput. Sci. Appl.*, vol. 14, no. 11, pp. 1208–1213, Nov. 2023.
- [5] R. T. Williams, “The ethical implications of using generative chatbots in higher education,” *Front. Educ.*, vol. 8, Jan. 2024.
- [6] S. Vaccino-Salvadore, “Exploring the ethical dimensions of using ChatGPT in language learning and beyond,” *Lang. 2023, Vol. 8, Page 191*, vol. 8, no. 3, p. 191, Aug. 2023.
- [7] M. J. Page *et al.*, “The PRISMA 2020 statement: An updated guideline for reporting systematic reviews,” *Int. J. Surg.*, vol. 88, pp. 1–11, 2021.
- [8] D. Moher *et al.*, “Preferred reporting items for systematic review and meta-analysis protocols (PRISMA-P) 2015 statement,” *Rev. Esp. Nutr. Humana y Diet.*, vol. 20, no. 2, 2016.
- [9] M. Aria and C. Cuccurullo, “Bibliometrix: An R-tool for comprehensive science mapping analysis,” *J. Informetr.*, vol. 11, no. 4, pp. 959–975, 2017.



---

## Decentralized Collaborative Multi-Agent Reinforcement Learning for Air Attack Scenarios

Berire Gunduz<sup>\*1</sup>, Mehmet Dikmen<sup>1</sup>

<sup>1</sup>Department of Computer Engineering, Baskent University, Ankara, Türkiye

---

### Abstract

Transforming virtual entities into collaborative artificial intelligence agents in military tactical simulations is of great importance for enhancing the realism and educational quality of simulations. In response to this need, the effectiveness of collaborative multi-agent reinforcement learning methods has been researched in a real-time military tactical environment simulation. Similar to real-time strategy games, this simulation dynamically portrays defense and attack scenarios, incorporating diverse inputs and actors. Within the scope of the study, air attack scenarios were designed on this simulation; featuring enemy aircrafts that make decisions using rule-based algorithms, and friendly aircrafts that learn to select various actions via multi-agent reinforcement learning methods. Through conducted experiments, the effectiveness and applicability of two primary training methodologies for friendly aircraft—Decentralized Training-Decentralized Execution and Centralized Training-Centralized Execution—was compared. While Centralized Training-Centralized Execution proved faster and displayed more stable learning, Decentralized Training-Decentralized Execution exhibited greater adaptability in the face of limited information. The comparison between decentralized and centralized training approaches provides valuable insights into the optimal methodologies for training collaborative artificial intelligence agents within simulated tactical environments. Furthermore, this study contributes to advancing the understanding of how multi-agent reinforcement learning methods can be applied within dynamic, real-time military simulations, offering potential pathways for future research and development in this domain. Ultimately, the findings of this study have implications not only for military training and education but also for the broader application of artificial intelligence in dynamic and collaborative decision-making scenarios.

**Keywords:** *Air attack scenarios, Multi-agent reinforcement learning, Cooperative, Decentralized*

---

## 1 INTRODUCTION

In military tactical simulations, enabling virtual entities to exhibit realistic behaviors is of great importance for enhancing the realism of the simulations and improving the quality of training. The use of rule-based algorithms to ensure realistic behaviors in virtual entities requires designs specific to the entity, scenario, and environment, which do not provide sufficient flexibility and require a significant amount of labor. Following the successes of reinforcement learning, one of the artificial intelligence development methods, on this and similar problems, many studies on making virtual entities intelligent with reinforcement learning in military tactical simulations have entered the literature. Within the scope of this thesis, the effectiveness of the decentralized collaborative multi-agent reinforcement learning method was examined in a real-time military tactical environment simulation (FIVE), developed by HAVELSAN.

The simulation, similar in nature to real-time strategy games, can simulate defense and attack scenarios against an enemy with adjustable inputs and various actors. Moreover, this simulation provides the opportunity to observe many intermediate states based on cause-and-effect relationships at specific time intervals. Transforming the virtual entities on the same team in the simulation into cooperative AI agents is crucial for increasing simulation realism and improving training quality. For the experiments conducted within this scope, air attack scenarios were created and used as a testing ground.

In the examined air attack scenarios, friendly aircraft aim to destroy the enemy's ground and air defense units. While enemy aircraft decide on actions through a rule-based decision-making mechanism, friendly aircraft with artificial intelligence decide on actions using reinforcement learning policies. The real-time nature of the simulation, the numerous parameters that can affect agents and intermediate states, increase the complexity of finding optimal policies for friendly aircraft. Additionally, the fact that each aircraft on the same team needs to

make individual decisions and cooperate with other aircraft despite this individuality further complicates the problem.

Multi-agent reinforcement learning methods used to solve such problems are divided into three, regarding the learning environment. One of these methods, the Decentralized Training-Decentralized Execution method, is a decentralized method, and experiments were conducted on the mentioned simulation using this method within the scope of the thesis. Subsequently, the findings obtained were compared with the data obtained from the Centralized Training-Centralized Execution method, and the advantages and disadvantages of these two methods were examined comparatively.

This thesis aims to provide significant literature contributions in this field by addressing the applicability of multi-agent reinforcement learning methods in real-time military simulations and comparing these methods with each other. Real-time military simulations play a critical role in the development of modern warfare strategies, and the results of this study will provide important contributions to future military training and strategy development processes.

## 2 MATERIAL AND METHOD

The problem examined within the scope of this thesis is the decentralized, collaborative, multi-agent reinforcement learning method in air attack scenarios. Multi-agent reinforcement learning methods are classified according to the task type, learning environment, and finally, the type of interaction. Considering the scenarios and actors created based on the FIVE, it can be said that the study was conducted on complex tasks and partially observable environments. In this study, analyses and comparisons were made between Centralized Training-Centralized Execution (CT-CE) and Decentralized Training-Decentralized Execution (DT-DE) environments.

### 2.1 Scenarios

#### 2.1.1 Scenario A

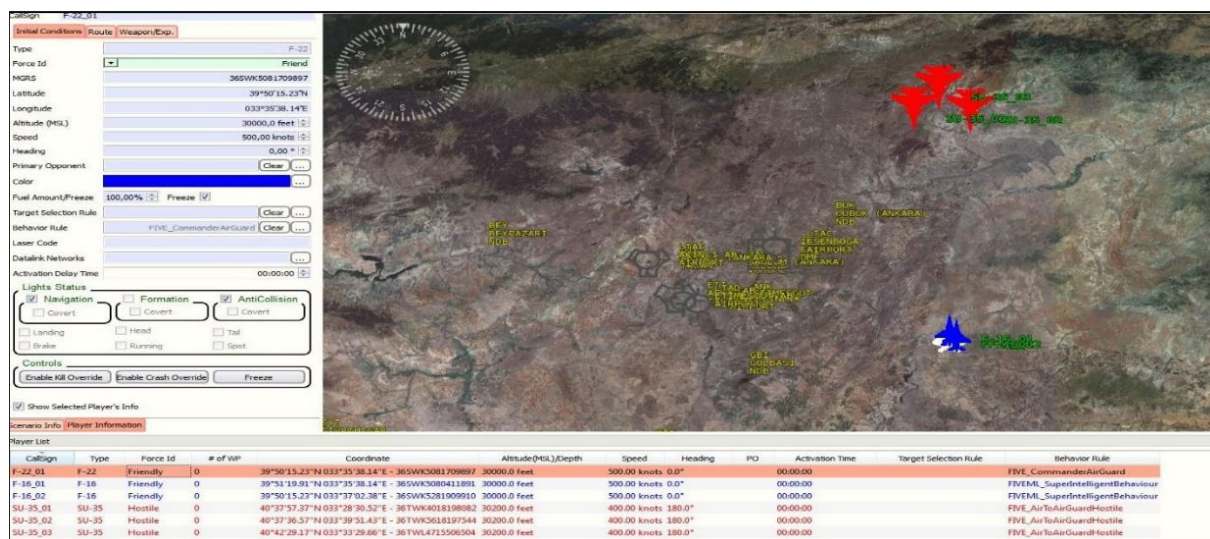
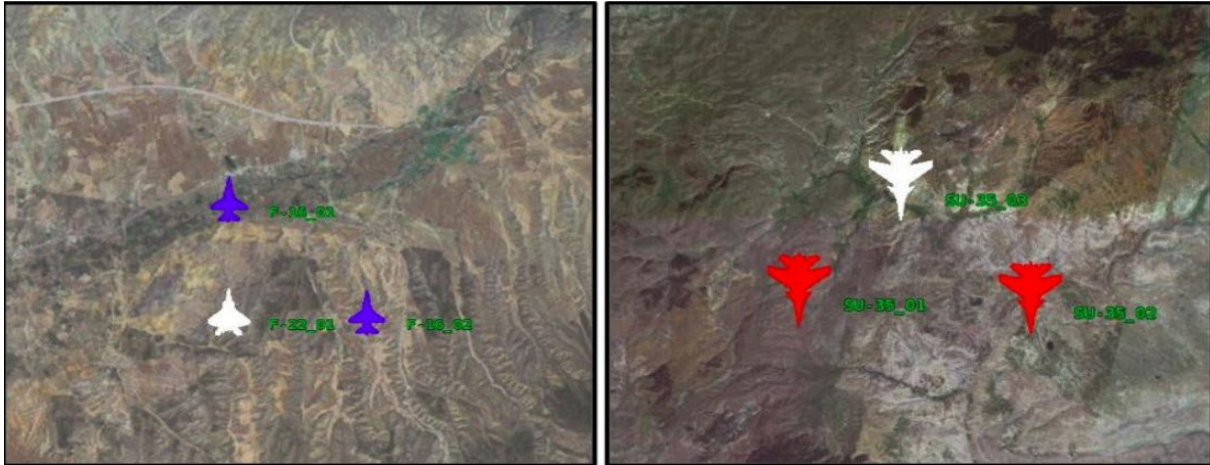


Figure 1. Scenario A from the GUI of FIVE

In the scenario shown in Figure 1, there are three fighter jets in the blue team and three fighter jets in the red team. The blue team consists of two F-16 jets and one F-22 jet serving as the commander. The red team consists of three SU-35 jets. The goal of both teams is to destroy all enemies in the opposing team. A more detailed examination of the actors in the teams is as follows:



**Figure 2.** Blue team (left) and red team (right) in Scenario A

### *Blue Team Actors*

a. Two F-16 jets with the same specifications; each has five hundred bullets, three radar-guided missiles, three heat-guided missiles, sixty chaff countermeasure missiles used to deceive enemy radar units, and eighty-eight flare countermeasure missiles used to deceive heat-guided missiles. Both jets are equipped with laser, radar, and optical sensors. At the beginning of the scenario, both jets have a speed value of 500 knots, a heading value of 0 degrees, and an altitude of 30,000 feet. The distance between the two jets is approximately 3 km. For the examination in Scenario A, only these two F-16 jets with the same specifications were assigned artificial intelligence.

b. The F-22 jet serving as the commander; for Scenario A, this jet was assigned the rule-based action function of the FIVE.

The actions taken by the F-22 in sequence according to this function are as follows:

- It declares itself as the commander to the other actors in the team.
- If it detects one or more undestroyed enemies nearby using its radar, laser, and other sensors, it sends a message to its teammates indicating the FIVE actor number of the detected enemy.
- If the teammates send a message that they have hit the enemy, it continues to move and search with sensors by changing its heading degree.
- As can be understood, this jet does not have the ability to actively attack. Its sole task is to identify detected enemies as targets for its teammates.

### *Red Team Actors*

Three SU-35 jets: Each jet has one hundred fifty bullets, three radar-guided missiles, three heat-guided missiles, eighty-eight chaff missiles, and eighty-eight flare missiles. All three jets are equipped with laser, radar, and optical sensors. For Scenario A, these three jets were assigned the rule-based action function of the FIVE.

According to this function, the actions taken by the SU-35 jets in sequence are as follows:

- Using its radar, laser, and other sensors, it identifies the closest undestroyed enemy it detects nearby as the target.
- If the distance to the target enemy is within the range of the heat-guided missiles, a heat-guided missile is fired at the enemy. If the distance to the enemy is greater than the range of the heat-guided missiles, radar-guided missiles and bullets are fired at the enemy.

### **2.1.2 Scenario B**

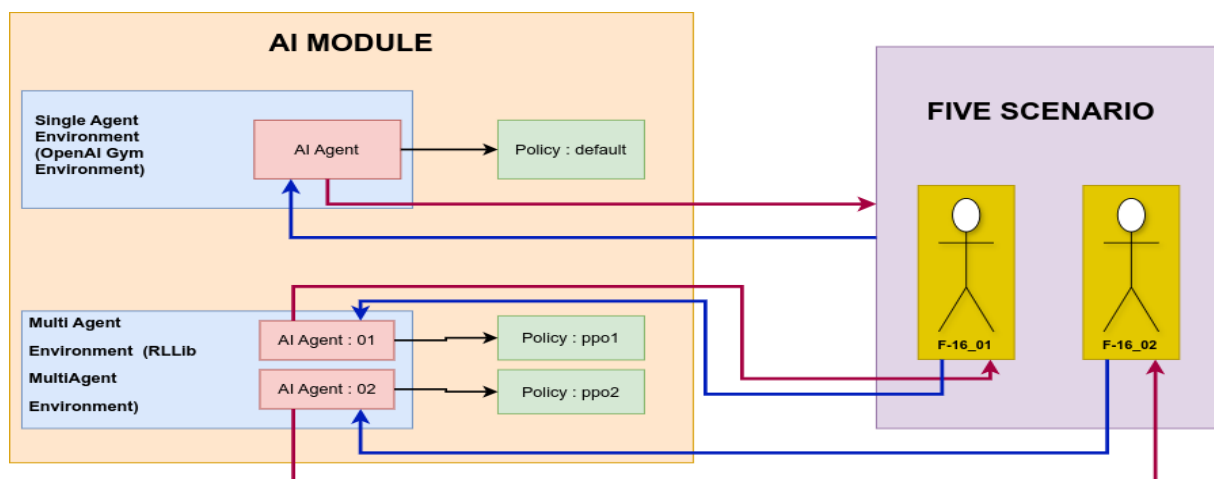
Scenario B is essentially the same as Scenario A. In the cooperative scenarios discussed in the thesis, to measure the effects of centralized command and messaging on reinforcement learning performance, in this scenario, the F-22 acting as the commander in the blue team is prevented from giving orders to the F-16 jets about potential enemies. This arrangement was made through the rule-based function assigned to the F-22 actor mentioned in Scenario A. The F-16 jets assigned with artificial intelligence are not prevented from messaging each other; the

actors can send messages by selecting “turn”, “target”, “fire”, “turn off radar”, and “enemy target identified” from their action spaces.

## 2.2 Software Design

RLLib is a comprehensive, open-source software library used for implementing, training, and deploying reinforcement learning (RL) algorithms. It is written in the Python programming language and is built on top of a distributed computing framework called Ray. Ray is a system designed for large-scale, parallel, and distributed applications. RLLib leverages this system to efficiently run a wide variety of RL algorithms for both single-agent and multi-agent environments [1]. The RLLib Environment Class is the fundamental class used to establish the relationship between RL algorithms and the environment discussed in the scenarios section. RLLib has basic environment classes labeled as "OpenAI Gym Environment" and the derived "RLLib MultiAgent Environment." These classes have two main functions: reset and step. A learning episode starts with the reset function, and the step function is called throughout the learning process. Here, the return values of these two functions are filled with information obtained from the FIVE. In order to train agents's policy networks for both CT-CE and DT-DE methods, Proximal Policy Optimization is used [2]

The aforementioned value spaces and functions are expressed with discrete values instead of continuous values. The reason for this is that discrete values both simplify the representation of the problem and accelerate computational operations on the RL side. With discrete values, observation and action spaces are expressed as finite, countable sets of probabilities, which significantly facilitates the convergence of rewards to a finite value compared to infinite, continuous data [3]. For example, the DQN (Deep Q Networks) algorithm, developed by working on Atari 2600 games, uses only discrete action spaces to utilize the neural network for searching action-value functions based on a table. However, it is impossible to create such a table if infinite-continuous values are used with DQN [4]. Many algorithms developed like DQN are based on discrete values, such as the Q-learning algorithm first introduced by Watkins in 1992 [5] and the RL study by David Silver in 2016 using deep neural networks and tree search in the game of Go [6]. There are many methods in the literature for discretizing continuous values such as speed and orientation angle. In the method called manual discretization by J. Kober and others [3], continuous data is divided into specific regions and made discrete. The data spaces and functions used in the thesis are also discretized using this method.



**Figure 3.** Simple diagram that shows design of the software

If we need to examine the types of data important for these environment classes:

### a. Actors

As previously mentioned, the differences between a centralized agent environment and a discrete multi-agent environment have been examined in the thesis study. The fundamental difference between these two environments on the software side is that the number of artificial intelligence actors is one in a centralized single-agent environment and two in a discrete multi-agent environment.

As shown in Figure 3, the data of the two entities in the FIVE scenario is sent integrally (blue arrow) to the single-agent environment. Subsequently, the rewards calculated inside are used to update a single policy, and the actions decided by the policy are sent back to the FIVE integrally (red arrow). In the context of multi-agent RL, this

architecture is known as Centralized Learning-Centralized Execution (CT-CE). In the multi-agent environment, two artificial intelligence actors and their policies are created. The data of the two artificial intelligence actors are matched with the data of the corresponding entities in the FIVE according to their names.

As shown in Figure 3, the observation data of the “F-16\_01” entity in the FIVE is used to train the artificial intelligence agent numbered “01”, and the observation data of the “F-16\_02” entity in the FIVE is used to train the artificial intelligence agent numbered “02” (blue arrows). The actions decided by the agents’ policies (ppo1 and ppo2) are sent to the corresponding entities in the FIVE (red arrows). This discrete multi-agent structure is classified as Decentralized Training-Distributed Execution (DT-DE) in the context of multi-agent RL. In the DT-DE design, the data spaces and functions detailed in the continuation of the section are defined separately for each actor in the environment and matched with the relevant actors.

### *b. Observation Space*

Observation data is created by processing the data collected from the FIVE environment into a form that RLlib can use. Some of these observation information are as follows: Actor position information, Actor ammunition information, Actor sensor information, Actor damage information, Actor communication information. Due to the multi-agent nature of the problem observation data about the other entities also added to actors’ observation spaces: Is other entity friendly/enemy information, other entity’s relative position information, Is other entity detected by sensors information, Is other entity within weapon range, other entity’s overall health information.

### *c. Action Space*

As mentioned earlier, the actions of an entity in the FIVE environment are possible using certain sub-functions written in the FIVE infrastructure. For this reason, the action space containing the actions that the RL algorithm can select is a subset of these sub-function sets, which are limited in number and scope. This set is defined as a “MultiDiscrete” space consisting of six categories within the scope of RLlib.

These categories are speed actions, orientation angle actions, altitude actions, sensor actions, weapon actions, message actions.

### *d. Reward Function*

As mentioned by G. Vevirko and others [7], there are infinite ways to define a reward function. Each different reward function can lead to completely different learning processes. While most successful RL studies use handcrafted reward functions, some studies are directly inspired by human learning processes. In many RL studies, rewards have a sparse reward structure. In a sparse reward structure, the agent only earns points when it completes its task. Solving problems using RL with such reward structures is difficult. To address this issue, a dense surrogate reward system has been developed. Dense surrogate rewards are calculated based on the agent’s current state and its distance to the goal. However, this method requires precise calculations and observations for adjusting intermediate rewards, as the agent may develop suboptimal policies that exploit these intermediate rewards and get stuck in a specific loop [7]. In all the experiments conducted within the scope of the thesis, predetermined rewards proportional to 0.5-2.0 per agent were used. The results of these rewards' magnitudes and existence were not evaluated within this thesis.

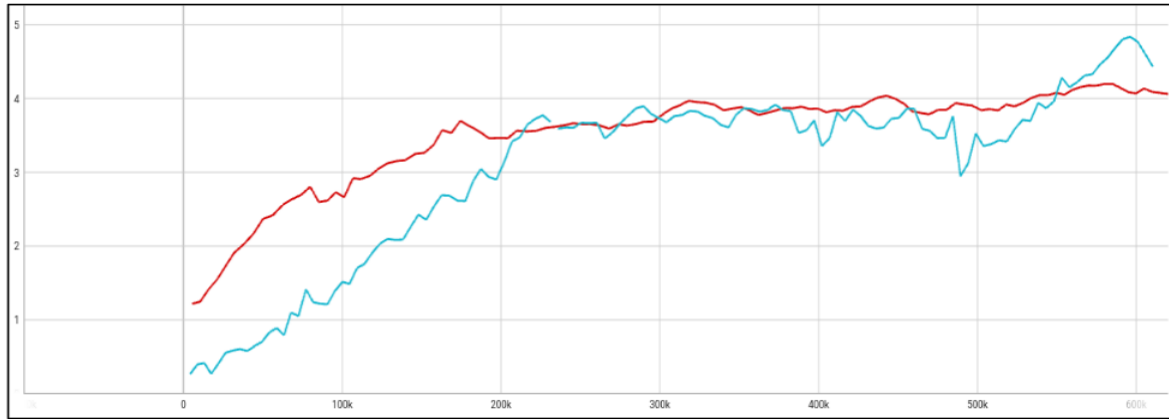
### *e. Episode Termination Indicator*

In Reinforcement Learning (RL), a signal is needed to indicate the end of an episode. In RLlib, this signal is referred to as the “done” flag. During the episode, this flag is set to false, and when the episode ends, it is set to true. In the thesis work, the end of the episode is determined by whether any agent in a multi-agent environment has completed its episode. Whether an agent has completed its episode is evaluated using the following conditions: Agent is eliminated, All enemies are eliminated, All teammates are eliminated, Attack area is abandoned.

## **3 RESULTS**

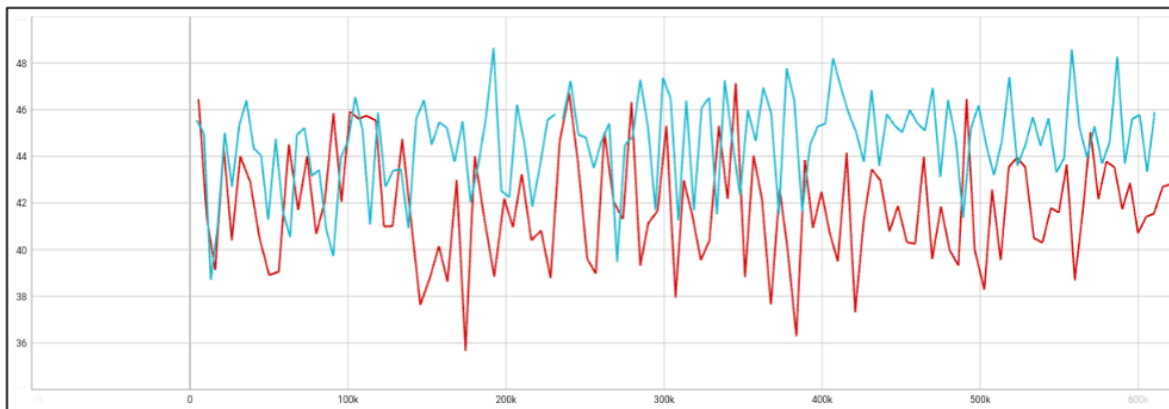
### **3.1 Experiment 1**

In the first experiment, learning environments CT-CE and DT-DE were compared using Scenario A.



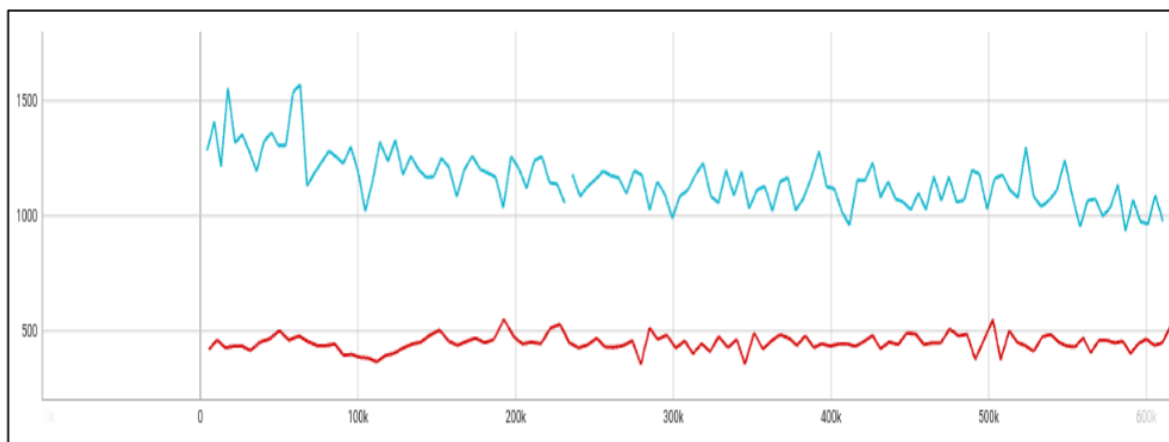
**Figure 4.** Comparison of the average episode reward (vertical axis) in Centralized training (red) and Decentralized training (blue) learning environments with respect to the number of steps (horizontal axis) in Scenario A

As can be seen in Figure 4, the CT-CE environment received higher rewards at the start of learning compared to the DT-DE environment. Assuming that both environments have two FIVE virtual entities and rewards per virtual entity are centered around values between 0 and 2.0, a reward value of 4 can be considered the target reward for Scenario A. The environment that first approached this value of 4 was CT-CE, which did so around 300,000 steps. DT-DE, on the other hand, reached this value at the 550,000th step.



**Figure 5.** Comparison of the average CPU usage (vertical axis) in Centralized training (red) and Decentralized training (blue) learning environments with respect to the number of steps (horizontal axis) in Scenario A

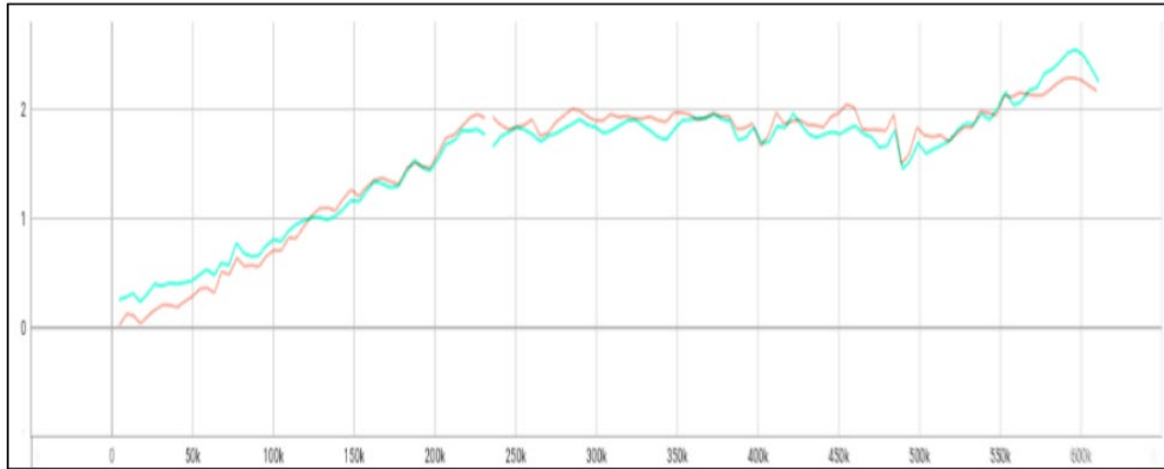
Figure 5 indicates that DT-DE is generally at a disadvantage compared to CT-CE in terms of CPU (resource) usage.



**Figure 6.** Comparison of the average time spent per training iteration (vertical axis) in Centralized training (red) and Decentralized training (blue) learning environments with respect to the number of steps (horizontal axis) in Scenario A



When evaluating training time, Figure 6 shows that the duration of a training iteration in CT-CE is approximately twice as short as in DT-DE. This is again due to training two policies simultaneously in the DT-DE environment.



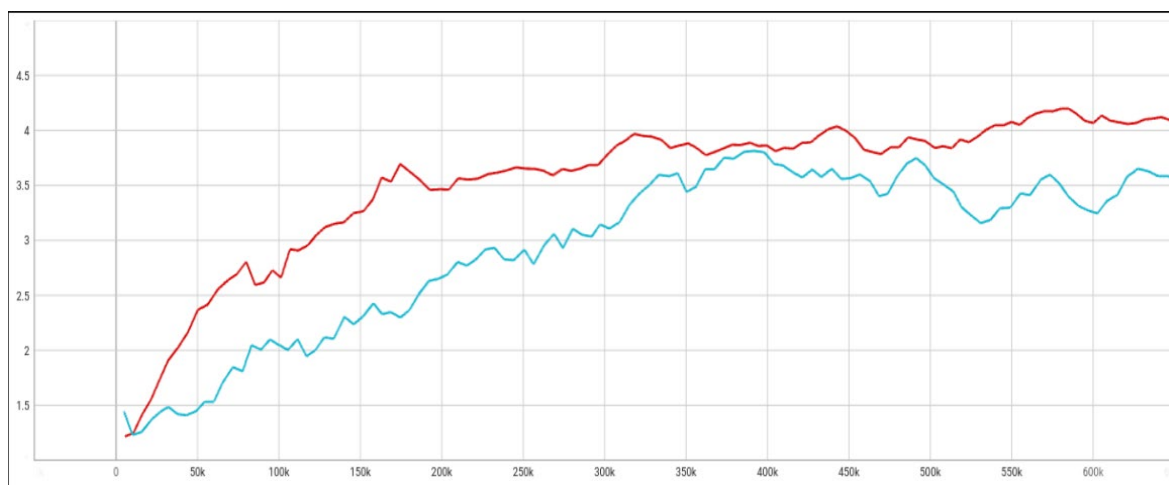
**Figure 7.** Comparison of the average episode rewards (vertical axis) of ppo1 (red) and ppo2 (green) in Decentralized training environments with respect to the number of steps (horizontal axis) in Scenario A

According to the policy-based metrics in Figure 7, the policy ppo1 (red), associated with the F-16\_01 virtual entity closer to the enemy in Scenario A of the DT-DE environment, learned faster compared to the policy ppo2 (green) associated with the F-16\_02 virtual entity farther from the enemy. Policy ppo1 reached a reward value of 2.0 in about 250,000 steps, while policy ppo2 took about 550,000 steps to achieve this reward value. This difference may be due to the greater distance of the enemy from the ppo2 virtual entity. An important assumption here is that non-identical (the virtual actors in the thesis have different distances from the enemy) actors show distinct learning outcomes in DT-DE environments.

In the CT-CE environment, due to the central structure, random actions assigned to these virtual entities (selected actions used in varying sequences sometimes for F-16\_01, sometimes for F-16\_02) might not leverage such individual advantages.

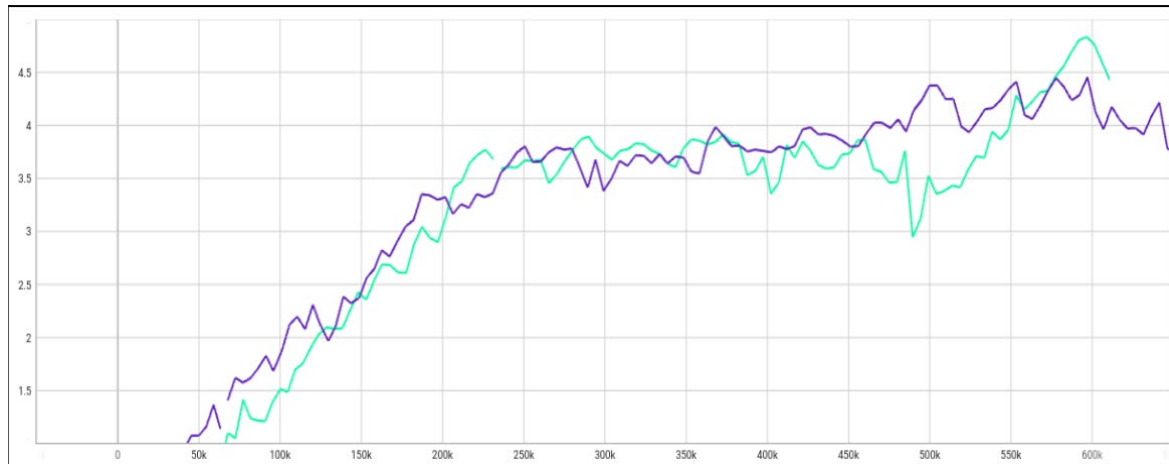
### 3.2 Experiment 2

In the second experiment, learning environments CT-CE and DT-DE were compared using Scenario B. As previously mentioned, the only difference between Scenario B and Scenario A is that the messaging feature of the commanding F-22 aircraft is turned off. This section will examine both the differences between CT-CE and DT-DE and the effects of having a directing virtual entity in these environments.



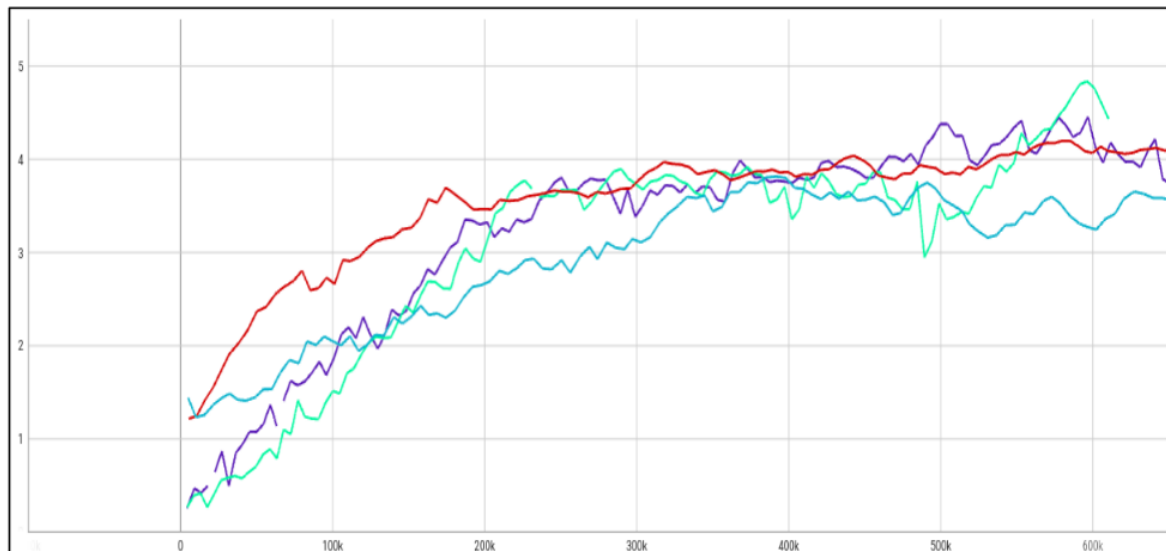
**Figure 8.** Comparison of Episode Reward Mean (vertical axis) against Steps (horizontal axis) for Scenario A (Red) where the commander can issue commands and Scenario B (Blue) where the commander cannot in Centralized environment

Primarily, as seen in Figure 8, having a commanding virtual entity (red) in the CT-CE environment provided a noticeable advantage in training compared to not having one (blue). With the commander's support, the central policy reached a reward value of 4 in approximately 350,000 steps, while without the commander, this reward amount could not be reached even after 650,000 steps.



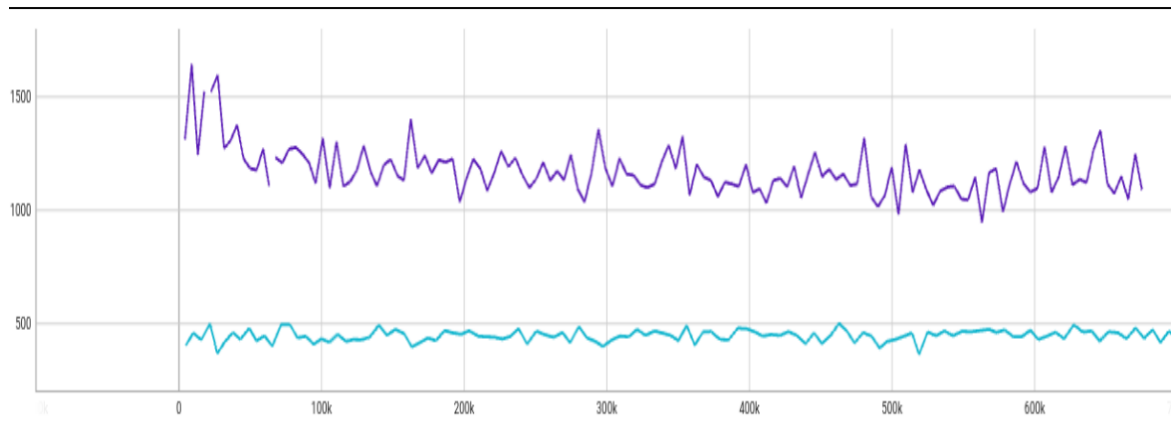
**Figure 9.** Comparison of Episode Reward Mean (vertical axis) against Steps (horizontal axis) for Scenario A (Red) where the commander can issue commands and Scenario B (Blue) where the commander cannot in Decentralized environment

Surprisingly, the average reward difference between the two scenarios in the DT-DE environment is much smaller compared to the CT-CE environment (see Figure 9). Indeed, up to the 550,000th step, Scenario B, where the commander cannot give orders, performed better in terms of reward value than Scenario A. This may be because the commander's command information in the CT-CE environment is significantly more effective compared to the DT-DE environment. In CT-CE, the agent establishes a faster and more precise relationship between the information received from the commander and the action to be performed, while in DT-DE, the effect of this message on individual policies might be reduced, making it harder to establish a relationship between individual actions and the commander's orders. The fact that the DT-DE environment reached much higher reward values towards the end of the training may point to this.



**Figure 10.** Comparison of the average episode reward for Scenario A (green) where the commander can give orders versus Scenario B (purple) where the commander cannot give orders in the Decentralized environment, and for Scenario A (red) versus Scenario B (blue) in the Centralized environment, with respect to the number of steps

To reach a more precise and general conclusion, as seen in Figure 10, in the CT-CE environment, training with the commander's orders in Scenario A reached a reward value of 4.0 most quickly and created the most stable training graph. Secondly, DT-DE scenarios showed better results compared to the CT-CE environment trained in Scenario B.



**Figure 11.** Comparison of the Average Time Spent per Training Iteration (vertical axis) against Steps (horizontal axis) for the DT-DE (purple) and CT-CE (blue) environments trained on Scenario B

Furthermore, as seen in Figure 11, DT-DE training took significantly longer than CT-CE training in Scenario B.

## 4 CONCLUSION

In this thesis, the effectiveness of a decentralized cooperative multi-agent reinforcement learning method was investigated in a real-time military tactical environment simulation developed by HAVELSAN. Similar to real-time strategy games, this simulation emulates defense and attack scenarios with various inputs and actors. Within the scope of the thesis, air attack scenarios were developed involving friendly aircraft learning action selection through multi-agent reinforcement learning methods and enemy aircraft making decisions based on rule-based algorithms. The results of the two main methods used in the training of friendly aircraft, Decentralized Training - Distributed Execution and Centralized Learning - Centralized Execution, were compared.

The study compared the CT-CE (Centralized Training, Centralized Execution) and DT-DE (Decentralized Training, Decentralized Execution) learning environments and highlighted the advantages and limitations of each method. DT-DE provides significant advantages, particularly in terms of scalability and flexibility, by allowing training to be parallelized across computer clusters located in different geographical locations, thus supporting a broader simulation environment.

The experiments initially showed that CT-CE achieved higher reward values. However, the adaptability of DT-DE and its performance improvements over time during the learning process have demonstrated that this method can also be highly effective in the long run. Additionally, as expected from the experiments, the DT-DE environment, which trains two different policies simultaneously, consumed more resources and time.

The thesis revealed that both DT-DE and CT-CE have their own unique advantages and disadvantages. For instance, CT-CE allows for fast and coordinated decision-making processes due to its centralized control mechanism; however, it also comes with the risk of affecting the entire system in case of a system-wide error or interruption. In contrast, DT-DE, with each agent making decisions independently, limits the impact on other agents even if a problem occurs within the system. This independence enhances system resilience while providing diversity in learning processes.

In conclusion, this thesis has demonstrated the applicability and potential of decentralized cooperative multi-agent reinforcement learning methods in air attack scenarios. The study has made significant contributions, particularly for military simulations and strategic training programs. Future work should involve comparing CT-CE and DT-DE methods over longer training periods to observe convergence to higher reward values. Additionally, the success of a Centralized Learning - Decentralized Execution environment, which combines Centralized and Distributed training methods, can be measured on these scenarios. Furthermore, instead of mixed-task scenarios used in this study, fully cooperative task scenarios can be compared in multi-agent training environments.

## References

- [1] E. Liang et al., "RLlib: Abstractions for distributed reinforcement learning," *arXiv (Cornell University)*, Jan. 2017, doi: 10.48550/arxiv.1712.09381.
- [2] J. Schulman, F. Wolski, P. Dhariwal, A. Radford, and O. Klimov, "Proximal policy optimization

- algorithms,” *arXiv*, 2017, <https://arxiv.org/abs/1707.06347>.
- [3] J. Kober, J. A. Bagnell, and J. Peters, “Reinforcement learning in robotics: A survey,” *The International Journal of Robotics Research*, vol. 32, no. 11, pp. 1238–1274, Aug. 2013, doi: 10.1177/0278364913495721.
  - [4] V. Mnih et al., “Human-level control through deep reinforcement learning,” *Nature*, vol. 518, no. 7540, pp. 529–533, Feb. 2015, doi: 10.1038/nature14236.
  - [5] C. J. C. H. Watkins and P. Dayan, “Q-learning,” *Machine Learning*, vol. 8, no. 3–4, pp. 279–292, 1992.
  - [6] D. Silver et al., “Mastering the game of go without human knowledge,” *Nature*, vol. 550, no. 7676, pp. 354–359, Oct. 2017, doi: <https://doi.org/10.1038/nature24270>.
  - [7] G. Vevurko, W. Bohmer, and M. de Weerd, “To the Max: Reinventing reward in reinforcement learning,” *arXiv (Cornell University)*, Feb. 2024, doi: 10.48550/arxiv.2402.01361.



---

## Phenotypic and Technological Characterization of Lactic Acid Bacteria Isolated from Algerian Artisanal Dairy Products

Roumaissaa Belkacem<sup>\*1</sup>, Qada Benameur<sup>2</sup>

<sup>1</sup>*Alimentary Sciences Department, Faculty of Sciences of Nature and Life, University of Abdelhamid Ibn Badis Mostaganem, 27000 Mostaganem, Algeria*

<sup>2</sup>*Agronomy Department, Faculty of Sciences of Nature and Life, University of Abdelhamid Ibn Badis Mostaganem, 27000 Mostaganem, Algeria*

---

### Abstract

Artisanal dairy products are versatile ecosystems composed mainly of pathogenic and lactic acid bacteria (LAB). These later can be isolated from animals, fruits and vegetables. The aim of this study was to isolate LAB from some Algerian artisanal dairy products and tested their technological properties.

Artisanal dairy products samples were collected from western Algeria. LAB strains were isolated and identified by classical phenotypic and biochemical analyses such as: Gram tasting, Catalase test, oxydase test, growth at different temperatures, at different pH and the ability to grow in the presence of 4% and 6.5% NaCl. strains isolated were evaluated for several technological activities (lipolytic potentiel, proteolytic potentiel and acidifying potentiel).

All strains have been isolated in this study were catalase negative, oxidase negative and gram positive. The microscopic examination showed different forms and arrangements: cocci and bacillus cells in pairs and clusters. Among the isolated LAB, 17 were grown at pH 5 and 12 at pH 4. Some of these strains were grown at a 37 °C, at a 15 °C and others at 45 °C. In the other hand some of strains were grown at a 4% and others at 6.5% NaCl. Technological activities showed that all strains were presented proteolytic actievity with diametre zones ranged from (12mm to 29mm) except S44 no activity was observed and lipolytic activity was observed by three strains. The result of acidifying potentiel revealed that some tested strains were able to reduce the pH of lactic acid bacteria to values lower than 5.5 progressively after 6h.

The findings were revealed that strains have been presented significant technological activities, they are considered as starter culture and can be used in food industry.

**Keywords:** *Lactic acid bacteria, Artisanal diary product, Starter culture, Proteolytic activity, Acidifying potentiel*

---



## Contribution of Lorentz Force in Cathode/Arc Coupling During TIG Welding

Merazi Sayah<sup>\*1</sup>, Leila Belgacem<sup>1</sup>

<sup>1</sup>Research Center in Industrial Technologies – CRTI, Algiers, Algeria

---

### Abstract

This paper presents an in-depth study of the TIG (Tungsten Inert Gas) welding process under direct current with the use of helium as a shielding gas, focusing on the coupling between cathode and arc. Using advanced modeling techniques, including the COMSOL Multiphysics software, we examine how Lorentz strength contributes to this coupling. The Lorentz force, which results from the interaction between the electric current and the magnetic field, plays a crucial role in the stability and dynamics of the electric arc. By incorporating this contribution into our model, we aim to improve the simulation accuracy of the TIG welding process. Our results highlight the importance of the Lorentz force in arc formation and maintenance, as well as its influence on the fusion bath characteristics. This research offers new perspectives to optimize welding parameters and improve the quality of welds made with direct current and helium as protective gas.

**Keywords:** *TIG welding, Modeling, Cathode/arc coupling, Direct current, Helium, Lorentz force*

---



---

## Structural, Morphological, and Optical Properties of Zinc Oxide Prepared by Sol-Gel Method

**Khemissi Lahouel<sup>\*1</sup>, Meriem Gasmi<sup>1</sup>, Saida Hoggas<sup>1</sup>, Sabiha Hakkar<sup>1</sup>**

<sup>1</sup>Laboratory of Structures, Proprieties and Inter Atomic Interactions, Faculty of Science and Technology, University of Abbes Laghrou, Khenchela 40000 Algeria

---

### Abstract

The study has been motivated by the remarkable characteristics of zinc oxide (ZnO): high exciton binding energy at 60 MeV and large band gap is 3.44 eV at low temperatures and 3.37 eV at room temperature, significant refractive index, high optical transparency and excellent electrical conductivity and low absorption coefficient in the visible region. ZnO has various application areas such as photocurrent, photocatalyst, light emitting diodes, gas sensors, transistors and solar cells Because of its excellent optical, electrical, and mechanical properties. ZnO thin film have been prepared by various deposited techniques such as Sol-Gel (dip coating, spin coating....), spray pyrolysis, Atomic Layer Deposition, Thermal Evaporation, Magnetron Sputtering and. Among these techniques for fabricated ZnO thin film, the Sol-Gel has various advantages such as cost-effective, controllable, simple, easy and large area applications.

In this study, synthesis of Zinc oxide (ZnO) thin film as a starting material dip-coating technique sol-gel method, this film of ZnO was annealed at 500 °C. The structural and optical properties of prepared ZnO thin film were measured by X-ray diffraction (XRD), Ultraviolet spectroscopy (UV-visible), FESEM image revealed morphology and the EDX verified the elemental respectively. These results; it was shown that thin film is hexagonal wurtzite phase and a preferred orientation along the [101] direction (JCPDS card no. 00-036-1451) and no secondary phases were observed.

**Keywords:** Dip-coating, Sol-gel, UV-visible, EDX, FESEM, XRD

---



---

## Effect of Extract Concentration on Green Synthesis of Silver Nanoparticles

Roufaida Aissa Brahim<sup>\*1</sup>, Hadjer Mabrouki<sup>1</sup>, Djamel-Eddine Akretche<sup>1</sup>

<sup>1</sup>Laboratory of Hydrometallurgy and Inorganic Molecular Chemistry (LHCIM), Faculty of Chemistry, USTHB, PO Box 32 El Alia, Bab Ezzouar, 16111, Algiers, Algeria

---

### Abstract

The green synthesis of silver nanoparticles (AgNPs) using plant extracts is an environmentally friendly and sustainable method for creating nanomaterials with special properties. However, synthesis factors such as extract concentration need to be optimized to produce stable, spherical AgNPs in high yields.

In this study, several plant extract concentrations (0.25 mg/ml, 5 mg/ml, 15 mg/ml, and 25 mg/ml) were investigated for the green synthesis of AgNPs. The reaction mixture included AgNO<sub>3</sub> (5 mM) as precursor, plant extract as biocatalyst, and borax buffer (pH 9). Results were obtained by measuring the absorbance of the solution after synthesis and 24 hours later.

The results showed that an extract concentration of 5 mg/ml was the optimum concentration to produce higher yields of stable spherical silver nanoparticles. The absorbance plot shows that nanoparticles produced at this concentration exhibit a high absorbance peak at 411 nm, indicating that more nanoparticles are being generated. Furthermore, after 24 hours, the absorbance peak at 411 nm was still greatest at this concentration, indicating greater nanoparticle stability over time. Lower concentrations (0.25 mg/ml) showed lower absorbance peaks, indicating reduced nanoparticle yields, while higher concentrations (15 and 25 mg/ml) showed lower absorbance peaks, probably due to nanoparticle aggregation at these concentrations.

In conclusion, an extract concentration of 5 mg/ml appears to be the best compromise between high yield and long-term stability of spherical AgNPs. This concentration should be used to further optimize the green silver nanoparticle synthesis method to produce AgNPs with enhanced biological activities.

**Keywords:** Silver nanoparticles, Green synthesis, Plant extract, UV-visible

---





## The Methode of Adobe in Building

Hammache Soumia<sup>\*1</sup>

<sup>1</sup>*Department of Civil and Hydraulic Engineering, University of Biskra, Algeria*

---

### Abstract

The adobe construction method, rooted in indigenous knowledge and widely used in various regions like Ethiopia, Colombia, and China, involves creating blocks from raw earth materials like soil, straw, and fibers. This sustainable technique has historical significance, offering simplicity, accessibility, and sustainability in building practices. Studies have shown that adobe blocks can exhibit excellent strength and durability, making them a viable alternative to traditional mud houses, especially in regions where conventional construction materials are scarce or economically challenging to access. The composition of adobe blocks typically includes a mix of soil, plant fibers, and binding agents, contributing to their mechanical strength and compact structure. By preserving the ancestral knowledge and techniques of adobe construction, communities can maintain their cultural heritage while addressing modern housing needs in a sustainable and environmentally friendly manner..

**Keywords:** *Soil, Earth materials, Construction method, Strength*

---



---

## CBD-Loaded Lipid-Based Nanoparticles for Topical Application Against Skin Cancer

Ana Paula Sanguinetti<sup>\*1,2</sup>, Mirian Scavone<sup>1,2</sup>, Magalí di Meglio<sup>1,2</sup>, Pablo Raies<sup>3</sup>, Paulo Maffia<sup>4,5</sup>, Jorge Montanari<sup>1,2,5</sup>, Maria Natalia Calienni<sup>1,2,5</sup>

<sup>1</sup>Laboratory of Nanosystems for Biotechnology Application (LANSAB), National University of Hurlingham, Villa Tesei, CP 1688, Argentina

<sup>2</sup>Scientific Research Commission of the Province of Buenos Aires (CIC), La Plata, CP 1900, Argentina

<sup>3</sup>National University of Hurlingham, Villa Tesei, CP 1688, Argentina

<sup>4</sup>Laboratory of Biotechnology and Microbiology Applications (LAByM), Universidad Nacional de Hurlingham, Villa Tesei, CP 1688, Argentina

<sup>5</sup>Autonomous City of Buenos Aires (CONICET), CP 1425, Argentina

---

### Abstract

There are indications that cannabidiol (CBD), present in the *Cannabis sativa L.*, inhibits the activation of the Hedgehog (Hh) signaling pathway associated with certain skin cancers. Given the anatomical location of the non-metastatic tumors, the topical cutaneous route allows for non-invasive and direct administration. Additionally, using smaller amounts of the drug and generating site-specific toxicity reduces the chances of producing side effects. However, as the *stratum corneum* barrier prevents the direct penetration of many molecules, the use of drug delivery systems is beneficial. The objective of this work is to optimize the encapsulation of CBD in solid lipid nanoparticles (SLN) and nanostructured lipid carriers (NLC) for future use in the topical treatment of skin tumors with Hh overactivation.

Two solid lipids, Witepsol<sup>®</sup> E85 and Compritol<sup>®</sup> 888 ATO (C888), and a liquid lipid for the NLC, Transcutol<sup>®</sup> HP (TRC), in combination with the surfactants Poloxamer 188 (P188) and Tween 80 (T80), were employed. Different concentrations and combinations of lipids and surfactants were tested while maintaining a constant CBD concentration. The obtained formulations were monitored over time and characterized using dynamic light scattering, TEM, Turbiscan Lab Expert, and RP-HPLC. Additionally, the cytotoxicity on the SK-Mel-28 cell line was determined using the MTT assay.

The main results demonstrated that CBD has been successfully encapsulated in SLN and NLC with high encapsulation efficiencies (>70%). The SLN composed of C888:T80:CBD presented the highest encapsulation efficiency (106 ± 4%), the lowest polydispersity (< 0.2), and an average hydrodynamic diameter of 180 nm. These SLNs showed a moderate tendency toward instability at 37°C; however, the mean size did not change considerably for 30 days at 4°C. The NLCs with C888:P188:TRC:CBD exhibited higher cytotoxicity than CBD, while SLNs with C888:T80:CBD had similar effects to CBD after 24 hours of incubation.

**Keywords:** *Cannabidiol, SLN, NLC, Skin, Cancer*

---



## Spatial Analysis of Soil Heavy Metals Based on Geostatistical Approach in the North of Iraq

Mohammed Oday Al Hamdani<sup>\*1</sup>, Ali Volkan Bilgili<sup>1</sup>, Sureyya Betul Rufaioglu<sup>1</sup>

<sup>1</sup>Department of Soil Science and Plant Nutrition, Harran University, Sanliurfa, Türkiye

### Abstract

Ecosystems and human health are both seriously threatened by soil contamination, especially when it comes to heavy metals. This study aims to investigate the geographical variability of lead (Pb), chromium (Cr), and cadmium (Cd) in the soils in the northern Iraqi district of Shekhan. The present study used geostatistical methods to examine the spatial distribution of heavy metals. The results are intended to further our knowledge of heavy metal offer guidance for managing and mitigating soil contamination. The Shekhan field is an oil field located in northern Iraq. It spans approximately 280km<sup>2</sup> and contains oil reserves in formations dating back to the Cretaceous, Jurassic, and Triassic periods. The majority of the production comes from the Upper Jurassic fractured carbonates. As of April 2020, over 70 million stock tank barrels of oil had been produced from the field, with estimated reserves of 578 million stock tank barrels. 60 soil samples of the plowing layer (0–20 cm) were taken. Geostatistical approaches based on ordinary kriging (OK) and Inverse distance weight (IDW) were used to the spatial distribution and map of heavy metals. The result indicated that significant variations in the heavy metals concentrations within the studied locations are shown by the coefficients of variation (CV) for cadmium (Cd), lead (pb), and chromium (Cr) (46.703%, 42.575%, and 46.627%, respectively). This variability suggests the complex relationship between different anthropogenic and environmental variables and soil contamination by heavy metals. The accuracy of the IDW and OK models were validated through high R<sup>2</sup> values obtained via cross-validation, demonstrating strong predictive performance with R<sup>2</sup> values of 0.79 for Cadmium (Cd), 0.85 for Lead (Pb), and 0.88 for Chromium (Cr). These results confirm the efficacy of IDW in accurately representing the spatial patterns of heavy metals in the area. The results are intended to further our knowledge of heavy metal mobility and offer guidance for managing and mitigating soil contamination.

**Keywords:** Soil pollution, Heavy metals, Geostatistic, ordinary kriging (OK), Inverse distance weigh (IDW), Shekhan region

## 1 INTRODUCTION

Ecosystems and human health are both seriously threatened by soil contamination, especially when it comes to heavy metals. A combination of man-made and natural processes contributes to the build-up of contaminants in the soil, including lead, mercury, cadmium, and arsenic. Many detrimental consequences, such as decreased productivity of soil, water quality issues, microbial community upheaval, long-term environmental repercussions, erosion, and even health hazards, can result from oil contamination of soil. Remediation methods, soil supplements, containment strategies, monitoring, and appropriate oil handling and transportation management are all necessary to lessen these consequences. Climate conditions, plant presence, geomorphology, and parent material all have an impact on natural pedagogical processes such organic matter decomposition and rock weathering. The complex and highly time-dependent soil structure is the result of these processes interacting over various geographical and temporal scales. The parent material of a soil has a major influence on its heavy metal content; some soils naturally have high concentrations of heavy metals because of the weathering of specific types of rock. For example, trace elements such as nickel, chromium, and manganese have been found in volcanic and metamorphic rock [1]. These minerals' basic crystalline structures disintegrate during weathering, releasing and transporting these elements into surface and groundwater systems as well as the topsoil. However, the amounts of heavy metals in soil have significantly grown due to human activity. Pollutants are introduced and soil structure is mechanically altered by urban and industrial activity. Significant quantities of lead and cadmium are released during industrial and transportation combustion processes, frequently in conjunction with zinc from tire wear. Zinc, copper, chromium, and nickel are introduced into the soil via industrial wastes, and contaminants from metal extraction mining activities are released into the atmosphere and end up in adjacent soils and rivers. A further factor in the pollution of soil with heavy metals is agricultural activities. Copper, nickel, zinc, and cadmium build up in the topsoil as a result of long-term, intense agricultural land usage, especially with regular pesticide

treatments [4]. Assessments of soil pollution are made more difficult by this contamination since it becomes more difficult to distinguish between anthropogenic and natural causes. Determining the causes of pollution and creating remediation plans need an understanding of the regional variability of heavy metal concentrations. Agricultural production and food safety may suffer if heavy metals are present in soil at hazardous amounts. For soil management and pollution mitigation to be effective, it is crucial to distinguish between anthropogenic contamination and natural background levels. Anthropogenic activities including smelting, driving, home activities, and garbage disposal cause heavy metal levels in soil to be raised, especially in urban areas. Heavy metal levels from these sources have often been shown to be high in studies on urban soil pollution in different cities. In order to alleviate these issues, soil contamination has been more thoroughly studied and mapped using geostatistical techniques. Geostatistics offers sophisticated techniques to measure the geographical characteristics of soil properties and facilitate spatial interpolation. With this method, the spatiotemporal fluctuation of soil parameters is seen as a random process that depends on both place and time. Geostatistics provides strong tools for analyzing geographical uncertainty and performing hazard evaluations by integrating spatial coordinates into data processing. The spatial distribution of heavy metals is modeled and concentrations in unsampled regions are predicted using geostatistical analysis techniques such as conventional kriging, disjunctive kriging, and indicator kriging. These techniques for interpolation and uncertainty estimates make use of the stochastic theory of spatial correlation. For environmental contamination research, indicator kriging—a nonparametric geostatistical technique is especially helpful since it employs a binary indicator modification of the data to lessen susceptibility to outliers.

The activities of a petroleum business involved in large-scale petrol mining have a considerable impact on soil degradation in the Shekhan Sub-district of Duhok City, located in the north of Iraq. A large agricultural region has been impacted by heavy metals. The geographical variability in soil concentrations of heavy metals caused by these human activities is thought to have a negative impact on agricultural productivity. The distribution patterns of heavy metals may be found by geostatistical analysis, which also makes it possible to determine the main sources of pollution and evaluate the total effect of these sources on environmental health and agriculture.

The purpose of this study is to predict the geographic variations of lead (Pb), chromium (Cr), and cadmium (Cd) in the soils of the Shekhan district in northern Iraq. In this study, the distribution of heavy metals was investigated using geostatistical techniques, namely inverse distance weighting (IDW) and ordinary kriging (OK). The findings should increase our understanding of the spatial variation of heavy metals and provide direction for controlling and reducing soil pollution.

## 2 MATERIAL AND METHOD

### 2.1 Study Area

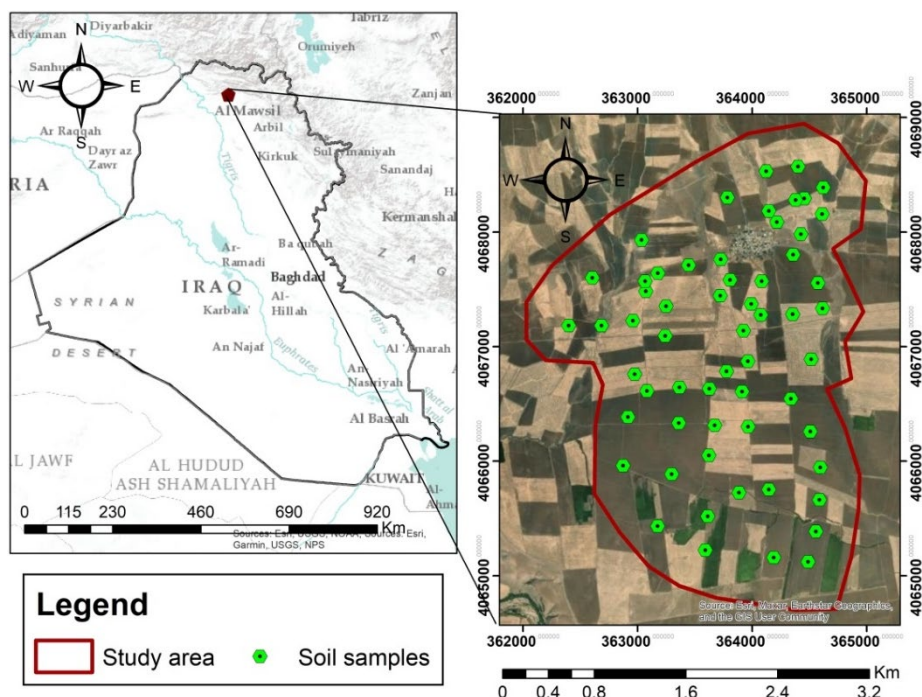


Figure 1. Study area

An oil field in northern Iraq is called the Shekhan field. With oil deposits found in minerals that date back to the Cretaceous, Jurassic, and Triassic eras, it covers an area of around 280 km<sup>2</sup> (figure 1). The cracked carbonates of the Upper Jurassic provide the majority of the output. The field produced more than 70 million stock tank barrels of oil as of April 2020, and its estimated reserves were 578 million stock tank barrels. The field has two production facilities, PF-1 and PF-2, each with five production wells and a combined capacity of 40,000 barrels per day. The field has been exporting crude oil since December 2013, initially by truck and later through spur pipelines connected to the Atrush export pipeline. The expansion project to increase production to 55,000 barrels per day was suspended in March 2020 due to market uncertainty caused by the Covid pandemic. Oil contamination in soil can have various negative effects, including reduced soil productivity, water pollution, disruption of microbial communities, long-term environmental impacts, erosion, and potential risks to human health. To mitigate these effects, containment measures, remediation techniques, soil amendments, monitoring, and proper management of oil handling and transportation are essential.

## 2.2 Soil Sampling and Laboratory Analysis

Sixty soil samples of the plowing layer (0–20 cm) were taken in the study region are shown in figure 1. Samples were dried in a 75°C oven for 72 hours. Each soil sample was digested in the presence of aqua regia (a 3:1 combination of nitric acid HNO<sub>3</sub> and HClO<sub>4</sub>) using 0.5 g of each soil sample. The analysis of the soil samples used to determine the presence of heavy metals follow. Shimadzu's atomic absorption spectrophotometer (AA-7000) and graphite furnace atomizer (GFA7000) were used to measure the presence of heavy metals in the filtrate of the samples at the Environment Directorate in Duhok City.

## 2.3 Descriptive Statistics of Soil Heavy Metals

The descriptive statistics of soil heavy metals (max. min., mean, standard deviation, kurtosis, skewness and CV %), were obtained using the SPSS program (IBM Corp., Armonk, NY, USA) for the heavy metals contained in the soil. Based on the SD and skewness values, the distribution pattern of three soil heavy metals of soil was calculated.

## 2.4 Ordinary Kriging Method

A geostatistical interpolation technique is ordinary kriging. The points that are closest to the estimated point are given more weight than those that are farther away if the data is spatially highly continuous. The weight is chosen so that the predicted variance is minimized. As a result, the semi variogram theory underlies the estimation of the value  $Z^*(x)$  of the point acquired by the conventional kriging method, which is derived by linearly combining sample points that fall within the estimated point's impact range (Equation 1). The calculation method is Equation [4].

$$Z_v^*(S_0) = \sum_{i=1}^n \lambda_i Z(S_i) \quad (1)$$

Where,  $\lambda_i$  is the weight for the observation  $z$  at location  $S_i$ . In kriging, the weights  $\lambda_i$  are calculated by equation (1) so that  $z^*(S_0)$  is unbiased and optimal (minimum squared error of estimation). The nugget and sill values were obtained to analyze the spatial dependence of the data. An appropriate variogram model was fitted, which allowed for the determination of the range, indicating the extent of spatial correlation within the dataset. Variogram analysis was conducted using software Python 3.8. Specific packages and libraries employed included pykrige in Python, which provided functions for variogram calculation and model fitting.

## 2.5 Inverse Distance Weight (IDW)

The interpolation mapping in this study was conducted using the IDW method with ArcGIS 9.2 software. The IDW method is based on the following interpolating function:

$$I_i = \frac{Z_i - Z(\text{avg})}{\sigma^2} + \sum_{j=1, j \neq i}^n [W_{ij} (z_j - z(\text{avg}))] \quad (2)$$

where  $Z_j$  is the value of variable  $Z$  at all other locations (where  $j \neq i$ );  $S_2$  is the variance of variable  $z$ ;  $z_i$  is the value of variable  $z$  at location  $i$ ;  $Z(\text{avg})$  is the average value of  $z$  with the sample number of  $n$ ; where  $W_{ij}$ , a weight, is the reciprocal of the distance  $d_{ij}$  between points  $i$  and  $j$ . A distance band may also be used to calculate weight  $Z_{ij}$ ; samples falling inside the band are assigned the same weight, while samples outside the band are assigned a

weight of zero (Equation 2). The IDW method is a straightforward interpolation technique that uses nearby measured values to estimate a value for an unmeasured location. It assigns greater weight to points closer to the prediction location, with the weights decreasing as distance increases [7]. In this study, the IDW method was applied with 12 neighboring samples for the estimation of each point, ensuring a robust and accurate spatial prediction of heavy metal concentrations in the study area.

## 2.6 Accuracy Assessment of the Estimations Model

Using the "Random selection within subsets" feature in GIS, the observation data set was randomly divided into 70% training and 30% testing. To evaluate the performance of the models, the coefficient of determination ( $R^2$ ), were obtained by R studio (Equation 3), mean absolute error (MAE) (Equation 5), root mean squared error (RMSE) (Equation 4), and mean absolute percentage error (MAPE) (Equation 6) were employed.

$$R^2 = 1 - \frac{\sum_{i=1}^n (y_i - \hat{y}_i)}{\sum_{i=1}^n (y_i - y_{\text{avg}})} \quad (3)$$

$$RMSE = \sqrt{\frac{\sum_{i=1}^n (\hat{y}_i - y_i)^2}{n}} \quad (4)$$

$$MAE = \frac{\sum_{i=1}^n (|\hat{y}_i - y_i|)}{n} \quad (5)$$

$$MAPE = \frac{1}{n} \sum_{i=1}^n \left| \frac{y_i - \hat{y}_i}{y_i} \right| \times 100 \quad (6)$$

## 3 RESULT AND DISCUSSION

### 3.1 Descriptive Statistic of Soil Heavy Metals

The analysis of heavy metal concentrations in soil samples from the study area provides valuable comprehensions into the environmental and industrial impact of metal pollution. Table 1 summarizes the descriptive statistics for Cadmium (Cd), Lead (Pb), and Chromium (Cr) concentrations, including minimum, maximum, mean, standard deviation, kurtosis, skewness, and coefficient of variation (CV). It was found that the soil samples had an average cadmium value of 1.705 mg/kg and a standard deviation of 0.796 mg/kg. A little platykurtic and negatively skewed distribution is indicated by the values of kurtosis and skewness, which are -0.521 and -0.705, respectively. According to these results, the research region may have a moderate degree of Cd contamination, which might have an impact on both ecological integrity and human health. However the mean concentration of lead was 2.643 mg/kg, with a standard deviation of 1.125 mg/kg. The contamination of lead (pb) in soil is frequently associated with past use of leaded gasoline and industrial pollutants. While the skewness number (0.266) shows a moderately positive skewness, the kurtosis value (-0.662) implies a somewhat platykurtic distribution. The relevance of lead pollution in the research region is highlighted by these data, emphasizing the necessity for environmental monitoring and remedial methods.

The mean concentration of chromium (Cr) was found to be 2.399 mg/kg, accompanied with a standard deviation of 1.118 mg/kg. This is in line with research conducted in industrialized regions, where Cr contamination in soil is frequently linked to waste disposal and metal processing [2]. A somewhat leptokurtic distribution is indicated by the kurtosis value of -0.941 and a moderately negative skewness is suggested by the skewness value of -0.667. The result of the current study is consistent with the finding of the previous study. [6] suggested that the industrial processes and agricultural methods have been linked to soil pollution with heavy metals including Cd, pb and Cr. Significant variations in the heavy metals concentrations within the studied locations are shown by the coefficients of variation (CV) for cadmium (Cd), lead (pb), and chromium (Cr) (46.703%, 42.575%, and 46.627%, respectively). This variability suggests the complex relationship between different anthropogenic and environmental variables and soil contamination by heavy metals. These findings are consistent with other research carried out in industrialized and urbanized areas when compared to earlier literature. Though they could differ from those in other geographic settings, it is crucial to identify the unique local causes and sources of heavy metal

contamination in the studied region. According to WHO, the concentration of cadmium considered safe in soil generally ranges between 1-2 mg/kg [8]. According to the results obtained, the mean value of cadmium is 1.705 mg/kg, which is within this limit and may threaten environmental health. In addition, the coefficient of variation is 46.703%, which indicates that cadmium distribution is highly variable.

In addition, WHO limits for lead are generally below 50 mg/kg [8]. As a result of the analysis, the mean value of lead was found to be 2.643 mg/kg, which is well below the WHO limits and at a safe level. The coefficient of variation of 42.575% indicates that the distribution of lead is also highly variable.

**Table 1.** Descriptive statistic of heavy metals (0-20 cm) depth

Heavy Metals	Min	Max	Mean	Standard Deviation	Kurtosis	Skewness	CV (%)
<b>Cadmium (Cd)</b>	0.121	2.75	1.705	0.796	-0.521	-0.705	46.703
<b>Lead (pb)</b>	0.752	0.493	2.643	1.125	-0.662	0.266	42.575
<b>Chromium (Cr)</b>	0.217	3.82	2.399	1.118	-0.941	-0.667	46.627

According to WHO, the limits for chromium are generally less than 100 mg/kg [8]. As shown in Table 1, the mean value of chromium was 2.399 mg/kg, which is well below the WHO limits and can be considered safe. The coefficient of variation is 46.627%, indicating that the distribution of chromium is highly variable.

Accordingly, the results obtained seem to be in line with the soil quality guidelines set by WHO. The average value of cadmium is approaching the WHO limits and is at a level that requires caution. For lead and chromium, the values are well below the WHO limits and are considered safer. The coefficients of variation for all metals are high and it is possible to say that these metals exhibit a heterogeneous distribution in the soil.

### 3.2 Spatial Distribution of Soil Heavy Metals

Geostatistical methods, such as ordinary kriging and inverse distance weighting (IDW), were used to evaluate the spatial distribution of soil heavy metals, namely cadmium (Cd), lead (Pb), and chromium (Cr). The capacity of these techniques to interpolate and display the geographical variability of pollutant concentrations in environmental investigations is well known.

The spatial distribution maps for cadmium (Cd), lead (Pb), and chromium (Cr) reveal distinct patterns of contamination in the study area (figure 2). Cadmium shows high concentrations in the northwest, extending through the center to the southeast, indicating significant sources possibly from industrial activities, agricultural practices. Lower concentrations in the northeast suggest less contamination there. The northeast and west-south regions have higher lead (pb) concentrations than the north. This pattern reflects a more concentrated distribution with discrete hotspots of high concentration and suggests several sources of pollution, such as industrial pollutants,

Although chromium is distributed rather evenly over the region, it is likely due to a variety of causes, including diffuse contamination from farming methods, natural soil levels, and industrial activity. With no notable hotspots, the homogeneity indicates a constant presence of chromium. Overall, these geographical distribution patterns show the causes and methods of heavy metal contamination dispersion, contribution important information for creating focused remediation plans and reducing the negative effects of heavy metal pollution on the environment and human health.

### 3.3 Ordinary Kriging Analysis

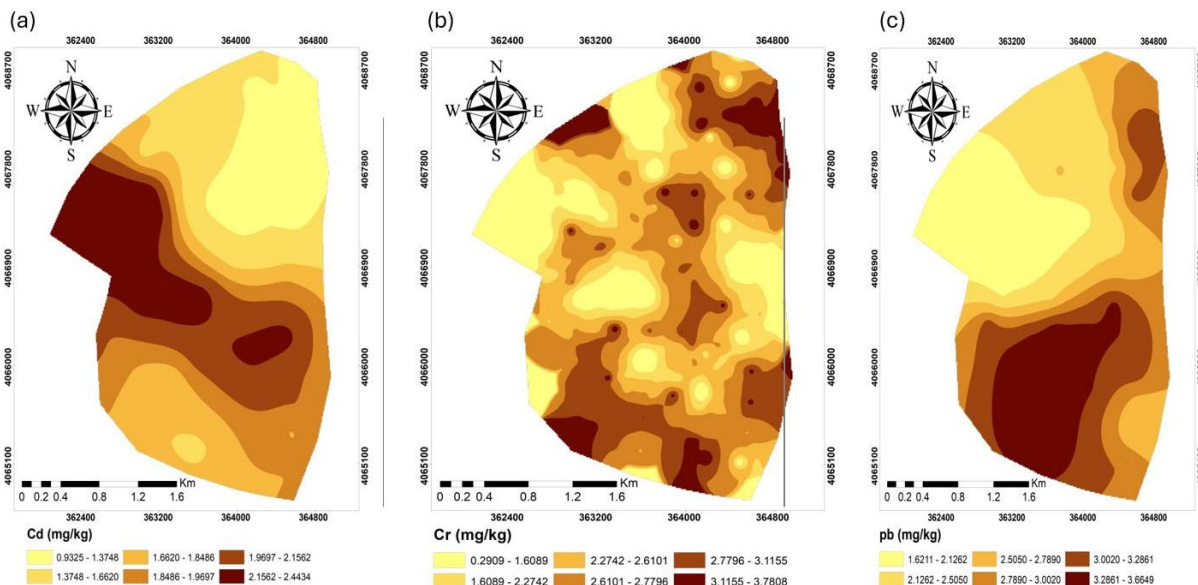
Heavy metals in soil samples are subjected to standard kriging analysis, which offers significant findings into the regional variability and dependency of lead (Pb), chromium (Cr), and cadmium (Cd). Table 2 provides specific information on the kriging model's parameters, such as fit model sill, nugget, range, and spatial dependency. The spherical model was selected as the best fit model due to its highest  $R^2$  value and the visual appearance of the variogram. The  $R^2$  value, which represents the proportion of the variance in the dependent variable that is predictable from the independent variable(s), indicated that the spherical model provided the most accurate fit to the data among the tested models. Additionally, the visual assessment of the variogram, which depicts the spatial dependence of the data, confirmed that the spherical model captured the spatial structure effectively. Thus, these combined criteria supported the choice of the spherical model for this analysis. The nugget value of Cadmium (Cd) is 0.61 and the sill value is 3.25, showing substantial fluctuation at short distances. The 1400 meter range represents the length of time during which the spatial connection is meaningful. With a spatial dependence of 18.77%, a moderate level of spatial dependence is suggested. Values of spatial autocorrelation between 25% and

75%, on the other hand, suggest moderate spatial dependence, while values below 25% indicate weak spatial dependence, according to [3]. Cadmium (Cd), therefore, exhibits a strong spatial dependency, corresponding to a somewhat uniform distribution with localized variability. The sill and nugget values for lead (pb) are 3.12 and 0.56 respectively. A longer spatial correlation than cadmium is shown by the range, which reaches 1560 meters. According to [3], lead has a 17.95% spatial dependency, which is similarly classified as poor spatial dependence. This suggests a rather consistent distribution of lead with minor regional variances throughout the research area. The sill and nugget values of chromium (Cr) are the lowest of the three heavy metals, 4.08 and 0.23, respectively, suggesting reduced fluctuation at short ranges. There is relatively little spatial autocorrelation, with a range of 1350 meters and a spatial dependence of 5.64%. This abnormally low spatial dependency points to a very homogenous distribution of chromium with very few contained variations, indicating a uniform distribution throughout the research region.

The results of conventional kriging analysis indicate that there is modest to very weak spatial dependency for all three heavy metals. In general, a uniform distribution with irregular restricted variations is suggested by the low spatial dependency values of chromium, lead, and cadmium. These results are in line with [3]'s categorization, which states that values less than 25% suggest weak spatial dependency. The very uniform distribution of these heavy metals in the soil samples is highlighted by this analysis, which offers important new information on their geographical variability and their effects on the environment and agricultural health in the research area.

**Table 1.** Ordinary kriging parameters for heavy metals (0-20 cm) depth

Heavy Metal	Model	Sill	Nugget	Range	Spatial Dependence
<b>Cadmium (Cd)</b>	Spherical	3.25	0.61	1400	18.7692
<b>Lead (pb)</b>	Spherical	3.12	0.56	1560	17.9487
<b>Chromium (Cr)</b>	Spherical	4.08	0.23	1350	5.63725



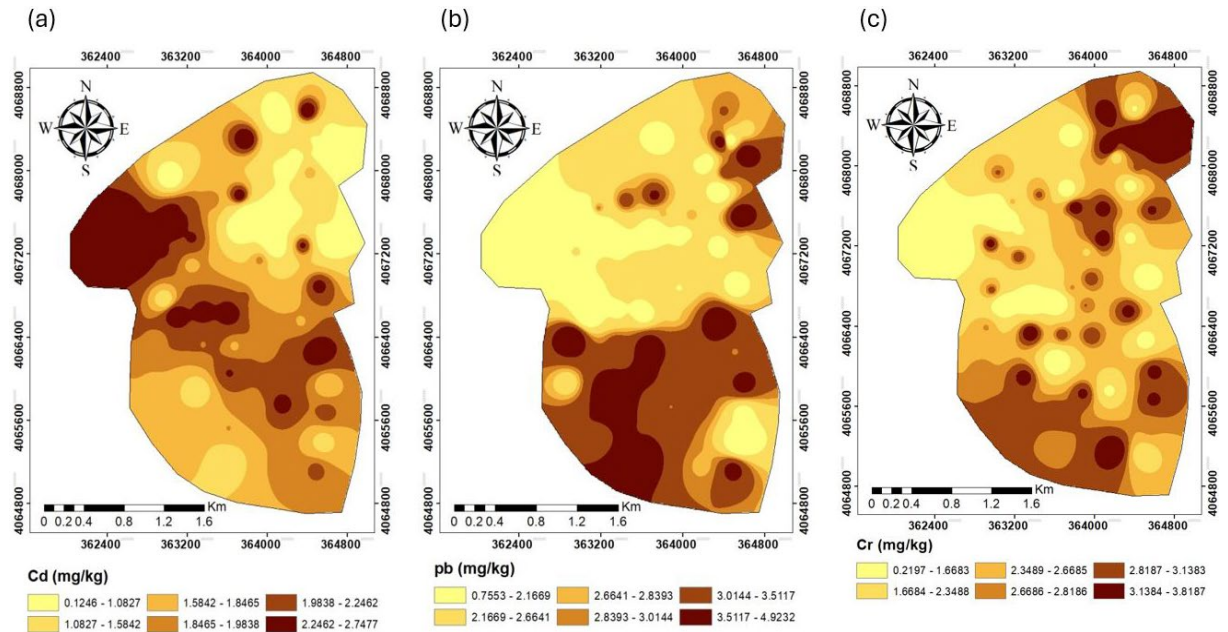
**Figure 2.** Spatial distribution of (a) Cadmium (Cd), (b) Chromium (Cr), and (c) Lead (Pb) respectively analysis by ordinary kriging (0-20cm) depth

### 3.4 Inverse Distance Weighting (IDW) Analysis

Geographical distribution maps for chromium (Cr), lead (Pb), and cadmium (Cd) were created using the Inverse Distance Weighting (IDW) geostatistical approach. IDW used nearby sampled points to estimate values in unsampled sites; with closer points having a stronger effect. Figure 3 illustrate the spatial distribution map of soil heavy metal (Cd, pb and Cr) at 2-20 cm depth obtained by IDW. High concentrations of cadmium (Cd) are mostly seen in the northwest, although they are also seen in the center and southeast. These concentrations are probably caused by industrial operations, agricultural activities, and natural formations. Reduced interpretations in the northeast indicate low levels of cadmium contamination in that area. As the distance from the high-value locations rises, the IDW interpolation displays a gradient from high to low concentrations. The lead (Pb) distribution map shows that the northeast and west-south regions have greater levels of lead concentrations than the northern region, suggesting that industrial pollutants, automobile exhaust, and agricultural runoff might be the possible causes. Low



results in the northern region point to low lead pollution; it is due to the result of close-fitting environmental restrictions or a decline in industrial activity. The distribution of chromium (Cr) on the globe is more consistent, indicating extensive sources including industrial processes, agricultural practices, or background levels of the element in nature. There are no notable hotspots, according to the constant distribution. The geographical distribution of heavy metals is successfully shown by IDW, which offers insights into the origins of pollution and dispersion mechanisms. To mitigate the effects on the environment and human health and to establish targeted remediation programs, this knowledge is essential.



**Figure 3.** Spatial distribution of Cadmium (a) Cd, (b) Lead (Pb), and (c) Chromium (Cr) respectively analysis by IDW (0-20 cm) depth

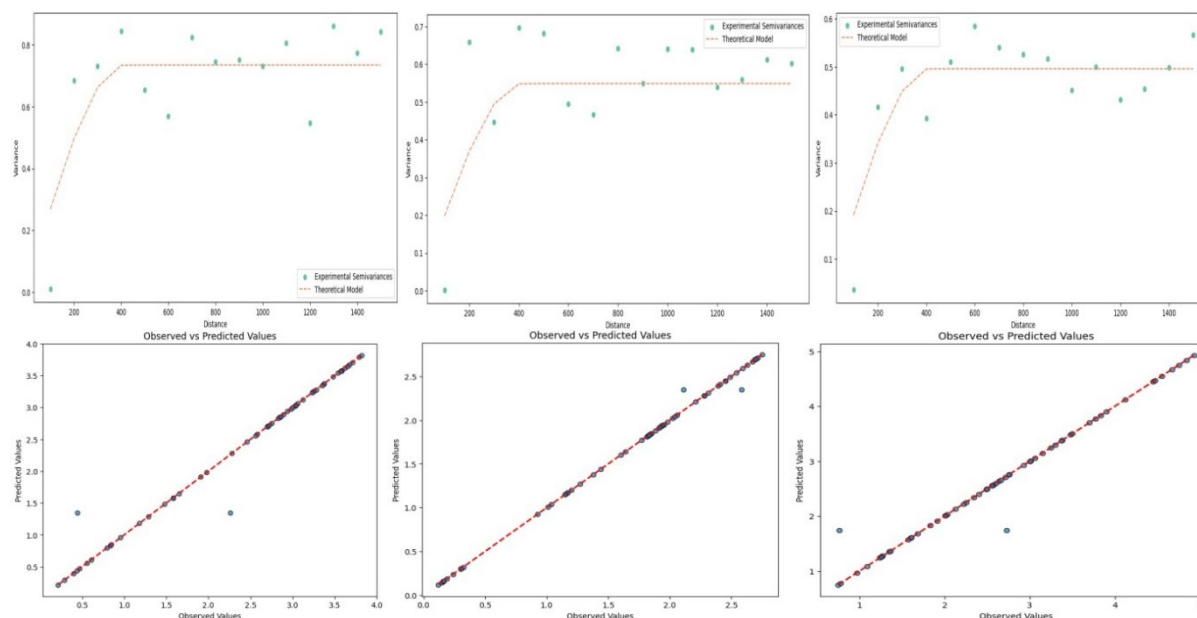
### 3.5 Accurate Assessment of Interpolation Models

The current study utilized two popular interpolation techniques, including Inverse Distance Weighting (IDW) and Ordinary Kriging, to map the spatial distribution of heavy metals in soil samples at 0-20 cm depth. These models were chosen because to their capacity to provide continuous surfaces of pollutant concentrations and effectively capture spatial variability. A geostatistical technique called ordinary kriging takes sample density variations and spatial autocorrelation into consideration. By taking the weighted average of the adjacent sample points into account, it offers a reliable estimate of the pollutant concentrations at unsampled sites. Taking spatial dependence into consideration and producing smoother and more accurate spatial predictions is one of the main benefits of ordinary kriging, however calculating the projected value at an unsampled site, inverse distance weighting (IDW) interpolation is used. This method assigns greater weight to sample locations that are closer to the source and less weight to them. This approach captures consistent changes in pollutant concentrations throughout the research region more effectively than kriging, although being less complex and computationally demanding. Table 3 illustrated the RMSE, MAE, and R<sup>2</sup> values for the three heavy metals: cadmium (Cd), lead (Pb), and chromium (Cr) for both the Ordinary Kriging (OK) and Inverse Distance Weighting (IDW) interpolation models.

The results of the Cadmium model comparison show that the IDW model is more accurate in forecasting the contents of Cadmium in soil samples than the OK model, with lower RMSE and MAE values. Additionally, the interpolation model appears to be able to explain 79% of the variance in Cadmium concentrations, as indicated by the R<sup>2</sup> value of 0.79 for IDW. This is indicative of a strong match. The IDW model predicts lead concentrations more accurately than the OK model, as seen by the reduced RMSE and MAE values for lead in comparison. In contrast to cadmium, lead concentration fluctuation is described by the interpolation model to the extent that it explains 85% of the variance, as indicated by the R<sup>2</sup> value of 0.85 for IDW. The IDW model has superior accuracy in forecasting Chromium concentrations, as seen by its lower RMSE and MAE values when compared to the OK model. Of the three heavy metals, IDW has the greatest R<sup>2</sup> value (0.88), indicating that the interpolation model fits the data quite well. the findings indicate that the IDW interpolation model performs better than the OK model in terms of goodness-of-fit and accuracy when it comes to estimating the spatial distribution of heavy metals in soil samples. This demonstrates the efficiency of IDW in collecting regional variations and generating accurate continuous surfaces of the amounts of pollutants.

**Table 2.** Accurate assessment of interpolation approaches (IDW and OK)

Heavy Metal	IDW			OK		
	RMSE	MAE	R2	RMSE	MAE	R2
Cadmium (Cd)	0.7509	0.01076	0.79	0.7646	0.00372	0.71
Lead (Pb)	1.1381	0.07111	0.85	1.0852	0.00798	0.66
Chromium (Cr)	1.1380	0.01023	0.88	1.1702	0.00038	0.57

**Figure 4.** Spatial analysis of heavy metals at 0- 20 cm depth by using variogram and simple graph, which illustrate the spatial distribution between observation value and predict value of heavy metals (Cd, Pb and Cr) respectively

## 4 CONCLUSION

This study provides a comprehensive understanding of the concentrations and geographical distribution of heavy metals such as lead (Pb), chromium (Cr) and cadmium (Cd) in soils (0-20 cm) depth in the Shekhan region of Northern Iraq. In this study, geostatistical methods were used to analyze the distribution and mobility of these heavy metals. The methods used include conventional kriging and inverse distance weighted (IDW) interpolation techniques. Soil sampling and laboratory analysis revealed that heavy metals vary significantly in different locations. The average concentration of cadmium was 1.705 mg/kg, lead 2.643 mg/kg and chromium 2.399 mg/kg. The coefficients of variation (CV) of these metals were 46.703% for cadmium, 42.575% for lead and 46.627% for chromium. These high variation values indicate that heavy metal pollution has a complex relationship and that both anthropogenic and environmental variables play an important role. In geographic distribution analyses, the IDW method was found to provide higher accuracy in determining the spatial distribution of heavy metals. The IDW model performed better for cadmium with 79%, for lead with 85% and for chromium with 88% of the ratios of explanation ( $R^2$ ). These results indicate that the IDW method is effective in capturing regional variability and making spatial estimates of heavy metal concentrations.

In conclusion, heavy metal pollution in the study area is significant and is caused by both natural sources and industrial and agricultural activities. These findings provide critical information for the development of targeted remediation strategies to protect environmental health and human health. Continuous environmental monitoring and implementation of effective pollution control methods are necessary for sustainable land management and public health protection in the future.

## References

- [1] B. J. Alloway, "Heavy metals in soils," *Blackie Academic and Professional, Chapman and Hall*, London p. 368, 1995.
- [2] S. L. Brown, R. L. Chaney, and G. M. Hettiarachchi, "Lead in urban soils: a real or perceived concern for urban agriculture," *Journal of Environmental Quality*, pp. 26-36, 2016.

- [3] Cambardella, "Field-scale variability of soil properties in central Iowa soils," *Soil Sci Soc Am J*, vol. 58, 1994.
- [4] S. E. Nicholson et al., "Validation of TRMM and other rainfall estimates with a high-density Gauge dataset for West Africa," *AMS Journal of Applied Meteorology and Climatology*, pp. 1337-1354, 2003.
- [5] C. O. Ogunkunle and P.O Fatoba. "Contamination and spatial distribution of heavy metals in topsoil surrounding a mega cement factory," *Atmos. Pollut. Res*, vol. 5, pp. 270–282, 2014.
- [6] Q. Yang, Z. Li, X. Lu, Q. Duan, L. Huang, and J. Bi, "A review of soil heavy metal pollution from industrial and agricultural regions in China: Pollution and risk assessment," *Science of The Total Environment*, pp. 690-700, 2018.
- [7] Shepard, "A two-dimensional interpolation function for irregularly-spaced data," in *1968 ACM National Conference*, New York, 1968, pp. 517-524.
- [8] WHO/FAO, Codex General Standard for Contaminants and Toxins in Food and Feed - CODEX STAN 193-1995. Joint FAO/WHO, 2001, doi: 10.13140/RG.2.1.4910.2560, 2001.



---

## A New Approach for the Degradation By-Products Pesticide Detection in Trace Level

**Chemseddine Zekkaoui<sup>\*1,2</sup>, Tarek Berrama<sup>1</sup>, Salima Dadou<sup>1</sup>, Assia Beriber<sup>1</sup>, Nassime Doufene<sup>1</sup>, Kadmi Yassine<sup>2</sup>**

<sup>1</sup>Industrial Process Engineering Sciences Laboratory, Houari Boumediene University of Science and Technology, BP 32, El-Alia, 16111, Bab-Ezzouar, Alger, Algeria

<sup>2</sup>Infrared and Raman Spectrochemistry Laboratory (LASIR), UMR-CNRS 8516, University of Science and Technology of Lille, France

---

### Abstract

The aims of this study is the identification of the by-products resulting from the degradation of an organophosphorus pesticide (Diazinon) using the photo-Fenton process. The initial concentration of this pollutant was set at 1 mg.L<sup>-1</sup> as an approach to the real case. A new concept based on the coupling of the two techniques was employed to identify the by-products of this degradation. QUEChERS extraction (quick, easy, cheap, effective, rugged, and safe) (Liq/Liq extraction technique) dispersive solid phase extraction (d-SPE) was performed. The extraction followed a well-defined protocol based on the principle of d-SPE extraction with an organic solvent in the presence of salts and tampons to ensure the transformation of the molecules in the effluent to the organic phase. The extract was evaporated (pre-concentration method) under a high-purity nitrogen stream. GC-MS/MS (gas phase chromatography coupled with a triple quadrupole mass spectrometry) was used for the identification of by-products resulting from the photo-degradation of Diazinon. The GC-MS/MS analysis method combined with the QuEChERS extraction approach and the pre-concentration method showed excellent performance in detecting by-products even at concentrations on the order of ng.L<sup>-1</sup>. Six by-products were identifier in this work: diazoxon, triethyl phosphate, triethyl thiophosphate, 2-isopropyl-5-ethyl-6-methylpyrimidine-4-ol, 2-isopropyl-6-methylpyrimidine-4-ol (IMP) and hydroxydiazinon. This methodology could be used to detect pesticides (at trace levels) and their by-products in waters at very low concentrations (at ultra-trace levels).

**Keywords:** GC-MS/MS, QUEChERS extraction, Pesticide, photo-Fenton degradation, By-products identification

---



## Application of Doehlert Design Experimental Methodology for the Optimal Emerging Pollutant Degradation with Fenton Process

**Chemseddine Zekkaoui<sup>\*1,2</sup>, Tarek Berrama<sup>1</sup>, Salima Dadou<sup>1</sup>, Assia Beriber<sup>1</sup>, Nassime Doufene<sup>1</sup>, Kadmi Yassine<sup>2</sup>**

<sup>1</sup>Industrial Process Engineering Sciences Laboratory, Houari Boumediene University of Science and Technology, BP 32, El-Alia, 16111, Bab-Ezzouar, Alger, Algeria

<sup>2</sup>Infrared and Raman Spectrochemistry Laboratory (LASIR), UMR-CNRS 8516, University of Science and Technology of Lille, France

---

### Abstract

This work aims to optimize the degradation of an emerging pollutant (veterinary drug) by an advanced oxidation process, namely Fenton. Preliminary tests have shown that the degradation yield can exceed around 60%, and 50% in terms of TOC, who reach equilibrium after 20 minutes. The setting up of an experimental design, which is the doehlert design, allowed us to optimize the degradation of this pollutant. The results of this plan are analyzed with the JMP software, which gives us the optimal conditions for a better degradation performance who can reach 78% in concentration and in 75% Totally Organic Carbon.

**Keywords:** *Advanced oxidation process, Fenton, Emerging pollutant, Experimental design, Doehlert design, Totally organic carbon*

---



## Optimization by the Surface Response Methodology of a Fenton Like Process by CrVI of an Anthraquinonic Dye Type Green Acid 25

Benidris Elbatoul<sup>\*1</sup>, Slamani Samira<sup>1</sup>, Hachemi Chaimaa<sup>1</sup>, Abdelmalek Fatiha<sup>1</sup>,  
Ghezzar Mouffek Redouane<sup>1</sup>

<sup>1</sup>Laboratory of Environmental Science and Valorization, Department of Process Engineering, University Abdelhamid Ibn Badis Mostaganem, Algeria

### Abstract

This study offers a comprehensive analysis of the optimization through the design of experiments methodology for the decolorization of Acid Green (Ag25) using a FENTON-like process with CrVI, a common organic dye in various industries. The primary aim of this research is to assess the impact of different variables on the efficiency of decolorizing Green Acid 25 (Ag25). The design of experiments approach is employed to systematically plan experiments that examine specific parameter combinations. These parameters encompass the concentrations of hydrogen peroxide (H<sub>2</sub>O<sub>2</sub>) and chromium (VI) ions, the pH of the reaction solution, and the reaction duration. The findings indicate intricate relationships among these parameters and their substantial influence on decolorization efficiency. Optimal conditions for maximal decolorization of Acid Green are identified using the design of experiments method with a standard "I. OPTIMAL" design. By applying these optimal conditions, effective decolorization of Acid Green 25 (Ag25) is achieved, underscoring the efficacy of the FENTON-like process in treating organic dyes. Furthermore, additional analyses are conducted to assess the energy efficiency and economic implications of decolorizing (Ag25) through the FENTON-like process. In summary, this study underscores the significance of experimental design in optimizing the decolorization of Green Acid 25 (Ag25) using the FENTON method. The results obtained offer valuable insights for devising efficient and economically feasible treatment strategies to eliminate organic dyes and chromate-containing wastewater, thereby advancing sustainable depollution technologies and contributing to environmental preservation in dye-reliant industries.

**Keywords:** Fenton like CRVI, Surface response, Acid green 25, Decolorization, I-optimal plan

## 1 INTRODUCTION

Human development and population growth have led to various changes in water resources and their distribution. Currently, several health problems (infections, illnesses, deaths) are linked to drinking water. Although most diseases such as typhoid and cholera are caused by classic pathogens, new pollutants causing similar diseases have also been detected in water, posing a great challenge for its treatment [1]. The study of the degradation of organic matter has been studied since the 1920s, which made it possible to develop biological purification. However, biological treatment plants cannot treat substances that are difficult to biodegrade or toxic (persistent organic pollutants) [2–4]. Conventional treatments (adsorption on activated carbon, membrane processes, coagulation-flocculation, chemical oxidations, etc.) have the disadvantage of transferring pollution from an aqueous phase to a new phase, thus creating a problem of secondary waste or regeneration of materials often very expensive [2]. For this, a lot of research has recently focused on a new class of oxidation techniques called: Advanced Oxidation Processes (AOP). These processes are based on the in-situ formation of hydroxyl radicals O which have an oxidizing power greater than that of oxidants. The objective of the study was to demonstrate the ability of the Fenton like process use a chromium hexavalent like catalyst and peroxide hydrogen like oxidant to remove Green Acid dye from textile industry wastewater using a design of experiments method to predict and optimize the main parameters that govern the process

## 2 MATERIAL AND METHOD

### 2.1 Chemicals Used

The chemicals used during this study are of analytical grade. We focused our study on textile dyes due to the excessive use of these products in Algeria and their harmful effect on the environment. We have green acid 25 as a model dye. The choice of dye studied meets the following criteria:

- High solubility in water,
- Easy analysis by UV/Visible spectrophotometer,
- Harmful to the environment in general and water in particular,
- Widely used as models to test the effectiveness of a water treatment process.

## 2.2 Methodology

All optimization experiments were carried out in 100 mL glass beakers under normal temperature and pressure conditions.

### 2.2.1 Fenton Like by CrVI

We treated a volume of 100 ml of a solution of green acid 25 with a concentration of 16 $\mu$ M (10 ppm), a solution of 1L with a concentration of 10ppm was prepared by ultra pur water on the other hand a solution mother of K<sub>2</sub>Cr<sub>2</sub>O<sub>7</sub> to make dilutions for a concentration of 1.5mM was prepared. All experiments based on ionized water being that solvent [5, 6].

During the long process for pH adjustment, we prepared 1N solutions of NaOH and H<sub>2</sub>SO<sub>4</sub>. The process consists of coupling an oxidant which is hydrogen peroxide and a non-ferrous catalyst which is hexavalent chromium. The optimization was carried out using the design of experiments methodology. In a 100ml beaker (25ml of CRVI solution + 25ml of AG25) then the H<sub>2</sub>O<sub>2</sub> is added for a concentration of 10mM.

Then after determining the optimal parameters ([H<sub>2</sub>O<sub>2</sub>] = 10mM; [CrVI] = 1.5mM; pH = 6) we followed the evolution of the treatment by monitoring using a UV-VISIBLE spectrophotometric technique. To better understand the system, we have done the scavenger effect and the effect of electrolytes on the process in question.

**Table 1.** Experiment matrix given by optimal plan I obtained by JMP PRO 14 (Real variables)

Test Number	pH	Contact Temp tc	[H <sub>2</sub> O <sub>2</sub> ] mM	[CrVI] mM	Discoloration%
1	6	35	10	2,475	75
2	4.5	35	10	1.5	80.52
3	3	35	19.4	1.5	88.37
4	4.5	67.5	14.7	2.25	93.93
5	4.5	35	19.4	3	90.52
6	4.5	67.5	14.7	2.25	93.93
7	6	100	10	1.5	98.15
8	3	67.5	10	1.5	84.21
9	4.5	100	14.7	3	86.31
10	3	100	19.4	1.5	92.66
11	3	75.3	19.4	3	78.42
12	3	100	10	2.25	92.68
13	4.5	67.5	14.7	2.25	93.93
14	4.5	67.5	14.7	2.25	93.93
15	4.5	67.5	14.7	2.25	93.93
16	6	35	19.7	1.5	69.18
17	6	67.5	14.7	3	84.21
18	6	100	19.4	2.25	80.00
19	4.5	67.5	14.7	2.25	93.93
20	4.5	67.5	10	3	86.31
21	4.5	67.5	14.7	2.25	93.93
22	3	35	14.7	3	78.42

### 2.2.2 Sample Analysis

Monitoring the decolorization of green acid 25 during the “Cr(VI)-mediated Fenton” process was carried out by removing an aliquot of the reaction mixture at the end of the treatment. The reading was carried out by UV-visible spectrophotometer at  $\lambda = 643$  nm. The decolorization efficiency of AG25 was calculated using the equation:

$$\text{Dec}\% = \frac{A_0 - A_t}{A_0} \times 100 \tag{1}$$

A<sub>0</sub>: absorbance of green acid dye 25 a initial state;

A<sub>t</sub>: absorbance of acid green dye 25 at a time t after the addition of H<sub>2</sub>O<sub>2</sub>

### 3 RESULTS

#### 3.1 Linear Regression Coefficient R<sup>2</sup>

The coefficient of determination provides information on the percentage of predicted variability. for the coefficient of our model equal to 0.98 which means that 98% of the variability was predicted with a Pvalue less than 0.05 for a confidence interval of 95%.

The graph (figure 1) confirms that the curve of the observed values as a function of the predicted values, perfectly resembles a straight line, we see the close agreement which exists between the experimental results and the predicted theoretical values. by the polynomial model.

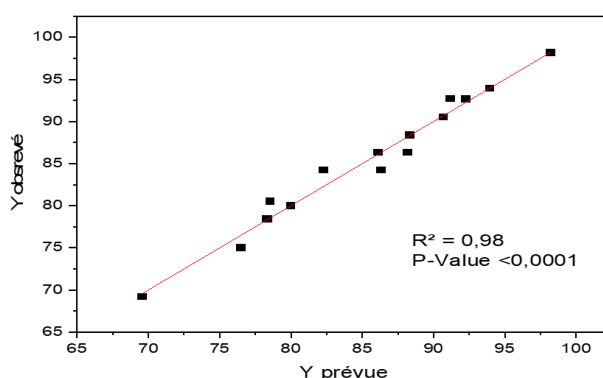


Figure 1. Predicted of experimental

#### 3.2 Overall Model and Lack of Fit

Table 2. Analysis of variance (ANOVAS) and lack of fit

Setting	Degree of Freedom	Sum of Squares	Mean Square	Report F	P-Value
Failure to fit	14	1231.6121	87.9723	30.0613	<0.0001*
Pure error	7	20.4850	2.9264	/	/
Total error	21	1252.0972		/	/

According to the above results, the model is significant with a (PValue <0.05), and hence the validity of the model is adequate. This model could probably predict the experimental results of our FENTON-mediated homogeneous oxidation process (in the presence of CrVI and H<sub>2</sub>O<sub>2</sub>) for the removal of green acid 25.

##### 3.2.1 Effect of Factors

- Linear Effect: From Table 3 we see that the results of the linear effect show that three factors have a significant influence on the discoloration of acid green dye 25 which represents our answer. The same results also show that the factor X2 (the contact time) presents the lowest P-value which highlights the great impact on the response (discoloration rate) and we clearly observe that there is an additional factor X4 ([CRVI] also presents a P-value low shows the influence on the discoloration rate (response).
- Interaction Effect: The results obtained from the study carried out show that the interaction between the contact time and the concentration of hydrogen peroxide has a great influence on the decoloration rate of green acid dye 25, the coefficient of this couple (X2,X3) is significant with a P-value which is equal to (0.0001\* < 0.05). on the other hand we note that the interaction between contact temperature and the CrVI concentration has a significant influence on the reduction of green acid 25 with a P value (0.0007\* < 0.05, subsequently the interaction between pH and hydrogen peroxide and the interaction between pH and CRVI is significant.



The effect of linear regression model factors is shown in the table below:

**Table 3:** Estimation of polynomial model regression coefficients

Term	Estimate	Standard error	t ratio	P-Value
Constant	93.9492992	0.646536	145.31	<.0001*
<b>Linearity</b>				
X1(3.6)	-1.279645	0.548382	-2.33	0.0523
X2(35,100)	4.5878472	0.543939	8.34	<0.0001*
X3(10,19.4)	-0.4836	0.532991	-0.91	0.3944
X4(1.5,3)	-2.615367	0.571538	-4.58	0.0026*
<b>Interaction</b>				
X1*X2	1.3816072	0.669301	2.06	0.0779
X1*X3	-3.267107	0.63276	-5.16	0.0013*
X1*X4	3.4658687	0.687884	5.04	0.0015*
X2*X3	-5.211896	0.623921	-8.35	<0.0001*
X2*X4	-3.963805	0.683364	-5.80	0.0007*
X3*X4	0.6357652	0.671368	0.95	0.3752
<b>Quadratic</b>				
X1*X1	-7.76982	0.956049	-8.13	<0.0001*
X2*X2	-0.315045	0.963337	-0.33	0.7532
X3*X3	-1.595266	1.10128	-1.45	0.1907
X4*X4	-3.469563	0.975923	-3.56	0.0093*

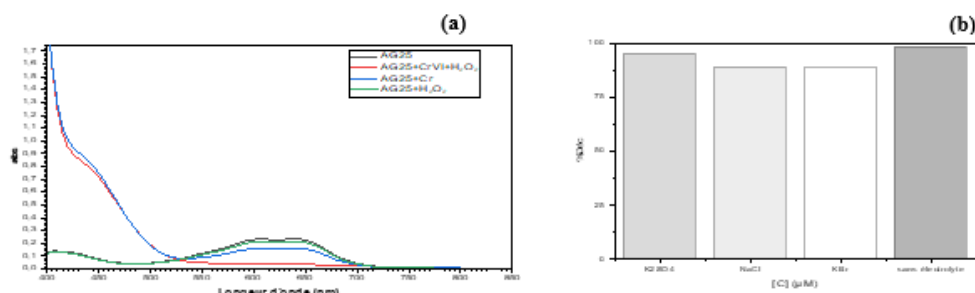
This influence means that the pH and the concentration of hexavalent chromium reach a maximum and then decrease, which is in agreement with our results.

### 3.2.2 Mathematical Model

The results obtained are summarized in the form of a second degree polynomial equation, given in reduced variables:

$$Y = 93.94 + 4.58 * X2 - 2.61 * X4 - 3.26 * X1 * X3 + 3.46 * X1 * X4 - 5.21 * X2 * X3 - 3.96 * X2 * X4 - 7.76 * X1 * X1 - 3.46 * X4 * X4 \tag{2}$$

### 3.2.3 Experimental Validation of the Fenton Like Process by CrVI and Monitoring of the Study



**Figure 2.** (a) Decolorization of acid green by Fenton like chromium hexavalent and (b) effect of electrolyte on process Fenton like

The study by the experiment design methodology allowed us to determine the optimal factors by the prediction model to validate this result it is necessary to repeat the same experiments in the same condition governed by the JMP pro14 software and continued the study of process, or even

- The effect of the oxidant alone,
- The catalyst effect alone,
- The effect of inhibition (scavenger),

- Study of the decolorization of green acid 25 by Fenton like process by CrVI for different combinations.

## 4 CONCLUSION

The results obtained also demonstrated that chromium can indeed be used successfully as a catalyst in the Fenton process for the degradation of green acid 25, it showed its reliability in an acidic medium pH = 4 and close to neutral pH =6 unlike the classic FENON which uses iron as a catalyst which works just at an acidic pH. We obtained an R2 = 0.98 and a P value < 0.05 which means that our process was carried out with a percentage of 98% and with an error < 5%.

However, it is important that the formation of hexavalent chromium can also have adverse effects on the environment, but this information was taken into consideration by the storage of CrVI and the medium was acidified in order to have the form of trivalent chromium which exists in nature without being a danger to the ecosystem. And based on our research on scientific articles and previously applied processes, we found that our process is responsible for the discoloration of 'Acid Vert 25' dye and also for the degradation of chromates, which reduces the hexavalent chromium in our solution.

On the other hand, every year, a large amount of wastewater containing Cr(VI) is produced by the electroplating, metal finishing, leather tanning and petroleum refining industries, requiring intensive treatment to prevent water contamination. The addition of H2O2 can be a solution to industrial wastewater contaminated with Cr(VI) can be used to degrade organic dyes before their pretreatment.

## References

- [1] I. Yahiaoui, F. Aissani-Benissad, F. Fourcade, and A. Amrane, "Removal of tetracycline hydrochloride from water based on direct anodic oxidation (Pb/PbO2 electrode) coupled to activated sludge culture," *Chemical Enginerin Journal*, vol. 221, pp. 418–4251, Apr. 2013.
- [2] A. Ozcan, "Degradation of hazardous organic compounds by using electro-fenton technology," Paris-Est University, Paris, 2010.
- [3] I. Yahiaoui, F. Aissani-Benissad, F. Fourcade, and A.Imrane, "Enhancement of the biodegradability of a mixture of dyes (methylene blue and basic yellow 28) using the electrochemical treatment on a glassy carbon electrode," *Desalination Water Treat*, vol. 57, pp. 12316–12323, May 2015.
- [4] S. Wardhani, M. Farid Rahman, D. Purwonugroho, R. Triandi Tjahjanto, C. Adi Damayanti, and I. Oktavia Wulandari, "Study of photocatalytic degradation of methylene blue by TiO2/Zeolite catalysts," *The Journal of Pure and Applied a Chemical Reaserch*, vol. 5, pp. 19–27, Feb. 2016.
- [5] T. Zhang, T. Oyama, and T. Ohmori, "Advanced oxidation processes (AOPs) for wastewater treatment: introduction, processes, applications, and future directions," *Environmental Materials Management*, 2017.
- [6] V. S. Watwe, S. D. Kulkarni, and P. S. Kulkarni "Cr(VI) mediated omoeneous Fenton oxidation for decolorization of methylene blue dye: Slude free and pertinenet to wide pH range," *ACS Omega*, vol 6, pp. 27288–2729, Oct. 2021.



## **Pellets from Olive Mill Waste: Densification and Characterization for Sustainable Waste Management Solutions**

**Zaina Izghri<sup>\*1</sup>, Fatima Ezzahra Yaacoubi<sup>1</sup>, Chaima Sekkouri<sup>1</sup>, Imad Rabichi<sup>1</sup>,  
Abdelaziz Ounas<sup>1</sup>, Karima Ennaciri<sup>1</sup>, Abdelaziz Bacaoui<sup>1</sup>, Abdelrani Yaacoubi<sup>1</sup>**

*<sup>1</sup>Laboratory of Applied Chemistry and biomass, Faculty of Sciences Semlalia, Cadi Ayyad University, B.P 2390, 40000, Marrakech, Morocco*

---

### **Abstract**

This research investigates the utilization of two-phase olive pomace, an abundant by product from olive oil production, as a renewable energy resource via an innovative method involving greenhouse drying and pelletization. The study evaluates the potential of greenhouse-dried olive pomace pellets as a sustainable biofuel. The process involves drying the olive pomace in a controlled greenhouse setting, followed by pelletization to improve its handling and combustion properties. The investigation assesses the energy content, combustion characteristics, and environmental impacts of the produced pellets. The study highlights the sustainability of greenhouse-dried olive pomace pellets as a renewable, eco-friendly energy option, his contributes to the valorization of food waste and the advancement of sustainable bioenergy solutions.

**Keywords:** *Pellets, Densification, Renewable energy, Greenhouse*

---



## Microplastic Pollution in Surface Waters of Ergene River: Sources and Spread

Enes Ozgenc<sup>\*1</sup>, Gunay Yildiz Tore<sup>2</sup>, Erdi Bulus<sup>3</sup>, Yesim Muge Sahin<sup>4</sup>

<sup>1</sup>Environmental Health Program, Vocational School of Health Services, Trakya University, Edirne, Türkiye

<sup>2</sup>Department of Environmental Engineering, Tekirdag Namik Kemal University, Tekirdag, Türkiye

<sup>3</sup>ArelPOTKAM (Polymer Technologies and Composite Application and Research Center), Istanbul Arel University, Istanbul, Türkiye

### Abstract

Microplastics, widely found in aquatic ecosystems, are a rapidly growing environmental issue in the modern world. These tiny plastic particles, smaller than 5 mm, enter natural environments through various human activities. The Ergene River, located in the Thrace region, is a significant waterway in an area with intense industrial and urban activities. This situation increases the risk of the river being exposed to microplastic pollution. This study examined the sources and distribution of microplastic pollution in the Ergene River's surface waters. Water samples taken from different river points were subjected to laboratory analyses, and the concentration, types, and potential sources of microplastics were identified. The study aims to reveal the effects of microplastic pollution on the river and to provide information on possible preventive measures by determining the sources of this pollution. Understanding the situation in the Ergene River is crucial, considering the environmental and ecological impacts of microplastics, their negative contributions to water quality, and their potentially harmful effects on aquatic life. In this context, the findings are expected to significantly contribute to developing strategies for combating and managing microplastic pollution.

**Keywords:** Aquatic ecosystems, Ergene river, Microplastic pollution, Sources, Distribution

## 1 INTRODUCTION

Microplastic pollution has emerged as a critical environmental issue in recent years, especially in aquatic ecosystems [1]. Microplastics are plastic particles smaller than 5 mm and commonly found in water bodies worldwide, originating from various human activities [2]. Their presence in aquatic ecosystems poses a significant threat due to their persistence and potential to cause ecological damage [3]. Microplastics can affect water's chemical composition [4], damage aquatic organisms' physical structure [5], and reach humans through the food chain [6]. The presence of microplastics, therefore, poses severe risks to water quality and biodiversity.

Various strategies and policies are being developed worldwide to reduce microplastic pollution. Efforts are underway in various countries to reduce plastic use, encourage recycling, and improve waste management [7]. In particular, physical, chemical, and biological methods are used to reduce microplastic pollution in water bodies [8]. However, the effectiveness and applicability of these methods vary depending on regional conditions and the characteristics of microplastics. The Ergene River, located in the Thrace region of Turkey, is a vital waterway passing through an area characterized by intense industrial and urban development. This geographical and economic context has increased the risk of exposure to microplastic pollution in the river's waters. This situation indicates that current solutions may be inadequate and that regional solutions should be developed. Considering the harmful effects of microplastics on water quality and aquatic organisms, understanding their distribution and origin in the Ergene River is of great importance.

This study focuses on the sources and spread of microplastic pollution in the surface waters of the Ergene River. The insights gained from this research are expected to contribute significantly to formulating effective measures to combat and manage microplastic pollution. By analyzing water samples collected from various points along the river, the study aims to identify potential sources of pollutants, quantify the factors contributing to microplastic pollution in the region, and identify the concentration and types of microplastics present. The analysis is vital not only to assess the river's current state but also to inform future strategies to reduce this form of pollution. By shedding light on microplastics' environmental and ecological impacts in the Ergene River, this study aims to provide a basis for future policy and conservation efforts to protect water quality and conserve aquatic life.

## 2 MATERIAL AND METHOD

### 2.1 Sampling Points of the Study Area

In this study, surface water analysis was carried out to assess the microplastic pollution in the Ergene River and specific regions around it. The sampling points in the study area were specifically selected to observe the interactions between industrial and rural areas. These points include Çerkezköy Organized Industrial Zone (OIZ) (41° 15' 59.40" N - 27° 56' 28.71" E), Uzunhacı Village (41° 20' 37.36" N - 27° 49' 43.18" E), Çorlu OIZ (41° 10' 48.39" N - 27° 46' 30.26" E) and Adasarhanlı (41° 03' 58.56" N - 26° 21' 44.02" E). Surface water samples were collected from these strategic points and analyzed to determine the density, size distribution, and types of microplastic particles. The data obtained played a critical role in understanding the level and distribution of microplastic pollution in the river. Furthermore, surface water analyses revealed the effects of seasonal variations and industrial and agricultural activities in the region on microplastic concentrations.

### 2.2 Surface Water Sampling

Sampling methods and frequency vary depending on the source and purpose. Samples taken at a specific time and place represent that time and place, while samples taken from sources whose composition does not change over time may represent a wider time period. Water samples from the sampling points were taken from different surface water depths by tying steel wire to sterilized 2-liter glass jars. Samples were collected 30-40 centimeters below the surface water, where mixing occurs fully. Sampling points were chosen to determine the effects of water inlets, outlets, and coastal activities. Parameters such as pH, temperature, dissolved oxygen, and conductivity were measured with a "Hach HQ40D Multimeter". Each sample was labeled with information such as place and time of collection. The samples were transported to the laboratory undisturbed and stored at +4°C [9]. Samples were preserved and analyzed by the 'TS EN ISO 5667-3 Water Quality' standard [10].

### 2.3 Pre-Treatment of Surface Water Samples

For MP characterization, 100 ml of surface water samples were taken. Each sample was passed through tared filters. Filtration was performed using a sieve set with pore sizes of 250-125-63 µm. The solids retained in the filters were backwashed with ultrapure water captured with a vacuum pump and then dried at 105°C for 1 hour to measure the solids concentration. After drying, excess water in the sample was evaporated at 70°C. For organic matter degradation by Fenton oxidation, 20 ml of 0.05M FeSO<sub>4</sub>·7H<sub>2</sub>O solution and 30% H<sub>2</sub>O<sub>2</sub> were added to the sample. The reaction was continued at 70-75°C for 30 minutes. After the H<sub>2</sub>O<sub>2</sub> was completely evaporated in an oven at 60°C, 6 g NaCl solution was added to the sample for every 20 ml. The microplastics were decomposed for 5-10 minutes, depending on the concentration. The supernatant microplastics were taken into centrifuge tubes and centrifuged at 3500 rpm for 5 minutes before filtration. After centrifugation, the samples were filtered through membrane filters with 0.45-1.2 µm pores; the filters were wrapped with aluminum foil and dried at room temperature [11]. Microplastics were characterized by Fourier-transform infrared (FTIR) spectroscopy and Scanning Electron Microscopy (SEM), and microplastics that could be airborne were detected with the witness sample.

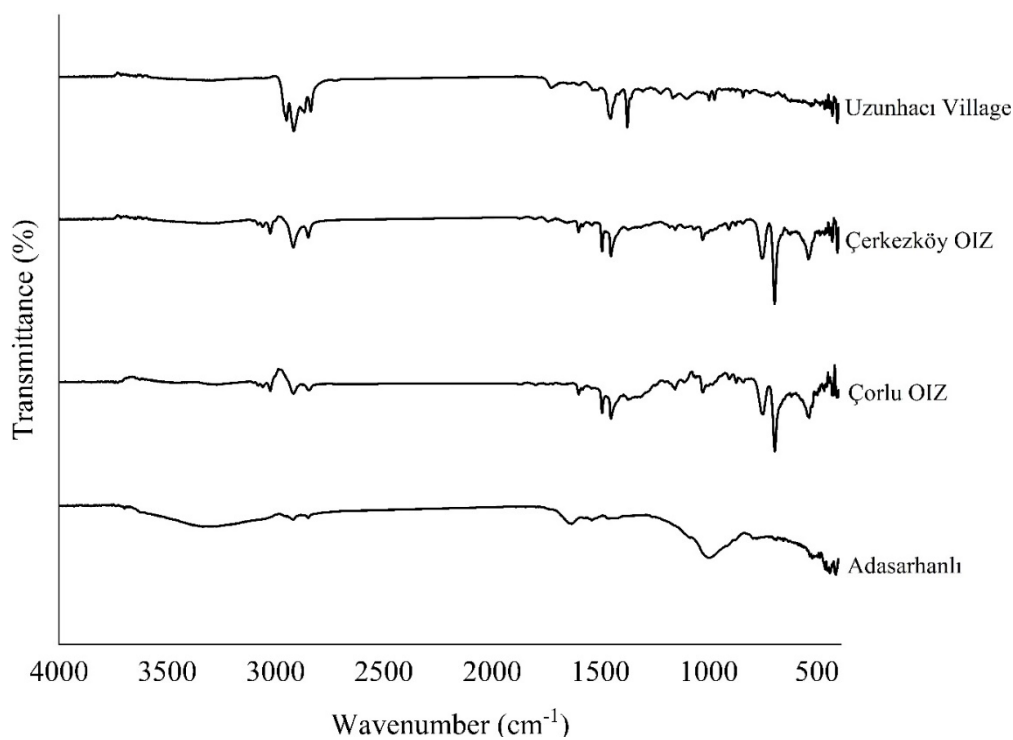
### 2.4 Identification of MPs

The presence of functional groups of MPs was determined in the wavelength range of 400-4400 cm<sup>-1</sup> in the JASCO brand 6600 model FTIR analyzer. As a result of this process, the chemical structures of MPs and the presence of functional groups were determined. To examine the surface morphology and structural features of the MPs in detail, the 500 nm, 1 µm, 5 µm, and 10 µm sized areas of the samples were imaged using high and low vacuum detectors on a Quanta brand FEI FEG450 model FEGSEM device.

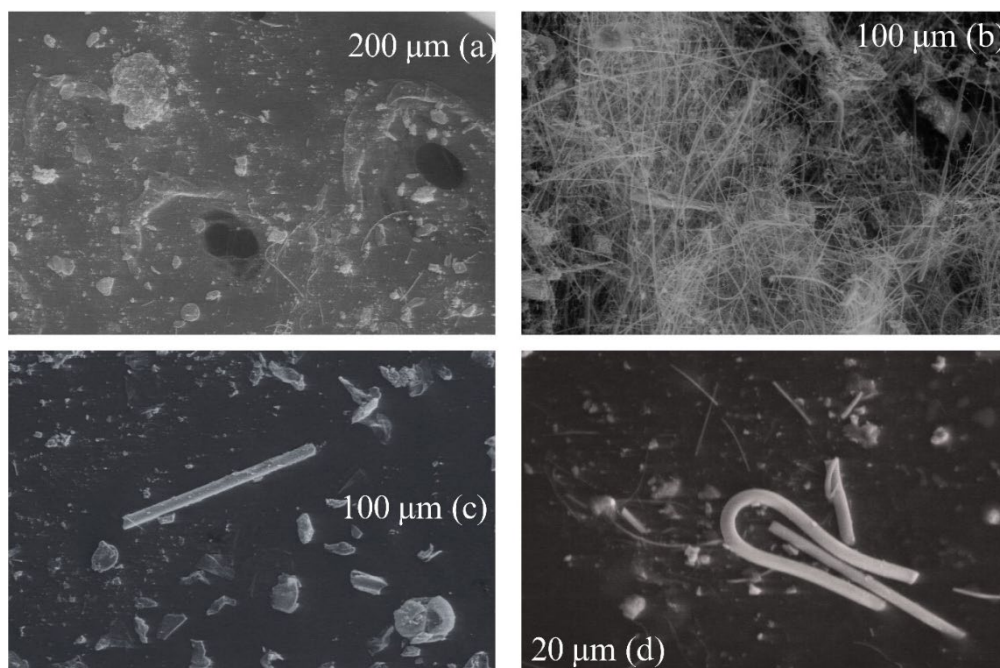
## 3 RESULTS

In the surface water analysis of Uzunhacı Village, 433.56 mg of the 671.12 mg sample consists of plastic material, while 237.56 mg of it consists of non-plastic materials. The polymer types in the sample include low-density polyethylene (LDPE), polypropylene (PP), and cellulose. The amount of LDPE was determined as 151.65 mg, and its density was 0.913 g/cm<sup>3</sup>. PP was 226.13 mg, and its density was 0.896 g/cm<sup>3</sup>. In addition, cellulose was detected in the sample as 55.78 mg, with a 1.231 g/cm<sup>3</sup> density. In the surface water analysis of Çerkezköy OSB, 124.78 mg of the 471.7 mg sample consists of plastic materials. The amount of non-plastic materials was measured as 346.92 mg. The polymer types detected are high-density polyethylene (HDPE), polystyrene (PS), and cellulose. HDPE was recorded as 43.83 mg, and its density was 0.937 g/cm<sup>3</sup>. The amount of PS was 43.12 mg, and its density

was  $0.998 \text{ g/cm}^3$ . The amount of cellulose was  $37.83 \text{ mg}$ , and its density was measured as  $1.231 \text{ g/cm}^3$ . In the Çorlu OSB surface water analysis,  $402.63 \text{ mg}$  of the  $639.12 \text{ mg}$  sample consisted of plastic materials, while the amount of non-plastic material was determined as  $236.49 \text{ mg}$ . The polymer types in the sample include HDPE, PS, and cellulose. The amount of HDPE was  $156.78 \text{ mg}$ , and its density was  $0.941 \text{ g/cm}^3$ ; the amount of PS was  $223.41 \text{ mg}$ , and its density was measured as  $0.998 \text{ g/cm}^3$ . In addition, cellulose was detected with an amount of  $22.44 \text{ mg}$  and a  $1.231 \text{ g/cm}^3$  density. In the Adasarhanlı surface water analysis,  $445.85 \text{ mg}$  of the  $665.91 \text{ mg}$  sample consisted of plastic materials, while  $220.06 \text{ mg}$  contained non-plastic materials. The polymer types in the sample include HDPE, polyamide (PA), and cellulose. The amount of HDPE was recorded as  $159.85 \text{ mg}$ , and its density was  $0.954 \text{ g/cm}^3$ ; the amount of PA was recorded as  $147.86 \text{ mg}$ , and its density was  $1.125 \text{ g/cm}^3$ . The amount of cellulose was measured as  $56.81 \text{ mg}$ , and its density was  $1.231 \text{ g/cm}^3$ . FTIR and SEM images of microplastic analyzes are shown in Figure 1 and Figure 2, respectively.



**Figure 1.** FTIR analysis



**Figure 2.** SEM images: (a) Uzunhacı Village, (b) Çerkezköy OIZ, (c) Çorlu OIZ, (d) Adasarhanlı

## 4 CONCLUSION

This study analyzed samples taken from different points of the Ergene River and revealed that microplastic pollution in the region has a wide range of polymer diversity and morphological forms. SEM images showed that microplastics are present in the form of particles, fibers, flocs, foam, and films. These results indicate that the river is affected by various sources of microplastic pollution and that this pollution has a complex structure. Polymers such as LDPE, PP, and cellulose were detected in the samples taken from Uzunhacı Village. LDPE can be found due to plastics commonly used in agriculture, while the high amount of PP indicates the use of packaging materials. The presence of cellulose may be due to the textile industry or agricultural waste. Since this region is known for intensive agricultural activities, microplastics are thought to originate from such activities. HDPE, PS, and cellulose were found in samples taken from the entrance of Çerkezköy OSB. HDPE may come from industrial packaging and rigid plastic products. The presence of PS indicates intensive use of food packaging and disposable products. Cellulose, which may originate from the textile industry, was also found in this area. The presence of intensive industrial activities at this point points to industrial wastes as the source of the detected microplastics. Polymer species such as HDPE, PS, and cellulose were also detected in samples taken from the entrance of Çorlu OSB. This indicates that hard plastics, food packaging, and textiles are entering the river. The fact that Çorlu OIZ has intensive industrial activities increases the likelihood of contributing to microplastic pollution. HDPE, PA, and cellulose were found in samples from Adasarhanlı. HDPE reflects the widespread use of rigid plastic packaging, while PA may be due to textiles. Cellulose indicates that natural fibers and textile wastes enter the river. The prevalence of both industrial and agricultural activities in this region increases the complexity of microplastic pollution. The microplastic species and morphological forms detected in the Ergene River result from various regional human activities. Agriculture, the textile industry, plastic production, and consumer products are the main sources of microplastic entering the river. Microplastics can negatively impact the environment and ecosystems, both physically and chemically. In particular, potential impacts on aquatic life can lead to the accumulation of toxic chemicals entering the food chain. The results obtained in this study show that microplastic pollution in the Ergene River is a severe environmental problem. Further research and environmental regulations are needed to solve this problem. Microplastic pollution should be tackled by considering the sustainability and environmental impacts of the activities in the region.

## Acknowledgments

We would like to sincerely thank AreIPOTKAM (Polymer Technologies and Composite Application and Research Center) for their invaluable contributions to this study's execution.

## References

- [1] A. Zhou *et al.*, "Microplastics and their potential effects on the aquaculture systems: A critical review," *Reviews in Aquaculture*, vol. 13, no. 1, pp. 719–733, 2021.
- [2] M. N. Issac and B. Kandasubramanian, "Effect of microplastics in water and aquatic systems," *Environmental Science and Pollution Research*, vol. 28, pp. 19544–19562, 2021.
- [3] Z. Yuan, R. Nag, and E. Cummins, "Human health concerns regarding microplastics in the aquatic environment-From marine to food systems," *Science of the Total Environment*, vol. 823, art. no. 153730, 2022.
- [4] Y. Xiang *et al.*, "Microplastics and environmental pollutants: Key interaction and toxicology in aquatic and soil environments," *Journal of Hazardous Materials*, vol. 422, art. no. 126843, 2022.
- [5] F. Xiong *et al.*, "Microplastics induce neurotoxicity in aquatic animals at environmentally realistic concentrations: A meta-analysis," *Environmental Pollution*, vol. 318, art. no. 120939, 2022.
- [6] X. Yao, X.-S. Luo, J. Fan, T. Zhang, H. Li, and Y. Wei, "Ecological and human health risks of atmospheric microplastics (MPs): A review," *Environmental Science: Atmospheres*, no. 5, 2022.
- [7] R. Muthuvairavasamy, *Microplastics: Footprints On The Earth and Their Environmental Management*, Springer Nature, 2022.
- [8] A. Talukdar, P. Kundu, S. Bhattacharya, and N. Dutta, "Microplastic contamination in wastewater: Sources, distribution, detection and remediation through physical and chemical-biological methods," *Science of The Total Environment*, vol. 916, art. no. 170254, 2024.
- [9] M. Cole, "A novel method for preparing microplastic fibers," *Scientific reports*, vol. 6, no. 1, pp. 1–7, 2016.
- [10] P. Krystek, A. Wimmer, R. Ritsema, and C. EngelhArd, "Sampling and pre-treatment in nanoparticle analysis in water," 2022.

- [11] J. Masura, J. Baker, G. Foster, and C. Arthur, "Laboratory methods for the analysis of microplastics in the marine environment: Recommendations for quantifying synthetic particles in waters and sediments," 2015.





---

## Diatomite Formation Associated with Sogucak Pyroclastics (Sandikli, Türkiye)

Bala Ekinci Sans<sup>\*1</sup>, Zeynep Doner<sup>1</sup>

<sup>1</sup>Department of Geological Engineering, Istanbul Technical University, Istanbul, Türkiye

---

### Abstract

In the study area, Paleozoic-aged Afyon Metamorphics, consisting mainly of schists and marbles, form the basement rock group. Miocene-Pliocene sedimentary units and volcanics unconformably overlie this group. Diatomite formations in the region are associated with the unit named Sogucak Pyroclastics (mainly andesitic agglomerates). The unit contains diatomite zones in the north of Basagac and Karadirek villages (north Sandikli-Afyonkarahisar). Pyroclastics are laterally and vertically transitional with other Pliocene-aged clastics and basaltic lavas. Diatomite lenses show morphology depending on paleotopography, between certain levels of pyroclastics. In diatomite zones, the color is mostly whitish, but there may also be variations in pink, yellowish pink, pinkish yellow, brownish yellow, and beige. The coloration likely varies due to secondary iron oxide/hydroxide additions and the humidity of the diatomites. Diatomites include opal bands, lenses and blocks in green, yellowish, and rarely reddish colors, which can be quite large locally. In the Akar and Ayrilikli stream localities, there is a white-beige colored diatomite zone in an area of 60 m x 30 m. The thickness of this zone is highly variable, ranging from 1.5 to 12 meters. Among the diatomite samples, some contain completely amorphous material, while others contain approximately 10% Ca-smectite in addition to the amorphous component, based on XRD analysis. Some samples also contain traces of illite-mica and quartz. There are changes in the chemistry of diatomites due to mineralogical differences and secondary iron. The versatility of diatomite makes it valuable in various industries. Considering that pure diatomite is preferred in some areas of use and smectite diatomites can be used in some areas, it is understood that there is a significant diatomite potential in the region.

**Keywords:** Diatomite, Sogucak pyroclastics, Opal, Sandikli-Afyonkarahisar, Türkiye

---



---

## Effects of Titanium Dioxide on the Ultrasonic and Structural Properties of Zinc–Strontium–Lithium Phosphate Glass

Nurhafizah Hasim<sup>\*1</sup>, Nur Hidayah Ahmad<sup>1</sup>, Nur Asilah Zulkifeli<sup>1</sup>, Anis Nazihah Mat Daud<sup>2</sup>

<sup>1</sup>Advanced Optical Materials Research Group, Department of Physics, Faculty of Science, Universiti Teknologi Malaysia, 81310 UTM Johor Bahru, Johor, Malaysia

<sup>2</sup>Department of Physics, Faculty of Science & Mathematics, Universiti Pendidikan Sultan Idris, 35900 Tanjong Malim, Perak, Malaysia

---

### Abstract

Zinc – strontium – lithium phosphate glass doped with titanium dioxide with the composition  $(50 - x) \text{P}_2\text{O}_5 - 20\text{ZnO} - 15\text{SrO} - 15\text{Li}_2\text{O} - (x)\text{TiO}_2$  where  $(0 \leq x \leq 2 \text{ mol}\%)$  is investigated. The glass was prepared via melt quenching method and their characterization of physical, structural, thermal, and mechanical properties are characterized by using density and molar volume, X-ray diffraction (XRD), Fourier transform infrared spectroscopy (FTIR), differential thermal analysis (DTA) and ultrasonic testing via pulse echo method. The densities are found having decrease and increase with addition of 0.0 to 2.0 mol%  $\text{TiO}_2$ . The molar volumes are found increase at 0.5 mol% and decrease from 1.0 to 2.0 mol%  $\text{TiO}_2$ . The absence of the broad humps at 20 to 30 degrees in XRD spectra, confirming the amorphous nature of the glasses. For the FTIR analysis, it found three obvious peaks it was at 861  $\text{cm}^{-1}$ , 1279  $\text{cm}^{-1}$  and 3636  $\text{cm}^{-1}$ . DTA values of  $T_g$ ,  $T_c$  and  $T_m$  shows decrease values from the curve due to decreasing in bond strength. The glass shows a good thermal stability due to the value of temperature more not lower than 100 °C. Longitudinal and shear velocity were measured for glass system using pulse echo method. Elastic properties such as longitudinal modulus, shear modulus, bulk modulus, young's modulus was calculated from the obtained values of ultrasonic wave velocities. There are two other physical parameters was also calculated from these ultrasonic properties it was Poisson's ratio and microhardness. The ultrasonic results and other parameters indicate the rigidity and the creation of cross-link density of covalent bonds glass system.

**Keywords:** *Ultrasonic properties, Structural properties, Titanium dioxide*

---



---

## Strategic Coordination of P2P Energy Trading in Smart Microgrids

Kubra Nur Sahin<sup>\*1</sup>, Muhammed Sutcu<sup>2</sup>

<sup>1</sup>Industrial Engineering, Abdullah Gul University, Kayseri, Türkiye

<sup>2</sup>Engineering Management, Gulf University of Science and Technology, Mishref, Kuwait

---

### Abstract

Managing energy resources within smart urban environments is a critical challenge in today's rapidly evolving urban landscape, characterized by swift urbanization and increasing environmental concerns. This study examines the challenges of optimizing peer-to-peer (P2P) energy trading within microgrids, presenting a comprehensive framework for sustainable urban energy management. The rise of local energy communities represents a significant shift, with prosumers actively adopting solar Photovoltaic (PV) systems and Battery Energy Storage (BES). This research aims to clarify the intricate relationship between traditional grid interactions and emerging P2P trading, all within the context of sustainable, community-focused energy practices.

The necessity to coordinate P2P energy trading within smart homes in microgrids is propelled by the significant transformation in the global energy landscape. This shift, marked by a growing emphasis on sustainability and decentralized energy systems, highlights the need to address the challenges of optimizing energy utilization patterns. Strategic coordination of P2P energy trading within microgrids is essential to enhance overall energy resilience, promote environmental sustainability, and fully exploit the potential of distributed energy resources. Using the systematic approach of Mixed-Integer Linear Programming (MILP), this study addresses these pressing coordination challenges comprehensively.

The findings highlight the crucial role of P2P systems in balancing supply and demand dynamics, democratizing energy distribution, and facilitating the seamless integration of renewable energy sources within microgrid environments. This research contributes to a greener and more resilient urban future by advancing our understanding of energy management practices.

**Keywords:** Energy management, Optimization, Peer-to-peer (P2P) energy trading, Renewable energy

---



---

# Advancing Turkish-to-English Translation: A Transformer-Based Neural Model Approach

Nurzhan Amantay<sup>\*1</sup>, Yasin Ortakci<sup>1</sup>

<sup>1</sup>Department of Computer Engineering, Karabuk University, Türkiye

---

## Abstract

Machine translation (MT) represents a pivotal area within the field of natural language processing, continuously striving for advancements. The transformer architecture, which employs the attention mechanism, has been surpassed the popular neural models such as Recurrent Neural Networks (RNNs) and Bidirectional Long Short Term Memory (BiLSTM) in terms of efficiency and memory usage. This paper investigates the application of the transformer in a neural machine translation model for Turkish-to-English. The neural model was trained using the Tatoeba Anki dataset, comprising 145,000 parallel Turkish-English sentence pairs. Our transformer model consists of six encoders and six decoders, each with eight multi-head self-attention mechanisms. After training over 30 epochs, the model achieved an accuracy of 0.95 and a BLEU score of 0.4208. This results underscore the potential of the transformer architecture in addressing the complexities of Turkish-English translation, particularly considering the linguistic disparities and grammatical intricacies between the two languages. The paper provides a detailed analysis of the model's architecture and implementation. The findings contribute to the understanding of transformer-based MT systems and their applicability to languages that do not have a sufficient amount of text corpora, such as Turkish.

**Keywords:** *Neural machine translation, Transformer, Self-attention, Encoder&decoder*

---

## 1 INTRODUCTION

The issue of linguistic barriers among individuals has been a long-standing concern for humanity. The act of communication between individuals who speak different languages is made possible through the intermediary of human translation. Nevertheless, the availability of high-quality human translation services remains a persistent challenge, largely due to the limited number and high cost of such skilled individuals. The unavailability and expense of human translation, coupled with the advances in Natural Language Processing (NLP) and computer science, have given rise to the concept of Machine Translation (MT), which aims to automate the process of translating languages.

MT is a significant task focused on using computers to translate text from one language to another. The early studies in this field includes rule-based and statistical approach. However these approaches have difficulties in the translation of long sentences. Then, deep learning based methods including Recurrent Neural Networks (RNNs) and Bidirectional Long Short Term Memory (BiLSTM) are started to be investigated in the MT. Nevertheless, these new techniques struggle with handling long text translations. A state-of-art neural model, transformers supported with the attention mechanism [1], has emerged as a powerful alternative MT architecture.

On the other hand, an examination of the existing literature on MT of the Turkish language revealed a research gap on translations from Turkish to English. The translation of Turkish into English is a challenging endeavour due to the distinct linguistic features of Turkish and the intricate lexical composition and grammatical structure of the language. Furthermore, the significant lack of Turkish-English text pair corpora represents another significant challenge. Although there are some studies on the translation of Turkish into English in the literature that do not employ transformer-based neural models, the quality of the resulting translations is still not optimal. Therefore, in this study, we present a novel approach to address the challenges of Turkish to English MT by developing a transformer-based neural network model.

Using the transformer in our MT model, we achieved a Bilingual Evaluation Understudy (BLEU) score of 0.4208 and an accuracy of 0.95 for Turkish to English translation. This high BLEU score and accuracy underscore the effectiveness of our model. The results demonstrate that the self-attention mechanism in transformers is highly

effective in capturing contextual information, resulting in notable enhancements in translation quality when compared to existing methodologies. The contribution of this study can be summarized as follows:

- A transformer-based Turkish to English MT model with high quality translation capability is developed.
- Deep insights into the encoder-decoder structures in the transformers used in the MT from Turkish to English, their numbers and the hyper-parameters to be used in the training are presented.
- This study has proposed an approach that greatly reduces the time cost of translation, which is one of the major limitations of initial statistical and expression-based methods.

The rest of this paper is structured as follows. Section 2 provides a detailed related studies regarding MT. Section 3 describes the methodologies of proposed model. Details regarding the datasets, hyperparameter tuning and evaluation metrics are presented in Section 4. Section 5 presents the results of study which covers the accuracy and BLEU metric evaluations of the proposed model. Section 6 provides a comprehensive discussion of the results of study, focusing on the interpretation and implications of the findings. Finally, the conclusion of the research is provided in Section 7.

## 2 RELATED WORK

The preliminary methodology employed in MT is predominantly based on manually crafted translation rules and linguistic expertise. Nevertheless, the intrinsic complexity of natural languages renders it difficult to account for all linguistic irregularities through the establishment of manual translation rules. With the advent of large-scale parallel corpora, an alternative approach, Statistical Machine Translation (SMT), which is based on the direct learning of underlying structural elements such as word alignments and phrase sequences from parallel corpora, has been proposed [2, 3]. Yildirim and Tantug explored an SMT-based method, re-ranking N-best lists in English-to-Turkish MT using Google Translate Research API, achieving an 11.81% relative improvement in BLEU scores by reordering candidate translations [4]. Similarly, El-Kahlout and Oflazer improved English-to-Turkish SMT by using morphological information and local word reordering, achieving a 62% relative improvement in BLEU scores with a score of 25.17 [5]. Yeniterzi and Oflazer put forth a methodology for translating from English to Turkish that incorporates syntactic analysis at the source text level. This approach yielded a 39% relative improvement in BLEU scores compared to a word-based baseline [6]. Yilmaz and Uguz developed a Turkish-English MT system using Moses and the BOUN-ITU Turkish-English Parallel Corpus, achieving a BLEU score of 17.02 and highlighting the benefits of shuffling corpus data and using a 4-gram language model [7]. Oflazer and El-Kahlout improved English-to-Turkish SMT by representing sub-lexical units, achieving a BLEU score of 25.08 using Moses, SRILM, and GIZA++ on a corpus from international relations and legal documents [8]. The findings of these studies have led to the conclusion that SMT is unable to model dependencies between words over long distances, which results in a suboptimal translation quality.

The deep learning paradigm has led to the emergence of Neural Machine Translation (NMT) which is replacing SMT as the dominant approach to MT [9–12]. The system offers a more straightforward end-to-end training process and showcases state-of-the-art performance on a multitude of language pairs [13]. The initial NMT architectures, including RCTM [10], RNNencDec [12], and Seq2Seq [9], employ a fixed-length approach, wherein the size of the source representation is fixed, irrespective of the length of the source sentences. These models typically employ recurrent neural networks (RNNs) as the decoder network for generating variable-length translations. However, it has been demonstrated that the efficacy of this methodology declines as the length of the input sentence increases [12]. Gülçehre et al. improved NMT by integrating language models trained on monolingual data using shallow and deep fusion, achieving up to 2 BLEU points improvement for low-resource Turkish-English and Chinese-English and 0.39-0.47 BLEU points for high-resource German-English and Czech-English [14]. Firat et al. developed a multi-way, multilingual NMT system that efficiently translates multiple language pairs, achieving better quality than conventional SMT for low-resource Turkish-English and Uzbek-English translations, with notable improvement for Uzbek-English due to linguistic similarities [15].

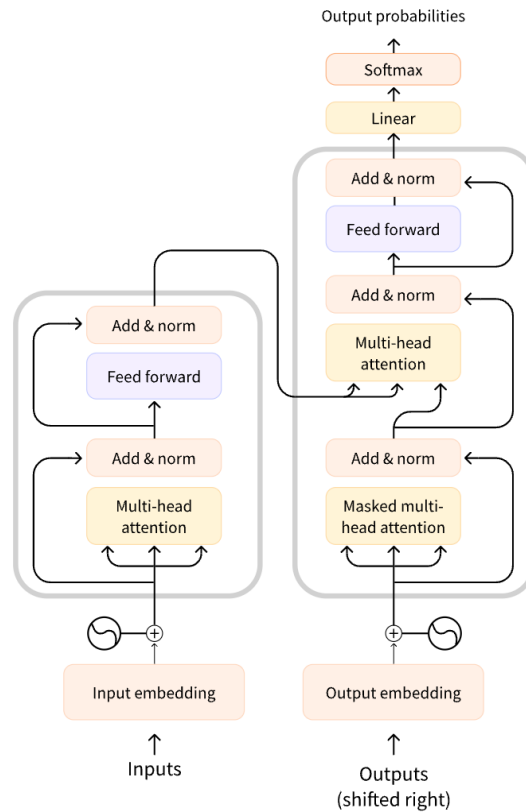
The limitations of classical NMT prompted the introduction of the attention mechanism by Bahdanau et al. [12], which represents a significant advancement in the field of RNN architectures. This mechanism enables the implementation of variable-length representations, a crucial aspect in the development of effective translation models. The attention mechanism guarantees that the distances between any given source and target words remain constant. As a result, the attention mechanism has facilitated the optimization process. The transformer employ multi-layered neural networks and rely entirely on self-attention networks which include encoder-decoder networks. Yirmibeşoğlu and Güngör improved Turkish-English translation using morphologically motivated input variations and data augmentation, achieving a BLEU score of 26.38 with a hybrid BiDeep and Transformer model

trained on the SETimes parallel corpus and augmented monolingual data [16]. These findings indicate a need for further investigation into the use of transformers in Turkish-English translation.

### 3 METHODOLOGY

#### 3.1 Overview of Transformer Architecture

The transformer architecture represented a significant advancement in the field of NLP due to its ability to achieve significantly faster training times and enhanced parallelization on Graphics Processing Units (GPUs). This was achieved by computing the self-attention mechanism in parallel for all words in a sequence. Consequently, larger models could be trained on extensive datasets, resulting in substantial enhancements in NLP performance.



**Figure 1.** The transformer - model architecture

The transformer architecture for NMT typically adheres to the conventional encoder-decoder paradigm. In comparison to RNN architectures, the Transformer employs a stack of identical self-attention-based layers in lieu of recurrent units, thereby facilitating superior parallelization. In particular, when presented with an input sequence,  $X = \{x_1, x_2, \dots, x_n\}$ , expressed in source language (e.g., Turkish), the model is tasked with predicting its corresponding translation,  $Y = \{y_1, y_2, \dots, y_m\}$ , in target language (e.g., English).

**Encoder:** A closer examination of the model reveals that a transformer encoder is comprised of  $N_e$  stacked layers of neural networks, with each layer containing two sub-layers: a multihead self-attention sub-layer and a position-wise Feed-Forward Network (FFN) sub-layer.

$$s^k = SelfAttn(X^k) + X^k, \tag{1}$$

$$F^e(X^k) = s^k + FFN(S^k), \tag{2}$$

where  $X^k \in \mathfrak{R}^{n \times d} + F^e(X^k) \in \mathfrak{R}^{n \times d}$  represents the inputs and outputs of the k-th encoder layer. d is the hidden dimension.

Decoder: The decoder employs a comparable architectural configuration, augmented with an additional multihead cross-attention sub-layer for each of the  $N_d$  decoder layers.

$$s^k = SelfAttn(Y^k) + Y^k, \tag{3}$$

$$c^k = CrossAttn(s^k, F^e(X^{Ne})) + s^k, \tag{4}$$

$$F^d(Y^k) = cc^k + FFN(c^k), \tag{5}$$

where  $Y^k \in \mathfrak{R}^{m \times d} + F^d(Y^k) \in \mathfrak{R}^{m \times d}$ , the inputs and outputs of k-th decoder layer.

### 3.2 Tensorflow Keras API

KerasNLP is a comprehensive NLP library designed to support the entire development cycle, from prototyping to deployment. It provides modular components with state-of-the-art preset weights and architectures that can be used out-of-the-box or customized for more control. As an extension of the core Keras API, KerasNLP integrates seamlessly with existing Keras workflows, offering high-level modules that are implemented as Layers or Models. This integration ensures ease of use and flexibility, making KerasNLP a powerful tool for developing and fine-tuning NLP models.

#### 3.2.1 Text Preprocessing and Text Vectorization

The text preprocessing involves defining a function Standardization to standardize text inputs by converting them to lowercase and stripping specified punctuation characters. The function is then applied within the TextVectorization layer for English text to ensure consistent and clean input data, improving the accuracy and efficiency of subsequent vectorization and model training processes.

Text vectorization is performed using the TextVectorization layer in TensorFlow/Keras, which converts raw text into integer sequences. For Turkish and English texts, separate TextVectorization layers are configured with specified vocabulary sizes with 15,000 words and with 20 tokens sequence lengths. The layers are adapted to the training texts to learn the vocabulary and prepare the text data for input into the neural network, enabling efficient handling of text as numerical data.

### 3.3 Vast.ai - Cloud Computing Platform

In the training, we used vast.ai which is cloud computing platform that offers cost-effective and flexible GPU resources for machine learning and AI tasks through a marketplace model that utilises surplus computing power. It provides a user-friendly interface for deploying and managing workloads with support for frameworks such as TensorFlow and PyTorch which allows for scalable resource allocation. Users can choose from a diverse range of GPU options, including both older and high-performance models, and benefit from automation via APIs.

## 4 EXPERIMENTAL STUDY

### 4.1 Setup

**Table 1.** The hyperparameters used in training our MT model

Name	Value
Encoder & Decoder	6
Multi Head Attention	8
Sequence lenth	512
Vocabulary size	30,000
Embedding dimension	256
Latent dimension	2048
Dropout rate	0.1
Batch size	128
Learning rate	1e-7
Number of Epoch	30

We trained our transformer model with six layers of both the encoder and decoder, each with eight self-attention heads, a sequence length of 512, a vocabulary size of 30,000, an embedding dimension of 256, a latent dimension of 2048, a dropout rate of 0.1, a batch size of 128, a learning rate of 1e-7, and with 30 epochs (Table 1).

## 4.2 Dataset

As a dataset for Turkish to English translation, we utilized Tatoeba Anki corpora (Tatoeba.org) which consists of 145K parallel sentences. Tatoeba a valuable resource for language learners and linguists, offering a comprehensive database of translated example sentence pairs in various languages. It is a collaborative source where members can contribute by adding, translating, and reviewing sentences to ensure accuracy and expand the repository. It also provides a wealth of diverse and comprehensive language content, which serves as an invaluable resource for advancing research and development in the field of MT studies. To validate the performance of our model, we splitted the dataset as training (70%), validation (15%) and test (15%) sets and the number of instances in each set is detailed in Table 2.

**Table 2.** Used dataset pairs sentences for Turkish to English translation task

Dataset Pairs	Count of Sentences Lines
Total Pairs	145105
Training Pairs	101575
Validation Pairs	21765
Test Pairs	21765

Dataset preparation involves creating datasets from the text pairs, batching, and mapping them using the formatdataset function to structure inputs and targets for the model. The datasets are then cached, shuffled, and prefetched for optimal performance during training. This organized data pipeline ensures efficient and scalable training and evaluation processes.

## 4.3 Evaluation Metrics

To measure effectiveness of our MT model, we utilized the BLEU score and accuracy evaluation metrics.

### 4.3.1 BLEU Score

BLEU scores are expressed on a scale of 0 to 1. It is rare for a translation to receive a score of 1 unless it is an exact replication of the reference text. It is unlikely that even a human translator would achieve a score of 1. The number of reference translations per sentence has been found to have a significant impact on the score, with higher scores being associated with more references [17]. BLEU was developed based on the premise that the closer a MT is to a professional human translation, the better it is. The BLEU metric is designed to measure the degree of alignment between SMT output and that of human reference translations. It should be noted that translations may differ in terms of word usage, word order, and phrase length [17]. BLEU is a metric that is used to evaluate the similarity between variable-length phrases in SMT output and reference translations. The weighted match averages determine the translation score. There are various versions of BLEU, but the fundamental metric necessitates a brevity penalty ( $P_b$ ), which is calculated as follows:

$$P_b \begin{cases} 1, c > r \\ e^{(1-r^c)}, c \leq r \end{cases} \tag{6}$$

where  $r$  represents the length of the reference corpus, while  $c$  denotes the candidate translation length. The fundamental BLEU metric is subsequently calculated according to the following formula:

$$BLEU = P_b \exp \sum_{n=0}^N w_n \log p_n \tag{7}$$

The n-gram precision  $p_n$  is calculated using n-grams with a maximum length of  $N$ .  $w_n$  are positive weights that sum to one. It should be noted that BLEU does not evaluate word and phrase position. This prevents SMT systems from increasing their scores by using words that are known with an elevated level of confidence. The number of permissible words for each candidate word is limited by the word count of the reference translation. The geometric mean of the sentence scores is calculated for the entire corpus. [18].



### 4.3.2 Accuracy

Accuracy is used to quantify the proportion of correct predictions made by a model in relation to the total number of predictions generated. In classification tasks, it is defined as:

$$\text{Accuracy} = \frac{\text{Number of Correct Predictions}}{\text{Total Number of Predictions}} \tag{8}$$

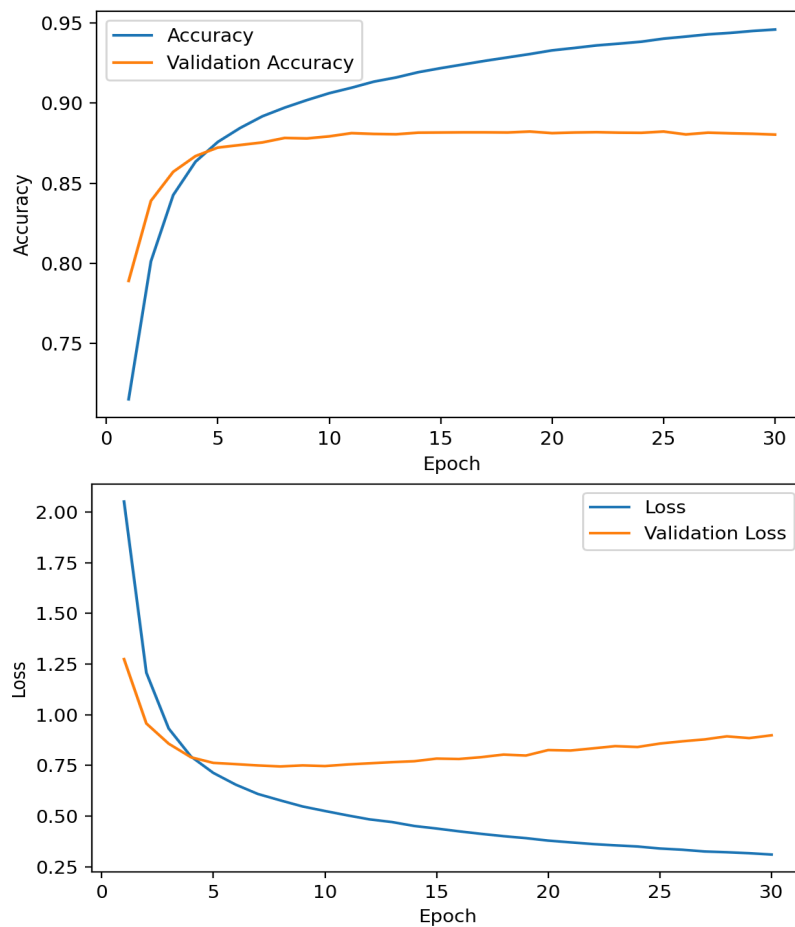
For sequence models like transformers, especially for tasks like MT, accuracy is typically computed at the token level. Each token in the predicted sequence is compared to the corresponding token in the reference (true) sequence. Tensorflow Keras API [19] can calculate accuracy automatically during training and validation. Accuracy metric in our model training context refers to token-level accuracy, which measures the proportion of correctly predicted tokens out of all tokens in the sequences. This metric provides a straightforward way to gauge the model's performance.

## 5 RESULTS

### 5.1 Accuracy and Loss Evaluation

During the training and validation process through 30 epochs, the changes in the accuracy and loss are shown on Figure 2. Our model managed to reach 95% accuracy, which indicates that the model learns effectively and is able to accurately predict the target outcomes on the training data. While it keeps increasing through the epochs, it levels off at around 88.1% from the 10th epoch onward. It is possible that the model is overfitting the training data, which impairs its ability to generalize effectively to new data. It is also possible that the model's architecture or training process is constrained, preventing it from attaining higher validation accuracy.

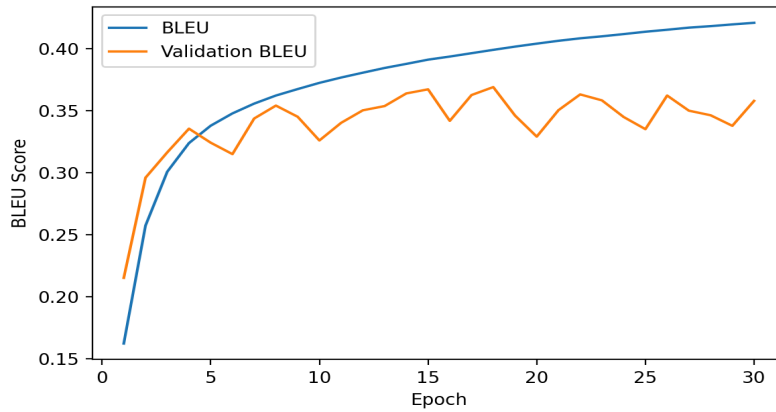
In terms of loss, it decreases consistently until epoch 10, suggesting that the model is getting better at minimizing prediction errors in the training data. However, from epoch 10 onwards, it remains constant and even starts to increase, raising concerns about potential overfitting.



**Figure 2.** Results of accuracy and loss respective to number of epoch during training and validation

## 5.2 BLEU Evaluation

For the BLEU metric, there is a steady increase during the training phase, reaching a score of 0.4208 after 30 epochs (Figure 3). This suggests that the model’s outputs are becoming increasingly grammatically correct and more similar to the reference translations over time. However, the BLEU metric during the validation phase follows a similar trend as observed in accuracy and loss. Specifically, it increases initially but then plateaus and exhibits minor fluctuations from the 10th epoch onward, which may indicate overfitting.



**Figure 3.** The results of the BLEU metric for both the training and validation sets are presented in relation to the number of epochs

## 6 DISCUSSION

The model exhibited effective learning from the training data, as evidenced by the high accuracy and BLUE score results in the validation phase. However, the stagnation observed after epoch 10 in the validation phase indicates the possibility of overfitting. The reason for this is that the data set is insufficient in terms of quantity and quality. Furthermore, this indicates the necessity for additional hyperparameter tuning. However, the high cost of each training process represents a significant challenge for these studies.

The observed overfitting underscores the necessity for meticulous observation of training dynamics and the implementation of strategies to mitigate this phenomenon. The objective is to enhance the model's generalization ability and achieve higher BLEU scores, which will ultimately result in more fluent and accurate translations. While a BLEU score of 0.4208 is a satisfactory starting point, future efforts will focus on incorporating higher-order n-grams to provide a more robust assessment of translation quality and achieve scores closer to those generated by human translators.

## 7 CONCLUSION

In this study, we developed and evaluated a transformer-based NMT model for Turkish-to-English translation. Leveraging the transformer architecture, which has demonstrated superior performance over traditional RNNs and BiLSTMs, our model successfully addressed the complexities inherent in translating between Turkish and English. Our experiments utilized the Tatoeba Anki dataset, consisting of 145,000 parallel Turkish-English sentence pairs, and achieved notable results. After training for 30 epochs, our model attained an accuracy of 0.95 and a BLEU score of 0.4208. These metrics underscore the effectiveness of the transformer architecture in capturing the contextual information necessary for high-quality translations. As a result, we developed an effective, efficient, and high-quality transformer-based translation system for Turkish to English. Additionally, we provided insight into the enhancement of MT with regard to the architecture and hyperparameter tuning. The findings from this study demonstrate the potential of transformer-based models in addressing the challenges associated with Turkish-to-English translation. This research not only advances the understanding of transformer applications in MT but also sets the stage for further exploration into optimizing such models for languages with limited text corpora.

On the other hand, despite the high accuracy and BLEU score, our results indicate potential overfitting, as evidenced by the leveling off of validation accuracy and the increase in validation loss after the 10th epoch. Future work should focus on strategies to mitigate overfitting, such as incorporating regularization techniques, expanding the dataset, or employing more sophisticated training regimens.

## Acknowledgments

We would like to thank the Aurora Bilişim Research Lab. Organisation for research funding and computing support. Additional thanks for Fatih Balkı, Enver Yıldırım, Salih Sarp and Vladislav Kuleykin.

## References

- [1] A. Vaswani *et al.*, “Attention is all you need,” *Adv Neural Inf Process Syst*, vol. 2017-December, pp. 5999–6009, Jun. 2017.
- [2] P. F. Brown *et al.*, “A statistical approach to machine translation,” *Computational Linguistics*, vol. 16, no. 2, pp. 79–85, 1990, Accessed: Jul. 13, 2024.
- [3] C. Callison-Burch, P. Koehn, C. S. Fordyce, and C. Monz, *Proceedings of the Second Workshop on Statistical Machine Translation*, Association for Computational Linguistics, 2007.
- [4] E. Yildirim and A. C. Tantug, “The feasibility analysis of re-ranking for N-best lists on English-Turkish machine translation,” in *2013 IEEE International Symposium on Innovations in Intelligent Systems and Applications, IEEE INISTA 2013*, 2013, doi: 10.1109/INISTA.2013.6577652.
- [5] I. D. El-Kahlout and K. Oflazer, “Exploiting morphology and local word reordering in English-to-Turkish Phrase-based statistical machine translation,” *IEEE Trans Audio Speech Lang Process*, vol. 18, no. 6, pp. 1313–1322, 2010, doi: 10.1109/TASL.2009.2033321.
- [6] R. Yeniterzi and K. Oflazer, “Syntax-to-Morphology Mapping in Factored Phrase-Based Statistical Machine Translation from English to Turkish,” *Association for Computational Linguistics*, pp. 454–464, 2010.
- [7] S. Yilmaz and I. Uguz, *Turkish-English Machine Translation System*, 2020.
- [8] K. Oflazer, I. Durgar, and D. El-Kahlout, “Exploring different representational units in English-to-Turkish statistical machine translation,” *Association for Computational Linguistics*, pp. 25–32, 2007.
- [9] I. Sutskever, O. Vinyals, and Q. V. Le, “Sequence to sequence learning with neural networks,” *Adv Neural Inf Process Syst*, vol. 4, no. January, pp. 3104–3112, Sep. 2014.
- [10] N. Kalchbrenner and P. Blunsom, “Recurrent continuous translation models,” *Association for Computational Linguistics*, pp. 1700–1709, 2013.
- [11] K. Cho *et al.*, “Learning phrase representations using RNN encoder–decoder for statistical machine translation,” in *EMNLP 2014 - 2014 Conference on Empirical Methods in Natural Language Processing*, pp. 1724–1734, 2014.
- [12] D. Bahdanau, K. H. Cho, and Y. Bengio, “Neural machine translation by jointly learning to align and translate,” in *3rd International Conference on Learning Representations, ICLR 2015*, Sep. 2014.
- [13] M. Junczys-Dowmunt, T. Dwojak, and H. Hoang, “Is neural machine translation ready for deployment? A case study on 30 translation directions,” in *13th International Conference on Spoken Language Translation*, Seattle, Washington D.C., 2016.
- [14] C. Gulcehre, O. Firat, K. Xu, K. Cho, and Y. Bengio, “On integrating a language model into neural machine translation,” *Comput Speech Lang*, vol. 45, pp. 137–148, Sep. 2017, doi: 10.1016/J.CSL.2017.01.014.
- [15] O. Firat, K. Cho, B. Sankaran, F. T. Yarman Vural, and Y. Bengio, “Multi-way, multilingual neural machine translation,” *Comput Speech Lang*, vol. 45, pp. 236–252, Sep. 2017, doi: 10.1016/J.CSL.2016.10.006.
- [16] Z. Yirmibesoglu and T. Gungor, “Morphologically motivated input variations and data augmentation in Turkish-English neural machine translation,” *ACM Transactions on Asian and Low-Resource Language Information Processing*, vol. 22, no. 3, Mar. 2023, doi: 10.1145/3571073/ASSET/AC619299-699C-4C6F-982F-EE94A8828F87/ASSETS/GRAPHIC/TALLIP-22-0214-T13.JPG.
- [17] K. Papineni, S. Roukos, T. Ward, and W.-J. Zhu, “Bleu: A method for automatic evaluation of machine translation,” *40th Annual Meeting on Association for Computational Linguistics - ACL’02*, 2002, pp. 311–318, doi: 10.3115/1073083.1073135.
- [18] A. E. Axelrod, *Factored Language Models for Statistical Machine Translation*, 2006.
- [19] KerasNLP Metrics. (2024, Jul. 13). [Online]. Available: [https://keras.io/api/keras\\_nlp/metrics/](https://keras.io/api/keras_nlp/metrics/)



## **Contribution to the Application of Condition Maintenance for Followed and Diagnostic Breakdowns of a Rotating Machine**

**Naima Tamaloussi<sup>\*1</sup>, Lamia Benzaid<sup>1</sup>, Zina Azzez<sup>1</sup>, Azzedine Bouzaouit<sup>2</sup>**

<sup>1</sup>*Department of Mechanical Engineering, Faculty of Technology, University of Skikda, Algeria*

<sup>2</sup>*LRPCSI Laboratory of Research, Department of Mechanical Engineering, Faculty of Technology, University of Skikda, Algeria*

---

### **Abstract**

The appropriate type of maintenance (corrective, preventive or predictive) is chosen for each rotating machine based on certain criteria, including: the cost of replacing equipment and the frequency of breakdowns, is one of the main causes of machine breakdown rotating. Which are monitored and diagnosed in real time to increase their lifespan and ensure their suitability.

The objective of this work is to study bearing fault diagnosis tools. We carried out precise and reliable machine condition measurements, based on vibration analysis, wear index tracking and thermal imaging, to discover faults and find suitable solutions to ensure the proper functioning of the machine.

**Keywords:** *Monitoring, Diagnostics, Infrared thermography, Vibration analysis, Rotating machine, Oil analysis*

---



## Recycling of Urban Waste in the Manufacture of Concretes

**Ben Khadda Ben Ammar<sup>\*1</sup>**

*<sup>1</sup>Civil and Hydraulic Engineering Department, Biskra, Algeria*

---

### **Abstract**

Recycling and recovery of waste have today become the right solution, which can offer new renewable and sustainable resources, which contribute to the construction process in the field of civil engineering to protect the environment. This work aims to recover brick waste in cementitious materials and their influence on the properties and performances of these materials. The substitution rates of 25%, 50%, 75% and 100% of sand by brick sand on the one hand and the same rate of natural gravel by those of crushed brick. The results of the mechanical characteristics at 7, 14 and 28 days of mortars and concretes indicate a reduction in mechanical resistance, acceptable for substitution does not exceed 25%.

**Keywords:** *Cementitious material, Valorization, Brick waste, Mechanical resistance, Environment*

---



# An Artificial Neural Network-Based Microwave Technique for Bianisotropic Materials Electromagnetic Property Extraction

Mehmet Akif Ozkaya<sup>\*1</sup>, Ugur Cem Hasar<sup>1</sup>

<sup>1</sup>Electrical and Electronics Engineering, Gaziantep University, Gaziantep, Türkiye

## Abstract

Materials characterization is a crucial area of study since precise understanding of a material's electromagnetic characteristics is necessary for a wide range of fascinating uses of the electromagnetic field. Accurate information of these properties can be obtained using a variety of microwave techniques. Artificial neural network (ANN)-based methods are crucial to these studies because they can accurately determine a material's electromagnetic properties even in the presence of insuppressible measurement noise or when measurement accuracies drop at critical frequencies like Fabry-Perot frequencies.

The ability to accurately extract electromagnetic properties from classical materials, such as dielectric, magnetic, or magnetodielectric materials, has been demonstrated by ANN-based microwave materials. It is noted that chiral or bianisotropic materials have not yet been treated with ANN-based microwave techniques. In order to accurately extract the electromagnetic properties of bianisotropic materials, we will use an ANN-based microwave approach of bianisotropic materials.

**Keywords:** ANN, Bianisotropic materials, Materials characterization, Electromagnetic properties

## 1 INTRODUCTION

Determining the electromagnetic properties of a material is essential for various applications, including food science [1], civil engineering [2], and biomedical engineering [3]. There are two types of microwave methods: resonant and non-resonant [4]. Resonant methods are more accurate, but they are limited in that they can only measure a small range of frequencies or a few different frequencies due to their frequency constraints [4]. The main focus of this study is on nonresonant techniques, which are wideband and offer relatively high accuracy [4, 5].

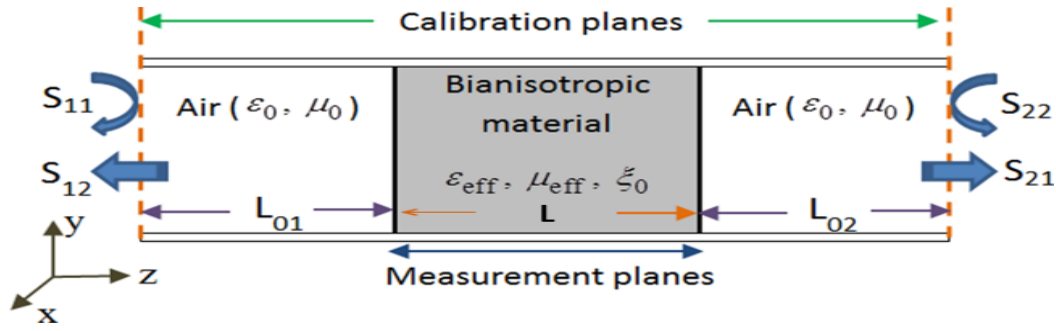
Random placement of the sample into the larger measuring cells of nonresonant techniques is a major drawback. In this case, transformation from planes the calibration is carried out (the calibration planes) to planes where the sample surfaces are present (the measurement planes) is a necessity [5]. Analytical expressions could be applied to eliminate such requirement [6]-[10]. In addition to this approach, artificial neural network (ANN) approach could as well be implemented to eliminate the effect of such transformation factors on measurements of electromagnetic properties of materials [11].

ANN approach is utilized in many diverse applications in recent studies [11–15]. In a recent study, we also implemented for the first time in the literature the ANN approach for electromagnetic property extraction of a special type of samples (bianisotropic materials) [16]. These materials have various properties including dissimilar forward and backward reflection properties and broaden transmission spectra [17]. However, this study [16] requires precise knowledge of sample thickness before starting to its electromagnetic property analysis. In this study, we present some preliminary results of ANN-based electromagnetic property extraction of bianisotropic materials without requiring the information of sample thickness.

## 2 MATERIAL AND METHOD

### 2.1 Problem Formulation

Fig. 1 illustrates a schematic view of a reflection-asymmetric bianisotropic material with length  $L$  located into a measurement cell with length  $L_g = L_{01} + L + L_{02}$ . It is positioned with no symmetry in the cell. In other words,  $L_{01} \neq L_{02}$ . Here,  $L_{01}$  and  $L_{02}$  the reference plane transformation distances.



**Figure 1.** S-parameters of a reflection-asymmetric bianisotropic material with length  $L$  randomly positioned within its waveguide cell ( $L_g = L_{01} + L + L_{02}$ )

In this work, we examine a biaxial bianisotropic MM slab with an interaction between the electric and magnetic fields that results in a nonzero magnetoelectric coupling coefficient  $\xi_0$  [16]. Under the assumption that the waveguide functions in the dominant mode ( $TE_{10}$  fundamental mode), a nonmagnetic substrate is used to construct the MM slab, which fills the entire waveguide's cross section [16]. For the time reference  $\exp(-i\omega t)$ , forward and backward reflection and transmission S-parameters ( $S_{11}^c$ ,  $S_{21}^c$ ,  $S_{22}^c$ , and  $S_{12}^c$ ) referenced to the calibration planes can be obtained as

$$S_{11}^c = R_{01}^2 \frac{\Gamma_1(1-T^2)}{1-\Gamma_1\Gamma_2T^2}, S_{22}^c = R_{02}^2 \frac{\Gamma_2(1-T^2)}{1-\Gamma_1\Gamma_2T^2} \quad (1)$$

$$S_{21}^c = S_{12}^c = R_{01}R_{02} \frac{T(1-\Gamma_1\Gamma_2)}{1-\Gamma_1\Gamma_2T^2} \quad (2)$$

$$\Gamma_1 = \frac{z_{ws}^+ - 1}{z_{ws}^+ + 1}, \Gamma_2 = \frac{z_{ws}^- - 1}{z_{ws}^- + 1}, z_{ws}^\mp = \frac{\mu_{eff}\beta_{0z}}{\beta_{sz} \mp ik_0\xi_0} \quad (3)$$

$$T = e^{+i\beta_{sz}L}, R_{01(2)} = e^{+i\beta_{0z}L_{01(2)}}, \beta_{0z} = \pi/a \quad (4)$$

$$\beta_{sz} = \sqrt{k_0^2(\epsilon_{eff}\mu_{eff} - \xi_0^2) - \mu_{eff}\beta_{0x}^2}, \beta_{0z} = \sqrt{k_0^2 - \beta_{0x}^2}. \quad (5)$$

Here,  $\Gamma_1$  and  $\Gamma_2$  are the semi-infinite reflection coefficients while  $T$  is the propagation factor;  $z_{ws}^+$  and  $z_{ws}^-$  are the normalized wave impedances whereas  $\beta_{0x}$ ,  $\beta_{0z}$ , and  $\beta_{sz}$  are, respectively, the air-filled region phase constants in the  $x$ - and  $z$ - directions and the sample-filled region phase constant in the  $z$ -direction;  $\epsilon_{eff}$  and  $\mu_{eff}$  are, respectively, the effective complex permittivity and effective complex permeability of the MM slab;  $k_0$  is the unbounded free-space wavenumber; and  $a$  is the width (broader dimension) of the guide.

Using the following RPI expressions:

$$A = \frac{S_{11}^c S_{22}^c}{S_{21}^c S_{12}^c}, B = \frac{S_{21}^c}{S_{21}^{c0}} \quad (6)$$

It is feasible to obtain the subsequent formula [16]:

$$(\Gamma_1\Gamma_2)^2 + \left[ (2-A)R_0^2B^2 - \frac{(1-R_0^2B^2)^2}{AR_0^2B^2} \right] \Gamma_1\Gamma_2 + 1 = 0 \quad (7)$$

which, when the passivity principle is applied, allows the product  $\Gamma_1\Gamma_2$  to be assessed; that is,  $|\Gamma_1\Gamma_2| \leq 1$ . Here,  $S_{21}^{c0}$  is the transmission S-parameter of the empty waveguide cell, and  $R_0 = e^{+i\beta_{0z}L}$ .

$\Gamma_1$  and  $\Gamma_2$  may not be separated from each other using (7) (no explicit solution for  $\epsilon_{eff}$ ,  $\mu_{eff}$ , and  $\xi_0$ ). In this work, we will first use an ANN-based machine learning algorithm to create a connection between the measured S-parameters and  $L_{01}$  and  $L_{02}$  without any information of  $L$ . Next, we will use these predicted  $L_{01}$  and  $L_{02}$  from [17] to calculate  $\epsilon_{eff}$ ,  $\mu_{eff}$ , and  $\xi_0$ .

$$\xi_0 = \frac{in\beta_{0z}}{k_0} \left( \frac{z_{ws}^+ - z_{ws}^-}{z_{ws}^+ + z_{ws}^-} \right), \mu_{eff} = z_{ws}^+ \left( n + \frac{ik_0\xi_0}{\beta_{0z}} \right) \quad (8)$$

$$\epsilon_{eff} = \frac{k_0^2 \xi_0^2 + \beta_{0z}^2 n^2 + \mu_{eff} \beta_{0z}^2}{k_0^2 \mu_{eff}}, n = \frac{\ln(T) \mp i2\pi m_b}{i\beta_{0z} L} \quad (9)$$

$$T = S_{21}^m / (1 - S_{11}^m \Gamma_2), z_{ws}^+ = \Omega_1 \mp \sqrt{\Omega_1^2 + \Omega_2} \quad (10)$$

$$z_{ws}^- = \frac{z_{ws}^+ + \Omega_3}{1 + \Omega_3 z_{ws}^+}, \Omega_1 = \frac{S_{22}^m - S_{11}^m}{S_{21}^m S_{12}^m - (1 - S_{11}^m)(1 - S_{22}^m)} \quad (11)$$

$$\Omega_2 = \frac{S_{21}^m S_{12}^m - (1 + S_{11}^m)(1 + S_{22}^m)}{S_{21}^m S_{12}^m - (1 - S_{11}^m)(1 - S_{22}^m)}, \Omega_3 = \frac{S_{11}^m - S_{22}^m}{S_{11}^m + S_{22}^m} \quad (12)$$

$$S_{11}^m = \frac{S_{11}^c}{R_{01}^2}, S_{22}^m = \frac{S_{22}^c}{R_{02}^2}, S_{21}^m = S_{12}^m = \frac{S_{21}^c}{R_{01} R_{02}} \quad (13)$$

Here,  $S_{11}^m$ ,  $S_{21}^m$ ,  $S_{22}^m$ , and  $S_{12}^m$  are the S-parameters referenced to the measurement planes,  $n$  is the refractive index of the MM slab, and  $m_b$  is the branch index term.

Our purpose is to determine electromagnetic properties of  $\epsilon_{eff}$ ,  $\mu_{eff}$ , and  $\xi_0$  of bianisotropic materials without using any knowledge of  $L$ .

## 2.2 ANN Model

Many neurons located in distinct layers of an artificial neural network (ANN) comprise the multilayer perception (MLP) architecture, which has demonstrated promise in investigating the correlation between input and output [8]. The input layer, hidden layer, and output layer are the three components that typically make up an artificial neural network model. There may be a large number of neurons in each stratum. An ANN model would require more time during the training phase the more layers it had.

In this study, the ANN Model was created using the 'nntool' package of MATLAB software. The 'nntool' selects data, builds and trains a network, and uses regression analysis and mean square error to assess the network's performance. There are three stages in the ANN model. These are training, validation and testing.

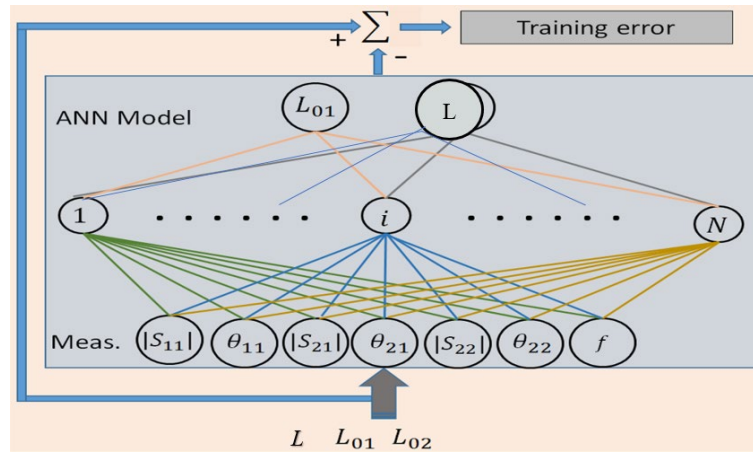
**Training:** The network is shown these during training, and its inaccuracy is taken into account to make necessary adjustments.

**Validation:** When generalization stops becoming better, these are used to stop training and measure the generalization of the network.

**Testing:** These offer an unbiased assessment of network performance both during and after training because they have no impact on training.

In our study, the ANN model has several features in the training phase. As seen schematically in Fig. 2, different combinations of L01 and L02 were taken into consideration as the outputs of the suggested ANN model during the training phase of our ANN model.





**Figure 2.** The proposed ANN model's training procedure

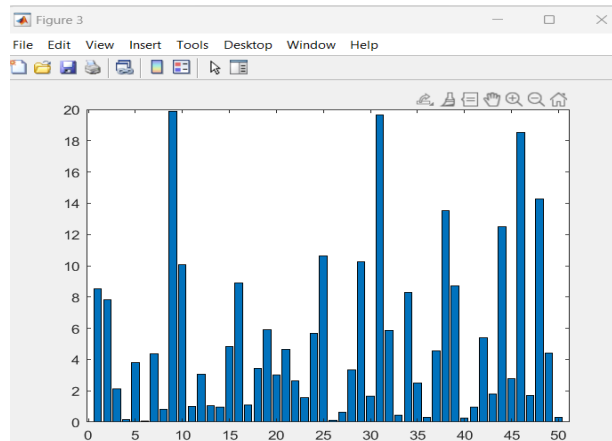
We implemented the following constraints during the training process:  $L_g = 11.00$  mm,  $L_{01} = [0.0:0.1:\lambda]$  and  $L_{02} = \lambda - L_{01}$  where  $\lambda = L_g - L$ . The input dataset for the training procedure has a size of  $7 \times 12505$  for  $[|S_{11}|, \theta_{11}, |S_{21}|, \theta_{21}, |S_{22}|, \theta_{22}, f]$  resulting in  $7 \times 12505 = 87535$ . The size of the training procedure's output dataset is  $3 \times 12505$  for  $[L_{01}, L_{02}, L]$  resulting in  $3 \times 12505 = 37515$ . To reduce overall fitting errors, roughly 70% of the data were utilized for training, 15% for validation, and the remaining portion was used for testing. All of the data were randomly selected from the total [11].

### 3 RESULTS

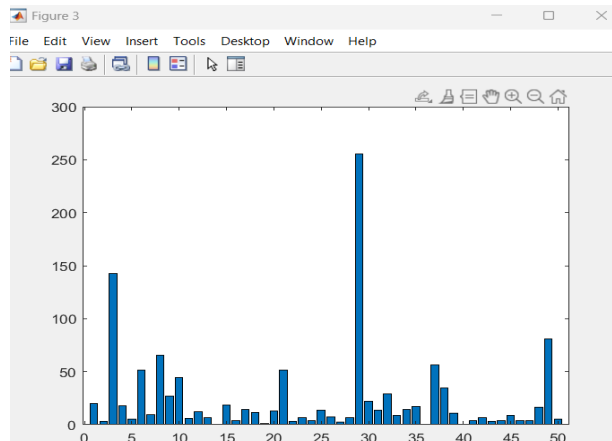
The data was randomly divided into training, validation and testing with 70%, 15% and 15%. Network Type: Feed-forward backprop, training function: TRAINLM, Adaptation learning function: LEARNNGDM, Performance function: MSE, Number of layers: 2, Number of neurons: 10 and Transfer Function: TANSIG were selected in ANN model.

In the Algorithms section of our ANN model, Data Division: Random, Training: The Levenberg-Marquard, Performance: Mean Squared Error and Calculations: MEX are determined. Additionally, epochs are specified as 1000 in the Progress section of the training phase. The Levenberg-Marquard algorithm takes less time but more memory. When a rise in the mean square error of the validation samples indicates that generalization is no longer improving, training automatically ends. There are 7 input neurons, 10 Hidden Layer neurons, 3 Output Layer neurons and 3 output neurons in the training algorithm of the ANN model.

The ANN model was trained using 1000 iterations in the training algorithm and the results of this training were produced appropriately. The best validation performance is 0.0026302(MSE) at epoch 588 and validation checks = 6, at epoch 594. Regression values of the trained network are Training = 99.964%, Validation = 99.963%, Test = 99.965% and All = 99.964%.



**Figure 3.** Percentage of the difference between the actual and predicted values of L in the ANN model  
 In our ANN model, output prediction was made in 3x50 dimension according to 7x50 input datasets randomly selected from the input dataset. Fig. 3 shows the percentage of the difference between the Actual and Predicted values of L in the ANN model.



**Figure 4.** Percentage of difference between actual and predicted values of L for SNR in ANN model

In the ANN model, when Signal-to-Noise Ratio (SNR) is added to the 7x50 input dataset randomly selected from the input dataset, an output prediction of 3x50 was made. Fig. 4 demonstrates the percentage difference between the True and Predicted values of L for SNR in the ANN model.

#### 4 CONCLUSION

An ANN model is proposed to ascertain the bianisotropic materials’ effective electromagnetic characteristics when thickness information of these materials is not known or precise. The ANN model has training, validation and testing stages. In this study, it has been noted that the applied ANN model with good results can be attained. The values  $L_{01}$ ,  $L_{02}$  and  $L$  cannot be expressed analytically and cannot be calculated all together, so we need an ANN model. ANN allows us to find these values. The model predicts  $L_{01}$ ,  $L_{02}$  and  $L$  from these datasets.  $\epsilon_{eff}$ ,  $\mu_{eff}$  and  $\xi_0$  were extracted from the formulas using the  $L_{01}$ ,  $L_{02}$  and  $L$  values determined by the ANN model.

#### References

- [1] Z. Meng, Z. Wu, and J. Gray, “Microwave sensor technologies for food evaluation and analysis: Methods, challenges and solutions,” *Trans. Inst. Meas. Control*, vol. 40, no. 12, pp. 3433–3448, Aug. 2018.
- [2] K. L. Chung and S. Kharkovsky, “Monitoring of microwave properties of early-age concrete and mortar specimens,” *IEEE Trans. Instrum. Meas.*, vol. 64, no. 5, pp. 1196–1203, May 2015
- [3] N. K. Nikolova, *Introduction to Microwave Imaging*, Cambridge: Cambridge University Press, 2017.
- [4] L. F. Chen, C. K. Ong, C. P. Neo, V. V. Varadan, and V. K. Varadan, *Microwave Electronics: Measurement and Materials Characterization*, West Sussex, U.K.: Wiley, 2004.
- [5] J. Baker-Jarvis, E. J. Vanzura, and W. A. Kissick, “Improved technique for determining complex

- permittivity with the transmission/reflection method,” *IEEE Trans. Microw. Theory Techn.*, vol. 38, no. 8, pp. 1096–1103, Aug. 1990.
- [6] K. Chalapat, K. Sarvala, J. Li, and G. S. Paraoanu, “Wideband reference-plane invariant method for measuring electromagnetic parameters of materials,” *IEEE Trans. Microw. Theory Techn.*, vol. 57, no. 9, pp. 2257–2267, Sep. 2009.
- [7] U. C. Hasar and Y. Kaya, “Reference-independent microwave method for constitutive parameters determination of liquid materials from measured scattering parameters,” *J. Electromagn. Waves Appl.*, vol. 25, nos. 11–12, pp. 1708–1717, Jan. 2011.
- [8] U. C. Hasar, J. J. Barroso, Y. Kaya, M. Ertugrul, and M. Bute, “Reference-plane invariant transmission-reflection method for measurement of constitutive parameters of liquid materials,” *Sens. Actuators A: Phys.*, vol. 203, pp. 346–354, Dec. 2013.
- [9] Z. Caijun, J. Shenhui, “Calibration-independent and position-insensitive transmission/reflection method for permittivity measurement with one sample in coaxial line,” *IEEE Trans. Electromagn. Compat.*, vol. 53, no. 3, pp. 684–689, Aug. 2011.
- [10] U. C. Hasar, G. Yildiz, M. Bute, and A. Muratoglu, “Reference-plane-invariant waveguide method for electromagnetic characterization of bi-axial bianisotropic metamaterials,” *Sens. Actuators A: Phys.*, vol. 283, pp. 141–150, Nov. 2018.
- [11] C. Yang and H. Huang, “Determination of complex permittivity of low-loss materials from reference-plane invariant transmission/reflection measurements,” *IEEE Access*, vol. 7, pp. 131865–131872, 2019.
- [12] T. Mosavirik, M. Hashemi, M. Soleimani, V. Nayyeri, and O. M. Ramahi, “Accuracy-improved and low-cost material characterization using power measurement and artificial neural network,” *IEEE Trans. Instrum. Meas.*, vol. 70, art. no. 2517209, 2021.
- [13] U. C. Hasar, G. Akkaya, M. Aktan, C. Gozu, and A. C. Aydin, “Water-to-cement ratio prediction using ANNs from non-destructive and contactless microwave measurements,” *Prog. Electromagn. Res.*, vol. 94, pp. 311–325, 2009.
- [14] A. M. Albishi, S. H. Mirjahanmardi, A. M. Ali, V. Nayyeri, S. M. Wasly, and O. M. Ramahi, “Intelligent sensing using multiple sensors for material characterization,” *Sensors*, vol. 19, no. 21, p. 4766, Nov. 2019
- [15] M. Baghelani, N. Hosseini, and M. Daneshmand, “Artificial intelligence assisted noncontact microwave sensor for multivariable biofuel analysis,” *IEEE Trans. Ind. Electron.*, vol. 68, no. 11, pp. 11492–11500, Nov. 2021.
- [16] U. C. Hasar, H. Ozturk, M. Ertugrul, J. J. Barroso and O. M. Ramahi, “Artificial neural network model for evaluating parameters of reflection-asymmetric samples from reference-plane-invariant measurements,” *IEEE Transactions on Instrumentation and Measurement*, vol. 72, pp. 1-8, art. no. 6005208, 2023.
- [17] U. C. Hasar, A. Muratoglu, M. Bute, J. J. Barroso, and M. Ertugrul “Effective constitutive parameters retrieval method for bianisotropic metamaterials using waveguide measurements,” *IEEE Trans. Microw Theory Techn.*, vol. 65, no. 5, pp. 1488–1497, May 2017.



## Improved Propagation Constant Determination Using Two-Line Measurements

Ugur Cem Hasar<sup>\*1</sup>, Husain Ali<sup>1</sup>

<sup>1</sup>Electrical and Electronics Engineering, Gaziantep University, Gaziantep, Türkiye

### Abstract

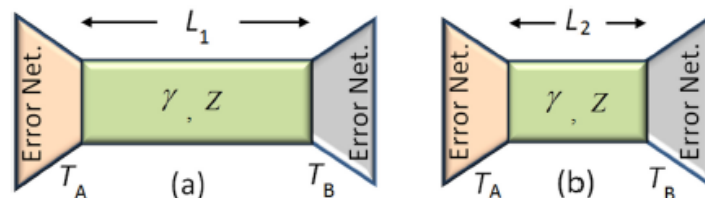
A new objective function has been derived for improved propagation constant  $\gamma$  measurement of uniform lines with symmetric reflections through calibration-free line-line measurements. Its advantage relies on the fact that it uses a term, which is in the product form of determinants of two characteristic terms, whose value is so close to unity both in theory and experiments. Eigen factor (complex exponential) and  $\gamma$  measurements of an X-band (8.2-12.4 GHz) uniform (empty) waveguide section with symmetric reflections were carried out to validate our proposed formalism.

**Keywords:** Propagation constant, Uniform lines, Unity-determinant value

## 1 INTRODUCTION

Many calibration techniques such as the Thru-ReflectLine (TRL) [1] call for accurate determination of frequency-dependent propagation constant ( $\gamma$ ) for electromagnetic characterization of microwave networks or devices (not only for determination of error-networks but also for evaluation of precise the reference planes for scattering-parameter (S-parameter) measurements). Measurement  $\gamma$  is also important for characterization of these networks or devices by calibration-free methods (no direct calibration process) [2–5] to extract relative complex permittivity ( $\epsilon_r$ ) or other equivalent parameters. These networks or devices can possess no-reflection property, symmetrical reflection property, or even asymmetric reflection property [1, 6–11].

The main problem in  $\gamma$  determination of uniform lines with symmetric reflections is assignment or allocation of correct eigenvalue and eigenfactor at a given frequency [1, 6–8, 10, 12]. There are two types of remedies for resolving this problem as direct approach and indirect approach. In the indirect approach, the terms  $a_m/c_m$  and  $b_m$  present in error networks are first determined by enforcing the passivity principle and then eigenfactors are calculated using one-to-one (unique) relation [1, 10]. In the direct approach, eigenfactors are directly determined by using different methodologies [6, 8, 12]. For example, in the study [8], between two eigenfactors, the one yielding a monotonous frequency-dependent variation (counterclockwise or clockwise manner) is kept, the other one is discarded for the analyzed frequency, and this process is repeated over the whole frequency band. The problem with this methodology is the assignment of reference eigenfactor at a given frequency from which monotonous variation of eigenfactors is evaluated for the remaining frequencies in the band.



**Figure 1.** A pair of uniform and identical lines between error boxes  $T_A$  and  $T_B$ . (a) Longer line with length  $L_1$  and (b) shorter line with length  $L_2$ .

On the other hand, in the studies [6, 12], accurate eigenfactor (positive or negative) at a given frequency is determined by using the property of cosine and sine hyperbolic functions and by exploiting the unique value of the cosine hyperbolic function. The problem associated with this methodology is the requirement of unity value of the determinant of an eigen matrix  $\det(T_M) = \det(T_{M2}T_{M1}^{-1})$  where  $\det(\star)$  denotes the determinant of ' $\star$ '. It will be demonstrated by measurements in Section IV that  $\det(T_M)$  is close but not totally equal to unity. In this letter, we derive a new objective function from which eigenfactors are extracted by considering that  $\gamma$ s in different directions of a uniform line with symmetric reflections are non-identical.

## 2 BACKGROUND AND PROBLEM DESCRIPTION

Fig. 1 illustrates a pair of uniform and identical lines with different lengths to determine  $\gamma$  by the proposed method. Here, it is assumed that the lines are sandwiched between two error boxes  $T_A$  and  $T_B$  referring to imperfections of vector network analyzers (VNAs), effect of transitions, source and load match errors, and tracking (frequency) errors. It is also assumed that only the dominant mode propagates through the microwave network [6]. Please refer to Section 4 about how this assumption is realized.

For each line in Fig. 1 we can write

$$T_{Mk} = T_A T_{Lk} T_B, \quad k = 1, 2 \quad (1)$$

$$T_{Lk} = \frac{1}{S_{21}^{(k)}} \begin{bmatrix} -\Delta_k & S_{11}^{(k)} \\ -S_{22}^{(k)} & 1 \end{bmatrix}, \quad \Delta_k = S_{11}^{(k)} S_{22}^{(k)} - S_{21}^{(k)} S_{12}^{(k)} \quad (2)$$

where  $T_M$ ,  $T_A$ , and  $T_B$  denote the wave cascading matrices of lines and error networks; and  $S_{11}^{(k)}$ ,  $S_{22}^{(k)}$ ,  $S_{21}^{(k)}$ , and  $S_{12}^{(k)}$  show the forward and backward reflection and transmission  $S$ -parameters of the  $k$ -th microwave network.

Using (1) and (2), the following eigen matrix and eigen equation can be formed [6, 12]

$$T_M = T_{M1} T_{M2}^{-1} = T_A \begin{bmatrix} e^{-\gamma L_d} & 0 \\ 0 & e^{+\gamma L_d} \end{bmatrix} T_A^{-1} \quad (3)$$

$$(e^{\pm\gamma L_d})^2 - \text{Tr}(T_M) e^{\mp\gamma L_d} + \det(T_M) = 0 \quad (4)$$

where  $L_d = L_1 - L_2$  and  $\text{Tr}(\star)$  shows the trace operation of the square matrix ' $\star$ '.

Assuming that  $\det(T_M) = 1$ , the following trigonometric expressions can be derived [6], [12]

$$e^{\mp\gamma L_d} = z \mp \sqrt{z^2 - 1} = \text{Ch}(\gamma L_d) \mp \text{Sh}(\gamma L_d) \quad (5)$$

$$\mp\gamma L_d = \log(e^{\mp\gamma L_d}) = \text{Ch}^{-1}(z) = \log[z \mp \sqrt{z^2 - 1}] \quad (6)$$

where  $z = \text{Tr}(T_M)/2 = \text{Ch}(\gamma L_d)$  and Ch and Sh denote the cosine and sine hyperbolic functions. The unique feature of expressions in (5) and (6) is that while Sh is two-valued due to sign-ambiguity, Ch is unique. This unique value of Ch is exploited to obtain unique value of Sh and thus  $e^{\mp\gamma L_d}$  [6] as

$$e^{\mp\gamma L_d} = [\text{Ch}(\alpha_T) \mp \text{Sh}(\alpha_T)][\cos(\beta_T) \mp i\sin(\beta_T)] \quad (7)$$

Where:

$$\text{Ch}^2(\alpha_T) = 0.5(|\text{Ch}(\gamma L_d)|^2 + |\text{Sh}(\gamma L_d)|^2 + 1.0) \quad (8)$$

$$\text{Sh}^2(\alpha_T) = 0.5(|\text{Ch}(\gamma L_d)|^2 + |\text{Sh}(\gamma L_d)|^2 - 1.0) \quad (9)$$

$$\cos^2(\beta_T) = 0.5(|\text{Ch}(\gamma L_d)|^2 - |\text{Sh}(\gamma L_d)|^2 + 1.0) \quad (10)$$

$$\sin^2(\beta_T) = 0.5(-|\text{Ch}(\gamma L_d)|^2 + |\text{Sh}(\gamma L_d)|^2 + 1.0) \quad (11)$$

and  $\alpha_T = \alpha L_d$  and  $\beta_T = \beta L_d$ .

A variant form for  $e^{\mp\gamma L_d}$  can be obtained [12] as

$$e^{\mp\gamma L_d} = z [1 \mp \sqrt{1 - 1/z^2}], \quad \alpha \geq 0, \text{ [passive]} \quad (12)$$

$$e^{\mp\gamma L_d} = z [1 \pm \sqrt{1 - 1/z^2}], \quad \alpha \leq 0, \text{ [active]} \quad (13)$$

The common premise of the expressions given in (5)-(13) is  $\det(T_M) = 1$ . Although ideally it is true, it is difficult to satisfy this by experiments. Therefore, the effect of non-unity  $\det(T_M)$  should be accounted for accurate  $\gamma$  extraction.

### 3 THE PROPOSED METHOD

In this section, we derive a new eigen factor expression accounting non-unity  $\det(T_M)$ . Toward this end, we define two propagation constants  $\gamma_1$  and  $\gamma_2 (\cong \gamma_1)$  in different directions and obtain the following eigen matrices

$$T_1 = T_{M1} T_{M2}^{-1} = T_A \begin{bmatrix} e^{-\gamma_1(L_1-L_2)} & 0 \\ 0 & e^{+\gamma_2(L_1-L_2)} \end{bmatrix} T_A^{-1} \quad (14)$$

$$T_2 = T_{M2} T_{M1}^{-1} = T_A \begin{bmatrix} e^{+\gamma_1(L_1-L_2)} & 0 \\ 0 & e^{-\gamma_2(L_1-L_2)} \end{bmatrix} T_A^{-1} \quad (15)$$

From (14) and (15), we find

$$\text{Tr}(M_1) = e^{-\gamma_1 L_d} + e^{+\gamma_2 L_d}, \quad \text{Tr}(M_2) = e^{+\gamma_1 L_d} + e^{-\gamma_2 L_d} \quad (16)$$

$$\det(M_1) = e^{-\gamma_1 L_d} e^{+\gamma_2 L_d}, \quad \det(M_2) = 1/\det(M_1) \quad (17)$$

$$\text{Tr}(M_1)\det(M_2) = e^{+\gamma_1 L_d} + e^{-\gamma_2 L_d} = \text{Tr}(M_2) \quad (18)$$

$$\text{Tr}(M_2)\det(M_1) = e^{-\gamma_1 L_d} + e^{+\gamma_2 L_d} = \text{Tr}(M_1) \quad (19)$$

$$\text{Tr}(M_1)\text{Tr}(M_2) = 2 + e^{-(\gamma_1+\gamma_2)L_d} + e^{+(\gamma_1+\gamma_2)L_d} \quad (20)$$

It is seen from (16) and (20) that some of these expressions are linearly dependent, some of them are not since  $\det(M_1)$  is inverse of  $\det(M_2)$ ,  $\text{Tr}(M_1)/\text{Tr}(M_2) = \det(M_1)$ , and  $\text{Tr}(M_2)/\text{Tr}(M_1) = \det(M_2)$ .

Using (17) and (20), we derive a new eigen function for finding  $\gamma$  as

$$(e^{\mp(\gamma_1+\gamma_2)L_d})^2 - [\text{Tr}(M_1)\text{Tr}(M_2) - 2]e^{\mp(\gamma_1+\gamma_2)L_d} + \det(M_1)\det(M_2) = 0 \quad (21)$$

The advantage of the new eigen function in (21) is that the coefficient after  $e^{\mp 2(\gamma_1+\gamma_2)L_d}$  term is identical to unity; that is,  $\det(M_1)\det(M_2) = 1$ . Therefore, by assuming that  $\gamma = (\gamma_1 + \gamma_2)/2$ , it is possible to apply the hyperbolic relations in (5) and (6) and thus the expressions in (12) and (13) to the new eigen function to derive

$$e^{\mp 2\gamma L_d} = z_2 \left[ 1 \mp \sqrt{1 - 1/z_2^2} \right], \quad \alpha \geq 0, \quad [\text{passive}] \quad (22)$$

$$e^{\mp 2\gamma L_d} = z_2 \left[ 1 \pm \sqrt{1 - 1/z_2^2} \right], \quad \alpha \leq 0, \quad [\text{active}] \quad (23)$$

where  $z_2 = \text{Tr}(M_1)\text{Tr}(M_2)/2 - 1$ .

Finally, the  $\gamma$  can be extracted from

$$\gamma = \alpha + i\beta = -(\ln(e^{-2\gamma L_d}) \pm 2\pi m)/(2L_d) \quad (24)$$

where  $m$  is the branch index ( $m = 0, 1, 2, \dots$ ) whose value can be ascertained by the stepwise method [13].

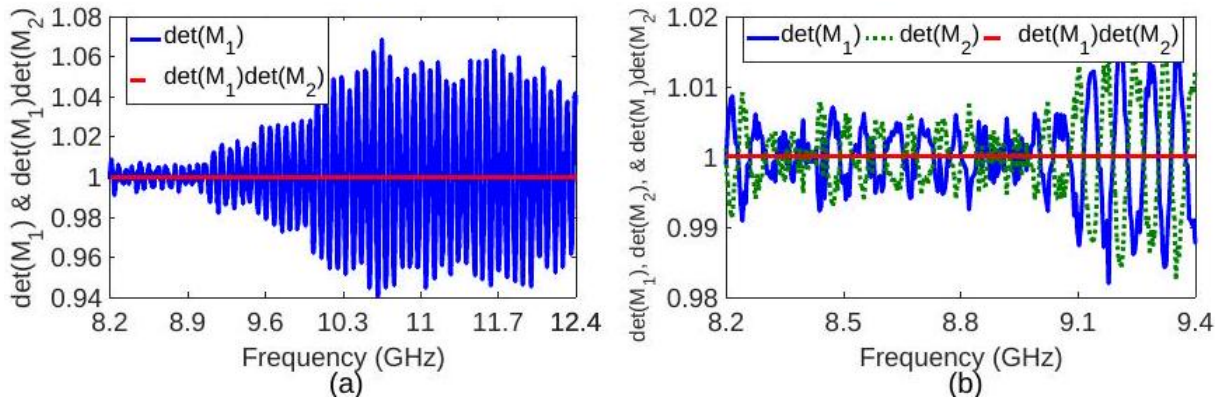
### 4 MEASUREMENT AND DISCUSSION

A general-purpose microwave measurement setup operating at X-band (8.2 – 12.4GHz) was constructed for validation of our formalism [11]. It involves a VNA (model N9918A from Keysight Instruments), two longer rugged phase-stable cables, two coaxial-to-waveguide adapter, and two waveguide straights with lengths greater than 2 times the wavelength at the minimum frequency of the X-band (8.2GHz). These straights were used in securing dominant mode propagation, as assumed in Section II. S-parameter measurements with 1001 points were

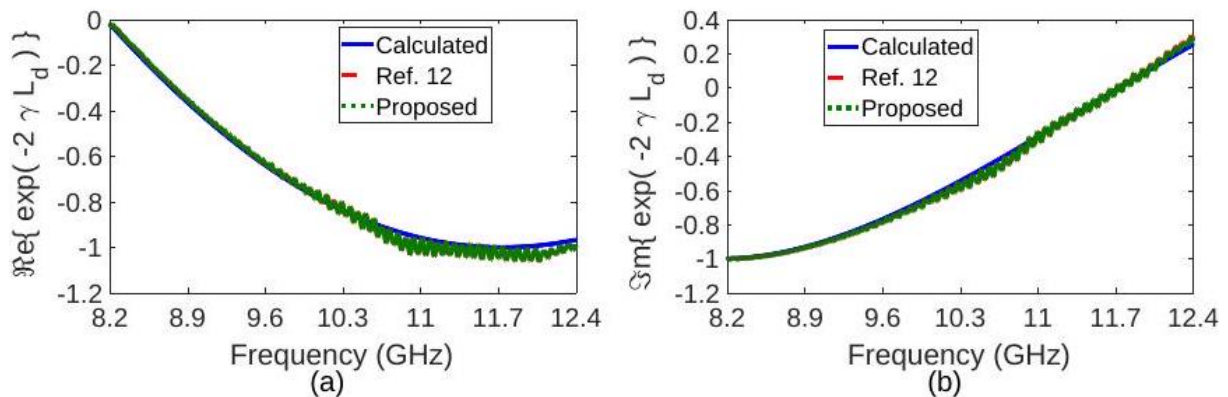
performed. In our measurements, we set the length of the second line ( $L_2$ ) to zero (thru connection) and considered the length of the first line (X-band waveguide cell) as  $L_1 = 7.7$  mm, yielding  $L_d = 7.7$  mm.

Before starting to  $\gamma$  measurements, we first examined the variation of  $\det(M_1)$  (or  $\det(T_M)$ ) and  $\det(M_2)$  over frequency. Fig. 2(a) and 2(b) illustrate the frequency dependencies of  $\det(M_1)$ ,  $\det(M_2)$ , and  $\det(M_1)\det(M_2)$  over whole band and over 8.2-9.4 GHz band. We note the following points from the dependencies in Figs. 2(a) and 2(b). First, both  $\det(M_1)$  and  $\det(M_2)$  are so close but do not attain unity value (less than  $1 \mp 0.06$ ) over whole band. Second, while  $\det(M_1)$  increases at a given frequency,  $\det(M_2)$  decreases at that frequency (or vice versa). Third,  $\det(M_1)\det(M_2)$  is so close to unity regardless how far  $\det(M_1)$  and/or  $\det(M_2)$  values are away from the unity.

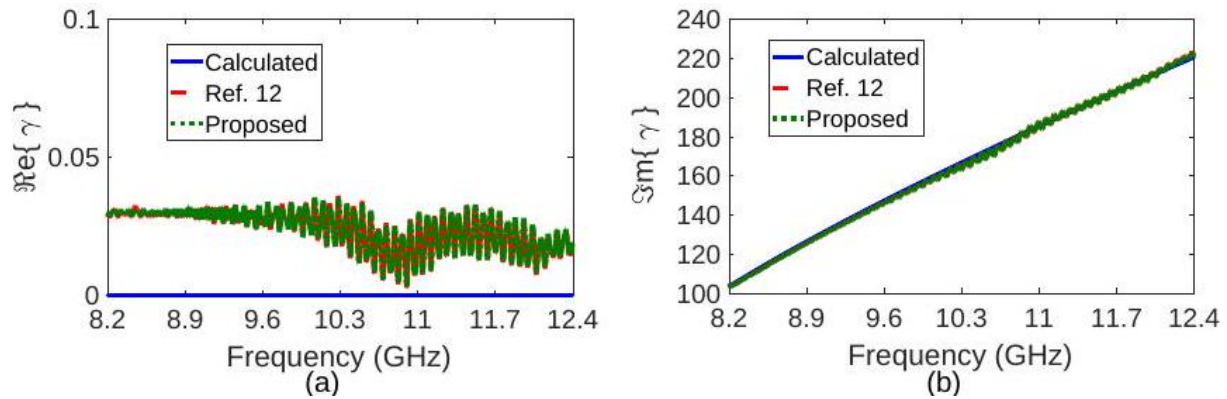
We then determined  $e^{-2\gamma L_d}$  and  $\gamma$  of the X-band line by the method [12] and the proposed method. Figs. 3 and 4 show, respectively, the real and imaginary parts of the determined  $e^{-2\gamma L_d}$  and extracted  $\gamma$  by the method [12] and the proposed method. Besides, imaginary parts of  $e^{-2\gamma L_d}$  and  $\gamma$  by the method [12] and the proposed method are also illustrated in Figs. 5(a) and 5(b) over 9.6-10 GHz frequency region for better comparison. In order to compare the accuracy of determined  $e^{-2\gamma L_d}$  values, we also computed  $e^{-2\gamma_{\text{cal}} L_d}$  using  $\gamma_{\text{cal}} = ik_0\sqrt{1 - (f_c/f)^2}$  where  $k_0$  is the free-space (unbounded) wavenumber and  $f_c \cong 6.557$  GHz. It is seen from Figs. 3 and 4 that extracted  $e^{-2\gamma L_d}$  and  $\gamma$  values by the method [12] and the proposed method are in good agreement with the calculated  $e^{-2\gamma_{\text{cal}} L_d}$  and  $\gamma_{\text{cal}}$  values. Besides, we note from Fig. 4(a) that extracted  $\alpha = \Re\{\gamma\}$  values by the method [12] and the proposed method are greater than zero for the whole frequency band, which is a requirement of the passivity principle. Finally, we note from Figs. 5(a) and 5(b) that the difference between  $\Im\{e^{-2\gamma L_d}\}$  (and  $\Im\{\gamma\}$ ) values extracted by the method [12] and the proposed method is arising from non-unity values of  $\det(M_1)$  and  $\det(M_2)$ . We think that our proposed method is more accurate in  $\gamma$  determination since  $\det(M_1)\det(M_2)$  is so close to unity, as validated from Fig. 2.



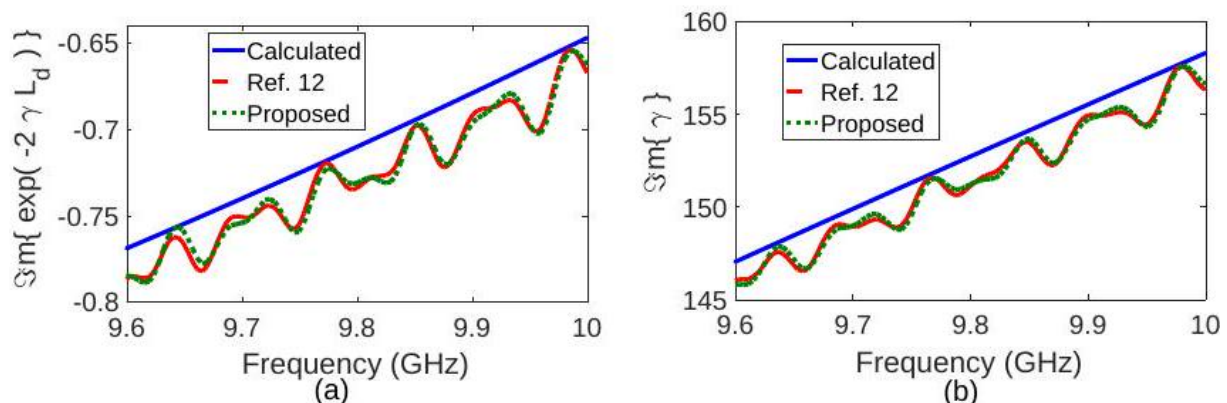
**Figure 2.** Frequency dependencies of (a) measured  $\det(M_1)$  and  $\det(M_1)\det(M_2)$  over whole X-band and (b)  $\det(M_1)$ ,  $\det(M_2)$ , and  $\det(M_1)\det(M_2)$  over 8.2 – 9.4GHz



**Figure 3.** (a) Real and (b) imaginary parts of the determined  $e^{-2\gamma L_d}$  by the method [12] and the proposed method in addition to its calculated value



**Figure 4.** (a) Real and (b) imaginary parts of the determined  $\gamma$  by the method [12] and the proposed method in addition to its calculated value



**Figure 5.** Frequency dependencies of determined (a)  $e^{-2\gamma L_d}$  and (b)  $\gamma$  over 9.6 – 10GHz by the method [12] and the proposed method in addition to its calculated value.

## 5 CONCLUSION

A new formalism has been devised for improved  $\gamma$  measurement of uniform reflection-symmetric lines from calibrationfree line-line measurements. As contrary to the methods [6] and [12] that both use the assumption  $\det(T_M) = 1$  which is difficult to satisfy in measurements due to the factors of imperfection, our method applies  $\det(M_1)\det(M_2) = 1$ , which is validated to be so close to unity by measurements in Fig. 2, for improved  $\gamma$  determination of uniform lines with symmetric reflections. S-parameter measurements of an X-band empty waveguide section with length 7.7 mm were performed for validation of our formalism.

## References

- [1] G. F. Engen and C. A. Hoer, "Thru-reflect-line: An improved technique for calibrating the dual 6-port automatic network analyzer," *IEEE Trans. Microw. Theory Techn.*, vol. 27, no. 12, pp. 983–987, Dec. 1979.
- [2] M. D. Janezic and J. A. Jargon, "Complex permittivity determination from propagation constant measurements," *IEEE Microw. Guided Wave Lett.*, vol. 9, no. 2, pp. 76–78, Feb. 1999.
- [3] C. Wan, B. Nauwelaers, W. D. Raedt, and M. V. Rossum, "Two new measurement methods for explicit determination of complex permittivity," *IEEE Trans. Microw. Theory Techn.*, vol. 46, no. 11, pp. 1614–1619, Nov. 1998.
- [4] I. Huynen, C. Steukers, and F. Duhamel, "A wideband line-line dielectrometric method for liquids, soils, and planar substrates," *IEEE Trans. Instrum. Meas.*, vol. 50, no. 5, pp. 1343–1348, Oct. 2001.
- [5] U. C. Hasar, "Self-calibrating transmission-reflection technique for constitutive parameters retrieval of materials," *IEEE Trans. Microw. Theory Techn.*, vol. 66, no. 2, pp. 1081–1089, Feb. 2018.
- [6] K. F. Fuh, "Broadband continuous extraction of complex propagation constants in methods using two-line measurements," *IEEE Microw. Wireless Compon. Lett.*, vol. 23, no. 12, pp. 671–673, Dec. 2013.
- [7] R. B. Marks, "A multiline method of network analyzer calibration," *IEEE Trans. Microw. Theory Techn.*, vol. 39, no. 7, pp. 1205–1215, Jul. 1991.
- [8] J. A. Reynoso-Hernandez, C. F. Estrada-Maldonado, T. Parra, K. Grenier, and J. Graffeuil, "An improved



- method for the wave propagation constant  $\gamma$  estimation in broadband uniform millimeter-wave transmission line,” *Microw. Opt. Technol. Lett.*, vol. 22, no. 4, pp. 268–271, Aug. 1999.
- [9] J. A. Reynoso-Hernandez, “Reliable method for computing the phase shift of multiline LRL calibration technique,” *IEEE Microw. Wireless Compon. Lett.*, vol. 12, no. 10, pp. 395–397, Oct. 2002
- [10] J. A. Reynoso-Hernandez, “Unified method for determining the complex propagation constant of reflecting and nonreflecting transmission lines,” *IEEE Microw. Wireless Compon. Lett.*, vol. 13, no. 8, pp. 351–353, Aug. 2003.
- [11] U. C. Hasar, “Propagation constant measurement of microwave networks with symmetric/asymmetric reflections,” *IEEE Sensors J.*, vol. 18, no. 12, pp. 4940–4946, Jun. 2018.
- [12] K. Fuh, “Identification and sign-ambiguity-free calculations of reciproca characteristic parameters in microwave applications,” *IEEE Microw. Wireless Compon. Lett.*, vol. 27, no. 9, pp. 773–775, Sep. 2017.
- [13] O. Luukkonen, S. I. Maslovski, and S. A. Tretyakov, “A stepwise Nicolson-Ross-Weir-based material parameter extraction method,” *IEEE Antennas Wireless Propag. Lett.*, vol. 10, pp. 1295–1298, 2011.



## Increasing the Reflection Parameter in Microstrip Patch Antennas by Trying Different Shapes

Hamdullah Ozturk<sup>\*1</sup>

<sup>1</sup>Department of Electrical and Electronics Engineering, Gaziantep Islam Science and Technology University, Gaziantep, 27010, Türkiye

### Abstract

Nowadays studies on antennas have increased significantly. In this study, microstrip patch antenna design and analysis were carried out. The frequency range of the designed antennas was selected as 0-2.4 GHz. FR-4 (dielectric constant 4.3 and thickness 1.6) material was preferred for the antenna design. The antenna consists of three different layers: ground, substrate and patch layer. CST microwave studio program was preferred for the design of the antenna. Different shapes were tried by taking into account the reflection parameter of the antenna. Considering the analysis results, a conclusion was reached as to what the best antenna shape should be.

**Keywords:** Antenna, Microstrip antenna, Electromagnetic, Reflection parameter

## 1 INTRODUCTION

An antenna is defined as a device used for transmitting or receiving electromagnetic waves in addition to allowing radio frequency communications between remote locations in free space or other material media [1]. In practice, it is known that antennas tend to scatter strongly because of their metal material and conspicuous placement [2]. Due to the development of wireless communication, the number of applications related to antennas is constantly increasing [3]. Today, wireless communication systems require antennas that require high performance and have some different features (For example; low profile, multi-operating band and low loss). Many different single-port multiband antennas have been presented in the literature [4].

Microstrip patch antennas have many attractive advantages such as low profile, ease of production, compatibility with shaped surfaces, and compatibility with integrated circuit technology. Due to such advantages, it has been widely researched and used in many devices [5]. Additionally, a microstrip patch antenna is capable of delivering reconfigurable radiation characteristics if an appropriate parameter controlling the radiation patterns can be used [6]. On the other hand, the traditional microstrip antenna has the disadvantage of narrow bandwidth, which limits its applications in wireless communications [5]. The problem of narrow bandwidth and interconnectivity that must be addressed and this remarks the researcher's attention for the past few years [7]. Different feeding methods, including the edge feed, the probe feed, the proximity-coupled feed, and the aperture-coupled feed, have been studied depend on various types of transmission lines, like the coaxial cables, microstrip lines, strip lines, coplanar waveguides (CPWs), and substrate integrated waveguides (SIWs) [8].

In this study, the effects of size parameters or shape changes of a microstrip patch antenna on the reflection parameter, which is one of the scattering parameters, were examined. During the analysis phase, a conclusion was reached about what the best antenna should be (size, shape, etc.) by taking into account different parameters such as current density, radiation pattern reflection parameter results in dB, and propagation direction.

## 2 MATERIAL AND METHOD

In this part of our study, we will focus on the properties of the materials used in the design phase and the software program used to design the study, and in another stage, we will focus on the explanations that include the analysis of the study.

### 2.1 Design of Microstrip Patch Antenna

In this section, detailed information is given about the software program preferred to realize the design and the materials used in the design phase to realize the antenna design.

CST microwave studio program was preferred to realize the design of the proposed antenna. The frequency of the designed antennas was chosen in the range of 0-2.4 GHz. The proposed antenna consists of 3 different layers. The first layer is the ground plane (copper), the second layer is the substrate (FR-4) material, and at the top is the patch part of the antenna consisting of copper material. Electrical conductivity for copper parts is  $5.8 \times 10^7$ . For FR-4 material, the dielectric constant was chosen as 4.3 and the layer thickness as 1.6 mm.

## 2.2 Analysis and Results of Microstrip Patch Antenna

The analysis and design part of the antenna was carried out using the CST microwave studio program, as mentioned in the previous section. The analysis of the antenna was made in the 0-2.4 GHz frequency range. Time domain was chosen for antenna analysis. The size of the antenna designed and the microstrip line width of the antenna were decided by taking into account some parameters such as the dielectric constant of the FR-4 material and its height. In the analysis of the antennas, the reflection parameter was taken into consideration. The first stage and different views of the proposed antenna, as well as the result of the designed antenna, are shown in the figures below.

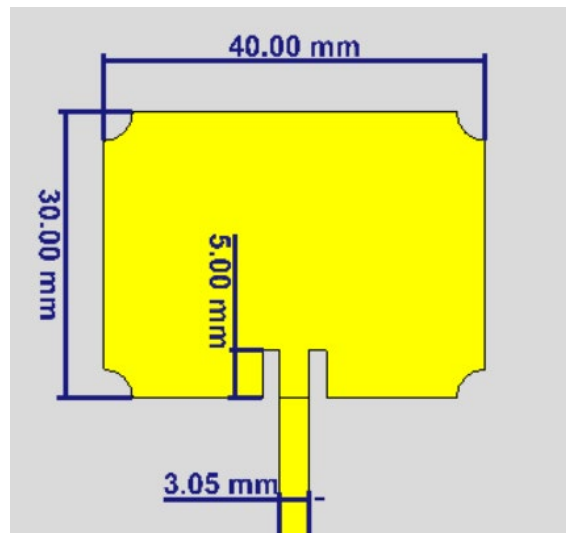


Figure 1. Microstrip patch antenna

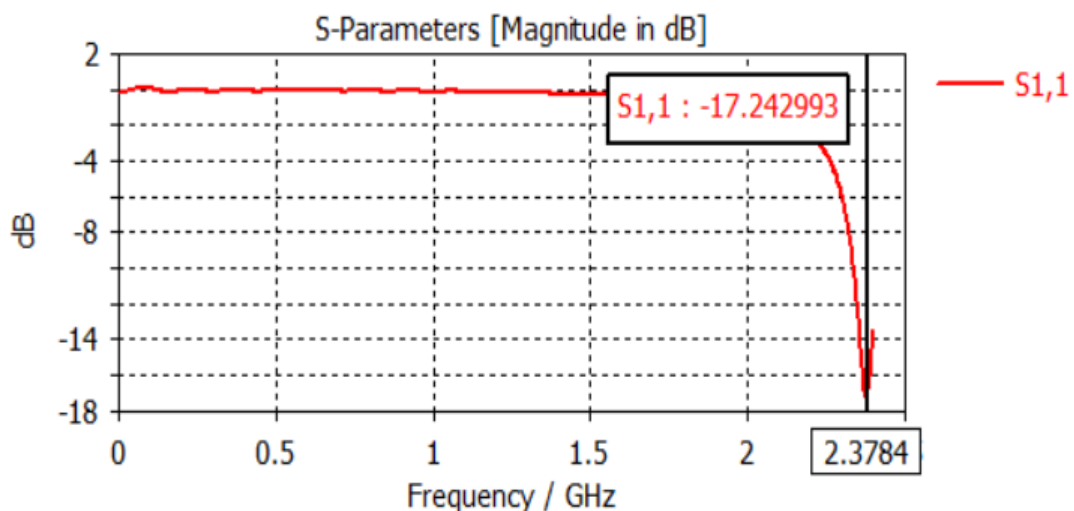


Figure 2. Result of microstrip patch antenna

When the result of the designed antenna is examined, it is seen that it is approximately 7 dB more than the 10 dB value determined as a reference. In other words, it can be seen that the reflection parameter of the proposed antenna at 2.3784 GHz is approximately -17.25 dB. However, the main purpose of the study is to obtain the best result for the reflection parameter S<sub>11</sub> by making changes in the size and shape of the antenna. For this purpose, different sizes and shapes were tried and the best result possible for this study was achieved. The simulation result and appearance of the changes made are given in the figures below, respectively.

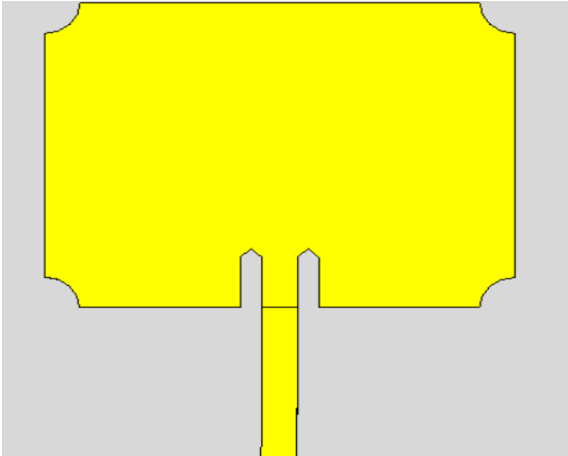


Figure 3. Microstrip patch antenna

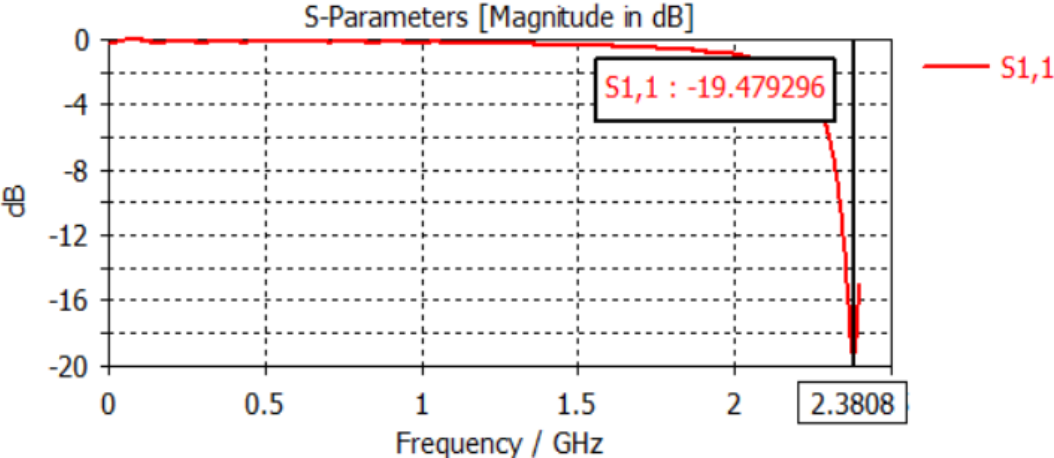


Figure 4. Result of the microstrip patch antenna

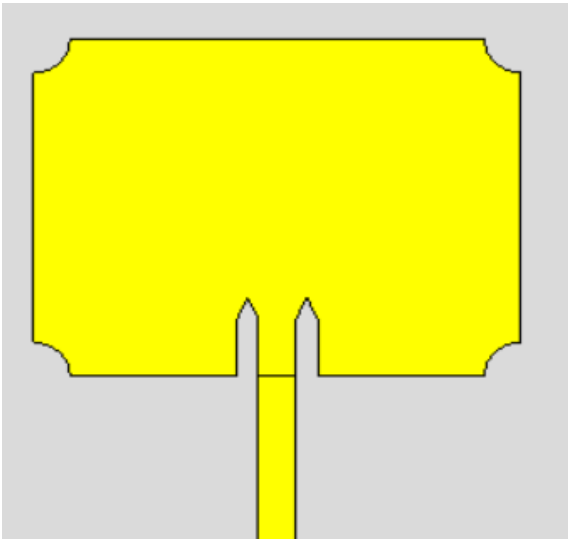


Figure 5. Proposed of the microstrip patch antenna

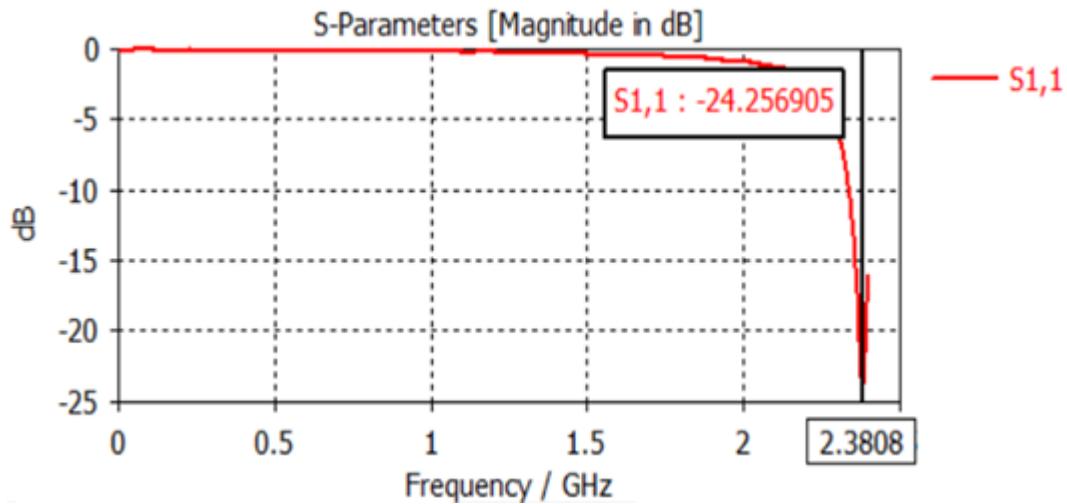


Figure 6. Result of the proposed antenna

When Figure 3 and Figure 5 are examined, it is clearly seen that the slightest change in size and shape in microstrip antennas has a huge impact on the results. Considering the changes made, it can be seen that our dB value was approximately (-19.48 dB) in the first change. In a second change, it is seen that our dB value is approximately (-24.3 dB). But these changes were not made randomly. It was done by taking into account parameters such as current density and direction of propagation etc. At the same time, according to the good reflection parameter result obtained, the shape of the antenna also showing the far field directivity is shown below. (For example, considering  $\phi = 0$ ). As can be seen in the figure, the propagation is seen to increase by expanding in one direction.

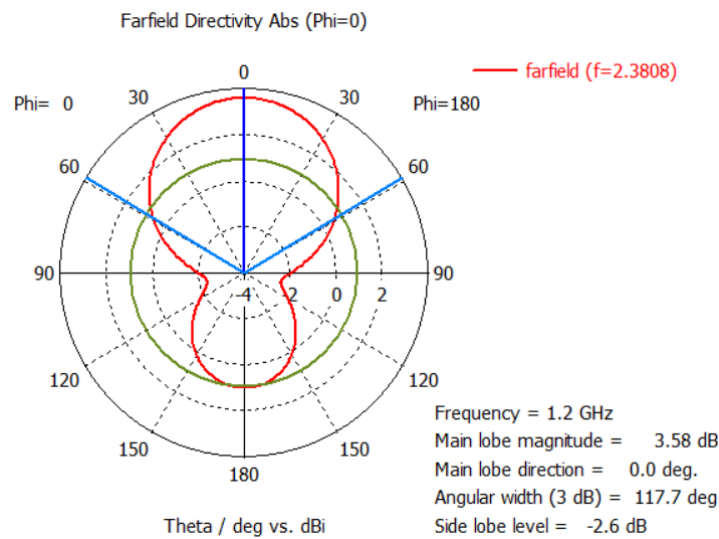


Figure 7. Result of the farfield directivity

### 3 CONCLUSION

As a result, microstrip patch antenna design and analysis were carried out. CST software was used in the study. By trying different shapes, the best reflection parameter result was obtained. The best result was obtained for the frequency value 2.3808, and the dB value for the reflection parameter for this frequency value was found to be approximately -24.3 dB. For these antennas, even a very small change in size and shape can change the result greatly during the antenna analysis phase.

### References

- [1] N. K. Das, "Antennas and radiation," in *The Electrical Engineering Handbook*, W.-K. Chen, Ed.: Elsevier, 2005.
- [2] Y. Yang, C. Wang, H. Yang, S. Li, X. Zhou, and J. Jin, "A hybrid mechanism water-based metasurface for

- antenna RCS reduction,” *IEEE Transactions on Antennas and Propagation*, 2024, doi: 10.1109/TAP.2024.3420079.
- [3] H. Wang, L. Chang, Y. Li, K. Wei, and Z. Zhang, “A deployable coplanar waveguide CoCo antenna,” *IEEE Antennas and Wireless Propagation Letters*, 2024.
- [4] J.F. Li, C.P. Zhen, X.X. Tian, F. Jiang, and L.H. Ye, “A Dual-polarization self-duplex antenna with high isolation and low profile,” *IEEE Antennas and Wireless Propagation Letters*. 2024.
- [5] Y. Cao, Y. Cai, W. Cao, B. Xi, Z. Qian, T. Wu, and L. Zhu, “Broadband and high-gain microstrip patch antenna loaded with parasitic mushroom-type structure,” *IEEE Antennas and Wireless Propagation Letters*, vol. 18, no.7, pp. 1405–1409, 2019.
- [6] T. Q. Tran and S. K. Sharma, “Radiation characteristics of a multimode concentric circular microstrip patch antenna by controlling amplitude and phase of modes,” *IEEE Transactions on Antennas and Propagation*, vol. 60, no.3, pp. 1601–1605, 2011.
- [7] B. Wang, Z. Zhao, K. Sun, C. Du, X. Yang, and D. Yang, “Wideband series-fed microstrip patch antenna array with flat gain based on magnetic current feeding technology,” *IEEE Antennas and Wireless Propagation Letters*, vol. 22, no. 4, pp. 834–838, 2022.
- [8] D. Cao, Y. Li, and J. Wang, “A millimeter-wave spoof surface plasmon polaritons-fed microstrip patch antenna array”. *IEEE Transactions on Antennas and Propagation*, vol. 68, no. 9, pp. 6811–6815, 2020.



---

## A Study on General Safety Precautions Against Electrical Accidents in Daily Life

Yunus Kaya<sup>\*1</sup>, Selahattin Kosunalp<sup>2</sup>

<sup>1</sup>Department of Electronics and Automation, Bayburt University, Bayburt, 69010 Türkiye

<sup>2</sup>Department of Computer Technologies, Gonen Vocational School, Bandirma Onyedi Eylul University, Bandirma/Balikesir, 10200 Türkiye

---

### Abstract

We are surrounded by electrical equipment both in our working environment and in our home, that is, in our daily lives. Therefore, electrical energy transmission and distribution lines surround us. It is only a matter of time before we are exposed to some dangers from both these lines and the electrical devices in our lives. In this study, brief and concise information about the dangers of electricity is given, and then the safety precautions that can be taken against electrical accidents are listed in general, and thus the aim is to prevent electrical accidents.

**Keywords:** Dangers of electricity, Electrical accidents, Precautions

---

## 1 INTRODUCTION

Electricity, which is effective in a wide range of areas from communication to telecommunication, from transportation to health, from education to almost all areas of our daily lives, has undoubtedly been one of the most important turning points in human life and is an indispensable part of human life today [1]. We are in a period where electrical appliances, vehicles, systems, and structures are increasingly entering our lives, electrification is becoming more widespread with digitalization, electrical energy is being carried everywhere, street lighting poles, billboards, bus stops, and mobile units are increasing, charging units are being installed in outdoor environments and more security measures are being taken [2]. For this reason, electricity is a source of risk that is used in almost all stages of our lives and everyone is exposed to its dangers [3]. Electricity-related accidents are among the most common problems encountered when using electrical energy, which is one of the types of energy that makes human life easier. Electrical accidents usually occur as a result of the carelessness, ignorance, and inexperience of individuals who use electrical appliances or who deal with these devices in their daily lives. As a result of electric shock, people can be injured, disabled or even lose their lives. Therefore, it is useful to learn the safety and protection measures that can be taken against electrical accidents in order to avoid the negative consequences of electricity, which makes our daily lives easier [4].

In this study, theoretical concepts such as electric current and voltage are not emphasized. Instead, the dangers of electricity are discussed in Section 2, and then general safety precautions against electrical accidents are listed in Section 3. This study, which approaches the subject in a concise and brief manner, aims to reduce electrical accidents to some extent.

## 2 DANGERS OF ELECTRICITY

Although the intensity of the current flowing through the transmission line depends on the voltage applied to the circuit, the cause of life-threatening electrical accidents is not the voltage but the current passing through the human body. Therefore, it is possible to divide accidents caused by electric current into three groups in terms of their effects [5]:

- The effect of electric current directly on the nerves, muscles, and the work of the heart.
- Damage resulting from heating caused by electric current (e.g. burns caused by arcing).
- In very small currents that are not harmful to humans, mechanical damages such as falling, hitting, etc. due to fear.

The effect and damage of an electric current intensity depends on many factors. These are the way electricity reaches the body, the type, amount and frequency of the current (if it is alternating current), the duration of exposure to current, and whether the skin is dry or damp. Water is generally a good conductor of electricity, and electrical conduction is easily achieved in humid environments. An electric shock can cause anything from mild

tingling to severe burns and even cardiac arrest. Table 1 below is important because it shows the results that would occur if the current were directed from hand to foot for one second at the mains frequency [6].

**Table 1.** Electric current intensity and effect [6]

Current Intensity	Effect
0–1 mA	Current is noticeable. Tickling is felt in the hand. Sensation is limited.
1–5 mA	Numbness is felt in the hand. Hand and arm movements become difficult.
5–15 mA	It is possible to release the object that is held. Cramps begin in the hand and arm. Blood pressure rises.
15–25 mA	It is not possible for the object that is held to be released on its own. However, the heart is not affected.
25–80 mA	It is the limit of the current that can be tolerated. Blood pressure increases. The heart starts to work irregularly. Breathing becomes difficult. The heart may stop, but it is possible to start it again. Consciousness is stable. Some people may faint after 50 mA.
80–100 mA	Depending on the duration of the effect of the electric current, fibrillation occurs in the heart. Loss of consciousness is observed.
$\geq 3000$ mA	Blood pressure rises. The heart stops. Severe burns and possible death occur.

### 3 GENERAL SAFETY PRECAUTIONS AGAINST ELECTRICAL ACCIDENTS

Knowing the precautions that can be taken against a situation before encountering it always provides an advantage during the event. In this section, general safety precautions that can be taken against electrical accidents in the work environment, at home, in the environment, in short in our daily lives, will be discussed in order to avoid the negative effects of electricity in the previous section. In this context, the precautions are detailed and listed below [2, 4, 5, 7]:

- In no work environment should you work under energy unless necessary (repair, maintenance, etc.), power should be cut off before working with electrical circuits or tools, and all precautions should be taken to prevent energy from being supplied while working.
- If it is necessary to work under energy, rubber or plastic shoes that do not conduct electricity (i.e. insulators) should be worn and the soles of the shoes should not be wet.
- The plugs of electrical machines and tools must be inserted with one hand (right hand).
- Before plugging in the power cables of various devices or lamps, it should be checked that these equipment or lamps are off (OFF/0).
- Before operating the machine or any suspicious electrical appliances, a voltage tester should be used to check for leaks, and leaking appliances and machines should never be used without being repaired.
- Electrical machines and buttons should not be touched with wet hands.
- Bare electrical wires or those with damaged sheaths should not be touched.
- It should be ensured that all electrical cables are tightened, clean, and tidy in case pets may chew the electrical cables and people may trip over them.
- All unused electrical outlets should be fitted with safety covers or, whenever possible, covered outlets should be used.
- A lot of electrical devices should not be connected to one outlet or extension cord as this could damage the electrical system or even cause a fire.
- A person who has been electrocuted should not be touched with bare hands.
- Mechanical fuses should not be repaired, these fuses must be replaced with new ones. If possible, automatic fuses should be used.



- Grounded plugs must be used in motorized and heated devices.
- A grounded outlet must be used.
- Tools or items not in use should be unplugged from outlets.
- Great care must be taken when working with electrical appliances or using a device that consumes electric current.
- If an abnormal change such as smoke or a burning smell is felt while an electrically operated device/machine is operating, the electrical power must be cut off immediately.
- Residual current relays should be used in all structures and their operation should be checked once a month.
- Do not attempt to repair any electrical equipment. Electrical work should be left to a trained and experienced electrician.
- The user manual of any electrical device must be studied and used under appropriate conditions.
- Electrical panel covers at home, at work or outside should not be opened, if there are open ones, they should not be tampered with, the warnings on the panels or poles should be paid attention to and stayed as far away as possible.
- High or medium voltage wires or poles should not be approached too close.
- Do not touch devices and tools that blow fuses, short circuit, produce arcs, or leak current. In case of arcing, detection of leakage, or blowing fuse, the electricity of the environment must be cut off from the panel immediately and support must be obtained from experts for testing.
- If open cables, connection points or panel covers are seen, the relevant units should be notified as soon as possible and these points should not be contacted in any way.
- We should act with the awareness that we are all responsible for electric shocks, and if a wrong, missing or threatening situation is detected, the relevant parties should be notified and the necessary precautions should be taken without delay. It should never be forgotten that simple precautions will reduce very serious dangers and protect our loved ones.

As a result, preventing risks from electrical sources is not difficult at all. After the above information is obtained, the risks should be kept under control by taking the necessary security measures. However, in case of any electrical accident, the authorized persons (for example, 112 Emergency Call Center for Türkiye) should be notified immediately, the person who has been electrocuted should not be touched with bare hands or if you do not have thick rubber-soled shoes, the injured person should not be touched without turning off the fuses, conductors such as cables near the person who has been electrocuted should be removed with an insulating rod, and the person who has been electrocuted should be removed from the area by pulling their clothes.

#### 4 CONCLUSION

In this study, the dangers of electricity, which is indispensable in our lives for the energy of the devices we use, work with and have around us every day, are first mentioned, and then the general safety precautions that can be taken against electrical accidents in daily life are briefly and concisely listed.

#### References

- [1] M. Fazlioglu. (2018, Jan. 8). *Elektrik Carpmalarında Alınabilecek Önlemler* [Online]. Available: <https://www.mustafafazlioglu.com.tr/2018/01/08/elektrik-carpmalarinda-alinabilecek-onlemler/>
- [2] S. Sagiroglu. (2023, Sep. 15). *Elektrik kazalari ve elektrik carpmasi ve dikkat edilmesi gereken hususlar* [Online]. Available: [https://www.emo.org.tr/genel/bizden\\_detay.php?kod=144455&tipi=3&sube=14](https://www.emo.org.tr/genel/bizden_detay.php?kod=144455&tipi=3&sube=14)
- [3] I. Aslan and Y. Celik. "Investigation of electric accidents in occupational health and safety," in *idRc 2019 - International Disaster & Resilience Congress*, Eskisehir, 2019, pp. 629–634.
- [4] ENOKS, "Elektrik kazalari ve guvenlik tedbirleri," [Online], May 24 2024. Available: <https://www.enoks.com.tr/wp-content/uploads/2019/03/Elektrik-KazalariTedbirleri.pdf>
- [5] "Elektrikle calismalarda ISG," [Online], May 25 2024. Available: <https://www.erbakan.edu.tr/storage/files/department/insaatmuhendisligi/editor/DersSayfalari/issagligi/elektrikleCalismalardaISG.pdf>
- [6] ADS Muhendislik. (2023, Feb. 14). *Elektrik akimi ve elektrik akiminin insan vucuduna etkileri* [Online]. Available: <https://www.adsmuhendislik.com.tr/blog/elektrik-akimi-etkileri>
- [7] Etki Akademi. (2021, Mar. 14). *Elektrik guvenligi icin ilk 10 kural* [Online]. Available: <https://etkiakademi.com/blog/elektrik-guvenligi-icin-ilk-10-kural>



## VO<sub>2</sub> Based Adaptive Wideband THz Metamaterial Absorber

Merve Kurt<sup>\*1</sup>, Gokhan Ozturk<sup>1</sup>

<sup>1</sup>Electrical and Electronics Engineering, Faculty of Engineering, Ataturk University, Erzurum, Türkiye

### Abstract

In this study, a broadband absorber device that can be actively tuned in the terahertz frequency range is proposed. In the design of the proposed structure, metal, dielectric and metal layers are used to provide the absorption of metamaterial design. Vanadium dioxide is used as metal on the upper surface of the design, silicon dioxide is used in the substrate that functions as a separator, and gold is used in the lower layer, which functions as a metal termination. Absorption analysis was performed with the simulation results obtained with the CST microwave program. In line with the simulation results, the absorption band gap values of the metamaterial absorber occur at 2.68 and 5.4 THz. When the predicted scan range absorptions were evaluated, it yielded a bandwidth of 2.72 THz. The adjustable range values of absorption are between 1.9% and 99.5% when the numerical conductivity of VO<sub>2</sub> is increased from 200 S/m to  $2 \times 10^5$  S/m. Performance analysis was presented by comparing the proposed design with other study reports in the literature in terms of bandwidth, efficiency and adjustable range performance criteria. In order to better understand the physical mechanism of the proposed design, electric field analysis at resonant frequencies was performed. Since the simulation results obtained with the CST microwave program show the same absorption performance in both TE and TM modes, the design works as polarization insensitive.

**Keywords:** Vanadium dioxide, Terahertz (THz), Metamaterial, Absorption

## 1 INTRODUCTION

Metamaterials used in electromagnetic studies related to semiconductor devices have modifiable properties and the ability to control electromagnetic waves [1]. While the electromagnetic properties of materials found in nature depend on the atomic or molecular structure, the electromagnetic properties of metamaterials are associated with the resonant element [2]. In addition, metamaterials show negative reflective properties [3]. Considering such properties of metamaterials, they are considered as hybrid properties depending on their composite components different from other materials. Thanks to their modifiable properties, metamaterials are preferred in application areas such as sensors, antennas, medical, signal absorption and image processing by taking part in specific designs within electromagnetic studies [4–8].

In 2008, Landy et al. [2] proposed an absorber device that realizes absorption using metamaterials for the first time. It was also observed that absorption was achieved at a single resonant frequency. Landy et al. [9–12], many researchers have created new designs to provide more efficiency and widen the bandwidth of the studies in this field. They have made progress in the electromagnetic field by conducting research on the absorption spectra of magnetic waves in visible light, infrared light, THz and GHz ranges [3, 13–16]. When the designs for the absorber were analyzed, it was seen that various materials were used as metamaterials. Composite structures such as vanadium dioxide (VO<sub>2</sub>), graphene and indium tin oxide were used in the studies [17–19].

When VO<sub>2</sub>-based studies in the literature are examined, Song et al. [20] proposed an absorber device with VO<sub>2</sub> material at THz frequency with adjustable conductivity to control the dynamic mechanism of metamaterials. When they changed the conductivity of VO<sub>2</sub> in certain ranges, they found the tunable absorption range between 30% and 100%. Wang et al. [21] realized a design for VO<sub>2</sub>-based THz band microwave devices using VO<sub>2</sub>, SiO<sub>2</sub> and gold materials. When Wang et al. analyzed this proposed design, they found the bandwidth to be 0.65 THz with an absorption rate above 90%. Song et al. [22] designed using a thin-layer VO<sub>2</sub> to actively regulate the absorption characteristics. They found simulated absorption results in the frequency range from 0.47 to 0.99 THz, achieving an efficiency rate above 90%. By gradually varying the conductivity of the VO<sub>2</sub>, they obtained a tunable level of the absorption peak between 5% and 100%. Bai et al. [23] analyzed the design they created from tunable broadband VO<sub>2</sub> metamaterial and stated in their study that they achieved absorption at a bandwidth of 1.25 THz. Dao et al. [24] proposed a design using polyimide, VO<sub>2</sub> and gold materials. By changing the conductivity of VO<sub>2</sub> used in this design, they found an adjustable absorption range between 4% and 100%. Song et al. [25] made a square-

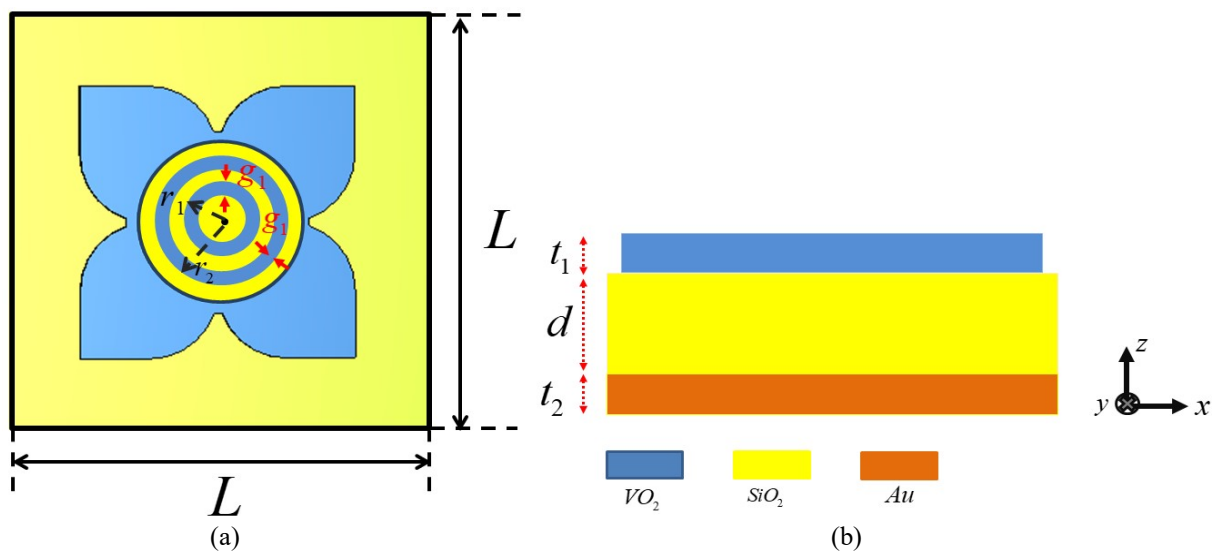
shaped design at THz frequencies based on VO<sub>2</sub>. In their proposed design, they found the absorption range values of the absorber they created by changing the conductivity of VO<sub>2</sub>, which shows phase change characteristics, between 20% and 90%. They found the reflection and absorption graphic efficiency rate as 80%. Huang et al. [26] proposed a broadband THz absorber based on hybrid patterned VO<sub>2</sub> metamaterial. The absorption band gap of their proposed design is 2.45 THz.

When the VO<sub>2</sub>-based THz metamaterial absorber studies in the literature are reviewed [20, 21, 22, 23, 24, 25, 26], the microwave bandwidth in which absorption is provided is provided for a narrow range. Again, the tunable absorption range of all these studies provides a change performance between 4% and 100%. Considering these studies, in this study, a device consisting of metal, dielectric and metal triode was designed to realize the signal absorption of metamaterials. In the designed structure, a tunable broadband THz absorber based on vanadium dioxide was studied. The bandwidth of the simulated device varies between 2.68 and 5.4 THz with an absorption rate of over 90% under different incident polarization angles. The conductivity of the vanadium dioxide metamaterial, which shows temperature-controlled phase change, was increased from 200 to  $2 \times 10^5$  and the conductivity value of VO<sub>2</sub>, which provides the best absorption, was found. To better understand the physical mechanism of the absorber, the electric field distribution at the absorption peak was analyzed. In addition, absorption graphs were plotted separately for TE and TM waves. The TE and TM absorption graph analysis confirmed that the structure is insensitive to polarization.

## 2 MATERIAL AND METHOD

### 2.1 Simulation Design subsections

The unit cell structure of the proposed design is shown in Fig. 1(a). In the unit cell design, a broadband terahertz absorber device based on vanadium dioxide as the metamaterial is proposed. During the design of the unit cell structure, VO<sub>2</sub> was used as the metal on the top surface, silicon dioxide (SiO<sub>2</sub>) was used as the dielectric layer and gold was used as the metal termination on the bottom layer. The unit cell period in the designed structure is  $l=30$  ( $\mu\text{m}$ ) micrometers.



**Figure 1.** (a) Top and (b) x-z view of the absorption scheme

As shown in Figs. 1 (a,b), the metamaterial layer design consisting of the VO<sub>2</sub> structure first consists of two nested circles with radii  $r_1 = 3.2 \mu\text{m}$  and  $r_2 = 4.8 \mu\text{m}$ , respectively. Following this design, 4 circles with a radius of  $6 \mu\text{m}$  and 4 squares of  $6 \mu\text{m}$  units were drawn around and stacked on top of each other. Then, a circle with a radius of  $7 \mu\text{m}$  and a width of  $1 \mu\text{m}$  and a rectangle with a width of  $12 \mu\text{m}$  and a height of  $2 \mu\text{m}$  were drawn and subtracted from the stacked drawing and the design shown in Fig. 1(a) was realized. The height of the VO<sub>2</sub> metamaterial in the top layer is  $t_1 = 0.25 \mu\text{m}$ . VO<sub>2</sub> is a composite material with temperature controlled phase change. The critical temperature of VO<sub>2</sub> is determined as 341K or 68 degrees. Vanadium dioxide, which shows phase change properties, functions as an insulator phase below the critical temperature of 341K and as a metal phase above the critical temperature. In this study, the temperature setting of VO<sub>2</sub> used as metamaterial was obtained by changing its conductivity. In the insulator phase state, its conductivity is less than 200S/m. In the metal phase state, its conductivity is of the order of  $10^5$ . Since the VO<sub>2</sub> used in the study was operated in the metal phase state,

conductivity values were evaluated around  $10^5$  [33]. In order to express the conductivity change and optical properties of VO<sub>2</sub>, the Drude model was defined. The expressions used for the Drude model description are given in equations 1 and 2 [34, 35].

$$\varepsilon(\omega) = \varepsilon(\infty) - \left( \frac{\omega_p^2(\sigma)}{\omega^2 + i\gamma\omega} \right) \quad (1)$$

The high frequency dielectric permittivity  $\varepsilon_\infty = 12$  and the collision frequency  $\gamma = 5.75 \times 10^{13}$  rad/s in the Drude model expression. The relation between plasma frequency  $\omega_p$  and conductivity  $\sigma$  can be expressed as in equation 2:

$$\omega_p^2(\sigma) = \left( \frac{\sigma}{\sigma_0} \right) * \omega_p^2(\sigma_0) \quad (2)$$

Here  $\sigma_0 = 3x \frac{(10^5)s}{m}$  and  $\omega_p(\sigma_0) = 1.4 \times 10^5$  rad/sn. By giving values to the  $\sigma$  expression in Equation 2, the change in the conductivity of the material is observed. In this study, optimized absorber results in the THz range were obtained by increasing the value of  $\sigma$ , which affects the conductivity, from  $2 \times 10^2$  to  $2 \times 10^5$ .

Silicon dioxide (SiO<sub>2</sub>) is used as the dielectric layer in the design. The height of this dielectric layer is  $d = 9 \mu m$  and the relative dielectric constant is  $\varepsilon = 3.8$ . Finally, at the bottom there is a gold coating with a height  $t_2 = 2 \mu m$  and a conductivity of  $4.56 \times 10^7$ .

In this study, simulation results were obtained with the CST microwave program to find the reflection and absorption of the designed system. Finite element analysis is performed by determining periodic boundary conditions for simulation graphs. The boundary conditions are determined as a unit cell structure in x and y direction and as a matching layer in z direction. The absorption of the predicted design is obtained as in equation (3) [36].

$$A(\omega) = 1 - R(\omega) - T(\omega) \quad (3)$$

$A(\omega)$  represents absorption,  $R(\omega)$  reflection and  $T(\omega)$  transmission. Since the thickness of the metal plane used in the design substrate is greater than the thickness of the surface plane, the transmission coefficient goes to zero. Impedance matching theory is an expression used to express the perfect absorption of the absorber. The impedance matching theory is given by equation (4) [12, 37].

$$z_w = \sqrt{\frac{(1+S_{11}^2) - S_{21}^2}{(1-S_{11}^2) - S_{21}^2}} \quad (4)$$

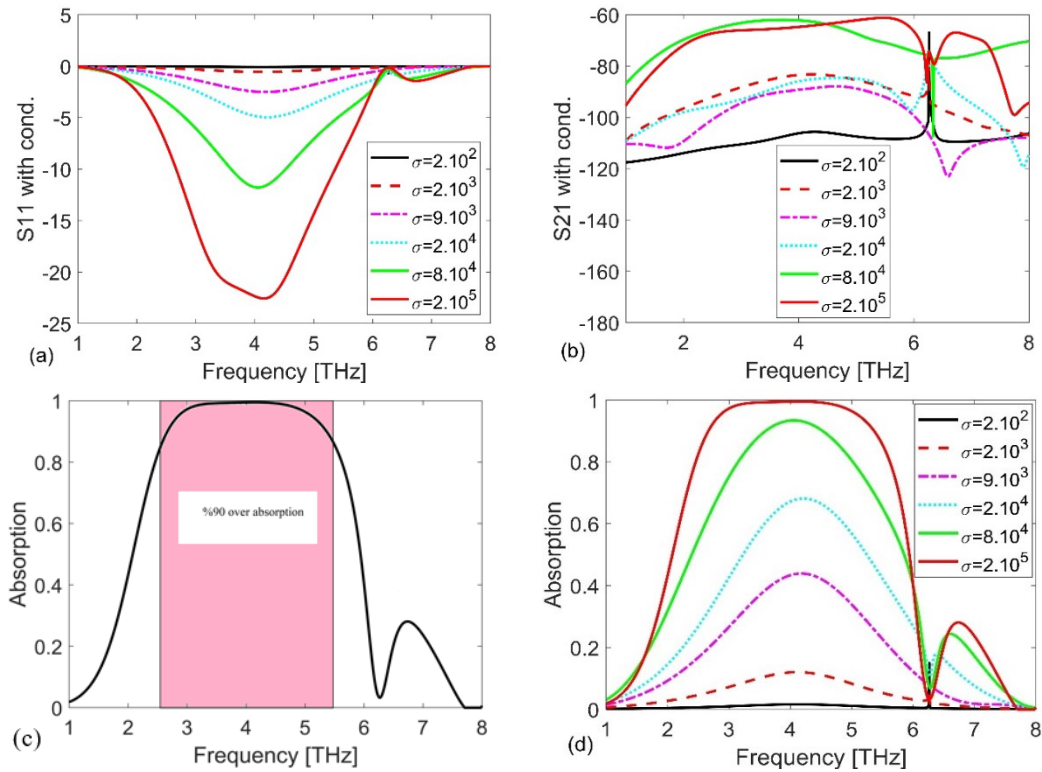
The parameter  $S_{11}$  in equation 4 is the reflection coefficient of the wave while  $S_{21}$  is the transmission coefficient of the wave.

### 3 RESULTS

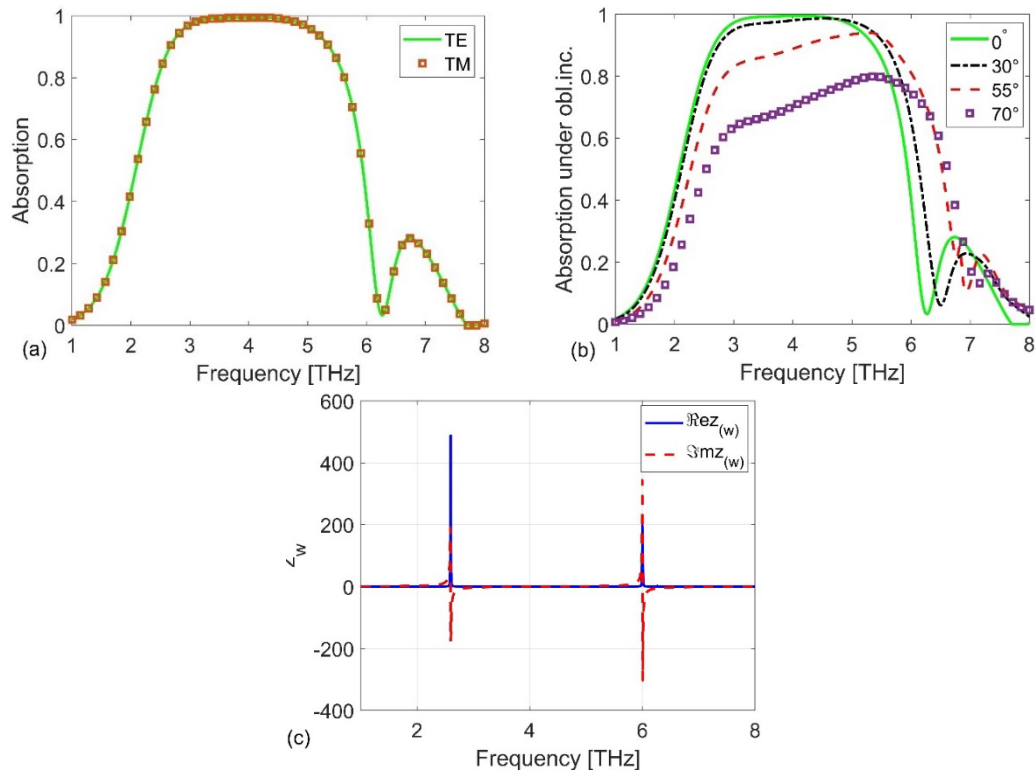
The design of the proposed absorber in Fig. 1 was realized and the simulation results were analyzed using the CST microwave program. The simulation was run in the range of 1-8 THz by applying unit cell boundary conditions in the frequency domain. Graphical analysis of the scattering parameters is presented by increasing the conductivity of VO<sub>2</sub> used in the top layer for the design from  $2 \times 10^2$  to  $2 \times 10^5$ .

Fig. 2(a,b) shows the reflection and transmission graphs of the incident wave for different conductivity values of VO<sub>2</sub> in the 1-8 THz range. In Fig. 2(a), as the conductivity value of VO<sub>2</sub> is increased, the  $S_{11}$  parameter value gradually decreases below -10 db. In Fig. 2(a), when the conductivity of VO<sub>2</sub> is optimized as  $2 \times 10^5$ , the peak of the  $S_{11}$  parameter jumps at 4.16 THz and reflects around -22 db. The  $S_{21}$  parameter graph obtained from the simulation results of the designed study is given in Fig. 2(b). For the  $S_{21}$  parameter graph, it is seen that VO<sub>2</sub> is below -60 db at different conductivity values. Fig. 2(c) shows the absorption performance plot for  $2 \times 10^5$  conductivity value where VO<sub>2</sub> gives the best results. The graph in Fig. 2(c) shows a range from 2.68 to 5.4 THz, resulting in a bandwidth of 2.72 THz. The resulting bandwidth provides an efficiency of around 99.5%.

In Fig. 2(d), the absorption graphs of VO<sub>2</sub> at different conductivity values are plotted. In Fig. 2(d), the absorption performance criterion increases from 1.9% to 100% when VO<sub>2</sub> conductivity value is started from  $2 \times 10^2$  and run up to  $2 \times 10^5$ . Fig. 2(d) shows that the widest bandwidth for absorption is for  $\sigma = 2 \times 10^5$ .



**Figure 2.** (a)  $S_{11}$  parameter and (b)  $S_{21}$  parameter spectra with different conductivities of VO2 (c) Spectrum of the absorber (d) Absorber spectrum with different conductivities of VO2

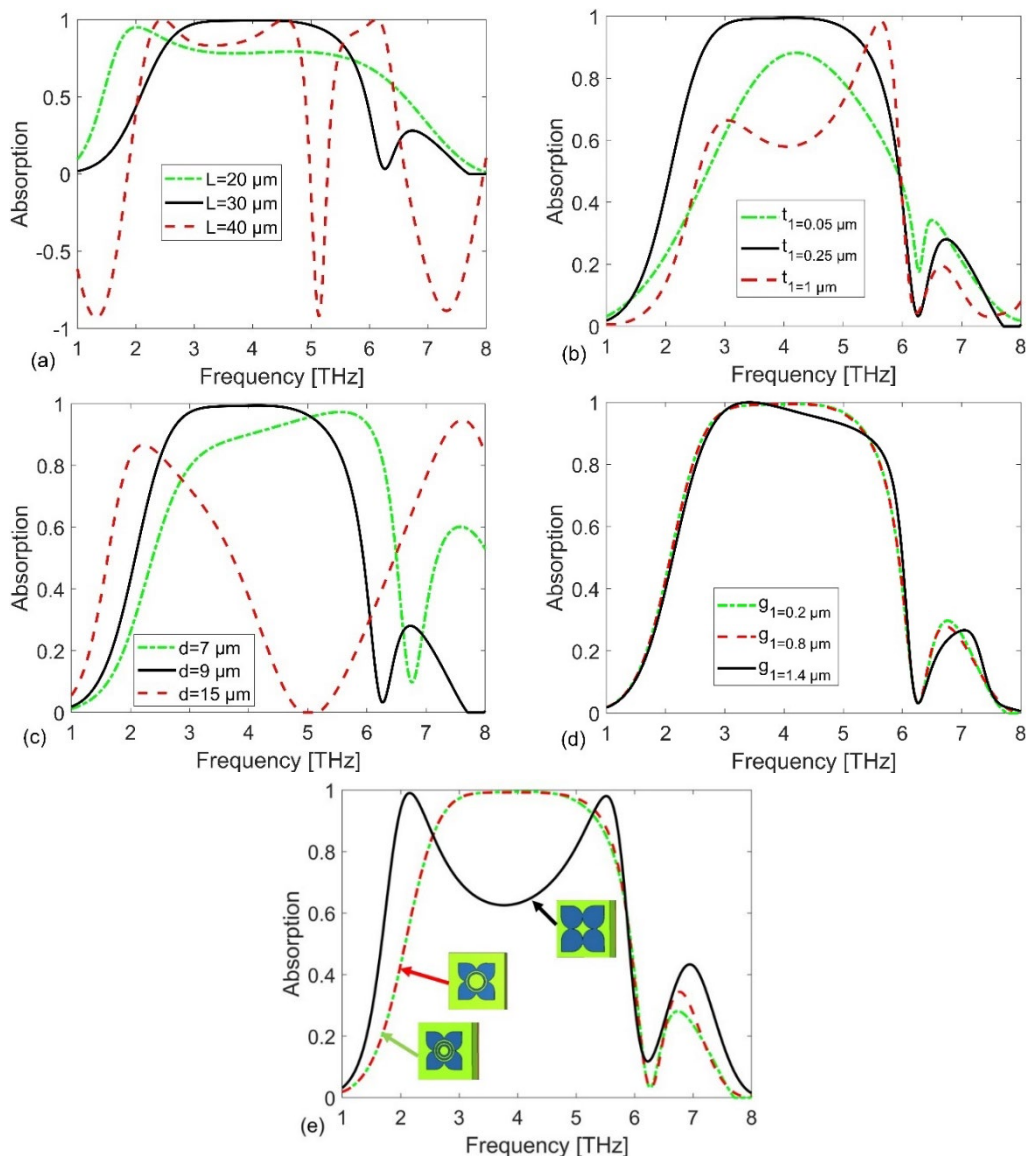


**Figure 3.** (a) Absorption spectra for TE and TM polarization and (b) under different polarization angles (c) relative impedance of VO2 for a conductivity of  $2 \times 10^5$

Fig. 3(a) shows that the absorption plots of the proposed design are identical in both x-polarized (TE) and y-polarized (TM) under normal index. The TE and TM modes in the same plot prove that the design is polarization insensitive. In addition, the symmetrical nature of the design proposed in this study makes it inevitable that the TE and TM modes show the same absorption performance. Fig. 3(b) shows the absorption performance for x-polarized

(TE) under different angles. In the absorption performance criterion in Fig. 3(b), it is seen that the incident waves provide around 80% absorption up to 70 degrees. Fig. 3(c) shows the normalized impedance value of the proposed model. In Fig. 3(c), the normalized impedance criterion is observed around 1 at positive values in the real part, while the negative part of the imaginary part is approximately in the region of 0. This leads to the conclusion that the impedance matching is realized.

In the simulation results obtained, when the conductivity of VO2 used in the metal phase state is selected as  $2 \times 10^5$ , the spectra of  $S_{11}$  and  $S_{21}$  parameters are given in Fig. 2(a,b). The simulation results for the proposed design cover the range from 2.68 to 5.4 THz, giving a bandwidth of 2.72 THz. For the design used in this study, the bandwidth of 2.72 THz provides an absorption performance of 99.5%, which is above 90%. In the absorption graph of the optimized parameter, there is a jump of around -22 db at the 4.16 THz resonance peak. In addition, since the designed structure has a symmetrical design, the same absorption graphs are obtained in TE and TM mode. When the wave absorption under different polarization angles is examined, it is observed that the absorption performance is around 80% up to 70 degrees.

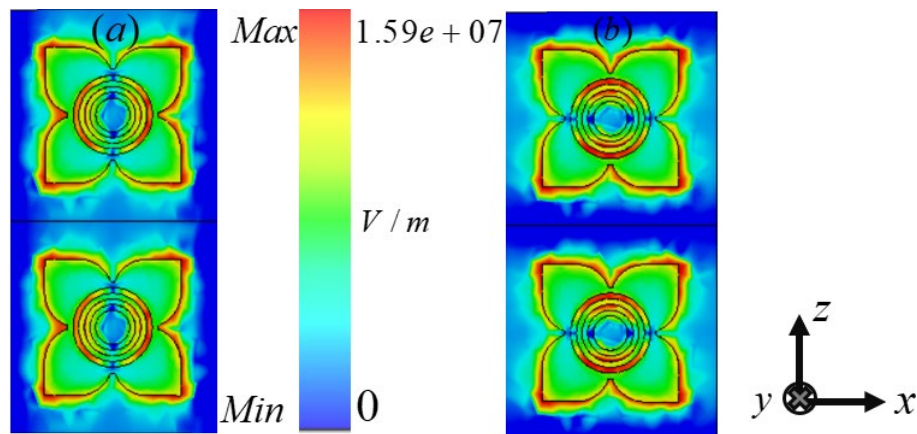


**Figure 4.** The effect of (a) the period  $l$  of the unit cell, (b) the height ( $t_1$ ) of vanadium dioxide, (c) the height  $d$  in the dielectric layer, (d) the width parameter  $g_1$  of the circles and (e) the structures at different stages on the absorption spectrum

In order to understand the physical mechanism of the proposed design, we analyzed the absorption variations obtained from the simulation results with the help of the CST microwave program. While analyzing the design, the parameter variables  $l$  period of the unit cell, the height of vanadium dioxide ( $t_1$ ), the height value  $d$  in the

dielectric layer and the width  $g_1$  of the circles were used. The optimum performance values used for the absorber are  $l = 30 \mu m$ ,  $r_1 = 3.2 \mu m$ ,  $r_2 = 4.8 \mu m$ ,  $g_1 = 0.8 \mu m$ ,  $t_1 = 0.25 \mu m$  and  $h = 9 \mu m$ . In this study, these optimum reference parameters are varied and the change graphs of the absorption are presented. Fig. 4(e) shows the absorbance changes for different VO2 layers.

In Fig. 5(a,b), the electrical distributions at the resonant frequency at the metasurface for the proposed design are analyzed. The resonant frequency value examined for the electrical distribution is 4.16 THz. Fig. 5(a) shows the electrical distributions for the incident wave in the x-polarized and Fig. 5(b) in the y-polarized direction. When the electrical distribution graphs given in Fig. 5(a,b) are examined, it is seen that the distributions for the horizontal and vertical position are homogeneously concentrated in almost the same layers on the metasurface. Although the electrical distributions are concentrated in the same layers in the horizontal and vertical position, it is observed that there are differences in regional concentrations. In Fig. 5(a), it is seen that the charge concentrations are distributed as right-left. In Fig. 5(b), it is shown that the charge distributions are located in the up-down direction.



**Figure 5.** Electric distribution of the metasurface at 4.16 THz for (a) x-polarized (b) y-polarized

Table 1 shows the comparison of absorption, bandwidth and efficiency performance between the proposed design and other studies in the literature [20–26] in order to perform the performance analysis of the proposed absorber. While making the comparison, it was taken into consideration that the structures used in the proposed design and other studies in the literature [20–26] have similar substrate, metal terminator and VO2 material at the metasurface. When the bandwidth ranges of the proposed design and other studies in the literature [20–26] are analyzed in Table 1, it is observed that the bandwidth of the proposed design is 2.72 THz and has a wider bandwidth than other studies. In the proposed design, when the conductivity of VO2 used in the metasurface is increased from  $2 \times 10^2$  to  $2 \times 10^5$ , the tunable range coverage reaches from 1.9% to 100%. In this context, when compared with other studies in the literature [20–26], the adjustable range level of the proposed study is superior. In addition, when the absorption performance criterion of the proposed design is evaluated, compared to some studies in the literature [25], it provides absorption performance above 90% in the frequency region where it works as an absorber.

**Table 1.** Comparison of absorption performances between VO2-based absorbers with different structures

Ref.	Bandwidth	Absorption efficiency	Adjustable range
Ref. [20]	0.33 THz	>90%	30%-100%
Ref. [21]	0.65 THz	>90%	30%-98%
Ref. [22]	0.52 THz	>90%	5%-100%
Ref. [23]	1.25 THz	>90%	15%-96%
Ref. [24]	1.23 THz	>90%	4%-100%
Ref. [25]	0.88 THz, 0.77 THz	>80%	20%-90%
Ref. [26]	2.45 THz	>90%	4%-100%
Proposed study	2.72 THz	>90%	1.9%-100%

## 4 CONCLUSION

In this paper, a broadband THz absorber device with three-layer metamaterial vanadium dioxide is presented. The proposed design has been finalized by running a simulation program. Vanadium dioxide, which shows phase

change properties and is used in the metal phase in the study, is used on the top surface of the design, and gold is used on the bottom layer. It is presented that the simulated absorption results of the proposed design cover the range from 2.68 THz to 5.4 THz and have a bandwidth reaching 2.72 THz. The  $S_{11}$  parameter and absorption graphs obtained from the simulation studies show that the design works with an efficiency of more than 90%. By increasing the conductivity of VO<sub>2</sub>, which is affected by temperature variation, from 200 S/m to  $2 \times 10^5$  S/m, the tunable peak intensity was obtained between 9% and 100%. The best absorber optimum results for the design were obtained by setting the conductivity to  $2 \times 10^5$  S/m. In addition, the electric field distribution analysis at the absorption frequency was performed to understand the physical mechanism of the structure. The simulation results of the proposed design are compared with the bandwidth, tunable range level and efficiency results of other designs in the literature and presented with their advantages. The designed absorber can be used in high potential applications such as modulators, power harvesting fields, imaging-sensing technology and photoelectric switches in the THz range.

## Acknowledgments

This study was supported by Atatürk University Scientific Research Projects (Project no: FDK-2022-10273).

## References

- [1] B. I. Wu *et al.*, "Anisotropic metamaterials as antenna substrate to enhance directivity," *Microwave and Optical Technology Letters*, vol. 48, no. 4, pp. 680–683, 2006.
- [2] N. I. Landy, S. Sajuyigbe, J. J. Mock, D. R. Smith, and W. J. Padilla, "Perfect metamaterial absorber," *Physical Review Letters*, vol. 100, no. 20, art. no. 207402, 2008.
- [3] C. M. Soukoulis, S. Linden, and M. Wegener, "Negative refractive index at optical wavelengths," *Science*, vol. 315, no. 5808, pp. 47–49, 2007.
- [4] X. He, S. Li, X. Yang, S. Shi, F. Wu, and J. Jiang, "High-sensitive dual-band sensor based on microsize circular ring complementary terahertz metamaterial," *Journal of Electromagnetic Waves and Applications*, vol. 31, no. 1, pp. 91–100, 2017.
- [5] B. I. Wu *et al.*, "Anisotropic metamaterials as antenna substrate to enhance directivity," *Microwave and Optical Technology Letters*, vol. 48, no. 4, pp. 680–683, 2006.
- [6] R. A. Shelby, D. R. Smith, and S. Schultz, "Experimental verification of a negative index of refraction," *Science*, vol. 292, no. 5514, pp. 77–79, 2001.
- [7] L. Zeng, B. Li, H. Li, and B. Wang, "Nano sensing based on transparency effect in planar metamaterial," *Journal of Modern Optics*, vol. 64, no. 12, pp. 1158–1163, 2017.
- [8] M. Papaioannou, E. Plum, and N. I. Zheludev, "All-optical pattern recognition and image processing on a metamaterial beam splitter," *ACS Photonics*, vol. 4, no. 2, pp. 217–222, 2017.
- [9] M. Rahmanshahi, S. Noori Kourani, S. Golmohammadi, H. Baghban, and H. Vahed, "A tunable perfect THz metamaterial absorber with three absorption peaks based on nonstructured graphene," *Plasmonics*, pp. 1–12, 2021.
- [10] J. Hendrickson, J. Guo, B. Zhang, W. Buchwald, and R. Soref, "Wideband perfect light absorber at midwave infrared using multiplexed metal structures," *Optics Letters*, vol. 37, no. 3, pp. 371–373, 2012.
- [11] H. Deng, L. Stan, D. A. Czaplewski, J. Gao, and X. Yang, "Broadband infrared absorbers with stacked double chromium ring resonators," *Optics Express*, vol. 25, no. 23, pp. 28295–28304, 2017.
- [12] G. Wu, X. Jiao, Y. Wang, Z. Zhao, Y. Wang, and J. Liu, "Ultra-wideband tunable metamaterial perfect absorber based on vanadium dioxide," *Optics Express*, vol. 29, no. 2, pp. 2703–2711, 2021.
- [13] X. Wang *et al.*, "A theoretical study of a plasmonic sensor comprising a gold nano-disk array on gold film with a SiO<sub>2</sub> spacer," *Chinese Physics B*, vol. 28, no. 4, art. no. 044201, 2019.
- [14] X. Chen, C. Cen, L. Zhou, R. Cao, Z. Yi, and Y. Tang, "Magnetic properties and reverse magnetization process of anisotropic nanocomposite permanent magnet," *Journal of Magnetism and Magnetic Materials*, vol. 483, pp. 152–157, 2019.
- [15] Z. Liu *et al.*, "Truncated titanium/semiconductor cones for wide-band solar absorbers," *Nanotechnology*, vol. 30, no. 30, art. no. 305203, 2019.
- [16] T. Van Huynh, B. S. Tung, B. X. Khuyen, S. T. Ngo, V. D. Lam, and N. T. Tung, "Controlling the absorption strength in bidirectional terahertz metamaterial absorbers with patterned graphene," *Computational Materials Science*, vol. 166, pp. 276–281, 2019.
- [17] X. Jiang, S. Wang, and H. Wu, "Metamaterial absorber with tunable absorption bandwidth based on vanadium dioxide," *Acta Photonica Sinica*, vol. 51, no. 1, art. no. 0151124, 2022.
- [18] J. Zhang, Z. Li, L. Shao, and W. Zhu, "Dynamical absorption manipulation in a graphene-based optically transparent and flexible metasurface," *Carbon*, vol. 176, pp. 374–382, 2021.
- [19] J. Xiao *et al.*, "Tunable terahertz absorber based on transparent and flexible metamaterial," *Chinese Optics*



- Letters*, vol. 18, no. 9, art. no. 092403, 2020.
- [20] Z. Song, K. Wang, J. Li, and Q. H. Liu, "Broadband tunable terahertz absorber based on vanadium dioxide metamaterials," *Optics Express*, vol. 26, no. 6, pp. 7148–7154, 2018.
- [21] S. Wang *et al.*, "Vanadium dioxide based broadband THz metamaterial absorbers with high tunability: simulation study," *Optics Express*, vol. 27, no. 14, pp. 19436–19447, 2019.
- [22] Z. Song, M. Wei, Z. Wang, G. Cai, Y. Liu, and Y. Zhou, "Terahertz absorber with reconfigurable bandwidth based on isotropic vanadium dioxide metasurfaces," *IEEE Photonics Journal*, vol. 11, no. 2, pp. 1–7, 2019.
- [23] J. Bai *et al.*, "Tunable broadband THz absorber using vanadium dioxide metamaterials," *Optics Communications*, vol. 452, pp. 292–295, 2019.
- [24] R.-N. Dao, X.-R. Kong, H.-F. Zhang, and X.-R. Su, "A tunable broadband terahertz metamaterial absorber based on the vanadium dioxide," *Optik*, vol. 180, pp. 619–625, 2019.
- [25] Z. Song, M. Jiang, Y. Deng, and A. Chen, "Wide-angle absorber with tunable intensity and bandwidth realized by a terahertz phase change material," *Optics Communications*, vol. 464, art. no. 125494, 2020.
- [26] J. Huang *et al.*, "Broadband terahertz absorber with a flexible, reconfigurable performance based on hybrid-patterned vanadium dioxide metasurfaces," *Optics Express*, vol. 28, no. 12, pp. 17832–17840, 2020.
- [27] A. S. Dalkilic, "Parametric study of energy, exergy and thermoeconomic analyses on vapor-compression system cascaded with lib<sub>r</sub>/water and nh<sub>3</sub>/water absorption cascade refrigeration cycle," *Anadolu University Journal of Science and Technology A-Applied Sciences and Engineering*, vol. 18, no. 1, pp. 78–96, 2017.
- [28] T. Parvin, K. Ahmed, A. M. Alatwi, and A. N. Z. Rashed, "Differential optical absorption spectroscopy-based refractive index sensor for cancer cell detection," *Optical Review*, vol. 28, pp. 134–143, 2021.
- [29] W. Li and J. G. Valentine, "Harvesting the loss: surface plasmon-based hot electron photodetection," *Nanophotonics*, vol. 6, no. 1, pp. 177–191, 2017.
- [30] P. H. Siegel, "Terahertz technology in biology and medicine," *IEEE Transactions on Microwave Theory and Techniques*, vol. 52, no. 10, pp. 2438–2447, 2004.
- [31] L. Cong, S. Tan, R. Yahiaoui, F. Yan, W. Zhang, and R. Singh, "Experimental demonstration of ultrasensitive sensing with terahertz metamaterial absorbers: A comparison with the metasurfaces," *Applied Physics Letters*, vol. 106, no. 3, 2015.
- [32] C. M. Watts *et al.*, "Terahertz compressive imaging with metamaterial spatial light modulators," *Nature Photonics*, vol. 8, no. 8, pp. 605–609, 2014.
- [33] Y. Zhao *et al.*, "Structural, electrical, and terahertz transmission properties of VO<sub>2</sub> thin films grown on c-, r-, and m-plane sapphire substrates," *Journal of Applied Physics*, vol. 111, no. 5, 2012.
- [34] M. Liu *et al.*, "Terahertz-field-induced insulator-to-metal transition in vanadium dioxide metamaterial," *Nature*, vol. 487, no. 7407, pp. 345–348, 2012.
- [35] Y. Zhu, Y. Zhao, M. Holtz, Z. Fan, and A. A. Bernussi, "Effect of substrate orientation on terahertz optical transmission through VO<sub>2</sub> thin films and application to functional antireflection coatings," *JOSA B*, vol. 29, no. 9, pp. 2373–2378, 2012.
- [36] X.-J. He, Y. Wang, J. Wang, T. Gui, and Q. Wu, "Dual-band terahertz metamaterial absorber with polarization insensitivity and wide incident angle," *Progress In Electromagnetics Research*, vol. 115, pp. 381–397, 2011.
- [37] D. R. Smith, S. Schultz, P. Markoš, and C. M. Soukoulis, "Determination of effective permittivity and permeability of metamaterials from reflection and transmission coefficients," *Physical Review B*, vol. 65, no. 19, art. no. 195104, 2002.



## The Impact of Telework on Gender Equality and Occupational Health

Mustafa Ozdemir\*<sup>1</sup>

<sup>1</sup>Department of Emergency and Disaster Management, Faculty of Applied Sciences, Bayburt University, Bayburt, Türkiye

### Abstract

This paper explores the multifaceted impacts of telework, also known as remote work, which has gained significant traction due to advancements in information and communication technologies (ICT) and the COVID-19 pandemic. Telework offers numerous benefits, including enhanced workforce flexibility, reduced commuting times, and improved work-life balance. It also aligns with sustainable development goals by mitigating environmental impacts. However, telework introduces challenges in terms of gender equality and occupational safety and health (OSH). This study examines how telework affects female employees, focusing on work-life balance, psychosocial risks, and working conditions. Additionally, it assesses telework regulations in European Union (EU) countries from a gender equality perspective. The findings underscore the need for flexible working hours, ergonomic work environments, social support, and policies that promote gender equality to optimise telework practices. By adopting these measures, employers and policymakers can enhance workforce productivity, employee satisfaction, and gender equality, ensuring telework's sustainable and effective implementation.

**Keywords:** Telework, Work-life balance, Gender equality, Occupational safety and health, Covid-19 pandemic

## 1 INTRODUCTION

Telework, or remote work, is an arrangement where employees use digital technologies to conduct their tasks outside the employer's premises, typically from home. This concept has gained importance with the advancement of information and communication technologies (ICT) and has become a more widespread practice in recent years [1]. Telework offers numerous advantages, such as increasing workforce flexibility, reducing employee commuting times, and improving work-life balance. Moreover, it can contribute to sustainable development goals by reducing environmental impacts. Understanding the importance of telework requires considering its effects on workforce flexibility and productivity. This working arrangement provides cost savings for employers while offering more flexible and suitable working conditions for employees [2].

During the COVID-19 pandemic, many businesses were compelled to adopt remote work models, highlighting telework's potential benefits and challenges. The pandemic accelerated the adoption of telework and created an awareness that this working arrangement could be permanent. The embrace of remote work necessitates employers and employees reevaluating how to integrate telework practices to make the workforce more flexible and efficient in the future [3, 4].

This paper examines the effects of telework practices on gender equality and occupational safety and health (OSH). Specifically, it addresses the impacts of telework on female employees in terms of work-life balance, psychosocial risks, and working conditions. Additionally, the paper evaluates telework regulations in European Union (EU) countries from a gender equality perspective.

This study aims to analyse the current state of telework practices concerning gender equality and OSH, identify potential risks, and propose recommendations to mitigate these risks. In this context, research conducted by EU institutions and current academic literature will be reviewed.

## 2 MATERIAL AND METHOD

In this study, a comprehensive literature review was conducted to examine the effects of remote work on gender equality and occupational health. The literature review includes existing academic studies, reports, and articles on remote work practices, gender equality, and occupational health. As part of the study, semi-structured interviews were conducted with 11 female and five male employees and three employers who have adopted remote work

practices. The interviews were designed to provide in-depth insights into employees' work-life balance, psychosocial risks, and working conditions.

### **3 RESULTS**

#### **3.1 Impact of the COVID-19 Pandemic on Telework**

The COVID-19 pandemic has led to the rapid and widespread adoption of telework practices. During the pandemic, millions of employees worldwide began working from home due to health and safety concerns. This shift occurred in parallel with the closure of physical workplaces and the implementation of social distancing measures. The pandemic demonstrated that work could be conducted remotely through digital technologies, making telework a more widely accepted and practised work arrangement than ever before [5].

With the widespread adoption of telework during the pandemic, employers and employees faced numerous new challenges. Employers had to ensure digital access for their employees, enhance cybersecurity measures, and manage remote work arrangements. On the other hand, employees encountered difficulties setting up a home working environment, maintaining a work-life balance, and adapting to digital technologies. However, telework's flexibility and productivity advantages also became evident during this period [6].

Initially, many businesses viewed telework as a temporary solution, but it has gradually become a permanent working model. In the post-pandemic era, hybrid working models have become more prevalent, and telework has established itself as a new norm in the business world. This shift has necessitated the development of better strategies by employers and employees to optimise telework practices. Telework is expected to become even more widespread and play a significant role in the labour market [7].

#### **3.2 The Relationship Between Telework and Gender Equality**

Telework presents significant opportunities and challenges in terms of gender equality. Telework, which can improve women's work-life balance, can increase women's participation in the workforce and support their career advancement. Flexible working hours and the ability to work from home allow women to manage better their caregiving and household responsibilities [8]. However, the effects of telework on gender equality are complex. Research indicates that telework can have disproportionately negative impacts on women. Women may experience more significant work-life conflict, stress, and health issues while working from home. These challenges can adversely affect their workplace positions and career development. Additionally, telework arrangements can impose a more significant burden on women due to their caregiving and household responsibilities [9].

To ensure gender equality, employers and policymakers must carefully plan and manage telework practices. Supportive measures such as flexible working hours, equal pay policies, and career development opportunities should be implemented to improve women's telework experiences. Additionally, the equitable sharing of caregiving and household responsibilities should be encouraged. Implementing telework arrangements that support gender equality can increase women's participation in the workforce and contribute to gender equality goals [10, 11].

#### **3.3 The Impact of Telework on Work-Life Balance**

Telework is a work arrangement with the potential to improve employees' work-life balance. Flexible working hours and the ability to work from home can help employees better balance their work and personal lives. Telework eliminates commuting times, allowing employees to spend more time with their families and pursue individual interests [12].

However, the impact of telework on work-life balance is complex. Factors such as the widespread use of digital technologies and extended working hours can negatively affect work-life balance. The expectation of constant online availability and blurring boundaries between work and personal life can limit employees' rest and personal time. This situation increases the risk of burnout, stress, and health problems among employees [13].

Employers must consider employees' work-life balance when managing telework practices. Setting flexible working hours and clear boundaries can help employees balance their work and personal lives. Additionally, supporting employees in digital access and cybersecurity matters can contribute to telework's efficient and sustainable implementation. Designing telework arrangements to improve employees' work-life balance can enhance workforce productivity and ensure employee satisfaction [14].

### 3.4. The Impact of Telework on Occupational Safety and Health

Telework introduces new challenges and risks in terms of occupational safety and health. The lack of ergonomically suitable home working environments increases employees' risk of physical health problems. Specifically, improper working postures, repetitive movements, and prolonged screen use can lead to musculoskeletal issues. Ergonomic arrangements of telework environments are essential to protect employees' physical health [15].

Telework also affects employees' psychological health. Isolation, lack of social support, and the expectation of constant online availability increase the risk of stress and burnout among employees. To minimise the psychological health impacts of telework, employers must provide social support to employees and regulate working hours. Additionally, encouraging employees to take regular breaks and clearly define their off-work time is crucial for protecting their psychological health [16].

Employers need to develop comprehensive policies and measures to manage telework's occupational safety and health risks. These measures include providing ergonomic working equipment to employees, supporting them in digital access and cybersecurity, and creating social support mechanisms to protect employees' psychological health. Evaluating telework arrangements from an occupational safety and health perspective and taking necessary precautions contribute to telework's sustainable and efficient implementation.

### 3.4 Differences in Telework Regulations Among Countries

Telework regulations vary significantly across countries. In some countries, telework is widely adopted; in others, it has yet to be fully embraced. For instance, while some European Union member states are advanced in telework practices, others maintain more traditional work arrangements. These differences stem from various factors, including national legal regulations, cultural norms, and economic conditions [17].

In the European Union, telework regulations generally encompass flexible working hours, occupational safety and health measures, and gender equality. However, the practices and policies among member states can differ significantly. In some countries, telework is legally regulated and widely practised; in others, no clear regulations exist. These differences substantially impact the prevalence and effectiveness of telework. The disparities in telework regulations among countries influence how employers and employees adopt and manage telework practices. Employers must comply with different legal regulations in various countries, while employees experience telework conditions and rights differently. Effective implementation of telework requires international cooperation and knowledge sharing. Sharing best practice examples among countries can contribute to the improvement and inclusiveness of telework regulations [18].

## 4 CONCLUSION

While telework has the potential to improve work-life balance, it also brings occupational safety and health risks. Differences in regulations across countries diversify the effects of telework. Employers need to develop flexible and supportive policies to optimise their employees' telework experiences. Additionally, strategies should be adopted to ensure telework regulations positively impact gender equality. To implement telework sustainably and efficiently, the following measures are recommended for employers and policymakers:

- Flexible working hours should be established, and clear boundaries should be set to help employees maintain their work-life balance.
- Employees should be provided with ergonomic working equipment and home working environments should be ergonomically arranged.
- Employees should have access to social support mechanisms, and measures should be taken to protect their psychological health.
- Telework regulations should be implemented to support gender equality.

Successful implementation of telework can enhance workforce productivity, ensure employee satisfaction, and contribute to gender equality goals. Careful planning and management of telework practices by employers and policymakers will help maximise the opportunities offered by this work arrangement.

## References

- [1] M. Vartiainen, “Telework and remote work,” in *Oxford Research Encyclopedia of Psychology*, Oxford: Oxford University Press, 2021.
- [2] R. E. Morgan, “Teleworking: An assessment of the benefits and challenges,” *European Business Review*, vol. 16, no. 4, pp. 344–357, 2004.
- [3] A. Abulibdeh, “Can COVID-19 mitigation measures promote telework practices?,” *Journal of Labor and Society*, vol. 23, no. 4, pp. 551–576, 2020.
- [4] O. Olawale, F. A. Ajayi, C. A. Udeh, and O. A. Odejide, “Remote work policies for IT professionals: review of current practices and future trends,” *International Journal of Management & Entrepreneurship Research*, vol. 6, no. 4, pp. 1236–1258, 2024.
- [5] M. C. Schall Jr and P. Chen, “Evidence-based strategies for improving occupational safety and health among teleworkers during and after the coronavirus pandemic,” *Human factors*, vol. 64, no. 8, pp. 1404–1411, 2022.
- [6] A. Belzunegui-Eraso and A. Erro-Garcés, “Teleworking in the context of the Covid-19 crisis,” *Sustainability*, vol. 12, no. 9, art. no. 3662, 2020.
- [7] J. Hopkins and A. Bardoel, “The future is hybrid: how organisations are designing and supporting sustainable hybrid work models in post-pandemic Australia,” *Sustainability*, vol. 15, no. 4, art. no. 3086, 2023.
- [8] D. G. Tremblay, “Balancing work and family with telework? Organizational issues and challenges for women and managers,” *Women in Management Review*, vol. 17, no. 3–4, pp. 157–170, 2002.
- [9] T. Alon, M. Doepke, J. Olmstead-Rumsey, and M. Tertilt, “The impact of COVID-19 on gender equality,” *National Bureau of Economic Research*, 2020.
- [10] S. S. El Ashry, “Flexible working practices for educated egyptian women in the digital era: A study on telework during the COVID-19 pandemic and its potential to reduce gender gap,” 2022.
- [11] S. Kley and T. Reimer, “Exploring the Gender gap in teleworking from home. The roles of worker’s characteristics, occupational positions and gender equality in europe,” *Social Indicators Research*, vol. 168, no. 1, pp. 185–206, 2023.
- [12] C. White and B. Maniam, “Flexible working arrangements, worklife balance, and working women,” *Journal of Business and Accounting*, vol. 13, no. 1, pp. 59–73, 2020.
- [13] V. B. Pedersen and S. Lewis, “Flexible friends? Flexible working time arrangements, blurred work-life boundaries and friendship,” *Work, Employment and Society*, vol. 26, no. 3, pp. 464–480, 2012.
- [14] C. Downes and E. Koekemoer, “Work-life balance policies: Challenges and benefits associated with implementing flexitime,” *SA Journal of Human Resource Management*, vol. 9, no. 1, pp. 1–13, 2011.
- [15] M. Ertel, E. Pech, and P. Ullsperger, “Telework in perspective—new challenges to occupational health and safety,” in *Health Effects of the New Labour Market*: Springer, 2000, pp. 169–181.
- [16] S. De Sio *et al.*, “Telework and its effects on mental health during the COVID-19 lockdown,” *European Review for Medical and Pharmacological Sciences*, vol. 25, no. 10, pp. 3914–3922, 2021.
- [17] S. Milasi, I. González-Vázquez, and E. Fernández-Macías, “Telework before the COVID-19 pandemic: Trends and drivers of differences across the EU,” 2021.
- [18] J. Plantenga, C. Remery, and F. Camilleri-Cassar, “Flexible working time arrangements and gender equality: A comparative review of 30 European countries,” 2009.

**SUPPORTERS** Bayburt University, Türkiye  
Gaziantep Islam Science and Technology University, Türkiye  
Citiedge University, Nigeria

**TITLE** Proceedings Book of International Conference on Engineering, Natural  
Sciences, and Technological Developments (ICENSTED 2024)

**ISSUED IN** Erdek/Balikesir, Türkiye

**ISSUED BY** Bayburt University

**EDITION** First, Pages LXXXIV + 1160

**ISBN** 978-605-9945-44-8